SECOND EDITION

TREATISE ON GEOPHYSICS

Volume 6

CRUSTAL AND LITHOSPHERE DYNAMICS

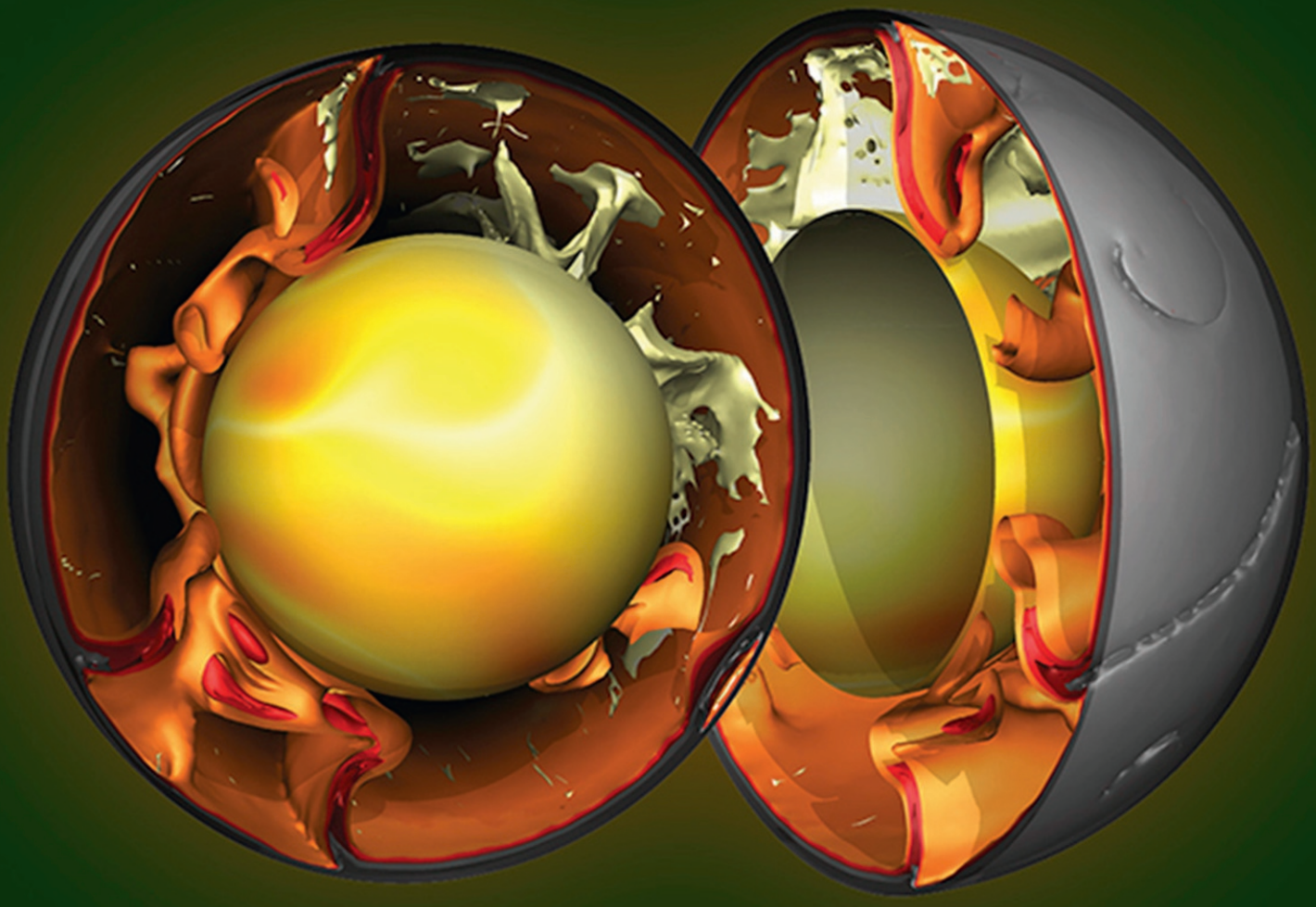

VOLUME EDITOR: ANTHONY WATTS

EDITOR-IN-CHIEF: GERALD SCHUBERT

TREATISE ON GEOPHYSICS

SECOND EDITION

This page intentionally left blank

TREATISE ON GEOPHYSICS

SECOND EDITION

EDITOR-IN-CHIEF

Gerald Schubert

Distinguished Professor Emeritus, Department of Earth, Planetary and Space Sciences, University of California, Los Angeles

VOLUME 6

CRUSTAL AND LITHOSPHERE DYNAMICS

VOLUME EDITOR

Professor Anthony Watts

Department of Earth Sciences, University of Oxford

Elsevier
Radarweg 29, PO Box 211, 1000 AE Amsterdam, The Netherlands
The Boulevard, Langford Lane, Kidlington, Oxford OX5 1GB, UK
30 Corporate Drive, Suite 400, Burlington MA 01803, USA

Copyright © 2015 Elsevier B.V. unless otherwise stated. All rights reserved.

Cover image created for this work by Fabio Crameri, University College London.
The figure depicts the temperature field from a convection calculation using the code STAG-YY, written by Paul Tackley.

The following chapters are US Government works in the public domain and not subject to copyright:

1.11 Crust and Lithospheric Structure - Global Crustal Structure; 3.09 Earth Rotation Variations – Long Period; 4.07 The Role of Fault-Zone Drilling; 5.11 The Time-Averaged Field and Paleosecular Variation; 10.21 Exoplanetary Geophysics: An Emerging Discipline; 11.12 Tools and Techniques: Gravitational Method.

No part of this publication may be reproduced or transmitted in any form or by any means, electronic or mechanical, including photocopying, recording, or any information storage and retrieval system, without permission in writing from the publisher. Details on how to seek permission, further information about the Publisher's permissions policies and our arrangements with organizations such as the Copyright Clearance Center and the Copyright Licensing Agency, can be found at our website: www.elsevier.com/permissions.

This book and the individual contributions contained in it are protected under copyright by the Publisher (other than as may be noted herein).

Notices
Knowledge and best practice in this field are constantly changing. As new research and experience broaden our understanding, changes in research methods, professional practices, or medical treatment may become necessary.

Practitioners and researchers may always rely on their own experience and knowledge in evaluating and using any information, methods, compounds, or experiments described herein. In using such information or methods they should be mindful of their own safety and the safety of others, including parties for whom they have a professional responsibility.

To the fullest extent of the law, neither the Publisher nor the authors, contributors, or editors, assume any liability for any injury and/or damage to persons or property as a matter of products liability, negligence or otherwise, or from any use or operation of any methods, products, instructions, or ideas contained in the material herein.

Library of Congress Cataloging-in-Publication Data
A catalog record for this book is available from the Library of Congress

British Library Cataloguing-in-Publication Data
A catalogue record for this book is available from the British Library

ISBN (print): 978-0-444-53802-4

For information on all Elsevier publications
visit our website at http://store.elsevier.com/

Editorial & Production: Gemma Tomalin, Richard Berryman, Marise Willis, Michael Nicholls, Ellen Bishop
Cover design: Matthew Limbert

Printed and bound in the United Kingdom

15 16 17 18 19 10 9 8 7 6 5 4 3 2 1

CONTENTS

Preface *vii*

Editor-in-Chief *ix*

Contributors *xi*

Contents of all Volumes *xiii*

6.01 Crustal and Lithosphere Dynamics: An Introduction and Overview 1
AB Watts

6.02 Plate Tectonics 45
P Wessel and RD Müller

6.03 Plate Rheology and Mechanics 95
EB Burov

6.04 Plate Deformation 153
R Sabadini

6.05 Heat Flow and Thermal Structure of the Lithosphere 217
C Jaupart and J-C Mareschal

6.06 Lithosphere Stress and Deformation 255
ML Zoback and M Zoback

6.07 Magmatism, Magma, and Magma Chambers 273
BD Marsh

6.08 The Dynamics of Continental Breakup and Extension 325
WR Buck

6.09 Mountain Building: From Earthquakes to Geologic Deformation 381
J-P Avouac

6.10 Fault Mechanics 433
CH Scholz

6.11 Mountain Building, Tectonic Evolution, Rheology, and Crustal Flow in the Himalaya, Karakoram, and Tibet 469
MP Searle

6.12 Tectonic Models for the Evolution of Sedimentary Basins 513
S Cloetingh, PA Ziegler, F Beekman, EB Burov, D Garcia-Castellanos, and L Matenco

6.13 Landscape Evolution 593
GE Tucker

This page intentionally left blank

PREFACE

The *Treatise on Geophysics* is a comprehensive and in-depth study of the physics of the Earth and of terrestrial-like planets residing both within and outside our solar system. Its breadth and detail of coverage are beyond what any single geophysics text can provide. The first edition of the *Treatise on Geophysics* was published in 2007, nearly a decade ago. Of course, there is much progress in science in that length of time and the field of geophysics has grown rapidly and developed new lines of inquiry. Accordingly, we have brought the *Treatise on Geophysics* up-to-date with this second edition. The new edition will continue to provide students and professionals with fundamental and state-of-the-art discussion of all aspects of geophysics. In this new edition, the reader will find updates to all the chapters contained in the first edition and new chapters that discuss topics missing from the first edition. In a few instances, chapters from the first edition have simply been reprinted in order to avoid gaps in coverage. Chapters that emphasized fundamental physics often required little updating.

A highlight of the second edition is a new volume on Resources in the Near-Surface Earth. The new volume discusses the role of geophysics in the exploitation and conservation of natural resources and the assessment of degradation of natural systems by pollution. The near surface is a zone where humans and natural systems interact. Understanding the effects of human impacts is a challenge particularly for the long term.

There are four new chapters in the volume on Deep Earth Seismology. One of them describes progress in seismic instrumentation in the last 30 years in the era of broadband digital sensor and recording systems. Another one addresses a new approach for the determination of crust and uppermost mantle structure, based on ambient noise cross-correlations. This has revolutionized the field, since it allows the study of regional structure at high resolution in areas where there are no earthquakes. The third new chapter is devoted to recent advances in characterizing the lithosphere–asthenosphere boundary under both oceans and continents. Finally, the last new chapter discusses the morphology of subducted slabs in the Earth's transition zone.

The Mineral Physics volume has new chapters on dynamic (shock-wave) compression methods, and on the mineralogy of the upper mantle and the D″ layer focusing on post-perovskite, and extrasolar super-Earths.

New material in the Geodesy volume expands the temporal resolution and latency of geodetic measurements to high-rate, real-time measurements and increases the spatial resolution to meter size pixels with optical and radar imaging systems. Application areas are extended with new material on the uses of Earth gravity measurements.

The Earthquake Seismology volume has a new chapter on rock mechanics that is a comprehensive account of modern rock mechanics with emphasis on the variation of frictional properties of rocks during an earthquake cycle. Many chapters have considerable updates reflecting the lessons from significant recent earthquakes (e.g., the 2011 Tohoku-Oki earthquake and the 2013 Okhotsk deep earthquake), new observations on slow slips and triggered earthquakes, and developments of new methods (e.g., back projection method). Some chapters are updated (e.g., paleoseismology and strong ground motion) with substantial new material.

Chapters in the Geomagnetism volume have been updated to include recent advances in the acquisition of larger data sets and higher quality data and in the construction of more reliable and sophisticated models. Improvements in data have occurred in areas such as magnetic anomalies, paleointensities, and planetary magnetism. Improvements in models of the present day field include so-called comprehensive models and models that incorporate data assimilation.

The Crustal and Lithosphere Dynamics volume has new contributions on mountain building and landscape evolution.

The Mantle Dynamics volume contains new chapters on the generation of plate tectonics from mantle convection and the core–mantle boundary region.

The Core Dynamics volume features a comprehensive update of this rapidly changing subject, including new chapters on turbulence and waves in the fluid outer core.

The volume on the Evolution of the Earth presents a new assessment on the role of volatiles in Earth evolution.

There are new chapters in the Physics of Terrestrial Planets and Moons volume on planetary atmospheres, planetary tectonics, extrasolar planets and asteroids and comets. The study of extrasolar planets has had explosive growth in the last decade and new spacecraft missions have significantly enhanced our knowledge of solar system planets and moons.

Finally, this is an opportunity for me to thank and acknowledge the editors of the individual volumes for their hard work, patience, dedication, and commitment in bringing this new edition of the Treatise to fruition. I am also indebted to Gemma Tomalin of Elsevier for her care and attention to the organization and production of the Treatise and to Deepa Arumugam for her careful coordination of the proofs from the copyeditor and typesetter. Of course, the authors of the individual chapters are the ones who are responsible for the excellence of the Treatise. We have all had some ups and downs in the process of producing the second edition of the Treatise but the final product is one that we can all view with pride.

Gerald Schubert
Editor-in-Chief

EDITOR-IN-CHIEF

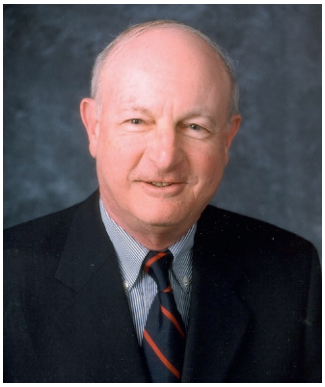

Gerald Schubert is Distinguished Professor Emeritus in the Department of Earth, Planetary and Space Sciences at the University of California, Los Angeles. His research interests encompass the physics of the interiors and atmospheres of the Earth, the Moon, and the other moons and planets of the solar system. He is co-author with Donald Turcotte of *Geodynamics* (ed. 3, Cambridge University Press, 2014) and with Turcotte and Peter Olson of *Mantle Convection in the Earth and Planets* (Cambridge University Press, 2001). He is the author of over 540 research papers. He has participated in a number of NASA's planetary missions, including Apollo, Pioneer Venus, Magellan, and Galileo, and has been editor and editorial board member of many journals, including *Icarus*, *Journal of Geophysical Research*, *Geophysical Research Letters*, and *Annual Reviews of Earth and Planetary Sciences*. Professor Schubert is a Fellow of the American Geophysical Union and a recipient of the Union's James B. MacElwane medal and the Harry H. Hess medal. He is a member of the National Academy of Sciences and the American Academy of Arts and Sciences.

This page intentionally left blank

CONTRIBUTORS

J-P Avouac
University of Cambridge, Cambridge, UK

F Beekman
Utrecht University, Utrecht, The Netherlands

WR Buck
Lamont-Doherty Earth Observatory of Columbia University, Palisades, NY, USA

EB Burov
Université Pierre et Marie Curie, Paris, France; Centre National de la Recherche Scientifique, Paris, France

S Cloetingh
Utrecht University, Utrecht, The Netherlands

D Garcia-Castellanos
Instituto de Ciencias de la Tierra Jaume Almera, Barcelona, Spain

C Jaupart
Institut de Physique du Globe de Paris, Paris, France

J-C Mareschal
Université du Québec à Montréal, Montréal, QC, Canada

BD Marsh
Johns Hopkins University, Baltimore, MD, USA

L Matenco
Utrecht University, Utrecht, The Netherlands

RD Müller
University of Sydney, Sydney, NSW, Australia

R Sabadini
University of Milan, Milan, Italy

CH Scholz
Columbia University, Palisades, NY, USA

MP Searle
University of Oxford, Oxford, UK

GE Tucker
Cooperative Institute for Research in Environmental Sciences (CIRES), Boulder, CO, USA; University of Colorado, Boulder, CO, USA

AB Watts
University of Oxford, Oxford, UK

P Wessel
University of Hawaii at Mānoa, Honolulu, HI, USA

PA Ziegler
University of Basel, Basel, Switzerland

M Zoback
Stanford University, Stanford, CA, USA

ML Zoback
US Geological Survey, Menlo Park, CA, USA

This page intentionally left blank

6.01 Crustal and Lithosphere Dynamics: An Introduction and Overview

AB Watts, University of Oxford, Oxford, UK

© 2015 Elsevier B.V. All rights reserved.

6.01.1	**Introduction**	1
6.01.2	**Isostasy and 'Steady-State' Equilibrium**	3
6.01.2.1	The Earth's Hypsometric Curve and Crustal Structure	3
6.01.2.2	Gravity Anomalies, Crustal Structure, and Local Models of Isostasy	4
6.01.2.3	Departures from Local Isostasy: Flexural Isostasy	7
6.01.3	**The Deformation of the Crust and Lithosphere**	11
6.01.3.1	Earthquake Loading, Postseismic Relaxation, and the Short-Term (i.e., up to a Few Years) Response	11
6.01.3.2	Glacial and Lake Loading and Unloading, Rebound, and the Intermediate-Term (a Few Tens of Thousand Years) Response	15
6.01.3.3	Volcano and Sediment Loading and the Long-Term (Greater than Several Hundreds of Thousand Years) Response	16
6.01.4	**Relationship Between Load and Plate Age and Rheological Structure**	22
6.01.4.1	The Relationship Between the Long-Term Elastic Thickness and Plate and Load Age	22
6.01.5	**Global Elastic Thickness**	25
6.01.5.1	T_e Map	25
6.01.5.2	Correlation of T_e with Temperature Structure and Shear-Wave Velocity	26
6.01.6	**Geologic Implications**	29
6.01.6.1	Toward an Integrated Model that Relates Elastic Thickness to Load Age on Short, Intermediate, and Long Timescales	29
6.01.6.2	Terranes, the Wilson Cycle, and Inheritance	31
6.01.6.3	Tectonic Setting of Geologic Features	33
6.01.6.4	Surface Processes, Flexure, and Landscape Evolution	34
6.01.6.5	The Relative Contributions of Lithospheric Flexure to the Earth's Topography and Gravity Anomaly Field and Mantle Convection	36
6.01.7	**Conclusions**	39
Acknowledgments		39
References		40

6.01.1 Introduction

It has been known since the pioneering works of Joseph Barrell during the early part of the twentieth century that the Earth's outermost layers comprise a strong upper layer, the lithosphere, which overlies a weak lower layer, the asthenosphere. Barrell (1914a) argued that because river deltas such as the Niger and Nile lack a flanking topographic depression, they must be supported by the strength of the lithosphere. He used (Barrell, 1914b) Pratt isostatic gravity anomalies over North America as a proxy for the magnitude of the stress differences that could be supported by the lithosphere and showed, using Darwin's equation (Darwin, 1882), that stresses increase and then decrease with depth in the lithosphere, passing by transition into the weak underlying asthenosphere.

Today, we distinguish the lithosphere from the asthenosphere on the basis of not only its strength but also its physical properties such as temperature, density, and seismic velocity structure. The lithosphere, for example, is generally associated with cooler temperatures, higher average densities, and higher average *S*-wave velocity anomalies than the asthenosphere.

Plate tectonics is based on the assumption that the lithosphere is rigid on long timescales and comprises a number of large plates that are moving with respect to each other across the Earth's surface. The positive density contrast between the lithosphere and the asthenosphere suggests that the rigid layer may be gravitationally unstable. Indeed, oceanic lithosphere – after it is created at a mid-oceanic ridge – cools, subsides, and sinks into the underlying asthenosphere, for example, at a deep-sea trench–outer-rise system.

Continental lithosphere may also be unstable. In rifts (e.g., East Africa), the lithosphere is regionally heated, thinned, and uplifted and may subside locally below sea level. In collisional systems (e.g., the Himalayas and Betics), however, continental lithosphere is thickened (Molnar et al., 1998) or is infiltrated by fluids released during metamorphic reactions (Le Pichon et al., 1997). Both processes may cause dense rocks of the lower crust to enter the eclogite stability field. As a result, the lower crust becomes denser than the underlying mantle, detaches, and, as at trenches, may sink into the underlying asthenosphere. The process of detachment unloads the lithosphere, which may cause regional uplift.

Isostatic considerations suggest that the crust – which comprises the uppermost part of the lithosphere – is buoyant and is in a state of flotation on the underlying mantle. Furthermore, flexure studies suggest that when it is subject to long-term geologic loads such as volcanoes, the lithosphere, rather than behaving as a number of independent floating blocks, as local

models of isostasy such as Airy and Pratt imply, responds by bending – in a similar manner as would an elastic plate that overlies an inviscid fluid substrate.

We are concerned in this volume with *crust and lithosphere dynamics*, which we may define as

> . . .the study of how the outermost layers of the Earth respond to loads that are emplaced on, within, and below it and its implications for plate mechanics and mantle flow.

Dynamics means, of course, *all* the loads and stresses and their resulting deformations and strains that are applied to the crust and lithosphere and the underlying asthenosphere. Unfortunately, there is no continuum that is representative of all the spatial and temporal scales of these stresses and their associated strains. This makes the determination of the thermal and mechanical properties of the lithosphere and asthenosphere a difficult, if not intractable, problem.

What we do have are 'snapshots' at particular temporal and spatial scales. They range from temporal scales by up to a few hundreds of seconds (e.g., during the coseismic deformation that results from earthquake triggering), to thousands of years (e.g., during the glacial isostatic adjustment that follows the waxing and waning of an ice sheet), to several tens of millions of years (e.g., during the flexural deformation due to sediment loading) and in spatial scales from a few, to a few tens, to several hundreds of kilometers.

Understanding the response of the lithosphere and asthenosphere system to particular loads and unloads is fundamental to our understanding of plate kinematics and mechanics and to predicting the response of the crust and lithosphere to more complex deformations such as those associated with erosion and sedimentation. It is also of importance in quantifying the relative contribution of the crust and lithosphere to surface observables such as gravity and topography and isolating the effects of processes on the surface and base of the lithosphere such as those associated with landscape evolution and mantle convection.

In this volume, we bring together contributions fundamental to 'crust and lithosphere dynamics.' The volume begins with a chapter by Wessel and Müller (Chapter 6.02) on plate kinematics. These authors show how new observations and methodologies have significantly improved the resolution of relative and absolute plate motions. By comparing these motions to predictions based on first-order rigid plate and fixed hot-spot reference frame models, the authors document the departures and their implications for the driving forces of plate tectonics. This chapter is followed by two contributions on plate mechanics. The first by Burov (Chapter 6.03) discusses the evidence that data from experimental rock mechanics have provided on the long-term rheology of the plates. By constructing strength profiles for both oceanic and continental lithosphere and then incorporating them into numerical models, he has been able to evaluate the role played by the vertically stratified rheological structure of the plates in such phenomena as orogeny and rifting, lithosphere-scale folding, and the development of convective instabilities. The second by Sabadini (Chapter 6.04) examines the evidence from geodetic data for the response of the plates to both relatively short-term loads such as those associated with coseismic and postseismic deformation and the waxing and waning of ice sheets and relatively long-term loads such as those associated with plate boundaries and continental collision. He shows that the response of the Eurasian Plate to boundary loads is best modeled by a thin viscous sheet with spatially varying viscosity, since such a model accounts well for the geodetically constrained velocity and stress fields. The next three chapters consider the evidence from surface heat flow, borehole breakouts, and magma models for the thermal and mechanical structure of the lithosphere. In their chapter, Jaupart and Mareschal (Chapter 6.05) review the evidence based on surface heat flow data for the thermal structure of the plates. They focus on two main issues: the first concerns the degree to which surface heat flow data are dependent on plate age, while the second involves the mechanisms by which heat is transported at the base of the plates. They argue that while the simple oceanic plate cooling model fails to explain the depth and surface heat flow of old seafloor, it has provided useful information on heat transport mechanisms at the base of the plate and helps explain why oceans, as well as continents, tend to a thermal steady state. In their chapter, Zoback and Zoback (Chapter 6.06) review the evidence from a variety of geologic and geophysical data, including *in situ* measurements, for the state of stress in the upper brittle crust. They show that on a continent-wide scale, stress orientation data are strikingly uniform, a fact that they attribute to the major forces that drive plate motions such as ridge push and trench pull. Deviations from these stress orientations are attributed to more local geologic features such as those associated with lateral density contrasts, topography and crustal thickness changes, and flexural loading. In his chapter, Marsh (Chapter 6.07) examines the evidence from the pattern and style of magmatism for processes that control magmatic activity. These include lithospheric extension that can make vast tracts of the continental crust accessible to melting and subduction that cause focused convective upwellings within the phase field of the source rock. The next two chapters examine the deformation of the lithosphere in extensional and compressional settings. In his chapter, Buck (Chapter 6.08) focuses on the effects of initial thermal and mechanical state of the lithosphere and magmatism on the styles of continental rifting. By considering processes such as thermal advection due to extension and viscous flow that localize and delocalize rifting, respectively, he addresses fundamental questions related to why some rifts are narrow and others wide and whether nonorogenic areas such as old cratons can rift in the absence of massive magmatic input. In his chapter, Avouac (Chapter 6.09) investigates the links between short-term deformation (e.g., earthquake cycle and neotectonics) and long-term deformation (e.g., the history of thrusting). He argues that deformation in the brittle crust tends to be localized and that different segments of mountains are active at different times. The next chapter by Scholz (Chapter 6.10) considers the structural styles of faulting in the shallow brittle part of the lithosphere, the brittle–ductile transition, and the shear zone in the ductile part of the lithosphere. By considering direct evidence for fault strength, he concludes that stress in the lithosphere is limited by faulting and is determined, to first-order, by Byerlee's law with hydrostatic pressure. The next two chapters consider how developments in crust and lithosphere dynamics have influenced our understanding of the rock record. Searle (Chapter 6.11) considers the evolution of

the Tibet–Himalayas collisional system and shows how careful geologic field mapping, sample ages, and *P*–*T* analysis of metamorphic terranes have been used to document flow in the middle continental crust. Cloetingh et al. (Chapter 6.12) review the formation and evolution of sedimentary basins in extensional, compressional, and strike-slip settings. By considering not only the effects of extension and compression but also phenomena such as structural inheritance, basin inversion, and far-field stresses, these authors argue that the preexisting thermal and mechanical structure of the lithosphere is the main control on the development of sedimentary basins. The final chapter by Tucker (Chapter 6.11) considers landscape evolution; the links between uplift, drainage patterns, and sedimentation; and the relationship between shallow and deep processes in the Earth.

We begin with this overview chapter in which the degree to which the Earth's outermost layers are in isostatic equilibrium is assessed. We do this by considering both the crustal structure and the gravity anomalies that would result from such equilibrium. By comparing these observables to calculations based on different local isostatic models (e.g., Airy and Pratt), the extent to which the Earth's crust tends to equilibrium can be determined. We then consider the departures from these first-order models, as evidenced by isostatic gravity anomalies. The short-term, intermediate, and long-term loads that might disturb isostasy are then reviewed and the implications of their deformation considered for both the elastic layer thickness of the lithosphere and the viscosity of the asthenosphere. We then examine the relationship between elastic layer thickness and load age and make an attempt to link the thicknesses that have been derived at the different timescales. The long-term elastic thickness is the focus of the remainder of the chapter since it is this timescale that is most relevant to geologic processes. First, we examine its correlation with other proxies for lithosphere temperature structure such as surface heat flow and shear-wave speeds. Finally, we will explore some of the implications of plate flexure for terrane structure and structural inheritance, tectonic setting, landscape evolution, and mantle dynamics.

6.01.2 Isostasy and 'Steady-State' Equilibrium

We know from isostasy (Bowie, 1927) that the outermost layers of the Earth tend toward a state of hydrostatic equilibrium. In simple terms, the crust appears to float on the underlying mantle, much like a block of wood on water. The height that such a block floats depends on its thickness and density. Thick and light blocks should float higher than thin and dense ones.

Probably the best-known models of flotation are those of Pratt (Hayford, 1909) and Airy (Heiskanen, 1931). These two models regard individual blocks of crust and mantle as capable of supporting surface and subsurface loads independently, without restraint from neighboring blocks. Within a loaded 'block,' pressure increases with depth, but there is some depth, known as the depth of compensation, at which pressures balance and below which pressures are hydrostatic.

In the Airy model, loads are compensated by variations in the thickness of a uniform density crust, while in the Pratt model, lateral variations in the density of either the crust or subcrustal mantle provide the necessary support. Both models are highly idealized in the sense that they only consider the state that the crust and subcrustal mantle would approach given a sufficiently long time. Nevertheless, they have, as we will see, been extremely useful.

One observable that is sensitive to the change in mass distributions that results from loading and its associated compensation is the geoid or gravity anomaly. Locally compensated loads, for example, would be expected to be associated with relatively small-amplitude free-air gravity anomalies that average to zero over large areas. This is because there is a competition between the gravity anomaly caused by a mass excess or deficiency and its compensating mass deficiency or excess. The magnitude of the anomalies depends on the wavelength of loading. Nevertheless, the existence of large-amplitude, long-wavelength, isostatic gravity anomalies, for example, in the vicinity of the plate boundaries, is a testament to the fact that local crustal-scale isostatic conditions do not prevail everywhere (Figure 1).

6.01.2.1 The Earth's Hypsometric Curve and Crustal Structure

We can evaluate the extent to which a planetary body approaches isostatic equilibrium by considering its topography. On Earth, topography is defined with respect to the geoid or mean sea level, which provides a convenient reference surface to calculate the magnitude of the loads that might disturb isostasy. Topography above and below sea level, for example, can be considered as such loads. We can therefore use these loads to compute the expected thickness of the crust and density of the subcrustal mantle based on different isostatic models and compare them to observations based on seismic refraction data.

Figure 2 shows that the Earth's topography has a distinctly bimodal distribution, which is unique among the terrestrial planets. One peak corresponds to a modal topography of 0.303 km above mean sea level, while the other peak correlates with a modal topography 4.301 km below mean sea level. These observations imply fundamental differences in structure of the crust and mantle and, hence, models of formation between continents and oceans.

Figure 3 compares histograms of the Earth's observed crustal thickness to calculations based on different models of isostasy. The crustal structure, which is based on the CRUST 2.0 compilation of Bassin et al. (2000), shows a clear bimodal distribution with the peak at ~40 km corresponding to the continents and the peak at ~6 km with the oceans. The calculated crustal thickness, T_s, is based on an Airy model and is given by

$$\begin{aligned} T_s &= T_c + \frac{h\rho_m}{(\rho_m - \rho_c)}, \quad \text{Continent} \quad h \geq 0 \\ T_s &= T_c + \frac{h(\rho_m - \rho_w)}{(\rho_m - \rho_c)}, \quad \text{Ocean} \quad h \leq 0 \end{aligned} \qquad [1]$$

where T_c is the zero-elevation crustal thickness, h is the topography (positive above sea level, negative below), and ρ_w, ρ_c, and ρ_m are the densities of the water, crust, and mantle, respectively. Figure 3(a) shows a 'standard' model with $T_c = 31.2$ km, $\rho_w = 1030$ kg m^{-3}, $\rho_c = 2800$ kg m^{-3}, and $\rho_m = 3330$ kg m^{-3}. This model predicts, like the observed data, a bimodal

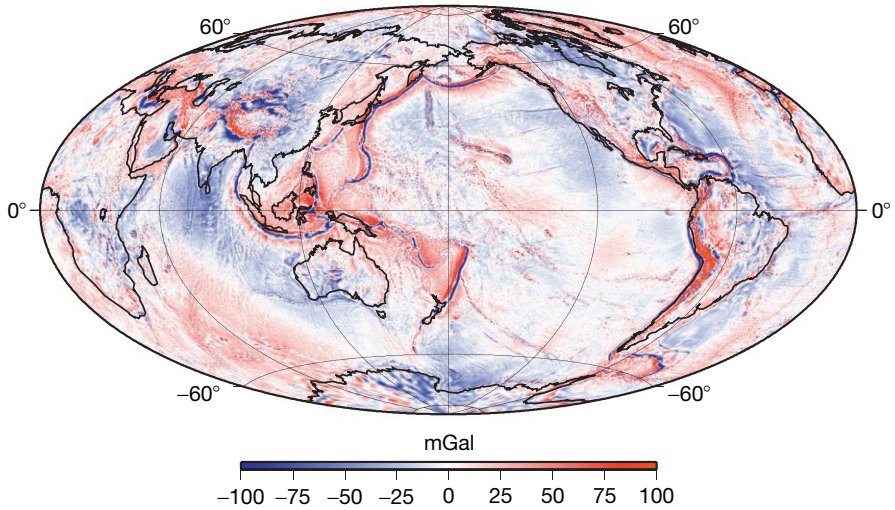

Figure 1 Global Airy isostatic gravity anomaly map. The anomaly has been calculated from the GEBCO 1 × 1 min topography grid (British Oceanographic Data Centre, 2003) and the EGM2008 2.5 × 2.5 min free-air gravity anomaly grid (Pavlis et al., 2008). The calculations assume a zero-elevation crustal thickness of 38.5 km and a density of water, crust, and mantle of 1030, 2700, and 3330 kg m^{-3}, respectively. The gravity effect of the topography and its Airy-type compensation have been computed using the fast Fourier transform (FFT) method of Parker (1973) and summed on a 15 × 15 min grid. The mean and root-mean-square (RMS) of the resulting grid are −0.56 and 29.51 mGal, respectively. Red shading indicates positive isostatic anomalies and regions of 'undercompensation' where Moho is shallower than would be expected on the basis of the Airy model. Blue regions indicate negative isostatic anomalies and regions of 'overcompensation' where Moho is deeper. White areas delineate regions of near-zero isostatic gravity anomalies where the crust appears to be in equilibrium and surface topography is fully compensated.

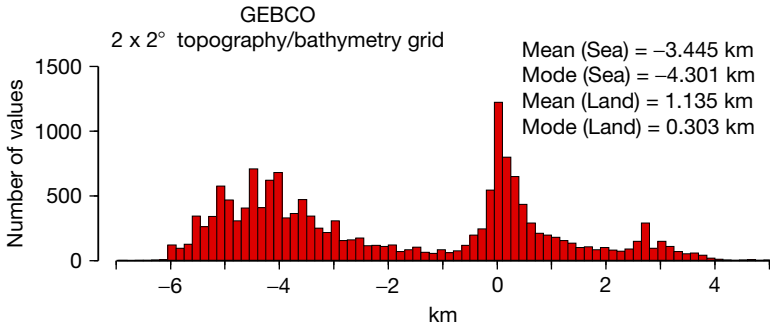

Figure 2 Histogram of the Earth's topography (land areas) and bathymetry (sea areas). The histogram is based on a 2 × 2° GEBCO (British Oceanographic Data Centre, 2003) grid and a bin size of 200 m. Positive values represent topography above the sea level. Negative values represent bathymetry below sea level. Note the distinct bimodal distribution of the data.

distribution. However, the calculated peaks are shifted with respect to the observed peaks. Continents appear to be thicker than the 'standard' model predicts and the oceans thinner.

The bimodal peaks in Figure 3(c) can be brought into agreement with the calculated isostatic model peaks (Figure 3(a), 3(b), and 3(d)) by adjusting the mantle density and zero-elevation crustal thickness. Figure 3(b) and 3(c) shows, for example, that a model with the same zero-elevation crustal thickness and water and crust density as the 'standard' model but with $\rho_m = 3180$ kg m^{-3} brings the observed and calculated oceanic peaks into agreement. However, the width of each peak differs. Oceanic crust is apparently thicker in deep, old, oceanic regions than the Airy model predicts and thinner in shallow, young, oceanic regions. This implies (for the same values of ρ_w, ρ_c, and T_c) that $\rho_m > 3180$ kg m^{-3} beneath old ocean and $\rho_m < 3180$ kg m^{-3} beneath young ocean and, hence, lateral density changes in the suboceanic crustal mantle between young and old oceanic lithosphere. Such a structure is more consistent with the predictions of the Pratt model than Airy.

Figure 3(c) and 3(d) shows that a model with the same water, crust, and mantle density as the 'standard model' but with $T_c = 40$ km brings both the location and width of the peak in the continent into agreement. Therefore, there does not appear to be a requirement, as there is in the case of the sub-oceanic mantle, for significant lateral density contrasts, and hence, we may conclude that the Airy model is a satisfactory description of continental crustal thickness.

6.01.2.2 Gravity Anomalies, Crustal Structure, and Local Models of Isostasy

The Earth's small mean isostatic gravity anomaly (the mean of the 15 × 15 min Airy isostatic gravity anomaly grid in Figure 1, e.g., is −0.56 mGal) suggests that isostatic equilibrium prevails

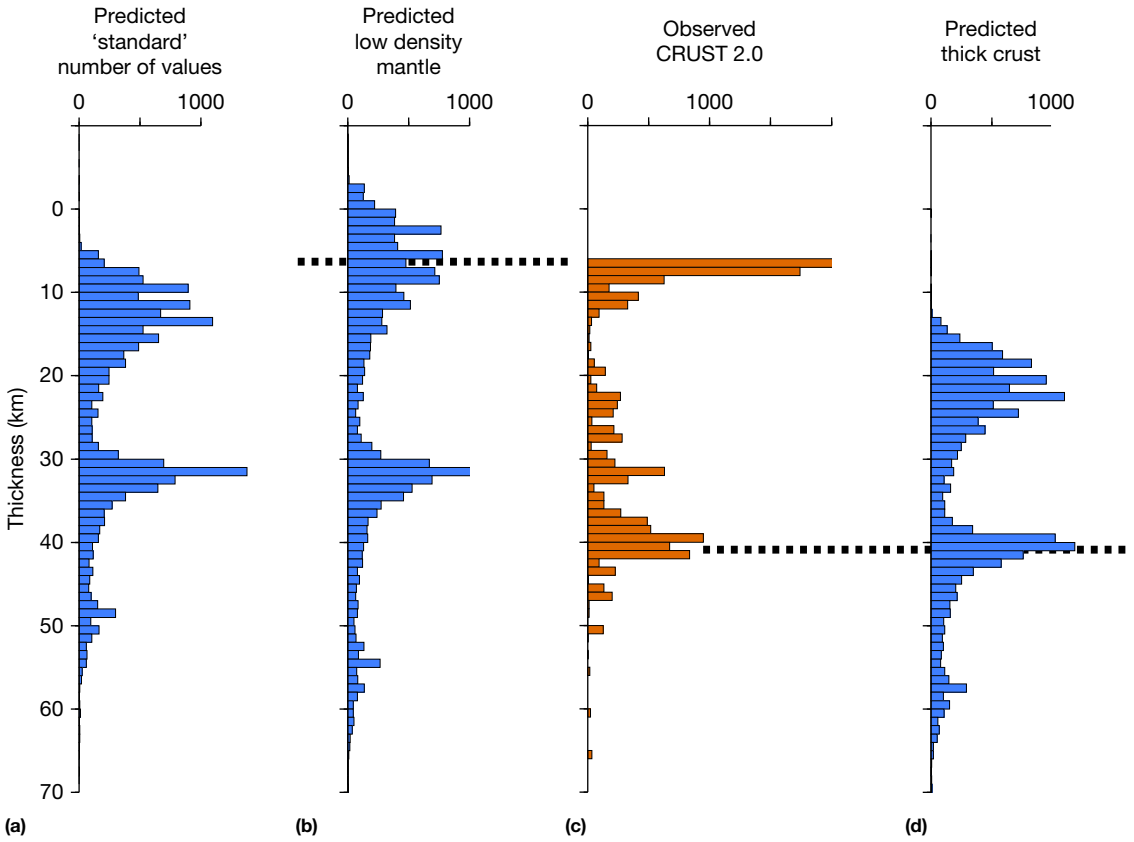

Figure 3 Histograms of observed and calculated crustal thickness. The observed thickness is based on CRUST 2.0 (Bassin et al., 2000). The calculated thickness is based on an Airy model of isostasy and a 2×2 min GEBCO topography and bathymetry grid. Different parameters have been assumed in the Airy model. (a) 'Standard' model with $\rho_w = 1030$ k gm^{-3}, $\rho_c = 2800$ k gm^{-3}, $\rho_m = 3330$ k gm^{-3}, and $T_c = 31.2$ km. (b) As in (a) except that $\rho_m = 3180$ k gm^{-3}. (c) Observed crustal thickness based on CRUST 2.0. (d) As in (a) except that $T_c = 40.0$ km.

to a significant extent. Not only does isostasy exist on the scale of the continents and the ocean basins, but also the small mean suggests a tendency toward equilibrium on the scale of individual geologic features such as some orogenic belts and rifts.

The applicability of local models of isostasy, such as Airy and Pratt, to individual geologic features can be tested by comparing their predicted gravity anomaly and crustal structure to observations. We will consider two features here: a mid-ocean ridge and a rifted continental margin. Although these features are linked in the sense that rifted margins form following the breakup of continents and the formation of new ocean basins, we will see that they are characterized by different modes of isostatic compensation.

Figure 4 shows a free-air gravity anomaly and topography profile, which intersects the Mid-Atlantic Ridge at latitude 48.8° N. The red-dashed line in Figure 4(b) shows the calculated gravity effect of the uncompensated seafloor topography. The gravity effect, $\Delta g_{\text{topo}}(x)$, was calculated using the expression of Parker (1973), which is given by

$$\Delta g_{\text{topo}}(x) = \Im^{-1}\left\{2\pi G(\rho_c - \rho_w)e^{-kd}\sum_{n=1}^{\infty}\frac{k^{n-1}}{n!}\Im\{h^n(x)\}\right\} \quad [2]$$

where $\Im$ denotes the Fourier transform, $\Im^{-1}$ the inverse Fourier transform, $h(x)$ is the topography, G is the gravitational constant, k is wave number (which is given by $2\pi/\lambda$, where λ is wavelength), n is the number of terms in the expansion of the gravity effect of the topography, and d is the mean seafloor depth. The mean seafloor depth in Figure 4(a) (dashed line) is 3.9 km, which yields a gravity anomaly that increases from about −50 mGal over the ridge flanks to >+100 mGal over the ridge crest, assuming $\rho_w = 1030$ kg m^{-3} and $\rho_c = 2650$ kg m^{-3}. These calculations are based on a first-order theory, that is, $n = 1$, since the gravity effect of higher-order terms in the series expansion is negligible. The figure reveals a strong correlation between the short-wavelength ($\lambda < \sim 200$ km) gravity anomaly and topography. The correlation at long wavelengths, however, is poor. This is well seen in Figure 4(c), which shows that the general level of the observed free-air gravity anomaly is approximately the same on either side of the ridge, despite the systematic deepening of the seafloor away from the crest of the ridge.

The differences in observed and calculated gravity anomalies in Figure 4(b) and 4(c) suggest that the gravity excess of the topography at mid-ocean ridges must be compensated by a mass deficiency at depth. The form of this compensation remains unclear. One possibility is that the ridge topography is in a state of Airy or Pratt isostatic equilibrium. We can test this assumption by computing the gravity effect of the different isostatic models and comparing them to the observed gravity anomalies. The first-order gravity effect of a variable crustal thickness Airy model, $\Delta g_{\text{Airy}}(x)$, for example, is given by

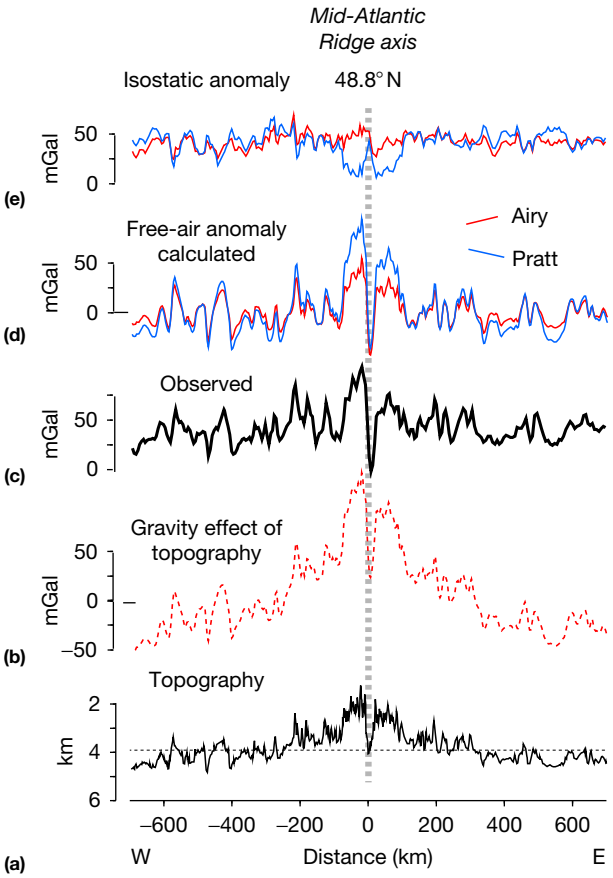

Figure 4 Gravity anomaly and topography profile of the Mid-Atlantic Ridge at 48.8° N. The data were acquired during cruise ss014 of R/V Snellius in 1965. (a) Topography. The dashed line shows the mean depth used to calculate the gravity anomaly. (b) Calculated gravity effect of the topography. (c) Observed free-air gravity anomaly. (d) Calculated gravity effect of the topography and its isostatic compensation. Red line, Airy model; blue line, Pratt model. Note the observed gravity anomaly is about 25–30 mGal higher than the calculated anomaly. This is due to the long-wavelength gravity anomaly 'high' that dominates the North Atlantic and is probably associated with the dynamics of the Iceland plume. (e) Airy (red line) and Pratt (blue line) isostatic anomalies. The calculated profiles assume two-dimensionality, ρ_w, ρ_c, and ρ_m of 1030, 2650, and 3330 kg m^{-3}, respectively, a zero-elevation crustal thickness, T_c, of 31.2 km (Airy model), and a mean depth of compensation, D_c, of 125 km (Pratt model).

$$\Delta g_{\text{Airy}}(x) = \Im^{-1}\left\{2\pi G(\rho_c - \rho_w)\Im\{h^n(x)\}e^{-kd}\left(1 - e^{-kt}\right)\right\} \quad [3]$$

where t is the mean thickness of the crust. The first-order gravity effect of a constant crustal thickness Pratt model, $\Delta g_{\text{Pratt}}(x)$, is given (e.g., Watts, 2001, eqn. [5.16]) by

$$\Delta g_{\text{Pratt}}(x) = \Im^{-1}\left\{2\pi G e^{-kd}\Im\{h^n(x)\}[(\rho_c - \rho_w) + (\rho_m - \rho_c)e^{-kt_c} - (\rho_m - \rho_w)e^{-k(D_c - t_c)}]\right\} \quad [4]$$

where t_c is the mean thickness of the crust and D_c is the depth of compensation.

Figure 4 shows that the observed free-air anomaly is explained well by either an Airy model with $T_c = 31.2$ km or a Pratt model with $D_c = 125$ km. This does not imply, however, that these models are the best description of the state of isostasy at the ridge.

In fact, we can dismiss an Airy model because it predicts that the oceanic crust thickens from ~11.7 km at the edge of the profile in Figure 4 to ~20.3 km beneath the ridge crest compared with the observed oceanic crustal thickness, which is the range 7–8 km (Mutter and Mutter, 1993). Moreover, there is no evidence that oceanic crust is thicker at the ridge crest than at the ridge flank. The compensation cannot therefore be attributed to crustal thickening of a uniform density crust and must therefore be due to lateral density variations in either 'layer 2' and/or 'layer 3' of the oceanic crust, the subcrustal mantle, or some combination of these factors.

These considerations suggest that the Pratt model, which implies lateral density variations, might be a better model to explain ridge compensation than the Airy model. In this model, which allows the possibility of a crust with uniform density and thickness, compensation is achieved by lateral density changes in the subcrustal mantle. The model implies lower density beneath the shallower ridge crest than beneath the deeper ridge flanks. Such a model is compatible with thermal models in which oceanic lithosphere is created at a hot, low-density, upwelling region beneath a mid-ocean ridge crest and then increases its density as it cools and subsides with age.

Figure 4(d) and 4(e) shows that there are departures, however, between the calculated gravity based on the Pratt model and observations in the region of the rift valley floor and its flanking uplifts. This is the shallowest part of the ridge crest, and apparently, there is no underlying lateral density change between the base of the crust and the depth of compensation that is able to explain it. One possibility is that the shallowest part of the ridge crest is underlain by much lower-density mantle than beneath the deeper ridge flanks. Another is that there are dynamic effects such that pressures do not necessarily balance at a particular depth. Rather, compensation is achieved at least in part by lateral flow.

While isostatic compensation at the mid-ocean ridge therefore appears compatible with a Pratt model of isostasy, at least beneath the ridge flanks, data from the margins of the ocean basins where oceanic crust abuts continental crust appear to be better described by an Airy model. This is well seen at the Nova Scotia passive margin, which formed following the rifting apart of the North American and Eurasian Plates during the Early Cretaceous and the formation of the Central Atlantic Ocean basin (Figure 5). Seismic refraction data reveal 'normal' thickness (~32.5 km) continental crust beneath the shelf offshore Nova Scotia, which is characterized by an upper-crust velocity of 5.2–5.7 km s^{-1} and lower-crust velocity of 6.8–6.9 km s^{-1} (Wu et al., 2006). The crust then thins abruptly beneath the continental slope to ~10 km over a horizontal distance of ~150 km. At ~325 km, the thin crust abuts normal thickness oceanic crust.

The thinning of the continental crust at the Nova Scotia rifted margin is in good agreement with the prediction of an Airy model with $T_c = 31.5$ km and densities of 1030, 2800, and 3300 kg m^{-3} for the water, crust, and mantle, respectively (Figure 5). The root-mean-square (RMS) difference, for example, between the observed and predicted depths and Moho is 2.16 km.

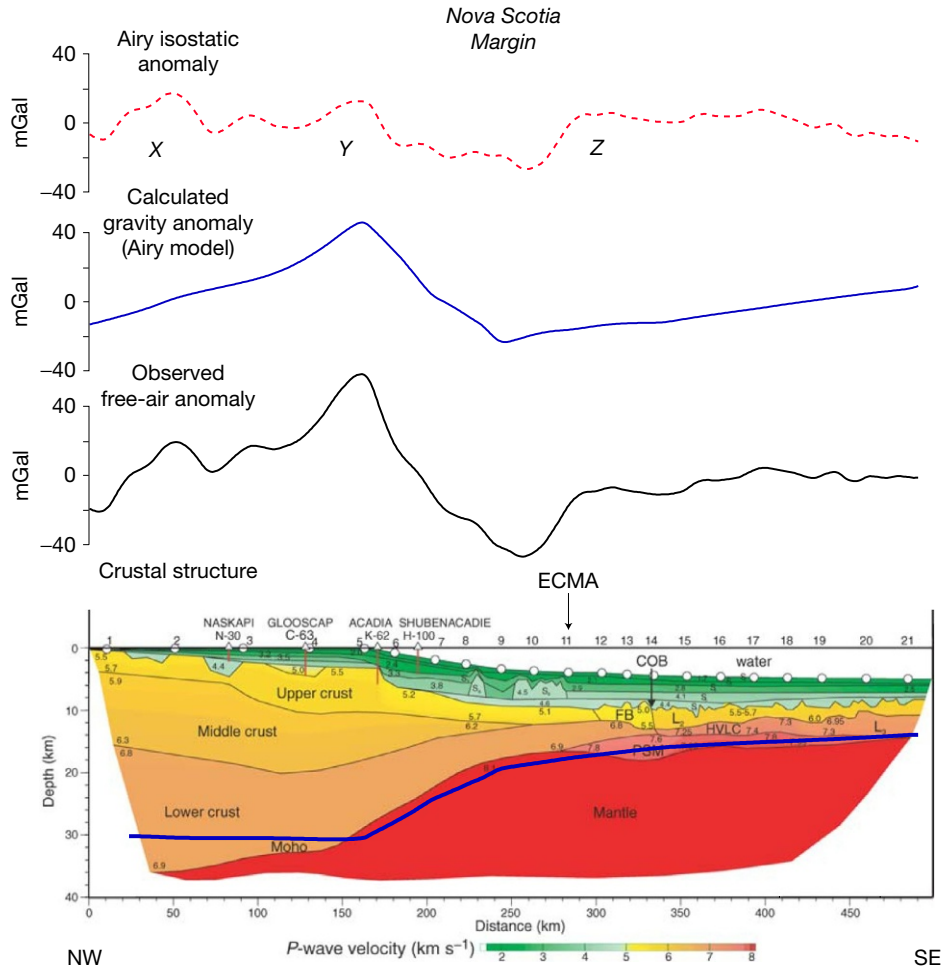

Figure 5 Gravity anomaly and seismic structure of the rifted continental margin offshore Halifax, Nova Scotia. The observed free-air gravity anomaly is based on the satellite-derived field of Sandwell and Smith (1997) and the seismically constrained crustal structure of Wu et al. (2006). The calculated base of the crust, which is based on the topography and its Airy-type compensation, is in good agreement with the seismic Moho. The calculated Airy gravity anomaly is also in reasonable agreement with the observed free-air gravity anomaly, as is seen by the relatively subdued Airy isostatic anomaly. ECMA, East Coast magnetic anomaly; COB, continent–ocean boundary.

An Airy model is also in accord with the observed free-air gravity anomaly at the margin. In particular, a model that incorporates the gravity effect of the topography and its Airy compensation explains well the long-wavelength component of the observed free-air gravity anomaly (Figure 5), especially the position of the edge effect 'high' and 'low.' This is seen in the Airy isostatic gravity anomaly, which is generally subdued across the margin. We attribute the short-wavelength anomalies (e.g., *X* and *Y*, Figure 5) in the region of shelf and slope to lateral density variations due, for example, to tilted blocks and intervening syn-rift basins.

The Airy and Pratt models represent a highly idealized condition that the Earth's crust and upper mantle would tend to, given sufficient time. They imply a weak crust that is unable to support geologic loads without yielding. The fact that the models account for gravity anomaly data at a mid-ocean ridge or a rifted margin does not, however, mean that the crust has no strength or that geologic processes such as sediment loading and unloading, and mantle upwelling and downwelling have not been operative at these features. Rather, they indicate that a state of isostatic equilibrium prevails despite the various geologic processes that have modified these features through time.

6.01.2.3 Departures from Local Isostasy: Flexural Isostasy

There are a number of locations on Earth where it is clear that the Pratt and Airy models of isostasy are unable to fully explain the gravity anomalies that are observed. Two such locations, which have featured prominently in previous isostatic studies, are the Hawaiian Islands, in the interior of the Pacific Plate, and northern India and the margins of the Tibetan Plateau, in the region of the Indian and Eurasian Plate boundary (see, e.g., Figure 1).

Figure 6 shows the isostatic anomalies in the region of the Hawaiian ridge as derived by Vening Meinesz (1941). He showed using submarine gravity measurements that an Airy model could not explain either the amplitude or wavelength of the free-air gravity anomaly across the Hawaiian ridge in the region of Oahu. In particular, he found that after correcting the free-air anomaly for the gravity effect of the topography

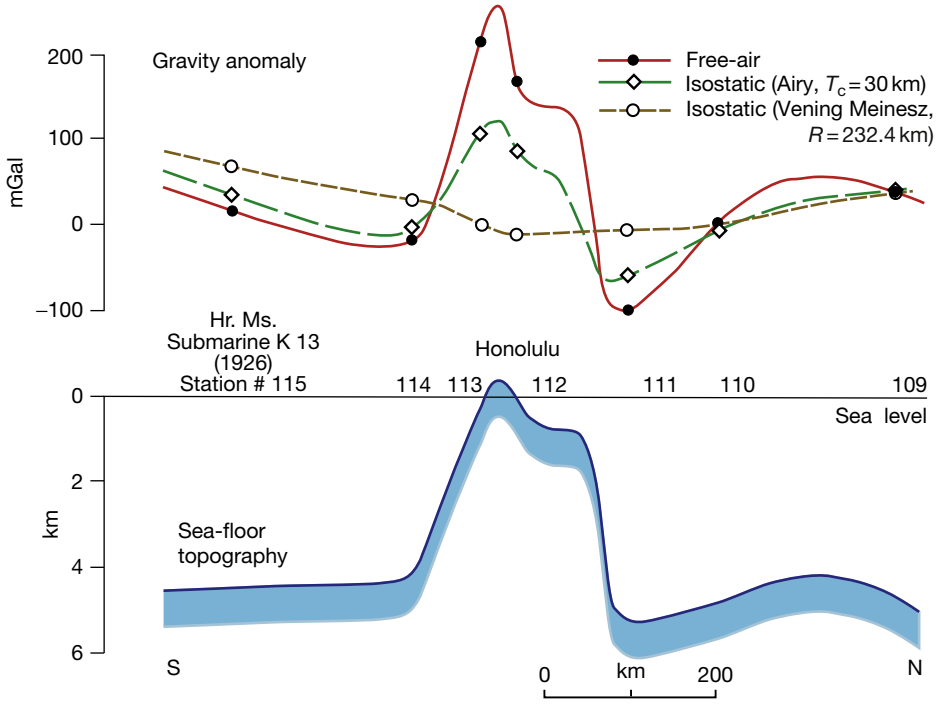

Figure 6 Gravity anomaly and topography profile of the Hawaiian ridge in the region of Oahu (Vening Meinesz, 1941). The free-air anomaly is based on gravity measurements acquired with a pendulum apparatus onboard the Royal Netherlands Navy Submarine K 13.

and its Airy compensation, a large-amplitude 'high' and 'low' remained over the ridge and flanking regions. The 'high' implies that the Moho is shallower under the ridge than the Airy model predicts, while the 'low' indicates it is deeper in flanking regions. Vening Meinesz (1941) demonstrated that a model in which the ridge was supported regionally, rather than locally, could better explain the observations.

In order to compute the gravity effect, Vening Meinesz set up a model in which the volcanoes that comprise the Hawaiian ridge load the surface of an elastic plate that overlies an inviscid substrate. The particular formulation that he used was that of Hertz (1884) who derived an analytic expression for the flexure of a thin elastic plate due to a concentrated 'point' load. The load-induced flexure comprised a subsidence or depression that was largest beneath the load but that extended into flanking regions because of the plate rigidity. Beyond the depression was a flexural uplift or bulge.

The flexure is determined by a parameter, β, which is related to the elastic parameters of the plate. In the Hertz (1884) formulation,

$$\beta = \left[\frac{D}{(\rho_{\text{substrate}} - \rho_{\text{infill}})}\right]^{1/4} \quad [5]$$

where $\rho_{\text{substrate}}$ is the density of the inviscid substrate, ρ_{infill} is the density of the material that infills the flexure, g is the gravitational acceleration, and D is the flexural rigidity of the plate. D is given by

$$D = \frac{ET_e^3}{12(1-\nu^2)} \quad [6]$$

where T_e is the elastic plate thickness, E is Young's modulus, and ν Poisson's ratio.

In the Hertz (1884) formulation, the distance to the first node (i.e., first point of no subsidence or uplift beyond the load) is given by 3.887β. Vening Meinesz (1941) used the flexure to compute the gravity effect of the compensation. However, he described the flexure in terms of the 'radius of regionality,' R, which is related to β by

$$R = 2.905\beta$$

Vening Meinesz (1941) set up tables to compute the flexure and gravity anomaly directly from the topography and found that $R = 234.4$ km best minimized the isostatic anomalies over the Hawaiian ridge. This corresponds to $T_e = 28.8$ km, assuming $\rho_{\text{substrate}} = 3330$ kg m^{-3}, $\rho_{\text{infill}} = 2800$ kg m^{-3}, and $g = 9.81$ m s^{-2}.

The advent of surface ship gravimeters in the mid-1960s led to a significant increase in the number of gravity anomaly profiles over the Hawaiian ridge. Figure 7 shows one such profile that intersects the ridge between Oahu and Molokai. Figure 7(b) shows a close agreement between the observed free-air gravity anomaly and the calculated anomaly based on $T_e = 20$ and $T_e = 30$ km. The calculated profiles based on $T_e = 10$ km produce an anomaly that has too small amplitude over the load and too short wavelength in the flanks, while $T_e = 75$ km produces an anomaly that is too high and too broad.

The elastic parameters that best describe flexure at an individual feature can be estimated from the isostatic gravity anomaly. Figure 7(b) shows, for example, the flexural isostatic anomalies at the Hawaiian ridge. The anomalies were calculated by subtracting the gravity effect of the topography and its flexural compensation from the observed free-air anomaly. The T_e that produces the most subdued isostatic anomaly and,

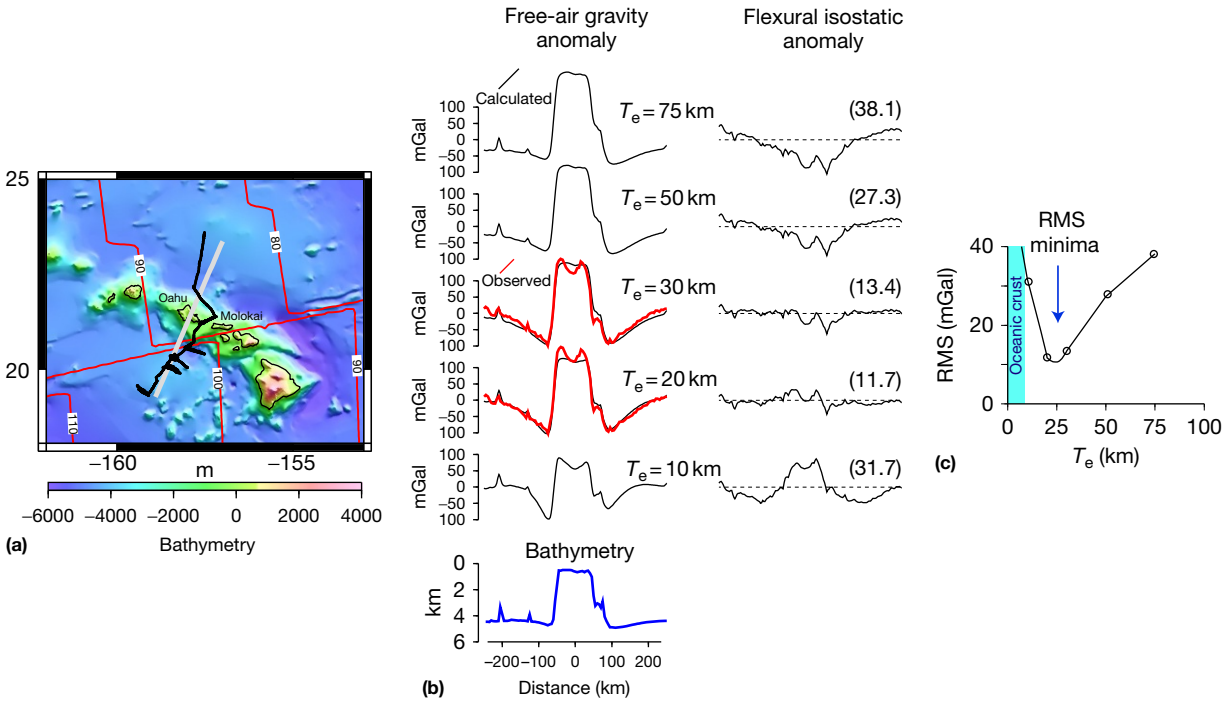

Figure 7 Comparison of observed and calculated gravity anomalies along a profile that intersects the Hawaiian ridge between Oahu and Molokai. The observed free-air gravity and bathymetry profile is based on data acquired during cruise KK088 of R/V Kana Keoki in 1982. The observed data have been projected onto a line centered on an origin at Honolulu (Lat: 21.32° N and Lon. 157.92° W) with an azimuth of 023°. The calculated gravity anomaly assumes two-dimensionality, $\rho_c = \rho_{infill} = \rho_{layer2} = 2700$ kg m^{-3}, $\rho_{layer3} = 2900$ kg m^{-3}, $\rho_m = 3330$ kg m^{-3}, and the T_e values shown. (a) Location map. The bathymetry has been constructed using a GEBCO 2 × 2 min grid. Black lines indicate gravity measurements. White line indicates the line of projection. Red lines indicate age isochrons based on Müller et al. (1997). (b) Left-hand panel shows bathymetry and observed and calculated free-air anomaly profiles. The right-hand panel shows bathymetry and flexural isostatic gravity anomaly profiles. (c) Plot of RMS difference between observed and calculated free-air gravity anomalies versus T_e.

hence, the best fit between observed and calculated free-air gravity anomalies is in the range 20–30 km. Figure 7(c) shows that the RMS difference of the flexural isostatic anomaly reaches its minimum value at $T_e = 25$ km, which is close to the estimate derived by Vening Meinesz (1941) from a much sparser gravity and topography data set. The isostatic anomalies that remain over the Hawaiian ridge are most likely due to shallow geologic structures that have not been included in the flexure model.

Figure 8 shows a detailed map of the Airy isostatic gravity anomalies in northern India and the Tibetan Plateau. Gravity data coverage is generally good in northern India but sparse over the Tibetan Plateau. The figure shows a prominent positive–negative isostatic anomaly 'couple' associated with the southern boundary of the Tibetan Plateau. The 'couple,' which is recognizable on earlier Airy and Pratt isostatic anomaly maps (e.g., Chugh and Bhattacharji, 1974), occurs to the south of the Indus–Tsangpo suture that separates the Indian and Eurasian Plates. The positive anomalies correlate with the Greater Himalayas that comprises rocks that underwent high-grade amphibolite facies metamorphism during the southward-directed thrusting that formed the Himalayas. The negative anomalies reach their minimum values just to the south of the Main Boundary Thrust (MBT) and extend to the distal edge of the Ganges foreland basin.

As we argued when considering the Hawaiian ridge, isostatic anomalies are indicative of the crustal structure. The belt of positive isostatic anomalies in Figure 8(b), for example, indicate that the Lesser and Greater Himalayas have a shallower Moho than is predicted by Airy, while the negative anomalies indicate that the Moho beneath the Ganges foreland basin is deeper. These observations have been interpreted by Karner and Watts (1983) and Lyon-Caen and Molnar (1983) as indicating that the Himalayas are supported, at least in part, by the strength of the subducting Indian lithospheric plate and that the Ganges foreland basin developed by flexure in front of the migrating thrusts and folds that comprise the mountain range.

We have used an iterative three-dimensional forward modeling technique to estimate the spatial distribution of T_e required to minimize the isostatic anomalies (Jordan and Watts, 2005). The main results, shown in Figure 8(c), suggest that the Tibetan Plateau and southern India are associated with relatively low T_e values ($0 < T_e < 20$ km), while northern India correlates with relatively high values ($T_e > 80$ km). They are also compatible with what is known about the regional geology and other geophysical observations in Tibet and northern India. For example, the Tibetan Plateau is associated with large amounts of shortening, a thick crust (70–80 km; Kind et al., 1996), high surface heat flow (~82 m Wm^{-2}; Wang, 2001), seismic reflection (Brown et al., 1996), and magnetotelluric survey (Chen et al., 1996) evidence for fluids in the mid-crust, while northern India correlates with normal thickness cratonic crust (~35–40 km; Hetenyi et al., 2006), low heat flow, high

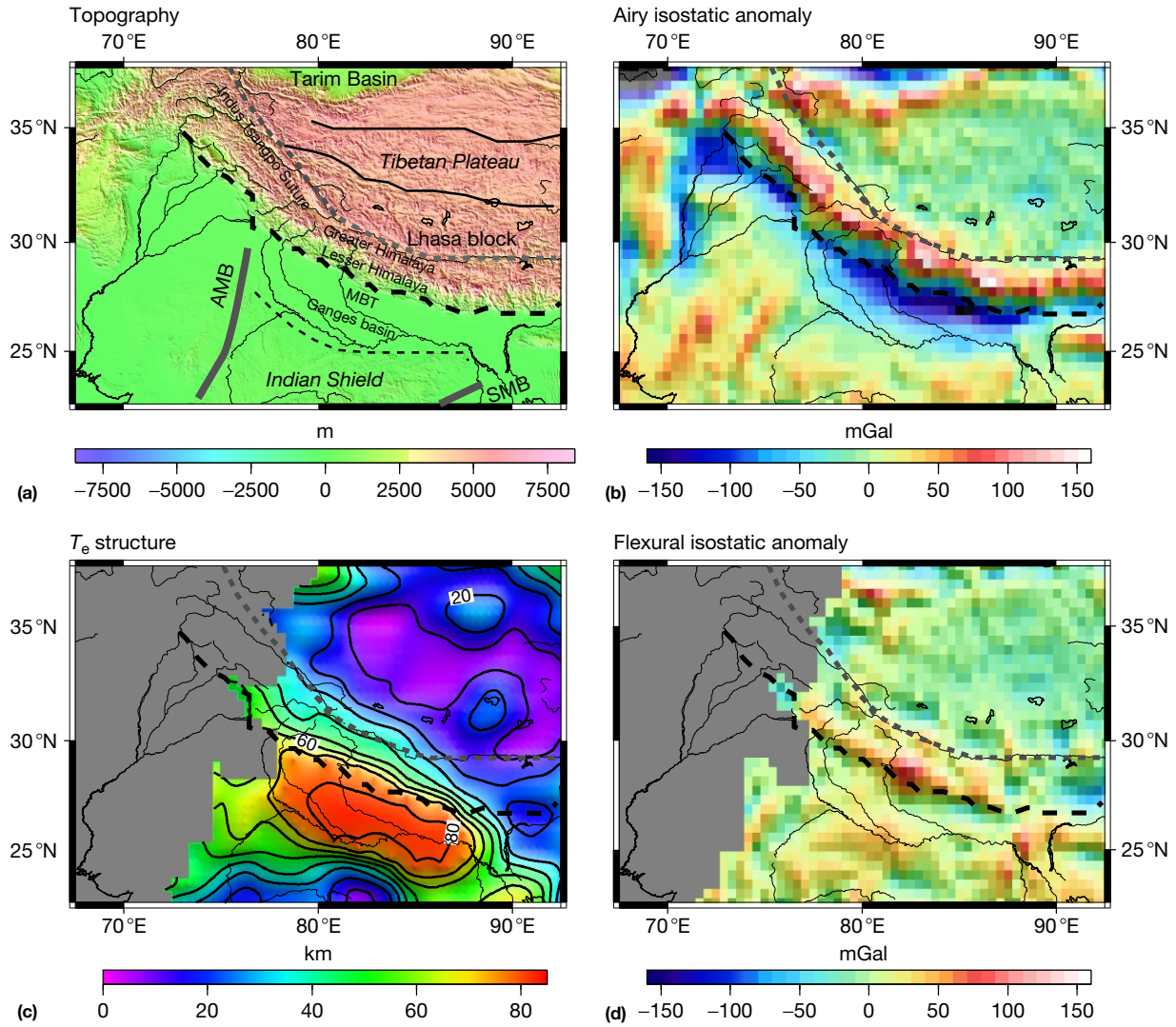

Figure 8 Topography, isostatic gravity anomalies, and the T_e structure of the northern Indian Shield, the Himalayas, and Tibetan Plateau. The thick black dashed line shows the location of the Main Boundary Thrust (MBT) and the gray dashed line the Indus–Tsangpo suture. The MBT marks the outermost thrust in the Himalayas. The suture separates the Indian and Eurasian Plates and formed as a result of a continent/continent collision during the Lower–Middle Eocene (Windley, 1988). AMB, Aravalli–Delhi mobile belt; SMB, Satpura mobile belt. (a) Topography based on a GEBCO 2 × 2 min grid. (b) Airy isostatic gravity anomaly. (c) T_e structure that best minimizes the Airy isostatic gravity anomaly. (d) Flexural isostatic gravity anomaly based on the T_e structure in (c). The isostatic anomalies and T_e structure are based on Jordan and Watts (2005).

elastic thickness (Trivedi et al., 2012; Watts et al., 2013), and an absence of any evidence for fluids within the crust.

The high and low T_e regions of northern India and the Tibetan Plateau are separated by a steep gradient that is located ~20 km to the north of the MBT (e.g., Jordan and Watts, 2005). A similar gradient has been deduced by Hetenyi et al. (2006) from thermomechanical modeling. By comparing model predictions based on an assumed rheology for the underthrust Indian Plate to the depth to the base of the Ganges basin and Moho, as determined by receiver functions, these authors have been able to estimate the T_e structure along a profile of the Himalayas and proximal Ganges basin at longitude 85° W. Their T_e gradient, however, is located ~180 km to the south of the MBT. Furthermore, their T_e values beneath the Himalayas are lower than those deduced by Jordan and Watts (2005) (~30 km compared to ~70 km). We are not certain of the reason for these discrepancies although they may be due to a lack of consideration by Hetenyi et al. (2006) of stronger rheologies, such as would be expected from a granulite lower crust or dry olivine mantle.

Recently, Li et al. (2008) used a new seismic tomography data set to show that the northern Ganges basin and high Himalayas are underlain by a region of a high *P*-wave velocity down to depths of at least 200 km. The high *P*-wave velocity region correlates closely with the high T_e region of Jordan and Watts (2005), Trivedi et al. (2012), and Watts et al. (2013) and is consistent with a model in which old, cold, strong Indian Plate is subducting beneath the high Himalayas at least as far as the Indus–Tsangpo suture where it abuts the Eurasian Plate.

6.01.3 The Deformation of the Crust and Lithosphere

We have been concerned thus far with the response of the Earth's outermost layers to long-term, large-scale, surface loads. In fact, these layers have been subject to a wide range of temporal and spatial scales of load. Each load scale provides different information about the response regime. Intermediate timescale loads, for example, are associated with a 'transient' regime in which the outermost layers would respond to loading (and unloading) by deforming over time (e.g., Figure 9). We will focus here therefore on three timescales: short-term (i.e., 0–120 s to a few years), intermediate (~10 ky), and long-term (>~1 My).

6.01.3.1 Earthquake Loading, Postseismic Relaxation, and the Short-Term (i.e., up to a Few Years) Response

The moment release in an earthquake can be considered as a short-term load on the crust and lithosphere that will respond by deforming. The pattern of deformation provides information not only on the fault slip plane that generates the earthquake but also on the rheological properties of the crust and lithosphere.

A model that has been particularly successful in explaining the deformation that occurs during an earthquake (i.e., the so-called coseismic deformation) is an elastic half-space model (Feigl et al., 1993; Okada, 1985; Savage and Burford, 1973). Okada (1985), for example, gave analytic expressions for the deformation that would be expected from slip on different types of faults embedded in an elastic half-space.

In general, there have been two main approaches to modeling coseismic deformation. In the forward approach, an elastic half-space model is used to compute the displacements on particular 'patches' of the fault that are then compared to observations such as those derived from Global Positioning System (GPS) and interferometric synthetic aperture radar (InSAR) data. In the inverse approach, the geodetic data are used to determine the displacements directly. Both approaches aim to constrain parameters such as the strike, dip, and rake of the fault that causes an earthquake and, hence, the geometry of the slip plane.

Examples of recent earthquakes that have been modeled using an elastic half-space model include Landers (Mojave Desert), 1992 (Miller et al., 1993); Dinar (Turkey), 1995 (Wright et al., 1999); Aiquile (Bolivia), 1998 (Funning et al., 2005); Hector Mine (Mojave Desert), 1999 (Hurst et al., 2000); Chi-Chi (Taiwan), 1999 (Johnson et al., 2001); Izmit (Turkey), 1999 (Reilinger et al., 2000); and Bam (Iran), 2003 (Motagh et al., 2005). These studies show that the vertical depth extent of slip on the fault plane varies with tectonic setting but is usually confined to the uppermost ~15 km of the brittle part of the crust.

The elastic half-space model has been modified to take into account a possible vertical stratification in the elastic properties. Ma and Kusznir (1995) and Hearn et al. (2002a), for example, used CRUST 5.0 to determine how the shear modulus might increase with depth and then applied it to the coseismic deformation associated with Izmit earthquake. They showed that a multilayer elastic model produces a greater slip at depth than the half-space model. In addition, Fialko (2004) had shown that multilayer elastic models explain well both the far-field and near-field symmetries and asymmetries in the

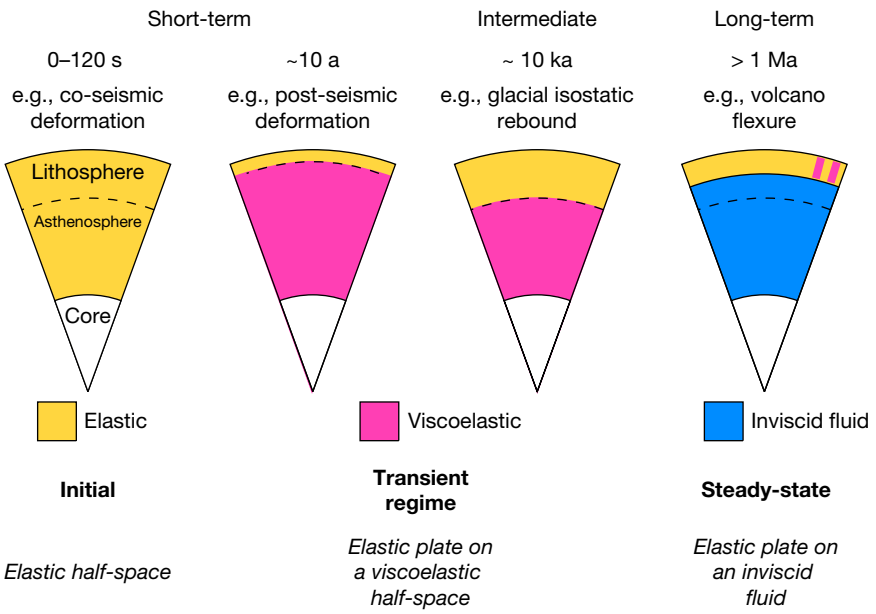

Figure 9 Schematic diagram illustrating how the Earth's outermost layers respond to loads of different timescales. The loads have been arbitrarily divided into: short-term, intermediate, and long-term timescales. Examples of short-term loads include the coseismic deformation associated with earthquake triggering and postseismic relaxation, intermediate loads include glacial isostatic adjustment, and long-term loads include volcano flexure. The bold text at the bottom of the diagram describes the deformation regime corresponding to each load duration. The italic text indicates the most commonly used deformation models at each timescale.

horizontal and vertical displacements derived from InSAR and GPS data associated with the Landers and Hector Mine earthquakes.

Despite its success, however, the elastic half-space model is limited because it ignores time-dependent contributions to the deformation. There are now a number of observations based on geodetic leveling, GPS, and InSAR data, for example, of a post-seismic deformation following an earthquake (e.g., Pollitz et al., 2000 and Savage et al., 2005). These data suggest some form of viscous relaxation process in the lithosphere–asthenosphere system.

Another model, therefore, is of a fault embedded in an elastic layer that overlies a viscoelastic half-space. The deformation in such a model (Dixon et al., 2003; Nur and Mavko, 1974; Pollitz, 2001; Savage and Prescott, 1978; Spence and Turcotte, 1979) is time-dependent and depends on the viscosity, the thickness of the elastic layer, and the time that has elapsed since the last earthquake compared to the viscous relaxation time.

Figure 10 shows an example of the deformation that would be expected during and following slip on a vertical normal fault that is confined to an elastic layer that overlies a viscoelastic half-space. The deformation reveals an uplift on the upthrown side of the fault (the footwall) and a subsidence on the downthrown side (the hanging wall). The initial, or coseismic, deformation is seen to be largely independent of the elastic layer thickness, h (note that we use h to indicate the short-term elastic layer thickness in order to distinguish it from the long-term thickness, T_e), and half-space viscosity, η_a. As time elapses, however, viscous effects dominate the initial elastic effects and the width of the uplift and subsidence region broadens. The width depends on the elastic layer thickness with the narrowest region of uplift and subsidence being associated with the thinnest plate and the widest region with the thickest.

The relationship between the width of deformation, w, and the elastic layer thickness, h, can be illustrated using a model of a discontinuous (i.e., broken) elastic plate over an inviscid substrate. We have (e.g., Watts, 2001, eqn [3.50])

$$w = \frac{\pi\alpha}{2} \qquad [7]$$

where α is the flexural parameter that is given by

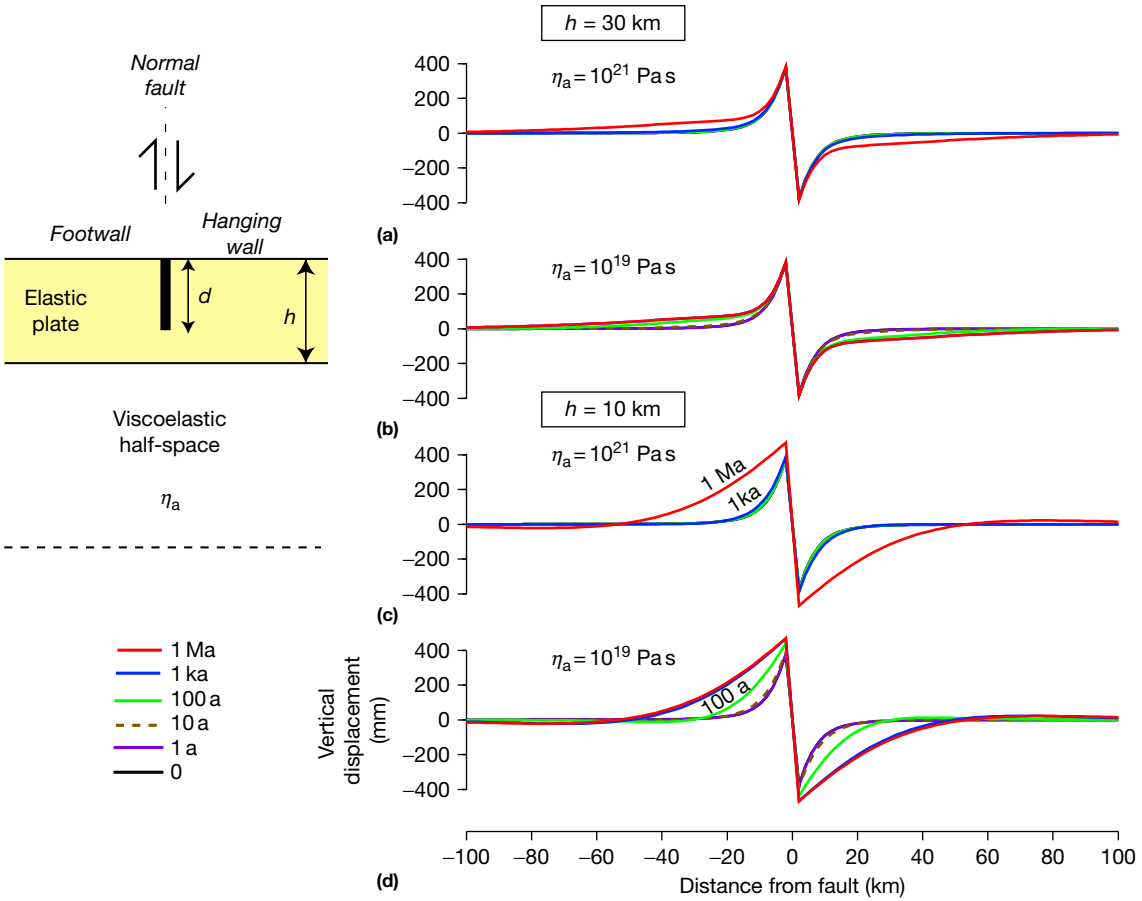

Figure 10 Simple model of the deformation due to a normal fault. The model is based on elastic layer ($E = 80$ GPa and $\sigma = 0.25$) that overlies a viscoelastic half-space. The fault plane extends from the surface to a depth, d, of 10 km and for a horizontal distance of ± 50 km orthogonal to the profile. The deformation is shown at 0 year, 1 year, 10 years, 100 years, 1 ky, and 1 My (solid colored lines) time intervals. (a) Thick plate, high viscosity ($h = 30$ km, $\eta_a = 10^{21}$ Pa s). (b) Thick plate, low viscosity ($h = 30$ km, $\eta_a = 10^{19}$ Pa s). (c) Thin plate, high viscosity ($h = 10$ km, $\eta = 10^{21}$ Pa s). (d) Thin plate, low viscosity ($h = 10$ km, $\eta_a = 10^{19}$ Pa s). The deformation was calculated by I. Ryder (pers. comm., 2006) using the code of Fukahata and Matsu'ura (2005) and Fukahata and Matsu'ura (2006).

$$\alpha = \left[\frac{ET_e^3}{3g\rho_m(1-\upsilon^2)}\right]^{1/4} \quad [8]$$

with $E = 80$ GPa, $\rho_m = 3330$ kg m^{-3}, $g = 9.81$ m s^{-2}, and $\upsilon = 0.25$. Equations [7] and [8] give w of 48.0 and 109.4 km for T_e of 10 and 30 km, respectively. These widths reproduce well the calculated widths in Figure 10.

We see from Figure 10 that the thickness, h, has a dampening effect on the postseismic deformation: thick elastic layers are associated with a smaller-amplitude deformation than are thin layers. The main control, however, on the deformation is the viscosity of the half-space. Low viscosity implies a more rapid response time than high viscosity.

The response time, τ_m, of a Maxwell viscoelastic half-space is given approximately (e.g., Mckenzie, 1967) by

$$\tau_m = \left[2(n+1)^2 + 1\right]\frac{\eta_a}{n\rho_m g a} \quad [9]$$

where n is the surface harmonic degree, η_a is the half-space viscosity, and a is the radius of the Earth. With $n = 400$ (which corresponds to $\lambda \sim 100$ km), $a = 6.378 \times 10^6$ m, $\rho_m = 3330$ kgm^{-3}, and $g = 9.81$ m s^{-2}. Equation [9] gives $\tau_m = 1.2$ ky and $\tau_m = 122.5$ ky for η_a of 10^{19} and 10^{21} Pa s, respectively. These calculated response times are consistent with Figure 10, which shows that for the low-viscosity case, deformation is essentially complete within ~ 1 ky, while for the high-viscosity case, it is not complete until ~ 1 My.

What is clear from Figure 10 is that the magnitude of the postseismic deformation is small, especially in the case of a thick elastic layer and a high underlying half-space viscosity. This makes it difficult to separate the time-dependent effects due to load-induced viscous relaxation from other effects such as those associated with pore-elastic rebound, afterslip, and regional tectonics.

Since the 1970s, more complex layered models have been proposed in order to account for postseismic deformation. Pollitz (1997), for example, developed a model (VISCO1D) of an elastic plate overlying a viscoelastic thin channel of finite thickness, which in turn overlies an elastic half-space. The main differences between the viscoelastic half-space and thin channel models have been discussed by Pollitz (1997) and Cohen and Kramer (1984), before him, who noted that the differences are largest early on in the earthquake cycle when displacements are smaller in the channel model than the half-space and there is a shift in the maximum displacement toward the fault.

Pollitz et al. (1998) applied a thin channel model to geodetic leveling and GPS data in the region of the Loma Prieta (Northern California) earthquake. By assuming an elastic upper-crust layer thickness of 16 km, they showed that the best fit to the geodetic data was for a Maxwell viscoelastic lower crust with a viscosity of 10^{19} Pa s, which in turn is underlain by a elastic layer. However, they also showed that a standard linear solid (i.e., a material with a viscous element that is elastic on both short and long timescales) lower-crust underlain by a viscoelastic mantle with 10^{19} Pa s could explain their data equally well.

Pollitz et al. (2000) and Pollitz et al. (2001) considered both linear (i.e., Maxwell viscoelastic and standard linear) and nonlinear (i.e., power law) models in their studies of GPS and InSAR data associated with the Landers and Hector Mine earthquakes. For Landers, they used a 30 km thick elastic layer (comprising a 16 km thick upper crust and a 14 km thick lower crust) and found an underlying moderate viscosity mantle with $\sim 7 \times 10^{18}$ Pa s between 30 and 50 km and $\sim 3 \times 10^{18}$ Pa s for greater depths. For Hector Mine, however, they used a 30 km thick upper layer that comprised a 16 km thick elastic layer, a 14 km thick lower viscoelastic crustal layer with 1.1×10^{19} Pa s, and a mantle viscosity that increases with time from $\sim 5 \times 10^{17}$ Pa s in the first few months to $\sim 2 \times 10^{19}$ Pa s after 1–3 years. The latter behavior, they argue, could arise from a nonlinear rheology.

The applicability of nonlinear rheologies to postseismic relaxation data has been critically discussed, most recently by Dalla Via et al. (2005) and Lorenzo-Martin et al. (2006). Dalla Via et al. (2005) preferred a Maxwell viscoelastic model in their analysis of the normal fault Irpinia (southern Apennines) earthquake, arguing that the availability of only two leveling data sets 1 and 5 years after the earthquake meant that it would not be possible to measure the transient effects associated with nonlinear rheologies. They found h of 18–20 km and $\eta_a \sim 10^{19}$ Pa s, which suggests a weak lower crust. Lorenzo-Martin et al. (2006) also used a Maxwell model in their analysis of the probable thrust fault Valdivia (Chile) earthquake, arguing that since their GPS data were acquired 35 years after the earthquake, the deformation probably had reached steady state by that time. They found a 46 km thick elastic plate overlying a 10^{20} Pa s mantle.

It is interesting to note that while the elastic layer thickness deduced for the Valdivia earthquake is significantly higher than for Landers and Hector Mine, it is of the order of the estimates of Nishimura and Thatcher (2003) derived from the 1959 Hebgen Lake (Northern Basin and Range, Western United States) earthquake. These authors used geodetic leveling data from two surveys after the earthquake and showed that the width of the uplift (up to 300 mm over several tens of kilometers) could be explained in terms of a single earthquake cycle model of an elastic plate overlying a Maxwell viscoelastic half-space (Figures 11 and 12). The best fits were for h of 38 km and η_a of 4×10^{19} Pa s. Similar results were obtained by Vergnolle et al. (2003) from the 1905 Bolnay–Tsetserleg and 1957 Bogd sequence of earthquakes in an intercontinental setting in central Mongolia ($h = 35$ km and $\eta_a = 1$–4×10^{19} Pa s).

Many earthquakes occur on plate boundaries where there has been a long history of seismicity, and so one question is how the temporal sequence and rupture lengths of past earthquakes cumulatively contribute to the present-day displacement field. Hearn et al. (2002b), for example, used the Savage (2000) multiple earthquake cycle model to analyze the displacements that would arise for 12 earthquakes during 1912–81 along the Anatolian strike-slip plate boundary separating the Eurasian and African Plates. They found $h = 25$ km and an asthenosphere viscosity, η_a, $> 5 \times 10^{20}$ Pa s, which implies a thin elastic plate and a high-viscosity mantle.

Smith and Sandwell (2006) used a new three-dimensional deformation model (Smith and Sandwell, 2004) to analyze the displacements from 37 historical (1800–2004) and prehistorical (after AD 1000) earthquakes on the San Andreas Fault system. They found $h = 70$ km and $\eta_a = 3 \times 10^{18}$ Pa s, which implies a thick plate and a relatively weak mantle.

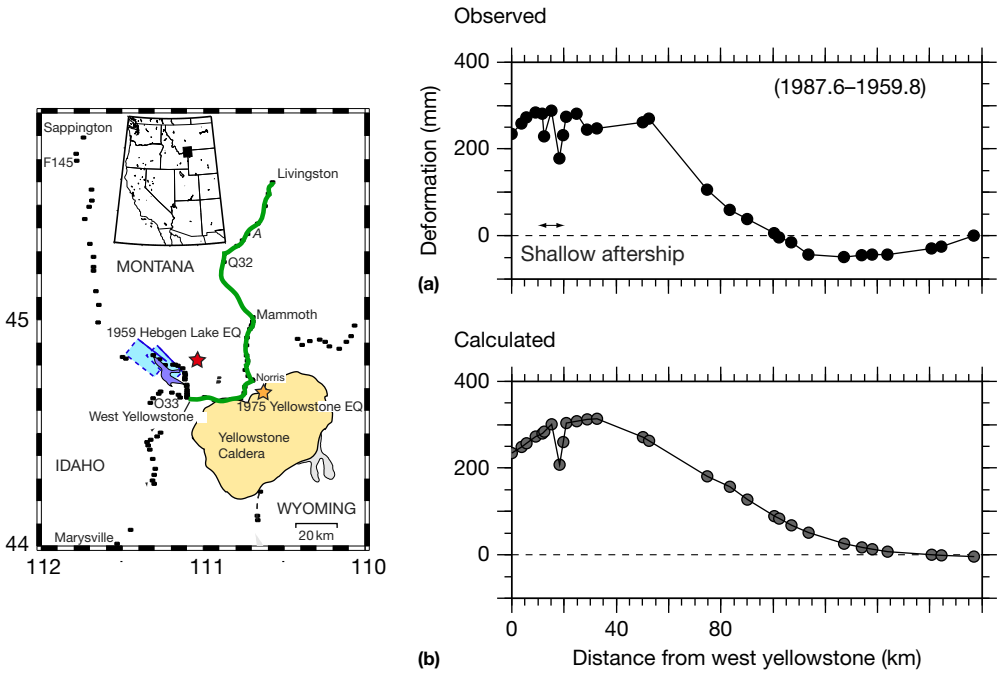

Figure 11 Comparison of the observed and calculated displacements that followed the 1959 Hebgen Lake earthquake. Blue-filled rectangles show the two fault planes of the earthquake. The observed displacement is based on geodetic measurements between West Yellowstone and Livingstone (green line on map). The vertical displacement reaches amplitudes of up to ~300 mm and extends for distances up to ~110 km from the fault plane. The calculated displacement is based on a model of an elastic layer overlying a viscoelastic half-space. Reproduced from Figures 1 and 8 of Nishimura T and Thatcher W (2003) Rheology of the lithosphere inferred from postseismic uplift following the 1959 Hebgen Lake earthquake. *Journal of Geophysical Research* 108, http://dx.doi.org/10.1029/2002JB002191.

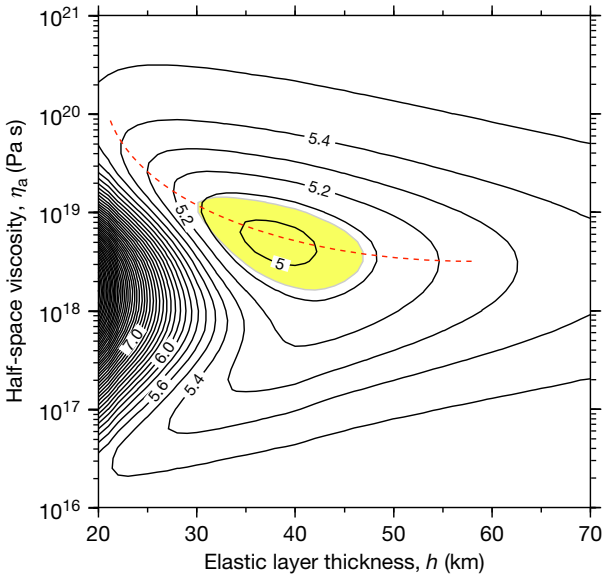

Figure 12 Plot of the RMS difference between observed and calculated displacements (in mm) for different values of the elastic layer thickness, h, and half-space viscosity η_a. The 'best fit' is for $h = 38$ km and $\eta_a = 4 \times 10^{19}$ Pa s. The figure illustrates the 'trade-off' between h and η_a. The dashed lines show the trend of the RMS minima. Lower thickness and higher viscosity and higher thickness and lower viscosity fit the data equally well. Reproduced from Figure 5(h) of Nishimura T and Thatcher W (2003) Rheology of the lithosphere inferred from postseismic uplift following the 1959 Hebgen Lake earthquake. *Journal of Geophysical Research* 108, http://dx.doi.org/10.1029/2002JB002191.

High elastic layer thickness is not, in fact, an uncommon result in geodetic studies. Johnson and Segall (2004) used the contemporary GPS velocity field across the Carrizo Plain and San Francisco Bay segments of the San Andreas Fault system and derived values of $44 < h < 100$ km. Cohen and Darby (2003) used geodetically constrained velocities across the Pacific and Australian Plate boundary in southern North Island, New Zealand, and derived h of ~45 km and 100–160 km for the Pacific and Australian Plates, respectively.

These differences between elastic layer thickness and mantle viscosity are interesting as they help explain why the patterns of deformation that follow earthquakes vary with regional tectonic setting. **Figure 10**, for example, shows that elastic layer thickness differences affect the amplitude and wavelength of the deformation – thick plates yield larger wavelength features than thin plates. This explains why the lobate vertical deformation patterns associated with the relatively thick elastic layer ($h > 60$ km) San Andreas system are wide ($w \sim 500$ km), while those associated with the relatively thin plate ($h \sim 15$ km) Landers and Hector Mine earthquakes are narrow ($w \sim 70$ km). Mantle viscosity, on the other hand, determines how quickly the plate relaxes – low viscosity yields shorter relaxation times compared with high viscosity. This explains why the relatively high-mantle-viscosity San Andreas and Landers earthquakes (Pollitz et al., 2000; Smith and Sandwell, 2006) are associated with a long relaxation time (3.6–7.0 years), while the relatively low-viscosity Hector Mine earthquake (Jacobs et al., 2002) correlates with shorter relaxation times (~135 days).

In a recent study, Yamasaki and Houseman (2012) used an InSAR data set of the deformation 165 days following the Manyi (Tibet) earthquake to infer the viscosity gradient in the crust and mantle underlying the thin elastic layer. Their best-fit model comprised a 10 km thick elastic layer that overlies a substrate with a viscosity of 1.2×10^{21} Pa s, which decreases exponentially to 1.6×10^{18} Pa s at the depth of the Moho (~60 km).

6.01.3.2 Glacial and Lake Loading and Unloading, Rebound, and the Intermediate-Term (a Few Tens of Thousand Years) Response

The waxing and waning of ice sheets load and unload the crust and lithosphere, which respond by flexure. The Last Glacial Maximum, for example, was ~21 ka when much of the Northern Hemisphere was covered by an ice sheet >1 km thick. As climates began to warm, the ice sheet retreated leaving in its wake vast meltwater lakes such as former Lake Agassiz and Lake Algonquin. The present-day Great Lakes, which straddle the US–Canada border, are remnants of these lakes. Deglaciation was interrupted ~13–11 ka when cold conditions briefly returned during the Younger Dryas. The final melting stages were more rapid, forced by rising temperatures. Today, grounded ice cover in the Northern Hemisphere is limited to Greenland; Baffin, Devon, and Ellesmere Islands; Svalbard; Franz Josef Land; and the Taymyr marginal zone (Siberia).

It has been known since the pioneering work of McConnell (1968) that the deformation following ice retreat provides information not only on the viscosity of the asthenosphere but also on the elastic thickness of the lithosphere. He found that there were two spectral peaks in the Fennoscandia uplift data: a primary long-wavelength ($\lambda \sim 800$ km) peak that required very long relaxation times and hence a viscous mantle to explain it and a secondary short-wavelength ($\lambda \sim 480$ km) peak that required short times and a less-viscous mantle. He found that the incorporation of a 120 km thick elastic layer that was underlain by a low-viscosity upper-mantle layer, which, in turn, was underlain by a more viscous lower mantle, explained both peaks in the spectral uplift data well.

Iwasaki and Matsu'ura (1982) used uplift data from the shorelines of former Lake Bonneville and Fennoscandia to estimate both the elastic layer thickness, H (note that we use H in this paper to define the intermediate-term elastic layer thickness in order to distinguish it from the short-term elastic layer thickness, h, and the long-term elastic thickness, T_e), and upper-mantle viscosity, η. They used a three-layer rheological model, similar to that of McConnell and estimated $H \sim 30$–40 km (Lake Bonneville) and $H \sim 100$ km (Fennoscandia) and a viscosity of the underlying layer of 1×10^{21} Pa s and 1.4×10^{20} to 1.4×10^{21} Pa s, respectively. Iwasaki and Matsu'ura (1982) found that changes in elastic layer thickness had a significant effect on the displacement in the loaded area: thin elastic layers gave relatively large displacements over small areas, while thick layers gave relatively small displacements over large areas. The similarity in upper-mantle viscosity and, hence, relaxation times between Lake Bonneville and Fennoscandia suggested to them, however, that H is the main factor that causes regional differences in their uplift patterns.

Fjeldskaar (1994, 1997) showed that the vertical crustal displacement field in Fennoscandia is particularly sensitive to H and helps explain observations such as regional differences in the tilting of former lake shorelines. He found, for example, that higher tilts required a lower H and lower tilts a higher H. The best-fit ice model implies that since the Helsinki, Finland, region has low tilts, it has a relatively thick elastic layer thickness ($H \sim 50$ km), while Western Norway, which has high tilts, requires a relatively low thickness ($H \sim 20$ km).

Most other estimates of H from glacial rebound studies, however, are significantly higher than 20–50 km. Davis and Mitrovica (1996), for example, used the ICE-3G model of Tushingham and Peltier (1991) and relative sea-level curves derived from tide gauges to suggest $H = 120$ km and an upper viscosity and lower viscosity of 1×10^{21} and 4×10^{21} Pa s, respectively, at the East Coast of the United States. They noted the importance of glacial isostatic rebound to the sea-level curves that include both a melting component and local tectonic component. Moreover, they showed that many of the features in the rebound corrected sea-level curves of previous workers are eliminated if the lower-mantle viscosity is increased.

Di Donato et al. (2000) noted, however, that an ICE-3G model with $H = 120$ km could not explain all the details of the sea-level curves along the East Coast, the United States. In particular, they noticed discrepancies in the rate of adjustment of up to 1 mm year^{-1}, which they attributed to the effects of a viscous layer that was embedded in the elastic layer. Their preferred model therefore was a 80 km thick elastic layer with a 15 km thick viscoelastic layer with viscosity of 10^{18} Pa s embedded in it.

Somewhat smaller elastic layer thicknesses were reported by Lambeck et al. (1998) and Peltier et al. (2002) for the ice sheet that, at its maximum, covered much of the British Isles. Lambeck et al. (1998) and Shennan et al. (2000), for example, found $65 < H < 85$ km, while Peltier et al. (2002) preferred $H = 90$ km. The Peltier et al. (2002) and Shennan et al. (2000) models are based on the same general constraints for the maximum thickness of the Scottish ice sheet (Ballantyne et al., 1998). It is not immediately clear therefore why these authors obtained such different H estimates. One possibility is the different viscoelastic structure assumed between the models and the trade-off that exists between upper-mantle viscosity and elastic layer thickness. Another is the different number of dated sea-level index points that were apparently used in the modeling.

Milne et al. (2004) used the rates of displacement constrained by GPS measurements to estimate the elastic layer thickness and mantle viscosity in Fennoscandia. They found the horizontal rates to be particularly sensitive to elastic thickness and mantle viscosity and that certain trade-offs existed between them. They showed, for example, that a combination of a high elastic layer thickness and high viscosity could explain the rate data as well as a combination of low elastic layer thickness and low viscosity. Their 'best-fit' upper-mantle viscosity structure (8×10^{20} Pa s) implies an elastic layer thickness of 120 km (**Figure 13(c)**).

Finally, Latychev et al. (2005) and van den Berg et al. (2006) had investigated the effects of a spatial variation in elastic layer thickness on the patterns of glacial rebound.

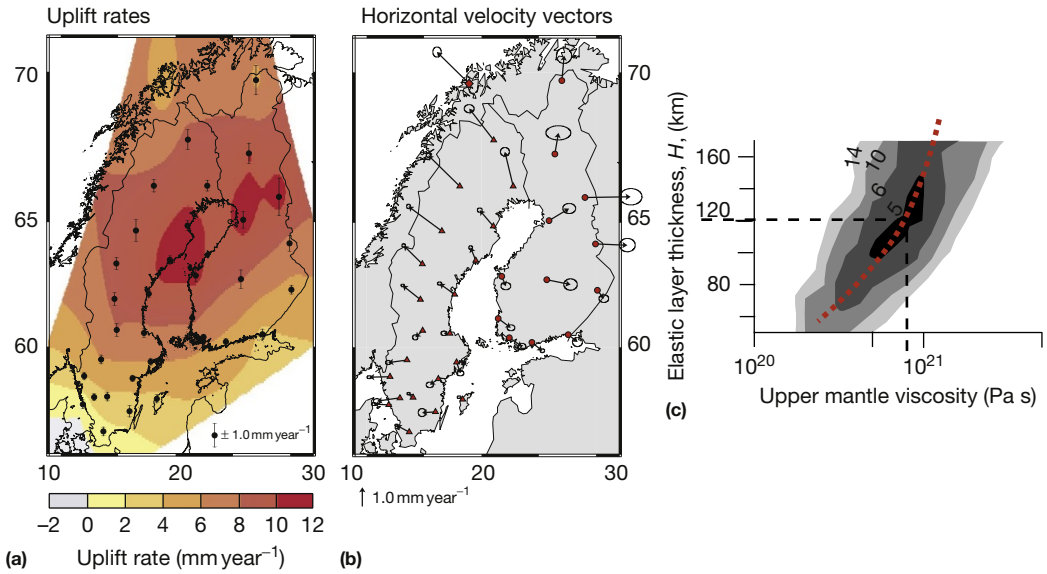

Figure 13 Crustal movements derived from the analysis of GPS data in Fennoscandia. (a) and (b) show vertical and horizontal rates of displacement, respectively. The scale of the velocity vectors in (b) is indicated at the base of the figure. Note that the horizontal rates are lowest where the uplift rates are highest and are directed outward from the main center of ice loading. (c) Normalized Chi-squared misfit between observed and calculated horizontal rates as a function of elastic layer thickness, H, and upper-mantle viscosity, η. Reproduced from Figure 1 of Milne GA, Mitrovica JX, Scherneck H-G, et al. (2004) Continuous GPS measurements of postglacial adjustment in Fennoscandia, *Journal of Geophysical Research* 109: B02412, http://dx.doi.org/10.1029/2003JB002619.

Latychev et al. (2005) showed that variations in elastic layer thickness across the continent–ocean boundary in the North Atlantic region could induce changes of up to 0.5 mm year^{-1} horizontal displacements rates. Stronger motions implied small elastic layer thickness, while weaker motions implied a large thickness. Their preferred model was a continental elastic layer thickness of 220 km and an oceanic elastic layer thickness of 70 km, which yielded an average thickness of ~120 km. Moreover, van den Berg et al. (2006) showed that spatial changes in elastic layer thickness could affect both the pattern of rebound and the spatial extent and the reconstructed volume of the ice.

That spatial variations in elastic layer thickness may be important in glacial loading and unloading can be demonstrated by considering a model of an elastic plate overlying an inviscid substrate. Although such a model is time-invariant, it is indicative of the deformation that the crust and lithosphere would approach given sufficient time. Walcott (1970a), for example, used the model to account for the present-day height of the ~12 ka shorelines of Lake Algonquin (**Figure 14**): an ~200 m deep lake that once infilled the flexural depression flanking the Laurentide ice sheet. He found a best-fit elastic layer thickness, T_e, of ~85 km.

Figure 15 shows the flexure that would be expected for a load, the approximate size of the Scottish ice sheet, which is superimposed on a lithosphere with a spatially varying elastic thickness structure. The calculations assume a disk-shaped ice load (radius = 75 km and height = 400, 500, and 600 m) centered near Fort William, Scotland, and the elastic thickness structure derived by Pérez-Gussinyé and Watts (2005) from a spectral analysis of Bouguer gravity anomaly and topography data. The observations comprise a data set of ~15–18 ka raised beaches (Sissons et al., 1966) and a 4 ka sea-level data set inferred mainly from peat deposits (Shennan and Horton, 2002). The figure shows general agreement between the uplift as indicated in the raised beach data and the pattern of uplift and subsidence as indicated by the sea-level data. In contrast, the flexure for a uniform T_e of 65 and 90 km (which correspond to the values of H used by Lambeck et al. (1998), Shennan et al. (2000), and Peltier et al. (2002) in their studies) does not fit as well. In particular, the uplift is too small and the width too broad. The fit to the uplift data could be improved by increasing the load height. Both Lambeck et al. (1998) and Peltier et al. (2002), for example, considered ice load heights of up to 1 km. The problem is that greater load heights predict an even wider region of uplift.

Therefore, the spatially varying T_e of Pérez-Gussinyé and Watts (2005), which predicts low values over the Caledonian orogenic belt north of the Iapetus Suture and high values over the Avalonian platform to the south, accounts for the magnitude of rebound, the width of the uplift, and the presence of a wide flanking region of subsidence. The model suggests a load height of ~500 m, but there are few constraints, except perhaps in northwest Scotland where the ice sheet appears to have formed a broad dome up to ~750 m high (Ballantyne et al., 1998). Irrespective, **Figure 14** illustrates the potential importance of a spatially varying elastic layer thickness structure in glacial rebound studies – not only for the pattern of flexure but also for the size of the ice load.

6.01.3.3 Volcano and Sediment Loading and the Long-Term (Greater than Several Hundreds of Thousand Years) Response

Volcanoes represent discreet loads on the surface of the lithosphere. They are associated with frequent eruptions, but they form over long periods of time. The large shield volcanoes that

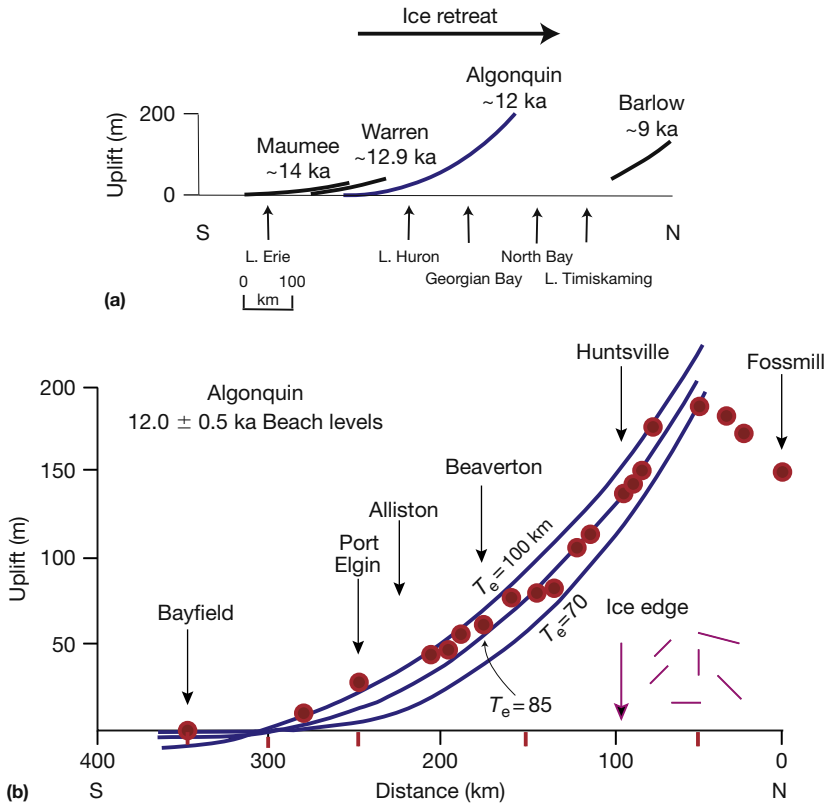

Figure 14 The flexure of the North American Plate that followed the retreat of the last Laurentide ice advance. (a) Profiles showing the heights of former shorelines of the lakes that once filled the 'moat' flanking the ice load (Walcott, 1972). (b) Comparison of the observed height of ~12 ka beach levels of Lake Algonquin with calculated profiles based on a flexure model with T_e of 70, 85, and 110 km (Walcott, 1970a). The decrease in the shoreline height at ~50 km was caused by the retreat of the ice load across the Fossmill outlet (Chapman, 1954). This led to the draining of Lake Algonquin out through the St. Lawrence River valley and into the Atlantic Ocean.

make up surface exposures on Hawaii, for example, range in age from 0 to 0.4 Ma. However, sampling of the submarine flanks of oceanic islands shows that they can take as long as ~1–2 My to form (Clague et al., 1989). Furthermore, there is evidence at some islands (e.g., the Marquesas) of volcanism that continues for some 2–4 My after the main tholeiite shield-building phase has ended (Duncan et al., 1986).

Figure 16 shows the volcano load-induced flexure northeast of Oahu (Hawaiian Islands), as seen in depth-converted seismic reflection profile data. The figure shows that at ~200 km from the northeast flank of the island, the top of Pacific Oceanic crust shallows to ~4.5 km, where it forms a bulge on the seafloor. At about 180 km, oceanic crust progressively deepens until beneath the island flank it is >3.5 km deeper than it is in the bulge region. The observed flexure of oceanic crust can be explained by an elastic plate model with a load defined by the bathymetry above a depth of 4.5 km and a thickness, T_e, of 25 km. The calculated flexure based on $T_e = 10$ km predicts too narrow and deep flexure compared to the observed, while $T_e = 50$ km predicts a flexure that is too broad and shallow.

The Hawaiian Islands form part of the Hawaiian–Emperor chain of submarine volcanoes, which formed as the Pacific Plate migrated over a deep mantle 'hot spot,' presently located beneath Loihi. As each new volcano in the chain has been emplaced on oceanic crust, its flexural effects have influenced the vertical motion history of preexisting 'upstream' islands and seamounts (Watts and ten Brink, 1989). For example, flexure due to the relatively young load of Hawaii (<0.4 Ma) has deformed older volcanoes in the Hawaiian Islands. Maui, for example, is in the flexural moat of Hawaii and therefore experiences subsidence. Oahu, however, is in its bulge region and therefore experiences uplift. As Grigg and Jones (1997) have shown, such uplift and subsidence patterns are consistent with observations, especially the raised fossil beach deposits on Oahu (Grossman and Fletcher, 1998) and the submerged wave-cut terraces (Faichney et al., 2010; Ludwig et al., 1991) on the flanks of Oahu and Maui, Hawaii.

Other examples of flexure due to a new load that influences preexisting loads have been described from the Southern Cook Islands (Figure 17). McNutt and Menard (1978) argued that the relatively young loads of Rarotonga and Aitutaki have deformed their preexisting neighboring islands. Atiu and Mauke, for example, are located on the bulge of both Rarotonga and Aitutaki and have been raised 63 and 19 m, respectively. While there is still some dispute about the relative ages of these islands (Jarrard and Turner, 1979), it is clear that flexure is capable of deforming preexisting oceanic islands and seamounts, depending on their distance from the main load centers.

Volcanoes onshore should show similar flexure features as are seen in oceanic regions (e.g., Smith et al., 2002). Unfortunately, it is more difficult to document the evidence for

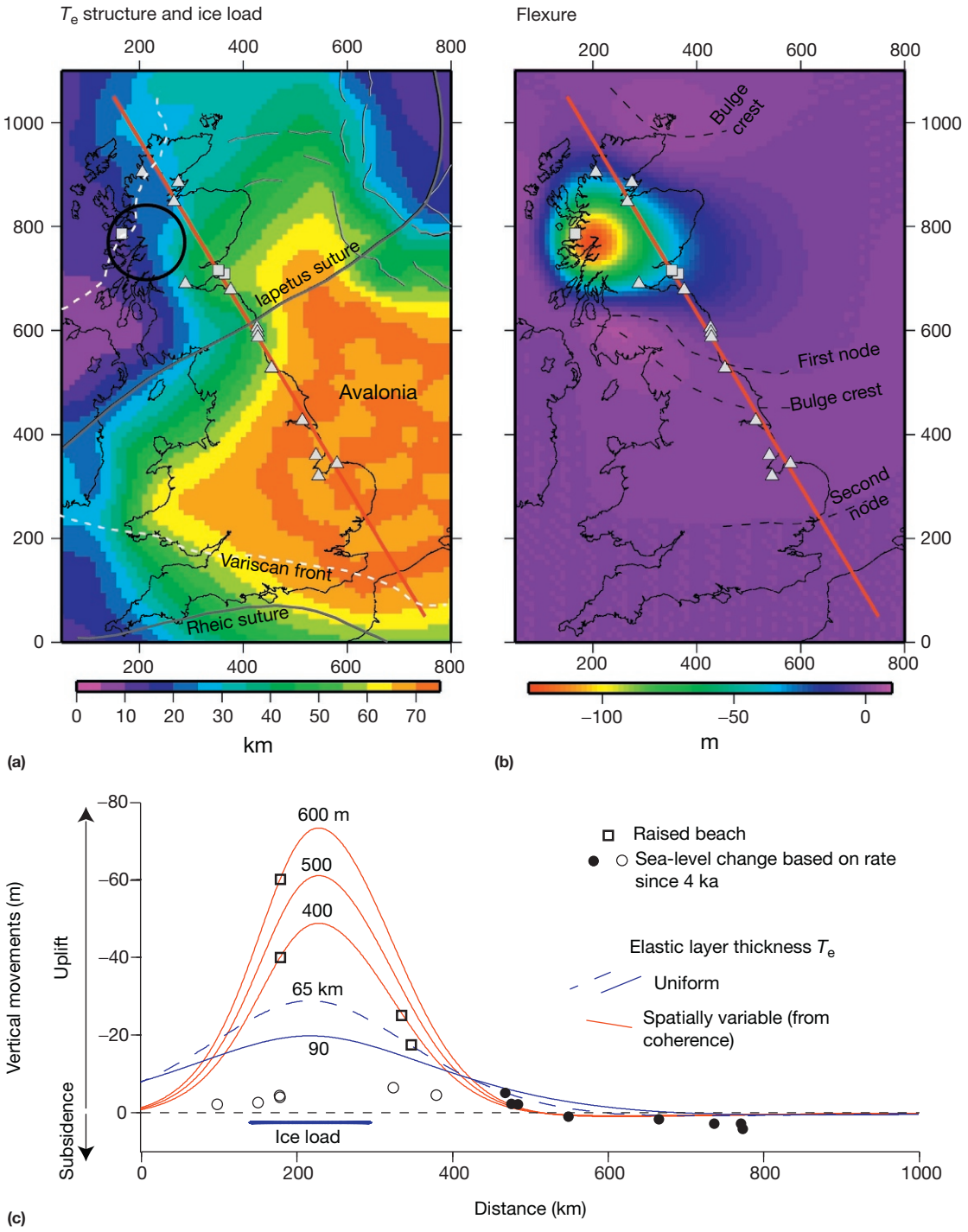

Figure 15 The flexure of the UK lithosphere caused by a simple model for the load of the Scottish ice sheet. (a) T_e structure based on the spectral (Bouguer coherence) results of Pérez-Gussinyé and Watts (2005). (b) Flexure due to a cylindrical load of height 500 m, radius 75 km, and density 947 kg m^{-3} that is emplaced on the T_e structures in (a). (c) Comparison of predicted flexure based on uniform T_e structures of 65 km (the value of H assumed by Lambeck et al. (1998)) and 90 km (the value of H assumed by Peltier et al. (2002)) (blue lines) and the spatially varying structure based on coherence (red lines) for load heights of 400, 500, and 600 m to observations of >14.7 ka raised beaches (squares) and late Holocene to Recent (i.e., 0–4 ka) sea-level change along the east coast of England (filled circles) and Scotland (open circles). The raised beach andsea-level data are based on Sissons et al. (1966), Shennan et al. (2002), and Shennan and Horton (2002).

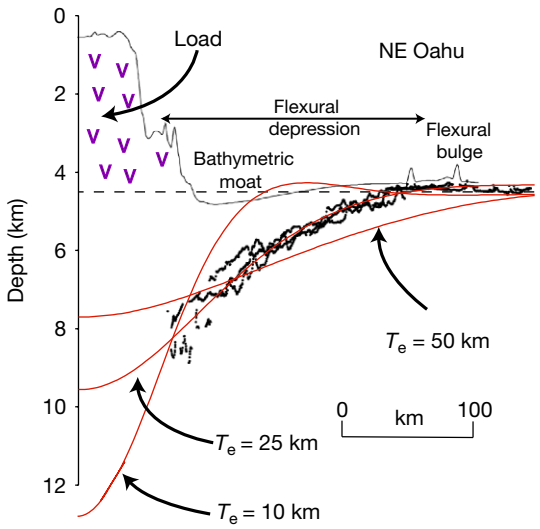

Figure 16 Comparison of observed and calculated flexure profiles northeast of Oahu, Hawaiian Islands. The observed flexure (black-filled circles) shows the top of oceanic crust as imaged on depth-converted seismic reflection profiles. The calculated flexure (red lines) is based on a three-dimensional elastic plate model, a load given by the bathymetry shallower than 4.5 km (dashed line), and an elastic thickness, T_e, of 10, 25, and 50 km. Reproduced from Figure 4.22 of Watts AB (2001) *Isostasy and Flexure of the Lithosphere*, p. 458. Cambridge: Cambridge University Press.

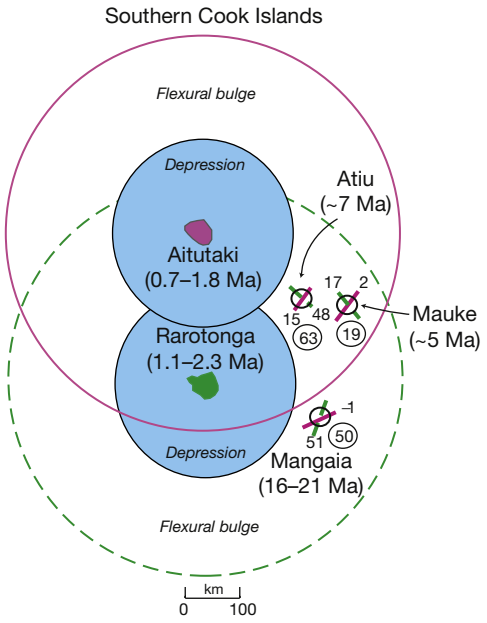

Figure 17 Comparison of the observed and calculated uplift at Mauke, Mangaia, and Atiu in the southern Cook Islands, Pacific Ocean. The 'rings' show the calculated flexure due to loading of the relatively young islands of Aitutaki and Rarotonga. Solid magenta ring shows the second node associated with the Aitutaki flexure. Dashed green ring shows the second node associated with the Rarotonga flexure. The short magenta and green lines show the magnitude of the flexural bulge at Atiu, Mauke, and Mangaia. Blue shaded regions show the flexural depressions. Reproduced from Figure 4 of McNutt MK and Menard HW (1978) Lithosphere flexure and uplifted atolls. *Journal of Geophysical Research* 83: 1206–1212.

flexure because of the modifying effects of erosion and sedimentation and the fact that many terrestrial volcanoes are superimposed on broad, sometimes quite complex, topographic swells. One example, however, where the volcano can be relatively easily isolated from the background regional topography is Kilimanjaro in Tanzania. This volcano, which has a relief of >4.5 km and is ~80 km wide at its base, is of Pleistocene age (~1.8–0.01 Ma) and has been emplaced on Precambrian basement of relatively low relief. Preliminary calculations (Humphreys, 2003) suggest that Kilimanjaro has depressed the underlying crust and lithosphere by upward of 4 km over horizontal distances of >200 km.

Unlike volcanoes, which form concentrated, short duration, loads, sediments represent broad loads emplaced over long periods of time. Nevertheless, they have provided useful information on the long-term deformation of the crust and lithosphere, especially at large river deltas.

One example is the Amazon River delta and associated deep-sea fan offshore northeast Brazil. Plate reconstructions show that the delta and fan have been deposited on a rift-type and shear-type margin that formed following the separation of South America and Africa and the opening of the Equatorial Atlantic Ocean in the Late Albian. The modern delta is limited in extent to the inner continental shelf and probably formed as a result of a high sediment flux that accompanied the last major sea-level rise (Hubscher et al., 2002). The deep-sea fan, however, extends across the outer shelf, slope, and upper rise and is believed to have formed during the Middle/Late Miocene, following the uplift and erosion in the Bolivian Andes (Damuth, 1975).

A difficulty with quantifying the role of flexure at delta–fan systems in rifted margin settings is that the original configuration of the margin and, hence, magnitude of the applied sediment load are unknown. However, it is possible to use sediment thickness and gravity anomaly data, together with combined three-dimensional flexural backstripping and gravity modeling techniques to determine the load and, hence, flexure (e.g., Stewart et al., 2000; Watts, 1988). Backstripping determines the initial, sediment unloaded, configuration of the margin for different assumptions on T_e, while gravity modeling of the restored crustal structure and the sediment load and its compensation constrains T_e.

Figure 18 shows a bathymetry, sediment thickness, and free-air gravity anomaly profile of the northeast Brazil margin in the region of the Amazon delta and deep-sea fan (Rodger et al., 2006). The figure shows that the margin comprises two main stratigraphic sequences: an older one of Early Cretaceous to Middle Miocene age and a younger one of Middle/Late Miocene to Recent age. Seismic reflection data suggest that the sediments overlie crystalline continental basement rocks on the landward end of the profile and unusually thin oceanic crust on its seaward end. The thick dash-dot line shows the tectonic subsidence, obtained by summing the backstrip of the older layer with $T_e = 13$ km, the backstrip of the younger layer with $T_e = 35$ km, and the present-day, unfilled, water depth. This subsidence yields the best fit between the observed and calculated gravity anomalies and permits the observed sediment accumulation at the margin to be divided into two parts: an upper part (light yellow shade), which defines the load, and a lower part (dark yellow shade), which is the flexure.

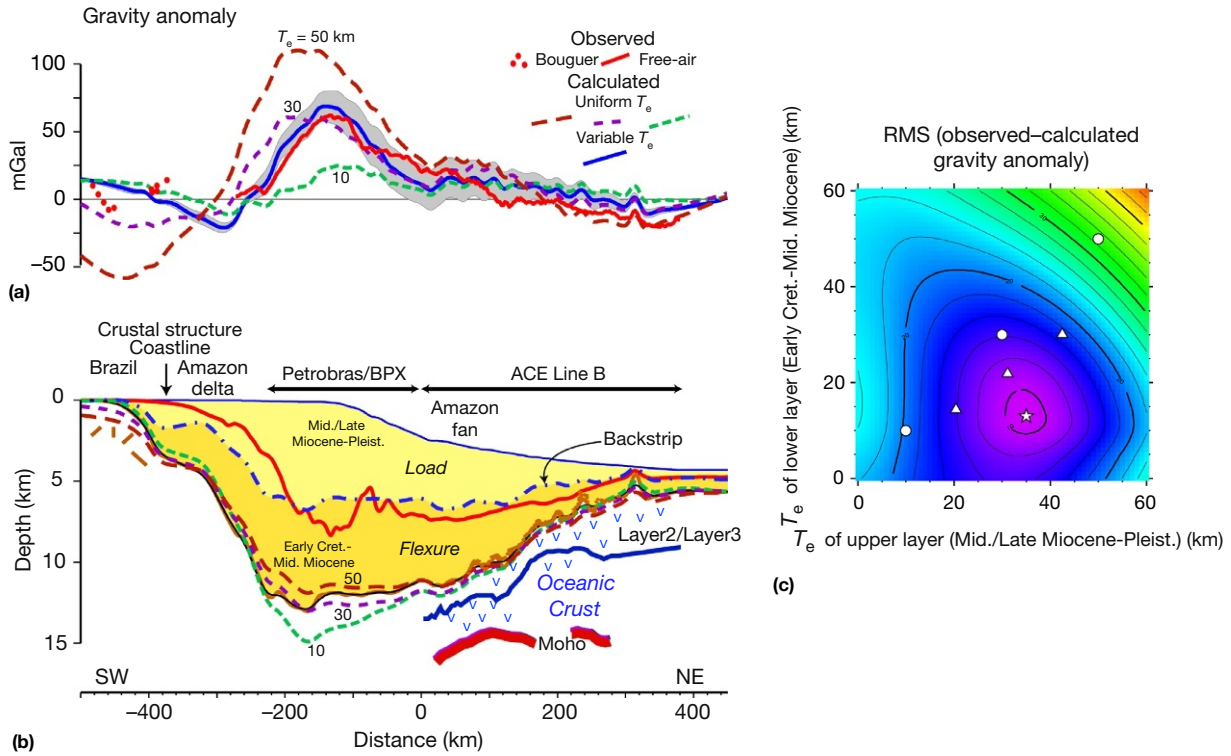

Figure 18 Crustal structure, bathymetry, and gravity anomaly profile of the Amazon delta and deep-sea fan system. (a) Gravity anomalies. The observed gravity is based on surface ship and land data, the sources of which are described in Rodger et al. (2006). The calculated gravity is based on combined three-dimensional backstripping and gravity modeling with uniform T_e of 10, 30, and 50 km (dashed colored lines). The blue solid is based on a variable T_e model in which the oldest, Early Cretaceous–Middle Miocene, layer formed on lithosphere with an average T_e of 13 km, while the youngest, Late Miocene–Recent, layer formed on lithosphere with an average T_e of 35 km. (b) Crustal structure. The 'v v v' symbols show the distribution of oceanic crust as inferred from the seismic refraction data. The solid red line shows the Middle/Late Miocene reflector. The dashed blue lines show the backstrip based on the variable T_e model. Other dashed lines show the flexure for the sediment load shown with uniform T_e of 10, 30, and 50 km. (c) Plot of the RMS difference between observed and calculated gravity anomalies for different values of the T_e for the older, lower layer, and the younger, upper layer.

Figure 19 shows the flexure due to only the younger, Middle/Late Miocene to Recent, delta and fan load (Watts et al., 2009). The figure shows that combined delta and fan loading has depressed the crust and lithosphere by >2 km over a horizontal distance of up to 1000 km. Beyond the depression, loading produces a bulge, which reaches amplitudes of up to 40 m. The first node, which separates the flexural depression and bulge, follows the general trend of the coastline remarkably well, suggesting a flexural control. Indeed, the embayment in the estuary region of the Amazon and Para Rivers appears to be controlled, at least in part, by the flexure due to the fan load, which extends across much of the outer and middle shelf. Onshore, the bulge corresponds to the position of the Gurupá arch, which is an eroded crystalline basement ridge with a drainage divide. Further onshore, there is evidence of back-bulges in the region of the Gurupá várzea (subsidence) and maybe the Monte Alegre arch (uplift).

We have, thus far, been discussing the deformation associated with long-term loading in terms of a thin elastic plate that overlies an inviscid substrate. While such a model is a good description of the surfaces of flexure associated with volcano and sediment loading, it is time-invariant and ignores the fact that the deformation may change with time.

Walcott (1970b) argued that a better description of the response of the crust and lithosphere to geologic loads might be a model of a Maxwell viscoelastic, rather than an elastic, plate overlying an inviscid substrate. Such a model is initially elastic but behaves as a viscous fluid on long timescales. Indeed, both Sleep and Snell (1976) and Beaumont (1978) used a viscoelastic model to describe the stratigraphic 'architecture' of sedimentary basins.

Watts and Cochran (1974) showed, however, that a Maxwell viscoelastic model with the same pair of elastic and viscous parameters was unable to explain the free-air gravity anomaly along both the Emperor seamounts and the Hawaiian ridge. While the older Emperor seamounts have a lower T_e than the younger Hawaiian ridge – as the viscoelastic model would predict – the values could be equally well explained by a purely elastic model in which the Emperor seamounts were emplaced on young, weak, lithosphere, while the Hawaiian ridge was emplaced on old, strong, lithosphere. Such a tectonic setting is consistent with sample ages along the seamount chain and with the age of the underlying seafloor, as inferred from marine magnetic anomalies and plate-tectonic reconstructions.

A basic tenet of plate tectonics is that the major plates behave rigidly on the long timescales of seafloor spreading

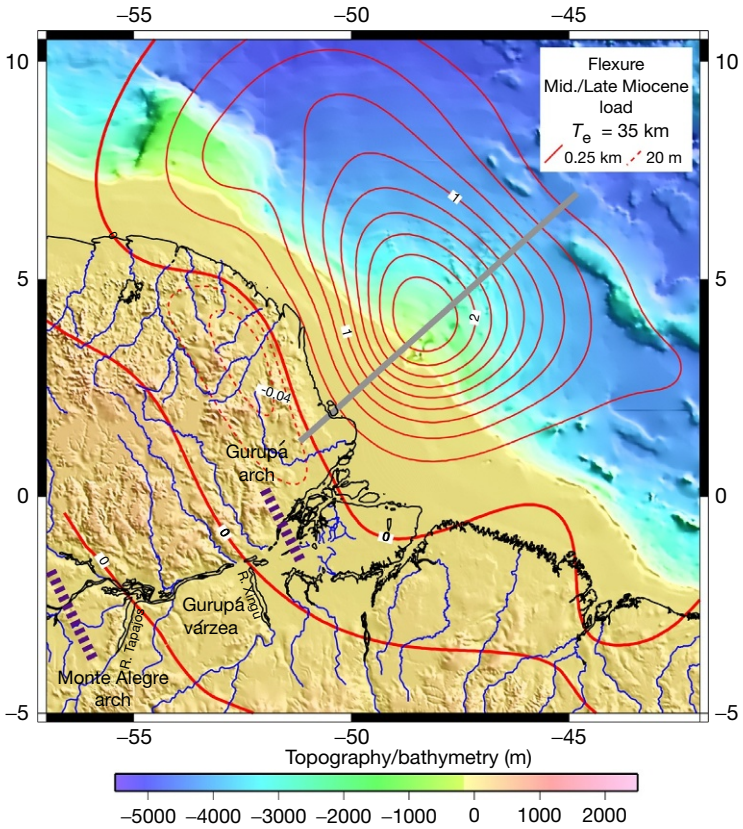

Figure 19 Flexure of the lithosphere caused by the Late Miocene–Recent Amazon River delta and submarine fan load. The flexure comprises a circular-shaped depression that is flanked by a bulge. The depression reaches a maximum of 2.1 km beneath the shelf break in slope, while the flanking bulge reaches a maximum of 40 m. Onshore, the bulge correlates with the Gurupá arch, an eroded crystalline basement ridge (Roddaz et al., 2005). Flanking the arch is a second depression (the so-called back-bulge of DeCelles and Giles (1996)). The depression correlates with the Gurupá várzea, a seasonally flooded savanna ecosystem.

and orogeny and that deformation is limited to their boundaries. Many oceanic plate boundaries (e.g., the mid-ocean ridge) are characterized by a narrow zone of deformation that extends over a few tens of kilometers or less. Deformation may extend over a wider region, but it is usually confined to a simple flexure, for example, on the flanks of rift valleys (Ebinger et al., 1991), fracture zone ridges and troughs (Sandwell and Schubert, 1982), and seaward of deep-sea trenches (Watts and Talwani, 1974).

It has long been recognized that some plate boundaries are characterized by deformation that is much more diffuse, being distributed over horizontal distances of up to a few thousand kilometers (Gordon, 1998). A good example is the Indian–Eurasian Plate boundary in northern India and the Tibetan Plateau. Geologic studies (e.g., Shen et al., 2001) suggest that the plateau comprises a number of crustal 'blocks' that are bounded by active faults, while geodetic studies (e.g., Zhang et al., 2004) suggest that it is deforming more as a continuum. Indeed, England and McKenzie (1982) had modeled the long-term deformation of the Tibetan Plateau using a thin viscous, rather than an elastic, sheet that overlies an inviscid substrate. They showed that such a model, when it is modified to include both Newtonian and non-Newtonian rheologies, is compatible not only with the observed topography and crustal structure but also with the strains and stresses implied by geodetic data. That the plateau is weak is in accord with the results of flexure studies, which suggest that the Tibetan lithosphere is a region of low elastic thickness and, hence, long-term strength (e.g., Braitenberg et al., 2003; Jordan and Watts, 2005; Masek et al., 1994).

The thin viscous sheet model of England and McKenzie (1982) is discussed in more detail by Sabadini in **Chapter 6.04**. He points out that a viscous sheet is a useful way to model active tectonics not only at plate boundaries but also in the plate interiors. He uses the model, for example, to model the deformation of the interior of the Eurasian Plate that is caused by plate boundary forces associated with Africa–Eurasian Plate convergence at the Alpine orogenic belt, Africa–Eurasia left-lateral shear at the Gloria fault, and North America–Eurasia extension at the Mid-Atlantic Ridge. The effect of a spatially varying long-term strength (e.g., due to the East European Craton) is taken into account in his model by considering lateral variations in the average viscosity. By computing the displacement velocities and then comparing them to changes in baseline rates, as inferred from pairs of GPS sites, he has constrained the spatial variations in long-term strength of the Eurasian Plate.

An outstanding question is whether the entire crust and lithosphere in diffuse plate boundaries are behaving as a continuum or only part of it. For example, Clark and

Royden (2000) used geomorphic observations at the eastern margin of the Tibetan Plateau to suggest that convergence is accommodated by extrusion and flow in the lower part of the crust. Searle et al. (2006), on the other hand, used field geologic observations of the juxtaposition of middle crust Barrovian-type metamorphic rocks and leucogranites with upper-crust undeformed sedimentary rocks in the Himalayas region to suggest that extrusion and flow are limited to the middle crust.

Another, perhaps more pertinent, question is the role the upper mantle plays in the long-term deformation of continental lithosphere (see, e.g., Burov and Watts, 2006; Jackson, 2002). Is it weak or strong? Most oceanic T_e estimates exceed the local crustal thickness, which suggests the mantle is strong and is involved in the support of long-term loads. In the continents, however, the role of the subcrustal mantle in supporting these loads is not as clear. Many cratonic shields yield a T_e that exceeds the local crustal thickness, and it is difficult to explain these high values without invoking at least some strength in the upper mantle. The continents, however, are also associated with many low T_e values, especially in rift settings, and it is not always clear whether they require a strong mantle or not. Burov and Watts (2006), for example, had shown that the incorporation of a strong mantle rheology in thermal and mechanical modeling does not necessarily lead to an increase in the equivalent T_e. This is because another control on T_e is the degree of coupling between the individual competent layers, and if the lower crust is weak and poorly coupled with the mantle, then T_e may remain low, irrespective of the mantle's actual strength.

6.01.4 Relationship Between Load and Plate Age and Rheological Structure

6.01.4.1 The Relationship Between the Long-Term Elastic Thickness and Plate and Load Age

Probably the best data we have that indicate a dependence of T_e on age have come from the oceans. By comparing the observed gravity and geoid anomalies, surfaces of flexure, and vertical motion histories of seamounts and oceanic islands, for example, to the results of calculations based on a model of an elastic plate overlying an inviscid substrate, constraints have been placed on oceanic T_e and its relationship to plate and load age in both intraplate and plate boundary settings.

The first plots of T_e versus age were limited to only a few estimates in the north Pacific Ocean (Watts, 1978). Nevertheless, they indicated that T_e was two to three times smaller than either the seismic or thermal thickness of oceanic lithosphere. Moreover, they suggested a relationship between T_e and the age of the oceanic lithosphere at the time loading such that loads emplaced on young lithosphere, for example, at or near a mid-ocean ridge crest, would be associated with lower T_e than a similar-sized loads emplaced on the older ridge flanks. Thus, as oceanic lithosphere ages, it becomes stronger. Indeed, Watts (1978) showed that T_e depends on the depth to the 300–600 °C isotherm based on a cooling plate model and is given approximately by

$$T_e = (3.0 \pm 1.5)t^{1/2}$$

where t is the age of the lithosphere at the time of loading. This result has generally been confirmed in subsequent studies (e.g., Watts et al., 1980b) that have been based on a larger number of T_e estimates and a wider, more representative, range of tectonic settings.

As pointed out by Bodine et al. (1981) and Lago and Cazenave (1981), a dependence of T_e on plate age is compatible with the extrapolation of data from experimental rock mechanics. These data imply that the strength of the lithosphere is limited by brittle failure in its uppermost part and ductile flow in its lowermost part (*see* **Chapter 6.03** by Burov for a more detailed discussion). Moreover, the data imply that since brittle deformation depends on confining pressure and ductile deformation is determined by *both* pressure and temperature, strength increases and then decreases with depth. Goetze and Evans (1979) used this result, together with the temperature structure as prescribed by a cooling plate model, to construct yield strength envelope (YSE) profiles for different thermal ages of oceanic lithosphere. They showed that the area under a YSE plot would increase with age and, since bending moment is the vertical integral of the stress profile, that T_e is a proxy for the integrated strength of the lithosphere. Individual loads are therefore supported by the both the brittle and ductile strength of the lithosphere and the strength of the intervening, undeformed, elastic 'core.'

Not all loads on the oceanic lithosphere, however, are described by a controlling isotherm in the range 300–600 °C. Flexure studies at seamounts and oceanic islands in the French Polynesia region, for example, suggest that T_e is controlled by a lower isotherm (Calmant and Cazenave, 1987; Maia and Arkani-Hamid, 2002), while studies at some deep-sea trench–outer-rise (Judge and McNutt, 1991) and fracture zone systems (Wessel and Haxby, 1990) imply a higher isotherm.

Figure 20(a), which is based on the 139 estimates listed in Table 6.2 in Watts (2001), shows that most T_e estimates fall within the range of the 300–600 °C controlling isotherms and that there is, indeed, a dependence of T_e on thermal age. The main departures are at some seamounts and oceanic islands in the French Polynesia region of the south-central Pacific (which includes the Society Islands, Tuamotu Plateau, Marquesas Islands, and Austral Islands) and some deep-sea trench–outer-rise systems and fracture zones. **Figure 20(b)**, which is based on a seamount and oceanic island subset of the data in **Figure 20(a)**, suggests that T_e might also depend on load age. Old seamounts and oceanic islands appear to have a low T_e, while young seamounts and oceanic islands have a high T_e.

Watts and Zhong (2000) showed that a dependence of T_e on both plate and load age can be explained by a multilayered viscoelastic model in which the viscosity is prescribed by the thermally activated creep laws and the temperature by a cooling plate model. Since temperatures increase with depth in the lithosphere, viscosities decrease, with low values at the base and high values at the top. The range of viscosities is such that the response time to loading in a multilayered viscoelastic model is mixed. Initially, subsidence is rapid and it then slows with time. **Figure 20(c)** shows that a multilayered viscoelastic model with a reference viscosity at the base of the lithosphere of 10^{20} Pa s and a creep activation energy of 120 KJ mol^{-1} can explain the seamount and oceanic island T_e data when account is taken of the age of oceanic lithosphere that these volcanoes have been emplaced on. The figure implies that as the lithosphere relaxes and the bending stresses

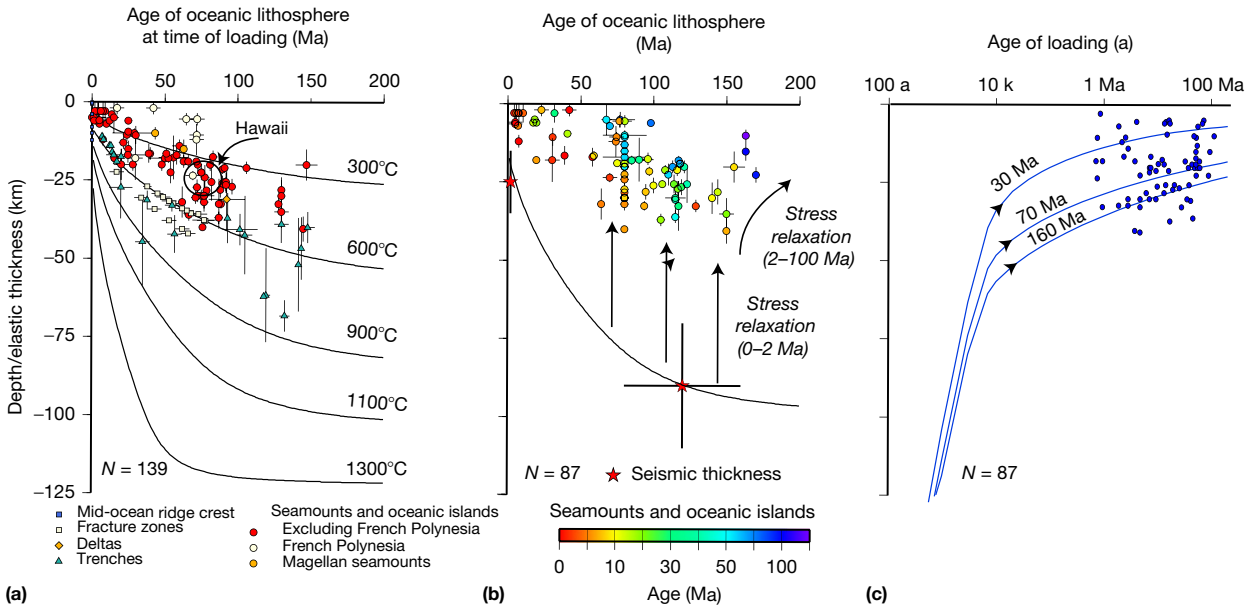

Figure 20 Plot of T_e versus age. The data are based on Table 6.2 of Watts (2001). (a) T_e versus age of the oceanic lithosphere at the time of loading. Solid lines show oceanic geotherms based on the cooling plate model (Parsons and Sclater, 1977). Data have been color-coded according to tectonic setting. Filled and open circles indicate seamounts and oceanic islands. Filled squares, open squares, and triangles are indicative of mid-ocean ridges, fracture zones, and trench–outer rises, respectively. Large unfilled circle shows the best-fit value at Hawaii (**Figure 7**). (b) T_e versus age of the oceanic lithosphere. The data, which comprise only seamounts and oceanic islands, have been color-coded according to load age. (c) T_e versus age of loading. Seamounts and oceanic islands only. Blue lines are predictions based on a multilayered viscoelastic model with an assumed 30, 70, and 160 Ma oceanic geotherm based on a cooling plate model, a reference viscosity, η, of 10^{20} Pa s, and an activation energy, Q, of 120 KJ mol^{-1} (Watts and Zhong, 2000).

migrate up through the plate, the elastic thickness that supports a volcano load decreases with load age. A consequence of this behavior is that the subsidence beneath a load would increase with time and the bulges move in toward it.

The morphology of the flexural moats that flank large oceanic islands shows evidence of a load-induced stress relaxation. The bathymetric moat of some islands (e.g., Oahu – **Figure 16**), for example, is located close to the edifice of the volcano load and is usually narrower than the flexural depression as defined by the best-fitting elastic plate model. Moreover, seismic reflection profiles of the Oahu, Hawaiian Islands (ten Brink and Watts, 1985), and Tenerife, Canary Islands (Collier and Watts, 2001), flexural moats reveal a wide pattern of onlap deep in the moat infill sequence and a narrow pattern of offlap in the shallow part, consistent with the predictions of a multilayered viscoelastic model.

To date, the largest number of oceanic T_e estimates derived from a single flexure study is that of Watts et al. (2006). These authors used the satellite-derived gravity field, together with inverse gravitational admittance functions, to predict the bathymetry for different values of T_e. They then compared the predicted bathymetry to observations and estimated T_e at 291 'sample' sites where both the age of the volcanic load and the underlying oceanic crust and lithosphere are known. The sites included a number of new bathymetric features that had not been included in previous compilations of T_e versus age.

Figure 21(a) shows those sample sites in the Pacific Ocean where T_e is lower than (white-filled circles), within (red-filled circles), and higher than (green-filled circles) the 300–600 °C controlling isotherms. As might be expected, the Hawaiian ridge, Marquesas Islands, and some seamounts in the Mid-Pacific Mountains and Marshall Islands fall within the controlling isotherms. However, many seamounts in the French Polynesia region show lower values.

Interestingly, the low values in French Polynesia occur in a region dubbed by Staudigel et al. (1989) the South Pacific Isotopic and Thermal Anomaly (SOPITA) (**Figure 21**). The region is characterized by unusually shallow seafloor and stable isotopic anomalies and incorporates the Pacific 'superswell' of McNutt and Fischer (1987). It is also a region of low T_e values, as Calmant and Cazenave (1987) and Maia and Arkani-Hamid (2002) had previously pointed out. **Figure 21(b)**, which has been constructed from all the estimates in Watts et al. (2006), shows a low T_e region in French Polynesia that extends northwestward to the Line Islands, Gilbert Ridge, Marshall Islands, and part of the Mid-Pacific Mountains. The Lines Islands and Gilbert Ridge, which range in age from 63.7 to 112.9 Ma, 'backtrack' along Pacific absolute motion paths into the SOPITA. Therefore, the SOPITA appears to be a long-lived feature.

We pointed out earlier (e.g., **Figure 20**) that deep-sea trench–outer-rise regions are generally associated with higher than expected T_e values. In principal, these regions should yield the best estimates of T_e and its relationship with age because, unlike volcano loads, the flexed lithosphere is not perturbed during loading by the thermal and mechanical effects of magma intrusion and magma chamber inflation and deflation. The bathymetry of the outer rise seaward of trenches has been the subject of many studies since the mid-1970s, most recently by Bry and White (2007) who, rather

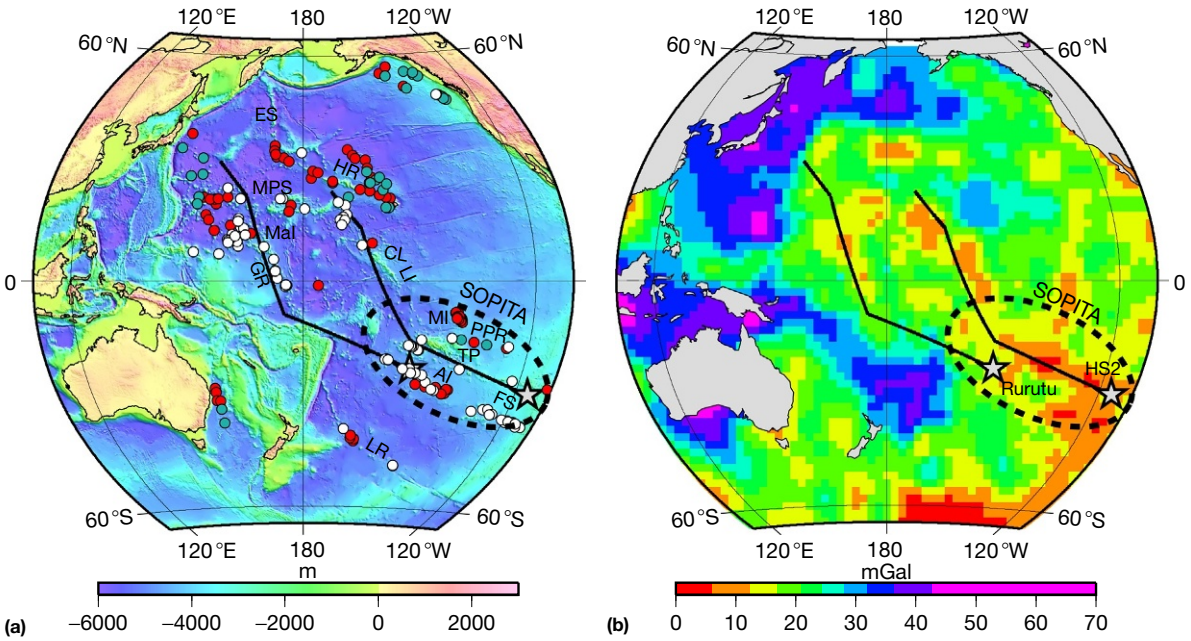

Figure 21 Bathymetry, topography, and T_e map of the central north Pacific Ocean region. Black lines show the seamount trails expected for a hot spot presently located at Rurutu (Austral Islands) (Koppers et al., 2001) and HS2 (near Easter microplate) (Searle et al., 1995). The trails have been computed assuming the Hawaiian 43–0 Ma, Emperor 80–43 Ma, and 100–80 Ma stage poles given in Koppers et al. (2001). Large stars show hot-spot locations. The dashed ellipse delineates the South Pacific Isotopic and Thermal Anomaly (SOPITA) (Staudigel et al., 1989). (a) Bathymetry and topography based on a 5 × 5 min GEBCO grid. Red-filled circles show bathymetric features with a T_e value that falls within the 300–600 °C controlling isotherms. White-filled circles show features that require a lower controlling isotherm and green-filled circles a higher isotherm. ES, Emperor seamounts; MPS, Mid-Pacific Mountains; HR, Hawaiian ridge; Mal, Marshall Islands; GR, Gilbert Ridge; CL Cross Lines; LI, Line Islands; MI, Marquesas Islands; PPR, Pukapuka Ridge; TP, Tuamotu Plateau; AI, Austral Islands; FS, Foundation Seamounts. (b) T_e map based on the data in Watts et al. (2006). Red, low T_e values; and blue, high T_e values.

surprisingly, found little dependence between T_e and age of oceanic lithosphere. Kalnins and Watts (2009), who used a moving window gravitational admittance technique, confirmed the forward modeling results in **Figure 21** that T_e is high seaward of the Japan, Izu-Bonin, and Mariana trenches where some of the oldest seafloor in the Pacific Ocean is presently being subducted, and we would expect high values. Finally, Hunter et al. (in prep.) have reexamined all the existing bathymetry and gravity data seaward of trenches and found that when profile length, curvature and yielding, and bending moments at the trench are considered, T_e does indeed depend on oceanic crustal age.

Unfortunately, it has not been as easy to demonstrate a dependence of T_e on age in the continents as it has in the oceans. Plots of continental T_e versus age since the last major thermal event (the so-called thermotectonic age) reveal considerable scatter, and no one set of thermal parameters can explain all the data (Watts, 2001). The reasons for this are complex, but they can be simplified to uncertainties in geothermal gradient and definitions of load. In the oceans, thermal age is the main control on T_e as it is on heat flow. Anomalies in both parameters are probably due to lateral variations in mantle temperature. In the continents, however, regions of the same thermotectonic age may have different geotherms because of spatial variations in crustal heat production. Therefore, continental T_e, like heat flow, may show only a weak relationship with thermotectonic age. In the oceans, loads and their associated flexures are relatively easily defined. In the continents, however, erosion and sedimentation act to modify loads and obscure the surfaces of flexure making it difficult to estimate T_e for a particular tectonic event.

Despite these difficulties, there are hints that continental T_e, like oceanic T_e, depends on age. In Europe, for example, spectral techniques (i.e., Bouguer coherence and free-air admittance) of analyzing gravity anomaly and topography data reveal that Archean and Early/Middle Proterozoic terranes are associated with $T_e > 70$ km, while adjacent Late Proterozoic and Phanerozoic terranes correlate with lower values in the range 15–40 km (Pérez-Gussinyé and Watts, 2005). Similar results have been obtained for the terranes of North and South America (e.g., Bechtel et al., 1990; Tassara et al., 2006).

Figure 22 shows a recent compilation of >85 continental T_e estimates, plotted against age of the load (Watts et al., 2013). The figure shows that thrust and fold and rim flank uplift loads that involve Archean lithosphere have a significantly higher T_e than similar types of loads formed on Phanerozoic lithosphere. One interpretation of the results in **Figure 22** therefore is that old cratonic Archean shields form strong, rigid, blocks, except at their edges where subsequent extensional and compressional events, for example, associated with Phanerozoic magmatism, rifting, and orogeny, have weakened them. Also shown in the figure is the predicted relationship between T_e and load age based on a multilayered viscoelastic model with the same values of the reference viscosity and creep activation energy parameter pair as used in **Figure 20(c)** but with a representative continental geotherm rather than an oceanic

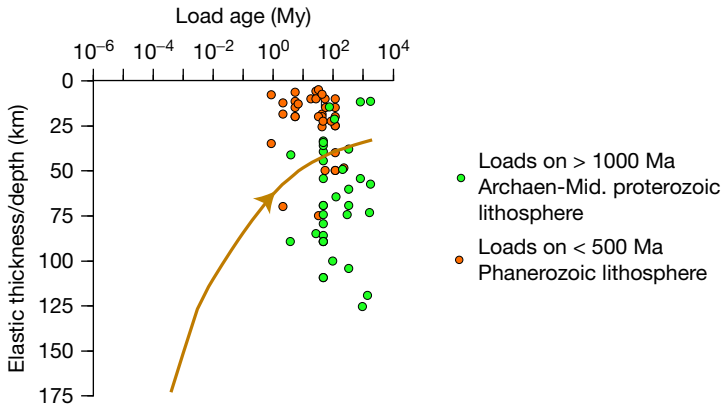

Figure 22 Plot of T_e against the age of load for foreland basin and rim flank uplift loads on continental lithosphere. The sources of data are given in Watts et al. (2013). Orange and green circles represent loads on lithosphere with thermotectonic age <500 and >1000 Ma, respectively. Brown line is a prediction based on a multilayered viscoelastic model with a kimberlite-derived continental geotherm, a reference viscosity, η, of 10^{20} Pa s, and an activation energy, Q, of 200 KJ mol^{-1} (Watts et al., 2013).

geotherm. The comparison of observations and model predictions suggests that high (i.e., >30–40 km) T_e values in the continents are expected even in the case of loads that are >100 My in duration. Lower values than the model predictions could then be explained by hotter geotherms and higher values by colder geotherms.

Data from experimental rock mechanics suggest that unlike the oceans, continents have a complex multilayer rheology. As is demonstrated by Burov in **Chapter 6.03**, compositional differences between the upper continental crust, lower crust, and mantle imply a vertically stratified rheology. The oceans, for example, have a single competent layer, but the continents may have more than one such layer. The actual continental yield strength envelope (YSE) profile will be a strong function not only of the composition but also of the geothermal gradient, crustal thickness, and strain rate. Burov and Diament (1995) have shown that T_e depends on the thickness of 'all' the competent layers and is relatively small for thick crust, low strain rates, and young thermotectonic age and relatively high for thin crust, high strain rates, and old ages.

One tectonic setting, however, where a relationship between T_e and age has been reasonably well documented is at the present-day margins of the continents. These features form following heating and thinning of continental lithosphere. When those margins are considered that have been subject at some stage during their evolution to a large discreet load, such as a fold and thrust belt or river delta, then evidence emerges of a dependence of T_e on age. The South China Sea, for example, is a young margin that was loaded by fold and thrust loads in Taiwan during the Late Miocene and has a low T_e (Lin and Watts, 2002), while northeast Brazil is an old margin that was loaded by the Amazon delta and fan system during the Middle/Late Miocene and has a high T_e (Rodger et al., 2006). Therefore, heating at the time of rifting weakens the lithosphere, while cooling following rifting strengthens it. Such a model is supported by YSE considerations (Pérez-Gussinyé and Reston, 2001) and by the results of numerical modeling (Burov and Poliakov, 2001).

6.01.5 Global Elastic Thickness

6.01.5.1 T_e Map

There now exist a sufficient number of estimates from both the oceans and continents to construct a global T_e map. Such a map is useful, for example, for determining how the lithosphere might respond to complex loads such as those associated with sedimentation and erosion. Other possible uses are in studies of the figure of the Earth, lunar and solar tides, and intraplate deformation. Mound et al. (2003) had pointed out that the T_e structure of the lithosphere might help explain some of the departures that are observed between the observed flattening of the Earth and the flattening predicted by hydrostatic theory. Shukowsky and Mantovani (1999) and Mantovani et al. (2005), on the other hand, suggested a link between T_e and the M2 (lunar semidiurnal) component of the tidal gravity anomaly. Finally, Dyksterhuis et al. (2005) suggested that T_e can be used to scale the viscosity in thin viscous sheet models that attempt to calculate intraplate deformation and stresses due to plate boundary forces.

Figure 23(b) shows a $2 \times 2^\circ$ global T_e map. The map has been constructed from >18 000 individual T_e estimates. Because it is difficult in the case that T_e is high to precisely constrain the value of T_e (see, e.g., the discussion in Pérez-Gussinyé and Watts (2005)), values of $T_e > 65$ km have been assigned to 65 km. **Figure 23(a)** shows that the data distribution is uneven, especially in the western Central Atlantic and parts of Africa, South America, and the former Soviet Union where there are few elastic thickness estimates.

Nevertheless, the map reflects the T_e structure in North America, Europe, India, and the central Pacific well. Most low T_e values are in the oceans, while most high values are in the continents. In general, low T_e values delineate the mid-ocean ridge and continental rift systems, while high values correlate with the old, cold, cratonic shields. Phanerozoic mobile belts are characterized by intermediate values. Perhaps one of the main surprises is the spatial variability in the T_e structure. The oceans show the lowest variability, while the continents show the highest.

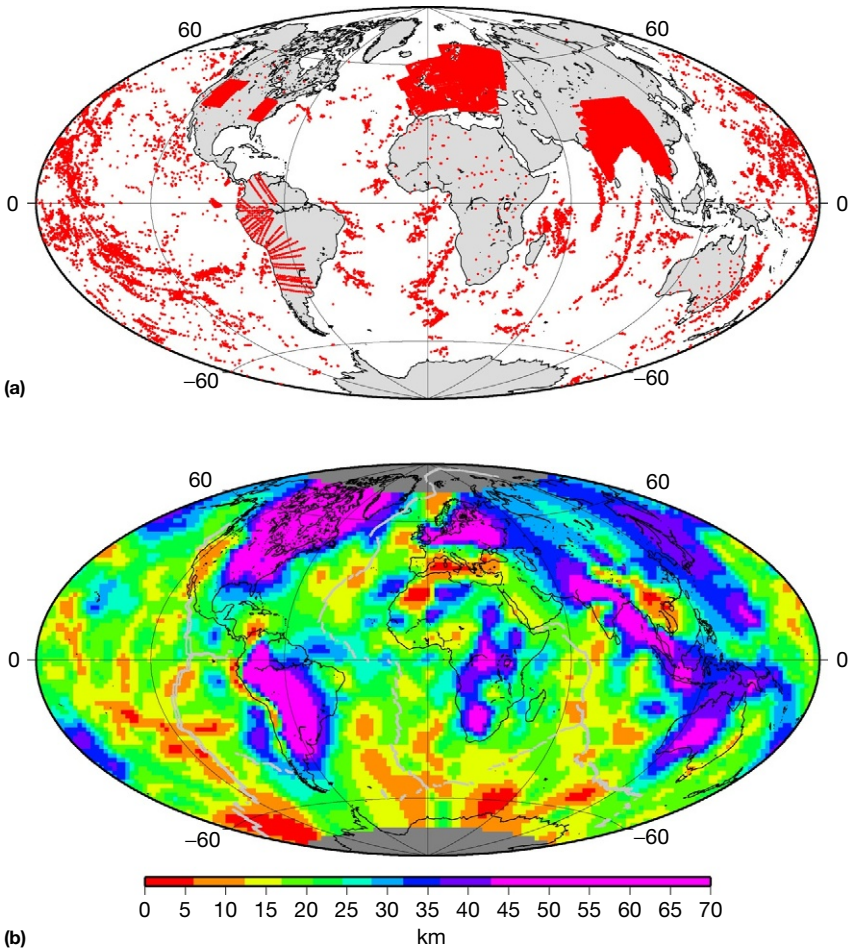

Figure 23 Global T_e map. (a) Location map of T_e estimates (red dots). The estimates are derived from studies of gravity anomaly and topography/bathymetry using both forward and inverse (i.e., spectral) modeling techniques. Principal data sources are Europe (Pérez-Gussinyé and Watts, 2005), Australia (Simons et al., 2003), Africa (Hartley et al., 1996), North America (Bechtel et al., 1990; Lowry and Smith, 1994; Armstrong and Watts, 2001), Ireland (Armstrong, 1997), former Soviet Union (Kogan et al., 1994), India and Tibetan Plateau (Jordan and Watts, 2005), South America (Stewart and Watts, 1997), and the ocean basins (Watts et al., 2006). (b) Global T_e map. The map is based on a $2 \times 2^\circ$ grid of the T_e estimates in (a).

Some of the variability in Figure 23(b) arises because T_e is a parameter that reflects both the past and present thermal and mechanical structure of the lithosphere. A new volcano load in the central Pacific Ocean, for example, where T_e is low because it reflects a frozen-in older loading event near the crest of the East Pacific Rise, will 'see' a high T_e rather than a low T_e because it has been emplaced in a ridge flank setting, some distance from the rise crest. There are, of course, many cases of young loads in the oceans, for example, at Hawaii, seaward of deep-sea trenches and river deltas where the T_e structure will reflect the current integrated strength of the lithosphere. Similar cases may arise in spectral studies in the continents where processes of sedimentation and erosion have occurred over long periods up until the present day and so obscure the signals of earlier loading events. Therefore, caution needs to be applied when using the global T_e map as a proxy for either the present or the past, long-term strength of the lithosphere.

6.01.5.2 Correlation of T_e with Temperature Structure and Shear-Wave Velocity

Since T_e is a proxy for the integrated strength, it is useful to compare it to other physical properties that reflect the thermal and mechanical structure of the lithosphere. We know, for example, that surface heat flow data reflect the temperature structure, at least in the oceans and, also, that seismic surface and body waves reflect temperature and composition. Therefore, there might be some relation between T_e and these properties.

We show in Figures 24 and 25 a comparison of the topography, crustal structure, depth to the 550 and 1300 °C isotherms, surface heat flow, T_e, and shear-wave velocity anomaly along two long profiles of equatorial regions. The sources of the data are summarized in the figure captions and Table 1. The temperature data are based on Artemieva and Mooney (2001) who used surface heat flow

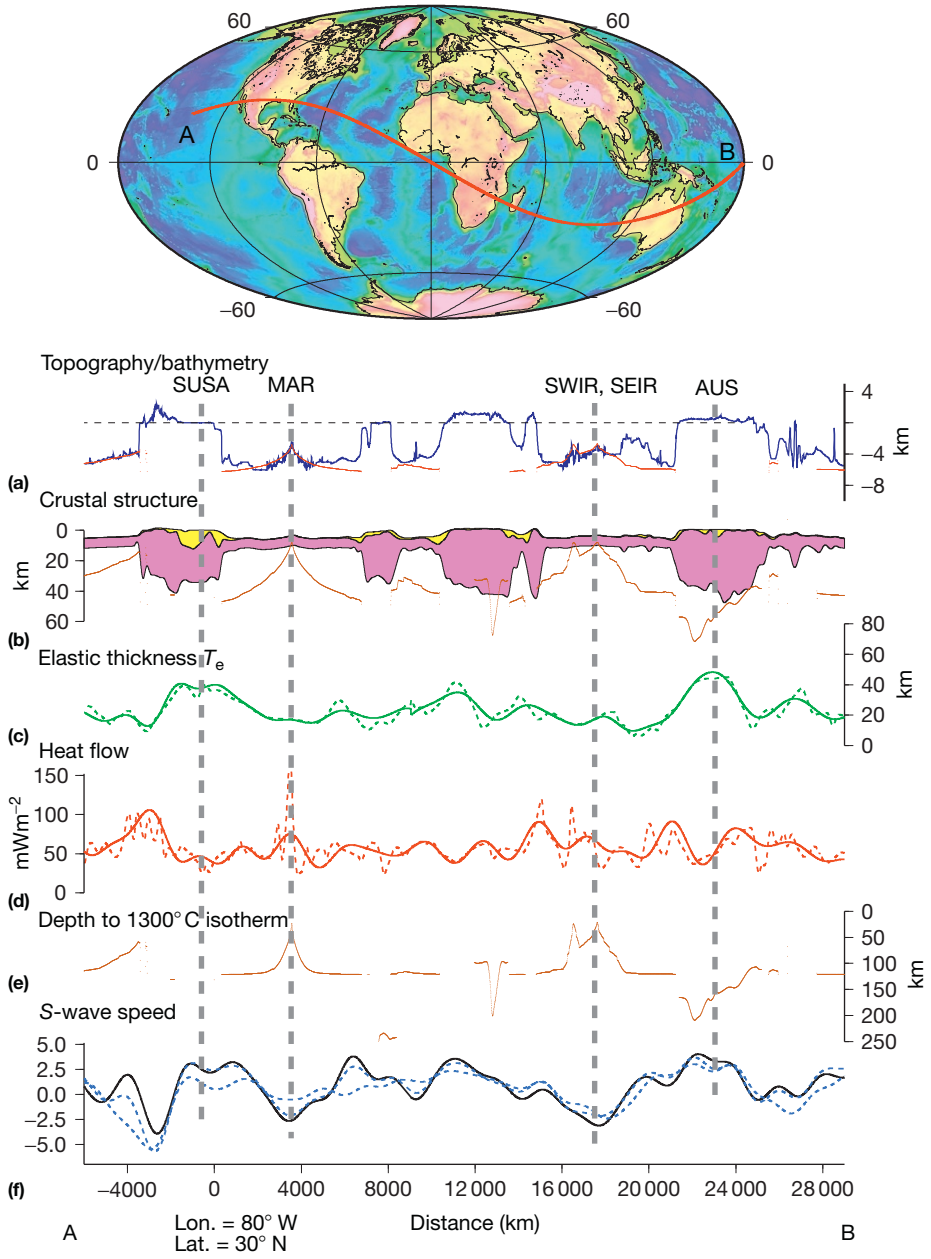

Figure 24 Comparison of the elastic, thermal, and seismic 'thickness' of the crust and lithosphere along profile AB. SUSA, Southern United States of America; MAR, Mid-Atlantic Ridge; SWIR, Southwest Indian Ridge; SEIR, Southeast Indian Ridge; AUS, Australia. (a) Topography/bathymetry (blue line) based on a 1 × 1 min GEBCO (British Oceanographic Data Centre, 2003) grid. Red lines show the calculated bathymetry based on the Müller et al. (1997) oceanic age grid and the Parsons and Sclater (1977) cooling plate model. (b) Crustal structure based on CRUST 2.0 (Bassin et al., 2000). Yellow fill shows sediment thickness based on the NOAA 5 × 5 min grid of Divins (2005). Brown lines show the depth to the 550 °C isotherm derived by Artemieva and Mooney (2001). The isotherm is constrained by the surface heat flow data of Pollack et al. (1993) and different assumptions on the thermal parameters within the crust and subcrustal mantle. (c) Elastic thickness, T_e. Dashed lines show original values based on the grid in **Figure 23(b)**. Solid line shows low-pass-filtered (high pass = 2100 km, high cut = 1900 km) grid values. (d) Surface heat flow. Dashed lines show original grid based on Pollack et al. (1993). Solid line shows low-pass-filtered (high pass = 2100 km, high cut = 1900 km) grid values. (e) Thermal thickness based on the depth to the 1300 °C isotherm of Artemieva and Mooney (2001). (f) Shear-wave velocity anomaly based on the SAW24B16 model of Megnin and Romanowicz (2000). Solid lines show the shear-wave anomaly, expressed as a percent relative to PREM (Dziewonski and Anderson, 1981), at 50 km. Dashed lines show the anomaly at 100 and 200 km depth.

data measured at boreholes (Pollack et al., 1993), together with the steady-state thermal conductivity equation, to calculate the temperature at different depths in the lithosphere. The accuracy of these calculations is limited by the uneven data distribution and the incomplete information on the contribution of crustal heat production. Nevertheless, Artemieva et al. (2004) estimated an accuracy of ±100 °C for these data. The shear-wave velocity data are based on

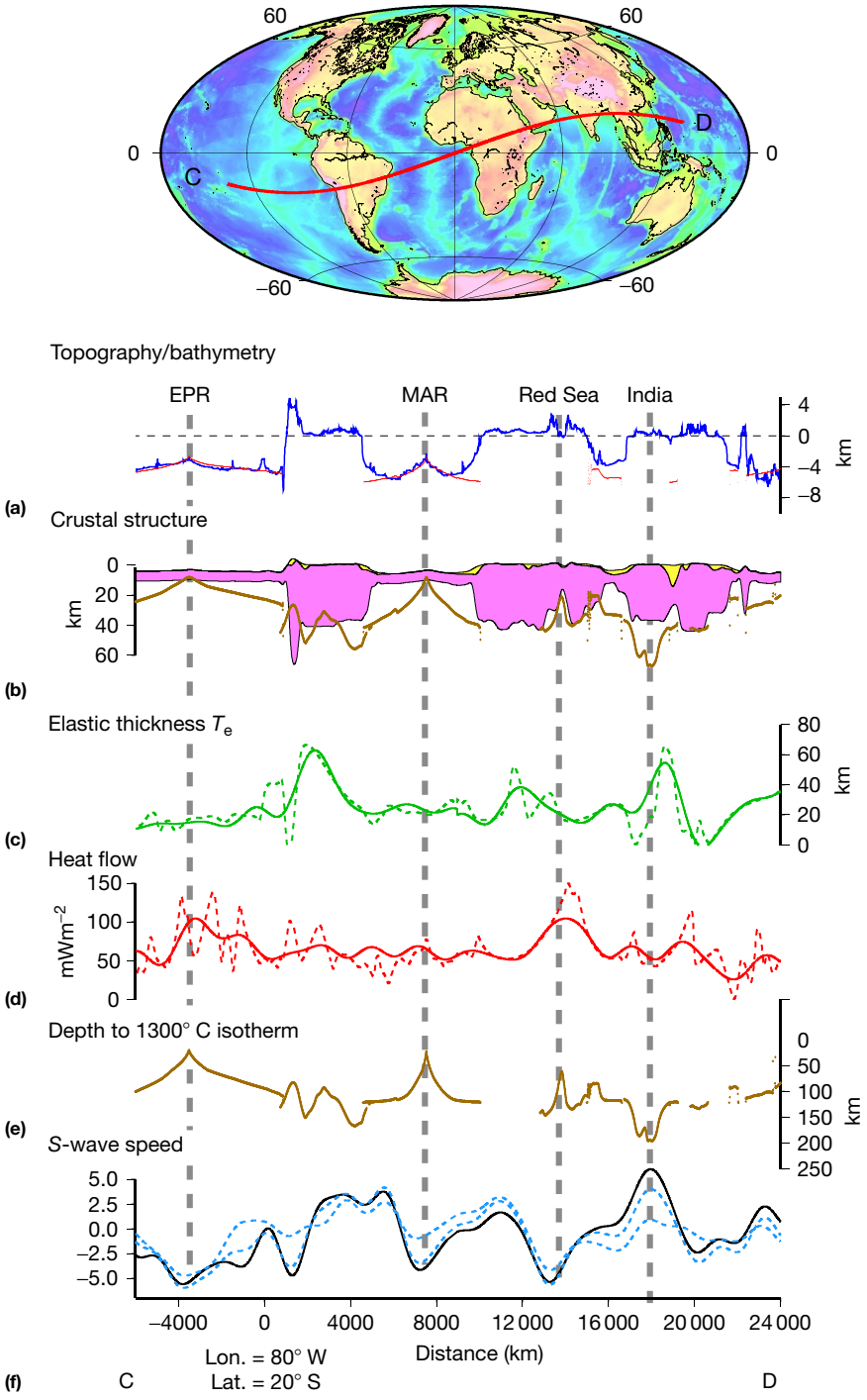

Figure 25 Elastic, thermal, and seismic 'thickness' of the crust and lithosphere along Profile CD. EPR, East Pacific Rise. Data sources and other labels are as in **Figure 24**.

SAW24B16: a 'high-resolution' tomographic model derived by Megnin and Romanowicz (2000) from the inversion of body, surface, and higher-mode waveforms. The model is complete to spherical harmonic degree 24, which corresponds to $\lambda > \sim 1600$ km. Shear-wave velocities are shown at different depths in the lithosphere as a variation in percent with respect to the preliminary reference Earth model (PREM) of Dziewonski and Anderson (1981).

Figures 24 and 25 show a good visual correlation along the profiles between T_e, surface heat flow, and shear-wave velocity anomaly, particularly in the region of the old, inactive, Archean cratons and the young, active, mid-ocean ridges. In cratonic regions, T_e is high, surface heat flow is low, and shear-wave velocity anomalies are high. This is well seen in Profile AB of Western Australia (Yilgarn block) and Profile CD of the Indian subcontinent (Bundelkhand block) and South America

Table 1 Internet resources for global profiles in Figures 24 and 25

Data	*Web address*
GEBCO 1 × 1 min bathymetry and topography	http://www.gebco.net/
Crustal thickness and velocity structure (CRUST 2.0, 1.0)	http://igppweb.ucsd.edu/~gabi/crust2.html http://igppweb.ucsd.edu/~gabi/crust1.html
Marine gravity from satellite altimetry	http://topex.ucsd.edu/WWW_html/mar_grav.html
Ship track gravity and bathymetry	http://www.geomapapp.org/
Surface heat flow	http://www.geo.lsa.umich.edu/IHFC/heatflow.html
Sediment thickness	http://www.ngdc.noaa.gov/mgg/sedthick/sedthick.html
Ocean floor isochrons	http://www.earthbyte.org/Research/Current/digit_isochrons.html
Temperature structure	http://www.lithosphere.info/JGR2001.html
Shear-wave velocity model SAW24B16	http://seismo.berkeley.edu/~pepe/saw24b16.html
Global T_e grid	ftp://ftp.earth.ox.ac.uk/pub/tony/TOG/global_te.grd

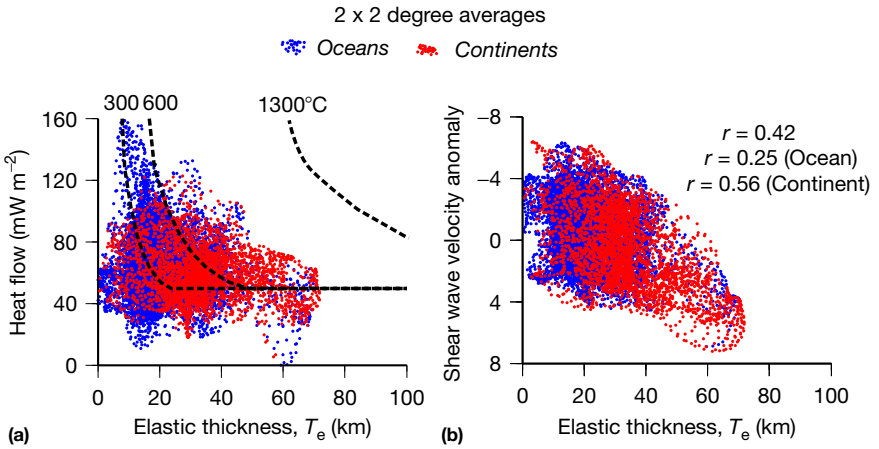

Figure 26 Scatter plots of 2 × 2° averages of surface heat flow against T_e and shear-wave velocity anomaly against T_e. The source of the surface heat flow and shear-wave velocity anomaly data is as in Figures 24 and 25. The T_e data are based on the grid used to construct the global map in Figure 23(b).

(Guaporé and San Francisco cratons). Here, $T_e > 65$ km, surface heat flow is close to the regional background value of 42 m Wm^{-2}, and the shear-wave velocity anomaly is >2.5%. In the region of mid-ocean ridges, T_e is low, heat flow is high, and shear-wave velocity anomalies are low. This is well seen in Profile CD of the East Pacific Rise and Southern Red Sea. Here, $T_e < 10$ km, surface heat flow is >100 mW m^{-2}, and the shear-wave velocity is <−4.0%. The South Atlantic mid-ocean ridge and the Southwest and Southeast Indian Ridges also correlate with low T_e and low shear-wave velocity anomalies, but the surface heat flow is low, probably because of hydrothermal circulation.

Figure 26(a) shows a scatter plot of 2 × 2° averages of T_e and surface heat flow. The figure shows the data to be poorly correlated (correlation coefficient, $r = 0.13$ for oceans and $r = 0.21$ for continents). This may be surprising, given the argument that T_e reflects the thermal structure. However, if T_e represents the depth to an isotherm, then we would not expect T_e and heat flow to be linearly correlated. Rather, they should follow an exponential curve. The figure still shows considerable scatter, however. This probably reflects the fact that even in the oceans, T_e maybe controlled by more than one isotherm. Oceanic data show two clusters: one of high heat flow and low T_e and the other of low heat flow and low T_e. The high heat flow/low T_e cluster would be expected for young seafloor at the mid-ocean ridge. Moreover, the low heat flow/low T_e cluster could be due to hydrothermal circulation that reduces the heat flow but has little effect on T_e.

Figure 26(b) shows a scatter plot of 2 × 2° averages of T_e and the shear-wave velocity anomaly. The figure shows these data to be better correlated, although r values are still low. We found, for example, $r = 0.42$ for the global data set and r of 0.56 and 0.25 for the continents and oceans, respectively. This compares to $r = 0.42$ for the global heat flow and shear-wave velocity anomaly data set and r of 0.46 (see also Artemieva et al. (2004) who obtained $r = 0.39$ for the same global heat flow data but a different seismic tomographic model) and 0.39 for the continents and oceans, respectively. The low correlation coefficients suggest that factors other than temperature (e.g., compositional inhomogeneities, fluids, and melts) may control the shear-wave velocity structure of the mantle.

6.01.6 Geologic Implications

6.01.6.1 Toward an Integrated Model that Relates Elastic Thickness to Load Age on Short, Intermediate, and Long Timescales

The inferences from oceanic flexure studies of a dependence of T_e on plate as well as load age suggest that there might be a link

between the different estimates of the elastic layer thickness discussed in this overview.

Indeed, such a link has already been discussed by Nishimura and Thatcher (2003) who considered the elastic layer thickness derived from postseismic deformation, glacial lake loading and unloading, and flexure in the same tectonic region of the Western United States. They pointed out that their postseismic estimate of elastic layer thickness of 38 km was greater than that calculated by Nakiboglu and Lambeck (1983) from the isostatic rebound that followed the draining of former Pleistocene Lake Bonneville (25–30 km), which, in turn, was greater than that calculated by Lowry and Smith (1995) from spectral analysis of gravity anomaly and topography data (5–15 km). In a related study, Cohen and Darby (2003) considered the relationship between elastic layer thickness based on geodetic data and flexure of the Wanganui foreland basin in North Island, New Zealand. These authors noted that the elastic layer thickness based on geodetic data (100–150 km) was significantly higher than that determined by Stern et al. (1992) from flexural studies (10 ± 10 km). They were not surprised by their result, pointing out that the geodetic elastic layer thickness 'should' be greater than the flexural, tectonic, one.

Figure 27 shows a log-linear plot of the elastic layer thickness as derived from coseismic and postseismic deformation, glacial isostatic rebound, and flexural studies against load age. The light blue-filled box shows the range of oceanic T_e values. The blue dashed lines show the predicted relationship between T_e and load age based on the multilayer viscoelastic model of Watts and Zhong (2000) with different assumed reference viscosities and lithosphere age (short dash – 30 Ma; long dash – 70 Ma). The orange- and green-filled circles show continental T_e values based on spectral and other techniques from Phanerozoic and Proterozoic and Archean terranes, respectively. The dark blue box shows the range of estimates from glacial isostatic rebound. Finally, the light and dark gray-filled boxes delineate the range of elastic layer thickness estimates from selected coseismic and postseismic deformation studies.

Figure 27 shows that there is no simple relationship between elastic layer thickness and load age. However, the figure shows that the elastic layer thickness derived from geodetic and glacial isostatic rebound can exceed those derived from flexural studies.

The blue- and brown-filled arrows in Figure 27(a) show possible relaxation paths linking the different timescales of

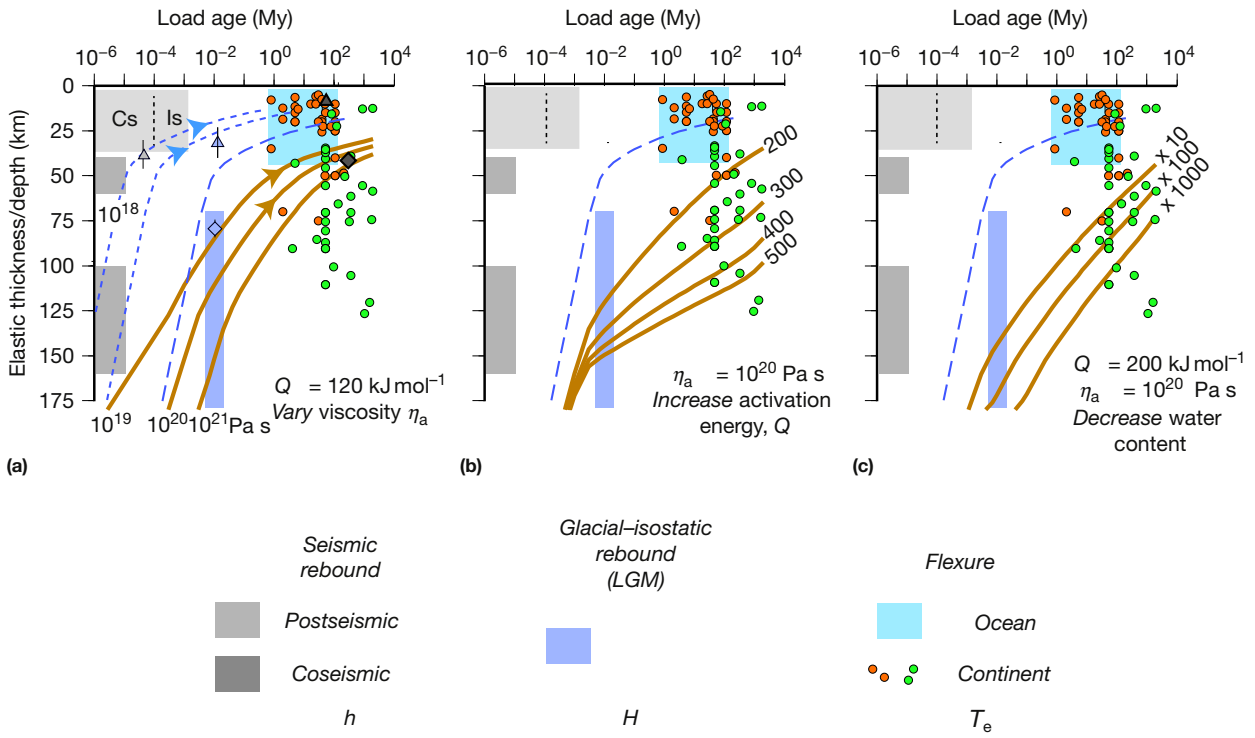

Figure 27 Plot of elastic layer thickness derived from coseismic and postseismic deformation (h), glacial isostatic rebound (H), and flexure studies (T_e) against the logarithm of load age. Light and dark gray boxes show the range of coseismic and postseismic deformation, respectively. The sources of data are given in Watts et al. (2013). Dark blue-filled box shows the range of elastic layer thickness from glacial isostatic rebound. Data sources based on Di Donato et al. (2000), East Coast, United States; Peltier et al. (2002), British Isles; and Milne et al. (2004), Fennoscandia. Light blue-filled box shows the range of oceanic T_e estimates plotted in **Figure 20(c)**. Orange- and green-filled circles show T_e estimates from Late Proterozoic/Phanerozoic and Archean and Early/Middle Proterozoic terranes, respectively. The sources of data are given in Watts et al. (2013). Blue-dashed lines indicate predictions based on a multilayered viscoelastic model with a 70 Ma (long dash) or a 30 Ma (short dash) oceanic geotherm. Thick brown lines indicate predictions based on a multilayered viscoelastic plate model with a kimberlite-derived continental geotherm. The predictions are based on different values of the effective activation energy, Q, and effective reference viscosity, η_a. (a) Constant Q (120 kJ mol^{-1}) and $10^{18} < \eta_a < 10^{21}$ Pa s. Triangles and diamonds show elastic layer thickness estimates for Western and Eastern United States, respectively. Cs, coseismic deformation. Is, interseismic deformation. (b) Constant η_a (10^{20} Pa s) and $200 < Q < 500$ kJ mol^{-1}. (c) Constant Q and η_a and decrease in water content by a factor of 10, 100, and 1000.

loading in the Western and Eastern United States. The Western US data set (filled triangles) includes geodetic estimates from Hebgen Lake (Nishimura and Thatcher, 2003), glacial rebound estimates from former Lake Bonneville (Nakiboglu and Lambeck, 1983), and flexural estimates from the eastern Rockies (Lowry et al., 2000). The plot suggests that elastic layer thickness decreases from ~40 km for geodetic timescales to ~10 km for flexural timescales. The Eastern US data set (filled diamonds) is based on Di Donato et al. (2000) who used tide gauge data for the glacial isostatic rebound estimates and Armstrong and Watts (2001) who used gravity anomaly and topography data for the flexural estimates. The plot suggests that elastic layer thickness decreases from 80 km for the glacial isostatic rebound timescale to ~40–50 km for the flexural timescale. **Figure 27(b)** and **27(c)** shows that these conclusions would not change significantly if we had increased the creep activation energy (**Figure 27(b)**) or water content (**Figure 27(c)**) of the subcrustal lithosphere, although the data from glacial isostatic rebound would not have been explained as well.

While the decrease in elastic layer thickness with load age within these two tectonically distinct regions of the United States is similar in form, their absolute values differ. This suggests that there are spatial variations in viscosity structure, and hence, relaxation times, between regions. In particular, the low elastic layer thickness in the Western United States suggests that the upper mantle here has a relatively low viscosity and short relaxation time, while the high elastic thickness in the Eastern United States implies that the upper mantle here has a relatively high viscosity and long relaxation time. This is in accord with the results of Nishimura and Thatcher (2003) and Di Donato et al. (2000) who suggested 4×10^{18} and 5×10^{20} Pa s for the viscosity of the upper mantle beneath the Western and Eastern United States, respectively. The Western United States has a higher regional elevation, thinner crust, and higher heat flow than the Eastern United States. Moreover, there is evidence from xenolith data (Dixon et al., 2004) that the mantle beneath the Western United States has high water content and is weak, possibly because of its long history of subduction.

These results from oceans and continents have implications for the way that the Earth's outermost rigid layers respond to loading. Initially, the lithosphere appears as a relatively strong structure that is able to support loads by bending over wide areas. With time, however, a load-induced stress relaxation sets in that causes the subsidence to increase in amplitude and decrease in width and the flanking flexural bulge to migrate inward toward the load center. The actual time that it takes for the lithosphere to relax depends on its viscosity structure. For example, because of its different tectonic setting, loads relax quicker in the Western United States than they would in the Eastern United States. Despite these differences, however, flexure studies suggest that the response to loads eventually stabilizes and appears to change little on very long timescales.

6.01.6.2 Terranes, the Wilson Cycle, and Inheritance

The continents are cored by the cratonic shields, which are 1.5 Ga and older. Geologic field mapping suggests that cratonic shields form the nucleus around which younger orogenic belts accrete. Continents therefore grow by a process of amalgamation. Central to this process is the 'Wilson cycle' in which the ocean basins repeatedly open and close, causing crustal thinning and thickening in response to extension and compression and the superposition on the lithosphere of loads and unloads through processes such as sedimentation and erosion, orogenic loading, and intracrustal thrusting.

Some insight into plate-forming processes has come from studies of T_e and its relationship to the terrane structure of the continents. In Europe, for example, it has been demonstrated first through the results of thermal and mechanical modeling (Cloetingh and Burov, 1996; *see also* **Chapter 6.12**) and then by spectral analysis of free-air and Bouguer gravity anomaly and topography data (Pérez-Gussinyé and Watts, 2005) that T_e varies from high values over the cratons ($T_e > 70$ km) to low values over flanking Caledonian (15–40 km), Variscan (20–40 km), and Alpine (10–25 km) orogenic belts (**Figure 28**). Thus, T_e and, hence, the integrated strength of the lithosphere appear to increase with age.

The mechanism by which long-term strength of continental lithosphere increases with age is not known. We know the Archean is a time of high temperature and volatile content that lead to high degrees of melting to greater depths. Indeed, forward modeling studies of the reconstructed geometry of the Wopmay foreland basin in the Superior Province of North America yield a low T_e that is thought to reflect locally high geothermal gradients at the time of orogenic loading (Grotzinger and Royden, 1990). Inverse (i.e., spectral) studies, however, reflect all the loads that have acted on the lithosphere through time, including loads such as sedimentation and erosion that have continued to modify it up to the present day. One possible explanation of the high Archean T_e values derived from spectral studies therefore is conductive cooling, which together with the Earth's secular cooling acts to strengthen the lithosphere. More difficult to explain are the low values associated with younger Late Proterozoic and Phanerozoic terranes. There should have been enough time for the oldest of these terranes to have cooled conductively to a stable state and hence strengthened. One possibility, as Pérez-Gussinyé and Watts (2005) had pointed out, is water during subduction, which weakens the lithosphere. Another is that the Late Proterozoic and Phanerozoic lithosphere is fundamentally weak due to the decrease in temperature and volatile content that occurred following the Archean.

Irrespective of how the cratons acquire their long-term strength, **Figure 28** suggests that processes such as rifting and breakup weaken continental lithosphere. While the west Iberia rifted margin appears to be little different in its T_e structure than flanking Variscan terranes, there is evidence that both the Norwegian and northwest Scotland rifted margins have a lower T_e and, hence, strength than the flanking Caledonian terranes. Both of these margins are characterized by seaward-dipping reflector sequences and high *P*-wave-velocity lower crustal bodies, and so one possibility is that magmatism accompanied rifting and breakup and assisted in reducing their long-term strength (Buck, 2004).

There is evidence in the North Atlantic of a genetic link between rifting and preexisting orogenic belts. For example, the breakup of Greenland and Norway during the Early Cenozoic appears to have followed the strike of the Caledonian

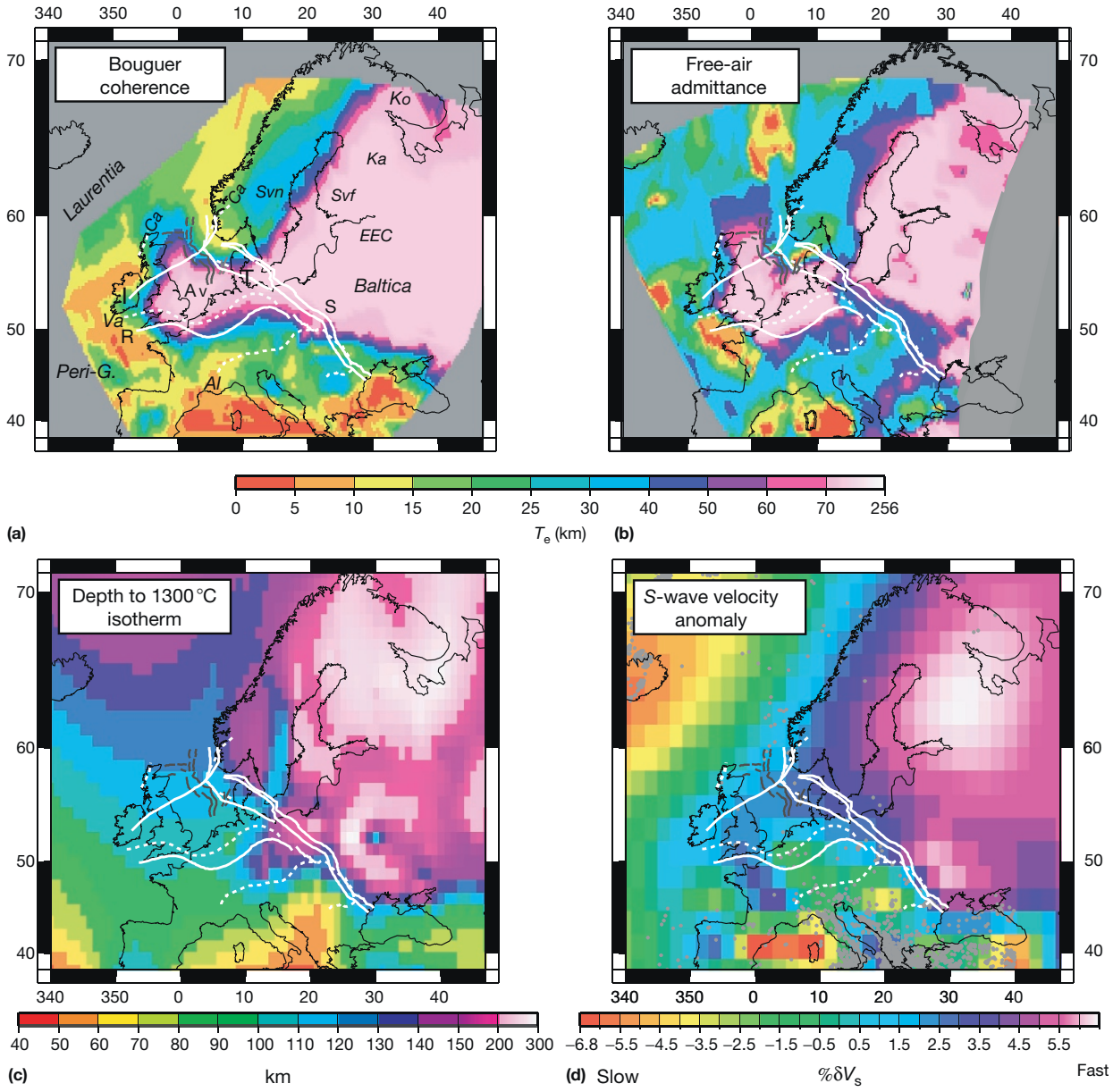

Figure 28 The elastic, thermal, and seismic structure of the European lithosphere. (a) T_e based on Bouguer coherence. (b) T_e based on free-air admittance. (c) Thermal structure, as indicated by surface heat flow evidence of the depth to the 1300° isotherm. (d) Seismic structure based on shear-wave velocity. Solid white lines indicate major sutures. I, Iapetus; R, Rheic. Dashed white lines indicate major deformation fronts. *Ca*, Caledonian front; *Va*, Variscan front, and *Al*, Alpine front. Reproduced from Pérez-Gussinyé M and Watts AB (2005) The long-term strength of Europe and its implications for plate-forming processes. *Nature* 436: 381–384, http://dx.doi.org/10.1038/nature03854.

orogenic belt. Indeed, as Vinck et al. (1984) pointed out, such an association is in accord with YSE considerations, which suggest that thick continental crust is mechanically weak. However, there is also evidence in the same tectonic setting of the contrary association – of orogenic belts that develop in close association with rifted margins. The Flannan thrust north of Scotland, for example, has been interpreted as a normal fault associated with a Late Precambrian–Cambrian rifted event on the Laurentia margin that was reactivated during the Caledonian orogeny (Brewer and Smythe, 1984).

A present-day example of an orogenic belt that developed on a rifted margin is Taiwan. Geologic and geophysical data (Lin et al., 2003) suggest that the west Taiwan foreland basin, for example, developed ~12 Ma due to orogenic loading of the Late Paleocene South China Sea rifted margin. Flexure modeling (Lin and Watts, 2002) shows that the observed depth to the base of the foreland basin sequence cannot be explained by surface loading alone and requires additional subsurface loads in order to explain it. By comparing the observed Bouguer gravity anomaly to the gravity effect of the topography and its Airy-type compensation, Lin and Watts (2002) were able to constrain the magnitude of the subsurface load and, hence, compute the deformation due to combined surface and buried loading. The best-fit model (Figure 29) suggests $T_e = 13$ km.

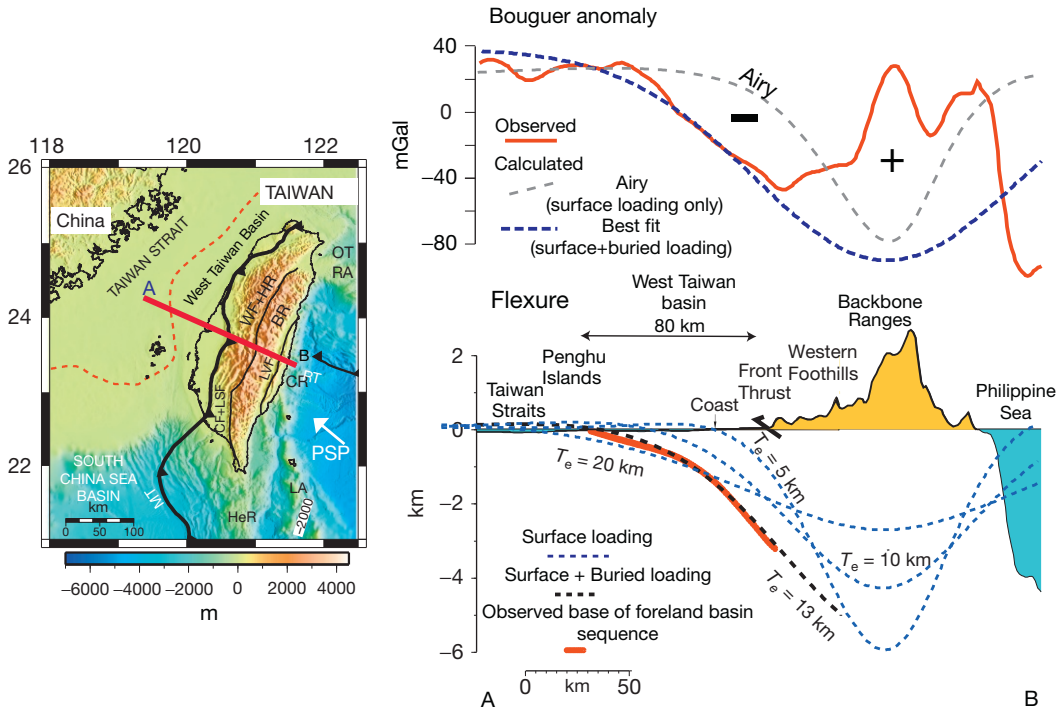

Figure 29 Comparison of the observed base of the west Taiwan foreland basin sequence to calculations based on an elastic plate model with surface and buried loading (Lin and Watts, 2002). The gravity anomaly profile shows the observed Bouguer anomaly (red solid line), the calculated gravity effect of the Airy compensating root (gray-dashed line), and the calculated gravity anomaly effect of the best-fit flexural surface (blue-dashed line). The Airy model assumes only surface loading and so the discrepancy between observed and calculated Airy gravity anomalies defines the load (indicated by '+') and flexure (indicated by '−') due to buried loading. The flexure profiles compare the depth to the base of the foreland sequence to calculated profiles with T_e of 5, 10, and 20 km. The best fit for a 'combined' surface and buried loading model is with $T_e = 13$ km (rms difference between observed base of foreland, corrected for compaction, and calculated flexure = 0.761 km). Reproduced from Figures 1, 6, and 9 of Lin AT and Watts AB (2002) Origin of the west Taiwan basin by orogenic loading and flexure of a rifted continental margin. *Journal of Geophysical Research* 107, http://dx.doi.org/10.1029/2001JB000669.

The low T_e value derived for the west Taiwan foreland basin is similar to values at extensional basins elsewhere and suggests that orogenic loading and foreland basin formation are influenced by the thermal and mechanical properties of the underlying rifted margin. The significance of preexisting structures being inherited during subsequent orogenic (or rifting) events has been recognized previously by Desegaulx et al. (1991) who pointed out the association of the Arzarcq (Aquitaine) foreland basin with the Permian–Early Cretaceous rifted crust of the Parentis basin and Bay of Biscay and by Watts (1992) who discussed how specific features of a rift margin, such as the hinge zone, might control the large-scale stratigraphic 'architecture' of foreland basins.

Recently, Mouthereau et al. (2013) have discussed the importance of inheritance in controlling orogenic belt structural style. They show that the amount of shortening measured from balanced cross sections is determined by the age of the preexisting lithosphere at the time of shortening. Shortening is smallest for young lithosphere and largest for old lithosphere. Since T_e may also be a function of age at the time of loading, then there should be a correlation between the amount of shortening and T_e. However, only a partial correlation between these parameters is observed. One explanation is that the amount of shortening is also sensitive to the depth of detachment. Irrespective of T_e then, shortening might be small when the detachment is deep (so-called thick-skin structural style) and large when the detachment is shallow (so-called thin-skin structural style).

6.01.6.3 Tectonic Setting of Geologic Features

One implication of an elastic plate model is that once acquired, T_e at a geologic feature is effectively 'frozen-in.' There may be changes due, for example, to a load-induced viscoelastic stress relaxation, but these effects will be small at long timescales compared to the changes that occur during the early stages of loading. This implies that present-day observations such as gravity and topography retain a memory of the elastic thickness.

This ability of a surface observable such as gravity or geoid to record the T_e at the time of loading is especially useful in the oceans where there are many bathymetric features of unknown tectonic setting. We have already pointed out that studies at sample sites where both load and crustal age are known suggest that a relation exists between T_e and the age of the oceanic lithosphere at the time of loading. Seamounts and oceanic islands emplaced on young oceanic lithosphere on or near a mid-ocean ridge, for example, are associated with low values of T_e, while similar age loads on old lithosphere off-ridge are associated with high values. Therefore, by using gravity and

topography data to estimate T_e at features of unknown age, it might be possible to determine their tectonic setting. Early studies based on predicting gravity from shipboard bathymetry data yielded some 100 estimates from the Pacific (Watts et al., 1980a), but a more recent study (Watts et al., 2006) based on predicting the bathymetry from satellite-derived gravity for different values of T_e and then comparing it to the observed bathymetry have yielded >9000 estimates from each of the world's main ocean basins.

Figure 30 shows an example of estimating the tectonic setting of bathymetric features in the region of the Musician Seamounts in the central Pacific Ocean. The filled circles have been color-coded according to their T_e value: red, $0 < T_e < 12$ km; green, $12 < T_e < 20$ km; and blue, $20 < T_e < 30$ km, which, as Figure 20 suggests, correspond to features that formed in an on-ridge, flank-ridge, and off-ridge setting, respectively. Figure 30 shows that while the Musician Seamounts, which comprise a number of individual seamounts and ridges, formed in either an on-ridge or flank-ridge setting, the Hawaiian ridge is distinctly off-ridge. This is consistent with sample ages that show the Musician Seamounts are 82–96 Ma (Kopp et al., 2003) and formed on 80–110 Ma oceanic lithosphere, while the Hawaiian Islands are 0–5 Ma and formed on lithosphere of similar age.

6.01.6.4 Surface Processes, Flexure, and Landscape Evolution

As we have already demonstrated, plate deformation associated with volcano and sediment loading comprises a broad depression that is flanked by a flexural (or peripheral) bulge. Bulges are an important feature of elastic and viscoelastic plate models, and although of much smaller amplitude than their neighboring depressions (usually <6%), they involve uplift and so are of significance, especially for landscape evolution.

Examples of such bulges are the ones that develop by flexure in front of migrating fold and thrust loads (Beaumont, 1981). These bulges form stratigraphic highs on which foreland basin sediments often onlap (Coakley and Watts, 1991). They control facies (Crampton and Allen, 1995) and may, in some cases, act as an additional source for clastic sediment or a 'raised' platform for carbonate growth (DeCelles and Giles, 1996).

Flexural bulges also appear to influence the river systems that exit orogenic belts. Figure 31 shows, for example, the flexure that would be expected from surface (i.e., topographic) loading in the bend region of the Central Andes. The calculation assumes the load has been emplaced on an elastic plate

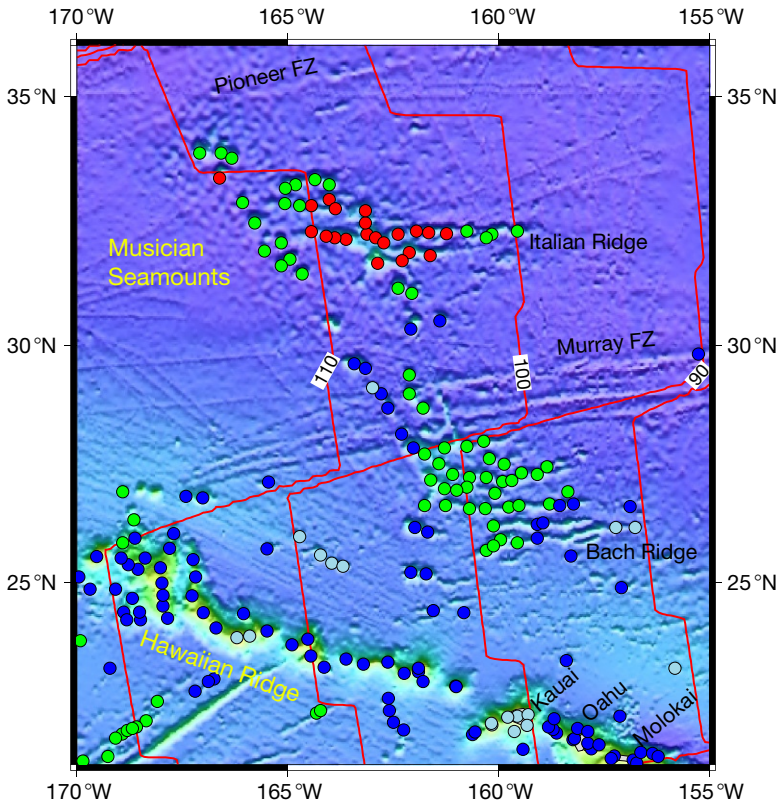

Figure 30 Bathymetric map of the central Pacific Ocean in the region of the Musician Seamounts. The filled circles show the bathymetric features that have yielded T_e estimates. Red-filled circles = $0 < T_e < 12$ km. Green-filled circles = $12 < T_e < 20$ km. Blue-filled circles = $T_e > 20$ km. Watts et al. (2006) attributed the low, intermediate, and high values to an on-ridge, flank-ridge, and off-ridge setting, respectively. Red lines indicate age isochrons based on Müller et al. (1997). Note that there is a mix of tectonic settings with some submarine volcanoes in on-ridge settings appearing in close proximity to those in off-ridge settings.

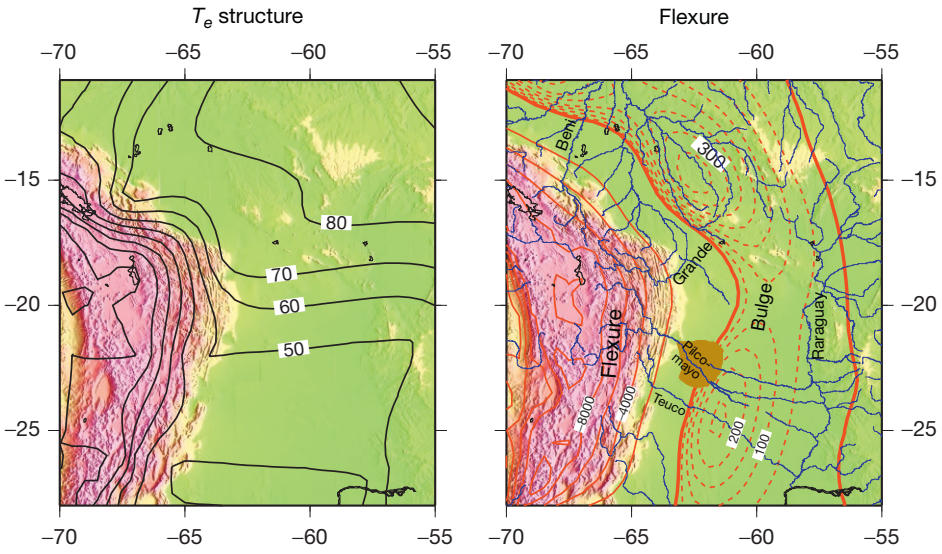

Figure 31 Relationship between the flexural bulge and drainage patterns in the bend region of the Central Andes. The flexure has been calculated using the finite difference method described in Wyer and Watts (2006) and assumes that the topography of the Andes represents a load on the surface of a spatially varying elastic thickness plate. (a) The topography is based on a GEBCO $2 \times 2^{\circ}$ grid and the T_e structure of Stewart and Watts (1997). (b) Flexure. Blue lines show the permanent rivers. Red lines show the flexure. Solid lines show the flexural depression. Contour interval, 2 km. Dashed lines show the flexural bulge. Contour interval, 50 m. Filled brown area shows the extent of the Pilcomayo megafan, as mapped by Leier et al. (2005).

with a spatially varying T_e structure that has been derived from forward modeling of Bouguer gravity anomaly and topography profile data (Stewart and Watts, 1997). As Sacek and Ussami (2009) have shown, the T_e structure derived by Stewart and Watts (1997) accounts well for the foreland basin subsidence in most of the sub-Andean system, especially in the bend region of the Central Andes.

Figure 31 shows that the calculated flexure reaches 3–4 km beneath the outermost (and youngest) thrust in the sub-Andean fold and thrust belt. The flexural bulge reaches amplitude of up to 200–300 m. The rivers that exit the fold and thrust belt in the bend region flow perpendicularly across the proximal foreland basin and then appear to be deflected by the bulge and flow axially across the distal part of the basin. A similar drainage pattern characterizes the Ganges foreland basin that flanks the Himalayas between longitude 76 and 88° E (**Figure 8(a)**; see also Garcia-Castellanos, 2002).

In contrast, the region to the south and north of the bend region shows exiting rivers that appear to flow perpendicularly across the foreland basin and, in some cases, to the crest of the flexural bulge. One explanation for this is that the sediment flux in the rivers has been sufficient to overfill the basin. This is well seen in the case of the Beni and Pilcomayo Rivers (**Figure 31**), which at the point of their exit from the sub-Andean fold and thrust belt form a 'megafan' (Horton and DeCelles, 2001; Leier et al., 2005). Indeed, the figure shows that the Pilcomayo megafan extends eastward to the crest of the bulge, which allows the river to continue eastward to its intersection with the Paraguay trunk river.

Burbank (1992) suggested that the presence or absence of axial rivers in foreland basins is indicative of the mechanisms of uplift in the adjacent fold and thrust belt. In his view, axial rivers reflect the effects of tectonic loading in the fold and thrust belt (due, e.g., to an increase in its mass) and hence subsidence and uplift in the flanking foreland basin and bulge. Perpendicular rivers, in contrast, are indicative of the increase in sediment flux and a regional uplift that would accompany erosional unloading in the fold and thrust belt.

Flexure due to erosional unloading may influence landscape evolution in the fold and thrust belt itself. Montgomery and Stolar (2006), for example, have shown that flexure due to erosional unloading controls the spacing of the river 'anticlines' that trend perpendicularly across fold and thrust belts (e.g., Himalayas): low values of T_e would favor a large-amplitude, narrow, response, while high values of T_e would favor a small-amplitude, wide, response.

Finally, in glacial landscapes (e.g., the Northern Hemisphere during the Pleistocene), plate flexure due to ice, water, and sediment loading and unloading has the potential to modify both the stress state and surface drainage patterns. Hampel and Hetzel (2006), for example, examined the flexural effects of ice unloading on stress patterns, faulting, and hence earthquake activity. Watts et al. (2000) examined the effects of sediment unloading due to river excavation by meltwater-charged rivers. These authors showed that flexure could induce rim uplifts in flanking regions, which, in turn, could modify drainage patterns.

An outstanding question is the extent to which erosional unloading in orogenic belts – and other elevated regions – contributes to their uplift. Uplift changes the base level of rivers, which respond by downcutting. The amount of material removed can be estimated from the depth and width of incised valleys and the height of the preincision surface. Depending on scale, this surface might correspond to a single river terrace or a plateau surface. Once the mass of eroded material has been estimated, then the expected flexural rebound can be

calculated for different assumed values of T_e. Such calculations have now been carried out in the Alps (Champagnac et al., 2007), the Transantarctic Mountains (Stern et al., 2005), and the Cascade Range (Mitchell et al., 2009) where it has been found that flexural rebound due to erosional unloading contributes a significant part (up to ~50%) to the observed uplift of these elevated features.

Unraveling the causes of erosion and determining whether climate change or tectonics is the main factor that drives surface uplift is a difficult problem. Molnar and England (1990) suggested that climate-induced erosion is a significant contributor. They attributed the surface uplift of Late Cenozoic mountain belts such as the Alps and Himalayas, for example, to climatic rather than tectonic-driven erosion. However, the factors that control surface erosion are complex, depending as they do on rock erodibility, precipitation, and vegetation, so determining the relative contribution of climate change and tectonics to surface topography is a challenging problem. What we can say is that isostasy, through its ability to refreshen a landscape, plays a significant role.

The role of isostasy is illustrated in the case of the Hangay Mountains of central Mongolia (West et al., 2013). Bounded by E–W-trending left-lateral strike-slip faults, this NW–SE-trending, 2–3 km high, mainly granitic massif is located in an intraplate setting that crosses different climate zones (**Figure 32**). West et al. (2013) estimated the amount of eroded material by differencing a high-resolution topography grid and a smoothed gridded surface of 'point' relict plateau heights. The spatial extent of eroded material generally correlates with mean annual precipitation, which is higher in the north and east of Hangay than in the south and west. Furthermore, variability in present-day peak heights across the north–south climatic and erosional gradient supports the view that climate-driven erosion increases peak heights by generating greater surface uplift through isostasy. However, when the actual eroded material is used to calculate the flexural uplift and this uplift is subtracted from the total surface uplift (the sum of the present-day topography and the eroded material), a significant residual uplift remains (**Figure 32(e)**). There is little relation between the peak values of this residual uplift and the region of maximum erosion (compare **Figure 32(b)** and **32(e)**). Therefore, the residual uplift can be interpreted as the result of nonisostatic dynamic processes. Indeed, the mountains are associated with a long-wavelength Bouguer gravity anomaly low, which cannot be explained by the gravity effect of an Airy-type crustal root (Petit et al., 2002), suggesting a hot buoyant upwelling region in the subcrustal mantle.

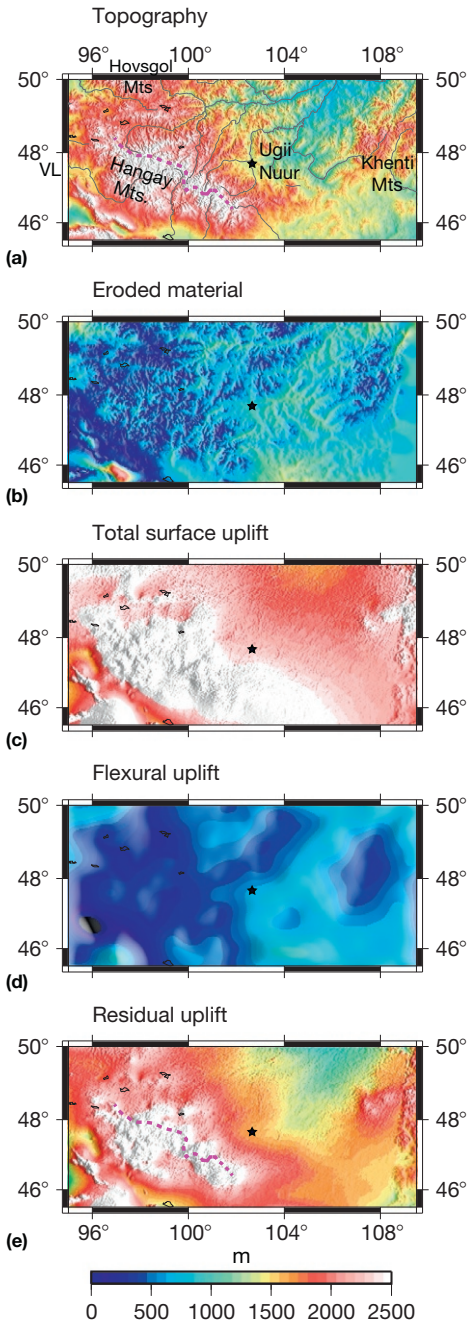

Figure 32 Topography, erosion, and uplift of the Hangay dome, Central Mongolia. (a) Present-day topography. (b) Eroded material as estimated by subtracting the present-day topography from a calculated surface derived from 'point' relict plateau heights (West et al., 2013). (c) Total surface uplift obtained by adding the amount of eroded material to the present-day topography. (d) Flexural uplift obtained by calculating the isostatic rebound due to the removal of the eroded material. (e) Residual uplift obtained by subtracting the flexural uplift from the total surface uplift.

6.01.6.5 The Relative Contributions of Lithospheric Flexure to the Earth's Topography and Gravity Anomaly Field and Mantle Convection

We have been concerned so far in this overview with the deformation of the crust and lithosphere by loads and unloads and their contribution to surface observables such as the Earth's gravity and topography field. These surface observables may, however, also reflect the effects of deeper sublithospheric processes such as those associated with mantle convection.

This is illustrated in **Figure 33**, which compares the observed spectrum of Earth's free-air gravity anomaly derived from EGM2008 (Pavlis et al., 2008) and an earlier satellite-derived model Kaula (1967) to the predicted spectrum based on different isostatic models. The figure shows that the observed power in the gravity anomaly is smaller than would be expected if topography is uncompensated (red circles,

Figure 33) and larger than expected if it is compensated by an Airy model of isostasy (green circles, Figure 33). The uncompensated case implies infinite T_e, while the compensated case implies $T_e = 0$. The figure shows that a finite T_e can explain the observed power at short wavelengths ($100 < \lambda < 900$ km where λ = wavelength), but not at long wavelengths. Indeed, no isostatic models, local or flexural, would be able to account for the observed power in the free-air gravity anomaly at long wavelengths, suggesting it is caused by non-isostatic processes, such as those associated with mantle dynamics.

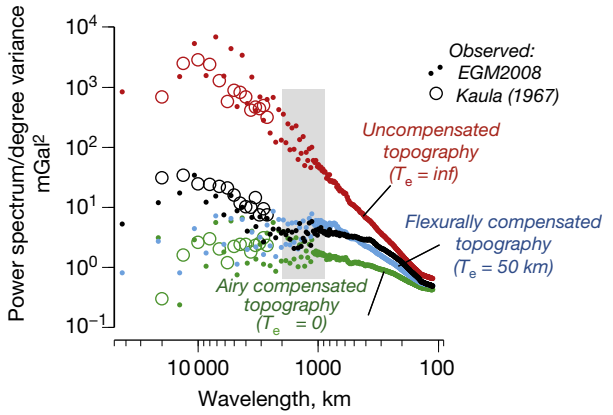

Figure 33 Power spectrum of the Earth's free-air gravity anomaly field compared to predictions based on different isostatic models. Red = uncompensated topography. Green = Airy isostatically compensated topography. Light blue = flexurally compensated topography. The numbers in brackets indicate the elastic thickness, T_e, implied in each model. The gray shade region shows the wavelength band (~900–1100 km) up to which flexurally compensated topography appears to explain the observations well. At longer wavelengths ($\lambda > 1100$ km), the power in the gravity anomaly decreases to zero, and there is no isostatic model that can explain the observations.

The long-wavelength components of the Earth's topography and gravity anomaly field data have been used, in the past, to infer the temperature structure of convection (Parsons and Daly, 1983), mantle viscosity (Panasyuk and Hager, 2000a,b; Zhong and Davies, 1999), and non-isostatic dynamic topography (Al-Hajri et al., 2009; Hager and Richards, 1989). The problem, however, has been in defining the 'cutoff' wavelengths so these surface observables can be used to isolate lithospheric effects such as flexure from the effects of deeper processes such as mantle dynamics (e.g., Watts and Daly, 1981).

Figure 34 shows the results of a spectral study of the relationship between free-air gravity anomaly and topography in the central Pacific Ocean where the 'cutoff' wavelengths can be reasonably well defined. The filled circles in Figure 34(b) show the isostatic response function, $\varphi_{\text{observed}}(k)$, for a range of analysis window sizes centered on Hawaii. $\varphi_{\text{observed}}(k)$ is given by

$$\varphi_{\text{observed}}(k) = \frac{\boldsymbol{Z}(k)}{2\pi G e^{-kd}(\rho_c - \rho_w)} \quad [10]$$

where

$$\boldsymbol{Z}(k) = \frac{\Delta \boldsymbol{g}(k)}{\boldsymbol{H}(k)}$$

and $\boldsymbol{Z}(k)$ is the gravitational admittance, $\Delta \boldsymbol{g}(k)$ is the Fourier transform of the free-air gravity anomaly, and $\boldsymbol{H}(k)$ is the Fourier transform of the topography. $\varphi_{\text{observed}}(k)$ is the wave number parameter that modifies the gravity effect of uncompensated topography so as to produce the free-air gravity

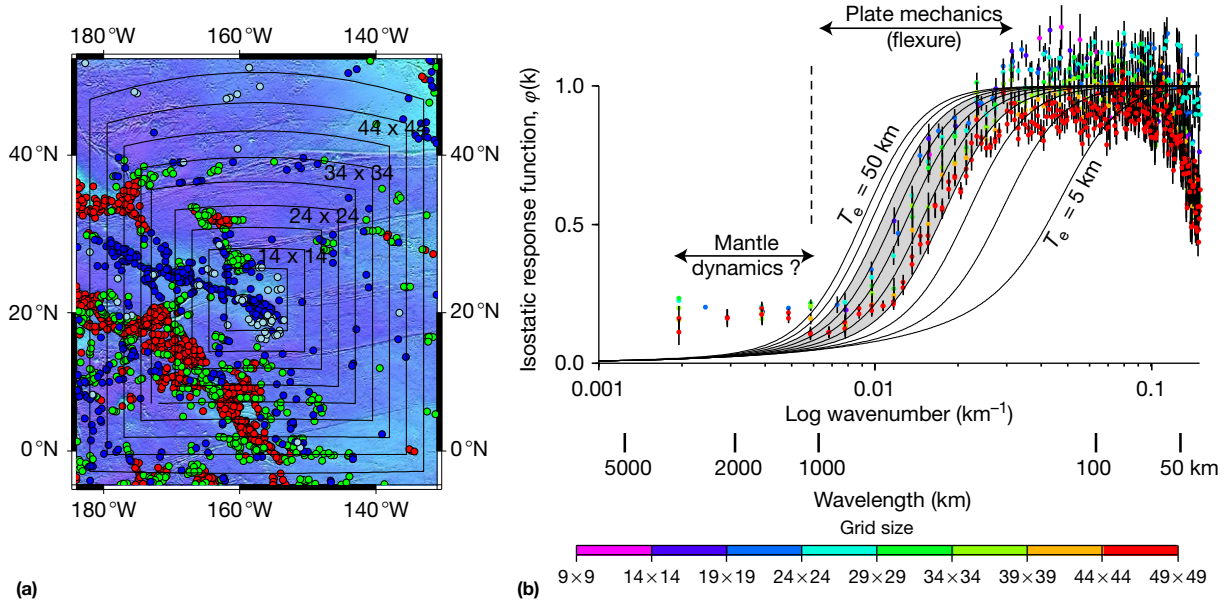

Figure 34 Isostatic response functions in the central Pacific Ocean. (a) Location map. Black lines indicate grids. (b) Comparison of observed and calculated isostatic response functions. The observed functions (filled circles with vertical bars) have been estimated from a spectral analysis of shiptrack gravity anomaly and bathymetry data within grids centered at latitude 21.5° N and longitude 157.5° W. The vertical bars indicate the error in the spectral estimate. The calculated functions are based on eqn [10] and the best-fit value of the density of oceanic crust, ρ_c, and mean depth, d, for each grid. The grids range in size from $9 \times 9°$ to $49 \times 49°$. Solid back lines show the calculated functions at 5 km intervals in the range 5–50 km. The gray shade shows the calculated functions within the region $20 < T_e < 40$ km. Modified from Wilson C (2004) *Long Wavelength Gravity and Topography Anomalies in the Pacific*, 93 pp. MESc. Thesis Oxford University.

anomaly due to the topography and its compensation. The solid lines in Figure 34(b) show the calculated flexural isostatic response function, $\varphi_{\text{flexure}}(k)$, which is given by

$$\varphi_{\text{flexure}}(k) = \left[1 - \phi_e(k) e^{-kt}\right]$$

where

t = undeformed thickness of the crust and $\phi_e(k) = \left[\frac{Dk^4}{(\rho_m - \rho_c)g} + 1\right]^{-1}$ [11]

We see from eqn [11] that as $k \to \infty$, $\varphi_{\text{flexure}}(k) \to 1$, and so at short wavelengths, the gravity anomaly is given by the gravity effect of the topography. As $k \to 0$, however, $\varphi_{\text{flexure}}(k) \to 0$, and so at long wavelengths, the gravity anomaly approaches zero because of flexural isostatic compensation. The wavelength 'band' defining the region that flexure contributes significantly to the free-air gravity anomaly field depends on D and, hence, T_e.

The comparisons of observed and calculated isostatic response functions in Figure 34 suggest that as the analysis window size increases, the best-fit T_e decreases. The highest values of T_e are for the relatively small $9 \times 9°$ grid, while the lowest values are for the relatively large $49 \times 49°$ grid. We attribute this to the fact that the grids are centered on the Hawaiian ridge that formed in an off-ridge tectonic setting where the load age is young and the oceanic lithosphere strong (see, e.g., Figure 30). These off-ridge estimates dominate the smallest grid, in contrast to the largest grid, which includes features formed in other settings, including many on-ridge estimates, and, hence, comprises mainly low T_e values. The figure shows that plate flexure contributes significantly to the central Pacific Ocean gravity field up to $\lambda \sim 1000$ km. Beyond this wavelength, there is a negligible contribution from flexure. The existence of a positive isostatic response function at $1000 < \lambda < 3000$ km is therefore unexpected and suggests that mechanisms other than flexure are operating at long wavelengths that cause gravity anomalies and topography to be correlated.

Figure 34(b) shows that the isostatic response function for $\lambda >= 1000$ km is ~ 0.175, which corresponds, using eqn [10] and $\rho_c = 2800$ kg m^{-3} and $\rho_w = 1030$ kg m^{-3}, to an admittance, $Z(k)$, of ~ 12.5 mGal km^{-1}. This agrees well with the ~ 13 mGal km^{-1} estimated by Wieczorek (Chapter 10.05) using a global SRTM topography grid and the EGRM96 gravity field that is based on satellite-derived GRACE and CHAMP data. The origin of these admittance values is not clear, but numerical models suggest they are most likely due to deep processes in the mantle such as those associated with mantle convection.

While Figure 34(b) suggests that it might be quite straightforward to use the 'rollover' in the gravitational admittance in the oceans to separate the effects of plate flexure and mantle dynamics, it has proved much more difficult in the continents. McKenzie (2010), for example, has shown that the continental

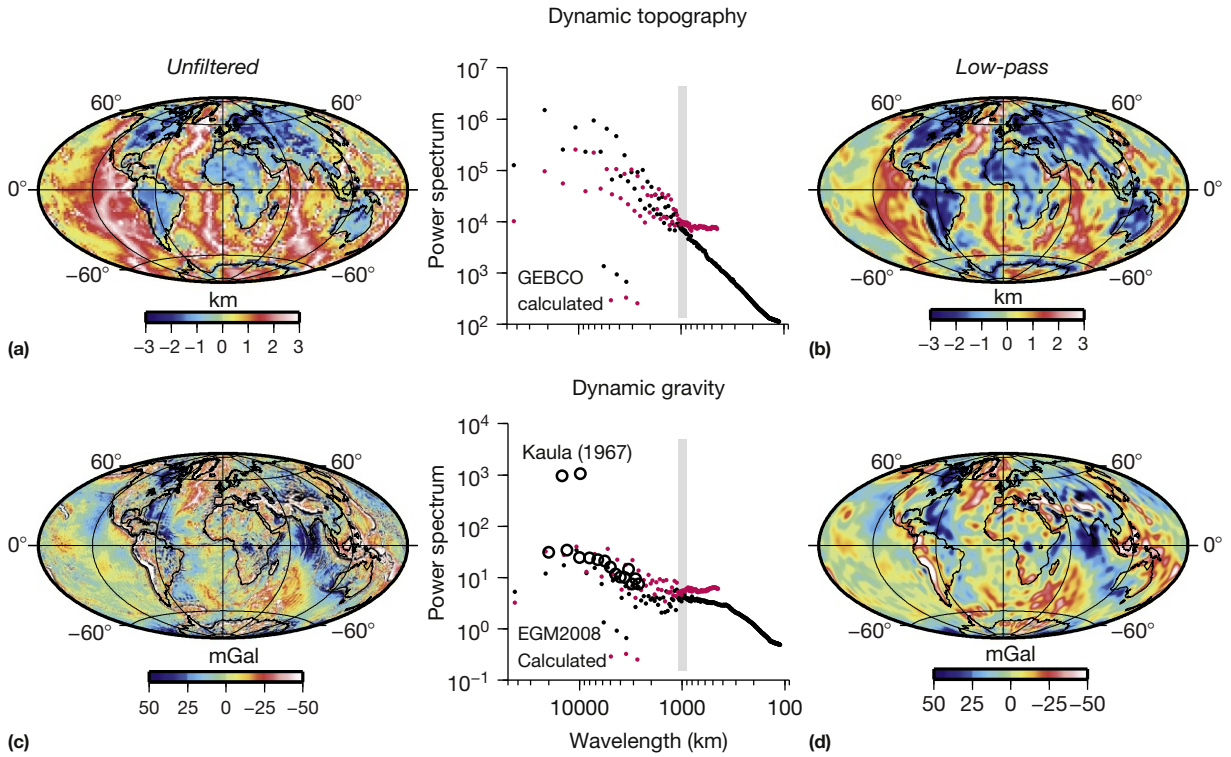

Figure 35 Dynamic topography and gravity. (a) Unfiltered dynamic topography. (b) Filtered dynamic topography using a low-pass filter, which passes $\lambda > 1100$ km and rejects $\lambda < 900$ km. (c) Unfiltered dynamic gravity. (d) Filtered dynamic gravity using a low-pass filter, which passes $\lambda > 1100$ km and rejects $\lambda < 900$ km. Dynamic topography has been calculated by subtracting the expected topography based on the CRUST 2.0 crustal structure from the observed topography and bathymetry defined by a GEBCO $2 \times 2°$ grid. Dynamic gravity has been calculated by summing the gravity effect of the expected topography and the Moho defined by CRUST 2.0 and subtracting it from the observed EGM2008 free-air gravity anomaly. The inset spectra compare the power spectra of the observed topography and free-air gravity anomaly (black symbols) to the power spectra of the dynamic topography and dynamic gravity (purple symbols).

admittance is strongly influenced by the effects of glacial isostatic rebound that also contributes to the long-wavelength admittance.

Other, non-spectral, ways of isolating the nonisostatic contribution to the Earth's gravity and topography and calculating dynamic topography and gravity have therefore been proposed that take into account both the actual crustal thickness, as determined, for example, from seismic refraction data (e.g., Panasyuk and Hager, 2000a,b), and the tendency of the crust to approach a state of isostatic equilibrium. The Earth's expected topography, h_e, is given, for example, by

$$\text{Continent}: \; h_e = \frac{(T_s - T_c)(\rho_m - \rho_c)}{\rho_m} \qquad [12]$$

$$\text{Ocean}: \; h_e = \frac{-(T_c - T_s)(\rho_m - \rho_c)}{(\rho_m - \rho_w)} \qquad [13]$$

where T_s is the observed crustal thickness (from CRUST 2.0), T_c is the Airy zero-elevation crustal thickness, and ρ_w, ρ_c, and ρ_m are the densities of the water, crust, and mantle, respectively. The non-isostatic, dynamic, topography is the topography that remains after subtracting the expected topography, h_e, from the observed topography. Dynamic gravity can then be calculated by summing the gravity effect of the expected topography and the Moho based on CRUST 2.0 and subtracting it from the observed free-air gravity anomaly.

Figure 35 shows global dynamic topography and gravity maps. The continents are dominated by dynamic topography lows. Topography here is therefore lower than would be expected for the observed crustal thickness. Dynamic gravity is more variable, with highs over some orogenic belts (Andes, Alps, and Himalayas) and some hot spots (Afar and Yellowstone) and lows over some cratonic (Congo and Hudson Bay) and foreland basins (Arabian Gulf and Rif). The correlation between dynamic topography and gravity is important to establish as it makes a good argument for convection. In this respect, the observation of dynamic topography and gravity highs over the Afar and lows over the Congo basin are significant as they can be interpreted with some confidence, in terms of mantle upwelling and downwelling, respectively.

The oceans, in contrast to the continents, are dominated by dynamic topography highs. The most prominent highs correlate with the mid-ocean ridge system, and they are, as would be expected, noticeably wider over the fast-spreading than the slow-spreading ridges. The highs indicate that topography is shallower than expected for normal oceanic crustal thickness, and so they reflect mantle upwelling. Dynamic gravity over the mid-ocean ridges is more variable, with only the hot-spot-influenced ridges (e.g., Iceland and Marion) associated with prominent highs. Other dynamic topography and gravity highs occur over the Hawaiian swell, the Pacific superswell region, and some subduction zone back-arc basins, suggesting mantle upwelling in these regions also.

6.01.7 Conclusions

We draw the following general conclusions from this overview:

- Crust and lithosphere dynamics involves a consideration of all the forces (or stresses) and resulting deformations (or strains) that have modified the Earth's outermost layers through time.
- There is no continuum of forces and deformations that can be studied that are representative of geologic processes such as those associated orogeny, continental rifting and breakup, and sedimentary basin formation.
- What we have are 'snapshots' at discreet timescales, the most important of which are coseismic and postseismic (a few seconds to a few hundreds of seconds) deformation, glacial isostatic adjustment (a few tens of thousands of a), and plate flexure ($>\sim 10^5$ years).
- There is evidence that a link might exist between the elastic layer thickness estimates inferred from the different timescales. For the same tectonic region, for example, geodetic and glacial isostatic rebound estimates of the elastic layer thickness appear to be some 30–40 km higher than flexural estimates.
- There are differences in the absolute value of elastic layer thickness and viscosity between regions, such that some areas relax quickly, while others relax slowly. We attribute these differences to regional variations in subcrustal mantle lithosphere viscosity.
- The regional variation in viscosity is large enough that even the elastic layer thickness derived from glacial loading and unloading may approach that expected from flexural loads. T_e is therefore a useful guide to the steady-state deformation.
- Global maps of T_e show significant spatial variations: high values are associated with cratonic regions, while low values correlate with mid-ocean ridges and some continental rifts. Phanerozoic orogenic belts have intermediate values – with both low and high values.
- There is a good correlation in some continents (e.g., Europe) between T_e and other proxies for the physical properties of the crust and lithosphere such as shear-wave velocity anomaly and surface heat flow.
- Geologic implications of a T_e that varies spatially include terrane mapping, the origin of bathymetric features, and the prediction of flexural bulges.
- Lithospheric flexure interacts with both the atmosphere and asthenosphere and so has implications for surface processes such as landscape evolution and for deep processes such as mantle convection.
- Isolating the effects of plate processes such as flexure from deep processes such as mantle convection from the Earth's gravity and topography field is a difficult but challenging problem that should be addressed in the future.

Acknowledgments

The author would like to thank Eugene Burov, Tom Jordan, James Humphreys, Johnny Hunter, Andrew Lin, Christine Peirce, Marta Pérez-Gussinyé, Matt Rodger, David Sandwell, Mike Searle, Josh West, Cian Wilson, and Shijie Zhong for their contributions. The author would also like to thank Isabelle Ryder who carried out the computations in Figure 9, Jonathan Stewart and Paul Wyer for their work on the finite difference code used to calculate the flexure in Figures 15 and

31, and Øyvind Engen for critically reading the original manuscript. The figures were constructed using the GMT software (Wessel and Smith, 1991).

References

Al-Hajri Y, White N, and Fishwick S (2009) Scales of transient convective support beneath Africa. *Geology* 37: 883–886.

Armstrong GD (1997) *Potential Field Signatures and Flexural Rigidity of the Lithosphere in Ireland*, p. 184. PhD Thesis, National University of Ireland, Galway.

Armstrong GD and Watts AB (2001) Spatial variations in T_e in the southern Appalachians, Eastern United States. *Journal of Geophysical Research* 106: 22009–22026.

Artemieva IM, Billien M, Leveque J-J, and Mooney WD (2004) Shear wave velocity, seismic attenuation, and thermal structure of the continental upper mantle. *Geophysical Journal International* 157: 607–628.

Artemieva IM and Mooney WD (2001) Thermal thickness and evolution of Precambrian lithosphere: A global study. *Journal of Geophysical Research* 106: 16387–16414.

Ballantyne CK, McCarroll D, Nesje A, Dahl SO, and Stone JO (1998) The last ice sheet in north-west Scotland: Reconstruction and implications. *Quaternary Science Reviews* 17: 1149–1184.

Barrell J (1914a) The strength of the Earth's crust. Part I: Geologic tests of the limits of strength. *Journal of Geology* 22: 28–48.

Barrell J (1914b) The strength of the Earth's crust. Part VII: Variations of strength with depth as shown by the nature of departures from isostasy. *Journal of Geology* 22: 729–741.

Bassin C, Laske G, and Masters G (2000) The current limits of resolution for surface wave tomography in North America. *Eos, Transactions of the American Geophysical Union* 81: F897.

Beaumont C (1978) The evolution of sedimentary basins on a viscoelastic lithosphere: Theory and examples. *Geophysical Journal of the Royal Astronomical Society* 55: 471–497.

Beaumont C (1981) Foreland basins. *Geophysical Journal of the Royal Astronomical Society* 65: 291–329.

Bechtel TD, Forsyth DW, Sharpton VL, and Grieve RAF (1990) Variations in effective elastic thickness of the North American lithosphere. *Nature* 343: 636–638.

Bodine JH, Steckler MS, and Watts AB (1981) Observations of flexure and the rheology of the oceanic lithosphere. *Journal of Geophysical Research* 86: 3695–3707.

Bowie W (1927) *Isostasy – The Science of the Equilibrium of the Earth's Crust*, p. 275. New York: E. P. Dutton.

Braitenberg C, Wang Y, Fang J, and Hsu HT (2003) Spatial variations of flexure parameters over the Tibet-Qinghai plateau. *Earth and Planetary Science Letters* 205: 211–224.

Brewer JA and Smythe DK (1984) MOIST and the continuity of crustal reflector geometry along the Caledonian-Appalachian orogen. *Journal of the Geological Society of London* 141: 105–120.

Brown LD, Zhao W, Nelson KD, et al. (1996) Bright spots, structure, and magmatism in southern Tibet from INDEPTH seismic reflection profiling. *Science* 274: 1688–1690.

Bry M and White N (2007) Reappraising elastic thickness variation at oceanic trenches. *Journal of Geophysical Research* 112: B08414. http://dx.doi.org/10.1029/2005JB004190.

Buck WR (2004) Consequences of asthenospheric variability on continental rifting. In: Karner GD, Taylor B, Driscoll NW, and Kobl stedt DL (eds.) *Rheology and Deformation of the Lithosphere at Continental Margins*, pp. 1–30. New York: Columbia University Press.

Burbank DW (1992) Causes of recent Himalayan uplift deduced from deposited patterns in the Ganges basin. *Nature* 357: 680–683.

Burov EB and Diament M (1995) The effective elastic thickness (T_e) of continental lithosphere. What does it really mean? *Journal of Geophysical Research* 100: 3895–3904.

Burov EB and Poliakov A (2001) Erosion and rheology controls on synrift and postrift evolution: Verifying old and new ideas using a fully coupled numerical model. *Journal of Geophysical Research* 106: 16461–16481.

Burov EB and Watts AB (2006) The long-term strength of continental lithosphere: Jelly sandwich of crème brûlée? *GSA Today* 16: 4–10.

Calmant S and Cazenave A (1987) Anomalous elastic thickness of the oceanic lithosphere in the south-central Pacific. *Nature* 32: 236–238.

Champagnac JD, Molnar P, and Anderson RN (2007) Quaternary erosion-induced isostatic rebound in the western Alps. *Geology* 35: 195–198.

Chapman LG (1954) An outlet of Lake Algonquin at Fossmill, Ontario. *Proceedings of the Geological Society of Canada* 6: 61–68.

Chen L, Booker JR, Jones AG, et al. (1996) Electrically conductive crust in southern Tibet from INDEPTH magnetotelluric surveying. *Science* 274: 1694–1696.

Chugh RS and Bhattacharji JC (1974) Study of isostasy in the Himalayan region. *Wadia Institute of Himalayan Geology* 4: 453–464.

Clague DA, Dalrymple GB, Wright TL, et al. (1989) The Hawaiian-Emperor chain. In: Winterer EL, Hussong DM, and Decker RW (eds.) *The Eastern Pacific Ocean and Hawaii, the Geology of North America*, pp. 187–287. Boulder, CO: Geological Society of America.

Clark MK and Royden LH (2000) Topographic ooze: Building the eastern margin of Tibet by lower crustal flow. *Geology* 28: 703–706.

Cloetingh S and Burov EB (1996) Thermomechanical structure of European continental lithosphere: Constraints from rheological profiles and EET estimates. *Geophysical Journal International* 124: 695–723.

Coakley BJ and Watts AB (1991) Tectonic controls on the development of unconformities: The North Slope, Alaska. *Tectonics* 10: 101–130.

Cohen SC and Darby DJ (2003) Tectonic plate coupling and elastic thickness derived from the inversion of a steady state viscoelastic model using geodetic data: Application to southern North Island New Zealand. *Journal of Geophysical Research* 108. http://dx.doi.org/10.1029/2002JB001687.

Cohen SC and Kramer MJ (1984) Crustal deformation, the earthquake cycle, and models of viscoelastic flow in the asthenosphere. *Geophysical Journal of the Royal Astronomical Society* 78: 735–750.

Collier J and Watts AB (2001) Lithospheric response to volcanic loading by the Canary Islands: Constraints from seismic reflection data in their flexural moats. *Geophysical Journal International* 147: 660–676.

Crampton SL and Allen PA (1995) Recognition of forebulge unconformities associated with early stage foreland basin development; example from the North Alpine foreland basin. *American Association of Petroleum Geologists* 79: 1495–1514.

Dalla Via G, Sabadini R, De Natale G, and Pingue F (2005) Lithospheric rheology in southern Italy inferred from postseismic viscoelastic relaxation following the 1980 Irpinia earthquake. *Journal of Geophysical Research* 110: B06311. http://dx.doi.org/10.1029/2004JB003539.

Damuth JE (1975) Amazon Cone: Morphology, sediments, age and growth pattern. *Geological Society of America Bulletin* 86: 863–878.

Darwin GH (1882) On the stresses caused in the interior of the Earth by the weight of continents and mountains. *Philosophical Transactions of the Royal Society* CLXXII: 187–230.

Davis JL and Mitrovica JX (1996) Glacial isostatic adjustment and the anomalous tide gauge record of Eastern North America. *Nature* 379: 331–333.

DeCelles PG and Giles KA (1996) Foreland basin systems. *Basin Research* 8: 105–123.

Desegaulx P, Kooi H, and Cloetingh S (1991) Consequences of foreland basin development on thinned continental lithosphere: Application to the Aquitaine basin (SW France). *Earth and Planetary Science Letters* 106: 116–132.

Di Donato G, Mitrovica JX, Sabadini R, and Vermeersen LLA (2000) The influence of a ductile crustal zone on glacial isostatic adjustment: Geodetic observables along the US East Coast. *Geophysical Research Letters* 27: 3017–3020.

Divins DL (2005) NGDC Total Sediment Thickness of the World's Oceans & Marginal Seas. http://www.ngdc.noaa.gov/mgg/sedthick/sedthick.html.

Dixon JE, Dixon TH, Bell DR, and Malservisi R (2004) Lateral variation in upper mantle viscosity: Role of water. *Earth and Planetary Science Letters* 222: 451–467.

Dixon TH, Norabuena E, and Hotaling L (2003) Paleoseismology and Global Positioning System: Earthquake-cycle effects and geodetic versus geologic fault slip rates in the Eastern California shear zone. *Geology* 31: 55–58.

Duncan RA, McCulloch MT, Barsczus HG, and Nelson DR (1986) Plume versus lithospheric sources for melts at Ua Pou, Marquesas Islands. *Nature* 322: 534–538.

Dyksterhuis S, Albert RA, and Muller RD (2005) Finite-element modelling of contemporary and paleo-intraplate stress using ABAQUS. *Computers and Geosciences* 31: 297–307.

Dziewonski AM and Anderson DL (1981) Preliminary reference Earth model. *Physics of the Earth and Planetary Interiors* 25: 297–356.

Ebinger CJ, Karner GD, and Weissel JK (1991) Mechanical strength of extended continental lithosphere: Constraints from the western rift system. *Tectonics* 10: 1239–1256.

England PC and McKenzie DP (1982) A thin viscous sheet model for continental deformation. *Geophysical Journal of the Royal Astronomical Society* 70: 295–321.

Faichney IDE, Webster JM, Clague DA, Paduan JB, and Fullagar PD (2010) Unraveling the tilting history of the submerged reefs surrounding Oahu and the Maui-Nui complex, Hawaii. *Geochemistry, Geophysics, Geosystems* 11: Q07002. http://dx.doi.org/10.1029/2010GC003044.

Feigl KL, Agnew DC, Bock Y, et al. (1993) Space geodetic measurement of crustal deformation in central and Southern California, 1984–1992. *Journal of Geophysical Research* 98: 21677–21712.
Fialko Y (2004) Probing the mechanical properties of seismically active crust with space geodesy: Study of the coseismic deformation due to the 1992 Mw7.3 Landers (Southern California) earthquake. *Journal of Geophysical Research* 109: B03307.
Fjeldskaar W (1994) Viscosity and thickness of the asthenosphere detected from Fennoscandian uplift. *Earth and Planetary Science Letters* 126: 399–410.
Fjeldskaar W (1997) Flexural rigidity of fennoscandia inferred from the postglacial uplift. *Tectonics* 16: 596–608.
Fukahata Y and Matsu'ura M (2005) General expressions for internal deformation fields due to a dislocation source in a multilayered elastic half-space. *Geophysical Journal International* 161: 507–521.
Fukahata Y and Matsu'ura M (2006) Quasi-static internal deformation due to a dislocation source in a multilayered elastic/viscoelastic half-space and an equivalence theorem. *Geophysical Journal International* 166: 418–434.
Funning GJ, Barke RMD, Lamb SH, Parsons B, and Wright TJ (2005) The 1998 Aiquile, Bolivia earthquake: A seismically active fault revealed with InSAR. *Earth and Planetary Science Letters* 232: 39–49.
Garcia-Castellanos D (2002) Interplay between lithospheric flexure and river transport in foreland basins. *Basin Research* 14: 89–104.
Goetze C and Evans B (1979) Stress and temperature in the bending lithosphere as constrained by experimental rock mechanics. *Geophysical Journal of the Royal Astronomical Society* 59: 463–478.
Gordon RG (1998) The plate tectonic approximation: Plate nonrigidity, diffuse plate boundaries, and global plate reconstructions. *Annual Review of Earth and Planetary Sciences* 26: 615–642.
Grigg RW and Jones AT (1997) Uplift caused by lithospheric flexure in the Hawaiian Archipelago as revealed by elevated coral deposits. *Marine Geology* 141: 11–25.
Grossman EE and Fletcher CH (1998) Sea level higher than present 3500 years ago on the northern main Hawaiian islands. *Geology* 26: 363–366.
Grotzinger J and Royden L (1990) Elastic strength of the Slave craton at 1.9Gyr and implications for the thermal evolution of the continents. *Nature* 347: 64–66.
Hager BH and Richards MA (1989) Long-wavelength variations in Earth's geoid: Physical models and dynamical implications. *Philosophical Transactions of the Royal Society* 328: 309–327.
Hampel A and Hetzel R (2006) Response of normal faults to glacial-interglacial fluctuations of ice and water masses on Earth's surface. *Journal of Geophysical Research* 111: B046406. http://dx.doi.org/10.1029/2005JB004124.
Hartley R, Watts AB, and Fairhead JD (1996) Isostasy of Africa. *Earth and Planetary Science Letters* 137: 1–18.
Hayford JF (1909) *The Figure of the Earth and Isostasy from Measurements in the United States*, p. 178. Washington, DC: Government Printing Office.
Hearn EH, Burgmann R, and Reilinger RE (2002a) Dynamics of Izmit earthquake postseismic deformation and loading of the Duzce earthquake hypocenter. *Bulletin of the Seismological Society of America* 92: 172–193.
Hearn EH, Hager BH, and Reilinger RE (2002b) Viscoelastic deformation from Anatolian Fault Zone earthquakes and the eastern Mediterranean GPS velocity field. *Geophysical Research Letters* 29: 44-1–44-4. http://dx.doi.org/10.1029/2002GL014889.
Heiskanen W (1931) Isostatic tables for the reduction of gravimetric observations calculated on the basis of Airy's hypothesis. *Bulletin Géodésique* 30: 110–129.
Hertz H (1884) On the equilibrium of floating elastic plates. *Wiedemann's Annalen* 22: 449–455.
Hetenyi G, Cattin R, Vergne J, and Nabelek JL (2006) The effective elastic thickness of the India plate from receiver function imaging, gravity anomalies and thermomechanical modelling. *Geophysical Journal International* 167: 1106–1118. http://www.1110.1111/j.1365-1246X.2006.03198.x.
Horton BK and DeCelles PG (2001) Modern and ancient fluvial megafans in the foreland basin system of the central Andes, southern Bolivia: Implications for drainage network evolution in fold-thrust belts. *Basin Research* 13: 43. http://dx.doi.org/10.1046/j.1365-2117.2001.00137.x.
Hubscher C, Figueiredo AG, Kruse L, and Spies V (2002) High-resolution analysis of the deposition pattern on the Amazon sub-aquatic delta and outer continental shelf. *Marine Geophysical Research* 23: 209–222.
Humphreys J (2003) *Lithospheric Flexure at Continental Volcanoes: Kilimanjaro, Tanzania and Mount Etna, Italy*, 88p. MESc Thesis, Oxford University.
Hurst KJ, Argus DF, Donnellan A, Heflin MB, and Jefferson DC (2000) The coseismic geodetic signature of the 1999 Hector Mine earthquake. *Geophysical Research Letters* 27: 2733–2736.
Iwasaki T and Matsu'ura M (1982) Quasi-static crustal deformations due to a surface load: Rheological structure of the Earth's crust and upper mantle. *Journal of Physics of the Earth* 30: 469–508.
Jackson J (2002) Strength of the continental lithosphere: Time to abandon the jelly sandwich? *GSA Today* 12: 4–10.
Jacobs A, Sandwell DT, and Sichoix L (2002) The 1999 (M_w 7.1) Hector Mine earthquake: Near-field postseismic deformation from ERS Interferometry. *Bulletin of the Seismological Society of America* 92: 1433–1442.
Jarrard RD and Turner DL (1979) Comments on 'Lithospheric flexure and uplifted atolls' by M. McNutt and H. W. Menard. *Journal of Geophysical Research* 84: 5691–5694.
Johnson KM, Hsu Y-J, Segall P, and Yu S-B (2001) Fault geometry and slip distribution of the 1999 Chi-Chi, Taiwan earthquake imaged from inversion of GPS data. *Geophysical Research Letters* 28: 2285–2288.
Johnson KM and Segall P (2004) Viscoelastic earthquake cycle models with deep stress-driven creep along the San Andreas fault system. *Journal of Geophysical Research* 109: B10403. http://dx.doi.org/10.1029/2004JB003096.
Jordan TA and Watts AB (2005) Gravity anomalies, flexure and the elastic thickness structure of the India-Eurasia collisional system. *Earth and Planetary Science Letters* 236: 732–750.
Judge AV and McNutt MK (1991) The relationship between plate curvature and elastic plate thickness: A study of the Peru–Chile trench. *Journal of Geophysical Research* 96: 16625–16640.
Kalnins LM and Watts AB (2009) Spatial variations in effective elastic thickness in the western Pacific Ocean and their implications for Mesozoic volcanism. *Earth and Planetary Science Letters* 286: 89–100.
Karner GD and Watts AB (1983) Gravity anomalies and flexure of the lithosphere at mountain ranges. *Journal of Geophysical Research* 88: 10449–10477.
Kaula WM (1967) Geophysical implications of satellite determinations of the Earth's gravitational field. *Space Science Reviews* 7: 769–794.
Kind R, Ni J, Zhao W, et al. (1996) Evidence from earthquake data for a partially molten crustal layer in southern Tibet. *Science* 274: 1692–1694.
Kogan MG, Fairhead JD, Balmino G, and Makedonskii EL (1994) Tectonic fabric and lithospheric strength of northern Eurasia based on gravity data. *Geophysical Research Letters* 21: 2653–2656.
Kopp H, Kopp C, Phipps Morgan J, Flueh ER, Weinrebe W, and Morgan WJ (2003) Fossil hotspot-ridge interaction in the Musicians seamount province: Geophysical investigations of hotspot volcanism at volcanic elongated ridges. *Journal of Geophysical Research* 108: 2160. http://dx.doi.org/10.1029/2002JB002015.
Koppers AAP, Phipps Morgan J, Morgan JW, and Staudigel H (2001) Testing the fixed hotspot hypothesis using $^{40}Ar/^{39}Ar$ age progressions along seamount trails. *Earth and Planetary Science Letters* 185: 237–252.
Lago B and Cazenave A (1981) State of stress in the oceanic lithosphere in response to loading. *Geophysical Journal of the Royal Astronomical Society* 64: 785–799.
Lambeck K, Smither C, and Johnston P (1998) Sea-level change, glacial rebound and mantle viscosity for northern Europe. *Geophysical Journal International* 134: 102–144.
Latychev K, Mitrovica JX, Tamisiea ME, and Tromp J (2005) Influence of lithospheric thickness variations on 3-D crustal velocities due to glacial isostatic adjustment. *Geophysical Research Letters* 32: L01304. http://dx.doi.org/10.1029/2004GL021454.
Le Pichon X, Henry P, and Goffe B (1997) Uplift of Tibet: From eclogites to granulites – Implications for the Andean Plateau and the Variscan belt. *Tectonophysics* 273: 57–76.
Leier AL, DeCelles PG, and Pelletier JD (2005) Mountains, monsoons and megafans. *Geology* 33: 289–292.
Li C, van der Hilst RD, Meltzer AS, and Engdahl ER (2008) Subduction of the Indian lithosphere beneath the Tibetan Plateau and Burma. *Earth and Planetary Science Letters* 274: 157–168.
Lin AT and Watts AB (2002) Origin of the west Taiwan basin by orogenic loading and flexure of a rifted continental margin. *Journal of Geophysical Research* 107. http://dx.doi.org/10.1029/2001JB000669.
Lin A-T, Watts AB, and Hesselbo SP (2003) Cenozoic stratigraphy and subsidence history of the South China Sea margin in the Taiwan region. *Basin Research* 15: 453–478.
Lorenzo-Martin F, Roth F, and Wang R (2006) Inversion for rheological parameters from post-seismic surface deformation associated with the 1960 Valdivia earthquake, Chile. *Geophysical Journal International* 164: 75–87. http://dx.doi.org/10.1111/j.1365-1246X.2005.02803.
Lowry AR, Ribe NM, and Smith RB (2000) Dynamic elevation of the Cordillera, Western United States. *Journal of Geophysical Research* 105: 23371–23390.
Lowry AR and Smith RB (1994) Flexural rigidity of the basin and range-Colorado Plateau-Rocky Mountain transition from coherence analysis of gravity and topography. *Journal of Geophysical Research* 99: 20123–20140.
Lowry AR and Smith RB (1995) Strength and rheology of the Western U.S. Cordillera. *Journal of Geophysical Research* 100: 17947–17963.

Ludwig KR, Szabo BJ, Moore JG, and Simmons KR (1991) Crustal subsidence rate of Hawaii determined from $^{234}U/^{238}U$ ages of drowned coral reefs. *Geology* 19: 171–174.

Lyon-Caen H and Molnar P (1983) Constraints on the structure of the Himalaya from an analysis of gravity anomalies and a flexural model of the lithosphere. *Journal of Geophysical Research* 88: 8171–8191.

Ma XQ and Kusznir NJ (1995) Coseismic and postseismic subsurface displacements and strains for a dip-slip normal fault in a three-layer elastic-gravitational medium. *Journal of Geophysical Research* 100: 12813–12830.

Maia M and Arkani-Hamid J (2002) The support mechanism of the young Foundation seamounts inferred from bathymetry and gravity. *Geophysical Journal International* 149: 190–210.

Mantovani MSM, Shukowsky W, de Freitas SRC, and Brito Neves BB (2005) Lithosphere mechanical behaviour inferred from tidal gravity anomalies: A comparison of Africa and South America. *Earth and Planetary Science Letters* 230: 397–412.

Masek JG, Isacks BL, and Fielding EJ (1994) Rift flank uplift in Tibet: Evidence for a viscous lower crust. *Tectonics* 13: 659–667.

McConnell RK (1968) Viscosity of the mantle from relaxation time spectra of isostatic adjustment. *Journal of Geophysical Research* 73: 7089–7105.

Mckenzie DP (1967) The viscosity of the mantle. *Geophysical Journal of the Royal Astronomical Society* 14: 297–305.

McKenzie D (2010) The influence of dynamically supported topography on estimates of T_e. *Earth and Planetary Science Letters* 295: 127–138.

McNutt MK and Fischer KM (1987) The south Pacific superswell. In: Keating BH (ed.) *Seamounts, Islands and Atolls*, pp. 25–34. Washington, DC: American Geophysical Union.

McNutt MK and Menard HW (1978) Lithosphere flexure and uplifted atolls. *Journal of Geophysical Research* 83: 1206–1212.

Megnin C and Romanowicz B (2000) The three-dimensional shear velocity structure of the mantle from the inversion of body, surface and higher-mode waveforms. *Geophysical Journal International* 143: 709–728.

Miller MM, Webb FH, Townsend D, Golombek MP, and Dokka RK (1993) Regional coseismic deformation from the June 28, 1992, Landers, California, earthquake; results from the Mojave GPS network. *Geology* 21: 868–872.

Milne GA, Davis JL, Mitrovica JX, et al. (2001) Space-Geodetic constraints on glacial isostatic adjustment in Fennoscandia. *Science* 291: 2381–2385.

Milne GA, Mitrovica JX, Scherneck H-G, et al. (2004) Continuous GPS measurements of postglacial adjustment in Fennoscandia. *Journal of Geophysical Research* 109: B02412. http://dx.doi.org/10.1029/2003JB002619.

Mitchell S, Montgomery D, and Greenberg H (2009) Erosional unloading, hillslope geometry, and the height of the Cascade Range, Washington State, USA. *Earth Surface Processes and Landforms* 34: 1108–1120.

Molnar P and England PC (1990) Late Cenozoic uplift of mountain ranges and global climate change: Chicken or egg?. *Nature* 346: 29–34.

Molnar P, Houseman GA, and Conrad CP (1998) Rayleigh-Taylor instability and convective thinning of mechanically thickened lithosphere: Effects of non-linear viscosity decreasing exponentially with depth and horizontal shortening of the layer. *Geophysical Journal International* 133: 568–584.

Montgomery DR and Stolar DB (2006) Reconsidering Himalayan river anticlines. *Geomorphology* 82: 4–15.

Motagh M, Tavakoli F, Djamour Y, Arabi S, and Zscau J (2005) Coseismic deformation from the 2003 $M_w = 6.5$ BAM earthquake as constrained by the InSAR and precise levelling data. *Geophysical Research Abstracts* 7, SRef-ID: 1607-7962/gra/EGU1605-A-01069.

Mound JE, Mitrovica JX, and Forte AM (2003) The equilibrium form of a rotating Earth with an elastic shell. *Geophysical Journal International* 152: 237–241.

Mouthereau F, Watts AB, and Burov E (2013) Structure of orogenic belts controlled by lithospheric age. *Nature Geoscience* 6: 785–789. http://dx.doi.org/10.1038/NGEO902.

Müller RD, Roest WR, Royer J-Y, Gahagan LM, and Sclater JG (1997) Digital isochrons of the world's ocean floor. *Journal of Geophysical Research* 102: 3211–3214.

Mutter CZ and Mutter JC (1993) Variations in thickness of layer 3 dominate oceanic crustal structure. *Earth and Planetary Science Letters* 117: 295–317.

Nakiboglu SM and Lambeck K (1983) A reevaluation of the isostatic rebound of Lake Bonneville. *Journal of Geophysical Research* 88: 439–447.

Nishimura T and Thatcher W (2003) Rheology of the lithosphere inferred from postseismic uplift following the 1959 Hebgen Lake earthquake. *Journal of Geophysical Research* 108: B8. http://dx.doi.org/10.1029/2002JB002191.

Nur A and Mavko G (1974) Postseismic viscoelastic rebound. *Science* 183: 204–206.

British Oceanographic Data Centre (2003) The GEBCO digital atlas, Centenary edition (CD-ROM), *Liverpool*.

Okada Y (1985) Surface deformation due to shear and tensile faults in a half-space. *Bulletin of the Seismological Society of America* 75: 1135–1154.

Panasyuk SV and Hager BH (2000a) Inversion for mantle viscosity profiles constrained by dynamic topography and the geoid, and their estimated errors. *Geophysical Journal International* 143: 821–836.

Panasyuk SV and Hager BH (2000b) Models of isostatic and dynamic topography, geoid anomalies and their uncertainties. *Journal of Geophysical Research* 105: 28,199–28,209.

Parker RL (1973) The rapid calculation of potential anomalies. *Geophysical Journal of the Royal Astronomical Society* 31: 447–455.

Parsons BE and Daly S (1983) The relationship between surface topography, gravity anomalies, and temperature structure of convection. *Journal of Geophysical Research* 88: 1129–1144.

Parsons B and Sclater JG (1977) Ocean floor bathymetry and heat flow. *Journal of Geophysical Research* 82: 803–827.

Pavlis NK, Holmes SA, Kenyon SC, and Factor JK (2008) An Earth gravitational model to degree 2160: EGM2008. In: *EGU General Assembly 2008, Vienna, Austria, April 13–18* .

Peltier WR, Shennan I, Drummond R, and Horton B (2002) On the postglacial isostatic adjustment of the British Isles and the shallow viscoelastic structure of the Earth. *Geophysical Journal International* 148: 443–475.

Pérez-Gussinyé M and Reston TJ (2001) Rheological evolution during extension at nonvolcanic rifted margins: Onset of serpentinization and development of detachments leading to continental breakup. *Journal of Geophysical Research* 106: 3961–3975.

Pérez-Gussinyé M and Watts AB (2005) The long-term strength of Europe and its implications for plate-forming processes. *Nature* 436: 381–384. http://dx.doi.org/10.1038/nature03854.

Petit C, Deverche J, Calais E, San'kov V, and Fairhead D (2002) Deep structure and mechanical behavior of the lithosphere in the Hangai–Hovsgol region, Mongolia: New constraints from gravity modeling. *Earth and Planetary Science Letters* 197: 133–149. http://dx.doi.org/10.1016/S0012-821X(02)00470-3.

Pollack HN, Hurter SJ, and Johnson JR (1993) Heat flow from the Earth's interior: Analysis of the Global Data Set. *Reviews of Geophysics* 31: 267–280.

Pollitz FF (1997) Gravitational viscoelastic postseismic relaxation on a layered spherical Earth. *Journal of Geophysical Research* 102: 17921–17941.

Pollitz FF (2001) Viscoelastic shear zone model of a strike-slip earthquake cycle. *Journal of Geophysical Research* 106: 26541–26560. http://www.2001JB000342.

Pollitz FF, Burgmann R, and Segall P (1998) Joint estimation of afterslip rate and postseismic relaxation following the 1989 Loma Prieta earthquake. *Journal of Geophysical Research* 103: 26975–26992.

Pollitz FF, Peltzer G, and Burgmann R (2000) Mobility of continental mantle: Evidence from postseismic geodetic observations following the 1992 Landers earthquake. *Journal of Geophysical Research* 105: 8035–8054.

Pollitz FF, Wicks C, and Thatcher W (2001) Mantle flow beneath a continental strike-slip fault: Postseismic deformation after the 1999 Hector Mine earthquake. *Science* 293: 1814–1818.

Reilinger RE, Ergintav S, Bürgmann R, et al. (2000) Coseismic and postseismic fault slip for the 17 August 1999, M = 7.5, Izmit, Turkey earthquake. *Science* 289: 1519–1524. http://www.1510.1126/science.1289.5484.1519.

Roddaz M, Baby P, Brusset S, Hermoza W, and Darrozes JM (2005) Forebulge dynamics and environmental control in Western Amazonia: The case study of the Arch of Iquitos (Peru). *Tectonophysics* 399: 87–108.

Rodger M, Watts AB, Greenroyd CJ, Peirce C, and Hobbs RW (2006) Evidence for unusually thin oceanic crust and strong mantle beneath the Amazon Fan. *Geology* 34: 1081–1084. http://www.1010.1130/G22966A.22961.

Sacek V and Ussami N (2009) Reappraisal of the effective elastic thickness for the sub-Andes using 3-D finite element flexural modelling, gravity and geological constraints. *Geophysical Journal International* 179: 778–786.

Sandwell DT and Schubert G (1982) Lithospheric flexure at fracture zones. *Journal of Geophysical Research* 87: 4657–4667.

Sandwell DT and Smith WHF (1997) Marine gravity anomaly from Geosat and ERS-1 satellite altimetry. *Journal of Geophysical Research* 102: 10039–10054.

Savage JC (2000) Viscoelastic coupling model for the earthquake cycle driven from below. *Journal of Geophysical Research* 105: 25525–25532.

Savage JC and Burford RO (1973) Geodetic determination of relative plate motion in Central California. *Journal of Geophysical Research* 78: 832–845.

Savage JC and Prescott WH (1978) Asthenosphere readjustment and the earthquake cycle. *Journal of Geophysical Research* 83: 3369–3376.

Savage JC, Svarc JL, and Yu S-B (2005) Postseismic relaxation and transient creep. *Journal of Geophysical Research* 110. http://dx.doi.org/10.1029/2005JB003687.
Searle RC, Francheteau J, and Cornaglia B (1995) New observations on mid-plate volcanism and the tectonic history of the Pacific plate, Tahiti to Easter microplate. *Earth and Planetary Science Letters* 131: 395–421.
Searle MP, Law RD, and Jessup MJ (2006) Crustal structure, restoration and evolution of the Greater Himalaya in Nepal-South Tibet: Implications for channel flow and ductile extrusion of the middle crust. *Journal of the Geological Society of London* 268: 355–378.
Shen F, Royden LH, and Burchfiel BC (2001) Large-scale crustal deformation of the Tibetan Plateau. *Journal of Geophysical Research* 106: 6793–6816.
Shennan I and Horton B (2002) Holocene land- and sea-level changes in Great Britain. *Journal of Quaternary Science* 17: 511–526.
Shennan I, Lambeck K, Horton B, et al. (2000) Late Devensian and Holocene records of relative sea-level changes in northwest Scotland and their implications for glacio-isostatic modelling. *Quaternary Science Reviews* 19: 1103–1135.
Shennan I, Lambeck K, Horton B, et al. (2002) Holocene isostasy and relative sea-level changes on the east coast of England. In: Shennan I and Andrews J (eds.) *Land–Ocean Interaction and Environmental Change Around the North Sea*, vol. 166, pp. 275–298. London: Geological Society of London.
Shukowsky W and Mantovani MSM (1999) Spatial variability of tidal gravity anomalies and its correlation with the effective elastic thickness of the lithosphere. *Physics of the Earth and Planetary Interiors* 114: 81–90.
Simons FJ, van der Hilst RD, and Zuber MT (2003) Spatio-spectral localization of isostatic coherence anisotropy in Australia and its relation to seismic anisotropy: Implications for lithospheric deformation. *Journal of Geophysical Research* 108: 2250. http://dx.doi.org/10.1029/2001JB000704.
Sissons JB, Smith DE, and Cullingford RA (1966) Lateglacial and postglacial shorelines in southeast Scotland. *Transactions of the Institute of British Geographers* 39: 9–18.
Sleep NH and Snell NS (1976) Thermal contraction and flexure of mid-continent and Atlantic marginal basins. *Geophysical Journal of the Royal Astronomical Society* 45: 125–154.
Smith GA, Moore JD, and McIntosh WC (2002) Assessing roles of volcanism and basin subsidence in causing Oligocene-Lower Miocene sedimentation in the northern Rio Grande Rift, New Mexico, USA. *Journal of Sedimentary Research* 72: 836–848.
Smith BR and Sandwell D (2004) A three-dimensional semi-analytic viscoelastic model for time-dependent analyses of the earthquake cycle. *Journal of Geophysical Research* 109: B12401. http://dx.doi.org/10.1029/2004JB003185.
Smith BR and Sandwell DT (2006) A model of the earthquake cycle along the San Andreas fault system for the past 1000 years. *Journal of Geophysical Research* 111: B01405. http://dx.doi.org/10.1029/2005JB003703.
Spence DA and Turcotte DL (1979) Viscoelastic damping of cyclic displacements on the San Andreas fault. *Proceedings of the Royal Society of London* 365: 121–144.
Staudigel H, Park KH, Pringle MS, Rubenstone JL, Smith WHF, and Zindler A (1989) The longevity of the south Pacific isotopic and thermal anomaly. *Journal of Geophysical Research* 94: 10501–10523.
Stern TA, Baxter AK, and Baxter PJ (2005) Isostatic rebound due to glacial erosion within the Transantarctic Mountains. *Geology* 33: 221–224.
Stern TA, Quinlan GM, and Holt WE (1992) Basin formation behind an active subduction zone: Three-dimensional flexural modelling of Wanganui basin, New Zealand. *Basin Research* 4: 197–214.
Stewart J and Watts AB (1997) Gravity anomalies and spatial variations of flexural rigidity at mountain ranges. *Journal of Geophysical Research* 102: 5327–5352.
Stewart J, Watts AB, and Bagguley J (2000) Three-dimensional subsidence analysis and gravity modelling of the continental margin offshore Namibia. *Geophysical Journal International* 141: 724–746.
Tassara A, Swain C, Hackney R, and Kirby J (2006) Elastic thickness structure of South America estimated using wavelets and satellite-derived gravity data. *Earth and Planetary Science Letters* 253: 17–36.
ten Brink US and Watts AB (1985) Seismic stratigraphy of the flexural moat flanking the Hawaiian Islands. *Nature* 317: 421–424.
Trivedi D, Singh Y, Maji TK, Kandpal SC, and Nair RR (2012) A new assessment of the elastic thickness (T_e) structure of the Indian shield, and its implications. *Annals of Geophysics* 55: 273–281. http://dx.doi.org/10.4401/ag-5172.
Tushingham AM and Peltier WR (1991) Ice-3G: A new global model of late Pleistocene deglaciation based upon geophysical predictions of post-glacial relative sea level change. *Journal of Geophysical Research* 96: 4497–4523.
van den Berg J, van de Wal, RSW, and Oerlemans J (2006) Recovering lateral variations in lithospheric strength from bedrock motion data using a coupled ice sheet-lithosphere model. *Journal of Geophysical Research* 111: D11104. http://dx.doi.org/10.1029/2005JB003790.
Vening Meinesz FA (1941) Gravity over the Hawaiian Archipelago and over the Madeira Area. In: *Proceedings of the Koninklijke Nederlandse Academie, Wetensia,* p. 44.
Vergnolle M, Pollitz F, and Calais F (2003) Constraints on the viscosity of the continental crust and mantle from GPS measurements and postseismic deformation models in western Mongolia. *Journal of Geophysical Research* 108: 2502. http://dx.doi.org/10.1029/2002JB002374.
Vinck GE, Morgan WJ, and Wu-Ling Z (1984) Preferential rifting of continents: A source of displaced terranes. *Journal of Geophysical Research* 89: 10072–10076.
Walcott RI (1970a) Isostatic response to loading of the crust in Canada. *Canadian Journal of Earth Sciences* 7: 716–727.
Walcott RI (1970b) Flexural rigidity, thickness, and viscosity of the lithosphere. *Journal of Geophysical Research* 75: 3941–3953.
Walcott RI (1972) Late Quaternary vertical movements in Eastern North America: Quantitative evidence of glacio-isostatic rebound. *Reviews of Geophysics and Space Physics* 10: 849–884.
Wang Y (2001) Heat flow pattern and lateral variations of lithosphere strength in China mainland: Constraints on active deformation. *Physics of the Earth and Planetary Interiors* 126: 121–146.
Watts AB (1978) An analysis of isostasy in the world's oceans. Part 1: Hawaiian-Emperor seamount chain. *Journal of Geophysical Research* 83: 5989–6004.
Watts AB (1988) Gravity anomalies, crustal structure and flexure of the lithosphere at the Baltimore Canyon Trough. *Earth and Planetary Science Letters* 89: 221–238.
Watts AB (1992) The effective elastic thickness of the lithosphere and the evolution of foreland basins. *Basin Research* 4: 169–178.
Watts AB (2001) *Isostasy and Flexure of the Lithosphere*, p. 458. Cambridge: Cambridge University Press.
Watts AB, Bodine JH, and Ribe NM (1980a) Observations of flexure and the geological evolution of the Pacific Ocean basin. *Nature* 283: 532–537.
Watts AB, Bodine JH, and Steckler MS (1980b) Observations of flexure and the state of stress in the oceanic lithosphere. *Journal of Geophysical Research* 85: 6369–6376.
Watts AB and Cochran JR (1974) Gravity anomalies and flexure of the lithosphere along the Hawaiian-Emperor seamount chain. *Geophysical Journal of the Royal Astronomical Society* 38: 119–141.
Watts AB and Daly SF (1981) Long wavelength gravity and topography anomalies. *Annual Review of Earth and Planetary Science Letters* 9: 415–448.
Watts AB, McKerrow WS, and Fielding E (2000) Lithospheric flexure, uplift and landscape evolution in south-central England. *Journal of the Geological Society of London* 157: 1169–1177.
Watts AB, Rodger M, Peirce C, Greenroyd CJ, and Hobbs RW (2009) Seismic structure, gravity anomalies, and flexure of the Amazon continental margin, NE Brazil. *Journal of Geophysical Research* 114: B07103. http://dx.doi.org/10.1029/2008JB006259.
Watts AB, Sandwell DT, Smith WHF, and Wessel P (2006) Global gravity, bathymetry, and the distribution of submarine volcanism through space and time. *Journal of Geophysical Research* 111: B08408. http://dx.doi.org/10.1029/2005JB004083.
Watts AB and Talwani M (1974) Gravity anomalies seaward of deep-sea trenches and their tectonic implications. *Geophysical Journal of the Royal Astronomical Society* 36: 57–92.
Watts AB and ten Brink US (1989) Crustal structure, flexure and subsidence history of the Hawaiian Islands. *Journal of Geophysical Research* 94: 10473–10500.
Watts AB and Zhong S (2000) Observations of flexure and the rheology of oceanic lithosphere. *Geophysical Journal International* 142: 855–875.
Watts AB, Zhong SJ, and Hunter J (2013) The behavior of the lithosphere on seismic to geologic timescales. *Annual Review of Earth and Planetary Sciences* 41: 443–468. http://dx.doi.org/10.1146/annurev-earth-042711-105457.
Wessel P and Haxby WF (1990) Thermal stresses, differential subsidence, and flexure at oceanic fracture zones. *Journal of Geophysical Research* 95: 375–391.
Wessel P and Smith WHF (1991) Free software helps map and display data. *Eos, Transactions of the American Geophysical Union* 72: 441–446.
West AJ, Fox M, Walker RT, et al. (2013) Links between climate, erosion, uplift, and topography during intracontinental mountain building of the Hangay Dome, Mongolia. *Geochemistry, Geophysics, Geosystems* 14: 5171–5193. http://dx.doi.org/10.1002/2013GC004859.
Wilson C (2004) *Long Wavelength Gravity and Topography Anomalies in the Pacific*, 93 pp. MESc Thesis, Oxford University.
Windley BF (1988) Tectonic framework of the Himalaya, Karakoram and Tibet. In: Shackleton RM, Dewey JF, and Windley BF (eds.) *Tectonic Evolution of the Himalayas and Tibet*, pp. 3–16. London: Philosophical Transactions of the Royal Society of London.

Wright TJ, Parsons BE, Jackson JA, et al. (1999) Source parameters of the 1 October 1995 Dinar (Turkey) earthquake from SAR interferometry and seismic bodywave modelling. *Earth and Planetary Science Letters* 172: 23–37.

Wu Y, Louden KE, Funck T, Jackson HR, and Dehler SA (2006) Crustal structure of the central Nova Scotia margin off eastern Canada. *Geophysical Journal International* 166: 878–906. http://dx.doi.org/10.1111/j.1365-1246X.2006.02991.x.

Wyer P and Watts AB (2006) Gravity anomalies and segmentation at the East Coast, USA continental margin. *Geophysical Journal International* 166: 1015–1038. http://dx.doi.org/10.1111/j.1365-1246X.2006.03066.x: 1015-1038.

Yamasaki T and Houseman GA (2012) The crustal viscosity gradient measured from post-seismic deformation: A case study of the 1997 Manyi (Tibet) earthquake. *Earth and Planetary Science Letters* 351–352: 105–114.

Zhang P-Z, Shen Z, Wang M, et al. (2004) Continuous deformation of the Tibetan Plateau from global positioning system data. *Geology* 32: 809–812.

Zhong S and Davies GF (1999) Effects of plate and slab viscosities on the geoid. *Earth and Planetary Science Letters* 170: 487–496.

6.02 Plate Tectonics

P Wessel, University of Hawaii at Mānoa, Honolulu, HI, USA
RD Müller, University of Sydney, Sydney, NSW, Australia

© 2015 Elsevier B.V. All rights reserved.

6.02.1	**Introduction**	46
6.02.2	**Studies of Relative Plate Motions**	46
6.02.2.1	Determination of the Present-Day Plate Motions	46
6.02.2.2	Techniques Used in Relative Plate Motion Studies	48
6.02.2.2.1	Uncertainties in relative plate rotations	51
6.02.2.2.2	Quantitative implementation of PURs	52
6.02.2.3	Example: Central North and South Atlantic Reconstructions	53
6.02.2.4	The Emergence of Reconstruction Tools	55
6.02.2.5	Diffuse Plate Boundaries	56
6.02.3	**Intraplate Volcanism**	57
6.02.3.1	The Morphology of the Ocean Floor	57
6.02.3.2	Seamount Provinces	59
6.02.3.3	Significance of Seamounts	61
6.02.3.4	The Ages of Seamounts and Oceanic Islands	64
6.02.3.5	Hot Spot Swells	64
6.02.4	**Studies of APMs**	64
6.02.4.1	Plume Theory, Seamount Chains, and the Fixed Hot Spot Hypothesis	64
6.02.4.2	Motion of the African Plate	65
6.02.4.3	Motion of the Pacific Plate	66
6.02.4.4	Quantitative Methods for Reconstructing APMs	66
6.02.4.4.1	The hot-spotting technique	68
6.02.4.4.2	PFRM: the polygonal finite rotation method	69
6.02.4.4.3	Moving hot spots	69
6.02.4.4.4	OMS: a modified Hellinger criterion for absolute plate rotations	70
6.02.4.4.5	Uncertainty in hot spot reconstructions using the OMS method	70
6.02.4.4.6	WHK: a hot-spotting–PFRM hybrid method	72
6.02.4.4.7	Comparison of the OMS and WHK modeling techniques	77
6.02.4.5	Global Ocean Basin Reconstructions	77
6.02.4.6	APM Models, Paleomagnetics, and TPW	79
6.02.5	**Driving Forces of Plate Tectonics**	84
6.02.5.1	Ridge Push	84
6.02.5.2	Slab Pull	84
6.02.5.3	Collisional Forces	86
6.02.5.4	Basal Shear Traction	86
6.02.5.5	Trench Suction	86
6.02.5.6	Plume Push	86
6.02.5.7	What Drives Plate Tectonics?	86
6.02.6	**Future Challenges**	88
Acknowledgments		88
References		88

Glossary

Hot-spotting A technique by Wessel and Kroenke (1997) that uses seafloor flow lines to infer hot spot locations.
OMS Modeling technique of O'Neill et al. (2005).
PFRM Polygonal finite rotation method of Harada and Hamano (2000).
WHK Hybrid modeling technique of Wessel et al. (2006).
WK97 An APM model proposed by Wessel and Kroenke (1997).

Abbreviations

APM	Absolute plate motion
APW	Apparent polar wander
GPS	Global Positioning System
PURs	Partial uncertainty rotations
RPM	Relative plate motion
TPW	True polar wander
VLBI	Very long baseline interferometry

6.02.1 Introduction

In geologic terms, a plate is defined based on mechanical and rheological arguments. The plate is that part of the outer shell of the Earth that moves coherently as a rigid body without significant internal deformation over geologic timescales. The word tectonics comes from the Greek root 'to build.' By combining these two words, we get the term plate tectonics, which refers to how the Earth's surface is composed of rigid plates that are moving relative to one another on top of hotter, more mobile mantle material. The idea of a lithosphere, representing a strong, outer layer of the Earth overlying a weak asthenosphere, was first introduced by Barrell (1914), long before the realization that the outer shell of the Earth forms a thermal boundary layer of a convecting system. The rise of the plate tectonic hypothesis led to the view that mid-ocean ridges may be associated with a cold, strong boundary layer and that trenches were sites where boundary layers became detached from the surface, being recycled back into the Earth's mantle (e.g., McKenzie, 1969). This approach led to some of the first successful attempts to create relatively simplistic, linear models for mantle convection (e.g., McKenzie et al., 1973), which agreed remarkably well with observations of bathymetry and heat flow from the ocean basins (Sclater and Francheteau, 1970; Sclater et al., 1971).

The concept of seafloor spreading was originally proposed by Hess (1962) and Dietz (1961) who suggested that new seafloor is created at mid-ocean ridges, spreads away from them as it ages, and is subducted at trenches. This idea borrowed some concepts from the much earlier (and in hindsight prescient) model suggested by Arthur Holmes (1944). Building on Hess and Dietz's contributions to understanding seafloor spreading and subduction, a major contribution came from Wilson (1965), who developed the concept of plates and transform faults. He suggested that the active mobile belts on the surface of the Earth are not isolated but continuous and that these mobile belts, marked by active seismicity, separate the Earth into a rigid set of plates. These active mobile belts consist of ridges where plates are created, trenches where plates are destroyed, and transform faults, which connect the other two belts to each other. **Figures 1** and **2** show bathymetry, modern ship track coverage, and gridded magnetic anomalies in two areas that served as keys for developing the seafloor spreading hypothesis in the North Atlantic (Heirtzler et al., 1968) and the East Pacific (Menard, 1964) oceans.

Central to the theory of plate tectonics is the concept of internal rigidity of tectonic plates together with Euler's theorem, which allows us to model the relative motion of plates quantitatively. All plates can be viewed as rigid caps on the surface of a sphere. The motion of a plate can be described by a rotation about a virtual axis that passes through the center of the sphere (Euler's theorem). In terms of the Earth, this implies that an angular velocity vector originating at the center of the globe can describe motions of plates. The most widespread parameterization of such a vector is using latitude and longitude to describe the location where the rotation axis cuts the surface of the Earth and a rotation rate that corresponds to the magnitude of the angular velocity (in degrees per million years or microradians per year). The latitude and longitude of the angular velocity vector constitute 'Euler's pole.'

The formal hypothesis of plate tectonics states that the Earth is envisioned as an interlocking internally rigid set of plates in constant motion. These plates are rigid except at plate boundaries, which are lines between contiguous plates. The relative motion between plates gives rise to earthquakes; these earthquakes in turn define the plate boundaries. There are three types of plate boundaries: (1) divergent boundaries, where new crust is generated as the plates diverge; (2) convergent boundaries, where crust is destroyed as one plate dives beneath another; and (3) transform boundaries, where crust is neither produced nor destroyed as the plates slide horizontally past each other. Not all plate boundaries are as simple as the main types discussed earlier. In some regions, the boundaries are not well defined because the deformation there extends over a broad belt, a plate-boundary zone (Gordon, 2000). Because plate-boundary zones involve at least two large plates and one or more microplates caught up between them, they tend to have complicated geologic structures and earthquake patterns.

6.02.2 Studies of Relative Plate Motions

6.02.2.1 Determination of the Present-Day Plate Motions

There are a number of different methods that can be used to determine instantaneous rotations for relative plate motions at the present. Such rotations can be described by angular velocity vectors and obey standard vector algebra, that is, the angular velocity vectors ${}_{A}\boldsymbol{\omega}_{B}$ and ${}_{B}\boldsymbol{\omega}_{C}$ describing the rotations of plate B relative to plate A and plate C relative to plate B can simply be added vectorially to obtain ${}_{A}\boldsymbol{\omega}_{C}$, the rotation of plate C relative to plate A. The present-day plate motions can now be measured in real time using satellite technology; hence, they are much better constrained than plate models for the geologic past. The methods used include the following:

1. The orientation of active transform faults between two plates can be used to compute their direction of relative motion. The relative motion of two plates sharing a mid-ocean ridge is assumed to be parallel to the transform faults, because the arcs of the faults are expected to be small circles. This would imply that the rotation pole must lie somewhere on the great circle perpendicular to the small circles defined by the transform faults. Hence, if two or more transform faults between a plate pair are used, the

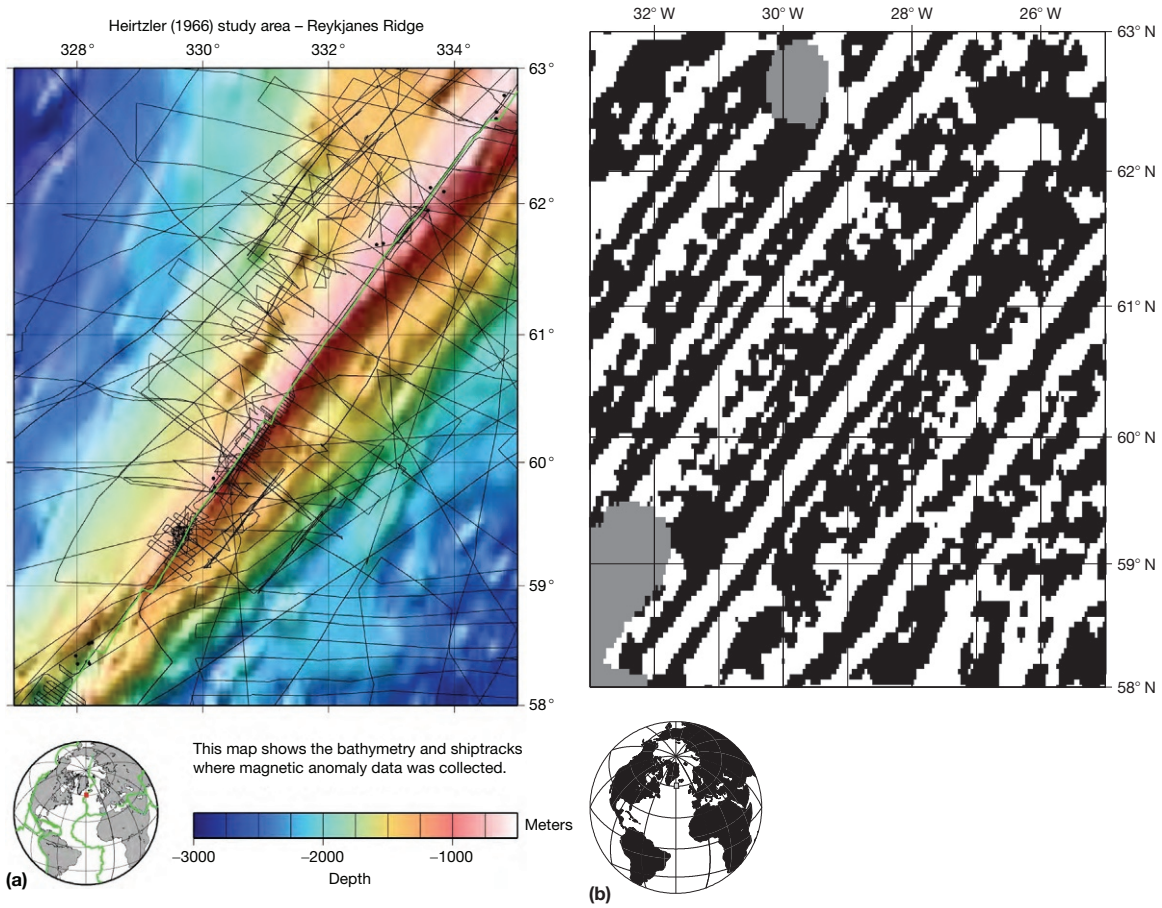

Figure 1 Gridded magnetic anomalies (b) based on magnetic anomaly ship track coverage in the National Geophysical Data Center (NGDC) database south of Iceland (a), a key area for plate tectonic theory development (Heirtzler et al., 1968). Black corresponds to magnetic anomalies due to a normal and white to a reversely polarized field (b).

intersection of the great circles approximates the position of the rotation pole (e.g., Morgan, 1968).

However, the reality of how well transform faults represent small circles about rotation poles has been found to deviate from plate tectonic theory for a number of reasons. For example, Müller and Roest (1992) investigated the North Atlantic Ocean to determine how well the azimuths of mapped ridge offsets correlate with small circles of synthetic fracture zone flow lines. They used gravity anomaly profiles obtained from satellite altimetry data to locate a large number of fracture zones as well as extinct spreading ridges and V-shaped structures and evaluated the agreement between the mapped fracture zones and synthetic flow lines as predicted from plate models for the opening of the North, central North, and South Atlantic. The geometry of many small- and medium-offset fracture zones indicates that the ridge axis discontinuities that produce them can migrate along the ridge, causing off-axis traces that deviate from tectonic flow lines. Recently, a global digital community dataset of oceanic fracture zones and other seafloor discontinuities was published by Matthews et al. (2011).

2. The spreading rates along a mid-ocean ridge as determined from magnetic anomaly patterns can be used to compute a rotation pole, since the spreading rate varies as the sine of the colatitude (i.e., angular distance) from the rotation pole. **Figure 3** illustrates a revised digital isochron chart of the ocean floor, based on Müller et al. (2008).
3. Fault plane solutions (focal mechanisms) of earthquakes at plate boundaries can be utilized to compute the direction of relative motion between plates. Only the location of the pole, but not the spreading rate, can be determined this way. A global model for current plate motions based on data of types (1)–(3) has been constructed and reviewed by DeMets et al. (2010).
4. Geologic markers are used along plate boundaries on land, in particular along strike-slip faults, to determine the neotectonic local relative motion. Markers used include streambed channels, roads, and field boundaries that have been offset by strike-slip motion.
5. A method that has been in use for quite a while is called very long baseline interferometry (VLBI). In this method, quasars are used for the signal source and terrestrial radio telescopes as the receivers. The difference in distance between two telescopes is measured over a period of years.
6. Satellites have made it possible to measure the present-day plate motions in real time at many more stations than

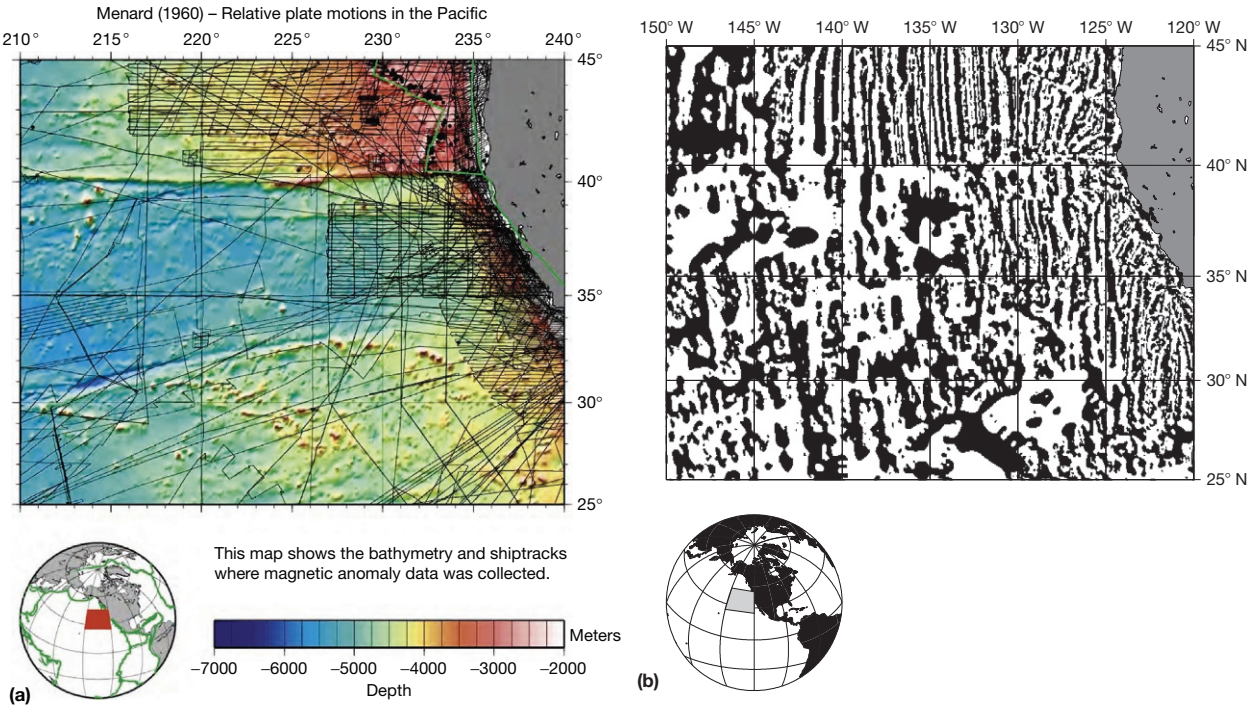

Figure 2 Gridded magnetic anomalies (b) based on magnetic anomaly ship track coverage in the NGDC database in the northeast Pacific, another key area for plate tectonic theory development (Menard, 1964) (a). Black corresponds to magnetic anomalies due to a normal and white to a reversely polarized field (b).

possible using the VLBI technique, which depends on permanent radio telescopes as the receivers. Satellite laser ranging techniques using the Global Positioning System (GPS) have been used very successfully recently to measure plate motions all over the world, especially in areas that are subject to earthquake hazards (see **Chapter 3.11**). GPS measurements are based on 24 satellites, resulting in full GPS coverage for navigation purposes anywhere in the oceans and providing opportunities better than ever before to monitor plate motions in real time with high-precision receivers. A survey time of about 1–2 years is sufficient to obtain a value outside of the error range. Using VLBI and GPS data jointly together with data such as SLR and DORIS (Argus et al., 2010) offers the possibility for rigorous kinematic analysis of regional deformation and strain accumulation along faults – however, this type of model derived from space-geodetic data over a few decades and differs significantly from the corresponding angular velocities averaged over several millions of years. A current plate motion model based solely on GPS data was constructed by Kogan and Steblov (2008); based on just a few decades of data, it differs significantly from the corresponding angular velocity averaged over the past 3.2 Myr, such as those of the MORVEL model (DeMets et al., 2010).

6.02.2.2 Techniques Used in Relative Plate Motion Studies

Unlike recent (instantaneous) plate motion, past plate motions require the use of finite rotations whose manipulation is considerably more complex. Some of the earliest quantitative efforts to model plate kinematics involved the fitting of coastlines on either side of the Atlantic by Bullard et al. (1965), who proposed a computer-generated prebreakup fit of the continents. Their fitting technique was based on the minimization of gaps and overlaps of isobaths that were assumed to be representative of the boundaries between continental crust and oceanic crust. A more advanced method is the Hellinger (1981) method that is based on fitting magnetic anomaly and fracture zone data. In this method, combined magnetic and fracture zone data are regarded as points on conjugate isochrons, which are considered to be great-circle segments. Even though fracture zones should ideally be represented by small-circle segments, the difference between short small and great-circle segments is negligible, and great-circle segments are computationally easier to handle. The best-fit reconstruction is computed by minimizing the sum of the misfits of conjugate sets of magnetic anomaly and fracture zone data points with respect to individual great-circle segments. Using this method, both the resulting rotation pole and the sum of the misfits depend critically on correctly identifying conjugate data points that belong to a common isochron segment. This represents a certain disadvantage compared with the method suggested by McKenzie and Sclater (1971), which minimizes the misfit area between two isochrons. In practice, the application of the Hellinger criterion of fit poses no problem, as observational errors are associated with individual data points, thus covering the relative differences in uncertainty between different groups of observations, for instance, magnetic crossings based on older, badly navigated cruises as compared with recent GPS-navigated cruises. Also, rotation poles have been published for most plates describing their late Cretaceous/Tertiary history of motion; therefore, an estimate for an initial rotation is always available.

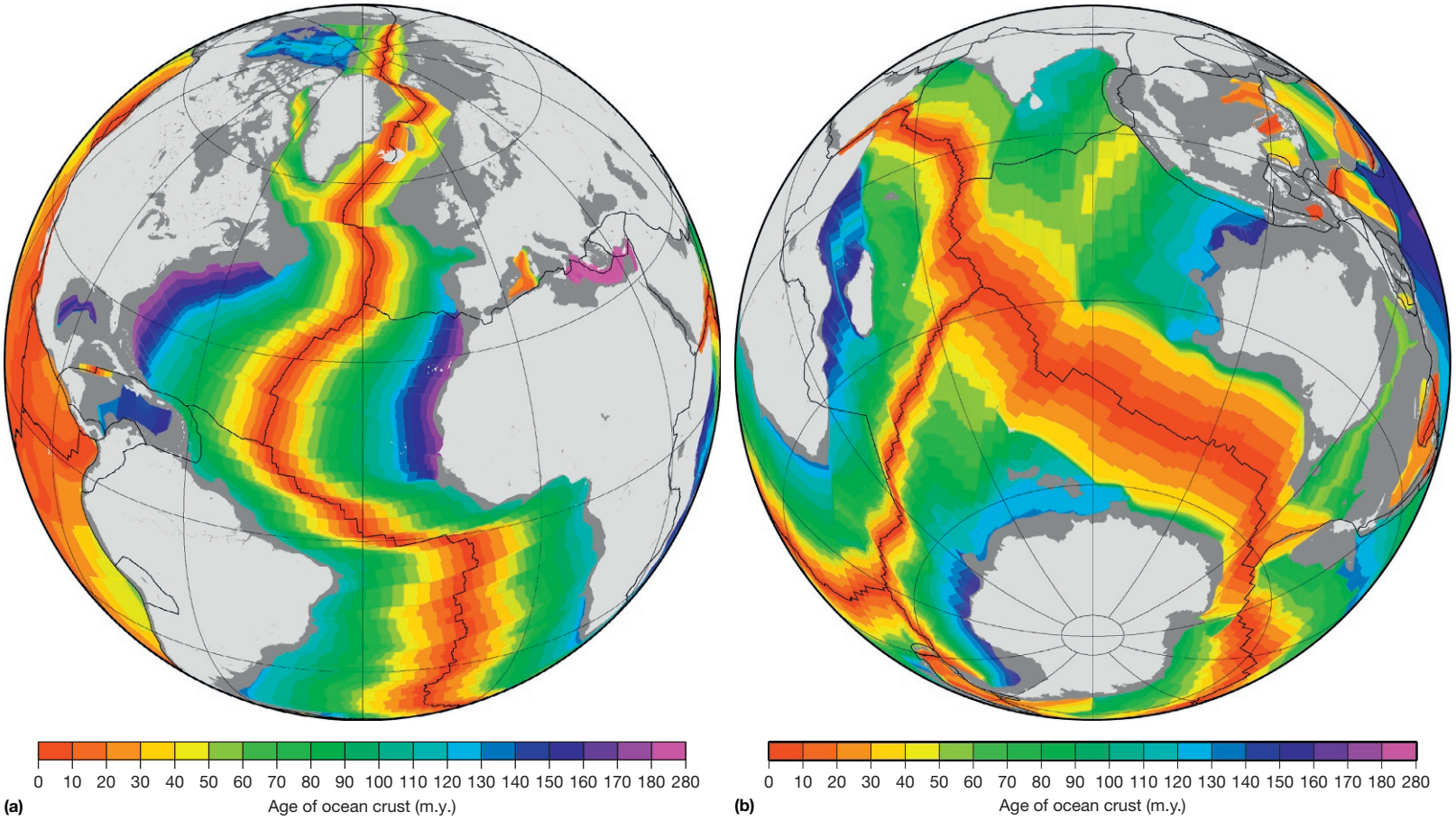

Figure 3 (Continued)

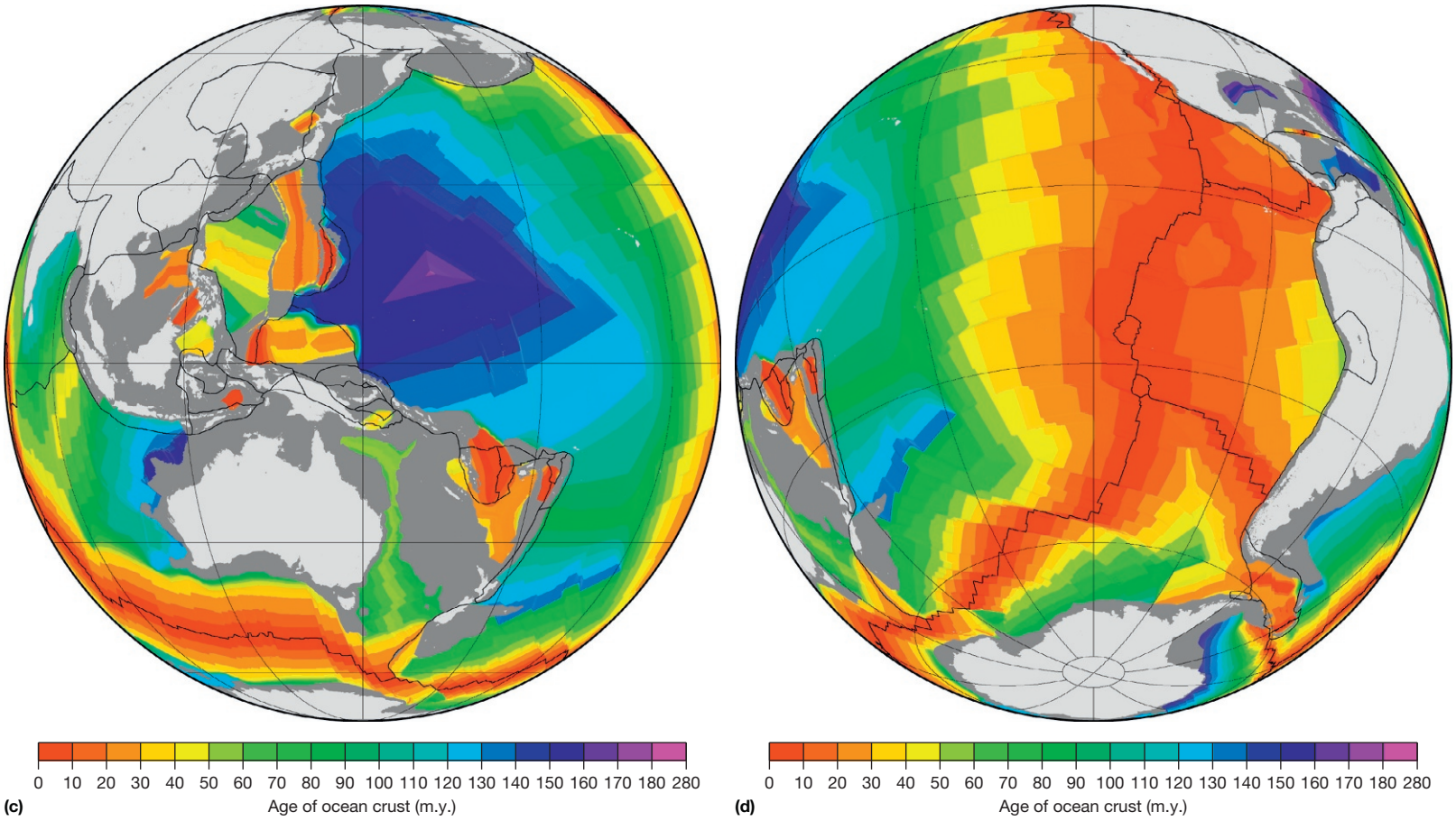

Figure 3 Revised age of the global ocean floor from Müller et al. (2008) with plate boundaries from Bird (2003) overlain. (a) Atlantic Ocean view, (b) Indian Ocean view, (c) West Pacific view, (d) East Pacific view.

Data from one plate (plate 2) are rotated to fit the data on another plate (plate 1) using the rotation $\hat{\mathbf{A}}$, an estimate of the true rotation $\mathbf{A}$ (Figure 4). This rotation is determined by minimizing the sum of the data misfits to great-circle segments.

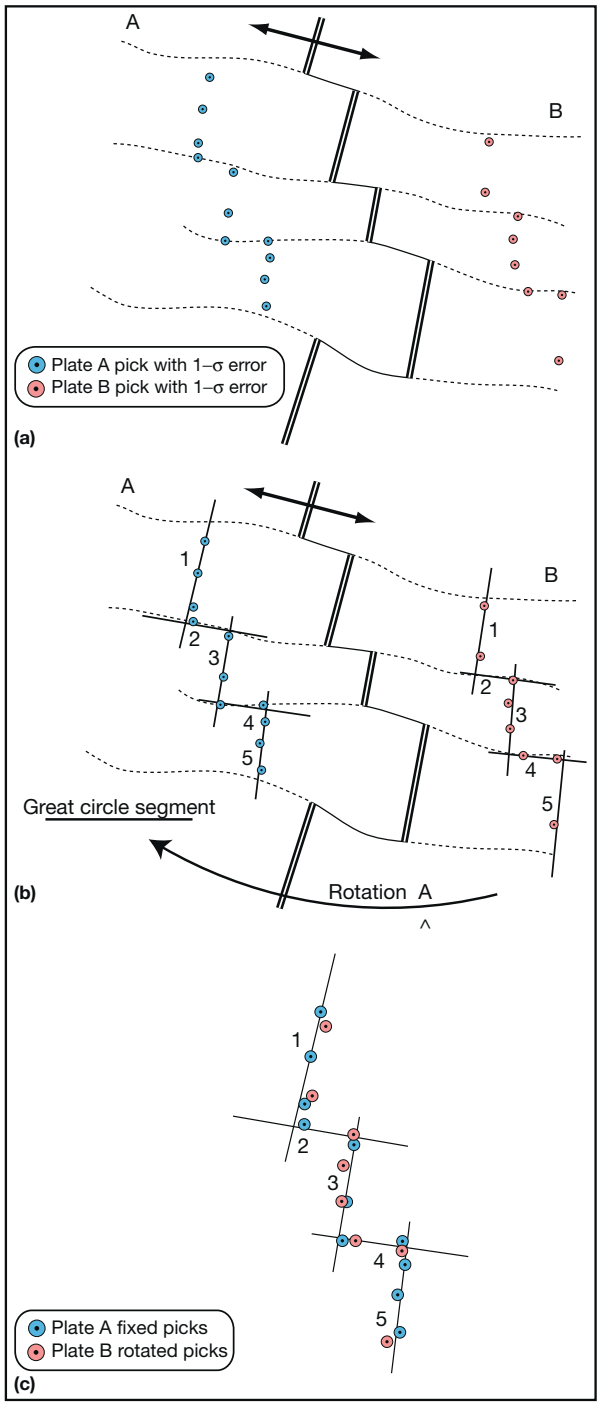

Figure 4 The Hellinger criterion of fit: (a) magnetic picks from two plates are identified, (b) conjugate picks are grouped, (c) data from one plate. Data from one plate (plate 2) are rotated to fit the data on another plate (plate 1) using the rotation $\hat{\mathbf{A}}$, an estimate of the true rotation $\mathbf{A}$. This rotation is determined by minimizing the sum of the data misfits to great-circle segments.

For a more comprehensive overview of fitting methodologies for tectonic reconstructions, see Matias et al. (2005). In terms of determining relative plate motions based on oceanic data, magnetic anomalies and fracture zones are critical.

6.02.2.2.1 Uncertainties in relative plate rotations

Plate kinematicists try to establish a relationship between their model parameters and the goodness of fit of the model with respect to the data. In the case of plate rotations, the model is given by a rotation, which may be represented by a three-dimensional (3-D) Cartesian unit vector (x, y, z), describing the location, and an angle (ω), corresponding to the length of this vector. In turn, the misfits of the data can be described by small Cartesian vectors, which correspond to an uncertainty ellipse about the rotation pole. Hence, the model is described by four parameters (x, y, z, ω) and the misfit in the data by three parameters (x, y, z).

This problem is conceptually similar to projecting the 3-D surface of the Earth onto a 2-D flat map surface. In the case of maps, the projection is not linear, that is, the projection cannot be accomplished without distortions unless one takes an area so small that the curvature of the Earth is negligible. Equivalently, the relationship between a rotation pole and the misfit of the data from two tectonic plates is only approximately linear for very small rotation angles. The reason is that rotations do not comprise a linear subspace in any Euclidean space. This causes a problem for calculating uncertainties of rotations, since the concepts of expected value and statistical parameters such as mean and variance require the fitted parameter to vary over some linear subspace.

Therefore, it would be impossible to establish a direct relationship between finite total reconstruction poles and misfits in the data, because this relationship is highly nonlinear with increasing rotation angles. This problem was first recognized by Stock and Molnar (1983), who proposed a recipe for calculating uncertainties in plate rotations in two steps:

1. Reconstruct the data by finding the best-fit reconstruction.
2. Estimate the uncertainties by the so-called partial uncertainty rotations.

Uncertainties of finite plate rotations are assumed to correspond to misfits in the reconstructed data points in terms of small rotations about three different rotation poles, which either misfit fracture zones and magnetic anomalies or skew the fit of all data (Stock and Molnar, 1983). **Figure 5** shows reconstructed magnetic anomaly and fracture zone identifications (crosses and dots represent identifications from two conjugate plates), and large bold dots show the locations of three rotation poles, which are used to express the misfit of the data with respect to isochron segments (ridge and transform segments approximated by great-circle segments).

Molnar and Stock (1985) noted that a measure of the uncertainty of a rotation is how much a small deviatoric rotation, when added to the best-fit rotation, affects the fit of the data. If a small deviatoric rotation significantly degrades the fit of the data, the uncertainty in the rotation is small. Conversely, if a small deviatoric rotation to the best-fit rotation does not significantly degrade the fit, the uncertainty in the rotation is larger. Molnar and Stock (1985) suggested that the best way to

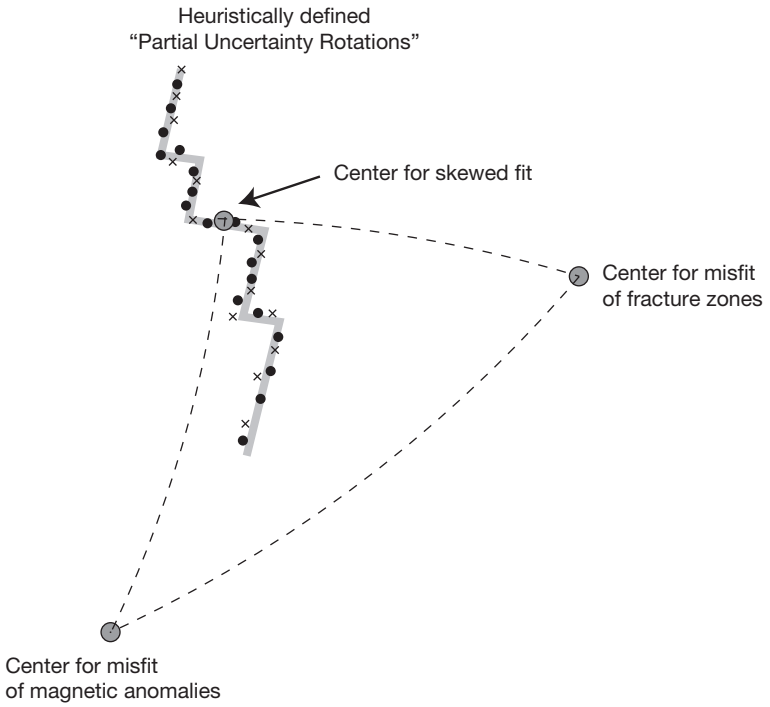

Figure 5 Partial uncertainty rotations. Reconstructed magnetic anomaly and fracture zone identifications (crosses and dots represent identifications from two conjugate plates) and large bold dots show the locations of three rotation poles, which are used to express the misfit of the data with respect to isochron segments (ridge and transform segments approximated by great-circle segments).

parameterize uncertainties in a rotation is by defining a group of small rotations $\Delta\mathbf{A}$, which can be added to the estimated rotation $\hat{\mathbf{A}}$ without significantly degrading the fit. They named the resulting rotations partial uncertainty rotations (PURs; see Figure 5). This eliminates the problem with parameterizing the rotation itself (any parameterization will do), and the problem becomes choosing a parameterization for the group of small rotations $\Delta\mathbf{A}$ that distorts it the least. This formulation is known as a moving parameterization, since rotations close to $\hat{\mathbf{A}}$ are parameterized by their differences from $\hat{\mathbf{A}}$.

6.02.2.2.2 Quantitative implementation of PURs

The method mentioned earlier is heuristic, and it is left to the scientist to decide which misfit is 'acceptable' and which one is 'unacceptable.' Hence, there is a need for an algorithm to rigorously compute uncertainties in plate rotations based on the misfit of the data, the geometry of the plate boundary, and the number of data points. This goal was accomplished by Ted Chang and coworkers (Chang, 1987, 1988; Chang et al., 1990; Kirkwood et al., 1999). In a nutshell, their approach is as follows:

1. Estimate the unknown rotation by minimizing a least squares criterion due to Hellinger (1981). The estimate for the unknown rotation is denoted by $\hat{\mathbf{A}}$.
2. Using a Taylor series centered at $\hat{\mathbf{A}}$, approximate the Hellinger criterion by the error sum squares of a suitable linear regression. As noted earlier, neither the data space, the surface of a sphere, nor the space of rotations is a Euclidean space, and hence, the problem of plate reconstruction is intrinsically nonlinear.
3. Let $\mathbf{A}$ denote the unknown true rotation, and write both $\mathbf{A}$ and $\hat{\mathbf{A}}$ as 3×3 matrices. Hopefully, $\hat{\mathbf{A}}$ is close to $\mathbf{A}$, and $\mathbf{A}^t\hat{\mathbf{A}}$ will be a small rotation. Let $\mathbf{u}$ be a 3 vector such that the direction of $\mathbf{u}$ gives the axis of $\mathbf{A}^t\hat{\mathbf{A}}$ and the length of $\mathbf{u}$ gives the angle of rotation of $\mathbf{A}^t\hat{\mathbf{A}}$. An approximate covariance matrix for $\mathbf{u}$ can be determined by applying standard least squares theory to the approximating linear regression found in step (2). This covariance matrix can be used, using standard statistical approaches, to express the uncertainties in $\mathbf{A}$.

This approach focuses on the deviation $\mathbf{A}^t\hat{\mathbf{A}}$ of the true rotation from the estimate $\hat{\mathbf{A}}$. Since the approximating linear regression is derived using a Taylor series centered at $\hat{\mathbf{A}}$, this approximating regression is naturally expressed in terms of deviations from $\hat{\mathbf{A}}$. This results in a covariance matrix for $\mathbf{u}$, a 3-component vector, which is determined by $\mathbf{A}^t\hat{\mathbf{A}}$, visualized as an ellipsoid (Figure 6). The fundamental insight gained from these concepts and approaches is that the uncertainties in a rotation are best expressed in terms of the deviations of the rotation from the best-fit rotation, not in terms of the error in the best-fit rotation itself.

The choice of parameterization of Chang (1988) is the moving exponential parameterization, based on the three-component vector $\mathbf{u}$. The advantage of the exponential parameterization is that it represents small rotations near the origin with minimal distortion. Parameterizations such as spherical coordinates (λ, θ, ρ) or Euler's angles (α, β, γ) have singularities near the origin and are not suitable for describing small

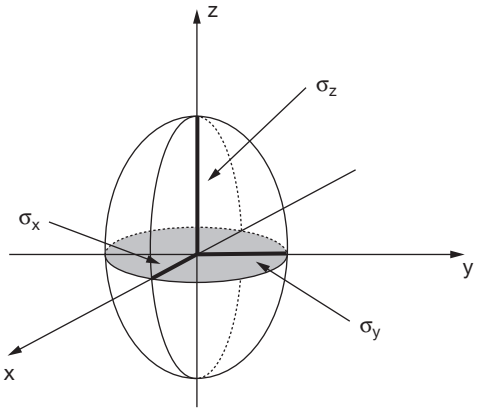

Figure 6 This ellipsoid reflects a fitted rotation uncertainty region expressed by a three-component vector **u** based on a 3×3 covariance matrix (see text for details).

rotations (Chang et al., 1990). The uncertainty of our estimated best-fit rotation is given by the covariance matrix cov (**u**). However, we also have uncertainties associated with our observations, that is, the errors in picking magnetic anomaly and fracture zone locations. The quality factor κ relates the uncertainties assigned to the data ($\hat{\sigma}$) to their true estimates (σ). The estimated factor $\hat{\kappa}$ is related to the uncertainties in the data by $\hat{\kappa} = (\hat{\sigma}/\sigma)^2$. Here, κ is unknown, but a method developed by Royer and Chang (1991) allows us to calculate $\hat{\kappa}$ from the misfit, the geometry of the plate boundary, and the number of data as

$$\hat{\kappa} = \frac{N - 2s - 3}{r}$$

where $N - 2s - 3$ represents the number of degrees of freedom, N is the number of points, s is the number of great-circle segments, and r is the total misfit (sum of squares of the weighted distances). The parameter $\hat{\kappa}$ indicates whether the assigned uncertainties are correct ($\hat{\kappa} \approx 1$), underestimated ($\hat{\kappa} \ll 1$), or overestimated ($\hat{\kappa} \gg 1$).

The confidence region of an estimated best-fit rotation $\hat{\mathbf{A}}$ is a three-dimensional ellipsoid (i.e., the axes are latitude, longitude, and angle). This ellipsoid can be projected onto a latitude–longitude plane using an algorithm described in Hanna and Chang (1990).

Chang (1988) observed that if one considers the eigenvectors of $(\text{cov}(\mathbf{u}))^{-1}$, these describe three axes at 90° to each other. Their respective eigenvalues constrain the maximum permissible rotation θ about these axes that will degrade the fit of the data to a specified limit. These rotations are roughly equivalent to the PURs described by Molnar and Stock (1985) (**Figure 5**). This analogy is useful for understanding what the matrix cov(**u**) actually represents.

6.02.2.3 Example: Central North and South Atlantic Reconstructions

The following example is taken from Müller et al. (1999), who combined magnetic anomaly data in the central North and South Atlantic Oceans with *Seasat* and *Geosat* satellite altimetry data to create a self-consistent dataset of magnetic and fracture zone identifications for the two ocean basins. This work builds on several decades of marine geophysical data collection and related papers in the central North and South Atlantic Oceans (e.g., Cande et al., 1988; Collette et al., 1984; Klitgord and Schouten, 1986; Roest, 1987; Roest et al., 1992; Shaw and Cande, 1990). The finite motion poles and their uncertainties were estimated for 15 times from chron 34 to the present using Chang's inversion method (Chang, 1987, 1988; Chang et al., 1990), allowing a simple parameterization of the rotation uncertainties along a plate circuit path. The rotations and their uncertainties were then combined to model the North–South American history of relative motion, and its effect on Caribbean tectonic history (Müller et al., 1999). The magnetic and fracture zone picks used in this model are shown in **Figures 7** and **8**.

A critical aspect in the reconstruction method is the correct assessment of the uncertainties in the location of the data that will propagate into the uncertainties of the rotation parameters (location of the rotation pole and rotation angle). Following a detailed analysis of the dispersion of magnetic anomaly C5 crossings in the Indian Ocean by Royer et al. (1997) and Müller et al. (1999) assigned $1-\sigma$ nominal uncertainties of 4 km to the magnetic anomaly crossings and of 5 km to fracture zone crossings following the Müller et al. (1991) analysis of depth to basement and geoid data along the Kane Fracture Zone.

Finite rotations for North American–African and South American–African plate motions were computed for 12 times from chron 34 to the present (**Figure 9**). The 95% confidence regions are three-dimensional ellipsoids in latitude, longitude, and rotation angle space. In order to represent them on a map, the ellipsoids are projected onto the latitude–longitude sphere. The projected uncertainty ellipses include uncertainties in latitude, longitude, and angle, but one must keep in mind that the true size of the rotation uncertainties (i.e., ellipsoids), which are described by the covariance matrices, might not be reflected well by their 2-D projection onto the sphere. For instance, in the case of the South Atlantic, the 2-D uncertainty in the location of the chron 5 best-fitting pole appears to be at least 10 times larger than the 2-D uncertainty in the location of the chron 21 rotation pole, whereas the volume of the 95% confidence region for chron 5 rotation is only about three times larger than for the chron 21 rotation (7838 vs. 2773 km^3, respectively). Conversely, the 95% uncertainty volume for chron 8 (19 705 km^3) is 2.5 larger than for chron 5, whereas its 2-D projection is about three times smaller than for chron 5.

The projected rotation confidence regions show a trend from larger uncertainties for younger chrons to more tightly constrained older reconstructions. This simply reflects the fact that when the rotation angle is small, changes in the position of the rotation pole only have small effects on the fit of the data, whereas the converse is true for large rotation angles. Somewhat ironically, older reconstructions are generally better constrained than younger reconstructions, even though this effect can be somewhat offset by relatively larger datasets for younger chrons.

The central North Atlantic and South Atlantic rotations can then be added, one with its angle reversed, to compute North–South American rotations (**Figure 10**). The resulting

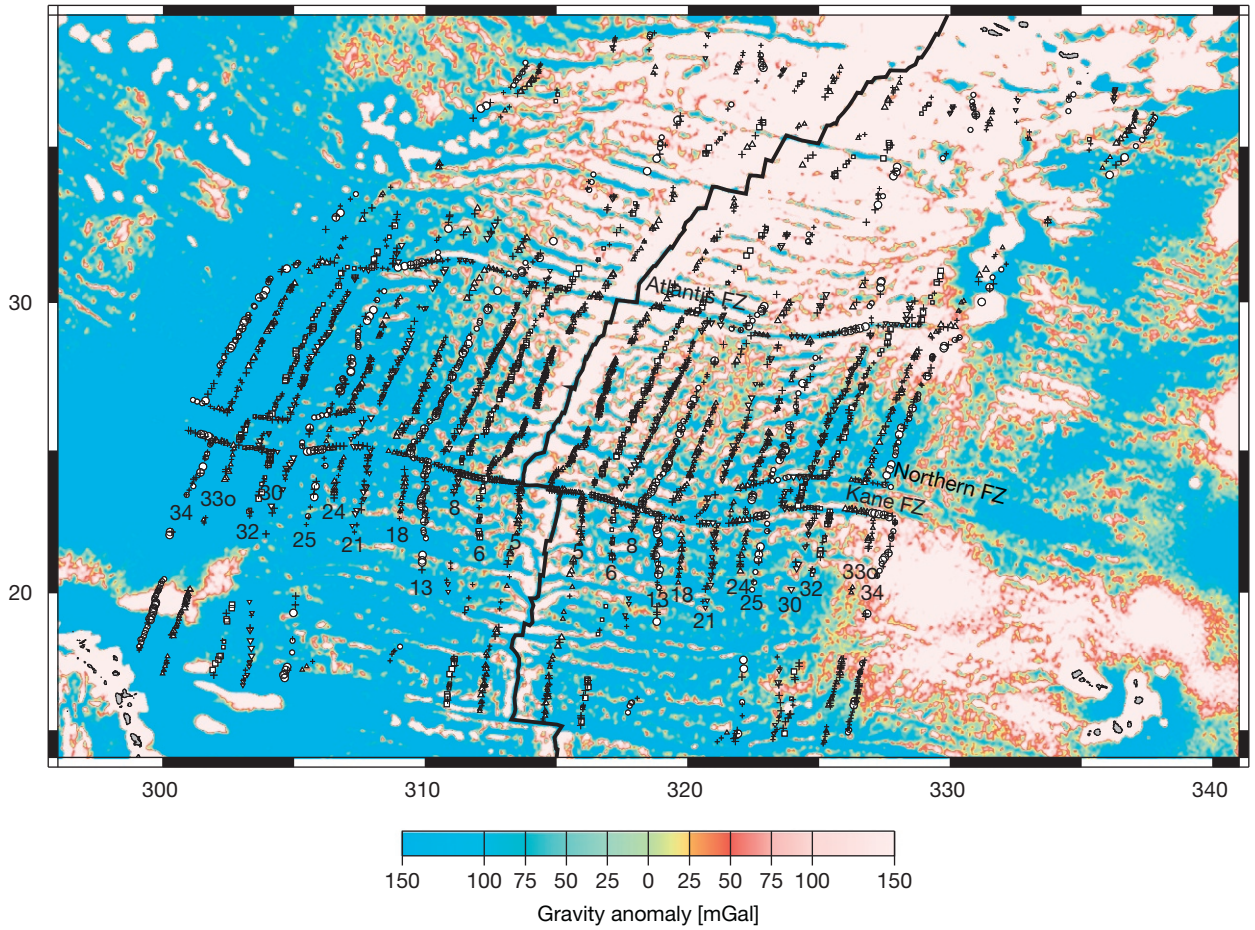

Figure 7 Gravity anomalies from satellite altimetry from Sandwell and Smith's (1997) grid, downward continued to the seafloor (Walter Smith, personal communications, 2006) and interpreted and rotated magnetic anomaly and fracture zone identifications in the central North Atlantic. The unrotated magnetic and fracture zone identifications are identified by the following symbols: triangle (C5, 9.74 Ma; C18, 38.43 Ma; C30, 65.58 Ma), square (C6, 19.05 Ma; C21, 46.26 Ma; C32, 71.59 Ma), upside down triangle (C8, 19.05 Ma; C24, 52.36 Ma; C33o, 79.08 Ma), and circle (C13, 33.06 Ma; C25, 55.90 Ma; C34, 83 Ma). All rotated data points are marked by crosses. Paleoridge or transform segments as defined by magnetic anomaly or fracture zone identifications, approximated as great circles in the inversion method used here, are denoted by alternating small and large symbols.

pole path shows (1) very stable poles of motion from chron 25 to 21 and from chron 18 to 8; (2) an important northward migration of the rotation poles from chron 34 to chron 18; and (3) a southward migration until chron 6. The North American–South American rotation stage poles always lie outside the Caribbean Plate; for the ages younger than chron 25 (55.9 Ma), they lie within or in the vicinity of the North American–South American plate boundary, implying a different sense of motion along strike of this plate boundary.

Figure 11 shows North American–South American plate motion through time, illustrated by the successive motion of three points attached to the North American Plate with respect to the South America Plate for 11 stages from chron 34 (83 Ma) to the present, including uncertainties of the location of rotated points. For each stage rotation vector, a simultaneous 95% confidence region is plotted about the young ends of the relative motion vectors, that is, the ellipse about points at chron 33o reflects the uncertainty for the chron 34–33o stage rotation. A simultaneous confidence region represents the area (on the surface of the Earth) in which a point on a given plate may have been located with equal likelihood for a particular reconstruction time, with 95% confidence. This means that with 95% confidence, there is an equal likelihood that a rotated point may end up anywhere within the 95% confidence region. The simultaneous 95% confidence regions increase in size with increasing distance from the stage pole of motion; in the Caribbean area, they increase in size correspondingly from east to west (Figure 11).

Even though the projected confidence ellipsoids of the finite rotation poles for North American–South American plate motion for chrons 18–6 show large overlaps (Figure 11), the simultaneous 95% confidence regions for the three rotated points shown indicate only little overlap. This may appear puzzling but only reflects the imperfect nature of the 3-D finite rotation pole error ellipsoid projections onto a spherical surface in Figure 10, as discussed before. In other words, this result shows that the covariance matrices and uncertainty ellipsoids for these reconstructions are different enough to distinguish different phases of convergence in the late Tertiary outside of the 95% error bounds. Combined

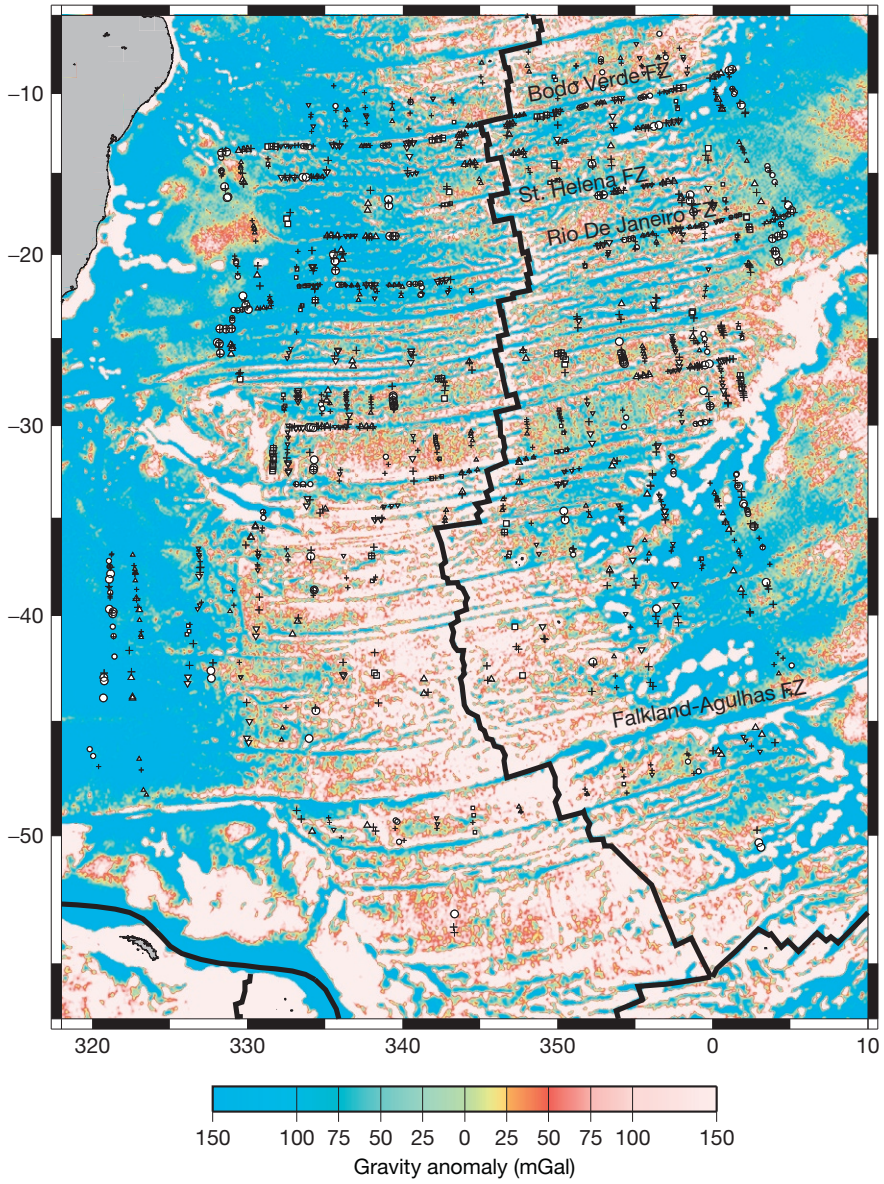

Figure 8 Gravity anomalies from satellite altimetry, downward continued to the seafloor as in **Figure 7** and interpreted and rotated magnetic anomaly and fracture zone identifications in the South Atlantic. The symbols used for plotting magnetic and fracture zone identifications follow the same convention as in **Figure 7**.

magnetic and fracture zone identifications and a rotation model can then be used to construct seafloor isochrons, which in turn can be gridded to produce a continuous map of seafloor ages (**Figure 3**) (Müller et al., 2008).

6.02.2.4 The Emergence of Reconstruction Tools

Traditionally the domain of specialists, the calculation of plate tectonic reconstructions has in recent years become much more accessible to a broad range of Earth scientists, students, and others. A key development is GPlates (www.gplates.org), an open-source paleogeographic information system running on Windows, Linux, and Mac OSX (Boyden et al., 2011; Qin et al., 2012; Williams et al., 2012). It enables the interactive manipulation of plate tectonic reconstructions and the visualization of geodata through geologic time (**Figure 12**). Developed originally as a standalone software, GPlates has gradually grown into an open innovation platform by employing an open standards-based information model, by implementing extensive data import/export capabilities, developing an emerging Python plug-in framework, and establishing links to web services. This extensible platform allows users to explore the evolution of the entire Earth system in accordance with past tectonic plate configurations by combining GPlates with a variety of research tools, data, and workflows. GPlates applications include tectonics, geodynamics, basin evolution, orogenesis, deep Earth resource exploration, paleobiology, paleoceanography, and paleoclimate. We believe such free tools will ultimately lead to the democratization of plate reconstructions.

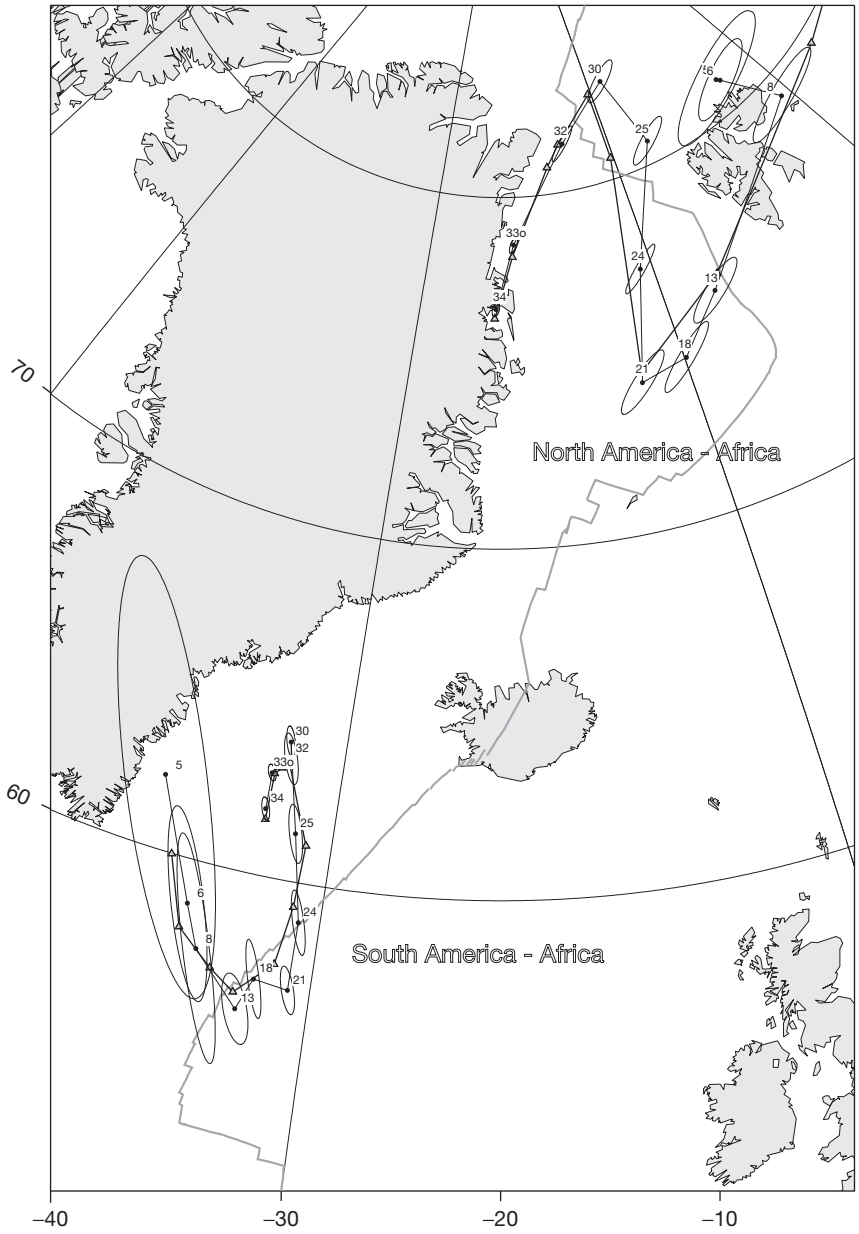

Figure 9 Total reconstruction poles and 95% confidence ellipses for North American–African (upper right) and South American–African (lower left) plate rotations for 12 reconstruction times from chron 34 (83 Ma) to the present. Note the sharp cusp in the North American–African pole path at chron 8 (25.8 Ma), marking a global plate reorganization, expressed, for example, also in the cessation of seafloor spreading in the Adare Trough between East Antarctica and West Antarctica.

6.02.2.5 Diffuse Plate Boundaries

As mentioned, the plate tectonic theory was developed using the approximation of rigid plates moving on a spherical Earth, separated by relatively narrow boundaries where much of the observable deformation is localized (e.g., McKenzie and Parker, 1967; Morgan, 1968; Wilson, 1965). The motions of plates were described with simple Euler's rotations on a sphere, and the motions were discontinuous only at the plate boundaries themselves. To a first approximation, this simplification has worked exceedingly well, particularly in the quest to understand the kinematic evolution of the ocean basins, but as both data and analyses have become more sophisticated, it is clear that there are departures from this simple, cartoonlike picture of how the Earth works. Early assessment of departures from the rigid plate model suggested that distributed deformation might be associated with zones of lithospheric weakness (such as fossil plate boundaries, fracture zones, and other scars in the oceanic lithosphere) (e.g., Bergman and Solomon, 1980; Sager and Keating, 1984; Stein, 1979; Sykes, 1978). However, as data of higher resolution have become available, a more complicated picture has emerged. For instance, the Indo-Australian Plate, once considered to have some weak zones associated with the Ninetyeast Ridge, has been shown to be better

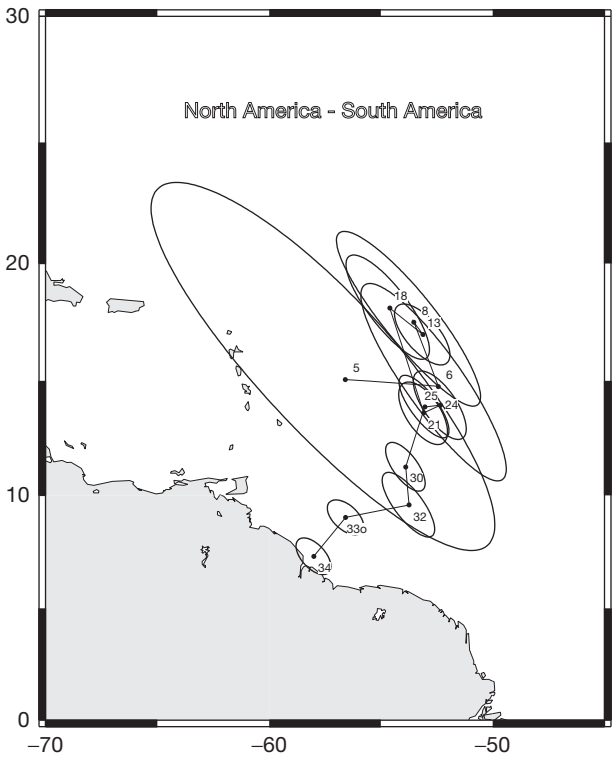

Figure 10 Total reconstruction poles for 12 reconstruction times for North American–South American relative plate motions since chron 34 (83 Ma). These rotations have been computed by combining the finite rotations and their 95% confidence regions shown in **Figure 9**. After Müller RD, Royer JY, Cande SC, Roest WR, and Maschenkov S (1999) New constraints on Carribean plate tectonic evolution. In: Mann P (ed.) *Caribbean Basins*. Amsterdam: Elsevier.

described as a composite plate made up of three-component plates (the Indian, Capricorn, and Australian Plates) separated by diffuse boundaries. Royer and Gordon (1997) coined the terms 'component' and 'composite' plates in order to allow a better description of the actual situation found in the oceans. When compared to predictions of stress modeling, it is seen that areas of high deviatoric compression roughly correspond with regions of observed crustal contraction, whereas areas predicted to have high deviatoric extension correspond to regions where stretching seems to be occurring. In detail, however, much of the deformation within these regions is accommodated by older weaknesses in the crust such as preexisting and reactivated faults (see **Chapter 6.04**) (Gordon, 2000).

The predicament of the Indo-Australian Plate is not unique. Africa, with its well-developed extensional activity in the Great Rift Valley, is now considered a composite plate made up of the two rigid component plates (Nubia and Somalia) (Chu and Gordon, 1999; Gordon, 1998), whereas North and South America can be considered component plates in the large American composite plate. It seems clear that diffuse plate boundaries are sites of strong plate coupling compared with narrow plate boundaries where the decoupling of mechanical properties is more complete; this is reflected in strain rates that are much higher across narrow plate boundaries (Gordon, 2000). **Figure 13** illustrates the distribution of diffuse plate boundaries. Indeed, the lowest strain rates at narrow plate boundaries exceed the upper strain rates from diffuse boundaries by two orders of magnitude. Such partitioning of strain may be a strong argument for describing plate evolution in terms of a non-Newtonian, self-lubricating rheology (e.g., Bercovici, 1993). It is interesting to note that the pole of rotation describing the relative motion between two component plates tends to lie within the diffuse boundary, and Gordon (2000) proposed the term 'convergent–divergent pivot' for such rotations that describes the change from extensional to compressional deformation within the short distance of the diffuse boundary. Work by Zatman et al. (2001, 2005) indicates that the location of such rotation poles within the diffuse boundary is favored by both geometric and rheological arguments.

6.02.3 Intraplate Volcanism

6.02.3.1 The Morphology of the Ocean Floor

In 1963, Tuzo Wilson noted that in certain locations around the world, such as Hawaii, volcanism has been active for very long periods of time (Wilson, 1963). This seemed to indicate that relatively small, long-lasting, and anomalously hot regions – called hot spots by Wilson – existed below the plates in the mantle that would provide localized sources of high heat energy (thermal plumes) to sustain volcanism (see **Chapter 7.10**). Specifically, Wilson hypothesized that the distinctive linear shape of the Hawaiian Island–Emperor seamount chain resulted from the Pacific Plate moving over a deep, stationary hot spot in the mantle, located beneath the present-day position of the Hawaiian Island. More than a hundred hot spots beneath the Earth's crust have been active during the past 10 Myr. Most of these are located under plate interiors (e.g., the African Plate), but some occur near diverging plate boundaries. Some are concentrated near the mid-oceanic ridge system, such as beneath Iceland, the Azores, and the Galápagos Islands. A widely used method of reconstructing plates relative to a fixed mesosphere utilizes linear chains of volcanoes that display age progression and are thought to be caused by focused spots of melting in the upper mantle. We will return to this topic shortly.

While it was the larger seamount chains that caught Wilson's eye, it had been known for some time that the oceans were littered with underwater volcanoes known as seamounts. Following the end of World War II, the rapid expansion of ocean-going expeditions with echo-sounding instruments promoted a major advance in the understanding of seafloor morphology, leading to the realization that the oceans had mountain chains of extraordinary length; this discovery was popularized by the early maps of Lamont Heezen and Tharp (1961, 1964). Also on those maps were the renditions of numerous seamounts. During World War II, Princeton geologist Harry Hess discovered and mapped several flat-topped seamounts that he named guyots; these were apparently former islands that had been eroded down to sea level and later drowned (Hess, 1946). Menard had surveyed many seamounts in the Pacific and suggested that there might be as many as 100 000 seamounts exceeding a height of 1 km in the Pacific

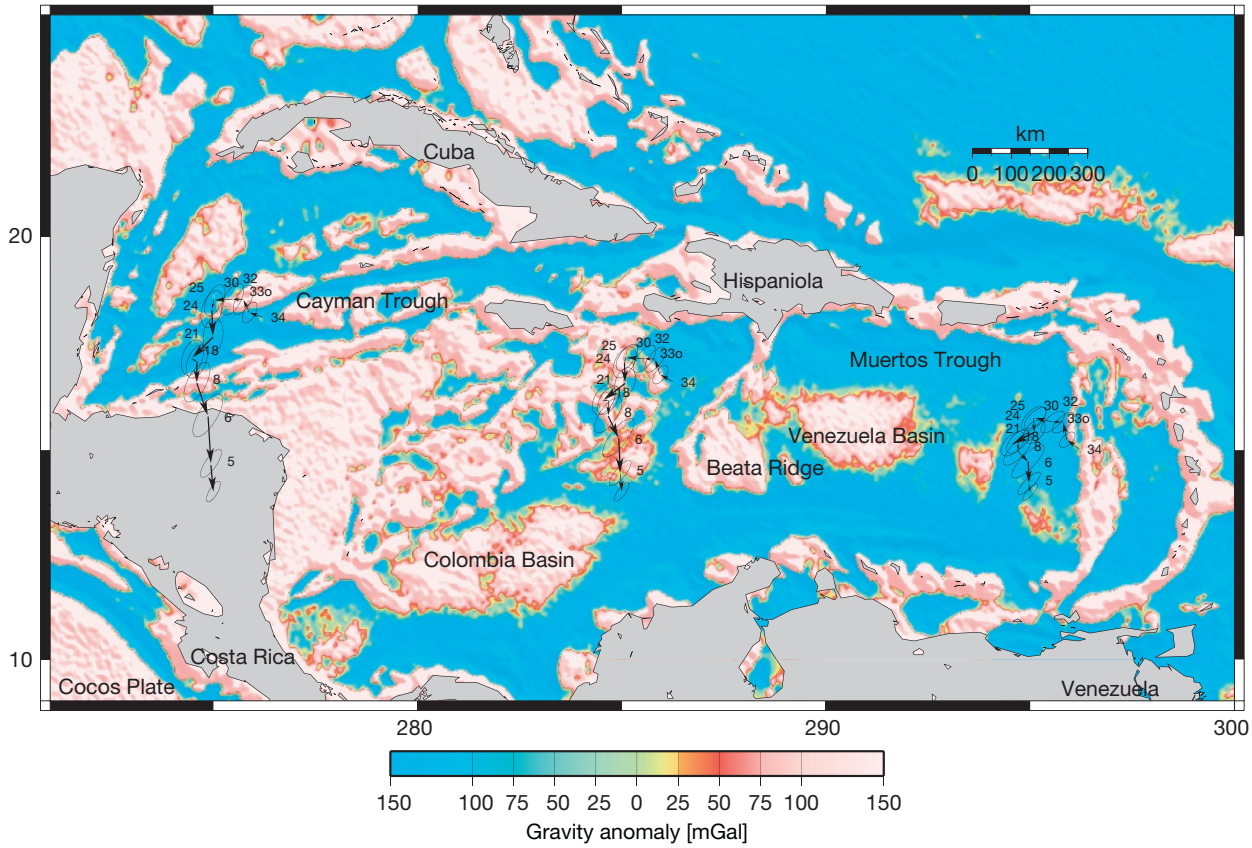

Figure 11 North American–South American plate motion through time of 3 points attached to the North American Plate with respect to the South American Plate for 11 stages from chron 34 (83 Ma) to the present. The simultaneous 95% confidence regions for each stage rotation vector are plotted about the young ends of the relative motion vectors, that is, the ellipse about points at chron 33o reflects the uncertainty for the chron 34–33o stage rotation. This figure demonstrates that this model cannot resolve very slow relative motions between chrons 25 and 24; some overlap between the confidence regions for chrons 32 and 30 and 18 and 13 is also observed. However, all other stage vectors are well resolved.

alone (Menard, 1964). However, because of the vastness of the oceans and the sparse sampling provided by surface ships, the majority of seamounts went uncharted. Most statistical treatments of seamount populations relied on extrapolations from smaller, well-surveyed areas by dense, single-beam echo-sounding tracks or by the improved coverage of the newer multibeam systems. With the advent of satellite altimetry, a new technique became available for the study of seamounts. **Figure 14** illustrates the leaps in resolution afforded by the new space-based techniques. The global gravity maps derived from the *Seasat* altimeter mission by Bill Haxby clearly depicted an impressive richness of seafloor fabric, in particular a plethora of underwater volcanoes (Haxby, 1987; Haxby et al., 1983). Using *Seasat* along-track profiles of sea surface heights, Craig and Sandwell (1988) were the first to undertake a truly global investigation of the seamount distribution, finding around 8500 individual edifices distributed throughout the world's oceans. They were able to confirm that the Pacific Ocean basin hosts the majority of the seamounts and that the western Pacific displays an unusual high density of large seamounts. However, due to the large track spacing (~100 km), many seamounts were only partially surveyed and many more fell within the gaps between tracks. The newer *Geosat*/*ERS-1* data vastly improved the coverage by having much closer track spacing, and by 1997, a new global gravity grid superior to the *Seasat* grids had been provided (Sandwell and Smith, 1997). Using this data, Wessel and Lyons (1997) were able to characterize almost 8900 seamounts in the Pacific Ocean alone, with most of the increase in population coming from smaller, hitherto uncharted seamounts. Wessel (2001) extended this analysis to all oceans, counting a total of almost 14 700 seamounts, later revised to 11 882 (Wessel et al., 2010) due to duplicates (**Figure 15**). Statistical treatment of the observed population suggests that the sizes of seamounts approximately follow a power-law relationship that, when extrapolated below the size of the smallest seamounts that are reliably identified by altimetry, matches Menard's earlier prediction of 100 000 seamounts of at least 1 km in height (**Figure 16**). Marine geologists now routinely study seamounts of much shorter stature (down to a few tens of meters), and if the inferred frequency–size relationship holds for even these smaller seamounts, one would predict a global total of more than one million seamounts, making these morphological features second in ubiquity only to the abyssal hills. Recent work, however, has suggested that the log–log relationship may not hold for smaller sizes, thus reducing the census downward to perhaps just 40–50 000 for seamounts whose heights exceed 100 m (Kim and Wessel, 2011).

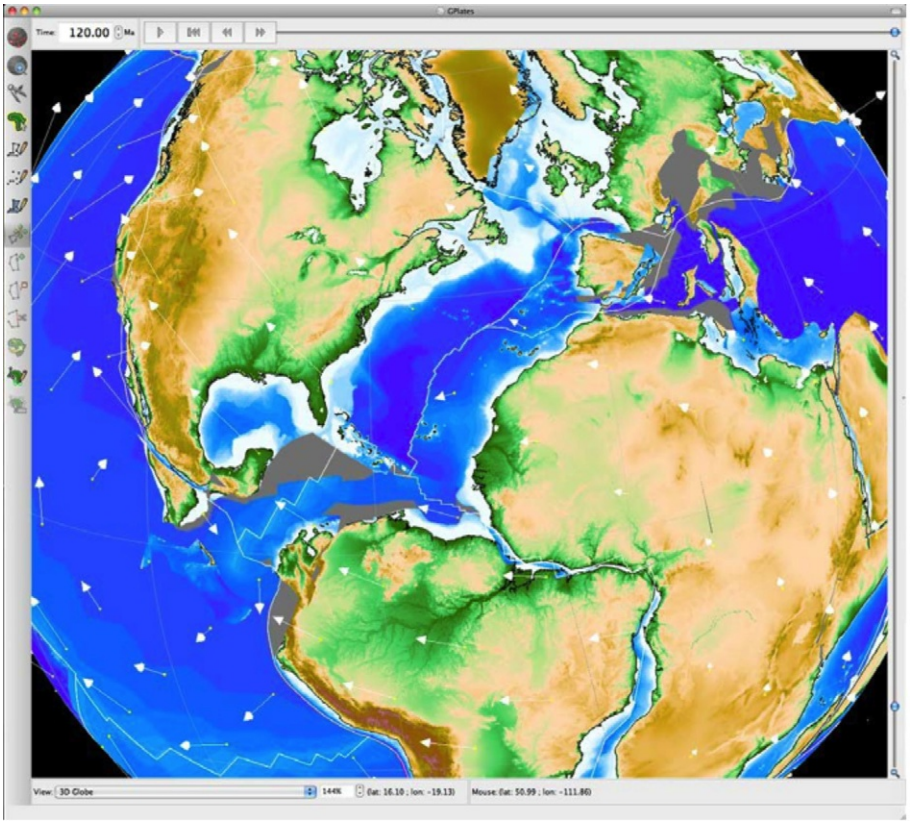

Figure 12 Interactive plate reconstructions. Snapshot at 120 Ma in GPlates showing the opening of the North Atlantic. Continents are shown with the present-day elevations, and the ocean depths are depicted in shades of blue (deep, dark blue; shallow, light blue). White arrows indicate predicted plate motion vectors.

6.02.3.2 Seamount Provinces

A closer examination of the spatial distribution of seamounts shows that there are at least three superimposed populations. The most numerous group is the smaller seamounts. Studies have indicated that the majority of these smaller seamounts were formed in close proximity to a spreading ridge, often right on the ridge flank and sometimes very close to transform offsets. Here, excess amounts of melt ascend through thin and fractured crust, forming small, subcircular seamounts – often just a few tens to hundreds of meters in elevation (e.g., Smith and Cann, 1990). Occasionally, somewhat larger seamounts can be formed. It is likely that most, if not all, smaller seamounts formed in this near-ridge tectonic environment since the rapid increase in lithospheric thickness away from the ridge would make the penetration of small amounts of melt from an increasingly deeper source less likely. Consequently, observed seamount production rates decrease with increasing crustal age and lithospheric thickness, being highest close to the ridge axis (e.g., Batiza, 1982). At fast-spreading ridges, such as the East Pacific Rise, small seamounts form on the flanks of the ridge where the crust is just 0.2–0.3 Myr old, and their abundance correlates with spreading rate (e.g., White et al., 1998). In contrast, at slow-spreading ridges such as the Mid-Atlantic Ridge, small seamounts appear to be produced almost exclusively within the median valley (e.g., Smith and Cann, 1990). Studies have shown that many of these new seamounts undergo extensive tectonic deformation by normal faulting that reduces their original heights considerably (Jaroslow et al., 2000). It is also evident that the increased sediment coverage on older seafloor (e.g., Ludwig and Houtz, 1979) is likely to bury the smallest and most numerous seamounts with height less than 100 m after a few tens of millions of years.

It seems to be a fact that the majority of larger seamounts found in the ocean basins were formed in an intraplate setting, far from the presence of active plate boundaries. Because of their frequent alignment into linear, subparallel chains that appear to correlate with the direction of current or past plate motions (e.g., Duncan and Clague, 1985; Koppers et al., 2001; O'Neill et al., 2005; Wessel and Kroenke, 1997), the most widely accepted origin of such seamounts remains that of the hot spot hypothesis, as mentioned earlier. The relative motion between plates and plumes leads to the formation of lines of extinct volcanoes; these exhibit monotonic age progressions, reflecting the history of past plate motions. Since the early formulation of the hot spot hypothesis, numerous hot spots have been proposed for sites of unusual volcanic activity (e.g., Burke and Wilson, 1976; Clouard and Bonneville, 2001; Sleep, 1990). Yet, conclusive imaging of the underlying mantle plumes using seismic tomography remains elusive (Nataf, 2000), despite tantalizing results from Iceland (Wolfe et al., 1997). For instance, the archetypal strong

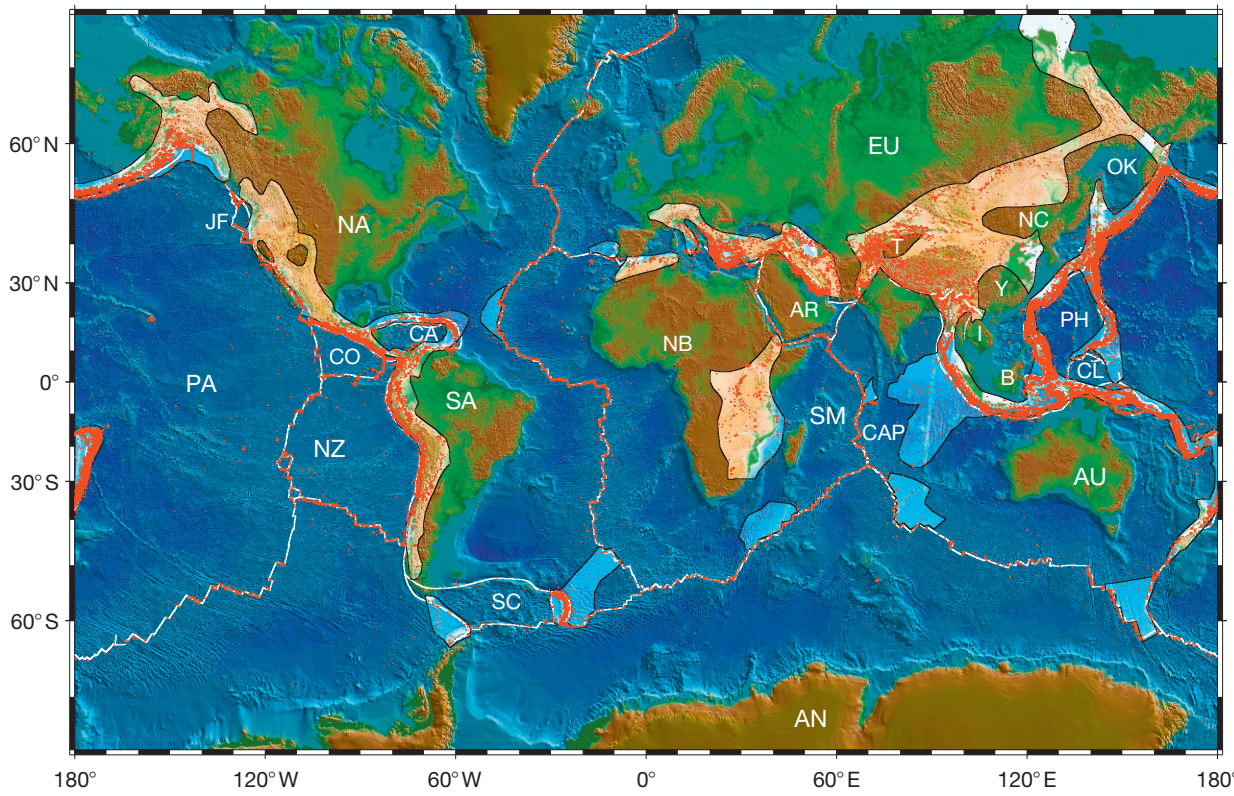

Figure 13 Map showing idealized narrow plate boundaries (Coffin et al., 1997), shallow (0–70 km depth) seismicity (red dots) (Engdahl et al., 1998), and regions of diffuse plate boundaries (areas of lighter illumination) based on Figure 1 of Gordon (2000) who inferred deformation from seismicity, topography, other evidence of faulting and nonclosure of plate motion circuits. These deforming regions, which constitute diffuse plate boundaries, cover ~15% of the Earth's surface. Plate abbreviations: B, Borneo; AN, Antarctica; AR, Arabia; AU, Australia; CA, Caribbean; CAP, Capricorn; CL, Caroline; CO, Cocos; EU, Eurasia; I, Indo-China; IN, India; JF, Juan de Fuca; NA, North America; NB, Nubia; NC, North China; NZ, Nazca; OK, Okhotsk; PA, Pacific; SA, South America; SC, Scotia Sea; SM, Somalia; Y, Yangtze; T, Tarim Basin; PH, Philippine.

plume that many believe has formed the Hawaiian–Emperor seamount chain and currently is assumed to underlie the Hawaiian hot spot at the southeast end of the Hawaiian Island is not well resolved (Cao et al., 2011; Wolfe et al., 2009), whereas other, less productive hot spots (e.g., Easter, Ascension, and Azores) appear more strongly manifested in the tomographic images (Montelli et al., 2004). Although the simple age progressions predicted by the hot spot hypothesis are reflected in the observations for several seamount chains (such as the Hawaiian–Emperor and Louisville chains), others exhibit a more complex age pattern that casts some doubt on the hot spot theory being the only explanation for such volcanism (e.g., Anderson et al., 1992; Dickinson, 1998; McNutt et al., 1997).

With some exceptions, the seamounts formed by hot spot volcanism tend to grow into the largest seamounts found in the oceans (**Figure 17**). In particular, intraplate seamounts formed on old (and hence thicker and thus stronger) oceanic lithosphere can in some cases reach almost 10 km (measured from the base on the seafloor to the tallest peak on an island). A case in point is Mauna Kea, one of five volcanoes that form the Hawaiian Island, which is the tallest mountain on Earth. Given the smallest features (~100 m) considered to be seamounts by most geologists, the sizes of observed seamounts span almost three orders of magnitude.

A few isolated, large intraplate seamounts are apparently not associated with any plume or hot spot seamount chain, such as Shimada Seamount in the Pacific (Gardner et al., 1984) and Vesteris Seamount in the North Atlantic (Haase and Devey, 1994). Because of their large sizes, they most likely formed on relatively thick and strong crust; this makes it likely that the available melt took advantage of preexisting zones of weakness in the lithosphere, probably made more vulnerable by extensional stresses related to plate motion changes (e.g., Sager and Keating, 1984).

The third group of seamounts is composed of those making up island arcs. Distinctly different from the two other classes of seamounts, the island arc seamounts form at subduction zones where one oceanic plate is being forced to subduct beneath the other. As subducting plates descend into the mantle, the higher pressure and increasing temperatures eventually cause decompressional melting of the old seafloor crust, the blanket of wet sediments (if any), and any preexisting seamounts to produce an ascending basaltic melt of a different magmatic composition than is available at spreading centers. In particular, the magma may be more volatile, increasing the chance of explosive eruptions. Geometrically, the distribution of these island arc seamounts and islands reflects the trend of the convergent plate boundaries, and the overall plate tectonic geometry places strong constraints on the evolution of such seamounts (e.g., Fryer, 1996).

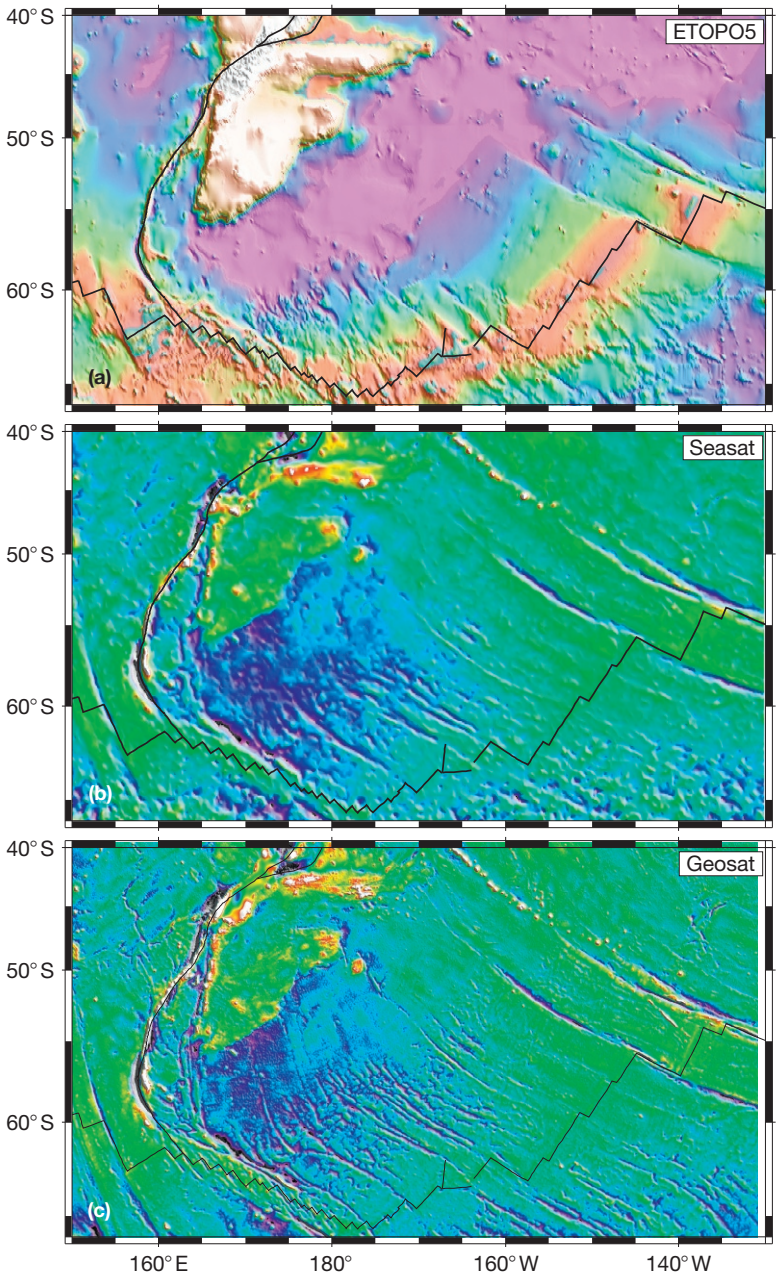

Figure 14 Improvements in mapping the large-scale morphology of the seafloor. (a) The ETOPO5 global 5 × 5 minute bathymetry grid, based largely on SYNBAPS (Van Wyckhouse, 1973), was derived from contour maps and yielded a coarse view of the seafloor, in particular in the remote southern oceans. However, it was a quantitative improvement from the more artistic map renditions of Heezen and Tharp (e.g., Heezen and Tharp, 1961). (b) The first global gravity field derived from *Seasat* altimetry was published by Haxby (1987) using the methodology of Haxby et al. (1983). In his map, fracture zones and seamounts were much better resolved. (c) The most recent version of *Geosat/ERS-1* altimetry-derived free-air anomalies (Sandwell and Smith, 1997) shows an order of magnitude more details, resolving morphological fabric hitherto only seen in dense ship surveys. The mapping of tectonic fabric such as fracture zones has allowed a marked improvement in plate tectonic modeling (e.g., Cande et al., 1995).

Geographically, these island arc seamounts are found in the relatively narrow collision zones between the converging tectonic plates, thus occupying a small area of the total seafloor. Like hot spot-produced seamounts, the island arc seamounts can reach considerable height and often form islands (hence the term island arcs). However, unlike the situation at hot spot-produced seamounts and oceanic islands, the volcanic activity along an active arc is essentially simultaneous, geologically speaking, with older seamounts constantly being overprinted by younger ones.

6.02.3.3 Significance of Seamounts

Seamounts present windows into the mantle, allowing scientists to examine in detail the nature of the magma that is

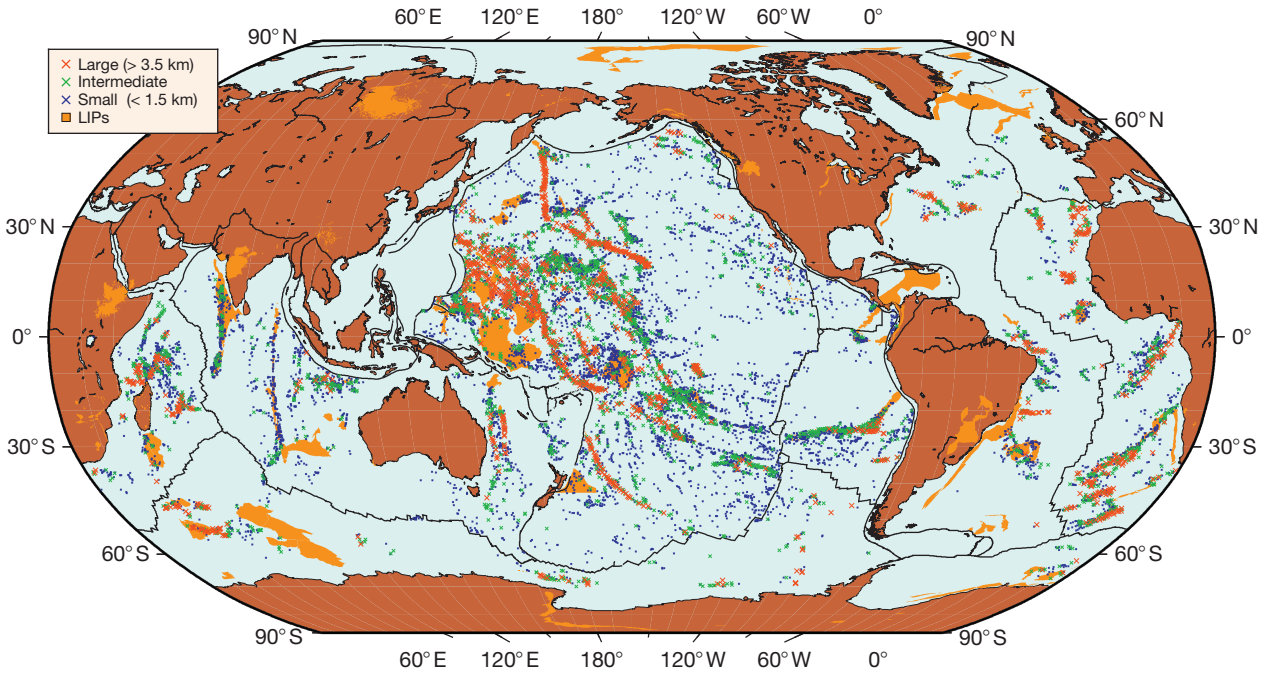

Figure 15 Global distribution of seamounts as identified by Wessel (2001) in a vertical gravity gradient grid (in units of mGal m^{-1} or Eötvös) derived from the *Geosat/ERS-1* satellite altimetry (Sandwell and Smith, 1997). Red crosses are large seamounts (>120 Eötvös, generally >3.5 km tall), blue are small seamounts (<60 Eötvös, generally <2.5 km tall), whereas green crosses are of intermediate size. The majority of seamounts can be found in the Pacific basin, with the remainder divided between the Atlantic and the Indian Oceans. Large igneous provinces are outlined in dark orange (e.g., Coffin and Eldholm, 1992); these are often associated with seamount provinces.

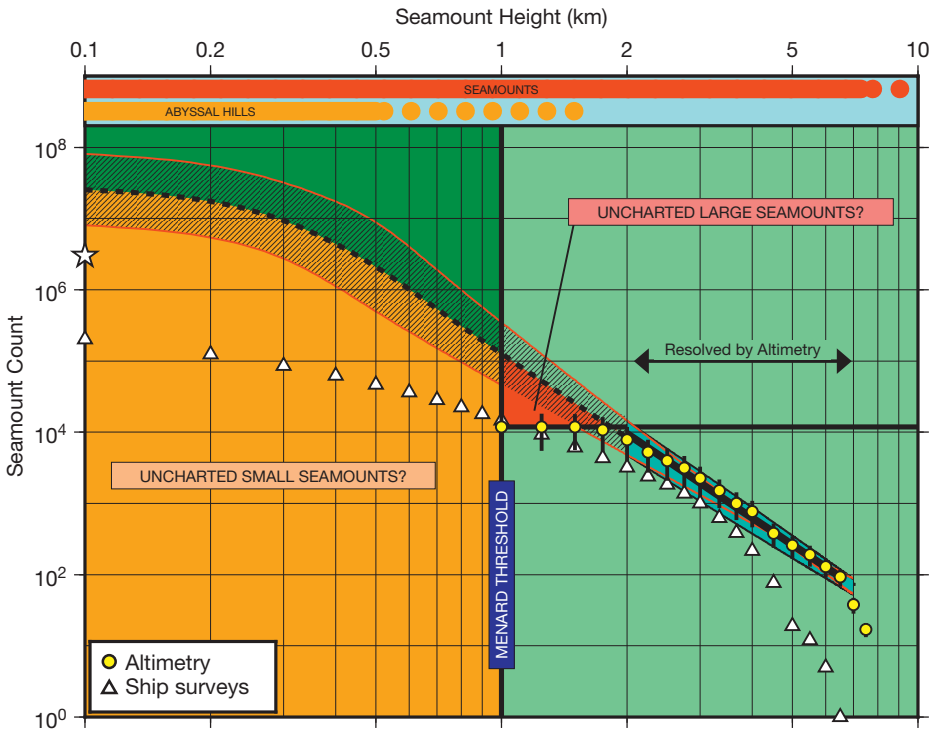

Figure 16 Global seamount size–frequency distribution. Height–frequency distributions of seamounts based on satellite altimetry (yellow circles) and single-beam bathymetry profiles (white triangles). Cyan band represents ±30% uncertainty in counts, yielding upper/lower extrapolations to smaller sizes (red lines with hachured uncertainty). The flattening of predictions for heights <500 m is due to sedimentation and area considerations (see text). There could be approximately 125 000 seamounts taller than 1 km and as many as 25 million taller than 100 m, but the uncertainties are considerable. White star (3 million) is adjusted prediction by Hillier and Watts (2007). Redrawn from Wessel et al. (2010).

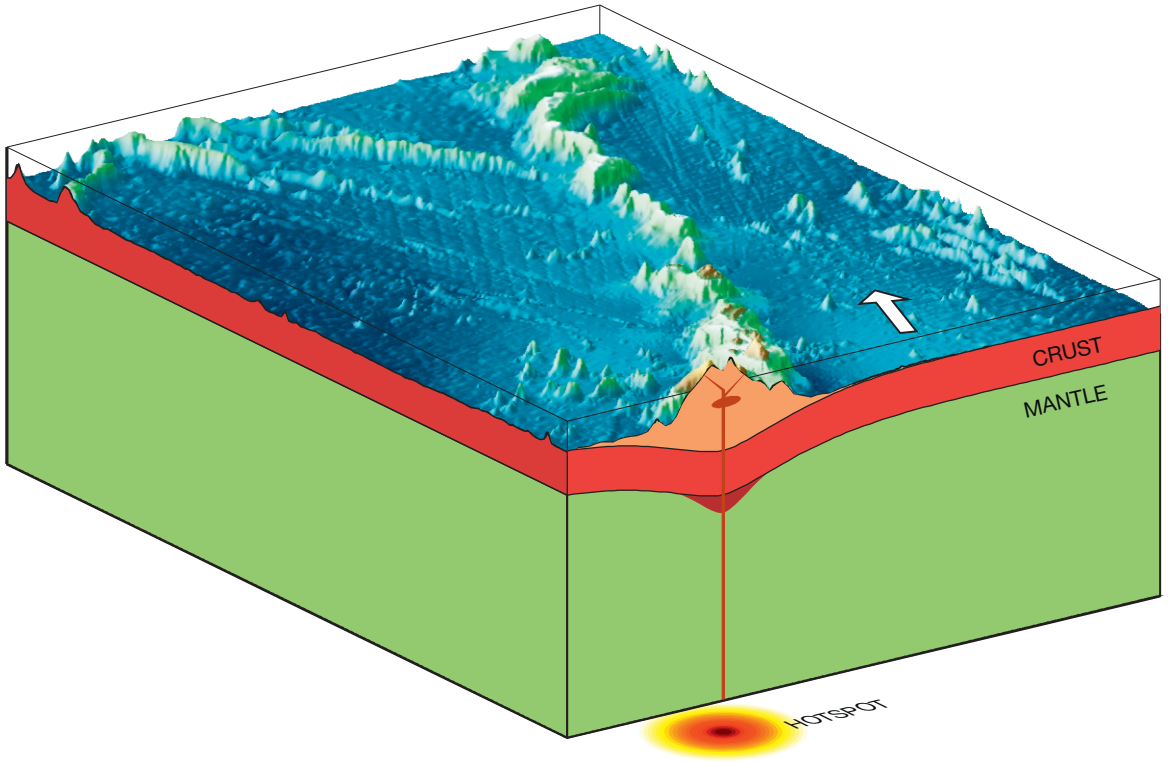

Figure 17 Sketch illustrating intraplate seamount (and island) formation over the Hawaiian hot spot. Given a thick and strong lithosphere (~90 Myr old), intraplate seamounts can grow very tall and even breach sea level to form oceanic islands. The large volcanic piles deform the lithosphere, which responds by flexure. The plume beneath the plate feeds the active volcanoes by a network of feeder dikes; some magma may pond beneath the crust as well (Watts and ten Brink, 1989). As the plate motion carries the volcanoes away from the hot spot (arrow indicates current direction of motion), they cease to be active and form a linear seamount or island chain.

erupting. While overwhelmingly basaltic, minor changes in the chemical and isotopic composition of lavas can be mapped and such patterns can be used to make inferences about the source, such as the depth of the magma and its ultimate composition (e.g., Janney et al., 2000). The extrusive volume represented by seamounts is a significant fraction of the entire crustal production, perhaps as much as 10% (Batiza, 1982), and both spatial and temporal variations in this intraplate volcanic budget shed light on the plate tectonic evolution of the ocean basins and the mechanisms by which the Earth gets rid of its excess heat. Furthermore, the alignment of seamounts into chains provides a means to decipher the motion of the tectonic plates over long geologic intervals, enabling a better understanding of the climatic changes experienced at islands that simply follow from latitudinal migration of plates carrying seamount provinces on their backs (e.g., Kroenke, 1996). Many seamounts have active hydrothermal convection systems that may have a significant effect on element cycles involving seawater (Batiza, 2001), and they also participate in the dissipation of residual heat from the formation of both seamount and seafloor (e.g., Harris et al., 2004). Finally, seamounts and islands act as measuring sticks for relative sea level variations, which can have both eustatic and tectonic components (Douglas, 1991; Tushingham and Peltier, 1992).

The bathymetry of the ocean floor influences the ocean circulation in several ways. Most importantly, the first-order bathymetric features such as ridges and plateaus steer the currents and in places provide barriers that prevent deep waters from mixing with warmer, shallower waters. However, there is a growing awareness that smaller-scale bathymetry, such as seamounts, may play a largely overlooked role in the turbulent mixing of the oceans (e.g., Kunze and Llewellyn Smith, 2004). In fact, measurements suggest that mixing around a shallow seamount is many orders of magnitude more vigorous than in areas far from seamounts (Lueck and Mudge, 1997). The precise understanding of how the Earth's climate will evolve depends on how quickly heat and carbon dioxide can penetrate into the deep oceans, and assumed rates of vertical mixing can affect model predictions considerably. Further mapping of seamounts and the inclusion of an accurate representation of the seafloor into models of global ocean circulation will be necessary in order to improve predictions of climate (e.g., Jayne et al., 2004).

Representing obstacles to flow, seamounts induce local currents, which can enhance the upwelling around the seamount. As this may bring up nutrient from the deeper ocean, primary productivity is enhanced, supporting a wide variety of life (Rogers, 1994). The importance of seamounts as habitats for ecological communities and in particular fish is being increasingly recognized, and a better understanding of the complex relationships between several parameters is required to develop well-founded policies on fisheries and conservation. Islands, as subset of seamounts that currently exceed sea level, also sustain unique flora and fauna and provide natural

laboratories for ecology, evolution, and cultural diversification (e.g., Price and Clague, 2002).

6.02.3.4 The Ages of Seamounts and Oceanic Islands

A key prediction of the hot spot hypothesis is that there should be a clear monotonic age progression along the seamount and island chains produced by hot spot volcanism. Consequently, the determination of actual ages from rock samples collected at these sites became of paramount importance early in the study of hot spot chains. Pioneering efforts by Turner, Duncan, McDougal, and others provided a valuable dataset whose importance cannot be overestimated (Duncan, 1981; Duncan and Clague, 1985; McDougall, 1971; Turner and Jarrard, 1982; Turner et al., 1980). A 2005 review by Clouard and Bonneville (2005) discusses a Pacific compilation of more than 1500 individual age determinations derived from almost 300 different volcanoes; since then, both Louisville (Koppers et al., 2011a) and Samoa (Koppers et al., 2011b) trails have seen renewed sampling. The picture that emerges from analyzing all the available data seems to be that, to first order, monotonic age progressions are observed at many of the Pacific chains, but for some, there is no clear pattern. Studies of age-progressive volcanism remain hampered by a lack of available samples; the realization that the field of radiochronology has made considerable advances since some of the earliest published dates, and hence, reanalysis is strongly recommended; and the discovery that volcanism at a given site can have an extended period of activity, making it difficult to say with certainty that the observed age is representative for the feature as a whole. In areas where new samples have been obtained and new, more sophisticated techniques have been applied to obtain the most accurate ages, significant discrepancies between the new and old dates are often found (e.g., Koppers et al., 2004). Such reanalysis not only is necessary but also suggests that caution must be used when combining old and new ages in age-progression studies. Some Pacific chains that geometrically seemed similar to the Hawaiian–Emperor bend (HEB) configuration have recently been dated, yielding ages that are difficult to understand in terms of hot spot volcanism (Koppers and Staudigel, 2005). It may be that volcanism caused by decompressional melting that rises up through new or existing cracks in the lithosphere, possibly helped by transient stresses during times of plate motion changes, is making studies of age-progressive volcanism more challenging.

The situation outside the Pacific is similar in the sense that tentative age progressions are often found for long seamount chains, but both the quality and the quantity of samples are much lower (e.g., Baksi, 1999). While new advances in dating technique promise to raise the quality of radiometrically determined ages to a higher level, the fact that reanalysis is a time-consuming and costly endeavor and the acquisition of new samples, in particular for older chains, is a difficult and costly proposition means that progress will come slowly. Consequently, the study of absolute plate motions (APMs) is a field that is in perpetual need of better data. New radiometric age data of high quality and from locations that are underrepresented in the database will, if collected, place the strongest constraints on the hot spot hypothesis.

6.02.3.5 Hot Spot Swells

The hot spot hypothesis states that seamount chains and oceanic islands are the surface expression of impinging mantle plumes. Upwelling mantle plumes are thought to form at either the core–mantle boundary (2900 km depth) or the boundary between the lower mantle and the upper mantle (670 km depth). One theory suggests that a 'plume head' develops, above a 'plume stem' (Bercovici and Kelly, 1997; Campbell and Griffiths, 1990; Coffin and Eldholm, 1993; Richards et al., 1989), but other scenarios of plume development with double plume heads (Bercovici and Mahoney, 1994) and time-varying magma output (Coffin et al., 2002) have also been suggested.

While most of our focus will be on assessing how the observed geometry and age progressions at such chains can be used to infer plate tectonic motions, another consequence of the hot spot hypothesis is the formation of hot spot swells around and downstream from the location of active hot spots (e.g., Crough, 1983; McNutt, 1998). Whereas the seamount chains are confined within a relatively narrow width (typically 100–200 km), the broader effect of the plume on the lithosphere and upper mantle can extend over a width of 1000 km or more. The most spectacular example of a hot spot swell is again coming from the Hawaiian chain where we find the aforementioned seamount chain located on top of a broad swell more that 3000 km long and 1200 km wide (e.g., Davies, 1992; Vidal and Bonneville, 2004; Wessel, 1993), but it should be noted that such thermal swells are present in all the oceans and associated with most of the hot spot chains. Observations suggest that the amplitude and extent of such swells are strongly dependent on the age of the underlying lithosphere; hence, Hawaii (located on seafloor of around 100 Ma) is much more pronounced than, say, the swells in French Polynesia (situated on seafloor of half that age) (Cazenave et al., 1988; Ceuleneer et al., 1988). Pioneering analysis of hot spot swells suggested the shallow bathymetry was a direct consequence of reheating of the lithosphere (Detrick and Crough, 1978), although some pointed out the possible role of compositional buoyancy (e.g., Jordan, 1979; Phipps Morgan et al., 1995), as well as the dynamic uplift (e.g., Olson, 1990). Modeling of the dynamic origin of hot spot swells is nontrivial but considerable progress has been made. The consensus view is that hot spot swells are best explained by the presence of a deep-seated upwelling plume, which explains both the broad swell and the focused volcanism (e.g., Ribe and Christensen, 1999).

6.02.4 Studies of APMs

6.02.4.1 Plume Theory, Seamount Chains, and the Fixed Hot Spot Hypothesis

As mentioned, Wilson (1963) hypothesized that the distinctive linear shape of the Hawaiian Island–Emperor seamount chain resulted from the Pacific Plate moving over a deep, stationary hot spot in the mantle, located beneath the present-day position of the Hawaiian Island. Heat from this hot spot produced a persistent source of magma by partly melting the overriding Pacific Plate. The magma, which is lighter than the surrounding

solid rock, then rises through the mantle and crust to erupt onto the seafloor, forming an active seamount. Over time, countless eruptions cause the seamount to grow until it finally emerges above sea level to form an island volcano. Wilson (1963) suggested that continuing plate movement eventually carries the island beyond the hot spot, cutting it off from the magma source, and volcanism ceases.

As one island volcano becomes extinct, another develops over the hot spot, and the cycle is repeated. This process of volcano growth and death, over many millions of years, has left a long trail of volcanic islands and seamounts across the Pacific Ocean floor. According to Wilson's hot spot hypothesis, the volcanoes of the Hawaiian chain should get progressively older and become more eroded the farther they travel beyond the hot spot. The oldest volcanic rocks on Kauai, the northwesternmost inhabited Hawaiian Island, are about 5.5 Myr old and are deeply eroded (McDougall, 1979). By comparison, on the Hawaiian Island – southeasternmost in the chain and presumably still positioned over the hot spot – the oldest exposed rocks are less than 0.7 Myr old and new volcanic rock is continually being formed. However, it is the monotonic age progression exhibited by dated rock samples dredged from submarine volcanoes all along the Hawaiian–Emperor chain that has convinced scientists of the general validity of the hot spot hypothesis (e.g., Clague and Dalrymple, 1989).

During the past 20 years, our knowledge of the Mesozoic and Cenozoic relative motion between the major tectonic plates has increased substantially even though 'absolute' plate motions relative to a 'fixed' mesosphere are still controversial. Identified marine magnetic anomalies, some as old as 165 Myr, along with seafloor tectonic lineations based on bathymetric and satellite altimetry data accurately define relative plate motions for most of the major plates. Paleomagnetic data and hot spot traces are among the concepts that have been used to attempt to constrain the 'absolute' plate motions. Paleomagnetic data can be used to determine the paleomeridian orientation and the paleolatitude of a plate, which together can be considered the paleopole for a given plate. However, since the Earth's dipole field is radially symmetrical, no paleolongitudinal information can be deduced from paleomagnetic data.

Seamount chains with a linear age progression (i.e., a hot spot track) can be used to restore plates to their paleopositions with the assumption that hot spots are either fixed or nearly fixed relative to each other ('fixed hot spot hypothesis'). Molnar and Stock (1987) showed though that during the Tertiary, the Hawaiian hot spot moved with an average velocity of 10–20 mm per year relative to the Iceland hot spot and to hot spots beneath the African and Indian Plates.

Numerous paleomagnetic datasets and models for the 'absolute' motions of the North American, African, and Eurasian Plates during the Mesozoic and Cenozoic have been published. Unfortunately, there are inconsistencies between different apparent polar wander (APW) paths and hot spot models. Especially for times older than about 45 Ma, large discrepancies are observed between APM models based on hot spot tracks and those based on APW paths from paleomagnetic data.

6.02.4.2 Motion of the African Plate

A widely used APM model based on fixed hot spots was proposed by Müller et al. (1993) who used a refined model for global relative plate motions and a compilation of the bathymetry and radiometric age dates of major hot spot tracks to test the 'fixed hot spot hypothesis.' They combined major hot spot tracks with well-documented age progression from the Atlantic and Indian Oceans and used an interactive technique to derive a 'best-fit' model in a qualitative sense for motions of the major plates in the Atlantic–Indian domain relative to hot spot tracks with a clear age progression.

Even though this model is widely used, it has some well-recognized shortcomings. The late Tertiary portion of this model was not well constrained by radiometric ages, based on the lack of published age dates for the post-30 Ma portion of most hot spot tracks involved at that time. For reconstruction times predating 80 Ma, the only available hot spot tracks with age progression in the Atlantic–Indian Oceans are the New England Seamount chain (linked to the Great Meteor hot spot) and the Walvis Ridge/Rio Grande Rise (linked to the Tristan hot spot) in the Atlantic Ocean. Therefore, the absolute motion of the Indian, Australian, and Antarctic Plates relative to the mantle has to be computed by plate circuit closure for these times. However, when the Müller et al. (1993) model was constructed, pre-80 Ma relative plate motions in the Indian Ocean were poorly known, due to a lack of data in crucial areas, in particular offshore Antarctica in the Enderby Basin and south of the Kerguelen Plateau. Here, a sequence of Mesozoic magnetic anomalies was subsequently mapped and modeled, starting at about 130 Ma (Gaina et al., 2003, 2007). However, the Müller et al. (1993) model was (incorrectly) based on the assumption of post-120 Ma breakup between India and Madagascar. Disagreements between hot spot and published paleomagnetic reference frames have been documented for India (Müller et al., 1994) and for Australia (Idnurm, 1985), suggesting that the mantle underlying the Indian Ocean may not have provided a fixed reference frame. Paleopoles for India from the Rajmahal Traps (Das et al., 1996; Rao and Rao, 1996) result in a paleolatitude of the traps at their time of formation (~117 Ma, Baksi, 1995) at 47° S (±400 km), whereas the Müller et al. (1993) model places them at about 40° S (±400 km).

A comparison of mid-Cretaceous (122–80 Ma) paleolatitudes of North America and Africa from paleomagnetic data with those from hot spot tracks (Van Fossen and Kent, 1992) has provided evidence for an 11–13° discrepancy, providing evidence that Atlantic hot spots were not fixed relative to the Earth's spin axis before 80 Ma, but moved southward as much as 18° (Torsvik et al., 2002) between 100 and 130 Ma. Others argue that this apparent southward movement was caused by true polar wander (TPW) (Prevot et al., 2002).

The Müller et al. (1993) APM model results in a relatively sharp bend of plate motion directions (e.g., of Australia and Antarctica) relative to the mantle at about 80 Ma, which originates from the bend between the New England Seamount chain and the Corner Rise seamounts at roughly 80 Ma in the central North Atlantic. An equivalent bend in fracture zones is not found in either the Atlantic or the Indian Ocean.

6.02.4.3 Motion of the Pacific Plate

The Pacific Plate is by far the largest tectonic plate on Earth, and its APM relative to the underlying mantle is predominantly determined by negative buoyancy forces related to subduction (e.g., Chapple and Tullis, 1977; Conrad and Lithgow-Bertelloni, 2002; Forsyth and Uyeda, 1975; Hager and O'Connell, 1981; Lithgow-Bertelloni and Richards, 1998). To first order, this assessment is well reflected in the north–south alignment of westward-dipping subduction zones along the Pacific Plate's western boundary and the generally westward motion of the plate during the last ~50 Myr. The Pacific Plate's only eastward-dipping subduction zone is found along the short Queen Charlotte margin north of the Juan de Fuca Plate (**Figure 13**); the slab pull exerted at this margin is considered to be relatively minor (Hyndman and Hamilton, 1993). As changes in buoyancy forces are expected to develop slowly (e.g., Hall et al., 2003; Mueller and Phillips, 1991), APM should consequentially be steady and change slowly. However, other forces acting on the plates, such as resistive forces associated with collisions, can develop more rapidly and thus influence plate motions over shorter time spans (e.g., Cloos, 1993; Lithgow-Bertelloni and Richards, 1998). Consequently, various collisions have been given as reason for inferred short-term APM changes (e.g., Knesel et al., 2008; Wessel and Kroenke, 2007).

Because the Pacific Plate is entirely oceanic with no continents on which to establish a paleomagnetically determined plate motion history, APM models for the plate typically have been derived from the geometry and chronology of hot spot chains. The Hawaiian chain is clearly the most studied hot spot chain and has as its most characteristic feature the prominent bend near longitude 172° E, here called the HEB. It was also noted that the Louisville chain in the far South Pacific also had a bend, albeit much gentler and consistent with an ~25° local change in Pacific APM (Lonsdale, 1988). Since Wilson (1963) first suggested it, the HEB has been explained by a dramatic ~60° change in direction of Pacific Plate motion over a stationary hot spot in the mantle (Morgan, 1971). Consequently, the geometries of the Hawaiian–Emperor chain and other coeval chains (**Figure 15**) have been used to model the Pacific APM (e.g., Duncan and Clague, 1985; Koppers et al., 2001; Wessel and Kroenke, 2008; Wessel et al., 2006; Yan and Kroenke, 1993). All these APM models assumed hot spots with negligible motion.

The analysis of rock samples obtained from drilling the Emperor seamounts has revealed a frozen-in paleomagnetic field best explained if the seamounts were formed significantly further north (5–10°) of the present-day location of Hawaii (Kono, 1980; Tarduno and Cottrell, 1997). Efforts to project the APM of Africa, via the global plate circuit, into the Pacific failed to reproduce the shape of the HEB (Cande et al., 1995; Raymond et al., 2000). These inconsistencies lead to alternative models where the plume sustaining the volcanism was no longer stationary (Steinberger, 2000; Steinberger and O'Connell, 1998). Such models can potentially fit both the changing latitude of the hot spot (as suggested by paleomagnetics) and the geometry and age progression of the seamount chain. Some researchers concluded that no change in Pacific APM had taken place at all: Since the trail records the vector sum of plate and plume motion, it could be reconstructed by a rapid slowdown in the southward motion of the plume, while Pacific Plate motion remained unchanged in direction and magnitude (Tarduno et al., 2003, 2009).

To reconcile African and Pacific Plate APM models requires their propagation via the global plate circuit (Acton and Gordon, 1994). Because the history of all RPM changes between conjugate plate pairs is not known, the projection of the African APM into the Pacific is subject to uncertainties that cannot easily be quantified. For instance, by choosing a different plate circuit for connecting the Pacific to Australia via the Lord Howe Rise, Steinberger et al. (2004) showed that the HEB did seem to require a plate motion component and thus could not be caused by plume drift alone. However, Matthews et al. (2012) pointed out that subduction took place east of Australia during this time period, making such a direct circuit between Pacific and Australia tenuous. Preliminary paleolatitude information from the Louisville chain (Koppers et al., 2012) implies much less southward hot spot motion than determined for Hawaii from the Emperor seamounts, suggesting that the coeval Louisville bend is predominantly caused by a change in plate motion. The great-circle distances between same-age samples in the Hawaiian–Emperor and Louisville chains (Wessel and Kroenke, 2009) provide independent estimates of the separation of these two hot spots through time. Changes in this separation appear insignificant back to 55 Ma, but for the critical time period 80–55 Ma, this separation decreased by as much as 3–5° (**Figure 18**). Recently, Doubrovine et al. (2012) presented evidence for two equal and antipodal TPW episodes affecting the 90–60 and 60–40 Ma intervals, complicating matters further. Combined, this information suggests that the HEB is most likely a combination of change in plate motion, plume motion, and perhaps TPW, with individual contributions still to be properly determined.

6.02.4.4 Quantitative Methods for Reconstructing APMs

In considering seamounts and island chains as markers of past plate motion over stationary hot spots, Morgan (1971, 1972) realized that such trails should form sets of copolar small circles on the Earth surface as a consequence of Euler's theorem for plate motions on a sphere. Much early works were concerned with determining stage rotations that would describe the consecutive sets of small-circle motions. Traditionally, segments from different seamount chains thought to represent the same-age interval would be used to determine a single Euler's rotation pole by solving for a best-fit rotation pole (**Figure 19**). The opening angle would be assessed separately by trial and error since the lack of complete age coverage makes it difficult to determine the beginning and end of each segment uniquely. Given the age range of a particular set of copolar segments, opening 'rates' can be determined. This method is best suited to determine first-order trends in APM, but as more details are sought, the difficulty with identifying increasingly shorter small-circle segments and correlating these across several seamount chains becomes insurmountable. Nevertheless, because the data portray small circles, it was natural to define the model in terms of stage rotations and not total reconstruction rotations.

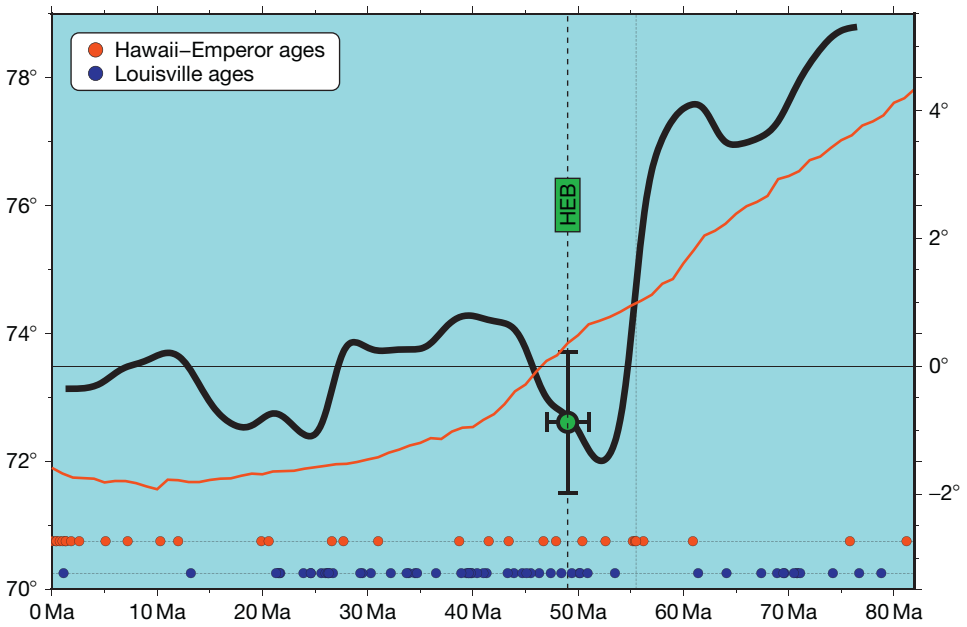

Figure 18 Variations in hot spot separation. Dated locations along the Hawaiian–Emperor and Louisville chains are used to infer the distance between these two hot spots as a function of time (heavy line). Circles show sample distribution, while green circle represents the $72.6 \pm 1.1^\circ$ separation between HEB and the Louisville bend (Wessel et al., 2006). At ~55 Ma, separation drops ~4° and remains stable until present day. Red line shows separation between moving hot spots in the Doubrovine et al. (2012) model.

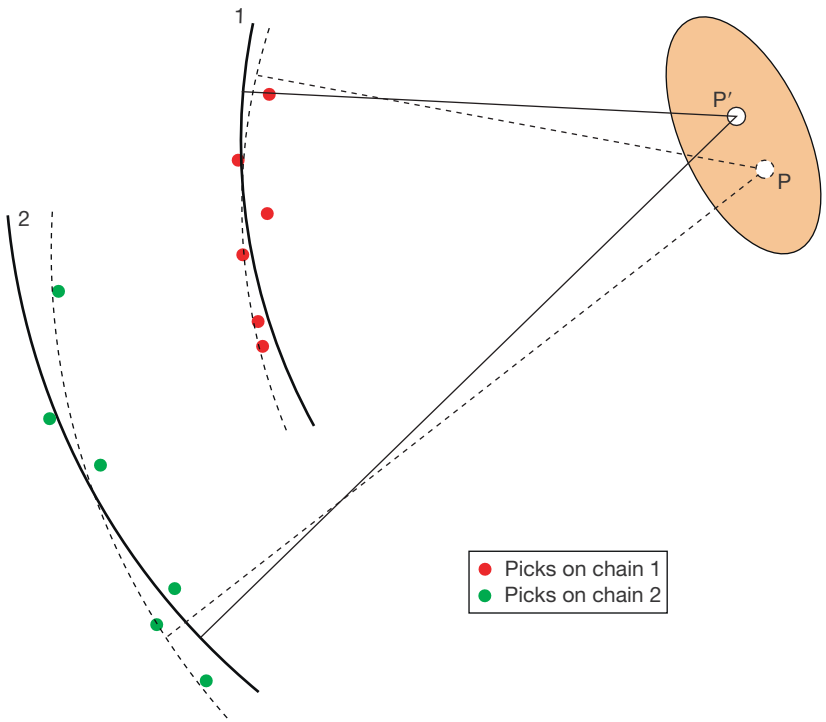

Figure 19 Traditional modeling of APM using stage rotations. Seamounts (red and green circles) are considered points that must approximately lie along small circles (heavy lines). Given a trial pole location (P′), a revised pole location P is found such that the misfit between seamounts and the local best-fitting small circle for each chain is minimized.

Although useful as an exploratory technique, the traditional APM modeling approach has many limitations: (1) short segments, possibly reflecting APM changes, are difficult to identify and correlate across several chains; (2) short small-circle segments become indistinguishable from great circles, and hence, angular distances to poles cannot be accurately determined; (3) without easily identifiable kinks that can be correlated between chain segments, ages are needed to define segments and make the correlation, and these are often lacking; (4) unlike RPM modeling, no rigorous approach for estimating APM uncertainties exists; (5) the method breaks down if hot spots are moving during a stage interval; and, finally, (6) no consistency check for hot spot locations is provided.

6.02.4.4.1 The hot-spotting technique

The last shortcoming was addressed by Wessel and Kroenke (1997) who discovered a simple geometric principle that allows researchers to assess the self-consistency of an APM model. Dubbed 'hot-spotting,' the technique accepts the APM model as correct and constructs seafloor flow lines backward in time from each location on the plate that has a seamount. Since seamounts are not singular points but rather have a finite size, Wessel and Kroenke (1997) convolved each seamount's shape with the corresponding flow line, resulting in a grid of values they called the cumulative volcano amplitude (CVA). The maximum CVA value is proportional to the amount of material produced by the hot spot. Because these flow lines illustrate the path of the seafloor over the mantle (and hence the hot spots, here assumed stationary), it follows that such flow lines must necessarily intersect at the locations of these hot spots (Figure 20). This is evidently true from geometric principles, but the application of the technique rests of several assumptions that must hold true for the result to be valid: (1) the hot spots must be fixed or moving very slowly, (2) the plate motion model must be approximately correct, (3) plates must be rigid over the time span represented by the hot spot volcanism, and (4) the seamounts considered must all have been produced over the hot spots in question. Departure from one or more of these assumptions will be highlighted by the hot-spotting calculations, such as mismatch between optimal and assumed hot spot locations; for a review of issues, see Wessel and Kroenke (1998a,b).

The hot-spotting technique has been identified with a particular plate motion model (called WK97) that was derived in the same article that introduced the geometric concept (Wessel and Kroenke, 1997). WK97 was based on the premise that Hollister Ridge, a site of ongoing eruptions, a site of acoustic noise, and the site of a geoid high, might possibly be the present-day location of the Louisville hot spot. From this assumption, one can derive a controversial plate motion model such as WK97, which added a new, 3 Ma rotation to an earlier APM model (Yan and Kroenke, 1993), which Wessel and Kroenke (2000) later revised to 6 Ma. The proposed 6 Ma change in Pacific APM coincided with numerous other pronounced changes along the plate's boundary (e.g., Krijgsman et al., 1999), including the development of microplates, extensional transform faults, and propagating ridges. While several earlier papers had proposed a late Neogene change in Pacific APM (e.g., Engebretson et al., 1985; Harbert and Cox, 1989; Pollitz, 1986), the WK97 model was much more radical,

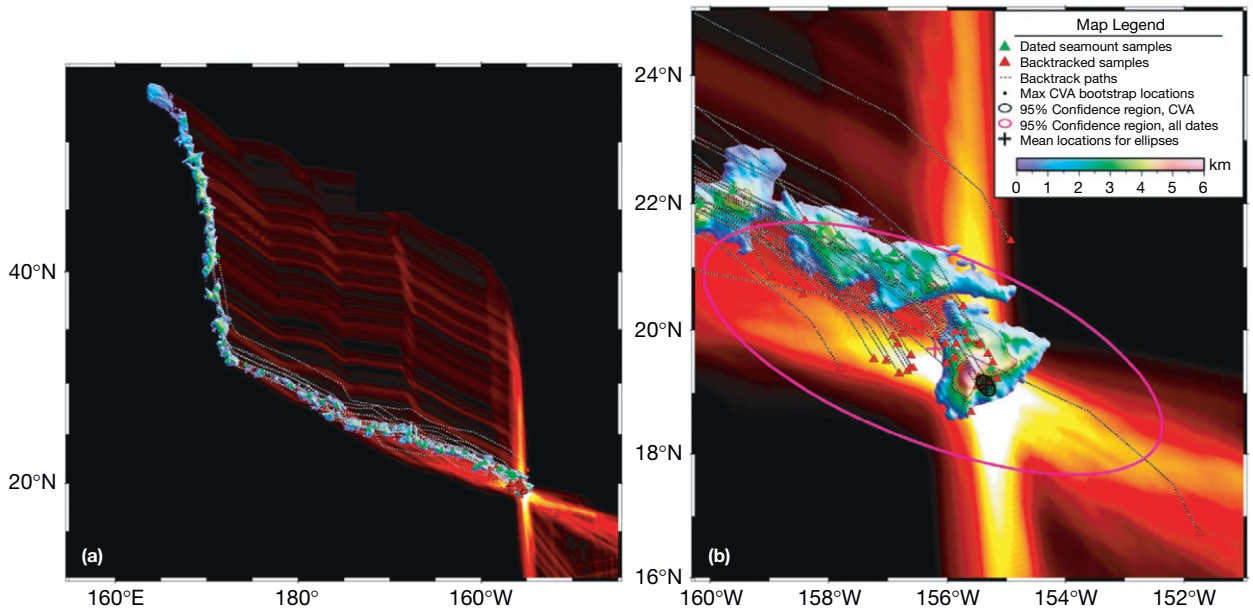

Figure 20 Hot-spotting is a geometric method that checks the self-consistency of an APM model (Wessel and Kroenke, 1997). By generating the flow lines of the seafloor back in time, it follows that seafloor with hot spot-produced seamounts has flow lines that must intersect at the hot spot location, provided hot spots are stationary and the plate is rigid. (a) Hot-spotting applied to all seamounts in the Hawaiian–Emperor chain (colored relief), resulting in a high density of flow line intersections just SE of the Hawaiian Island. Green triangles are dated seamounts, and red triangles are their reconstructed location based on their age. (b) Close-up of the hot spot region. Small black ellipse is the 95% confidence region (using a bootstrap approach) for the optional hot spot location based on the hot-spotting technique for this APM and the geometry of the chain. In contrast, the magenta ellipse is the 95% confidence ellipse for the relocated seamounts.

suggesting a low-latitude rotation pole to mimic the inferred pivoting of the Pacific Plate about the collision zone between the Ontong Java Plateau and the northern margin of the Australian Plate. As very recent changes in APM are subject to large uncertainties and much of the supporting evidence may also be explained in terms of RPM changes, their model remains speculative. Models of current APM are also sensitive to choice of seamount chains; if the recent change in the geometry of the Hawaiian chain is excluded, one will derive a model with a less pronounced change (e.g., Gripp and Gordon, 2002).

Hot-spotting is simply an application of Euler's theorem and is now understood to be related to the Hough transform used in pattern recognition (Wessel, 2008). As such, it takes the rotations of a plate motion model, constructs flow lines for all seamount locations, and lets their crossings reveal an optimal zero-age (hot spot) location. If given the WK97 rotations, it would find that the optimal hot spot location lies on Hollister Ridge since that is what the rotations were designed to do in the first place. Whereas hot-spotting is just a geometric test that can tell how *consistent* a plate motion model is given the data constraints, researchers that disagreed with the premise of WK97 tended to conclude that the hot-spotting technique itself was fundamentally flawed (Aslanian et al., 1998; Wessel and Kroenke, 1998c). A clearer presentation of what in hindsight is a simple procedure would have been preferable.

6.02.4.4.2 PFRM: the polygonal finite rotation method

Harada and Hamano (2000) made many of the other issues hampering traditional modeling irrelevant by introducing a new technique to determine total reconstruction rotations provided hot spot locations are known. Their polygonal finite rotation method (PFRM) was based on a simple geometric concept relating positions along the chains to the location of hot spots at the time the seamounts were formed (**Figure 21**). While their technique can be applied to the general case where hot spots are moving, their discussion and showcase of it were limited to the case of fixed hot spots. In that situation, the present location of N hot spots can be considered the vertices of an N-sided polygon. With hot spots fixed and plates rigid, there is a population of finite rotations that will rotate this polygon so that its vertices will each lie along the N seamount chains. Harada and Hamano (2000) found this population by a Monte Carlo approach, in which they assigned envelopes around the three seamount chains used in their analysis (Hawaiian–Emperor, Louisville, and Easter–Line Islands) and determined rotations by selecting points inside these envelopes and solving for rotations that reconstructed the selected points close to the corresponding hot spots. From this large set of rotations, one can determine representative rotations for a set of different opening angles. Unlike previous techniques, these rotations are purely geometric as no age constraints, other than the zero-age hot spot locations, went into their determination. Observed ages along the N seamount chains were then used to determine a smooth cubic spline function that relates opening angle to actual age. Their resulting APM model fits most chains in the Pacific fairly well, although the subjectively chosen width for the chain envelopes affected the smoothness and fit of the model. Since it was the envelopes and not the distribution of seamounts inside them that were used to derive rotations, the model was necessarily subjective.

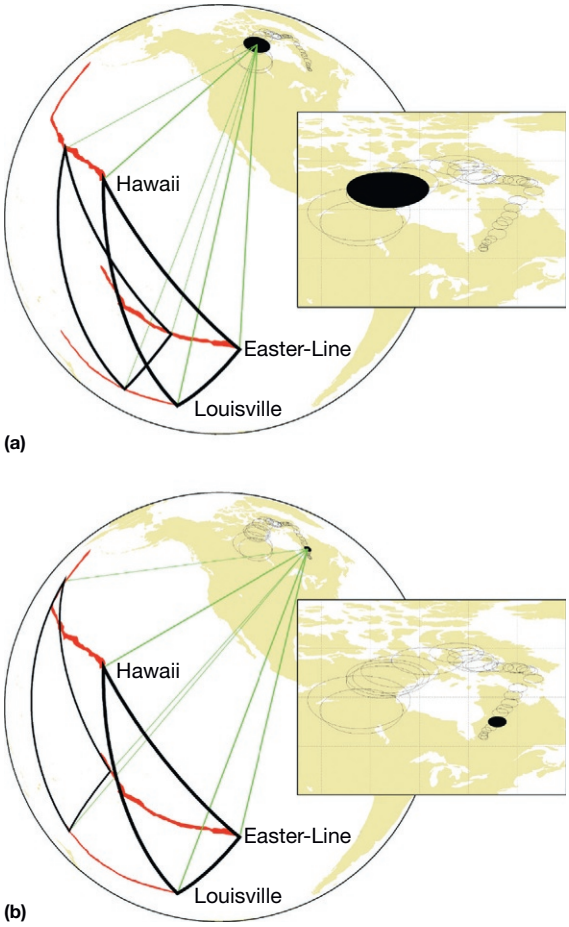

Figure 21 Almost continuous traces of poles for total rotation of the Pacific Plate can be calculated from more than two continuous hot spot tracks. By assuming fixed hot spots and a rigid plate, we know the spherical triangle whose vertices are the present hot spot locations can be recreated for earlier times. Using a Monte Carlo approach, Harada and Hamano (2000) were able to determine the locations of rotation poles for a swath of opening angles such that the shape of the spherical triangle would fit the chain. (a) For smaller opening angles, many rotation poles are found for each opening angle, resulting in larger uncertainties in the pole location. (b) For larger opening angles, the scatter in the locations of the rotation poles is much smaller. Redrawn from Harada and Hamano (2000).

6.02.4.4.3 Moving hot spots

Testing models for motions between individual and groups of hot spots requires mantle convection models, constrained by known plate motions. Steinberger and O'Connell (1997) were the first to develop models of hot spot motion and polar motion based on mantle flow models. Their novel model for the differential motion of individual hot spots is based on mantle density heterogeneities derived from seismic tomography and on known plate motions. Steinberger (2000) extended this type of modeling to a larger number of hot spots and flow models. These models combine large-scale mantle convection with smaller-scale features such as hot spots, whose

present-day locations are constrained by observations. This approach is most reliable in the Tertiary and has provided estimates for TPW, nondipole fields, and the motion of individual hot spots relative to each other for the last 68 Ma.

When these models are extended back to the Cretaceous, however, the advection of mantle density anomalies may result in runaway instabilities and other artifacts. Nevertheless, hot spot motion can still be computed prior to 68 Ma but with an additional uncertainty resulting from changes in mantle density structure and hence unaccounted mantle flow. Test runs for models from 120 Ma to the present, either including or excluding the advection of mantle density anomalies, have shown that there are many similarities between the two types of models. This indicates that meaningful predictions for relative hot spot motion can be made based on a simple mantle convection model constrained by time-dependent plate motions and constant mantle density heterogeneities. This strategy was used by O'Neill et al. (2003, 2005) to model the motion of plumes in a convecting mantle relative to each other, in the context of an 'interactive inversion' strategy. They explored the large parameter space inherent in these models to search for those mantle convection models that provide the best-fit to observed hot spot tracks and their age progression and minimize the disagreements between model-based paleolatitudes and paleolatitudes from paleomagnetic data. O'Neill et al. (2003, 2005) adopted the Hellinger criterion of fit (Hellinger, 1981) for deriving best-fit absolute plate rotations based on track geometries, radiometric ages, and the moving locations of plumes in a convecting mantle to derive covariance matrices for absolute rotations of plates in the Indo-Atlantic domain for the last 120 million years.

6.02.4.4.4 OMS: a modified Hellinger criterion for absolute plate rotations

The method proposed by O'Neill et al. (2005) for finding absolute plate rotations based on hot spot tracks with age progression is similar to that introduced by Hellinger (1981) for relative plate rotations; it is herein referred to as the OMS method. For relative plate rotations, the two datasets, isochrons and fracture zones, essentially describe two orthogonal types of data. Fracture zones are formed by the toroidal motion of two plates relative to one another; they effectively describe the flow lines of one plate relative to the other. Furthermore, they cut across isochrons; that is, many isochrons can be offset by the same amount by one fracture zone. Paleo-mid-ocean ridge segments of isochrons are reconstructed from the remanent magnetic signature of the ocean crust. Providing the reversal sequence has been identified correctly, the main sources of error are locations and the dates assigned by the reversal timescale.

However, there are important differences between data constraining the history of seafloor spreading and hot spot tracks. One problem with hot spot tracks is the relatively sparse temporal coverage of these tracks (e.g., Wessel and Kroenke, 1997). As a result, the focus of hot spot-based reconstructions has been the fitting of hot spot tracks to present inferred positions of these respective hot spots. These tracks essentially represent the flow lines of the plates relative to the position of the hot spots at the time of their formation. One the other hand, the dating of many hot spot tracks has reached a degree whereby the coverage rivals that of the magnetic anomaly sequence for some areas and times. The problem is that the dated tracks are not uniformly sampled; it is impossible to construct isochrons in the literal sense from sampled hot spot tracks. However, the age uncertainties can be considered along-track, based on the additional constraint that the tracks represent the flow lines. Conversely, assuming the profile normal to the hot spot track is made uniformly, we can say that the uncertainty in the position of the hot spot when it created a particular section is related to the geometry of the track cross section.

This provides us with two orthogonal datasets. We can date portions of hot spot tracks u_{ij} (green stars in Figure 22; i is the segment, j the point ($j = 1, \ldots, m_i$), and m_i the number of isochron points on the ith segment; in our case, 2). While the uncertainties for given 'isochrons' between tracks are likely to be extremely large, it is still possible to estimate the section of a track corresponding to a given time. We also have the track geometry itself (yellow stars in Figure 22), which represents the flow lines of plate motion relative to the underlying mantle, represented by the points v_{ik} ($k = 1, \ldots, n_i$, where n_i is the number of track points on segment i). The track sections are constrained in length, so that the track length considered is less than the converted 'length' of the along-track timing uncertainties. The best-fit rotation will be one that minimizes the misfit of these datasets and the present (or calculated) position of the hot spots responsible for them. The isochron segments are composed of data from two tracks, which must be fit to the two associated hot spot positions, while the track geometry dataset is uniquely fit to its associated hot spot. Thus, we have all the ingredients to estimate a rotation for a given time using the Hellinger criterion, which in modified form finds the rotation that minimizes

$$r(A,\eta) = \left[\overbrace{\sum_{i,j=1,2} \left(\frac{h^t_{i,j}\eta_i}{\sigma_{i,j}} \right)^2}^{\text{Hot spots}} + \overbrace{\sum_{i,j=1,2} \left(\frac{u^t_{i,j}A\eta_i}{\sigma_{i,j}} \right)^2}^{\text{Isochrons}} \right] + \left(\overbrace{\sum_{k} \left(\frac{h^t_k\eta_k}{\widetilde{\sigma}_k} \right)^2}^{\text{Hot spots}} + \overbrace{\sum_{k,h} \left(\frac{v^t_{k,h}A\eta_k}{\widetilde{\sigma}_{k,h}} \right)^2}^{\text{Track geometry}} \right)$$

Here, σ and $\widetilde{\sigma}$ are the uncertainties in the points interpolated from dated locations and digitized points along a track section. This assumes the data can be considered to approximate great-circle segments. This is obviously not true over the lifetime of a hot spot track; bends in the track, changes in rates of plate motion, and, most importantly, hot spot motion all introduce discrepancies into the great-circle approximation. However, if hot spots move an order of magnitude more slowly than their overriding plates, the deviations from the great-circle approximation for a given interval introduce errors much smaller than the errors inherent in the data.

6.02.4.4.5 Uncertainty in hot spot reconstructions using the OMS method

Hot spot reconstructions involve finding the best-fitting rotation that reconstructs volcanic chains to the present assumed position (or calculated past position) of the hot spot that formed them, for two or more hot spots. Thus, one can envisage two sources of error in such reconstructions – uncertainties

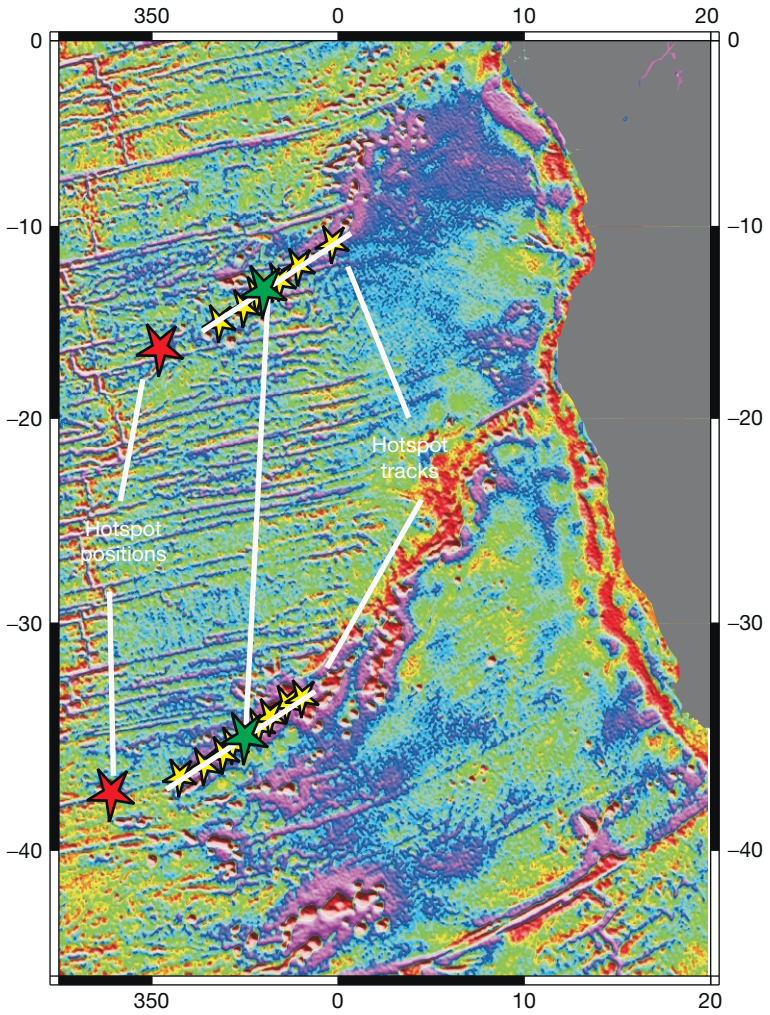

Figure 22 A modified Hellinger criterion of fit for hot spot track reconstructions (O'Neill et al., 2005). Red stars indicate the position of the hot spots, the digitized section of track within the uncertainties of the age we are interested in is shown as yellow stars, and best estimates of the position on the track of the age we want are shown as a green star. The track sections and age positions are considered conjugate datasets (hence, we have three sections here, black lines), and they are both reconstructed to the present position of the hot spot. Modified from O'Neill C, Müller D, and Steinberger B (2005) On the uncertainties in hot spot reconstructions and the significance of moving hot spot reference frames. *Geochemistry*, *Geophysics*, *Geosystems* 6: Q04003.

of the reconstructed sections of volcanic chains and uncertainties in the present-day or calculated past positions of the hot spots themselves.

In some cases, current volcanism has been used to infer the present-day position of a hot spot. For example, current volcanism on Réunion island has been inferred to represent the present surface expression of the Réunion plume (e.g., Müller et al., 1993). There are a number of possible departures from this simple plume–volcanism relationship that affect on our ability to constrain the position of mantle plumes. First is that melt produced by a plume may be advected laterally, either by asthenospheric conduits (Morgan, 1978; Müller et al., 1998) to active ridges or by sublithospheric topography (Ebinger and Sleep, 1998). This leads to the conclusion that volcanism can occur far from the actual position of a plume and that plumes can be responsible for volcanism over a wide area.

To give an example, the Walvis Ridge system is widely attributed to a plume located at Tristan da Cunha (Duncan, 1981; Morgan, 1971, 1972). However, present volcanism occurs on both Tristan da Cunha and Gough Islands (O'Connor and Le Roex, 1992), and both systems have left distinct lineations within Walvis Ridge, each with its own distinct age progression (see **Figure 23**). Which island better represents the position of the plume is unclear. Furthermore, O'Connor and le Roex (1992) suggested that the wide, distributed volcanism of the Tristan da Cunha and St. Helena hot spot systems may be due to the fact that the volcanic centers themselves are more spatially extensive, and more diffuse, than commonly assumed. One possible explanation of this is that plumes are larger than commonly assumed. Until recently, we have had no direct estimate of the diameter of plume conduits, only weak constraints based on their buoyancy flux and our inability to image them tomographically. Recently, Montelli et al. (2004) had presented tomographic images of upwelling plumes. Many of these plumes do not have resolvable features extending to the lower mantle. Others, for example,

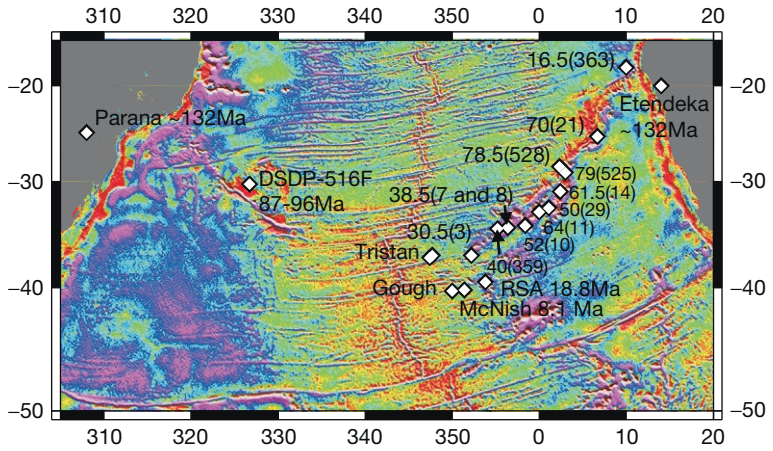

Figure 23 Gravity anomaly map of the South Atlantic, showing the Walvis Ridge and Rio Grande Rise hot spot system. Radiometric age for the ridge system is plotted based on a summary by O'Neill et al. (2003).

Kerguelen–Crozet, appear to have a common source in the lower mantle, suggesting that the initial conduit has split, similar to the suggestion of Coffin et al. (2002). The plume conduits themselves appear to be of the order ~200 km in the upper mantle, suggesting the volcanism we see is only the minor surface expression of fairly large mantle structures.

The uncertainty in the position of a hot spot is even greater for past times. O'Neill et al.'s (2003, 2005) mantle flow calculations and conduit modeling represent one attempt at constraining these past positions; however, the physical uncertainties in the input to these calculations, together with the uncertainties in modeling assumptions, make it difficult to constrain the uncertainties in these modeled positions in a meaningful way.

The uncertainties in reconstructing a volcanic chain can be divided into two groups: those related to the positional uncertainty of a hot spot at the time it created a specific portion of a ridge and those related to the age of that section. To use the Hellinger criterion, we require all the uncertainties in a spatial context, so we translate the age uncertainties into spatial uncertainties by combining them with the estimated angular velocities of the plates (and their uncertainties). Here, we make the assumption that the age uncertainties are larger than the inherent spatial uncertainties. This means that the positional errors need to be constrained by examining profiles across the hot spot chain and assume timing uncertainties, when converted to spatial uncertainties, fall along-track. The combined uncertainties for a given data point thus form an error ellipse centered on that point and elongate along the direction of the volcanic chain.

Figure 24 shows a gravity anomaly profile (Sandwell and Smith, 1997) across the Ninetyeast Ridge. This profile possesses a degree of uncertainty, in that we have inherent positional uncertainties of the satellite recording the data, and whatever geometric distortions are introduced by the gridding of the data. The highest peak of the ridge is assumed to represent the position of the plume at the time it formed this section. To find this, a one-dimensional low-pass filter is applied to the data, and a simple gradient algorithm is used to find the highest peak. For noncontinuous volcanic chains (e.g., seamount chains), this approach requires manual editing. To estimate the uncertainties in this position, we use the half-width of the profile. This is defined by the intersection of the profile with a point halfway between its maximum height and average background value (mean of the lower quartile).

The uncertainties of the ages of hot spot tracks stem first from the inherent uncertainties in radiometric ages. Given the great expense in obtaining oceanic samples, often, the quality of such samples is of small consequence in obtaining an age for them. The uncertainties in radiometric age are minor considering the systematic uncertainties in assigning an age to a particular portion of a volcanic chain.

A serious issue from a statistical point of view is due to the uneven sampling of volcanic chains and our inability to construct 'isochrons' in the standard sense. O'Neill et al. (2005) assumed a linear rate of spreading between dated points on hot spot tracks, to construct points for the times we are interested in. These points inherit uncertainties from the dates of the locations they are constrained from and from the assumption of spreading rate.

Finally, hot spot track age uncertainties must be converted into spatial uncertainties for use with the Hellinger criterion of fit. This involves combining the time error with the plate's angular velocity for that time, generally obtained from previous fixed hot spot reconstructions. This angular velocity has its own inherent uncertainty, and this must also be considered, and so the spatial uncertainty becomes

$$\Delta d = \Delta t \Omega + \Delta t \Delta \Omega$$

The error ellipses, for example, points along the Ninetyeast Ridge, at 10 Myr intervals, are shown in Figure 24. The elongate axis reflects the large time uncertainties of each point, expressed along the trend of the volcanic chain.

6.02.4.4.6 WHK: a hot-spotting–PFRM hybrid method

Wessel et al. (2006) extended the PFRM proposed by Harada and Hamano (2000) in several major ways, resulting in a hybrid method referred to as the WHK method. First, rather than relying on subjectively defined containment envelopes for each chain (since these become unconstrained where there are no significant surface expression of volcanism), they chose

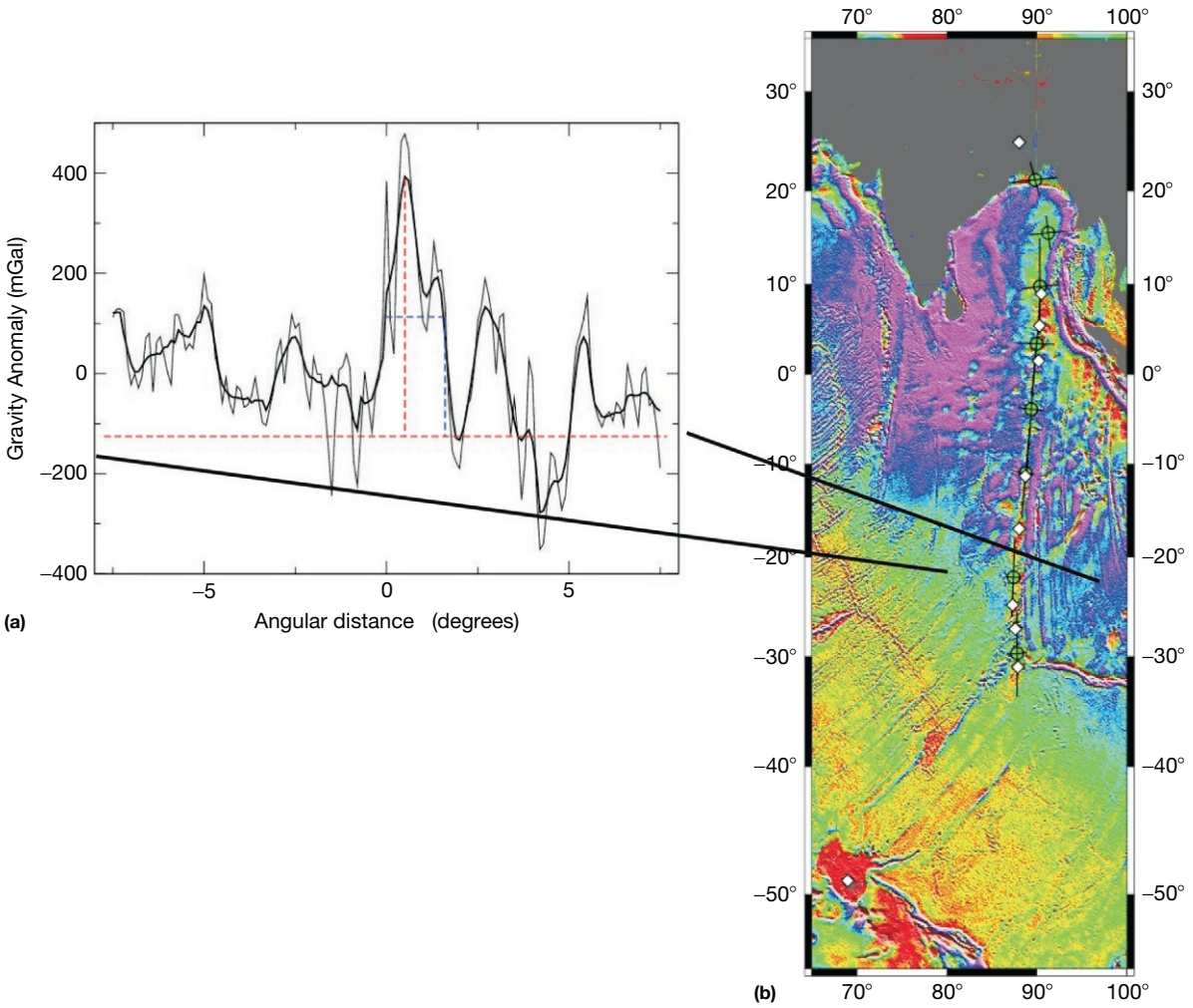

Figure 24 (a) Gravity anomaly cross section of the Ninetyeast Ridge, for the segment shown in (b). The highest point is defined by taking a 1-D filter of the data (thick line) and using a simple neighboring gradient method. The half-width of the profile is defined as the point where the profile crosses the average of the maximum and the average of the lower quartile (assumed base level of the profile). (b) Gravity anomaly map of the Ninetyeast Ridge, showing the profile half-widths as defined in (a) and the along-track errors, which are a combination of radiometric age errors, systematic time errors (see text), and plate velocities, together with their uncertainties, at 10 Myr intervals. The resulting error ellipses are extremely elongate along-track. Modified from O'Neill C, Müller D, and Steinberger B (2005) On the uncertainties in hot spot reconstructions and the significance of moving hot spot reference frames. *Geochemistry, Geophysics, Geosystems* 6: Q04003.

instead to use actual seamount signatures as expressed in high-resolution bathymetry grids to constrain the geometry. Specifically, the 2 min predicted bathymetry of Smith and Sandwell (1997) was high-pass-filtered to remove regional depth variations and isolate the seamount chains. Conservative envelopes were then used to exclude seamounts too far from any hot spot trail, resulting in their starting point for geometric modeling. This approach allows for gaps in coverage along trails. All grid nodes inside a seamount base contour were assigned unique chain identifiers so that overlapping trails could be handled (**Figure 25**). The number of chains that can be fitted for a given opening angle is thus variable. Rather than using a Monte Carlo inversion, they solved for all possible rotations using a grid search. The selected hot spot locations were rotated using the negative rotation so that the projected points would fall somewhere along the respective tails. Rotations that produced reconstructed points on or close to the trail (the cutoff depended on the uncertainty of the hot spot location) for two or more chains were kept; the remaining rotations were discarded. This procedure resulted in thousands of rotations for a wide range of opening angles.

Second, the population of rotations that were consistent with the given chain geometries was examined further in order to exclude rotations that were outliers with respect to the main trend. Because gaps along chains were explicitly treated, up to six chains could be included in the fitting, although the number varies with opening angle. Wessel and Kroenke (2008) extended this work to 12 chains, with a maximum of 6 chains fit simultaneously (**Figure 26**).

Third, they incorporated the hot-spotting principle to refine the locations of the starting points (hot spot locations) for each chain. This, of course, is only possible for long-lived chains reflecting significant changes in plate motion and furthermore is only valid for a situation in which the hot spots have not

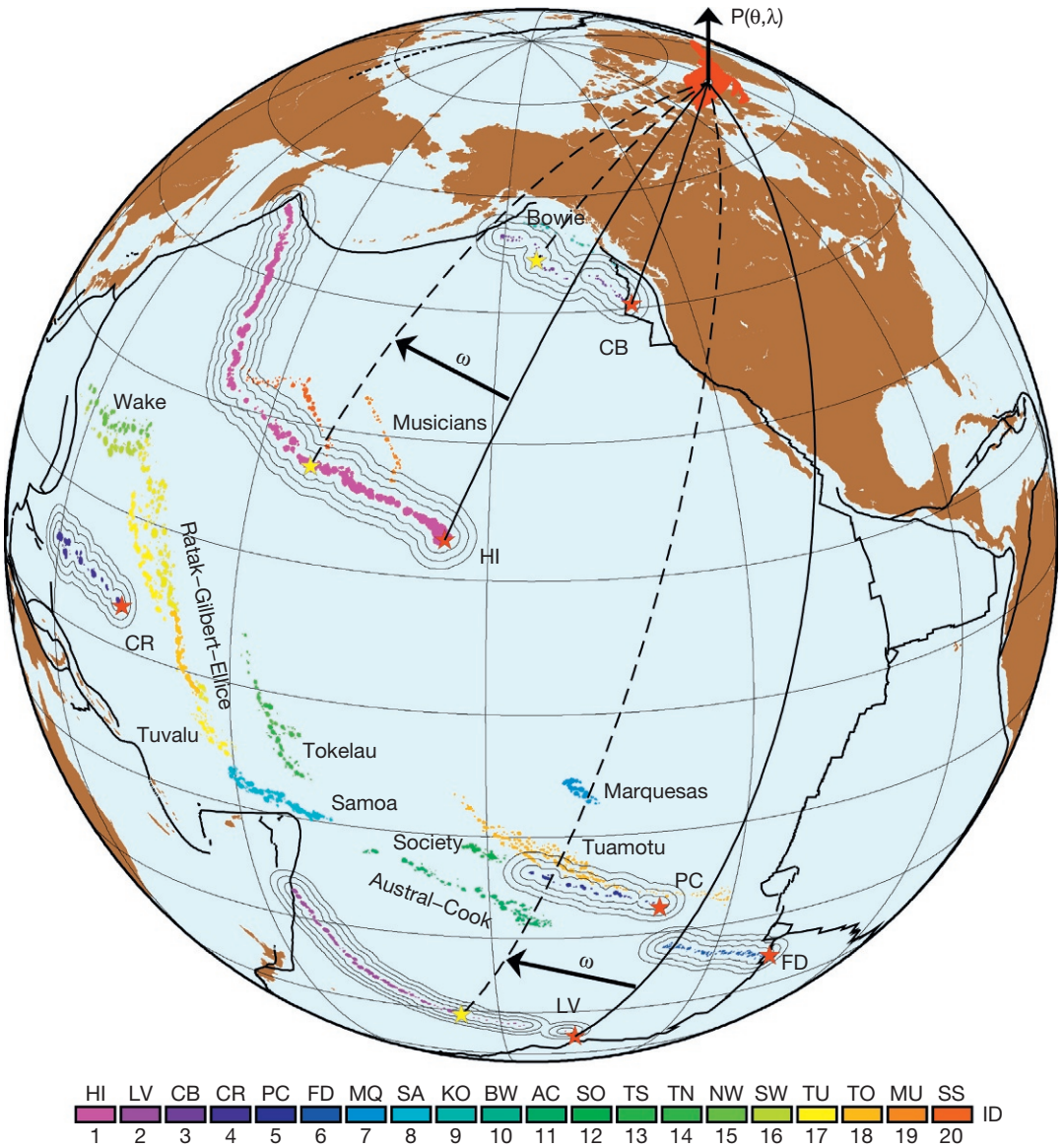

Figure 25 Seamount data constraints generated from the Wessel and Lyons (1997) seamount database. Unique chain ID numbers have been assigned to each seamount (as color-coded). The PFRM works by brute-force grid search of all possible rotations. For each trial rotation, here exemplified by the rotation pole P at (70° N, 66° W) with an opening angle of $\omega = 18°$, the M hot spot locations (red stars: HI, Hawaii; LV, Louisville; FD, Foundation; PC, Pitcairn; CR, Caroline; and CB, Cobb) are reconstructed (yellow stars). If two or more of these reconstructed points fall on or very close to their respective seamount chain, the rotation is included in the further analysis. The cluster of poles near P (red dots) represents all the rotations that passed the test for all opening angles in the $17° \leq \omega \leq 19°$ interval. Additional chains (shown but not used in the modeling) are Marquesas (MQ), Samoa (SA), Kodiak (KO), Bowie (BW), Austral–Cook (AC), Society Islands (SO), southern (TS) and northern (TN) Tokelau, southern (SW) and northern (NW) Wake, Tuvalu (TU), Tuamotu (TO), Musicians (MU), and Liliuokalani (SS). Figure redrawn from Wessel et al. (2006).

moved significantly. In essence, once a smooth geometric model of rotations was obtained, hot-spotting was applied to see if the optimal hot spot locations implied by the CVA maxima corresponded to the initial selection of hot spot locations. If a difference was discovered, the hot spot location would be moved accordingly and a new population of rotations was calculated using the modified hot spot locations. Several iterations were required before the process stabilized.

Finally, they improved the statistical treatment of the rotation population by determining representative average rotations for key isochron ages rather than for predetermined ranges of opening angles (as in Harada and Hamano, 2000). This was achieved by combining all age data (for all chains considered) on a single plot of age versus opening angle and then fitting a linear spline to represent the trend. Given the 95% confidence limits on the spline, they were able to project the age uncertainties into angle uncertainties and thus obtain the desired average rotations (**Figure 27**). Finally, their new technique included the construction of uncertainty covariance matrices for each total reconstruction rotation, allowing the uncertainty in the reconstruction to be quantified and displayed on maps. Their preliminary, high-resolution APM

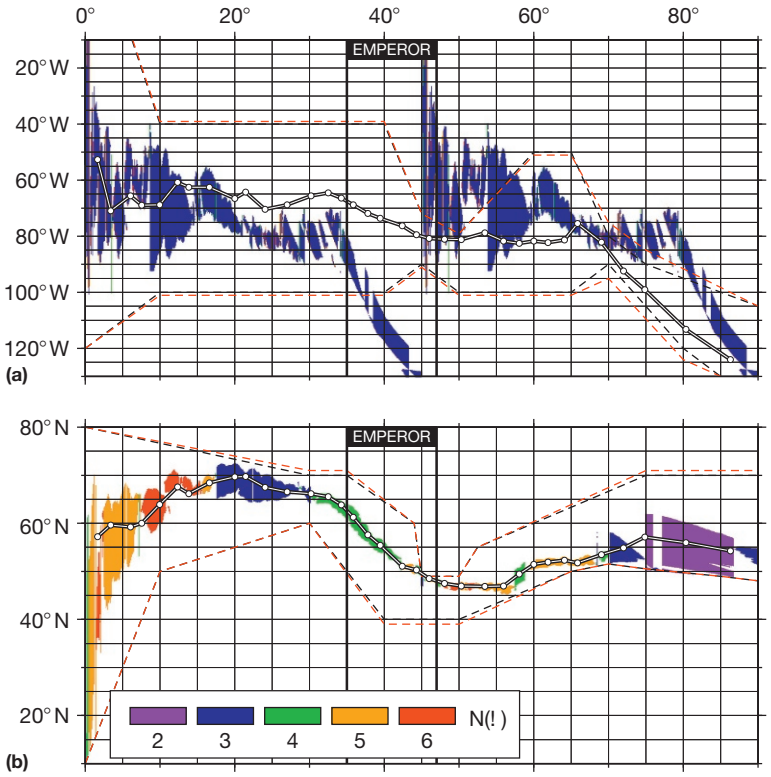

Figure 26 (a) All possible rotation pole coordinates as functions of opening angle (w), color-coded by how many chains were fitted simultaneously (black means rotations were deemed unsuitable on closer inspection). Trial rotations outside the dashed red lines were excluded as they always failed to fit the trails. (a) Longitude of rotation poles. Lines with white dots indicate smoothed model using the initial ~2° window for w. (b) Same for rotation pole latitudes. These estimates form the geometric part of the WK08-A model. Vertical lines delineate the range of angles corresponding to the 60–90 Ma Emperor stage. Figure redrawn from Wessel and Kroenke (2008).

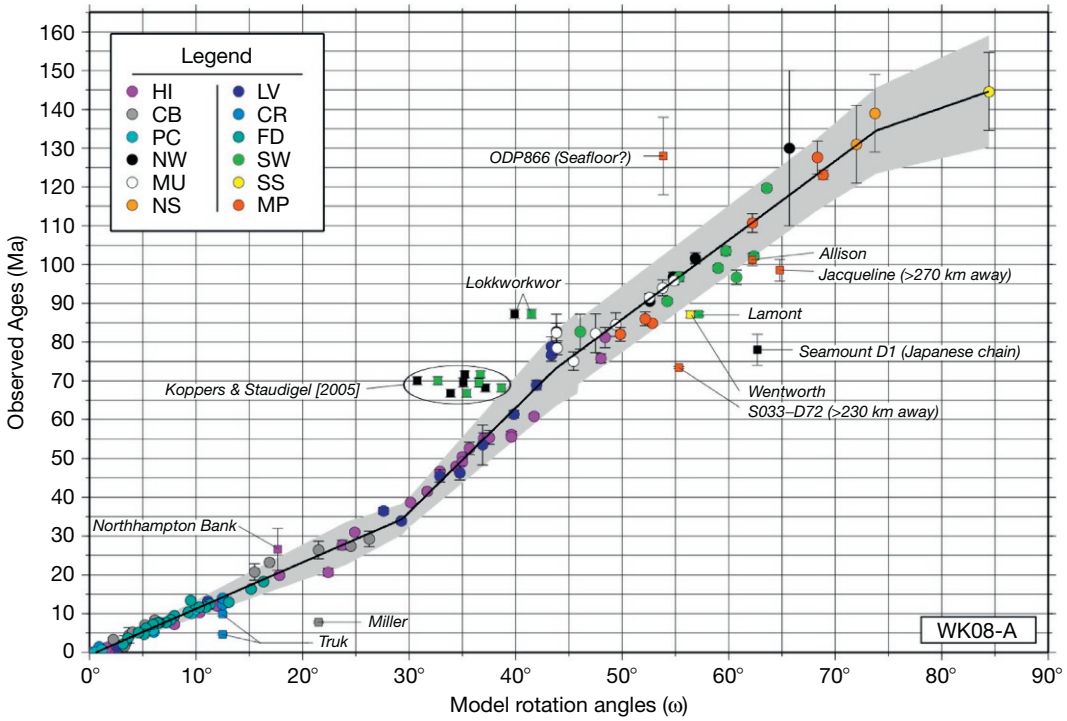

Figure 27 The $t(w)$ plot for the 12 Pacific chains used in the APM modeling with appropriate smoothing that reflects age uncertainties (WK08-A). The linear spline found four significant segments back to 144 Ma. Gray band represents a 95% confidence level for the spline. Given these uncertainties from ages, we project them onto the opening angle (w) axis to yield new w – windows to use for the smoothing of rotations (**Figure 26**). Circles represent samples used in the interpolation, whereas squares are samples rejected for reasons stated in the text. Some individual samples from the overlapping strands in the Ratak–Gilbert–Ellice chains appear twice (i.e., as both NW and SW with same age but different w) as they could belong to either chain. Figure redrawn from Wessel and Kroenke (2008).

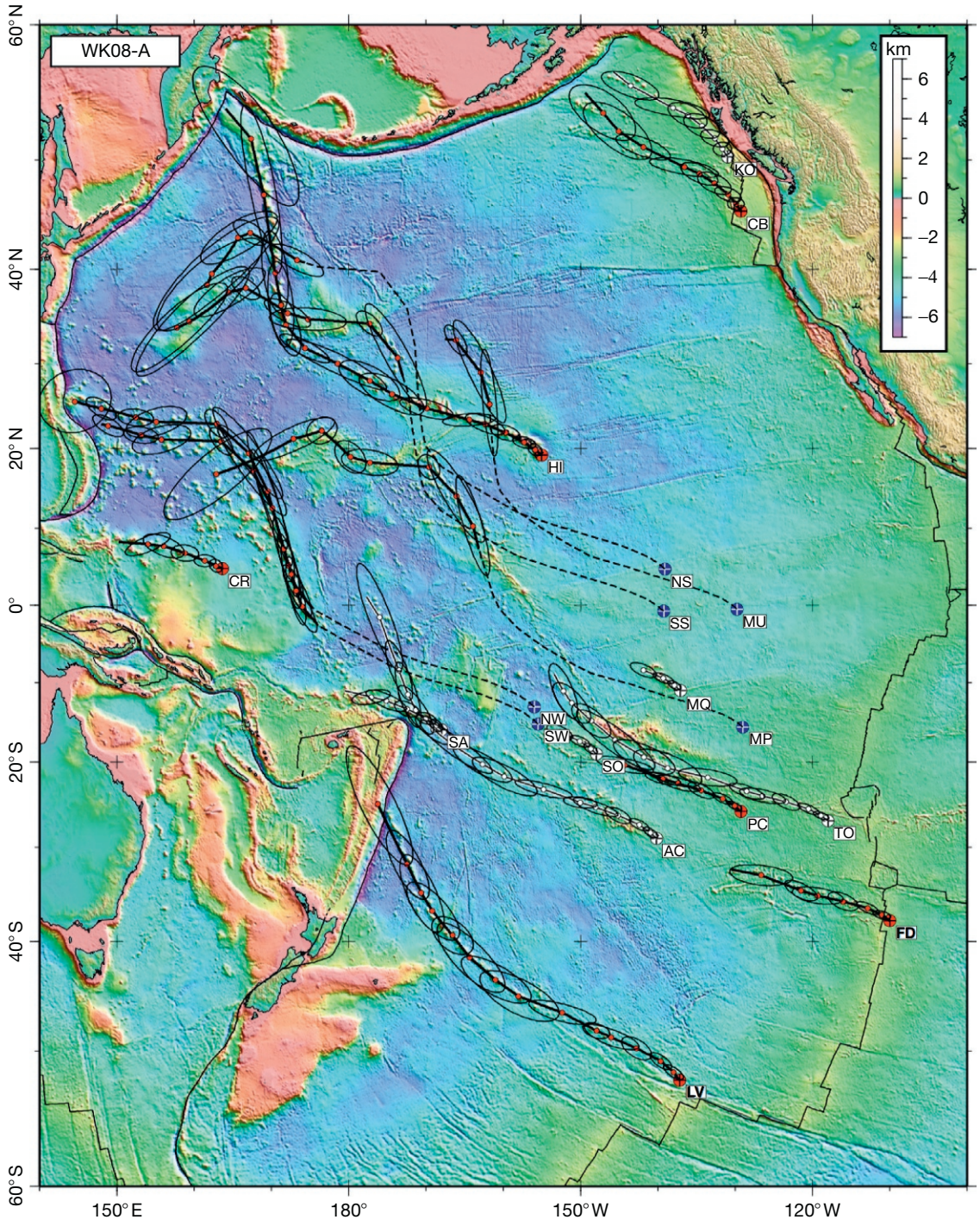

Figure 28 Pacific Plate with predicted tracks and 95% confidence ellipses on reconstructed points (red and white) along each trail for the WK08-A APM model. Solid black lines (and red points) are used for trails that constrained the model, with open lines (and white points) for prediction at other trails. Red (blue) circles indicate the model locations of active (extinct) hot spots; white circles show other hot spots not used in determining the APM. Long dashed lines connect extinct hot spots with assumed seamount chain. See caption of **Figure 25** for chain abbreviations. Figure redrawn from Wessel and Kroenke (2008).

model fits the data well, and its predictions for hot spot chains not used in the solution are satisfactory (**Figure 28**). Their findings suggest that the uncertainties or variability of radiometric ages makes it difficult to discern whether or not the Hawaiian or other Pacific hot spots have moved significantly with respect to each other based on geometry and age data alone. There is no age or geometry evidence that suggests significant motion of plumes since the formation of the HEB around chrons 21–22 (Sharp and Clague, 2006); this conclusion is corroborated by the paleolatitudes of Hawaiian

seamounts (Sager et al., 2005). However, prior to that time, the fewer seamount chain constraints and larger age scatter may suggest the need for additional model parameters (i.e., hot spot motion); the additional parameters would make it easier to reconcile the paleomagnetic data (Tarduno et al., 2003) and observed changes in the inter-hot spot separations (Wessel and Kroenke, 2009).

6.02.4.4.7 Comparison of the OMS and WHK modeling techniques

Since the OMS (O'Neill et al., 2005) and WHK (Wessel et al., 2006) techniques overlap in scope, we will compare them and discuss some of their similarities and differences. However, as both techniques have been introduced very recently, the approaches taken are somewhat different, and to date, they have been applied to different ocean basins; a direct comparison of model parameters is not yet possible.

Unlike classical APM modeling techniques, both techniques find total reconstruction rotations and provide rigorous covariance matrices that describe the uncertainties in the model rotations. The OMS method derives these from a modified Hellinger criterion, and thus, the parameterization of uncertainties is identical to that used in RPM studies; this is advantageous when combining APM and RPM rotations. The WHK technique, on the other hand, considers a different criterion of fit and hence is likely to yield a slightly different solution than OMS. Another advantage of the OMS method is that it works equally well with both fixed and moving hot spots (provided past hot spot locations are prescribed as functions of time), whereas the WHK method currently requires past hot spot locations as a function of opening angle; iterations will be required to extract a compatible angle–time relationship. The current locations of hot spots are input parameters for both methods. However, for fixed hot spots, the WHK method will adjust these locations for an optional fit using the hot-spotting test; this is not done in OMS. The OMS method needs to linearly interpolate between dated samples to determine points along the chain for the times of interest. The large uncertainties in ages therefore propagate directly into the locations chosen to determine the rotation. The WHK method does not need to use ages to determine points to be used in determining rotations; it first uses all points to determine an accurate motion path and only secondly analyzes the stacked ages to determine the history. The OMS technique must also make the approximation that the data can be considered great-circle segments; however, this is only likely to introduce minor errors. Finally, while the WHK method produces a smooth APM model by virtue of averaging thousands of rotations, the OMS technique has no mechanism for smoothing and consequently can generate a nonsmooth age progression along the hot spot track. Further development to address the shortcomings is likely to improve both techniques.

6.02.4.5 Global Ocean Basin Reconstructions

Because numerous plate pairs share divergent plate boundaries, it is possible to link plates not directly connected via intermediate plates that do share such boundaries, thus forming a plate circuit or plate chain (Cox and Hart, 1986). These relationships allow relative plate motions determined for one ocean to be propagated into other ocean basins. While limited versions of global models using plate circuits have been assembled since the beginning of plate tectonics (e.g., Le Pichon, 1968), more recent efforts have culminated in global models such as those presented by Torsvik et al. (2008) and Seton et al. (2012). In particular, Seton et al. (2012) constructed a new type of global plate motion model consisting of a set of continuously closing topological plate polygons with associated plate boundaries and plate velocities since the breakup of the supercontinent Pangaea. The uncertainties of reconstructing mid-ocean ridges and flanks in the Jurassic (~200–145 Ma) are substantial and arguably hard to quantify given that we depend on information preserved in the present-day ocean crust. However, even though the details of those mid-ocean ridge geometries are unknown, we can make reasonable estimates applying the principle of Occam's razor paired with the rules of plate tectonics as a guide to available geophysical and geologic data constraining mid-ocean ridge geometries through time.

Preserved magnetic lineations in the Pacific Ocean provide unequivocal evidence that a vast mid-ocean ridge system existed in the Pacific Ocean in the mid-Cretaceous/late Cretaceous, significantly longer than today's ridge system, and much of which is now subducted – this was first recognized by Larson and Chase (1972). Subsequent detailed mapping and compilation of magnetic M-sequence anomalies in the northwestern Pacific Ocean (Nakanishi et al., 1992) revealed the complete Mesozoic magnetic anomaly lineation pattern in this area. Nakanishi et al. (1992) wrote that "Reconstruction of the Late Jurassic lineations (e.g., in the East Mariana, Nauru and Central Pacific basins) reveals an exact shape of the Pacific plate in that period" – implying that the mid-ocean ridge system bounding the Pacific Plate can be reconstructed all the way back to the Jurassic. Their work also revealed the origin of the Pacific Plate as a triangularly shaped microplate at a triple junction in the Panthalassa Ocean basin, the predecessor of the Pacific Ocean. This forms the basis of Seton et al.'s (2012) Pacific Ocean reconstructions (**Figure 29**).

The longest now vanished mid-ocean ridge that once formed part of this ridge system is the Izanagi–Pacific ridge. Nakanishi et al. (1992) emphasized that the complete pattern of magnetic lineations preserved on the Pacific Plate reveals the configuration of the Pacific–Izanagi–Farallon triple junction, as the magnetic bight between the Japanese and the Hawaiian lineation sets is clearly identified. There are uncertainties associated with reconstructing the exact history of ridge subduction, asymmetries of spreading where we only have information on one plate preserved, and several other aspects of the exact mid-ocean ridge configuration in the Pacific Ocean in the Mesozoic. Seton et al. (2012) assumed that the triple junction between the Izanagi, Farallon, and Phoenix Plates that is known to have existed in the Late Jurassic based on magnetic lineations preserved in the West Pacific Ocean (Nakanishi et al., 1992), existed in similar form since the Early Jurassic at 200 Ma paired with an assumption of constant spreading rates between the Izanagi, Phoenix, and Farallon Plates between 200 and 170 Ma, corresponding to the time interval for which no magnetic lineations are preserved.

Seton et al.'s (2012) model includes recently proposed models for the opening of ocean basins between fragments of the Ontong Java–Manihiki–Hikurangi large igneous provinces

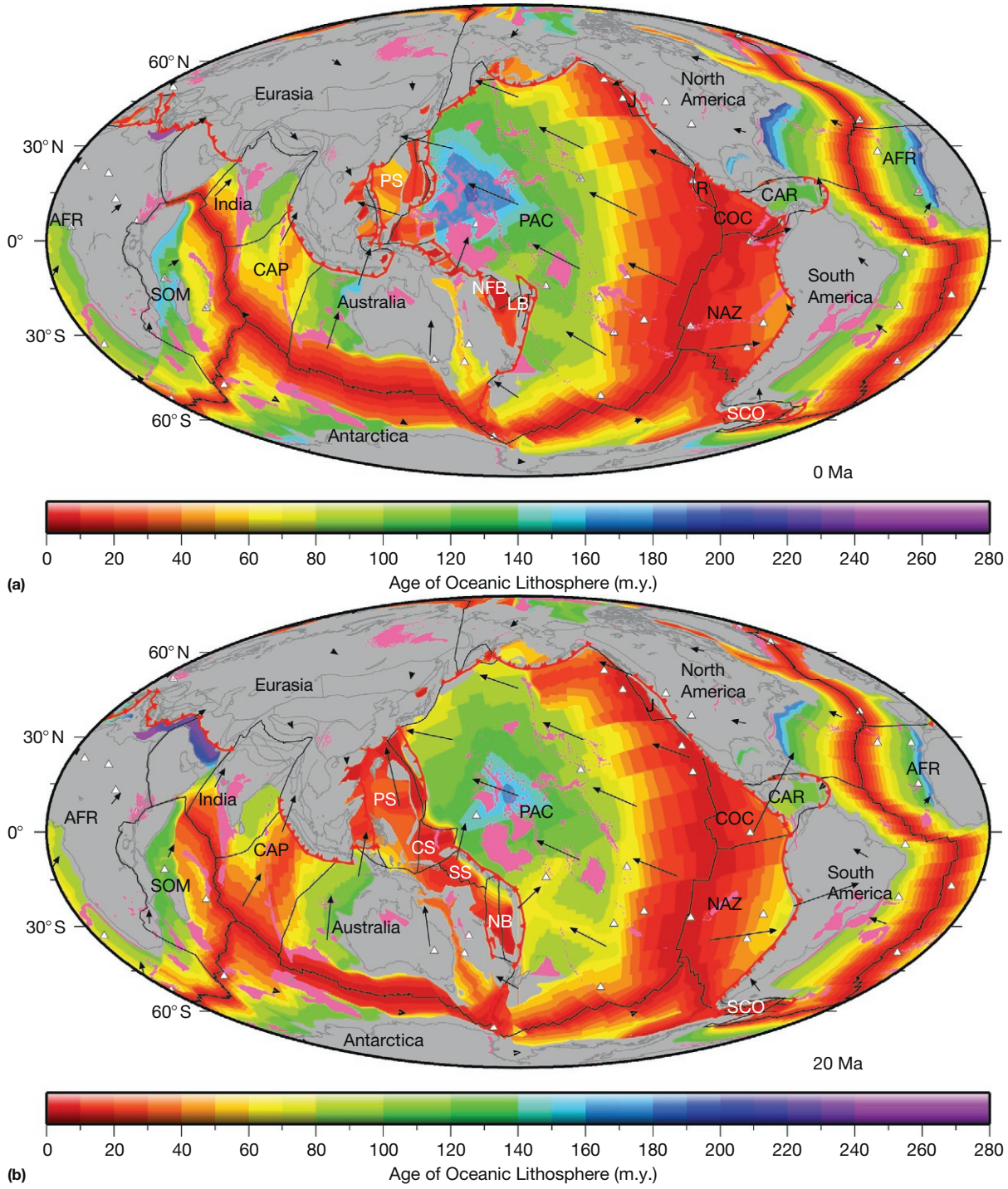

Figure 29 (Continued)

(Chandler et al., 2012; Taylor, 2006; Viso et al., 2005). In the Tethys, they follow the model by Stampfli and Borel (2002) and Golonka (2007), in which the Paleo-Tethys Ocean is closed in the Late Triassic/Early Jurassic, associated with the stepwise collision of a series of Gondwanaland ribbon continents with Eurasia. By using combined evidence from preserved magnetic lineations, and geologic data from accreted terranes such as 'Argo Land' and the rules of plate tectonics (Cox and Hart, 1986), it is possible to constrain the overall geometries of Tethys mid-ocean ridges quite well, as demonstrated by Heine et al. (2004). The closure of the Mongol–Okhotsk Ocean between 200 and 150 Ma is modeled after van der Voo et al. (1999). In their model, the breakup of the supercontinent Pangaea occurs in the central North Atlantic around 200 Ma (Labails et al., 2010) followed by the formation of the Pacific Plate about 190 Ma (Seton et al., 2012).

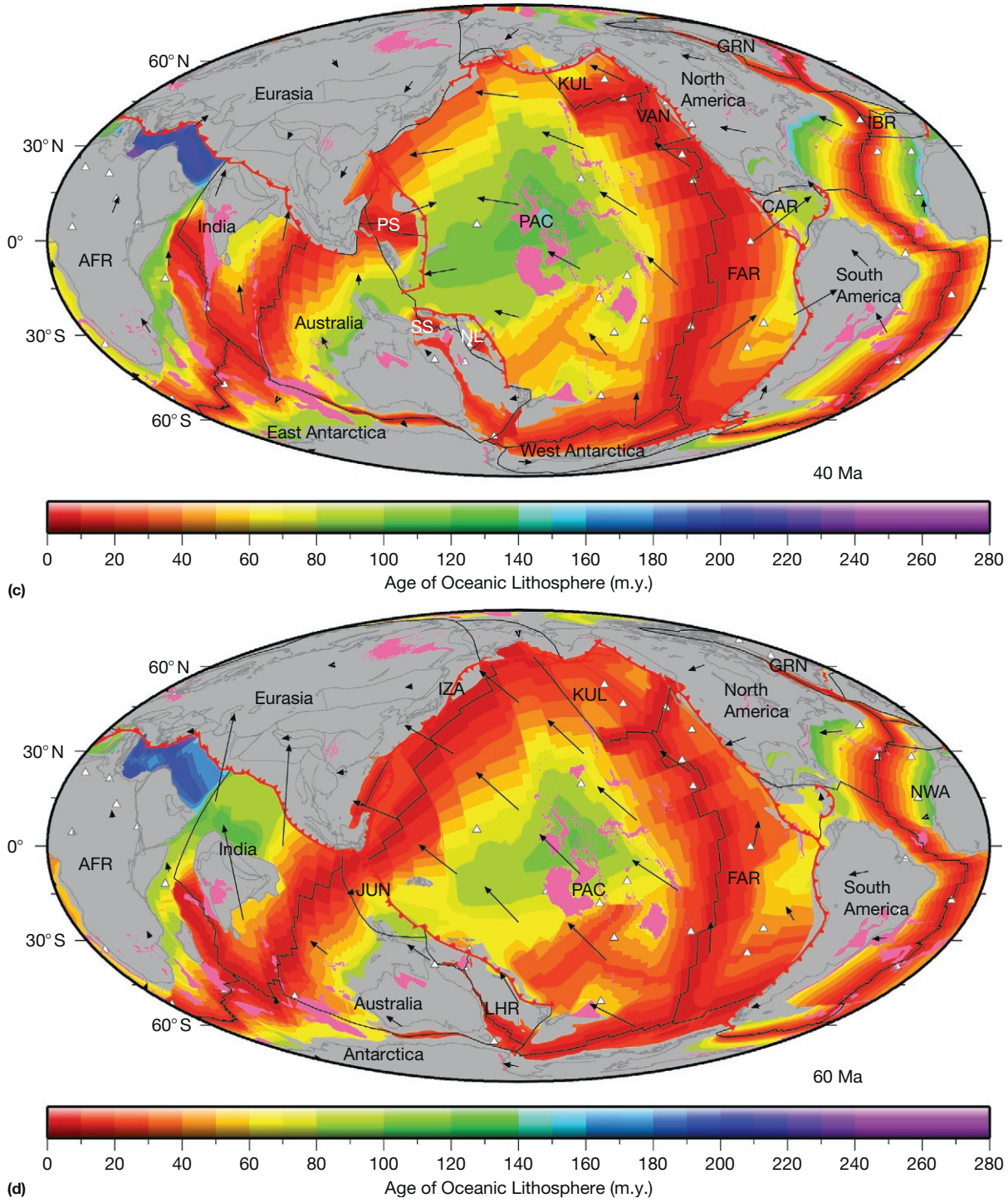

Figure 29 (Continued)

6.02.4.6 APM Models, Paleomagnetics, and TPW

APM models have traditionally been determined for a single plate (e.g., Pacific) or a set of plates connected by ridges (e.g., Africa and neighbor plates in the Indo-Atlantic). It is therefore of interest to propagate these predictions into other oceans using the plate circuits mentioned earlier so that APM models may be compared. As mentioned earlier, Molnar and Stock (1987) first showed that the hot spots in the Pacific appear to have moved relative to the set of hot spots used to determine Indo-Atlantic APM; however, Andrews et al. (2006) found that this relative motion is only significant prior to 68 Ma. There are two important issues that make these comparisons challenging. First, a key

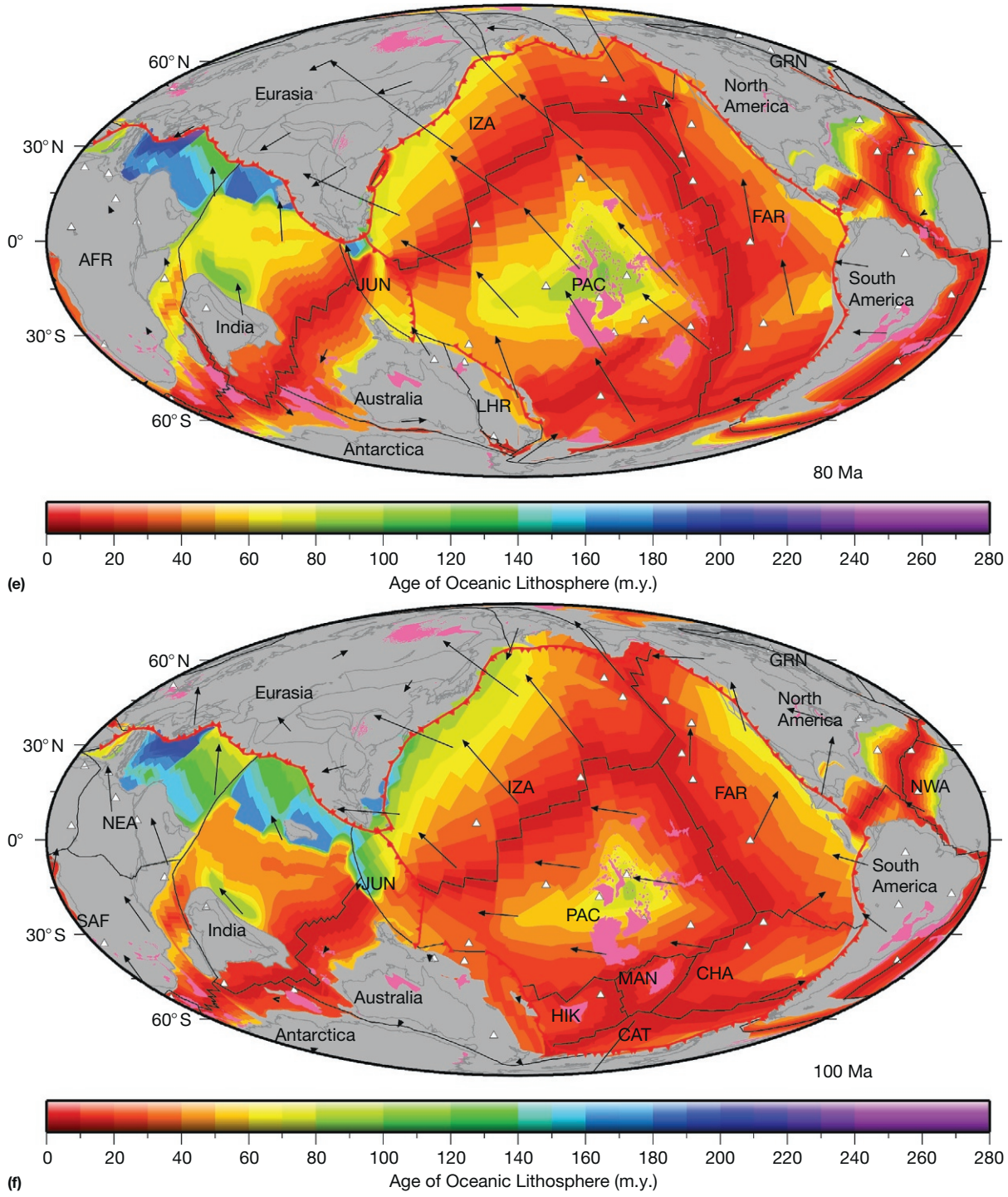

Figure 29 (Continued)

problem area in designing global plate circuits is the connection via West Antarctica. Because the boundary is located in the Ross Sea, the motion between East Antarctica and West Antarctica remains difficult to determine with precision. Seafloor spreading in the Adare Trough was first identified by Cande et al. (2000), but data remain sparse and relatively small changes in the RPM estimates propagate to give relative large changes elsewhere. In particular, continental deformation within the Transantarctic Mountains is difficult to reconstruct accurately, contributing to the total uncertainty. Second, relatively few hot spot chains have adequate (or any at all) sampling for paleomagnetic analysis, making the models incomplete.

A benchmark test for all global APM modeling has been how well an Africa-based APM, after projection via the plate

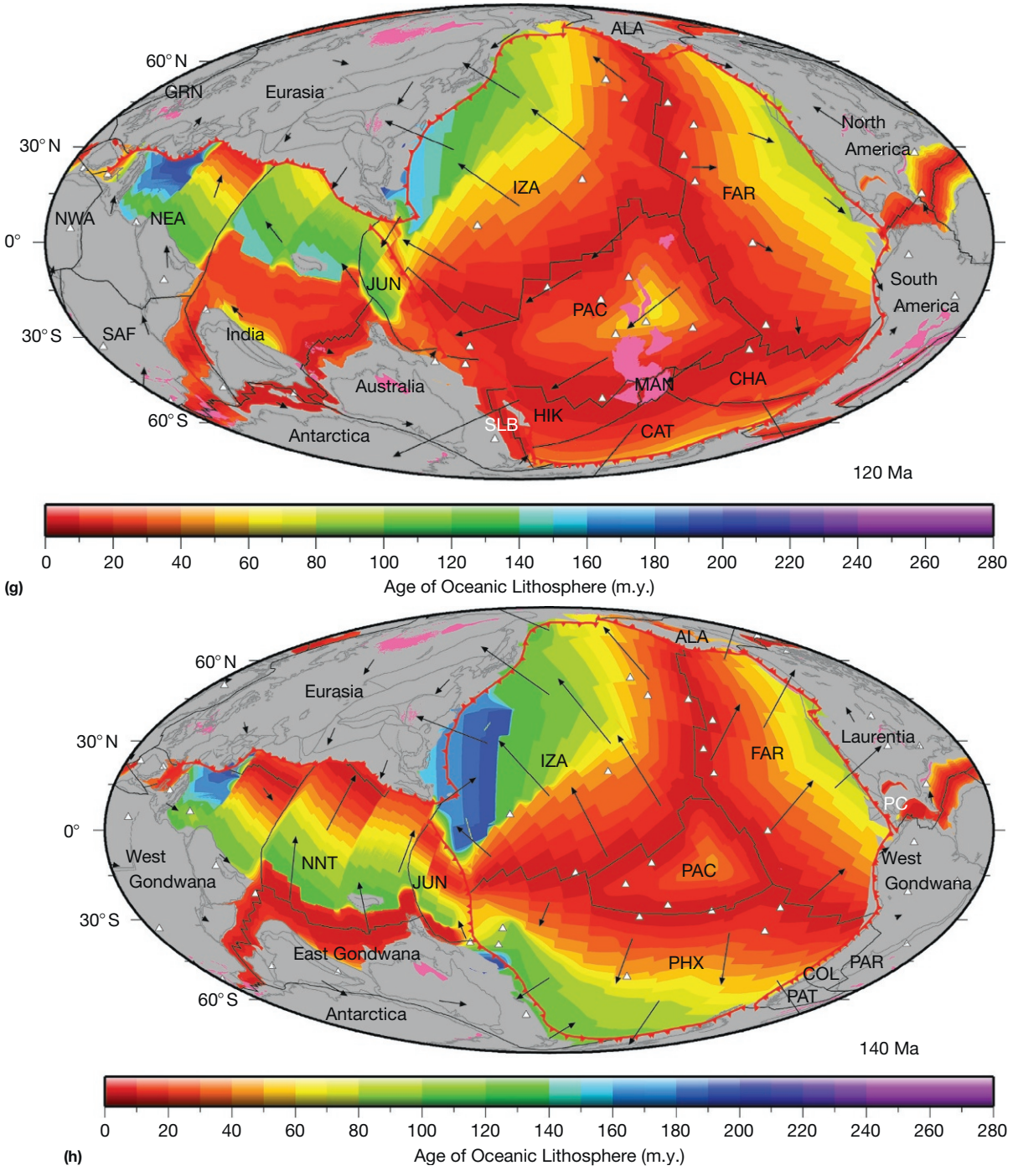

Figure 29 (Continued)

circuit, is able to reconstruct the trend of the Hawaiian–Emperor hot spot trail in the Pacific. Early efforts (Cande et al., 1995; Raymond et al., 2000) showed significant mismatch for reconstructions older than ~40 Ma and were unable to account for the geometry of the HEB. One approach to address this failure was to consider the effect of moving hot spots (Steinberger, 2000). The latitudinal component of such motions can be constrained by paleolatitudes, at least in the case of the Hawaiian plume (Tarduno et al., 2003). It is expected that recently published data from the Louisville chain (Koppers et al., 2012) will be used to constrain its hot spot motion as well. Steinberger et al. (2004) found that by using a moving hot spot APM model for Africa, the predictions in the Pacific depended on which plate circuit was used for the reconstruction. Using the East–West Antarctica circuit employed by Cande et al. (1995) again failed to match the

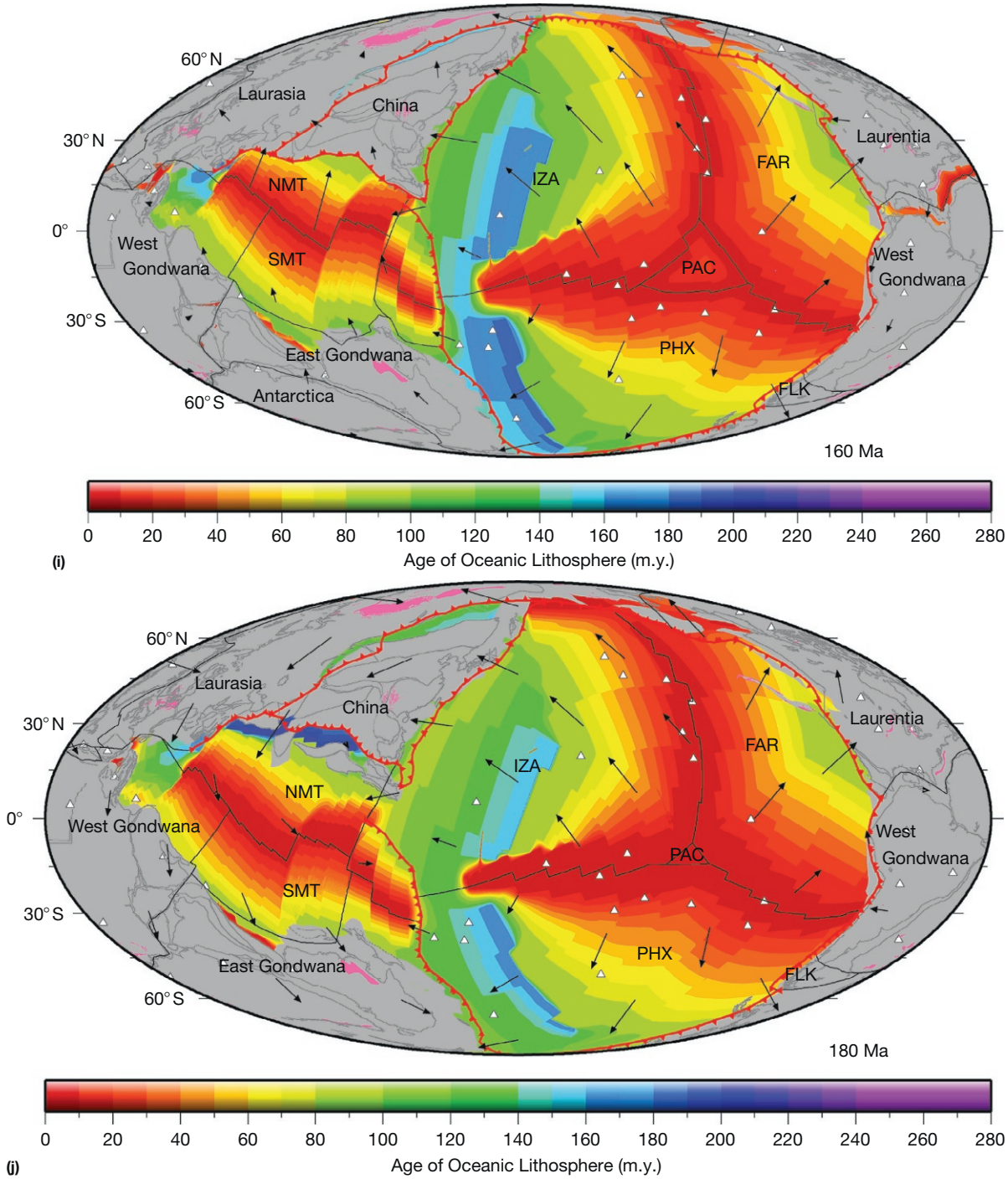

Figure 29 (Continued)

HEB geometry, but if a new circuit that connected Australia to the Pacific via Lord Howe Rise was used (thus bypassing West Antarctica entirely), the fit improved somewhat. This improvement led Doubrovine et al. (2012) to extend the approach of O'Neill et al. (2005) and determine a global APM that satisfied the geometry, age progression, and paleolatitude of five hot spot chains (Hawaii and Louisville on the Pacific Plate, Réunion and Tristan da Cunha on the African Plate, and the New England chain on the North American Plate). Their model championed the Lord Howe Rise circuit and represents a truly global moving hot spot APM model, despite some shortcomings in fitting the five individual hot spot trails. The Lord Howe Rise plate circuit is based on the assumption that there was no subduction east of the Lord

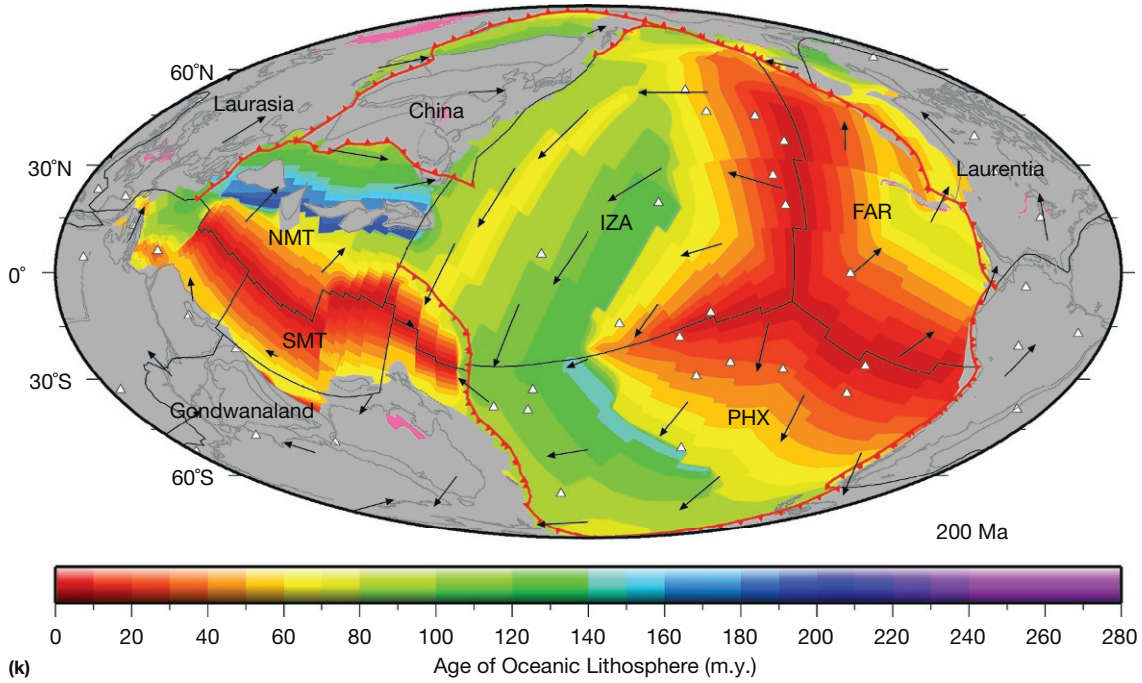

Figure 29 (a) Global plate reconstruction at selected periods. Base map shows the age–area distribution of oceanic lithosphere at the time of formation. Red lines denote subduction zones; black lines denote mid-ocean ridges and transform faults. Pink polygons indicate products of plume-related excessive volcanism, and white triangles are the present-day hot spot locations. Absolute plate velocity vectors are denoted as black arrows. (a) 200 Ma reconstruction: FAR, Farallon; IZA, Izanagi; NMT, North Meso-Tethys; PHX, Phoenix; SMT, South Meso-Tethys. (b) 180 Ma reconstruction: FAR, Farallon; FLK, Falkland; IZA, Izanagi; NMT, North Meso-Tethys; PAC, Pacific; PHX, Phoenix; SMT, South Meso-Tethys. (c) 160 Ma reconstruction: FAR, Farallon; FLK, Falkland; IZA, Izanagi; NMT, North Meso-Tethys; PAC, Pacific; PHX, Phoenix; SMT, South Meso-Tethys. (d) 140 Ma reconstruction: ALA, Alaska; COL, Colorado; FAR, Farallon; FLK, Falkland; IZA, Izanagi; JUN, Junction; NNT, North Neo-Tethys; PAC, Pacific; PAT, Patagonia; PAR, Parana; PHX, Phoenix. (e) 120 Ma reconstruction: ALA, Alaska; CAT, Catequil; CHA, Chasca; FAR, Farallon; GRN, Greenland; HIK, Hikurangi; IZA, Izanagi; JUN, Junction; MAN, Manihiki; NEA, Northeast Africa; NMT, North Meso-Tethys; NWA, Northwest Africa; PAC, Pacific; PHX, Phoenix; SAF, South Africa; SLB, South Loyalty; SMT, South Meso-Tethys. (f) 100 Ma reconstruction: ALA, Alaska; CAT, Catequil; CHA, Chasca; FAR, Farallon; GRN, Greenland; HIK, Hikurangi; IZA, Izanagi; JUN, Junction; MAN, Manihiki; NEA, Northeast Africa; NMT, North Meso-Tethys; NWA, Northwest Africa; PAC, Pacific; PHX, Phoenix; SAF, South Africa; SLB, South Loyalty; SMT, South Meso-Tethys. (g) 80 Ma reconstruction: AFR, Africa; FAR, Farallon; GRN, Greenland; IZA, Izanagi; JUN, Junction; LHR, Lord Howe Rise. (h) 60 Ma reconstruction: AFR, Africa; FAR, Farallon; GRN, Greenland; IZA, Izanagi; JUN, Junction; LHR, Lord Howe Rise; KUL, Kula; PAC, Pacific. (i) 40 Ma reconstruction: AFR, Africa; CAR, Caribbean; FAR, Farallon; GRN, Greenland; IBR, Iberia; JUN, Junction; NL, North Loyalty; PAC, Pacific; PS, Philippine Sea; SS, Solomon; VAN, Vancouver. (j) 20 Ma reconstruction: AFR, Africa; CAP, Capricorn; CAR, Caribbean; COC, Cocos; CS, Caroline; J, Juan de Fuca; JUN, Junction; NAZ, Nazca; NB, Norfolk; PAC, Pacific; PS, Philippine Sea; SCO, Scotia; SOM, Somalia; SS, Solomon. (k) Present-day reconstruction: AFR, Africa; CAP, Capricorn; CAR, Caribbean; COC, Cocos; J, Juan de Fuca; LB, Lau; NAZ, Nazca; NFB, North Fiji; PAC, Pacific; PS, Philippine Sea; R, Rivera; SCO, Scotia Sea; SOM, Somalia.

Howe Rise from about 100 to 50 Ma. However, recent work (Matthews et al., 2012) shows there is petrologic evidence for subduction in this region after 90 Ma, and there is clear seismological evidence of subducted slab material in the lower mantle underneath the Lord Howe Rise region that requires active subduction between the Pacific and the Lord Howe Rise after ~90–85 Ma. This argues for using the East–West Antarctica circuit despite its shortcomings.

The availability of paleolatitudes from the Louisville chain means two chains on the same plate now have considerable latitudinal constraints for their oldest sections. Combined with the time series of inter-hot spot distances (Wessel and Kroenke, 2009), there are now several types of data constraints available for APM models. Models of hot spot motion must broadly satisfy these independent datasets. In particular, the inter-hot spot distances can be computed given dated rock samples from several hot spot chains; such data are much more plentiful than the limited paleolatitude dataset that requires expensive oceanic drilling expedition that hopefully sample enough volcanic flow units to average out the paleosecular variation. Being independent datasets, additions of new chronology and paleolatitude measurements will be exceptionally valuable for future APM studies.

As more paleomagnetic data suggest changes in the latitudes of hot spots through time, approaches such as that of Doubrovine et al. (2012) will likely become refined over time. However, many challenges remain. For reconstructions that go back before 70 Ma, severe numerical artifacts tend to develop in mantle backward advection calculations (e.g., Conrad and Gurnis, 2003). Doubrovine et al. (2012) thus made the choice to limit the backward advection for their plumes to 70 Ma; for older times (i.e., up to 130 Ma), a constant flow field was assumed defined by the density structure reconstructed at 70 Ma. This necessary simplification creates additional uncertainty for the modeled hot spot motions. Further work will clearly be needed to refine global plate circuits and their effects

on global APM models, as well as improvements to the APM models themselves.

TPW is defined as the wholesale rotation of the Earth relative to its spin axis. TPW is believed to occur in response to changing mass distributions about the Earth's spin axis (e.g., Tsai and Stevenson, 2007) and has been called upon to explain tectonic and paleomagnetic puzzles in the Earth's past (e.g., Li et al., 2004). The possibility of TWP complicates the determination of global APM. For instance, in fitting their global APM model, Doubrovine et al. (2012) found evidence for significant amounts of TPW. In particular, they identified two nearly equal and antipodal rotations of the Earth relative to its spin axis for the 90–60 and 60–40 Ma intervals. Other workers have identified episodes of TPW around 100–110 Ma and several instances in the more distant past (e.g., Besse and Courtillot, 2002; Greff-Lefftz and Besse, 2012; Steinberger and Torsvik, 2008). Paleolatitude measurements from oceanic hot spot chains may contain components of TPW; hence, a key challenge of future work is to resolve the contributions from plume motions, TWP, and plate motions.

6.02.5 Driving Forces of Plate Tectonics

Even though it has been shown that surface tectonic plates can be self-consistently generated through 3-D mantle convection (Tackley, 1998), the relative importance of driving forces of the time-dependent plate geometries and velocities of plates is still controversial. The question of what drives plate motion is indeed regarded as one of the most important scientific problems yet to be solved (Maddox, 1998). Identifying the main set of forces is relatively straightforward, but resolving the relative importance of individual forces for driving plate breakup and motion more protracted. Ziegler (1993) argued for the dominance of basal shear traction for causing plate motion. Others argue that basal shear only plays a small role due to weak coupling between the lithosphere and asthenosphere (even though the magnitude and lateral variability of this coupling is still unknown). Forsyth and Uyeda (1975), Richardson (1992), and Carlson et al. (1983) argued that plate-boundary forces are the main driving mechanisms of plate motion. Exactly which boundary forces play the most important role, however, is still an area of hot debate. Forces acting along the boundaries of plates that presumably drive plate motions are mainly caused by the upwelling of hot, buoyant asthenosphere at the mid-ocean ridge and the subduction of cold, dense lithosphere at trenches.

6.02.5.1 Ridge Push

The ridge-push force is often regarded as the primary plate driving mechanism (Coblentz and Richardson, 1995; Meijer and Wortel, 1992; Richardson, 1992), although other authors regard it as secondary to other forces (Carlson et al., 1983; Forsyth and Uyeda, 1975). The ridge-push force originates from a distributed pressure gradient (i.e., a body force) that acts on the entire plate normal to the strike of a mid-ocean ridge. It arises from the isostatic sinking of the oceanic lithosphere away from the mid-ocean ridge as it cools and densifies (Wilson, 1993).

The contribution of this topographic force can be calculated in two ways (Richardson, 1992). Firstly, it can be calculated as a line force acting along the length of the ridge normal to the strike of the ridge. Secondly, it can be calculated as a pressure gradient integrated over a profile perpendicular to the strike of the mid-ocean ridge crossing an entire ridge flank. The second method provides a more accurate result. The ridge-push force F_{rp} can be calculated at a given location by the following equation based on a thermal boundary layer model (e.g., Turcotte and Schubert, 2002):

$$F_{rp} = g\rho_m\alpha_v(T_m - T_0)\left[1 + \frac{2}{\pi}\frac{\rho_m\alpha_v(T_m - T_0)}{(\rho_m - \rho_0)}\right]\kappa t$$

where $g = 10\ \mathrm{m\ s^{-2}}$, $\rho_m = 3300\ \mathrm{kg\ m^{-3}}$, $\rho_0 = 1000\ \mathrm{kg\ m^{-3}}$, $\kappa = 1\ \mathrm{mm^2}$, $(T_m - T_0) = 1200\ \mathrm{K}$, $\alpha_v = 3 \times 10^{-5}\ \mathrm{K^{-1}}$, and t is the age of the lithosphere.

If the plate model (McKenzie, 1967) is applied instead of a thermal boundary layer model, then it follows that that mainly oceanic crust younger than 80 Myr contributes to the ridge-push force as oceanic lithosphere older than this age does not cool considerably, resulting in the cessation of isostatic sinking of oceanic lithosphere older than 80 Myr.

Some authors have also found it advantageous to consider the ridge-push force as a torque acting on the plate. Richardson (1992) used the equation mentioned earlier, integrated over the plate for lithosphere younger than 80 Ma, to give

$$T_{rp} = \int^{A} r \times F_{rp}\,\mathrm{d}A$$

where T_{rp} is the torque from the ridge-push force and A is the area of the plate younger than 80 Ma. Richardson (1992) demonstrated a good correlation between the azimuth of the ridge torque pole and the pole of absolute plate velocity. The T_{rp} has also been shown to correlate well with the direction of the first-order intraplate stress field of the Indo-Australian Plate (Coblentz et al., 1995).

6.02.5.2 Slab Pull

The slab-pull force originates from the negative buoyancy of the downgoing dense oceanic lithosphere at subduction zones and is proportional to the excess mass of the cold slab in relation to the mass of the warmer displaced mantle (Spence, 1987). This density contrast, and therefore energy contribution of the downgoing slab, can also be enhanced by the phase change from olivine to the more dense spinel, which occurs in the downgoing slab earlier than the surrounding mantle (Bott, 1982; Spence, 1987). Negatively buoyant slabs also induce mantle convection as they penetrate the mantle, in turn driving lithospheric plates through shear traction at the base of plates (Conrad and Lithgow-Bertelloni, 2004; Lithgow-Bertelloni and Richards, 1998). Because subduction induces mantle flow toward the downwelling material, these tractions cause nearby plates to move toward subduction zones (Conrad and Lithgow-Bertelloni, 2004; Lithgow-Bertelloni and Richards, 1998).

Energy transmitted to the plate from the downgoing slab must be proportional to the excess mass M_e of the plate (Carlson et al., 1983). The excess mass is given by

$$M_e = \frac{1}{2}(\rho_L - \rho_m)\frac{LE}{\sin\psi}$$

where ρ_L is the density of the lithosphere, ρ_m is the density of the mantle, L is the thickness of the lithosphere, E is the depth at which the excess density vanishes, and Ψ is the dip of the slab (Carlson et al., 1983). The force on the lithospheric plate F_{sp} can then be calculated using

$$F_{sp} = M_e g$$

where g is gravitational acceleration.

Forsyth and Uyeda (1975) regarded slab pull as the main constraint on the velocity of plates (**Figure 30**). They considered the downgoing slab as having a 'terminal velocity' and that the potential energy stored in the downgoing slab is an order of magnitude greater than any other force acting on the plate. The

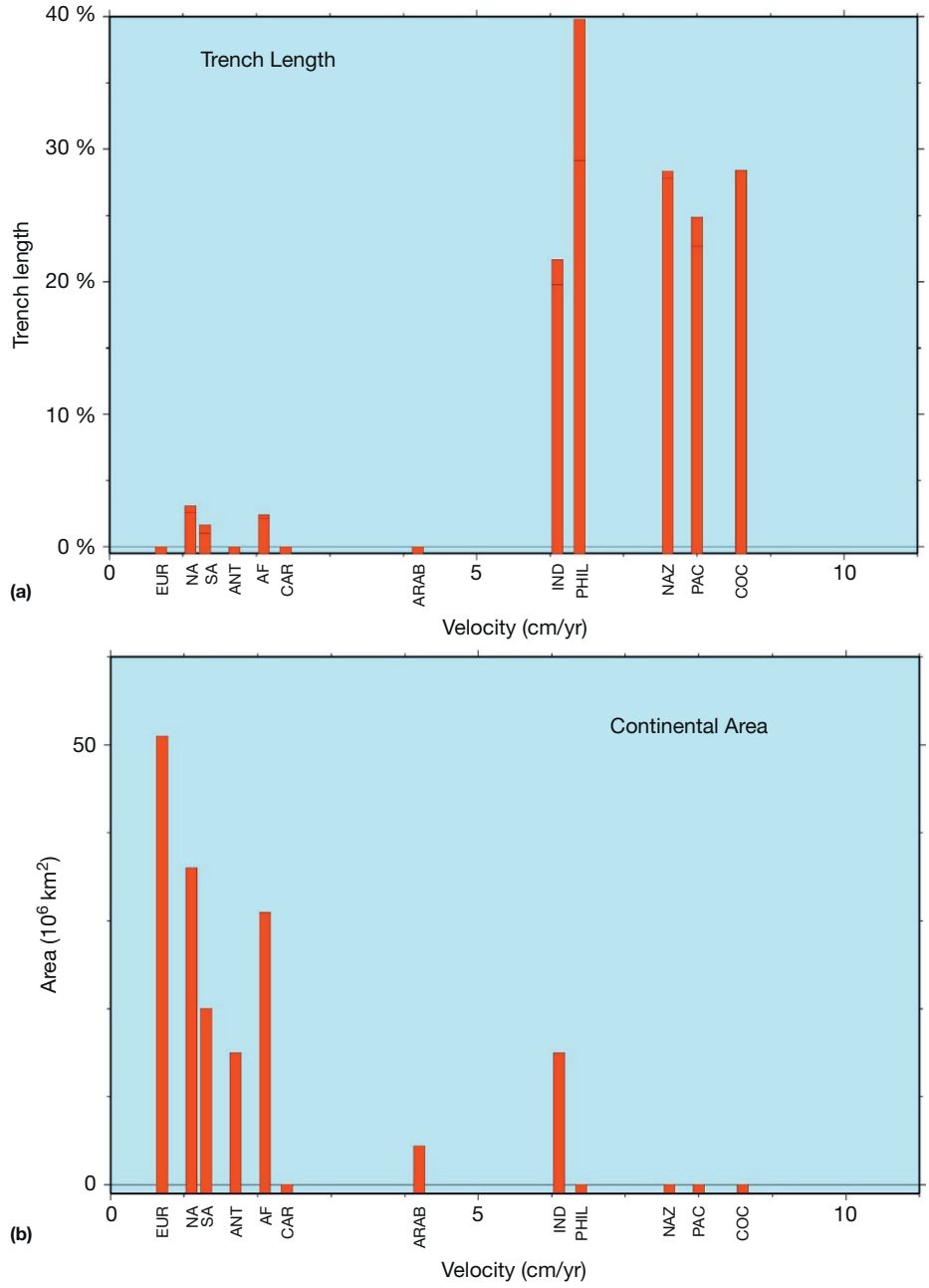

Figure 30 (a) Trench length as a percentage of plate circumference, plotted versus the plate velocity. There is a clear correlation between high velocities and high percentage of trench length, suggesting trench pull is one of the more significant plate driving forces. (b) Area of continental crust associated with a plate plotted versus plate velocity. It is seen that predominantly oceanic plates have significantly higher velocity than continental plates. Redrawn from Forsyth and Uyeda (1975).

exact magnitude of the energy contained in the downgoing slab has been disputed, with Spence (1987) suggesting it may only be three times the size of other forces acting on the plate. Carlson et al. (1983) suggested that the absolute plate speed is determined by the slab-pull force, as a function of the age of the oceanic lithosphere being subducted at trenches, with older subducted lithosphere resulting in higher absolute plate velocities.

The 'terminal velocity' of the plate, as discussed by Forsyth and Uyeda (1975), is due to high viscous drag forces acting on the downgoing slab that impede its entry into the mantle. Some authors have suggested that these viscous drag forces acting on the slab may actually be large enough to almost entirely balance out the negative buoyancy of the downgoing slab (Coblentz et al., 1995; Sandiford et al., 1995). In this case, the 'net force' experienced by the plate from the subducting slab may be of the same magnitude or less than other forces driving the plate. In contrast, Schellart's (2004) recent dynamic lab experiments suggest that the net slab-pull force may be up to twice as large as the ridge-push force, and Conrad and Lithgow-Bertelloni's models (2004) imply that slab suction and slab pull presently account for about 40% and 60% of the forces on plates, with ridge push globally playing a minor role.

6.02.5.3 Collisional Forces

Collisional forces do not act to drive the plate motions, but rather impede them. Collisional forces act along the boundary of plates and arise as a result of the frictional forces between the two colliding plates. At well-coupled subduction zones, there is a buildup of frictional strain energy between the subducting plate and the overriding plate. This energy is then released through earthquakes and crustal deformation. Where the collision of a continental landmass is also involved, loss of energy from plate momentum is converted into excess gravitational potential energy stored as thickened crust (Bott, 1982). For instance, in the case of the collision between India and Asia responsible for the Himalayan orogen, the amount of energy converted into crustal thickening is of the same order as the plate driving forces, as the velocity of the plate slowed upon collision (e.g., Copley et al., 2010; Sandiford et al., 1995).

6.02.5.4 Basal Shear Traction

The notion of shear forces acting at the base of the plates with the convecting mantle acting as a 'conveyor belt' driving the plates, while popular in the past, has fallen out of favor in preference to other plate driving mechanisms. While the relative importance of basal shear forces may be dominant under Pangaea-style megacontinents (Ziegler, 1993), they probably play only a minor role in the kinematics of dispersed plates (for discussion, see Wilson, 1993). Stoddard and Abbot (1996) argued that the crustal roots under cratons act like keels and penetrate a rapidly convecting mantle. This interaction with the rapidly convecting mantle then acts to drive the motion of the plate. However, given our lacking knowledge of the extent of coupling of the lithosphere to the mantle (Coblentz et al., 1995), it is difficult to quantify the relative importance of basal shear relative to other forces.

6.02.5.5 Trench Suction

Trench suction is regarded as a lifting pressure or suction on the upper surface of the downgoing plate caused by an asthenospheric corner flow that is induced by the motion of the descending plate. This force is balanced by the negative buoyancy of the descending lithospheric plate that acts to pull it vertically down by the motion of the descending plate. The balance of these two forces is thought to keep the plate at a finite descent angle (Stevenson and Turner, 1977).

6.02.5.6 Plume Push

Cande and Stegman (2011) extended the catalog of phenomena attributed to mantle plumes by suggesting that they are able to impart a substantial force on plates – a plume-push force – that can do more than just break up continents. Their hypothesis is that if a rising plume head impinges on the base of a tectonic plate long after supercontinent breakup and dispersal, then its pushing force may result in a substantial transient acceleration or deceleration of plates. The velocity of a plate being hit by a plume depends on how the plume-push force balances out with other forces acting on a given plate. Cande and Stegman (2011) developed their model by studying the effect of the Réunion plume, whose incipient head is thought to have reached the surface around 67 Ma, emplacing the Deccan flood basalts in India (Chenet et al., 2007). Using a careful analysis of marine geophysical data from the Indian Ocean, they noted several phenomena associated with this event: India sped up between 68 and 66 Myr ago and subsequently sustained APM speeds of 10–12 cm per year for about 15 million years, with peak speed reaching about 18 cm per year. Between 52 and 45 Myr ago, India's motion slowed down dramatically to less than 4 cm per year. In addition, Africa's motion slowed down while India sped up, only to return to its previous path and speed after India had decelerated (**Figure 31**).

6.02.5.7 What Drives Plate Tectonics?

A major debate concerns a 'top-down' versus mantle-driven mechanism for driving the organization of plates (Anderson, 2001). Abundant plume-driven continental breakup examples and hypotheses associated with magmatic provinces (Coffin and Eldholm, 1992; Dalziel et al., 2000; Ebinger and Sleep, 1998; Storey, 1995) emphasize mantle-driven tectonics. However, the good agreement between long-wavelength features of the intraplate stress field (Zoback, 1992) with the stress orientations predicted by ridge-push forces and large-scale APMs led to the view that plate motions and intraplate deformation result mainly from the balance between ridge-push and collisional forces, emphasizing a 'top-down' mechanism, but without a significant role for slab pull (Richardson, 1992). Alternatively, slab-pull forces have been advocated as the most important driving forces of current plate motions (Conrad and Lithgow-Bertelloni, 2002, 2004; Forsyth and Uyeda, 1975; Schellart, 2004) in a 'top-down' context.

Most analyses of plate driving forces and intraplate stresses are focused on the Earth's present dispersed plate geometry (e.g., Cloething, 1986; Richardson, 1992; Sandiford et al., 1995),

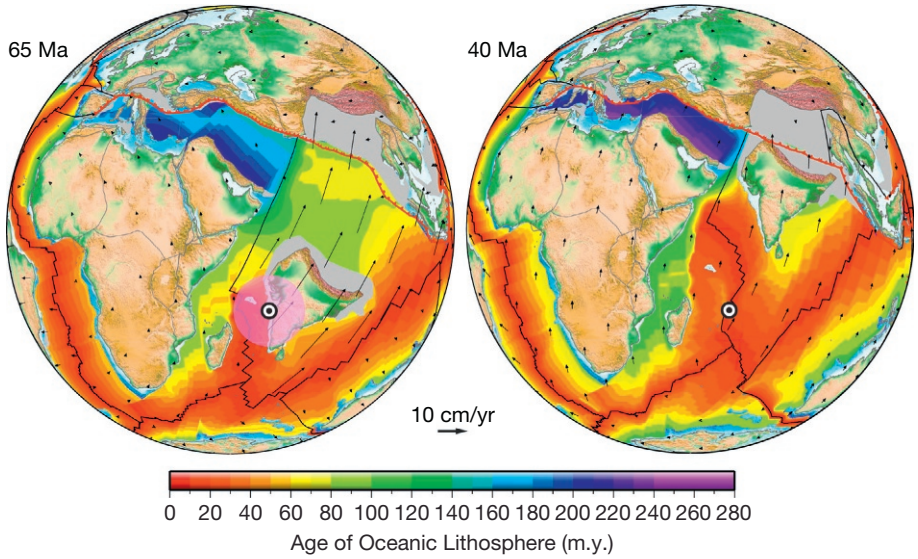

Figure 31 The Indian and African Plates at 65 and 40 Ma. Black arrows represent APMs, with the fast motion of India 65 Myr ago and the slow motion of Africa, corresponding to a time shortly after the Réunion plume head is thought to have arrived at the surface; plume head is hypothesized to have affected the plates' speeds. By 40 Ma, the influence of the plume had waned: The Indian Plate had slowed down considerably and the African Plate had resumed its former direction and speed. Rotated present-day topography is shown on the continents, and seafloor age is depicted in the ocean basins. The estimated extent of now-destroyed continental margins is represented by the gray areas; mid-ocean ridges and transform faults are shown as black lines; subduction zones are shown as a red line, with teeth on the overriding plate. (Plate reconstructions generated using the GPlates1.2 software, data, and rotations.)

where ridge push is a major contributor to plate motions; most continents are under gravity-controlled compression; and the most prominent intracontinental rift, the Afar Triangle in Africa, is driven by the excess gravitational potential produced by plume-driven uplift (Ebinger and Sleep, 1998). In contrast, the post-Devonian history of the Tethyan Ocean between Gondwanaland and Laurasia is characterized by a history of at least 12 continental blocks or plates of varying sizes that were rifted off the northern passive margin of Gondwanaland without much evidence for associated magmatism and accreted to Eurasia after crossing the Tethys (Audley-Charles et al., 1988; Metcalfe, 1999; Ricou, 1995). The absence of magmatism along the northeastern Gondwanaland passive margin during most of these continental breakup events precludes mantle upwelling as a dominating driving force and is difficult to understand if slab pull plays no significant role in driving continental breakup. Slab retreat was suggested by Collins (2003) as the main mechanism causing breakup of Pangaea, and based on a mantle convection model, Conrad and Lithgow-Bertelloni (2004) suggested that the importance slab pull has been increasing steadily through the Cenozoic because the mass and length of upper-mantle slabs have been increasing, causing subducting plates to double their speed relative to nonsubducting plates during this time period.

India's superfast motion has been puzzling. One model ascribed it to losing its continental roots due to mantle plume activity when Gondwanaland originally broke apart (Kumar et al., 2007). However, such an erosion and melting away of India's roots, thought to have occurred around 130 Ma, cannot be held responsible for the specific acceleration starting at 67 Ma. Moreover, some geodynamic models suggest that the maximum velocity that tectonic plates typically reach is 8 cm per year. The reason for this maximum speed is that plates are largely driven by the pull of slabs subducting in the mantle, especially upper-mantle slabs to which plates are attached (e.g., Goes et al., 2008; Schellart et al., 2007). The characteristic sinking velocity for upper-mantle slabs is about 7 cm per year with a maximum of 8 cm per year for the oldest, thickest, most negatively buoyant slabs (Goes et al., 2008). This work has been confirmed by sophisticated numerical models for the present-day plate motions (Stadler et al., 2010), which show a near-perfect agreement between observed plate motions and those predicted by driving plates with only upper-mantle slabs.

Therefore, geodynamic models raise the question how plates can achieve velocities in great excess of 8 cm per year. Cande and Stegman (2011) used their detailed kinematic models to make a conceptual argument that by adding a plume-push force, India can be sufficiently accelerated, while Africa is slowed down. This dichotomy is explained by considering the location of the Réunion plume relative to the two plates. In India's case, the plume-push force would act in unison with slab pull north of India, whereas in Africa's case, it would counteract slab pull, slowing the continent down. After exhaustion of the plume head and the waning of its presumed pushing force, Africa exhibits a speed-up synchronous with the slowdown of India.

Of course, this scenario is not without problems. One potential difficulty is that the Deccan Traps – emplaced as a direct consequence of the partial melts supplied by the Réunion plume head – were emplaced over a comparatively short period of time from 68 to 65 Ma (Chenet et al., 2007). The Indian Plate velocity anomaly, on the other hand, lasted for more than 15 Myr. Another potential problem comes from geodynamic modeling. Van Hinsbergen et al. (2011) recently

explored the magnitude of the plume-push force and concluded that while a plume head effect could account for an acceleration of India, it could only do so by a few cm per year, certainly not the 10 cm per year required to explain the Indian Plate velocities. Equivalently, their models indicate that a combination of reduced plume flux, reduced coupling with the plate and the plate moving away from the plume, can only account for a small portion of India's dramatic slowdown at 52 Ma. Whether the plume-push force model for India's superfast motion will stand the test of time remains to be seen.

6.02.6 Future Challenges

Perhaps, one of the key components to make significant progress in the analysis and testing of the hot spot hypothesis is the availability of samples from several hot spot chains. The study of APMs over hot spots remains a data-starved field, and it is to be expected that as more and better age data become available, particularly in key sections currently underrepresented and poorly constrained, they will play a major role in deciding among competing hypotheses. One of the particularly challenging tasks will be to develop an accepted approach that can be used to separate volcanism caused by hot spots from other volcanism unrelated to plume activity. A growing body of evidence suggests much surface volcanism can also occur as a consequence of extension. For instance, the Pacific Ocean has several linear volcanic ridges (e.g., Lynch, 1999) whose ages are not compatible with the hot spot paradigm and may be better explained in terms of transient extensional stresses during times of plate motion changes (Anderson et al., 1992; Sandwell et al., 1995; Wessel and Kroenke, 2007).

The field of relative plate motion studies has revealed much about the plate tectonic motions between oceanic plates. However, new discoveries are needed in areas where magnetic anomalies are scarce or of very low amplitude, such as in the Cretaceous quiet zone (e.g., Granot et al., 2012). It is possible that a combination of high-resolution magnetic profiling and multibeam bathymetric mapping of abyssal hill fabric can remedy this situation (e.g., Sandwell et al., 2002). Recent modeling improvements, such as Bayesian methods that can recover smooth plate motions in the presence of noisy finite rotations (Iaffeldano et al., 2012), are expected to take on a larger role in linking observed kinematics to mantle dynamics.

Over the last 10 years, new evidence has been gathered that seems to suggest that hot spots are far from being the stationary features originally envisioned. The best-documented case comes from the Emperor seamounts where drilling results have shown that the Emperor seamounts have paleolatitudes that are incompatible with formation over a hot spot at the current 19–20° latitude of the Hawaiian Island (Tarduno et al., 2003). More recently, paleolatitudes from the oldest section of the Louisville chain have become available (Koppers et al., 2012), showing a much more limited latitudinal motion. Modeling of APMs must allow for the possibility of such hot spot motion, as the techniques of O'Neill et al. (2005) and Wessel et al. (2006) both do. However, while hot spot motion paths predicted from mantle flow models (e.g., Doubrovine et al., 2012; Steinberger, 2000) are presently required, ideally, it should be possible to determine the optimal path of motion for hot spots from available geochronology, seamount chain geometry, and paleomagnetic data alone and then compare the results to the predictions of the flow models. Theoretical improvements along such lines seem pertinent to solving this problem.

Further advances in the mapping of seafloor morphology depend on better coverage of high-quality data. Given the size of the oceans, the pace of oceanic exploration, and the ever-increasing costs of ship fuel, it seems exceedingly unlikely that complete bathymetric coverage will be achieved in the next hundred years, despite the optimism in some quarters (Vogt and Jung, 2000). If this is true, more emphasis should be placed on obtaining the best possible data coverage using space-based techniques; for marine tectonic studies, this means collecting a new set of altimetry measurements capable of resolving much smaller wavelengths and amplitudes of the sea surface undulations from which the marine geoid is derived (Sandwell et al., 2002). From such data, the proven techniques of reconstructing the Earth's gravity field and from it undertaking bathymetric prediction will enable scientists to better classify seafloor fabric and complement the information inferred from traditional shipboard geophysical observations. Nevertheless, plate tectonic deciphering of seafloor formed during the Cretaceous Normal Superchron will require high-resolution imaging beyond what is attainable via satellite altimetry; hence, seagoing explorations will continue to be a key requirement to make progress in these difficult regions.

In order to advance our understanding of the coupling and feedbacks between deep Earth processes and plate kinematics, tools and workflows need to be established in which observations, plate kinematics through time, geodynamic modeling, and model/data visualization are seamlessly linked, based on open standards and open-source tools. With more and better data and the continued development of more sophisticated models that combine data and model outputs with powerful dynamic visualization, an additional need is the ability of scientists to better communicate and exchange information in well understood and suitable formats. The burgeoning field of geoinformatics is likely to enable key advances in all of the Earth sciences during the next decade. We are already seeing the results of this work with the release of user-friendly plate tectonic-specific software (Williams et al., 2012) that has the potential to elevate plate reconstructions from the purview of a few specialists to a common activity for everybody studying plate tectonics. For this transition to be successful, it is important that Earth scientists embrace the computational skills required to manage data and strive to communicate both data and results efficiently to the community.

Acknowledgments

This chapter was greatly improved by reviewer comments. We thank Christian Heine and Maria Seton for the help with **Figures 1–3** and **29**, respectively. This is SOEST contribution no. 9213.

References

Acton GD and Gordon RG (1994) Paleomagnetic tests of Pacific plate reconstructions and implications for motion between hotspots. *Science* 263: 1246–1254.
Anderson DL (2001) Top-down tectonics? *Science* 293: 2016–2018.
Anderson DL, Tanimoto T, and Zhang Y-S (1992) Plate tectonics and hotspots: The third dimension. *Science* 256: 1645–1651.

Andrews DL, Gordon RG, and Horner-Johnson BC (2006) Uncertainties in plate reconstructions relative to the hotspots; Pacific-hotspot rotations and uncertainties for the past 68 million years. *Geophysical Journal International* 166: 939–951.
Argus DF, Gordon RG, Heflin MB, et al. (2010) The angular velocities of the plates and the velocity of Earth's centre from space geodesy. *Geophysical Journal International* 180: 913–960.
Aslanian D, Géli L, and Olivet J-L (1998) Hotspotting called into question. *Nature* 396: 127.
Audley-Charles MB, Ballantyne PD, and Hall R (1988) Mesozoic–Cenozoic rift–drift sequence of Asian fragments from Gondwanaland. *Tectonophysics* 155: 317–330.
Baksi AK (1995) Petrogenesis and timing of volcanism in the Rajmahal flood basalt province, northeastern India. *Chemical Geology* 121: 73–90.
Baksi AK (1999) Reevaluation of plate motion models based on hotspot tracks in the Atlantic and Indian Oceans. *Journal of Geology* 107: 13–26.
Barrell J (1914) The strength of the Earth's crust, VIII, physical conditions controlling the nature of lithosphere and asthenosphere. *Journal of Geology* 22: 425–443.
Batiza R (1982) Abundances, distribution, and sizes of volcanoes in the Pacific Ocean and implications for the origin of non-hotspot volcanoes. *Earth and Planetary Science Letters* 60: 195–206.
Batiza R (2001) Seamounts and off-ridge volcanism. In: Steele J, Thorpe S, and Turekian K (eds.) *Encyclopedia of Ocean Sciences*. San Diego: Academic Press.
Bercovici D (1993) A simple model of plate generation from mantle flow. *Geophysical Journal International* 114: 635–650.
Bercovici D and Kelly A (1997) The non-linear initiation of diapirs and plume heads. *Physics of the Earth and Planetary Interiors* 101: 119–130.
Bercovici D and Mahoney J (1994) Double flood basalts and plume head separation at the 660-kilometer discontinuity. *Science* 266: 1367–1369.
Bergman EA and Solomon SC (1980) Oceanic intraplate earthquakes: Implications for local and regional intraplate stress. *Journal of Geophysical Research* 85: 5389–5410.
Besse J and Courtillot V (2002) Apparent and true polar wander and the geometry of the geomagnetic field over the last 200 Myr. *Journal of Geophysical Research* 107. http://dx.doi.org/10.1029/2000JB000050.
Bird P (2003) An updated digital model of plate boundaries. *Geochemistry, Geophysics, Geosystems* 4: 1027.
Bott MHP (1982) *The Interior of the Earth: Its Structure, Constitution and Evolution*. London: Arnold.
Boyden JA, Müller RD, Gurnis M, et al. (2011) Next-generation plate-tectonic reconstructions using GPlates. In: Keller GR and Baru C (eds.) *Geoinformatics: Cyberinfrastructure for the Solid Earth Sciences*. Cambridge: Cambridge University Press.
Bullard EC, Everett JE, and Smith AG (1965) Fit of continents around Atlantic. In: Blackett PMS, Bullard EC, and Runcorn SK (eds.) *A Symposium on Continental Drift, Roy. Soc. Lond*.
Burke KC and Wilson JT (1976) Hot spots on the Earth's surface. *Journal of Geophysical Research* 93: 7690–7708.
Campbell IH and Griffiths RW (1990) Implications of mantle plume structure for the evolution of flood basalts. *Earth and Planetary Science Letters* 99: 79–93.
Cande SC, Labrecque JL, and Haxby WF (1988) Plate kinematics of the south Atlantic: Chron C34 to present. *Journal of Geophysical Research* 93: 13479–13492.
Cande SC, Raymond CA, Stock J, and Haxby WF (1995) Geophysics of the Pitman fracture zone and Pacific–Antarctic plate motions during the Cenozoic. *Science* 270: 947–953.
Cande SC and Stegman DR (2011) Indian and African plate motions driven by the push force of the Réunion plume head. *Nature* 475: 47–52.
Cande SC, Stock JM, Müller RD, and Ishihara T (2000) Cenozoic motion between East and West Antarctica. *Nature* 404: 145–150.
Cao Q, Van Der Hilst R, De Hoop MV, and Shim S-H (2011) Seismic imaging of transition zone discontinuities suggests hot mantle west of Hawaii. *Science* 332: 1068–1071.
Carlson RL, Hilde TWC, and Uyeda S (1983) The driving mechanism of plate tectonics: Relation to age of lithosphere at trenches. *Geophysical Research Letters* 10: 297–300.
Cazenave A, Dominh K, Rabinowicz M, and Ceuleneer G (1988) Geoid and depth anomalies over ocean swells and troughs: Evidence of an increasing trend of the geoid to depth ratio with age of plate. *Journal of Geophysical Research* 93: 8064–8077.
Ceuleneer G, Rabinowicz M, Monnereau M, Cazenave A, and Rosemberg C (1988) Viscosity and thickness of the sub-lithospheric low-viscosity zone: Constraints from geoid and depth over oceanic swells. *Earth and Planetary Science Letters* 89: 84–102.
Chandler MT, Wessel P, Taylor B, Seton M, Kim S-S, and Hyeong K (2012) Reconstructing Ontong Java Nui: Implications for Pacific absolute plate motion, hotspot drift and true polar wander. *Earth and Planetary Science Letters* 331–332: 140–151.
Chang T (1987) On the statistical properties of estimated rotations. *Journal of Geophysical Research* 92: 6319–6329.
Chang T (1988) Estimating the relative rotation of two tectonic plates from boundary crossings. *Journal of the American Statistical Association* 83: 1178–1183.
Chang T, Stock J, and Molnar P (1990) The rotation group in plate tectonics and the representation of uncertainties of plate reconstructions. *Geophysical Journal International* 101: 649–661.
Chapple WM and Tullis TE (1977) Evaluation of the forces that drive the plates. *Journal of Geophysical Research* 82: 1967–1984.
Chenet AL, Quidelleur X, Fluteau F, Courtillot V, and Bajpai S (2007) ^{40}K–^{40}Ar dating of the Main Deccan large igneous province: Further evidence of KTB age and short duration. *Earth and Planetary Science Letters* 263: 1–15.
Chu D and Gordon RG (1999) Evidence for motion between Nubia and Somalia along the Southwest Indian Ridge. *Nature* 398: 64–67.
Clague D and Dalrymple GB (1989) The tectonic and geologic setting of the Hawaiian–Emperor volcanic chain. In: Winterer EL, Hussong DM, and Decker RW (eds.) *The Eastern Pacific Ocean and Hawaii*. Boulder, CO: Geological Society of America.
Cloething S (1986) Intraplate stresses: A new tectonic mechanism for fluctuations in sea level. *Geology* 14: 617–620.
Cloos M (1993) Lithospheric buoyancy and collisional orogenesis; subduction of oceanic plateaus, continental margins, island arcs, spreading ridges, and seamounts. *Geological Society of America Bulletin* 105: 715–737.
Clouard V and Bonneville A (2001) How many Pacific hotspots are fed by deep-mantle plumes? *Geology* 29: 695–698.
Clouard V and Bonneville A (2005) Ages of seamounts, islands, and plateaus on the Pacific plate. In: Foulger GR, Natland JH, Presnall DC, and Anderson DL (eds.) *Plates, Plumes, and Paradigms*. Boulder, CO: Geological Society of America.
Coblentz DD and Richardson RM (1995) Statistical trends in the intraplate stress field. *Journal of Geophysical Research* 100: 20245–20255.
Coblentz DD, Sandiford M, Richardson RM, Zhou S, and Hillis R (1995) The origins of the intraplate stress field in continental Australia. *Earth and Planetary Science Letters* 133: 299–309.
Coffin MF and Eldholm O (1992) Volcanism and continental breakup: A compilation of large igneous provinces. In: Storey BC (ed.) *Magmatism and the Causes of Continental Breakup*. London: Geological Society of London.
Coffin MF and Eldholm O (1993) Large igneous provinces. *Scientific American* 269: 42–49.
Coffin MF, Gahagan LM, and Lawver LA (1997) Present-day plate boundary digital data compilation. University of Texas Institute for Geophysics Technical Report.
Coffin MF, Prince MS, and Duncan RA (2002) Kerguelen hotspot magma output since 130 Ma. *Journal of Petrology* 43: 1121–1139.
Collette BJ, Slootweg AP, Verhoef J, and Roest WR (1984) Geophysical investigations of the floor of the Atlantic ocean between 10° and 38° N (kroonvlag-project). *Proceedings of the Royal Netherlands Academy of Sciences* 87: 1–76.
Collins WJ (2003) Slab pull, mantle convection, and Pangaean assembly and dispersal. *Earth and Planetary Science Letters* 205: 225–237.
Conrad CP and Gurnis M (2003) Seismic tomography, surface uplift, and the breakup of Gondwanaland: Integrating mantle convection backwards in time. *Geochemistry, Geophysics, Geosystems* 4: 1031.
Conrad CP and Lithgow-Bertelloni C (2002) How mantle slabs drive plate tectonics. *Science* 298: 207–209.
Conrad CP and Lithgow-Bertelloni C (2004) The temporal evolution of plate driving forces: Importance of "slab suction" versus "slab pull" during the Cenozoic. *Journal of Geophysical Research* 109: 1–14.
Copley A, Avouac J-P, and Royer JY (2010) India–Asia collision and the Cenozoic slowdown of the Indian plate: Implications for the forces driving plate motions. *Journal of Geophysical Research* 115. http://dx.doi.org/10.1029/2009JB006634.
Cox A and Hart RB (1986) *Plate Tectonics: How it Works*. Oxford, UK: Blackwell.
Craig CH and Sandwell DT (1988) Global distribution of seamounts from Seasat profiles. *Journal of Geophysical Research* 93: 10408–10420.
Crough ST (1983) Hotspot swells. *Annual Review of Earth and Planetary Sciences* 11: 165–193.
Dalziel IWD, Lawver LA, and Murphy JB (2000) Plumes, orogenesis, and supercontinental fragmentation. *Earth and Planetary Science Letters* 178: 1–11.
Das AK, Piper JDA, Bandyopadhyay G, and Mallik SB (1996) Polarity inversion in the Rajmahal lavas, north-east India: Trap emplacement near commencement of the cretaceous normal superchron. *Geophysical Journal International* 124: 427–432.
Davies GF (1992) Temporal variation of the Hawaiian plume flux. *Earth and Planetary Science Letters* 113: 277–286.
Demets C, Gordon RG, and Argus DF (2010) Geologically current plate motions. *Geophysical Journal International* 181: 1–80.

Detrick RS and Crough ST (1978) Island subsidence, hot spots, and lithospheric thinning. *Journal of Geophysical Research* 83: 1236–1244.

Dickinson WR (1998) Geomorphology and geodynamics of the Cook-Austral island-seamount chain in the south Pacific ocean: Implications for hotspots and plumes. *International Geology Review* 40: 1039–1075.

Dietz RS (1961) Evolution by spreading of the sea floor. *Nature* 190: 854.

Doubrovine PV, Steinberger B, and Torsvik TH (2012) Absolute plate motions in a reference frame defined by moving hot spots in the Pacific, Atlantic, and Indian oceans. *Journal of Geophysical Research* 117, B09101.

Douglas BC (1991) Global sea level rise. *Journal of Geophysical Research* 96: 6981–6992.

Duncan RA (1981) Hotspots in the Southern ocean – An absolute frame of reference for motion of the Gondwana continents. *Tectonophysics* 74: 29–42.

Duncan RA and Clague DA (1985) Pacific plate motion recorded by linear volcanic chains. In: Nairn AEM, Stehli FG, and Uyeda S (eds.) *The Ocean Basins and Margins*. New York: Plenum.

Ebinger CJ and Sleep NH (1998) Cenozoic magmatism throughout east Africa resulting from impact of a single plume. *Nature* 395: 788–791.

Engdahl ER, Van Der Hilst R, and Buland R (1998) Global teleseismic earthquake relocation with improved travel times and procedures for depth determination. *Bulletin of the Seismological Society of America* 88: 722–743.

Engebretson DC, Cox A, and Gordon RG (1985) Relative motions between oceanic and continental plates in the Pacific Ocean. *Special Paper, Geological Society of America* 206: 1–58.

Forsyth DW and Uyeda S (1975) On the relative importance of the driving forces of plate motion. *Geophysical Journal* 43: 163–200.

Fryer P (1996) Evolution of the Mariana convergent plate margin system. *Reviews of Geophysics* 34: 89–125.

Gaina C, Müller RD, Brown BJ, and Ishihara T (2003) Microcontinent formation around Australia. *Geological Society of America Special Paper* 372: 405–416.

Gaina C, Müller RD, Brown B, Ishihara T, and Ivanov S (2007) Breakup and early seafloor spreading between India and Antarctica. *Geophysical Journal International* http://dx.doi.org/10.1111/j.1365-246X.2007.03450.x.

Gardner JV, Dean WE, and Blakely RJ (1984) Shimada seamount: An example of recent mid-plate volcanism. *Geological Society of America Bulletin* 95: 855–862.

Goes S, Capitanio FA, and Morra G (2008) Evidence of lower-mantle slab penetration phases in plate motions. *Nature* 451: 981–984.

Golonka J (2007) Late Triassic and Early Jurassic palaeogeography of the world. *Palaeogeography, Palaeoclimatology, Palaeoecology* 244: 297–307.

Gordon RG (1998) The plate tectonic approximation: Plate nonrigidity, diffuse plate boundaries, and global plate reconstructions. *Annual Review of Earth and Planetary Sciences* 26: 615–642.

Gordon RC (2000) Diffuse oceanic plate boundaries: Strain rates, vertically averaged rheology, and comparisons with narrow plate boundaries and stable plate interiors. In: Richards MA, Gordon RC, and Van Der Hilst RD (eds.) *The History and Dynamics of Global Plate Motions*. Washington, DC: American Geophysical Union.

Granot R, Dyment J, and Gallet Y (2012) Geomagnetic field variability during the Cretaceous Normal Superchron. *Nature Geoscience* 5: 220–223.

Greff-Lefftz M and Besse J (2012) Paleo movement of continents since 300 Ma, mantle dynamics and large wander of the rotational pole. *Earth and Planetary Science Letters* 345–348: 151–158.

Gripp AE and Gordon RG (2002) Young tracks of hotspots and current plate velocities. *Geophysical Journal International* 150: 321–361.

Haase KM and Devey CW (1994) The petrology and geochemistry of Vesteris seamount Greenland basin – An intraplate alkaline volcano of non-plume origin. *Journal of Petrology* 35: 295–328.

Hager BH and O'Connell RJ (1981) A simple global model of plate dynamics and mantle convection. *Journal of Geophysical Research* 86: 4843–4867.

Hall CE, Gurnis M, Sdrolias M, Lavier LL, and Muller RD (2003) Catastrophic initiation of subduction following forced convergence across fracture zones. *Earth and Planetary Science Letters* 212: 15–30.

Hanna MS and Chang T (1990) On graphically representing the confidence region for an unknown rotation in three dimensions. *Computers & Geosciences* 16: 163–194.

Harada Y and Hamano Y (2000) Recent progress on the plate motion relative to hotspots. In: Richards MA, Gordon RG, and Hilst RDVD (eds.) *The History and Dynamics of Global Plate Motions. Geophysical Monograph*. Washington, DC: American Geophysical Union.

Harbert W and Cox A (1989) Late Neogene motion of the Pacific plate. *Journal of Geophysical Research* 94: 3052–3064.

Harris RN, Fisher AT, and Chapman DS (2004) Fluid flow through seamounts and implications for global mass fluxes. *Geology* 32: 725–728.

Haxby WF (1987) *Gravity Field of the World's Oceans*. Boulder, CO: National Geophysical Data Center, NOAA.

Haxby WF, Karner GD, Labrecque JL, and Weissel JK (1983) Digital images of combined oceanic and continental data sets and their use in tectonic studies. *Eos* 64: 995–1004.

Heezen BC and Tharp M (1961) *Physiographic Diagram of the South Atlantic, the Caribbean, the Scotia Sea, and the Eastern Margin of the South Pacific Ocean*. New York: Geological Society of America.

Heezen BC and Tharp M (1964) *Physiographic Diagram of the Indian Ocean, the Red Sea, the South China Sea, the Sulu Sea, and the Celebes Sea*. New York: Geological Society of America.

Heine C, Müller RD, and Gaina C (2004) Reconstructing the lost eastern Tethys ocean basin: Convergence history of the SE Asian margin and marine gateways. In: Clift PD (ed.) *Continent–Ocean Interactions Within East Asian Marginal Seas*. Washington, DC: American Geophysical Union.

Heirtzler JR, Dickson GO, Herron EM, Pitman WC III, and Le Pichon X (1968) Marine magnetic anomalies, geomagnetic field reversals, and motions of the ocean floor and continents. *Journal of Geophysical Research* 73: 2119–2136.

Hellinger SJ (1981) The uncertainties of finite rotations in plate tectonics. *Journal of Geophysical Research* 86: 9312–9318.

Hess HH (1946) Drowned ancient islands of the Pacific Basin. *American Journal of Science* 244: 772–791.

Hess HH (1962) History of ocean basins. *Geological Society of America Bulletin; Petrologic Studies: A Volume to Honour A.F. Buddington* 559–620.

Hillier JK and Watts AB (2007) Global distribution of seamounts from ship-track bathymetry data. *Geophysical Research Letters* 34(L13304). http://dx.doi.org/10.1029/2007GL029874.

Holmes A (1944) *Principles of Physical Geology*. Edinburgh: Thomas Nelson & Sons.

Hyndman RD and Hamilton TS (1993) Queen Charlotte area Cenozoic tectonics and volcanism and their association with relative plate motions along the northeastern Pacific margin. *Journal of Geophysical Research* 98: 14257–14277.

Iaffeldano G, Bodin T, and Sambridge M (2012) Reconstructing plate-motion changes in the presence of finite-rotations noise. *Nature Communications* 3: 1048.

Idnurm M (1985) Late Mesozoic and Cenozoic palaeomagnetism of Australia – II. Implications for geomagnetism and true polar wander. *Geophysical Journal of the Royal Astronomical Society* 83: 419–433.

Janney PE, Macdougall JD, Natland JH, and Lynch MA (2000) Geochemical evidence from the Pukapuka volcanic ridge system for a shallow enriched mantle domain beneath the South Pacific superswell. *Earth and Planetary Science Letters* 181: 47–60.

Jaroslow GE, Smith DK, and Tucholke BE (2000) Record of seamount production and off-axis evolution in the western North Atlantic Ocean, 25°25'–27°10'N. *Journal of Geophysical Research* 105: 2721–2736.

Jayne SR, St. Laurent LC, and Gille ST (2004) Connections between ocean bottom topography and Earth's climate. *Oceanography* 17: 65–74.

Jordan TH (1979) Mineralogies, densities, and seismic velocities of garnet lherzolites and their geophysical implications. In: Boyd FR and Meyer HOA (eds.) *The Mantle Sample: Inclusions in Kimberlites and Other Volcanics*. Washington, DC: American Geophysical Union.

Kim S-S and Wessel P (2011) New global seamount census from altimetry-derived gravity data. *Geophysical Journal International* 186: 615–631.

Kirkwood BH, Royer J-Y, Chang TC, and Gordon RG (1999) Statistical tools for estimating and combining finite rotations and their uncertainties. *Geophysical Journal International* 137: 408–428.

Klitgord K and Schouten H (1986) Plate kinematics of the central Atlantic. In: Vogt PR and Tucholke BE (eds.) *The Western North Atlantic Region, DNAG*. Boulder, CO: Geological Society of America.

Knesel KM, Cohen BE, Vasconcelos PM, and Thiede DS (2008) Rapid change in drift of the Australian plate records collision with Ontong Java plateau. *Nature* 454: 754–757.

Kogan MG and Steblov GM (2008) Current global plate kinematics from GPS (1995–2007) with the plate-consistent reference frame. *Journal of Geophysical Research* 113, B04416.

Kono M (1980) Paleomagnetism of DSDP Leg 55 basalts and implications for the tectonics of the Pacific plate. In: Jackson ED, Koizumi I, Kirkpatrick RJ, Avdeiko G, Clague D, Dalrymple GB, Karpoff A-M, Mckenzie J, Butt A, Ling HY, Takayama T, Greene HG, Morgan J, and Kono M (eds.) *Initial Reports DSDP*. Washington: US Government Printing Office.

Koppers AAP, Duncan RA, and Steinberger B (2004) Implications of a nonlinear $^{40}Ar/^{39}Ar$ age progression along the Louisville seamount trail for models of fixed and moving hot spots. *Geochemistry, Geophysics, Geosystems* 5. http://dx.doi.org/10.1029/2003GC000671.

Koppers AAP, Gowen MD, Colwell LE, et al. (2011a) New $^{40}Ar/^{39}Ar$ age progression for the Louisville hot spot trail and implications for inter-hot spot motion. *Geochemistry, Geophysics, Geosystems* 12. http://dx.doi.org/10.1029/2011GC003804.

Koppers AAP, Phipps Morgan J, Morgan JW, and Staudigel H (2001) Testing the fixed hotspot hypothesis using $^{40}Ar/^{39}Ar$ age progressions along seamount trails. *Earth and Planetary Science Letters* 185: 237–252.

Koppers AAP, Russell JA, Roberts J, et al. (2011b) Age systematics of two young en echelon Samoan volcanic trails. *Geochemistry, Geophysics, Geosystems* 12, Q07025.

Koppers AA and Staudigel H (2005) Asynchronous bends in Pacific seamount trails: A case for extensional volcanism? *Science* 307: 904–907.

Koppers AAP, Yamazaki T, Geldmacher J, et al. (2012) Limited latitudinal mantle plume motion for the Louisville hotspot. *Nature Geoscience* 5(12): 911–917.

Krijgsman W, Hilgen FJ, Raffi I, Sierro FJ, and Wilson DS (1999) Chronology, causes and progression of the Messinian salinity crises. *Nature* 400: 652–655.

Kroenke LW (1996) Plate tectonic development of the Western and Southwestern Pacific. In: Keast A and Miller SE (eds.) *The Origin and Evolution of Pacific Island Biotas*. Amsterdam: SPB Academic Publishing.

Kumar P, Yuan X, Kumar MR, Kind R, Li X, and Chadha R (2007) The rapid drift of the Indian tectonic plate. *Nature* 449: 894–897.

Kunze E and Llewellyn Smith SG (2004) The role of small-scale topography in turbulent mixing of the global ocean. *Oceanography* 17: 55–64.

Labails C, Olivet J-L, Aslanian D, and Roest WR (2010) An alternative early opening scenario for the Central Atlantic Ocean. *Earth and Planetary Science Letters* 297: 355–368.

Larson RL and Chase CG (1972) Late Mesozoic evolution of the western Pacific Ocean. *Geological Society of America Bulletin* 83: 3627–3644.

Le Pichon X (1968) Sea floor spreading and continental drift. *Journal of Geophysical Research* 73: 3661–3697.

Li ZX, Evans DAD, and Zhang S (2004) A 90° spin on Rodinia: Possible causal links between the Neoproterozoic supercontinent, superplume, true polar wander and low-latitude glaciation. *Earth and Planetary Science Letters* 220: 409–421.

Lithgow-Bertelloni C and Richards MA (1998) The dynamics of Cenozoic and Mesozoic plate motions. *Reviews of Geophysics* 36: 27–78.

Lonsdale P (1988) Geography and history of the Louisville hotspot chain in the southwest Pacific. *Journal of Geophysical Research* 93: 3078–3104.

Ludwig WJ and Houtz RE (1979) *Isopach Map of the Sediments in the Pacific Ocean Basin, Color Map with Text*. Tulsa, OK: American Association of Petroleum Geologist.

Lueck RG and Mudge TD (1997) Topographically induced mixing around a shallow seamount. *Science* 276: 1831–1833.

Lynch MA (1999) Linear ridge groups: Evidence for tensional cracking in the Pacific Plate. *Journal of Geophysical Research* 104: 29321–29333.

Maddox J (1998) *What Remains to be Discovered: Mapping the Secrets of the Universe, the Origins of Life, and the Future of the Human Race*. New York: Free Press.

Matias LM, Olivet J-L, Aslanian D, and Fidalgo L (2005) PLACA: A white box for plate reconstruction and best-fit pole determination. *Computers & Geosciences* 31: 437–452.

Matthews KJ, Müller RD, Wessel P, and Whittaker JM (2011) The tectonic fabric of the ocean basins. *Journal of Geophysical Research* 116(B12109): 1–28.

Matthews KJ, Seton M, Flament N, and Müller RD (2012) Late Cretaceous to present-day opening of the southwest Pacific constrained by numerical models and seismic tomography. In: *Eastern Australian Basins Symposium, IV*, pp. 105–119.

McDougall I (1971) Volcanic island chains and sea floor spreading. *Nature* 231: 141–144.

McDougall I (1979) Age of shield-building of Kauai and linear migration of volcanism in the Hawaiian island chain. *Earth and Planetary Science Letters* 46: 31–42.

McKenzie DP (1967) Some remarks on heat flow and gravity anomalies. *Journal of Geophysical Research* 72: 6261–6273.

McKenzie DP (1969) Speculations on the consequences and causes of plate motion. *Geophysical Journal* 18: 1–32.

Mckenzie DP and Parker RL (1967) The North Pacific: An example of tectonics on a sphere. *Nature* 216: 1276–1280.

Mckenzie DP, Roberts J, and Weiss N (1973) Numerical models of convection in the Earth's mantle. *Tectonophysics* 19: 89–103.

Mckenzie DP and Sclater JG (1971) The evolution of the Indian Ocean since the Late Cretaceous. *Geophysical Journal of the Royal Astronomical Society* 24: 437–528.

McNutt MK (1998) Superswells. *Reviews of Geophysics* 36: 211–244.

Mcnutt MK, Caress DW, Reynolds J, Jordahl KA, and Duncan RA (1997) Failure of plume theory to explain midplate volcanism in the southern Austral Islands. *Nature* 389: 479–482.

Meijer PT and Wortel M (1992) The dynamics of motion of the South American Plate. *Journal of Geophysical Research* 97: 11915–11931.

Menard HW (1964) *Marine Geology of the Pacific*. New York: McGraw-Hill.

Metcalfe I (1999) Gondwana dispersion and Asian accretion: An overview. In: Metcalfe I (ed.) *Gondwana Dispersion and Asian Accretion*. Rotterdam: A. A. Balkema.

Molnar P and Stock JM (1985) A method for bounding uncertainties in combined plate reconstructions. *Journal of Geophysical Research* 90: 12537–12544.

Molnar P and Stock J (1987) Relative motions of hotspots in the Pacific, Atlantic and Indian Oceans since Late Cretaceous time. *Nature* 327: 587–591.

Montelli R, Nolet G, Dahlen FA, Masters G, Engdahl ER, and Hung S-H (2004) Finite-frequency tomography reveals a variety of plumes in the mantle. *Science* 303: 338–343.

Morgan WJ (1968) Rises, trenches, great faults and crustal blocks. *Journal of Geophysical Research* 73: 1959–1982.

Morgan WJ (1971) Convection plumes in the lower mantle. *Nature* 230: 43–44.

Morgan WJ (1972) Plate motions and deep mantle convection. *Geological Society of America Memoirs* 132: 7–22.

Morgan WJ (1978) Rodriguez, Darwin, Amsterdam, . . ., a second type of hotspot island. *Journal of Geophysical Research* 83: 5355–5360.

Mueller S and Phillips RJ (1991) On the initiation of subduction. *Journal of Geophysical Research* 96: 651–665.

Müller RD and Roest WR (1992) Fracture zones in the north Atlantic from combined Geosat and Seasat data. *Journal of Geophysical Research* 97: 3337–3350.

Müller RD, Roest WR, and Royer JY (1998) Asymmetric sea-floor spreading caused by ridge–plume interactions. *Nature* 396: 455–459.

Müller RD, Royer JY, Cande SC, Roest WR, and Maschenkov S (1999) New constraints on Carribean plate tectonic evolution. In: Mann P (ed.) *Caribbean Basins*. Amsterdam: Elsevier.

Müller RD, Royer J-Y, and Lawver LA (1993) Revised plate motions relative to the hotspots from combined Atlantic and Indian Ocean hotspot tracks. *Geology* 21: 275–278.

Müller RD, Royer J-Y, and Lawver LA (1994) Revised plate motions relative to the hotspots from combined Atlantic and Indian Ocean hotspot tracks: Reply. *Geology* 22: 277–278.

Müller RD, Sandwell DT, Tucholke BE, Sclater JG, and Shaw PR (1991) Depth to basement and geoid expression of the Kane fracture zone: A comparison. *Marine Geophysical Research* 12: 105–129.

Müller RD, Sdrolias M, Gaina C, and Roest WR (2008) Age, spreading rates, and spreading asymmetry of the world's ocean crust. *Geochemistry, Geophysics, Geosystems* 9. http://dx.doi.org/10.1029/2007GC001743.

Nakanishi M, Tamaki K, and Kobayashi K (1992) A new Mesozoic isochron chart of the northwestern Pacific Ocean: Paleomagnetic and tectonic implications. *Geophysical Research Letters* 19: 693–696.

Nataf H-C (2000) Seismic imaging of mantle plumes. *Annual Review of Earth and Planetary Sciences* 28: 391–417.

O'Connor JM and Le Roex AP (1992) South Atlantic hot spot-plume systems: 1. Distribution of volcanism in time and space. *Earth and Planetary Science Letters* 113: 343–364.

Olson P (1990) Hot spots, swells and mantle plumes. In: Ryan MP (ed.) *Magma Transport and Storage*. New York: John Wiley.

O'Neill C, Muller D, and Steinberger B (2003) Geodynamic implications of moving Indian Ocean hotspots. *Earth and Planetary Science Letters* 215: 151–168.

O'Neill C, Müller D, and Steinberger B (2005) On the uncertainties in hot spot reconstructions and the significance of moving hot spot reference frames. *Geochemistry, Geophysics, Geosystems* 6, Q04003.

Phipps Morgan J, Morgan WJ, and Price E (1995) Hotspot melting generates both hotspot volcanism and a hotspot swell? *Journal of Geophysical Research* 100: 8045–8062.

Pollitz F (1986) Pliocene change in Pacific-plate motion. *Nature* 320: 738–741.

Prevot M, Mattern F, Camps P, and Daignieres M (2002) Evidence for a 20° tilting of the Earth's rotation axis 100 million years ago. *Earth and Planetary Science Letters* 179: 517–528.

Price JP and Clague DA (2002) How old is the Hawaiian biota? Geology and phylogeny suggest recent divergence. *Proceedings of the Royal Society of London* 269: 2429–2435.

Qin X, Müller RD, Cannon J, et al. (2012) The GPlates geological information model and markup language. *Geoscientific Instrumentation, Methods and Data Systems* 2: 163.

Rao GVSP and Rao JM (1996) Palaeomagnetism of the Rajmahal traps of India: Implication to the reversal in the cretaceous normal superchron. *Journal of Geomagnetism and Geoelectricity* 48: 993–1000.

Raymond CA, Stock JM, and Cande SE (2000) Fast paleogene motion of the Pacific hotspots from revised global plate circuit constraints. In: Richards MA, Gordon RG, and Van Der Hilst RD (eds.) *The History and Dynamics of Global Plate Motions*. Washington, DC: American Geophysical Union.

Ribe NM and Christensen UR (1999) The dynamical origin of Hawaiian volcanism. *Earth and Planetary Science Letters* 171: 517–531.

Richards MA, Duncan RA, and Courtillot V (1989) Flood basalts and hot spot tracks: Plume heads and tails. *Science* 246: 103–107.

Richardson RM (1992) Ridge forces, absolute plate motions, and the intraplate stress field. *Journal of Geophysical Research* 97: 11739–11748.

Ricou L-E (1995) The plate tectonic history of the past Tethys ocean. In: Nairn AEM (ed.) *The Ocean Basins and Their Margins*. New York: Plenum Press.

Roest W (1987) Seafloor spreading pattern of the north Atlantic between 10° and 40° N. PhD. Utrecht, Netherlands.

Roest WR, Dañobeitia JJ, Verhoef J, and Collette BJ (1992) Magnetic anomalies in the Canary Basin and the Mesozoic evolution of the central North Atlantic. *Marine Geophysical Research* 14: 1–24.

Rogers AD (1994) The biology of seamounts. *Advances in Marine Biology* 30: 305–350.

Royer J-Y and Chang T (1991) Evidence for relative motions between the Indian and Australian plates during the last 20 m.y. from plate tectonic reconstructions: Implications for the deformation of the Indo-Australian plate. *Journal of Geophysical Research* 96: 11779–11802.

Royer J-Y and Gordon RG (1997) The motion and boundary between the Capricorn and Australian plates. *Science* 277: 1268–1274.

Royer J-Y, Gordon RG, Demets C, and Vogt PR (1997) New limits on the motion between India and Australia since chron 5 (11 Ma) and implications for lithospheric deformation in the equatorial Indian Ocean. *Geophysical Journal International* 129: 41–74.

Sager WW and Keating B (1984) Paleomagnetism of Line Islands seamounts: Evidence for late Cretaceous and early Tertiary volcanism. *Journal of Geophysical Research* 89: 11135–11151.

Sager WW, Lamarche AJ, and Kopp C (2005) Paleomagnetic modeling of seamounts near the Hawaiian–Emperor bend. *Tectonophysics* 405: 121–140.

Sandiford M, Coblentz DD, and Richardson RM (1995) Ridge torques and continental collision in the Indian–Australian plate. *Geology* 23: 653–656.

Sandwell D, Gille ST, and Smith WHF (2002) *Bathymetry from Space: Oceanography, Geophysics, and Climate*. Bethesda, MD: Geoscience Professional Services.

Sandwell DT and Smith WHF (1997) Marine gravity anomaly from Geosat and ERS-1 satellite altimetry. *Journal of Geophysical Research* 102: 10039–10054.

Sandwell DT, Winterer EL, Mammerickx J, et al. (1995) Evidence for diffuse extension of the Pacific plate from Pukapuka ridges and cross-grain gravity lineations. *Journal of Geophysical Research* 100: 15087–15099.

Schellart WP (2004) Quantifying the net slab pull force as a driving mechanism for plate tectonics. *Geophysical Research Letters* 31. http://dx.doi.org/10.01029/02004GL019528.

Schellart WP, Freeman J, Stegman DR, Moresi L, and May D (2007) Evolution and diversity of subduction zones controlled by slab width. *Nature* 446: 308–311.

Sclater JG, Anderson RN, and Bell ML (1971) Elevation of ridges and evolution of the central Eastern Pacific. *Journal of Geophysical Research* 76: 7888–7915.

Sclater JG and Francheteau J (1970) The implications of terrestrial heat flow observations on current tectonic and geochemical models of the crust and upper mantle. *Geophysical Journal* 20: 509–542.

Seton M, Müller RD, Zahirovic S, et al. (2012) Global continental and ocean basin reconstructions since 200 Ma. *Earth Science Reviews* 113: 212–270.

Sharp WD and Clague DA (2006) 50-Ma initiation of Hawaii–Emperor bend records major change in Pacific plate motion. *Science* 313: 1281–1284.

Shaw PR and Cande SC (1990) High-resolution inversion for South Atlantic plate kinematics using joint altimeter and magnetic anomaly data. *Journal of Geophysical Research* 95: 2625–2644.

Sleep NH (1990) Hotspots and mantle plumes: Some phenomenology. *Journal of Geophysical Research* 95: 6715–6736.

Smith DK and Cann JR (1990) Hundreds of small volcanoes on the median valley floor of the Mid-Atlantic Ridge at 24–30°N. *Nature* 348: 152–155.

Smith WHF and Sandwell DT (1997) Global sea floor topography from satellite altimetry and ship depth soundings. *Science* 277: 1956–1962.

Spence W (1987) Slab pull and the seismotectonics of subducting lithosphere. *Reviews of Geophysics* 25: 55–69.

Stadler G, Gurnis M, Burstedde C, Wilcox LC, Alisic L, and Ghattas O (2010) The dynamics of plate tectonics and mantle flow: From local to global scales. *Science* 329: 1033–1038.

Stampfli GM and Borel GD (2002) A plate tectonic model for the Paleozoic and Mesozoic constrained by dynamic plate boundaries and restored synthetic oceanic isochrons. *Earth and Planetary Science Letters* 196: 17–33.

Stein S (1979) Intraplate seismicity on bathymetric features: The 1968 Emperor Trough earthquake. *Journal of Geophysical Research* 84: 4763–4768.

Steinberger B (2000) Plumes in a convecting mantle: Models and observations for individual hotspots. *Journal of Geophysical Research* 105: 11127–11152.

Steinberger BM and O'Connell RJ (1997) Changes of the Earth's rotation axis owing to advection of mantle density heterogeneities. *Nature* 387: 169–173.

Steinberger B and O'Connell RJ (1998) Advection of plumes in mantle flow: Implications for hot spot motion, mantle viscosity and plume distributions. *Geophysical Journal International* 132: 412–434.

Steinberger B, Sutherland R, and O'Connell RJ (2004) Prediction of Emperor–Hawaii seamount locations from a revised model of global plate motion and mantle flow. *Nature* 430: 167–173.

Steinberger B and Torsvik TH (2008) Absolute plate motions and true polar wander in the absence of hotspot tracks. *Nature* 452: 620–624.

Stevenson DJ and Turner JS (1977) Angle of subduction. *Nature* 270: 334–336.

Stock JM and Molnar P (1983) Some geometrical aspects of uncertainties in combined plate reconstructions. *Geology* 11: 697–701.

Stoddard PR and Abbot D (1996) Influence of the tectosphere upon plate motion. *Journal of Geophysical Research* 101: 5425–5433.

Storey BC (1995) The role of mantle plumes in continental breakup: Case histories from Gondwanaland. *Nature* 377: 301–308.

Sykes LR (1978) Intraplate seismicity, reactivation of preexisting zones of weakness, alkaline magmatism, and other tectonism postdating continental fragmentation. *Reviews of Geophysics* 16: 621–688.

Tackley PJ (1998) Self-consistent generation of tectonic plates in three-dimensional mantle convection. *Earth and Planetary Science Letters* 157: 9–22.

Tarduno JA, Bunge H-P, Sleep NH, and Hansen U (2009) The bent Hawaiian–Emperor hotspot track: Inheriting the mantle wind. *Science* 324: 50–53.

Tarduno JA and Cottrell RD (1997) Paleomagnetic evidence for motion of the Hawaiian hotspot during formation of the Emperor seamounts. *Earth and Planetary Science Letters* 153: 171–180.

Tarduno JA, Duncan RA, Scholl DW, et al. (2003) The Emperor Seamounts: Southward motion of the Hawaiian Hotspot plume in Earth's mantle. *Science* 301: 1064–1069.

Taylor B (2006) The single largest oceanic plateau: Ontong Java–Manihiki–Hikurangi. *Earth and Planetary Science Letters* 241: 372–380.

Torsvik T, Müller RD, Van Der Voo R, Steinberger B, and Gaina C (2008) Global plate motion frames: Toward a unified model. *Reviews of Geophysics* 46. http://dx.doi.org/10.1029/2007RG000227.

Torsvik TH, Van Der Voo R, and Redfield TF (2002) Relative hotspot motions versus True Polar Wander. *Earth and Planetary Science Letters* 202: 185–200.

Tsai VC and Stevenson DJ (2007) Theoretical constraints on true polar wander. *Journal of Geophysical Research* 112. http://dx.doi.org/10.1029/2005JB003923.

Turcotte DL and Schubert G (2002) *Geodynamics*. Cambridge, UK: Cambridge University Press.

Turner DL and Jarrard RD (1982) K–Ar dating of the Cook-Austral island chain: A test of the hot-spot hypothesis. *Journal of Volcanology and Geothermal Research* 12: 187–220.

Turner DL, Jarrard RD, and Forbes RB (1980) Geochronology and origin of the Pratt-Welker seamount chain, Gulf of Alaska: A new pole of rotation for the Pacific plate. *Journal of Geophysical Research* 85: 6547–6556.

Tushingham AM and Peltier WR (1992) Validation of the ICE-3G model of Würm-Wisconsin deglaciation using a global data base of relative sea level histories. *Journal of Geophysical Research* 97: 3285–3304.

Van Der Voo R, Spakman W, and Bijwaard H (1999) Mesozoic subducted slabs under Siberia. *Nature* 397: 246–249.

Van Fossen MC and Kent DV (1992) Paleomagnetism of 122 Ma plutons in New England and the Mid-Cretaceous paleomagnetic field in North America: True polar wander or large-scale differential mantle motion? *Journal of Geophysical Research* 97: 19651–19661.

Van Hinsbergen DJJ, Steinberger B, Doubrovine PV, and Gassmöller R (2011) Acceleration and deceleration of India–Asia convergence since the Cretaceous: Roles of mantle plumes and continental collision. *Journal of Geophysical Research* 116, B06101.

van Wyckhouse R (1973) *SYNBAPS*. Stennis Space Center, MS: U.S. Natl. Oceanogr. Office.

Vidal V and Bonneville A (2004) Variations of the Hawaiian hot spot activity revealed by variations in the magma production rate. *Journal of Geophysical Research* 109. http://dx.doi.org/10.1029/2003JB002559.

Viso RF, Larson RL, and Pockalny RA (2005) Tectonic evolution of the Pacific–Phoenix–Farallon triple junction in the South Pacific Ocean. *Earth and Planetary Science Letters* 233: 179.

Vogt PR and Jung W-Y (2000) GOMap: A matchless resolution to start the new millennium. *Eos, Transactions of the American Geophysical Union* 81: 254–258.

Watts AB and Ten Brink US (1989) Crustal structure, flexure, and subsidence history of the Hawaiian Islands. *Journal of Geophysical Research* 94: 10473–10500.

Wessel P (1993) Observational constraints on models of the Hawaiian hot spot swell. *Journal of Geophysical Research* 98: 16095–16104.

Wessel P (2001) Global distribution of seamounts inferred from gridded Geosat/ERS-1 altimetry. *Journal of Geophysical Research* 106: 19431–19441.

Wessel P (2008) Hotspotting: Principles and properties of a plate tectonic Hough transform. *Geochemistry, Geophysics, Geosystems* 9. http://dx.doi.org/10.1029/2008GC002058.

Wessel P, Harada Y, and Kroenke LW (2006) Towards a self-consistent, high-resolution absolute plate motion model for the Pacific. *Geochemistry, Geophysics, Geosystems* 7: Q03L12.

Wessel P and Kroenke LW (1997) A geometric technique for relocating hotspots and refining absolute plate motions. *Nature* 387: 365–369.

Wessel P and Kroenke LW (1998a) Factors influencing the locations of hot spots determined by the hot-spotting technique. *Geophysical Research Letters* 25: 555–558.

Wessel P and Kroenke LW (1998b) The geometric relationship between hot spots and seamounts: Implications for Pacific hot spots. *Earth and Planetary Science Letters* 158: 1–18.

Wessel P and Kroenke LW (1998c) Hotspotting called into question—Reply. *Nature* 396: 127–128.

Wessel P and Kroenke LW (2000) Ontong Java plateau and Late Neogene changes in Pacific plate motion. *Journal of Geophysical Research* 105: 28255–28277.

Wessel P and Kroenke LW (2007) Reconciling Late Neogene Pacific absolute and relative plate motion changes. *Geochemistry, Geophysics, Geosystems* 8. http://dx.doi.org/10.1029/2007GC001636.

Wessel P and Kroenke LW (2008) Pacific absolute plate motions since 145 Ma: An assessment of the fixed hotspot hypothesis. *Journal of Geophysical Research* 113. http://dx.doi.org/10.1029/2007JB005499.

Wessel P and Kroenke LW (2009) Observations of geometry and ages constrain relative motion of Hawaii and Louisville plumes. *Earth and Planetary Science Letters* 284: 467–472.

Wessel P and Lyons S (1997) Distribution of large Pacific seamounts from Geosat/ERS-1: Implications for the history of intraplate volcanism. *Journal of Geophysical Research* 102: 22459–22476.

Wessel P, Sandwell DT, and Kim S-S (2010) The global seamount census. *Oceanography* 23: 24–33.

White SM, Macdonald KC, Scheirer DS, and Cormier M-H (1998) Distribution of isolated semounts on the flanks of the East Pacific Rise, 15.3°S–20°S. *Journal of Geophysical Research* 103: 30371–30384.

Williams SE, Müller RD, Landgrebe TCW, and Whittaker JM (2012) An open-source software environment for visualizing and refining plate tectonic reconstructions using high-resolution geological and geophysical data sets. *GSA Today* 22: 4–9.

Wilson JT (1963) A possible origin of the Hawaiian islands. *Canadian Journal of Physics* 41: 863–870.

Wilson JT (1965) A new class of faults and their bearing on continental drift. *Nature* 207: 343–347.

Wilson M (1993) Plate-moving mechanisms – Constraints and controversies. *Journal of the Geological Society* 150: 923–926.

Wolfe CJ, Bjarnason IT, Vandecar JC, and Solomon SC (1997) Seismic structure of the Iceland mantle plume. *Nature* 385: 245–247.

Wolfe CJ, Solomon SC, Laske G, et al. (2009) Mantle shear-wave velocity structure beneath the Hawaiian Hot Spot. *Science* 326: 1388–1390.

Yan CY and Kroenke LW (1993) A plate tectonic reconstruction of the southwest Pacific, 0–100 Ma. *Proceedings of the Ocean Drilling Program. Scientific Results* 130: 697–709.

Zatman S, Gordon RG, and Mutnuri K (2005) Dynamics of diffuse oceanic plate boundaries: Insensitivity to rheology. *Geophysical Journal International* 162: 239–248.

Zatman S, Gordon RG, and Richards MA (2001) Analytic models for the dynamics of diffuse oceanic plate boundaries. *Geophysical Journal International* 145: 145–156.

Ziegler P (1993) Plate-moving mechanisms: Their relative importance. *Journal of the Geological Society (London)* 150: 927–940.

Zoback ML (1992) First- and second-order patterns of stress in the lithosphere: The world stress map project. *Journal of Geophysical Research* 97: 11703–11728.

This page intentionally left blank

6.03 Plate Rheology and Mechanics

EB Burov, Université Pierre et Marie Curie, Paris, France; Centre National de la Recherche Scientifique, Paris, France

© 2015 Elsevier B.V. All rights reserved.

6.03.1	**Introduction: Plate Rheology and Mechanics**	95
6.03.2	**Rock Mechanics Data and Conventional Rheology Models**	99
6.03.2.1	Elastic Properties	100
6.03.2.2	Brittle or Plastic Properties	101
6.03.2.3	Ductile (Viscous) Properties	103
6.03.2.3.1	Diffusion and dislocation creep	103
6.03.2.3.2	Pressure solution, cataclastic flow, Peierls plasticity, GBS flow, and other mechanisms	103
6.03.2.4	Yield Stress Envelopes	105
6.03.3	**Constitutive Models**	106
6.03.3.1	Maxwell Model	106
6.03.3.2	Kelvin Model	109
6.03.3.3	Mixed Models	109
6.03.4	**Uncertainties in the Experimental Rheology Laws**	109
6.03.4.1	Uncertainties of Rock Mechanics Data	109
6.03.4.2	Uncertainties in the Synthetic Yield Stress Envelopes	110
6.03.4.3	Uncertainties in Deformation Mechanisms in Nature	110
6.03.4.4	Role of Secondary Factors: Frictional Heating, Pressure, Fluid Content, Partial Melting, and Metamorphic Phase Changes	111
6.03.4.5	Possible Ways to Parameterize Rheology Data for Geologic Timescales	114
6.03.5	**Rheology and Structure of the Oceanic Lithosphere**	115
6.03.5.1	Goetze and Evans Yield Stress Envelopes: Age Dependence of the Integrated Strength	115
6.03.5.2	Rheology and Observations of Flexure (T_e Data)	116
6.03.5.3	Flexural Strength and Initiation of Oceanic Subduction	117
6.03.5.4	Intraplate Seismicity (T_s), T_e, and Brittle–Ductile Interactions	117
6.03.5.5	Intraplate Seismicity and Ductile Creep	121
6.03.5.6	Constraints on the Long-Term Viscosity from Subsidence Data	122
6.03.5.7	Large-Scale Lithospheric Folding	122
6.03.6	**Rheology and Structure of the Continental Lithosphere and Continental Margins**	122
6.03.6.1	Common Goetze and Evans Yield Stress Envelopes	122
6.03.6.2	Age Dependence and Other Dependences of the Integrated Strength of the Lithosphere	123
6.03.6.3	Seismicity, T_s, BDT, and Long-Term Strength	130
6.03.6.4	Physical Considerations Beyond the Observations of Flexure, Gravity Potential Theory, Intraplate Stresses	133
6.03.6.5	Gravitational Stability Analysis: Rayleigh–Taylor Instabilities or Survival of Cratons, Continental Margins, and Mountain Roots	133
6.03.6.6	Dynamic Stability Analysis Using Direct Numerical Thermomechanical Models	138
6.03.6.7	Resistance to Stable Deformation Under Compressional Tectonic Forces ('Simple Shear' Subduction versus 'Pure Shear' Collision)	138
6.03.6.8	Response to Large-Scale Compressional Instabilities (Folding)	141
6.03.6.9	Response to Extensional Tectonic Loading (Rifting)	143
6.03.7	**Relations Between Short-Term and Long-Term Properties**	143
6.03.7.1	Seismicity and Long-Term Deformation	143
6.03.7.2	Postseismic Relaxation Data and Long-Term Deformation	145
6.03.7.3	Field Observations and Geophysical Data	146
6.03.8	**Conclusions and Future Perspectives**	146
Appendix A	**Flexure of Continental Lithosphere with Multilayered Nonlinear Rheology**	147
Appendix B	**Thermal Model of the Lithosphere**	148
Acknowledgments		148
References		148

6.03.1 Introduction: Plate Rheology and Mechanics

The rheology and strength of the Earth's lithosphere has been a topic of debate since the beginning of the twentieth century when Joseph Barrell introduced the concept of a strong lithosphere overlying a fluid asthenosphere (Barrell, 1914), after the formulation of the continental drift theory by Wegener and first interpretations of regional isostasy by J. Barrell and Vening-Meinesz (Barrell, 1914; Watts, 2001; Watts, this volume). This concept constitutes an integral part of plate tectonics (e.g., Le Pichon et al., 1973; Turcotte and Schubert, 2002; Watts, 2001) and the question of how the strength of the plates varies spatially and temporally is fundamental to geology and geodynamics (e.g., Burov, 2007, 2010; Burov and Watts, 2006; Cochran, 1980; Jackson, 2002). As suggested on the basis of recent mantle–lithosphere interaction models (e.g., Schmeling et al., 2008), the elastic and plastic properties of the lithosphere essentially determine the geometry of lithospheric plates and the mechanisms of formation of constructive, destructive, and transform plate boundaries at a global scale. At smaller scales, the mechanical properties of the lithosphere condition formation and evolution of major geologic structures such as spreading centers, transform/strike-slip faults, rift and foreland basins, passive margins, mountain ranges, or plateaus. They also control short-term processes such as seismicity (Watts and Burov, 2003).

The fact that the lithosphere has finite measurable strength has been first demonstrated from observations and models of regional isostatic compensation of considerable topographic loads such as oceanic islands or continental mountain belts. Before that, the lithosphere was considered as either a very strong solid layer (Pratt's model) or, in turn, a weak fractured layer (Airy's model). Postglacial rebound studies of the early twentieth century have contributed to the definition of the 'mechanical lithosphere' as the uppermost layer of the solid Earth characterized by slow viscoelastic relaxation, in contrast to the underlying, relatively low-viscosity asthenosphere. The long-term mechanical base of the lithosphere, h_m, is limited by the depth to the 500–600 °C isotherm in oceans and the 700–800 °C isotherm in continents, while the base of the thermal lithosphere is almost twice as deep at the 1330 °C isotherm.

The strength of lithospheric plates depends on their structure and rheological properties exhibited in the particular geodynamic context. For a rock of given mineralogical composition and microstructure, the most important controlling parameters are pressure, temperature, strain, strain rate, strain history, fluid content and pore fluid pressure, grain size, fugacities of volatiles, and chemical activities of mineral components (Evans and Kohlstedt, 1995; Keefner et al., 2011).

Goetze and Evans (1979) were the first to combine the data of experimental rock mechanics and extrapolate them to geologic timescales and spatial scales. They introduced the yield strength envelope (YSE) for the oceanic lithosphere, that is, a vertical profile that predicts the maximum differential stress supported by rock as a function of depth. In YSE rheology models, the depth dependence of rock strength integrates multiple factors such as the increase of both brittle and ductile strength with pressure and the decrease of ductile strength with depth-increasing temperature, lithologic structure, and fluid content. YSEs are used both to validate rock mechanics data and to explain the mechanical behavior of lithospheric plates. The YSE concept has been proven to work fairly well for oceans where it explains the observed age and temperature dependence of plate responses to surface and subsurface loads. Yet, the same concept faces a number of difficulties in continents and at continental margins (Afonso and Ranalli, 2004; Burov, 2010, 2011; Burov and Diament, 1995; Burov and Watts, 2006; Handy and Brun, 2004; Jackson, 2002). However, a complete understanding of oceanic lithosphere dynamics requires a thorough account for thermomechanical response of its continental boundaries, as well as a study of continental dynamics itself.

One of the major experimental rheology laws used for construction of YSEs is Byerlee's law of brittle failure (Byerlee, 1978). Byerlee's law demonstrates that brittle rock strength is above all a function of pressure–depth and is almost independent of rock type (**Figure 1**). Byerlee's law shows that most common rocks exhibit a similar relationship between yield stress and normal stress and that this relationship resembles Mohr–Coulomb plasticity. That is, it refers to the classical Amonton's law of friction (e.g., Nadai, 1963). Byerlee's law has been confirmed by multiple studies, which show that most rocks have similar angles of internal friction (30–33°) and similar (small) dilatation angles (~10°). This explains why even highly stratified volumes of brittle rocks often behave as a mechanically uniform media: tectonic faults can propagate large distances at depth or horizontally, ignoring lithologic stratification and inherited structures. The fault dip or the angle between conjugate faults is a function of the internal friction angle; it is thus possible to constrain the properties of brittle rocks from direct observations of fault/fracture geometries. These properties do not depend on timescale. Hence, brittle failure parameters derived from laboratory experiments can be applied on geologic spatial and temporal scales. Of course, rheologically anomalous inclusions, variations in porous pressure, or stress concentrations can change fault geometries (e.g., Huismans et al., 2005; Lavier et al., 2000; Le Pourhiet et al., 2004; Melosh, 1990; Tirel et al., 2004). In particular, the formation of low-angle faults observed in a number of geologic contexts presents one of specific problem (e.g., Buck, 2007; Huet et al., 2011; Melosh, 1990; Cloetingh et al., this volume; Buck, this volume). Yet, in most cases, observations of 'abnormal' fault dips can be explained within Byerlee's law. For example, common interpretations of low-angle faulting compatible with Byerlee's law refer to local rotation of principal stress axis due to shear flow in the ductile crust (e.g., Melosh, 1990) or due to flexural rotation of originally steep faults (e.g., Buck, 1988). Other explanations refer to various special mechanisms of friction or cohesion softening applied to Byerlee's law (e.g., Huismans et al., 2005).

In contrast with brittle properties, ductile rock strength strongly depends on rock type and a large number of specific conditions such as grain size, macro- and microstructure, temperature, strain rate, fluid content, and many other factors. In particular, ductile behavior depends nonlinearly on strain rate and thus on the timescale of the deformation process. Laboratory experiments are conducted on human timescale (5–10 years). Their results are then extrapolated to geologic timescales ($>10^6$ years). From a mathematical point of view, such huge extrapolation cannot be justified, specifically because of the nonlinear character of ductile deformation. From a physical point of view, one also cannot be certain that the same mechanisms of ductile deformation act at both slow and high strain rates or at

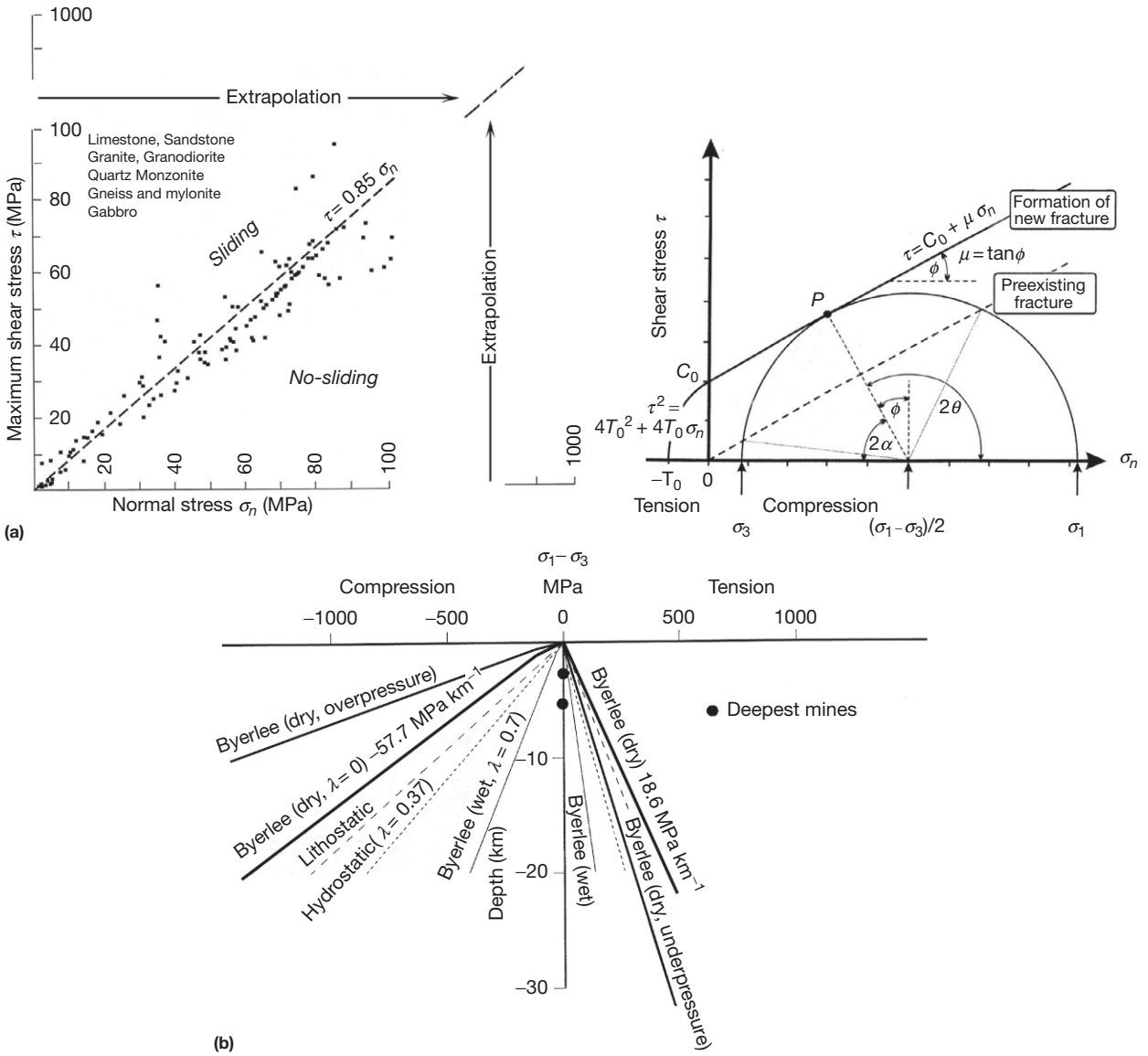

Figure 1 (a) (right) Experimentally established linear dependence between normal stress and shear stress for compressional failure of various rocks (modified from Byerlee JD (1978) Friction of rocks. *Pure and Applied Geophysics* 116: 615–626). These data demonstrate the applicability of Coulomb–Navier failure criterion $\tau = C_0 + \mu\sigma_n$ and relative independence of Byerlee's law on rock type. This law has been validated only for the first several kilometers of the upper crust (pressures of few MPa). However, it is commonly extrapolated to more important depth/pressure conditions (up to 40–50 km depth or 1–1.5 GPa), where other stress-limiting mechanisms such as Peierls law are likely to operate. (left) Two principal failure criteria (Coulomb–Navier and Griffith). Under general compression (here, $\sigma_n > 0$), Coulomb criterion predicts linear relation between normal stress σ_n and shear stress τ. Under general extension (here, $\sigma_n < 0$), parabolic Griffith criterion applies. C_0 is cohesion, T_0 is tension cutoff, μ is friction coefficient, β is friction angle, and σ_1 and σ_3 are principal stresses. 2α is angle between two conjugated faults forming under stress σ_1, and $\phi = \pi/2 - 2\alpha$ is friction angle ($\mu = \tan\phi$). For most dry rocks, $\phi = 30^\circ$ (modified from Price NJ and Cosgrove JW (1990) *Analysis of Geological Structures*. Cambridge: Cambridge University Press). It can be seen that Byerlee's law corresponds to Mohr–Coulomb plasticity with preexisting fractures. (b) Dependence of brittle strength on depth/pressure: lithostatic pressure (if not stated otherwise), fluid pressure, and tectonically induced over- or underpressure. Note that rocks are weaker under extension than under compression, which explains frequent deep seismicity in overall weak rift zones. Tectonic extension or compression may change total pressure and, consequently, brittle strength, by a factor of, respectively, 0.5–2. Combined from Watts (2001) and Petrini and Podladchikov (2000). λ is pore pressure factor.

both low and high temperatures (exaggerated temperatures are commonly used in experiments to accelerate deformation and to avoid brittle failure). Solid-state theory successfully reproduces some creep mechanisms such as diffusion creep or pressure solution (e.g., Poirier, 1985). However, this is not the case for major creep mechanisms such as dislocation creep (e.g., Hull and Bacon, 1984). Most of the Arrhenius-type constitutive laws proposed for ductile rocks are approximations of experimental data and are not physically formulated dependencies (e.g., Brace and Kohlstedt, 1980; Rutter and Brodie, 1991). The YSEs derived

for oceanic and continental lithosphere under the assumption of dry olivine rheology predict important strength in the mantle part, down to 50–60 km depth in oceans and to 100–120 km depth in cratons. However, some studies (e.g., Jackson, 2002) suggest that lithosphere mantle is mechanically weak below 40 km depth, or, more exactly, below the 500 °C isotherm. According to this hypothesis, the cratons are thin and hot (equilibrium thermal thickness $a = z(1330°) \sim 100$ km) and the continental plate strength is concentrated in the crust. These propositions arrive from conflicting interpretations of rock mechanics and intraplate seismicity data. Plate seismicity is detected mainly above 40 km depth (Jackson, 2002) in both continents and oceans. Jackson (2002) found that all continental microseismicity originates in the crust. Yet, reassessment of same data sets by Monsalve et al. (2006) shows earthquake locations as deep as 100 km, that is, well below the Moho depth. Nevertheless, most microseismic events do indeed occur above 40 km depth. In continents, the depth interval 0–40 km corresponds to diversely composed granite–diorite–feldspar–diabase–granulite crust, but in the oceans, it comprises 30 km of olivine-based uppermost mantle lithosphere and 7–10 km of basaltic crust. Hence, it can be logically concluded that in the 0–40 km depth interval, the maximum earthquake depth cannot be strongly related to rock type. The only rheological property that is largely rock type-independent is brittle strength (Byerlee, 1978), which is a linear function of pressure for all magmatic rocks. In contrast, ductile strength is strongly dependent on rock type and temperature and is expected to vary considerably at 40 km depth or 500 °C isotherm in different plates. Consequently, it is reasonable to assume that maximum earthquake depth is linked to depth-dependent brittle strength and should be conditioned by intraplate stress levels. Indeed, brittle strength is expected to be similar at the same depth in both oceans and continents. For this reason, a large number of studies (e.g., Handy and Brun, 2004; Watts and Burov, 2003) do not find any significant correlation between seismic depth and the long-term ductile strength of the lithosphere. It is pointed out that if a direct link between the two properties could exist, it would have to be an anticorrelation. According to this point of view, depth-dependent confining pressure precludes brittle failure explaining the scarcity of deep earthquakes. Hence, it is suggested that seismic deformation is a sign of mechanical weakness of shallow levels of the lithosphere. In addition, in continents, mechanical crust–mantle decoupling results in a stress drop at the Moho boundary making mantle earthquakes even less possible. The other part of this reasoning refers to the fact that seismicity is characteristic of short timescale behavior, which is physically unrelated to long-term rheology because at this short timescale, viscous–elastic–plastic lithosphere is expected to deform only in brittle–elastic mode.

Consequently, there may be no direct correlation between seismic behavior and long-term ductile behavior. Indeed, the observations of plate flexure below orogens (Watts, 2001) suggest that many continental plates have strong elastic cores (T_e), which are 2–2.5 times thicker than the seismogenic layer thickness, T_s. However, a number of points still need to be explained. In particular, maximum earthquake depth apparently correlates with the long-term brittle layer thickness, which vanishes, together with T_e, in the vicinity of oceanic spreading centers. The long-term thickness of the brittle layer is controlled by the depth to the brittle–ductile transition (BDT) and hence is temperature-dependent. Thermal gradients in hot lithosphere near spreading centers are much steeper than in normal lithosphere. As result, due the exponential dependency of the ductile strength on temperature, the BDT depth near ridges is close to the depth of 500–700 °C that defines the bottom of the mechanical lithosphere. Hence, near the ridges, plate strength is concentrated in the uppermost brittle layer; the YSE is saturated, that is, the deformation is largely nonflexural. In these specific conditions, integrated plate strength may correlate with T_s. With distance from spreading centers, BDT depth becomes shallower than the depth to 500–600 °C, an elastic core forms within the lithosphere, and the correlation rapidly breaks down. In particular, there is a large difference between the depths of extensional and compressional earthquakes (Watts and Burov, 2003).

However, driven by the idea of correlation between the seismogenic layer thickness and long-term strength of the lithosphere, a number of authors (Jackson, 2002; McKenzie and Fairhead, 1997; Zoback and Townend, 2001) challenge conventional rheology models for the lithosphere where ductile mantle provides an important contribution to the integrated plate strength. In continents, the conventional model is known as the 'jelly sandwich' because the assumption of strong mantle implies a stratified rheology profile with strong upper/lower crust and mantle layers separated by a weak 'jelly-like' ductile layer at the base of the lower crust. The previously mentioned authors stated that the 'jelly sandwich' model is incorrect, proposing instead a model in which all long-term strength is concentrated in the brittle layer. For continents, they have chosen a rheology envelope originally developed for Venus (Mackwell et al., 1998), in which the crust is strong, but the mantle is weak. This model (that I dubbed 'crème brûlée' model) suggests that continents are thin and hot (>800 °C at 60 km depth) and have a water-saturated mantle.

Historically, the 'crème brûlée' model has arisen because of conflicting results from rock mechanics, earthquake, and elastic thickness (T_e) data. Even if its validity is largely debated, its appearance illustrates the lack of reliable constraints on long-term rheology. Indeed, while one can systematically improve the precision and inherent consistence of rock mechanics experiments, it is difficult to prove, on the basis of laboratory experiments alone, that these data are relevant to long-term deformation (Kohlstedt et al., 1995). There is actually much confusion concerning the interpretation of brittle–elastic–ductile YSEs derived for the continental lithosphere. Even if the underlying rheology laws were robust, the common YSE profiles introduce additional uncertainties, because they are derived using strong assumptions regarding the shape of the geotherm, pressure, strain, and strain rate distribution at depth. For example, Jackson's (2002) suggestion that the depth of seismicity is limited by the depth of the BDT is based on interpretation of YSEs derived for geologic strain rates ($\sim 10^{-17}$–10^{-15} s^{-1}). Yet, long-term YSEs are not valid for seismic timescale deformation: when recomputed for seismic strain rates (10^{3}–10^{6} s^{-1}), YSEs predict that at this timescale, the lithosphere is entirely brittle–elastic, with BDT depth well below its bottom. Indeed, as revealed by postglacial rebound data (e.g., Peltier, 1974; Peltier and Andrews, 1976), the shortest ductile timescales in the lithosphere–asthenosphere system are on the order of thousands of years. Consequently, the

long-term BDT depth is not a direct proxy to maximum seismic depth. It can be only argued that since brittle earthquakes take place on the preexisting fractures or faults forming by coalescence of smaller fractures, they will more likely happen within a permanently brittle layer.

It becomes evident that independent large-scale constraints are needed to assess the long-term rheology of the lithosphere. In the following chapter, we summarize available experimental and observational data on lithosphere rheology and discuss possible approaches for parameterization and the application of data from experimental rock mechanics at geologic temporal and spatial scales.

6.03.2 Rock Mechanics Data and Conventional Rheology Models

For very small strains and/or short timescales (e.g., seismic), rocks deform elastically (Tables 1–4). Under stress, atomic bonds can be broken at quite small strains leading to inelastic deformation. Inelastic ductile deformation results from thermally activated creeping flow at long timescales. The most common mechanisms of ductile flow refer to atomic diffusion under pressure, sliding along intracrystal dislocations, point or planar defects, or sliding at grain boundaries. Inelastic brittle deformation results from coalescence of

Table 1 Commonly inferred parameters for diffusion creep in the mantle lithosphere, $n=1$ (Hirth and Kohlstedt, 2003; Karato et al., 1986)

Rock/mineral	A *(s^{-1} Pa^{-1} μm^m)*	*m*	Q *(kJ mol^{-1})*	*Comments*
Dry olivine	7.7×10^{-8}	1–3	536	Karato et al. (1986)
Dry olivine	1.5×10^{3}	3	375 ± 50	Hirth and Kohlstedt (2003)
Wet olivine	1.5×10^{-9}	1–3	498	Karato et al. (1986)
Wet olivine	2.5×10^{1}	3	375 ± 75	Hirth and Kohlstedt (2003)

These data are provided with primary goal to demonstrate characteristic values of parameters and to illustrate the scatter in experimental parameters.

Table 2 Commonly inferred parameters of dislocation creep

Rock/mineral	A *($MPa^{-n}s^{-1}$)*	n	Q *(kJ mol^{-1})*	*Comments*
Wet quartzite	10^{-4}	2.4	160	Brace and Kohlstedt (1980), Kirby and Kronenberg (1987), and Kohlstedt et al. (1995)
Wet quartzite	1.1×10^{-4}	4	223	Gleason and Tullis (1995), **Figure 4(b)**
Wet quartzite	1.25×10^{-5}	3 ± 0.2	242 ± 24	Rutter and Brodie (2004)
Dry feldspar (anorthite)	5.01×10^{12}	3	641	Rybacki et al. (2006)
Wet feldspar (anorthite)	1.58	3	345	Rybacki et al. (2006)
Dry diabase	$10^{-3.7}$	3.4	260	Kirby (1983)
Dry diabase	2.0×10^{-4}	3.4	260	Kirby (1983)
Columbia diabase (weak)	190 ± 110	4.7 ± 0.6	485 ± 30	Mackwell et al. (1998), **Figure 4(b)**
Maryland diabase (strong)	8 ± 4	4.7 ± 0.6	485 ± 30	Mackwell et al. (1998)
Granite(wet)	2×10^{-4}	1.9	140	Mackwell et al. (1998)
Wet diorite	3.2×10^{-2}	2.4	212	Ranalli (1995)
Dry mafic granulite	1.4×10^{4}	4.2	445	Wilks and Carter (1990)
Undried Adirondack granulite	3.18×10^{-4}	3.1	243	Wilks and Carter (1990)
Undried Pikwitonei granulite	1.4×10^{4}	4.2	445	Wilks and Carter (1990), **Figure 4(b)**
Dry olivine	10^{4}	3	520	Chopra and Paterson (1984)
Dry olivine	4.8	3.0	502	Evans and Kohlstedt (1995)
Dry olivine	5.0	3.5	530	Hirth and Kohlstedt (2003)
Dry dunite	4.85×10^{4}	3.5	535	Hirth and Kohlstedt (1996)
Microgabbro	5×10^{9}	3.4	497	Wilks and Carter (1990)
Wet olivine (dunite)	275.6	4.45	498	Chopra and Paterson (1981)
Wet olivine	4.876×10^{6}	3.5	515 ± 30	Hirth and Kohlstedt (1996)
Wet olivine	2.5×10^{7}	1.0	375 ± 75	Hirth and Kohlstedt (2003)
Wet Aheim dunite	2.6	4.5	498	Evans and Kohlstedt (1995)
Dry Anita Bay dunite	4.5	3.6	535	Chopra and Paterson (1981)
Wet synthetic San Carlos olivine	1.5×10^{6}	3	250	Karato et al. (1986)
Dry synthetic olivine	5.4	3.5	540	Karato et al. (1986)
Dry synthetic olivine	1.25×10^{6}	3.0 ± 0.1	510 ± 30	Karato and Jung (2003)
Wet synthetic olivine	3.3	3.0	420	Karato et al. (1986)
Wet synthetic olivine	794	3.0 ± 0.1	470 ± 40	Karato and Jung (2003)
Wet Anita Bay dunite	955	3.4	444	Chopra and Paterson (1984)
Wet Aheim dunite	417	4.48	498	Chopra and Paterson (1984), **Figure 4(b)**
Dry olivine	4.85×10^{4}	3.5	535	Chopra and Paterson (1981), **Figure 4(b)**
Olivine (Dorn's dislocation glide) at $\sigma_1-\sigma_3\geq200$ MPa	$\dot{\varepsilon}_0=5.7\times10^{11}\,s^{-1}$, $\sigma_0=8.5\times10^{3}$ MPa; $H^*=535$ kJ mol^{-1}			

These data are provided with primary goal to demonstrate characteristic values of parameters and to illustrate the scatter in experimental parameters; for recent updates, see, for example, Kohlstedt (2007).

Table 3 Peierls plasticity

Rock/mineral	τ_0 *(MPa)*	$\dot{\varepsilon}$ (s^{-1})	Q $(kJ\ mol^{-1})$	*Comments*
Synthetic olivine	8500	5.7×10^{-11}	536	Karato et al. (1998)
San Carlos peridotite	9100	1.3×10^{-12}	498	Goetze and Evans (1979)

Table 4 Summary of most common thermal and mechanical parameters of the lithosphere (also used in various model simulations shown in this paper)

Type	*Parameter*	*Value*
Thermal	T_{z0}, surface temperature	0 °C
	T_m, temperature at base of thermal lithosphere	1330 °C
	k_c, thermal conductivity of the upper crust	2.5 $Wm^{-1}\,°C^{-1}$
	k_{c2}, thermal conductivity of the lower crust	2.0 $Wm^{-1}\,°C^{-1}$
	k_m, thermal conductivity of mantle	3.5 $Wm^{-1}\,°C^{-1}$
	χ_c, thermal diffusivity of the upper crust	$8.3 \times 10^{-7}\ m^2\ s^{-1}$
	χ_{c2}, thermal diffusivity of the lower crust	$6.7 \times 10^{-7}\ m^2\ s^{-1}$
	χ_m, thermal diffusivity of mantle	$10^{-6}\ m^2\ s^{-1}$
	Hs, radiogenic heat production at surface	$9.5 \times 10^{-10}\ W\ kg^{-1}$
	h_r, radiogenic heat production decay depth constant	10 km
	H_{c2}/C_{c2} heat source term, lower crust	$1.7 \times 10^{-13}\ °K\ s^{-1}$
	a, equilibrium thermal thickness of the lithosphere	125–350 km
	t, thermotectonic age of the lithosphere	0–1000 My
Mechanical	ρ_c, density of upper crust	2700 kg m^{-3}
	ρ_{c2}, density of lower crust	2900 kg m^{-3}
	ρ_m, density of mantle (undepleted)	3330 kg m^{-3}
	ρ_a, density of asthenosphere	3310 kg m^{-3}
	Lamé elastic constants λ, G (here, $\lambda = G$)	30 GPa
	ϕ, Byerlee's law/Mohr–Coulomb criterion – friction angle	30°
	C_0, Byerlee's law /Mohr–Coulomb criterion – cohesion	20 MPa
	A,m,n,Q,H, ductile flow law parameters	**Tables 1–3**
	T_e, equivalent elastic thickness	0–110 km
	h_{1c},h_{2c},h_m, mechanical bottoms of the upper crust, lower crust, and mantle, respectively	<20; <40; <125 km, respectively
Divers	T_c, crustal thickness	7–70 km, 36–40 km (average in continents)
	T_s, seismogenic layer thickness	15–20 km; <50 km

preexisting microcracks and fractures into a single frictional shear band (fault) at sufficiently high strains (Byerlee, 1978; Lokhner, 1995). In nature, there is no pure elastic, viscous, or plastic deformation; all types of deformation take place simultaneously but in different proportions.

6.03.2.1 Elastic Properties

Elasticity arises from short-range interatomic forces that, when the material is unstressed, maintain the atoms in regular patterns. Stresses resulting from elastic deformation are linear function of strain, and the initial geometry of the material is fully recoverable after stress/strain relief. The elastic strain propagates with a speed of sound and goes ahead of viscous or plastic strain. This behavior is described by linear Hooke's law:

$$\sigma_{ij} = \lambda \varepsilon_{ii} \delta_{ij} + 2G\varepsilon_{ij} \qquad [1]$$

where λ and G are Lame's constants. Repeating indexes mean summation and δ is Kronecker's operator. λ and G are related to the incompressibility (bulk) modulus K_e:

$$K_e = {}^1/_3(3\lambda + 2G) \qquad [2]$$

An equivalent form of eqn [1] is

$$\begin{aligned} \varepsilon_{ij} &= E^{-1}\sigma_{ii}\delta_{ij} - E^{-1}\upsilon\sigma_{ij} \\ G &= E/2(1+\upsilon);\ \lambda = E\upsilon/((1+\upsilon)(1-2\upsilon)) \end{aligned} \qquad [3]$$

where E is Young's modulus and υ is Poisson's ratio. A number of direct observations suggest that the lithosphere maintains elastic stresses over long periods of time. These observations demonstrate that lithospheric plates behave as rigid blocks or shells for tens and hundreds My. Plate tectonics is the most evident demonstration of this phenomenon (DeMets et al., 1990). For normal loading, plate flexure, or regional isostasy, studies demonstrate that plates behave as thin rigid plates of finite thickness called equivalent elastic thickness of the lithosphere (T_e; **Figure 2(a)**). T_e varies from 0 km for very young areas (spreading centers) to 110 km for cratons (Audet and Burgmann, 2011; Forsyth, 1985; Watts, 2001). The continent average T_e is 30–50 km. For oceans, T_e is proportional to the square root of their age t (in My) (Le Pichon et al., 1973) and is generally smaller than 50 km:

$$T_{e\ oceans} \sim 5t^{1/2} \qquad [4]$$

The age t of the oceanic lithosphere is a proxy of its thermal state and thus of its ductile strength. The integrated strength of the oceanic lithosphere is largely controlled by its ductile

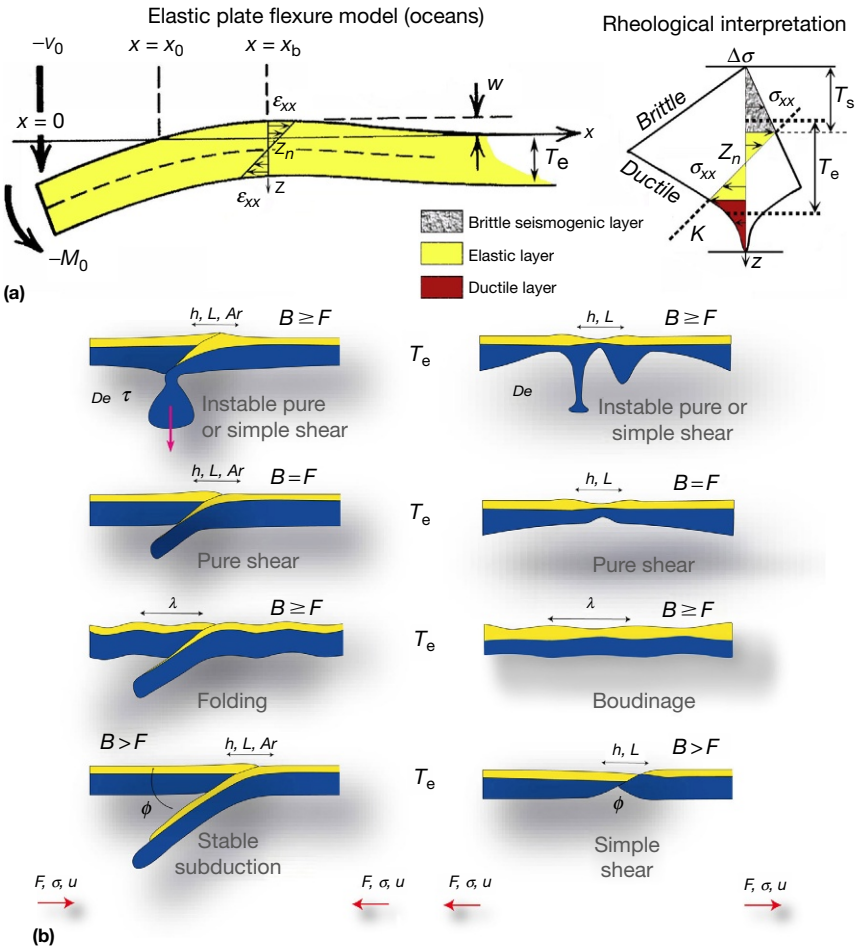

Figure 2 (a) Lithospheric flexure is the most widespread mode of deformation of the lithosphere since it is primarily related to the response of the lithosphere to permanently present vertical gravitational forces (and also boundary moments and vertical and horizontal boundary forces acting at plate boundaries). The figure shows a stress–strain distribution (σ_{xx}, ε_{xx}) in the classical elastic model of lithospheric flexure. w is vertical deflection of the plate, V_0 is cutting force, and M_0 is the boundary moment (both are associated with plate boundary conditions such as slab pull, loading from the upper plate, mantle drag, and other forces). z_n is the neutral plane. T_e is the equivalent elastic thickness of the plate, that is, the thickness of an ideal monolayer elastic plate that provides same observed geometry of bending $w(x)$ as the real lithosphere. Thickness of the real lithosphere may be essentially larger than T_e (modified from Turcotte DL and Schubert G (2002) *Geodynamics*, 2nd edn., p. 456. Cambridge: Cambridge University Press). (b) Observed modes of lithospheric deformation under horizontal forcing and related large-scale parameters used for estimation of lithospheric strength and rheology: T_e, F, σ, u, De, τ, h, L, λ, ϕ. T_e is equivalent elastic thickness. F, σ, u are, respectively, horizontal force, stress, and convergence/extension velocity that are linked to the lithospheric strength and possible deformation styles. De and τ are, respectively, Deborah number and relaxation/growth time related to viscosity contrasts in the lithosphere. λ is the characteristic wavelength of unstable deformation related to the thickness of the competent layers in the lithosphere. h, L are, respectively, the vertical and horizontal scales for process-induced topography supported by lithospheric strength, Argand number $Ar = \rho g h L / F$. ϕ is subduction or major fault angle that can be indicative of the brittle properties and of overall plate strength. In oceans, subduction and folding prevail at destructive boundaries and pure shear – at constructive boundaries (ridges). Compressive pure shear, boudinage, and RT instabilities are basically observed only in continents. In all cases, flexural deformation interferes with the other modes of deformation.

strength. In the continental domain, T_e is controlled by several factors and cannot be estimated from simple relations (Burov and Diament, 1995).

6.03.2.2 Brittle or Plastic Properties

Brittle failure occurs in different modes. One of them refers to tensile failure that results in fractures parallel to one of the axis of the principal stresses (σ_1, σ_3) and does not depend on confining pressure (Jaeger and Cook, 1976). However, tectonic fracturing is mostly related to shear failure, which is pressure-dependent plastic behavior (**Figure 1**; Nadai, 1963). Brittle deformation in shear described by Byerlee's law refers to frictional sliding on preexisting microfractures with either one or two fault planes forming an angle of $<45°$ with the direction of the maximum compression. Several empirical plastic yielding criteria exist that predict activation of brittle–plastic deformation for given conditions (Von Mises, Tresca, Mohr–Coulomb, Drucker–Prager, etc.). The Coulomb–Navier failure criterion (referred to as Mohr–Coulomb criterion when expressed in terms of Mohr's circle diagrams) best represents the brittle behavior of rocks in geologically relevant contexts (Byerlee, 1978). This criterion refers to Amonton's law of friction:

$$\tau = C_0 + \tan(\phi)\sigma_n \quad [5]$$

where C_0 is the cohesive strength (<20 MPa), $\tan(\phi)$ is the internal friction coefficient, ϕ is the internal friction angle (typically 30–33°), τ and σ_n are, respectively, the shear stress and normal stress on a selected surface within material. According to Cauchy's formulation for a Cartesian basis (x,y, z) (e.g., Kachanov, 1971),

$$\begin{aligned}\sigma_n &= \sigma_{xx}\cos^2(n,x) + \sigma_{yy}\cos^2(n,y) + \sigma_{zz}^2\cos(n,z) \\ &+ 2\left(\tau_{yx}\cos(n,x)\cos(n,y) + \tau_{yz}\cos(n,y)\cos(n,z)\right. \\ &\left. + \tau_{xz}\cos(n,z)\cos(n,x)\right)\end{aligned} \quad [6]$$

where subscripts refer to the global Cartesian stress components. The shear stress on a fault plane τ_n is $t_n^2 = X_n^2 + Y_n^2 + Z_n^2 - \sigma_n^2$, where X_n,Y_n,Z_n refer to the x,y,z components of $\boldsymbol{\sigma}_n$. Assigning the origin of the z-coordinate to Z_n, we obtain 2-D Mohr circles ($\theta = \text{angle}(\boldsymbol{n},\boldsymbol{x})$):

$$\begin{aligned}\sigma_n = \sigma_{xx}\cos^2\theta + \sigma_{yy}\sin^2\theta,\ \tau_n^2 = X_n^2 + Y_n^2 - \sigma_n^2, \\ \sigma_n^2 + \tau^2 - \sigma_n(\sigma_{xx} + \sigma_{yy}) + (\sigma_{xx}\sigma_{yy}) = 0\end{aligned} \quad [7]$$

Measurements *in situ* are referred to the (σ_1,σ_3) frame (**Figure 1**):

$$\begin{aligned}\sigma_n &= \tfrac{1}{2}(\sigma_1 + \sigma_3) + \tfrac{1}{2}(\sigma_1 - \sigma_3)\cos 2\theta \\ \tau &= \tfrac{1}{2}(\sigma_1 - \sigma_3)\sin 2\theta\end{aligned} \quad [8a]$$

σ_n and τ refer to a plane (e.g., fault plane), whose normal $\boldsymbol{n}$ forms an angle θ with the direction of σ_1; $\phi = 2\theta - \tfrac{1}{2}\pi = \tfrac{1}{2}\pi - 2\alpha$, where 2α is the angle between two conjugated shear planes $\alpha = \theta - \tfrac{1}{2}\pi$. Shear fractures are thus oblique to σ_1 and σ_3 and develop in two preferred orientations that form an angle of ~60° ($2\theta - \pi = \tfrac{1}{2}\pi - \phi$) to each other, constituting an 'X'-shaped conjugate set. Conjugated shear zones are bisected acutely by the maximum shortening direction and obtusely by the maximum extension direction. Their intersection is parallel to σ_2, which is normal to (σ_1,σ_3) plane. Large-scale shear bands and faults follow the same rule and may form by coalescence of various types of smaller fractures: shear fractures parallel to the sense of displacement along the conjugate shear zones, tensile fractures striking parallel to each other in both conjugate zones, and 'Riedel' shear fractures that make an angle of ~15° (or ~75°) to the bulk shear direction. These small-scale fractures may step en échelon along incipient shear zones.

The parabolic Griffith criterion extends the Mohr–Coulomb criterion to the domain of tensile stress:

$$\tau^2 = 4T_0^2 + 4T_0\sigma_n \quad [8b]$$

where $2T_0 = C_0$ is the tension cutoff (**Figure 1**). Tensile fractures open in normal to the maximum extension direction. They next dilate and get filled (healed) with minerals (quartz and calcite) precipitated from fluids circulating within the host rock to form extensional veins.

The point where the yield criterion function is tangent to the largest of Mohr circles (σ_1,σ_3) defines failure stress and angles θ and α. A third parameter, Ψ, dilatation angle, accounts for dilatation in shear that occurs due to sliding over interface aspherities. Hence, Ψ characterizes the degree of compressibility ($\Psi = 0$ for incompressible rock). For simple shear, Ψ is defined from the ratio of volume strain rate $\dot{\varepsilon}_{ii}$ to shear strain rate $\dot{\varepsilon}_{ij}$:

$$\tan\Psi = \dot{\varepsilon}_{ii}/\dot{\varepsilon}_{ij} \quad [8c]$$

Plasticity is associative if $\Psi = \phi$ or nonassociative if $\Psi \neq \phi$. More precisely, plasticity is nonassociative if the plastic potential function differs from the plastic failure function. For Mohr–Coulomb or Drucker–Prager plasticity, this is the case when $\Psi \neq \phi$. Most rocks are nonassociative: $\Psi < 10°$ and $\phi = 30°$–$40°$ (Vermeer and de Borst, 1984). This explains localization of shear bands due to the rheological instabilities even without material softening. These instabilities occur because the nonassociative materials do not deform homogeneously in a postpeak stress regime, but bifurcate into two states: plastic deformation within a shear band and elastic unloading outside. This leads to a stress discontinuity across the shear band and, consequently, to instabilities. Normal stresses parallel to the shear band decrease in a postpeak regime, which results in a decrease in vertical stress as well. This stress drop is called 'nonassociated softening' (Vermeer, 1990), as distinct from material softening, which occurs when some intrinsic material parameters (cohesion and friction angle) decrease as a function of strain or stress.

Byerlee (1978) experimentally demonstrated that for the majority of rocks, the Coulomb failure criterion applies in the form (**Figure 1**)

$$\begin{aligned}\tau &= 0.85\sigma_n,\ \sigma_n \le 200\,\text{MPa} \\ \tau &= 50\,\text{MPa} + 0.6\sigma_n,\ 1700\,\text{MPa} > \sigma_n > 200\,\text{MPa}\end{aligned} \quad [9]$$

or

$$\begin{aligned}\sigma_1 &= 4.7\sigma_3,\ \sigma_3 \le 114\,\text{MPa} \\ \sigma_1 &= 3.1\sigma_3 + 177\,\text{MPa},\ 1094\,\text{MPa} > \sigma_3 > 114\,\text{MPa}\end{aligned} \quad [10]$$

Byerlee (1978) had also shown that frictional properties of rocks are nearly independent of rock type. This explains why tectonic faults may intersect lithologically heterogeneous structures. However, brittle strength depends highly on pressure variations caused by tectonic stresses and fluids. The latter are described by the fluid pressure factor $\lambda = \rho_w/\rho$, where ρ_w is the density of water and ρ is rock density:

$$\Delta\sigma = \sigma_1 - \sigma_3 = \alpha\rho g z(1 - \lambda) \quad [11]$$

where $\alpha = 1 - R^{-1}$ for normal faulting, $\alpha = R - 1$ for thrusting, and $\alpha = (R-1)/(1 + \beta\ (R-1))$ for strike-slip faulting, with $R = ((1+\phi^2)^{1/2} - \phi)^{-2}$ and $\tan\beta = (\sigma_2 - \sigma_3)/(\sigma_1 - \sigma_3) < 1$.

It is noteworthy that Byerlee's data can also correspond to a weak power law (Lokhner, 1995):

$$|\tau| = \sigma_n^{0.94} \quad [12]$$

Deep drilling has provided direct evidence in support of Byerlee's law for the first few km of the crust (1–14 km) (e.g., Zoback et al., 1993). However, this law is probably not applicable at depths exceeding 30–50 km (e.g., Kirby et al., 1991). At high depth/pressure or temperature, brittle failure may change to semibrittle (e.g., Bos and Spiers, 2002; Chester, 1995) or to some form of ductile–superplastic regime (e.g., Goetze and Evans, 1979). One of the discussed possibilities refers to Peierls plasticity (Goetze and Evans, 1979, see also next section) or to grain boundary sliding (GBS) that is specific to upper mantle rocks (e.g., Drury, 2005). Peierls plasticity takes place at high differential stresses (>100–200 MPa), when mixed dislocation glide and climb occur (Karato, 1998; Karato et al., 1986).

Parameters of the Peierls mechanism are not well known since they have been obtained only in a few experiments (Evans and Goetze, 1979; Goetze and Evans, 1979) at room pressure. Synthetic parameters (e.g., Karato, 1998; Karato et al., 1986) can be used only as rough estimates (**Table 3**). GBS creep may occur at large strains in relatively cold (<700–800 °C) upper mantle lithosphere (e.g., Precigout et al., 2007; Precigout and Gueydan, 2009; Terry and Heidelbach, 2004). This flow law may eventually explain the absence of distributed seismicity in the mantle, as well as the difference between crustal and mantle seismicity (no GBS creep in the crust). Despite the lack of experimental data for near-Moho and mantle conditions, there is a general agreement that brittle strength reaches maximum values at 30–50 km depth, below which Byerlee's law is apparently replaced by some other behavior such as Peierls flow and the rock strength no longer increases (Kirby, 1991; Kirby et al., 1996). However, some phenomena, such as discovery of apparently brittle ultrahigh-pressure pseudotachylites in exhumed deep fault zones (Austrheim and Bondy, 1994), suggest that brittle-like failure may have been occasionally produced at great depth in large shear zones.

6.03.2.3 Ductile (Viscous) Properties

Viscous behavior applies when the deformational stress is a function of strain rate and does not depend on the strain itself. The term 'ductile,' often associated with strain rate-dependent properties of the rocks, is not related to a particular constitutive relationship but to the ability of materials to change form irreversibly without fracturing. Actually, if the strain rate–stress dependence is not negligible, the material is considered as ductile–plastic if it deforms irreversibly without fracture. When the ductile deformation is characterized by linear strain rate–stress dependence, one speaks of Newtonian viscous deformation. When this dependence is nonlinear, the term 'non-Newtonian viscosity' is applied. At temperatures >300 °C, strain rate-dependent nonlinear dislocation creep is dominant. At very high temperatures (>1330 °C), the deformation appears to be dominated by linear diffusion creep (note, however, that a number of studies have suggested that the upper mantle is partly driven by the dislocation creep (Van Hunen et al., 2005)).

6.03.2.3.1 Diffusion and dislocation creep

The dominant ductile flow mechanisms in the lithosphere–asthenosphere system are associated with the diffusion and dislocation creep. In contrast to brittle deformation, the ductile deformation is extremely dependent on rock type (e.g., Kirby and Kronenberg, 1987). Even small variations in mineral composition may have a strong impact on ductile properties (Brace and Kohlstedt, 1980; Bürgmann and Dresen, 2008; Hier-Majumder et al., 2005; Kirby and Kronenberg, 1987; Kohlstedt, 2007; Mackwell et al., 1998; **Tables 1–2**). The mechanisms of ductile deformation are variable and abundant: diffusion creep, numerous variants of dislocation creep (dislocation climb, glide, screw, edge, etc.), pressure solution, GBS, and so on. Grain size-sensitive (GSS) diffusion creep (Nabarro-Herring (volume diffusion)) or Coble creep (surface diffusion) (Ashby and Verall, 1978) is associated with temperature-dependent directional diffusivity of rocks and minerals under applied stress (**Table 1**):

$$\dot{\varepsilon}^d = Aa^{-m} f_w \Delta\sigma^n \exp\left(-H(RT)^{-1}\right) \quad [13]$$

where $\dot{\varepsilon}^d$ is shear strain rate; A is a material constant; a is a grain size; m is a diffusion constant; f_w is the water fugacity factor; n is a power law constant; $\Delta\sigma = \sigma_1 - \sigma_3$ is differential stress; R is Boltzmann's gas constant; H is creep activation enthalpy, $H = Q + PV$, where Q is activation energy, P is pressure, and V is activation volume; and T is temperature in K. For olivine-rich rocks at high-temperature–low-stress conditions, $m = 3$ and $n = 1$ so that the constitutive law is linear Newtonian.

At high stresses and moderate temperatures <1330 °C, $m = 0$ and $n = 3$, the creep rate is dominated by grain size-insensitive (GSI) dislocation creep (power law and Dorn's law). The power flow law is strongly non-Newtonian (**Table 2**) for $\Delta\sigma < 200$ MPa:

$$\dot{\varepsilon}^d = Af_w \Delta\sigma^n \exp\left(-H(RT)^{-1}\right) \text{ for } \Delta\sigma < 200\,\text{Mpa}(\text{Power law}) \quad [14]$$

$$\dot{\varepsilon}^d = Af_w \exp\left(-H\left(1 - \Delta\sigma/\sigma_p\right)^2/RT\right) \text{ for } \Delta\sigma > 200\,\text{Mpa}(\text{Dorn law}) \quad [15]$$

where $\dot{\varepsilon}_0$ and σ_p are, respectively, maximum strain rate and Peierls stress (lattice resistance to dislocation glide, on the order of several GPa). For tectonically relevant $\Delta\sigma/\sigma_p$ ratios (<0.1), Dorn's behavior is close to plastic behavior (Peierls plasticity) and tends to limit ductile strength in a high-stress regime (**Figure 3**). This law is not sufficiently well studied and its application may be subject to large uncertainties (Goetze and Evans, 1979).

The effective viscosity μ_{eff} for power flow law can be defined from

$$\tau_{ij} \equiv \mu_{eff} \dot{\varepsilon}^d_{ij} \quad [16]$$

which yields

$$\mu_{eff} = \dot{\varepsilon}^{d(1-n)/n}_{ij} A^{-1/n} \exp\left(H(nRT)^{-1}\right) \quad [17]$$

The laws [14] to [15] are derived for uniaxial deformation. They should be converted, with all possible reservations, to a form valid for triaxial deformation, via the second invariant (J_2) of strain rate $\dot{\varepsilon}^d_{ij}$ and geometric proportionality factors:

$$\mu_{eff} = \dot{\varepsilon}^{d(1-n)/n}_{II} (A^*)^{-1/n} \exp\left(H(nRT)^{-1}\right) \quad [18]$$

$$\dot{\varepsilon}^d_{II} = \left(J_2\left(\dot{\varepsilon}^d_{ij}\right)\right)^{1/2} \text{ and } A^* = \tfrac{1}{2}A \cdot 3^{(n+1)/2}$$

where $\dot{\varepsilon}^d_{II}$ is the effective shear strain rate. The diffusion creep takes over for small grain size that is specific for highly sheared material (ductile shear zones) or for very high temperatures. Grain size reduction is believed to be an important mechanism of rock softening and localization in mantle shear zones or in the upper mantle (Karato et al., 1986). Creep mechanisms are strongly dependent on water, water fugacities, and mineralogical and melt content (Karato, 1986).

6.03.2.3.2 Pressure solution, cataclastic flow, Peierls plasticity, GBS flow, and other mechanisms

While dislocation and diffusion creep are the dominant flow mechanisms in the lithosphere and the underlying asthenosphere, a number of secondary but contextually important ductile creep mechanisms are also present at specific pressure–temperature conditions.

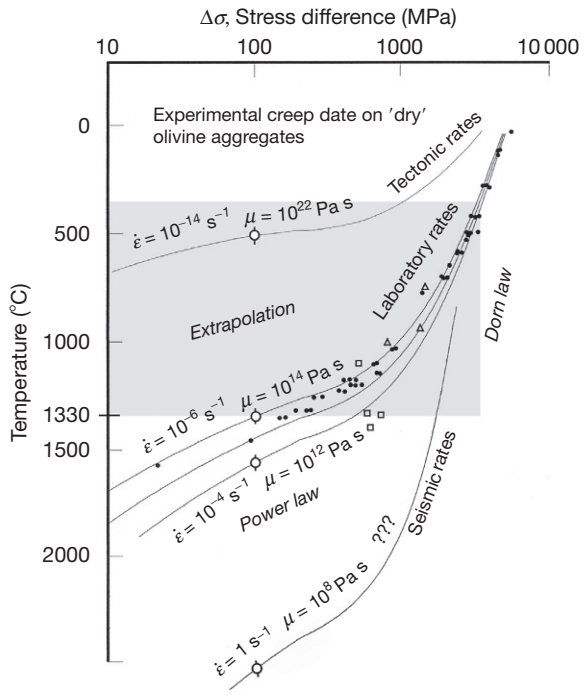

Figure 3 Typical example of experimental data on ductile flow in rocks (olivine aggregates and power and Dorn's flow laws for different temperature–stress domains). Shown also are predicted viscosity values, μ, for 100 MPa stress level (open circles). Note sensitivity to strain rate $\dot{\varepsilon}$ and rock composition (triangles, squares, and black dots correspond to different variants of principally the same olivine aggregates). The typical strain rates used in experiments (10^{-6}–10^{-4} s^{-1}) are ten orders of magnitude higher than those in nature (10^{-14}–10^{-17} s^{-1}), which poses a serious question on the possibility of extrapolation of these data onto geologic timescales (modified from Goetze C and Evans B (1979) Stress and temperature in bending lithosphere as constrained by experimental rock mechanics. *Geophysical Journal of the Royal Astronomical Society* 59: 463–478; Watts AB (2001) *Isostasy and Flexure of the Lithosphere*, p. 458. Cambridge: Cambridge University Press). Hypothetical extrapolation of experiential data to seismic timescales (1 s) predicts very low-viscosity values, yet at these timescales, creep takes place at temperatures that are higher than maximum lithospheric temperature (1330 °C). Consequently, it is unlikely that seismic movements can activate ductile creep in lithospheric mantle.

Pressure solution is one of 'cold' ductile flow mechanisms that may occur at shallow depths and at temperatures below 200 °C and thus can compete with brittle deformation. This mechanism refers to the enhanced solubility of minerals under stress/pressure. Application of mechanical stress provokes directional solution of minerals in pore water, which leads to reduction of volume of solid phase equivalent to deformation:

$$\dot{\varepsilon}^d = 12\delta\rho_w D_s \sigma \left(h^3 \rho \sigma_0\right)^{-1} \qquad [19a]$$

where δ is width of the grain boundary, ρ_w is density of solvent (water), D_s is the diffusion coefficient, σ is stress, h is the initial dimension of the crystal and ρ is the density of the soluble mineral (e.g., silica), and σ_0 is maximum stress. Silica, for example, is perfectly soluble in water at $\sigma_0 \sim 500$ MPa and $T = 500$ °C. Some experimental studies (e.g., Gratier et al., 2006) have found that eqn [19a] should be corrected to include an exponential term depending on temperature and σ. The resulting flow law is weakly nonlinear power law with $n = 1.7$.

Cataclastic flow or semibrittle flow in porous rocks or at fault surfaces is another well-known example of 'cold' ductile behavior that occurs in high-strain regime. Cataclastic flow is associated with strain rate-dependent reduction of friction. It involves distributed microfractures at grain level, such that at a mesoscopic level or hand specimen scale, the rock appears to flow. This flow is often associated with semibrittle flow and treated in conjunction with crystal–plastic flow (Chester, 1988):

$$\tau = \tanh(\alpha\sigma_n)\left(\beta^{-1}\ln\left(\dot{\varepsilon}B^{-1}e^{(Q/RT)}\right)\right) + (1 - \tanh(\alpha\sigma_n))\tau_f \qquad [19b]$$

where α, β, B are material constants and τ_f is frictional stress that corresponds to the Mohr–Coulomb stress (eqn [5]) at low deformation rates and becomes rate-dependent at higher rates (Rice and Tse, 1986):

$$\tau_f = \sigma_n\left(\mu_r - C\ln\left(\frac{\dot{\delta}}{\dot{\delta}_r} + 1\right)\right) \qquad [19c]$$

where $\dot{\delta}$ and $\dot{\delta}_r$ is shear displacement and reference shear displacement rate, respectively, C is an experimental constant, and μ_r is a high-rate friction coefficient.

Peierls plasticity (see also eqn [15]) applies when the stress in the rock reaches a specific limit called Peierls stress. The latter is associated with Peierls energy, which changes with a transition of a dislocation line between the adjacent valleys of the potential relief, by a distance smaller than Burger's vector. At this moment, the dominant creep mechanism becomes dislocation glide and climb. The extended constitutive equation for Peierls plasticity relates to a form of Dorn's law (Evans and Goetze, 1979; Goetze and Evans, 1979):

$$\dot{\varepsilon}_{ij}^d = \dot{\varepsilon}_0 \exp\left(-\frac{Q + p(V - \beta\Delta V_w)}{RT}\left(1 - \frac{\tau_{ij}}{\tau_p}\right)\right) \qquad [20a]$$

where $\dot{\varepsilon}_0 = A\alpha$, A,Q,V,P,R, and T are defined in the same way as for the ductile creep laws (see eqn [15]), α is an experimentally defined weakening parameter controlled by water content, β is an adjustable experimental parameter, ΔV_w is molar volume change due to incorporation of hydroxyl ions in the main rock, and τ_p is the shear stress limit (~Peierls stress) that characterizes transition to plastic failure. Regenauer-Lieb et al. (2001) suggested that Peierls plasticity and water-induced weakening may play a major role in localization of deformation at important depth or in subduction/collision zones. However, as mentioned, Peierls rheology is poorly constrained, while Peierls stress is significantly higher than typical tectonic stress, which limits the applicability of this law to high-strain zones.

During dynamic recrystallization, the accommodation of grain size reduction occurs by three competing deformation mechanisms, that is, GSI dislocation creep, GSS diffusion creep, and dry-GBS (GBS) GSS creep (Durham et al., 2009; Precigout et al., 2007). It involves grain size reduction controlled by diffusion creep at high temperatures (>800 °C), whereas dislocation creep and dry-GBS creep are the accommodating

mechanisms at lower temperatures (500–800 °C). GBS creep has been only recently considered in terms of its potential importance for tectonic-scale deformation (e.g., Precigout et al., 2007). Now, a growing number of studies suggest that like Peierls flow, it can replace Byerlee's law and dislocation creep in lithosphere mantle in a quite important depth range (e.g., Drury, 2005) corresponding, in continents, to a 20–30 km layer of sub-Moho mantle and, in the oceans, to the bottom of the mechanical lithosphere. It is suggested that this mechanism may be responsible for softening and aseismic localization of shear deformation in the uppermost strong lithosphere mantle (e.g., Precigout et al., 2007), allowing, for example, for formation of narrow rifts without a necessity for large far-field forces. Dry-GBS creep has been shown to accommodate grain size reduction during dynamic recrystallization and to induce significant weakening at low temperatures. The phenomenological equation for the GBS creep has the same form as for the diffusion creep, yet with highly different parameters, in particular with n in the order of 3:

$$\dot{\varepsilon}^d = A_{\mathrm{GBS}} a^{-m} \tau^n \exp\left(-H(RT)^{-1}\right) \qquad [20b]$$

where A_{GBS} is the preexponential constant, a is grain size, m is the GBS grain size exponent (typically $m=2$), n is the GBS power law constant (typically $n=3.5$), τ is shear stress, H is creep activation enthalpy, and T is temperature in °K. GBS creep thus combines features of both the diffusion and dislocation power law creep. Analogously to dislocation creep, it operates at high stresses and is highly nonlinear, with n close to that for dislocation power law creep in dry olivine. Yet, similarly to the diffusion creep, GBS creep is highly GSS, which makes of it an efficient mechanism of strain localization in strong mantle. By itself, diffusion creep cannot play a strain localization role in the mantle lithosphere since it operates at high temperatures and small stresses (<10 MPa) and thus cannot result in important strength/stress drops. Diffusion creep also corresponds to Newtonian linear flow ($n=1$); hence, its localizing properties are more limited. Ductile shear band strain localization resulting from the GBS creep may occur in the depth range corresponding to 500–800 °C (40–60 km depth in continents, e.g., Terry and Heidelbach, 2004) and therefore provide some explanation for the scarcity of earthquakes below this depth. Nevertheless, the hypothesis of the potential role of GBS creep mechanism in the mantle lithosphere needs further investigation.

6.03.2.4 Yield Stress Envelopes

By combining three major rheology laws (elastic, brittle, and ductile), Goetze and Evans (1979) had introduced the YSE for the lithosphere (**Figure 4**) defined as a differential stress contour $\sigma^f(z)$, or $\Delta\sigma_{\max}(z)$, such that

$$\begin{aligned}\sigma^f(z) &= \Delta\sigma_{\max}(z) \\ &= \mathrm{sign}(\varepsilon)\min\left(\left|\sigma^b(x,z,t,\dot{\varepsilon},\mathrm{sign}(\varepsilon))\right|, \left|\sigma^d(x,z,t,\dot{\varepsilon})\right|\right)\end{aligned} \qquad [21a]$$

where $\sigma^b(x,z,t,\dot{\varepsilon},\mathrm{sign}(\varepsilon))$, $\sigma^d(x,z,t,\dot{\varepsilon})$ are the maximum brittle and ductile yielding stresses; sign(ε) is a sign function equal to 1 for extension and −1 for compression; t is time; and x refers to the possibility of not only depth (z) but also spatial strength variations. The differential stress $\Delta\sigma(\varepsilon)$ for the strain $\varepsilon=\varepsilon(x,y,t,\dot{\varepsilon})$ is

$$\Delta\sigma(\varepsilon) = \mathrm{sign}(\varepsilon)\min\left(\left|\sigma^f\right|, \left|\sigma^e(\varepsilon)\right|\right) \qquad [21b]$$

where $\sigma^e(\varepsilon)$ is the value of elastic stress for the given strain ε. The lithosphere deforms elastically if $\sigma^e(z,\varepsilon)<\sigma^f(z)$. This implies the existence of a pertinent elastic 'core,' where inelastic strains are negligible. This core, associated with the equivalent elastic thickness, T_e, provides the main contribution to the integrated plate strength, B:

$$B = \int_0^\infty \sigma^f(x,y,t,\dot{\varepsilon})\mathrm{d}z \le \int_0^\infty \sigma^e(\varepsilon)\mathrm{d}z \qquad [22]$$

Depth dependence of $\Delta\sigma_{\max}(z)$ stems from many factors among which are temperature, pressure, and composition. The YSEs are computed for a fixed background strain rate (typically, 10^{-15} s^{-1}). As suggested by McAdoo et al. (1985) for oceanic lithosphere and by Burov and Diament (1992) for continental lithosphere, the YSEs can be linearized, which allows for simple parameterization of rheology laws from direct observations of flexure. Linearized YSEs have been used in inelastic flexural models (Burov and Diament, 1992,1995; McAdoo et al., 1985; **Appendix A**). This has allowed for the prediction of T_e for regional studies, as a function of YSE, surface and subsurface loading, thermal distribution, plate structure, and other parameters. By fitting nonlinear flexural models to the observed deformation, it has become possible to test and validate rheological profiles derived from experimental rock mechanics. These models have confirmed the validity of rheological envelopes for a number of regions (e.g., Central Asia (Burov and Diament, 1992; Watts and Burov, 2003) and European lithosphere (Cloetingh and Burov, 1996; Tesauro et al., 2009a,b,c)).

The formulation of the YSE and its interpretation in terms of the observed equivalent elastic thickness (T_e) of the lithosphere constitutes a major breakthrough in our understanding of the long-term behavior of the lithospheric plates. Computed oceanic YSEs show a remarkable correlation with the measured values of T_e. The predicted depth of the BDT also correlates with deepest microseismicity in the oceanic domain (e.g., Watts and Burov, 2003).

While the composition and thermal structure of oceanic plates are well established, it is not the case for the continental domains. Continents have a thick crust of diverse structure and properties that vary from region to region. In addition, it is argued (Jackson, 2002) that in continents, the resistance of mantle olivine is strongly reduced due to the presence of fluids (**Figure 4(b)**; **Table 2**). Yet, more recent studies have detected high water content only in deep upper mantle below the lithosphere but not in the lithosphere itself (Katayama et al., 2005). Inspection of the CB ('crème brûlée') YSE published by Jackson (2002) shows that it is not the assumption of wet olivine rheology that makes this YSE exceptionally weak but that of a very thin hot continental lithosphere (800 °C at 60 km depth, estimated equilibrium plate thickness $a=z(1330\ ^\circ\mathrm{C})$ ~100 km). Such conditions may exist in a few places on the Earth but not in the thick old Indian Craton targeted by Jackson (2002). Wet olivine rheology preserves important strength (**Figure 4(b)**, right) in the case of a geotherm computed for a more appropriate equilibrium plate

thickness ($a = z(1330\,^{\circ}\mathrm{C}) \sim 200$ km) and taking into account radiogenic heat sources.

6.03.3 Constitutive Models

Elastic and brittle (plastic) rheologies are strain rate-independent, whereas viscous rheology is strain-independent. However, in the lithosphere, the behavior of elastic and brittle domains becomes strain rate-dependent via interaction with the viscous domain, which, in turn, becomes strain-dependent. Thus, even if the rheological parameters (elastic, ductile, or brittle) were well constrained, the next question would be how to combine these rheological terms in a constitutive model. There are various possible constitutive models based on either the Maxwell, Voigt, or Kelvin model or their various possible combinations (Figure 4(c)).

6.03.3.1 Maxwell Model

In a Maxwell solid, total strain ε^{M} equals a sum of the elastic strain ε^{e} and viscous strain $\varepsilon,^{v}$ while viscous and elastic stresses are equal:

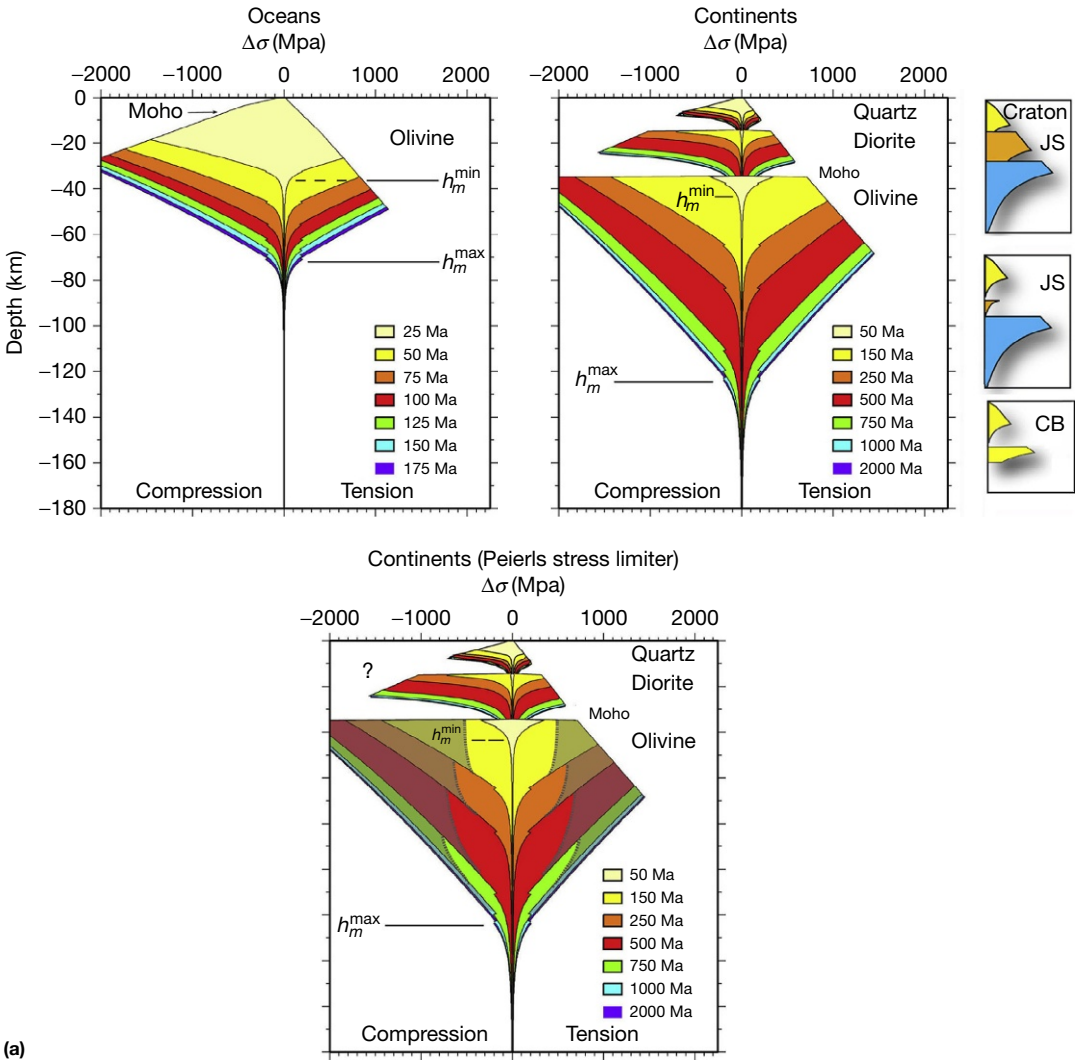

Figure 4 (a) Examples of rheological yield stress envelopes for oceans (as introduced by Goetze and Evans (1979)) and continents (modified from Burov EB and Diament M (1995) The effective elastic thickness (T_e) of continental lithosphere: What does it really mean? *Journal of Geophysical Research* 100: 3895–3904). The YSE is shown as a function of the thermotectonic age. The main difference between the oceanic and continental lithosphere refers to the thick crust and multilayered structure of the latter, which may lead to mechanical decoupling between the rheological layers and horizontal ductile flow in the intermediate or lower crust. The right panel illustrates different variants of continental YSE: cratonic jelly sandwich (JS, strong lower crust is coupled with strong mantle), classic JS (strong crust is decoupled from strong mantle), crème brûlée (CB, very weak mantle). The bottom panel shows YSE for continental lithosphere under hypothetic assumption that Peierls flow takes place in mantle olivine at high-stress conditions. Although Peierls flow may also occur in other rocks/minerals, the laboratory data are not robust enough for lithosphere-scale interpolation (actually this is also partly the case of olivine/peridotite). The ductile strength of crustal rocks is highly uncertain; in particular, the rheology of quartz-rich upper crustal rocks is subject to large variations.

$$\begin{aligned}\varepsilon_{ij}^{M} &= \varepsilon_{ij}^{e} + \varepsilon_{ij}^{v} \\ \sigma_{ij}^{e} &= \sigma_{ij}^{v}\end{aligned} \quad [23]$$

The strain relation is often written in the incremental form

$$e_{ij}^{M} = e_{ij}^{e} + e_{ij}^{v} = S_{ij}/\left(2G^{M}\right) + \sigma_{ij}/\left(2\mu^{M}\right) \quad [24]$$

where e is $\partial\varepsilon/\partial t$ (incremental strain, or strain rate) and S is $\partial\sigma/\partial t$ (incremental stress, or stress rate). The behavior of this solid is dominated by the rheological term developing larger strain or strain rate. Thus, for most materials, in case of instantaneous strain, the first reaction is elastic and is associated with maximum stress, but in later stages, stress decays due to viscous relaxation at a rate controlled by the Maxwell relaxation time τ_m:

$$\tau_m = \mu/E \quad [25]$$

If τ_m is considerably shorter than the life span of the system, then deformation is effectively viscous (small Deborah number). For the asthenosphere, τ_m is known from postglacial rebound data (e.g., Peltier, 1974). This time is about 10–100 years implying effective viscosity of $1\text{–}5 \times 10^{19}$ Pa s. In the lithosphere, τ_m is on the order of several My, as indicated by data on volcanic island loading (Watts, 2001).

In 'extended' Maxwell viscous–elastic–plastic models, the total incremental strain ε^{M_ext} equals a sum of the elastic, plastic, and viscous strain increments:

$$\varepsilon_{ij}^{M\_ext} = \varepsilon_{ij}^{M} + \varepsilon_{ij}^{p} \quad [26a]$$

If several ductile flow law mechanisms can be activated at the same time, the viscous term ε_{ij}^{v} in the Maxwell term ε_{ij}^{M} is often written as

$$\varepsilon_{ij}^{v} = \varepsilon_{ij}^{vdc} + \varepsilon_{ij}^{vdf} + \varepsilon_{ij}^{vgbs} + \varepsilon_{ij}^{vp} \quad [26b]$$

where $\varepsilon_{ij}^{vdc}, \varepsilon_{ij}^{vdf}, \varepsilon_{ij}^{vgbs}, \varepsilon_{ij}^{vp}$ are contributions from dislocation, diffusion, GBS, and Peierls creep, respectively. It follows from eqn [26b] that for deformation with constant stress, the effective viscosity is

$$\mu^{eff} = \left(\left(\mu^{vdf}\right)^{-1} + \left(\mu^{vdc}\right)^{-1} + \left(\mu^{vp}\right)^{-1} + \left(\mu^{vgbs}\right)^{-1}\right)^{-1} \quad [26c]$$

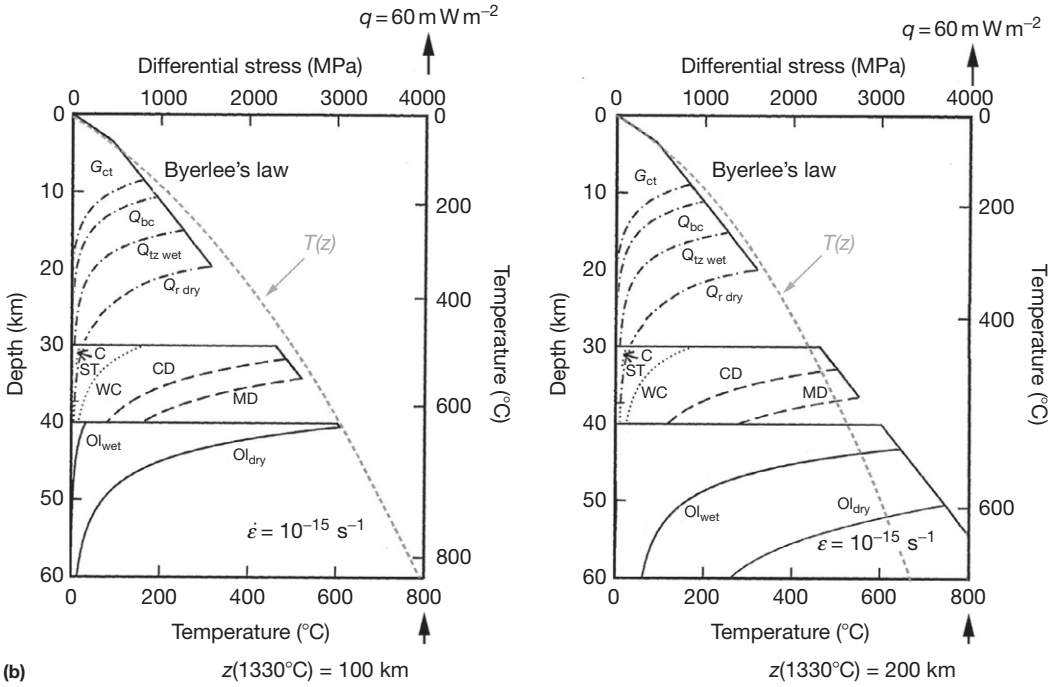

Figure 4 (Continued) (b) Influence of compositional variation, plate thickness $a = z$ (1330 °C), and fluid content on continental yield stress envelope (YSE) computed for typical surface heat flow, q, of 60 mW m^{-2} but two different thermal models: equilibrium thermal plate thickness of 100 km (left; Chapman, 1986) and of 200 km (right; plate cooling model, **Appendix B** (Burov and Diament, 1995)). CD, dry Columbia diabase; MD, dry Maryland diabase; WC, Pikwitonei granulate; ST and C, diabase from Shelton and Tullis (1981) and Caristan (1982). The upper crust is wet quartzite from Gleason and Tullis (1995); Ol_{dry} and Ol_{wet} are dry and wet dunites from Chopra and Paterson (1984). Q_{bc} refers to dry quartzite from Brace and Kohlstedt (1980). G_{gt} is wet granite from Carter and Tsenn (1987). Q_r is for extra strong dry quartz from Ranalli (1995). Comparison of the YSE computed for two different thermal plate thicknesses demonstrates large ambiguities in estimation of the mantle strength: the continental heat flux used as a common surface boundary condition mainly affects crustal temperature distribution. The mantle part of the geotherm primarily depends on the position of the thermal bottom of the lithosphere. The left 'weak' YSE results from erroneous assumption that continents have the same or even smaller thickness then the oceans (Jackson, 2002). The use of the left YSE results in ridiculously small predictions of the mantle strength. Left part of the figure is based on Mackwell et al. (1998). The continental YSEs based on the assumption of weak mantle rheology (left) are dubbed 'crème brûlée' models, whereas those that include strong crustal and mantle layers are dubbed 'jelly sandwich' rheology. The failure envelopes shown in the left match those from Jackson (2002). The Jackson's (2002) envelopes are based on Figure 4 from Mackwell et al. (1998). The parameters are given in **Tables 2–3**.

(Continued)

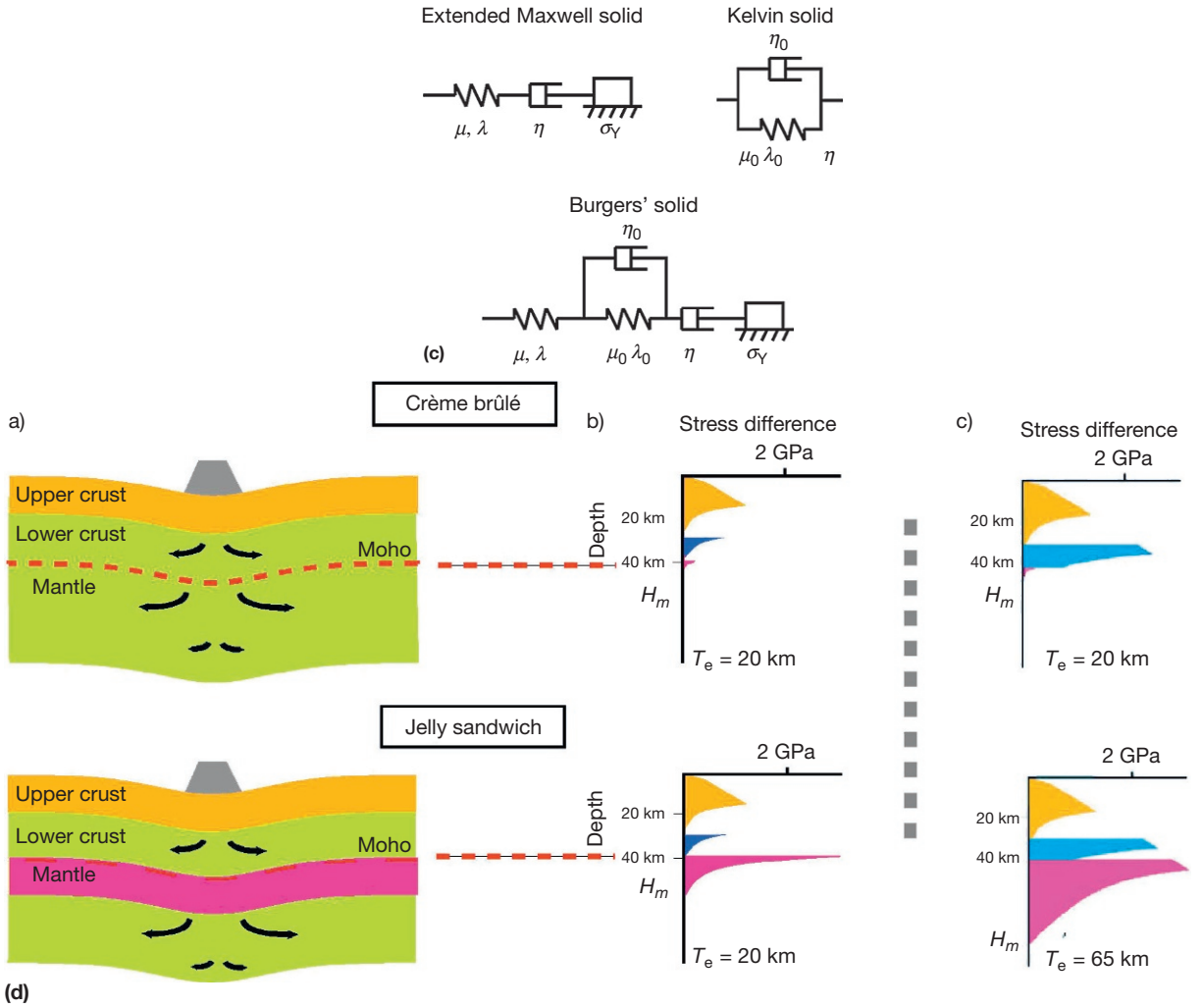

Figure 4 (Continued) (c) Various ways to combine rheological terms in constitutive models of materials: the extended Maxwell serial model, Kelvin parallel model, and Burger's combined model (and so on). The resulting properties of solids largely depend on how the rheological terms are interconnected. Knowledge of the parameters of each rheological term is not sufficient for the prediction of the mechanical behavior of materials. (d) Schematic diagram illustrating contrastingly different models for the long-term strength of continental lithosphere (Burov and Watts, 2006). In the crème brûlée model, the strength is confined to the uppermost brittle layer of the crust, and compensation is achieved mainly by flow in the weak upper mantle. In the jelly sandwich model, the mantle is strong and the compensation for surface loads occurs mainly in the underlying asthenosphere. a – Models of deformation. The arrows schematically show the velocity field of the flow. b – Brace–Goetze failure envelopes for a thermotectonic age of 150 My, a weak undried granulite lower crust, a uniform strain rate of 10^{-15} s^{-1}, and either a dry (jelly sandwich) or wet (crème brûlée) olivine mantle. H_m is the short-term mechanical thickness of the lithosphere and T_e is the long-term elastic thickness. Other parameters are as given in **Table 2**. The two envelopes match those in Figure 5(b) and 5(d) of Jackson (2002). They yield a T_e of 20 km (e.g., Burov and Diament, 1995), which is similar to the thickness of the most competent layer. This is because the competent layers are mechanically decoupled by weak ductile layers and so the inclusion of a weak lower crust or strong mantle contributes little to T_e. c – Brace–Goetze failure envelopes for a thermotectonic age of 500 My. Other parameters are as in – b – except that a strong, dry, Maryland diabase has been assumed for the lower crust. The two envelopes show other possible rheological models: one in which the upper and lower crust are strong and the mantle is weak (upper panel) and another in which the upper and lower crust and the mantle are strong (lower panel). The assumption of a strong lower crust in the weak mantle model again contributes little to T_e because of decoupling, although T_e would increase from 20 to 40 km if the upper crust was strong at its interface with the lower crust. In contrast, a strong lower crust contributes significantly to the T_e of the strong mantle model. This is because the lower crust is strong at its interface with the mantle and so the crust and mantle are now mechanically coupled.

It should be noted, however, that there is no direct evidence for the applicability of the rule [26c] in nature. For example, the logarithmic average of the effective viscosities is sometimes used following the hypothesis that the weakest flow mechanism dominates the overall ductile behavior. The contribution of each ductile flow mechanism can also be estimated from general physical considerations, for example, from total work minimization.

6.03.3.2 Kelvin Model

The alternative Kelvin (Voigt) model implies that the total stress equals the sum of the elastic σ^e and viscous stress σ^v, while ε^e_{ij} and ε^v_{ij} are equal:

$$\begin{aligned}\sigma^K_{ij} &= \sigma^e_{ij} + \sigma^v_{ij} = 2\mu e^k_{ij} + 2G^k\varepsilon^k_{ij}\\ \varepsilon^e_{ij} &= \varepsilon^v_{ij}\end{aligned} \quad [27]$$

Its extended viscous–elastic–plastic version is

$$\begin{aligned}\sigma^{K\_ext}_{ij} &= \sigma^K_{ij} + \sigma^p_{ij}\\ \varepsilon^e_{ij} &= \varepsilon^v_{ij} = \varepsilon^p_{ij}\end{aligned} \quad [28]$$

Although the minerals most probably do not behave as Kelvin solids at microscale, their aggregates and macrostructural assemblages may do.

6.03.3.3 Mixed Models

Observations of long-term loading of the lithosphere such as by seamounts (Watts, 2001) demonstrate a complex behavior, which involves initially Maxwell-type response with an exponential stress drop followed (after several My) by slowdown of stress relaxation so that long-term stress achieves some nearly constant level. This behavior evokes a generalized linear (Maxwell + Kelvin) model, or Burger's model, which represents a serial combination of a Kelvin model with an extended Maxwell model:

$$e^B_{ij} = e^M_{ij} + e^K_{ij} + e^P_{ij} \quad [29]$$

The viscous and elastic parameters of the Kelvin unit are not the same as those of the Maxwell unit. It is possible that relaxation of postseismic deformation may be controlled by the Kelvin term characterized by a viscosity several orders smaller than the Maxwell term (e.g., Pollitz et al., 2001). Present failure to establish any links between the Kelvin and Maxwell viscosities restricts interpretation of postseismic data in terms of the long-term properties of the lithosphere–asthenosphere system.

6.03.4 Uncertainties in the Experimental Rheology Laws

The uncertainties involved in the long-term rheological properties derived from experimental rheology data have produced confusing propositions for the long-term rheological strength of the crustal and mantle parts of the lithosphere (**Figure 4(b)** and **4(d)**). These uncertainties derive from (1) uncertainties in rock mechanics data, (2) uncertainties in the thermal and other data used for construction of YSEs, (3) poor knowledge of the deformation mechanisms that really occur at depth, (4) uncertainties on the constitutive models, (5) additional (unaccounted for) factors influencing rock strength such as frictional heating, pressure variations, fluid content, chemical, or thermodynamic transformations (such as melanitization of shear bands), and (6) micro- and macrostructural effects, for example, layering and anisotropy, from 0.01 to 10^4 m scale.

6.03.4.1 Uncertainties of Rock Mechanics Data

Elastic and Byerlee's brittle parameters are relatively well constrained, with an uncertainty of 10–30% for the relevant depth intervals. Although the validity of Byerlee's law is questionable for fault zones (e.g., Chester, 1995) or at depths/pressures below 30–50 km (Kirby et al., 1991, 1996), this would primarily affect fault and seismic distribution but not regional deformation.

Ductile flow properties are the most uncertain, although modern techniques of experimental rock mechanics allow for sufficiently robust and cross compatible measurements of creep parameters (e.g., Kohlstedt, 2007; Kohlstedt et al., 1995), specifically after the advent of new techniques such as Paterson-type deformation testing machines (e.g., Bürgmann and Dresen, 2008). Yet, it is not the precision of experiments but extrapolation of their results to natural conditions that create major difficulties:

1. With rare exceptions, experiments refer to simplified conditions such as uniaxial deformation or torque, whereas real rocks are deformed in several planes. In general, to accelerate deformation yet avoiding brittle failure, experiments are conducted at much higher temperatures than in nature. Extrapolation to lower-temperature conditions is not straightforward, since it is possible that other creep mechanisms may dominate at lower temperature (e.g., in olivine, power law dislocation creep may be replaced by GBS creep at temperatures below 800 °C). Creep mechanisms that take place in each particular experiment are not always well identified. It is not guaranteed that the same mechanisms are activated in natural conditions (e.g., at slower strain rates or lower temperatures). Recent studies based on new techniques (e.g., Patterson triaxial press) suggest that rock strength (e.g., for quartzite) may be twice as high as estimates obtained before the turn of the twentieth century (e.g., Bürgmann and Dresen, 2008). Yet, other studies show that accounting for some additional factors such as oxygen fugacity (Keefner et al., 2011) results in a factor of 5 smaller effective viscosity for dislocation creep (in dunite) than suggested by previous data. This indicates that further, probably significant revisions of rock properties are possible in the near future.
2. Experimental strain rates are on the order of 10^{-9}–10^{-4} s^{-1}, which is on average 10^{10} times faster than geologic strain rates (10^{-18}–10^{-14} s^{-1}). Extrapolation of these data to geologic timescales is mathematically 'illegal' because the errors of such extrapolation may be of the same order as or larger than the predicted rock strength.
3. The experiments refer to simple monophase minerals or synthetic or selected 'representative' rocks. Extension of their results to real aggregate compositions has to be justified (e.g., Kohlstedt et al., 1995). It is often assumed that the weakest of the most abundant mineral species defines the mechanical behavior of the entire rock. For granites, this is quartz, often replaced by quartzite in laboratory experiments. It was shown, however, that lower amounts of weak phases such as micas or albites may result in significantly smaller strength than that of quartz or quartzite (see discussion in Burov, 2002). It was also noted that polyphase aggregates are weaker than their constituents and that

different mineral species may take a lead in the experiments and nature (e.g., Kenis et al., 2005; Kohlstedt et al., 1995).
4. Experimental strain rates may vary in a different way from nature.
5. Experiments are conducted on small rock samples of homogeneous structure. At larger scales (>0.1–1 m), rocks, specifically crustal, may be highly structured. Their mechanical resistance may depend on their macrostructure more than on the rheological properties of the microconstituents (Evans, 2005; Ji et al., 2000; Kohlstedt et al., 1995). For example, in strong mantle peridotites, strain may localize on weak mylonitic shear zones leading to overall weaker behavior (e.g., Jin et al., 1998).
6. Water content influences rock strength. In general, rocks contain 0.05–0.1 wt% H_2O. The experiments usually consider 'wet,' 'undried,' or 'dry' rock samples (Chen et al., 2006; Mackwell et al., 1998). However, for each particular region, it is difficult to know whether the rock is dry, wet, or partially wet (e.g., Karato, 1986). It is also argued that 'dry' experiments never reach the 'dryness' of some natural conditions (D. McKenzie, personal communication).
7. Volatile fugacities and chemical and thermodynamic reactions modify the mechanical behavior of rocks. These factors are basically unknown or poorly controlled in nature.
8. Temperature–pressure (P–T) conditions of experiments do not represent natural P–T conditions or loading paths (e.g., Goetze and Evans, 1979). Basically, it is only the 'P' or 'T' condition that is respected at any time. For example, in many cases, temperatures used in experiments are significantly higher than in nature.

Due to these uncertainties, Brace and Kohlstedt (1980) and Kohlstedt et al. (1995) had suggested that real crustal rocks may be significantly 'softer' than the experimental estimates. As a highly encouraging point, it should be noted, however, that the oceanic YSEs based on the dry olivine flow law demonstrate a very good correlation with the observed T_e values, age, and thermal state of the lithosphere (e.g., Watts, 2001). For continents, one can attempt to validate or reparameterize rock mechanics data by using observations of long-term deformation, T_e data, and thermomechanical models (Burov and Watts, 2006; Watts and Burov, 2003).

6.03.4.2 Uncertainties in the Synthetic Yield Stress Envelopes

In addition to the uncertainties involved in the rheology laws, there are many specific YSE uncertainties arising from various assumptions on thermal distribution, background strain rate, plate structure, and rheological composition of the lithosphere.

One of the most misleading, if not disastrous, assumptions is that of the homogeneous background strain rate. Analytic and numerical models (e.g., Burov and Poliakov, 2001; Kusznir, 1991) predict strong (orders of magnitude) vertical and horizontal variations in strain rate in deforming lithosphere, for example, in the ductile lower crust of continents. As a result, the effective strength may deviate by up to 30–80% from that predicted from constant-rate YSEs.

Ductile behavior is extremely sensitive to temperature and the presence of fluids (e.g., Chen et al., 2006). A slight variation in the background geotherm, thermal conductivity, or fluid content may 'transform,' for example, hard dry quartzite (Kirby and Kronenberg, 1987) to some equivalent of soft calcite (Kohlstedt et al., 1995). In power law materials, shear stress weakly depends on the strain rate but strongly depends on temperature, T, and activation energy Q. A simple increase in Q by a factor of 2 'converts' weak quartzite into the hardest olivine or clinopyroxene (**Table 2**). In the continental crust, behaviors predicted by the strongest dry flow laws can be turned into those predicted by the weakest wet flow laws by a small adjustment of the poorly constrained concentration of radiogenic heat sources. Internal heat production, not accounted for in laboratory experiments, may also influence long-term creep mechanisms (softening).

The geotherm, $T(z)$, controls not only the ductile strength of the lithosphere but also, indirectly, its brittle strength through the influence of temperature on the depth of the BDT. Different assumptions on $T(z)$ produce important differences in the predicted strength (**Figure 4(b)**). In continents, age has no unique relation with thermal structure, and the surface heat flow is 'polluted' by up to a 50% contribution from crustal radiogenic heat production (Turcotte and Schubert, 2002). The equilibrium thermal (or geochemical, seismic, or gravimetric) thickness of continental plates, a (defined as the depth to 1330 °C), is an important parameter needed for consistent introduction of bottom boundary conditions in thermal models. For continents, a may vary from 150 to 350 km. a controls the mantle part of the geotherm much more than the surface heat flux, q. This explains why for the same value of heat flux, q, and identical rheological parameters, some authors predict very 'hot' geotherms and, consequently, weak mantle behavior (Jackson, 2002; Mackwell et al., 1998), whereas others (e.g., Jaupart and Mareschal, 1999; Jaupart and Mareschal, 2007 and this study) predict colder geotherms, hence stronger behavior. Seismic and seismic tomography data and geothermal data (e.g., Jaupart and Mareschal, 1999, 2007) suggest that continental lithosphere should be on average thicker than oceanic lithosphere (150–350 km compared to 100–125 km). However, it is not uncommon that, for simplicity, the same small thickness is imposed for both continents and oceans (Jackson, 2002; **Figure 4(b)**, right). This assumption potentially results in largely underestimated (50–100%) mantle strength.

6.03.4.3 Uncertainties in Deformation Mechanisms in Nature

There is a growing understanding that ductile, elastic, or brittle deformation cannot be treated separately from each other. In general, mixed behaviors should prevail. Semibrittle/semiductile behaviors can be developed near zones of BDT or large shear bands. A number of studies argue that under upper crustal conditions, 'non-Byerlee's' strain rate-dependent frictional mechanisms may be activated simultaneously with ductile creep. This leads to a weak, ductile-like constitutive law for the brittle regime. According to these studies (e.g., Chester, 1995), upper crustal strength may be limited to maximum 50 MPa at 6–15 km depth. Observations of crustal rebound (Bills et al., 1994) indicate that the strength of the upper crust

may be strongly reduced below 3 km depth, with an estimated maximum viscosity below 10^{23} Pa s, which suggests stress levels <50 MPa. Many known natural examples show that ductile creep can start (even in pure quartz) at 5–6 km depth (S. Patterson, 2002, personal communication). 'Conventional' quartzite rheology (Ranalli, 1995) used for the upper crust is about 4 times stronger than 'weakest' estimates found in literature. Yet, it is twice weaker than last estimates obtained using modern Patterson testing equipment (e.g., Bürgmann and Dresen, 2008).

6.03.4.4 Role of Secondary Factors: Frictional Heating, Pressure, Fluid Content, Partial Melting, and Metamorphic Phase Changes

Fluid pressure reduces brittle strength (**Figure 1(b)**), and a small (<0.1 wt% H_2O) amount of fluids can (e.g., **Figure 4(b)**; **Table 2**) decrease ductile rock strength by a factor of 2–3 (e.g., Mackwell et al., 1998). Yet, it is practically impossible to estimate fluid content *in situ*. The experimental data generally include only two sets for each type of rock: 'wet,' 'undried,' and 'dry.' 'Dry' rock may still have traces of fluid and 'wet' rock may be 'wet' to different degrees. When fluid content is unknown, the prediction for rock strength remains rather indefinite, between 'wet' and 'dry' states. Metamorphic phase changes and free fluids are the major factors that affect the lithosphere density and strength of subduction channels (Angiboust et al., 2012). First, activated by fluids, these changes lead to formation of a very weak serpentinite layer that reduces friction in the subduction channel (e.g., Yamato et al., 2007). Second, dehydration of eclogitized crust leads to creation of a weak mantle wedge with the back-arc zone additionally weakened by associated partial melting. Third, lithosphere bending near subduction zones is greatly enhanced by flexural brittle–plastic yielding (**Figure 5(c)** and **5(f)**; Burov and Diament, 1995) resulting in the formation of a series of water-saturated (lithostatic pressure drop = lower brittle strength) serpentinized (weak) normal faults that provide considerable additional weakening of the plate (Faccenda et al., 2009; Regenauer-Lieb et al., 2001). Combined, these three factors create the necessary conditions for one-sided oceanic subduction. Metamorphic phase changes and fluids also play a similar role at passive margins and in many other contexts. For example, melanitization of shear bands is sought to play a major role in strain localization in a variety of tectonic settings. In this case, the rheology of the host rock is of minor importance, while the deformation is conditioned by very particular properties of ultraweakened shear zones. In general, prograde metamorphic phases are denser and mechanically weaker than the parent rock. Thus, eclogitization of the crust may play an important role in the force balance acting on the subducting slab. Metastable reactions at the 410 km phase transition boundary have a double effect: depleted downwellings and fertile upwellings push–pull the slab in opposite directions.

Frictional heating $\partial T_{shear}/\partial t$ at fault zones (Regenauer-Lieb et al., 2001) may decrease ductile (including Peierls and GBS)

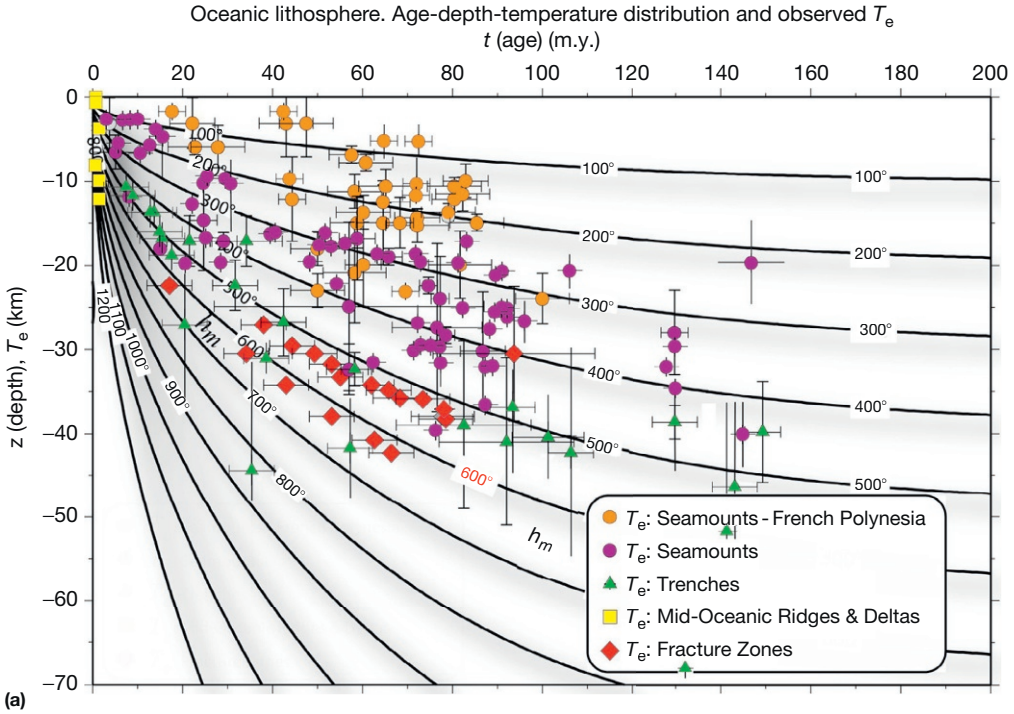

Figure 5 (a) Revealed correlation between the observed flexural strength T_e and age–temperature of the oceanic lithosphere. Thermal distribution is computed according to the plate cooling model (Burov and Diament, 1995; Parsons and Sclater, 1977). The T_e data are superimposed with computed geotherms. The relevant estimates refer to zones with normal thermal gradient such as fracture zones and trenches. Naturally, the cases of seamount loading cannot be fitted with the standard cooling model due to both viscoelastic relaxation (younger mountains) and local thermal rejuvenation of the underlying lithosphere by hot-spot activity (Watts, 2001). However, locally adjusted thermal models confirm T_e correlation with the depth of the geotherm 400–500 °C, specifically for seamounts older than 10 My (Watts, 2001).

(Continued)

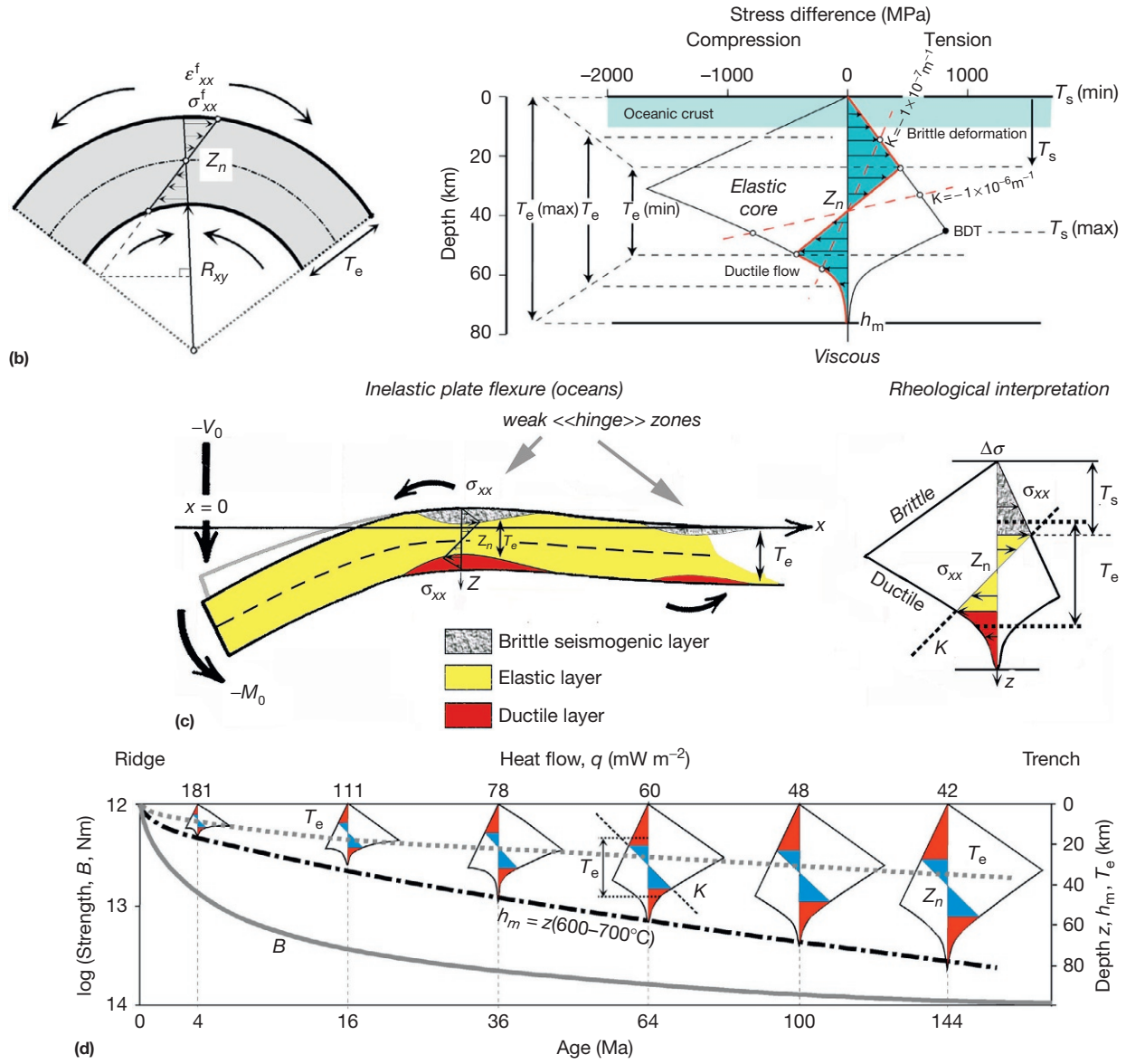

Figure 5 (Continued) (b) (left) Sketch of stress distribution due to bending of an ideal elastic plate. (right) Sketch of stress distribution in a bending viscous–elastic–plastic oceanic plate and interpretation of the seismogenic layer, T_s, and equivalent elastic thickness, T_e, of the oceanic lithosphere in terms of rheology (YSE) and its dependence on flexural stress gradient (reproduced from Watts AB and Burov E (2003). Lithospheric strength and its relationship to the elastic and seismogenic layer thickness. *Earth and Planet Science Letters* 213: 113–131). ε^f_{xx}, σ^f_{xx}, and R_{xy} are flexural strain, stress, and local radius of flexure ($R_{xy} = -K^{-1}$), respectively. Thin solid line shows the YSE for 80 Ma oceanic lithosphere. The brittle behavior is controlled by Byerlee's law, the ductile behavior by olivine power flow law ($n = 3$, $A = 7 \times 10 - 14$ Pa^{-3} s^{-1}, $Q = 512$ kJ mol^{-1} (Kirby and Kronenberg, 1987)), and the thermal structure by the cooling plate model (Parsons and Sclater, 1977). The solid red line shows the stress difference for a load that generates a moment, M, of 2.2×1017 N m^{-1} and curvature, K, of 5×10^{-6} m^{-1}. The figure shows that the load is supported partly by an elastic 'core' and partly by the brittle and ductile strength of the lithosphere. The red-dashed lines show the cases for K of 1×10^{-7} m^{-1} and 1×10^{-6} m^{-1}, which bracket the range of observed values at trench–outer rise systems (Goetze and Evans, 1979; Judge and McNutt, 1991; McNutt and Menard, 1982). The figure shows that T_s corresponds to the depth of the intersection of the moment–curvature curve with the brittle deformation field but could extend from the surface, T_s (min), to the brittle–ductile transition (BDT), T_s (max). T_e, in contrast, could extend from the thickness of the elastic core, T_e (min), to the thickness of the entire elastic plate, T_e (max). Both T_s and T_e depend on the moment generated by the load and, hence, the plate curvature. Yet, T_s increases with curvature, while T_e decreases. This figure represents an ideal case of pure bending stress in which T_e and T_s can be interrelated. Generally, lithospheric regions where strain is sufficient to define T_s are in state of failure that may be largely produced by in-plane tectonic stress rather than by bending stress. In this case, T_s and T_e anticorrelate or have no direct relation. (c) Reinterpretation of flexure of an oceanic plate (**Figure 2(a)**) under assumption of realistic rheology (see also (b)). Inelastic flexure results in 'plastic hinging,' for example, formation of weak hinge zones at the inflection points. The observed T_e is thus horizontally variable and differs from that of an elastic plate. Flexural weakening is supposed to help initialization of subduction of cold old lithosphere. (d) Variation of the mechanical strength, of integrated strength B and equivalent elastic thickness, T_e, of the oceanic lithosphere as function of age and thermal structure. T_e of the lithosphere actually depends on the gradient of bending stress related to local plate curvature, K. T_e approximately equals the size of the 'elastic core' plus half size of the underlying brittle zone and half size of the ductile zone beneath. Note that B correlates with T_e. Note also that T_e cannot be interpreted as a depth to some specific level in the lithosphere. Yet, it correlates well with h_m or geotherm to 400–500 °C (reproduced from Watts AB (2001) *Isostasy and Flexure of the Lithosphere*, p. 458. Cambridge: Cambridge University Press).

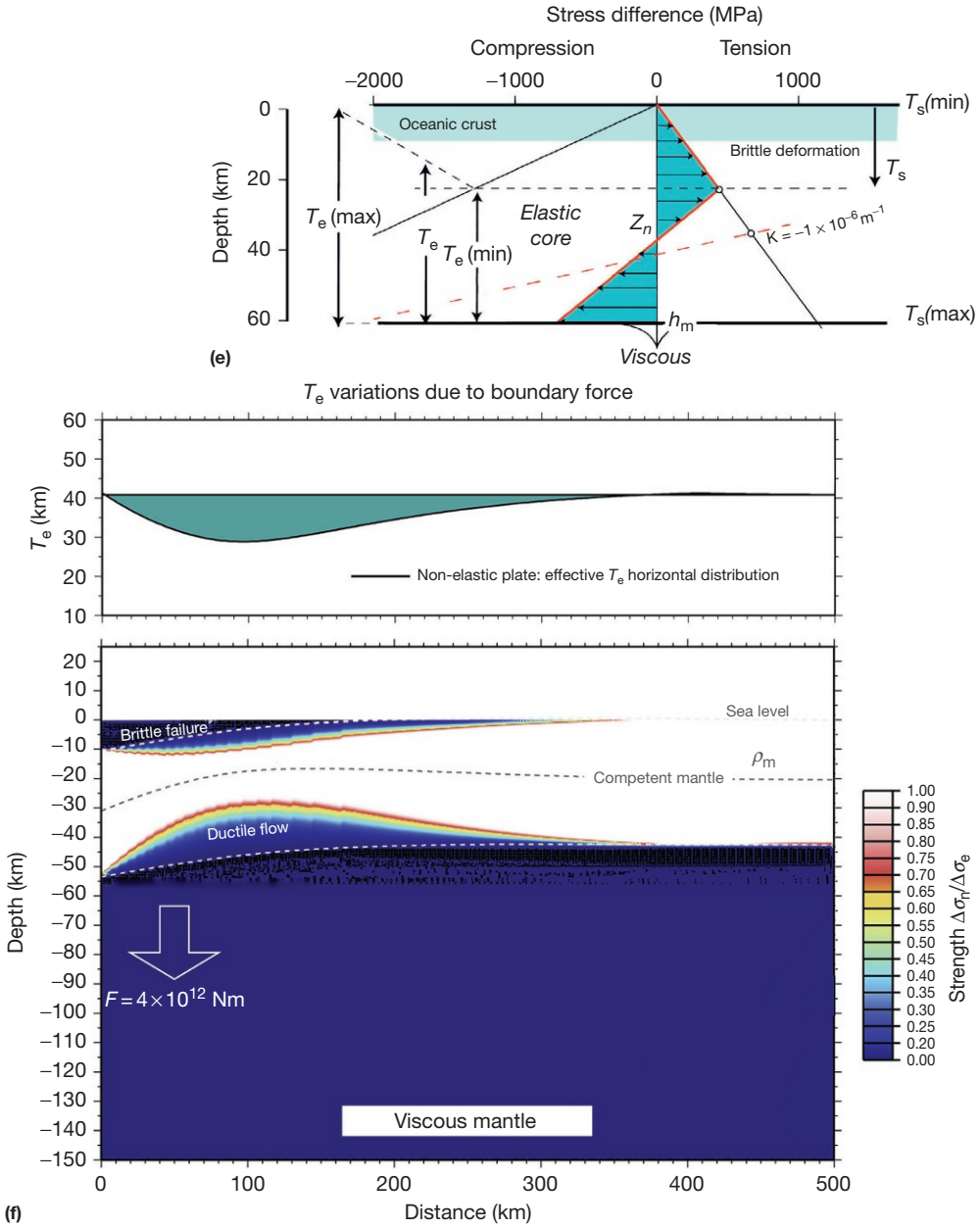

Figure 5 (Continued) (e) YSE based on the 'crème brûlée' rheology model: interpretation of the seismogenic layer, T_s and equivalent elastic thickness, T_e, under assumption of Jackson (2002) that the mechanical strength of the lithosphere is concentrated in the brittle layer. This case considers brittle–elastic lithosphere with zero strength ductile part, for the same typical amount of flexure ($K = 5 \times 10 - 6$ m^{-1}) and T_s value (20 km) as in the case shown in (b). The figure demonstrates inconsistence of two simultaneous assumptions: of weak ductile mantle and $T_e = T_s$, due to geometric incompatibility between seismogenic layer (T_s) and elastic thickness (T_e). If $T_s = 20$ km, then $T_e > 40$ km. (f) Computed variations of oceanic lithosphere strength and elastic thickness in a bending viscous–elastic–plastic plate of 70 Ma (see also (c)). Plate flexure is caused by a boundary force of 4×10^{12} N per unit length. Note the formation of a large weakened zone including normal faulting at top. It is believed that water penetrates in the flexurally induced normal faults resulting in additional drastic weakening of the lithosphere (reduction of brittle strength due to fluid pressure and serpentinization). Together with inelastic yielding, these factors allow for easy bending of oceanic plates at subduction zones, thus making subduction possible (without that strong old oceanic plates even though negatively buoyant will not subduct (i.e., flex down), due their high strength) (reproduced from Burov EB and Diament M (1995) The effective elastic thickness (T_e) of continental lithosphere: What does it really mean? *Journal of Geophysical Research* 100: 3895–3904).

strength, provoking metamorphic changes resulting in the appearance of softer phases or a change in fluid content (and thus in strength) through hydration/dehydration reactions:

$$\partial T_{\text{shear}}/\partial t = \text{frac} \times \left(\rho C_p\right)^{-1} \sigma_{II} \partial \dot{\varepsilon}_{II}^{v,p}/\partial t \qquad [30]$$

where $\partial \dot{\varepsilon}_{II}^{v,p}/\partial t$ is an inelastic contribution to the effective shear strain rate. Slow (geologic rates) friction may produce about 100 °C temperature rise in shear zones such as major faults or subduction channels (Turcotte and Schubert, 2002). This would result in a local 30–50% strength reduction in quartz-rich and metamorphic rocks. Rapid seismic slip may generate,

at short timescales, very high temperatures resulting in melting (pseudotachylites) and hence in very low resistance to shear (e.g., John et al., 2009). Accounting for frictional weakening is an ambiguous problem because the strength drop due to ductile shear primarily depends on the absolute value of the temperature anomaly. Yet, while it is easy to estimate the total amount of thermal energy generated by shear, quantitative evaluation of the associated temperature anomaly is difficult due its strong dependence on the thickness of the shear band, stress, slip rate, and secondary factors such as fluids.

Rock behavior is also strongly conditioned by elastic properties. Although the criteria for brittle–plastic failure do not depend on elasticity, viscous–elastic behavior and shear heating do depend on it. Hence, behavior of the whole brittle–ductile–elastic system depends on elastic properties. Elastic modules increase with pressure and density, changing the effective behavior of the system. These parameters control stress relaxation in the lithosphere and may be responsible for transient states lasting for several My. Elasticity is responsible for the accumulation of mechanical energy; the elastic contribution to the shear strain rate is thus less than the total strain rate in the computation of shear heating.

Partial melting may play an important role in the evolution of spreading centers, passive margins, and rift and subduction systems. It can result in significant weakening and localization of deformation. Partial melting is usually addressed using the approach developed by McKenzie and Bickle (1988) and Katz et al. (2003).

The behavior of lithospheric plates is largely conditioned by deformation at their boundaries (e.g., collision). These boundaries are characterized by specific conditions. In particular, the subduction channel undergoes continuous phase changes and, consequently, rheology changes. Unfortunately, data on the rheology of metamorphic rocks are not abundant. As mentioned, the very few ideas that we can learn from direct observations in outcrops and rare laboratory experiments suggest that metamorphic rocks (e.g., micas; schists, serpentine, and eclogite) are considerably weaker than their parent phases.

6.03.4.5 Possible Ways to Parameterize Rheology Data for Geologic Timescales

There may be several ways to constrain rock rheology for geologic timescales (**Figure 2(b)**):

1. Observations of deformation in response to tectonic loading.
   - Observations of isostatic compensation: flexure, estimates of the equivalent elastic thickness of the lithosphere, T_e (e.g., Burov and Diament, 1995, 1996; Forsyth, 1985; Pérez-Gussinyé and Watts, 2005; Watts, 2001).
   - Neotectonic vertical motions related to postglacial rebound and lake and submarine volcanic loading (e.g., Bills et al., 2007; Kaufmann and Amelung, 2000; Larsen et al., 2005; Passey, 1981; Peltier, 1974; Watts, 2001).
   - Physical estimates of minimal integrated strength of the lithosphere required for (1) subduction, (2) transmission of tectonic stresses over large spatial scales, and (3) stability of large geologic structures such as seamounts over their respective life spans (e.g., Bott, 1993; England and Molnar, 1997, 2005; Lachenbruch and Morgan, 1990).
   - Observations of lithospheric folding (wavelength as a function of the integrated strength; Cloetingh et al., 1999; Gerbault et al., 1999; Lambeck, 1983; **Table 5**).
   - Indirect geophysical and geologic data tracing the geometry of deformed lithosphere and anomalous (e.g., low viscosity or high water content) zones: attenuation of *S*-waves, seismic anisotropy, petrology (P–T–t) paths, magnetotelluric sounding, gravity, observations of ductile and brittle behaviors in the outcrops including exhumed fault, fossil shear zones and crustal roots, and paleostress estimates (e.g., Austrheim and Boundy, 1994; Bürgmann and Dresen, 2008; Chen and Molnar, 1983; Cloetingh and Banda, 1992; Govers et al., 1992; Jolivet et al., 1998; Molnar and Tapponnier, 1981; Wei et al., 2001; Wever, 1989).
   - Estimates of the minimal integrated strength of the lithosphere required for long-term stability of geologic structures, subduction or transmission of tectonic stresses, and forces over large spatial scales, including horizontal pressure gradients caused by lateral variations in lithospheric density structure and topography (gravity potential energy theory, e.g., England and Molnar, 2005). For example, lithosphere must be strong enough to transmit ridge push and slab pull forces in the order of 10^{11}–10^{13} N per unit length.
   - Lithosphere-scale numerical thermomechanical models of tectonic processes integrating multidisciplinary data, which allows for physical testing of the validity of data and hypotheses on lithosphere rheology; direct mechanical or thermomechanical models testing the stability of geologic structures or tectonic deformation styles as a function of implied rheological properties (e.g., Bassi, 1995; Beuchert and Podladchikov, 2010; Beuchert et al., 2010; Bird, 1991; Brun, 2002; Burov and Watts, 2006; Toussaint et al., 2004).
2. Observations of deformation in response to short-term loading.
   - Tidal deformation (e.g., Bills et al., 1994).
   - Postseismic relaxation (e.g., Avoauc, 2007; DallaVia et al., 2005; Sabadini and Vermeersen, 2004).
   - Geodetic (GPS-INSAR) data (e.g., England and Molnar, 2005; Montesi, 2004).

Some authors argue about possible relationships between maximum depths of intraplate seismicity and long-term rheology (e.g., Jackson, 2002; Maggi et al., 2000). However, due to the different timescales of seismic events and long-term deformation, these relationships, if real, are not straightforward (e.g., Bürgmann and Dresen, 2008; Burov and Watts, 2006; Watts and Burov, 2003) and can hardly be exploited in practice.

Data based on observations of long-term deformation allow one to constrain a number of parameters such as T_e, F, σ, u, De, τ, h, L, λ, ϕ (**Figure 2(b)**), where T_e is directly related to the integrated plate strength (B) and F, σ, u are respectively horizontal force, stress, and convergence/extension velocity that are ultimately linked to maximum stress/strain values supported by the lithosphere, as well as to possible deformation styles: for example, continental subduction is virtually impossible for values of u below 2–3 cm year^{-1} for a

Table 5 Estimates (Cloetingh et al., 1999 and references therein) for wavelengths of lithospheric folding (λ), effective elastic thickness (T_e), thermal age, t_o, the onset of folding (Ma), duration of folding (Ma)

λ *(km)*	T_e *(km)*	λ/T_e	*Thermal age (Ma)*	t_o, *Onset of folding (My BC)*	*Present state of folding*	*Type*
200–250 (1)	<40	>4–5	60	8	Active deformation	B
500–600(2)	50–70	10	400–600	60	Preserved	N
200 (3)	30	6–7	200	60	Preserved	B
200 (present)–>400–500 (preserved) (4)	25 (after recent reheating at 200 Ma)	8	>700	400–700	Preserved	B
300–360 (5)	>15*	>20	175–400	8–10	Active deformation	B
100–200 (6)	Not available, approx. >30	4–6	>100	60	Preserved	B/N
200? (7)	20–35	10–15	300	6	Active subsidence	N
200–250 (8)	15	13	175	8–10	Active deformation	B/N
350–400 (9)	6–9*	>30	<20	4–6	Active deformation	N
300 (10)	10–30	10	30	6–8	Active deformation	B/N
40 (11)	20–25*	2	<20	6–8	Active deformation	N
50 (12)	20–25*	2	20	6–8	Active subsidence	N
600 (13)	>100	6	>1200	1200	Preserved?	B
60 (14)	<10	6	65	35–8 My	Active deformation	B/N

Numbers in brackets refer to data sources: (1) Indian Ocean, (2) Russian platform, (3) Arctic Canada, (4) Central Australia, (5) Western Goby, (6) Paris Basin, (7) North Sea Basin, (8) Ferghana and Tajik basins, (9) Pannonian Basin, (10) Iberian Basin, (11) Southern Tyrrhenian Sea, (12) Gulf of Lion, (13) Transcontinental Arch of North America, (14) Norwegian Sea. 'B' means regular folding style, 'N' means 'irregular,' and 'B/N' stands for the cases displaying both types of folding behavior. It is noteworthy that cases of abnormally high (>10) or low (<4) λ/T_e ratios (marked with '*') correspond to hot (thermally reset) lithospheres, which implies dominant crustal folding. The high ratios often correspond to very weak lithospheres loaded by large amounts of sediment, which increases the wavelength of folding. Small λ/T_e ratios (<4) may refer to plastic hinging achieved at large amounts of shortening, for which wavelength is a simple function of the amount of shortening and does not depend on h or T_e.

three-layer lithosphere (Burov and Yamato, 2008; Toussaint et al., 2004) or 1 cm year^{-1} for a four-layer lithosphere (Yamato et al., 2007). *De* and τ are, respectively, the Deborah number and the relaxation/growth time of Rayleigh–Taylor instabilities related to viscosity and density contrasts in the lithosphere. λ is the characteristic wavelength of unstable deformation (folding or boudinage; see later **Section 6.03.5.7**), which is a function of the thickness of the competent layers within the lithosphere. h and L are, respectively, the characteristic height and horizontal size of process-induced topography, related to plate strength and rheology. ϕ is the subduction or major fault angle that can be indicative of the brittle properties and overall plate strength (subduction) of the plate.

Interpretations of short-term deformation data are not certain, because there is no evidence that mechanisms of short-term deformation are the same as the mechanisms of long-term deformation. As mentioned, this concerns first of all not only intraplate seismicity data but also postseismic relaxation data (e.g., Freed et al., 2007). For example, it is suspected that accelerated postseismic creep may occur due to cavitation in fine-grained mylonitic shear zones in the lower crust. By comparison with rock mechanics experiments, one can expect that the duration of deformation should exceed several years to assure that it is relevant to long-term properties.

6.03.5 Rheology and Structure of the Oceanic Lithosphere

6.03.5.1 Goetze and Evans Yield Stress Envelopes: Age Dependence of the Integrated Strength

Yield stress envelopes (**Figure 4(a)**) for oceanic lithosphere are based on Byerlee's law for the brittle part and on the dry olivine flow law for the ductile part. A single olivine flow law is generally used as thin basaltic oceanic crust deforms in the brittle regime and does not need a separate flow law. The geotherms $T(z)$ used for computation of the ductile strength are derived from a half-space cooling plate model assuming constant surface and bottom temperature boundary conditions (Parsons and Sclater, 1977; Turcotte and Schubert, 2002):

$$\frac{T-T_{z0}}{T_m-T_{z0}}=\mathrm{erf}\left(\frac{z}{2\sqrt{\chi t}}\right)$$
$$\frac{z}{2\sqrt{\chi t}}\equiv\eta \qquad [31a]$$

where t is time (age), χ is thermal diffusivity, and erf is error function,

$$\mathrm{erf}(\eta)=\frac{2}{\sqrt{\pi}}\int_0^{\eta}e^{-\lambda^2}\,\mathrm{d}\lambda \qquad [31b]$$

$$\gamma(T_{z0}) \approx z|_{x=0} + A\sqrt{\chi t} \qquad [31c]$$

T_m is both the initial and bottom temperatures (e.g., 1330 °C), T_{z0} is the surface temperature (e.g., 0 °C), and $z|_{x=0}$ is the depth of the spreading center (e.g., 2500 m). γ (T_{z0}) is model-predicted depth of sea bottom derived under the assumption of simple local isostasy (i.e., $T_e = 0$), for which the value of the parameter A varies from 0.0625 to 0.0825 depending on the assumed reference density. As can also be seen from **Figure 4(a)**, the mechanical bottom h_m of the lithosphere roughly follows the isotherm of 500 °C:

$$h_m \approx z(500\,^\circ\mathrm{C}) \approx (\chi t)^{1/2} \qquad [32]$$

Predictions of sea bottom depths based on eqns [31] and the hypothesis of local isostasy fit the observations only for ages smaller than 70–100 Ma. For older ages (yet far from subduction zones), the predicted bottom depths are 20–30% larger than the observed bathymetry, mainly because the lithospheric strength increases with age, resulting in growing contribution from regional isostatic compensation that locally negates a part of thermal subsidence, and because the lithosphere reaches nearly stationary state, for which the half-space cooling model is no more applicable. Some authors also point to the effect of small-scale convection below the lithosphere that may be equivalent to constant basal heat flow boundary condition, instead of constant temperature boundary condition (Doin and Fleitout, 1996). Assumption of small-scale convection, whose existence is yet to be proved, would shift the geotherms of 500–600 °C up by about 100 °C. It provides a slightly better fit between the predicted and observed bathymetry for old lithosphere (>100 Ma). However, as mentioned previously, a similar effect can be expected from strengthening of the lithosphere with age or due to the fact that the lithosphere approaches a permanent regime.

6.03.5.2 Rheology and Observations of Flexure (T_e Data)

The lithosphere responds to surface and subsurface loads by bending (**Figure 2(a)**). Bending is characterized by vertical deflection, $w(x)$ with a local radius of curvature, R_{xy} (x) or curvature, $K(x) = -R_{xy}{}^{-1} = \partial^2 w/\partial x^2$. The amplitude and wavelength, λ, of bending depend on the flexural rigidity D or equivalent elastic thickness T_e. D actually provides a direct measure for the *integrated long-term strength* of the lithosphere and is linked to the *equivalent elastic thickness* of the lithosphere, T_e: $D = ET_e^3(12(1-\nu^2)^{-1})$. The flexural equation, when written in the form that uses bending moment $M_x(x)$, is rheology-independent. The elasticity is then used as the simplest rheological interpretation of bending strength. D and hence T_e are estimated by fitting the observed flexural profiles (Moho depression for continents or bathymetry for oceans) to the solution of thin plate equation:

$$\frac{\partial^2}{\partial x^2}\overbrace{\left(\underbrace{\frac{ET_e{}^3}{12(1-\nu^2)}}_{D(x)}\underbrace{\frac{\partial^2 w(x)}{\partial x^2}}_{K(x)}\right)}^{M_x} + \frac{\partial}{\partial x}\left(F_x\frac{\partial w(x)}{\partial x}\right) + \Delta\rho g w(x) = \rho_c g h(x) + p(x) \qquad [33]$$

where F_x is the horizontal fiber force, $\Delta\rho$ is the density contrast between surface material (topography/sediment) and asthenosphere, ρ_c is the density of surface material, $h(x)$ is the initial topographic elevation, and $p(x)$ is any additional surface or subsurface load. For inelastic plates, T_e and D represent the 'condensed' plate strength linked to the integrated plate strength B (eqn [22]). T_e is therefore a direct proxy for the long-term integrated strength of the lithosphere, B (see Watts, 2001). For example, for a single-layer plate of thickness h_m with $T_e = T_{e\_ocean}$,

$$B = \int_0^\infty \sigma^f(x, y, t, \dot{\varepsilon})\mathrm{d}z \text{ while } T_{e\_ocean} = \left(12\left(\frac{\partial\sigma_{xx}^f}{\partial\gamma}\right)^{-1}\overbrace{\int_0^{h_m}\sigma_{xx}^f(z-Z_n)\mathrm{d}z}^{M_x(x)}\right)^{\frac{1}{3}};\ T_{e\_ocean} < h_m \qquad [34]$$

where σ_{xx}^f is bending stress (Burov and Diament, 1995). For an inelastic rheology, T_e is smaller than h_m (**Figure 5(b)**) and has no direct geometric interpretation but is derived from D and M. D and T_e may spatially vary due to their dependence on local bending that leads to localized plate weakening (called *plastic or ductile hinging*) in the areas of utmost flexure (**Figures 2(b)** and **5(c)**), for example, near *subduction zones* or below mountains and islands. M and D are obtained from depth integration of bending stress σ_{xx}^f, which is a function of local plate curvature $K(x) = \partial^2 w/\partial x^2$ (e.g., Burov and Diament, 1995):

$$\sigma_{xx}^f(z, K) \approx \min\left(\sigma_b(z), \sigma_d(z), K(z - z_n(K))E(1-\nu^2)^{-1}\right)$$
$$D(x, K) = \left|\frac{M(x, K)}{K}\right|$$
$$T_e(x, K) = \left(M(x, K)\frac{12(1-\nu^2)}{EK}\right)^{\frac{1}{3}} \qquad [35]$$

Here, $z_n(K)$ is the 'floating' depth to the neutral stress free plane: $z_n(K) \to 0.5h_m$ as $K \to 0$. By comparing observations of flexure in the regions of long-term surface loading by, for example, ice, sediment, and volcanoes, to the predictions of simple elastic plate models, it has been possible to estimate T_e and thus B, in a wide range of geologic settings. Oceanic flexure studies suggest that T_e is in the range 2–40 km and depends on load and plate age (**Figure 5(a)**). These results are consistent with the predictions of rock mechanics, so that T_e values follow the age-controlled depth to 400–500 °C (**Figure 5(d)**). The Brace–Goetze YSEs (Brace and Kohlstedt, 1980; Goetze and Evans, 1979) predict that strength should increase until the depth of the BDT and then decrease in accordance with the brittle and ductile deformation laws. In oceanic regions, the failure curves are approximately symmetrical about the BDT where the brittle–elastic and elastic–ductile layers contribute equally to the strength. Since both T_e and BDT generally exceed the mean thickness of the crust (~7 km), there is a little doubt that the largest contribution to the strength of oceanic lithosphere comes from the mantle, not the crust.

McAdoo et al. (1985) used eqns [35] to calculate the ratio of $T_e(K)$ to h_m for the middle value of oceanic thermal age of 80 Ma, a dry olivine rheology, and a strain rate of 10^{-14} s^{-1}. They showed that for low curvatures (i.e., $K < 10^{-8}$ m^{-1}), the ratio is 1, indicating little difference between the elastic thickness values. However, as plate curvature increases, the ratio

decreases as T_e (K) decreases. For $K = 10^{-6}\,m^{-1}$, the ratio is ~0.5, indicating a 50% reduction in the elastic thickness.

The tendency of the oceanic lithosphere to yield in the seaward walls of trenches can be understood in terms of simple mechanical considerations. Ideal elastic materials support any stress level. In the case of real materials, stress levels are limited by rock yield strength at corresponding depths. Flexural strain in a bending plate increases with distance from the neutral plane. Consequently, the uppermost and lowermost parts of the plate are subject to higher strains and may experience brittle or ductile deformation as soon as the strain cannot be supported elastically. These deforming regions constitute zones of mechanical weakness since the stress level there is lower than it would be if the material maintained elastic behavior and, importantly, the stress there is not greater or not lower than it would be at the limits of the elastic core that separates brittle and ductile regions. The level of brittle and ductile stress, however, is very far from being negligible. A load emplaced on the oceanic lithosphere will therefore be supported partly by the strength of the elastic core and partly by the brittle and ductile strength of the plate. The significance of T_e values that have been estimated at trenches is that it reflects this combined, integrated, strength of the plate.

As the topography of the Moho is accessible only from indirect observations, flexural models use various techniques to compute the geometry of the Moho or of the basement from gravity anomalies. Departures of these anomalies from those predicted by local isostatic models (e.g., Airy and Pratt) have long played a key role in the debate concerning the strength of the lithosphere. Modern isostatic studies follow either a forward or inverse modeling approach. In forward modeling, the gravity anomaly due, for example, to a surface (i.e., topographic) load and its flexural compensation is calculated for different values of T_e and compared to the observed gravity anomaly. The 'best fit' T_e is then determined as the one that minimizes the difference between observed and calculated gravity anomalies (e.g., Watts, 2001). In inverse (e.g., spectral) models, gravity and topography data are used to estimate T_e *directly* by computing the transfer function between them as a function of wavelength (e.g., admittance or coherence) and comparing it to model predictions. As for all potential field data, the inversion of gravity data has no unique solution. This makes inverse gravity–flexural methods generally less reliable than direct models in complex continental settings, although recent developments in this domain are marked by very significant improvements (Kirby and Swain, 2009, 2011) so that one has to draw a distinction between most admittance and early coherence analyses, which often used incorrect loading models or bias-prone windowing approaches, and the latest generation of synthetic-tested studies. Nevertheless, since inverse methods do not take into account boundary forces and moments at plate boundaries, they are still prone to biased results in the areas affected by active tectonics.

In oceanic regions, however, forward modeling and inverse modeling yield similar values of T_e. This is no better demonstration of this along the Hawaiian–Emperor seamount chain. Forward modeling reveals a mean T_e of 25 ± 9 km, while inverse (spectral) modeling based on the free-air admittance method yields 20–30 km (Watts, 1978). When the T_e estimates are plotted as a function of load and plate age (**Figure 5(a)** and **5(d)**), they yield the same result: T_e increases with age of the lithosphere at the time of loading, being small (2–6 km) over young lithosphere and large over old lithosphere (>30 km).

6.03.5.3 Flexural Strength and Initiation of Oceanic Subduction

Strengthening of the lithosphere with age creates a number of difficulties for explanation of initialization of oceanic subduction (Cloetingh et al., 1982). Despite the widespread view that lithosphere subducts when it reaches maximum negative buoyancy due to cooling with age, at this moment, it also reaches a maximum flexural strength (**Figure 5(d)**) that normally should prevent downward bending of the plate and hence subduction. It has been argued (Cloetingh et al., 1982) that conditions for oceanic subduction initiation could be optimal for a narrow time interval around an age of 30 Ma after seafloor spreading, when gravitational instability and relatively low strength occur simultaneously. Later, McAdoo et al. (1985) and then Burov and Diament (1995) had provided a mechanism (**Figures 2(a), 5(c)**, and **5(f)**) that explains the possibility of downward bending of strong lithosphere due localized weakening cased by bending strains in the brittle and ductile parts of the plate. This phenomenon, called plastic hinging, results in local 30–50% T_e reduction allowing the plate to 'turn' over the weakened zone. Finally (see also **Section 112.4.4**), Faccenda et al. (2009) had suggested that flexural weakening of the lithosphere is further enhanced by fluids penetrating in the brittle part of the plastic hinge zone (**Figure 5(c)** and **5(f)**). Fluids result in reduction of lithostatic pressure and hence of brittle strength and also reduce the ductile strength through serpentinization.

6.03.5.4 Intraplate Seismicity (T_s), T_e, and Brittle–Ductile Interactions

Intraplate seismicity is concentrated in a specific depth interval called the seismogenic layer (**Figure 6(a)**). The thickness, T_s, of this layer averages 15–20 km and rarely exceeds 40–50 km in both oceanic and continental lithosphere. In continents, most earthquakes thus naturally happen in the crust, since its average thickness is on the order of 40 km. Sub-Moho continental mantle earthquakes are rare (e.g., Deverchere et al., 1991; Monsalve et al., 2006; Tesauro et al., 2008; **Figure 6(b)**) to a point that their very existence is sometimes doubted (Jackson, 2002; Maggi et al., 2000).

According to rock mechanics data, brittle properties of the oceanic and continental lithosphere cannot significantly differ from each other. Hence, the similarity of T_s in oceans and adjacent continents might be suggestive of similar stress levels and thus of transmission of tectonic stress from oceanic to continental domain. However, some authors suggest that T_s is related to long-term lithospheric strength and thus to T_e (Jackson, 2002; Maggi et al., 2000; **Figure 6(a)**). These authors go further by suggesting that these parameters are equivalent thus inferring that the strength of the lithosphere resides only in its brittle part. For continents, this means that all plate strength is concentrated in the crust and implies that all previous T_e estimates for old continental plates that exceed crustal

thickness are incorrect. These ideas gave birth to the 'crème brûlée' rheology model for continents (strong crust–weak mantle), in contrast to the 'jelly sandwich' rheology model (strong upper crust–strong mantle).

From the mechanical point of view, it can be demonstrated that T_s and T_e cannot correspond to the same layer in the lithosphere (Burov and Watts, 2006; Watts and Burov, 2003). Mechanical considerations suggest that T_s has its own significance. Of course, this does not exclude the possibility that T_s and T_e may have similar values. Yet, it was shown (Burov and Watts, 2006) that if $T_s \approx T_e$, then about half of the plate strength has to be supported by its ductile part. In this particular case, the quasielastic resistant core of the plate includes brittle and ductile layers in similar proportions.

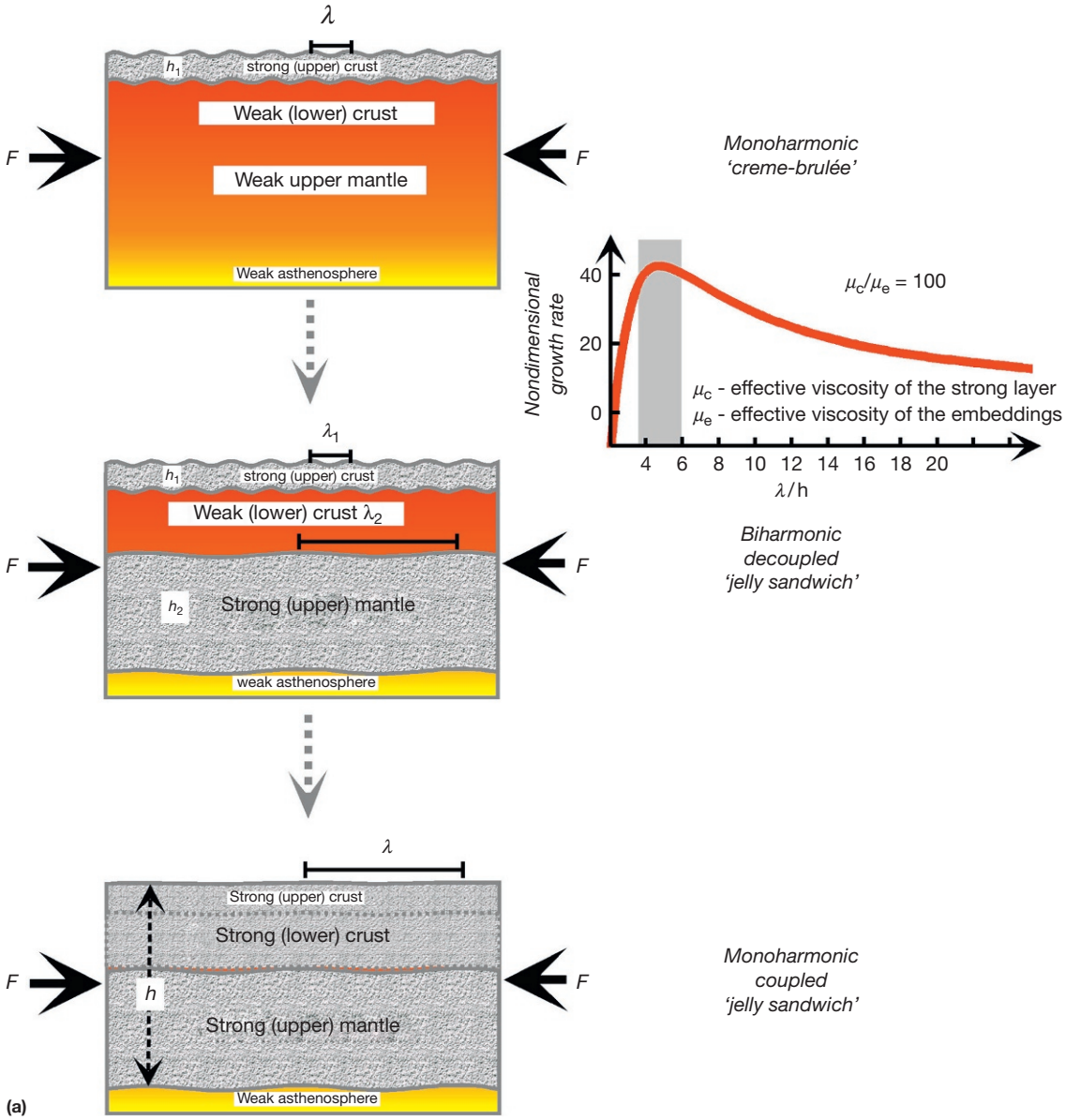

Figure 6 (a) Sketch of typical folding models for continental lithosphere (h_1 and h_2 are thicknesses of the competent crust and mantle, respectively). The system is submitted to compression by horizontal tectonic force F. In the case when the lower crust is weak ('crème brûlée' rheology model), the upper crust may fold independently of the mantle part (wavelength λ_2), with a wavelength λ_1 (decoupled, or biharmonic folding), which corresponds to the 'jelly sandwich' rheology model *sensu stricto*. Very young (<150 Ma) and very old (>1000 Ma) lithospheres (single competent layer or coupled crust and mantle) develop monoharmonic folding. Note that we call 'jelly sandwich' all rheological profiles that include both strong upper crust and mantle; thus, the case of very old coupled lithosphere from the bottom of the figure also corresponds to the 'jelly sandwich' concept. Inset shows the analytic estimate for the growth rate of strongly non-Newtonian folding (coupled layers, non-Newtonian rheology) as a function of λ/h for a typical ratio of the effective viscosities of the competent layer and embeddings (100 (reproduced from Burov EB, Lobkovsky LI, Cloetingh S, and Nikishin AM (1993) Continental lithosphere folding in Central Asia (part 2), constraints from gravity and topography. *Tectonophysics* 226: 73–87)). Shaded rectangle shows the range of the dominating λ/h ratios (4–6).

It was found, from force balance considerations (e.g., Bott, 1993; Cloetingh and Wortel, 1986; Molnar and Lyon-Caen, 1988; Zoback, 1992), that representative tectonic stresses and intraplate forces cannot exceed 100–600 MPa and 10^{13}N per unit length (meter), respectively. Byerlee's law predicts that brittle strength linearly increases with pressure and, hence, depth (Figures 1, 4(a), 4(b), and 5(b)). Near the surface, brittle strength is 0–20 MPa, but it is 30–100 times higher in oceanic and continental mantle at 40 km depth: 0.6–2 GPa in oceans (depending on fluid pressure) and around 2 GPa in continents (no fluid pressure). Figure 5(b) demonstrates that bending stress, and thus the probability to reach brittle strength limits, decreases while approaching the neutral surface. For the previously mentioned two reasons, the upper crustal layers fail more easily than mantle layers. At 50 km depth (the maximum depth of distributed seismicity), dry brittle rock strength is 2 GPa. Assuming a 100 km thick lithosphere, one needs a horizontal tectonic force of 10^{14} Nm to reach this strength. This value is improbable since it is one or two orders of magnitude higher than estimates for intraplate forces. A 2 GPa stress level may probably be reached only exceptionally, for example, at location of inflection points, where the sum of tectonic and bending stress is maximum. Yet, as mentioned, the absence of preexisting fractures in temperature–pressure healed mantle rock would prohibit Byerlee's failure even if the differential stress level meets the required limit.

Discussions on continental rheology stem from both the uncertainties in the rheology laws and the conflicting results on T_e from continental studies. In contrast, oceanic T_e estimates are considered to be robust. T_e–T_s relations thus can be best understood using oceanic data. When all oceanic T_s data and T_e data are plotted on the same depth plot, they appear to correlate (Figure 6(a)). Yet, when one separates the extensional and compressional events, the correlation is not observed: extensional earthquakes are systematically found at two times shallower depth than the corresponding T_e values (Watts and Burov, 2003). This can be understood if one remembers that brittle (Byerlee's law) extensional failure requires nearly two times smaller stress than compressional failure. This leads to the conclusion that earthquake depths are primarily controlled by intraplate stress level. Contrary to T_e, for a fixed intraplate force per unit length F, T_s must decrease with increasing integrated strength of the lithosphere B ($F<B$):

$$T_s \approx \Upsilon\left(F/T_e + \sigma^f_{xx}|_{z=Ts}\right)/\rho g$$
$$T_e(\text{oceans}) <\approx 0.7h_m \qquad [36]$$

The factor $\Upsilon=0.6^{-1}$–0.85^{-1} comes from eqn [9], and $\sigma^f_{xx|_z}=T_s$ is flexural stress (eqns [35]) at the depth $z=T_s$. Equation [36] shows that T_s decreases with increasing T_e. Thus, T_s and T_e do not correlate but anticorrelate for all $F<B$ ($F=B$ corresponds to whole-scale plate failure and is incompatible with flexural deformation; $F>B$ is not possible). For an unbent plate, T_s can be equal to T_e only if $T_e=(0.8\,F/\rho g)^{1/2}$. If $F=10^{13}$ N m, T_s is <15–16 km, but $T_e=30$ km (Figure 5(b)). For smaller F, $T_s<\frac{1}{2}T_e$. If one accepts the CB rheology model where ductile mantle has no contribution to the bending strength (Figure 5(e)), then $T_e\geq 2T_s$, which means that this hypothesis is mechanically inconsistent with the assumption that T_e and T_s are equivalent. Flexural stress σ^f_{xx} may increase the value of T_s by a factor of 2–3, but at the same time, it would decrease T_e by the same factor (Figure 5(e)). As result, in oceans,

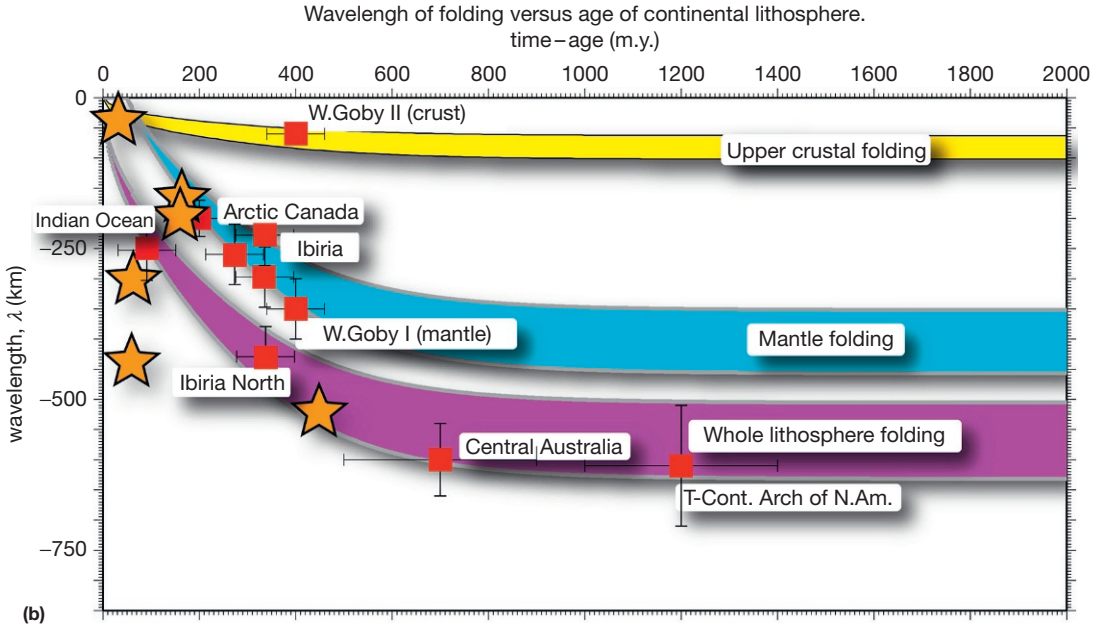

Figure 6 (Continued) (b) The observed wavelength of folding (Table 5) as a function of thermal age (calculated according to the model of Burov et al. (1993)). Numbers correspond to the ones used in the Table 5. Squares show the cases of 'regular' folding, whereas the stars mark 'irregular' cases (variable wavelengths, large amounts of shortening, important sedimentary loads, etc.). Different theoretical curves correspond to the crustal, mantle (supporting the presence of the decoupled rheology), and 'welded' folding (modified from Cloetingh S, Burov E, and Poliakov A (1999) Lithosphere folding: Primary response to compression? (from central Asia to Paris Basin). *Tectonics* 18: 1064–1083).

(Continued)

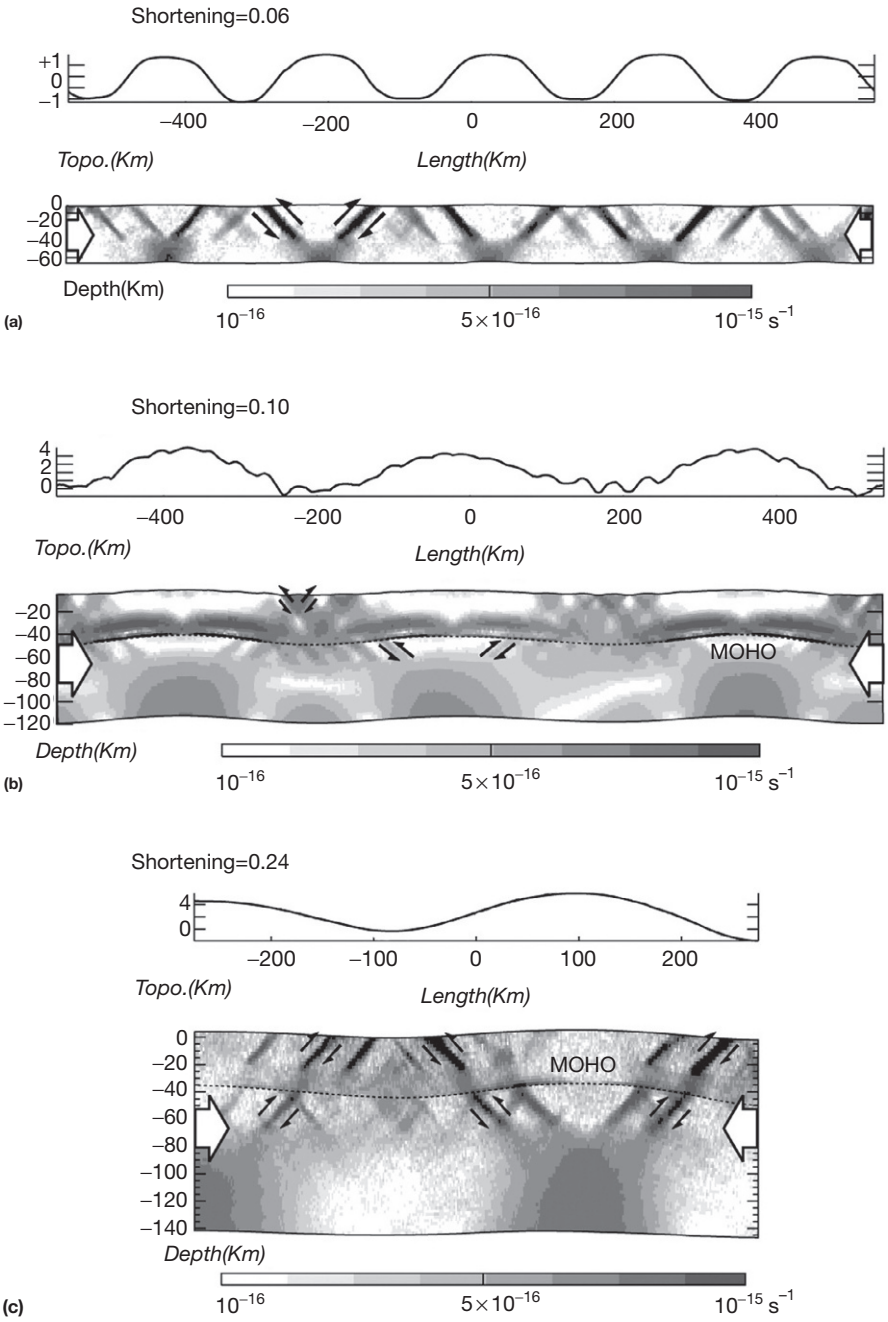

Figure 6 (Continued) (c) Topography and logarithm of strain rate field predicted from the direct numerical thermomechanical experiments on high-amplitude folding in brittle–elastic–ductile for oceanic lithosphere, in case 'a' ($T_e \sim 40$ km rheology profile 4 for 50–75 Ma in **Figure 9(a)**), and continental lithosphere in case 'b' ($T_e \sim 60$ km, rheology profile 2 for 250 Ma in **Figure 9(a)**) and case 'c' ($T_e \sim 80$ km, rheology profile 2 for 750–1000 Ma in **Figure 9(a)**). All snapshots correspond to ~7 My since the onset of shortening (modified from Gerbault M, Burov EB, Poliakov A, and Dagnieres M (1999) Do faults trigger folding in the lithosphere? *Geophysical Research Letters* 26: 2271–2274). Cases 'b' and 'c' correspond to the 'jelly sandwich' lithorheological structures from **Figure 4(a)** and **4(d)**. The experiments confirm the ideas presented in (a) (e.g., biharmonic folding in case 'b' with two different wavelengths developing together) and demonstrate the possibility of the development of large-scale folding despite of concurrent intense brittle faulting. *De facto*, folding controls localization of brittle faults that tend to localize at the inflection points of folds.

T_s and T_e cannot approach each other until the plate preserves some elastic core ($F < B$). The maximum intraplate stress ($\sigma^f_{xx} + F/T_e$) is limited to 2 GPa in compression and about 1 Ga in extension (**Figure 4(a)**). This yields $T_s < 40$–50 km, which is compatible with the observations (Maggi et al., 2000).

As seen from **Figure 5(b)** and **5(c)**, the strong mechanical core associated with T_e is centered at the neutral plane of the plate, z_n, whereas the seismogenic layer T_s is shifted toward the surface. This shows why T_s cannot have same geometric interpretation as T_e. Since bending stresses are minimal near z_n, the

earthquakes are favored only at some depth above or below z_n (Figure 5(b) and 5(c)). The brittle strength linearly increases with depth, making deeper earthquakes less probable. It is thus natural that earthquakes are more frequent above z_n. For a pure elastic plate, z_n is located in the middle of the plate. For a brittle–elastic–ductile plate with a typical YSE, z_n is only roughly located in its middle, depending on the proportion between the integrated strengths of the brittle and ductile domains (Figure 5(b) and 5(c)). In most common case, the sizes of these domains are comparable, $z_n \approx \frac{1}{2}T_e(\max)$ and $T_s < \frac{1}{2}T_e$. If the ductile part is very weak (e.g., near the ridges, age $<$ 4–10 Ma), the plate strength is concentrated in the brittle–elastic layer T_s. In this case, earthquakes must occur at depths $< \approx (T_e(\max) - T_e)$ (Figure 5(c)), while $T_e(\max) - T_e < \frac{1}{2}T_e$ except for extreme amounts of flexure. Hence, in a plate with a very weak ductile part, the equality $T_s = T_e$ is impossible unless the plate undergoes a strong nonflexural deformation. Yet, in the latter case, T_e has no meaning. T_s may be equal to T_e only if the plate has a quasi*symmetrical* strength distribution, that is, comprises *equally* strong brittle and ductile part (Figure 5(b)). Needless to say, this configuration is incompatible with the crème brûlée rheology model.

It is noteworthy that the previous considerations are valid only under the hypothesis that T_s and T_e are both related to flexural deformation of the lithosphere, the only context a link between these two quantities may have some sense. If the lithosphere undergoes important nonflexural deformation or just transmits important tectonic stress, T_s would not be expected to have any relation to T_e.

6.03.5.5 Intraplate Seismicity and Ductile Creep

Rock mechanics data suggest that in addition to Byerlee's friction law, a semibrittle/semiductile strain rate-dependent plastic flow may increasingly occur beginning at 10–15 km depth, with a frictional component that is not observed at depths $>$ 40–50 km (Bos and Spiers, 2002; Chester, 1995; Ranalli, 1995). Starting from this depth, Peierls and GBS creep is more likely than brittle failure. This probably explains why intraplate earthquakes are rare below 40–50 km depth in both the oceanic and continental lithosphere.

The most puzzling point refers to the observation that in the oceans, for given plate age, the maximum earthquake depth appears to correlate with the depth to the isotherm ~400–500 °C. This depth is about 40–50 km for plate ages between 70 and 180 Ma but is much shallower near spreading centers. Thermal models of lithosphere are quite uncertain, so quite a few earthquakes may also occur below the 500 °C isotherm depth (e.g., Watts, 2001). At any rate, correlation of the maximum earthquake depth with temperature cannot be directly linked to the long-term ductile strength because at seismic strain rates, the entire upper mantle behaves as an elastic material (Figure 4). One possible explanation may be related to the fact that brittle failure can be activated only on preexisting microfractures. Microfractures are likely to be healed under pressure in hot ductile mantle below the depth to 500 °C. Ductile healing occurs in all kinds of rocks, particularly in the presence of fluids. However, there is an essential difference between the dislocation creep characteristic of both hot lower crustal and mantle rocks and the GSS GBS (grain boundary sliding) creep that is more specific for olivine and can be activated in relatively narrow temperature–pressure interval between 500 and 800 °C, thus at 40–70 km depth just below the continental Moho (Drury, 2005). GBS creep is strongly favored by a reduction in grain size under large strains and may result in localized strength drop and formation of ductile shear bands in the sub-Moho mantle. Meanwhile, rock retains considerable strength (~200–400 MPa), which, however, is smaller than for dislocation creep and is much smaller than the hypothetical brittle strength at 40 km depth (several GPa). The rock recovers its initial strength and deforms by dislocation creep as the grains regrow.

Hence, weak ductile shear bands will likely form in the sub-Moho mantle instead of high-stress brittle shear bands. Then, sub-Moho rocks will not be able to accumulate significant elastic stresses and seismogenic stress release becomes improbable. Since the GBS creep is specific for mantle and not for crustal rocks, this might explain the scarcity of earthquakes below the continental Moho and sharp seismic transition between the crust and mantle.

That said, continental subcrustal earthquakes are rare but not unknown (e.g., Monsalve et al., 2006; Tesauro et al., 2011; Figure 6(b)). There are also cases where earthquakes extend to really great depths (more than 300 km) while producing conventionally looking focal-depth solution mechanisms corresponding to simple shear sliding. The physical mechanisms of deep earthquakes are still not understood, but it is agreed that deep seismicity is not related to Byerlee's brittle sliding, for obvious reasons such as ultimate growth of brittle strength with increasing pressure and healing of the preexisting fractures under combined increase of temperature and pressure with depth (John et al., 2009; Kirby et al., 1991; Scholz, 1990, 2002). As pointed out (Green, 2007), the only high-pressure shearing instabilities identified by experiment require generation *in situ* of a small fraction of very weak material differing significantly in density from the 'parent material.' Growing evidence (Green, 2007) suggests that earthquakes shallower than 400 km are most probably initiated by breakdown of hydrous phases and those below 400 km depth, as a shearing instability associated with breakdown of metastable olivine to its higher-pressure polymorphs. For example, intermediate depth earthquakes (below 300–400 km) may be caused by sliding on ductile shear bands that get weakened due to fluid-induced metamorphic reactions and due to shear heating that under these conditions may lead to thermal runaway (John et al., 2009). These mechanisms are only weakly related to the initial rock strength, and it has been known for some time that, unlike shallow (i.e., depths $<$ 50–70 km) earthquakes, deep earthquakes produce very few aftershocks. This aftershock behavior is an important argument that the earthquake generating mechanism differs between shallow and deep earthquakes. Indeed, in contrast to brittle shear bands, ductile shear bands are expected to self-weaken allowing for continuous sliding until all elastic energy accumulated in surrounding rock is realized, which reduces the possibility of further aftershocks. The observation of double seismic zones in subductioning slabs, one of which is the slab/mantle wedge interface but

the second one is located near the neutral plane of the plate, also adds to the arguments in favor of the nonbrittle mechanisms of deep seismicity.

6.03.5.6 Constraints on the Long-Term Viscosity from Subsidence Data

Volcanic islands such as Hawaii present an ideal example of point loading that can be used to evaluate long-term lithospheric strength (Watts, 2001). Acting as an almost instantaneous surface load, islands produce local depression, whose geometry and amplitude are reflected in seismic stratigraphic data. It was shown that the primary response of the lithosphere involves the integrated strength that is different from the long-established strength. In general, the lithosphere exhibits high flexural strength within the first 10 My after loading (e.g., for Hawaii, $T_e(t=0)=90$ km; Watts, 2001), which progressively decays toward some asymptotic value (for Hawaii, $T_e(t\to\infty)=30$ km; Walcott, 1970). It is remarkable that the strength decay is exponential, as for a Maxwell solid, only within interval of a few My; after that, strength remains unchanged or slowly increases with time following the common thermal age dependence. The subsidence data suggest that the characteristic relaxation times in the lithosphere are on the order of several My. Compared to the Maxwell relaxation times in the asthenosphere (10–100 years), it suggests that the average lithosphere viscosity is 10^4–10^5 higher than the asthenospheric viscosity (10^{19}–5×10^{19} Pa s). This yields a rough estimate of 10^{23}–10^{24} Pa s for the depth-averaged viscosity of oceanic lithosphere and suggests that elastic strain plays an important role in long-term deformation.

6.03.5.7 Large-Scale Lithospheric Folding

A number of observations (e.g., Weissel et al., 1980) reveal periodic undulations of the seafloor in zones of intraplate compression such as the Indian Ocean (see also discussion on continental folding in the following sections). These undulations may reflect compressional instabilities that develop in stiff layers overlying weaker layers or embedded in a weaker matrix (Figure 7). The minimal stiffness (viscosity) ratio needed for development of folding is ~100 (Biot, 1961). The wavelength, λ, of folding is roughly proportional to 5–10 thicknesses of the competent layer, h_m:

$$\begin{aligned}
&\lambda = 2\pi h_m(\mu_1/\mu_2)^{1/3} \text{ (viscous rheology, no gravity)}\\
&\lambda = 2\pi(F/\Delta\rho g)^{1/2},\ F\approx B\approx 2\mu_1\dot{\varepsilon}h_m \text{ (viscous gravity folding)}\\
&\lambda = 2\pi(Gh_m/F)^{1/2} \text{ (elastic buckling, no gravity)}\\
&\lambda = 2\pi(2D/F)^{1/2},\ F\approx(4D\Delta\rho g h_m)^{1/2} \text{ (elastic gravity buckling)}
\end{aligned} \qquad [37]$$

where μ_1 is the average viscosity of the lithosphere and μ_2 is the viscosity of the asthenosphere. In the case of the Indian Ocean, the observed λ is on the order of 250 km (Weissel et al., 1980), implying a 50 km thick stiff layer. This value agrees with eqn [36] and is close to T_e estimates for Indian Ocean (40–50 km; Watts, 2001; Figure 5(a)). The wavelength of lithosphere folding thus can be used as a proxy for long-term strength of the lithosphere, in the same way as T_e (compare Figure 7(b) with Figures 5(a) and 8). According to both theory and experiments, noticeable folding develops in layered systems with competence contrasts higher than 100. The viscosity of the underlying asthenosphere is known to be on the order of $1–5\times10^{19}$ Pa s. Hence, one can conclude that the average viscosity of the oceanic lithosphere is $>10^{21}$–10^{22} Pa s. This estimate provides only a lower bound on the mean viscosity of the lithosphere since λ is weakly dependent on μ_1/μ_2 in the range $10^2<\mu_1/\mu_2<10^4$. Consequently, μ_2 can vary from 10^{21} to 10^{24} Pa s.

6.03.6 Rheology and Structure of the Continental Lithosphere and Continental Margins

6.03.6.1 Common Goetze and Evans Yield Stress Envelopes

Similar to the oceanic lithosphere, the continental YSEs are derived from common assumptions such as the rheological structure, crustal thickness, lithosphere thickness $a=z(1330\,^\circ\text{C})$, thermal structure, and strain rate field. Since the continental crust is much more variable in its structure and composition than the oceanic crust, there is much larger variety of possible continental YSEs (Figure 9). In contrast to the oceanic lithosphere, the thermal structure of continental plates is not well constrained because (1) they may have undergone several major thermal events in their history, (2) the thermal thickness, a, of continents is not well defined, and (3) about 50% of the continental surface heat flux is due to relatively variable radiogenic heat production in the upper crust and it is also influenced by surface processes and spatial variation in thermal properties. The common thermal model refers to cooling of a multilayer plate heated from below (Afonso and Ranalli, 2004; Burov and Diament, 1992, 1995; Appendix B). This model is characterized by a time of cooling t, also called thermotectonic age, has a vertically heterogeneous structure, and accounts for radiogenic heat production in the crust. According to this model, the thermal structure of the continental lithosphere becomes stationary after 400–700 Ma since the last major thermal event (e.g., Burov and Diament, 1995; Jaupart and Mareschal, 2007).

The assumed difference in the mechanical properties of the upper crust, lower crust, and mantle may lead to the appearance of weak ductile zone(s) in the lower crust that allows for mechanical decoupling of the upper crust from the mantle (e.g., Bird, 1991; Chen and Molnar, 1983; Kuznir and Park, 1986; Lobkovsky and Kerchman, 1992). Crust–mantle decoupling occurs if the lower crust is mechanically weaker than mantle olivine at the Moho boundary. This decoupling implies the possibility of lateral flow in the lower crust, enhanced by dissipative heating, grain size reduction, and possible metamorphic changes (Burov et al., 1993; Lobkovsky and Kerchman, 1992). For 'common' quartz-dominated crust, decoupling should always occur, except for thin (e.g., rifted) crust (<20 km). For other crustal compositions (diabase, feldspar, quartz-diorite, etc; Figures 4(a) and 9), decoupling might take place in most cases, except in very old cold lithospheres (age > 750 Ma). The presence of fluids (wet/dry rheology) also promotes crust–mantle decoupling.

A number of independent data sources provide additional constraints on the choice of crustal rheology. These include T_e and other deformation data, seismicity distributions (Chen and Molnar, 1983; Cloetingh and Banda, 1992; Deverchere et al., 1993; Govers et al., 1992; Molnar and Tapponnier, 1981), seismic reflectivity and velocity anomalies (P and S),

attenuation of S velocities associated with ductile zones or fluids (e.g., Kusznir and Matthews, 1988; Wever, 1989), petrology data (Cloetingh and Banda, 1992), and data from magnetotelluric soundings, which serve as indicators of the presence of melts and fluids (Wei et al., 2001).

6.03.6.2 Age Dependence and Other Dependences of the Integrated Strength of the Lithosphere

As for the oceans, T_e data are the main proxy for the long-term strength of continental lithosphere (Figure 8). In continents, T_e ranges from 0 to 110 km and shows only partial relationship with age. Although the continental lithosphere should strengthen while getting colder with time (Figure 8), there is no such a clear T_e age dependency in continents as in oceans (Figure 5(a) and 5(d)). Many plates have experienced thermal events that have changed their thermal state so that it does not correlate anymore with their geologic age (e.g., Kazakh shield (Burov et al., 1990) and Adriatic lithosphere (Kruse and Royden, 1994)). On the other hand, after 400–750 Ma (Figure 8), the temperature distribution in the lithosphere approaches equilibrium state and does not evolve with age. As mentioned, the interpretation of the surface heat flux in the continental domain is ambiguous because of uncertain crustal heat generation and thermal effects associated with erosion, sedimentation, and climatic changes (Jaupart and Mareschal,

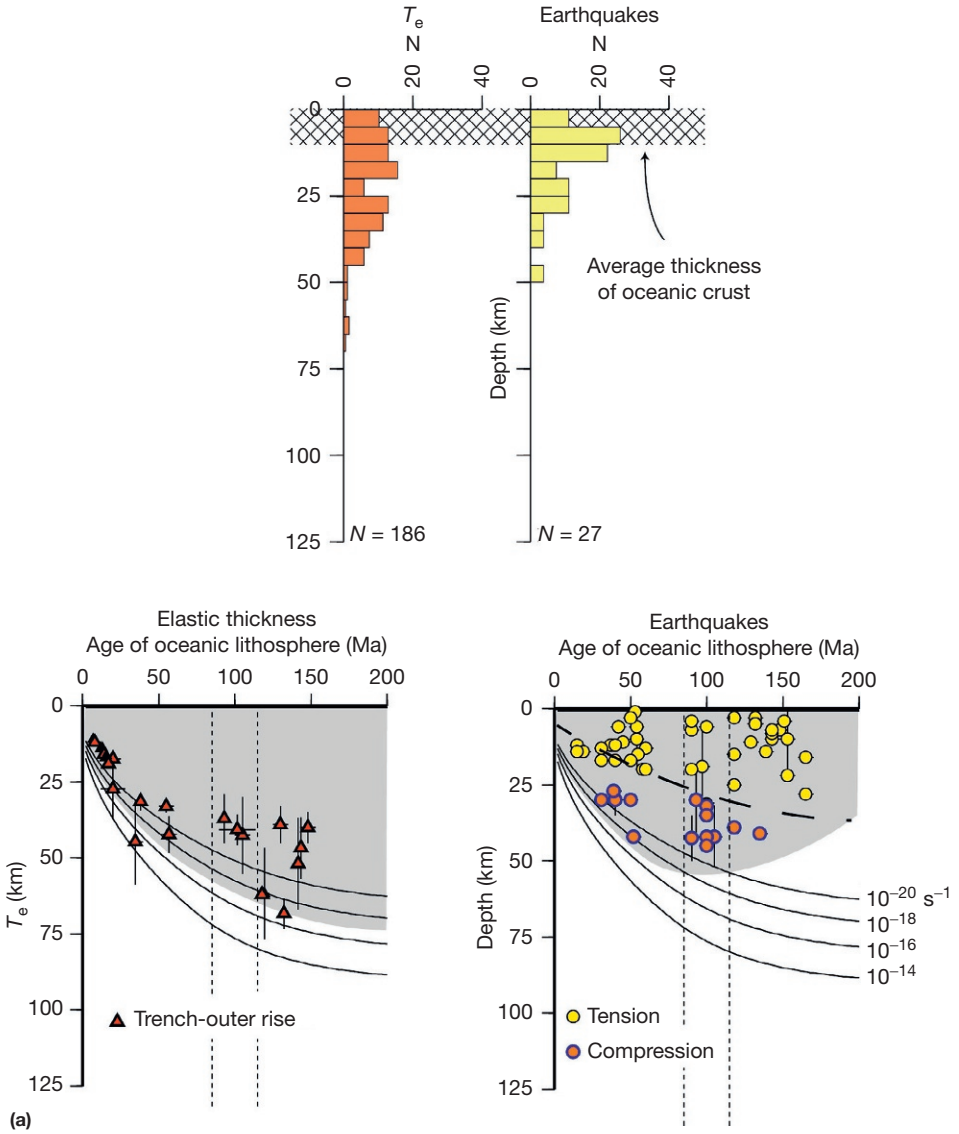

Figure 7 (a) Summary of T_e and T_s estimates for deep-sea trench–outer rise systems (reproduced from Watts AB and Burov E (2003). Lithospheric strength and its relationship to the elastic and seismogenic layer thickness. *Earth and Planet Science Letters* 213: 113–131). Data based on Table 6.1 of Watts (2001) and **Table 1** of Seno and Yamanaka (1996). The T_e estimates have been corrected for curvature. Solid lines show the YSE based on the same rheological structure as assumed in **Figure 4(a)**, a stress difference of 10 MPa, and thermal ages of oceanic lithosphere of 0–200 Ma.

(Continued)

2007). Surface heat flow mainly reflects crustal processes and should not be used to infer the subcrustal geotherm (England and Richardson, 1980).

The base of the mechanical lithosphere in continents, h_m, is referred to the isotherm of 700–750 °C, below which the yielding stress is <10–20 MPa (higher than in oceans; temperature at the base of the mechanical lithosphere results from pressure effect on ductile strength, since in continents, the depth to 500–750 °C is greater than in the oceans). The mean background strain rates are typically known within one order of accuracy. As can be seen from **Figure 9(b)**, such uncertainty is acceptable, since it affects the yield stress limits by no more than 10%.

As mentioned, the rheological meaning of T_e in the continents is not as clear as it is in the oceans (**Figures 5** and **8**). The T_e data show a somewhat bimodal distribution, with low values clustering at 30–40 km and high values clustering at 80 km (Burov and Diament, 1995; Watts, 2001). The reason for this clustering probably refers to the influence of plate structure. That is, depending on the ductile strength of the lower crust, the continental crust can be mechanically coupled or decoupled with the mantle resulting in highly differing T_e. Burov and Diament (1992) had shown for 'typical' continental lithosphere that the weak ductile zones in the lower crust do not allow flexural stresses to be transferred between the strong (brittle, elastic, or ductile) layers of the jelly 'sandwich.' As result, there are several 'elastic' cores inside the bending plate. In such a multilayer plate, flexural stress and strain levels are significantly smaller than in an equivalently bent monolith plate of same thickness. Consequently, its T_e, which is a measure of integrated bending stress, is also reduced. T_e of a multilayer plate reflects the combined strength of all the brittle, elastic, and ductile layers. Yet, it is not a simple sum of thicknesses of these layers (h_1, $h_2 \ldots$, h_n) (**Figure 10(a)**; **Appendices A** and **B**):

$$T_e(\mathrm{YSE}) \sim \left(h_1^3 + h_2^3 + h_3^3 \cdots\right)^{1/3} = \left(\sum_{l=1}^{n} h_1^3\right)^{1/3} \quad [38]$$

Thus, in the case of two equally strong but decoupled layers ($n=2$) of total thickness h (e.g., crust and mantle), $T_e \approx 0.6\,h$ instead of h, that is, the integrated strength is reduced roughly by a factor of 2 compared to a monolayer plate (e.g., old craton with strong coupled lower crust). The meaning of T_e (YSE) in the continents thus becomes clearer. It reflects the integrated effect of *all* competent layers that are involved in the support of a load, including the weak ones.

If the multilayered continental lithosphere is subject to large loads, it flexes, and the curvature of the deformed plate, K, increases. T_e (YSE) is again a function of K and is given (Burov and Diament, 1995, 1996) by (**Figure 10(b)**)

$$T_e(\mathrm{YSE}) = T_e(\mathrm{elastic})C(K, t, h_{c1}, h_{c2}, \ldots) \quad [39]$$

where C is a function of the curvature, K, the thermal age, t, and the rheological structure. A precise analytic expression for C is bulky (Burov and Diament, 1992), although Burov and Diament (1996) provided a first-order approximation for a 'typical' case of continental lithosphere with a mean crustal thickness of 35 km, a quartz-dominated crust, and an olivine-dominated mantle, which, they indicate, is valid for $10^{-9} < K < 10^{-6}$ m^{-1}. T_e (YSE) then simplifies to

$$T_e(\mathrm{YSE}) \approx T_e(\mathrm{elastic})\left(1-(1-K/K_{\max})^{1/2}\right)^{(1/2+1/4(T_e(\mathrm{elastic})/T_e(\max)))} \quad [40]$$

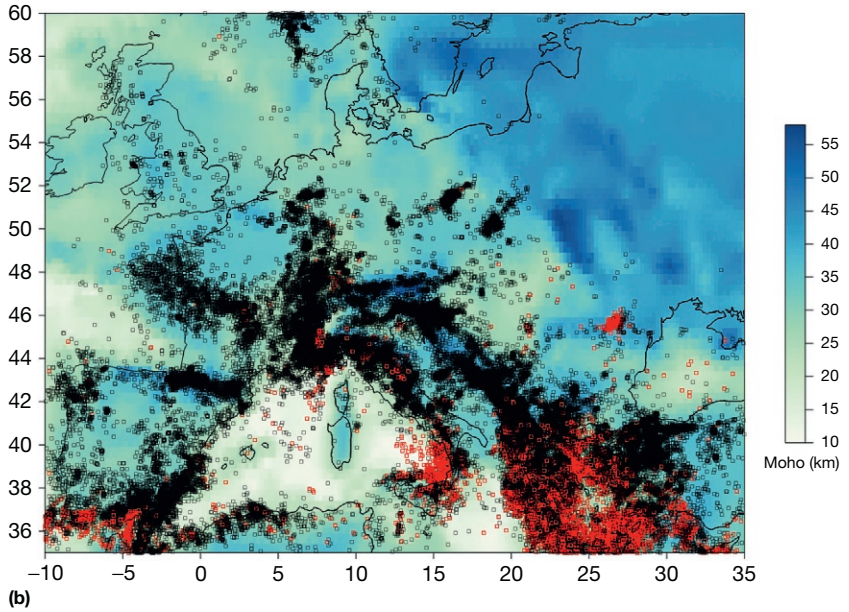

Figure 7 (Continued) (b) Seismicity distribution in Europe (Tesauro et al., 2008). The database contains more than 100 000 seismic events with magnitude between 1 and 9 for the time period 1973–2010. Black and red circles correspond to the earthquakes located in the crust and mantle lithosphere, respectively. The data on crustal thickness come from EuCRUST-07 (Tesauro et al., 2009a,b,c). Intraplate sub-Moho earthquakes in continental domain are rare but not exclusive, specifically in the areas with crustal thickness $<$20–30 km.

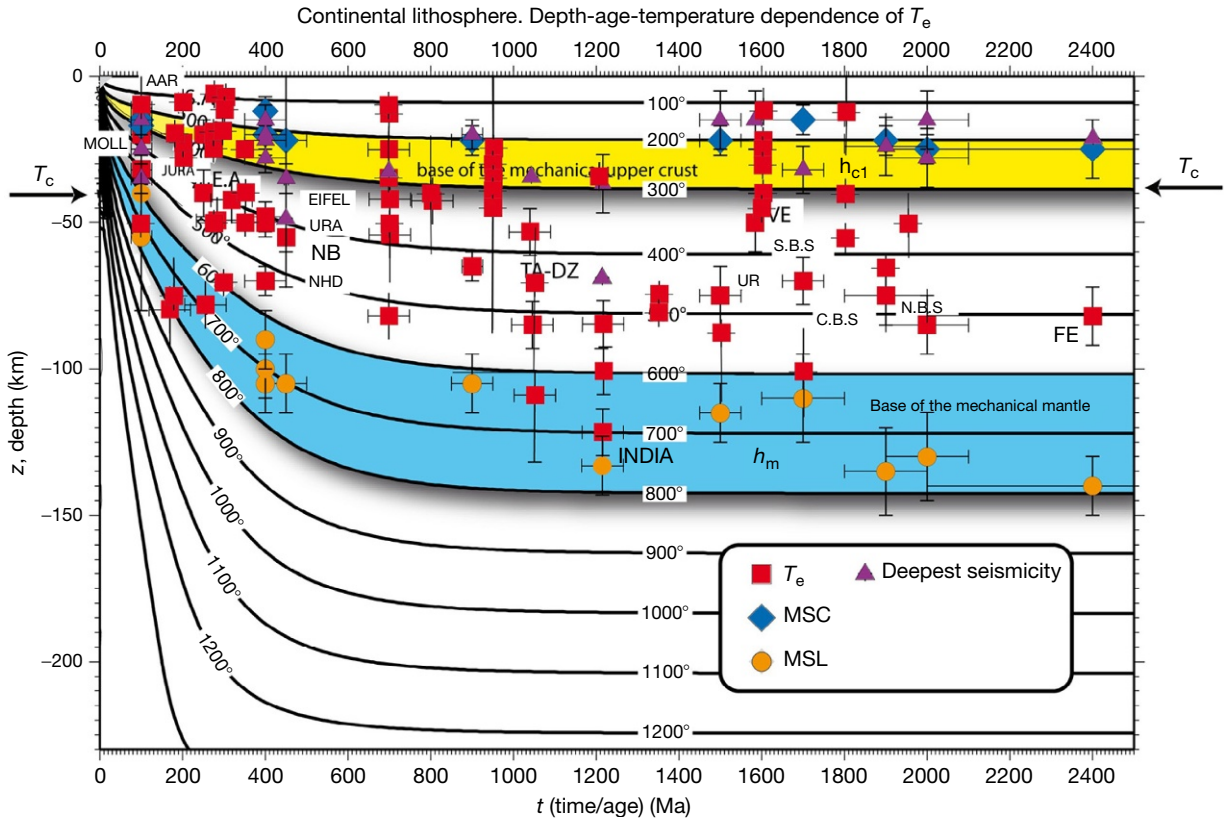

Figure 8 Compilation of observed elastic thickness (T_e) against age of the continental lithosphere at the time of loading and the thermal model of the continental lithosphere (equilibrium thermal thickness, $a = z(1330\ ^\circ\text{C})$, of 250 km (**Appendix B**). Also shown is the depth to the mechanical base of the lithosphere and maximum depths of seismicity (where available). The data refer to the studies that have taken into account – at minimum – surface topography loads. Where available, we preferred estimates based on robust forward models rather than on debated spectral models. In particular, common variants of FAA admittance technique (e.g., Jackson, 2002; McKenzie and Fairhead, 1997) are not applicable in areas of elevated topography (e.g., mountain ranges and plateaus), as well as near plate boundaries (since it cannot account for boundary forces associated with collision and slab pull) (Burov and Watts, 2006; Jordan and Watts, 2005; Lowry and Smith, 1994; Watts, 2001; Watts and Burov, 2003)). The lines are isotherms with account for radiogenic heat production in the crust. Filled squares are estimates of T_e in collision zones (foreland basins and thrust belts); filled circles correspond to postglacial rebound data. Isotherms 250–300 °C mark the base of the mechanically strong upper crust (quartz). The isotherms 700 – 750 °C mark h_m, the base of the competent mantle (olivine). Note that there are no significant changes in the thermal structure of the lithosphere after ~750 Ma, though there are significant reductions in T_e even for these ages. These reductions are obviously caused by differences in crustal structure and rheology. The notations are foreland basins/mountain thrust belts data: E.A., Eastern Alps; W.A., Western Alps; AD, Andes (sub-Andean); AN, Apennines; AP, Appalachians; CR, Carpathians; CS, Caucuses; DZ, Dzungarian basin; HM, Himalayas; GA, Ganges; KA, Kazakh shield (north Tien Shan); KU, Kunlun (south Tarim); NB, north Baikal (chosen since this part of the Baikal rift zone is believed to represent a 'broken' rift currently dominated by flexural deformations); TA, central and north Tarim; PA, Pamir; TR, Transverse Ranges; UR, Urals; VE, Verkhoyansk; ZA, Zagros. Postglacial rebound zones: L.A., Lake Algonquin; FE, Fennoscandia; L.AZ, Lake Agassiz; L.BO, Lake Bonneville; L.HL, Lake Hamilton. Data sources: S.A., AN., CR., HM, NB, KA, TA, PA,KU, GA, AD, TA, W.A, E.A., DZ, AP, GA, TR, VE, FE: (Burov and Diament, 1995 and references therein; Watts, 2001). Other data sources (ZA, L.A., L.AZ, L.BO, L.HL): (Watts, 1992, 2001).

where K_{max} (in m^{-1}) $= (180 \times 10^3\ (1 + 1.3T_e(\text{min})/T_e(\text{elastic}))^6)^{-1}$, T_e (max) = 120 km, T_e (min) = 15 km, and T_e (elastic) is the initial elastic thickness prior to flexure, which can be evaluated from eqn [38].

We show in **Figure 10(d)** and **10(e)**, therefore, how T_e and T_s would be expected to change using the more precise analytic formulations of Burov and Diament (1992, 1995, **Appendix A**). The Figure illustrates how the thickness of the brittle and ductile layers evolve with different loads and, hence, curvatures. On bending, brittle failure and, hence, the potential for seismicity preferentially develop in the uppermost part of the crust. The onset of brittle failure in the mantle is delayed, however, and does not occur until the amount of flexure and, hence, curvature is very large. Observations of curvature in regions of large continental loads provide constraints on the brittle strength of continental lithosphere. Curvatures range from $10^{-8}\ m^{-1}$ for the sub-Andean to $5 \times 10^{-7}\ m^{-1}$ for the West Taiwan foreland basins (Watts and Burov, 2003 and references therein). The highest curvatures are those reported by Kruse and Royden (1994) of $4–5 \times 10^{-6}\ m^{-1}$ for the Apennine and Dinarides forelands. **Figure 10(d)** and **10(e)** shows, however, that plate curvatures of $10^{-6}\ m^{-1}$ may not be sufficiently large to cause brittle failure in the subcrustal mantle, *unless* the flexed plate is subject to an externally applied tectonic stress. In the case illustrated in **Figure 10(d)**, the stress required to cause failure in the subcrustal mantle for this plate curvature is 350 MPa

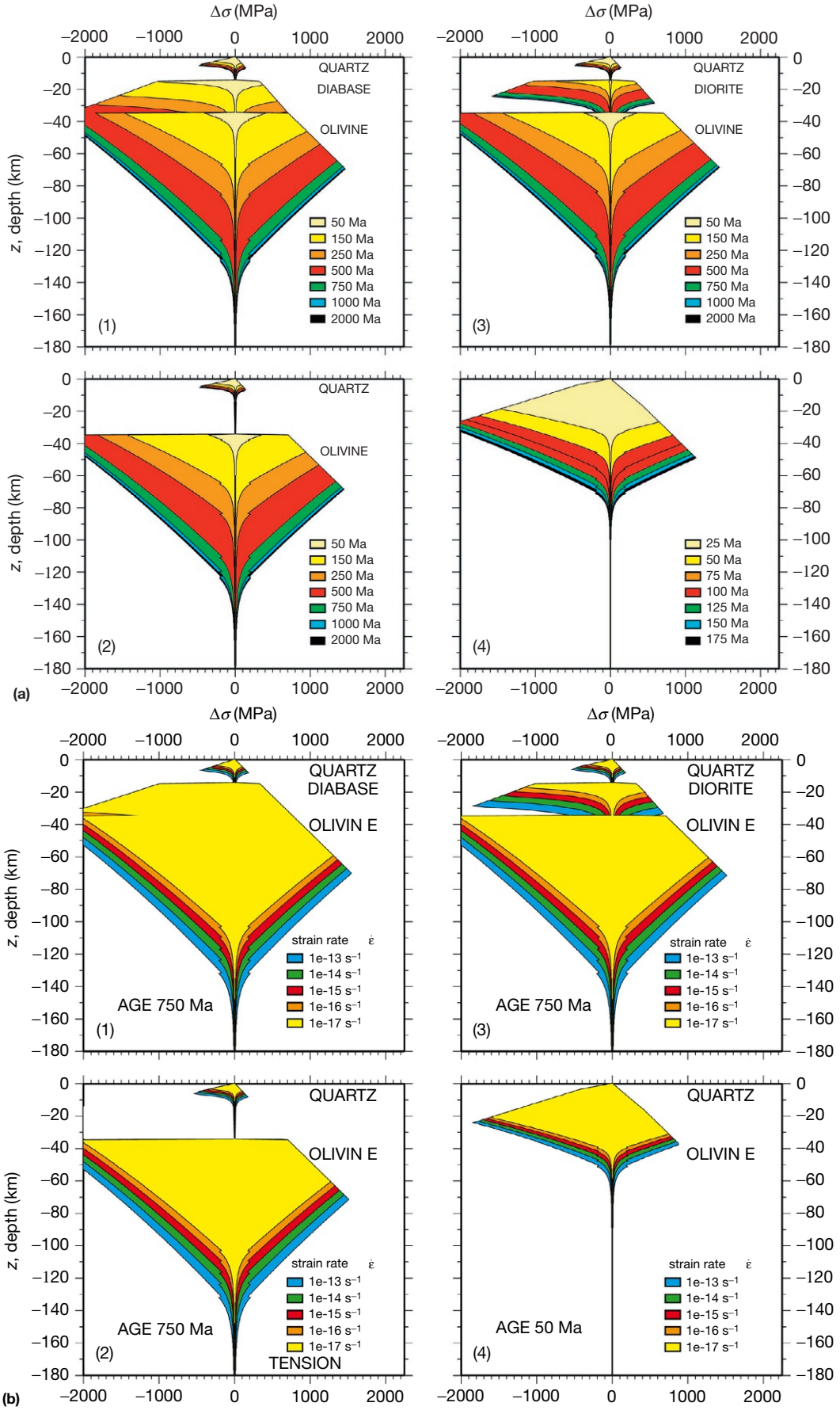

Figure 9 (a) Continental YSE as a function of thermotectonic age and crustal composition (reproduced from Burov EB and Diament M (1995) The effective elastic thickness (T_e) of continental lithosphere: What does it really mean? *Journal of Geophysical Research* 100: 3895–3904). Equilibrium thermal thickness 250 km. Upper crust is controlled by quartz rheology, and mantle lithosphere is controlled by dry olivine rheology. Cases 1, 2, and 3 – rheological envelopes for different lower crustal compositions: diabase, quart-diorite, and quartz, respectively. For comparison, oceanic YSE case (4) is shown in right bottom corner (thermal thickness 150 km). (b) Continental YSEs as function of the background strain rate and crustal composition (see also (a)).

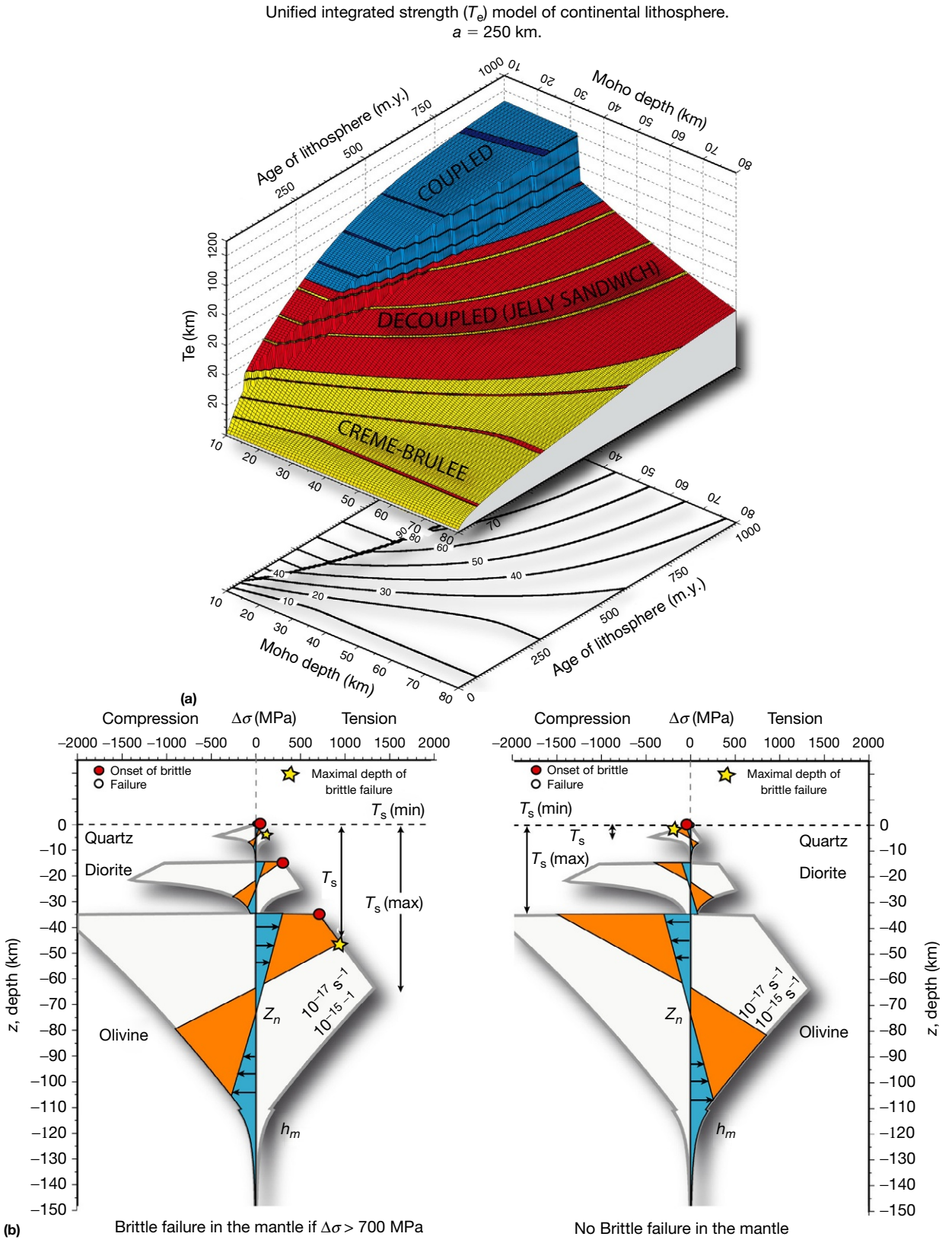

Figure 10 (a) Unified model of flexural strength of lithosphere, computed using equations of **Appendixes A** and **B**, for dry quartz upper crust, quartz-diorite lower crust, and dry olivine mantle (**Tables 3–4**). Equilibrium thermal thickness, $a = 250$ km (**Appendix B**). (b) Stress distribution within continental YSE for concave upward and concave downward flexure (see text).

(Continued)

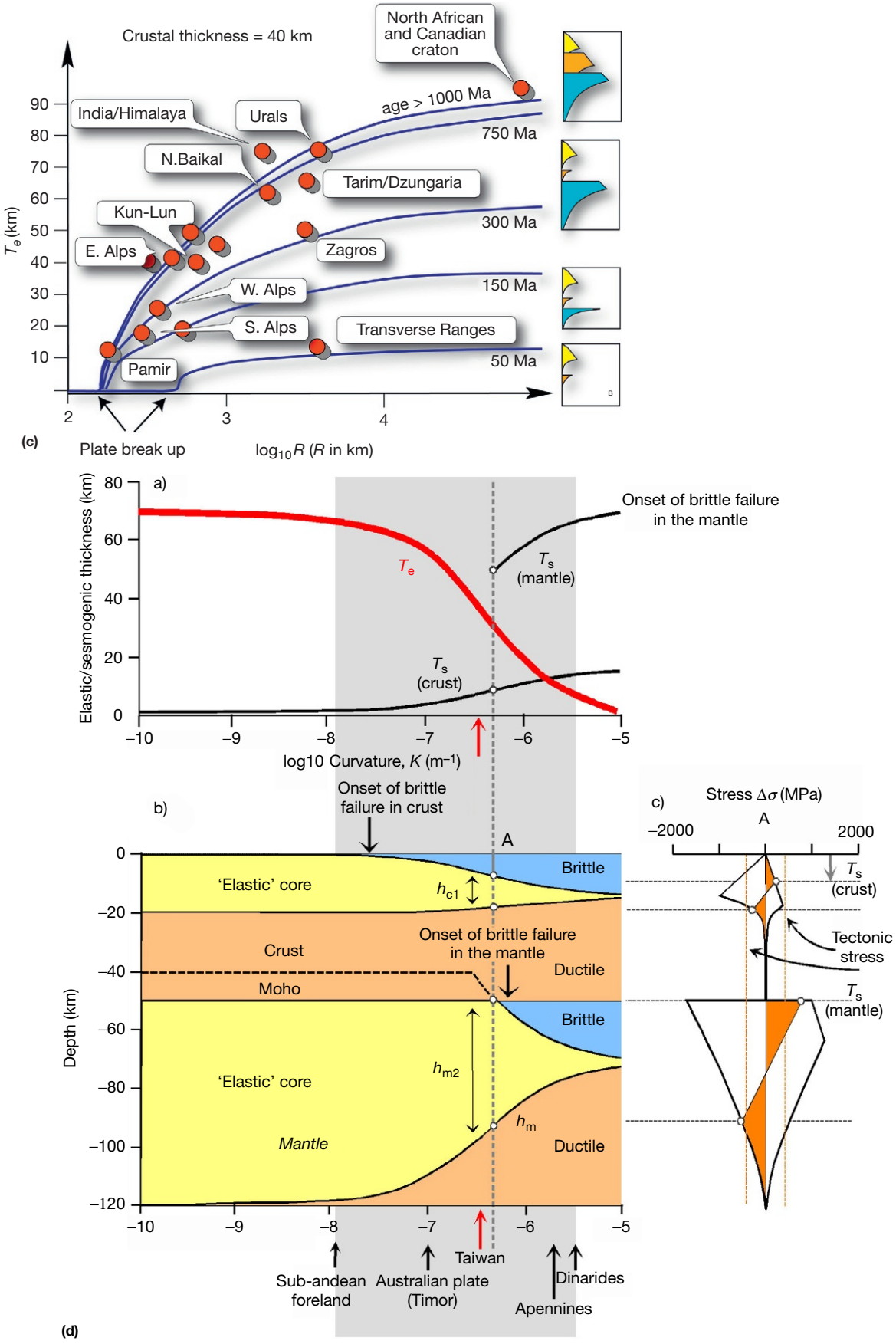

Figure 10 (Continued) (c) Predicted dependence of continental T_e on age and curvature of the lithosphere, computed for normal crustal thickness, T_c, of 40 km and compared with the data for continental plates with normal crustal thickness. Right: geometry of corresponding YSEs (same rheological parameters as in (a)). (d) Predicted relationships between the rheology structure, age, plate curvature K, T_e, and T_s for continental lithosphere with two-layer rheological structure. T_e and T_s as a function of curvature in a two-layer classical 'jelly sandwich' plate (strong upper crust, weak lower and intermediate crust, and strong mantle).

assuming 'dry' Byerlee's law. This is already close to the maximum likely value for tectonic boundary loads (e.g., Bott, 1993), suggesting that brittle failure and, hence, earthquakes in the mantle will be rare. Instead, seismicity will be limited to the uppermost part of the crust where rocks fail by brittle deformation, irrespective of the stress level. This limit does not apply, of course, to T_e. For curvatures up to $10^{-6}\,m^{-1}$, **Figure 10(d)** and **10(e)** shows that for the observed plate curvature range, T_e is always larger than T_s. Only for the highest curvatures (i.e., $K > 10^{-6}\,m^{-1}$) will $T_e < T_s$. Of course, stress estimates shown in **Figure 10(d)** and **10(e)** depend on the assumed rheology. In particular, frictional strength at depth may be several times smaller than the prediction of Byerlee's law in case of pore fluid pressure (reduction by a factor of 5; **Figure 1**). Yet the presence of fluids will also reduce the ductile rock strength by the same or higher amount. As a result, the rock may choose to flow rather than to break; T_e will be reduced and plate curvature would be higher for the same load. It thus appears difficult to favor mantle 'seismicity' by simple brittle strength reduction due to the presence of fluids.

Finally, it should be noted that the dependence of T_e and T_s on the state of stress and plate curvature may result in strong lateral variations of T_e and T_s at both local and regional scales (**Figure 10(d)–10(g)**). The computations (Burov and Diament, 1995) demonstrate that surface loads (elevated topography or sedimentary loading and plate boundary forces) may result in strong lateral variations of both T_e and T_s. Surface or subsurface loading may decrease T_e (and increase T_s) by 30–50% (or more in case of initially weak plates). In particular, the lithosphere beneath mountain ranges or large sedimentary basins (rifts and forelands) may be significantly weakened resulting in more 'local' compensation of the surface loads. In subduction/collision zones, localized weakening due to plate bending under boundary forces may result in steeper slab dip

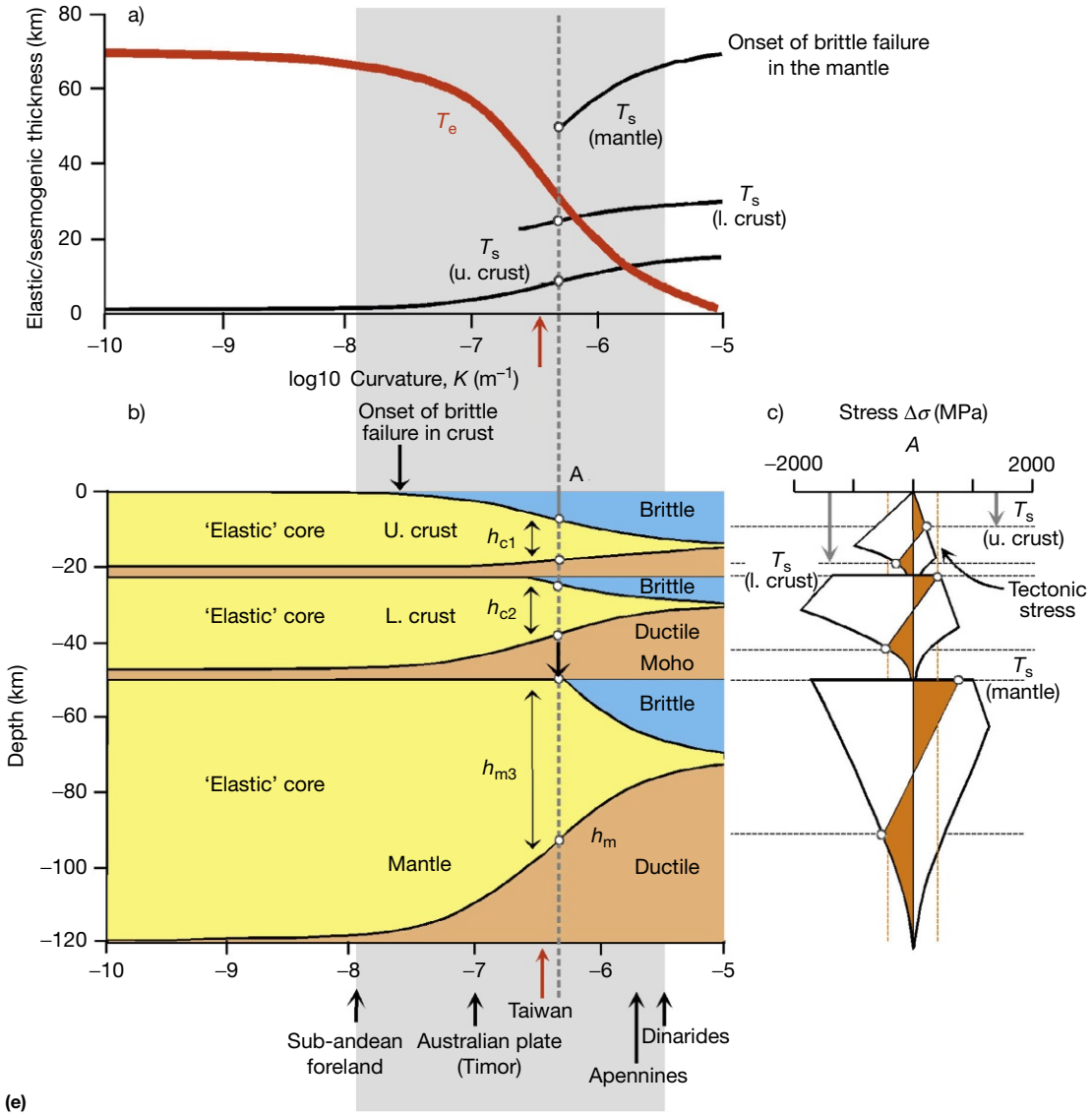

Figure 10 (Continued) (e) Predicted relationships between the rheology structure, age, plate curvature K, T_e, and T_s for continental lithosphere in a three-layer continental plate (strong upper crust, strong lower or intermediate crust, and strong mantle).

(Continued)

and accelerated slab breakoff. In case of weakened lithosphere (e.g., abnormal heat flux and metamorphic reactions leading to strength drop), loading may result in total failure of the plate (local isostasy). Similar results are expected in active rift zones and metamorphic core complexes (e.g., Buck, 2007; Burov and Cloetingh, 2007).

6.03.6.3 Seismicity, T_s, BDT, and Long-Term Strength

The considerations of the previous section (see also Figure 10) suggest a dual role for the continental subcrustal mantle. In regions of low curvature, the mantle may be devoid of earthquakes but largely involved in the support of long-term flexural-type loads. In regions of high curvature, however, the mantle may be seismic, but the support of long-term loads is confined mainly to the crust rather than the mantle. Despite differences in their timescales, we may therefore be able to use the presence or absence of mantle earthquakes, at least in the plate interiors, as a proxy for whether it is the crust or mantle that is mainly involved in the support of long-term loads. This discussion should be considered in strict relation to the common, but probably incorrect (at least for great depths), assumption that prefractured 'Byerlee's' rock provides a more favorable background for activation of unstable catastrophic sliding than geologically ductile rock. At seismic timescales, all rock down to lower mantle behaves as an elastic or elasto-plastic media. Any zones of mechanical weakness (fractures or ductile shear zones) may thus serve for nucleation of short-term brittle failure.

Figure 11 summarizes the data and the expected the relationship between T_s and curvature for thermal ages of the continental lithosphere of 50, 500, and 1000 Ma. The circles show the maximum observed curvatures and, hence, the maximum likely value of T_s. In the decoupled case, T_s does not exceed 15 km, which corresponds well with observations. Moreover, as for the oceans, T_e and T_s are more likely to anti-correlate than correlate. T_e always exceeds T_s, irrespective of thermal age and curvature. High T_e values limit the amount of curvature due to flexure, and hence, the ratio of T_e to T_s increases with thermal age (and strength). The coupled case has the potential to yield higher values of T_s, but as T_e

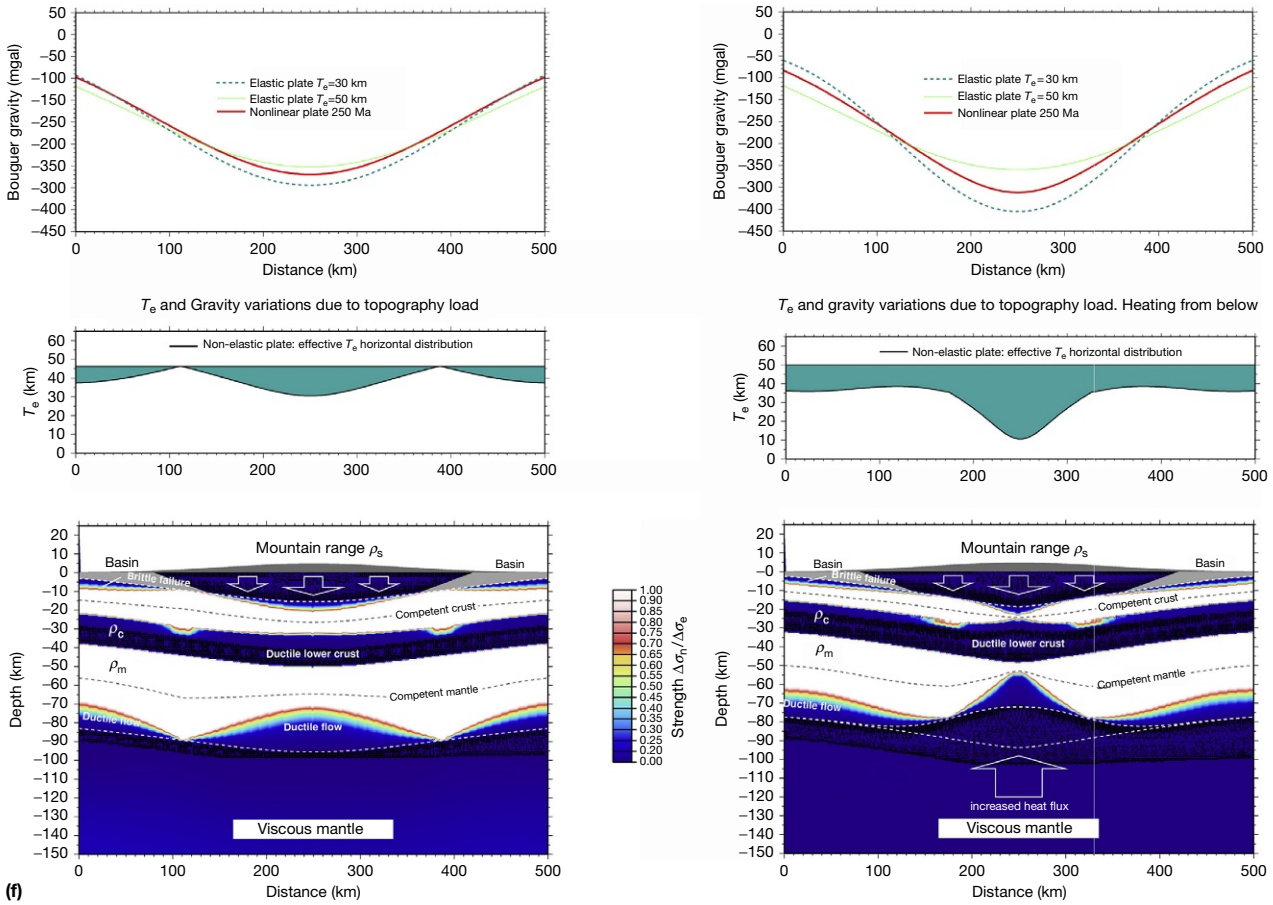

Figure 10 (Continued) (f) Computed lateral strength (T_e) variations in continental lithosphere (strength envelope from (d)) caused by surface loading (i.e., Gaussian mountain range 3 km height, Gaussian width 200 km) (reproduced from Burov EB and Diament M (1995) The effective elastic thickness (T_e) of continental lithosphere: What does it really mean? *Journal of Geophysical Research* 100: 3895–3904). The color code corresponds to the ratio of the elastic stress for given amount of strain (elastic prediction) to the real stress value (inelastic correction). The zones characterized by stress ratio 1 are effectively elastic. The zones with smaller ratio correspond to inelastic deformation (weakening), brittle or ductile.

increases, then curvature decreases. The ratio of T_e to T_s is therefore maintained. Interestingly, it is the oceanic lithosphere (**Figure 11**) that is associated with the highest values of T_s. The reason for this is that the oceanic crust is much thinner than its continental counterpart, and Byerlee's friction law extends, uninterrupted, without the assistance of weak zones such as ductile lower crust in continents, from the uppermost part of the crust to the underlying mantle.

As discussed in **Section 112.5.5**, intraplate seismicity in continental areas is mainly located in the upper crust, while it is often suggested that the lower crust or intermediate crust is too weak to deform in the brittle regime (e.g., Chen and Molnar, 1983). As also mentioned in **Section 112.5.5**, a number of studies have also indicated the presence of seismic events in the lower crust as well as in the upper mantle (Cloetingh and Banda, 1992; Deverchere et al., 1991, 1993; Doser and Yarwood, 1994; Monsalve et al., 2006; Shudofsky, 1985; Shudofsky et al., 1987). Even if sub-Moho seismicity exists, it is clear that mantle microearthquakes are rare and do not form a distinct population (e.g., Aldersons et al., 2003). There is evidence from seismic reflection profiles that the continental Moho is sometimes offset by faults (Burov and Molnar, 1998; Cloetingh and Banda, 1992; Klemperer and Hobbs, 1991), although the significance of this observation is not entirely clear.

Even though experiments suggest that brittle shear instabilities are unlikely at pressures corresponding to continental Moho depths (40 km) while mantle peridotites are prone to aseismic ductile shear banding due to specific localizing mechanisms such as GBS creep (**Section 112.5.5**), there is also an alternative explanation for little or absent mantle seismicity (Jackson, 2002). This author suggests that the mantle has a very low short-term ductile strength and thus deforms in ductile regime at seismic timescale. This, we believe, is a confusion. Even if one admits that the mantle is fluid at geologic timescale, it does not mean that it may flow at seismic timescale. Extrapolation of rock mechanics data (**Figure 3**) suggests that at seismic timescale, ductile creep cannot be activated within the lithospheric temperature–stress range: one needs temperatures higher than 1500–2000°C or stresses > 1 GPa (Burov and Watts, 2006; Watts and Burov, 2003). On the other hand, there is little doubt that mantle is stronger than the asthenosphere, which has a viscosity of $\sim 5 \times 10^{19}$ Pa s at a strain rate of 10^{-15} s^{-1}. Recomputing flow stress for seismic timescale (eqn

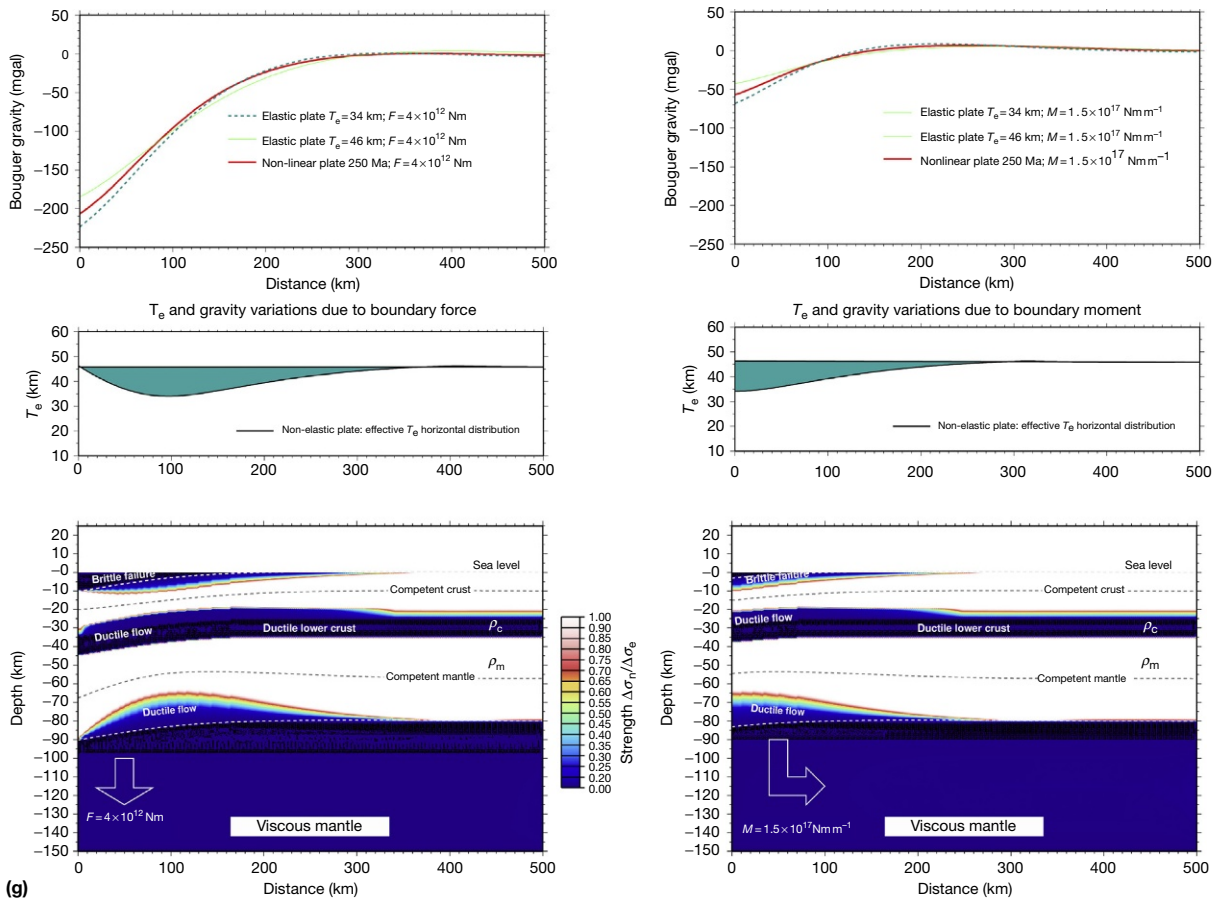

Figure 10 (Continued) (g) Computed lateral strength (T_e) variations in continental lithosphere, loaded on the end (cutting force F, right, or flexural moment M, left (Burov and Diament, 1995)). The color code corresponds to the ratio of the elastic stress for given amount of strain (elastic prediction) to the real stress value (inelastic correction). The zones characterized by stress ratio 1 are effectively elastic. The zones with smaller ratio correspond to inelastic deformation (weakening), brittle or ductile. Note the absence of brittle failure in the uppermost mantle (compare with **Figure 5(f)** for the oceanic lithosphere).

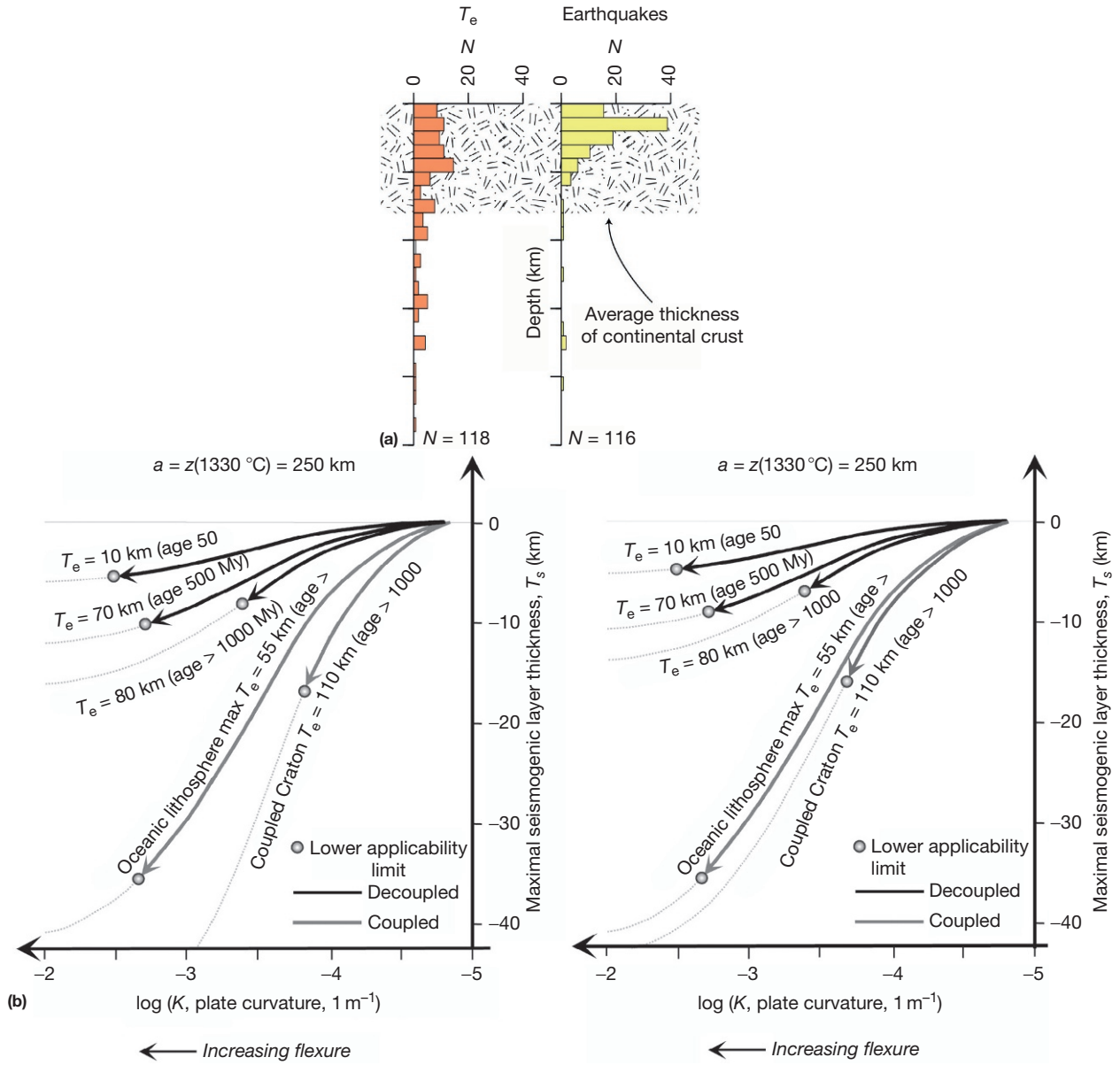

Figure 11 (a) Compilation of data on continental T_s compared with the data on T_e (reproduced from Watts AB and Burov E (2003) Lithospheric strength and its relationship to the elastic and seismogenic layer thickness. *Earth and Planet Science Letters* 213: 113–131). (b) Relationships between the plate curvature, T_e, and T_s for different ages of the lithosphere. (left) Assumption of equilibrium thermal thickness of the lithosphere, $a = 250$ km. (right) $a = 125$ km. Black curves are for decoupled rheology, while gray curves are for coupled rheology.

[13], strain rates of 10^{1}–10^{4} s^{-1}) shows that even for such a 'weak' rheology, the yield stress must be on the order of 10–100 GPa, that is, 10 to 1000 times higher than any imaginable tectonic stress. This proves that in no case, the absence of seismicity cannot be regarded as a sign of rheological weakness. Finally, it should be kept in mind that seismicity is related to frictional release of elastic strain accumulated during the interseismic period (Scholz, 1990). Hence, if one assumes that mantle is so weak that it prevents deep brittle seismicity, then it should be characterized by Maxwell relaxation times on the timescale of postseismic rebound (from several seconds to 1 month). This would lead to an inconsistent conclusion that the lithosphere mantle is 3 orders of magnitude weaker ($\mu = 10^{16}$ Pa s) than the asthenosphere, where relaxation times are 100–1000 years.

The assumption of weak mantle rheology clearly does not hold in regions where T_e is greater than crustal thickness ($T_e \sim 40$–110 km), ductile, instead of brittle, shear strain localization in the mantle (**Section 112.5.5**), and/or insufficient level of intraplate stress compared to high brittle strength resulting from strong confining pressure at Moho depth (Scholz, 1990). According to Byerlee's law, the brittle rock strength, σ_b, scales as lithostatic pressure or $\sigma_b \approx 0.6\rho gz$–$0.85\rho gz$. The level of intraplate stress is limited to several hundreds of MPa. For a stress level of 500 MPa, maximum seismic depth is 15 km. For exceptionally high stress levels of

1 GPa, this depth extends to 30 km, which is still above normal Moho. In the case of weak lower crust, transition of deviatoric stresses between crust and mantle is attenuated. Then, the mantle stress level is reduced, specifically in case of bending. **Figure 10** shows, for example, that bending stresses may exceed ductile limits in the lower crust inducing flow and decoupling even in initially coupled system. The horizontal far-field stresses that are detected, for example, in Europe (see Müller et al., 1992), may also result in crust–mantle decoupling. The vertical gradient of bending stress can be calculated from the observed radius of plate flexure. Therefore, it is possible to predict the conditions for brittle crustal or mantle seismicity from direct observations of flexure (Burov and Diament, 1992; Cloetingh and Burov, 1996).

The rare cases of lower crustal or sub-Moho mantle intraplate seismicity can be roughly classified as follows:

1. Zones of more or less homogeneous lower crustal seismicity (e.g., Albert rift, East Africa (Doser and Yarwood, 1994; Morley, 1989; Seno and Seito, 1994; Shudofsky, 1985; Shudofsky et al., 1987; Seno and Seito, 1994)).
2. Zones of localized seismicity, generally along deep faults (Baikal rift (Deverchere et al., 1991), Rhine graben (Brun and Gutscher, 1992; Brun et al., 1991; Fuchs et al., 1987)).

Cases of deep seismicity are more frequent in extensional settings and more rare in compressional settings. This confirms once again the idea that depth of seismicity is related to intraplate stress level. Indeed, the level of tectonic stresses is limited by available plate driving forces and by rock strength. One needs two to three times higher stress for brittle failure in compression than in tension (**Figure 1**), with or without fluid pressure. Under homogeneous compression, brittle rock strength, and thus stress needed to break the rock, may increase by a factor of 2, whereas under extension, it may be reduced by a factor 2 (Petrini and Podladchikov, 2000; **Figure 1**), with or without fluid pressure. Under homogeneous compression, brittle rock strength, and thus stress needed to break the rock, may increase by a factor of 2, whereas under extension, it may be reduced by a factor 2 (Petrini and Podladchikov, 2000; **Figure 1**). Consequently, for the same intraplate stress level, maximum seismic depth is two to five times deeper for tension than for compression.

The differentiation between zones of distributed and localized seismicity can be related to various conditions associated with seismogenic stress release:

a. A more 'basic' composition (Cloetingh and Banda, 1992; Stephenson and Cloetingh, 1991). In the areas where the lower crust has low temperature of creep activation (diabase, granulites, diorite, etc.), it may favor distributed cracking at depths corresponding to 300–400 °C (20–35 km). There may be also instabilities caused by compositional differences in the lower crust (e.g., Sibson, 1980).
b. Variation of unstable-to-stable frictional slip on deeply penetrating faults (Tse and Rice, 1986). The BDT refers to a bulk rheological property, while earthquakes are associated with frictional instabilities. Localized strain rate acceleration along the faults may keep material brittle even at Moho depths (40–50 km). Deep mantle-penetrating faults are suspected, for example, in the northern Baikal rift or in Ferghana basin (Burov and Molnar, 1998; Deverchere et al., 1993)
c. Nonbrittle metastable mechanisms of seismogenic stress release. This may be related, for example, to ductile shear banding potentially associated with unstable phase changes and thermal runaway, reorientation of crystalline grids, and a few other mechanisms, which are subject of intensive discussions (e.g., Govers et al., 1992; Green, 2007; John et al., 2009; Kirby et al., 1991). The inapplicability of Byerlee's law at depths exceeding 40–50 km was outlined in a number studies (e.g., Goetze and Evans, 1979; Kirby et al., 1991).

6.03.6.4 Physical Considerations Beyond the Observations of Flexure, Gravity Potential Theory, Intraplate Stresses

Simple physical considerations can be used to estimate minimal strength of the lithospheric plates needed to support surface topography and tectonic loads or to deform in accordance with the observed deformation styles. The tectonic forces are limited by the energy of plate driving motions and by lithospheric strength. The ratio of surface topography loads to horizontal tectonic forces (Argand number (Ar)) indicates whether a mountain range is mechanically stable or it collapses under its own weight. The maximum short-term height, and thus weight of mountains, is limited by gravity forces and by brittle strength of surface rocks. The long-term height, and the amplitude of crustal roots, also depends on the long-term strength of the supporting crust and mantle. Based on these considerations, a number of authors (e.g., Artyushkov, 1973; Dahlen, 1981; England and Houseman, 1989; Fleitout and Froidevaux, 1983) have developed conceptually elegant models allowing estimates of the minimal average stress levels in the lithosphere. This approach is based on computation of intraplate gravity-driven stresses caused by horizontal variations in plate thickness and by density contrasts $\Delta\rho$. Isostatically compensated topography creates lateral pressure and potential energy differences that have to be balanced by horizontal tectonic stresses (σ_{xx}) to keep the topography at surface:

$$\int_0^{h_m} \Delta\rho g y \mathrm{d}y = \int_0^{h_m} \sigma_{xx} \mathrm{d}y = B_{\min} \qquad [41]$$

This allows us to put lower bounds on the integrated plate strength $B_{\min}$. It was found that gravity-driven forces, and thus counterbalancing tectonic forces F and $B_{\min}$, should vary from 10^{12} to 10^{13} N per meter (i.e., per unit length in out-of-plane direction). Depending on plate thickness, this yields average intraplate stresses σ_{xx} of 10–100 MPa, on the order of values (yet smaller) obtained by Cloetingh and Wortel (1986) from dynamic plate modeling.

6.03.6.5 Gravitational Stability Analysis: Rayleigh–Taylor Instabilities or Survival of Cratons, Continental Margins, and Mountain Roots

The crème brûlée and the alternative jelly sandwich rheology models imply fundamental differences in the mechanical properties of mantle lithosphere. One can explore the stability of mantle lithosphere by posing the question, 'What do the different rheological models imply about the persistence of topography for long periods of geologic time?' (Burov and Watts, 2006).

The most stable continental lithosphere units are cratons. Their stability is favored by the presumed positive buoyancy of the depleted cratonic mantle and, as can be suggested, by its high integrated strength resulting from a cold thermal structure and mantle dehydration (resulting in dry olivine rheology). The mean heat flow in Archean cratons is ~40 mW m^{-2}, which increases to ~60 mW m^{-2} in flanking Phanerozoic orogenic belts (Jaupart and Mareschal, 1999). As Pinet et al. (1991) had shown, a significant part of this heat flow is derived from radiogenic sources in the crust. Therefore, temperatures at the Moho are relatively low (~400–600 °C). The mantle must therefore maintain a fixed, relatively high viscosity that prevents convective heat advection to the Moho. Otherwise, surface heat flow would increase to >150 mW m^{-2}, which would be the case in an actively extending rift (e.g., *Sclater et al.*, 1980). Since heat flow this high is not observed in cratons and orogens, then a thick, cool, stable mantle layer should remain that prevents direct contact between the crustal part of the lithosphere and the convective upper mantle.

The positive or neutral buoyancy of Mg-rich depleted cratonic mantle is largely accepted, but not well quantified, because most data come from mantle xenoliths, whose representativeness for the bulk mantle lithosphere is discussible (e.g., Artemieva, 2009a,b), and also because these data are not unambiguous (i.e., there are cases when xenoliths predict negative buoyancy for composite depleted mantle (Watremez et al., 2013)). The second factor of craton stability, the presumably high integrated strength of their mantle, is confirmed from flexural studies (e.g., Watts, 2001). Yet, most commonly used stagnant lid stability models based on viscous rheology fail to explain long-term thermal survival of cratons. Recently, Beuchert et al. (2010) had shown that accounting for realistically high temperature-dependent viscosity ratio in the cratonic mantle can provide conditions for thermal craton stability for billions of years. Yet, it should be noted that the problem of survival of cratons also refers to their capability to support tectonic forces and significant buried loads such as inherited crustal heterogeneities over long time spans (e.g., Burov et al., 1998). Thermomechanical models accounting for crustal heterogeneities indicate high integrated strength of the cratonic mantle (Burov et al., 1998; Francois et al., 2013) and confirm previously obtained T_e data (e.g., Watts, 2001).

Young fertile oceanic mantle lithosphere is expected to have a negative buoyancy starting from an age of 30 to 50 My. The negative buoyancy of the mantle lithosphere at subduction zones is widely considered as a major driving force in plate tectonics. The evidence that, in contrast to depleted cratonic mantle, normal, undepleted continental mantle is in average 20 kg m^{-3} denser than the underlying asthenosphere and is gravitationally unstable has been reviewed by Stacey (1992), among others. This instability is commonly accepted for Phanerozoic and younger lithosphere. Irrespective, volumetric seismic velocities, which are generally considered a proxy for density, are systematically higher in the lithospheric mantle than in the asthenosphere. Depending on its viscosity, the undepleted mantle lithosphere therefore has the potential to sink as the result of Rayleigh–Taylor (RT) instability (e.g., Buck and Toksöz, 1983; Houseman et al., 1981).

One can estimate the instability growth time (i.e., the time it takes for a mantle root to be amplified by e times its initial value) using Chandrasekhar's (1961) formulation. In this formulation, a mantle Newtonian fluid layer of viscosity, μ, density, ρ_m, and thickness, d, is placed on top of a less dense fluid asthenospheric layer of density ρ_a and the same thickness. (This formulation differs from that of Conrad and Molnar (1997) who used a fluid layer that is placed on top of a viscous half-space. However, both formulations are valid for instability amplitudes $< d$.) The most rapidly growing instability wavelength, λ, is Ad where $2.5 < A < 3.0$ and the corresponding growth time, t_{min}, is $B\mu[(\rho_m - \rho_a)gd]^{-1}$ where $6.2 < B < 13.0$ and g is average gravity. One can evaluate t_{min} for a particular μ by assuming $(\rho_m - \rho_a) = 20$ kg m^{-3} and $80 < d < 100$ km. If the continental mantle can support large stresses (>2 GPa) and has a high viscosity (10^{22}–10^{24} Pa s), as the jelly sandwich model implies, then t_{min} will be long (> 0.05–2 Ga), that is, comparable with age of cratons. If, on the other hand, the stresses are small (0–10 MPa) and the viscosity is low (10^{19}–10^{20} Pa s), as the crème brûlée model suggests, then it will be short (0.2–2.0 My).

The consequences of these growth times for the persistence of surface topographic features and their compensating roots or antiroots are profound. The long growth times implied by the jelly sandwich model imply that orogenic belts, for example, could persist for up to several tens of My and longer, while the crème brûlée model suggests collapse within a few My.

We have discussed earlier a constant viscosity and a large viscosity contrast between the lithosphere and asthenosphere. A temperature-dependent viscosity and power law rheology result in even shorter growth times than the ones derived here for constant viscosity (Conrad and Molnar, 1997; Molnar and Houseman, 2004). If either the viscosity contrast is small or a mantle root starts to detach, then eqn [1] in Weinberg and Podladchikov (1995) suggests that the entire system will begin to collapse at a vertical Stokes flow velocity of ~1 mm $year^{-1}$ for the jelly sandwich model and ~100–1000 mm $year^{-1}$ for the crème brûlée model (note that these flow velocities depend strongly on the characteristic wavelength of the instability, that is, width of the mantle root, which is assumed here to be λ). Therefore, our assumptions imply that a surface topographic feature such as an orogenic belt would disappear in less than 0.02–2 My for the crème brûlée model, whereas it could be supported for as long as 100 My–2 Gy for a jelly sandwich model.

A most straightforward way to discriminate between different thermorheological concepts for cratons is to test their implications for craton stability using forward thermomechanical models. Unlike conventional studies, which impose a rigid top as upper boundary condition, thus forcing zero topography, Francois et al. (2013) implemented free-surface boundary condition, which allows for analysis of stability of surface and Moho topography, in addition to that of the LAB. The possibility to track subtle variations in surface (>10 m) and Moho topography presents a prime feature of this approach. The second novelty for lithosphere stability analysis refers to account for inherited crustal heterogeneities that represent very substantial subsurface loads and hence play an essential role in the mechanical equilibrium of cratonized lithosphere. These models also implemented explicit viscous(ductile)–elastic–plastic(brittle) rheology laws in large-strain numerical formulation, instead of common viscous or

viscous–pseudoplastic rheologies (Lenardic et al., 2003) or viscoelastic rheologies (Beuchert et al., 2010) used for lithosphere stability analysis. Finally, a petrologically consistent density structure (computed using the reference thermodynamic code Perple_X) (see Appendix Supplementary Item D) has been used for full consistency with mineralogical data.

In all experiments, the initial 'model box' is 3000 km long and 600 km deep. The mechanical boundary conditions are as follows: (1) the upper surface is free (free stress and free slip condition in all directions), (2–3) constant horizontal velocity, v_x, at the lateral sides ($v_x - 0$ in most experiments), and (4) pliable hydrostatic Winkler basement (Burov et al., 1998). The experiments exploring the impact of a laterally heterogeneous crust in the absence of far-field tectonic forcing show large differences between the three thermorheological models (Figure 12). Surface topography is highly unstable for both the IM and CB rheologies (Figure 12) with differences in topographic heights on the order of 5000–8000 m (at 200 My, Figure 12), which are inconsistent with stratigraphic data for the Canadian and Australian cratons (see Francois et al., 2013 and references therein). In contrast, for the JS rheology, the differences in topographic height do not exceed 200 m (Figure 12) and remain within the observed range of topographic roughness. The Moho geometry also shows marked differences between all three models after 200 My. For the JS model, the initially prescribed 10 km Moho steps are well preserved. For the IM model, the Moho geometry is partly preserved but locally diverges strongly from the initial geometry. For the CB model, the initial steps are flattened to only 1–2 km after 200 My. The LAB boundary shows a similar trend and is increasingly unstable from the JS to IM and CB rheology. The CB model exhibits 40–80 km LAB undulations that progressively lead to small-scale convective instabilities and the removal of a large portion of the mantle lithosphere. For the IM and CB models, the mantle lithosphere is thinned in a number of places by a factor of 1.5–2 after 200 My. Given that the growth rate of viscous instabilities is an exponential function of time (Houseman et al., 1981), this indicates that 200 My constitutes the maximum half-life time span of a compositionally positively buoyant CB mantle (Figure 12). It is

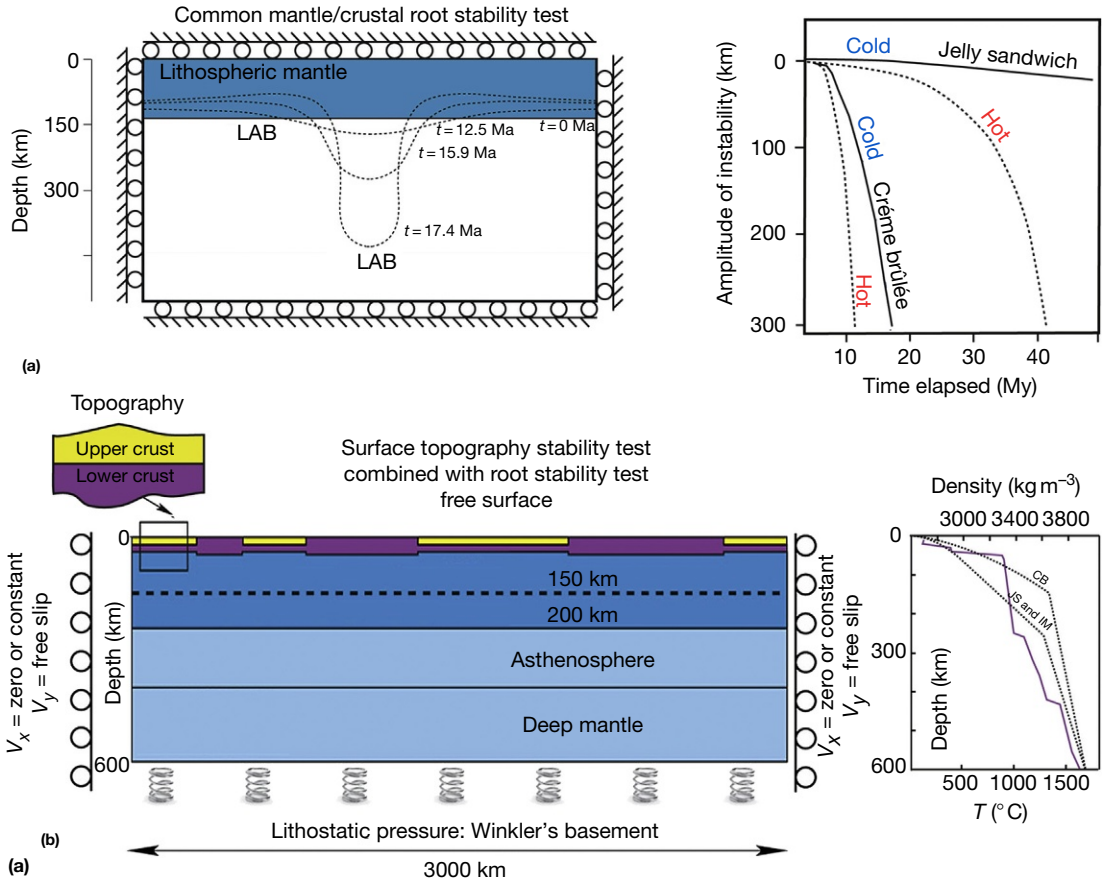

Figure 12 (a) (a – left) The conventional model for stability analysis of lithosphere (Rayleigh–Taylor instability) with negatively buoyant depleted mantle. LAB: lithosphere–asthenosphere boundary. (a – right) Typical model geometry. Predicted amplitudes of mantle root as a function of time for end-member rheological concepts (JS, 'jelly sandwich,' and CB, 'crème brûlée'). Amplitudes are computed for two end-member geotherms, 'cold' and 'hot' (see Burov and Watts, 2006). (b – left) The alternative surface topography stability model for a cratonic lithosphere with positively buoyant undepleted mantle (Francois et al., 2013). Compared with the conventional models, this model tests surface topography sensitivity to large lateral heterogeneities in crustal structure that are widespread in cratons. (b – right) Density and tested thermal structures ('hot' and 'cold' corresponding to contrasting thermal models of the lithosphere behind the 'CB' and 'JS' rheology (Watts and Burov, 2003). The density is computed in accordance with petrologic thermodynamic data on lithosphere and mantle composition.

(Continued)

noteworthy that the half-life time of negatively buoyant mantle is five to ten times shorter (Burov and Watts, 2006; Houseman et al., 1981), confirming the idea that compositional buoyancy is a crucial – yet not sufficient – controlling factor in the preservation of cratons (e.g., Burov and Watts, 2006).

The comparison between the models involving CB or JS rheology with a homogenous or heterogeneous crust shows that the strength of the mantle lithosphere is a major stabilizing factor for both surface topography and subsurface interfaces (i.e., Moho and LAB), while a strong crust alone is insufficient to keep topography stable over significant time spans. The experiments without far-field tectonic forces indicate that the buoyancy and strength of the strong mantle lithosphere are both necessary to allow for the long-term preservation of cratons. While the previous studies have already shown that lithospheric strength matters for cratonic stability, these experiments show that it is the subcrustal mantle lithosphere and not the thick cratonic crust that plays a major role in cratonic stability. It has been concluded (Francois et al., 2013) that dry olivine dislocation creep rheology is most appropriate for cratonized mantle lithosphere.

In addition to the analysis of craton stability, a number of authors (e.g., Burov and Molnar, 2008; Burov and Watts, 2006; Burov et al., 1998; Okaya et al., 1996; Willingshofer and Cloetingh, 2003) have made estimates of strength of normal (undepleted) lithosphere needed for support of long-term normal loads such as orogenic topography, crustal roots, or inherited heterogeneities and/or tectonic forces (**Figure 13(a)**). These estimates show that strong lithosphere mantle with at least 20–30 km thick mechanical core is needed for stability of crustal and topographic structures during characteristic life spans of geodynamic processes.

Figure 13(b) summarizes resultants of numerical experiments with normal orogenic loading exerted on lithosphere with undepleted mantle part. The surface load is represented

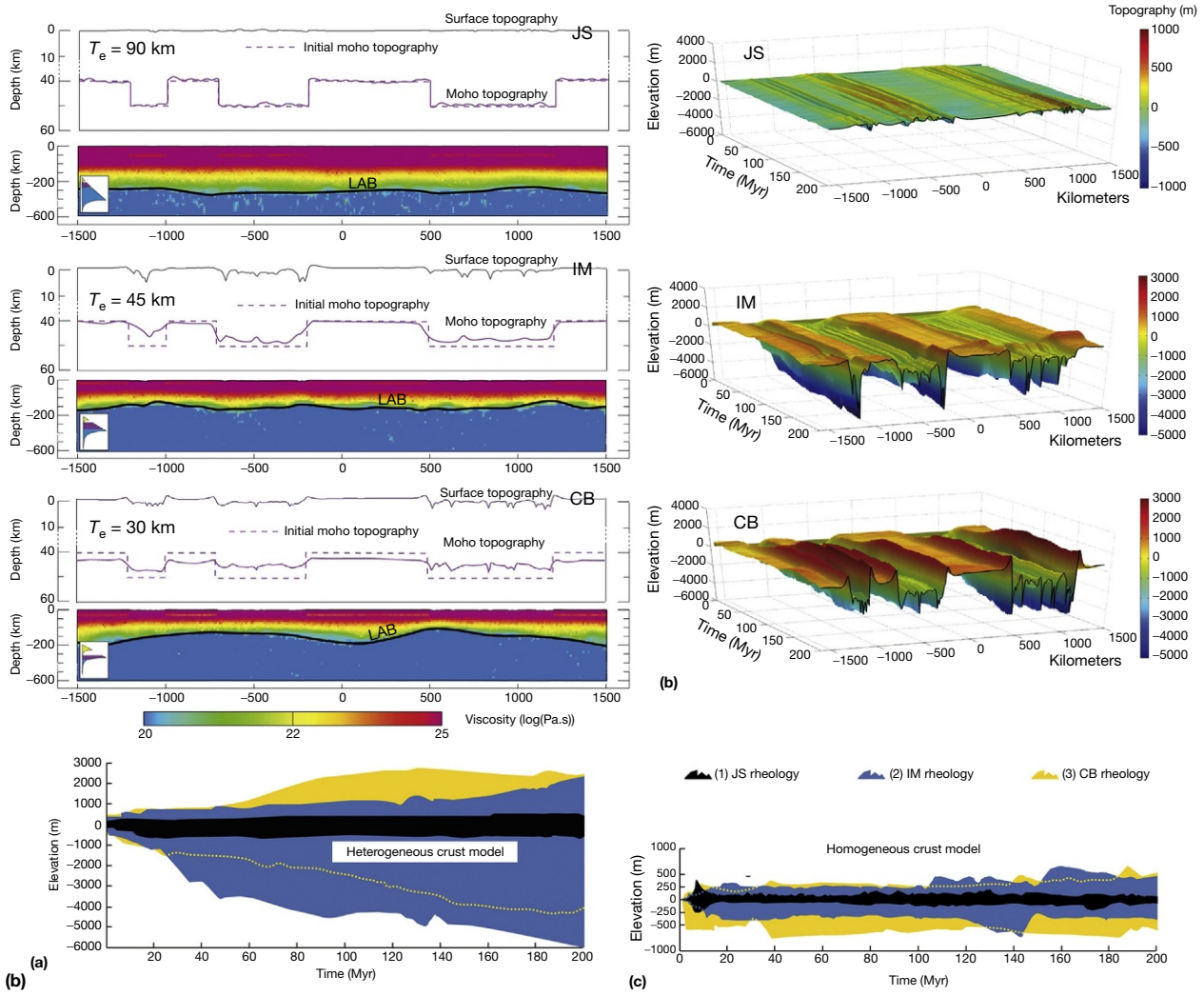

Figure 12 (Continued) (b) Numerical experiments on craton stability corresponding to the settings shown in (a). Top figure displays model setup. (a) Equivalent viscosity and surface and Moho topography evolution for three rheological assumptions: JS; CB, and intermediate case (IM). (b) Predicted surface topography evolution (note that in real cratons, surface topography undulations rarely exceed 100 m in the absence of strong external forcing. Hence, JS model is the most appropriate). (c) Average topography evolution as a function of time.

by a Gaussian-shaped mountain, 3 km high, 200 km wide, of uniform density (2650 kg m^{-3}). As can be seen, for the crème brûlée model, the crust and mantle already become gravitationally and mechanically unstable after 1.5–2.0 My. By 10 My (Figure 13(b) and 13(c)), the lithosphere disintegrates due to delamination of the sub-Moho mantle followed by its convective removal and replacement with hot asthenosphere. This leads to flattening of the Moho and tectonic erosion of the crustal root that initially supported the topography. The jelly sandwich model, on the other hand, is stable, and there are

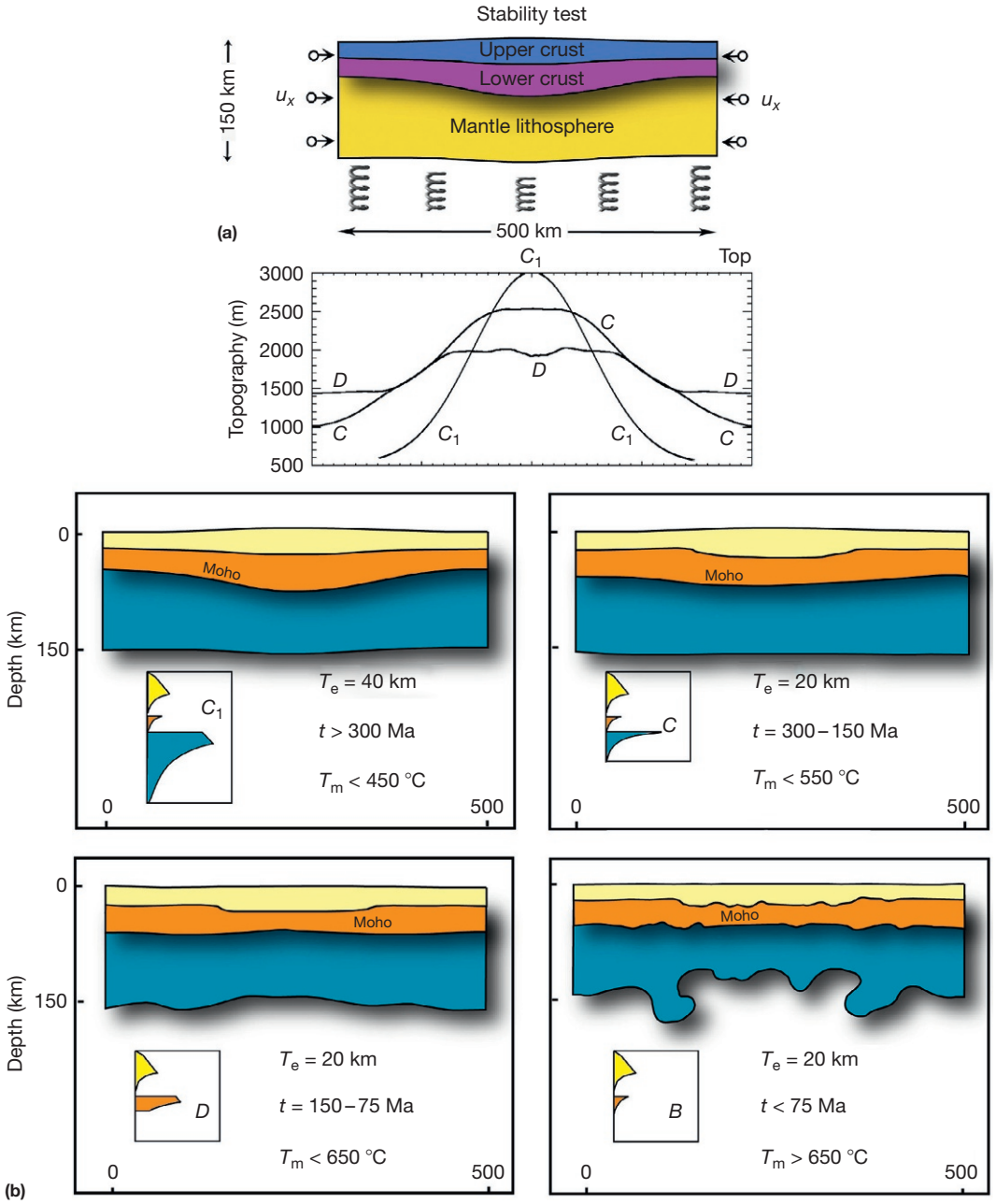

Figure 13 (a) Setup of the numerical thermomechanical model aimed to study gravitational mechanical stability of the lithosphere. Thermomechanical numerical tests of the stability of a mountain range are based on yield stress envelopes corresponding to the 'jelly sandwich' and 'crème brûlée' rheology models (Figure 4(a) and 4(d); see also Jackson (2002)). The thermal structure is equivalent to that of a 150-My-old plate. The numerical model is based on fully coupled thermomechanical large-strain viscous–elastic–plastic finite element code Paro(a)voz v.9 based on the FLAC algorithm (Cundall, 1989). This code allows for explicit testing of ductile, brittle, and elastic rheology laws. The models assume a free upper surface and a hydrostatic boundary condition at the lower surface (depicted by springs in the figure). The stability test was based on a mountain range of height 5 km and width 200 km that is initially in isostatic equilibrium with a zero elevation 36 km thick crust. The isostatic balance has been disturbed by applying a horizontal compression to the edges of the lithosphere at a rate of 5 mm $year^{-1}$. The displacements of both the surface topography and Moho were then tracked through time. (b) Crustal and mantle structure after 10 My has elapsed. Middle of the figure shows surface topography evolution for rheologies C_1, C (jelly sandwich) and D (crème brûlée), left, and effective shear stress distribution for the case C. Note rapid topography collapse in case D, whereas cases C_1 and C are stable.

(Continued)

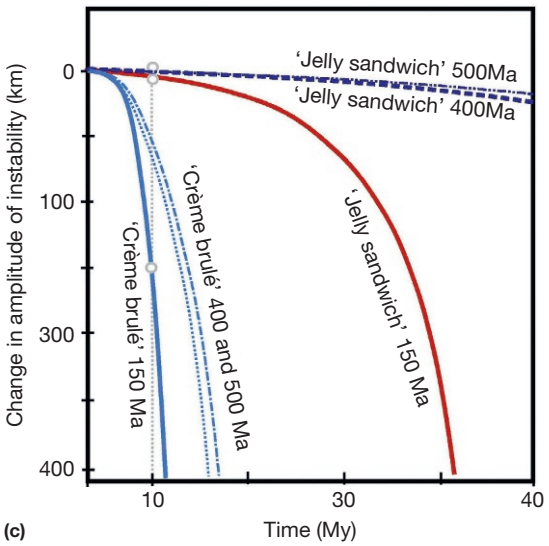

Figure 13 (Continued) (c) The amplitude of the mantle root instability as a function of time. The figure shows the evolution of a marker that was initially positioned at the base of the mechanical lithosphere (i.e., the depth where the strength = 10 MPa). This initial position is assumed to be at 0 km on the vertical plot axis. The sold and dashed lines show the instability for a weak, young (thermotectonic age = 150 My) and strong, old (thermotectonic age = 400- or 500-My-old) plates, respectively.

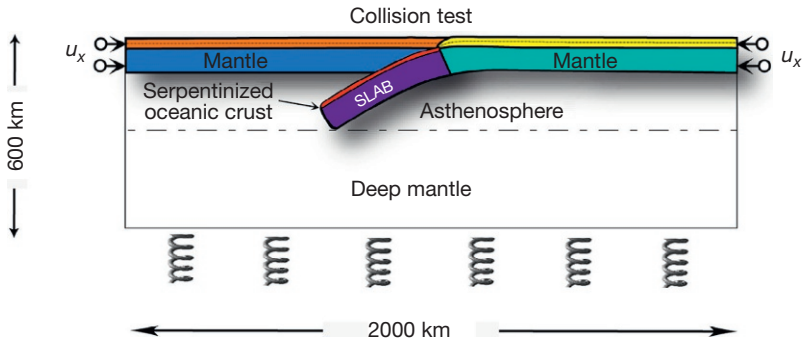

Figure 14 Setup of numerical thermomechanical models aimed to study rheological sensitivities of continental collision mechanisms. The collision test was based on a continent/continent collision initiated by subduction of a dense, downgoing, oceanic plate. Assumed normal thickness of the oceanic crust is 7 km, with serpentinized crust–mantle interface in the slab (Rupke et al., 2002). Total convergence rate of 60 mm year^{-1}. Rheological properties and other parameters are as given in **Tables 1–3**.

only few signs of crust and mantle instability for the duration of the experiments (10 My).

6.03.6.6 Dynamic Stability Analysis Using Direct Numerical Thermomechanical Models

In order to substantiate the growth times of convective instabilities derived from simple viscous models, and response of the lithosphere to horizontal shortening, Burov and Watts (2006) carried out sensitivity tests using a large-strain thermomechanical numerical model that allows the equations of mechanical equilibrium for a viscous–elastic–plastic plate to be solved for *any* prescribed rheological strength profile (e.g., Cundall, 1989; Poliakov et al., 1993). Similar models have been used by Toussaint et al. (2004), for example, to determine the role that the geotherm, lower crustal composition, and metamorphic changes in the subducting crust may play on the evolution of continental compressional zones. Burov and Watts (2006) ran separate series of tests (**Figure 14**) using rheological properties that matched cases with weak mantle rheology (crème brûlée; **Figure 4(d)**) and strong mantle rheology (jelly sandwich; **Figure 4(d)**), as well as some intermediate rheology profiles with weak or strong mantle. The goal of these experiments is to test what these and intermediate rheology models imply about the stability of mountain ranges and the structural styles that develop. The next sections show the results of stability tests and continental collision tests.

6.03.6.7 Resistance to Stable Deformation Under Compressional Tectonic Forces ('Simple Shear' Subduction versus 'Pure Shear' Collision)

Figure 15 shows the results of the collision tests for five various YSEs considered in Jackson (2002) and Mackwell et al. (1998) (see also **Figure 4(b)** and **4(d)**). **Figure 15(a)** shows a snapshot of the deformation after 300 km of shortening, which at

60 mm year^{-1} takes 5 My. The jelly sandwich models (three cases marked JS1, JS2, and JS3) are stable and subduction occurs by the underthrusting of a continental slab that, with or without the crust, maintains its overall shape. In addition, the predicted deformation style in the accretion prism appears to be highly realistic (**Figure 15(b)** and **15(c)**; Burov and Yamato, 2008). The crème brûlée models (two cases in the bottom, one strong and another with weak lower crust), on the other hand, are unstable. There is no subduction and convergence is taken up in the suture zone that separates the two plates. The crème brûlée model is therefore unable to explain those features of collisional systems that require subduction such as kyanite- and sillimanite-grade metamorphism. The jelly sandwich model, on the other hand, can explain not only the metamorphism and development of fold-and-thrust structures (**Figure 15(b)** and **15(c)**) but also some of the gross structural styles of collisional systems such as those associated with slab flattening (e.g., western North America; Humphreys et al., 2003), crustal doubling (e.g., Alps; Giese et al., 1982), and arc subduction (e.g., southern Tibet; Boutelier et al., 2003).

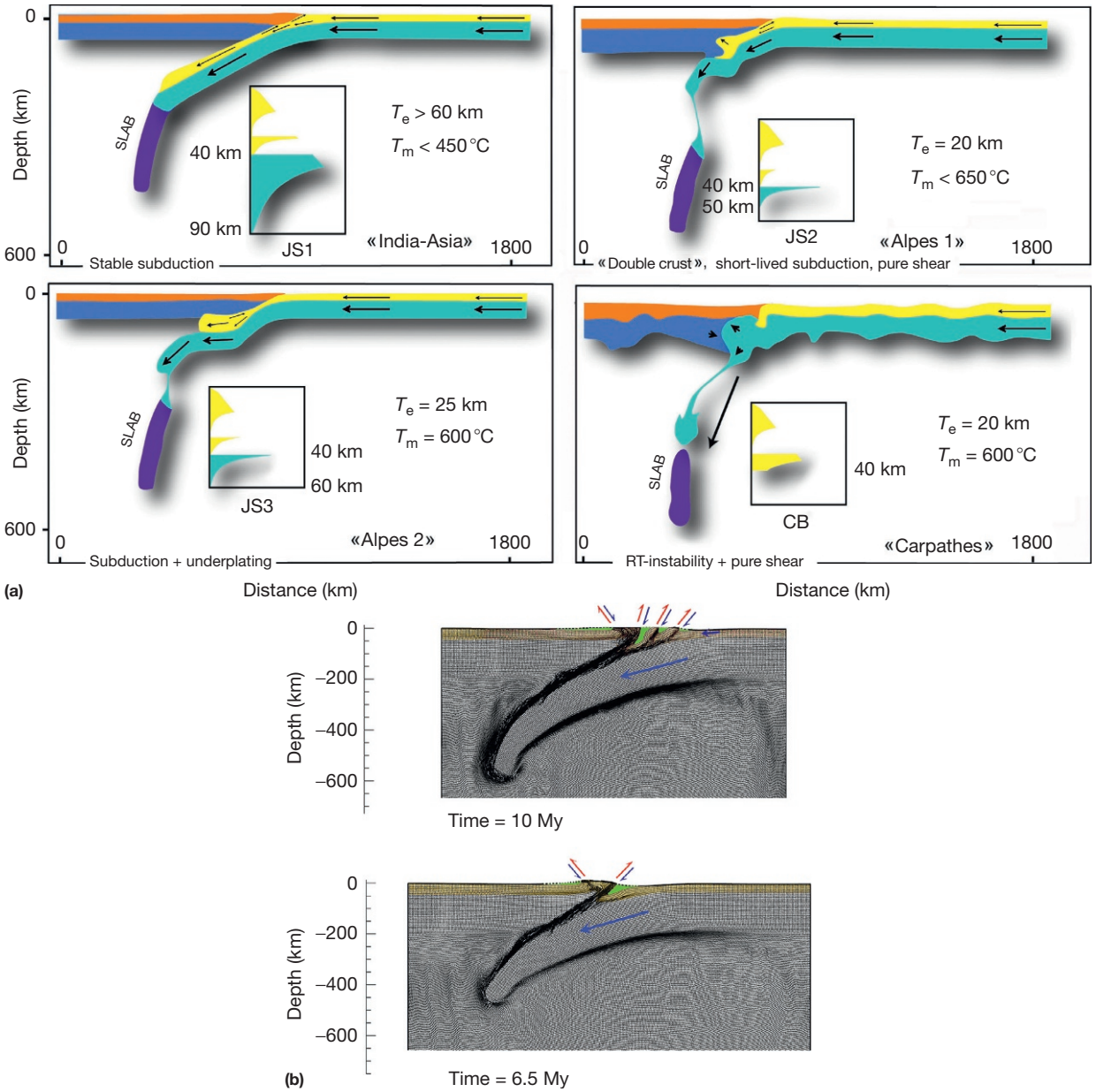

Figure 15 (a) Numerical tests of the stability of a continental collisional system using various failure envelopes. The figure shows a snapshot at 5 My of the structural styles that develop after 300 km of shortening. (b) Deformation of the passive marker grid highlighting multiple thrust-and-fold structures forming at different stages of continental subduction, for the experiment corresponding to the rheology profile 'C_1' from (a). Formation of such structures requires a relatively low strength of the near-Moho zone in the lower crust (possibility of crust–mantle decoupling) and a strong mantle as a sliding surface. This explains the eventual complexity of some of the resulting *P–T–t* paths. For the sake of space, the image is cut horizontally at 650 km depth (the bottom is not shown). Green color corresponds to sedimentary depots.

(Continued)

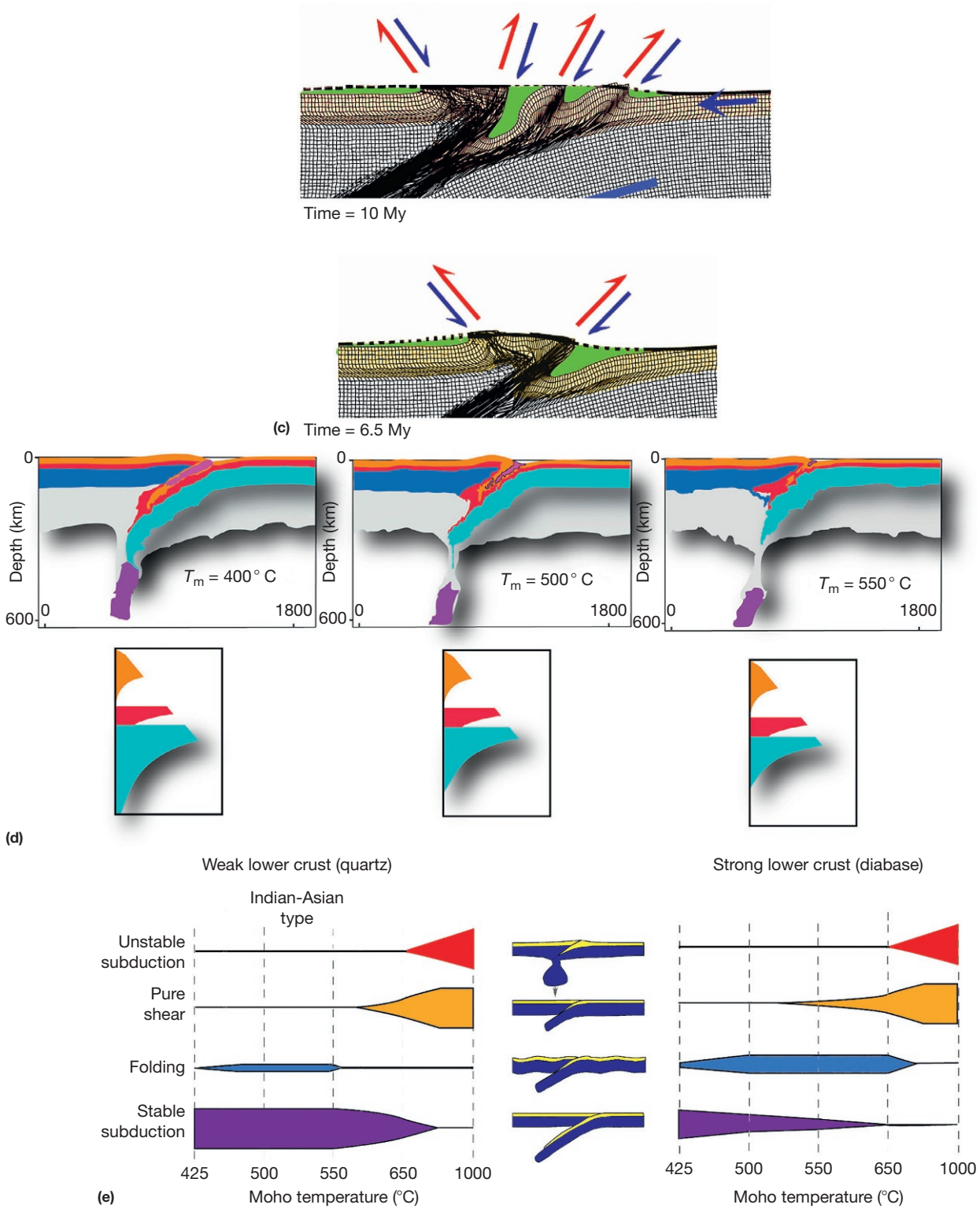

Figure 15 (Continued) (c) Zoom to the central part of (b) (Burov and Yamato, 2008). Purple color corresponds to the created sedimentary matter, orange color marks the upper crustal material, and red color marks the lower crustal material. The gradation of the scale bar is 50 km. (d) Experiments of (a) (profile C_1), (b), and (c) repeated for the case of strong dry diabase lower crust (quartz–diabase–dry olivine rheology) at 5.5 My. Moho temperatures are, respectively, 400, 500, and 550 °C. All other parameters and details are exactly the same as in the experiments from (a). Note important buckling of the plates imposed by the presence of strong diabase crust that results in mechanical coupling between the plates. Purple color corresponds to the sedimentary matter or to the oceanic slab, orange color marks the upper crustal material, and red color marks lower crustal material. Blue (dark or light) color marks mantle lithosphere; gray color marks the asthenosphere. (e) Comparison of shortening styles of continental lithosphere in case of weak lower crust (right) and strong dry diabase lower crust (left, det diabase rheology profile from **Figure 4(b)**). As also shown in (d), strong lower crust promotes large-scale folding instead of subduction. Similarly to (a), Moho temperature characterizes the geotherm and thus the rheology profile.

Slow-rate continental collision settings such as western Alpine orogeny present a particularly rich context for testing different rheological hypothesis. The continental convergence in the Alpine collision zone goes at rates that are in average smaller than 1 mm year^{-1} (Yamato et al., 2007) and have hardly exceeded 1–2 cm year^{-1} at the initial stages of the continent–continent phase of collision. Under these conditions, thermal diffusion strongly competes with thermal advection in the submerging part of the lithosphere. This significantly hampers the chances for stable subduction since high thermal Péclet numbers (ratio of advection rate to diffusion rate) are needed to keep subduction going (Burov et al., 2014a, b, c; Toussaint et al., 2004). In case when thermal diffusion contributes in heat balance as much as thermal advection, the slab heats up at a same rate as it goes down, its buoyancy increases, while its ductile strength decreases. Both factors prevent subduction, whose possibility becomes strongly dependent on subtle peculiarities of the rheological properties and structure of not only the continental mantle lithosphere but also its crust. Or petrology data on exhumation of ultrahigh-pressure metamorphic rocks that where initially buried to depths in excess of 110 km attest that at least at its initial stages, Alpine subduction did take place and continued for at least 5–10 My. Thermomechanical models (Burov et al., 2014a, b, c; Yamato et al., 2007) show that in this case, it is possible to constrain not only the rheological strength of mantle lithosphere but also some fine details of the rheological structure of the crust of both the subducting plate and overriding plate. **Figure 16** shows the results of several experiments where different crustal rheological profiles were tested with the goal to determine their compatibility with one-sided continental subduction. Despite the fact that all of the tested profiles are consistent in terms of rock mechanics data, only some of them are compatible with subduction scenario in the Alpine settings. It has been shown that the evolution of the Alpine orogeny can be best explained under the assumption of a three-layer decoupled rheological structure with quartz-dominated upper crust, quartz-diorite lower crust, and dry olivine mantle lithosphere that has a strong mechanical core with effective mechanical thickness of at least 30 km. When this structure is determined, parameterization of the appropriate rheology laws becomes rather straightforward.

6.03.6.8 Response to Large-Scale Compressional Instabilities (Folding)

Analysis of the subsidence and uplift history of sedimentary basins for a number of sites worldwide suggests that lithospheric folding is a primary response of the lithosphere to recently induced compressional stresses (e.g., Burov et al., 1993; Cloetingh et al., 1999; Cloetingh and Ziegler, 2007; **Table 5**; **Figure 7**). Despite the widely held view that folding occurs only over a short time interval, it was shown (Cloetingh et al., 1999; Gerbault et al., 1999) that it can persist over very long periods of time (>10 My) independently of presence of inhomogeneities such as crustal faults (**Figure 7(c)**). The numerical experiments on brittle–elastic–ductile folding implemented in these studies show that the formation of large-scale faults does not prevent folding. In turn, the localization and spacing of the faults are controlled by the wavelength of folding (faults tend to localize at the inflection points of folds). As suggested on the base of analytic considerations (eqn [37], section on the oceanic folding), and confirmed by the numerical experiments, the characteristic wavelengths, λ, of small-amplitude folding are proportional to 5–10× thickness of the competent layers and thus are indicative of the lithospheric strength:

$$\lambda < 5 - 10h \sim 5T_e - 10T_e \qquad [42]$$

These wavelengths are determined by the presence of young lithosphere in large parts of Europe or Central Asia or by that of old lithosphere in the Canadian or Australian craton, as well as by the geometries of the sediment bodies acting as a load on the lithosphere in basins. The proximity of some of these sites to the areas of active tectonic compression suggests that the tectonically induced horizontal stresses are responsible for the large-scale warping of the continental lithosphere. The persistence of periodical undulations in Central Australia (700 Ma since onset of folding) or in the Paris Basin (60 Ma) long after the end of the initial tectonic compression requires a strong rheology compatible with the effective elastic thickness values of about 100 km in the first case and 50–60 km in the second case (Cloetingh and Burov, 2010; Cloetingh et al., 1999). **Figure 7(b)** and **Table 5** show recent compilation of the observed wavelength of continental folding (Cloetingh et al., 1999) compared to the predictions of analytic models (e.g., Burov et al., 1993). In continental lithosphere, there may be several competent layers that yield different folding wavelengths. In such cases, observed folding wavelengths allow one to separate between strong crustal and mantle layers. For example, in the case of Central Asian lithosphere, two wavelengths can be depicted: crustal (50–100 km) and mantle (300–350 km). These wavelengths suggest the existence of roughly 10 km thick strong crustal 'core' and 30–50 km thick strong mantle layer. In case of cratons (Central Australia), the folding wavelength reaches 600–700 km indicating a 60 km thick competent layer. In both cases, the thickness of the strongest folded layer appears to be higher than the crustal thickness, confirming the idea that plates maintain considerable strength concentrated in their mantle part. The observations of folding suggest thicknesses of competent layers comparable with the corresponding T_e estimates (**Figures 5** and **8**). It is noteworthy, however, that there are some cases when λ/T_e ratios are abnormally high (>10) or low (<4). The high ratios mostly correspond to very weak lithospheres loaded by large amounts of sediment, which increases the wavelength of folding. The linear folding theory (eqn [37] or [42]) also does not apply in case of high amplitude-to-wavelength ratios (basically small λ/T_e), because in this case, plastic hinging at the weakened inflection points results in transition from unstable-to-stable folding, for which the wavelength is a simple function of the amount of shortening and does not depend on h or T_e. Wavelength of folding may be additionally influenced by superposition of various geodynamic events, for example, post-compressional extension and mantle dynamics.

As an illustration, **Figure 17** shows the results of thermomechanical modeling experiments for a 250-Ma-old lithosphere shortened at a slow rate of 1.25 cm year^{-1} (Smit et al., 2013). In this case, some strongly decoupled low-amplitude short=wavelength (50–100 km) folding superimposed on large-wavelength mantle folding (300–400 km) develops, leading to crustal thickening above synclinal mantle folds.

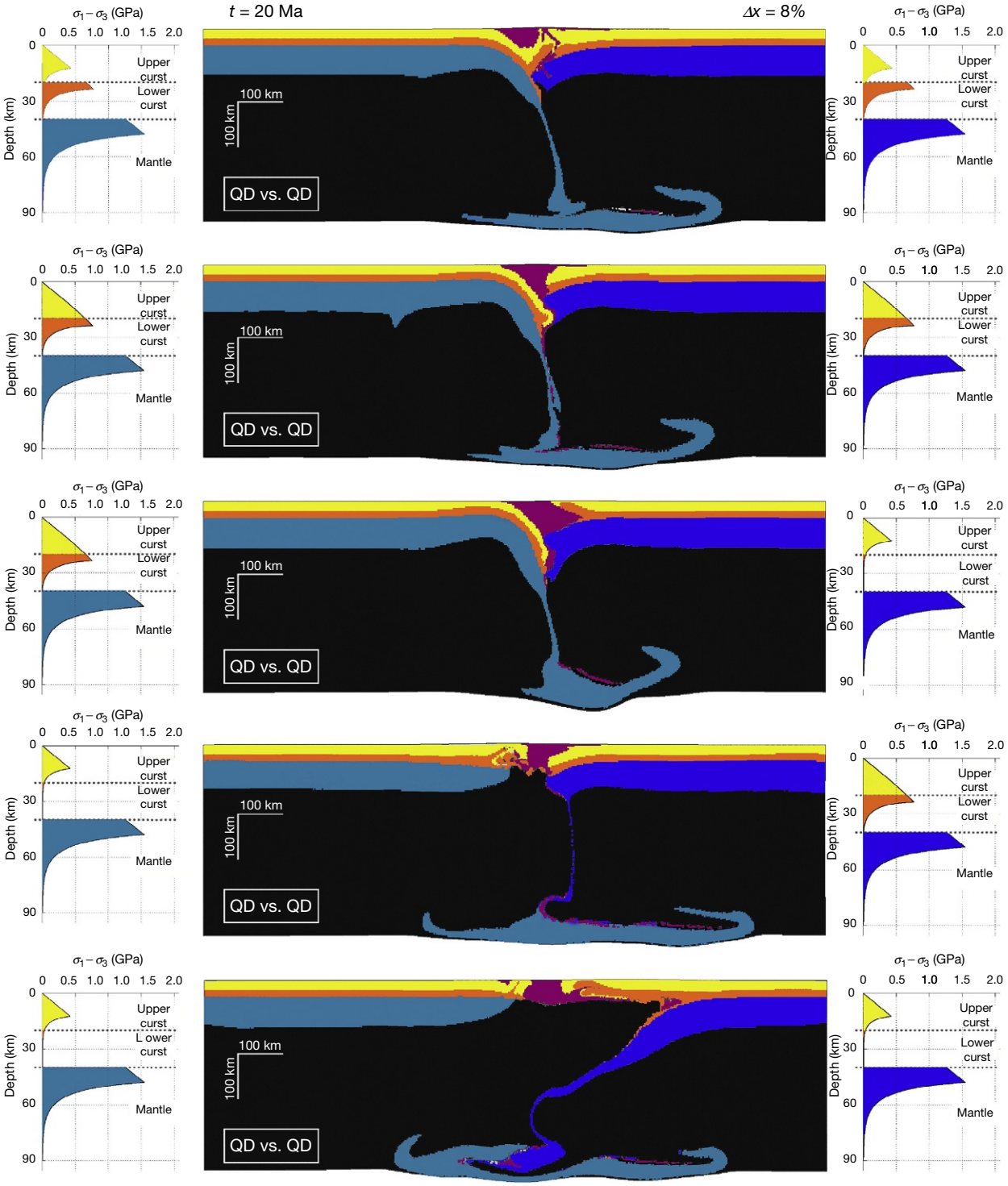

Figure 16 Influence of crustal rheology on the collision style in case of slow (6 mm year^{-1}) Alpine-type collision (weak lithosphere; Burov et al., 2012). Shown are morphologies for the models at 20 My for different crustal strength profiles. QD, quartz–diabase double-layer crustal structure (upper and lower crust, respectively); QQ, quartz–quartz double-layer crustal structure; DD, strong single-layer structure simulated by diabase. Color code: blue, mantle; orange, lower crust; yellow, upper crust; dark, asthenosphere and sublithosphere mantle.

The experiments shown in Figure 17 put further emphasis on the effect of rheological decoupling on the observed surface topography wavelengths, specifically in case of 500-Ma-old lithosphere. For small convergence rates, mantle folding may not develop or will occur with reduced wavelength due to low Péclet number of the system, which leads to heat diffusion and weakening of the folds. The observed folding wavelengths are directly related to the thickness of the mechanical cores in the crust and mantle. Hence, it becomes possible to parameterize leading crustal and mantle rheologies by varying tested rheological profiles until the model-predicted wavelength spectra start to match the observations.

6.03.6.9 Response to Extensional Tectonic Loading (Rifting)

A number of authors (e.g., Bassi, 1995; Buck, 2007; Huismans et al., 2005) have studied possible rifting modes as a function of the rheological profile. The results show that the narrow rifting mode is only possible in case of substantial mantle strength. If the lithospheric mantle is weak, the system switches to the wide rifting mode (e.g., Basin and Range) that may be characterized by periodic instabilities such as boudinage. These models suggest that not only narrow rifting mode but also other rifting styles (wide rifting mode and metamorphic core complex mode), except very wide delocalized rifts, require at least a 20–30 km thick competent mantle layer. Application of common dry olivine flow laws in the direct numerical models of tectonic deformation yields generally coherent results for predicted rifting styles (Figure 18). Certainly, strength in the mantle may not always be needed to form metamorphic core complexes. In this case, rather thick, weak lower crust may be required (Block and Royden, 1990; Buck, 1988, 1991). In this case, it is suggested that the lack of a pronounced basin, associated with the large extension inferred for core complexes, may indicate that crust has flowed into the extending region. The crust in such cases would decouple the mantle from the surface so mantle strength would have very little effect on core complex development.

6.03.7 Relations Between Short-Term and Long-Term Properties

6.03.7.1 Seismicity and Long-Term Deformation

Handy and Brun (2004) argued that seismicity is an ambiguous indicator of strength, that is, it is an indicator of mechanical weakness of the relevant layer that is not capable of sustaining tectonic or bending stress. The models of previous sections show that T_s is also an indicator of current stress level (eqn [36]) and probably reflects the thickness of the uppermost weak

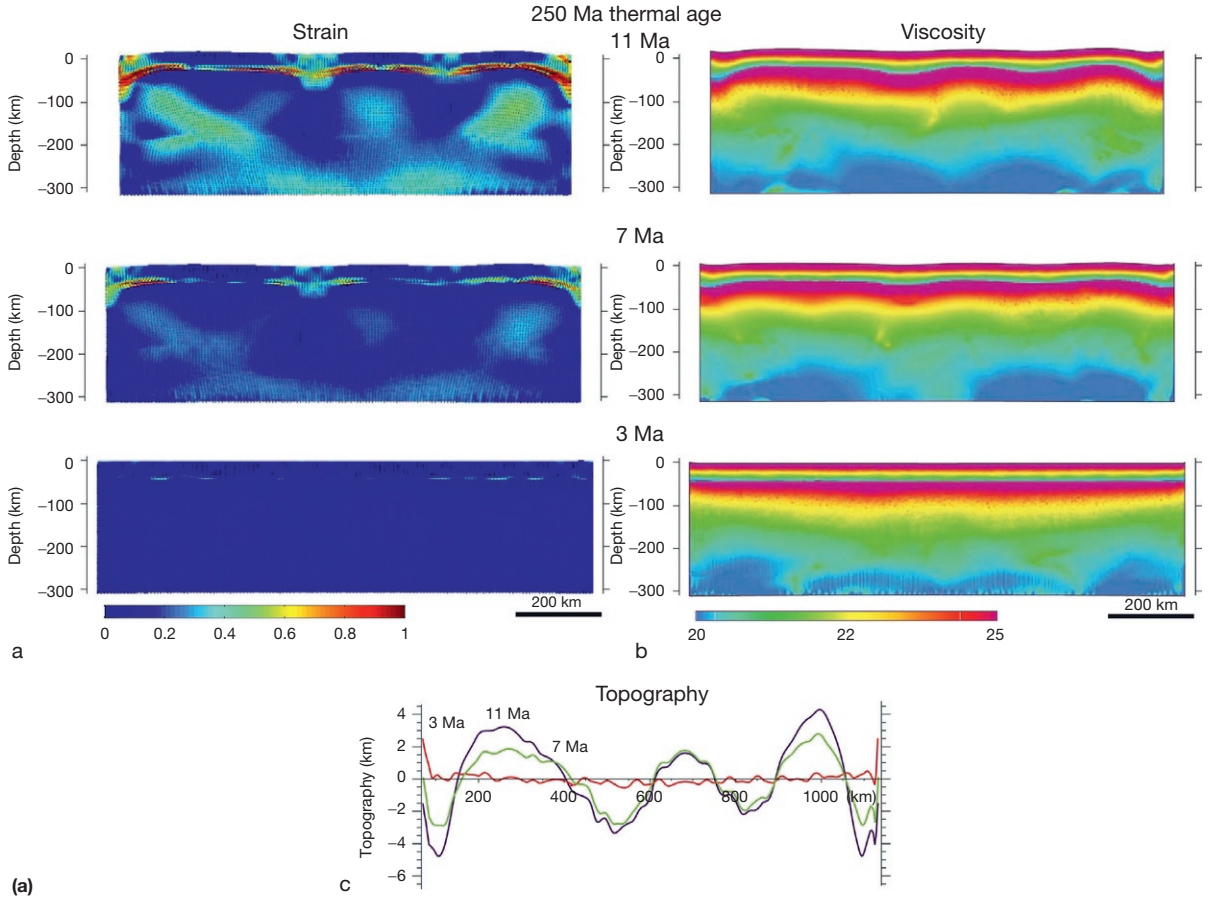

Figure 17 (a) Example of continental folding models for thermotectonic age of 250 Ma. Shown are finite strain, effective viscosity, and surface topography (Smit et al., 2012). Shortening at 1.25 cm year^{-1}. The horizontal scale of the model is identical to the vertical scale.

(Continued)

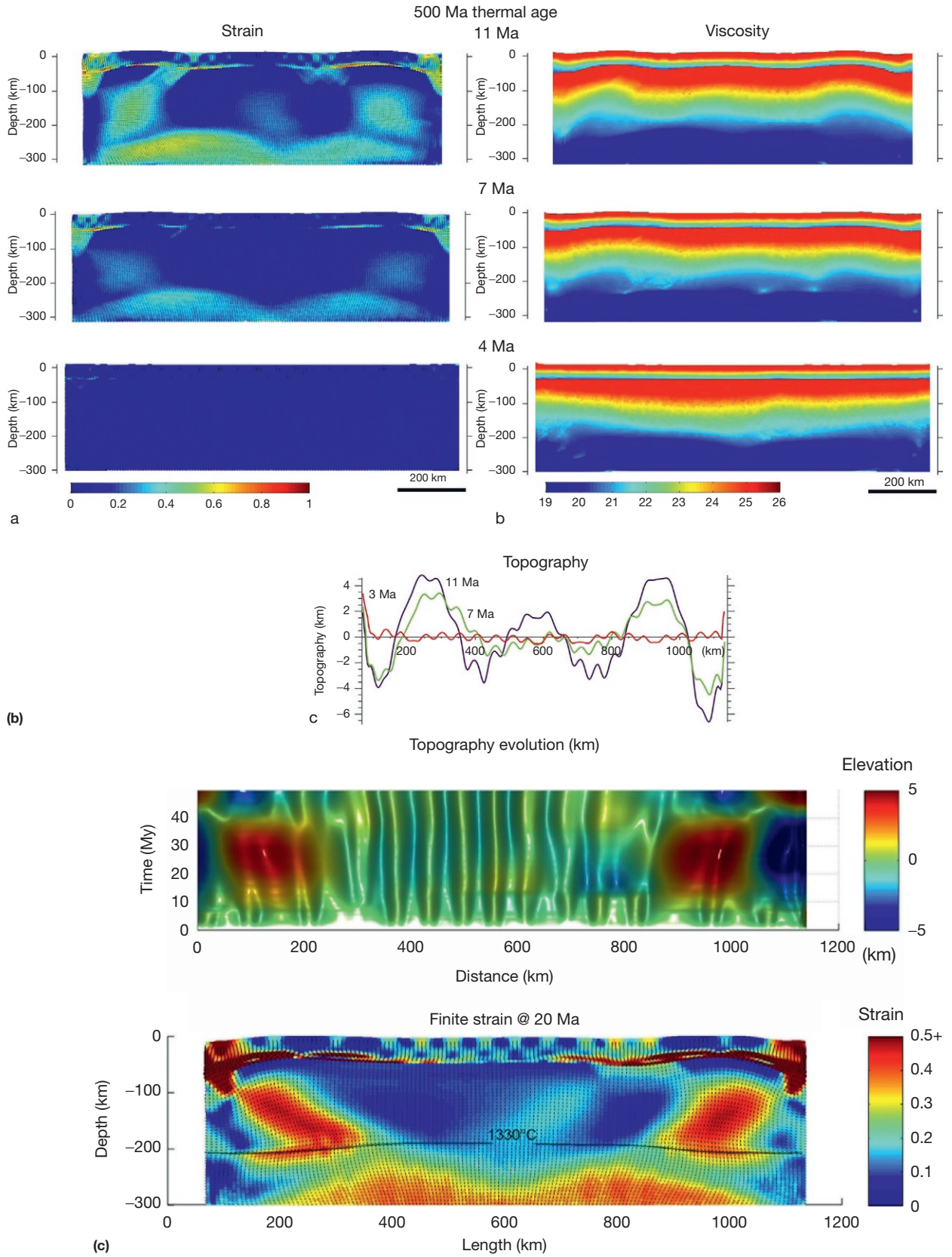

Figure 17 (Continued) (b) Numerical models of continental folding models for thermotectonic age of 500 Ma. Shown are finite strain, effective viscosity, and surface topography (Smit et al., 2012). Shortening at 1.25 cm year^{-1}. The horizontal scale of the model is identical to the vertical scale. (c) Surface topography evolution at 20 Ma for the experiment shown in **Figure 16(a)** (Smit et al., 2012). The horizontal scale of the model is identical to the vertical scale.

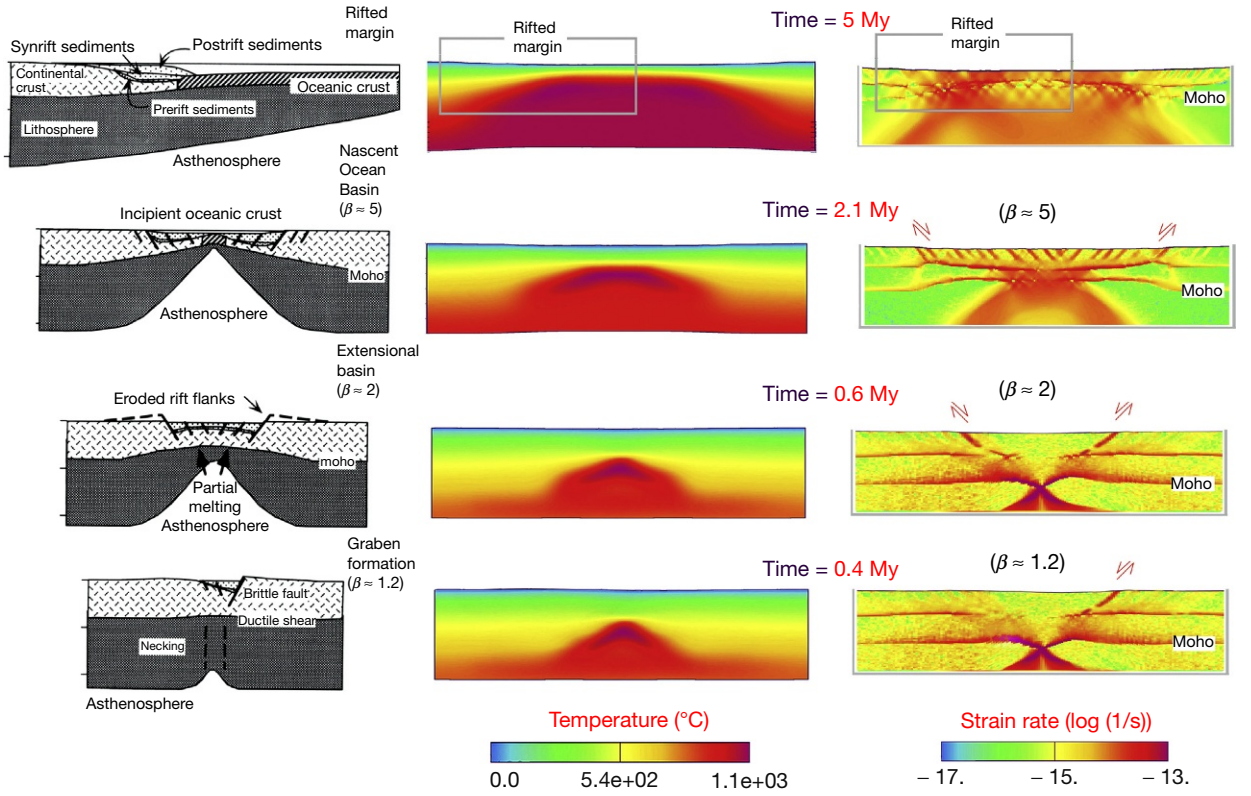

Figure 18 Stable and unstable extension styles predicted from direct numerical viscous–elastic–plastic thermomechanical models (Burov and Poliakov, 2001) and compared with the typically observed extension styles. Application of common dry olivine flow laws for mantle lithosphere yields generally coherent results for predicted styles of rifting. (right) Rifting styles as a function of the amount of extension (factor β) according to the geologic observations (Salveson, 1978). (left) Model predicted rifting styles (log strain rate) computed from the viscous–elastic–plastic numerical model based on 'jelly sandwich' rheology with strong upper crust (quartz) and upper mantle (olivine) (reproduced from Burov EB and Poliakov ANB (2001) Erosion and rheology controls on synrift and postrift evolution: Verifying old and new ideas using a fully coupled numerical model. *Journal of Geophysical Research* 106: 16,461–16,481). The rheology profile used for thermomechanical modeling corresponds to 150–200 My profile 3 from **Figure 9(a)**.

brittle layers that respond on historical timescales to stresses by faulting and earthquakes. T_e, in contrast, is proxy for the integrated strength of the entire lithosphere that responds to long-term ($>10^5$ year) geologic loads by flexure. A number of seismic tomography studies (e.g., Soureau et al., 2001) have also demonstrated that when compared with the distribution of seismicity, tomography reveals that earthquake depths are often limited by density or compositional boundaries, specifically those between the upper and lower crust. This may be related to stress drops caused by mechanical inconsistencies between these layers.

Seismic patterns do not allow for discrimination between the brittle and hypothetical nonbrittle–ductile earthquakes. Although the absence of earthquakes beneath the seismic Moho remains enigmatic, the simplest explanation refers to the insufficiency of tectonic and bending stresses to reach high brittle strength at Moho depth and below, healing of microfractures, and dominance of GBS shear strain localization that is specific for mantle in temperature range of 500–800 °C. As shown in **Figure 10**, for continental crust of typical thickness and a crust–mantle detachment, the bending stresses at the crust–mantle boundary are lower than the yielding strength, whereas the weight of the thickened crust increases the brittle strength of the mantle lithosphere.

From field observations, it is argued (Handy and Brun, 2004; see also **Section 112.5.5**) that earthquakes can be reasonably interpreted as a manifestation of a transient mechanical instability within shear zones. According to observations of outcropping fault surfaces, most shear zones have very specific rheological properties that distinguish them from normal rocks. For example, in these zones, ductile mylonitic creep is punctuated by ephemeral high-stress events involving fracture, frictional melting, and episodic local loss of cohesion.

6.03.7.2 Postseismic Relaxation Data and Long-Term Deformation

A number of studies interpret postseismic relaxation data in terms of the long-term viscosity of the crust or mantle (e.g., DallaVia et al., 2005; Pollitz et al., 2001; Sabadini and Vermeersen, 2004). Most of these studies yield 'subsurface' viscosities of 5×10^{16} to 2×10^{19} Pa s. These values are smaller than the estimates of asthenospheric viscosity derived from postglacial rebound data but considerably higher (8 orders of magnitude) than predictions of rock mechanics for seismic timescale (**Figure 3**). They are also 3–6 orders of magnitude lower than what can be inferred for long-term deformation from the data of rock mechanics, except for some quartz-dominated lower

crustal compositions. We conclude that postseismic viscosity values are either not indicative of the long-term behavior, referring to early Kelvin reaction according to Burger's rheology model (eqn [29]), or indicative of highly nonlinear behavior, which yields disproportionally small viscosities at high deformation rates. Several mechanisms may be considered, for example, preferential deformation due to cavitation in fine-grained mylonitic shear zones that results in porosity increase and major ductile weakening of the shear zone (Bürgmann and Dresen, 2008). Such deformation may only occur at seismic and postseismic timescales. Since postseismic deformation rates may vary with time, the effective Kelvin viscosities might be also nonlinear. For example, one of the alternative explanations of the low postseismic viscosity values refers to strain rate-dependent deformation caused by postseismic equilibration of fluid pressure in seismically modified fracture networks. In all cases, postseismic data are most probably not related to the long-term behavior.

6.03.7.3 Field Observations and Geophysical Data

Geophysical transects of plate margins and structural studies of exhumed fault rocks generally validate the rheology laws derived from experimental rock mechanics (Handy and Brun, 2004; Mouthereau et al., 2013) assuming 'jelly sandwich' parameters. Seismically observed crustal and mantle lithosphere structures are largely indicative of cases of ductile lower crust and stronger mantle lithosphere. In particular, this refers to the geophysical traverses NFP20 and ECORS-CROP across the Alps (Bayer et al., 1989; ECORS-CROP group, 1989; Frei et al., 1990; Kissling and Spakman, 1996) and DEKORP-ECORS across the Rhine Graben (Brun et al., 1991, 1992; Meissner and Bortfeld, 1990). The Alpine part of the transects shows that the lower crust of the Apulian Plate is detached from its underlying mantle and forms a north-tapering wedge between the downgoing European lithosphere and partly exhumed nappe edifice of the Alpine orogen (Handy and Brun, 2004). Burov et al. (1999) had studied the mechanical stability of this structure to find that high mantle resistance compatible with a 30 km thick competent mantle lithosphere layer is required to ensure its long-term stability. Similar considerations concerning the presence of strong mantle can be derived from seismic cross sections of the Rhine Graben and those across the Altyn Tagh fault system (Wittlinger et al., 1998) and Ferghana basin (Central Asia; Burov and Molnar, 1998), across the Abitibi–Wawa belts and Kapuskasing uplift system in the Canadian craton (LITHOPROBE). In the case of the Altyn Tagh fault system, oblique convergence of the bounding plates is accommodated by the Altyn Tagh strike-slip and thrust system, indicating that the lithospheric mantle was displaced along the fault as a rigid media. Remarkable direct evidence of high mantle strength is based on the data on the Kapuskasing uplift (Burov et al., 1998). The Kapuskasing structural zone cuts structures of the Superior Province in the Canadian Shield: the Abitibi–Wawa granite–greenstone belts to the south and Quetico–Opatica metasedimentary belts to the north. The geophysical and seismic transect LITHOPROBE reveals enormous volumes of dense granulates thrust upward along the ancient Kapuskasing thrust fault that was active about 2700 My ago. Despite the load of the granulite body, which exceeds that of an 'average' mountain belt, Moho boundary shows a small depression with an amplitude of just a few kilometers, which implies T_e of 100 km and viscosities $>10^{24}$ Pa s. It was concluded that independently of crustal strength, the mantle part of the lithosphere of the Canadian craton should include a strong layer with a minimum thickness of 60 km and thus rheology corresponding to strongest of the dry olivine rheologies (**Table 2**). This conclusion has been drawn (Burov et al., 1998) from the results of thermomechanical numerical models testing the mechanical stability of the Kapuskasing structure for a wide spectrum of rheology laws. It is also noted that in the collision zones (e.g., Himalaya), the lower crust is practically never exposed at the surface. Since the lower crust is lighter than the mantle, the simplest explanation would be that it is dragged down by the downgoing mantle lithosphere, which requires high mantle strength.

6.03.8 Conclusions and Future Perspectives

Although rheology laws based on experimental data of rock mechanics may be partly representative for long-term and large-scale deformation, they need validation and re-parameterization for geologic temporal and spatial scales. This particularly refers to the flow laws for crustal rocks, due to the diversity of mineralogical composition of continental crust (Burov, 2002). Long-term rheological properties can be scaled on the basis of observations of long-term/large-scale deformation such as the deformation of the lithosphere under known geologic loads (flexure, collision–subduction, folding, boudinage, and rifting), tectonic deformation styles, seismic and geodetic data, postglacial rebound data, and so on. The laboratory data serve as a 'first guess' for construction of long-term rheological models. Parameterization of these data requires better constraints on some major structural parameters such as the equilibrium thermal thickness of continents, $a=z(1330\,^{\circ}\mathrm{C})$, and density contrasts between the lithospheric mantle and asthenosphere. The data on the equivalent elastic thickness (T_e) and other large-scale data confirm that the rheology of the oceanic lithosphere is in acceptable agreement with rock mechanics data for dislocation creep in dry olivine. For continents, rock mechanics data are largely compatible with the observation that T_e varies from 0–10 km in young plates to 110–120 km in cratons. If $T_e > T_c$, the strongest rheological layer refers to the mantle and fits dry olivine rheology. If $T_e < T_c$, the strength is likely to be shared between crust and mantle. 'Jelly sandwich' (decoupled) or 'dried jelly sandwich' (coupled) rheology models appear to be the most applicable for continents. The data and models suggest that for equivalent conditions, the integrated strength of continental mantle does not significantly differ from that of the oceanic lithosphere. After the thermal structure, the second major control on the mechanical behavior of continental plates refers to the diverse structure and rheology of their crusts. Depending on the crustal strength and thickness, continents may be either stronger or weaker than the oceanic plates. 'Weak or moderate' continental plate strength ($T_e < 1–1.5T_c$) refers to the cases of 'generalized jelly sandwich' rheology with ductile lower or intermediate crust (most orogenic belts and some cratons, plateaus, and most postrift basins). Strong 'dried jelly sandwich' applies to old cratons ($T_e = 1.5–2.5T_c$) where the lower crust is strong

and thus crust and mantle are mechanically coupled. 'Crème brûlée' rheology ($T_e < T_c$, strong crust–weak mantle) is extremely weak and may apply only for young or rejuvenated lithospheres or some active rift zones (e.g., Salton Sea, Southern California, and Taupo Volcanic Zone, North Island New Zealand).

The primary question related to the interpretation of the T_s data is 'why is there little or no microseismicity below the depth to 500 °C or at most 40–50 km, in both the oceans and continents?.' The T_s data, we believe, are indicative of limited tectonic stress levels in the lithosphere and of small brittle strength of its upper layers compared to that of the deeper mantle. Since Byerlee's brittle failure becomes less probable with growing pressure (depth) and with healing of the pre-existing fractures due to increasing pressure–temperature, it is highly probable that aseismic (e.g., grain size-dependent GBS creep; Drury, 2005) deformation replaces Byerlee's brittle failure in the mantle at temperatures above 500–600 °C. GBS creep is specific for mantle olivine and is efficient in the 'cold' sub-Moho temperature range (500–600–700 °C), which explains why the probability of earthquakes in the continental mantle is lower than in the crust. T_s is thus not a proxy for the integrated strength of the lithosphere or T_e. T_s anticorrelates with T_e if intraplate force $F < B$ (integrated plate strength). If $F = B$, the entire plate is in the yield state and T_e has no mechanical meaning, while T_s equals BDT depth. The only possible relation between T_s and T_e is related to the influence of T_e on the mean intraplate stress level: for a given value of normal load or tectonic force $F < B$, T_s decreases with increasing T_e. In most cases, simple consideration suggests, as a rule of thumb, $T_s \leq \Upsilon(F/T_e + \sigma_{xx}^f)/\rho g \leq \frac{1}{2}T_e$ (eqn [36]). In oceans, the only possibility for $T_s = T_e$ refers to nearly broken plates having equally strong brittle and ductile parts. This invalidates the proposition that plate strength is concentrated in the brittle part. In continents, $T_s = T_e$ may happen in 'thermally young' plates because there, in contrast to oceans, T_s and T_e may refer to different lithologic layers, upper crust, lower crust, and mantle (e.g., broken brittle crust supported by strong ductile mantle).

Even provided that rheology laws based on experimental rock mechanics are robust, continental YSEs based on these laws are subject to large uncertainties due to differing assumptions on the geotherm, background strain rate, hydrous conditions, and crustal structure. It is largely these factors that mainly determine the long-term mechanical properties of the lithosphere. Hence, future investigations should focus on finding better observational and model constrains on these key conditions. In particular, the cross compatibility of estimates of continental plate strength obtained from the observations of (1) flexure (for T_e values coming from the models accounting for all surface and subsurface loads), (2) folding, (3) mechanical stability models, and (4) field and indirect geophysical data supports YSE profiles derived for dry olivine and (with more reservations) granite upper crust assuming plate cooling model for 200–250 km thick lithosphere.

There is almost certainly no one type of strength profile that characterizes all continental lithosphere. It was shown that jelly sandwich rheology models (and their variants that include strong mantle and various crustal structures) are mechanically compatible with long-term support of tectonic loads and major structural styles, whereas crème brûlée models, or any models with weak mantle, are mechanically unstable. Thermomechanical modeling of lithospheric deformation suggests that the persistence of surface topographic features and their compensating roots requires that the subcrustal mantle is strong and able to act as both a stress guide and a support for surface loads. It might be thought that it would not matter which competent layer in the lithosphere is the strong one. However, the models show that the density contrast between the crust and mantle is sufficient to ensure that it is the mantle, rather than the crust, which provides both the stress guide and support. In our view, subduction, orogenesis, or narrow to normal rifting *requires* a strong mantle layer. We have found this to be true irrespective of the actual strength of the crust. Weak mantle is mechanically unstable and tends to delaminate from the overlying crust because it is unable to resist forces of tectonic origin. Once it does delaminate, hotter and lighter mantle asthenosphere can flow upward to the Moho. The resulting increase in Moho temperature would lead to extensive partial melting and magmatic activity as well as further weakening (e.g., Karato, 1986) such that, for example, subduction is inhibited and surface topography collapses in a relatively short interval of time.

Appendix A Flexure of Continental Lithosphere with Multilayered Nonlinear Rheology

The rheology-independent form of 2-D plate bending equation is

$$-\frac{\partial^2 M_x}{\partial x^2} + \frac{\partial}{\partial x}\left(T_x \frac{\partial w}{\partial x}\right) + p_- = p_+ \qquad [A.1]$$

$$M = -\int_{h_m} \sigma_{xx} \gamma \mathrm{d}\gamma$$

where M_x is bending moment, h_m is the total thickness of the plate, F_x is horizontal fiber force, w is the vertical deflection of the plate (bathymetry, geometry of Moho), and p_- and p_+ are negative and positive normal loads, respectively. The equivalent elastic thickness T_e of a plate with arbitrary rheology (yet compatible with static bending) is

$$M = -D\frac{\partial^2 w}{\partial x^2} = -E\frac{{T_e}^3}{12(1-\nu^2)}\frac{\partial^2 w}{\partial x^2}$$

or

$$T_e = \sqrt[3]{-M\frac{12(1-\nu^2)}{E}\left(\frac{\partial^2 w}{\partial x^2}\right)^{-1}} = \sqrt[3]{\mathrm{MK}^{-1}\mathrm{G}} \qquad [A.2]$$

where E and ν are the assumed elastic parameters, K is plate curvature, and $G = 12(1-\nu^2)E^{-1}$.

For a single-layer plate (e.g., oceanic lithosphere, $T_e \leq h_m$) composed of n mechanically coupled rheological layers of thickness h_i, $i = 1, \cdots n$,

$$T_e \approx h_1 + h_2 \cdots = \sum_n h_i \qquad [A.3]$$

For a lithosphere composed of n mechanically decoupled layers,

$$T_e \approx \left(h_1^3 + h_2^3 \cdots\right) = \sqrt[3]{\sum_n h_i^3} < \sum_n h_i \qquad [A.4]$$

In case of equally thick decoupled layers ($h_1 \approx h_2 \approx h_3 \ldots = h$), $T_e \approx n^{1/3}h$ instead of $T_e = nh$ for a coupled plate (eqn [A.3]). Layer decoupling thus reduces T_e by a factor

of $n^{3/4}$, that is, by 40–50% for $n<4$. The effective rigidity $D(x,w''\ldots)$ of a plate with nonlinear rheology can be estimated as

$$D(\phi)\frac{\partial^2 w(x)}{\partial x^2}\approx -D(\phi)R_{xy}^{-1}=-M_x(\phi) \qquad [A.5]$$

Accordingly, $T_e=T_e(x, w''\ldots)$ of such a plate is

$$T_e=\left(\frac{D(\phi)}{D_0}\right)^{\frac{1}{3}}=\left(-\frac{M_x(\phi)R_{xy}}{D_0}\right)^{\frac{1}{3}}\approx\left(\frac{M_x(\phi)}{D_0}\left(\frac{\partial^2 w(x)}{\partial x^2}\right)^{-1}\right)^{\frac{1}{3}} \qquad [A.6]$$

where $D_0=E(12(1-\nu^2))^{-1}$ and $\phi=(x, w''\ \ldots)$. R_{xy} is local radius of bending $R_{xy}\approx-(w'')^{-1}$. For a multilayer plate composed of $i=1,\ldots n$ lithologic layers with $j=1\ldots m_i$ rheological zones (brittle, elastic, ductile, etc.) per each layer, D and T_e can be obtained from the following system:

$$\begin{cases}\dfrac{\partial^2}{\partial x^2}\overbrace{\left(D_0T_e^3(\phi)\underbrace{\dfrac{\partial^2 w(x)}{\partial x^2}}_{K}\right)}^{M_x(\phi)}+\dfrac{\partial}{\partial x}\left(F_x(\phi)\dfrac{\partial w(x)}{\partial x}\right)+p_-(\phi)w(x)=p_+(x)\\ T_e(\phi)=\left(\dfrac{M_x(\phi)}{D_0}\left(\dfrac{\partial^2 w(x)}{\partial x^2}\right)^{-1}\right)^{\frac{1}{3}}\\ M_x(\phi)=-\displaystyle\sum_{i=1}^{n}\sum_{j=1}^{m_i}\int_{z_{ij}^-(\phi)}^{z_{ij}^+(\phi)}\sigma_{xx}^{(j)}(\phi)z_i{}^*(\phi)\mathrm{d}z\\ F_x(\phi)=-\displaystyle\sum_{i=1}^{n}\sum_{j=1}^{m_i}\int_{z_{ij}^-(\phi)}^{z_{ij}^+(\phi)}\sigma_{xx}^{(j)}(\phi)\mathrm{d}z\end{cases} \qquad [A.7]$$

The boundaries of the rheological zones z_{ij} are not predefined *a priori* but are computed, using an iterative procedure, as function of ϕ. Mechanical decoupling of rheological layers has three major consequences:

Up to 50% reduction of the flexural resistance, T_e
Maintenance of high resistance to cutting loads
T_e mainly controlled by thickness of the strongest layer

Appendix B Thermal Model of the Lithosphere

The thermal structure of the oceanic lithosphere is described in detail in Section 6.03.5.1. The thermal structure of multilayer continental lithosphere is estimated using a similar half-space cooling model that is subdivided on three layers (upper and lower crust, and mantle) and incorporates radiogenic heat sources:

$$\begin{cases}\dot{T}-\chi_{c1}\Delta T=\chi_{c1}\rho_{c1}H_sk_{c1}^{-1}e^{-zh_r^{-1}}, & 0\le z\le h_{c1}\\ \dot{T}-\chi_{c2}\Delta T=H_{c2}C_{c2}^{-1}, & h_{c1}\le z\le T\\ \dot{T}-\chi_m\Delta T=0, & T_c\le z\le a\end{cases} \qquad [B.1]$$

where the overdot means differentiation with respect to time. h_{c1} is thickness of the upper crust, and T_c is total crustal thickness (see Table 4 for other parameters). The boundary and initial conditions are

$T(0,t)=0$ (surface temperature),
$T(a,t)=T_m=1350°C$ ($a\approx250$ km is the depth to the thermal bottom, or *equilibrium thermal thickness*),
$T(z,0)=T_m$ (homogeneous temperature distribution at the beginning).

The solution of the system (eqn [B.1]) is obtained under assumption of heat flux and temperature continuity across the upper and lower crust and mantle lithosphere.

Acknowledgments

A large part of this review study has benefited from author's collaboration with A. B. Watts. I am very much thankful to Mary Ford, Roger Buck, and Antony Watts for their many helpful discussions and comments on initial versions of the manuscript. I also thank P. Molnar, C. Jaupart, L. Jolivet, Y. Podladchikov, and S. Cloetingh for their many helpful discussions. The first edition of this study was funded by the ANR EGEO program and by ISTEP internal project funding. The second edition is supported by the Advanced ERC Grant RHEOLITH.

References

Afonso JC and Ranalli G (2004) Crustal and mantle strengths in continental lithosphere: Is the jelly sandwich model obsolete? *Tectonophysics* 394: 221–232.
Aldersons F, Ben-Avraham Z, Hofstetter A, Kissling E, and Al-Yazjeen T (2003) Lower-crustal strength under the Dead Sea basin from local earthquake data and rheological modelling. *Earth and Planetary Science Letters* 214: 129–142.
Angiboust S, Wolf S, Burov E, Agard Ph, and Yamato P (2012) Effect of fluid circulation on subduction interface tectonic processes: Insights from thermo-mechanical numerical modelling. *Earth and Planetary Science Letters* 357–358: 238–248.
Artemieva IM (2009a) Are xenoliths representative of the "intact" cratonic mantle? A geophysical perspective. *Geophysical Research Abstracts* 11, EGU2009–1717, 2009, EGU General Assembly.
Artemieva IM (2009b) The continental lithosphere: Reconciling thermal, seismic, and petrologic data. *Lithos* 109: 23–46.
Artyushkov EV (1973) Stresses in the lithosphere caused by crustal thickness inhomogeneities. *Journal of Geophysical Research* 78: 7675–7708.
Ashby MF and Verall RA (1978) Micromechanisms of flow and fracture, and their relevance to the rheology of the upper mantle. *Philosophical Transactions of the Royal Society of London* 288: 59–95.
Audet P and Burgmann R (2011) Dominant role of tectonic inheritance in supercontinent cycles. *Nature Geoscience* 4(3): 184–187. http://dx.doi.org/10.1038/NGEO1080.
Austrheim H and Boundy T (1994) Pseudotachylytes generated during seismic faulting and eclogitization of the deep crust. *Science* 265: 82–83.
Avoauc J-P (2007) Mountain building. In: *Treatise on Geophysics*. Amsterdam: Elsevier.
Barrell J (1914) The strength of the Earth's crust. I. Geologic tests of the limits of strength. *Journal of Geology* 22: 28–48.
Bassi G (1995) Relative importance of strain rate and rheology for the mode of continental extension. *Geophysical Journal International* 122: 195–210.
Bayer R, Carozzo MT, Lanza R, Miletto M, and Rey D (1989) Gravity modelling along the ECORS-CROP vertical seismic reflection profile through the Western Alps. *Tectonophysics* 162: 203–218.
Beuchert MJ and Podladchikov YY (2010) Viscoelastic mantle convection and lithospheric stresses. *Geophysical Journal International* 183(1): 35–63. http://dx.doi.org/10.1111/j.1365-246X.2010.04708.x.
Beuchert MJ, Podladchikov YY, Simon NSC, and Ruepke LH (2010) Modeling of craton stability using a viscoelastic rheology. *Journal of Geophysical Research* 115: B11413. http://dx.doi.org/10.1029/2009JB006482.
Bills BG, Adams KD, and Wesnousky SG (2007) Viscosity structure of the crust and upper mantle in western Nevada from isostatic rebound patterns of Lake Lahontan shorelines. *Journal of Geophysical Research* 112: B08411.

Bills BG, Currey D, and Marshall GA (1994) Viscosity estimates for the crust and upper mantle from patterns of lacustrine shoreline deformation in the Eastern Great Basin. *Journal of Geophysical Research* 99(B11): 22,059–22,086.

Biot MA (1961) Theory of Folding of Stratified viscoelastic media and its implications in tectonics and orogenesis. *Geological Society of America Bulletin* 72: 1595–1620.

Bird P (1991) Lateral extrusion of lower crust from under high topography in the isostatic limit. *Journal of Geophysical Research* 96: 10275–10286.

Block L and Royden LH (1990) Core complex geometries and regional scale flow in the lower crust. *Tectonics* 9: 557–567.

Bos B and Spiers CJ (2002) Frictional-viscous flow in phyllosilicate-bearing fault rock: Microphysical model and Implications for crustal strength profiles. *Journal of Geophysical Research* 107(B2): 2028. http://dx.doi.org/10.1029/2001JB000301.

Bott MHP (1993) Modelling the plate-driving mechanism. *Journal of the Geological Society of London* 150: 941–951.

Boutelier D, Chemenda A, and Burg J-P (2003) Subduction versus accretion of intra-oceanic volcanic arcs: Insight from thermo-mechanical analogue experiments. *Earth and Planetary Science Letters* 212: 31–45.

Brace WF and Kohlstedt DL (1980) Limits on lithospheric stress imposed by laboratory experiments. *Journal of Geophysical Research* 85: 6248–6252.

Brun J-P (2002) Deformation of the continental lithosphere: Insights from brittle-ductile models. In: De Meer S, Drury MR, De Bresser JHP, and Pennock GM (eds.) *Deformation Mechanisms, Rheology and Tectonics: Current Status and Future Perspectives*, pp. 355–370, Spec. Publ.-Geol. Soc. Lond., 200.

Brun J-P and Gutscher MADEKORP-ECORS teams (1992) Deep crustal structure of the Rhine Graben from DEKORP-ECORS seismic reflection data: A summary. *Tectonophysics* 208: 139–147.

Brun J-P and Wenzel Fthe ECORS-DEKORP Team (1991) Crustal structure of the southern Rhine Graben from ECORS-DEKORP seismic reflection data. *Geology* 19: 758–762.

Buck WR (1988) Flexural rotation of normal faults. *Tectonics* 7: 959–973.

Buck WR (1991) Modes of continental extension. *Journal of Geophysical Research* 96: 20161–20178.

Buck WR (2007) Continental break-up and building. In: *Treatise on Geophysics*. New York: Elsevier.

Buck WR and Toksöz MN (1983) Thermal effects of continental collisions: Thickening a variable viscosity lithosphere. *Tectonophysics* 100: 53–69.

Bürgmann R and Dresen G (2008) Rheology of the lower crust and upper mantle: Evidence from rock mechanics, geodesy, and field observations. *Annual Review of Earth and Planetary Sciences* 36: 531–567. http://dx.doi.org/10.1146/annurev.earth.36.031207.124326.

Burov E (2002) The upper crust is softer than dry quartzite. *Tectonophysics* 361: 321–326.

Burov EB (2007) Plate rheology and mechanics. In: Watts AB and Schubert G (eds.) *Treatise on Geophysics*. *Crust and Lithosphere Dynamics*, vol. 6, pp. 99–152. Elsevier, ISBN: 978-0-444-51928-3, TOGP00102. 611 pp.

Burov E (2010) The equivalent elastic thickness (T_e), seismicity and the long-term rheology of continental lithosphere: Time to burn-out "crème brûlée"? Insights from large-scale geodynamic modeling. *Tectonophysics* 484(4): 26.

Burov E (2011) Rheology and strength of the lithosphere. *Marine and Petroleum Geology* 28(8): 1402–1443. http://dx.doi.org/10.1016/j.marpetgeo.2011.05.008, Invited paper.

Burov E and Cloetingh S (2010) Plume-like upper mantle instabilities drive subduction initiation. *Geophysical Research Letters* 37, L03309.

Burov EB and Cloetingh S (1997) Erosion and rift dynamics: New thermomechanical aspects of post-rift evolution of extensional basins. *Earth and Planetary Science Letters* 150: 7–26.

Burov EB and Diament M (1992) Flexure of the continental lithosphere with multilayered rheology. *Geophysical Journal International* 109: 449–468.

Burov EB and Diament M (1995) The effective elastic thickness (T_e) of continental lithosphere: What does it really mean? *Journal of Geophysical Research* 100: 3895–3904.

Burov EB and Diament M (1996) Isostasy, effective elastic thickness (EET) and inelastic rheology of continents and oceans. *Geology* 24: 419–423.

Burov E, Francois T, Yamato P, and Wolf S (2014a) Mechanisms of continental subduction and exhumation of HP and UHP rocks. *Gondwana Research* 25: 464–493. http://dx.doi.org/10.1016/j.gr.2012.09.010.

Burov E, Francois T, Agard P, et al. (2014b) Mechanisms of subduction and HP/UHP exhumation of continental crust: Rheological and geodynamic controls. *Tectonophysics* 631: 212–250. http://dx.doi.org/10.1016/j.tecto.2014.04.033.

Burov E, Francois T, Yamato P, and Wolf S (2014c) Advances and challenges in geotectonic modeling. *Societé Geologique de France* 185: 147–168. http://dx.doi.org/10.2113/gssgfbull.185.3.147.

Burov EB, Kogan MG, Lyon-Caen H, and Molnar P (1990) Gravity anomalies, the deep structure, and dynamic processes beneath the Tien Shan. *Earth and Planetary Science Letters* 96: 367–383.

Burov EB, Lobkovsky LI, Cloetingh S, and Nikishin AM (1993) Continental lithosphere folding in Central Asia (part 2), constraints from gravity and topography. *Tectonophysics* 226: 73–87.

Burov EB, Mareschal J-C, and Jaupart C (1998) Large scale crustal inhomogeneities and lithospheric strength in cratons. *Earth and Planetary Science Letters* 164: 205–219.

Burov EB and Molnar P (1998) Gravity anomalies over the Ferghana Valley (central Asia) and intracontinental deformation. *Journal of Geophysical Research* 103: 18,137–18,152.

Burov EB and Molnar P (2008) Rayleigh-Taylor instability of a viscoelastic (Maxwell solid): Dependence of growth rates on wave number and elastic constants. *Earth and Planetary Science Letters* 275(3–4): 370–381.

Burov E, Podladchikov Y, Grandjean G, and Burg J-P (1999) Validation of multidisciplinary data using thermo-mechanical modelling: Application to the Western and Northern Alps. *Terra Nova* 11: 124–131.

Burov EB and Poliakov ANB (2001) Erosion and rheology controls on synrift and postrift evolution: Verifying old and new ideas using a fully coupled numerical model. *Journal of Geophysical Research* 106: 16,461–16,481.

Burov E and Watts AB (2006) The long-term strength of continental lithosphere: "jelly-sandwich" or "crème-brûlée"? *GSA Today* 16: 4–10.

Burov E and Yamato P (2008) Continental plate collision, P-T-t-z conditions and unstable vs. stable plate dynamics: Insights from thermo-mechanical modelling. *Lithos* 103: 178–204.

Byerlee JD (1978) Friction of rocks. *Pure and Applied Geophysics* 116: 615–626.

Caristan Y (1982) The transition from high temperature creep to fracture in Maryland diabase. *Journal of Geophysical Research* 87: 6781–6790.

Carter NL and Tsenn MC (1987) Flow properties of continental lithosphere. *Tectonophysics* 136: 27–63.

Chandrasekhar S (1961) *Hydrodynamic and Hydromagnetic Stability*, p. 704. Oxford: Oxford University Press.

Chapman Y (1986) Thermal gradient in the continental crust. In: Dawson JB, et al. (eds.) *The Nature of the Continental Crust*, pp. 63–70, Spec. Publ. Geol. Soc. London, 24.

Chen S, Hiraga K, and Kohlstedt DL (2006) Water weakening of clinopyroxene in the dislocation creep regime. *Journal of Geophysical Research* 111: B08203.

Chen W-P and Molnar P (1983) Focal depths of intracontinental and intraplate earthquakes and their implications for the thermal and mechanical properties of the lithosphere. *Journal of Geophysical Research* 88: 4183–4214.

Chester FM (1988) The brittle-ductile transition in a deformation-mechanism map for halite. *Tectonophysics* 154: 125–136.

Chester FM (1995) A rheologic model for wet crust applied to strike-slip faults. *Journal of Geophysical Research* 100(B7): 13,033–13,044.

Chopra PN and Paterson MS (1981) The experimental deformation of dunite. *Tectonophysics* 78: 453–473.

Chopra PN and Paterson MS (1984) The role of water in the deformation of dunite. *Journal of Geophysical Research* 89: 7861–7876.

Cloetingh S and Banda E (1992) Europe's lithosphere – Physical properties. Mechanical structure. In: Blundell D, Freeman R, and Mueller S (eds.) *A Continent Revealed: The European Geotraverse*, pp. 80–91. New York: Cambridge University Press/ European Science Foundation.

Cloetingh S and Burov EB (1996) Thermomechanical structure of the European continental lithosphere: Constraints from rheological profiles and EET estimates. *Geophysical Journal International* 124: 695–723.

Cloetingh S and Burov E (2010) Lithospheric folding and sedimentary basin evolution: A review and analysis of formation mechanisms. *Basin Research* 23: 257–290. http://dx.doi.org/10.1111/j.1365-2117.2010.00490.x.

Cloetingh S, Burov E, and Poliakov A (1999) Lithosphere folding: Primary response to compression? (from central Asia to Paris Basin). *Tectonics* 18: 1064–1083.

Cloetingh S and Wortel R (1986) Stress in the Indo-Australian plate. *Tectonophysics* 132: 49–67.

Cloetingh S and Ziegler P (2007) Tectonic models of sedimentary basins. In: Watts AB (ed.) *Treatise on Geophysics*, vol. 6, pp. 485–611. Amsterdam: Elsevier.

Cloetingh S, et al. (1982) Evolution of passive continental margins and initiation of subduction zones. *Nature* 297: 139–142.

Cochran JR (1980) Some remarks on isostasy and the long-term behavior of the continental lithosphere. *Earth and Planetary Science Letters* 46: 766–2711.

Conrad CP and Molnar P (1997) The growth of Rayleigh-Taylor-type instabilities in the lithosphere for various rheological and density structures. *Geophysical Journal International* 129: 95–112.

Cundall PA (1989) Numerical experiments on localization in frictional materials. *Archive of Applied Mechanics* 59: 148–159.

Dahlen FA (1981) Isostasy and the ambient state of stress in the oceanic lithosphere. *Journal of Geophysical Research* 86: 7801–7807.

DallaVia G, Sabadini R, DeNatale G, and Pingue F (2005) Lithospheric rheology in southern Italy inferred from postseismic viscoelastic relaxation following the 1980 Irpinia earthquake. *Journal of Geophysical Research* 110: B06311. http://dx.doi.org/10.1029/2004JB003539.

DeMets C, Gordon RG, Argus DF, et al. (1990) Current plate motions. *Geophysical Journal International* 101: 425–478.

Deverchere J, Houdry F, Diament M, Solonenko NV, and Solonenko AV (1991) Evidence for a seismogenic upper mantle and lower crust in the Baikal rift. *Geophysical Research Letters* 18(6): 1099–1102.

Deverchere J, Houdry F, Solonenko NV, Solonenko AV, and Sankov VA (1993) Seismicity, active faults and stress field of the North Muya Region, Baikal Rift: New insights on the rheology of extended continental lithosphere. *Journal of Geophysical Research* 98: 19895–19912.

Doin M and Fleitout L (1996) Thermal evolution of the oceanic lithosphere: An alternative view. *Earth and Planetary Science Letters* 142: 121–136.

Doser D and Yarwood DR (1994) Deep crustal earthquakes associated with continental rifts. *Tectonophysics* 229: 123–131.

Drury MR (2005) Dynamic recrystallization and strain softening of olivine aggregates in the laboratory and the lithosphere. *Geological Society London Special Publications* 243: 143–158.

Durham WB, Meib S, Kohlstedt DL, Wang L, and Dixon NA (2009) New measurements of activation volume in olivine under anhydrous conditions. *Physics of the Earth and Planetary Interiors* 172: 67–73.

ECORS-CROP Deep Seismic Sounding Group (1989) A new picture of the Moho under the western Alps. *Nature (London)* 337: 249–251.

England PC and Houseman GA (1989) Extension during continental convergence, with application to the Tibetan Plateau. *Journal of Geophysical Research* 94: 17561–17579.

England P and Molnar P (1997) Active deformation of Asia: From kinematics to dynamics. *Science* 278: 647–650.

England PC and Molnar P (2005) Late Quaternary to decadal velocity fields in Asia. *Journal of Geophysical Research* 110: B12401. http://dx.doi.org/10.1029/2004JB003541.

England P and Richardson SW (1980) Erosion and age dependence of continental heat flow. *Geophysical Journal of the Royal Astronomical Society* 62: 421–437.

Evans B (2005) Creep constitutive laws for rocks with evolving structure. *Geological Society London Special Publications* 245: 329–346.

Evans B and Goetze C (1979) The temperature variation of hardness of olivine and its implication for polycrystalline yield stress. *Journal of Geophysical Research* 84: 5505–5524.

Evans B and Kohlstedt DL (1995) Rheology of rocks. In: Ahrens TJ (ed.) *Rock Physics and Phase Relations: A Handbook of Physical Constants*. *AGU Reference Shelf*, vol. 1, pp. 149–165. Washington, DC: AGU.

Faccenda M, Gerya TV, and Burlini L (2009) Deep slab hydration induced by bending related variations in tectonic pressure. *Nature Geoscience* 2: 790–793.

Fleitout L and Froidevaux C (1983) Tectonic stresses in the lithosphere. *Tectonics* 3: 315–334.

Forsyth DW (1985) Subsurface loading and estimates of the flexural rigidity of continental lithosphere. *Journal of Geophysical Research* 90: 12,623–12,632.

Francois T, Burov E, Meyer B, and Agard P (2013) Survival and rheological structure of cratons: Key constraints from surface topography. *Tectonophysics* 602: 106–223. http://dx.doi.org/10.1016/j.tecto.2012.10.009.

Freed AM, Burgmann R, and Herring TA (2007) Far-reaching transient motions after Mojave earthquakes require broad mantle flow beneath a strong crust. *Geophysical Research Letters* 34: L19302.

Frei W, Heitzmann P, and Lehner P (1990) Swiss NFP20 research program of the deep structure of the Alps. *Mémoires de la Société géologique de France* 156: 29–46.

Fuchs K, Bonjer K-P, Gajewski D, et al. (1987) Crustal evolution of the Rhinegraben area, I. Exploring the lower crust in the Rhinegraben rift by unified geophysical experiments. *Tectonophysics* 141: 261–275.

Gerbault M, Burov EB, Poliakov A, and Dagnieres M (1999) Do faults trigger folding in the lithosphere? *Geophysical Research Letters* 26: 2271–2274.

Giese P, Nicolich R, and Reutter K-J (1982) Explosion crustal seismic studies in the Alpine-Mediterranean region and their implications to tectonic processes. In: Berckhemer H and Hsu KJ (eds.) *Alpine-Mediterranean Geodynamics*, pp. 347–376. Washington, DC: American Geophysical Union.

Gleason GC and Tullis J (1995) A flow law for dislocation creep of quartz aggregates determined with the molten salt cell. *Tectonophysics* 247: 1–23.

Goetze C and Evans B (1979) Stress and temperature in bending lithosphere as constrained by experimental rock mechanics. *Geophysical Journal of the Royal Astronomical Society* 59: 463–478.

Govers R, Wortel MJR, Cloetingh SAPL, and Stein CA (1992) Stress magnitude estimates from earthquakes in oceanic plate interiors. *Journal of Geophysical Research* 97: 11749–11759.

Gratier J, Guiguet R, Renard F, and Jenatto L (2006) Experimental pressure solution creep of quartz by indenter technique. *Eos, Transactions of the American Geophysical Union* 87(52). Fall Meet. Suppl., Abstract T23D-0525.

Green HW II (2007) Shearing instabilities accompanying high-pressure phase transformations and the mechanics of deep earthquakes. *PNAS* 104(22): 9133–9138.

Handy MR and Brun JP (2004) Seismicity, structure and strength of the continental lithosphere. *Earth and Planetary Science Letters* 223: 427–441.

Hier-Majumder S, Mei S, and Kohlstedt DL (2005) Water weakening of clinopyroxenite in diffusion creep. *Journal of Geophysical Research* 110: B07406. http://dx.doi.org/10.1029/2004JB003414.

Hirth G and Kohlstedt DL (1996) Water in the oceanic upper mantle: Implications for rheology, melt extraction and the evolution of the lithosphere. *Earth and Planetary Science Letters* 144: 93–108.

Hirth G and Kohlstedt DL (2003) Rheology of the upper mantle and the mantle wedge: A view from the experimentalists. In: Eiler J (ed.) *Inside the Subduction Factory*, pp. 83–105, American Geophysical Union Monograph.

Houseman GA, McKenzie DP, and Molnar P (1981) Convective instability of a thickened boundary layer and its relevance for the thermal evolution of continental convergent belts. *Journal of Geophysical Research* 86: 6135–6155.

Huet B, Le Pourhiet L, Labrousse L, Burov E, and Jolivet L (2011) Post-orogenic extension and metamorphic core complexes in a heterogeneous crust: The role of crustal layering inherited from collision. Application to the Cyclades (Aegean domain). *Geophysical Journal International* 184(2): 611–625.

Huismans RS, Buiter S, and Beaumont C (2005) Effect of plastic-viscous layering and strain softening on mode selection during lithospheric extension. *Journal of Geophysical Research* 110: B02406. http://dx.doi.org/10.1029/2004JB003114.

Hull D and Bacon DJ (1984) *Introduction to Dislocations*, 3rd edn., p. 255. Oxford: Pergamon Press.

Humphreys ED, Hessler E, Dueker K, Farmer GL, Erslov E, and Atwater T (2003) How Laramide-age hydration of North American lithosphere by the Farallon slab controlled subsequent activity. *International Geology Review* 45: 575–595.

Jackson J (2002) Strength of the continental lithosphere: Time to abandon the jelly sandwich? *GSA Today* September: 4–10.

Jaeger JC and Cook NGW (1976) *Fundamentals of Rock Mechanics*, 2nd edn, p. 585. NY: Chapman and Hall.

Jaupart C and Mareschal JC (1999) The thermal structure and thickness of continental roots. *Lithos* 48: 93–114.

Jaupart C and Mareschal JC (2007) Heat flow and thermal structure of the lithosphere. In: *Treatise on Geophysics*. Amsterdam: Elsevier.

Ji S, Wirth R, Rybacki E, and Jiang Z (2000) High-temperature plastic deformation of quartz-plagioclase multilayers by layer-normal compression. *Journal of Geophysical Research* 105(B): 16,651–16,664.

Jin D, Karato S, and Obata M (1998) Mechanisms of shear localization in the continental lithosphere: Inference from the deformation microstructures of peridotites from the Ivrea zone, northwestern Italy. *Journal of Structural Geology* 20: 195–209.

John T, Medvedev S, Rüpke LH, Andersen TB, Podladchikov Y, and Austrheim H (2009) Generation of intermediate-depth earthquakes by self-localizing thermal runaway. *Nature Geoscience* 2: 137–140.

Jolivet L, Faccenna C, Goffé B, et al. (1998) Mid-crustal shear zones in post-orogenic extension: The northern Tyrrhenian Sea case. *Journal of Geophysical Research* 103: 12123–12160.

Jordan TA and Watts AB (2005) Gravity anomalies, flexure and the elastic thickness structure of the India-Eurasia collisional system. *Earth and Planetary Science Letters* 236: 732–750.

Judge A and McNutt MK (1991) The relationship between plate dip and elastic plate thickness: A study of the Peru-Chile Trench. *Journal of Geophysical Research* 96: 16,625–16,639.

Kachanov LM (1971) *Foundations of the Theory of Plasticity*, p. 324. Amsterdam: North-Holland Publications.

Karato S-I (1986) Does partial melting reduce the creep strength of the upper mantle? *Nature* 319: 309–310.

Karato S-I (1998) Effects of pressure on plastic deformation of polycrystalline solids: Some geological applications. *Materials Research Society Symposium Proceedings* 499: 3–14.

Karato S (1998) Effects of pressure on plastic deformation of polycrystalline solids: Some geological applications. *Materials Research Society Symposium Proceedings* 499: 3–14.

Karato S-I and Jung H (2003) Effects of pressure on high-temperature dislocation creep in olivine. *Philosophy Magazine* 83: 401–414.

Karato S-I, Paterson MS, and FitzGerald JD (1986) Rheology of synthetic olivine aggregates: Influence of the grain size and water. *Journal of Geophysical Research* 91: 8151–8176.
Katayama I, Karato S-I, and Brandon M (2005) Evidence for high water content in the deep upper mantle inferred from deformation microstructures. *Geology* 33(7): 613–616.
Katz RF, Spiegelman M, and Langmuir CH (2003) A new parameterization of hydrous mantle melting. *Geochemistry, Geophysics, Geosystems* 4(9): 1073. http://dx.doi.org/10.1029/2002GC000433.
Kaufmann G and Amelung F (2000) Reservoir-induced deformation and continental rheology in the vicinity of Lake Mead, Nevada. *Journal of Geophysical Research* 105: 16341–16358.
Keefner JW, Mackwell SJ, Kohlstedt DL, and Heidelbach F (2011) Dependence of dislocation creep of dunite on oxygen fugacity: Implications for viscosity variations in Earth's mantle. *Journal of Geophysical Research* 116: B05201. http://dx.doi.org/10.1029/2010JB007748.
Kenis I, Urai JL, van der Zee W, Hilgers C, and Sintubin M (2005) Rheology of fine-grained siliciclastic rocks in the middle crust – Evidence from structural and numerical analysis. *Earth and Planetary Science Letters* 233: 351–360.
Kirby SH (1983) Rheology of the lithosphere. *Reviews of Geophysics* 21: 1458–1487.
Kirby SH, Durham W, and Stern L (1991) Mantle phase changes and deep-earthquake faulting in subducting lithosphere. *Science* 252: 216–225.
Kirby SH and Kronenberg AK (1987) Rheology of the lithosphere: Selected topics. *Reviews of Geophysics* 25: 1219–1244, correction 1680–1681.
Kirby SH, Stein S, Okal EA, and Rubie DC (1996) Metastable mantle phase transformations and deep earthquakes in subducting oceanic lithosphere. *Reviews of Geophysics* 34: 261–306.
Kirby JF and Swain CJ (2009) A reassessment of spectral T_e estimation in continental interiors: The case of North America. *Journal of Geophysical Research* (114): B08401. http://dx.doi.org/10.1029/2009JB006356.
Kirby JF and Swain CJ (2011) Improving the spatial resolution of effective elastic thickness estimation with the fan wavelet transform. *Computers & Geosciences* 37(9): 1345–1354. http://dx.doi.org/10.1016/j.cageo.2010.10.008.
Kissling E and Spakman W (1996) Interpretation of tomographic images of uppermost mantle structure: Examples from the Western and Central Alps. *The Journal of Geodynamics* 21: 97–111.
Klemperer S and Hobbs R (1991) *The BIRPS Atlas*, p. 124. Cambridge: Cambridge University Press.
Kohlstedt DL (2007) Constitutive equations, rheological behavior, and viscosity of rocks. In: Schubert G and Schubert G (eds.) *Treatise on Geophysics. Miner. Phys.*, vol. 2.14, pp. 389–417. Amsterdam: Elsevier.
Kohlstedt DL, Evans B, and Mackwell SJ (1995) Strength of the lithosphere: Constraints imposed by laboratory experiments. *Journal of Geophysical Research* 100: 17587–17602.
Kruse S and Royden L (1994) Bending and unbending of an elastic lithosphere: The Cenozoic history of the Apennine and Dinaride fordeep basins. *Tectonics* 13: 278–302.
Kusznir NJ (1991) The distribution of stress with depth in the lithosphere: Thermo-rheological and geodynamic constraints. *Philosophical Transactions of the Royal Society of London* A337: 95–110.
Kusznir NJ and Matthews DH (1988) Deep seismic reflections and the deformational mechanics of the continental lithosphere. *Journal of Petrology* Special_Volume (1) : 63–87.
Kuznir NL and Park RG (1986) Continental lithosphere strength: The critical role of lower crustal deformation. In: Dawson JB, Carswell DA, Hall J, and Wedepohl KH (eds.) *The Nature of the Lower Continental Crust*, pp. 79–94, Special Publication-Geological Society, 24.
Lachenbruch AH and Morgan P (1990) Continental extension, magmatism and elevation; formal relations and rules of thumb. *Tectonophysics* 174: 39–62.
Lambeck K (1983) Structure and evolution of intracratonic basins in central Australia. *Geophysical Journal of the Royal Astronomical Society* 74: 843–886.
Larsen CF, Motyka RJ, Freymueller JT, Echelmeyer KA, and Ivins ER (2005) Rapid viscoelastic uplift in southeast Alaska caused by post–Little Ice Age glacial retreat. *Earth and Planetary Science Letters* 237: 548–560.
Lavier LL, Buck WR, and Poliakov ANB (2000) Factors controlling normal fault offset in ideal brittle layer. *Journal of Geophysical Research* 105: 23,431–23,442.
Le Pichon X, Francheteau J, and Bonnin J (1973) *Plate Tectonics*, p. 300. New York: Elsevier Scientific.
Le Pourhiet L, Burov E, and Moretti I (2004) Rifting through a stack of inhomogeneous thrusts (the dipping pie concept). *Tectonics* 23(4): TC4005. http://dx.doi.org/10.1029/2003TC001584.
Lenardic A, Moresi LN, and Muhlhaus H (2003) Longevity and stability of cratonic lithosphere: Insights from numerical simulations of coupled mantle convection and continental tectonics. *Journal of Geophysical Research* 108(B6). http://dx.doi.org/10.1029/2002JB001859.
Lobkovsky LI and Kerchman VI (1992) A two-level concept of plate tectonics: Application to geodynamics. *Tectonophysics* 199: 343–374.
Lokhner DA (1995) Rock failure. In: Ahrens TJ (ed.) *Rock Physics and Phase Relations: A Handbook of Physical Constants, AGU Reference Shelf 1*, pp. 127–147. Washington, DC: AGU.
Lowry AR and Smith RB (1994) Flexural rigidity of the Basin and Range-Colorado Plateau-Rocky Mountain transition from coherence analysis of gravity and topography. *Journal of Geophysical Research* 99: 20,123–20,140.
Mackwell SJ, Zimmerman ME, and Kohlstedt DL (1998) High-temperature deformation of dry diabase with applications to tectonics on Venus. *Journal of Geophysical Research* 103: 975–984.
Maggi A, Jackson JA, Priestley K, and Baker C (2000) A re-assessment of focal depth distributions in southern Iran, the Tien Shan and northern India: Do earthquakes occur in the continental mantle? *Geophysical Journal International* 143: 629–661.
McAdoo DC, Martin CF, and Polouse S (1985) Seasat observations of flexure: Evidence for a strong lithosphere. *Tectonophysics* 116: 209–222.
McKenzie D and Bickle MJ (1988) The volume and composition of melt generated by extension of the lithosphere. *Journal of Petrology* 29: 342–532.
McKenzie DP and Fairhead D (1997) Estimates of the effective elastic thickness of the continental lithosphere from Bouguer and free-air gravity anomalies. *Journal of Geophysical Research* 102: 27,523–27,552.
McNutt MK and Menard HW (1982) Constraints on yield strength in the oceanic lithosphere derived from observations of flexure. *Geophysical Journal of the Royal Astronomical Society* 71: 363–395.
Meissner R and Bortfeld RK (eds.) (1990) *DEKORP-Atlas, Results of Deutsches Kontinentales Reflexionsseismisches Programm*. Berlin, Heidelberg, New York: Springer Verlag, 18p and 80 plates.
Melosh HJ (1990) Mechanical basis for low-angle normal faulting in the Basin and Range province. *Nature* 343: 331–335.
Molnar P and Houseman GA (2004) The effects of buoyant crust on the gravitational instability of thickened mantle lithosphere at zones of intracontinental convergence. *Geophysical Journal International* 158: 1134–1150.
Molnar P and Lyon-Caen H (1988) Some simple physical aspects of the support, structure, and evolution of mountain belts. *Geological Society of America Special Paper* 218: 179–207.
Molnar P and Tapponnier (1981) A possible dependence of the tectonic strength on the age of the crust in Asia. *Earth and Planetary Science Letters* 52: 107–114.
Monsalve G, Sheehan A, Schulte-Pelkum V, Rajaure S, Pandey MR, and Wu F (2006) Seismicity and one-dimensional velocity structure of the Himalayan collision zone: Earthquakes in the crust and upper mantle. *Journal of Geophysical Research* 111: B10301. http://dx.doi.org/10.1029/2005JB004062.
Montesi LGJ (2004) Controls of shear zone rheology and tectonic loading on post seismic creep. *Journal of Geophysical Research* 109: B10404. http://dx.doi.org/10.1029/2003JB002925.
Morley CK (1989) Extension, detachments, and sedimentation in continental rifts (with particular reference to East Africa). *Tectonics* 8: 1175–1192.
Mouthereau F, Watts AB, and Burov E (2013) Collisional orogens, structural inheritance and the long-term strength of continental lithosphere. *Nature Geoscience* 6(9): 785–789.
Müller B, Zoback ML, Fuchs K, et al. (1992) Regional patterns of stress in Europe. *Journal of Geophysical Research* 97: 11783–11803.
Nadai A (1963) *Theory of Flow and Fracture of Solids*, vol. 2, p. 705. New York: McGraw-Hill.
Okaya N, Cloetingh S, and Mueller St (1996) A lithospheric cross section through the Swiss Alps – II. Constraints on the mechanical structure of a continent-continent collision zone. *Geophysical Journal International* 127: 399–414.
Parsons BE and Sclater JG (1977) An analysis of the variation of ocean floor bathymetry and heat flow with age. *Journal of Geophysical Research* 82: 803–827.
Passey QP (1981) Upper mantle viscosity derived from the difference in rebound of the Provo and Bonneville shorelines, Lake Bonneville basin. *Journal of Geophysical Research* 86: 11701–11708.
Peltier WR (1974) The impulse response of a Maxwell Earth. *Reviews of Geophysics and Space Physics* 12: 649–669.
Peltier WR and Andrews JT (1976) Glacial-isostatic adjustment – I. The forward problem. *Geophysical Journal of the Royal Astronomical Society* 46: 605–646.
Pérez-Gussinyé M and Watts AB (2005) The long-term strength of Europe and its implications for plate-forming processes. *Nature* 436(7049): 381–384. http://dx.doi.org/10.1038.
Petrini K and Podladchikov Yu (2000) Lithospheric pressure-depth relationship in compressive regions of thickened crust. *Journal of Metamorphic Geology* 18: 67–78.

Pinet C, Jaupart C, Mareschal J-C, Gariepy C, Bienfait G, and Lapointe R (1991) Heat flow and lithospheric structure of the eastern Canadian shield. *Journal of Geophysical Research* 96: 19,923–19,941.

Poirier JP (1985) *Creep of Crystals*, p. 260. Cambridge: Cambridge University Press.

Poliakov ANB, Cundall P, Podladchikov Y, and Laykhovsky V (1993) An explicit inertial method for the simulation of visco-elastic flow: An evaluation of elastic effects on diapiric flow in two- or three-layers models. In: Stone DB and Runcorn SK (eds.) *Flow and Creep in the Solar System: Observations, Modelling and Theory, Dynamic Modelling and Flow in the Earth and Planets Series*, pp. 175–195.

Pollitz FF, Wicks C, and Thatcher W (2001) Mantle flow beneath a continental strike-slip fault: Postseismic deformation after the 1999 hector mine earthquake. *Science* 293: 1814–1818.

Précigout J and Gueydan F (2009) Mantle weakening and strain localization: Implications for the long-term strength of the continental lithosphere. *Geology* 37(2): 147–150. http://dx.doi.org/10.1130/G25239A.1.

Precigout J, Gueydan F, Gapais D, Garrido CJ, and Essaifi A (2007) Strain localisation in the subcontinental mantle – A ductile alternative to the brittle mantle. *Tectonophysics* 445: 318–336.

Ranalli G (1995) *Rheology of the Earth*, 2nd edn., p. 413. London: Chapman and Hall.

Regenauer-Lieb K, Yuen DA, and Branlund J (2001) The initiation of subduction: Criticality by addition of water? *Science* 294(5542): 578–580.

Rice JR and Tse ST (1986) Dynamic motion of a single degree of freedom system following a rate and state dependent friction law. *Journal of Geophysical Research* 91: 521–530.

Rupke LH, Morgan JP, Hort M, and Connolly JAD (2002) Are the regional variations in Central American arc lavas due to differing basaltic versus peridotitic slab sources of fluids? *Geology* 30: 1035–1038.

Rutter EH and Brodie KH (1991) Lithosphere rheology – A note of caution. *The Journal of Structural Geology* 13: 363–367.

Rutter EH and Brodie KH (2004) Experimental grain size-sensitive flow of hot-pressed Brazilian quartz aggregates. *Journal of Structural Geology* 26: 2011–2023.

Rybacki E, Gottschalk M, Wirth R, et al. (2006) Influence of water fugacity and activation volume on the flow properties of fine-grained anorthite aggregates. *Journal of Geophysical Research* 111: B03203. http://dx.doi.org/10.1029/2005JB003663.

Sabadini R and Vermeersen LLA (2004) Global dynamics of the earth: Applications of normal mode relaxation theory to solid-earth geophysics. *Modern Approaches Geophys*, vol. 30. New York: Springer.

Salveson JO (1978) Variations in the geology of rift basins: A tectonic model. In: *Conf. Proc. Los Alamos Natl. Lab., 7487, Los Alamos, N.M.*, pp. 82–86.

Schmelling H, Babeyko AY, Enns A, et al. (2008) A benchmark comparison of spontaneous subduction models – Toward a free surface. *Physics of the Earth and Planetary Interiors* 171: 198–223.

Scholz CH (1990) Mechanics of faulting. *Annual Review of Earth and Planetary Sciences* 17: 309–334.

Scholz CH (2002) *The Mechanics of Earthquakes and Faulting*, 2nd edn. Cambridge, England: Cambridge University Press.

Sclater JG, Jaupart C, and Galson D (1980) The heat flow through oceanic and continental crust and the heat loss of the Earth. *Journal of Geophysical Research* 18: 269–311.

Seno T and Seito A (1994) Recent East African earthquakes in the lower crust. *Earth and Planetary Science Letters* 121: 125–135.

Seno T and Yamanaka Y (1996) Double seismic zones, compressional deep trench-outer rise events and superplumes. In: Bebout GE, Scholl DW, Kirby SH, and Platt JP (eds.) *Subduction Top to Bottom, Geophysical Monograph Series*, vol. 96, pp. 347–355. Washington, D.C.: AGU.

Shelton G and Tullis JA (1981) Experimental flow laws for crustal rocks. *Eos, Transactions, American Geophysical Union* 62: 396.

Shudofsky GN (1985) Source mechanisms and focal depths of east African earthquakes using Rayleigh-wave inversion and body-wave modelling. *Geophysical Journal of the Royal Astronomical Society* 83: 563–614.

Shudofsky GN, Cloetingh S, Stein S, and Wortel R (1987) Unusually deep earthquakes in east Africa: Constraints on the thermo-mechanical structure of a continental rift system. *Geophysical Research Letters* 14(7): 741–744.

Sibson RH (1980) Transient discontinuities in ductile shear zones. *Journal of Structural Geology* 2: 165–171.

Smit J, Cloetingh S, Burov E, et al. (2013) Interference of lithospheric folding in western Central Asia by simultaneous Indian and Arabian plate indentation. *Tectonophysics* 602: 176–193. http://dx.doi.org/10.1016/j.tecto.2012.05.030.

Souriau A, Chevrot S, and Olivera C (2008) A new tomographic image of the Pyrenean lithosphere from teleseismic data. *Tectonophysics* 460: 206–214.

Stacey FD (1992) *Physics of the Earth*, p. 513. Brisbane: Brookfield Press.

Stephenson RA and Cloetingh S (1991) Some examples and mechanical aspects of continental lithospheric folding. *Tectonophysics* 188: 27–37.

Terry M and Heidelbach F (2004) Superplasticity in garnet from eclogite facies shear zones in the Haram Gabbro, Haramsøya, Norway. *Geology* 32(4): 281–284. http://dx.doi.org/10.1130/G20157.1.

Tesauro M, Burov E, Kaban M, and Cloetingh S (2011) Ductile crustal flow in Europe's lithosphere. *Earth and Planetary Science Letters* 312(1–2): 254–265.

Tesauro M, Kaban MK, and Cloetingh SAPL (2008) EuCRUST-07: A new reference model for the European crust. *Geophysical Research Letters* 35: LXXXXX. http://dx.doi.org/10.1029/2007GL032244.

Tesauro M, Kaban MK, and Cloetingh S (2009a) How rigid is Europe's lithosphere? *Geophysical Research Letters* 36, L16303.

Tesauro M, Kaban MK, and Cloetingh SAPL (2009b) A new thermal and rheological model of the European lithosphere. *Tectonophysics* 476: 478–495.

Tesauro M, Kaban MK, Cloetingh SAPL, Hardebol NJ, and Beekman F (2009c) 3D strength and gravity anomalies of the European lithosphere. *Earth and Planetary Science Letters* 263: 56–73.

Tirel C, Brun J-P, and Burov E (2004) Thermo-mechanical modeling of extensional gneiss dome. In: *Gneiss Domes and Orogeny*, pp. 67–78 Geological Society of America Special Paper, 380.

Toussaint G, Burov E, and Jolivet J (2004) Continental plate collision: Unstable vs. stable slab dynamics. *Geology* 32: 33–36.

Tse ST and Rice JR (1986) Crustal earthquake instability in relation to the depth variation of friction slip properties. *Journal of Geophysical Research* 91: 9452–9472.

Turcotte DL and Schubert G (2002) *Geodynamics*, 2nd edn., p. 456. Cambridge: Cambridge University Press.

Van Hunen J, Zhong S, Shapiro N, and Ritzwoller HR (2005) New evidence for dislocation creep from 3-D geodynamic modelling of the Pacific upper mantle structure. *Earth and Planetary Science Letters* 238: 146–155.

Vermeer PA (1990) The orientation of shear bands in biaxial tests. *Geotechnique* 40(2): 223–236.

Vermeer PA and de Borst R (1984) Non-associated plasticity for soils, concrete and rocks. In: *Heron*, pp. 1–75. Rijswijk, The Netherlands: Stevin-laboratory of Civil Engineering, University of Technology, Delft Institute TNO for Building Materials and Building Structures, 29(3à).

Walcott RI (1970) Isostatic response to loading of the crust in Canada. *Canadian Journal of Earth Sciences* 7: 716–727.

Watremez L, Burov E, d'Acremont E, et al. (2013) Buoyancy and localizing properties of continental mantle lithosphere: Insights from thermomechanical models of the eastern Gulf of Aden. *Geochemistry, Geophysics, Geosystems* 14: 2800–2817. http://dx.doi.org/10.1002/ggge.20179, ISSN: 15252027.

Watts AB (1978) An analysis of isostasy in the world's oceans: 1. Hawaiian-Emperor Seamount Chain. *Journal of Geophysical Research* 83: 5,989–6,004.

Watts AB (1992) The elastic thickness of the lithosphere and the evolution of sedimentary basins. *Basin Research* 4: 169–178.

Watts AB (2001) *Isostasy and Flexure of the Lithosphere*, p. 458. Cambridge: Cambridge University Press.

Watts AB and Burov E (2003) Lithospheric strength and its relationship to the elastic and seismogenic layer thickness. *Earth and Planetary Science Letters* 213: 113–131.

Wei W, Unsworth M, Jones A, et al. (2001) Detection of widespread fluids in the Tibetan crust by magnetotelluric studies. *Science* 292(5517): 716–719. http://dx.doi.org/10.1126/science.1010580.

Weinberg RF and Podladchikov Y (1995) The rise of solid state diapirs. *The Journal of Structural Geology* 17: 1183–1195.

Weissel J, Anderson RN, and Geller C (1980) Deformation of the Indo-Australian plate. *Nature* 287: 284–291.

Wever T (1989) The Conrad discontinuity and the top of the reflective lower crust – Do they coincide? *Tectonophysics* 157: 39–58.

Wilks KR and Carter NL (1990) Rheology of some continental lower crustal rocks. *Tectonophysics* 182: 57–77.

Willingshofer E and Cloetingh S (2003) The present-day lithospheric strength of the Eastern Alps and its relationship to neotectonics. *Tectonics* 22: 1075. http://dx.doi.org/10.1029/2002TC001463.

Wittlinger G, Tapponnier P, Poupinet G, et al. (1998) Tomographic evidence for localized lithospheric shear along the Altyn Tagh fault. *Science* 282: 74–76.

Yamato P, Agard P, Burov E, Le Pourhiet L, Jolivet L, and Tiberi C (2007) Burial and exhumation in a subduction wedge: Mutual constraints from thermo-mechanical modelling and natural p-t-t data (sch. Lustres, w. Alps). *Journal of Geophysical Research* 112, B07410.

Zoback ML (1992) First- and second-order patterns of stress in the lithosphere: The World Stress Map project. *Journal of Geophysical Research* 97: 11,703–11,728.

Zoback MD, Apel R, Baumgartner J, et al. (1993) Upper-crustal strength inferred from stress measurements to 6 km depth in the KTB borehole. *Nature* 365: 633–635.

Zoback MD and Townend J (2001) Implication of hydrostatic pore pressures and high crustal strength for the deformation of intraplate lithosphere. *Tectonophysics* 336: 19–30.

6.04 Plate Deformation

R Sabadini, University of Milan, Milan, Italy

© 2015 Elsevier B.V. All rights reserved.

6.04.1	**Introduction**	153
6.04.2	**Postglacial Rebound**	154
6.04.2.1	Introduction	154
6.04.2.2	PGR Mathematical Modeling	154
6.04.2.3	Global Vertical and Horizontal Displacements from PGR	157
6.04.2.4	PGR in GPS Analyses	159
6.04.2.5	Present-Day Glacier Shrinkage and Uplift of the Alps	163
6.04.2.6	Sea-Level Changes	165
6.04.3	**Continental Plates**	168
6.04.3.1	Introduction	168
6.04.3.2	Modeling Intraplate Deformation	169
6.04.3.3	Monitoring Intraplate Deformation via GPS Analyses	172
6.04.4	**Plate Deformation at Subduction Zones**	178
6.04.4.1	Introduction	178
6.04.4.2	The Mediterranean: A Natural Laboratory for Understanding Plate Behavior at Subduction Zones	178
6.04.4.3	The Fingerprint of Subduction in GPS Data	180
6.04.4.4	Stress Pattern in the Mediterranean	184
6.04.4.5	Blending Seismic, GPS, and Stress Data	185
6.04.5	**Coseismic and Postseismic Deformations**	186
6.04.5.1	Introduction	186
6.04.5.2	Modeling Global Coseismic and Postseismic Plate Deformations	186
6.04.5.3	Postseismic Deformation from Shallow Earthquakes	189
6.04.5.4	The Example of the 1997 Umbria–Marche Earthquake	190
6.04.5.5	DInSAR-Retrieved Coseismic Displacements	193
6.04.5.6	The 1980 Irpinia Earthquake	195
6.04.6	**Interseismic and Preseismic Deformation**	198
6.04.6.1	The Pollino and Emilia-Romagna Seismogenic Regions	199
6.04.7	**The 2004 Sumatra and 2011 Giant Tohoku-Oki Earthquakes**	206
6.04.7.1	Modeling the 2004 Sumatra Earthquake	206
6.04.7.2	The GRACE Data	208
6.04.7.3	Constraining the 2004 Sumatra Earthquake	210
6.04.7.4	The 2011 Great Tohoku-Oki Earthquake: Gravitational Seismology	211
6.04.8	**Conclusions**	212
References		213

6.04.1 Introduction

Focusing on plate-deformation properties will provide a close look at the lithosphere and crust. Indeed, it should be noted that when studying postglacial rebound (PGR), the Earth's outermost elastic layer cannot be isolated from the mantle since a great deal of the latter's material is required to fill mass deficiency in deglaciated areas during the process of isostatic readjustment. This means that equations of motion must necessarily be applied to the whole spherical volume, including the lithosphere and underlying mantle. When studying continental collision, which involves only the outermost part of the planet, the mantle can be considered as totally decoupled from the lithosphere. In this case, to a good approximation, the spherical volume considered in PGR can thus be shrunk to the outermost lithosphere, where differential equations of motion are solved within a thin outer layer. This concept is the basis of the mathematical developments for PGR and continental collision, as it will be shown.

In modeling geophysical phenomena such as plate deformation, the choice of the rheology, or the way the Earth's material behaves under an applied deviatoric stress, depends essentially on the characteristic timescale over which such deformation occurs. In what follows, the main questions at issue in attempting to study transient and long-timescale geodynamic phenomena are addressed in a wide arc of timescales. These range from seconds, characteristic of coseismic deformation, to hundreds of millions of years, as in the case of subduction, making use of results based on the analytic normal-mode theory in viscoelasticity or finite-element schemes.

Figure 1 sketches out the entire geodynamic spectrum spanning the whole range of phenomenological timescales. One of

 http://dx.doi.org/10.1016/B978-0-444-53802-4.00113-5

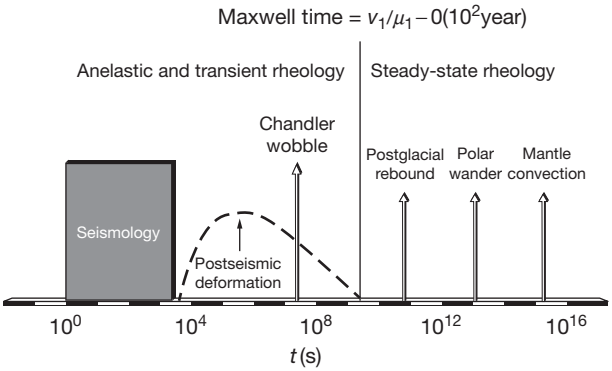

Figure 1 Diagram illustrating the relation of the characteristic timescale for several geophysical phenomena to the Maxwell time of the mantle defined as v_1/μ_1 – with v_1 and μ_1 denoting, respectively, the steady-state mantle viscosity and rigidity – which separates the steady state and the transient regimes of the mantle creep. Reproduced from Figure 1.1 of Sabadini R and Vermeersen B (2004) *Global Dynamics of the Earth*, 328 pp. Kluwer Academic Publisher, with kind permission of Springer Science and Business Media.

the key questions is whether one can implement a constitutive law that can satisfactorily model all these phenomena, from the anelastic transient regime to the steady-state domain. Analyzing plate deformation thus requires the implementation of the appropriate constitutive relation between stress and strain, which is capable of reproducing the mechanical behavior of the crust–lithosphere system over the widest range of timescales characterizing the geodynamic process under study.

The appropriate constitutive relation that is to be employed in analyzing transient geodynamic phenomena, like PGR, is currently a matter of controversy in geophysics. There is evidence from modeling (Spada et al., 1991) that PGR-induced stress level in the mantle is less than O(100 bar), or O(10 MPa), which implies that the creep mechanism may be linear for polycrystalline aggregates since grain boundary processes such as Coble creep may become dominant.

Since there is no unambiguous evidence either in the PGR event or in other types of geodynamic data that absolutely requires a nonlinear viscoelastic rheology, geophysicists tend to prefer the simple linear models in viscoelasticity, which allow for a considerably simpler mathematical treatment of the dynamics.

The simplest viscoelastic model, which can describe the Earth as an elastic body for short timescales and as a viscous fluid for timescales characteristic of plate deformation during continental collision or subduction, is the linear Maxwell solid, portrayed in Figure 2. It shows a standard one-dimensional (1-D) spring and dashpot analog of the Maxwell rheology. The speed for shear-wave propagation depends on the square root of the instantaneous rigidity μ_1, whereas the strength of the lithosphere and mantle, over timescales of 10^3–10^6 years, depends on the viscosity v_1, characterizing the planet's ability to propagate deformation over such long timescales. In order to gain a deep insight into the physics of plate-deformation processes, the mathematical equations describing the mechanical behavior of the whole set of geophysical phenomena, from

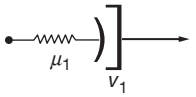

Figure 2 Mechanical analog of Maxwell rheology. The elastic response is governed by the shear modulus μ_1 of the spring while the long-term creep is controlled by the viscosity v_1 of the dashpot. Reproduced from Sabadini R and Vermeersen B (2004)*Global Dynamics of the Earth*, 328 pp. Dordrecht: Kluwer Academic Publisher.

PGR to plate behavior in continental collision and subduction, are implemented.

6.04.2 Postglacial Rebound

6.04.2.1 Introduction

Using oxygen isotope analysis of ocean sediments, Shackleton and Opdyke (1976) showed that great ice ages have repeatedly occurred over the Earth and are characterized by a growth period of about 90 000 years and a decay period of about 10 000 years, leading to a total period of 100 000 years for one complete cycle. These findings are based on the relative concentration of the oxygen isotopes ^{16}O and ^{18}O in seawater. Depending on the amount of ice that has accumulated on land, the relative abundance of the two isotopes incorporated in ocean sediments varies due to their specific mass difference. Since the lighter isotope evaporates more easily from the oceans, yielding an overabundance of this isotope in ice with respect to ocean water, an overabundance of the heavier isotope is created in the oceans and recorded in the sediments during glacial times.

Mathematical simulation via appropriate geophysical models of the Earth's response to this huge redistribution of ice and water masses occurring over timescales of 10^3–10^4 years makes it possible to retrieve the mechanical and deformation properties of the lithosphere, the outermost portion of our planet, including the underlying mantle. In modeling PGR, the plate under consideration is thus the entire outermost elastic shell of the Earth rather than a part of it as in continental collision or subduction, as will become clear later in the text. Given that it is such a huge, global readjustment of the Earth to surface loads, PGR mainly involves the deformation properties of the mantle, rather than the outermost plate, though the latter certainly plays the role of fine-tuning the visible surface effects of rebound on Global Positioning System (GPS) data, as shown in the following for PGR modeling.

PGR is responsible for the largest vertical motions occurring over the Earth, such as those in the Hudson Bay or in the Gulf of Bothnia, and the largest global gravity changes, like those nowadays seen from satellite data.

6.04.2.2 PGR Mathematical Modeling

For long-timescale processes like PGR, the inertial forces vanish and the conservation of linear momentum requires that the body forces **F** per unit mass acting on the element of the body be balanced by the stresses acting on the surface of the element. The stress tensor σ acting on the infinitesimal block with density ρ satisfies the following momentum equation:

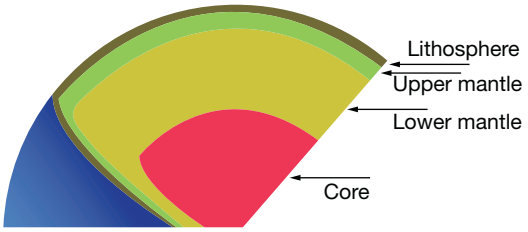

Figure 3 Four-layered Earth model, consisting of the outermost elastic lithosphere (gray), upper mantle (green), lower mantle (light green), and core (red).

$$\nabla\cdot\sigma + \rho\mathbf{F} = 0 \qquad [1]$$

at each instant of time. At the start, the Earth is assumed compressible, laterally homogeneous, radially stratified, hydrostatically prestressed, and not rotating. PGR models shown in the succeeding text will be based on the assumption that the Earth's material is incompressible, since in this case, solutions to eqn [1] can be treated analytically, as detailed in Sabadini and Vermeersen (2004).

Equation [1] holds in each volume element of the Earth shown in Figure 3. Elastic equations of motion are considered since any linear viscoelastic problem that is of interest to us is equivalent to an elastic problem in the Laplace domain (see Sabadini and Vermeersen, 2004 for details). Momentum and gravity equations are thus solved for an elastic medium, and only at the end, with the elastic solution in hand, is the solution derived in the time domain by antitransformation from Laplace to time domain.

The stress tensor σ is the sum of the initial pressure due to the hydrostatically prestressed condition, plus a perturbation σ_1, so that σ reads

$$\sigma = \sigma_1 - p_0\mathbf{I} \qquad [2]$$

where σ_1 denotes a tensor that describes the acquired, nonhydrostatic stress related to the strain by means of the appropriate constitutive equations that mathematically describe the mechanical analog depicted in Figure 2. The hydrostatic pressure p_0, with $\mathbf{I}$ the identity matrix, enters the equation in the preceding text with the minus sign since it denotes a compressive stress, which is negative according to the convention that stresses are positive when they act in the same direction as the outward normal to the surface embedding the Earth's volume under study. On the elementary surface enclosing the elementary volume in which the equation of equilibrium holds, the pressure, or stress due to the load of the overlying material, is negative. According to this convention, the equation of conservation of linear momentum thus becomes

$$\nabla\cdot\sigma_1 - \nabla p_0 + \rho\mathbf{F} = 0 \qquad [3]$$

If the body is subject to an elastic displacement $\mathbf{u}$ at t_0, the pressure at $t_0+\delta t$ at a fixed point in space is

$$p_0(t_0+\delta t) = p_0(t_0) - \mathbf{u}\cdot\nabla p_0 \qquad [4]$$

The minus sign accounts for the fact that the pressure increases at a fixed point in space if the elastic displacement occurs in the opposite direction with respect to the pressure gradient.

The equation of conservation of linear momentum after elastic displacement becomes, with $p_0(t_0+\delta t)$ instead of $p_0(t_0)$,

$$\nabla\cdot\sigma_1 - \nabla p_0(t_0) + \nabla(\mathbf{u}\cdot\nabla p_0) + \rho\mathbf{F} = 0 \qquad [5]$$

The gradient of the initial pressure is given by

$$\nabla p_0 = -\rho_0 g\hat{\mathbf{e}}_r \qquad [6]$$

where $\hat{\mathbf{e}}_r$ denotes the unit vector, positive outward from the Earth's center. By working eqn [6] into eqn [5], the equation of equilibrium becomes

$$\nabla\cdot\sigma_1 - \nabla p_0(t_0) - \nabla(\rho_0 g\mathbf{u}\cdot\hat{\mathbf{e}}_r) + \rho\mathbf{F} = 0 \qquad [7]$$

The force $\mathbf{F}$ can usually be split into gravity and all kinds of other terms that represent the forcing due to a variety of geophysical phenomena as tidal forces and loads due to ice-sheet disintegration and ice–water redistribution and earthquakes. For the moment, it is assumed that the force $\mathbf{F}$ is gravity, thus simulating the condition of a free, self-gravitating Earth with no other forcings or loads acting on its surface or interior, and that, being a conservative force, it can be expressed as the negative gradient of the potential field ϕ:

$$\mathbf{F} = \cdots\nabla\phi \qquad [8]$$

The potential field ϕ can be written as the sum of two terms

$$\phi = \phi_0 + \phi_1 \qquad [9]$$

with ϕ_0 as the field in the initial state and ϕ_1 the infinitesimal perturbation. The linearized equation of momentum becomes, with ρ_1 the perturbation in the density and g the gravity,

$$\nabla\cdot\sigma_1 - \nabla(\rho_0 g\mathbf{u}\cdot\hat{\mathbf{e}}_r) - \rho_0\nabla\phi_1 - \rho_1 g\hat{\mathbf{e}}_r = 0 \qquad [10]$$

the second term of eqn [7] being canceled by the term $-\rho_0\nabla\phi_0$.

The first term of eqn [10] describes the stress contribution, the second term the advection of the hydrostatic prestress, the third the changed gravity (self-gravitation), and the fourth the changed density due to compressibility. In cases where self-gravitation is neglected, the third term will be zero, while in the case of incompressibility, as considered hereafter, the fourth term will be zero.

The perturbed gravitational potential ϕ_1 satisfies the Poisson equation

$$\nabla^2\phi_1 = 4\pi G\rho_1 \qquad [11]$$

with G as the universal gravitational constant. In the case of incompressibility, the right-hand term will be zero since $\rho_1 = 0$, and eqn [11] reduces to the Laplace equation

$$\nabla^2\phi_1 = 0 \qquad [12]$$

The earlier-mentioned equations need to be supplemented by a constitutive equation describing how stress and strain (or strain rate) are related to each other. For PGR modeling, the Maxwell rheological model depicted in Figure 2 is considered. The momentum and Poisson equations for an elastic solid will first be expanded in spherical harmonics and only afterward is transformation from the Laplace to the time domain performed in order to retrieve the viscoelastic solution specialized for an incompressible material in PGR (see results in the succeeding text).

The equilibrium and Poisson equations can be written in spherical coordinates, as shown in Schubert et al. (2001, p. 281). By denoting derivatives with respect to r and θ by means of ∂_r and ∂_θ, respectively, and assuming that there is no longitudinal component in the fields or in their derivatives, with symmetrical deformation around the polar axis as appropriate for a point loading the north pole of the Earth model in Figure 3, and by taking into account of the continuity equation,

$$\rho_1 = -\nabla\cdot(\rho_0\mathbf{u}) = -\mathbf{u}\cdot\hat{\mathbf{e}}_r\partial_r\rho_0 - \rho_0\nabla\cdot\mathbf{u} \qquad [13]$$

with $\Delta = \nabla\cdot\mathbf{u}$ and ρ_1 denoting the perturbed density, the two r and θ components of the momentum and Poisson equations become

$$\begin{aligned} &-\rho_0\partial_r\phi_1 + \rho_0 g_0\Delta - \rho_0\partial_r(ug_0) + \partial_r\sigma_{rr} \\ &+ r^{-1}\partial_\theta\sigma_{r\theta} + r^{-1}(2\sigma_{rr} - \sigma_{\theta\theta} - \sigma_{\theta\theta} + \sigma_{r\theta}\cot\theta) = 0 \end{aligned} \qquad [14]$$

$$\begin{aligned} &-\rho_0 r^{-1}\partial_\theta\phi_1 - \rho_0 g_0 r^{-1}\partial_{\theta u} + \partial_r\sigma_r\theta \\ &+ r^{-1}\partial_\theta\sigma_{\theta\theta} + r^{-1}\left((\sigma_{\theta\theta} - \sigma_{\phi\phi})\cot\theta + 3\sigma_{r\theta}\right) = 0 \end{aligned} \qquad [15]$$

$$r^{-2}\partial_r\left(r^2\partial_r\phi_1\right) + \left(r^2\sin\theta\right)^{-1}\partial_\theta(\sin\theta\partial_\theta\phi_1) = -4\pi G(\rho_0\Delta + u\partial_r\rho_0) \qquad [16]$$

where σ_{rr}, $\sigma_{\theta\theta}$, $\sigma_{\phi\phi}$, and $\sigma_{r\theta}$ denote the stress components in spherical coordinates. In principle, deformation, stress field, and gravity field can be solved by means of numerical integration techniques. Sabadini and Vermeersen (2004) showed how it is possible to solve these equations analytically by means of viscoelastic normal-mode modeling in the Laplace-transformed domain, as stated by the 'correspondence principle,' thereby providing deep insights into the physics of relaxation processes; the explicit expression for the singular part of the Green function for spheroidal, incompressible deformation, necessary for modeling a multilayered Earth, was derived for the first time in Sabadini et al. (1982).

By following the normal-mode approach fully described in Sabadini and Vermeersen (2004), the momentum and Poisson equations given in the preceding text are expanded in spherical harmonics defined by

$$Y_l^m(\theta,\phi) = (-1)^m p_l^m(\cos\theta)\exp(im\phi) \qquad [17]$$

with $l = 0, 1, 2, \ldots$ and $m = -l, -l+1, \ldots l$ and $P_l^m(\cos\theta)$ denoting the associated Legendre function:

$$P_l^m(\cos\theta) = \frac{(1-\cos^2\theta)^{m/2}}{2^l l!}\frac{d^{l+m}}{d(\cos\theta)^{l+m}}\left(\cos^2\theta - 1\right)^l \qquad [18]$$

For the spheroidal part, of importance in PGR problems, the radial displacement u, the tangential (colatitudinal) component v, and the perturbation in the gravitational potential ϕ_1 as functions of the scalars U_l, V_l, and ϕ_l, which depend solely on the harmonic degree l and on the radial distance r from the center of the Earth, are

$$u = \sum_{l=0}^{\infty} U_l(r)P_l(\cos\theta) \qquad [19]$$

$$v = \sum_{l=0}^{\infty} V_l(r)\partial_\theta P_l(\cos\theta) \qquad [20]$$

$$\phi_1 = -\sum_{l=0}^{\infty}\phi_l(r)P_l(\cos\theta) \qquad [21]$$

where the Legendre polynomial $P_l(\cos\theta)$ is obtained from the Rodrigues formula

$$P_l(\cos\theta) = \frac{1}{2^l l!}\frac{d^l}{d(\cos\theta)^l}\left(\cos^2\theta - 1\right)^l \qquad [22]$$

or from $m=0$ in the previous definition [18] of the associated Legendre function. Note that the spheroidal solution does not carry any longitudinal displacement, as anticipated earlier in the text.

The toroidal displacement components v' along colatitude and w along longitude entering plate-deformation processes activated by earthquakes are defined by the following expansion in spherical harmonics:

$$v' = \sum_{l=0}^{\infty} W_l(r)\sum_{m=-l}^{l}\nabla_\phi Y_l^m(\theta,\phi) \qquad [23]$$

$$w = -\sum_{l=0}^{\infty} W_l(r)\sum_{m=-l}^{m=l}\nabla_\theta Y_l^m(\theta,\phi) \qquad [24]$$

which provide the toroidal components of the latitudinal and longitudinal displacements v' and w as a function of the W_l scalar harmonic coefficients. Collectively, U_l, V_l, W_l, and ϕ_l are named scalar eigenfunctions and satisfy linear systems of homogeneous ordinary differential equations in the radial variable r. Spheroidal deformations belong to the same category as those the reader can produce in a football balloon by pressing it with her or his finger, while toroidal deformations are those produced by turning around the two hemispheres of the balloon in the opposite directions.

Transforming in the Laplace domain the following relationship between 1-D strain rate ϵ and stress σ, valid for the Maxwell rheology of Figure 2,

$$\frac{d\varepsilon}{dt} = \frac{\sigma}{2\nu} + \frac{1}{2\mu}\frac{d\sigma}{dt} \qquad [25]$$

with ν being the viscosity of the dashpot of the mantle or lower crust (LC), leads to

$$\tilde{\sigma}_{ij}(s) = 2\tilde{\mu}(s)\tilde{\varepsilon}_{ij}(s) \qquad [26]$$

with the Laplace-transformed rigidity $\mu(s)$ being

$$\tilde{\mu}(s) = \frac{\mu s}{s + \mu/\nu} \qquad [27]$$

formally identical to the elastic stress–strain relationship; the right member of eqn [25] represents the sum of the strain rates occurring within the dashpot, $\sigma/2\nu$, and within the spring, $(1/2\mu)$ $(d\sigma/dt)$. Equation [26] indicates that the solution to the time-dependent viscoelastic problem is obtained first in the Laplace transform domain as an equivalent elastic solution. This elastic solution in the Laplace transform domain is then transformed back into the time domain. It should be reminded that this approach is valid only for linear viscoelastic problems,

for which the linear relation is provided by eqn [26], in which μ does not depend on stress or strain.

In the Laplace transform domain, viscoelastic normal-mode theory provides the tools to obtain the time-dependent viscoelastic solution.

The core of that theory stands on the result that in the Laplace transform domain, the solution for the stress-free boundary conditions at the Earth's surface is singular at points of the Laplace variable s-axis that correspond to real, negative numbers. For an incompressible Earth model, these numbers represent a finite ensemble of M real inverse relaxation times s_j, with M depending on the numbers of viscoelastic layers in which the Earth's model itself is stratified. For compressible models, this ensemble is infinite.

These singularities of the solution in the s-domain are first-order poles, so that each singularity s_j provides a relaxing exponential $e^{s_j t}$, once antitransformed in the time domain.

These s_j numbers are named viscoelastic relaxation modes; the viscoelastic solution in the time domain becomes, for the radial displacement pertaining to this chapter,

$$U_l(t) = U_{le}\delta(t) + \sum_{j=1}^{M} U_{lj} e^{s_j t} \qquad [28]$$

where l denotes the harmonic degree l, U_{le} the elastic contribution from the spring of Figure 2, and $\sum_{j=1}^{M} U_{lj} e^{s_j t}$ the summation over the modes representing the (viscoelastic) contribution from the dashpot, coupled with the spring.

Similar expression holds for the horizontal displacement and perturbation in the gravitational potential V_l, ϕ_l, also of interest in this chapter.

For the simple four-layer Earth model, as sketched in Figure 3, it can be seen, as explained in Sabadini and Vermeersen (2004), that eight modes are excited by density and rigidity contrasts at the various interfaces separating the lithosphere from the atmosphere, the mantle from the core, the lithosphere from the mantle, and the upper mantle from the lower mantle.

These relaxation modes, which ultimately constrain the characteristic deformation timescales of the Earth's model forced by any kind of geophysical processes, are plotted in Figure 4 as a function of the harmonic degree l, entering the series given by eqns [19]–[21].

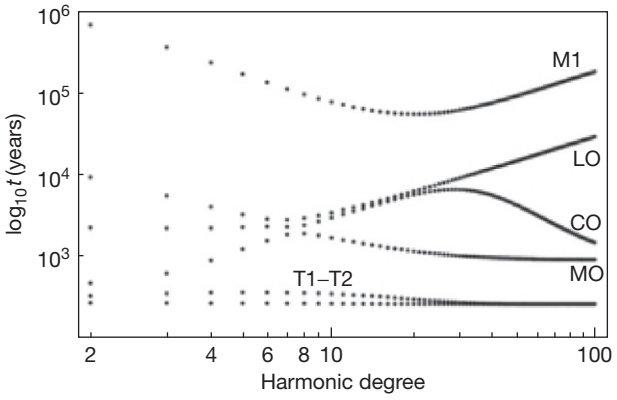

Figure 4 Viscoelastic normal modes triggered by the density and rigidity contrasts of the four-layered Earth model in Figure 3.

They span timescales from hundred to million years, with the labeling referring to the interface triggering that mode, with M0 denoting the mode excited by the density contrast between the Earth and the atmosphere, L0 that due to the rheological contrast between the elastic outer lithosphere and underlying viscoelastic mantle, C that due to the density contrast between the core and the mantle, M1 that due to the density contrast between the upper mantle and lower mantle, and T denoting fast relaxing modes due to discontinuities in viscosity and rigidities at the various interfaces. These modes are those of the Earth's model used in Barletta and Sabadini (2006) to simulate upwelling of superplumes from the mantle, which reach the bottom of the lithosphere.

6.04.2.3 Global Vertical and Horizontal Displacements from PGR

PGR is responsible not only for vertical and horizontal displacements at the Earth's surface but also for secular components of the change of sea level and the Earth's gravity field. These variations can also be affected by present-day mass instability in Antarctica and Greenland. For PGR analyses, the multilayered, spherically stratified self-gravitating relaxation model, outlined in Vermeersen and Sabadini (1997) and based on the normal-mode relaxation theory described in the preceding text, is used. The redistribution of the glacial meltwater on the viscoelastic Earth is solved within the ICE-3G model (Tushingham and Peltier, 1991), by using the spectral analysis first implemented by Mitrovica and Peltier (1991), appropriate for sea-level change calculations, as shown later in the text.

The results in Figure 5 (Marotta, 2003), portraying the modeled global deformation pattern induced by PGR, show that vertical and horizontal velocities associated with PGR are sensitive to the rheological or viscosity stratification of the mantle, where the viscosity denotes the flow properties of the mantle, as depicted by the ν parameter in the dashpot shown in Figure 2. Figure 5(a) corresponds to an upper-mantle viscosity of $\mu_{UM} = 0.5 \times 10^{21}$ Pa s and a lower-mantle viscosity of $\mu_{LM} = 1.0 \times 10^{21}$ Pa s defining the PGR-21 model; the bottom panel corresponds to $\mu_{UM} = 0.5 \times 10^{21}$ Pa s and $\mu_{LM} = 1.0 \times 10^{22}$ Pa s, defining the PGR-22 model. The elastic lithosphere is 80 km thick, and both lithosphere and mantle are assumed incompressible, as stated earlier in the text, which means that density remains constant within each layer of the radially stratified Earth model and that, at a fixed position in space, density changes can occur only via displacements of interfaces separating material with different density. Both PGR-21 and PGR-22 are built as per the Earth in Figure 3, but each layer representing the lithosphere, the upper mantle, and the lower mantle is in turn subdivided into thinner layers such that, taken collectively, these parts of the planet contain 31 layers whose physical properties are volumetrically averaged from realistic, seismologically retrieved Earth stratification (Dziewonski and Anderson, 1981).

The vertical deformation represented by the colors is characterized by uplifting centers over deglaciated areas in North America, northern Europe, and Antarctica, where ice-sheet complexes where located, in agreement with ICE-3G, and by subsidence in the periphery of these deglaciation centers. It should be recalled that these global deformation patterns

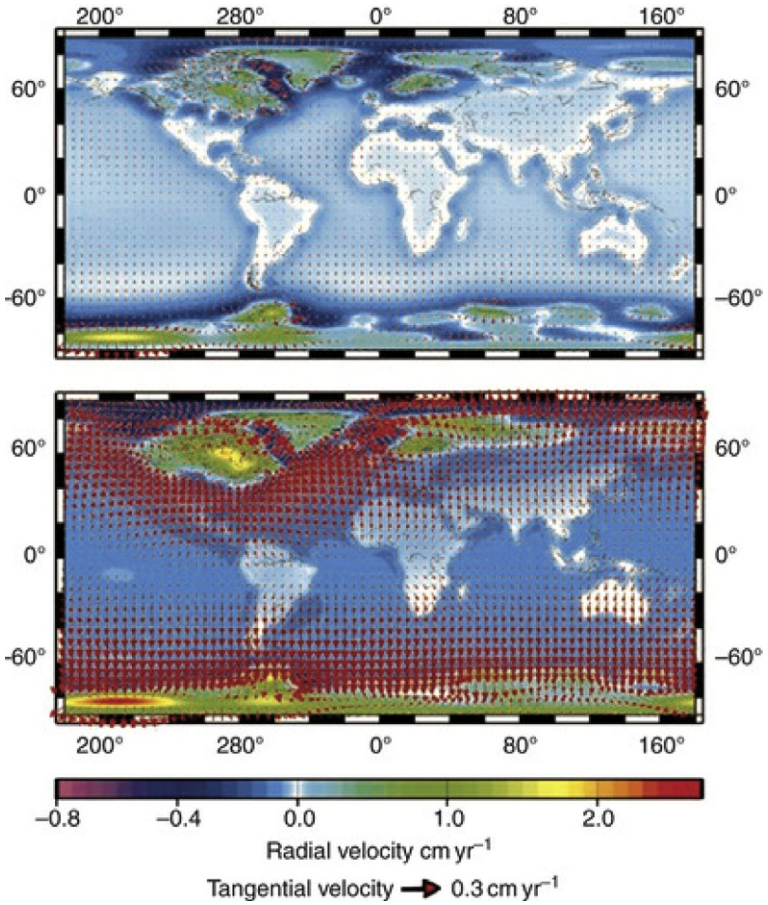

Figure 5 (a) Corresponds to an upper-mantle viscosity of $\mu_{UM} = 0.5 \times 10^{21}$ Pa s and a lower-mantle viscosity of $\mu_{LM} = 1.0 \times 10^{21}$ Pa s (PGR-21). (b) Corresponds to $\mu_{UM} = 0.5 \times 10^{21}$ and $\mu_{LM} = 1.0 \times 10^{22}$ Pa s (PGR-22). The elastic lithosphere is 80 km thick, and both lithosphere and mantle are incompressible. Redrawn from Figure 1 of Marotta AM (2003) Benefits from GOCE within solid earth geophysics. *Space Science Reviews* 108: 95–104. ISSN: 0038-6308, http://dx.doi.org/10.1023/A:1026273832697.

represent, in terms of vertical and horizontal velocities in millimeters per year, the mathematical simulation of present-day deformation of the Earth, forced by ice-sheet disintegration during the Pleistocene, which ended about 7000 years ago, and are going on today because of the viscous memory of the Earth, as sketched by the dashpot in Figure 2.

The horizontal velocity field is characterized by two different components: a global one, directed northward or southward with respect to the Earth's equatorial region because of the suction effect of the mantle material toward the deglaciated regions of the Northern and Southern Hemispheres, and a regional one directed radially outward from the center of the different deglaciation zones. The relative strengths of these components, as the intensity of vertical motions, depend on the viscosity ratio between the upper mantle and lower mantle, as the comparison of panel (b) and panel (a) shows.

Increasing the viscosity in the lower mantle to 10^{22} Pa s, with respect to 10^{21} Pa s, makes mantle material more difficult to relax after deglaciation, which maintains larger horizontal and vertical velocities for the present-day situation, as portrayed in Figure 5(b). For lower-mantle viscosity 10^{21} Pa s, it is remarkable that the outward horizontal velocity from deglaciation centers is larger than the global velocity due to material flow from the equatorial region of the mantle, particularly visible in North America. Increasing the lower-mantle viscosity makes the global flow from the equatorial region larger, as anticipated in the preceding text, which in turn dampens, at deglaciation centers, the outward velocity directed toward the equator. This effect can be better visualized in Figure 6, which focuses on PGR velocity patterns in Europe.

Figure 6 is an enlargement of Fennoscandia from Figure 5, showing vertical and horizontal velocity fields in Europe for the two Earth models introduced in Figure 5, namely, PGR-21 (a) and PGR-22 (b). Two different components of the horizontal velocity field can be distinguished, a global north-trending one, due to the suction effect of mantle material from the equator toward the deglaciated regions of the Northern Hemisphere, as anticipated in the preceding text, and a regional one directed radially outward from the center of deglaciation in the Gulf of Bothnia. Each component prevails over the other depending on the viscosity ratio between the upper mantle and lower mantle. For PGR-21, top panel, the two deformation styles in the deglaciated region and in the far field are well separated, as indicated by the outward horizontal velocities of at most 0.6 mm year^{-1} in proximity of the deglaciated region and by the north-trending lower values, less than

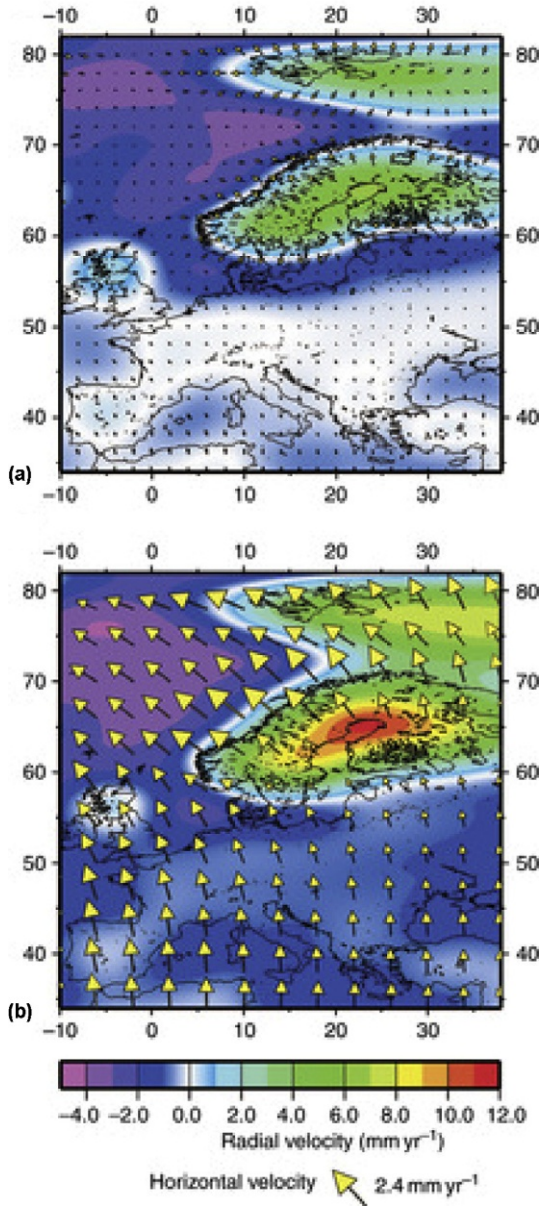

Figure 6 (a,b) Enlargements of the European region taken from **Figure 5**.

0.2 mm year^{-1}, in the far field. The vertical deformation is characterized by two uplifting centers in the northeastern region where ice-sheet complexes were located. The Mediterranean region is affected by a subsidence of −1 mm year^{-1}, with the adjacent European continental region essentially unaffected by vertical motions. The deformation pattern portrayed in panel (a) agrees with the findings of Mitrovica et al. (1994) (their Figure 3), except for the slightly smaller rates due to the overall reduction in the upper- and lower-mantle viscosities by a factor 2 in this analysis.

For PGR-22 (bottom panel), the high north-trending component of the horizontal velocity, which exceeds the local outward velocity in the southern part of the deglaciation region, is due to the larger global isostatic disequilibrium of the planet with respect to PGR-21 that is caused by increased viscosity. The latter induces a substantial increase in the horizontal velocity, up to 2.4 mm year^{-1} in the north and 1.2–1.6 mm year^{-1} in the far field. In comparison with the top panel, there is a notably substantial intensification of the uplift, affecting a wider region. Subsidence increases in the Mediterranean region to 2 mm year^{-1}, extending its influence even in central Europe, at a rate of 1 mm year^{-1}. Generally speaking, these PGR patterns of 3-D deformation predicted by models have proved to be consistent among the various analyses (James and Ivins, 1997; Mitrovica et al., 1993, 1994; Peltier, 1998).

6.04.2.4 PGR in GPS Analyses

In order to help the reader appreciate the quality of PGR geophysical modeling and thus its ability to correctly reproduce the physical properties of the lithosphere–mantle system and the characteristics of the deformation pattern at the Earth's surface, a comparison is performed between PGR predictions and two classes of geodetic observables retrieved from GPS data analyses, rates of change of baselines, and strain rates. The first observable, shortened into baseline rate, denotes the rate of change of the distance, or baseline, between two GPS sites, along the direction connecting the two sites; in the following, only the style of this change, extension or equivalent lengthening of the baseline, and compression, or equivalent shortening of the baseline, will be considered, leaving to the analysis of strain-rate patterns, within triangular domains connecting three GPS sites, a detailed analysis of the deformation.

Baseline analyses thus yield a 1-D picture of the deformation between two GPS sites, while strain-rate analysis portrays a 2-D picture within the area surrounded by the three segments connecting the three GPS sites, thus providing a precise picture of the deformation style of the area under study. The region has been monitored by using permanent GPS receivers of the ITRF2000 network established by the International Earth Rotation and Reference Systems Service (Altamini et al., 2002). BIFROST data provide additional stations not included in the ITRF2000 network (Johansson et al., 2002; Milne et al., 2001). The reader should be aware that sites quoted as BIFROST sites in the following figures include, in addition to sites in the actual BIFROST network, a set of some other sites, namely, HERS, MADR, BRUS, KOSG, POTS, WETT, and RIGA, not officially belonging to this network.

Consistency between model predictions and geodetic deformation patterns can thus be viewed as an indicator that plate-deformation properties have been properly accounted for in terms of those parameters that are particularly relevant for the present analyses, such as plate thickness, elasticity, viscosity, or its coupling with the underlying mantle. Baseline rates obtained from geodetically retrieved data are first shown with respect to the VAAS reference site. **Figure 7** shows, in fact, the location of baselines associated with ITRF2000 and BIFROST data sets, respectively, where the observed dominant extension is denoted by blue and the observed shortening by red. Both panels indicate a well-defined extensional pattern for all baselines, independently on their length, except for a few of them, thereby indicating compression.

Figure 8 shows PGR predictions based on the PGR compressible model detailed in Milne et al. (2001) and used also in

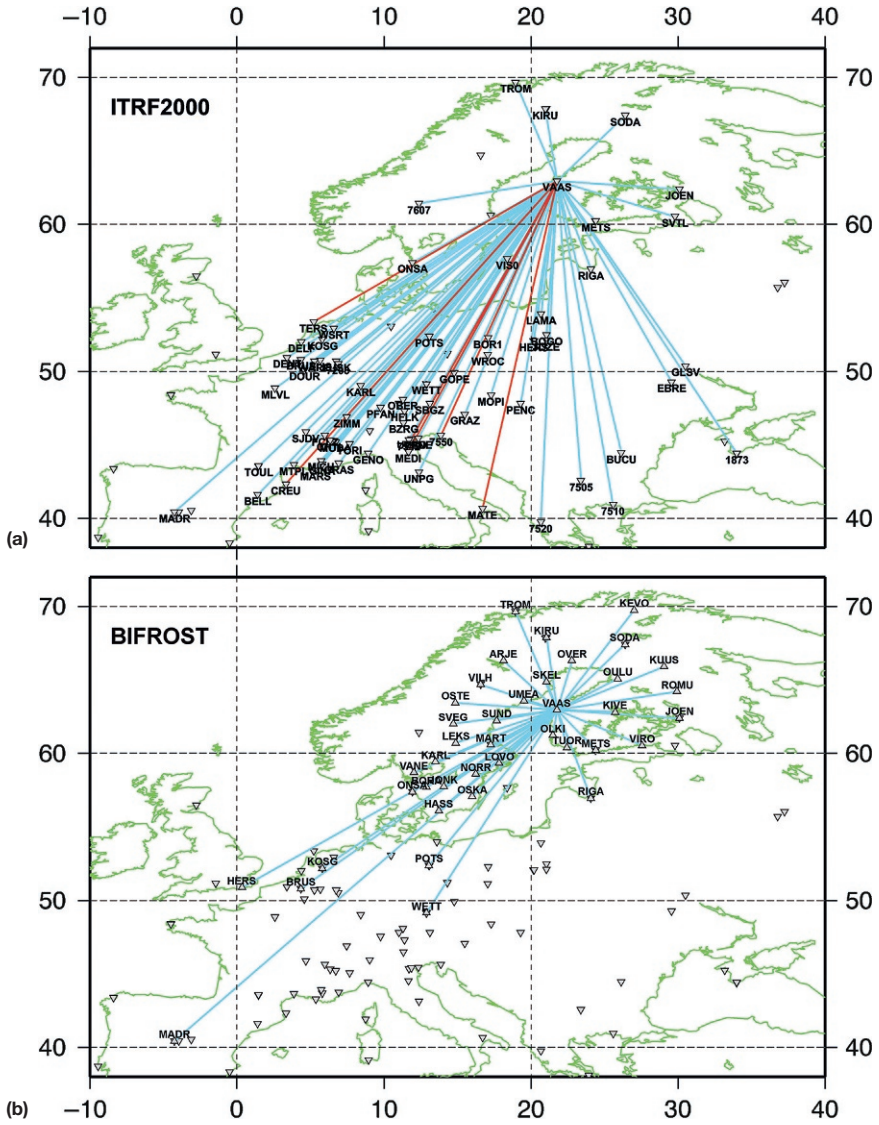

Figure 7 Observed baseline rates for baselines referenced to the site VAAS, where blue indicates extension and red shortening, according to ITRF2000 (a) and BIFROST data sets (b). Gray inverse triangles indicate the ITRF2000 sites while the upright ones indicate BIFROST sites. Reproduced from Marotta AM, Miltrovica JX, Sabadini R, and Milne G (2004) Combined effects of tectonics and glacial isostatic adjustment on intraplate deformation in central and northern Europe: Application to geodetic baseline analyses. *Journal of Geophysical Research* 109: B01413. http://dx.doi.org/10.1029/2002JB002337, with permission from AGU.

Marotta et al. (2004); it provides the style of changes in the baseline rate for all VAAS-referenced baselines in Figure 7, with blue indicating extension and red shortening. Except for some inconsistencies with a few southerly directed baselines, PGR modeling well reproduces the major feature of Figure 7, which is the dominant extension in the ITRF2000 and BIFROST data.

Since postglacial adjustment in Fennoscandia is characterized by horizontal motions directed outward from the center of the ancient ice complex in proximity of VAAS, as shown in Figure 6, widespread lengthening of baselines or extension along the short BIFROST baselines in Figure 7 is expected. On the other hand, the origin of the widespread extension for the longer ITRF2000 or BIFROST baselines for central and southern Europe, visible in Figure 8, is not as clear as the lengthening along short baselines. Explanation for this behavior can be found in Marotta et al. (2004) and is repeated herein. For the PGR-21 model, for example, carrying a viscosity profile similar to that defining the Milne et al. (2001) model considered in Figure 8, the horizontal velocity field is characterized by outward-directed motions within Fennoscandia, changing to motions toward Fennoscandia at the periphery, as shown in Figure 6(a) in detail. On this basis, it could be expected that PGR would induce shortening in the longer baselines, VAAS to Central or southern Europe, in Figures 7 and 8. Yet it should be recalled that both horizontal and radial motions contribute to changes in baseline length. From Figure 6, VAAS is predicted in uplift at a rate close to 1 cm year^{-1}, while Central and southern European sites, which lie within the peripheral bulge of Fennoscandia, are subsiding at lower rates. The net contribution of this uplift and moderate

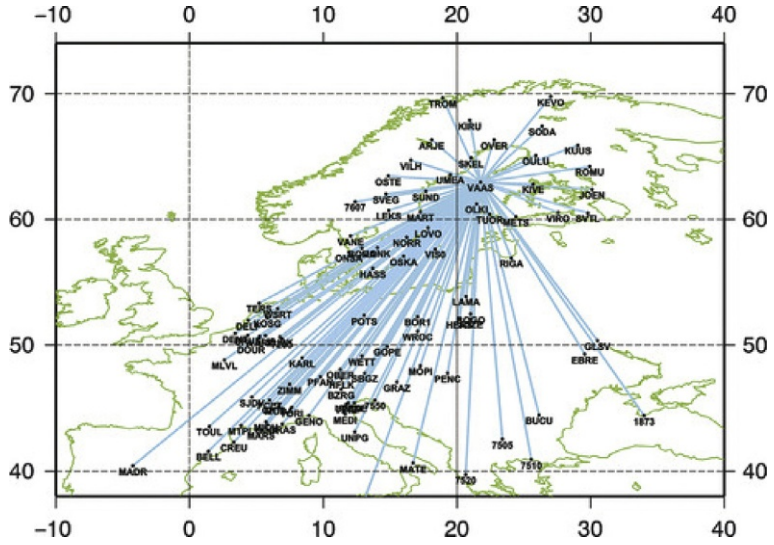

Figure 8 Predicted baseline rates for baselines referenced to VAAS for PGR. Reproduced from Marotta AM, Miltrovica JX, Sabadini R, and Milne G (2004) Combined effects of tectonics and glacial isostatic adjustment on intraplate deformation in central and northern Europe: Application to geodetic baseline analyses. *Journal of Geophysical Research* 109: B01413. http://dx.doi.org/10.1029/2002JB002337, with permission from AGU.

subsidence extends to the baselines, thus counteracting the baseline shortening associated with the PGR-induced horizontal velocity field. The net effect of baseline lengthening is consistent with the pattern of widespread extension evident in the longer baselines in Figure 7(a).

For ITRF2000 and BIFROST data sets, Figure 9 shows the pattern of baseline rates referenced to Potsdam (POTS) in northern Europe. Short BIFROST baselines defined by sites between 55° and 60° N are primarily in compression, while baselines extending to more northerly located sites are in extension, as visible in Figure 9(b). The same pattern is evident in the ITRF2000 baselines extending into Fennoscandia, as in Figure 9(a). ITRF2000 baselines are subject to changes in deformation style from northern, Central, and southern Europe. In fact, baselines south of POTS are predominantly in compression, with some exceptions showing extension as for the cluster of baselines defined by sites in the southeast portion of Figure 9(a). North of POTS, extension is the dominant mechanism, as shown by baselines connecting POTS with sites north of it, except for a few cases, essentially NE-directed cases.

Figure 10 shows predictions for the same set of baselines generated using the PGR model described in the preceding text. This model reconciles the pattern evident in the northern baselines, in particular a transition from shortening to extension as one considers more northerly sites. In the following figures, the impact of PGR is shown on strain-rate tensor in the horizontal plane, as done in Marotta and Sabadini (2004), rather than on baselines connecting pairs of sites, as done in Marotta and Sabadini (2002) and Marotta et al. (2004). In what follows, we shall consider the results on strain-rate eigenvalues and eigendirections, computed for a set of triangular domains covering the study area and compared with the corresponding ones obtained from the ITRF2000 velocity solutions.

Strain rates, within the triangles whose vertices correspond to permanent GPS sites in Europe, can be retrieved from the gradients of the horizontal velocities at GPS sites from standard strain-rate mathematical expressions as defined in continuum mechanics. In our approach, this is accomplished assuming that the horizontal velocity components vary linearly with distance within each triangle. This constant space gradient provides a first-order approximation of the strain rate in each tectonic region embedded within the vertices of the triangles. This approximation can be improved by increasing the spatial resolution of the geodetic network by introducing new geodetic sites. The intersection point of the bisectors of the triangles is taken as the reference point where strain-rate tensor is evaluated. Strain-rate eigenvalues are in units of nanostrain per year, meaning, for example, shortening of 1 mm year^{-1} over a distance of 1000 km along the eigendirection corresponding to that eigenvalue, for compression, or lengthening of the same relative amount for extension; strain means relative deformation, so the same strain rate would be obtained for shortening (or lengthening) of 1 cm over 10 000 km and so on.

Once the strain-rate tensor is obtained, standard procedures of matrix algebra are used to obtain eigenvalues and eigendirections. Within each triangular domain, strain-rate eigenvalues $\dot{\epsilon}_1$ and $\dot{\epsilon}_2$, for both data and model predictions, are computed as per the procedure described in Devoti et al. (2002). The latter requires the inversion of a system of linear equations into six unknowns: four tensor components plus two velocity components at the reference point. The velocity gradient tensor can then be decomposed into its symmetrical part and antisymmetric part, the former providing the strain-rate eigenvectors and eigenvalues after diagonalization and the latter a rigid rotation rate. The errors associated with the geodetic strain-rate tensor are obtained by means of the covariance matrix associated with the velocity components at each site.

In the selected triangulation, the geodetic ITRF2000 solution pattern obtained from GPS data is shown in Figure 11 in terms of strain-rate eigenvalues and eigendirections and relative error bounds, which are provided by the radii of the circular sectors for the eigenvalues and by the azimuths bounding the colored areas for the eigendirections. The strain-rate

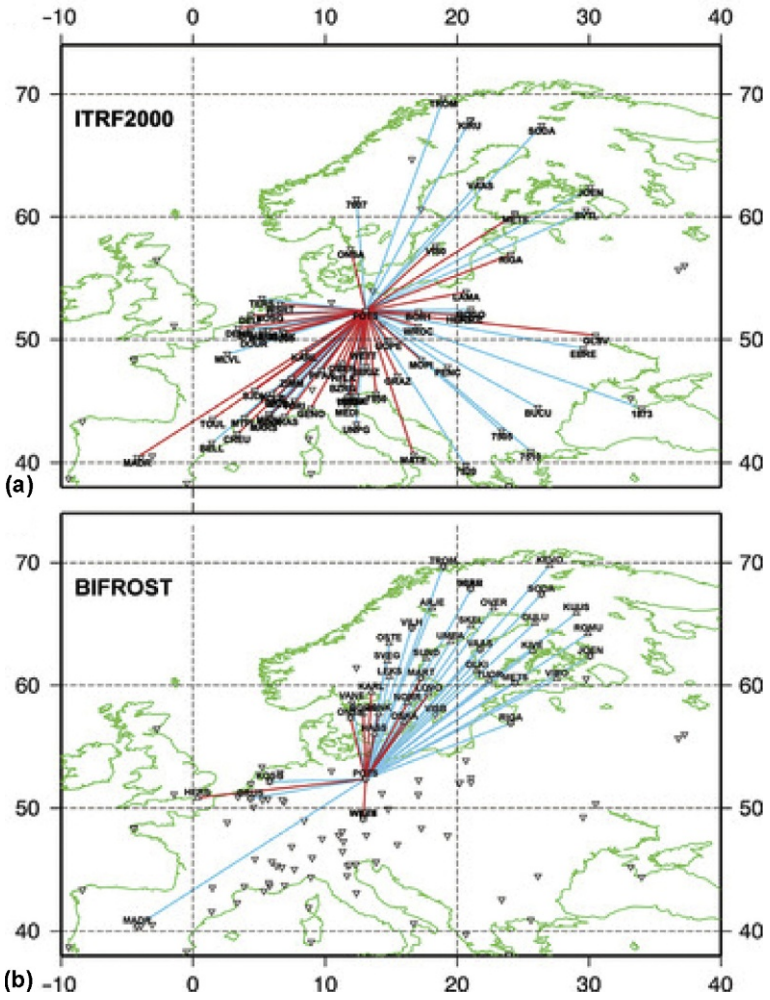

Figure 9 Observed baseline rates for baselines referenced to the site POTS according to ITRF2000 (a) and BIFROST (b) data sets. Gray inverse triangles indicate the ITRF2000 sites while the upright ones indicate BIFROST sites. Reproduced from Marotta AM, Miltrovica JX, Sabadini R, and Milne G (2004) Combined effects of tectonics and glacial isostatic adjustment on intraplate deformation in central and northern Europe: Application to geodetic baseline analyses. *Journal of Geophysical Research* 109: B01413. http://dx.doi.org/10.1029/2002JB002337, with permission from AGU.

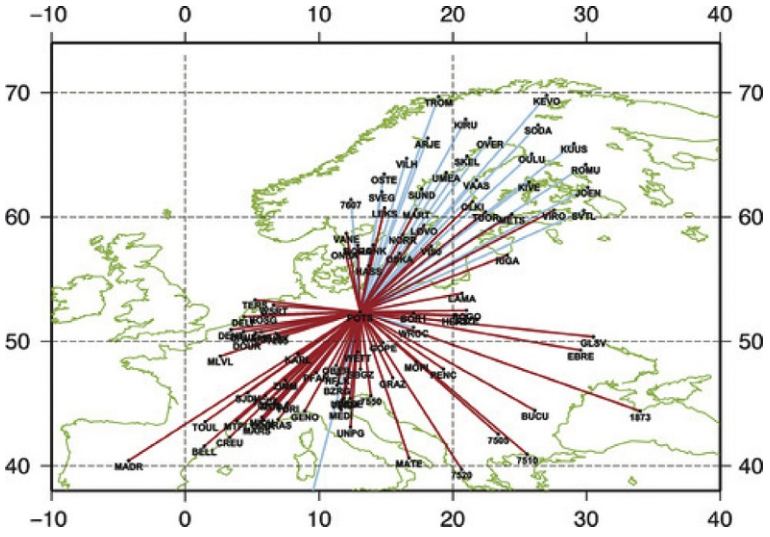

Figure 10 Predicted baseline rates for baselines referenced to POTS for PGR. Reproduced from Marotta AM, Mitrovica JX, Sabadini R, and Milne G (2004) Combined effects of tectonics and glacial isostatic adjustment on intraplate deformation in central and northern Europe: Application to geodetic baseline analyses. *Journal of Geophysical Research* 109: B01413. http://dx.doi.org/10.1029/2002JB002337, with permission from AGU.

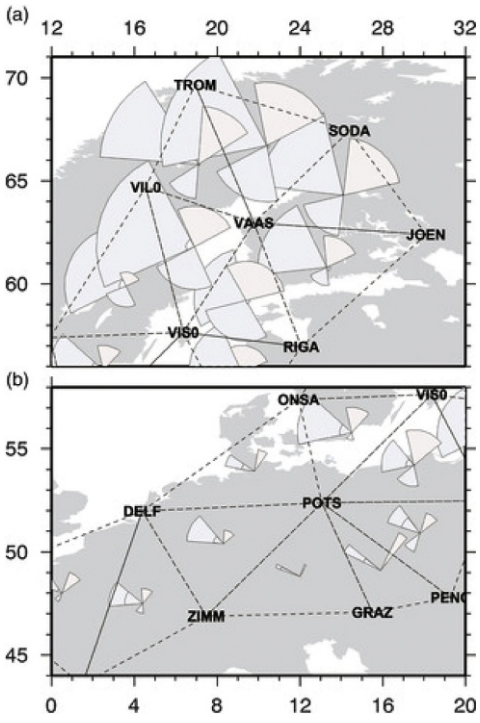

Figure 11 (a,b) Observed strain rates in units of nanostrain from ITRF2000. Reproduced from Marotta AM and Sabadini R (2004) The signatures of tectonics and glacial isostatic adjustment revealed by the strain rate in Europe. *Geophysical Journal International* 157: 865–870. http://dx.doi.org/10.1111/j.1365-246X.2004.02275.X.

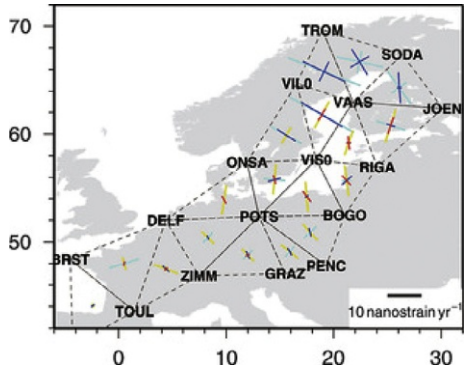

Figure 12 Strain rates in units of nanostrain predicted from PGR models, with lower-mantle viscosities of 10^{21} Pa s (blue, extension; and red, compression) and with lower-mantle viscosities of 10^{22} Pa s (cyan, extension; and yellow, compression). Reproduced from Marotta AM and Sabadini R (2004) The signatures of tectonics and glacial isostatic adjustment revealed by the strain rate in Europe. *Geophysical Journal International* 157: 865–870. http://dx.doi.org/10.1111/j.1365-246X.2004.02275.X.

pattern is characterized by global SE–NW-directed extension and SW–NE-directed compression at both low and high latitudes. Another characteristic of this pattern is the ratio between extension and compression, which is significantly higher in Fennoscandia than in central Europe. Uncertainties in strain-rate predictions are generally high, both in magnitude and in direction. Because of the African–Eurasian convergence, the tectonic contribution to the strain rate is considered in a following section, where PGR and tectonic contributions will be integrated, within the framework of a final comparison between modeled and geodetic strain-rate patterns. In this section, attention will focus on PGR strain-rate patterns. Particular care is devoted to defining the final set of triangular domains. Although several criteria could be followed for choosing the triangulation, a combination of geometric and reliability criteria has been adopted. The subset of sites, which are uniformly distributed through the study area, is selected first from the best geodetic GPS sites of ITRF2000 so that velocity is known with the lowest variance. This most representative geodetic triangulation must be compliant with representative homogeneous tectonic units; this requirement is particularly important when the African–Eurasian convergence, or active tectonics, is considered, as done in the following sections.

The models shown in Figure 12 are similar to PGR-21 and PGR-22 in Figures 5 and 6, in terms of mantle viscosity, except for the 120 km thick lithosphere; the blue and red bars refer to a lower-mantle viscosity of 10^{21} Pa s, similar to PGR-21, and cyan and yellow bars to a lower-mantle viscosity of 10^{22} Pa s, similar to PGR-22.

The 10^{21} Pa s lower-mantle viscosity model in Figure 12 predicts SE–NW extension in Fennoscandia (blue bars) in agreement with the geodetic data and negligible SE–NW compression in the south (red bars). A peculiar situation is visible south of VIS0 and north of POTS, where PGR modeling predicts an SSE–NNW compression comparable in magnitude to that induced by the tectonic model characterized by the stiff Baltic Shield, with no ridge push, as will be shown afterward. Extension in the north and a small compression between 52° and 58° north latitudes are due to the outward motion from the deglaciation center and from the small northerly oriented velocities from equatorial regions due to PGR, as shown in Figure 5.

Stiffening of the lower mantle to 10^{22} Pa s (cyan and yellow) is responsible for an increase in extension in all the triangles (as shown by the cyan bars) that improves the fit with geodetic strain rates north of VIS0. South of the line connecting ONSA and VIS0 and north of POTS, compression (yellow bars) is increased with respect to the 10^{21} Pa s lower-mantle viscosity model. South of POTS, the contribution of this PGR model to both compression and extension is larger than the 10^{21} Pa s lower-mantle viscosity model, but compression points in the SE–NW direction, in contrast with the observation. After having analyzed the effects of active tectonics on strain rate, we shall consider the combined effects of PGR and the African–Eurasian convergence, showing that both geophysical processes contribute to observed geodetic strain rates.

6.04.2.5 Present-Day Glacier Shrinkage and Uplift of the Alps

Sizable signatures on Earth's surface displacements are induced not only by the melting of the huge ice sheets of the Pleistocene but also by the present-day decline of glaciers covering mountain belts. In this section, the decline of Alpine glaciers beginning in AD 1850, inferred from the analysis of regional and national glacier inventories, is implemented within the normal-mode viscoelastic theory to estimate the uplift of the

Earth's crust due to this glacier shrinkage, following the study of Barletta et al. (2006a). Alpine glacier shrinkage is consistent with worldwide large ice-mass reductions (Haeberli et al., 1999; Paul et al., 2002) and is an indicator of global climate change (IPCC, 2001). Uplift rates from Alpine glacier wasting can be compared with those predicted for larger ice complexes, for example, the Patagonian ones treated by Ivins and James (2004), thus providing testable tools for modeling lithosphere–cryosphere interaction, within two different environments, the Alps and the Andes.

World Glacier Inventory (WGI) data are used in Barletta et al. (2006a) to evaluate the mass loss affecting the Alpine glaciers on a known time interval. WGI data (surface area, length, and main dimensional parameters) collected between the 1950s and the 1980s and more recent glacier area reduction factors have been used. Updated glacier areas are evaluated for the years 1996, 1997, 1998, and 1999 by applying a surface reduction factor specific for each glacier, considering the Alpine region where it is located. This factor is obtained from the available literature, mainly national and regional glacier inventories, dealing with glacier shrinkage rate in the different Alpine regions (Biancotti and Motta, 2001; Kääb et al., 2002; Paul et al., 2002). In AD 1999, the glaciers considered in this section covered an area of 2215 km^2. A mean mass-balance value per year has been obtained by averaging the mass balances for each Alpine region. These yearly values have then been averaged over the considered 4 years to obtain a unique value for each Alpine region to be used within the high spatial resolution normal-mode scheme according to Barletta et al. (2006a). The average of these regional values is −0.71 mm $year^{-1}$ water equivalent, or 1.54 Gt $year^{-1}$, representing an estimate of the mean mass loss affecting the entire Alpine chain.

Uplift rates are based on a spherical and radially stratified, viscoelastic Earth model and linear Maxwell rheology, as in Figure 2, similar to that used for the postseismic calculations of the following section and tuned to the viscosity profile considered in Burov et al. (1999) and volume-averaged rigidities from Preliminary Reference Earth Model (PREM) (Dziewonski and Anderson, 1981).

Figure 13, in the main color scale, shows the modeled elastic uplift rates for the present-day mass balance in Table 1, while the inset, red color scale, shows the measured uplift rates, corresponding to the same years of the considered mass balance, from high-precision leveling lines, limited to Switzerland, after Schlatter et al. (2005); contour white lines from the modeling are superimposed in the inset for comparison. Uplift rates of the order of 0.1–0.2 mm $year^{-1}$ characterize the response of the whole Alpine belt to present-day glacier reduction, encircling patches of high uplift rates corresponding to the major glacial complexes. The largest uplift of 0.9 mm $year^{-1}$, indicated by the arrow, occurs in the French Alps, in proximity to Mont Blanc, where the largest mass loss is located. Uplift values of about 0.4 mm $year^{-1}$, a factor of 2 lower than the maxima in the west, are found in Austria. In the inset, the white contours from the modeling and the measured uplift rate pattern are similar in shape, indicating that present-day glacier shrinkage contributes a substantial fraction to the observed uplift rate. The 0.1 mm $year^{-1}$ white contour in the north almost overprints the 0.4 mm $year^{-1}$ measured one, indicating that in the periphery of the uplifting region, about 20% of the uplift is due to present-day glacier shrinkage. The largest patches of the modeled uplift overlap the regions of the largest observed ones, although the highest modeled uplift rates of about 0.4–0.5 mm $year^{-1}$, dark blue patches in the main panel of Figure 13, are about a factor of

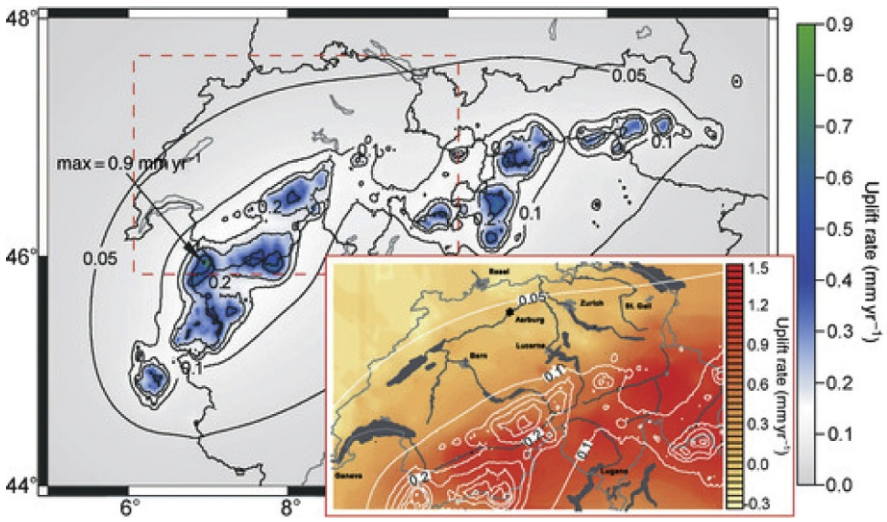

Figure 13 Computed high-resolution vertical rates (elastic response) to ice-mass loss are represented in the main color scale, from (gray) 0.0 mm $year^{-1}$ to (green) 0.9 mm $year^{-1}$. Vertical rates, obtained from the new national height network (LHN95) system of Switzerland, are portrayed in the inset in red color scale ranging from −0.3 to 1.5 mm $year^{-1}$. In the inset (corresponding to the dashed box in main figure), our computed (white) contour lines are superimposed to the vertical rates obtained from the adjustment of high-precision leveling observations, for comparison. Details on observation error bars are found in Schlatter et al. (2005). Reproduced from Barletta VR, Ferrari C, Diolaiuti G, Carnielli T, Sabadini R, and Smiraglia C (2006) Glacier shrinkage and modeled uplift of the Alps. *Geophysical Research Letters* 33: L14307. http://dx.doi.org/10.1029/2006GL026490, with permission from AGU.

2 lower than the measured ones. These findings show that glacier shrinkage contributes substantially to the Alpine chain uplift and that there are other phenomena, such as active tectonics, drainage, and erosion, that could affect the uplift pattern.

Figure 14 shows the effects of viscous relaxation in the LC and in the asthenosphere on uplift rates, assuming a constant volume loss since AD 1850 for a total of 155 km^3, equally distributed over the representative glacier distribution of 1973, and rheological parameters in Table 2. According to Haeberli and Beniston (1998), the estimated total glacier volume in the European Alps was about 130 km^3 for the mid-1970s and since the end of the Little Ice Age (LIA), glacierization has lost about half of its original volume, implying 130 km^3 since 1850, plus 25 km^3 since 1973, according to Paul et al. (2002). The viscous uplift simulated represents an upper bound, since pre-LIA built-up of the load signal, not considered here, acts to partially counteract the post-LIA unloading effects. The viscous uplift pattern is notably smoother than the elastic one. In the western Alps, where the elastic part is the most important, the largest viscous uplift rates are concentrated as well, reaching 0.32 mm $year^{-1}$. Summing up the largest elastic contribution and the geographically corresponding viscous one, an uplift of 0.7–0.8 mm $year^{-1}$ is obtained in the western Alps, half of the largest observed one of 1.5 mm $year^{-1}$. The estimate of the viscous contribution, on the other hand, can be affected by uncertainties in the rheological parameters and thus must be taken with caution. Reducing the viscosities of layers 2–5 by a factor of 2 with respect to Table 2, for example, increases uplift rates by a factor of 1.5, without modifying the pattern. The dimension of the patches where uplift is concentrated, tens of kilometers, is comparable with the 40 km crustal thickness, indicating that contributions to uplift originate from stress relaxation in the soft LC of 2.15×10^{19} Pa s (Table 2).

Present-day glacier reduction in the Alps, estimated from glacier inventories and induced viscoelastic response of a stratified Earth model, is responsible for sizable uplift rates. Patches of 0.4–0.5 mm $year^{-1}$, due to ice-mass loss in the largest ice complexes, overprint a characteristic area of slower uplift of 0.1–0.2 mm $year^{-1}$, representing the signature of the phenomenon in the whole Alpine chain. Viscous stress relaxation in the LC, due to glacier mass loss after the end of the LIA, produces an uplift of 0.32 mm $year^{-1}$, leading to a total viscoelastic response, spring plus dashpot in Figure 2, of 0.8 mm $year^{-1}$. This section shows that viscoelastic response to present-day glacier shrinkage is a substantial fraction, about half, of the observed uplift. These results are thus essential for a correct interpretation of uplift data in the Alpine chain and for the quantification of the contributions from different drivers of uplift, such as present-day glacier instability, active tectonics, and drainage.

6.04.2.6 Sea-Level Changes

If the ice sheets of Antarctica and Greenland melt, sea level is expected to rise. This is in fact a major concern that global warming of the Earth might induce melt of the present-day large ice sheets, thus inducing a global sea-level rise, leading to

Table 1 The coefficient of glacier area reduction per year and the mass balance, averaged over 1996–99

Region	*Area yearly reduction (%)*	*Mass balance (mm $year^{-1}$, w.e.)*
Austria	0.63	−0.64
France	0.47	−0.97
Italy	0.47	−1.19
Switzerland	0.84	−0.40
Germany	0.63	−0.64

Table 2 Rheological structure

Layer	r *(km)*	ρ *(kg m^{-3})*	μ *(Pa)*	ν *(Pa s)*
1	6371.0	2650.0	2.97×10^{10}	1.00×10^{35}
2	6352.5	2750.0	5.58×10^{10}	2.15×10^{19}
3	6341.0	2900.0	6.81×10^{10}	5.00×10^{21}
4	6331.0	3439.3	7.27×10^{10}	4.64×10^{20}
5	5951.0	3882.3	1.09×10^{11}	4.64×10^{20}
6	5701.0	4890.6	2.21×10^{11}	1.000×10^{21}
7	3480.0	10932	0.00	0.0

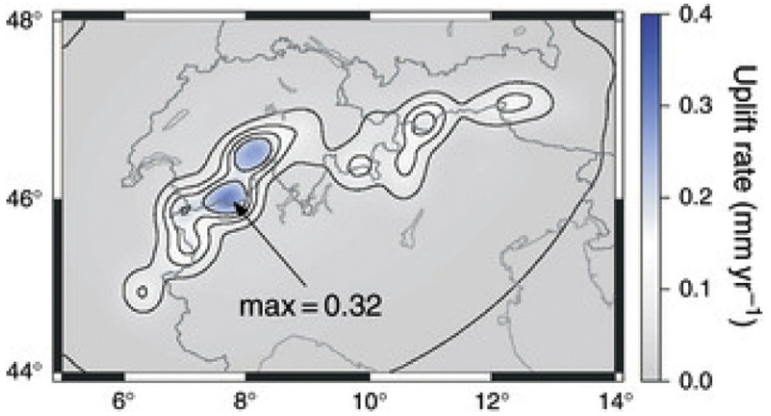

Figure 14 High-resolution viscous contribution, for 155 km^3 of ice volume loss since AD 1850. Reproduced from Barletta VR, Ferrari C, Diolaiuti G, Carnielli T, Sabadini R, and Smiraglia C (2006) Glacier shrinkage and modeled uplift of the Alps. *Geophysical Research Letters* 33: L14307. http://dx.doi.org/10.1029/2006GL026490, with permission from AGU.

floodings of lowlands: it is thus relevant to study the effects of ice-sheet melting on sea-level changes.

The link between ice melt and sea-level rise might seem obvious, but it is not, once it is realized that ice melt could actually induce a sea-level drop at some places on the Earth's surface, rather than sea-level rise.

In fact, an ice sheet on a continent attracts the water of the ocean, due to its own mass: the water near the ice sheet will be elevated with respect to a situation in which this gravitational interaction between the masses of the ice and of the water does not occur, because of the absence of the ice sheet. If the ice-sheet melts, this gravitational attraction effect, or self-gravitation, would disappear. Woodward (1888) showed that this effect is not negligible and derived the following formula for the ratio of the change in sea level with self-gravitation taken into account and the sea-level change without the self-gravitation of the ice sheet, treated as a point source:

$$\left(\frac{1}{2\sin(\theta/2)} - 1 - \frac{\rho_E}{3\rho_w}\right) \Big/ \frac{\rho_E}{3\rho_w} \qquad [29]$$

where θ is the angular distance from the ice sheet, ρ_E the mean density of the Earth, and ρ_w the density of the water. Expression [29] shows that the ratio is not dependent on the total mass of the ice sheet. A derivation of [29] can also be found in Farrell and Clark (1976). From [29], it can be easily shown that sea level will drop in the oceans as a result of ice melt within a distance of about 20°, which on the Earth's surface corresponds to about 2200 km from the former ice sheet. Even within 60°, about 6700 km, sea level will rise less than if the amount of water from the ice sheet had been distributed uniformly, or eustatically, over the oceans. At distances exceeding 60°, sea level will rise more than the eustatic value. The relation between ice melt and sea-level change is clearly not so simple as the reader might think. In fact, even though the mass of ice that melts equals that of the total amount of water that is added to the oceans, the redistribution of the meltwater is not uniform.

The situation becomes even more complicated, once it is realized that the solid Earth is not rigid, as shown in **Figure 5**.

The relation between ice melt and sea-level rise, modified by [29] because of self-gravitation, must so be expanded to a three-component relation involving continental ice, sea level, and the solid Earth. Ice melt will cause a sea-level change that will induce solid-Earth deformation. But solid-Earth deformation in turn will induce a sea-level change again. This sea-level change will induce solid-Earth deformation, and so on. It is thus clear that this relationship is a nonlinear one: the formulation for this relationship has been derived in the 1970s and has become known as the sea-level equation, which is an integral equation. This equation for sea-level change reads (Farrell and Clark, 1976)

$$S = \rho_I \frac{\phi}{g} * L + \rho_W \frac{\phi}{g} * S + C \qquad [30]$$

in which S denotes the change in sea level, L the change in (continental) ice thickness, ϕ the Green function for the variation in the gravitational potential, ρ_I the density of the ice, and g surface gravity. C is a constant that is to be determined by invoking the condition that the total amount of ice change is equal to the total amount of sea-level change. The asterisk denotes time convolution. Sea-level change S is both on the left-hand side and on the right-hand side of eqn [30], which makes the latter an integral equation.

Thanks to this sea-level equation, by which the sea-level change and solid-Earth deformation interrelationship as function of ice-mass variations and solid-Earth models can be taken into account, present-day sea-level variations can be modeled adequately, both for sea-level changes due to Pleistocene deglaciation and for those induced by recent continental ice-mass changes (e.g., Di Donato et al., 1999; Farrell and Clark, 1976; Johnston, 1993; Lambeck et al., 1990; Mitrovica and Peltier, 1991; Nakada and Lambeck, 1987; Peltier and Andrews, 1976; Wu and Peltier, 1983).

The importance of PGR on the interpretation of sea-level variabilities has been addressed by several authors. Lambeck and Nakiboglu (1984) found that PGR contributes between 30% and 50% of the present-day secular rise in sea level of 1.8 mm year^{-1} (Douglas, 1995). Although there are many uncertainties in estimating such a percentage, these findings show the potential importance of including solid-Earth deformation processes in studying sea-level changes.

Figure 15 shows a global picture of sea-level changes in millimeters per year due to PGR, based on the same kind of modeling that has been used to produce previous figures of PGR-induced deformation, in terms of surface vertical and horizontal velocities, baseline rates, and strain rates. These results show that sea-level changes are highly correlated with vertical deformation rates of the lithosphere, as indicated, for example, by the result that the largest values of sea-level drop coincide with the deglaciation centers of **Figure 5**, where the lithosphere is subject to uplift. In fact, since the surface of the sea has to remain an equipotential surface and vertical displacement of this surface is about one order of magnitude lower than the vertical displacement of the lithosphere, or sea bottom, sea-level change S decreases, since the distance between the equipotential and the sea bottom is reduced in uplifting areas. **Figure 16** deals with the vertical displacement of the surface of the sea that moves up or down, with respect to the Earth's center, in order to remain an equipotential, even though ice, water, and solid-Earth material is redistributed, thus modifying the gravity field.

The redistribution of mass caused by PGR, in fact, is responsible not only for vertical and horizontal displacements of sites over the Earth's surface but also for perturbation of the gravitational potential, as on the other hand indicated by the equations of previous sections. Uplifting of the Earth's crust, for example, over North America, Fennoscandia, and Antarctica, causes dense crustal material replacing the air or the water, thus infilling the mass deficit left by ice-sheet disintegration. This growing positive mass over such wide continental areas is responsible for increasing the gravity over these areas, by Newton's law. PGR has thus the effect of changing the position of surfaces of constant gravity potentials, or equipotentials, with respect to the Earth's center. In particular, one of these equipotentials, namely, geoid, representing the surface of mean sea level, excluding dynamic phenomena such as currents, waves due to winds, and tides, is displaced due to PGR, as shown in **Figure 16**. This figure shows the vertical displacement of such a surface, or geoid, in millimeters per year, as

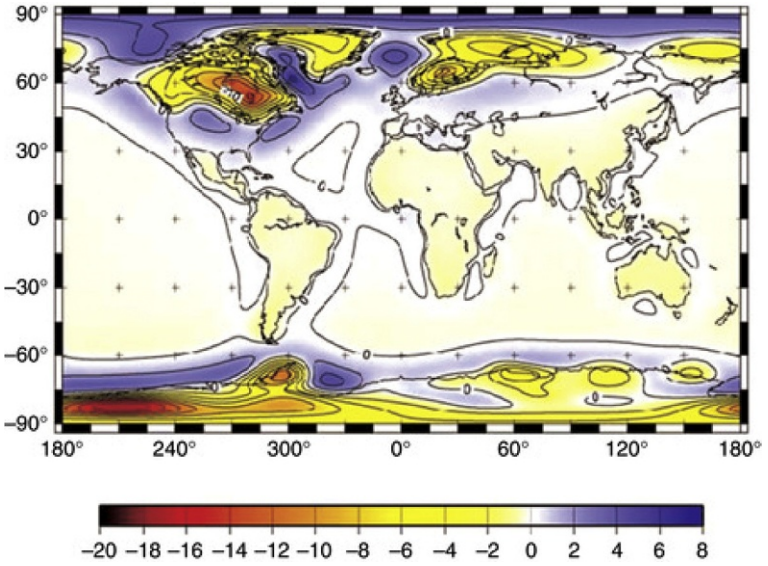

Figure 15 Global sea-level changes in millimeters per year from PGR.

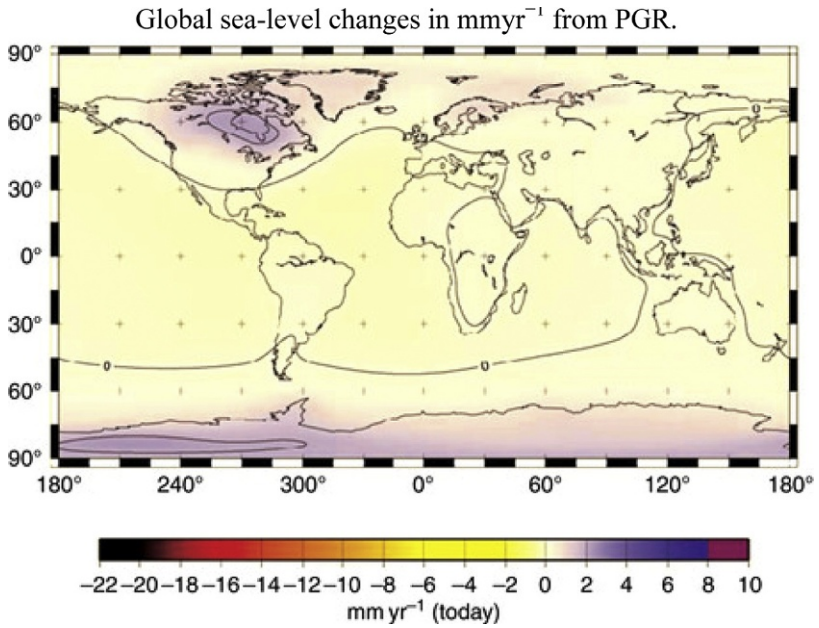

Figure 16 Global geoid changes in millimeters per year from PGR.

predicted by the same kind of modeling used in previous figures. As stated earlier in the text, the geoid is increasing, by a few millimeters per year, over the deglaciation centers, while it is subject to a small decline at far distances from these centers. As anticipated, geoid changes are smaller than sea-level changes, since the latter is mainly controlled by the vertical displacement of the Earth's surface, or sea bottom.

Of course, such an increase of gravity cannot be felt by human beings, but modern satellites do sense such an increase of gravity. The secular component or drift in the geoid variations obtained from Gravity Recovery and Climate Experiment (GRACE) mission from NASA, for example, shows that gravity, and thus the geoid, is presently growing over the Hudson Bay, in agreement with previous picture, as portrayed by **Figure 17** obtained from GRACE data (Barletta et al., 2006b). The figure portrays the displacement rate, in millimeters per year, of the geoid that represents the real changes of the Earth's gravity obtained by extracting the secular trend or drift from GRACE data, smoothed by means of a Gaussian filter of 500 km, which can be directly compared with **Figure 16**. This geoid change is obtained by extracting the linear trend in each harmonic coefficient of the gravity field obtained from GRACE data (Barletta et al., 2006b). A comparison between **Figures 16** and **17** shows on the other hand that such a correlation of increasing geoid is

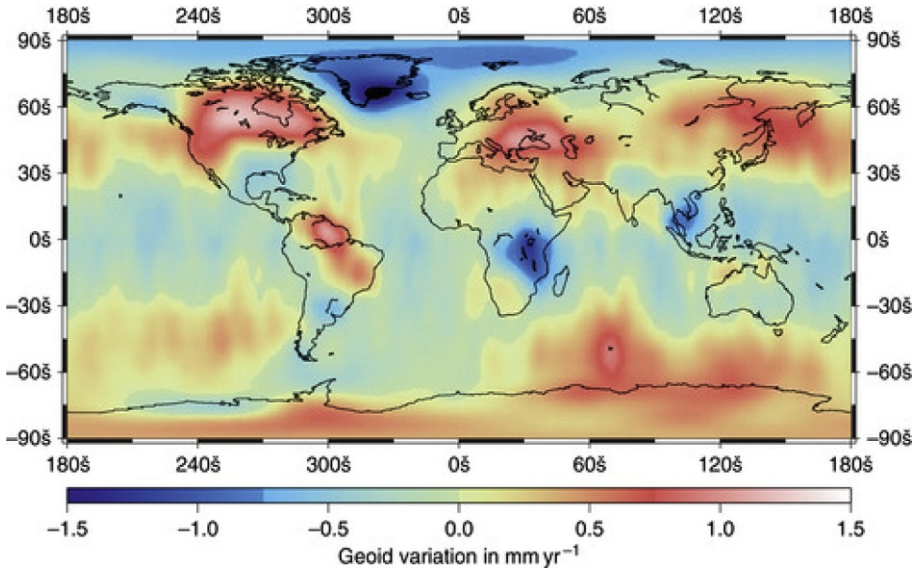

Figure 17 Global geoid changes in millimeters per year, secular component, from GRACE.

not so obvious when the other two deglaciation centers, Fennoscandia and Antarctica, are considered and the reason for that can be found in other phenomena, such as present-day melting in Antarctica, that mask the effects of PGR. In any case, it is the first time after Newton that scientists have the possibility to monitor global gravity changes of the Earth, thanks to gravity space missions.

Similarly to what it has been done for displacement patterns in **Figures 5** and **6**, relative to global and European perspectives, **Figure 18(a)** and **18(b)** now focuses on modeled present-day rates of sea-level change, in northern Europe and in the Mediterranean region. The lower-mantle viscosity considered for these sea-level changes' calculation is consistent with inferences based on postglacial relative sea-level variations in northern Europe (Lambeck et al., 1990) and numerical predictions of postglacial sea-level change in southern Europe (Mitrovica and Davis, 1995). The sea-level equation [30] has been solved by using the pseudo-spectral algorithm by Mitrovica and Peltier (1991) with a truncation at degree and order 256, so the spatial resolution is sufficient to model sea-level increase in small regions, such as those considered herein.

As expected, the highest rates are obtained in the center of deglaciation, the Gulf of Bothnia, where uplift of the land causes a sea-level fall of -11 mm year^{-1}. In the periphery of the uplifting region, the land is subsiding due to the collapse of the peripheral bulge, and sea level thus increases along the coastal areas of northern Europe, by as much as 1–2 mm year^{-1}. This sea-level increase along the coasts of northern continental Europe is not constant but is subject to large variabilities, from 0.4 mm year^{-1} near the French coast to 1–1.5 mm year^{-1} along the coasts of the Netherlands and Germany. It should be noted that the collapse of the peripheral bulge decreases in central Europe and, further to the south, sea level is actually increasing, with rates in the order of 0.6–0.8 mm year^{-1} in the central Mediterranean, due to the subsidence of sea bottom caused by the water load of the Mediterranean itself.

The periphery of the Mediterranean is characterized by a weak sea-level rise, with rates from 0.2 to 0.4 mm year^{-1} in the Adriatic Sea and about 0.4 mm year^{-1} along the Mediterranean coast of France. Here, the rates of sea-level change have small values due to the levering effect, as discussed in Nakada and Lambeck (1989), for example. Such an effect implies that subsidence of ocean basins is accompanied by uplift of surrounding continents. This ocean-basin subsidence is due to mantle material presently flowing from the Mediterranean region toward the Fennoscandia in northern Europe, concordant with the main stream from the Earth's equatorial regions to deglaciation centers, as anticipated in previous sections. These values are comparable with the sea-level changes due to active tectonics in the central Mediterranean. Finite-element calculations of active tectonics in the Italian Peninsula have indicated in fact that overthrusting of the Apennines onto the Adriatic Plate is responsible for sea-level increases of about 0.4 mm year^{-1}, as detailed in Negredo et al. (1997). Sea-level change values in central Mediterranean due to PGR are thus comparable with those due to active tectonics, as first enlightened by Di Donato et al. (1999).

6.04.3 Continental Plates

6.04.3.1 Introduction

Crustal deformation in Europe is influenced not only by PGR, as shown in previous sections, but also by plate tectonic forces, including boundary forces associated with the African–Eurasian convergence, spreading at the Mid-Atlantic Ridge, and subduction-related ones.

The reader can thus wonder whether there are regions in Europe where PGR or tectonic effects on baseline rates or strain rates can be ignored or whether there are regions where both phenomena act in concert, in order to investigate the nature and origin of intraplate deformation in continental Europe. More generally, it is relevant to analyze the complex geometric

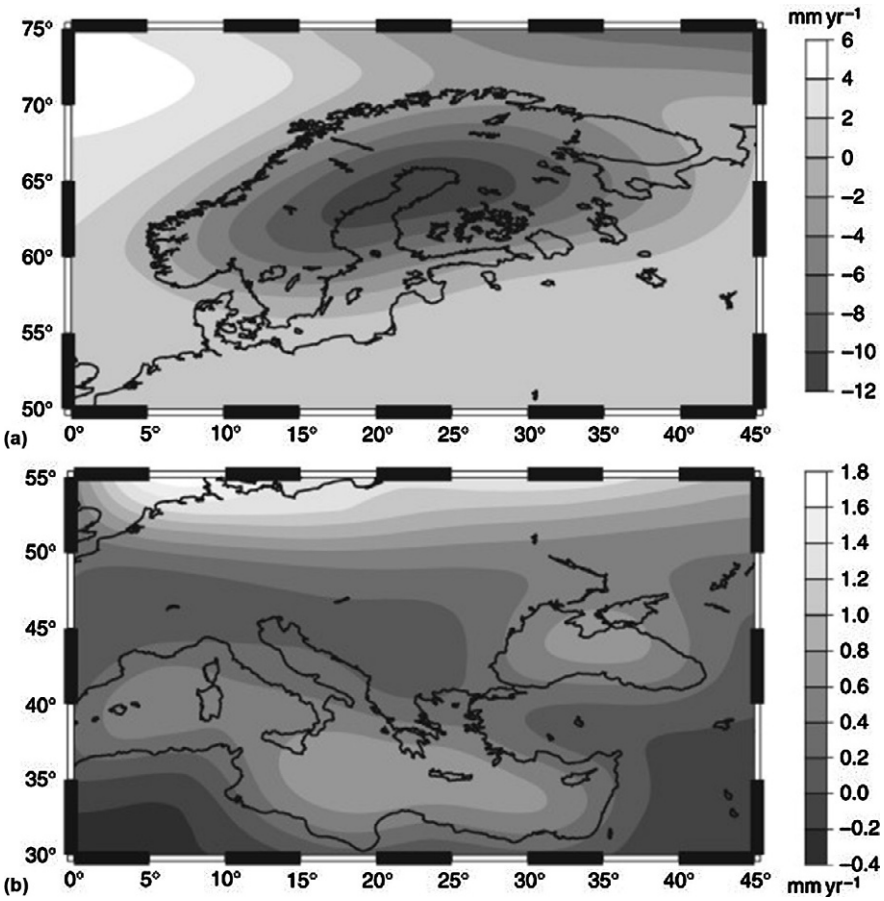

Figure 18 The present-day rates of sea-level change (a) in northern Europe and (b) in the Mediterranean region due to PGR. Reproduced from Figure 6.5 of Sabadini R and Vermeersen B (2004) *Global Dynamics of the Earth*, p. 328, Kluwer Academic Publisher, with kind permission of Springer Science and Business Media.

interplay between tectonics and PGR in European continental deformation.

These issues are now considered in this section, in order to compare predictions generated from thin-sheet tectonic models and PGR simulations.

6.04.3.2 Modeling Intraplate Deformation

The mathematical model of continent–continent collision, to simulate the effects of active tectonics in Europe due to the African–Eurasian convergence, is based on the thin-sheet scheme (England and McKenzie, 1983; Marotta et al., 2001). This mathematical scheme allows us to analyze the sensitivity of modeling results on changes in velocity forcing along the Mid-Atlantic Ridge and variations in the lithospheric strength, or rheology, of various European subdomains. Thanks to the adopted finite-element numerical scheme for solving the following thin-sheet differential equations [35] and [36], the viscosity can be appropriately chosen for each subdomain, in order to account for lateral variations in lithospheric strength. The analysis finally highlights a combined tectonic model plus PGR that best fits ITRF2000 data.

An incompressible, viscous model is adopted to investigate tectonic deformation in the Mediterranean–Fennoscandia driven by the African–Eurasian convergence and Mid-Atlantic Ridge opening (**Figure 19**). The figure shows the finite-element mesh, used to solve the differential equations of motion by means of the finite-element scheme first presented in Marotta et al. (2004). This section is based on the studies by Marotta and Sabadini (2004) and Marotta et al. (2004), where for the first time, intraplate deformation in central Europe was interpreted in terms of self-consistent geophysical models. Once compared with **Figure 2**, this purely viscous model includes only the dashpot, as appropriate for long-lasting tectonic processes of million years. The treatment of the lithosphere as an incompressible, viscous fluid is in fact adopted in models of long-timescale geologic processes (Turcotte and Schubert, 1982).

The deformation field, sampled at the nodes of the finite-element mesh, is expressed in terms of crustal velocities and baseline rates obtained from the thin-sheet approximation implemented by Marotta et al. (2001) and modified in Marotta et al. (2004) in such a way to include spherical geometry. Stratification of the lithosphere is taken into account when we vertically average the lithospheric viscosity to build the thin viscous sheet modeling of the lithosphere with constant total thickness, overlying an inviscid asthenosphere, which assures a stress-free condition at the base of the plate. The thin-sheet approximation assumes that wavelengths

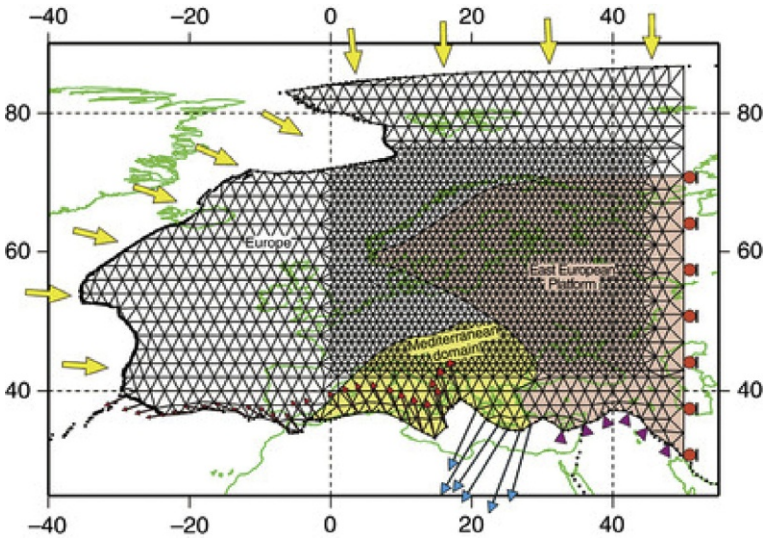

Figure 19 Finite-element grid adopted for the tectonic predictions described in this study. The grid distinguishes three major blocks, or subdomains: the European, East European Platform, and Mediterranean. The thick yellow arrows at the left side of the domain represent ridge push forces. The counterclockwise rotation of the African Plate with respect to the European Plate, adopted from NUVEL-1A, is reflected by the red arrows at the bottom left. The velocities along the Aegean trench (blue arrows) were geodetically determined by McClusky et al. (2000). The southern border between the model domain and the Arabian region is held fixed (pink triangles), while the right (eastern) boundary of the model is assumed to be shear stress-free (red dots). Reproduced from Marotta AM, Mitrovica JX, Sabadini R, and Milne G (2004) Combined effects of tectonics and glacial isostatic adjustment on intraplate deformation in central and northern Europe: Application to geodetic baseline analyses. *Journal of Geophysical Research* 109: B01413. http://dx.doi.org/10.1029/2002JB002337, with permission from AGU.

characterizing plate deformation are larger than plate thickness. Other thin-plate approximations are based on the assumption that the lithosphere is isostatically compensated and on the vertical averaging of lithospheric rheology. Three-dimensional problems are thus reduced to 2-D ones, where horizontal velocity components do not depend on the depth: horizontal components of the momentum equation are vertically integrated through the plate and are then solved using a 2-D finite-element mesh, as shown in **Figure 19**, thus estimating only velocity horizontal components.

The western and southern borders of the model domain coincide with the Mid-Atlantic Ridge and African–Eurasian Plate contact, respectively, where velocity boundary conditions are applied. The eastern border of the model ends at 45° E meridian, within the intracratonic East European Platform, where stress transmission from boundary forcing is expected to be negligible. The domain is discretized using planar finite triangular elements sufficiently small in size so that the surface of each individual grid element can be considered as flat.

In the tectonic modeling under study, the differential equations describing the mechanical behavior of the plates are eqn [1] in spherical geometry and coincide with those of PGR only for the radial r and colatitudinal θ components of the divergence of the stress tensor $\nabla\cdot\sigma$, since plate-deformation modeling under applied horizontal tectonic forces includes the longitudinal component ϕ of the momentum equations. Differently from PGR where due to the type of forcing and symmetry of the problem, only the radial and colatitudinal equations are relevant, in the tectonic modeling, the longitudinal equation must be included, since horizontal tectonic forces have, in general, both θ and ϕ components. In the same coordinate system, the θ, ϕ, and r components of the momentum equations are then (Schubert et al., 2001)

$$\frac{1}{r}\frac{\partial}{\partial\theta}\sigma_{\theta\theta}+\frac{1}{r\sin\theta}\frac{\partial}{\partial\phi}\sigma_{\theta\phi}+\frac{\partial}{\partial r}\sigma_{\theta r}+\frac{1}{r}\left[\left(\sigma_{\theta\theta}-\sigma_{\phi\phi}\right)\cot\theta+3\sigma_{\theta r}\right]=0 \quad [31]$$

$$\frac{1}{r}\frac{\partial}{\partial\theta}\sigma_{\phi\theta}+\frac{1}{r\sin\theta}\frac{\partial}{\partial\phi}\sigma_{\phi\phi}+\frac{\partial}{\partial r}\sigma_{\phi r}+\frac{1}{r}\left(3\sigma_{\phi r}+2\sigma_{\phi\theta}\cot\theta\right)=0 \quad [32]$$

$$\frac{1}{r}\frac{\partial}{\partial\theta}\sigma_{r\theta}+\frac{1}{r\sin\theta}\frac{\partial}{\partial\phi}\sigma_{r\phi}+\frac{\partial}{\partial r}\sigma_{rr}+\frac{1}{r}\left(2\sigma_{rr}-\sigma_{\theta\theta}-\sigma_{\phi\phi}+\sigma_{r\theta}\cot\theta\right)+f_r=0 \quad [33]$$

where f_r denotes the gravitational body force term. As usual, the stress can be written as

$$\sigma_{ij}=\tau_{ij}-p_0\delta_{ij} \quad [34]$$

where p_0 is the hydrostatic pressure.

Under the assumptions that only horizontal tectonic forces are active and are associated with the African–Eurasian convergence and that there is no shear stress or basal drag at the base of the lithosphere, the components $\sigma_{r\theta}$ and $\sigma_{r\phi}$ within these general equations are neglected. By applying the constitutive equation for an incompressible, viscous material and the conditions for isostatic balance, the momentum equations become, after integration over the thickness of the lithosphere (Marotta et al., 2004),

$$\frac{\partial}{\partial\theta}\left[2\overline{\mu}\left(\frac{\partial}{\partial\theta}u\theta+u_r\right)\right]+\frac{1}{\sin\theta}\frac{\partial}{\partial\phi}\times\left[\overline{\mu}\left(\frac{1}{\sin\theta}\frac{\partial}{\partial\phi}u\theta+\frac{\partial}{\partial\theta}u_\phi-u_\phi\cot\theta\right)\right]+\left[2\overline{\mu}\left(\frac{\partial}{\partial\theta}u\theta-\frac{1}{\sin\theta}\frac{\partial}{\partial\phi}u_\phi-u_\theta\cot\theta\right)\right]\cot\theta=\frac{g\rho_c R}{2L}\left(1-\frac{\rho_c}{\rho_m}\right)\frac{\partial}{\partial\theta}S^2 \quad [35]$$

$$\frac{\partial}{\partial\theta}\left[\overline{\mu}\left(\frac{1}{\sin\theta}\frac{\partial}{\partial\phi}u\theta+\frac{\partial}{\partial\theta}u_\phi-u_\phi\cot\theta\right)\right]$$
$$+\frac{1}{\sin\theta}\frac{\partial}{\partial\phi}\left[2\overline{\mu}\left(\frac{1}{\sin\theta}\frac{\partial}{\partial\phi}u_\phi+u_\theta\cot\theta+u_r\right)\right]$$
$$+\left[2\overline{\mu}\left(\frac{\partial}{\partial\theta}u_\phi+\frac{1}{\sin\theta}\frac{\partial}{\partial\phi}u_\theta-u_\phi\cot\theta\right)\right]\cot\theta \quad [36]$$
$$=\frac{g\rho_c R}{2L}\left(1-\frac{\rho_c}{\rho_m}\right)\frac{1}{\sin\theta}\frac{\partial}{\partial\phi}S^2$$

where $\overline{\mu}$ denotes the vertically averaged viscosity of the lithosphere, S denotes the crustal thickness, L is the lithospheric thickness, ρ_c and ρ_m denote the densities of the crust and lithosphere, respectively, g is the gravity, and R is the radius of the Earth.

The third unknown, u_r, is eliminated from these equations by invoking incompressibility and by assuming that the radial strain rate $(\partial/\partial r)u_r$ vanishes. As detailed in Marotta et al. (2004), u_r can thus be expressed as

$$u_r=-\frac{1}{2}\left\{\frac{\partial u\theta}{\partial\theta}+\frac{1}{\sin\theta}\frac{\partial u\phi}{\partial\phi}+u_\theta\cot\theta\right\} \quad [37]$$

The thin-sheet model is appropriate for estimating horizontal components of velocity field u_θ, u_ϕ only: the radial component of the differential equation ensures the condition of isostatic equilibrium, requiring that mass excess is supported in the radial direction by radial stress.

By specifying crustal thickness S and boundary conditions, numerical integration of previous equations yields the stationary tectonic deformation field. Velocity is approximated by linear polynomial interpolating functions within each finite element and numerical integration is performed by Gaussian quadrature with seven integration points (Marotta et al., 2004).

A series of numerical tectonic deformation models are summarized in **Table 1** as models 1–7, distinguished in terms of lithospheric viscosity and velocity boundary condition along the North Atlantic Ridge. Model inputs are discussed next.

Lateral variations in lithospheric strength can be taken into account in the modeling by specifying distinct viscosity values at each element of the grid. Lateral viscosity variations are referred to the European lithosphere, treated as the reference domain where a prescribed reference viscosity is fixed.

In the homogeneous viscosity model, the velocity pattern is shaped by velocity boundary conditions and is unaffected by changes in the lithospheric viscosity in the range 10^{23}–10^{25} Pa s; the value of 10^{25} Pa s is the reference viscosity that ensures numerical stability when lateral viscosity variations are introduced.

Two isoviscous lithospheric domains are considered: The first corresponds to the Mediterranean domain, extending from the Tyrrhenian Sea to the eastern limit of the Pannonian Basin through the Adriatic Plate, while the second is the East European Platform, as shown in **Figure 19**.

This modeling has some similarities with earlier work by Grunthal and Stromayer (1992), who modeled the stress field in central Europe by means of elastic rheology with laterally varying rigidities that simulate different tectonic units. A viscous fluid with laterally varying viscosity is considered herein, to compare model predictions with geodetic observations.

Velocity boundary conditions are relative to the Eurasian Plate. The velocity of Africa relative to Eurasia is prescribed by NUVEL-1A (red arrows at the bottom border of the finite-element mesh; **Figure 19**), the pattern reflecting the African–Eurasian continental convergence of the order of 1 cm year^{-1}. These velocities impose a counterclockwise rotation of the African Plate with respect to Eurasia. Relative to a fixed Eurasia, ridge push forces acting along the North Atlantic Ridge are also modeled. In the simulations, these forces are parameterized in terms of velocity boundary conditions applied along the ridge, to simulate the effects of the line forces acting along the plate boundary, as described in Richardson et al. (1979). These ridge velocities are represented by thick yellow arrows, to make it clear that they are derived in a different manner with respect to those related to the African–Eurasian convergence.

Line forces normal to the ridge, resulting from applied velocity boundary conditions, can be estimated from the eigenvalues of the stress tensor within those elements whose left sides define the ridge, in order to verify that boundary conditions induce realistic forces within the lithospheric model. Along the westernmost part of the Mid-Atlantic Ridge, predicted ridge push forces range from $\sim10^{12}$ N m^{-1}, for an imposed velocity boundary condition of about 1 mm year^{-1}, to $\sim10^{13}$ N m^{-1} for 5 mm year^{-1}, the latter representing an upper bound for ridge push forces, as shown by Richardson and Reding (1991). Ridge velocities are not constant along the ridge, but are scaled with respect to the spreading velocities deduced from NUVEL-1A, so that imposed ridge velocities of 1 and 5 mm year^{-1} are of the order of 1/20th and 1/4th of the full spreading rate ($\sim$2 mm year^{-1}) according to NUVEL-1A.

Along the Aegean trench, geodetically determined velocities by McClusky et al. (2000) are applied as velocity boundary conditions to an equal number of nodes, as indicated by the blue arrows in **Figure 19**, from west to east. These sites are LOGO (25 mm year^{-1}), LEON (33 mm year^{-1}), OMAL (30 mm year^{-1}), ROML (32 mm year^{-1}), KAPT (33 mm year^{-1}), and KATV (30 mm year^{-1}). These velocities reflect trench subduction forces along this boundary and represent the velocity of these geodetic sites with respect to Eurasia.

The eastern boundary of the model domain is held fixed, and to avoid large effects from artificial stress accumulation, due to this boundary condition, a shear stress-free boundary condition is imposed at this border, as indicated by the red dots along the right boundary of the model. The imposed conditions at the eastern boundary would be consistent with a possible decoupling between the western and eastern parts of the Eurasian Plate, as suggested by Molnar et al. (1973). This condition clearly implies that intraplate deformation of Eurasia due to the African–Eurasian convergence and Mid-Atlantic Ridge push takes place within the model domain.

The contact between the East European Platform and Arabian Plate is fixed in the simulations carried out in this section, as indicated by the pink triangles in the southeastern part of **Figure 19**. This condition will be released in the following sections, focused on strain rate in the Mediterranean.

Crustal thickness variations have been obtained from linear interpolation onto the adopted grid of model CRUST 2.0 by Bassin et al. (2000).

6.04.3.3 Monitoring Intraplate Deformation via GPS Analyses

Here, we shall explore the effects of lateral viscosity variations and varying velocity boundary condition along the Mid-Atlantic Ridge on intraplate deformation in Europe from active tectonics. The first three models in Table 3 correspond to different imposed velocity boundary conditions along the North Atlantic Ridge, while the other boundary conditions are as described in the preceding text. The horizontal velocities predicted within the modeled domain for these three models are shown in Figure 20.

Figure 20(a) focuses on the effects of the African–Eurasian convergence on intraplate velocity pattern within the model domain, where crustal velocity gradually diminishes from ~2 mm year^{-1} at latitudes of 45° along the Alpine front to 0.2 mm year^{-1} in central Fennoscandia. The velocity field driven by the African indenter extends throughout central Europe, approximately in the northwestern direction, with velocity isocontours roughly parallel to the collision front.

For 1 mm year^{-1} along the North Atlantic Ridge, Figure 20(b) a rotation from NW to NE in the global velocity direction is obtained in central and northern Europe. With respect to Figure 20(a), the velocity is increased throughout the western part of the study domain and an increase from 0.2 to 0.5 mm year^{-1} is obtained at the latitude of Fennoscandia. When the velocity along the Mid-Atlantic Ridge is increased to 5 mm year^{-1}, an upper bound in terms of ridge push forces as discussed in the preceding text (Figure 20(c)), tectonic velocity in England and Fennoscandia reaches magnitudes of ~3–~2 mm year^{-1}, respectively. The imprints of western and southern boundary forcings are evident in this tectonic velocity pattern. In the Alpine front, north-directed motions up to ~4 mm year^{-1} are obtained in Figure 20(c), and to the north of this region, sites in central Europe are now characterized by an eastern velocity component.

The velocity patterns in Figure 20 represent intraplate deformation for homogeneous viscosity models, with Figure 20(c) portraying unrealistic deformation magnitudes for large ridge push forces. The effect of incorporating lateral variations in lithospheric stiffness into the tectonic model is exploited in Figure 21, corresponding to viscosity increase of two orders of magnitude in the East European domain with respect to the reference viscosity of 10^{25} Pa s. The two simulations differ in terms of boundary condition along the North Atlantic Ridge, which is 0.0 mm year^{-1} in Figure 21(a) and model 4 and 5.0 - mm year^{-1} in Figure 21(b) and model 5. Stiffening of the lithosphere within the East European Platform has a prominent effect on tectonic velocities within that region. From north to south across the platform, velocity gradients are reduced considerably in Figure 21(a) with respect to Figure 20(a). A nearly constant crustal velocity of ~0.6 mm year^{-1} thus characterizes a large portion of the stiffened craton, including Fennoscandia.

Table 3 Tectonic models

Model	*Rheological heterogeneities*	*Ridge velocity b.c. (mm year^{-1})*
1	No rheological heterogeneities	0.0
2	No rheological heterogeneities	1.0
3	No rheological heterogeneities	5.0
4	Stiff East European Platform	0.0
5	Stiff East European Platform	5.0
6	Soft Mediterranean domain	0.0
7	Soft Mediterranean domain	5.0

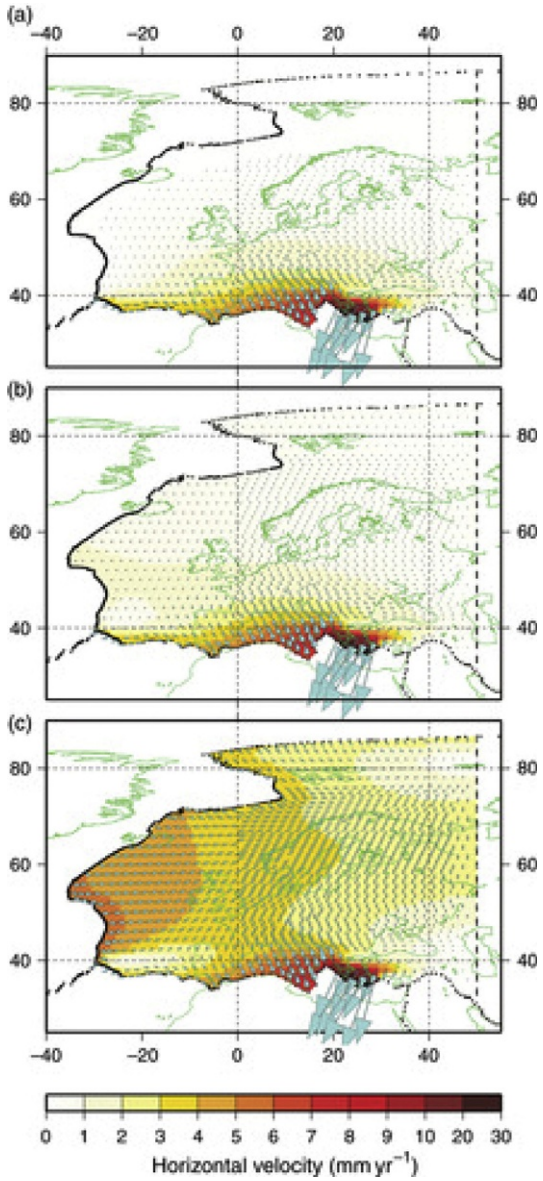

Figure 20 Predictions of horizontal crustal velocities generated using our finite-element tectonic model (arrows and color contouring). The models are all based on a homogeneous lithosphere with viscosity of 10^{25} Pa s and they are distinguished on the basis of the velocity boundary conditions applied on the North Atlantic Ridge. Specifically, these conditions are (a) 0, (b) 1/20, and (c) 1/4 of the full spreading velocity given by the NUVEL-1A model at each point on the ridge. These models are labeled 1–3, respectively, in Table 3. Reproduced from Marotta AM, Mitrovica JX, Sabadini R, and Milne G (2004) Combined effects of tectonics and glacial isostatic adjustment on intraplate deformation in central and northern Europe: Application to geodetic baseline analyses. *Journal of Geophysical Research* 109: B01413. http://dx.doi.org/10.1029/2002JB002337, with permission from AGU.

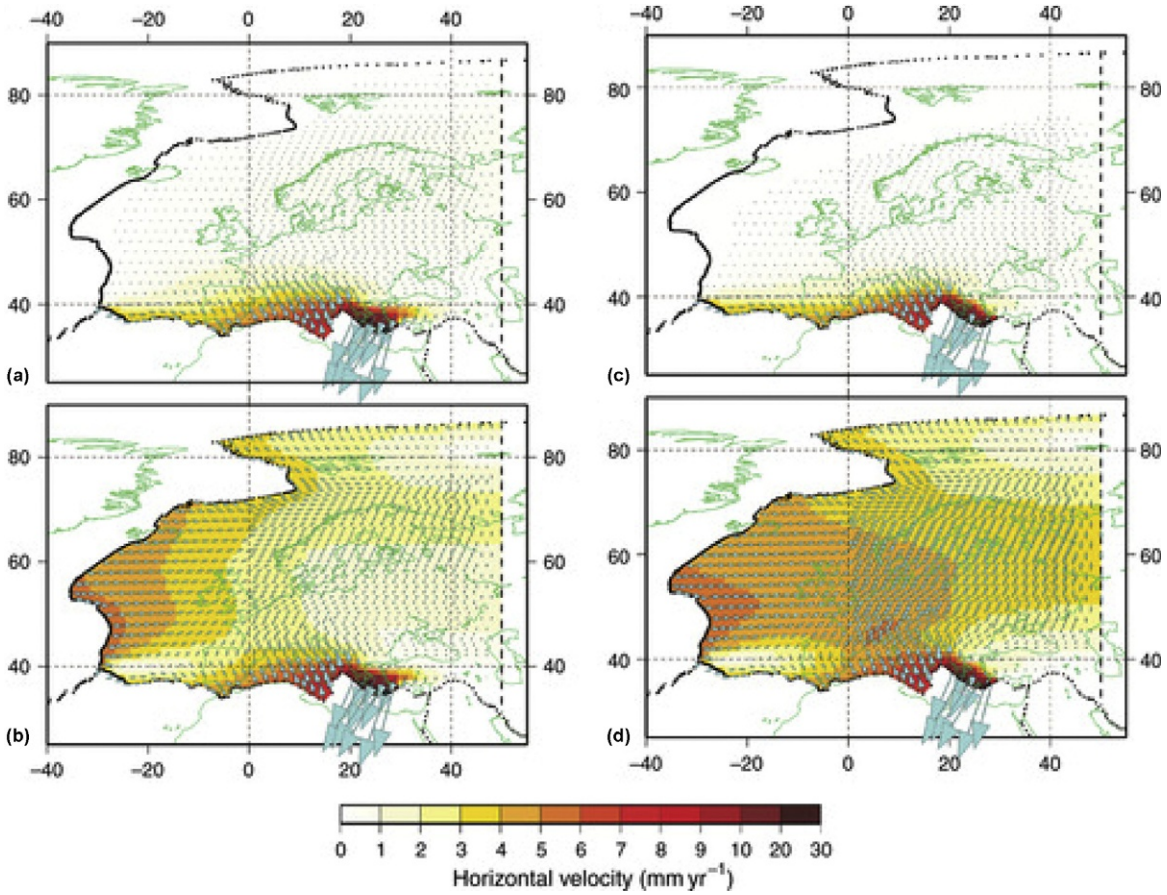

Figure 21 As in **Figure 20**, except for models 4–7 of **Table 3**. In particular, panels (a) and (b) correspond to models in which the East European Platform is two orders of magnitude stiffer than the reference European domain (models 4 and 5). In panels (c) and (d), the viscosity of the Mediterranean subdomain is reduced by one order of magnitude relative to the reference value of the European domain (models 6 and 7, respectively). Furthermore, these models sample cases in which the velocity condition applied along the North Atlantic Ridge (in order to model ridge push forces) is either zero (panels (a) and (c)) or 1/4 (panels (b) and (d)) of the NUVEL-1A full spreading velocities, approximately 0.0 or 5.0 mm year^{-1}. Reproduced from Marotta AM, Mitrovica JX, Sabadini R, and Milne G (2004) Combined effects of tectonics and glacial isostatic adjustment on intraplate deformation in central and northern Europe: Application to geodetic baseline analyses. *Journal of Geophysical Research* 109: B01413. http://dx.doi.org/10.1029/2002JB002337, with permission from AGU.

The stiffened lithosphere shields the Baltic region and Fennoscandia from the velocity driven by the ridge and dampens the velocity gradients within the East European Platform, as shown in **Figure 20(c)** and model 3 compared with **Figure 21(b)** and model 5. Increasing the viscosity of the East European Platform results in a substantial reduction, in northern Europe and Fennoscandia from North Atlantic Ridge-induced velocity. Models 6 and 7 are characterized by one order of magnitude viscosity reduction within the Mediterranean lithosphere (**Figure 21(c)** and **21(d)**, respectively). A comparison of **Figures 21** and **20**, for example, shows that a large amount of the deformation driven by the push of Africa is accommodated in the weakened lithosphere, with velocity gradients concentrated in the Mediterranean. The relatively small velocities within Fennoscandia in **Figure 20** (panel (a)) now extend well southward into central Europe in **Figure 21(c)**. As expected, intraplate deformation in Europe due to the African–Eurasian convergence is sensitive to the amount of deformation that takes place within the Mediterranean lithosphere.

A velocity along the North Atlantic Ridge introduced in model 7 and weakened Mediterranean lithosphere are considered in **Figure 21(d)**; the result in **Figure 21(d)** can be compared with **Figure 20(c)**. A weakening of the Mediterranean subdomain favors the diffusion into Europe of the eastward-directed velocity driven by the Atlantic spreading. Note the pronounced eastward migration of the 4 mm year^{-1} contour in **Figure 21(d)** relative to **Figure 20(c)**.

Deformation style in Europe from tectonics is first analyzed in terms of baseline rates, as done for PGR. Baseline rate modeling is first compared to ITRF2000 data predictions, with respect to VAAS. **Figures 22** and **23** show predictions of baseline rates generated from a tectonic model subset. **Figure 22** is based on model 1 of **Table 3** and is characterized by a homogeneous lithosphere, by the African–Eurasian convergence and no Mid-Atlantic Ridge forcing. For this homogeneous viscosity, VAAS-referenced baselines show a general pattern of shortening, except for a limited extension for short baselines connecting three sites east of VAAS. It is thus

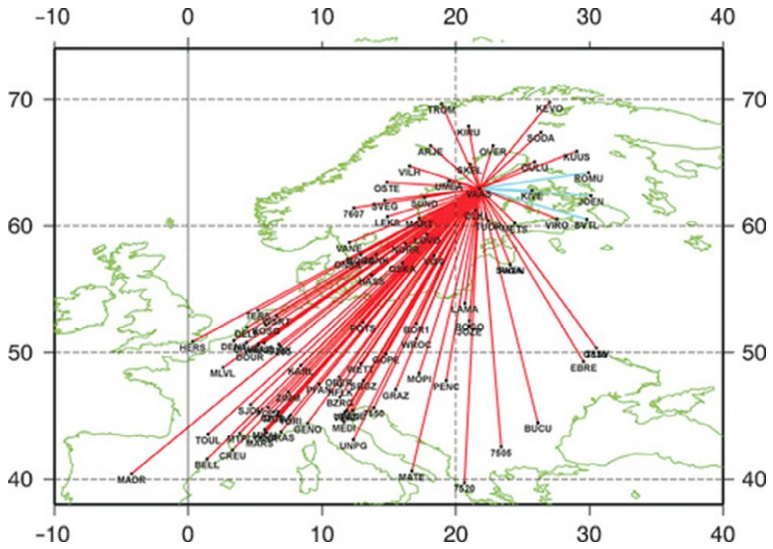

Figure 22 Predicted baseline rates for baselines referenced to the site VAAS model 1. Reproduced from Marotta AM, Mitrovica JX, Sabadini R, and Milne G (2004) Combined effects of tectonics and glacial isostatic adjustment on intraplate deformation in central and northern Europe: Application to geodetic baseline analyses. *Journal of Geophysical Research* 109: B01413. http://dx.doi.org/10.1029/2002JB002337, with permission from AGU.

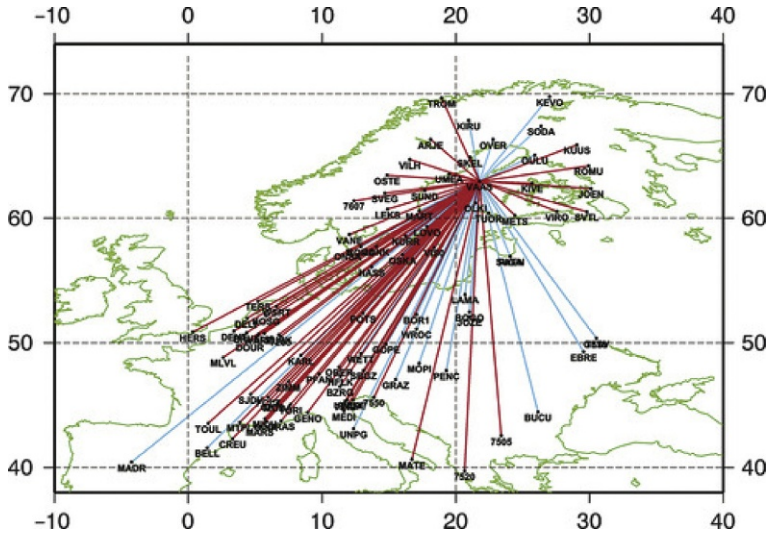

Figure 23 Predicted baseline rates for baselines referenced to the site VAAS for model 5. Reproduced from Marotta AM, Mitrovica JX, Sabadini R, and Milne G (2004) Combined effects of tectonics and glacial isostatic adjustment on intraplate deformation in central and northern Europe: Application to geodetic baseline analyses. *Journal of Geophysical Research* 109: B01413. http://dx.doi.org/10.1029/2002JB002337, with permission from AGU.

remarkable that, except for this limited extension, the style of baseline rates is opposite to the observed pattern in Figure 7.

Figure 23 shows the results for lateral variations in plate strength, model 5, characterized by stiffening of the East European Platform. With respect to homogeneous model results, model 1 (Figure 22) and model 5 (Figure 23) improve the fit to the observed baseline rate pattern by yielding extension for baselines directed southeast to southwest from VAAS. These findings too are unsatisfactory since modeling predicts shortening for other baselines, in contrast to geodetically retrieved baseline rates. These results from models 1 and 5 show that tectonic modeling has the tendency to predict too much compression, even at high latitudes, and that such modeling performs better at intermediate latitudes in central Europe, as shown in the succeeding text.

Figures 24–26 show POTS-referenced baseline rate results generated using the same tectonic models in Figures 22 and 23, plus model 7. The uniform lithosphere model 1 in Figure 24 is driven by forcing along the southern African–Eurasian boundary, and the resulting northward decrease in velocity shown in Figure 20 (panel (a)) yields a shortening of all baselines, which is similar to what was observed for VAAS-referenced baselines in Figure 22 and thus fails to reproduce the extension of the baselines connecting sites north of POTS.

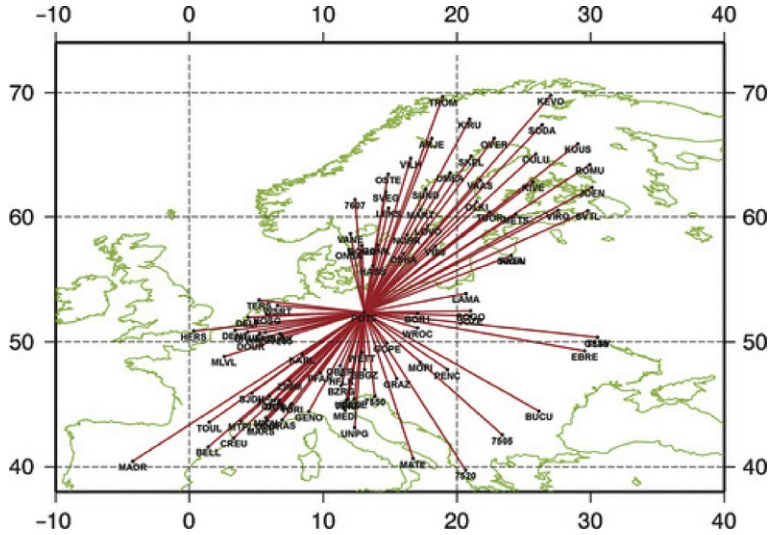

Figure 24 Predicted baseline rates for baselines referenced to the site POTS for model 1. Reproduced from Marotta AM, Mitrovica JX, Sabadini R, and Milne G (2004) Combined effects of tectonics and glacial isostatic adjustment on intraplate deformation in central and northern Europe: Application to geodetic baseline analyses. *Journal of Geophysical Research* 109: B01413. http://dx.doi.org/10.1029/2002JB002337, with permission from AGU.

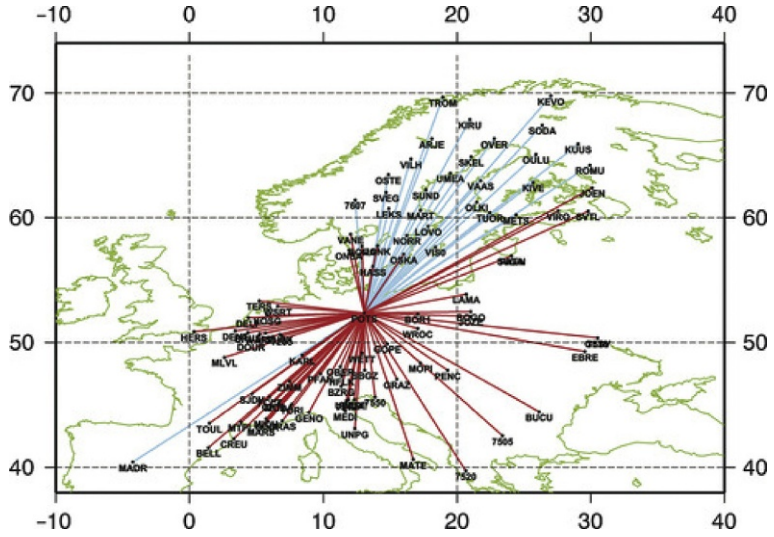

Figure 25 Predicted baseline rates for baselines referenced to the site POTS for model 5. Reproduced from Marotta AM, Mitrovica JX, Sabadini R, and Milne G (2004) Combined effects of tectonics and glacial isostatic adjustment on intraplate deformation in central and northern Europe: Application to geodetic baseline analyses. *Journal of Geophysical Research* 109: B01413. http://dx.doi.org/10.1029/2002JB002337, with permission from AGU.

Figure 25 shows the impact on POTS-referenced baselines of increasing the viscosity in the East European Platform, model 5. The combined effect of viscosity increase in the Baltic Shield and push from the Mid-Atlantic Ridge reproduces the observed pattern characterized by dominant shortening between POTS and the Mediterranean and extension between POTS and Fennoscandia. The effect of the high viscosity in the shield is to maintain into southern and central Europe, south of POTS, the north-directed motion driven by the African indenter. The stronger platform acts to significantly reduce the modeled tectonic deformation across central and northern Europe, including Potsdam. Sites clustered near the African–European Plate boundary in the southwest for latitudes 43–48 °N are thus expected to move toward a relatively more stationary Potsdam, which results in baseline shortening. Figure 25 thus shows that realistic tectonic modeling, such as that characterizing model 5 with lithospheric stiffening in the Baltic Shield and with velocity applied along the Mid-Atlantic Ridge to simulate ridge push forces, is able to reproduce the dominant shortening of baselines from south of POTS and to contribute to extension north of it.

For the final tectonic model of this sequence (model 7, Figure 26), the weakened Mediterranean domain, in contrast to the strong Baltic Shield case, is responsible for the

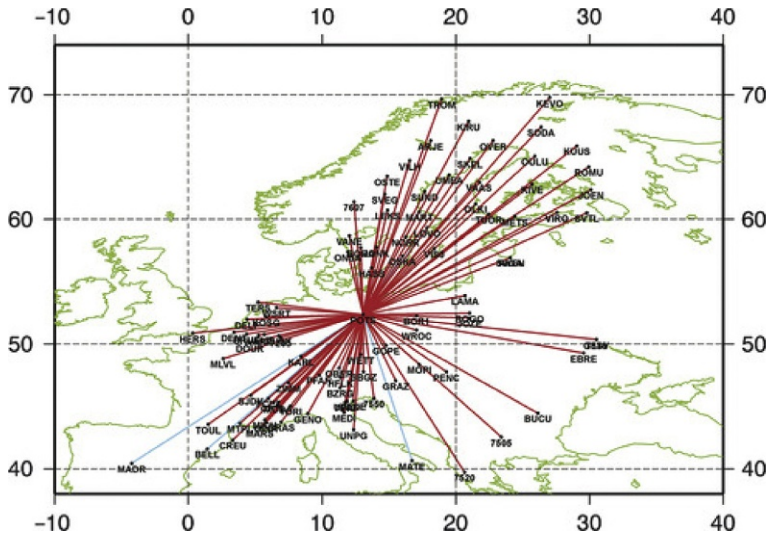

Figure 26 Predicted baseline rates for baselines referenced to the site POTS for model 7. Reproduced from Marotta AM, Mitrovica JX, Sabadini R, and Milne G (2004) Combined effects of tectonics and glacial isostatic adjustment on intraplate deformation in central and northern Europe: Application to geodetic baseline analyses. *Journal of Geophysical Research* 109: B01413. http://dx.doi.org/10.1029/2002JB002337, with permission from AGU.

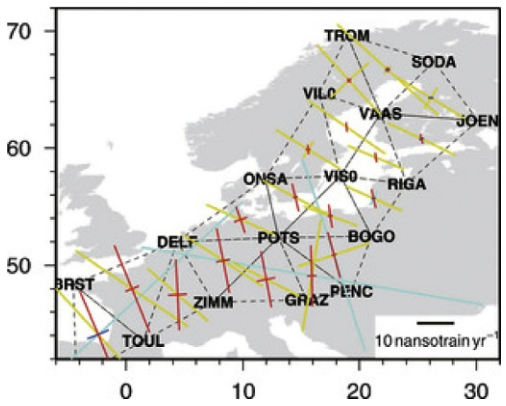

Figure 27 Strain rates in units of nanostrain predicted for tectonic model 3 (cyan, extension; yellow, compression) and model 1 (blue, extension; red, compression). Reproduced from Marotta AM and Sabadini R (2004) The signatures of tectonics and glacial isostatic adjustment revealed by the strain rate in Europe. *Geophysical Journal International* 157: 865–870. http://dx.doi.org/10.1111/j.1365-246X.2004.02275.x.

appearance of limited extension south of POTS, in contrast with observations. By analogy with PGR analyses, strain-rate patterns will now be considered for tectonic modeling.

Figure 27 shows strain-rate results from tectonic models 3 and 1. Except for POTS–PENC–BOGO and POTS–GRAZ–PENC, where extension dominates, as indicated by cyan bars, model 3 predicts SE–NW compression (yellow bars) due to the combined effects of the African–Eurasian convergence and Mid-Atlantic Ridge spread. The striking result of model 3 is that modeled compression acts at right angles with respect to that derived from geodetic data. The two triangles noted earlier in the text are the only ones yielding complete agreement in terms of extensional eigendirections and eigenvalues between modeling results and observations, shown in Figure 11. Another major problem of this model is that it predicts compression north of VIS0, whereas ITRF2000 data indicate extension. This inconsistency suggests that the effects of ridge push are too large and that reducing them should also reduce the misfit. This hypothesis is tested by taking the end-member model 1, in which no ridge push is considered (see Table 3). This extreme case implicitly assumes that deformation due to ridge push is completely adjusted in the part of the domain between the ridge and the area under study. As expected, in model 1, the previous disagreement between data and prediction is significantly reduced, with compression becoming negligible at high latitudes (red bars) and subject to a clockwise rotation in central Europe, in agreement with geodetic data analysis of Figure 11.

The introduction of rheological heterogeneities in the tectonic model is crucial for securing the best-fit model for the stiff Baltic Shield, as shown in Figure 28, corresponding to model 5 (cyan, extension; yellow, compression) and model 4 (blue, extension; red, compression). Even in the presence of a velocity boundary condition of 5.0 mm year^{-1} along the Mid-Atlantic Ridge, a substantial modification results in the strain-rate patterns north of the line connecting DELF to BOGO, where compression is reduced with respect to Figure 27 (yellow bars) and SSW–NNE extension appears. The reduction of compression in the stiff Baltic Shield and south of it is easily understood in terms of the reduced flow within the high-viscosity region, which acts as a barrier that annihilates the propagation of the velocity driven by the African–Eurasian convergence and Mid-Atlantic Ridge push within the shield. When zero-velocity boundary conditions are assumed along the western boundary, as in model 4, the ridge push effects disappear everywhere, leaving space to the African indenter and to an increase in compression with respect to Figure 27, as indicated by the red bars. Rotation from NNW to NNE of compressive eigendirections occurs now south of Potsdam, in good agreement with ITRF2000 analyses. Due to the stiffening of the Baltic Shield, the compressive effects of the African–Eurasian push almost disappear north of VIS0, supporting

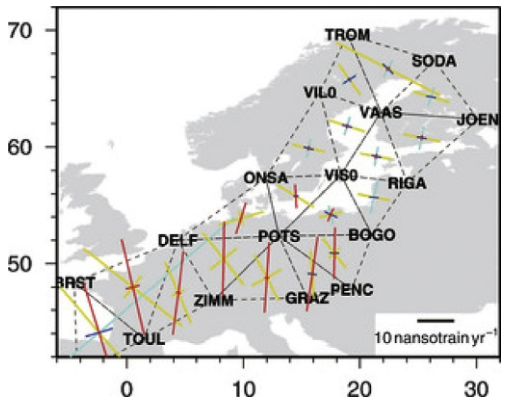

Figure 28 Strain rates in units of nanostrain predicted for tectonic model 3 (cyan, extension; yellow, compression) and model 4 (blue, extension; red, compression). Reproduced from Marotta AM and Sabadini R (2004) The signatures of tectonics and glacial isostatic adjustment revealed by the strain rate in Europe. *Geophysical Journal International* 157: 865–870. http://dx.doi.org/10.1111/j.1365-246X.2004.02275.X.

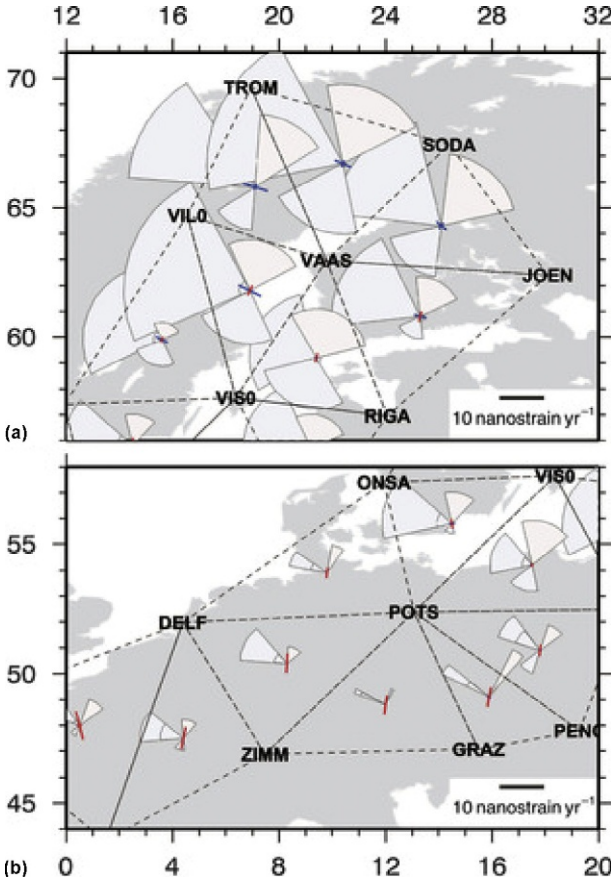

Figure 29 (a, b) Strain rates in units of nanostrain from PGR and tectonics (blue, extension; red, compression). Reproduced from Marotta AM and Sabadini R (2004) The signatures of tectonics and glacial isostatic adjustment revealed by the strain rate in Europe. *Geophysical Journal International* 157: 865–870. http://dx.doi.org/10.1111/j.1365-246X.2004.02275.X.

the hypothesis that another geophysical process must be invoked to explain the large SE–NW extension, which is PGR.

Note that comparing Figures 12 and 28 for PGR effects on strain rates, the tectonic model with the stiff Baltic Shield influences the compression south of ONSA–VIS0, with the largest contributions south of DELF–POTS–BOGO, while PGR contributes to the compression in the central European region between ONSA–VIS0 and DELF–POTS–BOGO and to the extension north of ONSA–VIS0. These findings show that tectonics dominates the strain-rate pattern south of POTS, while PGR is the dominant mechanism north of VIS0 in Fennoscandia, and that both tectonics and PGR contribute to the deformation in the European continental region between the latitudes of POTS and VIS0. That this is the case is better shown in Figure 29, where the combined effects of tectonic model 5 and PGR are portrayed, with panels (a) and (b) referring to the northern and southern domains, respectively. Model predictions denoted by the bars are superimposed on strain rates resulting from ITRF2000, represented with their errors in the magnitude and azimuth, with light blue denoting extension and light red compression. Note that the data are portrayed with only one side of the admissible area of variability of the magnitude, to leave room for depicting the already elucidated possible change from compression into extension, or vice versa, caused by some errors being larger in absolute value than the corresponding datum, as shown by the sectors changing color along the same eigendirection. Model results reproduce well the general pattern of NW extension in panel (a), while, in panel (b), only the NE compression is reproduced.

Agreement in the azimuth is obtained by combining tectonic model 5 with the PGR model characterized by the lower-mantle viscosity of 10^{22} Pa s for high latitudes, as shown in the top panel, and with the 10^{21} Pa s lower-mantle viscosity PGR model for intermediate latitudes, as in the bottom panel, which supports the existence of lateral variations in mantle viscosity, with a stiffer mantle underneath the Baltic Shield that is coherent with the laterally heterogeneous tectonic model. It is worthwhile remarking that modeling has the tendency to reproduce lower bounds of observed strain rates.

Findings from this section indicate that the African–Eurasian convergence has the dominant role in determining plate-deformation patterns south of 52° north latitude, which corresponds to that of Potsdam (POTS). This tectonic mechanism has no effect north of about 58° north latitude, corresponding to the latitude of Onsala (ONSA), in Fennoscandia. PGR is the only mechanism that has a signature north of Onsala. Strain rate in central Europe between Onsala and Potsdam is affected by both mechanisms. Strain-rate analysis thus reinforces the results of the previous section on baseline rates, where plate deformation in Europe is the result of an interplay between forces induced by tectonics and PGR. Lateral variations in lithospheric strength in the East European Platform play a crucial role in separating the two domains, south of Potsdam and north of Onsala, where tectonics and PGR have their major influence. The combination of tectonic modeling, characterized by a stiff East European Platform and Mid-Atlantic Ridge push effects that are completely absorbed within the western oceanic portion of the model's domain, and PGR modeling is the best performing one

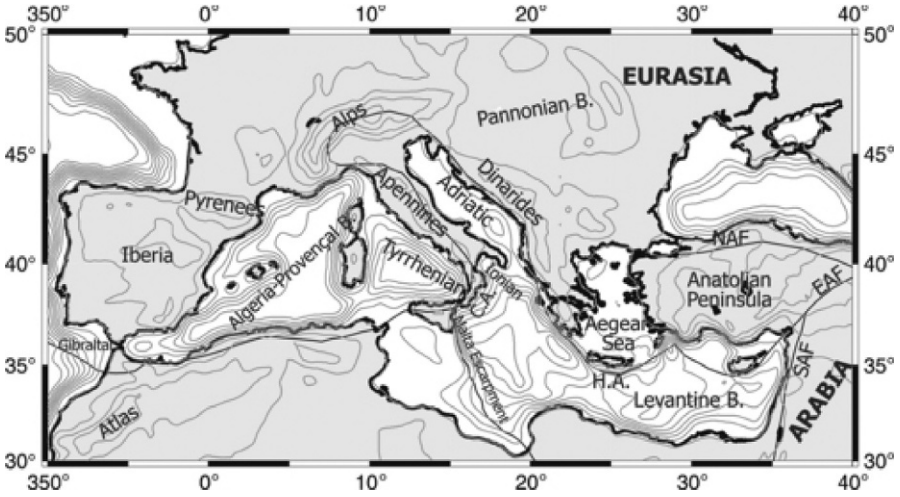

Figure 30 Elevation (ETOPO5), in kilometers with isolines every 0.5 km, and tectonic sketch map of the study region. H.A., Hellenic arc; C.A., Calabrian Arc; B, basin; NAF, North Anatolian Fault; SAF, South Anatolian Fault; EAF, East Anatolian Fault. Reproduced from Jiménez-Munt I, Sabadini R, Gardi A, and Bianco G (2003) Active deformation in the Mediterranean from Gibraltar to Anatolia inferred from numerical modeling and geodetic and seismological data. *Journal of Geophysical Research* 108: B1. http://dx.doi.org/10.1029/2001JB001544, with permission from AGU.

when geodetic strain rates are compared and reproduce well the major features of compression south of Onsala and SE–NW extension north of Onsala.

6.04.4 Plate Deformation at Subduction Zones

6.04.4.1 Introduction

The tectonic setting of the Mediterranean is controlled by the collision of the African and Arabian Plates with Eurasia and by subduction in the Hellenic arc and Calabrian Arc (Jackson and McKenzie, 1998; McKenzie, 1970). **Figure 30** portrays the major tectonic structures, the solid line indicating the African–Eurasian Plate boundary and such major faults as the North Anatolian Fault (NAF), East Anatolian Fault (EAF), and South Anatolian Fault (SAF). In spite of the African–Arabian versus Eurasian convergence, several regions exhibit extension in the Earth's crust, such as the Alboran Sea, the Algero-Provençal Basin, the Tyrrhenian Sea, and the Aegean Sea (topography is given in kilometers by contour lines). This section focuses on the geophysical modeling of continental collision between Africa and Eurasia on the basis of thin-plate theory, which is generalized so as to include the effects of subduction in the Hellenic arc and Calabria Arc and on strain rates from permanent GPS receivers in the Mediterranean. Such velocity fields are based on GPS measurements from Clarke et al. (1998) and McClusky et al. (2000) and from the Space Geodesy Center (CGS) of the Italian Space Agency (ASI) in Matera.

6.04.4.2 The Mediterranean: A Natural Laboratory for Understanding Plate Behavior at Subduction Zones

Earthquakes in the Mediterranean are not confined to a single fault, which implies that deformation in this region cannot simply be described by relative motions of rigid blocks. Within the broad deforming belts in the continents, some large, flat, aseismic regions like central Turkey or the Adriatic Sea behave like rigid blocks and can usefully be thought of as microplates (Jiménez-Munt and Sabadini, 2002). This section focuses on the numerical modeling of the major tectonic processes active in the Mediterranean and on the comparison between model predictions and geodetic data. The modeling in the present analysis includes convergence between the African–Arabian and Eurasian Plates and the additional forces acting at plate boundaries due to subduction and is based on the study by Jiménez-Munt et al. (2003), where for the first time GPS data for the whole Mediterranean region were interpreted by means of self-consistent geophysical modeling. Unlike PGR modeling, vertical motions cannot be reliably modeled by thin-plate approximation and, hence, are not taken into account.

The geodetic data set includes 190 vector velocities, as shown in **Figure 31**, with respect to fixed Eurasia. Of these geodetic velocities, gray arrows in **Figures 31** and **33** were obtained by the Space Geodesy Center of the Italian Space Agency (ASI-CGS) in Matera using GPS, satellite laser ranging (SLR), and very long baseline interferometric (VLBI) data (Devoti et al., 2002). These data have been completed in the eastern Mediterranean with the GPS measurements for the period 1988–97 carried out by McClusky et al. (2000) (black arrows; also referred to Eurasia). A description of how geodetic data of different nature, such as GPS, SLR, and VLBI techniques, have been combined so as to obtain reliable velocities at each site is given in Devoti et al. (2002). The ASI-CGS solution in **Figure 31(a)** and **31(b)** represents the residual velocity with respect to Eurasia obtained by subtracting the rigid motion of Eurasia expressed in the NUVEL-1A reference frame. The large error ellipses in the western and central Mediterranean, especially in the Iberian Peninsula and in the northern sector of the Adriatic Plate, are an indication that the geodetic data are sparse and variable in these areas. In the eastern Mediterranean, error ellipses are provided only for the ASI-CGS solution.

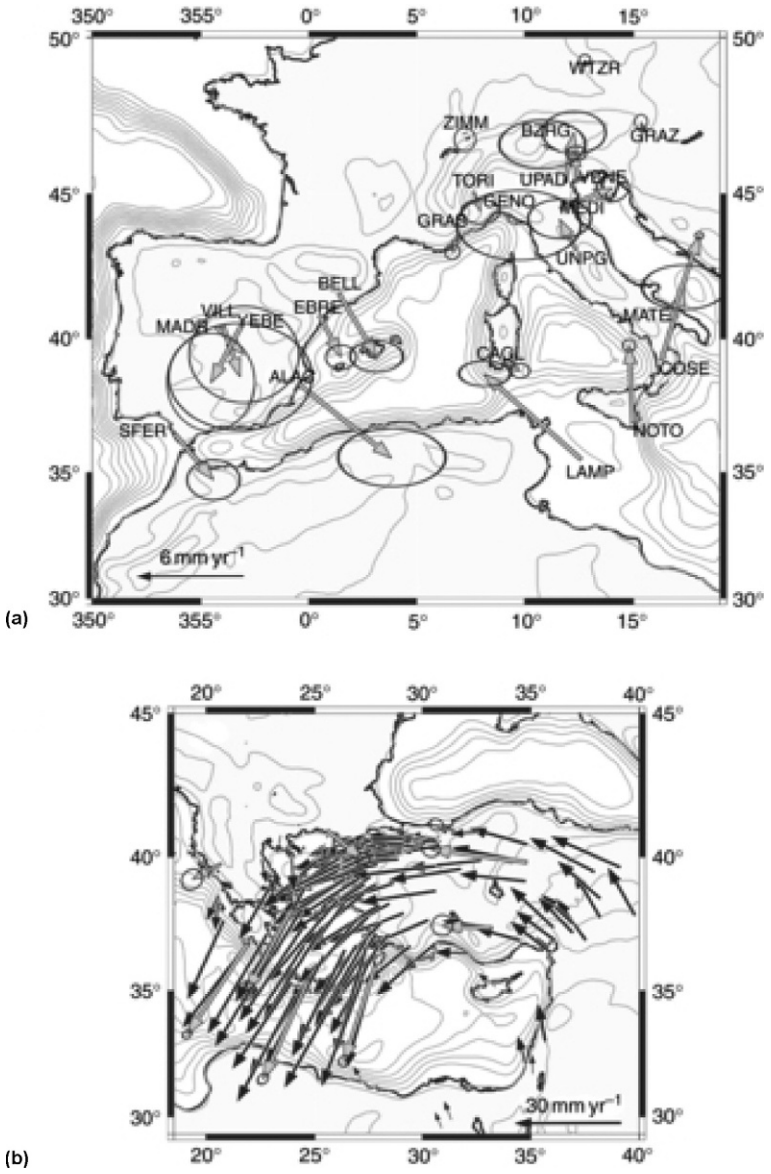

Figure 31 Geodetic data. Gray arrows have been obtained by the Space Geodesy Center (CGS) in Matera (Devoti et al., 2002) and black arrows by the GPS measurements made by McClusky et al. (2001). (a) Western Mediterranean. (b) Eastern Mediterranean. Reproduced from Jiménez-Munt I, Sabadini R, Gardi A, and Bianco G (2003) Active deformation in the Mediterranean from Gibraltar to Anatolia inferred from numerical modeling and geodetic and seismological data. *Journal of Geophysical Research* 108: B1. http://dx.doi.org/10.1029/2001JB001544, with permission from AGU.

Figure 31(a) and 31(b), from west to east, highlights three different styles for the direction of the horizontal velocity field: a generally south-trending direction in the Iberian Peninsula and Ligurian coast of Italy, a north-trending direction for southern Italy and the Italian Peninsula, with a rotation from NW to NNE from Lampedusa Island (LAMP) between Africa and Sicily to Matera (MATE) through Calabria (COSE), as shown in Figure 31(a) and a rotation from NNW to SSW from eastern Anatolia to the southern Aegean. The NE direction in southern Italy agrees with the suggestion of the counterclockwise rotation of the Adriatic Plate, as suggested by Ward (1994) and Anderson and Jackson (1987).

Another major feature, such as the magnitude of the velocity, characterizes the geodetic pattern, which shows a substantial increase from the west to the east and from the north to the south. In central and northeast Italy, the motion has a large north component, except in the Po Plain, with the site MEDI showing a large eastward component probably due to local tectonic effects, for example, thrusts associated with the buried Apenninic chain or to the water table. Lampedusa, Sicily, and the Italian Peninsula, except its westernmost coastal area, show a dominant north-trending component, in agreement with the major NUVEL-1A velocity component at these longitudes.

In moving to the eastern Mediterranean, Figure 31(b) evinces high velocities, of the order of $\sim$30 mm year^{-1}, with SSW direction in the Aegean Region and with west-directed velocities in the Anatolian Peninsula. Figure 31(b) also

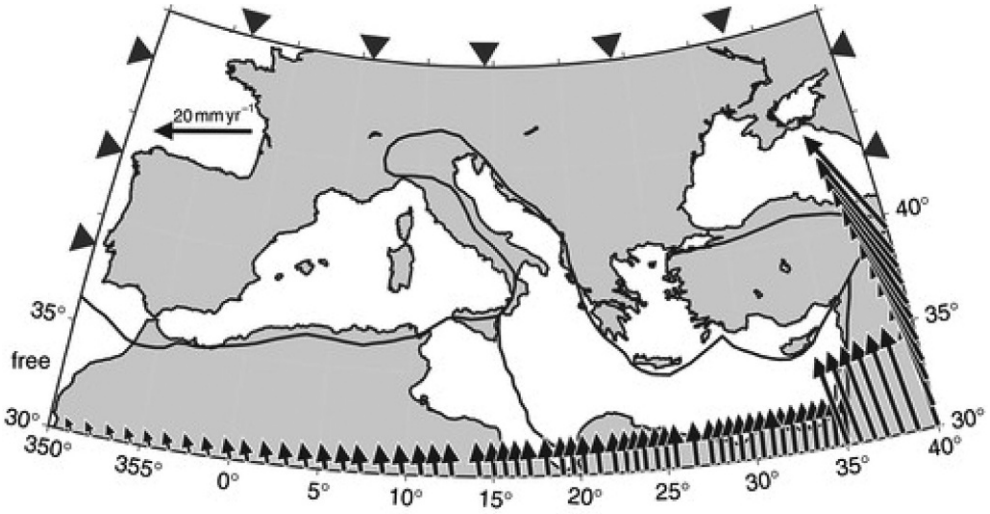

Figure 32 Boundary conditions corresponding to African–Eurasian convergence. Reproduced from Jiménez-Munt I, Sabadini R, Gardi A, and Bianco G (2003) Active deformation in the Mediterranean from Gibraltar to Anatolia inferred from numerical modeling and geodetic and seismological data. *Journal of Geophysical Research* 108: B1. http://dx.doi.org/10.1029/2001JB001544, with permission from AGU.

highlights the northward motion of the Arabian Plate and counterclockwise rotation of central–western Anatolia and the southern Aegean, a rotation that is bounded to the north by the NAF and its extension into the Aegean Sea.

Active convergence between Africa–Arabia and Eurasia is modeled as shown in Figure 32. The global kinematics of these plates is governed by the counterclockwise rotation of Africa and Arabia relative to Eurasia, based in this section on the results of the global model of plate motion NUVEL-1A (DeMets et al., 1994). In the following results, Eurasia is fixed, as indicated by the bold triangles along the northern, northwestern, and northeastern boundaries of the domain under consideration, and the velocity boundary conditions are taken relative to this plate, as shown by the black arrows. Velocity increases from west to east, with 3.3 mm year^{-1} in the direction of 35° W on the westernmost part and around 10 mm year^{-1} in the north direction in the proximity of the Arabian Plate boundary. Figure 32 shows that the Arabian Plate, located between the southern boundary from 35° E to 40° E and eastern boundary south of 40° N, moves with velocities ranging from 20 to 24 mm year^{-1}, varying their directions from south to north, from 10° W to 26° W. Only major faults are considered and treated as continuous along plate boundaries, as represented in Figure 32 by the solid line, along North Africa, the Calabrian Arc, the Malta Escarpment, the Apennines, the Alps, Dinarides, the Hellenic arc, and Anatolian faults.

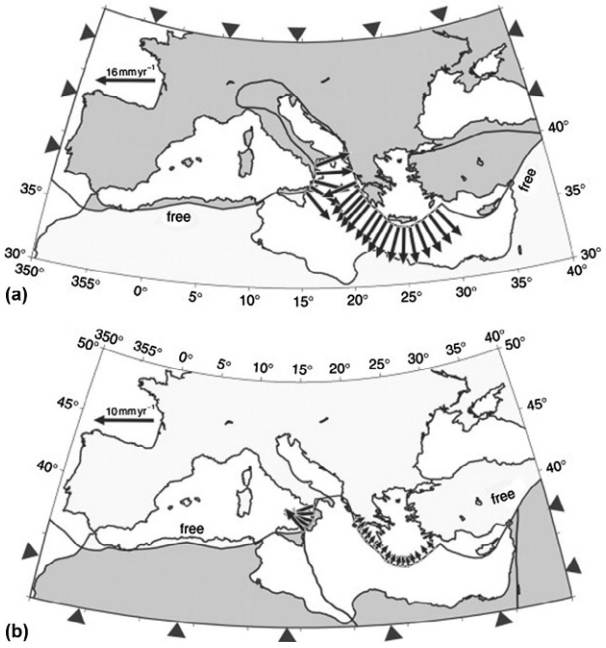

Figure 33 Boundary conditions corresponding to the subduction forces. (a) North model, velocities due to the suction force applied at the overriding plate, Tyrrhenian Sea, and Aegean Sea. (b) South model, velocities due to the slab pull applied at the subducting plate. Reproduced from Jiménez-Munt I, Sabadini R, Gardi A, and Bianco G (2003) Active deformation in the Mediterranean from Gibraltar to Anatolia inferred from numerical modeling and geodetic and seismological data. *Journal of Geophysical Research* 108: B1. http://dx.doi.org/10.1029/2001JB001544, with permission from AGU.

6.04.4.3 The Fingerprint of Subduction in GPS Data

The model of continental convergence shown in Figure 32 must be supplemented with the effects of subduction in the Aegean (Hellenic arc) and southern Italy (Calabrian Arc). Within a thin-plate formulation, this can be achieved by applying the appropriate horizontal velocities at the plate boundaries so as to simulate the effects of tectonic forces due to trench suction on the overriding plate and slab pull on the subducting plate (Bassi et al., 1997). This implies that the plate boundary must coincide with a boundary of the finite-element mesh, which can be achieved by subdividing the model between the Eurasian and African domains, as shown in Figure 33(a) and 33(b). The appropriate velocity boundary conditions

simulating subduction forces can thus be applied where subduction is active in the Hellenic arc and Calabrian Arc, as shown by the arrows in Figure 33.

While the reader will find a detailed description of the forces that are active at subduction zones, it may be relevant to provide here a brief description of the physical process that is responsible for the appearance of the velocities along the Hellenic arc and Calabrian Arc, as shown in Figure 33(a) and 33(b). Subduction denotes the penetration of oceanic lithosphere into the mantle under another plate, called an overriding plate. Specifically, in Figure 33(a) and 33(b), along the arcs, two pieces of lithosphere are pushed by Africa and enter the mantle in approximately northwest and northeast directions in the Calabrian Arc and Hellenic arc, respectively. By falling down in the mantle, the two subducted plates should leave an empty space underneath the overriding plates, which are the Tyrrhenian and Aegean Basins, north of the two arcs. Since cavitation, or empty volume, cannot exist, the overriding plates are sucked toward the arcs to fill the volume left by the subducting plates.

In the modeling, these suction forces toward the arcs are simulated by the black arrows directed southeast in the Calabrian Arc and southwest in the Hellenic arc. This process is also responsible for extra velocities toward the arcs as shown in Figure 33(b) that supplements the velocities induced by Africa in the same regions. The velocities plotted in Figure 33 are thus taken from another family of subduction models, not shown in these sections, in vertical cross sections, as in Giunchi et al. (1996) or Negredo et al. (1997, 1999), where the effects of trench suction and slab pull are taken self-consistently into account. The slab pull effects are evaluated using positive density contrasts based on the petrologic studies of Irifune and Ringwood (1987). These models are purely gravitational, driven solely by the negative buoyancy of the subducted portion of the slab. The velocities, parameterizing subduction forces, are portrayed by the black arrows perpendicular to the arcs, for the Eurasian Plate (Figure 33(a)) and African Plate (Figure 33(b)). These velocity boundary conditions yield suction and slab pull forces that agree, in magnitude, with the tectonic forces applied by Meijer and Wortel (1992) to simulate the effects of subduction in the Andes. The remaining plate boundaries (North Africa and eastern Anatolia), where subduction is not presently occurring, are subject to free-boundary conditions, where the only effects are those due to lithostatic stress.

For the Calabrian Arc, the horizontal velocities are obtained by means of previous 2-D dynamic models in the Tyrrhenian Sea (see Figure 4(b) of Giunchi et al., 1996). A velocity of 10 mm year^{-1} is applied at the edge of the overriding plate (Eurasia) along the arc and of 5 mm year^{-1} at the edge of the subducting plate (Africa). These velocities are applied perpendicularly to the arc, as in Figure 33(a) and 33(b), for the overriding (Eurasian domain) and underthrusting (African domain) plates, respectively.

For the Hellenic arc, a new series of 2-D subduction models, in vertical cross section, are implemented in order to elucidate the effects of the geometry of the subducted slab on velocity boundary conditions to be applied at the arcs. This class of subduction models is based on the distribution of earthquakes (Kiratzi and Papazachos, 1995; Papazachos et al., 2000) and on seismic tomography. It has been verified that rollback, the motion of the edge of the arc toward the subducting plate, is sensitive to the geometry of the slab and to the depth of subduction.

Once the relative velocities due to subduction are evaluated along the arcs, they can be applied to the Eurasian and African Plates, as shown in Figure 33(a) and 33(b), in order to retrieve the velocity field induced by subduction that must be added to the velocity due to convergence. Figure 34 portrays the eigenvectors and eigenvalues of the modeled and geodetic strain-rate tensor. The western, central, and eastern Mediterranean (panels (a)–(d)) are subdivided into triangles with vertices connecting the sites where the horizontal velocity components are available in order to estimate the strain rate, from the numerical and geodetic standpoint, and to characterize the style of deformation in the area within each triangle.

The following panels in Figure 34 show the eigendirections as two perpendicular arrows oriented with respect to the meridian; the length of the arrow is scaled to provide the eigenvalue in units of 10^{-9} year^{-1} (1 nanostrain year^{-1}). Red stands for compression and black for extension, with arrows in bold representing the geodetic strain rates and the hollow arrows the numerically retrieved strain rate. From west to east, the geodetically retrieved strain rate is compared with the numerical one. In the western Mediterranean (Figure 34(a)), SFER–ALAC–CAGL–LAMP, compression predominates in the NNW direction. The eigendirection relative to this compression is well reproduced by the model, between 5° W and 10° E longitude, as indicated by the triangle SFER–ALAC–LAMP, where the geodetic and modeled eigendirections agree within the standard deviation σ, represented by the gray surface surrounding the eigenvectors of the geodetic strain tensor. The modeled eigenvalue is a factor of 2 lower than the geodetic one, indicating that the model underestimates the compression. This eigenvalue is well reproduced in the central Mediterranean, within the triangle ALAC–CAGL–LAMP. The NNW compression in the western Mediterranean agrees well with observed stress data, in the following Figure 35, as indicated by the thrust events (blue bars) in North Africa and in the western part of Sicily. This compression is clearly induced by the relative motion between Africa and Eurasia (DeMets et al., 1994). South of LAMP, the geodetic compression rotates 90° with respect to the compression in the western Mediterranean and is not reproduced by the model, which severely underestimates the accompanying extension.

In the region from LAMP to MATE, the ENE compression is now well reproduced by the model. The north-trending extension is in fact underestimated in the modeling, except for the triangle with vertices in LAMP and NOTO where the best fit is obtained, as far as the magnitude and direction of compression and extension are concerned. Change in strain style from LAMP to the northeast is evident also in the stress data in Figure 35, where there is a change from the eastern part of Sicily to the Calabrian Arc from thrust–compression to normal fault–extension; this change is well reproduced by the geodetic strain rate and, to a lesser extent, by modeling. A wide zone of strike-slip events in WSM2000 correlates well with the 90° rotation in the eigendirection from west to east with respect to LAMP.

In the Iberian Peninsula, modeling and observation are in complete disagreement, which suggests that some major

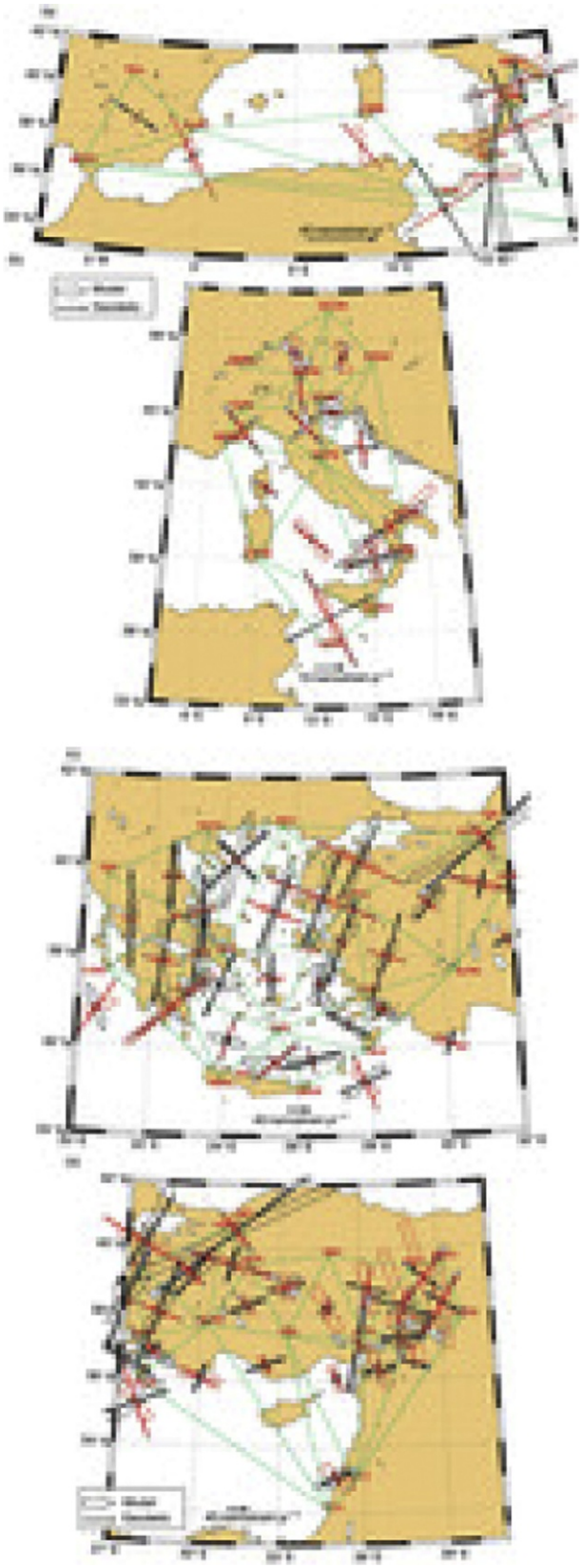

Figure 34 Horizontal principal strain rates: geodetic ones (solid arrows) and modeled ones (empty arrows) resulting from model C, with the associated errors. Extension is represented in black and compression in red. (a) Western Mediterranean; (b) central Mediterranean; (c) Aegean Region; and (d) Anatolian Peninsula. Reproduced from Jiménez-Munt I, Sabadini R, Gardi A, and Bianco G (2003) Active deformation in the Mediterranean from Gibraltar to Anatolia inferred from numerical modeling and geodetic and seismological data. *Journal of Geophysical Research* 108: B1. http://dx.doi.org/10.1029/2001JB001544, with permission from AGU.

tectonic features are not properly modeled in the westernmost part of the domain or that the quality of geodetic data is currently insufficient. Several competing models have been proposed to explain the region's geodynamic evolution, including escape tectonics, subduction and slab retreat, lithosphere–mantle delamination, and orogenic collapse (e.g., Marotta et al., 1999; Platt and Vissers, 1989). So far, however, there is no consensus among the possible active mechanisms since their numerical modeling has produced unsatisfactory results.

The eigendirections of modeled and geodetic strain rate are best reproduced within the SFER–CAGL–LAMP triangle, even though the dominant compression is underestimated. In the eastern part of the studied area, the nature of the fit improves, with generally well-reproduced eigenvalues but some deviation between the eigendirections. The compression in the triangles located to the east vis-à-vis the Calabrian Arc rotates 90° with respect to the western Mediterranean, leading to an extension that is roughly perpendicular to the arc, appears as a surface fingerprint of subduction.

In the center of the Tyrrhenian Sea (**Figure 34(b)**), CAGL–UNPG–NOTO and NOTO–UNPG–COSE, the geodetic and the model strain rates, are in close agreement to both eigendirections and eigenvalues. In proximity to this region, UNPG–MATE–COSE portrays the worst fit, with the modeled compression aligned with geodetic extension due to the mismatch between the modeled and geodetic velocity directions of MATE. The geodetic EW extension UNPG–NOTO–MATE, not reproduced by the model, agrees well with the extensional tectonics perpendicular to the Apenninic chain, indicated by the normal-fault events (yellow bars) appearing in the WSM2000 in **Figure 35**. The observed extension, perpendicular to the chain, seems to indicate that subduction is also active underneath the Central Apennines, a process that has not been parameterized in the modeling. This would explain the failure of the model to reproduce geodetic and WSM2000 extensions.

In proximity to the Calabrian Arc, the principal strain rate is extensional (UNPG–COSE–NOTO), with complete coherence between geodetic and modeled eigenvalues and eigendirections, which are roughly perpendicular to the arc, probably indicating rollback of the arc itself. This pattern is in agreement with the radial extension stress regime proposed by Rebaï et al. (1992), which also appears in the WSM2000 in the Calabrian Arc region, indicated by the yellow bars parallel to the arc. The geodetic strain rate within the GRAS–TORI–UNPG–NOTO–CAGL pentagon portrays a NW compression as the dominant tectonic mechanism, which changes into a dominant ENE extension in the CAGL–NOTO–LAMP and UNPG–COSE–NOTO triangles. The model reproduces well all these features, except the high ENE extension in the CAGL–NOTO–LAMP triangle. The dominant NW compression in the pentagon in the preceding text is also evident in the WSM2000, as indicated

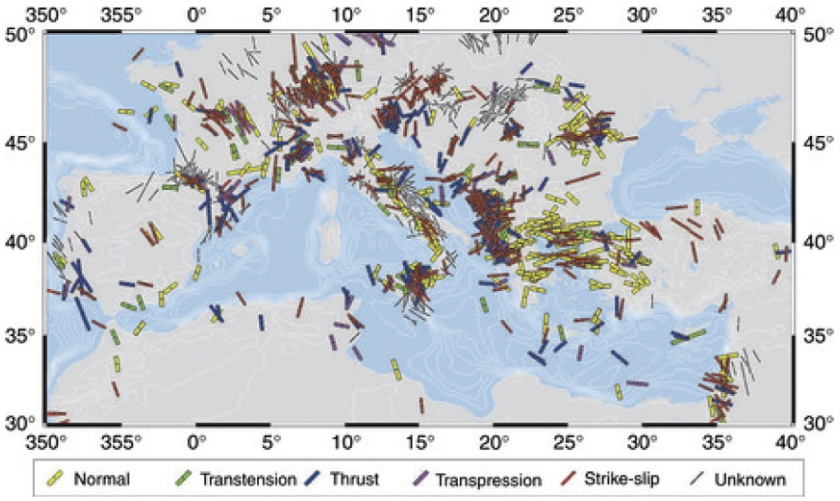

Figure 35 Directions of the most compressive horizontal principal stress from the World Stress Map (WSM2000) project (Mueller et al., 2000). The color of the symbol represents the tectonic regime and its length is proportional to the quality of data. Reproduced from Jiménez-Munt I, Sabadini R, Gardi A, and Bianco G (2003) Active deformation in the Mediterranean from Gibraltar to Anatolia inferred from numerical modeling and geodetic and seismological data. *Journal of Geophysical Research* 108: B1. http://dx.doi.org/10.1029/2001JB001544, with permission from AGU.

by thrust events in western Sicily and the Ligurian coast of Italy (blue bars).

If we now look at northern Italy and the Alpine front, we see a deterioration in the quality of the geodetic strain, as shown by the large errors. Geodetic and modeled strain-rate values are subject to a substantial reduction with respect to the southern values, in agreement with the reduction of deformation from south to north due to the increase in distance from the African–Eurasian collision front and subduction zones. While the eigendirections are generally well reproduced, the fit is poor for both TORI–VENE–UNPG and VENE–GRAZ–UNPG, with a 90° mismatch in this latter triangle in the eigendirections and modeling predicting negligible strain rates in the former. This mismatch may be due to limitations in the model or to the quality of the geodetic strain, both possibly related to the small size of area's strain rates. There may also be effects associated with the hydrologic cycle of the crust, which is not considered in the modeling. The geodetic compression in the TORI–VENE–UNPG triangle agrees well with thrusts events (blue bars) of the WSM2000. Within the ZIMM–WTZR–GRAZ–VENE–BZRG pentagon, the style of the compressive strain rates is well reproduced by the modeling, in both eigendirections and eigenvalues. The geodetic data and geophysical model agree in fact with the WSM2000 that portrays a cluster of thrust events in the region corresponding to the WZTR–GRAZ–VENE triangle. A mismatch between geodetic and modeled strain rates is notable within the VENE–GRAZ–UNPG and GRAZ–MATE–UNPG triangles: A west-directed extension, rather than compression, is predicted in the former and an EW extension is not satisfactorily reproduced in the latter.

In the Aegean Region, Figure 34(c), a general improvement in the coherence between the eigendirections and eigenvalues is obtained from the geodetic data and from the numerical modeling in comparison to Figure 34(a) and 34(b). The dominant mechanism is NNE extension, compatible with north-trending normal-faulting deformation, which is in fact the major feature of the stress pattern in this region (Figure 35). This extension can be viewed as the surface expression of suction forces induced by the sinking slab in the Aegean. Details of such a widespread extensional pattern show that the largest deviation in the eigendirection occurs in LEON–7515–TWR triangle in Greece and CAMK–BURD–7512 in western Anatolia, with a mismatch of about 90°, and in SOXO–7510–7515, with a mismatch of about 30°. Except for these three triangles, geodetic and modeled strain-rate eigendirections are in good agreement, in both Greece and western Anatolia. The eigenvalues are also in fairly good agreement, but it should be noted that when mismatch occurs, the numerical model has the tendency to underestimate geodetic extension, as, for example, in the 7520–NEZA–LOGO triangle in eastern Greece or in the D7DU–CAMK–CEIL and D7DU–BURD–CAMK triangles in western Anatolia.

Difficulties are also encountered in reproducing the isotropic extension for SOXO–7510–7515. In general, a good agreement is found between eigendirections and the largest eigenvalues. Moving to the east, we see that the NNE extension in Greece and the Aegean Region shows the tendency to rotate to the NE in Anatolia and that, in concert with this rotation in the eigendirection of the extension, compression at right angles with respect to the previous WNW direction becomes the dominant mechanism in eastern Anatolia. If we draw a parallel with the major driving tectonic mechanism of extension in the Aegean Region, we see that the increase in compression in eastern Anatolia agrees well with the concept that push from the Arabian Plate is a major controlling mechanism in easternmost Anatolia. It thus becomes clear that the peculiar pattern of extension in the Aegean and compression in Anatolia is largely due to the combined effects of suction induced by deep Aegean subduction and by push from Arabia. Predominant extension in the Aegean Sea and increasing compression to the east explain the tectonic regime observed in the WSM2000, with normal faulting in the Aegean and strike-slip in the east.

Close to the Hellenic arc, the modeled extension parallel to the arc overestimates the geodetic one and, on the contrary, considerable geodetic compression perpendicular to the arc, especially in its western part, is underestimated by the model. North of Crete, compression in the geodetic strain perpendicular to the arc and extension parallel to it is notable, in agreement with the numerically modeled eigendirections (LEON–OMAL–TWR and TWR–ZAKR–7512). Modeling reproduces the compression perpendicular to the arc south of Greece (LOGO–LEON–OMAL), but not north of Crete. The extensional strain-rate regime parallel to the arc resulting from the modeling is also visible in the WSM2000. This case is mentioned as a situation in which there is a better agreement between modeling and stress data than between modeling and geodetic data or between geodetic and stress data. In this arc region, the worst fit occurs in westernmost Crete (LEON–OMAL–TWR), where predominantly, WNW extension is found from modeling rather than NNE geodetic compression.

East of Crete, modeled extension in the TWR–7512–ZAKR triangle is consistent with observations. Deviations between eigendirections are observed west of the Peloponnesus and east of Crete, certainly due to edge effects of the Hellenic subduction and thus to difficulties encountered by the 2-D modeling in reproducing the real 3-D tectonic structures at the edges of the subducting plate. In spite of this limitation, it is remarkable that the intensity of the geodetic strain rate is well reproduced, denoting compression directed outward from the subduction zone and extension along the hinge line, where the subducting plate encounters the Earth's surface.

The largest geodetic and modeled strain-rate eigenvalues of about 10^2 nanostrain year^{-1} in northwestern Anatolia close to the NAF agree well with the geodetic strain rate found by Ward (1998) in the Aegean–Anatolian Region. The pattern of geodetic and modeled strain release by Ward (1998) is not comparable in detail with ours due to the larger set of geodetic data considered and to the higher spatial resolution herein with respect to Ward's study.

Figure 34(d) portrays geodetic and modeled strain rates for Anatolia. Modeled eigendirections are best reproduced in the western part, with a rotation from NNE (CAMK–D7DU–BURD) to NE (AGOK–SIVR–7587) and from a longitude of 28° to 32°, in good agreement with the largest geodetic eigenvalues denoting extension. The geodetic and modeled strain rates are in complete agreement with the cluster of normal-fault events in western Anatolia, denoting extension in the NNE direction, as shown in the WSM2000 (**Figure 35**). From west to east, it is remarkable that, at least for the largest eigenvalue, dominant extension changes into dominant compression, both in the modeling and in the geodetic data.

An intermediate zone of visibly reduced strain rate is centered at approximately 33° E, in which the dominant NE extension in the west, though reduced, changes into NE compression in the east. Modeling reproduces well the reduction in geodetic strain-rate eigenvalues, but in the SIVR–7585–7580 triangle in the center of Anatolia, the model eigenvectors are rotated by 90° with respect to the geodetic ones, a negative result that is not unexpected due to low strain rate. In the center of Anatolia, the model thus reproduces well the reduction in strain rate and the transition from extension in the west to compression in the east, but fails to reproduce the eigendirections in the center of this zone. The reduction in strain rate is well imaged by the WSM2000.

In the eastern part, NNW compression is the dominant mechanism, in agreement with the important push of Arabia. The magnitude of the largest eigenvalue is generally overestimated by the modeling, clearly controlled by the push of the Arabian Plate. The model fails to simulate the extension observed in the data; though it has the capability to reproduce the largest eigenvalues, it has difficulties to reproduce the smallest ones. In eastern Anatolia, the geodetic eigendirection is rotated counterclockwise with respect to the modeled one. This discrepancy in the eigendirections could be due to edge effects since this region is close to the boundary where the velocity conditions are applied, as shown in **Figure 33**. A comparison with WSM2000 is not as robust as in western Anatolia since it is based on a single stress data in the easternmost region denoting thrusting, with an eigendirection roughly in agreement with the geodetic observation and modeled NE compression.

6.04.4.4 Stress Pattern in the Mediterranean

Geophysical and geologic techniques have made it possible to determine, for example, the approximate nature (compressional or extensional) and orientation of the tectonic stress acting in Europe and the Mediterranean. Compressive horizontal principal stress orientations and local tectonic regimes have in fact been compiled from the World Stress Map (WSM2000; Mueller et al., 2000; **Figure 35**). Four different types of stress indicators – earthquake focal mechanisms, wellbore breakouts and drilling-induced fractures, *in situ* stress measurements, and young geologic data – are considered here. These data generally show that one of the principal axes of the stress tensor is approximately vertical. Stress orientation is thus defined by the azimuth of one of the horizontal principal stress axes, and 1384 principal stress directions are used to draw a comparison with modeling and geodetic strain-rate eigendirections.

In western and central Mediterranean and northern Europe, west of 15° E longitude, the maximum compressive horizontal stress is NNW-directed, parallel to the red bars and to the relative displacement between the European and African Plates, as in **Figure 34**, except on arc structures such as the western Alps and the Gibraltar arcs, where small stress deviations can be found. This pattern differs from what is observed in the central and eastern Mediterranean, where the stress field presents several deviations at collision zones associated with large-scale faults and mountain belts and at active subduction zones beneath the Calabrian Arc and Hellenic arc.

The tectonic regime along the plate boundary in North Africa and in a large part of Sicily reflects the convergence between Africa and Eurasia, showing a dominantly NW compressive trend. In the Calabrian Arc, the stress regime is complex, being characterized by large variability in orientation and depth and in the style of deformation, and, according to Rebaï et al. (1992), it is close to radial extension. In the southern Apennines, normal faulting and strike-slip faulting prevail, with extension perpendicular to the chain, as indicated by the yellow bars parallel to it. In terms of tectonic regime, the northern Apenninic belt shows a clear distinction between an area of extension in the inner portion of the belt and an area under horizontal compression or transpression along the

Adriatic margin. Northern Italy coincides with the Alpine orogenic belt and is subject mostly to compression (Rebaï et al., 1992). For the entire European and Mediterranean domains, the general style of stress is thus characterized by general compression and extension, the latter perpendicular to the Apennines and spread in the Aegean.

Stress direction within Anatolia undergoes a progressive counterclockwise rotation from a NE-trending compression in eastern Anatolia to a northerly directed extension in western Anatolia. This stress pattern is consistent with the westward movement of the Anatolian Peninsula, which is pushed away from the collision zone along the North Anatolian right-lateral strike-slip Fault (NAF) to the north and the East Anatolian left-lateral Fault (EAF) (Kahle et al., 2000). It is also being pulled toward the Aegean by suction forces associated with subduction, in agreement with previous strain-rate geodetic and modeling results. The extensional tectonics along the Aegean back-arc basin and western Anatolia indicates that coupling between the African Plate and the Anatolian block is weak.

6.04.4.5 Blending Seismic, GPS, and Stress Data

Seismic strain provides a major constraint for plate-deformation properties since it gives the amount of strain released by the sequence of elastic shots associated with the earthquakes. The estimate of seismic strain is based on the scalar moment M_0 of the earthquakes as related to the seismic part of the strain (Kostrov, 1974). **Figure 36** shows the geographic distribution of earthquakes, with magnitudes M_s ranging between 2.8 and 8 superimposed on the seismic strain rates, in units of s^{-1} obtained from Kostrov's (1974) methodology, which gives a measure of the brittle deformation according to

$$\dot{\varepsilon} = \frac{1}{2\mu V \Delta t} \sum_{n=1}^{N} M_0^n \qquad [38]$$

where $\dot{\varepsilon}$ is the strain rate, V is the deforming volume, μ is the shear modulus, and M_0^n is the seismic moment of the nth earthquake from the N total earthquakes occurring during the time interval Δt. The earthquake data are compiled from the NEIC for the period between 1903 and 1999. The seismic moment has been calculated according to Ekström and Dziewonski (1988) using the surface magnitude, M_s:

$$\log M_0 = \begin{cases} 19.24 + M_s & \text{for } M_s < 5.3 \\ 30.2 - (92.45 - 11.4 M_s)^{1/2} & \text{for } 5.3 \le M_s \le 6.8 \\ 16.14 + \frac{3}{2} M_s & \text{for } M_s > 6.8 \end{cases} \qquad [39]$$

Each earthquake involves a strain-rate effect that follows a Gaussian function, as shown in Jiménez-Munt et al. (2001). The most appropriate value for the Gaussian width in this area yields a value of 150 km, representing the diameter of the circular area around the earthquake where the elastic effects of the earthquake rupture are felt. **Figure 36** shows the seismic strain rate and the epicenters of the earthquakes included in these calculations. The largest seismic strain-rate release is of the order of 10^{-16}–10^{-15} s^{-1}, and it occurs from west to east along the plate boundaries in North Africa, in southern and northeastern Italy, along the Alps and Dinarides, in the Aegean Region, and in western and eastern Anatolia. Due to the combined effects of the real earthquake distribution and of the Gaussian distribution, this seismic strain pattern is characterized, except for a localized maxima in Algeria, by a peculiar pattern portraying a region of 10^{-16}–10^{-15} s^{-1}, embedding northeastern Italy, Dinarides, Aegean, and western Anatolia that is surrounded by a region of lower strain-rate release of 10^{-17} s^{-1}. The pattern in **Figure 36** is consistent with that of

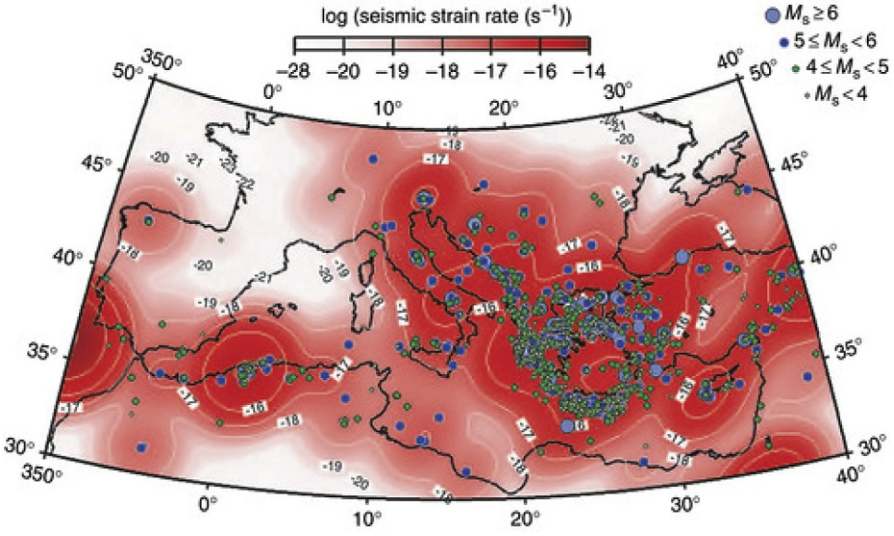

Figure 36 Calculated seismic strain rate using the methodology described by Kostrov (1974). Reproduced from Jiménez-Munt I, Sabadini R, Gardi A, and Bianco G (2003) Active deformation in the Mediterranean from Gibraltar to Anatolia inferred from numerical modeling and geodetic and seismological data. *Journal of Geophysical Research* 108: B1. http://dx.doi.org/10.1029/2001JB001544, with permission from AGU.

the seismic moment rate density, in units of N m year^{-1} m^{-2}, depicted in Figure 3 of Ward (1998), also based on the NEIC catalog.

Figure 34 shows that, once converted into strain rate in time units of seconds rather than years, obtained by dividing the results of Figure 34 by 3.153×10^7, denoting the number of seconds in 1 year, a level of about 10^{-15} s^{-1} is obtained in both modeled and geodetic strain rates. Modeling is thus coherent with geodetic findings, but model and geodetic strain rates are higher than the seismic ones in Figure 36. This general finding should not be surprising, since geodetic strain is the sum of the deformation released by earthquakes and of that due to ductile creep of the crust and lithosphere, which may be larger than seismic deformation alone. Another cause for seismic strain being generally lower than geodetic and modeled ones may be the short time interval of 100 years spanned by the seismic catalog, as compared with the characteristic time scale of rheological modeling that is appropriate for 10^3–10^6 years.

Some general features in modeling and geodetic strain-rate patterns (Figure 34) are well correlated with seismic strain rate (Figure 36) as are the high values in southern Italy that decrease to the north and the high strain rate in the Aegean that decreases in central Anatolia and increases again near the EAF.

The coherence between modeled, geodetic, and seismological strain rates and stress patterns reveals the capability of geophysical modeling to reproduce plate-deformation characteristics in terms of the mechanical properties of the crust and lithosphere and to provide an estimate of seismic deformation release.

6.04.5 Coseismic and Postseismic Deformations

6.04.5.1 Introduction

Faulting in the lithosphere causes an instantaneous deformation of the Earth's surface, called coseismic deformation. In response to coseismically induced elastic stress in the mantle, slow creep occurs in these deep parts of the planet, or in the viscous portion of the crust, via viscoelastic stress relaxation, as required by the dashpot sketched in Figure 2. Just after the earthquake, stress release due to flow in the viscous parts of the Earth starts to operate, leading to a mechanism called postseismic deformation. The latter is thus associated with the delayed deformation of the lithosphere caused by stress relaxation in the mantle or in the low-viscosity layers of the crust.

This section deals with the effects of a realistic PREM-based (Dziewonski and Anderson, 1981) lithosphere and mantle stratification on postseismic deformation. Relaxation, considered here to occur within the mantle, will then be taken up and the effects of stress relaxation in the viscous portion of the crust will be considered thereafter.

6.04.5.2 Modeling Global Coseismic and Postseismic Plate Deformations

The analysis carried out in this section is key to the understanding of plate–mantle interaction, especially for the correct interpretation of GPS and differential interferometry synthetic aperture radar (DInSAR) data of plate deformation, when earthquakes occur within the plate or at its boundaries. Improvements in satellite differential radar interferometry (Massonnet et al., 1993) or in precise GPS monitoring of crustal motions necessitate in fact realistic and precise models of coseismic and postseismic effects, which must include sphericity, self-gravitation, and stratification of the crust, lithosphere, and mantle, as outlined in the present analysis and based on a completely analytic approach using the mathematical formulation outlined in the preceding text, when the appropriate expression of the body force equivalents for seismic sources is in place for normal-mode solution. These body force equivalents, whose explicit expression was first given by Smylie and Manshina (1971), can be demonstrated to induce the same dynamic effects of the earthquake fault in the Earth's material, as prescribed by dislocation theory. With respect to PGR, normal-mode summation in coseismic modeling and postseismic modeling must go up to harmonic degrees of the order of 10^3, one order of magnitude higher than in PGR, as the peaks of the total strength of the modes as a function of harmonic degree can be situated at degrees of several thousands for shallow earthquakes at plate boundaries between the African and Eurasian domains, as we shall see. Unlike PGR, the toroidal solution must also be considered, as described in Sabadini and Vermeersen (2004). The procedure for solving postseismic problems in viscoelasticity, as shown herein, was first described by Sabadini et al. (1984).

Figure 37 deals with the relaxation times as a function of harmonic degree and shows that these relaxation modes form neat continuous-like patterns with increasing harmonic degree. The model used in this calculation is a ten-layer one averaged from PREM, as detailed in Table 4. The fastest transient viscoelastic modes superimpose at the bottom of the scale. Note that not all the modes are important since, for example, the top four modes for each harmonic degree in Figure 37, which are the internal-mantle buoyancy modes, have extremely long relaxation times, some even exceeding the age of the Earth and, hence, play no role in postseismic deformation.

To elucidate the influence of lithospheric and mantle stratification on postseismic deformation, the following figures portray displacement patterns for a vertical, point-like, dip-slip source embedded 100 km deep at the base of the lithosphere; the seismic moment of the source is fixed at 10^{22} N m, which is characteristic of a large earthquake. The radial displacement fields are sampled at an azimuth of 90° with respect to the strike of the fault in the subsiding portion of the Earth's surface; tangential displacements are sampled at 45°. The same displacement patterns would be found at 180° from these directions, but with the reverse sign. Figure 38 shows the radial and tangential displacement components (panels (a) and (b), respectively) for a fixed distance of 200 km from the epicenter of the fault and varying time after the occurrence of the earthquake. Notable differences can be observed among the four- and ten-layer volume-averaged models and P1 model as used in analyses by Sabadini and Vermeersen (1997) where the rigidity and density parameters were taken by imposing specific density contrasts at internal interfaces rather than averaging the density and elastic parameters from PREM, as done here. The parameters for the four-layer volume-averaged model are given in Table 5.

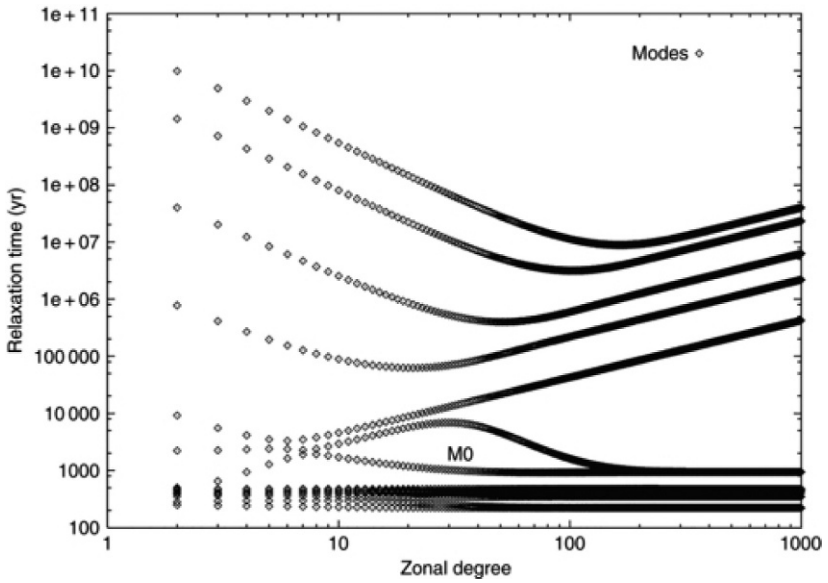

Figure 37 Relaxation times, in years, as a function of the harmonic zonal degree for the ten-layer model averaged from PREM and described in **Table 4**; the elastic lithosphere has three layers and the uppermost mantle is divided into four viscoelastic layers with a viscosity of 10^{21} Pa s, which is also the value for the viscosity of the homogeneous transition zone (TZ) and lower mantle. The fundamental mantle modes are indicated by M0. Reproduced from Sabadini R and Vermeersen LLA (1997) Influence of lithospheric and mantle layering on global post-seismic deformation. *Geophysical Research Letters* 24: 2075–2078, with permission from AGU.

Table 4 Parameters for the ten-layer volume-averaged Earth model

Layer	r *(km)*	ρ *(kg m^{-3})*	μ *(N m^{-2})*	ν *(Pa s)*	
1	6371–6356	2283	2.66×10^{10}		
2	6356–6331	3194	5.91×10^{10}		Elastic lithosphere
3	6331–6251	3372	6.77×10^{10}		
4	6251–6221	3372	6.69×10^{10}	1.5×10^{20}	
5	6221–6151	3372	6.61×10^{10}	2.5×10^{20}	Uppermost mantle
6	6151–6061	3462	7.56×10^{10}	4.5×10^{20}	
7	6061–5971	3515	7.89×10^{10}	7.0×10^{20}	
8	5971–5701	3857	1.06×10^{11}	3.0×10^{21}	Transition zone
9	5701–3480	4878	2.19×10^{11}	2.4×10^{22}	Lower mantle
10	3480–0	10932			Inviscid fluid core

r is the distance with respect to the center of the Earth, ρ the density of the layer, and μ the rigidity. The viscosity ν is given for the convex profile models, as shown in Sabadini and Vermeersen (2004).

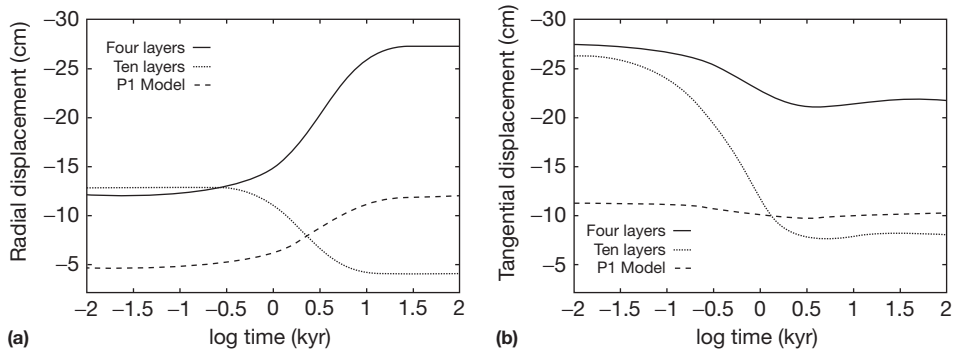

Figure 38 Radial displacement (a) and tangential displacement (b) in centimeters as a function of time in years after the occurrence of the faulting, at $t = 0$ year; the source is a vertical, point-like, dip-slip, with a seismic moment of 10^{22} N m. Negative values denote subsidence; the distance from the epicenter of the fault is $D = 200$ km. The parameters for the four- and ten-layer volume-averaged models are given in **Tables 5** and **4**. Viscosity is fixed at 10^{21} Pa s in each viscoelastic mantle layer of all models. Reproduced from Sabadini R and Vermeersen LLA (1997) Influence of lithospheric and mantle layering on global post-seismic deformation. *Geophysical Research Letters* 24: 2075–2078, with permission from AGU.

Table 5 Parameters for the four-layer volume-averaged Earth model

Layer	r *(km)*	ρ *(kg m^{-3})*	μ *(N m^{-2})*	ν *(Pa s)*	
1	6371–6250	3234	5.99×10^{10}		Elastic lithosphere
2	6250–5701	3631	8.60×10^{10}	1.6×10^{21}	Upper mantle
3	5701–3480	4878	2.17×10^{11}	2.4×10^{22}	Lower mantle
4	3480–0	10932			Inviscid fluid core

r is the distance with respect to the center of the Earth, ρ the density of the layer, and μ the rigidity. The viscosity ν is given for the convex profile models.

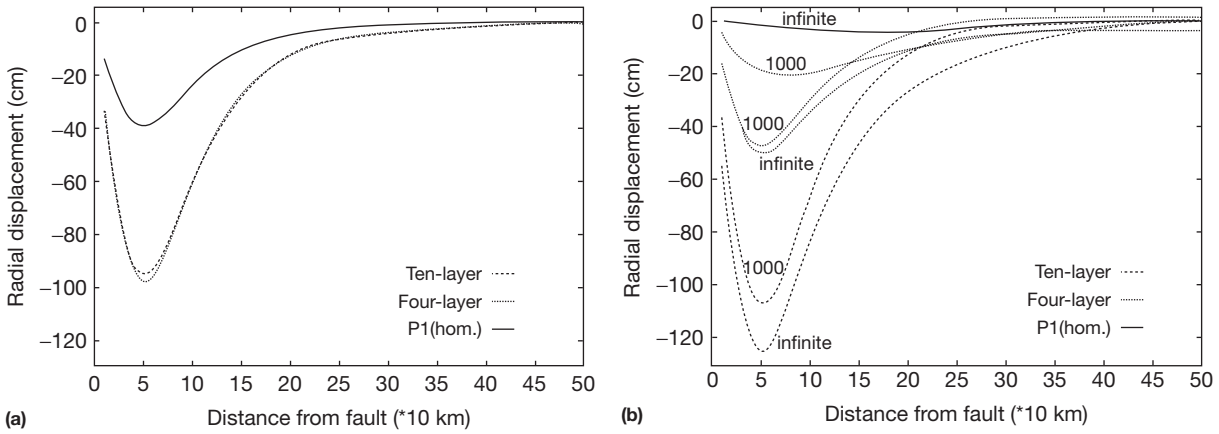

Figure 39 Radial displacement as a function of the distance from the fault in the elastic limit (a) and at $t = 1000$ year after the earthquake together with the long-timescale $t = \infty$ limit (b). The curves depict the cases for the ten-layer model (solid curve), four-layer model (dashed curve), and P1 model (short-dashed curve). The mantle viscosity of the four- and ten-layer models is given in **Tables 5** and **4**. P1 model has a uniform mantle viscosity of 10^{21} Pa s. In all cases, the lithosphere is elastic. Reproduced from Sabadini R and Vermeersen LLA (1997) Influence of lithospheric and mantle layering on global post-seismic deformation. *Geophysical Research Letters* 24: 2075–2078, with permission from AGU.

For radial displacement (panel (a)), the volume-averaged models predict an increase in postseismic deformation, while P1 model (short-dashed curve) predicts the opposite behavior, that is, a reduction in postseismic signals. Although similar to the ten-layer model in the amplification of the postseismic deformation, the four-layer model (portrayed by the solid curve) predicts, in both the elastic limit and long-timescale limit, a radial displacement that is higher by a factor of 2 in comparison with the ten-layer models, as shown by the dashed curve. The behavior of the old P1 model is due to the absence of elastic stratification between the lithosphere and the mantle, responsible for an overestimated lithospheric rigidity. Deviations in the four-layer model with respect to the ten-layer one are due to the absence of stratification in the elastic lithosphere in the four-layer model. These findings indicate the importance in correctly taking into account the realistic stratification of the plate in dealing with global postseismic deformation.

It has been verified that further refinement in lithospheric layering does not modify these findings with respect to the ten-layer model. The largest rigidity and density contrasts within the lithosphere are located at the base of the UC and LC, with the remaining portion of the lithosphere essentially homogeneous, which ensures that a three-layered lithosphere, as here, is sufficient to provide realistic estimates of the effects of earthquakes on global coseismic and postseismic deformations.

In **Figure 38(b)**, the same kind of analysis is carried out for the tangential displacement in the outward direction with respect to the fault at 45° from the fault's strike. By analogy with the findings from **Figure 38(a)**, the tangential displacement of P1 model is also subject to a substantial reduction during postseismic deformation. This is in distinct contrast to the results of volume-averaged models, which show a small reduction in the signal with respect to the coseismic deformation. A comparison of the four- and ten-layer models reinforces the conclusion drawn from panel (a) about the importance of stratifying the outer elastic layer of the Earth for realistic estimates of postseismic displacements.

Figure 39 shows the displacement as function of the distance from the source for the Earth's models portrayed in **Figure 38** but for fixed-time intervals after the earthquake. Four- and ten-layer viscosity models are averaged from a convex viscosity profile; the viscosity values can be found in **Tables 4** and **5**. The panels depict three snapshots of the deformation, with panel (a) showing the elastic limit, panel (b) an intermediate time when postseismic deformation is operative, and the long-timescale limit. The most striking result in the figure is that the ten-layer model behaves in a completely different fashion from the simplified P1 and four-layer models. In the elastic limit, in fact, both the P1 and four-layer models overestimate the radial displacement by more

than a factor of 2. During the transient at $t = 10^3$ years, the P1 model predicts a substantial reduction rather than a smooth amplification of the postseismic signal, as predicted by the volume-averaged four- and ten-layer models. In the far field is an upwarping of the lithosphere for the ten-layer model that is not reproduced by the four-layered model due to the overestimated rigidity of the outer elastic layer. In the long-timescale configuration, the ten-layer model does not show a visible increase in the deformation in the near field, but in the far field, it has rebounded with an annihilation of the upwarping noted in the transient regime.

This result indicates, as expected, that mantle relaxation has a strong control over postseismic deformation in the far field from the epicenter of large earthquakes and thus ultimately controls plate–mantle interaction. In this final state, the old P1 model predicts a pattern that does not show any resemblance to the more realistically stratified models, providing a smooth deformation of a few centimeters, in comparison with the 50 cm at 50 km from the epicenter as predicted by the ten-layer model. Except for the far field, the drastically different behavior of the three models is due to whether the lithosphere has been stratified or not.

Figure 40 shows the effects of mantle viscosity stratification based on the comparison between two ten-layer models, with the same lithospheric stratification, but different viscosities, such as a uniform mantle viscosity of 10^{21} Pa s and a varying one like the convex viscosity profile. The elastic and long-timescale limits of the homogeneous and convex viscosity mantle models are the same, as shown by the short-dashed and dotted curves. Since the elastic profiles of the mantle and lithosphere are identical, the initial and final configurations of the Earth models are the same since even the long time state of the model is determined by its elastic structure. In proximity to the source, at distances in the order of 10–100 km, the two models behave similarly, except for a 10% smaller signal at 50 km for the homogeneous model caused by a higher viscosity in the upper mantle, whereas in the far field, the homogeneous and convex viscosity mantle models produce a quite different response at intermediate timescales of 1–1000 year.

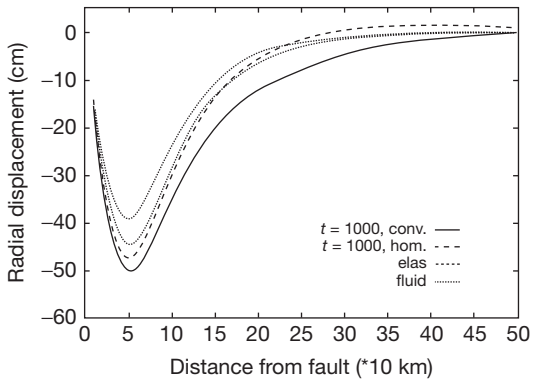

Figure 40 Comparison between a ten-layer model with a uniform viscosity of 10^{21} Pa s (dashed curve) and convex viscosity (solid curve) at $t = 1000$ year after the earthquake. The short-dashed and dotted curves denote the elastic and long-timescale limits of the two models. Reproduced from Sabadini R and Vermeersen LLA (1997) Influence of lithospheric and mantle layering on global post-seismic deformation. *Geophysical Research Letters* 24: 2075–2078, with permission from AGU.

As noted in Figure 39(b), displacement in the far field occurs in the opposite direction with respect to that experienced in the near field. The convex viscosity profile model predicts in fact positive vertical displacements of about 3 cm, while the homogeneous viscosity model does not show any visible evidence of relaxation. This result demonstrates the importance of mantle rheological stratification in controlling the deformation of the plate in the far field during postseismic deformation. The upward deflection of the lithosphere in the far field caused by the convex viscosity mantle is due to the upper mantle, which is softer than the homogeneous model. The elastic stratification of the lithosphere has thus a major influence on postseismic deformation. Three layers in the lithosphere, at the least, averaged from PREM, are found to be necessary to obtain correct estimates of the deformation following large earthquakes, in both the near field and far field.

Further increase in the 11 lithospheric layers of PREM produces a minor refinement in postseismic deformation estimates in comparison with the major improvement that is gained from 1 to 3 lithospheric layers. Modifications in deformation patterns during the time evolution from the initial elastic state to the long timescales are mainly controlled by mantle rheology. Viscoelastic stratification of the mantle has in fact major influences on the rebound of the lithospheric plate in the far field following the earthquake. In comparison to the required stratification of the lithosphere, the same fineness of layering is not needed for the mantle, in agreement with the result that mantle rheological stratification controls the global pattern of postseismic deformation in the far field.

6.04.5.3 Postseismic Deformation from Shallow Earthquakes

The previous section looked at large and deep earthquakes to elucidate the global properties of postseismic deformation by considering, in particular, stress relaxation in the mantle. Normal-mode theory will now be applied to analyze stress relaxation in the LC. By dealing with shallow sources and rheologically stratified crusts, normal-mode expansion must be performed to high harmonic degrees to correctly simulate postseismic displacements for earthquakes whose faults cut a thin upper elastic crust overlying viscoelastic layers. Even higher resolution is necessary for coseismic calculations for shallow sources, so that summation over 400 000 spherical harmonics must be performed, whereas summation over spherical harmonics of a few times 10^3 is adequate for estimating the rates of deformation due to stress relaxation in the LC. The reader can find details for implementing improvements in normal-mode theory for dealing with such high degrees like 10^4 in Riva and Vermeersen (2002), who first developed the necessary mathematical tools. The modeling results in this section represent a novelty in terms of both the large number of layers dealt with, first made possible by the grid-spacing procedures to detect the normal modes in the Laplace domain described in Vermeersen and Sabadini (1997), which represent the real heart of this new family of postseismic deformation models, and then by the high spatial resolution of viscoelastic solution described in Riva and Vermeersen (2002).

6.04.5.4 The Example of the 1997 Umbria–Marche Earthquake

The stress relaxation process in the LC is studied here via the moderate-size 1997 Umbria–Marche earthquake, which is characteristic of slowly deforming plate boundaries in the central Mediterranean like that in central Italy between the Tyrrhenian and Adriatic domains. This section is thus based on the studies of Riva et al. (2000) and Aoudia et al. (2003) where postseismic relaxation was considered for the first time within the context of shallow normal faulting.

Central Italy is undergoing continental extension, as noted in the preceding text, when dealing with tectonic forces applied at plate boundaries, and experienced the moderate, normal-faulting 1997 Umbria–Marche earthquake sequence. Deep seismic reflection studies and this earthquake sequence clearly show a seismogenic layer decoupled from the LC by a sizable transition zone (TZ). In accord with these observations, normal-mode modeling is based on a three-layer crust divided into an elastic upper crust (UC), a TZ, and a low-viscosity LC, as shown in **Figure 41**, in agreement with nearly all viscoelastic relaxation studies (Ma and Kusznir, 1995; Pollitz, 1996), assuming brittle UC, LC, and mantle.

Seismological and geologic observations from regions of active faulting suggest that the seismogenic UC could be separated from the LC by an extra layer, called TZ, representing the place of occurrence of both brittle and ductile processes; these observations are frequent in regions of active continental extension. The structure of the crust of **Figure 41** agrees with seismic reflection profiles (Pialli et al., 1998) purposely designed to study the deep crust in the northern Apennines. Below the Umbria–Marche extensional belt, the top of the LC is placed at a depth of 20 km, while the Moho is at a depth of 35 km.

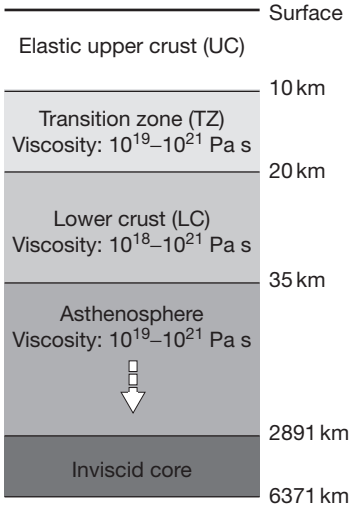

Figure 41 Earth model and viscosity parameters used for the 1997 Umbria–Marche earthquake. Reproduced from Riva REM, Aoudia A, Vermeersen LLA, Sabadini R, and Panza GF (2000) Crustal versus asthenospheric relaxation and post-seismic deformation for shallow normal faulting earthquakes: The Umbria–Marche (central Italy) case. *Geophysical Journal International* 141: F7–F11.

An abrupt cutoff of the 1997 Umbria–Marche aftershock sequence is placed about 9 km deep, which seems to indicate that seismic activity is largely restricted to the uppermost 10 km of the deforming continental crust and leaves room for a 10 km thick TZ above 15 km of the LC as imaged by the seismic reflection profiles (**Figure 41**). The TZ acts in the normal-mode modeling as a layer that decouples the elastic UC from the low-viscosity LC. Modeling is thus based on the five layers shown in **Figure 41**. This stratification is also consistent with the range of regional velocity models estimated via surface-wave dispersion analyses, gravity, and heat-flow anomalies.

The Umbria–Marche earthquake sequence started on 26 September 1997 in a complex deforming zone along a normal-fault system in the Central Apennines. Only the strongest earthquake of the Umbria–Marche sequence that took place on this date at 9:40 UTC (11:40 CEST) ($M_S = 6.0$) is considered in the modeling, the seismic moment estimate being based on the solution in Saraó et al. (1998) and retrieved from broadband waveform inversion, in good agreement with the CMT solution (Ekstrom et al., 1998). The application in the succeeding text provides a first-order estimate of the expected vertical velocities caused by postseismic relaxation in the area.

To illustrate first the sensitivity of the results on the source's depth, the finiteness of the source in the vertical direction is neglected, and besides the source depth of 7 km, in agreement with the seismological solution (Saraó et al., 1998), a case in which the source is embedded at a depth of 3 km is considered in order to simulate the effects of a fault almost reaching the Earth's surface. The seismic moment is distributed along a line of dislocations whose length along-strike is 10 km. The source has thus the infinitesimal extension of a point in the down-dip direction. The dip of the fault is 37°, in agreement with the seismological solution by Saraó et al. (1998). To resolve the deformation produced by this shallow fault, summation of 4000 normal modes is performed so as to ensure convergence of the normal-mode solution.

Vertical deformation is considered as being the most relevant to normal-faulting simulations, and the results are computed at the Earth's surface along a line perpendicular to the strike of the fault and crossing its center. The fault is dipping to the left, and the distance is measured from the intersection of the upward prolongation of the fault with the Earth's surface. **Figure 42(a)** shows the depth at 7 km and the modeled coseismic and postseismic vertical deformations measured at the surface. The coseismic component (solid line) shows the deformation pattern characterizing normal faulting, with uplifted, localized footwall and broad subsidence in the hanging wall. The postseismic component (dashed line) accounting for both coseismic deformation and postseismic viscoelastic relaxation is responsible for a broadening of the subsidence affecting the footwall.

Postseismic displacements are evaluated after complete viscoelastic relaxation. The largest coseismic displacement is −8 cm 10 km from the fault. Due to viscoelastic relaxation, the maximum displacement increases to −12 cm, and a broad area, which remained at rest during the coseismic deformation, is now subject to subsidence at distances of tens of kilometers due to the decoupling of the uppermost part of the crust with respect to the lower layers. Normal faulting and extension at

the bottom of the UC, below the neutral plane of the uppermost elastic layer, are responsible for down-flexure of this elastic layer, imaged by the broad subsidence in Figure 42(a). Figure 42(b) portrays modeled vertical velocities at different times after the earthquake. A wide region of negative velocity marks the broad down-flexure, or subsidence, of the UC, while two regions of low velocity represent the peripheral flexure response of this plate to subsidence. The short-wavelength feature at the center of the subsiding area can be recognized as a relative maximum corresponding to the footwall and the subsidence of the hanging wall, within a generalized subsidence.

The highest velocity is -0.85 mm year^{-1} in the hanging wall at $t=0$ and, because of the relatively high viscosity of the TZ (10^{19} Pa s), is subject to a minor reduction after 10 years. After 50 years, there is still a visible velocity signal of about -0.25 mm year^{-1}. A viscosity of 10^{18} Pa s is considered for the TZ, which is thus coupled to the LC, and velocity is subject to an increase of one order of magnitude, attaining the value of -8.5 mm year^{-1}. Since the TZ and LC viscosities are largely uncertain, ranging between 10^{18} and 10^{19} Pa s, it is likely that the largest subsidence rates in the highly deforming area of the hanging wall vary in the range obtained in this figure. These findings show that a comparison between

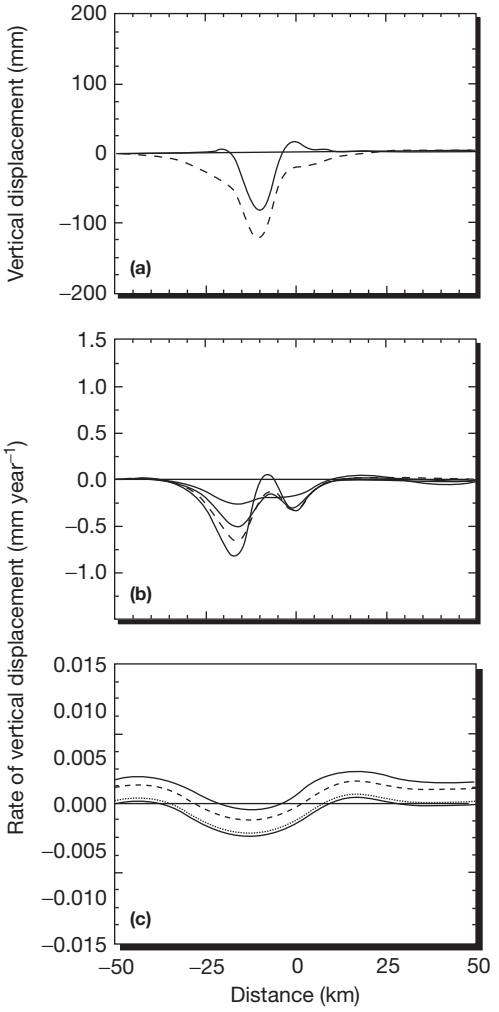

Figure 42 Coseismic and postseismic vertical surface displacements and rates calculated for a 7 km deep normal-faulting line source. The profiles are across the center of the fault ($x=0$ km) and perpendicular to its strike. The fault is dipping to the left and is buried in the upper layer. (a) Coseismic (solid line) and postseismic (dashed line) displacements. (b) Postseismic rates due to relaxation in the TZ expected at different times after the earthquake, with $t=0$, 10, 20, 50 years; solid, dashed, dash-dotted, and dotted, respectively. (c) Postseismic rates due to relaxation in the mantle expected at $t=0$, 100, 500, 1000 years; solid, dashed, dash-dotted, and dotted, respectively, after the earthquake. Redrawn from Riva REM, Aoudia A, Vermeersen LLA, Sabadini R, and Panza GF (2000) Crustal versus asthenospheric relaxation and post-seismic deformation for shallow normal faulting earthquakes: The Umbria–Marche (central Italy) case. *Geophysical Journal International* 141: F7–F11.

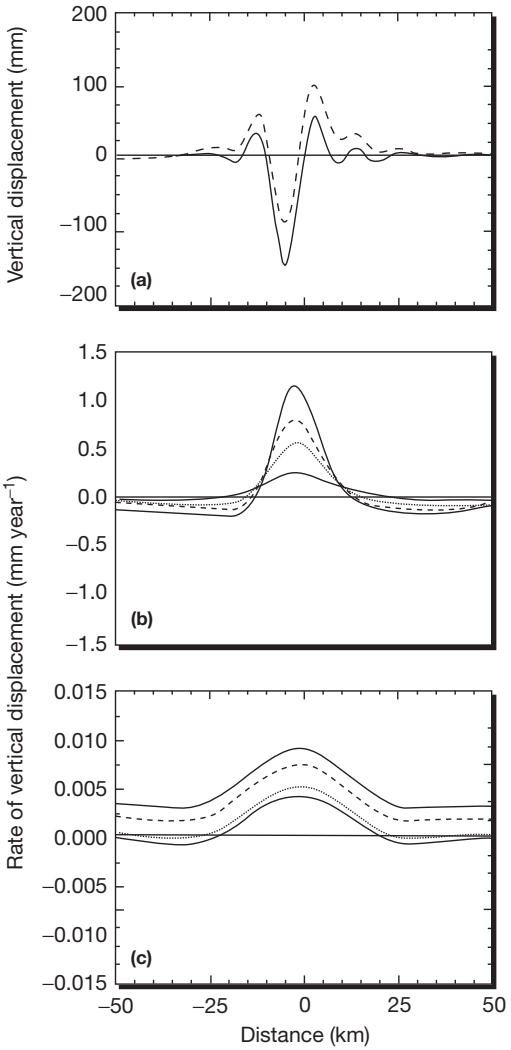

Figure 43 (a–c) Coseismic and postseismic vertical surface displacements and rates calculated for a 3 km deep normal-faulting line source. Redrawn from Riva REM, Aoudia A, Vermeersen LLA, Sabadini R, and Panza GF (2000) Crustal versus asthenospheric relaxation and post-seismic deformation for shallow normal faulting earthquakes: The Umbria–Marche (central Italy) case. *Geophysical Journal International* 141: F7–F11.

ongoing GPS campaigns and model predictions is crucial for estimating the effective viscosity of the TZ and LC layers.

Figure 42(c) deals with stress relaxation in the mantle; sampling times increased with respect to previous cases. The deformation pattern is broadened by stress relaxation involving larger portions of the Earth, with substantially reduced vertical velocities when compared to those in Figure 42(b). Notable in Figure 42(b) and 42(c) is that for shallow normal faulting, TZ and LC play a major role in comparison with the mantle, whose role is insignificant in present analyses.

In Figure 43, the source is embedded at the shallow depth of 3 km in the top half of the UC. The pattern of both coseismic displacement and postseismic displacement is now sharper than in Figure 42, and the largest coseismic subsidence in the hanging wall is increased by a factor of 2 with respect to the case of 7 km depth considered in Figure 42(a). The uplift in the footwall, with respect to Figure 42(a), is three times larger. Such an increase in the amplitude of the displacement and the sharpening of its pattern are due to the shallow depth of the source. With respect to Figure 42, note the upward migration of postseismic displacement pattern vis-à-vis coseismic displacement. Such an effect is caused by the extensional sources being located above the neutral plane of the UC, which induce a bending moment opposite to that induced by the deeper source in Figure 42 and, hence, a general uplift rather than subsidence. In Figures 42(a) and 43(a), depending on whether the source is located beneath or above the neutral plane, the postseismic curves lie completely either above or below the coseismic ones. These findings differ from those reported by Ma and Kusznir (1995), where, due to the finiteness of the source in the vertical direction, the fault cuts the whole UC through its neutral plane and the postseismic curves thus intermingle with coseismic ones. These findings represent a clear example of the sensitivity of plate-deformation properties, especially the Earth's crust, in seismogenic areas.

The velocity pattern in Figure 43(b) is also affected by the global upwarping observed in postseismic displacements, as noted in previous observations on the UC's flexural properties, with uplift velocities of 1.2 mm year^{-1} in the hanging wall close to the footwall. This tendency of a general upwarping can also be seen in Figure 43(c), where relaxation involves only the mantle. The same observations as those for Figure 42(c) can be applied to Figure 43(c), excepting the uplift of the footwall being enhanced with respect to the subsidence in the hanging wall. These results suggest that detection of postseismic deformation in the Umbria–Marche area is a challenging task due to the smallness of the expected velocity signal, of the order of a few millimeters per year, for vertical and horizontal components.

To reveal postseismic effects in the area and, in particular, to detect the horizontal deformation components, a series of GPS campaigns have been undertaken. The results of this surveying, along a baseline perpendicular to the major fault activated during the 1997 Umbria–Marche seismic sequence, are shown in Figure 44, where displacements are evaluated with respect to the town of Spello, indicated by A_0. These findings represent evidence for horizontal postseismic deformation triggered by shallow earthquakes, in the Mediterranean region, as first shown in Aoudia et al. (2003). Figure 44 (redrawn from Aoudia et al., 2003) compares GPS baseline variations with

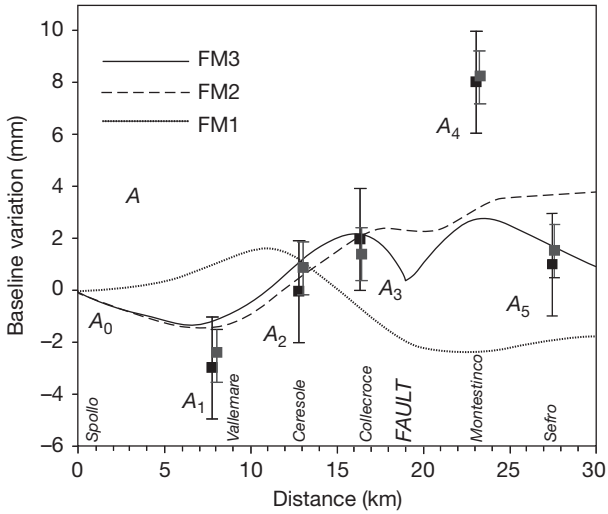

Figure 44 2002–1999 baseline length variations along the GPS section with respect to the A_0 site using GIPSY and Bernese solutions, gray and black vertical bars, respectively, versus viscoelastic model predictions for FM1 (Salvi et al., 2000), FM2 (Zollo et al., 1999), and FM3 (Basili and Meghraoui, 2001), using a viscosity of 10^{18} and 10^{17} Pa s for the TZ and lower crust, respectively. Reproduced from Figure 8.8 of Sabadini R and Vermeersen B (2004) *Global Dynamics of the Earth*, p. 328. Kluwer Academic Publisher, with kind permission of Springer Science and Business Media.

modeled ones as a function of baseline length in kilometers from the reference site of Spello (A_0).

All baseline variations are positive, except A_0–A_1, which indicates a general trend of postseismic extension across the fault. Estimates for GPS data reduction are shown with one-sigma error bar, together with model results corresponding to a TZ viscosity of 10^{18} Pa s and an LC viscosity of 10^{17} Pa s. Different fault models, indicated by FM1, FM2, and FM3, are considered, as indicated in the caption. FM1 (dotted) is not consistent with observations at different sites and does not reproduce the general pattern of baseline variations from the analyses. While FM2 (dashed) reproduces only part of the observations and the general trend, FM3 (solid) evidences the best fitting, reproducing well almost all the observations and the general baseline variation pattern. These findings demonstrate the important role of GPS survey in seismogenic zones in revealing the physics of postseismic deformation and providing a fundamental tool to unravel plate-deformation properties in active fault areas.

This section thus provides a first estimate of expected rates of vertical postseismic deformation in a characteristic seismogenic zone of the central Mediterranean. Fine rheological layering in the crust has a major role in the interplay of relaxation in the TZ and LC with respect to relaxation in the mantle when shallow sources are considered in normal-mode relaxation theory. Unlike large and generally deep earthquakes (Melosh, 1983; Thatcher and Rundle, 1979), shallow and moderate normal-faulting earthquakes are unaffected by lower lithospheric viscous coupling, while the TZ and low-viscosity LC impose a pattern and a spatial scale on postseismic deformation. For normal faulting, these applications show the relevance of source depth with respect to thickness and the

neutral plane of the elastic layer in controlling postseismic upwarping or downwarping, as emphasized by Thatcher and Rundle (1979) and Melosh (1983) for thrust faults. Since the elastic layer here is the UC rather than the whole lithosphere, this section shows that the results from Thatcher and Rundle (1979) and Melosh (1983) are scale-invariant and applicable to dip-slip sources embedded in an elastic layer of any thickness overlying a viscoelastic one. Furthermore, the pattern of widening and narrowing of the deformation due to stress relaxation at different depths (**Figures 42** and **43**) agrees with King et al.'s (1988) findings from simpler models. We have also seen that an appropriate test area for dealing with viscoelastic normal-mode theory at high harmonic degrees and for studying TZ and LC relaxation effects is the central Mediterranean, the Italian Peninsula in particular, where a clear cutoff in the depth distribution of earthquakes indicates that the seismogenic layer is limited to the first 10 km of the crust and a well-developed TZ lies below it and above, a low-viscosity LC.

6.04.5.5 DInSAR-Retrieved Coseismic Displacements

DInSAR techniques have demonstrated their potential as land deformation measurement tools. In particular, their capability has been considerably improved by using large stacks of synthetic aperture radar (SAR) images acquired over the same area, instead of the classical two images for standard configurations. Thanks to these improvements, DInSAR techniques became quantitative geodetic tools for land deformation monitoring. This section begins with a concise description of some basic DInSAR concepts, followed by results on coseismic displacements of the 1997 earthquake that struck the Umbria–Marche seismogenic zone.

Only for coseismic deformation are the DInSAR results considered since they release a continuous deformation pattern over areas whose spatial dimensions are those characterizing the spatial pattern of such a geophysical process and provide extra information with respect of GPS data, which are sparse over sites where GPS antennas are located. In fact, the pixels in DInSAR analysis are distributed with a spatial resolution of tens of meters, wherein the differential interferometric phase is recorded from two or more images so as to yield a sort of continuous deformation pattern of the Earth.

DInSAR techniques exploit the information contained in the phase of the radar microwave of 2.8 cm half-wavelength, of at least two complex SAR images acquired in different epochs over the same area, forming an interferometric pair. Unlike a simple amplitude SAR image, containing the amplitude of the SAR signal only, a complex SAR image contains two components, the phase and amplitude of signal per pixel. The phase is the key observable of all interferometric SAR techniques. The repeated acquisition of images over a given area is usually performed by using the same sensor. Besides the compatibility of the systems, the condition of forming interferometric pairs constraints the acquisition geometry.

Figure 45 summarizes the basic principle of DInSAR technique, considering a single-pixel footprint P. The sensor acquires a first SAR image at the time t_0, measuring the phase Φ_M of the microwave. The first satellite and the corresponding image are usually referred as the master one, indicated by M. If the land is subject to a displacement $D(t)$, the point P moves to

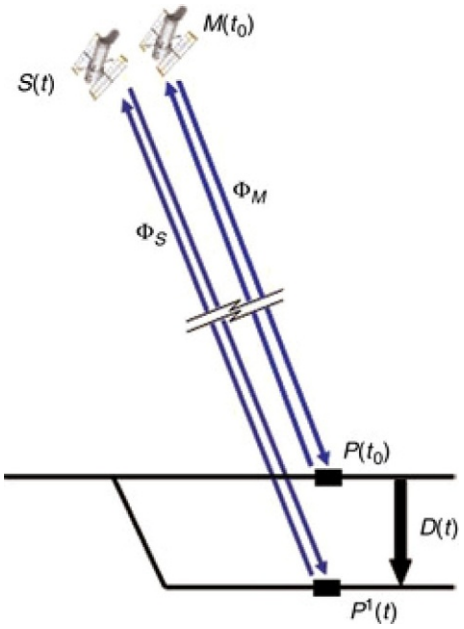

Figure 45 Principle of DInSAR for measuring the $D(t)$ displacement.

P'. The sensors acquire a second SAR image at the time t, measuring the phase Φ_S. The second satellite is usually referred as the slave, indicated by S. DInSAR techniques exploit the phase difference $\Phi_{int} = \Phi_M - \Phi_S$, called interferometric phase, containing information of land displacement, thus finally retrieving the land displacement $D(t)$. For a general review of DInSAR interferometry, see Rosen et al. (2000).

These DInSAR techniques and inverse geophysical modeling have been used by Crippa et al. (2006) to constrain coseismic slip over the two faults of the 1997 seismic sequence in the Umbria–Marche region, in central Italy, exploiting the characteristics of these data, especially their dense spatial sampling.

DInSAR analysis of the 1997 earthquake coseismic displacement from Crippa et al. (2006) is based on a 35-day interferogram, the images having been acquired on 7 September and 12 October 1997, thus including coseismic displacements of the terrain. Other nine coseismic interferograms originally available for the study were discarded, due to their low coherence over the studied area.

The following results are based on a careful analysis of DInSAR errors that can potentially affect single interferogram analyses, as detailed in Crippa et al. (2006). Besides the deformation component, a generic DInSAR-derived displacement field contains in fact other components like the atmospheric component, the residual topography component due to DEM errors, the component related to orbit errors, the unwrapping-related errors, and the decorrelation noise (Hanssen, 2001). These components can be important sources of errors, severely degrading the quality of the DInSAR-derived deformation field. The best way to avoid this degradation is to use multiple observations, that is, multiple interferograms of the same deformation area, as, for example, in Ferretti et al. (2001). Either the errors can thus be estimated or their effects can be reduced, thereby improving the quality of the results. However, there are several geophysical applications that must rely on a

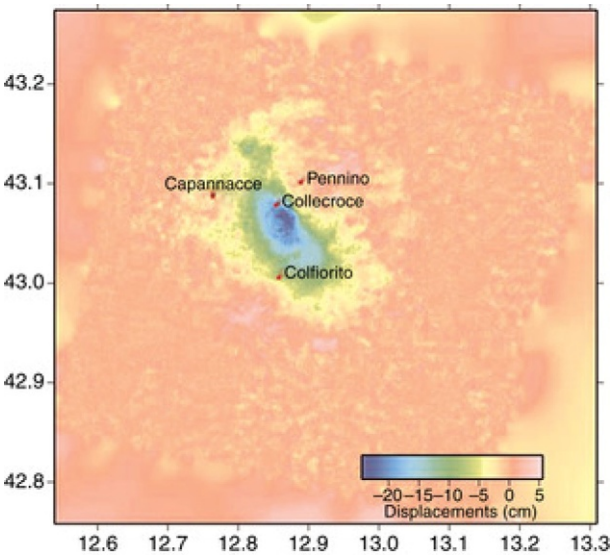

Figure 46 DInSAR-retrieved vertical displacement in the 1997 Umbria–Marche earthquake area. Reproduced from Crippa B, Crosetto M, Biescas E, Troise C, Pingue F, and De Natale G (2006) An advanced slip model for the Umbria–Marche earthquake sequence: Coseismic displacement observed by SAR inteferometry and model inversion. *Geophysical Journal International* 164: 36–45. http://dx.doi.org/10.1111/j.1365-246X.2005.02830.x.

single interferogram, as done here. Crippa et al. (2006) described in detail the techniques that have been used to minimize the impact of these error sources over the DInSAR-retrieved coseismic displacement portrayed in the following analysis of the 1997 Umbria–Marche seismic sequence.

The DInSAR vertical displacement map of **Figure 46** is derived in Crippa et al. (2006) by undersampling the original DInSAR solutions, so that it contains about 9000 points or pixels, instead of the potentially available 100 000. In comparison with previous SAR results over the same area, the major advantage of this DInSAR solution is its high sampling density of the coseismic field. These displacement values are relative displacement measurements with respect to an arbitrary reference point, which is chosen at 15 km from the mainshock. In **Figure 46**, the displacement of about 25 cm in the hanging wall of the normal fault represents the most evident feature of vertical deformation pattern. This figure enlightens the power of this technique for measuring crustal displacements in seismogenic zones, once it is realized that each pixel, represented by a unitary square in the diagram, represents a sampling point, where vertical displacement can be precisely measured. It should be noted that each pixel has the dimension of about 80–90 m, and plenty of them concur to build the DInSAR image.

Inversion of DInSAR displacement solution portrayed in **Figure 46**, to retrieve the slip over the faults, is based on the inversion scheme from De Natale and Pingue (1991), providing heterogeneous seismic moment distributions on rectangular faults based on unidirectional slip and fixed fault locations.

The fault parameters are described in Crippa et al. (2006); the two fault models are based on individual source points spaced by 0.25 km on both length and width; rigidity is fixed at $\mu = 3.12 \times 10^{10}$ Pa.

The left top panel of **Figure 47** shows the surface displacement from the slip over the faults obtained from the inversion, to be compared with the DInSAR-retrieved image in the right top panel of **Figure 47**. Observed and modeled surface displacement patterns resemble closely each other, both being characterized by a well-developed displacement in the hanging wall and smooth uplift in the footwall of the fault, in good agreement with what is expected for normal-fault earthquakes. The high quality of the fit becomes even more evident in the bottom panel, where the modeled vertical displacement is subtracted from the observed one, portraying small residuals.

The seismic moment distribution from the DInSAR solution (**Figure 48**) is compatible with previous results from purely seismological analyses (Capuano et al., 2000) but it should be emphasized that this DInSAR-retrieved distribution is much better resolved. The relation between seismic moment M and slip Δs shown in the figures is $M = \mu A \Delta s$, where μ denotes the rigidity of the crust and A the area of the fault, which establishes the linear relationship between seismic moment and slip, as given in the color scale of the figure. Both DInSAR and seismological models portray good agreement between their estimated areas of maximum dislocation on the two faults. The reconstruction of the event from seismological data (Capuano et al., 2000) implies that the fracture nucleation for the second event (9:40 UTC (11:40 CEST)) started close to the southernmost edge of the northern fault (left in figure) several hours after the 00:33 UTC (2:33 CEST) event, which nucleated from the southernmost fault (right in figure). The presence of the largest patch of slip in the southernmost part of the northern fault is likely to correspond to the nucleation area of the 9:40 event. The effectiveness of using rigorous unwrapping for DInSAR data inversion can also be demonstrated by comparing these results to those recently obtained by Lundgren and Stramondo (2002), who inverted sampled DInSAR fringes by a simulated annealing method. Their slip distribution, for example, included fault patches with up to about 2 m of dislocation, a very high value, hardly compatible with geologic fault scarp and seismological data (Capuano et al., 2000). In the present analysis, peak dislocation computed using the rigidity value = 31.2 GPa is around 0.75 m, with realistic values generally lower than 0.5 m. The total seismic moment obtained by DInSAR data inversion is $M = 5 \times 10^{17}$ N m and $M = 8 \times 10^{17}$ N m for the southern and northern faults, respectively, in agreement with the seismically derived ones by Capuano et al.'s (2000) $M = 4 \times 10^{17}$ N m and $M = 10 \times 10^{17}$ N m. Another key feature of the model from the DInSAR solution is the clustering of slip on the northernmost part of the southern fault, which should correspond, according to the seismological model of Capuano et al. (2000), to the first shock (00:30). The occurrence of two mainshocks on adjacent parts of the two faults after a few hours suggests that the second shock was triggered by the static stress loading caused by the first one.

The joint use of DInSAR and advanced inversion techniques can open a new perspective in seismotectonic modeling and in the understanding fault processes in both coseismic and interseismic phases.

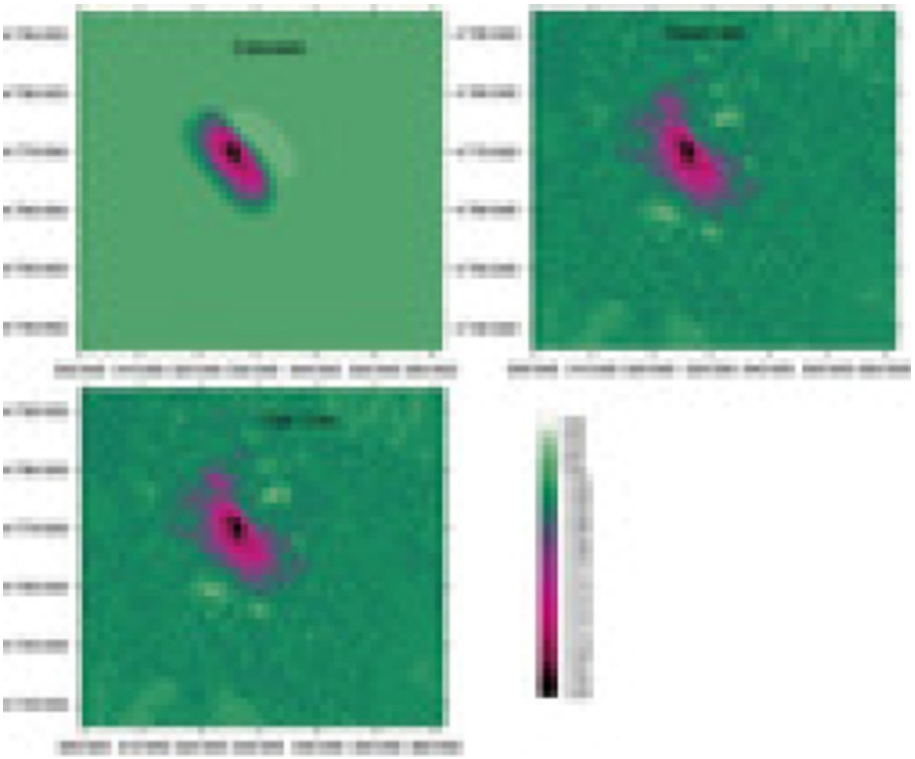

Figure 47 Modeled (top, left panel) and DInSAR (top, right panel) vertical displacements and residuals (bottom panel) in the Umbria–Marche earthquake area. Reproduced from Crippa B, Crosetto M, Biescas E, Troise C, Pingue F, and De Natale G (2006) An advanced slip model for the Umbria–Marche earthquake sequence: Coseismic displacement observed by SAR inteferometry and model inversion. *Geophysical Journal International* 164: 36–45, http://dx.doi.org/10.1111/j.1365-246X.2005.02830.x.

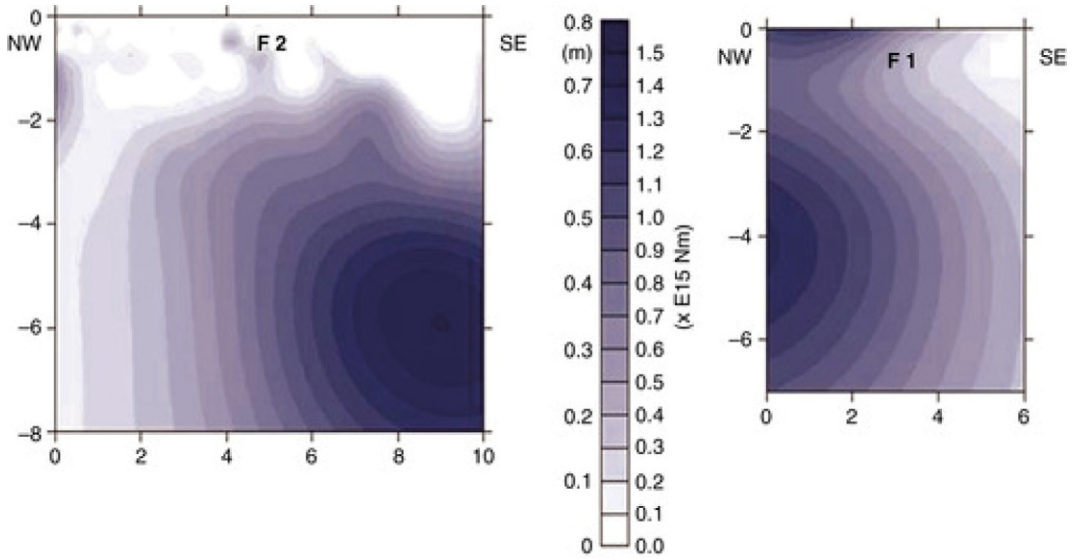

Figure 48 Seismic moment and slip release on the northern and southern fault surfaces, left and right, respectively. Reproduced from Crippa B, Crosetto M, Biescas E, Troise C, Pingue F, and De Natale G (2006) An advanced slip model for the Umbria–Marche earthquake sequence: Coseismic displacement observed by SAR inteferometry and model inversion. *Geophysical Journal International* 164: 36–45. http://dx.doi.org/10.1111/j.1365-246X.2005.02830.x.

6.04.5.6 The 1980 Irpinia Earthquake

A comparison of the measured vertical displacements from two leveling campaigns carried out in 1981 and 1985 in the epicentral area of the 1980 Irpinia earthquake ($M_s = 6.9$) and predictions from viscoelastic Earth model results reveals the occurrence of postseismic deformation due to stress relaxation in the ductile part of the crust south of the area explored in the

preceding text. In proximity of the major fault, leveling lines show a peculiar upwarping of the crust, accumulated during the time interval 1981–85. Here, we explore the mechanism of stress relaxation in the ductile parts of the crust after the 1980 Irpinia earthquake, following the study by Dalla Via et al. (2003, 2005), where postseismic deformation was discovered in the southern Apennines (Italy). The joint use of local and worldwide seismological data, static deformations, and geologic evidences provides a detailed picture of the complex mechanism of this event. The main event consisted of at least three distinct subfaults that ruptured at intervals of about 20 s from each other. Surface faulting linked to this earthquake was notably evident at several places, particularly on the main fault (first subevent), with dislocation up to 1.2 m. The total seismic moment inferred for this event is 3×10^{19} N m.

Viscoelastic relaxation theory for an incompressible, self-gravitating, spherical, viscoelastic Earth, presented in the first part of this chapter, has been modified as detailed in Riva and Vermeersen (2002) to increase the spatial resolution for high harmonic degrees. Summation in eqns [19] and [20] and eqns [23] and [24] is carried out to 40 000 spherical harmonic contributions in the coseismic case and to 6000 spherical harmonics in the postseismic case. This approach ensures the highest spatial resolution in both coseismic and postseismic components. The Earth model described in Table 6 consists of five layers, including a purely elastic UC, a viscoelastic LC, a lower crust bottom, mantle, and an inviscid core.

The depths of the crustal layers and their elastic values are taken from the average depths of the seismogenic crust and MOHO in the southern Apennine area, while the deeper layers are based on standard global Earth models. The upper limit of the LC, 18.5 km, has been chosen to match the maximum depths of earthquakes in this area on the assumption that the viscoelastic, ductile LC inhibits seismic fracture. Viscosity in the LC has been varied from typical values of 10^{19} Pa s (Pollitz et al., 1998). In order to mimic the reduction of the viscosity within the LC and the decoupling between the LC and M, as expected on the basis of strength reduction with depth for the continental lithosphere under extension (Lynch and Morgan, 1987), the bottom of the lower crust, LCB, in Table 6, has been reduced by one order of magnitude with respect to the normal value of 10^{19} Pa s. Due to the simplified viscosity profile within the LC, only the effective viscosity resulting from the volumetric average within the two viscoelastic layers characterizing the LC can be compared with postseismic results from other tectonic environments (Pollitz et al., 1998). A standard M of 10^{21} Pa s below the LC does not portray any sizable deformation over the timescale of postseismic deformation.

Table 6 Viscoelastic model parameters for the 1980 Irpinia earthquake

Layer	*Depth (km)*	ρ *(kg dm^{-3})*	ν *(Pa s)*	μ *(GPa)*
UC	0–18.5	2.65	∞	32.5
LC	18.5–28.5	2.75	1×10^{18} 0.75×10^{19} 1×10^{19} ∞	33.7
LCB	28.5–32.5	2.90	10^{18} ∞	35.5
M	32.5–2891	3.39	10^{21}	73.5
IC	2891–6372	10.93		

UC, upper crust; LC, lower crust; LCB, lower crust bottom; M, mantle; IC, inviscid core.

The assumed fault system consists of three normal subfaults as shown in Figure 49, including the three leveling lines CZT2 (diamonds), CZT3 (crosses), and IGM81 (circles) measured immediately after the mainshock and 4 years later; the thin curve in Figure 49, starting from Eboli and routing to Grottaminarda through Potenza and the IGM81 profile, represents the leveling line along which the coseismic vertical displacement has been measured (Arca et al., 1983; De Natale et al., 1988). The surface projections of the three faults F1, F2, and F3 are shown by the light gray; the fault parameters of this model, shown in Table 7, are taken from Pingue and De Natale (1993). The total seismic moment is inferred from seismological and geodetic data; for the main fault F1, the seismic moment M_0 is fixed at 24.4×10^{18} N m, at $25. \times 10^{18}$ N m for F2, and at 3.2×10^{18} N m for F3. The slip angle is fixed at $-90°$ for each fault. Slip on the three subfaults is considered homogeneous in the first tests. Subsequently, by maintaining the seismic moment constant to $M_0 = 3.0 \times 10^{19}$ N m, the slip distribution on the main fault is varied with depth in order to reduce the misfit between model predictions and observations.

Figure 50 shows the observed displacements resulting from the leveling lines in Figure 49, where the black vertical bars reproduce the observations and their average errors; the curves represent the modeled vertical displacements due to viscoelastic relaxation for various combinations of slip distribution and viscosities and not including the coseismic component. In order to carry out a comparison independent of the choice of the zero in the leveling, each model result is uniformly shifted so that the mean residual vanishes. The gray curves correspond to the reference model characterized by a uniform distribution of the seismic moment over the fault and by a LC viscosity between 18.5 and 28.5 km depth, of 10^{19} Pa s (Table 6).

Although the trends shown by this model agree with some basic features of the three lines, such as the subsidence along points 1–20 and the following uplift of IGM81, the general uplift along CZT2, and the uplift between points 1 and 50 of CZT3, the gray curves always underestimate the observations, especially the upward bulge of 20–30 mm of CZT3 and the drastic increase in the uplift at point 20 of IGM81. To increase the upwarping of the crust along CZT3, where this line crosses the major fault, it is necessary to distribute the seismic moment such that the maximum slip occurs at depths of about 10 km, as shown in Table 8, resulting in the dotted curves in Figure 50.

This best-fit seismic moment distribution was chosen by minimizing the residuals between observations and model predictions for all the three lines simultaneously. The long-wavelength uplift between points 1 and 35 of CZT3 increases with respect to the dotted curve to 12 mm; the same is true for CZT2 for points 1–25, where uplift reaches 10 mm. Particularly evident is the tendency to reproduce the change from subsidence to uplift along IGM81 from the benchmarks 15 to 35.

The fit between the observations and model results can be substantially improved by reducing the viscosity in the LC

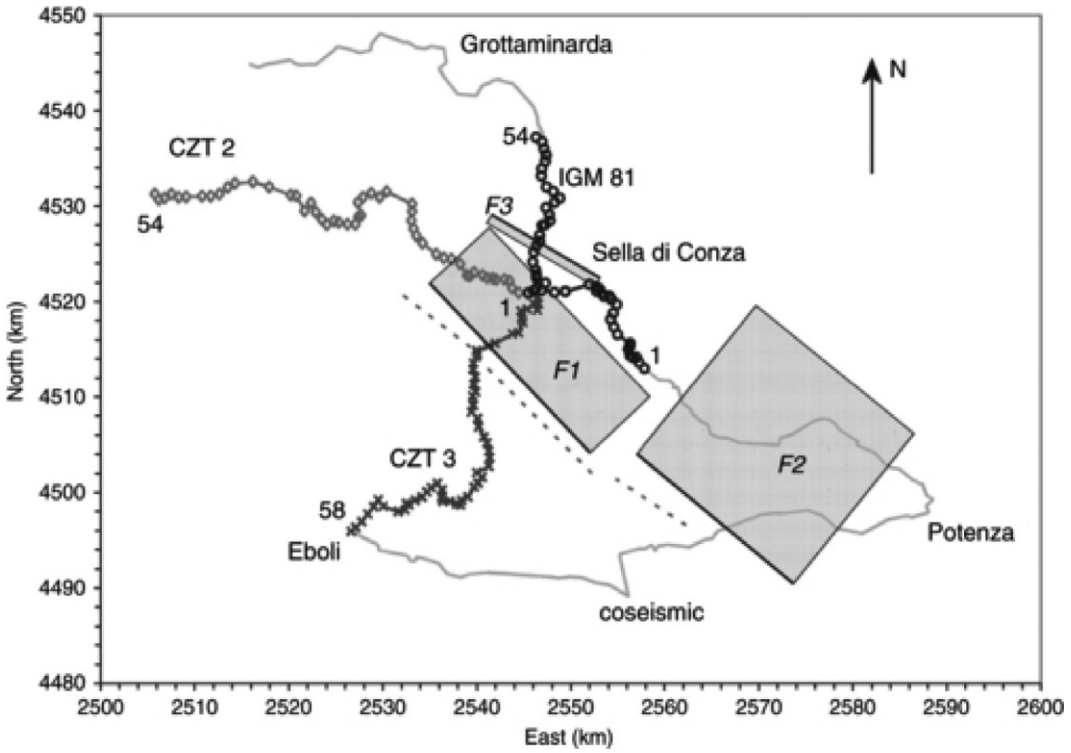

Figure 49 Fault model of the 1980 Irpinia earthquake. The leveling lines IGM81 (black dots), CZT2 (squares), and CZT3 (gray dots) are also indicated. F1, F2, and F3 indicate the three faults, at 0, 18, and 40 s, respectively, as given in **Table 7**; the dashed lines provide the surface evidence of the faults. The first (1) and last (54 and 58) benchmarks of each leveling line are also shown. Reproduced from Dalla Via G, De Natale G, Troise C, et al. (2003) First evidence of post-seismic deformation in the central Mediterranean: Crustal viscoelastic relaxation in the area of the 1980 Irpinia earthquake (southern Italy). *Geophysical Journal International* 154(3): F9–F14. http://dx.doi.org/10.1046/j.1365-246X.2003.02031.x.

Table 7 Fault parameters

Subevent	*L1 (km)*	*L2 (km)*	*Top (km)*	*Disl. (cm)*	*Str. (°)*	*Dip (°)*
F1 (0 s)	25	20	1.0	150	317	60
F2 (18 s)	22	14	1.0	25	310	20
F3 (40 s)	13	10	1.3	75	120	85

L1, fault length; L2, fault width along slip direction; Top, depth of fault top margin; Disl., mean dislocation; Str., strike.

from 10^{19} Pa s to 0.75×10^{19} Pa s as indicated by the black solid curves. The increase to 23 mm in the maximum along CZT3 is accompanied by an increase to 15 and 10 mm along CZT2 and IGM81, respectively. The general trend of observed displacements now appears well reproduced by the best-fit model, except for some high-frequency signals at very localized zones and a rather systematic underestimation of displacements in the northernmost zone of IGM81.

Figure 51 provides an aerial view of the postseismic vertical displacement accumulated in the period 1981–85, with characteristic zones of uplift and subsidence; this figure corresponds to the same viscosity model of Figure 50 and is characterized by LC relaxation (solid curves). Two major features are notable: the broadness of the area affected by subsidence and uplift and the amplitude of the displacement, in the order of 10 and 40 mm for uplift and subsidence. These effects are indicative of stress release at depth and of the ability of the viscoelastic part of the crust to channel the flow at large distances from the fault. The expected present-day peak-to-peak postseismic vertical displacement, 22 years after the earthquake, is 120 cm and characterized by the same pattern as in Figure 51.

In the case averaged over the thickness of the LC of 14 km, the effective average viscosity of 0.6×10^{19} Pa s agrees within the order of magnitude with the 'normal' LC viscosity of about 10^{19} Pa s obtained by Pollitz et al. (1998) from postseismic relaxation following the 1989 Loma Prieta earthquake. The characteristic wavelength of the postseismic deformation in the Irpinia area is supporting evidence for viscoelastic relaxation in the LC rather than in the uppermost part of the mantle, unlike the 1992 Landers earthquake where there are indications that relaxation also involves a weak upper mantle. An additional result from postseismic displacement modeling in this area consists of further details about the fault slip with respect to the previous results. It appears that higher slip concentration at around 10 km depth is able to provide the best fit to the observed data.

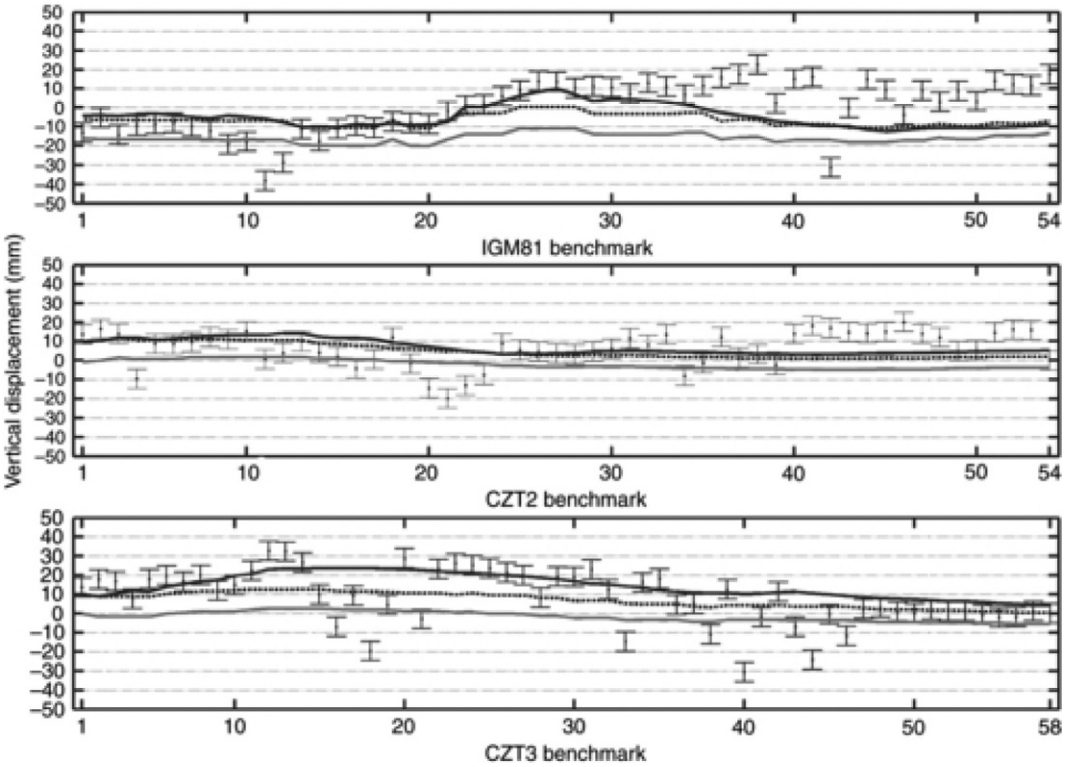

Figure 50 Leveling data for the three lines and modeling results: The gray curves correspond to a TZ viscosity of 10^{19} Pa s and a uniformly distributed seismic moment and the dotted ones to the same viscosity but nonhomogeneous seismic moment according to **Table 8**. The black solid curves correspond to a lower crust (LC) viscosity of 0.75×10^{19} Pa s and the seismic moment distribution in **Table 8**. From Dalla Via G, De Natale G, Troise C, et al. (2003) First evidence of post-seismic deformation in the central Mediterranean: Crustal viscoelastic relaxation in the area of the 1980 Irpinia earthquake (southern Italy). *Geophysical Journal International* 154(3): F9–F14. http://dx.doi.org/10.1046/j.1365-246X.2003.02031.x.

Table 8 Seismic moment distribution along the fault width (L2)

Fault fraction	*F1*	*F2*	*F3*
1/5	$0.8 \times M$	$2.0 \times M$	$2.0 \times M$
2/5	$1.2 \times M$	$2.0 \times M$	$2.0 \times M$
3/5	$1.5 \times M$	$1.0 \times M$	$1.0 \times M$
4/5	$1.0 \times M$	$0.0 \times M$	$0.0 \times M$
5/5	$0.5 \times M$	$0.0 \times M$	$0.0 \times M$

$M = M_0/5$, where M_0 is given in the text; the fault description is given in **Table 7**.

6.04.6 Interseismic and Preseismic Deformation

The understanding of plate-deformation dynamics represents nowadays a necessary step leading to the comprehension of the physical processes ending into an earthquake from the detection, interpretation, and modeling of the seismic cycle, but once considered for the interseismic and preseismic phases, it will have a major impact also on the society and on the economy: in fact, GPS and DInSAR time series anomalies detecting the behavior of the plates in active seismogenic regions, compared to the stationary trends attributable to steady-state tectonics analyzed in the preceding text, represent a promising new frontier for the use of these data, and hopefully of space gravity data too, in the monitoring of the preseismic phase of the earthquakes.

Modeling of the complete seismic cycle will in fact improve the safety of the population subject to the earthquake extreme natural events thanks to the new elements arising from the joint geophysical and geodetic data during the earthquake preseismic phase. Decision makers will in fact gain new diagnostic elements that will complement the classical seismological ones to safeguard the population and civil and industrial infrastructures in the surveyed active seismogenic regions. It is obvious how such a development perspective overcomes the limitations of the traditional probabilistic approach, based on generally incomplete catalogs of historical seismicity. The latter, in fact, is limited to define the likelihood of an earthquake of magnitude higher than a certain threshold in a certain interval of time and thus provides a 'static' description of reality, demonstrably inadequate for some recent events that occurred in the Mediterranean region, such as the 2012 Emilia-Romagna one, and for the detection of the dynamic behavior of another important seismogenic region in the southern Apennines, the Pollino one, both proposed in the following as examples for enlightening the importance of the understanding of plate-deformation dynamics as carried out in this chapter.

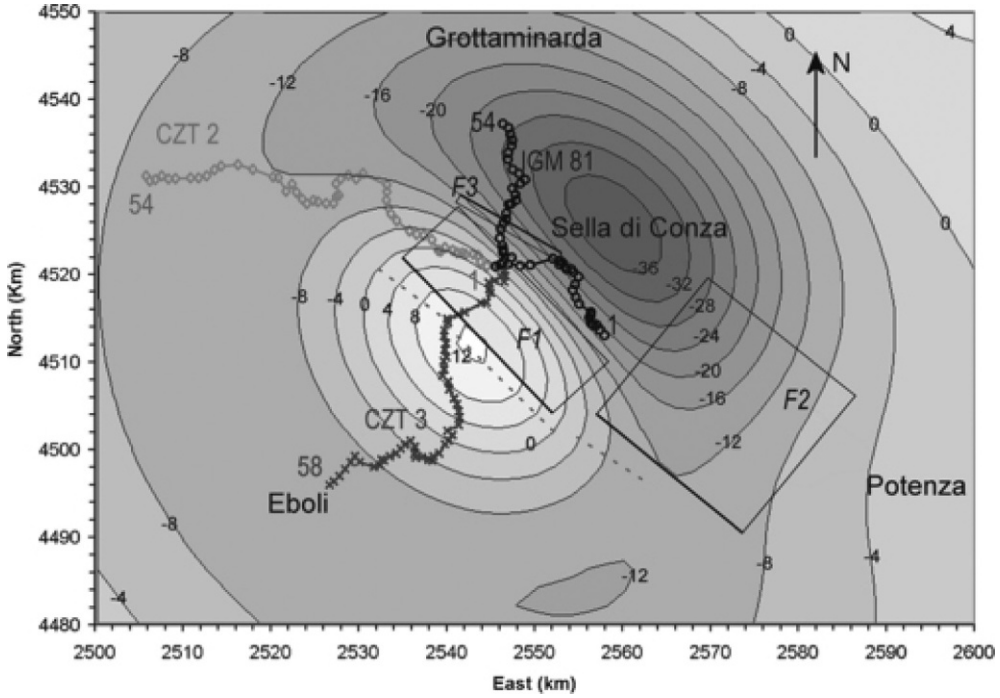

Figure 51 Postseismic displacement accumulated in the period 1981–85 (in millimeters) due to crustal relaxation. Redrawn from Dalla Via G, De Natale G, Troise C, et al. (2003) First evidence of post-seismic deformation in the central Mediterranean: Crustal viscoelastic relaxation in the area of the 1980 Irpinia earthquake (southern Italy). *Geophysical Journal International* 154(3): F9–F14. http://dx.doi.org/10.1046/j.1365-246X.2003.02031.x.

6.04.6.1 The Pollino and Emilia-Romagna Seismogenic Regions

Section 6.04.5 focused mainly on co- and postseismic deformations: within the frame of the SISMA (SISMA, 2011, Seismic Information System for Monitoring and Alert, Italian Space Agency, http://www.asi.it/it/eventi/workshop/progetto_sisma) activities, attention is drawn hereinafter to the inter- and preseismic phases of the Castrovillari fault embedded in the Pollino seismogenic region in Calabria, southern Apennines, an active but slowly extensional deforming zone within the diffuse plate boundary between Africa and Eurasia, and to recent inter- and preseismic strain-rate findings in the northern Apennines, involving the Emilia-Romagna region.

These phases are relevant for the behavior of active faults, which can remain locked or slip and creep aseismically. This behavior has been discovered by some pioneering works on strike-slip faults, the San Andreas in California and the NAF in the Mediterranean, in the last 50 years (Ambraseys, 1970; Bürgmann et al., 1998, 2000; Cakir et al., 2005; Rosen et al., 1998; Steinbrugge et al., 1960). Creep occurs at different spatial and timescales, involving various depths within the seismogenic layer, at rates that may differ from the background tectonic ones, as shown in the following. Fault creep patterns, including the creep intensity, provide important information on the seismic cycle, being the stress accumulation mode leading to the earthquake dependent on the interplay between creeping and locked parts of the fault. Works on the San Andreas and NAF creeps have also made use of DInSAR and GPS technologies, but Sabadini et al. (2009) were the first to exploit these data within the slowly deforming African and Eurasian Plate boundary from the comparison between regional deformations and those occurring at the spatial scale of a normal fault embedded in the former. The surveyed fault is the long-lasting quiescent Castrovillari normal fault, over which a campaign GPS network composed of ten sites covering an area of about 30 km × 17 km has been set up, centered in the normal-faulting area (Figures 52 and 54). Implementation of the campaign sites was carefully performed to ensure a submillimeter forced centering of the antennas. The GPS measurements started in 2003 and five campaigns have been performed up to 2008. Station coordinates have been framed in IGS05 using the IGS transformation parameters at the end of the processing analysis; repeatability of the coordinates has been improved to 1.1 mm. Measured strain rates of Figure 52(a) at the spatial scale of the fault, obtained from the GPS campaign velocities as shown in Figure 54, are compared with modeled strain rates at tectonic regional scales, Figure 52(b), according to Marotta et al. (2004), based on thin-sheet modeling and ITRF2005 African–Eurasian relative motion and to continuous GPS strain rates at the regional scale. As continuous GPS data surrounding the Castrovillari fault are not available, a tectonic finite-element modeling has been set up to zoom into the Pollino range, indicated by the thin square in Figure 52(b). This makes it possible to verify whether the extension perpendicular to the fault, as in Figure 52(a), is coherent with tectonic strain rates. This is the case, in fact, as shown by the outward arrows indicating strain rates in terms of eigenvalues and eigenvectors, evaluated from the finite-element model, following the procedure described in Marotta and Sabadini (2004), providing an extension of 5 nanostrain year^{-1}. This extension at the regional scale of the

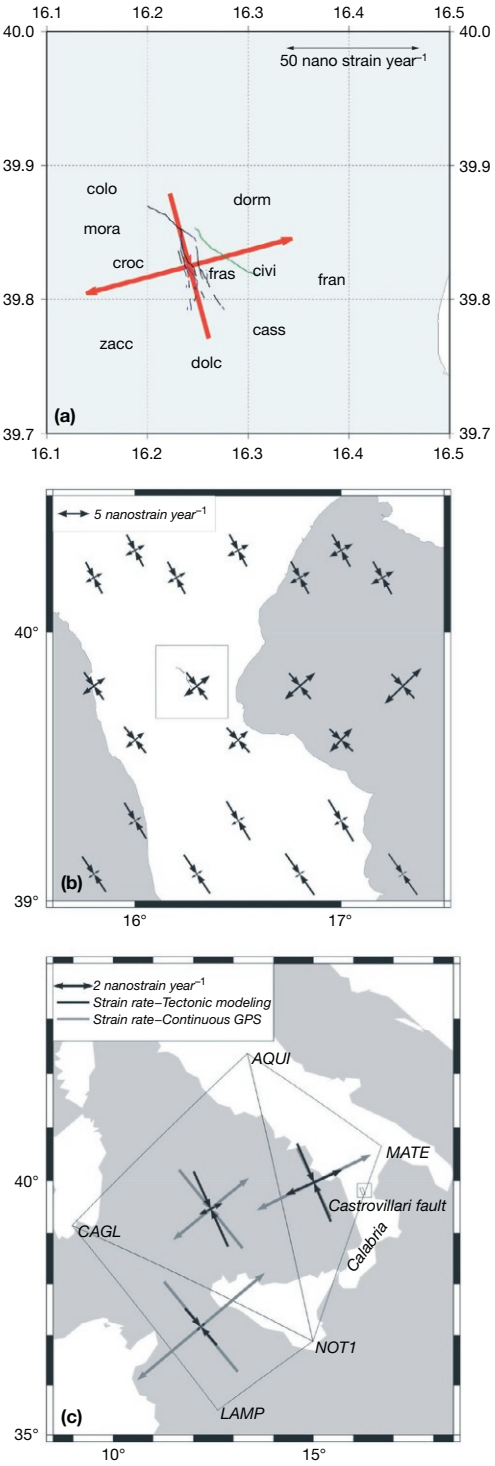

Figure 52 Panel (a), mean strain rates (e.g., in nanostrain year^{-1}, corresponding to a change in length of 1 part over 10^9, or 1 mm over 1000 km) from GPS surveying, at the ten GPS sites, *colo* (Coloreto), *croc* (Crocefisso), *dorm* (Dolcedorme), *mora* (Morano), *fras* (Frascineto), *civi* (Civita), *zacc* (Zaccalia), *dolc* (Dolcetti), *cass* (Cassano), and *fran* (Francavilla), in the Pollino range. The thin gray lines indicate the Castrovillari fault scarps (Cinti et al., 2002), attesting its recent activity and where trenches have been opened. The red arrows represent the principal strain-rate axes, converging for compression and diverging for extension. Strain rate does not include the contribution of *civi* station. Panel (b), strain rates from thin-sheet tectonic (finite-element) modeling; the Pollino range area is indicated by the square, while the Castrovillari fault is indicated by the thin line denoting the fault scarps. Panel (c), strain rate (in nanostrain year^{-1}) from continuous GPS (gray) and tectonic modeling (black). Converging arrows denote compression and diverging ones extension. Continuous GPS sites are AQUI (Aquila), CAGL (Cagliari), LAMP (Lampedusa), NOT1 (Noto), and MATE (Matera). The thin square zone in Calabria denotes the Pollino range area, including the Castrovillari fault (small rectangle). Redrawn from Figure 4 of Sabadini R, Aoudia A, Barzaghi R, et al. (2009) First evidences of fast creeping on a long-lasting quiescent earthquake normal-fault in the Mediterranean. *Geophysical Journal International* 179: 720–732. http://dx.doi.org/10.1111/j.1365 246X.2009.04312.x.

Pollino range is fully concordant with that of 3–6 nanostrain year^{-1} from continuous (2001–06) GPS, gray arrows, and from global-scale finite-element modeling (**Figure 52(c)**, black arrows) within the NOTO–MATE–AQUI triangle, evaluated for the strain rates of **Figure 52(b)**. The horizontal principal strain-rate axes of **Figure 52(a)** show an extension perpendicular to the strike of the fault in agreement with normal faulting and fully concordant with the extensional tectonics from thin-sheet modeling and continuous GPS. **Figure 52(a)** shows that strain rates at the scale of the fault are around 50 nanostrain year^{-1}, one order of magnitude higher than regional and tectonic strain rates.

Zooming into the rectangle of **Figure 52(b)** embedding the Pollino seismogenic zone, the surface projection of the Castrovillari normal fault is depicted by the rectangle of **Figure 53**, with the blue line indicating the fault scarps, from Cinti et al. (2002): this figure provides the DInSAR vertical velocity from ERS1 and ERS2 SAR images covering the period 1995–2000. The color scale ranges from the largest subsidence of −6 to −2 mm year^{-1} (blue) to the highest uplift of 4–7 mm year^{-1} (red). These vertical rates are derived from an interferogram stack applying an advanced DInSAR procedure separating the linear deformation component of the observed interferometric phases from other contributions such as the topographic and atmospheric ones, including orbital effects and phase noise (Biescas et al., 2007). The rates were estimated only over the pixels showing high coherence in the entire stack of processed interferograms. A broad subsidence overprints the surface projection of the hanging wall of the Castrovillari fault, whose right-hand border corresponds to the northwest–southeast trending thin line depicting the fault scarps; uplift stands over the footwall, in agreement with normal fault-like motion.

Figure 54 portrays the GPS campaign velocities and relative 1σ confidence error ellipses (in millimeters per year) in the Eurasian reference frame. The computed velocities, after datum shift to ITRF2005, were computed with respect to the Eurasian reference frame using the APKIM2005 model (Drewes, 2006). This GPS velocity field shows significantly nonzero velocities and a different behavior across the fault. The velocity vectors of the sites in the footwall (*dorm*, *civi*, *cass*, and *fran*) differ, in both magnitude and direction, from those in the hanging wall (*colo*, *mora*, *croc*, *zacc*, *dolc*, and *fras*). Assuming a homogeneous deformation field, the horizontal strain rates of **Figure 52(a)** have been computed via a least-square approach using the GPS velocities of each site of **Figure 54**.

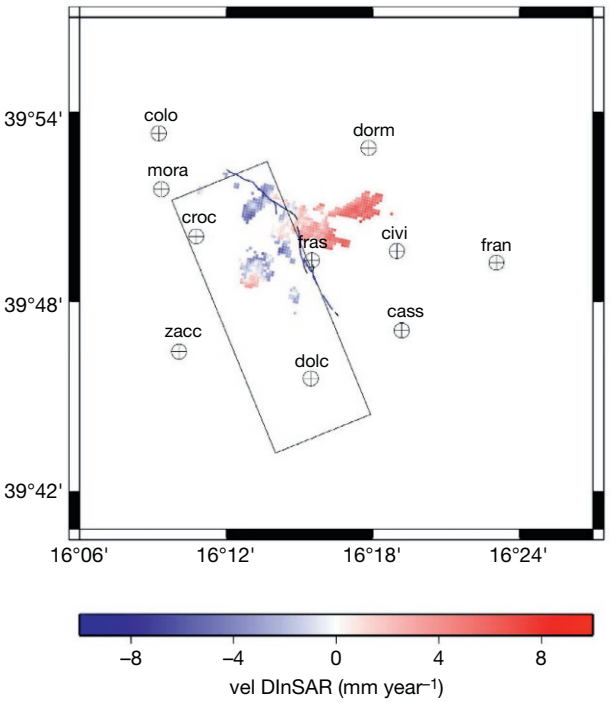

Figure 53 DInSAR vertical velocity from SAR images covering the period 1995–2000. Each pixel represents the unit of the SAR image, containing information on the amplitude and phase of the reflected radar signal. The surface projection of the Castrovillari normal fault is depicted by the rectangle, with the blue line indicating the fault scarps, from Cinti et al. (2002). GPS sites are also shown, as in **Figure 52**. Redrawn from Figure 2 of Sabadini R, Aoudia A, Barzaghi R, et al. (2009) First evidences of fast creeping on a long-lasting quiescent earthquake normal-fault in the Mediterranean. *Geophysical Journal International* 179: 720–732. http://dx.doi.org/10.1111/j.1365 246X.2009.04312.x.

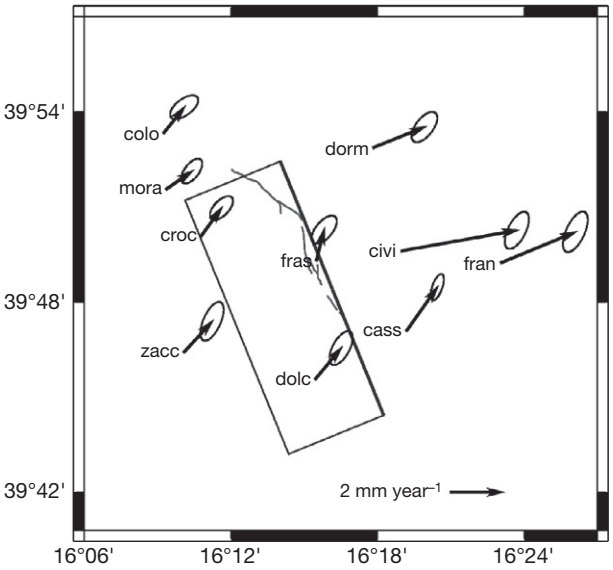

Figure 54 GPS campaign velocities in the Eurasian reference frame, defined by the geodetic plate kinematic model APKIM2005 and relative 1σ confidence error ellipses (in millimeters per year). Redrawn from Figure 3 of Sabadini R, Aoudia A, Barzaghi R, et al. (2009) First evidences of fast creeping on a long-lasting quiescent earthquake normal-fault in the Mediterranean. *Geophysical Journal International* 179: 720–732. http://dx.doi.org/10.1111/j.1365 246X.2009.04312.x.

Vertical and horizontal velocities of **Figures 53** and **54** are used for slip or creep rate inversion over the fault. A purely normal fault-like slip over the Castrovillari fault is assumed in accordance with the most updated Database of Individual Seismogenic Sources (DISS Working Group 2007) and Basili et al. (2008) and based on active tectonics data from Cinti et al. (2002). Fault parameters and geometry are thus characterized by length and width of the fault of 16.0 and 12.0 km and strike, dip, and rake of 157.0°, 60.0°, and 270.0°, respectively. The lack in literature of a variable rake model for the Castrovillari fault and the dominant extensional behavior over the fault suggests us to adopt a simple purely normal-faulting mechanism.

Vertical (DInSAR) and horizontal (GPS) constant rates from the linear fit of the data are interpreted in terms of relative motion across the fault of its southwest hanging wall, with respect to the northeast footwall. As for the surface data, this relative motion is constant in time, at least for the time window of surveying, and is thus interpreted in terms of slip or specifically in terms of creep, in analogy with the already-known cases of strike-slip Californian fault and NAF. A linear model is thus assumed both for surface data and, consequently, for slip over the fault. A brief description of the inversion scheme, which images creep over the fault from surface velocity data, is now provided.

Creep over the fault is thus portrayed in terms of slip over the Castrovillari fault, as seen in the perpendicular direction from the western, or Tyrrhenian, side of the fault, which is the subsiding hanging wall. The fault is subdivided into 1 km × 1 km patches being the reference fault 16 km × 12 km, the slip rate over each patch corresponding to a component of the vector of model unknowns. Surface velocities at the observation points, both DInSAR and GPS, are then evaluated as a linear superposition of elementary surface signals due to each patch, calculated on the basis of the forward Okada elastic half-space model (Okada, 1992). Inversion is carried out following Occam's inversion method (deGroot-Hedlin and Constable, 1990), which states that in the inversion, given an acceptable degree of misfit between modeled results and observed data, the less complex solution has to be chosen. Complexity of the solution is measured by a parameter, namely, roughness, that quantifies slip changes among the patches. Roughness is chosen in such a way to make the slip pattern over the fault rather smooth, in order to avoid localized, probably unrealistically detailed, spots of slip; this roughness is one order of magnitude smaller than the one used for slip pattern due to coseismic displacements (Dalla Via et al., 2006), expected to be larger with respect to the creep one. In this perspective, we allow for the possibility of slip rates different from zero at the fault edges, in full accordance with dislocation theory, which underlies the forward modeling, and with the limited fault dimensions, obtained from active tectonic data.

In **Figures 55** and **56**, a detailed analysis of the creep pattern over the fault, separately for DInSAR and GPS inversion, is

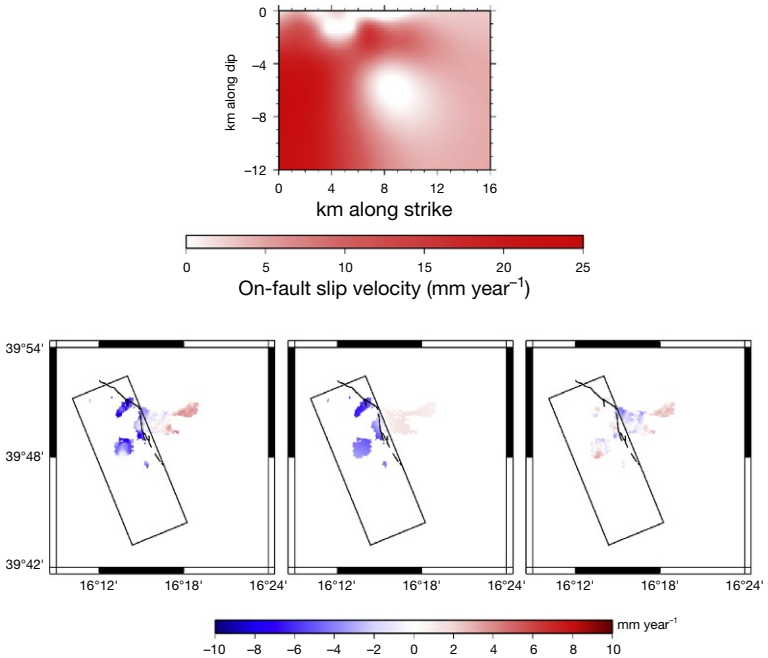

Figure 55 Slip rate over the Castrovillari fault from DInSAR, top panel, with the left-hand border of the fault plane corresponding to its northern edge and the right-hand border to the southern one, as in the following panels. At the bottom panel, DInSAR data including an offset (left-hand panel), model results (center panel), and misfit (right-hand panel). Roughness is 1 mm km^{-1}, the offset is −2.7 mm year^{-1}, and other parameters can be found in Sabadini et al. (2009), from which the figure is redrawn. The maximum slip rate is 24 mm year^{-1} while the average is 8.5 mm year^{-1}. Redrawn from Figure 5 of Sabadini R, Aoudia A, Barzaghi R, et al. (2009) First evidences of fast creeping on a long-lasting quiescent earthquake normal-fault in the Mediterranean. *Geophysical Journal International* 179: 720–732. http://dx.doi.org/10.1111/j.1365 246X.2009.04312.x.

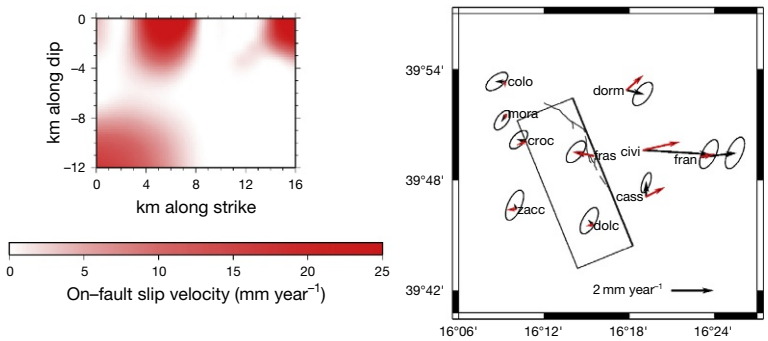

Figure 56 Slip rate over the Castrovillari fault from GPS (left-hand panel). In the right-hand panel, GPS velocities (black arrows), including 1σ error ellipses and modeled ones (red arrows). The offset with respect to APKIM2005 is detailed in Sabadini et al. (2009), from which the figure is redrawn. The maximum slip rate is 35.3 mm year^{-1}, while the average slip is 3.7 mm year^{-1}. Only six patches show a slip larger than 20 mm year^{-1}. Roughness is the same of **Figure 55**. Redrawn from Figure 7 of Sabadini R, Aoudia A, Barzaghi R, et al. (2009) First evidences of fast creeping on a long-lasting quiescent earthquake normal-fault in the Mediterranean. *Geophysical Journal International* 179: 720–732. http://dx.doi.org/10.1111/j.1365 246X.2009.04312.x.

carried out, enabling the reader to capture the intimate nature of fault creep, reaching in particular a deep insight into its variability over the fault surface in terms of data coverage on the Earth's surface.

Since DInSAR vertical motions are evaluated with respect to an arbitrarily fixed zero, in our case given by an average velocity of four points placed near the center of the measuring area, as a general rule, it is allowed to add a uniform vertical velocity offset. This offset is chosen in such a way to balance the positive and negative residuals between data and vertical rates obtained from the forward model, since the forward model is not likely carrying the same zero vertical velocity used for DInSAR referencing; this offset can be chosen to minimize the misfit.

Figure 55 (top panel) shows the inverted creep rate distribution over the Castrovillari fault for normal fault-like motion using DInSAR velocities. The rates are given in millimeters per year, according to the color scale, over the patches of the fault. The largest amount of slip is localized in the northernmost (left-hand side) part of the fault from 0 to 7 km along-strike, with maximum rates of about 20 and 24 mm year^{-1} over a limited number of patches and an average one of 8.5 mm year^{-1}. From the vertical rate pattern, it is notable that the large slip rates in the northernmost part of the Castrovillari

fault are required to accommodate the large subsidence in the fault's hanging wall, between *mora* and *fras* (Figure 53). Slip rate is subject to a substantial decrease in the half-southern (right-hand side) part of the fault, with a central locked zone. Creep rates do not vanish at the left and bottom edges of the fault mainly for three reasons: first, dislocation theory allows for displacement discontinuities at the edges; second, by limiting roughness, slip is smoothed over the fault, which leads in turn to slip discontinuities between the fault and its surrounding; and third, fault dimensions inferred from active tectonics could underestimate the creeping surface.

The three panels at the bottom of Figure 55 show the data, including the offset (left-hand panel), the modeled vertical rates at the Earth's surface (central panel), and the misfit (right-hand panel). The average misfit, that is, the average of the difference between data and model values at each pixel, is very low, of the order of 0.01 mm year^{-1}; the model reproduces well the data, although some deviations, of about 1 mm year^{-1}, remain in the hanging wall. The pattern of vertical rates well reproduces the regions of subsidence and uplift, the former affecting the hanging wall. The model shows the tendency for a sharper transition between subsidence and uplift when compared to the broader pattern from DInSAR analysis in the top left-hand panel. The large slip rates noted above in the top panel in the northern and deepest part of the fault is responsible for the large subsidence (blue) observed in these DInSAR model results and, in conjunction with the locked central sector of the fault, for the smooth uplift (red) in the footwall.

For GPS inversion, only 20 horizontal displacement components are available, but inversion is well determined by the regularization conditions imposed by assuming an upper bound for the allowed average slip gradient over the fault. Similarly to the vertical offset of the DInSAR case, a horizontal offset, with respect to the geodetic plate kinematic model, is introduced in the north and east horizontal displacements, in order to minimize the misfit between GPS data and model predictions, since the zero horizontal displacements assumed for GPS do not necessarily coincide with the zero motion predicted by modeling. Except for the slip-rate spot in the top, right-hand part of the fault, required to accommodate *dolc*–*cass* relative motion, Figure 56 shows that GPS is concordant with DInSAR in terms of localization of the largest amount of slip in the northernmost (left-hand panel) part of the fault from 0 to 7 km along-strike, with the highest rates of about 20 mm year^{-1}. Differently from DInSAR, slip is not uniformly distributed in depth, but it is rather localized at the top and bottom zones of the northern part of the fault. These slip rates are required by the large extension between *colo*, *mora*, *croc*, and *fras* on the hanging wall with respect to *civi*, *dorm*, and *fran* in the footwall, characterizing the normal fault-like pattern of the horizontal motions in the Castrovillari area. The deep creep, at 8–12 km, is required to accommodate the extension between *colo*, *mora*, and *croc* with respect to *dorm*, whose distance is comparable with fault dimensions, while the shallow creep in the northern part accommodates the *fras* with respect to *civi* and *fran* extensions, whose distance is smaller than fault dimensions.

The lack of creep at the 4–8 km depth, from GPS inversion differently from DInSAR's one, could thus be ascribed to a nonuniform coverage of GPS distribution at the Earth's surface and to incomplete DInSAR data coverage of the surface area overlying the fault. The slip-rate spot in the southernmost (right-hand panel) part of the fault at 14–16 km along the strike, at the very shallow depth of about 2 km, is required to accommodate the motion between the *cass* and *dolc* sites. Within the creeping northern part of the fault, GPS shows the tendency to focus the highest creep rates at shallow depths with respect to DInSAR, the latter being more uniformly distributed in depth, suggesting a different depth-resolving power from GPS horizontal and DInSAR vertical motions.

The incomplete coincidence of slip-rate patterns from DInSAR and GPS could also be partially ascribed to the different data coverage of GPS and DInSAR data at the Earth's surface. As a matter of fact, there is a spot of subsidence in the vertical DInSAR pattern, which is in fact responsible for some slip in the part of the fault between 8 and 12 km, with respect the locked central and southern parts of the fault, but it is evidently not sufficient to drive the larger slip required by the GPS motion between the *cass* and *dolc* more to the south. The two techniques are recording fast aseismic creeping within the seismogenic layer with a persistent velocity-weakening locked southern part of the fault for at least a decade, the entire time span covered by the DInSAR and GPS data. It is not possible to establish when creeping started on the fault, and a detailed comparison between DInSAR and GPS creep inversions may indicate a different depth-resolving power of the two techniques or an upward migration of creep, the latter suggesting that creep is diminishing, since a smaller number of patches are affected by creep from GPS with respect to DInSAR.

The magnitude of the vectors, except for *civi* and *fran*, is well reproduced within the 1σ ellipses (red arrows), as shown in Figure 56 (right-hand panel), when the slip rates resulting from the inversion in Figure 56 (left-hand panel) are used in the Okada-based forward model to reproduce the surface geodetic deformation. Azimuths are more severely affected by modeling, particularly at the *dorm* and *cass* sites. It is likely that pure normal faulting does not account for some 3-D aspects of fault creep.

The combined use of DInSAR and GPS data has made possible to capture the first evidences of fast creeping over a normal fault in the Mediterranean, the Castrovillari fault, during its interseismic and possibly preseismic deformation phases. Creep occurs over all depths of the seismogenic layer, embedded in a generally slowly deforming zone. The velocity creeping zone reaches rates as high as 20 mm year^{-1}, within an average background of 3–9 mm year^{-1}, and limits to the north a southern part that shows the tendency to be locked, from which an earthquake could depart: these rates are higher than the average slip rate of 1 mm year^{-1} of the Castrovillari fault from paleoseismology (Cinti et al., 2002), suggesting that we are detecting a fast transient characterizing the interseismic or preseismic phases of the fault. The creep rates are comparable with those along the (strike-slip) NAF (Ambraseys, 1970; Cakir et al., 2005): creep is now first evidenced and shown to be feasible also for normal faulting. Although the onset of creep over the Castrovillari fault cannot be established, creep over there is a long-lasting phenomenon, of at least one decade, the time interval covered by DInSAR-GPS data: such a timescale is suggested herein to characterize transient phenomena for

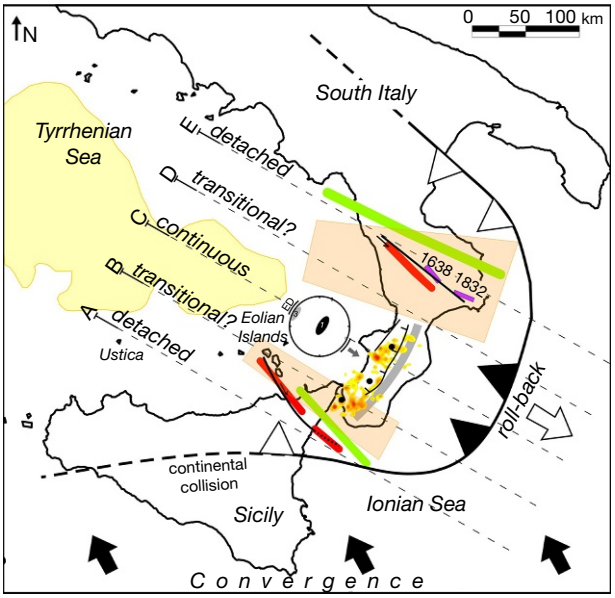

Figure 57 Tectonic setting of the southern Apennines, including the Pollino seismogenic zone in the north. Redrawn from Figure 16 of Neri G, Marotta AM, Orecchio B, et al. (2012) How lithospheric subduction changes along the Calabrian Arc in southern Italy: Geophysical evidences. *International Journal of Earth Sciences (Geologische Rundschau)* 101:1949–1969. http://dx.doi.org/10.1007/s00531-012-0762-7.

normal faulting. This decade creep seems in fact to reflect another similarity with the strike-slip faults, since the former over the NAF has also been observed to be long-lasting, over decades (Cakir et al., 2005). These findings are of importance for establishing that creep is a general rule for active faults, not limited to strike-slip environments. They also shed light on the mode in which deformation is distributed among the various parts of the whole seismogenic zone or single fault, which has of course implications on the pattern of stress built-up and thus earthquake generation. Aseismic slip can in fact exert a strong influence on the moment budget of faults, which needs to be quantified for accurate seismic hazard estimates; stress redistribution in the crust due to creep affects the locations of future earthquakes.

The Pollino seismogenic zone is at the northern boundary of a complex subduction environment, as sketched in Figure 57, redrawn from Neri et al. (2012), showing the main tectonic engines represented by NW–SE plate convergence and gravity induced southeastward rollback of the Ionian lithosphere subducting beneath the Tyrrhenian. The subduction modes detected along the profiles A–E by the intermediate-depth seismic tomography and gravity thermomechanical modeling in the quoted paper are reported, providing evidences of a change from a continuous slab, black triangles, into a detached slab, green thick lines, with the Pollino seismogenic zone north of it, which suggests a possible explanation for the extensional tectonics over there.

The subduction mode changes along the Arc from 'continuous' (C) to 'detached' (E) slab modes; dashed lines contour the transitional area D between sectors C and E according to gravity analysis, such as those of Figure 58 (left), providing in panel (b) the surface residual gravity anomaly predicted by the 2-D continuous-slab thermomechanical model (black line) and by the 2-D detached-slab model (green line) as that in panel (a), detached between 200 and 300 km depth, in agreement with the seismic tomography along the A and E profiles of Figure 57. The general subsidence of the residual gravity profile for the detached slab, green line with respect to the black one, is also visible in the same quantity, that is, the residual gravity anomaly, obtained from observed data along profiles perpendicular to the arc when moving from the center of the arc to the north over the detached slab; the residual gravity anomaly from observed data is obtained by subtracting from the observed Bouguer anomaly the component due to isostatic compensation evaluated from the compensated Moho corresponding to the bathymetry, assuming a simple Airy model (see Figure 7 in Neri et al., 2012). Details on the thermomechanical modeling are found in Marotta et al. (2007). The dipolar gravity pattern of Figure 58 (left) is typical for all subduction zones. The continuous-slab thermomechanical model, black (Figure 58 left, panel (b)), where the gap of panel (a) is filled, is based on the tomography model of Figure 58 (right, from Neri et al., 2012) along the C profile of Figure 57.

After the analysis shown in Section 6.04.6.1, which appeared in the international literature in 2009 (Sabadini et al., 2009), the Pollino seismogenic zone, indicated by the square in Figure 52(c), has been struck by a normal fault Mw = 5.2 earthquake on 26 October 2012, epicenter in Mormanno, a locality around 10 km roughly northwest with respect to the site of Morano (the *mora* (Morano) site of Figures 52–56). This earthquake did not occurred in the southern part of the Castrovillari fault of the previous figures, which, according to our results, was already prone to generate a sizable earthquake, which means magnitude of Mw = 5.0 at the least, in the white part of the fault plane of Figures 55 and 56: although the epicenter of this quake was northwest with respect to the locked part of the Castrovillari fault as envisaged by our findings, the 50 nanostrain year^{-1} measured in the area (Figure 52(a)) suggests that this large extensional activity is more widespread with respect to the SISMA surveyed area, so that the results of this section represent an underestimate, in space, of the seismic hazard of the whole Pollino seismogenic zone. These findings indicate that large strain rates in surveyed seismogenic zones overriding the regional strain rate from the steady-state background tectonic activity, as for the clear case shown in the figure, must be taken as indicators that the seismogenic zone itself is ready to generate earthquakes.

Similar arguments are applicable to another portion of the Apennines in the Italian Peninsula, struck on 20 May 2012 by a thrust fault Mw = 5.9 earthquake in its northern part, in Emilia-Romagna, at the southern boundary of the Po Plain embedded between the Apennines and the Alps.

Regarding this issue, Figure 59 compares the triangular strain-rate eigenvectors predicted by the thin-sheet finite-element model *NU* model (red bars for compression and blue bars for extension) of Marotta and Sabadini (2008), forced at the bottom by the NUVEL-1A (DeMets and Dixon, 1999) velocity boundary conditions applied at the southern African–Eurasian boundary. These computational strain rates are compared with the geodetically retrieved ones from GPS ITRF2005 solutions according to Marotta and Sabadini (2008)

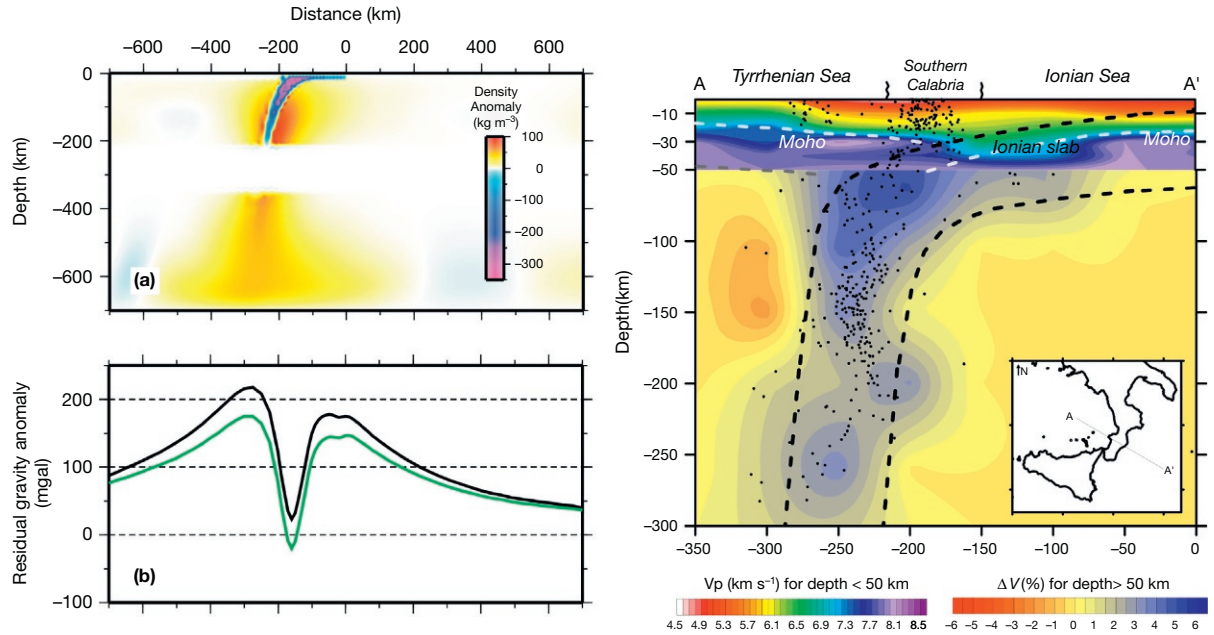

Figure 58 Deep density anomaly obtained assuming the mechanical rupture of the subducted slab between 200 and 300 km depth. Black and green curves show the surface gravity anomalies predicted by the 2-D detached-slab model (green line) compared to the surface gravity anomalies predicted by the 2-D continuous-slab model (black line). Redrawn from Figures 6 and 13 of Neri G, Marotta AM, Orecchio B, et al., (2012) How lithospheric subduction changes along the Calabrian Arc in southern Italy: Geophysical evidences. *International Journal of Earth Sciences (Geologische Rundschau)* 101: 1949–1969. http://dx.doi.org/10.1007/s00531-012-0762-7.

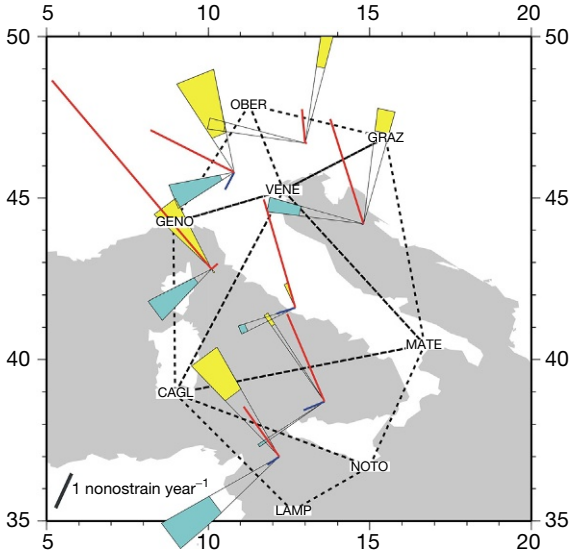

Figure 59 Triangular strain-rate eigenvectors predicted by model *NU* (red bars for compression and blue bars for extension), compared with the geodetic triangular strain-rate eigenvectors from ITRF2005 (available at http://lareg.ensg.ign.fr/ITRF_solutions/2005//ITRF2005.php), where yellow indicates compression and cyan extension, with the size of the circular sectors proportional to the magnitude of the eigenvector magnitude and azimuth uncertainties, in nanostrain year^{-1}. Redrawn from Figure 10 of Marotta AM and Sabadini R (2008) Africa–Eurasia kinematics control of long-wavelength tectonic deformation in the Central Mediterranean. *Geophysical Journal International* 175: 742–754. http://dx.doi.org/10.1111/j.1365-246X.2008.03906.x.

(their Figure 1(b)), where yellow indicates compression and cyan extension. The 2012 Emilia-Romagna earthquake epicenter is within the GENO–OBER–VENE triangle, roughly west of VENE. Although modeling overestimates the compressive component of the triangular strain rate in the GENO–CAGL–VENE and CAGL–MATE–VENE triangles, within the triangle GENO–OBER–VENE embedding the Po Plain where we are interested in the estimate of the strain rate to provide arguments for the 2012 Emilia-Romagna earthquake, compression is well reproduced in amplitude, with discrepancy limited to the azimuth. Figure 60 portrays a different perspective of the deformation within the Italian Peninsula with respect to Figure 59, showing the baseline rates predicted by model *NU*, as in Figure 59, compared with the baseline rates obtained from ITRF2005 (yellow for shortening and cyan for elongation); red indicates predicted shortening, whereas blue indicates predicted elongation, from the same thin-sheet finite-element model as for Figure 59.

In general, the predicted deformation has the same style as indicated by the data, as for CAGL–LAMP, CAGL–NOTO, GENO–NOTO, VENE–NOTO, VENE–MATE, GENO–CAGL, VENE–GRAZ, OBER–VENE, and GRAZ–MATE baselines shortening while CAGL–MATE, GENO–OBER, and LAMP–NOTO baselines undergoing elongation, in agreement with GPS baseline rates. The baseline and strain-rate patterns of Figures 60 and 59 show that the African–Eurasian convergence, driven in these figures by the NUVEL-1A model, is majorly responsible for the dominant compression within the Po Plain area, embedded between the northern Apennines and the Alps.

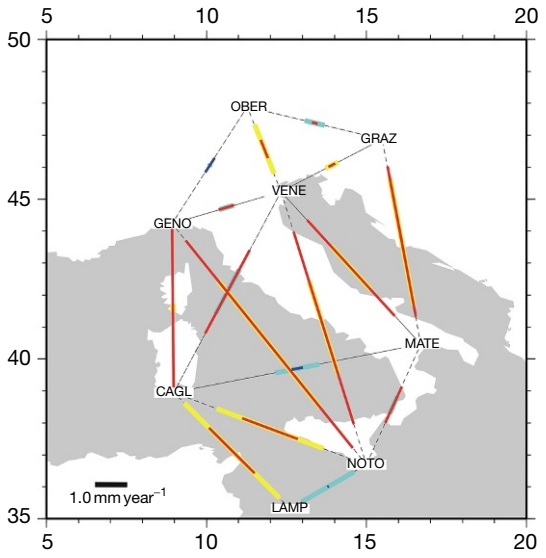

Figure 60 Baseline rates predicted by model *NU*, compared with the baseline rates obtained from ITRF2005 (yellow for shortening and cyan for elongation). Red indicates predicted shortening, whereas blue indicates predicted elongation. Redrawn from Figure 9 of Marotta AM and Sabadini R (2008) Africa–Eurasia kinematics control of long-wavelength tectonic deformation in the Central Mediterranean. *Geophysical Journal International* 175: 742–754. http://dx.doi.org/10.1111/j.1365-246X.2008.03906.x.

Figures 59 and 60, fully concordant with the previous analysis of Figure 34 (second panel) based on a different GPS data set, having been obtained from the Centre for Space Geodesy (CGS) in Matera (Devoti et al., 2002) rather than from the updated and enriched ITRF2005 data set, show that the Po Plain, embedded within the GENO, OBER, and VENE sites, is subject to a dominant compression in the north–north–west direction of about 3 nanostrain year^{-1} (Figure 59) and around 2 mm year^{-1} baseline shortening (Figure 60), confirming the style of compression of Figure 34 (second panel), where the compression in the triangle TORI–BRGZ–VENE, about 7 nanostrain year^{-1}, is in the same direction and is comparable in terms of amplitude to the extension perpendicular to the central and southern Apennines, as also shown in Figure 34 (second panel), in the triangle PG–MATE–COSE of about 10 nanostrain year^{-1}. This extensional pattern well agrees with the most recent findings of Figure 52 (b) and 52(c), where the strain rate is 3–5 nanostrain year^{-1} in the region surrounding the Pollino seismogenic region, representative of the whole southern Apennines. As for the central and southern Apennines, struck by the 2009 L'Aquila Mw = 6.0 earthquake, and the Pollino seismogenic zone, struck by the 2012 Mormanno Mw = 5.2 earthquake, the Po Plain too has to be considered an active seismogenic zone, on the basis of these strain-rate values comparable in amplitude to those of the Central Apennines. Neglecting these first evidences of high strain rates in the northern Apennines and Po Plain, known since the works of Jiménez-Munt et al. (2003) and Marotta and Sabadini (2004, 2008) and the results of the SISMA project (SISMA, 2011), the latter reporting on the strain rate in the northern Apennines in greater details with respect to Figures 34 and 59, has led to the severe underestimation of the seismic hazard in this region, struck by the Mw = 5.9 earthquake that caused the collapse of civil and industrial infrastructure and human losses, since the seismic hazard described by the official map (http://zonesismiche.mi.ingv.it/mappa_ps_apr04/italia.html) underestimates the potential of this seismogenic zone, not accounting for the earlier-mentioned results on present-day, high strain and deformation rates of that area at the edge of the northern Apennines.

6.04.7 The 2004 Sumatra and 2011 Giant Tohoku-Oki Earthquakes

Mass redistributions caused by great earthquakes are made visible nowadays by their long-wavelength gravity signature, detectable by space gravity missions, such as the GRACE space mission (Gross and Chao, 2006): these gravity data provide a new physics for understanding the behavior of the plates during the occurrence of extreme natural events, such as giant earthquakes of magnitude Mw higher than 9.0. The scientific community has used GRACE data for studying the three major seismic events in the past decade, the 2004 Sumatra (Broerse et al., 2011; Cambiotti et al., 2011; de Linage et al., 2009; Han et al., 2006; Panet et al., 2007), the 2010 Maule (Han et al., 2010; Heki and Matsuo, 2010), and the 2011 Great Tohoku-Oki (Cambiotti and Sabadini, 2011, 2013; Han et al., 2011; Matsuo and Heki, 2011; Zhou et al., 2012) earthquakes. These megathrust earthquakes occur within subduction environments of fast converging oceanic and continental plates and cause volume changes of rocks in the region surrounding the fault, as well as deformation of the Earth surface and internal layer boundaries carrying density contrasts. Furthermore, due to the uplift of the ocean floor, they also displace ocean water away from the near field, the gravitational effect of which is comparable with that from mass rearrangement within solid Earth (Broerse et al., 2011; Cambiotti et al., 2011; de Linage et al., 2009). It is not possible to treat the topic of plate deformation without considering the giant earthquakes that struck our planet in the most destructive way, affecting the margins of the plates at the fast converging zones of the Indian and Pacific Oceans. Mass changes due to these events have been so huge to be detectable from space in terms of permanent signatures affecting the Earth's gravity field.

6.04.7.1 Modeling the 2004 Sumatra Earthquake

The coseismic geoid and gravity anomalies from the 2004 Sumatra earthquake are obtained from a new, compressible self-gravitating Earth model that is fully realistic as it builds on PREM (Dziewonski and Anderson, 1981) and represents the elastic limit of viscoelastic models, recently used for PGR studies (Cambiotti et al., 2010) and developed for coseismic studies by Smylie and Manshina (1971) and Sun and Okubo (1993). This approach differs from that followed by Gross and Chao (2006) and de Linage et al. (2009), both using compressible models based on a free oscillation scheme. The gravitational part of the phenomenon is dealt with self-consistently and the effects of compressibility are taken into account both in the initial state and during the perturbations (Cambiotti and Sabadini, 2010), on the basis of the Runge–Kutta integration in the radial variable of the differential equations describing momentum conservation and self-gravitation.

Because the gravitational effect of sea-level feedback has been important for the 2004 Sumatra earthquake (de Linage et al., 2009), a self-consistent treatment of the global ocean layer of PREM is included. In this way, the approaches used by Han et al. (2006) and de Linage et al. (2009) are refined in the results shown in this section although, from a quantitative point of view, the approach used in the present analysis does not significantly change the results presented by these authors.

This novel theoretical treatment in the modeling is accompanied by new efforts in the treatment of the GRACE data time series that are aimed at optimizing the estimate of the coseismic gravitational component of the 2004 Sumatra earthquake, thus providing a realistic comparison between observations and models. The 2004 Sumatra earthquake was one of the strongest nonperiodic gravity variations that occurred at the Earth's surface in the last decade. However, the analysis of the earthquake signature in GRACE data is quite challenging because of the steplike shape of the phenomenon. Additional contamination may originate from other phenomena occurring in the Sumatran region, such as hydrologic and residual ocean circulation cycles. Moreover, the peculiar noise associated with GRACE data is particularly strong at equatorial latitudes, and its north–south shape is troublesome. Particular attention has been devoted at removing those signals other than the coseismic jump from GRACE data time series to quantify the asymmetry between the negative coseismic gravity anomaly northeast of the Sumatran trench and the positive one southwest of it, which has been proposed by de Linage et al. (2009) to be due to the sea-level feedback. This asymmetry is then discussed in terms of the physical processes that are responsible for this feature that appeared for the first time in the study of the Earth's gravity field, and similar to the concept suggested by Gross and Chao (2006) for space-based Earth rotation measurements, gravity data from the GRACE space mission are exploited to help constraining the seismic source model of the 2004 Sumatra earthquake obtained by centroid–moment–tensor (CMT) source analyses.

Figure 61 shows the coseismic geoid anomalies for compressible self-gravitating Earth models based on PREM (Dziewonski and Anderson, 1981), both eliminating (**Figure 61(a)**) and including (**Figure 61(b)**) the ocean layer of PREM; these models are named S-PREM (Solid PREM) and O-PREM (Ocean PREM). In order to gain insight into the physics of the coseismic gravitational perturbations, we first consider geoid anomalies rather than gravity ones, in order to compare them with radial displacements and to quantify sea-level variations, which are the difference between the geoid variation and the radial displacement of the sea bottom and describe the water redistribution responsible for the sea-level feedback on the geoid anomalies themselves. Results shown in the following are based on the seismic source model of Tsai et al. (2005), which is composed of five point-like sources with total seismic moment $N_s = 1.17 \times 10^{23}$ N m, and on the use of an isotropic 350 km Gaussian filtering (Wahr et al., 1998). Although more realistic slip distributions over the fault are typically used to explain seismic waves and ground motions from GPS (Ammon et al., 2005), the along-strike five seismic source model used by Tsai et al. (2005) is adequate since, at the limited spatial resolution of GRACE data, the difference with respect to more realistic slip distributions is expected to be small. Slip distribution along dip instead affects the long-wavelength seismic signal, a sensitivity that can be used to obtain information about the depth at which the largest seismic

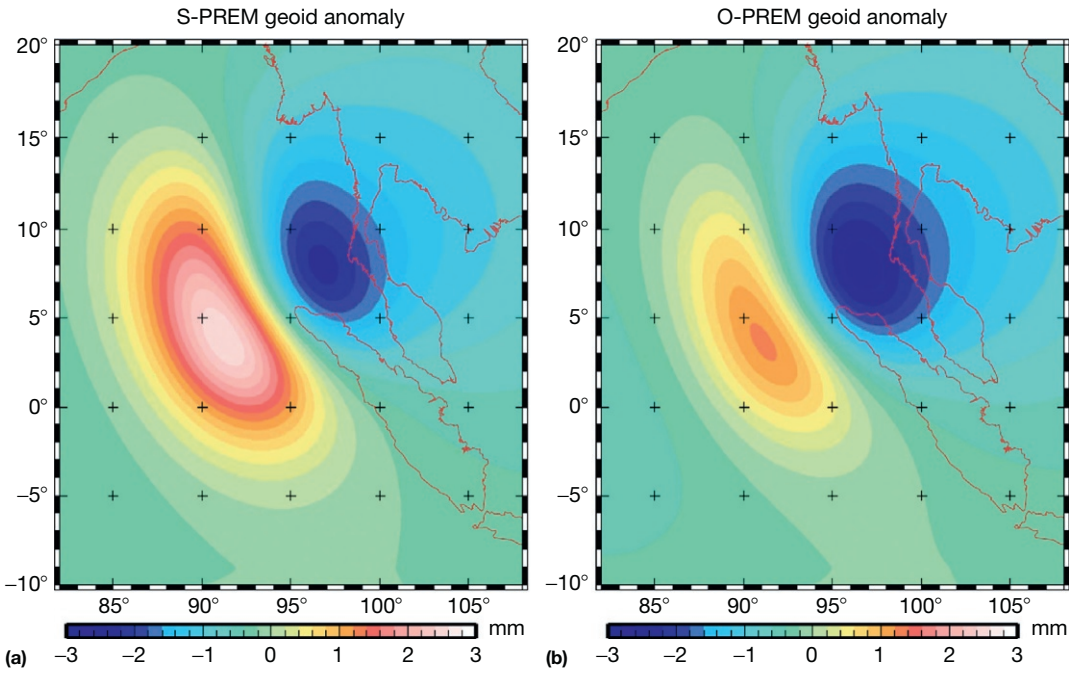

Figure 61 Coseismic geoid anomalies for compressible (a) S-PREM and (b) O-PREM, after the 350 km Gaussian filtering. Redrawn from Figure 1 of Cambiotti G, Bordoni A, Sabadini R, Colli L (2011) GRACE gravity data help constraining seismic models of the 2004 Sumatran earthquake. *Journal of Geophysical Research* 116: B10403. http://dx.doi.org/10.1029/2010JB007848.

moment has been released. To better isolate the main features of the coseismic phenomenon, the maximum and minimum geoid anomalies deserve particular attention to address the main physical processes affecting the asymmetry coefficient AS, defined as the ratio between the absolute values of the minimum negative and maximum positive geoid anomalies.

For S-PREM, the pattern of geoid anomalies is bipolar as expected for a dip-slip source within a spherically symmetrical, self-gravitating Earth model (Sun and Okubo, 1993); maximum and minimum geoid anomalies are +2.57 and −2.28 mm, respectively, and the asymmetry coefficient is AS = 0.88. The positive geoid anomaly is slightly higher in the absolute value than the negative one. For O-PREM, maximum and minimum geoid anomalies of +1.24 and −2.52 mm are obtained leading to an asymmetry coefficient AS = 2.03.

The difference between the two models is the sea-level feedback to the geoid anomalies, which is obtained by subtracting the geoid anomalies for O-PREM (**Figure 61(b)**) from those for S-PREM (**Figure 61(a)**) and is negative almost everywhere as shown in **Figure 62**. It is of the same order of magnitude of the geoid anomalies for S-PREM, with a minimum value of −1.36 mm. In order to better understand this issue, in **Figure 63**, we show the radial displacements at the solid-Earth surface for both S-PREM (**Figure 63(a)**) and O-PREM (**Figure 63(b)**), after the 350 km Gaussian filtering for the sake of comparison with the geoid anomalies shown in **Figure 61**.

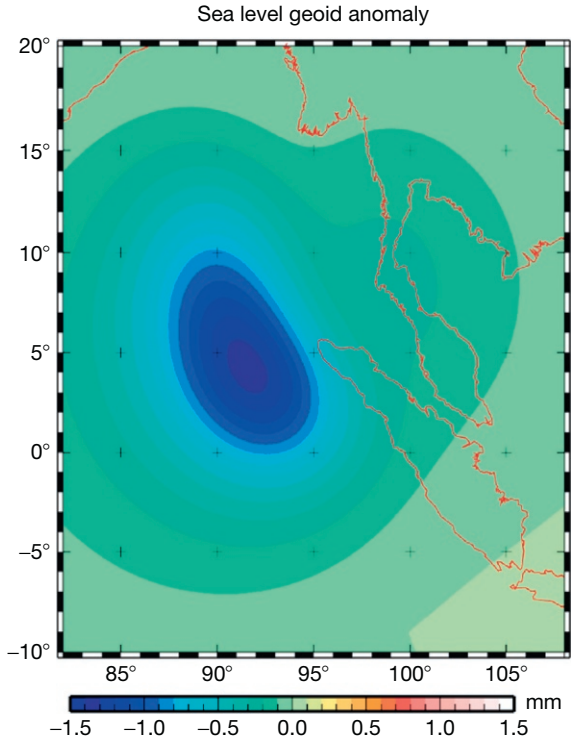

Figure 62 Coseismic geoid anomalies due to the sea-level feedback, obtained by subtracting compressible O-PREM and S-PREM geoid anomalies shown in **Figure 61**, after the 350 km Gaussian filtering. Redrawn from Figure 2 of Cambiotti G, Bordoni A, Sabadini R, Colli L (2011) GRACE gravity data help constraining seismic models of the 2004 Sumatran earthquake. *Journal of Geophysical Research* 116, B10403. http://dx.doi.org/10.1029/2010JB007848.

Note (**Figure 63(a)**) that the predicted maximum uplift, +93.1 mm, has an absolute value that is much larger than the maximum down-drop, −18.3 mm, by about a factor of 5 for S-PREM. Furthermore, the loading due to water redistribution has a negligible effect on the radial displacement because the maximum uplift, +97.0 mm, and down-drop, −18.6 mm, for O-PREM (**Figure 63(b)**) differ from those for S-PREM by less than 3%. These differences are, however, comparable with the geoid anomalies shown in **Figure 61**. The fact that the radial displacement is larger than the geoid anomaly by almost two orders of magnitude indicates that the coseismic sea-level variation is mainly due to the variation of the topography rather than that of the geoid and that the uplifted crust displaces away the ocean water, thus reducing the geoid anomalies in the near field of the 2004 Sumatra earthquake, in agreement with de Linage et al. (2009) who first suggested that the asymmetry toward the negative pole of the coseismic gravity anomalies observed in GRACE data is due to the sea-level feedback.

6.04.7.2 The GRACE Data

The peculiar steplike shape of the signature due to an earthquake is quite difficult to resolve in gravitational data analyses using standard approaches. The one-month time resolution of the GRACE data is the highest ever achieved by a satellite-only campaign on gravity variations, but it still poorly resolves coseismic phenomena in detail due to contamination from postseismic effects and from any other phenomena that occurred in the same geographic area during and immediately after the earthquake. Moreover, the peculiar noise of GRACE data, the so-called stripes, is particularly strong at equatorial latitudes; thus, its typical north–south shape can make data in the Sumatran region less clear. A good treatment of the stripes is therefore important. Among the various solutions proposed recently, the anisotropic filtering described by Kusche (2007) and Kusche et al. (2009) has been used to extract the earthquake gravity signal. Kusche et al. (2009) provide three anisotropic filters with different spatial resolutions, and to better address the main features of the local scale signature of the 2004 Sumatra earthquake, we have chosen the DDK3 filter at the highest spatial resolution. Depending on the comparison criterion, this filter is roughly equivalent to an isotropic Gaussian filter of about 240–330 km half-width, close to the limit of the GRACE nominal resolution; the main features of the 2004 Sumatra earthquake as recorded in GRACE data are provided on the basis of the gravity anomaly representation. The other natural choice, the geoid representation, which is more global, is prone to leakage of signals from nearby regions as for the case of hydrology: the gravity anomaly representation is less sensitive to this kind of contamination.

GRACE level 2 data are processed and provided to the scientific community by three official analysis centers: the Center for Space Research (CSR, University of Texas at Austin), the GeoForschungsZentrum (GFZ, Potsdam), and the Jet Propulsion Laboratory (JPL, California Institute of Technology). The solutions that they provide are of similar quality, though there are some differences. In order to optimize the information from these different solutions, the analysis is performed on the average of CSR and GFZ data, for each (common) month of the two time series. Separate usage of the two time

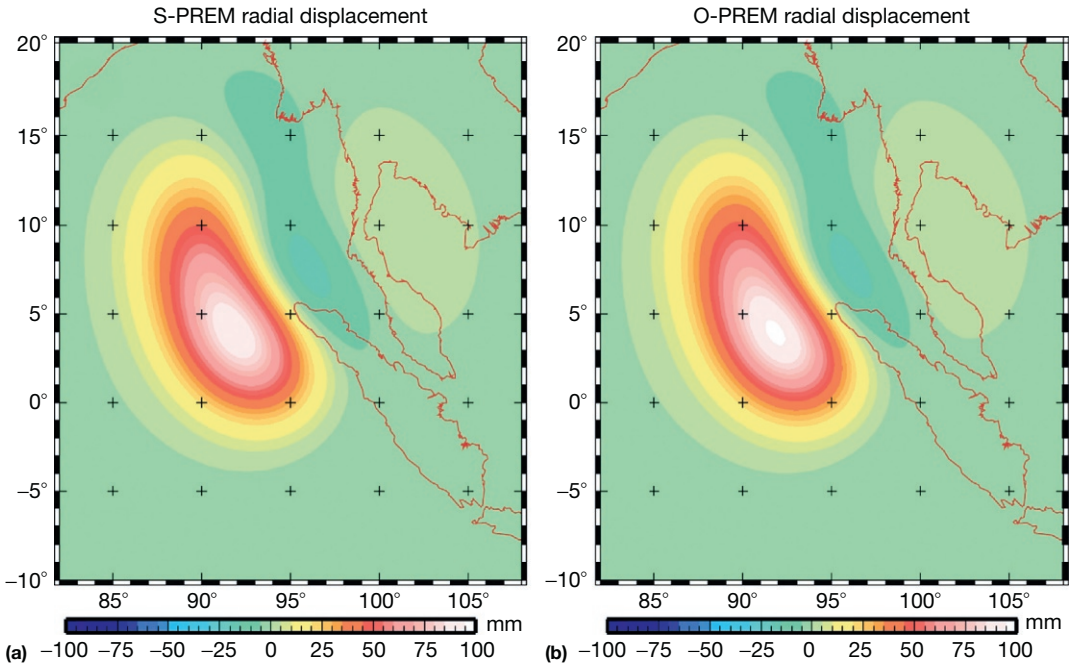

Figure 63 Coseismic radial displacements for compressible (a) S-PREM and (b) O-PREM, after the 350 km Gaussian filtering for the sake of comparison with the geoid anomalies shown in **Figure 61** in terms of sea-level variations. Redrawn from Figure 3 of Cambiotti G, Bordoni A, Sabadini R, and Colli L (2011) GRACE gravity data help constraining seismic models of the 2004 Sumatran earthquake. *Journal of Geophysical Research* 116: B10403. http://dx.doi.org/10.1029/2010JB007848.

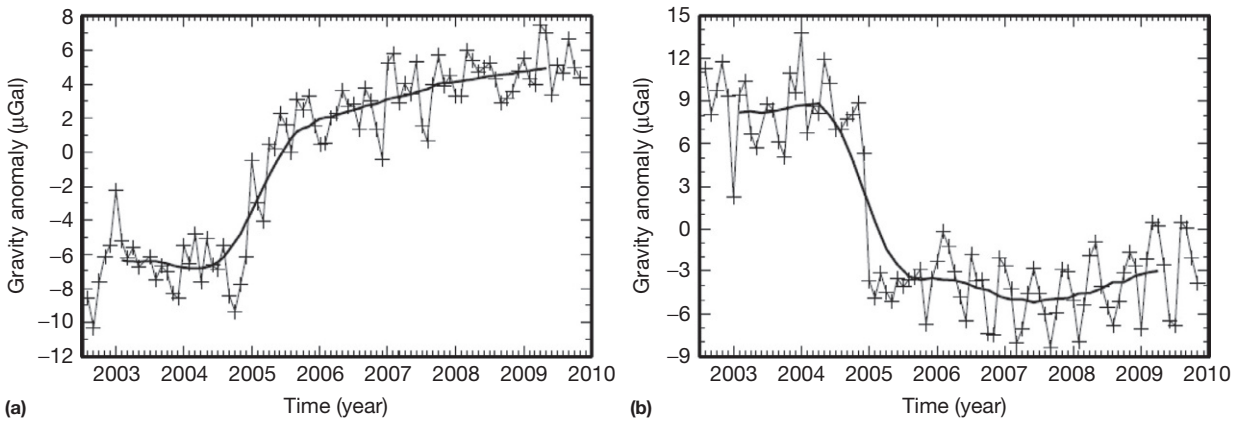

Figure 64 Original (thin solid lines, cross-shaped points) and smoothed (thick solid lines) DDK3-filtered GRACE data time series at points (94.2°, 2.1°) and (97.0°, 7.7°), in the (a) south–west and (b) north–east near field of the Sumatran trench. Redrawn from Figure 5 of Cambiotti G, Bordoni A, Sabadini R, and Colli L (2011) GRACE gravity data help constraining seismic models of the 2004 Sumatran earthquake. *Journal of Geophysical Research* 116: B10403. http://dx.doi.org/10.1029/2010JB007848.

series is not expected to impact the results of the study. The average is done after applying the corrections prescribed to the Stokes coefficients of the two data sets and replacing the degree-2 order-0 Stokes coefficient with its more stable estimate from the SLR constellation satellites as recommended. The GFZ solution is truncated at the harmonic degree-60 in order to conform to the lower spatial resolution of the CSR solution.

Figure 64 shows the original GRACE data time series in gravity anomaly representation (thin solid line, cross-shaped points) at the two points (94.2°, 2.1°) and (97.0°, 7.7°) in the south–west and north–east near fields of the Sumatran trench.

GRACE data time series are then smoothed in the time domain by means of a Gaussian filter, to reduce the variability due to seasonal and interannual signals due to hydrology from the continent and to the residual ocean circulation component present in the data while preserving permanent co- and post-seismic signatures and signals due to medium and long-period hydrologic cycles of periods greater than 2 years. After the Gaussian smoothing in the time domain (black solid line in

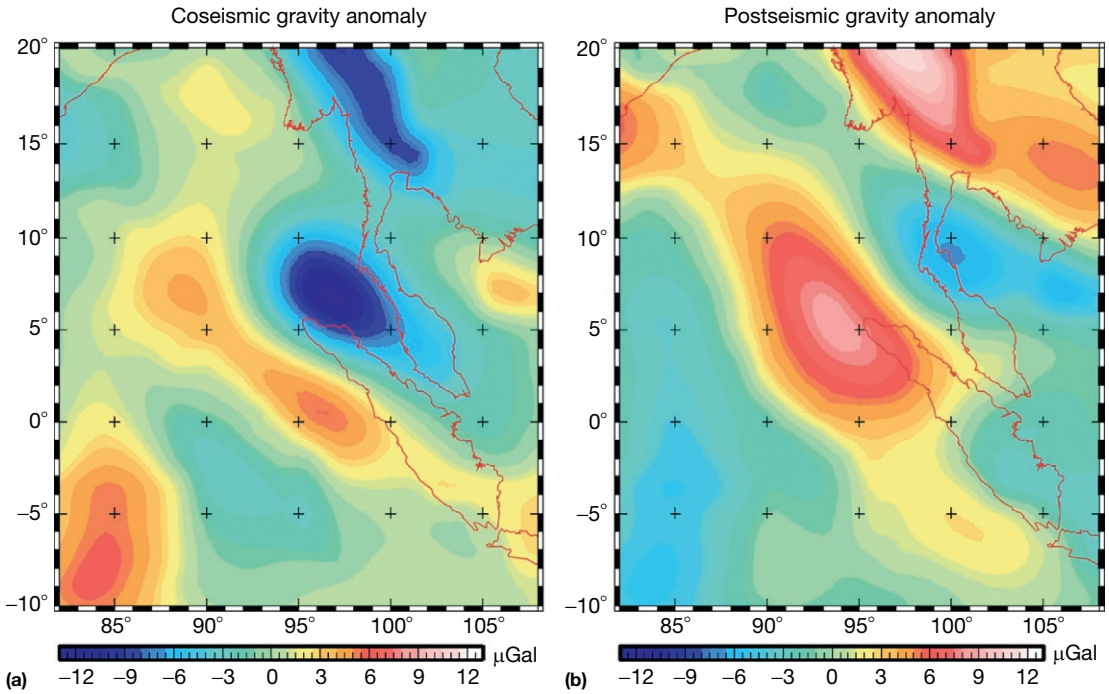

Figure 65 (a) Coseismic gravity anomalies and (b) postseismic contribution 5 years after the earthquake obtained by the nonlinear fitting to the smoothed DDK3-filtered GRACE data time series. Redrawn from Figure 7 of Cambiotti G, Bordoni A, Sabadini R, and Colli L (2011) GRACE gravity data help constraining seismic models of the 2004 Sumatran earthquake. *Journal of Geophysical Research* 116: B10403. http://dx.doi.org/10.1029/2010JB007848.

Figure 64), the latter shows evident long-term signals that cannot be considered as only coseismic jumps. Therefore, in order to remove these signals and to estimate only the coseismic jump, the smoothed time series are fitted by means of a coseismic discontinuity and a linear trend, representing the simplest approximation of postseismic signatures. On this basis, Figure 65 is generated, representing the coseismic jump (Figure 65(a)) and the postseismic signal (Figure 65(b)).

Figure 65 shows the estimated coseismic jump and postseismic contribution 5 years after the earthquake. The maximum coseismic gravity anomaly is $+6.1 \pm 1.5$ μGal and the minimum is -12.7 ± 0.9 μGal at points (95.6°, 0.7°) and (97.0°, 6.3°). The peak-to-peak coseismic jump is thus $+18.8 \pm 1.7$ μGal, and the asymmetry coefficient is $AS = 2.1 \pm 0.5$. The postseismic contribution can be as important as the coseismic one, with maximum, $+8.7 \pm 0.7$ μGal, and minimum, -7.1 ± 1.6 μGal, values at points (94.2°, 4.9°) and (99.8°, 9.1°), respectively.

6.04.7.3 Constraining the 2004 Sumatra Earthquake

In order to make the comparison between coseismic jump estimates from observations with those from significant models, it is important to apply the same spatial filter used to deal with GRACE data to models because the spatial features of the seismic signature make the gravity anomalies very sensitive to the type of filtering. The use of different filters would yield unphysical differences, which would make the comparison less effective. For this reason and owing to the easy implementation of the filter DDK3, made available by Kusche et al. (2009), DDK3-filtered CSR–GFZ solutions are compared with equivalently filtered coseismic models.

To be compared with the coseismic jump obtained from observations shown in Figure 65(a), Figure 66(a) portrays the coseismic gravity anomalies obtained for compressible O-PREM including the sea-level feedback and based on the seismic source model of Tsai et al. (2005), after the DDK3 filtering. Maximum and minimum gravity anomalies are +8.6 and −10.0 μGal at points (92.8°, 2.1°) and (97.0°, 6.3°). The peak-to-peak gravity anomaly obtained from the model, +18.6 μGal, is in agreement, within one-sigma error, with the observed one, $+18.8 \pm 1.7$ μGal, while the asymmetry coefficient $AS = 1.2$ differs from the observed one, $AS = 2.1 \pm 0.5$, by about two-sigma error. In view of the fact that the asymmetry coefficient AS depends mainly on the sea-level feedback and that the latter is strongly characterized by variations of topography at the bottom of the ocean, which is in turn dependent on the depth of the source, the depth of the latter is decreased to 15 km in Figure 66(b), with respect to the original Tsai et al. (2005) solution located at 25 km depth.

Figure 66(b) is now in better agreement with observations. In this case, both the peak-to-peak gravity anomaly and the asymmetry coefficient AS from modeling match the best estimates from observations, 18.8 μGal and 2.1, respectively, suggesting that the physics of this giant earthquake is represented correctly.

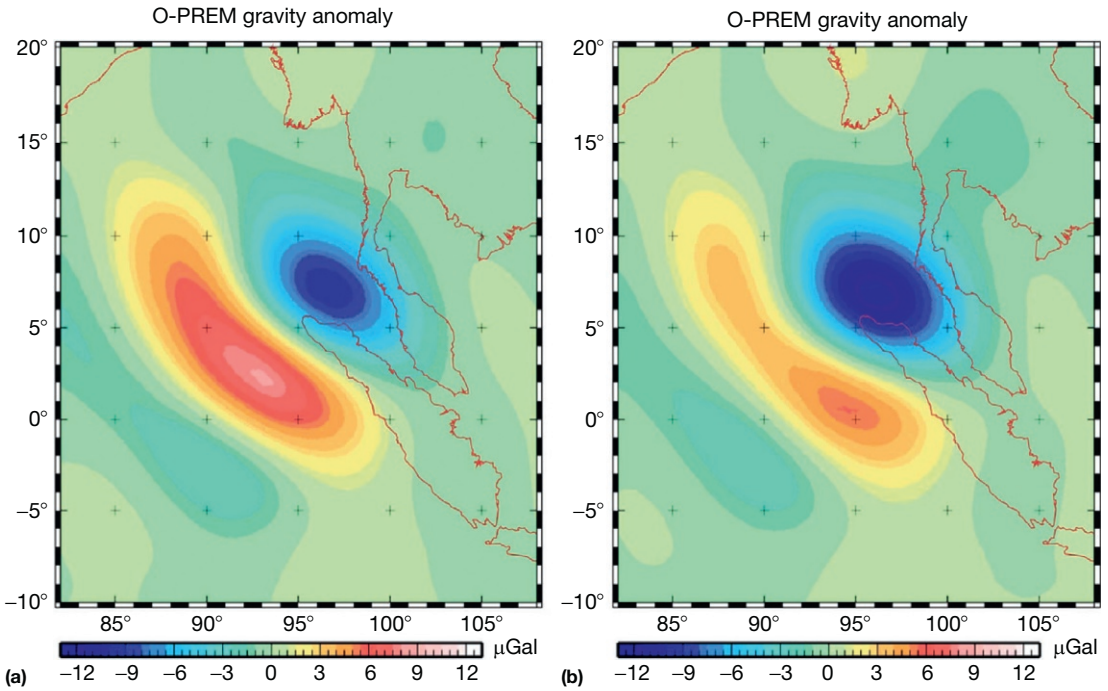

Figure 66 DDK3-filtered coseismic gravity anomalies for compressible O-PREM obtained using the (a) original and (b) modified seismic source models of Tsai et al. (2005), with source depths below, 25 km, and above, 15 km, the Moho discontinuity, respectively. The dip angles for the modified seismic source models have been increased by 50%. Redrawn from Figure 9 of Cambiotti G, Bordoni A, Sabadini R, and Colli L (2011) GRACE gravity data help constraining seismic models of the 2004 Sumatran earthquake. *Journal of Geophysical Research* 116: B10403. http://dx.doi.org/10.1029/2010JB007848.

6.04.7.4 The 2011 Great Tohoku-Oki Earthquake: Gravitational Seismology

A novel procedure for estimating the principal seismic source parameters (hypocenter and moment tensor) relying solely on space gravity data from GRACE has been applied for the first time to the 2011 Great Tohoku-Oki earthquake in Cambiotti and Sabadini (2013). It yields a seismic source model that is consistent with a thrust earthquake and geologic information of the subduction zone and closely resembles the Global CMT (Centroid–Moment–Tensor) Project solution based on teleseismic body-wave inversion: The moment magnitude is slightly higher, 9.13 ± 0.11 compared with the CMT 9.08 one, and the hypocenter is further offshore about 40 km within the oceanic plate. This procedure has thus become an important tool in seismology, complementing centroid–moment–tensor analyses by exploiting the new gravity data from GRACE.

Within the context of a CMT solution, coseismic gravity changes is modeled for a point-like seismic sources by means of a previously developed first-order theory (Cambiotti et al., 2011; Sun and Okubo, 1993; Takeuchi and Saito, 1972) implemented in a self-gravitating, compressible one-dimensional Earth model based on PREM (Dziewonski and Anderson, 1981), where the crust and the lithospheric mantle are substituted by a regional average of CRUST2.0 (Bassin et al., 2000).

Following the probabilistic approach to the nonlinear inverse problem by Mosengard and Tarantola (2002) and

Table 9 Best principal seismic source parameters of GCMT, Global CMT Project, and USGS Solutions

Solution	*GCMT*	*Global CMT Project*	*USGS*
Hypocenter			
Depth (km)	16.1	20.0	10.0
Latitude	37.75° N ± 0.46	37.5° N	38.5° N
Longitude	143.47° E ± 0.46	143.1° E	142.6° E
Moment tensor (10^{22} N m)			
M_{rr}	2.45 ± 1.15	1.730	2.03
$M_{\theta\theta}$	−0.12 ± 0.70	−0.281	−0.16
$M_{\varphi\varphi}$	−2.33 ± 0.91	−1.450	−1.87
$M_{r\theta}$	2.17 ± 0.59	2.120	2.06
$M_{r\varphi}$	5.33 ± 0.95	4.550	3.49
$M_{\theta\varphi}$	−1.07 ± 0.31	−0.657	−0.60
Seismic moment (10^{22} N m)			
Double couple	6.32 ± 2.94	5.31	4.54
Residual dipoles	0.32 ± 0.55	0.01	−0.05
Moment magnitude			
Double couple	9.13 ± 0.11	9.08	9.04
Residual dipoles	8.34 ± 0.32	0.01	−0.05
Fault plane geometry			
Dip (°)	12.2 ± 3.1	10	14
Slip (°)	89.7 ± 8.5	88	68
Strike (°)	201.9 ± 7.8	203	187

Taken from Table 2 of Cambiotti G and Sabadini R (2013) Gravitational seismology retrieving Centroid–Moment–Tensor solution of the 2011 Great Tohoku-Oki earthquake. *Journal of Geophysical Research* 118. http://dx.doi.org/10.1029/2012JB009555

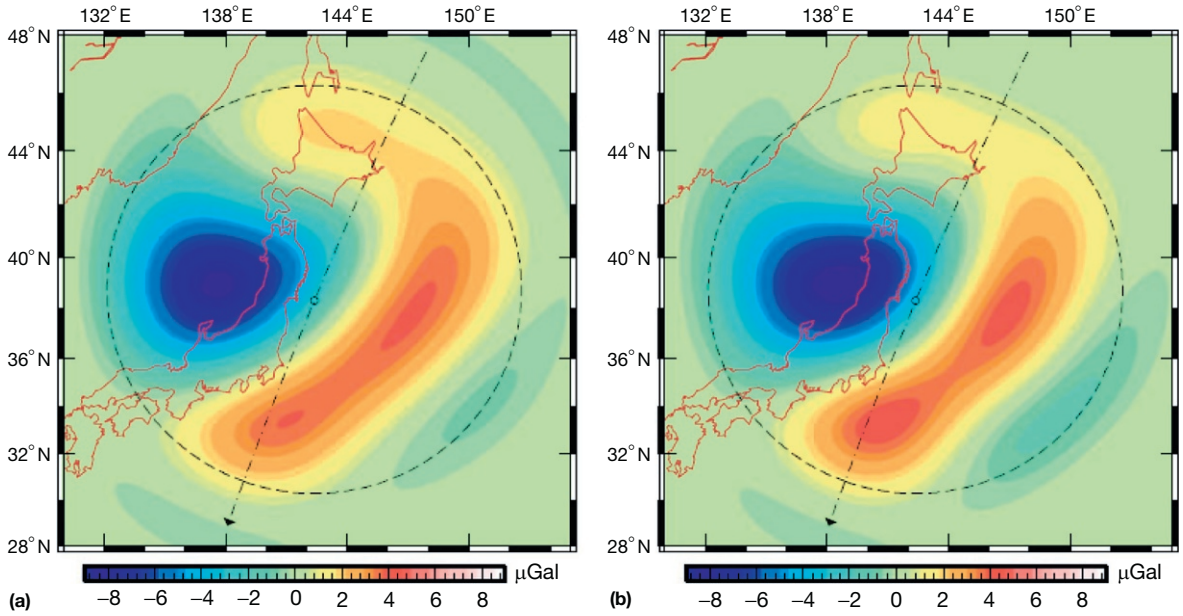

Figure 67 Coseismic gravity anomalies (a) estimated from GRACE data and (b) modeled using the GCMT solution, after DDK3 filtering and spatial localization within a circular cup (dashed circle) of half-width 8° and centered at the USGS mainshock. Redrawn from Figure 2 of Cambiotti G and Sabadini R (2013) Gravitational seismology retrieving Centroid–Moment–Tensor solution of the 2011 Tohoku earthquake. *Journal of Geophysical Research* 118: http://dx.doi.org/10.1029/2012JB009555.

localizing in space the DDK3-filtered GRACE and synthetic gravity anomalies on the basis of the optimally concentrated Slepian functions as described in Cambiotti and Sabadini (2011), the earthquake CMT parameters are obtained for the best model, thus providing the first self-consistent GCMT (Gravitational Centroid–Moment–Tensor) solution, as given in **Table 9**. The synthetic gravity pattern based on these inverted parameters is given in **Figure 67(b)**, closely resembling that from the GRACE data given in **Figure 67(a)**. It is worthwhile to note that the bipolar shape of the gravity is the same as that of the 2004 Sumatra earthquake, with minima and maxima inverted with respect to **Figure 66** due to the opposite direction of plate convergence of the Indian and Pacific Oceans underneath Eurasia. The negative pole in the hanging-wall side has the minimum gravity anomaly of -8.3 ± 1.6 μGal at point 38.9° N, 138.6° E and the positive pole in the footwall side that is characterized by two maxima of $+4.2 \pm 1.5$ and $+4.1 \pm 1.1$ μGal at points 33.3° N, 140.8° E and 37.8° N, 146.9° E, respectively. Note that this two-dome structure of the positive pole in the offshore region is also present in the observations of **Figure 67(a)**. It is due to the use of the anisotropic DDK3 filter and to the gravity reduction caused by ocean water removal from the uplifted crust, a phenomenon that leaves two small domes, remnants of the broader and higher central positive pole caused by mass rearrangement of the solid Earth (Cambiotti and Sabadini, 2011).

Table 9 compares our solution, which we name Gravitational Centroid–Moment–Tensor (GCMT) solution, with two classical seismological CMT solutions, the Global CMT Project and the USGS (United States Geological Survey). The GCMT and Global CMT Project solutions well agree with each other within one-sigma error: the GCMT moment magnitude 9.13 ± 0.11 is slightly higher compared with the 9.08 Global CMT Project solution. Our higher estimate of the moment magnitude may, in part, reflect the influence of after-slip in GRACE measurements. This after-slip is thought to be a substantial fraction of the seismic moment in the weeks following the mainshock (Ozawa et al., 2012).

The GCMT solution instead differs from the USGS solution especially for the location of the epicenter (**Figure 68**) and the geometry of the fault discontinuity. The USGS solution is indeed characterized by a strike angle of 187°, which is not well aligned with the local trench and by a significant along-strike component of slip, the rake angle being 68° (**Table 9**).

6.04.8 Conclusions

Comparison between GPS, DInSAR, and GRACE space data, and displacements and velocities inferred from geophysical modeling of various geodynamic processes, is a feasible tool to gain insight into the physics of plate-deformation mode. Geophysical modeling has been applied to the Earth's global response to surface loads during ice-sheet disintegration or major tectonic processes and to localized phenomena, such as co- and postseismic deformations or crustal deformation during present-day shrinkage of mountain glaciers.

The capability of geophysical modeling to reproduce plate-deformation characteristics in terms of their mechanical properties has been exploited, for example, in PGR models, which correctly reproduce the deformation pattern in Europe in terms of GPS baseline rates and strain rates. Such a modeling, in particular, involves the deformation properties of the

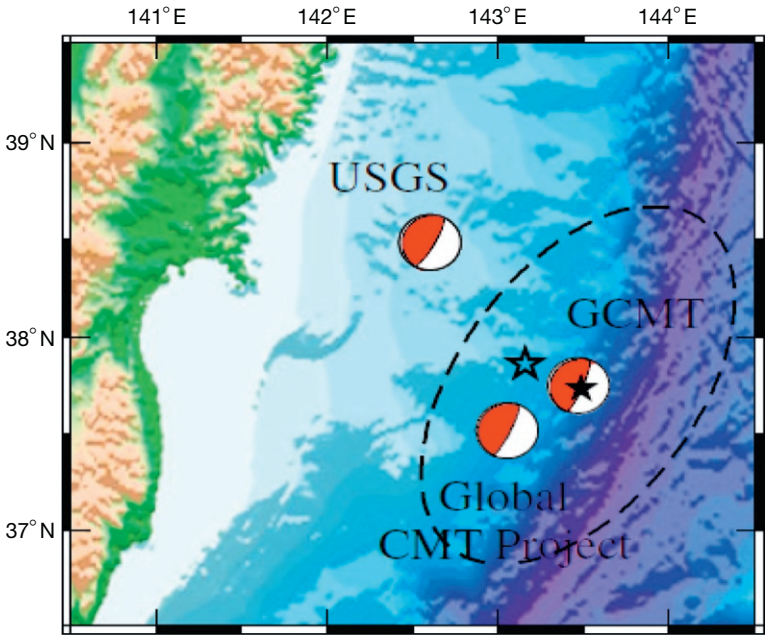

Figure 68 GCMT, Global CMT Project, and USGS focal mechanisms and mean epicenters within the crust and the lithospheric mantle (white and black stars, respectively). The dashed ellipse indicates the two-sigma errors of the GCMT solution. Redrawn from Figure 4 of Cambiotti G and Sabadini R (2013) Gravitational seismology retrieving Centroid–Moment–Tensor solution of the 2011 Tohoku earthquake. *Journal of Geophysical Research* 118. http://dx.doi.org/10.1029/2012JB009555.

lithosphere–mantle coupled system, rather than only the outermost plate, which implies that the mathematical modeling required solving the differential equations for the motion of the Earth's material within both the lithosphere and mantle. PGR has thus allowed to constrain the thickness of the Earth's outer plate jointly with mantle viscosity, the latter providing the global mechanical and rheological properties of the Earth. PGR is such a huge phenomenon that is expected to be visible even from space in the global, time-dependent gravity field of the Earth, as shown by flying space missions.

The same kind of modeling, but at shorter wavelengths than PGR, has allowed us to constrain, when considering postseismic deformation, the viscosity of the shallowest part of the plates, thus revealing that the latter cannot be considered as fully elastic, even at shallow depths of kilometers.

The mathematical model of continent–continent collision and subduction, to simulate the effects of active tectonics in Europe and in the Mediterranean due to the African–Eurasian convergence, based on the thin-sheet scheme, has carried into coincidence modeled baseline rates and strain rates with those retrieved from GPS analyses. Such a good correlation shows that mathematical modeling of plate properties is correct and that the major tectonic processes have been properly taken into account. This mathematical scheme, in fact, has allowed us to analyze the sensitivity of modeling results on plate-strength variations jointly with changes in tectonic forcing, such as those related to Mid-Atlantic ridge opening or subduction.

This chapter has shown that at the beginning of the third millennium, the joint use of geophysical modeling and GPS–DInSAR–space gravity data can be used to unravel the plate's physical properties and the characteristics of plate-deformation mode in a wide range of wavelengths and timescales. Modeling and detecting plate deformation are now a powerful tool to implement new and modern strategies to safeguard the population and civil and industrial infrastructures from the hazard of natural events.

References

Altamini Z, Sillard P, and Boucher C (2002) ITRF2000: A new release of the International Terrestrial Reference Frame for Earth Science applications. *Journal of Geophysical Research* 107(B10): 2214. http://dx.doi.org/10.1029/2001JB000561.

Ambraseys NN (1970) Some characteristic features of the Anatolian fault zone. *Tectonophysics* 9: 143–165.

Ammon CJ, Chen J, Hong-Kie T, et al. (2005) Rupture process of the 2004 Sumatra–Andaman earthquake. *Science* 308: 1133–1139. http://dx.doi.org/10.1126/science.1112260.

Anderson H and Jackson J (1987) Active tectonics in the Adriatic regions. *Geophysical Journal of the Royal Astronomical Society* 91: 937–983.

Aoudia A, Borghi A, Riva REM, et al. (2003) Postseismic deformation following the 1997 Umbria–Marche (Italy) moderate normal faulting earthquakes. *Geophysical Research Letters* 30(7): 1390. http://dx.doi.org/10.1029/2002GL016339.

Arca S, Bonasia V, Gaulon R, Pingue F, Ruegg JC, and Scarpa R (1983) Ground movements and faulting mechanism associated to the November 23, 1980 southern Italy earthquake. *Bollettino di Geodesia e Science Affini* XLII(2): 137–147.

Barletta VR, Ferrari C, Diolaiuti G, Carnielli T, Sabadini R, and Smiraglia C (2006a) Glacier shrinkage and modeled uplift of the Alps. *Geophysical Research Letters* 33: L14307. http://dx.doi.org/10.1029/2006GL026490.

Barletta VR and Sabadini R (2006) Investigating superswells and sea level changes caused by superplumes via normal mode relaxation theory. *Journal of Geophysical Research* 111: B04404. http://dx.doi.org/10.1029/2005JB003926.

Barletta VR, Sabadini R, and Bordoni A (2006b) Ice mass loss in the polar regions of the Earth and mantle viscosity from GRACE data. In: *3rd International GOCE User Workshop, ESA ESRIN 6–8 November 2006*.

Basili R and Meghraoui M (2001) Coseismic and postseismic displacements related with the 1997 earthquake sequence in Umbria–Marche (central Italy). *Geophysical Research Letters* 28: 2695–2698.

Basili R, Valensise G, Vannoli P, et al. (2008) The Database of Individual Seismogenic Sources (DISS), version 3: Summarizing 20 years of research on Italy's earthquake geology. *Tectonophysics* 453: 20–40. http://dx.doi.org/10.1016/j.tecto.2007.04.014.

Bassi G, Sabadini R, and Rebaï S (1997) Modern tectonic regime in the Tyrrhenian area: Observations and models. *Geophysical Journal International* 129: 330–346.

Bassin C, Laske G, and Masters G (2000) The current limits of resolution for surface wave tomography in North America. *Eos, Transactions of the American Geophysical Union* 81: F897.

Biancotti A and Motta M (2001) L'evoluzione recente ed attuale dei ghiacciai italiani. *Bollettino Geofisico* 3–4: 273.

Biescas E, Crosetto M, Agudo M, Monserrat O, and Crippa B (2007) Two Radar interferometric approaches to monitor slow and fast land deformation. *Journal of Surveying Engineering* 133: 66–71.

Broerse DBT, Vermeersen LLA, Riva REM, and van der Wal W (2011) Ocean contribution to co-seismic crustal deformation and geoid anomalies: Application to the 2004 December 26 Sumatran–Andaman earthquake. *Earth and Planetary Science Letters* 305: 341–349. http://dx.doi.org/10.1016/j.epsl.2011.03.011.

Bürgmann R, Fielding E, and Sukhatme J (1998) Slip along the Hayward fault, California, estimated from space-based synthetic aperture radar interferometry. *Geology* 26(6): 559–562.

Bürgmann R, Schmidt D, Nadeau RM, et al. (2000) Earthquake potential along the northern Hayward Fault, California. *Science* 289: 1178–1182.

Burov E, Podladchkov Y, Grandjean G, and Burg JP (1999) Thermo-mechanical approach to validation of deep crustal and lithospheric structures inferred from multidisciplinary data: Application to the Western and Northern Alps. *Terra Nova* 11(2–3): 124–131. http://dx.doi.org/10.1046/j.1365-3121.1999.00236.X.

Cakir Z, Akoglu AM, Belabbes S, Ergintav S, and Meghraoui M (2005) Creeping along the Ismetpasa section of the North Anatolian fault (Western Turkey): Rate and extent from InSAR. *Earth and Planetary Science Letters* 238: 225–234.

Cambiotti G, Bordoni A, Sabadini R, and Colli L (2011) GRACE gravity data help constraining seismic models of the 2004 Sumatran earthquake. *Journal of Geophysical Research* 116: B10403. http://dx.doi.org/10.1029/2010JB007848.

Cambiotti G, Ricard Y, and Sabadini R (2010) Ice age True Polar Wander in a compressible and non-hydrostatic Earth. *Geophysical Journal International* 183(3): 1248–1264.

Cambiotti G and Sabadini R (2010) The compressional and compositional stratifications in Maxwell Earth models: The gravitational overturning and the long period tangential flux. *Geophysical Journal International* 180: 475–500. http://dx.doi.org/10.1111/j.1365-246X.2009.04434.x.

Cambiotti G and Sabadini R (2011) A source model for the great 2011 Tohoku earthquake (Mw=9.1) from inversion of GRACE gravity data. *Earth and Planetary Science Letters* 335(2012): 72–79. http://dx.doi.org/10.1016/j.epsl.2012.05.002.

Cambiotti G and Sabadini R (2013) Gravitational seismology retrieving Centroid–Moment–Tensor solution of the 2011 Tohoku earthquake. *Journal of Geophysical Research* 118. http://dx.doi.org/10.1029/2012JB009555.

Capuano P, Zollo A, Emolo A, Marcucci S, and Milana G (2000) Rupture mechanism and source parameters of Umbria–Marche mainshocks from strong motion data. *Journal of Seismology* 4: 463–478.

Cinti FR, Moro M, Pantosti D, Cucci L, and D'Addezio G (2002) New constraints on the seismic history of the Castrovillari fault in the Pollino gap (Calabria, southern Italy). *Journal of Seismology* 6: 199–217.

Clarke PJ, Davies RR, England PC, et al. (1998) Crustal strain in central Greece from repeated GPS measurements in the interval 1989–1997. *Geophysical Journal International* 135: 195–214.

Crippa B, Crosetto M, Biescas E, Troise C, Pingue F, and De Natale G (2006) An advanced slip model for the Umbria–Marche earthquake sequence: Coseismic displacement observed by SAR interferometry and model inversion. *Geophysical Journal International* 164: 36–45. http://dx.doi.org/10.1111/j.1365-246X.2005.02830.x.

Dalla Via G, Crippa B, Toraldo Serra EM, Giacomuzzi G, and Sabadini R (2006) Exploitation of high-density dinsar data points of the Umbria-Marche (Italy) 1997 seismic sequence for fault characteristics. *Geophysical Research Letters* 34: L17301. http://dx.doi.org/10.1029/2007GL030718.

Dalla Via G, De Natale G, Troise C, et al. (2003) First evidence of post-seismic deformation in the central Mediterranean: Crustal viscoelastic relaxation in the area of the 1980 Irpinia earthquake (southern Italy). *Geophysical Journal International* 154(3): F9–F14. http://dx.doi.org/10.1046/j.1365-246X.2003.02031.x.

Dalla Via G, Sabadini R, De Natale G, and Pingue F (2005) Lithospheric rheology in southern Italy inferred from postseismic viscoelastic relaxation following the 1980 Irpinia earthquake. *Journal of Geophysical Research* 110: B06311. http://dx.doi.org/10.1029/2004JB003539.

de Linage C, Rivera L, Hinderer J, et al. (2009) Separation of coseismic and postseismic gravity changes for the 2004 Sumatran earthquake from 4.6 yr of GRACE observations and modelling of the coseismic change by normal mode summation. *Geophysical Journal International* 176: 695–714. http://dx.doi.org/10.1111/j.1365246X.2008.04025.x.

De Natale G and Pingue F (1991) A variable slip fault model for the 1908 Messina straits (Italy) earthquake by inversion of levelling data. *Geophysical Journal International* 104: 73–84.

De Natale G, Pingue F, and Scarpa R (1988) Seismic and ground deformation monitoring in the seismogenetic region of southern Apennines, Italy. *Tectonophysics* 152: 165–178.

deGroot-Hedlin C and Constable S (1990) Occam's inversion to generate smooth, two dimensional models from magnetotelluric data. *Geophysics* 55: 1613–1624.

DeMets C and Dixon TH (1999) New kinematic models for Pacific-North America motion from 3 Ma to present; I: Evidence for steady motion and biases in the NUVEL-1A model. *Geophysical Research Letters* 26: 1921–1924.

DeMets C, Gordon RG, Argus DF, and Stein S (1994) Effect of recent revisions to the geomagnetic reversal time scale on estimates of current plate motions. *Geophysical Research Letters* 21: 2191–2194.

Devoti R, Ferraro C, Gueguen E, et al. (2002) Geophysical interpretation of geodetic deformation in the central Mediterranean area. *Tectonophysics* 346: 151–167.

Di Donato G, Negredo AM, Sabadini R, and Vermeersen LLA (1999) Multiple processes causing sea level rise in the central Mediterranean. *Geophysical Research Letters* 26: 1769–1772.

Douglas BC (1995) Global sea level change: Determination and interpretation. *Reviews of Geophysics* 33(Supplement (July)): 1425–1432.

Drewes H (2006) The APKIM2005, basis for a non-rotating ITRF. International IAG Symposium "Geodetic Reference Frame, GRF2006", LVG, München, 2006-10-11.

Dziewonski AM and Anderson DL (1981) Preliminary reference Earth model. *Physics of the Earth and Planetary Interiors* 25: 297–356.

Ekström G and Dziewonski AM (1988) Evidence of bias in estimations of earthquakes size. *Nature* 332: 319–323.

Ekstrom G, Morelli A, and Dziewonski AM (1998) Moment tensor analysis of the central Italy earthquake sequence of September–October 1997. *Geophysical Research Letters* 25: 1971–1974.

England P and McKenzie D (1983) Correction to: A thin viscous sheet model for continental deformation. *Geophysical Journal of the Royal Astronomical Society* 73: 523–532.

Farrell WE and Clark JA (1976) On postglacial sea-level. *Geophysical Journal of the Royal Astronomical Society* 46: 647–667.

Ferretti A, Prati C, and Rocca F (2001) Permanent scatterers in SAR interferometry. *IEEE Transactions on Geoscience and Remote Sensing* 39(1): 8–20.

Giunchi C, Sabadini R, Boschi E, and Gasperini P (1996) Dynamic models of subduction: Geophysical and geological evidence in the Tyrrhenian Sea. *Geophysical Journal International* 126: 555–578.

Gross RS and Chao BF (2006) The rotational and gravitational signature of the December 26, 2004 Sumatran earthquake. *Surveys in Geophysics* 27: 615–632. http://dx.doi.org/10.1007/s10712-006-9008-1.

Grunthal G and Stromayer D (1992) The recent crustal stress field in central Europe: Trajectories and finite element modelling. *Journal of Geophysical Research* 97: 11805–11820.

Haeberli W and Beniston M (1998) Climate change and its impacts on glaciers and permafrost in the Alps. *Ambio* 27(4): 258–265.

Haeberli W, Fraunfelder R, Hoelzle M, and Maish M (1999) Rates and acceleration trend of global mass changes. *Geografiska Annaler* 810: 585–591.

Han SC, Sauber J, and Riva R (2011) Contribution of satellite gravimetry to understanding seismic source processes of the 2011 Tohoku-Oki earthquake. *Geophysical Research Letters* 38: L24312. http://dx.doi.org/10.1029/2011GL049975.

Han SC, Shum CK, Bevis M, Ji C, and Kuo CY (2006) Crustal dilatation observed by GRACE after the 2004 Sumatran–Andaman earthquake. *Science* 313: 658–662. http://dx.doi.org/10.1126/science.1128661.

Han SC, Shum CK, Bevis M, Ji C, and Kuo CY (2010) Regional gravity decrease after the 2010 Maule (Chile) earthquake indicates large-scale mass redistribution. *Geophysical Research Letters* 37: LL23307. http://dx.doi.org/10.1029/2010GL045449.

Hanssen R (2001) *Radar Interferometry*. Dordrecht: Kluwer Academic Publisher.

Heki K and Matsuo K (2010) Coseismic gravity changes of the 2010 earthquake in central Chile from satellite gravimetry. *Geophysical Research Letters* 37: L24306.

IPCC (2001) A contribution of Working Groups I, II, and III to the third assessment report of the intergovernmental panel on climate change. In: Watson RT and the

Core Writing Team (eds.) *Climate Change 2001: Synthesis Report*, p. 398. New York, NY: Cambridge University Press.
Irifune T and Ringwood AE (1987) Phases transformations in a harzburgite composition to 26GPa: Implications for dynamical behavior of the subducting slab. *Earth and Planetary Science Letters* 86: 365–376.
ITRF2005, available at http://lareg.ensg.ign.fr/ITRF_solutions/2005//ITRF2005.php.
Ivins ER and James TS (2004) Bedrock response to Llanquihue Holocene and present-day glaciation in southernmost South America. *Geophysical Research Letters* 31: L24613. http://dx.doi.org/10.1029/2004GL021500.
Jackson J and McKenzie D (1998) The relationship between plate motions and seismic tremors, and the rates of active deformation in the Mediterranean and Middle East. *Geophysical Journal of the Royal Astronomical Society* 93: 45–73.
James TS and Ivins ER (1997) Global geodetic signatures of the Antarctic ice sheet. *Journal of Geophysical Research* 102: 605–633.
Jiménez-Munt I, Fernandez M, Torne M, and Bird P (2001) The transition from linear to diffuse plate boundary in the Azores–Gibraltar region: Results from a thin sheet model. *Earth and Planetary Science Letters* 192: 175–189.
Jiménez-Munt I and Sabadini R (2002) The block-like behaviour of Anatolia envisaged in the modeled and geodetic strain rates. *Geophysical Research Letters* 29: 1979. http://dx.doi.org/10.1029/2002GL015995.
Jiménez-Munt I, Sabadini R, Gardi A, and Bianco G (2003) Active deformation in the Mediterranean from Gibraltar to Anatolia inferred from numerical modeling and geodetic and seismological data. *Journal of Geophysical Research* 108: B1. http://dx.doi.org/10.1029/2001JB001544.
Johansson JM, Davis JL, Scherneck HG, et al. (2002) Continuous GPS measurements of postglacial adjustment in Fennoscandia. Part 1: Geodetic results. *Journal of Geophysical Research* 107. http://dx.doi.org/10.1029/2001JB000400.
Johnston P (1993) The effect of spatially non-uniform water loads on prediction of sea-level change. *Geophysical Journal International* 114: 615–634.
Kääb A, Paul F, Maisch M, Hoelzle M, and Haeberli W (2002) The new remote-sensing-derived Swiss glacier inventory. Part II: First results. *Annals of Glaciology* 34: 362–366.
Kahle H-G, Cocard M, Peter Y, et al. (2000) GPS-derived strain rate field within the boundary zones of the Eurasian, African and Arabian Plates, 2000. *Journal of Geophysical Research* 105: 23353–23370.
King GCP, Stein RS, and Rundle GB (1988) The growth of geological structures by repeated earthquakes: Conceptual framework. *Journal of Geophysical Research* 93: 13307–13318.
Kiratzi A and Papazachos C (1995) Active deformation of the shallow part of the subducting lithospheric slab in the southern Aegean. *Journal of Geodynamics* 19: 65–78.
Kostrov V (1974) Seismic moment and energy of earthquakes, and seismic flow of rock. *Izvestiya Academy of Sciences USSR Physics of Solid Earth* 1: 23–44.
Kusche J (2007) Approximate decorrelation and non-isotropic smoothing of the time-variable GRACE-type gravity field models. *Journal of Geodesy* 81: 733–749. http://dx.doi.org/10.1007/s00190-007-0143-3.
Kusche J, Schmidt R, Petrovic S, and Rietbroek R (2009) Decorrelated GRACE time-variable gravity solutions by GFZ, and their validation using a hydrological model. *Journal of Geodesy* 83: 903–913. http://dx.doi.org/10.1007/s00190-009-0308-3.
Lambeck K, Johnston P, and Nakada M (1990) Holocene glacial rebound and sea-level change in NW Europe. *Geophysical Journal International* 103: 451–468.
Lambeck K and Nakiboglu SM (1984) Recent global changes in sea level. *Geophysical Research Letters* 11: 959–961.
Lundgren P and Stramondo S (2002) Slip distribution of the 1997 Umbria–Marche earthquake sequence: Joint inversion of GPS and synthetic aperture radar interferometric data. *Journal of Geophysical Research* 107(B11): 2316.
Lynch HD and Morgan P (1987) The tensile strength of the lithosphere and the localization of extension. In: Coward MP, Dewey JF, and Hancock PL (eds.) *Continental Extensional Tectonics*, pp. 53–65. Oxford: Blackwell Science, Geological Society Special Publication, 28.
Ma XQ and Kusznir NJ (1995) Coseismic and postseismic subsurface displacements and strains for a dip-slip normal fault in a three layer elastic-gravitational medium. *Journal of Geophysical Research* 100: 12813–12828.
Marotta AM (2003) Benefits from GOCE within solid earth geophysics. *Space Science Reviews* 0038-6308. 108: 95–104. http://dx.doi.org/10.1023/A:1026273832697.
Marotta AM, Barzaghi R, Borghi A, and Spelta E (2007) Gravity constraints on the dynamics of the crust–mantle system during Calabrian subduction. *Geophysical Journal International* 171: 977–985.
Marotta AM, Bayer U, Scheck M, and Thybo H (2001) The stress field below the NE German Basin: Effects induced by the Alpine collision. *Geophysical Journal International* 144: F8–F12.
Marotta AM, Fernandez M, and Sabadini R (1999) The onset of extension during lithospheric shortening: A two-dimensional thermomechanical model for lithospheric unrooting. *Geophysical Journal International* 139: 98–114.
Marotta AM, Mitrovica JX, Sabadini R, and Milne G (2004) Combined effects of tectonics and glacial isostatic adjustment on intraplate deformation in central and northern Europe: Application to geodetic baseline analyses. *Journal of Geophysical Research* 109: B01413. http://dx.doi.org/10.1029/2002JB002337.
Marotta AM and Sabadini R (2002) Tectonic versus glacial isostatic deformation in Europe. *Geophysical Research Letters* 29(10). http://dx.doi.org/10.1029/2001GL013865.
Marotta AM and Sabadini R (2004) The signatures of tectonics and glacial isostatic adjustment revealed by the strain rate in Europe. *Geophysical Journal International* 157: 865–870. http://dx.doi.org/10.1111/j.1365-246X.2004.02275.X.
Marotta AM and Sabadini R (2008) Africa–Eurasia kinematics control of long-wavelength tectonic deformation in the Central Mediterranean. *Geophysical Journal International* 175: 742–754. http://dx.doi.org/10.1111/j.1365-246X.2008.03906.x.
Massonnet D, Rossi M, Carmona C, et al. (1993) The displacement field of the Landers earthquake mapped by radar interferometry. *Nature* 364: 138–142.
Matsuo K and Heki K (2011) Coseismic gravity changes of the 2011 Tohoku-Oki earthquake from satellite gravimetry. *Geophysical Research Letters* 38: L00G12. http://dx.doi.org/10.1029/2011GL049018.
McClusky S, Balassanian S, Barka A, et al. (2000) Global Positioning System constraints on plate kinematics and dynamics in the eastern Mediterranean and Caucasus. *Journal of Geophysical Research* 105: 5695–5719.
McKenzie DP (1970) Plate tectonics of the Mediterranean region. *Nature* 226: 239–243.
Meijer PTh and Wortel MJR (1992) The dynamics of motion of the South American plate. *Journal of Geophysical Research* 97: 11915–11931.
Melosh HJ (1983) Vertical movements following a dip-slip earthquake. *Geophysical Research Letters* 10: 47–50.
Milne GA, Davis JL, Mitrovica J, et al. (2001) Space geodetic constrains on glacial isostatic adjustment in Fennoscandia. *Science* 291: 2381–2385.
Mitrovica JX and Davis JL (1995) Present day post-glacial sea level change far from the late Pleistocene ice sheets: Implications for recent analyses of tide gauge record. *Geophysical Research Letters* 18: 2529–2532.
Mitrovica JX, Davis JL, and Shapiro II (1993) Constraining proposed combinations of ice history and Earth rheology using VLBI determined baseline rates in North America. *Geophysical Research Letters* 20: 2387–2390.
Mitrovica JX, Davis JL, and Shapiro II (1994) A spectral formalism for computing three-dimensional deformations due to surface loads. Part 2: Present-day glacial isostatic adjustment. *Journal of Geophysical Research* 99: 7075–7101.
Mitrovica JX and Peltier WR (1991) On postglacial geoid subsidence over the equatorial oceans. *Journal of Geophysical Research* 96: 20053–20071.
Molnar P, Fitch TJ, and Wu FT (1973) Fault plane solutions of shallow earthquakes and contemporary tectonics in Asia. *Earth and Planetary Science Letters* 19: 101–112.
Mosengard K and Tarantola A (2002) Probabilistic approach to inverse problems. In: *International Handbook of Earthquake & Engineering Seismology (Part A)*, pp. 237–265. New York: Academic Press.
Mueller B, Reinecker J, and Fuchs K (2000) *The 2000 Release of the World Stress Map*. http://www.world-stress-map.org.
Nakada M and Lambeck K (1987) Glacial rebound and relative sea-level variations: A new appraisal. *Geophysical Journal of the Royal Astronomical Society* 90: 171–224.
Nakada M and Lambeck K (1989) Late Pleistocene and Holocene sea-level change in the Australian region and mantle rheology. *Geophysical Journal International* 96: 497–517.
Negredo AM, Sabadini R, Bianco G, and Fernandez M (1999) Three-dimensional modeling of crustal motions caused by subduction and continental convergence in the central Mediterranean. *Geophysical Journal International* 136: 261–274.
Negredo AM, Sabadini R, and Giunchi C (1997) Interplay between subduction and continental convergence: A three-dimensional dynamic model for the Central Mediterranean. *Geophysical Journal International* 131: F1–F5.
Neri G, Marotta AM, Orecchio B, et al. (2012) How lithospheric subduction changes along the Calabrian Arc in southern Italy: Geophysical evidences. *International Journal of Earth Sciences (Geologische Rundschau)* 101: 1949–1969. http://dx.doi.org/10.1007/s00531-012-0762-7.
Okada Y (1992) Internal deformation due to shear and tensile faults in a half-space. *Bulletin of the Seismological Society of America* 82: 1018–1040.
Ozawa S, Nishimura T, Munekane H, et al. (2012) Preceding, coseismic, and postseismic slips of the 2011 Tohoku earthquake, Japan. *Journal of Geophysical Research* 117: B07404. http://dx.doi.org/10.1029/2011JB009120.
Panet I, Mikhailov V, Diament M, et al. (2007) Co-seismic and post-seismic signatures of the Sumatra December 2004 and March 2005 earthquakes in GRACE satellite

gravity. *Geophysical Journal International* 171: 171–190. http://dx.doi.org/10.1111/j.1365-246X.2007.03525.x.
Papazachos BC, Karakostas VG, Papazachos CB, and Scordilis EM (2000) The geometry of the Wadati-Benioff zone and lithospheric kinematics in the Hellenic arc. *Tectonophysics* 319: 275–300.
Paul F, Kääb A, Maisch M, Kellenberger T, and Haeberli W (2002) The new remote-sensing derived Swiss glacier Inventory. Part I: Methods. *Annals of Glaciology* 34: 355–361.
Peltier WR (1998) Postglacial variations in the level of the sea: Implications for climate dynamics and solid-Earth geophysics. *Reviews of Geophysics* 36: 603–689.
Peltier WR and Andrews JT (1976) Glacial isostatic adjustment. Part I: The forward problem. *Geophysical Journal of the Royal Astronomical Society* 46: 605–646.
Pialli G, Barchi M, and Minelli G (eds.) (1998) *Memorie della Societa Geologica Italiana*, vol. LII. *Results of the CROP03 Deep Seismic Reflection Profile*, p. 657.
Pingue F and De Natale G (1993) Fault mechanism of the 40s subevent of the 1980 Irpinia (southern Italy) earthquake from levelling data. *Geophysical Research Letters* 20: 911–914.
Platt JP and Vissers RLM (1989) Extensional collapse of thickened continental lithosphere: A working hypothesis for the Alboran Sea and Gibraltar Arc. *Geology* 17: 540–543.
Pollitz FF (1996) Coseismic deformation from earthquake faulting on a layered spherical Earth. *Geophysical Journal International* 125: 1–14.
Pollitz FF, Burgmann R, and Segall P (1998) Joint estimation of afterslip rate and post-seismic relaxation following the 1989 Loma Prieta earthquake. *Journal of Geophysical Research* 103: 26975–26992.
Rebaï S, Philip H, and Taboada A (1992) Modern tectonics stress field in the Mediterranean region: Evidence for variation in stress directions at different scales. *Geophysical Journal International* 110: 106–140.
Richardson RM and Reding L (1991) North American plate dynamics. *Journal of Geophysical Research* 96: 12201–12223.
Richardson RM, Solomon SC, and Sleep NH (1979) Tectonic stress in the plates. *Reviews of Geophysics* 17: 981–1019.
Riva REM, Aoudia A, Vermeersen LLA, Sabadini R, and Panza GF (2000) Crustal versus asthenospheric relaxation and post-seismic deformation for shallow normal faulting earthquakes: The Umbria–Marche (central Italy) case. *Geophysical Journal International* 141: F7–F11.
Riva REM and Vermeersen LLA (2002) Approximation method for high-degree harmonics in normal mode modeling. *Geophysical Journal International* 151: 309–313.
Rosen PA, Hensley S, Joughin IR, et al. (2000) Synthetic aperture radar interferometry. *Proceedings of the IEEE* 88(3): 333–382.
Rosen P, Werner C, Fielding E, Hensley S, Buckley S, and Vincent P (1998) Aseismic creep along the San Andreas fault northwest of Parkfield, CA measured by radar interferometry. *Journal of Geophysical Research* 25: 825–828.
Sabadini R, Aoudia A, Barzaghi R, et al. (2009) First evidences of fast creeping on a long-lasting quiescent earthquake normal-fault in the Mediterranean. *Geophysical Journal International* 179: 720–732. http://dx.doi.org/10.1111/j.1365246X.2009.04312.x.
Sabadini R and Vermeersen LLA (1997) Influence of lithospheric and mantle layering on global post-seismic deformation. *Geophysical Research Letters* 24: 2075–2078.
Sabadini R and Vermeersen B (2004) *Global Dynamics of the Earth*, p. 328. Dordrecht: Kluwer Academic Publisher.
Sabadini R, Yuen DA, and Boschi E (1982) Polar wandering and the forced responses of a rotating, multilayered, viscoelastic planet. *Journal of Geophysical Research* 87: 2885–2903.
Sabadini R, Yuen DA, and Boschi E (1984) The effects of postseismic motions on the moment of inertia of a stratified viscoelastic Earth with an asthenosphere. *Geophysical Journal of the Royal Astronomical Society* 79: 727–745.
Salvi S, Stramondo S, Cocco M, et al. (2000) Modeling coseismic displacements resulting from SAR interferometry and GPS measurements during the 1997 Umbria–Marche seismic sequence. *Journal of Seismology* 4: 479–499.
Saraó A, Romanell F, Costa G, and Panza GF (1998) Source inversion and macroseismic modelling for the Umbria–Marche main events. *Annales Geophysicae* 16(I): C164.
Schlatter A, Schneider D, Geiger A, and Kahle HG (2005) Recent vertical movements from precise levelling in the vicinity of the city of Basel, Switzerland. *International Journal of Earth Sciences* 94: 507514. http://dx.doi.org/10.1007/s00531-004-0049-9.
Schubert G, Turcotte DL, and Olson P (2001) *Mantle Convection in the Earth and Planets*, p. 940. Cambridge, UK: Cambridge University Press.
Shackleton NJ and Opdyke ND (1976) Oxygen isotope and paleomagnetic stratigraphy of Pacific core V28–239 late Pliocene to latest Pleistocene. *Geological Society of America Memoir* 145: 449–464.
SISMA, Final Workshop held in Rome on May, 4 2011, ASI web page: http://www.asi.it/it/news/progetto_sisma_una_storia_di_successo.
Smylie DE and Manshina L (1971) The elasticity theory of dislocations in real Earth models and changes in the rotation of the Earth. *Geophysical Journal of the Royal Astronomical Society* 23: 329–354.
Spada G, Yuen DA, Sabadini R, and Boschi E (1991) Lower-mantle viscosity constrained by seismicity around deglaciated regions. *Nature* 351: 53–55.
Steinbrugge KV, Zacher EG, Tocher D, Whitten CA, and Clair CN (1960) Creep on the San Andreas fault. *Bulletin of the Seismological Society of America* 50: 396–404.
Sun WK and Okubo SH (1993) Surface-potential and gravity changes due to internal dislocations in a spherical earth—1. Theory for a point dislocation. *Geophysical Journal International* 114: 569–592.
Takeuchi H and Saito M (1972) Seismic surface waves. *Methods in Computational Physics* 11: 217–295.
Thatcher W and Rundle JB (1979) A model for the earthquake cycle in underthrust zones. *Journal of Geophysical Research* 84: 5540–5556.
Tsai VC, Nettles M, Ekström G, and Dziewonski AM (2005) Multiple CMT source analysis of the 2004 Sumatran earthquake. *Geophysical Research Letters* 32: L17304. http://dx.doi.org/10.1029/2005GL023813.
Turcotte DL and Schubert G (1982) *Geodynamics: Applications of Continuum Physics to Geological Problems*, p. 450. New York: John Wiley and Sons.
Tushingham AM and Peltier WR (1991) ICE-3G: A new global model of late Pleistocene deglaciation based upon geophysical predictions of postglacial relative sea level change. *Journal of Geophysical Research* 96: 4497–4523.
Vermeersen LLA and Sabadini R (1997) A new class of stratified viscoelastic models by analytical techniques. *Geophysical Journal International* 129: 531–570.
Wahr J, Molenaar M, and Bryan F (1998) Time variability of the Earth's gravity field: Hydrological and oceanic effects and their possible detection using GRACE. *Journal of Geophysical Research* 108: 30205–30229.
Ward SN (1994) Constraints in the seismotectonics of the central Mediterranean from very long baseline interferometry. *Geophysical Journal International* 117: 441–452.
Ward SN (1998) On the consistency of earthquake moment release and space geodetic strain rates: Europe. *Geophysical Journal International* 135: 1011–1018.
Woodward RS (1888) On the form and position of mean sea level. *United States Geological Survey Bulletin* 48: 87–170.
Wu P and Peltier WR (1983) Glacial isostatic adjustment and the free air gravity anomaly as a constraint on deep mantle viscosity. *Geophysical Journal of the Royal Astronomical Society* 74: 377–449.
Zhou X, Sun W, Zhao G, Fu G, Dong J, and Nie Z (2012) Geodetic observations detecting coseismic displacements and gravity changes caused by the Mw = 9.0 Tohoku-Oki earthquake. *Journal of Geophysical Research* 117: B05408.
Zollo A, Marcucci S, Milana G, and Capuano P (1999) The 1997 Umbria–Marche (Central Italy) earthquake sequence: Insights on the mainshock ruptures from near source strong motion records. *Geophysical Research Letters* 26: 3165–3168.

6.05 Heat Flow and Thermal Structure of the Lithosphere

C Jaupart, Institut de Physique du Globe de Paris, Paris, France
J-C Mareschal, Université du Québec à Montréal, Montréal, QC, Canada

© 2015 Elsevier B.V. All rights reserved.

6.05.1	**Introduction**	218
6.05.2	**Surface Heat Flux and Heat Transport in the Earth**	218
6.05.2.1	Mechanisms of Heat Transport	218
6.05.2.2	Distribution of Heat Flux: Large-Scale Overview	219
6.05.2.3	Thermal Boundary Layer Structure	220
6.05.2.4	Basal Boundary Conditions	221
6.05.2.5	Controls on Lithospheric Thickness	222
6.05.2.6	The Thermal Lithosphere as Opposed to the Seismically Defined Lithosphere	222
6.05.2.7	Summary: Two Different Approaches to Thermal Studies of the Lithosphere	223
6.05.3	**Oceanic Heat Flux, Topography, and Cooling Models**	223
6.05.3.1	Hydrothermal Circulation	223
6.05.3.2	Heat Flux Measurements near Rift Zones	223
6.05.3.3	Cooling Half-Space Model	224
6.05.3.4	Old Ocean Basins. Flattening of the Heat Flow Versus Age Curve	225
6.05.3.5	The Plate Model for the Oceanic Lithosphere	226
6.05.3.6	Variations of Lithospheric Thermal Structure due to Factors Other Than Age	227
6.05.3.6.1	Large-scale variations of mantle temperature	227
6.05.3.6.2	Hot spots	228
6.05.3.7	Summary	228
6.05.4	**Continental Lithosphere in Steady State**	228
6.05.4.1	Vertical Temperature Distribution	228
6.05.4.2	Crustal Heat Production	229
6.05.4.3	Mantle Heat Flux	232
6.05.4.4	Regional Variations of Heat Flow and Lithospheric Temperatures	235
6.05.4.5	Variations of Crustal Thickness	235
6.05.4.6	Summary	237
6.05.5	**Continental Lithosphere in Transient Thermal Conditions**	237
6.05.5.1	General Features	237
6.05.5.2	Compressional Orogens	237
6.05.5.3	Rifts and Zones of Extension	237
6.05.5.4	Thermal Relaxation of Thick Continental Lithosphere	238
6.05.5.4.1	Sedimentary basins	238
6.05.5.4.2	Tectonic and magmatic perturbations	238
6.05.5.5	Long-Term Transients	239
6.05.5.5.1	Archean conditions	239
6.05.5.5.2	Secular cooling in the lithosphere	239
6.05.6	**Thermal Control on Lithospheric Thickness**	239
6.05.7	**Other Geophysical Constraints on the Thermal Regime of the Continental Lithosphere**	242
6.05.7.1	Constraints from Seismology	242
6.05.7.2	Seismicity, Elastic Thickness, and Thermal Regime of the Lithosphere	243
6.05.7.3	Depth to the Curie Isotherms	246
6.05.7.4	Thermal Isostasy	246
6.05.8	**Conclusions**	246
Appendix A	**Measurement Techniques**	247
Appendix B	**Corrections**	247
Appendix C	**Climatic Effects**	248
Appendix D	**Physical Properties**	248
Acknowledgments		249
References		249

6.05.1 Introduction

The concept of lithosphere is as old as geophysics and was initially introduced in studies of isostatic compensation (Barrell, 1914; Love, 1911). The region of compensation sustains topographic loads and induced stresses: it is made of material that behaves as solid rock and hence was christened lithosphere. It was found to extend to a depth of about 100 km for the large-scale equilibrium that exists between oceans and continents. By definition, the region that lies below has to be such that stresses and horizontal pressure gradients get canceled by flow. It was recognized that such a change of rheological behavior can be explained by a temperature increase but that the competing effects of pressure must also be accounted for. With the data available at the time, it was thought that crustal rocks could in fact be stronger at depth than at the surface, which led to the hypothesis that melting was the most likely culprit (Barrell, 1915). Early workers were weary of this hypothesis because they could see that volcanoes and batholiths are not ubiquitous on Earth and because downward extrapolation of shallow temperature profiles placed melting conditions at a depth of only 50 km or so, significantly less than the compensation depth (Barrell, 1915). They expressed their concern by avoiding any connection with melting and coined the term asthenosphere ('zone of weakness'). The discovery of the seismic low-velocity zone at a depth of about 80 km by Gutenberg (1926, 1948) provided confirmation that there was indeed a weak zone at the expected depth. Further work revealed that this zone was well defined only beneath young oceans and that it did not exist beneath cratons (Brune and Dorman, 1963), which was taken as a setback at the time. Since then, it has become clear that there are fundamental differences between oceanic and continental lithospheres on the one hand and between old and young continental lithospheres on the other hand. This short historical perspective illustrates the challenge of reconciling different strands of information. We shall see that, in fact, different geophysical properties and variables lead to different lithospheric thicknesses and that the simple lithosphere–asthenosphere dichotomy fails to account for the complex thermal and rheological structure of the upper 200–300 km of silicate Earth. Part of the difficulty stems from terminology that is not self-consistent: Lithosphere refers to a material ('rock'), whereas asthenosphere refers to rheology ('weakness').

Rheological behavior and melting strongly depend on temperature, so that it is logical to begin any discussion of lithosphere and asthenosphere with an evaluation of the thermal structure of Earth beneath oceans and continents. Different kinds of geophysical data provide constraints on temperature, but we shall focus here on thermal models derived from heat flow data. Despite many decades of heat flow measurements, many geologic provinces on the continents and large parts of the oceans remain poorly sampled. Two methods have been used to circumvent this data gap. One has been to search for a simple control variable on lithospheric temperatures, such as age. Another has been to develop increasingly precise and detailed seismic velocity profiles and to invert them for temperature.

To set the stage for this chapter, we recapitulate briefly advances made in one generation, as measured against a comprehensive review paper (Sclater et al., 1980). When that review was published, the oceanic heat flow problem was essentially solved. Since then, the model has passed a series of critical tests. For young seafloor, this has entailed documenting and understanding hydrothermal circulation through fractured oceanic crust buried by variable thickness of low-permeability sediments and determination of small-scale heat flux variations. For old seafloor, this has involved precise measurements of heat flux through areas with flat topography unaffected by sedimentary perturbations (slumping and turbidity currents) and deep oceanic currents. On continents, progress has been made, thanks to systematic measurements of heat flux and heat production in old cratons and determination of (P, T) conditions in the lithospheric mantle through xenolith studies. Additionally, subsidence studies in a large number of sedimentary basins have documented the transient response of the continental lithosphere to thermal perturbations. For both continents and oceans, detailed seismic velocity profiles have been interpreted in terms of the thermal structure of the lithosphere and mantle. Complementary information has come from many disciplines, leading to a very large data set and to a sound understanding of key issues.

Here, we review these advances focusing on two issues. One is to assess the reliability of age as a control variable on heat flow and lithospheric thermal structure. In continents, variations of crustal heat production are large in both the horizontal and the vertical directions and prevent the calculation of a single typical 'geotherm' for all provinces of the same age. In oceans, age is indeed the main control variable. The other issue is the control on lithospheric thickness and the mechanism of heat transport at the base of the lithosphere, in other words the bottom boundary condition to be used in thermal models. In steady state, this boundary condition is of small concern because the thermal structure can be determined by downward continuation of surface measurements. It is a major factor, however, if the thermal regime is transient.

We have not aimed this chapter at heat flow specialists and pursue two different goals. One is to show how to use heat flux data, which involves an analysis of available measurements and their uncertainties and a discussion of missing information. Our other goal is to illustrate the controls on the different thermal regimes that are observed and to describe the key steps in data interpretation. This will be achieved with simple physical arguments instead of complicated numerical calculations. In the following, for simplicity, data and measurements refer only to heat flow studies unless otherwise specified.

6.05.2 Surface Heat Flux and Heat Transport in the Earth

6.05.2.1 Mechanisms of Heat Transport

In the solid Earth, three mechanisms of heat transport must be accounted for. Ordered by increasing depth, these are hydrothermal convection, conduction, and convection. Hydrothermal circulation develops in fractures and pores, which get closed by the confining pressure deeper than 10 km. This mechanism is of small importance at the lithospheric scale but plays a crucial role in shallow environments where heat flux measurements are made. Conduction dominates over regions that

are cold and cannot be deformed over geologic timescales. One can see here the strong link between thermal and mechanical processes. At sufficient depth, the temperature is high enough for rocks to deform at significant rates and convective heat transfer dominates. In active volcanic areas, one must account for yet another heat transport mechanism: magma ascent.

6.05.2.2 Distribution of Heat Flux: Large-Scale Overview

More than 58 000 heat flux measurements at the Earth's surface are included in the most recent catalog of the International Heat Flow Commission (http://www.heatflow.und.edu/). This number includes ≈23 000 marine heat flux measurements in the oceans and ≈35 000 values for the continents. All these measurements rely on Fourier's law of heat conduction and hence cannot account for heat that is transported by other mechanisms. The land values have been obtained by both measurements in boreholes in steady state and estimates from bottom hole temperature (BHT) data in oil exploration wells on land and on the continental margins (see **Appendix A**). The continental database includes all available measurements regardless of their quality and should be used with extreme caution. For example, the database includes a large number (>100) of very shallow measurements in lake sediments in a small area of the western Superior Province, Canada. The values obtained are unreliable and are much higher than values from precise measurements in deep boreholes from the same area (Rolandone et al., 2003b). Using the former data set or the unsorted global database leads to erroneous values of lithospheric thickness and unfounded conclusions on thermal events in that part of the Canadian Shield. For reasons that will be explained later, the marine measurements cannot be used directly to infer thermal structure beneath the seafloor.

Due to the many limitations of the raw data, the world heat flow map (**Figure 1**) was obtained by combining reliable land heat flux data with values calculated from a model of cooling of the oceanic seafloor. The heat flow map of North America (**Figure 2**; see also Blackwell and Richards, 2004) was derived from reliable data that were selected from simple quality criteria and illustrates the differences between continental heat flow and oceanic heat flow. Except in tectonically active regions (Basin and Range, Yellowstone, Rio Grande Rift, etc.), heat flux is low throughout the North American continent and lowest in the Canadian Shield. In contrast, heat flux is higher in the oceans than in the continent and higher on the western than on the eastern margin. In addition to these large-scale differences, many other features need detailed interpretation. We shall see that one cannot apply the same physical framework and the same interpretation methods to oceans and continents. From a global perspective, the oceanic lithosphere is in a transient thermal state over most of its short residence time at the Earth's surface, contrary to continents that are mostly in, or close to, thermal steady state. Oceanic heat flux follows a decreasing trend as a function of age that parallels that of elevation (or bathymetry). The continental lithosphere has experienced a longer evolution and is characterized by a complicated structure and composition. More importantly, the

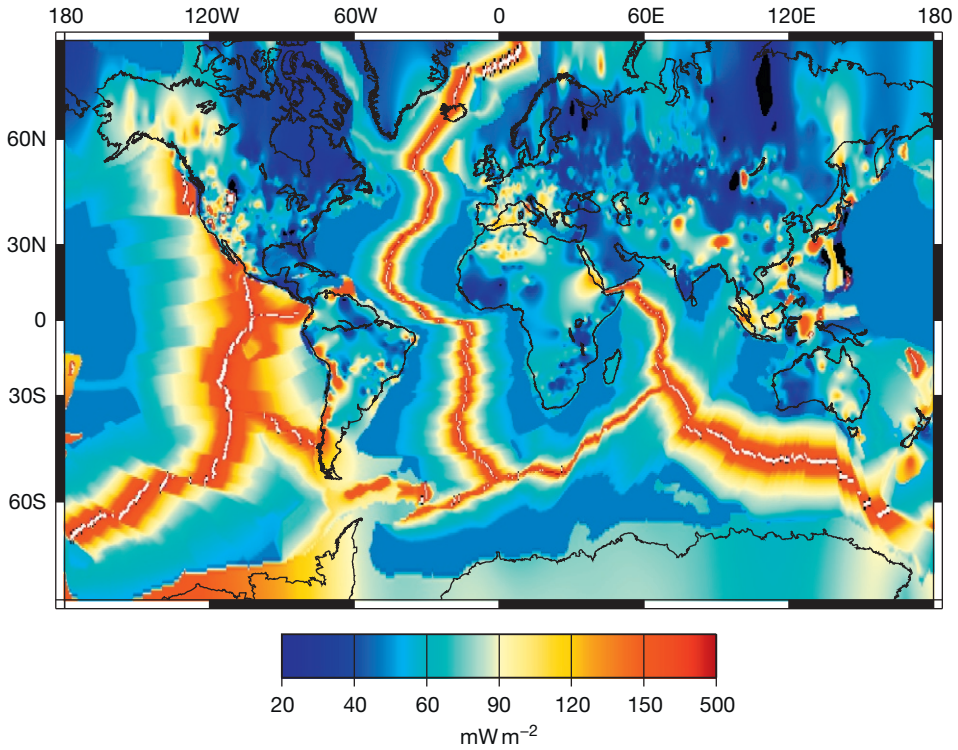

Figure 1 World heat flow map adapted from Jaupart and Mareschal (2011). Land and continental margin data are taken from the latest data compilations by Francis Lucazeau and Derrick Hasterok. The data set includes ≈35 000 standard heat flux measurements and bottom hole temperature estimates in the continents and their margins. For the oceans, heat flux is calculated using equation 8 with seafloor ages from Müller et al. (2008).

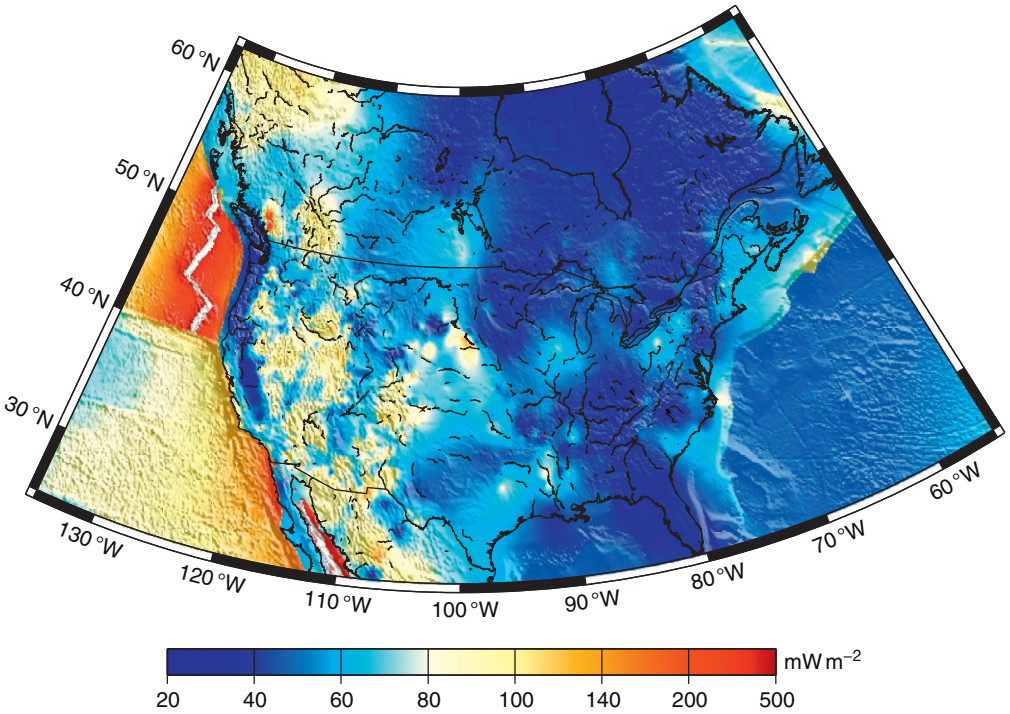

Figure 2 Heat flow map of North America with recent data added to the compilation by Blackwell and Richards (2004).

continental crust is enriched in radioactive elements that contribute the largest component to the surface heat flux. One consequence is that one loses the simple relationship between heat flow and elevation that is so clear in the oceans. Continental elevation is controlled primarily by variations of crustal thickness and composition, and its dependence on thermal structure can be detected only after careful analysis.

The raw average of oceanic and continental heat flux data are 70 and 80 mW m^{-2}, respectively (Harris and Chapman, 2004; Pollack et al., 1993; Sclater et al., 1980). These numbers are biased for several reasons. Only the conductive component of the heat flow has been measured and reported. In the oceans, heat flux measurements are made in sediments where conductive conditions prevail, but hydrothermal circulation and associated advective heat transport may be very active in the igneous crust beneath. For this reason, raw heat flux data are not reliable in lithospheric studies and one must depend on small-scale experiments to account for the effects of hydrothermal convection. Once this is done, the average oceanic heat flux is found to be 101 mW m^{-2}. In the continents, high-heat-flow regions that cover a small surface are oversampled. Excluding the values from the United States, where many values were obtained in the Basin and Range Province, the mean continental heat flux drops to only 65 mW m^{-2}. Another bias comes from the selection and geographic distribution of BHT data that are almost exclusively located in the oil-rich provinces of North America (Alberta and the Gulf Coast states in the United States). The sampling bias can be removed by weighting the data by area as demonstrated in Table 1. Averaging over $1^\circ \times 1^\circ$ windows yields a mean continental heat flux of 65 mW m^{-2}. This mean value does not decrease significantly when averaging is done over wider windows. The histograms of heat flux values or averages over $1^\circ \times 1^\circ$ windows have identical shapes, except for the extremely high values (>200 mW m^{-2}). Excluding the BHT data does not affect these statistics. Another method to reduce the bias consists of binning the heat flux data by geologic type and weighting accordingly (Davies and Davies, 2010; Pollack et al., 1993). It yields the same mean value of 65 mW m^{-2}.

Table 1 Continental heat flux statistics[a]

	μ(Q) mW m^{-2}	σ(Q) mW m^{-2}	N(Q)
All measurements			
All values	70.1	152.0	35 065
Averages $1^\circ \times 1^\circ$	64.5	64.7	4261
Averages $2^\circ \times 2^\circ$	63.7	53.9	1955
Averages $3^\circ \times 3^\circ$	62.6	34.4	1205
Standard measurements only			
All values	80.3	215.1	17 256
Averages $1^\circ \times 1^\circ$	64.8	79.8	3391
Averages $2^\circ \times 2^\circ$	63.0	57.4	1673
Averages $3^\circ \times 3^\circ$	62.6	37.3	1051

[a] μ is the mean, σ is the standard deviation, and N is the number of values.

6.05.2.3 Thermal Boundary Layer Structure

As will be shown later, heat is brought to the base of the lithosphere by convection in the mantle beneath both continents and oceans. The vertical temperature profile must be divided in two parts: an upper part where heat is transported by conduction and a lower convective boundary layer. In steady state and in the absence of heat-producing elements, heat flow is constant in the conductive upper part, implying a constant temperature gradient for constant thermal conductivity.

In contrast, the temperature gradient is not constant in the convective boundary layer and progressively tends to a small value in the mantle beneath. For definition of the thermal lithosphere, we must consider three different depths (Figure 3). The shallowest boundary, h_1, corresponds to the lower boundary of the conductive upper part and of what we shall call the thermal lithosphere. The deepest boundary, h_3, corresponds to the lower limit of the thermal boundary layer. This boundary may also be regarded as the transition between the lithospheric regime and the fully convective mantle regime, such that the mantle thermal structure below is not related to that of the lithosphere. An intermediate depth, h_2, is obtained by downward extrapolation of the conductive geotherm to the isentropic temperature profile for the convecting mantle. With no knowledge of boundary layer characteristics, one can only determine h_2 and h_3, the former from heat flow data and the latter from seismic velocity anomalies. Such determinations are associated with two major caveats. One is that they cannot be equal to one another, which does not permit cross-checks. The other caveat is that they say nothing about h_1. Yet, it is h_1 that defines the mechanically coherent unit (the 'plate') that moves at the Earth's surface and sets the thermal relaxation time that follows tectonic and magmatic perturbations. Uncertainty on this thickness has severe consequences because the diffusive relaxation time is $\propto h^2$. A final remark is that h_1 characterizes the upper boundary condition at the top of the convecting mantle.

We shall discuss later the controls on thickness h_1, which include the increasing strength of mantle material with decreasing temperature, intrinsic buoyancy due to composition, and enhanced strength due to dehydration.

6.05.2.4 Basal Boundary Conditions

In steady state, the heat flux at the Earth's surface is equal to

$$Q_0 = Q_{\text{crust}} + Q_{\text{lith}} + Q_b \qquad [1]$$

where Q_{crust} and Q_{lith} stand for the contributions of heat sources in the crust and in the lithospheric mantle and Q_b is the heat flux at the base of the lithosphere. In the oceans, one may ignore the first two with negligible error and surface heat flux is a direct measure of the basal heat flux. In the continents, the procedure is more complex because it involves estimating the potentially large crustal contribution, Q_{crust}. In both cases, steady state cannot be taken for granted because it depends on the lithospheric thickness, which is part of the solution. Thus, in practice, one must first demonstrate that transient thermal effects are negligible.

Far from steady-state conditions, the surface heat flux includes a large transient component and identifying the different components is an underconstrained problem. In other words, a purely empirical approach is not sufficient and measurements can only be interpreted within a theoretical framework. This major difficulty has been at the core of heat flux studies from the beginning. From a physical point of view, one must introduce three temperatures, T_0 at the upper boundary (the Earth's surface), which, for all practical purposes, may be taken as fixed and equal to 0 °C; T_b at the base of the lithosphere; and T_w in the well-mixed convective interior. In steady state and in the absence of heat sources, one has

$$Q_0 = Q_b = \lambda \frac{T_b - T_0}{h_1} \qquad [2]$$

with λ is the thermal conductivity. A closure equation relates this flux to the temperature difference across the convective boundary layer, $(T_w - T_b)$ (Figure 3). Note that the problem has two unknowns, T_b and h_1, and two input variables, Q_b and T_0. In the general case, one must solve for the fully coupled heat transfer problem, which requires comprehensive convection models involving a variety of scales. Numerical models of this kind remain tentative because of the uncertainties in the setup (initial conditions; rheological properties, accounting for

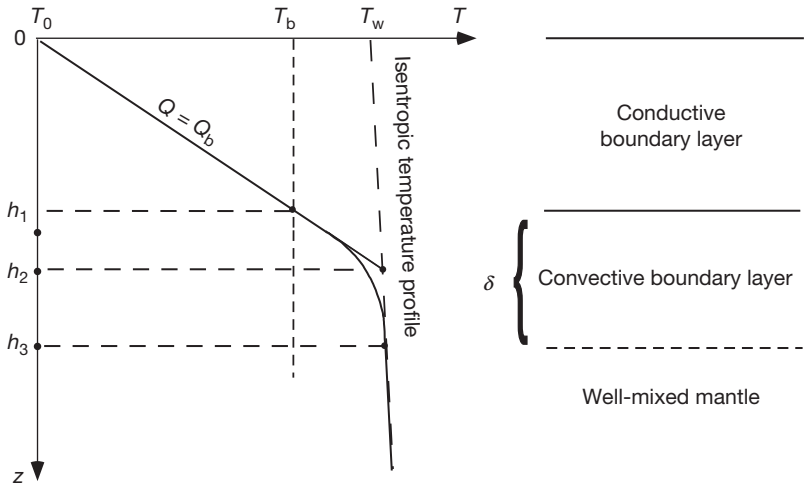

Figure 3 Schematic structure of the thermal boundary layer at the top of Earth convecting mantle. The boundary layer must be split in two parts. In the effectively rigid upper part of thickness h_1, heat is transported by conduction. In the unstable lower part of thickness $\delta = h_3 - h_1$, heat is brought to the base of the upper part through convection. The vertical profile obtained by downward extrapolation of shallow temperature data intersects the well-mixed isentropic profile at yet another depth, h_2. The temperature at the base of the conductive upper part is T_b, which is significantly smaller than the well-mixed potential temperature T_w. The temperature difference across the unstable boundary layer of thickness δ is $T_w - T_b$.

continents and oceans; etc.) as well as inherent computer limitations. For this reason, two simple models have been developed, corresponding to two end-member cases for the efficacy of heat transport at the base of the lithosphere. This can be understood by introducing heat transfer coefficient B such that

$$Q_b = B(T_w - T_b) \quad [3]$$

For perfectly efficient heat transfer, $B \to \infty$, implying that $T_b \to T_w$. This is the fixed temperature boundary condition. Another limit case is when the convective mantle can only maintain a fixed heat flux. In this case, Q_b is set to a constant. Both boundary conditions allow straightforward solutions to the heat equation if the lithospheric thickness is fixed. One additional problem is to ascertain whether or not the lithospheric thickness changes with time, which requires an understanding of the physical controls on lithospheric thickness.

6.05.2.5 Controls on Lithospheric Thickness

Here, we discuss controls on thickness h_1. We know of three such factors, which have been studied to varying degrees of complexity. One is the strong temperature dependence of rheological properties, such that only the least viscous (and hence hottest) part of the thermal boundary layer breaks down and sustains small-scale convection at the base of a strong upper layer (Parsons and McKenzie, 1978). With a reliable rheological law, one can calculate all characteristics of the thermal boundary layer, including thickness h_1 and basal heat flux Q_b. Uncertainties in upper mantle properties have led to reversing the approach, in such a way that heat flux data have in fact been used to obtain constraints on mantle rheology (Davaille and Jaupart, 1994; Huang and Zhong, 2005; Lévy and Jaupart, 2011; Solomatov and Moresi, 2000). A second mechanism relies on an intrinsic density difference such that the plate is made of buoyant material that cannot become unstable upon cooling (Jordan, 1975, 1981; Oxburgh and Parmentier, 1977). In a third mechanism, a 'compositional' rheological contrast stabilizes the plate, such that it is more viscous than the mantle below (Hirth and Kohlstedt, 1996; Pollack, 1986). All three mechanisms are relevant in the Earth but have rarely been included together in convection calculations so far. The interesting question is to assess the importance of each one. Current limitations on the resolving power of geophysical studies and on how the physical properties of lithospheric material vary as a function of temperature, composition, and water content prevent firm conclusions. Useful information can be gained by invoking the physical processes of continental root formation and evolution.

Mantle material upwelling beneath an oceanic ridge undergoes partial melting and basalt extraction, leaving a residue that is both slightly buoyant (Oxburgh and Parmentier, 1977; Schutt and Lesher, 2006) and more viscous than the underlying mantle (Hirth and Kohlstedt, 1996). Depending on mantle temperature and water content, melting may start at depths between about 60 and 80 km, which sets the thickness of the buoyant and viscous residue. Naturally, one must ask whether this is equal to h_1, the thickness of the thermal lithosphere. The continental problem is more complicated because there is no consensus on the mechanism of the formation of cratonic roots. One popular model is inspired by the oceanic one and invokes melting and melt extraction at the top of large mantle plumes. According to an alternative model, continental lithosphere is generated by melting above subduction zones (Carlson et al., 2005). The key consequence is that the protoroot may remain hydrated, in which case it is intrinsically buoyant but not intrinsically more viscous. The processes of melting and melt extraction account for the changes of physical properties that are required for stabilization but do not specify thickness. One must allow for two, and possibly three, phases of lithosphere formation. Following partial melting, the buoyant residue may thicken due to tectonic compression or thrusting and may then thin due to convective breakdown or erosion. Even if its thickness does not change, the lithosphere may be chemically modified by the invasion of fluids or melts from below (Lee et al., 2011).

There can be no doubt that continental and oceanic lithospheres are not alike. Because of its limited time span at the Earth's surface, oceanic lithosphere has its characteristics set by melting at a mid-ocean ridge and cooling only, with only minor and local modifications due to mantle plumes. For the much older continental lithosphere, composition and thickness may change with time and may vary with position within a single landmass. Today, we know that it is much thicker than its oceanic analogue and that it is made of intrinsically buoyant material (Doin et al., 1996; Turcotte and McAdoo, 1979; Jordan, 1975).

6.05.2.6 The Thermal Lithosphere as Opposed to the Seismically Defined Lithosphere

As will be illustrated in this chapter, knowledge of the Earth's shallow thermal structure remains subject to large uncertainties, which has motivated the use of alternative methods. Among them, seismic methods are the most powerful and precise, but do not discriminate well between the different thicknesses involved (**Figure 3**).

On a worldwide scale, with very few exceptions, cratons are systematically associated with fast regions extending to depths of about 200–300 km. With reference to the schematic lithospheric structure given in **Figure 3**, such estimates correspond to depths $\geq h_3$ and hence provide upper bounds to both h_1 and h_2. The lithosphere preserves compositional heterogeneities in contrast to the well-mixed asthenosphere. Thus, its thickness can be defined by seismology as the depth where small-scale lateral heterogeneities disappear. Such depth would be $\geq h_1$. Discontinuities in the depth range 80–240 km have been observed by seismic reflection and refraction experiments and by teleseismic body wave studies. They cannot be explained by thermal effects but could be due to higher hydration in the asthenosphere, in which case they would correspond to h_1.

Independent information comes from the vertical distribution of seismic anisotropy. One may expect different anisotropy characteristics and orientation depending on depth (Gung et al., 2003). Below the base of the lithosphere, anisotropy is due to convective shear stresses and should be aligned with the direction of plate motion. Within the lithosphere, anisotropy probably reflects a fabric inherited from past tectonic events (Silver, 1996). The depth at which the anisotropy characteristics change may therefore be interpreted as the base of the lithosphere, that is, $\geq h_1$.

Electrical conductivity profiles provide yet another means of constraining lithospheric thickness. Conductivity is sensitive to both the temperature and the water content of mantle rocks. The analysis of data from the Archean Slave Province, Canada, and the northeastern Pacific shows that old continental lithosphere contains less water than the oceanic mantle in the depth range 150–250 km (Hirth et al., 2000).

6.05.2.7 Summary: Two Different Approaches to Thermal Studies of the Lithosphere

The thermal boundary layer at the Earth's surface must be divided into two parts with different rheologies and heat transport mechanisms. These differences are significant for three reasons. One is that different geophysical methods provide constraints on different parts of the boundary layer and hence cannot be compared without care. Another reason is that heat flow is not sensitive to the same parts of the boundary layer in transient and steady-state conditions. A third reason is that these two parts play different roles for the dynamics of mantle convection and for the secular cooling of the Earth. For example, mantle plumes must first go through the convective boundary layer before reaching the base of the lithosphere. Thus, for studies of plume penetration through the lithosphere, the relevant thermal perturbation is the sum of the temperature anomaly driving plume ascent through the deep mantle and the temperature difference across the boundary layer, which may be large.

For these reasons, a purely empirical approach to heat flux data is doomed to fail. The problem is more acute in continents because of crustal heat production, an independent variable unrelated to heat transport mechanisms. At the very least, heat flux data provide quantitative constraints on models derived from other observables. At best, when used in conjunction with other methods and some consideration of heat transport mechanisms, they provide insight on mantle dynamics.

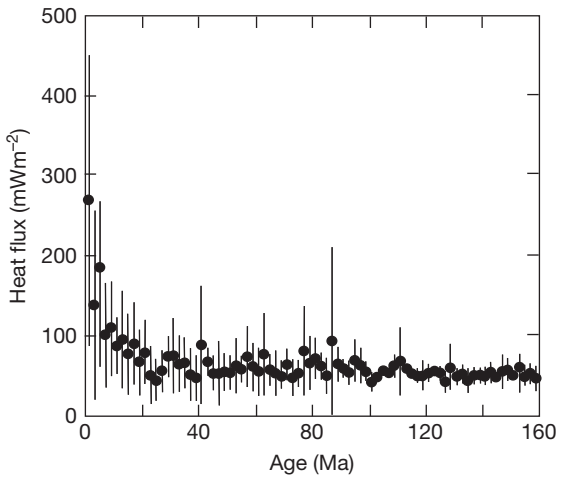

Figure 4 Oceanic heat flux data in 2 My interval bins as a function of age, from the compilation by Stein and Stein (1992). Note the non-monotonic variation of the mean heat flux and the extremely large data scatter at young ages.

6.05.3 Oceanic Heat Flux, Topography, and Cooling Models

Heat flow data through seafloor of all ages exhibit considerable scatter (Figure 4), which has generated a lot of confusion and debate. Very high values in excess of 200 mW m^{-2} have been recorded on young seafloor, in many cases in association with much lower values. Such high values are absent from seafloor older than about 10 My and provide key evidence for studies of the oceanic lithosphere. Four decades of measurements in all the world's ocean basins have confirmed that the large scatter of oceanic heat flow values is due neither to limited sampling nor to measurement errors and is a fundamental feature of heat transport processes in the oceanic crust and its sedimentary cover. Such shallow processes affect heat flow measurements but do not modify greatly the cooling of oceanic lithosphere as a whole, which proceeds on a much larger depth range.

6.05.3.1 Hydrothermal Circulation

Submarine observations of mid-ocean ridges have revealed spectacular plumes of hot aqueous solutions oozing out of the seafloor. Measurements on samples from DSDP and ODP boreholes and ophiolite massifs have shown that the oceanic crust is pervasively fractured and chemically altered. Mass balance calculations demonstrate that large volumes of fluid circulate through the crust, carrying large amounts of energy (e.g., Davis and Elderfield, 2004). *In situ* quantitative assessment of hydrothermal circulation can only be achieved by establishing the energy budget of a vast area, such that it encompasses both downwellings and upwellings. For young ocean floor, upwellings carry hot fluids into the sea, and a proper heat loss estimate can only be made by simultaneously measuring the discharge rate and the temperature anomaly (Ramondec et al., 2006). A single black smoker can evacuate as much as 0.1 MW (Barreyre et al., 2012), but diffuse venting through thin crack networks and bacterial mats account for an even larger power, $\approx$ 90% at the Tour Eiffel vent site in the Lucky Strike hydrothermal field of the Mid-Atlantic Ridge (Mittelstaedt et al., 2012). The average heat flux through that site is about 10^7 mW m^{-2} (Mittelstaedt et al., 2012). These large amounts of heat lost by very young oceanic lithosphere cannot be measured by conventional heat flow techniques. Because of this, one strategy is to avoid sites with hydrothermal convection, but this would exclude seafloor younger than 60 My. The other strategy is to seek sites with thick sedimentary cover. Hydrothermal convection is mostly active through the fractured oceanic crust. With a thick sedimentary cover, upwellings are slowed down and become diffuse and hence tend towards thermal equilibrium with the surrounding matrix. In this case, conduction is the dominant heat transport mechanism and conventional heat flow techniques can be used.

6.05.3.2 Heat Flux Measurements near Rift Zones

Several detailed surveys have led to a thorough understanding of the mass and heat balance of young oceanic basement and sedimentary cover. Figure 5 shows a comparison between a heat flux profile on very young seafloor near the Juan de Fuca

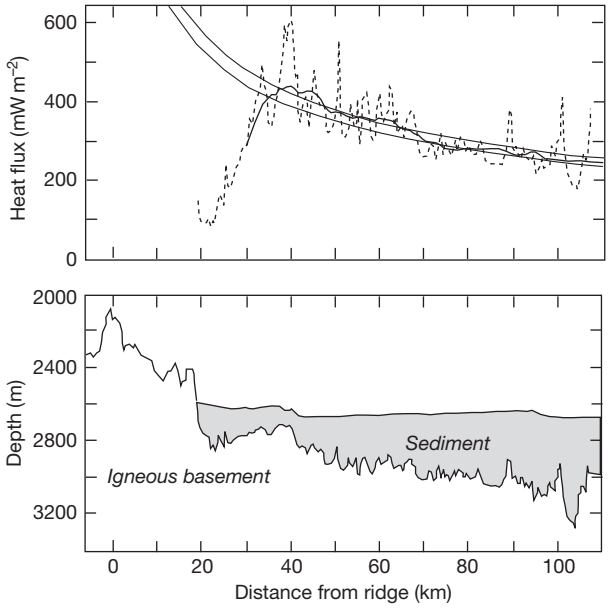

Figure 5 (top) Horizontal variation of heat flux away from Juan de Fuca Ridge (adapted from Davis EE, et al. (1999) Regional heat flow variations across the sedimented Juan de Fuca ridge eastern flank: Constraints on lithospheric cooling and lateral hydrothermal heat transport. *Journal of Geophysical Research* 104: 17,675–17,688). (bottom) Structure of young seafloor beneath the measurement sites, showing the lack of sedimentary cover at small distance from the ridge. The heat flux profile was obtained with a running average over 15 km windows. The two curves correspond to the half-space cooling model, such that $Q = C_Q \tau^{-1/2}$ with the two extreme values that have been proposed for $C_Q = 470$ and 510 mW m^{-2} My^{-1}.

Ridge and a cross section showing the sediment thickness and basement depth from Davis et al. (1999). The heat flux fluctuates on the scale of station spacing (2 km), which implies that surveys with large station spacing do not yield meaningful results. To emphasize the long-wavelength trends, a 15 km running average was applied on the heat flux profile. This profile shows two distinct trends: Near the basement outcrop, to the left, the heat flux increases with age and reaches a maximum value in excess of 400 mW m^{-2}; further away from the outcrop, the heat flux decreases with age. In the latter region, the total heat flux variation is large enough to allow comparison with theoretical models for the cooling of the ocean lithosphere.

Direct observation of the seafloor shows that the basement outcrop region is a zone of recharge and that, beneath the sedimentary cover, flow is dominantly horizontal. Because the basement surface is maintained approximately isothermal by vigorous convection, variations of heat flux seem mostly controlled by sediment thickness. Focused discharge with very large heat flux values occurs at a few locations in association with basement topographic highs. Elsewhere, water flow is diffuse, such that it equilibrates with the sediments. Rates of flow deduced from chemical concentration gradients are consistent with theoretical hydrologic calculations (Davis et al., 1999). In order to evaluate the deep-seated heat flux, it is thus important to make measurements in a sufficiently large area with small sampling distance to filter out the effect of sediment thickness variability and of the ventilation areas.

6.05.3.3 Cooling Half-Space Model

Oceanic ridges are associated with mantle upwellings feeding plate-scale horizontal flow. Such flow occurs in a variety of settings and has been studied extensively. Flow is dominantly horizontal with negligible variations of horizontal velocity with depth. The large wavelengths of heat flow variations imply that heat transfer is dominantly vertical. In a 2-D rectangular coordinate system, with x distance from the ridge and z depth from the seafloor, the temperature obeys the following equation:

$$\rho C_p \left(\frac{\partial T}{\partial t} + u \frac{\partial T}{\partial x} \right) = \frac{\partial}{\partial z} \left(\lambda \frac{\partial T}{\partial z} \right) \quad [4]$$

where u is the horizontal velocity, ρ the density of the lithosphere, C_p the heat capacity, and λ the thermal conductivity. We have neglected viscous heat dissipation and radiogenic heat production, which is very small in mantle rocks. Over the timescale of an oceanic plate, steady state can be assumed (i.e., the temperature remains constant at a fixed distance from the ridge). In steady state with constant thermal conductivity, the heat equation [4] reduces to

$$\rho C_p u \frac{\partial T}{\partial x} = \lambda \frac{\partial^2 T}{\partial z^2} \quad [5]$$

It is better to work in a reference frame attached to the oceanic plate and involves the age of the sea floor τ

$$\frac{\partial T}{\partial \tau} = \kappa \frac{\partial^2 T}{\partial z^2} \quad [6]$$

where κ is thermal diffusivity

For a constant spreading rate, age is proportional to distance to the ridge:

$$\tau = x/u \quad [7]$$

This is the one-dimensional heat diffusion equation, whose solution requires a set of initial and boundary conditions. The upper boundary condition and the initial condition can be specified with little error. The high efficiency of heat transport in the water column ensures that the seafloor surface is kept at a fixed temperature T_0 of about 4 °C. The initial condition is set by a model for the ascent of hot material (Davis and Lister, 1974; Roberts, 1979). Over the horizontal scale of a mantle upwelling, one may neglect dissipation. Neglecting further lateral heat transfer, one can use solutions for isentropic pressure release (McKenzie and Bickle, 1988). For such an initial geotherm, temperature decreases with increasing height above the melting point. The total temperature drop depends on the starting mantle temperature, which sets the depth at which melting starts, and estimates for the heat of fusion, but never exceeds 200 K. This is much smaller than the difference ΔT between the surface temperature and the starting temperature, and it may be neglected in a first approximation. For uniform initial temperature $T_i = T_0 + \Delta T$, this model yields a heat flux proportional to $1/\sqrt{\tau}$:

$$Q = \lambda \frac{\Delta T}{\sqrt{\pi \kappa \tau}} = C_Q \tau^{-1/2} \quad [8]$$

where $C_Q = \lambda \Delta T / \sqrt{\pi \kappa}$ is a constant. As shown by Carslaw and Jaeger (1959) and Lister (1977), this simple age dependence

also holds when physical properties are temperature-dependent. In this model, by definition,

$$h_2 = \sqrt{\pi\kappa\tau} \quad [9]$$

With this simple model, the heat flux solution diverges as the seafloor age tends to zero. This is due to the choice of initial temperature profile at the ridge, which does not account for lateral heat transport at the ridge and specifies that mantle at high temperature gets emplaced against cold seawater instantaneously. A better condition is such that the heat brought in at the ridge by the mantle upwelling is lost horizontally to the oceanic plate (Davis and Lister, 1974). In this modified model, the heat flux at the ridge is finite. Calculated heat flux values differ significantly from those of the previous model only for ages <1 My (Sclater et al., 1980). For studies of oceanic lithosphere as a whole, this is completely negligible.

The validity of the cooling model can be assessed by going back to the Juan de Fuca heat flux data (**Figure 5**). The 15 km running average of heat flux measured over thick sediments fits the theoretical prediction beautifully. Three additional verifications may be made. From heat flux data, the constant C_q has been estimated to be 490 ± 20 mW m^{-2} My$^{1/2}$. From well-known values of thermal conductivity and thermal diffusivity, we obtain an estimate for the mantle temperature $\Delta T = 1350$ °C, which is very close to values deduced from the chemical composition of mid-ocean ridge basalts (Kinzler and Grove, 1992).

A second verification is provided by bathymetry data. Using an isostatic balance condition,

$$\frac{dh}{dt} = \frac{\alpha}{C_p(\rho_m - \rho_w)} q(0,t) \quad [10]$$

where α is the volume thermal expansion coefficient, ρ_m the density of the mantle, and ρ_w the density of sea water. Thus,

$$h(\tau) = H_0 + C_h\sqrt{\tau} \quad [11]$$

with

$$C_h = \frac{2\alpha\rho_m\Delta T}{(\rho_m - \rho_w)}\sqrt{\frac{\kappa}{\pi}} \quad [12]$$

Bathymetry records the total cooling of the oceanic lithosphere since its formation at the mid-ocean ridges. The bathymetry data are far less noisy than the heat flux data and fit extremely well the model predictions for oceanic lithosphere younger than ≈ 100 My (**Figure 6**). Again, the constant C_h can be calculated from the value of constant C_Q in the heat flux equation and checked against the observations. This was done by Davis and Lister (1974) following the theoretical analysis by Parker and Oldenburg (1973). In a recent study of young (i.e., <80 My) seafloor bathymetry, Crosby and McKenzie (2009) found that the values $C_h = 325 \pm 20$ mMy$^{-1/2}$ and $H_0 = 2600 \pm 200$ fit relatively well the data. The value of C_h/C_Q from measurements is close to that calculated from standard values of the physical properties ($C_h/C_Q \approx 700$ m^{3}W^{-1} My^{-1}).

A third verification is possible, thanks to geoid anomalies that decrease linearly with age. As before, the observed C_Q value can be used together with well-known values of physical properties to predict these anomalies, with excellent results

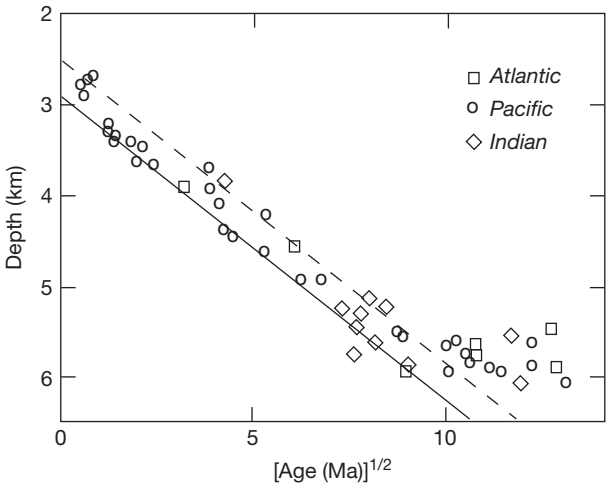

Figure 6 Depth to the seafloor basement as a function of the square root of age (data from Carlson RL and Johnson HP (1994) On modeling the thermal evolution of the oceanic upper mantle: An assessment of the cooling plate model. *Journal of Geophysical Research* 99: 3201–3214). These data correspond to DSDP holes and are not affected by uncertainties on sediment thickness. The dashed lines represent the two extreme linear relationships that are consistent with data.

(Cadio and Korenaga, 2012; Cazenave, 1984; Haxby and Turcotte, 1978; Sandwell and Schubert, 1980).

Surface wave tomography models of the upper mantle (Debayle et al., 2005; Shapiro and Ritzwoller, 2002) show variations in shear wave velocities in the upper mantle down to 400 km. In the oceans, these variations are directly related to temperature variations in the cooling plate. Global and regional studies have shown that, for young oceans, the increase in shear wave velocity with age fits well a half-space cooling model (e.g., Maggi et al., 2006; Priestley and McKenzie, 2006).

The cooling model therefore accounts for all the observations on young seafloor and can be used to determine the mantle temperature. Should cooling proceed unhampered, the thermal boundary layer would thicken and reach a thickness of about 130 km by 180 My.

6.05.3.4 Old Ocean Basins. Flattening of the Heat Flow Versus Age Curve

Heat flux data depart from eqn [1] on seafloor older than *ca.*100 My and tend to a constant value of ≈ 48 mW m^{-2} (**Figures 7** and **8**). Depth to the ocean floor also departs from the theoretical predictions and tends to a constant value. These observations have been hotly debated and have important consequences that are discussed in the next section. Because heat flux data are scarce and subject to large experimental uncertainties, one could choose to focus on bathymetry. Depth values also exhibit significant scatter, however, due to inaccurate estimates of sediment thickness and inherent basement roughness (Johnson and Carlson, 1992). Another issue is the influence of seamounts and large hot spot volcanic edifices, which obscure the behavior of 'normal' lithosphere, if such a thing exists (Heestand and Crough, 1981). From the

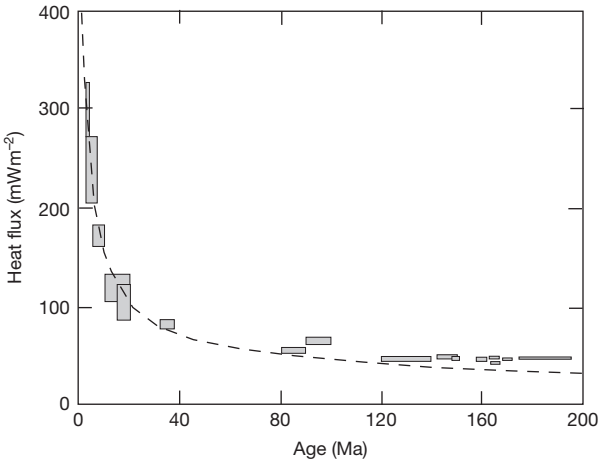

Figure 7 Reliable oceanic heat flux data as a function of age (adapted from Lister CRB, Sclater JG, Nagihara S, Davis EE, and Villinger H (1990) Heat flow maintained in ocean basins of great age – Investigations in the north-equatorial West Pacific. *Geophysical Journal International* 102: 603–630). The boxes represent the average heat flux in well-sedimented areas of the seafloor. The height of each box is the 90% confidence interval for the mean heat flux, and the width represents the age range or uncertainty. The dashed line is the best-fit half-space cooling model. Note that heat flux data through old seafloor are systematically higher than the model predictions.

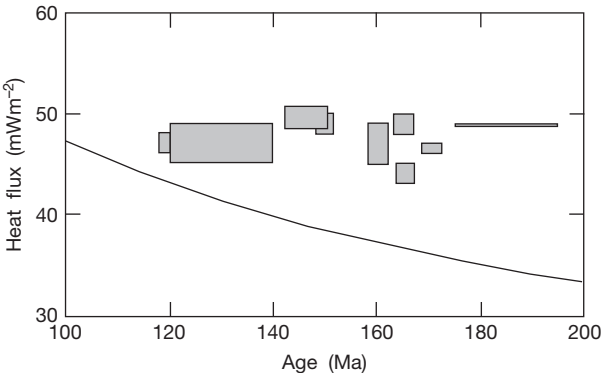

Figure 8 Close-up of the reliable oceanic heat flux data through seafloor older than 100 My (adapted from Lister CRB, Sclater JG, Nagihara S, Davis EE, and Villinger H (1990) Heat flow maintained in ocean basins of great age – Investigations in the north-equatorial West Pacific. *Geophysical Journal International* 102: 603–630). Within measurement uncertainty, these data suggest that heat flux is constant and about 48 mW m^{-2}.

general standpoint of mantle convection, depth to the seafloor is sensitive to the thermal structure of the whole upper mantle and to stresses at the base of the lithosphere, which depend on the dynamics of plate-scale convection (Davies, 1988). It turns out, therefore, that the flattening of the bathymetry does not allow straightforward conclusions.

Perhaps ironically, it is probably best to go back to heat flux because it is sensitive neither to deep mantle temperature anomalies nor to convective stresses. Over the limited age range of oceanic lithosphere, heat flow records shallow thermal processes within and just below the lithosphere (Davaille and Jaupart, 1994). This motivated detailed and accurate heat flux surveys through old seafloor (Lister et al., 1990). New measurement techniques relying on longer temperature probes and *in situ* conductivity measurements are affected by much smaller uncertainties (Becker and Davis, 2004). **Figure 8** shows reliable heat flux data including measurements specifically collected to detect age-related variations if there were any. It is clear that heat flux departs from the $1/\sqrt{\tau}$ behavior and exhibits no detectable variation at ages larger than about 120 My. This indicates that heat is supplied to the lithosphere from below.

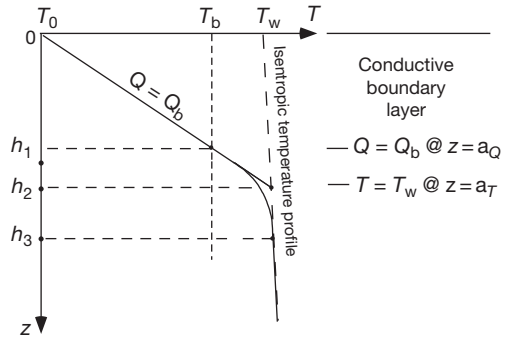

Figure 9 (left) Schematic structure of the thermal boundary layer at the top of Earth's convecting mantle. (right) Two simple plate models and their relationships to the true boundary layer structure. The fixed temperature model corresponds to thickness h_2 and to temperature T_w. The fixed heat flux model corresponds to thickness h_1 and to temperature T_b.

6.05.3.5 The Plate Model for the Oceanic Lithosphere

Data on old seafloor indicate that heat is brought into the lithosphere from below, which has led to the 'plate' model such that a boundary condition is specified at some fixed depth (the base of the plate). **Figure 9** illustrates the relationships between the thermal boundary layer structure and the plate model characteristics. The original plate model of McKenzie (1967) is such that the plate is initially at a fixed temperature ΔT_T, the surface is maintained at $T=0$, and the base of the plate at depth a_T is maintained at ΔT_T. With reference to **Figure 3**, one has $a_T = h_2$, showing that the fixed temperature model does not specify the thickness of the unstable boundary layer at the base of the lithosphere.

Assuming for simplicity that physical properties are constant, an important point to which we shall return, temperature within the plate obeys the following equation:

$$T(z,t) = \Delta T_T \left(\frac{z}{a_T} + \frac{2}{\pi} \sum_{n=1}^{\infty} \frac{1}{n} \sin\left(\frac{n\pi z}{a_T}\right) \exp\left(\frac{-n^2\pi^2\kappa t}{a_T^2}\right) \right) \quad [13]$$

which defines a characteristic time:

$$\tau_T = \frac{a_T^2}{\kappa} \quad [14]$$

For $t \gg \tau_T$, the series can be approximated by its leading term as follows:

Table 2 Parameter values for the oceanic plate model

ΔT (°C)	a (km)	Method	Reference
1333	125	Constant properties – fixed T	Parsons and Sclater (1977)
1450	95	Constant properties – fixed T	Stein and Stein (1992)
1350	118	T-dependent properties – fixed Q at variable depth[a]	Doin and Fleitout (1996)
1315	106	T-dependent properties – fixed T	McKenzie et al. (2005)

[a]In this model, heat flux is fixed at the base of the growing thermal boundary layer.

$$T(z,t)=\Delta T_{\mathrm{T}}\left(\frac{z}{a_{\mathrm{T}}}+\frac{2}{\pi}\sin\left(\frac{\pi z}{a_{\mathrm{T}}}\right)\exp\left(-\frac{\pi^2\kappa t}{a_{\mathrm{T}}^2}\right)\right) \quad [15]$$

which shows straightforward relaxation behavior. Surface heat flux and depth to the seafloor are readily calculated from this solution and are in good overall agreement with the observations (Parsons and Sclater, 1977). There are small systematic differences between model predictions and observations, however, indicating that the model is only an approximation (Johnson and Carlson, 1992; Carlson and Johnson, 1994). Depending on the data set and on model specifications (such as temperature-dependent physical properties), the analysis provides estimates of $\approx$100 km and 1300 °C for a_T and ΔT, respectively (**Table 2**). As in the case of the half-space model, the model can be tested against direct petrologic estimates (Kinzler and Grove, 1992; McKenzie and Bickle, 1988). This test invalidates the widely used model of Stein and Stein (1992), which requires $\Delta T = 1450$ °C.

An alternative plate model corresponds to the fixed flux boundary condition. In this case, the plate is initially at temperature ΔT_{q} and fixed flux $\lambda\Delta T_{\mathrm{Q}}/a_{\mathrm{Q}}$ is maintained at the base a_{Q}, which is in fact h_1 (**Figure 9**). The solution is

$$T(z,t)=\frac{\Delta T_{\mathrm{Q}}z}{a_{\mathrm{Q}}}+\frac{8\Delta T_{\mathrm{Q}}}{\pi^2}\sum_{n=0}^{\infty}\frac{1}{(2n+1)^2}\cos\left(\frac{(2n+1)\pi z}{2a_{\mathrm{Q}}}\right)\exp\left(\frac{-(2n+1)^2\pi^2\kappa t}{4a_{\mathrm{Q}}^2}\right) \quad [16]$$

where the temperature difference ΔT_{Q} corresponds to steady state with basal heat flux Q_{b}

$$\Delta T_{\mathrm{Q}}=\frac{Q_{\mathrm{b}}a_{\mathrm{Q}}}{\lambda} \quad [17]$$

and where the characteristic relaxation time is

$$\tau_{\mathrm{Q}}=4\frac{a_{\mathrm{Q}}^2}{\kappa} \quad [18]$$

With this solution, the leading term in the series expansion for the age dependence of heat flux and bathymetry exhibits the same type of relaxation than for a fixed basal temperature but with a different value for the characteristic relaxation time. A fit to the data forces the two relaxation times to take the same value of about 80 My, the age at which the subsidence departs from boundary layer cooling subsidence. This leads to

$$a_{\mathrm{Q}}=\frac{a_{\mathrm{T}}}{2}\approx 50\,\mathrm{km} \quad [19]$$

This model does not specify the characteristics of the unstable boundary layer. With reference to **Figure 3**, one has $a_{\mathrm{T}}=h_2$ and $a_{\mathrm{Q}}=h_1$. Thus, the solutions for the two plate models are consistent with the fundamental inequality $h_2>h_1$. The estimate for h_1 may be compared to the thickness of depleted mantle, which depends on the well-mixed mantle potential temperature (T_{w}). For $T_{\mathrm{w}}\approx 1300$ °C, this is $\approx$60 km. Accounting for the various uncertainties involved, the two estimates may be considered in satisfactory agreement.

The point of this discussion is not to dwell on precision, which would require more complex calculations with temperature-dependent properties, but to show how to interpret thickness estimates deduced from thermal models. It makes it clear, for example, that the fixed temperature model cannot be used to determine the thickness of melt-depleted mantle. This model, however, provides an approximate description of the whole oceanic boundary layer. **Figure 10** shows the temperature cross section based on this model calculated by McKenzie et al. (2005), which accounts for temperature-dependent physical properties.

From a physical standpoint, the fixed temperature and fixed heat flux models must both be considered as crude simplifications. The former requires a specific time variation of heat flux at the base of the lithosphere, which may not be consistent with true mantle dynamics. The latter model requires that heat is brought into the lithosphere at small ages. More complex models have a fixed heat flux brought to the base of a growing thermal boundary layer (Doin and Fleitout, 1996), at which point it is perhaps best to turn to full numerical simulations (Dumoulin et al., 2001; Huang and Zhong, 2005). One should note, however, that the oceanic lithosphere is made of depleted mantle, such that it already has a finite thickness at zero age. We shall evaluate later how its thickness can increase due to cooling and eventually stabilize at some value such that conduction can evacuate heat input due to convection in the asthenosphere.

6.05.3.6 Variations of Lithospheric Thermal Structure due to Factors Other Than Age

6.05.3.6.1 Large-scale variations of mantle temperature

The chemical composition of mid-ocean ridge basalts varies within a restricted range, but these variations are highly significant (Klein and Langmuir, 1987) because they require that the mantle temperature is not uniform along a ridge axis. Detailed petrologic studies yield a range of 1300–1450 °C for the source temperature (Kinzler and Grove, 1992). This range does not correspond to experimental errors, but to compositional variations among mid-ocean basalts that are due to variations in source temperature. Depending on which scale these variations occur, their causes and consequences differ strongly. Small-scale heterogeneities are of local significance only and have no effect on geophysical observables. Large-scale heterogeneities indicate

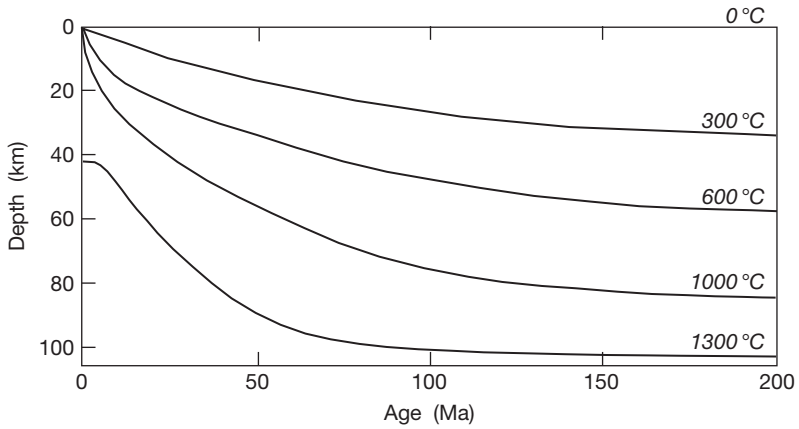

Figure 10 Isotherms in the oceanic lithosphere from the plate model of McKenzie et al. (2005). Earthquake hypocenters are confined to shallow regions above the 600 °C isotherm.

the existence of large mantle domains and imply variations in plate temperatures and physical properties.

Heat flux data allow accurate determination of the heat flux cooling constant, C_Q, between 470 and 510, corresponding to an uncertainty of only ≈4%. In terms of mantle temperature, assuming no uncertainty on the thermal properties entering the expression for C_Q, this corresponds to an uncertainty for T_i of ≈±60 °C. This is compatible with the petrologic estimates but does not allow an independent constraint. Bathymetry data exhibit large-scale trends with along-strike variations of ridge topography as well as of subsidence rate (Marty and Cazenave, 1989). With a modified plate model, one may estimate that the mantle temperature varies by about ±100 °C (Lago et al., 1990). Such variations occur on a large scale and may be traced from the ridge to old seafloor (Humler et al., 1999).

6.05.3.6.2 Hot spots

Hot spots are associated with spectacular swells on the seafloor (Crough, 1983). Debate has been on whether mantle plumes are involved and on the extent of lithospheric thinning. Several mechanisms can be invoked for a bathymetric swell, involving heating of lithospheric material or a normal stress applied to the base of the lithosphere by an active mantle upwelling (i.e., a dynamic stress) or by ponded buoyant (hot) plume material (Jurine et al., 2005).

The search for heat flux anomalies over hot spot swells has led to mixed results. Courtney and White (1986) found a weak anomaly over Cape Verde. Bonneville et al. (1997) had to resort to closely spaced measurements to detect a small anomaly of about 8 mW m^{-2} over the Réunion hot spot track. A global analysis shows that swells are associated with above normal heat flux values (Stein, 1995). Without lithospheric thinning, it would take about 100 My for a basal thermal perturbation to be detectable in surface heat flux data. No heat flux anomaly above the error level has been observed along the Hawaiian hot spot track, probably due to hydrothermal convection within the sedimentary moat surrounding the island (Harris et al., 2000; Von Herzen et al., 1989). The thermal state of the oceanic lithosphere near hotspots can now be studied with surface wave tomography (Priestley and McKenzie, 2006). For example, Li et al. (2004) found thinning by ≈50 km of the lithosphere beneath the island of Kauai. Low-velocity anomalies have been found beneath Iceland and the Azores hotspots in the Atlantic (Pilidou et al., 2005), but seismic evidence for an anomaly related to the Pacific superswell remains elusive (Maggi et al., 2006).

The data indicate large modifications of lithospheric thickness and thermal structure above mantle plumes, as expected on physical grounds (Jurine et al., 2005; Moore et al., 1999). Such modifications, however, depend on plume strength and lithospheric thickness and must be evaluated on a case by case basis.

6.05.3.7 Summary

At small ages, heat flux data are noisy and their small-scale variations are not sensitive to deep thermal conditions. For ages < 100 My, heat flux data are consistent with conductive cooling of the oceanic lithosphere and yield an estimate of the mantle temperature. The deepening of bathymetry with age provides a direct measure of the time-integrated cooling of the lithosphere. The observed bathymetry *versus* age relationship is the strongest supporting evidence for the cooling model. For old ages, plate models relying on specific choices for the basal boundary condition must be considered as approximate, and they cannot specify how the lithospheric thickness stabilizes to a constant value. Heat flux data provide important insight into convective processes because they specify the rate at which heat is brought to the base of the lithosphere. Determination of plate thickness from a thermal model is subject to some ambiguity because it depends on assumed boundary conditions.

6.05.4 Continental Lithosphere in Steady State

6.05.4.1 Vertical Temperature Distribution

There is now no doubt that the continental lithosphere is much thicker than its oceanic counterpart. The choice of a boundary condition at the base of the lithosphere is important when considering the transient regime and the return to equilibrium. For a 200 km thick lithosphere with constant temperature at its

base, the thermal relaxation time is ≈300 My. As shown earlier, it would be four times as long for a constant heat flux boundary condition. Gass et al. (1978) and Jaupart et al. (1998) had also pointed out that for lateral changes in basal heat flux to reach the surface, they must remain immobile relative to the lithosphere for more than 1 Gy. Basal boundary conditions varying on a timescale <500 My have little or no effect on surface heat flux. A thick lithosphere introduces two additional complexities. One is that even very small concentrations of radioelements in the lithospheric mantle may account for a nonnegligible fraction of the total heat flow. Another is that the surface heat flux cannot be in equilibrium with the present heat production in the lithospheric mantle (Michaut and Jaupart, 2004).

In the crust, the progressive rundown of radioactivity is slow compared to thermal equilibration time, and steady state may be assumed in many situations. Because heat production varies at all scales, the approach must depend on the scale of the study (Jaupart and Mareschal, 2012; Mareschal and Jaupart, 2004). Deep horizontal variations of heat production (and also of basal heat flux) are smoothed out by diffusion. Conventional wisdom from potential theory is that short-wavelength variations are associated with shallow sources, whereas long-wavelength ones might be due to deep sources. For heat flow, the former is certainly true but not the latter: crustal sources reflect the surface geology, which follows the long-wavelength pattern of accretion. Starting from the surface, downward continuation is unstable for small wavelengths. In practice, one must use an averaging window 100 km wide for crustal temperatures and 500 km wide for the deep lithosphere.

With a reliable model for the vertical variation of the horizontally averaged heat production, $A(z)$, the surface heat flux Q_0 can be written as

$$Q_0 = Q_M + \int_0^{z_m} A(z')\mathrm{d}z' \qquad [20]$$

where z_m is depth to Moho. Note that one may not assume that Q_b, the heat flux at the base of the lithosphere, is equal to Q_M, the heat flux at the Moho, because of long thermal transients and heat production in the lithospheric mantle. Such issues will be discussed separately. In steady state, vertical temperature profiles are obtained by integration:

$$\lambda(T)\frac{\mathrm{d}T}{\mathrm{d}z} = Q_0 - \int_0^z A(z')\mathrm{d}z' \qquad [21]$$

where $\lambda(T)$ is the temperature-dependent thermal conductivity. In practice, the function $A(z)$ is not well known, but one may obtain constraints on the Moho heat flux, as will be explained later. As a first approximation, one may neglect heat production in the lithospheric mantle. Specifying the values of heat flux at the surface and at the Moho then sets the total amount of crustal heat production, which leaves only one unknown: the vertical variation of heat production in the crust.

Figures 11–13 illustrate the effects of changing the three main variables: the surface heat flux, the Moho heat flux, and the vertical distribution of crustal heat production. For accurate predictions, calculations must account for temperature-dependent conductivity in the crust and mantle (see Appendix D). For a stratified crust with an enriched upper layer and a fixed Moho heat flux, increasing the surface heat flux from 30 to 75 mW m^{-2} leads to small temperature differences in the mantle (≈100 K). Temperatures are more sensitive to changes of the vertical distribution of heat production (Figure 12). As discussed later, current estimates for the Moho heat flux beneath cratons range from 12 to 18 mW m^{-2}. This range of variations leads to large differences in temperatures in the lowermost lithosphere (≈250 K).

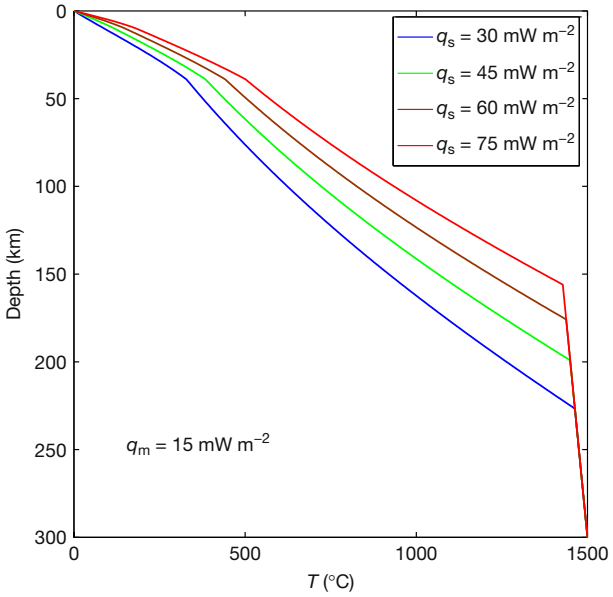

Figure 11 Four continental geotherms calculated for surface heat flux = 30, 45, 60, and 75 mW m^{-2}. Calculations are made with temperature-dependent conductivity in the crust and mantle (see **Appendix D**) and for the same Moho heat flux of 15 mW m^{-2}. Crustal heat production is assumed to be distributed in two layers of equal thickness with a fixed value of 0.4 μW m^{-3} for heat production in the lower crust. With such models, changing the surface heat flux by 15 mW m^{-2} leads to changes of ≈50 °C for temperatures at the Moho and ≈20 km for lithospheric thickness defined by the intersection of the conductive geotherm with the isentrope for a 1350°C potential temperature.

6.05.4.2 Crustal Heat Production

It is now clear that there is no 'universal' law that relates crustal heat production to surface heat flux or that allows the heat flux and heat production to be determined from crustal age. In principle, the distribution of radiogenic heat production could be obtained by sampling all representative rocks in a geologic province. This is rarely feasible in practice because of a lack of samples from the lower crust (Jaupart and Mareschal, 2012). The vagaries of geochemical studies are seldom consistent with those of heat flow studies, implying that one must deal with poorly matched data sets. For these reasons, some authors have searched for shortcuts and have tried to derive the crustal heat production directly from the heat flux data.

Early work on continental heat flux revealed, within certain provinces, a linear relationship between the local values of heat flux Q and heat production A_0 (Birch et al., 1968):

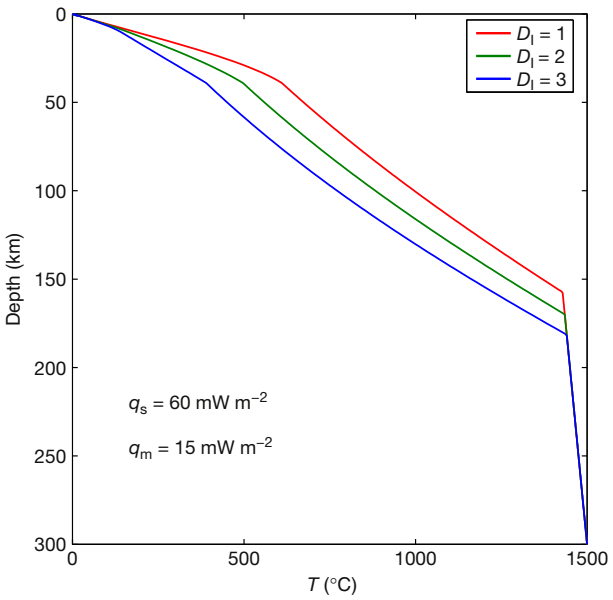

Figure 12 Three continental geotherms for the same heat flux value of 60 mW m^{-2} and three different vertical distributions of crustal heat production. The vertical distribution is characterized by the differentiation index D_I (eqns [23] and [24]). D_I is the relative radioelement enrichment of the uppermost 10 km relative to the bulk crust, that is, $D_I = 1$ corresponds to a homogeneous crust. Calculations are made with temperature-dependent conductivity (see text) and for the same Moho heat flux of 15 mW m^{-2}. Increasing the vertical differentiation from 1 to 3 leads to a >250 °C decrease in Moho temperature.

$$Q = Q_r + A_0 D \qquad [22]$$

The slope D, which has dimension of length and is usually ≈10 km, is related to the thickness of a surficial heat-producing layer. Q_r is called the reduced heat flux. The region where the relationship holds defines a heat flux province characterized by D and Q_r. Within the relatively large errors in both heat flux and heat production values, several such provinces were defined, including the Sierra Nevada and the Basin and Range, which are not in steady state. Among the many heat source distributions that fit this relationship, the exponentially decreasing one, $A(z) = A_0 \exp(-z/D)$, was favored because it is independent of the erosion level (Lachenbruch, 1970). With this model, the total heat production in the crust is $\approx A_0 \times D$ and $Q_M \approx Q_r$ if D is < 10 km. This (and other) simple models based on the linear relationship imply that the vertical distribution of heat production can be described by a single universal function with well-defined parameters within each province. If this concept was verified, it would be possible to infer the vertical distribution of heat production as well as the mantle heat flux directly from surface heat flux. For instance, Artemieva and Mooney (2001) had followed this approach to determine the thickness and temperature in the continental lithosphere on a worldwide scale from the global heat flux compilation.

With the large data sets now available, it is clear that the concept of a universal vertical heat production distribution is not valid. The correlation between local values of surface heat flux and heat production only holds over exposed plutons very enriched in radioactive elements. Over other rock types, it is weak at best, as demonstrated by data from large Precambrian

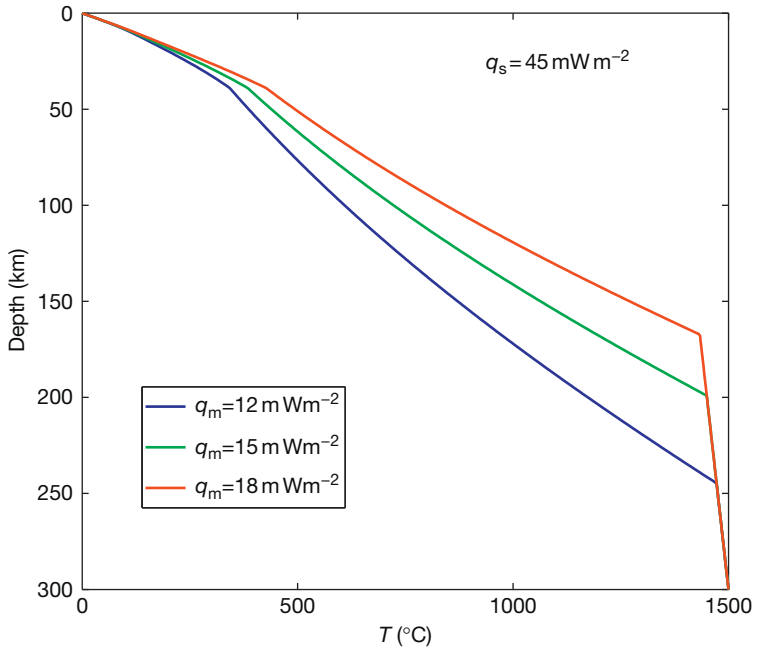

Figure 13 Three continental geotherms for the same surface heat flux value of 60 mW m^{-2} and three different values of the Moho heat flux (12, 15, and 18 mW m^{-2}). Calculations are made with temperature-dependent conductivity (see text) and for the same stratified crustal model as in Figure 11. Changing the Moho heat flux by +/− 3 mW m^{-2} leads to changes of ≈40 °C for temperatures at the Moho and 35–40 km for lithospheric thickness.

provinces of India (Roy and Rao, 2000, 2003), Canada (Perry et al., 2010), and South Africa (Jones, 1987, 1988). Theory shows that, for the rather small wavelengths involved, surface heat flux is only sensitive to shallow heat production contrasts (Jaupart, 1983a). In fact, the linear relationship is an artifact because horizontal heat transport smoothes out deep differences in heat production rates. Values of D are not related to other physical dimensions in a geologic province, such as pluton thickness, and are related to the horizontal correlation distance of heat production (Jaupart, 1983b; Nielsen, 1987; Vasseur and Singh, 1986). One unfortunate consequence is that the reduced heat flux is not the mantle heat flux, but the heat flux at some intermediate crustal depth. Thus, one cannot get around the problem of estimating heat production in the mid and lower crust.

Following a related approach, Pollack and Chapman (1977a,b) noted a correlation between the reduced heat flux and the average heat flux $\overline{Q}$ in a few geologic provinces. They added estimates of lower crustal heat production and obtained a model in which the mantle and surface heat fluxes are nearly proportional to each other. This relationship is not valid at short spatial scales by construction and is not consistent with data from several well-sampled regions, as shown in the succeeding text.

Sampling of different structural levels in the crust, studies of lower crustal xenoliths, and studies in very deep boreholes have given us much needed estimates of the vertical distribution of heat generation. Samples from the lower crust show that heat production is not negligible. Xenoliths lead to a global average heat production of 0.28 $\mu W\,m^{-3}$ (Rudnick and Fountain, 1995), while exposed rocks from lower crustal levels yield 0.4–0.5 $\mu W\,m^{-3}$ (**Figure 14**). These values are much too high to be consistent with an exponential decrease of heat sources. Studies of exposed crustal sections suggest a general trend of decreasing heat production with depth, but this trend is not a monotonic function (Ashwal et al., 1987; Fountain et al., 1987; Ketcham, 1996). Even for the Sierra Nevada Batholith where the exponential model had initially been proposed, a recent compilation has shown that the heat production does not decrease exponentially with depth (Brady et al., 2006). In the Sierra Nevada, heat production first increases, then decreases, and remains constant in the lower crust beneath 15 km. Measurements in very deep boreholes (Kola and KTB) have shown that the concentration of heat sources does not systematically decrease with depth. At Kola, Baltic Shield, Russia, the Proterozoic supracrustal rocks (above 4 km) have much lower heat production (0.4 $\mu W\,m^{-3}$) than the Archean basement (1.47 $\mu W\,m^{-3}$) (Kremenentsky et al., 1989). At KTB, Bavaria, Germany, heat production decreases with depth at shallow levels, reaches a minimum between 3 and 8 km, and increases again in the deepest part of the borehole. Likewise, heat production was found to increase from <0.1 $\mu W\,m^{-3}$ near the surface to ≈ 1.5 $\mu W\,m^{-3}$ at 5 km depth in the hole drilled through the Dabie–Sulu ultrahigh metamorphic terrane, in China (He et al., 2008).

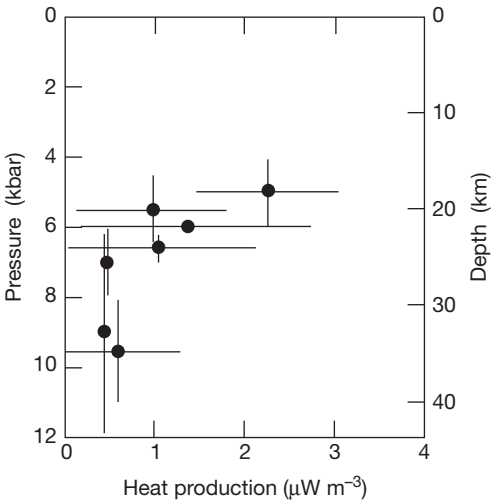

Figure 14 Radiogenic heat production in granulite facies rocks from the Baltic and Canadian Shields as a function of peak metamorphic pressure (data from Joeleht TH and Kukkonen IT (1998) Thermal properties of granulite facies rocks in the Precambrian basement of Finland and Estonia. *Tectonophysics* 291: 195–203). Note that heat production does not drop below 0.4 $\mu W\,m^{-3}$.

These results may perhaps seem obvious to geologists trained to deal with the complexities of crustal structure and processes. A universal function describing the vertical distribution of heat production requires a ubiquitous mechanism affecting all crustal rocks in the same manner everywhere. A natural candidate would be fluid redistribution accompanying metamorphic reactions, but we know that it does not affect uranium and thorium (Bea and Montero, 1999; Bingen et al., 1996). It is now clear that heat production in the lower crust depends mostly on prior geologic history. One cannot expect that tectonic and magmatic processes somehow manage to redistribute heat production in a systematic fashion on a scale of a few to a few tens of kilometers.

As shown earlier, one key step is to derive reliable average values for both the surface and the Moho heat fluxes. Their difference yields the total amount of heat produced in the crust. Adding an estimate of the average heat production at the surface, one can further obtain a measure of its vertical variations. For that reason, Perry et al. (2006a) introduced a differentiation index:

$$D_I = \frac{A_0}{<A>} \qquad [23]$$

where A_0 is the surface heat production and $<A>$ is the mean crustal heat production. If Moho heat flux is Q_M and crustal thickness H,

$$D_I = \frac{A_0 H}{Q_0 - Q_M} \qquad [24]$$

How to obtain estimates of the Moho heat flux is discussed in the next section. Crustal stabilization requires vertical differentiation of the radioelements. This operates as a self-regulating system: high heat production with uniform vertical distribution gives rise to elevated temperatures favoring melting in the lower crust and differentiation (Sandiford and McLaren, 2002). One can thus expects the differentiation index to be high when average crustal heat production and surface heat flux are high. For example, $D_I \approx 3$ and 1 for the Phanerozoic Appalachian and Grenville Provinces, North America, respectively (**Figure 15** and **Table 3**). It is expected that crustal differentiation should

lead to $D_I > 1$. This is not always the case, because the rocks exposed at the surface can be brought up by other processes than magmatic differentiation. For instance, in the Flin Flon volcanic belt of the Proterozoic Trans-Hudson orogen, North America, $D_I \approx 0.4$. A similar value is obtained at the Kola superdeep hole. In both cases, the Proterozoic supracrustal rocks were tectonically transported over a more radiogenic Archean basement.

6.05.4.3 Mantle Heat Flux

When the lithosphere is thick, variations in basal heat flux are unlikely to be reflected in the surface heat flux. Indeed, except for very long wavelengths, any basal heat flux variation of amplitude ΔQ_b is attenuated when upward continued to the surface (Mareschal and Jaupart, 2004):

$$\Delta Q_0 = \frac{\Delta Q_b}{\cosh(2\pi L/\Lambda)} \quad [25]$$

where L is the lithospheric thickness and Λ the wavelength of the variation. As mentioned earlier, ΔQ_b must be understood as a time average over >500 My. Likewise, for wavelengths <500 km, horizontal temperature variations in the lithosphere induced by changes in the basal heat flux would be larger than the ±200 K inferred from xenoliths and seismic data. Mareschal and Jaupart (2004) concluded that variations in the basal heat flux account for $<\pm 2$ mW m^{-2} of the surface heat flux variations, that is, they are comparable to the uncertainty on the heat flux determination. As shown in Figure 16, variations in crustal heat production account for the variability of surface heat flux in all the major provinces of North America (Jaupart et al., 1998; Lewis et al., 2003; Pinet et al., 1991). Such a correlation leaves little room for variations of the mantle heat

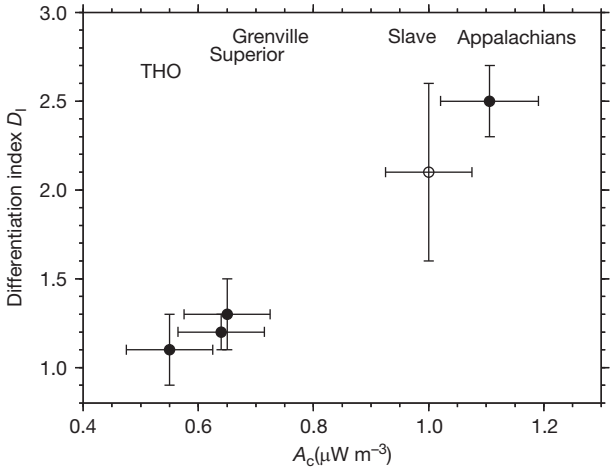

Figure 15 Crustal differentiation index D_I as a function of average crustal heat production in five large geologic provinces of North America. Adapted from Perry HKC, Jaupart C, Mareschal JC, and Bienfait G (2006) Crustal heat production in the Superior Province, Canadian Shield, and in North America inferred from heat flow data. *Journal of Geophysical Research* 111: B04,401, http://dx.doi.org/10.1029/2005JB003,893.

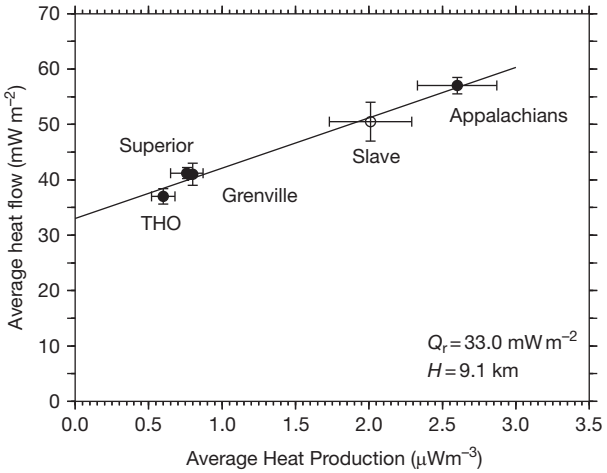

Figure 16 Relationship between the average values of surface heat flux and heat production for five large geologic province of North America. Adapted from Perry HKC, Jaupart C, Mareschal JC, and Bienfait G (2006) Crustal heat production in the Superior Province, Canadian Shield, and in North America inferred from heat flow data. *Journal of Geophysical Research* 111: B04,401, http://dx.doi.org/10.1029/2005JB003,893.

Table 3 Average heat flux, crustal heat production, and differentiation index for different provinces and subprovinces of the Canadian Shield

Province	*Age (Ga)*	$<Q> \pm \sigma_q$ *(mW m^{-2})*	N_q	$<A> \pm \sigma_A$ *(μW m^{-3})*	N_A	z_m *(km)*	D_I
Slave	3.1–2.9	51 ± 6	3	2.3	[a]	36	2.3 ± 0.5
Superior	2.9–2.6	40 ± 10	79	0.72 ± 0.6	62	40	1.2 ± 0.1
Abitibi	2.7	38 ± 7	30	0.4 ± 0.3	24	40	0.7 ± 0.1
Trans-Hudson Orogen	2.1–1.8	42 ± 11	49	0.7 ± 0.5	48	40	1.1 ± 0.2
Thompson Belt	2.1–1.9	53 ± 6	10	1.1 ± 0.3	10	40	1 ± 0.1
FlinFlon Snow Lake Belt	1.9–1.8	42 ± 5	15	0.3 ± 0.2	14	40	0.7 ± 0.1
Lynn Lake Belt	1.8	32 ± 7	9	0.7 ± 1	9	36	2.3 ± 0.1
Grenville	1.3–1.1	41 ± 11	0.8	[a]	40		1.3 ± 0.2
Appalachians	0.4	57 ± 13	79	2.6 ± 1.9	50	40	2.5 ± 0.2

$<Q>$, average surface heat flux; N_Q, number of sites; $<A>$, average surface heat production; N_A, number of values; z_m, crustal thickness; D_I, differentiation index. See text for the definition of differentiation index D_I

[a]Area-weighted average.

Data from Perry et al. (2010) and references therein

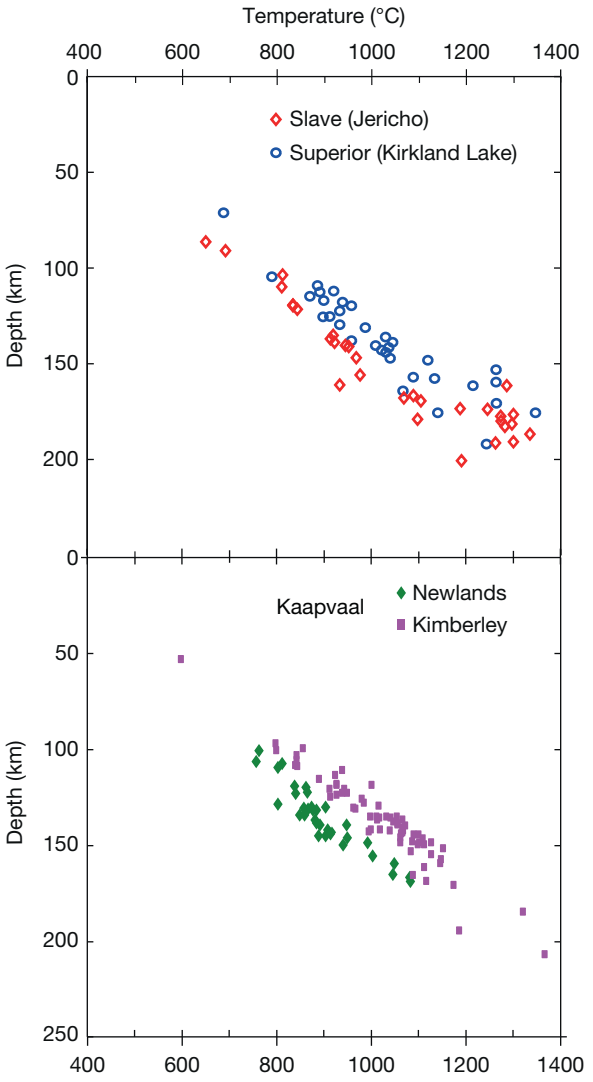

Figure 17 Temperature and pressure values for equilibrium mineral assemblages in xenoliths from deep continental lithosphere. (top) Two kimberlite pipes from two different cratons in the Canadian Shield. (bottom) Two kimberlite pipes from the same craton, Kaapvaal, South Africa. Data from Rudnick and Nyblade (1999) and Michaut et al. (2007).

flux, which is an independent variable. The sharpness of the variations in surface heat flux between provinces also requires that they originate in the crust. For example, the transition between the Grenville and the Appalachians takes place over <50 km (Mareschal et al., 2000).

Values of the mantle heat flux may be obtained using two independent methods. In the Abitibi Province of the Archean Superior Province, Canada, xenolith suites from the Kirkland Lake kimberlite pipe yield temperatures and pressures corresponding to a wide depth range. The temperature estimates are lower than temperatures in the convecting mantle at depths <200 km (**Figure 17**). With an estimate of thermal conductivity in the mantle, Rudnick and Nyblade (1999) found a best-fit Moho heat flux ≈ 18 mW m^{-2}, within a range of 17–25 mW m^{-2}. Another method relies on the variations of heat flux and crustal structure combined with heat production data for the various rock types. For the same Abitibi area, Guillou et al. (1994) incorporated constraints from seismic and gravity data to arrive at a range of 7–15 mW m^{-2} for Q_M. These two independent estimates can be combined to reduce the uncertainty: Values lower than 15 mW m^{-2} would not be consistent with the xenolith data, and values higher than 18 mW m^{-2} would not be compatible with heat flux and heat production data.

Similar agreement between these two methods has been obtained in other provinces, in South Africa, for example. There, the deep crustal section exposed in the Vredefort structure allowed an estimate of 18 mW m^{-2} for the Moho heat flux in the Kaapvaal Craton (Nicolaysen et al., 1981), very close to the value deduced from xenolith (P, T) data (Rudnick and Nyblade, 1999; **Figure 17**).

There are now enough data to directly assess whether the mantle heat flux varies as a function of age or as a function of distance across a craton. In the Canadian Shield, xenolith samples from the Jericho kimberlite pipe of the Archean Slave Province, more than 2000 km northwest of the Abitibi, give a best-fitting value of 15 mW m^{-2} for mantle heat flux (Russell et al., 2001). As shown in **Figure 17**, the (P, T) data from the Superior and Slave Provinces cannot resolve lateral variations of lithospheric geothermal gradient across the Canadian Shield. In the Lac de Gras kimberlite pipes, which also belong to the Slave Province, surface heat flux data are available and allow tighter constraints of 12–15 mW m^{-2} for Q_M (Mareschal et al., 2004). Crustal models lead to mantle heat flux values of 10–15 mW m^{-2} for the *c.*1.8 Ga Trans-Hudson orogen (Rolandone et al., 2002) and for the *c.* 1.0 Ga Grenville Province (Pinet et al., 1991). The same conclusions hold for the Kaapvaal Craton, South Africa (**Figure 17**).

Lower and upper bounds on Q_M can be derived using other arguments. Rolandone et al. (2002) calculated lower crustal temperatures when different provinces of the Canadian Shield stabilized, which depend on the crustal heat production. Requiring that temperatures were below melting, they found that Q_M could not be less than about 12 mW m^{-2}. Upper bounds on the mantle heat flow can be derived from the lowest heat flux measured in the shield. Heat flux values of 22–23 mW m^{-2} are found in the center of the shield, in the Trans-Hudson orogen (Mareschal et al., 1999), and at the eastern edge of the shield, at Voisey's Bay, Labrador (Mareschal et al., 2000). Because of horizontal heat diffusion, such values include the contribution of crustal heat production averaged over large volumes (Mareschal and Jaupart, 2004). Using a lower bound of 0.2 μW m^{-3} on crustal heat production leads to a refined upper bound of 15 mW m^{-2} for Q_M.

Using these constraints simultaneously, the mantle heat flux beneath the Canadian Shield cannot vary by more than ± 3 mW m^{-2} around a value of 15 mW m^{-2}, implying that variations of lithospheric thickness do not exceed $\approx \pm 50$ km.

Similar results have been obtained in other continents and are listed in **Table 4**. In the Baltic and Siberian Shields, the lowest regional average heat flux values are 15 and 18 mW m^{-2}, respectively (**Table 5** and references). Such measurements provide upper limits on mantle heat flux that are even lower than in Canada.

Table 4 Mean heat flux and heat production in major provinces

	<Q>[a] ($mW\ m^{-2}$)	σ_Q[b]	N_Q[c]	<A>[a] ($\mu W\ m^{-3}$)	σ_A[b]	N_A[c]	*References*
Archean							
Dharwar (India)	36 ± 2.1	6	8	1.6		690	Roy and Rao (2000, 2003)
Witwatersrand (S. Africa)	51 ± 0.7	6	81				Ballard et al. (1987), Jones (1988)
Lesotho (S. Africa)	61 ± 5.3	16	9				Jones (1992)
Tanzanian Craton (Africa)	33 ± 3	10	9	2.4	1.9	5	Nyblade et al. (1990); Nyblade (1997)
Western Shield (Australia)	49 ± 2.1	13	37	2.6	2.1	12	Cull (1991)
Ukrainian Shield	32 ± 0.7	7	106				Cermak (1993)
Superior (N. America)	40 ± 1.0	10	79	0.72	0.6	62	Lévy et al. (2010); Perry et al. (2010), and references therein
Slave (N. America)	51 ± 1.0	10	3	2.3	1.0	20	Lewis et al. (2003); Mareschal et al. (2004)
Total Archean	41.5 ± 0.7	11	332				Jaupart and Mareschal (2012)
Proterozoic							
Aravali (India)	68 ± 4.9	13	7				Roy and Rao (2000)
Southern Granulite Province (India)							
Northern Block	36 ± 0.3	4	14	0.5	0.3		Ray et al. (2003)
Southern Block	44 ± 1	6	6	2.53		177	Ray et al. (2003)
Namaqua (S. Africa)	61 ± 2.5	11	20	2.3		10	Jones (1987)
Central Shield (Australia)	83 ± 2.2	20	32	3.6	1.9	38	Cull (1991); Neumann et al. (2000)
Baltic Shield	31 ± 1.2	9	68				Cermak (1993)
Trans-Hudson (N. America)	42 ± 2.0	11	49	0.73	0.50	47	Mareschal et al. (2005)
Wopmay (N. America)	90 ± 1.0	11	12	4.8	1.0	20	Lewis et al. (2003)
Grenville (N. America)	41 ± 2.0	11	30	0.80	[d]	17	Mareschal et al. (2000)
North China (China)	50 ± 1.1	11	99				Hu et al. (2000)
Upper Yangtze Block (China)	53 ± 0.8	9	119				Hu et al. (2000)
Tarim Block (China)	44 ± 2.1	10	22				Hu et al. (2000)
Qaidam Basin (China)	52 ± 3.4	13	16				Hu et al. (2000)
Total Proterozoic	48 ± 0.8	16	675				[e]
Proterozoic							
Aravali (India)	68 ± 4.9	13	7				Roy and Rao (2000)
Southern Granulite Province (India)							
Northern Block	36 ± 0.3	4	14	0.5	0.3		Ray et al. (2003)
Southern Block	44 ± 1	6	6	2.53		177	Ray et al. (2003)
Namaqua (S. Africa)	61 ± 2.5	11	20	2.3		10	Jones (1987)
Central Shield (Australia)	83 ± 2.2	20	32	3.6	1.9	38	Cull (1991); Neumann et al. (2000)
Baltic Shield	31 ± 1.2	9	68				Cermak (1993)
Trans-Hudson (N. America)	42 ± 2.0	11	49	0.73	0.50	47	Mareschal et al. (2005)
Wopmay (N. America)	90 ± 1.0	11	12	4.8	1.0	20	Lewis et al. (2003)
Grenville (N. America)	41 ± 2.0	11	30	0.80	[d]	17	Mareschal et al. (2000)
North China (China)	50 ± 1.1	11	99				Hu et al. (2000)
Upper Yangtze Block (China)	53 ± 0.8	9	119				Hu et al. (2000)
Tarim Block (China)	44 ± 2.1	10	22				Hu et al. (2000)
Qaidam Basin (China)	52 ± 3.4	13	16				Hu et al. (2000)
Total Proterozoic	48 ± 0.8	16	675				[e]
Paleozoic							
Appalachians (N. America)	57 ± 1.5	13	79	2.6	1.9	50	Jaupart and Mareschal (1999)
Mainland United Kingdom	54[d]	12	188				Lee et al. (1987)
Dnieper aulacogen (Russia)	45 ± 0.6	8	165				Cermak (1993)
Pripyat depression (Russia)	66 ± 2.2	17	59				Cermak (1993)
Platforms (Russia)	68 ± 0.9	16	323				Cermak (1993)
Altai-Ergula Belt (China)	60 ± 2.2	9	18				Hu et al. (2000)
Junggar–Higgan Belt (China)	47 ± 2.1	10	22				Hu et al. (2000)
Total Paleozoic	58.3 ± 0.5	22	2213				[e]

[a]Mean ± one standard error.
[b]Standard deviation on the distribution.
[c]Number of sites.
[d]Area-weighted average value.
[e]Total in the compilation by Nyblade and Pollack (1993) excluding the more recent measurements including here.

6.05.4.4 Regional Variations of Heat Flow and Lithospheric Temperatures

Table 4 shows the average heat flux from different provinces grouped according to age. The trend of decreasing heat flux with age is weak at best and shows remarkable exceptions. In North America, variations of heat flux can be accounted for by changes of crustal heat production, as explained earlier. For stable continents, the very wide range of average heat fluxes within each age group (Archean, 36–61 mW m^{-2}; Proterozoic, 31–90 mWm^{-2}; and Paleozoic, 45–68 mW m^{-2}) implies that age is not a proxy for heat flux. This range suggests that surface heat flux reflects the structure and composition of the continental crust, which vary due to the competing mechanisms of crustal extraction from the mantle and crustal recycling. In the Proterozoic provinces, high heat flux and crustal heat production (e.g., Wopmay orogen, Thompson Belt in the Trans-Hudson orogen, and Gawler Craton in Australia) are always associated with recycled (Archean) crust. By contrast, juvenile Proterozoic crust is characterized by low heat flux (e.g., all the juvenile belts of the Trans-Hudson orogen in Canada and the Proterozoic rocks of the Kola Peninsula in Russia).

Within each province, there is regional (on a scale on the order of 400 km) variability that must be considered when calculating geotherms. This is illustrated in Table 5 that shows that the regional variability is high within all provinces. Thus, there is no geotherm characteristic of a single province. To illustrate this point, we have calculated geotherms from selected regions from stable North America. The selection covers the extreme regimes within each age group. The crustal models are described in Table 6 and the variations in thermal conductivity are described in Appendix D. Geotherms shown on Figure 18 illustrate two points: (1) There is no direct relation between the geotherm and the age as the profiles from different age groups overlap; (2) there is also no simple relationship between the surface heat flux and the temperature profiles. For example, there may be no difference in mantle temperature between the Grenville and the Appalachians in spite of the higher surface heat flux in the Appalachians than in the Grenville (58 vs. 41 mW m^{-2}). The high heat flux in the Appalachians is mostly accounted for by high heat production (3 μW m^{-3}) at shallow depth resulting in a differentiation index $D_I = 3$. In contrast, the Grenville whose crust is made up of stacked slices from all levels appears to be more homogeneous at crustal scale with $D_I = 1$. Thus, the vertical differentiation of the radioelements must be understood in order to estimate Moho and mantle temperatures.

Xenoliths (P, T) data support these inferences. As shown in Figure 17, horizontal variations of temperature in a 100–200 K range are found within a single craton, such as the Kaapvaal Craton, South Africa, as well as between two crayons, such as the Slave and Superior Provinces, Canada.

On the scale of the whole North American continent, the average heat production and the crustal differentiation index are positively correlated (Perry et al., 2006a). Thus, regions with large heat production (and hence high surface heat flux) are systematically associated with an enriched upper crust. In most cases, this is due to highly radiogenic granites that do not extend very deep, as in the Appalachian Province, for example. All else being equal, temperatures decrease with increasing differentiation index and increase with increasing heat production. With the correlation between heat production and differentiation index (Figure 15), variations of crustal temperatures are much smaller than for a single universal model for the vertical distribution of radioelements. From the standpoint of large-scale geophysical models, the relations between surface heat flux, Moho heat flux, and Moho temperature are nonlinear and cannot be reduced to simple correlations.

Table 5 Regional variations of the heat flux in different cratons

	Minimum	*Maximum*
	(mW m^{-2})	
Superior Province	22	48
Trans-Hudson orogen	22	50
Australia	34	54
Baltic Shield	15	39
Siberian Shield	18	46

Minimum and maximum values obtained by averaging over 200 × 200 km windows

6.05.4.5 Variations of Crustal Thickness

Independent evidence for significant horizontal variations of crustal temperatures is provided by the topography of the Moho discontinuity. The characteristic time of relaxation for topography on an interface between two layers with a density difference $\Delta\rho$ is (Chandrasekhar, 1961)

Table 6 Heat flux and crustal heat production used for geotherm calculations

Region	Q_o	A_1	H_1	A_2	h_2	A_3	H_3	*Moho depth*	T_m
Archean									
E. Abitibi (Mareschal et al., 2000)	29	0.4	40					40	325
W. Abitibi (Mareschal et al., 2000)	45	1.2	20	0.4	20			40	422
Slave (Mareschal et al., 2004)	50	1.7	10	1.2	10	0.4	20	40	428
Proterozoic									
Labrador (Mareschal et al., 2000)	22	0.2	40					40	287
THO (Flin Flon Belt) (Mareschal et al., 2005)	40	0.3	8	1.2	12	0.25	20	40	434
Wopmay (Lewis et al., 2003)	90	4.8	10	1.0	10	0.4	20	40	705
Grenville (Mareschal et al., 2000)	40	0.7	40					40	440
Paleozoic									
Appalachians (Mareschal et al., 2000)	58	3.1	8	1.1	10	0.4	22	40	426

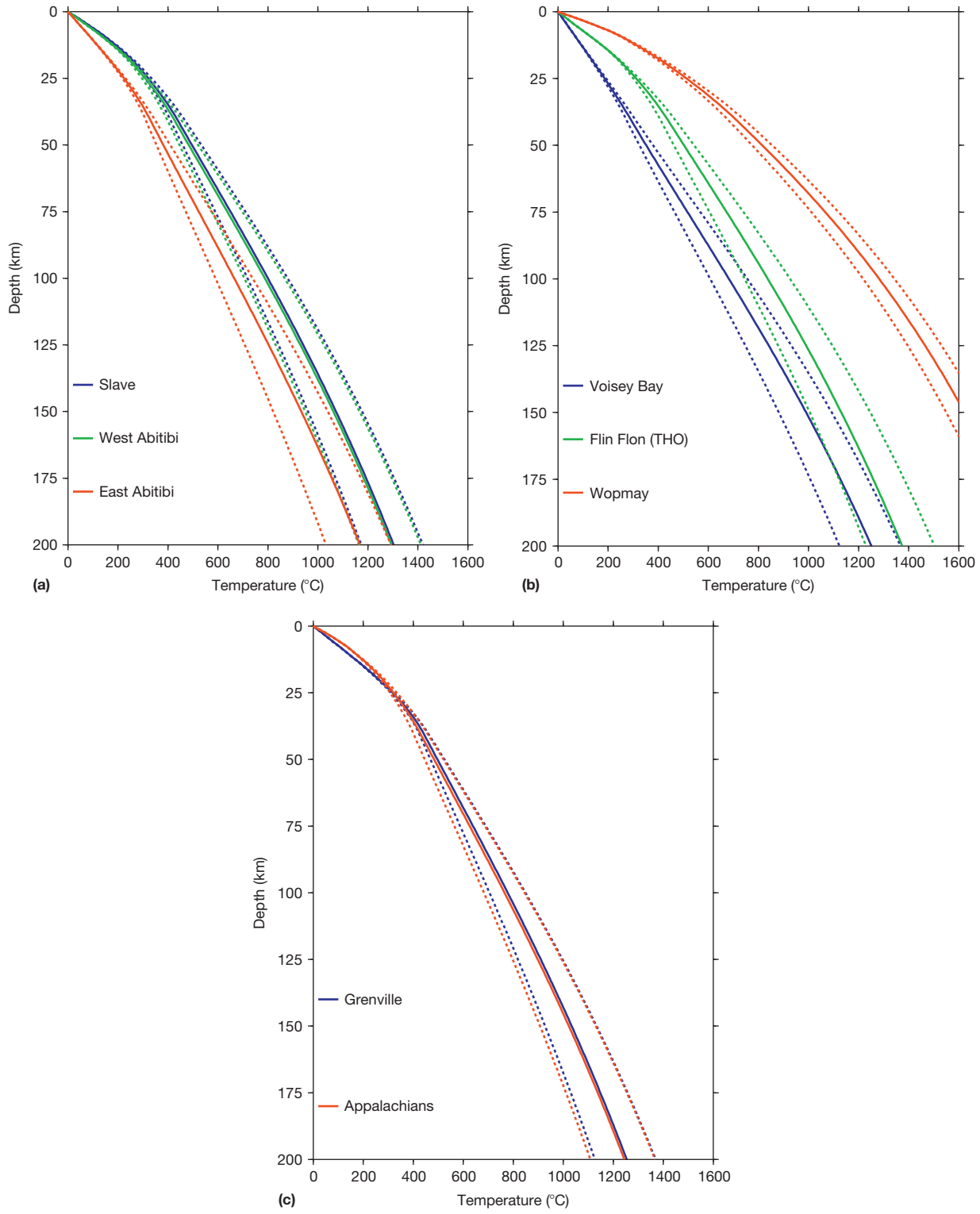

Figure 18 Geotherms for different regions in the Canadian Shield: (a) eastern Abitibi, western Abitibi, and Slave Province (Archean); (b) Voisey's Bay, Flin Flon Belt, and Wopmay orogen (Proterozoic); (c) Grenville (mid-Proterozoic) and Appalachians (Paleozoic). Thick lines are the geotherm calculated for the crustal models in **Table 6**. Thin dotted lines are for the same models with ± 2 mW m^{-2} change in Moho heat flow.

$$\tau \approx \frac{8\pi\mu_{\text{eff}}}{g\Delta\rho\Lambda} \qquad [26]$$

where g is the acceleration of gravity, μ_{eff} is the effective viscosity, and Λ is the wavelength of the interface topography. The value mentioned earlier yields only an order of magnitude because the relaxation time is modulated by a function depending on the geometry and the boundary conditions (Chandrasekhar, 1961). For representative crustal rheologies, temperature differences of

100–200 K that are predicted imply that the effective viscosity varies by up to three orders of magnitude. Thus, relaxation of tectonic deformation proceeds at different rates depending on the crustal heat production. Higher crustal heat production and heat flow during the Archean might thus explain the observation that the Archean Moho is flat, even in regions that have experienced compression. However, a few areas that were deformed during the Proterozoic have preserved thick crustal roots: the Kapuskasing uplift in the Superior Province, the Lynn Lake area in the Trans-Hudson orogen, and the eastern part of the Grenville front. Thick crust with the same bulk crustal composition than elsewhere would lead to high temperatures at the Moho and in the underlying mantle, which would allow flow in the lower crust and relaxation of the crustal root. The persistence of crustal roots demonstrates that temperatures have remained low for a very long time (a minimum of 1.8 Gy at both Lynn Lake and Kapuskasing and 1.0 Gy in the Grenville), which can be only explained by anomalously low crustal heat production. Mareschal et al. (2005) had indeed noted that heat flux was anomalously low in these three areas of the Canadian Shield. More generally, there is absolutely no correlation between heat flux and crustal thickness suggesting that regions with a thicker crust have a lower than average crustal heat production (Mareschal and Jaupart, 2013).

6.05.4.6 Summary

Continental heat flow is sensitive to the local geology and crustal structure and hence must be used with precaution for studies at the lithospheric scale. In stable continents, high heat flux is always associated with high heat production and an enriched upper crustal layer. Thus, one cannot build geotherms with the same function for the vertical distribution of heat production regardless of the local geologic context. Heat flux data alone are not sufficient and must be supplemented by additional information on crustal heat production or mantle heat flux. On a large scale, three key control variables on lithospheric temperatures are correlated: the average surface heat flux, the average crustal heat production, and the vertical variation of heat production. In contrast, variations in the basal heat flux are small ($\sim\pm3$ mW m^{-2}).

Steady-state thermal models are only valid if heat flux is less than about 90 mW m^{-2}. Higher values imply melting in the crust or weak lithospheric mantle that can deform easily, suggesting that other heat transport mechanisms are effective. In a thick lithosphere, long-term thermal transients are inevitable.

6.05.5 Continental Lithosphere in Transient Thermal Conditions

6.05.5.1 General Features

In tectonically active regions, advection of heat usually dominates over conduction and temperatures are strongly time-dependent. Thermal evolution models depend very much on the choice of the boundary conditions at the base of the lithosphere and cannot be assessed against heat flux data for several reasons. One difficulty comes from the variable quality and density of heat flow data in active regions. In the western United States, the numerous heat flux data from the Basin and Range and Rio Grande Rift are very noisy because of hydrologic perturbations (Lachenbruch and Sass, 1978), a situation reminiscent of young seafloor. Furthermore, the inclusion in the data set of measurements made for geothermal energy exploration has introduced a strong bias towards excessively high values. Far from thermal steady state, one may not use heat flux data to estimate lithospheric temperatures by downward extrapolation of shallow heat flux measurements.

In a continent that is being deformed, heat flow and temperatures depend on the competing effects of crustal thickness changes, which imply changes of crustal heat production, and deformation, which affects the temperature distribution. Thus, erosion or crustal extension initially causes steeper geotherms and enhanced heat flux. After these transient effects decay, the reduced crustal thickness leads to a lower heat flux than initial. Conversely, crustal thickening causes the geothermal gradient and the heat flux to decrease at first and then to increase due to higher crustal heat production. In many cases, heat flux also records shallow processes such as the cooling of recently emplaced plutons. Because crustal composition is often affected by syn- or postorogenic magmatism, there is no general rule to predict the final crustal thickness, composition, and heat production distribution.

Following the cessation of tectonic and magmatic activity, one must distinguish between two types of transients. Crustal temperatures return to equilibrium with local heat sources in <100 My. This is followed by a much slower transient associated with reequilibration of the lithospheric mantle. For thick lithosphere, such transients may last as long as 500 My (Hamdani et al., 1991; Kaminski and Jaupart, 2000; Nyblade and Pollack, 1993) and result in negative or positive heat flow anomalies. Such slow thermal relaxation has two important features. Firstly, it involves deep thermal anomalies whose lateral variations are efficiently smoothed out by heat conduction and that do not lead to spatial variations of surface heat flux over distances <500 km. Secondly, it is linked to changes of thermal boundary layer thickness that may be detectable by other methods (Jaupart et al., 1998).

6.05.5.2 Compressional Orogens

Unless the crust has anomalous composition, the total radiogenic heat production increases with crustal thickness. Steady-state conditions have not been reached in young orogens where heat flow is also enhanced by erosion. High heat flux values have been measured in Tibet and parts of the Alps (Jaupart et al., 1985). These values imply high temperatures in the shallow crust. Because these variations are of short wavelengths, they have been attributed to the cooling of shallow plutons. One should note that crustal melting and emplacement of granite intrusions in the upper crust modify the vertical distribution of radioelements. Thus, one should not use the same heat production model before and after orogenesis (Mareschal and Jaupart, 2005; Sandiford and McLaren, 2002).

6.05.5.3 Rifts and Zones of Extension

Crustal extension and lithospheric thinning will instantly result in a steeper temperature gradient and an increase in heat flux. Thermal conduction cannot account for the rapid thinning of the lithosphere and mechanical processes such as delamination or diapiric uprise of the asthenosphere are

necessary to account for the rapid development of extension zones (Mareschal, 1983). The thermal effects of extension are transient and after return to equilibrium, the heat flux at the surface of thinned crust will reflect the smaller amount of radioactive elements and hence will be lower than before extension. Further changes of crustal heat production may occur due to the injection of basaltic melts, which are depleted in radioelements with respect to average continental crust. This explains, for example, why heat flux is slightly lower in the 1000 My Keweenawan Rift than in the surrounding Superior Province (Perry et al., 2004).

In the Basin and Range Province of the southwestern United States (Morgan, 1983; Sass et al., 1994), high heat flux values (110 mW m^{-2}) are consistent with an extension rate of 100% (Lachenbruch and Sass, 1978; Lachenbruch et al., 1994). The high temperatures that are implied must cause thermal expansion of the crust and parts of the mantle and hence should lead to an elevated topography. On the other hand, crustal thinning has the opposite effect. For the Basin and Range, the calculated thermal expansion in the lithospheric mantle is not sufficient to account for the high elevation. According to Lachenbruch et al. (1994), the mantle lithosphere beneath the Basin and Range has been delaminated and not simply stretched.

A striking feature of the zones of extension is that the transition between the region of elevated heat flux and the surrounding is as sharp as the sampling allows to determine. This is observed across the boundaries of the Colorado Plateau and the Basin and Range in North America (Bodell and Chapman, 1982), between the East African Rift and the Tanzanian Craton (Nyblade, 1997), and between the Baikal Rift and the Siberian Craton (Poort and Klerkx, 2004). Where the sampling is sufficient, heat flux exhibits short-wavelength variations. These variations are probably due to shallow magmatic intrusions, a hypothesis well justified by the numerous volcanic edifices that dot such areas; they also may reflect groundwater movement (Poort and Klerkx, 2004). For studies of lithospheric structure, one must separate between a high background heat flux due to extension and local anomalies reflecting shallow magmatic heat input, which requires measurements at close spacings.

6.05.5.4 Thermal Relaxation of Thick Continental Lithosphere

Once active deformation and magmatism have ceased, the return to thermal equilibrium takes a long time. The thermal relaxation time depends on the thermal structure at the end of activity, the lateral extent of the perturbed region, and the boundary condition at the base of the lithosphere.

6.05.5.4.1 Sedimentary basins

The subsidence of sedimentary basins and passive continental margins provides a good record of the relaxation of thermal perturbations in the lithosphere and is sensitive to lithospheric thickness. Such transients have been recorded in intracratonic basins located away from active plate boundaries and have generated a lot of interest (Ahern and Mrkvicka, 1984; Haxby et al., 1976; Nunn and Sleep, 1984). Subsidence is also affected by tectonic, metamorphic, and eustatic effects. In order to identify these effects, some authors have assumed that the continental lithosphere has a well-defined characteristic cooling time of 60 My (Bond and Kominz, 1991) and that subsidence phases that are significantly longer than this require other than thermal effects, such as renewed extension. These assumptions are not justified for thick continental lithosphere with long thermal relaxation time.

Theoretical subsidence models that have been developed differ by their initial conditions and their basal boundary conditions (Hamdani et al., 1991, 1994; McKenzie, 1978). Although this has not been sufficiently emphasized, the latter is the important factor determining the duration of thermal subsidence. The duration of the subsidence episode varies by a factor of 3 between various intracratonic basins of North America. For a fixed temperature at the base of the lithosphere, theory would imply that the continental lithospheric thickness is about 115 and 270 km beneath the Michigan and Williston Basins, respectively (Ahern and Mrkvicka, 1984; Haxby et al., 1976). For two basins of similar age located on the Precambrian basement of the same continent, such a large difference is surprising. This motivated Hamdani et al. (1994) to investigate the influence of thermal boundary conditions at the base of the lithosphere. They showed that subsidence is slower for a fixed flux than for a fixed temperature and attributed the different subsidence responses to different thermal processes at the base of the lithosphere. However, these arguments rely on 1-D thermal models that have recently been questioned (Kaminski and Jaupart, 2000). According to Haxby et al. (1976), for example, the initial perturbation beneath the Michigan Basin has a radius of about 120 km, which is less than the thickness of the North American lithosphere. In this case, the assumption of purely vertical heat transfer is not tenable.

Accounting for horizontal heat transfer, the solution may be cast in the form of a relationship between the width of the thermal perturbation and the lithospheric thickness. No solution can be found for lithospheric thicknesses < 170 km and the observations are best fitted for a model with fixed heat flux basal boundary condition (Kaminski and Jaupart, 2000).

6.05.5.4.2 Tectonic and magmatic perturbations

The large relaxation time of thick continental lithosphere might lead one to conclude that all thermal perturbations decay slowly and leave a heat flow anomaly for a long time. In some cases where the thermal perturbation is narrow, a large thickness may in a sense be self-defeating as it enhances lateral heat transfer. Thus, thermal relaxation of some tectonic or magmatic perturbations may in fact be more sensitive to width than to thickness.

Gaudemer et al. (1988) and Huerta et al. (1998) had shown that temperatures in orogenic belts depend on belt width and on local values of heat production and thermal conductivity. One consequence is that (P, T, t) metamorphic paths may record belt width as well as other characteristics. Another striking example is provided by flood basalt provinces where large volumes of magma rose through the lithosphere. For a laterally extensive thermal perturbation, one should detect a relict thermal signal for more than 200 My. There is no heat flow anomaly over the Deccan Traps, India, which erupted at about 65 My (Roy and Rao, 2000). The same is true over the Paraná Basin in Brazil that saw the emplacement of large magma volumes at

120 My (Hurter and Pollack, 1996). It seems that, in both cases, eruptive fissures are localized in relatively small areas, suggesting that the zone affected by magma ascent may be a few 100 km in width. In this case, thermal perturbations decay rapidly by horizontal heat transport. One consequence is that lithospheric seismic velocity anomalies that are associated with large magmatic events cannot be accounted for by thermal effects and hence reflect compositional variations. In several cases, it seems that the lithosphere has been modified over a large depth interval. For example, a pronounced low-velocity anomaly of narrow width (120 km) extends through the whole mantle part of the lithosphere beneath the south central Saskatchewan kimberlite field in the Trans-Hudson orogen, Canada (Bank et al., 1998). Similar anomalies have been found beneath the Monteregian–White Mountain–New England hotspot track in northeastern America or beneath the Bushveld intrusion in South Africa (James et al., 2001; Rondenay et al., 2000).

6.05.5.5 Long-Term Transients

The large thickness of continental lithosphere implies very large thermal relaxation times with some interesting consequences.

6.05.5.5.1 Archean conditions

The Archean era saw the stabilization of large cratons and the emergence of geologic processes that are still active today. In the Archean, crustal metamorphism was biased towards high-temperature low-pressure conditions in contrast to more recent analogues, indicating that crustal temperatures were higher than today. In apparent contradiction, cratons achieved stability because they had strong lithospheric roots, indicating that temperatures in the lithospheric mantle were not much hotter than today. Proposed mechanisms of formation of lithospheric roots involve either stacking of subducted slabs (Abbott, 1991; Helmstaedt and Schulze, 1989) or melting of mantle over hot spots (Griffin et al., 2003). These mechanisms result in different initial thermal conditions and evolution for the stabilized lithosphere.

In the Archean, heat production in the Earth was double the present, which might suggest higher temperatures in the crust and in the mantle as well as higher heat flux at the base of young continental lithosphere. On average, however, the Archean crust of today is associated with less heat-producing elements than its modern analogues. When corrected for age, the total amount of crustal heat production in Archean times was close to that presently observed in Paleozoic provinces. Save for a few anomalous regions with high radioactivity, crustal heat production in the Archean is thus not sufficient to account for crustal temperatures that are higher than those of modern equivalents. The origin of the high-temperature–low-pressure metamorphic conditions must thus be sought in other mechanisms, perhaps widespread magmatic perturbations.

Crustal radioactivity heats the crust in a geologically short time, but a much longer time is required to heat up the lower lithosphere. In Archean times, continental lithosphere was never very old and its thermal structure remained sensitive to initial conditions, that is, conditions that led to the extraction of continental material from the mantle and to the stabilization of thick roots. If the lithospheric mantle is formed by the underthrusting of subducted slabs beneath the crust, it will initially be colder than in steady state. Mareschal and Jaupart (2005) had estimated the time needed for time-dependent crustal radioactivity to heat up the entire lithosphere. When the half-life of crustal radioactivity is of the same order as the thermal time of the lithosphere, lithospheric temperatures cannot adjust to the time-dependent radiogenic heat production and remain lower than predicted by steady-state calculations. Following isolation of a continental root from the convecting mantle, the 'radiogenic' temperature component at the base of the lithosphere reaches a maximum after 1–2 Gy, depending on lithospheric thickness (**Figure 19**). The peak temperature is $\approx$70% of what one would infer from steady-state models. Thus, temperatures in the crust and deep in the continental root are effectively decoupled for a long time. If the root forms with its initial temperature below steady state, the mantle temperature will always be below steady state for the crustal production. Depending on the mechanism of root formation, the lithospheric mantle could well remain sufficiently cold and strong to preserve Archean features (van der Velden et al., 2005).

6.05.5.5.2 Secular cooling in the lithosphere

In thick continental lithosphere, the timescale for diffusive heat transport is comparable to the half-lives of uranium, thorium, and potassium, implying that temperatures are not in equilibrium with the instantaneous rate of radiogenic heat generation. The lithospheric mantle undergoes secular cooling even when thermal conditions at the base of the lithosphere remain steady. The magnitude of transient effects depends on mantle heat production as well as on lithospheric thickness. Even large values of heat production do not introduce large transients in a shallow lithosphere. Conversely, even small values of heat production lead to significant transient effects in a thick lithosphere.

In lithosphere that is thicker than 200 km, the geotherm is transient and sensitive to past heat generation. For the same parameter values, and in particular for the same values of present heat production, the deeper part of the temperature profile diverges from a steady-state calculation because of the long time to transport heat to the upper boundary. Depending on the amount of radioelements in the lithospheric mantle, the vertical temperature profile may exhibit significant curvature and may be hotter than a steady-state profile by as much as 150 K (**Figure 20**). For typical values of heat production in the lithospheric mantle, this secular cooling contributes about 3 mW m^{-2} to the total heat flow. Predicted cooling rates for lithospheric material are in the range of 50–150 K Gy^{-1}, close to values reported recently for mantle xenoliths from the Kaapvaal Craton, South Africa (Albarède, 2003; Bedini et al., 2004).

One important consequence of such long-term transient behavior stems from the shape of the vertical temperature profile. Applying a steady-state thermal model to xenolith (P, T) data leads to an overestimate of the mantle heat flux and an underestimate of the lithospheric thickness.

6.05.6 Thermal Control on Lithospheric Thickness

We have seen that oceanic and continental lithospheres have different thicknesses and also that they appear to be in thermal

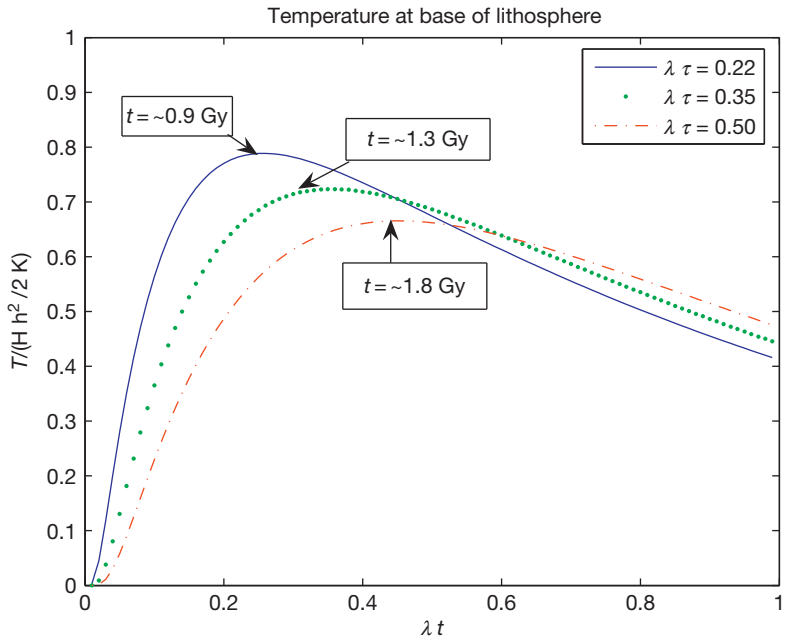

Figure 19 Temperature increase at the base of the lithospheric root after its stabilization beneath the crust. The temperature is divided by the maximum temperature increase due to crustal heat production at the time of stabilization. λ is the average decay constant of the radioelements (corresponding to a half-life of about 2.5 Gy). τ is the thermal relaxation time of the root. The chosen values of $\lambda\tau$ correspond to root thicknesses of 170, 215, and 255 km. The arrow points to the time when the temperature reaches its maximum.

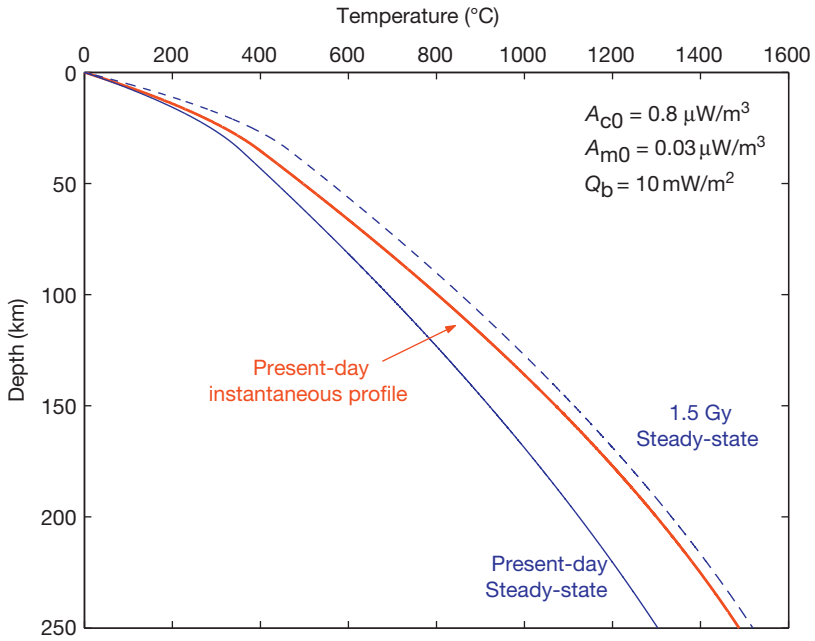

Figure 20 Transient geotherm with decaying heat sources in the lithospheric mantle. Two steady-state calculations corresponding to the same values of heat production today and to values of heat production at 1.5 Ga. Due to the large relaxation time of thick lithosphere, temperatures are not in equilibrium with radioactive heat sources.

steady state at old ages. Thermal equilibrium requires that asthenospheric convection supplies the amount of heat that is lost by conduction through the lithosphere. The different thicknesses imply different steady-state basal heat fluxes, $\approx$48 and 15 mW m^{-2} for oceans and continents, respectively, and yet it is the same asthenospheric material that lies beneath the two types of lithospheres. We now discuss how such different heat fluxes and thermal equilibrium conditions can be maintained. One possibility that was entertained by early workers is that continental lithosphere is simply oceanic

lithosphere that has grown very old and that has become very thick due to uninterrupted cooling. This is not consistent with the observations in the oceans, for example, which provide no evidence for any decrease of heat flux in the 120–190 My age range (Figures 7 and 8). The same straightforward approach is harder to apply to continents, as explained earlier, but no meaningful time-dependent trend can be extracted out of continental heat flow data for ages older than about 500 My. To understand how two different thermal steady states can be achieved, we resort to theoretical considerations.

Denoting by Q_b the convective heat flux and by T_b the temperature at the base of the lithosphere, the heat flux balance at the base of the lithosphere is such that

$$Q_b = \lambda \frac{\Delta T_\delta}{\delta} \qquad [27]$$

where δ is the thickness of the convective boundary layer at the base of the lithosphere and $\Delta T_\delta = T_w - T_b$ is the temperature difference across it. Robust scaling laws for the convective heat flux from laboratory experiments and theory and numerical calculations specify Q_b and ΔT_δ for all types of mantle rheological laws (Jaupart and Mareschal, 2011). To close the problem, we first rely on heat conduction in its simplest form:

$$Q_b = \lambda \frac{T_b - T_o}{h_1} \qquad [28]$$

where the effects of crustal heat production have been neglected. Using these two equations, one can solve for both T_b and h_1. The asthenosphere viscosity μ and the driving temperature difference for convection, ΔT_δ, depend on pressure, implying that the convective heat flux decreases with increasing depth and increasing lithospheric thickness. So does the conductive heat flux through the lithosphere, which also decreases as the lithosphere thickens. The pressure dependences of the two types of heat fluxes are different and allow two solutions to the heat flux balance equation, one for small depth, corresponding to high heat flux and thin lithosphere, and another for a larger depth with a larger viscosity, corresponding to low-heat-flux and thick lithosphere (Figure 21). It is tempting to associate these two equilibrium states with oceanic and continental lithospheres, respectively. One must evaluate how each state is achieved in practice, however, and whether it is stable or not to thermal and tectonic perturbations. This is best carried out by considering how the conductive heat flux changes when it is not in equilibrium with the convective one.

If we ignore the intrinsic buoyancy of the lithospheric mantle, the lithosphere behaves rigidly because it is cold and its thickness can change as its temperatures evolve. Let us imagine that some perturbations have moved the lithosphere away from its equilibrium thermal state, such that the convective heat flux is no longer equal to the conductive heat flux at the base of the lithosphere. On the one hand, if the convective heat flux is larger than the conductive one, the lithosphere heats up and thins, and hence, the conductive heat flux increases. On the other hand, if the convective heat flux is less than the conductive one, the lithosphere cools down and hence thickens, so that the conductive heat flux decreases. This shows how lithospheric thickness and heat flux can adjust to bring the system back to an equilibrium state. As shown in Figure 21, however, the thickness changes in two different

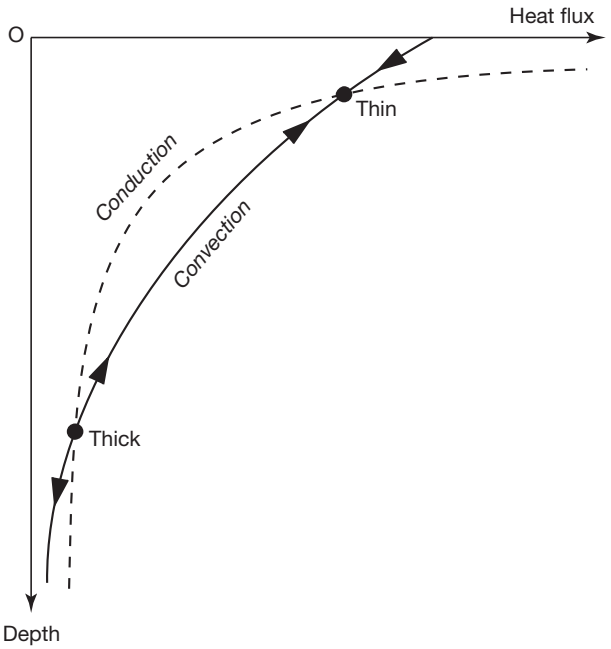

Figure 21 Schematic plot of the local convective heat flux beneath the lithosphere as a function of depth for a viscosity that depends on pressure and temperature. The heat flux sustained by convection depends on the local viscosity, which depends on pressure. With increasing lithospheric thickness, the convective heat flux decreases due to the pressure dependence of viscosity. The dashed line shows the heat flux that is carried by conduction across the lithosphere, which also decreases with depth. A stable thermal state requires equality of the convective and conductive heat fluxes. There are two such states, but only one of them is stable to perturbations. Arrows denote how the convective heat flux varies when the lithospheric thickness is not at an equilibrium value.

ways in the vicinity of the two equilibrium states. The shallow equilibrium state may be attained from both thin and thick starting lithospheres and is stable to perturbations. In contrast, the deep equilibrium situation can only be achieved if the lithosphere is created with precisely the right thickness. Starting from lithosphere that is either too thick or too thin, one cannot reach the deep equilibrium state and it is not a stable one. This argument led Doin et al. (1997) to conclude that continental lithosphere is not in an equilibrium state and that it is indeed oceanic lithosphere that has been thickening for a long time. This model is attractive because it explains how the same starting material and the same initial mechanism can lead to two very different types of lithospheres. In order to kick thin oceanic lithosphere out of its thermal equilibrium state, one can appeal to tectonic thickening or thrusting or underplating by plumes, but the amount of thickening required is large (Figure 21). This argument, however, is outside the scope of this chapter and we focus on purely thermal considerations.

The model fails because the closure equation for the conductive heat flux eqn [28] does not account for the large amounts of heat-producing elements in the continental crust. With radiogenic heat production in the crust, stable solutions correspond to the thickness of continental lithosphere (Figure 22). Calculations involve many variables, including the potential mantle temperature and the activation volume

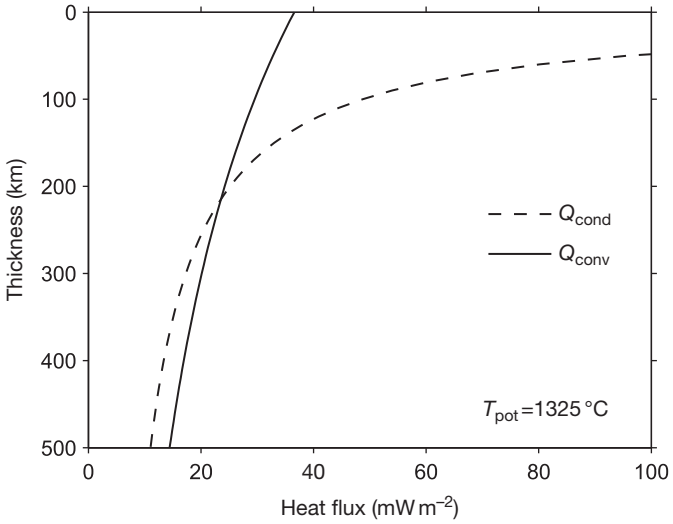

Figure 22 Conductive (Q_{cond}) and convective (Q_{conv}) heat fluxes as a function of lithospheric thickness, for a mantle potential temperature of 1325 °C and an average crustal radioactivity of 0.5 μW m^{-3} (adapted from Lévy F and Jaupart C (2011) Temperature and rheological properties of the mantle beneath the North American craton from an analysis of heat flux and seismic data. *Journal of Geophysical Research* 116: B01, 408). The asthenosphere deforms by wet dislocation creep with an activation volume of 10 cm^3 mol^{-1}.

for creep. Using the constraints of heat flow and seismic data on the one hand and various rheological laws and their parameters on the other hand, Lévy and Jaupart (2011) arrived at self-consistent models for North America.

The two ingredients that are required for the generation of both thin and thick stable lithospheres are an activation volume for creep that is sufficiently large and marked differences of crustal heat production. The impact of the former is straightforward: with a nonzero activation volume, asthenospheric material stiffens with increasing depth, which accounts for the different values of the basal heat flux beneath oceanic and continental lithospheres. The role of the latter is subtle and may well tell us a lot about continental evolution, as it introduces a relationship between crustal heat production and lithospheric thickness. This discussion illustrates the added value of studying oceanic and continental lithospheres within the same thermal framework. It also shows clearly the importance of accounting for continental crust and its large amounts of radioactive elements.

6.05.7 Other Geophysical Constraints on the Thermal Regime of the Continental Lithosphere

6.05.7.1 Constraints from Seismology

The 3-D seismic velocity structure of the upper mantle determined by seismic tomography has shown strong correlation with the geology. In particular, the presence of lithospheric roots beneath cratons is associated with higher seismic velocity than outside (e.g., Goes and vanderLee, 2002; Goes et al., 2005; Poupinet and Shapiro, 2009; Poupinet et al., 2003). Heat production in the lithospheric mantle is often assumed to be negligible but a very small difference in heat production between the depleted cratonic mantle and surrounding areas leading to 1–2 mW m^{-2} difference in Moho heat flux leads to large temperature differences in the lower lithosphere (Hieronymus and Goes, 2010, see also **Figure 13**).

For North America, upper mantle shear wave velocities derived from surface wave tomography (Bedle and van der Lee, 2009) are clearly correlated with surface heat flux. The map of vertical shear wave travel delays calculated between 260 and 60 km shows negative travel time anomalies beneath the craton and positive anomalies in active regions (**Figure 23**), which can be directly compared with the North American heat flow map (**Figure 2**).

Seismic tomography models of the upper mantle that are directly obtained by inversion of surface wave data are nonunique. Heat flux data and thermodynamic constraints can be used to narrow down the range of seismic tomography models that are consistent with mantle temperatures. Shapiro and Ritzwoller (2004) inverted surface wave data to obtain vertical profiles of *S*-wave velocity through both continents and oceans. For a given compositional model, these data can be converted to temperature. In a given area, the solution domain allows for nonmonotonous variations of temperature with depth, that is, with zones where temperature decreases with depth, which are not physically realistic. The range can be further narrowed down with constraints from heat flux by eliminating solutions outside the range of Moho temperatures and mantle heat flux allowed by thermal models. One striking result is that this procedure gets rid of the nonphysical solutions with negative vertical temperature gradients (**Figure 24**).

Further comparison between seismic and thermal models must allow for errors in both types of variables and for differences in the spatial resolutions of seismic and thermal models. Converting seismic wave speed into temperature or temperature into wave speed is affected by significant uncertainties due to the compositional model and to the effects of anelasticity and fluids (e.g., Goes et al. (2000); Sobolev et al. (1996)). The relationship between wave speed and temperature can be calibrated empirically, however, in areas with extensive data

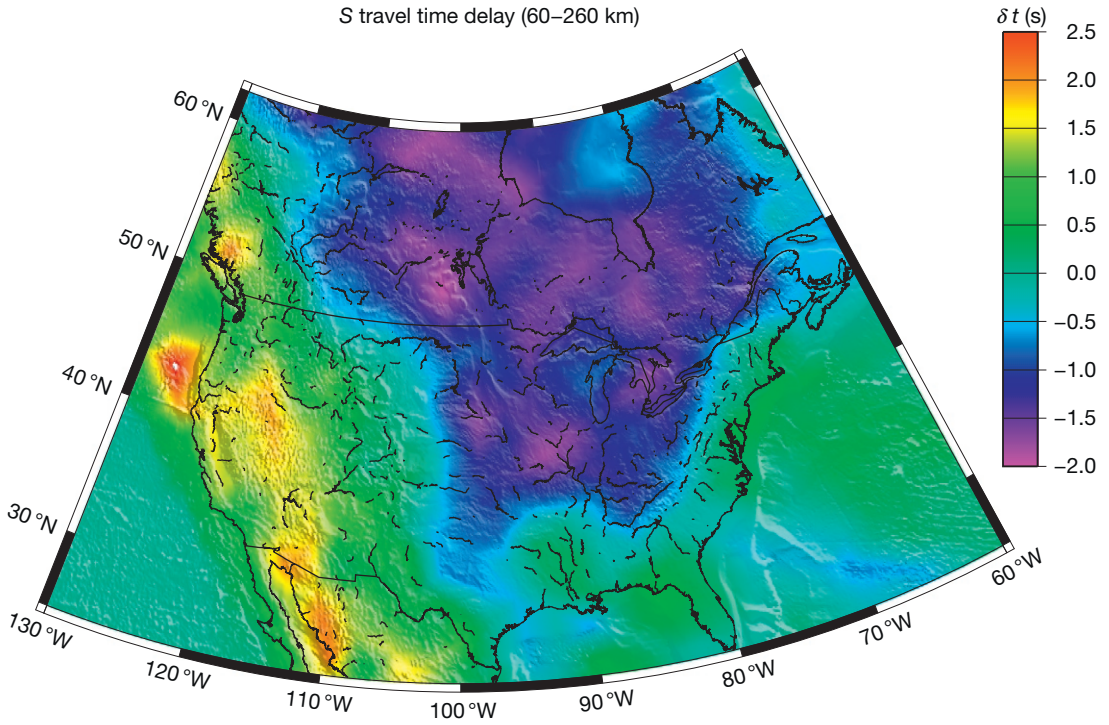

Figure 23 Shear wave travel time delays between 60 and 300 km based on the seismic tomography model NA07 of Bedle and van der Lee (2009). The delay is the difference between the vertical propagation time of shear waves calculated with the NA07 model and the vertical travel time for the reference ak135 velocity profiles.

coverage. Perry et al. (2006b) used such approach in the southern part of the Archean Superior Province of the Canadian Shield, where a large number of heat flux data are available and several seismic surveys have been conducted. They used P_n velocities of the refracted wave that propagates through the mantle just below the Moho discontinuity. Such velocities are determined locally and are not affected by spatial smoothing inherent to tomographic analyses. Spatial resolution along the seismic line depends on the receiver spacing and on local heterogeneity and is typically $\approx$100 km. Perry et al. (2006b) compiled all available P_n velocity data and determined upper mantle temperatures from heat flow data on a $2^\circ \times 2^\circ$ grid. On this scale, they obtained correlations between P_n and upper mantle temperature (**Figure 25**). These data imply that $\partial V(P_n)/\partial T \approx -6.0 \times 10^{-4} \pm 10\%\,\mathrm{km\,s^{-1}\,K^{-1}}$, within the range of temperature derivatives obtained in laboratory studies of ultramafic rocks. Such a close agreement provides confidence in the absolute temperature values deduced from heat flow and seismic studies. This study shows that the Moho temperature varies by about 300 K in the southern Superior Province, due to differences in crustal heat production and crustal thickness.

6.05.7.2 Seismicity, Elastic Thickness, and Thermal Regime of the Lithosphere

In the oceans, both the effective elastic thickness (T_e) and the maximum depth of earthquakes increase with the age of the oceanic lithosphere (Seno and Yamanaka, 1996; Watts, 2001). The dependence of T_e on the age of the oceanic lithosphere (at the time of loading) was examined in many studies (Calmant et al., 1990; Lago and Cazenave, 1981; Watts, 2001, see also **Chapter 6.01** and references therein) that show that, with few exceptions, oceanic T_e is given approximately by the depth to the 450 °C isotherm of the cooling plate model. The effective elastic thickness of the oceanic lithosphere is related to the yield strength envelope that is useful to understand how the temperature profile affects the strength of the lithosphere. The depth where the strength begins to decrease corresponds to the transition from brittle to ductile. In the oceans, this depth is strongly controlled by temperature, that is, by the age of the plate (McKenzie et al., 2005). The thickness of the seismogenic layer has been determined for intraplate settings or seaward of deep trenches (Emmerson and McKenzie, 2007; Seno and Yamanaka, 1996; Wiens and Stein, 1984). This thickness follows closely the T_e estimates suggesting that in the ocean, the brittle to ductile transition occurs at $<$600 °C.

For the continents, it had been expected that the depth distribution of earthquakes would be bimodal with earthquakes occurring in the brittle upper crust and in the upper mantle. But it was found that mantle earthquakes are exceptionally rare in the continents (Emmerson et al., 2006; Maggi et al., 2000). The conclusion that in the continents the seismogenic zone is confined to the upper crust appears inconsistent with some large values of T_e ($>$80 km) that have been observed beneath cratons.

In the continents, the strength profile is complicated by the rheological stratification in the lithosphere (Burov and Diament, 1995; see also **Chapter 6.03**). A relationship between age, thermal regime, and strength of the continental lithosphere was suggested by Karner et al. (1983). This clearly

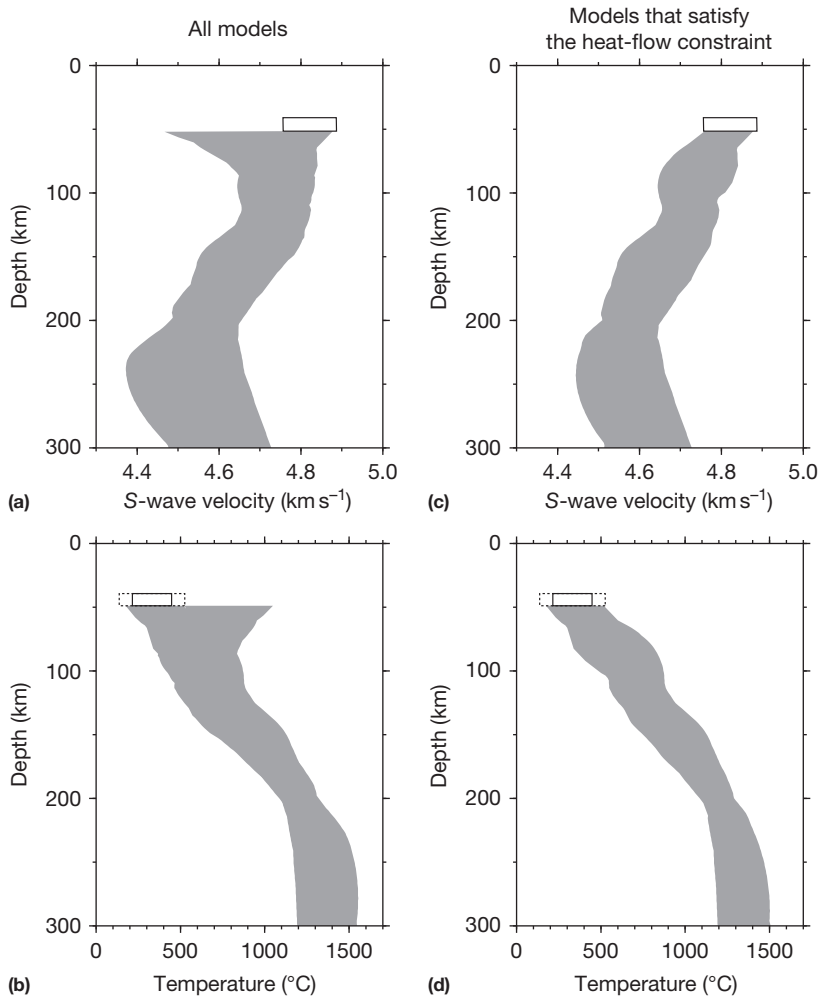

Figure 24 (top) Vertical profiles of *S*-wave velocity through the Canadian Shield obtained by diffraction tomography. (bottom) Vertical temperature profiles deduced from the velocity data. The left panel shows the whole solution domain, which includes nonphysical temperature profiles such that temperature decreases with depth at shallow levels. The right panel shows the solutions that are consistent with bounds of the Moho temperature deduced from heat flow studies. All the nonrealistic temperature profiles have been eliminated.

holds for the very young lithosphere and explains differences between the elastic thicknesses in the Basin and Range and stable North America (Lowry and Smith, 1995) or the Canadian Cordillera and the Canadian Shield (Flück et al., 2003; Hyndman et al., 2009). The temperature differences inferred from thermal models are consistent with the very long-wavelength variations in elastic thickness. Small-scale variations in T_e often seem difficult to account for by the thermal regime, but some high-resolution studies of the elastic thickness show a very good correlation with the thermal regime. For example, the study of the elastic thickness in Africa by Pérez-Gussinyé et al. (2009) shows a good qualitative correlation with the heat flow data including sharp variations between the East African Rift and the Tanzanian Craton.

A systematic comparison of heat flux and T_e estimates in the continents is complicated because both data sets are noisy. T_e is usually estimated by the coherence method, but the results strongly depend on the spectral method that is used to calculate the coherence (Audet and Mareschal, 2004; Simons et al., 2000; see also **Chapter 10.05**). The compilation of all the regional estimates of T_e includes values that have been obtained by various spectral methods and shows only a weak correlation with continental heat flux data even when the data are averaged over $2 \times 2^\circ$ windows (Watts, 2013). When the same method is used to determine the variations in effective elastic thickness worldwide, the correlation remains poor (Audet and Bürgmann, 2011, see also **Figure 26**). However, when T_e estimates are binned by heat flux values, their means exhibit a well-defined decrease with increasing heat flux (**Figure 26**). Detailed analysis of anomalies is beyond the objectives of this report, but it must be pointed out that high T_e and high heat flux are found in the Gawler Craton and the Proterozoic provinces of Australia where the high heat flux is accounted for by the very high radioactivity of the shallow crust and does not imply elevated temperature at depth. This emphasizes that surface heat flux values are not sufficient to determine lithospheric temperatures accurately and that one must also account for the vertical distribution of heat sources, which varies from province to province.

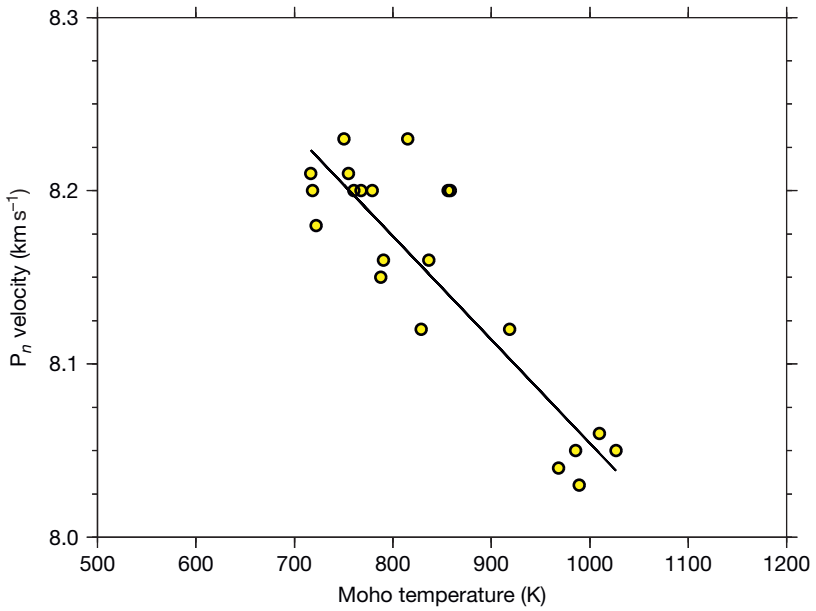

Figure 25 Relationship between P_n velocity and temperature at the Moho in the southern Superior Province of the Canadian Shield (adapted from Perry HKC, Jaupart C, Mareschal JC, and Shapiro NM (2006) Upper mantle velocity-temperature conversion determined from seismic refraction and heat flow. *Journal of Geophysical Research* 111: B07,301, http://dx.doi.org/10.1029/2005JB003,921). Moho temperature is calculated for a Moho heat flux of 15 mW m^{-2}. Solid line is the best-fit linear relationship with a slope of -6.0×10^{-4} km s^{-1} K^{-1}, within the range of values for ultramafic rocks determined in the laboratory.

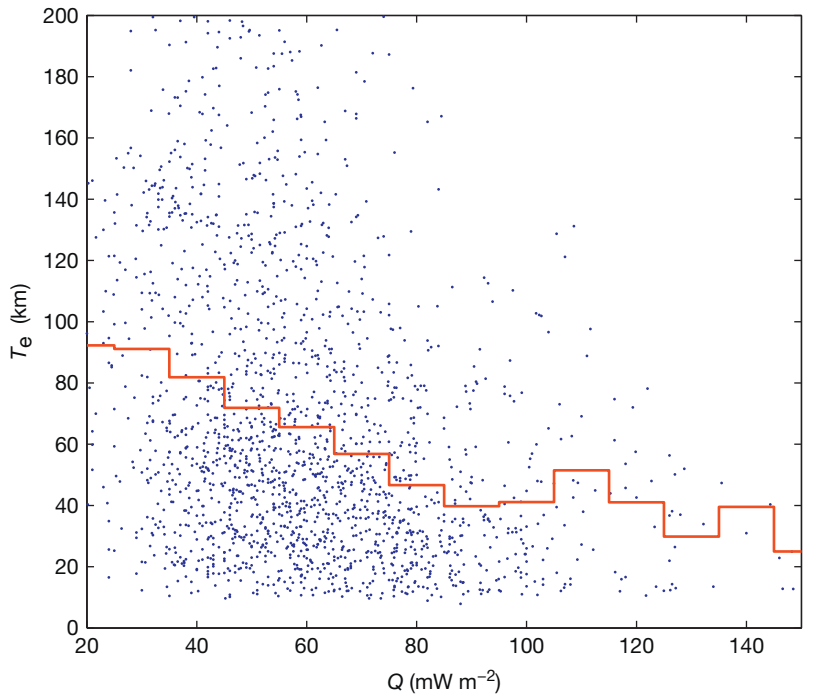

Figure 26 Variations in elastic thickness T_e with surface heat flux in the continents. Elastic thickness estimates using the wavelet transform from Audet and Bürgmann (2011) and heat flux data averaged over $2 \times 2^\circ$ cells are shown as blue dots. The solid red line represents the average T_e when the data are binned in 10 mW m^{-2} wide intervals.

A different approach consists of predicting T_e from a thermal and rheological model and comparing with 'observed' T_e values. This comparison shows that, although there is a good correlation between the two values, there is a significant difference between the two distributions. The thermal–rheological estimates show a bimodal distribution with two peaks, one over the cratons and one over young provinces, while the distribution of 'observed' T_e values is unimodal (Tesauro et al., 2012).

6.05.7.3 Depth to the Curie Isotherms

The main sources of magnetic anomalies are present in the crust and not in the mantle. The Curie isotherm for magnetite, ≈580 °C, will normally be located in the upper mantle beneath continents and oceans. However, high surface heat flux and elevated temperatures in the lower crust will cause a shallow Curie isotherm with thinning of the magnetic crust and an upper crustal source of magnetic anomaly. Satellite magnetic data have been used to confirm the elevated lower crustal temperatures beneath the Basin and Range (Mayhew, 1982) or to delineate the edge of the North American craton (Purucker et al., 2002 see also **Chapter 5.06** by Purucker and Whaler). The high-quality magnetic data obtained by recent satellite missions have sufficient resolution to be useful for detailed lithospheric studies (Maus et al., 2006). In regions that are covered by ice sheets where heat flow measurements are impractical, the magnetic data can be used to infer the depth of the Curie isotherm (Fox Maule et al., 2005), but the surface heat flux cannot be deduced without information on the vertical distribution of heat-producing elements.

6.05.7.4 Thermal Isostasy

In the oceans, the depth of seafloor below sea level is directly related to the average lithospheric density and temperature. Note that the oceanic geotherm is not in steady state. Crough and Thompson (1977) had applied similar concepts to the continental lithosphere. In the continents, density variations are due both to changing crustal thickness (and composition) and to differences in temperature. Low mantle temperature beneath the cratons should increase the density of the mantle and keep the elevation much lower than the observed mean elevation. This led Jordan (1981) to propose that the cratonic mantle is made up of refractory residual mantle with lower intrinsic density than the off-cratonic mantle. This compositional effect balances the thermal effect to give to the cratons their present elevation.

In the Basin and Range, where the typical crustal thickness is 30 km, the average elevation of 1750 m requires the upper mantle density to be anomalously low. Differences in temperature can account only for part of the elevation, and low-density magma intrusions are thought to also contribute to the buoyancy of the mantle (Lachenbruch and Morgan, 1990). The high heat flux in the Canadian Cordillera suggests that thermal isostasy contributes to part of the elevation (Hyndman, 2010; Lewis et al., 2003).

If isostasy was achieved by Airy's mechanism, one expects elevation to be correlated with crustal thickness (and mean density). After adjusting the elevation data for the differences in mean crustal density, one can compare elevation with crustal thickness and identify two different regimes in North America (Hyndman, 2010). For the same crustal thickness, regions with low heat flux stand on average 1.4 km lower than tectonically active regions with high heat flux (**Figure 27**).

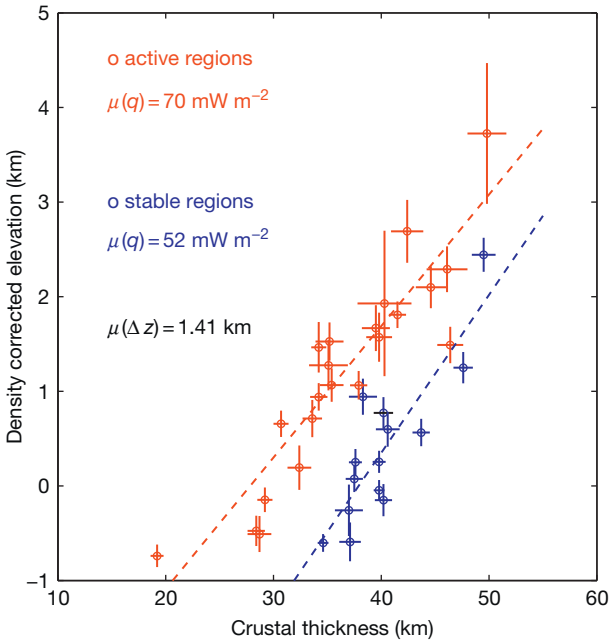

Figure 27 Mean elevation as a function of crustal thickness for different provinces in North America. Elevation has been corrected to account for the differences in mean crustal density. The average elevation of tectonically active regions with high heat flow is about 1.4 km higher than that of stable regions with normal heat flow. Adapted from Hyndman RD (2010) The consequences of Canadian Cordillera thermal regime in recent tectonics and elevation: A review. *Canadian Journal of Earth Sciences* 47: 621–632.

The relationship between the thermal regime and the surface elevation of the continents has been further studied by Hasterok and Chapman (2007a,b). These authors calculated the median elevation and heat flux for different geologic provinces in North America, and they adjusted the mean elevation to account for the variations in crustal thickness and density. After such a correction has been performed, a clear correlation can be observed between the average elevation and heat flux in these regions in spite of some scatter in the values (**Figure 28**). Two anomalies stand out. One is the Pacific Coast Range where heat flux is low and adjusted elevation high possibly because of the support of the topography by the subducting slab. The other apparent anomaly is provided by the Wopmay orogen where high heat flux is accounted for by the very high heat production in the shallow crust and does not imply elevated temperature at depth (Lewis et al., 2003). This illustrates again the importance of the vertical distribution of the heat-producing elements for calculating thermal models.

6.05.8 Conclusions

The failure of the simple 'half-space' cooling model to account for heat flux and bathymetry of old seafloor provides very

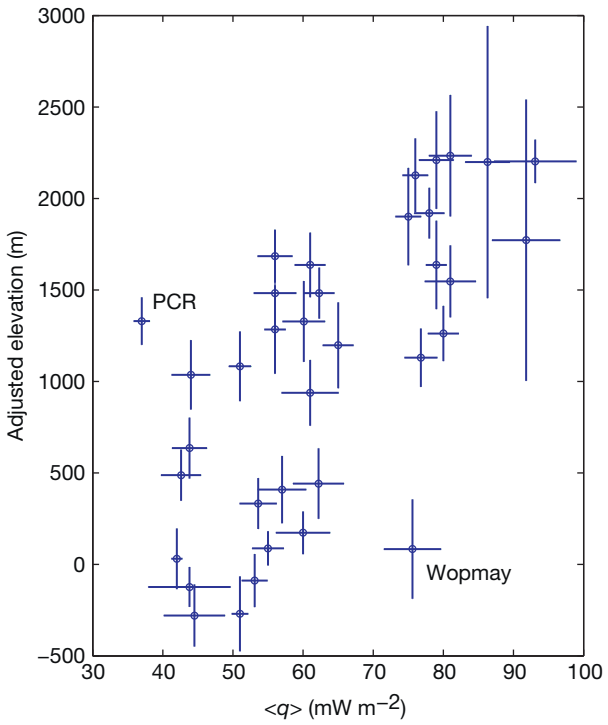

Figure 28 Elevation versus mean surface heat flux for different geologic provinces in North America. Elevation has been adjusted to account for differences in crustal thickness and density. The Pacific Coast Range (PCR) and the Wopmay orogen stand out as anomalies. Adapted from Hasterok D and Chapman DS (2007) Continental thermal isostasy: 2. Application to North America. *Journal of Geophysical Research* 112: 6415.

useful information on the heat transport mechanisms that are active in the mantle and helps addressing the more complex problem of continents. The mechanism that brings heat to the base of the oceanic lithosphere is probably also active beneath the continental lithosphere and explains why continents tend to thermal steady state.

Lithospheric thickness is in many ways an ill-defined variable. Not only does its value vary from one geophysical method to the next, but also from the thermal perspective, it may also change depending on the basal boundary condition. Furthermore, it may be different for steady-state and transient thermal models. Such complexities are not merely a problem of vocabulary and reflect important features of heat transport in the upper boundary layer of mantle convection.

For lithospheric studies, one should regard heat flow data as affected by large geologic noise. The sources of this noise are hydrothermal circulation in the oceans and crustal radiogenic heat production in the continents. Unfortunately, this noise is locally controlled (i.e., local topography and sediment thickness for oceans, geologic evolution, and crustal structure for continents). Thus, one may not propose generic lithosphere models valid for continents or oceans of given age without carefully accounting for the local environment. One may not determine lithosphere structure without additional constraints and without a heat transport model. Heat flow data, however, do provide strong constraints on heat transport mechanisms.

Appendix A Measurement Techniques

Heat flux is never directly measured but its vertical component is obtained by Fourier's law:

$$Q = \lambda \frac{\partial T}{\partial z} \qquad [A.1]$$

Continental or oceanic heat flux measurements thus require the determination of the vertical temperature gradient and of the thermal conductivity (Beck, 1988; Jessop, 1990).

A.1 Conventional Land Heat Flow Measurements

On land, conventional heat flux measurements are obtained by measuring temperature in drill holes (usually holes of opportunity, mostly mining exploration). Continuous core samples are routinely kept in mining exploration and conductivity can be measured on samples from the hole. The divided bar method provides the most robust method to measure the bulk rock conductivity because it involves relatively large samples and is insensitive to small-scale variations in lithology, but it is time-consuming and only a limited number of samples can be processed. Continuous measurement of conductivity on the entire core can be made with an optical scanning device (Popov et al., 1999). The heat flux is commonly obtained as the slope of the best-fitting line to the 'Bullard plot' of temperature versus thermal resistance to depth z, $R(z)$:

$$R(z) = \int_0^z \frac{\mathrm{d}z'}{\lambda(z')} \qquad [A.2]$$

Alternatively, heat flux can be obtained from Fourier's law over depth intervals where the conductivity is constant. Both methods give comparable results even when the fit is poor or when heat flow varies between depth intervals. Because the temperature field in the upper 200 m is often perturbed by surface effects, including the effect of recent climate change, reliable heat flux measurements require deep boreholes (at least 300 m).

A.2 Bottom Hole Temperature Data

Temperature measurements are routinely available from oil exploration wells, as either BHT or drill stem tests (DST), with a precision never better than 5–10 K after corrections. In deep wells, the gradient can thus be estimated with a precision of 10–15%. The other difficulty with oil exploration wells is the lack of core samples for thermal conductivity, which has to be estimated from the lithology or from other physical properties (density, porosity, etc.) that are routinely logged (Goutorbe et al., 2006). Although less precise than conventional methods, oil exploration data have provided most of the estimates of heat flux in sedimentary basins and on many continental margins.

Appendix B Corrections

Heat flux determinations assume that heat is transported vertically in steady state and thus require no lateral variations in surface boundary conditions or physical properties. Changes in vegetation, the proximity to a lake, and topography can distort the shallow temperature field and affect the heat flow estimate

(Jeffreys, 1938). Rapid erosion (or sedimentation) also affects the temperature field (Benfield, 1949). These effects are largest near the surface and the error on the heat flow is small in sufficiently deep boreholes. The topographic perturbation can be accounted for and corrections can be made. If the erosion rate is known, a correction can also be applied (Carslaw and Jaeger, 1959, p. 388). The effect of a lake or change in vegetation cannot be estimated without extensive data coverage in the horizontal direction, and the only practical solution is to restrict measurements to boreholes that are deep enough.

Appendix C Climatic Effects

Temperatures near the Earth surface keep a memory of the past surface boundary conditions. This was understood by Kelvin who tried to use this effect to determine the age of the Earth (Thomson, 1864). For periodic variations of the surface temperature, the temperature wave is attenuated exponentially as it propagates downward with a skin depth $\delta = \sqrt{\kappa T/\pi}$ (Carslaw and Jaeger, 1959, p. 66) where T is the period and κ the thermal diffusivity. The daily and annual temperature cycles are damped over <0.5 and 10 m respectively. They do not affect temperature at the depth of land heat flux measurements. Long-term variations in surface temperature could potentially significantly affect the temperature gradient. Birch (1948) had already pointed out that, following the last glacial episode that ended *c.*10 000 years BP, surface temperature warming could affect the temperature gradient down to 2000 m and, if not accounted for, lead to underestimating the heat flow. If the time-varying surface boundary condition was known, it would be easy to account for it and make a correction. For the part of Canada covered by the Laurentide Ice Sheet, Jessop (1971) proposed a correction for a detailed climate history of the past 400 000 years with temperature equal to present during the interglacials and to $-1\,^{\circ}\mathrm{C}$ during the glacial episodes. Because the present temperature of the ground surface in Canada is quite low, the correction is usually small (<10% the heat flux). Measurements in deep boreholes in Canada have indeed shown that heat flow does not increase much at depth and that the effect of last glaciation is small (Chouinard and Mareschal, 2009; Rolandone et al., 2003a; Sass et al., 1971). These measurements also show that the thermal boundary condition at the base of the glacier might have been quite variable (possibly because it depends on the heat flow). Without detailed information on this past boundary condition, identical corrections have been applied to all the data from Canada. Similar but larger corrections are needed for data from northern Eurasia (Demezhko et al., 2007).

During the past 200 years, there has been a general warming trend following the 'Little Ice Ages' with an acceleration since 1960. This recent warming affects temperature profiles down to 200 m. In regions where heat flux is low and the warming has been particularly strong, the temperature gradients are negative down to 50–80 m. Borehole temperature profiles have been inverted to determine the surface temperature of the past centuries (Cermak, 1971; Lachenbruch and Marshall, 1986; Lewis, 1992). For measuring heat flux, it is now clear that reliable estimates require relatively deep boreholes (>300 m) to filter out the effect of recent warming and measure a stable temperature gradient over >100 m.

Appendix D Physical Properties

The calculation of the geotherm requires thermal conductivity to be known. Thermal conductivity depends on composition: it increases with the quartz content (Clauser and Huenges, 1995, and references therein). Table D.1 gives values of thermal conductivity for some important rocks and minerals. The lattice conductivity decreases with temperature. Over the range of crustal temperatures, the thermal conductivity can vary by as much as 50%. Durham et al. (1987) had measured the thermal conductivity variations for samples of different crustal rocks and proposed the following law for the thermal conductivity in the crust:

$$\lambda = 2.26 - \frac{618.241}{T} + \lambda_0 \left(\frac{255.576}{T} - 0.30247 \right) \qquad [D.1]$$

where λ is thermal conductivity (in $\mathrm{W\,m^{-1}\,K^{-1}}$), T is the absolute temperature, and λ_0 is the conductivity at the surface (for $T = 273$ K). Clauser and Huenges (1995) proposed similar equations to determine the lattice conductivity. The temperature dependence of conductivity cannot be neglected. When calculated with temperature-dependent conductivity, Moho temperatures in elevated heat flux regions could be up to $\approx$150 K higher than for constant conductivity.

At temperature higher than 1000 K, the radiative component of the thermal conductivity must be included. For mantle rocks, Schärmeli (1979) obtained the following relationship:

$$\lambda_r = 0.37 \times 10^{-9} T^3 \qquad [D.2]$$

More recent measurements by Hofmeister (1999) suggest lower values than given by eqn [D.2] for the radiative component of the thermal conductivity in mantle rocks. Based on these measurements, McKenzie et al. (2005) had proposed that the thermal conductivity in the mantle can be approximated by the following series expansion that accounts for both the lattice and the radiative components:

$$\lambda = \frac{b}{1 + cT} + \sum_{m=0}^{3} d_m T^m \qquad [D.3]$$

where T is absolute temperature and the constants $b = 8.98$, $c = 0.0228$, $d_0 = 1.753 \times 10^{-2}$, $d_1 = -1.0365 \times 10^{-4}$, $d_2 = 2.2451 \times 10^{-7}$, and $d_3 = -3.4071 \times 10^{-11}$.

Table D.1 Thermal conductivity of some rocks at room temperature

Rock type	*Mean ($W\,m^{-1}\,K^{-1}$)*	*Min–max ($W\,m^{-1}\,K^{-1}$)*	*References*
Basalt	2.0	1.8–2.5	Clark (1966)
Gabbro	2.2	1.8–2.5	Clark (1966)
Gneiss	3.6	2.0–5.0[a]	Clauser and Huenges (1995)
Granite	3.2	2.8–3.6	Clark (1966)
Granulite facies rocks	–	3.01–3.48	Joeleht and Kukkonen (1998)
Peridotite	2.8	2.3–3.4	Clark (1966)

[a]Thermal conductivity of gneiss in direction perpendicular to foliation is 0.6 that in direction parallel to foliation.

Within the lithosphere, one can use the simpler approximation for the mantle thermal conductivity proposed by Xu et al. (2004):

$$\lambda = \lambda_{298}\sqrt{\frac{298}{T}} \qquad [D.4]$$

with $\lambda_{298} = 4.49\ \mathrm{W\ m^{-1}\ K^{-1}}$.

The specific heat of crustal rocks is $1000\ \mathrm{J\ kg^{-1}\ K^{-1}}$. The thermal diffusivity $\approx 10^{-6}\ \mathrm{m^2\ s^{-1}}$, that is, $31.5\ \mathrm{m^2\ year^{-1}}$.

Acknowledgments

We are grateful to Francis Lucazeau who provided his compilation of world heat flow data, Derrick Hasterok who provided his results on thermal isostasy in digital format, Tony Watts for his compilations of effective elastic thicknesses worldwide, and Pascal Audet for his grid of effective elastic thickness on continents.

References

Abbott D (1991) The case for accretion of the tectosphere by buoyant subduction. *Geophysical Research Letters* 18: 585–588.

Ahern J and Mrkvicka S (1984) A mechanical and thermal model for the evolution of the Williston basin. *Tectonics* 3: 79–102.

Albarède F (2003) The thermal history of leaky chronometers above their closure temperature. *Geophysical Research Letters* 30: 1015.

Artemieva IM and Mooney WD (2001) Thermal thickness and evolution of Precambrian lithosphere: A global study. *Journal of Geophysical Research* 106: 16,387–16,414.

Ashwal LD, Morgan P, Kelley SA, and Percival J (1987) Heat production in an Archean crustal profile and implications for heat flow and mobilization of heat producing elements. *Earth and Planetary Science Letters* 85: 439–450.

Audet P and Bürgmann R (2011) Dominant role of tectonic inheritance in supercontinent cycles. *Nature Geoscience* 4: 184–187.

Audet P and Mareschal J-C (2004) Variations in elastic thickness in the Canadian Shield. *Earth and Planetary Science Letters* 226: 17–31.

Ballard S, Pollack HN, and Skinner NJ (1987) Terrestrial heat flow in Botswana and Namibia. *Journal of Geophysical Research* 92: 6291–6300.

Bank C-G, Bostock MG, Ellis RM, Hajnal Z, and VanDecar JC (1998) Lithospheric mantle structure beneath the Trans-Hudson Orogen and the origin of diamondiferous kimberlites. *Journal of Geophysical Research* 103: 10,103–10,114.

Barrell J (1914) The strength of the earth's crust. *Journal of Geology* 22: 655–683.

Barrell J (1915) The strength of the earth's crust viii. Physical conditions controlling the nature of lithosphere and asthenosphere. *Journal of Geology* 23: 425–443.

Barreyre T, Escartin J, Garcia R, Cannat M, Mittelstaedt E, and Prados R (2012) Structure, temporal evolution, and heat flux estimates from the lucky strike deep-sea hydrothermal field derived from seafloor image mosaics. *Geochemistry, Geophysics, Geosystems* 13: Q04007.

Bea F and Montero P (1999) Behaviour of accessory phases and redistribution of Zr, REE, Y, th, and U during metamorphism and partial melting of metapelites in the lower crust: an example from the Kinzigite formation of Ivrea-Verbano, northwestern Italy. *Geochimica et Cosmochimica Acta* 63: 1133–1153.

Beck AE (1988) Methods for determining thermal conductivity and thermal diffusivity. In: Haenel R, Rybach L, and Stegena L (eds.) *Handbook of Terrestrial Heat Flow Density Determination*. Kluwer: Dordrecht.

Becker K and Davis E (2004) In situ determinations of the permeability of the igneous oceanic crust. In: Davis E and Elderfield H (eds.) *Hydrogeology of the Oceanic Lithosphere*. Cambridge: Cambridge University Press.

Bedini R-M, Blichert-Toft J, Boyet M, and Albarède F (2004) Isotopic constraints on the cooling of the continental lithosphere. *Earth and Planetary Science Letters* 223: 99–111.

Bedle H and van der Lee S (2009) S velocity variations beneath North America. *Journal of Geophysical Research* 114: 7308.

Benfield AE (1949) The effect of uplift and denudation on underground temperatures. *Journal of Applied Physics* 20: 66–70.

Bingen B, Demaiffe D, and Hertogen J (1996) Redistribution of rare earth elements, thorium, and uranium over accessory minerals in the course of amphibolite to granulite facies metamorphism: The role of apatite and monazite in orthogneisses from southwestern Norway. *Geochimica et Cosmochimica Acta* 60: 1341–1354.

Birch F (1948) The effects of Pleistocene climatic variations upon geothermal gradients. *American Journal of Science* 246: 729–760.

Birch F, Roy RF, and Decker ER (1968) Heat flow and thermal history in New England and New York. In: An-Zen E (ed.) *Studies of Appalachian Geology*, pp. 437–451. New York: Wiley-Interscience.

Blackwell D and Richards M (2004) *Geothermal Map of North America*. Tulsa, OK: American Association of Petroleum Geologists.

Bodell JM and Chapman DS (1982) Heat flow in the north central Colorado plateau. *Journal of Geophysical Research* 87: 2869–2884.

Bond G and Kominz M (1991) Disentangling middle Paleozoic sea level and tectonic events in cratonic margins and cratonic basins of North America. *Journal of Geophysical Research* 94: 6619–6639.

Bonneville A, Von Herzen RP, and Lucazeau F (1997) Heat flow over Reunion hot spot track: Additional evidence for thermal rejuvenation of oceanic lithosphere. *Journal of Geophysical Research* 102: 22,731–22,748.

Brady RJ, Ducea MN, Kidder SB, and Saleeby JB (2006) The distribution of radiogenic heat production as a function of depth in the Sierra Nevada batholith, California. *Lithos* 86: 229–244.

Brune J and Dorman J (1963) Seismic waves and earth structure in the canadian shield. *The Bulletin of the Seismological Society of America* 53: 167–210.

Burov EB and Diament M (1995) The effective elastic thickness (t_e) of the lithosphere: What does it really mean? *Journal of Geophysical Research* 100: 3905–3927.

Cadio C and Korenaga J (2012) Localization of geoid anomalies and the evolution of oceanic lithosphere: A case study from the Mendocino Fracture Zone. *Journal of Geophysical Research* 117: 10,404.

Calmant S, Francheteau J, and Cazenave A (1990) Elastic layer thickening with age of the oceanic lithosphere. *Geophysical Journal International* 100: 59–67.

Carlson RL and Johnson HP (1994) On modeling the thermal evolution of the oceanic upper mantle: An assessment of the cooling plate model. *Journal of Geophysical Research* 99: 3201–3214.

Carlson RW, Pearson DG, and James DE (2005) Physical, chemical, and chronological characteristics of continental mantle. *Reviews of Geophysics* 43: RG1001. http://dx.doi.org/10.1029/2004RG000156.

Carslaw HS and Jaeger JC (1959) *Conduction of Heat in Solids*, 2nd edn. Oxford, UK: Clarendon Press.

Cazenave A (1984) Thermal cooling of the oceanic lithosphere – New constraints from geoid height data. *Earth and Planetary Science Letters* 70: 395–406.

Cermak V (1971) Underground temperature and inferred climatic temperature of the past millennium. *Palaeogeography, Palaeoclimatology, Palaeoecology* 98: 167–182.

Cermak V (1993) Lithospheric thermal regimes in Europe. *Physics of the Earth and Planetary Interiors* 79: 179–193.

Chandrasekhar S (1961) *Hydrodynamic and Hydromagnetic Stability*. New York: Oxford university press.

Chouinard C and Mareschal JC (2009) Ground surface temperature history in southern Canada: Temperatures at the base of the Laurentide ice sheet and during the Holocene. *Earth and Planetary Science Letters* 277: 280–289.

Clark SP (1966) Thermal conductivity. In: Clark SP (ed.) *Handbook of Physical Constants*, pp. 459–482. Boulder, CO: GSA.

Clauser C and Huenges E (1995) Thermal conductivity of rocks and minerals. In: Ahrens TJ (ed.) *A Handbook of Physical Constants: Rock Physics and Phase Relations*, pp. 105–126. Washington, DC: AGU.

Courtney R and White R (1986) Anomalous heat flow and geoid across the Cape Verde Rise: Evidence of dynamic support from a thermal plume in the mantle. *Geophysical Journal of the Royal Astronomical Society* 87: 815–868.

Crosby AG and McKenzie D (2009) An analysis of young ocean depth, gravity and global residual topography. *Geophysical Journal International* 178: 1198–1219.

Crough ST (1983) Hotspot swells. *The Annual Review of Earth and Planetary Sciences* 11: 165–193.

Crough ST and Thompson GA (1977) Thermal model of continental lithosphere. *Journal of Geophysical Research* 81: 4857–4862.

Cull JP (1991) Heat flow and regional geophysics in Australia. In: Cermak V and Rybach L (eds.) *Terrestrial Heat Flow and the Lithosphere Structure*, pp. 486–500. Berlin: Springer Verlag.

Davaille A and Jaupart C (1994) Onset of thermal convection in fluids with temperature-dependent viscosity: Application to the oceanic mantle. *Journal of Geophysical Research* 99: 19,853–19,866.

Davies GF (1988) Ocean bathymetry and mantle convection, 1. Large-scale flow and hotspots. *Journal of Geophysical Research* 93: 10,467–10,480.

Davies JH and Davies DR (2010) Earth's surface heat flux. *Solid Earth* 1: 5–24.

Davis EE and Elderfield H (2004) *Hydrogeology of the Oceanic Lithosphere*. Cambridge, UK: Cambridge University Press.

Davis EE and Lister CRB (1974) Fundamentals of ridge crest topography. *Earth and Planetary Science Letters* 21: 405–413.

Davis EE, Chapman DS, Wang K, et al. (1999) Regional heat flow variations across the sedimented Juan de Fuca ridge eastern flank: Constraints on lithospheric cooling and lateral hydrothermal heat transport. *Journal of Geophysical Research* 104: 17,675–17,688.

Debayle E, Kennett B, and Priestley K (2005) Global azimuthal seismic anisotropy and the unique plate-motion deformation of Australia. *Nature* 433: 509–512.

Demezhko DY, Ryvkin DG, Outkin VI, Duchkov AD, and Balobaev VT (2007) Spatial distribution of Pleistocene/Holocene warming amplitudes in Northern Eurasia inferred from geothermal data. *Climate of the Past Discussions* 3: 607–630.

Doin M-P and Fleitout L (1996) Thermal evolution of the oceanic lithosphere: An alternative view. *Earth and Planetary Science Letters* 142: 121–136.

Doin M-P, Fleitout L, and Christensen U (1997) Mantle convection and stability of depleted and undepleted continental lithosphere. *Journal of Geophysical Research* 102: 2771–2787.

Doin M-P, Fleitout L, and McKenzie D (1996) Geoid anomalies and the structure of continental and oceanic lithospheres. *Journal of Geophysical Research* 101: 16,119–16,136.

Dumoulin C, Doin M, and Fleitout L (2001) Numerical simulations of the cooling of an oceanic lithosphere above a convective mantle. *Physics of the Earth and Planetary Interiors* 125: 45–64.

Durham WB, Mirkovich VV, and Heard HC (1987) Thermal diffusivity of igneous rocks at elevated pressure and temperature. *Journal of Geophysical Research* 92: 11,615–11,634.

Emmerson B, Jackson J, McKenzie D, and Priestley K (2006) Seismicity, structure and rheology of the lithosphere in the Lake Baikal region. *Geophysical Journal International* 167: 1233–1272.

Emmerson B and McKenzie D (2007) Thermal structure and seismicity of subducting lithosphere. *Physics of the Earth and Planetary Interiors* 163: 191–208.

Flück P, Hyndman RD, and Lowe C (2003) Effective elastic thickness T_e of the lithosphere in western Canada. *Journal of Geophysical Research* 108: 2430.

Fountain DM, Salisbury MH, and Furlong KP (1987) Heat production and thermal conductivity of rocks from the Pikwitonei-Sachigo continental cross section, central Manitoba: Implications for the thermal structure of Archean crust. *Canadian Journal of Earth Sciences* 24: 1583–1594.

Fox Maule C, Purucker ME, Olsen N, and Mosegaard K (2005) Heat flux anomalies in Antarctica revealed by satellite magnetic data. *Science* 309: 464–467.

Gass IG, Thorpe RS, Pollack HN, and Chapman DS (1978) Geological and geophysical parameters for mid-plate volcanism. *Philosophical Transactions of the Royal Society A* 301: 581–597.

Gaudemer Y, Jaupart C, and Tapponier P (1988) Thermal control on post-orogenic extension in collision belts. *Earth and Planetary Science Letters* 89: 48–62.

Goes S, Govers R, and Vacher P (2000) Shallow mantle temperatures under Europe from *p* and *s* wave tomography. *Journal of Geophysical Research* 105: 11,153–11,169.

Goes S, Simmons FJ, and Yoshizawa K (2005) Seismic constraints on temperature of the Australian uppermost mantle. *Earth and Planetary Science Letters* 236: 227–237.

Goes S and vanderLee S (2002) Thermal structure of the north American uppermost mantle inferred from seismic tomography. *Journal of Geophysical Research* 107: 2050.

Goutorbe B, Lucazeau F, and Bonneville A (2006) Using neural networks to predict thermal conductivity from geophysical well logs. *Geophysical Journal International* 166: 115–125.

Griffin WL, O'Reilly SY, Abe N, et al. (2003) The origin and evolution of Archean lithospheric mantle. *Precambrian Research* 127: 19–41.

Guillou L, Mareschal JC, Jaupart C, Gariépy C, Bienfait G, and Lapointe R (1994) Heat flow and gravity structure of the Abitibi belt, Superior Province, Canada. *Earth and Planetary Science Letters* 122: 447–460.

Gung Y, Panning M, and Romanowiz B (2003) Global anisotropy and the thickness of the continents. *Nature* 422: 707–710.

Gutenberg B (1926) Untersuchungen zur frage, bis zu welcher tiefe die erde kristallin ist. *Zeitschrift für Geophysik* 2: 24–29.

Gutenberg B (1948) On the layer of relatively low wave velocity at a depth of about 80 kilometers. *The Bulletin of the Seismological Society of America* 38: 121–148.

Hamdani Y, Mareschal J-C, and Arkani-Hamed J (1991) Phase change and thermal subsidence in intracontinental sedimentary basins. *Geophysical Journal International* 106: 657–665.

Hamdani Y, Mareschal J-C, and Arkani-Hamed J (1994) Phase change and thermal subsidence of the Williston basin. *Geophysical Journal International* 116: 585–597.

Harris RN and Chapman DS (2004) Deep-seated oceanic heat flow, heat deficits, and hydrothermal circulation. In: *Hydrogeology of the Oceanic Lithosphere*, pp. 311–336. New York: Cambridge University Press.

Harris RN, Garven G, Georgen J, McNutt MK, Christiansen L, and Von Herzen RP (2000) Submarine hydrogeology of the Hawaiian archipelagic apron 2. Numerical simulations of coupled heat transport and fluid flow. *Journal of Geophysical Research* 105: 21,353–21,370.

Hasterok D and Chapman DS (2007a) Continental thermal isostasy: 1. Methods and sensitivity. *Journal of Geophysical Research* 112: 6414.

Hasterok D and Chapman DS (2007b) Continental thermal isostasy: 2. Application to North America. *Journal of Geophysical Research* 112: 6415.

Haxby WF and Turcotte DL (1978) On isostatic geoid anomalies. *Journal of Geophysical Research* 83: 5473–5478.

Haxby W, Turcotte D, and Bird J (1976) Thermal and mechanical evolution of the Michigan basin. *Tectonophysics* 36: 57–75.

He L, Hu S, Huang S, et al. (2008) Heat flow study at the chinese continental scientific drilling site: Borehole temperature, thermal conductivity, and radiogenic heat production. *Journal of Geophysical Research* 113: 2404.

Heestand RL and Crough ST (1981) The effect of hot spots on the oceanic age-depth relation. *Journal of Geophysical Research* 86: 6107–6114.

Helmstaedt HH and Schulze DJ (1989) Southern African kimberlites and their mantle sample: implications for Archean tectonics and lithosphere evolution. In: Ross J (ed.) *Kimberlites and Related Rocks: Volume 1. Their Composition, Occurrence, Origin, and Emplacement. Geological Society of Australia Special Publication*, vol. 14, pp. 358–368. Perth: Geological Society of Australia, Geological Society of Australia Special Publication.

Hieronymus CF and Goes S (2010) Complex cratonic seismic structure from thermal models of the lithosphere: Effects of variations in deep radiogenic heating. *Geophysical Journal International* 180: 999–1012.

Hirth G, Evans R, and Chave A (2000) Comparison of continental and oceanic mantle electrical conductivity: Is the Archean lithosphere dry? *Geochemistry, Geophysics, Geosystems* 1, 2000GC000,048.

Hirth G and Kohlstedt DL (1996) Water in the oceanic upper mantle: Implications for rheology, melt extraction and the evolution of the lithosphere. *Earth and Planetary Science Letters* 144: 93–108.

Hofmeister AM (1999) Mantle values of thermal conductivity and the geotherm from phonon lifetimes. *Science* 283: 1699.

Hu S, He L, and Wang J (2000) Heat flow in the continental area of China: A new data set. *Earth and Planetary Science Letters* 179: 407–419.

Huang J and Zhong S (2005) Sublithospheric small-scale convection and its implications for the residual topography at old ocean basins and the plate model. *Journal of Geophysical Research* 110: B05,404. http://dx.doi.org/10.1029/2004JB003153.

Huerta AD, Royden LH, and Hodges KV (1998) The thermal structure of collisional orogens as a response to accretion, erosion, and radiogenic heating. *Journal of Geophysical Research* 103: 15,287–15,302.

Humler E, Langmuir C, and Daux V (1999) Depth versus age: New perspectives from the chemical compositions of ancient crust. *Earth and Planetary Science Letters* 173: 7–23.

Hurter SJ and Pollack HN (1996) Terrestrial heat flow in the Paraná Basin, southern Brazil. *Journal of Geophysical Research* 101: 8659–8672.

Hyndman RD (2010) The consequences of Canadian Cordillera thermal regime in recent tectonics and elevation: A review. *Canadian Journal of Earth Sciences* 47: 621–632.

Hyndman RD, Currie CA, Mazzotti S, and Frederiksen A (2009) Temperature control of continental lithosphere elastic thickness, T_e vs V_s. *Earth and Planetary Science Letters* 277: 539–548.

James DE, Fouch MJ, VanDecar JC, and van der Lee S (2001) Tectospheric structure beneath southern Africa. *Geophysical Research Letters* 28: 2485–2488.

Jaupart C (1983a) Horizontal heat transfer due to radioactivity contrasts: Causes and consequences of the linear heat flow-heat production relationship. *Geophysical Journal of the Royal Astronomical Society* 75: 411–435.

Jaupart C (1983b) The effects of alteration and the interpretation of heat flow and radioactivity data – A reply to R.U.M. Rao. *Earth and Planetary Science Letters* 62: 430–438.

Jaupart C, Francheteau J, and Shen X-J (1985) On the thermal structure of the Southern Tibetan Crust. *Geophysical Journal of the Royal Astronomical Society* 81: 131–155.

Jaupart C and Mareschal JC (1999) The thermal structure and thickness of continental roots. *Lithos* 48: 93–114.

Jaupart C and Mareschal JC (2011) *Heat Generation and Transport in the Earth*. Cambridge: Cambridge University Press.

Jaupart C and Mareschal JC (2012) Constraints on crustal heat production from heat flow data. In: Rudnick RL (ed.) *Treatise on Geochemistry*. 2nd edn., *The Crust*, 2nd edn., vol. 3, pp. 65–84. New York: Permagon.

Jaupart C, Mareschal JC, Guillou-Frottier L, and Davaille A (1998) Heat flow and thickness of the lithosphere in the Canadian Shield. *Journal of Geophysical Research* 103(103): 15,269–15,286.
Jeffreys H (1938) The disturbance of the temperature gradient in the earth's crust by inequalities of height. *Monthly Notices of the Royal Astronomical Society (MNRAS) and Geophysical Journal* (Suppl. 4): 309–312.
Jessop AM (1971) The distribution of glacial perturbation of heat flow in Canada. *Canadian Journal of Earth Sciences* 8: 162–166.
Jessop AM (1990) *Thermal Geophysics*. Amsterdam: Elsevier.
Joeleht TH and Kukkonen IT (1998) Thermal properties of granulite facies rocks in the Precambrian basement of Finland and Estonia. *Tectonophysics* 291: 195–203.
Johnson HP and Carlson RL (1992) Variation of sea floor depth with age: A test of models based on drilling results. *Geophysical Research Letters* 19: 1971–1974.
Jones MQW (1987) Heat flow and heat production in the Namaqua mobile belt, South Africa. *Journal of Geophysical Research* 92: 6273–6289.
Jones MQW (1988) Heat flow in the Witwatersrand Basin and environs and its significance for the South African Shield geotherm and lithosphere thickness. *Journal of Geophysical Research* 93: 3243–3260.
Jones MQW (1992) Heat flow anomaly in Lesotho: Implications for the southern boundary of the Kaapvaal craton. *Geophysical Research Letters* 19: 2031–2034.
Jordan TH (1975) The continental tectosphere. *Reviews of Geophysics* 13: 1–12.
Jordan TH (1981) Continents as a chemical boundary layer. *Royal Society of London Philosophical Transactions Series A* 301: 359–373.
Jurine D, Jaupart C, Brandeis G, and Tackley PJ (2005) Penetration of mantle plumes through depleted lithosphere. *Journal of Geophysical Research* 110: B10,104.
Kaminski E and Jaupart C (2000) Lithospheric structure beneath the Phanerozoic intracratonic basins of North America. *Earth and Planetary Science Letters* 178: 139–149.
Karner GD, Steckler MS, and Thorne J (1983) Long-term mechanical properties of the continental lithosphere. *Nature* 304: 250–253.
Ketcham RA (1996) Distribution of heat-producing elements in the upper and middle crust of southern and west central Arizona: Evidence from the core complexes. *Journal of Geophysical Research* 101: 13,611–13,632.
Kinzler RJ and Grove TL (1992) Primary magmas of Mid-Ocean ridge basalts 2. Applications. *Journal of Geophysical Research* 97: 6907–6926.
Klein EM and Langmuir CH (1987) Global correlations of ocean ridge basalt chemistry with axial depth and crustal thickness. *Journal of Geophysical Research* 92: 8089–8115.
Kremenentsky AA, Milanovsky SY, and Ovchinnikov LN (1989) A heat generation model for the continental crust based on deep drilling in the Baltic shield. *Tectonophysics* 159: 231–246.
Lachenbruch AH (1970) Crustal temperature and heat production: implications of the linear heat flow heat production relationship. *Journal of Geophysical Research* 73: 3292–3300.
Lachenbruch AH and Marshall BV (1986) Changing climate: Geothermal evidence from permafrost in Alaska. *Science* 234: 689–696.
Lachenbruch AH and Morgan P (1990) Continental extension, magmatism and elevation; formal relations and rules of thumb. *Tectonophysics* 174: 39–62.
Lachenbruch AH and Sass JH (1978) Models of an extending lithosphere and heat flow in the Basin and Range province. *Memoir – Geological Society of America* 152: 209–258.
Lachenbruch AH, Sass JH, and Morgan P (1994) Thermal regime of the southern Basin and Range Province: 2. Implications of heat flow for regional extension and metamorphic core complexes. *Journal of Geophysical Research* 99: 22,121–22,133.
Lago B and Cazenave A (1981) State of stress of the oceanic lithosphere in response to loading. *Geophysical Journal of the Royal Astronomical Society* 64: 785–799.
Lago B, Cazenave A, and Marty J-C (1990) Regional variations in subsidence rate of lithospheric plates: Implication for thermal cooling models. *Physics of the Earth and Planetary Interiors* 61: 253–259.
Lee MK, Brown GC, Webb PC, Wheildon J, and Rollin KE (1987) Heat flow, heat production and thermo-tectonic setting in mainland UK. *Journal of the Geological Society* 144: 35–42.
Lee C-TA, Luffi P, and Chin EJ (2011) Building and destroying continental mantle. *The Annual Review of Earth and Planetary Sciences* 39: 59–90.
Lévy F and Jaupart C (2011) Temperature and rheological properties of the mantle beneath the North American craton from an analysis of heat flux and seismic data. *Journal of Geophysical Research* 116: B01,408.
Lévy F, Jaupart C, Mareschal J, Bienfait G, and Limare A (2010) Low heat flux and large variations of lithospheric thickness in the Canadian Shield. *Journal of Geophysical Research* 115: 6404.
Lewis TJ (ed.) (1992) *Climatic Change Inferred from Underground Temperatures, Palaeogeography, Palaeoclimatology, Palaeoecology (Global and Planetary Change Section)* 98: 78–282.
Lewis TJ, Hyndman RD, and Fluck P (2003) Heat flow, heat generation and crustal temperatures in the northern Canadian Cordillera: Thermal control on tectonics. *Journal of Geophysical Research* 108: 2316.
Li X, Kind R, Yuan X, Wölbern I, and Hanka W (2004) Rejuvenation of the lithosphere by the Hawaiian plume. *Nature* 427: 827–829.
Lister CRB (1977) Estimators for heat flow and deep rock properties based on boundary layer theory. *Tectonophysics* 41: 157–171.
Lister CRB, Sclater JG, Nagihara S, Davis EE, and Villinger H (1990) Heat flow maintained in ocean basins of great age – Investigations in the north-equatorial West Pacific. *Geophysical Journal International* 102: 603–630.
Love AEH (1911) *Some Problems of Geodynamics*. Cambridge, UK: Cambridge University Press.
Lowry AR and Smith RB (1995) Strength and rheology of the western US Cordillera. *Journal of Geophysical Research* 100: 17,947–17,963.
Maggi A, Debayle E, Priestley K, and Barruol G (2006) Multimode surface waveform tomography of the Pacific Ocean: A closer look at the lithospheric cooling signature. *Geophysical Journal International* 166: 1384–1397.
Maggi A, Jackson JA, McKenzie DP, and Preistley K (2000) Earthquake focal depths, effective elastic thickness, and the strength of the continental lithosphere. *Geology* 28: 495–498.
Mareschal JC (1983) Mechanisms of uplift preceding rifting. *Tectonophysics* 94: 51–66.
Mareschal JC and Jaupart C (2004) Variations of surface heat flow and lithospheric thermal structure beneath the North American craton. *Earth and Planetary Science Letters* 223: 65–77.
Mareschal JC and Jaupart C (2013) Radiogenic heat production, thermal regime and evolution of continental crust. *Tectonophysics* 609: 524–534.
Mareschal JC and Jaupart C (2005) Archean thermal regime and stabilization of the cratons. In: Benn K, Condie K, and Mareschal JC (eds.) *Archean Geodynamic Processes*, pp. 61–73. Washington, DC: AGU.
Mareschal JC, Jaupart C, Cheng LZ, et al. (1999) Heat flow in the Trans-Hudson Orogen of the Canadian Shield: Implications for Proterozoic continental growth. *Journal of Geophysical Research* 104: 29,007–29,024.
Mareschal JC, Jaupart C, Gariépy C, et al. (2000) Heat flow and deep thermal structure near the southeastern edge of the Canadian Shield. *Canadian Journal of Earth Sciences* 37: 399–414.
Mareschal JC, Jaupart C, Rolandone F, et al. (2005) Heat flow, thermal regime, and rheology of the lithosphere in the Trans-Hudson Orogen. *Canadian Journal of Earth Sciences* 42: 517–532.
Mareschal JC, Nyblade A, Perry HKC, Jaupart C, and Bienfait G (2004) Heat flow and deep lithospheric thermal structure at Lac de Gras, Slave Province, Canada. *Geophysical Research Letters* 31: L12,611. http://dx.doi.org/10.1029/2004GL020,133.
Marty JC and Cazenave A (1989) Regional variations in subsidence rate of oceanic plates: A global analysis. *Earth and Planetary Science Letters* 94: 301–315.
Maus S, Rother M, Hemant K, et al. (2006) Earth's lithospheric magnetic field determined to spherical harmonic degree 90 from CHAMP satellite measurements. *Geophysical Journal International* 164: 319–330.
Mayhew MA (1982) Application of satellite magnetic anomaly to Curie isotherm mapping. *Journal of Geophysical Research* 87: 4846–4854.
McKenzie D (1967) Some remarks on heat flow and gravity anomalies. *Journal of Geophysical Research* 72: 6261–6273.
McKenzie D (1978) Some remarks on the development of sedimentary basins. *Earth and Planetary Science Letters* 40: 25–32.
McKenzie D and Bickle MJ (1988) The volume and composition of melt generated by extension of the lithosphere. *Journal of Petrology* 29: 625–679.
McKenzie D, Jackson J, and Priestley K (2005) Thermal structure of oceanic and continental lithosphere. *Earth and Planetary Science Letters* 233: 337–349.
Michaut C and Jaupart C (2004) Nonequilibrium temperatures and cooling rates in thick continental lithosphere. *Geophysical Research Letters* 31: L24,602.
Michaut C, Jaupart C, and Bell DR (2007) Transient geotherms in archean continental lithosphere: New constraints on thickness and heat production of the subcontinental lithospheric mantle. *Journal of Geophysical Research* 112: B04,408.
Mittelstaedt E, Escartin J, Gracias N, et al. (2012) Quantifying diffuse and discrete venting at the tour eiffel vent site, lucky strike hydrothermal field. *Geochemistry, Geophysics, Geosystems* 19: Q04008.
Moore WB, Schubert G, and Tackley PJ (1999) The role of rheology in lithospheric thinning by mantle plumes. *Geophysical Research Letters* 26: 1073–1076.

Morgan P (1983) Constraints on rift thermal processes from heat flow and uplift. *Tectonophysics* 94: 277–298.

Müller RD, Sdrolias M, Gaina C, and Roest WR (2008) Age, spreading rates, and spreading asymmetry of the world's ocean crust. *Geochemistry, Geophysics, Geosystems* 9: 4006.

Neumann N, Sandiford M, and Foden J (2000) Regional geochemistry and continental heat flow: implications for the origin of the South Australian heat flow anomaly. *Earth and Planetary Science Letters* 183: 107–120.

Nicolaysen LO, Hart RJ, and Gale NH (1981) The Vredefort radioelement profile extended to supracrustal strata at Carletonville, with implications for continental heat flow. *Journal of Geophysical Research* 86: 10,653–10,662.

Nielsen SB (1987) Steady state heat flow in a random medium and the linear heat flow-heat production relationship. *Geophysical Research Letters* 14: 318–322.

Nunn JA and Sleep NH (1984) Thermal contraction and flexure of intracratonic basins: A three dimensional study of the Michigan Basin. *Geophysical Journal of the Royal Astronomical Society* 79: 587–635.

Nyblade AA (1997) Heat flow across the East African Plateau. *Geophysical Research Letters* 24: 2083–2086.

Nyblade AA and Pollack HN (1993) A global analysis of heat flow from Precambrian terrains – Implications for the thermal structure of Archean and Proterozoic lithosphere. *Journal of Geophysical Research* 98: 12,207–12,218.

Nyblade AA, Pollack HN, Jones DL, Podmore F, and Mushayan-debvu M (1990) Terrestrial heat flow in east and southern Africa. *Journal of Geophysical Research* 951: 17,371–17,384.

Oxburgh ER and Parmentier EM (1977) Compositional and density stratification in oceanic lithosphere; causes and consequences. *Journal of the Geological Society* 133: 343–355.

Parker RL and Oldenburg DW (1973) Geophysics-Thermal model of ocean ridges. *Nature* 242: 137–141.

Parsons B and McKenzie D (1978) Mantle convection and thermal structure of plates. *Journal of Geophysical Research* 83: 4485–4496.

Parsons B and Sclater JG (1977) An analysis of the variation of ocean floor bathymetry and heat flow with age. *Journal of Geophysical Research* 82: 803–827.

Pérez-Gussinyé M, Metois M, Fernández M, Vergés J, Fullea J, and Lowry AR (2009) Effective elastic thickness of Africa and its relationship to other proxies for lithospheric structure and surface tectonics. *Earth and Planetary Science Letters* 287: 152–167.

Perry HKC, Jaupart C, Mareschal JC, and Bienfait G (2006a) Crustal heat production in the Superior Province, Canadian Shield, and in North America inferred from heat flow data. *Journal of Geophysical Research* 111: B04,401. http://dx.doi.org/10.1029/2005JB003,893.

Perry HKC, Jaupart C, Mareschal JC, Rolandone F, and Bienfait G (2004) Heat flow in the Nipigon arm of the Keweenawan Rift, northwestern Ontario, Canada. *Geophysical Research Letters* 31: L15,607. http://dx.doi.org/10.1029/2004GL020,159.

Perry HKC, Jaupart C, Mareschal JC, and Shapiro NM (2006b) Upper mantle velocity-temperature conversion determined from seismic refraction and heat flow. *Journal of Geophysical Research* 111: B07,301. http://dx.doi.org/10.1029/2005JB003,921.

Perry C, Rosieanu C, Mareschal J-C, and Jaupart C (2010) Thermal regime of the lithosphere in the Canadian Shield. *Canadian Journal of Earth Sciences* 47: 389–408.

Pilidou S, Priestley K, Debayle E, and Gudmundsson Ó (2005) Rayleigh wave tomography in the North Atlantic: High resolution images of the Iceland, Azores and Eifel mantle plumes. *Lithos* 79: 453–474.

Pinet C, Jaupart C, Mareschal J-C, Gariepy C, Bienfait G, and Lapointe R (1991) Heat flow and structure of the lithosphere in the eastern Canadian shield. *Journal of Geophysical Research* 96: 19,941–19,963.

Pollack HN (1986) Cratonization and thermal evolution of the mantle. *Earth and Planetary Science Letters* 80: 175–182.

Pollack HN and Chapman DS (1977a) On the regional variations of heat flow, geotherms, and lithospheric thickness. *Tectonophysics* 38: 279–296.

Pollack HN and Chapman DS (1977b) Mantle heat flow. *Earth and Planetary Science Letters* 34: 174–184.

Pollack HN, Hurter SJ, and Johnston JR (1993) Heat flow from the earth's interior: Analysis of the global data set. *Reviews of Geophysics* 31: 267–280.

Poort J and Klerkx J (2004) Absence of a regional surface thermal high in the Baikal rift; new insights from detailed contouring of heat flow anomalies. *Tectonophysics* 383: 217–241.

Popov YA, Pribnow DFC, Sass JH, Williams CF, and Burkhardt H (1999) Characterization of rock thermal conductivity by high resolution optical scanning. *Geothermics* 28: 253–276.

Poupinet G, Arndt N, and Vacher P (2003) Seismic tomography beneath stable tectonic regions and the origin and composition of the continental lithospheric mantle. *Earth and Planetary Science Letters* 212: 89–101.

Poupinet G and Shapiro NM (2009) Worldwide distribution of ages of the continental lithosphere derived from a global seismic tomographic model. *Lithos* 109: 125–130.

Priestley K and McKenzie D (2006) The thermal structure of the lithosphere from shear wave velocities. *Earth and Planetary Science Letters* 244: 285–301.

Purucker M, Langlais B, Olsen N, Hulot G, and Mandea M (2002) The southern edge of cratonic North America: Evidence from new satellite magnetometer observations. *Geophysical Research Letters* 29: 56-1–56-4.

Ramondec P, Germanovich L, Damm KV, and Lowell R (2006) The first measurements of hydrothermal heat output at 9°50′N, East Pacific Rise. *Earth and Planetary Science Letters* 245: 487–497.

Ray L, Kumar PS, Reddy GK, et al. (2003) High mantle heat flow in a Precambrian granulite province: Evidence from southern India. *Journal of Geophysical Research* 108: 2084.

Roberts GO (1979) Fast viscous Bénard convection. *Geophysical and Astrophysical Fluid Dynamics* 12: 235–272.

Rolandone F, Jaupart C, Mareschal JC, et al. (2002) Surface heat flow, crustal temperatures and mantle heat flow in the Proterozoic Trans-Hudson Orogen, Canadian Shield. *Journal of Geophysical Research* 107: 2314. http://dx.doi.org/10.1029/2001JB000,698.

Rolandone F, Mareschal JC, and Jaupart C (2003a) Temperatures at the base of the Laurentide ice sheet inferred from heat flow data. *Geophysical Research Letters* 30: 1944.

Rolandone F, Mareschal JC, Jaupart C, Gosselin C, Bienfait G, and Lapointe R (2003b) Heat flow in the western Superior Province of the Canadian shield. *Geophysical Research Letters* 30: 120,000–120,001.

Rondenay S, Bostock MG, Hearn TM, White DJ, and Ellis RM (2000) Lithospheric assembly and modification of the SE Canadian Shield: Abitibi-Grenville teleseismic experiment. *Journal of Geophysical Research* 105: 13,735–13,754.

Roy S and Rao RUM (2000) Heat flow in the Indian shield. *Journal of Geophysical Research* 105: 25,587–25,604.

Roy S and Rao RUM (2003) Towards a crustal thermal model for the Archean Dharwar craton, southern India. *Physics and Chemistry of the Earth* 28: 361–373.

Rudnick RL and Fountain DM (1995) Nature and composition of the continental crust: A lower crustal perspective. *Reviews of Geophysics* 33: 267–310.

Rudnick RL and Nyblade AA (1999) The thickness of Archean lithosphere: Constraints from xenolith thermobarometry and surface heat flow. In: Fei Y, Bertka CM, and Mysen BO (eds.) *Mantle Petrology; Field Observations and High Pressure Experimentation: A Tribute to Francis R. (Joe) Boyd*, pp. 3–11. Geochemical Society.

Russell JK, Dipple GM, and Kopylova MG (2001) Heat production and heat flow in the mantle lithosphere, Slave craton, Canada. *Physics of the Earth and Planetary Interiors* 123: 27–44.

Sandiford M and McLaren S (2002) Tectonic feedback and the ordering of heat producing elements within the continental lithosphere. *Earth and Planetary Science Letters* 204: 133–150.

Sandwell D and Schubert G (1980) Geoid height versus age for symmetric spreading ridges. *Journal of Geophysical Research* 85: 7235–7241.

Sass JH, Lachenbruch AH, and Jessop AM (1971) Uniform heat flow in a deep hole in the Canadian shield and its paleoclimatic implications. *Journal of Geophysical Research* 76: 8586–8596.

Sass JH, Lachenbruch AH, Jr SPG, et al. (1994) Thermal regime of the southern Basin and Range: 1. Heat flow data from Arizona and the Mojave desert of California and Nevada. *Journal of Geophysical Research* 99: 22,093–22,120.

Schärmeli G (1979) Identification of radioactive thermal conductivity in olivine up to 25 kbar and 1500K. In: Timmerhauf KD and Barber MS (eds.) Proceedings of the 6th AIRAPT Conference, pp. 60–74. New York: Plenum Press.

Schutt D and Lesher C (2006) The effects of melt depletion on the density and seismic velocity of garnet and spinel lherzolite. *Journal of Geophysical Research* 111: B05,401. http://dx.doi.org/10.1029/2003JB002,950.

Sclater JG, Jaupart C, and Galson D (1980) The heat flow through oceanic and continental crust and the heat loss from the earth. *Reviews of Geophysics* 18: 269–311.

Seno T and Yamanaka Y (1996) Double seismic zones, compressional deep trench outer rise events, and superplumes. In: Bebout GE, Scholl DW, Kirby SH, and Platt JP (eds.) *Subduction Top to Bottom Monograph*, vol. 36, pp. 347–355. Washington, DC: AGU.

Shapiro NM and Ritzwoller MH (2002) Monte-Carlo inversion for a global shear-velocity model of the crust and upper mantle. *Geophysical Journal International* 151: 88–105.

Shapiro NM and Ritzwoller MH (2004) Thermodynamic constraints on seismic inversions. *Geophysical Journal International* 157: 1175–1188.
Silver P (1996) Seismic anisotropy beneath the continents: Probing the depths of geology. *The Annual Review of Earth and Planetary Sciences* 24: 385–432.
Simons FJ, Zuber MT, and Korenaga J (2000) Isostatic response of the Australian lithosphere: Estimation of effective elastic thickness and anisotropy using multitaper spectral analysis. *Journal of Geophysical Research* 105: 19,163–19,184.
Sobolev SV, Zeyen H, Stoll G, Werling F, Altherr R, and Fuchs K (1996) Upper mantle temperatures from teleseismic tomography of french massif central including effects of composition, mineral reactions, anharmonicity, anelasticity and partial melt. *Earth and Planetary Science Letters* 157: 193–207.
Solomatov V and Moresi L-N (2000) Scaling of time-dependent stagnant lid convection: Application to small-scale convection on the earth and other terrestrial planets. *Journal of Geophysical Research* 105: 21,795–21,818.
Stein CA (1995) Heat flow of the earth. In: *Global Earth Physics: A Handbook of Physical Constants*, pp. 144–158.
Stein CA and Stein S (1992) A model for the global variation in oceanic depth and heat flow with lithospheric age. *Nature* 359: 123–129.
Tesauro M, Audet P, Kaban MK, Bürgmann R, and Cloetingh S (2012) The effective elastic thickness of the continental lithosphere: Comparison between rheological and inverse approaches. *Geochemistry, Geophysics, Geosystems* 13: 9001.
Thomson W (1864) On the secular cooling of the earth. *Transactions of the Royal Society of Edinburgh* 23: 295–311.
Turcotte DL and McAdoo DC (1979) Geoid anomalies and the thickness of the lithosphere. *Journal of Geophysical Research* 84: 2381–2387.
van der Velden AJ, Cook F, Drummond BJ, and Goleby BR (2005) Reflections of the Neoarchean: A global perspective. In: Benn K, Mareschal JC, and Condie K (eds.) *Geophys. Mono. Archean Geodynamics and Environments*, vol. 164, pp. 255–265. AGU.
Vasseur G and Singh RN (1986) Effects of random horizontal variations in radiogenic heat source distribution on its relationship with heat flow. *Journal of Geophysical Research* 91: 10,397–10,404.
Von Herzen RP, Cordery MJ, Detrick RS, and Fang C (1989) Heat flow and the thermal origin of hot spot swells: The Hawaiian Swell revisited. *Journal of Geophysical Research* 94: 13,783–13,799.
Watts AB (2001) *Isostasy and Flexure of the Lithosphere*. Cambridge, UK: Cambridge University Press.
Watts AB (2013) An overview. In: Watts AB (ed.) *Treatise on Geophysics. The lithosphere*, 2nd edn., vol. 6. Amsterdam: Elsevier.
Wiens DA and Stein S (1984) Intraplate seismicity and stresses in young oceanic lithosphere. *Journal of Geophysical Research* 89: 11,442–11,464.
Xu Y, Shankland TJ, Linhardt S, Rubie DC, Langenhorst F, and Klasinski K (2004) Thermal diffusivity and conductivity of olivine, wadsleyite and ringwoodite to 20 GPa and 13730 K. *Physics of the Earth and Planetary Interiors* 143: 321–336.

This page intentionally left blank

6.06 Lithosphere Stress and Deformation

ML Zoback, US Geological Survey, Menlo Park, CA, USA
M Zoback, Stanford University, Stanford, CA, USA

© 2007 Elsevier B.V. All rights reserved.

This chapter is reproduced from the previous edition, Volume 6, pp. 253–273, © 2007, Elsevier B.V.

6.06.1	Introduction	255
6.06.2	Global Patterns of Tectonic Stress	255
6.06.3	Sources of the Lithospheric Stress Field	258
6.06.4	Absolute Stress Magnitudes and the Critically Stressed Crust	261
6.06.5	Stress Field Constraints on Lithospheric Deformation	262
6.06.6	Concluding Remarks	268
Appendix A	Indicators of Contemporary Stress	268
References		269

6.06.1 Introduction

The advent of plate tectonics brought a new meaning and understanding to the mechanically defined lithosphere. Lithosphere became synonymous with the Earth's outer thermal boundary, the mobile 'plates' of plate tectonics. Motion of the plates was soon understood to be the result of a balance of forces that both drove and resisted their movement. While convection in the Earth is the ultimate source of the energy to drive plate tectonics, large-density inhomogeneities associated with plate subduction and generation of new oceanic lithosphere create the major driving forces. Other potentially important forces include viscous drag at the base of plates (either driving or resisting) and frictional resistance along plate boundaries.

Lithospheric deformation, the 'tectonics' of plate tectonics, is a result of the stress state within the lithosphere. In this chapter, we review the evidence for, and the implications of, field and laboratory data on the state of stress in the lithosphere and the forces acting upon and within it. Intensive investigation over the past few decades has revealed that the lithospheric state of stress is remarkably uniform both with depth and over vast regions of plate interiors. The broad uniformity of observed stress orientations and relative magnitudes, even across major bends in old orogenic belts, indicates that the lithospheric stress field is the result of present-day forces and is not due to residual stresses from past tectonic activity. Modeling has shown us that the same forces acting on and within the plates to drive plate motion are the same forces responsible for the state of stress in the lithosphere. Direct measurement of stress magnitudes at depth confirms a simple model in which stress differences in the crust are close to and limited by the frictional strength of the most well-oriented faults.

In contrast to the relative uniformity of intraplate stress fields, deformation rates in plate interiors vary by about eight orders of magnitude. We show how knowledge of the stress field, combined with mechanical, thermal, and rheological properties, can be used to constrain both the rate and style of lithospheric deformational processes.

6.06.2 Global Patterns of Tectonic Stress

Early attempts to map the state of stress in the lithosphere were largely based on earthquake focal mechanisms and very sparse, and usually quite shallow, in situ stress measurements (e.g., Pavoni, 1961, 1980; Raleigh, 1974; Richardson et al., 1976, 1979). Despite a relatively low density of stress data, these early investigations hinted at the broad-scale uniformity of stresses. In 1980, Zoback and Zoback introduced an integrated stress mapping strategy utilizing a variety of geologic and geophysical data: earthquake focal plane mechanisms, young geologic data on fault slip and volcanic alignments, in situ stress measurements, and stress-induced wellbore breakouts and drilling-induced tensile fractures. The initial effort to apply this integrated mapping strategy to the conterminous United States (Zoback and Zoback, 1980) revealed two fundamental characteristics of the crustal stress field:

1. To first order, the stress field is uniform with depth throughout the upper brittle crust as indicated by the consistency of stress orientations inferred from the different data types that sampled different volumes of rock at different depths: geologic and in situ stress measurement data sampled the surface or very near surface (less than 1–2 km depth), earthquake focal mechanisms provide coverage for depths between about 5 and 20 km, whereas wellbore breakout and drilling-induced fracture data commonly sample 1–4 km deep and in some cases as deep as 5–6 km, providing a valuable link between the near-surface and the focal mechanism data.
2. Stress orientations are remarkably uniform over broad regions (length scales up to thousands of kilometers), despite large changes in crustal geology, tectonic history, and crustal thickness.

A brief description of how the state of stress is inferred from the different types of stress indicators used is given in **Appendix A**: More information on the assumptions, difficulties, and uncertainties of inferring stress orientations from these different data types can be found in Zoback and Zoback (1980, 1991) and Zoback et al. (1989).

 http://dx.doi.org/10.1016/B978-0-444-53802-4.00115-9

A quality-ranking scheme was developed by Zoback and Zoback (1989, 1991) to assess how reliably an individual determination records the tectonic stress field. The quality-ranking scheme also permits comparison of orientations inferred from very different types of stress indicators that sample different depth intervals. This quality criterion was subsequently utilized in the International Lithosphere Program's World Stress Map (WSM) project, a large collaborative effort of data compilation and analyses by over 40 scientists from 30 different countries (Zoback, 1992). A special issue of the *Journal of Geophysical Research* (vol. 97, pp. 11703–12014) summarized the overall results of this project and presented the individual contributions of many of these investigators in various regions of the world. Today, the WSM database includes more than 10000 entries and is maintained by a research group of the Heidelberg Academy of Sciences and Humanities.

The global stress orientation data continue to reveal striking regional uniformity (**Figure 1(a)**). The success of the WSM project has validated this integrated stress mapping strategy using a variety of data types and demonstrated that with careful attention to data quality, coherent stress patterns over large regions of the Earth can be mapped with reliability and interpreted with respect to large-scale lithospheric processes.

Similar to stress orientations, stress regime (relative magnitude of the three principal stresses) also shows marked regional uniformity. Because stress is a tensor quantity, a full description of the state of stress requires information on both magnitudes and orientation. Direct stress measurements at depth as well as the style of faulting at depth revealed by earthquakes indicate that, in general, the state of stress at depth can be described by three principal stresses ($S_1 > S_2 > S_3$) that lie in approximately horizontal and vertical planes (e.g., Zoback, 1992; Zoback and Zoback, 1989). The magnitude of the vertical principal stress is generally taken as the weight of the overburden.

Following Anderson (1951) in his classic paper on faulting, we define stress regime by the relative magnitude of the vertical stress (S_v) to the two maximum and minimum horizontal stresses (respectively, S_{Hmax} and S_{hmin}). Three distinct regimes are possible:

- *Normal faulting stress regime*: When the vertical stress dominates ($S_1 = S_v$), gravity drives normal faulting and creates horizontal extensional deformation:

$$S_v > S_{Hmax} > S_{hmin} \quad [1]$$

- *Reverse faulting stress regime*: When both horizontal stresses exceed the vertical stress ($S_3 = S_v$), compressional deformation and shortening is accommodated through thrust or reverse faulting:

$$S_{Hmax} > S_{hmin} > S_v \quad [2]$$

- *Strike-slip faulting stress regime*: An intermediate stress state ($S_2 = S_v$), where the difference between the two horizontal stresses (horizontal shear) dominates deformation, resulting in strike-slip faulting:

$$S_{Hmax} \geq S_v \geq S_{hmin} \quad [3]$$

Relative stress magnitude information can be obtained from direct in situ stress measurements as well as from the style of tectonic faulting inferred from earthquake focal mechanisms and geologic observations of young faulting. While global coverage is quite variable, the relative uniformity of both stress orientation and relative magnitudes in different parts of the world is striking and permits mapping of regionally coherent tectonic stress regimes.

Figure 1(b) presents a generalized version of the global stress map that is quite similar to that presented by Zoback (1992). Tectonic stress regimes are indicated in **Figure 1(b)** by both color and arrow type. Blue inward-pointing arrows indicate S_{Hmax} orientations in areas of compressional (strike-slip and thrust) stress regimes. Red outward-pointing arrows give S_{hmin} orientations (extensions direction) in areas of normal faulting regimes. Regions dominated by strike-slip tectonics are distinguished with green thick inward-pointing and orthogonal, thin outward-pointing arrows. Overall, arrow sizes in **Figure 1(b)** represent a subjective assessment of 'quality' related to the degree of uniformity of stress orientation and also to the number and density of data (Zoback, 1992).

The data shown in **Figure 1(a)** and **1(b)** reinforce the broad-scale patterns and general conclusions regarding the global database summarized in Zoback et al. (1989):

- The interior portions of most plates (variously called intraplate and midplate regions) are dominated by compression (thrust and strike-slip stress regimes) in which the maximum principal stress is horizontal.
- Active extensional tectonism (normal faulting stress regimes) in which the maximum principal stress is vertical generally occurs in topographically high areas in both the continents and the oceans.
- Regional consistency of both stress orientations and relative magnitudes permits the definition of broad-scale regional stress provinces, many of which coincide with physiographic provinces, particularly in tectonically active regions. These provinces may have lateral dimensions on the order of 10^3–10^4 km, many times the typical lithosphere thickness of 100–300 km.

Zoback (1992) referred to these broad regions subjected to uniform stress orientation or a uniform pattern of stress orientation (such as the radial pattern of stress orientations in China) as 'first-order' stress provinces. For example, the uniform ENE S_{Hmax} orientation in midplate North America covers nearly the entire continental portion of the plate lying at an average elevation of less than 1000 m (excluding the west coast) and may also extend across much of the western Atlantic Basin (Zoback et al., 1986). Thus, here, the stress field is uniform over roughly 5000 km in both an E–W direction and an N–S direction. As we will see in **Section 6.06.3**, most of these first-order stress fields are consistent with the balance of forces acting on and within the plates, which drive plate motions.

Once the first-order stress patterns are recognized, the so-called 'second-order' patterns or local perturbations can be identified (Zoback, 1992). These second-order stress fields are often associated with specific geologic or tectonic features, for example, lithospheric flexure, lateral strength contrasts, and lateral density contrasts within the lithosphere, which give rise to buoyancy forces derived from lateral variations in gravitational potential energy (e.g., Artyushkov, 1973; Bai et al., 1992;

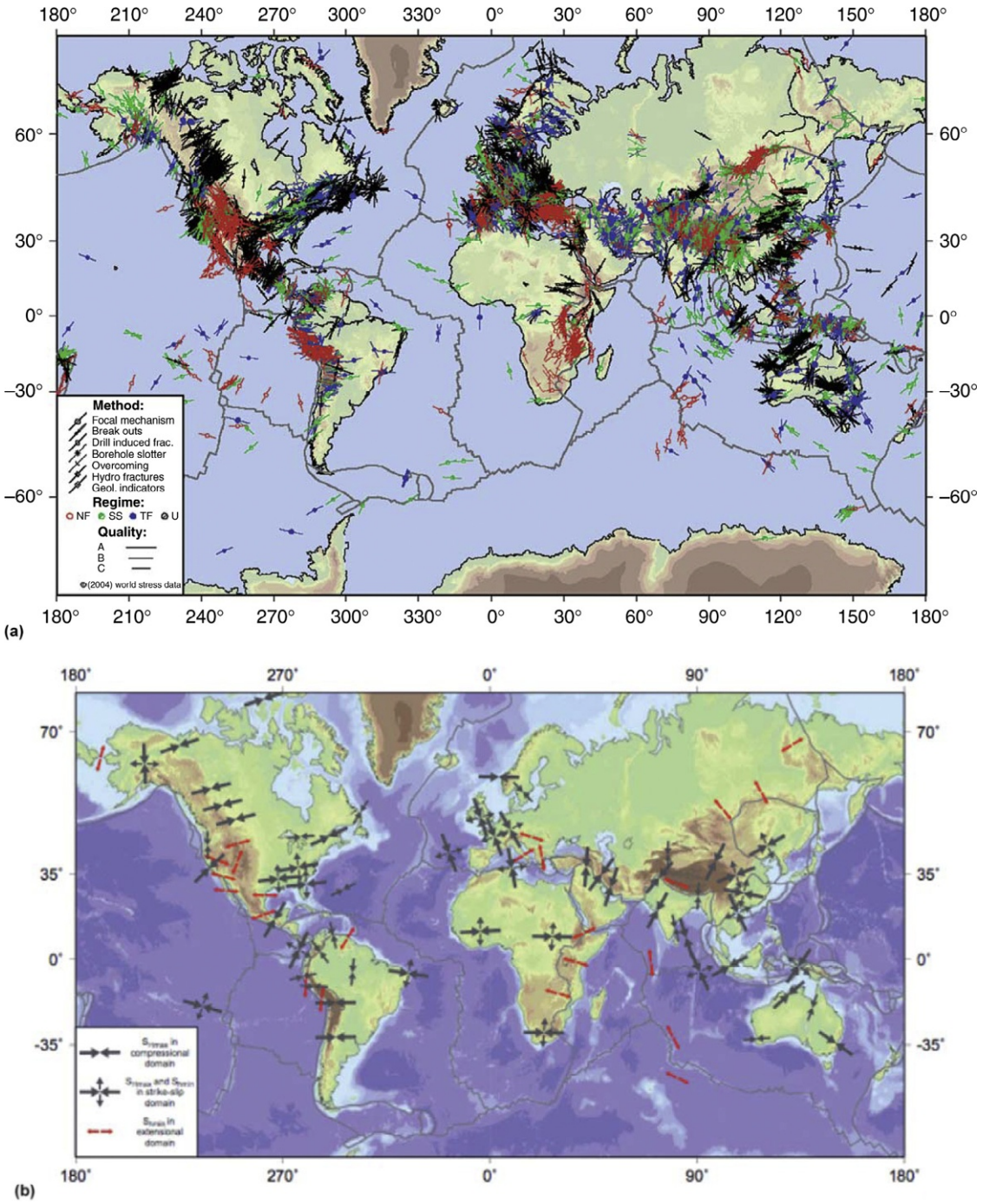

Figure 1 (a) Maximum horizontal stress orientations from the World Stress Map project plotted on a base of average topography. Line lengths of data are proportional to quality. Stress regimes are indicated by color: red, normal faulting; green, strike-slip faulting; blue, reverse faulting. (b) Generalized stress map mean stress directions based on averages of clusters of data shown in (a). A single set of thick inward-pointing arrows indicate S_{Hmax} orientations in a reverse faulting stress regime. A single set of outward-pointing arrows indicate S_{hmin} orientations in a normal faulting stress regime. Strike-slip faulting stress regime indicated by thick inward-pointing arrows (S_{Hmax} direction) and thin outward-pointing arrows (S_{hmin} direction). Symbol sizes in all cases are proportional to the number and consistency of data orientations averaged from World Stress Map project (The current version of the World Stress Map database can be found at http://www-wsm.physik.uni-karlsruhe.de/.) Reproduced from Zoback ML (1992) First- and second-order patterns of stress in the lithosphere: The World Stress Map project. *Journal of Geophysical Research* 97: 11703–11728, with permission from American Geophysical Union.

Coblentz et al., 1994; Fleitout, 1991; Fleitout and Froidevaux, 1982, 1983; Jones et al., 1996; Sonder, 1990; Wortel et al., 1991; Zoback and Mooney, 2003). These second-order stress patterns typically have wavelengths ranging from 5 to 10 (or more) times the thickness of the brittle upper lithosphere.

Stress mapping has shown a number of second-order processes that can produce rotations of S_{Hmax} orientations. Few examples include the following:

- A 75–85° rotation on the northeastern Canadian continental shelf possibly related to margin-normal extension derived from sediment-loading flexural stresses (Zoback, 1992).
- An ~45° rotation of stress directions along the mid-Norwegian margin, apparently due to lithospheric flexure associated with deglaciation (see Grollimund and Zoback, 2001).
- A 50–60° rotation within the East African Rift relative to Western Africa due to extensional buoyancy forces caused by lithospheric thinning (Zoback, 1992) and an approximately 90° rotation along the northern margin of the Paleozoic Amazonas rift in central Brazil (Zoback and Richardson, 1996). In this final example, this rotation is hypothesized as being due to deviatoric compression oriented normal to the rift axis resulting from local lithospheric support of a dense mass in the lower crust beneath the rift ('rift pillow').
- An ~50° counterclockwise rotation of S_{Hmax} directions in the southern San Joaquin basin of California that is associated with the 'big bend' of the San Andreas Fault (Castillo and Zoback, 1995).
- A clockwise rotation of horizontal principal stress directions (and a progressive decrease in horizontal stress magnitudes) going clockwise around the northern boundary of South America. This large-scale rotation of stress directions appears to be at least in part associated with the gravitational effect of a section of the Caribbean Plate subducted to the south beneath continental South America (Colmenares and Zoback, 2003).

An even larger-scale example of a 'second-order' stress rotation can be found in the stress orientations in much of the westernmost United States, which are consistent with the combined effects of right-lateral shear along the San Andreas plate boundary and extensional buoyancy forces driven by the topographically high regions of the Western United States (e.g., Zoback and Thompson, 1978). Flesch et al. (2000) had shown with lithospheric deformational modeling that this superposition is 'capable' of explaining the north–northeast maximum horizontal orientations and relative magnitudes and can also predict the rates of deformation. This final example demonstrates that much can be learned by using the observed stress data to constrain the sources of stress acting on the lithosphere (as discussed in a later section). It also demonstrates that large-scale lithospheric heterogeneities can be as important as plate-driving forces in determining the state of stress within the plates.

6.06.3 Sources of the Lithospheric Stress Field

The most likely sources of the observed, regionally uniform first-order patterns of stress orientations and relative magnitudes are the large-scale forces acting on and within the plates to drive their motion. Solomon et al. (1975) and subsequent studies by Richardson et al. (1976, 1979) were the first to attempt to predict global intraplate stress orientations and relative magnitudes by modeling plate-driving forces. Following Forsyth and Uyeda (1975) and Chapple and Tullis (1977), the forces they considered included

- constant value forces acting generally perpendicular to plate boundaries – ridge push (a symmetrical force at ridges creating compression far within the plates), slab pull (the balance of the negative buoyancy of the subducting slab and the viscous and frictional resistance to subduction), trench suction (a traction on plates induced by mantle flow moving toward downwelling at subduction zones), and collisional resistance and
- tractions on the base of plates – drag forces proportional to plate velocity.

For a detailed discussion of each of the previously mentioned plate-driving forces, see **Chapter 6.02**.

These forces were incorporated in thin-shell finite-element models of constant-thickness lithosphere to calculate internal stresses in the plates. Richardson et al. (1979) constrained their results by a relatively sparse sampling of the global stress field based on earthquake focal mechanisms. They concluded that ridge push and net slab pull were of comparable size and that shear tractions on the base of the plates were resistive.

Zoback et al. (1989) showed a correlation between S_{Hmax} orientation and the azimuth of both absolute and relative plate velocities for several intraplate regions. However, Richardson (1992) demonstrated that the ridge push torque pole is very similar to the absolute velocity pole for most plates; thus, a comparison with absolute velocity trajectories can do little to distinguish between ridge push and basal drag as a source of stress. In fact, comparison between stress directions and local azimuths computed from velocity poles is an overly simplistic approach to evaluating the influence of plate-driving force on the intraplate stress field. At best, these correlations demonstrate the important role of the plate boundary forces and can be used to conclude that the net balance of forces driving the plates also stresses them (Zoback et al., 1989).

As the intraplate stress database improved, a number of single-plate finite-element models were produced, following a similar approach to Richardson et al. (1979) and assuming a no-net torque constraint (Cloetingh and Wortel, 1985, 1986; Coblentz and Richardson, 1996; Coblentz and Sandiford, 1994; Coblentz et al., 1998; Flesch et al., 2000; Govers and Meijer, 2001; Grunthal and Stromeyer, 1992; Meijer and Wortel, 1992; Meijer et al., 1997; Richardson, 1978; Richardson and Cox, 1984; Richardson and Reding, 1991; Stefanick and Jurdy, 1992). In many of these models, the ridge push force was often used to calibrate the magnitude of all forces acting on the plates as ridge push is the best quantified of the driving forces since it can be calculated directly from bathymetry and the crust/lithosphere structure in the oceans. Over time, these models became increasingly more sophisticated and incorporated gravitational potential energy forces (so-called buoyancy forces) within the plates related to lateral variations in lithospheric density and/or thickness (including realistic representations of ridge push force).

Most studies found ridge push to be a significant force and concluded that internal buoyancy body forces due to lateral variations in lithospheric structure and density (lithospheric buoyancy) were also significant. Some studies found significant compressive stress transmitted across convergent margins and transforms; others found drag to be an important balancing force, either resistive or driving, often depending on how the drag force was formulated (e.g., restricted only to continental portions of plates). The influence of slab pull on the intraplate stress field was generally found to be no larger than (and sometimes smaller than) the magnitude of the other forces acting on the plates. While such models are illuminating, they generally suffer from the lack of well-constrained boundary conditions. Hence, the results of single-plate stress modeling tend to be rather nonunique.

Lithospheric buoyancy forces arise from lateral variations in both crust thickness and mantle-lid thickness. As pointed out by Fleitout and Froidevaux (1982, 1983), regions of high topography (due to either thick crust or thin mantle lid) have high potential energy and hence have a tendency to 'spread' or extend. In contrast, thick, cold mantle lid tends to 'sink' into less-dense asthenosphere, generating compression within the upper lithosphere. Several lines of evidence indicate that buoyancy forces due to inhomogeneities in lithospheric density structure can be significant and comparable in magnitude to plate-driving forces:

1. Ridge push (recognized as a key force in determining stress orientation in a number of plates, particularly those with no attached slab) is actually a buoyancy force acting over the entire profile of cooling oceanic lithosphere.
2. The dominance of extensional tectonics in tectonically active areas at high elevations ($>\sim 2$ km) (e.g., the Western United States, the East African Rift System, and the Baikal Rift) indicates that positive buoyancy forces (positive potential energy) derived from unusually low densities in the upper mantle (and/or thin lithosphere) are probably the primary force in these regions, overcoming general intraplate compression (Zoback and Mooney, 2003).
3. As noted earlier, Flesch et al. (2000) demonstrated that stress orientations in the Western United States are consistent with a balance of right-lateral shear along the San Andreas plate boundary and extensional buoyancy forces generated by the elevated crust and thin lithosphere beneath the Western Cordillera.

Over the past two decades, significant advances in our understanding of the crustal stress field have been matched by greatly increased knowledge of the three-dimensional (3-D) structure and lateral variations and inhomogeneities in the lithosphere as well as structure and physical properties inferred from tomographic and other seismic studies. This increased knowledge of Earth structure has been incorporated in modeling stress patterns within the plates using basal shear tractions determined from mantle flow models. Bai et al. (1992) were the first to attempt a combined approach that predicted both the plate velocities and the stresses within plates using a relatively low-resolution model of mantle density anomalies to induce flow in a Newtonian viscous mantle. Bai et al. also included buoyancy forces within the lithosphere induced by variations of Moho depth. They imposed a no-net torque constraint to compute plate velocities; these velocities were then used as the shear tractions on the base of the plates to determine internal stresses. Their models showed a relatively poor correlation between the predicted stress directions and the observed regional stress field, possibly due to the coarse spacing (15°) of their grid. However, their models were the first to really investigate the importance of sublithospheric density anomalies on the upper lithosphere stress field.

Bird (1998) implemented a global model in which laterally heterogeneous plates of nonlinear rheology were separated by faults with low friction. He found that driving forces that result only from elevation differences between ocean ridges and trenches (balanced by passive basal drag and fault friction) are not compatible with observed plate velocities. His best models to match both stress orientations and plate velocities required forward drag acting on the continents only, with dense descending slabs pulling oceanic plates and stirring the more viscous mantle. Steinberger et al. (2001) also attempted to match plate velocities and stress orientations by calculating a mantle flow field from density structures inferred from seismic tomography. In this model, computed stresses also included the effects of buoyancy forces within the lithosphere due to lateral variations in lithospheric and crustal density and structure. However, their results were somewhat equivocal. While mantle flow models were found to be generally in accord with observed stress directions and plate motion, they also predicted stress directions in the absence of any effects of mantle flow, which explained the stress observations nearly as well.

In a comprehensive study, Lithgow-Bertelloni and Guynn (2004) attempted to match the observed intraplate stress patterns with a set of 3-D global finite-element models that included mantle flow, lithospheric heterogeneity, and topography. They tested two versions of lithospheric heterogeneity – one based directly on seismic and other constraints (Crust 2.0, Laske et al., 2002) and another assuming a simple model of isostatic compensation. They also implemented mantle tractions computed from two models of mantle density heterogeneity – one based on the history of subduction for the last 180 Myr (which successfully reproduces the present-day geoid and Cenozoic plate velocities) and a second inferred from seismic tomography (Grand et al., 1997). Furthermore, they investigated effects of variable viscosity structure, including the case of a low-viscosity channel between 100 and 200 km depth. The results of this study are also somewhat equivocal. Their mantle traction-only models consistently predict large extensional stresses in the center of the Pacific Plate and over much of the Atlantic – in sharp contrast to the compressional tectonism in these areas inferred from intraplate earthquake focal mechanisms (e.g., Wiens and Stein, 1985). Because their predicted stresses from mantle tractions are a factor two to four times greater than stresses due to lithospheric structure (i.e., buoyancy forces), even when they combine the two sources, the predicted stress field does not match large-scale features of the observed stresses very well, particularly in the oceans. They found the best fits for the observed stress field were predicted from models of lithosphere heterogeneity alone (these models include ridge push forces as it is a buoyancy force resulting from lateral variations of density and structure within the lithosphere).

Zoback and Mooney (2003) implemented a simple model tying lithosphere buoyancy to surface elevation to predict stress regime within continental plate interiors. They determined the

crustal portion of lithospheric buoyancy (density × thickness) using the USGS global database of crustal structure determinations (Mooney et al, 2002; **Chapter 1.11**). Adopting a mid-ocean ridge as a reference column (following Lachenbruch et al., 1985; Lachenbruch and Morgan, 1990), they computed elevations due only to the crustal component of buoyancy and found the predicted elevations exceed observed elevations in nearly all cases (97% of the data), consistent with the existence of a cool lithospheric mantle lid denser than the asthenosphere on which it floats. The difference between the observed and predicted crustal elevation is a measure of the decrease in elevation produced by the negative buoyancy of the mantle lid. This negative buoyancy was combined with a simple thermal model for the density of the mantle lid to compute mantle-lid thickness. They then computed gravitational potential energy differences relative to mid-ocean ridges by taking a vertical integral over the computed complete lithosphere density structure. Their results are shown in **Figure 2(a)** and show broad agreement with observed stress regime data, given in **Figure 2(b)**. They found that thick mantle roots beneath shields lead to strong negative potential energy differences relative to surrounding regions resulting in additional

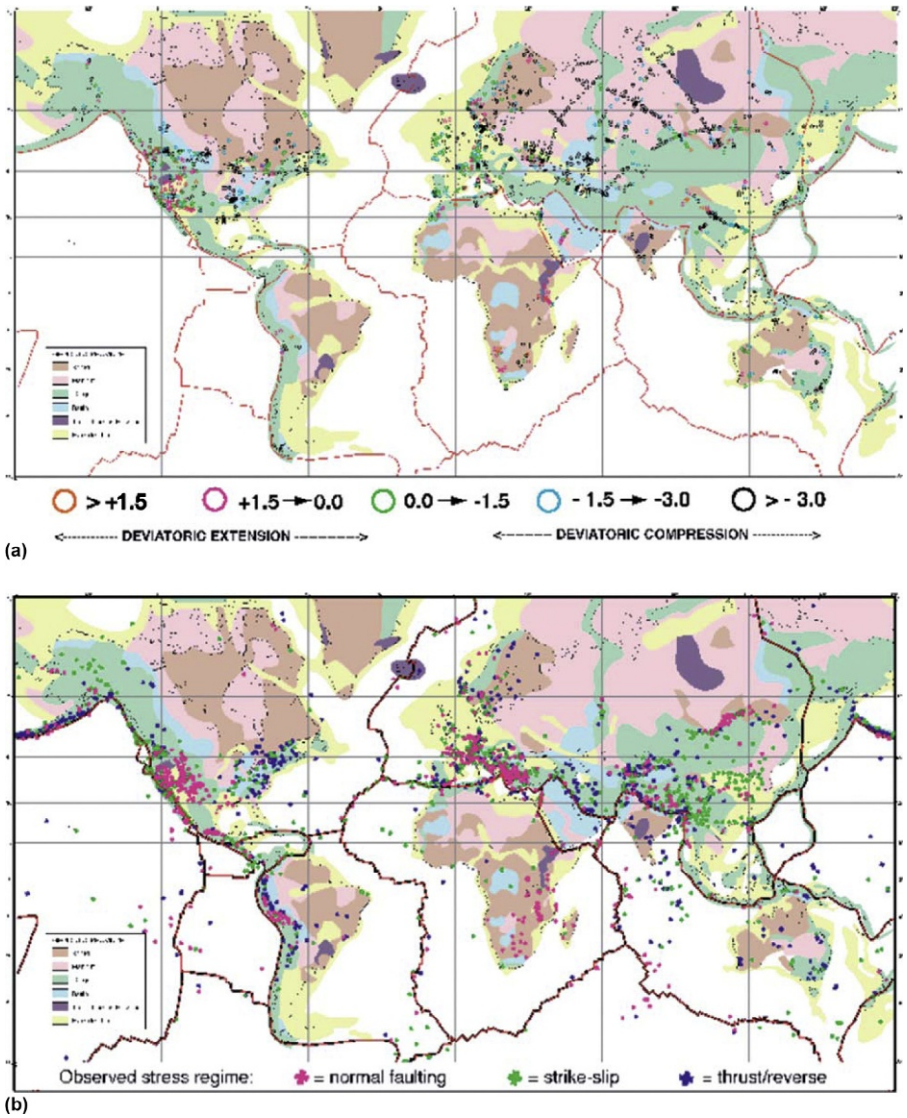

Figure 2 (a) Map of computed potential energy differences relative to a reference asthenosphere geoid shown on a base of tectonic provinces (after Goodwin, 1996). Positive potential energy differences giving rise to deviatoric extensional stresses are shown in red and magenta, weak negative potential energy differences are shown in green, and negative potential energy differences are shown in cyan, and blue represent the largest deviatoric compression values implying strong deviatoric compressional stresses. (b) Observed stress regime data from the World Stress Map database. These represent a subset of the entire database and are those data points with stress regime information, primarily earthquake focal mechanisms and geologic stress indicators. Magenta indicates an extensional stress regime, characterized by normal faulting. Green shows data indicating strike-slip faulting. Blue points represent areas of a strongly compressional stress regime, characterized by thrust or reverse faulting. Reproduced from Zoback ML and Mooney WD (2003) Lithospheric buoyancy and continental intraplate stress. *International Geology Review* 45: 95–118, with permission from American Geophysical Union.

compressive stresses superimposed on the intraplate stresses derived from plate boundary forces – consistent with the dominance of reverse faulting earthquakes in the intraplate shield regions. Areas of high elevation and a thin mantle lid (e.g., Western US Basin and Range, East African Rift, and Baikal Rift) are predicted to be in extension, consistent with the observed stress regime in these areas.

The simplicity of the observed crustal stress field thus appears most consistent with buoyancy-related forces acting directly on and within the lithosphere – in particular, ridge push and internal lithosphere density heterogeneities. Possible contributions from deep-mantle density heterogeneities, or tractions, from the flow they induce seem to be small or even unresolvable. More detailed stress data coverage and more accurate mantle/lithosphere models will be needed to determine the exact balance of forces, as well as the potential significance of drag forces. The body of work modeling stresses over the past 30 years seems to generally support the broad conclusions of the very first comprehensive modeling attempt by Richardson et al. (1979) – that ridge push and net slab pull (downwelling pull balanced by viscous and frictional resistance to subduction) were of comparable size and that shear tractions on the base of the plates are relatively small. As Richardson and Reding pointed out in 1981 in their modeling of stresses within the North American Plate, the large lateral gradients in stress magnitudes (up to an order of magnitude variation) across large plates, required by models in which drag dominates, are not observed.

6.06.4 Absolute Stress Magnitudes and the Critically Stressed Crust

Direct measurements of stress to depths of ~8 km have confirmed a simple yet profound model of how stress magnitudes vary with depth within the crust. This simple model is one of frictional faulting equilibrium or 'critically stressed crust' in which actual stress differences in the crust are very close to the values required for slip on the most well-oriented preexisting faults. This model is based on classic Coulomb faulting theory and confirmed by laboratory tests of rock failure. It is also the basis for the linear portion of lithospheric strength curves first developed by Brace and Kohlstedt (1980) that show maximum stress differences (i.e., strength) as a function of depth; the integral of these stress-difference profiles yields lithospheric strength. As reviewed by Zoback et al. (2002) and summarized in the succeeding text, the implications of a critically stressed crust are profound.

According to Coulomb theory, fault slippage will occur when the shear stress on the fault τ equals the sum of the inherent fault strength S_o and the frictional resistance to sliding (the product of μ, the coefficient of friction on the fault, and σ_n, the stress acting normal to the fault plane):

$$\tau = S_o + \mu\sigma_n \qquad [4]$$

The maximum shear stress is given as $(S_1 - S_3)/2$ and corresponds to the most well-oriented fault planes for slip.

Actual stress magnitudes in the Earth's crust are modified by internal pore pressure in the rock. The concept of 'effective stress' is used to incorporate the influence of pore pressure at depth; a component of effective stress σ_{ij} is related to the total stress S_{ij} via

$$\sigma_{ij} = S_{ij} - \delta_{ij}P_p \qquad [5]$$

where δ_{ij} is the Kronecker delta and P_p is the pore pressure.

By applying the concept of effective stress to Anderson faulting theory, we can predict stress magnitudes at depth for different stress regimes. Two-dimensional faulting theory assumes that failure on preexisting faults is a function only of the difference between the least and greatest principal effective stresses σ_1 and σ_3. In this case, the ratio of stress magnitudes of σ_1 and σ_3 can be shown to be a constant, related to the frictional coefficient of the most favorably oriented faults:

$$\sigma_1/\sigma_3 = (S_1 - P_P)/(S_3 - P_p) = \left(\left(\mu^2 + 1\right)^{1/2} + \mu\right)^2 \qquad [6]$$

Since the coefficient of friction is relatively well defined for most rocks and ranges between ~0.6 and 1.0 (Byerlee, 1978), eqn [6] indicates that frictional sliding will occur when $\sigma_1/\sigma_3 \sim 3$.

Assuming hydrostatic pore pressure (a common assumption for which a complete justification is given later in this section) and that the vertical stress is equal to the weight of the overburden, we can compute absolute stress magnitudes for the three main Anderson faulting regimes:

- Normal faulting, extensional regimes: $S_{hmin} \sim 0.6\ S_v$
- Reverse faulting, compressional regimes: $S_{Hmax} \sim 2.3\ S_v$
- Strike-slip faulting regimes: (when $S_v \sim 1/2\ S_{Hmax} + S_{hmin}$) $S_{Hmax} \sim 2.2\ S_{hmin}$

This simple model of crustal stress magnitude has been validated by a large number of in situ stress measurements in deep wells and scientific boreholes (see review by Townend and Zoback, 2000). The deepest and most complete set of stress magnitude data (collected to ~8 km depth in a scientific borehole in Germany) is shown in **Figure 3**. The measured stresses indicate a strike-slip stress regime, and the stress differences throughout the entire depth range sampled are consistent with frictional faulting equilibrium with a frictional coefficient of ~0.7 (dashed line above 10 km) (Brudy et al., 1997; Zoback et al., 1993). Further evidence for such a 'frictional failure' stress state is provided by a series of earthquakes that were triggered at ~9 km depth in rock surrounding the borehole with extremely low perturbations of the ambient, approximately hydrostatic pore pressure (Zoback and Harjes, 1997).

Figure 4 (from Townend and Zoback, 2000; Zoback and Townend, 2001) shows a compilation of stress measurements in relatively deep wells and boreholes from a variety of tectonic provinces around the world. As shown in **Figure 4(a)**, the ratio of the measured maximum and minimum effective stresses (as shown in eqn [6]) corresponds to values predicted from frictional faulting equilibrium with a coefficient of friction ranging between 0.6 and 1.0, the same range as that observed in the laboratory (Byerlee, 1978). Additional data collected at shallower depths in the crust (<3 km) substantiate the observation that the upper crust is critically stressed according to Mohr–Coulomb frictional failure theory (see reviews by McGarr and Gay, 1978; Zoback and Healy, 1992). **Figure 4(b)** shows the same stress measurement as presented in **Figure 3(a)** but this time as a function of apparent depth (see Townend and

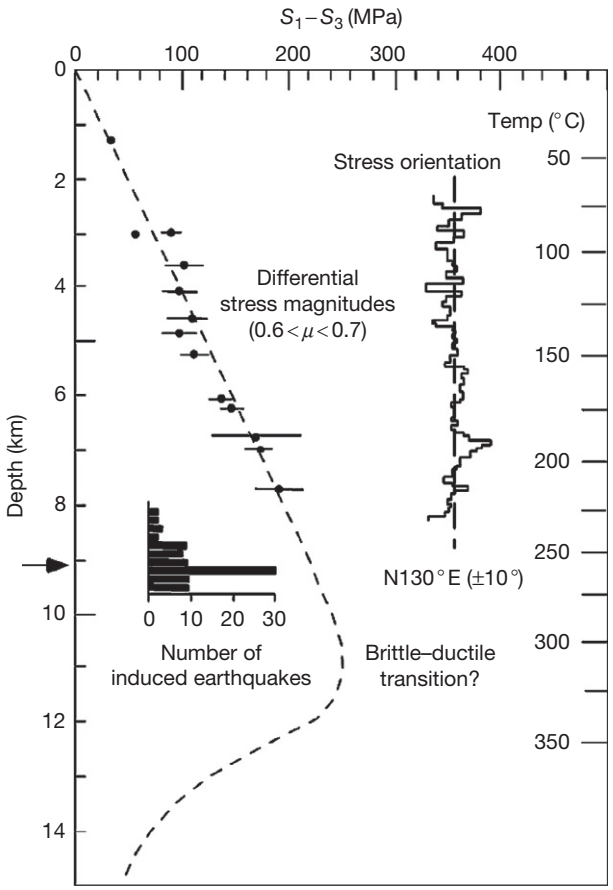

Figure 3 Stress measurements in the German scientific research well, KTB, indicate a strong crust, in a state of failure equilibrium as predicted by Coulomb theory and laboratory-derived coefficients of friction of 0.6–0.7. The arrow at 9.2 km depth indicates where the fluid injection experiment occurred. Reproduced from Zoback MD and Harjes HP (1997) 'Injection induced earthquakes and crustal stress at 9 km depth at the KTB deep drilling site, Germany.' *Journal of Geophysical Research* 102: 18477–18491, with permission from American Geophysical Union.

Zoback, 2000). As shown, stress magnitudes increase rapidly with depth in the brittle crust.

Two important implications of the data in Figure 4 are worth noting. First, 'Byerlee's law' (i.e., that the coefficient of frictional sliding is in the range 0.6–1.0 in the brittle crust, independent of rock type) was defined on the basis of hundreds of laboratory experiments, yet it appears to correspond to faults in situ equally well. This is a surprising result given the large difference between the size of samples used for friction experiments in the laboratory, the size of real faults in situ, the variability of roughness of the sliding surface, and the idealized conditions under which laboratory experiments are conducted. Second, despite the fact that the Earth's brittle crust contains a spectrum of widely distributed faults, fractures, and planar discontinuities at many different scales and orientations, it appears that stress magnitudes at depth (specifically, the differences in magnitude between the maximum and minimum principal stresses) are limited by the frictional strength of the most well oriented of these planar discontinuities.

Because frictional strength depends on pore pressure, it is important to note that the measured stress data shown in Figure 4 are all associated with essentially hydrostatic pore pressures, suggestive of relatively high permeability throughout the upper crust. By analyzing the results of in situ hydraulic tests conducted at length scales of 10–1000 m and to depths as great as 9 km as well as the migration rates of induced seismicity over distances of up to several kilometers, Townend and Zoback (2000) inferred upper-crustal permeabilities between $\sim 10^{-17}$ and 10^{-16} m^2, three to four orders magnitude higher than that of core samples studied in the laboratory at equivalent pressures. Geothermal and metamorphic data also indicate that the permeability of the upper crust is high ($>10^{-18}$ m^2) throughout the brittle regime (Manning and Ingebritsen, 1999).

In fact, we believe that the mechanism responsible for creating and maintaining high crustal permeability is fundamentally related to the observation that the crust is in a state of frictional faulting equilibrium. Using data from several scientific boreholes, Barton et al. (1995) demonstrated that optimally oriented planes are hydraulically conductive, whereas nonoptimally oriented planes are nonconductive. This conclusion is supported by data collected subsequently from even deeper boreholes in other tectonic settings (Barton et al., 1998; Hickman et al., 1997) and the 8 km deep borehole in Germany (Ito et al., 2001). Another way of saying this is that the active faults that limit crustal strength are also responsible for maintaining pore pressures at hydrostatic values. These results clearly indicate that critically stressed faults act as fluid conduits and control large-scale permeability (Townend and Zoback, 2000; Zoback and Townend, 2001). Thus, the presence of critically stressed faults in the crust keeps the brittle crust permeable and upper-crustal pore pressures close to hydrostatic values.

Three independent lines of evidence support the in situ measurements in indicating a critically stressed crust at frictional faulting equilibrium:

- The widespread occurrence of crustal seismicity induced by either reservoir impoundment or fluid injection (cf. Healy et al., 1968; Pine et al., 1990; Raleigh et al., 1972; Zoback and Harjes, 1997)
- Earthquakes triggered by small stress changes (~0.1–0.3 MPa) associated with other earthquakes (cf. Stein et al., 1992)
- Relatively small stress drops in crustal earthquakes (1–10 MPa) (Hanks, 1977) typically an order of magnitude smaller than expected stress differences at seismogenic depths (as shown in Figure 4(b))

All these observations imply that the stress driving and released in earthquake faulting involves relatively small fluctuations around frictional faulting equilibrium values.

6.06.5 Stress Field Constraints on Lithospheric Deformation

It might seem surprising that stress in the crust is generally in a state of incipient frictional failure, especially in relatively stable intraplate areas. A significant implication of this observation is that observed variations in rates of active lithospheric

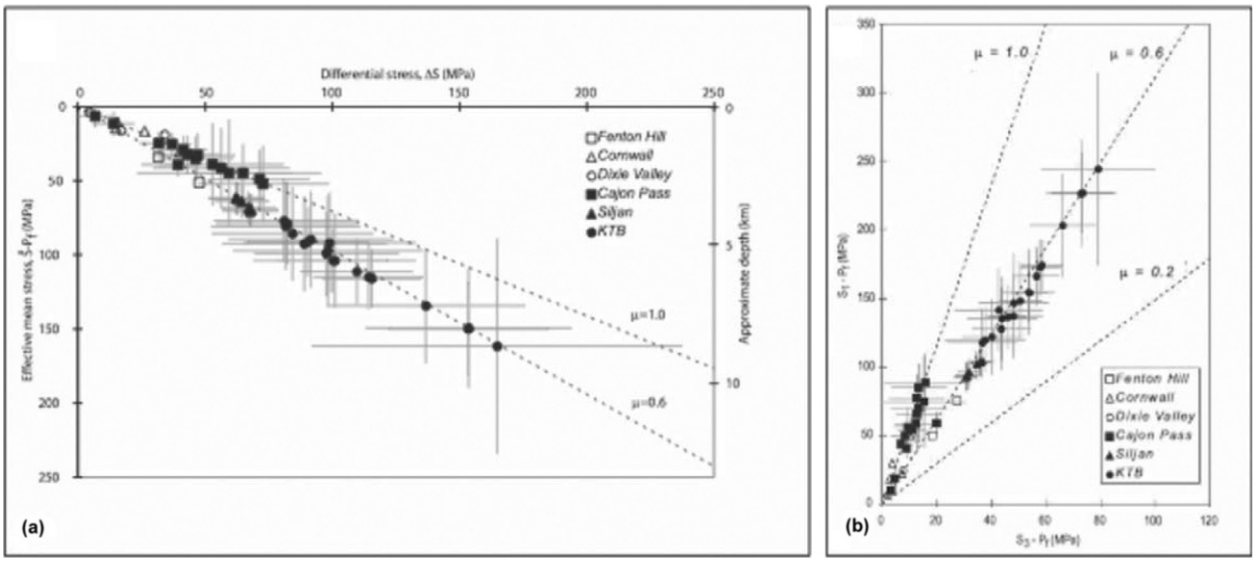

Figure 4 (a) In situ stress measurements in relatively deep wells in crystalline rock indicate that stress magnitudes seem to be controlled by the frictional strength of faults with coefficients of friction between 0.6 and 1.0. (b) When converted to approximate depth, the deep borehole stress measurements indicate a rapid increase in depth, as seen in lithospheric strength profiles. (a) Reproduced from Zoback MD and Townend J (2001) Implications of hydrostatic pore pressures and high crustal strength for the deformation of intraplate lithosphere. *Tectonophysics* 336: 19–30, with permission from American Geophysical Union. (b) Reproduced from Townend J and Zoback MD (2000) How faulting keeps the crust strong. *Geology* 28(5): 399–402, with permission from American Geophysical Union.

deformation must be directly linked to lithospheric strength, not to large variations in stress state. One of the strongest parameters controlling integrated lithospheric strength is Moho temperature (e.g., England and Molnar, 1991). Using surface heat flow as a proxy for Moho temperature, we can observe the strong correlation between lithospheric strength and deformation rate by comparing a map of US heat flow (Blackwell and Steele, 1992; Blackwell et al., 1991) with the US National Seismic Hazard Map (Frankel et al., 2002; **Figure 5**). The seismic hazard map is not directly a strain-rate map, it portrays shaking hazard, which is proportional to the rate of seismicity as well as the potential size of likely earthquakes in a region, so it too is a proxy. Nonetheless, it is clear that in general within the regions of warmest crust are those deforming most rapidly.

The reason for the correlation between lithospheric strength and rate of deformation can be visualized in terms of a simple conceptual model of deforming lithosphere that is in balance with the forces acting on it. The lithosphere is generally represented as three distinct layers – brittle upper crust, ductile lower crust, and ductile uppermost mantle (**Figure 6**, from Zoback and Townend, 2001 following previous workers). Deformation in the ductile lower crust and upper mantle is governed by power-law creep law (e.g., Brace and Kohlstedt, 1980). Because any applied force to the lithosphere will result in steady-state creep in the lower crust and upper mantle, as long as the 'three-layer' lithosphere is coupled, stress will build up in the upper brittle layer due to the creep at deeper levels. Stress in the upper crust builds over time, eventually to the point of brittle failure. The fact that intraplate earthquakes are relatively infrequent results simply from the fact that the rate of ductile strain rate is low in the lower crust and upper mantle (Zoback et al., 2002).

The detailed manner in which stress in the lithosphere is related to deformation and deformation rate can be investigated using lithospheric strength envelopes that incorporate brittle strength (based on frictional faulting equilibrium) and power-law creep with appropriate rheologies to represent the ductile behavior. Depending on thermal regime, there may be zones of brittle deformation in the lower crust and upper mantle as well as the upper crust, if the stress differences for brittle deformation are lower than those required for ductile deformation. Integrating this differential stress profile over the thickness of the lithosphere gives the cumulative strength (or force/length in these 2-D models) of the lithosphere.

Typically, investigators select a strain rate for the lithosphere and compute the total strength (force/length) required to deform the lithosphere at that rate (e.g., Kohlstedt et al., 1995; Ranalli and Murphy, 1987; Sibson, 1983). Zoback and Townend (2001) proposed an alternate approach to modeling lithospheric deformation by assuming a value for the cumulative force deforming the lithosphere and then calculating the resulting strain rate as a function of temperature and rheology. They applied this force-limited, steady-state deformation model to two end-member intraplate regions that differ markedly in their average surface heat flow, but with identical lithosphere structures – both have a 40 km thick crust and a 60 km thick mantle lid (**Figure 7**). The temperature profiles in **Figure 7** were computed assuming simple heat productivity models and downward continuation of surface heat flow and allowing thermal conductivity to be a function of both temperature and depth. A strike-slip/reverse faulting stress state (i.e., $S_1 > S_2 > S_3 \sim S_v$) was also assumed, consistent with the general compressional state of stress observed in most midplate and intraplate regions (see Zoback, 1992). Pore pressures in the lower crust were assumed to be near-lithostatic,

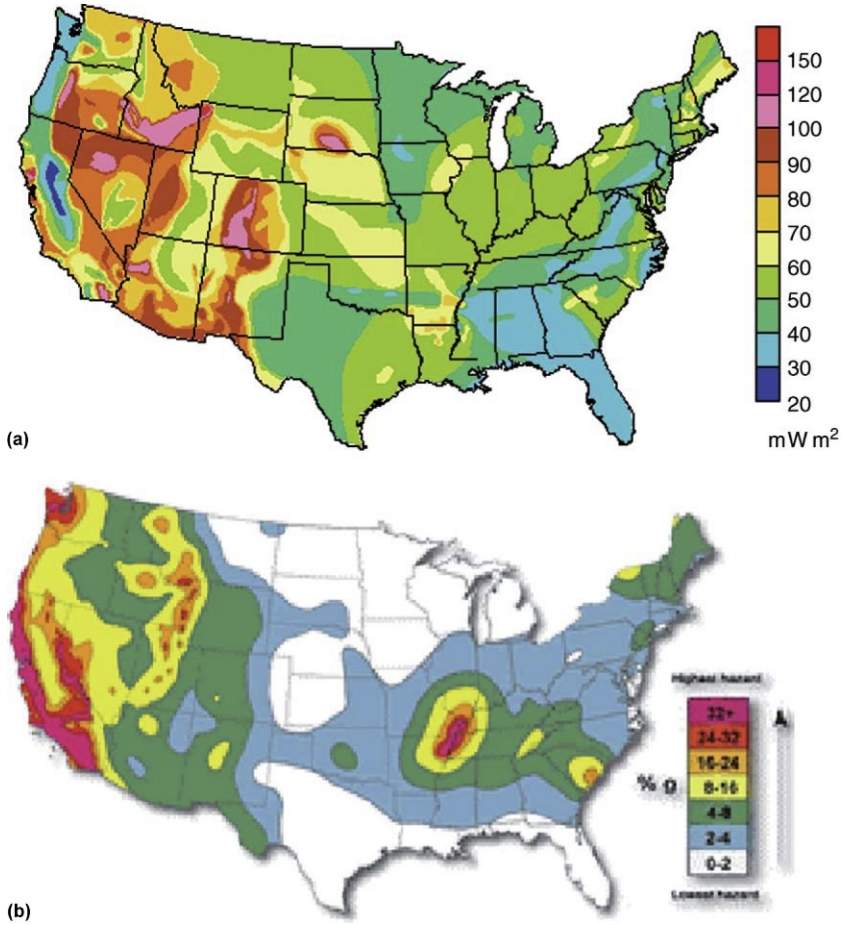

Figure 5 Comparison of (a) US heat flow (from Blackwell and Steele, 1992) with (b) the US National Seismic Hazard Map (Frankel et al., 2002). Note the strong correlation between regions of high crustal temperature and regions of high deformation rate as indicated by high seismic hazard.

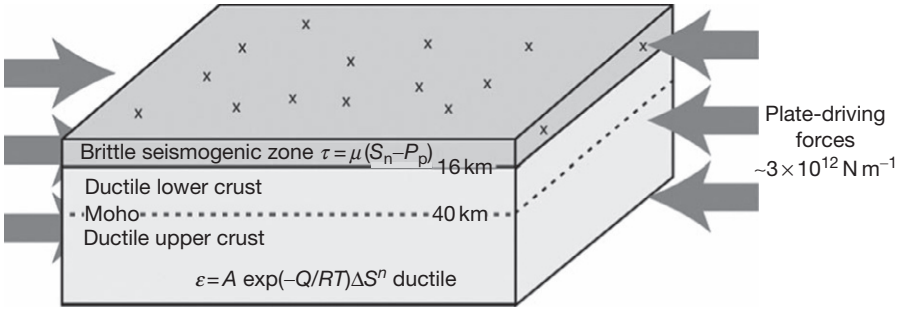

Figure 6 Schematic illustration of how the forces acting on the lithosphere keep the brittle crust in frictional equilibrium through creep in the lower crust and upper mantle. Reproduced from Zoback MD and Townend J (2001) Implications of hydrostatic pore pressures and high crustal strength for the deformation of intraplate lithosphere. *Tectonophysics* 336: 19–30, with permission from American Geophysical Union.

following the arguments presented by Nur and Walder (1990) and consistent with the conclusions of Manning and Ingebritsen (1999) that permeability of the lower crust probably does not exceed 10^{-19} m^2 at 30 km depth implying relatively long characteristic diffusion times ($>10^5$ years) consistent with maintaining near-lithostatic pore pressures.

Using the temperature–depth profiles shown in Figure 7, Zoback and Townend calculated differential stresses in the ductile portion of the upper and lower crust and lithospheric mantle and the corresponding ductile strain rate, such that the cumulative area under the stress profile (lithospheric strength) does not exceed the assumed total force/length available to deform the lithosphere, $\sim 3 \times 10^{12}$ N m^{-1}. The rationale for limiting the deforming force/length to this value is based on the extensive stress modeling summarized in the previous section indicating that the magnitude of the cumulative forces

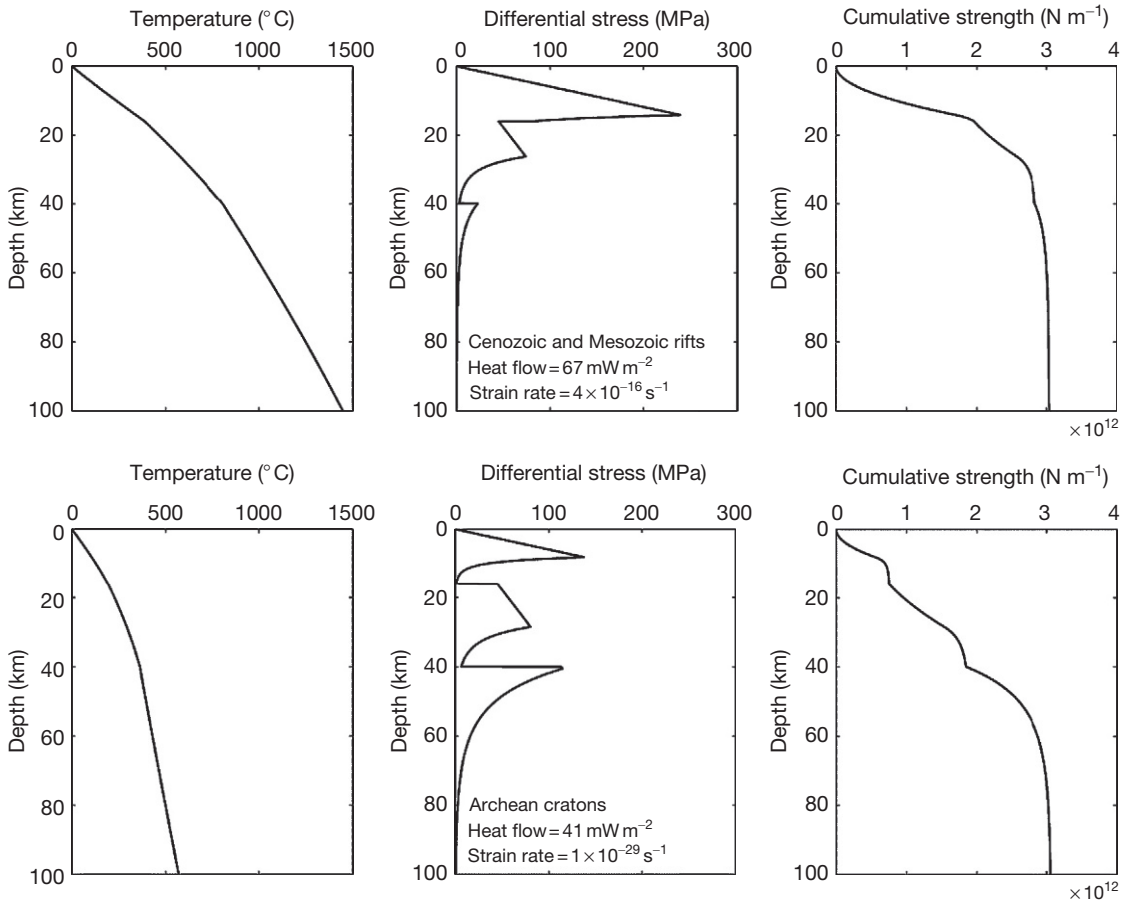
Temperature (°C)
Differential stress (MPa)
Cumulative strength (N m^{-1})
Depth (km)
Cenozoic and Mesozoic rifts
Heat flow = 67 mW m^{-2}
Strain rate = 4 × 10^{-16} s^{-1}
× 10^{12}
Archean cratons
Heat flow = 41 mW m^{-2}
Strain rate = 1 × 10^{-29} s^{-1}

Figure 7 A comparison between theoretical temperature, differential stress, and cumulative strength profiles for two representative intraplate regions, an area of moderate heat flow (67 mW m^{-2}) and a shield area with very low heat flow (41 mW m^{-2}). As detailed in Zoback and Townend (2001), a lithospheric structure composed of a 16 km thick felsic upper crust (with the rheological properties of dry Adirondack granulite), a 24 km thick mafic lower crust (dry Pikwitonei granulite), and a 60 km thick lithospheric mantle (wet Aheim dunite) are assumed. Reproduced from Zoback MD, Townend J, and Grollimund B (2002) Steady-state failure equilibrium and deformation of intraplate lithosphere. *International Geology Review* 44: 383–401, with permission from American Geophysical Union.

acting on the lithosphere is generally on the order of the ridge push force, which is fairly well constrained between 1 and 5×10^{12} N m^{-1} based on oceanic crust and lithosphere density and structure data.

The more than 12 orders of magnitude difference in the computed strain rates between the two regions subjected to the same force/length is thus related to their relative strengths. As seen in the upper half of Figure 7, a situation representative of intraplate Cenozoic and Mesozoic rifted crust with moderately high heat flow (~67 mW m^{-2}) exhibits relatively high strain rates (~10^{-16} s^{-1}). This is due to the relatively high temperatures in the lower crust and upper mantle, so that relatively little force is required to cause deformation there. Note too that in this case, most of the total tectonic force is carried in the strong brittle crust. On geologic timescales, this region would appear to deform as a viscous continuum.

In contrast, in a cold shield region (lower half of Figure 7), the lower crust and upper mantle are considerably stronger and the total force available is sufficient to only strain the lithosphere at a rate of ~10^{-29} s^{-1}, a negligible rate (even over billions of years!) and thus consistent with a rigid plate assumption. Differences in strength of the two regions are largely driven by the >400 K difference in temperature at the Moho (40 km depth) (Figure 7).

A test of such a force-limited, steady-state model is that the estimated intraplate lithospheric strain rates must not exceed approximately 10^{-17} s^{-1}, in order to be consistent with plate tectonic reconstructions assuming 'rigid' plates (e.g., Gordon, 1998). Because calculations such as those in Figure 7 involve a large number of parameters (surface heat flow, thermal conductivity, upper-crustal heat productivity, the frictional coefficient of the crust, and the rheological parameters of each layer), Zoback and Townend (2001) treated uncertainties in each of these parameters using a Monte Carlo technique: 1000 estimates of each parameter were drawn at random from normal distributions, and 1000 separate models were constructed. Composite temperature–depth, differential stress–depth, and strength–depth profiles were then constructed by stacking the different models' results.

Figure 8 illustrates the intraplate lithosphere modeling results for surface heat flow of 60 ± 6 mW m^{-2} (mean ± 10%), representative of stable continental heat flow (Pollack et al.,

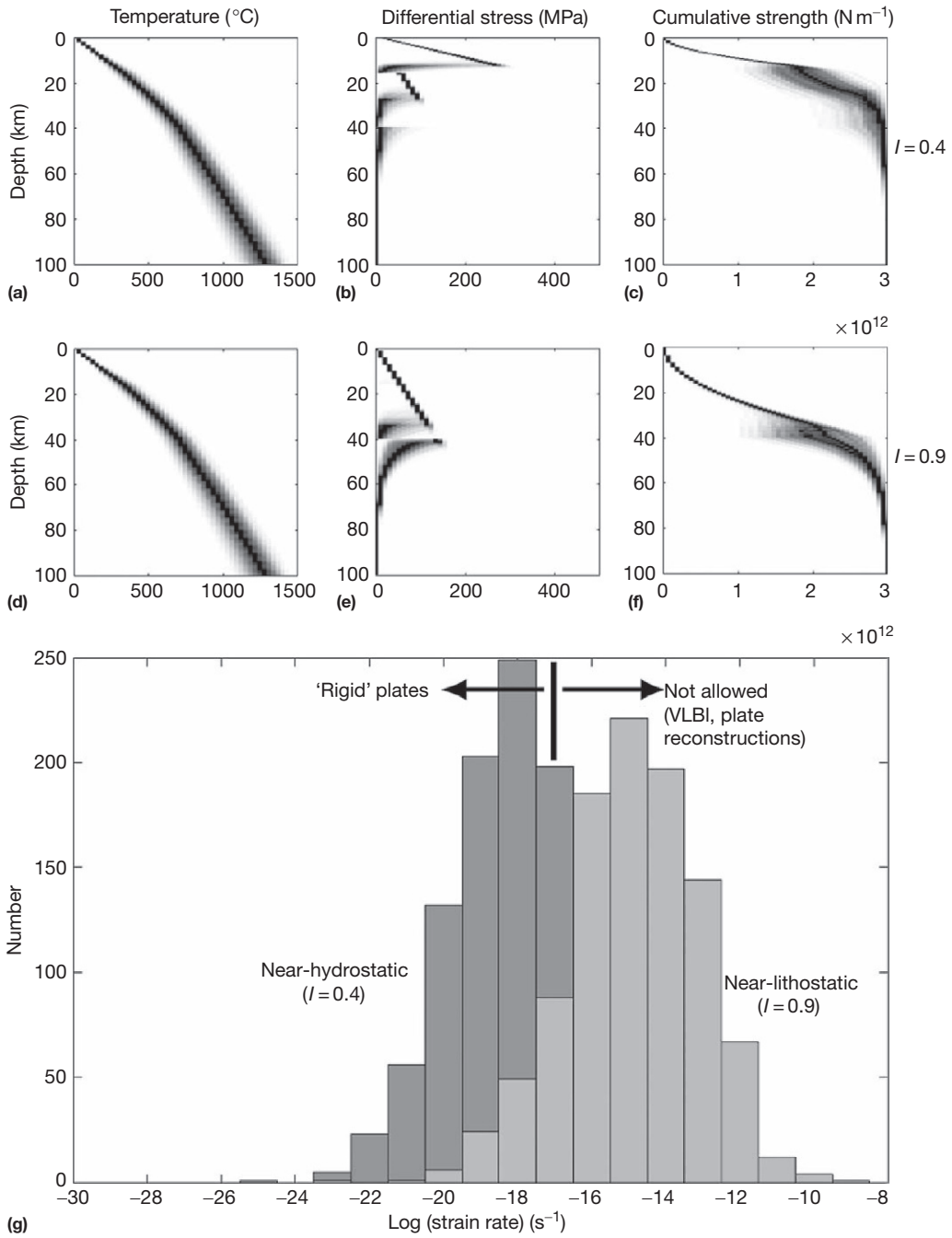

Figure 8 (a–g) Results of 1000 Monte Carlo strain-rate calculations for a strike-slip stress state and surface heat flow of 60 ± 6 mW m^{-2}, subject to the constraint that the total strength of the lithosphere is 3×10^{12} N m^{-1}. Reproduced from Zoback MD and Townend J (2001) Implications of hydrostatic pore pressures and high crustal strength for the deformation of intraplate lithosphere. *Tectonophysics* 336: 19–30, with permission from American Geophysical Union.

1993). The uppermost plots (Figure 8(a)–8(c)) display the model results incorporating hydrostatic pore pressures in the upper crust, and the three middle plots (Figure 8(d)–8(f)) display the corresponding results for near-lithostatic pore pressures. Note that the temperature–depth profiles are the same in both cases. At the bottom of Figure 8 is a histogram (Figure 8(g)) illustrating the range of estimated strain rates under each pore-pressure condition: the strain rates are distributed log-normally about a geometric mean of approximately 10^{-18} s^{-1} under 'near-hydrostatic upper-crustal pore-pressure' conditions and approximately 10^{-15} s^{-1} for near-lithostatic pore-pressure conditions. This latter value is much too high to be consistent with geologic and geodetic observations and demonstrates the importance of near-hydrostatic fluid pressures in the upper crust for maintaining the strength of intraplate lithosphere. Although we do not illustrate

it here, it is important to note that for very low surface heat flow ($<50 \pm 5$ mW m^{-2}) such as is characteristic of Proterozoic and Archean cratonic crust (Pollack et al., 1993), strain rates lower than 10^{-20} s^{-1} are expected under either pore-pressure regime.

Thus, at the relatively low strain rates characterizing intraplate regions, there is sufficient plate-driving force available to overcome the integrated strength of the lithosphere, causing ductile deformation and maintaining the 'strong' brittle crust in a state of frictional failure equilibrium. One manifestation of high crustal strength is the efficient transmission of tectonic stress over distances of thousands of kilometers in intraplate regions documented by the stress orientation and relative magnitude data. Thus, in essence, the upper crust acts as a very efficient stress guide.

As an example of how lithospheric strength variations concentrate deformation, consider the partition of deformation along the San Andreas Fault system in Central California. As pointed out by Page et al. (1998), deformation along the San Andreas system is transpressional; in addition to the right-lateral shear accommodating relative motion between the Pacific and North American Plates, appreciable fault-normal convergence has been occurring since about 3.5 Ma. This convergence has resulted in uplift, folding, and reverse faulting over a broad zone about 100 km wide and corresponding to the Coast Ranges adjacent to the San Andreas.

This type of distributed deformation could be categorized as a diffuse plate boundary (e.g., Gordon, 1998; Wessel and Mueller, 2007), but it is interesting to consider more specifically why the transpressional deformation is distributed so broadly and why there is such an abrupt cessation of this deformation at the eastern boundary between the Coast Ranges and the Great Valley. The sharpness of this transition is particularly distinctive given that the entire region is subject to a relatively uniform compressive stress field acting at a high angle to the San Andreas Fault and subparallel strike-slip faults (**Figure 9**). This high angle implies that the San Andreas Fault (and perhaps other plate boundaries) has low frictional strength, in marked contrast to the high frictional strength exhibited by intraplate faults (briefly summarized by Zoback, 2000).

The stress observations shown in **Figure 9** (primarily from wellbore breakout measurements in oil and gas wells and earthquake focal mechanisms not associated with right-lateral slip along transform faults; see Mount and Suppe, 1987; Zoback et al., 1987) are remarkably consistent with modeled stress directions across the region and shown by dashed trajectories, interpolated from the results of Flesch et al. (2000). As previously discussed, the Flesch et al. model incorporates the combined effects of buoyancy-related stresses in the Western United States (principally due to the thermally uplifted Basin and Range Province) and right-lateral shear in the far field associated with plate interaction.

The abrupt change in the rate of deformation at the eastern boundary between the Coast Ranges and Great Valley coincides with a marked decrease in heat flow and therefore with lower-crustal and upper-mantle temperatures. Zoback et al. (2002) thus inferred that the rate of deformation is high throughout the Coast Ranges because temperatures in the lower crust and upper mantle are high. In contrast, heat flow in the Great Valley is extremely low (comparable to that of shield areas); hence, the available force is insufficient to cause deformation at appreciable rates. In fact, as revealed by undeformed seismic reflectors corresponding to formations as old

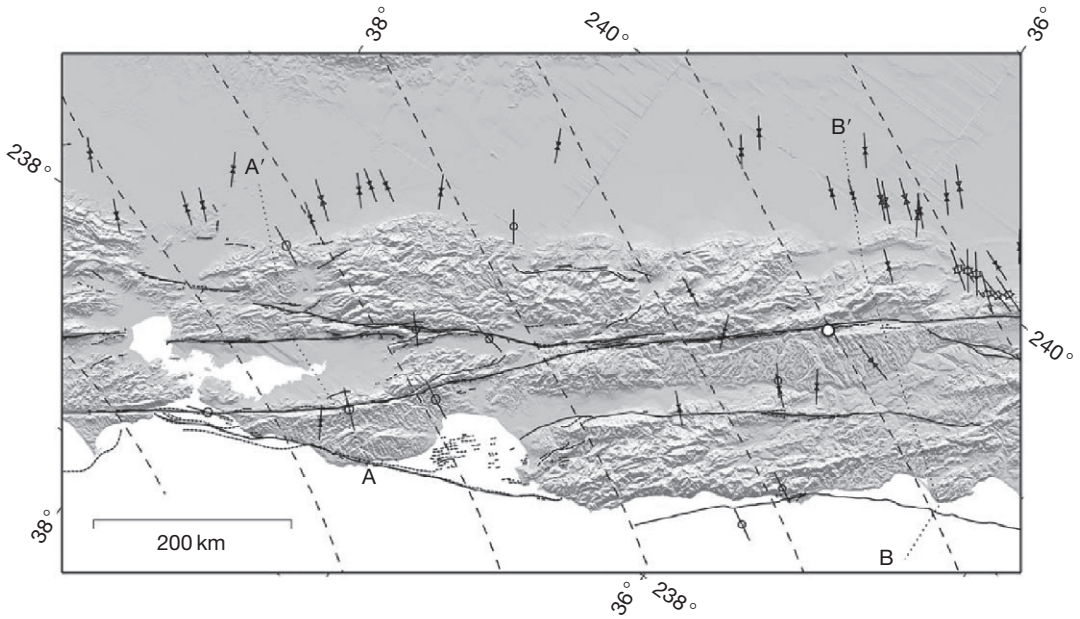

Figure 9 Topographic map of western California in an oblique Mercator projection about the NUVEL 1A North America–Pacific Euler pole (DeMets et al., 1990). In this projection, relative plate motion is parallel to the upper and lower margins of the map. The major right-lateral strike-slip faults comprising the San Andreas Fault system are also shown. The data show the direction of maximum horizontal stress from earthquake focal mechanism inversions (lines with a circle in the middle) or borehole stress measurements (bowtie symbols). The dashed trajectories are interpolations of stress directions calculated by Flesch et al. (2000) using a model based on lithospheric buoyancy and plate interaction. Reproduced from Townend and Zoback MD (2004) with permission from American Geophysical Union.

as Cretaceous in age, it is remarkable how little deformation has occurred in the Great Valley during the Cenozoic (e.g., Wentworth and Zoback, 1989).

6.06.6 Concluding Remarks

Several decades of study have produced a surprisingly simple and consistent picture of the lithospheric state of stress:

- The lithospheric stress field is the result of present-day active tectonics, and not related to residual stresses from past tectonic activity – this is indicated by remarkably uniform stress orientations over broad regions of the lithosphere (scales up to thousands of kilometers) including consistency across major bends in old orogenic belts.
- The same forces acting on and within the plates to drive plate motion are largely responsible for the stress state within the plates – this is demonstrated by the consistency of broad regional intraplate stress field with stresses predicted by models of these driving forces. Buoyancy forces due to lateral variations in lithospheric structure and density are also a significant contributor to the intraplate stress field. Most regions of intraplate extension are in regions of high topography generated by a thinned mantle lid.
- Direct stress measurements to depths of 8.1 km in deep wells and scientific research boreholes confirm the fact that stress magnitudes within the brittle crust are controlled by frictional strength. In fact, stress differences within the upper brittle layer indicate a state of incipient frictional failure on well-oriented preexisting fault planes.
- Because the brittle crust appears to be in a state of incipient frictional failure, the rate of deformation in a region is determined by the overall strength of the lithosphere; hence, young, hot lithosphere (e.g., along active plate boundaries) deforms much more rapidly than colder, stronger lithosphere in midplate regions. However, measured stress magnitudes in the two contrasting tectonic regions would be identical.
- Balancing observed rates of lithospheric deformation with applied forces suggests that most of the stress within the lithosphere is carried in its strong, uppermost brittle crustal layer (from the surface to ~15–20 km depth).

Appendix A Indicators of Contemporary Stress

Zoback and Zoback (1980) developed an integrated stress mapping strategy in the lithosphere based on data from a variety of sources: earthquake focal plane mechanisms, young geologic data on fault slip and volcanic alignments, in situ stress measurements, and stress-induced wellbore breakouts and drilling-induced tensile fractures. Each stress indicator is explained briefly later.

A.1 Earthquake Focal Mechanisms

While earthquake focal plane mechanisms are the most ubiquitous indicator of stress in the lithosphere, determination of principal stress orientations and relative magnitudes from these mechanisms must be done with appreciable caution. The pattern of seismic radiation from the focus of an earthquake permits construction of earthquake focal mechanisms. Perhaps the most simple and straightforward information about in situ stress that is obtainable from focal mechanisms and in situ stress is that the type of earthquake (i.e., normal, strike-slip, or reverse faulting) defines the relative magnitudes of S_{Hmax}, S_{hmin}, and S_v. In addition, the orientation of the fault plane and auxiliary plane (which bound the compressional and extensional quadrants of the focal plane mechanism) defines the orientation of the P (compressional), B (intermediate), and T (extensional) axes. These axes are sometimes incorrectly assumed to be the same as the orientation of S_1, S_2, and S_3.

For cases in which laboratory-measured coefficients of fault friction of ~0.6–1.0 are applicable to the crust, there is usually not a large error if one uses the P, B, and T axes as approximations of average principal stress orientations, especially if the orientation of the fault plane upon which the earthquake occurred is known (Raleigh et al., 1972). However, if friction is negligible on the faults in question, there can be considerable difference between the P, B, and T axes and principal stress directions (McKenzie, 1982). An earthquake focal plane mechanism always has the P and T axes at 45° to the fault plane and the B axes in the plane of the fault. With a frictionless fault, the seismic radiation pattern is controlled by the orientation of the fault plane and not the in situ stress field. One result of this is that just knowing the orientation of the P-axis of earthquakes along weak, plate-bounding strike-slip faults (like the San Andreas) does not allow one to define principal stress orientations from the focal plane mechanisms of the strike-slip earthquakes occurring on the fault (Zoback et al., 1987).

Principal stress directions can be determined directly from a group of earthquake focal mechanisms (or set of fault striae measurements) through the use of inversion techniques that are based on the slip kinematics and the assumption that fault slip will always occur in the direction of maximum resolved shear stress on a fault plane (cf. Angelier, 1984; Gephart and Forsyth, 1984; Michael, 1987). Such inversions yield four parameters, the orientation of the three principal stresses and the relative magnitude of the intermediate principal stress with respect to the maximum and minimum principal stresses.

The analysis of seismic waves radiating from an earthquake also can be used to estimate the magnitude of stress released in an earthquake (stress drop), although not absolute stress levels (Brune, 1970). In general, stress drops of crustal earthquakes are on the order of 1–10 MPa (Hanks, 1977). Equation [6] can be used to show that such stress drops are only a small fraction of the shear stresses that actually cause fault slip if pore pressures are approximately hydrostatic at depth and Coulomb faulting theory (with laboratory-derived coefficients of friction) is applicable to faults in situ. This is discussed in more detail in the succeeding text.

A.2 Geologic Stress Indicators

There are two general types of 'relatively young' geologic data that can be used for in situ stress determinations: (1) the

orientation of igneous dikes or cinder cone alignments, both of which form in a plane normal to the least principal stress (Nakamura, 1977), and (2) fault slip data, particularly the inversion of sets of striae (i.e., slickensides) on faults as described earlier. Of course, the term 'relatively young' is quite subjective but essentially means that the features in question are characteristic of the tectonic processes currently active in the region of question. In most cases, the WSM database utilizes data that are Quaternary in age but in all areas represent the youngest episode of deformation in an area.

A.3 In Situ Stress Measurements

Numerous techniques have been developed for measuring stress at depth. Amadei and Stephansson (1997) and Engelder (1993) discussed many of these stress measurement methods, most of which are used in mining and civil engineering. Because we are principally interested here in regional tectonic stresses (and their implications) and because a variety of nontectonic processes affect in situ stresses near the Earth's surface (Engelder and Sbar, 1984), we do not utilize near-surface stress measurements in the WSM or regional tectonic stress compilations (these measurements are given the lowest quality in the criteria used by WSM since they are not believed to be reliably indicative of the regional stress). In general, we believe that only in situ stress measurements made at depths greater than 100 m are indicative of the tectonic stress field at midcrustal depths. This means that techniques utilized in wells and boreholes, which access the crust at appreciable depth, are especially useful for stress measurements.

When a well or borehole is drilled, the stresses that were previously supported by the exhumed material are transferred to the region surrounding the hole. The resultant stress concentration is well understood from elastic theory. Because this stress concentration amplifies the stress difference between far-field principal stresses by a factor of 4, there are several other ways in which the stress concentration around boreholes can be exploited to help measure in situ stresses. The hydraulic fracturing technique (e.g., Haimson and Fairhurst, 1970; Zoback and Haimson, 1983) takes advantage of this stress concentration and, under ideal circumstances, enables stress magnitude and orientation measurements to be made to about 3 km depth (Baumgärtner et al., 1990).

The most common method of determining stress orientation from observations in wells and boreholes is stress-induced wellbore breakouts. Breakouts are related to a natural compressive failure process that occurs when the maximum hoop stress around the hole is large enough to exceed the strength of the rock. This causes the rock around a portion of the wellbore to fail in compression (Bell and Gough, 1979; Zoback et al., 1985). For the simple case of a vertical well drilled when S_v is a principal stress, this leads to the occurrence of stress-induced borehole breakouts that form at the azimuth of the minimum horizontal compressive stress. Breakouts are an important source of crustal stress information because they are ubiquitous in oil and gas wells drilled around the world and because they also permit stress orientations to be determined over a great range of depth in an individual well. Detailed studies have shown that these orientations are quite uniform with depth and independent of lithology and age (e.g., Castillo and Zoback, 1994).

Another form of naturally occurring wellbore failure is drilling-induced tensile fractures. These fractures form in the wall of the borehole at the azimuth of the maximum horizontal compressive stress when the circumferential stress acting around the well locally goes into tension, and they are not seen in core from the same depth (Brudy and Zoback, 1993, 1999; Brudy et al., 1997; Lund and Zoback, 1999; Moos and Zoback, 1990; Peska and Zoback, 1995).

References

Amadei B and Stephansson O (1997) *Rock Stress and Its Measurement*. London: Chapman and Hall.

Anderson EM (1951) *The Dynamics of Faulting and Dyke Formation with Applications to Britain*. Edinburgh: Oliver and Boyd, 206 pp.

Angelier J (1979) Determination of the mean principal directions of stresses for a given fault population. *Tectonophysics* 56: T17–T26.

Angelier J (1984) Tectonic analysis of fault slip data sets. *Journal of Geophysical Research* 89: 5835–5848.

Artyushkov EV (1973) Stresses in the lithosphere caused by crustal thickness inhomogeneities. *Journal of Geophysical Research* 78: 7675–7708.

Bai W, Vigny C, Ricard Y, and Froidevaux C (1992) On the origin of deviatoric stresses in the lithosphere. *Journal of Geophysical Research* 97: 11729–11737.

Barton CA, Hickman SH, Morin R, Zoback MD, and Benoit D (1998) Reservoir-scale fracture permeability in the Dixie Valley, Nevada, geothermal field: abstracts volume. In: *Society of Petroleum Engineers Annual Meeting, Trondheim*, pp. 315–322, Paper Number 47371.

Barton CA, Zoback MD, and Moos D (1995) Fluid flow along potentially active faults in crystalline rock. *Geology* 23: 683–686.

Baumgärtner J, Rummel F, and Zoback MD (1990) Hydraulic fracturing *in situ* stress measurements to 3 km depth in the KTB pilot hole VB. A summary of a preliminary data evaluation, in KTB Report 90–6a: 353–400.

Bell JS and Gough DI (1979) Northeast–southwest compressive stress in Alberta: Evidence from oil wells. *Earth and Planetary Science Letters* 45: 475–482.

Bird P (1998) Testing hypotheses on plate-driving mechanisms with global lithosphere models including topography, thermal structure and faults. *Journal of Geophysical Research* 103: 10115–10129.

Blackwell DD and Steele JL (1992) *Geothermal Map of North America*. Geological Society of America, DNAG Map No. 006.

Blackwell DD, Steele JL, and Carter LS (1991) Heat flow patterns of the North American continent: A discussion of the DNAG geothermal map of North America. In: Slemmons DB, Engdahl ER, and Blackwell DD (eds.) *Neotectonics of North America: Geological Society of America DNAG Decade Map*, vol. 1, pp. 423–437. Boulder, CO: Geological Society of America (498 pp).

Brace WF and Kohlstedt DL (1980) Limits on lithospheric stress imposed by laboratory experiments. *Journal of Geophysical Research* 85: 6248–6252.

Brudy M and Zoback MD (1993) Compressive and tensile failure of boreholes arbitrarily-inclined to principal stress axes: Application to the KTB boreholes, Germany. *International Journal Rock Mechanics Mining Sciences* 30: 1035–1038.

Brudy M and Zoback MD (1999) Drilling-induced tensile wall-fractures: Implications for the determination of *in-situ* stress orientation and magnitude. *International Journal of Rock Mechanics and Mining Sciences* 36: 191–215.

Brudy M, Zoback MD, Fuchs K, Rummel F, and Baumgärtner J (1997) Estimation of the complete stress tensor to 8 km depth in the KTB scientific drill holes: Implications for crustal strength. *Journal of Geophysical Research* 102: 18453–18475.

Brune JN (1970) Tectonic stress and the spectra of seismic shear from earthquakes. *Journal of Geophysical Research* 75: 4997–5009.

Byerlee JD (1978) Friction of rock. *Pure and Applied Geophysics* 116: 615–626.

Castillo DA and Zoback MD (1994) Systematic variations in stress state in the Southern San Joaquin Valley: Inferences based on well-bore data and contemporary seismicity. *American Association Petroleum Geologists Bulletin* 78(8): 1257–1275.

Castillo D and Zoback MD (1995) Systematic stress variations in the Southern San Joaquin valley and along the White Wolf fault: Implications for the rupture mechanics of the 1952 Ms 7.8 Kern County earthquake and contemporary seismicity. *Journal of Geophysical Research* 100(B4): 6249–6264.

Chapple WM and Tullis TE (1977) Evaluation of the forces that drive the plates. *Journal of Geophysical Research* 82: 1967–1984.

Cloetingh SAPL and Wortel MJR (1985) Regional stress field of the Indian Plate. *Geophysical Research Letters* 12: 77–80.

Cloetingh SAPL and Wortel MJR (1986) Stress in the Indo-Australian plate. *Tectonophysics* 132: 49–67.

Coblentz DD and Richardson RM (1996) Analysis of the South American intraplate stress field. *Journal of Geophysical Research* 101: 8643–8657.

Coblentz DD, Richardson RM, and Sandiford M (1994) On the gravitational potential of the Earth's lithosphere. *Tectonics* 13: 929–945.

Coblentz DD and Sandiford M (1994) Tectonic stresses in the African plate: Constraints on the ambient lithospheric stress state. *Geology* 22: 831–834.

Coblentz DD, Zhou S, Hillis RR, Richardson RM, and Sandiford M (1998) Topography, boundary forces, and the Indo-Australian intraplate stress field. *Journal of Geophysical Research* 103: 919–931.

Colmenares LB and Zoback MD (2003) Stress field and seismotectonics of Northern South America. *Geology* 31: 721–724.

DeMets C, Gordon RG, Argus DF, and Stein S (1990) Current plate motions. *Geophysical Journal International* 101: 425–478.

Engelder T (1993) *Stress Regimes in the Lithosphere*. Princeton, NJ: Princeton University Press.

Engelder T and Sbar ML (1984) Near-surface *in situ* stress: Introduction. *Journal of Geophysical Research* 89: 9321–9322.

England PC and Molnar P (1991) Inferences of deviatoric stress in actively deforming belts from simple physical models. *Philosophical Transactions of the Royal Society of London A* 337: 73–81.

Fleitout L (1991) The sources of lithospheric tectonic stresses. *Philosophical Transactions of the Royal Society of London Series A* 337: 73–81.

Fleitout L and Froidevaux C (1982) Tectonics and topography for a lithosphere containing density heterogeneities. *Tectonics* 1: 21–56.

Fleitout L and Froidevaux C (1983) Tectonic stresses in the lithosphere. *Tectonics* 2: 315–324.

Flesch LM, Holt WE, Haines AJ, and Shen-Tu B (2000) Dynamics of the Pacific-North American plate boundary in the Western United States. *Science* 287: 834–836.

Forsyth DW and Uyeda S (1975) On the relative importance of driving forces of plate motion. *Geophysical Journal of the Royal Astronomical Society* 43: 163–200.

Frankel AD, Petersen MD, Mueller CS, et al. (2002) Documentation for the 2002 Update of the National Seismic Hazard Maps: USGS Open-File Report 02-420, 33 pp.

Gephart JW and Forsyth DW (1984) An improved method for determining the regional stress tensor using earthquake focal mechanism data: Application to the San Fernando earthquake sequence. *Journal of Geophysical Research* 89: 9305–9320.

Goodwin AM (1996) *Principles of Precambrian Geology*. London: Academic Press, 327 pp.

Gordon RG (1998) The plate tectonic approximation: Plate non-rigidity, diffuse plate boundaries, and global plate reconstructions. *Annual Review of Earth and Planetary Sciences* 26: 615–642.

Govers R and Meijer PT (2001) On the dynamics of the Juan de Fuca plate. *Earth and Planetary Science Letters* 189: 115–131.

Grand S, van der Hilst RD, and Widiyantoro S (1997) Global seismic tomography: A snapshot of convection in the Earth. *GSA Today* 7: 1–7.

Grollimund BR and Zoback MD (2001) Impact of glacially-induced stress changes on hydrocarbon exploration offshore Norway. *American Association of Petroleum Geologists Bulletin* 87(3): 493–506.

Grunthal G and Stromeyer D (1992) The recent crustal stress field in central Europe – Trajectories and finite-element modeling. *Journal of Geophysical Research* 97: 11805–11820.

Haimson BC and Fairhurst C (1970) *In situ* stress determination at great depth by means of hydraulic fracturing. In: Sumerton W (ed.) *Proceedings of the 11th US Symposium on Rock Mechanics*, pp. 559–584. New York: Society of Mining Engineers of AIME.

Hanks TC (1977) Earthquake stress drops, ambient tectonic stresses and stresses that drive plate motions. *Pure and Applied Geophysics* 115: 441–458.

Healy JH, Rubey WW, Griggs DT, and Ralieg CB (1968) The Denver earthquakes. *Science* 161: 1301–1310.

Hickman SH, Barton CA, Zoback MD, Morin R, Sass J, and Benoit R (1997) In-situ stress and fracture permeability along the Stillwater fault zone, Dixie Valley, Nevada. *International Journal of Rock Mechanics and Mining Sciences* 34: 3–4 (Paper No. 126).

Ito T, Zoback MD, and Peska P (2001) Utilization of mud weights in excess of the least principal stress to stabilize wellbores: Theory and practical examples. *Society of Petroleum Engineers Drilling and Completions* 16: 221–229.

Jones CH, Unruh JR, and Sonder LJ (1996) The role of gravitational potential energy in active deformation in the Southwestern United States. *Nature* 381: 37–41.

Kohlstedt DL, Evans B, and Mackwell SJ (1995) Strength of the lithosphere: Constraints imposed by laboratory experiments. *Journal of Geophysical Research* 100: 17587–17602.

Lachenbruch AH and Morgan P (1990) Continental extension, magmatism and elevation; formal relations and rules of thumb. *Tectonophysics* 174: 39–62.

Lachenbruch AH, Sass JH, and Galanis SP Jr. (1985) Heat flow in southernmost California and the origin of the Salton Trough. *Journal of Geophysical Research* 90: 6709–6736.

Lithgow-Bertelloni C and Guynn JH (2004) Origin of the lithospheric stress field. *Journal of Geophysical Research* 109: B01408. http://dx.doi.org/10.1029/2003JB002467.

Lund B and Zoback MD (1999) Orientation and magnitude of *in situ* stress to 6.5 km depth in the Baltic Shield. *International Journal of Rock Mechanics and Mining Sciences* 36: 169–190.

Manning CE and Ingebritsen SE (1999) Permeability of the continental crust: Implications of geothermal data and metamorphic systems. *Reviews of Geophysics* 37: 127–150.

McGarr A and Gay NC (1978) State of stress in the Earth's crust. *Annual Review of the Earth and Planetary Sciences* 6: 558–562.

McKenzie DP (1982) The relation between fault plane solutions for earthquakes and the directions of the principal stresses. *Bulletin of Seismological Society of America* 59: 591–601.

Meijer PT, Govers R, and Wortel MJR (1997) Forces controlling the present-day state of stress of the Andes. *Earth and Planetary Science Letters* 148: 157–170.

Meijer PT and Wortel MJR (1992) The dynamics of motion of the South American plate. *Journal of Geophysical Research* 97: 1915–1932.

Michael AJ (1987) The use of focal mechanisms to determine stress: A control study. *Journal of Geophysical Research* 92: 357–368.

Mooney WD, Prodehl C, and Pavlenkova N (2002) Seismic velocity structure of the continental lithosphere from controlled source data. In: Lee WHK (ed.) *International Handbook of Earthquake and Engineering Seismology*, vol. 81A, pp. 887–910. San Diego, CA: Academic Press.

Moos D and Zoback MD (1990) Utilization of observations of well bore failure to constrain the orientation and magnitude of crustal stresses: Application to Continental Deep Sea Drilling Project and Ocean Drilling Program Boreholes. *Journal of Geophysical Research* 95: 9305–9325.

Mount VS and Suppe J (1987) State of stress near the San Andreas Fault: Implications for wrench tectonics. *Geology* 15: 1143–1146.

Nakamura K (1977) Volcanoes as possible indicators of tectonic stress orientation – Principle and proposal. *Journal of Volcanology and Geothermal Research* 2: 1–16.

Nur A and Walder J (1990) *Time-dependent hydraulics of the Earth's Crust*. *The Role of Fluids in Crustal Processes*. Washington, DC: National Research Council, pp. 113–127.

Page BM, Thompson GA, and Coleman RG (1998) Late Cenozoic tectonics of the Central and Southern Coast Ranges of California. *Geological Society of America Bulletin* 110: 846–876.

Pavoni N (1961) Faltung durch Horizontal verschiebung. *Ecolgae Geologicae Helvetiae Basel* 54: 515–534.

Pavoni N (1980) Crustal stress inferred from fault-plane solutions of earthquakes and neotectonic deformation in Switzerland. *Rock Mechanics* 9(Suppl.): 63–68.

Peska P and Zoback MD (1995) Compressive and tensile failure of inclined wellbores and determination of in situ stress and rock strength. *Journal of Geophysical Research* 100(B7): 12791–12811.

Pine RJ, Jupe A, and Tunbridge LW (1990) An evaluation of *in situ* stress measurements affecting different volumes of rock in the Carnmenellis granite. In: Cunha PD (ed.) *Scale Effects in Rock Masses*, pp. 269–277. Rotterdam: Balkema.

Pollack HN, Hurter SJ, and Johnson JR (1993) Heat flow from the Earth's interior: Analysis of the global data set. *Reviews of Geophysics* 31: 267–280.

Raleigh CB (1974) Crustal stress and global tectonics. In: International Society for Rock Mechanics and US National Committee for Rock Mechanics (eds.) Advances in Rock Mechanics: Proceedings of the 3rd Congress, vol. 1A, pp. 593–597. Washington, DC: National Academy of Sciences.

Raleigh CB, Healy JH, and Bredehoeft JD (1972) Faulting and crustal stress at Rangely, Colorado. In: Heard HC (ed.) *Geophysical Monograph Series 16: Flow and Fracture of Rocks*, pp. 275–284. Washington, DC: AGU.

Ranalli G and Murphy DC (1987) Rheological stratification of the lithosphere. *Tectonophysics* 132: 281–295.

Richardson RM (1978) Finite element modeling of stress in the Nazca plate: Driving forces and plate boundary earthquakes. *Tectonophysics* 50: 223–248.

Richardson RM (1992) Ridge forces, absolute plate motions, and the intraplate stress field. *Journal of Geophysical Research* 97: 1739–1748.

Richardson RM and Cox BL (1984) Evolution of oceanic lithosphere: A driving force study of the Nazca plate. *Journal of Geophysical Research* 89: 10043–10052.
Richardson RM and Reding LM (1991) North American plate dynamics. *Journal of Geophysical Research* 96: 12201–12223.
Richardson RM, Solomon SC, and Sleep NH (1976) Intraplate stress as an indicator of plate tectonic driving forces. *Journal of Geophysical Research* 81: 1847–1856.
Richardson RM, Solomon SC, and Sleep NH (1979) Tectonic stress in the plates. *Reviews of Geophysics* 17: 981–1019.
Sibson RH (1983) Continental fault structure and the shallow earthquake source. *Journal of the Geological Society of London* 5: 741–767.
Solomon SC, Sleep NH, and Richardson RM (1975) On the forces driving plate tectonics: Inferences from absolute plate velocities and intraplate stress. *Geophysical Journal of the Royal Astronomical Society* 42: 769–801.
Sonder LJ (1990) Effects of density contrasts on the orientation of stresses in the lithosphere: Relation to principal stress directions in the Transverse ranges, California. *Tectonics* 9: 761–771.
Stefanick M and Jurdy DM (1992) Stress observations and driving force models for the South American plate. *Journal of Geophysical Research* 97(B8): 11905–11913.
Stein RS, King GC, and Lin J (1992) Change in failure stress on the Southern San Andreas fault system caused by the 1992 magnitude 7.4 Landers earthquake. *Science* 258: 1328–1332.
Steinberger B, Schmeling H, and Marquart G (2001) Large-scale lithospheric stress field and topography induced by global mantle circulation. *Earth and Planetary Science Letters* 186: 75–91.
Townend J and Zoback MD (2000) How faulting keeps the crust strong. *Geology* 28(5): 399–402.
Wentworth CM and Zoback MD (1989) The style of late Cenozoic deformation at the eastern front of the California Coast Ranges. *Tectonics* 8: 237–246.
Wessel P and Mueller RD (2007) Plate tectonics. In: Schubert G and Watts AB (eds.) *Treatise on Geophysics*, vol. 6. pp. 49–98. Elsevier: Amsterdam.
Wiens DA and Stein S (1985) Implications of oceanic intraplate seismicity for plate stresses, driving forces, and rheology. *Tectonophysics* 116: 143–162.
Wortel MJR, Remkes MJN, Govers R, Cloetingh SAPL, and Meijer PT (1991) Dynamics of the lithosphere and the intraplate stress-field. *Philosophical Transactions of the Royal Society of London Series A* 337: 111–126.
Zoback ML (1992) First- and second-order patterns of stress in the lithosphere: The World Stress Map project. *Journal of Geophysical Research* 97: 11703–11728 (The current version of the World Stress Map database can be found at: http://www-wsm.physik.uni-karlsruhe.de/).
Zoback MD (2000) Strength of the San Andreas. *Nature* 405: 31–32.
Zoback MD, Apel R, Brudy M, et al. (1993) Upper crustal strength inferred from stress measurements to 6 km depth in the KTB borehole. *Nature* 365: 633–635.
Zoback MD and Haimson BC (eds.) (1983) *Hydraulic Fracturing Stress Measurements, US National Committee for Rock Mechanics, 270*. Washington, DC: National Press.
Zoback MD and Harjes HP (1997) Injection induced earthquakes and crustal stress at 9 km depth at the KTB deep drilling site, Germany. *Journal of Geophysical Research* 102: 18477–18491.
Zoback MD and Healy JH (1992) *In situ* stress measurements to 3.5 km depth in the Cajon Pass scientific-research borehole: Implications for the mechanics of crustal faulting. *Journal of Geophysical Research* 97: 5039–5057.
Zoback ML and Mooney WD (2003) Lithospheric buoyancy and continental intraplate stress. *International Geology Review* 45: 95–118.
Zoback MD, Moos D, Mastin L, and Anderson RN (1985) Wellbore breakouts and *in situ* stress. *Journal of Geophysical Research* 90: 5523–5530.
Zoback ML, Nishenko SP, Richardson RM, Hasegawa HS, and Zoback MD (1986) Mid-plate stress, deformation, and seismicity. In: Vogt PR and Tucholke BE (eds.) *The Geology of North America, vol. M: The Western North Atlantic Region*, pp. 297–312. Boulder, CO: Geological Society of America.
Zoback ML and Richardson RM (1996) Stress perturbation associated with the Amazonas and other ancient continental rifts. *Journal of Geophysical Research* 101: 5459–5475.
Zoback ML and Thompson GA (1978) Basin and Range rifting in northern Nevada: Clues from a mid-Miocene rift and its subsequent offsets. *Geology* 6: 111–116.
Zoback MD and Townend J (2001) Implications of hydrostatic pore pressures and high crustal strength for the deformation of intraplate lithosphere. *Tectonophysics* 336: 19–30.
Zoback MD, Townend J, and Grollimund B (2002) Steady-state failure equilibrium and deformation of intraplate lithosphere. *International Geology Review* 44: 383–401.
Zoback ML and Zoback MD (1980) State of stress of the conterminous United States. *Journal of Geophysical Research* 85: 6113–6156.
Zoback ML and Zoback MD (1989) Tectonic stress field of the conterminous United States. *Geological Society of America Memoir* 172: 523–539.
Zoback MD and Zoback ML (1991) Tectonic stress field of North America and relative plate motions. In: Slemmons DB, et al. (ed.) *The Geology of North America, Neotectonics of North America*, pp. 339–366. Boulder, CO: Geological Society of America.
Zoback MD, Zoback ML, Mount VS, et al. (1987) New evidence on the state of stress of the San Andreas fault system. *Science* 238: 1105–1111.
Zoback ML, et al. (1989) Global patterns of tectonic stress. *Nature* 341: 291–298.

Relevant Websites

http://mahi.ucsd.edu – UCSD Department of Mathematics.
http://www-wsm.physik.uni-karlsruhe.de – World Stress Map Project.

This page intentionally left blank

6.07 Magmatism, Magma, and Magma Chambers

BD Marsh, Johns Hopkins University, Baltimore, MD, USA

© 2015 Elsevier B.V. All rights reserved.

6.07.1	**Introduction**	274
6.07.2	**The Nature of Magma**	275
6.07.2.1	Transport Characteristics	276
6.07.2.2	Phase Equilibria	277
6.07.2.3	Solidification Fronts	277
6.07.3	**Crystals in Magma**	278
6.07.3.1	Solidification Front Crystallization or Phenocryst-Free Magmas	279
6.07.3.2	Phenocryst-Bearing Magma	280
6.07.3.3	Kilauea Iki Lava Lake	282
6.07.3.4	Primitive versus Primary Magmas	285
6.07.3.4.1	Historical concept of solidification front fractionation	285
6.07.4	**Magma Chambers**	285
6.07.4.1	The Problem: The Diversity of Igneous Rocks	285
6.07.4.2	George Becker's Magma Chamber	285
6.07.5	**Historical Setting**	287
6.07.5.1	Lifetime Lines	288
6.07.6	**Initial Conditions of Magmatic Systems**	290
6.07.6.1	Cooling from the Roof	290
6.07.6.2	Style of Crystal Nucleation and Growth	291
6.07.6.3	The Critical Connection between Space and Composition	292
6.07.6.3.1	Temperature space, phase space, and spatial position	292
6.07.6.4	The Sequence of Emplacement or Delivery of the Magma	294
6.07.6.4.1	Forms of magmatic bodies	294
6.07.6.4.2	Internal transport style	295
6.07.6.4.3	Eruptive timescales and fluxes	295
6.07.6.4.4	Filling times	295
6.07.6.4.5	Magmatic deliveries, episodes, periods, and repose times	296
6.07.6.5	Thermal Ascent Characteristics and the Role of Thermal Convection	296
6.07.6.5.1	Superheat	297
6.07.6.6	Summary of Magmatic Initial Conditions	300
6.07.7	**End-Member Magmatic Systems**	300
6.07.7.1	The Sudbury Igneous Complex (SIC)	300
6.07.7.2	Ferrar Dolerites, Antarctica	302
6.07.8	**Lessons Learned from Sudbury and the Ferrar Dolerites**	305
6.07.9	**Ocean Ridge Magmatism**	306
6.07.10	**Island Arc Magmatism**	307
6.07.10.1	Introduction	307
6.07.10.2	Arc Form	308
6.07.10.2.1	Spacing of the volcanic centers	308
6.07.10.2.2	Arc segmentation	309
6.07.10.3	Character of the Volcanic Centers	310
6.07.10.4	Magma Transport	311
6.07.10.5	Subduction Regime	311
6.07.10.6	Subducting Plate Internal State	312
6.07.10.6.1	Thermal regime	312
6.07.10.6.2	Hydrothermal flows	313
6.07.10.7	The Source of Arc Magma	313
6.07.10.7.1	Slab quartz-eclogite	314
6.07.10.8	Diapirism, Rayleigh–Taylor Instability, and Volcano Spacing	316
6.07.10.9	Alkali Basalts Posterior to Arcs	316
6.07.10.10	The Arc Magmatic System	316
6.07.11	**Solidification Front Differentiation Processes**	317
6.07.11.1	Introduction	317
6.07.11.2	Solidification Front Instability	317

 http://dx.doi.org/10.1016/B978-0-444-53802-4.00116-0

6.07.11.3 Silicic Segregations and Crust Reprocessing in Iceland 317
6.07.11.4 Sidewall Upflow 318
6.07.11.5 Fissure Flushing 319
6.07.12 Magmatic Systems 320
Acknowledgments 320
References 320

6.07.1 Introduction

Magmatism is perhaps the single most critical ingredient in molding and understanding planetary evolution. It is a direct reflection of a planet's internal thermal state and its chemical and physical constitution. On Earth, magmatism is closely linked to tectonism, which itself is directly linked to the larger-scale process of thermal convection within the mantle and core. Magma itself is a product of thermal and density instabilities within the mantle and crust. It is primarily produced by convection through a phase boundary, which is due to the striking differences in slopes as a function of pressure of silicate rock melting curves and the adiabatic temperature during uprise. The inevitable net result of any material uprise is the encountering of the rock solidus, promoting melting, magma production, plutonism, and volcanism. Once magma is produced, its temperature trajectory favors superheating and continued melting, and the magma takes on a life of its own with myriad secondary manifestations. One vital fundamental process is crystal growth and separation, commonly called fractionation or differentiation, which, in effect, distills magma, creating the major divisions of Earth and the vast spectrum of rock types, including, indirectly, metamorphic and sedimentary rocks. Remelting of crustal materials brought in prolonged contact with magma fresh from the mantle also readily produces secondary magmas (e.g., Bergantz, 1989). These magmas go to building and reorganizing the crust and to creating sedimentary and metamorphic provenances.

On planets like Moon, Io, and Europa, processes distinct from those on Earth generate magmatism. Sufficiently large meteoroid impacts have efficiently generated, especially early on, voluminous sheets of magma on all the terrestrial planets and even occasionally on the younger Earth, such as at Sudbury 1.85 Ga. Extreme tidal dissipation within Io, a body the size of today's thermally inert Moon, due to the close proximity of Jupiter has sustained almost daily volcanism for the history of the solar system. And cryovolcanism on icy Europa stems mysteriously from a thick (~100 km) aqueous mantle beneath a much thinner (~25 km) ice crust or 'lithosphere.' Europa magmatism does not enjoy the strong increase in silicate melting point with pressure leading to superheating, but instead, the slight decrease in ice melting point with pressure tends to supercool rising magma, suppressing volcanism, yet it does occur. And equally surprising, internally generated Earth magmas are never superheated.

Most magma thus arises through partial melting of a source or parent rock regardless of composition. The collected buoyant magma ascends, contributing to volcanism or, more often, when becoming stalled at depth, plutonism. This overall process is 'magmatism.' Within any process of magmatism, there are certain physical and chemical processes that are truly fundamental to shaping the behavior and outcome of the magma, and it is these magmatic processes that are considered herein.

Volcanism is the last, in effect, split second dramatic end result of certain magmatisms. Volcanoes, regardless of where they are found, reflect the physical processes at depth of magma production, collection, and transport. They are vital physical probes into planetary interiors. The most voluminous and steady volcanic magmatisms of Earth, like those of the ocean ridges and Hawaii, erupt magma at or near the liquidus, but never superheated. The low crystallinity and high fluidity of these magmas reflect this high-temperature, near-liquidus eruptive state, whereas many island arc magmas, especially the andesitic ones, can be of high crystallinity; the most dangerous ones, as at Merapi, flirt with the point of critical crystallinity at 55 vol.%. As the phenocryst or crystal content approaches maximum packing at critical crystallinity, the magma becomes a dilatant solid, expanding upon shear. High-crystallinity magma in a volcanic neck, in effect, corks or plugs the vent causing potentially highly explosive eruptions. High-temperature, low-crystallinity basaltic magmas are not generally explosive, but the exceeding mobility of the lavas is dangerous. Cinder cone volcanism, commonly areally sporadic and associated with alkali basalts, is just the reverse. The early volatile-rich phase is explosive, almost regardless of crystal content, but the associated lavas are sluggish and immobile. Magma explosiveness can thus reflect an enhanced volatile content, high crystallinity, or high silica content, each reflecting a particular effect on magma rheology and its effect on transport.

The spatial pattern and style of volcanic magmatism intimately reflects the nature of the causative process. Globally widespread magmatism, as on Io, reflects planetwide melting as in tidal pumping or a heavy impact flux. Linear arrays or strings of magmatism, as along ocean ridges, island arcs, and some ocean islands, reflect melting associated with thermoconvective flows tightly focused within the phase field of the source rock. Either the thermal regime or the source material (or both) is spatially focused. Areally widespread, small volume magmatism, exemplified by cinder cone fields, reflects a pervasive, marginally focused convective flow, much like a broad low-pressure system in the atmosphere, where sporadic melting instabilities are mainly due to detailed local irregularities in source rock composition. Typical convective flows of this nature are broad, gently upwelling flows associated with the wedge flows driven by subduction near and behind island arcs. Widespread, but voluminous magmatisms, as in the silicic volcanism of the Western United States over the past 50 Ma, reflect convective stretching and thermal destabilization of the continental lithosphere. The high-temperature asthenosphere thermal regime reaches the Moho where vast regions of continental crust of irregular thickness and composition are accessible to melting and remobilization. This leads to voluminous production

of rhyolitic magmas, batholiths, and crustal reorganization (Bachmann and Bergantz, 2004, 2008; Dufek and Bergantz, 2005).

Volcano edifices themselves in a simple way measure the hydrostatic (i.e., magma-static) head and power or strength of the system, the mobility of the source relative to the surface plate, the strength or age of the local lithosphere, and the intensity of the gravitational field. The largest volcanoes in the solar system are in the Tharsis bulge region of Mars. The extreme size of Olympus Mons at ~30 km tall and 850 km in basal diameter reflects a weak gravity field, an old, cold, and strong lithosphere, and the immobility of the source relative to the surface plate. For a given areal extent, the volcanoes of Venus are the shortest, reflecting the high-temperature, weak nature of the Venusian lithosphere. This is broadly similar to the volcanoes within the rift zones of Iceland, where isostasy is rapid (~1 km Ma^{-1}) due to the thin, hot, and weak crust.

Magmatic plumbing systems begin in the source regions and end at plutons and volcanoes. Knowledge of the structure of volcanoes and plutons comes mainly from direct observations of field relations in deeply eroded terrains. The ultimate source regions can be sensed, in terms of depth, degree of melting upon extraction, and source material, through geochemistry. Detailed knowledge of the physical state of these systems comes mainly from modeling and rare well-exposed crustal rocks. Temporal hypocenter distributions, particularly in active, voluminous systems, like Hawaii, are valuable in inferring the deeper geometric form, extent, and sense of connection between eruptions and deep transport. A comprehensive study of their nature is given by Wright and Klein (2014). Some styles of harmonic tremor, which sometimes occurs during eruptive stages, seem to indicate the preeruptive state of magma held in vertically oriented cylindrical conduits. Ground deformation associated with tumescence prior to eruption consistently indicates through elastic modeling a local, near-surface staging region, which is commonly identified with the concept of a magma chamber. This is reinforced by the very nature and pervasiveness of plutons. Overall, the most commonly held conceptualization of a generic magmatic plumping system has a deep source region linked to a near-surface magma chamber through a poorly discerned transport region, which for simplicity is often illustrated as an extended pipelike feature. Aside from the gross inferences from seismic studies, the actual intervening plumping linking source to near surface, the ascent path, has been difficult to ascertain. Although magma perhaps spends most of its life in this part of the system, it has, *per force*, been largely ignored physically and chemically due to lack of a clear and detailed conception of this important feature. This basic magmatic architecture, source, ascent path, chamber, and pluton or volcano, is found in different forms in most magmatic systems (Figure 1).

Magma chamber is a particularly important concept. Volcanologists use the mechanics of magma chambers to handle all the major and subtle chemical and textural transitions necessary to link one lava to another. Successive lavas may give a time record of the operation of a magma chamber, although the actual chamber can never be sensed. Plutons are, in a strong sense, actual magma chambers, but evidence of how they operated in real time has been largely lost through protracted crystallization and annealing, and the nature of the connection of plutons to either volcanoes or the deeper, ascent path of the system is not at all clear. It is the coupling of field spatial relationships of rock texture to the instantaneous time record of volcanism that promises to give a clearer picture of the overall process of magmatism. This is central thrust of this chapter.

6.07.2 The Nature of Magma

Magma is a viscous fluid consisting most often of polymerized silicate melt, crystals, dissolved gases, and sometimes bubbles and foreign chunks of crystals and rocks. Of all the fluids provided by nature, magma is the most intriguing. In traversing

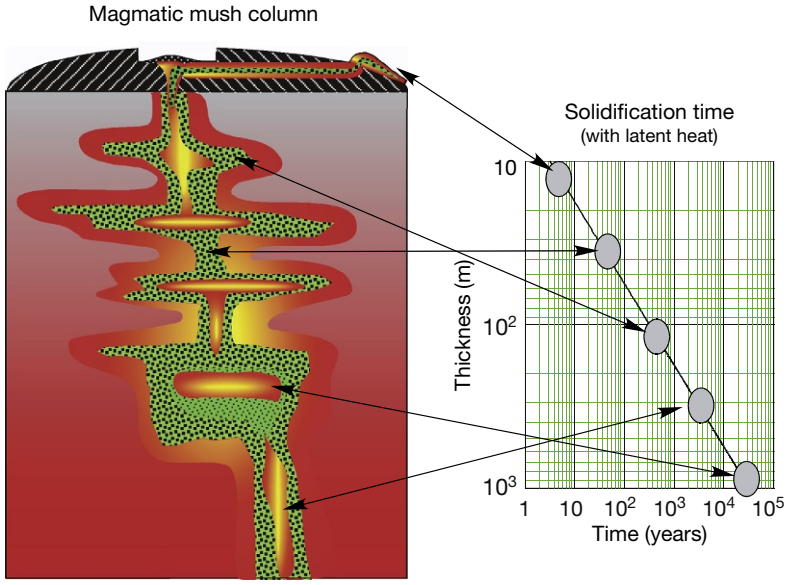

Figure 1 Magmatic systems (left) are an integrated collection of sills and connecting conduits linking a source region to the near-surface and volcanic centers. The thermal timescales (right) for solidification vary throughout the system due to the local thermal regime and the length scale of the system.

the melting range, a span of ~200 °C, magma viscosity increases by a factor of 10^{18} (mks or cgs), which is the largest change of any physical parameter for any equivalent temperature change. Crystals spontaneously nucleate and grow, modifying both the local buoyancy and melt composition, furnishing swarms of particles of a wide range of sizes that sort by size and density and stick together, welding tightly to form strong, truss-like, networks at many degrees of crystallinity. The corresponding rheology reflects this astounding diversity. At the lowest crystallinities, magma is linear or Newtonian in viscosity (μ) with stress (τ) proportional to strain (σ) ($\tau = \mu\sigma$), but with increasing crystal or particle content, rheology becomes increasingly nonlinear with magma becoming a shear-thinning power-law fluid. Beyond the crystallinity of maximum packing (~55 vol.%), viscosity becomes effectively infinite, turning the material from a highly viscous fluid into a porous medium.

6.07.2.1 Transport Characteristics

Heat and mass transport are slow in magma. Thermal (K) and chemical (D) diffusivities are small (typically $\sim 10^{-2}$ and $\sim 10^{-6}$ cm^2 s^{-1}, respectively) and kinematic viscosity (ν) is large, making the Prandtl ($Pr = \nu/K$, always very large), Schmidt ($Sc = \nu/D$), and Lewis ($Le = K/D$) numbers each large as opposed to molten metals with small Pr. That is, vorticity, heat, and mass can each be described by a transport or diffusion equation of the form

$$\frac{\partial A}{\partial t} = B\frac{\partial^2 A}{\partial X_i^2} \qquad [1]$$

where A can be vorticity, temperature, or mass concentration; B is a kinematic viscosity, thermal diffusivity, or mass diffusivity; and X_i is a spatial dimension. A scaling analysis of this equation relates the characteristic distance (δ) of diffusion associated with each of these processes to the associated transport property B and time (t), yielding

$$\delta = C(Bt)^{1/2} \qquad [2]$$

where C is a constant near unity in magnitude. The dimension δ is a measure of the diffusive layer thickness during the flow of momentum, heat, or mass. For heat, for example, $\delta_T = C(Kt)^{1/2}$. And the relative thicknesses of these layers is thus measured by

$$\frac{\delta_\nu}{\delta_T} \approx \frac{\nu}{K} = Pr \quad \text{(Prandtl no.)} \qquad [3]$$

$$\frac{\delta_\nu}{\delta_D} \approx \frac{\nu}{D} = Sc \quad \text{(Schmidt no.)} \qquad [4]$$

$$\frac{\delta_D}{\delta_T} \approx \frac{D}{K} = Le \quad \text{(Lewis no.)} \qquad [5]$$

Notice also that $Pr = Sc\,Le$; so these dimensionless numbers are not entirely independent of one another.

As an example of the value of these relatives measures, for magma with a kinematic viscosity of 10^2 cm^2 s^{-1} moving 1 km along a wall at the rate of 0.1 cm s^{-1}, the momentum boundary thickness will be about 400 m. The thermal boundary layer will have a thickness of about 4 m, and the mass boundary layer thickness will be about 4 cm.

With Pr being a measure of the relative thicknesses of viscous or momentum to thermal boundary layers, momentum boundary layers are much thicker than thermal boundary layers, making the boundary layer approach for momentum transfer in fluid mechanics generally inappropriate, unlike in metallurgy where Pr is small. Thermal boundary layer approaches, on the contrary, are highly valuable. Likewise, from the Schmidt and Lewis numbers, chemical boundary layers due to chemical diffusion are much thinner than both momentum and thermal boundary layers (see Figure 2). Diffusion halos about growing and dissolving crystals and xenoliths, for example, are exceedingly thin, making these halos of low buoyancy and contamination highly local. In many ways, this makes solving magmatic transport problems straightforward. Thin thermal and chemical boundary layers are

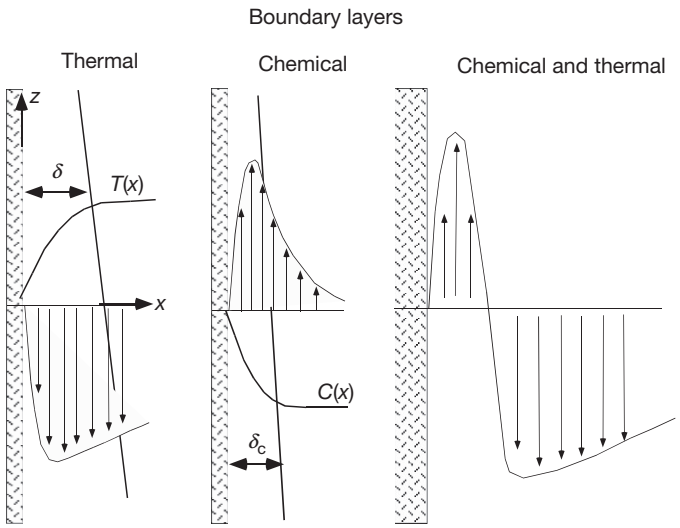

Figure 2 The types of boundary layers and their characteristic length scales operating in magmatic systems.

embedded in wide shear zones where the variation in velocity is broad and gentle. We shall soon see, however, that the unusually strong effects of variable viscosity, as mentioned already, partly mitigate this attractive feature of many magmatic flows. Some of this viscosity effect comes from the increasing silica content of the melt as crystallization proceeds, but by far, the most serious effect comes from the increasing concentration of crystals themselves and the interactions among these solids. These characteristics affect all aspects of magma generation, transport, differentiation, and eruption.

6.07.2.2 Phase Equilibria

The melting behavior of a typical basaltic magma, in terms of phase equilibria, as a function of pressure is shown in Figure 3. The high-temperature boundary beyond which (in temperature) no crystals exist is the *liquidus* and the lower boundary below which the magma is completely solid is the *solidus*. In between these boundaries are phase fields delineating the stability of various mineral phases. Two magmas are indicated, one is free of dissolved water (dry magma) and the other (wet magma) contains a few percent dissolved water, where the point of saturation occurs at about 2 kb (0.2 GPa, 200 MPa). The solubility of water (and CO_2 and SO_2, the other principal volatile species) is directly proportional to the confining pressure, or depth in Earth, and there is also a point (~10–15 kb) at which no more water can be dissolved in the magma. At this point, the magma contains about 25 wt% water, which is equivalent to the molar proportion of water in seawater (~96%). Magma in this condition, should it ever be achieved, is an aqueous solution with a silicate solute. At pressures above the indicated point of saturation at 2 kb, the wet magma is undersaturated with water, and the phase diagram is geometrically similar to that of the dry magma, except that it is at a significantly lower temperature. This difference, as will be treated later, has a profound effect on the characteristics of ascent and eruption.

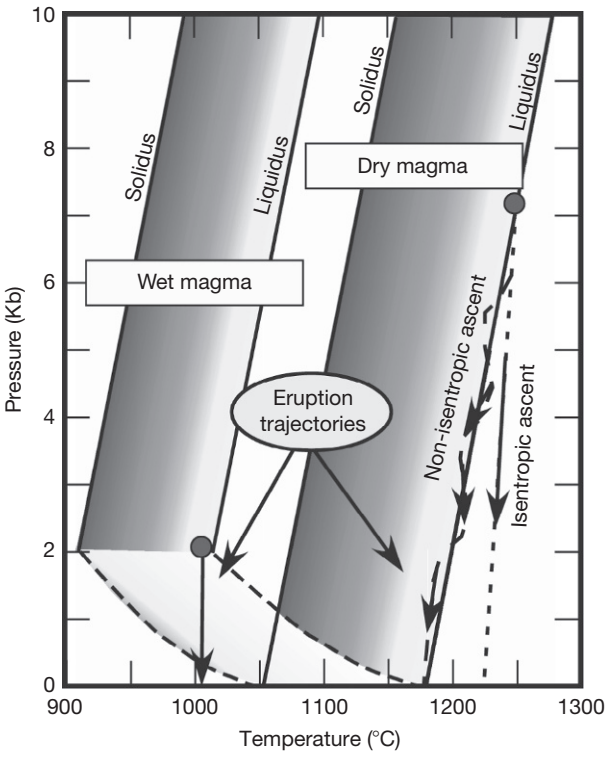

Figure 3 The general phase equilibria for basaltic magma as a function of pressure for dry and wet magmas. The adiabatic ascent path is indicated for the dry magma and also is the effect of rapid cooling due to superheating and convection. For the wet magma, the near-surface liquidus may be below the 1 atm solidus temperature.

6.07.2.3 Solidification Fronts

Between the liquidus and solidus, the magma is a physical and chemical mixture of liquid (melt) and crystals (and perhaps bubbles). The properties of this mixture are complex and exceedingly important at every stage in a magma's life in determining the set of dominant physical and chemical processes involved in shaping the magma's behavior and chemical evolution. Figure 4 shows the buildup of crystals with decreasing temperature between the liquidus and solidus for typical basalts. Nucleation and growth of crystals begins at the liquidus, by definition, and with decreasing temperature crystallinity (ϕ, or crystal fraction) at first builds up slowly and then more rapidly as crystallinity reaches 50 vol.% after which it again builds increasingly slowly with approach to the solidus. Near the liquidus, where crystallinity is low and crystals are small, the magma is a *suspension*. Here, the crystals can settle relative to one another without much hindrance from one another, but since they are small, settling is slow. This state holds to a crystallinity of about 25 vol.% where the viscosity of the mass (see the succeeding text) has increased by a factor of ten over that at the liquidus and the crystals now 'feel' the presence of one another as they move. Motion of a single crystal causes a shear flow extending out ~10 radii, which entrains neighboring crystals. There is also some observational (Marsh, 1998) and experimental (Philpotts and Carroll, 1996) evidence that, especially in plagioclase-bearing basaltic magmas, a 'chicken-wire' network of crystals may develop that gives a certain structure and strength to the magma. Beyond the suspension zone where crystals are (ideally) still separated from one another is the *mush* zone, which persists until the crystallinity reaches the state of maximum packing where the crystals are all touching. This occurs when crystallinity reaches about 55 vol.% ($\phi \sim 0.55$). At this point, the crystals are tacked or welded together to form a solid

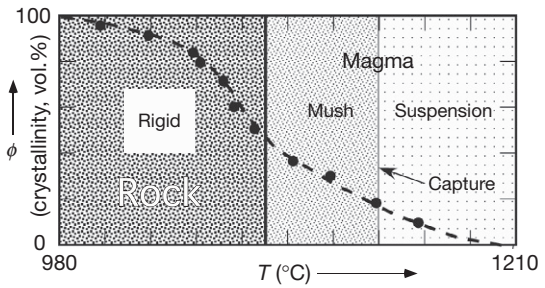

Figure 4 The variation of crystallinity in basaltic magma at any pressure as a function of temperature.

framework of some strength (e.g., Marsh, 2002). In essence, the magma is now a partially molten rock and can no longer flow as a viscous fluid. The remaining melt, which is interstitial to the crystals, can still move as a porous or the Darcy flow (e.g., Hersum et al., 2005). Because of this overall strength, which is found in Hawaiian lava lakes to be drillable, this cooler region is called the *rigid crust*. These three zones, then, suspension, mush, and rigid crust, make up all magmatic *solidification fronts*. A solidification front (see **Figure 5**) is the active zone of crystallization that forms the perimeter of all magmas. Solidification fronts are dynamic in the sense that they continually move in response to the prevailing thermal regime or state of heat transfer from (or sometimes to) the magma. All crystallization, by definition, takes place within solidification fronts. And it is within these fronts that all physical and chemical processes take place to modify the magma composition and texture. Beyond the solidification fronts, in the magma interior, there are no new crystals and hence no processes operate there to separate crystals and melt (more in the succeeding text).

As magma approaches the point of maximum crystal packing, where $\phi \sim 0.55$, it undergoes a dramatic rheological transition. It becomes a dilatant solid, which means that the mass of crystals and melt upon being sheared expands as neighboring solids try to move outward and around one another to accommodate the shear. When this condition is reached for magma in the throat of a volcano, the volcano becomes plugged and can no longer emit lava. With continued cooling and crystallization in the magma below, gases exsolve that can build pressure to the point of catastrophic failure of the entire edifice. This condition will be discussed again shortly. The dynamics of solidification fronts measure the dynamics, especially the rate of cooling, of every magma from deep chambers to lava flows.

6.07.3 Crystals in Magma

All magmas can be separated into two broad groups according to the sources of the constituent crystals: (1) crystals grown in the present cycle of active solidification fronts and (2) crystals inherited or entrained from prior crystallization events, including crystals from disaggregated wall rock. It is fundamental to the study of every magmatic rock to recognize the provenance of the constituent crystals. Crystals have historically been separated texturally into phenocrysts and groundmass. Phenocrysts are unusually large or otherwise distinctive crystals and groundmass are commonly tiny crystals interstitial to any phenocrysts. This distinction is most apparent in volcanic rocks but is also often clear in many plutonic rocks producing textures called porphyritic. It has long been assumed (e.g., Carmichael et al., 1974; Turner and Verhoogen, 1951) that phenocrysts represent crystallization at depth under slow, protracted cooling and groundmass crystals the latest rapid phase of cooling associated, in volcanic rocks, with eruptive processes or emplacement processes in plutons. The apparent sharp change in crystal size between phenocrysts and groundmass upon quantitative examination using measured crystal size distributions (CSDs; Marsh, 1988a,b, 1998, 2007a,b) shows most crystal populations to be more nearly continuous in size from phenocrysts to groundmass. This feature is characteristic of active crystallization where ongoing nucleation followed by crystal growth first spawns and then grows a wide spectrum of crystal sizes, just as in a human population. Yet there are many magmas that have also inherited crystals from earlier solidification events, and these crystals are valuable indicators of dynamic processes involving crystal entrainment, transport, and sorting. Recognizing the distinction between these two classes of crystals is of critical importance to understanding

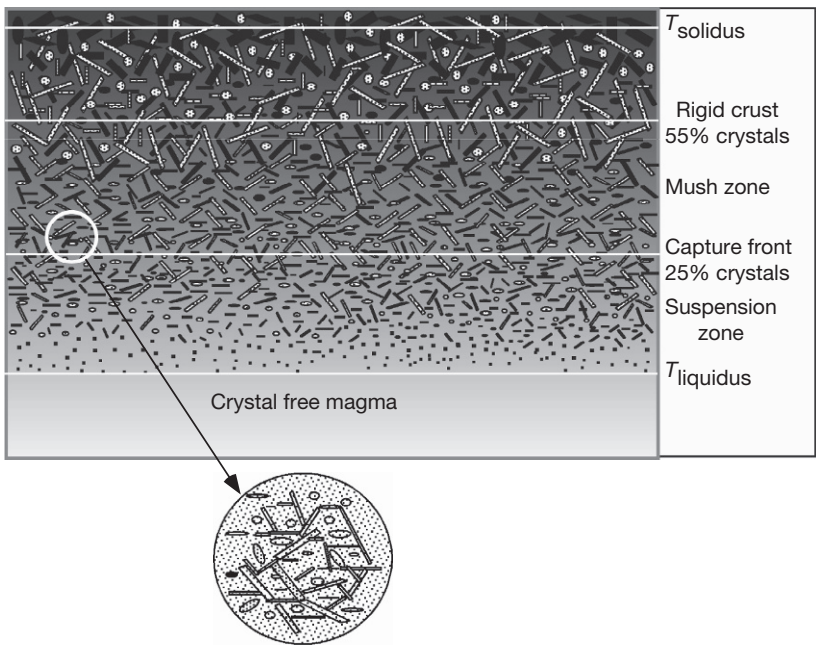

Figure 5 A typical solidification front in basaltic magma.

magmatic processes. Yet it has proven elusive in some magmatic bodies to recognize imported crystals, which leads to faulty reasoning in deciphering magmatic history. These two regimes, which for convenience are henceforth referred to as phenocryst-free and phenocryst-bearing, are next considered in some detail to emphasize this importance, beginning first with crystallization controlled by solidification fronts.

6.07.3.1 Solidification Front Crystallization or Phenocryst-Free Magmas

Solidification fronts are packaged between the liquidus isotherm at the leading edge and the solidus isotherm at the trailing edge. Nuclei and superclusters already present begin to grow in earnest at the leading edge of the solidification front, and these crystals continue to grow as the front passes through the region of melt. In the strictest sense, the melt is stationary and the solidification front moves through the melt transforming it into a crystalline mass. In the leading part of the solidification front, the suspension zone, crystals can settle easily without hindrance, but individual crystals are small and settle slowly. This settling is well described by Stokes' law:

$$V_S = C_S \frac{\Delta\rho g a^2}{\mu} \quad [6]$$

where C_S is a constant of order one ($\sim 2/9$ for spherical solids) depending on the shape of the crystal, $\Delta\rho$ is density contrast, g is gravity, a is crystal radius, and μ is magma viscosity. To escape the solidification front, the crystal must settle faster than the rate of advancement of the solidification front itself. Early in the cooling history, especially for magma emplaced in cool upper crustal wall rock, solidification fronts move rapidly and it is impossible for newly formed crystals to escape. Only in very slow-moving solidification fronts are crystals sometimes able to escape. And once a crystal becomes deeply embedded in a solidification front, melt viscosity and hindrance from neighboring crystals increase to the point that escape is not possible. The region where this transition occurs marks the boundary between the suspension and mush zones and is called the *capture front*. Crystals outward of the capture front are forever trapped in the solidification front.

As cooling proceeds, the distance between the isotherms defining the solidification front increases with the square root of time, just as in any conductive process. That is, even though solidification fronts involve heat production from latent heat of crystallization, from solutions to Stefan-type problems (e.g., Carslaw and Jaeger, 1959; Mangan and Marsh, 1992; Turcotte and Schubert, 2002), the position $S(t)$ of the front is given exactly by

$$S(t) = 4b(Kt)^{1/2} \quad [7]$$

where b is a constant and K is thermal diffusivity. The rate of advance is given by the time derivative of this equation:

$$V_F = \frac{dS(t)}{dt} = b\left[\frac{K}{t}\right]^{1/2} \quad [8]$$

Equating this with the rate of crystal settling from Stokes' law gives a relation for minimum size crystal that can escape from the solidification front as a function of time. That is,

$$a(t) = \left[\frac{b}{C_S}\frac{\mu(K/t)^{1/2}}{\Delta\rho g}\right]^{1/2} \quad [9]$$

The larger the viscosity, the larger the crystal must be to escape, and the larger the density contrast, the sooner the escape is possible. The constant b measures the effect of latent heat relative to the enthalpy of the magma and can be adequately represented from its original transcendental equation as (e.g., Zieg and Marsh, 2002)

$$b = \left[\frac{C_P(T_m - T_w)}{5H(\pi)^{1/2}}\right]^{2/5} \quad [10]$$

where C_P is specific heat, T_m is magma initial temperature, T_w is wall rock initial temperature, and H is latent heat.

To relate this escaping crystal size to the size of an actual body of magma, this measure of crystal size can be compared to the actual size of crystals growing in the suspension zone of the thickening solidification front. This is done by estimating the time taken by the capture front isotherm to traverse the suspension zone as a function of time. The position of the capture front isotherm is a large fraction ($f_{CF} \sim 0.9$) of the position of the leading edge of the solidification front given by eqn [7]:

$$S(t) = 4bf_{CF}(Kt)^{1/2} \quad [11]$$

and the difference of these two equations gives an estimate of the thickness of the suspension zone:

$$\Delta S(t) = (1 - f_{CF})4b(Kt)^{1/2} \quad [12]$$

The time spent traversing this zone is given by the quotient of [12] and [8]:

$$\Delta t(t) = \frac{\Delta S(t)}{V_F(t)} = 4(1 - f_{CF})t \quad [13]$$

The time for the solidification front to traverse the suspension zone is thus a linear function of time and independent of the thermal properties of the system. The size ($a(t)$) of a typical crystal grown during this time can be found using a general growth law for crystal growth. Although this choice is completely arbitrary, a convenient and realistic formula is the linear relation (e.g., Marsh, 1998; Zieg and Marsh, 2002)

$$a(t) = G\Delta t(t) = 4G(1 - f_{CF})t \quad [14]$$

Solving this equation simultaneously with that given by eqn [9] gives the time at which the first crystals escape from the solidification front:

$$t = \left[\frac{(b/C_S)\mu K^{1/2}}{(4G(1 - f_{CF}))^2 \Delta\rho g}\right]^{2/5} \quad [15]$$

This time can also be inserted into the growth law of eqn [14] to yield the size of the crystal at the time of escape, which is

$$a(t) = \left[\frac{(b/C_S)(4G(1 - f_{CF}))^{1/2}\mu K^{1/2}}{\Delta\rho g}\right]^{2/5} \quad [16]$$

The time of escape and size of crystal escaping are shown in Figure 6. For a magma viscosity of 10^3 poise and where crystals are growing at 10^{-10} cm s^{-1}, escape begins after about

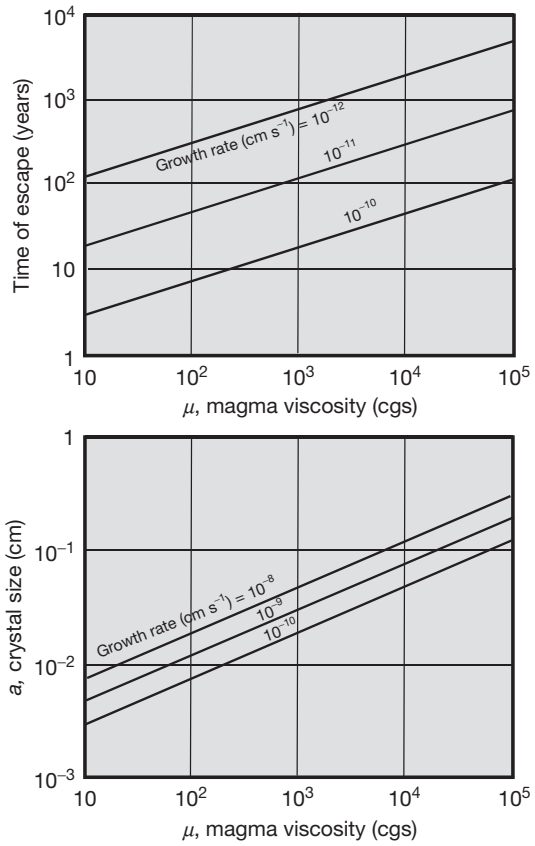

Figure 6 (upper) The time of escape of a crystal from a solidification front as a function of magma viscosity and crystal growth rate. (lower) The size of the first escaping crystal as a function of magma viscosity and crystal growth rate.

30 years, and the crystal size (radius) is about 0.03 cm. As might be expected, the size of the crystal at first escape is relatively insensitive to growth rate, but the escape time is much more sensitive to growth rate. The sooner a crystal can reach the critical size to sink faster than the rate of advancement of the capture front, the sooner it can escape. As magma viscosity increases, the time of first escape and the crystal size at escape each increase. For granitic magmas where the viscosity might be 10^5–10^6 poise, escaping crystals must be about 1 cm in radius, which for the growth rates indicated takes on the order of 10^3–10^4 years. This indicates why differentiation by crystal escape from solidification fronts is unlikely in granitic magmas.

Crystal escape from solidification fronts is much more likely in basaltic magmas once the crystals reach about 0.1 mm in size, which can occur after about 30 years when the solidification front has a thickness of about 50 m, depending on the cooling regime. The question then arises: What happens to these crystals once they escape the solidification front? Since the magma below the advancing front is the hottest part of the system, crystals entering this region will begin melting and dissolving back into the magma (see **Figure 7**). This process was originally recognized by Jaeger and Joplin (1955) and examined by Mangan and Marsh (1992) who, through a different approach, found results similar to those in the preceding text. Fractionation begins after about 25 years when capture front advancement has slowed to 1–2 m year^{-1}. For intrusions thinner than about 30 m, this condition is never achieved and no escape is possible, but for magmatic sheets thicker than about 100 m, this process may often occur. They also followed the course of the sinking crystals into the magma interior and estimated the time and distance settled for complete resorption. Survival through the hotter interior depends also on the proximity of the lower solidification front rising from the floor of the magma. Crystal accumulation on the floor of the magma is not possible until the lower solidification front has advanced to intercept the descending crystals prior to resorption. Interception is likely after about 75% solidification, which is when the lower front is about midway through the original magma (**Figure 7**). These intercepted escaped crystals will be small, and they join a part of the lower front having crystals of a broadly similar size. So, at best, a microcumulate layer may develop near the centerline of the body.

The net result of crystallization of a magma initially containing only nuclei and no large phenocrysts is a body of rock of essentially uniform composition and with a crystal size that increases inward in accord with the local growth or transit time of the solidification front. Many dolerite (diabase) sills throughout the world ranging in thickness from 1 to 350 m are often of uniform composition with a grain size that increases gradually in response to the slowing of the solidification front as it moves into the body from top to bottom. Actual CSDs can be calculated in detail to characterize this process (see Marsh, 1988a,b; Zieg and Marsh, 2002).

6.07.3.2 Phenocryst-Bearing Magma

That some magmas carry significant loads of large crystals that suddenly settle when the magma comes to rest upon emplacement and strongly chemically differentiate the magma became apparent with the controversy over the origin of the sequence of rock at Shonkin Sag laccolith in north central Montana. It is also from early studies of this body that came most of the basic concepts on the critical magmatic processes assumed to control magmatic chemical evolution. And it is these same processes that have been used, rightly or wrongly, to this day. Although much more on this crucial history will be covered later, it is important here to consider this classic magmatic body to set the stage for understanding this large class of magmas, which includes exotically layered bodies.

Shonkin Sag is a relatively small circular laccolith, 70 m thick and 3 km in diameter. Yet, in spite of its small size and relatively rapid cooling time, it is strongly differentiated (**Figure 8**). The obvious curiosity is that many much thicker and more areally extensive dolerite sills throughout the world, also of basaltic composition, show almost no differentiation. In the initial study of Shonkin Sag, Pirsson (1905) realized that a large mass of crystals had settled and formed a thick pile of cumulates on the floor. Many bodies show similar distributions of cumulate crystals, and most commonly, it has been assumed, like Pirsson, that these cumulate crystals grew after emplacement in response to strong cooling from the sill roof and simply settled to the floor. When the body was restudied in the 1930s independently by Hurlbut (1939) at Harvard and Barksdale (1937) at Yale, a spirited debate sprung up.

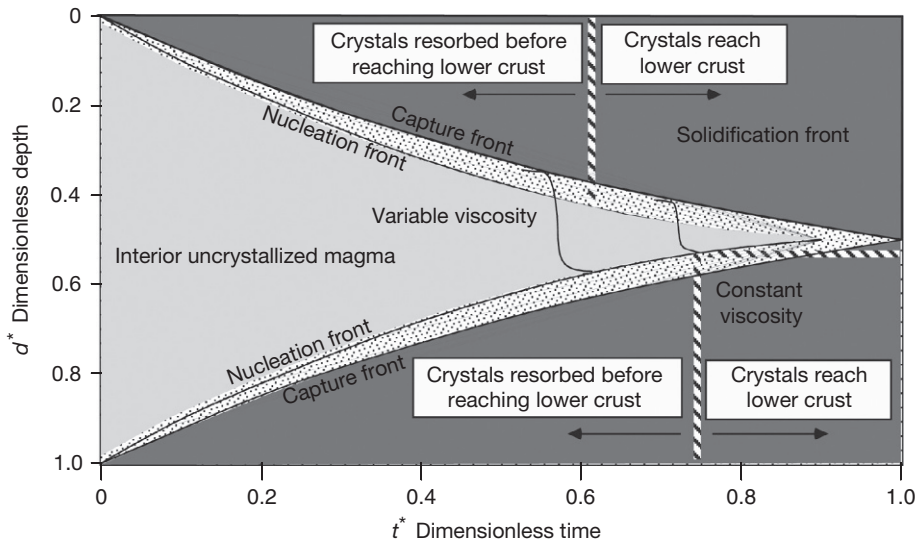

Figure 7 The thickening of upper and lower solidification fronts in a sheetlike body and their relationship to capturing settling crystals.

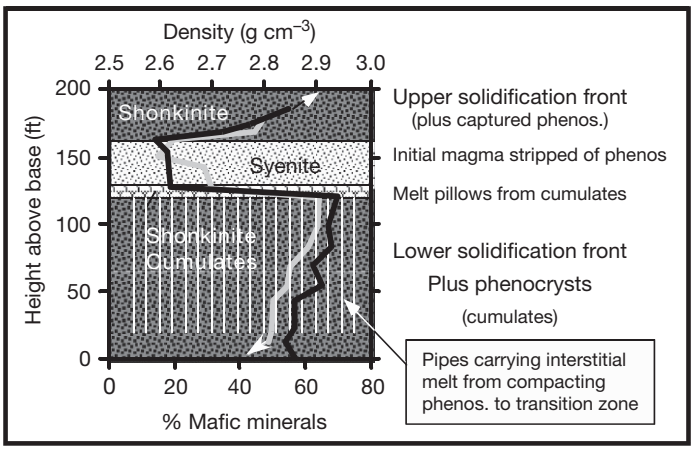

Figure 8 The stratigraphic field relations between rock types of Shonkin Sag laccolith.

Hurlbut made the critical observation that the initial magma carried a high concentration (~35 vol.%) of large crystals *prior* to emplacement. The cumulate crystals did not grow after emplacement but the cumulates formed almost as a snowfall from the rapid injection of a slurry of phenocrysts. This may well be the origin of the extremely important idea of the role of magma in carrying crystals. Barksdale, on the other hand, was deeply impressed by the presence of what appeared to be an internal contact where the transition zone rocks (see Figure 8) directly overlay the basal cumulates. This feature in the field does, indeed, look very much like an internal contact possibly formed by the later injection of a separate magma. This was the point of contention: Hurlbut said the entire stratigraphic distribution of rocks could be formed in place from simply an initially crystal-laden magma. Barksdale insisted that multiple injections of magma are necessary. These two points of view, *in situ* differentiation versus multiple injections, are still often points of contention in explaining igneous sequences. And, as will be seen here, there is clearly room and good reason for both views. In short, as the large load of phenocrysts was settling and accumulating in a thick pile on the laccolith floor, interstitial melt was forced upward through a series of pipelike conduits and expelled on top of the compacting cumulate pile (Marsh et al., 1991). Being too dense to rise higher in the sequence, the expelled essentially crystal-free melt established a series of overlapping pillows of melt forming the transition zone. This expelled, residual melt now being in the hottest part of the body and being multiply saturated because of its intimate prior contact with the cumulates went on to crystallize into unusually coarse crystals. The net result is a layer of rock in sharp textural contrast to the underlying cumulates of clinopyroxene phenocrysts. For all intents, this looks like an internal contact from a separate injection of magma. And in a very real way, it is, but this is an auto- or internal injection. Barksdale was very impressed by this feature and his arguments center on many facets of this observation. It is important to note that, whereas the basic geologic observation is correct, it is the interpretation of this

feature in terms of a magmatic process that is faulty. This is a fairly common pitfall in magmatology, and it appears even more strongly when the meaning of a thick cumulate pile of crystals on the floor of a magmatic body is interpreted (see succeeding text).

On more general grounds, when magma-carrying phenocrysts are emplaced, there is a competition between the rate of crystal settling and the rate of solidification. Just as in the previous section, when considering crystal capture and escape by inward-propagating solidification fronts, the same process operates here except that with crystals *initially* distributed vertically throughout the body, a large population of crystals easily escapes capture and settles freely into the lower, upcoming solidification front. It is important to consider some end-member situations for magma laden with crystals emplaced as a sheet (see **Figure 9**). If the magma could cool instantaneously regardless of its thickness, which physically is impossible, all crystals would be trapped in place before they could settle. The final distribution of crystals would be one of uniformity throughout the sheet. At the other extreme, if the body did not crystallize at all, all the crystals would settle to the floor and form a thick pile of constant abundance like a bed of clastic sedimentary rock. Although very thin (~1 m) and very thick (~100s m) sheets of magma may approximate these extremes, actual magmas are somewhere in between. Inward-advancing solidification fronts from the top and bottom compete with crystal settling. The initial advance of the upper and lower solidification fronts is infinitely rapid, which is what leads to the fine-grained chilled margins around igneous bodies, and any phenocrysts near the margins are immediately captured. But because the rate of solidification front advance decreases inversely with distance into the body (i.e., from eqn [2], an isotherm advance velocity (V) can be formed that leads to $V \sim K/Z$, where K is thermal diffusivity and Z is distance into the body), with increasing depth, more and more crystals escape capture, and all crystals initially in the center of the body settle into the lower rising solidification front. The net result is an S-shaped profile of phenocryst abundance vertically through the body (see **Figure 8**). This basic form of phenocryst distribution is seen in many magmatic sheets, and it is a clear indication of solidification of a phenocryst-charged body of magma. Moreover, there are many variations on this basic theme, and one readily accessible system of this nature that was studied in real time is Kilauea Iki lava lake in Hawaii.

6.07.3.3 Kilauea Iki Lava Lake

Lava lakes form in Hawaii when erupting magma fills naturally occurring pits or sink holes due to collapsing deeper lava tubes. Kilauea Iki lava lake formed from the late 1959 eruption of a crystal (olivine)-laden basalt, filling an ~2 km wide pit to a depth of about 125 m (e.g., Helz, 1986; Helz et al., 1989). Because the eruptive flux repeatedly waxed and waned during filling, the load of large olivine crystals delivered to the lava lake also varied over time. In a now-classic observation, Murata and Richter (1966) found that the magnitude of the eruptive flux at Kilauea is proportional to the size and the abundance of olivine crystals entrained by the erupting magma. In other words, the larger the eruptive flux and the stronger the eruption, the more and the larger olivine carried by the erupting magma. This is like a river in flood stage. The bigger and more dramatic the flood, the bigger the bed load of solids that it can move, and the larger the size of the individual solids that can be moved. Kilauea's historic record back for the past 200 years also shows these clear correlations (Garcia et al., 2003). The olivines entrained are not necessarily phenocrysts but are all sorts of crystals contained within the plumbing system; some are phenocrysts from earlier magmatic events, others are xenocrysts from peridotitic wall rock, and everything in between. When the crystals in a single sample are examined, they go from Fo_{75} to Fo_{92}, and the latter compositions are clearly from mantle wall rock (e.g., Garcia et al., 2003; Maaloe et al., 1989, 1992). In Hawaii, these crystals are called 'tramp' crystals to reflect their perhaps vagrant and varied origins (e.g., Wright and Fiske, 1971). Tramp crystals are found in systems all over the world at, for example, Jan Mayen (Imsland, 1984), Reunion (Upton and Wadsworth, 1967), and the Ferrar Dolerites (see succeeding text). And in a series of studies, Davidson and coworkers have shown through microsampling of individual crystals that neighboring crystals of similar bulk composition may be strikingly out of isotopic equilibrium (e.g., Davidson et al., 2005a,b, 2007). Considering that all magmas everywhere must ascend and erupt through crystalline mantle and/or crustal wall rock, which are in effect gravel piles, every magmatic system should contain some kind of tramp crystals.

The surprising aspect of magma carrying this heterogeneous collection of crystals is that if the lava chemical composition is plotted on a conventional diagram of CaO versus MgO (in wt%) or a typical oxide subtraction diagram, the variation appears as that due to perfect fractionation of olivine crystals indigenous to the magma (see **Figure 10**). Wright (1971) had shown that when these relations are considered in more detail for individual eruptions, the variations due to olivine control are even cleaner and tighter. Wright calls these trends olivine control lines. That is, all of the variation in MgO can be effected purely by the addition or loss of olivine tramp crystals. These exotic crystals have a strong effect on magma composition also through diffusional exchange.

As soon as a tramp crystal enters the ascending magma, it begins to chemically exchange Fe and Mg with the melt. The melt is much poorer in Mg and richer in Fe than typical tramp crystals. The time for these crystals to come to equilibrium with the melt can be estimated from eqn [2]: $t \sim a^2/D$, where a is crystal radius (~1 mm) and D is the chemical diffusivity controlling the exchange ($\sim 10^{-6}$ cm^2 s^{-1}). It takes only about a month or so to erase the original compositional identity of the tramp crystal and bring it into equilibrium with the melt. The melt has lost Fe to the crystal and gained Mg, which has made the apparent magma composition *more primitive*, exactly opposite to a normal (and commonly assumed) liquid line of descent or fractionation. Conversely, for these tramp crystals to have sustained their exotic compositional identity, the period of time from entrainment until eruption must be very short, perhaps only days.

Given the eruptive compositional variability of the lavas, especially in terms of the entrained crystal compositions, the magma filling Kilauea Iki lava lake varied daily during the eruption. As the eruptive flux waxed and waned, so did the crystal input. The initial conditions in the lava lake sheet of

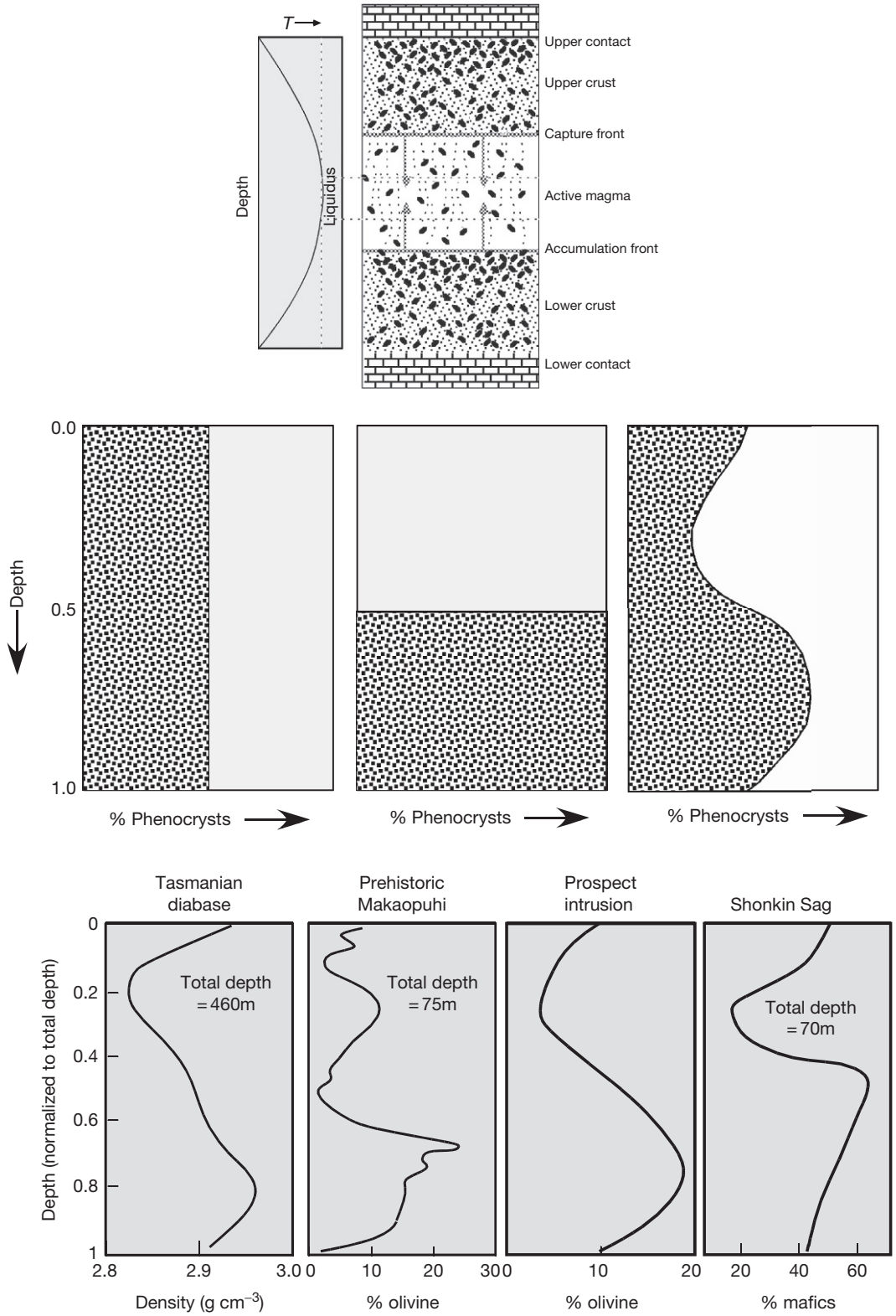

Figure 9 The process of settling of phenocrysts leading to formation of various final distributions of crystals. (upper) A schematic depiction of the process. (middle) The formation of idealized or end-member distributions. (lower) Actual distributions of crystals observed in some intrusions.

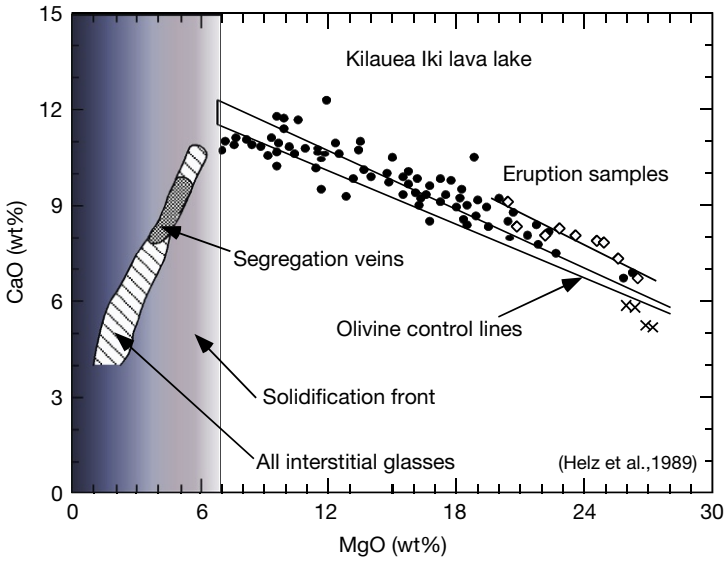

Figure 10 Variation of CaO and MgO in samples from Kilauea Iki lava lake. Note the olivine control lines, which show the effects of gains and losses in entrained olivine crystals. All compositions at MgO less than about 7 wt% are from drilling of the upper solidification front.

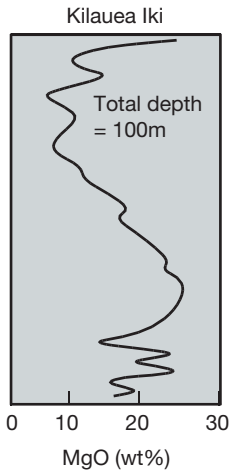

Figure 11 The S-shaped profile for Kilauea Iki where the detailed variations reflecting variations in eruption flux are clear.

magma, in terms of the abundance of tramp crystals, are in striking contrast to Shonkin Sag. At Shonkin Sag, the magma ascended from depth and the crystals were presumably flow-sorted and mixed prior to emplacement and the sequence of crystal settling leading to the final S-shaped profile. But at Kilauea Iki, the S-shaped profile will also reflect detailed variations due to the eruptive filling process (see Figure 11). Similar small-scale variations in intrusive complexes, as is seen in the Basement Sill of the Ferrar Dolerites of the McMurdo Dry Valleys, thus reflect periodic filling and repose times and may be a critical link between the similarity of intrusive and volcanic processes of magma transport.

Once the tramp olivine crystals have settled to form a cumulative pile on the floor of the lava lake, they begin to diffusionally exchange with the interstitial melt left in the bed, and in a matter of a few months, they have lost their original compositional heritage. A later analysis of this series of rocks would be difficult to unravel the true magmatic history due to this late, postemplacement, reequilibration. The clearest record of the role of tramp crystals, and their compositional diversity, is best recorded in the rapidly chilled rocks at the upper margin.

The sequence of chemical differentiation is controlled by two key processes: The first is the loss of the load of entrained tramp crystals once the magma came to rest. The magma in the center of the body after loss of the tramp crystals is a melt containing only tiny crystals and has differentiated from ~20% MgO to ~7 wt% MgO. It is essential to note that the change in composition took place, in essence, instantaneously as the tramp crystals settled out. This is *punctuated crystal fractionation and differentiation*. The second is the fact that after the loss of the tramp crystals, the center of the lava lake contains only crystal-free melt, and the system now resembles a phenocryst-free system discussed earlier. The system continues to cool and solidify without further differentiation. And if by chance this magma were to be erupted, only the low-viscosity, crystal-free core melt would be eruptible. The ensuing lava would thus show extensive chemical signs of differentiation, but it would mainly be due to the role of the entrained tramp crystals. Moreover, in all of these considerations, the role of melt as simply a 'carrier fluid' becomes clear, where the true identity or physical–chemical behavior of the magma only comes from the addition and loss of crystals regardless of the source.

The dramatic contrast in evolution of magma with and without initial concentrations of large crystals is central to understanding all magmas. Yet the importance of this distinction, and even the recognition of this feature itself, was not appreciated in the formative stages of magmatology. The essential concepts of differentiation and, especially, the evolution of magma in chambers were conceived and put into scientific play, in many ways, on faulty reasoning. The field relations were clearly recognized, but the physical processes giving rise to these field relationships were unknown. Through these considerations is where the concept came about of magma chambers, undoubtedly the most universal concept in magmatology.

6.07.3.4 Primitive versus Primary Magmas

When considering a magmatic complex or system, petrologists are literally obsessed with identifying the magmatic composition from which all other related compositions in the suite could have arisen by crystal fractionation processes. Norman Bowen himself, as we will see later, incited this obsession by discovering the crystallization reaction series whereby, starting with basalt, granite could be formed by growing and progressively settling out crystals with silica contents less than that of the adjacent magma. The natural tendency has thus been to automatically take the rock with the highest MgO content and assume it is the primary magma of the series. Magma MgO content has become synonymous with primitiveness. This reflects the direct connection between all basaltic magmas and mantle peridotitic rock. After all, there is no doubt whatsoever that basalts generally come from partial melting of the mantle and every other igneous rock, continents included, comes from basalt. It also reflects the observation that in Hawaii, there is a clear succession from MgO-rich picrites right on to tholeiitic basalts with 5–7 wt% MgO. It is naturally assumed and inherently adhered to, without even having to defend the proposition, that any basaltic rock with low MgO must be a differentiate. It cannot be a primary composition.

The general fallacy of this line of reasoning comes from not recognizing the fundamental mechanical role of tramp crystals in deciding magma bulk composition. We shall see repeatedly in the succeeding text that virtually any basalt can be a primary magma regardless of its MgO content. Any such basalt traversing the lithosphere has the opportunity to entrain high concentrations of nonindigenous crystals of olivine or other mafic phases. The new bulk composition certainly appears primitive, but it is not primary, and to assume that it is short-circuits the reasoning process leading to understanding magmatic processes. It is much more appropriate to consider magmatic processes as being characterized by a 'carrier magma' that is subjected to the mechanical gain and loss of crystals throughout its life. The carrier magma itself can be, within reason, of almost any composition. It certainly need not be inherently primitive, and it may be challenging to recognize the carrier magma, which, depending on the age and size of the system, may be of several different types. This concept is particularly important when considering the role of magma chambers in magmatic processes.

6.07.3.4.1 Historical concept of solidification front fractionation

The possible role of solidification fronts in capturing phenocrysts was first noticed by Pirsson (1905) in studying Shonkin Sag. Two of his students (Osborne and Roberts, 1931) were the first to analytically model the growth of the solidification front and compare this with the rate of settling of crystals due to Stokes' law. They compared their results to observations at Shonkin Sag, but due to a misnumbered sample, the calculated profile did not match that observed. Jaeger and Joplin (1955) made a substantial contribution when they realized that newly grown crystals falling from the advancing solidification front will dissolve as they sink into the hotter interior magma and will not contribute to fractionation. When Jaeger suggested this process might be general and be taking place in sill like the Palisade Sill, he was taken to task for this quaint point of view by Walker (1956) and Hess (1956) who could not understand Jaeger's straightforward analysis. Walker and Hess firmly held the assumption that, in essence, "it is well known by petrologists that crystals grow in the interiors of magmas and commonly settle to fractionate the system." They did not realize that the effect they were thinking of came from systems injected with phenocrysts from the start. J. C. Jaeger was the author, with H. S. Carslaw, of the fundamental, sterling treatise on heat conduction in solids, and his analytic insight into cooling and solidification of magma was unprecedented. The inability of leading petrologists of the day to recognize the truly original and valuable contributions by Jaeger set back the development of magma physics by several decades. The production of S-shaped profiles was analyzed again by Gray and Crain (1969) and Fujii (1974).

6.07.4 Magma Chambers

Magma chambers are the conceptual cornerstones of every magmatic process. They are high-level staging areas that charge volcanoes for eruption. They are cavernous pools wherein complex patterns and cycles of crystallization take place to transform initially homogeneous melt into spatially differentiated sequences, which may or may not be erupted. They are enormously versatile in size, shape, and function and can produce layered intrusions, a layered oceanic crust, and homogeneous diabase sills and granitic plutons. The central feature of this dynamic versatility is the pervasive nucleation and growth of crystals throughout the chamber that can be separated, sorted, or reentrained in a vast array of processes (see **Figure 12**). This valuable and useful concept of magma chambers has been adhered to for over 100 years. It is based on an exceedingly fundamental and misleading premise of how silicate melts solidify. Here, we examine this concept in detail, to strengthen it fundamentally and to show that all magmatic systems function by a common, basic, and simple set of processes.

6.07.4.1 The Problem: The Diversity of Igneous Rocks

The abundant variety of igneous rocks found on Earth's surface has long spawned an innate curiosity into the processes responsible for this variety and, moreover, how these same processes might have shaped the very structure of Earth itself. A strong burst of intellectual activity concerning the origin and evolution of magma was brought on by the advent of thin section-making and western exploration in the United States and by the general intense activity in chemistry and physics taking place at the beginning of the twentieth century. The rapid discovery of new elements, radioactivity, black body radiation and the development of chemical thermodynamics by J. Willard Gibbs, for example, set the stage for fundamental advances in understanding magma.

6.07.4.2 George Becker's Magma Chamber

In 1897, George Becker (1847–1919) set forth the basic concept of magma chamber differentiation that is still largely

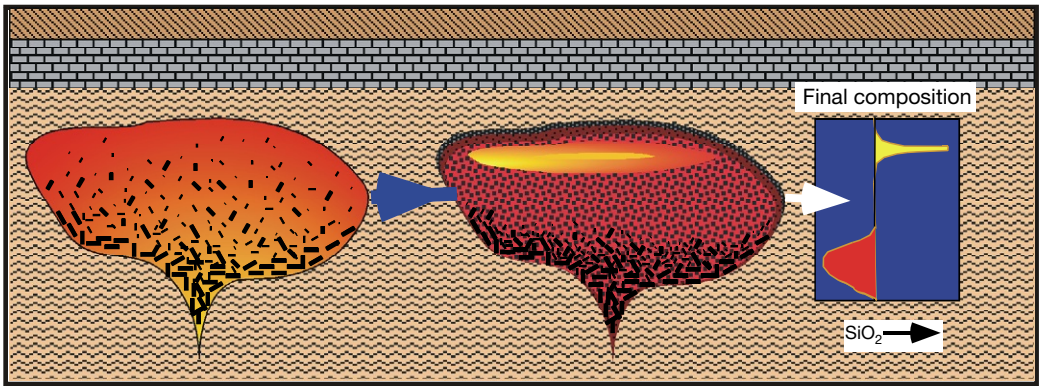

Figure 12 The historically imagined or classical magma chamber showing crystals settling from the center of the chamber leading to a pile of cumulates on the floor and a silica-rich sandwich horizon at the interface of the upper and lower crystallization zones.

adhered to this day (Becker, 1897). Becker was a physical chemist and mining geologist with the U.S. Geological Survey. He was impressed by how a cooled bottle of wine grows ice crystals around the edges, and as crystallization proceeds, the mother liquor or residual melt toward the center becomes increasingly rich in alcohol, the component with the lowest freezing temperature. If the temperature is progressively lowered, the container could become compositionally zoned to form, in effect, a differentiation sequence, which he said would be a perfect analogue of a laccolith. Becker said: "A bottle of wine or a barrel of cider exposed to low temperature deposits nearly pure ice on the walls, while a stronger liquor may be tapped from the center. If still a lower temperature were applied the central and more fusible portion would also solidify. Such a mass would be, so far as I can see, a very perfect analogue to a laccolith." He had in mind the rock sequence displayed by Shonkin Sag laccolith, which had been discovered in north central Montana during mapping of the 49th parallel. This style of fractional crystallization was well known from ancient times and was practiced by Native Americans in concentrating maple sap prior to boiling down to syrup. Charles Darwin noticed on his visit to the Galapagos during the Beagle Voyage that large olivine crystals had clearly settled to the base of lobes of basalt. Fouque realized in 1879, in his chemical study of the eruptives of Santorini, that the separation of plagioclase enriched the lava in silica. Crystal fractionation was a common chemistry laboratory technique in the late nineteenth century. Madam Curie used it to isolate radium and Becker, having been trained as a chemist, certainly knew of the effectiveness of this process (e.g., McBirney, 1993).

Becker's idea undoubtedly describes the most fundamental concept in magmatic processes. The fact that crystals in multicomponent, multiphase systems always have compositions different than the host liquids allows a systematic evolution in melt composition with crystallization. This feature of solutions is what makes metallurgy, ceramics, and igneous petrology the rich fields that they are. Although this feature of solutions was long known, Becker made the important realization that this same process might also give rise to a *spatial* variation in final rock composition. Spatial variations in rock composition are fundamental to magmatic systems.

The downside to Becker's idea, which has been overlooked in deference to its conceptual usefulness, is that the process really only works with dendritic crystals, which are the rule in molten alloys and aqueous solutions but not silicate magmas. The whole essence of magmatic processes, and rocks themselves in the broadest possible sense, rests on the fact that magmas and rocks consist of very small crystals or clusters of small crystals that grow in essentially parasitic chemical relationships (e.g., Marsh, 1998). This simple subtlety in crystal size and form, known so well by every petrologist, coupled with a spatially varying thermal regime is the basis of all magmatic processes. It simplifies and changes completely Becker's concept of magma chambers, and it exposes a robust continuum linking all magmatic events.

Louis Pirsson (1860–1919) picked up on Becker's idea and significantly extended it to explain the lithologic variations seen at Shonkin Sag laccolith. Pirsson, a petrologist at Yale, R. A. Daly, W. H. Weed, and others visited Shonkin Sag and found it, as introduced already, to be remarkably differentiated for such a small (70 m) sheetlike body. Pirsson combined Becker's idea with his own insight on thermal convection in fluids to give a plausible explanation of how Shonkin Sag might have evolved. His mistaken but detailed and brilliant exposition (Pirsson, 1905, pp. 187–188) of this process is at the very root of today's common beliefs of magmatic processes:

> It seems almost impossible to resist the view that in an enclosed mass of magma sufficiently mobile for local differentiation to take place convection currents due to unequal cooling would occur. On the upper surface and along the outer walls cooling would take place more rapidly; on the floor of the chamber, protected by the heated mass above and with heated rocks below, less rapidly. Thus there would be a tendency along the top and sides for the magma to grow heavier and to descend. Material from the more highly heated central part would tend to rise and replace this, and thus currents would be established in the magma, rising in the center, flowing off to the sides at the top, and descending along the cooler walls. ..... Such currents, once established, would continue as long as sufficient mobility remained in the magma to permit them.
>
> At some period crystallization would take place, and this most naturally would begin at the outer walls. It would not begin at the top because the material would arrive there from below at its highest temperature. Moving off toward the sides the material begins to cool and descend and becomes coolest as it nears the floor; here crystallization would commence. The first substance to crystallize is the solvent, which in this case would be the femic minerals, chiefly augite. Part of the material solidified would remain attached to the outer wall and form a gradually increasing crust, and part would be in the form of free crystals swimming in the liquid and carried on in

the current. Probably at first, as the liquid moved inward over the floor of the laccolith and became reheated, these crystals would remelt, giving rise to numerous small spots of magma of a different composition, which would slowly diffuse. As time went on, however, there would be a constantly increasing tendency for the crystals to endure; they would be carried greater and greater distances. But as they are solid objects and of greater specific gravity than the liquid, there might be a tendency for the crystals to drag behind and accumulate on the floor of the chamber. Moreover, from the heat set free at the time of their crystallization and from the resulting concentration of the chemically combined water vapor in the magma, the residual liquid would tend to have its mobility kept undiminished, since these would be factors which would tend to counteract the increase in viscosity due to cooling. In this manner it may be possible to understand how there would form a femic marginal crust and a great thickness of the femic material at the bottom of the laccolith. As the cooling went on the edges of the outer crust would rise more and more toward the top, finally spreading over it, and as a result the crust should be thinner on the top than elsewhere, as in the Shonkin Sag laccolith, in which the upper crust of femic rock is still preserved.

Beginning with a crystal-free, apparently superheated melt, Pirsson suggested that crystals nucleate and grow inward from the edges of the laccolith, convecting melt moves through the growing marginal band of crystals, chemically exchanging with them freely, and unattached crystals pile up on the floor. He reasoned that crystallization will be most intense near the roof where cooling is strongest and that these crystals will be carried downward by convection along the walls and then outward over the floor and deposited as the melt itself keeps circulating and differentiating. The end result is a thick pile of crystals on the floor, a thin rind of crystals welded to the roof, and a layer of highly differentiated rock just below the roof in what later has come to be called a sandwich horizon. *This basic idea, which was given root by Louis Pirsson to explain Shonkin Sag, has pervaded all of igneous petrology, with only minor modification to this day.* This is a powerful, well-reasoned, and clearly stated idea. It is based on seemingly straightforward, but faulty, reasoning, which inherently exists, without any clear enunciation or realization, in the reasoning behind almost every present-day petrologic scenario. The key features of this reasoning are an assumption of the knowledge of the *initial conditions* of the system at the time of emplacement, the *spatial style of crystallization* of magma, and the *size of crystals* that can be grown after emplacement. These concepts remain elusive to this day and need to be examined in detail. Before doing this, however, in order to understand how this idea flourished, it is essential to appreciate the historical context and activity of the petrologists alive at this time.

6.07.5 Historical Setting

The propagation of ideas very often rests on the random happenstance of how people appear and disappear from science. And it is in the mix of expertise lost and gained with the loss and gain of these people that ideas become taken seriously, become modified, and inadvertently become fundamental principles of the science itself. A corollary to this is the remark often attributed to Max Planck that beliefs in science mainly change through the loss by death of the holders of the old, out of date ideas. But it is also sometimes true that with the loss of these people, a vast resource of experience in observation is also lost. And some of these lost observations may be those that present serious obstacles to the acceptance of the newer ideas. This is especially serious in petrology where a great deal of the fundamental observations reside in a life's experience in studying field relations and gaining impressions of processes that may be impossible to quantify or record in any permanent way. So the science may sometimes suddenly proceed not because of the establishment of a new fundamental principle, but by the inadvertent removal of an obstacle through the loss of understanding of a fundamental observation or of the loss of the observer himself or herself. It was this nature of events that largely defined the research field of igneous petrology for all of the twentieth century. And the period of 1905–1915, in particular, was perhaps the most critical of all in shaping the concepts of magmatic processes and, especially, magma chambers.

Prior to about 1905, arguably, the greatest advance in understanding magma was in the development of thin sections and the establishment of the CIPW Norm. Thin sections allowed a detailed inspection of the intimate relationships between minerals quenched in the act of crystallizing. Although discovered and developed by the Britains W. Nicol (1768–1851) and H. C. Sorby (1826–1908) (e.g., Dawson, 1992), it was principally the Germans K.H.F. Rosenbusch and F. Zirkel who quickly and systematically developed petrography into a science and trained a cadre of petrographers. The exceedingly fundamental realization that a rock composition could be expressed in any number of textures and crystal sizes spawned the need for some way to normalize texture, or remove its influence altogether, in order to put all rocks on a common footing for useful classification. The CIPW Norm was the outgrowth of this need, whereby each whole rock composition could be represented by its equivalent plutonic texture. This removed the mystery of falsely classifying rocks due to overall crystallinity rather than simply due to chemical composition. The CIPW Norm was a monumental product of the penetrating petrologic insight of G. H. Williams (1856–1894) of Johns Hopkins, W. Cross (1854–1949) of the U.S. Geological Survey, J. P. Iddings (1857–1920) of the University of Chicago, and L. V. Pirsson (1860–1919) of Yale and the analytical chemistry insight of H. S. Washington (1867–1934) of the Carnegie Institute's Geophysical Laboratory. Williams died in 1894 before full development and publication of what became the CIPW Norm in 1903 (Cross et al., 1903). These men quantitatively combined rock chemistry with their intuitive understanding of observational phase equilibria to predict with uncanny accuracy the crystallization sequence of virtually every igneous rock. In light of the fact that no systematic experimental phase equilibria were yet known for igneous rocks, this was a monumental and sophisticated scientific achievement. Nowadays, we have the equivalent operation in the form of comprehensive thermodynamic models of crystallization, two of which are, among others, the MELTS program by Ghiorso and associates (Ghiorso et al., 1983) and COMAGMAT by Ariskin and associates (Ariskin, 1999). This is a direct reflection of the rapid development of experimental petrology beginning in about 1910.

In 1900, the level of petrologic insight within single individuals from the perspectives of field and thin section studies was very possibly more sophisticated than it is today. There

were, however, three major undeveloped areas that critically impeded the understanding of magmatic processes. These were (1) mechanics of viscous fluids, (2) experimental phase equilibria, and (3) kinetics of crystal nucleation and growth. First, although George Gabriel Stokes (1819–1903) and Claude-Louis-Marie-Henri Navier (1785–1836) beginning in about 1850 (e.g., Stokes, 1851) had developed the basic equations of motion of viscous fluids, which set forth a stream of analysis involving both viscous and inviscid fluids, including Stokes' famous result for the drag on a sphere, it was not until 1916 that J. W. Strutt (1842–1919) (Lord Rayleigh) solved the problem of simple thermal convection in a layer of constant viscosity fluid heated from below (Rayleigh, 1916). Second, on phase equilibria, there were many bits and pieces of experimental information scattered about on natural systems starting with James Hall (1798) to F. A. Fouque in 1879 (McBirney, 1998) and Frederick Guthrie's (1884) experiments on melting of metal alloys who stated: "I submit that, according to analogy, we should regard compound rocks and minerals [i.e., multicomponent systems], other than sedimentary rocks, as representing various kinds of eutectic alloys." But there was no general understanding of the structure of phase diagrams for magmas. Many petrologists believed because of the apparent preponderance of granites and basalts that this reflected the presence of pole compositions in the solution chemistry of silicate magmas. That is, in a phase diagram of temperature versus solution silica content, there might exist two eutectic regions, one for basalt and the other for granitic or silicic residual compositions. Cooling and crystallizing magma inevitably ends up at one or the other compositional end point. Earth as a planet is essentially bimodal in granitic continents and basaltic ocean basins, observed R.A. Daly (1871–1957), which reflects this process (e.g., Daly, 1914). And third, there was no general appreciation of how the rate of solidification is related to the size and number of crystals in a rock. The distinction between crystals nucleated and grown in place over phenocrysts carried in with the magma was not appreciated. The role of rapid quenching at the contacts of sills and dikes producing chilled margins, laced with large numbers of small crystals, and slower cooling in the interior producing larger crystals was clearly long recognized. But there was no realization that inordinately large crystals in small sills like Shonkin Sag could not have grown after emplacement. In fact, there was little understanding of the need to isolate and define the initial conditions of a newly emplaced magma. Although not explicitly discussed until two or three decades later, it was apparently assumed that all magmas arrived for emplacement essentially free of crystals. Today, these three areas are each mature fields in and of themselves, but the complex interplay of these areas, considered as one dynamic continuum, still remains as the foremost frontier to understanding magmatic processes.

6.07.5.1 Lifetime Lines

The life spans of the principal petrologists of this time are shown in Figure 13. Nearly all of those mentioned so far were born in the middle 1800s, and by about 1915, they were either dying or retiring from the field. The new wave of petrologists (e.g., Bowen, Grout, and Wager) was emerging from graduate school with a desire to apply new methods, mainly phase equilibria, to solve classical magmatic problems. Although Becker and Pirsson had clearly defined the dynamics of magma chambers, the usefulness of this concept was yet to be measured against the phase equilibria of real silicate systems, which hitherto was completely unknown in any quantitative sense. This entire area was ripe for development in the wake of the seminal experimental work by Arthur L. Day on the plagioclase binary. N. L. Bowen (1887–1955) rapidly became the leader in this area and in 1915 he published one of the most important papers of the century (Bowen, 1915).

Armed with a relative wealth of basic information on silicate phase equilibria, diffusion constants, and elementary thermodynamic constants (e.g., heats of fusion), which he had extracted from phase diagrams, Bowen systematically evaluated, one by one, all the various suggested mechanisms thought to effect the differentiation of magma. His logical, detailed, and quantitative approach of coupling experiment, theory, and field inferences swept away a host of processes as being ineffective. He established fractional crystallization by crystal settling as the primary means of differentiation. That is, prior to knowing silicate phase equilibria, nearly any mechanism known to chemistry had been argued to be important in explaining the diversity of igneous rocks. Diffusional exchange with wall rock, Soret effect, wall rock assimilation, and gas fluxing, among many other processes had been suggested to be important. Prior to Bowen, they were all equal competitors. Bowen evaluated each of these in a fashion that is remarkably similar to the modern method of scaling analysis in applied mathematics. He was forceful and thorough in his Socratic approach and conclusions and he left no room for argument. He demolished all competing theories on differentiation. He even attacked the Becker–Pirsson model where the residual convecting melt continual reacts through diffusion with dendritic crystals growing on the walls. Instead, he said that only by crystal growth and settling could significant differentiation proceed. He overlooked the fact that this is exactly what Pirsson himself had said in applying Becker's wine bottle model to Shonkin Sag.

In this 90-page treatise, Bowen showed (see Figure 14) that it is principally the phase relations of solid solutions and not eutectics that control igneous systems and that there is therefore no practical end to how far differentiation can proceed as long as crystals can settle or be otherwise physically separated from the melt. There were, however, many petrologists who did not believe that crystals could settle in viscous magma. Bowen not only showed experimentally in a large experimental charge that olivine in picritic magma did clearly settle but also deduced the viscosity of melts and used Stokes' law to calculate settling velocities (Bowen, 1947). He performed novel experiments and produced data crucial to answering the central question posed by the earlier generation. The amount of printed material he turned out was enormous and a great deal of it is still pertinent.

The bottom line is that Bowen pushed and promoted his model thoroughly and hard. He said crystals grow in the middle of a charge or a magma chamber. They settle to the bottom and the residual liquid compositionally evolves from basalt to granite. It is simply an unavoidable fact of silicate phase equilibria. Although acceptance was reluctant at the start, with time, as opponents died, this concept of

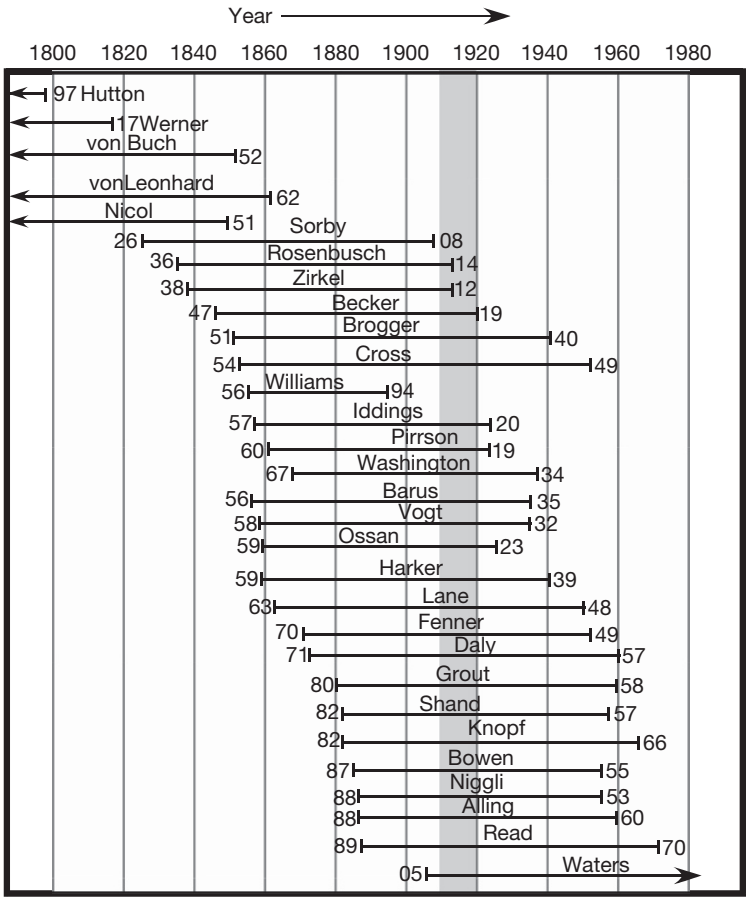

Figure 13 The names and dates of existence of prominent geologists and petrologists of the late nineteenth and early twentieth centuries.

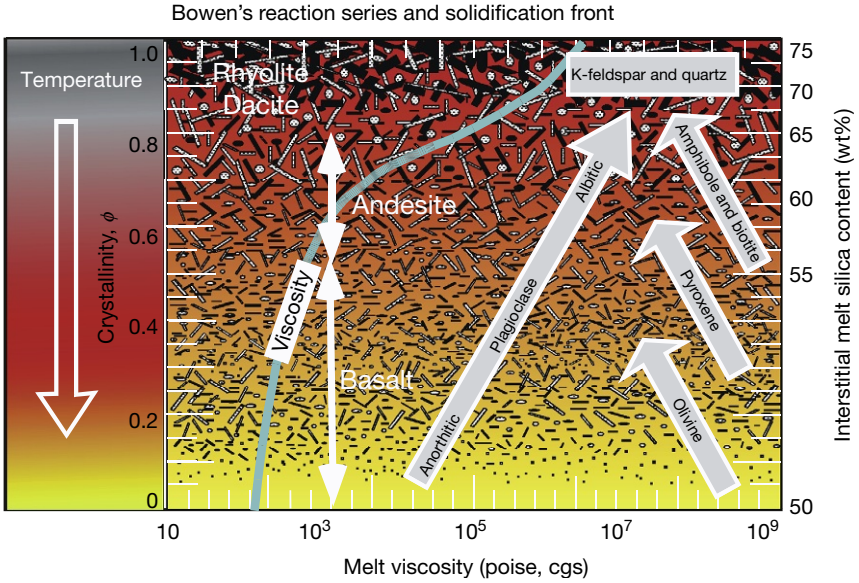

Figure 14 Bowen's reaction series superimposed on an active basalt solidification front at the roof of a sheet of magma. Variations of composition and viscosity as a result crystallization are also shown.

fractionation prevailed, and in its simplest dynamic sense, petrologists have stuck with this to the present. No one today would refute that the separation of crystals from melt causes chemical differentiation, but what is still unclear is how this actually takes place in a physical sense. For magma, bodies are not at all like large laboratory crucibles of constant temperature throughout, where crystallization is uniform and early crystals can fall to the floor. In real magmas, there are large spatial variations in temperature, and the center of the body is the hottest area where crystallization occurs last. Then, if all significant nucleation and growth of crystals are in marginal fronts and there are no crystals in the interior, how does crystal–liquid separation take place? To his credit, Bowen did worry about this, and he proposed that melt buried in high-crystallinity mushes might be kneaded out by tectonic processes. But later, he realized that this would probably be ineffective because the timescale of deformation is generally so much longer than that for solidification. The positive impact of Norman Bowen on igneous petrology cannot be overemphasized. He was to igneous petrology what Charles Darwin, also a geologist, was to biology (see Young (1998) for a particularly insightful biography of Bowen).

6.07.6 Initial Conditions of Magmatic Systems

All natural processes involve time. And the most critical part of analyzing and understanding magmatic processes involves a clear and concise knowledge of the nature of the system at the outset when it all began. The ensuing process itself, especially including the eventual final outcome, reflects in every detail the initial state of the magma. The final product, more than anything else, simply reflects the initial conditions. The importance of these conditions has been routinely overlooked, and the processes conjured up to explain rock sequences, especially complicated ones, are often unrealistic and overly complicated. They are complicated mainly because the assumed, unrealistic initial conditions are so far from the final state of the system and are hence impossibly difficult to sensibly connect in any logical construct. The necessary initial conditions, as mentioned earlier, are

1. the spatial pattern of cooling and crystallization (i.e., body shape and size),
2. the composition and initial crystallinity of the magma,
3. the sequence of emplacement of the magma,
4. the final distribution of crystal sizes throughout the body.

These are, in and of themselves, often exceedingly difficult conditions to ascertain without first knowing what evidence in the rocks clearly reflects these conditions. In early studies, the critical importance of these conditions to the final outcome was unknown and the simplest possible conditions were assumed. In their classic study of the chemical evolution and layering of the Skaergaard intrusion, for example, Wager and Deer (1939) and Wager and Brown (1968) stated at the outset that crystal-free magma was instantaneously injected, perhaps in a violent fashion. For the initial composition of the magma, they took the composition of that chilled against the wall rock, gabbro. Skaergaard contains about 250 km^3 of magma in a body of the shape of a laccolithic loaf of bread of dimensions ~3–4 km thick, 5–8 km wide, and 9–11 km long. This is not volumetrically a large body of magma, and many large dolerite sills are this large, although none are as thick. But why does it exhibit such well-formed layering? Is it the form of the container holding the magma, the style of cooling, the chemical composition of the magma, or the conditions of emplacement of the magma? Given the initial conditions assumed for the formation and condition of the initial magma, a host of processes involving sorting of crystals existing in the initial magma are excluded, as are also processes associated with the emplacement sequence itself.

Given the assumed initial conditions of no or very few initial crystals, Wager and Deer explained Skaergaard as due to crystal growth starting somewhere in the middle of the body in response to strong cooling from the roof. This is exactly Pirsson's original explanation for Shonkin Sag. The melt mingles with any crystals that are around the edges and keeps reacting like the bottle of wine so that the middle of the body chemically evolves with time. Cumulous crystals, like snowfalls, build up on the floor and form sequences of modally layered rocks in response to periodic loading and unloading of the system with crystals due to roofward cooling. The geometric form of the body encourages cascades of crystal-laden currents down the sloping walls. Within the piles of cumulate crystals on the floor, compaction, continued crystal growth, and melt migration physically modify the textures and chemically evolve the rock to fit the final product. Additional liquid may leak out, but eventually, some refined residual melt is left near the roof, Pirsson's 'sandwich horizon,' with some marginal rind on the top. This is fully the Shonkin Sag perspective. Wager and Deer got this perspective from Harry Hess who was working on the massive, heavily layered Stillwater intrusion. Although Hess's memoir was published much later in 1960, Wager and Deer cited his incidental reports on his Stillwater work. Faced with similar sequences of modally layered rocks, Hess went back to the early work of Becker, Pirsson, and Grout and incorporated the overall process spelled out by Pirsson. The important point here is that the Pirsson model is the fundamental idea from which all explanations for the evolution of layered intrusions have emanated. It is thus important to examine this model in more detail in light of discerning the importance of magmatic initial conditions.

6.07.6.1 Cooling from the Roof

When an opening is made in the crust for emplacement of a magmatic body, the upper and lower contacts of country rock initially have exactly the same temperature. The magma is generally so much hotter than the country rock that the difference in temperature between magma and country rock is virtually identical at upper and lower contacts, regardless of the thickness of the body. The rate of cooling of the magma by conduction through the upper and lower wall rock is also virtually identical. The body thus cools at the same rate from top to bottom. This is shown by considering the central temperature in identical hot sheets emplaced far from, near, and on Earth's surface. There is no difference, especially in early times, in the rate of cooling for deeply buried and shallow intrusions and only a slight difference for a body (e.g., lava or

lava lake) on the surface. The sheets of magma are so much hotter than their surroundings that the thermal state of the surroundings is essentially immaterial to the geometric pattern of cooling. This also holds for all the other margins of the body, that is, sidewalls. Other processes of cooling, like hydrothermal convection, will influence differently the upper and lower contacts, but mainly only in the later stages of cooling when solidification is no longer important (e.g., Marsh, 1989). The conclusion is, thus, that magmas in general do not cool more strongly from the roof and crystallization is no more intense along the roof than it is elsewhere along the margins of the body. Cooling is characterized by heat flow from all outer margins of the magma at *approximately* similar rates, and this cooling is characterized everywhere by crystallization. For every unit of thermal energy flowing from the magma, a specific mass of crystals is produced in a specific spatial pattern (e.g., Irvine, 1970).

6.07.6.2 Style of Crystal Nucleation and Growth

In the original Becker–Pirsson model of magma chamber crystallization, for example, liquid moves freely in and out of the mass of growing crystals, carrying nutrients to the crystals. The residual melt becomes increasingly depleted in time in crystalline components, thereby becoming enriched in unwanted or residual components. The center of a crystallizing bottle of wine becomes brandy. This is essentially what happens in any system where dendritic crystal growth prevails as in metallic alloys and aqueous solutions. These solutions are also commonly of low-viscosity melt and low Prandtl number. Compared to silicates, dendritic crystals are unusually large and can span a significant distance within a solidification front. If these dendritic systems are scaled up to the size of typical bodies of magma, dendritic crystals might reach sizes of tens or hundreds of meters long. On the large crystals, proportionally large, highly buoyant compositional boundary layers develop that are highly mobile and highly effective in carrying 'used up' fluid from the crystals. This is very much unlike crystallization in silicate magmas.

A curious aspect of silicate crystallization is that the size of crystals in most igneous rocks is on the order of tenths of a millimeter to a centimeter. The crystals are always tiny relative to the body size. This reflects the multisaturated, multicomponent nature of silicate magmas where chemical diffusion is slow and the melts are highly viscous (e.g., large Prandtl number). Within thickening solidification fronts, crystals nucleate and grow at the leading edge near the liquidus. Nucleation certainly does not start here, for magmas are essentially dirty systems, always laced with nuclei. Only in rare circumstances, as in impact melt sheets, do magmas ever become sufficiently superheated to be free of nuclei as an initial condition. This reflects the fact that endogenous magmas are never found to be superheated. Nuclei are thus always present and serve as seeds for crystallization regardless of the exact phase involved. Once the cooling front arrives, existing nuclei increase in size outward through the solidification front. The tiny growing crystals are in a parasitic relationship with one another where what chemical components one crystal does not use another one will utilize for nucleation and growth. Diffusion is so slow in silicate liquids that if an olivine crystal is growing on the liquidus of tholeiitic basalt, for example, unwanted components like CaO, Al_2O_3, Na_2O, Fe_2O_3 SiO_2, and K_2O soon build up in the surrounding melt. This increases the chemical potentials of clinopyroxene and plagioclase, spawning nucleation and crystal growth. This reflects the common perpetual state of near multiple saturation in many basaltic magmas; a slight enhancement in concentration of rejected components saturates the melt in another solid phase. Continual growth of these crystals enhances nucleation and growth of the other phases and vice versa. This creates local intense clusters of crystals of several phases and, eventually, from these clusters appears single large, well-formed crystals (see **Figure 15**). The small crystals combine through aggregation and grain boundary migration into large, optically continuous crystals. The process is akin to Ostwald ripening where touching grains combine in response to lowering of the net surface free energy (Marsh, 1998). This is, in effect, a form of high-temperature annealing, which happens so rapidly that it is difficult to observe except in samples quenched from lava lakes. The long-believed perception of crystals nucleating and growing at widely separate locations and only eventually impinging on one another at the close of solidification is a reflection of an assumption of homogeneous nucleation, which rarely occurs in magma. Heterogeneous nucleation is the rule in magma. This style of coarsening has been observed experimentally in titania (Penn and Banfield, 1999) and in real time during plagioclase growth in basaltic andesite by Schiavi et al. (2009).

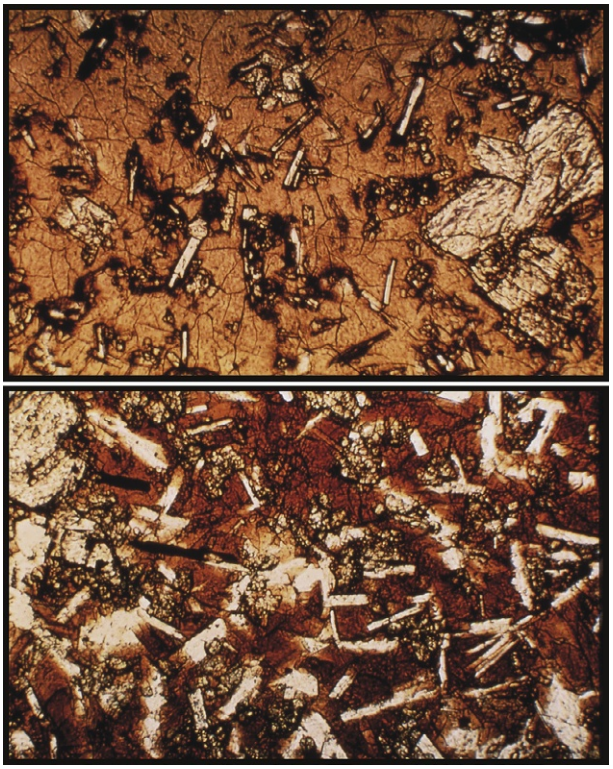

Figure 15 Thin sections (~5 × 2 cm) from Makaopuhi lava lake (courtesy of Dr. T. L. Wright) at crystallinities of about 20 and 40 vol.% (upper to lower) showing the tendency for crystallization to occur in dense clusters.

6.07.6.3 The Critical Connection between Space and Composition

The variations in melt silica content and viscosity with distance or crystallinity within a typical tholeiitic basalt solidification front are shown in Figure 16. Both silica content and viscosity increase dramatically with the degree of crystallinity or distance outward in the solidification front. It is especially notable that silica enrichment increases gradually for the first 50 vol.% of crystallization, increasing by only about 5 wt%. It is only outward of this point, at much higher crystallinities, that strong enrichment occurs. But once the level of crystallinity reaches 50 vol.%, the point of critical crystallinity has been reached where the magma is a rigid network of crystals laced with melt. At this point and beyond, the melt and crystals cannot be easily separated, and certainly not by conventional crystal settling. Andesitic, dacitic, and rhyolitic melts occur interstitially at increasingly higher states of crystallinity, where the separation of melt and solids is increasingly difficult. The key to chemical differentiation of the magma is to isolate the enriched melt at a separate body of magma. But how does this occur?

Out in the center of the body, nothing is happening; there is no crystallization. Crystals only begin growing here once the inward-propagating solidification front arrives. Even small crystals escaping from the suspension zone of the solidification front will have no effect on the overall magma composition. Tiny crystals falling from the suspension zone are resorbed in the inner hotter magma and do nothing to change melt composition. Even a plume of crystals and slightly cooler melt dropping from the suspension zone, which might survive transit of the hot inner magma, simply enters the suspension zone of the lower solidification front with no net spatial change in the composition of the system. It just goes from one part of the system to another. Low-density melt might escape from the lower solidification front, but the viscous chemical boundary layers on the tiny crystals have little buoyancy and are stabilized by the cluster style of nucleation and growth and the advancement of the solidification front itself. In a chemical sense, little to nothing is going on out in the center of the body. It is within the solidification fronts that any differentiation will take place.

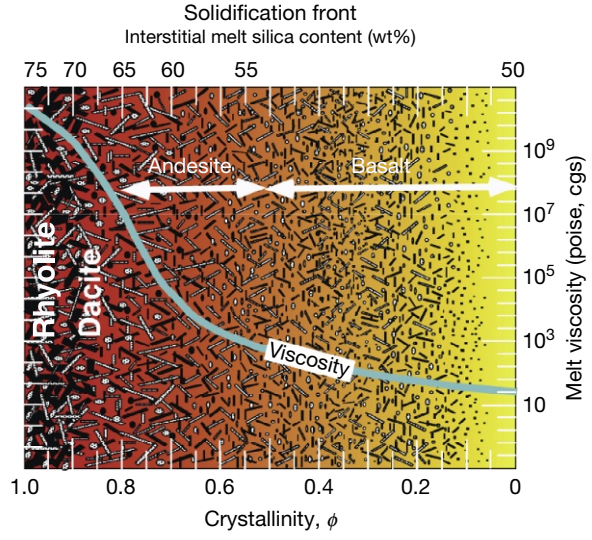

Figure 16 A solidification front on the sidewall of a basaltic magma showing the variations in composition, viscosity, and crystal mass as a function of position.

6.07.6.3.1 Temperature space, phase space, and spatial position

The most critical relationship to appreciate in understanding magmatic processes is the relationship between moving across a conventional phase diagram and moving in space in a magmatic system. Because the temperature field of any magma is closely tied to space, phase diagrams are also tied to space. Moving on a phase diagram in composition and temperature ($T(x,y,z)$), thus, always involves moving in space ($X(x,y,z)$) in a magma, and these moves are almost always within solidification fronts because that is where temperature varies the strongest with spatial coordinates.

This critical relationship can be readily appreciated by considering a Coombs–Walker normative ternary phase diagram involving the normative components olivine, diopside, and silica at the apices and full saturation with plagioclase (see Figure 17). These phase relations fit a wide range of basaltic magmas from tholeiites to high alumina basalts (HABs). There is a single major cotectic boundary separating the two major phase fields of olivine, or alternatively orthopyroxene at higher silica contents, and diopside or clinopyroxene. Because of the one to one mapping between temperature and space, any movement on this phase diagram, along the cotectic or anywhere else, involves a spatial move in magma space. And any spatial move constrains what physical processes are possible. Beginning in the middle of the magmatic system, the corresponding point on the phase diagram is the beginning bulk magma composition on the cotectic boundary (see the large block dot). (If the system has just been emplaced and is laden with a slurry of, say, olivine, the initial bulk composition will be out in the olivine field, toward the olivine corner, but just as soon as this crystal load settles out, the bulk composition will migrate to the cotectic.) Moving in space from the center outward into the upper solidification front involves no move on the phase diagram because temperature and composition are each constant. Once the solidification front is entered, there is a choice on the phase diagram whether to follow the bulk composition (crystals plus melt) or only the interstitial melt composition. If the local bulk composition is followed, all points map onto the same initial starting bulk composition (i.e., the same starting black dot). This is because there has been no separation of crystals and melt. If, on the other hand, the local residual melt composition is monitored, then the compositions migrate, with increasing crystallization or depth outward (i.e., toward lower temperatures) within the solidification front, along the cotectic toward the silica corner of the ternary. The silica corner will, in fact, be closely approached as the very last bit of melt crystallizes near the solidus at the back end of the advancing solidification front. It is important to realize that these late-stage, highly fractionated melt compositions do not exist separately, in and of themselves, as an actual physical entity that could be erupted as lava or reemplaced as a pluton. These melts are locked within the crystalline framework of the solidification front

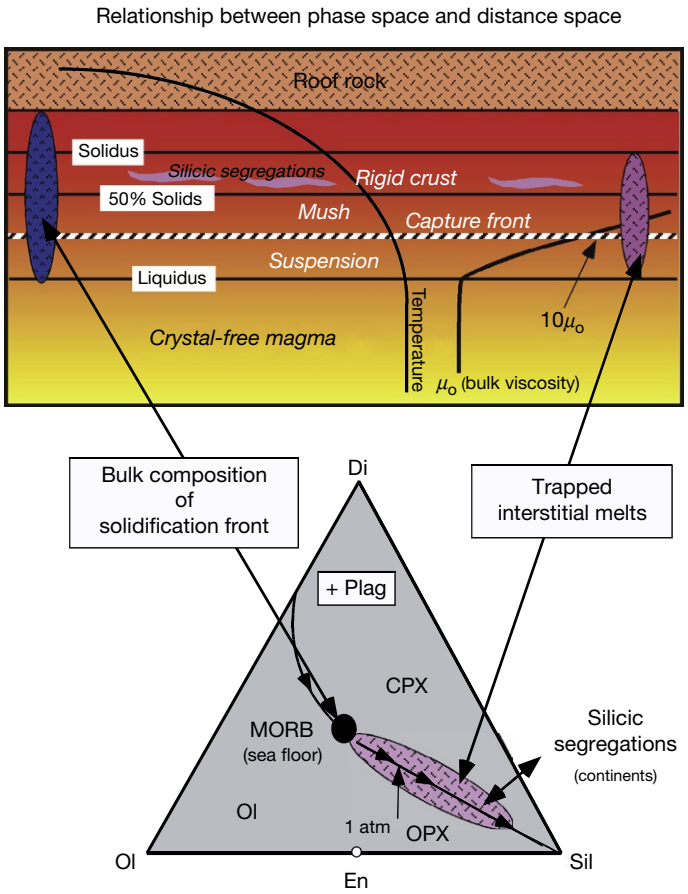

Figure 17 The fundamental relationship between spatial position (upper) in a solidification front and phase position in the normative basalt ternary system.

and cannot be separated by any simple means; more on these processes later.

An understanding of this critical relationship between spatial variations within a magmatic system and movement on a phase diagram makes solving, or at least understanding, many fundamental petrologic occurrences straightforward. Magmatism at ocean ridges the world over is predominantly tholeiitic with subtle variations of many kinds (e.g., Klein and Langmuir, 1987). Surprising enough, for such a prodigious system, no silicic differentiates are ever seen as lava. The volumetrically overwhelming composition is stuck, essentially motionless on the cotectic, and does not move toward the silica corner as might be expected from the viewpoint of classical crystal fractionation theory. No continent-like rocks are produced; the oceanic magmatic system operates in a compositional phase space separate from what is needed to build continents. The ocean ridge magmatic system, as will be seen later, is essentially a sill or stack of sills, called the axial ridge magma chamber, perched at the top of a vertically extensive magmatic mush column. When the plates move apart, aliquots of essentially crystal-free magma are withdrawn or pulled from the subjacent sill by disrupting the roofward solidification front. No differentiated magma comes from within the solidification fronts, so the lavas are generally monotonically basaltic. Once the system is activated in this way, more magma is peristaltically replenished from below, which may contain 'tramp' or dynamically entrained crystals from the underlying mush column. Upon entering the axial sill, these crystals will settle from the magma, which is an example of *punctuated differentiation* discussed earlier, and the magma will rest there surrounded by solidification fronts.

This process also explains why large volume basaltic centers in oceanic settings, like Hawaii, produce such a paucity of silicic differentiates. The summit lavas from Kilauea, for example, are mysteriously never more fractionated than about 51.5 wt% SiO_2 and 7 wt% MgO (see **Figure 18**). If this composition is traced from the chemical variation diagram to a solidification front, it is found that this composition defines the inner, leading edge of the suspension zone of the solidification front. The more fractionated, more siliceous compositions are, again, locked within the front and are not available by any simple means for withdrawal and eruption. The magma available for eruption is that which is most volumetric and most mobile (i.e., lowest viscosity), which is that deep within the interior. If the magma has arrived carrying an abundance of entrained forsterite-rich olivine xenocrysts or tramp crystals, once these crystals fall from the magma as in punctuated differentiation, the usual magma type of ~51.5 wt% SiO_2 and 7 wt% MgO is immediately produced. There are sometimes mildly differentiated lavas erupted from the Kilauea rift

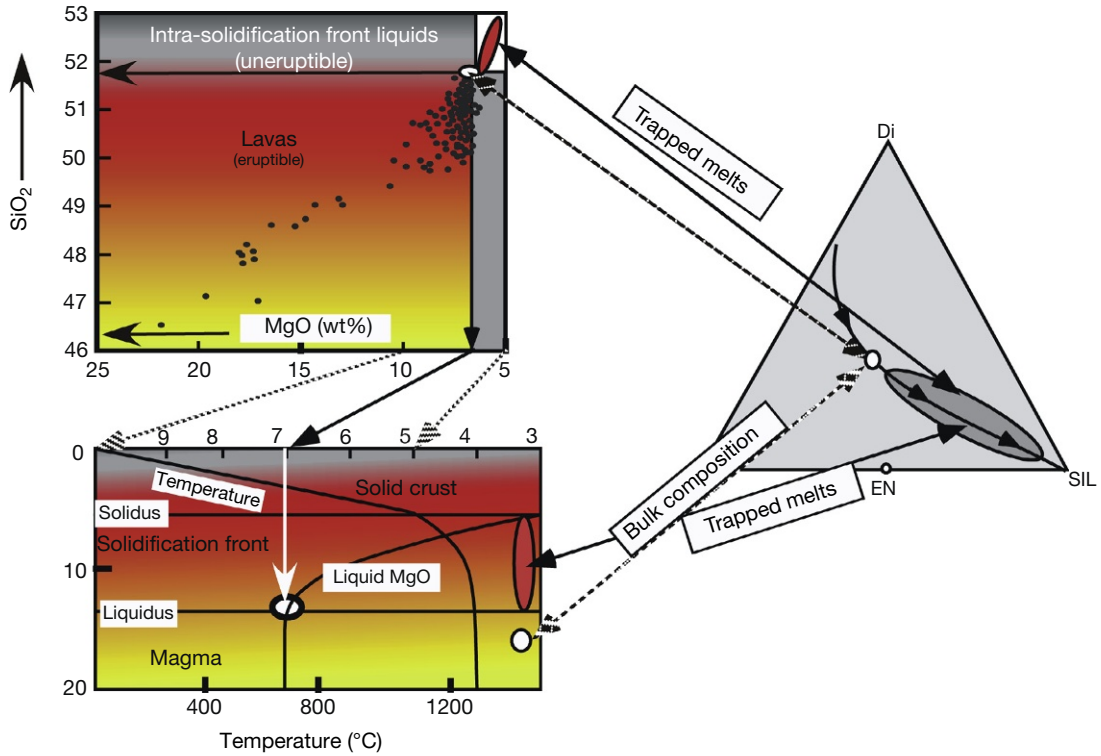

Figure 18 The explanation for the absence of lavas erupted from Kilauea summit with silica greater than about 51.5 wt% is found in tracing the magma composition to the spatial position at the leading edge of the solidification front.

system, silicic pods are also found in the crusts of the Hawaiian lava lakes, and on Iceland, about 18% of the surface lavas are true rhyolites and processes leading to these effects will be examined later. Bimodal differentiation comes from gravitationally unstable solidification fronts tearing open and forming lenses of silicic liquids or silicic segregations. Once established, this material is uneruptible unless it can be collected into masses large enough to be thermally viable for transport and eruption.

6.07.6.4 The Sequence of Emplacement or Delivery of the Magma

The fundamental question always lurking about but rarely answered in analyzing exhumed magmatic systems is: How was the system built? What was the overall nature of the event in time span and volumes of individual deliveries of batches of magma that made the system? How did the system operate on a year-to-year basis? These are difficult questions and the postmortem evidence in exhumed magmatic systems is rarely conclusive. Rather, the most direct evidence of the timescales and volumes of individual batches of magma comes from volcanic systems. Volcanic systems, on the other hand, lack all information on the details of the internal arrangement and local physical environments of the system in which the volcanic products formed. It is no wonder, then, that volcanologists and plutonists have widely divergent views on the basic structure and workings of magmatic systems. Yet it is the coupling of this evidence that gives critical insight into the real-time dynamics of the establishment and sustaining of magmatic systems. The quantitative connection between volcanism and plutonism is the product of observed erupted flux and the volume of individual plutonic complexes. This product measures the *filling time* or times to establish a magmatic complex. To estimate this product, something of the form and volumes of plutonic systems must be appreciated along with the temporal pulse of volcanic systems.

6.07.6.4.1 Forms of magmatic bodies

Magmatic systems come in all shapes and sizes, but the most common shape is sheetlike for plutons, sills, and certainly lavas. This reflects the common vertical orientation of the least principal stress in the upper crust. Magma ascends as fluid filled cracks (dikes) or viscous blobs (diapirs) or as a combination of each. Dike and fissure propagation is common in young or developing systems, where the country rock is cool and brittle, or in systems where the crust is in tension as in continuous rifting at ocean ridges. Magma ascends due to its low density relative to the wall rock and the influence of gravity. Ascension is a gravitational instability, which is impeded by loss of hydrostatic head (e.g., Ryan, 1994). The leading mass of magma reaches a level of neutral buoyancy, which may be due more to the vertically integrated buoyancy than to merely to local density contrast, and is forced to spread laterally by the continual rise of magma deeper in the rising column, thus forming sheetlike bodies, which in the upper crust are known as sills. Sheetlike forms are fundamental to all magma, regardless of level of emplacement in Earth. Magmatic systems are, to first order, a series of sheets connected by circular conduits and dike-like fissures.

Diapirism is more the rule in relatively stationary, well-developed magmatic systems, as beneath older volcanic centers in island arcs where the system has had ample time to develop and the underlying lithosphere has had ample time to heat up from the long-term passage of many magmatic bodies. But here, too, stalling diapirs mushroom-out and go to form sheet-like bodies.

6.07.6.4.2 Internal transport style

Once a magmatic system is established and has formed a mush column (Figure 1), the form of magma transport is more a combination of processes driven by density variations reflecting basic differences in chemical composition and the abundance and type of crystals carried by the melt. Local transport at every level, although broadly similar, may vary over time from diapiric on many length scales to slurry flow as in a pipe to dike flow. The style of the process itself and time series of repetition is certainly chaotic. But since the material is a viscous fluid of a relatively narrow range of composition and crystallinity, the outcome, almost regardless of the details of transport, is distinct to the tectonic setting and to a large extent is thus predictable.

Because of the strong effect of annealing during prolonged solidification, it is almost impossible to gauge the importance of repetitive reinjection during building of a plutonic complex. Internal chilled margins as indicators of the sudden juxtaposition of magmas batches of contrasting temperature only survive solidification in smaller bodies, and the strong textural changes that do survive in large bodies are almost universally interpreted as reflecting internal solidification dynamics (e.g., Patwardhan and Marsh, 2011; Zieg and Marsh, 2012). Thus, there are few if any true indicators in intrusive complexes of the nature of the time series of deliveries of the batches of magma that collected to make the final magma. This is where some knowledge of the fluxes and eruptive timescales is absolutely critical to understanding magmatic systems.

6.07.6.4.3 Eruptive timescales and fluxes

The observed durations of volcanic eruptions have been summarized by Simkin (1993). By far, the most common eruption lasts from about a month to a year, with the overall spectrum of times spanning about 100 years.

Measures of eruption flux come from mass balances on both large and small scales. The flux of magma from global ocean ridge system can be estimated from the product of the average rate of spreading (double sided, ~5 cm year^{-1}), the thickness of the oceanic crust (~8 km), and the length of the ridge system (~40 000 km), which amounts to about 15 km^3 year^{-1}. This is clearly a minimum estimate, for the actual amount of magma existing in the system at any time because a significant amount of magma probably gets trapped in the deeper parts of the system and is recycled back into the mantle source rock. The flux establishing Hawaii must have been, on average, about 1 km^3 year^{-1}. The age of the island is about 1 Ma and it has a volume of about 10^6 km^3, yet observed fluxes are only ~0.10 km^3 year^{-1}. The apparent fluxes that established large igneous provinces fall in this range of ~1–15 km^3 year^{-1}. For examples, consider the Columbia River flood basalts (~1 km^3 year^{-1}), the Deccan Traps (~3 km^3 year^{-1}), and Ontong Java (~15 km^3 year^{-1}) (see Coffin and Eldholm, 1992). The volumes of these lava sequences are generally much larger (~1–50 × 10^6 km^3) than any known magmatic intrusions, the largest of which are Bushveld (S. Africa) and Dufek (Antarctica) each at about 500 000 km^3. The Sudbury impact melt sheet may originally have had a volume of about 35 000 km^3, and Skaergaard is on the order of 250 km^3. By far, the largest single 'day' eruptions are those of silicic pyroclastic ash flows. The Fish Canyon ash flow is about 3000 km^3, the Toba Tuff is about 2000 km^3, and the two Timber Mountain tuffs are 1200 and 900 km^3 (e.g., Smith and Roobol, 1982). The huge flux of these silicic events undoubtedly reflects the mode of transport of uncapping an overpressured, near-surface system containing large amounts of dissolved volatiles. It would be difficult imagining any similar single intrusive event of this magnitude.

6.07.6.4.4 Filling times

Given the final volume of a pluton or sill, the filling time is a multiple of the input flux. For a body of the size of Skaergaard (~250 km^3), for example, the filling time is ~17 years if all the magma produced at the ocean ridges (15 km^3 year^{-1}) were directed to this location. For a Hawaiian rate (1 km^3 year^{-1}), the filling time is longer, 250 years. There is no simple way to decide the actual filling time; U–Th and Po–Pb–Ra isotopic disequilibrium techniques may offer some information, but the context of the materials measured is often unclear. The only direct, firm physical constraint comes from rates of solidification. The rate of filling must be significantly greater than the rate of solidification. For these sheetlike systems, it is straightforward to show by scaling the heat equation (see eqn [1]) and including the effect of latent heat (e.g., Jaeger, 1968) that the solidification time (t) is well approximated by the simple formula

$$t = 0.694\frac{(L)^2}{K} \qquad [17]$$

where L is the half-thickness of the sheet and K is the thermal diffusivity (e.g., ~10^{-2} cm^2 s^{-1}). The half-thickness of a sill or pluton can be estimated by noting that the aspect ratio (n) of sills is 100 or more, whereas that of plutons is about 10; there are of course large variances in these values, especially for plutons. Nevertheless, for a given volume (V) of magma, the half-thickness of the equivalent rectangular sheet of dimensions $n2L \times n2L \times 2L$, is given by $L = (V/8n^2)^{1/3}$. Under this approximation, for a given volume of magma, sills will be thinner than plutons and the solidification time of sills will be significantly smaller than for plutons. The competition in filling time and solidification time for a range of fluxes operating over the characteristic eruptive times found by Simkin (1993) is shown in Figure 19. In light of the earlier discussion of the controls of crystallinity on magma fluidity, the calculated time for solidification has been lessened by a factor of 10 to ensure that the body is sufficiently fluid to ensure reinjection without creating an internal chilled margin or also to ensure that the sequence of arrivals of magmatic parcels can mix to make a single body. From this constraint, the characteristic thickness of a sill is ~100 m and ~1000 m for a pluton, and the filling times are, respectively, about 10 and 300 years. These are geologically reasonable results, but the actual filling times

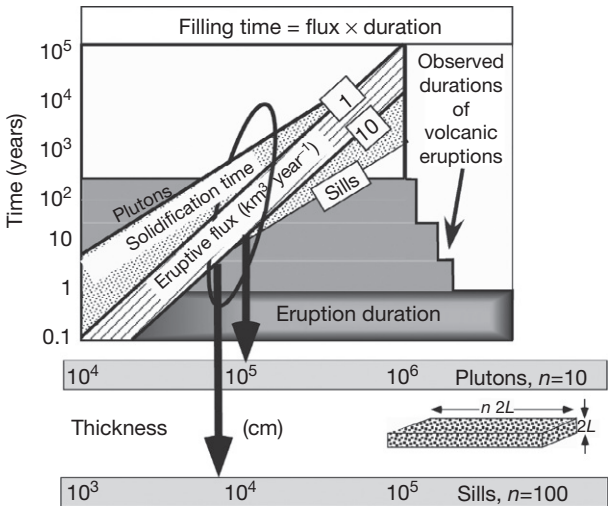

Figure 19 The time to fill sheetlike plutons and sills of a given aspect ratio (lower axis area) found using observed durations of eruptions and the estimated fluxes from large igneous outpourings. The time of solidification as a function of body size (half-thickness) is also shown as a constraint on the time of filling.

may be much less. This sequence of events for sills will be revisited later when discussing the Ferrar Dolerites.

6.07.6.4.5 Magmatic deliveries, episodes, periods, and repose times

At a more detailed level, it is also clear, in keeping with the typical episodic style of volcanic eruptions, that the full volume of the body is seldom delivered in a single event but, instead, individual batches of magma arrive serially perhaps every few weeks or months. The accumulated volume from the full series of deliveries amounts to a volcanic episode, which gives rise to the final body of magma. This is an important distinction as a series of episodes may also be strung together to make up a much longer magmatic period giving rise to a sequence of sills or a compound pluton consisting of multiple lobes each associated with one another but, due to varying sizes or shapes, having distinct cooling times (e.g., Bergantz, 2000). The episodes themselves reflect volcanic repose times, which for many active volcanoes may occur for tens to hundreds or perhaps thousands of years. Moreover, the longer the series of deliveries, the more chance there is for variations in phenocryst content in the batch of arriving magma, which, as already mentioned for Hawaii, is highly dependent on the magnitude of the eruptive flux. Thus, the larger the final body of magma, the larger is the probable variance in the concentration of large crystals, both phenocrysts and tramp crystals, contained in the ensemble of the individual delivered batches of magma. An excellent example of this expected variance in deliveries is found in the ~500 000 year 3 km deep drill hole record from Hawaii shown in **Figure 20** (Rhodes and Vollinger, 2004; Stolper et al., 2009). The strong variation in lava MgO content with depth is a direct reflection of the modal olivine content, much of which is certainly inherited tramp or xenocrystic crystals. From such considerations, a general principle emerges: The more variance in the deliveries, the more variance to be expected in the final sequence of the rock within the pluton or sill. Moreover, the obvious corollary is: It is exactly these variances that give rise to exotic sequences of layering from modal sorting during deposition of crystal-laden deliveries of magma in the building of large igneous bodies. Nevertheless, in this context, what is perhaps also surprising is the abundance in volume flood basalt provinces of extensive lavas containing low concentrations of phenocrysts (e.g., Holden and Hooper, 1987; Hooper, 1987).

6.07.6.5 Thermal Ascent Characteristics and the Role of Thermal Convection

From the earliest models of magma chambers, as in Pirsson's discussion of Shonkin Sag, convection has always played a role in establishing the final product. The exact nature of this convection, whether it was driven by thermal, compositional, or sedimentation effects, has never been clear. Convection has been a necessary convenience in magmatic histories, and it has taken on a multifaceted physical nature most often without explicitly defining its specific form. The process of ascent, transport, and emplacement of magma is certainly a form of convection or advection. Fluid motions accompanying the deposition of phenocrysts, however complicated this might be due to the dynamics of slurries (e.g., Marsh, 2004, 2013), are also certainly a form of convection. But most often, perhaps in response to the concerted attention on mantle convection in driving plate tectonics, magmatic convection has been assumed to be primarily thermal and has often been called upon to orchestrate the many details of petrologic outcomes. The physics of conventional thermal convection in a crystallizing solution is not entirely straightforward as has been summarized by Zieg and Marsh (2005), from which the following summary comes.

The importance of thermal buoyancy relative to viscous drag and heat transfer by conduction is a measure of the tendency for thermal convection to occur in a layer of fluid. These effects are collectively measured by the dimensionless Rayleigh number (Ra). The physics of thermal convection in many types of constant viscosity fluids with various forms of heat sources, geometries, and boundary conditions is well known (e.g., Turner, 1973). Relatively little is known, however, about thermal convection in fluids undergoing crystallization in marginal solidification fronts, especially in fluids as diverse as silicate magmas (Marsh, 1989). This uncertainty has spurred debate over the occurrence of thermal convection in common magmas (e.g., Marsh, 1991). With no direct experimental observations of magmatic thermal convection, experimental attention has been focused on analogue fluids that might be similar to magma. These systems are molten paraffin (Brandeis and Marsh, 1989, 1990; Viskanta and Gau, 1982) and solutions of isopropanol and water (Hort et al., 1999; Kerr et al., 1989). This work collectively shows that in an initially superheated melt, convection sets in rapidly and persists only until all the superheat has been dissipated. Thermal convection steadily wanes with approach to the liquidus and ceases at the liquidus itself. All further cooling is by conduction, which may be the behavior of many crystallizing fluids. The strong contrast with nonsolidifying systems is marked by the kinetics of crystallization (Hort, 1997; Hort et al., 1999; Marsh, 1996). There is indirect evidence that it is also the case in magma in comparing the cooling of Hawaiian lava lakes with lava flows.

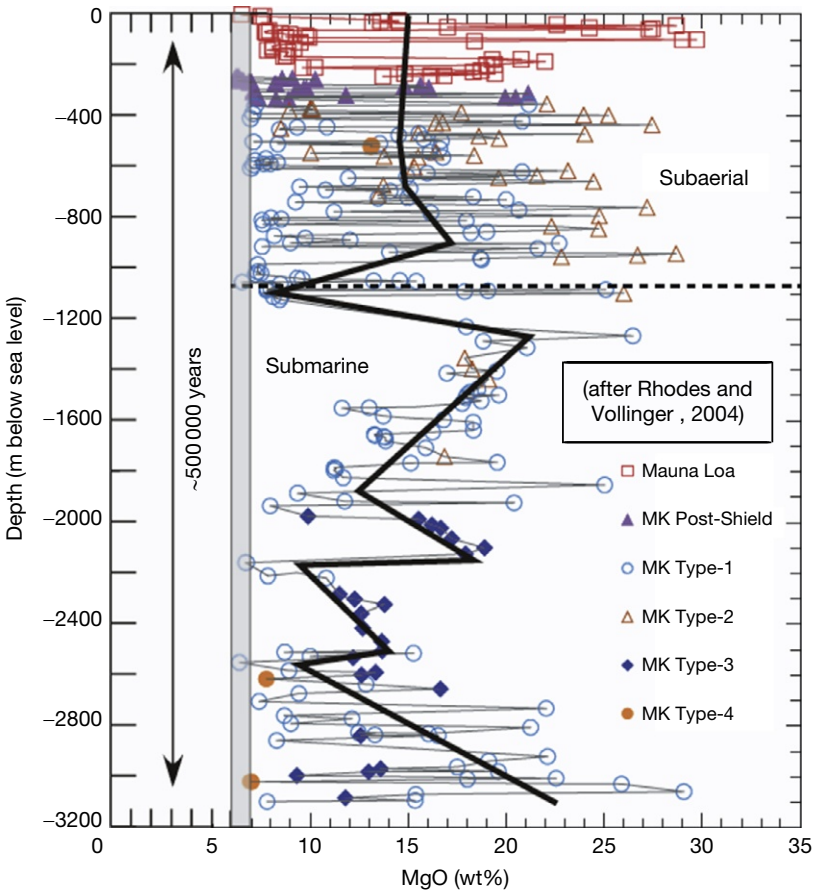

Figure 20 The variation in CaO and MgO in lavas encountered in the 3 km Hilo, Hawaii, drill hole covering a time span of ~500 000 years. The large range in MgO content reflects a similar range in modal olivine. No lavas are found with MgO less that ~7 wt% MgO, which is the residual composition after loss of all primocrysts of olivine. Reproduced from Rhodes JM and Vollinger MJ (2004) Composition of basaltic lavas sampled by phase-2 of the Hawaii Scientific Drilling Project: Geochemical stratigraphy and magma types. *Geochemistry Geophysics Geosystems*, p. 38. American Geophysical Union.

The growth of the crust of the lava lakes, measured through direct drilling (e.g., Wright and Okamura, 1977), shows the same pattern (see **Figure 21**) of growth for lavas as measured by Hon et al. (1994). This is fundamentally significant for, as will be seen in the succeeding text, the magnitude of the Rayleigh number (*Ra*) depends on the characteristic length scale to the third power and *Ra* must be much larger than about 10^3 for convection to be possible. Since most lavas are quite thin (~5 m), *Ra* is small, certainly subcritical, which suggests the same for the much thicker (~100 m) lava lakes where *Ra* might be expected to be strongly supercritical.

6.07.6.5.1 Superheat

This apparent lack of thermal convection may also be a reflection of the lack of superheat in terrestrial magma, which always erupts at or below the liquidus temperatures. This is because crystal-free magma adiabats are steeper than liquidi, which promotes superheating. The appearance of any superheat at all leads to enormous values of *Ra*, which brings on vigorous thermal convection, dissipating the superheat heat to the wall rock and bringing the temperature strongly back to the liquidus (see **Figure 3**). With the loss of superheat, thermal convection ceases, and the process repeats itself on a timescale governed by the rate of ascent. The thermal ascent trajectory thus asymptotically adheres to the liquidus. For sufficiently rapid ascent rates, magma temperature is, in effect, buffered at the liquidus. When ascent is sufficiently slow, heat loss by conduction sustains magma temperature at subliquidus values, but here, the magma flirts with stagnation through critical increases in viscosity due to crystallization (note shading in figure). 'Dry' magmas, like in Hawaii, erupt at near liquidus temperatures. No magma is ever bone-dry, and Hawaiian MgO-rich lavas (as in **Figure 20**) contain significant amounts of 'phenocrysts,' which are a combination of the so-called 'tramp' crystals entrained from earlier crystallization cumulates and even wall rock materials (e.g., Garcia et al., 1989, 2003; Marsh, 2006; Wright and Fiske, 1971). The relatively low volatile content makes the ensuing eruption of low explosivity, but the lavas are exceedingly mobile. This is just the reverse for 'wet' magmas. Here, 'wet' means magma containing significant amounts of dissolved volatiles, especially water, which for alkali basalts may amount to 2–3 wt%.

Wet magmas similarly follow the liquidus, but only as long as they remain undersaturated. At the depth of volatile saturation, the liquidus and adiabat cross (see **Figure 3**). At this point, the liquidus, depending on the exact water content,

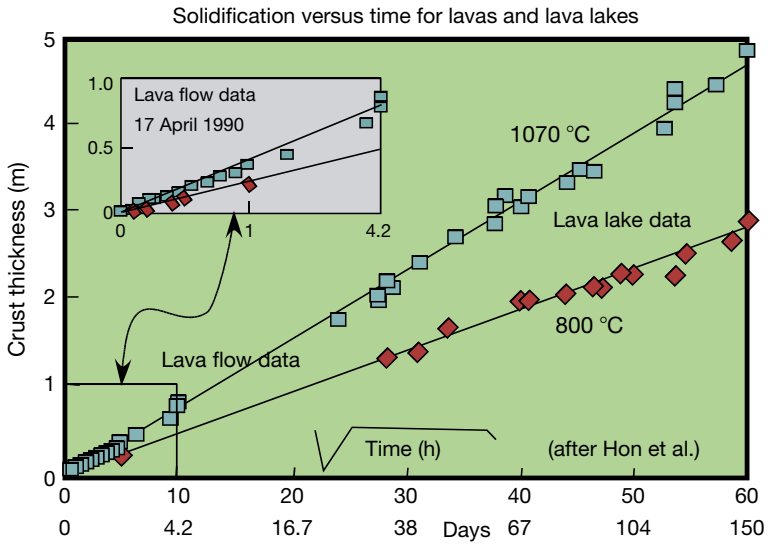

Figure 21 The thickness as a function of time (square root of time) of the upper solidification front or crust on Hawaiian lavas and lava lakes as measured by tracking isotherms at temperatures of 1070 °C and 800 °C. It is significant that the rate of thickening is the same, even for thin lavas where the Rayleigh number (Ra) is expected to be small with no chance of thermal convection, also suggesting no convection in the much thicker lava lakes. Reproduced from Hon K, Kauahikaua J, et al. (1994) Emplacement and inflation of pahoehoe sheet flows: Observations and measurements of active lava flows on Kilauea Volcano, Hawaii. *Geological Society of America Bulletin* 106: 351–370.

may be at or below the 1 atm solidus. Further adiabatic ascent is, at best, isothermal (allowing for some crystallization; see details later), and the magma undergoes progressive devolatilization, bubble nucleation, bubble coalescence, fragmentation, and extensive ash and tephra formation. The eruption is highly explosive, but the ensuing lavas are sluggish and highly immobile. By analogy with siliceous systems (e.g., Dobran, 2001; Jaupart, 1998; Melnik et al., 2005), the magma degasses and slowly squeezes out as a viscous sludge.

The universal lack of superheat in endogenetic magma bodies may thus be a fundamental reflection of the efficiency of convection in eliminating superheat as it occurs during ascent (Marsh, 1989). Magmas formed by impacts, however, can become instantly superheated *in situ*; this is by the transfer of kinetic energy through friction to heat. This results in vigorous magmatic convection lasting until the magma has cooled to its liquidus temperature. The initial temperature of Sudbury impact melt sheet, as to be presently considered, was approximately 1700 °C, well above the liquidus temperature (~1200 °C). It is in this context, and also perhaps for the lavas on Io, it is useful to consider the role of thermal convection in superheated magma.

The magnitude of the governing *Ra* at the onset of convection determines the timescales for convection to become fully developed and also for the superheat to be removed from the system. *Ra* can be estimated directly from the definition

$$Ra = \frac{\alpha g \Delta T L^3}{\nu \kappa} \qquad [18]$$

where g is the gravity, ΔT is the initial amount of superheat (~500 °C for Sudbury), α is the coefficient of thermal expansion ($\sim 5 \times 10^{-5}\ ^\circ C^{-1}$), L is the thickness of an individual layer (norite ~1 km, granophyre ~1.5 km for Sudbury), ν is the kinematic viscosity of the melt layers (norite $\sim 10\ cm^2\ s^{-1}$, granophyre $\sim 100\ cm^2\ s^{-1}$), and κ is the thermal diffusivity ($\sim 10^{-2}\ cm^2\ s^{-1}$). With these values,

$$Ra = 10^{15} - 10^{17} \qquad [19]$$

For reference, the *Ra* governing convection in Earth's mantle is $\sim 10^5$, and convection commences in a layer of fluid contained between two solid boundaries heated from below and cooled from above when $Ra = 1708$. For one solid boundary (floor) and one fluid boundary (roof), $Ra = 1100$, which is appropriate for Sudbury. This implies that convection in the Sudbury melt sheet was initially in the regime of vigorous turbulence (e.g., Khurana, 1988). This means that the thermal regime was chaotic and the layers would have been rapidly mixed and homogenized (Kadanoff, 2001). It is important to emphasize that, during convection, all the main dynamic features of the system (e.g., convective velocity and rate of heat transfer) depend intimately on *Ra*. It is also important to realize that even for a magma with a very small amount of superheat (~1 °C), *Ra* could be enormous if L is sufficiently large. In the earlier estimate of *Ra* for Sudbury, reducing ΔT to this level only brings *Ra* down to about 10^{12}–10^{13}. This suggests that any amount of superheat whatsoever will bring on vigorous convection and rapidly bring the temperature back to the liquidus. Because of crystallization and the absence of superheat, thermal convection cannot be expected as a common process in magma chambers. Nevertheless, for completeness, especially in considering ascending magmas, extraterrestrial magmas, and impact melt sheets, it is essential to consider the start-up time and rate of cooling in convecting magma.

The time (t) for convection in a layer to start and become fully established, for example, is given by (e.g., Jhaveri and Homsy, 1982)

$$t = \frac{L^2}{\kappa}\left[\frac{B}{Ra}\right]^{2/3} \quad [20]$$

where B (~350) is a constant and the other symbols are as in the preceding text. Using Ra as found earlier, thermal convection in the Sudbury melt sheet, a layer in excess of 2.5 km thick, became fully established within about an hour. This reflects the potential strength of convection due to the presence of such a large degree of superheat in a thick, relatively low-viscosity sheet. The rate of cooling also reflects this extreme vigor of thermal convection.

There are two extremes for the emplacement and cooling environment of magma. The first is magma cooled rapidly at the margins due perhaps to hydrothermal transfer in the roof and footwall, and the second is magma deeply embedded in a purely conductive medium.

6.07.6.5.1.1 Rapid convective cooling

The average temperature (T) in a rapidly convecting layer, strongly cooled from its margins, especially from above, is given by (Jaupart and Brandeis, 1986)

$$T = T_L + \Delta T_o\left[1 + \frac{t}{\tau}\right]^{-1/b} \quad [21]$$

where T_L is the liquidus temperature, ΔT_o is the amount of superheat, t is time, and τ is a group of parameters characterizing the overall cooling time. That is,

$$\tau = \frac{L^2}{2Cb\kappa'}Ra^{-b} \quad [22]$$

The symbols used here are as defined earlier, except for C and b, which come from the parametric relationship ($Nu = C\,Ra^b$) between the rate of heat transfer, as measured by the dimensionless Nusselt number (Nu), and Ra. (Nu measures the magnitude of heat transfer by convection relative to that by conduction.) For high Ra convection, typical values of these constants are $b = 1/3$ and $C = 0.4$ (e.g., Marsh, 1989; Turner, 1973). The thermal diffusivity ($\kappa' = K_c/\rho C_p$) derived here contains mixed properties; the thermal conductivity (K_c) is of the wall rock and the density (ρ) and specific heat (C_p) are of the magma, but a representative value of about 10^{-2} cm^2 s^{-1} is still appropriate.

The drop in temperature, as calculated using eqn [21], is shown in Figure 22. Even in a body as massive as the Sudbury impact melt sheet, which may have contained ~35 000 km of magma, albeit in a thin sheet (~3 km × 200 km), the initial superheat could have dissipated in approximately 10 years. This reflects the great efficiency of thermal convection in removing heat from a layer when there is little resistance to heat flow at the margins. For a body buried deeply in a conductive environment, as in continental crust, cooling is significantly slower.

6.07.6.5.1.2 Convective cooling in a layer embedded in a conductive medium

For this extreme, consider a melt sheet sandwiched between upper and lower rock units that transfer heat only by conduction. To assure that this is the slowest possible rate of convective cooling and to simplify the problem, assume that the upper and lower layers of country rock are infinitely thick. The temperature of the magma as a function of time is given by (Carslaw and Jaeger, 1959; see also Marsh, 1989)

$$\frac{T - T_w}{T_m - T_w} = \exp\left(hx + h^2\kappa t\right)\mathrm{erfc}\left(\frac{x}{\sqrt{4\kappa t}} + h\sqrt{\kappa t}\right) \quad [23]$$

where exp and erfc are, respectively, the exponential and complementary error functions, T_m is the initial magma temperature, T_w is the initial wall rock temperature, x is the vertical spatial coordinate, and $h = \rho C_p/MC_p'$, where ρ is wall rock density, C_p and C_p' are the specific heats of, respectively, the wall rock and magma, and M is the mass of magma (of density ρ') in contact with a unit area of wall rock. For a melt sheet of thickness L cooling from above and below where $C_p \sim C_p'$, $M = \rho' L/2$, and $\rho \sim \rho'$, whence $h = 2/L$, the temperature of the magma over time is found by setting $x = 0$:

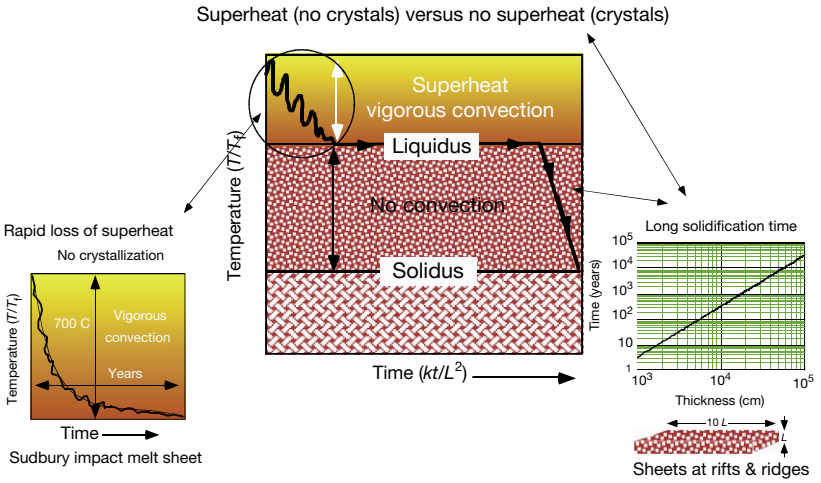

Figure 22 Modes of magmatic cooling for superheated magmas, like impact melt sheets (thermal convection), and for all other magmatic bodies (conduction). The scales are in nondimensional temperature versus nondimensional time, where T_f is the final temperature, t is time, L is body half-thickness, and K is thermal diffusivity.

$$\frac{T - T_w}{T_m - T_w} = \exp(4F)\mathrm{erfc}\left(\sqrt{4F}\right) \quad [24]$$

where $F = \kappa t/L^2$. Since the magma is always well mixed and of uniform temperature, the contact temperature is also the overall magma temperature. In this example, the magma reaches its liquidus temperature in about 10 000 years; still a relatively short time, but much longer than the previous estimate (~10 years).

These two bounding examples demonstrate how rapidly highly vigorous magmatic convection dissipates superheat, and itself lasts a relatively short period of time, probably between a few tens of years and a few hundred years. Once convection ceases, the magma continues to cool solely by conduction of heat.

Early petrologists believed superheating to be common in magmas, or at least there was confusion on this issue. And, as mentioned already, even though crystal-laden volcanic eruptions are the rule, the meaning of this feature relative to magma chamber evolution was not appreciated. Coupled with the inaccuracy in assuming the importance of cooling mainly from the roof, these misconstrued initial conditions set the stage for a century of research on magma chamber processes.

6.07.6.6 Summary of Magmatic Initial Conditions

Like most Earth processes, including the formation of Earth itself, the initial conditions of magmatic systems are well-nigh impossible to ascertain. And because the initial conditions, regarding timing, mode of delivery, volume, and, especially, the concentration of phenocrysts, of each input are only rarely known, it is critically important not to assume initial conditions that are unrealistic. For in any physical process, identifying the correct or reasonably correct initial conditions is absolutely critical to the outcome. The assumption by early petrologists of large magmatic bodies being 'instantaneously emplaced free of crystals' is not only incorrect and untenable but also an impossibly difficult starting point from which to reach the observed end result of an exotically layered body. The most obvious cause of layering in intrusive bodies is the periodic influx of crystal-laden magma (e.g., Marsh, 2006), and not due to some form of periodic overturning related to thermal convection during crystallization. In fact, from all experimental evidence on analogue systems and circumstantial field evidence, magmas only thermally convect if they are superheated, which is a state never been observed for any endogenetic magma. Convection in response to the density contrasts of periodic injections of deliveries of magma, some containing heavy concentrations of crystals, leading to establishment of a large body, must certainly occur. This particle density-driven convection would clearly be periodic, short-lived, and related to crystal deposition and layer formation. In this fashion, the larger the body, the higher the probability of acquiring textural diversity.

6.07.7 End-Member Magmatic Systems

Perhaps the most revealing and insightful means of understanding magmatic processes is to examine unusually complete, well-exposed systems where the initial conditions and outcomes are especially clear. Here, we will examine two such systems that in a strong sense define the end-members of magmatic system establishment and evolution. The two examined in the succeeding text are the Sudbury impact melt sheet and the Ferrar Dolerite system of the McMurdo Dry Valleys, Antarctica. When deciphering these and any other magmatic system, it is critically important to keep in mind the role of solidification fronts in forming the final product and also the major controls that the initial conditions have on deciding the final outcome. In trying to recognize the initial conditions, two features must be sought. One is the concentration of large crystals in the initial magma forming the body, and the other is the number of possible injections that gave rise to the body.

6.07.7.1 The Sudbury Igneous Complex (SIC)

The Sudbury impact melt sheet is the closest example on Earth of a massive magmatic laboratory bench experiment. *This is a body that was emplaced instantaneously and free of crystals, which are the exact initial conditions postulated by early petrologists*. In this context alone, it is enormously valuable to examine the end product.

The SIC was produced 1.85 Ga in a matter of minutes (~5) by impact of 10–12 km bolide (e.g., Grieve et al., 1991). Perhaps originally containing as much as 35 000 km^3 of magma ~3 km deep and spread across a crater ~200 km in diameter, the melt sheet had the aspect ratio of a compact disk. For all intents and purposes, this is an infinite flat sheet of magma. Moreover, the initial temperature, which can be ascertained by several methods, at ~1700 °C, was well beyond the magma liquidus (~1200 °C), thus providing ~500 °C of superheat and destroying all existing crystals (Zieg and Marsh, 2005). The body today (see **Figure 23**) has been deformed by continent-to-continent collision during Grenville time, folding it from south to north much as one would fold a sandwich. This folding, along with glaciation, has made the stratigraphy particularly accessible, as has extensive drilling associated with mining (~1.5 billion metric tons) of massive deposits of Ni–Cu sulfide ores along the crater floor.

The final section of igneous rock is an upper layer of ~2 km of granophyre (~70 wt% SiO_2) and a lower ~1 km layer of norite (~57 wt% SiO_2) separated by a transition zone of quartz gabbro of several hundred meters, which is the densest rock in the entire section (**Figures 23** and **24**). The most surprising aspect of this body is the degree of homogeneity of the norite and granophyre. The same stratigraphy is laterally continuous across the entire body with no modal layering anywhere. Trace element and isotopic ratios are much too similar to ascribe to pure chance or a protracted igneous process. For example, isotopic ratios, like $^{87}Sr/^{86}Sr$ (Dickin et al., 1999) and La/Sm, Gd/Yb, and Th/Nb, are nearly identical in the two main units (Lightfoot et al., 1997). Although sill-like in form, which is similar to other large bodies, like Bushveld, Dufek, and Stillwater, it has none of the feature of major sills. The average composition is ~64% SiO_2 but this material is not found as extensive chilled margins at the top and bottom, and there is no systematic chemical progression inward to suggest any form of differentiation by crystal fractionation. These features, among many others (see Zieg and Marsh, 2005), along with

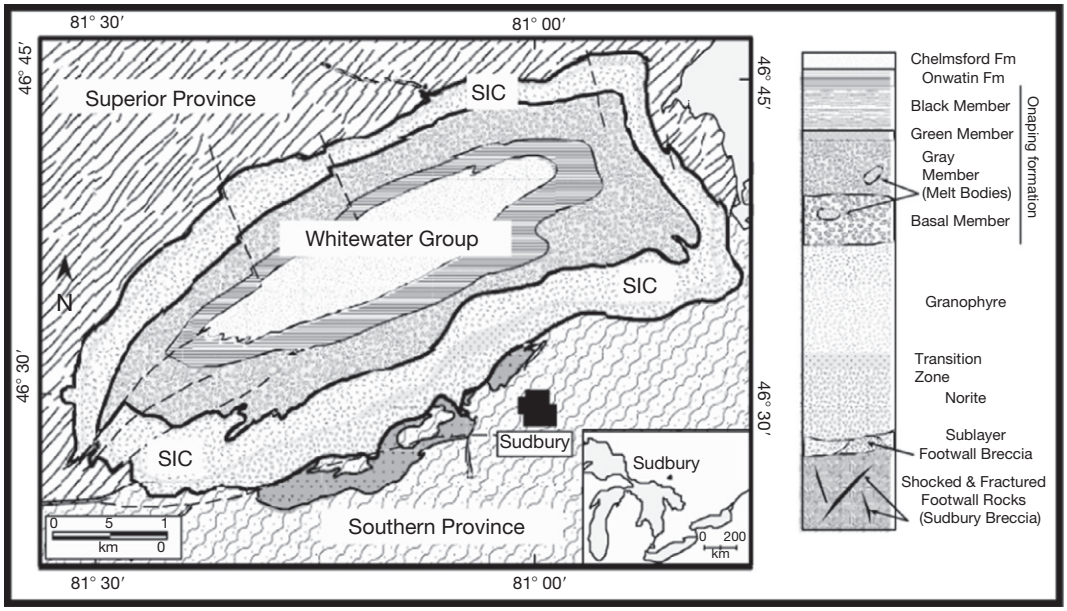

Figure 23 Geologic map of the Sudbury Igneous Complex, Ontario, Canada. At the right is the general stratigraphy of the crater. Reproduced from Zieg MJ and Marsh BD (2005) The Sudbury Igneous Complex: Viscous emulsion differentiation of a superheated impact melt sheet. *Bulletin of the Geological Society of America* 117: 1427–1450.

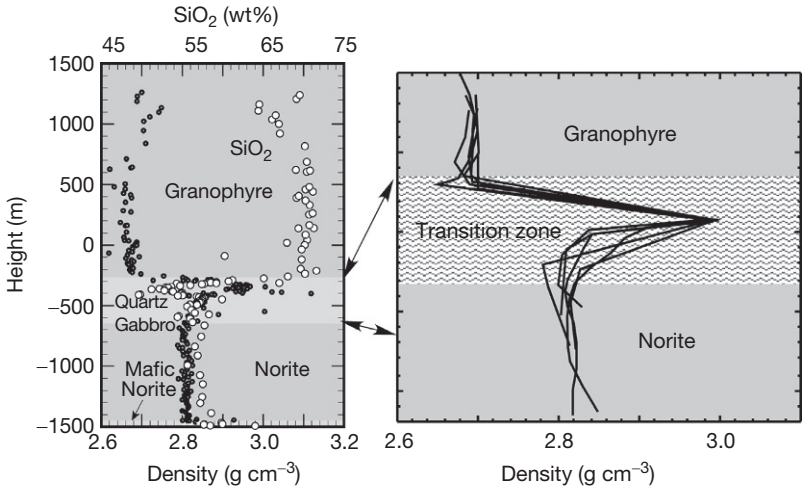

Figure 24 The variations (left) in density and bulk rock silica content through the Sudbury impact melt sheet, showing the granophyre and norite units, and a detailed view (right) of the density structure in the transition zone where the profiles have been normalized for position to the maximum density at each drill hole location. The remarkable similarity throughout the body suggests a delicate mechanical equilibrium.

unusually uniform textural homogeneity suggest that, once formed, the body did not evolve at all along the lines long assumed for magmatic bodies. In fact, to a close first approximation, once formed, the main units did not evolve at all, but simply crystallized in place. All of these features are likely natural consequences of the initial conditions imposed by the impact process.

Impacts of this size generate an outward-moving shock wave of ~500 GPa (5 Mbar), which is equivalent to the pressure at Earth's center. Temperatures reached about 4000 °C at the center of the impact, vaporizing the impactor and adjacent silicate crust. Beyond the vaporization zone, an extensive melting front existed and beyond this a fracture front. The production of breccia of all sizes (tens of meters to nanometers), in states of vapor, liquid, and solid, characterizes all aspects of the cratering event. As the impactor penetrated downward, it produced within a few minutes a transient cavity ~30 km deep and ~90 km in diameter. The target materials from which the breccias were made consisted of highly evolved continental crust. The crust was granitic overall, but in detail, it consisted of granitic plutons, gneisses, swarms of diabase dikes and sills, gabbroic plutons, quartzose sediments, and untold other lithologic varieties. These materials form an extensive 3 km thick sequence of 'fallback' breccia (Onaping Formation) capping the magma that cascaded in from the crater rim and atmosphere as the crater relaxed over a few

minutes into the final shallow impact melt sheet (~6 × 200 km). The magmatic part of this sheet is the molten breccia (Zieg and Marsh, 2005), which is more properly described as a magmatic viscous emulsion. That is, it consisted of blobs of silicate melt of a wide spectrum of chemical composition and thus density and viscosity. Although certainly not chemically immiscible, small density and compositional differences gave rise to an exceedingly heterogeneous melt where each blob had the freedom to sink or rise. In emulsions, large volumes of near-identical composition parcels rapidly coalesce into an extensive 'continuous phase' within which are other smaller chemically and physically distinct blobs, which form a 'dispersed phase.' Because of the inherent granitic nature of the crust here, the continuous phase was granitic and the dispersed phase basaltic. Once the sheet formed, this superheated magmatic emulsion immediately began to separate and coalesce into an upper granitic layer and a lower basaltic layer. Emulsion separation and coalescence processes are rapid, in a system this large taking place within a few years. Although a rapid process, this process also allowed extensive intimate chemical exchange between the dispersed and continuous phases.

Melt parcels smaller than a certain critical size (~1 cm) rose or fell so slowly that they were chemically resorbed by diffusion into the surrounding melt. Moreover, the vast surface area available to chemical exchange allowed the entire melt sheet to chemically interact by diffusion during coalescence of the emulsion. And once the two layers had separated, each superheated layer went into vigorous thermal convection, which thoroughly homogenized each layer. Prior to this time, the strong upward and downward flow of melt parcels suppressed thermal convection. As already demonstrated, this convective phase of cooling lasted at most a few tens of years (Zieg and Marsh, 2005). The net result is two layers of strongly contrasting chemical composition that have intimately and thoroughly exchanged trace chemical components to a high degree, and then, each has been thoroughly homogenized internally by exceedingly vigorous convection. The high temperature and the vigorous convection stripped the entire body of volatiles, making it unusually dry for magmas of these compositions.

Once the superheat had been dissipated from each layer through thermal convection, convection ceased and crystallization commenced in the form of inward-propagating solidification fronts from the top and bottom. These fronts were unusual in that the contact temperatures at the base and roof were each near the solidus temperature of the respective magmas, granophyre and norite. This pinned the solidus at or near the boundaries, while the liquidus, defining the leading edge of the front, freely propagated inward to meet, perhaps coincidentally, at the juncture of the two layers. This allowed for unusually thick solidification fronts to form, which made unusually thick crystal mushes at the top and bottom that acted to retard the descent and rise of solid breccia debris from, respectively, the roof and floor. Rafts of Onaping breccia foundering from the roof fell in the less dense granitic magma and descended until reaching the lower layer of basaltic magma, where they collected. At the same time, rafts of breccia and individual large blocks from granitic plutons forming the crater floor rose until encountering the upper granitic magma. The net result of the movement of all this debris is a zone of collection at the interface between the two layers. This debris, some of which further disaggregated and dissolved in surrounding magma, and mafic melt squeezed from slight compaction of the lower solidification combined in the end to make the transition zone. The collection of all this debris formed an unusual environment in terms of chemical compositions and also oxidation state and collection of volatiles. Some of this debris carried hydrous minerals that dehydrated upon heating, further shattering the breccias into smaller fragments and freeing volatiles to collect and form miarolitic cavities. This all produced an oxidized environment of heterogeneous composition of strong density contrasts that may have allowed internal gravity waves to propagate along this interface. The culmination of this collection process occurred as the lower solidification front reached the interface, structurally supporting this unit, which is the densest horizon in the entire body. This strong density gradient and overall structure of the transition zone is remarkably consistent everywhere it has been measured (see **Figure 24**).

The net result of generating a large body of magma instantaneously and free of all crystals is to produce two essentially homogeneous layers with no internal modal sorting or layering whatsoever. This is a dramatic confirmation of the *null hypothesis*, which postulates that any sheetlike magma initially free of crystals will crystallize to homogeneous rock with only slight internal variations (Zieg and Marsh, 2005). Magmas of these initial conditions do not become exotically layered and show strong differentiation trends from basaltic to granitic compositions by present generation crystal fractionation. Then, how does layering happen? It happens by injections of magma laden with large crystals. The extent and degree of layering are a direct indication of the extent of injection of crystal-laden magma.

The Sudbury record is also valuable in showing what happens to true granite target rock once it is heated beyond its liquidus and then allowed to crystallize as dry high silica magma. The surprising result is that the final texture is not typical coarse-grained granite, but fine-grained granophyre. This is likely due to the loss of its textural template due to superheating and higher viscosity, and thus slower diffusion rates, under anhydrous conditions.

Sudbury is also a prime example of how the continental crust became organized early in Earth's history. Ongoing impacts extensively melted the fledgling crust, allowing it to continually reorganize through emulsion sorting and coalescence.

As mentioned earlier, Sudbury is critically important in clearly showing what happens to magma when the initial conditions are explicitly known. In this regard, it is an end-member example. Many thinner, featureless diabase sills the world over are examples of this type of magmatic body.

6.07.7.2 Ferrar Dolerites, Antarctica

A second end-member is represented by systems that are multiply or serially injected with magma alternately free of large crystals and literally choked with large crystals. An excellent example of such a system that is unusually well exposed is the Ferrar Dolerites of the McMurdo Dry Valleys, Antarctica. A careful examination of this system enables evaluation of the astonishing role of large crystals in controlling differentiation and in producing a vast assortment of layering.

The Ferrar Dolerites, like similar systems worldwide, were emplaced during the breakup of Gondwana ~180 Ma. Instead

of the magma occupying a central rift and eventually being lost due to ongoing rifting, these magmas were emplaced in the stable west continental shoulder of the rifted continent. The magmas were mainly injected into a thick section of Mesozoic sediments called the Beacon Supergroup, consisting of sandstones and associated sediments including coal deposits. The overall package dips slightly (~5°) west and is remarkably unfaulted, intact, and exceedingly well exposed. The McMurdo Dry Valleys are Earth's most ancient landscapes and have remained since the early Tertiary essentially unchanged (e.g., Wilch et al., 1993). Deep and long east–west river-cut valleys expose ~4 km vertical sections over an area of ~10 000 km^2 revealing four major mafic sills each ~300 m thick. Sill composition is broadly similar to dolerite/diabase sills of this age and type emplaced with the Gondwana breakup worldwide. And with ~55 wt% SiO_2, they are similar compositionally to the norites of the lower part of the Sudbury melt sheet, but the overall result could not have been more different. The fundamental reason for this difference is the presence of a rich abundance of large orthopyroxene (Opx) crystals and the piecemeal injection of the system as sills rather than as a single large body (Marsh, 2004).

A general geologic map of the Dry Valleys showing the distribution of the dolerite sills is given in Marsh (2007b). The four-sill system is capped by extensive flood basalts called the Kirkpatrick Basalt (e.g., Fleming et al., 1992), which are directly connected in age, composition, and field relations to the underlying sills. The general stratigraphic layout is shown in Figure 25. Besides the unusually clean exposures, the singularly valuable and telling feature of this system is the presence of an extensive distribution of large Opx crystals in the lowermost sill, the Basement Sill, which can be used as tracers to follow sill emplacement and solidification. These Opx crystals in every way play the same role here as do the olivine tramp crystals in Hawaiian lavas and lava lakes. These Opx crystals along with, strictly speaking, about 15 vol.% Cpx crystals are from earlier magmatic events deeper in the underlying magmatic mush column and also likely from subcontinental mantle wall rock that have been entrained by the rising magma. Sills and dikes containing similar concentrations of phenocrysts have been long recognized (e.g., Drever and Johnston, 1967; Gibb and Henderson, 1996), and Simkin (1967), building on an idea by Baragar (1960), generalized the concept of flow differentiation to suggest a sequence of ascent and emplacement as sills of crystal-laden magma. This *Simkin sequence* is also shown in Figure 25.

A fundamental property of particles in ascending fluid is the tendency to sort themselves by buoyancy and drag (i.e., size, shape, and density contrast) relative to the walls containing the flow. Heavy particles move away from walls and fall, relatively speaking, in the ascending fluid establishing a central high concentration or tongue of particles. The detailed physics of this process is not entirely clear, but migration is associated with small inertial effects in an otherwise essentially inertia-free flow. Because the crystal tongue falls progressively behind the leading tip of the ascending column of magma, the leading

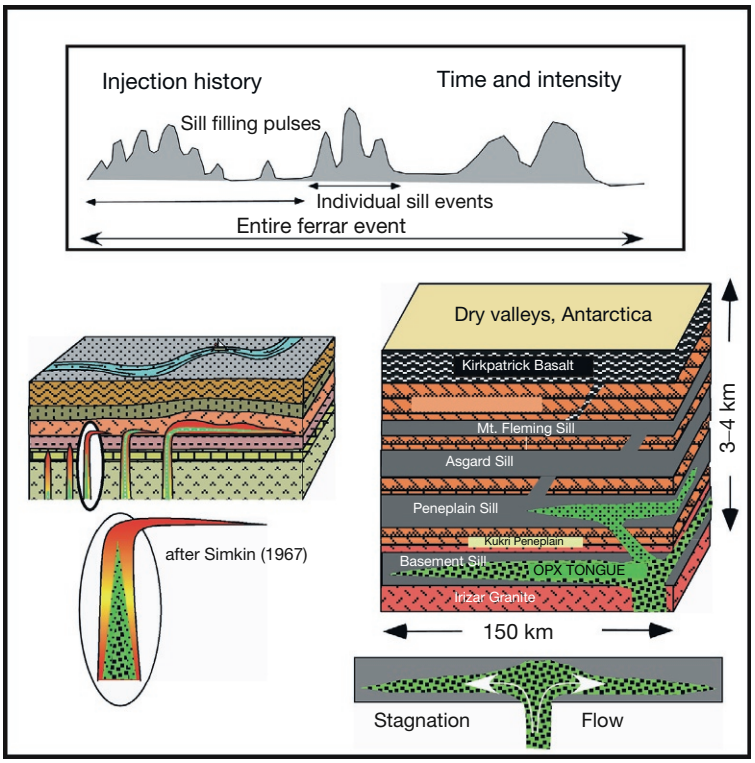

Figure 25 The stratigraphy of the dolerite sills of the McMurdo Dry Valleys, showing (left) the process of filling a sill by magma laden with entrained crystals, as envisioned by Simkin (1967). The inferred time sequence of filling of individual sills as a series of pulses leading to a prolonged periodic episode of sill formation is depicted at the top.

magma and the magma on the margins are the most refined, having been stripped of crystals, and are positioned to cool and solidify first after emplacement. That is, once ascent stalls and the magma begins to spread laterally, the leading crystal-free magma coats and essentially cauterizes the wall rock as the sill wall rock is progressively opened. All the crystal-free magma about the sill margins is quickly chilled into fine-grained rock. The tongue of crystals is uniformly deposited along the lower solidification front, forming a classic S-shaped profile after solidification. Seminal fluid mechanical experiments realistically depicting this process have been performed by Bhattacharji (1967).

This Simkin sequence of emplacement is found in the Basement Sill where an extensive Opx tongue is found throughout the Dry Valleys. Although the locus of emplacement of sills is rarely found, the distribution of the Opx tongue gives direct insight into this point. The Opx tongue diminishes in thickness in all directions outward from the general area of Bull Pass, a pass in the Olympus Range forming the north wall of Wright Valley. From this area, a series of petallike lobes propagated outward from a central funnel-like magmatic feeder zone to establish the Basement Sill. Profiles of MgO concentration through the Basement Sill and the upper sills are shown in **Figure 26**. The chilled margins and the leading tip of the Basement Sill all have low MgO contents of ~7 wt%, similar to Hawaiian basalts free of large crystals, but the composition at the sill center reaches about 20 wt% MgO, reflecting the high concentration (~40 vol.%) of entrained Opx crystals. The shape of the MgO concentration profile is parabolic, and the sizes and abundance of Opx crystals are also of this form, which is due to the emplacement flow field.

Upward in the sequence of sills, the maximum MgO content decreases systematically (**Figure 26**) with less and less modal evidence of any Opx involvement. The compositional progression blends into the composition of the overlying Kirkpatrick flood basalts. Coupled with the field relations, the overall system appears to have developed from the top down with the flood basalts first arriving from a plexus of regional dikes. Thickening of the basalts progressively capped the dikes forcing later arriving magma into sills that intruded increasingly deeper in concert with the magma density. The Basement Sill intruded last in a slow sluggish fashion due to its high crystal content. This slow ascent and lateral emplacement was aided by prior heating of the country rock by earlier magma. That the emplacement process was very likely pulsatile is indicated by internal irregularities in the MgO profiles. Stopping and restarting the emplacement process, as in volcanic reposes, causes resorting due to the steady advance of the upper and lower solidification fronts.

Everywhere within the Opx tongue are clear signs of further detailed crystal sorting between Opx and plagioclase. Plagioclase is the other major mineral phase in the Opx tongue, but it differs greatly in size as it nucleated and grew mainly during ascent and emplacement. It is generally about ten times smaller in grain size than the Opx (~2–5 mm). This large contrast in size allows plagioclase, given the chance, to sieve through the Opx and collect in pockets and layers; petrographic images are given by Marsh (2000) and Bedard et al. (2007). In most places, this sorting reflects the granular shearing nature of the magmatic flow with plagioclase forming thin undulating horizontal stringers or schlieren. That is, in shearing of dense particle-laden slurries, the flow dilates as the larger particles attempt to move past one another (e.g., Aronson and Tsimring, 2009). The dilation allows the smaller particles to sieve into the shear zones to form stringers or schlieren. Many processes of this nature occur in granular materials and all of them lead to sorting or layering of the final assemblage; it is an unavoidable process in granular materials (e.g., Makse et al., 1997; Savage and Lun, 1988). Signs of these processes are evident everywhere in the Basement Sill culminating in the Dais section in central Wright Valley. Here, the Basement Sill literally cascades downward and ponds at the deepest part of the body

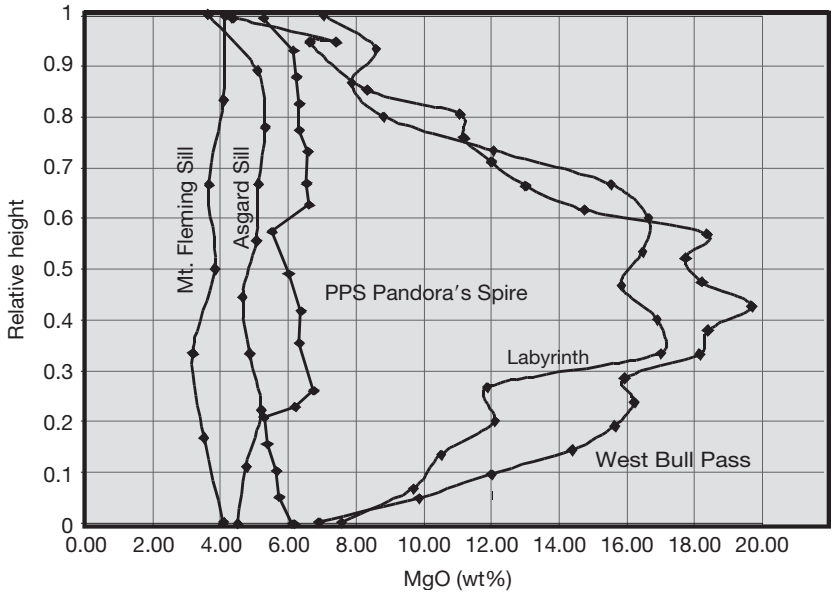

Figure 26 Variations of bulk rock MgO (wt%) through the McMurdo Dry Valleys sills showing the large concentrations in the Basement Sill, reflecting the high concentration of entrained orthopyroxene, and the monotonically decreasing average composition in each higher in the sequence.

to form an intricately layered complex called the Dais Intrusion (Marsh, 2004). The layering ranges between Opx-rich zones, called orthopyroxenite or Websterite, and almost pure anorthosite layers up to 0.5 m thick and laterally continuous for hundreds of meters (Bedard et al., 2007). This general style of layering between Opx and plagioclase is common in many large layered intrusions like Bushveld, Stillwater, and Dufek, but here, it has been preserved in an unusually pristine form due to the relatively rapid cooling of a body of this size. Cooling and solidification took place overall in about 2000 years, but much quicker locally. In the noted large layered bodies, cooling and solidification, like at Sudbury, took hundreds of thousands of years, during which time the initial textures annealed, destroying detailed indications of how the layers were formed. Layering has generally been historically ascribed to local internal nucleation and growth of crystals that have been subsequently resorted due to magma flow or simply crystal settling, but not as an obvious result of injection of a crystal-laden slurry.

Considered overall, this magmatic system is chemically similar to Hawaii. Plots of CaO versus MgO for Hawaii and the Dry Valleys Ferrar system are shown in **Figure 27**. Each system shows strong MgO control at high concentrations of MgO due to the mechanical addition or loss of olivine (Hawaii) and orthopyroxene (Ferrar). The other major difference in these two systems is in the context of the samples. All Hawaiian samples are of erupted lava, and *perforce*, only magmas with less than about 50 vol.% crystals can be erupted. Where exactly they came from in the underlying magmatic column and how they achieved their final chemical state are unknown, although it can be conjectured through geochemical methods. In the Ferrar case, the context of each sample is known exactly. In short, all of the rocks richer than 7 wt% MgO come from the Opx tongue, with the richest in MgO coming from the central part of the Opx tongue, and all rocks with less than 7 wt% MgO come from either the chilled margins or the upper sills that are free of entrained Opx. The mechanical and chemical processes by which these compositional states were reached can be traced by the spatial context of the rocks themselves within the overall system. In this sense, it is revealing that none of the upper sills, nor the Kirkpatrick Basalt, carry any Opx phenocrysts and there is no other physical indication of the role of Opx in their evolution. Yet it is clearly evident in their chemical compositions, being so similar to the fractionated compositions of the Basement Sill, that these magmas are products of an underlying magmatic mush column dominated by Opx.

An additional fortunate characteristic of the Ferrar system is the occurrence of four separate interconnected massive sills and a contiguous overlying sheet of flood basalts. The overall structure of the system is a stack of sills forming a fir tree-like magmatic system. This has allowed substantial volumes of magma, each perhaps representing a volcanic episode, to be serially emplaced as separate aliquots that cooled relatively rapidly to preserve an accurate magmatic record. If, on the other hand, all of this magma had gone to fill a single reservoir, with the time between each episode being short relative to the full solidification time, a massive layered intrusion would have resulted and all the revealing textures would have been lost to annealing (see **Figure 28**). Internal chill zones would not be evident as it is in the detailed textures (Zieg and Marsh, 2012) and the layering would be ascribed to different processes.

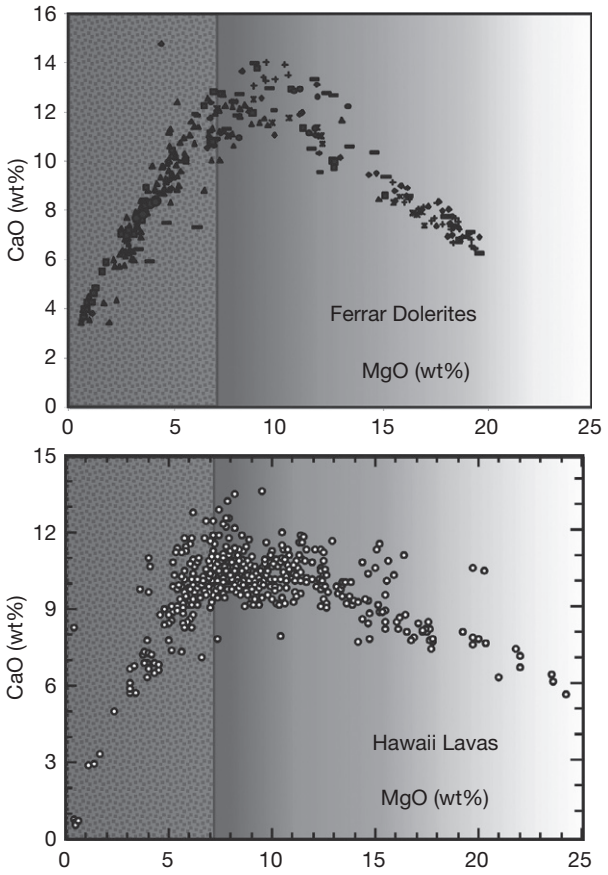

Figure 27 A comparison of the field of compositions (CaO vs. MgO in wt%) of the Ferrar Dolerites and the lavas from the island of Hawaii.

6.07.8 Lessons Learned from Sudbury and the Ferrar Dolerites

Magmatic systems are made of individual batches of magma delivered in amounts and over time as expected from volcanic processes. If the accumulated body is made of crystal-free contributions and is roughly sheetlike, it will crystallize to an essentially uniform mass of rock, regardless of size. This is the null hypothesis. In the strictest sense, there are of course many local chemical and textural aberrations due to untold local hydrothermal and solidification front processes, but these are second-order features. Strong textural and chemical variants come from variations in the nature of the injected magma. The bigger the body, the more injections necessary to build it and the more chance for strong variations in the crystal content of the incoming magma. Pervasive and exotic layering, clearly, reflects the deposition, sorting, and subsequent chemical annealing, including refinement of the incipient texture (e.g., Boudreau, 1994), of large crystals carried into the body by incoming magma. The old adage that only large bodies cool slowly enough to grow crystals large enough to become layered is untenable. Shonkin Sag at 70 m and the Basement Sill at

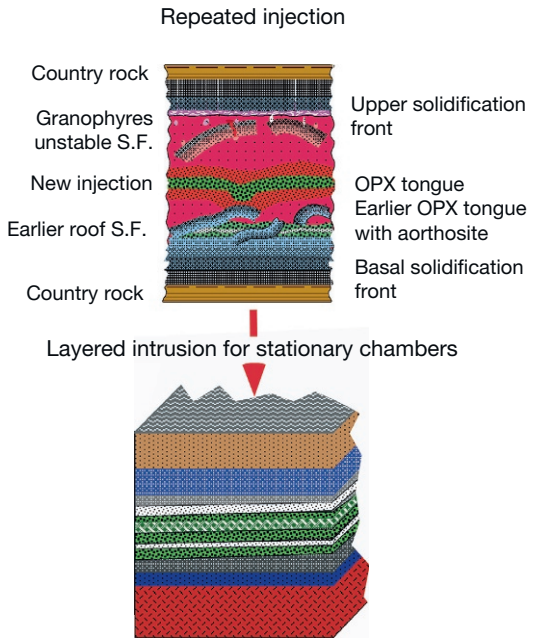

Figure 28 A schematic depiction of the repeated injection of basaltic magmas into a single reservoir where the crystal content can vary strongly from one injection to the next. In the end, this leads to an intricately layered pluton.

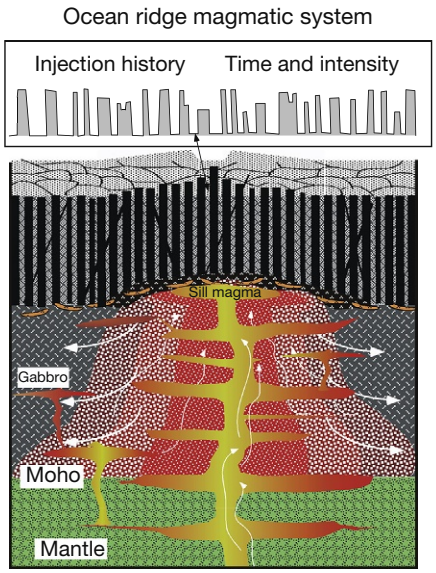

Figure 29 The mush column magmatic system at ocean ridges. The system is characterized by a thin sill (axial magma chamber, AMC) capping a vertically extensive system of thin sills and conduits within a massive column of mush. The sheeted dike complex at the top records the history of extraction of magma from the AMC as the plates suddenly pull apart over time periods depicted at the top. Note the small plagiogranite lenses within the upper gabbros formed by solidification front instability (SFI).

330 m negate this premise. Featureless sills and plutons, on the other hand, simply reflect their initial conditions of formation from phenocryst-free magma. The common occurrence of featureless granitic intrusions also reflects this state because of the inefficiency of crystal sorting in highly viscous magma. In essence, the final state of most magmas is not too far different than their initial state. And an important indicator of magmatic heritage is the nature and provenance of the 'tramp' crystals, which are indigenous to most magmas.

With this basic understanding of magmatic systems gained from systems well exposed and relatively straightforward to understand, it is useful to extend this insight to other magmatic systems. The two most common and extensive magmatic systems of Earth are those represented by ocean ridges and island arcs. These systems are mainly studied from a purely chemical point of view that, in and of itself, can be misleading as to the physical basis behind the outcome, and the following will emphasize more the physical workings of these systems.

6.07.9 Ocean Ridge Magmatism

In concert with the classical concept of magma chambers as giant vats of magma undergoing slow progressive cooling, crystallization, thermal convection, and crystal deposition into systematic layers reflecting the history of the system, vast reservoirs of magma were expected at the level of the oceanic crust beneath ocean ridges. When these features were sought using seismic methods, they were not found. Instead, thin (50–100 m), wide (2–3 km) ribbons of magma, or sills, were found (Sinton and Detrick, 1992). This spawned a general model of ridge magmatism more consistent with what is found for systems like the Ferrar and even Sudbury, albeit on a smaller scale, and the structure of the oceanic crust is an intimate reflection of the combined process of magmatism in response to plate tectonics.

This general system is shown schematically in **Figure 29**. This depiction stems from the general form of magmatic sill complexes found in the Ferrar system, in old continental crust, in ophiolites (e.g., Nicolas, 1995), and in 3-D multichannel seismic studies in the North Atlantic (e.g., Cartwright and Hansen, 2006), and it is also consistent with what should be expected on a mechanical basis in this tectonic region (e.g., Teagle et al., 2012). This is a magmatic mush column operating under quasi-steady-state conditions in response to upwelling and lateral flow (i.e., rifting) due to large-scale mantle convection. The mush column (**Figure 1**) stands in partially molten ultramafic mantle rock modally dominated by olivine with subordinate orthopyroxene, clinopyroxene, and plagioclase, with spinel and pyrope-rich garnet at successive higher pressures. At deeper levels (~50–100 km), significant partial melting due to adiabatic decompression (McKenzie, 1984) forms an anastomosing complex of melt veins and channels concentrating upward into a main mush column stalk with periodic sills (Korenaga and Kelemen, 1998; Marsh, 1996). The axial magma chamber beneath the ridge axis caps the mush column.

The system works through hydrostatic head produced in response to, in effect, suction at the top associated with the abrupt splitting and spreading of the lithospheric plates. From an initial state of slight overpressuring or near hydrostatic equilibrium, this abrupt motion splits the brittle oceanic crust, withdrawing magma from the underlying axial magma chamber, some of which erupts as pillow lavas and that in the feeder solidifies as a dike. The loss of hydrostatic equilibrium at

the head of the system propagates as a pressure pulse downward throughout the system, perhaps partly as solitons, drawing magma upward in the mush column and reestablishing stability. Because all parts of the contiguous ridge plates do not move at exactly the same time and to the same degree, the process of melt motion at depth is certain to be complicated. Magma at some depths may sometimes be transported laterally as it ascends, making its overall trajectory significantly nonvertical. The intimate time-series history of this process is recorded in the vast sheeted dike complex, which is a characteristic by-product of ridge magmatism well known from ophiolites. Because these dikes are random samples of the axial magma chamber, they give an excellent inventory of the general state of this magma, in terms of both composition and crystallinity. These dikes are typically fine-grained and of low phenocryst content; any phenocrysts are mostly plagioclase. The axial magma chamber or sill is a passive body that experiences bursts of withdrawals followed by recharging from below. Some recharges undoubtedly carry massive amounts of entrained large crystals, which sediment to the floor, undergoing punctuated differentiation, immediately upon entering the sill. Layering is thus an indirect reflection of dike formation.

The basalts erupting at the ocean ridges worldwide are tholeiitic basalts, with low K_2O (~0.2 wt%), modest TiO_2 (~1.5 wt%), and low and unfractionated REE (rare earth elements), and are commonly called MORBS (mid-ocean ridge basalts). To first order, these basalts are chemically among the most globally uniform of any class of magmas. These are called N-MORBs for normal MORBS. But at a more detailed level of inspection, they show significant variations in many facets, the most common of which is enrichments in K_2O and TiO_2 and sometimes iron (e.g., Klein and Langmuir, 1987; Langmuir et al., 1992). These are called E-MORBs or enriched MORBs and also sometimes Fe-Ti MORBS.

The first-order bulk composition of these basalts reflects the underlying magmatic process of prolonged intimate contact with an extensive mass of solids in the magmatic mush column. In effect, the chemical composition is buffered by the mechanics of the overall process, much as in a water purification system. This uniformity also reflects the uniformity of mantle composition itself, which has probably not changed drastically over Earth history. That is, at the present rate of ridge magmatism (~20 km^3 $year^{-1}$), with about 10% melting, the mantle will be recycled about once every 5 Ga, which, even allowing for the role of contamination by subduction, suggests the mantle composition has been, to first order, fairly constant. But as a result of initial inhomogeneities, subduction, and other styles of magma generation, there are certainly subtle and significant chemical variations in the mantle source rock. In addition to these variations, there are also regional variations in the thermal regime as a result of the form of mantle convection. These effects cause the depth of the principal melting region to vary in extent and depth, which altogether causes distinct fluctuations in the bulk composition of the magmatic product and the amount of magma produced, which is reflected in the local thickness of the oceanic crust (Klein and Langmuir, 1987). Another major factor is the rate of spreading, which may strongly affect strength of the melting anomaly and thus the overall mass and activity of the mush column.

It is interesting to consider ridge magmatism from the past classical point of view of magma chambers, where primitive (MgO-rich) magma is generated at depth, emplaced in a large vat, and differentiates by crystal growth and settling, generating a long 'liquid line of decent' and a large chemical diversity of products from picrites to olivine basalts and tholeiites and possibly even granites. Instead, there is exceedingly little diversity. Even picrites (olivine-rich basalt) are not found at ridges, and arguments have always persisted that if picrites are parental to MORB, then why are they never seen? Why do they not erupt more often, or at all? This is not an uncommon situation in petrologic studies where critically important parts of the hypothesized dynamic puzzle are not seen, but are postulated to be in a hidden zone or uneruptible due to density difficulties or other factors. On the other hand, the fact that critically important magmatic parts of the system are never seen may simply mean that they as actual physical processes do not, *per se*, exist as postulated. Instead, a more reasonable process achieves the desired chemical effect, like uniformity. In the present understanding of ridge magmatism, the magmas are chemically fractionated by contact with olivine, and other phases, through prolonged intimate, diffusional, contact within the mush column, not classical crystal fractionation. The lack of presence of an actual massive, 6–8 km thick magma chamber, as postulated on chemical grounds, is replaced by a virtual magma chamber, which is an integrated chemical process taking place over the full extent of the mush column.

6.07.10 Island Arc Magmatism

6.07.10.1 Introduction

Arc magmatism contrasts fundamentally with ocean ridge magmatism. The points of volcanism, the volcanic centers and surrounding crust, can remain fixed for long periods of time (~1–10 Ma, depending on location), and the flux of magma is much lower (~10^{-2} km^3 $year^{-1}$). Also, there is a universal relationship between the rate of subduction and volcanism. Where there is no subduction, there is no volcanism. There are also some close similarities and these are in the spatial trace of volcanism on the surface, both are long, sharp narrow welts, and the compositions of the most voluminous magmas are to first order similar, tholeiitic basalt and high alumina basalt (HAB). But unlike at the ridges, where there is no choice in the ultimate source of the magma, in arcs, a wedge of asthenosphere sandwiched between the arc lithosphere and the subducting oceanic crust provides almost any number of end-members and combinations, with and without continental crust, from which to get magma. As at ridges, the main approach to understanding arc magmatism has been, and is, mainly through geochemistry, but here, the focus will be more on the fundamental geophysical controls. Moreover, petrologists have long assumed, as based on early thermal models, that the subducting plate is too cold to melt and that the source of arc magma must thus be from the mantle above the plate, forming in response to fluxing by volatiles rising form the dehydrating plate. Again, intricate physical processes are postulated to explain chemical evidence. The question must always be asked: Are these processes reasonable and sensible?

A perusal of the principal volcanic arcs of the world (Figure 30) shows arcs existing in a diverse range of geologic environments. There are arcs built on thick continental crust in South America, arcs built on oceanic crust in the Scotia Arc off southeastern South America, arcs traversing from continental to oceanic crust as in the Aleutian Islands, and arcs on young mixed crust in Kamchatka and Japan. The ages of the arcs also vary a great deal from those like the Aleutians that may be as old as 40 Ma to those as a young as the Scotia Arc at ~3 Ma. This is not to say that the arc has been in continual operation for long periods of time. In fact, from the evidence of ashes deposited on the seafloors around arcs, there is an apparent periodicity of eruptive activity, especially around the Pacific, of about 2 Ma (e.g., Hein et al., 1978; Scheidegger et al., 1980). Coupled with a record of continuous subduction over much longer periods of time, this may indicate that the arc systems periodically load with magma and then discharge over and over again.

The force of the volcanism, even within a single arc, can also vary significantly as can the nature of the dominant lavas. In South America, there are major gaps along the strike of the arc where there is no volcanism. These correlate closely with shallowness in the angle of subduction. If the plate subducts too shallow, essentially adhering to the keel of the continental lithosphere, there is no wedge of asthenosphere and no volcanism. That subduction is an absolute necessary condition for volcanism is clearly seen in the Aleutians where the volcanic flux is directly proportional to the downward flux of the Pacific Plate (see Figure 31). The depth of the top of the subducting plate is most commonly ~125 km, but it can be as large as ~150–160 km. And the detailed structure of the volcanic front of any arc often intimately reflects the structural morphology of the subducting plate. Arc volcanic fronts are not simple continuous arcs, but are almost always segmented into a collection of individual short segments forming a piecewise continuous arc. And major fracture zones or structural irregularities in the subducting plate usually bound the arc segments.

6.07.10.2 Arc Form

There are two spatial characteristics of island arc volcanism that set it apart from all other forms of volcanism. These are the regular spacing of the arc volcanic centers and the segmentation of the volcanic front. Although when built on continental crust, the form of island arcs can appear cluttered and unclear, it is always there and clearest in young and tectonically uncomplicated regions.

6.07.10.2.1 Spacing of the volcanic centers

The basic structure of island arcs in terms of the positions and form of the volcanic centers is exceptionally clear. The arc begins with a single sharp line of volcanoes. This is the volcanic front as named by Sugimura (1968), which is, by far, the principal locus of volcanism. The front fills as a series of unusually regularly spaced volcanic centers separated by 50–65 km. The relatively young Scotia Arc shows this basic developmental form rather clearly (see Figure 32). After existing for about 3 Ma, secondary volcanic centers may appear behind the front, forming a weak secondary front. These are always smaller and spaced closer to the front than the principal spacing (d) of centers along the front. There is some sign that this secondary spacing (d') follows the relation $d' = d\cos(\theta)$,

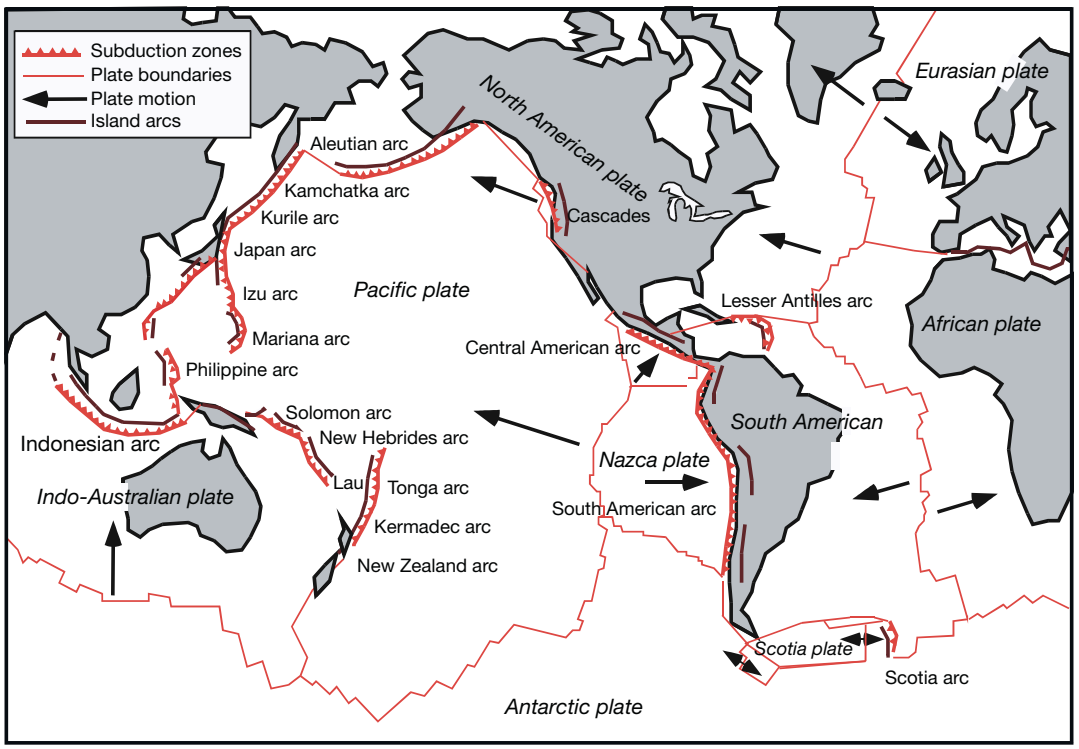

Figure 30 Islands arcs of the world.

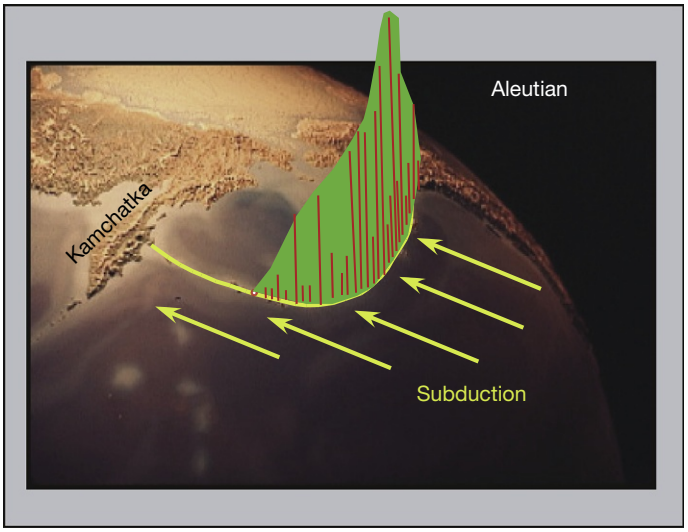

Figure 31 The striking variation in volcanic flux from the Aleutian Island Arc volcanic front as a function of the variation in the rate of subduction or flux of the Pacific Plate beneath the arc. Beyond Buldir Island on the western end of the arc, the relative plate movement is strike-slip and all volcanism ceases. Subduction begins again along the Kamchatkan Arc.

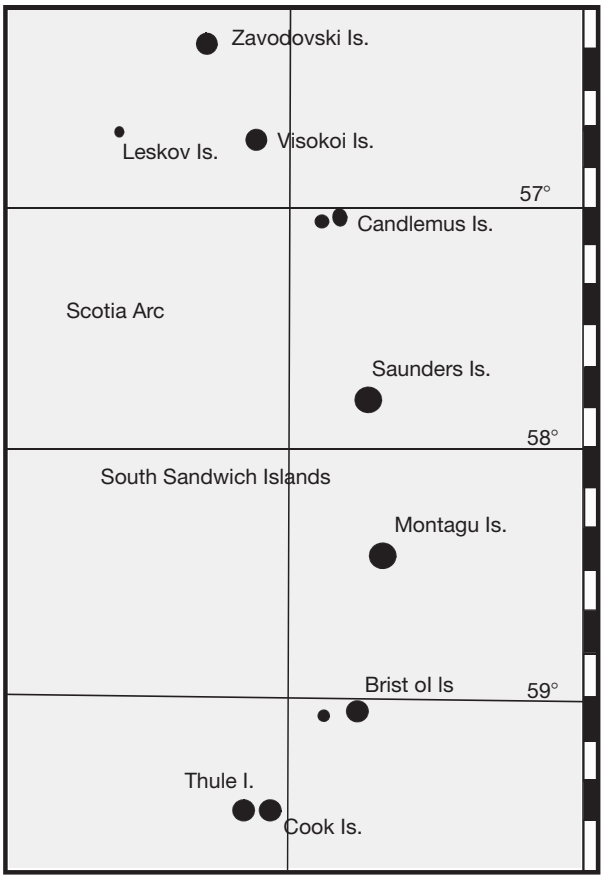

Figure 32 Detailed view of the Scotia Arc or South Sandwich Islands. Note the prominent volcanic front, the even spacing of volcanic centers, and the location of the secondary volcanic center, Leskov.

where θ is the angle of dip of the subducting plate (Marsh, 1979a,b). Leskov Island in the Scotia Arc and Amak and Bogoslof Islands in the Aleutians are prime examples of these secondary centers. Every arc seems to have them, although other forms of volcanism especially scattered cinder cones on continents, like in Mexico, sometimes complicate identification. On a similar timescale, young centers also appear within the main front at points approximately midway between the older initial and well-developed centers. These centers never reach the strength of the main centers. Bobrof Island and the doublet Koniuji–Kasatochi Islands in the central Aleutians are such late centers.

6.07.10.2.2 Arc segmentation

That the arc volcanic front can be broken up into piecewise continuous segments reflecting a similar structure in the underlying subducting plate was perceptively noticed and developed by Richard Stoiber (e.g., Stoiber and Carr, 1971) and Michael Carr (e.g., Carr et al., 1973). Every arc shows this basic from and it is especially clear for the Aleutian Arc (see Figures 33 and 34). To be clear, these alignments are between only the *active vents* of the front and not simply the volcanic centers, which often contain a series of waning and waxing vents. Although some segments contain only two or three vents, most segments are well defined by many vents, and this is much more than simply the correlation of large dots on a map. The alignments are particularly striking and delicate if viewed from the exact summit of an active vent. Stepping away ~10 m from a vent within a segment will lose the alignment, which can often be seen for 200 km of or more in each direction. Considering that the principal active vent within any center usually migrates slowly (~10 km Ma^{-1}) in time away from the original front and that the alignment exists at any time is suggestive of a deep-seated fundamental cause.

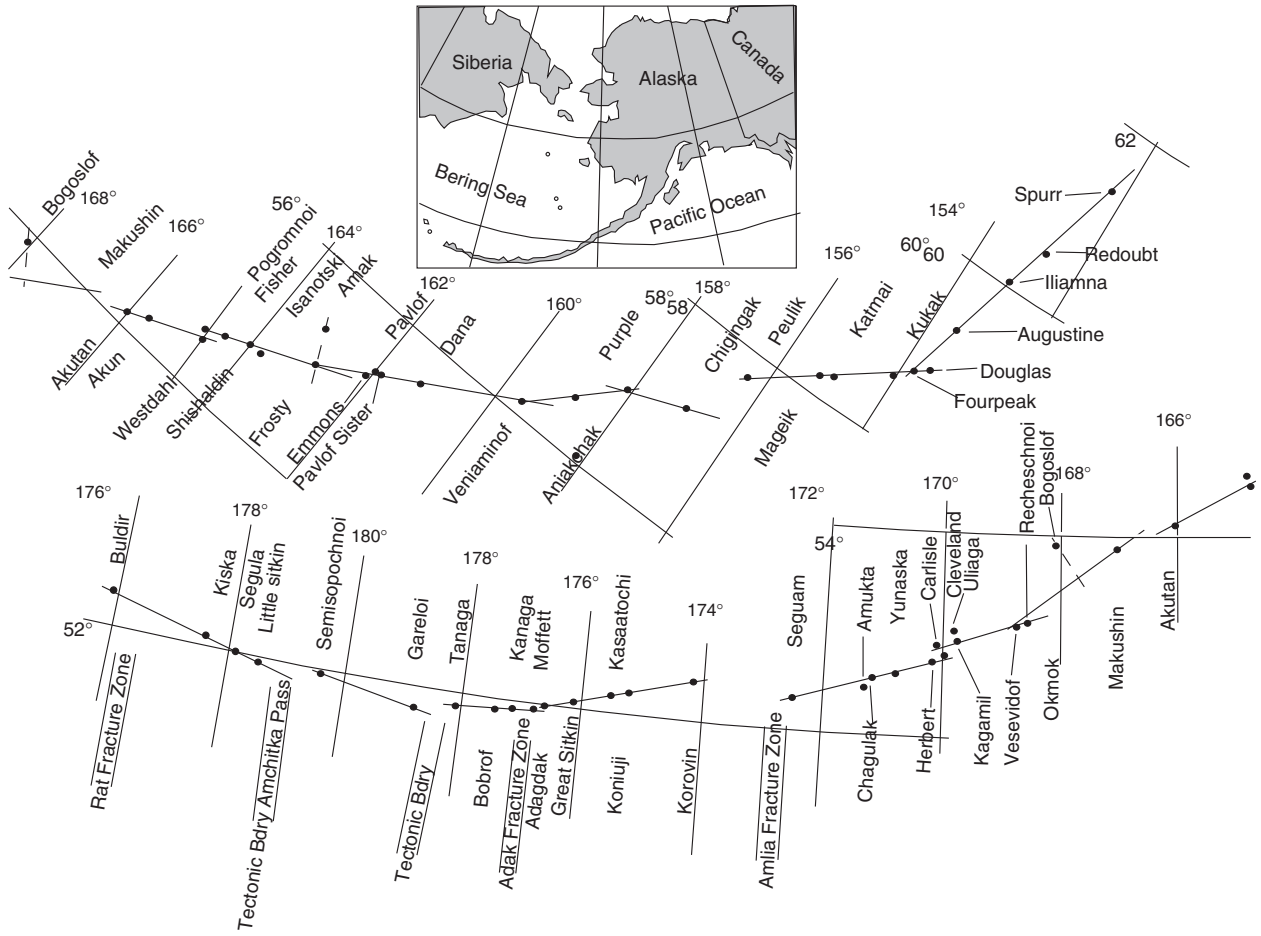

Figure 33 Segmentation of the Aleutian Island Arc volcanic front.

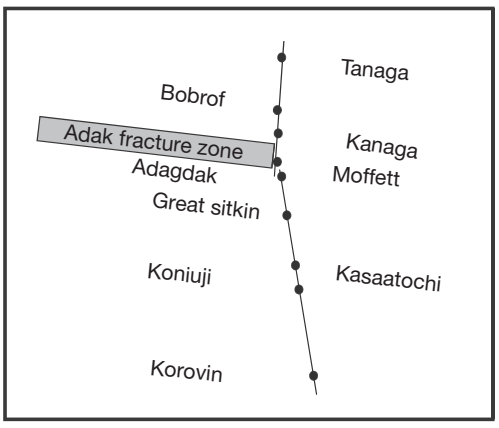

Figure 34 View of the detailed relations between two segments of the Aleutian volcanic front at the island of Adak and the position of the prominent fracture zone in the subducting plate.

6.07.10.3 Character of the Volcanic Centers

The general pattern of development of individual volcanic centers often shows a similar progression from initiation to final size and this progression can be arrested at any stage. These stages can be called young, mature, and supercenters. The final form, which is reflected by strength or volume of the center, depends critically on the position of the center within the front and within the arc itself. The stronger the rate of subduction, the larger the centers. Centers deeply within a segment are generally larger than those at the ends of segments. Centers begin, as can be seen from the appearance of secondary centers, as essentially large multiple domes; the magma is of low volume, highly crystalline, and sluggish. Others begin with the eruption of a series of highly mobile basaltic lavas interbedded with thin deposits of tephra to form a low profile shield. Continued growth adds more to the shield and then sharply transitions into a steeper-sided cone of primarily (50–70 vol.%) volcaniclastic debris trussed together with occasional lavas. Low crystallinity basaltic flows may be thin (~1 m, especially near the vent) and of limited extent (hundreds of meter), whereas high-crystallinity andesitic flows may be thick (~100 m), massive, and extensive (kms). This basic transition from shield to steep cone forms the classic composite cone of island arcs, consisting of a stratocone built on the foundation of a shield cone of basaltic lavas. Many volcanoes go no further in development. Reposes in activity allow erosion to deeply incise the cone; summit craters of tall stratocones commonly become glacial cirques breaching the crater and digging deep U-shaped valleys. In the next phase of activity, the cone reconstructs itself with the lavas and debris

filling the topographic voids, making the field relations challenging. This is a mature volcanic center. Further development often results in a series of domes and fumaroles ringing the cone at an elevation of about 50–70% of the cone relief. This is commonly encouraged by deep erosion that may weaken the cone near the main vent, allowing stagnant, high-crystallinity magma to sluggishly extrude laterally. This signals the solfataric stage of development. These locations also sometimes develop into a series of satellite cones and domes, evicting a series of flows that may mimic the development of the central cone.

Supercenters develop when activity is particularly strong and the stratocone phase outstrips erosion, forming volcanoes of unusually large relief like Mt. Fuji, Mt. Rainier, and Mt. Shishaldin (~3000 m) in the Aleutians. Beyond this point, the cone can become structurally unstable due to size and subsurface magma ponding and catastrophic caldera collapse often occurs (e.g., Smith and Bailey, 1968; Williams, 1941). The majority of the cone relief is destroyed through collapse and violent ejection, leaving a low relief, distinctive crater as at Crater Lake, Oregon (e.g., Bacon and Lanphere, 2006). Further activity builds domes and new cones within the caldera, generally not of a size commensurate to the original cone, but sometimes even larger. This cycle of growth and collapse may repeat itself many times until the locus of volcanism migrates to a new nearby location.

The style of eruption for arc volcanoes, unlike for Hawaiian and Icelandic volcanoes where fissure eruptions are common, is most often from the central vent. These central vents are highly concentrated and cylindrical that may fill and empty repeatedly during an eruptive episode. A ~300 m wide vent at Korovin in the central Aleutians has been observed empty to a depth of ~1.5 km and later brimming with magma and then spilling over into lavas. Acoustic echoing due to explosions at the base of the vent when evacuated can be heard for hundreds of kilometers. Although commonly ascribed simply to high volatile concentrations, the highly explosive nature of stratocone eruptions may more reflect this concentrated plumbing system coupled with high-crystallinity magmas, making them unusually viscous and difficult to discharge. Large regional dikes are uncommon, although they do sometimes accompany inflation and the precursory events attending caldera collapse. Small local dikes are common near vents, and deeply eroded cones sometimes show dikes radiating from the central vent that have trussed together the volcaniclastics of the stratocone, sometimes themselves serving as conduits for flank domes and lavas.

Ash flows or ignimbrite deposits, so common to continental volcanism and caldera collapse eruptions, are also common to arc volcanism especially in continental terrains like at Novarupta–Katmai, the largest eruption of the twentieth century (Hildreth and Fierstein, 2012). But because of their high mobility and erosiveness, evidence of these events is often difficult to find and trace, especially in oceanic environments.

6.07.10.4 Magma Transport

The strong centralization of arc volcanoes and the lack of dispersion on the surface of vents over periods of millions of years suggest deep magma transfer by diapirism rather than by dike propagation. Deeply eroded terrains also show bulbous plutons and a paucity of dikes. When built on continental crust, expansive welts of plutons forming vast linear batholiths, like the Sierra Nevada, form in the subsurface from foundered magma and from reprocessing of crustal wall rock. The dominant type of magma emitted is also affected by the density of the underlying crust. Arcs on continental terrains are dominantly andesitic (i.e., ~60 wt% SiO_2), whereas arcs on oceanic crust are dominated by HAB (~50 wt% SiO_2). This sensitivity to density contrast is locally critical in diapiric transport and much less so in dike transport. That is, standing dikes in elastic cracks operate more on an integrated, column-wide, density and the strength of the walls rather than on the local buoyancy at each horizon. The extreme paucity of mantle-like ultramafic xenoliths may also reflect the slow diapiric mode of transfer where the same conduit is used over and over, making the column traveled thermally and chemically insulated from access to primitive lithospheric rock.

6.07.10.5 Subduction Regime

Perhaps the most unusual aspect of arc magmatism is the deep presence of the wedge flow of asthenospheric mantle driven by the subducting plate (**Figure 35**). At shallow depths, the subducting lithosphere is in fault contact with the adjacent arc lithosphere. The depth extent of this contact is commonly 70–100 km but may be much longer in continental terrains where the lithosphere or tectosphere can be very old and thicker as in some places along the subduction zone of South America. The thickness of the arc lithosphere is also not well known in many areas. Below this depth of fault contact, the subducting plate is in contact with the mantle wedge or asthenosphere, a high viscosity fluid (~10^{17} Pa s). In most regions, this is the so-called seismic 'low-velocity zone,' reflecting incipient melting at the solidus of the regional mantle country rock. The asthenosphere in this wedge-shaped region adheres to the upper boundary with the arc lithosphere and at the same time is dragged downward by the motion of subduction. The streamlines, depicting the mass transfer, due to this dragging tilt upward in direct response to the angle of subduction. This flow field is found by solving the biharmonic equation for viscous flow, which comes from the Navier–Stokes equation. A key feature of this flow is that the associated stress field creates a traction or coupling between the two plates that, in effect, welds them together along the lithosphere-to-lithosphere fault contact. This junction is locked in place, and the volcanic front, as we have already seen, reflects this intimate connection by remaining relatively fixed for long periods of time.

This is an unusual flow in several regards. First, the form of the flow is the same at all distances from the corner. The upper part is essentially a parabolic flow between parallel plates and the lower half is a shear flow. For conservation of mass, all the fluid in the top half must turn and flow through the lower half of the flow field. Along the plane of symmetry, fluid moves from one side of the flow to the other. This flow is directed normal to the face of the subducting plate. Although normally at great distances from the plate interface, with approach to the corner, this flow becomes arbitrarily close to the plate. It is exactly above this corner region where the volcanic front is

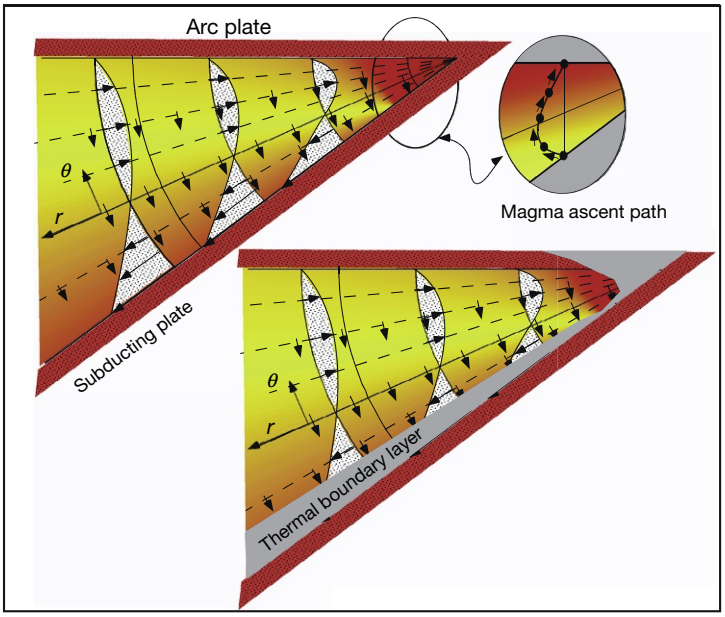

Figure 35 (upper) The flow of mantle material within the asthenospheric wedge induced by subduction, with the streamlines shown. (lower) The position and development of the cold thermal boundary layer at the slab–wedge interface, with also shown the strong thinning in the boundary layer near the corner and directly beneath the volcanic front. The inset diagram shows the trajectory of ascent of a diapir of mush form the slab as it traverses the wedge flow and repeatedly enters the same spot within the overlying arc lithosphere.

found. Second, since the downgoing plate is cold and the flow above it is mostly a shear flow, with streamlines parallel to the plate, a cold thermal boundary layer develops near the corner and thickens down the plate. This thickness δ_T can be estimated from eqn [2] as a function of distance (x) from the corner, which is measured by $x = t/V$, where t is time and V is the subduction velocity. Then,

$$\delta_T = C\sqrt{K}\left[\frac{x}{V}\right]^{1/2} \qquad [25]$$

where C is a constant of order one and K is thermal diffusivity. The boundary layer thickens downward (see **Figure 34**) along the plate with $x^{1/2}$, and it thins or thickens inversely with $V^{1/2}$. At a common distance from the corner, slow plates have much thicker boundary layers than fast-moving plates. This behavior is very much akin to the growth of the lithosphere itself as it moves away from ocean ridges. In this respect, it is also critical to recognize that any diffusive process associated with the plate, including chemical diffusion involving volatiles, will have a similar boundary layer development. The third unusual feature of this environment is the corner region where the motion goes from a fault interface controlled by friction to a fluid–solid interface dominated by a shear flow where friction is also involved but to a lesser extent. In this shear flow, heat flow is produced by viscous dissipation of energy within the flow according to $q = V\tau$, where τ is the local shear stress ($\tau = \mu(dV/dy)$ where μ is viscosity and y is the coordinate normal to the plate). But within the arc plate, with approach to the surface, the effective thermal boundary thickness becomes very large.

There are thus two key features in this regime that fundamentally affect the production of magma. One is that the corner flow continually brings into the wedge region hotter mantle material from greater depths, and this material is continually brought in contact with the subducting plate. It continually coats the plate, and the cold thermal boundary layer is never allowed to become unusually large, as it would if the corner were stagnant. Second, the thermal boundary layer becomes pinched near the corner as the corner flow turns and becomes a shear flow. This thermal pinch is exactly below the volcanic front, and it, in effect, intimately ties the spatial position of the front to the position of the plate. The thermal regime inside the subducting plate is also central to understanding how magma might be produced.

6.07.10.6 Subducting Plate Internal State

Two key processes within the downgoing plate affecting the production of magma are the thermal regime and the transport of hydrothermal fluids. The tholeiitic oceanic crust at the surface of the plate has a strong chemical affinity to arc basalts and is clearly a prime potential location for magma production. But as mentioned already, it is commonly considered too cold to undergo melting. This impression stems from early thermal models (e.g., Toksoz and Bird, 1977) and also from the fact that the slab interface was once on the seafloor, the coldest part of the lithosphere (Hsui et al., 1983).

6.07.10.6.1 Thermal regime

This latter impression can be appreciated by recalling that if two solids at contrasting temperatures T_1 and T_2 are abruptly brought into contact, the temperature of the interface (T_i) immediately becomes the average of the two initial temperatures, $T_i = 0.5\ (T_1 + T_2)$ (e.g., Turcotte and Schubert, 1982). For seafloor rock at 0 °C brought up against mantle wedge at, say,

1300 °C, the crust interface would thus achieve a temperature of about 650 °C, which is well below the solidus. The problem with this result is that the thermal path that the slab takes between leaving the seafloor and reaching a depth of ~125 km must be considered. The section where the two plates are in fault contact is especially critical as the frictional interaction produces heat and there is strong evidence that at shallow depths (0–50 km), the preponderance of earthquakes is along this interface, and at great depths, the strong band of earthquakes migrates slightly deeper into the plate to depths of ~10–20 km below the interface. So the temperature calculated earlier is an absolute minimum; frictional heating will preheat the oceanic crust allowing it to attain a significantly higher temperature when it enters the asthenosphere. And the inclusion of the flow in the wedge is essential to include in achieving any realistic estimate of the prevailing temperature along the slab interface. The full problem is quite involved and of the many studies that of Kincaid and Sacks (1997) is notable for its thoroughness. (They also give an extensive review of associated seismic and tectonic studies.) They find that near the corner, in the location indicated by the flow in **Figure 35**, there is positive temperature anomaly of about 80–100 °C at the slab–asthenosphere interface, over a thin (maybe only tens of meter) layer where the oceanic crust may be brought to a temperature of about 1350 °C. This is enough to initiate melting, and that this spot is exactly below the volcanic front is important. This spot is also tied to the plate-to-plate junction and may well determine the position of the volcanic front.

6.07.10.6.2 Hydrothermal flows

Being a solid, the thermal regime internal to the subducting plate is usually considered as solely due to heat conduction and this is certainly true to first order. But there is also hydrothermal circulation in response to dehydration. This reflects extensive hydrothermal circulation starting at the ridge and extensive alteration and exchange between the seawater and the oceanic crust. This exchange takes place over tens of millions of years. The principal effect is to alter the original minerals to hydrothermal equivalents, thus partially hydrating the oceanic crust. For example, olivine is partly altered to serpentine, plagioclase feldspar to forms of sericite, and clinopyroxene to hornblende. Although this alteration can be extensive in local areas, overall, these effects probably do not affect more than about 15–20 vol.% of the crust. What is much more pervasive is exchange at the isotopic level involving, for example, oxygen ($^{18}O/^{16}O$) and strontium ($^{87}Sr/^{86}Sr$), which can take place at high temperature and leave little to no visual trace. Fresh glassy MORBs erupted at the ridges commonly have, for example, initial $^{87}Sr/^{86}Sr$ near 0.7025, and with ocean water at 0.7090, after about 30–40 Ma, the oceanic crust, which has migrated to significant distances from the ridge crest, now has $^{87}Sr/^{86}Sr$ closer to 0.7040. These variations with depth are found in ophiolites (e.g., Gregory and Taylor, 1981) where a net increase is found in $^{87}Sr/^{86}Sr$, but $\delta^{18}O$ increases at the crust top (~+12‰) due to low-temperature exchange and decreases at the crust base due to high-temperature exchange such that the integrated effect is ~5.8‰, which is the normal value of fresh MORB. Thus, there is no net exchange in $\delta^{18}O$.

As the plate subducts and becomes heated, a new hydrothermal circulation system sets up due to phase transformations associated with dehydration. Because of the large horizontal temperature gradient across the inclined oceanic crust, the form of this flow is horizontal and upward, which makes it helical. This flow is confined only to parts of the plate where there is sufficient permeability to allow flow. Similar hydrothermal flows have been studied over extensive regions about solidifying plutons and the patterns and basic mechanics of these flows are well known (see e.g., Phillips, 1991; Taylor and Forester, 1979). Permeability is directly tied to the temperature and brittleness of rocks, and from these studies, it is abundantly clear that rocks are sealed beyond temperatures of about 700 °C. For this reason, this hydrothermal flow is confined wholly within the oceanic crust, which is the coldest, most brittle part of the subducting slab. Moreover, the region has been (and is being) subjected to extreme fracturing in response to earthquakes; each cubic km experiences about 10 000 events during subduction. This makes a strong permeability guide within the oceanic crust. At the same time, for these same reasons, the overlying asthenosphere in the wedge is tightly sealed; it is hot and weak and has nil permeability. Hydrothermal fluids released from the plate do not enter the overlying mantle wedge; they travel upward and repeatedly cycle across the oceanic crust (see **Figure 36**). This flow has a critical effect on the chemical nature of the subducting plate.

This intense, internally confined flow redistributes the initial variations in $\delta^{18}O$ and $^{87}Sr/^{86}Sr$. Because from the interaction with seawater there has been no net gain in $\delta^{18}O$, it is reset to its normal value of ~5.8. But because the crust has gained ^{87}Sr from seawater, there is a net increase throughout the crust in $^{87}Sr/^{86}Sr$ to a value of ~0.7040. The low solubility of isotopes like $^{143}Nd/^{144}Nd$ in seawater does not produce a corresponding effect on the oceanic crust. But perhaps the most remarkable and underappreciated effect of this flow is to produce an unusual skarn as it comes in contact with the slab-mantle interface. The flow cannot penetrate the mantle, but this interface, due to all the ongoing faulting and shear, is certainly a mechanical breccia of both rock types, namely, high-pressure MORB (i.e., quartz-eclogite) and garnet peridotite. The hydrothermal flow is in approximate chemical equilibrium with the MORB crust, but far from equilibrium with the peridotite. As soon as it touches this hot heterogeneous rock, it precipitates out phases to bring it closer to equilibrium. Although the nature of this *slab–skarn* assemblage is not as yet known with any exactness, it will be rich in trace elements like Ba, Rb, and elements with similar geochemical affinities. Thus, the most likely area of magma production has a MORB-like bulk composition with an enrichment of some trace elements.

6.07.10.7 The Source of Arc Magma

Although the more popular source of arc magmas is from melting of peridotitic material within the asthenospheric wedge due to fluxing from volatiles escaping from the subducting plate, this is highly unlikely for several fundamental reasons. First, because of its high temperature, the wedge is sealed to hydrothermal flows. Second, the composition of the predominant basalt found in island arcs has an exceedingly close chemical affinity to subducted MORB and virtually none to the wedge peridotite. Third, the strong focusing of arc volcanic

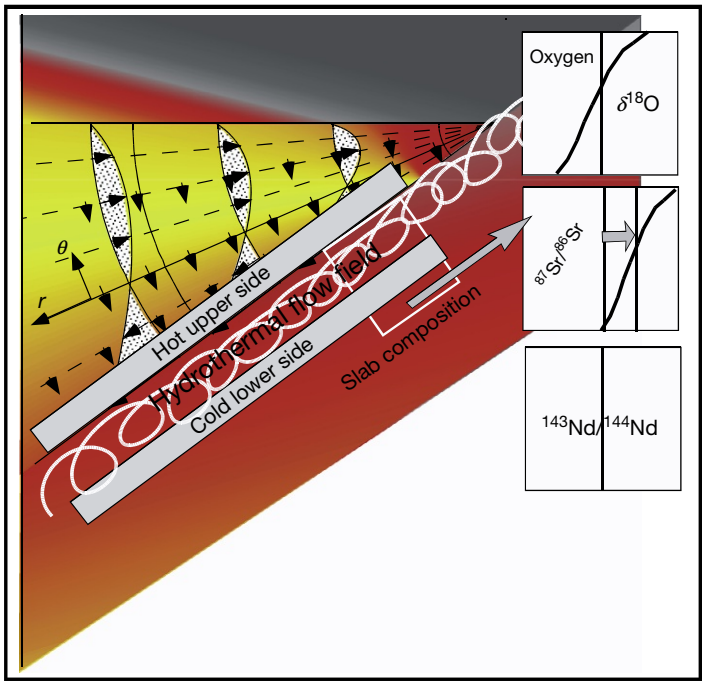

Figure 36 The helical hydrothermal flow up the coldest, most brittle, and most permeable part of the subducting plate. This flow redistributes the concentrations of certain isotopes and trace elements within the slab. No fluid penetrates the overlying asthenospheric wedge.

centers at the surface, with very little dispersion, over millions of years, links it to a magmatic source that is virtually static with respect to the plate–plate subduction configuration. This cannot be achieved through magma production within the wedge flow regime.

The major elements of magma dominate the mass of the magma, take the most energy to change, and are therefore the most diagnostic deciding source characteristics. The close chemical affinity of melts from the plate to HAB, the arc parental magma, can be seen by comparing HAB lava compositions with melt compositions from both the plate and the wedge. This is shown in Figure 37, where melt composition is shown as a function of degree of melting at 30–40 kb (3–4 GPa). Across each panel are horizontal lines representing HAB composition and intersections or matches with melt from either of the two source rocks are indicated. No matches are found for melt from the peridotitic wedge material, but matches are almost complete for each of the major elements for slab melting. It is particularly notable that slab melts are low in MgO content. This reflects a fundamental chemical property of this source rock in that the MgO content cannot exceed about 7.5 wt%. This is also a fundamental property of HAB. That is, arc basalts are characteristically low in MgO. For HAB from mature volcanic centers at $SiO_2 \sim 50$ wt%, MgO content is typically about 4–5 wt%. Some arc basalts are also found with significantly higher MgO, but these can almost universally be demonstrated to have suffered contamination with tramp olivine debris from lithospheric wall rock. Moreover, these basalts are also almost always from arc supercenters where there has been an unusually large eruptive flux. Large eruptive fluxes, like at Kilauea, lead to strong heating of the lithosphere wall rock, which causes structural weakening and collapse, furnishing peridotitic debris for entrainments by ascending arc HAB. Careful petrographic inspection of basalts with elevated MgO and/or Ni commonly reveals fragments of unzoned, often slightly strained, highly forsteritic ($\sim Fo_{92}$) olivine from the lithosphere. Because of the inherent assumption that magmas of high MgO contents are primitive and thus parental to the lower MgO suite, these contaminated basalts are often mistakenly assumed to be fundamental to the arc magmatic system. A second distinctive chemical feature of arc HAB is the elevated Al_2O_3 content (16–20 wt%), which is reflected by high modal contents of plagioclase in the plutons and lavas. These high plagioclase contents give arc basalts their characteristic gray appearance.

6.07.10.7.1 Slab quartz-eclogite

These chemical features also reflect the basic high-pressure mineralogy of the subducted oceanic crust. At pressures of 2–3 GPa, the MORB mineral assemblage of plagioclase, olivine, clinopyroxene, and Fe–Ti oxides transforms to quartz, garnet, jadeitic pyroxene, rutile, sanidine, and possibly kyanite, which is a quartz-eclogite. In comparison with the pervasive peridotitic country rock of the mantle at these depths, this quartz-bearing source rock is highly unusual. Melting of this assemblage produces the characteristic arc HAB bulk composition. A notable feature of this assemblage is the high modal content of garnet, which will strongly fractionate the concentration of REE in the ensuing melt. That this is not observed in arc HAB has long been taken to be evidence that garnet, and hence also the slab itself, is not a reasonable source rock. But this conclusion assumes melt extraction takes place at a

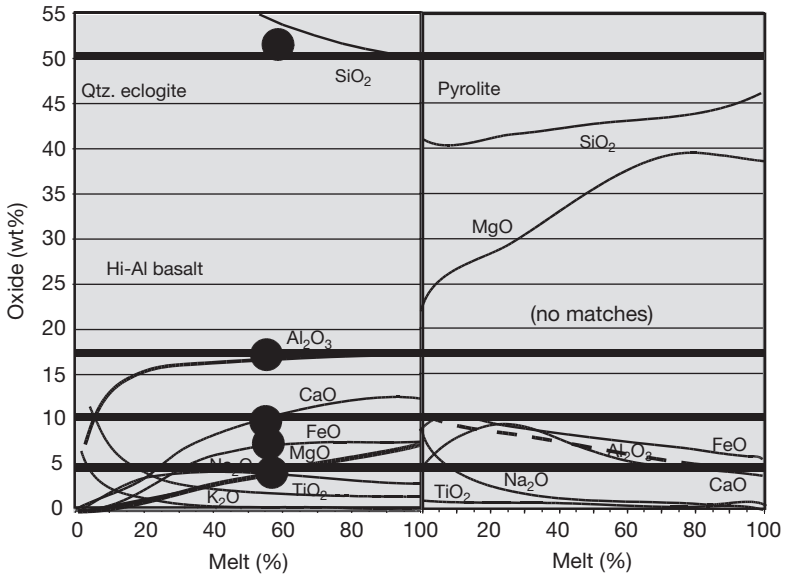

Figure 37 The compositions (oxides and curves) of melts as a function of degree of melting produced from quartz-eclogite subducted oceanic crust and pyrolite of the asthenospheric wedge. The straight horizontal lines show the composition of typical high alumina basalt (HAB) of island arcs (Aleutians) and the large dots show matching points between the observed HAB and the calculated melts. There is almost perfect agreement with the slab source and no agreement whatsoever with the mantle wedge.

sufficiently high pressure to assure that garnet is still a dominant phase, which is dynamically unlikely. That is, magma ascends because it is buoyant relative to its surroundings. And to become buoyant, or gravitationally unstable, sufficient melting is necessary to make the mushy assemblage less dense than the surroundings. Additional extensive melting takes place during ascension. The requisite amount of melting necessary to extract a melt free of solids will be, as in solidification fronts, near 50 vol.%. Melt extraction is also possible at lower degrees of melting due to compaction (e.g., Mckenzie, 1984), but in the slab, this is probably inoperative because of the highly limited thickness of material involved, which makes compaction weak. Gravitational instability may take place after only about 10–15 vol.% melting, and the mushy assemblage may rise 20–30 km before enough additional melting takes place to enable the solids to repack and free a nearly crystal-free melt. By this point (i.e., ~2–2.5 GPa), garnet, although still present, is a relatively minor phase, and the REE pattern fits that observed in the arc HAB (Brophy and Marsh, 1986). A critically important physical aspect of this process is the unusually narrow liquidus–solidus relation of quartz-eclogite, which may be as small as 50–70 °C. This means that, once the temperature reaches this point, partial melting, melt production, and instability take place rapidly with relatively little rise in temperature. The process, in effect, has a trigger point that may spontaneously generate magma and diapirs once the melting point is reached. This is in striking contrast to peridotitic mantle rock where the melting range is 500–600 °C and melt production is gradual.

The corollary of this deep phase equilibria is the phase equilibria of arc HAB itself, which is shown for Aleutian basalt in Figure 38 as determined by Baker and Eggler (1983). A striking feature of this phase diagram is the phase rosette near 2 GPa defined by plagioclase, garnet, and clinopyroxene.

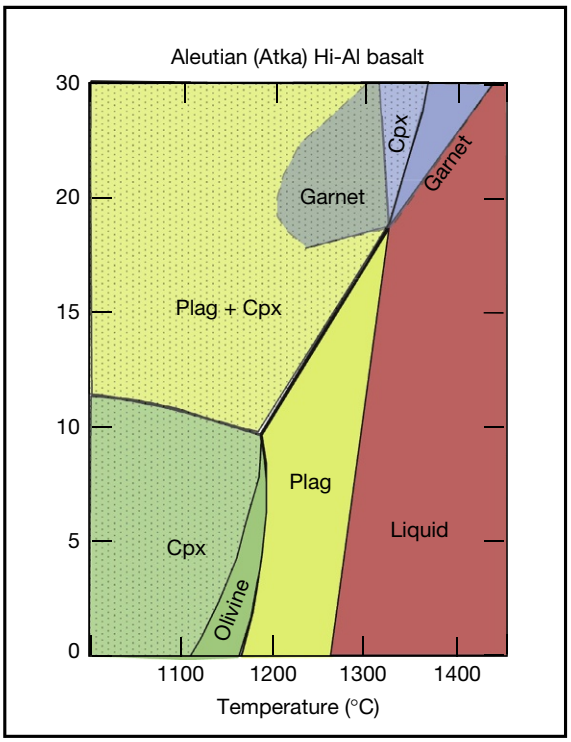

Figure 38 Phase diagram for typical Aleutian high alumina basalt. Note the rosette phase relations near 20 kb.

These are phases also common to quartz-eclogite, which suggests that at this point, these two rocks (i.e., HAB and quartz-eclogite mush) would be in equilibrium. This also suggests, alternatively, that this arc HAB may have been extracted from a mush of quartz-eclogite that rose buoyantly to this level.

Similar rosette features were long looked for (to no avail) in MORB phase equilibria to identify the point of extraction from peridotitic mantle, and here, in arc HAB, this feature seems to have been overlooked.

6.07.10.8 Diapirism, Rayleigh–Taylor Instability, and Volcano Spacing

In this process of magmatism triggered by the temperature of the slab surface reaching a critical point, a thin band or ribbon of buoyant mush is produced everywhere beneath the arc on the surface of the subducting plate. A layer of lower-density material beneath higher-density material initiates a collective gravitational instability that leads to the formation of a family of (ideally) evenly spaced plumes or diapirs of the buoyant material (see **Figure 39**). The distance between the diapirs is given by (Marsh, 1979a,b)

$$d = \frac{2\pi h_2}{2.15}\left(\frac{\mu_1}{\mu_2}\right)^{1/3} \quad [26]$$

where h_2 is the buoyant layer thickness and μ_1 and μ_2 are, respectively, the viscosity of the overlying mantle and the mush. And the radius of the diapir is given by

$$a = 0.53 h_2\left(\frac{\mu_1}{\mu_2}\right)^{1/4} \quad [27]$$

If these equations are used in concert along with conservation of mass and the observed spacing of arc volcanic centers, an estimate can be made of the nature of the source region (Marsh, 1979a,b). The source region is thin 50–100 m and highly viscous ($\sim 10^{10}$ Pa s), and the diapirs have a radius of ~3 km. Not only do these estimates seem reasonable, but there also are dynamic features of this process that fit or correlate well with the generally observed style of magmatism.

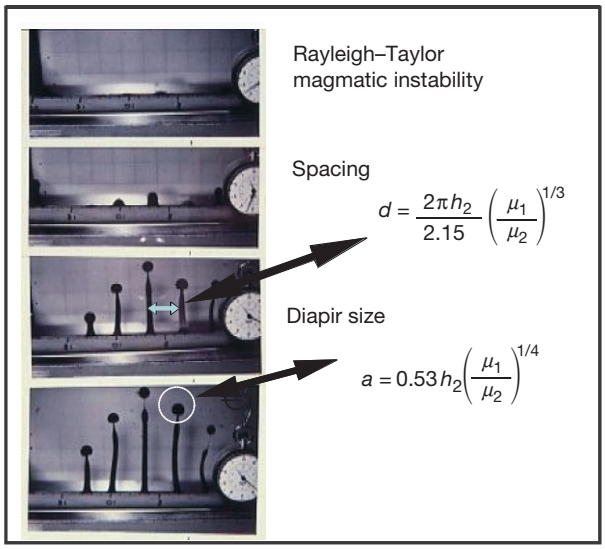

Figure 39 The process of Rayleigh–Taylor gravitational instability when a less dense fluid (black) lies beneath a more dense fluid (clear). Plumes automatically form as the most efficient form of fluid transfer. The equations at the right show the relationship between plume spacing and plume radius and the fluid viscosities and source thickness (h_2).

The overall magmatic process is driven by the production of buoyant mush, loading the system to the point of systematic instability, which relatively rapidly unloads the system over and over. Simply, the temperature at the slab interface slightly exceeding the solidus of the quartz-eclogite triggers this entire process. Evenly spaced diapirs of mush rise into the convecting mantle wedge, traverse it, and essentially burn a hole upward through the overlying lithosphere. The hot diapirs soften the wall rock allowing it to flow around the diapir (Marsh, 1982). Early diapirs undoubtedly stagnate before reaching the surface, but continued use by later diapirs eventually makes a path to the surface. This process eventually chemically and thermally insulates the pathway, allowing later magmas to travel to the surface without suffering undue thermal and chemical contamination. Extraction of standard arc HAB unavoidably takes place during ascent. Diapirs can traverse the mantle wedge and repeatedly enter exactly the same pathway point at the base of the arc lithosphere because the flow through the wedge, across any vertical section, obeys conservation of mass. Any diapir ascending at constant velocity entering this flow on one margin will exit the flow at exactly the same vertical point on the opposite margin. This will not be so for a magma generated *within* the wedge region. Moreover, the ribbon of melting on the slab surface will spread down-dip at the rate of subduction. Once the melt ribbon reaches a distance d down-dip, a new instability will commence. For typical subduction rates, this will occur about 3 Ma after the first instability, which is the time of appearance of the sporadic volcanoes of the secondary arcs, like Leskov in the Scotia Arc and Amak in the Aleutians. Because of the angle of dip (θ) of the unstable layer, the spacing of these centers will be $d\cos(\theta)$, which is also observed.

6.07.10.9 Alkali Basalts Posterior to Arcs

Scattered behind many island arcs are contemporary alkali basalt volcanoes. These are very much unlike arc magmas in composition and spatial distribution. They are scattered over a vast region, are silica-poor, are alkali-rich, commonly contain ultramafic nodules, and have an isotopic identity closely linking them to peridotitic source rock. Unlike arc HAB, everything about them suggests a mantle, not a slab, identity. These are exactly the characteristic magmas expected to be generated within the flowing mantle wedge. The streamlines of flow in the wedge are inclined upward as the flow moves into the corner region above the subducting plate. Already at the point of melting, this convective rise initiates further melting resulting in sporadic, disorganized volcanism on the surface.

6.07.10.10 The Arc Magmatic System

Arc magmatism is a mechanical system controlled by subduction of a MORB-like crust that is intimately coupled, physically and thermally, to the flow induced in the wedge region above the plate. Melting is initiated by this flow, which triggers a collective gravitational instability bringing magma periodically to the surface at prescribed locations over long periods of time. Chemical processes that reflect, but do not control, the

dominating physical processes buttress the entire process. The detailed chemical processes, at all levels, are best understood through an appreciation of the overall physical dynamics of the full system.

6.07.11 Solidification Front Differentiation Processes

6.07.11.1 Introduction

Magmatic systems, regardless of setting, are all broadly similar in the basic nature of the physical and chemical processes that shape the final product. The gain and loss of crystals, both indigenous and exotic or xenocrystic, their type, size, concentration, and length of time in contact with the melt are fundamental to the chemical evolution of the magma. But it is the dynamic role of solidification fronts that sets at any time the prevailing magmatic processes that go to determine the spatial pattern of rocks seen in the field and the temporal eruptive sequence of lavas. Crystal fractionation from the interiors of magma chambers, the classical approach to chemical differentiation, is not a realistic process. We have seen that the fundamental difficulty in achieving high degrees of chemical fractionation is that the silica-rich residual melt resides deep within solidification fronts where it is inaccessible to extraction accumulation, transport, and eruption. Given the observed diversity of igneous rocks on Earth and even at some small volcanoes, there are, clearly, other processes operating within solidification fronts that produce strong, bimodal chemical fractionation effects. The tearing open of solidification fronts under gravitational instability, flushing of residual melt from the front, and the sidewall upflow of residual melt are three key differentiation processes. These are processes that operate on relatively small spatial scales (1–10 m) but lead to planetary-scale differentiation effects.

6.07.11.2 Solidification Front Instability

A detailed examination of almost any thick basaltic sill reveals in the upper parts the presence of interdigitating lenses of silicic material (see Figure 40). The lenses often begin thin and small near the sill roof and increase in thickness and length up to, respectively, ~1 m and 20–30 m at a depth of about 25% full sill thickness. These bodies have been called by many names from pegmatitic segregations to silicic segregations to silicic schlieren to granophyres (e.g., Walker, 1956). As these names suggest, silicic segregations are significantly enriched in silica over the bulk composition of the sill, commonly ~60–65 wt% SiO_2 versus ~55 wt% SiO_2. They are also coarser-grained and their physical form often suggests that they fill tears and fractures in the sill. A likely mechanism of formation is by internal failure or tearing of the solidification front (Marsh, 2002).

Roof solidification fronts are generally denser than the underlying uncrystallized magma, and as they thicken, they will eventually fail under the action of gravity, producing internal gashes that fill with local residual melt. The process is similar to hanging an old rug from the ceiling and fastening weights along the lower edge. As more and more weight is added, the rug will eventually tear horizontally at the weakest spots. Solidification fronts tear where there is enough strength to fracture, which is within the rigid crust (see Figures 4 and 5). The internal distribution of both weight and strength within the solidification front is determined by the spatial increase in crystallinity with decreasing temperature. To avoid tearing, the local strength of the solidification front must increase proportionally with weight, and strength comes from increasing crystallinity. But crystallinity changes are dictated by phase equilibria and not by strength constraints. The noncovariant variation of strength and crystallinity sets the physical conditions for solidification front instability (SFI). With initiation of tearing, local interstitial melt is drawn into the tears. Due to conservation of mass, the infilling melt must come from below the tear, and the texture of the segregation reflects the filling process.

Prior to the tearing, from phase equilibrium considerations, the interstitial melt is contained in the solidification front at a crystallinity of about 60–65 vol.%. The melt is multiply saturated with solid phases, and with tearing, the local melt can now grow large (~1–10 cm) pegmatitic crystals of clinopyroxene, often in symplectic intergrowths with plagioclase. The melt arriving from lower in the solidification front is also slightly hotter, and as it cools, it forms progressively smaller crystals downward in the segregation. The texture of the segregation is, thus, coarse at the top and fine downward, reflecting the filling process. This is just the opposite expected if the segregations were blobs of residual melt from the lower solidification front that escaped and entered the upper solidification front.

Once generated, the silicic differentiates are almost impossible to remove or assimilate back into the basaltic magma. If the whole system becomes molten, they will maintain their physical and chemical identity due to their high contrast in viscosity, and being at near chemical equilibrium, they will not be assimilated by diffusion. Due to their density contrast, they will, however, given the chance, tend to collect at the top of the system and undergo compaction into large silicic masses as first recognized by Grossenbacher (1994). Some large dolerite sills have large bulbous masses of such rock at the upper contacts (e.g., Grossenbacher, 1994; McDougal, 1962). The inordinately large volume of these masses relative to the associated sill, the thin chilled margins of dolerite separating the mass from the country rock, and the often sharp contacts between the dolerite and the granophyre all suggest that these bodies have formed from reprocessing of basaltic bodies containing silicic segregations. This may be a process operating on many scales that contributes to building continental crust. It may today be operating at the ocean ridges in the formation of plagiogranite lenses and also in the crust of Iceland to form large bodies of rhyolite.

6.07.11.3 Silicic Segregations and Crust Reprocessing in Iceland

Silicic segregations form essentially unavoidably within any basaltic solidification front, yet they are spatially distributed and can only be collected if they are freed from the rock through wholesale melting. Large-scale systematic melting as in rifting provides a setting where this process can operate efficiently. The ideal locality for repeated rifting of basaltic

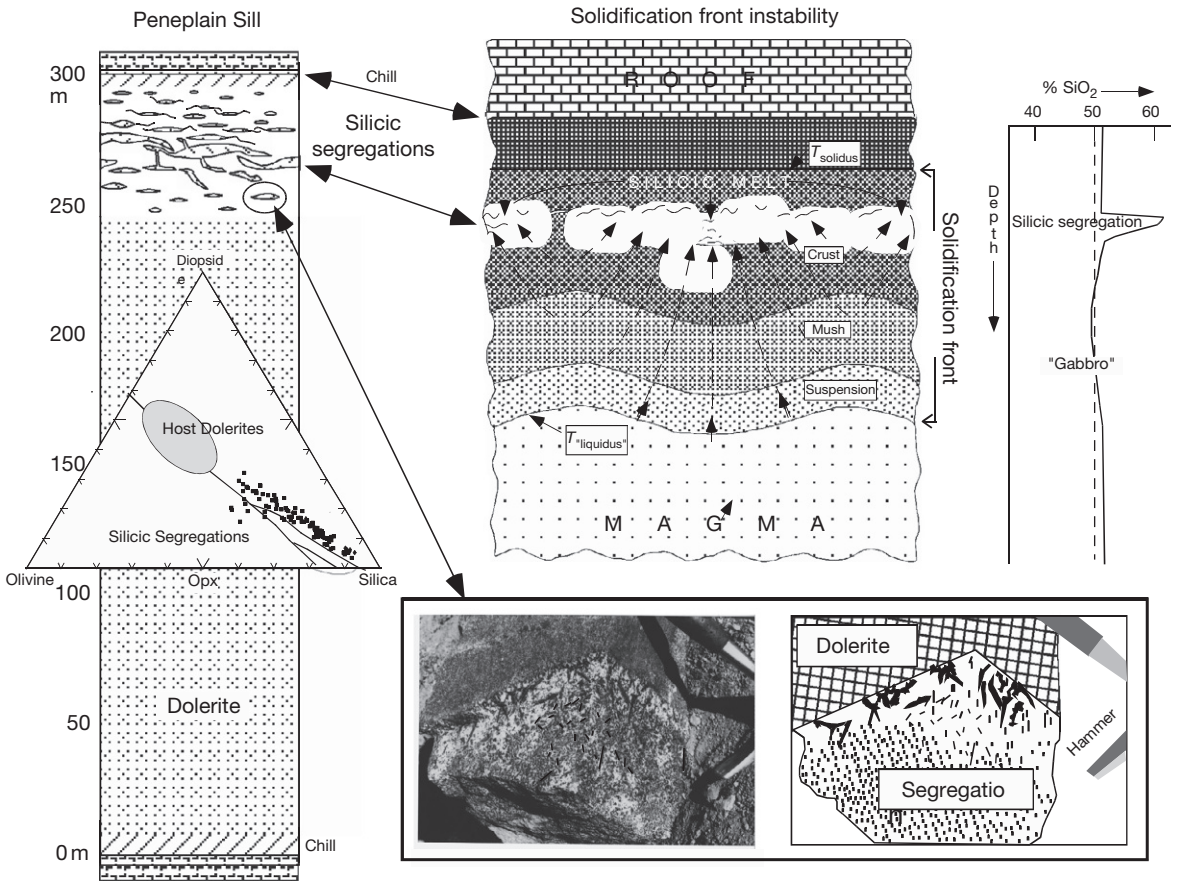

Figure 40 The process of SFI in the Peneplain sill at Solitary Rocks. The left section shows the location and nature of the silicic segregations along with a normative ternary showing the range of segregation compositions relative to the dolerite sill compositions. The SFI process is shown schematically (upper center) and the nature of an actual segregation is also shown (lower right). Reproduced from Marsh BD (2002) On bimodal differentiation by solidification front instability in basaltic magmas, I: Basic mechanics. *Geochimica et Cosmochimica Acta* 66: 2211–2229.

terranes is at immobile oceanic volcanic centers where the crust can be reprocessed over and over. This promotes a strong bimodality of crustal composition. About 18% of the surface rocks of Iceland are highly silicic rhyolites. This is in striking contrast to Hawaii where there are no rhyolitic rocks at all. Deep drilling in Iceland shows the crust laden with lenses and pockets of silicic segregations and coupled with a local ocean ridge that has periodically relocated into older crust allows for widespread remelting and conditions ideal for accumulating large amounts of silicic material. Detailed petrologic studies of the 200 km^3 rhyolite mass at Torfajökull caldera show that this body was formed by this process (Gunnarsson et al., 1998). Fissures propagating into older crust bring hot basaltic magma into thin warm crust, which promote progressive wholesale melting via melting fronts propagating outward into the country rock. These are prograde solidification fronts as opposed to common magmatic retrograde solidification fronts. Because of heterogeneous melting, the wall rock undergoes large-scale failure, freeing silicic segregations that collect into large masses of rhyolitic magma and sometimes erupt from the same craters as the basalts. This process is depicted in Figure 41. This overall process of collecting silicic segregations is very much akin to the emulsion coalescence that occurred in the Sudbury impact melt sheet. The net result of magmatic processes of this type is a bimodal suite of compositions characterized at each end by a basaltic and a silicic member.

6.07.11.4 Sidewall Upflow

Another means of escape of residual silicic melts from deep within solidification fronts is by upward flow along steep lateral walls. Since all magmas are contained within solidification fronts, some bodies will have tall steep lateral margins where low-density residual melt can flow upward under Darcy dynamics and collect at higher levels (see Figure 42). This can only happen if the advance of the solidification front is slow enough to allow upward flow through the porous solidification front. In the upper crust, solidification fronts move rapidly in response to high cooling rates, but with increasing depths in the crust, cooling becomes increasing slow. This retards the inward advance of the solidus, marking the rear of the solidification front, allowing ample time for upward flow of viscous melt. Unlike the idealized flows that are depicted in Figure 2, these realistic flows occur deep within the solidification front and not along hard walls

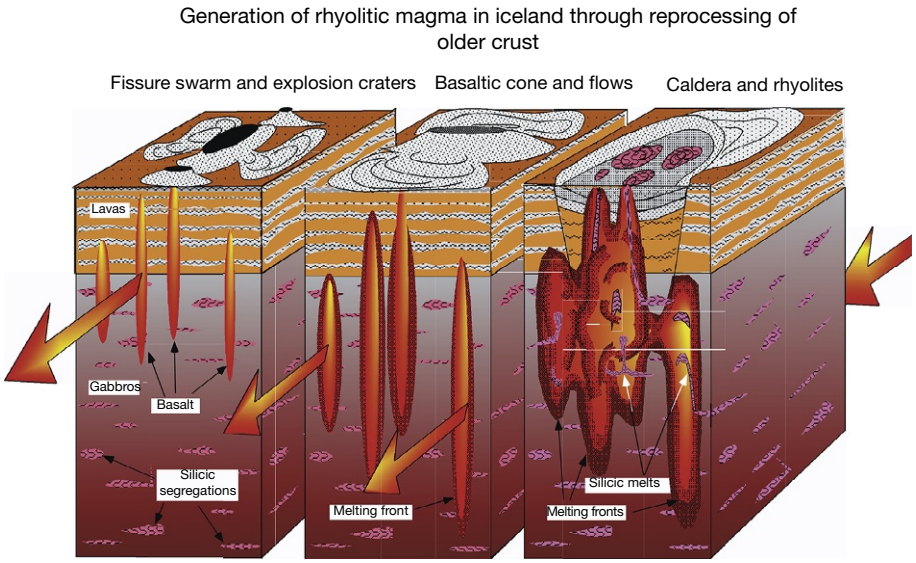

Figure 41 Reprocessing of the Icelandic crust due to propagation of basaltic fissures into older crust containing silicic segregations and the formation of large bodies of silicic material from the freeing and collection of these individual silicic segregations.

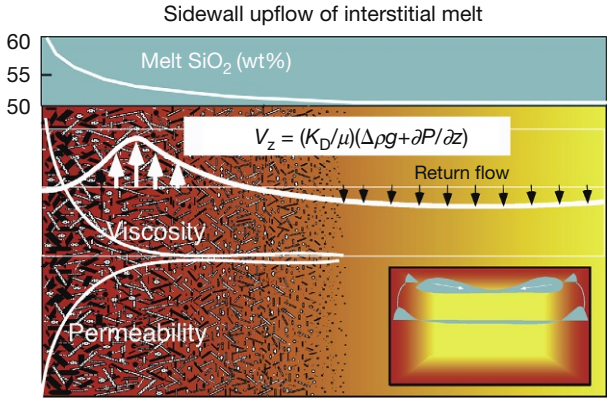

Figure 42 The flow up a vertical wall of interstitial residual, silica-rich melt deep within a solidification front. The variations in permeability and melt viscosity are indicated as is the form of the Darcy equation governing the flow.

where residual fluid can essentially stream upward and collect rapidly at the roof of the system. The flow is governed by the Darcy equation,

$$V_m = \frac{K_D}{\mu}\left[\frac{\partial P}{\partial z} + \Delta\rho g\right] \qquad [28]$$

where V_m is the Darcy velocity, which is a measure of the melt flux per unit area, K_D is permeability, μ is melt viscosity, P is pressure, z is the spatial coordinate, $\Delta\rho$ is density contrast, and g is gravity. It is critical to note there that both μ and K_D change strongly with distance outward in the solidification front; μ increases and K_D decreases such that the quantity K_D/μ decreases strongly with approach to the solidus (Figure 42). This regulates the flow and there is an optimum position within the rear of the solidification front where melt is most efficient at flowing upward. The slower the solidification front moves, the more silicic is the optimum melt. In the upper crust, the dominant melt has a composition of about 55 wt% SiO_2, and in the lower crust, it approaches 65 wt%. The buildup of volatiles in the residual melt helps the overall process.

6.07.11.5 Fissure Flushing

A broadly similar process to melt flow through the rear of a steep solidification front is the flushing of residual melt from an aging solidification front spanning a fissure or other sheet-like body. The process is depicted in Figure 43. During times of repose in magmatic systems, the driving pressure relaxes, conduit walls press in on the remaining magma, and solidification fronts move in from the lateral walls. The fronts eventually meet and form a bridge of crystals across the conduit. As solidification proceeds, the interstitial melt becomes progressively enriched in silica as a function of position within the conduit. When the repose periods end and magma flow resumes, magma coursing this conduit will flush the residual melt from the crystalline matrix of solids. This melt will be distinctive in its differentiated chemical composition, which will appear chemically indistinguishable to crystal fractionation, and also in the telltale clots of crystals torn from the solidification front during eviction. It is processes like these that undoubtedly give rise to mildly differentiated magmas at many locations in large, long-lived magmatic systems like Hawaii. Another characteristic of these events is their optimum near-surface location on flanks of the volcano where magma transport in fissures is common. The 1955 Kilauea eruption produced lava with these characteristics (Ho and Garcia, 1988; Wright and Fiske, 1971), and the ongoing eruptions of Puu Ōō also show some of these features (e.g., Garcia et al., 1989).

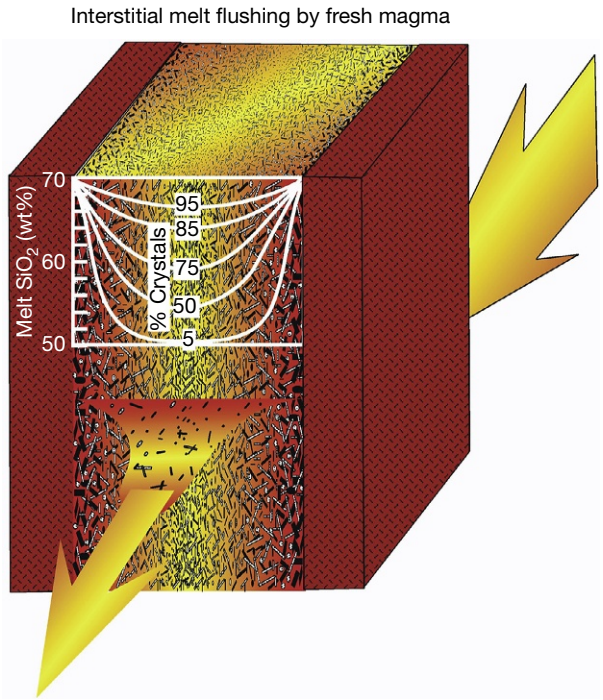

Figure 43 The process of flushing residual melt from a partially solidified fissure by reactivation of magma flow after a repose period. The curves show the variation in residual melt silica content as a function of position and degree of crystallinity within the fissure.

6.07.12 Magmatic Systems

Earth's surface displays a rich diversity of igneous rock from which most other rocks are derived. The majority of igneous rocks are either ocean floor basalts or continental granitics. The processes that produce this strong bimodality are physical processes, buttressed by chemical processes, associated with a prevailing tectonic theme. Mantle convection gives rise to seafloor spreading and a distinct style of magma production and evolution in a steady-state standing magmatic mush column capped by passive thin sills. No continental silicic material is produced. The seafloor is an enormous gabbroic batholith. Silicic noise is produced within the solidification fronts of basaltic systems on small local scales. The key to accentuating and enhancing this silicic signal is through systematic reprocessing. Remelting of the oceanic crust in subduction zones, during massive bolide impacts, in areas like Iceland, and in other immobile crustal welts accumulates this silicic material into viable rock masses.

Magmatic processes in and of themselves operate within a vast array of tectonic environments, but the processes involved in the behavior and evolution of magma are finite and understandable within a clear physical and chemical framework. The key to analyzing magmatic systems is to gain an integrated physical perspective of the overall process of magma production, transport, and emplacement or eruption. Magmas chemically evolve through the gain and loss of crystals, which is governed by entrainment of exotic crystals in addition to those nucleated and grown within the magma itself. But it is the understanding of the intimate coupling of spatial physical processes with phase equilibria that furnishes the greatest insight into the true processes that shape magma and Earth itself.

Acknowledgments

This work on magmatic processes is supported by the National Science Foundation Office of Polar Programs through grant ANT0944043 to the Johns Hopkins University. Unless otherwise noted, all figures are from the forthcoming book *Magma Physics* by this author.

References

Ariskin AA (1999) Phase equilibria modeling in igneous petrology: Use of COMAGMAT model for simulating fractionation of ferro-basaltic magmas and the genesis of high-alumina basalt. *Journal of Volcanology and Geothermal Research* 90: 115–162.

Aronson IS and Tsimring LS (2009) *Granular Patterns*, p. 343. Oxford University Press.

Bachmann O and Bergantz GW (2004) On the origin of crystal-poor rhyolites: Extracted from batholithic crystal mushes. *Journal of Petrology* 45(8): 1565–1582.

Bachmann O and Bergantz GW (2008) Rhyolites and their source mushes across tectonic settings. *Journal of Petrology* 49(12): 2277–2285.

Bacon CR and Lanphere M (2006) Eruptive history and geochronology of Mount Mazama and the Crater Lake region, Oregon. *Geological Society of America Bulletin* 118(11–12): 1331–1359.

Baker DR and Eggler DH (1983) Fractionation paths of Atka (Aleutians) high-alumina basalts: Constraints from phase relations. *Journal of Volcanology and Geothermal Research* 18: 387–404.

Baragar WRA (1960) Petrology of basaltic rocks in part of the Labrador Trough. *Bulletin of the Geological Society of America* 71: 1589–1644.

Barksdale JD (1937) The Shonkin Sag laccolith. *American Journal of Science* 33: 321–359.

Becker GF (1897) Fractional crystallization of rocks. *American Journal of Science* 4: 257–261.

Bedard JHJ, Marsh BD, Hersum TG, Naslund HR, and Mukasa SB (2007) Large-scale mechanical redistribution of orthopyroxene and plagioclase in the Basement Sill, McMurdo Dry Valleys, Antarctica: Petrological, mineral-chemical and field evidence for channelized movement of crystals and melt. *Journal of Petrology* 48: 2289–2326.

Bergantz GW (1989) Underplating and partial melting: implications for melt generation and extraction. *Science* 245: 1093–1095.

Bergantz GW (2000) On the dynamics of magma mixing by reintrusion: Implications for pluton assembly processes. *Journal of Structural Geology* 22(9): 1297–1309.

Bhattacharji S (1967) Mechanics of flow differentiation in ultramafic and mafic sills. *Journal of Geology* 75: 101–112.

Boudreau AE (1994) Mineral segregation during crystal aging in two-crystal, two-component systems. *South Africa Journal of Geology* 4: 473–485.

Bowen NL (1915) The later stages of the evolution of the igneous rocks. *Journal of Geology* 23: 1–89.

Bowen NL (1947) Magmas. *Bulletin of the Geological Society of America* 58: 263–280.

Brandeis G and Jaupart C (1986) On the interaction between convection and crystallization in cooling magma chambers. *Earth and Planetary Science Letters* 345–361.

Brandeis G and Marsh BD (1989) The convective liquidus in a solidifying magma chamber: A fluid dynamic investigation. *Nature* 339: 613–616.

Brandeis G and Marsh BD (1990) Transient magmatic convection prolonged by solidification. *Geophysical Research Letters* 17(8): 1125–1128.

Brophy JG and Marsh BD (1986) On the origin of high-alumina basalts and the mechanics of melt extraction. *Journal of Petrology* 27(4): 763–789.

Carmichael ISE, Turner FJ, and Verhoogen J (1974) *Igneous Petrology*. McGraw-Hill Book Company.

Carr MJ, Stoiber RE, et al. (1973) Discontinuities in the deep seismic zone under the Japanese Arcs. *Bulletin of the Geological Society of America* 84: 2917–2930.

Carslaw HS and Jaeger JC (1959) *Conduction of Heat in Solids*. Oxford: Clarendon Press.

Cartwright J and Hansen DM (2006) Magma transport through the crust via interconnected sill complexes. *Geology* 34(11): 929–932.
Coffin MF and Eldholm O (1992) Volcanism and continental break-up: A global compilation of large igneous provinces. In: Storey BC, Alabaster T, and Pankhurst RJ (eds.) *Magmatism and the Causes of Continental Break-up*, pp. 17–30. Boulder, CO: Geological Society of America.
Cross W, Iddings JP, Pirsson LV, and Washington HS (1903) Quantitative classification of igneous rocks. *Journal of Geology*: 286 pp. (spec. issue).
Daly RA (1914) *Igneous Rocks and Their Origin*, p. 563. New York: McGraw-Hill.
Davidson JP, Charlier B, Hora JM, and Perlroth R (2005a) Mineral isochrons and isotopic fingerprinting: Pitfalls and promises. *Geology* 33(1): 29–32.
Davidson JP, Hora JM, Garrison JM, and Dungan MA (2005b) Crustal forensics in arc magmas. *Journal of Volcanology and Geothermal Research* 140: 157–170.
Davidson JP, Morgan DJ, Charlier BLA, Harlou R, and Hora JM (2007) Microsampling and isotopic analysis of igneous rocks: Implications for the study of magmatic systems. *Annual Review of Earth and Planetary Sciences* 35: 274–310.
Dawson JB (1992) First thin sections of experimentally melted igneous rocks: Sorby's observations on magma crystallization. *Journal of Geology* 100: 251–257.
Dickin AP, Nguyen T, and Crocket JH (1999) Isotopic evidence for a single impact melting origin of the Sudbury Igneous Complex. In: Dressler BO and Sharpton VL (eds.) *Large Meteorite Impacts and Planetary Evolution II*, pp. 361–371. Geological Society of America, Special Paper 339.
Dobran F (2001) *Volcanic Processes, Mechanisms in Material Transport*. Kluwer Academic.
Drever HL and Johnston R (1967) Picritic minor intrusions. In: Wyllie PJ (ed.) *Ultramafic and Related Rocks*, pp. 71–82. New York: Wiley.
Dufek J and Bergantz GW (2005) Lower crustal magma genesis and preservation: A stochastic framework for the evaluation of basalt–crust interaction. *Journal of Petrology* 46(11): 2167–2195.
Fleming TH, Elliott DH, et al. (1992) Chemical and isotopic variations in an iron-rich lava flow from the Kirkpatrick Basalt, north Victoria Land, Antarctica: Implications for low-temperature alteration. *Contributions to Mineralogy and Petrology* 111: 440–457.
Fujii T (1974) Crystal settling in a sill. *Lithos* 7: 133–137.
Garcia MO, Ho RA, et al. (1989) Petrologic constraints on rift-zone processes. Results from episode 1 of the Puu Oo eruption of Kilauea volcano, Hawaii. *Bulletin of Volcanology* 52: 81–96.
Garcia MO, Pietruszka AJ, and Rhodes JM (2003) A petrologic perspective of Kilauea volcano's summit magma reservoir. *Journal of Petrology* 44: 2313–2339.
Ghiorso MS, Carmichael ISE, et al. (1983) The Gibbs free energy of mixing of natural silicate liquids; an expanded regular solution approximation for the calculation of magmatic intensive variables. *Contributions to Mineralogy and Petrology* 84: 107–145.
Gibb FGF and Henderson CMB (1996) The Shiant Isles Main Sill: Structure and mineral fractionation trends. *Mineralogical Magazine* 60: 67–97.
Gray NH and Crain IK (1969) Crystal settling in sills: A model for suspension settling. *Canadian Journal of Earth Sciences* 6: 1211–1216.
Gregory RT and Taylor HPJ (1981) An oxygen isotope profile in a section of Cretaceous Oceanic Crust, Samail Ophiolite, Oman: Evidence for $d^{18}O$ buffering of the oceans by deep (>5 km) seawater-hydrothermal circulation at mid-ocean ridges. *Journal of Geophysical Research* 86(B4): 2737–2755.
Grieve RAF, Stoffler D, et al. (1991) The Sudbury structure: Controversial or misunderstood? *Journal of Geophysical Research* 96(E5): 22,753–22,764.
Grossenbacher KA (1994) Origin of large granophyre pods in a Mesozoic diabase sheet near Gettysburg, Pennsylvania. PhD Thesis, Johns Hopkins University, p. 395.
Gunnarsson B, Marsh BD, et al. (1998) Generation of Icelandic rhyolites: Silicic lavas from the Torfajokull central volcano. *Journal of Volcanology and Geothermal Research* 83: 1–45.
Hall J (1798) Experiments on whinstone and lava. *Transaction of Royal Society of Edinburgh* 8: 43–76.
Hein JR, Scholl DW, et al. (1978) Episodes of Aleutian ridge explosive volcanism. *Science* 199: 137–141.
Helz RT (1986) Differentiation behavior of Kilauea Iki lava lake, Kilauea volcano, Hawaii: An overview of past and current work. *Geochemical Society Special Publication* 1: 241–258.
Helz RT, Kirschenbaum H, and Marinenko JW (1989) Diapiric transfer of melt in Kilauea Iki lava lake, Hawaii: A quick, efficient process of igneous differentiation. *Geological Society of America Bulletin* 101: 578–594.
Hersum T, Hilpert M, and Marsh B (2005) Permeability and melt flow in simulated and natural partially molten basaltic magmas. *Earth and Planetary Science Letters* 237: 798–814.
Hess HH (1956) The magnetic properties and differentiation of dolerite sills – Discussion of dolerite sills. *American Journal of Science* 254: 446–451.
Hildreth W and Fierstein J (2012) The Novarupta-Katmai eruption of 1912-largest eruption of the twentieth century. *U.S. Geological Survey professional Paper 1791*, 259 pp.
Ho RA and Garcia MO (1988) Origin of differentiated lavas at Kilauea Volcano, Hawaii: Implications from the 1955 eruption. *Bulletin of Volcanology* 50: 35–46.
Holden GS and Hooper PR (1987) Petrology and chemistry of a Columbia River basalt section, Rocky Canyon, west-central Idaho. *Geological Society of America Bulletin* 87: 215–225.
Hon K, Kauahikaua J, et al. (1994) Emplacement and inflation of pahoehoe sheet flows: Observations and measurements of active lava flows on Kilauea Volcano, Hawaii. *Geological Society of America Bulletin* 106: 351–370.
Hooper PR (1987) The Columbia River Flood Basalt Province: Current status. In: Mahoney JJ and Coffin MF (eds.) *Large Igneous Provinces: Continental, Oceanic, and Planetary Flood Volcanism: American Geophysical Union Monograph 100,* pp.1–27.
Hort M (1997) Cooling and crystallization in sheet-like magma bodies revisited. *Journal of Volcanology and Geothermal Research* 76: 297–317.
Hort M, Marsh BD, et al. (1999) Convection and crystallization in a liquid cooled from above: An experimental and theoretical study. *Journal of Petrology* 40(8): 1271–1300.
Hsui AT, Marsh BD, et al. (1983) On melting of the subducted oceanic crust: Effects of subduction induced mantle flow. *Tectonophysics* 99: 207–220.
Hurlbut CSJ (1939) Igneous rocks of the Highwood Mountains, Montana. Part I. The laccoliths. *Bulletin of the Geological Society of America* 50: 1043–1112.
Imsland P (1984) *Petrology, Mineralogy and Evolution of the Jan Mayen Magma System*. Reykjavik: Prentsmidjan Oddi.
Irvine TN (1970) Heat transfer during solidification of layered intrusions. I. Sheets and sills. *Canadian Journal of Earth Sciences* 7: 1031–1061.
Jaeger JC (1968) Cooling and solidification of igneous rocks. In: Hess HH and Poldervaart A (eds.). *Basalts: The Poldervaart Treatise on Rocks of Basaltic Composition*, vol. 2, pp. 503–536. New York: Interscience.
Jaeger JC and Joplin GA (1955) Rock magnetism and the differentiation of dolerite sill. *Journal of the Geological Society of Australia* 2: 1–19.
Jaeger JC and Joplin GA (1956) The magnetic properties and differentiation of dolerite sills – Discussion. *American Journal of Science* 254: 443–446.
Jaupart C (1998) Gas loss from magmas through conduit walls during eruption. *The Physics of Explosive Volcanic Eruptions*, vol. 145, pp. 73–90. Geological Society of London, Special Publication.
Jaupart C and Brandeis J (1986) The stagnant bottom layer of convecting magma chambers. *Earth and Planetary Science Letters* 80: 183–199.
Jhaveri B and Homsy GM (1980) Randomly forced Rayleigh–Benard convection. *Journal of Fluid Mechanics* 98: 329–348.
Jhaveri BS and Homsy GM (1982) The onset of convection in fluid layers heated rapidly in a time-dependent manner. *Journal of Fluid Mechanics* 114: 251–260.
Kadanoff LP (1991) Complex structures from simple systems. *Physics Today:* 9–10.
Kadanoff L (2001) Turbulent heat flow: Structures and scaling. *Physics Today* 54: 34.
Kerr RC, Huppert HE, et al. (1989) Disequilibrium and macrosegregation during solidification of a binary melt. *Nature* 340: 357–367.
Khurana A (1988) Rayleigh–Benard experiment probes transition from chaos to turbulence. *Physics Today* 41(6): 17–21.
Kincaid C and Sacks IS (1997) Thermal and dynamical evolution of the upper mantle in subduction zones. *Journal of Geophysical Research* 102: 12295–12315.
Klein EM and Langmuir CH (1987) Global correlation of ocean ridge basalt chemistry with axial depth and crustal thickness. *Journal of Geophysical Research* 92: 8089–8115.
Korenaga J and Kelemen PB (1998) Melt migration through the oceanic lower crust: A constraint from melt percolation modeling with finite solid diffusion. *Earth and Planetary Science Letters* 156: 1–11.
Langmuir CH, Klein EM, and Plank T (1992) Petrological systematics of mid-ocean ridge basalts: Constraints on melt generation beneath oceanic ridges. In: Morgan JP, Blackman DK, and Sinton JM (eds.) *Mantle Flow and Melt Generation at Mid-Ocean Ridges*. *Geophysical Monograph 71,* pp. 183–280. Washington, DC: American Geophysical Union.
Lightfoot PC, Keays RR, et al. (1997) Geochemical relationships in the Sudbury Igneous Complex: Origin of the main mass and offset dikes. *Economic Geology* 92: 289–397.
Maaloe S, James D, et al. (1992) The Koloa volcanic suite of Kauai, Hawaii. *Journal of Petrology* 33(4): 761–784.
Maaloe S, Tumyr O, et al. (1989) Population density and zoning of olivine phenocrysts in tholeiites from Kauai, Hawaii. *Contributions to Mineralogy and Petrology* 101: 176–186.

Makse HA, Shlomo H, et al. (1997) Spontaneous stratification in granular mixtures. *Nature* 286: 379–382.

Mangan MT and Marsh BD (1992) Solidification front fractionation in phenocryst-free sheet-like magma bodies. *Journal of Geology* 100: 605–620.

Marsh BD (1979a) Island arc development: Some observations, experiments, and speculations. *Journal of Geology* 87: 687–713.

Marsh BD (1979b) Island-arc volcanism. *American Scientist* 67: 161–172.

Marsh BD (1982) On the mechanics of igneous diapirism, stopping, and zone melting. *American Journal of Science* 282: 803–855.

Marsh BD (1988a) Crystal size distribution (CSD) in rocks and the kinetics and dynamics of crystallization I. Theory. *Contributions to Mineralogy and Petrology* 99: 277–291.

Marsh BD (1988b) Crystal capture, sorting, and retention in convecting magma. *Geological Society of America Bulletin* 100: 1720–1737.

Marsh BD (1989) On convective style and vigor in sheet-like magma chambers. *Journal of Petrology* 30: 479–530.

Marsh BD (1991) Reply to comments "On convective style and vigor in sheet-like magma chambers". *Journal of Petrology* 32(4): 855–860.

Marsh BD (1996) Solidification fronts and magmatic evolution. *Mineralogical Magazine* 60: 5–40.

Marsh BD (1998) On the interpretation of crystal size distributions in magmatic systems. *Journal of Petrology* 39: 553–599.

Marsh BD (2000) Magma Chambers. In: *Encyclopedia of Volcanoes*, pp. 191–206. Academic Press.

Marsh BD (2002) On bimodal differentiation by solidification front instability in basaltic magmas, I: Basic mechanics. *Geochimica et Cosmochimica Acta* 66: 2211–2229.

Marsh BD (2004) A magmatic mush column Rosetta Stone: The McMurdo Dry Valleys of Antarctica. *Eos, Transactions American Geophysical Union* 85(47): 497–502.

Marsh BD (2006) Dynamics of magma chambers. *Elements* 2: 287–292.

Marsh BD (2007a) Crystallization of silicate magmas deciphered using crystal size distributions. *Journal of the American Ceramic Society* 90(3): 746–757.

Marsh BD (2007b) Magmatism, magma, and magma chambers. In: *Treatise on Geophysics*, 1st edn, pp. 276–333. Elsevier, Chapter 6.

Marsh BD (2013) On some fundamentals of igneous petrology. *Contributions to Mineralogy and Petrology* 166: 665–690.

Marsh BD, Gunnarsson B, et al. (1991) Hawaiian basalt and Icelandic rhyolite: indicators of differentiation and partial melting. *Geologische Rundschau* 80(2): 481–510.

McBirney AR (1993) *Igneous Petrology*. Boston: Jones and Bartlett Publishers.

McBirney AR (1998) *Santorini and Its Eruptions*, by Ferdinand A. Fouqué translated by A. R. McBirney, p. 495. Johns Hopkins University Press.

McDougal I (1962) Differentiation of the Tasmanian dolerites: Red Hill dolerite-granophyre association. *Geological Society of America Bulletin* 73: 279–316.

McKenzie D (1984) The generation and compaction of partially molten rock. *Journal of Petrology* 25: 713–765.

Melnik O, Barmin AA, and Sparks RSJ (2005) Dynamics of magma flow inside volcanic conduits with bubble overpressure buildup and gas loss through permeable magma. *Journal of Volcanology and Geothermal Research* 143: 53–68.

Murata KJ and Richter DH (1966) The settling of olivine in Kilauean magma as shown by lavas of the 1959 eruption. *American Journal of Science* 264: 194–203.

Nicolas A (1995) *The Mid-Oceanic Ridges Mountains Below Sea Level*. Berlin, Heidelberg: Springer-Verlag.

Osborne FF and Roberts EJ (1931) Differentiation in the Shonkin Sag laccolith, Montana. *American Journal of Science* 22: 331–353.

Patwardhan K and Marsh BD (2011) Dynamics of the development of the Isle au Haut gabbro-diorite layered complex: Quantitative implications for mafic-silicic magma interactions. *Journal of Petrology* 52(12): 2365–2395.

Penn RL and Banfield JF (1999) Morphology development and crystal growth in nanocrystalline aggregates under hydrothermal conditions: Insights from titania. *Geochimica et Cosmochimica Acta* 63(10): 1549–1557.

Phillips OM (1991) *Flow and Reactions in Permeable Rocks*. Cambridge University Press.

Philpotts AR and Carroll M (1996) Physical properties of partly melted tholeiitic basalt. *Geology* 24(11): 1029–1032.

Pirsson LV (1905) *Petrography and Geology of the Igneous Rocks of the Highwood Mountains, Montana*. United States Geological Survey Bulletin no. 237.

Rayleigh L (J.W. Strutt) (1916) On convection currents in a horizontal layer of fluid when the higher temperature is on the under side. *Philosophical Magazine* 32: 529–546.

Rhodes JM and Vollinger MJ (2004) Composition of basaltic lavas sampled by phase-2 of the Hawaii Scientific Drilling Project: Geochemical stratigraphy and magma types. In: *Geochemistry Geophysics Geosystems*, p. 38. American Geophysical Union.

Ryan MP (1994) Neutral-buoyancy controlled magma transport and storage in mid-ocean ridge magma reservoirs and their sheeted-dike complex: A summary of basic relationships. In: Ryan MP (ed.) *Magmatic Systems*, pp. 97–138. San Diego, California: Academic Press.

Savage SB and Lun CKK (1988) Particle size segregation in inclined chute flow of dry cohesionless granular solids. *Journal of Fluid Mechanics* 189: 311–335.

Scheidegger KF, Corliss JB, et al. (1980) Compositions of deep-sea ash layers derived from North Pacific Volcanic arcs: Variations in time and space. *Journal of Volcanology and Geothermal Research* 7: 107–137.

Schiavi F, Walte N, and Keppler H (2009) First in situ observation of crystalline processes in basaltic-andesitic melt with the moissanite cell. *Geology* 37(11): 963–966.

Simkin T (1967) Flow differentiation in the prictic sills of North Skye. In: Wyllie PJ (ed.) *Ultramafic and Related Rocks*, pp. 64–69. New York: Wiley.

Simkin T (1993) Terrestrial Volcanism in space and time. *Annual Review of Earth and Planetary Sciences* 21: 427.

Sinton JM and Detrick RS (1992) Mid-ocean ridge magma chambers. *Journal of Geophysical Research* 97(B1): 197–216.

Smith RL and Bailey RA (1968) Resurgent cauldrons. In: Coats RR, Hay RL, and Anderson CA (eds.) *Studies in Volcanology: A Memoir in Honor of Howell Williams*, pp. 613–662. Geological Society of America.

Smith AL and Roobol MJ (1982) Andesitic pyroclastic flows. In: Thorpe RS (ed.) *Andesites Orogenic Andesites and Related Rocks*, pp. 415–436. Wiley.

Stoiber RE and Carr MJ (1971) Lithospheric plates, Benioff zones, and volcanoes. *Geological Society of America Bulletin* 82: 515–522.

Stokes GG (1851) On the effect of the internal friction of fluids on the motion of pendulums. *Transactions of the Cambridge Philosophical Society* 8: 8.

Stolper EM, DePaolo DJ, and Thomas DM (2009) Deep drilling into a mantle plume volcano: The Hawaii scientific drilling project. *Scientific Drilling*, no. 7, pp. 4–14.

Sugimura A (1968) Spatial relations of basaltic magmas in island arcs. In: Hess HH and Poldervaart A (eds.). *Basalts: The Poldervaart Treatise on Rocks of Basaltic Composition*, vol. 2, pp. 537–572. New York: Interscience Publishers.

Taylor HP and Forester RW (1979) An oxygen and hydrogen isotope study of the Skaergaard intrusion and its country rocks: A description of a 55 my old fossil hydrothermal system. *Journal of Petrology* 20: 355–419.

Teagle DAH, Ildefonse B, Blum P and the IODP Expedition 335 Scientists (2012) IODP Expedition 335: Deep Sampling in ODP Hole 1256D. *Scientific Drilling*, no. 13, April, pp. 28–34.

Toksoz MN and Bird P (1977) Modeling of temperatures in continental convergence zones. *Tectonophysics* 41: 181–193.

Turcotte DL and Schubert G (1982) *Geodynamics*. New York: Wiley.

Turcotte DL and Schubert G (2002) Geodynamics, p. 451. New York, NY: Cambridge University Press.

Turner JS (1973) *Buoyancy Effects in Fluids*. New York: Cambridge University Press.

Turner FJ and Verhoogen J (1951) *Igneous and Metamorphic Petrology*, p. 602. New York: McGraw-Hill Book Co., Inc.

Upton BGJ and Wadsworth WJ (1967) A complex basalt-mugearite sill in Piton des Neiges volcano, Reunion. *American Mineralogist* 52: 1475–1492.

Viskanta R and Gau C (1982) Inward solidification of a superheated liquid in a cooled horizontal tube. *Warme-Stoffubertrgung* 17: 39–46.

Wager LR and Brown GM (1968) *Layered Igneous Rocks*. San Francisco: W.H. Freeman.

Wager LR and Deer WA (1939) Geological investigations in East Greenland, Part III: The petrology of the Skaergaard intrusion, Kangerdlagssuaq, East Greenland. *Medd Eroenl* 105(4): 1–346.

Walker F (1956) The magnetic properties and differentiation of dolerite sills – Critical discussion. *American Journal of Science* 254: 433–443.

Wilch TI, Lux DR, et al. (1993) Minimal pliocene-pleistocene uplift of the dry valleys sector of the Transantarctic Mountains: A key parameter in ice-sheet reconstructions. *Geology* 21: 841–844.

Williams H (1941) Calderas and their origin. *Bulletin of the Department of Geological Sciences, University of California* 25(6): 239–346.

Wright TL (1971) Chemistry of Kilauea and Mauna Loa lava in space and time. *Geological Survey Professional Paper 735*, p. 40.

Wright TL and Fiske RS (1971) Origin of the differentiated and hybrid lavas of Kilauea volcano, Hawaii. *Journal of Petrology* 12(1): 1–65.

Wright TL and Klein FW (2014) Two hundred years of magma transport and storage at Kīlauea volcano, Hawaii, 1790–2008. *U.S. Geological Survey Professional Paper* 1676, p. 273.

Wright TL and Okamura RT (1977) Cooling and crystallization of tholeiitic basalt, 1965 Makaopuhi lava lake, Hawaii. *U.S. Geological Survey Professional Paper no. 1004*.

Young DA (1998) *N.L. Bowen and Crystallization – Differentiation*, p. 276. Washington, D.C.: Mineralogical Society of America.

Zieg MJ and Marsh BD (2002) Crystal size distributions and scaling laws in the quantification of igneous textures. *Journal of Petrology* 43(1): 85–101.

Zieg MJ and Marsh BD (2005) The Sudbury Igneous Complex: Viscous emulsion differentiation of a superheated impact melt sheet. *Bulletin of the Geological Society of America* 117: 1427–1450.

Zieg MJ and Marsh BD (2012) Multiple reinjections and crystal-mush compaction in the Beacon Sill, McMurdo Dry Valleys, Antarctica. *Journal of Petrology* 53(12): 2567–2591.

This page intentionally left blank

6.08 The Dynamics of Continental Breakup and Extension

WR Buck, Lamont-Doherty Earth Observatory of Columbia University, Palisades, NY, USA

© 2015 Elsevier B.V. All rights reserved.

6.08.1	**Introduction**	325
6.08.2	**Processes Affecting the Dynamics of Continental Extension**	326
6.08.2.1	Tectonic Force for Extension	327
6.08.2.2	Localizing Processes	330
6.08.2.2.1	Thermal advection due to stretching	330
6.08.2.2.2	Magmatic intrusion	331
6.08.2.2.3	Magmatic heat input	331
6.08.2.2.4	Cohesion loss	332
6.08.2.3	Delocalizing Processes	332
6.08.2.3.1	Thermal diffusion	332
6.08.2.3.2	Viscous flow	332
6.08.2.3.3	Local (crustal) isostasy	333
6.08.2.3.4	Regional isostasy	333
6.08.2.3.5	Additional effects	334
6.08.3	**High-Angle Versus Low-Angle Normal Faults**	334
6.08.3.1	Rift Shoulder Uplift	334
6.08.3.2	Low-Angle Fault Development and Stress Rotation	336
6.08.3.3	Fault Rotation	337
6.08.3.4	Large Offset of Normal Faults	337
6.08.3.5	Two-Dimensional Models of Fault Formation and Offset	338
6.08.4	**Core Complex Formation: Constraints and Models**	340
6.08.4.1	Fault Orientation and Rotation in Oceanic Core Complexes	340
6.08.4.2	'Riders Blocks' and Constraints on Fault Strength	342
6.08.4.3	Crustal Flow and Doming in Core Complexes	342
6.08.4.4	Exhumation of High-Pressure Rocks in Core Complexes	345
6.08.4.5	The Shape of Core Complex Domes	348
6.08.5	**Pure Versus Simple Shear Rifting**	349
6.08.6	**Wide Versus Narrow Rifts**	353
6.08.6.1	Slow Rifting and Thermal Diffusion	354
6.08.6.2	Viscous Stresses	354
6.08.6.3	Local Isostatic Crustal Thinning	354
6.08.7	**Hyperextended Margins**	356
6.08.8	**Rifting an Active Margin**	360
6.08.9	**Small-Scale Convection and Rifting**	361
6.08.9.1	Rift Subsidence, Seismic Structure, and Flank Uplift	362
6.08.9.2	Convective Partial Melting	362
6.08.10	**Dikes Versus Stretching to Initiate Rifting**	365
6.08.10.1	Force Available for Driving Rifting	368
6.08.10.2	Force Needed for Tectonic Rifting	368
6.08.10.3	Force Needed for Magmatic Rifting	370
6.08.10.4	The Meaning of Rift Straightness	372
6.08.10.5	The Distance of Dike/Rift Propagation	372
6.08.10.6	Magma Volumes Needed for Nonorogenic Rifting	373
6.08.11	**Conclusions and Future Work**	373
References		373

6.08.1 Introduction

Plate tectonics involves the creation of new plates at spreading centers and the return of those plates to the Earth's interior at subduction zones. No terrestrial spreading centers have been active for more than 200 million years, and spreading centers are constantly being subducted, as the Chile Rise is now being lost beneath South America. Without the development of new spreading centers, plate tectonics might cease. New spreading centers primarily develop either by the splitting of intact plates or when regions of plate convergence begin to extend.

 http://dx.doi.org/10.1016/B978-0-444-53802-4.00118-4

Both plate splitting and extension of convergent regions occur most often in continental, and not oceanic, lithosphere. Rifts are places where the breakup process either did not or has not yet progressed to seafloor spreading. Thus, they give us a snapshot of the early phase of continental extension. Passive margins (sometimes called rifted margins) are places where extended and/or intruded continent grades the ocean basin formed by postrift spreading, and they give us some constraints on the state of the crust and lithosphere when breakup ended.

Even before the acceptance of plate tectonics, nearly a half century ago, and since then, much effort has been made to characterize rifts and rifted margins and understand the processes affecting them. The pattern of faults, magmatic intrusive and extrusive constructs, uplifted rift flanks, and sediment-filled basins are used to reconstruct what happened during the extension of continents. One of the clearest messages from such observations is that continental rifts form with a variety of geometries, faulting patterns, and subsidence histories. For example, some rifts are narrow, like the Red Sea (e.g., Cochran, 1983a; see **Figure 1**), and some are wide, like the Basin and Range Province (e.g., Stewart, 1978; see **Figure 2**). Some areas of apparently narrow rifting, such as metamorphic core complexes (MCC), do not subside locally (e.g., Davis and Lister, 1988; Coney and Harms, 1984; see **Figure 3**), while some rifts, like those in East Africa, form deep basins even with modest amounts of extension (e.g., Ebinger et al., 1987; Rosendahl, 1987; see **Figure 4**). It has become accepted that the condition of the lithosphere at the time of rifting, its thermal structure and crustal thickness, can have a profound effect on the tectonic development of a rift (e.g., Bassi, 1991; Braun and Beaumont, 1989a,b; Buck, 1991; Dunbar and Sawyer, 1989; Gueydan et al., 1987; Sonder et al., 1987).

Some rifts and rifted margins were affected by copious magmatism, such as large parts of the East African Rift or the East Greenland margin, while others appear to have been little affected by magmatism, such as the Northern Red Sea or the margin of the US East Coast (Sengor and Burke, 1978). Simple kinematic models of lithospheric 'stretching' (e.g., McKenzie, 1978) reproduce the gross pattern of subsidence across rifts and margins. Thus, most models of rifting, including complex numerical ones, treat tectonic stretching and neglect magmatic processes. However, as better data have been collected in rifts (e.g., Maguire et al., 2006) and across rifted margins (e.g., Hinz, 1981; Holbrook et al., 2001), the importance of magmatism has become increasingly clear (**Figure 5**). A number of margins that were formerly thought to be nonvolcanic, like much of the South American–African margin, were affected by huge volumes of pre- and synrift volcanism and magmatic intrusion. Seismic observations and in some cases drilling have been used to identify these volcanic packages since they are buried by thick layers of sediment. Also, many nonvolcanic rifts and margins are along-strike continuations of volcanic rifts. This raises the question of whether some of the nonvolcanic sections were affected by magmatism early in their development.

The issues of the initial state of the lithosphere and the influence of magmatism on rift development are central themes in this chapter. These broad questions necessitate that we investigate the possible meaning of smaller-scale structures such as faults and the mechanics of magmatic intrusion as well as a plethora of observations concerning rift structure and rifted margin history. Given the great variety of rifts and the wealth of data relating to their formation, it is not surprising that controversies have arisen. In this short chapter, only a few of these controversies and only a small fraction of the observations relating to them can be discussed. Among the questions that will be touched on are the following: Do some extensional (i.e., normal) faults slip with low dip angles (i.e., $<30°$)? Are wide rifts formed by slow extension or due to the extension of hot, weak lithosphere? Can nonorogenic areas rift without massive magmatic input? Before discussing these controversies, an overview of some of the processes that may affect rifting is given.

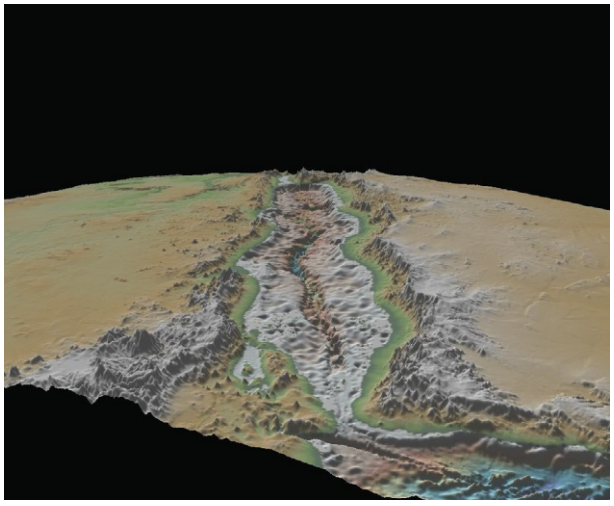

Figure 1 Shaded topographic relief image of the Red Sea viewed from the south with a vertical exaggeration of 20. The green to off-white transition marks the boundary between above and below sea level. Highlands such as the Ethiopian plateau and Yemen are in the foreground along with the low-elevation Afar Triangle. The Gulf of Suez is just visible in the distance (made with GeoMapApp).

6.08.2 Processes Affecting the Dynamics of Continental Extension

A simple way to study the mechanics of rifting builds on kinematic models. The initial pattern of lithospheric extension is specified, and the changes in the force needed to continue extension are estimated. If the force decreases, then extension should stay localized where it initiated. If the force increases, then it should be easier for the locus of extension to migrate laterally, resulting in a wide rift. The advantage of this approach is that many parameter combinations can be tested in a short time. The disadvantage is that underlying assumptions and approximations may not always be valid.

Two properties of the lithosphere control how it deforms in response to applied tectonic forces and to the addition of material such as magma. One is the intrinsic strength or yield stress of the lithospheric material. The yield stress is the applied stress required to produce strain at a given rate. The other property is the density distribution in the lithosphere. The density distribution, including topographic relief, controls the gravitational stresses that must be overcome to deform the lithosphere.

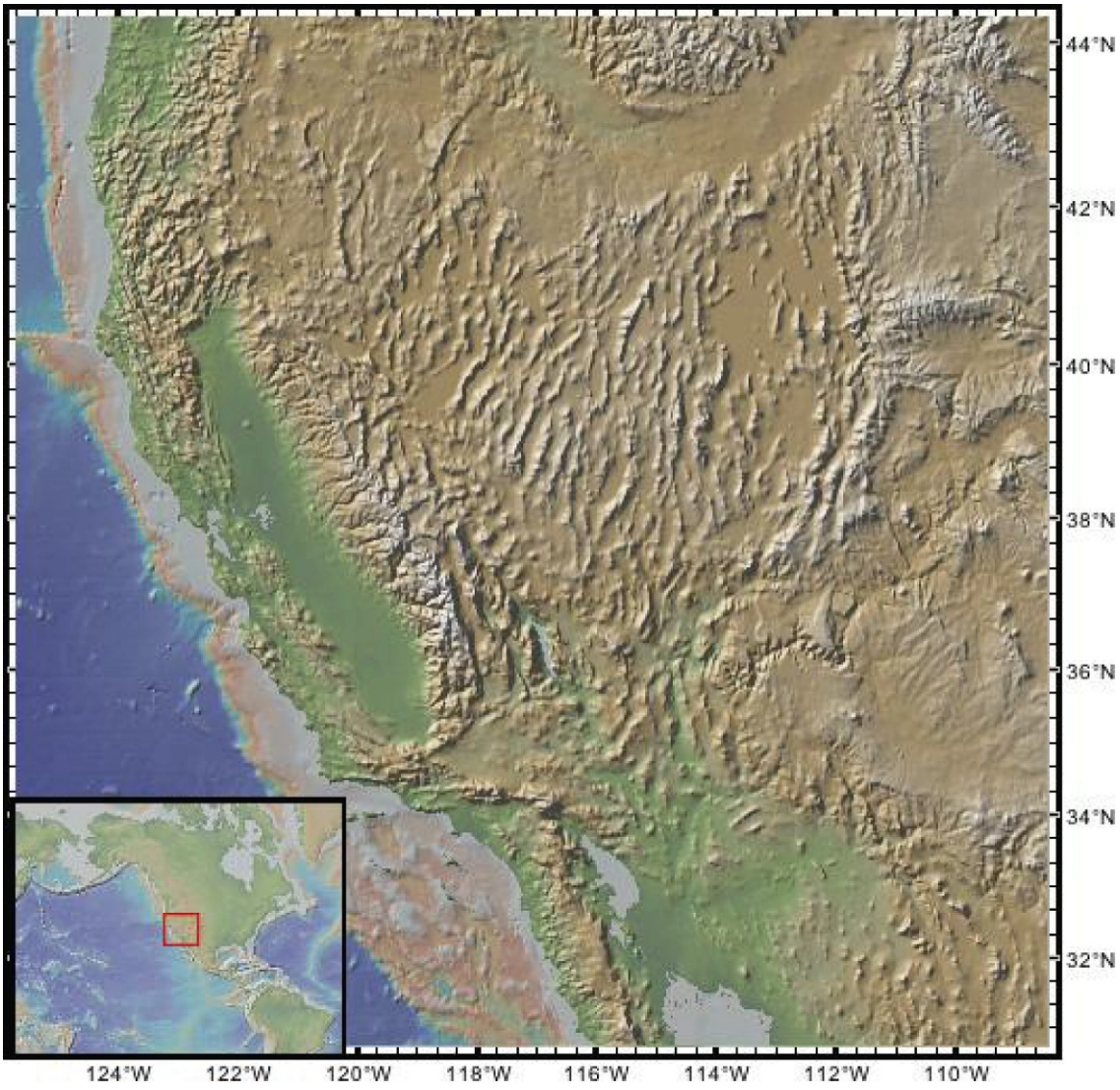

Figure 2 Shaded topographic relief image of western North America shown in plan view. The Basin and Range Province is bounded by the Sierra Nevada on the west and the Colorado Plateau on the east (made with GeoMapApp).

A number of processes can affect the yield strength and the density distribution of the lithosphere. Models of rifting describe one or more of these processes and how they interact to produce the kinds of rifts that are observed. It is convenient to think of these processes in terms of ones that promote or impede localized deformation of the lithosphere. To do this requires definition of a reference lithospheric state so that the effect of processes can been looked at in light of how much they change the extensional tectonic force needed to continue rifting. The reference lithosphere is taken to be laterally uniform in composition (i.e., crustal thickness) and in thermal structure (so isotherms are horizontal). Since the first infinitesimal increment of deformation does no work against gravity, the reference tectonic force for extension involves only the intrinsic strength of the lithosphere.

6.08.2.1 Tectonic Force for Extension

Separation of lithospheric plates requires extensional stresses. At any depth, those stresses can cause yielding by fault slip, ductile flow, or magmatic dike intrusion, whichever takes the least stress. Here, we assume that the reference state does not involve magmatism and so defer discussion of magma intrusion. The difference between the maximum and minimum principal stresses required to cause rock to deform at a given depth, the yield stress, is taken often to be the lesser of two stresses: the stress to produce brittle failure and the stress to cause ductile flow at a specified strain rate.

The extensional state of stress is approximated using the usual assumption that the vertical or z-direction is the largest principal stress and equals the lithostatic stress (Anderson, 1951) given by

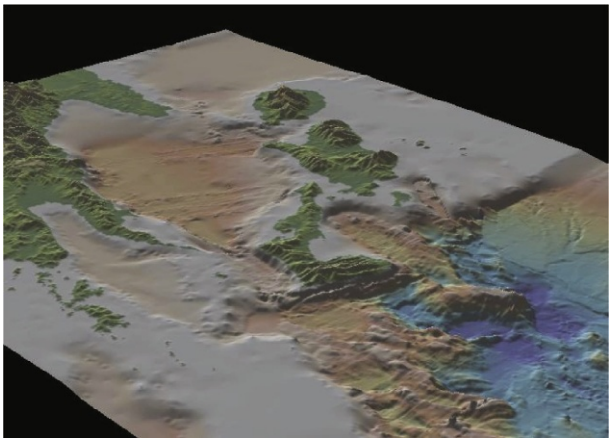

Figure 3 Shaded topographic relief image of the D'Entrecasteaux Islands of the Woodlark Basin. These islands are thought to be the youngest continental metamorphic core complexes on Earth (made with GeoMapApp).

$$\sigma_1(z) = g\int_0^z \rho_r(z')\mathrm{d}z' \qquad [1]$$

where g is the acceleration of gravity and ρ_r is the density of rock in the lithosphere. In the crust, the assumed density is 2800 kg m^{-3}; and in the mantle, density is 3300 kg m^{-3}.

At low temperatures and moderate confining pressure, rocks can break on faults. Continued application of stress can cause slip on those faults. If one component of the horizontal stress is the minimum stress (σ_3), then dip-slip faults should form with a normal sense of slip. Following Brace and Kohlstedt (1980), the stress difference ($\sigma_1 - \sigma_3$) needed for normal faulting is estimated under the assumption that cohesionless fractures exist in all directions to accommodate fault slip. Then, the minimum stress difference for faulting, the yield stress, is

$$\sigma_f(z) = B\left(\sigma_1(z) - P_p\right) \qquad [2]$$

where $B = 2f/[(1+f^2)^{1/2}+f]$, where f is the coefficient of friction. P_p is the pore pressure. Assuming $f = 0.85$, which is the average

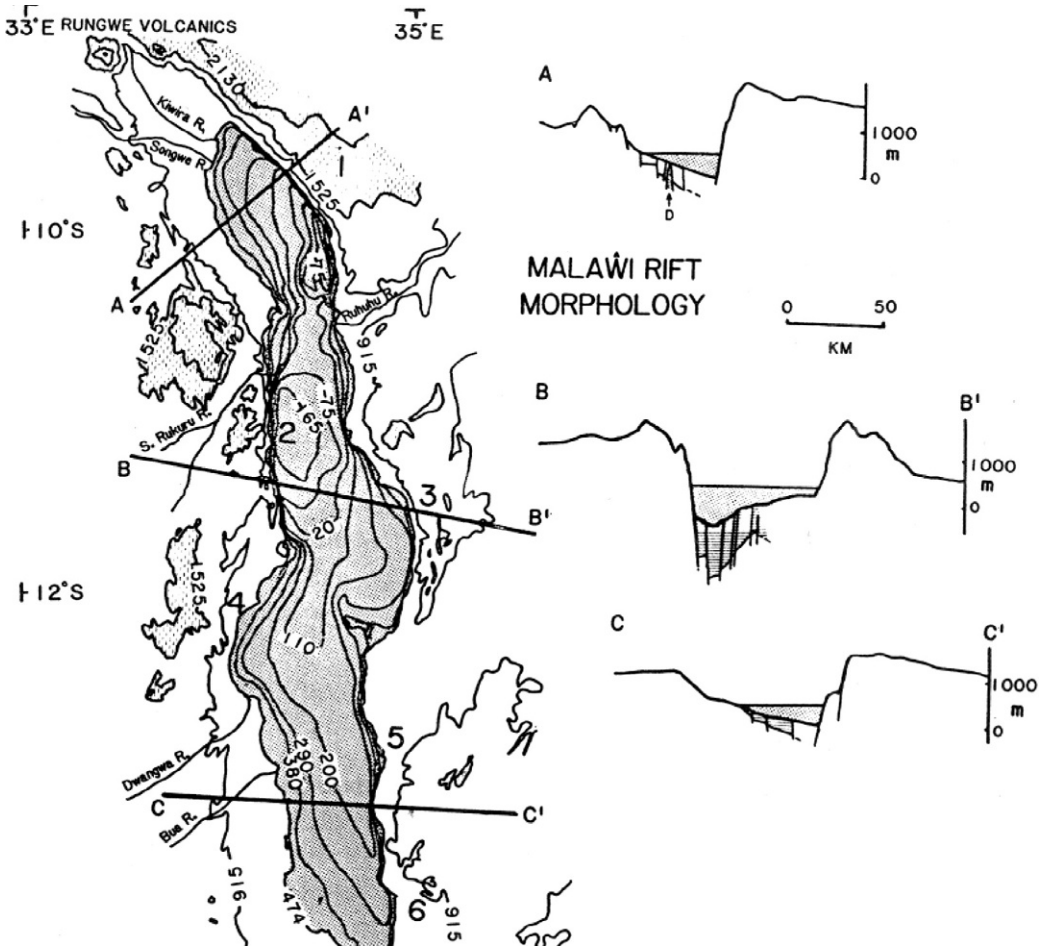

Figure 4 Topographic relief and profiles across the Malawi Rift of the East African Rift System. Note the change in polarity of the half-graben comprising the rift. Reproduced from Ebinger CJ, Rosendahl BR, et al. (1987) Tectonic model of the Malawi rift, Africa. *Tectonophysics* 141: 215–235.

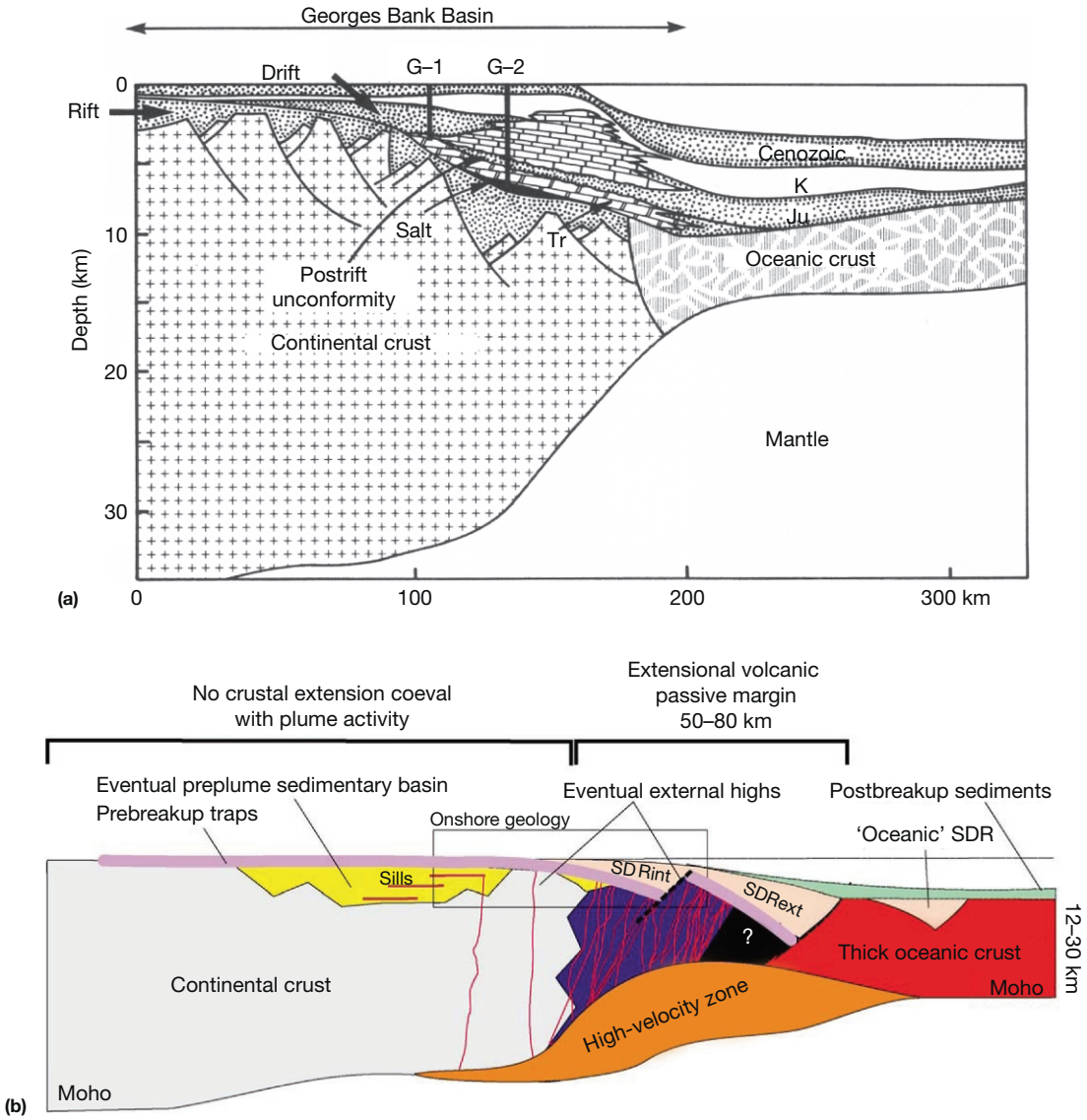

Figure 5 Schematic cross sections of representative (a) nonvolcanic (reproduced from Manspeizer W and Cousminer HL (1988) Late Triassic-Early Jurassic synrift basins of the U.S. Atlantic margin. In: Sheridan RE and Grow JA (eds.) *The Atlantic Continental Margin; U.S.*, *v*, pp. 197–216. Boulder, CO: Geological Society of America.) and (b) volcanic margins (reproduced from Geoffroy L (2005) Volcanic passive margins, Comptes Rendus – Academie des sciences. *Geoscience* 337(16): 1395–1408). SDRint and SDRext refer to internal and external seaward-dipping reflectors. The high-velocity zone may represent mafic intrusives.

friction coefficient for a wide range of rocks (Byerlee, 1978), makes the constant $B = 0.8$.

If the pore pressure in the rock, P_p, is taken to be hydrostatic, then the faulting or brittle yield stress should increase linearly with depth in a constant density lithosphere:

$$\sigma_f(z) = Cz \qquad [3]$$

For crust with a constant density of 2800 kg m^{-3}, the gradient of increase of the faulting yield stress with depth, C, is 14.1 MPa km^{-1}.

At high temperature, rocks can flow in response to stress differences without forming macroscopic fractures. For such ductile flow, the stress difference for ductile flow, σ_d, and strain rate, $\dot{\varepsilon}$, are found to be related through a flow law:

$$\sigma_d = (\dot{\varepsilon}/A)^{1/n} \exp(E/nRT) \qquad [4]$$

where T is absolute temperature, R is the universal gas constant, E is activation energy (e.g., Goetze and Evans, 1979), and A is a constant for given material. The ductile yield stress depends on the composition of rock as well as temperature. Dry anorthite rheology is assumed for the crust and a dry olivine rheology for the mantle. For anorthite, $E = 238$ kJ mol^{-1}, $A = 5.6 \times 10^{-23}$ Pa^{-n} s^{-1}, and $n = 3.2$; for olivine, $E = 500$ kJ mol^{-1}, $A = 1.0 \times 10^{-15}$ Pa^{-n} s^{-1}, and $n = 3$ (Kirby and Kronenberg, 1987).

To estimate the stress difference for extension (the yield stress) as a function of depth, z, we must specify the temperature profile through the lithosphere. This is done by assuming temperatures are in steady state with a constant heat flow from below and radioactive heat production within the crust. For the illustrative examples shown here, the thermal conductivity is set to 2.5 W m^{-1} °C^{-1} for the crust and 3.0 W m^{-1} °C^{-1} for the

mantle. The crustal heat production is set to 3.3×10^{-7} W m^{-3}, which contributes 10 mW m^{-2} to the surface heat flow for a 30 km thick crust. The mantle heat flow is adjusted to provide a given surface heat flow for a specific crustal thickness. Figure 6(a) shows yield stress profiles for a moderate heat flow temperature profile, assuming a 30 km thick crust.

The horizontal force per unit length required to cause tectonic extensional yielding of the entire model lithosphere, F_T, is estimated by integrating yield stress over depth (Figure 6(b)). This force depends strongly on the temperature profile and, thus, on the surface heat flow. To extend continental lithosphere with a heat flow of about 40 mW m^{-2}, as is seen adjacent to some rifts like the Red Sea (Martinez and Cochran, 1988), may require as much as 30 teraNt m^{-1} of tectonic force if no magma were intruded.

A number of factors can affect where extensional strain is concentrated in a continental region. Extension may, and probably does, nucleate in a site of a previous weakness. A prime question for us is whether extensional strain remains concentrated in that initial site or migrates to other places. Here, we will not consider propagation of rifting orthogonal to the direction of extension, but we will concentrate on simplified versions of two-dimensional (2-D) models concerned with the vertical plane parallel to the direction of extension.

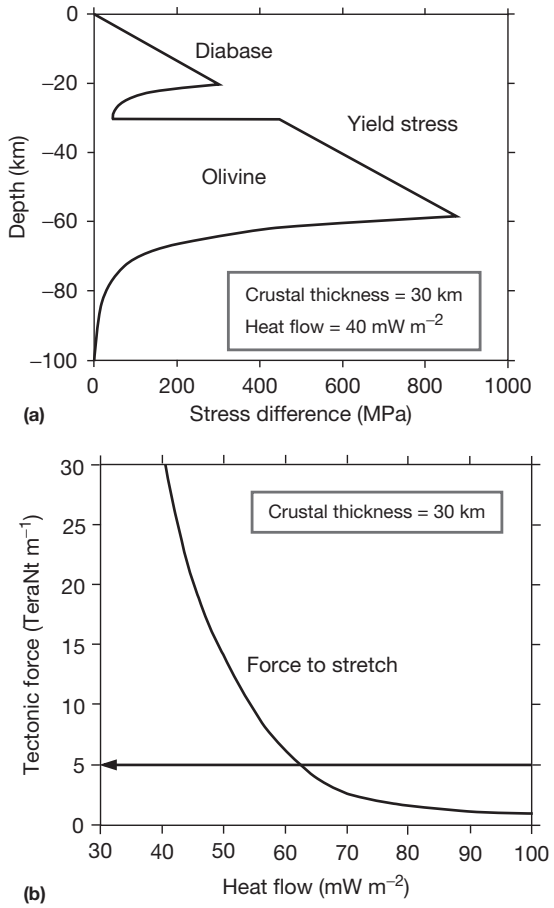

Figure 6 (a) Yield stress profile for diabase rheology crust over olivine rheology mantle for a typical continental thermal profile with an average value of surface heat flow. (b) Tectonic force for extension (the integral of yield stress with depth) as a function of surface heat flow for 30 km thick crust. The horizontal line gives the approximate maximum tectonic force available to drive rifting.

We discuss eight processes that may affect concentration or delocalization of strain during continental extension. Though this may seem like a bewilderingly large number of things that could affect extension, it should become clear that some of these processes can be insignificant. In an effort to show what may control the importance of each process, we derive scaling relations that show what parameters should control the effect of the process. The derivations attempt to show the approximate change in horizontal tectonic force needed for continued rifting due to a particular process. Each process is viewed in terms of how it affects the lithospheric strength or the gravitational force to continue extension. For example, a small amount of lithospheric thinning will reduce the strength of the lithosphere in proportion to the initial strength of the lithosphere times the square of the fractional amount of thinning. Local lithospheric thinning will produce gravitational stresses that also make continued extension easier, but the magnitude of the change in gravitational stresses is typically less than a few percent of the weakening effect. Familiarity with these scaling relations may make it easier to interpret complex numerical models of continental extension in which many parameters may affect the results.

6.08.2.2 Localizing Processes

6.08.2.2.1 Thermal advection due to stretching

The most obvious thing that may keep extension focused in one area is the localized thinning of lithosphere as it extends. Extension implies that material points horizontally offset from each other move apart. Conservation of mass requires vertical motion in response to this lateral extension. This implies some upward movement of the material within the lithosphere and so advection of heat. If this heat advection is significantly faster than thermal diffusion, then isotherms at the base of the lithosphere should move up. The lithosphere is thinned and so it is weakened. This process of 'necking' is self-reinforcing. The weaker the thinned or necked area, the more concentrated, and perhaps more rapid, the extension. The more concentrated the extensional strain, the faster the rift becomes weaker.

To quantify the necking-related reduction in brittle lithospheric yield strength, ΔF_N, we ignore thermal diffusion and relate lithospheric thinning to extensional strain, ε. The base of the brittle lithosphere is the place where the ductile and brittle yield strengths are equal. The ductile stress depends strongly on temperature, so that when heat is advected upward, the depth of the base of the lithosphere moves up. The contribution to the yield force (the integral of the yield strength envelope) due to the ductile part of the lithosphere is a small fraction of the total. Thus, in the interest of simplicity, all the strength is taken to be in the brittle part of the lithosphere. Assume that the base of the brittle lithosphere, where $z = H_b$, is marked by an isotherm. The new brittle lithospheric thickness is $(1-\varepsilon)H_b$. Since the brittle lithospheric strength is proportional to the square of the brittle layer thickness, the change in strength is

$$\Delta F_N = CH_b^2 - C(1-\varepsilon)^2 H_b^2 \sim 2C\varepsilon H_b^2 \qquad [5]$$

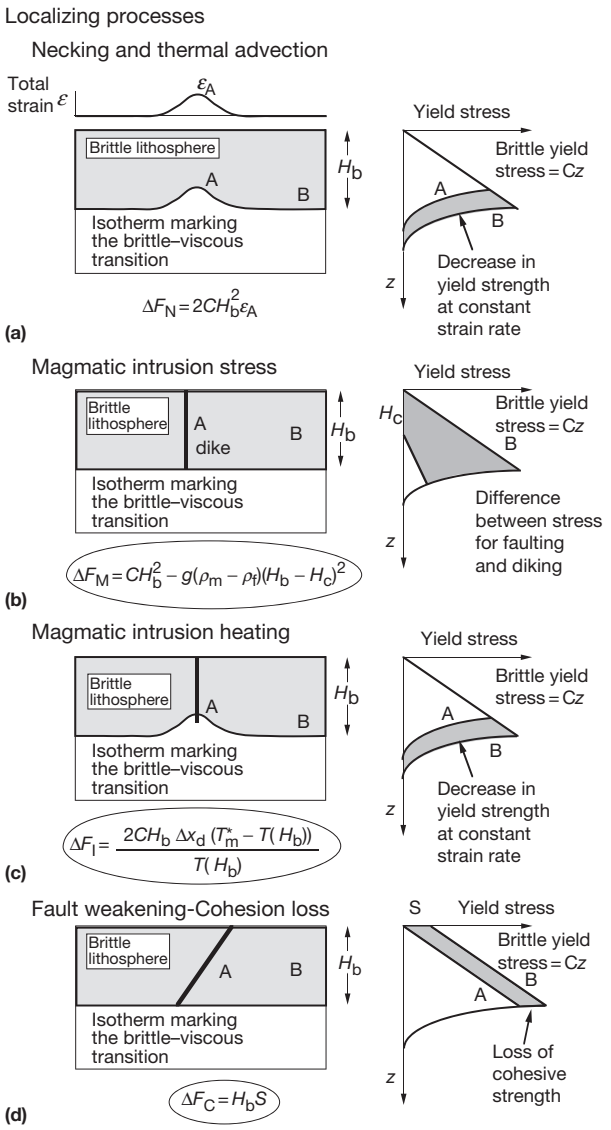

Figure 7 Schematic illustrations of processes that may lead to localization of strain during continental lithospheric extension. Plots to the right show the approximate distribution of yield stress with depth both at the center of a rift (A) and at an area unaffected by the rifting (B). The difference in the two curves is marked with vertical hatchers and that area is proportional to the change, here reduction, in the tectonic force needed for continued rifting. The scaling of these force changes is given within ovals. See text for further explanation.

Figure 7 illustrates the reduction in strength due to advective lithospheric thinning. In doing this, we ignore the effect of strain rate on yield stress, which is treated in the succeeding text on viscous stresses. The key result is that the first-order reduction in strength depends on two times the strain times the initial strength of the lithosphere.

6.08.2.2.2 Magmatic intrusion

Dikes are magma intrusions with a thickness much smaller than their width or length. Molten basalt is assumed to be the material filling rift-related dikes since mantle melting can produce basaltic magma and because more felsic dikes might be too high in viscosity to easily propagate. Dikes should form in planes perpendicular to the least principal stress, σ_3; for a rift, this should be in vertical planes parallel to the rift (Anderson, 1951). It is assumed that preexisting vertical fractures are prevalent in order to avoid the complications of fracture mechanisms (e.g., Rubin and Pollard, 1987). However, the extra stress needed to break open dikes in unbroken rock should be limited by the rock tensile strength, which would make a small contribution to the tectonic forces estimated here. Neglected also are the viscous stresses associated with the flow of magma in a dike, since the goal is to estimate the minimum stress difference (defined as $\sigma_1 - \sigma_3$, where σ_1 is the maximum principal stress) required to have magma stop and freeze at a given depth in a dike.

Before freezing, magma in a dike can cease moving up or down when the static pressure in the dike equals the horizontal stress at the dike wall (Lister and Kerr, 1991). The vertical pressure variation in a static column of fluid magma is related to its density, ρf, so for magma emplacement, $\partial\sigma_3/\partial z = \rho fg$. To specify the level of fluid magma pressure, it is assumed that dikes always cut to the surface, where the pressure is zero. In that case, the stress difference required for dike emplacement is

$$\sigma_M(z) = \sigma_1(z) - g\rho fz \qquad [6]$$

Clearly, with these simplifications, the stress difference for magma to allow extensional separation between blocks of lithosphere depends only on the density difference between the lithosphere and fluid magma. If the crustal rock density and fluid magma density are taken to be equal, the stress difference for crustal diking is zero. In mantle of density $\rho_m = 3300\ \mathrm{kg\ m^{-3}}$, the stress difference required for intrusion of fluid magma with density $\rho_f = 2700\ \mathrm{kg\ m^{-3}}$ increases at a rate of 6 MPa $\mathrm{km^{-1}}$ of depth into the mantle. If the ductile mantle is too weak to maintain such stresses, then the magma cannot be emplaced at depth and will be extruded. Then, the force to emplace magma is just related to the difference in brittle layer thickness and the crustal layer thickness:

$$F_M = g(\rho_m - \rho_f)\frac{(H_b - H_c)^2}{2} \qquad [7]$$

The decrease in force needed for rifting if there is enough magma to reach the surface is then

$$\Delta F_M = F_T - F_M = \left[CH_b^{2-} g(\rho_m - \rho_f)(H_b - H_c)^2\right]/2 \qquad [8]$$

6.08.2.2.3 Magmatic heat input

Basaltic magma is hotter than lithosphere so that dike intrusion advects heat into the lithosphere and can weaken it. Magma also releases a considerable quantity of latent heat when it crystallizes. We can define an effective temperature of magma as T_m^*, which is equal to the actual magma temperature plus the latent heat times the specific heat. A reasonable value of the added effective temperature due to latent heat is 300 °C so that liquid magma with an actual temperature of 1300 °C would have an effective temperature of 1600 °C. Since the temperature at the base of the brittle lithosphere is likely to be 600–800 °C, the intrusion of magma could heat the rock sufficiently to cause it to flow ductilly. To estimate the reduction in lithospheric thickness on intrusion of a set of dikes of

total width Δx_d requires that we specify the width of region of lithosphere that is heated. Taking a conservative estimate that this width of region of intrusion is equal to the lithospheric thickness results in a thinning of the lithosphere of approximately $\Delta x_d(T_m^* - T(H_b))/T(H_b)$ given a linear geotherm in the lithosphere. Thus, the reduction in lithospheric strength due to dike intrusions totaling Δx_d in width is

$$\Delta F_l = 2CH_b\Delta x_d(T_m^* - T(H_b)/T(H_b) \quad [9]$$

The lithospheric strength here is defined as the strength with no further magmatism. Thus, dike intrusions totaling 10 km wide could very significantly reduce the lithospheric thickness and strength and allow rifting to proceed at moderate levels of forces even if no more magma is supplied.

6.08.2.2.4 Cohesion loss

Within a rift, extension is not smoothly distributed, at least in the near surface, but is concentrated on normal faults. For faults to accommodate so much strain, they must be weaker than the surrounding less deformed rock. One possibility is that faults have lost some or all of the cohesion of the surrounding rocks.

The failure of brittle materials, such as cold rock, has been described by a number of criteria. We assume the Coulomb–Navier criterion, which states that failure occurs when the shear stress exceeds cohesion, S, plus a friction coefficient, μ, multiplied by the normal stress. In deriving the brittle yield stress in the succeeding text, we followed Brace and Kohlstedt (1980) and others, who adopted this criterion with $S = 0$.

When the yield criterion is reached, the rock may break as cohesion is lost. The optimum orientation of faults is controlled by the friction coefficient. Then, for cohesion loss, the yield stress on optimally oriented faults is reduced by an amount equal to $2S/[(1+\mu^2)^{1/2}/2+\mu]$. For μ close to 0.75, the reduction in yield stress is approximately equal to S. Laboratory-measured values of rock cohesion, also known as inherent shear strength, range from almost zero for weak sediments to nearly 50 MPa for some igneous rocks (Handin, 1966). The existence of large vertical cliffs requires cohesion in large volumes of rock that are of order 10 MPa.

Assuming that strain weakening results in noncohesive faults, then they would be weaker by approximately S. Multiplying this cohesion drop by the thickness of the brittle layer gives the amount of reduction in the yield strength of a fault compared to unfaulted rock. Thus, the reduction in force due to cohesion loss is approximately

$$\Delta F_C = SH_b \quad [10]$$

For a brittle layer thickness that is over 10 km, the reduction in strength due to cohesion loss should be fairly small compared to the strength that remains due to rock friction. It is possible that faults develop a lower frictional coefficient or become weaker due to pore pressure increases, though these are difficult to quantify.

6.08.2.3 Delocalizing Processes

6.08.2.3.1 Thermal diffusion

Thermal diffusion can lead to thickening, and so strengthening of the brittle lithosphere when the lithosphere is out of thermal equilibrium. Lithosphere may be in equilibrium with basal heat flux, which is presumably delivered by mantle convection. Thermal disequilibrium may be produced by several types of extension-related heat advection, such as lithosphere stretching or dike intrusions. Diffusion tends to return isotherms perturbed by advection to their previous configuration.

It is difficult to derive simple analytic expressions for the rate of lithospheric thickening due to thermal diffusion except for the simplest of boundary and initial conditions. The problem of cooling of a half-space, with no heat sources, gives a simple result that captures important features of more complex model configurations. For half-space cooling, the depth to an isotherm marking the base of the lithosphere increases proportional to $\sqrt{\kappa t}$ where κ is thermal diffusivity (see Turcotte and Schubert, 2002). Thus, the velocity of lithospheric thickening is proportional to κ/H_b, where H_b is the thickness of the lithosphere. In a time interval Δt, the lithosphere is thickened by roughly $\Delta t\kappa/H_b$. The yield stress at the base of the lithosphere is CH_b. and the lithospheric strengthening due to thermal diffusion is that stress times the increase in thickness:

$$\Delta F_d \approx C\kappa(\varepsilon/\dot{\varepsilon}) \quad [11]$$

where the time interval Δt is replaced by the ration of the strain, ε, and the strain rate of extension, $\dot{\varepsilon}$. For a typical rock diffusivity of 10^{-6} m^2 s^{-1}, a million years of cooling would produce an increase in strength of about 5×10^{11} Nt m^{-1}, which is a small fraction of the strength of lithosphere a few tens of kilometers thick.

6.08.2.3.2 Viscous flow

By definition, the strength of viscous material is proportional to strain rate or a strain rate raised to a power. This means that when viscous material strains faster, its flow stress is larger. This results in stress being delocalized in a viscous layer. A thought experiment can help illustrate this effect. Assume that the strain rate is greater in one region, as shown in Figure 8. Since the viscous flow stresses are greater in the region of high strain rate, the transition between brittle and viscous behavior (sometimes called the brittle–ductile transition) is deeper there. Clearly, where the transition depth is deeper, the total yield strength is greater. Thus, the area straining the fastest will be the strongest.

The amount of deepening of this transition and the lithospheric strengthening depends on two things: the contrast in strain rate and the length scale for changes in viscosity. At constant stress, the vertical distance Z_e over which the viscosity changes by a factor e (2.72) is related to the temperature gradient in the region of the transition, dT/dz, and to the temperature there (T_0) as $Z_e = RT_0^2/(EdT/dz)$. To get an expression for the related force increase, we assume constant stress at the transition depth and then estimate the vertical distance change in that depth for a given contrast in strain rate. Also, we assume a linear temperature gradient through the lithosphere so that $dT/dz = T_0/H_b$. Doing this gives a force increase of

$$\Delta F_V = \frac{CH_b^2RT_0^2}{E(T_0 - T_s)} \ln\left(\frac{\dot{\varepsilon}_A}{\dot{\varepsilon}_B}\right) \quad [12]$$

where T_s is the surface temperature. $\dot{\varepsilon}_B$ and $\dot{\varepsilon}_A$ are the background and local strain rates, respectively.

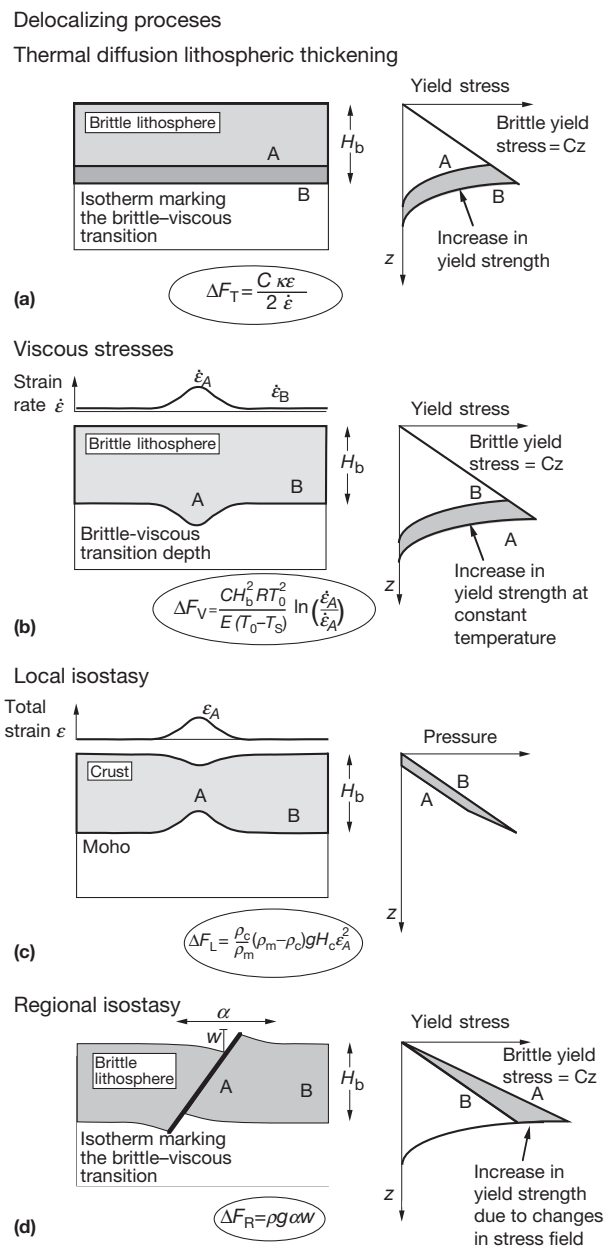

Figure 8 Same as **Figure 7** except that the processes could promote delocalization of strain during extension.

It is the viscous stress effect that can lead to both folding and boudinage structures in layered rocks (Biot, 1961; Ramberg, 1955; Smith, 1977). It is this viscous delocalization that has been suggested to contribute to the boudinage like structure of the wide Basin and Range Province of the Western United States (Fletcher and Hallet, 1983), as discussed in the succeeding text.

6.08.2.3.3 Local (crustal) isostasy

Local isostasy is an idealized description of how lithosphere floats on underlying fluid asthenosphere (Watts, 2001). The term 'local' implies that the surface elevation at a point depends only on the average density of the column of lithosphere below that point. Essentially, the shear stress on vertical planes is taken to be zero. However, horizontal stresses should be continuous across vertical planes. Vertical stresses at a given depth should depend on the topography and average density of material in a column. Thus, where there is topographic relief in local equilibrium, there will be nonzero stress differences ($\sigma_1 - \sigma_3$). For example, an elevated area will be in relative tension. Conversely, a low area will be in relative compression as material tries to flow into it.

Localized extension results in crustal thinning. Because crust is less dense than underlying mantle, local crustal thinning should produce lowered elevations in the center of a rift (e.g., McKenzie, 1978). This puts the center of the rift into relative compression, and this makes continued extension harder.

To estimate the magnitude of this effect, we follow previous workers (e.g., Artemjev and Artgushkov, 1971; Fleitout and Froidevaux, 1983) and assume that the wavelength of crustal thickness variations is large compared to crustal thickness. Then, the increase in the tectonic force for extension due to crustal thinning, ΔF_c, equals the integral over depth of the difference in lithostatic pressure, ΔP. This pressure difference equals $\Delta w \rho_c\, g$, where Δw is the change in surface elevation between the center of the rift and the adjacent, unrifted area. Here, ρ_o is the density of crust and g is the acceleration of gravity. Topographic relief Δw in local isostatic equilibrium has an amplitude of $\varepsilon_a H_c(\rho_m - \rho_o)/\rho_m$ where ρ_m is the density of the mantle and $\varepsilon_a H_c$ is the amount of crustal thinning at the center of a rift. As long as the strains are not too large, then the local crustal buoyancy force, ΔF_L approximately equals $\Delta P\, H_o$, can be expressed as

$$\Delta F_L = \rho_c g \varepsilon_a H_c^2 (\rho_m - \rho_o)/\rho_m \qquad [13]$$

Just as thermal diffusion may act to diminish the effect of thermal advection during lithospheric necking, lower crustal flow can act to even out crustal thickness variations and so reduce the crustal buoyancy effect. The idea that lateral crustal flow may be important in some areas is discussed in Block and Royden (1990), Buck (1991), and Bird (1991).

Isostatic topography in a rift can be caused by temperature differences. However, the thermal buoyancy force change due to lithospheric stretching is usually much smaller than that due to crustal thinning. This is because density changes due to a temperature change of 500 °C are ten times smaller than the density difference between crust and mantle. The thermal buoyancy force change scales with the thermal lithospheric thickness squared. Thus, when the lithosphere is thick, thermal buoyancy effects can be of larger magnitude than the crustal buoyancy force change because the depth extent of temperature anomalies can be much greater than the depth to Moho, as noted by Turcotte and Emmerman (1983) and LePichon and Alvarez (1984). Thermal and crustal buoyancy are of opposite sign for a rift.

6.08.2.3.4 Regional isostasy

Fault offset results in stress changes around and on the fault. Forsyth (1992) argued that those stress changes should inhibit continued offset on the fault. Eventually, it could be easier to break a new fault in adjacent lithosphere than for continued slip on an original fault.

Figure 8(d) illustrates this effect. As described in a later section, the scaling between the force and the vertical deflection is directly proportional to the horizontal wavelength of the response of the lithosphere to vertical loads, represented by the flexural parameter, α. It is approximately

$$\Delta F_R = g\rho_c \alpha w \qquad [14]$$

where w is the vertical offset across the fault.

6.08.2.3.5 Additional effects

Other factors may have a considerable effect on the geometry of extension, but they are even harder to quantify than the factors discussed here. For example, erosion and sedimentation may reduce both the local isostatic (crustal buoyancy) effect and the regional isostatic effect due to fault offset. This could therefore diminish those delocalizing effects (Burov and Cloetingh, 1997). However, it is difficult to quantify the rate of erosion or to specify either the distribution of sediment or its density.

The rest of this chapter is concerned with the several controversies that continue to exercise researchers in the field of continental extension. Each of these controversies can be cast in terms of a pair of end-member concepts, and the title of the following sections emphasizes these extreme possibilities.

6.08.3 High-Angle Versus Low-Angle Normal Faults

One of the most exciting and contentious areas of work on extensional tectonics in the last 20 years involves the interpretation of subhorizontal normal faults (Figure 9). These 'low-angle normal faults' were first recognized in continental MCCs (e.g., Coney and Harms, 1984) but now have been seen on the ocean floor near some mid-ocean ridges (e.g., Cann et al., 1997; Tucholke et al., 1997, 1998). The next section of the chapter focuses on the formation of core complexes, while this section deals with the mechanics of normal faulting.

Normal faults appear to fall into two distinct populations. High-angle normal faults dip at an angle of $>30°$ and are offset <10 km (Stein et al., 1988; Vening-Meisnez, 1950). Low-angle normal faults dip between 30° and subhorizontal, and some appear to have accommodated horizontal throws as much as 50 km or more (e.g., Davis and Lister, 1988; Davis et al., 1986; John and Foster, 1993; Wernicke, 1992; Yin and Dunn, 1992). Under the tenets of classical fault mechanics, normal faults in the brittle upper crust should initiate at dips $>45°$ and should be active at dips of no $<30°$ (Anderson, 1951; Byerlee, 1978; Sibson, 1985). Thus, there is great interest in whether some faults actively slipped at low dip angles ($<30°$). Before discussing ideas for the origin of low-angle normal faults, the question of how topographic relief is produced by offset of high-angle normal faults will be surveyed.

6.08.3.1 Rift Shoulder Uplift

Active rifts are primarily identified by their characteristic topographic relief; with a depression or rift valley surrounded by elevated flanks or shoulders (Figures 1 and 5).

Geologic and geophysical data indicate that the shoulder of a rift is typically footwall of a major, rift-bounding normal fault. Vening-Meisnez (1950) considered how normal fault offset might produce topographic relief. He assumed that the load was related to a fault cutting low-density crust floating on the asthenosphere. In this formulation, the force supporting uplift depends on the crustal thickness, h_c, and the density contrast between crust and mantle. To quantify the model, imagine that two floating blocks cut by a fault are moved apart and denser fluid upwells to fill the space between them. If the blocks are crust with density ρ_c and the fluid mantle has a density ρ_m, then the triangular parts of the blocks will be subject to buoyancy forces related to their shape. The upward force on the triangle of the footwall block is given by

$$V_0 = \frac{g h_c^2 \rho_c (\rho_m - \rho_c)}{2\rho_m \tan\theta} \qquad [15]$$

where g is the acceleration of gravity, h_c is the thickness of the crust, and θ is the dip of the fault cutting the blocks. Applying this load to the end of a thin elastic plate floating on the mantle would produce a vertical deflection of the plate of

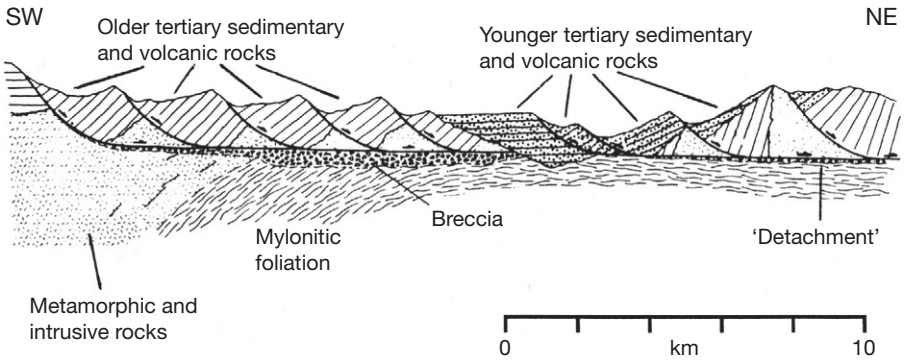

Figure 9 Interpretive cross section of the Whipple Mountains metamorphic core complex, though to be a site of large magnitude extension with no local subsidence. The detachment fault appears to have accommodated tens of kilometers extension and is not in a subhorizontal position. Reproduced from Davis GA (1980) Problems of intraplate extensional tectonics, western United States. *Continental Tectonics*, pp. 84–95. Washington, DC: National Academy of Science.

$$w(x) = \frac{2V_0}{\rho_m g \alpha} e^{-x/\alpha} \cos\frac{x}{2} \quad [16]$$

where α is the flexural parameter of the flexed plate (e.g., Turcotte and Schubert, 2002). Neglecting the distance from the point of application of the load and the edge of the region with full crustal thickness, the maximum deflection occurs at $x = 0$ and equals

$$w(0) = \frac{h_c^2 \rho_c (\rho_m - \rho_c)}{\alpha \rho_m^2 \tan\theta} \quad [17]$$

For a typical (i.e., moderate heat flow) continental region, the model appears to work. For such a region, it is reasonable to assume $h_c = 30$ km, $\alpha = 60$ km, $\rho_c = 2900$ kg m^{-3}, and $\rho_m = 3300$ kg m^{-3}, so the uplift of the footwall given by eqn [3] is 1.6 km. Even though the load of sediments filling the hangingwall basin would reduce the footwall uplift, the model fit is in reasonable agreement with the observed uplift magnitude for continental rifts.

This model does not work for oceanic rifts, since oceanic crust is much thinner and denser than continental crust. However, the topographic relief at mid-ocean ridges is comparable to that seen in continental rifts. Taking $h_c = 6$ km, $\alpha = 12$ km, and $\rho_c = 3000$ kg m^{-3} with other values held the same, eqn [17] predicts maximum footwall uplift of 0.16 km. This is far smaller than that observed for oceanic rifts.

Vening-Meisnez (1950) was right that the loads produced by normal fault offset should be supported regionally, but he did not consider the load produced by the offset of the Earth's surface. This load is even more important than the load caused by offset of the Moho, which was treated by Vening-Meisnez (1950). The slip of a normal fault should deflect the surface of the Earth and create topographic relief even if the crustal thickness is zero and the lithosphere has the same density as the asthenosphere.

Basic rock mechanics (Anderson, 1951) predicts that shear displacement should be easier than opening displacement at depth in the earth. The top and bottom sides of a normal fault should remain in contact as the fault shears. The offset of the fault pushes the footwall block up and the hangingwall block down. Flexing in response to the loads should result in a curved fault so it is not immediately clear how to formulate a thin-plate flexural approximation to the effect of fault offset. Weissel and Karner (1989) formulated the problem by conceptually turning off gravity when the fault offsets half the Earth's surface down relative to the other side of the fault. The offsets can be considered loads equal to the vertical offset times gravity times density. When gravity is 'turned on,' these loads deflect the lithosphere, resulting in a topographic pattern as shown in **Figure 10**.

Using the Weissel and Karner (1989) approach, an analytic solution for the deflection of the surface can be derived assuming thin elastic plate flexure theory. For the geometry in which a normal fault drops the hangingwall down (**Figure 10**), the load distribution is

$$V(x) = \begin{cases} \rho g \tan\theta x & 0 < x < \Delta x \\ \rho g \tan\theta x_0 & x > \Delta x \end{cases} \quad [18]$$

where $x = 0$ is the position of the intersection of the fault with the surface on the footwall (the breakaway) and $x = \Delta x$ is the intersection of the fault with the surface on the hangingwall. The vertical deflection at position x due to a localized load V at position x' is

$$w(x) = \frac{V(x')\rho g}{4\alpha} e^{-x/\alpha} \left(\cos\frac{(x'-x)}{\alpha} + \sin\frac{(x'-x)}{\alpha} \right) \quad x' \geq x \quad [19]$$

The maximum uplift of the footwall occurs at $x = 0$, and this can be calculated by integrating equation [19] from $x = 0$ to $x = \infty$:

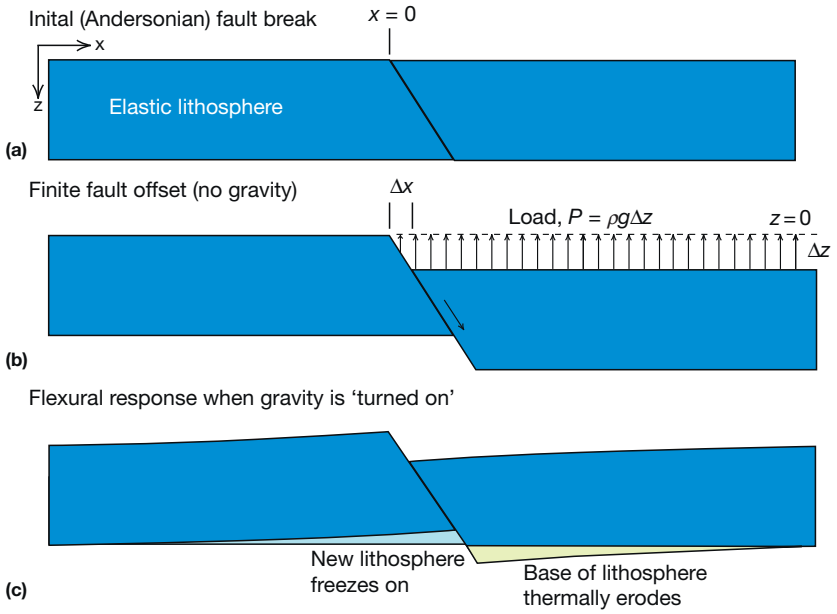

Figure 10 Schematic of a way to treat the effect of normal fault offset on topographic relief. (a) An ideally oriented fault and (b) how one side of the fault would move down in the absences of gravity. The magnitude of the load, P, would exist if gravity were 'turned on.' (c) The flexural response to that load.

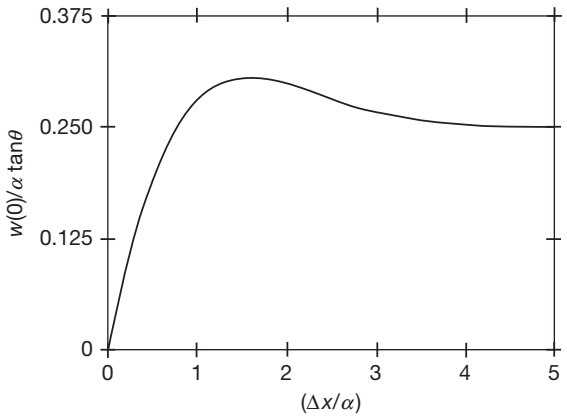

Figure 11 The results of an analytic calculations (eqn [20]) of the uplift of the footwall breakaway of a normal fault as a function of the horizontal offset, Δx, of the fault. The offset is normalized by the flexure parameter, α, and the vertical uplift is normalized by $\alpha \tan\theta$, where θ is the fault dip angle.

$$w(0) = \frac{\alpha \tan\theta}{4}\left\{ e^{-\Delta x/\alpha}\left(\sin\frac{\Delta x}{\alpha} - \cos\frac{\Delta x}{\alpha}\right) + 1 \right\} \qquad [20]$$

Figure 11 plots the value of the breakaway uplift versus horizontal fault offset. The uplift increases with offset up to the point where fault offset $\Delta x = (\pi/2)\alpha$ and then diminishes slightly. The maximum uplift is $\sim 0.3\alpha \tan\theta$. For a fault dip angle of 45° and a flexure parameter $\alpha = 10$ km, the maximum uplift given by eqn [6] is about 3 km. This is on the high end of the range of uplifts seen for oceanic or continental rifts. Several things can limit the development of topographic uplift across a normal fault, including sedimentary loading of the down-dropped side of a fault to produce the kind of half-graben basin seen for many continental rifts (e.g., Stein et al., 1988).

Braun and Beaumont (1989a,b) used numerical models of extension of a 2-D viscous–plastic layer to show that local extensional thinning of the layer (necking) could produce reasonable uplift of rift shoulders. They also interpreted their results in terms of a two-stage process in which stretching would produce a topographically low basin without gravity, but with gravity it uplifts rift shoulders (see Figure 12). Braun and Beaumont (1989a,b) also noted that such uplift might explain the 'breakup unconformity' seen at many rifted margins (Figure 13).

6.08.3.2 Low-Angle Fault Development and Stress Rotation

On the basis of geologic mapping of inactive faults, many authors have contended that slip has occurred along some normal faults with dip angles <30° (Davis and Lister, 1988; Miller and John, 1988; Wernicke, 1981). There is no clear evidence, however, for low-angle normal faults that are active today. Focal mechanism studies indicate the orientation of seismogenic faults. Information such as aftershock locations or the relation between surface fault breaks and hypocenters is needed to determine which nodal plane is the fault plane. Well-constrained fault-plane solutions indicate that most seismogenic normal faults dip at angles >30° (Jackson, 1987;

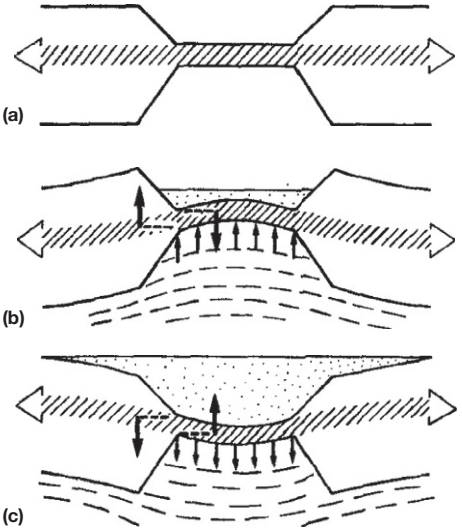

Figure 12 Schematic of the mechanism of (a) lithospheric necking and (b) resultant uplift caused by the gravitational response to the lowering of the surface due to plate stretching. (c) How continued sediment input (combined with thermal subsidence) can lead to subsidence of once elevated rift flanks. Reproduced from Braun J and Beaumont C (eds.) (1989) Contrasting styles of lithospheric extension: Implications for differences between Basin and Range Province and rifted continental margins. Extensional tectonics and stratigraphy of the north Atlantic margins. *American Association of Petroleum Geologist Memoir* 46: 53–79; Braun J and Beaumont C (1989) A physical explanation of the relation between flank uplifts and the breakup unconformity at rifted continental margins. *Geology* 17: 760–764.

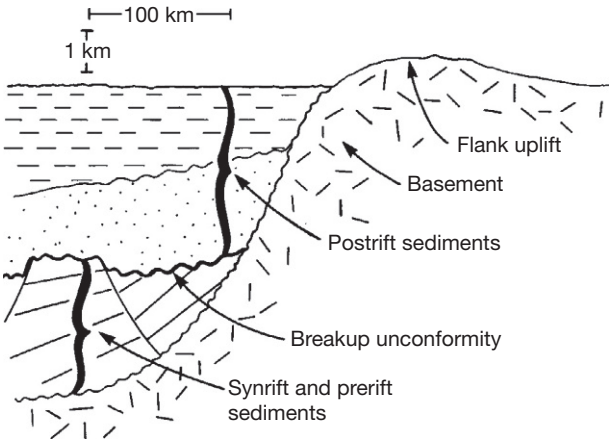

Figure 13 Illustration of typically observed rift flank uplift and rift margin syn- and postrift sediments with an intervening 'breakup unconformity.' Reproduced from Braun J and Beaumont C (eds.) (1989) Contrasting styles of lithospheric extension: Implications for differences between Basin and Range Province and rifted continental margins. Extensional tectonics and stratigraphy of the north Atlantic margins. *American Association of Petroleum Geologist Memoir* 46: 53–79; Braun J and Beaumont C (1989) A physical explanation of the relation between flank uplifts and the breakup unconformity at rifted continental margins. *Geology* 17: 760–764.

Thatcher and Hill, 1991), although at least one has been interpreted as a low-angle fault (Abers, 1991).

Several authors have suggested that normal faults could initiate with low dips if unusual loads reoriented the tectonic stress field itself (Parsons and Thompson, 1993; Spencer and Chase, 1989; Yin, 1989). Under the right set of regional or local loading conditions, the principal stresses might be rotated to a configuration at least geometrically compatible with low-angle normal faulting under the assumption that faulting occurs at an angle of $\sim 30^\circ$ to the maximum principal stress, a well-established result of Mohr–Coulomb fracture mechanics. These stress rotation models have a strong intuitive appeal. They tie a ubiquitous and puzzling feature of the Basin and Range Province, regional detachment faulting, to conditions known or strongly suspected to have existed there at the onset of extensional deformation: orogenic loading, ductile flow below the brittle layer, and widespread calc-alkaline magmatism. They also demonstrate that unusual boundary conditions can alter stress orientations.

The papers advocating initiation of normal faults at low dip angles (Parsons and Thompson, 1993; Spencer and Chase, 1989; Yin, 1989) did not address the question of whether the magnitudes of the reoriented stresses would allow regional low-angle normal faulting under geologically realistic conditions. Wills and Buck (1997) carried out simple analyses designed to test this aspect of several stress-field rotation models. Their results show that the areas at which these models predict low-angle normal fault development are the least favorable places for fault slip to occur. They also quantified the magnitude of spatial variations in cohesive strength and pore pressure required to initiate slip on low-angle normal faults, variations that are implausible.

6.08.3.3 Fault Rotation

An alternative to slip on low-angle normal faults is that the upper parts of some actively slipping high-angle normal faults rotate to shallower dips. Spencer (1984) first suggested that the isostatic response to offset of a normal fault would tend to decrease the dip of the fault. However, Spencer (1984) confined his discussion to the rotation of active low-angle faults. Hamilton (1988) and Wernicke and Axen (1988) argued that large rotation of high-angle faults is consistent with the structures seen in two different extensional settings. Buck (1988) also argued that rotation could explain low-angle fault structures and calculated the flexural response of lithosphere to the loads caused by the offset of a high-angle normal fault. This model produced realistic low-angle fault geometries only when (1) the lithospheric yield strength was finite and (2) the offset of the model fault was about twice the lithospheric thickness.

To get the inactive, up-dip parts of model normal faults to rotate to a low-angle orientation, Buck (1988) assumed that large offsets, relative to the lithospheric thickness, could occur on a high-angle normal fault to produce low-angle fault structures. A major question is why such large offsets might occur on some high-angle normal faults and not on others.

6.08.3.4 Large Offset of Normal Faults

The offset of a dip-slip fault produces topography and so changes the stresses around the fault. For a high-angle normal fault, the topographic relief should build up quickly as the fault is offset. Vening-Meisnez (1950) recognized this and was among the first to suggest that the stress changes related to normal fault offset could result in new faults being formed. Offset of an elastic layer by slip of one fault produces maximum bending stresses at about a flexural wavelength from the fault. Vening-Meisnez (1950) assumed the next fault would break where the bending stresses at the surface were maximally extensional and result in a graben. This assumption is reasonable, since the yield stress (the stress needed to break and slip on a fault) is minimum at the surface.

A different approach to analyzing the effect of normal fault offset on stresses was suggested by Forsyth (1992). In contrast to Vening-Meisnez (1950), he ignored the direct effect of bending stresses on promoting layer breaking and instead estimated the increase in the average regional tectonic stress in a layer due to the buildup of fault-related topography. Forsyth (1992) noted that Anderson's theory for normal faulting is only valid for infinitesimal fault slip because it only considers the work done overcoming friction on the fault surface. The initial orientation of a fault requiring the least regional stress is the one that dissipates the least friction on the fault per unit of horizontal displacement. When a fault is displaced, work is done in the bending of the lithospheric plate cute by the fault. To estimate this work, Forsyth (1992) approximated the lithosphere as a perfectly elastic layer floating on an inviscid substrate. The deflection of the layer caused by fault offset is estimated by using the thin-plate flexure equation. To do this analytically, the fault is treated as a vertical boundary cutting the lithosphere. The topographic step across the fault is the horizontal fault throw, Δx, times tan θ, where θ is the fault dip.

Because of the work done bending the lithosphere, it takes extra horizontal tensional stress to keep the slip occurring on the fault. Forsyth (1992) found that the extra horizontal stress increases linearly with Δx depending on $\tan^2\theta$. He estimated that after only a few hundred meters of slip on a typical high-angle fault, it is easier to break a new fault rather than to continue slip on the original fault. On a low-angle fault, the extra horizontal stress needed for continued motion builds up more slowly with offset. Forsyth (1992) suggested that an initially low-angle normal fault could buildup much more offset than a high-angle fault.

Buck (1993) used the approach of relating work building topography to tectonic forces suggested by Forsyth (1992), but he modified the way fault dip was considered (**Figure 14**). As in the description of topographic relief produced by fault offset, described earlier, the nonvertical dip of the fault significantly reduces the topography-related work to continue fault displacement. Another important change in formulation was the inclusion of the effect of finite yield strength on bending stresses. A Mohr–Coulomb plate will bend more easily than a purely elastic plate, since bending stresses cannot exceed the yield stress. Inclusion of finite yield stress in this model radically lowers the size of the tectonic force increase due to fault-related topography (as shown in **Figure 15**). Using reasonable values for friction and cohesion for a 10 km thick layer, the Buck (1993) model predicts possibly unlimited fault offset. For a thicker layer, the fault offset may be limited to an amount smaller than the layer thickness (**Figure 16**).

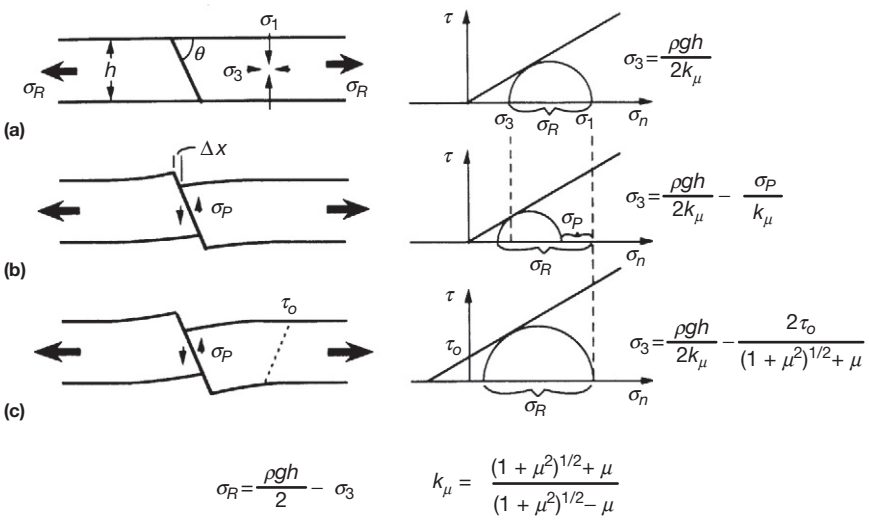

Figure 14 Illustration of the effect of plate bending stresses on the stress state required for slip on a normal fault. (a) The initial Andersonian stress state for slip on a cohesionless, optimally oriented fault. (b) The lowering of the minimum stress, σ_3, required for slip when the plate bending stress can be considered to reduce the vertical stress by an amount σ_p. (c) The regional stress difference needed to break a new fault with a shear strength τ_0. Here μ is the friction coefficient. Reproduced from Buck WR (1993) Effect of lithospheric thickness on the formation of high- and low-angle normal faults. *Geology* 21: 933–936.

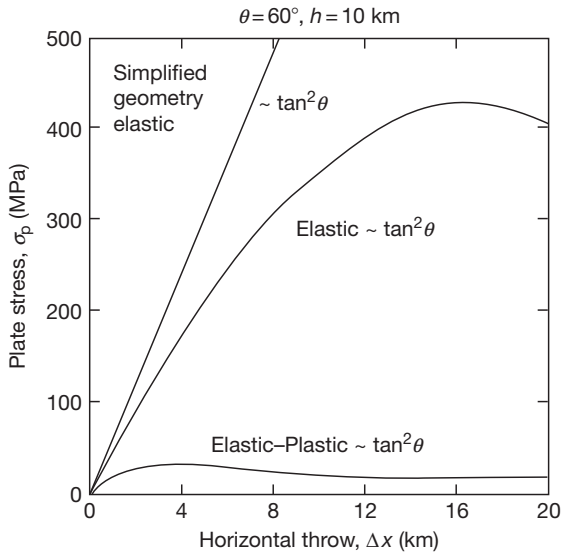

Figure 15 Results of analytic and thin-plate flexure numerical calculation of the change of plate stress with horizontal fault offset for a floating brittle layer 10 km thick and a 60° dipping normal fault. The straight line is from Forsyth (1992), while the elastic curve includes the effect of finite fault dip. The inclusion of finite yield strength of the brittle layer greatly reduces the magnitude of the plate bending stress. Reproduced from Buck WR (1993) Effect of lithospheric thickness on the formation of high- and low-angle normal faults. *Geology* 21: 933–936.

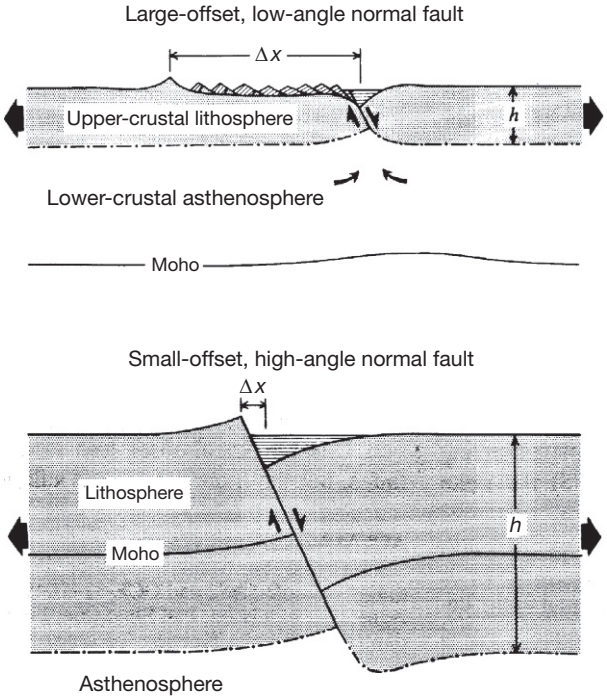

Figure 16 Cartoons of possible implications of the calculations of plate bending stresses given in **Figure 15**. Because plate bending stresses scale with the square of plate thickness, while the cohesive strength of the plate scales linearly with thickness, a noncohesive fault in a thick layer could accrue very large offset. A noncohesive fault cutting a thick cohesive layer might not achieve large offset before another fault replaced it.

6.08.3.5 Two-Dimensional Models of Fault Formation and Offset

The thin-plate approximation used in the studies described earlier is clearly not valid for large fault offset. To be confident of internal consistency in normal fault evolution models requires treatment of the 2- or 3-D stress and strain field. Analog models are useful for simulating the early, small-offset stage of fault development (e.g., Brun et al., 1994; Corti et al., 2003; Supak et al., 2006; Tirel et al., 2006; Tron and Brun, 1991; Withjack and Schlische, 2006), but cannot easily simulate the thermally controlled strength field evolution likely to

affect large-offset faults. Ideally, models could follow the development of faults in an extending, 3-D, viscous–elastic–plastic layer. Given the numerical cost of such models, groups have first developed 2-D models (Figure 17).

Early studies numerically simulated normal fault offset in 2-D cross sections of elastic layers, assuming that the fault offset varies slowly in the third dimension (e.g., King and Ellis, 1990; Melosh and Williams, 1989). Those studies assumed a pre-existing weak fault embedded in a purely elastic layer and solved for the topographic relief and stress changes around the offset faults. Given the potential importance of the finite brittle yield strength (here described as plastic deformation) in controlling how lithosphere can bend in response to fault offset, there has been great effort to include plastic deformation in numerical models. Braun and Beaumont (1989a,b) and Bassi (1991, 1995) treated the lithosphere as a viscous–plastic layer, but were not concerned with localized fault development. Behn et al. (2002) and Huismans et al. (2005) allowed strain rate- or strain-dependent weakening that led to localized zones of concentrated deformation (model 'faults'). Poliakov

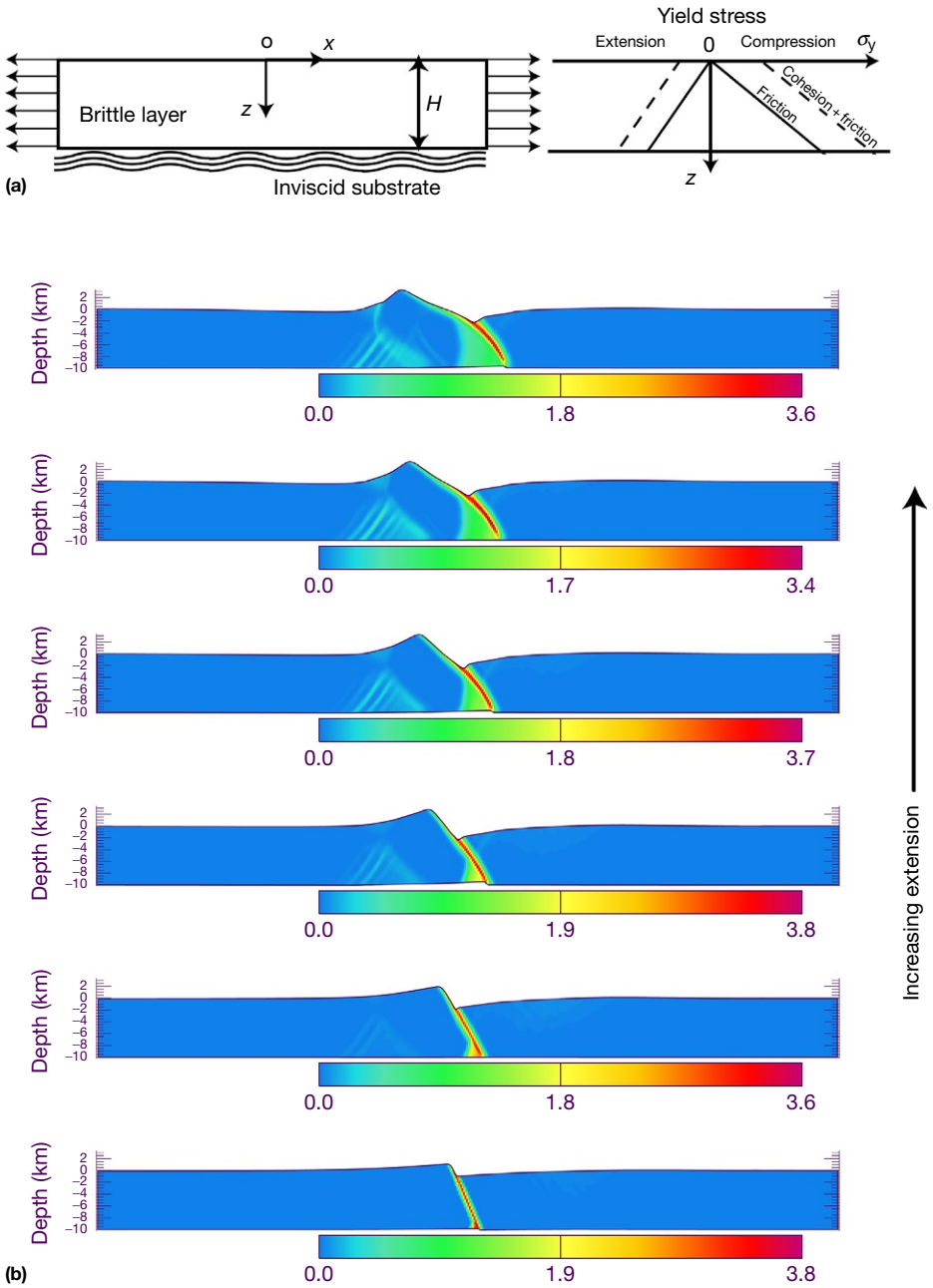

Figure 17 (a) Setup for a numerical model of extension of a floating brittle Mohr–Coulomb layer with a single normal fault seeded at the center of the model layer. Grid spacing is 250 m through this 10 km thick layer and a cohesion of 20 MPa is reduced to 2 MPa over a fault offset of 1500 m. (b) Results of numerical calculation showing the development of plastic (brittle strain) and surface topography. Note that the model is similar in setup to the conceptual model pictures in Figure 10.

and Buck (1998) adapted a numerical treatment of viscous–elastic–plastic deformation to normal fault development. They showed that a sequence of high-angle faults might form and accommodate extension at a simple model mid-ocean ridge structure. In the Poliakov and Buck (1998) formulation, the faults weaken as a function of their offset-related strain, up to a maximum amount of weakening.

Figure 17 shows results of 2-D numerical experiments of extending an elastic–plastic layer that stays nearly uniform in thickness, while a fault forms due to strain-dependent cohesion loss (see Section 6.08.2.2.4). The fault offset produces topography very much like that predicted by eqn [19] except that the wavelength of deformation appears to evolve in the early stage of model fault offset. The maximum fault-produced topographic relief, shown in Figure 18, also follows the pattern predicted by the simple analytic expression derived in the preceding text (eqn [20]).

Numerical experiments also have addressed the question of fault offset and rotation. Lavier et al. (1999, 2000) used an elastic–plastic formulation and investigated how much fault weakening is needed to get large offset of a normal fault. The base of the extending layer was kept at a constant depth to simulate cooling of asthenosphere pulled up as the footwall of the fault moved out and up. Figure 19 shows the results of one model experiment that produced a large-offset fault. The inactive, up-dip part of the footwall side of the fault was rotated into a flat lying position. Lavier et al. (2000) showed large-offset faults could only form when the fault weakening was above a minimum level, but that the rate of fault weakening with strain had to be within bounds. If the maximum amount of fault strain weakening is independent of the thickness of the brittle layer being extended, then large-offset faults will only happen when a layer is thinner than a given thickness. Figure 20 illustrates the force changes due to normal fault offset estimated for thin and thick layers based on the numerical models. Only for a thin layer do we expect to get a large-offset fault. Figure 21 (from Lavier and Buck, 2002) shows two model cases of normal fault offset in an extending viscous–elastic–plastic layers where the thermal structure is allowed to vary due to advection and diffusion of heat. It shows that a thin layer could develop a large-offset fault, while multiple, basin-bounding faults develop in a thicker layer. This is consistent with the observation that large-offset normal faults are only seen in areas of higher than average heat flow where one expects thinner than average lithosphere.

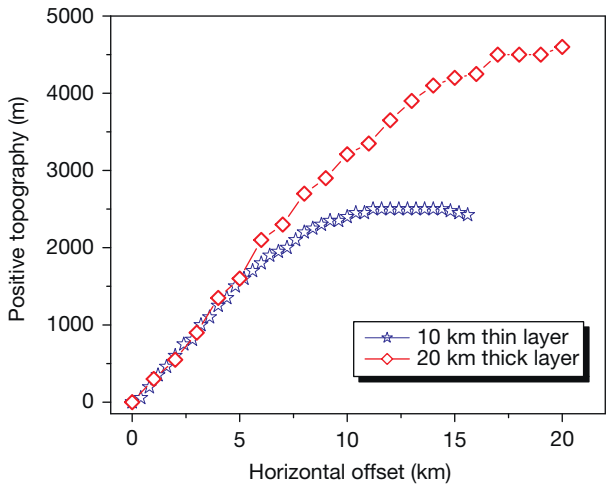

Figure 18 Results of the uplift of the footwall breakaway point as a function of horizontal fault offset. The 10 km layer case is pictured in Figure 17, while the results of a 20 km thick layer with similar setup are also shown. The numerical results are fit very well by the analytic estimate shown in Figure 11 for a flexure parameter of about 0.8 times the layer thickness and for a fault dip of ~50°.

6.08.4 Core Complex Formation: Constraints and Models

Many of the observations that sparked debate over the mechanics of low-angle normal faults come from MCCs. In recent years, we have learned a great deal about these most recently recognized major tectonic features. Core complexes of a new kind have been found and studied in the oceans. Also, ultrahigh-pressure rocks have been found within MCCs leading to interest in the relation between the subduction of continental crust and the formation of core complexes. Highlights of new observations in core complexes and models inspired by those observations are discussed here. A recent review of core complexes by Whitney et al. (2013) gives a more thorough review of core complex locations, constraints, and idea about their formation.

6.08.4.1 Fault Orientation and Rotation in Oceanic Core Complexes

As noted earlier, there is uncertainty over the dip of the detachment faults that are central to the formation of core complexes. Data from continental core complexes either are equivocal or support an initial fault dip of about 30° (e.g., Axen and Bartley, 1997; John and Foster, 1993). However, similar detachment structures associated with domal core complexes are also seen in oceanic crust (see Figure 22). Though this chapter is not focused on oceanic extensional processes, these new data from the oceans shed light on the long-standing controversy over the mechanics of large-offset normal faults.

Oceanic core complexes have been identified along the Mid-Atlantic Ridge, the Southwest Indian Ridge, and the Caribbean–North American Ridge (Hayman et al., 2011), at the Australian–Antarctic discordance (Christie et al., 1998), and along parts of some back-arc spreading centers (Ohara et al., 2001). These core complexes may comprise 50–60% of much of the Mid-Atlantic Ridge (Escartin et al., 2008; Smith et al., 2006, 2008) and 70% of part of the Australian–Antarctic discordance (Okino et al., 2004).

Oceanic core complexes have almost no potentially complicating prehistory of deformation, since they form from 'new' material rising from the asthenosphere. These features are subject to little erosion that can obscure structures and fault-generated topography. Also, mafic and ultramafic minerals in oceanic core complexes allow paleomagnetic determination of fault rotation.

The deployment of ocean-bottom seismometers has allowed monitoring of microseismicity, providing information

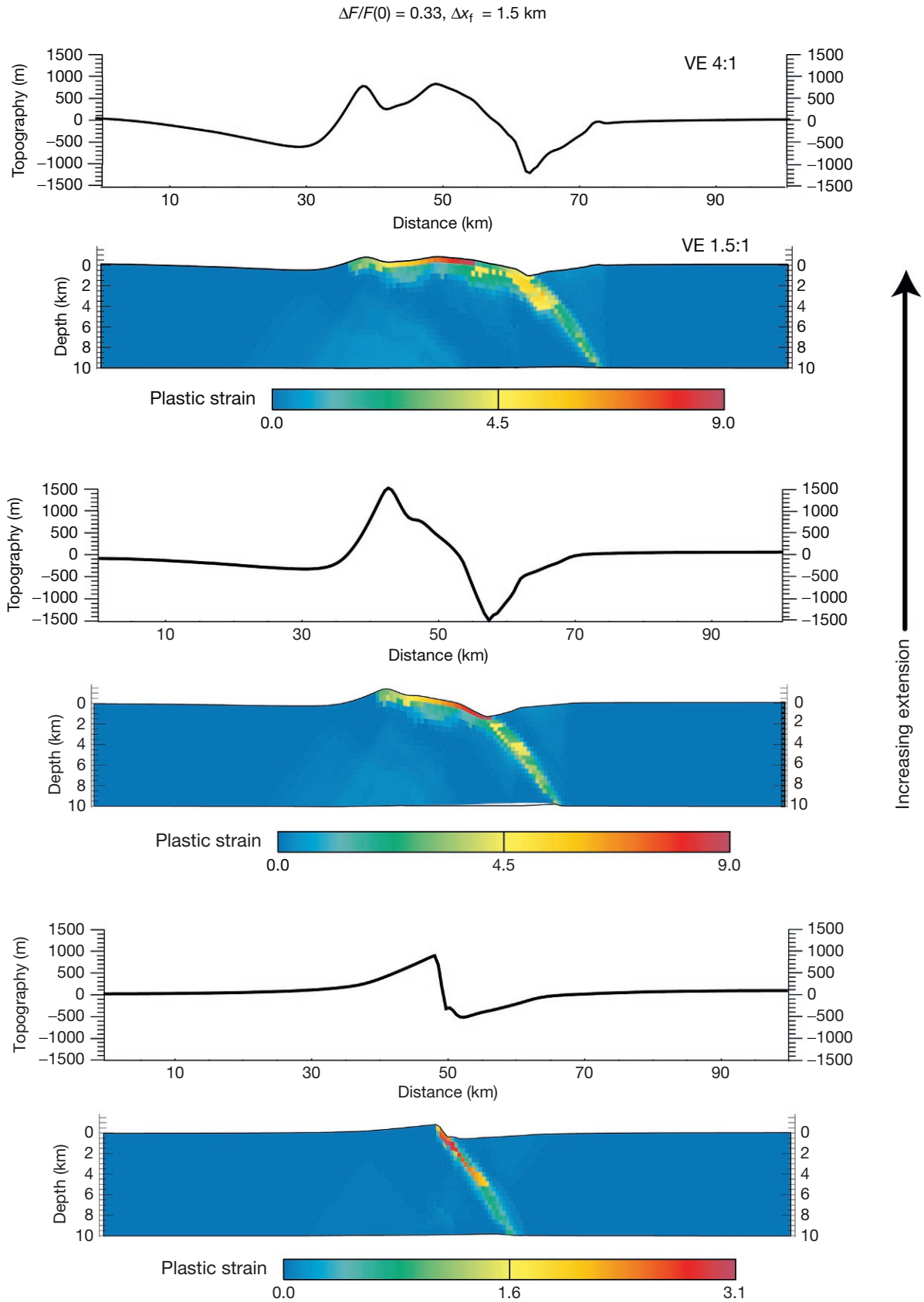

Figure 19 Results of a numerical model of extension of a floating brittle Mohr–Coulomb layer with a single seeded normal fault. The model is similar to that shown in **Figure 17**, but the calculated amount of extension is large enough to allow the footwall of the fault to rotate so that abandoned parts of the fault rotate to, and even past, horizontal. The cohesion loss of the fault was a function of strain with a decrease of 1/3 of the initial layer brittle yield strength occurring linearly with fault offset up to 1.5 km. Reproduced from Lavier LL, Buck WR, and Poliakov ANB (2000) Factors controlling normal fault offset in an ideal brittle layer. *Journal of Geophysical Research* 105(B10): 23431–23442.

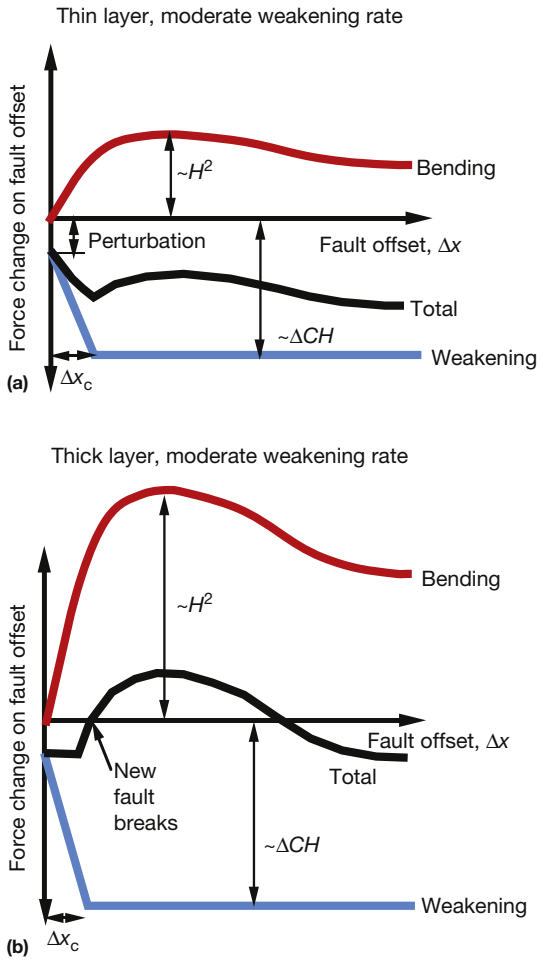

Figure 20 Schematic explanation of the reason that thin layers might allow unlimited normal fault offset, while a thicker layer would not. The force change due to bending is compared to the assumed (or model input) fault weakening amount. If the summed force change is negative, then the fault can continue slip (a), while if the force change becomes positive, the fault should be replaced by another fault.

to help understand detachment geometry and mechanics at depth. For example, in the hydrothermal field associated with the Trans-Atlantic Geotraverse (TAG) on the Mid-Atlantic Ridge, microseismicity defines a fairly planar swarm of earthquakes that dips steeply (70°), extends to ~7 km depth below the seafloor, and projects upward to the locus of hydrothermal activity (Canales et al., 2007; de Martin et al., 2007).

Paleomagnetism has been used to evaluate the rotation history that footwall rocks of oceanic detachment faults experienced during their exhumation. At the TAG hydrothermal field, a rotation of ~50° has been documented based on the reconstruction of magnetic vectors (MacLeod et al., 2011). Using a technique involving correlation between core structures and borehole wall imagery, paleomagnetic data of cores from the Atlantis Massif oceanic core complex require a rotation of $46 \pm 6°$ (Morris et al., 2009). These high rotation values about a nearly horizontal axis, and the seismicity data described earlier, suggest that some large-offset normal faults form and slip at steep dip angles.

6.08.4.2 'Riders Blocks' and Constraints on Fault Strength

Faults must be weaker than surrounding rocks to explain observed localization of strain on faults. There is disagreement over just how weak faults are and particularly whether they can be characterized as having normal versus low values of friction (Collettini et al., 2009; Escartin et al., 1997). Laboratory measurements indicate that for most rocks, the friction coefficient is between 0.6 and 0.8 (Byerlee, 1978). Supporting evidences for this 'normal' range of friction include the dips of active, seismogenic normal faults that range between ~45° and 60° (Collettini and Sibson, 2001; Jackson, 1987; Jackson and White, 1989) and stress differences measured in boreholes (Brace and Kohlstedt, 1980; McGarr and Gay, 1978; Townend and Zoback, 2000).

The recognition of large-offset normal faults, or detachments, in MCCs (Coney, 1980) that presently dip at a low angle (<30°), or are flat, has been used as an argument that these faults have a very low friction coefficient (e.g., Numelin et al., 2007). Analytic (e.g., Buck, 1993; Forsyth, 1992) and numerical simulations of lithospheric extension (e.g., Lavier et al., 1999; Rey et al., 2011) produce large-offset, core complex-forming, normal faults only when the faults were weaker than a given threshold.

In continental core complexes, wedge-shaped blocks of largely clastic and volcaniclastic, syntectonic rocks are seen on top of the high-metamorphic-grade footwall of the detachments (**Figure 23**). These rocks are generally assumed to be pieces of the hangingwall carried on top of the moving footwall (e.g., Rehrig and Reynolds, 1980). Similar 'rider' blocks have been recognized in oceanic core complexes by bathymetric and seismic studies (Dannowski et al., 2010; Reston and Ranero, 2011).

Based on the observation that parts of some oceanic core complexes lack rider blocks, Reston and Ranero (2011) suggested that this could result from detachments with especially weak mineral phases. They also suggested that the lack of syn-extensional clastic or volcanic infill above the fault could preclude rider block formation. Choi and Buck (2012) analyzed these suggestions and gave theoretical predictions of the range of conditions that would allow rider block formation. High-resolution numerical simulations done by Choi et al. (2013) confirmed the Reston and Ranero (2011) suggestions but went on to show that the formation of large-offset normal faults with rider blocks puts tight constraints on the strength of these faults. If the faults were too weak, rider blocks do not form; if they are too strong, large-offset faults do not form. A narrow range of fault weakening, relative to intact surrounding rock, allows for a consecutive series of rider blocks to emerge in a core complex-like geometry (**Figure 24**). Also, Choi et al. (2013) showed that rider blocks develop when the dominant form of weakening is by reduction of fault cohesion, while faults that weaken primarily by friction reduction do not form distinct rider blocks.

6.08.4.3 Crustal Flow and Doming in Core Complexes

Evidence of ductile deformation is recorded in the fabrics of rocks in the cores of MCCs. The most widely discussed idea is that warm, weak lower crust flows into the region of upper

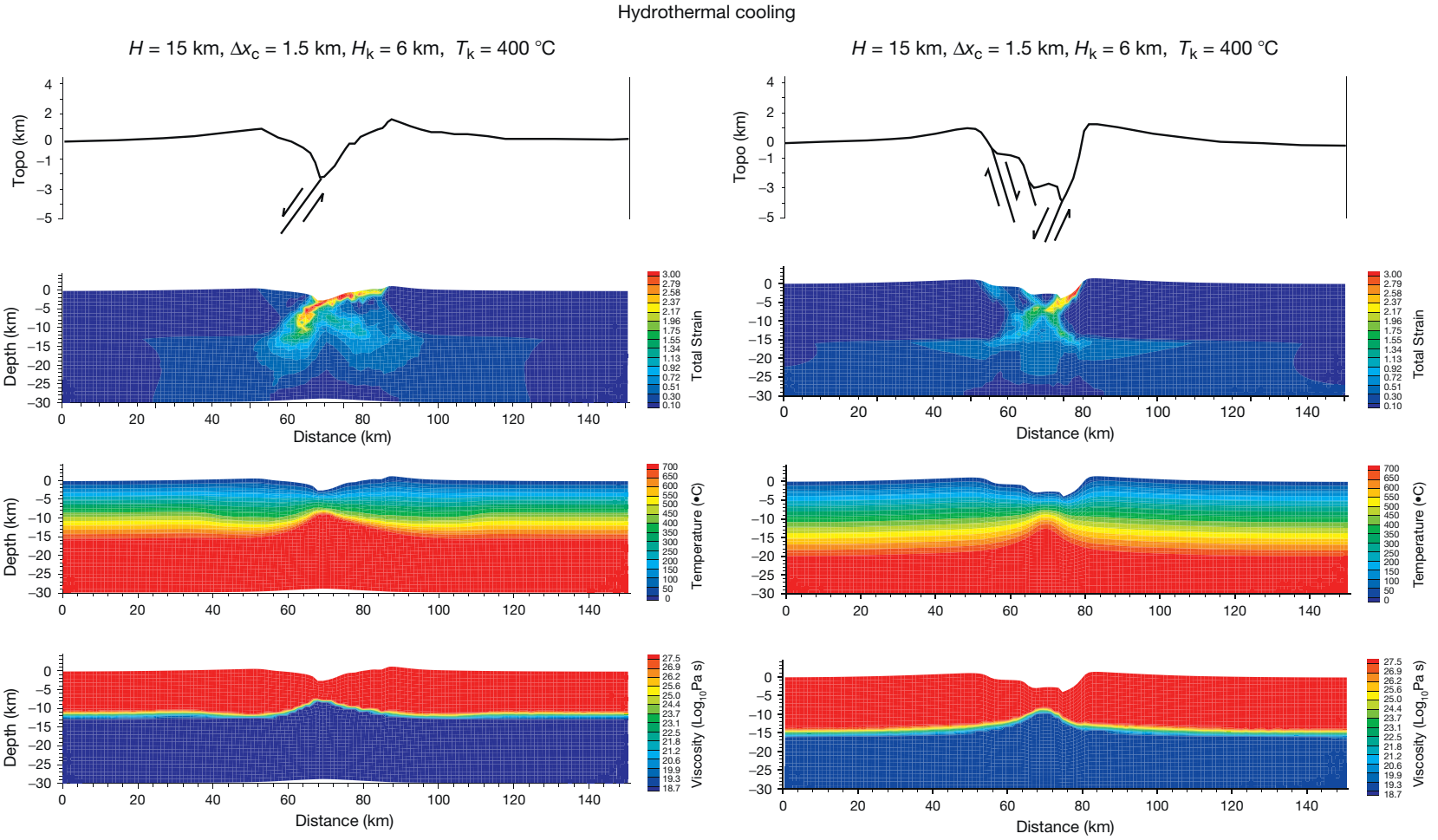
Hydrothermal cooling
H = 15 km, Δx_c = 1.5 km, H_k = 6 km, T_k = 400 °C
H = 15 km, Δx_c = 1.5 km, H_k = 6 km, T_k = 400 °C
Topo (km)
Depth (km)
Distance (km)
Total Strain
Temperature (•C)
Viscosity (Log10Pa s)

Figure 21 Results of numerical model calculations for extension of thin and thick brittle lithosphere. For both cases, the rheology is viscous–elastic–plastic with the viscous strength depending strongly on temperature. The evolving temperature field is computed under the assumption that hydrothermal circulation cools the shallow part of the lithosphere. Extension of the hotter, thinner lithosphere leads to a single, large-offset fault. With extension of the cooler thicker layer multiple normal faults. Reproduced from Lavier L and Buck WR (2002) Half graben versus large-offset low-angle normal fault: The importance of keeping cool during normal faulting. *Journal of Geophysical* 107, http://dx.doi.org/10.1029/2001JB000513.

crustal faulting (e.g., Block and Royden, 1990). Crustal flow may be a necessary requirement for keeping extension focused on a single upper crustal detachment since the local isostatic crustal thinning is to increase the force needed to continued extension concentrated in one region (Buck, 1991). As discussed in **Section 6.08.6**, the lack of fast crustal flow can lead to the formation of wide continental rifts. The smaller thickness of oceanic crust and the lesser contrast in density between oceanic crust and mantle mean that the isostatic force change on crustal thinning is enough to cause abandonment of an active normal fault.

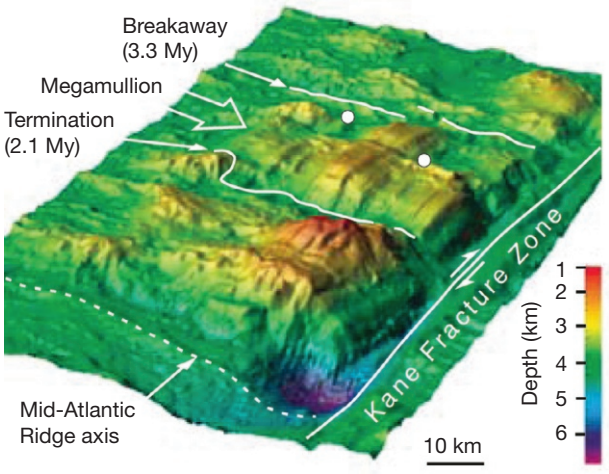

Figure 22 Three-dimensional shaded relief image showing the corrugated surface and dome shape of the oceanic core complex, sometimes called a megamullion, next to the Kane Transform and the Mid-Atlantic Ridge (MAR). View is from the northeast. Reproduced from Tucholke BE, Behn MD, Buck WR, and Lin J (2008) The role of melt supply in detachment faulting and the formation of megamullions. *Geology* 35: 455–458, http://dx.doi.org/10.1130/G24639A.1.

Mapping of fabrics in some core complexes indicates one or more gneiss domes, typically beneath a carapace of high- to medium-grade metamorphic rocks (Brun and van den Driessche, 1994; Vanderhaeghe and Teyssier, 2001; Whitney et al., 2004); these have been called migmatite-cored MCCs (Rey et al., 2009a,b). Such observations have prompted a renewed debate over the importance of local buoyancy versus regional lithospheric extension in driving formation of MCCs. In some cases, extension-normal folds are present indicating contraction normal to the extension direction (e.g., Jolivet et al., 2004; Singleton, 2013).

Gneiss domes are structural domes of foliation that typically display simple structural patterns on a large scale (e.g., Kruckenberg et al., 2011; Vanderhaeghe, 2004). Some domes have a 'double dome' pattern consisting of two main compartments defined by foliation and divided by a steep, median high-strain zone (see **Figure 25**). Two-dimensional models that explain the double dome structure propose that extension of the upper crust drives convergent flow of weak (partially molten) deep crust (Wdowinski and Axen, 1992). Lateral pressure gradients drive the lower crust toward regions of upper crustal extension and thinning. Beneath an active detachment,

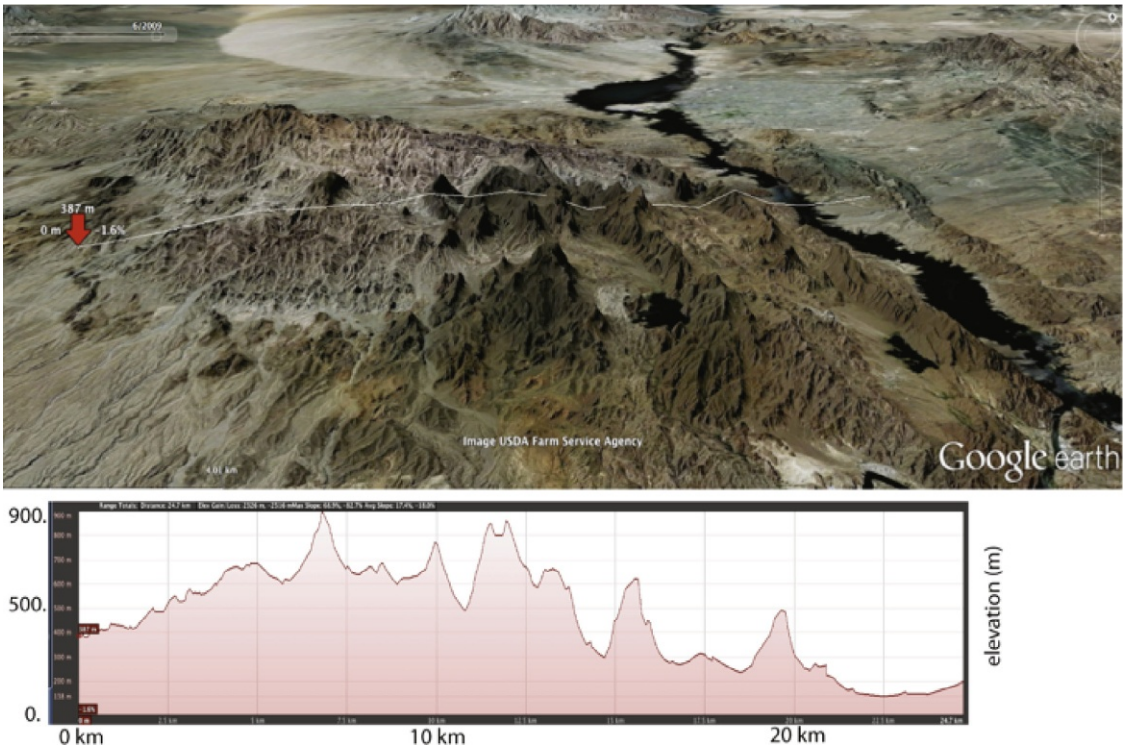

Figure 23 The dome and rider blocks of the Whipple Mountains metamorphic core complex in eastern California are shown in this image draped over topographic relief made using Google Earth. The view is from the south. The white line marks the location of the topographic profile shown in the lower panel. The darker rocks are rider blocks, some of which are continuous for ~10 km along strike. The very dark area is the Lake Havasu section of the Colorado River separating California and Arizona.

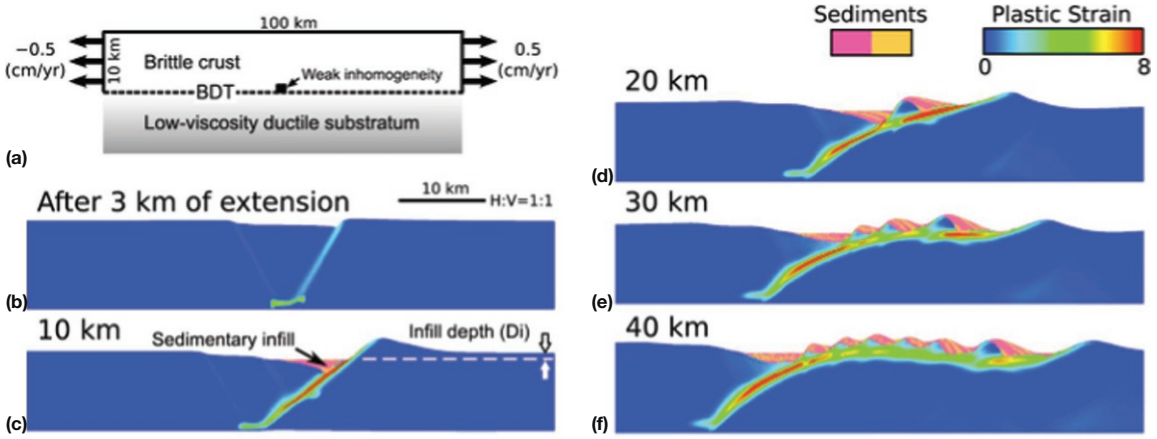

Figure 24 The sequence of the formation of consecutive rider blocks from the high-resolution numerical model study of Choi et al. (2013). (a) Model setup. (b–f) Snapshots of plastic strain and infill distribution in increasing offset. Lamé's constants are both 30 GPa, the initial value of cohesion C_i is 20 MPa, the final values of cohesion after strain C_f is 4 MPa, the initial and final friction angles are equal to 30°, the characteristic offset is 1.5 km, and the densities of crust and infill are 2800 and 2400 kg m^{-3}, respectively.

such pressure-driven flow can produce a viscous collision and the development of a vertical high-strain zone, which separates two subdomes of foliation (Rey et al., 2011; **Figure 26**). Such models predict that deep crustal rocks (such as eclogite and granulite) and possibly lithospheric mantle can be entrained and carried upward in steep high-strain zones.

6.08.4.4 Exhumation of High-Pressure Rocks in Core Complexes

Evidence that buoyant flow is important in core complex formation comes from the youngest known MCCs: the D'Entrecasteaux Islands of Papua New Guinea (**Figures 3** and **27**). These islands are located just west of the Woodlark Basin spreading center in the most rapidly extending rift system on Earth (e.g., Taylor et al., 1999; Wallace et al., 2004). The D'Entrecasteaux Islands rise to elevations up to 2500 m, though the average elevations are much lower. The Trobriand Platform north of the islands is very shallow, while the Goodenough Basin, which separates the islands from Papua New Guinea to the south, has average water depths of 1000–1200 m. There is also asymmetry in the age and thickness of the sediments flanking the islands with the Trobriand sedimentary sequence up to 5 km thick, while the sediments in Goodenough Bay are much thinner (Fitz and Mann, 2013). Boreholes on the Trobriand Platform indicate that sediments there are Eocene to present, while seismic stratigraphy indicates that the Goodenough sediments are Pliocene and younger (Fitz and Mann, 2013). Heat flow is low in the marine areas surrounding the islands, averaging 42 mW m^{-2} in Goodenough Bay (Martinez et al., 2001).

The D'Entrecasteaux Islands and Papua New Guinea lie close to the zone where oblique convergence between the north-moving Indo-Australian Plate and the northwest-moving Pacific Plate has been ongoing since the Eocene, though present-day convergence is concentrated on the New Britain Trench some 500 km north of the islands (e.g., Davies and Warren, 1988). GPS shows that the islands are moving away from the Papuan Peninsula and that the Trobriand Islands are moving away from the islands, with a total extension rate of 1–2 cm year^{-1} and seismicity marks zones of active deformation immediately north and south of the islands and on the north side of the Papuan Peninsula (Wallace et al., 2004).

The islands consist of a lower plate of complexly deformed gneissic domes separated from an upper plate of largely undeformed mafic and ultramafic rocks by shear zones and detachment faults (e.g., Baldwin et al., 2004; Little et al., 2011). The maximum metamorphic grade on Normanby Island is greenschist, while eclogites and granulites are found on Goodenough and Fergusson Islands. The metamorphic rocks form domal structures defined by an increase in grade toward the eroded centers of the domes (Davies and Warren, 1986). Rocks exhumed from ~90 km depth are found on Fergusson Island. Goodenough and Fergusson Islands granites were partially molten in the last few Ma, and geochronological and geobarometric measurements done on samples from these islands indicate steady exhumation of the rock in the last 7 Ma (Baldwin et al., 2008). Seismic measurements show that the crust and lithosphere under the islands are thinner than are seen on the Papuan Peninsula (Abers et al., 2002).

Stretching lineations interpreted to represent late-stage ductile deformation in the domes have a complex 3-D pattern, with dominant east–west trends near the center of the domes rotating to south-trending farther away from the dome centers (Little et al., 2011). The east–west ductile stretching directions in the domes, approximately parallel to the rift margins, are contrary to the expected orientation (parallel to the extension direction) if ductile deformation mirrored that seen at the surface (e.g., Ellis et al., 2011). This is not consistent with flow driven solely by lithospheric extension and may indicate that buoyant diapiric flow contributed to the emplacement of the ductile core of these island core complexes.

Ellis et al. (2011) investigated how the buoyancy and viscosity of partially molten crust might affect the deformation pattern in rock exhumed from great depth. They assumed that this rock was brought to great depth as continental crust that was attached to and carried with a subducted slab of cold lithosphere. The subducted crust warms

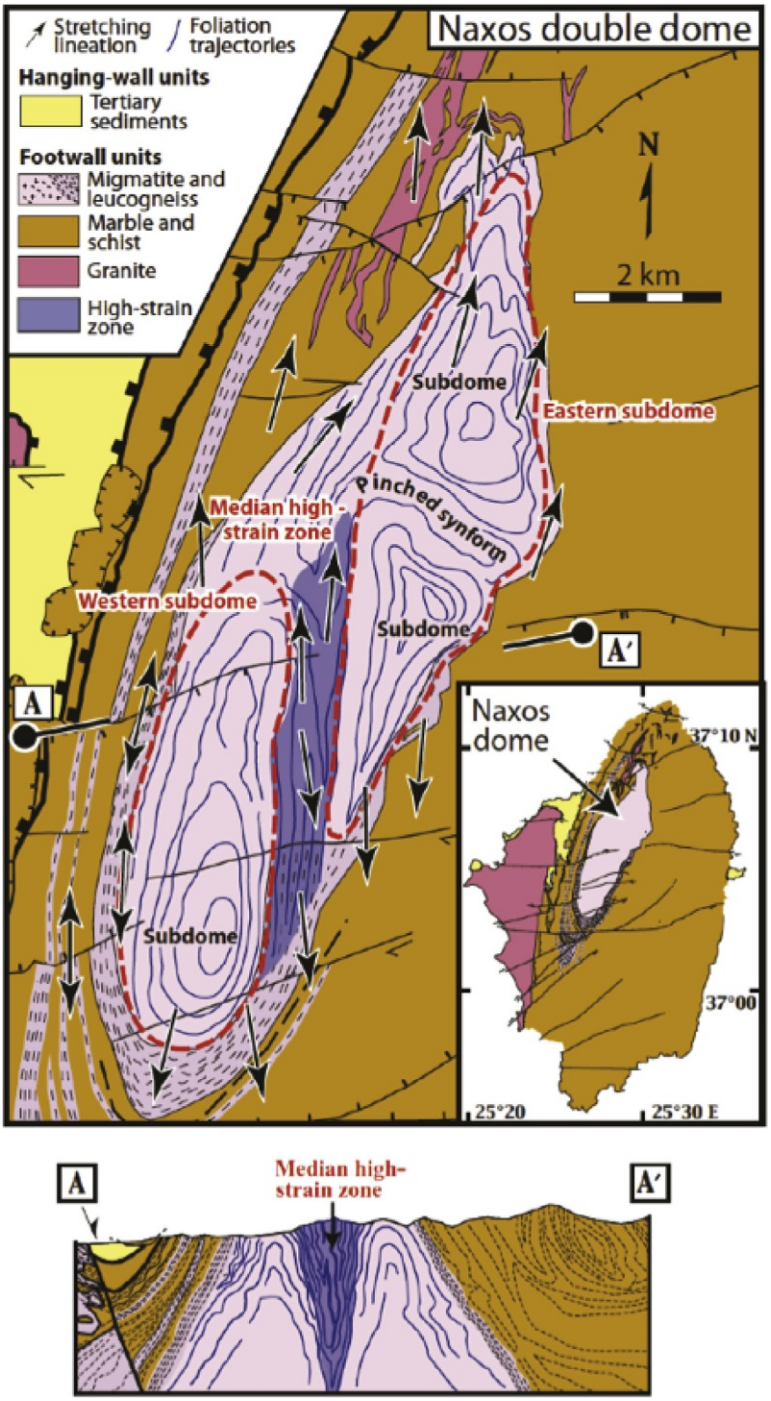

Figure 25 Simplified geologic maps and cross sections of domal structures within the Naxos metamorphic core complex in the central Aegean Sea of Greece. Reproduced from Rey PF, Teyssier C, Kruckenberg SC, and Whitney DL (2011) Viscous collision in channel explains double domes in metamorphic core complexes. *Geology* 39: 387–390.

and so weakens enough to flow and detach from the slab and move upward as a diapir. Ellis et al. (2011) did not consider the subduction process explicitly, but started their 2-D and 3-D models with a mass of hot, low-density, low-viscosity crust already at depth (see Figure 28). They showed that deeply subducted crustal material cannot rise through cold, strong lithosphere even if it has a very low density and viscosity compared to the overlying mantle and crust. Extension is needed to thin the lithosphere and let the buoyant, low-viscosity crustal material flow upward through the rift zone. They inferred that a combination of diapiric rise plus lithospheric extension is responsible for the exhumation of the high-pressure rocks in the D'Entrecasteaux Islands.

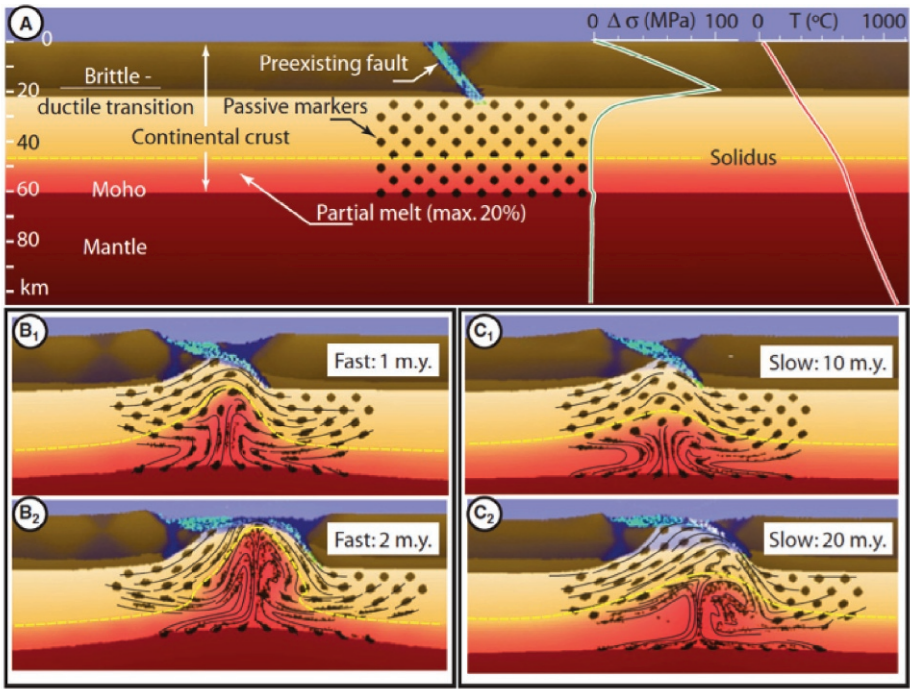

Figure 26 Illustrations of numerical models of extensional gneiss domes. A. model setup. B_{1-2} cases are for sides moving at 11.3 mm a. C_{1-2} are for sides moving ten times slower than for the case shown in B, so the amount of extension is the same in the corresponding panels of B and C. Solid lines through the strain markers represent foliation trajectories. Reproduced from Rey PF, Teyssier C, Kruckenberg SC, and Whitney DL (2011) Viscous collision in channel explains double domes in metamorphic core complexes. *Geology* 39: 387–390.

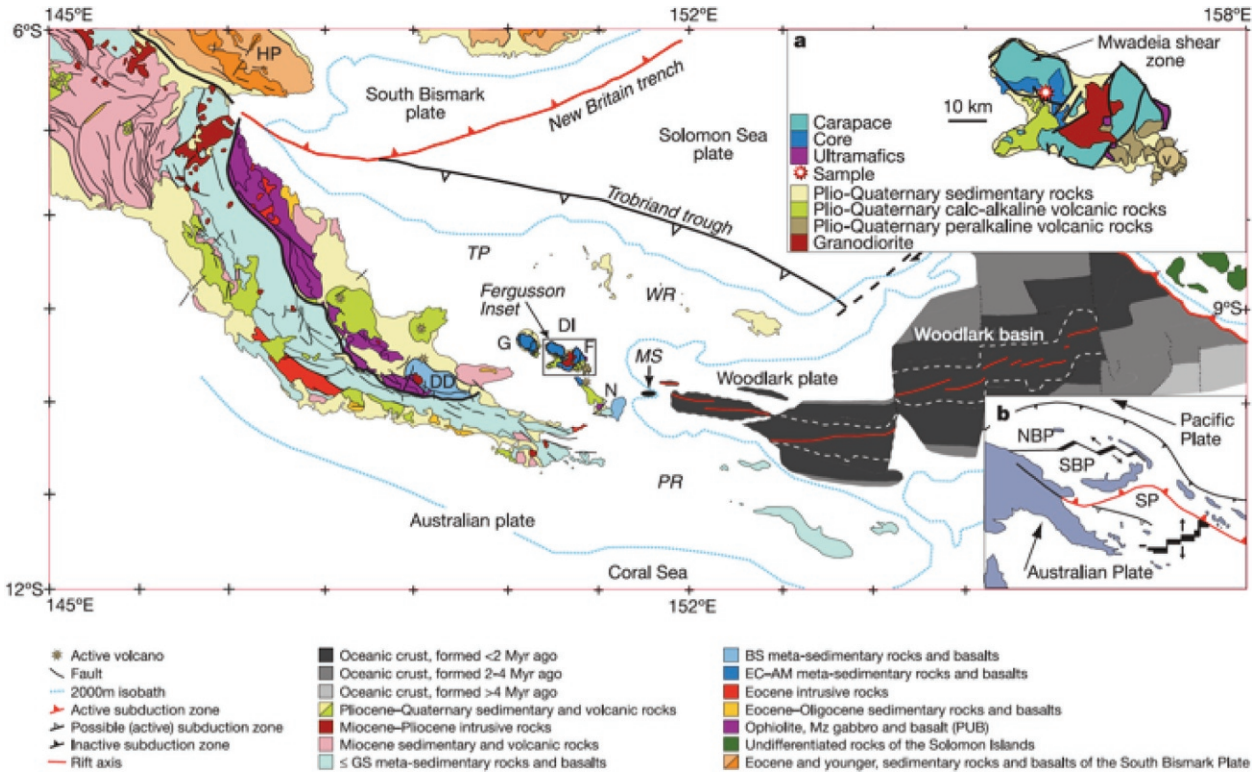

Figure 27 Map showing the geologic units in the region around the D'Entrecasteaux Islands (labeled DI) metamorphic core complexes and the Woodlark Basin of Papua New Guinea (reproduced from Baldwin SL, Monteleone B, Webb LE, Fitzgerald PG, Grove M, and Hill J (2004) Pliocene eclogite exhumation at plate tectonic rates in eastern Papua New Guinea. *Nature* 431: 263–267). DD is the Daymon dome core complex; G is Goodenough Island; F is Fergusson Island; N is Normanby Island; MS is Moresby Island seamount; TP is the Trobriand Platform; WR is Woodlark Rise; PP is Pocklington Rise; HP is the Huon Peninsula; PUB is the Papuan ultramafic belt; OC is oceanic crust; GS is greenschist; BS is blueschist; AM is amphibolite. Insert (a) shows Fergusson Island geology in more detail. (b) Shows the plate boundary zone of the Australian–Pacific Plate boundary. NBP is North Bismarck Plate; SBP is South Bismarck Plate; SP is the Solomon Plate.

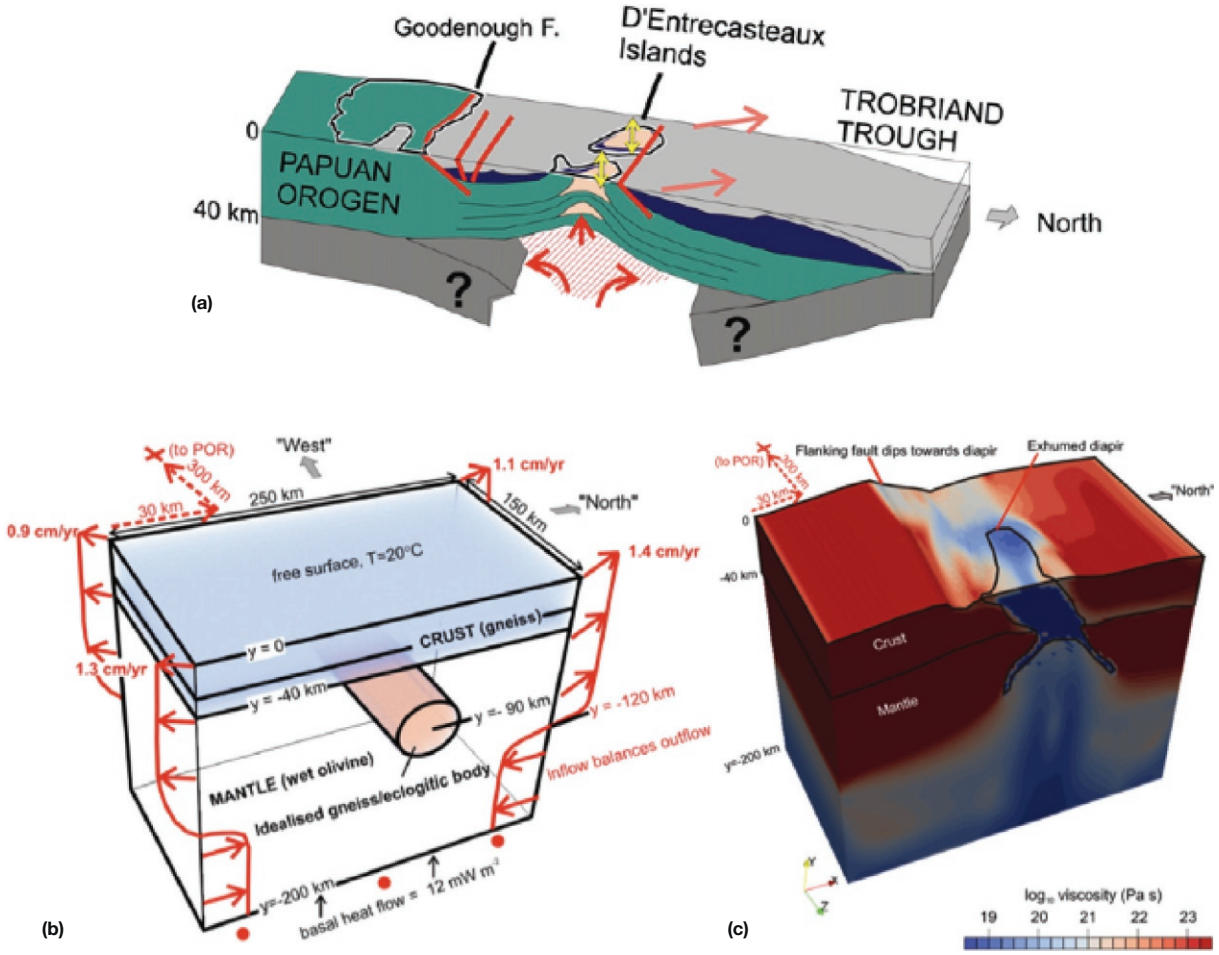

Figure 28 (a) Schematic of the conceptual model of subducted crust diapirically ascending into a rift to make the D'Entrecasteaux Islands. (b) Setup of the 3-D model of the rise of a buoyant crustal cylinder beneath extending crust and lithosphere. (c) Results of a calculation after 1.9 Ma of model time showing the lithospheric structure in terms of viscosity. Eclogite facies diapiric body outlined in bold black line. Reproduced from Ellis SM, Little TA, Wallace LM, Hacker BR, and Buiter SJH (2011) Feedback between rifting and diapirism can exhume ultrahigh-pressure rocks. *Earth and Planetary Science Letters* 311: 427–438.

The model of Ellis et al. (2011) does produce the pattern of flow inferred from geologic mapping of structures within the islands. However, the amount of extension in the models is limited to <60 km. Greater extension would produce a wider region of exhumed hot crust than is consistent with the low observed heat flow in the basins adjacent to the islands (e.g., Martinez et al., 2001). The models also predict several kilometers of subsidence in the region adjacent to the islands, and this is not consistent with the observed bathymetry or the seismic stratigraphy of those basins (e.g., Fitz and Mann, 2013). Finally, the small amount of extension needed in the Ellis et al. (2011) model is not consistent with the findings of Taylor et al. (1999) who inferred about 120 km of extension for the region of the D'Entrecasteaux Islands in the last 8 Ma based on the pattern of magnetic lineations in the oceanic crust of the adjacent Woodlark Basin.

One alternative to the diapir intrusion model of Ellis et al. (2011) is that eduction played a role in the exhumation of high-pressure rocks in the islands. Eduction is effectively reverse subduction in which subducted continental lithosphere moves upward coherently. Davies and Warren (1986) suggested that eduction occurred in the Eocene, but that is not consistent with dating showing that it occurred in the last few Ma and is ongoing (Baldwin et al., 2004). Webb et al. (2008) suggested that eduction in the region occurred since the Late Miocene and was likely related to the ongoing opening of Woodlark Basin. Eduction has the potential to account for the large magnitude of extension indicated for the region of the islands by Taylor et al. (1999). Numerical models showing the general rheological and tectonic conditions for eduction have recently been published (e.g., Duretz et al., 2012), but the specific constraints for the D'Entrecasteaux Islands region have not yet been considered in model studies.

6.08.4.5 The Shape of Core Complex Domes

The domes of MCCs show a variety of shapes (e.g., Jolivet et al., 2004). The dome axis, recognized by mapping the schistosity pattern in the exhumed metamorphic rocks, can be either elongated parallel to the stretching lineation (a-type domes in Figure 29 shown in orange) or normal to this direction (b-type domes in Figure 29 shown in blue). In the first case, the schistosity strikes mainly parallel to the direction of stretching, while in the second case, it strikes normal to it.

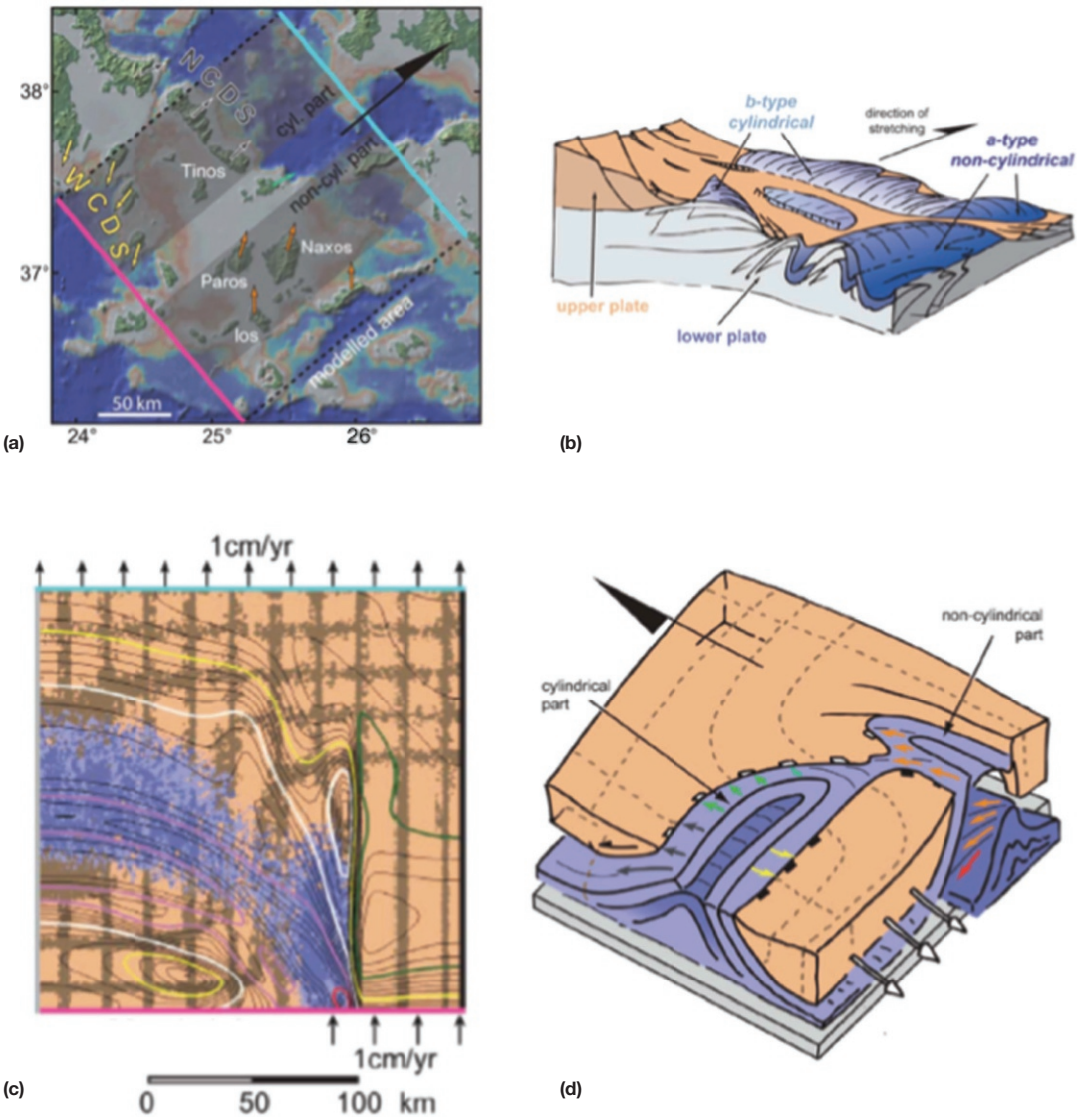

Figure 29 (a) Location map showing Aegean core complexes of two kinds defined in (b) with the south facing arrows indicating b-type cylindrical and north directed arrows indicating a-type noncylindrical. (c) Top view of boundary conditions and results for a 3-D model of continental core complex development. Blue is lower crust and tan is upper crust. (b) Interpretive block diagram of results. Reproduced fro Le Pourhiet L, Huet B, May DA, Labrousse L, and Jolivet L (2012) Kinematic interpretation of the 3D shapes of metamorphic core complexes. *Geochemistry*, *Geophysics*, *Geosystems* 13: Q09002. http://dx.doi.org/10.1029/2012GC004271.

Hence, b-type domes are nearly cylindrical structures and may be modeled in 2-D plane strain cross section, while the a-type domes are intrinsically 3-D structures since local horizontal constriction occurs normal to stretching (**Figure 29**).

These variations in the pattern of topographic doming of the well-studied Miocene MCCs of the central Aegean Sea have prompted a numerical study of the 3-D MCCs by Le Pourhiet et al. (2012). They noted that domes with a long axis orthogonal to the extension direction are consistent with 2-D model of core complexes (e.g., Lavier et al., 1999) with a peak in lower plate topography a set distance from the upper plate that is controlled by flexure of the plates. Le Pourhiet et al. (2012) focused on the impact of 3-D kinematic extensional boundary conditions on the 3-D shape of these domes. They considered a change in extensional boundary velocity as indicated in **Figure 29** and showed that this produces a transtensional boundary between two regions of the model. Such a boundary condition produces an extensionally exhumed 'core' of lower crustal rocks that is elongated in the direction of extension similar to a-type domes. Le Pourhiet et al. (2012) showed that domes formed in a transtensional step over, or at the tip of propagating strike-slip faults, display a finite strain field that can be interpreted as characteristic of transpressive domes, although in their model, no shortening was applied in the far field.

6.08.5 Pure Versus Simple Shear Rifting

Rift valleys are partly filled with sediment and rifted margins are characterized by syn- to postrifting sedimentary units that may be more than ten kilometers thick. Such thick piles of sediment can only be accommodated if the rifted region

subsides by several kilometers. The sediments act as a load that pushes down the surface and amplifies the amount of subsidence that would occur with no sedimentary infill. If a rift basin is narrow compared to the flexural wavelength of lithospheric response, then the load is regionally compensated. As noted in the last section, sediment loading can pull down the rift shoulders as it fills in the rift basin. If the rift is wider than the flexural wavelength, then the sediment can be treated as a locally compensated load.

To illustrate local compensation of sediment, consider the simple case of an air-filled rift basin with an initial depth of d_i. Imagine that gravity is 'turned off' as the basin is filled with sediment. When gravity is turned on, the sediment load pressure is the fill depth, d_s ($=d_i$), times the sediment density, ρ_s, times the acceleration of gravity, g. This load will push down the surface, and if we assume that sediment inflow keeps the basin filled to sea level, then the basin will continue to deepen until the sediment load is 'compensated.' Local compensation implies that the crust and mantle lithosphere floats on fluid mantle asthenosphere. This means that that the weight of a column of crust and mantle to an arbitrary 'depth of compensation' must be constant. As sediment fills the hole, it displaces mantle that is denser than sediment. Equating the column weight before and after basin fill, the ultimate basin fill depth d_s is related to the unfilled depth as

$$d_s = d_i \rho_m / (\rho_m - \rho_s) \qquad [21]$$

where ρ_m is the density of mantle. Taking $\rho_s = 2600\ \mathrm{kg\ m^{-3}}$ and $\rho_m = 3250\ \mathrm{kg\ m^{-3}}$, a 1 km deep air-filled basin would be filled with locally compensated sediment to 5 km. Deep holes might be likely to be filled in by water before being filled with sediment, but this intermediate step does not change the results of this simple analysis.

To get thick sedimentary packages requires a depression or hole. Wells drilled into rifted margins showed two interesting things about the thick sedimentary sequences (**Figure 30**). The sediments were deposited over a long time (10s to 100s of million years), and the infilling sediments were generally deposited at shallow water depths in a lake or in an ocean basin (Sleep, 1971; Steckler and Watts, 1978). Since compensation should occur on a timescale of thousands of years, these observations imply that the hole the sediments were filling had subsided with time.

To understand the mechanism by which rift basins and rifted margins subside, we need to understand subsidence of ocean basins. One of the most striking features of the ocean basins is the smooth pattern of depth increase with distance from the mid-ocean ridges. The depth of seafloor increases with the square root of its age (Parsons and Sclater, 1977). This is a clear confirmation of plate tectonics, which holds that the oceanic plates are formed when hot a mantle and magma upwells at a spreading center and then cools as they move away. Since most plates move laterally much faster than they thicken by cooling (except very close to the spreading center), this cooling may be approximated by the cooling of a half-space of hot material. Lithospheric material contracts and so becomes denser as it cools. Thus, as the lithosphere cools and shrinks, it will float lower on the asthenosphere. Combining half-space cooling with thermal contraction and local compensation predicts subsidence that is proportional to the square root of lithospheric age (e.g., Langseth and Taylor, 1967; McKenzie, 1967; Parsons and Sclater, 1977).

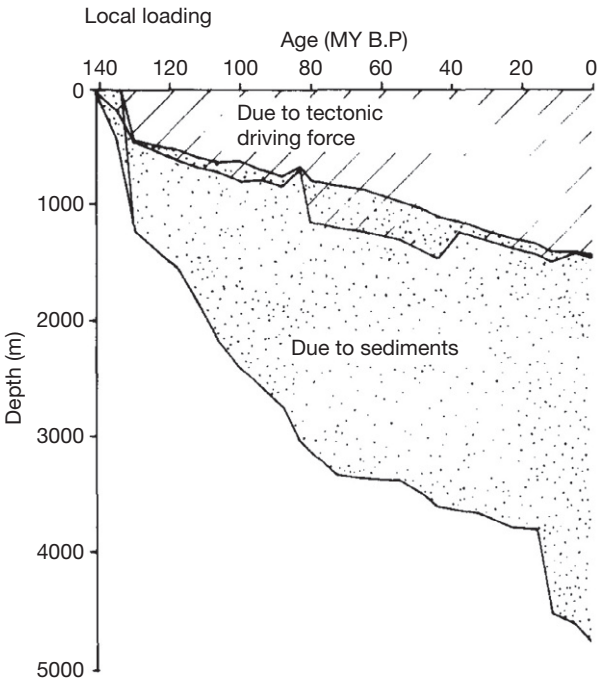

Figure 30 Subsidence data for the margin of the western Mediterranean showing that subsidence was not driven just by sediment loading. Estimated components of subsidence with time due to the isostatic response to sediment loading compared to the subsidence that would occur without sediment infill, here labeled as being due to an (unspecified) tectonic driving force. Reproduced from Watts AB and Ryan WBF (1976) Flexure of the lithosphere and continental margin basins. *Tectonophysics* 36: 25–44.

Sleep (1971) noted that the rate of subsidence of rifted margins also is related to the square root of sediment age. This suggested that rift margin subsidence might be controlled by lithosphere cooling down from a hot state at the time of rifting. However, there is still the problem of how to get an initially hot region to cool. Sleep reasoned that if continental lithosphere, with a surface close to sea level, were heated and thinned, thermal expansion would float the surface above sea level. The surface would gradually subside back to sea level and no marine sediments could fill in. Something had to happen to lower the surface. The idea favored by Sleep (1971) was erosion of the uplifted surface. If a layer of low-density crust (compared to mantle) were removed, then the surface could subside below sea level as cooling proceeded. However, the sediments that would be eroded off the elevated region are not seen.

Several authors (Artemjev and Artgushkov, 1971; McKenzie, 1978; Salveson, 1978) suggested that thinning of the lithosphere by pure shear extension created the thermal input needed to explain the later thermal subsidence. Because there is no active asthenospheric heating of the lithosphere in these models, they are termed 'passive.' The crustal thinning allows subsidence below sea level, or the original level of the continent, and sediment accumulation.

Mckenzie (1978) quantified the effects of uniform pure shear extension or 'stretching' of the entire lithosphere. Stretching should thin both the crust and thermal lithosphere

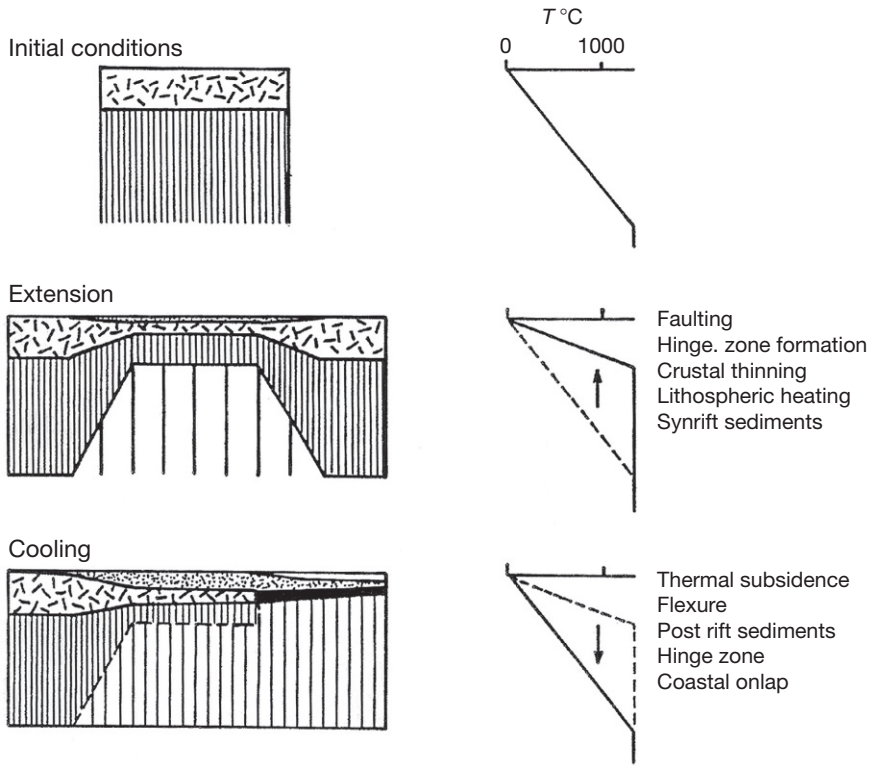

Figure 31 Schematic illustration of the McKenzie (1978) lithospheric stretching model. Reproduced from Steckler MS, Berthelot F, et al. (1988) Subsidence in the Gulf of Suez: implications for rifting and plate kinematics. *Tectonophysics* 153: 249–270; Steckler MS, Watts AB, et al. (1988) Subsidence and basin modeling at the U.S. Atlantic passive margin. In: Grow JA and Sheridan RE (eds.) *The Atlantic Continental Margin*. *The Geology of North America*, vol. I-2, pp. 399–416. Boulder, CO: U.S. Geological Society of America.

(see Figure 31). Local compensation of crustal thinning gives 'tectonic subsidence' on the timescale of the thinning. Lithospheric thinning causes immediate uplift followed by slow 'thermal subsidence.' In the McKenzie stretching model, the rift is approximated as a rectangular region of extensional pure shear. Pure shear describes homogeneous thinning of an entire block of material by a stretching factor β given by the ratio of the initial to final thickness ($\beta > 1$ for extensional thinning).

If the initial thermal gradient in the lithosphere is given by dT/dz, instantaneous pure shear thinning will result in steepening of the gradient to $\beta dT/dz$. After rifting, time-dependent conductive cooling of the lithosphere eventually results in reequilibration of the thermal gradient to its initial value. The stretching model is useful since it gives a 1-D description of the effect of lithospheric extension and so is easy to implement mathematically. McKenzie's (1978) model neglects lateral heat flow and heat loss during the finite time duration of extension but matches the main characteristics of the subsidence histories of many margins (see Figure 32).

The instantaneous uniform pure shear extension model was further generalized by Jarvis and McKenzie (1980) to include the effects of vertical heat loss during a finite duration extension event. They were able to model the heat flow and subsidence through a finite period of lithospheric stretching and thinning and the subsequent evolution after the end of the extension event. In general, the heat flow and subsidence history differed little from the instantaneous extension model, provided the time during which extension occurs is not too

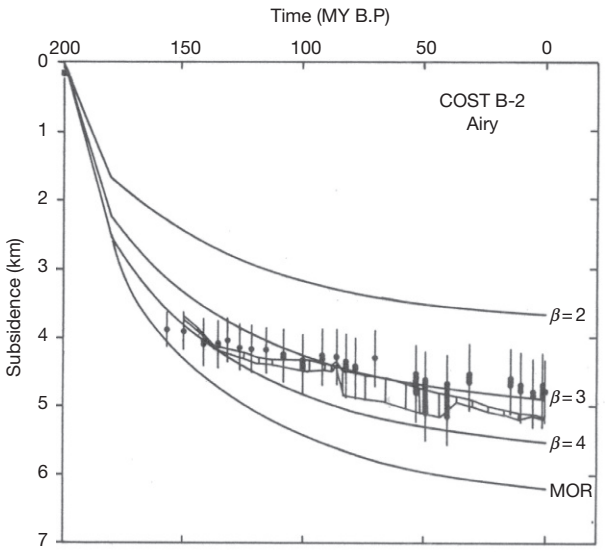

Figure 32 Comparison of subsidence data for the COST-B2 well on the US East Coast with predictions of the stretching model with different stretching factors, β. Reproduced from Steckler MS, Berthelot F, et al. (1988) Subsidence in the Gulf of Suez: implications for rifting and plate kinematics. *Tectonophysics* 153: 249–270; Steckler MS, Watts AB, et al. (1988) Subsidence and basin modeling at the U.S. Atlantic passive margin. In: Grow JA and Sheridan RE (eds.) *The Atlantic Continental Margin*. *The Geology of North America*, vol. I-2, pp. 399–416. Boulder, CO: U.S. Geological Society of America.

long. For a lithosphere thinned to half of its original thickness, for example, they found good agreement with the instantaneous case provided the duration of extension is < 15 Ma.

Though the stretching model gives a simple explanation of the approximate pattern of subsidence seen at most rifts, it fails to explain the details of the subsidence. Where constraints on subsidence are good, the ratio of thermal subsidence to tectonic subsidence is greater than predicted by the stretching model (e.g., Davis and Kusznir, 2004; Royden and Keen, 1980; see **Figure 33**). The problem is even worse if the effects of lateral heat conduction are added to the model (Alvarez et al., 1984; Cochran, 1983b). The synrift subsidence is augmented owing to the additional lateral heat loss, and the postrift subsidence is diminished compared to the 1-D model.

It appears that extra lithospheric thinning is needed compared to a standard stretching model. This observation led to the proposal of a two-layer stretching model (Royden and Keen, 1980) in which the subcrustal lithosphere is decoupled from the crust and can be extended by a greater amount than the crust (see **Figure 34**). Although this model provides a simple way to specify the amount of lithospheric heating independently of the amount of crustal extension, it lacks a physical mechanism for this process.

Another way to explain the observed increase in thermal relative to initial subsidence is to horizontally offset the locus of crustal versus lithospheric thinning. This is a key feature of the 'simple shear model' of lithospheric extension that was advanced by Wernicke (1985). One side of the rift is viewed as the upper plate, and the other is the lower plate of gently dipping normal fault or detachment (see **Figure 35**). Offset of the detachment would lead to very asymmetrical syn- and postrift subsidence. On the upper plate side, areas of little crustal thinning occur over places where the lithosphere is greatly thinned. Thus, the upper plate side could be a place of little initial tectonic subsidence and large magnitude thermal subsidence, fitting the general pattern of observed rifted margin subsidence.

Several geologic and geophysical observations have suggested the importance of simple shear extension in the crust, which gives rise to asymmetrical structures. Low-angle normal faults exposed at the Earth's surface have been traced to midcrustal levels using seismic reflection techniques. Seismic data for the eastern Basin and Range show low-angle normal faults that penetrate the upper and middle crust (Allmendinger et al., 1987). The Bay of Biscay, which has been considered a classic example of a pure shear margin (de Charpel et al., 1978), is interpreted by LePichon and Barbier (1987) to show evidence of crustal-scale simple shear along a detachment. MCCs show that rocks can come up from midcrustal levels apparently in association with extensional shear zones (Davis, 1983). The observation of synthetically dipping normal faults over broad areas (e.g., the southern Basin and Range; Stewart, 1978) has been taken as evidence for simple shear (Wernicke, 1981).

Strong topographic and volcanic asymmetries exist across some rifts and conjugate passive margins, among them the Red Sea Rift (Wernicke, 1985), East African Rift (Bosworth, 1987), and the Southeast Australian–Lord Howe Rise conjugate margin (Lister et al., 1986). The direct observations of simple shear extension are confined to the crust. However, the observation of normal faults extending to great depth in the crust combined with observations of topographic asymmetries across rifts has led to the suggestion that normal faults and/or ductile shear zones may extend through the entire lithosphere (Lister et al., 1986; Wernicke, 1981, 1985). Such lithospheric detachment models imply that much of the deformation in an extending region occurs as simple shear rather than pure shear.

Particularly good data to test the predictions of the simple shear model come from studies of the Northern Red Sea. The

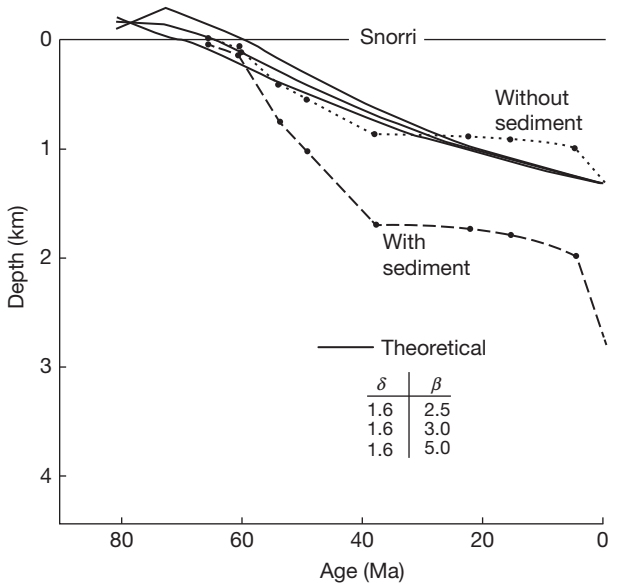

Figure 33 Subsidence data (dashed and dotted lines) for a well on the Labrador continental margin. Solid lines are predictions of a model with greater stretching of the lithosphere (factor β) compared to stretching of the crust (by a factor δ). Reproduced from Royden L and Keen CE (1980) Rifting process and thermal evolution of the continental margin of eastern Canada determined from subsidence curves. *Earth and Planetary Science Letters* 51: 343–361. http://dx.doi.org/10.1016/0012-821X(80)90216-2.

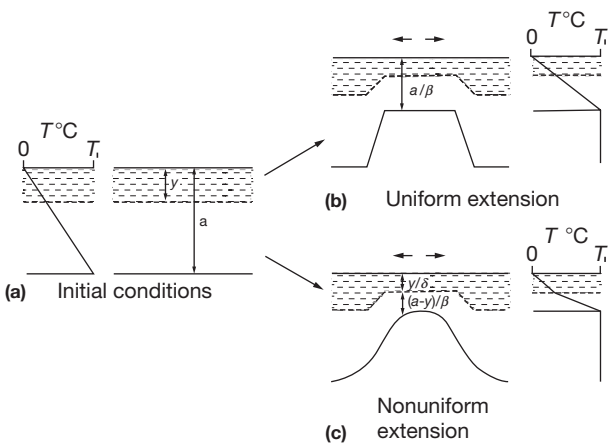

Figure 34 Schematic of the 'two-layer' stretching model in which the lithosphere is stretched by a different from the crust. Reproduced from Royden L and Keen CE (1980) Rifting process and thermal evolution of the continental margin of eastern Canada determined from subsidence curves. *Earth and Planetary Science Letters* 51: 343–361. http://dx.doi.org/10.1016/0012-821X(80)90216-2.

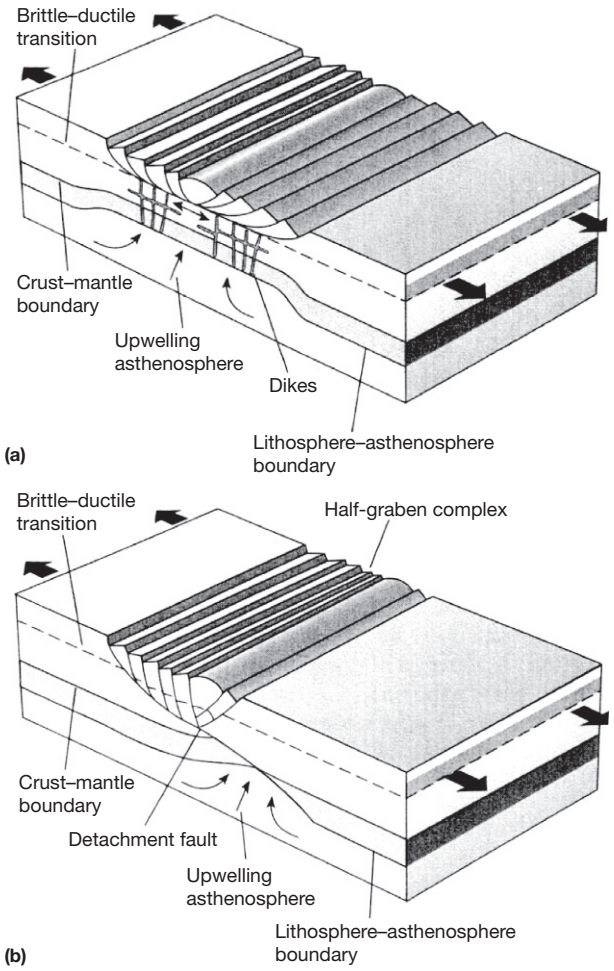

Figure 35 Schematic of structures formed by either pure shear or simple shear lithospheric extension. Reproduced from Lister GS and Davis GA (1989) Models for the formation of metamorphic core complexes and mylonitic detachment terranes. *Journal of Structural Geology* 11: 65–94.

asymmetrical uplift and volcanism bordering the Red Sea are well known and have been cited as evidence for a throughgoing lithospheric detachment (Wernicke, 1985). The kinematic history of opening of the Northern Red Sea is well constrained by geologic and geophysical data. Although rifting in the Red Sea began around the end of the Oligocene–Early Miocene (Cochran, 1983a), evidence from the Gulf of Suez and Gulf of Aqaba (Steckler et al., 1988a) suggests that in the Northern Red Sea, most of the extension has occurred within the last 19 My and that it continues to the present. The young age of this rift is particularly important for discriminating between models of its formation because many of the effects are transient and will not be observable tens of millions of years after rifting.

Geophysical fieldwork in the Northern Red Sea provided excellent heat flow coverage of this area (Cochran et al., 1986; Martinez and Cochran, 1988). To compare the predictions of the simple shear model to this data, Buck et al. (1988) used a numerical technique that solved for 2-D conductive and advective heat transport through time. Simple shear extension of the lithosphere was modeled as occurring along a straight shear zone, and the topographic response to simple shear could be described in terms of local isostasy.

The long wavelength topographic asymmetry across the Red Sea, which has been cited as evidence for simple shear extension of the lithosphere, was not matched by any of the simple shear model cases. The observed high heat flow anomalies in the Red Sea require a large component of pure shear lithospheric extension centered under the region of maximum crustal extension. In contrast, at the plate separation rate of the Northern Red Sea, simple shear extension of the lithosphere along a shallow ($<30°$) dip detachment is ineffective in reproducing the observed heat flow anomalies. Only a narrowing region of pure shear extension can satisfy the width of the rift and the peak observed heat flow values of $\sim$300 mW m^{-2}.

Other, older continental margins have been studied in terms of whether various kinematic extensional models can explain their structure and subsidence patterns. However, as conjugate margins have been studied, it seems that both rifted margins subside the way this model predicts for the upper plate margin. This has been described by Driscoll and Karner (1998) as the 'upper plate paradox.'

6.08.6 Wide Versus Narrow Rifts

It has long been recognized that extension of continents can result in either narrow or wide rifts (e.g., England, 1983). For narrow rifts, such as the Rhine Graben (Illies and Greiner, 1978), the Gulf of Suez (Steckler et al., 1988b), the East African Rift System (e.g., Ebinger et al., 1989), the Baikal Rift (e.g., Zorin, 1981), and the Rio Grande Rift (e.g., Morgan et al., 1986), the region of intense normal faulting is on the order of 100 km wide. For wide rifts, the type example of which is the Basin and Range Province of western North America, the region of significant normal faulting is as much as 800 km wide (Hamilton, 1987). The Basin and Range is characterized by small lateral gradients in crustal thickness, while narrow rifts may show large lateral gradients in thickness of crust and in topography.

Most rifts are relatively narrow (**Figures 1** and 4), and this is generally ascribed to the weakening effect of thermal advection. The lithosphere can be thinned by stretching or heated by injection of magma. Since hot crust and mantle materials flow at lower yield stresses (eqn [4]), a hotter region will be weaker. Extension should stay concentrated in the region of weakest lithosphere. The zone of extensional strain should remain confined to a region that is about as wide as the lithosphere is thick.

If a region of focused extension should become effectively stronger than the surrounding region, then one might expect the locus of extension to migrate to the weaker regions. If this continued, then a region of rifting that is wider than the lithospheric thickness might develop. Three delocalizing processes have been suggested as ways to get wide rifts: thermal diffusion strengthening, viscous strain rate strengthening, and the change in gravitational stresses due crustal buoyancy. The scaling relations derived in an earlier section help us to evaluate the potential of each of these mechanisms to produce a wide rift.

6.08.6.1 Slow Rifting and Thermal Diffusion

England (1983) used the thin-layer approximate to investigate whether wide rifts could occur due to thermal diffusion strengthening. He considered the evolution of continental yield strength during extension and noted that if the mantle is much stronger than the crust, then very slow extension could lead to a strength increase in the extending area. The basic idea is that weak crust is thinned by stretching and isostatically 'replaced' by intrinsically stronger mantle. Diffusive cooling has to be significant to have this compositional strengthening trump the advective weakening effect. To get this effect to produce strengthening during extension, England (1983) had to assume that mantle is much stronger than crust and that extension rates were very slow.

According to England (1983) as well as other workers (Kusznir and Park, 1987; Sonder and England, 1989), the diffusive strengthening effect explains the occurrence of wide regions of continental extension like the Aegean Sea and the Basin and Range Province. However, observations do not seem to confirm this prediction since some wide rifts did not extend at a slower velocity than did some narrow rifts.

Sawyer (1985) questioned the validity of the England (1983) analysis since it did not consider the effect of finite brittle yield strength of the crust and mantle. The yield strength in the England (1983) model only involved the viscous yield strength. Sawyer (1985) had questioned whether the crust–mantle strength contrast is likely to be as large as assumed by England (1983). At a range of temperatures likely to be found at the base of the crust, the ductine yield strength of crust can be thousands of MPa lower than that of the mantle. Sawyer (1985) noted that the brittle failure stress may be independent of rock type so that the contrast in crust and mantle strength is limited. When even conservative brittle yield strength values are included, it greatly lowers the threshold extension rates that would lead to lithospheric strengthening and so widening of a rift. Also, if the crust and mantle are dry, then the viscous yield strength of the crust may not be significantly different from that of the mantle (Kohlstedt et al., 1995; Mackwell et al., 1998).

Naturally, the importance of diffusion relative to advection of heat depends strongly on the rate of deformation. Scaling arguments can give a good idea of the strain rates that could produce extensional strengthening. The force for continued extension is reduced due to advective thinning by roughly $2\varepsilon CH_b^2$. The best case to make the slow-strain strengthening mechanism work is when the brittle layer thickness H_b is close to the crustal thickness H_c. The force for continued extension is reduced due to advective thinning by $\sim 2Ck(\varepsilon/\dot{\varepsilon})$. A ratio of the advective and diffusive force changes should be <1 for cases where the diffusive effect dominates. This occurs when $\dot{\varepsilon} < \kappa/H_c^2$. For $H_c = 40$ km and $\kappa = 10^{-6}$ m^2 s^{-1}, the maximum estimated strain rate is 10^{-15} s^{-1}. This is an extremely low extensional strain rate. To get such a low strain rate, the side of a 40 km wide zone of extension would have to be separating at a velocity of <1 mm year^{-1}! This scaling shows that the diffusive strengthening effect becomes more important for thinner crust, assuming that the base of the crust is hot enough for the crust there to be ductile and so weaker than the mantle. Still, White (2004) suggested that England's (1983) mechanism might explain the abandonment of many intracratonic rifts that seem to have extended at very low strain rates.

6.08.6.2 Viscous Stresses

Another possible effect to explain how wide rifts form relates to the stresses needed for yielding by viscous flow. The ductile yield stress in a representative flow law (eqn [4]) depends on strain rate. Thus, any area extending at a high rate will extend at higher stresses. This idea prompted Bassi et al. (1993) to suggest that wide rifts could be a product of viscous stress resisting localization of deformation.

It is difficult to consider using simple scaling relations to look at competition between viscous strain rate strengthening and other effects. The difficulty is that the viscous effect is independent of strain and most weakening (localizing) effects increase with increasing strain. To analyze the effect of viscosity on deformation, a linear stability approach is often used. The linearization of the model equations, implicit in these calculations, means that these results are strictly applicable only to the earliest phase of extension when strains are small. These models predict only two forms of extension of an initially uniform lithosphere, both of which could be termed a wide rift (e.g., Fletcher and Hallet, 1983; Martinod and Davy, 1992; Zuber and Parmentier, 1986). The lithosphere extends either in a uniform pure shear mode or with laterally periodic variation in the rate of extension. This second type of extension, often called 'lithospheric boudinage,' is suggested to explain the development of a series of basins and ranges in a broad region of continental extension.

Linear stability analysis does not predict a narrow rift mode of extension. Since many rifts, like the Rhine Graben and the Red Sea, are narrow, one wonders what situations lead to their development as compared to wide rifts like the Basin and Range. Zuber and Parmentier (1986) and Bassi (1991) showed that a large initial perturbation in lithospheric thickness or strength might cause localization in a single narrow rift, as opposed to a sequence of basins and ranges.

The effect of viscous stresses on the distribution of extension in finite amplitude (as opposed to linear stability) numerical model has been treated by a number of workers (e.g., Bassi, 1995; Buck et al., 2003; Buiter et al., 2008; Huismans and Beaumont, 2003; Huismans et al., 2005; Nagel and Buck, 2006). **Figure 36** shows the distribution of strain in a series of basins and ranges in a model with viscous effects driving delocalization. The viscous effects depend both on the viscosity variation with depth at the base of the lithosphere and on the extent to which viscous material weakens as a functions of strain or strain rate. In no models with large viscous delocalization do we get model large-offset faults (e.g., Nagel and Buck, 2006). Thus, the existence of localized large-offset strike-slip and normal faults argues against the importance of viscous delocalization.

6.08.6.3 Local Isostatic Crustal Thinning

The gravitational stresses related to local thinning of the crust could lead to wide rifting. To do this, the stretching-related gravitational delocalizing effect has to be larger than the localizing (weakening) effect of lithospheric advective thinning. The scaling relations derived in the 'Processes' section of this chapter give an indication of what controls these two effects. The force for continued extension is reduced due to advective thinning by roughly $2\varepsilon CH_b^2$ (eqn [5]). For reasonable friction

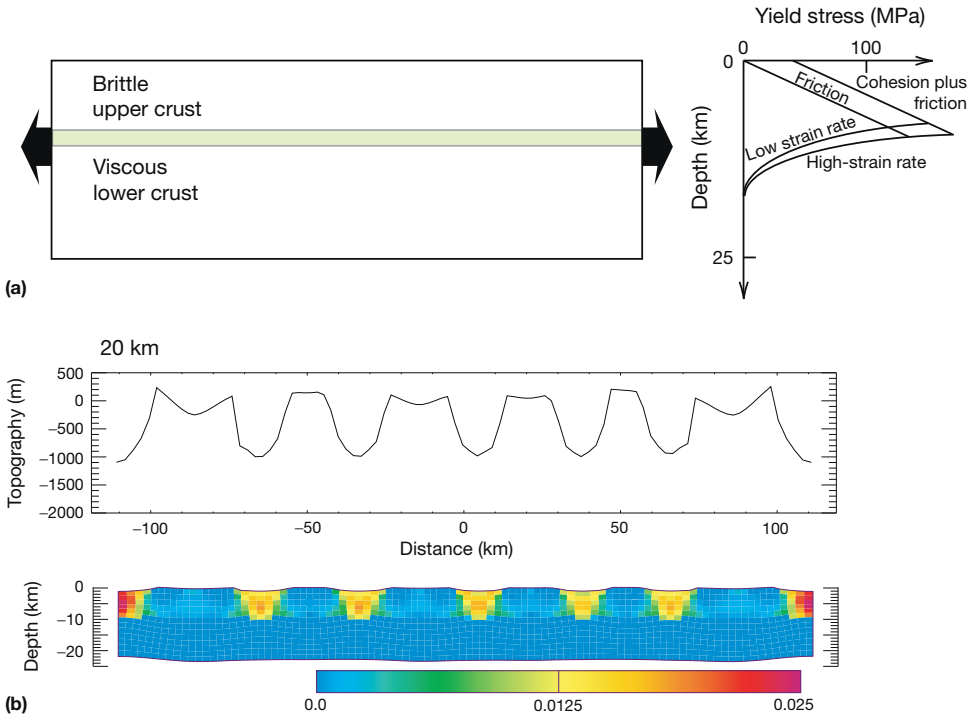

Figure 36 (a) Numerical setup and (b) results for a model in which the viscosity of the lithosphere forces a distributed pattern of extension. Color scale indicated brittle plastic strain in a series of local basins that are separated by higher ranges. Reproduced from Buck WR, Lavier LL, et al. (2003) A numerical model of lithospheric extension producing fault bounded basins and ranges. *International Geology Review* 45(8): 712–723.

coefficients and hydrostatic pore pressures in the crust, the brittle yield constant $C \sim 14 \times 10^3$ Pa m^{-1}. For a brittle layer thickness, $H_b = 20$ km, and a strain, $\varepsilon = 10\%$, this scaling estimate for the weakening is $\sim 5 \times 10^{11}$ Nt m^{-1}.

As discussed in the 'local isostasy' section, the local isostatic gravitational force change for crustal stretching is $2\varepsilon(\rho_c/\rho_m)(\rho_m - \rho_c)gH_b^2$ (eqn [13]). For crust 50 km thick with density 2800 kg m^{-3} overlying mantle with a density of 3200 kg m^{-3}, a 10% strain would produce a force increase of $\sim 10^{12}$ Nt m^{-1}. Thus, these simple scalings indicate that the wide rift mode should occur when the continental crust is thicker and hotter than normal. Extension of lithosphere with normal crustal thickness and average heat flow gives a narrow rift because the advective weakening dominates.

The main question about the crustal buoyancy mechanism for wide rifting concerns the hot lower crust. The mechanism should only produce wide rifting if the lower crust has to be weak, but not too weak. To understand this, we need to consider how flow of the lower crust will tend to fill in any area of crustal thinning. Crustal thinning lowers pressures in the crust where the crust is thinned. Surrounding crust will pour into this region if any part of the crust is weak enough to flow. The lower crust should be the hottest part of the crust, and so, if there is little or no compositional stratification of the crust, the lower crust should have the lowest effective viscosity. Hot, low-viscosity lower crust may flow into the region of crustal stretching, thus reducing the crustal thickness variations needed for buoyancy resistance to continued extension. If the lower crust is extremely hot and weak, then this model predicts a 'core complex mode' of extension, in which the locus of upper crustal extension remains fixed in one place, while the lower crust thins over a broad region.

To more quantitatively access this idea for wide rifting, Buck (1991) combined simple calculations of four of the processes discussed in the earlier section on rift processes: local isostatic crustal buoyancy, lower crustal flow, thermal advection, and thermal diffusion. Extension was assumed to be concentrated in a single region of pure shear stretching and the width of the region equaled the lithospheric thickness. The strain rate of stretching was fixed, and changes in the vertical thermal structure of the straining region were computed using a 1-D heat equation. Changes of crustal thickness and buoyancy were calculated using a 1-D thin channel equation to describe advective crustal thinning and lower crustal flow. After a small amount of extension, the change in force was computed. If the force decreased, the extension was considered to remain in the initial location, while if the force increased, the extension was taken to migrate. Migration of extension would eventually produce a wide rift. Because of the simplifying approximations of the model, millions of parameter combinations could be tested using modest amounts of computer time. Thus, maps of the wide rifting mode could be plotted in terms of crustal thickness and model heat flow for different crustal rheologies and assumed extension rates (**Figure 37**). The model predicts that wide rifting could result from crustal buoyancy for reasonable rheologies. The range of conditions for model wide rifts is broadly consistent with observations (**Figure 38**).

The possibility that wide rifting cold be controlled by crustal buoyancy has been suggested by more complete thin-layer calculations (Hopper and Buck, 1996) and by fully 2-D

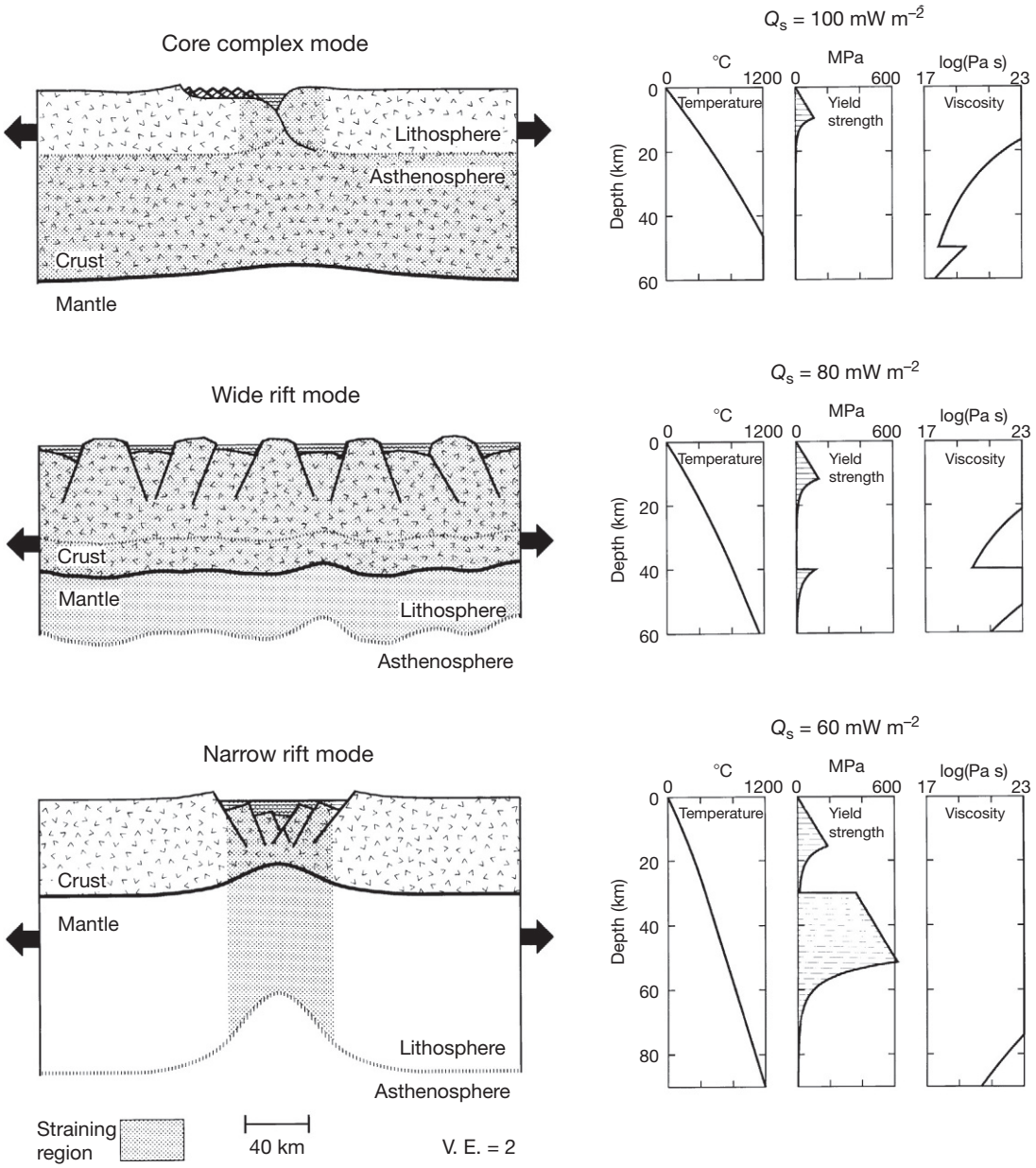

Figure 37 Illustration of model results predicting different forms of extension depending on the initial lithospheric thermal structure and crustal thickness (reproduced from Buck WR (1991) Modes of continental lithospheric extension. *Journal of Geophysical Research, B, Solid Earth and Planets* 96(12): 20161–20178). Both the core complex model and the wide rift mode are cases where warm crust is driven by gravity (local isostatic forces) to deform over a region that may be wider than the lithospheric thickness.

thermomechanical calculations (e.g., Christensen, 1992). For all these approaches, the wide rift and the 'core complex' modes are only predicted for thick, hot crust.

As noted in the chapter introduction, the main place where crust is thickened and heated is in orogens; thus, it is not surprising that most wide regions of rifting like the Basin and Range Province and the Aegean occur in regions where the crust was orogenically thickened. Indeed, it appears that extension driven by collapse of high mountains can occur even while convergence is still occurring across those mountains (see Dewey, 1988; Willett and Pope, 2004). Wide rifts may just be the result of extension of particularly wide orogenic belts where the crust has become fairly uniformly thick and hot as for the Tibetan Plateau (Royden et al., 1997).

6.08.7 Hyperextended Margins

Seismic refraction and reflection data collected at a number of nonvolcanic margins around the world indicate zones of crust <10 km thick over widths of 50–130 km (e.g., **Figure 39**). Among the margins with such broad zones of very thin crust are Iberia (e.g., Dean et al., 2000), Newfoundland (Shillington et al., 2006; van Avendonk et al., 2006, 2009), Congo

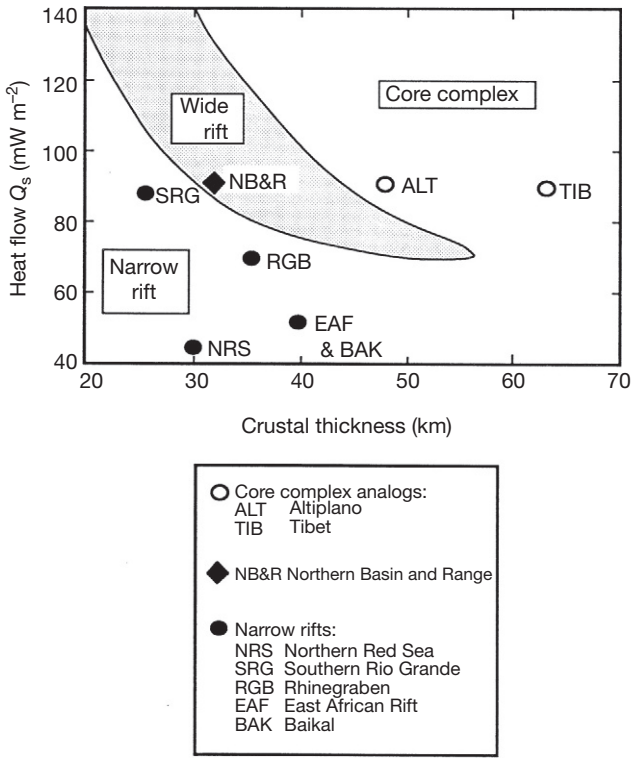

Figure 38 Predicted modes of extension as a function of crustal thickness and surface heat flow compared to data for regions showing those modes of extension, or in the case of the Altiplano and Tibet having the conditions that might lead to core complex formation. Reproduced from Buck WR (1991) Modes of continental lithospheric extension. *Journal of Geophysical Research, B, Solid Earth and Planets* 96(12): 20161–20178.

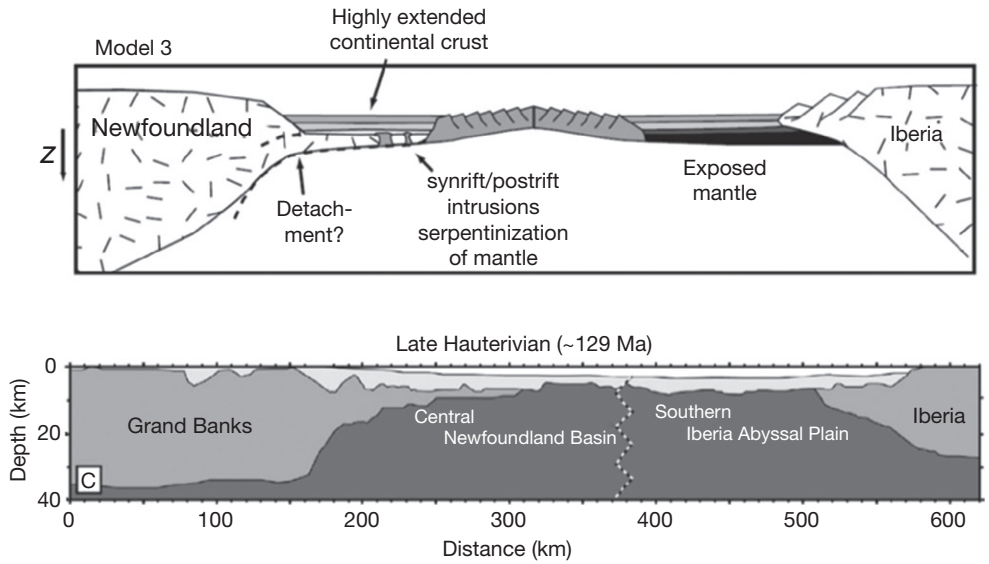

Figure 39 Schematic diagrams based on interpretation of seismic and drilling data indicating hyperextended crust and asymmetrical overall structure of the Newfoundland–Iberian margins. Top: Reproduced from Shillington DJ, Holbrook WS, Avendonk HJAV, et al. (2006) Evidence for asymmetric nonvolcanic rifting and slow incipient oceanic accretion from seismic reflection data on the Newfoundland margin. *Journal of Geophysical Research* 111: B09402. http://dx.doi.org/10.1029/2005JB003981; Bottom: van Avendonk HJA, Holbrook WS, Nunes GT, et al. (2006) Seismic velocity structure of the rifted margin of the eastern Grand Banks of Newfoundland, Canada. *Journal of Geophysical Research* 111: B11404. http://dx.doi.org/10.1029/2005JB004156.

(Contrucci et al., 2004), the Gulf of Aden (Leroy et al., 2010), and the Bay of Biscay (Jammes et al., 2010). These wide regions of apparently hyperextended crust are not easy to fit into simple models of rifting. Another interesting feature of some of the margins is that the crust is cut into blocks by a series of faults that dip oceanward (e.g., Ranero and Pérez-Gussinyé, 2010). Palinspastic reconstruction of structures across the Newfoundland–Iberian conjugate margin pair

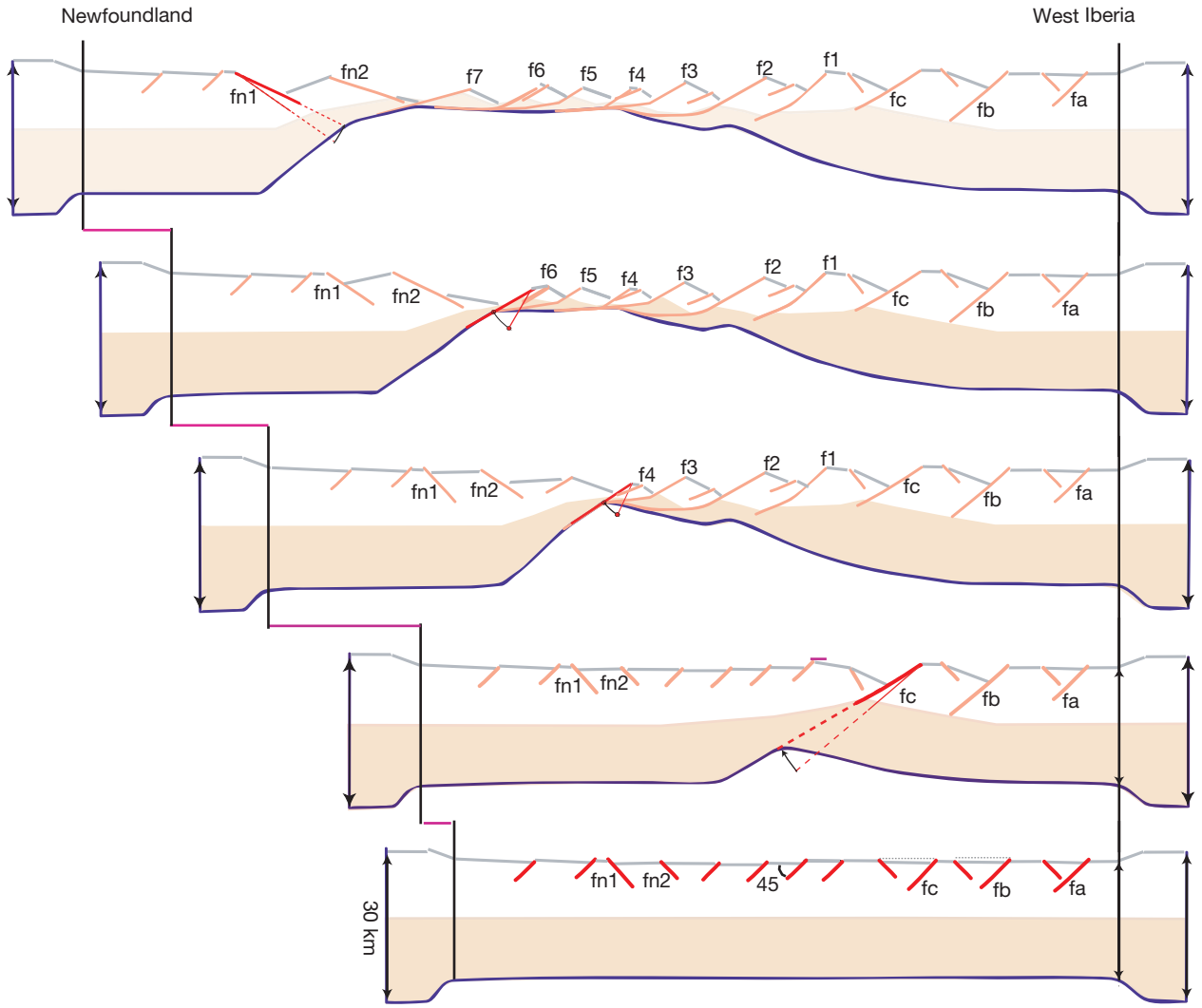

Figure 40 Steps of the kinematic balanced cross-section model for the development of the Newfoundland–Iberian margin of Ranero and Pérez-Gussinyé (2010).

based on seismic sections has led them to suggest that hyperextended margins are affected by a particular style of faulting (**Figure 40**). According to the Ranero and Pérez-Gussinyé (2010) kinematic model, a sequence of faults are each the only active for a time and are abandoned after they have accommodated a certain amount of offset. New faults form on the down-dip side of the old fault, always cutting into previously unextended crust. Eventually, an ocean basin forms at the sire of active faulting leaving very asymmetrical conjugate margins.

Numerical models have attempted to reproduce wide regions of hyperextended crust and in some cases mantle exhumation by incorporating rather special rheological conditions. For example, Nagel and Buck (2004) assumed a preexisting ductile detachment in the midcrust to decouple upper crustal and lower crustal deformation. Lavier and Manatschal (2006) assumed that a ductile detachment forms in response to shear at the brittle–ductile transition. Either of these models can reproduce some of the structures observed in hyperextended domains, including synthetic normal faults with some upper crustal blocks overlying exhumed mantle. However, why special weak zones develop on certain margins and not others is not clear.

Recent numerical models show the kind of migration normal faulting in a geometry similar to that suggested by Ranero and Pérez-Gussinyé (2010). Brune et al. (2014) showed that a layered crustal rheology and fairly cool initial conditions combined with moderate fault strain weakening could produce hyperextended continental margins (**Figure 41**). They suggested that advective heating of the lower crust allows limited oceanward crustal flow. The Brune et al. (2014) models also show that the width of the strongly extended margin is greater for faster rifting. They noted that this fits the trend of increasing margin width with increasing rifting velocity for the part of the South Atlantic margin.

A hint of this kind of asymmetrical margin development has been seen in numerical models with a single rheology for the crust, but only for particular cases of prerift thermal and

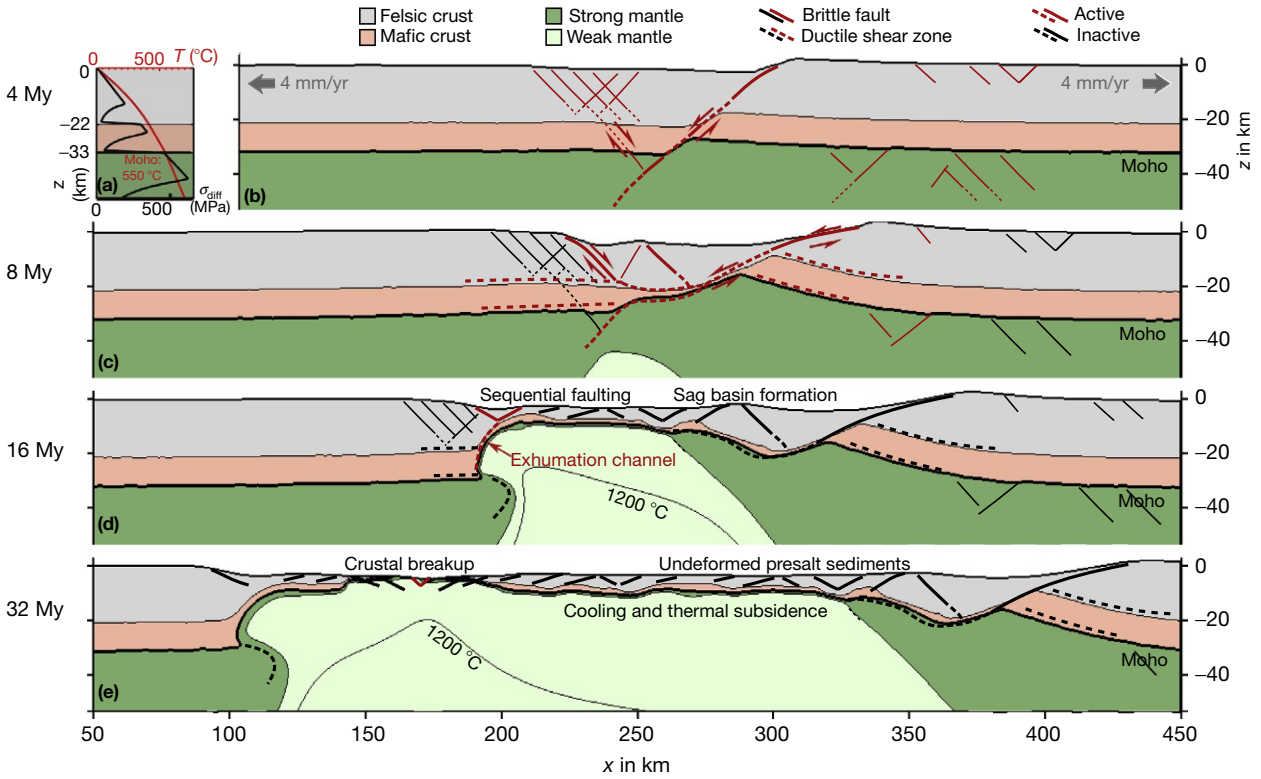

Figure 41 Illustration of the numerical lithospheric extension model of Brune et al. (2014) showing a period of asymmetrical extension leading to hyperthinned crust. (a) The initial model temperatures and yield stresses with depth. The process of steady-state rift migration is shown in (b)–(e). The wide margin is formed through rift migration and sequentially active faulting toward the future ocean. The model suggests an explanation for thick, undisturbed presalt sediments predating breakup deposited in the landward part of the margin.

crustal structure. Bialas et al. (2007) considered the extensional collapse wide regions of very thick (plateau-forming) crust to determine what cases could fit observation for the Trans-Antarctic Mountains and the adjacent Ross Sea. However, in a few cases, in which the temperature of the lower 10 km of crust was around 700 °C, Bialas et al. (2007) saw a different and asymmetrical mode develop. In those cases, the zone of extension progressively migrated into the adjacent thicker crust. This highlights that uncertainties in lithospheric rheology can lead to uncertainty in the relation between initial thermal state and the form of extensional deformation.

A different way to explain exposure of mantle at non-volcanic margins, such as the Iberian Margin (e.g., Whitmarsh et al., 2001), that involves compositionally buoyant lower lithosphere that is warm enough to flow into an extending rift has been advanced (Beaumont and Ings, 2012; Huismans and Beaumont, 2011). In most studies, the lithosphere is considered to be compositionally less dense, colder, drier, and therefore stronger than the underlying asthenosphere (e.g., Jordan, 1978; Nielsen and Hopper, 2002; Sleep, 2007). Huismans and Beaumont (2011) suggested that partly refertilized lower cratonic lithosphere may be sufficiently chemically depleted such that it is lower in density by 10–15 kg m^{-3} than the asthenosphere. This layer may be warm and so weak enough that its low density will cause it to flow toward the rift axis under gravity during rifting (Figure 42). If correct, this implies that the mid and outer

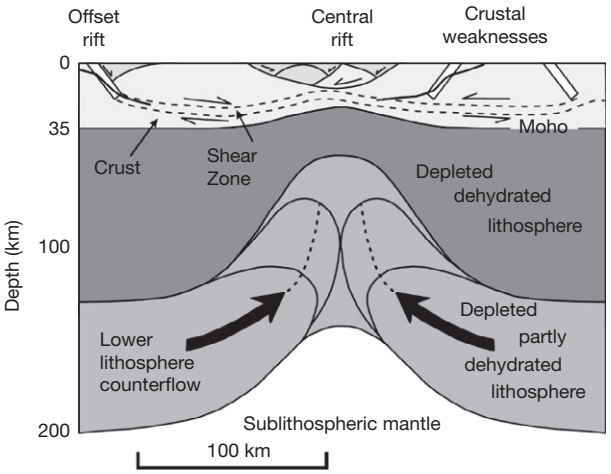

Figure 42 Illustration of the idea that depleted, but fairly weak, lower lithosphere can flow counter to the direction of plate separation at a rift. The figure also implies that reactivation of inherited crustal weak zones can produce offset rift basins. The authors suggest that 'counterflow' of the depleted lower lithosphere may strongly reduce the amount of mantle partial melting below nonmagmatic rifts. Reproduced from Beaumont C and Ings SJ (2012) Effect of depleted continental lithosphere counterflow and inherited crustal weakness on rifting of the continental lithosphere: General results. *Journal of Geophysical Research* 117: B08407. http://dx.doi.org/10.1029/2012JB009203.

regions of some continental margins will be underplated by thick lower cratonic lithosphere. They proposed that this process applies to the flow of thick cratonic lithosphere and cited the examples of the West African margin outboard of the Congo Craton and the Exmouth Plateau margin of Australia outboard of the Pilbara Craton.

Beaumont and Ings (2012) went further and proposed that thick depleted continental mantle lithosphere in general, not just cratonic lithosphere, may flow in the manner suggested by Huismans and Beaumont (2011). They termed this the 'Lower Lithosphere Counterflow' hypothesis because the lower lithosphere flows in the opposite direction from the motion of the overlying rifting margins (**Figure 42**).

6.08.8 Rifting an Active Margin

The Gulf of California (**Figure 43**) is an example of a young oblique rift formed on a volcanic arc with an extensional back-arc (Umhoefer, 2011). It is one of the best modern examples of rupture of continental lithosphere to form a narrow continental fragment or terrane outboard of a narrow sea (Umhoefer and Dorsey, 1997; Wilson, 1966). The Gulf of California is an oblique rift system with short spreading segments connected by long transform faults (**Figure 43**) (Lonsdale, 1989). Rifting in the gulf began 12–15 My when subduction ended as the East Pacific Rise intersected with and the Pacific Plate became attached to the Baja California peninsula (e.g., Atwater, 1970; Menard, 1978; Michaud et al., 2006; Stock and Lee, 1994). The peninsula now moves nearly completely with the Pacific Plate, with 48 mm year^{-1} of spreading across the Gulf of California representing 92% of the Pacific–North America relative motion (DeMets and Dixon, 1999; Dixon et al., 2000).

The Gulf of California transitioned to active seafloor spreading faster than most other rifts and passive margins. It also shows great variation along the rift axis in the width of the thinned crust making up the nascent pairs of passive margins (see **Figure 44** from Lizarralde et al., 2007). In the southern Gulf of California, seafloor spreading commenced ~6–10 My

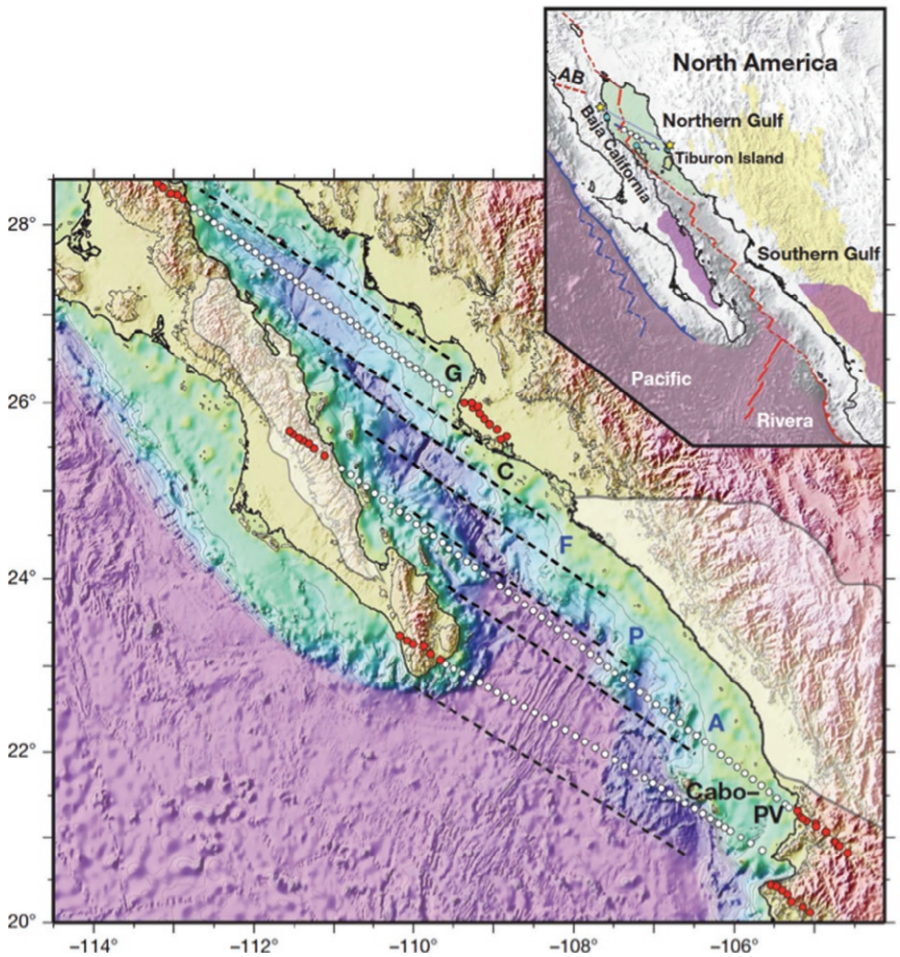

Figure 43 Map of the Gulf of California showing the obliquely spreading subbasins of that rift system. Red dots indicate onland seismometers, while white dots represent the locations of ocean-bottom seismometers in three transects of the PESCADOR experiment described in Lizarralde et al. (2007) and the figure is from that paper. The Guaymas (G), Carmen (C), Farallon (F), Pescadero (P), Alarcon (A), and the San Jose to Puerto Vallarta (Cabo–PV) segments are separated by dashed lines.

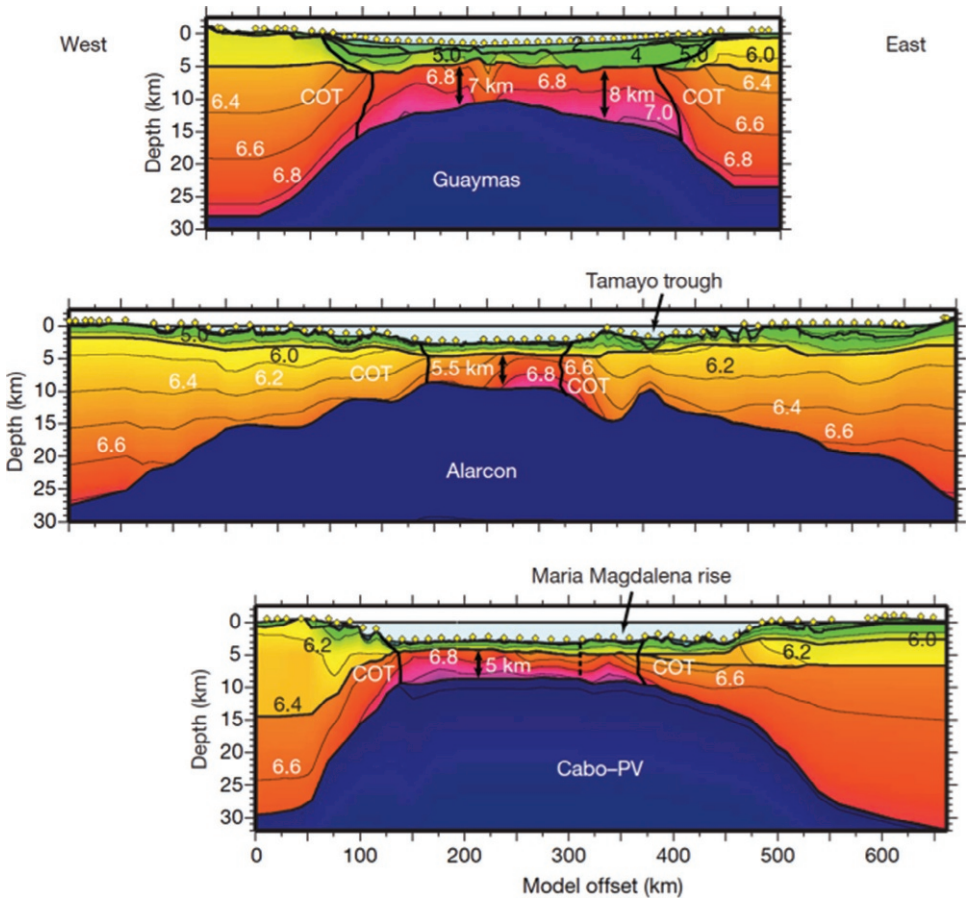

Figure 44 Models of the seismic velocity structure under three basins of the Gulf of California shown in **Figure 42**. Velocities are color codes and contours are labeled in nits of kilometer per second. COT indicates the interpreted continent ocean transition. Yellow diamonds are seismometer positions for each transect. Reproduced from Lizarralde D, Axen GJ, Brown HE, et al. (2007) Variable styles of rifting in the Gulf of California. *Nature* 448: 466–469.

after the formation of the oblique-divergent plate boundary at 12–12.5 Ma (Lonsdale, 1989; Stock and Hodges, 1989; Stock and Lee, 1994).

According to Umhoefer (2011), three main factors may have contributed to this rapid rupture: (1) an inherited long, narrow belt of hot, weak crust from a volcanic arc that was active immediately before formation of the oblique-divergent plate boundary and that lay between two strong batholith belts; (2) relatively rapid plate motion resulting in high strain rates; and (3) a dominant role of strike-slip faulting in the highly oblique-divergent setting that formed large pull-apart basins with rapid and focused crustal thinning in a linked en echelon system.

The causes of the variability in the width of the margins bordering the gulf remain a topic of debate. As shown in Figure 44, only the Alarcon Basin in the central southern Gulf has a very wide transition in crustal thickness (at least 200 km wide on each side of the rift). The more northerly Guaymas Basin has transitions that are as little as 50 km wide. The more southerly Cabo–Puerto Vallarta basin is narrow on the west side and moderately wide on the east. Lizarralde et al. (2007) noted that the greater rate and amount of sedimentation in the northern basin may have led to insulation and therefore warming of the center of the rift, thereby making the center weaker and causing extension to concentrate there. Bialas and Buck (2009) suggested that sedimentation may affect rift width but not because of a thermal blanketing effect. They emphasized the role of sedimentation in affecting buoyancy forces (see **Figure 45**). Bialas and Buck (2009) used a suite of numerical models to demonstrate that sedimentation can exert a great control on rift width when the crust is warm enough that in the absence of sedimentation, the lithosphere would extend in the wide rift mode.

It is possible that other processes may affect the rift margin width including variation in prerift structure and thermal state. Magma input may not be constant along the rift and also may affect the width of a rifted margin. As described in the next section, the observation of very broad zones of thinned crust at some passive margins has sparked considerable effect to explain what controls the width of rifted margins.

6.08.9 Small-Scale Convection and Rifting

Rifting, whether caused by stretching or magma intrusion, results in lateral temperature and therefore density variations. If the lower lithosphere flows as a viscous fluid, then lateral density

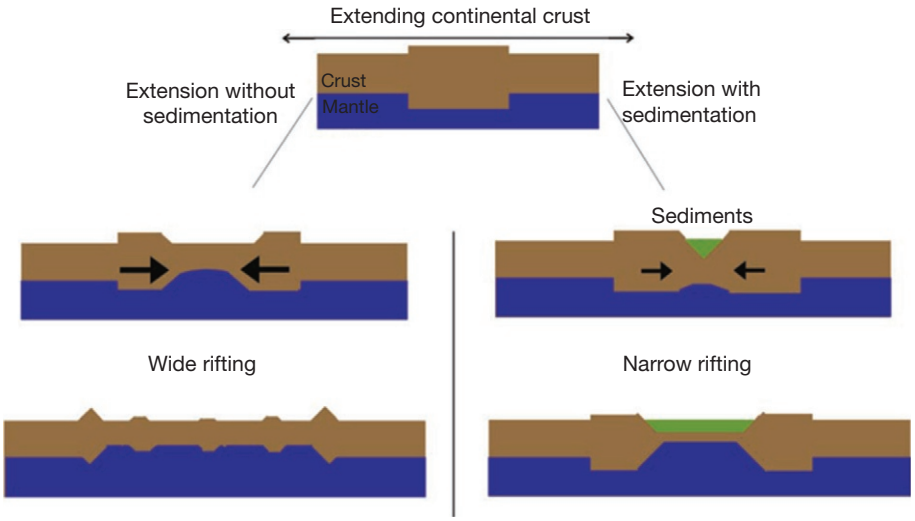

Figure 45 Illustration of the idea that in some conditions sedimentation can promote narrow rifting. Arrows represent the size of the buoyancy force difference and a greater force difference makes it harder for extension to stay concentrated in a region where the crust is thinned. Without sedimentation, the force differences are large and a wide rift results. With sedimentation, the crust is thickened from the top, reducing the buoyancy force difference and allowing continued focused extension. Reproduced from Bialas R and Buck WR (2009) The role of sedimentation in the development of rifts: Applications to the Gulf of California. *Tectonics* 28: TC4014. http://dx.doi.org/10.1029/2008TC002394.

differences will drive flow, with the cold, dense lower lithosphere at the side of a rift moving downward relative to the hotter, less dense center of the rift (Buck, 1986; Keen, 1985; **Figure 46**). Whether such 'small-scale' convection induced by rifting has observable effects depends on the shallow mantle viscosity and density structure (e.g., Nielsen and Hopper, 2002).

6.08.9.1 Rift Subsidence, Seismic Structure, and Flank Uplift

That rift-induced convection could affect the subsidence of a passive margin was first proposed by Keen (1985) and is still a subject of interest. For example, Petersen et al. (2010) showed that the stratigraphy of some rifts can be fit by variations in vertical motions of the lithosphere caused by small-scale convection. Such convection may also explain the seismic structure of young rifts like the Rio Grande Rift, which is flanked by what appear to be 'drips' of cold, high-velocity mantle lithosphere (e.g., van Wijk et al., 2008).

The convective removal of cold lower lithosphere beneath the flanks of a rift may contribute to the uplift of 'rift shoulders' (Buck, 1986; Wallner and Schmeling, 2010). However, gradual cooling of the lithospheric rift flanks thinned by convection should produce subsidence of those shoulders. Weissel and Karner (1989) noted that that some rift shoulders stay elevated for longer than would be expected for a thermal convective origin of the flanking highs. They suggested that places like Broken Ridge, the elevated flank of a Cretaceous rift in the Indian Ocean, are produced by the flexural response to normal fault offset as described in **Section 6.08.3.1**.

van Wijk et al. (2010) suggested that the uplift of the edge of the Colorado Plateau may result from small-scale convection (**Figure 47**). The contrast in lithospheric thickness driving the flow is taken to be produced by extensional stretching of the adjacent Basin and Range Province and the Rio Grande Rift. van Wijk et al. (2010) also suggested that the progression of volcanism inward from the edge of the plateau may result from propagation of the region of convective thinning of the lithosphere.

6.08.9.2 Convective Partial Melting

It is not surprising that rifts are commonly sites of volcanism and basaltic magma intrusion since the lithosphere is almost certainly thinned under most rifts. Basalt is produced when hot asthenosphere moves up to shallow depths, and the higher (i.e., shallower) the asthenosphere rises, the more it melts (e.g., White and McKenzie, 1989). Stretching thins the lithosphere and pulls up the mantle to depths where melting occurs. The depth where melting begins depends on temperature and hotter mantle starts melting deeper than cooler magma. Normal mantle is thought to begin significant melting at depths of 60–80 km (e.g., Klein and Langmuir, 1987).

Since the thinnest lithosphere occurs at spreading centers, we expect the greatest fraction of partial melting and so the greatest thickness of crust to form there. Ocean crust averages ~7 km thick (White et al., 1992) and presumably reflects the maximum pressure release melting of normal temperature mantle. Only in Iceland and the Afar, spreading centers thought to be underlain by actively upwelling, hotter-than-normal mantle plumes (e.g., Chang and Van der Lee, 2011; Wolf et al., 1997), is the crustal thickness around 20 km thick (e.g., Bastow et al., 2008; Bryndís Brandsdóttir et al., 1997; Hammond et al., 2011; Makris and Ginzburg, 1987).

The rift-related igneous crust of some volcanic passive margins is more than 20 km thick (e.g., Franke et al., 2010; Hinz, 1981; Holbrook and Kelemen, 1993; Hopper et al., 2003; Mutter et al., 1982). This is about three times the thickness of typical oceanic crust. In contrast, some rifted margins, such as the well-studied Iberian Margin, appear to have been intruded

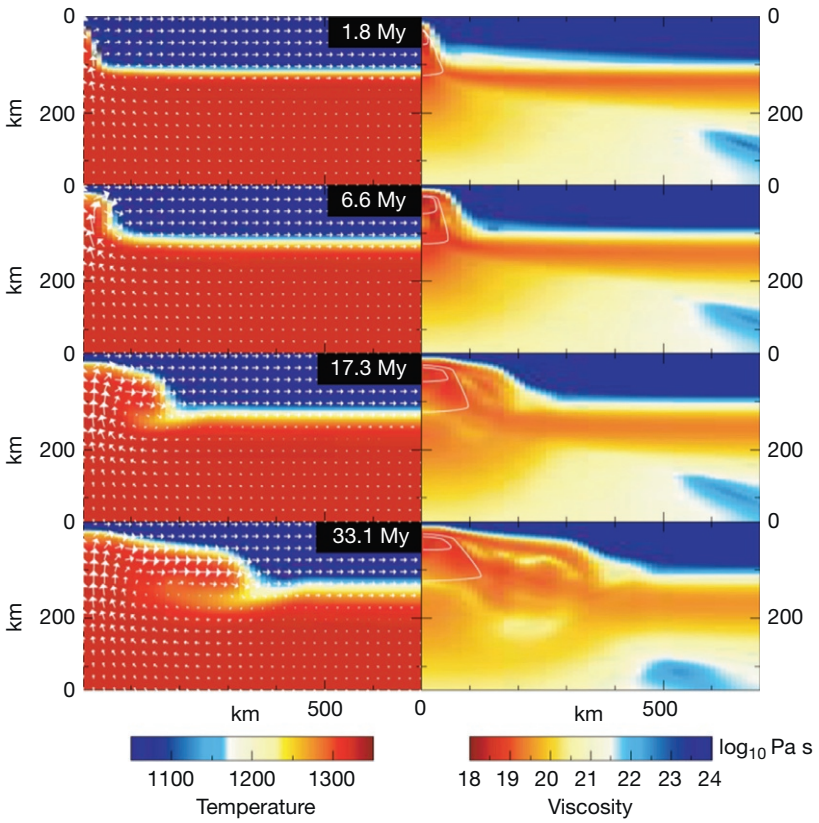

Figure 46 Illustration of the evolving pattern of small-scale convection and melting in a numerical thermomechanical rift model with a low enough mantle viscosity that flow is rapid (reproduced from Nielsen TK, and Hopper JR (2004) From rift to drift: Mantle melting during continental breakup. *Geochemistry*, *Geophysics*, *Geosystems* 5: Q07003. http://dx.doi.org/10.1029/2003GC000662). The left side is a symmetry boundary in the center of a zone of stretching with the surface of the 'plate' made to move at 10 mm a^{-1}. White arrows on left indicate the solid velocity. White contours on right show regions of 2% and 10% melt fraction. Convection in this particular case strongly affects the lithospheric structure. Extraction of melt decreases the density and increases the viscosity of the residual so that this model does not produce significantly more melt than does passive rifting.

by almost no magma (e.g., Reston, 2009). Variations in the vigor of small-scale convection are one explanation for this observed variability.

Lithosphere under rifts should be thicker than spreading centers. Thus, one expects that normal mantle would upwell less, melt less, and produce thinner basaltic crust in rifts than a spreading center. It is then a problem to explain why so many passive margins have great thicknesses of basaltic crust.

The idea that small-scale convection might explain the great thickness of igneous crust seen at volcanic passive margins was first suggested by Mutter et al. (1988). Those authors developed numerical models to show that much increased melt volumes could be produced due to convection driven by lateral temperature gradients at the side of a rift (**Figure 48**). Initial temperature structures were derived from an analytic model of lithospheric stretching. Density in their calculations only depended on temperature, and mantle viscosity was Newtonian and temperature-dependent. Mutter et al. (1988) suggested that volcanic passive margins developed when the contrast in lithospheric thickness was extreme, while a more gradual change in lithospheric thickness might result in less convective partial melting.

King and Anderson (1995, 1998) also suggested that lithospheric thickness variations might control convective partial melt production, but they emphasized the role of extremely thick cratonic lithosphere. They suggested that rifts formed next to thick, cold cratonic lithosphere would drive enough convective melting to produce a volcanic margin. King and Anderson (1995, 1998) used a more realistic non-Newtonian rheology but considered the same kind of imposed initial thermal structures considered by Mutter et al. (1988).

The next generation of models of rift-induced convection included dynamically driven lithospheric stretching along with convective flow. These self-consistent rift models produced large mantle melt fluxes as long as the mantle viscosity was low enough and the density depended only on temperature (Boutilier and Keen, 1999; Huismans et al., 2001; van Wijk et al., 2001). Boutilier and Keen (1999) assumed that the viscosity of the mantle is increased suddenly after 132 km of continental lithospheric extension. Ghods (2002) concluded that the addition of more realistic mantle viscosity would make it impossible for small-scale convection to produce large melt fluxes.

Nielsen and Hopper (2002, 2004) took similar rift calculations to those of Boutilier and Keen (1999) out to longer times where a spreading center developed. However, the changes in physical properties are treated in a more self-consistent manner in the models of Nielsen and Hopper (2002, 2004). They tested how weak the mantle must be to induce small-scale

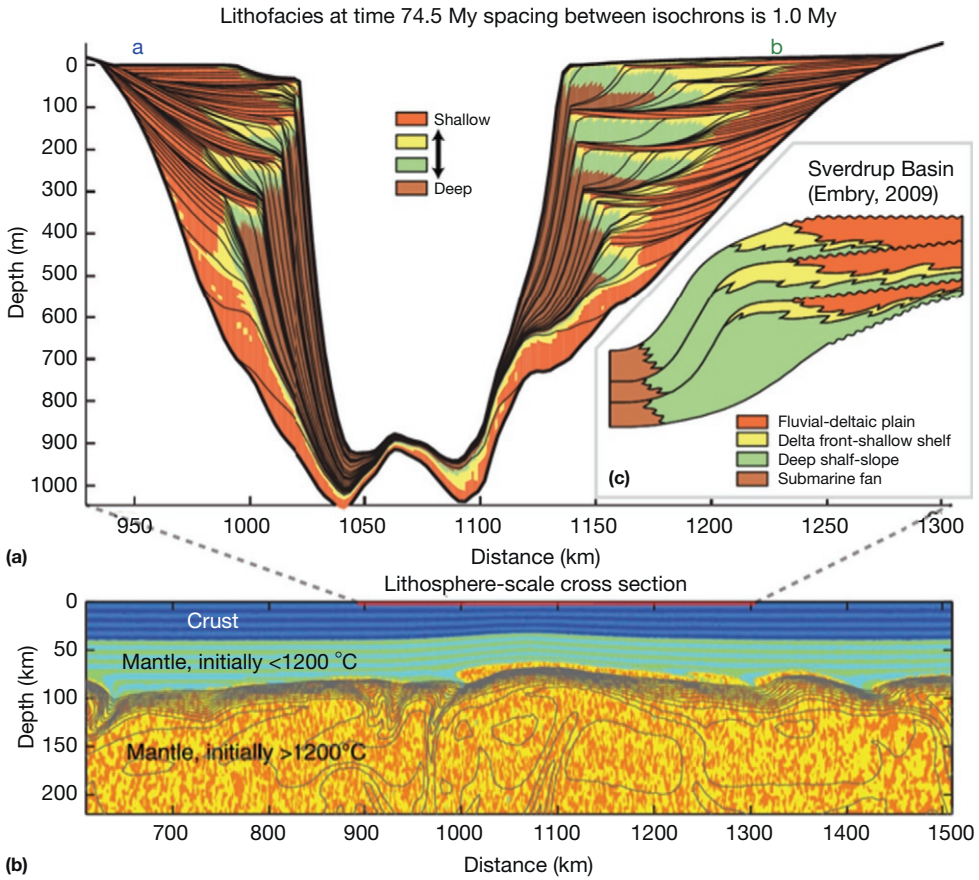

Figure 47 Results from a rift model with small-scale convection in the mantle (reproduced from Petersen KD, Nielsen SB, Clausen OR, Stephenson R, and Gerya T (2010) Small-scale mantle convection produces stratigraphic sequences in sedimentary basins. *Science* 329: 827–830. http://dx.doi.org/10.1126/science.1190115). The convection causes fluctuations in the surface topography that affects where sediment is deposited even though the sediment input is constant. (a) Lithofacies show cyclic deposition, evident from unconformities and lateral migration of lithofacies. (b) Lithospheric cross section showing gently thinned crust and mantle lithosphere and isotherms from 1200° to 1400 °C as solid lines.

convection and thus enhance melt production during breakup. Nielsen and Hopper (2002, 2004) found that the mantle reference viscosity required to generate a breakup instability is sufficiently low that an unrealistic time dependence develops in the subsequent oceanic spreading system. That is, the temporal variations in convection would produce larger changes in oceanic crustal thickness than are observed. Nielsen and Hopper (2002) then modified their model to include effects related to extraction of melt form the mantle. They prescribed that the mantle viscosity increase and density decrease with increasing amounts of melt extraction. Nielsen and Hopper (2002) found that these effects not only prevented oscillations of melt rate for the spreading center phase but also eliminated most of the convective partial melting.

Experimental data indicate that melt extraction from the mantle should decrease density and increase viscosity and both effects should reduce the vigor of small-scale convection. Oxburgh and Parmentier (1977) noted that the extraction of melt should leave the residual mantle lower in density than undepleted mantle. This occurs because elements such as iron, which densifies several mantle minerals, and aluminum, which contributes to the formation of denser phases like garnet and spinel, are partitioned into the melt. The extraction of 20% melt should decrease the mantle density by ~1% (e.g., Oxburgh and Parmentier, 1977). This is comparable to the density change produced by a 300 °C increase in temperature assuming a thermal expansion coefficient of $3.3 \times 10^{-5}\,^{\circ}\mathrm{C}^{-1}$ (e.g., Turcotte and Schubert, 2002). Thus, mantle depleted by extraction of 10% melt would have to be 150 °C colder than undepleted mantle to be negatively buoyant. Models show that this depletion density effect could help focus upwelling flow under spreading centers (e.g., Rabinowicz et al., 1984; Scott and Stevenson, 1989; Sotin and Parmentier, 1989).

Extraction of water from the mantle due to partial melting beneath mid-ocean ridges may increase the viscosity of the residuum by two to three orders of magnitude (e.g., Hirth and Kohlstedt, 1996). Several studies have shown that this effect could profoundly affect shallow mantle the flow pattern both related to active plume flow (e.g., Ito et al., 1999) and passive plate separation at a spreading center (e.g., Choblet and Parmentier, 2001; Phipps Morgan, 1997). The presence of melt in the mantle should lower mantle viscosity (e.g., Cooper and Kohlstedt, 1986; Hirth and Kohlstedt, 1995a,b; Karato, 1986) and may counter the dehydration effect on viscosity. This is likely to be important in a fairly localized zone beneath a spreading center or rift where high melt fractions should be present (e.g., Choi and Buck, 2010; Su and Buck, 1993). Even if there is a melt-rich zone under a rift, the dehydration effect

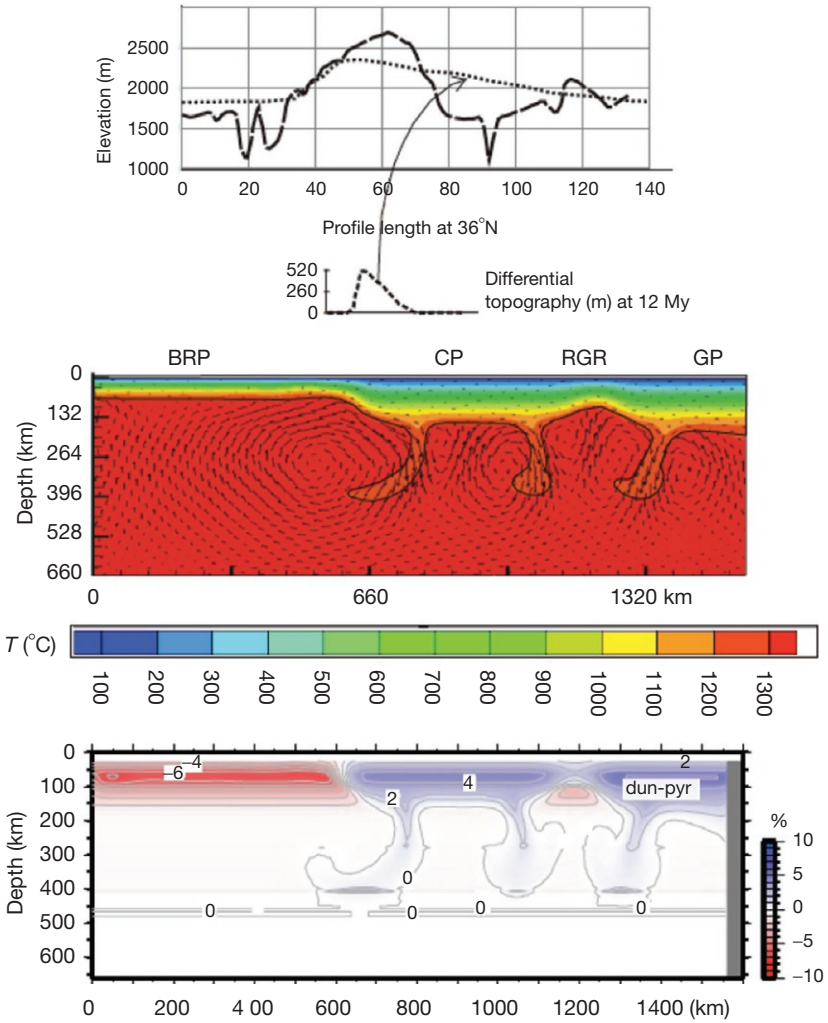

Figure 48 Results of a numerical model of small-scale convection driven by lateral variations in lithospheric structure estimated from seismic data (reproduced from van Wijk JW, Baldridge WS, van Hunen J, et al. (2010) Small-scale convection at the edge of the Colorado Plateau: Implications for topography, magmatism, and evolution of Proterozoic lithosphere. *Geology* 38: 611–614. http://dx.doi.org/10.1130/G31031.1). The model is set up to represent a cross-section from the Basin and Range Province (BRP) to the Colorado Plateau (CP) and through the Rio Grande Rift (RGR) to the Great Plains (GP). The plot at top shows the topography resulting from lithospheric thinning at 12 Ma in the numerical model and is compared to a line of topography at the edge of the plateau at 36 °N, from 112.8 to 111.3 °W. The lower panel shows the S-wave velocity structure predicted from the thermal structure shown in the middle panel. The conversion from temperature and composition to velocity is given in van Wijk et al. (2010).

should still act to stabilize lithosphere on the sides of a rift (Nielsen and Hopper, 2002, 2004).

Sleep (2007) developed models similar to those of Nielsen and Hopper (2002) in which mantle viscosity and density were affected by depletion. Sleep (2007) agreed with those authors that such effects would make it impossible for rift-induced small-scale convection to greatly contribute to melt production at a passive margin. Schmeling (2010) also agreed with Nielsen and Hopper (2002) that hotter-than-normal mantle supplied to the top of the asthenosphere by a mantle plume was the most likely cause for volcanic passive margins (**Figure 49**). In the absence of considerable convective partial melting, the observed differences in magma volumes between volcanic and magma-starved margins require differences in mantle temperature of about 200 °C (e.g., White and McKenzie, 1989, 1995).

Another major problem for the small-scale model of excess basalt production is the timing of rifting versus basalt production. As noted in the next section, the extrusion of massive amounts of basalt predates the development of the rifts for recent major continental rifting events such as the opening of the North and South Atlantic Margins and the opening of the Red Sea (e.g., Courtillot and Renne, 2003). These observations favor a plume model for the generation of excess mantle melting under volcanic rifts and margins.

6.08.10 Dikes Versus Stretching to Initiate Rifting

Areas of initially thin lithosphere should rift at very low levels of tectonic force. Further, some areas of high heat flow and initially thick crust, such as the North American Basin and Range Province, start extending with little or no basaltic volcanism. Models neglecting magmatism do predict the general patterns of observed extensional strain inferred for such areas.

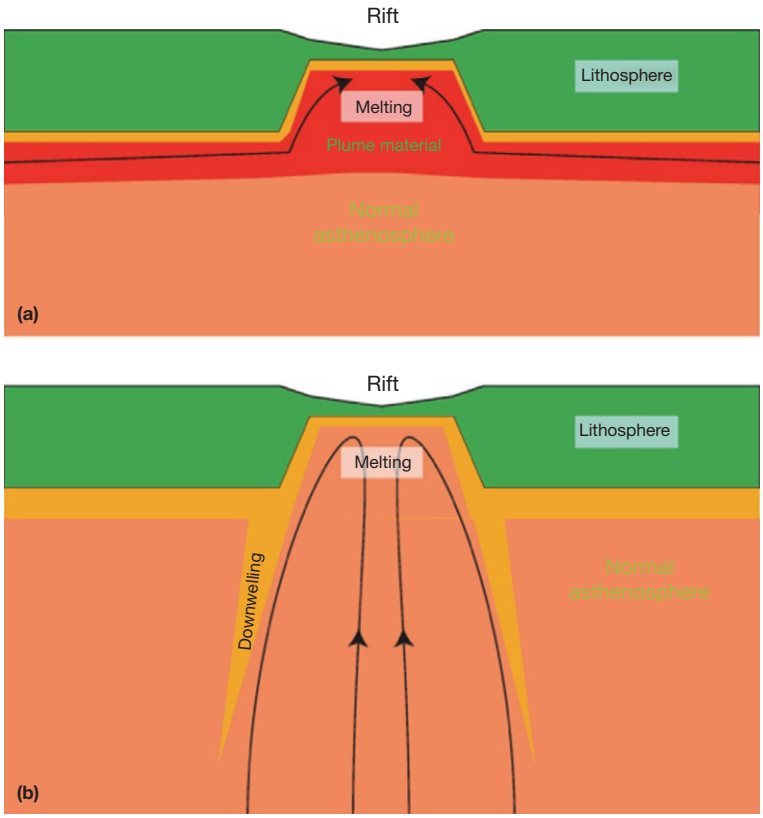

Figure 49 Illustration of two ideas for the formation of extra melt at magmatic passive margins (reproduced from Sleep NH (2007) Edge-modulated stagnant-lid convection and volcanic passive margins. *Geochemistry, Geophysics, Geosystems* 8: Q12004. http://dx.doi.org/10.1029/2007GC001672). (a) Hot plume material pounded under continental lithosphere flows into a rift where it reaches shallow enough depths for significant partial melting. Hot mantle melts more than normal mantle. (b) Small-scale convection carries more normal mantle to shallow enough depth under a rift for partial melting to occur. The cycling of large volumes of normal mantle through the melting region gives more total melt than would be produced by passive upwelling.

It should be noted that these 'hot' weak areas are not typical, but may require some kind of preheating. The effect of orogenesis, especially thickening of radiogenic crust, has been implicated as a way of heating regions such as the Basin and Range Province and the Aegean Sea extensional province (e.g., Sonder et al., 1987). However, in areas of low to normal heat flow, the earliest phase of rifting is often accompanied by basaltic magmatism.

Though it has long been known that many rifts are associated with volcanism (**Figure 50**), a fundamental change in our understanding of rifted margins has been driven by new observations concerning the volume and flux of magmatism associated with those margins. There has been a gradual realization that most rifted margins are temporally and spatially associated with very large magma input. Seismic data have been one of the key inputs that have led to a change from emphasis from passive lithospheric stretching to active magma-assisted rifting. It was the seismic imaging of 'seaward-dipping reflectors' along many margins that led to increased interest in the role of magma during rifting.

Large igneous provinces, where there are thick layers of subaerial extruded basalt, account for a small fraction of the length of rift associated with them. Seaward-dipping reflectors (see **Figure 51**) are seismically bright layers that dip oceanward on many rifted margins such as parts of the South Atlantic margin (Hinz, 1981) and the North Atlantic margin of Greenland (e.g., Holbrook et al., 2001). Drilling into the units has confirmed that these are basalt flows (Larsen et al., 1993). These dipping reflectors are thought to form the same way tilted basalt flows form on Iceland where flows from a rift center load and depress the surface isostatically. As the rift widens, the center of magmatic fissure eruptions moves away from the margin resulting in the kinds of pattern schematically shown in **Figure 52**. The imaging of seaward-dipping reflectors and deeper high-velocity units that may be mafic intrusives (see **Figure 5**) indicates that many more margins may be considered to be 'volcanic' than was previously thought. It is estimated that many millions of cubic kilometers of basalt are intruded and extruded along some rift systems (e.g., Holbrook et al., 2001).

There are several models for the origin of magma that affects volcanic margins. A key controversy is whether the magmatism causes the rifting or vice-versa. The idea that rifting causes volcanism comes from considering the way lithospheric stretching advects hot mantle upward and so can lead to melting of that passively flowing mantle (e.g., White and McKenzie, 1989). However, several lines of evidence support the idea of some kind of active mantle upwelling to trigger rifting. First, volcanism is often spread over regions that do not include apparently significant rifting and therefore stretching

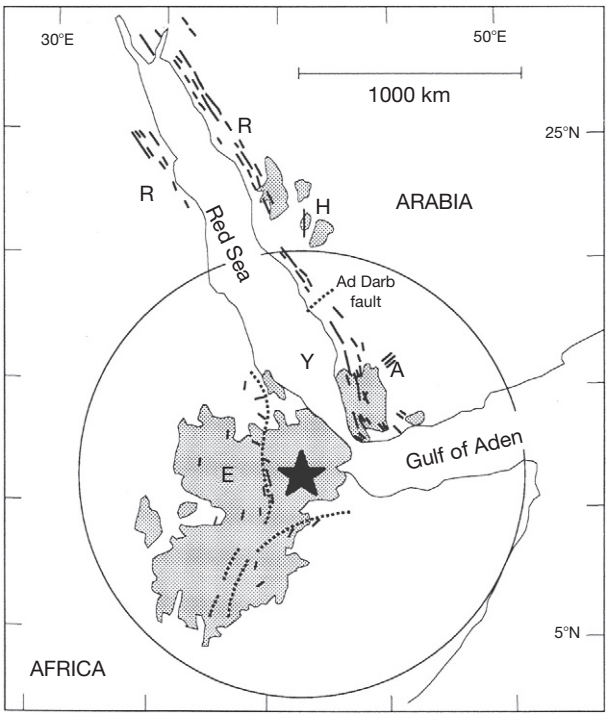

Figure 50 Map of the distribution of the Ethiopian flood basalts and related dikes along the Red Sea. Reproduced from Ernst RE and Buchan KL (1997) Giant radiating dyke swarms: Their use in identifying pre-Mesozoic large igneous provinces and mantle plumes. In: Mahoney JJ and Coffin MF (eds.) *Large Igneous Provinces; Continental, Oceanic, and Planetary Flood Volcanism*, pp. 297–333. Washington, DC: American Geophysical Union. Geophysical Monograph.

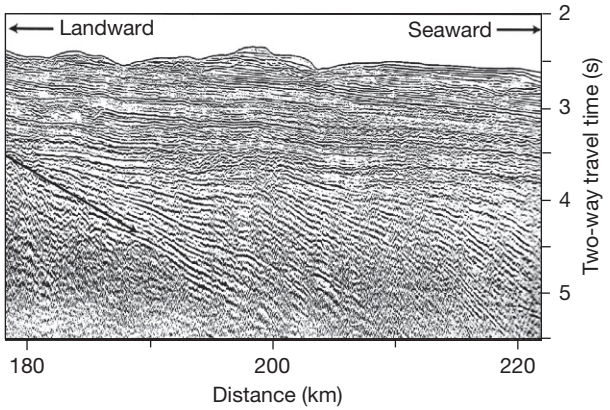

Figure 51 Example of a multichannel seismic profile with arrow showing the prominent seaward-dipping reflectors along the East Greenland margin. Reproduced from Hopper JR, Dahl JT, et al. (2003) Structure of the SE Greenland margin from seismic reflection and refraction data: Implications for nascent spreading center subsidence and asymmetric crustal accretion during North Atlantic opening. *Journal of Geophysical Research* 108: 2269.

(Figures 53 and 54). Dikes appear to radiate from a central location that may be the locus of plume upwelling (Figures 54 and 55). Also, the volcanism seems to predate rifting in many rifts (Figure 56).

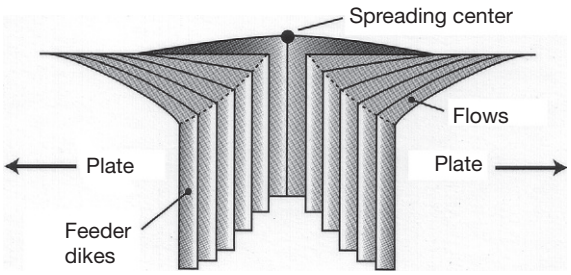

Figure 52 Illustration of the isostatic model of formation of seaward-dipping reflectors as basalt flows coming out of a rift spreading center. Reproduced from Palmason G (1980) A continuum model of crustal generation in Iceland: Kinematic aspects. *Journal of Geophysical Research* 47: 7–18.

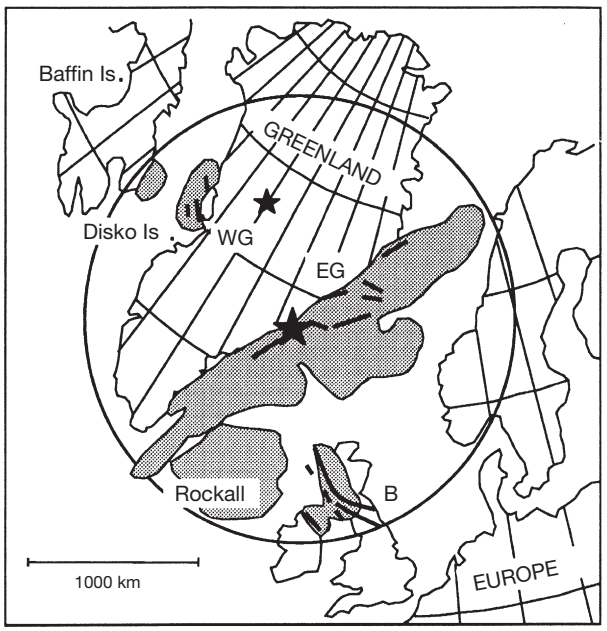

Figure 53 Distribution of basalts and dikes for East Greenland (EG), West Greenland (WG), and the British Tertiary Volcanic Province (B). Reproduced from Ernst RE and Buchan KL (1997) Giant radiating dyke swarms: Their use in identifying pre-Mesozoic large igneous provinces and mantle plumes. In: Mahoney JJ and Coffin MF (eds.) *Large Igneous Provinces; Continental, Oceanic, and Planetary Flood Volcanism*, pp. 297–333. Washington, DC: American Geophysical Union. Geophysical Monograph.

Rifts and passive margins associated with large igneous provinces tend to be nearly straight. No rift is perfectly straight, but if a great circle can pass through part of every segment of a rift, then that rift could be said to be straight. For many rifts, like the Aden rift, the small-scale segments of the rift do not parallel the coastline or the border faults of the rift (e.g., Leroy et al., 2004). This is not surprising since the stress orientation and opening direction can change after the initial phase of opening.

The Red Sea is the clearest example of a straight rift with the coastlines showing only slight deviations from a great circle over 2000 km and the axis of spreading and rifting is even straighter than the coast. The South Atlantic margins of South America and Africa, associated in space and time with the

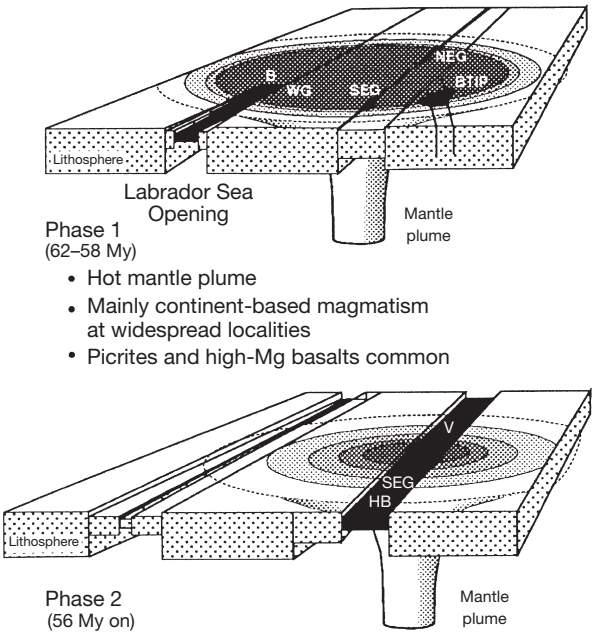

Figure 54 Illustration of the idea that plumes may have fed magma to West and East Greenland during the formation of that large igneous province and those rifted margins. Reproduced from Saunders AD, Fitton JG, et al. (1997) The North Atlantic igneous province. In: Mahoney JJ and Coffin MF (eds.) *Large Igneous Provinces: Continental, Oceanic, and Planetary Flood Volcanism*, vol. 100, pp. 45–93. Washington, DC: American Geophysical Union.

Paraná flood basalts (Hinz, 1981), are another very straight margin. The dike-intruded and volcanic-covered North Atlantic margins of Greenland (e.g., Holbrook et al., 2001) and the conjugate European margins are also remarkably straight on a scale of thousands of kilometers.

A magmatic rift does not have to be volcanic. The Northern Red Sea and the Gulf of Suez lack evidence of massive synrift volcanism (forming many kilometer thick seaward-dipping seismic reflector packages) that has been documented along much of the South Atlantic and Greenland margins (Hinz, 1981; Mutter and Zehnder, 1988). However, synrift dikes striking parallel to the rift are seen as far north as the Gulf of Suez and valley-filling, synrift volcanics are common there as well (Patton et al., 1994).

In this section, simple estimates of the effect of copious magma on the force to rift will be made and compared to the estimated force available for rifting.

6.08.10.1 Force Available for Driving Rifting

Many authors have discussed ways that plate tectonic-related and plume-related processes could produce relative tension at a rift (e.g., Forsyth and Uyeda, 1975; Solomon et al., 1980), and these approaches give similar estimates of rift-driving forces. The simplest of these approaches relates to the uplift that may occur over a region of abnormally hot mantle. The radiation of rift branches away from the uplifted plateau areas of Ethiopia and Yemen is consistent with the extensional driving force being related to the uplift of that region (e.g., Ernst and Buchan, 1997; Sengor and Burke, 1978).

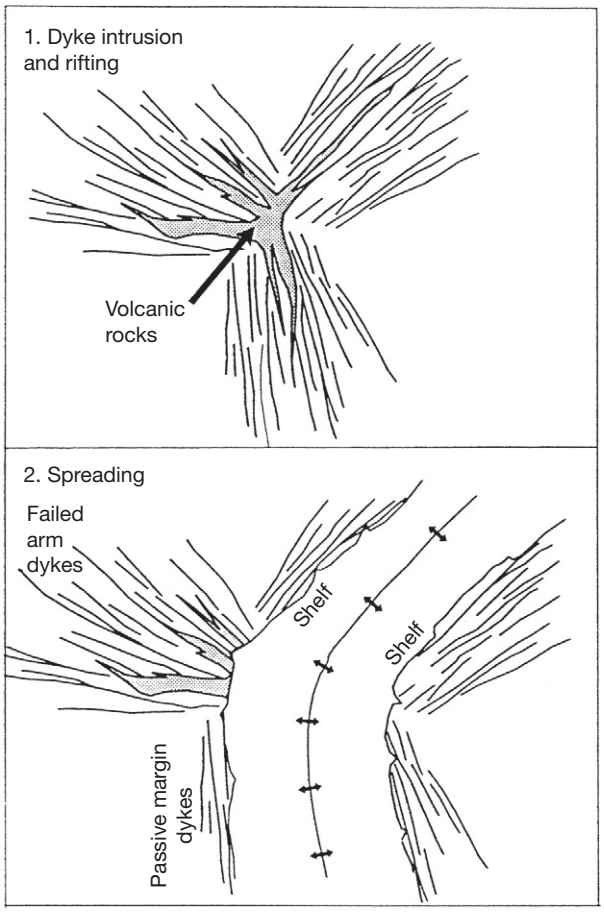

Figure 55 Illustration of how giant radiating dike swarms are often seen to relate to the geometry of subsequent rifting. Reproduced from Ernst RE and Buchan KL (1997) Giant radiating dyke swarms: Their use in identifying pre-Mesozoic large igneous provinces and mantle plumes. In: Mahoney JJ and Coffin MF (eds.) *Large Igneous Provinces; Continental, Oceanic, and Planetary Flood Volcanism*, pp. 297–333. Washington, DC: American Geophysical Union. Geophysical Monograph.

For uplift due to a low-density root, the extensional force scales with the magnitude of the uplift, e, and the depth of the low-density compensation layer, d (Bott, 1991; Spohn and Schubert, 1982). The force is roughly $e\rho_m g d$, where ρ_m is the mantle density and g is the acceleration of gravity. For a root of uniform density, hot mantle between 100 and 200 km d would be 150 km. Then, ~1 kilometer of uplift compensated at 150 km depth gives $\sim 5 \times 10^{12}$ Nt m^{-1} of rift-driving force. Higher elevations and deeper compensation depths are possible, but the force may be spread over a longer rift than the width of the uplifted area. Thus, the average level of rift force is likely to be less than about 5×10^{12}Nt m^{-1}.

6.08.10.2 Force Needed for Tectonic Rifting

Recall from the 'Processes' section of this chapter that the tectonic yield strength depends on the thermal structure of the lithosphere and to a lesser extent on the composition of the lithosphere. To compare the force for tectonic extension to that required for magmatic extension, it is sufficient to ignore the possibility that crust is weaker in terms of ductile

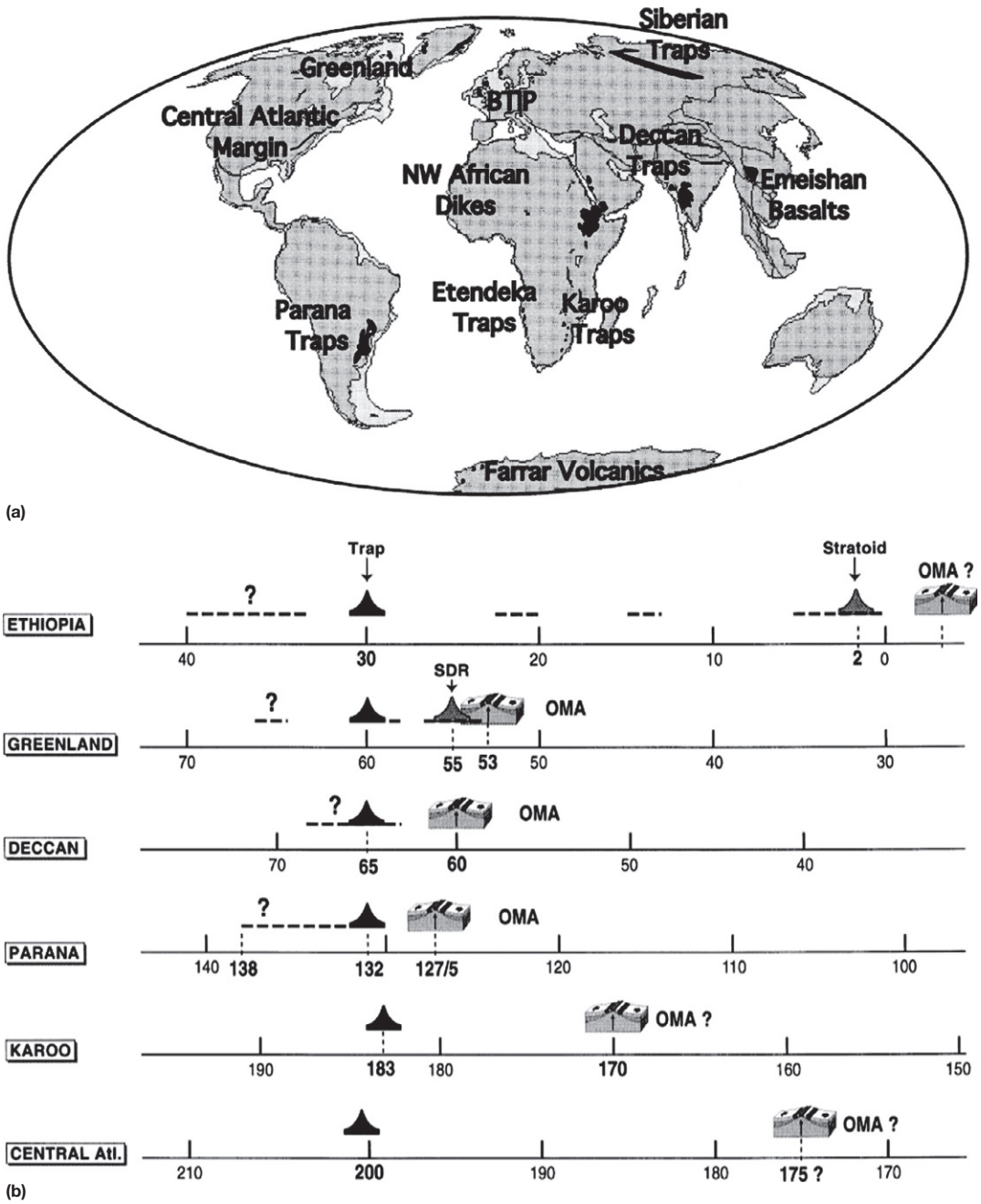

Figure 56 (a) The distribution of large igneous provinces over the last 300 My. (b) The temporal relation between the major (trap) phase of volcanism in these provinces and the onset of ocean floor spreading (as seen by oceanic magnetic anomalies (OMA)). Reproduced from Courtillot V, Jaupart C, et al. (1999) On causal links between flood basalts and continental breakup. *Earth and Planetary Science Letters* 166: 177–195.

flow than mantle. To the extent that we can ignore the contribution of ductile yield stress to the lithospheric strength and if we take the density of the lithosphere constant with depth, we can get a simple estimate of the tectonic force for rifting:

$$F_T = \frac{CH_b^2}{2} \qquad [22]$$

where H_b is the thickness of the brittle lithosphere and C is a constant defined in eqns [2] and [3] and is $\sim 1.4 \times 10^4$ Pa m^{-1}. Neglecting hydrostatic pore pressures increases the value of C, and so the estimated force, by about 50%, and taking a mantle density for the lithospheric density increases it a further 10%. Assuming the creeping part of the lithosphere contributes to the tectonic force also increases this estimate, but for crust creeping more easily than the mantle, the tectonic force is reduced by an amount that depends on the crustal thickness, rheological constants, and thermal state (e.g., Brace and Kohlstedt, 1980; Kusznir and Park, 1987; Sawyer, 1985). For the purpose of making simple comparisons with the force needed to open a magmatic rift in this paper, eqn [4] is sufficient.

6.08.10.3 Force Needed for Magmatic Rifting

As long as the magma is less dense than the rock it intrudes, then some extensional stress has to be applied to keep the magma from rising to the surface and extruding (Buck, 2004). Only when the magma is 'kept down' by this stress difference will the dike open at depth and so allow plates to move apart (Figure 57). Neglecting any stress needed to open a crack, as discussed earlier, the minimum stress difference needed to open a magma-filled dike is

$$\sigma_M(z) = \int_0^{H_b} g(\rho_s(z) - \rho_f)dz \qquad [23]$$

Equation [23] is valid only when the fluid magma density is less than or equal to the average lithospheric density. For example, for constant lithospheric density that is less than the magma density, an extensional force would be required to pull dense magma up from the asthenosphere and magma could not rise to the surface and the limits of integration would have to be changed. Such cases are not likely to be important for lithosphere thicker than a few kilometers and for basaltic magma densities, so they are not discussed further.

The extensional tectonic force to open a magma-filled dike through denser lithosphere with a thickness h_l is

$$F_M = \int_0^{H_b} \sigma_M(z)dz \qquad [24]$$

Consider the simple case that the densities of the crust and mantle, ρ_c and ρ_m, respectively, are constant with depth. If the entire crust is brittle down to its base at $z = H_c$ and the thickness of mantle lithosphere is H_m (so the total lithospheric thickness $H_b = H_c + H_m$), then

$$F_M = g(\rho_c - \rho_f)\frac{H_c^2}{2} + g\left[(\rho_c - \rho_f)H_c + (\rho_m - \rho_f)\frac{H_m}{2}\right]H_m \qquad [25]$$

The density of continental crust is not likely to be very different from the density of basaltic magma. If that is true, then it takes no force to open a dike in the crust, but it still takes considerable force to open a dike into the mantle lithosphere. For $\rho_c = \rho_f$, we get the further simplification that gives eqn [7] (given in an earlier section).

For reasonable density values, we plot this estimate of the force to dike through the entire lithosphere versus the lithospheric thickness (Figure 58), and we compare this to the quadratic relation between tectonic force and lithospheric thickness for tectonic stretching (eqn [22]). For a density contrast

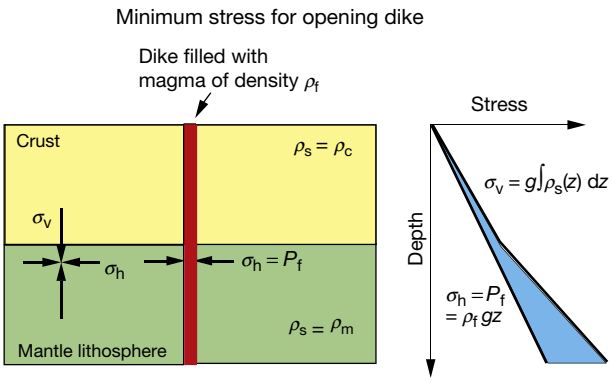

Figure 57 The stress distribution for extensional separation of two lithospheric blocks by a vertical magmatic intrusion (a dike). Here, the solid lithosphere has a density, ρ_s, that is greater than the fluid magma density, ρ_f. The yellow region represents crust with a density, ρ_c, close to that of basaltic magma in dikes and the green represents mantle lithosphere with a density, ρ_m, greater than that of the crust. The horizontal stress, σ_h, equals the pressure in the dike, P_f, while the vertical stress, v_v, equals the overburden pressure. The area between these two stresses (highlighted in blue) equals the force that must be applied to keep the dike open. Reproduced from Buck WR (2006) The role of magma in the development of the Afro-Arabian rift system. In: Yirgu G, Ebinger CJ, and Maguire PKH (eds.) *The Afar Volcanic Province Within the East African Rift System*, vol. 259, pp. 43–54. London: Geological Society.

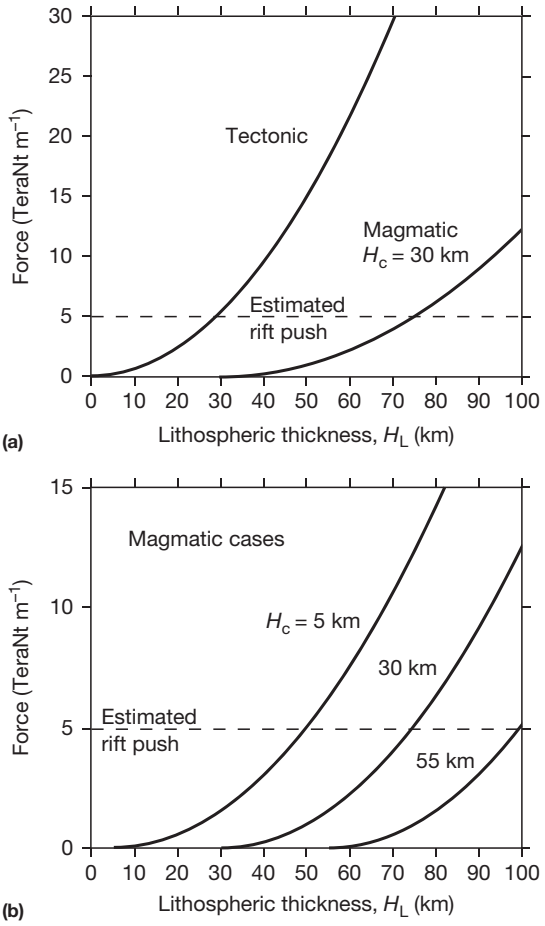

Figure 58 Illustration of estimated force required for lithospheric extension for either tectonic or magmatic rifting as a function of lithospheric thickness lithosphere. Equation [22] was used to compute the tectonic force and eqn [7] was used to compute the magmatic force. (a) The forces as a function of lithospheric thickness assuming a 30 km thick crust. The dashed line is an estimate of the force available to drive lithospheric extension. (b) How the crustal thickness affects the estimated magmatic force. It is the mantle lithospheric thickness, which equals the total lithospheric thickness minus the crustal thickness, that controls this force. Reproduced from Buck WR (2006) The role of magma in the development of the Afro-Arabian rift system. In: Yirgu G, Ebinger CJ, and Maguire PKH (eds.) *The Afar Volcanic Province Within the East African Rift System*, vol. 259, pp. 43–54. London: Geological Society.

between solid mantle and fluid magma of 500 kg m^{-3} (based on mantle density of 3250 kg m^{-3} and magma density of 2750 kg m^{-3}), it would take 4×10^{12} Nt m^{-1} to dike through a 40 km thick lithospheric mantle layer. To dike through 100 km of mantle lithosphere would take 2.5×10^{13} Nt m^{-1}, and this is considerably more force than is likely to be available to drive rifting. The term magmatic rifting will be used to describe lithospheric extension that is aided by dike intrusion, and the force for magmatic rifting is taken to be the force to open dikes through the lithosphere.

Dikes may not open through the entire thickness of the lithosphere if insufficient magma is available, and for such cases, the force required to rift would be intermediate between the force for tectonic rifting and the force for magmatic rifting. Figure 59 shows how different these forces are likely to be as a function of lithospheric thickness. The tectonic force depends on the square of the whole thickness of the lithosphere (times ~6000 Nt m^{-3}), while the magmatic force depends on the square of the mantle lithospheric thickness (times ~2500 Nt m^{-3}). For reasonable driving force levels,

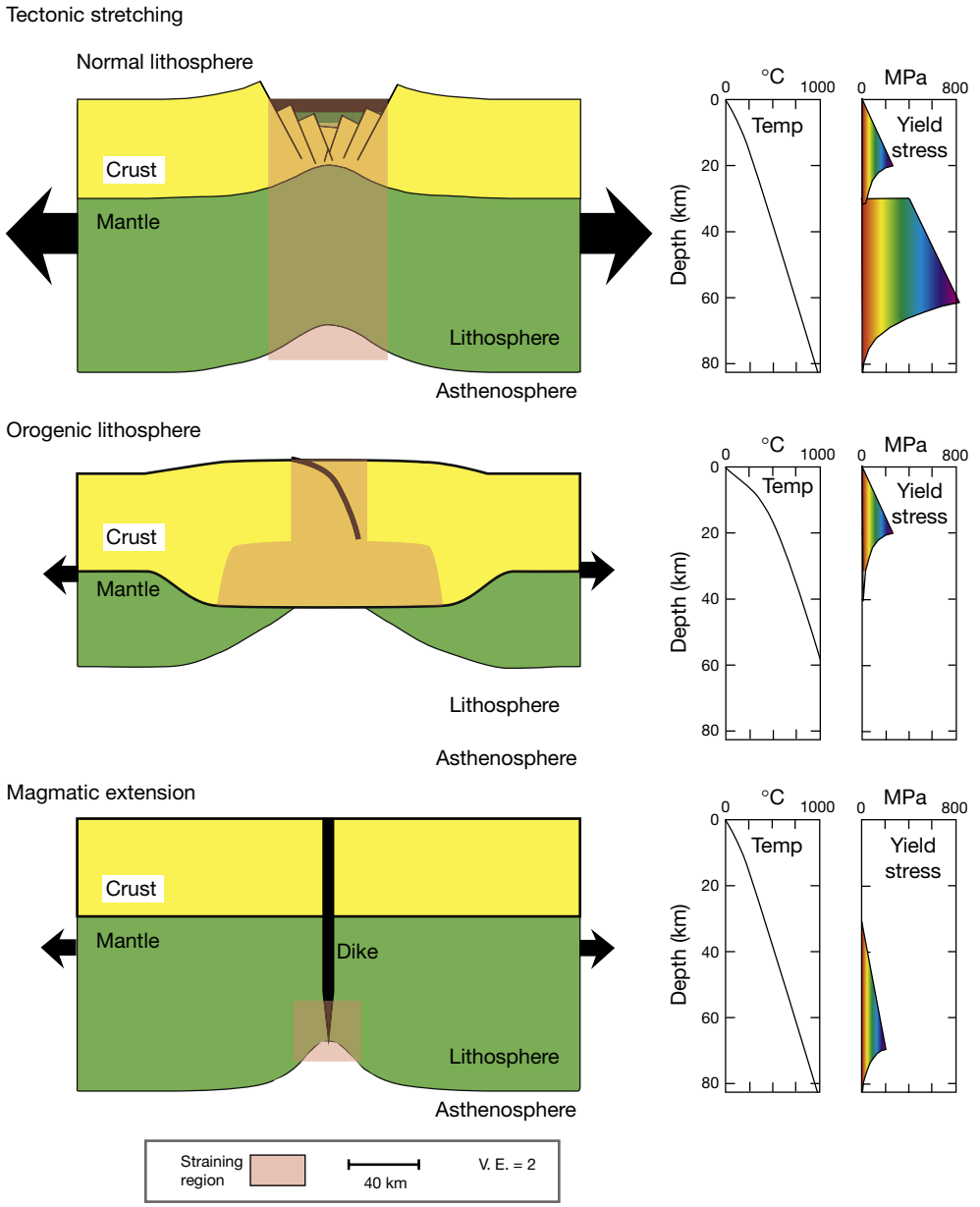

Figure 59 Schematic of stresses needed for extension of continental lithosphere. Note the large difference in the yield stress, the stress difference needed to get extensional separation of two lithospheric blocks. Tectonic extension of (a) normal continental lithosphere should require very large yield stresses and correspondingly large tectonic extensional forces. (b) Orogenically, lithosphere should have a higher geotherm and much lower lithospheric strength. (c) Magmatic intrusion may allow extension of normal lithosphere at modest tectonic force levels. Modified from Buck WR (2004) Consequences of the asthenospheric variability on continental rifting. In: Karner GD, et al. (eds.) Rheology and Deformation of the Lithosphere at Continental Margins, pp. 1–31. New York: Columbia University Press.

only lithosphere thinner than ~30 km thick should rift tectonically (i.e., in the absence of magmatic dike intrusion). For a normal continental crustal thickness of 40 km, the base of the lithosphere could be as deep as ~80 km and still allow magmatic rifting at reasonable force levels. **Figure 59** shows that lithosphere with thicker continental crust should rift magmatically with much less force than for lithosphere with thin crust.

Rifts intruded by large volumes of basaltic magma should subside little during the intrusion phase of extension. If sufficient dike intrusion occurs to heat the lithosphere appreciably, then its strength could be lowered to the point where tectonic extensions can proceed at moderate stress levels. Such combined magmatic and tectonic extension could give a rifted margin with less tectonic subsidence and more thermal subsidence than predicted by a McKenzie stretching model. As noted earlier, this is the pattern of subsidence most commonly seen at rifted margins.

6.08.10.4 The Meaning of Rift Straightness

The straightness of many rifts may indicate that they were initiated by magmatic dike intrusions. Lithospheric extension can be accomplished by either dike opening or fault slip. Both dikes and faults form in response to stress difference in the lithosphere. Faults form and slip where the shear stress is great enough to overcome the strength of the material and allow brittle deformation. Faults change orientation where the stress orientations change or where there are strength variations. So, rifts where faults accommodate the extension do not have to be straight. They can curve where the stresses change or 'sidestep' into weaker areas.

Dikes are narrow magma-filled tension cracks (e.g., Lister and Kerr, 1991), and as such, the plane of the dike must be orthogonal to the least principal stress in a strong, brittle layer. When the least principal stress is horizontal, the dike is vertical and these are the kinds of dikes discussed here. The key to the straightness of dikes may be that dikes, unlike faults, need a source of magma and a connection to that magma source. The open part of the dike is the conduit connecting the source area to the tip of the dike. If dikes are fed from a distributed magma source below a brittle layer, then the dikes do not have to be straight except on the scale of the layer thickness. One way to produce dikes that are straight over lateral distances longer than the brittle layer thickness is if the magma source is localized. The dikes can only remain connected to the source if they are straight.

If the magma does come from a central source, then the dike cannot propagate if it loses connection to the magma supply because the connection is the open, unfrozen, straight dike behind the propagating tip. If a dike tip were to step laterally away from the plane of the open dike by more than the width of the dike, it would no longer be fed magma. Dikes exposed in ophiolites and bordering rifts are typically about a meter wide (e.g., Varga, 2003), so very small offsets are viable.

Straight dikes have been observed propagating from a central magma chamber along a subaerial segment of the Mid-Atlantic Ridge in Iceland. In 1975, an episode of ~15 dike intrusion and magma extrusion events began, with the longest dike propagating 70 km from the Krafla central volcano (Tryggvason, 1980). Seismic and geodetic measurements unequivocally show that the dikes are sourced from a central magma chamber that subsided while the dike was propagating (Einarsson, 1991). Dikes on the flanks of active volcanoes, like those propagating down the east rift zone of Kilauea Volcano in Hawaii, are seen to be straight (e.g., Cervelli et al., 2002). Ancient dikes in the MacKenzie dike swarm of Canada are straight and traceable for thousands of kilometers (Fialko and Rubin, 1999).

The fact that most mid-ocean ridge segments are straight and nearly orthogonal to the spreading direction may reflect dikes fed from central magma chambers. New data on ridge segments suggest that at the slowest spreading rates, there are nonmagmatic segments that are not straight. Dick et al. (2003) noted that the slowest spreading centers, such as the Gakkel Ridge in the Arctic and oblique sections of the Southwest Indian Ridge, show an alteration of volcanic segments and nonvolcanic ones. Peridotite samples dredged from the surface of the nonvolcanic segments indicate that the mantle there is stretched with little or no input of magma. When these nonvolcanic segments are along oblique sections of the ridge, the usual pattern of ridge segments orthogonal to transform faults is not seen. Such segments are cut by numerous faults that trend oblique to the spreading direction.

6.08.10.5 The Distance of Dike/Rift Propagation

Dike propagation may be controlled by a dauntingly large number of thermal and mechanical processes. Among them are the pressure and flux of magma coming out of a source region, the viscous resistance to magma flow along the body of the dike and into the tip region, elastic stresses in lithosphere, and the freezing of magma (e.g., Lister and Kerr, 1991; Rubin, 1995). Although the details of dike mechanics are controversial (e.g., Delaney and Pollard, 1982; Fialko and Rubin, 1999; Ida, 1999), there is no doubt that the distance of dike propagation should be related to the supply of magma. The volume of magma intruded into the thick lithosphere along a several thousand kilometer long rift has to be massive.

The size of a magma chamber should play a major role in determining how much magma can be supplied to dikes as they propagate. The magma pressure is likely to be reduced as volume is extracted from a magma chamber. Buck et al. (2006) argued that lithosphere-cutting dikes stop when the 'driving stress' (defined as the difference between magma pressure and tectonic stress orthogonal to the dike) becomes too small, either because the dike slows and the tip freezes or because the driving stress is not enough to break open a new section of dike. The larger and shallower the magma chamber, the smaller the pressure drop on extraction of a given volume of magma. Large magma chambers should supply large amounts of basalt to a propagating dike and so could be necessary to the production of long dikes.

Simple thermal arguments would suggest that the size and depth of a magma chamber should correlate with the flux of magma coming into a region. The greatest known fluxes of magma occur during the geologically short periods when large igneous provinces form. The volumes are up to several million cubic kilometers and the time interval of high rate magma output is 1 My or less (Courtillot and Renne, 2003,

and references therein). Very large, near-surface magma chambers are likely to form during periods of high melt flux from localized mantle upwellings. Magma chambers the size of large gabbroic layered intrusions found near the centers of some large igneous provinces could feed dikes propagating thousands of kilometers. For example, the Skaergaard layered intrusion of East Greenland is estimated to have a volume of $\sim$300 km^3 (Nielsen, 2004), sufficient to fill a dike 2000 km long, 50 km high, and 3 m thick.

The regions where the mantle lithosphere is very thick may not rift even if copious, high-pressure basaltic magma is present (see **Figure 58(b)**). Recall that extrusion of magma on the surface limits the maximum magma pressure. Cratonic regions, where the lithosphere may be well over a hundred kilometers thick (Jordan, 1975; Venkataraman et al., 2004), and old oceanic lithosphere, where the mantle lithosphere may be $\sim$60 km thick (e.g., Wiens and Stein, 1984), should be too thick to rift.

Dikes and associated magmatic rift propagation can stop because either the magma pressure gets too low or the stress is not sufficient to open a dike through the lithosphere. For the Afro-Arabian Rift System, it may be the lack of extensional stress sufficient to open dikes through very thick mantle lithosphere that limits dike propagation. Previous workers have noted that changes in lithospheric strength may have controlled the termination of the Red Sea branch (e.g., Steckler and ten Brink, 1986) or affected the structure of the East African branch (e.g., Rosendahl, 1987). Those workers were concerned with the difference in tectonic strength of the lithosphere. It is possible that similar arguments may apply for magma-assisted rifting. It may be the increase in force for magmatic rifting related to mantle lithosphere thickening that limits rift propagation.

This is suggested by the observation that the Northern and Southern Branches of the system end close to regions of thick mantle lithosphere. The Northern Red Sea branch ends close to the Mediterranean Sea where old oceanic lithosphere may be too thick to be cut by dikes.

6.08.10.6 Magma Volumes Needed for Nonorogenic Rifting

Most models of rifting are driven by kinematic boundary conditions: the sides of the model domain are pulled apart at a set rate regardless of the force needed. To investigate rifting with a set, moderate extensional force, Bialas et al. (2010) developed a numerical approach that included simulated dike intrusions adding mass and heat to the lithosphere. In that 2-D model, magma-filled dikes open periodically in continental lithosphere in response to an evolving model stress field. The long-term viscous–elastic–plastic deformation as well as the advection and diffusion of heat is tracked using a finite difference-based scheme. At set time intervals, the opening of a vertical dike filled with inviscid magma is computed using a boundary element method. After the instantaneous dike opening event, the change in elastic stresses is then passed back to the long-term model calculation. The available rifting force, lithospheric structure, and magma flux are varied in the numerical simulations.

If the applied extensional force is less than that needed for tectonic stretching, the rate of extension is controlled by the rate of magma injection. The heat emplaced by the dikes eventually weakens the lithosphere so that extension can continue even without additional magma. Bialas et al. (2010) found that the amount of magma required for this transition to tectonic stretching is nearly independent of the rate of magmatic injection, with the exception of highly extrusive cases. For a force of 4 TN m^{-1}, the transition takes about 100 km^3 of magma emplaced by dikes along 1000 km of rift through 80 km thick lithosphere (as defined by the 1200 °C isotherm).

These model results suggest that for the 2000 km long Red Sea Rift, the amount of magma required to allow extension at moderate force levels is less than two-thirds the estimated $3.5^\circ \times 10^5$ km^3 of basalt present today, post erosion, on the Ethiopian and Yemen Plateau at 30 Ma (Mohr, 1983). Thus, a fraction of the magma produced in short-lived volcanic pulses associated with LIPs could be enough to initiate a rift in moderately old continental lithosphere. Magma-assisted rifts may transition to tectonic rifts with rapid magma injection over a short period of time ($\sim$1 Ma as seen for some volcanic margins like the North Atlantic) or with slow rates over longer timescales (>10–20 Ma similar to 'magmatic rifts' like the Red Sea).

6.08.11 Conclusions and Future Work

The questions discussed here are certainly not settled and new observations and models are clarifying the arguments. Several other major problems of continental extension have not been discussed here. For example, what controls the time interval between major rifting events? What controls the length of rifts? Why are fault patterns at rifts so variable? New observations and improved numerical models should allow us to address these and other rift-related questions.

More geologic and geophysical data are needed on rift and margin structure and history. The amount and timing of magmatism must be constrained. To understand the fault structures forming margins, we need better constraints on actual distribution of faults and their offset histories. It appears that we are still in the discovery phase of finding out what rifts are like.

Continuum numerical models are good for studying some of the problems of large-scale rift structure. New techniques need to be developed to deal with. A great challenge is to combine models of highly localized processes such as fault zone evolution and dike propagation with larger regional-scale models of continental extension. On the other end of the spectrum, detailed rift models need to be embedded into global-scale numerical models to test ideas about the ways large-scale convective processes may be linked to the formation of continental rifts.

References

Abers GA (1991) Possible seismogenic shallow-dipping normal faults in the Woodlark-D'Entrecasteaux extensional province, Papua New Guinea. *Geology* 19.
Abers GA, Ferris A, Craig M, et al. (2002) Mantle compensation of active metamorphic core complexes at Woodlark rift in Papua New Guinea. *Nature* 418: 862–865.

Allmendinger RW, Hauge TA, et al. (1987) Overview of the COCORP 40°N Transect Western United States: The fabric of an orogenic belt. *Geological Society of America Bulletin* 98: 308–319.

Alvarez F, Virieux J, et al. (1984) Thermal consequence of lithosphere extension: The initial stretching phase. *Geophysical Journal of the Royal Astronomical Society* 78: 389–411.

Anderson EM (1951) *The Dynamics of Faulting and Dyke Formation, with Applications to Britain*. London: Oliver and Boyd.

Artemjev ME and Artgushkov EV (1971) Structure and isostasy of the Baikal rift and the mechanism of rifting. *Journal of Geophysical Research* 76: 1197–1211.

Atwater TM (1970) Implications of plate tectonics for the Cenozoic evolution of western North America. *Geological Society of America Bulletin* 81: 3513–3536.

Axen GJ and Bartley JM (1997) Field tests of rolling hinges: Existence, mechanical types, and implications for extensional tectonics. *Journal of Geophysical Research* 102(B9): 20515–20537.

Baldwin SL, Monteleone B, Webb LE, Fitzgerald PG, Grove M, and Hill J (2004) Pliocene eclogite exhumation at plate tectonic rates in eastern Papua New Guinea. *Nature* 431: 263–267.

Baldwin SL, Webb LE, and Monteleone BD (2008) Late Miocene coesite–eclogite exhumed in the Woodlark Rift. *Geology* 36: 735–738.

Bassi G (1991) Factors controlling the style of continental rifting: Insights from numerical modelling. *Earth and Planetary Science Letters* 105(4): 430–452.

Bassi G (1995) Relative importance of strain rate and rheology for the mode of continental extension. *Geophysical Journal International* 122(1): 195. http://dx.doi.org/10.1111/j.1365-246X.1995.tb03547.x.

Bassi G, Keen CE, and Potter P (1993) Contrasting styles of rifting: Models and examples from the Eastern Canadian Margin. *Tectonics* 12(3): 639. http://dx.doi.org/10.1029/93TC00197.

Bastow ID, Nyblade AA, Stuart GW, Rooney TO, and Benoit MH (2008) Upper mantle seismic structure beneath the Ethiopian hotspot: Rifting at the edge of the African low velocity anomaly. *Geochemistry, Geophysics, Geosystems* 9: Q12022.

Beaumont C and Ings SJ (2012) Effect of depleted continental lithosphere counterflow and inherited crustal weakness on rifting of the continental lithosphere: General results. *Journal of Geophysical Research* 117: B08407. http://dx.doi.org/10.1029/2012JB009203.

Behn MD, Lin J, et al. (2002) A continuum mechanics model for normal faulting using a strain-rate softening rheology: Implications for thermal and rheological controls on continental and oceanic rifting. *Earth and Planetary Science Letters* 202(3–4): 725–740.

Bialas R and Buck WR (2009) The role of sedimentation in the development of rifts: Applications to the Gulf of California. *Tectonics* 28: TC4014. http://dx.doi.org/10.1029/2008TC002394.

Bialas R, Buck WR, and Qin R (2010) How much magma is required to rift a continent? *Earth and Planetary Science Letters* 292: 68–78.

Bialas R, Buck WR, Studinger M, and Fitzgerald P (2007) Plateau collapse model for the Transantarctic Mountains/West Antarctic Rift System: Insights from numerical experiments. *Geology* 35(8): 687–690.

Biot MA (1961) Theory of folding of stratified, visco-elastic media and its application in tectonics and orogenesis. *Geological Society of America Bulletin* 72: 1595–1632.

Bird P (1991) Lateral extrusion of lower crust from under high topography, in the isostatic limit. *Journal of Geophysical Research, B, Solid Earth and Planets* 96(6): 10275–10286.

Block L and Royden LH (1990) Core complex geometries and regional scale flow in the lower crust. *Tectonics* 9: 557–567.

Bosworth W (1987) Off-axis volcanism in the Gregory rift, east Africa: Implications for models of continental rifting. *Geology* 15: 397–400.

Bott MHP (1991) Ridge push and associated plate interior stress in normal and hot spot regions. *Tectonophysics* 200: 17–32.

Boutilier RR and Keen CE (1999) Small-scale convection and divergent plate boundaries. *Journal of Geophysical Research* 104: 7389–7403.

Brace WF and Kohlstedt DL (1980) Limits on lithospheric stress imposed by laboratory experiments. *Journal of Geophysical Research* 85(B11): 6248–6252.

Braun J and Beaumont C (eds.) (1989a) Contrasting styles of lithospheric extension: Implications for differences between Basin and Range Province and rifted continental margins. Extensional tectonics and stratigraphy of the north Atlantic margins. *American Association of Petroleum Geologist Memoir* 46: 53–79.

Braun J and Beaumont C (1989b) A physical explanation of the relation between flank uplifts and the breakup unconformity at rifted continental margins. *Geology* 17: 760–764.

Brun JP, Sokoutis D, et al. (1994) Analog modeling of detachment fault systems and core complexes. *Geology* 22: 319–322.

Brun J-P and van den Driessche J (1994) Extensional gneiss domes and detachment fault systems – Structure and kinematics. *Bulletin de la Societe Geologique de France* 165: 519–530.

Brune S, Heine C, Perez-Gussinye M, and Sobolev SV (2014) Rift migration explains continental margin asymmetry and crustal hyper-extension. *Nature Communications*. http://dx.doi.org/10.1038/ncomms5014.

Bryndís Brandsdóttir B, Menke W, Einarsson P, White RS, and Staples RK (1997) Färoe-Iceland Ridge Experiment 2. Crustal structure of the Krafla central volcano. *Journal of Geophysical Research* 102: 7867–7886. http://dx.doi.org/10.1029/96JB03799.

Buck WR (1986) Small-scale convection induced by passive rifting: The cause for uplift of rift shoulders. *Earth and Planetary Science Letters* 77: 362–372.

Buck WR (1988) Flexural rotation of normal faults. *Tectonics* 7: 959–973.

Buck WR (1991) Modes of continental lithospheric extension. *Journal of Geophysical Research, B, Solid Earth and Planets* 96(12): 20161–20178.

Buck WR (1993) Effect of lithospheric thickness on the formation of high- and low-angle normal faults. *Geology* 21: 933–936.

Buck WR (2004) Consequences of the asthenospheric variability on continental rifting. In: Karner GD, et al. (eds.) *Rheology and Deformation of the Lithosphere at Continental Margins*, pp. 1–31. New York: Columbia University Press.

Buck WR (2006) The role of magma in the development of the Afro-Arabian rift system. In: Yirgu G, Ebinger CJ, and Maguire PKH (eds.). *The Afar Volcanic Province Within the East African Rift System*, vol. 259, pp. 43–54. London: Geological Society.

Buck WR, Einarsson P, et al. (2006) Tectonic stress and magma chamber size as controls on dike propagation: Constraints from the 1974–1989 Krafla rifting Episode. *Journal of Geophysical Research* 111: B1240.

Buck WR, Lavier LL, et al. (2003) A numerical model of lithospheric extension producing fault bounded basins and ranges. *International Geology Review* 45(8): 712–723.

Buck WR, Martinez F, et al. (1988) Thermal consequences of lithospheric extension: Pure and simple. *Tectonics* 7: 213–234.

Buiter SJH, Huismans RS, and Beaumont C (2008) Dissipation analysis as a guide to mode selection during crustal extension and implications for the styles of sedimentary basins. *Journal of Geophysical Research* 113: B06406. http://dx.doi.org/10.1029/2007JB005272.

Burov E and Cloetingh S (1997) Erosion and rift dynamics: New thermomechanical aspects of post-rift evolution of extensional basins. *Earth and Planetary Science Letters* 150(1–2): 7–26.

Byerlee JD (1978) Friction of rocks. *Pure and Applied Geophysics* 116: 615–626.

Canales JP, Sohn RA, and De Martin BJ (2007) Crustal structure of the Trans-Atlantic Geotraverse (TAG) segment (Mid-Atlantic Ridge, 26°10′ N): Implications for the nature of hydrothermal circulation and detachment faulting at slow spreading ridges. *Geochemistry, Geophysics, Geosystems* 8: Q08004.

Cann JR, Blackman DK, Smith DK, et al. (1997) Corrugated slip surfaces formed at ridge-transform intersections on the Mid-Atlantic Ridge. *Nature* 385: 329–332. http://dx.doi.org/10.1038/385329a0.

Cervelli P, Segall P, et al. (2002) The 12 September 1999 upper east rift zone dike intrusion at Kilauea Volcano, Hawaii. *Journal of Geophysical Research, B, Solid Earth and Planets* 107(7): 13.

Chang S-J and Van der Lee S (2011) Mantle plumes and associated flow beneath Arabia and East Africa. *Earth and Planetary Science Letters* 302: 448–454.

Choblet G and Parmentier E (2001) Mantle upwelling and melting beneath slow spreading centers: Effects of variable rheology and melt productivity. *Earth and Planetary Science Letters* 184: 589–604.

Choi E and Buck WR (2010) Constraints on shallow mantle viscosity from morphology and deformation of fast-spreading ridges. *Geophysical Research Letters* 37: L16302. http://dx.doi.org/10.1029/2010GL043681.

Choi E and Buck WR (2012) Constraints on the strength of faults from the geometry of rider blocks in continental and oceanic core complexes. *Journal of Geophysical Research* 117. http://dx.doi.org/10.1029/2011JB008741.

Choi E, Buck WR, Lavier L, and Petersen KD (2013) Using core complex geometry to constrain fault strength. *Geophysical Research Letters* 40: 3863–3867. http://dx.doi.org/10.1002/grl.50732.

Christensen UR (1992) An Eulerian technique for thermomechanical modeling of lithospheric extension. *Journal of Geophysical Research, B, Solid Earth and Planets* 97(2): 2015–2036.

Christie DM, West BP, Pyle DG, and Hanan BB (1998) Chaotic topography, mantle flow and mantle migration in the Australian–Antarctic discordance. *Nature* 394: 637–644.

Cochran JR (1983a) Effects of finite rifting times on the development of sedimentary basins. *Earth and Planetary Science Letters* 66: 289–303.

Cochran JR (1983b) A model for the development of the Red Sea. *Bulletin of the American Association of Petroleum Geologists* 67: 41–69.

Cochran JR, Martinez F, et al. (1986) Conrad Deep: A new Northern Red Sea deep: Origin and implications for continental rifting. *Earth and Planetary Science Letters* 78: 18–32.

Collettini C, Niemeijer A, Viti C, and Marone C (2009) Fault zone fabric and fault weakness. *Nature* 462(7275): 907–910. http://dx.doi.org/10.1038/nature08585.

Collettini C and Sibson RH (2001) Normal faults, normal friction? *Geology* 29((10): 927–930. http://dx.doi.org/10.1130/0091-7613(2001) 029<0927:NFNF>2.0.CO;2.

Coney PJ (1980) Cordilleran metamorphic core complexes: An overview. In: Crittenden MD Jr, Coney PJ, and Davis GH (eds.) *Cordilleran Metamorphic Core Complexes*, pp. 7–31. Boulder, CO: Geological Society of America, Memoir 153.

Coney PJ and Harms TA (1984) Cordilleran metamorphic core complexes: Cenozoic extensional relics of Mesozoic compression. *Geology* 12: 550–554.

Contrucci I, Matias L, Moulin M, et al. (2004) Deep structure of the West African continental margin (Congo, Zaire, Angola), between 5 S and 8 S, from reflection/refraction seismics and gravity data. *Geophysical Journal International* 158: 529–553. http://dx.doi.org/10.1111/j.1365-246X.2004.02303.x.

Cooper RF and Kohlstedt DL (1986) Rheology and structure of olivine-basalt partial melts. *Journal of Geophysical Research* 91: 9315–9323.

Corti G, Bonini M, et al. (2003) Analogue modelling of continental extension: A review focused on the relations between the patterns of deformation and the presence of magma. *Earth-Science Reviews* 63: 169–247.

Courtillot V, Jaupart C, et al. (1999) On causal links between flood basalts and continental breakup. *Earth and Planetary Science Letters* 166: 177–195.

Courtillot VE and Renne PR (2003) On the ages of flood basalt events. *Comptes Rendus Geoscience* 335: 113–140.

Dannowski A, Grevemeyer I, Ranero CR, et al. (2010) Seismic structure of an oceanic core complex at the Mid-Atlantic Ridge, 22°19′N. *Journal of Geophysics Research* 115: B07107.

Davis GA (1980) Problems of intraplate extensional tectonics, western United States. In: *Continental Tectonics*, pp. 84–95. Washington, DC: National Academy of Science.

Davis GH (1983) Shear zone model for the origin of metamorphic core complexes. *Geology* 11: 342–347.

Davies HL and Warren RG (1988) Origin of eclogite-bearing, domed, layered metamorphic complexes ('core complexes') in the D'Entrecasteaux Islands, Papua New Guinea. *Tectonics* 7: 1–21.

Davis M and Kusznir NJ (2004) Depth dependent extension at rifted margins. In: Karner GEA (ed.) *Rheology and Deformation of the Lithosphere at Continental Margins*. New York: Columbia University Press.

Davis GA and Lister GA (1988) Detachment faulting in continental extension: Perspective from the southwestern U.S. Cordillera. In: Clark SP, Burchfield BC, and Suppe J (eds.) *Processes in Continental Lithospheric Deformation*, pp. 133–159. Boulder, CO: Geological Society of America, Special Paper 218.

Davis GA, Lister GS, and Reynolds SJ (1986) Structural evolution of the Whipple and South mountains shear zones, southwestern United States. *Geology* 14(1): 7–10. http://dx.doi.org/10.1130/0091-7613(1986)14<7:SEOTWA>2.0.CO;2.

de Charpel O, Guennoc P, et al. (1978) Rifting, crustal attenuation and subsidence in the Bay of Biscay. *Nature* 275: 706–711.

de Martin BJ, Canales RAR, Canales JP, and Humphris SE (2007) Kinematics and geometry of active detachment faulting beneath the Trans-Atlantic Geotraverse (TAG) hydrothermal field on the Mid-Atlantic Ridge. *Geology* 35: 711–714.

Dean SM, Minshull TA, Whitmarsh RB, and Louden KE (2000) Deep structure of the ocean-continent transition in the southern Iberia Abyssal Plain from seismic refraction profiles: The IAM-9 transect at 40°20′N. *Journal of Geophysical Research* 105: 5859–5885. http://dx.doi.org/10.1029/1999JB900301.

Delaney PT and Pollard DD (1982) Solidification of basaltic magma during flow in dike. *American Journal of Science* 282: 856–885.

DeMets C and Dixon TH (1999) New kinematic models for Pacific-North America motion from 3 Ma to present. I. Evidence for steady motion and biases in the NUVEL-1A model. *Geophysical Research Letters* 26: 1921–1924.

Dewey JF (1988) Extensional collapse of orogens. *Tectonics* 7(6): 1123–1139.

Dick HJB, Lin J, et al. (2003) An ultraslow-spreading class of ocean ridge. *Nature* 426(6965): 405–412.

Dixon TH, Farina F, DeMets C, et al. (2000) New kinematic models for Pacific-North America motion from 3 Ma to present. II. Evidence for a "Baja California shear zone". *Geophysical Research Letters* 26: 1921–1924.

Driscoll NW and Karner GD (1998) Lower crustal extension across the Northern Carnarvon basin, Australia: Evidence for an eastward dipping detachment. *Journal of Geophysical Research* 103(B3): 4975–4991.

Dunbar JA and Sawyer DS (1989) How preexisting weaknesses control the style of continental breakup. *Journal of Geophysical Research, B, Solid Earth and Planets* 94(6): 7278–7292.

Duretz T, Gerya TV, Kaus BJP, and Andersen Gerya TB (2012) Thermomechanical modeling of slab eduction. *Journal of Geophysical Research* 117: B08411. http://dx.doi.org/10.1029/2012JB009137.

Ebinger CJ, Deino AL, et al. (1989) Chronology of volcanism and rift basin propagation: Rungwe volcanic province, East Africa. *Journal of Geophysical Research* 94: 15785–15803.

Ebinger CJ, Rosendahl BR, et al. (1987) Tectonic model of the Malawi rift, Africa. *Tectonophysics* 141: 215–235.

Einarsson P (1991) The Krafla rifting episode 1975–1989. In: *Náttúra Myvatns (The Nature of Lake Myvatn)*. Reykjavík: Icelandic Nature Science Society.

Ellis SM, Little TA, Wallace LM, Hacker BR, and Buiter SJH (2011) Feedback between rifting and diapirism can exhume ultrahigh-pressure rocks. *Earth and Planetary Science Letters* 311: 427–438.

England P (1983) Constraints on extension of continental lithosphere. *Journal of Geophysical Research* 88: 1145–1152.

Ernst RE and Buchan KL (1997) Giant radiating dyke swarms: Their use in identifying pre-Mesozoic large igneous provinces and mantle plumes. In: Mahoney JJ and Coffin MF (eds.) *Large Igneous Provinces: Continental, Oceanic, and Planetary Flood Volcanism*, pp. 297–333. Washington, DC: American Geophysical Union, Geophysical Monograph.

Escartin J, Hirth G, and Evans B (1997) Nondilatant brittle deformation of serpentinites: Implications for Mohr–Coulomb theory and the strength of faults. *Journal of Geophysical Research* 102(B2): 2897–2913.

Escartin J, Smith DK, Cann J, Schouten H, Langmuir CH, and Escrig S (2008) Central role of detachment faults in accretion of slow-spreading oceanic lithosphere. *Nature (London)* 455(7214): 790–794.

Fialko YA and Rubin AM (1999) Thermal and mechanical aspects of magma emplacement in giant dike swarms. *Journal of Geophysical Research* 104(B10): 23033–23049.

Fitz G and Mann P (2013) Evaluating upper versus lower crustal extension through structural reconstructions and subsidence analysis of basins adjacent to the D'Entrecasteaux Islands, eastern Papua New Guinea. *Geochemistry, Geophysics, Geosystems* 14: 1800–1818. http://dx.doi.org/10.1002/ggge.20123.

Fleitout L and Froidevaux Claude (1983) Tectonic stresses in the lithosphere. *Tectonics* 2(3): 315–324.

Fletcher RC and Hallet B (1983) Unstable extension of the lithosphere: A mechanical model for Basin and Range structure. *Journal of Geophysical Research* 88: 7457–7466.

Forsyth DW (1992) Finite extension and low-angle normal faulting. *Geology* 20: 27–30.

Forsyth DW and Uyeda S (1975) On the relative importance of the driving forces of plate motion. *Geophysical Journal of the Royal Astronomical Society* 43(1): 163–200.

Franke D, Ladage S, Schnabel M, et al. (2010) Birth of a volcanic margin off Argentina, South Atlantic. *Geochemistry, Geophysics, Geosystems* 11: Q0AB04. http://dx.doi.org/10.1029/2009GC002715.

Geoffroy L (2005) Volcanic passive margins, Comptes Rendus - Academie des sciences. *Geoscience* 337(16): 1395–1408.

Ghods A (2002) Is small scale convection responsible for the formation of thick igneous crust along volcanic passive margins? *Geophysical Research Letters* 29(10): 1365. http://dx.doi.org/10.1029/2001GL014408.

Goetze C and Evans B (1979) Stress and temperature in the bending lithosphere as constrained by experimental rock mechanics. *Geophysical Journal of the Royal Astronomical Society* 59: 463–478.

Gueydan F, Morency C, and Brun J-P (2008) Continental rifting as a function of lithosphere mantle strength. *Tectonophysics* 460: 83–93.

Hamilton WB (ed.) (1987) Crustal extension in the Basin and Range province, southwestern United States. In: *Continental Extensional Tectonics*. London: Geological Society, Special Publication.

Hamilton W (1988) Extensional faulting in the Death Valley region (abstract). In: *Geological Society of America Abstracts with Programs, vol. 20*, pp. 165–166.

Hammond JOS, Kendall J-M, Stuart GW, et al. (2011) The nature of the crust beneath the Afar triple junction: Evidence from receiver functions. *Geochemistry, Geophysics, Geosystems* 12. http://dx.doi.org/10.1029/2011GC003738.

Handin J (1966) Strength and ductility. In: Clark SP Jr (ed.). *Handbook of Physical Constraints*, vol. 97, pp. 223–290. New York: Geological Society of America, Memoir.

Hayman NW, Grindlay NR, Perfit MR, Mann P, Leroy S, and de Lépinay BM (2011) Oceanic core complex development at the ultraslow spreading Mid-Cayman Spreading Center. *Geochemistry, Geophysics, Geosystems* 12: Q0AG02. http://dx.doi.org/10.1029/2010GC003240.

Hinz K (1981) A hypothesis on terrestrial catastrophes: Wedges of very thick oceanward dipping layers beneath passive margins. *Geologisches Jahrbuch Reihe B* 22: 3–28.

Hirth G and Kohlstedt DL (1995a) Experimental constraints on the dynamics of the partially molten upper mantle 1: Deformation in the diffusion creep regime. *Journal of Geophysical Research* 100: 1981–2001.

Hirth G and Kohlstedt DL (1995b) Experimental constraints on the dynamics of the partially molten upper mantle 2: Deformation in the dislocation creep regime. *Journal of Geophysical Research* 100: 15441–15449.

Hirth G and Kohlstedt DL (1996) Water in the oceanic upper mantle: Implications for rheology, melt extraction, and the evolution of the lithosphere. *Earth and Planetary Science Letters* 144: 93–108.

Holbrook W and Kelemen P (1993) Large igneous province on the US Atlantic margin and implications for magmatism during breakup. *Nature* 364: 433–436.

Holbrook WS, Larsen HC, et al. (2001) Mantle thermal structure and active upwelling during continental breakup in the North Atlantic. *Earth and Planetary Science Letters* 190: 251–266.

Hopper J and Buck WR (1996) Effects of lower crustal flow on continental extension and passive margin formation. *Journal of Geophysical Research* 101: 20175–20194.

Hopper JR, Dahl JT, et al. (2003) Structure of the SE Greenland margin from seismic reflection and refraction data; implications for nascent spreading center subsidence and asymmetric crustal accretion during North Atlantic opening. *Journal of Geophysical Research* 108: 2269.

Huismans RS and Beaumont C (2003) Symmetric and asymmetric lithospheric extension: Relative effects of frictional-plastic and viscous strain softening. *Journal of Geophysical Research, B, Solid Earth and Planets* 108(10): 22.

Huismans R and Beaumont C (2011) Depth-dependent extension, two stage breakup and cratonic underplating at rifted margins. *Nature* 473: 74–78. http://dx.doi.org/10.1038/nature09988.

Huismans RS, Buiter SJH, et al. (2005) Effect of plastic-viscous layering and strain softening on mode selection during clothes extension. *Journal of Geophysical Research* 110(B2): 17.

Huismans RS, Podladchikov YY, and Cloetingh S (2001) Transition from passive to active rifting: Relative importance of asthenospheric doming and passive extension of the lithosphere. *Journal of Geophysical Research* 106(B6): 11271–11291.

Ito G, Shen Y, Hirth G, and Wolfe CJ (1999) Mantle flow, melting, and dehydration of the Iceland mantle plume. *Earth and Planetary Science Letters* 165: 81–96. http://dx.doi.org/10.1016/S0012-821X(98)00216-7.

Ida Y (1999) Effects of the crustal stress on the growth of dikes: Conditions of intrusion and extrusion of magma. *Journal of Geophysical Research* 104(B8): 17897–17910.

Illies JH and Greiner G (1978) Rhinegraben and the Alpine system. *Geological Society of America Bulletin* 89(5): 770–782.

Jackson JA (1987) Active normal faulting and crustal extension. In: Coward MP, Dewey JF, and Hancock PL (eds.) *Continental Extensional Tectonics*, vol. 28, pp. 3–17. London, Oxford: Geological Society/Blackwell Scientific, Special Publications.

Jackson JA and White NJ (1989) Normal faulting in the upper continental crust: Observations from regions of active extension. *Journal of Structural Geology* 11: 15–36.

Jammes S, Lavier L, and Manatschal G (2010) Extreme crustal thinning in the Bay of Biscay and the Western Pyrenees: From observations to modeling. *Geochemistry, Geophysics, Geosystems* 11: Q10016. http://dx.doi.org/10.1029/2010GC003218.

Jarvis GT and McKenzie DP (1980) Sedimentary basin formation with finite extension rates. *Earth and Planetary Science Letters* 48: 42–52.

John BJ and Foster DA (1993) Structural and thermal constraints on the initiation angle of detachment faulting in the southern Basin and Range: The Chemehuevi Mountains case study. *Geological Society of America Bulletin* 105: 1091–1108.

Jolivet L, Famin V, Mehl C, et al. (2004) Strain localization during crustal-scale boudinage to form extensional metamorphic domes in the Aegean Sea. In: Whitney DL, Teyssier C, and Siddoway CS (eds.) *Gneiss Domes in Orogeny*, pp. 185–210. Boulder, CO: Geological Society of America, Special Paper No. 380.

Jordan TH (1975) The continental tectosphere. *Reviews of Geophysics and Space Physics* 13(3): 1–12.

Jordan TH (1978) Composition and development of the continental tectosphere. *Nature* 274: 544–548. http://dx.doi.org/10.1038/274544a0.

Karato S (1986) Does partial melting reduce the creep strength of the upper mantle. *Nature* 319: 309–310.

Keen CE (1985) The dynamics of rifting: Deformation of the lithosphere by active and passive driving forces. *Geophysical Journal of the Royal Astronomical Society* 80: 95–120.

King SD and Anderson DL (1995) An alternative mechanism of flood basalt formation. *Earth and Planetary Science Letters* 136: 269–279.

King SD and Anderson DL (1998) Edge driven convection. *Earth and Planetary Science Letters* 160: 289–296.

King G and Ellis M (1990) The origin of large local uplift in extensional regions. *Nature* 348: 689–692.

Kirby SH and Kronenberg AK (1987) Rheology of the lithosphere: Selected topics. *Reviews of Geophysics* 25: 1219–1244.

Klein EM and Langmuir CH (1987) Global correlations of ocean ridge basalt chemistry with axial depth and crustal thickness. *Journal of Geophysical Research* 92: 8089–8115.

Kohlstedt DL, Evans B, and Mackwell SJ (1995) Strength of the lithosphere: Constraints imposed by laboratory experiments. *Journal of Geophysical Research* 100: 17587–17602.

Kruckenberg SC, Vanderhaeghe O, Ferré EC, Teyssier C, and Whitney DL (2011) Flow of partially molten crust and the internal dynamics of a migmatite dome, Naxos, Greece. *Tectonics* 30: TC3001. http://dx.doi.org/10.1029/2010TC002751.

Kusznir NJ and Park RG (1987) The extensional strength of the continental lithosphere: Its dependence on geothermal gradient, and crustal composition and thickness. In: Coward MP, Dewey JF, and Hancock PL (eds.) *Continental Extensional Tectonics*, pp. 35–52. London: Geological Society, Special Publication 28.

Langseth MG and Taylor PI (1967) Recent heat flow measurements in the Indian Ocean. *Journal of Geophysical Research* 85: 3740–3750.

Larsen HC, Saunders AD, et al. (1993) Preliminary results from drilling on the SE Greenland margin: ODP Leg 152. In: AGU 1993 Fall Meeting, vol. 74, Supplement, p. 606. Washington, DC: American Geophysical Union.

Lavier L and Buck WR (2002) Half graben versus large-offset low-angle normal fault: The importance of keeping cool during normal faulting. *Journal of Geophysical Research* 107, http://dx.doi.org/10.1029/2001JB000513.

Lavier LL, Buck WR, and Poliakov ANB (1999) Self-consistent rolling-hinge model for the evolution of large-offset low-angle normal faults. *Geology* 27(12): 1127–1130.

Lavier LL, Buck WR, and Poliakov ANB (2000) Factors controlling normal fault offset in an ideal brittle layer. *Journal of Geophysical Research* 105(B10): 23431–23442.

Lavier LL and Manatschal G (2006) A mechanism to thin the continental lithosphere at magma-poor margins. *Nature* 440(7082): 324–328.

Le Pourhiet L, Huet B, May DA, Labrousse L, and Jolivet L (2012) Kinematic interpretation of the 3D shapes of metamorphic core complexes. *Geochemistry, Geophysics, Geosystems* 13: Q09002. http://dx.doi.org/10.1029/2012GC004271.

LePichon X and Alvarez F (1984) From stretching to subduction in back-arc regions: Dynamic considerations. *Tectonophysics* 102: 343–357.

LePichon X and Barbier F (1987) Passive margin formation by low-angle faulting within the upper crust: The northern Bay of Biscay margin. *Tectonics* 6: 133–150.

Leroy S, Gente P, et al. (2004) From Rifting to Spreading in the Eastern Gulf of Aden: A geophysical survey of young oceanic basin from margin to margin. *Terra Nova* 16: 184–192.

Leroy S, Lucazeau F, d'Acremont F, et al. (2010) Contrasted styles of rifting in the eastern Gulf of Aden: A combined wide-angle, multichannel seismic, and heat flow survey. *Geochemistry, Geophysics, Geosystems* 11: Q07004. http://dx.doi.org/10.1029/2009GC002963.

Lister GS and Davis GA (1989) Models for the formation of metamorphic core complexes and mylonitic detachment terranes. *Journal of Structural Geology* 11: 65–94.

Lister GS, Etheridge MA, et al. (1986) Detachment faulting and the evolution of passive continental margins. *Geology* 14: 246–250.

Lister JR and Kerr RC (1991) Fluid-mechanical models of crack propagation and their application to magma transport in dykes. *Journal of Geophysical Research* 96: 10049–10077.

Little TA, Hacker BR, Gordon SM, et al. (2011) Diapiric exhumation of Earth's youngest (UHP) eclogites in the gneiss domes of the D'Entrecasteaux Islands, Papua New Guinea. *Tectonophysics* 510: 39–68.

Lizarralde D, Axen GJ, Brown HE, et al. (2007) Variable styles of rifting in the Gulf of California. *Nature* 448: 466–469.

Lonsdale P (1989) Geology and tectonic history of the Gulf of California (2009). In: Winterer EL, Hussong DM, and Decker RW (eds.). *The Eastern Pacific Ocean and Hawaii*, 1989: pp. 499–521. Boulder, CO: Geological Society of America.

Mackwell SJ, Zimmerman ME, et al. (1998) High-temperature deformation of dry diabase with application to tectonics on Venus. *Journal of Geophysical Research* 103: 975–984.

MacLeod CJ, Carlut J, Escartin J, Horen H, and Morris A (2011) Quantitative constraint on footwall rotations at the 15°45′N oceanic core complex, Mid-Atlantic Ridge: Implications for oceanic detachment fault processes. *Geochemistry, Geophysics, Geosystems* 12: Q0AG03.

Makris J and Ginzburg A (1987) The Afar Depression: Transition between continental rifting and sea floor spreading. *Tectonophysics* 141: 199–214.

Manspeizer W and Cousminer HL (1988) Late Triassic-Early Jurassic synrift basins of the U.S. Atlantic margin. In: Sheridan RE and Grow JA (eds.) *The Atlantic Continental Margin; U.S., v*, pp. 197–216. Boulder, CO: Geological Society of America.

Martinez F and Cochran JR (1988) Structure and tectonics of the northern Red Sea: Catching a continental margin between rifting and drifting. *Tectonophysics* 150: 1–32.

Martinez F, Goodliffe A, and Taylor B (2001) Metamorphic core complex formation by density inversion and lower crustal extrusion. *Nature* 411: 930–933.

Martinod J and Davy P (1992) Periodic instabilities during compression or extension of the lithosphere: 1. Deformation modes from an analytical perturbation method. *Journal of Geophysical Research* 97: 1999–2014.

McGarr A and Gay NC (1978) State of stress in the Earth's crust. *Annual Review of Earth and Planetary Sciences* 6(1): 405–436. http://dx.doi.org/10.1146/annurev.ea.06.050178. 002201.

Maguire PHK, Keller GR, Klemperer SL, et al. (2006) Crustal structure of the northern Main Ethiopian Rift from the EAGLE controlled-source survey; a snapshot of incipient lithospheric break-up. In: Yirgu G, Ebinger CJ, and Maguire PKH (eds.) *The Afar Volcanic Province within the East African Rift System: Special Publications*, vol. 259, pp. 269–291. London: Geological Society.

McKenzie DP (1967) Some remarks on heat flow and gravity anomalies. *Journal of Geophysical Research* 72(24): 6261–6273.

McKenzie DP (1978) Some remarks on the development of sedimentary basins. *Earth and Planetary Science Letters* 40: 25–32.

Melosh HJ and Williams CA (1989) Mechanics of graben formation in crustal rocks: A finite element analysis. *Journal of Geophysical Research* 94(B10): 13961–13973.

Menard HW (1978) Fragmentation of the Farallon plate by pivoting subduction. *Journal of Geology* 86: 99–110.

Michaud F, et al. (2006) Oceanic-ridge subduction vs. slab break off: Plate tectonic evolution along the Baja California Sur continental margin since 15 Ma. *Geology* 34: 13–16.

Miller JMG and John BE (1988) Detachment strata in a Tertiary low-angle normal fault terrane, southeastern California: A sedimentary record of unroofing, breaching, and continued slip. *Geology* 19: 645–648.

Mohr P (1983) Ethiopian flood basalt province. *Nature* 303: 577–584.

Morgan P, Seager WR, et al. (1986) Cenozoic mechanical and tectonic evolution of the Rio Grande Rift. *Journal of Geophysical Research* 91: 6263–6276.

Morris A, Gee JS, Pressling N, et al. (2009) Footwall rotation in an oceanic core complex quantified using reoriented Integrated Ocean Drilling Program core samples. *Earth and Planetary Science Letters* 287: 217–228.

Mutter JC, Buck WR, and Zehnder CA (1988) Convective partial melting 1: A model for the formation of thick basaltic sequences during the initiation of spreading. *Journal of Geophysical Research* 93: 1031–1048.

Mutter JC, Talwani M, et al. (1982) Origin of seaward-dipping reflectors in oceanic crust off the Norwegian margin by "subaerial seafloor spreading". *Geology* 10: 353–357.

Mutter JC and Zehnder CM (1988) Deep crustal structure and magmatic processes: The inception of seafloor spreading in the Norwegian-Greenland Sea. In: Morton AC and Parsons B (eds.) *Early Tertiary Volcanism and the Opening of the NE Atlantic*, pp. 34–38. London: Geological Society.

Nagel TJ and Buck WR (2004) Symmetric alternative to asymmetric rifting models. *Geology* 32: 937–940.

Nagel TJ and Buck WR (2006) Channel flow and the development of parallel-dipping normal faults. *Journal of Geophysical Research* 111: B08407. http://dx.doi.org/10.1029/2005JB004000.

Nielsen TFD (2004) The shape and volume of the Skaergaard Intrusion, Greenland: Implications for mass balance and bulk composition. *Journal of Petrology* 45(3): 507–530.

Nielsen TK and Hopper JR (2002) Formation of volcanic rifted margins: Are temperature anomalies required? *Geophysical Research Letters* 29(21): 2022. http://dx.doi.org/10.1029/2002GL015681.

Nielsen TK and Hopper JR (2004) From rift to drift: Mantle melting during continental breakup. *Geochemistry, Geophysics, Geosystems* 5: Q07003. http://dx.doi.org/10.1029/2003GC000662.

Numelin T, Marone C, and Kirby E (2007) Frictional properties of natural fault gouge from a low-angle normal fault, Panamint Valley, California. *Tectonics* 26(2): TC2004. http://dx.doi.org/10.1029/2005TC001916.

Ohara Y, Yoshida T, Kato Y, and Kasuga S (2001) Giant megamullion in the Parece Vela Backarc Basin. *Marine Geophysical Researches* 22: 47–61.

Okino K, Matsuda K, Christie DM, Nogi Y, and Koziumu K (2004) Development of oceanic detachment and asymmetric spreading at the Australian-Antarctic Discordance. *Geochemistry, Geophysics, Geosystems* 5: Q12012.

Oxburgh ER and Parmentier EM (1977) Compositional and density stratification in the oceanic lithosphere – Causes and consequences. *Journal of the Geological Society of London* 133: 343–354.

Palmason G (1980) A continuum model of crustal generation in Iceland: Kinematic aspects. *Journal of Geophysical Research* 47: 7–18.

Parsons B and Sclater JG (1977) Ocean floor bathymetry and heat flow. *Journal of Geophysical Research* 82: 803–827.

Parsons T and Thompson GA (1993) Does magmatism influence low-angle normal faulting? *Geology* 21: 247–250.

Patton TL, Moustafa AR, et al. (1994) Tectonic evolution and structural setting of the Suez Rift. In: Landon SM (ed.) *Interior Rift Basins*. Tulsa. OK: American Association of Petroleum Geologists Memoir.

Petersen KD, Nielsen SB, Clausen OR, Stephenson R, and Gerya T (2010) Small-scale mantle convection produces stratigraphic sequences in sedimentary basins. *Science* 329: 827–830. http://dx.doi.org/10.1126/science.1190115.

Phipps Morgan J (1997) The generation of a compositional lithosphere by mid-ocean ridge melting and its effect on subsequent off-axis hotspot upwelling and melting. *Earth and Planetary Science Letters* 146: 213–232. http://dx.doi.org/10.1016/S0012-821X(96)00207-5.

Poliakov A and Buck WR (1998) Mechanics of stretching elastic–plastic-viscous layers: Applications to slow-spreading mid-ocean ridges. In: Buck WR, Delaney PT, Karson JA, and Lagabrielle Y (eds.) *AGU Monograph: Faulting and Magmatism at Mid-Ocean Ridges*, vol. 106, pp. 305–324. Washington, DC: AGU.

Rabinowicz M, Nicolas A, and Vigneres JL (1984) A rolling mill effect in asthenosphere beneath oceanic spreading centers. *Earth and Planetary Science Letters* 67: 97–108.

Ramberg H (1955) Natural and experimental boudinage and pinch-and-swell structures. *Journal of Geology* 63: 512–526.

Ranero CR and Pérez-Gussinyé M (2010) Sequential faulting explains the asymmetry and extension discrepancy of conjugate margins. *Nature* 468: 2–8. http://dx.doi.org/10.1038/nature09520.

Rehrig WA and Reynolds SJ (1980) Geologic and geochronologic reconnaissance of a northwest-trending zone of metamorphic core complexes in southern and western Arizona. In: Crittenden MD, Coney PJ, and Davis GH (eds.) *Cordilleran Metamorphic Core Complexes*, vol. 153, pp. 131–157. Boulder, CO: Geological Society of America, Geological Society of America Memoir 153.

Reston TJ (2009) The structure, evolution and symmetry of the magma poor rifted margins of the North and Central Atlantic: A synthesis. *Tectonophysics* 468: 6–27. http://dx.doi.org/10.1016/j.tecto.2008.09.002.

Reston TJ and Ranero CR (2011) The 3-D geometry of detachment faulting at mid-ocean ridges. *Geochemistry, Geophysics, Geosystems* 12: Q0AG05. http://dx.doi.org/10.1029/2011GC003666.

Rey PF, Teyssier C, Kruckenberg SC, and Whitney DL (2011) Viscous collision in channel explains double domes in metamorphic core complexes. *Geology* 39: 387–390.

Rey P, Teyssier C, and Whitney DL (2009a) Crustal melting and core complex dynamics. *Geology* 37: 391–394.

Rey P, Teyssier C, and Whitney DL (2009b) The role of partial melting and extensional strain rates in the development of metamorphic core complexes (McMCC). *Tectonophysics* 477: 135–144.

Rosendahl BR (1987) Architecture of continental rifts with special reference to East Africa. *Annual Review of Earth and Planetary Sciences* 15: 443–503.

Royden LH, Burchfiel BC, et al. (1997) Surface deformation and lower crustal flow in eastern Tibet. *Science* 276(5313): 788–790.

Royden L and Keen CE (1980) Rifting process and thermal evolution of the continental margin of eastern Canada determined from subsidence curves. *Earth and Planetary Science Letters* 51: 343–361. http://dx.doi.org/10.1016/0012-821X(80) 90216-2.

Rubin AM (1995) Propagation of Magma-filled cracks. *Annual Review of Earth and Planetary Sciences* 23: 287–336.

Rubin AM and Pollard DD (1987) Origins of blake-like dikes in volcanic rift zones. *U.S. Geological Survey Professional Paper* 1350: 1449–1470.

Salveson JO (1978) Variations in the geology of rift basins: A tectonic model. In: Olsen KH and Chapin CE (eds.). *Conference Proceedings*, vol. 7487*, 1978 International Symposium on the Rio Grande Rift: Program and Abstracts*, pp. 82–86. Los Alamos Scientific Laboratory.

Saunders AD, Fitton JG, et al. (1997) The North Atlantic igneous province. In: Mahoney JJ and Coffin MF (eds.) *Large Igneous Provinces; Continental, Oceanic, and Planetary Flood Volcanism*, vol. 100, pp. 45–93. Washington, DC: American Geophysical Union.

Sawyer DS (1985) Brittle failure in the upper mantle during extension of continental lithosphere. *Journal of Geophysical Research* 90(4): 3021–3025.

Schmeling H (2010) Dynamic models of continental rifting with melt generation. *Tectonophysics* 480: 33–47. http://dx.doi.org/10.1016/j.tecto.2009.09.005.

Scott DR and Stevenson DJ (1989) A self-consistent model of melting, magma migration, and buoyancy-driven circulation beneath a mid-ocean ridge. *Journal of Geophysical Research* 94: 2973–2988.

Sengor AMC and Burke K (1978) Relative timing of rifting and volcanism on Earth and its tectonic implications. *Geophysical Research Letters* 5: 419–421.
Shillington DJ, Holbrook WS, Avendonk HJAV, et al. (2006) Evidence for asymmetric nonvolcanic rifting and slow incipient oceanic accretion from seismic reflection data on the Newfoundland margin. *Journal of Geophysical Research* 111: B09402. http://dx.doi.org/10.1029/2005JB003981.
Sibson RH (1985) A note on fault reactivation. *Journal of Structural Geology* 7(6): 751–754.
Singleton JS (2013) Development of extension-parallel corrugations in the Buckskin–Rawhide metamorphic core complex, west-central Arizona. *Geological Society of America Bulletin* 125: 453–472.
Sleep NH (1971) Thermal effects of the formation of Atlantic continental margins by continental breakup. *Geophysical Journal of the Royal Astronomical Society* 24: 325–350.
Sleep NH (2007) Edge-modulated stagnant-lid convection and volcanic passive margins. *Geochemistry, Geophysics, Geosystems* 8: Q12004. http://dx.doi.org/10.1029/2007GC001672.
Smith RB (1977) Formation of folds, boudinage, and mullions in non-Newtonian materials. *Geological Society of America Bulletin* 88: 312–320.
Smith DK, Cann JR, and Escartin J (2006) Widespread active detachment faulting and core complex formation near 13°N on the Mid-Atlantic Ridge. *Nature* 442: 440–443.
Smith DK, et al. (2008) Fault rotation and core complex formation: Significant processes in seafloor formation at slow spreading mid-ocean ridges (Mid-Atlantic Ridge, 13-15°N). *Geochemistry, Geophysics, Geosystems* 9, http://dx.doi.org/10.1029/2007GC001699.
Solomon SC, Richardson RM, et al. (1980) Tectonic stresses: Models and magnitudes. *Journal of Geophysical Research* 85: 6086–6092.
Sonder LJ and England PC (1989) Effects of a temperature-dependent rheology on large-scale continental extension. *Journal of Geophysical Research, B, Solid Earth and Planets* 94(6): 7603–7619.
Sonder LJPCE, Wernicke BP, and Christiansen RL (1987) A physical model for Cenozoic extension of Western North America. In: *Continental extensional tectonics, Durham, UK, April 18–20, 1985*. London: Geological Society of London.
Sotin C and Parmentier EM (1989) Dynamical consequences of compositional and thermal density stratification beneath spreading centers. *Geophysical Research Letters* 16: 835–838.
Spencer JE (1984) Role of tectonic denudation in warping and uplift of low-angle normal faults. *Geology* 12(2): 95–98.
Spencer JE and Chase CG (1989) Role of crustal flexure in initiation of low-angle normal faults and implications for structural evolution of the Basin and Range province. *Journal of Geophysical Research* 94: 1765–1775.
Spohn T and Schubert G (1982) Convective thinning of the lithosphere: A mechanism for this initiation of continental rifting. *Journal of Geophysical Research* 87: 4669–4681.
Spyropoulos C, Griffith WJ, et al. (1999) Experimental evidence for different strain regimes of crack populations in a clay model. *Geophysical Research Letters* 26(8): 1081–1084.
Steckler MS, Berthelot F, et al. (1988a) Subsidence in the Gulf of Suez: Implications for rifting and plate kinematics. *Tectonophysics* 153: 249–270.
Steckler MS and ten Brink US (1986) Lithospheric strength variations as a control on new plate boundaries: Examples from the northern Red Sea region. *Earth and Planetary Science Letters* 79: 120–132.
Steckler MS and Watts AB (1978) Subsidence of the Atlantic-type continental margin off New York. *Earth and Planetary Science Letters* 41: 1–13.
Steckler MS, Watts AB, and Thorne JA (1988b) Subsidence and basin modeling at the U.S. Atlantic passive margin. In: Grow JA and Sheridan RE (eds.) *The Atlantic Continental Margin. The Geology of North America*, vol. I-2, pp. 399–416. Boulder, CO: U.S. Geological Society of America.
Stein R, King G, et al. (1988) The growth of geological structures by repeated earthquakes. 2: Field examples of continental dip-slip faults. *Journal of Geophysical Research* 93(B11): 13319–13331.
Stewart JH (1978) Basin-range structure in western North America: A review. In: Smith RB and Eaton GP (eds.) *Cenozoic Tectonics and Regional Geophysics of the Western Cordillera*, pp. 1–31. Boulder, CO: Geological Society of America.
Stock JM and Hodges KV (1989) Pre-Pliocene extension around the Gulf of California and the transfer of Baja California to the Pacific Plate. *Tectonics* 8: 99–115. http://dx.doi.org/10.1029/TC008i001p00099.
Stock JM and Lee J (1994) Do microplates in subduction zones leave a geological record? *Tectonics* 13: 1472–1487.
Su W and Buck WR (1993) Buoyancy effects on mantle flow under mid-ocean ridges. *Journal of Geophysical Research* 98: 12191–12205.
Supak SK, Bohnenstiehl DR, et al. (2006) Flexing is not stretching: An analog study of bending induced cracking. *Earth and Planetary Science Letters* 246: 125–137.
Taylor B, Goodliffe AM, and Martinez F (1999) How continents break-up: Insights from Papua New Guinea. *Journal of Geophysical Research* 104: 7497–7512.
Thatcher W and Hill DP (1991) Fault orientations in extension and conjugate strike-slip environments and their implications. *Geology* 19: 1116–1120.
Tirel C, Brun JP, et al. (2006) Extension of thickened and hot lithospheres: Inferences from laboratory modeling. *Tectonics* 25: 1.
Townend J and Zoback MD (2000) How faulting keeps the crust strong. *Geology* 28(5): 399–402. http://dx.doi.org/10.1130/0091-7613.
Tron V and Brun JP (1991) Experiments on oblique rifting in brittle–ductile systems. In: Cobbold PR (ed.). Experimental and numerical modelling of continental deformation. *Tectonophysics* 188: 71–84.
Tryggvason E (1980) Subsidence events in the Krafla area, north Iceland 1975–1979. *Journal of Geophysics* 47: 141–153.
Tucholke B, Lin J, et al. (1997) Segmentation and crustal structure of the western Mid-Atlantic Ridge flank, 25 degrees 25′-27 degrees 10′N and 0–29 m.y. *Journal of Geophysical Research, B, Solid Earth and Planets* 102(5): 203–210.
Tucholke B, Lin J, et al. (1998) Megamullions and mullion structure defining oceanic metamorphic core complexes on the Mid-Atlantic Ridge. *Journal of Geophysical Research* 103: 9857–9866.
Tucholke BE, Behn MD, Buck WR, and Lin J (2008) The role of melt supply in detachment faulting and the formation of megamullions. *Geology* 35: 455–458. http://dx.doi.org/10.1130/G24639A.1.
Turcotte D and Emmerman SH (1983) Mechanisms of active and passive rifting. *Tectonophysics* 94: 39–50.
Turcotte D and Schubert G (2002) *Geodynamics: Application of Continuum Physics to Geological Problems*. New York: Wiley.
Umhoefer PJ and Dorsey RJ (1997) Translation of terranes: A perspective from the central domain of the Baja California peninsula, Mexico. *Geology* 25: 1007–1010.
Umhoefer PJ (2011) Why did the Southern Gulf of California rupture so rapidly? Oblique divergence across hot, weak lithosphere along a tectonically active margin. *GSA Today* 21.
van Avendonk HJA, Holbrook WS, Nunes GT, et al. (2006) Seismic velocity structure of the rifted margin of the eastern Grand Banks of Newfoundland, Canada. *Journal of Geophysical Research* 111: B11404. http://dx.doi.org/10.1029/2005JB004156.
van Avendonk HJA, Lavier L, and Shillington D (2009) Extension of continental crust at the margin of the eastern Grand Banks, Newfoundland. *Tectonophysics* 468(1–4): 131–148. http://dx.doi.org/10.1016/j.tecto.2008.05.030.
van Wijk JW, Baldridge WS, van Hunen J, et al. (2010) Small-scale convection at the edge of the Colorado Plateau: Implications for topography, magmatism, and evolution of Proterozoic lithosphere. *Geology* 38: 611–614. http://dx.doi.org/10.1130/G31031.1.
van Wijk JW, Huismans RS, Ter Voorde M, and Cloetingh S (2001) Melt generation at volcanic continental margins: No need for a mantle plume. *Geophysical Research Letters* 28: 3995–3998.
van Wijk J, van Hunen J, and Goes S (2008) Small-scale convection during continental rifting: Evidence from the Rio Grande rift. *Geology* 36: 575–578. http://dx.doi.org/10.1130/G24691A.1.
Vanderhaeghe O (2004) Structural development of the Naxos migmatite dome. In: Whitney DL, Teyssier C, and Siddoway CS (eds.) *Gneiss Domes in Orogeny*, pp. 211–227. Boulder, CO: Geological Society of America, Special Paper 380.
Vanderhaeghe O and Teyssier C (2001) Partial melting and flow of orogens. *Tectonophysics* 342: 451–472.
Varga RJ (2003) The sheeted dike complex of the Troodos Ophiolite and its role in understanding mid-ocean ridge processes. In: Dilek Y and Newcomb S (eds.) *Ophiolite Concept and the Evolution of Geological Thought*, pp. 323–336. Boulder, CO: Geological Society of America, Special Paper 373.
Vening-Meisnez FA (1950) Les grabens Africains résultants de compression ou de tension de la croûte terrestre? *Mémoires de l'Institut Royal Colonial Belge* 21: 539–552.
Venkataraman A, Nyblade AA, et al. (2004) Upper mantle Q and thermal structure beneath Tanzania, East Africa from teleseismic P wave spectra. *Geophysical Research Letters* 31: 15.
Wallace LM, Stevens C, Silver E, et al. (2004) GPS and seismological constraints on active tectonics and arc-continent collision in PNG: Implications for mechanics of microplate rotations in a plate boundary zone. *Journal of Geophysical Research* 109: B05404. http://dx.doi.org/10.1029/2003JB002481.
Wallner H and Schmeling H (2010) Rift induced delamination of mantle lithosphere and crustal uplift: A new mechanism for explaining Rwenzori Mountains' extreme elevation? *International Journal of Earth Sciences* 99: 1511–1524. http://dx.doi.org/10.1007/s00531-010-0521-6.
Watts AB (2001) *Isostasy and Flexure of the Lithosphere*. Cambridge: University of Cambridge.

Watts AB and Ryan WBF (1976) Flexure of the lithosphere and continental margin basins. *Tectonophysics* 36: 25–44.
Wdowinski S and Axen GJ (1992) Isostatic rebound due to tectonic denudation: A viscous flow model of a layered lithosphere. *Tectonics* 11: 303–315.
Webb LE, Baldwin SL, Little TA, and Fitzgerald PG (2008) Can microplate rotation drive subduction inversion? *Geology* 36: 823–826.
Weissel JK and Karner G (1989) Flexural uplift of rifts flanks due to mechanical unloading of the lithosphere during extension. *Journal of Geophysical Research* 94: 13919–13950.
Wernicke B (1981) Low-angle normal faults in the Basin and Range province: Nappe tectonics in an extending orogen. *Nature* 291: 645–648.
Wernicke B (1985) Uniform-sense normal simple shear of the continental lithosphere. *Canadian Journal of Earth Sciences* 22: 108–125.
Wernicke BP (1992) Cenozoic extensional tectonics of the U.S. Cordillera. In: Burchfield BC, Lipman PW, and Zoback ML (eds.). *The Cordilleran Orogen: Conterminous U.S*, vol. G-3, pp. 553–583. Boulder, CO: Geological Society of America.
Wernicke B and Axen GJ (1988) On the role of isostasy in the evolution of normal fault systems. *Geology* 16: 848–851.
White NJ (2004) Using prior subsidence data to infer basin evolution. In: Curtis A and Wood R (eds.) *Geological Prior Information: Informing Science and Engineering*, pp. 211–224. London: Geological Society, Special Publication No. 239.
White RS, MacKenzie D, and O'Nions RK (1992) Oceanic crustal thickness from seismic measurements and rare earth element inversions. *Journal of Geophysical Research* 97: 19683–19715. http://dx.doi.org/10.1029/92JB01749.
White RS and McKenzie DP (1989) Magmatism at rift zones: The generation of volcanic continental margins and flood basalts. *Journal of Geophysical Research* 94: 7685–7729.
White RS and McKenzie DP (1995) Mantle plumes and flood basalts. *Journal of Geophysical Research* 94: 17543–17585.
Whitmarsh RB, Manatschal G, and Minshull TA (2001) Evolution of magma-poor continental margins from rifting to seafloor spreading. *Nature* 413(6852): 150–154. http://dx.doi.org/10.1038/35093085.
Whitney DL, Teyssier C, Rey P, and Buck WR (2013) Continental and oceanic core complexes. *Geological Society of America Bulletin* 125: 273–298. http://dx.doi.org/10.1130/B30754.1.
Whitney DL, Teyssier C, and Vanderhaeghe O (2004) Gneiss domes and crustal flow. In: Whitney DL, Teyssier C, and Siddoway CS (eds.) *Gneiss Domes in Orogeny*, p. 393. Boulder, CO: Geological Society of America, Special Paper 380.
Wiens DA and Stein S (1984) Intraplate seismicity and stresses in young oceanic lithosphere. *Journal of Geophysical Research* 89: 11442–11464.
Willett SD and Pope DC (2004) Thermo-mechanical models of convergent orogenesis: Thermal and rheologic dependence of crustal deformation. In: Karner GD, Taylor B, Driscoll NW, and Kohlstedt DL (eds.) *Rheology and Deformation of the Lithosphere at Continental Margin*, pp. 179–222. New York, NY: Columbia University Press.
Wills S and Buck WR (1997) Stress field rotation and rooted detachment faults: A test of fault initiation models. *Journal of Geophysical Research* 102(20): 20503–20514.
Wilson JT (1966) Did the Atlantic close and then re-open? *Nature* 211: 676–681.
Withjack MO and Schlische RW (2006) Geometric and experimental models of extensional fault-bend folds. In: *Analogue and Numerical Modelling of Crustal-Scale Processes*, pp. 285–305. London: Geological Society Special, Publication No. 253.
Wolf CJ, Bjarnason ITh, VanDecar JC, and Solomon SC (1997) Seismic structure of the Iceland mantle plume. *Nature* 385: 245–247.
Yin A (1989) Origin of regional, rooted low-angle normal faults: A mechanical model and its tectonic implications. *Tectonics* 8: 469–482.
Yin A and Dunn J (1992) Structural and stratigraphic development of the Whipple-Chemehuevi detachment fault system, southeastern California; implications for the geometrical evolution of domal and basinal low-angle normal faults. *Geological Society of America Bulletin* 104: 659–674
Zorin YA (1981) The Baikal Rift: An example of the intrusion of asthenospheric material into the lithosphere as the cause of disruption of lithospheric plates. *Tectonophysics* 73(1–3): 91–104.
Zuber MT and Parmentier EM (1986) Lithospheric necking: A dynamic model for rift morphology. *Earth and Planetary Science Letters* 77: 373–383.

This page intentionally left blank

6.09 Mountain Building: From Earthquakes to Geologic Deformation

J-P Avouac, University of Cambridge, Cambridge, UK

© 2015 Elsevier B.V. All rights reserved.

6.09.1	**Introduction**	382
6.09.2	**Geodynamic Setting of the Himalayas**	382
6.09.2.1	The Himalayas as a Result of the India–Asia Collision	382
6.09.2.2	Variation of Crustal Thickness Across the Himalayas	383
6.09.2.3	Geologic Architecture of the Himalayan Range and Southern Tibet	385
6.09.2.4	Metamorphism	388
6.09.2.5	Topography Across the Himalayan Range	389
6.09.2.6	Crustal-Scale Structural Models of the Himalaya	389
6.09.2.7	Geophysical Constraints on the Structure of the Crust	390
6.09.3	**Holocene Deformation and Erosion**	390
6.09.3.1	Active Thrusting and Folding in the Sub-Himalayas	390
6.09.3.1.1	Structural evolution of the sub-Himalayas	391
6.09.3.1.2	River incision across the sub-Himalayas	391
6.09.3.1.3	Converting incision rates to uplift rates in the sub-Himalayas	392
6.09.3.1.4	Converting uplift rates to horizontal shortening from area balance	393
6.09.3.1.5	Converting uplift rates to horizontal shortening from the fault-bend fold model	394
6.09.3.2	River Incision, Erosion, and Uplift Across the Range	395
6.09.3.2.1	Fluvial incision across the whole range	395
6.09.3.2.2	Denudation across the whole range	395
6.09.3.2.3	Holocene kinematics of overthrusting along the MFT–MHT	396
6.09.4	**Longer-Term Geologic Deformation and Exhumation**	397
6.09.4.1	Foreland Deposition: A Record of Underthrusting	397
6.09.4.2	Structural Evolution of the Thrust Package	398
6.09.4.3	Exhumation of the Lesser and High Himalayas: A Record of Overthrusting	399
6.09.4.4	Overthrusting, Underthrusting, and Accretion	400
6.09.5	**Kinematic and Mechanical Models of Crustal Deformation**	401
6.09.5.1	Thermokinematic Model of the Evolution of the Range Since 15 Ma	402
6.09.5.2	Modeling the Topography	403
6.09.5.3	Modeling Deformation and Surface Processes Based on Continuum Mechanics	403
6.09.5.3.1	Model implementation	403
6.09.5.3.2	Modeling results	406
6.09.6	**Geodetic Deformation and the Seismic Cycle**	407
6.09.6.1	Large Earthquakes in the Himalayas	407
6.09.6.2	Geodetic Deformation in the Nepal Himalayas	409
6.09.6.3	Microseismic Activity in the Nepal Himalayas	410
6.09.6.4	What Controls Interseismic Coupling on the MHT?	411
6.09.6.5	A Model of the Seismic Cycle in the Central Nepal Himalayas	413
6.09.6.6	Geodetic Deformation, Seismic Coupling, and Recurrence of Large Earthquakes in the Himalayas	413
6.09.6.7	Is Interseismic Strain Stationary?	415
6.09.7	**Discussion**	417
6.09.7.1	The Critical Wedge Theory: Does It Apply to the Himalayas?	417
6.09.7.2	Low Friction on the Main Himalayan Thrust	420
6.09.7.3	Importance of the Brittle–Ductile Transition	421
6.09.7.4	Metamorphism During Underthrusting	421
6.09.7.5	How Does the Steep Front of the High Himalayas Relate to Tectonics, Erosion, and Climate?	423
6.09.7.6	The Elevation and Support of Mountain Ranges: Effect of Climate and Lower Crustal Flow	424
6.09.7.6.1	Height and width of a critical brittle wedge	424
6.09.7.6.2	Effect of ductile deformation in the lower crust	424
6.09.7.6.3	The fate of the Indian crust and mantle lithosphere	425
6.09.8	**Conclusions**	425
Acknowledgments		426
References		426

6.09.1 Introduction

Mountain ranges are the most spectacular manifestation of continental dynamics. The fact that some mountain ranges were able to maintain their topography over tens of millions years, while their erosion was feeding large sedimentary basins, is unambiguous evidence that tectonic forces can cause sustained uplift of subsidence of the continental crust. Geologists noticed quite early on that most mountain ranges are contractional orogens, the result of horizontal contraction of the continental crust, and that they tend to form long belts separating domains with often quite different geologic history (e.g., Argand, 1924; Willis, 1891). A tour of active mountain ranges on earth today shows that contractional mountain ranges can arise in a variety of contexts. Some have formed along converging plate boundaries as the result of collisions that can involve two continents (along the Himalayas, e.g., as detailed in this chapter), a continent and an island arc (in Taiwan, e.g., Malavieille et al., 2002a), or a continent and an oceanic plateau (the Southern Alps of New Zealand, e.g., Walcott, 1998). Contractional mountain ranges can also form along subduction zones without necessarily having such collisional features. In the Andes, for example, the stresses transmitted across a subduction zone appear to be sufficient to cause trench-perpendicular shortening (e.g., Lamb, 2006), probably because high heat flow in the back-arc zone weakens the continental lithosphere (Hyndman et al., 2005). Mountain ranges are thus often closely associated with converging plate boundaries. However, active mountain building can also occur far away from plate boundaries, the Tian Shan, in central Asia, being an outstanding example (e.g., Avouac et al., 1993; Hendrix et al., 1992).

Mountains are major players in the interactions between solid Earth and its climate. Surface processes play a key role in the mechanics of mountain building not only because of the isostatic response to erosion (Molnar and England, 1990a) but also because they contribute to focalizing crustal deformation leading to a positive feedback between erosion at the surface and shortening of the crust (Avouac and Burov, 1996; Koons, 1987). Climate may also influence the mechanics of mountain building along subduction zones, through its influence on the amount of sediments delivered to the trench and hence on the mechanical coupling across the plate boundary (Lamb and Davis, 2003). Mountain ranges affect atmospheric circulation and the distribution of precipitation and consequently drainage patterns (Ramstein et al., 1997; Raymo and Ruddiman, 1992; Ruddiman and Kutzbach, 1991). Their erosion influences eventually their elevation through isostasy and influences the chemistry of the atmosphere through a variety of chemical reactions and through burial of organic matter (Derry and France-Lanord, 1997; France-Lanord and Derry, 1997; Kerrick and Caldeira, 1993, 1999). Finally, mountain ranges and their piedmonts are also a primary locus of geohazards, earthquakes, landslides, and floods in particular.

For all these reasons, understanding better orogenic processes is a fundamental issue in geology. The anatomy of mountain ranges, and the tectonic processes at work deep in the crust, might be studied from the investigation of the exhumed core of ancient orogens. A lot of insight on orogenic processes can also be gained by ausculting orogens that are actively deforming. This chapter illustrates that the study of active processes can shed light on how mountain ranges form and evolve over a geologic period of time.

This chapter focuses on the Himalayas which is undoubtedly the world's most impressive example of an active collisional orogen. This incomparably long and high mountain arc is the setting of rapid, ongoing crustal shortening and thickening, intense denudation driven by the monsoon climate, and frequent large earthquakes. The relation of this range to plate tectonics has long been recognized (Dewey and Bird, 1970). As reviewed in this chapter, we now have a reasonably solid understanding of the structure of the range, of its petrometamorphic history, and of the kinematics of its active deformation. The long-term geologic history of the range – from several millions to a few tens of millions of years – has been documented by structural, thermobarometric, and thermochronological studies. Morphotectonic investigations have revealed its evolution over the past several thousands or tens of thousands of years. And, finally, geodetic measurements and seismological monitoring have revealed the pattern of strain and stress buildup over several years. This chapter shows that the results of these investigations can be assembled into a simple, coherent picture of the structure and evolution of the range. Some emphasis is put on surface processes. These processes carved the morphological features that are used to deduce vertical displacements. They generated the molasse deposits that filled the subsiding foreland basin, providing a stratigraphic record of mountain building. They influenced the evolution of the range by changing its thermal structure and stress field via redistribution of surface mass. Surface processes therefore contribute to recording the geologic history of an orogen, and they also participate in the mountain-building process itself.

The Himalayas is consequently one of the best places on Earth where the geologic history of a mountain belt can be analyzed in view of currently ongoing tectonic processes. Although some aspects might be specific to the setting of this mountain range, the tectonic processes at work there are presumably the same as those at work in any other contractional mountain range.

6.09.2 Geodynamic Setting of the Himalayas

6.09.2.1 The Himalayas as a Result of the India–Asia Collision

The Himalayan arc and the Tibetan Plateau formed as a result of the collision between India and Asia (e.g., Powell and Conaghan, 1973). The two continents were once separated by the Tethys Sea, which was subducted beneath the southern margin of Asia (**Figure 1**). The age of the onset of collision is still debated. It is estimated to be between ~65 and 45 Ma depending on the chosen approach to that question, but most observations point to an age of about 50 Ma (e.g., DeSigoyer et al., 2000; Ding et al., 2005; Jaeger et al., 1989; Najman et al., 2010; Patriat and *Achache*, 1984; Rowley, 1996; Searle et al., 1990). A recent analysis of paleolatitudes from sites just north and south of the suture zone in southwestern Tibet shows that the collision occurred in that area between

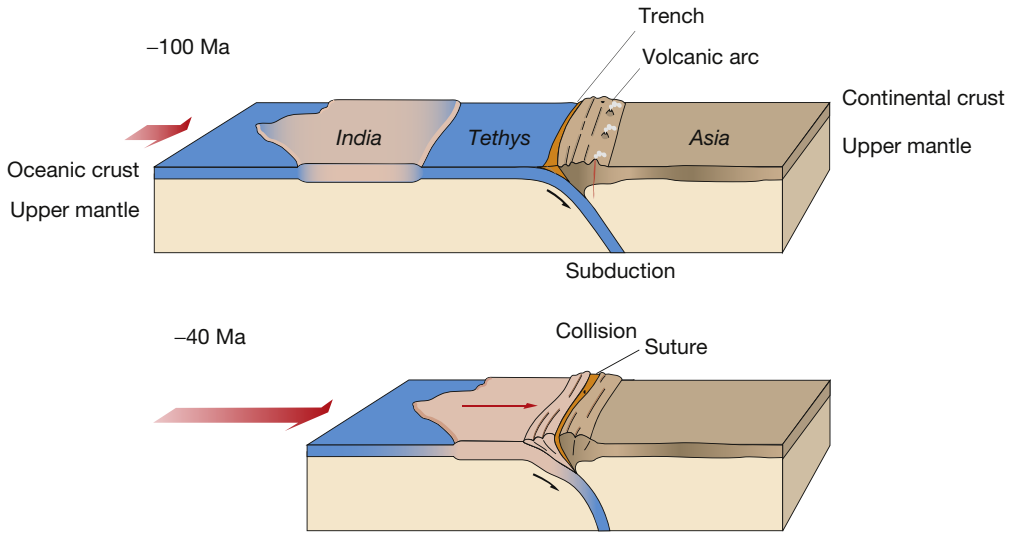

Figure 1 Prior to the collision, an ocean, the Tethys Sea, used to separate the northern margin of India and Eurasia. The southern margin of Asia was an active margin with a subduction zone similar, for example, to the Andean subduction zone bordering the western margin of South America. Modified from Malavieille J, Marcoux J, and De Wever P (2002) L'ocean perdu. In: *Himalaya-Tibet*, *Le choc des continents*, pp. 32–39. Paris, France: CNRS Editions et Museum national de'Histoire naturelle.

44 and 55 Ma (95% confidence interval; Meng et al., 2012). The timing and paleolatitude of the collision (~24° N) require that the northern margin of continental India used to lay about 1500 km north of present Indian Craton (defining 'Greater India'). In fact, it seems that the rise of the topography during a continental collision might postdate significantly the onset of the tectonic collision, defined as the time when the continental margin on the subducting plate first encounters the trench. For example, the northern Australian margin has started colliding with the Banda Arc in the Pliocene resulting in a well-developed fold-and-thrust belt, but no significant mountain range has formed yet (Bowin et al., 1980). This is probably because, in the early stage of a collision, subduction of the cold continental crust can occur as required from the observation of high-pressure metamorphic rocks exhumed quite early in the history of the collision that has been suggested from analogue (Chemenda et al., 2000) and thermomechanical modeling (Toussaint et al., 2004a). The first stratigraphic evidence for the rise of the topography, namely, the transition from passive margin sedimentation to forearc sedimentation, is observed in the Ypresian (50.7 Ma) in the western Himalayas (Beck et al., 1995) and seems younger than middle Lutetian (40 Ma) in the central eastern Himalayas, suggesting that suturing began in the west and migrated in the east (e.g., Rowley, 1996). Reconstruction of the plate motion of India relative to Asia (**Figure 2(a)**) shows an abrupt decrease in the convergence rate, probably resulting from the collision, from ~15 to 4–5 cm year^{-1} at *c*.50 Ma (**Figure 2(b)**; Copley et al., 2010; Molnar and Tapponnier, 1975; Patriat and Achache, 1984). Since that time, India has indented ~3000 km into Asia, producing a combination of lateral escape and crustal thickening that has given rise to the highest topographic features on Earth (e.g., Harrison et al., 1992; Molnar and Tapponnier, 1975; Tapponnier et al., 2001; **Figure 3**). The pattern and kinematics of active faults in Asia and geodetic measurements clearly show a combination of strike-slip faulting and crustal shortening, but the respective contribution of these two mechanisms to the overall deformation remains a matter of debate (Avouac and Tapponnier, 1993; Larson et al., 1999; Meade, 2007; Molnar and Tapponnier, 1975; Wang et al., 2001; Zhang et al., 2004; **Figure 4**). At present, northern India is moving ~35 mm year^{-1} along a N15° E azimuth (31 mm year^{-1} along a N10° E azimuth for a point located at the western Himalayan syntaxis and 38 mm year^{-1} along a N20° E azimuth for a point located at the eastern Himalayan syntaxis; Bettinelli et al., 2006; **Figure 2(b)**). This rate is nearly 25% less than that suggested by the Indian Plate motion model derived from the opening of the Indian Ocean (**Figure 2(b)**). Crustal shortening across the Himalayas, estimated at 19 ± 2.5 mm year^{-1} (see **Section 6.09.6**), absorbs nearly half of the current convergence rate between India and Eurasia.

6.09.2.2 Variation of Crustal Thickness Across the Himalayas

The remarkable elevation of the Himalayas and Tibetan Plateau unambiguously results from an extremely thick crust. Various seismic experiments conducted in southern Tibet all suggest a crustal thickness on the order of 70–80 km (Him et al., 1984; Kind et al., 1996; Mitra et al., 2005; Wittlinger et al., 2009; Zhao et al., 1993). For comparison, the crustal thickness of the Indian shield is estimated at 40–44 km (Mitra et al., 2005; Saul et al., 2000; **Figure 5**). Receiver function studies across the Himalayas of central Nepal (Hetenyi et al., 2006, 2007; Nabelek et al., 2009; Wittlinger et al., 2009), eastern Nepal (Schulte-Pelkum et al., 2005), and northeastern India (Mitra et al., 2005) show the Moho can be traced as a continuous feature across the arc. This observation agrees with the modeling of gravity measurements: The Bouguer anomaly in India and in Tibet primarily indicates local Airy compensation, but important deviations from Airy isostasy are observed in the Himalayan range and its foreland (Cattin et al., 2001; Jin

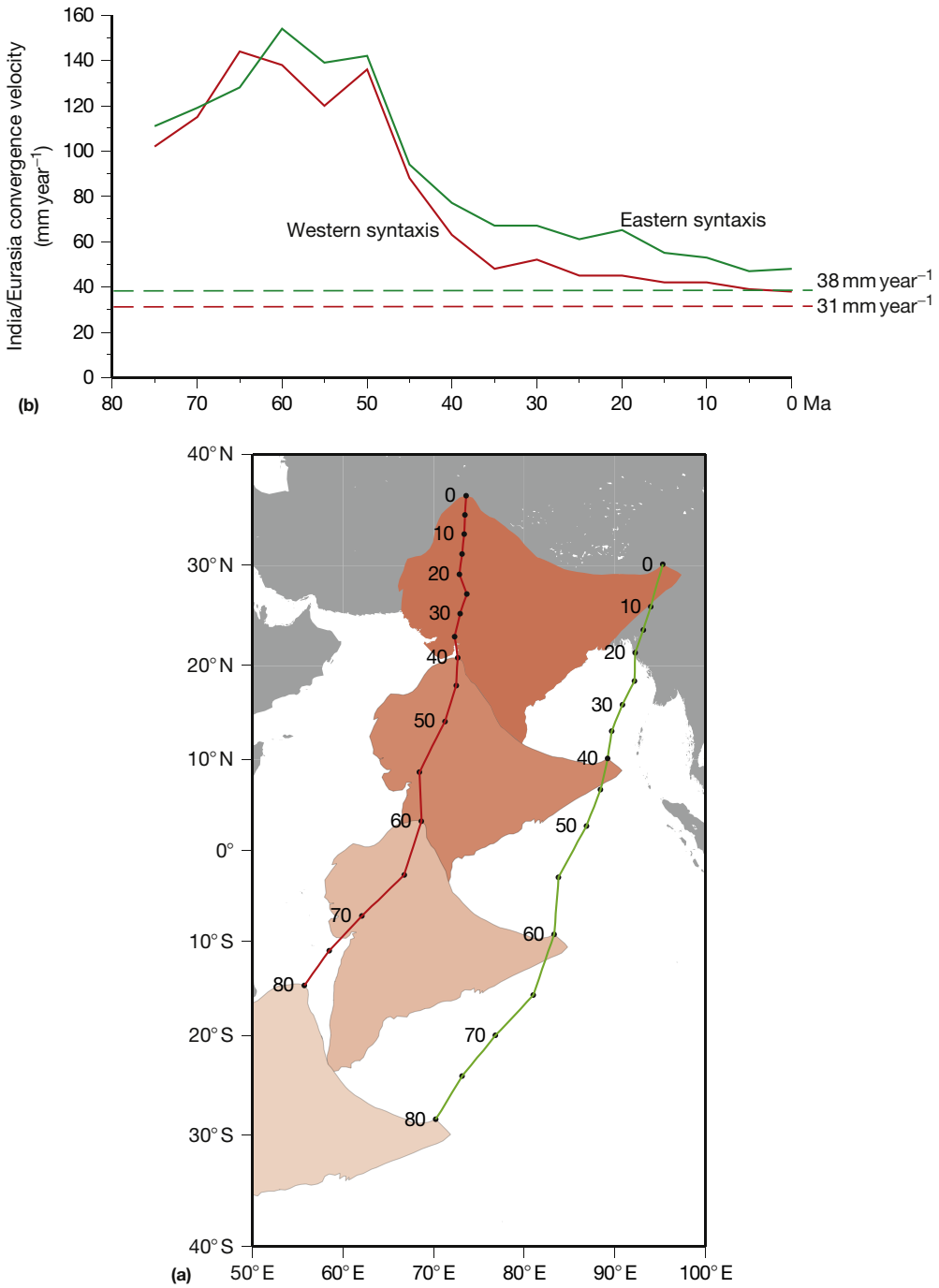

Figure 2 Plate motion of India relative to Eurasia (a) and convergence rates (b) over the last 80 Ma. This kinematics was obtained from the recent synthesis of the magnetic anomalies of the Indian Ocean (Royer and Patriat, 2002; see Patriat and Segoufin, 1988, for a former similar analysis). The India/Africa relative motion derived from the analysis of this data set was referenced to Eurasia through an Africa/North America and North America/Eurasia plate circuit across the Atlantic sea. Convergence rates were computed at points attached to the Indian Plate located at the current position of the eastern and western Himalayas. The modern velocities computed at these same points from a plate model determined from geodetic measurements (Bettinelli et al., 2006) are shown for comparison (dashed lines). The abrupt decrease of the convergence rate starting at about 50 Ma is thought to relate to the onset of the India–Asia continental collision (Molnar and Tapponnier, 1975).

et al., 1996; Lyon-Caen and Molnar, 1983, 1985) and are particularly evident in the gravity data across the central Nepal Himalayas (Figure 5). Values more negative than those expected from local isostasy are observed over the Gangetic Plain, indicating some mass deficit there. By contrast, mass excess is indicated below the adjacent Himalayan range. These deviations are the signature of flexural support of the range, meaning that the weight of the Himalayas is supported

by the strength of the underthrusting Indian Plate. The steep gravity gradient, on the order of mGal km^{-1}, beneath the High Himalayas, suggests a local steepening of the Moho dip. Flexural modeling of a thin elastic plate overlying an inviscid fluid (Lyon-Caen and Molnar, 1983; 1985; Maggi et al., 2000) successfully reproduces the observed gravity anomalies. However, this kind of model requires that some forces or momentum be exerted on the flexed plate in addition to the load of the high topography (Lyon-Caen and Molnar, 1983). In order to account for the locally steeper gradient of gravity anomalies (Figure 5), this kind of modeling also requires an abrupt weakening of the Indian Plate beneath the high range. This weakening could reflect the influence of the thermal structure of the range on crustal rheology. The kinematics of underthrusting results in a thermal structure with relatively high temperatures at midcrustal depths, favoring ductile flow within the crust and implying some decoupling between the upper crust and the upper mantle and an abrupt decrease of the apparent flexural rigidity of the lithosphere (Burov and Diament, 1995). If the thermal structure and its influence on crustal rock density and rheology are taken into account, there is indeed no need for additional forces other than the weight of the topography to result in the downwarping of the Indian lithosphere under the load of the range and sediments in the foreland (Figure 5), as is shown in thermomechanical models (Cattin et al., 2001; Hetenyi et al., 2006).

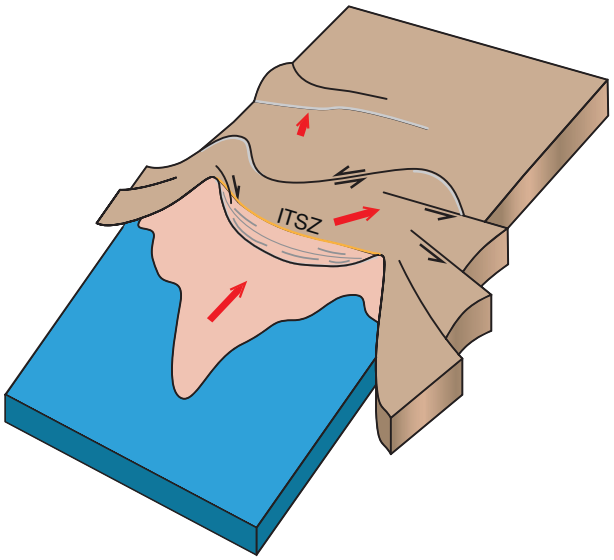

Figure 3 Sketch showing how indentation of India into Eurasia since the onset of the collision has been absorbed by a combination of crustal thickening and lateral escape.

6.09.2.3 Geologic Architecture of the Himalayan Range and Southern Tibet

Relics of the Tethys Sea can now be traced along the Indus–Tsangpo suture zone (ITSZ) (e.g., Burg, 1983; Searle et al., 1987) well north of the Himalayan summits (Figure 6). To the south, Cambrian to Eocene Tethyan sediments deposited on the northern passive margin of the Indian continent were sutured to the volcanic and plutonic rocks of the once-active margin of Eurasia (Burg et al., 1987; Searle et al., 1987). Now uplifted to elevations of ~5000 m, they were intensely deformed, probably mostly in the early 'Alpine' period of the collision (Burg et al., 1984; Ratschbacher, 1994), although there is evidence that thrust faulting in southern Tibet probably persisted until Middle Miocene time (Yin et al., 1999).

A major normal fault separates the Tethyan sedimentary cover from the High Himalayan crystalline units; initially called the North Himalayan Normal Fault (Burg et al., 1984),

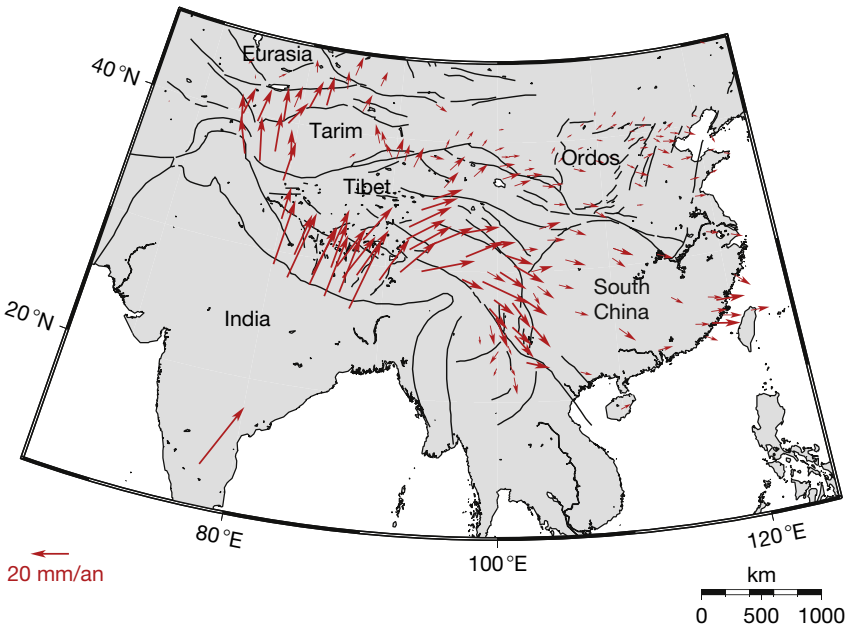

Figure 4 Velocities, relative to stable Eurasia, measured from GPS over an ~10-year period. Data from Wang et al. (2001).

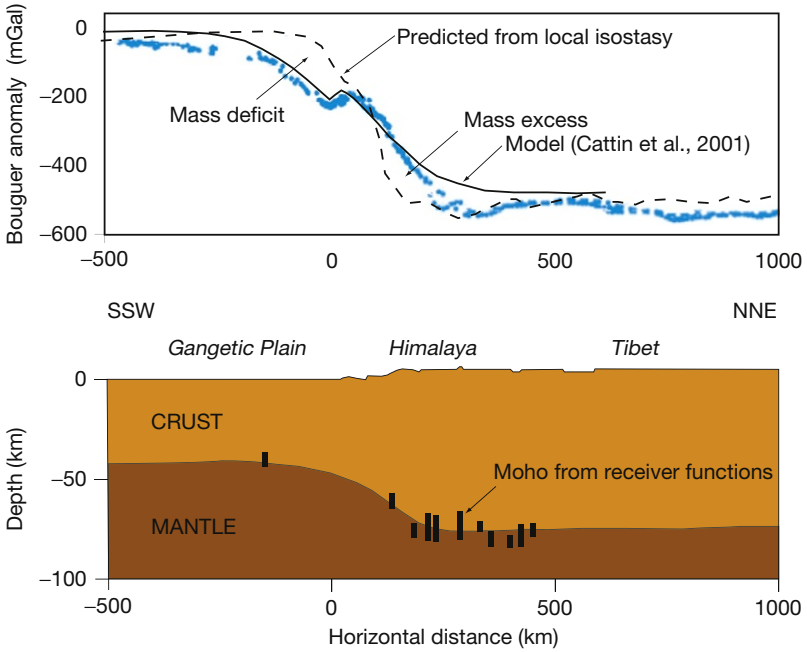

Figure 5 The Bouguer anomalies along an N18° E profile across the Himalayas of central Nepal (modified from Cattin R, Martelet G, Henry P, Avouac JP, Diament M, and Shakya TR (2001) Gravity anomalies, crustal structure and thermo-mechanical support of the Himalaya of Central Nepal. *Geophysical Journal International* 147(2): 381–392 and Hetenyi G, Cattin R, Vergne J, and Nabelek JL (2006) The effective elastic thickness of the India Plate from receiver function imaging, gravity anomalies and thermomechanical modelling, *Geophysical Journal International* 167(3): 1106–1118) (approximately section AA′ in **Figure 7**). All the data within a 30 km wide swath were projected onto the section. Several data sets were merged with accuracies ranging from about 0.5 to 7 mGal (Bureau Gravimétrique International database; Abtout, 1987; Sun, 1989; Van de Meulebrouck, 1983). Thick vertical bars show Moho picks on receiver functions beneath Tibet (Kind et al., 1996) and beneath the Indian shield (Saul et al., 2000). Also shown is the Moho across eastern Nepal Himalayas determined from the HIMNT experiment (dashed line; Schulte-Pelkum et al., 2005) and from the Hi-CLIMB experiment (Hetenyi et al., 2006). The thick line shows the expected Bouguer anomaly in the case of isostatic compensation of a crust with 2.67 density over an upper mantle with 3.27 density (computed from the topography smoothed with a 50 km wide Gaussian). The thin line is the Moho computed from a mechanical model that accounts for the low-density sediments in the foreland, the rheological layering of the crust, and its dependence on the thermal structure (Cattin et al., 2001).

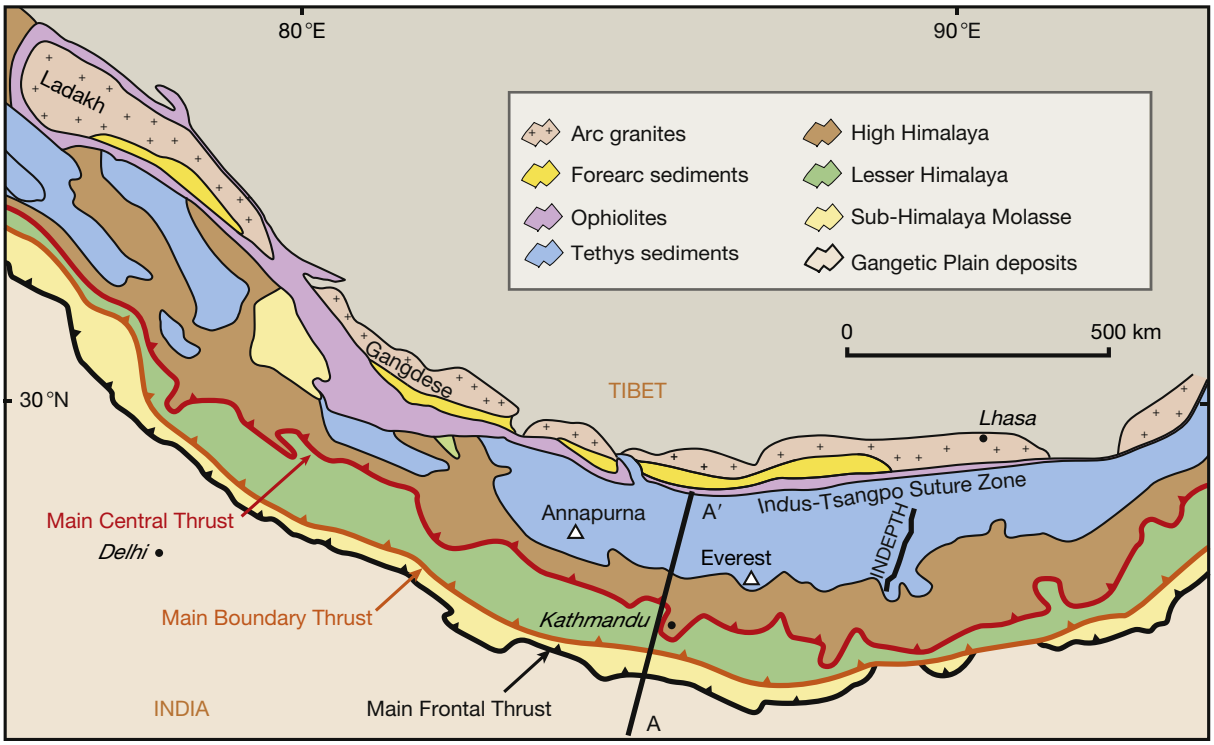

Figure 6 Simplified geologic map of Himalayan arc. For clarity, High Himalayan nappes over the Lesser Himalayas are not represented. Locations of section AA′ and INDEPTH I reflection line (e.g., Hauck et al., 1998) are indicated. Geologic map modified from Malavieille et al., 2002b.

its later appellation as the South Tibetan Detachment (STD) is more commonly used in the *literature* (Burchfiel et al., 1992). Motion on the STD is thought to have resumed sometime between 15 and 20 Ma (e.g., Searle et al., 1997).

To the south, crustal shortening chiefly resulted from deformation on a limited number of major thrust faults. From north to south, these are the Main Central Thrust (MCT), the Main Boundary Thrust (MBT), and the Main Frontal Thrust (MFT) faults (**Figures 7** and **8**; e.g., Gansser, 1964; Le Fort, 1975; Meigs et al., 1995; Nakata, 1989; Yeats et al., 1992). These faults were likely activated in a forward-propagating sequence.

The major Himalayan thrust faults separate domains with contrasting geology:

The foreland basin. The Indo-Gangetic Plain is a 200–300 km wide foreland basin in which a fraction of the material eroded from the neighboring rising topography is trapped. Most of the material is transported by the Ganges drainage system and ultimately delivered to the Bengal fan. Several kilometers of Cenozoic molasse deposits have accumulated over the Archean to Early Proterozoic metamorphic Indian basement rocks.

The foreland fold-and-thrust belt. North of the Indo-Gangetic Plain, the sub-Himalayas is a zone of thin-skinned tectonics bounded to the south by the MFT and to the north by the MBT (e.g., Delcaillau, 1986; Lavé and Avouac, 2000; Mugnier et al., 1999). Tertiary siltstones, sandstones, and conglomerates have been scraped off the basement, folded, and faulted at the front of the advancing range, forming a typical foreland fold-and-thrust belt. In central Nepal, the sections along Surai Khola (Appel and Rossler, 1994; Corvinus, 1988), Tinau Khola (Gautam and Appel, 1994), Arung Khola (Tokuoka et al., 1986), and Bakeya Khola (Harrison et al., 1993) expose a 3500–5500 m thick sedimentary sequence that was deposited between 14 and 1 Ma. In places, the fold belt involves slices of pre-Tertiary sediments, which are reddish-maroon quartzites and gray shales with some doleritic intrusions (Lavé and Avouac, 2000), similar to Vindhyan units drilled at Raxaul (Sastri et al., 1971). Pre-Tertiary units involved in the sub-Himalayan fold belt are also reported 50 km east of the section along the Bagmati, north of the Kamla Khola (Mascle and Hérail, 1982). These observations indicate that the decollement underlying the fold belt must lie on top of the Indian basement, at 5–6 km depth along the section across central Nepal (**Figure 8**).

The internal zones. North of the MBT, the Lesser Himalayan units consist of low-grade metasediments: phyllite, quartzite, and limestone of Devonian or older ages (Upreti, 1999; **Figures 7** and **8**). In some places, overlying Tertiary units have been preserved, particularly sandstones and siltstones of the Dumri Formation (Sakai, 1985). This formation consists of Himalayan foreland sediments that were deposited between *c.*16 and 21 Ma, as indicated by dating of detrital muscovite and magnetostratigraphy (DeCelles et al., 1998). The section across the Himalayas of central Nepal near Kathmandu is characterized by a crystalline sheet forming a klippe, usually referred to as the Kathmandu Klippe, on top of the Lesser Himalayan units (Stöcklin et al., 1980). The resistance to erosion of the crystalline units, combined with its uplift along the MBT, is chiefly responsible for the impressive relief of the Mahabharat south of the Kathmandu basin (**Figure 8**). The crystalline units, consisting mainly of schist and gneiss intruded by Late Cambrian to Ordovician granites (Schärer and Allegre, 1983), are overlain by Cambrian to Eocene Tethyan sediments (Stöcklin et al., 1980). Thermobarometric studies indicate that this crystalline sheet was thrust over the Dumri Formation, particularly in the Tansen area (Bollinger et al., 2004a; Sakai et al., 1999). The basal 'Mahabharat' thrust can be interpreted as the southern extension of the MCT, although the possibility that it is a distinct thrust fault rooting below the MCT cannot be excluded (e.g., Upreti, 1999). North of the klippe, the foliation in the Lesser Himalayan schist describes a large antiformal structure, called the Pokhara–Gorkha anticlinorium (Pêcher, 1989). This structure, as

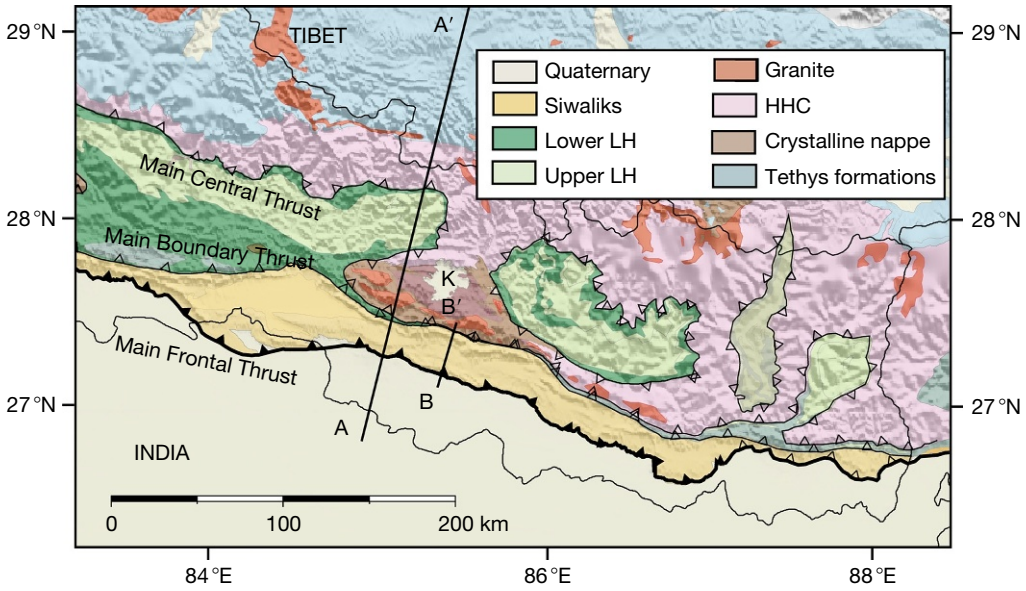

Figure 7 Geologic map of central and eastern Nepal (source data: Department of Mines and Geology, Nepal) with location of sections AA′ (**Figure 8**) and BB′ (**Figure 11**). K, Kathmandu basin.

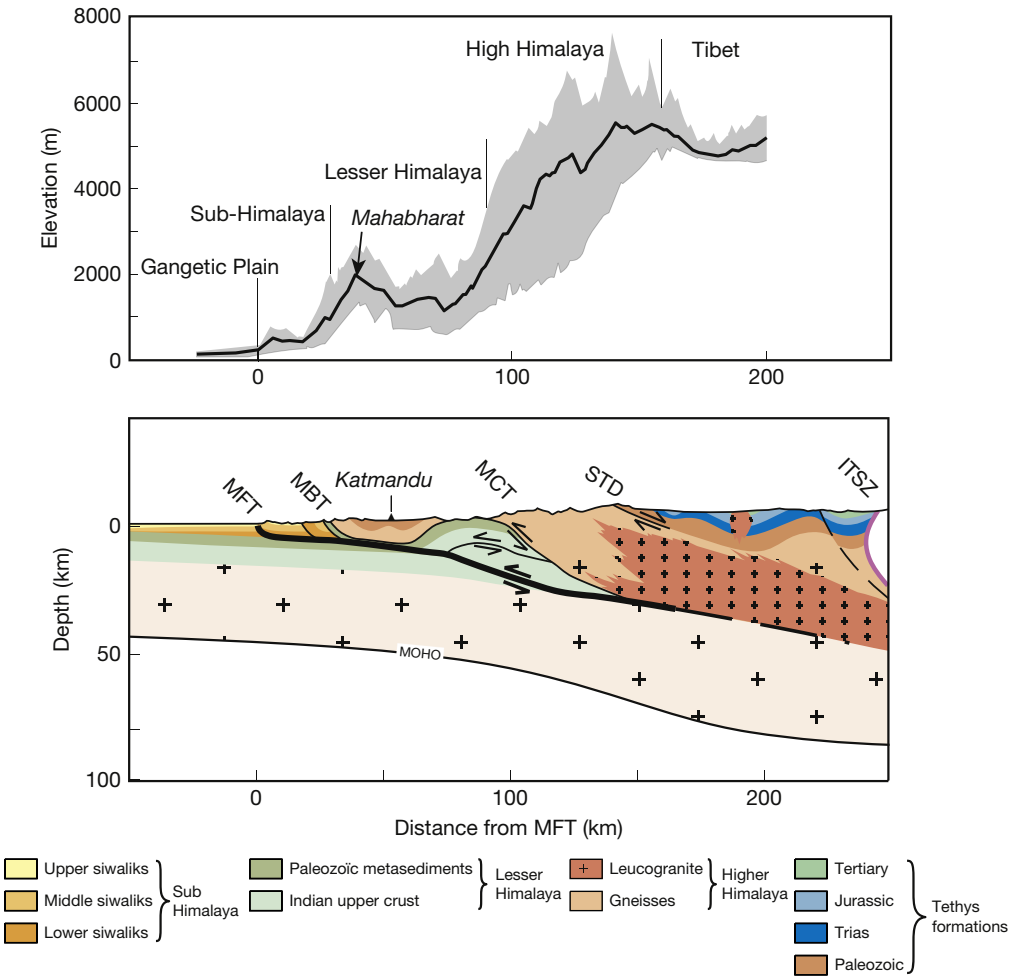

Figure 8 Geologic section across central Nepal Himalayas at the longitude of Kathmandu. Thick line shows the Main Himalayan Thrust fault, MHT, which reaches the surface at the front of the Siwalik Hills, where it coincides with the MFT. The Main Boundary Thrust fault separates Lesser Himalayan metasediments from the molasse deposits of the sub-Himalayas (the Siwalik Hills). The Main Central Thrust fault (MCT) places the higher-grade metamorphic rocks of the High Himalayan crystalline units over the Lesser Himalayan metasediments. (top) Mean, maximum, and minimum elevation within a 50 km wide swath centered on section AA′ (see **Figures 6** and **7** for location of section). Several geographical domains are distinguished from north to south: Tibet, High Himalayas, Lesser Himalayas, sub-Himalayas, and the Gangetic Plain.

shown in **Figure 8**, has been interpreted as a hinterland dipping duplex structure (Brunel, 1986), and it has been recognized on most sections across the Nepal Himalayas (DeCelles et al., 2001; Robinson et al., 2003; Schelling and Arita, 1991; Schelling, 1992) and in Kumaon, India (Celerier et al., 2009; Srivastava and Mitra, 1994). The High Himalayan units consist of amphibolite-grade schist intruded by large leucogranitic plutons. Neodymium isotopic provenance studies suggest that Lesser Himalayan metasediments were derived from the Indian Craton, while the High Himalayan rocks most probably correspond to an exotic terrane accreted onto India in the early Paleozoic (Robinson et al., 2001).

6.09.2.4 Metamorphism

As early as the mid-nineteenth century, field geologists noticed an upward increase of metamorphic grade across the Himalayas (Mallet, 1874; Medlicott, 1864; Oldham, 1883a). A number of field studies have since documented this 'inverted' gradient (e.g., Le Fort, 1975; Pêcher, 1989). The inverted gradient is most obvious within and close to the MCT zone, especially along the Everest section, which has received particular attention (Brunel and Kienast, 1986; Catlos et al., 2002; Law et al., 2004; Lombard, 1953; Lombardo and Rolfo, 2000). Metamorphic grade increases upward from chlorite- to biotite-, garnet-, kyanite-, and sillimanite-grade rocks over a structural distance of a few kilometers (**Figure 9**). The metamorphic grade of the Lesser Himalaya, on the other hand, was only recently documented because of the poor mineralogy of these rocks. This limitation was recently overcome by means of the calibrated RSCM thermometric technique (Beyssac et al., 2002), which uses the degree of graphitization of carbonaceous matter, measured by Raman microspectroscopy, to determine peak metamorphic temperatures. These temperatures in the LH typically vary between 550 °C near the MCT and ~350 °C at deeper structural levels (**Figure 9**) (Beyssac et al., 2004; Bollinger et al., 2004a). Combined with local structural measurements, these data indicate that the peak

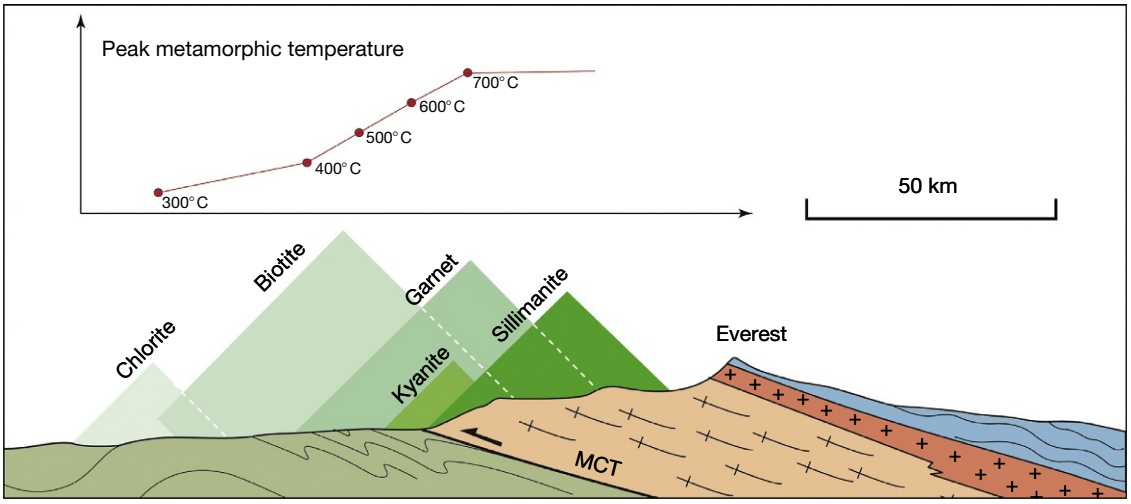

Figure 9 Simplified section of the MCT zone in the Everest area. Metamorphic grade across the MCT zone shows an apparently inverted gradient together with metamorphic peak temperatures increasing upward (based on Brunel and Kienast, 1986; Catlos et al., 2002; Law et al., 2004; Lombard, 1953; Lombardo and Rolfo, 2000).

metamorphic temperatures increase upward in the section. This apparently inverted gradient was first documented near the MCT zone and is observed to actually encompass the topmost 5–7 km of the Lesser Himalayan units. The inverted metamorphic gradient has been interpreted as either evidence for a thermal structure with recumbent isotherms (Le Fort, 1975) or the result of postmetamorphic shearing of isograds (e.g., Brunel et al., 1979; Hubbard, 1996), and it has stimulated a variety of thermal modeling studies (Harrison et al., 1998a; Jaupart and Provost, 1985; Molnar and England, 1990b; Royden, 1993).

6.09.2.5 Topography Across the Himalayan Range

The easily erodible molasse of the sub-Himalayas forms foothills reaching elevations of a few hundred meters. The very rough relief of these hills attests to rapid erosion and tectonic uplift (Hurtrez et al., 1999). North of the foothills, in the Lesser Himalayan domain, the topography of the range reaches elevations up to 2500 m, with the higher topography correlating strongly with remnants of High Himalayan crystalline klippes (**Figure 8**). In fact, the morphology in the Lesser Himalayas is generally 'inverted,' with synclinal crests and anticlinal valleys (Valdiya, 1964), suggesting moderate tectonic activity.

Focusing on the Himalayas of Nepal, we observe that north of a line trending ~N108° E, roughly coinciding with the trace of the MCT, the topography rises abruptly from elevations of ~1000 m to more than 6000 m. The abrupt break in slope that marks the front of the High Himalayas can be traced all along the Nepal Himalayas. A unique feature of the range's morphology is the position of the front of the high range well to the north of the main bounding thrust faults along the foothills. This feature has been interpreted as evidence for out-of-sequence thrusting at the front of the High Himalayas that would be either active (e.g., Wobus et al., 2003) or Late Miocene (e.g., Catlos et al., 2001; Harrison et al., 1997), the presence of a ramp along the sole thrust fault at base of the Himalayan wedge associated to a duplex system (e.g., Lavé and Avouac, 2001). These interpretations are discussed in **Section 6.09.7**.

6.09.2.6 Crustal-Scale Structural Models of the Himalaya

A variety of crustal-scale sections across the Himalayas have been proposed based on surface geology. One early view was that all the major thrust faults are crustal-scale faults that developed following a forward propagation sequence after the collision along the ITSZ (e.g., Le Fort, 1975; Mattauer, 1975; 1986; Molnar and Lyon-Caen, 1988; Molnar, 1990). According to this view, all faults would be parallel to one another and reach to the Moho. Subsequent studies proposed the alternative that all the major faults root into a common midcrustal decollement (Brunel, 1983; Schelling and Arita, 1991). This geometry was initially inferred from the Lesser Himalayan antiformal structure, and it appears to be consistent with the pattern of exhumation recorded in the metamorphism of the Lesser and Higher Himalayan formations. Indeed, peak metamorphic pressures documented in the Nepal Himalayas never exceed ~8 kbar (see Guillot (1999) for a review), suggesting that rocks were exhumed from depths of 30 to 35 km at most. This hypothesis forms the basis of the cross section constructed in **Figure 8**, which is similar to the 'balanced' sections that have been constructed along several transects across the Himalayas of Kumaon (Srivastava and Mitra, 1994), far western Nepal (DeCelles et al., 2001), central Nepal (Robinson et al., 2001), and eastern Nepal (Schelling and Arita, 1991). The main point is that these balanced sections all suggest some duplex structure in the Lesser Himalaya, with all the major thrust faults rooting into a midcrustal decollement beneath the high range. The decollement must have developed after the emplacement of the crystalline thrust sheets. It should be realized that the geometric rigor used to balance these sections may give a misleading impression of accuracy. The following underlying assumptions do not strictly hold in this case: (1) Deformation occurs by bedding slip with constant width and length of the various units maintained and

(2) the footwall is nondeformable basement. Not only have the Lesser Himalayan units developed an intense foliation and experienced a significant amount of pure shear, but also the basement itself might actually deform as it is underthrust below the range. The details of the balanced sections, though they have the merit of being based on a plausible kinematics, should therefore be regarded with caution.

6.09.2.7 Geophysical Constraints on the Structure of the Crust

The structure of the crust across the central Himalayas has been investigated through a variety of techniques, including gravimetry, magnetotellury, and seismology. A major feature revealed by seismic experiments in southern Tibet is a strong midcrustal reflector at a depth of 35–40 km. The existence of this reflector was first suggested by wide-angle seismic reflection studies (Him and Sapin, 1984); later, it was better imaged by the common midpoint deep seismic profiles run during the INDEPTH experiment (Brown et al., 1996; Nelson et al., 1996; Zhao et al., 1993). As shown in **Figure 10**, this conspicuous reflector was found to coincide with the midcrustal decollement inferred from the structural sections across the range, and it was consequently termed the Main Himalayan Thrust fault, or MHT (Brown et al., 1996).

The deep electrical structure of the central Nepal Himalayas was imaged by magnetotelluric sounding (Lemonnier et al., 1999; **Figure 10**). Variations of electrical conductivity in the crust can result from changes in fluid content, pore geometry, or lithology. Conductive zones in the crust are generally thought to reflect well-connected conductive phases, such as brines or melts, or conductive minerals like graphite (Marquis et al., 1995). The section shows a high conductivity in the foreland (~30 Ω m) consistent with the geometry of the molassic foreland basin and contrasting with the resistive Indian basement (>300 Ω m) and Lesser Himalayan units (>1000 Ω m). A continuous shallow-dipping conductor that can be traced northward coincides relatively well with the position of the decollement beneath the Lesser Himalayas inferred from structural studies. It may well reflect some dragging of fluid-rich sediments along the thrust fault, a process expected as the rugged topography of the Indian basement underthrusts the Lesser Himalaya.

Farther north, the magnetotelluric section shows a major conductive zone (~30 Ω m) at ~15 km depth under the front of the High Himalayas. This zone coincides with the position of the midcrustal ramp beneath the front of the High Himalayas, as well as with a zone of intense microseismic activity (**Figure 10**) revealed from local seismic monitoring (Cattin and Avouac, 2000; Pandey et al., 1995, 1999).

These geophysical data thus indicate the MHT is a major thrust fault that can be traced nearly continuously from the MFT, along the foothills, and under southern Tibet, but the detailed geometry remains elusive yet. Contrary to early views, the MCT, MBT, and MFT should not be seen as equivalent major thrust faults cutting through the whole crust, but are more likely splay faults rooting in a single midcrustal decollement. The geometry of the MHT is characterized by a ramp–flat geometry, probably with two major ramps. One ramp is very shallow and corresponds to where the fault emerges with a dip angle of ~30° at the surface along the MFT. The position of the other ramp is more conjectural, possibly lying at midcrustal depths beneath the front of the high range and dipping northward by an estimated 15°.

6.09.3 Holocene Deformation and Erosion

6.09.3.1 Active Thrusting and Folding in the Sub-Himalayas

The kinematics of thrusting along the front of the Nepal Himalayas can be interpreted from the study of deformed river terraces. The methodology is reviewed here, followed by a summary of results obtained from the study of terraces along the Bagmati River along section BB′ south of the Kathmandu basin (see location in **Figure 7**). For more details and results from other sections, the reader is referred to Lavé and Avouac (2000).

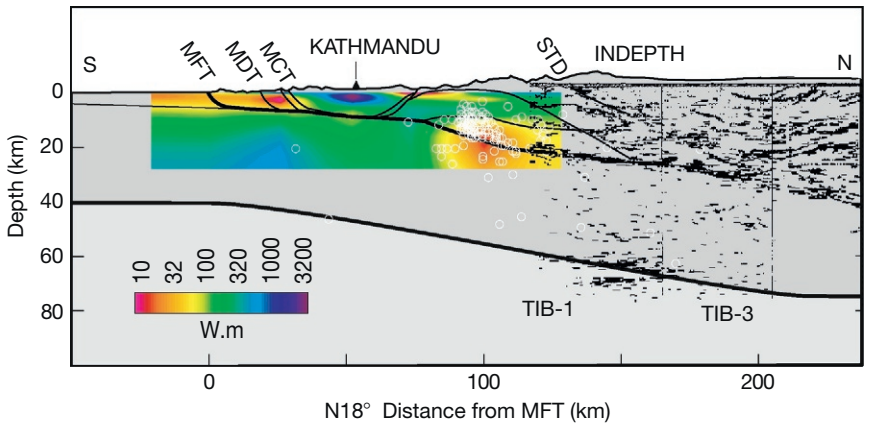

Figure 10 Geophysical constraints on the crustal structure across central Nepal. The conductivity section was obtained from a magnetotelluric experiment carried out along the section AA′ across central Nepal (Lemonnier et al., 1999). Also reported are the INDEPTH seismic sections run about 300 km east of section AA′ (see location in **Figure 7**; Brown et al., 1996; Nelson et al., 1996; Zhao et al., 1993). All the thrust faults are inferred to root at depth in a subhorizontal ductile shear zone that would correspond to the prominent midcrustal reflector.

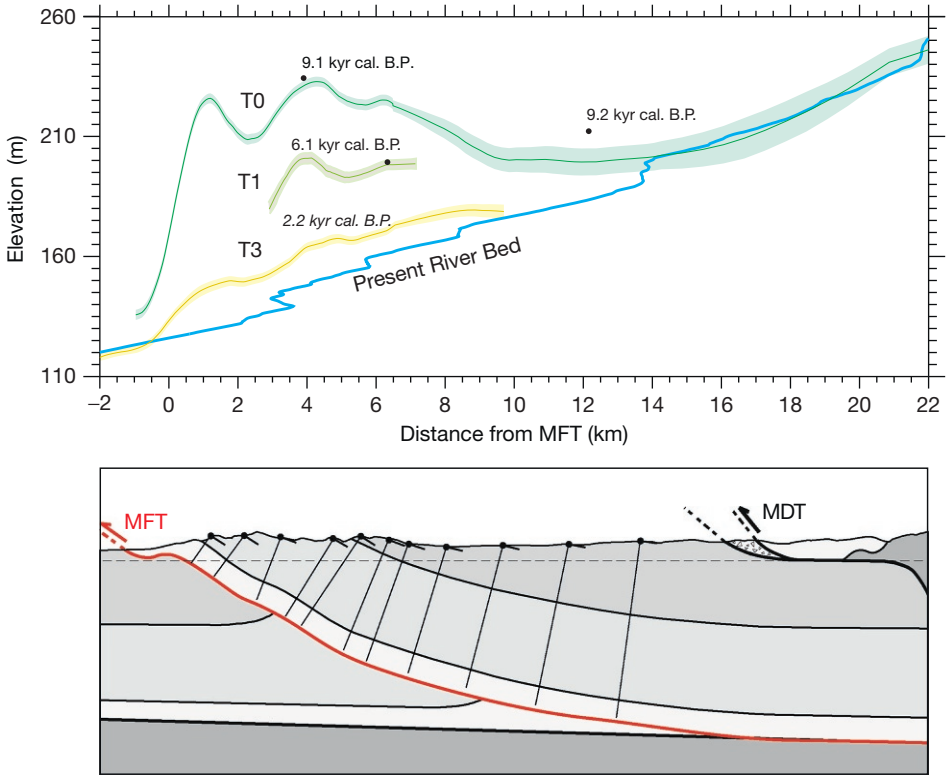

Figure 11 Structural section with elevation of abandoned terraces along the Bagmati River across the Siwalik Hills south of the Kathmandu basin, approximately along section AA′ (see location in **Figure 7**) (modified from Lavé J and Avouac JP (2000) Active folding of fluvial terraces across the Siwaliks Hills, Himalayas of central Nepal. *Journal of Geophysical Research-Solid Earth* 105(B3): 5735–5770). Also indicated are ages of terrace abandonment from C14 dating after calibration to calendar ages. The age of T_3 (in italics) was indirectly inferred from the age of the same terrace level along the nearby Bakeya River.

6.09.3.1.1 Structural evolution of the sub-Himalayas

Several structural cross sections were constructed along the Bagmati River and nearby rivers (Lavé and Avouac, 2000). In this area, the Siwalik Hills are divided in two fold belts (**Figures 7** and **11**). The southern one is the topographic expression of the MFT fault, which reaches the surface, or close to it, along the front of the foothills (Nakata, 1989). The other fold belt, ~15 km north of the MFT fold belt, is associated with the Main Dun Thrust (Mugnier et al., 1992; **Figure 11**). The MFT fold belt makes a gently inclined monocline with dips varying between 25° and 50° to the NNW (**Figure 11**). At the front of the fold belt, Lower Siwalik clay and siltstones are disrupted by meter-scale faults and folds. The section can be balanced easily using the fault-bend fold model (Suppe, 1985). The model assumes that deformation occurs by bed-parallel shear only, so that bed lengths and bed thicknesses are preserved during folding. The observed dip angles then imply a curved ramp that roots into the decollement on top of the Indian basement (**Figures 11**). Restoration of the Bagmati and nearby Bakeya sections suggests a minimum shortening of 11 km due to slip on the MFT and 12 km of further shortening due to slip on the MDT. The relief of the fold shows that ~90% of the material uplifted along the MFT and MDT has been eroded away. So, on average over a geologic period of a few million years, denudation must have balanced tectonic uplift.

Although this particular section shows the MFT reaching the surface, it should be noted that the MFT is often blind. This is probably because before a fold develops into a fault-bend fold, there is a prior phase of fault-tip folding (Mitra, 2003; Suppe and Medwedeff, 1990). During this phase, the fault remains blind, and shortening of the unfaulted sedimentary layer is probably accomplished solely by folding with some component of pure shear likely (as illustrated in **Figure 12**). As a result, deciphering the kinematic evolution of deformation from structural and geomorphic studies is challenging, and a more elaborate approach than the one outlined here is needed (Bernard et al., 2007; Daeron et al., 2007; Simoes et al., 2007b).

6.09.3.1.2 River incision across the sub-Himalayas

Abandoned fluvial terraces are ubiquitous in the sub-Himalayas of central Nepal and have been most extensively surveyed along the Bagmati, Bakeya, Narayani, and Ratu Rivers (Delcaillau, 1986; Lavé and Avouac, 2000). These terraces are strath terraces, with the bedrock tread (the 'strath'; Bull, 1991) being overlain by a few meters of gravel very similar to the bed load of the modern rivers. The gravel is generally overlain by overbank sands and silts with, in places, mixed colluvium or fanglomerates fed from adjacent valley slopes. The difference in elevation between the abandoned terrace and the present riverbed provides some direct estimate of the incision since the

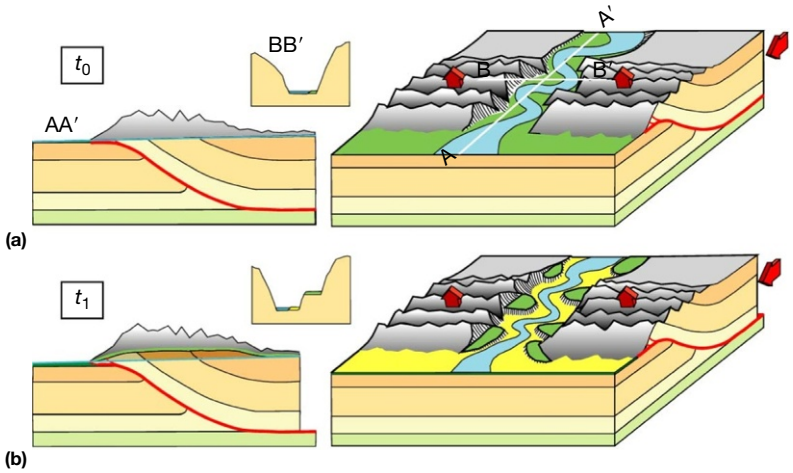

Figure 12 Diagram showing the formation, abandonment, and warping of fluvial terraces during fold growth (modified from Lavé J and Avouac JP (2000) Active folding of fluvial terraces across the Siwaliks Hills, Himalayas of central Nepal. *Journal of Geophysical Research-Solid Earth* 105(B3): 5735–5770). (a) Initially, the river has enough stream power to bevel a wide channel at the rate imposed by the growing fold (tectonic uplift minus sedimentation rate at the front of the fold). At time t_0, due to some decrease of its stream power (of possibly climate origin), the river starts entrenching into a narrower channel. (b) At time t_1, a paired terrace, corresponding to the river channel at time t_0, is preserved in the landscape (labeled T_0). This terrace overhangs the active riverbed by a quantity that depends on the amount of tectonic uplift induced by the folding between t_0 and t_1 and on the change of base level due to sedimentation at front of the fold.

terrace abandonment. Charcoal samples collected from the various preserved terraces in the study area all yielded Holocene (<10 ka) ^{14}C ages.

The chronological data obtained in this way indicate four major episodes of terrace abandonment, dated to 9.2 ± 0.15, 6.1 ± 0.15, 3.7 ± 0.1, and 2.2 ± 0.2 ka (^{14}C ages converted to calendar ages). These dates probably correspond to wet-to-dry climate transitions during the Holocene period (Lavé and Avouac, 2000). The uppermost level, labeled T_0 in Figure 11, is generally the most prominent in the landscape because it corresponds to particularly wide terrace treads. The second most prominent level is T_3, dated to ~2.2 ka. Along the Bagmati River, the T_2 terrace is not well preserved and could not be mapped and measured easily in the field. Figure 11 shows the elevation above the present riverbed of the three other terraces along the Bagmati River. These data provide an estimate of the average incision, $i(x,y,t)$, at any point (x,y) along the river since the abandonment of terrace T at time t of incision,

$$i(x, y, t) = T(x, y, t) - r(x, y) \quad [1]$$

where $r(x,y)$ is the present river profile and $T(x,y,t)$ is the present elevation profile of the abandoned river terrace.

6.09.3.1.3 Converting incision rates to uplift rates in the sub-Himalayas

The geometry of the abandoned terraces (Figure 11) clearly demonstrates that since these terraces were abandoned, they have recorded some amount of folding and faulting associated with thrusting along the MFT. By contrast, the terraces are not affected by any clear deformation across the MDT. They also can be traced farther upstream across the MBT without any evidence of tectonic activity (Lavé and Avouac, 2000).

The determination of tectonic uplift relative to some chosen reference frame, here chosen to be the footwall of the MFT, requires some estimate of the geometry of the riverbed at the time it was deposited (Figure 12). It may simply be assumed that the river has maintained a constant profile during deformation, with river incision counterbalancing tectonic uplift. Accordingly, tectonic uplift since terrace abandonment would then be equal to incision, that is, the difference of elevation between the abandoned terrace and the present river:

$$u(x, y, t) = i(x, y, t) \quad [2]$$

This equation assumes that the term that arises from the apparent uplift of the riverbed due to the horizontal component of the displacement field can be neglected. This is a valid assumption because of the generally low stream gradient cutting across the sub-Himalayas. In this case, this term is <1% of the estimated uplift.

Given that on average over many seismic cycles the fold might be assumed to grow more or less steadily, $u(x,y,t)$ may be assumed to be proportional to the time elapsed since the terrace abandonment. It follows that the incision deduced from two terraces abandoned at different times, t and t', should match:

$$i(x, y, t)/t = i(x, y, t')/t' \quad [3]$$

The incision profiles deduced from T_0 and T_3 along the Bagmati section are similar, but some mismatch on the northern limb of the fold, due to an incision deficit, was observed (Lavé and Avouac, 2000). This suggests that the simple assumption of eqn [3] does not hold.

Actually, the cumulative uplift since terrace deposition at time t with respect to a point attached to the footwall of the MFT ought to be written as

$$u(x, y, t) = i(x, y, t) + b(x, y, t) \quad [4]$$

where $b(x,y,t)$ accounts for the change in the geometry of the riverbed with the sign convention illustrated in Figure 13.

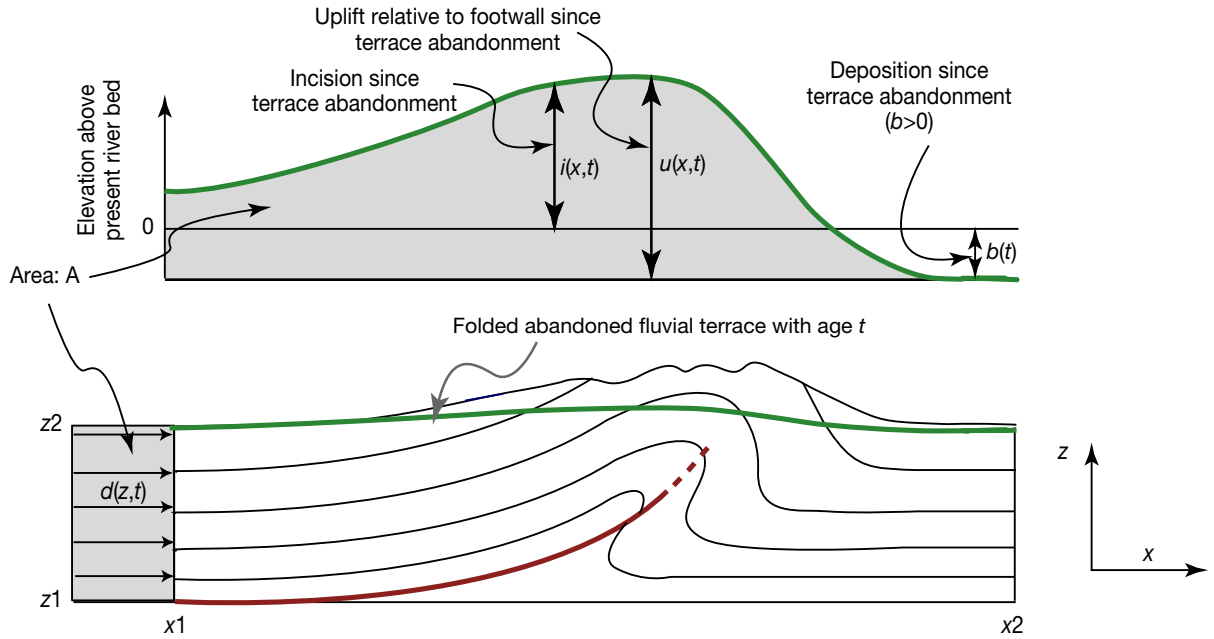

Figure 13 Sketch defining the relationship between fluvial incision, i, base level change, b, and uplift relative to the footwall, u, since the abandonment of fluvial terrace across a growing anticline.

This term might vary along the section (something ignored in Figure 13) and should be written as

$$b(x, y, t) = p(x, y, t) + q(x, y, t) \quad [5]$$

where $q(x,y,t)$ is the local base level change since time t and $p(x,y,t)$ is the change in elevation at (x,y) due to possible changes of the river gradient and river sinuosity. The term $q(x,y,t)$ is equal to the sedimentation rate (or incision rate) at the front of the MFT (Lavé and Avouac, 2000). There are no uplifted Holocene terraces south of the MFT, and rivers clearly aggrade where they exit the Siwalik Hills. Based on the magnetostratigraphic sections (Appel et al., 1991; Harrison et al., 1993), the sedimentation rate can be estimated to 0.45 ± 0.5 mm year^{-1}.

In the absence of any way to assess possible changes in the stream gradient during the Holocene, this parameter is assumed to be constant and equal to the present 0.27% value. It should be realized that the Holocene trend toward a drier climate in this part of Asia may have forced hydrologic modifications, including gradient changes, but these are not easily analyzed.

The paleochannel corresponding to each terrace level can be estimated from the terrace remnants within the steep flanks of the canyon (Lavé and Avouac, 2000). Study of these channels reveals that river sinuosity has increased during the Holocene. The river was least sinuous ($s = 1.8$) at the time of T_0 strath beveling. At the time of T_1 abandonment, the sinuosity had increased to ~2.0. At the time of T_3 abandonment, it was ~2.1. The present riverbed shows the narrowest and most sinuous channel ($s = 2.4$). This sinuosity increase must have resulted in a gradual increase of the apparent slope of the river, and hence an incision deficit, on a projection perpendicular to the fold axis.

To account for sinuosity changes, $p(x,y,\ t)$ might be written as

$$p(x, y, t) = s\Delta L(x, y, t) \quad [6]$$

where $\Delta L(x,y,t)$ is the change in longitudinal distance along the river due to the sinuosity change since t and s is the channel gradient, which is assumed to be constant along that particular river reach and unchanged with time.

If the fold geometry is locally cylindrical and if the x-axis is perpendicular to the azimuth of the axial surface, then the uplift rate is only a function of x.

The uplift rate profiles in Figure 14 were computed from eqn [4], taking sinuosity and base level changes into account. The two curves derived from the two best preserved terraces along that section are identical within the error bars. Together with the uplift rate profiles deduced from other terrace levels along the Bagmati and Bakeya Rivers (Lavé and Avouac, 2000), these data suggest that the anticline has been growing more or less steadily during the Holocene. The zone of active uplift is 1–14 km wide and the uplift rate reaches a maximum of ~11 mm year^{-1}.

It should be emphasized that this section shows that it is possible to estimate tectonic uplift rates from river incision rates but that these two rates generally differ due to possible base level and sinuosity changes. In certain cases where the tectonic signal is not as large as in the Himalaya, climate-driven hydrologic changes can be the main factor governing river incision (Poisson and Avouac, 2004).

6.09.3.1.4 Converting uplift rates to horizontal shortening from area balance

A simple way to deduce horizontal shortening from uplift profiles across the MFT fold is to assume conservation of

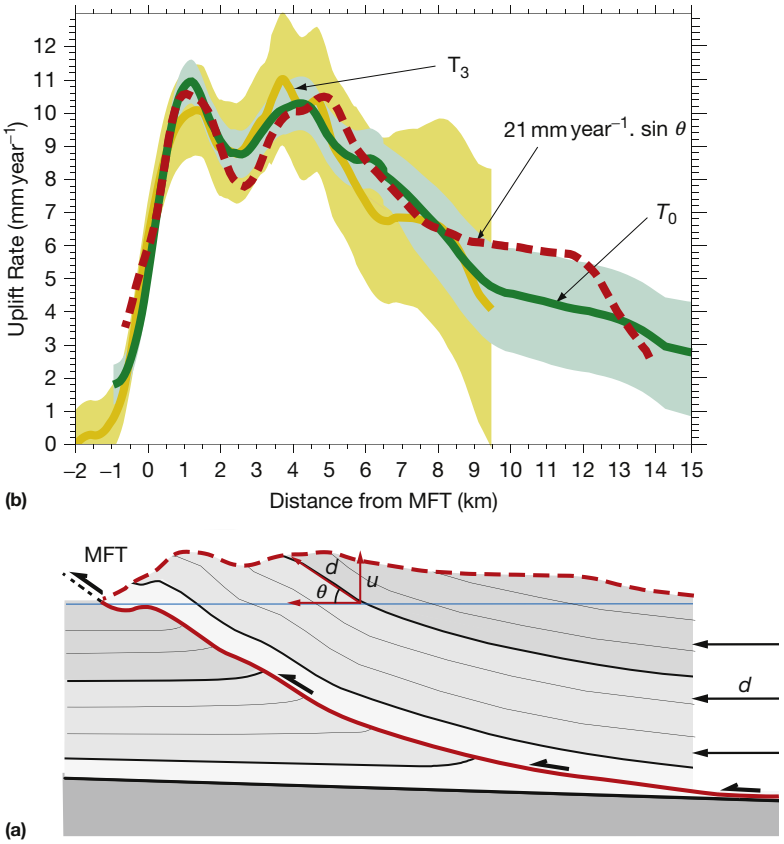

Figure 14 (a) Relationship between horizontal shortening and uplift assuming conservation of area. A is the area between the abandoned terrace tread and the profile of the riverbed at the time t it was abandoned. h is the thickness of the units detached from the basement. Conservation of area implies that the cumulative shortening, d, since terrace abandonment is $d=A/h$. (b) Relationship between horizontal shortening and uplift rates, assuming fault-bend folding. At any point with abscissa x along the section, the fault-bend fold model predicts that local dip angle, θ, and local cumulative uplift, u, should relate to the amount of bed-parallel displacement, d, of the bed outcropping at that point according to $u=d\sin\theta$. The sketch assumes no bed-parallel shear above the decollement, implying that all beds have experienced the same displacement d. It should be noticed that the relation still holds if d varies with depth.

mass, that is, conservation of area in cross section if the effect of tectonic transport perpendicular to the section can be neglected (Molnar et al., 1994). Let A be the area between the present profile of an abandoned terrace tread and the profile of the same terrace level at the time, t, it was abandoned (Figure 15). Let h be the thickness of the units detached from the basement. Assuming plane strain and conservation of mass, we derive the mean horizontal displacement, d, necessary to account for the deformation of the terrace

$$d(t)=\frac{A(t)}{h}=\frac{\int_0^x u(x,t)\mathrm{d}x}{h} \qquad [7]$$

This approach requires a continuous terrace tread across the growing fold. The only such terrace is the T_0 level along the Bagmati River. Deformation of that level corresponds to an area of $A(T_0)=1.05\pm0.25$ km^2. According to the structural description earlier, the depth of the basement is 5.0 ± 0.3 km beneath the MFT, and it dips northward with a slope of 2.9° (corresponding to a grade of 2.5%). Given that the MFT ramp merges with the decollement ~18 km north of its trace at the surface, the depth to the decollement beneath the fold is 5.5 ± 0.3 km. The accumulated shortening since

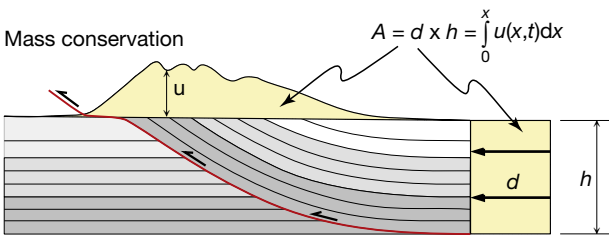

Figure 15 Uplift rate (top) along the Bagmati section (bottom) deduced from terrace T_0 and T_3 after correction for 0.45 mm year^{-1} base level change due to sedimentation south of the MFT and sinuosity changes. Dashed line shows the predicted uplift rate pattern assuming fault-bend folding. For a cylindrical fold, it would correspond to $U(x,y)=d(t)\sin\theta(x,y)$. It yields a good fit to the observed uplift rates for a horizontal shortening rate across the MFT of 21 mm year^{-1}.

9.2 ± 0.2 cal ky is then estimated to be $d-192$ m (+60/−50 m), yielding a shortening rate of $21+7/-6$ mm year^{-1}.

6.09.3.1.5 Converting uplift rates to horizontal shortening from the fault-bend fold model

Figure 14 suggests that the uplift profiles recorded by the Holocene terraces are closely related to the geologic structure

of the fold. Indeed, the small variation of the uplift rate within ~1 km of the middle of the fold correlates with a variation in bedding dip angles and thus of the dip of the ramp at depth. The correlation between structural geology and recent uplift is in fact expected for a fault-bend fold. According to this model, the hanging wall accommodates deformation imposed by the fault geometry at depth via bedding plane slip, with no change of the length and width of the beds (Figure 14). It follows that, on the back limb, uplift rate depends on the dip of the fault at depth, which equals the local bedding dip angle. In the case of a fold with cylindrical geometry (with beds striking perpendicular to the section, taken to be parallel to the y axis), assuming that the slip increment since terrace abandonment is small, one may write

$$U(x,t) = \mathrm{d}(t)\sin\theta(x) \qquad [8]$$

where $\theta(x)$ is the dip angle at point (x,y) and $\mathrm{d}(t)$ is the displacement measured parallel to the decollement outside the fold zone of the bed outcropping at point (x,y). The equation holds insofar as the dip angle does not vary significantly over a distance of d, that is, $1/d \gg (\mathrm{d}(\sin\theta)/\mathrm{d}x)$.

The fault-bend model leads to a testable correlation between structural geology and terrace warping. The uplift profiles deduced from terraces T_0 and T_3 along the Bagmati River are in close agreement with the bedding dip angles, as expected from eqn [8] (Figure 14).

This model makes it possible to estimate the cumulative shortening since the abandonment of each terrace by least-squares adjustment of the model to the uplift profiles, with $\mathrm{d}(t)$ being the only adjustable variable. Each abandoned terrace yields a point on the plot in Figure 16, which shows d as a function of elapsed time since the abandonment of each terrace. The points are seen to follow a linear trend. A least-squares fit yields 20.4 ± 1 mm year^{-1}, which may be taken to represent the rate of fault slip on the MFT, or alternatively the horizontal shortening rate across the fold over the Holocene period, since the decollement is nearly horizontal (within a few degrees) according the structural model. This rate is much better constrained than the estimate deduced from conservation of mass in the previous paragraph. The uncertainty neglects the uncertainty related to the applicability of the fault-bend fold model, because this source of uncertainty is difficult to incorporate formally. However, this estimate ignores the fact that the slip along the MFT is not linear as a function of time, because it has most probably resulted from recurring coseismic slip events. When this stick-slip behavior is taken into account, assuming slip events between 4 and 6 m (with a uniform probability in this range), the long-term slip rate is revised to 21 ± 1.5 mm year^{-1} (Lavé and Avouac, 2000).

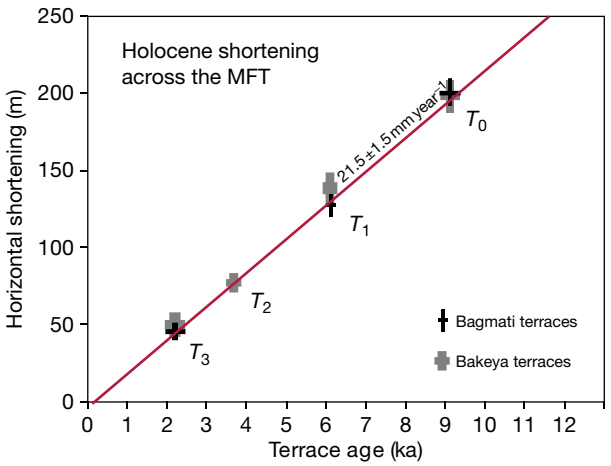

Figure 16 Plot of horizontal shortening deduced from the various terrace treads along the Bagmati and Bakeya section as a function of age of terrace abandonment (Lavé and Avouac, 2000). These data are consistent with a uniform 21 ± 1 mm year^{-1} shortening rate over the Holocene period. If the fold is assumed to have been growing by incremental deformation during large earthquakes, the mean shortening rate is slightly modified since some amount of elastic straining at the large scale may yet remain to be released or may not have been released by the time of emplacement of the different terraces. Assuming that these increments can be as large as 5 m of horizontal shortening and that all values between 0 and 5 m are equiprobable, we obtain a long-term averaged shortening rate, offering a best fit to the terrace record, of 21.5 ± 1.5 mm year^{-1}.

6.09.3.2 River Incision, Erosion, and Uplift Across the Range

6.09.3.2.1 Fluvial incision across the whole range

In the previous section, we saw that the pattern of river incision could be used to determine tectonic uplift in the sub-Himalayas. The same approach might be applied at the scale of the whole range, although there are several limiting factors. In the Lesser Himalayas, strath terraces are sparse. There are, however, prominent fill terraces >100 m thick and probably of Pleistocene age (Fort et al., 1983; Iwata, 1976). Close to the front of the high range, the valleys become steep and narrow and the terraces are no longer preserved. Such a terrace pattern suggests a slow rate of fluvial incision in the Lesser Himalayas and an abrupt increase at the front of the high range (Lavé and Avouac, 2001), as first inferred from the observation that most Himalayan rivers have developed knickpoints where they cross the front of the high range (Seeber and Gornitz, 1983). Due to the difficulty of using the terrace record to determine incision rates, another approach has been adopted. The principle of the approach is that fluvial incision rate can be estimated from the shear stress exerted by the flowing water at the bottom of the channel (*Lavé and Avouac*, 2001). The model was calibrated from a few sites in the Lesser Himalayas and sub-Himalayas, where Holocene strath terraces could be dated. This approach has been shown to yield results consistent with the terrace record of river incision at sites where both approaches could be applied. Figure 17 shows the average profiles obtained from river incision estimated along six major rivers running across the central Nepal Himalayas. It turns out that river incision in the Lesser Himalayas does not exceed a few mm year^{-1}, and it increases abruptly at the front of the high range to reach values between 3 and 8 mm year^{-1}. The zone of rapid river entrenchment is only ~50 km wide, and it coincides with the front of High Himalayas.

6.09.3.2.2 Denudation across the whole range

In the sub-Himalayas, the rivers cutting across the active folds incise at approximately the rate of tectonic uplift (minus the sedimentation rate, which is only a minor term in this case).

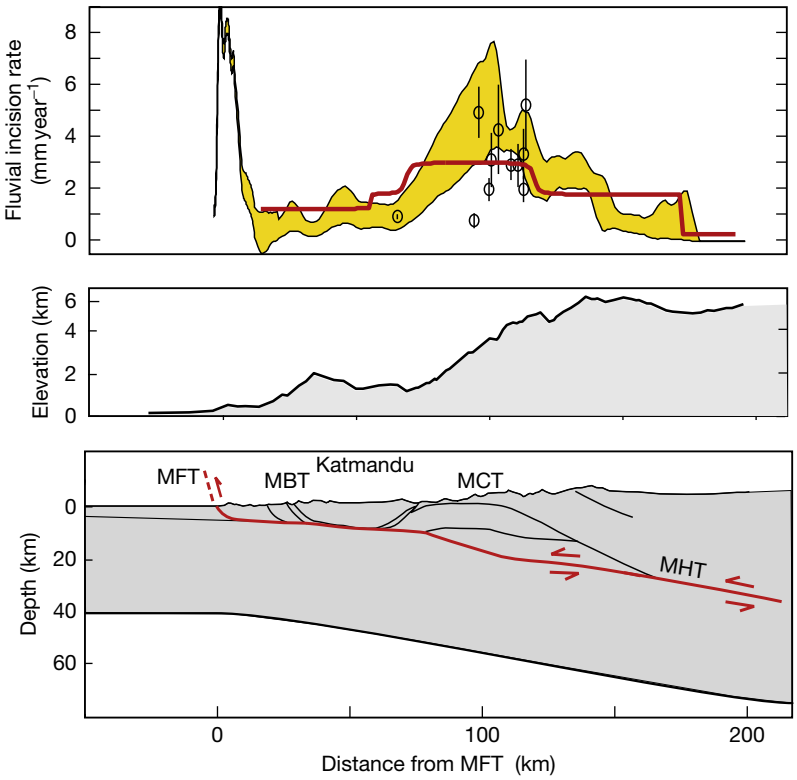

Figure 17 Rate of river incision across the Himalayas of central Nepal (Lavé and Avouac, 2001). Dark shading shows river incision across the Siwalik Hills deduced from three Holocene terraces along the Bagmati River. River incision across the Lesser Himalayas (gray shading) was derived from the computation of river incision along the major rivers of central Nepal based on their present hydrologic regime. Also shown are erosion rates over the last about 1 Ma derived from fission track data from the Annapurna area (Burbank et al., 2003). These data were converted into erosion rates using the thermal model of Henry et al. (1997), which is close to the more recent thermal model derived from a formal inversion of the thermochronological and thermobarometric data of central Nepal (model 1 of Herman et al. (2010)). Also shown is the erosion predicted from this thermokinematic model over the last 10 Ma.

Since the present topography accounts for <10% of the total volume of rock uplifted by thrusting since fold inception, this implies that denudation must also be in equilibrium with tectonic uplift (Hurtrez et al., 1999).

Current denudation rates are estimated for the 11 catchments within the Lesser and Higher central Nepal Himalayas for which measurements of suspended load are available (Lavé and Avouac, 2001). These rates were found to be smaller by ~20% than estimates assuming that denudation equals river incision rates along the main drainages in each watershed. This misfit is insignificant in view of the large uncertainties in both the measurements of suspended load and estimates of sediment discharge and may partly be offset by the contribution of the bed load.

Mass processes are probably the dominant erosional process in the Himalayas of Nepal, especially in the high range, where the bare, steep hillslopes often show evidence of recent landslides. As has been suggested for the High Himalayas of northern Pakistan, hillslopes in Nepal are probably near their critical slopes for mass movement (Burbank et al., 1996). In this setting, fluvial downcutting is probably the rate-limiting process driving hillslope erosion, and denudation is expected to equal fluvial incision on average.

Denudation rates in the Nepal Himalayas can also be compared with the sediment volume delivered to the foreland basins and to the Bengal fan. The pattern of fluvial incision of **Figure 17** predicts a sediment flux of 375 km^2 My^{-1}. This rate may be compared with the $1 \pm 0.5 \times 10^6$ m year^{-1} rate proposed by Metivier, et al. (1999) to be eroded from the Himalayas over the last 2 My and deposited in the Gangetic Plain and Bengal fan. Given that the Ganges and Brahmaputra Rivers drain the Himalayas over an ~1800 km long stretch, this value implies 280 ± 110 km My^{-1} of denudation on average across a section of the range. To the first order, this suggests that denudation of the whole landscape matches the pace of fluvial downcutting and that fluxes have not varied dramatically over the Quaternary period.

6.09.3.2.3 Holocene kinematics of overthrusting along the MFT–MHT

The average slip rate on the MFT over the Holocene appears to be very close to the total shortening rate across the range, as measured from GPS. It also compares well with geologic estimates of the shortening rate across the Lesser Himalayas of Nepal, which range from 16 to 25 mm year^{-1} (DeCelles et al., 2001; Hauck et al., 1998). This estimate also compares well

with the Quaternary shortening rate across the Himalayas deduced from E–W extension in southern Tibet. If this Quaternary extension is assumed to accommodate the lateral variation of the direction of thrusting along the arcuate Himalayan front (Armijo et al., 1986; Baranowski et al., 1984; McCaffrey and Nabelek, 1998), the estimated extension rate of about 10 mm year^{-1} implies a Late Quaternary shortening rate of 20 ± 10 mm year^{-1} (Armijo et al., 1986).

The observed pattern of erosion is found to closely mimic the uplift predicted by slip along the flat–ramp–flat geometry of the Main Himalayan Thrust fault. The theoretical pattern of uplift can be simply estimated by assuming that the hanging wall is thrust along the MHT and accommodates the MHT geometry simply by vertical shear (Molnar, 1987). If the topography is approximately steady state, as argued in the previous section, the flexural loading of the Indian Plate does not vary and this model does not require any computation of the flexural response of the lithosphere. This approach predicts an uplift pattern that fits reasonably with the fluvial incision pattern of Figure 17 (Lavé and Avouac, 2001). It thus seems that over the Holocene period, all the shortening across the Himalayas has been absorbed by slip along one major thrust fault.

6.09.4 Longer-Term Geologic Deformation and Exhumation

We now compare the kinematics of deformation established for the Holocene period with the kinematics of deformation and exhumation over a longer geologic period. We review first how this kinematics can be inferred by combining (1) the history of deposition in the foreland, (2) the structural architecture of the Himalayan internal zones, and (3) the cooling histories and metamorphic grades in the Lesser and High Himalayas.

6.09.4.1 Foreland Deposition: A Record of Underthrusting

Sedimentation in the foreland basin provides indirect information on orogenic growth. As the Himalayan wedge grows, it overthrusts the Indian basement, forming a 'foreland flexural basin' in which a fraction of the material eroded from the range accumulates with a stratigraphic organization that depends on the kinematics of overthrusting (Lavé, 1997; Lyon-Caen and Molnar, 1985; Figure 18). Several kilometers of Cenozoic molasse sediments (the Murree and Siwalik Formations) have thus accumulated on the Precambrian Indian basement. They consist of an upward coarsening sequence (claystone, siltstone, sandstone, and conglomerates) of the Upper Miocene to Pleistocene age. As shown in Figure 18, the development of the flexural basin during underthrusting implies some progradation of sedimentary facies and of the contact between the basement and the most distal sediments away from the mountain front. This model implies, as observed, an upward gradation from distal to more proximal facies.

If the age of the oldest sediments overlying the pre-Tertiary basement is plotted as a function of the distance perpendicular to the range, the rate of sediment progradation can be deduced (Figure 18). The southward progradation over the last 15 My was first estimated with this method to be between 10 and 15 mm year^{-1} (Lyon-Caen and Molnar, 1985), based on a compilation of well data in the Gangetic foreland. The more recent compilation by Mugnier and Huyghe (2006) suggests a rate of progradation, V_{pr}, between 15 and 20 mm year^{-1} (Figure 19).

Assuming that the geometries of the Himalayan wedge and of the flexed Indian Plate have not changed with time, as initially proposed by Lyon-Caen and Molnar (1985), V_{pr} might be taken as equal to the overthrusting rate V_0 (the convergence rate between India and southern Tibet; Figure 19). This reasoning, however, ignores retreat or advance of the mountain front as a result of erosion or of crustal thickening.

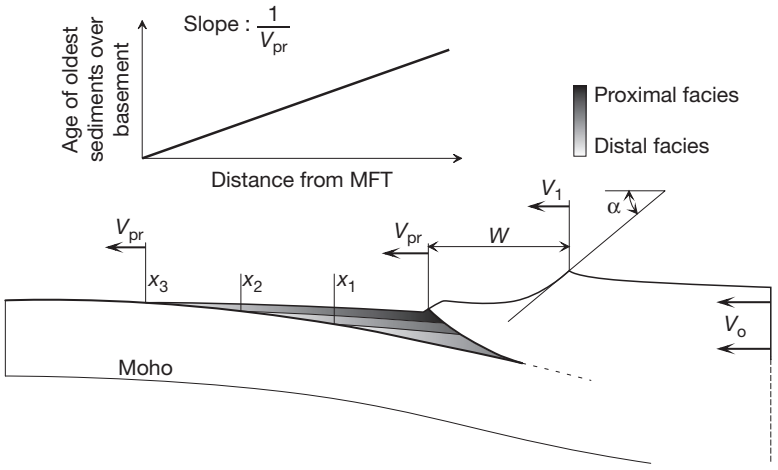

Figure 18 Sketch showing how dated outcropping sections in the sub-Himalayas can be used to infer horizontal displacement of the foreland due to underthrusting. The present thickness of unit 1, h^*, represents, after decompaction, the depth of the foreland basin, h, at the time of the onset of deposition of unit 2, t_{1-2}. If the geometry of the basin is assumed to have remained stationary, this section was at that time at a distance $(\Delta x_1 + \Delta x_2)$ from its present position. We can then estimate by how much the Indian Plate has underthrust the Himalayan topography since time t_{1-2}.

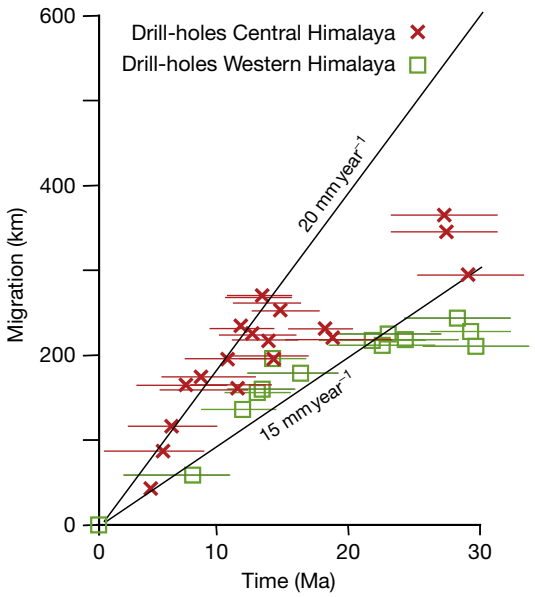

Figure 19 Age of oldest Cenozoic foreland deposits overlying the Indian basement versus distance from edge of Ganges basin (reproduced from Mugnier JL and Huyghe P (2006) Ganges basin geometry records a pre-15 Ma isostatic rebound of Himalaya. *Geology* 34(6): 445–448). These data indicate that the sediments are prograding over the Indian basement at a rate between 15 and 20 mm year^{-1} as the Indian crust is thrust under the Himalayan wedge.

A more general formulation should account for internal deformation of the range as well as for possible erosional retreat of the front of the high range. This is shown in **Figure 18** to represent the edge of the overriding load that flexes down the plate (Avouac, 2003). We then write

$$V_{pr} = V_1 + \alpha \frac{dW}{dt} \quad [9]$$

where V_1 represents the velocity of the front of the high range and W is the width of the accretionary prism (**Figure 18**). It is assumed that the center of mass of the topographic load flexing the Indian basement depends on the position of the crest of the Himalayan wedge, the width and shape of the orogenic wedge, and the partial support of topography by the buoyant crustal root. For this reason, α is a geometric factor between 0 and 1. The rate at which the Indian basement underthrusts the high range is V_1. This velocity is hereafter termed the 'underthrusting rate.' It equals the rate of sediment progradation, V_{pr}, in the case of an orogenic wedge with constant width.

The retreat, if positive, or advance, if negative, of the front of the high range is then

$$V_2 = V_0 - V_1 \quad [10]$$

This velocity represents the rate at which the hanging wall rides over the MHT and is termed here the 'overthrusting' rate. This term can be large, and it could have varied during Himalayan orogenesis. In the absence of any crustal thickening or isostatic response, if eroded at a vertical rate of e, the mountain front would apparently retreat by

$$V_2 = \frac{e}{\tan\alpha} \quad [11]$$

The denudation rate in the High Himalayas is estimated to be 4–8 mm year^{-1} (Lavé and Avouac, 2001), and the gradient at the front of the high range is ~10%. These figures would yield a very rapid retreat of as much as 40–80 mm year^{-1}. In reality, erosion is compensated by some uplift, u, due to isostatic response and crustal thickening, so that the apparent retreat is less and should be written as

$$V_2 = \frac{e-u}{\tan\alpha} \quad [12]$$

Some estimate of V_2 is therefore needed, in addition to the description of the internal deformation of the wedge, to fully describe the kinematics of mountain building and its relation to rates of sediment progradation and deposition in the foreland.

6.09.4.2 Structural Evolution of the Thrust Package

The structural architecture of the Himalayas can be used to infer the kinematics of deformation through the technique of palinspastic restoration (Dahlstrom, 1969). The chronology can be constrained from crosscutting relationships and provenance data from the molasse (Siwalik and Dumri Formations) and thermochronology. A complete discussion of this issue is beyond the scope of this chapter, but a few key results are reported here. Compressional deformation north of the Himalayas started in the early 'Alpine' time of the collision, and there is evidence that crustal thickening in southern Tibet persisted until Middle Miocene time (e.g., Ratschbacher, 1994; Yin et al., 1999). Farther south, deformation and anatexis in the MCT zone occurred at *c.*22 Ma (Copeland et al., 1991; Hodges et al., 1996), an age consistent with a slightly younger cooling in the rocks of the hanging wall attributed to emplacement along the MCT (Copeland et al., 1991; Hodges et al., 1996; Hubbard, 1989; Hubbard et al., 1991). Such a timing is also consistent with conventional and isotopic provenance data from the Dumri Formation that indicate an Early Miocene age for the onset of erosion of the High Himalayan crystalline rocks (Robinson et al., 2001). Out-of-sequence reactivation of the MCT may have taken place by Late Miocene to Early Pliocene time, as indicated from monazite ages of rocks exhumed from midcrustal depths (Catlos et al., 2001; Harrison et al., 1997). This reactivation has been proposed to be responsible for the inverse thermal gradient and for the steep morphological front of the High Himalayan range (Harrison et al., 1997, 1998a,b). However, there is no direct, reliable estimate of the timing of thrusting on the MBT. Age estimates and the provenance of Siwalik sandstones in northern India, west of our study area, indicate that exhumation of the LH commenced some 10 My ago (Meigs et al., 1995). This observation was interpreted to indicate motion on the MBT began as early as 10 Ma (Meigs et al., 1995). Alternatively, exhumation of LH rocks could have resulted from the development of the LH duplex, requiring a much younger (possibly 5 Ma) activation of the MBT (DeCelles et al., 1998; Robinson et al., 2001).

Finally, deformation in the sub-Himalayas due to motion on the MFT and the various thrust faults between the MFT and the MBT has proceeded from Middle Miocene time to the present.

The chronological constraints discussed earlier, when considered with various restored balanced cross sections across the

central Himalayas (DeCelles et al., 2001; Schelling and Arita, 1991; Srivastava and Mitra, 1994), provide some idea of the kinematics over the last 20 Myr. Figure 20 presents the kinematic model proposed for far western Nepal (Robinson et al., 2001). This model also applies, with some minor variations, to central Nepal (Bollinger et al., 2004a; Robinson et al., 2003).

Over the last 15 Ma, the Himalayan orogen has developed as a result of frontal accretion at the toe, internal deformation of the wedge, and underplating. Underplating, associated with duplex formation of the Lesser Himalayan units at mid-crustal depths, has likely been the dominant process contributing to the volume of the Himalayan wedge since Middle Miocene time.

6.09.4.3 Exhumation of the Lesser and High Himalayas: A Record of Overthrusting

Exhumation rates across the range can be used to determine the tectonic evolution of the orogenic wedge. The reader is referred to Bollinger et al. (2004a, 2006) for a more detailed discussion of the approach outlined here.

The most complete picture of the chronology of exhumation in the area comes from $^{39}Ar/^{40}Ar$ ages of muscovite (Figure 21). This technique provides an estimate of the age of a rock sample when it cooled through the muscovite blocking temperature, ~350 °C. Several authors, in particular Peter Copeland and his colleagues, have analyzed samples collected along the central Nepal section from the high range to the southern edge of the Kathmandu Klippe (Figure 21). These data indicate that the trailing edge of the Kathmandu thrust sheet cooled below 350 °C at *c.*20–22 Ma, an age consistent with the onset of deformation and anatexis in the MCT zone. Ages follow a nearly linear trend corresponding to a slope of about 0.23 My km^{-1}, gradually decreasing northward to ~5 Ma at the front of the high range (Figure 21). As a first step, we may ignore accretion and assume steady-state topography and thermal structure defining the reference frame used to describe the kinematics.

Given the shallow dip angle of the MHT below the Lesser Himalayas and the likelihood of a steep 350 °C isotherm, the rocks now outcropping along a section perpendicular to the range must have all crossed the isotherm near the same location (Figure 22). The cooling ages should then follow a linear trend, as observed in Figure 21 (Avouac, 2003). The slope of the age–distance relationship thus provides an estimate of the rate of overthrusting of the hanging wall, which is the inverse of the age gradient

$$V_2 = V_0 - V_1 \sim 4.3\,\text{mm year}^{-1}$$

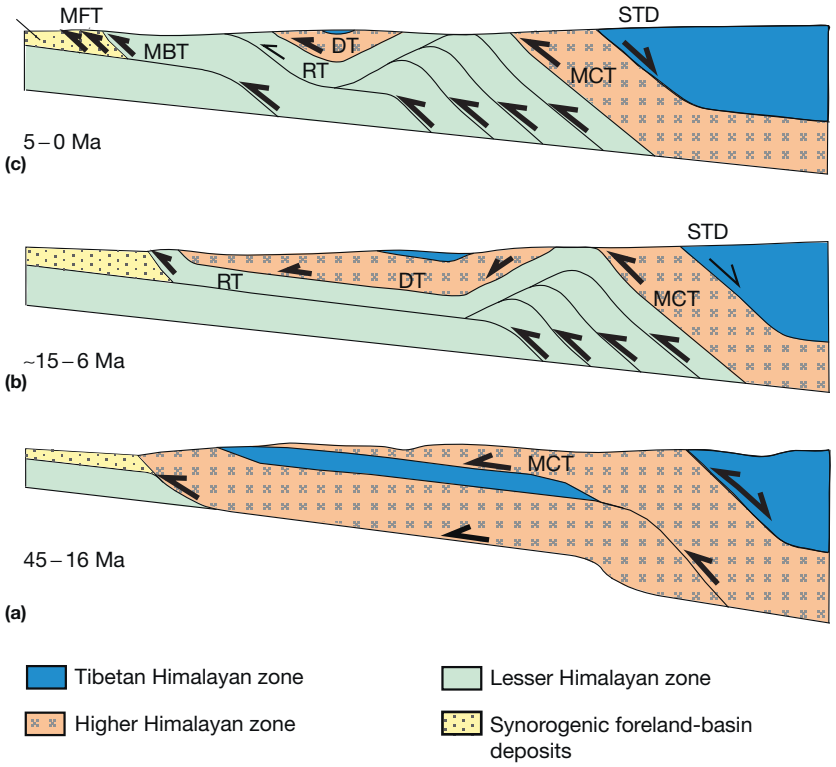

Figure 20 Schematic model of the structural evolution of the Himalayan orogen (modified from Robinson DM, DeCelles PG, Patchett PJ, and Garzione CN (2001) The kinematic evolution of the Nepalese Himalaya interpreted from Nd isotopes. *Earth and Planetary Science Letters* 192: 507–521). This scheme is based mainly on observations along a section across the Himalayas of western Nepal. MCT, Main Central Thrust; DT, Dadeldhura thrust; RT, Ramgarh thrust; MBT, Main Boundary Thrust; MFT, Main Frontal Thrust; STD, South Tibetan Detachment. 45–16 Ma: emplacement of the MCT and then of the DT crystalline thrust sheets, coeval with motion on the STD. Deposition of the Dumri and Bhainskati foreland formations. 156 Ma: emplacement of the Lesser Himalayan RT thrust sheet and development of the duplex; deposition of the Lower and Middle Siwaliks. 5–0 Ma: motion on the MBT and MFT; deposition of the Upper Siwaliks; major phase of exhumation of the LH duplex.

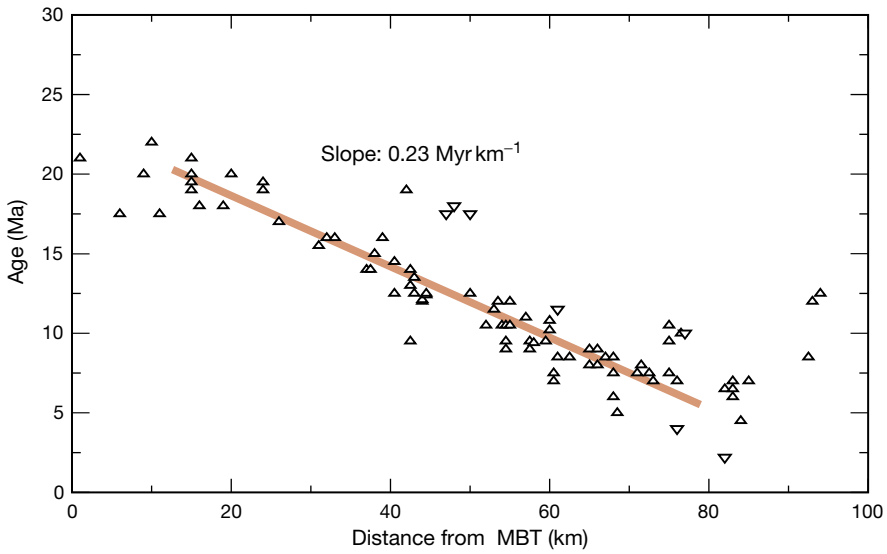

Figure 21 Cooling ages in central Nepal as a function of distance from MBT along a N018°E section. All samples collected from the LH and the overlying crystalline thrust sheets are reported. The Ar^{39}/Ar^{40} muscovite ages appear to approximately follow a linear trend with ages increasing southward by about 0.2 My km^{-1}. Data compilation by Bollinger (2002) from Arita et al. (1997), Arita and Ganzawa (1997), Copeland (1997), Macfarlane et al. (1992), and Herman et al. (2010). The origin is taken at the MBT. All samples collected from the LH and the overlying crystalline thrust sheets are reported.

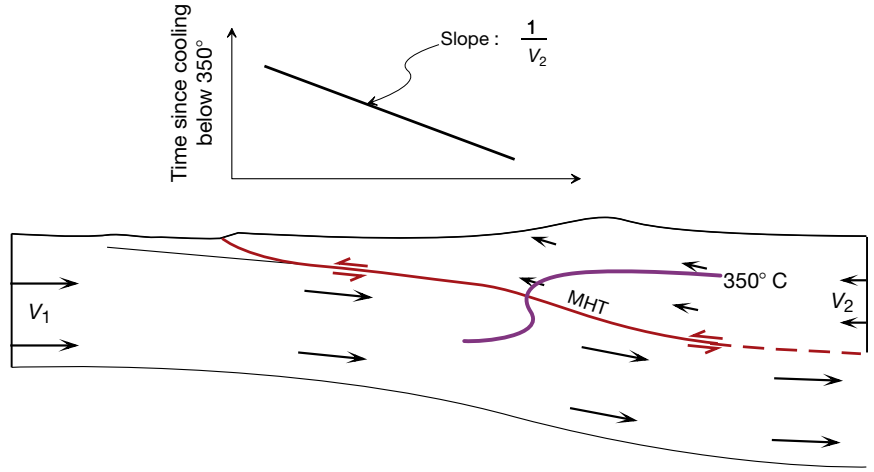

Figure 22 Kinematic model for a convergence rate V_0, an overthrusting rate $V_0 - V_{HR}$, and an underthrusting at rate V_{HR}. The topography and thermal structure are assumed to be in a steady state. This kinematics predicts that cooling ages (e.g., for Ar/Ar dating on muscovites) along a section perpendicular to the range should follow approximately a linear trend with an age gradient of $1/V_0 - V_{HR}$. The isotherm corresponding to the Muscovite-blocking temperature for $^{39}Ar/^{40}Ar$ is estimated at 350 °C.

6.09.4.4 Overthrusting, Underthrusting, and Accretion

In the previous section, the development of the foreland basin, the structural architecture of the internal zones, and the geochronological data required that (1) the footwall underthrusts the MHT, (2) part of the footwall be accreted to the hanging wall, and (3) the wedge itself overthrusts the MHT and is eroded (Figure 23). The kinematics of shortening across a mountain range should thus generally be described in terms of 'underthrusting,' 'overthrusting,' and 'accretion.'

The kinematics in Figure 22 might be modified to fit the structural evolution model of Figure 20 by assuming that some accretion occurs by underplating due to the development of a duplex at midcrustal depths (Figure 23). The particle path trajectories shown in Figure 24 assume a continuous process of accretion (Avouac, 2003). The top of the underthrusting plate is accreted, while the lower part underthrusts the orogenic wedge. In reality, the process of accretion might be discontinuous.

When the overthrusting rate derived from the thermochronological data, ~ 4.3 mm year^{-1}, is added to the rate of underthrusting determined from the sediment progradation rate in the foreland, $\sim$17.5 mm year^{-1}, we obtain an estimate of the shortening rate across the whole range, V_0. The shortening rate is thus

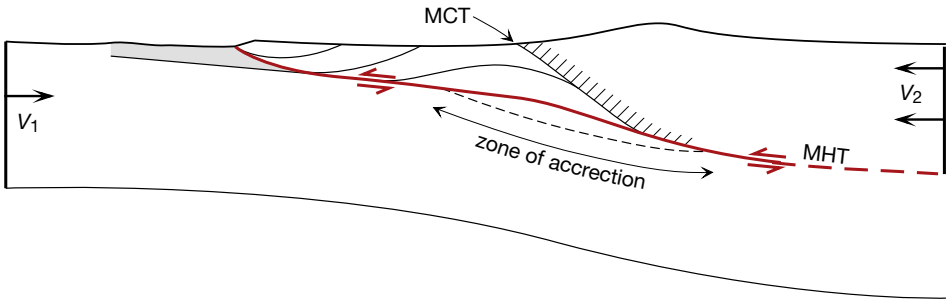

Figure 23 Schematic model of duplexing in the Lesser Himalayas. Thick line shows the geometry of the active thrust fault at a time just before it migrates to a new position farther south (dashed line). This migration induces accretion of material from the footwall to the hanging wall. Thin dashed line shows the geometry of other thrust sheets accreted before time t. The position of the midcrustal ramp, the 'accretion window,' is taken as a reference to define velocities V_{pr} and $V_0 - V_{HR}$, assuming that it controls the topography of the range and the load flexing the Indian lithosphere.

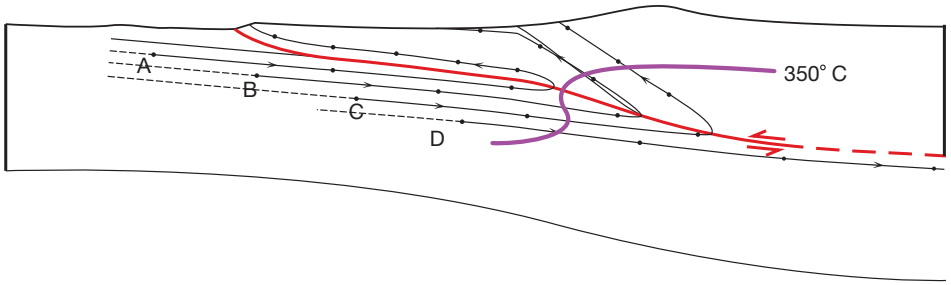

Figure 24 Particle trajectories expected from the model of duplexation shown in **Figure 17**, assuming that ramp migration is a continuous process. Dots show approximate positions about every 5 My. This model also predicts diachronic exhumation with an age gradient of $1/V_0 - V_{HR}$.

averaged to be ~22 mm year^{-1} over the last 15 Ma. The uncertainty associated with that rate is difficult to estimate because of the number of assumptions made to reach it. It could be as high as 30%. In any case, this rate is remarkably consistent with the current ~20 mm year^{-1} convergence rate across the Himalayas derived from morphotectonics and GPS geodesy.

The kinematics may be compared with two end-member cases of a steady-state regime without accretion:

1. If the hanging wall is assumed to overthrust an undeformable footwall by 20 mm year^{-1}, there would be no sediment progradation and no subsidence of the foreland, and we should observe a diachronous exhumation corresponding to

$$V_2 \sim 20 \text{ mm year}^{-1}$$
$$V_{pr} = V_1 \sim 0 \text{ mm year}^{-1}$$

2. In the opposite case, if the convergence is assumed to be entirely accommodated by underthrusting of the Indian basement below a rigid hanging wall without any erosion at the surface (a 'subduction zone' kinematics), we get

$$V_2 \sim 0 \text{ mm year}^{-1}$$
$$V_{pr} = V_1 \sim 20 \text{ mm year}^{-1}$$

The simple kinematics obtained from the analysis described here lies between these two end-members and reconciles the rate of sediment progradation and subsidence of the foreland with the retreat of the mountain front driven by erosion.

When comparing this to the Holocene kinematics described in the previous section, we conclude that the long-term shortening rate is approximately equal to the Holocene shortening rate. The rate of accretion and the partitioning of Holocene shortening into underthrusting and overthrusting are more difficult to assess. However, the pattern of exhumation provides some keys. These issues will be addressed in the modeling section, in which it is suggested that the partitioning of the convergence for Holocene kinematics is approximately the same as over the long term.

6.09.5 Kinematic and Mechanical Models of Crustal Deformation

The data reviewed in the previous sections suggest that the shortening rate across the Himalayas determined from geodetic measurements (19 ± 2.5 mm year^{-1}; Bettinelli et al., 2006) and the averaged rate over the last 15 Ma (~22 mm year^{-1}) are remarkably close and equal to the Holocene slip rate on the MHT (21 ± 1.5 mm year^{-1}; Lavé and Avouac, 2000). These findings suggest that the Himalayan wedge has probably suffered little internal shortening, at least over the Holocene period, and that the shortening rate across the range has not varied much over the last 15 Ma. This section will describe numerical models consistent with these two key hypotheses. To start, an outline of the thermokinematic model of the long-term deformation of Bollinger et al. (2006) is provided. In this approach, the kinematics is prescribed, the thermal evolution is computed, and the

model parameters are adjusted by trial and error until they fit the observations. This approach provides a way to test more rigorously, and to refine, the kinematic model of Section 6.09.4.4. The next section describes how the Holocene kinematics can be reproduced from a mechanical model that accounts for both the erosion and the effect of temperature on the rheology of the crust (e.g., Cattin and Avouac, 2000).

Attempts at reproducing the long-term evolution of mountain range from thermomechanical modeling are not reviewed here because this work is more relevant to the geologic and geophysical data reviewed in the previous section. Readers interested in this kind of modeling, in which the kinematics of deformation is computed from the force balances, assuming some temperature-dependent rheology, and the mechanical and thermal evolutions are coupled, are referred, for example, to Beaumont et al. (2004), Toussaint et al. (2004a), and Toussaint et al. (2004b).

6.09.5.1 Thermokinematic Model of the Evolution of the Range Since 15 Ma

In this section, we describe a thermokinematic model that assumes that shortening across the range has been entirely taken up by slip along the MHT and that the growth of the Himalayan wedge has resulted from underplating only. Here, we refer to model KTM11 of Bollinger et al. (2006). An updated model has been obtained from a formal inversion of the large data set of thermochronological and thermobarometric data available from central Nepal and yielded a very similar kinematics (model 1 of Herman et al. (2010)).

A finite element model has been used to solve the heat advection–diffusion equation in transient state (Zienkiewicz and Taylor, 1989). The time-varying temperature field is thus computed from the assumed velocity field, boundary conditions, and material properties. The velocity field satisfies the continuity equation $\left(\vec{\nabla}\,\vec{v}=0\right)$, which implies continuity of the velocity normal to the fault along the underplating window. Vertical shear along hinge lines is allowed to accommodate variations in accretion rate (Figure 26). Peak T and cooling ages are then computed by particle tracking through the time-dependent temperature field.

The thermal structure is computed using based on the kinematics sketched in Figure 25, taking into account the effects of erosion, accretion, and shear heating. The topography is assumed to be steady state. For simplicity, the possible flat–ramp geometry is ignored, and the MHT is given a constant dip angle of 10°. A zone of underplating allows transfer of material from the footwall to the hanging wall (Figure 25). The thermal parameters, also indicated in Figure 25, were taken from Henry et al. (1997). The formal inversion of Herman et al. (2010) yielded an only slightly different radiogenic production of 2.2 μ Wm^{-3} for the Higher and Lesser Himalayan units and a value of 0.8 μ Wm^{-3} for the middle and lower crust of India.

The sum V_1+V_2, which represents the convergence rate across the range, V_0, was chosen to match the 21 mm $year^{-1}$ Holocene shortening rate. As inferred from the pattern of $^{39}Ar/^{40}Ar$ ages, the overthrusting rate was chosen to be $V_2=4$ mm $year^{-1}$, implying an underthrusting rate of $V_1=17$ mm $year^{-1}$. Because the model assumes steady-state topography, the underthrusting rate V_1 should be equal to the rate of progradation of sediments in the foreland. The position of the window of underplating was adjusted to fit the position and shape of the accreted LH units and to correspond with peak metamorphic temperatures in the 300°–550 °C range of observed values in the LH. The position of the window and the rate of underplating determine the gradient of peak metamorphic temperatures and the geometry of the accreted units. Because the topography is assumed to be steady state, they also determine the pattern of erosion at the surface. The metamorphic gradient observed near the front of the high range (Figure 26(a)), where peak metamorphism in the MCT zone was reached over the last 5–10 Ma, is different from that observed below the klippes farther south (Figure 26(b)), where peak metamorphism was reached *c.*15 Ma. The history of underplating was adjusted to fit these different gradients and to meet the structural constraint that the LH duplex developed over the last *c.*8 Ma (DeCelles et al., 2001; Robinson et al., 2001; Figure 20). The model fits both patterns by assuming an increase of rate of accretion via underplating at *c.*8 Ma.

The model that fits the data best and accounts for underplating of the Lesser Himalayan units (model 1 of Herman et al. (2010)) yields an erosion pattern grossly consistent with that derived from river incision across the Himalayas although rates are somewhat smaller (Figure 17). The model predicts a cooling history consistent with the various thermochronological data, including data from lower temperature

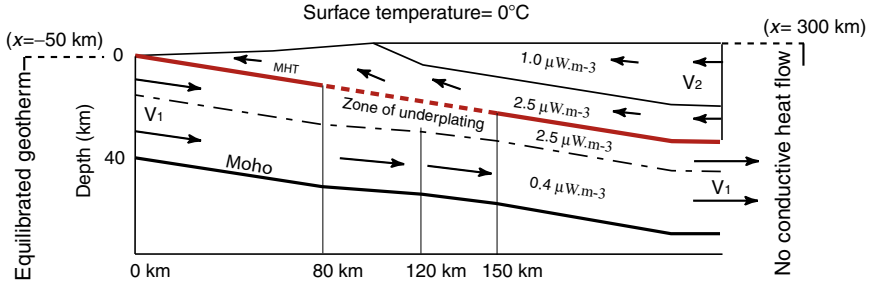

Figure 25 Model geometry, kinematics, and thermal parameters used for modeling cooling history corresponding to model KTM11 of Bollinger et al. (2006). Shear stress along the MHT is assumed to be the minimum between the ductile and the brittle shear stresses. We assume an effective friction $\mu=0.1$, and ductile stresses the ductile shear zone is taken to be 100 m thick and obeys a Quartz-type flow law (Henry et al., 1997). In the model, shear stresses do not exceed 50 MPa, values consistent with constraints obtained by comparing seismicity and current geodetic strain on maximum deviatoric stresses (Bollinger et al., 2004b). The reader is referred to Bollinger et al. (2006) for more details regarding the modeling.

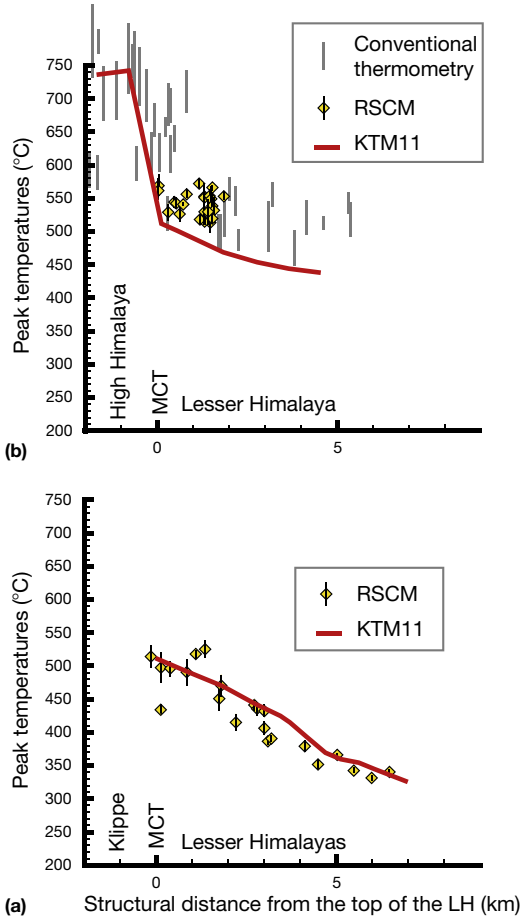

Figure 26 Peak temperatures estimated from RSCM thermometry and conventional thermometry at, respectively, 80 km (a) and 50 km (b) from the front of the range in central–western Nepal (data from Bollinger et al. (2004a) and reference therein). These data show an inverted metamorphic gradient, which the peak metamorphic temperature increasing upward, which encompasses the topmost 7–8 km of Lesser Himalayan units. Red curves show the prediction of model KTM11 (Bollinger et al., 2006).

thermochronological techniques than the $^{39}Ar/^{40}Ar$ data described earlier (Figure 27). These data are well distributed both in time (spanning the last 20 My) and in space covering a 400 km wide span of the Himalayan range.

The predicted peak temperatures also fit the observations reasonably well (Figure 26). It should be noted that the model predicts peak temperatures lower than 350 °C in the core of the anticlinorium at structural distances as short as 5 km from the top of the LH; this prediction is consistent with the report that muscovites were not reset for $^{39}Ar/^{40}Ar$ dating at this distance from the MCT (Bollinger et al., 2006; Wobus et al., 2005).

The model thus accounts for the inverted metamorphic gradient and is consistent with the thermochronological data available to date. It also reconciles the kinematics of recent crustal deformation deduced from morphotectonic and geodetic studies with the evolution of the range over the last 20 million years. According to this model, the Himalayan range has grown primarily by underplating with little internal shortening of the wedge, through the development of a midcrustal duplex straddling the brittle–ductile transition on the MHT.

This model, however, ignores possible activity along the STD between 16 and 20 Ma. Coeval thrust motion along the MCT and normal motion along the STD at this time would possibly have allowed rapid exhumation of the HHC as a result of midcrustal channel flows (e.g., Grujic et al., 1996; Searle et al., 2006). This effect is neglected, as most of the data we analyze here pertain to the more recent tectonic history of the range.

6.09.5.2 Modeling the Topography

The topography can be used to assess the model of crustal deformation described in the previous sections. In an attempt at doing so, Herman et al. (2010) had modeled the temporal evolution of the topography using a landscape evolution model (Braun and Sambridge, 1997). The kinematic field derived from the inversion of the thermochronological and thermometric data was used to impose horizontal advection and vertical uplift. Surface erosion was computed neglecting orographic forcing on rainfall, and the erosion parameters were estimated so as to ensure an overall balance between erosion and surface uplift for the present topography. This simulation reproduces the topographic break between the Lesser and the Higher Himalayas due to the locally higher uplift rate that results about equally from thrusting along the midcrustal ramp and from underplating (Figure 28). In this experiment, it only takes about 1 My to produce a topographic break that is dynamically steady in space and time. The short memory time is due to the relatively high erosion rate of about 3 mm $year^{-1}$ (Figure 17).

6.09.5.3 Modeling Deformation and Surface Processes Based on Continuum Mechanics

The data on recent deformation and the thermometric and thermochronological data from the central Nepal Himalayas all suggest that the shortening across the range has been taken up primarily by thrusting along the Main Himalayan Thrust fault, with negligible internal shortening of the Himalayan orogenic wedge.

Here, this kinematics is shown to be not only plausible from a mechanical point of view, provided that friction along the MHT is low, but also quantitatively consistent with the observed pattern of erosion and the present morphology of range. The modeling should therefore be seen primarily as a test of the internal consistency of the various data sets and as a validation of the hypotheses used to design the models. Furthermore, the modeling provides some insight into the mechanical properties required to fit the various observations, and it sheds light on the coupling between erosion and crustal deformation.

6.09.5.3.1 Model implementation

The models discussed here were computed from a 2-D finite element code (Hassani et al., 1997) initially designed to account for the mechanical layering of the crust. The code was modified to incorporate surface processes and the dependency of rheology on local temperature (Cattin and Avouac,

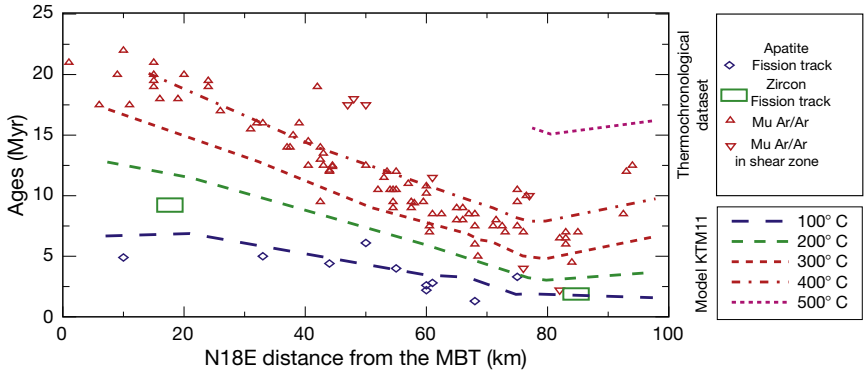

Figure 27 Synthesis of thermochronological ages from the Lesser Himalayas and HHC across the Himalayas of central Nepal. Data from Arita et al. (1997), Arita and Ganzawa (1997), Bollinger et al. (2004a), Catlos et al. (2001), Copeland et al. (1991), Macfarlane (1993), Wobus et al. (2003), and peter Copeland pers. comm. (1999) as in Bollinger et al. (2004a). The data are compared with the predicted cooling ages from model KTM11 for different closure temperatures. See **Figure 8** for location of section.

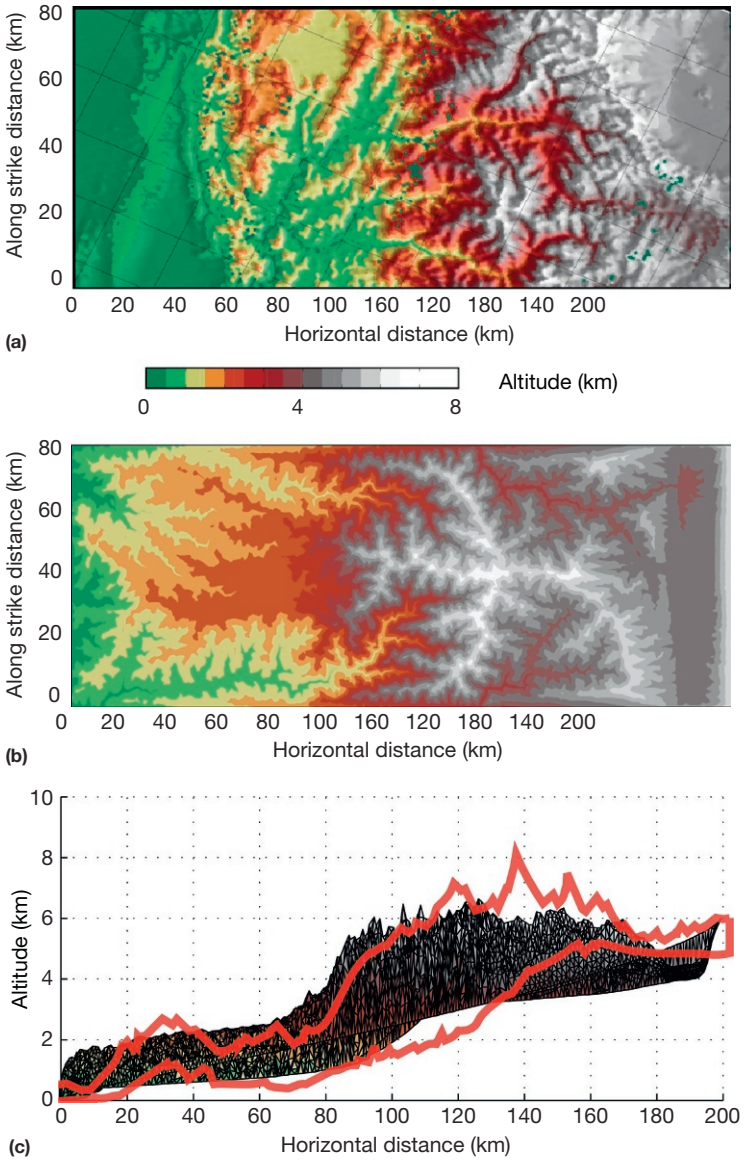

Figure 28 (a) Topography of the Himalayas of central Nepal, Kathmandu basin area. (b) Topography predicted from a landscape evolution model, imposing the kinematics derived from the inversion of the thermochronological and thermometric data. (c) Comparison of observed topography (red lines show minimum and maximum elevations) and modeled topography (black lines). Note that the model reproduces quite well the physiographic transition from the Lesser to the Higher Himalayas. Modified from Herman F, Copeland P, Avouac JP, et al. (2010) Exhumation, crustal deformation, and thermal structure of the Nepal Himalaya derived from the inversion of thermochronological and thermobarometric data and modeling of the topography. *Journal of Geophysical Research, Solid Earth* 115.

2000). We focus here on the initial model of Cattin and Avouac (2000), referred to here as CA2000. This model has been updated later on and several types of erosion laws were tested more recently (Godard et al., 2004, 2006).

The model CA2000 assumes a prescribed geometry for the MFT, with its characteristic geometry of ramps and flats along which quasistatic frictional sliding is allowed. Outside of the MFT proper, the medium is assumed to deform according to a combination of brittle failure and thermally activated ductile flow. Deformation thus depends on the boundary conditions, assumed rheology, and local temperature. The thermal structure is assumed a priori and was computed from a thermokinematic model similar to that predicted by KTM11 of Bollinger et al. (2006) or model 1 Herman et al. (2010).

A 700 km long section is initially loaded with the present average topography along section AA′ (**Figure 29**). A fault is introduced with a prescribed geometry representing the flat beneath the Lesser Himalayas and the midcrustal ramp at the front of the High Himalayas (**Figure 30**). The southern end of the model is fixed. At the northern end, vertical displacements are free and the upper crust is subjected to 20 mm year^{-1} of horizontal shortening by imposing a southward horizontal velocity of 20 mm year^{-1} between the surface and 40 km depth. At depths below 40 km, horizontal displacements are null so that the Indian mantle lid does not shorten. It should be noticed that these boundary conditions favor simple shear beneath Tibet.

The model is loaded with gravitational body forces ($g = 9.81$ m s^{-2}) and is supported at its base by hydrostatic pressure to allow for isostatic restoring forces.

Denudation of the range is modeled using 1-D linear diffusion, which assumes that the southward flux of sediments at the surface is proportional to the local slope. Conservation of mass then yields the erosion rate

$$e = k\frac{\partial^2 h}{\partial x^2} \qquad [13]$$

where k is the mass diffusivity coefficient, h is the elevation, and x is the horizontal distance.

The value of k was chosen to ensure an average denudation rate consistent with the 250–675 m^2 year^{-1} flux of sediments eroded from the range (Lavé and Avouac, 2001; $k = 10^4$ m^2 year^{-1}).

In the foreland ($x \leq 0$), the model assumes that sedimentation maintains a flat topography at a constant elevation.

The model assumes a depth-varying viscoelasto-plastic rheology. Brittle failure is determined by the Drucker–Prager criterion:

$$\frac{1}{2}(\sigma_1 - \sigma_3) = \left[c(\cot\phi) + \frac{1}{2}(\sigma_1 + \sigma_3)\right]\sin\phi \qquad [14]$$

where c is the cohesion and ϕ is the internal friction angle.

Viscous deformation is assumed to obey a power-creep law, consistent with laboratory experiments (Carter and Tsenn, 1987; Kirby and Kronenberg, 1987; Tsenn and Carter, 1987):

$$\dot{\varepsilon} = A_P(\sigma_1 - \sigma_3)^n \exp(-E_P/RT) \qquad [15]$$

where R is the universal gas constant, T is the temperature, E_P is the activation energy, and A_P and n are empirically determined constants (assumed not to vary with stress and (p, T) conditions). The ductile flow law thus depends on the rock type and on temperature.

The rheology of the mantle is thought to be governed by olivine and that of the upper crust by quartz (see parameters in

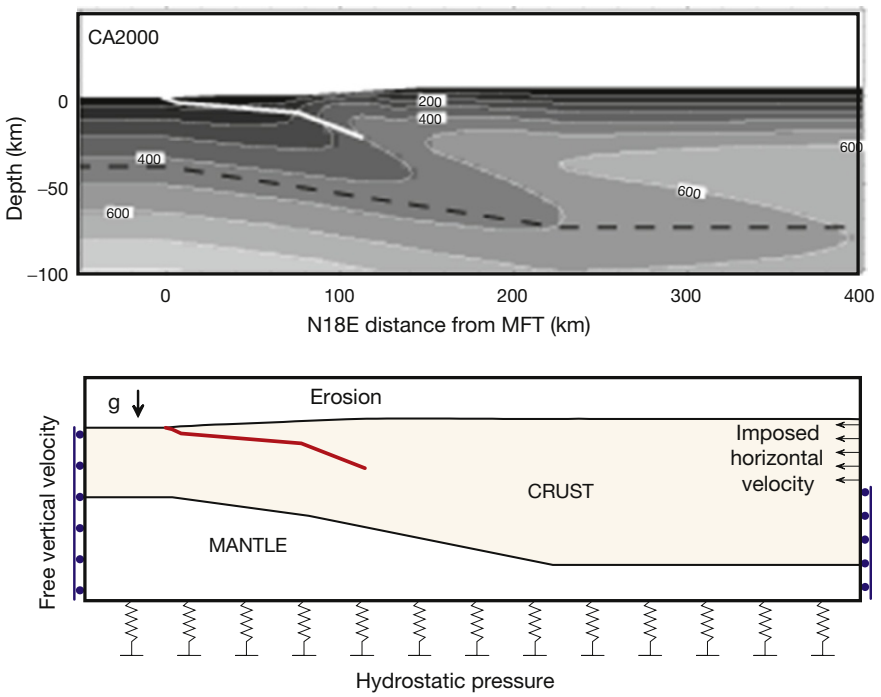

Figure 29 Setting of the numerical model of Cattin and Avouac (2000), referred here as CA2000. Bottom shows the boundary conditions. Top shows the assumed steady-state thermal structure.

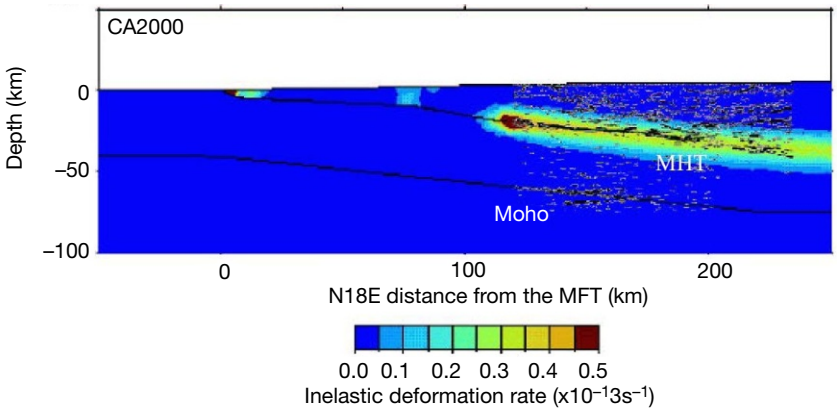

Figure 30 Shear strain rates over the long term computed by assuming a diabase rheology for the lower crust and quartz rheology for the upper crust (Cattin and Avouac, 2000). It shows a subhorizontal shear zone that closely follows the midcrustal reflector imaged by the INDEPTH experiment (Zhao et al., 1993).

Table 1 Physical parameters and material properties used in the mechanical models

Parameter	*Quartz*	*Diabase*	*Olivine*
ρ (kg m^{-3})	2900	2900	3300
E (GPa)	20	20	70
ν	0.25	0.25	0.25
c (MPa)	10	10	10
ϕ	30°	30°	30°
A_p (Pa^{-n}s^{-1})	6.03×10^{-24}	6.31×10^{-20}	7×10^{-14}
n	2.72	3.05	3
E_p (kJ mol^{-1})	134	276	510

ρ, density; E, Young's modulus; ν, the Poisson ratio; c, cohesion; ϕ, internal friction angle; A_p, power-law strain rate; n, power-law exponent; E_p, power-law activation energy (Carter and Tsenn, 1987; Kirby, 1987; Tsenn and Carter, 1987).

Table 1). For the lower crust, the two end-members have considered either a soft 'quartz' rheology or a stronger 'diabase' rheology (Table 1).

Fault friction

The MHT is assumed to follow a simple static friction law:

$$|\tau| - \mu\sigma_n \leq 0 \qquad [16]$$

where τ and σ_n are the shear and normal stress, respectively, on the fault, and μ is the effective friction coefficient.

6.09.5.3.2 Modeling results

Figure 30 shows the strain rate field in CA2000, obtained assuming a diabase rheology for the lower crust. The 'MHT,' along which quasistatic frictional slip occurs, roots into a subhorizontal shear zone that fits the prominent midcrustal reflector imaged from the INDEPTH profiles. This is a result of the position of the downdip end of the prescribed fault's geometry and of the a priori thermal structure that implies a subhorizontal zone locally weakened by higher temperatures (Figure 29).

Sensitivity tests have revealed that the effective friction, μ, along the MHT must be lower than 0.15. If basal friction is too high, the hanging wall shortens as it overrides the MHT. If friction is low enough, the hanging wall can ride over the MHT without much internal deformation. Distributed plastic deformation then only occurs in the vicinity of the kinks along the MHT ramp–flat geometry (Figure 30). The horizontal velocities are therefore nearly constant, with the exception of the discontinuity at the point where the fault meets the surface (Figure 31).

In CA2000, the 20 mm year^{-1} of horizontal shortening across the range is partitioned into ~15 mm year^{-1} of underthrusting and ~5 mm year^{-1} of overthrusting (Figure 31). This partitioning is thus quite close to that derived from the long-term kinematic evolution of the range.

The model leads to some natural balance between denudation and uplift rate. This balance is seen in Figure 31, in which denudation rate, modeled here from a simple linear diffusion equation, approximately equals the modeled uplift rate, and both are close to the pattern of fluvial incision. The model reproduces reasonably well the zone of localized uplift and erosion observed at the front of the high range. The modeled topography rapidly reaches steady state, or close to it. As expressed in eqn [12], uplift and erosion differ at steady state because erosio must compensate for uplift and for the horizontal transport of the hanging wall topography. The difference is small, less than ~1 mm year^{-1}, because the overthrusting rate is only ~20% of the convergence rate and the slope of the topography is 10–20% at most.

In fact, the assumption of a diffusive erosion law leads to a modeled topography in CA2000 that departs somewhat from the observed average topography in the study area (Figure 32). The predicted topography fails in particular in reproducing the break in slope at the front of the High Himalayas. Godard et al. (2004, 2006) were able to solve this problem and predict a more accurate topography by considering an erosion model (Lavé, 2005) that is still 2-D but takes into account river valleys and interfluves (Figure 32). Their model, which otherwise is the same as that of Cattin and Avouac (2000), assumes that fluvial incision is proportional to the shear stress in excess of some threshold (Lavé and Avouac, 2001) and that denudation of hillslope is driven by fluvial incision. An unexpected

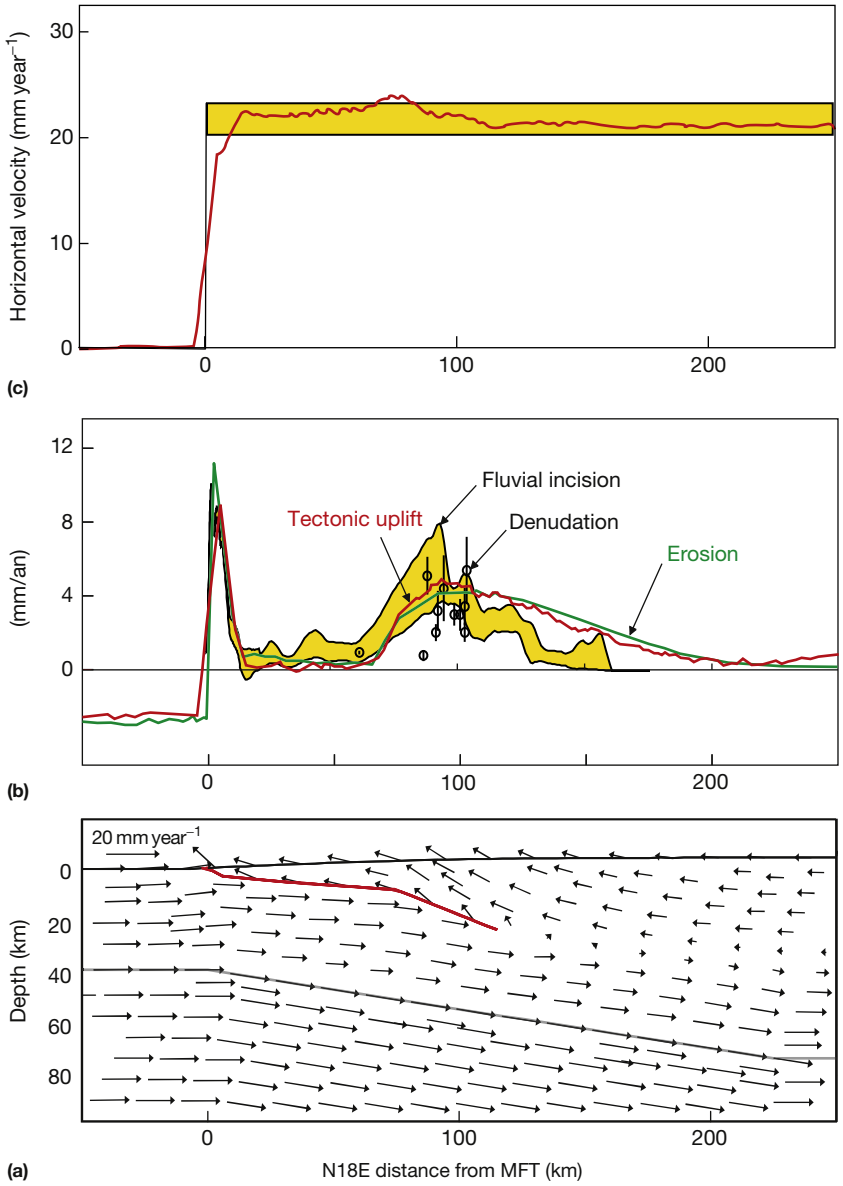

Figure 31 Velocity and horizontal and vertical displacement rates predicted by the FEM model of Cattin and Avouac (2000). (a) Velocity field relative to India. (b) Predicted uplift and erosion rates are compared to the measured river incision profile of Lavé and Avouac (2001) and to the erosion rates derived from thermochronological data (Burbank et al., 2003). (c) Horizontal velocity relative to India as derived from the slip rate on the MFT and predicted by the FEM model (red line).

result of this modeling is that relatively high viscosity in a lower crustal diabase rheology was found to better reproduce the topographic profile across the range than did the softer, quartz-like rheology applied by Cattin and Avouac (2000). This shows that rheology should not be assessed independently of the erosion law.

6.09.6 Geodetic Deformation and the Seismic Cycle

In the previous sections, crustal deformation was described as a continuous, steady process resulting from a combination of viscous deformation at depth and quasistatic plastic deformation in the upper crust. This is probably a reasonable approximation for deformation over a geologic period of time longer than 10 ka. However, the recurrence of large earthquakes associated with mountain building in the Himalayas (**Figure 33**) shows that deformation is not a steady process. It must result in part from seismic events or aseismic transients, like afterslip, and from viscous deformation that may not necessarily be stationary. Geodetic measurements offer a way to assess how this nonstationary deformation proceeds.

6.09.6.1 Large Earthquakes in the Himalayas

Three destructive $M_w > 8$ earthquakes have occurred in the Himalayan region since the end of the nineteenth century (Ambraseys and Bilham, 2000; Ambraseys and Douglas,

2004; Hough et al., 2005): the $M_w \sim 8.1$ 1897 Shillong earthquake that did not really occur along the Himalayan arc, the $M_w \sim 8.2$ Bihar–Nepal earthquake of 1934, and the $M_w \sim 8.5$ Assam earthquake of 1950. A number of more moderate earthquakes have been quite destructive including the $M_w \sim 7.8$ Kangra earthquake of 1905 and the $M_w \sim 7.6$ Kashmir earthquake of 2005 that claimed about 85 000 lives (**Figure 33**).

Considerable uncertainty remains as to the exact location and size of the 1934 Bihar–Nepal earthquake, the most recent large historical event in the study area (e.g., Chen and Molnar, 1977; Pandey and Molnar, 1988). Long-period seismic data indicate a released seismic moment of about 4.1×10^{21} N m., corresponding to $M_w \sim 8.4$ earthquake, could have occurred along a thrust fault with an $\sim 5^\circ$ northward dip (Molnar, 1984). Macroseismic intensities and subsidence of the foreland revealed from leveling data suggest that the earthquake ruptured a 250–300 km along-strike segment of the arc (Bilham et al., 1998; **Figure 33**). There are historical indications that Kathmandu has been struck repeatedly by severe earthquakes in the past (Pant, 2002; Rana, 1935). Major destruction was reported in 1255, 1344, 1408, 1681, and 1833. The 1833 event, estimated to $M_w \sim 7.7$, apparently ruptured the western part of the segment that ruptured again during the 1934 quake (Bilham, 1995), but the extent of damage in Kathmandu suggests a slightly smaller or more distant event. The 1255 earthquake was a major disaster that caused the death of King Abhaya Malla and killed about one-third of the population of Kathmandu Valley (Pant, 2002). Very little is known about the 1344 event, which may have caused the death of King Arimalla (Pant, 2002). When assessing these historical earthquakes, it should be noted that some palaces and temples in Kathmandu Valley built after the mid-fifteenth century remained intact until the 1934 event. These constructions had deep foundations (up to 15 m deep) and were reinforced by wooden frames so that they could resist significant shaking. The Temple of Shiva in Bhaktapur was one such building, built in 1458 CE but totally destroyed in 1934 (Pandey and Molnar, 1988). Some other temples built less strongly in the end of the fourteenth century or in the early fifteenth century survived until they were destroyed in 1934, suggesting that the 1681 and 1408 events were smaller than the 1934 earthquake. On this basis, the return period of earthquakes with magnitudes similar to or larger than the 1934 event may fall between 100 and 475 years.

The area between the locations of the 1934 and 1905 events represents an ~800 km long seismic gap. The most recent event that ruptured its eastern portion was probably the 1833 event.

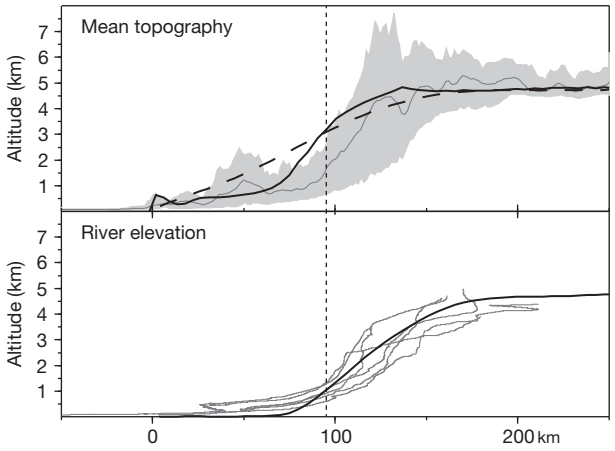

Figure 32 (Top) Comparison of the average topography across the central Nepal Himalayas with that predicted by model CA2000 and that of Godard et al. (2004). CA2000 assumes a linear diffusion model of erosion and a quartz rheology for the lower crust. Godard et al.'s (2004) model assumes that river erosion drives denudation of hillslopes and a diabase rheology for the lower crust. (Bottom) Comparison of river profiles along major rivers from central Nepal with the theoretical river profile predicted by the modeling of Godard et al. (2004).

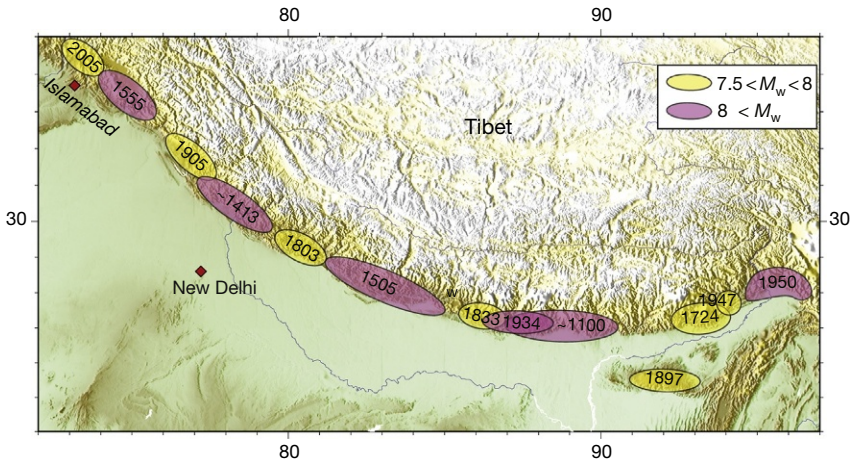

Figure 33 Estimated rupture area of major earthquakes along the Himalayas. Based on Ambraseys (2000), Ambraseys and Bilham (2000), Ambraseys and Jackson (2003), and Bilham (2004). The ~1100 and ~1413 AD events were both documented from paleoseismic studies (Kumar et al., 2006; Lavé et al., 2005; Upreti et al., 2000). There is a possibility that the paleoruptures along the front of the northwestern Himalayas, which were only loosely dated to ~1413 AD, might in fact relate to the 1505 historical earthquake (Kumar et al., 2006). If so, the magnitude of that event might have been close to M_w 9.

A large magnitude event along the western portion of the Himalayas was reported in 1803 (Oldham, 1883b). The magnitude of this earthquake is estimated to $M_w \sim 7.5$ by Ambraseys and Douglas (2004) but might be underestimated, in particular because the historical data are difficult to interpret due to the political situation in the area at that time (Bilham and Wallace, 2005). This earthquake ruptured an arc segment probably between Dehra Dun and far western Nepal, and its moment magnitude may have reached as high as 7.8 or 8. (Bollinger, 2002). Further back in time, historical accounts suggest a 'giant' earthquake in 1505, with a magnitude estimated to 8.2 by Ambraseys and Douglas (2003) but possibly >8.5 (Bilham and Wallace, 2005).

It has long been believed that large Himalayan earthquakes were not rupturing the surface (e.g., Seeber and Armbruster, 1981). In fact, the M_w 7.6 earthquake that ruptured the Himalayan front east of the Kashmir basin in 2005 (Avouac et al., 2006; Kaneda et al., 2008; Pathier et al., 2006) was the first example of a large Himalayan earthquake with documented surface ruptures. Surface ruptures extend over a distance of about 75 km, and the mean coseismic slip was measured to 4 m. It has recently been discovered that the 1934 earthquake actually broke the surface along the MFT over a distance of may be up to 150 km east of the Kathmandu basin (Sapkota et al., 2013). The MFT ruptured also during the 1255 historical earthquake (Sapkota et al., 2013). Evidence for even possibly much larger than the $M_w \sim 8$ historical events has also been reported. Along the Himalayan foothills in Nepal, there is evidence for a $17+5/-3$ m slip event on the MFT *c.*1100 *CE* at locations separated by 240 km along strike (Lavé et al., 2005; Nakata et al., 1998; Upreti et al., 2000). Evidence for a similar event with an age loosely constrained to *c.*1413 *CE* was also found in the Kumaon and Garhwal Himalayas (Kumar et al., 2006). In fact, there is a possibility that these paleoruptures might in fact relate to the 1505 historical earthquake (Ambraseys and Jackson, 2003), which would then be inferred to have ruptured the Himalayan front from western Nepal to Garhwal over a distance possibly as large as 800 km. If so, the magnitude of that event might have been close to M_w 9.

6.09.6.2 Geodetic Deformation in the Nepal Himalayas

The pattern of active deformation across the Nepal Himalayas has been documented from GPS geodetic measurements (Ader et al., 2012; Bettinelli et al., 2006; Bilham, 1997; Chen et al., 2004; Jouanne et al., 1999; Larson et al., 1999). Velocities relative to northern India rise from ~0 mm year^{-1} along the foothills, to ~3 mm year^{-1} around the Kathmandu basin, to ~15–17 mm year^{-1} north of the High Himalayas (**Figures 34** and **35**). The contraction perpendicular to the range is thus confined to a 100 km wide zone centered at the front of the High Himalayas. These data show that the MFT–MHT has remained nearly fully locked from where it emerges along the foothills to below the high range. Such data can be used to assess the current convergence rate across the Himalayas and the creep rate along the MHT (Ader et al., 2012; Bettinelli et al., 2006). This kind of analysis assumes that interseismic deformation can be modeled as the result of slip along a discontinuity embedded in a purely elastic medium. Deformation is computed based on the dislocation theory, generally using the formulation of Okada (1992). This is only a first-order approximation as the zone of deformation within the crust might have some finite width, and some fraction of interseismic strain of the medium might be anelastic (Meade, 2010). In practice, the data are adjusted reasonably well from a model in which the MHT is assumed to be fully locked from the surface to beneath the front of the High Himalayas, over a width of about 100 km, and creeping a uniform rate along its downdip continuation (**Figure 35**). Early analysis of this sort yielded a convergence rate of the order of 20 mm year^{-1} (Ader et al., 2012; Bettinelli et al., 2006; Bilham, 1997; Chen et al., 2004; Jouanne et al., 1999; Larson et al., 1999). In effect, simple 2-D models assuming complete locking of the MHT account for most of the data variance (**Figure 35**). The position of the best-fitting creeping dislocation inferred from such modeling was found to coincide remarkably well with the midcrustal reflector imaged beneath southern Tibet (**Figure 35**; Bettinelli et al., 2006). This observation adds further support to the interpretation of this reflector as the northward continuation of the basal detachment beneath the Himalayan wedge. The most recent geodetic data set assembled by Ader et al. (Ader et al., 2012; Bettinelli et al., 2006; Bilham, 1997; Chen et al., 2004; Jouanne et al., 1999; Larson et al., 1999) was used to solve jointly for the pattern of creep of the MHT and the convergence rate across the range. The Nepal Himalayas was divided into a western and eastern segments, respectively, west and east of the Kali Gandaki River that flows into the Thakkhola graben. Contraction across each segment is close to being perpendicular to the range and the prominent N–S-trending Thakkhola graben probably resulted from the E–W extension associated to the change of strike of the Himalayan front (Bettinelli et al., 2006; Bollinger et al., 2004b). The modeling yields a convergence rate of ± 1.0 mm year^{-1} across western Nepal and 17.8 ± 0.5 mm year^{-1} across eastern Nepal (**Figure 34**; Ader et al., 2012). The uncertainties stated here take into account the uncertainties on the original geodetic measurements and also on the plate motion of India. However, as is commonly done in tectonic geodesy, the uncertainty related to the geometry of the elastic dislocation model itself is ignored, as is the uncertainty related to the overall applicability of the model. The uncertainty in the geometry is probably the major source of error ignored in this analysis. The uncertainties on the elastic properties of the medium itself, which probably vary laterally and with depth in a setting such as the Himalaya, are ignored as well.

Despite the uncertainties in these estimates, the current rate of shortening across the Nepal Himalayas determined from geodesy appears remarkably close to the 21.5 ± 1.5 mm year^{-1} Holocene rate determined from morphotectonics (**Section 6.09.3**) or the ~22 mm year^{-1} rate estimated from foreland sediment progradation during underthrusting and thermochronological constraints on overthrusting over the last 15 Ma (**Section 6.09.4**). An implication is that most of the interseismic strain must actually be elastic so that slip rate along the deeper portion of the MHT be equal to the slip rate determined from the folding of the Holocene terraces in the Himalayan foothills (**Figure 36**).

Figure 34 shows the pattern of interseismic coupling on the MHT determined from the formal inversion of the geodetic data (Ader et al., 2012). The interseismic coupling is defined as

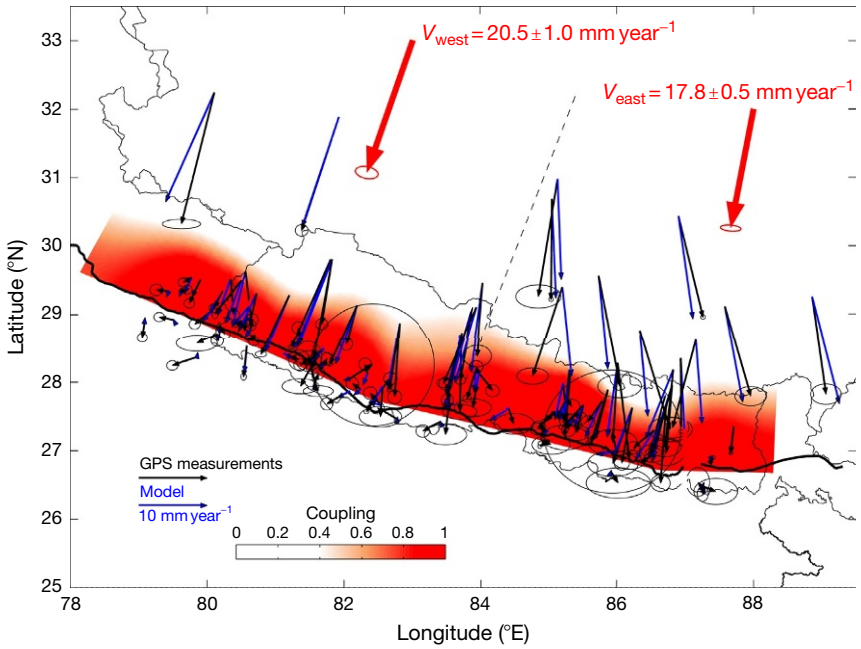

Figure 34 Horizontal velocities relative to stable India measured from geodetic measurements collected between 1991 and 2010 (Ader et al., 2012). Black arrows represent velocities determined from campaign and continuous GPS measurements. Ellipses show 87% confidence uncertainties. Color coding shows the degree of locking of the MHT derived from the inversion of these data, and the blue arrows show surface velocities predicted from this model on interseismic coupling. Red arrows show convergence velocities across the Himalayas determined for east and west Nepal, respectively (the areas, respectively, west and east of the dashed line).

the ratio of the slip rate deficit (the difference between the local creep rate on the MHT and the slip rate at depth needed to account for the total convergence rate across the Himalaya) divided by the slip rate at depth. A value of 1 means that the fault is purely locked and a value of 0 that the fault is creeping at the same rate as that required to account for the total convergence across the range. A striking result of this analysis is that the MHT appears fully locked updip of the front of the High Himalayas and that the transition to a fully creeping zone is very sharp (Figure 37). It occurs over a distance of <30 km. This value is close to the resolution power of the inversion suggesting that the transition could in reality be even sharper (Ader et al., 2012).

6.09.6.3 Microseismic Activity in the Nepal Himalayas

Local seismic monitoring in the Kathmandu area (Pandey et al., 1995, 1999) has revealed intense microseismic activity (Figure 38). Most events cluster in a narrow zone beneath the front of the high range at depths between 5 and 30 km. Initial observations suggest that the belt of seismicity ends abruptly to the north as soon as the elevation exceeds 3500 m, suggesting some cutoff effect due to the topography (Avouac, 2003).

This zone with high microseismic activity coincides with high uplift rates recorded in leveling measurements (Jackson and Bilham, 1994) and measured from SAR interferometry (Grandin et al., 2012) and lies quite close to the tip of the creeping zone as determined from the modeling of the geodetic deformation (Figures 39 and 40). This correlation suggests that the microseismic activity is triggered by stress buildup near the downdip end of the locked fault zone (Bollinger et al., 2004b; Cattin and Avouac, 2000).

The mechanical consistency of the simple model described earlier was tested using the FEM model CA2000 described in Section 6.09.5. To simulate the effect of the locked fault zone from this model, friction on the MHT was increased slightly (from 0.15 to 0.17) after the regime of quasistatic sliding along the MHT had been reached. At this stage in the model, frictional sliding along the fault was suddenly inhibited, while ductile shear extended along the subhorizontal shear zone beneath the high range and southern Tibet. The model successfully predicts horizontal displacement and uplift rates consistent with geodetic measurements (Figure 39), as well as stress accumulation near the northern edge of the locked fault. It turns out that 83% of the microearthquakes fall within this area of enhanced Coulomb stress (Cattin and Avouac, 2000).

The correspondence of seismicity cutoff to a particular elevation (3500 m) can be simply explained by the effect of elevation on the ambient stress tensor. Where topographic elevation gets higher than 3500 m, the north–south horizontal compression is no more the maximum horizontal stress. As a result, deviatoric stresses are no longer affected or even decrease during interseismic stress buildup (Bollinger et al., 2004b). Figure 40 compares the seismicity relocated from the double difference technique with the stress change computed from the model of interseismic deformation (Ader et al., 2012). Shear stress is counted positive if thrusting along the MHT is promoted. Seismicity is triggered where interseismic strain promotes north–south horizontal compression and where the elevation is <3500 m (so that north–south

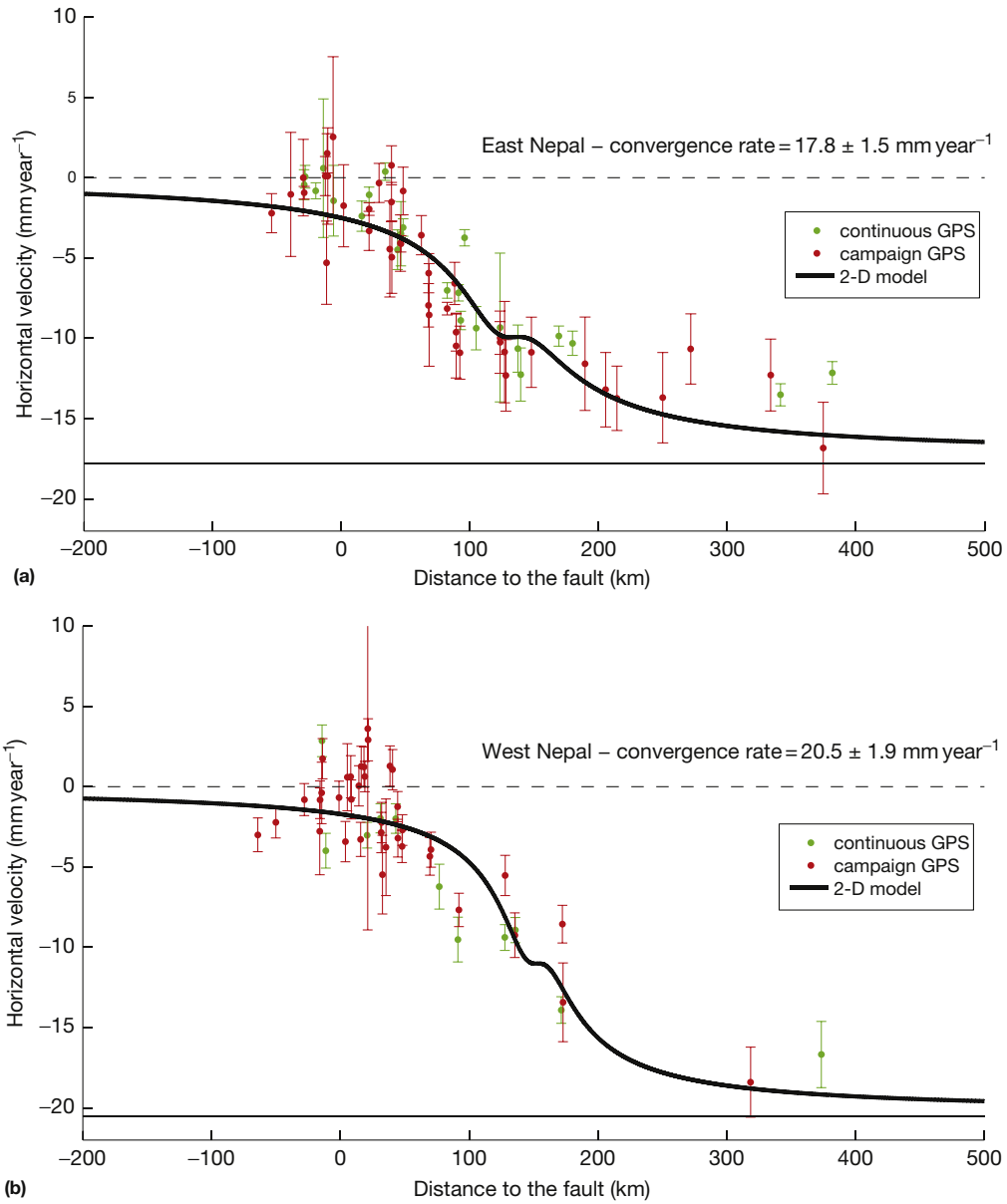

Figure 35 Horizontal velocities across the Himalayas of eastern (a) and western (b) Nepal. All data were projected on sections perpendicular to the range. Continuous lines show velocities computed from a simple 2-D model of interseismic strain that assumes a creeping dislocation embedded in an elastic half-space using the convergence rates derived by Ader et al. (2012) for eastern and western Nepal, respectively, east and west of the dashed line in **Figure 34**.

compression is the maximum horizontal stress). The deviatoric stresses in the 5–15 km depth range of the seismicity are thus estimated to a maximum of 35 MPa (Bollinger et al., 2004b).

Because the seismicity in this region releases an accumulated moment that amounts to, at most, a few % of the upper crustal strain revealed from geodetic monitoring, it holds that these earthquakes release an amount of strain that is insignificant compared to crustal deformation over the long term. The measured geodetic deformation therefore must be either permanent and aseismic or elastic. Significant nonrecoverable deformation of the upper crust in the interseismic period can be excluded, since localized slip on the MFT accounts for most, if not all, of the shortening across the range. The deformation measured over the last few years across the Kathmandu section thus necessarily reflects elastic strain of the upper crust that will be ultimately released by slip on the MHT. This stress transfer is probably chiefly the result of recurring major earthquakes rupturing the MHT.

6.09.6.4 What Controls Interseismic Coupling on the MHT?

To first order, the pattern of interseismic coupling along the MHT is binary. The MHT is essentially fully locked south of the front of the Higher Himalayas and fully creeping north of it. The transition occurs over a distance of <30 km. It thus appears that, in the

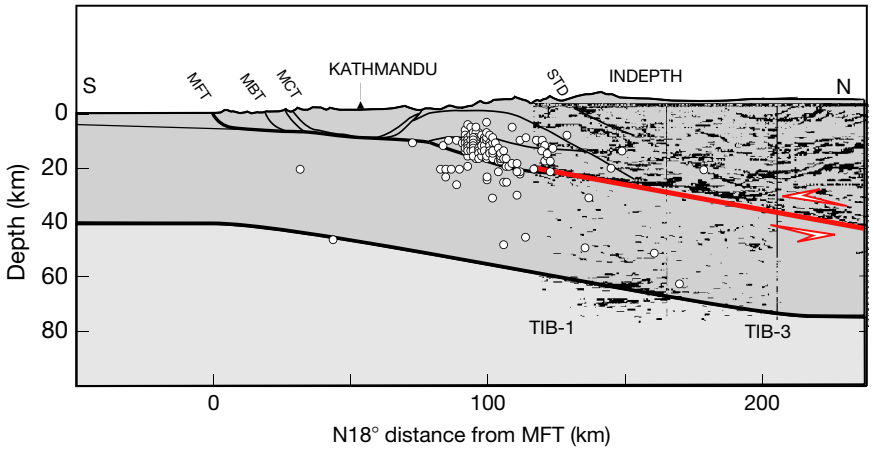

Figure 36 Outline of the structural cross section across central Nepal and the seismic sections, TIB-1 and TIB-3 of the INDEPTH profile (Hauck et al., 1998; Nelson et al., 1996; Zhao et al., 1993; see location in **Figure 6**). Thick continuous line shows the geometry of the creeping dislocation determined from the joined inversion of all geodetic data for central and eastern Nepal (Bettinelli et al., 2006). Hypocenters from well-constrained events recorded during the temporary deployment, in 1995, of three 3-component seismic stations in addition to the permanent seismic network (Cattin and Avouac, 2000).

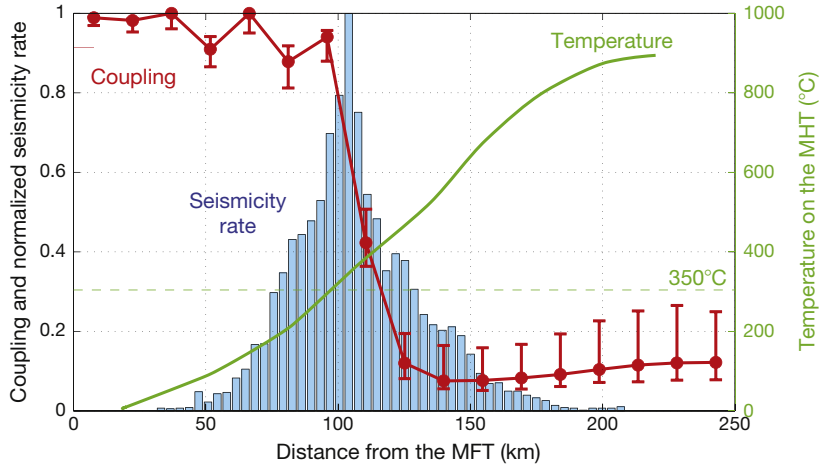

Figure 37 Comparison between interseismic coupling and temperature along the MH and seismicity across the Nepal Himalayas (Ader et al., 2012). Red line with error bars shows coupling along a section at the location of the Kathmandu basin where resolution is best due to the density of GPS data and vertical rates constrained from a leveling line. Blue histogram shows the seismicity rate, normalized to a maximum value of 1. Green curve shows temperature along the MHT determined from thermochronological and thermometric data (model 1 of Herman et al. (2010)). The thin dashed green line indicates for reference the critical temperature of 350 °C, above which frictional sliding is dominantly rate strengthening, promoting stable sliding, in laboratory experiments on quartzofeldspathic rocks (Blanpied et al., 1995; Marone, 1998).

Himalayan context, interseismic coupling varies essentially along the downdip direction. The homogeneous pattern of coupling along the MHT is very different from the strongly heterogeneous coupling observed on subduction megathrust characterized by both downdip and along-strike variations (Chlieh et al., 2008; Freymueller et al., 2000; Loveless and Meade, 2010; Moreno et al., 2010; Suwa et al., 2006; Wallace et al., 2004).

Temperature, pressure, metamorphic grade, and fluid contents are all factors that vary primarily along the downdip direction and that play a key role in controlling downdip variations of interseismic coupling along the MHT. It is commonly thought that temperatures would be the dominant controlling factor. Laboratory experiments on quartzofeldspathic rocks show that frictional sliding transitions from rate weakening, favoring unstable slip sliding hence locking in the interseismic period, to rate strengthening, favoring stable sliding hence aseismic creep in the interseismic period, at a temperature around 350 °C (Blanpied et al., 1991; 1995; Marone and Scholz, 1988; Marone, 1998). The thermal control has therefore been advocated as an explanation for the seismicity cutoff generally observed at a depth of around 15 km within continents. However, observational data supporting the theory have remained scant or inconclusive, in particular in the well-studied strike-slip context of the San Andreas Fault system (e.g., Magistrale, 2002). The theory would hold well for the Himalayas as shown by the comparison of interseismic coupling and temperature on the MHT along a section across the range where both quantities are well constrained (**Figure 37**): the transition from unstable sliding to stable sliding occurs where the temperature is estimated to increase from about

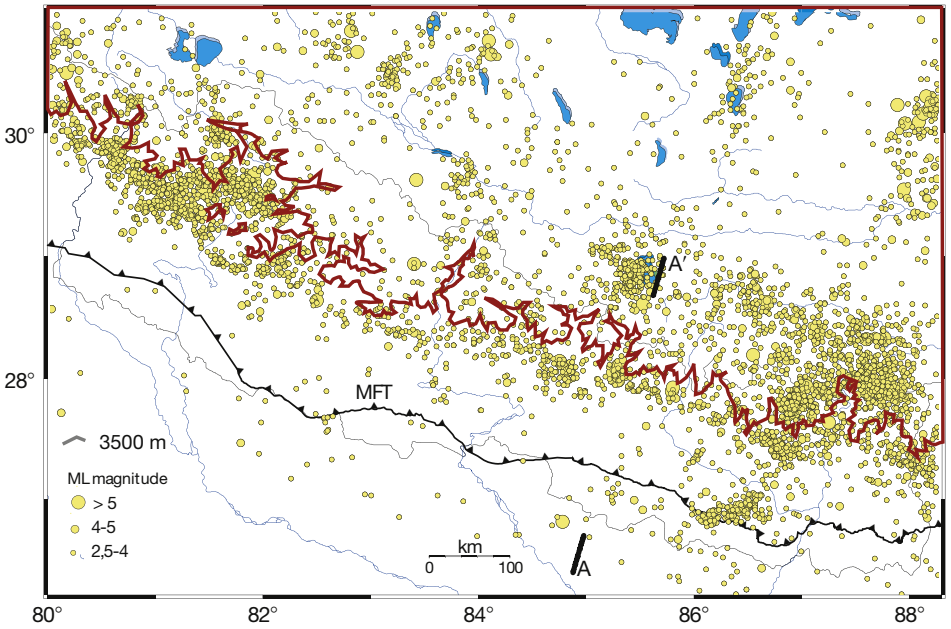

Figure 38 Seismicity of Nepal recorded by the DMG seismological network between April 1995 and October 1999 (Pandey et al., 1999). The red line follows the 3500 m elevation contour line. Seismic activity north of this zone is mostly related to active normal faulting in southern Tibet. South of this line seismic activity, due to NS compression, is most probably triggered by interseismic strain.

300 to 500 °C. This consistency does not warrant that the temperature effect observed in the laboratory experiments is the key mechanism at play along the MHT, however. Note that the coincidence between the transition to stable sliding and the zone of higher-conductivity images from the magnetotelluric sounding experiment described previously also suggests that fluids and possible metamorphic reactions may influence the position of the downdip end of the locked fault portion. It fact, because of the cylindrical geometry of the system, it is challenging to identify with any certainty what is the controlling factor of the mode of slip on the MHT.

6.09.6.5 A Model of the Seismic Cycle in the Central Nepal Himalayas

While motion along the locked portion of the MHT is probably stick slip and results from recurring large earthquakes, aseismic creep prevails on the deeper part of the interface. The elastic strain accumulated in the upper crust during the interseismic period must be transferred to slip on the MFT at the surface. This strain transfer most probably results from large earthquakes that activate the portion of the MHT that remains locked in the interseismic period. Trenching investigations have now shown evidence for coseismic surface ruptures along the front of the Nepal Himalayan foothills due to past events whose moment magnitude probably exceeded M_w 8.0 (Lavé et al., 2005; Sapkota et al., 2013). In fact, seismicity is continuously triggered by interseismic stress buildup near the downdip end of the locked fault zone, and some of these earthquakes probably occur on the MHT. As this seismicity obeys the Gutenberg–Richter magnitude–frequency distribution (Pandey et al., 1999; **Figure 42**), only a very small fraction of these earthquakes do evolve into large events. Most events actually fail to propagate up to the surface. For example, the M_w 6.8 1991 Uttarkashi earthquake nucleated beneath the front of the High Himalayas and ruptured the MHT (Cotton et al., 1996). It thus probably ruptured the downdip edge of the locked fault zone. This event, as most events nucleating there, did not propagate all the way to the Himalayan piedmont, possibly because the elastic stresses in the surrounding elastic medium were too low to sustain the propagation of the seismic rupture. It might then be conjectured that events of $M=7$ contribute to loading of the shallow-dipping decollement below the Lesser Himalayas, raising elastic stresses there until one event ruptures all the way to the surface. These $M>7.5$ events probably account for most of the stress transfer to the front of the thrust fault system (**Figure 41**). Aseismic creep could also contribute to some fraction of fault slip within the area that has remained locked over the period covered by the geodetic measurements. Aseismic creep could occur as spontaneous slip event or as afterslip following large earthquakes. There are no examples yet documented of significant aseismic transient on continental thrust fault. By contrast, seismic afterslip is probably quite systematic. For example, most of the postseismic deformation following the Kashmir earthquake or the Chi-chi earthquake in Taiwan resulted from afterslip downdip of the ruptured fault patches (Hsu et al., 2002; Jouanne et al., 2011). In these examples, afterslip released an equivalent moment of <60% of the coseismic moment.

6.09.6.6 Geodetic Deformation, Seismic Coupling, and Recurrence of Large Earthquakes in the Himalayas

The average return period of the largest Himalayan earthquakes might then be estimated by assuming that the

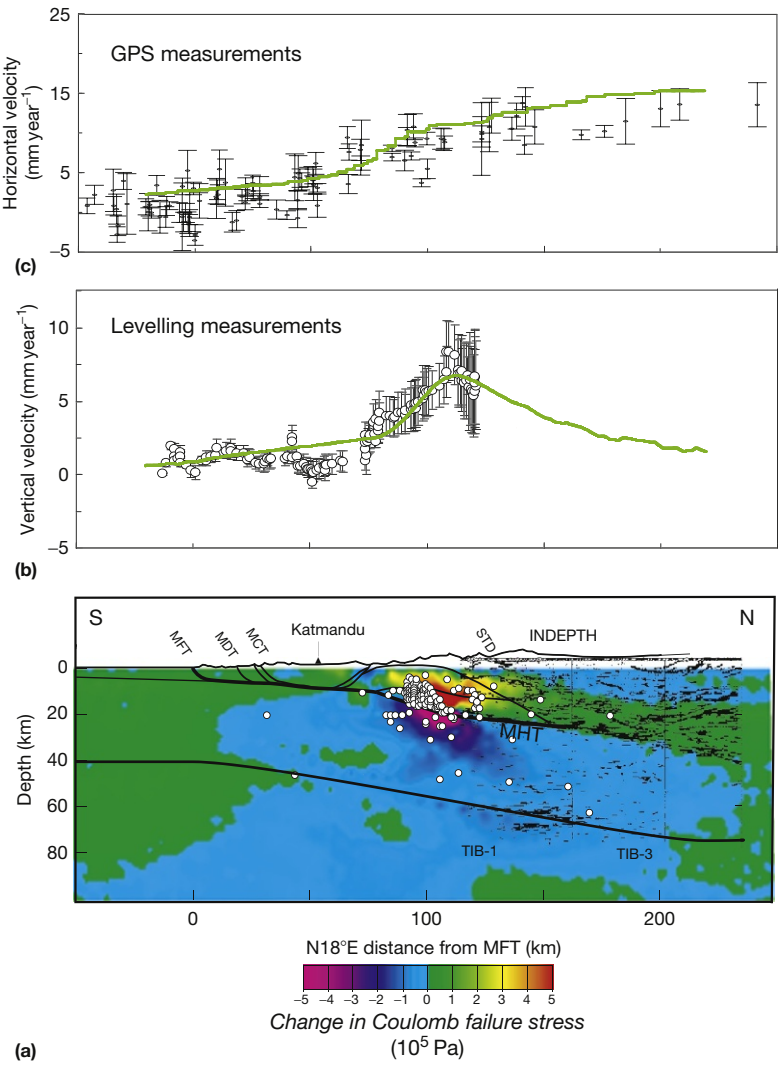

Figure 39 (a) Horizontal velocities relative to India along section AA′ computed from CA2000 (Cattin and Avouac, 2000; continuous line) compared with velocities estimated from GPS measurements (Ader et al., 2012). (b) Measured uplift rates (circles; Jackson and Bilham, 1994) and theoretical uplift rates (continuous line) computed from CA2000 (Cattin and Avouac, 2000), assuming a shortening rate of 16 mm year^{-1}. (c) Coulomb stress changes due to 350 year of interseismic strain computed from model CA2000 and observed seismicity projected on section AA′ (white dots; Cattin and Avouac, 2000).

interseismic deficit of slip, which accumulates in the Nepal Himalayas at the rate of 6.5×10^{19} Nm year^{-1} when converted into a moment rate, is entirely balanced by seismic slip and associated afterslip (*Ader et al., 2012*). This analysis suggests that the known historical earthquakes, which reached M_w 8.2 in Nepal in 1934, fall well short of balancing interseismic strain (**Figure 42**). One possibility would be that $M_w > 8$ be more frequent in the longer run than what the historical data suggest. If the largest earthquakes are assumed to reach up to M_w 8.5, the magnitude of the 1950 Assam earthquake, their return period in the Nepal Himalayas would need to be of the order of 50 years to balance interseismic strain. This seems inconsistent with the historical record as $M_w > 8$ is documented to have struck Nepal only in 1934, 1505, and probably 1255. Another option would be that even larger earthquakes, with $M_w > 8.5$ as some paleoseismic studies have suggested (Lavé et al., 2005), might occur. None would have occurred over the historical period owing to their long (>1000 year) return period. The fact that no segmentation is seen in the interseismic coupling model (**Figure 40**) makes it possible that a large rupture could propagate laterally over a distance larger than the typical 200–300 km inferred for historical $M_w \sim 8$ events (**Figure 33**). The problem of the deficit of seismic moment probably holds for the whole Himalayan arc (Bilham et al., 2001), and the prospect for possibly very large ($M_w > 8.5$) infrequent earthquakes is a looming perspective for the whole region. The reasoning could be partly flawed because of a possible overestimation of the average convergence rate and of the degree of interseismic locking and ignorance of possible aseismic transient slip. The uncertainties involved with the various estimated quantities of these reasonings thus provide the possibility that a fraction of the slip on the locked portion of the MHT is in fact aseismic. Better monitoring of geodetic deformation in the Himalayas will help address that

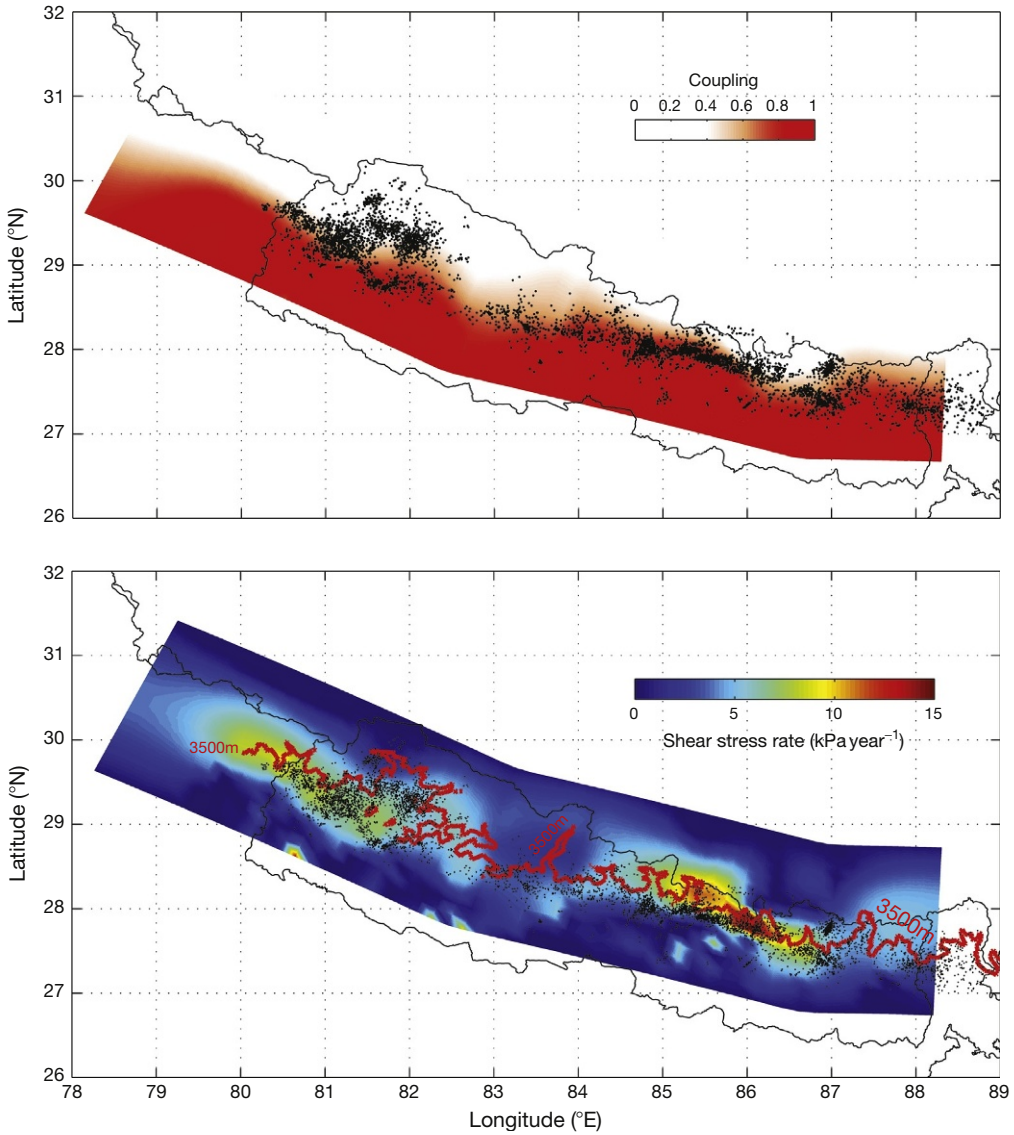

Figure 40 Comparison between seismicity distribution, interseismic coupling (top), and interseismic shear stress increase rate on the MHT (bottom; Ader et al., 2012). The seismicity reported here was relocated by the double difference technique (courtesy of Sudhire Rajaure, DMG/NSC). The thick red line represents the 3500 m elevation contour line above which the seismicity seems to drop. Seismicity follows approximately the downdip end of the locked zone of the MHT. Closer inspection reveals that seismicity is clustered where shear stress increases in the interseismic period and where the elevation does not exceed 3500 m.

question in the future and help constrain better the rate of accumulation of moment deficit, at the scale of the whole Himalayan arc, due to be released by future earthquakes.

6.09.6.7 Is Interseismic Strain Stationary?

The model of interseismic coupling described earlier is based on geodetic data collected between 1991 and 2010. This period represents probably only a small fraction of the average time span between the largest earthquakes in the area. Interseismic coupling has been observed to be nonstationary on subduction megathrust (e.g., Nishimura et al., 2004).

In addition due to stress transfer associated with the seismic cycle, strain rates during the interseismic period should not be stationary. Indeed, there should be some time variation in crustal straining in the period between two large recurring earthquakes due to both frictional afterslip and ductile flow (e.g., Cohen, 1999; Pollitz et al., 1998; Smith and Wyss, 1968). In the case of the Himalayas, a strong asymmetry of the postseismic relaxation should be expected due to the presumably much lower viscosity beneath southern Tibet. In this setting, a viscous strain wave would be expected to propagate north of the range following each large earthquake rupturing at the front of the Himalayas (Bott and Dean, 1973). The result of the apparent shortening rate across the range might appear larger in the early postseismic period than in end of the interseismic period. This mechanism has been analyzed based on a simplified 1-D model of the seismic cycle (Perfettini and Avouac, 2004) and in 2-D models

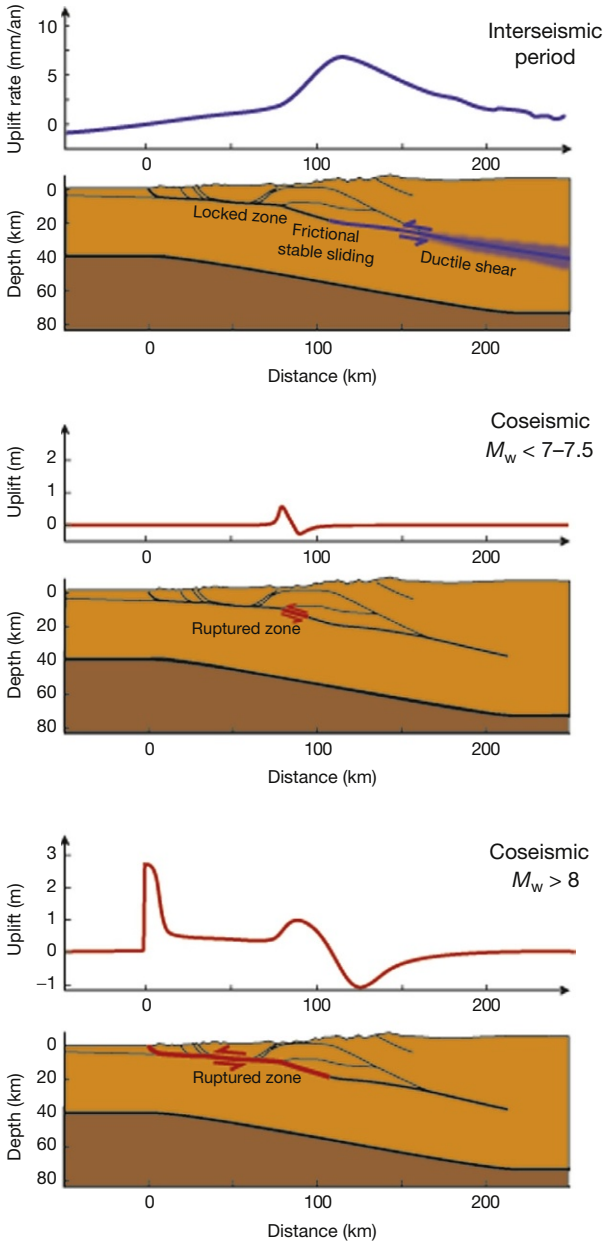

Figure 41 Model of the seismic cycle in the Nepal Himalayas. Slip along the locked portion of the Main Himalayan Thrust fault is thought to result from ductile at depth greater than about 20 km, where temperature exceeds about 350 °C. The shallower portion of the MHT is thought to slip either during blind thrust earthquakes with magnitude typically <7.5 or during larger earthquakes breaking the surface along the trace of the MFT. Seismicity off the MHT is thought to play a negligible role in the strain budget.

(Hilley et al., 2009; Johnson and Segall, 2004). In the 1-D simple model, the behavior of the thrust fault system is simplified and modeled as a simple spring-and-slider system loaded by a constant force. Three main domains with different rheologies are considered, with the springs allowing stress transfer between them during the seismic cycle. The upper fault portion is assumed to undergo unstable frictional sliding and is modeled by slider 1 with a state-and-rate friction law (Dieterich, 1979; Rice and Tse, 1986). Its behavior is obtained by solving the following equations:

$$\tau_1 = \sigma_1(\mu_* + a_1 \log(V/V_*) + b_1 \log(\theta V_*/D_c)) \quad [17]$$

$$d\theta/dt = 1 - (\theta V/D_c) \quad [18]$$

where τ_1 is the shear stress; σ_1 is the effective normal stress set to some arbitrary value of 250 MPa (corresponding to a depth of about 10 km); μ_* is the steady-state friction coefficient corresponding to some reference sliding velocity V_*; and a_1, b_1, and D_c are frictional parameters that were chosen together with the spring rigidity in order for slip to be unstable and to obtain a coseismic slip of the order of 5 m.

The deeper fault portion is assumed to undergo rate-strengthening brittle creep. This process is modeled from a rate-strengthening friction law associated with slider 2:

$$\tau_1 = \sigma_2(\mu_* + a_2 \log(V/V_*)) \quad [19]$$

where $a_2 > 0$ to ensure stable sliding.

The fault roots at depth in a ductile shear zone with viscosity η, arbitrarily assumed to be about $w = 5$ km thick. This fault portion is modeled from a viscous slider so that

$$\tau_3 = \eta^* V_3 \quad [20]$$

where $\eta^* = \eta/w$. Motion of the most frontal slider, slider 1, would represent the slip along the seismogenic fault portion. Motion of slider 3 represents the convergence across the fault system. A constant force, F, is applied on slider 3, which was adjusted in order to produce an average slip rate $V_0 = 20$ mm year^{-1}.

The behavior of the system is then characterized by the following:

- The coseismic slip: ΔU
- The duration of the interseismic period: $\Delta t = \Delta U/V_0$
- The Maxwell relaxation time defined here as $T_M = k/\eta^*$
- The brittle relaxation time defined here as $t_R = a_2\sigma_2/kV_0$

If the driving force, F, exceeds some critical value, F_c, determined by the frictional coupling between the upper plate and the lower plate, the system produces recurrent slip events, with a return period T, followed by afterslip (due to the second slider) and viscous relaxation (due to the third slider).

If the viscosity is high, that is, if the Maxwell time is of the order of the duration of the interseismic period, slider 3 has a nearly uniform motion. If the Maxwell time is much shorter than the duration of the interseismic period, then some significant variations are observed. More precisely, the model predicts that the shortening rate at the end of the interseismic period, v_f, relates to the shortening rate at the beginning of the postseismic relaxation, v_i, according to

$$\frac{v_i}{v_f} = \exp\left(\frac{T}{T_M}\right) \propto \frac{\Delta\tau}{F - F_C} \quad [21]$$

where $d\tau$ is the coseismic stress drop. So if the coseismic stress drop is large compared with the preseismic deviatoric stresses driving viscous flow at depth, variation of strain in the interseismic period might be significant.

The Maxwell time is difficult to estimate in the absence of geodetic measurements of postseismic relaxation following

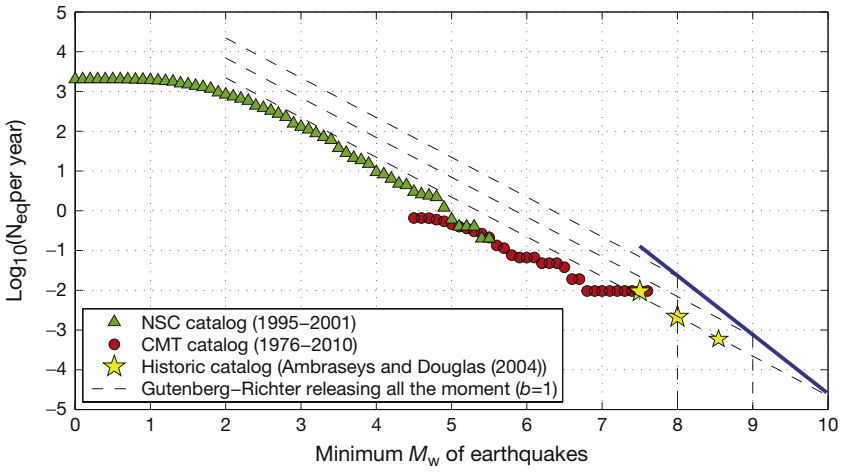
Log10(Neq per year)
Minimum Mw of earthquakes
NSC catalog (1995–2001)
CMT catalog (1976–2010)
Historic catalog (Ambraseys and Douglas (2004))
Gutenberg–Richter releasing all the moment (b=1)

Figure 42 Frequency–magnitude distribution of Himalayan earthquakes. Different catalogs are plotted that all show the typical Gutenberg–Richter distribution with a *b*-value close to 1. The green symbols represent the 1995–2001 catalog of local earthquakes recorded by the Nepal seismic network (Pandey et al., 1999). Red symbols show frequency–magnitude distribution of thrust events (with a rake between 45° and 135°) from the CMT catalog (1976–2010). Seismicity recorded along the whole Himalayan arc was rescaled to the size of Nepal territory (which covers about a third of whole Himalayan arc). This catalog is dominated by the aftershocks of the 2005 M_w 7.6 Kashmir earthquake (45 out of the 69 events). Yellow symbols show historical earthquakes in the Nepal Himalayas based on the catalog of Ambraseys and Douglas (2004). To compensate for the incompleteness of this catalog, the last 500 years were considered for $M_w > 8$ earthquakes and the last 200 years for $M_w > 7.5$ earthquakes. The thick blue line shows the return period of the maximum magnitude earthquake required for seismicity to balance the moment deficit due to locking of the MHT in the interseismic period. The three dashed lines show the distribution that the seismicity should follow for an assumed maximum magnitude of either 8, 9, or 10.

Himalayan earthquakes. The modeling of the interseismic and longer-term kinematics of deformation across the range provides some constraints but is not very discriminant (Cattin and Avouac, 2000; Godard et al., 2004). The fact that 'quartz'-like rheology (**Table 1**) seems too weak (Godard et al., 2004) places a lower bound on the possible value of the Maxwell time. Given the thermal structure of the range, such a nonlinear rheology leads to a postseismic relaxation similar to the relaxation of a linear viscous body with a Maxwell time of the order of several years. The evidence for time variation of the interseismic strain pattern might be better found by looking at lateral variations of the interseismic strain or by comparing the long-term rate with the current rate of convergence across the range. The data are insufficiently precise to detect significant difference. In fact, the shortening rate across western Nepal Himalayas, where no large earthquake is known to have occurred for several centuries, is apparently slightly larger than across eastern Nepal Himalayas, which ruptured in 1934, while the opposite would be expected. This discussion that is based on a simple 1-D model is only tentative at this point. In reality, stress transfer occurs in 3-D, and coseismic stress drop due to the rupture of a particular arc segment would be compensated by increased stresses on adjacent segment and elastic response of the whole surrounding medium (not only of the thrust sheet as modeled here). Also the northward propagation of the postseismic strain wave is ignored. A proper analysis of this possible mechanism would require better geodetic measurements, especially across southern Tibet, where the gradient of horizontal displacement should vary during the seismic cycle, and 3-D viscoelastic modeling.

6.09.7 Discussion

6.09.7.1 The Critical Wedge Theory: Does It Apply to the Himalayas?

The geometry of the Himalayan orogen, together with the early view that the MCT, MBT, and MFT were crustal-scale thrust faults that formed in a forward propagation sequence (**Figure 43**), has inspired the idea that the Himalayas could be a crustal-scale equivalent of an accretionary prism, an analogue to the wedge of sand that forms in front of a moving bulldozer (Davis et al., 1983). The formation of this wedge can be easily reproduced in 'sandbox' experiments (e.g., Davis et al., 1983; Malavieille, 1984). When sand layers are detached from a rigid basement and pushed by a moving buttress, they form a wedge with a nearly constant slope (**Figure 44**). This wedge is critical, meaning that any point within the wedge is at the verge of failure. In this experiment, the geometry of the wedge is dictated by the balance between frictional stresses at the base of the wedge and stresses induced by the slope of the wedge (Chapple, 1978; Dahlen, 1990; Dahlen and Suppe, 1988; Davis et al., 1983). The self-similar growth of the wedge results from frontal accretion by southward propagation of the deformation front and from thickening and shortening of the wedge (**Figure 43**).

For a homogeneous, noncohesive, brittle wedge obeying the Coulomb–Mohr failure criterion (e.g., Jaeger and Cook, 1979; which is close to the Drucker–Prager criterion mentioned earlier), the taper angle, $\alpha + \beta$, assumed small, is approximately given by Davis et al. (1983), Barr and Dahlen (1990), and Dahlen et al. (1984):

$$\alpha = \frac{\mu'_b - 2\mu'\beta}{1 + 2\mu'} \quad [22]$$

where α is the slope of the topography and β is the slope of the basement. μ'_b and μ' characterize the basal friction and the compressive strength of the wedge, respectively, and are referred to as the effective basal friction and effective wedge strength (Barr and Dahlen, 1989). These values depend on the ratio λ of the pore-fluid pressure to the lithostatic pressure (Hubbert and Rubey, 1959), according to

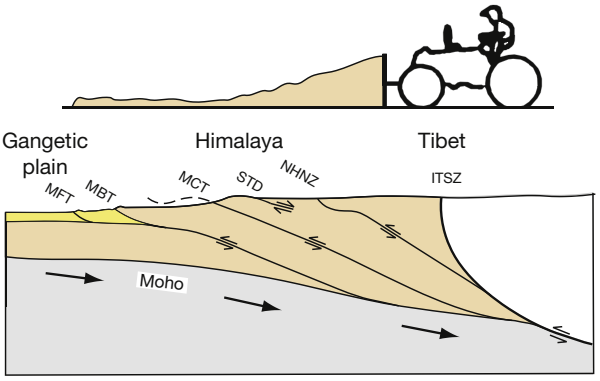

Figure 43 Schematic geologic section across the Himalayas of central Nepal reflecting early interpretation of the major thrust faults as crustal-scale parallel faults. Analogy with the geometry of a sand wedge at front of a bulldozer.

$$\mu'_b = (1 - \lambda_b)\mu_b \quad [23]$$

$$\mu' = (1 - \lambda)\frac{\sin\phi}{1 - \sin\phi} \quad [24]$$

where ϕ the internal friction angle (the coefficient of internal friction is $\mu = \tan\phi$) and μ_b is the basal coefficient of friction.

Equation [22] expresses how the topographic slope of a critical wedge depends on the dip angle of the basement and on the basal friction and strength of the wedge. It shows in particular that the slope of the wedge increases with the basal friction.

Without erosion (as in Figure 44), the wedge would grow indefinitely and the force needed to drive deformation would increase as the square of the thickness of the wedge. This is because the force transmitted at the interface between the underthrusting basement and the overthrusting wedge is the integral of the basal shear stress along the length of the basal contact, which both increase linearly with the thickness of the self-similar wedge.

If erosion is taken into account, as it should be to reproduce the evolution of a subaerial fold-and-thrust belt or of a mountain range as whole, the wedge reaches some steady-state geometry with particle trajectories like those pictured in Figure 45. It is then possible to derive an analytic expression of the velocity field (Barr and Dahlen, 1989). Horizontal shortening is distributed throughout the prism and the horizontal velocity at the surface can be derived from a simple mass balance (Avouac, 2003), yielding

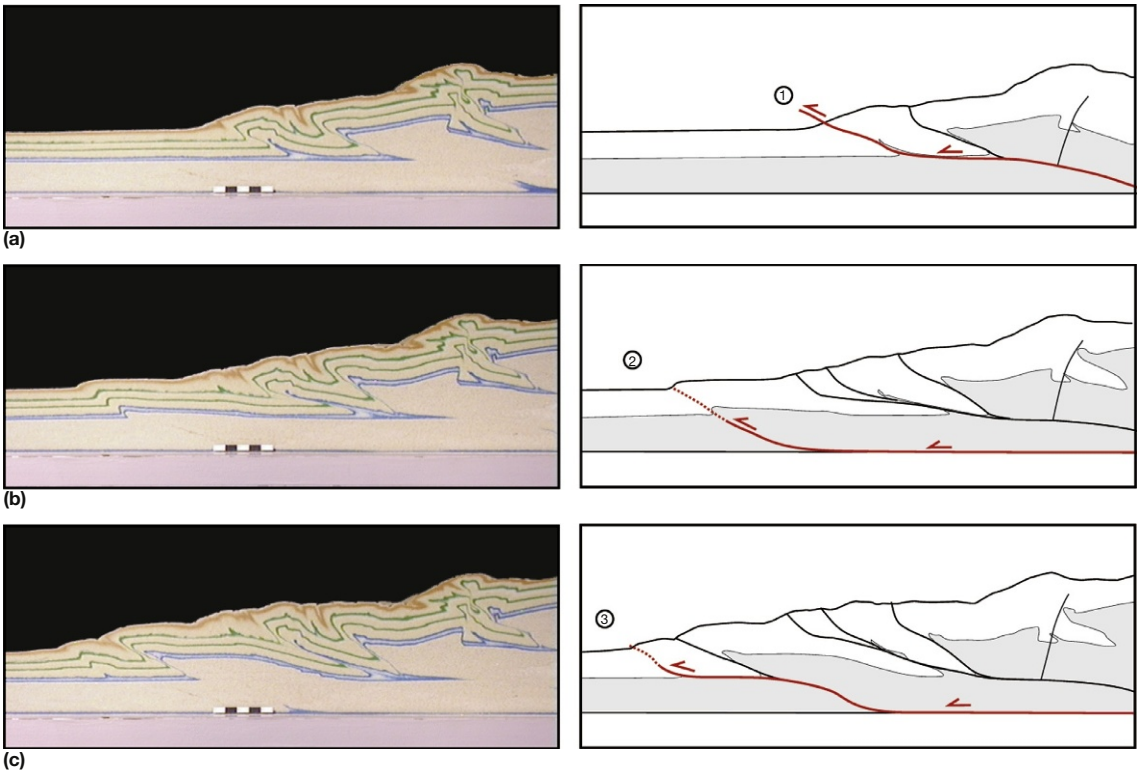

Figure 44 Example of an analogue modeling of growth of a brittle wedge. A rigid backstop moves to the left over a fixed rigid basement inducing detachment of the sand layers. Note the forward propagation sequence of thrusting. Courtesy of Stephane Dominguez, ISTEEM, Montpellier.

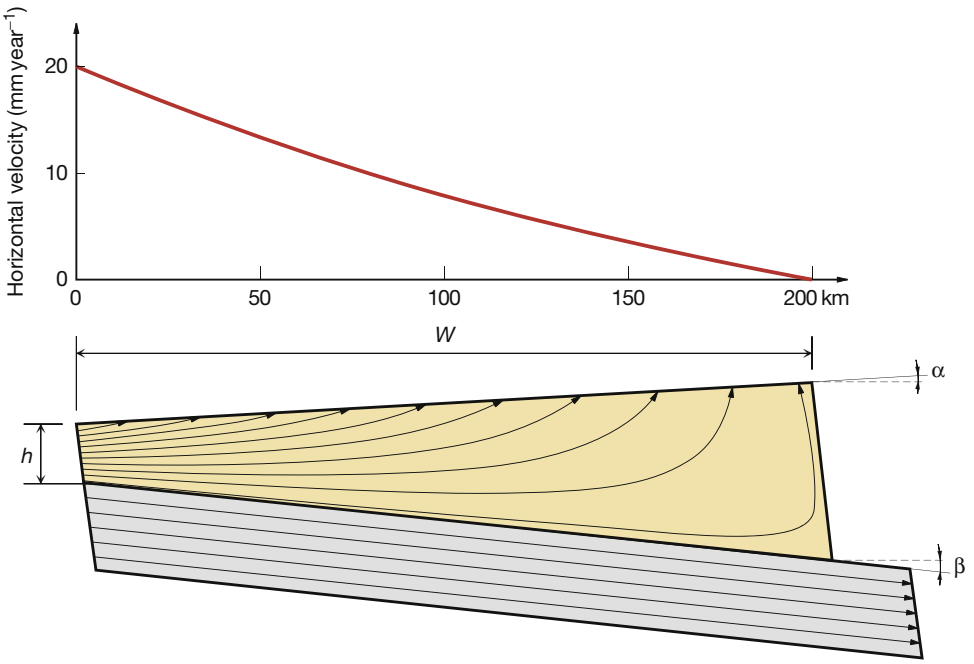

Figure 45 Particle trajectories in a steady-state critical accretionary prism subjected to erosion (Barr et al., 1991). Horizontal surface velocities computed from eqn [25] for $h = 15$ km, $W = 200$ km, tg $(\alpha + \beta) = 4\%$, and $V_0 = 20$ mm year^{-1}.

$$V(x) = \frac{V_0 h(W - x)}{W(h + x\tan\phi)} \qquad [25]$$

where the origin of the abscissa is taken at the backstop, assumed to be fixed. V_0 is the convergence rate, hence the velocity of the leading edge of the wedge. This equation assumes that the erosion rate is uniform. In Figure 45, the predicted horizontal surface velocity was computed for $h = 15$ km, $W = 200$ km, tg $(\alpha + \beta) = 4\%$, and $V_0 = 20$ mm year^{-1}. This set of parameters corresponds approximately to the geometry and size of the Himalayan wedge of central Nepal, assuming that about half of the Indian crust is incorporated into the Himalayan wedge. For the wedge to be steady state, a 2-D erosion flux of 300 m^2 year^{-1} is then required (per unit length of the Himalayan arc). This is in the range of possible values inferred from the sediment budget over the last 2 My at the scale of the whole Himalayan range (Metivier et al., 1999) or from denudation rates derived from river sediment discharge in central Nepal (Lavé and Avouac, 2001). This value corresponds to an erosion rate of ~1.5 mm year^{-1} on average over the section.

Based on the analytic expression of the velocity field, it is possible to compute the thermal structure from a thermokinematic approach and to estimate pressure–temperature–time ('*P*–*T*–*t*') paths (Barr and Dahlen, 1989; Barr et al., 1991). This kinematics predicts that in a steady-state orogenic prism, the peak metamorphic conditions increase from the toe to the rear of the wedge (Figure 46). This model can thus account for the northward increase of metamorphic grade from the Lesser to the High Himalayas across the MCT zone, a metamorphic zonation that is in fact quite common across mountain ranges.

The critical wedge model provides a simple and rigorous mechanical framework to analyze the structure and deformation of an orogen and its sensitivity to erosion and to the mechanical properties of the wedge. A number of possible variations around the initial ideas were explored by assuming different possible rheological laws, including the effects of (1) cohesion, (2) the transition to ductile deformation at depth, (3) different kinds of boundary conditions, (4) extending the model into 3-D, and (5) including more realistic erosion laws (e.g., Dahlen et al., 1984; Koons, 1994, 1989; Willett et al., 1993; Willett, 1999; Williams et al., 1994b).

The data reviewed earlier show that the kinematics of deformation across the Nepal Himalayas turns out to be quite different from that predicted by the critical taper theory for a homogeneous wedge. Crustal shortening across the Nepal Himalayas has resulted in apparently little internal deformation of the orogenic wedge over the Holocene or over the longer geologic period modeled with KTM11. In the KTM11 model, erosion maintains a balance between denudation and tectonic uplift, and a steady state can thus be reached through underplating of material. Although the possibility for underplating has been considered in some thermokinematic models (Barr and Dahlen, 1989), there is no theoretical analysis in the literature of why this mode of accretion arises and what controls the respective contribution of underplating and frontal accretion to the total flux of material into a wedge. This issue has been addressed from analogue experiments, which have shown that underplating can be reproduced under some conditions (Gutscher et al., 1998). Recently, Konstantinovskaia and Malavieille (2005) were able to reproduce underplating by the formation of a duplex. The structural evolution in their model shows striking similarities to that of the Himalayan orogen (Figure 47). The key factors in this experiment were (1) the introduction of a weak horizontal layer of glass microbeads and (2) erosion at the surface so that the

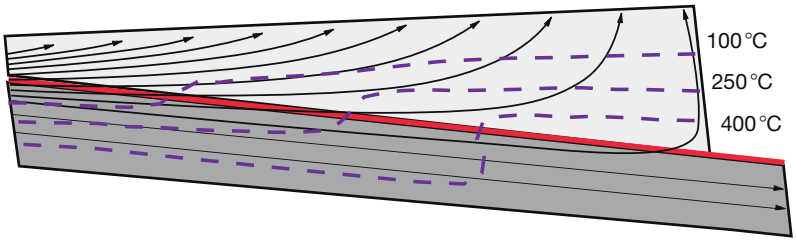

Figure 46 Particle trajectories and thermal structure in a steady-state critical wedge subjected to erosion and underplating. Adapted from Barr TD and Dahlen FA (1989) Brittle frictional mountain building. 2. Thermal structure and heat-budget. *Journal of Geophysical Research-Solid Earth and Planets* 94(B4): 3923–3947.

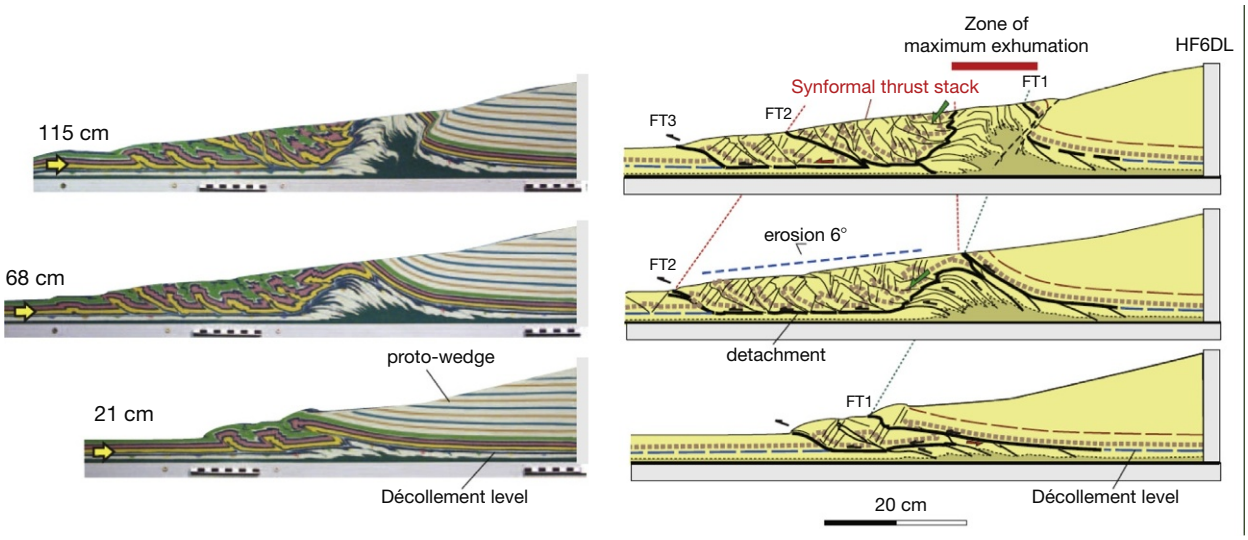

Figure 47 Evolution of an analogue sand wedge with a glass bed decollement (Konstantinovskaia and Malavieille, 2005). Note the similarity with the proposed structural evolution of the Himalayan orogen.

topography was always maintained close to the critical slope (here controlled by the weaker layer). The model leads first to the development of a frontal wedge by frontal accretion, while the rear of the wedge is uplifted due to the growth of a duplex a depth, all accomplished with little shortening (**Figure 47**). The weak detachment is key to the formation of the duplex since it becomes the roof thrust of the system. There is no shortening of the medium above the roof thrust probably because the critical slope of the topography is controlled by the weak layers and is thus steeper than the slope required for brittle failure of the stronger sand layers above the roof thrust.

So, the Himalayas is a case of an orogenic wedge in which the slope of the topography is steeper than, or equal to, the critical slope that would arise if the wedge were homogeneous and everywhere at the verge of brittle failure. Accretion through the development of a duplex at depth, coupled with erosion at the surface, is a viable mechanical explanation as demonstrated from the analogue experiments of Konstantinovskaia and Malavieille (2005). Because the frontal slope results from the erosional retreat of the advancing range front, erosion might play the key role of maintaining a slope steeper than the critical value for brittle deformation of the wedge. Combined with the effect of a weak basal friction, the topography must induce stresses that do not exceed the brittle strength of the medium within the wedge above the MHT.

6.09.7.2 Low Friction on the Main Himalayan Thrust

The observation that the overhanging wall of the MHT does not shorten during overthrusting allows the possibility of inferring the friction along the MHT. This geometry means that the slope of the topography must be overcritical. If the friction was too high, or the topographic slope too shallow, the wedge would be undercritical and the hanging wall would deform. There would be no slip on the MFT at the surface until the wedge topography reached the critical value. Given the slope of the Himalayan wedge in the Lesser Himalayas and the estimated dip angle of the MHT (~4° at most beneath the Lesser Himalaya), and assuming an internal friction of 0.85, the effective basal friction, μ_b', on the flat portion of the MHT is inferred from eqn [22] to be smaller than ~0.12 (Cattin and Avouac, 2000). This is in keeping with the numerical model CA2000, which was found to require a basal effective friction less than ~0.13. This value is consistent with the analysis of Davis et al. (1983) who considered the whole Himalayan wedge (which has a steeper slope than the Lesser Himalayan portion) and obtained a somewhat larger effective basal friction of 0.25.

Another constraint on friction along the MHT zone comes from the observation that microseismic activity along the front of the high range shows a cutoff at an elevation of 3500 m

(Section 6.09.6.3). This threshold is interpreted to correspond to the point where Coulomb stresses no longer increase during the interseismic period of increasing N–S compressive stress. This is achieved if the N–S deviatoric stress is of the order of magnitude of the vertical stress variation due to the increase in elevation across the range. When the elevation rises higher than 3500 m, the principal compressive stress is vertical and decreases during interseismic elastic strain (the effect of the Poisson coefficient is that vertical stress decreases as horizontal compression increases). Isostatic restoring forces and elastic stresses cause difficulties in estimating the effect of topography on the stress field at depth. To a first order, the 2500 m elevation difference between the area with intense microseismic activity in the Lesser Himalayas and the cutoff elevation must correspond to a σ_{zz} increase of 70 MPa at most (for a crustal density of 2.6 g cm^{-3}). We infer that the shear stresses on the decollement cannot exceed 35 MPa. Given that the decollement lies at a depth of ~10 km, this corresponds with a friction of the order of 0.1 (Bollinger et al., 2004b).

The formal inversion of the thermochronological and thermobarometric data from central Nepal (Herman et al., 2010) also provides constraints on friction along the MHT. This analysis indeed places an upper bound on shear heating induced by frictional sliding that in turn requires the effective friction coefficient, μ_b', to be lower than 0.07.

A classical interpretation of low friction at the base of thrust sheets invokes fluid pressurization (Hubbert and Rubey, 1959). This seems a reasonable scenario if some foreland sediments along with free water are underthrust beneath the Himalayan wedge, as the relatively high conductivity along the MHT might suggest (Figure 10). Fluid pressurization could then result from sediment compaction during shear (Segall and Rice, 1995; Sleep and Blanpied, 1992). Fluid pressure does not need to be permanently high however, as it could rise only during seismic slip events. In that case, thermal pressurization (Rice, 2006), due to thermal expansion of pore fluids induced by transient frictional heating during seismic slip, could also be a factor.

Given that the MHT probably slips mainly during seismic slip events, the low apparent friction could well be due to other dynamic effects such as frictional melting and hydrodynamic lubrication (Kanamori and Brodsky, 2004). Once these dynamic weakening mechanisms trigger an earthquake at some point on the MHT, the rupture could propagate along the MHT even if the preseismic stress is far from the critical stress needed for static slip.

6.09.7.3 Importance of the Brittle–Ductile Transition

The variation with depth of rheology probably controls a number of aspects of the Himalayan orogen, including its seismicity, its pattern of geodetic deformation, and even its topography. Regarding this last point, it is noteworthy that the transition from the Himalayan range to the flat Tibetan Plateau takes place close to where the mechanical coupling between the wedge and the underthrusting basement transitions from brittle to ductile behavior. The transition probably leads to a reduction of the basal shear stress and thus to a shallower critical topographic slope (Williams et al., 1994a). This feature arises naturally in thermomechanical models of orogens (e.g., Toussaint et al., 2004a), as it does in the FEM models discussed in Section 6.09.5 (Figure 32). Temperature is probably the major controlling factor on this transition in behavior, as demonstrated from the discussion of geodetic deformation and its relation to the thermal structure. In this regard, observational data from the Himalayas are remarkably consistent with the wealth of laboratory data on the rheology of crustal rocks (e.g., Kohlstedt et al., 1995; Marone, 1998). As we have seen, the development of a midcrustal duplex is a key feature in the structural evolution of the Himalayas. Although this feature can be reproduced from sandbox experiments (Konstantinovskaia and Malavieille, 2005), it is probable that, in nature, the development of a duplex relates to the brittle–ductile transition, as suggested from the analysis of ancient exhumed analogue systems (Dunlap et al., 1997). It is possible that rheological layering due to the thermal structure of an active orogen might be a primary factor allowing this kinematics, as suggested from the observation of a similar kinematics in thermomechanical modeling (Toussaint et al., 2004a).

6.09.7.4 Metamorphism During Underthrusting

The rocks cropping out in the High Himalayas and in the Lesser Himalayas have without question experienced metamorphic reactions during the development of the orogen. We have seen that model KTM11 predicts a *P*–*T*–*t* path in reasonably good agreement with the estimated peak temperatures and cooling histories along the section. The portion of the crust that underthrusts the high range and southern Tibet should also experience petrologic transformations as the rocks are transported to greater depth and higher temperatures.

Returning now to the interpretation of the electrical conductivity of Figure 10 (Lemonnier et al., 1999), the comparison with the thermal structure is instructive. Because the midcrustal zone of high conductivity does not follow any particular isotherm, in particular since it does not extend to the north, a thermometamorphic control model can be excluded. This conductive body, which becomes prominent where the underthrusting footwall reaches temperatures ~350 °C, may instead result from the presence of fluids released by metamorphic reactions, especially those involving chlorite breakdown. The isotopic composition of hot springs located at the front of the high range, on top of the conductivity anomaly, does suggest some contamination by metamorphic fluids (Evans et al., 2001; Kotarba, 1986). The fluids released by metamorphic reactions would percolate upward through the zone where intense microseismic activity is triggered by interseismic strain, allowing for some connectivity of the fluid phase that is required for it to be detectable by magnetotelluric sounding.

The thermal structure might also be used to estimate how the crustal density should vary given the predicted *P*–*T* conditions along the section (Cattin et al., 2001; Henry et al., 1997; Figure 48). A prediction of the model is that, provided that the kinetics of metamorphic reaction can be neglected, the underthrusted crust should enter the granulite and then the eclogite facies. However, the resulting density distribution would be inconsistent with the observed gravity. The misfit between the predicted and observed Bouguer anomaly is as high as 150 mgal in southern Tibet (model 1 in Figure 48), suggesting

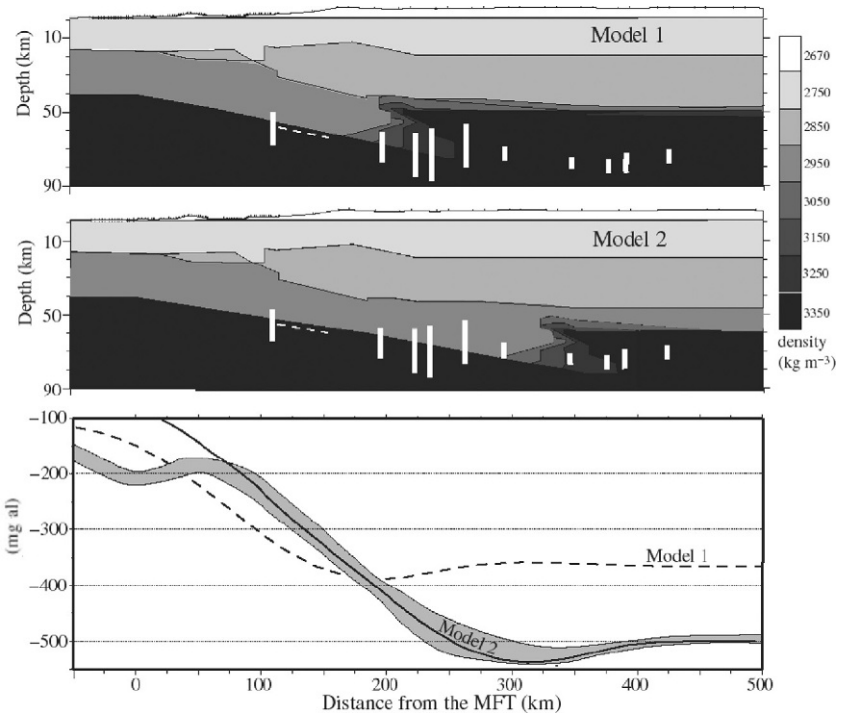

Figure 48 Density model deduced from a steady-state thermopetrologic model showing eclogitization of the lower crust beneath the Himalayan range (Cattin et al., 2001) computed based on the petrogenetic grid of Bousquet et al. (1997). White lines show constraints on Moho depths derived from INDEPTH (dashed line from seismic profile and vertical bars from receiver functions). The Bouguer anomaly (dashed line) associated with the density of model 1 is found to be inconsistent with the data (gray shading), by as much as 150 mgal under Tibet. It therefore suggests that eclogitization does not occur as south as shown in model 1. The dashed curve exhibits a warped anomaly (km 100–250) with wavelength and amplitude strikingly comparable with those observed in the data north of the high range (km 200–350). Model 2 (black line) was modified assuming that eclogitization is delayed by 6.5–8.5 My, possibly due to the kinetics of petrologic changes.

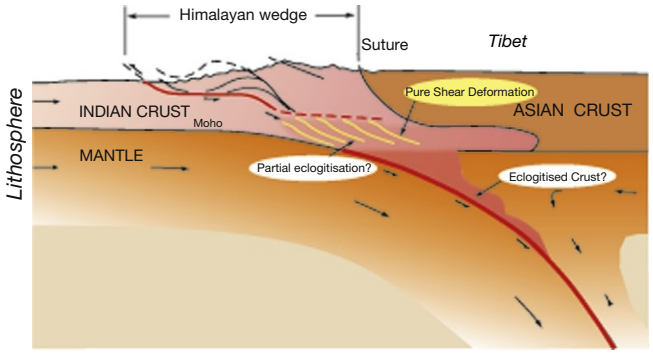

Figure 49 Cartoon of the collision zone illustrating the possibility for partial eclogitization of the underthrusted Indian crust and continental subduction. A fraction of the Indian crust is incorporated into the Himalayan wedge and is ultimately eroded away. The remaining fraction is either injected beneath southern Tibet, as suggested, for example, by Zhao and Morgan (1985), or eclogitized and subducted, as suggested, for example, by Le Pichon et al. (1992).

that eclogitization does not occur as extensively as this model would imply. A much better fit, the gravity measurements is obtained if the lower crust is assumed to be metastable (model 2 in **Figure 48**; Cattin et al., 2001; Hetenyi et al., 2007). As argued by Cattin et al. (2001) and Jackson et al. (2004), one possible explanation of this is that eclogitization is limited by the availability of water, which is known to be the critical factor-limiting metamorphic processes in the lower crust (Austrheim, 1990). In any case, the seismic velocity structure of the deep crust beneath the Himalayas of eastern Nepal (Schulte-Pelkum et al., 2005) and beneath southern Tibet (Hetenyi et al., 2007; Wittlinger et al., 2009) points to partial eclogitization of the Indian lower crust. It is possible that some fraction of the underthrusting Indian crust becomes eclogitized and subducted into the mantle, as shown schematically in **Figure 49**.

6.09.7.5 How Does the Steep Front of the High Himalayas Relate to Tectonics, Erosion, and Climate?

The sudden 2–3 km increase in the topography at the front of the high range, almost 100 km north of the trace of the Main Frontal Fault (**Figure 8**), has been interpreted in various ways. Because this area coincides with a zone of localized ongoing uplift, as revealed from leveling data, the topographic step has been attributed to active thrusting at the front of the high range (Bilham et al., 1997). There is indeed evidence for some neotectonic activity at the front of the high range (Hodges et al., 2004). It has been proposed that the lower crust of Tibet would be extruded from below the high plateau toward the front of the high range due to coupling between intense localized erosion and uplift (Beaumont et al., 2001). The steep front of the High Himalayas has also been interpreted as the preserved morphological signature of a Late Miocene reactivation of the MCT zone (Harrison et al., 1997). Others have proposed that headward regressive erosion along the rivers cutting the edge of the Tibetan Plateau would have induced uplift of the Himalayan peaks through isostatic rebound, enhancing orographic precipitation and hence denudation (Burbank, 1992; Masek et al., 1994; Molnar, 1990; Montgomery, 1994; **Figure 50**).

The morphology of the front of the High Himalayas of Nepal undoubtedly reflects some dynamic equilibrium between tectonic deformation and surface processes. Indeed, in the absence of tectonic uplift, the various rivers cutting across the Himalayas would be retreating at very different rates and the edge of the Tibetan Plateau, instead of having the straight and sharp edge that is observed today, would rapidly evolve a sinuous geometry (Lavé and Avouac, 2001). The steep relief and the high uplift rates in the High Himalayas must therefore correlate with a zone of more localized uplift. This reasoning implies that the present morphology of the front of the high range more probably reflects present tectonics and erosion than it does a Late Miocene reactivation of the MCT (Catlos et al., 2001; Harrison et al., 1997). It is improbable that a significant contribution to uplift takes place by active thrusting at the front of the high range, as suggested by some authors (Bilham et al., 1997; Hodges et al., 2004; Meade, 2010; Wobus et al., 2005). This scenario would imply some amount of shortening rate to be added to the 21 mm year^{-1} absorbed at the MFT, and the total shortening rate across the range would subsequently exceed the geodetic rate significantly. This is in keeping with low-temperature thermochronological data, which also rule out significant thrusting at front of the High Himalayas of central Nepal (Nadin and Martin, 2012). The idea that the Himalayas would currently be uplifted by extrusion of the lower crust from beneath the high plateau can therefore also be excluded. However, there is geologic evidence that such a channel-flow tectonics (Beaumont et al., 2001) may have happened in the past, at the time of coeval motion on the MCT and STD (Grujic et al., 1996; Searle et al., 2006).

As we have seen, the present topography of the range can be reproduced reasonably well, as well as the observed pattern of erosion, if localized uplift is assumed to result simply from thrusting over a midcrustal ramp possibly in association with underplating (**Figures 28, 32**, and **33**; Godard et al., 2006; Herman et al., 2010). The available data on active tectonics in the Himalayas and on fluvial incision are thus consistent with the simple view that active tectonics in the Himalayas are primarily controlled by localized slip along the MHT, with topography being close to steady state, as denudation driven by fluvial downcutting balances *tectonic* uplift.

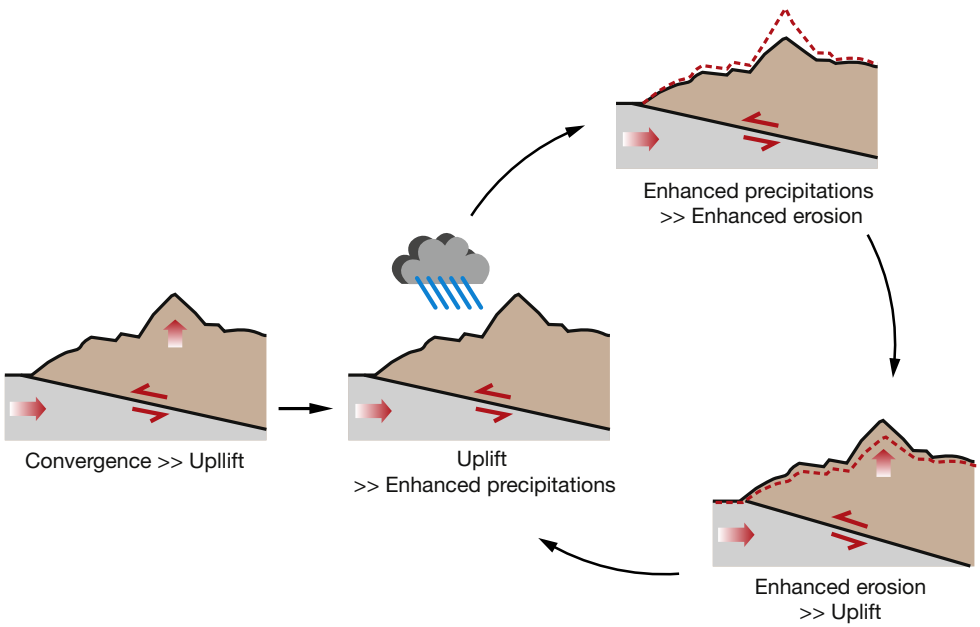

Figure 50 Diagram illustrating the coupling between mountain uplift, climate, and erosion due to the isostatic response to erosion. Modified from Masek JG, Isacks BL, Gubbels TL, and Fielding EJ (1994) Erosion and tectonics at the margins of continental plateaus. *Journal of Geophysical Research 99*: 13941–13956.

6.09.7.6 The Elevation and Support of Mountain Ranges: Effect of Climate and Lower Crustal Flow

It has long been recognized that isostasy is a major factor allowing for the support of high topography (Airy, 1855; Pratt, 1855). In this view, by virtue of Archimedes' principle, some deficit of mass at depth compensates for the excess of mass due to the topography. In the case of the Himalayas and southern Tibet, the deficit of mass is clearly due primarily to the exceptional Moho depth, which permits an almost local isostatic balance (**Figure 5**). At first glance, this means the elevation of the range is directly related to the thickness and density of the crust. But this is only an approximation because the presence of elastic bending stresses means that balance is only achieved at a regional scale. The mass deficit below the foreland and the mass excess below the high topography are a direct manifestation of this effect (e.g., Lyon-Caen and Molnar, 1985).

6.09.7.6.1 Height and width of a critical brittle wedge

Let us consider first that the critical brittle wedge theory applies at the scale of the whole orogen. Let us then imagine a brittle wedge over a basement at isostatic balance (the inclusion or exclusion of flexural stresses in the basement makes no difference in this reasoning), with a rigid backstop. Examples of such numerical experiments can be found in Hilley and Strecker (2004) and Whipple and Meade (2004). The width and height of such an orogen depend on these two factors in a rather simple way, which is amenable to analytic formulations. If the parameters characterizing erosion rates ('climate') are kept constant, the wedge will tend toward a steady-state geometry in which the eroded flux balances the accreted flux. Accordingly, the volume and maximum height of the orogenic wedge depend on the rate of accretion of material. If 'climate' changes the internal deformation of the wedge, the wedge adjusts its width so that the critical slope is still maintained and the eroded flux and accretion flux balance each other. In this case, the climate would have no influence on the steady-state erosion flux. Similarly, if the accreted flux is varied, the wedge will also adjust its width. This means that, except for transients, a change in erosion flux can only relate to a change in tectonic forcing.

It should be noted that the tectonic forcing in this reasoning is described in terms of an accretion flux that depends on the convergence rate, which is assumed constant. The assumption of a constant convergence rate implies that any change in the wedge geometry has to be associated with a change in the driving force. Namely, if climate change is assumed to lead to more rapid erosion, the wedge will shrink so that the force transmitted by friction along the basal decollement will decrease (as the square of the width or height of the orogen). The assumption of a constant convergence rate might be appropriate in the case of a small orogen, for example, Taiwan, which would not affect the force balance at the scale of the tectonic plates. In the case of a mountain range the size of the Himalayas, the assumption of a constant driving force can be argued as more appropriate. Let us now characterize tectonic forcing as the force applied to the system. In this case, a constant tectonic forcing implies constant wedge geometry. If climate change leads to increased erosion, the convergence rate would need to increase so that the accretion flux would still compensate erosion.

According to this reasoning, the height and width of a critical brittle wedge are ultimately determined by the force applied to the system, that is, the horizontal forces associated with plate tectonics (which presumably vary less rapidly than climate, only on timescales longer than geologic periods). In the case of the Himalayas, it would be primarily the force arising from the excess buoyancy of the Indian Ocean ridge system that is transmitted across the Indian continent (excluding the eventual effect of drag at the base of the Indian lithosphere; e.g., Coblentz et al., 1998; Sandiford et al., 1995). Climate then determines both the erosion flux (with some complex transfer function that depends on surface processes) and the convergence rate.

6.09.7.6.2 Effect of ductile deformation in the lower crust

In the real world, an orogenic wedge cannot be considered a brittle wedge at the scale of the crust. One implication of the dominantly ductile rheology is that an isostatically compensated mountain range is not in hydrostatic balance. The result is that the ductile lower crust will tend to be expelled from below the high topography (Avouac and Burov, 1996; Bird, 1991; Gratton, 1989; McKenzie and Jackson, 2002; **Figure 51**). This process is advocated to explain the eastward growth of the Tibetan Plateau, for example (Clark and Royden, 2000; Clark et al., 2004).

In the absence of erosion, a mountain range collapses with a decay time that depends only on the rheology of the lower crust. Let us consider an isolated mountain range, one the size of the

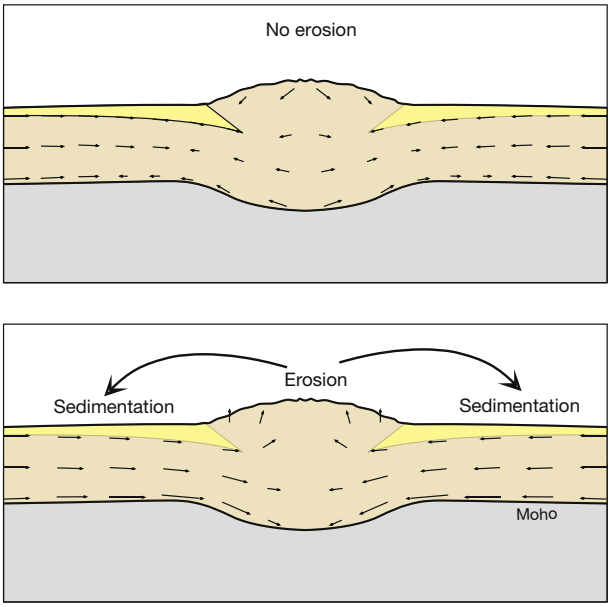

Figure 51 Coupling between mountain building and erosion in case of horizontal crustal flow (Avouac and Burov, 1996). In the absence of erosion, any mountain range is expected to collapse as a result of ductile flow in the lower crust (top). In the presence of erosion and sedimentation, a positive feedback can arise favoring focused shortening below the mountain range, where vertical advection of heat results in thermal weakening the crust (bottom). In that case, a mountain range can grow until some steady-state geometry is reached.

Tian Shan, that is, 300 km wide, and not associated with a plateau like the Himalayas. It would take between 3 and 10 Ma for an initial average relief of 3000 m to be reduced to half as a result of this process alone (Avouac and Burov, 1996). The decay time increases with the wavelength of the topography (Bird, 1991). If we now consider the same isolated mountain range submitted only to erosion, the relief would also decay with a similar or somewhat shorter decay time, assuming erosional parameters consistent with the current (<1 mm year^{-1}) erosion rate in this particular mountain range (Avouac and Burov, 1996; Métivier and Gaudemer, 1997). Now, when crustal shortening and erosion are considered together, a positive feedback arises (Avouac and Burov, 1996; **Figure 51**). Rather than resulting in a topography decaying even more rapidly, this feedback allows an initial topography to grow until it reaches some steady state. The dynamic equilibrium between denudation and tectonic uplift then arises naturally from the coupling between surface processes and ductile flow at depth and also contributes to localizing the deformation (Avouac and Burov, 1996). It should be noted that the thermal evolution of the range is a key factor in allowing for this feedback to happen (Koons, 1987). The hotter and weaker crust below the range deforms more easily, favoring localized deformation there, and enhanced erosion leads to upward advection of heat and hence further thermal weakening of the crust below the range.

In this case, the relationship between the geometry of the orogen and climate forcing is more complex than it is in the case of a critical brittle wedge, because the geometry of the range is dependent on strain rates (due to the power-law rheology ascribed to the ductile crust) and the relative contribution of brittle and ductile stresses to the force balance varies as the geometry of the wedge and its thermal structure change. Qualitatively, the model yields that if the system is submitted to constant driving forces, like enhanced erosion due to climate, the shortening rate across the range should increase just as in the reasoning based on the critical brittle wedge model. The elevation and width of the orogen should then be reduced to compensate for the strain rate hardening effect, which is presumably small.

The coupling described here is more complex but included the isostatic adjustment to erosion (e.g., Molnar and England, 1990a), but it does include such a component. The coupling leads to the additional fundamental implication that a change in climate might also induce a change in convergence rate. To a first order, the topography of a range should directly gauge the driving tectonic forces and depend only marginally on climate. Again, if the system is to be driven by constant tectonic forces, climate would affect primarily the erosion flux. If the system is assumed to be driven by a constant convergence rate, then the erosion flux would depend only weakly on climate.

6.09.7.6.3 The fate of the Indian crust and mantle lithosphere

Most of the crust was most probably detached from the mantle lithosphere as India collided with Eurasia. Over the last 15 Ma, a fraction, estimated at $\sim$1/3, of the Indian crust has been incorporated into the Himalayan wedge and was ultimately eroded away. The remaining fraction was either injected beneath southern Tibet, as suggested by Zhao and Morgan (1985), or eclogitized and subducted (**Figure 49**). What happened to the lithospheric mantle remains poorly known. It is probable that at the onset of the collision, subduction continued for a while until the oceanic slab broke away and sunk into the mantle under its own weight. Slab break-off seems necessary because the subducting continental mantle lithosphere is already quite hot and weak and will therefore tend to resist subduction, due to its buoyancy, and instead neck easily (Davies and Vonblanckenburg, 1995). There is indication that slab break did indeed occur in the early stages of the India–Asia collision (Kohn and Parkinson, 2002).

It is also possible that the mantle lithosphere may have continued to subduct (Mattauer, 1986; **Figure 49**), as argued from the interpretation of tomographic results and crustal volume budget (Replumaz et al., 2004, 2010a,b). It should be noted that while continental subduction might be taking place beneath southern Tibet, it is not associated with the kind of seismicity that characterizes oceanic subduction zones (e.g., the 'Benioff zone'), probably because the subducting mantle lithosphere is too hot to be seismogenic. Also, the presumably small density contrast between the subcontinental lithosphere and the upper Mantle makes it difficult to detect from tomographic studies.

Another possibility is that the mantle lithosphere thickened homogeneously (England and McKenzie, 1983; Houseman and England, 1986) and ultimately became unstable and was removed by convection (Houseman et al., 1981). It has been proposed that convective removal of the mantle lithosphere beneath Tibet would have occurred at *c.*8 Ma, leading to a sudden increase of the elevation of the plateau, which would in turn have strengthened the monsoon (Molnar et al., 1993). This scenario seems at odds with evidence that the Tibetan Plateau had reached close to its present elevation probably before *c.*15 Ma (Currie et al., 2005; Garzione et al., 2000; Spicer et al., 2003) or even before 35 Ma (Aikman et al., 2008; Rowley and Currie, 2006). Also, it has been argued based on thermomechanical modeling that surface erosion not only contributes to localize deformation within the crust but also favors continental subduction and inhibits the possibility for thickening of the mantle and its subsequent delamination (Pysklywec, 2006). Finally, the lithospheric mantle lid seems to be still present beneath most of the Tibetan Plateau according to surface tomography studies and body wave tomography (Bourjot and Romanowicz, 1992; Griot et al., 1998; Priestley et al., 2008).

6.09.8 Conclusions

Various multidisciplinary efforts have provided important information on the subsurface structure of the range and on the kinematics of deformation over different timescales. The available data can be assembled in a relatively consistent way in light of our current understanding of the mechanics of the lithosphere and of the seismic cycle. The kinematics observed in the Nepal Himalayas, described in some detail in this chapter, might be specific to some aspect of the Himalayan setting. Other mountain ranges located in a different climatic and tectonic setting might evolve quite differently, and analyzing these differences would probably help in the understanding of some aspect of the mechanics governing collisional mountain building. One example of a persisting puzzle is that shortening

across the Himalayas of central Nepal has been absorbed by localized thrusting on only one single major fault along its piedmont, the MFT, but it is clear that shortening across the Tian Shan is absorbed by thrusting on a number of faults distributed within the range and along its northern and southern piedmont (Thompson et al., 2002). The example of Taiwan is closer to that of an intermediate Himalayas, with shortening being absorbed on several thrust faults within the western foothills (Simoes et al., 2007a). The mechanical reasons for these differences are unclear and need to be clarified.

Another persisting puzzle is related to the early history of the Himalayan orogen. The focus has been put here on active deformation and on geologic deformation over the last *c.*15 Ma. This time covers less than half the life of the Himalayan orogen. A number of fundamental geodynamic processes occurred earlier and have also imprinted the Himalayan orogen, in particular through their influence on magmatism. The Tethys oceanic slab probably detached early on in subduction (Kohn and Parkinson, 2002) and likely induced a significant change in the balance of forces across the collision zone. Some crustal materials underthrusted to depths >100 km were exhumed quite early in the history of the collision (DeSigoyer et al., 2000; Guillot et al., 1997); this scenario requires a tectonic regime fundamentally different from the one that has prevailed over the last 15 Ma. Later on, slip on a major normal fault, the STD, coeval with the onset of motion on the MCT at *c.*20 Ma, led to a rapid episode of unroofing of the High Himalayas (Searle et al., 2006) just before the current tectonic regime was established.

The observation that nearly half the convergence between stable Eurasia and India is currently being absorbed by thrusting along the Himalayan arc is a clear indication that deformation of the brittle upper crust is highly localized. This finding does not conflict with the observation that the zone with finite strain across the Himalayas and southern Tibet is more than one hundred kilometers wide. Indeed, the locus of active localized deformation has moved with time as the material was accreted onto the orogen. In the author's view, highly localized active deformation most probably also reflects localized strain at the scale of the lithosphere, possibly the result of coupling between surface erosion and crustal deformation.

Acknowledgments

A number of PhD students, postdoc, and collaborators have contributed to the results that are summarized in this chapter. I would like to acknowledge in particular the contributions from Thomas Ader, Laurent Bollinger, Rodolphe Cattin, Jérome Lavé, Genia Burov Hugo Perfettini, S. Dominguez, Mireille Fouzat, Thierry Héritier, Frédéric Perrier, Pierre Bettinelli, M. R. Pandey, Suhire Rajaure, and Umesh, Tiwari. An earlier version of this manuscript has benefited from useful comments by An Yin and Rodolphe Cattin and Gyorgy Hetenyi and editing by Elisabeth Nadin. Roger Bilham and Simon Lamb are thanked for their insightful reviews.

References

Abtout A (1987) *La détermination des anomalies des champs de potentiel (magnétisme, gravimétrie) et la structure de la lithosphere continentale en Asie*. Thèse de 3ième cycle, Université Paris VII, Paris.

Ader T, Avouac JP, Liu-Zeng J, et al. (2012) Convergence rate across the Nepal Himalaya and interseismic coupling on the Main Himalayan Thrust: Implications for seismic hazard. *Journal of Geophysical Research, Solid Earth* 117.

Aikman AB, Harrison TM, and Lin D (2008) Evidence for early (>44 Ma) Himalayan crustal thickening, Tethyan Himalaya, southeastern Tibet. *Earth and Planetary Science Letters* 274(1–2): 14–23.

Airy GB (1855) On the computations of the effect of the attraction of the mountain masses as disturbing the apparent astronomical latitude of stations in geodetic surveys. *Philosophical Transactions of the Royal Society of London* 145: 101–104.

Ambraseys N (2000) Reappraisal of north-Indian earthquakes at the turn of the 20th century. *Current Science* 79(9): 1237–1250.

Ambraseys N and Bilham R (2000) A note on the kangra M-s = 7.8 earthquake of 4 April 1905. *Current Science* 79(1): 45–50.

Ambraseys NN and Douglas J (2004) Magnitude calibration of north Indian earthquakes. *Geophysical Journal International* 159(1): 165–206.

Ambraseys N and Jackson D (2003) A note on early earthquakes in northern India and southern Tibet. *Current Science* 84(4): 570–582.

Appel E, Rosler W, and Corvinus G (1991) Magnetostratigraphy of the Miocene Pleistocene Surai-Khola Siwaliks in West Nepal. *Geophysical Journal International* 105(1): 191–198.

Appel E and Rossler W (1994) Magnetic polarity stratigraphy of the Neogene Surai Khola section (Siwaliks, SW Nepal). *Himalayan Geology* 15: 63–68.

Argand E (1924) La tectonique de l'Asie. *13th International Geological Congress*: *Brussels*, pp. 170–372.

Arita K, Dallmeyer RD, and Takasu A (1997) Tectonothermal evolution of the Lesser Himalaya, Nepal: Constraints from Ar-40/Ar-39 ages from the Kathmandu Nappe. *Island Arc* 6(4): 372–385.

Arita K and Ganzawa Y (1997) Thrust tectonics and uplift process of the Nepal Himalaya revealed from fission-track ages (in Japanese with English abstract). *Journal of Geography* 106: 156–167.

Armijo R, Tapponnier P, Mercier JL, and Han TL (1986) Quaternary extension in Southern Tibet – Field observations and tectonic implications. *Journal of Geophysical Research-Solid Earth and Planets* 91(B14): 13803–13872.

Austrheim H (1990) The Granulite Eclogite Facies Transition – A comparison of experimental work and a natural occurrence in the Bergen Arcs, Western Norway. *Lithos* 25(1–3): 163–169.

Avouac JP (2003) Mountain building, erosion and the seismic cycle in the Nepal Himalaya. In: Dmowska R (ed.) *Advances in Geophysics*, pp. 1–79. Amsterdam: Elsevier.

Avouac JP, Ayoub F, Leprince S, Konca O, and Helmberger DV (2006) The 2005, M-w Kashmir earthquake: Sub-pixel correlation of ASTER images and seismic waveforms analysis. *Earth and Planetary Science Letters* 249(3–4): 514–528.

Avouac JP and Burov EB (1996) Erosion as a driving mechanism of intracontinental mountain growth. *Journal of Geophysical Research, Solid Earth* 101(B8): 17747–17769.

Avouac JP and Tapponnier P (1993) Kinematic model of active deformation in Central-Asia. *Geophysical Research Letters* 20(10): 895–898.

Avouac JP, Tapponnier P, Bai M, You H, and Wang G (1993) Active thrusting and folding along the northern Tien-Shan and Late Cenozoic rotation of the Tarim relative to Dzungaria and Kazakhstan. *Journal of Geophysical Research, Solid Earth* 98(B4): 6755–6804.

Baranowski J, Armbruster J, Seeber L, et al. (1984) Focal depths and fault plane solutions of earthquakes and active tectonics of the Himalaya. *Journal of Geophysical Research* 89(NB8): 6918–6928.

Barr TD and Dahlen FA (1989) Brittle frictional mountain building. 2. Thermal structure and heat-budget. *Journal of Geophysical Research-Solid Earth and Planets* 94(B4): 3923–3947.

Barr TD and Dahlen FA (1990) Constraints on friction and stress in the Taiwan fold-and-thrust belt from heat flow and geochronology. *Geology* 18: 111–115.

Barr TD, Dahlen FA, and McPhail DC (1991) Brittle frictional mountain building. 3. Low-grade metamorphism. *Journal of Geophysical Research-Solid Earth and Planets* 96(B6): 10,319–10,338.

Beaumont C, Jamieson RA, Nguyen MH, and Lee B (2001) Himalayan tectonics explained by extrusion of a low-viscosity crustal channel coupled to focused surface denudation. *Nature* 414(6865): 738–742.

Beaumont C, Jamieson RA, Nguyen MH, and Medvedev S (2004) Crustal channel flows: 1. Numerical models with applications to the tectonics of the Himalayan-Tibetan orogen. *Journal of Geophysical Research, Solid Earth* 109(B6): B06406.

Beck RA, Burbank DW, Sercombe WJ, et al. (1995) Stratigraphic evidence for an early collision between northwest India and Asia. *Nature* 373(6509): 55–58.

Bernard S, Avouac JP, Dominguez S, and Simoes M (2007) Kinematics of fault-related folding derived from a sandbox experiment. *Journal of Geophysical Research, Solid Earth* 112(B3).

Bettinelli P, Avouac JP, Flouzat M, et al. (2006) Plate motion of India and interseismic strain in the Nepal Himalaya from GPS and DORIS measurements. *Journal of Geodesy* 80(8–11): 567–589.

Beyssac O, Bollinger L, Avouac JP, and Goffe B (2004) Thermal metamorphism in the Lesser Himalaya of Nepal determined from Raman spectroscopy of carbonaceous material. *Earth and Planetary Science Letters* 225(1–2): 233–241.

Beyssac O, Goffe B, Chopin C, and Rouzaud J-N (2002) Raman spectra of carbonaceous material in metasediments: A new geothermometer. *Journal of Metamorphic Geology* 20: 859–871.

Bilham R (1995) Location and magnitude of the 1833 Nepal Earthquake and its relation to the rupture zones of contiguous Great Himalayan earthquakes. *Current Science* 69(2): 101–128.

Bilham R (1997) *The Elusive Height of Mount Everest: Everest*, pp. 26–27. New York: National Geographic Society.

Bilham R (2004) Earthquakes in India and the Himalaya: Tectonics, geodesy and history. *Annals of Geophysics* 47(2–3): 839–858.

Bilham R, Blume F, Bendick R, and Gaur VK (1998) Geodetic constraints on the translation and deformation of India: Implications for future great Himalayan earthquakes. *Current Science* 74(3): 213–229.

Bilham R, Gaur VK, and Molnar P (2001) Earthquakes – Himalayan seismic hazard. *Science* 293(5534): 1442–1444.

Bilham R, Larson K, Freymueller J, et al. (1997) GPS measurements of present-day convergence across the Nepal Himalaya. *Nature* 386(6620): 61–64.

Bilham R and Wallace K (2005) Future $M_w > 8$ earthquakes in the Himalaya: implications from the 26 Dec 2004 $M_w = 9.0$ earthquake on India's eastern plate margin. *Geological Survey of India Special Publication* 85: 1–14.

Bird P (1991) Lateral extrusion of lower crust from under high topography, in the isostatic limit. *Journal of Geophysical Research-Solid Earth and Planets* 96(B6): 10275–10286.

Blanpied ML, Lockner DA, and Byerlee JD (1991) Fault stability inferred from granite sliding experiments at hydrothermal conditions. *Geophysical Research Letters* 18(4): 609–612.

Blanpied ML, Lockner DA, and Byerlee JD (1995) Frictional slip of granite at hydrothermal conditions. *Journal of Geophysical Research, Solid Earth* 100(B7): 13045–13064.

Bollinger L (2002) *Déformation de l'Himalaya du Népal*. PhD thesis, 400 pp, P. XI.

Bollinger L, Avouac JP, Beyssac O, et al. (2004a) Thermal structure and exhumation history of the Lesser Himalaya in Central Nepal. *Tectonics* 23: TC5015. http://dx.doi.org/10.1029/2003TC001564.

Bollinger L, Avouac JP, Cattin R, and Pandey MR (2004b) Stress buildup in the Himalaya. *Journal of Geophysical Research, Solid Earth* 109(B11): 51.

Bollinger L, Henry P, and Avouac JP (2006) Mountain building in the Nepal Himalaya: Thermal and kinematic model. *Earth and Planetary Science Letters* 244(1–2): 58–71.

Bott MHP and Dean DS (1973) Stress diffusion from plate boundaries. *Nature* 243(5406): 339–341.

Bourjot L and Romanowicz B (1992) Crust and upper mantle tomography in Tibet using surface waves. *Geophysical Research Letters* 19(9): 881–884.

Bousquet R, Goffe B, Henry P, LePichon X, and Chopin C (1997) Kinematic, thermal and petrological model of the Central Alps: Lepontine metamorphism in the upper crust and eclogitisation of the lower crust. *Tectonophysics* 273(1–2): 105–127.

Bowin C, Purdy GM, Johnston C, et al. (1980) Arc-continent collision in banda sea region. *AAPG Bulletin* 64(6): 868–915.

Braun J and Sambridge M (1997) Modelling landscape evolution on geological time scales: A new method based on irregular spatial discretization. *Basin Research* 9(1): 27–52.

Brown LD, Zhao WJ, Nelson DK, et al. (1996) Bright spots, structure, and magmatism in southern Tibet from INDEPTH seismic reflection profiling. *Science* 274(5293): 1688–1690.

Brunel M (1983) *Etude pétro-structurale des chevauchements ductiles en Himalaya (Népal oriental et Himalaya du Nord-Ouest)*. Thése doctorat d'État thesis, Paris VII, Paris.

Brunel M (1986) Ductile thrusting in the Himalayas – Shear sense criteria and stretching lineations. *Tectonics* 5(2): 247–265.

Brunel M, Colchen M, Le Fort P, Mascle G, and Pêcher A (1979) Structural analysis and tectonic evolution of the Central Himalaya of Nepal. In: Saklani PS (ed.) *Structural Geology of the Himalaya*, pp. 247–264. New-Delhi: Today and Tomorrow's Printers and Publishers.

Brunel M and Kienast JR (1986) Etude pétro-structurale des chevauchements ductiles himalayens sur la transversale de l'Everest-Makalu (Népal oriental). *Canadian Journal of Earth Sciences* 23: 1117–1137.

Bull W (1991) *Geomorphic Response to Climatic Change*, p. 326. Oxford: Oxford University Press.

Burbank DW (1992) Causes of recent Himalayan Uplift deduced from deposited patterns in the Ganges basin. *Nature* 357(6380): 680–683.

Burbank DW, Blythe AE, Putkonen J, et al. (2003) Decoupling of erosion and precipitation in the Himalayas. *Letters to Nature* 426: 652–655.

Burbank DW, Leland J, Fielding E, et al. (1996) Bedrock incision, rock uplift and threshold hillslopes in the northwestern Himalayas. *Nature* 379(6565): 505–510.

Burchfiel BC, Zhiliang C, Hodges KV, et al. (1992) The southern Tibetan detachment system, Himalayan Orogen: Extension contemporaneous with and parallel to shortening in a collisional mountain belt. *Geological Society of America Special Paper* 269: 1–41.

Burg JP (1983) Himalayan orogen and global tectonics seen from the Tsangpo suture zone of Tibet (China). In: Sinha AK (ed.) *Himalayan Orogen and Global Tectonics*, pp. 35–44. New Delhi: Oxford & IBH Publ. Co.

Burg JP, Brunel M, Gapais D, Chen GM, and Liu GH (1984) Deformation of leucogranites of the crystalline Main Central Sheet in southern Tibet (China). *Journal of Structural Geology* 6: 532–542.

Burg JP, Leyreloup A, Girardeau J, and Chen GM (1987) Structure and metamorphism of a tectonically thickened continental-crust – The Yalu Tsangpo suture zone (Tibet). *Philosophical Transactions of the Royal Society A: Physical, Mathematical and Engineering Sciences* 321(1557): 67–86.

Burov EB and Diament M (1995) The effective elastic thickness (T-E) of continental lithosphere – What does it really mean. *Journal of Geophysical Research, Solid Earth* 100(B3): 3905–3927.

Carter NL and Tsenn MC (1987) Flow properties of continental lithosphere. *Tectonophysics* 136: 27–63.

Catlos EJ, Harrison TM, Kohn MJ, et al. (2001) Geochronologic and thermobarometric constraints on the evolution of the Main Central Thrust, central Nepal Himalaya. *Journal of Geophysical Research, Solid Earth* 106(B8): 16177–16204.

Catlos EJ, Harrison TM, Manning CE, et al. (2002) Records of the evolution of the Himalayan orogen from in situ Th-Pb ion microprobe dating of monazite: Eastern Nepal and western Garhwal. *Journal of Asian Earth Sciences* 20(5): 459–479.

Cattin R and Avouac JP (2000) Modeling mountain building and the seismic cycle in the Himalaya of Nepal. *Journal of Geophysical Research, Solid Earth* 105(B6): 13389–13407.

Cattin R, Martelet G, Henry P, Avouac JP, Diament M, and Shakya TR (2001) Gravity anomalies, crustal structure and thermo-mechanical support of the Himalaya of Central Nepal. *Geophysical Journal International* 147(2): 381–392.

Celerier J, Harrison TM, Webb AAG, and Yin A (2009) The Kumaun and Garwhal Lesser Himalaya, India: Part 1. Structure and stratigraphy. *Geological Society of America Bulletin* 121(9–10): 1262–1280.

Chapple WM (1978) Mechanics of thin-skinned fold-and-thrust belts. *Geological Society of America Bulletin* 89(8): 1189–1198.

Chemenda AI, Burg JP, and Mattauer M (2000) Evolutionary model of the Himalaya-Tibet system: Geopoem based on new modelling, geological and geophysical data. *Earth and Planetary Science Letters* 174(3–4): 397–409.

Chen QZ, Freymueller JT, Wang Q, Yang ZQ, Xu CJ, and Liu JN (2004) A deforming block model for the present-day tectonics of Tibet. *Journal of Geophysical Research, Solid Earth* 109(B1): B01403.

Chen WP and Molnar P (1977) Seismic moments of major earthquakes and average rate of slip in Central Asia. *Journal of Geophysical Research* 82(20): 2945–2969.

Chlieh M, Avouac JP, Sieh K, Natawidjaja DH, and Galetzka J (2008) Heterogeneous coupling of the Sumatran megathrust constrained by geodetic and paleogeodetic measurements. *Journal of Geophysical Research, Solid Earth* 113(B5): B05305.

Clark MK and Royden LH (2000) Topographic ooze: Building the eastern margin of Tibet by lower crustal flow. *Geology* 28(8): 703–706.

Clark MK, Schoenbohm LM, Royden LH, et al. (2004) Surface uplift, tectonics, and erosion of eastern Tibet from large-scale drainage patterns. *Tectonics* 23(1): TC1006.

Coblentz DD, Zhou SH, Hillis RR, Richardson RM, and Sandiford M (1998) Topography, boundary forces, and the Indo-Australian intraplate stress field. *Journal of Geophysical Research, Solid Earth* 103(B1): 919–931.

Cohen SC (1999) Numerical models of crustal deformation in seismic zones. *Advances in Geophysics* 41: 134–231.

Copeland P (1997) The when and where of the growth of the Himalaya and the Tibetan plateau. In: Ruddiman WF (ed.) *Tectonic Uplift and Climatic Change*, pp. 19–40. New York: Plenum Press.

Copeland P, Harrison TM, Hodges KV, Maruejol P, Lefort P, and Pecher A (1991) An early Pliocene thermal disturbance of the main central thrust, central Nepal – Implications for Himalayan tectonics. *Journal of Geophysical Research-Solid Earth and Planets* 96(B5): 8475–8500.

Copley A, Avouac JP, and Royer JY (2010) India-Asia collision and the Cenozoic slowdown of the Indian plate: Implications for the forces driving plate motions. *Journal of Geophysical Research, Solid Earth* 115: B03410.

Corvinus G (1988) The Mio-Plio-Pleistocene litho- and bio-stratigraphy of the Surai khola Siwaliks in west Nepal: first results. *Comptes rendus des séances de l'Académie des sciences. Série D* 306: 1471–1477.

Cotton F, Campillo M, Deschamps A, and Rastogi BK (1996) Rupture history and seismotectonics of the 1991 Uttarkashi, Himalaya earthquake. *Tectonophysics* 258(1–4): 3551.

Currie BS, Rowley DB, and Tabor NJ (2005) Middle Miocene paleoaltimetry of southern Tibet: Implications for the role of mantle thickening and delamination in the Himalayan orogen. *Geology* 33(3): 181–184.

Daeron M, Avouac JP, and Charreau J (2007) Modeling the shortening history of a fault tip fold using structural and geomorphic records of deformation. *Journal of Geophysical Research, Solid Earth* 112(B3): B03S13.

Dahlen FA (1990) Critical taper model of fold-and-thrust belts and accretionary wedges. *Annual Review of Earth and Planetary Sciences* 18: 55–99.

Dahlen FA and Suppe J (1988) Mechanics, growth and erosion of mountain belts. *Special Paper – Geological Society of America* 218: 161–178.

Dahlen FA, Suppe J, and Davis D (1984) Mechanics of fold-and-thrust belts and accretionary wedges: Cohesive Coulomb theory. *Journal of Geophysical Research* 89(B12): 10087–10101.

Dahlstrom CDA (1969) Balanced cross sections. *Canadian Journal of Earth Sciences* 6: 743–757.

Davies JH and Vonblanckenburg F (1995) Slab breakoff – A model of lithosphere detachment and its test in the magmatism and deformation of collisional orogens. *Earth and Planetary Science Letters* 129(1–4): 85–102.

Davis D, Suppe J, and Dahlen FA (1983) Mechanics of fold-and-thrust belts and accretionary wedges. *Journal of Geophysical Research* 88: 1153–1172.

DeCelles PG, Gehrels GE, Quade J, Ojha TP, Kapp PA, and Upreti BN (1998) Neogene foreland basin deposits, erosional unroofing, and the kinematic history of the Himalayan fold-thrust belt, western Nepal. *Geological Society of America Bulletin* 110(1): 2–21.

DeCelles PG, Robinson DM, Quade J, et al. (2001) Stratigraphy, structure, and tectonic evolution of the Himalayan fold-thrust belt in western Nepal. *Tectonics* 20: 487–509.

Delcaillau B (1986) Dynamique et evolution structurale du piémont frontal de l'Himalaya: les Siwaliks du Népal oriental. *Revue de géologie dynamique et de géographie physique* 27: 319–337.

Derry LA and France-Lanord C (1997) Himalayan weathering and erosion fluxes: Climate and tectonic controls. In: Ruddiman WF (ed.) *Tectonic Uplift and Climatic Change*, pp. 289–312. New York: Plenum.

DeSigoyer J, Chavagnac V, Blichert-Toft J, et al. (2000) Dating the Indian continental subduction and collisional thickening in the northwest Himalaya: Multi chronology of the Tso Morari eclogites. *Geology* 28(6): 487–490.

Dewey JF and Bird JM (1970) Mountain belts and new global tectonics. *Journal of Geophysical Research* 75(14): 2625–2685.

Dieterich JH (1979) Modeling of rock friction, 1, experimental results and constitutive equations. *Journal of Geophysical Research* 84: 2161–2168.

Ding L, Kapp P, and Wan XQ (2005) Paleocene–Eocene record of ophiolite obduction and initial India-Asia collision, south central Tibet. *Tectonics* 24(3): TC3001.

Dunlap WJ, Hirth G, and Teyssier C (1997) Thermomechanical evolution of a ductile duplex. *Tectonics* 16(6): 983–1000.

England PC and McKenzie DP (1983) A thin viscous sheet model for continental deformation. *Geophysical Journal of the Royal Astronomical Society* 73: 523–532.

Evans MJ, Derry LA, Anderson SP, and France-Lanord C (2001) Hydrothermal source of radiogenic Sr to Himalayan rivers. *Geology* 29: 803–806.

Fort M, Freytet P, and Colchen M (1983) The Quaternary sedimentary evolution of the intra-montane basin of Pokhara in relation to the Himalaya Midlands and their hinterland (west central Nepal). In: Sinha AK (ed.) *Contemporary Geoscientific Researches in Himalaya*, pp. 91–96. Dehra-Dun, India: Wadia Institute of Himalayan Geology.

France-Lanord C and Derry LA (1997) Organic carbon burial forcing of the carbon cycle from Himalayan erosion. *Nature* 390: 65–67.

Freymueller JT, Cohen SC, and Fletcher HJ (2000) Spatial variations in present-day deformation, Kenai Peninsula, Alaska, and their implications. *Journal of Geophysical Research* 105: 8079–8101.

Gansser A (1964) *Geology of the Himalayas*, p.289. London: Interscience Publishers.

Garzione CN, Dettman DL, Quade J, DeCelles PG, and Butler RF (2000) High times on the Tibetan plateau: Paleoelevation of the Thakkhola graben, Nepal. *Geology* 28: 339–342.

Gautam P and Appel E (1994) Magnetic polarity stratigraphy of Siwalik Group sediments of Tinau khola section in west central Nepal, revisited. *Geophysical Journal International* 17: 223–234.

Godard V, Cattin R, and Lavé J (2004) Numerical modeling of mountain building: Interplay between erosion law and crustal rheology. *Geophysical Research Letters* 31: L23607. http://dx.doi.org/10.1029/2004GL021006.

Godard V, Lave J, and Cattin R (2006) Numerical modelling of erosion processes in the Himalayas of Nepal: Effects of spatial variations of rock strength and precipitation. In: Buiter SJH and Schreurs G (eds.) *Analogue and Numerical Modelling of Crustal-Scale Processes*, pp. 341–358. London: Geological Society Special Publications.

Grandin R, Doin MP, Bollinger L, et al. (2012) Long-term growth of the Himalaya inferred from interseismic InSAR measurement. *Geology* 40(12): 1059–1062.

Gratton J (1989) Crustal shortening, root spreading, isostasy, and the growth of orogenic belts: A dimensional analysis. *Journal of Geophysical Research* 94(B11): 15627–15634.

Griot DK, Montagner JP, and Tapponnier P (1998) Phase velocity structure from Rayleigh and Love waves in Tibet and its neighboring regions. *Journal of Geophysical Research, Solid Earth* 103(B9): 21215–21232.

Grujic D, Casey M, Davidson C, et al. (1996) Ductile extrusion of the Higher Himalayan Crystalline in Bhutan: Evidence from quartz microfabrics. *Tectonophysics* 260(1–3): 21–43.

Guillot S (1999) An overview of the metamorphic evolution in central Nepal. *Journal of Asian Earth Sciences* 17: 713–725.

Guillot S, De Sigoyer J, Lardeaux JM, and Mascle G (1997) Eclogitic metasediments from the Tso Morari area (Ladakh, Himalaya): Evidence for continental subduction during the India-Asia convergence. *Contributions to Mineralogy and Petrology* 128: 197–212.

Gutscher MA, Kukowski N, Malavieille J, and Lallemand S (1998) Material transfer in accretionary wedges from analysis of a systematic series of analog experiments. *Journal of Structural Geology* 20(4): 407–416.

Harrison TM, Copeland P, Hall SA, et al. (1993) Isotopic preservation of Himalayan/Tibetan uplift, denudation, and climatic histories of two Molasse deposits. *The Journal of Geology* 101: 157–175.

Harrison TM, Copeland P, Kidd WSF, and Yin A (1992) Raising Tibet. *Science* 255: 1663–1670.

Harrison TM, Grove M, Lovera OM, and Catlos EJ (1998a) A model for the origin of Himalayan anatexis and inverted metamorphism. *Journal of Geophysical Research* 103: 27017–27032.

Harrison TM, Ryerson FJ, Le Fort P, Yin A, Lovera OM, and Catlos EJ (1997) A late Miocene-Pliocene origin for the central himalayan inverted metamorphism. *Earth and Planetary Science Letters* 146: E1–E8.

Harrison TM, Yin A, and Ryerson FJ (1998b) Orographic evolution of the Himalaya and Tibet. In: Crowley TJ and Burke K (eds.) *Tectonic Boundary Conditions for Climate Reconstructions*. New York: Oxford University Press.

Hassani R, Jongmans D, and Chery J (1997) Study of plate deformation and stress in subduction processes using two-dimensional numerical models. *Journal of Geophysical Research* 102: 17951–17965.

Hauck ML, Nelson KD, Brown LD, Zhao W, and Ross AR (1998) Crustal structure of the himalayan orogen at 90 deg east longitude from project INDEPTH deep reflection profiles. *Tectonics* 17: 481–500.

Hendrix MS, Graham SA, Caroll AR, et al. (1992) Sedimentary record and climatic implications of recurrent deformation in the Tien Shan: Evidence from Mesozoic strata of the north Tarim, south Junggar, and Turpan basins, northwest China. *Geological Society of America Bulletin* 104: 53–79.

Henry P, Le Pichon X, and Goffe B (1997) Kinematic, thermal and petrological model of the Himalayas: Constraints related to metamorphism within the underthrust Indian crust and topographic elevation. *Tectonophysics* 273: 31–56.

Herman F, Copeland P, Avouac JP, et al. (2010) Exhumation, crustal deformation, and thermal structure of the Nepal Himalaya derived from the inversion of thermochronological and thermobarometric data and modeling of the topography. *Journal of Geophysical Research, Solid Earth* 115.

Hetenyi G, Cattin R, Brunet F, et al. (2007) Density distribution of the India plate beneath the Tibetan plateau: Geophysical and petrological constraints on the kinetics of lower-crustal eclogitization. *Earth and Planetary Science Letters* 264(1–2): 226–244.

Hetenyi G, Cattin R, Vergne J, and Nabelek JL (2006) The effective elastic thickness of the India Plate from receiver function imaging, gravity anomalies and

thermomechanical modelling. *Geophysical Journal International* 167(3): 1106–1118.
Hilley GE, Johnson KM, Wang M, Shen ZK, and Burgmann R (2009) Earthquake-cycle deformation and fault slip rates in northern Tibet. *Geology* 37(1): 31–34.
Hilley GE and Strecker MR (2004) Steady state erosion of critical Coulomb wedges with applications to Taiwan and the Himalaya. *Journal of Geophysical Research* 109: B011411.
Him A, Jobert G, Xu ZX, and Gao EY (1984) Main features of the upper lithosphere in the unit between the High Himalayas and the Yarlung Zangpo Jiang suture. *Annals of Geophysics* 2: 113–118.
Him A and Sapin M (1984) The Himalayan zone of crustal interaction. *Annals of Geophysics* 39: 205–249.
Hodges KV, Parrish R, and Searle MP (1996) Tectonic evolution of the central Annapurna range, Nepalese Himalaya. *Tectonics* 15: 1264–1291.
Hodges KV, Wobus C, Ruhl K, Schildgen T, and Whipple K (2004) Quaternary deformation, river steepening, and heavy precipitation at the front of the Higher Himalayan ranges. *Earth and Planetary Science Letters* 220(3–4): 379–389.
Hough S, Bilham R, Ambraseys N, and Feldl N (2005) Revisiting the 1897 Shillong and 1905 Kangra earthquakes in northern India: Site response, Moho reflections and a Triggered earthquake. *Current Science* 88(10): 1632–1638.
Houseman G and England P (1986) Finite strain calculations of continental deformation, 1, Method and general results for convergent zones. *Journal of Geophysical Research* 91: 3651–3663.
Houseman GA, McKenzie DP, and Molnar P (1981) Convective instability of a thickened boundary-layer and its relevance for the thermal evolution of continental convergent belts. *Journal of Geophysical Research* 86(NB7): 6115–6132.
Hsu YJ, Bechor N, Segall P, Yu S-B, Kuo LC, and Ma KF (2002) Rapid afterslip following the 1999 Chi-Chi, Taiwan earthquake. *Geophysical Research Letters* 29: 1–4. http://dx.doi.org/10.1029/2002GL014967.
Hubbard MS (1989) Thermobarometric constraints on the thermal history of the Main Central Thrust zone and Tibetan Slab, Eastern Nepal. *Journal of Metamorphic Geology* 7: 19–30.
Hubbard MS (1996) Ductile shear as a cause of inverted metamorphism: Example from the Nepal Himalaya. *The Journal of Geology* 104: 493–499.
Hubbard MS, Royden L, and Hodges K (1991) Constraints on unroofing rates in the High Himalaya, Eastern Nepal. *Tectonics* 10: 287–298.
Hubbert MK and Rubey WW (1959) Role of fluid pressure in mechanics of overthrust faulting. I. Mechanics of fluid-filled porous solids and its application to overthrust faulting. *Geological Society of America Bulletin* 79: 115–166.
Hurtrez JE, Lucazeau F, Lavé J, and Avouac JP (1999) Investigation of the relationships between basin morphology, tectonic uplift, and denudation from the study of an active fold belt in the Siwalik Hills, central Nepal. *Journal of Geophysical Research, Solid Earth* 104(B6): 12779–12796.
Hyndman R, Currie CA, and Mazzotti SP (2005) Subduction zone backarcs, mobile belts, and orogenic heat. *GSA Today* 15(2): 4–10.
Iwata S (1976) Late Pleistocene and Holocene moraines in the Sagarmatha region, Khumbu Himal. *Journal of the Japanese Society of Snow and Ice* 38: 115–119.
Jackson JA, Austrheim H, McKenzie D, and Priestley K (2004) Metastability, mechanical strength, and the support of mountain belts. *Geology* 32(7): 625–628.
Jackson M and Bilham R (1994) Constraints on Himalayan deformation inferred from vertical velocity fields in Nepal and Tibet. *Journal of Geophysical Research* 99: 13897–13919.
Jaeger JC and Cook NGW (1979) *Fundamentals of Rocks Mechanics*, 3rd edn. London: Chapman and Hall.
Jaeger JJ, Courtillot V, and Tapponnier P (1989) Paleontological view of the ages of the deccan traps, the cretaceous tertiary boundary, and the India-Asia collision. *Geology* 17(4): 316–319.
Jaupart C and Provost A (1985) Heat focussing, granite genesis and inverted metamorphic gradients in continental collision zones. *Earth and Planetary Science Letters* 73: 385–397.
Jin Y, McNutt MK, and Zhu Y (1996) Mapping the descent of Indian and Eurasian plates beneath the Tibetan Plateau from gravity anomalies. *Journal of Geophysical Research* 101: 11275–11290.
Johnson KM and Segall P (2004) Viscoelastic earthquake cycle models with deep stress-driven creep along the San Andreas fault system. *Journal of Geophysical Research, Solid Earth* 109(B10).
Jouanne F, Awan A, Madji A, et al. (2011) Postseismic deformation in Pakistan after the 8 October 2005 earthquake: Evidence of afterslip along a flat north of the Balakot-Bagh thrust. *Journal of Geophysical Research, Solid Earth* 116: B07401.
Jouanne F, Mugnier JL, Pandey MR, et al. (1999) Oblique convergence in the Himalayas of western Nepal deduced from preliminary results of GPS measurements. *Geophysical Research Letters* 26(13): 1933–1936.
Kanamori H and Brodsky EE (2004) The physics of earthquakes. *Reports on Progress in Physics* 67(8): 1429–1496.
Kaneda H, Nakata T, Tsutsumi H, et al. (2008) Surface rupture of the 2005 Kashmir, Pakistan, earthquake and its active tectonic implications. *Bulletin of the Seismological Society of America* 98(2): 521–557.
Kerrick DM and Caldeira K (1993) Paleoatmospheric consequences of CO_2 released during early cenozoic regional metamorphism in the tethyan orogen. *Chemical Geology* 108(1–4): 201–230.
Kerrick DM and Caldeira K (1999) Was the Himalayan orogen a climatically significant coupled source and sink for atmospheric CO_2 during the Cenozoic? *Earth and Planetary Science Letters* 173: 195–203.
Kind R, Ni J, Zhao W, et al. (1996) Mid-crustal Low-velocity zone beneath the southern Lhasa block: Results from the INDEPTH-II earthquake recording program. *Science* 274: 1,692–1,694.
Kirby SH and Kronenberg AK (1987) Rheology of the lithosphere: Selected topics. *Reviews of Geophysics* 25: 1219–1244.
Kohlstedt DL, Evans B, and Mackwell SJ (1995) Strength of the lithosphere: Constraints imposed by laboratory experiments. *Journal of Geophysical Research* 100: 17587–17602.
Kohn MJ and Parkinson CD (2002) Petrologic case for Eocene slab breakoff during the Indo-Asian collision. *Geology* 30(7): 591–594.
Konstantinovskaia E and Malavieille J (2005) Erosion and exhumation in accretionary orogens: Experimental and geological approaches. *Geochemistry, Geophysics, Geosystems* 6: Q02006.
Koons PO (1987) Some thermal and mechanical consequences of rapid uplift – An example from the southern Alps, New-Zealand. *Earth and Planetary Science Letters* 86(2–4): 307–319.
Koons PO (1989) The topographic evolution of collisional mountain belts – A numerical look at the southern Alps, New-Zealand. *American Journal of Science* 289(9): 1041–1069.
Koons P (1994) Three-dimensional critical wedges: Tectonics and topography in oblique collisional orogens. *Journal of Geophysical Research* 99(B6): 12301–12315.
Kotarba M (1986) Origin and possibilities of utilization of thermal waters in the central Nepal Himalayas. In: Le Fort P, Colchen M, and Montenat C (eds.) *Évolution des domaines orogéniques d'Asie meridionale (de la Turquie a l'Indonésie)*, pp. 183–189. Nancy: Sciences de la Terre.
Kumar S, Wesnousky SG, Rockwell TK, Briggs R, Thakur VC, and Jayangondaperumal R (2006) Paleoseismic evidence of great surface-rupture earthquakes along the Indian Himalaya. *Journal of Geophysical Research* 111. http://dx.doi.org/10.1029/2004JB003309.
Lamb S (2006) Shear stresses on megathrusts: Implications for mountain building behind subduction zones. *Journal of Geophysical Research* 111: B07401. http://dx.doi.org/07410.01029/02005JB0003916.
Lamb S and Davis P (2003) Cenozoic climate change as a possible cause for the rise of the Andes. *Nature* 425(6960): 792–797.
Larson K, Bürgmann R, Bilham R, and Freymueller JT (1999) Kinematics of the India-Eurasia collision zone from GPS measurements. *Journal of Geophysical Research* 104: 1077–1093.
Lavé J (1997) *Tectonique et érosion: L'apport de la dynamique fluviale à l'étude sismotectonique de l'Himalaya du Népal central*. Thèse de doctorat thesis, Paris 7.
Lavé J (2005) Analytic solution of the mean elevation of a watershed dominated by fluvial incision and hillslope landslides. *Geophysical Research Letters* 32(11): L11403.
Lavé J and Avouac JP (2000) Active folding of fluvial terraces across the Siwaliks Hills, Himalayas of central Nepal. *Journal of Geophysical Research, Solid Earth* 105(B3): 5735–5770.
Lavé J and Avouac JP (2001) Fluvial incision and tectonic uplift across the Himalayas of central Nepal. *Journal of Geophysical Research, Solid Earth* 106(B11): 26561–26591.
Lavé J, Yule D, Sapkota S, et al. (2005) Evidence for a great medieval earthquake (approximate to 1100 AD) in the Central Himalayas, Nepal. *Science* 307(5713): 1302–1305.
Law RD, Searle MP, and Simpson RL (2004) Strain, deformation temperatures and vorticity of flow at the top of the Greater Himalayan Slab, Everest Massif, Tibet. *Journal of the Geological Society* 161: 305–320.
Le Fort P (1975) Himalayas: The collided range: Present knowledge of the continental arc. *American Journal of Science* 275A: 1–44.
Le Pichon X, Fournier M, and Jolivet L (1992) Kinematics, topography, shortening, and extrusion in the India-Eurasia collision. *Tectonics* 11(6): 1085–1098.

Lemonnier C, Marquis G, Perrier F, et al. (1999) Electrical structure of the Himalaya of Central Nepal: High conductivity around the mid-crustal ramp along the MHT. *Geophysical Research Letters* 26(21): 3261–3264.

Lombard A (1953) Presentation d'un profil géologique du Mt. Everest a la plaine du Gange (Népal oriental). *Bulletin de la Societe belge de geologie, de paleontologie et d'hydrologie* 42: 123–128.

Lombardo B and Rolfo F (2000) Two contrasting eclogite types in the Himalayas: Implications for the Himalayan orogeny. *Journal of Geodynamics* 30: 37–60.

Loveless JP and Meade BJ (2010) Geodetic imaging of plate motions, slip rates, and partitioning of deformation in Japan. *Journal of Geophysical Research, Solid Earth* 115: B02410.

Lyon-Caen H and Molnar P (1983) Constraints on the structure of the Himalaya from an analysis of gravity anomalies and a flexural model of the lithosphere. *Journal of Geophysical Research* 88: 8171–8191.

Lyon-Caen H and Molnar P (1985) Gravity anomalies, flexure of the Indian plate and the structure, support and evolution of the Himalaya and Ganga Basin. *Tectonics* 4: 513–538.

Macfarlane AM (1993) Chronology of tectonic events in the crystalline core of the Himalaya, Langtang national park, central Nepal. *Tectonics* 12: 1004–1025.

Macfarlane A, Hodges KV, and Lux D (1992) A structural analysis of the Main Central Thrust zone Langtang National Park, Central Nepal Himalaya. *Geological Society of America Bulletin* 104: 1389–1402.

Maggi A, Jackson JA, McKenzie D, and Priestley K (2000) Earthquake focal depths, effective elastic thickness, and the strength of the continental lithosphere. *Geology* 28(6): 495–498.

Magistrale H (2002) Relative contributions of crustal temperature and composition to controlling the depth of earthquakes in Southern California. *Geophysical Research Letters* 29(10).

Malavieille J (1984) Modelisation experimentale des chevauchements imbriques: Application aux chaines de montagnes. *Bulletin de la Societe geologique de France* XXVI(1): 129–138.

Malavieille J, Lallemand SE, Dominguez S, et al. (2002a) Arc-continent collision in Taiwan: New marine observations and tectonic evolution. *Geological Society of America, Special Paper* 358: 189–213.

Malavieille J, Marcoux J, and De Wever P (2002b) L'ocean perdu. In: *Himalaya-Tibet, Le choc des continents*, pp. 32–39. Paris, France: CNRS Editions et Museum national de'Histoire naturelle.

Mallet FR (1874) On the geology of the Darjiling district and the Western Duars. *Memoirs of the Geological Survey of India*, vol. 11. (part 1). Geological Survey of India.

Marone C (1998) Laboratory-derived friction laws and their application to seismic faulting. *Annual Review of Earth and Planetary Sciences* 26: 643–696.

Marone C and Scholz CH (1988) The depth of seismic faulting and the transition from stable to unstable slip regimes. *Geophysical Research Letters* 15: 621–624.

Marquis G, Jones AG, and Hyndman RD (1995) Coincident conductive and reflective middle and lower crust in southern British Columbia. *Geophysical Journal International* 120: 111–131.

Mascle GH and Hérail G (1982) Les Siwaliks: le prisme d'accretion tectonique associe a la subduction intracontinentale himalayenne. *Geologiya Alpine Grenoble* 58: 95–103.

Masek JG, Isacks BL, Gubbels TL, and Fielding EJ (1994) Erosion and tectonics at the margins of continental plateaus. *Journal of Geophysical Research* 99: 13941–13956.

Mattauer M (1975) Sur le mécanisme de formation de la schistosité dans l'Himalaya. *Earth and Planetary Science Letters* 28: 144–154.

Mattauer M (1986) Intracontinental subduction, crust-mantle décollement and crust-stacking wedge in the Himalayas and other continental belts. In: Coward MP and Ries AC (eds.) *Collision Tectonics*, pp. 37–50. London: Geological Society of London, Special Publications.

McCaffrey R and Nabelek J (1998) Role of oblique convergence in the active deformation of the Himalayas and southern Tibet plateau. *Geology* 26: 691–694.

McKenzie D and Jackson J (2002) Conditions for flow in the continental crust. *Tectonics* 21(6): 1055.

Meade BJ (2007) Present-day kinematics at the India-Asia collision zone. *Geology* 35(1): 81–84.

Meade BJ (2010) The signature of an unbalanced earthquake cycle in Himalayan topography? *Geology* 38(11): 987–990.

Medlicott HB (1864) On the geological structure and relations of the southern portion of the Himalayan range between river Ganges and Ravee. *Memoirs of the Geological Survey of India* 3(2): 1–206.

Meigs AJ, Burbank DW, and Beck RA (1995) Middle-late Miocene (>10 Ma) formation of the main boundary thrust in the western Himalaya. *Geology* 23(5): 423–426.

Meng J, Wang CS, Zhao XX, Coe R, Li YL, and Finn D (2012) India-Asia collision was at 24 degrees N and 50 Ma: Palaeomagnetic proof from southernmost Asia. *Scientific Reports* 2: 1–11.

Métivier F and Gaudemer Y (1997) Mass transfer between eastern Tien Shan and adjacent basins (central Asia): Constraints on regional tectonics and topography. *Geophysical Journal International* 128: 1–17.

Metivier F, Gaudemer Y, Tapponnier P, and Klein M (1999) Mass accumulation rates in Asia during the Cenozoic. *Geophysical Journal International* 137: 280–318.

Mitra S (2003) A unified kinematic model for the evolution of detachment folds. *Journal of Structural Geology* 25(10): 1659–1673.

Mitra S, Priestley K, Bhattacharyya AK, and Gaur VK (2005) Crustal structure and earthquake focal depths beneath northeastern India and southern Tibet. *Geophysical Journal International* 160(1): 227–248.

Molnar P (1984) Structure and tectonics of the Himalaya: Constraints and implications of geophysical data. *The Annual Review of Earth and Planetary Sciences* 12: 489–518.

Molnar P (1987) Inversion of profiles of uplift rates for the geometry of dip-slip faults at depth, with examples from the Alps and the Himalaya. *Annales Geophysicae Series B-Terrestrial and Planetary Physics* 5(6): 663–670.

Molnar P (1990) A review of the seismicity and the rates of active underthrusting and deformation at the Himalaya. *Journal of Himalayan Geology* 1: 131–154.

Molnar P, Brown ET, Burchfiel BC, et al. (1994) Quaternary climate-change and the formation of river terraces across growing anticlines on the north flank of the Tien-Shan, China. *Journal of Geology* 102(5): 583–602.

Molnar P and England P (1990a) Late Cenozoic uplift of mountain ranges and global climate change: Chicken or egg. *Nature* 346: 29–34.

Molnar P and England P (1990b) Temperatures, heat flux, and frictional stress near major thrust fault. *Journal of Geophysical Research* 95: 4833–4856.

Molnar P, England P, and Martinod J (1993) Mantle dynamics, uplift of the Tibetan plateau, and the Indian monsoon. *Reviews of Geophysics* 31(4): 357–396.

Molnar P and Lyon-Caen H (1988) Some simple physical aspects of the support, structure, and evolution of mountain belts. *Processes in Continental Lithospheric Deformation*, vol. 218, pp. 179–207. Boulder, CO: Geological Society of America, Special Paper.

Molnar P and Tapponnier P (1975) Cenozoic tectonics of Asia: Effects of a continental collision. *Science* 189: 419–426.

Montgomery DR (1994) Valley incision and uplift of mountain peaks. *Journal of Geophysical Research* 99: 13913–13921.

Moreno M, Rosenau M, and Oncken O (2010) 2010 Maule earthquake slip correlates with pre-seismic locking of Andean subduction zone. *Nature* 467(7312): 198–202.

Mugnier JL and Huyghe P (2006) Ganges basin geometry records a pre-15 Ma isostatic rebound of Himalaya. *Geology* 34(6): 445–448.

Mugnier J-L, Leturmy P, Mascle G, et al. (1999) The Siwaliks of western Nepal 1: Geometry and kinematics. *Journal of Asian Earth Sciences* 17: 629–642.

Mugnier JL, Mascle G, and Faucher T (1992) La structure des Siwaliks de l'Ouest Népal: un prisme d'accrétion intracontinental. *Bulletin de la Societe Geologique de France* 163: 585–595.

Nabelek J, Hetenyi G, Vergne J, et al. (2009) Underplating in the Himalaya-Tibet collision zone revealed by the Hi-CLIMB experiment. *Science* 325(5946): 1371–1374.

Nadin ES and Martin AJ (2012) Apatite thermochronometry within a knickzone near the Higher Himalaya front, central Nepal: No resolvable fault motion in the past one million years. *Tectonics* 31.

Najman Y, Appel E, Boudagher-Fadel M, et al. (2010) Timing of India-Asia collision: Geological, biostratigraphic, and palaeomagnetic constraints. *Journal of Geophysical Research, Solid Earth* 115.

Nakata T (1989) Active faults of the Himalaya of India and Nepal. In: Malinconico LL Jr., and Lillie R (eds.) *Tectonics of the Western Himalayas*, pp. 243–264. Boulder, CO: Geological Society of America.

Nakata T, Yagi H, Okumura K, et al. (1998) First successful Paleoseismic trench study on active faults in the Himalaya. *Eos* 79: F615.

Nelson KD, Zhao WJ, Brown LD, et al. (1996) Partially molten middle crust beneath southern Tibet: Synthesis of project INDEPTH results. *Science* 274(5293): 1684–1688.

Nishimura T, Hirasawa T, Miyazaki S-I, et al. (2004) Temporal change of interplate coupling in northeastern Japan during 1995-2002 estimated from continuous GPS observations. *Geophysical Journal International* 157: 901–916.

Okada Y (1992) Internal deformation due to shear and tensile faults in a half-space. *Bulletin of the Seismological Society of America* 82(2): 1018–1040.

Oldham RD (1883a) The geology of Jaunsar and the lower Himalayas. *Records of the Geological Survey of India* 16: 193–198.

Oldham T (1883b) Catalog of Indian earthquakes. *Memoir of the Geological Survey of India* 19: 163–215.
Pandey MR and Molnar P (1988) The distribution of intensity of the Bihar-Nepal earthquake of 15 january 1934 and bounds on the extent of the rupture zone. *Journal of Nepal Geological Society* 5: 23–45.
Pandey MR, Tandukar RP, Avouac JP, Lavé J, and Massot JP (1995) Interseismic strain accumulation on the Himalaya crustal ramp (Nepal). *Geophysical Research Letters* 22(7): 751–754.
Pandey MR, Tandukar RP, Avouac J-P, Vergne J, and Héritier T (1999) Seismotectonics of Nepal himalayas from a local seismic network. *Journal of Asian Earth Sciences* 17: 703–712.
Pant MR (2002) A step toward a historical seismicity of Nepal. *Adarsa* 2: 29–60.
Pathier E, Fielding EJ, Wright TJ, Walker R, Parsons BE, and Hensley S (2006) Displacement field and slip distribution of the 2005 Kashmir earthquake from SAR imagery. *Geophysical Research Letters* 33(20): L20310.
Patriat P and Achache J (1984) India-Eurasia collision chronology has implications for crustal shortening and driving mechanism of plates. *Nature* 311: 615–621.
Patriat P and Segoufin J (1988) Reconstruction of the Central Indian-Ocean. *Tectonophysics* 155(1–4): 211–234.
Pêcher A (1989) The metamorphism in Central Himalaya. *Journal of Metamorphic Geology* 7: 31–41.
Perfettini H and Avouac JP (2004) Stress transfer and strain rate variations during the seismic cycle. *Journal of Geophysical Research, Solid Earth* 109(B6): B06402.
Poisson B and Avouac JP (2004) Holocene hydrological changes inferred from alluvial stream entrenchment in North Tian Shan (Northwestern China). *Journal of Geology* 112(2): 231–249.
Pollitz FF, Burgmann R, and Segall P (1998) Joint estimation of afterslip rate and postseismic relaxation following the 1989 Loma Prieta earthquake. *Journal of Geophysical Research, Solid Earth* 103(B11): 26975–26992.
Powell CMA and Conaghan PJ (1973) Plate tectonics and the Himalayas. *Earth and Planetary Science Letters* 20: 1–12.
Pratt JH (1855) On the attraction of the Himalaya Mountains, and of the elevated regions beyond them, upon the plumb line in India. *Philosophical Transactions of the Royal Society of London* 145: 53–100.
Priestley K, Jackson J, and McKenzie D (2008) Lithospheric structure and deep earthquakes beneath India, the Himalaya and southern Tibet. *Geophysical Journal International* 172(1): 345–362.
Pysklywec RN (2006) Surface erosion control on the evolution of the deep lithosphere. *Geology* 34(4): 225–228, http://dx.doi.org/210.1130/G21963.21961.
Ramstein G, Fluteau F, Besse J, and Joussaume S (1997) Effect of orogeny, plate motion and land sea distribution on Eurasian climate change over the past 30 million years. *Nature* 386(6627): 788–795.
Rana BSJB (1935) *Nepalako Mahabhukampa (1990 sala) Nepal's Great Earthquake*.
Ratschbacher Lea (1994) Distributed deformation in southern and western Tibet during and after the India-Asia collision. *Journal of Geophysical Research* 99: 19917–19945.
Raymo ME and Ruddiman WF (1992) Tectonic forcing of late Cenozoic climate. *Nature* 359(6391): 117–122.
Replumaz A, Karason H, van der Hilst RD, Besse J, and Tapponnier P (2004) 4-D evolution of SE Asia's mantle from geological reconstructions and seismic tomography. *Earth and Planetary Science Letters* 221(1–4): 103–115.
Replumaz A, Negredo AM, Guillot S, and Villasenor A (2010a) Multiple episodes of continental subduction during India/Asia convergence: Insight from seismic tomography and tectonic reconstruction. *Tectonophysics* 483(1–2): 125–134.
Replumaz A, Negredo AM, Villasenor A, and Guillot S (2010b) Indian continental subduction and slab break-off during Tertiary collision. *Terra Nova* 22(4): 290–296.
Rice JR (2006) Heating and weakening of faults during earthquake slip. *Journal of Geophysical Research, Solid Earth* 111(B5).
Rice JR and Tse ST (1986) Dynamic motion of a single degree of freedom system following a rate and state dependent friction law. *Journal of Geophysical Research* 91: 521–530.
Robinson DM, DeCelles PG, Garzione CN, Pearson ON, Harrison TM, and Catlos EJ (2003) Kinematic model for the Main Central thrust in Nepal. *Geology* 31(4): 359–362.
Robinson DM, DeCelles PG, Patchett PJ, and Garzione CN (2001) The kinematic evolution of the Nepalese Himalaya interpreted from Nd isotopes. *Earth and Planetary Science Letters* 192: 507–521.
Rowley DB (1996) Age of initiation of collision between India and Asia: A review of stratigraphic data. *Earth and Planetary Science Letters* 145: 1–13.
Rowley DB and Currie BS (2006) Palaeo-altimetry of the late Eocene to Miocene Lunpola basin, central Tibet. *Nature* 439(7077): 677–681.
Royden LH (1993) The steady state thermal structure of eroding orogenic belts and accretionary prisms. *Journal of Geophysical Research* 98: 4487–4507.
Royer JY and Patriat P (2002) L'Inde part a la derive. In: *Himalaya-Tibet, Le choc des continents*, pp. 25–31. Paris, France: CNRS Editions et Museum national de'Histoire naturelle.
Ruddiman WF and Kutzbach JE (1991) Plateau uplift and climatic-change. *Scientific American* 264(3): 66–75.
Sakai H (1985) Geology of the Kali Gandaki Supergroup of the Lesser Himalayas in Nepal. *Memoirs of the Faculty of Science, Kyushu University, Series D, Geology* 25: 337–397.
Sakai H, Takigami Y, Nakamuta Y, and Nomura H (1999) Inverted metamorphism in the Pre- Siwalik foreland basin sediments beneath the crystalline nappe, western Nepal Himalaya. *Journal of Asian Earth Sciences* 17: 727–739.
Sandiford M, Coblentz DD, and Richardson RM (1995) Ridge torques and continental collision in the Indian-Australian plate. *Geology* 23(7): 653–656.
Sapkota SN, Bollinger L, Klinger Y, Tapponnier P, Gaudemer Y, and Tiwari D (2013) Primary surface ruptures of the great Himalayan earthquakes in 1934 and 1255. *Nature Geoscience* 6(1): 71–76.
Sastri VV, Bhandari LL, Raju ATR, and Datta AK (1971) Tectonic framework and subsurface stratigraphy of the Ganga basin. *Journal of the Geological Society of India* 12: 222–233.
Saul J, Kumar MR, and Sarkar D (2000) Lithospheric and upper mantle structure of the indian shield, from teleseismic receiver functions. *Geophysical Research Letters* 27: 2357–2360.
Schärer U and Allegre CJ (1983) The Palung granite (Himalaya); high resolution U-Pb systematics in zircon and monazite. *Earth and Planetary Science Letters* 63: 423–432.
Schelling D (1992) The tectonostratigraphy and structure of the eastern Nepal Himalaya. *Tectonics* 11: 925–943.
Schelling D and Arita K (1991) Thrust tectonics, crustal shortening, and the structure of the far-eastern Nepal Himalaya. *Tectonics* 10(5): 851–862.
Schulte-Pelkum V, Monsalve G, Sheehan A, et al. (2005) Imaging the Indian subcontinent beneath the Himalaya. *Nature* 435(7046): 1222–1225.
Searle MP, Law RD, and Jessup MJ (2006) Crustal structure, restoration and evolution of the Greater Himalaya in Nepal-South Tibet: Implications for channel flow and ductile extrusion of the middle crust. In: Law RD, et al. (eds.) *Channel Flow, Ductile Extrusion and Exhumation in Continental Collision Zones*, pp. 355–378.
Searle MP, Parrish RR, Hodges KV, Hurford MW, Ayres MW, and Whitehouse MJ (1997) Shisha Pangma leucogranite, South Tibetan Himalaya: Field relations, geochemistry, age, origin, and emplacement. *The Journal of Geology* 105: 295–317.
Searle MP, Pickering KT, and Cooper DJW (1990) Restoration and evolution of the intermontane Indus molasse basin, Ladakh Himalaya, India. *Tectonophysics* 174(3–4): 301–314.
Searle MP, Windley B, Coward M, et al. (1987) The closing of Tethys and the tectonics of the Himalaya. *Geological Society of America Bulletin* 98: 678–701.
Seeber L and Armbruster JG (1981) Great detachment earthquakes along the Himalayan arc and long-term forecasting. In: Simpson DE and Richards PG (eds.) *Earthquake Prediction: An International Review. Maurice Ewing Series*, vol. 4, pp. 259–277. Washington, DC: The American Geophysical Union.
Seeber L and Gornitz V (1983) River profiles along the himalayan arc as indicators of active tectonics. *Tectonophysics* 92: 335–367.
Segall P and Rice JR (1995) Dilatancy, compaction, and slip instability of a fluid-infiltrated fault. *Journal of Geophysical Research, Solid Earth* 100(B11): 22155–22171.
Simoes M, Avouac JP, and Chen YG (2007a) Slip rates on the Chelungpu and Chushiang thrust faults inferred from a deformed strath terrace along the Dungpuna river, west central Taiwan. *Journal of Geophysical Research, Solid Earth* 112(B3): B03S10.
Simoes M, Avouac JP, Chen YG, et al. (2007b) Kinematic analysis of the Pakuashan fault tip fold, west central Taiwan: Shortening rate and age of folding inception. *Journal of Geophysical Research, Solid Earth* 112(B3).
Sleep NH and Blanpied ML (1992) Creep, compaction and the weak rheology of major faults. *Nature* 359(6397): 687–692.
Smith SW and Wyss M (1968) Displacement on the San Andreas fault subsequent to the 1966 Parkfield earthquake. *The Bulletin of the Seismological Society of America* 58(6): 1966–1973.
Spicer RA, Harris NBW, Widdowson M, et al. (2003) Constant elevation of southern Tibet over the past 15 million years. *Nature* 421(6923): 622–624.
Srivastava P and Mitra G (1994) Thrust geometries and deep structure of the outer and Lesser Himalaya, Kumaon and Garhwal (India): Implications for evolution of the Himalayan fold-and-thrust belt. *Tectonics* 13: 89–109.

Stöcklin J, Bhattarai KD, Chettri VS, and Bhandari AN (1980) *Geologic Map of Kathmandu Area and Central Mahabharat Range*. Kathmandu, Nepal: Department of Mines and Geology.

Sun W (1989) *Bouguer Gravity Anomaly Map of the People's Republic of China*. Chinese Academy of Geoexploration, Beijing.

Suppe J (1985) *Principles of Structural Geology*. p.537. Englewood cliffs, NJ: Prentice-Hall, Inc.

Suppe J and Medwedeff DA (1990) Geometry and kinematics of fault-propagation folding. *Eclogae Geologicae Helvetiae* 83(3): 409–454.

Suwa Y, Miura S, Hasegawa A, Sato T, and Tachibana K (2006) Interplate coupling beneath NE Japan inferred from three-dimensional displacement field. *Journal of Geophysical Research, Solid Earth* 111(B4): B04402.

Tapponnier P, Xu ZQ, Roger F, et al. (2001) Oblique stepwise rise and growth of the Tibet plateau. *Science* 294(5547): 1671–1677.

Thompson SC, Weldon RJ, Rubin CM, Abdrakhmatov K, Molnar P, and Berger GW (2002) Late Quaternary slip rates across the central Tien Shan, Kyrgyzstan, central Asia. *Journal of Geophysical Research, Solid Earth* 107(B9): 2203.

Tokuoka T, Takayasu K, Yoshida M, and Hisatomi K (1986) The Churia (Siwalik) group of the Arung khola area, west central Nepal. *Memoirs of the Faculty of Science, Shimane University* 20: 135–210.

Toussaint G, Burov E, and Avouac JP (2004a) Tectonic evolution of a continental collision zone: A thermomechanical numerical model. *Tectonics* 23(6): TC6003.

Toussaint G, Burov EB, and Jolivet L (2004b) Continental plate collision: Unstable vs. stable slab dynamics. *Geology* 32(1): 33–36.

Tsenn MC and Carter NL (1987) Upper limits of power law creep of rocks. *Tectonophysics* 136: 1–26.

Upreti BN (1999) An overview of the stratigraphy and tectonics of the Nepal Himalaya. *Journal of Asian Earth Sciences* 17: 577–606.

Upreti BN, Nakata T, Kumahara Y, et al. (2000) The latest active faulting in southeast Nepal. In: Okumura KTK and Goto H (eds.) *Active Fault Research for the New Millennium*. Proceedings of the Hokudan International Symposium and School on Active Faulting, pp. 533–536. Hiroshima, Japan: Letter Press Ltd.

Valdiya KS (1964) The unfossiliferous formations of the Lesser Himalaya and their correlation. In: *Paper Presented at 22nd International Geological Congress, Delhi* .

Van de Meulebrouck J (1983) Reconnaissance geophysique des structures crustales de deux segments de chaine de collision: le Haut Allier (Massif Central français) et le Sud Tibet (Himalaya).

Walcott RI (1998) Modes of oblique compression: Late Cenozoic tectonics of the South Island of New Zealand. *Reviews of Geophysics* 36(1): 1–26.

Wallace LM, Beavan J, McCaffrey R, and Darby D (2004) Subduction zone coupling and tectonic block rotations in the North Island, New Zealand. *Journal of Geophysical Research, Solid Earth* 109(B12): B12406.

Wang Q, Zhang P, Freymueller JT, et al. (2001) Present-day crustal deformation in China constrained by global positioning system measurements. *Science* 294(5542): 574–577.

Whipple KX and Meade BJ (2004) Controls on the strength of coupling among climate, erosion, and deformation in two-sided, frictional orogenic wedges at steady state. *Journal of Geophysical Research: Earth Surface* 109(F1): F01011.

Willett SD (1999) Orogeny and topography: The effects of erosion on the structure of mountain belts. *Journal of Geophysical Research* 104(B12): 28957–28981.

Willett S, Beaumont C, and Fullsack P (1993) Mechanical model for the tectonics of doubly vergent compressional orogens. *Geology* 21(4): 371–374.

Williams CA, Conners C, Dahlen FA, Price EJ, and Suppe J (1994a) Effect of the brittle-ductile transition on the topography of compressive mountain belts on Earth and Venus. *Journal of Geophysical Research, Solid Earth* 99(B10): 19947–19974.

Williams CA, Connors C, Dalhen FA, Price EJ, and Suppe J (1994b) The effect of brittle-ductile transition on the topography of compressive mountain belts on Earth and Venus. *Journal of Geophysical Research* 99: 19,947–19,974.

Willis B (1891) *The Mechanics of Appalachian Structure*, 281 pp. U. S. Geol. Surv. 13th Annual Report 1891–1892, Part 2.

Wittlinger G, Farra V, Hetenyi G, Vergne J, and Nabelek J (2009) Seismic velocities in Southern Tibet lower crust: A receiver function approach for eclogite detection. *Geophysical Journal International* 177(3): 1037–1049.

Wobus C, Heimsath A, Whipple K, and Hodges K (2005) Active out-of-sequence thrust faulting in the central Nepalese Himalaya. *Nature* 434(7036): 1008–1011.

Wobus CW, Hodges KV, and Whipple KX (2003) Has focused denudation sustained active thrusting at the Himalayan topographic front? *Geology* 31(10): 861–864.

Yeats RS, Nakata T, Farah A, Mizra MA, Pandey MR, and Stein RS (1992) The Himalayan frontal fault system. In: DeJong KA and Farah A (eds.) *Geodynamics of Pakistan, Geological Survey of Pakistan: Seismicity of the Hazara Arc in northern Pakistan: Decollement vs. Basement Faulting*, *Annales Tectonicae, Special Issue Supplement to Volume VI,* Supp. to Vol. 6, pp. 85–98.

Yin A, Harrison TM, Murphy MA, et al. (1999) Tertiary deformation history of southeastern and southwestern Tibet during the Indo-Asian collision. *Geological Society of America Bulletin* 111(11): 1644–1664.

Zhang PZ, Shen Z, Wang M, Gan WJ, Burgmann R, and Molnar P (2004) Continuous deformation of the Tibetan Plateau from global positioning system data. *Geology* 32(9): 809–812.

Zhao WL and Morgan J (1985) Uplift of Tibetan plateau. *Tectonics* 4: 359–369.

Zhao W, Nelson KD, and project INDEPTH Team (1993) Deep seismic-reflection evidence continental underthrusting beneath southern Tibet. *Nature* 366: 557–559.

Zienkiewicz OC and Taylor RL (1989) *The Finite Element Method*, 4th edn. New York: McGraw-Hill.

6.10 Fault Mechanics

CH Scholz, Columbia University, Palisades, NY, USA

© 2007 Elsevier B.V. All rights reserved.

This chapter is reproduced from the previous edition, Volume 6, pp. 441–483, © 2007, Elsevier B.V.

6.10.1	**Introduction**	433
6.10.2	**Elementary Fault Theory**	434
6.10.2.1	Anderson's Theory of Faulting	434
6.10.2.2	Overthrust Faults and the Hubert–Rubey Theory	435
6.10.3	**Fracture Mechanics of Faults**	436
6.10.3.1	Linear Elastic Fracture Mechanics	436
6.10.3.2	The Dugdale–Barenblatt Model	437
6.10.3.3	Critical Fault Tip Taper Model	437
6.10.3.4	Experimental Studies of Fault Propagation	437
6.10.3.5	Fault Scaling Laws and the Mechanics of Fault Growth	438
6.10.3.6	Displacement–Length Scaling	438
6.10.3.7	Fault Tip Taper Scaling	439
6.10.3.8	Process Zones and Their Scaling	440
6.10.3.9	Cataclasite Zone Scaling	442
6.10.3.10	Interpretation of the Scaling Laws in Terms of Crack Models	442
6.10.4	**Fault Interactions**	445
6.10.4.1	Mode III Interactions: Normal Faults	445
6.10.4.1.1	Pinning	445
6.10.4.1.2	Coalescence	448
6.10.4.1.3	Nucleation inhibition	448
6.10.4.2	Mode II Interactions	448
6.10.4.2.1	Interactions at strike-slip jogs	450
6.10.4.2.2	Strike-slip splay faults	450
6.10.5	**Fault Populations**	451
6.10.5.1	Observations of Fault Populations	453
6.10.5.1.1	Power law distributions	453
6.10.5.1.2	Exponential distributions	454
6.10.5.1.3	Periodic distributions	455
6.10.5.2	The Formation of Fault Populations	455
6.10.6	**Strain and Faulting**	457
6.10.6.1	Calculation of Brittle Strain from Fault Data	457
6.10.6.2	Fault Rotation and Lockup	458
6.10.7	**Fault Rocks and Structures**	459
6.10.7.1	Shallow Schizosphere	459
6.10.7.2	Deep Schizosphere	460
6.10.7.3	Brittle–Plastic Transition Region	461
6.10.7.4	Plastosphere Shear Zones	461
6.10.7.4.1	Mylonite fabric elements	462
6.10.7.4.2	Shear localization and strain softening in mylonite zones	462
6.10.7.5	Synoptic Model for Faults and Shear Zones	463
6.10.8	**The Strength of Faults**	463
6.10.8.1	Direct Evidence for Fault Strength	463
6.10.8.2	The Weak SAF Fallacy	464
References		465

6.10.1 Introduction

The continental crust may be considered to be composed of two mechanical units: an upper region, the schizosphere, which responds to large deformations in a brittle manner, and below that, the plastosphere, which deforms by plastic flow. There is a gradual transition between the two. The schizosphere constitutes the upper 10 to several tens of kilometers of the crust, depending on the heat flow and hence age of the crust. Below 1–2 km, stresses are compressive and macroscopic deformation is by shear fracture. Such shear fractures, which have friction between their walls, are called faults. The oceanic lithosphere may be similarly divided.

Brittle deformation of the schizosphere takes place on two timescales. The long timescale corresponds to the formation

 http://dx.doi.org/10.1016/B978-0-444-53802-4.00119-6

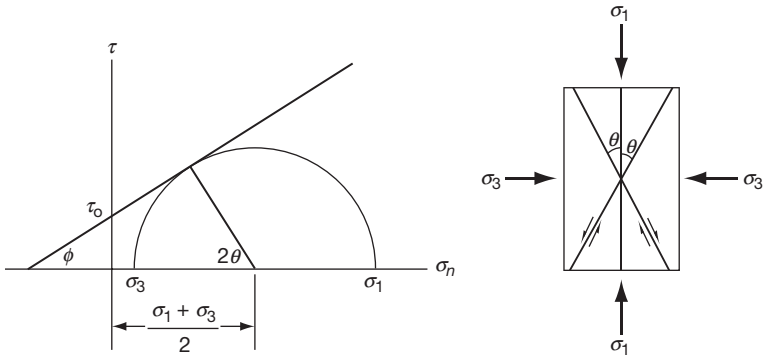

Figure 1 The Mohr diagram illustrating the Coulomb fracture criterion and the orientation of shear fractures.

and propagation of faults and the short timescale to the nucleation and propagation of earthquakes. Earthquakes are dynamically propagating shear cracks that propagate on faults due to a stick-slip frictional instability. The shear displacement on faults is usually the result of the cumulative slip of many earthquakes. Because of these different timescales, the two phenomena, faulting and earthquakes, are usually studied separately and by different disciplines. This chapter is concerned primarily with faults, which are treated as quasistatic features.

When a fault reaches the dimensions of the schizosphere, it will generate, by virtue of the stress concentration at its base, a ductile shear zone within the plastosphere, which will further develop and deepen as the fault continues to grow. This ductile shear zone thus becomes an integral part of the structure. For compatibility of their boundary conditions, the two must act as a unit at long timescales, but at the short (earthquake) timescales, they interact. Thus, for large faults, which include such shear zones, both the brittle/frictional and ductile/plastic regions must be considered as interacting parts of the same fault system, and both should be discussed in any treatment of faults. Much of the material in this chapter is expanded and updated from Scholz (2002).

6.10.2 Elementary Fault Theory

The first recognition of faults as tectonic agents was made by Nicolaus Steno in his *prodromus* of 1669, in his discussion of the origin of mountains (Adams, 1938). Faults were known by early miners; in fact, fault is an English mining term (Lyell, 1832). Lyell was the first to associate earthquakes with faults, in a study of the earthquakes of 1783 in Calabria. However, the modern theory of faulting did not arise until the early twentieth century.

6.10.2.1 Anderson's Theory of Faulting

Early in his career, E. M. Anderson proposed that faults are brittle fractures that occur according to the Coulomb criterion (Anderson, 1905). The Coulomb criterion relates the shear stress τ to normal stress σ_n on a plane within the material:

$$\tau = \tau_0 + \mu\sigma_n \qquad [1]$$

where the parameters τ_0 and μ are called the cohesion and coefficient of internal friction, respectively. The angle $\phi = \tan^{-1}\mu$ is called the angle of internal friction. Figure 1 shows this criterion with a Mohr circle representation. From the Mohr circle, it can be seen that failure will occur on two conjugate planes oriented at acute angles on either side of the maximum principal compressive stress σ_1

$$\theta = \pi/4 - \phi/2 \qquad [2]$$

with opposite senses of shear. The intersection of the two planes is in the direction of the intermediate principal stress, σ_2.

Recognizing the condition that near the free surface, one of the principal stresses must be vertical, Anderson showed that the three classes of faults, normal, thrust, and strike-slip, result from the three types of inequality that arise between the three principal stresses.

Figure 2(a) shows a section through a Coulomb fracture envelope at a fixed value of the vertical principal stress σ_v. The two horizontal principal stresses are assumed to be north–south and east–west for convenience, denoted σ_{NS} and σ_{EW}. Each side of this six-sided envelope defines a different regime of faulting, as shown in Figure 2(b). Side 1, for example, is the failure locus for $\sigma_N s > \sigma_V > \sigma_{EW}$, hence for strike-slip faults striking at an acute angle from N, as shown in Figure 2(b). In the figure, it is assumed that $\mu = 0.6$; hence, $\phi = 30°$.

At the end of his career, Anderson (1951) produced a monograph in which, to support his hypothesis, he described many examples from Britain of conjugate fault systems in which the angular relationships conform to the expectations of the Coulomb criterion.

The angular relations of conjugate faults to the stress field apply only to the stress state at the time of the formation of the faults. In many cases of the old faults discussed by Anderson, it is not possible to prove the simultaneity of their origin. Furthermore, as will be discussed later, faults rotate away from the σ_1 direction as they accrue slip, so that their included angle at a later time may be larger than given in eqn [2].

Figure 3 shows an example of currently active faults in Japan. The figure depicts the Izu peninsula, which lies on the Philippine Sea Plate and is currently colliding with the plate (unknown) on which NE Japan sits (Nakamura et al., 1984; Somerville, 1978). Many sets of conjugate strike-slip faults occur on Izu, of which the ones that have recently ruptured in large earthquakes with known slip directions are shown. The alignments of parasitic cone emanating from the Hakone and

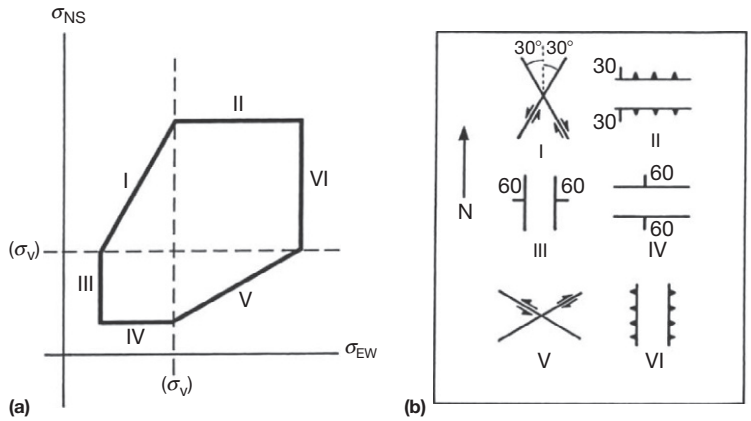

Figure 2 (a) Slice through the Coulomb fracture envelop at a fixed level of vertical stress σ_v. (b) Orientation of faults for the various sides of the fracture envelop. Reproduced from Scholz CH (2002) *The Mechanics of Earthquakes and Faulting*, 2nd edn. Cambridge: Cambridge University Press.

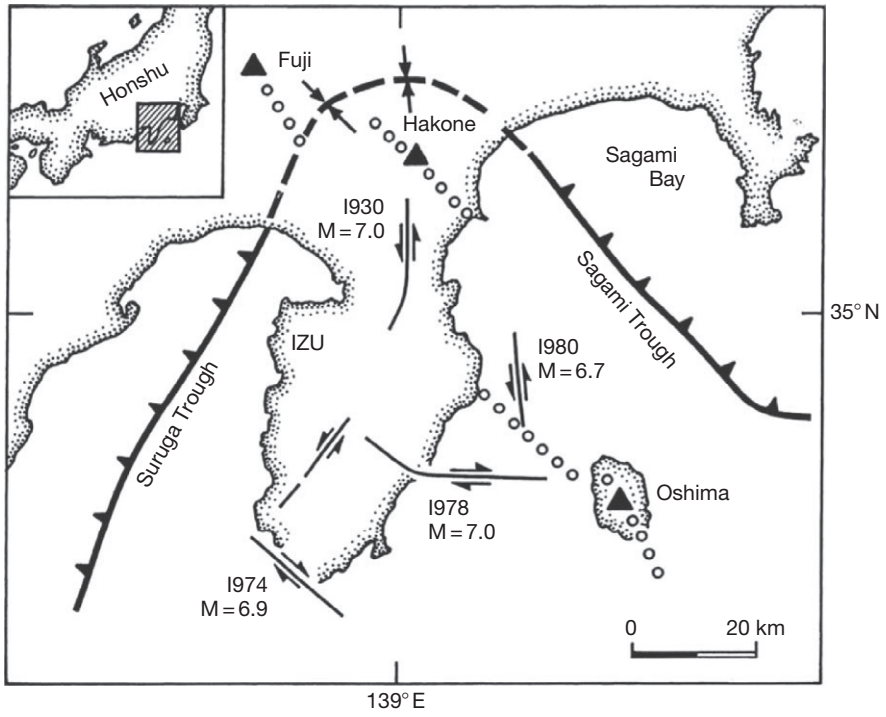

Figure 3 Map of the Izu peninsula, Japan, showing the faults ruptured in recent strike-slip earthquakes and the orientation of parasitic volcanoes (open circles) associated with major volcanoes (filled triangles). Reproduced from Scholz CH (2002) *The Mechanics of Earthquakes and Faulting*, 2nd edn. Cambridge: Cambridge University Press.

Oshima volcanoes bisect the angle between the conjugate faults. These cones overlie dikes that are produced by hydraulic fracturing and hence lie parallel to σ_1 (Anderson, 1936; Nakamura, 1969), thus providing independent evidence for the stress direction.

6.10.2.2 Overthrust Faults and the Hubert–Rubey Theory

An important category of faults that does not conform with Andersonian mechanics is overthrusts. These are nearly horizontal thrust faults, common in foreland fold and thrust belts, that are observed to have transported their upper plates large distances over their lower plates. These faults do not conform in their orientation with Anderson's theory, and they also present a fundamental mechanical difficulty. Figure 4 shows a schematic diagram of a thrust sheet on height z and length l is pushed along a friction surface by a horizontal stress σ_h. The force balance for this is

$$F = \sigma_h = (\sigma_z - p)l\mu \qquad [3]$$

where μ is the friction, p is the pore pressure, and a simple effective stress law is assumed. Let $\sigma_v = \rho g z$, the lithostatic overburden, and let pore pressure $p = \lambda \rho g z$, where λ is a constant. Then, the maximum length of a block that can be pushed without σ_h exceeding the compressive strength of the rock C is

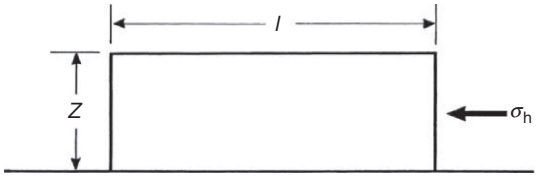

Figure 4 Diagram illustrating the Hubert–Rubey theory of overthrust faulting. Reproduced from Scholz CH (2002) *The Mechanics of Earthquakes and Faulting*, 2nd edn. Cambridge: Cambridge University Press.

$$l = C/(1-\lambda)\rho g\mu \qquad [4]$$

If we assume that p is hydrostatic, then $\lambda = 0.4$. Assuming reasonable values of $C = 200$ MPa, $\mu = 0.85$, and $\rho = 2.5$, we obtain from eqn [4] that $l = 16$ km.

Many overthrust sheets, however, are observed to be much longer than that, in the range of 50–100 km. In some cases, overthrusts, called decollements, slide on a layer of a weak ductile material such as salt or gypsum. The Jura overthrust in Switzerland, for example, moved on a gypsum layer, which was plastically deformed to form a mylonite. In such cases, the right-hand side of [3] is replaced by $\tau_{max}l$, where τ_{max} is the yield strength of the weak material. Then, [4] becomes

$$l = Cz/\tau_{max} \qquad [5]$$

and because $C \gg \tau_{max}$, $l \gg z$.

Hubbert and Rubey (1959) suggested that under certain circumstances, p could exceed hydrostatic and, in the case of overthrusts, could reach the lithostatic pressure without hydrofracturing intervening. Thus, as λ in eqn [4] approaches 1, the constraint on the length of the overthrust sheet vanishes.

The mechanism by which pore pressure could be so elevated was controversial at the time. Voight (1976) contains a collection of papers debating this issue. It is now well known, from oil-field data, that such overpressures are found in sedimentary basins that contain abundant shale that can seal in the pressures produced by compaction of the sediments. Typical geologic terranes in which this mechanism, and overthrusts, occurs are foreland fold and thrust belts and the accretionary prisms of subduction zones.

6.10.3 Fracture Mechanics of Faults

Anderson's theory is concerned only with the orientation of faults with respect to the principal stress directions. He did not consider how faults grow. Faults occur in lengths ranging from a few centimeters to hundreds of kilometers, so they must grow in length as they accrue slip. To understand this behavior, we need to treat faults as shear cracks, which is treated here in a simplified form.

6.10.3.1 Linear Elastic Fracture Mechanics

This form of fracture mechanics assumes the fault to be a crack in a linear elastic medium. Because the stress and displacement distributions around such a crack have been solved analytically, this theory is the most attractive mathematically and is the one most often used. For a more complete treatment see, for example, Lawn and Wilshaw (1975) and, for geologic applications, Pollard and Segall (1987).

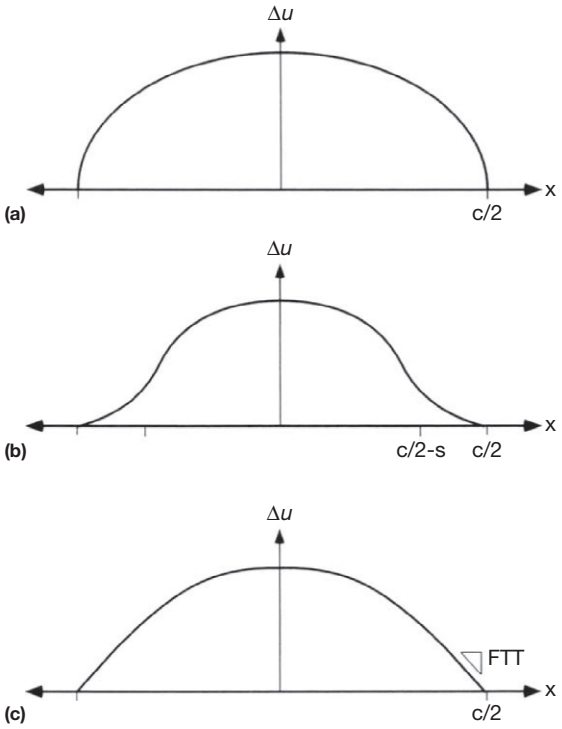

Figure 5 Three types of crack models discussed in the text: (a) elastic model, (b) Dugdale model, and (c) small-scale yielding model. Reproduced from Scholz CH (2002) *The Mechanics of Earthquakes and Faulting*, 2nd edn. Cambridge: Cambridge University Press.

In this model, the crack tip is assumed to be a mathematically sharp slit. The displacement D between the crack walls is given by

$$D = \Delta\sigma\frac{2(1-\upsilon)}{\mu}\left(L^2 - x^2\right)^{1/2} \qquad [6]$$

where L is the length of the crack, x is the position along its length, υ and μ are the elastic constants, and the stress drop $\Delta\sigma = (\Delta\sigma_y - \Delta\sigma_f)$, the yield stress of the intact rock less the residual friction stress. The displacement distribution is thus elliptical, as shown in **Figure 5(a)**. The maximum displacement is thus

$$D_{max} = \Delta\sigma\frac{2(1-\upsilon)}{\mu}L \qquad [7]$$

The stress at the tip of the crack is

$$\sigma = K(2\pi r)^{-1/2}f(\theta) \qquad [8]$$

where r is the distance from the crack tip, K is called the stress intensity factor, and $f(\theta)$ is a function that describes the dependence with the angle θ from the plane of the crack. The functions $f(\theta)$ depend on crack mode. They can be found tabulated in standard sources such as Lawn and Wilshaw (1975). The stress intensity factor is given by

$$K = \Delta\sigma(\pi L)^{1/2} \qquad [9]$$

The Griffith fracture criterion is included by assuming that the crack propagates when K reaches a critical value K_c defined by the point at which the critical energy release rate G_c equals the surface energy:

$$G_c = K_c^2/2(1+\upsilon)\mu = 2\alpha \qquad [10]$$

where α is the specific surface energy of the material. This is the Griffith equilibrium equation. Notice that [9] indicates that K increases with L. Because the right-hand side of [10] is constant, equilibrium requires that $\Delta\sigma$ decrease as the crack grows: that is, the crack weakens as it lengthens. This feature results in the Griffith instability: if the driving stress is maintained, the crack will run without limit after reaching its critical length.

Combining [7] with [9], we obtain

$$D_{max} = \frac{2(1-\upsilon)}{\mu} L^{1/2} K_c \qquad [11]$$

Because K_c is constant at equilibrium, this implies that D_{max} scales as $L^{1/2}$.

6.10.3.2 The Dugdale–Barenblatt Model

The elastic crack model, while convenient for calculating stress and displacement fields around faults, has several problems when it comes to applying it to crack propagation. The first is the square root singularity in the crack tip stress [8]. No real materials, of course, can support such a stress singularity. Materials such as steel and rock are likely to inelastically yield in some volume around the crack tip by plastic flow or microcracking and thus relax the singularity.

Dugdale (1960) and Barenblatt (1962) were the first to address this problem. They modified the elastic crack model by assuming a breakdown or yielding region s in the vicinity of the tip. They did this by imposing a resistive cohesion stress up to the yield stress σ_y in the breakdown region. The resulting displacement distribution is shown in **Figure 5(b)**.

Cowie and Scholz (1992a) applied this model to faulting. There are two ways of scaling s. If one assumes that s is constant, then the breakdown regions become comparatively small as the fault grows and the behavior approaches that of the elastic crack model. This is not realistic, however, because as L increases, the size of the stress concentration at the tip increases, so we should expect that s will increase likewise. For an elastic, purely plastic material, for example, the radius of the zone of yielding at the crack tip is (Atkinson, 1987)

$$r_y = (1/2\pi)(\mu/\sigma_y)^2 = \frac{L}{8}\left(\frac{\sigma_a}{\sigma_y}\right)^2 \qquad [12]$$

where σ_a is the applied stress and σ_y the yield stress. Because the ratio of these two is scale-independent, we see that r_y scales with L. Therefore, we should scale s with L in the Dugdale–Barenblatt model. For this case, Cowie and Scholz (1992a) showed that the stress in the breakdown zone $(\sigma_y - \sigma_f)$ remains constant during fault growth. Thus, unlike the elastic crack model, the fault remains of constant strength during growth. The displacement at the inner end of the breakdown zone, D_0, scales with L. The breakdown energy is

$$G = (\sigma_y - \sigma_f) D_0 \qquad [13]$$

Using the expression for D_0 from Cowie and Scholz (1992a), [13] becomes

$$G = \frac{2(1-\nu)L(\sigma_y - \sigma_f)^2 \cos\theta_2}{\pi\mu} \ln(\sec\theta_2) \qquad [14]$$

where $\cos\theta_2 = (\langle l\rangle L - s)/L$. Thus, G scales with L, rather than being constant, as in the elastic crack model. In this case, the right-hand side of the equilibrium equation scales with L, so that there is no Griffith instability: the fault grows quasistatically. K_c then scales with $L^{1/2}$ (see eqn [10]) and so the equivalent of [11] will show that D scales linearly with L. Specifically,

$$\frac{D_{max}}{L} = \frac{(1-\nu)(\sigma_y - \sigma_f)}{2\pi\mu} \text{fnct}(\theta_2) \qquad [15]$$

we see that the faults are self-similar and that the D_{max}/L ratio is a strain that corresponds to the stress drop $(\sigma_y - \sigma_f)$.

6.10.3.3 Critical Fault Tip Taper Model

The Dugdale–Barenblatt model is unrealistic in that, for mathematical facility, it restricts the inelastic deformation to the plane of the crack. A more realistic elastic–plastic model that allows inelastic deformation within a volume surrounding the crack tip is called the crack tip opening angle model (Kanninen and Popelar, 1985). Because we are applying this to faults rather than opening-mode cracks, we call it the critical fault tip taper (CFTT) model. This is a numerical model so that we can discuss only its results. The displacement profile for the CFTT model is shown in **Figure 5(c)**. The displacements near the crack center are similar to the elastic crack, but near the tips, they taper linearly, as the name suggests. This CFTT remains constant as the fault propagates in a material of uniform σ_y and the value of the taper increases with σ_y. Like the Dugdale–Barenblatt model, both G and D_{max} scale linearly with L. These predictions agree very well with experimental results for cracking in ductile materials like steel and aluminum. Under the conditions of fault propagation, rock does not undergo crystalline plasticity like those materials. Rock is rather a granular aggregate of several anisotropic crystalline phases that result in a highly heterogeneous stress field at the grain scale. At sufficiently high stresses, this will result in dilatant microcracking at the grain scale. This should occur near the tips of faults, resulting in a high concentration of inelastic deformation there, forming what is known as a brittle process zone.

6.10.3.4 Experimental Studies of Fault Propagation

It is difficult to study fault propagation in the laboratory because in compression tests, an instability usually occurs just at the beginning of the falling part of the stress–strain curve, so that data cannot be taken beyond that point. Lockner et al. (1991) were able to avoid this by using a dynamic feedback system to stiffen the system and suppress the instability. **Figure 6** shows the complete stress–strain curve for one of their experiments and the locations of acoustic emissions during each stage. In stage (a) on the ascending part of the loading curve, acoustic emissions produced by dilatant microcracking

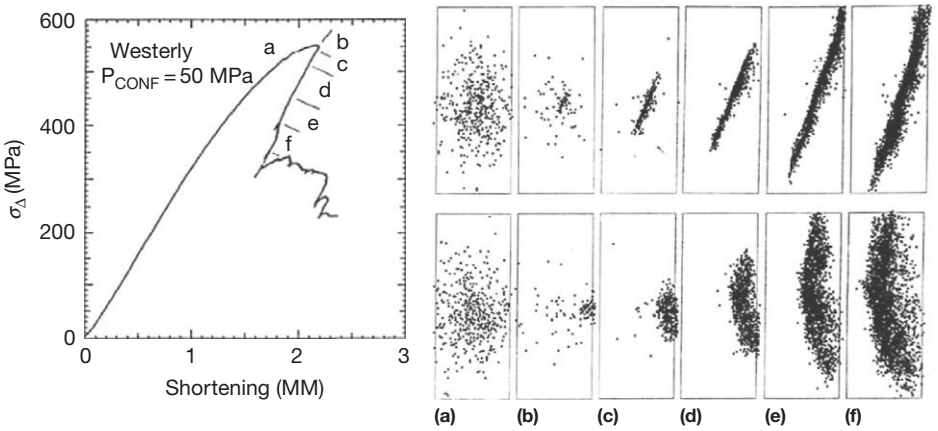

Figure 6 Left: complete stress–strain curve for failure of granite. Right: orthogonal views of the locations of acoustic emission for each stage of the stress–strain curve. Reproduced from Lockner DA, Byerlee JD, Kuksenko V, Ponomarev A, and Sidorin A (1991) Quasi-static fault growth and shear fracture energy in granite. *Nature* 350: 39–42.

(Scholz, 1968b) are uniformly distributed in the central region of the test specimen. The linear concentration of acoustic emissions in (b) indicates the nucleation of a fault, which subsequently propagates through the sample amid a cloud of acoustic emissions. The stress plateau following (f) in **Figure 6** reflects the residual friction as the fully formed fault slides.

Subsequent microscopic study of one of their experiments by Moore and Lockner (1995) showed that a brittle process zone about 40 mm wide had formed around the fault (**Figure 7**). The crack density increases exponentially as the fault is approached (**Figure 7(a)**). The cracks are primarily intergranular tensile cracks. Their orientation peaks at about 30° from the fault on its compressional side (**Figure 7(b)**). These results show that inelastic deformation occurs near the tip of the fault and the fault evidently forms by the breakdown of this process zone when a critical crack density occurs within it. In the next section, we will examine field data to see if this process occurs for natural faults.

6.10.3.5 Fault Scaling Laws and the Mechanics of Fault Growth

Because faults are shear cracks with friction, as displacement D accrues on the fault, it must also grow in length L. In order to identify the proper crack model to use for faults, the scaling laws between D and L and other fault parameters must be determined. In this section, the observations will be presented and then discussed in the light of crack models. This will lead to an understanding of how faults propagate.

6.10.3.6 Displacement–Length Scaling

Early attempts to find a relationship between D and L consisted of collecting data on D and L from the literature and trying to fit it to a relationship of the form

$$D = \gamma L'' \qquad [16]$$

Walsh and Watterson (1988) and Marrett and Allmendinger (1991) concluded that n is 2.0 and 1.5, respectively. However, for theoretical reasons, it is not possible for n to exceed 1, regardless of the crack model considered. If $n > 1$, eqns [7] and [15] show that stress drop will have to increase with length. The strength of the fault would thus increase with length. If this were the case, faults would not grow: the rock would crush at the grain scale.

Cowie and Scholz (1992a,b) studied this scaling relation from the viewpoint of the Dugdale–Barenblatt elastic–plastic crack model. They concluded that for this model, $n = 1$ and that γ should increase linearly with rock strength. This latter conclusion indicates that the attempt to fit a universal law of the type given by eqn [16] is incorrect: rather, because faults occur in different rock types and depths that there should be a family of curves with different values of γ that should describe the scaling. They were able to show that the data of Marrett and Allmendinger were consistent with $n = 1$: the greater slope found by Marrett and Allmendinger was because the longer faults sampled deeper into the crust and hence stronger rocks and because their data included plate boundaries, which have no tips and hence need not obey the scaling law.

In order to separate the variables in eqn [16], Dawers et al. (1993) studied a population of isolated (noninteracting) normal faults in a 200 m thick welded tuff in the Volcanic Tablelands of eastern California. In that locality, there was a wide range of lengths of faults in a single rock type, which propagated at the surface, so the strength variable γ should be constant. They were also careful to select faults that were not interacting with other faults. As will be discussed in **Section 6.10.5**, the interaction of faults through their stress fields can severely distort their displacement profiles and hence their value of γ. The along-strike displacement profiles for a number of their faults, ranging in length from 690 to 2200 m, normalized to fault length, are shown in **Figure 8**. A very good data collapse is achieved, indicating that these faults are self-similar. A plot of D versus L is shown in **Figure 9**. These data show that $n = 1$ with a crossover phenomenon occurring where $L > 200$ m, the layer thickness. When fault length is less than the layer thickness, the displacement profiles are peaked, whereas when $L > 200$ m, they are more flat-topped, as in **Figure 8**. This difference results in a slight change in γ at the crossover. Thus, when the faults are

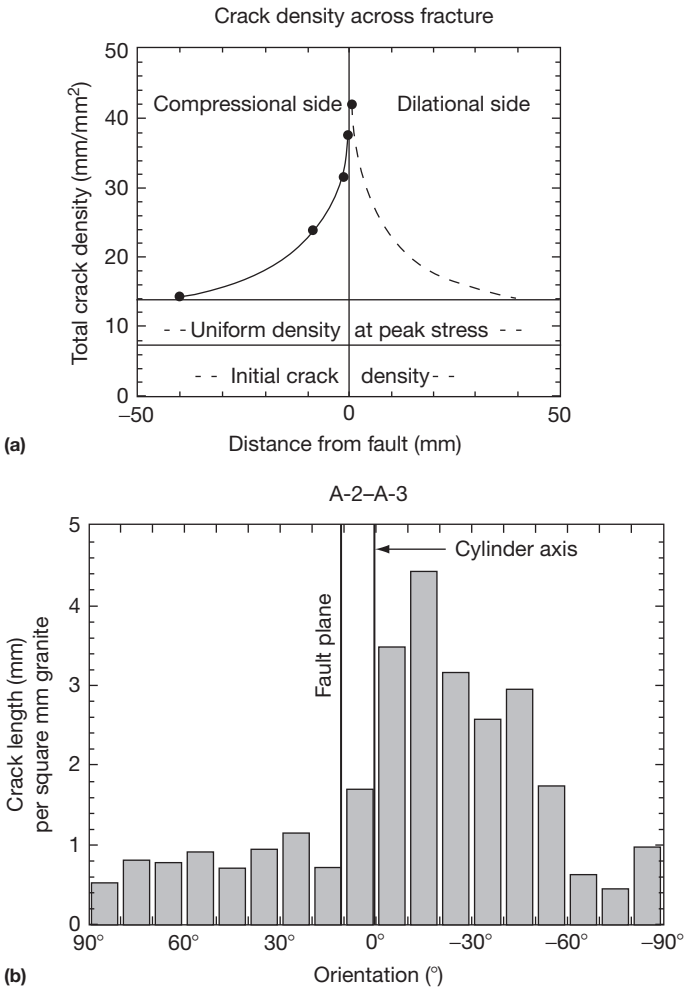

Figure 7 (a) Crack density as a function of distance from the fault formed in an experiment like that shown in **Figure 6**. (b) Orientation of cracks as a function of angle from the rock cylinder and fault. Reproduced from Moore DE and Lockner DA (1995) The role of microcracking in shear-fracture propagation in granite. *Journal of Structural Geology* 17: 95–114.

3-D cracks, propagating in two directions, they are not self-similar with the 2-D cracks that have breached the brittle layer thickness and propagate only in the horizontal direction.

A summary diagram showing D/L scaling using the global data set is shown in **Figure 10**. Here, the data have been edited much more carefully than in the earlier compilations of Walsh and Watterson and Marrett and Allmendinger. For example, faults that are plate boundaries have been removed. Plate boundary faults do not have defined lengths and hence do not need to obey this scaling law. A ridge–ridge transform fault, for example, is stress-relieved by the spreading ridges at both ends and hence can accrue slip with no need to grow longer because it does not have tips where displacement must go to zero, producing there a large stress concentration. The linear scaling of D with L is still apparent in **Figure 10**, though with more scatter than in **Figure 9**. Much of this has to do with strength variations between the different faults, because the scaling parameter γ is a stress drop between the yield strength of the rock and the residual friction. For example, the longer faults (>10 km) penetrate the crust and therefore rupture crystalline rock at high pressure and therefore have higher γ values. The faults with $\gamma < 10^{-2}$ are in soft sedimentary rocks like sandstones and shales. Another source of scatter is that there has been no attempt to separate interacting from noninteracting faults (Schlische et al., 1996), which also influences the γ value. The effects of fault interactions will be discussed in **Section 6.10.5**.

6.10.3.7 Fault Tip Taper Scaling

The data in **Figure 8** indicate that for noninteracting faults in a uniform rock type, the displacement profiles are symmetrical with linear, scale-invariant fault tip tapers (FTTs). The linear displacement tapers of faults have also been noticed elsewhere (Burgmann et al., 1994; Cartwright and Mansfield, 1998; Cowie and Shipton, 1998). FTT is plotted versus length for a variety of faults and earthquake ruptures in **Figure 11** (Scholz and Lawler, 2004). **Figure 11(a)** shows the tapers from the Volcanic Tablelands data illustrated in **Figures 8** and **9**. These data show that FTT is scale-independent over the two orders of magnitude range of fault length. **Figure 11(b)** shows data from other sites, separated into isolated and interacting faults and

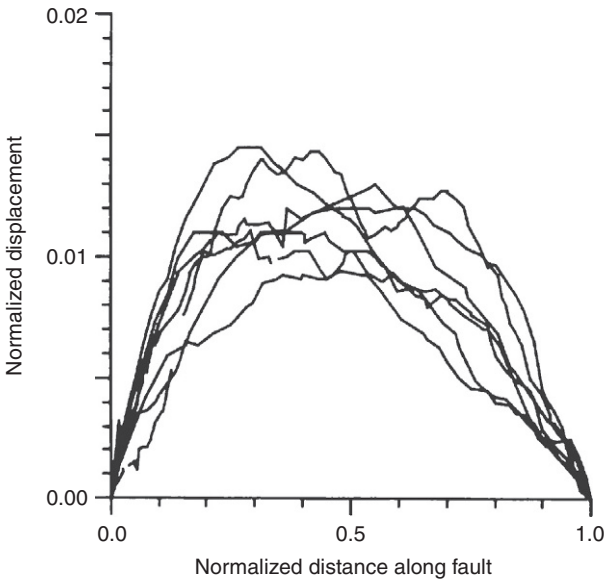

Figure 8 Displacement profiles normalized to fault length for normal faults in the Volcanic Tablelands, eastern California. The faults range in length from 690 to 2200 m. Modified from Dawers NH, Anders MH, and Scholz CH (1993) Growth of normal faults: Displacement–length scaling. *Geology* 21: 1107–1110.

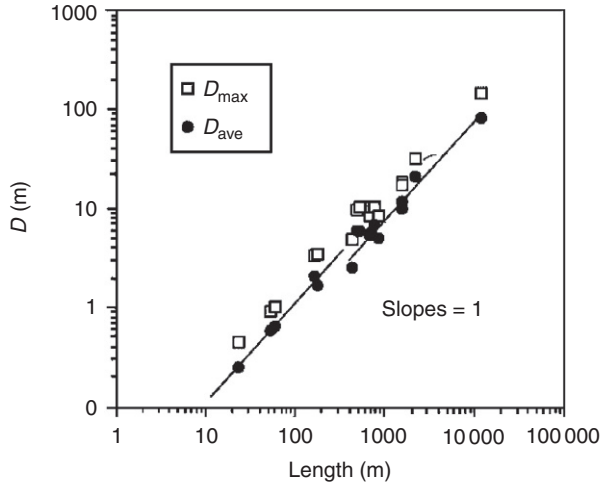

Figure 9 Displacement–length scaling for the Volcanic Tableland faults. Modified from Dawers NH, Anders MH, and Scholz CH (1993) Growth of normal faults: Displacement–length scaling. *Geology* 21: 1107–1110.

earthquake ruptures. The interacting faults are overlapping subparallel normal faults that will be discussed in the next section. The tapers for interacting rupture tips are always greater, by up to a factor of 10, than for the isolated ruptures. The scatter of FTT for the isolated faults is much greater than for the data from the Volcanic Tablelands because they are in a variety of rock types. The data are broken out by rock type in Figure 12. There, we see that, among the isolated faults, FTT is greater for faults in granite than for faults in sedimentary rock, averaging 8×10^{-2} and 1×10^{-2}, respectively. The tapers in the welded tuff (Figure 11(a)) are intermediate, averaging 5×10^{-2}.

Thus, like the D/L ratio, FTT increases with rock strength. Both parameters for earthquake ruptures are about two orders of magnitude less than for faults. The D/L ratio for earthquake ruptures is in the range 10^{-5}–10^{-4} (Scholz, 2002, p. 207). This is because the $\Delta\sigma$ for earthquakes is the difference between static friction and dynamic friction and hence is much smaller than stress drip for faulting.

6.10.3.8 Process Zones and Their Scaling

Just as in the case of the laboratory experiments shown in Figure 7, faults are known to have brittle process zones, or regions of intense microcracking surrounding them (Anders and Wiltschko, 1994; Chernyshev and Dearman, 1991). Scholz et al. (1993) proposed that the process zone is dominated by dilatant grain-scale microcracks formed by the fault tip stresses. Such cracks are opening-mode (tensile) cracks that form parallel to the local σ_1 direction. An empirical dilatancy–stress relation (from Scholz, 1968a) was convolved over the fault tip stresses as the fault propagated past the point in question. This predicts an exponential increase of crack density as the fault is approached. For a mode II (strike-slip) shear crack, the crack tip stresses are asymmetrical across the fault. As shown in Figure 13, this predicts different orientation of microcracks on either side: with a maximum peak at about 30° from the fault on the compressional side and 70° on the extensional side. These model results agree quite well with the experimental results of Moore and Lockner (1995) shown in Figure 7.

To test this model for natural faults, Vermilye and Scholz (1998) measured microcrack densities in traverses across several strike-slip faults in quartzite in the Shawangunk Mountains of New York. This rock type was chosen because quartz has no cleavage that would influence microcrack orientation and because microcracks are well preserved in it. Microcrack density is plotted versus log distance from the fault in Figure 14 for two faults, one 40 m long (circles) and the other 2 m long (squares). Microcrack density increases exponentially as the faults are approached, in agreement with the theory and experimental results.

A nearby exposure of a dextral strike-slip fault exposed on a cliff face is shown in Figure 15. Lower hemisphere contoured microcrack pole plots are shown for several locations, projected onto the horizontal surface. Background microcracks measured several meters from the fault (MC16) show a girdle pattern. This is interpreted as dilatant microcracks parallel to the regional stress, inclined about 25° to the fault. The near-fault microcracks (MC1 and MC2) have different orientations on either side of the fault, those in MC1 striking at low angles to the fault and those in MC2 at high angles. This is consistent with a dextral fault propagating toward the viewer, with MC1 being on the compressional side and MC2 on the extensional side. At the tip of the fault (MC5-W and MC5-E), the microcracks are fault-parallel. This is interpreted as due to tensile-mode release of fault dilation during unroofing from the 5 to 7 km depth at which this fault was formed.

The data in Figure 14 indicate that the maximum microcrack density, which occurs where the rock breaks down to cataclasite, does not depend on fault length, but that the width of the process zone P, as measured by the distance

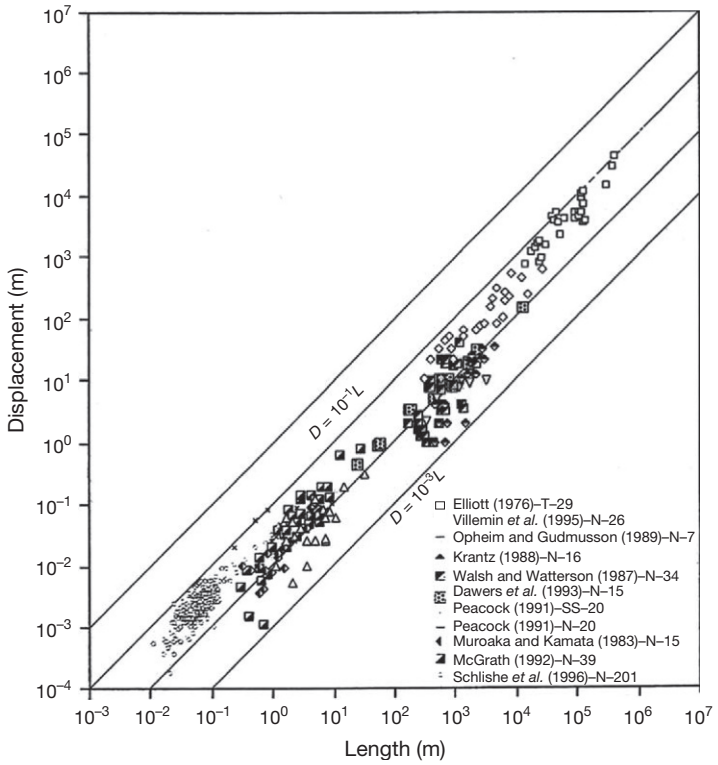

Figure 10 Summary diagram displacement–length scaling for faults. Modified from Schlische RW, Young SS, Ackermann RV, and Gupta A (1996) Geometry and scaling relations of a population of very small rift-related normal faults. *Geology* 24: 683–686.

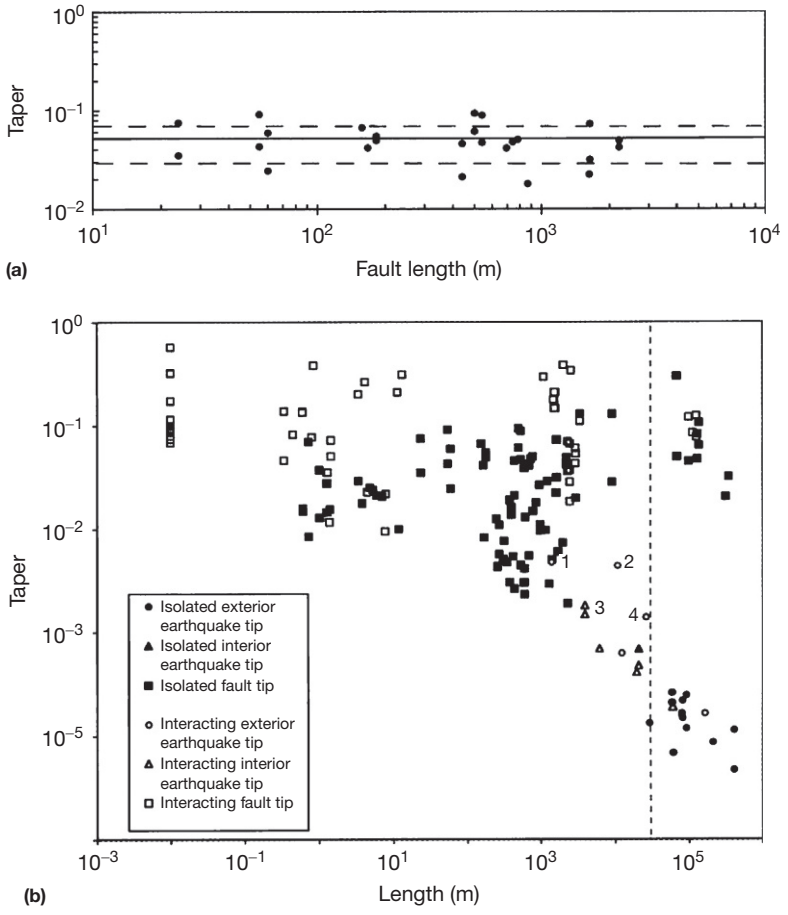

Figure 11 (a) Fault tip tapers for isolated faults from the Volcanic Tablelands versus length. (b) The same for other faults and earthquakes, sorted according to interacting or not. Modified from Scholz CH and Lawler TM (2004) Slip tapers at the tips of faults and earthquake ruptures. *Geophysical Research Letters* 31: L21609.

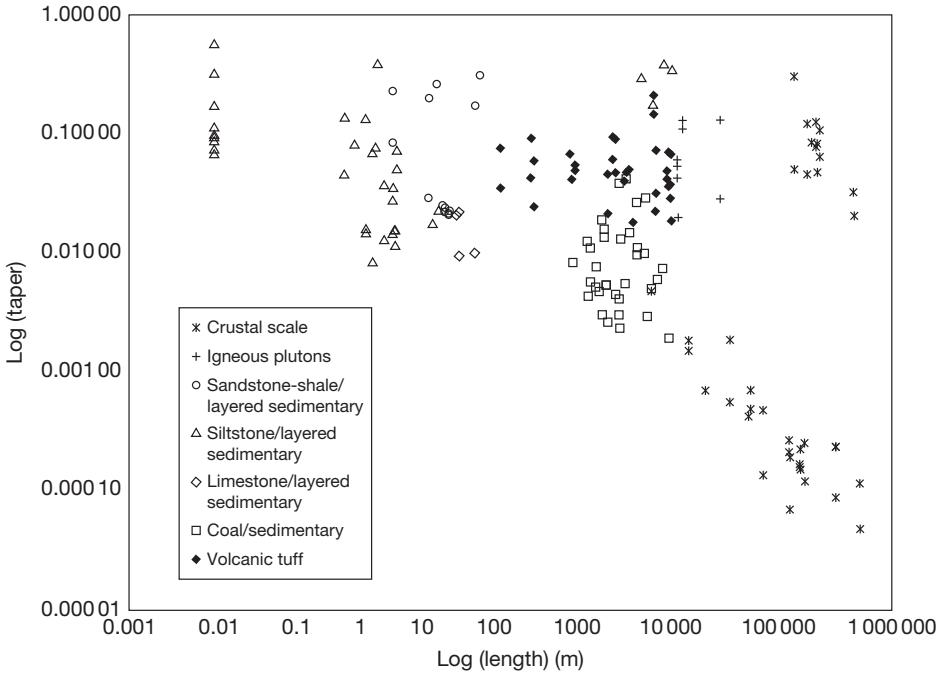

Figure 12 Fault tip tapers for other faults and earthquakes except sorted according to rock type. Modified from Scholz CH and Lawler TM (2004) Slip tapers at the tips of faults and earthquake ruptures. *Geophysical Research Letters* 31: L21609.

from the fault at which microcrack density reaches the background level, does depend on L. Data collected from various sources (**Figure 16**) indicate that this scaling is linear.

In porous rocks such as the Berea and Navajo sandstones, in which the porosity is nearly 20%, shearing induces porosity reduction rather than dilatancy (Lockner et al., 1992). This results in the formation of deformation bands, local regions of reduced porosity (Aydin and Johnson, 1978; Mair et al., 2000). The damage zones of faults in such rocks consist of numerous deformation bands, with little increase of microcrack density, and the damage zone width increases with throw on an individual fault (Shipton and Cowie, 2001). The deformation thus appears to consist mainly of grain sliding and rotation, resulting in compaction, rather than internal microcracking in grains, and the damage zone development does not appear primarily as a crack tip phenomenon but increases with strain.

6.10.3.9 Cataclasite Zone Scaling

The cataclasite zone is the band of ground rock fragments found in the core of the fault. If the grain size is clay-sized, it is often called fault gouge, which may or may not contain clay minerals. Some material of this type is initially formed in the innermost part of the process zone where the crack density reaches a critical value to fragment the rock and form the fault.

As displacement occurs on the fault, additional cataclasite is formed by frictional wear. A simple model for steady-state wear predicts (Scholz, 2002, p. 78) that the thickness of wear material T scales as

$$T = \frac{\kappa \sigma D}{3b} \qquad [17]$$

where σ is the normal stress, D is the fault displacement, κ is a dimensionless parameter called the wear coefficient, and b is a measure of the rock strength or friability. This wear law is confirmed by experiment (Wang and Scholz, 1994; Yoshioka, 1986). Observational data for faults, shown in **Figure 17**, indicate linear scaling between T and D (Evans, 1990; Hull, 1988; Scholz, 1987). There is a large scatter in the data, which may reflect variations in the other parameters in eqn [17]. Even for a single fault, there is a large variation in T along strike: for example, along the San Andreas Fault (SAF in **Figure 17**), the cataclasite thickness varies by more than an order of magnitude. This may reflect variations of rock type and fault geometry and structure.

Wilson et al. (2005) had pointed out a zone some 70–100 m wide adjacent to the SAF consisting of rock that has been pulverized *in situ*. This is well outside the cataclasite zone in this region. They argue that this is due to dynamic pulverization produced by the passage of earthquakes, by either the rupture tip stress field or fault normal loading and unloading. They report that the surface energy in this process is an appreciable fraction of the work of faulting, but this has been contradicted by similar work on the nearby Punchbowl fault (Chester et al., 2005).

6.10.3.10 Interpretation of the Scaling Laws in Terms of Crack Models

The scaling laws for faults are summarized in **Table 1**. In all cases, the scaling laws are linear. Typical values are given by order of magnitude. In all cases, the actual value of the scaling parameters depends upon rock strength. The D/L ratio increases with strength, and the T/L and P/L ratios should decrease with strength. The scale-independent FTT increases with strength.

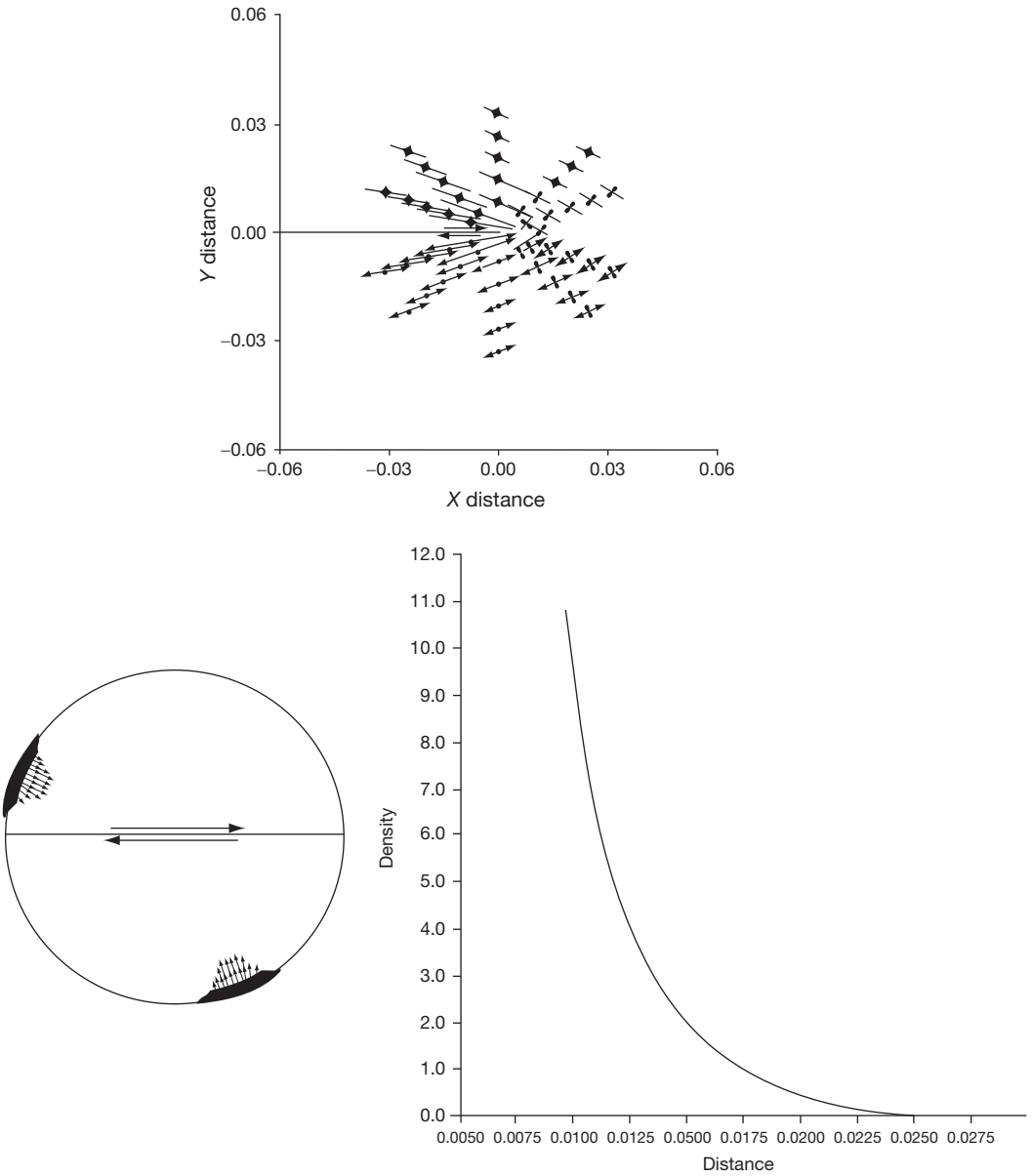

Figure 13 Predictions of the process zone model of Scholz et al. (1993). Top: stresses around a strike-slip fault tip: dashed, compression, solid, and tension. Lower left: orientation of expected microcracks on each side of the fault. Lower right: expected crack density as a function of distance from the fault. Modified from Scholz CH, Dawers NH, Yu JZ, and Anders MH (1993) Fault growth and fault scaling laws: Preliminary results. *Journal of Geophysical Research*, *Solid Earth* 98: 21951–21961.

We can now compare these observations with the crack models discussed earlier. The elastic crack model can immediately be eliminated: it does not predict a linear D/L scaling, a linear fault tip displacement taper, or a process zone. Both the Dugdale–Barenblatt and CFTT models predict linear D/L scaling but the presence of a linear FTT and a volumetrically extended process zone are consistent only with the CFTT model. This model predicts also that G scales linearly with L, which is independently confirmed by the finding that P scales linearly with L. This model also predicts a linear FTT and that FTT should increase with rock strength.

A consistent picture emerges regarding the mechanism of fault propagation. The crack tip stress field produces pervasive cracking in the adjacent rock. This is primarily in the form of dilatant microcracks at the grain scale: opening-mode cracks parallel to the local σ_1 direction. Most cracking is at the grain scale because it is at that scale that stress heterogeneity, caused by elastic mismatches between grains, is highest and hence where the highest stress concentrations are found (Scholz, 1968a). Macroscopic deformation features, such as secondary faults and pressure solution bands, are also found within the process zone and exhibit the same falloff with distance from the fault as the microcracks, but they are not nearly as ubiquitous (Vermilye and Scholz, 1998).

When the microcrack density reaches a critical level, the rock fragments into a cataclasite on which the fault may then

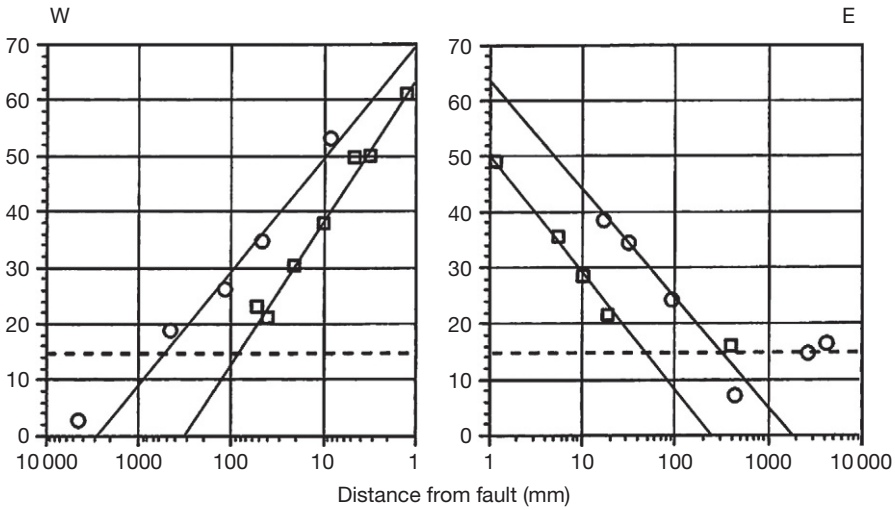

Figure 14 Microcrack density as a function of distance from two strike-slip faults in quartzite in the Shawangunk Mountains, New York, one 40 m long (circles) and the other 2 m long (squares). Dashed line is the background density. Modified from Vermilye JM and Scholz CH (1998) The process zone: A microstructural view of fault growth. *Journal of Geophysical Research*, *Solid Earth* 103: 12223–12237.

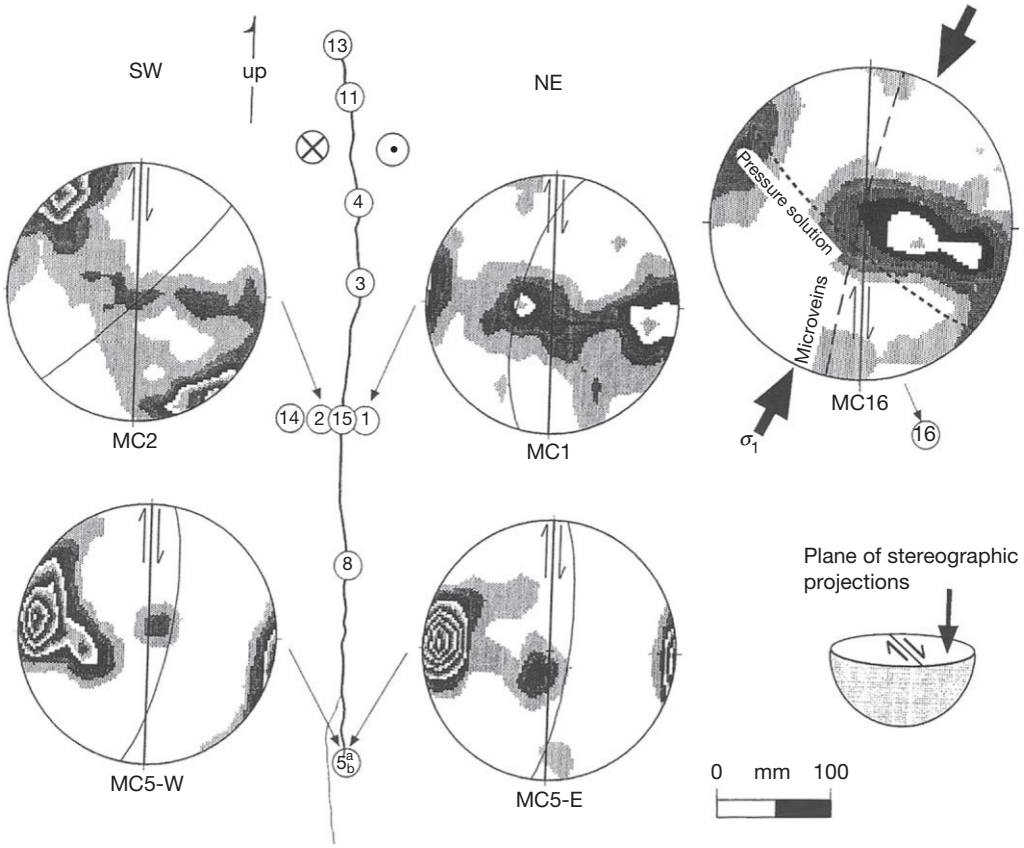

Figure 15 Contoured pole plots of microcrack orientations around a strike-slip fault in the Shawangunks. Reproduced from Vermilye JM and Scholz CH (1998) The process zone: A microstructural view of fault growth. *Journal of Geophysical Research*, *Solid Earth* 103: 12223–12237.

slide frictionally, and the process continues. This is the breakdown fault-forming process as originally visualized by Cowie and Scholz (1992a) and observed in the laboratory experiments of Lockner et al. (1991) and Moore and Lockner (1995). It results in a wide zone of distributed fractures containing a narrow zone of comminuted rock within which the main shearing occurs (Chester et al., 1993; Chester and Logan, 1986). According to the scaling parameters of **Table 1**, the cataclasite zone width is typically about 10^{-2} of the process zone width, although, as mentioned in the preceding text, the

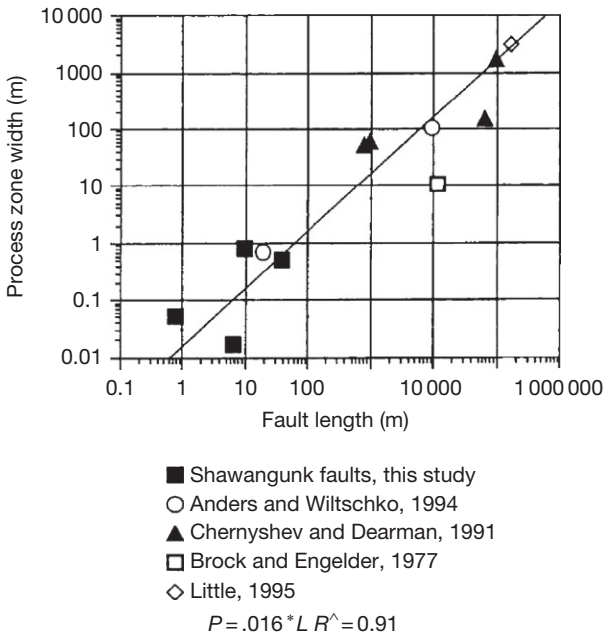

Figure 16 Scaling of process zone width with fault length. Reproduced from Vermilye JM and Scholz CH (1998) The process zone: A microstructural view of fault growth. *Journal of Geophysical Research, Solid Earth* 103: 12223–12237.

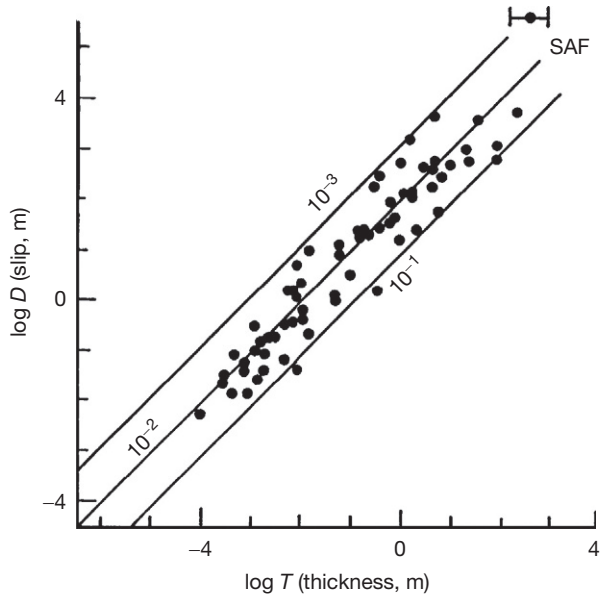

Figure 17 Scaling of cataclasite zone thickness with fault displacement. Reproduced from Scholz CH (1987) Wear and gouge formation in brittle faulting. *Geology* 15: 493–495.

former may vary considerably along strike. That however is a 2-D view, whereas the actual scaling is 3-D. Imagine a fault of finite length that initiated at its center and propagated bilaterally in both directions. Because the width of the process zone scales with the length of the fault at the time the fault passed the particular point in question, it is narrowest in the center of the fault and widens to maxima at both tips. On the other hand, the width of the cataclasite zone scales with fault slip, so it will be widest at the fault center and narrowest at the tips. However, no one has yet made enough fault traverses to verify these conclusions.

Table 1 Typical values of fault scaling parameters

	Length (L)	*Displacement* (D)	*Process zone width* (P)	*Cataclasite zone width* (T)
L	1	10^2	10^2	10^4
D	10^{-2}	1	1	10^2
P	10^{-2}	1	1	10^2
T	10^{-4}	10^{-2}	10^{-2}	1

6.10.4 Fault Interactions

Slip on a fault produces stress changes in the surrounding regions. One example is shown in Figure 18 (Das and Scholz, 1981), which shows the change of fault-parallel shear stress adjacent to a vertical strike-slip fault. Because faults usually grow in populations or systems rather than as isolated features, they commonly grow within the stress change region of other faults. This will affect the behavior of the fault. If it propagates into a region of stress enhancement, it will be induced to propagate more readily. If it propagates into a stress-drop region, its propagation will be impeded and it may become pinned, unable to propagate further. The displacement distribution on the fault, as mentioned earlier, will become distorted from what would be expected for a crack in a uniform stress field. Crack tip stress for mode II cracks, such as the strike-slip fault shown in Figure 18, is different from that of mode III cracks, such as normal faults, so the stress interactions will differ between them and we treat them here separately. Fault forming in a given tectonic environment, and hence stress field, is usually subparallel, so the most common interactions, and those the most studied, are between subparallel faults. With one exception, we will be limited to these types of interactions.

6.10.4.1 Mode III Interactions: Normal Faults

The most extensive studies of fault interaction have been done for subparallel normal faults. This is because for normal faults, if they are not highly eroded, one can easily measure the slip distribution from scarp height. To do this for strike-slip faults, one needs offset markers, which are seldom frequent enough.

6.10.4.1.1 Pinning

Peacock (1991) and Peacock and Sanderson (1994) pointed out that the displacement distribution of overlapping normal faults is, unlike the examples shown in Figure 8, asymmetrical. The peak in displacement is shifted toward the overlapping end and the FTT at that end is steeper than at the distal end. Figure 19 shows the displacement profiles for three different times for the main bounding fault system of the East African Rift on the west side of Lake Malawi. These profiles were obtained by seismically backstripping seismic profiles in the

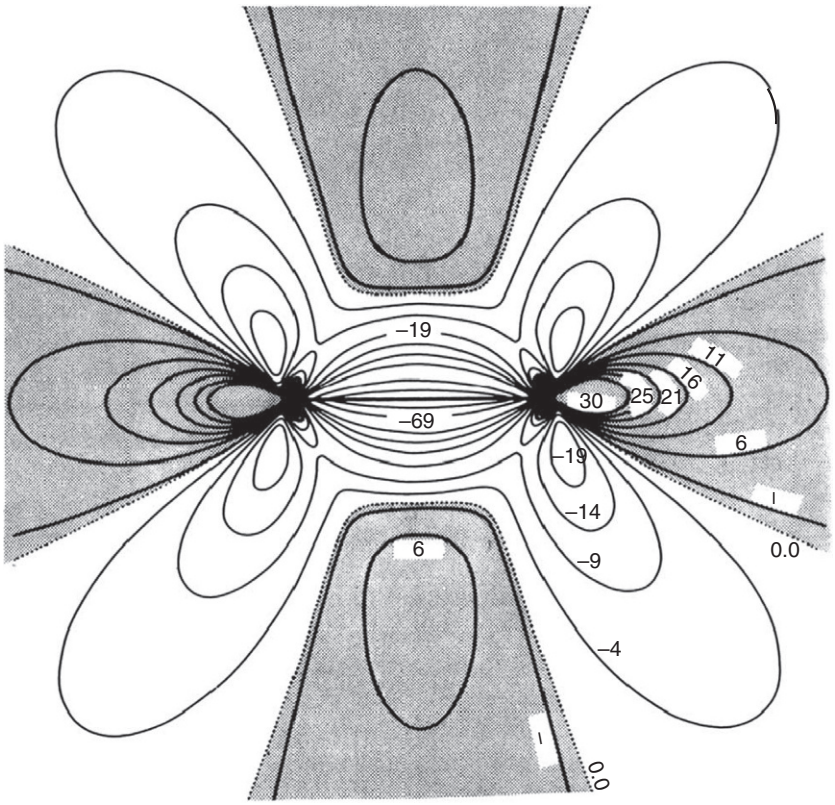

Figure 18 Change in fault-parallel shear stress due to slip on a strike-slip fault. Stress drop, 100 MPa; contours in MPa. Reproduced from Das S and Scholz CH (1981) Off-fault aftershock clusters caused by shear stress increase? *Bulletin of the Seismological Society of America* 71: 1669–1675.

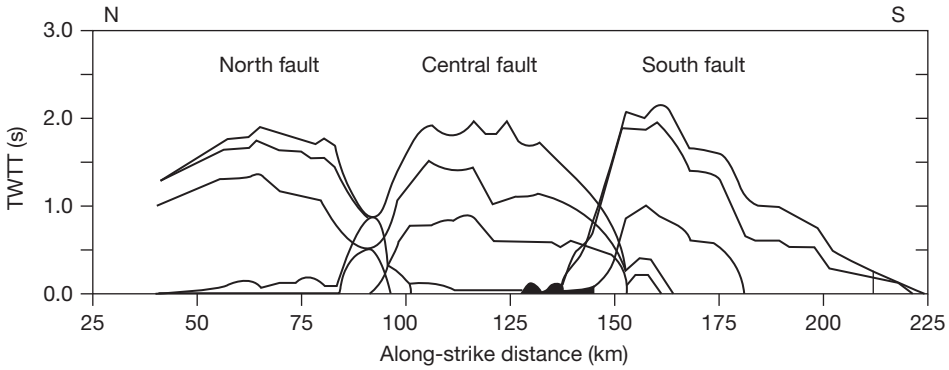

Figure 19 Displacement profiles for the three main bounding faults on the west side of Lake Malawi at three different times separated by several million years. Reproduced from Contreras J, Anders MH, and Scholz CH (2000) Growth of a normal fault system: Observations from the Lake Malawi basin of the east African rift. *Journal of Structural Geology* 22: 159–168.

lake at three time markers several million years apart (Contreras et al., 2000). For the two-way travel time, 1 s is approximately 1 km. This fault system is composed of three overlapping subparallel normal faults, the South fault and the North fault offset 5 and 7 km to the east of the Central fault, respectively. The temporal information allows us to observe the progression of interaction between the individual faults as slip accrues on them. As time progresses, the overlap of the South and Central faults increases, and as it does so, the FTT at the north end of the South fault steepens, whereas the FTT on its noninteracting southern tip remains much less steep. Its displacement profile becomes more and more asymmetrical and most of the propagation is to the south, the rate of propagation of the overlapping tip becoming progressively slower as the overlap increases, until finally the fault becomes completely pinned. Much the same thing happens with the North fault, whereas the Central fault becomes pinned at both ends, accumulating displacement without becoming longer. The effect of the pinning is that the D/L ratio of this fault grows with time. This increased D/L ratio is not because the fault is becoming stronger, but because its tips are prevented from growing because they are in the stress-drop shadow of the overlapping faults. This is one of the effects that

introduces scatter in D/L plots like Figure 10. The high FTTs at interacting tips shown in Figure 12(b) are also the result of this pinning mechanism.

Gupta and Scholz (2000a) studied the systematics of this interaction from a population of centimeter- to decimeter-scale normal faults exposed on the bedding planes of siltstones in the Solite Quarry in North Carolina. They measured the degree of disturbance of the displacement profiles for interacting tips compared with a noninteracting standard. They found this to be a function of offset and separation in such a way that the more highly interacting tips were deeper in the stress-drop region of the adjacent fault. This is shown in Figure 20, where the displacement anomaly is measured in standard deviations from the standard and the stress drop is calculated from an elastic crack model using the offset and separation.

A simple diagram illustrating the pinning mechanism is shown in Figure 21. The stress field for the driving shear stress of a mode III crack is symmetrical, with a stress-drop region (solid contours) on either side of the crack and stress increase regions beyond the tips. Imagine fault F′ to be stationary and being approached by a propagating fault F. Fault F will first be attracted to fault F′ by the enhanced fault tip stress (negative stress drop) of the latter. Once fault F passes the tip of F′, it will enter its stress-drop region and be repulsed, that is, its further growth will be inhibited. In order to continue to propagate, the stress concentration at its tip must increase, to overcome both the rock strength and the stress drop from fault F′. This stress concentration is determined by the FTT, so this must become steeper at the interacting end and steepen further as the tip grows deeper into the stress shadow. As a result, the displacement profile becomes asymmetrical. A similar result has been obtained by modeling using the elastic crack model (Willemse, 1997; Willemse et al., 1996). As faults more likely interact than not, asymmetrical profiles are more common than symmetrical ones (Manighetti et al., 2004).

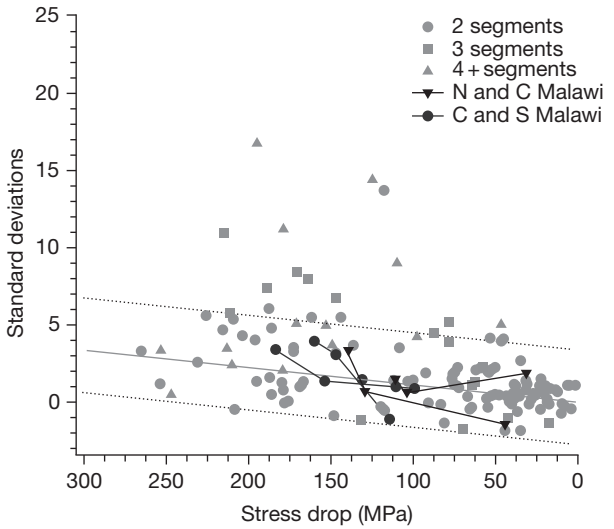

Figure 20 Distortion of the fault tip of interacting normal faults, in standard deviations from noninteracting faults versus the magnitude of their stress shadows calculated from an elastic model. The lines and symbols show the temporal change in the same measurements from the Malawi fault segments shown in Figure 19. Reproduced from Gupta A and Scholz CH (2000a) A model of normal fault interaction based on observations and theory. *Journal of Structural Geology* 22: 865–879.

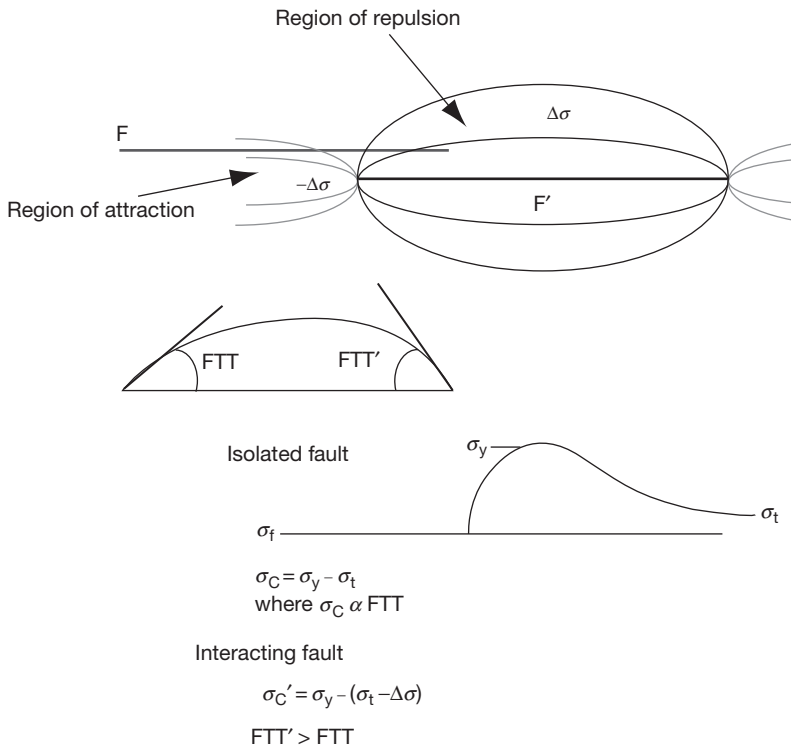

Figure 21 A diagram illustrating the fault pinning interaction.

6.10.4.1.2 Coalescence

Figure 22 shows the summed displacement profiles for the three interacting Malawi faults shown in Figure 19. The dashed profile is the expected profile for a single fault with a net length equal to the three fault segments. Notice that as the faults grow and their interactions increase, their summed profiles become closer to that of a single fault. This indicates that the interacting faults increasingly act as a single unit. This coalescence is a gradual process; it can occur by the faults 'soft linking' through their stress fields or through connecting by means of secondary faults, that is, hard linking.

Figures 23 and 24 show three faults in the Volcanic Tablelands that are in the process of coalescing (Dawers and Anders, 1995). In the vicinity of the relay ramps between the overlapping tips of the major segments, many smaller faults have formed, some of which cross the relay ramps obliquely. Their combined effect (Figure 24) is to eliminate the displacement minima that would be expected in the relay ramp regions, thus smoothing out the overall displacement profile so that it appears more like that on a single long fault, just as in the case shown in Figure 22. One of course sees only a portion of the linking phenomena in a section such as shown in this example, one needs information in three dimensions to observe the total picture (Crider and Pollard, 1998).

6.10.4.1.3 Nucleation inhibition

If a fault lies entirely within the stress-drop region of another, larger, fault, it will become inactive. Figure 25 shows several examples for normal faults in the Solite Quarry (Ackermann and Schlische, 1997). In this case, the larger faults predated the smaller ones, as there is an absence of the smaller ones in their stress-drop regions (stress shadows). Otherwise, there would be inactivated small faults in their stress shadows and one would not be able to observe this phenomenon.

These three interaction mechanisms are illustrated in Figure 26. As we shall see in Section 6.10.6, these three mechanisms, working together in a system of growing faults, result in the development of populations of faults with distinct statistical properties.

6.10.4.2 Mode II Interactions

Unlike mode III cracks, mode II cracks, such as strike-slip faults in horizontal section, have asymmetrical stress fields on either side of their tips. One side is extensional; the other, compressional. There are therefore different interactions for overlapping jogs depending on their sign, compressional or extensional.

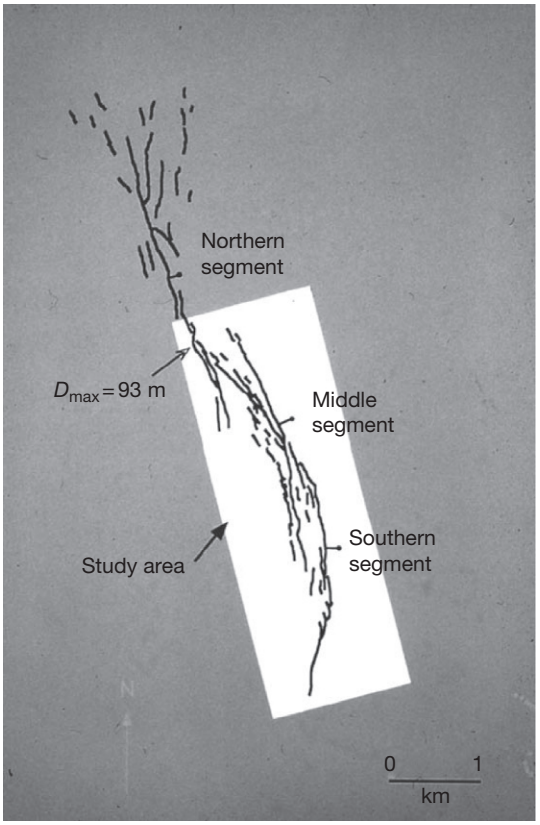

Figure 23 Map view of interacting normal faults in the Volcanic Tablelands, eastern California. Modified from Dawers NH and Anders MH (1995) Displacement–length scaling and fault linkage. *Journal of Structural Geology* 17: 607–614.

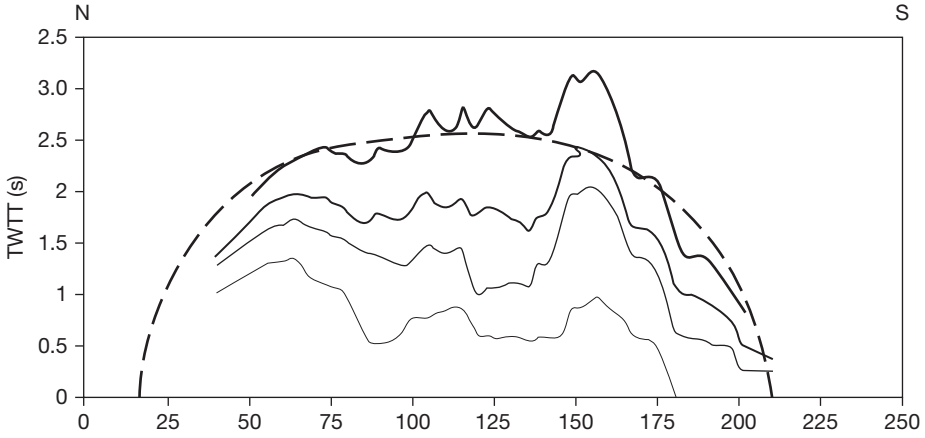

Figure 22 Summed displacement profiles for the three Malawi faults of Figure 19 at different time intervals. The dashed curve is the expected profile for a single fault with length equal to the summed lengths. Modified from Contreras J, Anders MH, and Scholz CH (2000) Growth of a normal fault system: Observations from the Lake Malawi basin of the east African rift. *Journal of Structural Geology* 22: 159–168.

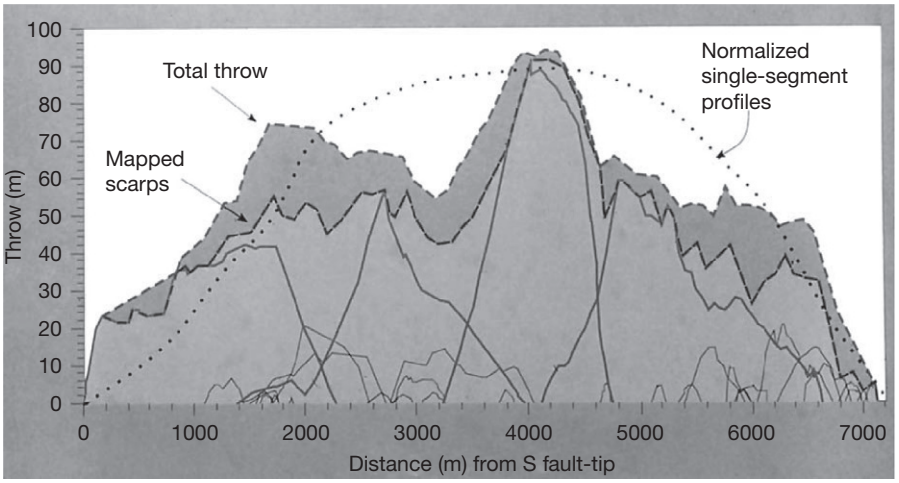

Figure 24 Displacement profiles for the faults of **Figure 23**. The summed throw and the expected displacement profile for a single noninteracting fault are also shown. Reproduced from Dawers NH and Anders MH (1995) Displacement–length scaling and fault linkage. *Journal of Structural Geology* 17: 607–614.

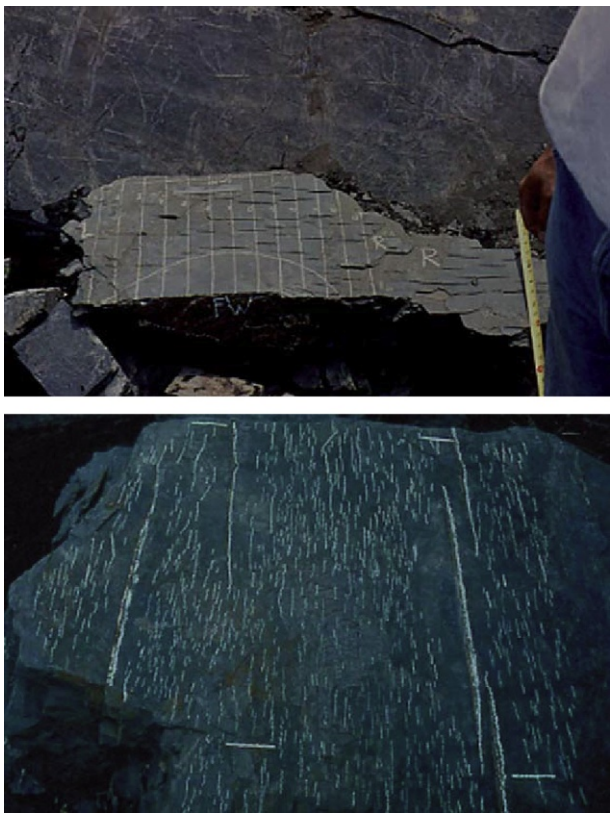

Figure 25 Photos of nucleation inhibition in small normal faults from the Solite Quarry, North Carolina. Top: a normal fault footwall (FW) with a dearth of smaller faults in its stress shadow region, outlined in chalk. Bottom: view of three larger faults with no small faults in their stress shadow regions – faults are highlighted with chalk for visibility. Reproduced from Ackermann RV and Schlische RW (1997) Anticlustering of small normal faults around larger faults. *Geology* 25: 1127–1130.

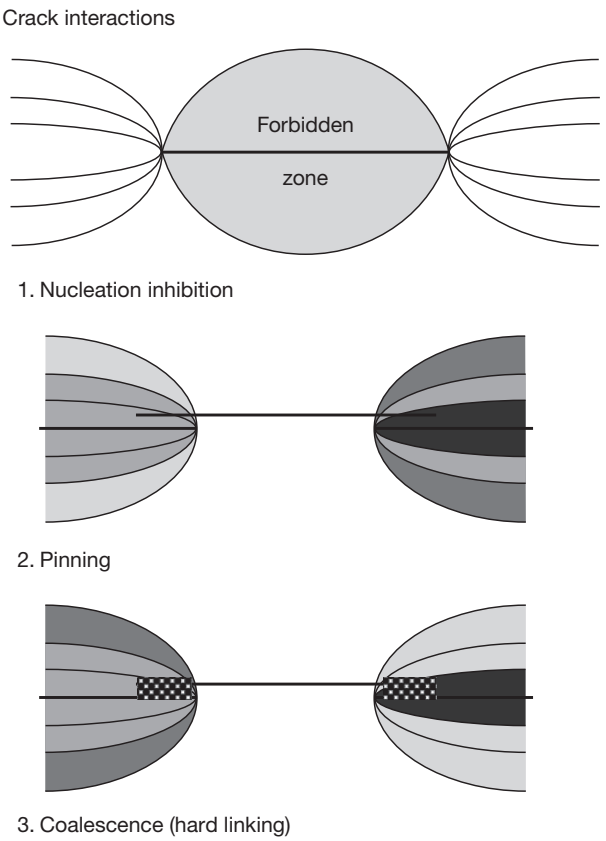

Figure 26 Illustration of the modes of interactions of overlapping normal faults.

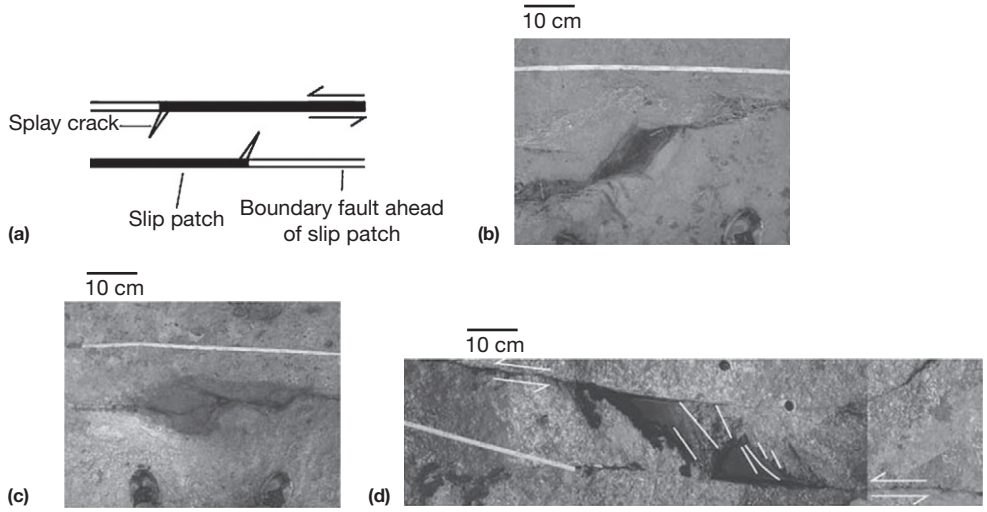

Figure 27 Illustrations of jogs in strike-slip faults. (a) Schematic diagram of jog formation between joints reactivated in shear (from Martel and Pollard, 1989). (b) An extensional jog in a left lateral fault. (c) An extensional jog containing a shunt fault. (d) A compressional jog. White lines highlight the orientation of pressure solution selvages. Jogs (b)–(d) are from the quartzite in the Shawangunk Mountains.

6.10.4.2.1 Interactions at strike-slip jogs

Jogs are offsets of strike-slip faults and are the primary reason for the segmentation of such faults. If the sign of the step over between the fault segments (right or left) is the same as the sign of the fault (right lateral or left lateral), the jog is extensional; if opposite, it is compressional. Both kinds of jogs are observed.

Figure 27 shows a number of small-scale jogs. Figure 27(a) is a schematic diagram of an extension jog in the Sierra Nevada granite (Martel and Pollard, 1989). In that locality, the strike-slip faults are reactivated joints, so they have very small D/L ratios as compared to features that originated as strike-slip faults. The jog forms at what they call splay faults and wing cracks that originate from the tips of the fault on the extensional side and propagate across the gap between the faults. When this occurs, a rhomboid cavity is formed (Figure 27(b)). Such jogs have been modeled numerically by Martel et al. (1988), Burgmann and Pollard (1994), and Pachell and Evans (2002) and with an analog model by Dooley and McClay (1997). They occur on a wide range of scales, forming pull-apart basins at the larger scale. One of the larger of these is the basin containing the Dead Sea on the Dead Sea Transform (Al-zoubi and ten Brink, 2002). At these crustal-scale cases, inward-facing normal faults lie in the place of the wing cracks shown in Figure 27(a). Aydin and Nur (1982) claimed that pull-apart basins are self-similar structures, always being about twice as long as wide. However, they may have various temporal histories, which can produce some variability in this (Wakabayashi et al., 2004). The Hanmer Basin on the Hope Fault in New Zealand, for example, has a particularly complex history (Wood et al., 1994).

Figure 27(c) shows a rhombic cavity crosscut by a 'shunt' fault. The 1992 Landers earthquake ruptured across such a shunt fault, the Kickapoo Fault, that crosses the extensional jog between the Johnson Valley and Homestead Valley faults in California (Figure 28) (Sowers et al., 1994). Slip on the right lateral Johnson Valley and Homestead Valley faults both tapered to zero in their overlap regions (Figure 28, lower panel), but slip on the Kickapoo Fault was just enough to keep the overall summed slip constant at about 3 m (Figure 28, middle panel). Thus, the action of the shunt fault precluded the development of much extension at this jog during the earthquake. Notice the very high tip tapers of the Kickapoo Fault as it approaches (but does not touch) the other faults. This FTT is about a factor to 10 greater than that for noninteracting earthquake ruptures (Figure 11(b)).

A small compressive jog in quartzite is shown in Figure 28(d). Within the rhombic deformation zone, fine pressure solution lamellae occur in orientations highlighted by the white lines. These are perpendicular to the maximum compression direction in the jog. At the crustal scale, thrusts or anticlines (Campagna and Aydin, 1991) occur with these orientations. They have been studied with analog models by McClay and Bonora (2001).

6.10.4.2.2 Strike-slip splay faults

Splay faults are common in strike-slip systems. Prominent examples from the Alpine and San Andreas Fault systems in New Zealand and California are compared in Figure 29, where the figures have been rotated such that their relative plate motion directions are nearly parallel. Both the Alpine Fault and the Big Bend region of the SAF are oblique in a transpressive sense from the plate motion direction. The Marlborough Fault System of New Zealand, such as the Hope, Awatere, and Wairau, and the splay faults of southern California, such as the San Jacinto, Elsinore, and San Clemente, are, in contrast, pure strike-slip faults oriented parallel to the plate motion direction. Similarly, in northern California, the Calaveras and Hayward Faults splay from the San Andreas where it too is transpressive.

In Figure 30, Global Positioning System (GPS) velocities and the geologic slip rates for the various faults in the San Andreas Fault system in southern California are shown. In this region, only 22 of the entire 50 mm year^{-1} plate motion is taken up in the SAF proper, the rest occurring on the splay

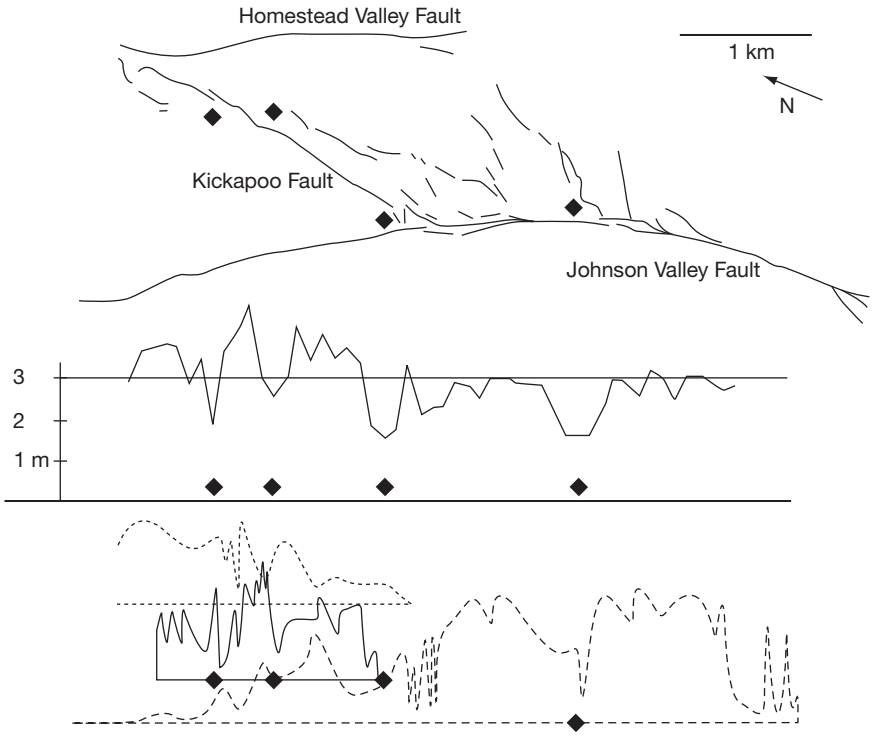

Figure 28 The Kickapoo Fault is a shunt fault between the right lateral Homestead Valley and Johnson Valley faults activated in the 1992 Landers earthquake. Top: map view; bottom: slip on each fault during the earthquake; middle:summed slip on the three faults. Modified from Sowers JM, Unruh JR, Lettis WR, and Rubin TD (1994) Relationship of the Kickapoo Fault to the Johnson Valley and Homestead Valley Faults, San-Bernardino County, California. *Bulletin of the Seismological Society of America* 84: 528.

faults (Bourne et al., 1998b). A very similar slip distribution occurs in the New Zealand case (Bourne et al., 1998a).

A detail of the junction between the San Jacinto Fault and SAF is shown in **Figure 31**. The GPS data indicate that north of this juncture the San Andreas moves at a rate of 34 and 12 mm year^{-1} of that is transferred to the San Jacinto. It is common to think of such transfers as kinematic, that is, the slip divides between two contacting faults, a part continuing on the master fault, the other part on the splay. This would require that the splay offset the master fault, which **Figure 31** shows not to be the case. This cannot be because the San Jacinto is too young to have produced an offset, because its net slip is about 20 km, measured some 100 km south of the junction (Kendrick et al., 2002). Furthermore, close examination shows that the San Jacinto Fault does not touch the San Andreas. If it is considered to be continuous with the Glen Helen fault, it curves to near parallelism with the San Andreas before disappearing. At its tip, of course, the slip must be zero. This noncontacting and nonoffsetting nature of splay junctions is a feature of all the splays of the San Andreas Fault and Alpine Fault systems.

No one has attempted to model the splay interaction, but some conjectures can be made. If the slip transfer is not kinematic, it must be dynamic, that is, facilitated by the interacting stress fields of the two faults. The splay fault presumably forms later than the master fault and is prevented from touching it by the stress shadow of the master fault. Its tip is therefore pinned. The slip rate on the San Jacinto Fault must be zero at its tip and increase with distance to the south, up to its full 12 mm year^{-1}. Similarly, the slip rate on the SAF must not suddenly decrease, but gradually do so as the slip rate on the San Jacinto Fault increases. As net slip increases on the San Jacinto Fault, the slip gradient at its tip increases, producing an ever-increasing stress concentration in the vicinity of its tip. This will cause its tip to propagate, but at an ever decreasing velocity as it goes deeper into the stress shadow of the SAF. Some effects of this resulting large stress concentration can be seen in **Figure 31**. Just NE of the tip, where the stresses should be extensional, is the San Bernardino Basin. This 1.7 km deep basin has basement vertically offset 1.2 km, down to the east, on the San Jacinto Fault (Stephenson et al., 2002). On the other, compressive side, are the uplifted San Gabriel Mountains and the Cucamonga thrust fault. Is the Cucamonga thrust just another transverse range bounding fault, or does it owe its existence to the San Jacinto Fault tip stress field? In its corresponding position at the nearly identical splay junction of the Hope and Alpine Faults, the 1996 M 6.7 Arthur's Pass earthquake occurred. It had a thrust mechanism, dipping in to the Alpine Fault (Abercrombie et al., 2000).

6.10.5 Fault Populations

It has long been known that earthquakes obey a well-defined size distribution, the Gutenberg–Richter relation. When defined in terms of seismic moment, it is a power law. This kind of distribution is typical of fractal objects, and it can be argued from a geometric point of view that this arises because

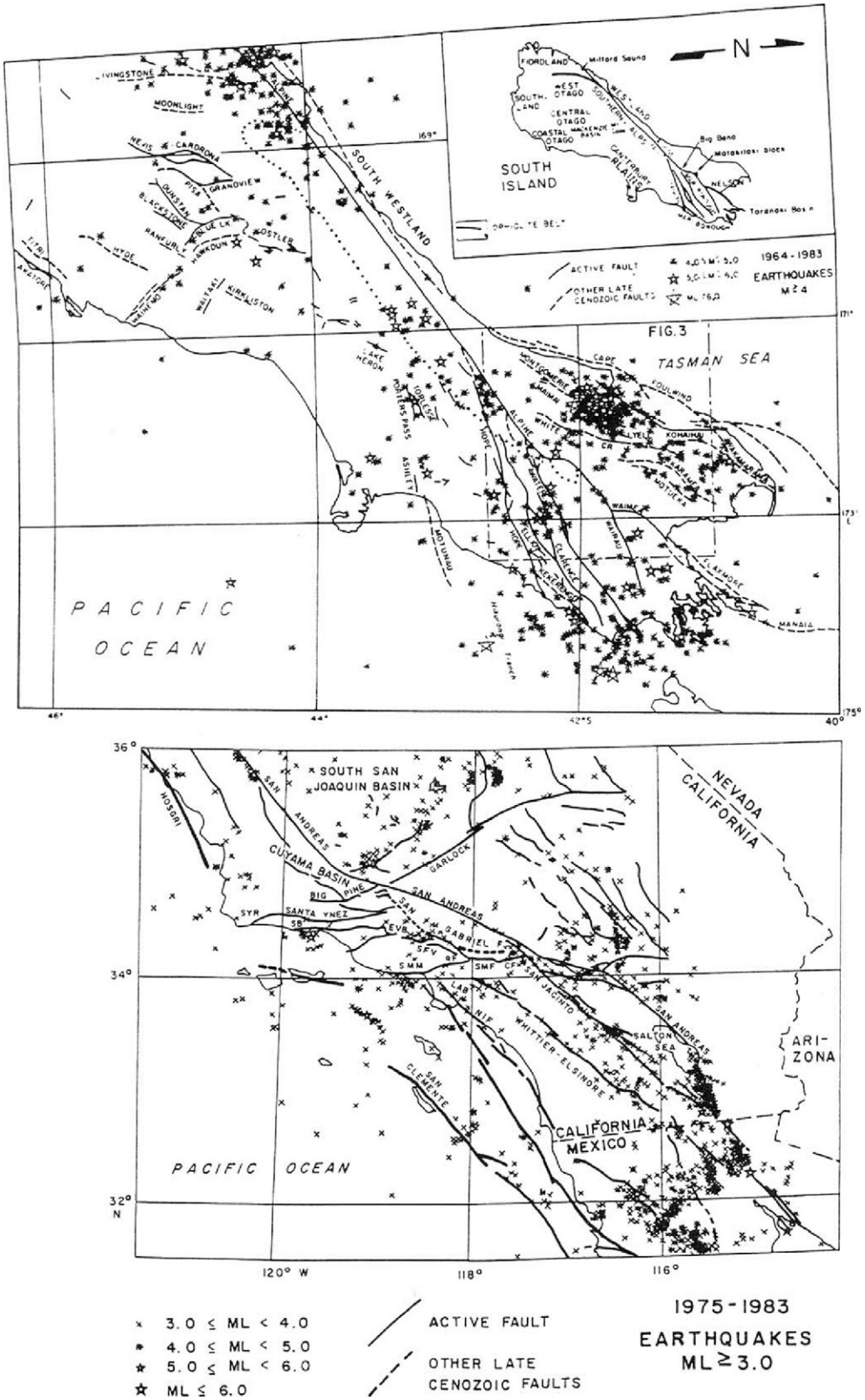

Figure 29 The Alpine Fault system (top) compared with the San Andreas Fault system (bottom). The top map has been rotated for comparison. Reproduced from Yeats R and Berryman K (1987) South Island, New Zealand and transverse Ranges, California, a seismotectonic comparison. *Tectonics* 6: 363–376.

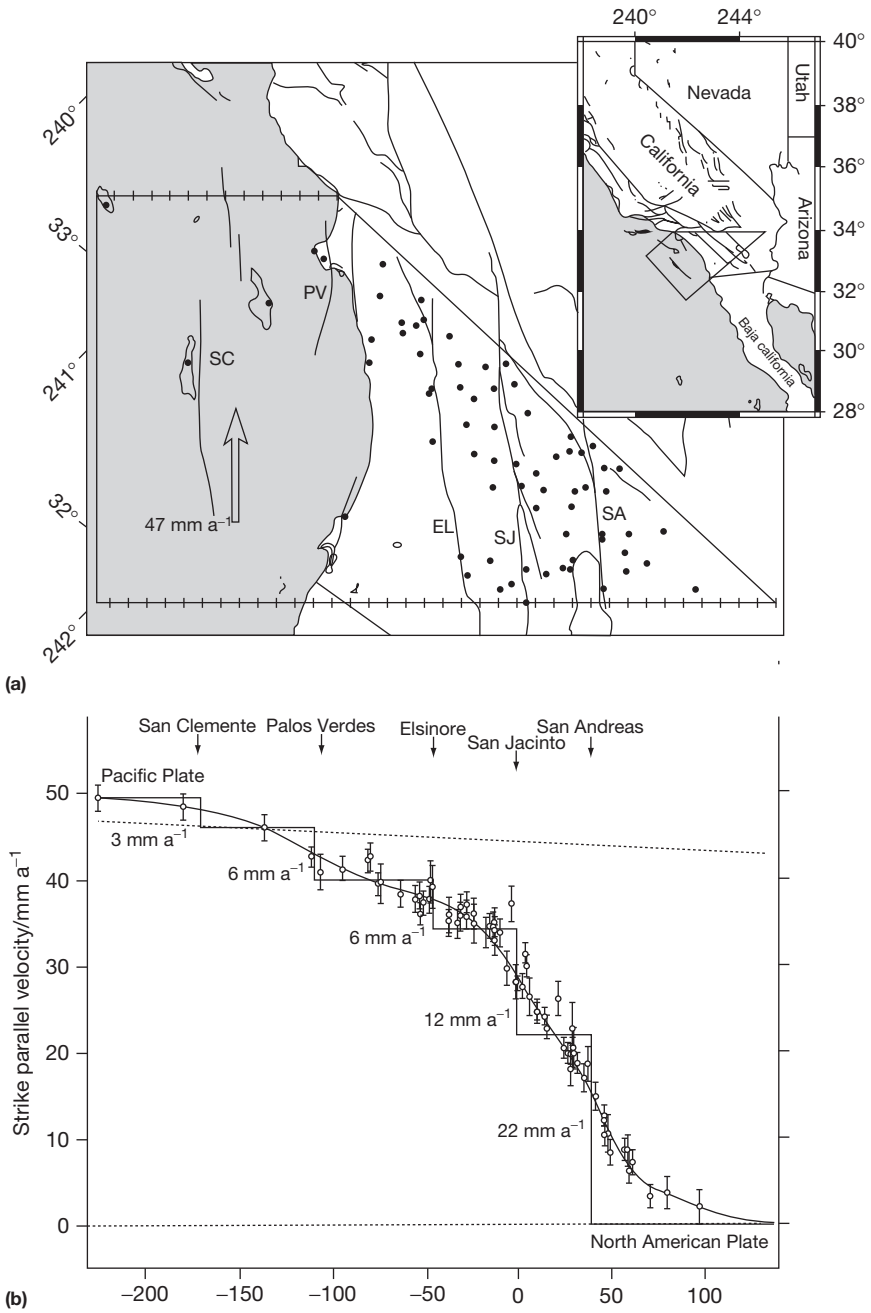

Figure 30 (a) Map of the San Andreas Fault (SAF) system in southern California, with location of GPS sites as dots. (b) Strike-parallel velocities from GPS data. Staircase is the geologic slip rates of the faults. Curve is velocities expected from a model. Reproduced from Bourne SJ, England PC, and Parsons B (1998b) The motion of crustal blocks driven by flow of the lower lithosphere and implications for slip rates of continental strike-slip faults. *Nature* 391: 655–659.

they are self-similar (Turcotte, 1992). Earthquakes are self-similar: like faults, the slip in an earthquake scales linearly with its length (Scholz, 1982).

We might then expect faults to have populations with similar power law statistical properties. It turns out, though, that faults can have more than one kind of population. In this section, we describe these populations and the mechanisms by which they are generated.

6.10.5.1 Observations of Fault Populations

6.10.5.1.1 Power law distributions

Power law distribution for faults has the form

$$N(L) = aL^{-c} \qquad [18]$$

where $N(L)$ is the number of faults greater than length L. This is a fractal distribution and has been described many times for

faults (for a collection of papers on this topic, see Cowie et al., 1996). However, the data are seldom convincing that this is the correct distribution or what is the correct value of the exponent (Cladouhos and Marrett, 1996). A major problem is that the data are usually obtained from mapping, which has very little dynamic range. An example is shown in **Figure 32**. There, the size distribution of faults in the Volcanic Tablelands was measured at three scales. For each scale range, there is a limited straight section below which the data roll off because of a lack of resolution of the smallest faults. At the top end, there is another roll-off, for which there are two causes. The first is data censoring: The faults become larger than the map size, and hence, their lengths are underestimated. The second problem is that because the number of faults measured was limited, a cumulative distribution was plotted. Burroughs and Tebbens (2001) showed that a cumulative plot of a power law distribution with an upper cutoff produces a roll-off at the upper end and an overestimate of the exponent of the straight segment. As a result of these various problems, plots such as in **Figure 32** are not very convincing of a power law and overestimate the exponent.

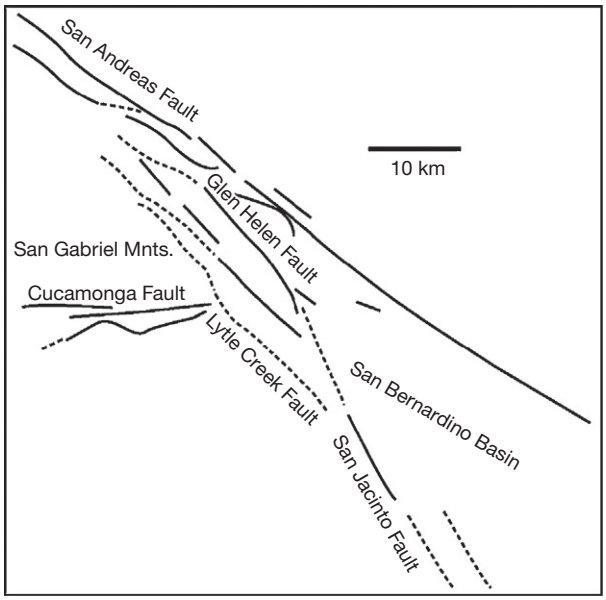

Figure 31 Map of the confluence of the San Jacinto Fault with the SAF.

These problems are overcome in **Figure 33**. The data are from normal faults in the low plains of Venus, obtained by the synthetic aperture radar of the Magellan spacecraft (see Scholz, 1997, for an illustration of the image used). There is no dynamic range problem because the image was 200×200 km and the pixel size was 70 m. The image analysis software neglected faults that touched the edge of the image, which removed the censoring problem, and there were enough faults in the population, 1750, that a frequency plot could be used, avoiding the Burroughs and Tebbens problem. One can see that it is clearly a power law distribution with an exponent of -2. The equivalent exponent for a cumulative distribution would then be -1, a little smaller than the exponent of -1.2 obtained in **Figure 32**, illustrating the overestimation problem with cumulative distributions.

6.10.5.1.2 Exponential distributions

Cowie et al. (1993) were the first to discover that exponential fault distributions exist. Their data came from sonar swath mapping of the normal faults on the flanks of the East Pacific Rise and are shown in **Figure 34** as semilog plots. The data clearly do not fit a power law; instead, they are fit by

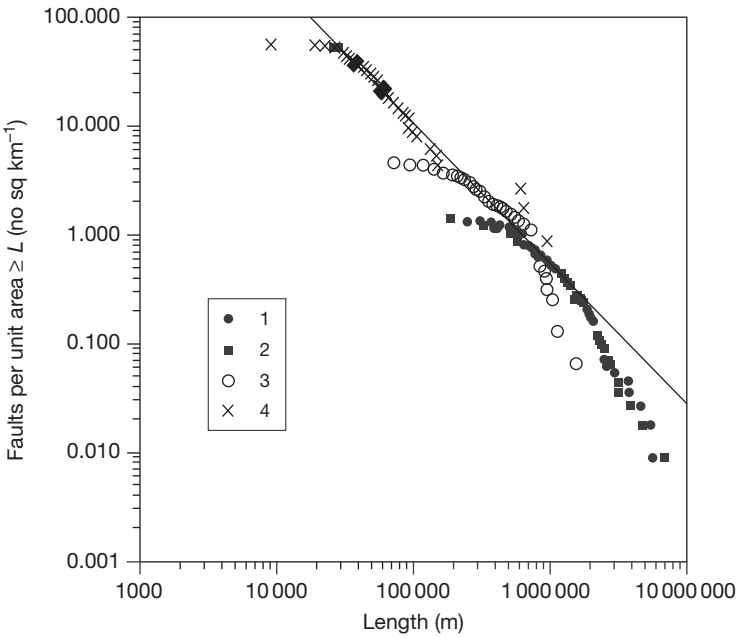

Figure 32 The length distribution of faults for the Volcanic Tablelands mapped at three scales. Reproduced from Scholz CH, Dawers NH, Yu JZ, and Anders MH (1993) Fault growth and fault scaling laws: Preliminary results. *Journal of Geophysical Research*, *Solid Earth* 98: 21951–21961.

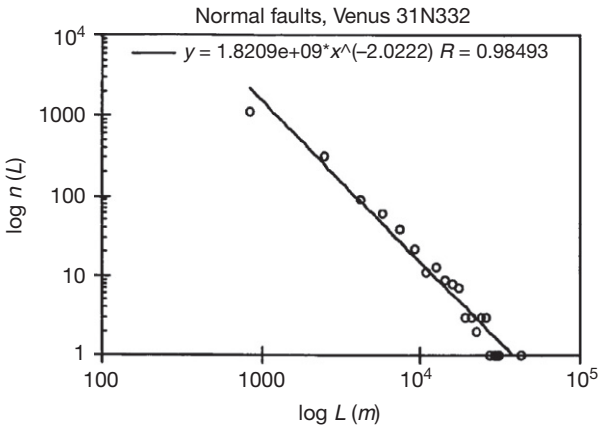

Figure 33 Frequency plot of the length distribution of faults of the low plains of Venus. Taken from a synthetic aperture radar image from the Magellan mission. Reproduced from Scholz CH (1997) Earthquake and fault populations and the calculation of brittle strain. *Geowissenshaften* 15: 124–130.

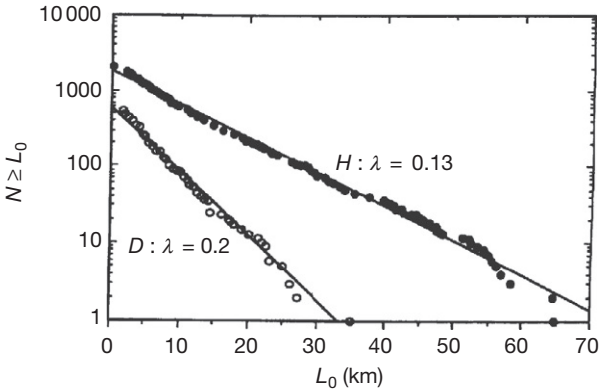

Figure 34 Length distribution of faults on the flanks of the East Pacific Rise, from sonar swath mapping data. Reproduced from Cowie PA, Scholz CH, Edwards M, and Malinverno A (1993) Fault strain and seismic coupling on midocean ridges. *Journal of Geophysical Research, Solid Earth* 98: 17911–17920.

$$N(L) = N_T \exp(-\lambda L) \quad [19]$$

where N_T is the total number of faults and λ is the reciprocal of the mean fault length.

6.10.5.1.3 Periodic distributions

It has long been known that joints in layered sedimentary rock are often evenly spaced with a spacing proportional to the bed thickness (Price, 1966, p. 144). Periodic distributions like this are seldom seen for faults. One example, shown in Figure 30, is the subparallel strike-slip faults of the San Andreas Fault system in southern California. There, the faults have a fairly even spacing of 40–50 km. Another example is the ~100 km long normal faults that form the evenly spaced basins and ranges in Nevada.

Hu and Evans (1989) experimentally studied the cracking of adhesive brittle films on ductile substrates subject to tension. They found that the cracks reached a saturated population of evenly spaced system-sized cracks. The spacing of the cracks is proportional to the thickness of the brittle layer. They showed that the spacing is such that the cracks occur just outside on each other's stress shadow. Their results are consistent with those for the faults in Figure 30, which are spaced about three times the brittle thickness of 15 km.

Soliva et al. (2006), in a study of a population of normal faults restricted to a single sedimentary layer, found a periodic distribution with closer spacing than that expected for a layer bounded at one edge by the free surface.

As we shall see later in the text, these different populations are transition regimes that occur as brittle strain increases. Brittle strain is the strain due to faulting and is determined by summing the moments of the faults, as will be discussed in Section 6.10.7. Thus, the power law distributions shown in Figures 32 and 33 were for regions in which the brittle strain was 1–2%. The data for the East Pacific Rise had strains of 5% for the data at 3° S (lower curve) and 10% at 13–15° N (upper curve).

6.10.5.2 The Formation of Fault Populations

Cowie et al. (1995) studied a model simulating a brittle elastic plate undergoing stretching. For large strains, this model converges on a single system-size crack, but at small strains, power law (fractal) size distributions were observed forming in geometrically fractal populations.

Spyropoulos et al. (2002), continuing this approach, studied a numerical model of stretching a brittle layer supported by a ductile substrate. It was a discrete spring-block model, illustrated in Figure 35. The blocks were connected by leaf springs to a lower substrate that acted as a ductile layer that was stretched. Each block could rupture, following a slip-weakening fracture criterion. The strength of slip weakening was the only tunable parameter in the model, and over a broad range, it produced very similar results.

Figure 36 shows the fraction of active sites versus strain normalized to disorder. The fraction of active sites is the sum of crack lengths that are opening over a time window. This parameter first increases rapidly with strain as many new cracks are nucleated. The rate of increase in active sites gradually decreases until it reaches a peak, and then the number of active sites gradually declines to an asymptotic level at high strain. As new cracks nucleate and grow, the number of sites in stress shadows increases, so that the probability of nucleation of new cracks decreases and the probability of the death of old cracks and probability of the coalescence of cracks both increase, leading to the peak and eventual decrease in active sites. Thus, the rising part of the curve is dominated by nucleation and growth of cracks, and the falling part is dominated by coalescence and the inactivity of small cracks caught in the stress shadows of longer cracks.

Figure 37 shows the evolution of the frequency–size distribution of cracks with strain in the rising part of the curve in Figure 36. It begins as exponential, mimicking the noise introduced initially in the model, and evolves asymptotically to a power law shown as the heavy line. The dashed line has slope −2 for comparison. The distribution of sizes for the large strain falling part of the curve is shown in Figure 38. Here, it becomes an exponential distribution for all but the

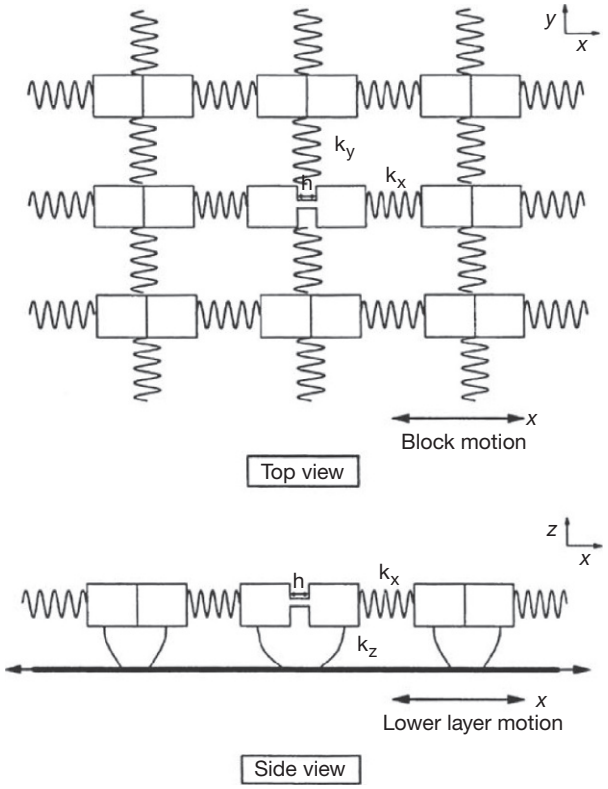

Figure 35 Schematic diagram of a model of fracture of a brittle layer over a ductile substrate. Reproduced from Spyropoulos C, Scholz CH, and Shaw BE (2002) Transition regimes for growing crack populations. *Physical Review E* 65: 056105. http://dx.doi.org/10.1103/PhysRevE.65.056105.

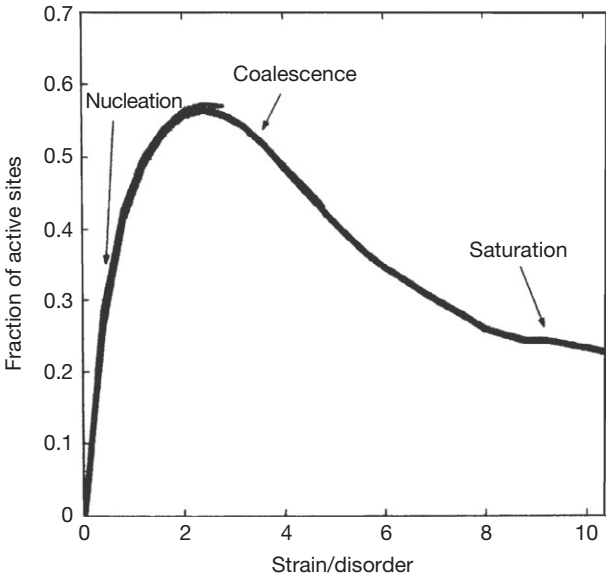

Figure 36 Fraction of active sites versus strain for the model shown in Figure 35. Reproduced from Spyropoulos C, Scholz CH, and Shaw BE (2002) Transition regimes for growing crack populations. *Physical Review E* 65: 056105. http://dx.doi.org/10.1103/PhysRevE.65.056105.

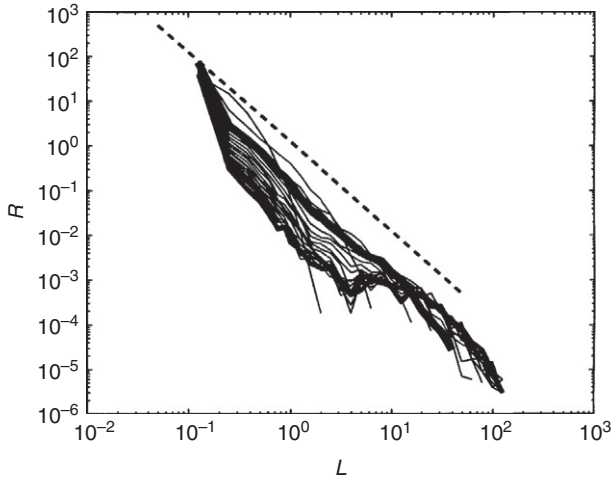

Figure 37 Length distribution of faults from the model at low strains. Reproduced from Spyropoulos C, Scholz CH, and Shaw BE (2002) Transition regimes for growing crack populations. *Physical Review E* 65: 056105. http://dx.doi.org/10.1103/PhysRevE.65.056105.

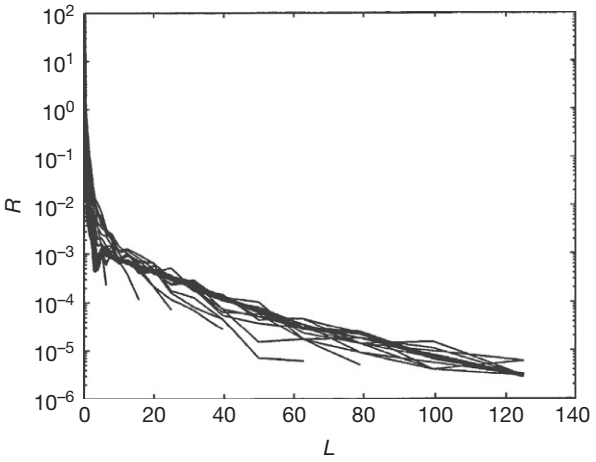

Figure 38 Length distribution of faults from the model at high strains. Reproduced from Spyropoulos C, Scholz CH, and Shaw BE (2002) Transition regimes for growing crack populations. *Physical Review E* 65: 056105. http://dx.doi.org/10.1103/PhysRevE.65.056105.

smallest cracks. At saturation, the crack distribution was dominated by evenly spaced system-size cracks.

This numerical model was validated by physical models in the form of a clay cake stretched on a rubber substrate by Spyropoulos et al. (1999). Both the peaked form of the crack density versus brittle strain curve and the evolution from power law to exponential size distribution were observed. Ackermann et al. (2001) reproduced these results in similar experiments.

Gupta and Scholz (2000b) observed this transition for the Asal rift in Djibouti. Using data from a digital elevation model, they found that the brittle strain increased to a maximum of 12% in the center of the rift. As shown in **Figure 39(a)**, the strain was accommodated at first by increasing fault density, but after 6% strain, the fault density no longer increased. After that point, further strain was accommodated by an increasing

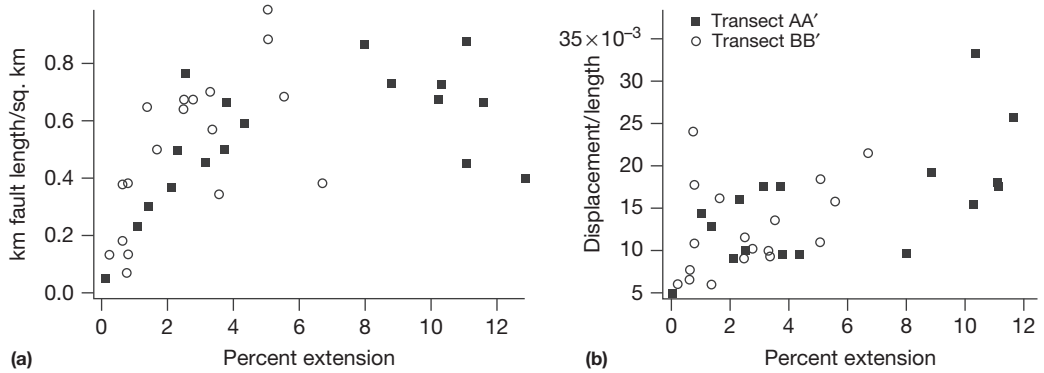

Figure 39 Fault data from the Asal rift, Djibouti. (a) Fault density versus brittle strain. (b) Displacement/length ratio versus strain. Reproduced from Gupta A and Scholz CH (2000b) Brittle strain regime transition in the Afar depression: Implications for fault growth and seafloor spreading. *Geology* 28: 1087–1090.

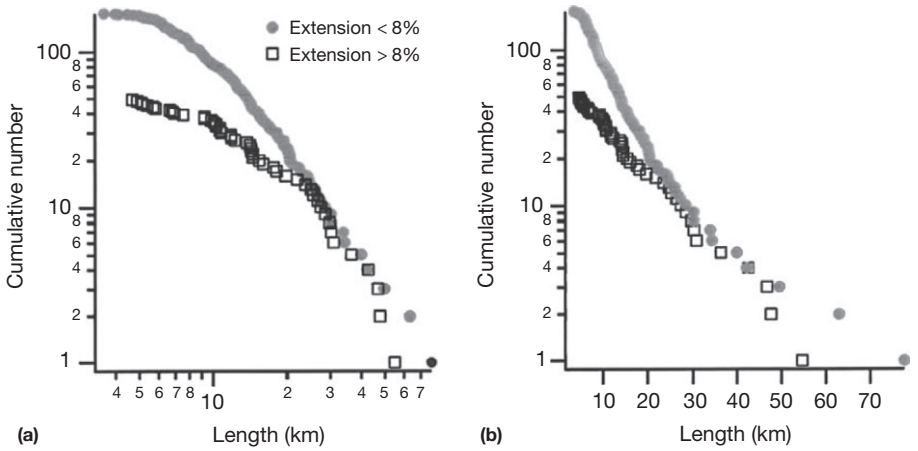

Figure 40 The length distribution of faults for the Asal rift, at low and high strains. (a) In log-log coordinates. (b) In semilog coordinates. Reproduced from Gupta A and Scholz CH (2000b) Brittle strain regime transition in the Afar depression: Implications for fault growth and seafloor spreading. *Geology* 28: 1087–1090.

D/L ratio (Figure 39(b)) indicating that all faults had become pinned at 6% strain. The size distribution was power law for low strains and exponential for high strains (Figure 40). Because the faults in the Asal rift are highly interacting, their displacement profiles are often highly contorted (Manighetti et al., 2001).

6.10.6 Strain and Faulting

6.10.6.1 Calculation of Brittle Strain from Fault Data

The brittle strain due to faulting may be determined by summing the geometric moments of the faults in a population, where geometric moment is defined as

$$M = uA \qquad [20]$$

where u is the mean fault displacement and A is the fault area. The geometric moment is the magnitude of the tensor moment:

$$M_{ij} = M\left(u_i n_j + u_j n_i\right) \qquad [21]$$

where u_i is the unit vector in the direction of displacement and n_i is the unit normal to fault plane.

The formula (Kostrov, 1974) for calculating the net strains from a volume V of rocks that have been active over a geologic period is

$$\varepsilon_{ij} = \frac{1}{2V}\sum_{k=1}^{N}\left[M_{ij}\right]_k \qquad [22]$$

To illustrate this compact tensor equation, consider the simple case of a plate of brittle thickness W^* and length and width l_1 and l_2 being extended in the x_1 direction by a population of parallel normal faults of dip φ (Figure 41). The mean displacement $\hat{u}_1$ of the right-hand face is

$$\hat{u}_1 = \sum_{k=1}^{N}\frac{u_k \cos\varphi L_k^2 \sin\varphi}{W^* l_2} \qquad [23]$$

for small faults that do not rupture the entire thickness and are assumed to be equant of side L. We then have

$$\varepsilon_{11} = \frac{\hat{u}_1}{l_1} = \frac{\cos\varphi \sin\varphi}{V}\sum_{k=1}^{N} u_k L_k^2 \qquad [24]$$

a simple form of eqn [22]. If the faults become large such that they rupture the entire thickness of the brittle layer, they will

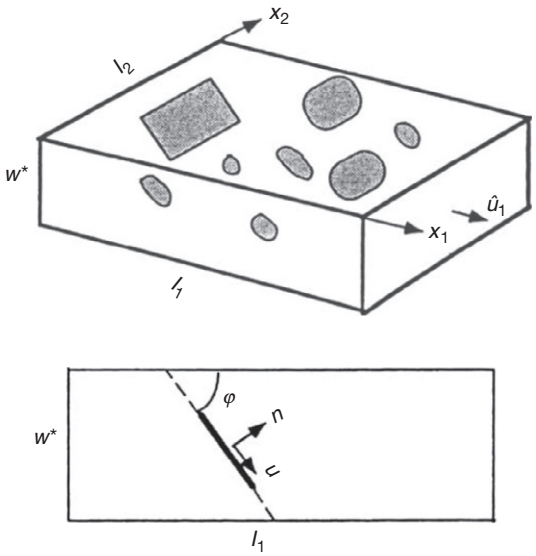

Figure 41 Schematic diagram for calculating fault strain. Reproduced from Scholz CH (1997) Earthquake and fault populations and the calculation of brittle strain. *Geowissenshaften* 15: 124–130.

have a width $W = W^*/\sin\varphi$ and the equivalent expression becomes

$$\varepsilon_{11} = \frac{\cos\varphi}{A}\sum_{k=1}^{N} u_k L_k \qquad [25]$$

where V and A are the volume and area of the deformed region, respectively.

Cowie et al. (1993) used this method, with exactly this geometry, to calculate the fraction of seafloor spreading that results from normal faulting. The strain shown in Figure 39 was also calculated in this way. In the former study, the data source was from sonar swath mapping and in the latter case, from a digital elevation model. They therefore had quite good information on both u and L. For more incomplete data sets, for example, from geologic mapping, several scaling results can be included to make the procedure much less demanding (Scholz and Cowie, 1990).

It is usually easier to determine fault length than displacement. Since we have already established the linear scaling $u = \gamma L$, it is not necessary to measure u and L independently for every fault. One needs only to determine the scaling parameter for a few faults in the region and then to apply it throughout. A further simplification results from a property of fault populations. For most continental settings, the strains are low and the fault populations are power law. Integrating over eqn [18] and using the scaling law, we find that for large faults ($L \geq W^*$),

$$\sum_{K=1}^{N} M_k = aW^*\gamma C\int \frac{dN(L)}{dL}L^2\,dL = \frac{aW^*\gamma C}{2-C}L^{2-C} \qquad [26]$$

and for small faults ($L \leq W^*$),

$$\sum_{k=1}^{N} M_k = aW^*\gamma C\int \frac{dN(L)}{dL}L3\,dL = \frac{aW^*\gamma C}{3-C}L^{3-C} \qquad [27]$$

We have previously found (Figures 32 and 33) that the value of C is approximately (or perhaps exactly) 1. Inserting this value into the proper integrals in the preceding text, we see that they are convergent. Almost all the moment is carried by the longest faults, so we need only evaluate the integrals at their upper bounds. The remaining moment in the smaller faults can be calculated (Scholz and Cowie, 1990) so we need not be concerned with the lack of resolution at the smaller scales.

6.10.6.2 Fault Rotation and Lockup

As faults accrue displacement, they rotate such that the angle between the fault plane and σ_1 increases. The most familiar cases are where systems of subparallel faults occur, the so-called bookshelf faulting (Savage et al., 2004; Sigmundsson et al., 1995; Tapponnier et al., 1990), but any individual fault will also rotate in this manner. Martel (1999) had analyzed fault rotation at an infinitesimal scale with an elastic crack model: the basic physics behind it is correct for the finite scale. This rotation means that the fault becomes progressively less favorable-oriented for slip. Eventually, it will become frictionally locked. The stress condition for reactivating a fault inclined at an angle θ_R to σ_1 is (Sibson, 1985)

$$\frac{(\sigma_1 - p)}{(\sigma_3 - p)} = \frac{(1 + \mu\cot\theta_R)}{(1 - \mu\tan\theta_R)} \qquad [28]$$

where p is the pore pressure and μ is the friction coefficient. This stress ratio has a minimum at the optimum angle for fault reactivation θ_R^* and goes to infinity at the lockup angle $2\theta_R^*$. This is the maximum angle of the fault to σ_1. This angle may be reached as p approaches σ_3 but may not be exceeded, because p cannot exceed σ_3 without hydrofracturing occurring and the consequent draining of the pore fluid.

We can evaluate this for dip-slip faults because in that case, we can assume one of the principal stresses is vertical and the others are horizontal. Figure 42 shows the dip angles of large reverse (a) and normal (b) fault earthquakes in which the fault plane is known unambiguously from aftershock, geodetic, or surface faulting evidence (Jackson, 1987; Sibson and Xie, 1998). Also shown are the optimal and lockup angles for a typical laboratory friction coefficient of 0.6. The lockup angle predicted by this friction value agrees well with the data. This is strong evidence that this laboratory value is appropriate for faults. The most common angles are somewhat farther from the fault than the optimum angle, as expected from finite rotation. The fact that some faults are active at or near the lockup angle indicates that p does sometimes approach σ_3. Direct evidence for this comes from the relationship of veins to high-angle reverse faults near the lockup angle (Sibson et al., 1988).

Because faults are embedded in an elastic medium, when they rotate, we might expect there to be an elastic restoring force that resists further rotation and hence causes the fault to lock up before reaching the lockup angle as calculated in the preceding text. This problem has been evaluated in the case of crustal-scale normal faults (Buck, 1988; Cowie et al., 2005; Scholz and Contreras, 1998). Displacement on such a normal fault results in flexure of the crust, which is responsible for the footwall uplift and hanging wall basins that arise. For further

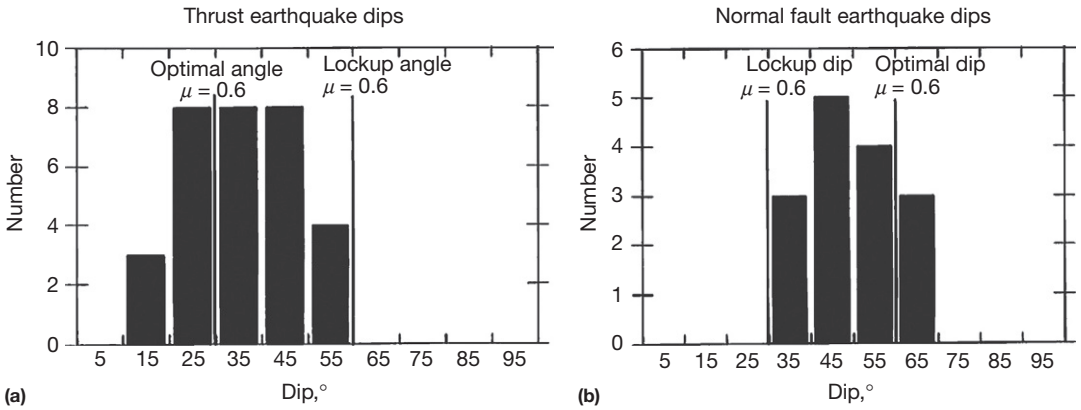

Figure 42 Histogram dip angles of active (a) thrust and (b) normal-faulting earthquakes. Reproduced from Scholz CH (2000) Evidence for a strong San Andreas fault. *Geology* 28: 163–166.

displacement, the shear stress on the fault must exceed both friction and the elastic flexural restoring stress. Thus, the lockup in this case will occur before the one solely due to friction given by eqn [28]. These analyses indicate that such faults have a maximum displacement and hence length, which are functions of the seismogenic thickness and the effective elastic thickness of the crust.

There of course may be other reasons why faults stop propagating; stress shadowing, as mentioned earlier, may cause this, as well as changes in thermal structure or tectonic loading (Bull et al., 2006; Cowie et al., 2005).

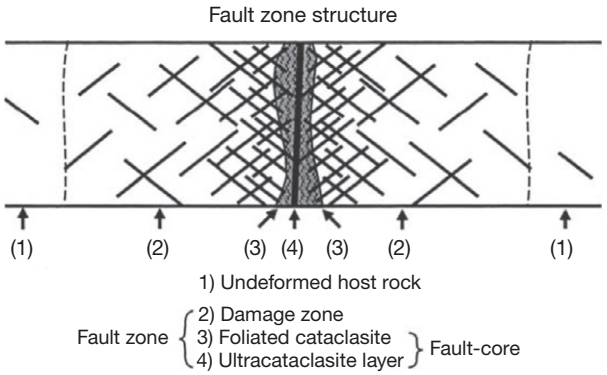

Figure 43 Schematic diagram of the structure of the San Gabriel Fault, California, at a depth of 3–5 km. Reproduced from Chester FM, Chester JS, Kirschner DL, Schulz SE, and Evans JP (2004) Structure of large-displacement strike-slip fault zones in the brittle continental crust. In: Karner G, Taylor B, Driscoll N, and Kohlstedt D (eds.) *Rheology and Deformation of the Lithosphere at Continental Margins*, pp. 223–260. New York: Columbia University Press.

6.10.7 Fault Rocks and Structures

Rocks found in fault zones are characteristic of them, indicating modes of deformation unique to faults. Snoke et al. (1998) had produced a photographic atlas of such rocks. Fault-related rocks are, of course, dependent upon their protolith and they vary with depth. Here, we attempt to restrict the discussion to faults in crystalline protoliths. The discussion is divided into sections of increasing depth: shallow schizosphere, deep schizosphere, brittle–plastic transition region, and plastosphere.

6.10.7.1 Shallow Schizosphere

In the upper half of the seismogenic layer, faults are completely brittle structures. A schematic diagram of the components of such a fault is shown in **Figure 43**. A broad damage zone surrounds a fault core consisting of cataclasites, often foliated, containing narrower bands of ultracataclasites within which discrete sliding surfaces may be found (Chester et al., 1993).

The San Gabriel Fault, an ancestral strand of the SAF in California, has been studied by Chester et al. (1993, 2004). This fault has a strike-slip offset of 20 km and is exposed at a depth of 2–5 km. Its damage zone is several hundred meters wide, the cataclasite zone is several meters wide, and the ultracataclasite zone width is in the centimeter to decimeter range. Both the cataclasites and ultracataclasites are often foliated, with the foliation near parallel to the fault. Almost all shearing has occurred in the fault core, with it being concentrated in the ultracataclastic layer and along slip surfaces. This narrowness of the zone of principal slip has been emphasized by Sibson (2003), who provided many examples.

The density of microcracking and mesoscopic features decreases exponentially with distance from the ultracataclastic layer (**Figure 44**). This is similar to that observed for process zones (**Figure 14**), so it is likely that the damage zone is the wake of a process zone produced by the fault tip, perhaps augmented by further damage from earthquakes, as suggested by Wilson et al. (2005). There is also an increase in mineralization and volatile content as the ultracataclastic layer is approached (Chester et al., 2004). The grain size distribution of the cataclastic rocks is power law, or fractal, with the fractal dimension increasing with strain (**Figure 45**; see also Di Toro and Pennacchioni, 2005). This occurs due to the production of fine grains at the expense of coarse grains during comminution, as expected from theory (Sammis et al., 1986) and experiment (Marone and Scholz, 1989).

The Punchbowl fault, another large-displacement (40 km) strike-slip forerunner of the SAF exposed to a depth of 2–4 km,

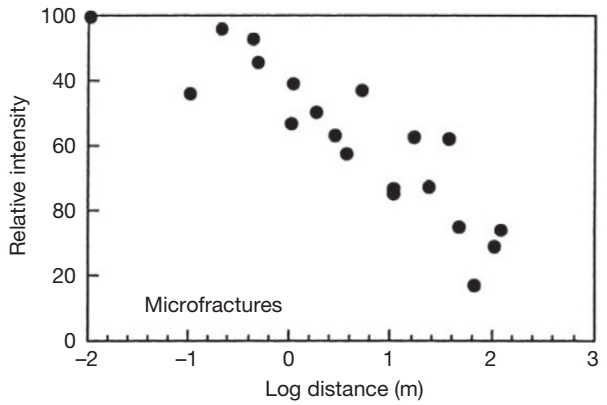

Figure 44 Microfracture density as a function of distance from the San Gabriel Fault. Reproduced from Chester FM, Chester JS, Kirschner DL, Schulz SE, and Evans JP (2004) Structure of large-displacement strike-slip fault zones in the brittle continental crust. In: Karner G, Taylor B, Driscoll N, and Kohlstedt D (eds.) *Rheology and Deformation of the Lithosphere at Continental Margins*, pp. 223–260. New York: Columbia University Press.

has been described by Chester and Chester (1998) and Chester et al. (2004). It has two fault cores, about 125 m apart. Deformation increases as each core is approached, in a similar way as the San Gabriel Fault, but remains high in the sliver between the two cores. The northern of these two cores occurs at the contact between crystalline basement and sandstone. Ultracataclasites derived from each protolith are juxtaposed in the core but not mixed, suggesting that slip occurs on a discrete principal fault surface.

There is no evidence, in the form of pseudotachylytes, clastic dikes, or explosion breccia, of seismic rupture for either of these faults. Indeed, the delicacy of the structures suggests that slip, at the depths exposed, may have been aseismic.

6.10.7.2 Deep Schizosphere

The Gole Larghe Fault Zone of northern Italy is exposed at a depth of 9–11 km and an estimated ambient temperature of 250–300 °C (Di Toro and Pennacchioni, 2005). This fault, with a net displacement of 1100 m, is extremely well preserved on glacially polished surfaces. It does not show the extreme

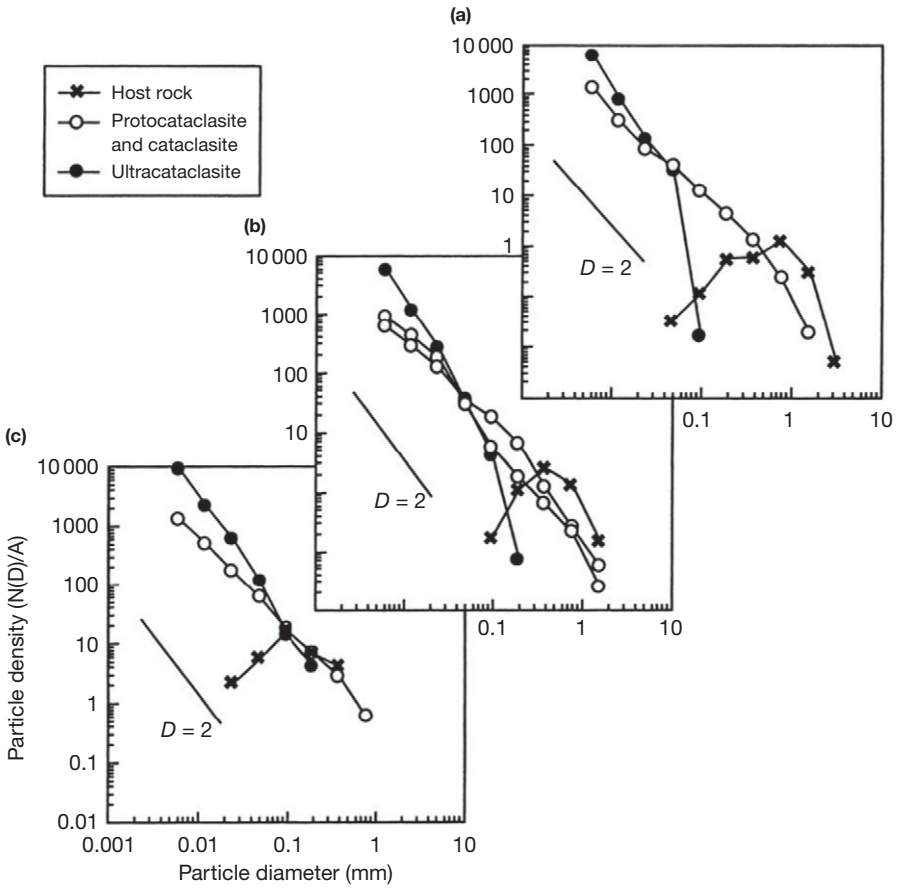

Figure 45 Particle size distribution for three different distances from the San Gabriel Fault. Reproduced from Chester FM, Chester JS, Kirschner DL, Schulz SE, and Evans JP (2004) Structure of large-displacement strike-slip fault zones in the brittle continental crust. In: Karner G, Taylor B, Driscoll N, and Kohlstedt D (eds.) *Rheology and Deformation of the Lithosphere at Continental Margins*, pp. 223–260. New York: Columbia University Press.

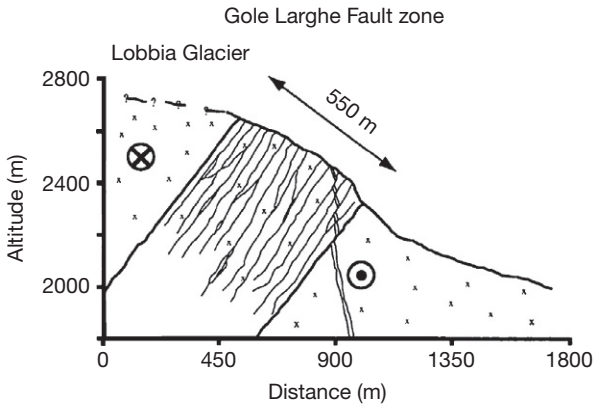

Figure 46 Schematic diagram of the Gole Larghe Fault Zone, northern Italy, at a depth of 9–11 km. Fault-parallel lines indicated pseudotachylyte veins. Reproduced from Di Toro G and Pennacchioni G (2005) Fault plane processes and mesoscopic structure of a strong-type seismogenic fault in tonalites (Adamello batholith, Southern Alps). *Tectonophysics* 402: 55–80.

localization of slip associated with the San Gabriel Fault and Punchbowl fault described in the preceding text. It appears as a 550 m wide zone in which hundreds of pseudotachylyte veins and cataclasite layers are distributed evenly throughout the host tonalite (**Figure 46**). Pseudotachylytes are the products of friction melting and hence are evidence of ancient seismic faulting (Sibson, 1975).

The pseudotachylytes in the Gole Larghe Fault often reactivated cataclasite layers that had been indurated prior to reactivation. The cataclasites in turn reactivated joints. The pseudotachylyte veins are not reactivated, however, suggesting that each represents an individual earthquake. The veins have thicknesses in the millimeter–centimeter range and are associated with displacements in the decimeter–meter range. If the entire work of faulting τd goes into melting, then their thickness/displacement (t/d) should be proportional to τ (Di Toro and Pennacchioni, 2005). Their thickness increases with displacement, but like Sibson's (Sibson, 1975) data, the scaling appears closer to $d \propto t^2$ than linear, implying that τ decreases with d. Di Toro et al. (2005a,b) attempted to determine this and other earthquake source properties from them, but with limited success because the displacement associated with the cataclasite phase of faulting could not be separated from that in the purely pseudotachylyte phase. Di Toro et al. (2005a,b) were able to infer, however, the direction and velocity of propagation from the orientation of pseudotachylyte injection veins.

Although pseudotachylytes sometimes occur at shallower depth (Sibson, 2003), they are primarily found in the deeper, higher-stress part of the schizosphere. Like the case of the Gohle Larghe Fault, deep, pseudotachylyte-bearing faults are not localized but are often hundreds of meters to kilometers wide with distributed deformation (Allen, 2005; Grocott, 1981; Swanson, 1988). Di Toro and Pennacchioni (2005) suggested that the delocalization mechanism of such faults is the strong welding by pseudotachylytes that prevents their reactivation.

Pachell and Evans (2002) studied a smaller displacement (100 m) fault in the Sierra Nevada of California that was active at the same depth range as the Gole Larghe Fault but with distinctively different properties. It was a brittle feature consisting of fractures spanning a width of meters to tens of meters, with abundant jogs and with little developed cataclasite. They did not report any pseudotachylyte veins.

In contrast to the cases discussed in the preceding text, many crustal-scale large-displacement strike-slip faults exposed in the middle crust are several kilometers wide, with no single concentrated core in which the bulk of the slip occurs. Examples are the Carboneras Fault in southeastern Spain (Faulkner et al., 2003) and the Damxung-Jiali Shear Zone in Tibet (Edwards and Ratschbacher, 2005). Both of these shear zones have multiple anastomosing zones of concentrated shear extending over widths of 3–5 km. The Tibetan case is clearly seismogenic: multiple pseudotachylyte veins, ~1–10 mm thick, are scattered throughout the depth range 5–15 km. Both these faults cut sedimentary and metasedimentary rocks, often having phyllitic textures, which may have a bearing on their different developments.

6.10.7.3 Brittle–Plastic Transition Region

Within the brittle–plastic transition regime, pseudotachylytes can be observed to penetrate into mylonites (Camacho et al., 1995; Lin et al., 2005; Passchier, 1984). Lin et al. (2005) described pseudotachylytes in the Woodroffe Thrust, a 1.5 km thick mylonitized shear zone separating granulite facies from amphibolite facies gneisses. The shear zone, exposed at a depth of 25–30 km, contains large volumes of millimeter- to centimeter-scale pseudotachylyte veins. They are of two types, cataclasite-related, similar to those described in the preceding text, and mylonite-related. The mylonite-related veins penetrate into mylonites and ultramylonites and are themselves overprinted by subsequent mylonitization, with foliation parallel to that of the mylonites.

The earthquakes that produce these pseudotachylyte veins nucleate in the deep schizosphere but are able to propagate to some distance into the plastically deforming mylonite zone by virtue of the extremely high strain rates at the tip of the propagating rupture, which temporarily embrittles the rock. Plastic deformation during the subsequent slow shearing of the interseismic period resulted in the mylonitization of the pseudotachylyte veins (e.g., Tse and Rice, 1986). The cataclastic-related veins overprint the mylonite-related ones and were produced subsequent to the unroofing of the fault through the brittle–plastic transition.

6.10.7.4 Plastosphere Shear Zones

Major faults have been seismically imaged to extend well into the plastosphere as ductile shear zones. Examples include the SAF, which has been imaged to the Moho by Henstock et al. (1997) and Parsons (1998), and the Wind River thrust, which has been imaged continuously to 24 km by Smithson et al. (1978). In deeply exposed terrain, these have been found to be mylonite belts and can be found to be traced all the way from greenschist grade all the way to granulite-grade metamorphism (Bak et al., 1975a,b; Hanmer et al., 1995).

6.10.7.4.1 Mylonite fabric elements

Mylonites are products of plastic deformation and have distinctive fabrics. Figure 47 shows a schematic diagram of a shear zone and its associated fabric elements. If the material within the shear zone deforms cataclastically or plastically, then, regardless of the magnitude of the external stresses, the internal stresses will always be pure shear, as shown by Byerlee and Savage (1992). If the material is a cataclasite or mylonite, it will develop a foliation on the plane of maximum shortening (S), which, with finite strain, will rotate to within parallelism with the shear zone. In the cataclastic regime, Riedel shears develop in the R_1 and R_2 direction. In both regimes, zones of concentrated shear may develop in the C orientation (Chester et al., 1993; Lister and Snoke, 1984; Lister and Williams, 1979; Simpson and Schmid, 1983), and in the plastic regime, a foliation or cleavage, called C', may also develop in the R_1 direction.

Mylonites have a single foliation with a lineation on the foliation plane. They are the product of shear under semibrittle to plastic condition. They may form from any protolith, but here, we will restrict the discussion to those formed from granite rock. The foliation is initially on the plane of maximum shortening but with finite strain rotates toward the plane of shear, of the shear zone itself (Figure 48). The lineation is in the direction of shear. S–C mylonites have concentrated shear on C surfaces, which are hence shear discontinuities (Figure 48(b)).

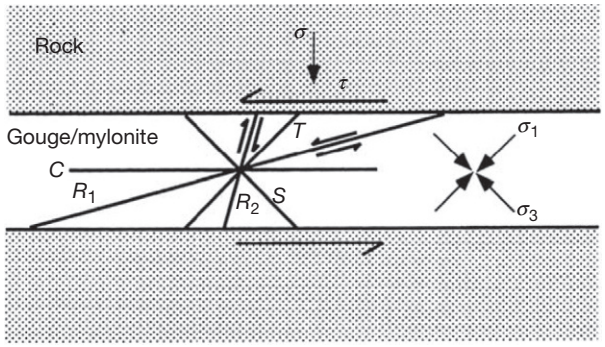

Figure 47 Schematic diagram of fabric elements in a cataclasite or mylonite shear zone. Reproduced from Scholz CH (2002) *The Mechanics of Earthquakes and Faulting*, 2nd edn. Cambridge: Cambridge University Press.

6.10.7.4.2 Shear localization and strain softening in mylonite zones

The localization of shear in mylonite zones indicates that the mylonites must be undergoing some kind of strain softening. Although there has been some experimental work on the formation of mylonites in analog materials (Kawamoto and Shimamoto, 1998), there has been little discussion of the mechanism for this softening in the literature. We therefore take this opportunity to speculate on it, in the particular case of granitoid mylonite zones.

Consider the case of a shear zone in the greenschist metamorphic facies, that is, in the temperature range of approximately 300–450 °C. Under those conditions, quartz can flow plastically and feldspar cannot. Thus, the material we are trying to shear is composed mainly (say 70–80%) of feldspar, which behaves as a hard strong brittle material, with the rest consisting of quartz and some other ductile minerals like mica, which behave as ductile and relatively soft components.

The question is what controls the strength, the strong component or the weak component? This depends on the rock fabric: the way the different components are arranged (Jordan, 1988). The starting granite has an igneous fabric; the quartz grains are arranged tightly and randomly in the interstices between the more frequent feldspar grains. In this state, the feldspar determines the strength of the rock, just as the sand and gravel determines the strength of concrete, rather than the soft mortar, which only serves to hold the aggregate together. All the forces in the material are being transmitted between the contacts of the hard grains.

Once shearing begins, the mylonitic fabric begins to be developed, which changes the ordering of the mineral phases. The ductile minerals, quartz and mica, form undulous sheets between layers of feldspar (such sheets being called 'quartz ribbons' because of their appearance in thin section). Almost all subsequent deformation of the rock takes place on these quartz sheets: after an initial period of cataclastis, the feldspars, often forming augen, act as rigid particles. Thus, the strength of the rock will decrease progressively as the mylonitic fabric develops and rotates toward the plane of shear, on which it

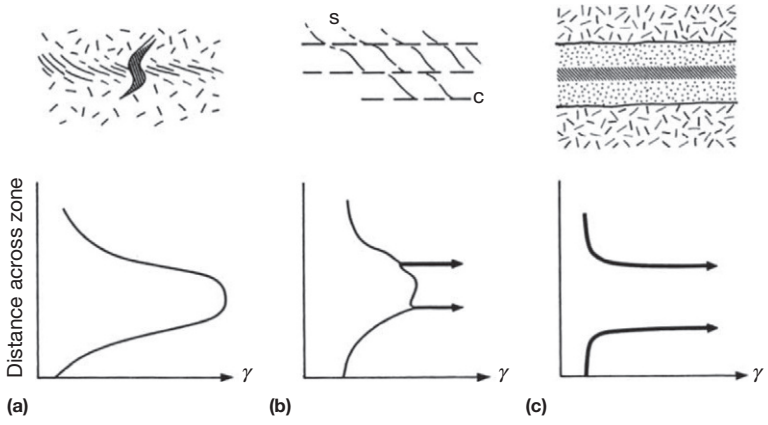

Figure 48 Rotation of fabric elements and shear strain in three types of shear zones. (a) Mylonite zone, (b) S–C mylonite zone, and (c) cataclasite zone. Reproduced from Scholz CH (2002) *The Mechanics of Earthquakes and Faulting*, 2nd edn. Cambridge: Cambridge University Press.

will have the greatest resolved shear stress. So, although this softening occurs with increase in shear strain, it should be more properly called fabric softening rather than strain softening.

It has also been observed, however, that mylonite zones, like brittle fault zones, widen with net shear across them (Hull, 1988). This is a form of strain delocalization, which implies some sort of hardening mechanism. The shear zone is widening by adding new mylonite from its boundaries as net shear increases. This presumable means the high-strain mylonites in the center of the shear zone have hardened and can no longer provide sufficient strain (Means, 1984). This may be strain hardening of the usual type, produced by high dislocation density.

In the few cases where one can trace a ductile shear zone with depth, it is usually found that it broadens with depth (Bak et al., 1975a,b). The Nagssugtoqidian shear zone in Greenland, for example, reported to have a strike-slip shear offset in the 100 km range, is almost 25 km wide in the granulite facies depth range (Bak et al., 1975a,b). This broadening may result from the effect of increasing temperature in weakening and making the mylonites less fabric softening.

6.10.7.5 Synoptic Model for Faults and Shear Zones

A model that illustrates many properties of fault zones is shown in **Figure 49** (Scholz, 1988). The temperature-depth scale is based on the geotherm measured for the SAF and hence may differ in other regions. A granitic protolith is assumed. The left panel shows the expected fault rocks, ranging from cataclasites in the upper, seismically active region to mylonites below the onset of quartz plasticity at ~11 km.

Pseudotachylytes occur in the lower part of the former region and the upper part of the latter. Although mylonites are formed within the Greenschist regime, the rock there flows in a semibrittle manner: full plasticity does not occur until feldspar begins flowing in the upper part of amphibolite metamorphism (Simpson, 1985). Thus, the strength profile on the right panel does not show the typical parrot beak shape obtained by extrapolating laboratory plasticity data from high temperature (e.g., Brace and Kohlstedt, 1980). The inner panel indicates the seismic behavior interpreted from rate/state variable friction laws. Earthquakes can only nucleate within the unstable region where the friction parameter $A–B$ is negative. They can, however, dynamically rupture shallower or deeper than that. Thus, there is a region of alternating plasticity and seismic slip just below the nucleation zone. For more discussion, see Scholz (2002).

6.10.8 The Strength of Faults

Faults are, of course, planes of weakness in the crust. The strength of a fault $\sigma_f = \mu(\sigma_n - p)$ may be calculated as a function of depth provided that we know the correct value of friction coefficient μ and pore pressure p. In this section, we will examine evidence pertaining to these parameters.

6.10.8.1 Direct Evidence for Fault Strength

The only direct evidence for the absolute value of fault strength comes from stress measurements made in deep (>1 km) boreholes in the crystalline basement. Results from the deepest of these, the KTB borehole in Germany (Brudy et al., 1997), are shown in **Figure 50**. They indicate that shear stress increases with depth consistent with a friction coefficient of $\mu = 0.65$ and that pore pressure is hydrostatic at all depths. This same result has universally been found in all deep borehole measurements, which have been made in a variety of tectonic settings: extensional, compressional, transcurrent, plate boundary, and intraplate (Lund and Zoback, 1999; McGarr and Gay, 1978; McGarr et al., 1982; Shamir and Zoback, 1992; Townend and Zoback, 2000, 2001; Zoback and Harjes, 1997; Zoback and Healy, 1984, 1992; Zoback et al., 1980).

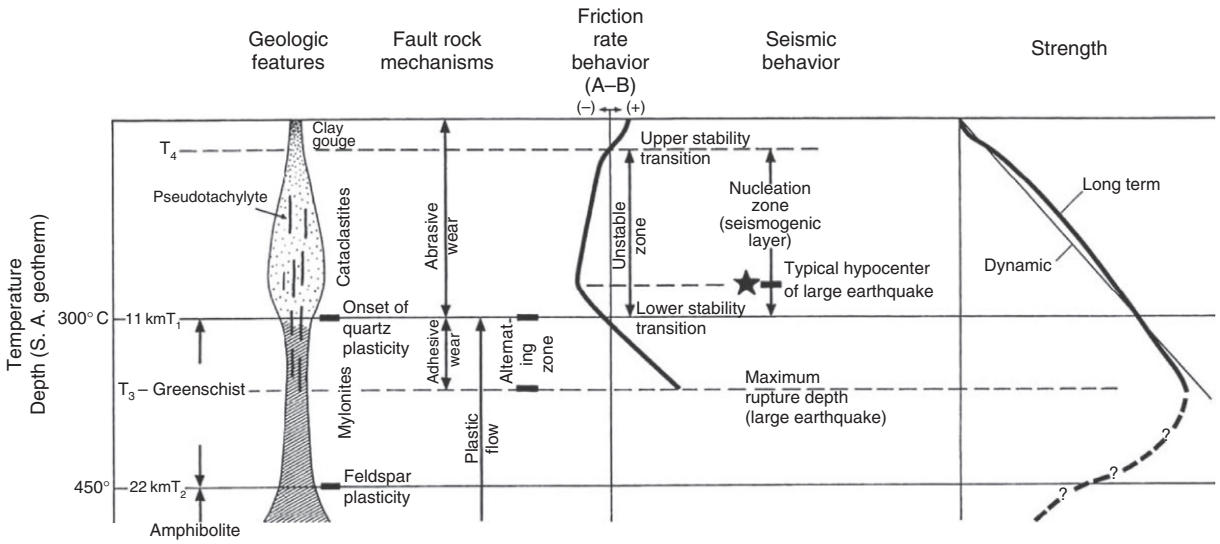

Figure 49 Synoptic fault model. See text for discussion. Reproduced from Scholz CH (1988) The brittle–plastic transition and the depth of seismic faulting. *Geologische Rundschau* 77: 319–328.

The straightforward interpretation of these results is that stresses in the continental crust are limited by the ubiquitous presence of favorably oriented faults with friction $0.6 \leq \mu \leq 0.7$. This hypothesis was verified by a fluid injection test near the bottom of the KTB hole that produced microearthquake activity with induced pore pressures of only 1% of the ambient stresses (Zoback and Harjes, 1997).

This value of μ agrees with laboratory measurements (Byerlee, 1978). It is quite expected that the friction coefficient should be the same on the field- and laboratory-scale. Friction is scale-independent (Amonton's first law) and it is independent of lithology (Byerlee, 1978) and temperature (Blanpied et al., 1995), up to the onset of plasticity.

That pore pressure is hydrostatic in the crystalline rock of the crust is a consequence of the high permeability of the crust resulting from the presence of faults (Townend and Zoback, 2000). This simple result, that is, the strength of the crust is determined by Byerlee's law with hydrostatic pore pressures, thus comes as no surprise (except to seismologists, who from the time of Tsuboi (1933) had believed that the strength of faults was the stress drop of earthquakes, $\sim$10 MPa). This result is consistent with the orientation of active faults with respect to σ_1, as shown in **Figure 42**.

Information regarding the strength of faults relative to the surrounding crust can be obtained from stress orientation data. If a fault is very weak with respect to the surrounding crust, then it will act as a principal plane and then σ_1 must rotate, within several fault depths, to near perpendicularity with it. On the other hand, if the fault strength is comparable with the surrounding crust, then σ_1 must rotate in the opposite manner and approach the fault at an angle less than the lockup angle, which for $\mu = 0.6$ is 60°. Hardebeck and Hauksson (1999) did this exercise for all of southern California. They found that the strong fault sense of stress rotation prevailed at all crossing of the faults of the San Andreas Fault system. An example is shown in **Figure 51**. Unfortunately, they misinterpreted their data. The correct interpretation was given by Scholz (2000).

Stress measurements from paleopiezometers such as dislocation density indicate that shear stresses of order 100 MPa also are typical of ductile shear zones beneath the seismogenic zone (Kohlstedt and Weathers, 1980). At the Stack of Glencoul on the Moine thrust, the differential stress remains constant with distance for 100 m from the fault even though strain increases greatly as the center of the shear zone is approached (Weathers et al., 1979). Unfortunately, for the past 35 years, a pall of controversy has been cast over this topic, which has been more misleading than illuminating.

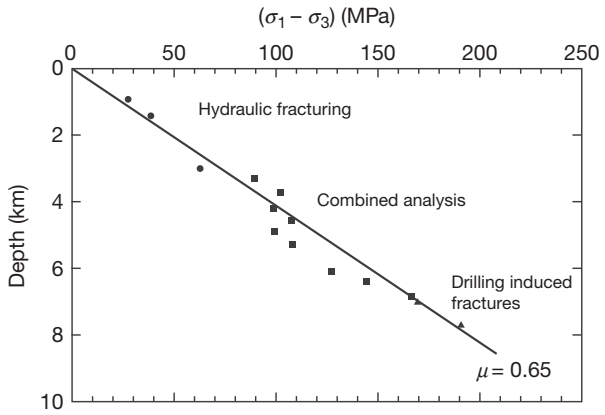

Figure 50 Stress as a function of depth in the KTB borehole in Germany. Line is the predicted stress for a friction of $\mu = 0.65$. Modified from Brudy M, Zoback MD, Fuchs K, Rummel F, and Baumgartner J (1997) Estimation of the complete stress tensor to 8 km depth in the KTB scientific drill holes: Implications for crustal strength. *Journal of Geophysical Research Solid Earth* 102: 18453–18475.

6.10.8.2 The Weak SAF Fallacy

Brune et al. (1969) measured heat flow in a profile across the SAF in the Mojave sector and no sign of a heat flow anomaly centered on the fault of the type expected if heat transport was by conduction. They concluded that the shear stress on the fault could not be greater than that necessary to account for the stress drop in earthquakes, $\sim$20 MPa, in accord with the traditional seismological belief.

Explaining this so-called San Andreas heat flow paradox became a major research program in the United States. It has been, however, a singularly unsuccessful one: no explanation for a weak SAF has been proposed that is not either internally contradictory or inconsistent with observations.

Proponents of the weak SAF hypothesis brush aside the borehole stress measurements discussed earlier in the text with the argument that it is only well-developed faults like the SAF that are weak, without defining the term 'well developed' in a manner that can be tested. The stress orientation data mentioned in the preceding text (Scholz, 2000) are dismissed with the argument that the lack of a heat flow anomaly is definitive (Zoback, 2000).

To be sure, if there is friction, there must be heat generated. But to say that there is no heat flow anomaly associated with the SAF is incorrect. There is in fact a pronounced heat flow

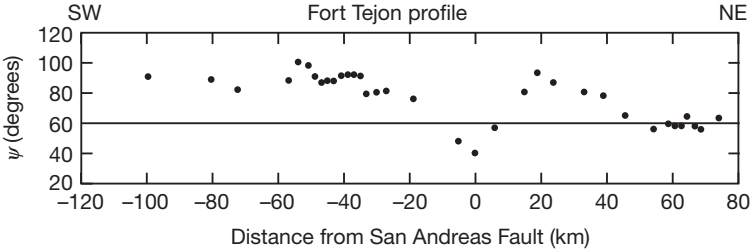

Figure 51 Angle between σ_1 and the SAF in a profile across the fault in the vicinity of Fort Tejon. Reproduced from Scholz CH (2000) Evidence for a strong San Andreas fault. *Geology* 28: 163–166.

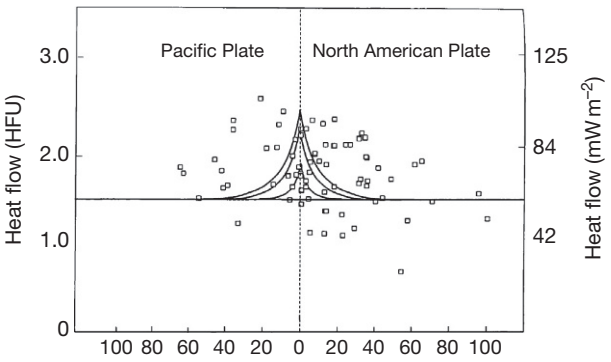

Figure 52 Heat flow data projected onto a profile perpendicular to the SAF. They are compared with the prediction of models of conductive heating from fault friction. Modified from Lachenbruch A and Sass J (1980) Heat flow and energetics of the San Andreas fault zone. *Journal of Geophysical Research* 85: 6185–6222.

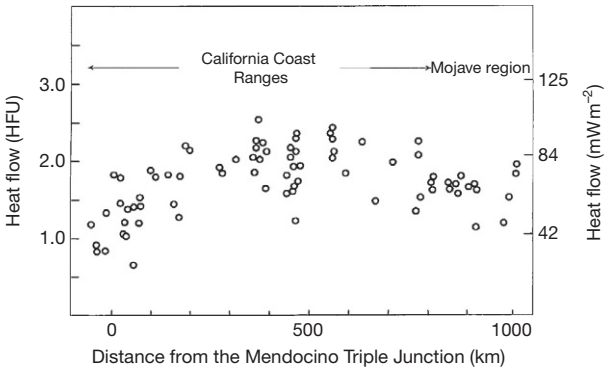

Figure 53 The heat flow data projected along strike of the SAF. Modified from Lachenbruch A and Sass J (1980) Heat flow and energetics of the San Andreas fault zone. *Journal of Geophysical Research* 85: 6185–6222.

anomaly associated with the SAF, shown in **Figures 52** and **53** (Lachenbruch and Sass, 1980). **Figure 52** shows the data projected onto a profile across the fault. A conductive anomaly is drawn for comparison: this certainly does not match the data, which show a much broader anomaly. **Figure 53** shows the data projected along strike. Its most striking feature is its smooth decrease to zero as the Mendocino Triple Junction is approached.

The SAF has been propagating to the north for the past 30 my (Atwater, 1970), and its northern tip has just reached Cape Mendocino, where it has zero age and displacement. If frictional work is what generates the heat in the anomaly in **Figure 53**, then its decrease as Cape Mendocino is approached is just what is expected. The other mechanisms proposed to explain this (Lachenbruch and Sass, 1980) have failed the test of time (Scholz and Hanks, 2004).

The fallacy in the weak SAF hypothesis is the assumption that conduction is the mechanism of heat transport. There is no known crustal-scale conductive heat flow anomaly. The crust is simply too permeable to support one. The thermal generating power of the fault is τv, the shear stress times the sliding velocity. The conduction models such as Brune et al. (1969) are steady-state models that assume that v is 34 mm year^{-1}, the geologic slip rate of the SAF. However, the SAF does not slip this way but at $v \sim 1$ ms^{-1} for several seconds every 150 years or so, a thermal flux 10^9 times higher. It is hard to imagine that this heat would not be advected by transport of water away from the fault at depth, where the stresses are highest.

The reader should be aware that the arguments expressed in this section represent the author's opinions and they are distinctively in the minority at present. For a more detailed discussion of this entire issue, see Scholz and Hanks (2004) and Scholz (2006).

References

Abercrombie RE, Webb TH, Robinson R, McGinty PJ, Mori JJ, and Beavan RJ (2000) The enigma of the Arthur's Pass, New Zealand, earthquake 1. Reconciling a variety of data for an unusual earthquake sequence. *Journal of Geophysical Research, Solid Earth* 105: 16119–16137.

Ackermann RV and Schlische RW (1997) Anticlustering of small normal faults around larger faults. *Geology* 25: 1127–1130.

Ackermann RV, Schlische RW, and Withjack MO (2001) The geometric and statistical evolution of normal fault systems: An experimental study of the effects of mechanical layer thickness on scaling laws. *Journal of Structural Geology* 23: 1803–1819.

Adams FD (1938) *The Growth and Development of the Geological Sciences*. Baltimore, MD: Williams & Wilkins.

Allen JL (2005) A multi-kilometer pseudotachylyte system as an exhumed record of earthquake rupture geometry at hypocentral depths (Colorado, USA). *Tectonophysics* 402: 37–54.

Al-zoubi A and ten Brink U (2002) Lower crustal flow and the role of shear in basin subsidence: An example from the Dead Sea basin. *Earth and Planetary Science Letters* 199: 67–79.

Anders MH and Wiltschko DV (1994) Microfracturing, paleostress and the growth of faults. *Journal of Structural Geology* 16: 795–815.

Anderson EM (1905) The dynamics of faulting. *Transactions of the Edinburgh Geological Society* 8: 340–387.

Anderson EM (1936) The dynamics of the formation of cone-sheets, ring-dykes, and cauldron-subsidences. *Proceedings of the Royal Society of Edinburgh* 56: 125–128.

Anderson EM (1951) *The Dynamics of Faulting*, 2nd edn. Edinburgh, UK: Oliver and Boyd.

Atkinson BK (ed.) (1987) Introduction to fracture mechanics and its geophysical applications. In: *Fracture Mechanics of Rock*, pp. 1–26. London: Academic Press.

Atwater T (1970) Implications of plate tectonics for the Cenozoic tectonic evolution of western North America. *Geological Society of America Bulletin* 81: 3513–3536.

Aydin A and Johnson AM (1978) Development of faults as zones of deformation bands and as slip surfaces in sandstone. *Advances in Applied Mechanics* 116: 922–929.

Aydin A and Nur A (1982) Evolution of pull-apart basins and their scale independence. *Tectonics* 1: 91–105.

Bak J, Korstgard J, and Sorensen K (1975a) Major shear zone within Nagssugtoqidian of West Greenland. *Tectonophysics* 27: 191–209.

Bak J, Sorensen K, Grocott J, Korstgard JA, Nash D, and Watterson J (1975b) Tectonic implications of precambrian shear belts in Western Greenland. *Nature* 254: 566–569.

Barenblatt GI (1962) The mathematical theory of equilibrium cracks in brittle fracture. *Advances in Applied Mechanics* 7: 55–80.

Blanpied ML, Lockner DA, and Byerlee JD (1995) Frictional slip of granite at hydrothermal conditions. *Journal of Geophysical Research, Solid Earth* 100: 13045–13064.

Bourne SJ, Arnadottir T, Beavan J, et al. (1998a) Crustal deformation of the Marlborough fault zone in the South Island of New Zealand: Geodetic constraints over the interval 1982–1994. *Journal of Geophysical Research, Solid Earth* 103: 30147–30165.

Bourne SJ, England PC, and Parsons B (1998b) The motion of crustal blocks driven by flow of the lower lithosphere and implications for slip rates of continental strike-slip faults. *Nature* 391: 655–659.

Brace WF and Kohlstedt D (1980) Limits on lithospheric stress imposed by laboratory experiments. *Journal of Geophysical Research* 85: 6248–6252.

Brudy M, Zoback MD, Fuchs K, Rummel F, and Baumgartner J (1997) Estimation of the complete stress tensor to 8 km depth in the KTB scientific drill holes: Implications for crustal strength. *Journal of Geophysical Research, Solid Earth* 102: 18453–18475.

Brune J, Henyey T, and Roy R (1969) Heat flow, stress, and rate of slip along the San Andreas fault, California. *Journal of Geophysical Research* 74: 3821–3827.

Buck WR (1988) Flexural rotation of normal faults. *Tectonics* 7: 959–973.

Bull JM, Barnes PM, Lamarche G, et al. (2006) High-resolution record of displacement accumulation on an active normal fault: Implications for models of slip accumulation during repeated earthquakes. *Journal of Structural Geology* 28: 1146–1166.

Burgmann R and Pollard DD (1994) Strain accommodation about strike-slip-fault discontinuities in granitic rock under brittle-to-ductile conditions. *Journal of Structural Geology* 16: 1655–1674.

Burgmann R, Pollard DD, and Martel SJ (1994) Slip distributions on faults – Effects of stress gradients, inelastic deformation, heterogeneous host-rock stiffness, and fault interaction. *Journal of Structural Geology* 16: 1675–1690.

Burroughs SM and Tebbens SF (2001) Upper-truncated power laws in natural systems. *Pure and Applied Geophysics* 158: 741–757.

Byerlee JD (1978) Friction of rocks. *Pure and Applied Geophysics* 116: 615–626.

Byerlee JD and Savage JC (1992) Coulomb plasticity within the fault zone. *Geophysical Research Letters* 19: 2341–2344.

Camacho A, Vernon RH, and Fitz Gerald JD (1995) Large volumes of anhydrous pseudotachylyte in the Woodroffe Thrust, Eastern Musgrave Ranges, Australia. *Journal of Structural Geology* 17: 371–383.

Campagna DJ and Aydin A (1991) Tertiary uplift and shortening in the basin and range – The Echo Hills, Southeastern Nevada. *Geology* 19: 485–488.

Cartwright JA and Mansfield CS (1998) Lateral displacement variation and lateral tip geometry of normal faults in the Canyonlands National Park, Utah. *Journal of Structural Geology* 20: 3–19.

Chernyshev SN and Dearman WR (1991) *Rock Fractures*. London: Butterworth-Heinemann.

Chester FM and Chester JS (1998) Ultracataclasite structure and friction processes of the Punchbowl fault, San Andreas system, California. *Tectonophysics* 295: 199–221.

Chester FM, Chester JS, Kirschner DL, Schulz SE, and Evans JP (2004) Structure of large-displacement strike-slip fault zones in the brittle continental crust. In: Karner G, Taylor B, Driscoll N, and Kohlstedt D (eds.) *Rheology and Deformation of the Lithosphere at Continental Margins*, pp. 223–260. New York: Columbia University Press.

Chester JS, Chester FM, and Kronenberg AK (2005) Fracture surface energy of the Punchbowl fault, San Andreas system. *Nature* 437: 133–136.

Chester FM, Evans JP, and Biegel RL (1993) Internal structure and weakening mechanisms of the San Andreas fault. *Journal of Geophysical Research, Solid Earth* 98: 771–786.

Chester FM and Logan JM (1986) Implications for mechanical properties of brittle faults from observations of the Punchbowl fault zone, California. *Pure and Applied Geophysics* 124: 79–106.

Cladouhos TT and Marrett R (1996) Are fault growth and linkage models consistent with power-law distributions of fault lengths? *Journal of Structural Geology* 18: 281–293.

Contreras J, Anders MH, and Scholz CH (2000) Growth of a normal fault system: Observations from the Lake Malawi basin of the east African rift. *Journal of Structural Geology* 22: 159–168.

Cowie PA, Knipe RJ, and Main IG (1996) Special issue: Scaling laws for fault and fracture populations – Analyses and applications – Introduction. *Journal of Structural Geology* 18: R5–R11.

Cowie PA and Scholz CH (1992a) Physical explanation for the displacement–length relationship of faults using a post-yield fracture mechanics model. *Journal of Structural Geology* 14: 1133–1148.

Cowie PA and Scholz CH (1992b) Displacement–length scaling relationship for faults: Data synthesis and discussion. *Journal of Structural Geology* 14: 1149–1156.

Cowie PA, Scholz CH, Edwards M, and Malinverno A (1993) Fault strain and seismic coupling on midocean ridges. *Journal of Geophysical Research, Solid Earth* 98: 17911–17920.

Cowie PA and Shipton ZK (1998) Fault tip displacement gradients and process zone dimensions. *Journal of Structural Geology* 20: 983–997.

Cowie PA, Sornette D, and Vanneste C (1995) Multifractal scaling properties of a growing fault population. *Geophysical Journal International* 122: 457–469.

Cowie PA, Underhill JR, Behn MD, Lin J, and Gill CE (2005) Spatio-temporal evolution of strain accumulation derived from multiscale observations of Late Jurassic rifting in the northern North Sea: A critical test of models for lithospheric extension. *Earth and Planetary Science Letters* 234: 401–419.

Crider JG and Pollard DD (1998) Fault linkage: Three-dimensional mechanical interaction between echelon normal faults. *Journal of Geophysical Research, Solid Earth* 103: 24373–24391.

Das S and Scholz CH (1981) Off-fault aftershock clusters caused by shear stress increase? *Bulletin of the Seismological Society of America* 71: 1669–1675.

Dawers NH and Anders MH (1995) Displacement–length scaling and fault linkage. *Journal of Structural Geology* 17: 607–614.

Dawers NH, Anders MH, and Scholz CH (1993) Growth of normal faults: Displacement–length scaling. *Geology* 21: 1107–1110.

Di Toro G, Nielsen S, and Pennacchioni G (2005a) Earthquake rupture dynamics frozen in exhumed ancient faults. *Nature* 436: 1009–1012.

Di Toro G and Pennacchioni G (2005) Fault plane processes and mesoscopic structure of a strong-type seismogenic fault in tonalites (Adamello batholith, Southern Alps). *Tectonophysics* 402: 55–80.

Di Toro G, Pennacchioni G, and Teza G (2005b) Can pseudotachylytes be used to infer earthquake source parameters? An example of limitations in the study of exhumed faults. *Tectonophysics* 402: 3–20.

Dooley T and Mcclay K (1997) Analog modeling of pull-apart basins. *American Association of Petroleum Geologists Bulletin* 81: 1804–1826.

Dugdale DSJ (1960) Yielding of steel sheets containing slits. *Journal of the Mechanics and Physics of Solids* 8: 100–115.

Edwards MA and Ratschbacher L (2005) Seismic and aseismic weakening effects in transtension: Field and microstructural observations on the mechanics and architecture of a large fault zone in SE Tibet. In: Bruhn D and Burlini L (eds.) *High-Strain Zones: Structure and Physical Properties*, pp. 109–141. London: The Geological Society of London.

Evans JP (1990) Thickness displacement relationships for fault zones. *Journal of Structural Geology* 12: 1061–1065.

Faulkner DR, Lewis AC, and Rutter EH (2003) On the internal structure and mechanics of large strike-slip fault zones: Field observations of the Carboneras Fault in southeastern Spain. *Tectonophysics* 367: 235–251.

Grocott J (1981) Fracture geometry of pseudotachylyte generation zones: A study of shear fractures formed during seismic events. *Journal of Structural Geology* 3: 169–178.

Gupta A and Scholz CH (2000a) A model of normal fault interaction based on observations and theory. *Journal of Structural Geology* 22: 865–879.

Gupta A and Scholz CH (2000b) Brittle strain regime transition in the Afar depression: Implications for fault growth and seafloor spreading. *Geology* 28: 1087–1090.

Hanmer S, Williams M, and Kopf C (1995) Modest movements, spectacular fabrics in an intracontinental deep-crustal strike-slip fault: Striding-Athabasca mylonite zone, NW Canadian Shield. *Journal of Structural Geology* 17: 493–507.

Hardebeck JL and Hauksson E (1999) Role of fluids in faulting inferred from stress field signatures. *Science* 285: 236–239.

Henstock TJ, Levander A, and Hole JA (1997) Deformation in the lower crust of the San Andreas fault system in northern California. *Science* 278: 650–653.

Hu MS and Evans AG (1989) The cracking and decohesion of thin-films on ductile substrates. *Acta Metallurgica* 37: 917–925.

Hubbert MK and Rubey WW (1959) Role of fluid pressure in the mechanics of overthrust faulting. *Bulletin of the Geological Society of America* 70: 115–166.

Hull J (1988) Thickness–displacement relationships for deformation zones. *Journal of Structural Geology* 10: 431–435.

Jackson JA (1987) Active normal faulting and crustal extension. In: Coward M, Dewey J, and Hancock P (eds.) *Continental Extensional Tectonics*, pp. 3–18. London: Blackwell.

Jordan P (1988) The rheology of polymineralic rocks – An approach. *Geologische Rundschau* 77: 285–294.

Kanninen MF and Popelar CH (1985) *Advanced Fracture Mechanics*. Oxford: Oxford University Press.

Kawamoto E and Shimamoto T (1998) The strength profile for bimineralic shear zones: An insight from high-temperature shearing experiments on calcite–halite mixtures. *Tectonophysics* 295: 1–14.

Kendrick KJ, Morton DM, Wells SG, and Simpson RW (2002) Spatial and temporal deformation along the northern San Jacinto fault, southern California: Implications for slip rates. *Bulletin of the Seismological Society of America* 92: 2782–2802.

Kohlstedt DL and Weathers MS (1980) Deformation-induced microstructures, paleopiezometers, and differential stresses in deeply eroded fault zones. *Journal of Geophysical Research* 85: 6269–6285.

Kostrov B (1974) Seismic moment and energy of earthquakes, and seismic flow of rock. *Izvestiya, Academy of Sciences, USSR Physics, Solid Earth* 1: 23–40.

Lachenbruch A and Sass J (1980) Heat flow and energetics of the San Andreas fault zone. *Journal of Geophysical Research* 85: 6185–6222.

Lawn BR and Wilshaw TR (1975) *Fracture of Brittle Solids*. Cambridge: Cambridge University Press.

Lin AM, Maruyama T, Aaron S, Michibayashi K, Camacho A, and Kano KI (2005) Propagation of seismic slip from brittle to ductile crust: Evidence from pseudotachylyte of the Woodroffe thrust, central Australia. *Tectonophysics* 402: 21–35.
Lister G and Snoke A (1984) S-C mylonites. *Journal of Structural Geology* 6: 617–638.
Lister GS and Williams PF (1979) Fabric development in shear zones: Theoretical controls and observed phenomena. *Journal of Structural Geology* 1: 283–297.
Lockner DA, Byerlee JD, Kuksenko V, Ponomarev A, and Sidorin A (1991) Quasi-static fault growth and shear fracture energy in granite. *Nature* 350: 39–42.
Lockner DA, Byerlee JD, Kuksenko V, Ponomarev A, and Sidorin A (1992) Observations of quasistatic fault growth from acoustic emissions. In: Evans B and Wong T-F (eds.) *Fault Mechanics and Transport Properties of Rock*, pp. 3–32. San Diego, CA: Academic Press.
Lund B and Zoback MD (1999) Orientation and magnitude of in situ stress to 6.5 km depth in the Baltic Shield. *International Journal of Rock Mechanics and Mining Science* 36: 169–190.
Lyell C (1832) *Principles of Geology*. London: J. Murray.
Mair K, Main I, and Elphick S (2000) Sequential growth of deformation bands in the laboratory. *Journal of Structural Geology* 22: 25–42.
Manighetti I, King GCP, Gaudemer Y, Scholz CH, and Doubre C (2001) Slip accumulation and lateral propagation of active normal faults in Afar. *Journal of Geophysical Research, Solid Earth* 106: 13667–13696.
Manighetti I, King G, and Sammis CG (2004) The role of off-fault damage in the evolution of normal faults. *Earth and Planetary Science Letters* 217: 399–408.
Marone C and Scholz CH (1989) Particle-size distribution and microstructures within simulated fault gouge. *Journal of Structural Geology* 11: 799–814.
Marrett R and Allmendinger RW (1991) Estimates of strain due to brittle faulting: Sampling of fault populations. *Journal of Structural Geology* 13: 735–738.
Martel SJ (1999) Mechanical controls on fault geometry. *Journal of Structural Geology* 21: 585–596.
Martel SJ and Pollard DD (1989) Mechanics of slip and fracture along small faults and simple strike-slip-fault zones in granitic rock. *Journal of Geophysical Research* 94: 9417–9428.
Martel SJ, Pollard DD, and Segall P (1988) Development of simple strike-slip-fault zones, Mount Abbot quadrangle, Sierra-Nevada, California. *Geological Society of America Bulletin* 100: 1451–1465.
Mcclay K and Bonora M (2001) Analog models of restraining stepovers in strike-slip fault systems. *American Association of Petroleum Geologists Bulletin* 85: 233–260.
McGarr A and Gay NC (1978) State of stress in the Earth's crust. *Annual Review of Earth and Planetary Science* 6: 405–436.
McGarr A, Zoback MD, and Hanks TC (1982) Implications of an elastic analysis of *in situ* stress measurements near the San Andreas fault. *Journal of Geophysical Research* 87: 7797–7806.
Means WD (1984) Shear zones of type I and II and their significance for reconstructing rock history. *Geological Society of America Abstract with Programs* 16: 50.
Moore DE and Lockner DA (1995) The role of microcracking in shear-fracture propagation in granite. *Journal of Structural Geology* 17: 95–114.
Nakamura K (1969) Arrangement of parasitic cones as a possible key to a regional stress field. *Bulletin of the Volcanology Society of Japan* 14: 8–20.
Nakamura K, Shimazaki K, and Yonekura N (1984) Subduction, bending, and education. Present and quaternary tectonics of the northern border of the Philippine Sea plate. *Bulletin de la Societe Geologique de France* 26: 221–243.
Pachell MA and Evans JP (2002) Growth, linkage, and termination processes of a 10-km-long strike-slip fault in jointed granite: The Gemini fault zone, Sierra Nevada, California. *Journal of Structural Geology* 24: 1903–1924.
Parsons T (1998) Seismic-reflection evidence that the Hayward fault extends into the lower crust of the San Francisco Bay Area, California. *Bulletin of the Seismological Society of America* 88: 1212–1223.
Passchier C (1984) The generation of ductile and brittle defommation bands in a low-angle mylonite zone. *Journal of Structural Geology* 6: 273–281.
Peacock DCP (1991) Displacements and segment linkage in strike-slip-fault zones. *Journal of Structural Geology* 13: 1025–1035.
Peacock DCP and Sanderson DJ (1994) Geometry and development of relay ramps in normal-fault systems. *American Association of Petroleum Geologists Bulletin* 78: 147–165.
Pollard DD and Segall P (1987) Theoretical displacements and stresses near fractures in rock: With applications to faults, joints, dikes, and solution surfaces. In: Atkinson BK (ed.) *Fracture Mechanics of Rock*, pp. 277–348. London: Academic Press.
Price NJ (1966) *Fault and Joint Development in Brittle and Semi-Brittle Rock*. Oxford: Pergamon.
Sammis CG, Osborne R, Anderson J, Banerdt M, and White P (1986) Self-similar cataclasis in the formation of fault gouge. *Pure and Applied Geophysics* 124: 53–78.
Savage JC, Svarc JL, and Prescott WH (2004) Interseismic strain and rotation rates in the northeast Mojave domain, eastern California. *Journal of Geophysical Research, Solid Earth* 109. http://dx.doi.org/10.1029/2003JB002705.
Schlische RW, Young SS, Ackermann RV, and Gupta A (1996) Geometry and scaling relations of a population of very small rift-related normal faults. *Geology* 24: 683–686.
Scholz CH (1968a) Microfracturing and the inelastic deformation of rock in compression. *Journal of Geophysical Research* 73: 1417–1432.
Scholz CH (1968b) Experimental study of the fracturing process in brittle rock. *Journal of Geophysical Research* 73: 1447–1454.
Scholz CH (1982) Scaling laws for large earthquakes: Consequences for physical models. *Bulletin of the Seismological Society of America* 72: 1–14.
Scholz CH (1987) Wear and gouge formation in brittle faulting. *Geology* 15: 493–495.
Scholz CH (1988) The brittle–plastic transition and the depth of seismic faulting. *Geologische Rundschau* 77: 319–328.
Scholz CH (1997) Earthquake and fault populations and the calculation of brittle strain. *Geowissenshaften* 15: 124–130.
Scholz CH (2000) Evidence for a strong San Andreas fault. *Geology* 28: 163–166.
Scholz CH (2002) *The Mechanics of Earthquakes and Faulting*, 2nd edn Cambridge: Cambridge University Press.
Scholz CH (2006) The strength of the San Andreas Fault: A critical analysis. In: Abercrombie R, McGarr A, Kanamori H, and Toro GD (eds.) *Radiated Energy and the Physics of Earthquake Faulting*. Washington, DC: American Geophysical Union.
Scholz CH and Contreras JC (1998) Mechanics of continental rift architecture. *Geology* 26: 967–970.
Scholz CH and Cowie PA (1990) Determination of total strain from faulting using slip measurements. *Nature* 346: 837–839.
Scholz CH, Dawers NH, Yu JZ, and Anders MH (1993) Fault growth and fault scaling laws: Preliminary results. *Journal of Geophysical Research, Solid Earth* 98: 21951–21961.
Scholz CH and Hanks TC (2004) The strength of the San Andreas fault: A discussion. In: Karner GD, Taylor B, Driscoll NW, and Kohlstedt DL (eds.) *Rheology and Deformation of the Lithosphere at Continental Margins*, pp. 261–283. New York: Columbia University Press.
Scholz CH and Lawler TM (2004) Slip tapers at the tips of faults and earthquake ruptures. *Geophysical Research Letters* 31: L21609.
Shamir G and Zoback MD (1992) Stress orientation profile to 3.5 km depth near the San Andreas fault at Cajon Pass, California. *Journal of Geophysical Research* 97: 5059–5080.
Shipton ZK and Cowie PA (2001) Damage zone and slip-surface evolution over μm to km scales in high-porosity Navajo sandstone, Utah. *Journal of Structural Geology* 23: 1825–1844.
Sibson RH (1975) Generation of pseudotachylyte by ancient seismic faulting. *Geophysical Journal of the Royal Astronomical Society* 43: 775–794.
Sibson RH (1985) A note on fault reactivation. *Journal of Structural Geology* 7: 751–754.
Sibson RH (2003) Thickness of the seismic slip zone. *Bulletin of the Seismological Society of America* 93: 1169–1178.
Sibson RH, Roberts F, and Poulsen KH (1988) High-angle reverse faults, fluid pressure cycling, and mesothermal gold-quartz deposits. *Geology* 16: 551–555.
Sibson RH and Xie GY (1998) Dip range for intracontinental reverse fault ruptures: Truth not stranger than friction? *Bulletin of the Seismological Society of America* 88: 1014–1022.
Sigmundsson F, Einarsson P, Bilham R, and Sturkell E (1995) Rift-transform kinematics in south Iceland: Deformation from global positioning system measurements, 1986 to 1992. *Journal of Geophysical Research, Solid Earth* 100: 6235–6248.
Simpson C (1985) Deformation of granitic rocks across the brittle–ductile transition. *Journal of Structural Geology* 5: 503–512.
Simpson C and Schmid SM (1983) An evaluation of criteria to deduce the sense of movement in sheared rock. *Geological Society of America Bulletin* 94: 1281–1288.
Smithson SB, Brewer J, Kaufman S, Oliver J, and Hurich C (1978) Nature of wind river thrust, Wyoming, from cocorp deep-reflection data and from gravity data. *Geology* 6: 648–652.
Snoke AW, Tullis J, and Todd VR (1998) *Fault-Related Rocks*. Princeton, NJ: Princeton University Press.
Soliva R, Benedicto A, and Maerten L (2006) Spacing and linkage of confined normal faults: Importance of mechanical thickness. *Journal of Geophysical Research, Solid Earth* 111: B01402. http://dx.doi.org/10.1029/2004JB003507.
Somerville P (1978) The accommodation of plate collision by deformation in the Izu block, Japan. *Bulletin of the Earthquake Research Institute, University of Tokyo* 53: 629–648.

Sowers JM, Unruh JR, Lettis WR, and Rubin TD (1994) Relationship of the Kickapoo Fault to the Johnson Valley and Homestead Valley Faults, San-Bernardino County, California. *Bulletin of the Seismological Society of America* 84: 528.

Spyropoulos C, Griffith WJ, Scholz CH, and Shaw BE (1999) Experimental evidence for different strain regimes of crack populations in a clay model. *Geophysical Research Letters* 26: 1081–1084.

Spyropoulos C, Scholz CH, and Shaw BE (2002) Transition regimes for growing crack populations. *Physical Review E* 65: 056105. http://dx.doi.org/10.1103/PhysRevE.65.056105.

Stephenson WJ, Odum JK, Williams RA, and Anderson ML (2002) Delineation of faulting and basin geometry along a seismic reflection transect in urbanized San Bernardino Valley, California. *Bulletin of the Seismological Society of America* 92: 2504–2520.

Swanson MT (1988) Pseudotachylyte-bearing strike-slip duplex structures in the Fort Foster Brittle Zone, S Maine. *Journal of Structural Geology* 10: 813–828.

Tapponnier P, Armijo R, Manighetti I, and Courtillot V (1990) Bookshelf faulting and horizontal block rotations between overlapping rifts in Southern Afar. *Geophysical Research Letters* 17: 1–4.

Townend J and Zoback MD (2000) How faulting keeps the crust strong. *Geology* 28: 399–402.

Townend J and Zoback MD (2001) Implications of earthquake focal mechanisms for the frictional strength of the San Andreas fault system. In: Holsworth RE (ed.) *Geological Society of London Spec. Publication 186: The Nature and Tectonic Significance of Fault Zone Weakening*, pp. 13–21. London: Blackwell.

Tse S and Rice J (1986) Crustal earthquake instability in relation to the depth variation of frictional slip properties. *Journal of Geophysical Research* 91: 9452–9472.

Tsuboi C (1933) Investigation of deformation of the crust found by precise geodetic means. *Japanese Journal of Astronomy and Geophysics* 10: 93–248.

Turcotte DL (1992) *Fractals and Chaos in Geology and Geophysics*. Cambridge: Cambridge University Press.

Vermilye JM and Scholz CH (1998) The process zone: A microstructural view of fault growth. *Journal of Geophysical Research, Solid Earth* 103: 12223–12237.

Voight B (1976) *Mechanics of Thrust Faults and Decollements*. Stroudsburg, PN: Dowden, Huchinson, and Ross.

Wakabayashi J, Hengesh JV, and Sawyer TL (2004) Four-dimensional transform fault processes: Progressive evolution of step-overs and bends. *Tectonophysics* 392: 279–301.

Walsh JJ and Watterson J (1988) Analysis of the relationship between displacements and dimensions of faults. *Journal of Structural Geology* 10: 238–347.

Wang WB and Scholz CH (1994) Wear processes during frictional sliding of rock: A theoretical and experimental study. *Journal of Geophysical Research, Solid Earth* 99: 6789–6799.

Weathers MS, Bird JM, Cooper RF, and Kohlstedt DL (1979) Differential stress determined from deformation-induced microstructures of the Moine Thrust Zone. *Journal of Geophysical Research* 84: 7495–7509.

Willemse EJM (1997) Segmented normal faults: Correspondence between three dimensional mechanical models and field data. *Journal of Geophysical Research, Solid Earth* 102: 675–692.

Willemse EJM, Pollard DD, and Aydin A (1996) Three-dimensional analyses of slip distributions on normal fault arrays with consequences for fault scaling. *Journal of Structural Geology* 18: 295–309.

Wilson B, Dewers T, Reches Z, and Brune J (2005) Particle size and energetics of gouge from earthquake rupture zones. *Nature* 434: 749–752.

Wood R, Pettinga J, Bannister S, LaMarche G, and McMorran T (1994) Structure of the hanmer strike-slip basin, Hope fault, New Zealand. *Geological Society of America Bulletin* 106: 1459–1473.

Yoshioka N (1986) Fracture energy and the variation of gouge and surface roughness during frictional sliding of rocks. *Journal of Physics of the Earth* 34: 335–355.

Zoback MD (2000) Strength of the San Andreas. *Nature* 405: 31–32.

Zoback MD and Harjes H-P (1997) Injection induced earthquakes and crustal stress at 9 km depth at the KTB deep drilling site, Germany. *Journal of Geophysical Research* 102: 18477–18491.

Zoback MD and Healy JH (1984) Friction, faulting, and *in situ* stress. *Annales Geophysicae* 2: 689–698.

Zoback MD and Healy JH (1992) *In situ* stress measurements to 3.5 km depth in the Cajon Pass scientific research borehole: Implications for the mechanics of crustal faulting. *Journal of Geophysical Research* 97: 5039–5057.

Zoback MD, Tsukahara H, and Hickman S (1980) Stress measurements at depth in the vicinity of the San Andreas fault: Implications for the magnitude of shear stress at depth. *Journal of Geophysical Research* 85: 6157–6173.

6.11 Mountain Building, Tectonic Evolution, Rheology, and Crustal Flow in the Himalaya, Karakoram, and Tibet

MP Searle, University of Oxford, Oxford, UK

© 2015 Elsevier B.V. All rights reserved.

6.11.1	**Introduction**	469
6.11.2	**Lithospheric Structure and Rheology**	470
6.11.2.1	Jelly Sandwich Model	470
6.11.2.2	Crème Brûleé Model	470
6.11.3	**Deep Structure of the Himalaya and Tibet**	472
6.11.3.1	Seismic Constraints	472
6.11.3.2	Petrologic and Thermobarometric Constraints from Volcanics and Xenoliths	476
6.11.4	**Tectonic Evolution of the Himalaya**	476
6.11.4.1	Precollisional Ophiolite Obduction	476
6.11.4.2	Accretion of Kohistan Island Arc	477
6.11.4.3	India–Asia Collision	478
6.11.4.4	Continental Subduction and UHP Metamorphism	478
6.11.4.5	Crustal Thickening and Kyanite-Grade Metamorphism in the Himalaya	479
6.11.4.6	Sillimanite–Cordierite Migmatites and Decompression Melting of the Crust along the Himalaya	480
6.11.4.7	Miocene Channel Flow along the Himalaya	480
6.11.4.8	Pliocene–Pleistocene Metamorphism and Melting in the Himalayan Syntaxis Regions	485
6.11.5	**Tectonic Evolution of Tibet**	485
6.11.5.1	Precollisional Crustal Thickening	489
6.11.5.2	Precollisional Magmatism	490
6.11.5.3	Shoshonite and Adakite Volcanism	491
6.11.5.4	Strike-Slip Faults in Tibet	494
6.11.5.4.1	Karakoram fault	494
6.11.5.4.2	Altyn Tagh fault	494
6.11.5.4.3	Haiyuan fault	496
6.11.5.4.4	Kunlun fault	496
6.11.5.4.5	Xianshuihe fault	496
6.11.5.4.6	Jiale fault	497
6.11.5.5	East–West Extension in Tibet	497
6.11.6	**Tectonic Evolution of the Karakoram**	498
6.11.6.1	Precollisional Magmatism and Metamorphism	498
6.11.6.2	Postcollisional Metamorphism	498
6.11.6.3	Postcollisional Crustal Melting	501
6.11.7	**Discussion: Lithospheric Models**	502
6.11.8	**Conclusions**	504
Acknowledgments		506
References		506

6.11.1 Introduction

Plate tectonic theory assumes that Earth's lithosphere can retain strength to behave as coherent and relatively rigid plates for long periods (>1 Myr). The rheology or strength of the lithosphere depends on rock composition, temperature, pressure, viscosity, water/fluid/melt content, strain, and deformation rates through time (Burov, 2010; Turcotte and Schubert, 2002; Watts and Burov, 2003). Conventional thermal models of the oceanic lithosphere show that the lithosphere cools conductively and thickens as it moves away from the mid-ocean ridge. The youngest and hottest rocks occur along the active ridge axis and the oldest, coldest, and thickest oceanic lithosphere occurs farthest from the ridge along continental margins. Intraoceanic subduction can result in initiation of an island arc and a back-arc spreading center, the tectonic setting of most obducted ophiolites in the geologic record.

The continental lithosphere is much more complex than the oceanic lithosphere and there is no single strength profile that characterizes all regions. In general, experimental rock mechanics show that strength increases with depth through the brittle upper crust (Byerlee's law) and then decreases below the brittle–ductile transition where deformation is more diffuse and rocks deform by flow (Brace and Kohlstedt,

1980; Goetz and Evans, 1979). The brittle–ductile transition can be a thick zone of intermediate strain where brittle–elastic and elastic–ductile processes can operate. Brittle failure results in frictional slip and faulting, whereas ductile flow results from some combination of dislocation glide, grain-boundary sliding, and diffusion creep (Nabarro-Herring or Coble creep) (Passchier and Trouw, 1996). Ductility depends on mineral composition and grain size as well as temperature and pressure. Quartz, for example, starts to deform plastically at c. 300 °C, whereas feldspars start to deform plastically at around 500 °C (Sibson, 1983).

Earthquakes are generally restricted to the brittle upper crust (the seismogenic layer; T_s) although deeper earthquakes are common along active mountain belts where thrusting and subduction processes operate. The effective elastic thickness (T_e) is the integrated strength of the entire lithosphere that responds to long-term loads by flexure (Watts, 2001). In the oceans, the effective elastic thickness (T_e) ranges from 2 to 40 km and correlates with plate age and earthquake depths, according to a conductive thermal model of oceanic lithosphere. In the continents, however, T_e ranges from 0 to 100 km and there is no correlation with age (Burov and Watts, 2006; Watts and Burov, 2003). Flexure of the lithosphere occurs as a result of loading by ice sheets, volcanic outpourings, or tectonic collisions, for example.

The thickness of the seismogenic zone T_s is a short-term proxy for the strength of the lithosphere, whereas T_e is a long-term proxy dependant on geologic loading. Old stable shields have thicker, colder, more stable lithosphere with low temperatures (as low as c. 500 ± 100 °C) at the Moho, whereas active mountain belts and orogenic plateaus such as Tibet have more complex lithospheric structure, are much hotter with Moho temperatures as high as >1000 °C, and evolve rapidly as orogenic conditions change through time. Of particular importance are a series of deep earthquakes beneath the Himalaya and South Tibet, which have been interpreted as occurring either within the strong upper mantle (e.g., Chen and Yang, 2004; Monsalve et al., 2009) or in the deepest parts of the crust (Jackson, 2002; Jackson et al., 2008; Maggi et al., 2000).

The Himalaya and Tibetan Plateau is probably the most important and largest region where recent and ongoing continent–continent collision has formed a mountain belt and a large orogenic plateau (**Figure 1**). The zone of collision, the Indus–Yarlung Tsangpo suture zone, runs around the western (Nanga Parbat) syntaxis through the mountains of north Pakistan and Ladakh along South Tibet to the eastern (Namcha Barwa) syntaxis (**Figure 2**). South of the suture, the Himalaya are made up entirely of Neoproterozoic–Phanerozoic rocks of the Indian Plate upper crust that have been folded, thrust, and shortened by several hundred kilometers. Nowhere along the Himalaya are deeper Archean–Paleoproterozoic rocks found, suggesting that the 'basement' that originally underlay the Himalayan upper crust (mainly strong Precambrian granulites) must have been subducted at a shallow angle to the north and underplated South Tibet. The Tibetan Plateau to the north of the Himalaya is a vast uplifted plateau at an average elevation of just over 5 km and crustal thickness (from c. 85 to 70 km thick) double that of normal continental crust. Because of very low erosion and exhumation rates in Tibet, lower crustal rocks are very sparsely exposed, but in the Karakoram Range of northern Pakistan, geologically laterally equivalent to the central Tibetan Qiangtang terrane, most of the rocks exposed are deep crustal metamorphic and granitic rocks (Searle et al., 2010a). The geologic and thermal evolution of the Karakoram and the Pamir holds the key to rocks that are deeply buried and unexposed in Tibet.

This chapter reviews the main models that attempt to describe the lithospheric structure and rheology and then reviews the geologic data that contribute toward these models. Two end-member models have been proposed to explain the long-term (>1 Ma) strength of continental lithosphere, dubbed the 'jelly sandwich' and the 'crème brûleé' models. Much of the evidence that constrains these models relies on earthquakes, seismic data, gravity modeling, and geology. For Tibet, two types of crustal flow models will also be discussed, the lower crust flow models developed for eastern Tibet (Clark and Royden, 2000; Royden et al., 1997) and the channel flow models developed for the Himalaya (Beaumont et al., 2001, 2004; Godin et al., 2006; Jessup et al., 2006; Law et al., 2004, 2010; Searle and Rex, 1989; Searle and Szulc, 2005; Searle et al., 2003, 2006, 2010a,b).

6.11.2 Lithospheric Structure and Rheology

Two end-member models to explain the rheology and structure of the lithosphere are the so-called 'jelly sandwich' and 'crème brûleé' models.

6.11.2.1 Jelly Sandwich Model

In the 'jelly sandwich' model, the strength of the lithosphere resides in the upper crust and upper mantle with a relatively weak lower crust (Burov, 2010; Burov and Watts, 2006; Watts and Burov, 2003). Earthquakes are restricted to the upper crust, and the contentious deep earthquakes beneath the Himalaya are interpreted to be within the upper mantle (Chen and Molnar, 1983; Monsalve et al., 2009). High values of T_e (up to 70 km) over the Ganges basin and Himalaya suggest that the lithospheric mantle beneath the downgoing Indian Plate is strong enough to support the loading of the Himalayan thrust sheets (Hetényi et al., 2007; Jordan and Watts, 2005). The presence of deep earthquakes (c. 70–90 km) beneath the Himalaya requires brittle deformation, although the upper mantle can still be strong if it bears a significant fraction of the stresses required to support the observed loads (Monsalve et al., 2009). The problem is that temperatures in the upper mantle need to be less than c. 600 °C in order to explain the seismicity (McKenzie et al., 2005; Priestley et al., 2008), a figure that seems unrealistically low for Tibet. On the other hand, weak mantle is mechanically unstable and could delaminate from the crust allowing hotter, lighter asthenospheric mantle to flow upward (Houseman et al., 1981).

6.11.2.2 Crème Brûleé Model

The 'crème brûleé' model proposes that the strength of the lithosphere is confined to the seismogenic upper crust with a ductilely deforming lower crust and a weak upper mantle. The deep earthquakes beneath the Himalaya are thought to be in the lower part of the Indian Shield crust as it underthrusts Tibet, and not in the mantle at all (Jackson, 2002; Jackson

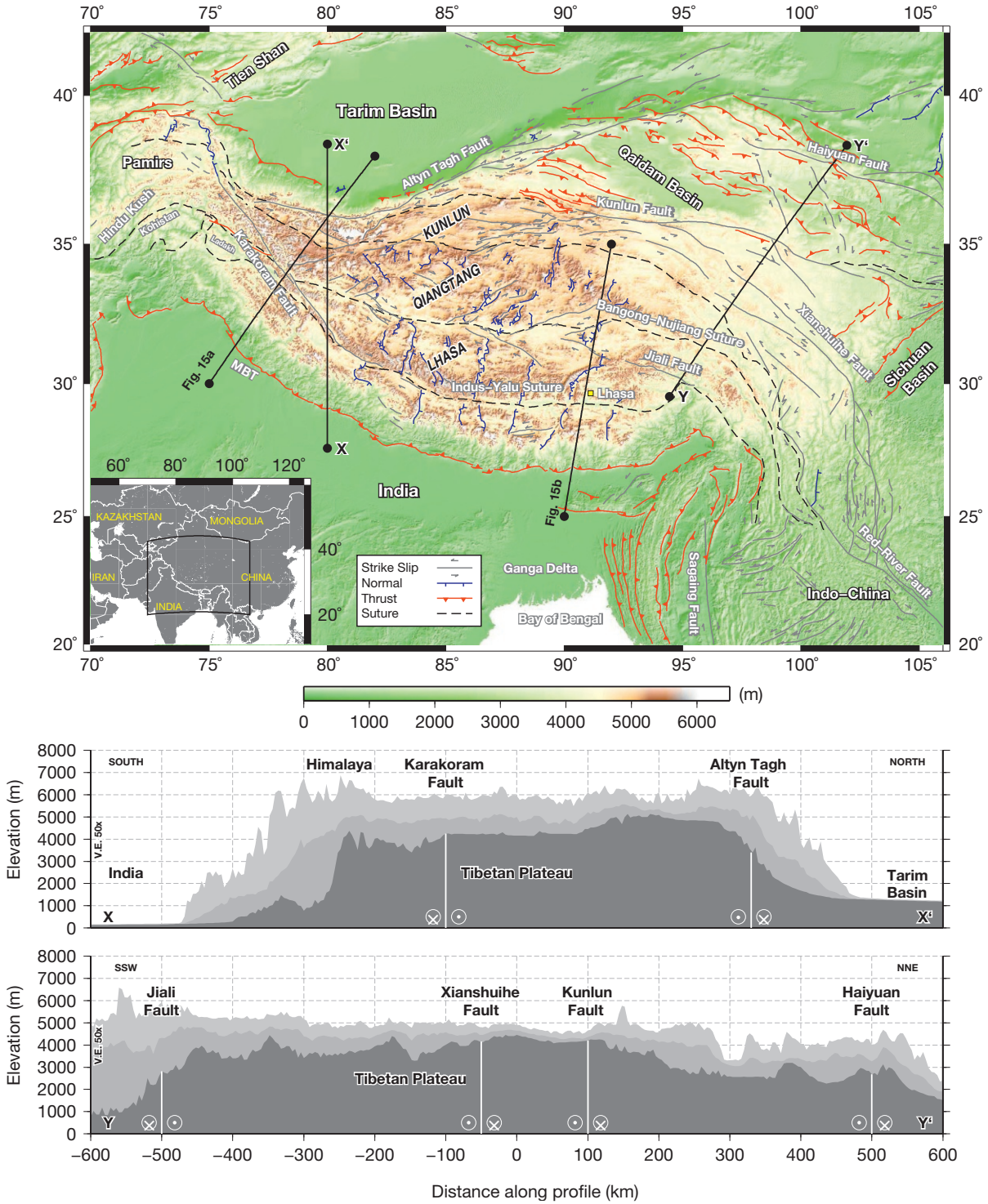

Figure 1 Digital elevation map of the Tibetan Plateau region showing active and recent thrust faults (red), normal faults (blue), and strike-slip faults (gray) together with major suture zones (black, dashed), after Taylor and Yin (2009). Two topographic profiles (X–X′ and Y–Y′) are shown with positions of the major strike-slip faults.

et al., 2008; Maggi et al., 2000). In this model, T_e values in the Himalaya are thought to be similar to the thickness of the seismogenic layer. The lowermost crust is composed of mechanically strong granulite facies rocks that are metastable at eclogite facies pressures (70–80 km; 20 kbar). Granulites are dry and thus strong, but as the Indian lower crust is subducted northward to deeper levels beneath the Himalaya and South Tibet, the granulites would convert to eclogites with the addition of a hydrous phase and therefore a decrease in strength (Austrheim, 1987). If no water entered the system, the Indian

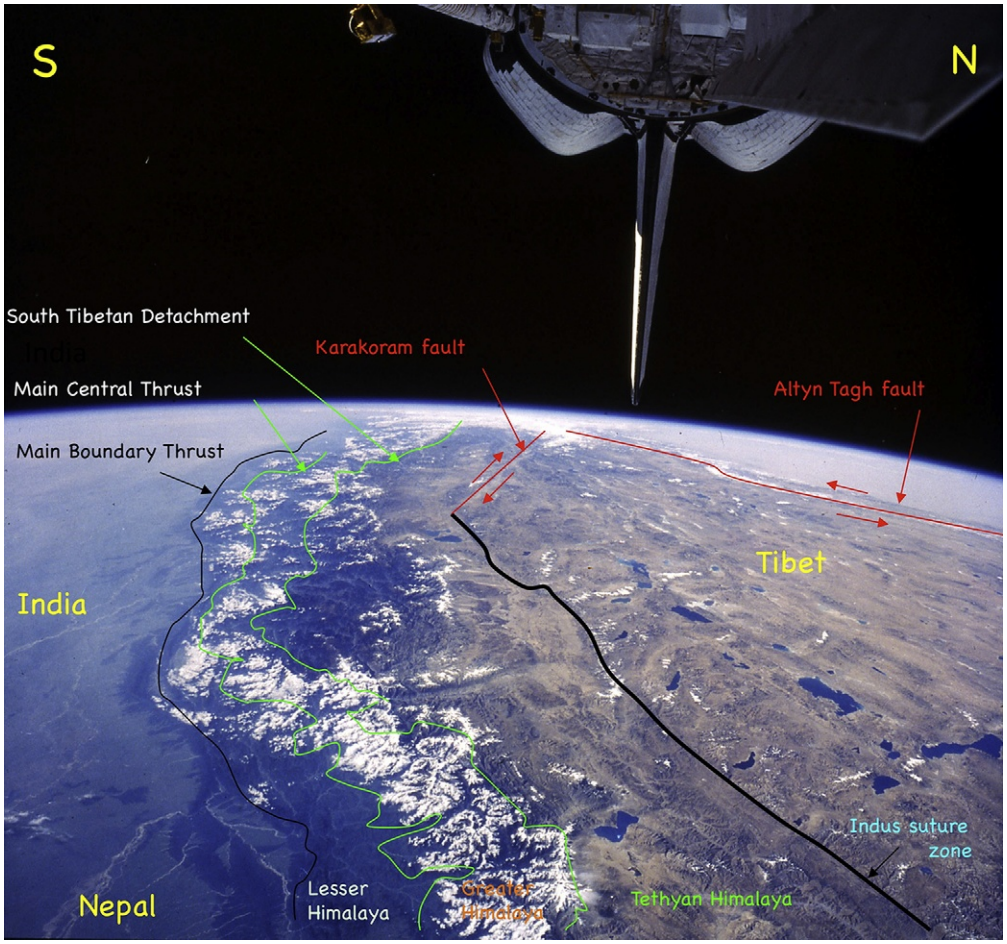

Figure 2 Photo showing the Himalayan mountains (snow-covered) and Tibetan Plateau, looking west showing the major structural features. Courtesy of NASA.

Shield granulites would simply retain the same mineralogy but be at higher pressures and maintain their strength. Seismic profiles across Tibet show that relatively cold Indian lithospheric mantle extends north beneath the Tibetan Plateau at least as far as ~32 N (Nabelek et al., 2009; Tilmann et al., 2003).

6.11.3 Deep Structure of the Himalaya and Tibet

6.11.3.1 Seismic Constraints

Figure 3 shows two profiles across the western Himalaya–Karakoram–west Tibet (a) and across the central Nepal Himalaya and central Tibet, constructed using geologic and geophysical data. In the western profile (**Figure 3(a)**), crustal thickness was determined using teleseismic receiver functions (Rai et al., 2006). The crust beneath India was found to be 40 km thick, increasing to ~50 km depth beneath the Himalayan foothills and 65 km beneath the highest peaks. North of the high Himalaya, the Moho deepens further to 70–75 km beneath the Karakoram. North of the Karakoram, Wittlinger et al. (2004) used receiver functions to map the Moho to depths of 80 km beneath the Bangong suture zone and as much as 90 km depth beneath central Tibet. Across North Tibet to the Kunlun, the Moho shallows to ~50–60 km beneath the Altyn Tagh fault and ~50 km beneath the stable Tarim Basin. In the central Himalaya–Tibet profile (**Figure 3(b)**), Schulte-Pelkum et al. (2005) imaged the Indian Moho descending smoothly to ~45 km in southern Nepal to ~75 km beneath southern Tibet. The unusual deep earthquakes (70–90 km) beneath the Himalaya and South Tibet would then be located within the lower crust (Jackson, 2002; Jackson et al., 2008; Maggi et al., 2000) and not, as previously thought, within the mantle (Chen and Molnar, 1983; Monsalve et al., 2009).

An alternative explanation of the deep earthquakes could come from metamorphic phase changes. During crustal subduction, the transformation of a metastable granulite to an eclogite involves the infiltration of hydrous fluids that may lead to brittle fracture and formation of pseudotachylyte (Austrheim, 1987; Austrheim and Boundy, 1994). This process could explain the deep earthquakes under the Himalaya where Precambrian Indian Shield granulite facies rocks were transported to depths of 70–90 km by northward subduction and transformed into either high-pressure granulite (dry) or eclogite (wet) due to the increase in lithostatic pressure.

The mantle structure under Tibet has also been the focus of much discussion. McKenzie et al. (2005) suggested that the mantle is seismogenic only when it is colder than 600 °C in

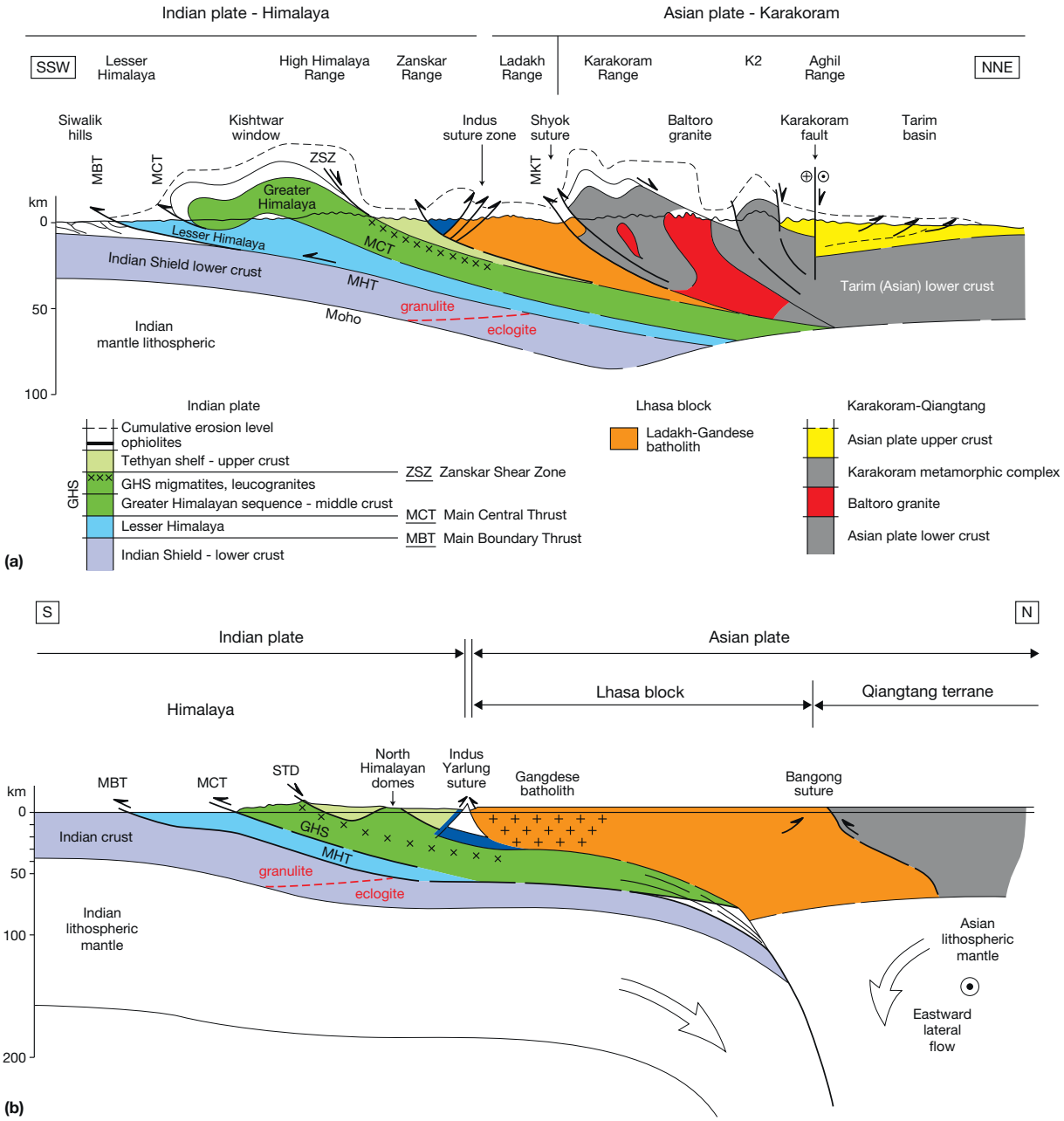

Figure 3 Two crustal-scale profiles across (a) western Himalaya, Ladakh, and Karakoram Ranges, Tarim Basin, and (b) central Tibetan Plateau region. Reproduced from Searle MP, Elliott JR, Phillips RJ, and Chung SL (2011) Crustal-lithospheric structure and continental extrusion of Tibet. *Journal of the Geological Society*, *London*, 168: 633–672, http://dx.doi.org/10.1144/0016-76492010-139.

both the oceans and the continents. Although it is possible that Moho temperatures beneath the Indian Shield could be as low as this, Moho temperatures beneath the Tibetan Plateau are much hotter. Early models for the Tibetan lithospheric evolution suggested that following lithospheric thickening, wholesale delamination of the thickened lithospheric mantle occurred, which was replaced by hot asthenospheric mantle (England and Houseman, 1989; Houseman et al., 1981). However, Priestley and McKenzie (2006), Priestley et al., (2008) and McKenzie and Priestley (2008) used surface-wave tomography to show that the whole of Tibet is underlain by high-wave speed upper mantle material to a depth of 225–250 km (Figure 4). These new data do not support the lithospheric delamination model, but are consistent with a relatively cold upper mantle beneath Tibet and support the model of underthrusting of cold Indian lithosphere from the south as originally proposed by Argand (1924). The only exception is a narrow band along the northernmost Tibetan

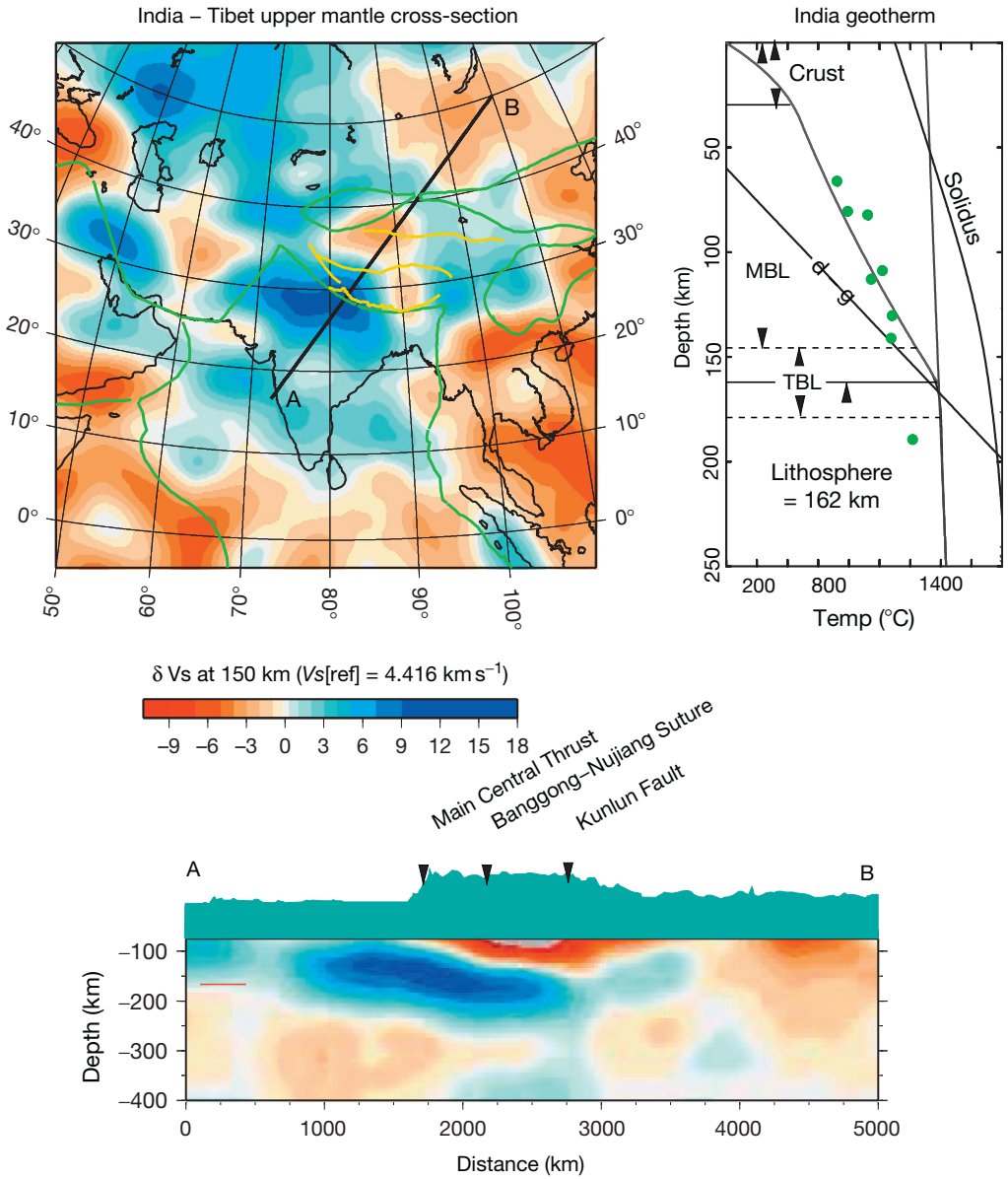

Figure 4 Depth section through the surface-wave tomography model of Priestley et al. (2008) for Tibet showing the positions of the main faults. Fast mantle underlies India and South Tibet at 125 km depth and underlies all of Tibet at 175 km depth. North of Tibet, the high-velocity mantle lid extends to 175–200 km depth but dips to the south beneath northern Tibet.

Plateau in the Kunlun where Pliocene–Recent shoshonitic volcanics indicate a hot mantle source (Chung et al., 2005) and seismic tomography shows anisotropy that might be indicative of easterly flow (Owens and Zandt, 1997). Mantle S-wave birefringence indicates the flow direction where fast polarization planes and olivine axes are E–W.

Kosarev et al. (1999) presented seismic evidence for a detached Indian lithospheric mantle beneath Tibet. Later, broadband seismic experiments showed a major variation in lithospheric structure across the Tibetan Plateau. Owens and Zandt (1997) interpreted the Indian continental crust and mantle lithosphere as underthrusting north as far as the Bangong suture zone at c.32 N from shear-coupled teleseismic P-waves (**Figure 5(a)**). Thus, South Tibet is underlain by relatively cold Indian mantle, whereas North Tibet is underlain by hot, low-density mantle and characteristic east–west anisotropy. This anisotropy is thought to reflect the eastward extrusion of North Tibetan lithosphere, assuming that the crust and mantle were coupled. The INDEPTH seismic data (Haines et al., 2003; Nelson et al., 1996; Tilmann et al., 2003; Zhao et al., 1994) (**Figure 5(b)**) also showed a major difference in lithospheric structure between North and South Tibet, with cold Indian lithospheric mantle penetrating north as far as the Bangong suture zone and relatively hot Asian lithospheric

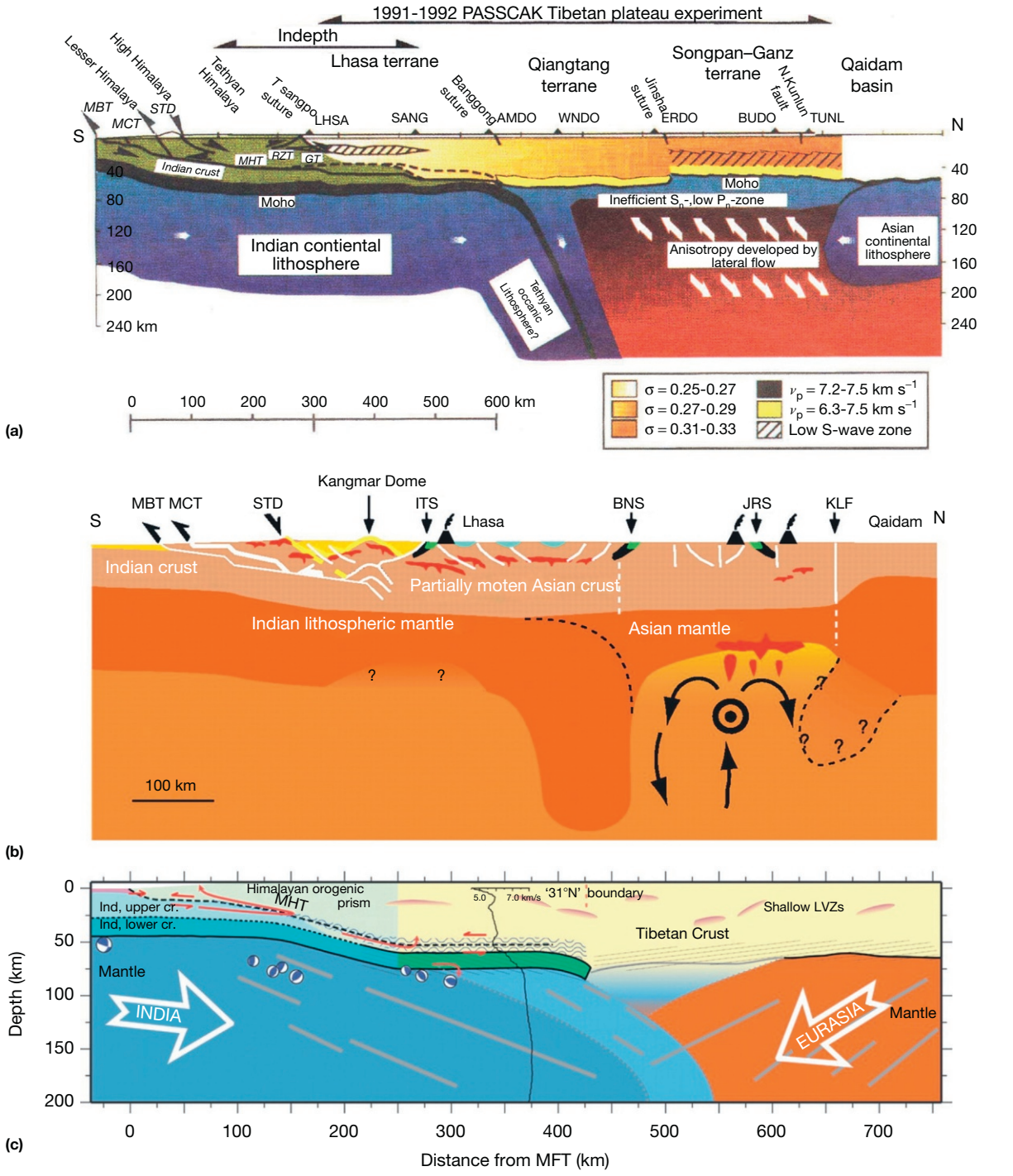

Figure 5 Three interpretative profiles across the Tibetan Plateau as interpreted from deep seismic experiments. (a) Owens and Zandt (1997) profile at ~92°E to 93°E showing Indian crust (green) extending north beneath southern part of the Lhasa Block. MHT is Main Himalayan Thrust imaged on seismic reflection data. Blue indicates mantle lithosphere. Red areas indicate region teleseismic tomography suggest that mantle is lower velocity than South Tibet. (b) Tilmann et al., (2003) profile showing the downwelling of Indian lithosphere beneath the Bangong suture (BNS). The convection cell beneath North Tibet is superimposed on eastward extrusion. Red patches indicate pockets of partial melts. (c) Nábelek et al. (2009) interpretation of the receiver function profile, also showing underthrusting of Indian lithosphere as far as 31°N. The eclogitized lower crust of India is shown in green. Prominent lineations of the upper mantle fabric are shown in gray. Also shown are the possible mantle earthquake focal mechanisms, after Chen and Yang (2004).

mantle beneath North Tibet as far north as the Kunlun. The INDEPTH III profile across the northern Tibetan Qiangtang terrane suggested the presence of a weak lower crust infiltrated by fluids corresponding to low-viscosity ductile flow. The INDEPTH IV profile extended north across into the Qaidam Basin where a 15 km offset in the Moho marks the northern boundary of the thick crust of Tibet. Moho depths of up to about 80 km beneath the South Tibet Lhasa terrane reduce to about 65 km beneath the North Tibetan Qiangtang terrane and to about 48 km beneath the Qaidam Basin (Nabelek et al., 2009; Vergne et al., 2002).

The 2002–2005 Hi-CLIMB receiver function experiment involved an 800 km long linear array of broadband seismometers extending from the Indian foreland and Ganges basin across the Himalaya and Lhasa terranes to the middle of the Qiangtang terrane (Hetényi et al., 2006, 2007; Nabelek et al., 2009). The Hi-CLIMB profile also showed deepening of the Moho from 50 km beneath the Himalaya, to 70 km beneath South Tibet, rising to 65 km beneath the Qiangtang block (**Figure 5(c)**). The profile also suggests that the lowermost Indian crust underthrusts the plateau north as far as 31 N, becoming eclogitized at depths greater than c. 50 km. North-dipping mantle fabrics suggest mantle subduction along several subparallel diffuse shear zones (Nabelek et al., 2009). Nabelek et al. (2009) also inferred southward subduction of Tarim–Qaidam (Eurasian) lithosphere beneath the Kunlun, although this interpretation has recently been challenged by Liang et al. (2012). Certainly, the lack of major Cenozoic crustal shortening across the Kunlun, unlike the Himalaya, suggests that southward subduction of Asian lithosphere was very limited. Recent surface-wave tomography studies imply a high-velocity lithospheric mantle beneath almost the whole plateau to a depth of 225–250 km, except for a narrow band along the Kunlun in the far north (Priestley and McKenzie, 2006; Priestley et al., 2008).

6.11.3.2 Petrologic and Thermobarometric Constraints from Volcanics and Xenoliths

The presence of Cenozoic potassic volcanism on the Tibetan Plateau has been linked to the model of convective thinning of excessively thickened lithosphere, delamination, and replacement by hotter asthenosphere (England and Houseman, 1989; Houseman et al., 1981). Since then, potassium-rich shoshonites and less common sodic-rich volcanic rocks have been mapped across most of the Tibetan Plateau and are known to have erupted from 50 Ma onward (Chung et al., 1998, 2003, 2005; Ding et al., 2004; Wang et al., 2010). The spatial and temporal extent of these volcanic rocks and xenoliths brought up from the lower crust within the volcanics can give a more precise idea of the thermal conditions of the lithosphere during the India–Asia collision.

Felsic and mafic granulites from the lower crust, preserved as small xenoliths in Upper Miocene ultrapotassic dikes in South Tibet, show that temperatures above the ~80 km deep (pressures of 2.6–2.2 GPa) Moho were 1330–1130 °C during the Upper Miocene (Chan et al., 2009). Similar granulite and eclogite xenoliths erupted in Miocene ultrapotassic dikes show similar ultrahigh temperatures and pressures in the Pamir (Ducea et al., 2003; Gordon et al., 2012). Hacker et al. (2005) obtained ultrahigh temperatures and pressures (1000–1100 °C; 2.8–2.5 GPa) from xenoliths of crustal origin hosted in the Miocene Dunkeldik ultrapotassic dikes in the southern Pamir. The *P–T* conditions of crustally derived xenoliths from the Pamir, as well as central and South Tibet (20–27 kbar; 800–1200 °C), suggest the entire region has had thick crust at least from Middle Miocene times. It is quite likely that the deep, lower crust of parts of the Pamir, Karakoram, and Tibet could presently be enjoying UHT–UHP metamorphism.

6.11.4 Tectonic Evolution of the Himalaya

The Himalayan range runs for more than 2500 km along the northern borders of Pakistan, India, Nepal, Sikkim, Bhutan, and Arunachal Pradesh with southern Tibet (**Figure 6**). Two major episodes of mountain-building tectonic activity are evident along the Himalaya. Firstly, a major episode of ophiolite obduction from Neotethys southward to the passive continental margin of India and associated accretion of large island arc complexes (Kohistan–Dras island arc) in the west occurred during the Late Cretaceous and Paleocene, prior to the India–Asia collision. Secondly, the Early Eocene (c.50 Ma) India–Asia collision resulted in widespread Middle Eocene to Miocene crustal shortening, thickening, regional metamorphism, migmatization, and production of crustal melt leucogranites along the Greater Himalaya and an Upper Miocene active thrust–fold belt along the Lesser Himalaya (Hodges, 2000; Yin and Harrison, 2000). The youngest metamorphic rocks exposed at the surface are Pliocene–Quaternary high-grade rocks in the Nanga Parbat syntaxis in Pakistan. Much of the evidence for the earlier ophiolite obduction orogenic phase has been destroyed by metamorphic and deformational overprinting, or by erosion.

6.11.4.1 Precollisional Ophiolite Obduction

A major episode of deformation along the North Indian continental margin is recorded by pre-Paleocene folding and thrusting of Mesozoic rocks in the Tethyan zone. Several disrupted ophiolite complexes are present along the North Indian margin, the latest and most intact of which is the Early Jurassic (177.1 ± 1 Ma; U–Pb zircon, Pedersen et al., 2001) Spontang ophiolite of Ladakh–Zanskar in NW India. The Spontang ophiolite consists of upper mantle peridotites and crustal gabbros, sheeted dikes, and pillow lava sequences that were obducted onto the passive continental margin of India during the Late Cretaceous (Corfield et al., 2001; Searle, 1986; Searle et al., 1999). An 88 ± 5 Ma andesitic island arc sequence above the ophiolite indicates that the ophiolite was formed and emplaced in a subduction zone setting (Pedersen et al., 2001). Intense folding and thrusting of the Mesozoic shelf carbonate rocks beneath the Spontang ophiolite indicate a major phase of crustal shortening and thickening during the Late Cretaceous prior to deposition of the unconformably overlying Paleocene–Eocene shallow water carbonates (Searle and Treloar, 2010). By analogy with the Semail Ophiolite in the Oman mountains, an area that has not yet undergone continent–continent collision, it is possible that the Indian

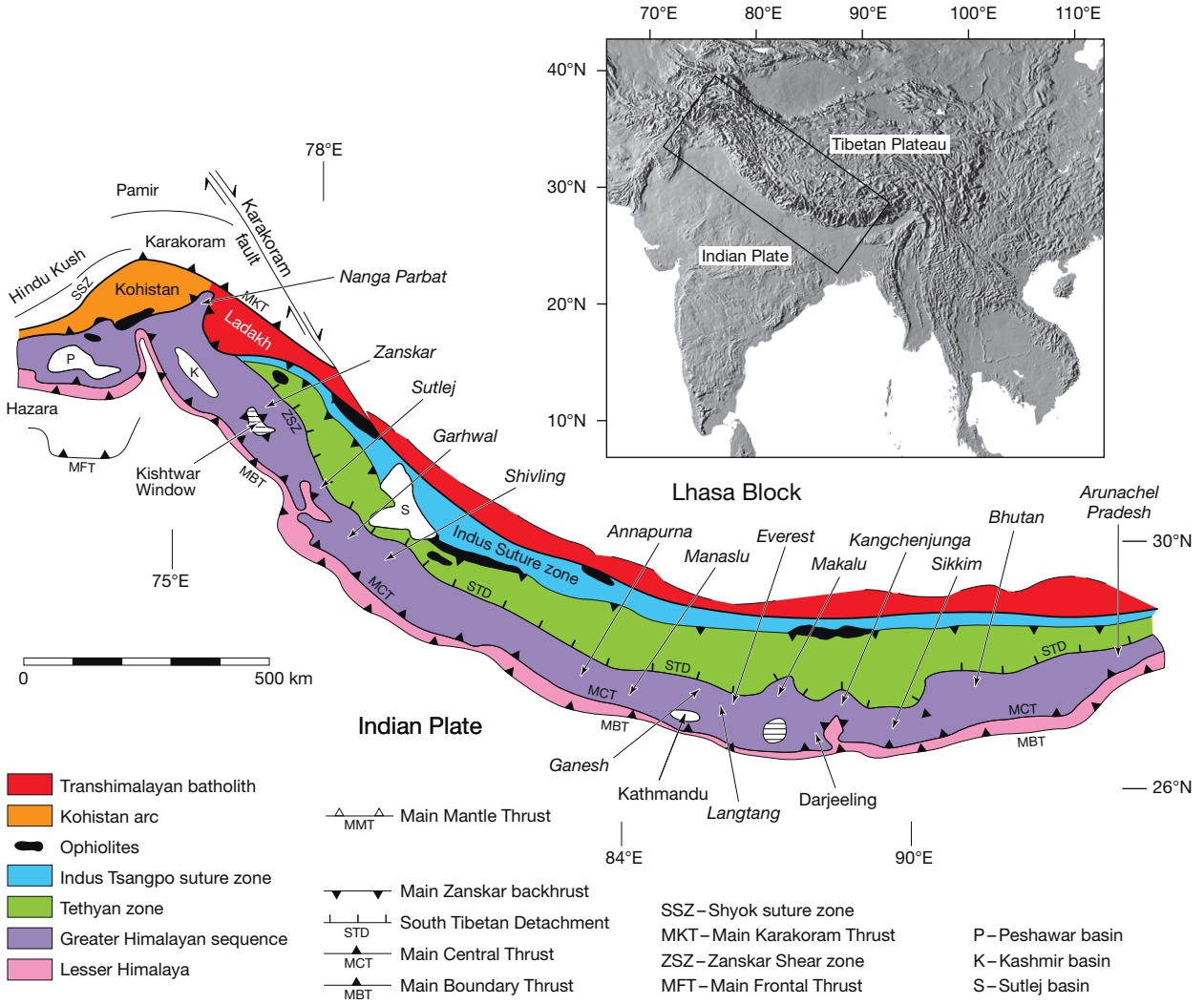

Figure 6 Geologic map of the Himalaya showing the major structural units and major faults as well as the most prominent mountains.

continental margin suffered hundreds of kilometers of crustal shortening, intense folding, thrusting, and crustal thickening during this episode of orogenesis. It is probably no coincidence that the two regions recording Early Eocene ultrahigh-pressure metamorphism along the leading margin of the Indian Plate, similar in structural setting to the Oman (ultra-) high-pressure event, are located adjacent to the obducted Kohistan arc in Pakistan and Spontang ophiolite in Ladakh.

6.11.4.2 Accretion of Kohistan Island Arc

In the western Himalaya, a large-scale Late Cretaceous to Eocene island arc complex, the Kohistan–Dras island arc, crops out within the Tethyan suture zone between India and Asia, bounded by two sutures, the Shyok suture to the north and the Indus suture (Main Mantle Thrust) to the south (Dhuime et al., 2007; Garrido et al., 2006; Jagoutz and Schmidt, 2012; Jagoutz et al., 2007; Jan and Howie, 1981; Khan et al., 1993; Pettersen and Treloar, 2004). The Kohistan arc comprises a complete upper mantle and crust section through an island arc (**Figure 7**). The mantle component includes the ultramafic lower part of the Jijal complex (layered dunite, wehrlite, and Cr-rich pyroxenites overlain by websterites and pyroxenites; Dhuime et al., 2007; Garrido et al., 2007) and the Sapat ultramafic (dunite and harzburgite) thrust slices. The crustal component includes the upper part of the Jijal complex, Kamila complex (garnet granulites and basal amphibolites of MORB affinity), Chilas complex (gabbronorites and diorites), and overlying andesitic-dacitic volcanic complexes (Dir, Utror, Shamran, and Chalt volcanic suites). All these rocks are intruded by extensive biotite- and hornblende-bearing monzogranites, granodiorites, and tonalites of the Kohistan batholith. The Kohistan arc was an intraoceanic island arc formed above a north-dipping subduction zone and obducted onto the northern margin of India. A second long-lived subduction zone dipping northward beneath the Asian margin lasted from at least Late Jurassic through Cretaceous time to the Early Eocene. Subduction-related I-type granite magmatism, typical of Andean-type settings, characterizes the magmatic evolution of both northern Kohistan terrane and the Karakoram terrane to the north (Searle et al., 1999). Much of the upper crustal sedimentary

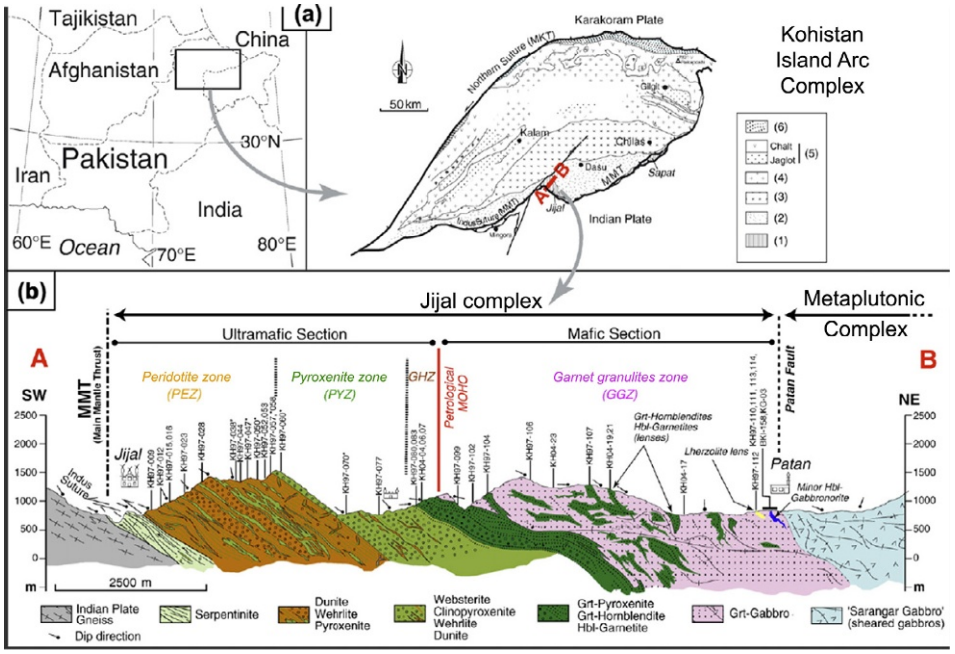

Figure 7 Simplified geologic map and cross section across the basal part of the Kohistan arc, north Pakistan, after Dhuime et al. (2007). The basal high-pressure Jijal complex comprises mantle sequence peridotites and pyroxenites overlain by lower crustal sequence garnet granulites and gabbros of the Chilas complex.

rocks of the North Indian Plate margin (Tethyan Himalaya), up to 5 km stratigraphic thick in Ladakh, have been removed in Pakistan, such that the Kohistan arc lies above high-grade regional metamorphic rocks of the Greater Himalayan sequence (GHS). Thus, the main geologic evidence for the timing of India–Asia collision lies in Ladakh and along the suture zone of South Tibet.

6.11.4.3 India–Asia Collision

The timing of the India–Asia collision and the closing of Neotethys along the main Himalayan chain are constrained by several factors, including the abrupt slowing of the northward drift of India from paleomagnetic data (Dupont-Nuvet et al., 2010; Najman et al., 2010; van Hinsbergen et al., 2011a,b), the abrupt ending of marine sedimentation within the Indus suture zone and along the North Indian Plate margin (Garzanti et al., 1987; Green et al., 2008; Searle et al., 1997a, 1988), the ending of subduction-related I-type granite magmatism along the South Asian margin in the Ladakh Range (St-Onge et al., 2010), and the beginning of terrestrial fluviatile and lacustrine sedimentation along the Indus suture zone (Garzanti et al., 1987; Searle et al., 1990). All of these events occurred at, or close to, 50 Ma, and it is widely thought that this marks the timing of closing the Neotethys seaway that once lay between India and the Lhasa Block (Asia). The most precise age of closure of Tethys comes from the biostratigraphic dating of the final marine sediments within the Indus suture zone of Ladakh, at 50.5 Ma (Ypresian stage of the Early Eocene) where marine limestones contain foraminifera belonging to the planktonic zone P8 (Green et al., 2008). There is no hard evidence for diachronous collision with an almost identical biostratigraphic record from South Tibet as that from Ladakh (Zhu et al., 2005).

Figure 8 shows a diagrammatic representation of the Indus molasse basin in Ladakh with the ages of mapped unconformities. The nummulitic limestone horizon along the southern part of the suture zone, dated at 50.5 Ma, is the youngest shallow marine deposit known, and these rocks are overlain by continental redbeds (Nurla Formation) and conglomerates (Hemis and Choksti Formations). Along the northern part of the suture zone, a prominent unconformity shows the redbeds of the Nurla Fm. overlying granites of the Ladakh batholith. U–Pb ages of the host I-type hornblende-bearing granodiorites show intrusion occurred at 57.7 ± 0.2 Ma. These granodiorites are cut by leucogranite dikes, the youngest magmatic units in the Ladakh batholith along the South Asian plate margin, dated at 47.1 ± 0.1 Ma (St-Onge et al., 2010). By this time, India and Asia had collided, the Neotethys ocean that lay between them had closed, and north-directed oceanic subduction resulting in intrusion of I-type granites along the Kohistan–Ladakh–Gangdese batholith had ceased.

6.11.4.4 Continental Subduction and UHP Metamorphism

The earliest metamorphism recorded along the North Indian Plate margin is an (ultra-)high-pressure eclogite facies metamorphic event seen in the Kaghan region, north Pakistan, and in the Tso Morari complex, NW India. In both areas, widespread eclogite blocks and boudins are encased within basement gneisses (Kaghan) or in regional high-grade sillimanite–cordierite gneisses (Puga gneisses at Tso Morari). Both eclogite boudins and blocks and metamorphic host rocks must have been subducted to depths in excess of 100 km, either during the final phase of ophiolite obduction or during the earliest phase of

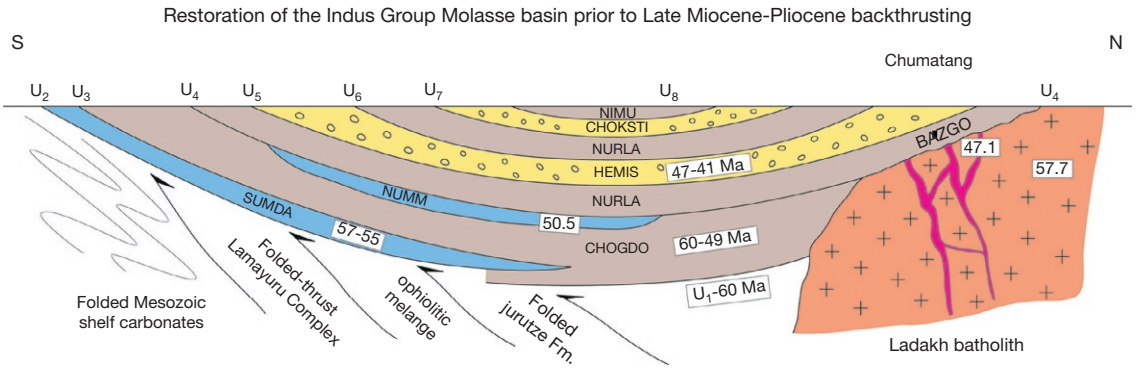

U8 ~2 Ma. Quaternary alluvial terraces overlying folded Nimu Fm; Zanskar River.

U7 ~ ? Base of Nimu Fm. Ending of massive conglomerates; return to fine- rained sandstones, mudstones, siltstones.

U6 ~41 Ma. Return to Nurla facies floodplain muds, silts and lower-energy rivers.

U5 ~47 Ma. Base of Hemis - Choksti conglomerates, high-energy fluvial channels derived from north; uplift Ladakh batholith.?Initiation of Indus River.

U4 50.5 Ma. Final marine transgression (Nummultic limestones), followed by sub-aerial fluvial and floodplain deposition (Nurla Fm.).

U3 ~54 Ma. Marine to continental transition (top Sumda Fm.).

U2 ~57 Ma. Neo-autochthonous marine transgression

U1 60 Ma. Base of chogdo Fm purple-red sandstones, siltstones, mudstones (60-49 Ma detrital zircons). Unconformity truncates folded and thrust Lamayuru, Nindam, Jurutze. Tar Fms. End of ophiolite-obduction related deformation.

Late Cretaceous-Palaeocene thrusts, folds

Figure 8 Restoration of the Indus molasse basin along the Indus suture zone in Ladakh, NW India, prior to the Late Miocene–Pliocene backthrusting phase, after Searle et al. (1988). U1–U8 marks major unconformities. Ages shown are U–Pb zircon ages from Ladakh granites and Chumatang dikes (St-Onge et al., 2010) and detrital zircons and age range of nummulitic limestones in the final marine sedimentary rocks along the suture zone (Green et al., 2008).

continental collision. O'Brien et al. (2001) discovered coesite in the Kaghan eclogites and determined UHP pressures of 27 kbar along the leading margin of the Indian Plate crust. U–Pb zircon and allanite ages from coesite-bearing eclogites from Kaghan show that UHP metamorphism occurred at 46.4 ± 0.1 Ma at peak *P*–*T* conditions of >27.5 kbar (>100 km depth) and 720–770 °C (Parrish et al., 2006). Lower-pressure growth of titanite occurred at 46.4 and 44 Ma, implying extremely rapid exhumation through the mantle from >100 km to c. 35 km depth, presumably during slab break-off and buoyant rebound of subducted Indian crust.

For the Tso Morari eclogites in Ladakh, *P*–*T* conditions of 550 ± 50 °C and 20 ± 3 kbar were initially documented by de Sigoyer et al. (2000), and peak HP metamorphism was proposed to be 55 ± 12 Ma from Lu–Hf (Grt–Cpx–Rt), Sm–Nd (Grt–Gln–Rt), and U–Pb allanite dating (de Sigoyer et al., 2000). Kaneko et al. (2003) measured U–Pb ion microprobe ages of 46.2 ± 0.7 Ma from zircon rims, interpreted as dating the timing of UHP metamorphism. St-Onge et al. (2013) integrated PTt paths from phase diagram modeling combined with SHRIMP U–Pb zircon and monazite age dating from the Tso Morari eclogites and determined prograde (burial) eclogite facies garnet growth at 58.0 Ma, followed by peak HP/UHP conditions of 25.5–27.5 kbar and 630–645 °C at 50.8 ± 1.4 Ma (zircons encased in garnet rim in the eclogite matrix) (**Figure 9**). Th–Pb SHRIMP dating of monazite cores surrounded by allanite rims in the host Puga gneiss constrains equilibration of the garnet–cordierite–sillimanite–biotite–plagioclase–quartz + melt assemblage at 45.3 ± 1.1 Ma (St-Onge et al., 2013). Earlier reports of microdiamonds within eclogites from Tso Morari (Mukherjee et al., 2005) are not supported by any petrologic, thermobarometric, or other data, and phase diagram modeling suggests that pressures did not extend into the microdiamond field (St-Onge et al., 2013).

It seems likely that following Late Cretaceous–Early Paleocene obduction of ophiolites onto the northern passive continental margin of India, the collision of India with Asia during the Early Eocene led to the final closing of Tethys at 50 Ma and the beginning of crustal thickening and regional metamorphism along the Indian Plate margin (**Figure 10(a)** and **10(b)**). The leading margin of India was dragged down the subduction zone and metamorphosed to coesite–eclogite conditions during the Late Paleocene–Early Eocene. Buoyant rebound of the subducted crustal slice requires some sort of slab break-off to trigger rapid exhumation. The eclogites then became encased within lower and middle crustal kyanite- and sillimanite-bearing gneisses of the main Himalayan metamorphic event (**Figure 10(c)** and **10(d)**).

6.11.4.5 Crustal Thickening and Kyanite-Grade Metamorphism in the Himalaya

Following India–Asia collision, folding and thrusting along the North Indian continental margin resulted in crustal shortening and thickening. Intense tight to isoclinal folding in sedimentary rocks of the upper crustal Tethyan zone resulted in several hundred kilometers of shortening (Corfield and Searle, 2000). Similar thickening in the lower crust led to regional Barrovian facies metamorphism at deeper levels along the GHS. Initially, metamorphic isograds were right way up, as reflected by the geometry in the North Himalayan domes, but along the Greater Himalaya, isograds were subsequently deformed by south-vergent recumbent folding. The entire base of the GHS

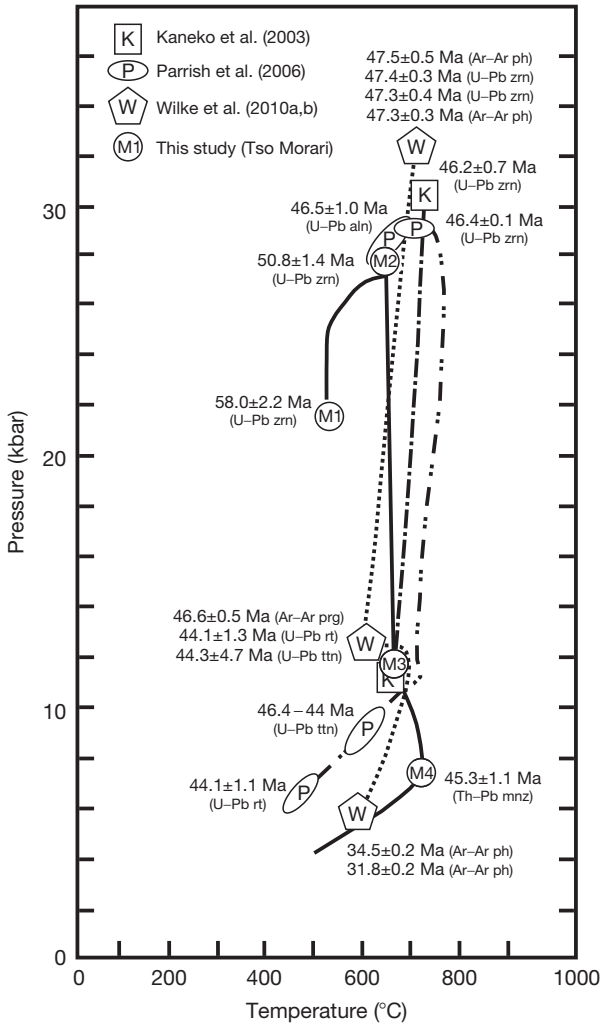

Figure 9 Integrated PTt path for the Tso Morari eclogites in Ladakh, NW India, showing all U–Pb age data. Reproduced from St-Onge MR, Rayner N, Palin RM, Searle MP, and Waters DJ (2013) Integrated pressure–temperature–time constraints for the Tso Morari dome (Northwest India): Implications for the burial and exhumation path of UHP units in the Western Himalaya. *Journal of Metamorphic Geology*, in press.

now shows an inverted metamorphic field gradient from biotite-grade rocks through garnet- and staurolite-grade schists to kyanite gneisses above a crustal-scale south-directed thrust the Main Central Thrust (MCT) (**Figures 11** and **12**). Fabrics and kinematic shear-sense indicators all indicate south-directed thrusting placed deeper, hotter rocks over shallower, colder rocks. The entire top of the GHS shows sillimanite-grade gneisses, sillimanite ± cordierite + K-feldspar migmatites, and partial melting beneath a large-scale low-angle normal fault, the South Tibetan Detachment (STD) or Zanskar shear zone (ZSZ) in the western Himalaya. These rocks show widespread fabrics and shear-sense indicators showing top-to-north shearing placing lower-pressure rocks onto higher-pressure rocks.

Thermobarometry of kyanite-grade gneisses from Zanskar has revealed peak *P*–*T* conditions of 10.5–9.5 kbar and 620–650 °C (Searle et al., 1992, 1999; Walker et al., 2001). U–Pb dating of metamorphic monazites reveals that peak kyanite-grade metamorphism in Zanskar and the Indian Himalaya occurred between 37 and 29 Ma (Walker et al., 1999). Similar U–Pb monazite dating of kyanite gneisses from the Annapurna Himalaya of Nepal recording ages between 35 and 32 Ma (Godin et al., 2001) and from the Everest region of 38.9 ± 0.2 Ma (Cottle et al., 2009) suggests that this was a regional Late Eocene–Early Oligocene event along the Greater Himalaya. Both muscovite and biotite breakdown reactions resulted in formation of early Himalayan kyanite + K-feldspar + melts and the formation of migmatites and leucogranites. Kyanite is the stable aluminum silicate across 35 km width of the western Himalaya in Zanskar–Kishtwar; along the central Himalaya, it is widespread not only along the GHS mainly south of the sillimanite zone but also at higher structural levels beneath the STD.

6.11.4.6 Sillimanite–Cordierite Migmatites and Decompression Melting of the Crust along the Himalaya

Following Late Eocene–Oligocene crustal thickening and regional kyanite-grade metamorphism along the Himalaya, decompression led to a decrease in pressure and an increase in temperature along the Greater Himalaya. Initial coexistence of both kyanite and sillimanite led to sillimanite + muscovite metamorphism with increased exhumation and decompression. During the Early Miocene, the GHS rocks crossed the muscovite dehydration reaction, producing widespread migmatites with the assemblage: sillimanite ± cordierite ± garnet + K-feldspar + leucogranitic melt. At pressures < 5 kbar, cordierite, sillimanite, and andalusite are present as either magmatic or restitic components in the melts. Leucogranites typically contain quartz, K-feldspar, and plagioclase with varying amounts of garnet, tourmaline, muscovite, biotite, cordierite, andalusite, and sillimanite. Himalayan leucogranites are 100% crustal melts derived from melting of sedimentary source rocks (most likely the Neoproterozoic Haimanta–Cheka sequences, preserved in low-grade outliers above the GHS). Melting of boron-rich shales resulted in tourmaline-rich granites, whereas melting of both pelites and psammites is apparent throughout the GHS. K-feldspar augen gneisses may be relic orthogneiss horizons (e.g., Cambro–Ordovician S-type granites) but could also be the result of the second muscovite melting reaction in pelitic or psammitic assemblages. There is abundant field evidence for *in situ* melting of both pelitic and psammitic assemblages as well as K-feldspar augen gneisses (Searle et al., 2010b).

6.11.4.7 Miocene Channel Flow along the Himalaya

The channel flow model was developed by field geologists mapping the regional metamorphic rocks of the Greater Himalaya, combined with metamorphic petrology, thermobarometry, phase diagram modeling, and U–Pb geochronology. During the 1980s and 1990s, it was recognized that the GHS rocks were bounded by two crustal-scale ductile shear zones and brittle faults, both dipping at shallow angles to the north (Grasemann et al., 1999; Grujic et al., 2002; Searle and Rex, 1989; Searle and Szulc, 2005; Searle et al., 1992, 1999). The MCT zone is a large ductile shear zone associated with an

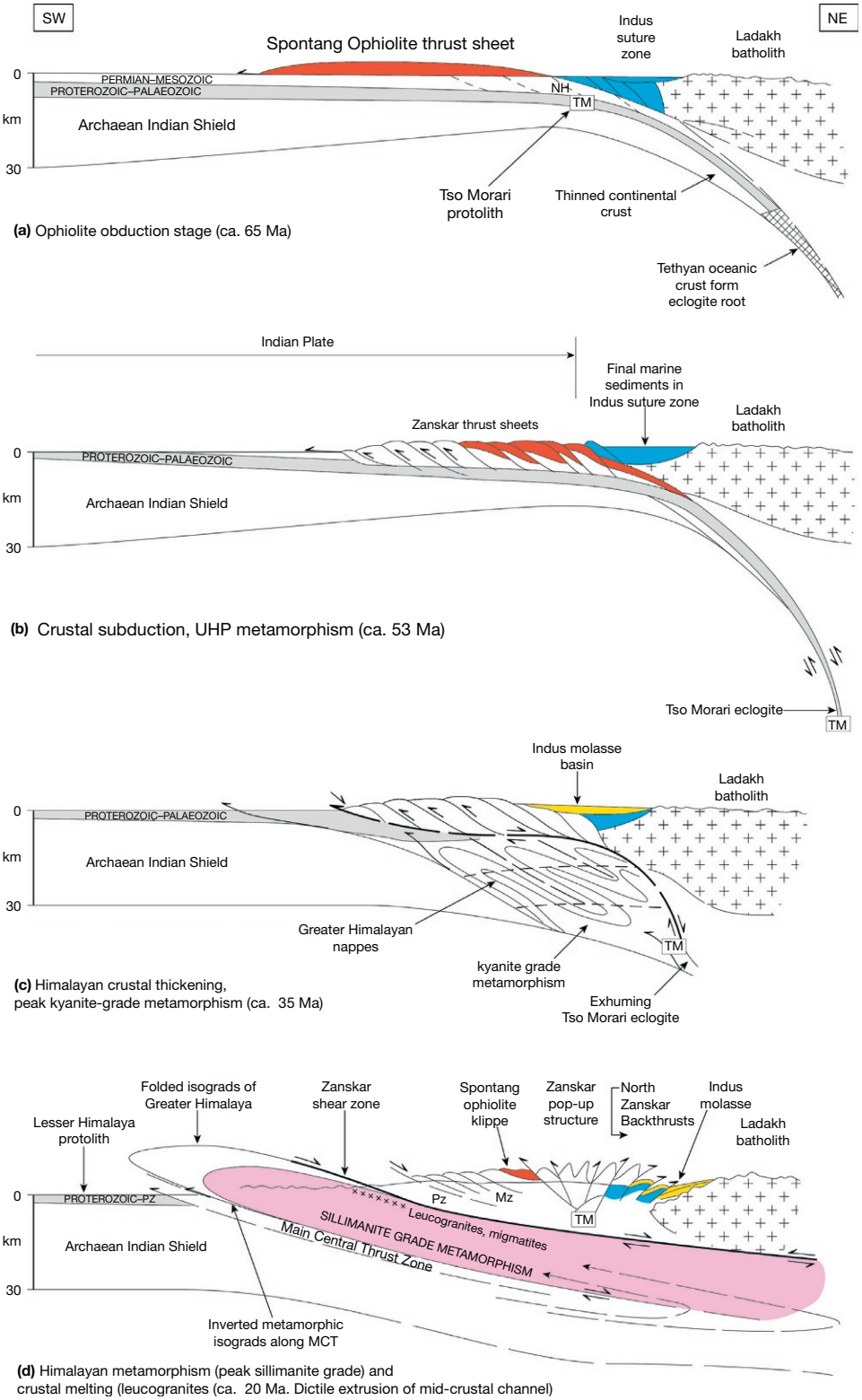

Figure 10 Four stages in the tectonic evolution of the Himalaya: (a) Late Cretaceous ophiolite obduction stage; obduction of the Spontang ophiolite and Kohistan ophiolites and island arc onto the Indian continental margin. (b) Early Eocene India–Asia collision and deep subduction of the continental margin to form UHP eclogites (TM = Tso Morari). (c) Late Eocene–Early Oligocene crustal thickening stage to form regional Barrovian kyanite metamorphism. (d) Late Oligocene–Middle Miocene regional sillimanite-grade metamorphism and partial melting to form migmatites and leucogranites, initiation of the Main Central Thrust and South Tibetan Detachment; channel flow.

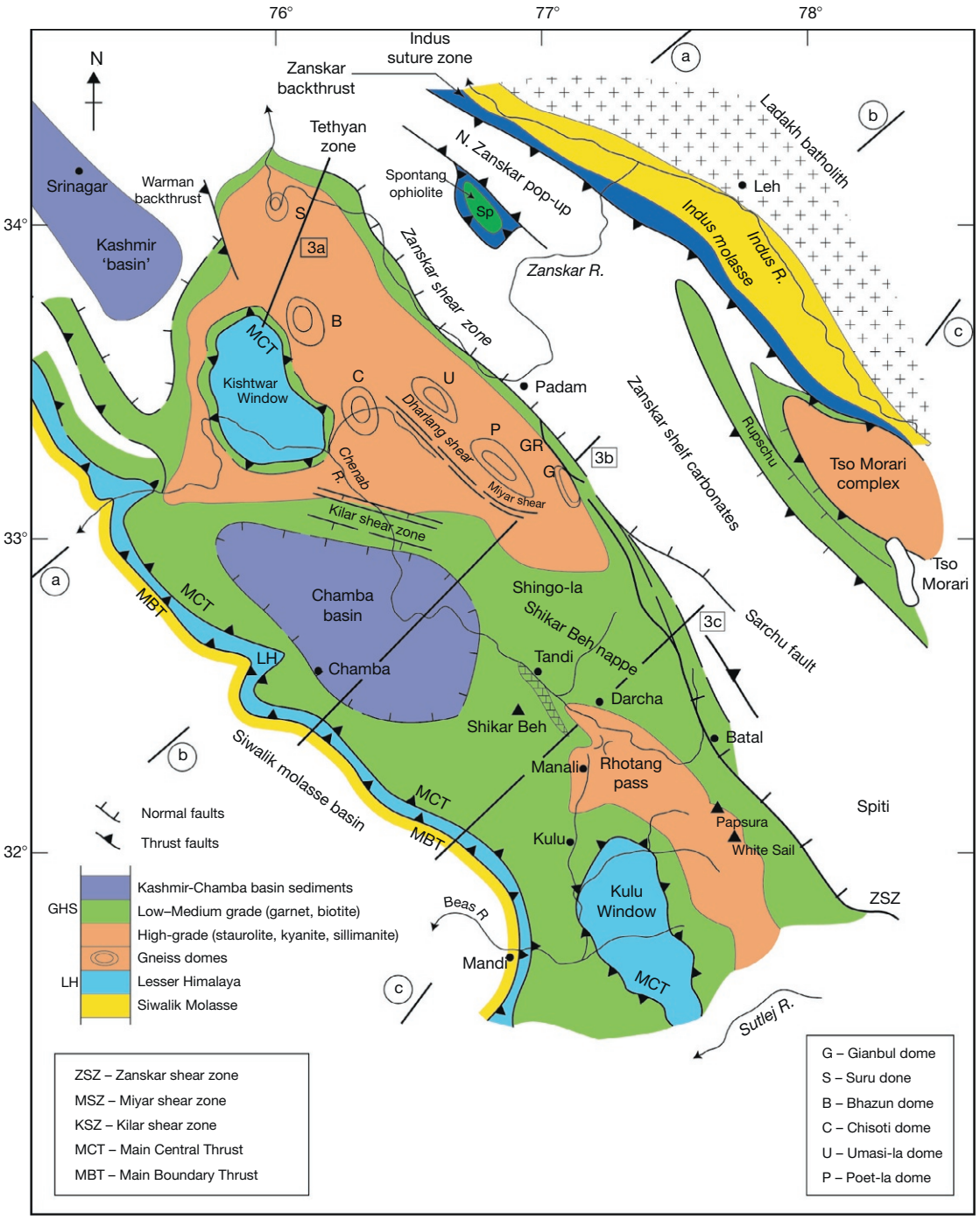

Figure 11 Geologic map of the Greater Himalayan sequence in the western Himalaya (Kashmir, Zanskar, Kishtwar, Lahoul; N. India), after Searle et al. (1992, 1999). Metamorphic rocks are shaded amphibolite facies (brown) with sillimanite-grade gneiss domes individually labeled, greenschist facies (green) and low-grade metasedimentary (dark blue), with the major faults.

inverted metamorphic field gradient and inverted *P–T* conditions from biotite-grade along the base through garnet, staurolite, and kyanite to sillimanite + muscovite isograds up to the partial melt zone of sillimanite + K-feldspar migmatites and associated migmatites (Searle et al., 2008). The STD is a large-scale low-angle normal fault associated with a right-way-up isograd sequence from sillimanite + K-feldspar migmatites and *in situ* leucogranite melts up through the same isograds to the base of the Tethyan sedimentary sequence above. In between these two faults, an up to 10–15 km structural thickness of partially melted kyanite- or sillimanite- (±cordierite) grade rocks shows that this midcrustal layer was riddled with partial melts during the Miocene (Figure 13).

Only in the western Zanskar–Kishtwar Himalaya in NW India can the right-way-up isograds beneath the STD (locally called the Zanskar Shear Zone (ZSZ)) be mapped around a

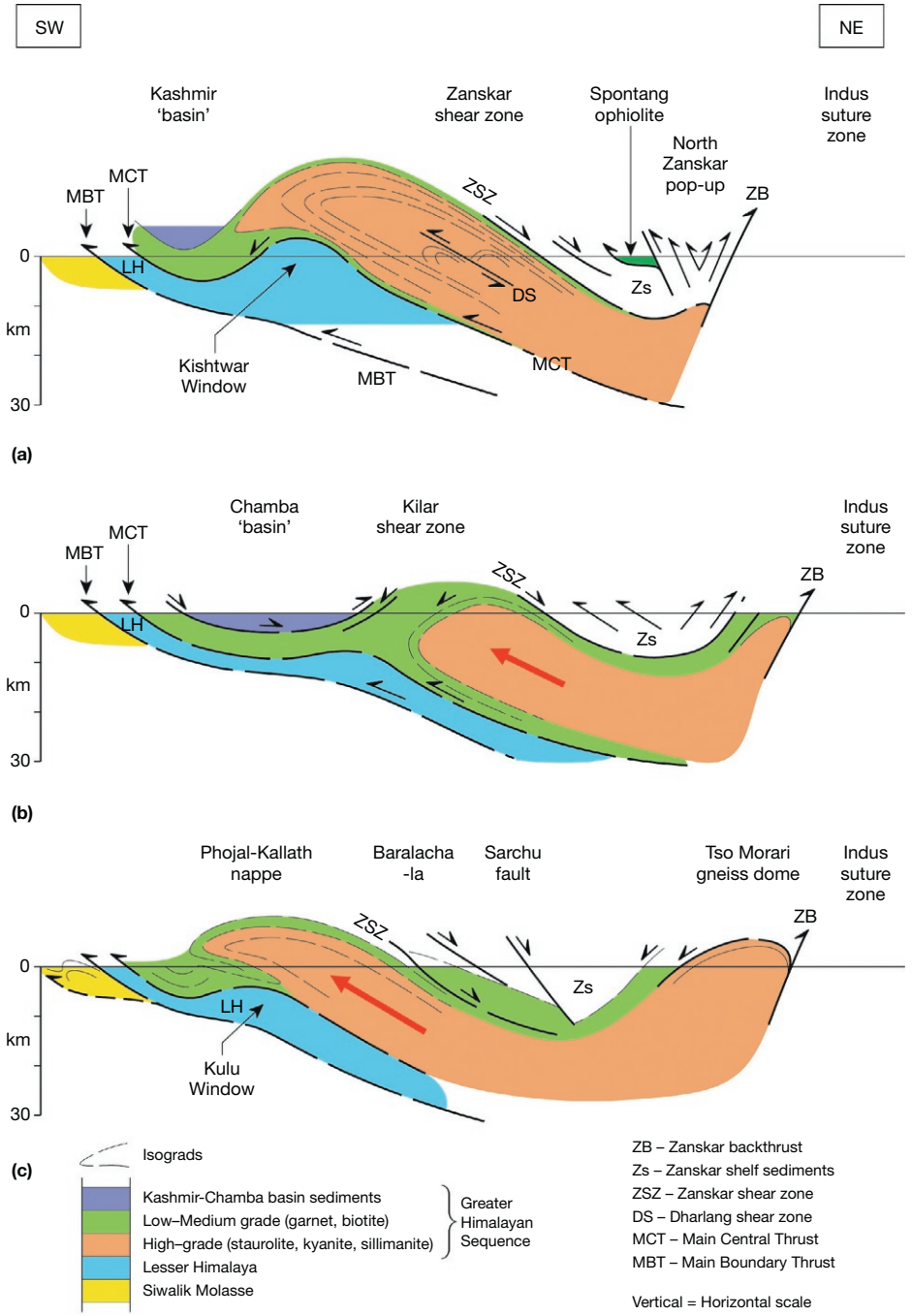

Figure 12 Cross sections of the Greater Himalayan sequence metamorphic rocks, lines of section are shown in **Figure 11**.

large-scale SW-vergent recumbent fold to link with the inverted isograd sequence along the hanging wall of the MCT (Searle and Rex, 1989; Searle et al., 1992, 1999) (**Figure 11**). Geologic offsets along the MCT and STD are hard to tie down but pressure–depth constraints suggest at least 100–130 km of southward motion of the GHS relative to the Tethyan rocks above and the Lesser Himalayan rocks below occurred along the Everest profile (Searle et al., 2003, 2006). Quantitative strain analyses suggest that a major component of pure shear flattening was associated with both shear zones bounding the partially molten core (Jessup et al., 2006; Law et al., 2004, 2011). This flattening accounts for the narrow zone of condensed isograds in ductile shear zones above and below the channel. Isotopic and trace element modeling shows that the Himalayan leucogranites formed by the incongruent melting of muscovite during decompression (Harris et al., 1995; Harris and Inger, 1992; Harris and Massey, 1994).

U–Pb dating of metamorphic monazites and igneous minerals within leucogranites showed that the Himalayan melts formed over the period c. 24–11 Ma, with the majority intruded during the period 21–19 Ma (e.g., Cottle et al., 2009; Godin et al., 2001, 2006; Searle et al., 1997a, 1999,

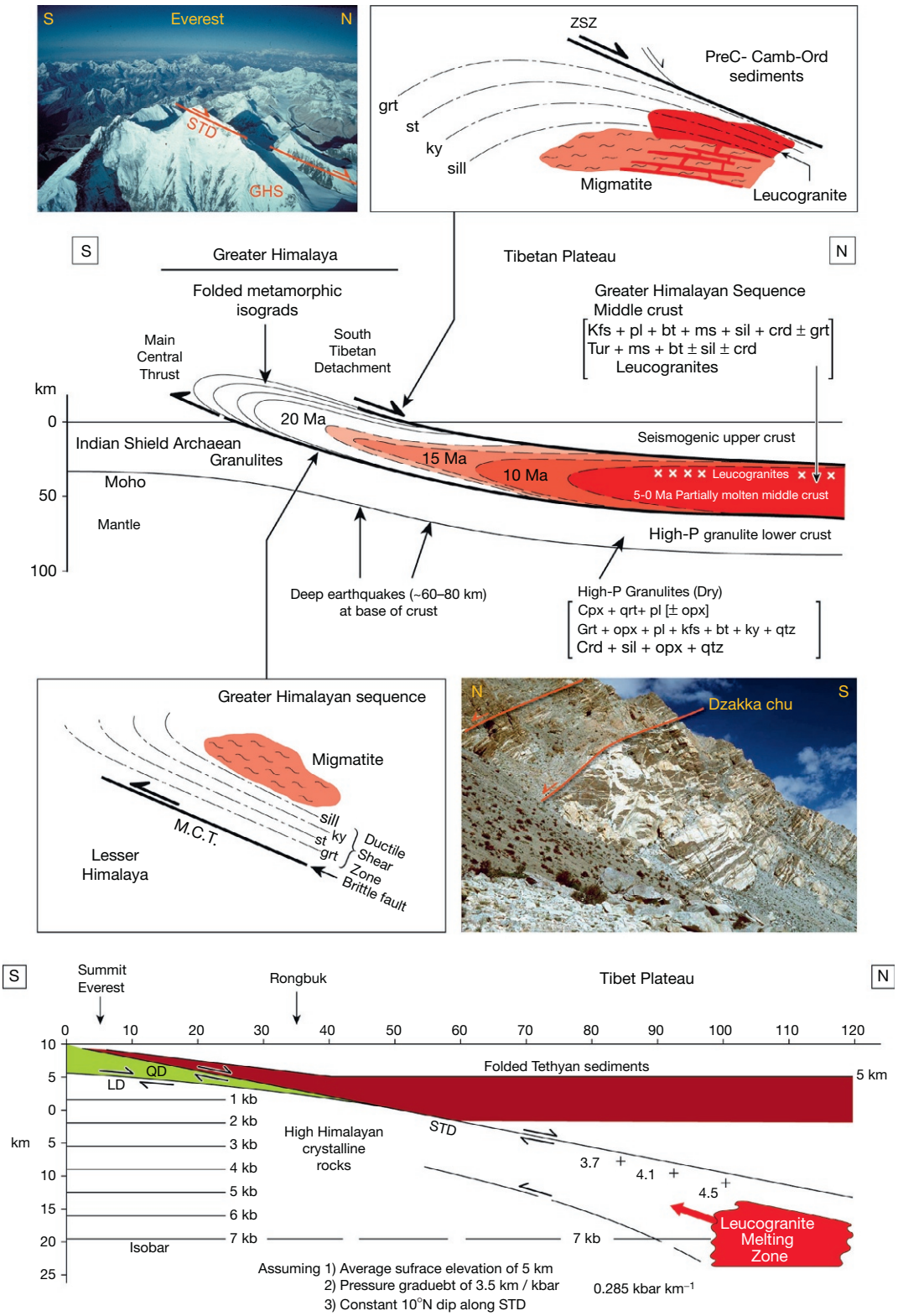

Figure 13 The channel flow model based on regional mapping combined with strain analyses, thermobarometry, and U–Pb geochronology of Greater Himalayan rocks along the Everest transect, Nepal, and South Tibet, after Searle et al. (2003, 2006), Law et al. (2006, 2011), and Jessup et al. (2006, 2008). Insets show alignment of inverted metamorphic isograds in the MCT zone along the base and right-way-up isograds along the STD low-angle normal fault along the top of the extruding midcrustal layer.

2003, 2006). Leucogranites formed by *in situ* melting in the core migmatite zone, and then melts segregated and were intruded along giant sill complexes, fed by a few crosscutting dikes within the sillimanite zone (Figure 14). In the Everest region, some of these leucogranite sills can be mapped for over 50 km across strike (Jessup et al., 2006; Searle et al., 2003, 2006, 2010b). Channel flow along the Himalaya ended when crustal melting stopped around 14–11 Ma (Cottle et al., 2009; Streule et al., 2010). This marks a period of rapid cooling along the GHS when exhumation and erosion reached a peak. $^{40}Ar/^{39}Ar$ and fission track data from vertical sampling up several leucogranites show abrupt cooling during this period, notably in the Shishapangma (Searle et al., 1997a), Shivling (Searle et al., 1999) and Everest massifs (Streule et al., 2012; Figure 15).

Channel flow involves a viscous, fluid-filled channel bounded by rigid sheets above and below. The driving force behind channel flow is gravitational potential, governed by the topographic and crustal thickness variation between the Tibetan Plateau hinterland (~5 km elevation; 65–75 km thick crust) and the Indian foreland (<0.5 km elevation; ~35–40 km thick crust). Two end-member models of crustal flow for the Himalaya are (a) Couette flow (simple shear) where the velocity profile is caused by shearing along the MCT and (b) Poiseuille flow (also called 'pipe flow'), in which friction produces a velocity gradient that reaches a maximum in the middle of the channel (Figure 16). Although partial melting and channel flow were initiated at depths of c. 30–40 km under kyanite-grade conditions during the Oligocene, it is thought that the Miocene thermal structure across the Himalaya corresponds more closely to Poiseuille flow. Maximum flow occurred from the middle to the top of the partial melt zone where the migmatites and leucogranites are concentrated (Searle et al., 2006, 2010b). Kinematic indicators and S-C fabrics across the GHS show top-south thrust-related fabrics from the MCT zone and in the kyanite-grade rocks, where deeper, higher-pressure rocks are thrust over shallower, lower-pressure rocks, but in the sillimanite gneisses and migmatites show top-north 'extensional' fabrics where shallow lower-pressure rocks are placed above higher-pressure kyanite gneisses (Figure 17). There is actually no net extension in the Himalaya; the exhumation of the Greater Himalayan metamorphic sequence occurred beneath a passive roof stretching fault (STD) in a wholly compressional environment (Cottle et al., 2007; Jessup et al., 2006; Law et al., 2004, 2010; Searle et al., 2003, 2006). In the Dhaulagiri–Annapurna Himalaya in Nepal, metamorphism increases up section to partially melted kyanite- and sillimanite-grade rocks (Figure 18). The STD cuts out up to 20–22 km of structural thickness by juxtaposing 10–12 kbar kyanite-grade migmatites next to 9 kbar clinopyroxene + tremolite + K-feldspar marbles, and both these rocks adjacent to Cambrian limestones are affected only by burial metamorphism (Figure 19(a) and 19(b)).

Beaumont et al. (2001) and Jamieson et al. (2004) used all the geologic and thermobarometric constraints as parameters in their thermal–mechanical simulation of channel flow in the Himalaya. They suggested that channel flow was dynamically linked to focused erosion along the high Himalaya. As Klemperer (2006) noted, their model does fit all the observations, "inevitably, since the model was designed *a posteriori* to fit the observations." Neither erosion nor climate (specifically rainfall), however, can be a driving force for channel flow. Tectonics and gravitational forces drive channel flow, and erosion and rainfall are governed by topography along the Himalayan front. The major questions remaining are why did melting occur at such shallow levels in the Himalaya and not at depth and why did melting suddenly end? It has been speculated that the high concentration of high heat-producing elements in the Neoproterozoic source rocks caused shallow level melting and that batch melting during the Early Miocene exhausted the supply of muscovite- and biotite-rich shale–psammite around 14–11 Ma ago when the youngest leucogranites were intruded across ductile flow-related fabrics (Cottle et al., 2009; Searle et al., 2010b). Himalayan leucogranites have extremely high $^{87}Sr/^{86}Sr$ ratios indicating a wholly crustal origin and highly radiogenic Pb isotopic compositions implying a source enriched in U and Th (Gariepy et al., 1985).

6.11.4.8 Pliocene–Pleistocene Metamorphism and Melting in the Himalayan Syntaxis Regions

Kyanite- and sillimanite-grade metamorphic rocks are present along the entire 2500 km length of the Greater Himalaya, but in the two syntaxial regions in the far NW (Nanga Parbat syntaxis, Pakistan) and far NE (Namcha Barwa syntaxis, SE Tibet), Pliocene–Pleistocene sillimanite and cordierite gneisses, migmatites, and leucogranites indicate younger high-temperature metamorphism. Both of these regions have extremely high erosion–exhumation rates and show the youngest exhumed deep crustal rocks exposed in the Himalaya. U–Pb dating of metamorphic monazite, xenotime, and zircon revealed astonishingly young ages of high-grade metamorphism exposed in this 8125 m high Nanga Parbat massif. Exhumation rates of ~11–13 mm/a were calculated from migmatites that formed at 1.7 Ma and 5.0 kbar by biotite dehydration melting and decompression and from garnet + cordierite melt veins that crystallized at 1.0 Ma and 3.5 kbar (Crowley et al., 2009). The youngest granite melts dated at Nanga Parbat are tourmaline-bearing leucogranite dikes that separated from the source and ascended to crystallize near their solidus at 0.7 Ma. The geometry of the steep bounding shear zones and faults suggests that Nanga Parbat may record local vertical channel flow with compression in all horizontal directions.

The eastern Namcha Barwa syntaxis has a similar core of partially melted kyanite- and sillimanite-grade metamorphic rocks with young monazite and titanite U–Pb ages of 10–3 Ma (Booth et al., 2008; Zeitler et al., 2001a,b). The precise boundary between Indian Plate metamorphic rocks and Asian plate metamorphic rocks is not well defined in the eastern syntaxis region so there is some confusion whether the high-grade gneisses and migmatites to the west belong to deeper levels of the Gangdese batholith along the southern margin of Asia (Guo et al., 2007; Palin et al., 2013; Xu et al., 2010; Zhang et al., 2009, 2010) or whether they are part of the Himalaya.

6.11.5 Tectonic Evolution of Tibet

The Tibetan Plateau is the largest area of high elevation (about 5000 m) and thick crust (between 65 and 90 km) anywhere in

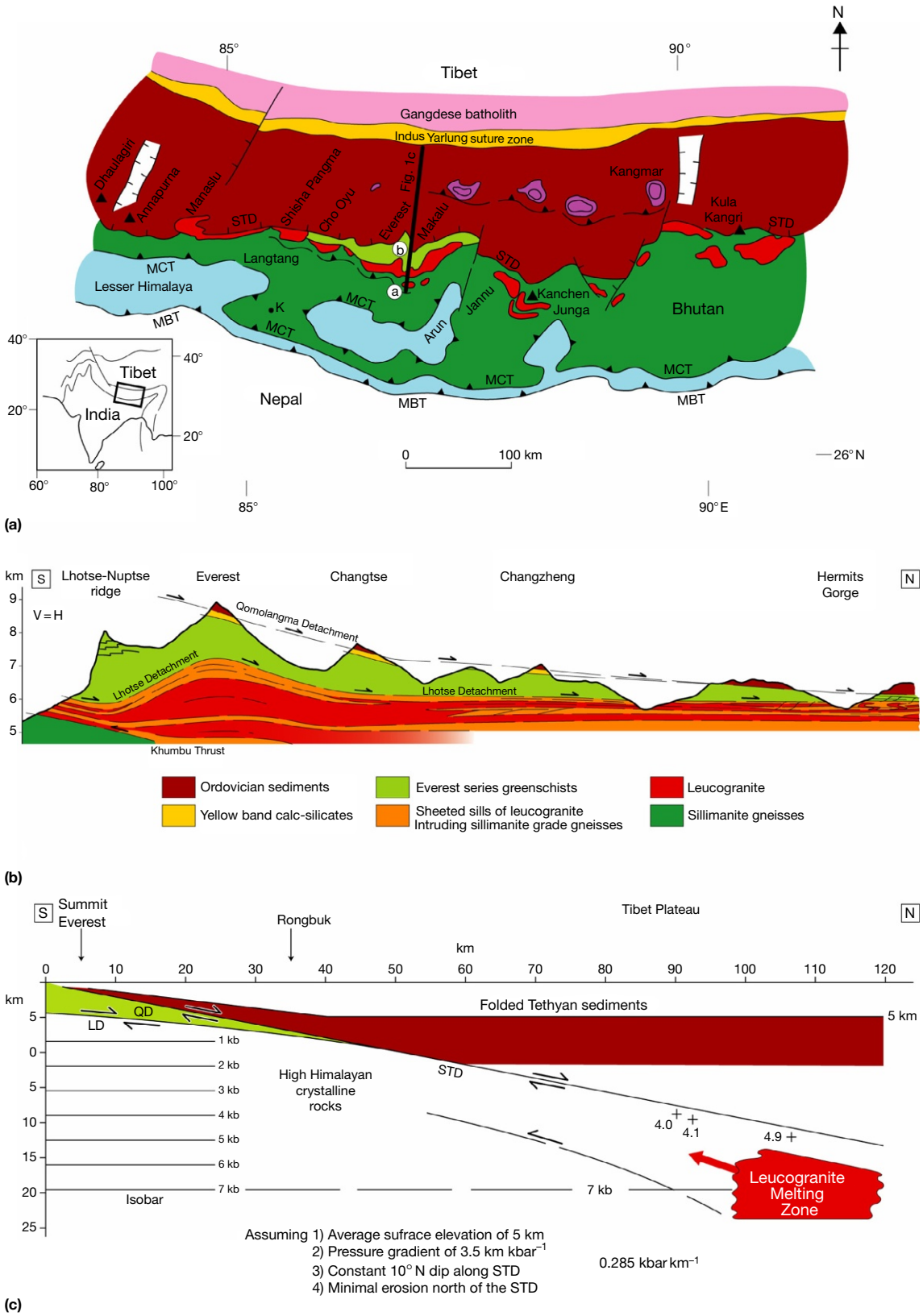

Figure 14 Geologic map and cross section of the Everest profile, Nepal, and South Tibet, after Searle (2007). Bottom diagram shows a simply restoration of the STD using pressures to constrain depth of melting and assuming constant dip on STD. Results of restoration suggest a minimum southward extrusion of c.100 km along the footwall of the STD.

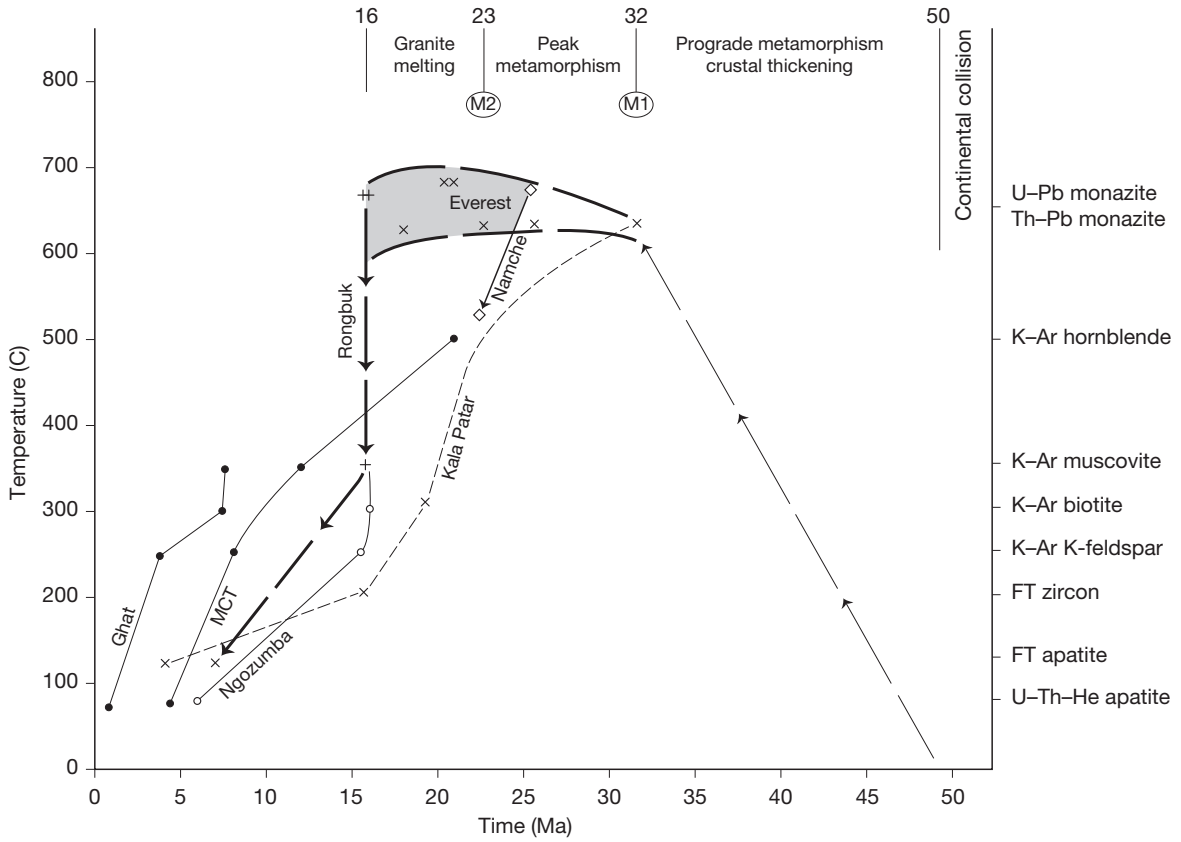

Figure 15 Temperature versus time diagram showing geochronological data from the Everest Himalaya, after Searle et al. (2003). Crustal thickening led to increasing temperature and pressure from 50 to 30 Ma, when kyanite metamorphism peaked. Slight decompression and temperature increase from 30 to 16 Ma led to sillimanite-grade metamorphism and partial melting. Rapid extrusion of the partially molten midcrustal Greater Himalayan sequence during the Miocene led to rapid cooling during the Late Miocene–Pliocene.

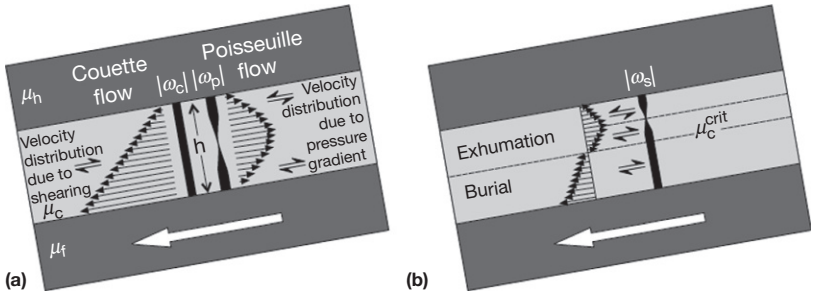

Figure 16 End-member models of crustal flow in a viscous channel, after Grujic et al. (2002), Godin et al. (2006), and Law et al. (2011). (a) Couette flow with velocity profile caused by shearing (left) and Poiseuille flow where the velocity gradient is due to the pressure gradient and maximum flow occurs in the middle of the channel (right). (b) Diagram illustrating the metamorphic and strain pattern expected in an extruding midcrustal channel. For the Himalaya, the lower part of the GHS shows burial, prograde metamorphic conditions, and top-to-south kinematic indicators, whereas the top of the GHS shows exhumation-related top-to-north 'extensional' kinematic indicators. Most migmatites and Himalayan leucogranites are contained with the top part of the GHS during the decompression, exhumation stage.

the world. The area of high elevation lies north of the Himalaya and includes the Karakoram and Pamir ranges in the west, the Kunlun and Altyn Tagh ranges in the north, and the Longmenshan range along the eastern border of the plateau. It includes the northernmost part of the Indian Plate, the Tethyan Himalaya, the Indus–Yarlung Tsangpo suture zone, and the Lhasa and Qiangtang terranes of south and central Tibet and the Jinsha suture and Kunlun terrane of North Tibet. The timing of uplift of the plateau is important not only for tectonic models of continental collision but also for links with climate evolution and environmental changes across Asia.

GPS velocities derived from measurements spanning 1998 to 2004 show mostly orthogonal motion across the western and central Himalaya, swinging gradually toward the NE and

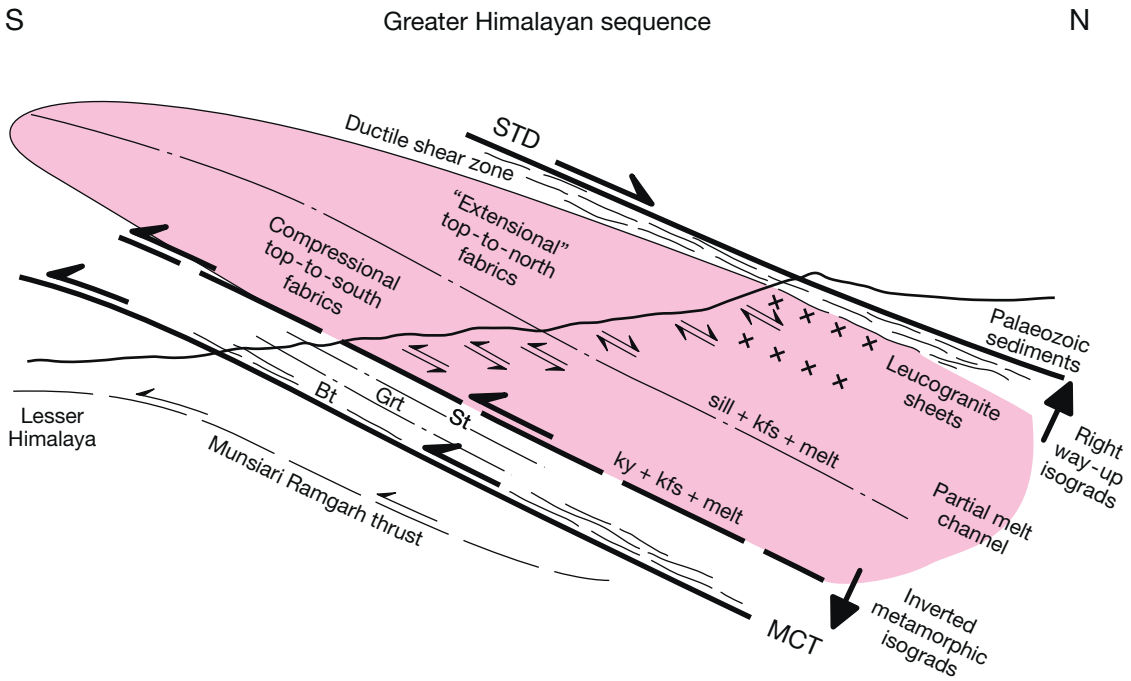

Figure 17 Diagrammatic representation of the GHS along the Langtang–Ganesh Himalaya, Nepal, showing the predominance of top-to-south fabrics in the lower part of the GHS above the Main Central Thrust with associated inverted metamorphic isograds, and the predominance of top-to-north kinematic indicators and right-way-up metamorphic isograds in the upper part of the GHS beneath the South Tibetan Detachment low-angle normal fault.

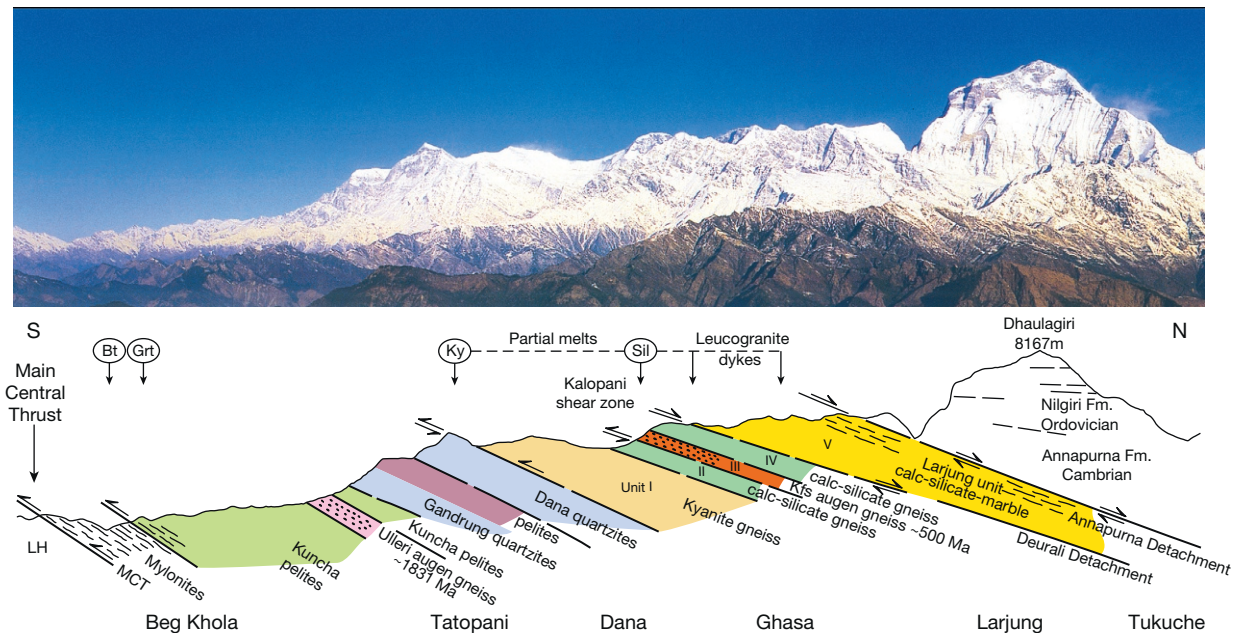

Figure 18 Photograph and sketch of the geologic profile along the Dhaulagiri Himal in Nepal showing location of the high-strain Main Central Thrust and South Tibetan Detachment ductile shear zones and distribution of metamorphism across the GHS, after Searle (2010).

east-directed motion across the eastern part of the plateau (Gan et al., 2007; **Figure 20**). GPS data show north–south shortening rates of 40 mm year^{-1} across the plateau, with almost 20 mm year^{-1} east–west motion with respect to India and stable Asia. However, GPS data only reveal relative motions of the surface at the present time; they do not provide information on past motions or on flow in the deeper crust that may be decoupled from the upper crust, as is known to be the case beneath the Himalaya and South Tibet. It is therefore dangerous to assume coupling of upper and lower crust in eastern Tibet, and GPS data do not provide any information on lower crustal flow.

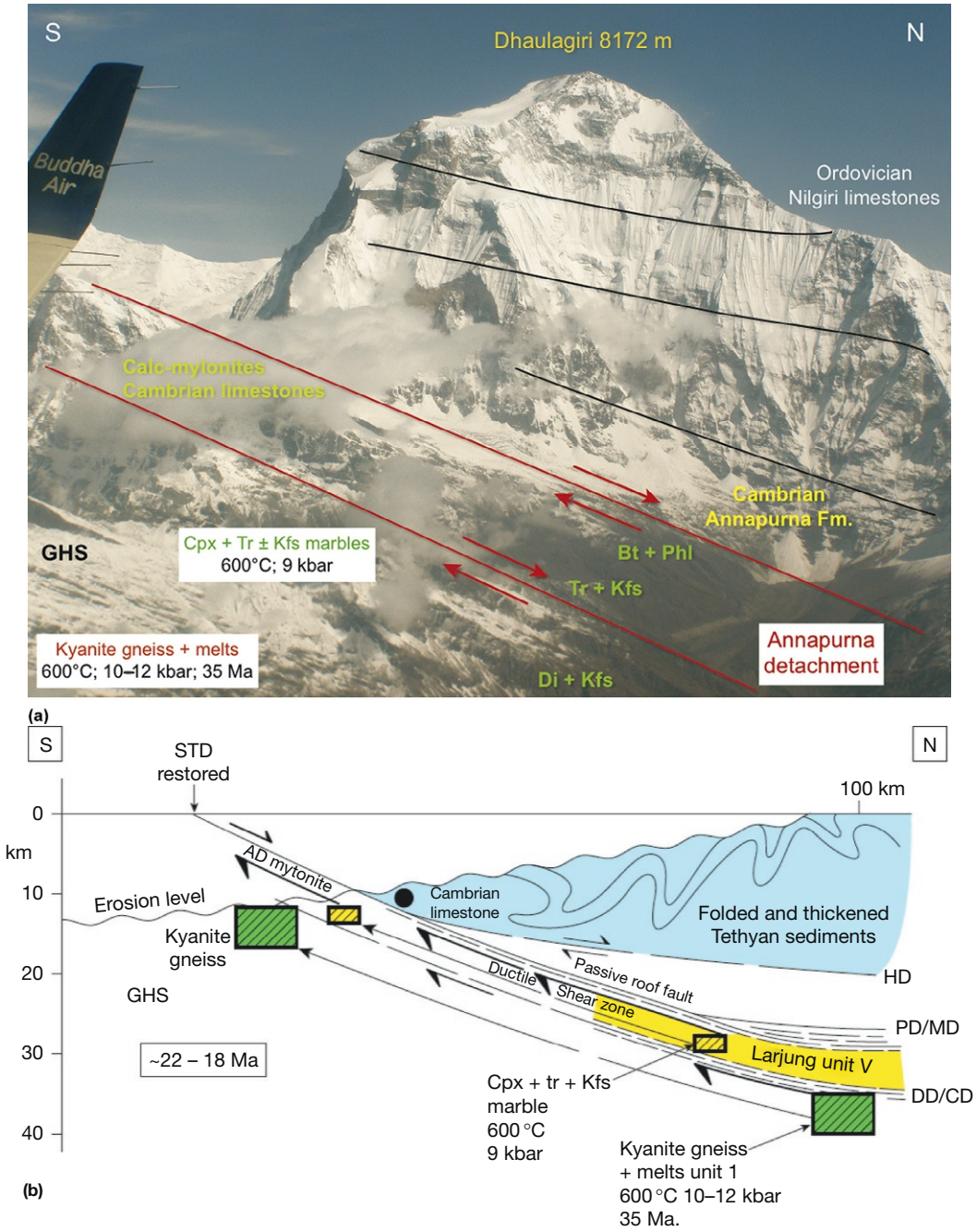

Figure 19 (a) Aerial photograph of Dhaulagiri (8172 m) in western Nepal view toward west, showing the main faults and shear zones with temperatures, pressures, and timing of each rock unit across the South Tibetan Detachment low-angle normal fault. (b) Reconstruction of the STD low-angle normal fault in Dhaulagiri showing the pressures–depths of each unit (Larjung unit clinopyroxene + tremolite + K-feldspar marble (yellow) and kyanite gneiss (green)) and the inferred motion of exhumation during Miocene (22–18 Ma) channel flow, after Searle (2011). Resulting top-to-north kinematic indicators and S-C fabrics show how apparently extensional fabrics are formed in an exhumation channel in a compressive tectonic environment.

6.11.5.1 Precollisional Crustal Thickening

The youngest marine sedimentary rocks in the Lhasa Block of South Tibet are Albian–Aptian (~125–100 Ma) shallow marine limestones of the middle Takena Formation (Kapp et al., 2007; Leier et al., 2007). After this time, the entire region was lifted above sea level and continental fluvial and lacustrine sedimentation predominated. A regional unconformity across the Lhasa Block shows folded Takena Formation redbeds truncated beneath flat-lying Linzizong calc-alkaline andesites, suggesting that crustal shortening must have occurred prior to 60 Ma, before the India–Asia collision (Kapp et al., 2007; Searle et al., 2011). Regional thermochronological data ($^{40}Ar/^{39}$, apatite fission track and apatite (U–Th)/He ages) show relatively old ages across the plateau (depths of <3 km

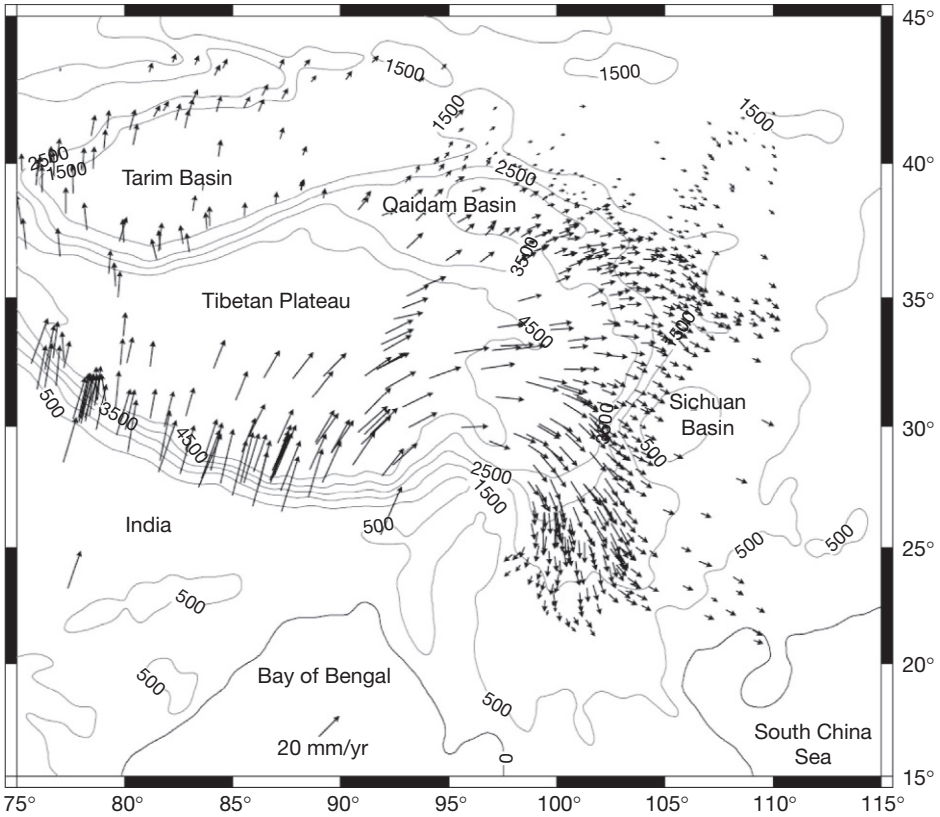

Figure 20 GPS velocities across Tibet relative to a stable Eurasia, after Gan et al. (2007); Chen et al. (2000) and Wang et al. (2001). Contour lines indicate smoothed surface elevations using a 200 km wide Gaussian filter.

between 85 and 45 Ma; Hetzel et al., 2011; Rohrmann et al., 2012). The ages show that plateau growth during the Late Cretaceous in central Tibet expanded to cover to whole plateau by 45 Ma and strongly suggest the presence of a high, elevated plateau since then.

Unlike the Karakoram and the Pamir, there is little field evidence of Cenozoic crustal shortening across Tibet, casting doubt on models involving postcollisional homogeneous thickening of the Tibetan Plateau (Dewey and Burke, 1973; Houseman et al., 1981). Whereas there is abundant evidence for Cenozoic shortening, thickening, and regional metamorphism in the Karakoram (Searle et al., 2010a) and Pamir (Schmidt et al., 2011; Stearns et al., 2013), there is little evidence for regional metamorphism during the Cenozoic across the plateau as would be expected for postcollisional homogeneous thickening. In fact, most of the metamorphism in Tibet is related to either the Triassic–Early Jurassic Indosinian orogeny (Pullen et al., 2011; Weller et al., 2013) or an earlier Permian subduction-related high-pressure event recorded by Permian eclogites across the middle of the Lhasa Block (Yang et al., 2009). The only record of Neogene metamorphism and magmatism in Tibet is some enigmatic metamorphic rocks and leucogranitic dikes in the West Nyenchen Tanglha range, north of Lhasa (Kapp et al., 2005).

The almost complete lack of Neogene deformation and metamorphism in Tibet, as well as the exhumation history of the rocks as revealed by low-temperature thermochronological data across Tibet (Hetzel et al., 2011; Rohrmann et al., 2012), contrasts strongly with the Cenozoic metamorphic and magmatic history of the Karakoram (Fraser et al., 2001; Searle et al., 1992, 2010a) and Pamir (Schmidt et al., 2011; Stearns et al., 2013) to the west. Geologic and geochronological data support the model of passive uplift of Tibet by underthrusting of Indian lower crust and mantle lithosphere beneath the south and central part of the plateau (Argand, 1924; Searle et al., 2011), whereas data from the Karakoram and Pamir support underthrusting as well as Cenozoic crustal thickening, regional metamorphism, and widespread crustal melting forming the giant Baltoro granite batholith in northern Pakistan.

6.11.5.2 Precollisional Magmatism

Along the southern margin of the Lhasa terrane (South Asian margin), a 2500 km long batholith composed mainly of I-type hornblende- and biotite-bearing granites, granodiorites, and diorites crops out from northern Kohistan (Pakistan) across Ladakh and southern Tibet to the eastern Himalayan syntaxis. These Ladakh–Gangdese granites are related to the northward subduction of Tethyan oceanic lithosphere beneath the South Asian continental margin. The granites have an extensive calc-alkaline volcanic superstructure comprising andesites, rhyolites, and ignimbrite flows (Linzizong volcanic rocks; Chiu et al., 2009; Ding et al., 2007; Kapp et al., 2007; Mo et al., 2007, 2008; Wen et al., 2008a,b), of similar composition and areal extent to the Central Andean volcanic province. U–Pb zircon ages of Gangdese granites range from Early

Jurassic to Early Eocene (198–49 Ma), suggesting long-lasting I-type magmatism (Chu et al., 2006; Chung et al., 2005). Zircon U–Pb ages from the Gangdese granites and ^{40}Ar–^{39}Ar ages from the Linzizong volcanics show two distinct phases of volcanism, a widespread Cretaceous stage (~133–110 Ma) and an intense magmatic 'flare-up' in the Paleocene (66–57 Ma) when compositions vary from low-K tholeiite through calc-alkaline andesite to shoshonitic suites (Chiu et al., 2009; Lee et al., 2009).

Both Ladakh–Gangdese granitoids and Linzizong-type andesite–ignimbrite volcanic rocks ceased around the time of Indian Plate collision as oceanic subduction beneath the South Asian margin ended. Thinned Indian crust along the leading northern margin was dragged down the subduction zone between 57 and 47 Ma (U–Pb ages of the UHP eclogites from Kaghan and Tso Morari; Parrish et al., 2006; St-Onge et al., 2013), which rapidly choked the subduction zone leading to slab break-off and rapid buoyant return flow of the deeply buried eclogites. Final magmatism along the Kohistan–Ladakh–Gangdese batholith was a series of garnet-bearing leucogranitic dikes (Indus confluence dikes in Kohistan and Chumathang dikes in Ladakh) formed by extreme differentiation of the initial calc-alkaline batholith or possible mixing with a sedimentary protolith in the source. After 47 Ma, no subduction-related calc-alkaline magmatism is recorded. Plutons younger than 47 Ma have an alkaline chemical composition and are related to postcollisional adakites (Chung et al., 2005).

6.11.5.3 Shoshonite and Adakite Volcanism

Postcollisional intrusive dikes and alkalic volcanic rocks are distributed widely across the whole Tibetan Plateau, and the age and geochemistry allow us to interpret the evolution of the mantle beneath Tibet in space and time (**Figure 21**). Some of these dikes contain xenoliths of granulites, eclogites, and peridotites sourced from the lower crust and upper mantle (Chan et al., 2009; Hacker et al., 2000). Potassium-rich shoshonites and subordinate sodium-rich lavas were erupted across the Qiangtang terrane between 50 and 30 Ma (Chung et al., 2005). Ultrapotassic volcanic rocks requiring a hot, enriched mantle lithosphere were erupted across the Lhasa Block between 30 and 10 Ma (Chung et al., 1998, 2003, 2009; Nomade et al., 2004; Wang et al., 2010).

Adakites were originally found in thick island arcs, such as the Aleutians (Kay and Kay, 2002), but have more recently been found across the Tibetan Plateau (Chung et al., 2003, 2005). Tibetan adakites are intermediate to felsic lavas, lack a mafic phase, are generally sodium-rich, and have other geochemical characteristics (high MgO and Sr, low Y, and heavy REE) similar to island arc adakites. The geochemistry of adakites requires a garnet-bearing source, either eclogite or garnet amphibolite of lower crustal origin (elevated La/Yb and Sr/Y ratios, strongly fractionated rare-earth elements), and hence, their presence suggests a thick crust. They are generally thought to be modern equivalents of the tonalite–trondhjemite–granodiorite (TTG) suites dominant across many Archean terranes (Foley et al., 2003; Martin, 1988).

Miocene potassic to ultrapotassic volcanism is widespread across southern Tibet between 26 and 8 Ma (Chung et al., 2005), indicating a hydrous (phlogopite-bearing) hot and weak mantle lithosphere beneath southern Tibet during the Miocene. Felsic and mafic granulite and pyroxenite xenoliths entrained in 17–14 Ma ultrapotassic dikes suggest very high pressures and temperatures (1330–1130 °C; 26–22 kbar) in the lower crust at that time (16.8 ± 0.9, 15.6 ± 0.6, and 14.4 ± 0.4 Ma from $^{206}Pb/^{238}U$ dating of zircons; Chan et al., 2009). The xenolith compositions enable us to propose a schematic crustal section through Tibet (**Figure 22**) where the lower crust is composed of felsic and mafic granulites, ultramafic hornblende- and biotite-rich restites, and garnet and clinopyroxene eclogites (Searle et al., 2011). Shoshonitic volcanics together with ultrapotassic lamproites and lamprophyres are sourced from a harzburgite–lherzolite mantle, whereas adakites are sourced from the garnet-bearing amphibolites and eclogites. The middle crust is composed dominantly of precollisional tonalites and granodiorites hosting shallow level reservoirs of postcollisional late adakitic melts.

In the Qiangtang terrane, central Tibet, both peraluminous rhyolites and dacites and metaluminous andesitic porphyries have adakitic geochemical characteristics. North–south-aligned andesitic porphyry dikes have been dated at 47–38 Ma, suggesting that not only had the Tibetan crust already been thickened by that time but also east–west extension was operative (Wang et al., 2010). Geochemical and Sr–Nd isotopic data suggest that the dikes were derived from partial melting of enriched lithospheric mantle with some metasomatism related to continental crustal subduction. Hacker et al. (2000) described several localities in the Qiangtang terrane where lower crustal metasedimentary xenoliths and xenocrysts were found within 2.5–3.2 Ma shoshonitic lavas. These anhydrous granulite facies xenoliths include ortho- and clinopyroxene, garnet, biotite, K-feldspar, and quartz with the more aluminous samples containing sillimanite, cordierite, orthopyroxene, and quartz. These metapelitic or psammitic granulites equilibrated at temperatures of 800–1100 °C and depths of 30–50 km (Hacker et al., 2000). No eclogite or mantle-derived peridotite xenoliths seem to be present in the Qiangtang volcanic rocks. In the Karakoram terrane, the western extension of the Qiangtang terrane, numerous lamprophyric dikes (biotite-bearing minettes and hornblende-bearing vogesites) with similar Oligocene–Early Miocene ages intrude the northern Karakoram terrane (Searle et al., 1992, 2010a).

The youngest magmatic rocks in Tibet are seen across the Kunlun terrane in the far north of the plateau, where potassium-rich shoshonitic volcanic rocks erupted in the Middle Miocene to Quaternary. The spatial distribution and ages of the volcanic rocks across Tibet suggest that Tibet was underlain by thick crust with an eclogite or garnet amphibolite root and hot mantle throughout the Late Eocene to Middle–Late Miocene. As Indian lower crust and cold lithospheric mantle progressively underthrust to the north, jacking up the plateau, the hot, weak mantle was progressively pushed to the north. In the last few million years, only the northern plateau region along the Kunlun retains this hot mantle. This region also coincides with the area showing strong east–west seismic anisotropy (Owens and Zandt, 1997) suggesting some eastward escape of Kunlun lithosphere.

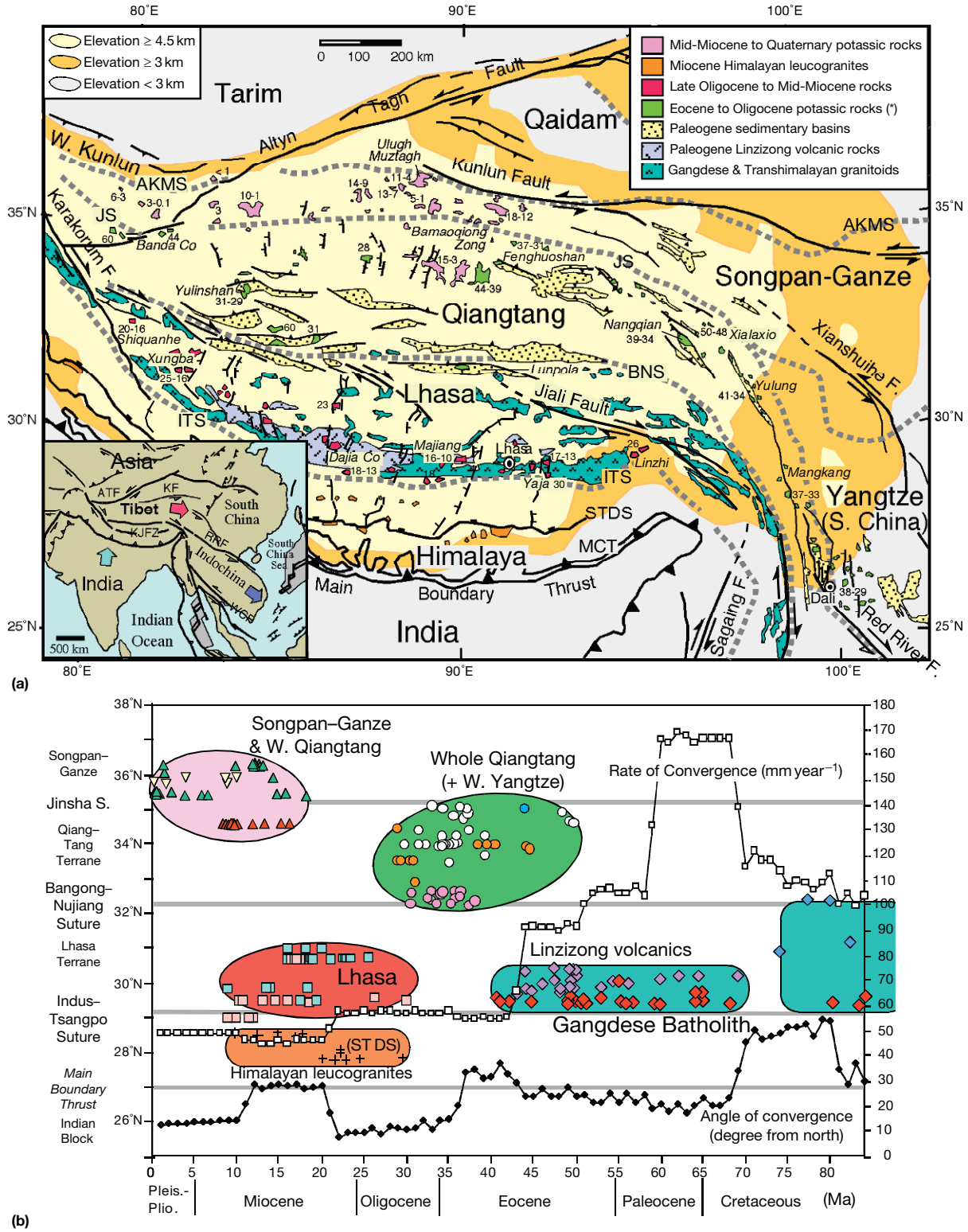

Figure 21 (a) Simplified geologic map of the Tibetan Plateau and surrounding areas, modified after Chung et al. (2005) showing distribution of postcollisional (potassic) magmatism across Tibet with their age ranges in numerals (see text and Chung et al., 2005, 2009; Lee et al., 2009; Wang et al., 2010 for sources of data). MBT, Main Boundary Thrust; MCT, Main Central Thrust; STDS, South Tibetan Detachment system; ITS, Indus–Yarlung Tsangpo suture zone; BNS, Bangong–Nujiang suture; JS, Jinsha suture; AKMS, Anyimaqin–Kunlun–Muztagh suture; ATF, Altyn Tagh fault; KF, Kunlun fault; KJFZ, Karakoram–Jiale fault zone; RRF, Red River Fault; WCF, Wang Chao fault. (b) Spatial variation in Tibetan magmatism across Tibet, showing geographic distribution of volcanic rocks (left margin) against time, after Chung et al. (2005). Precollisional Gangdese granites and calc-alkaline Linzizong volcanics (blue) end soon after closure of Neotethys and India–Asia collision. Postcollisional adakites and shoshonites span the whole period following India–Asia collision with the youngest rocks along the Kunlun ranges, northern Tibet.

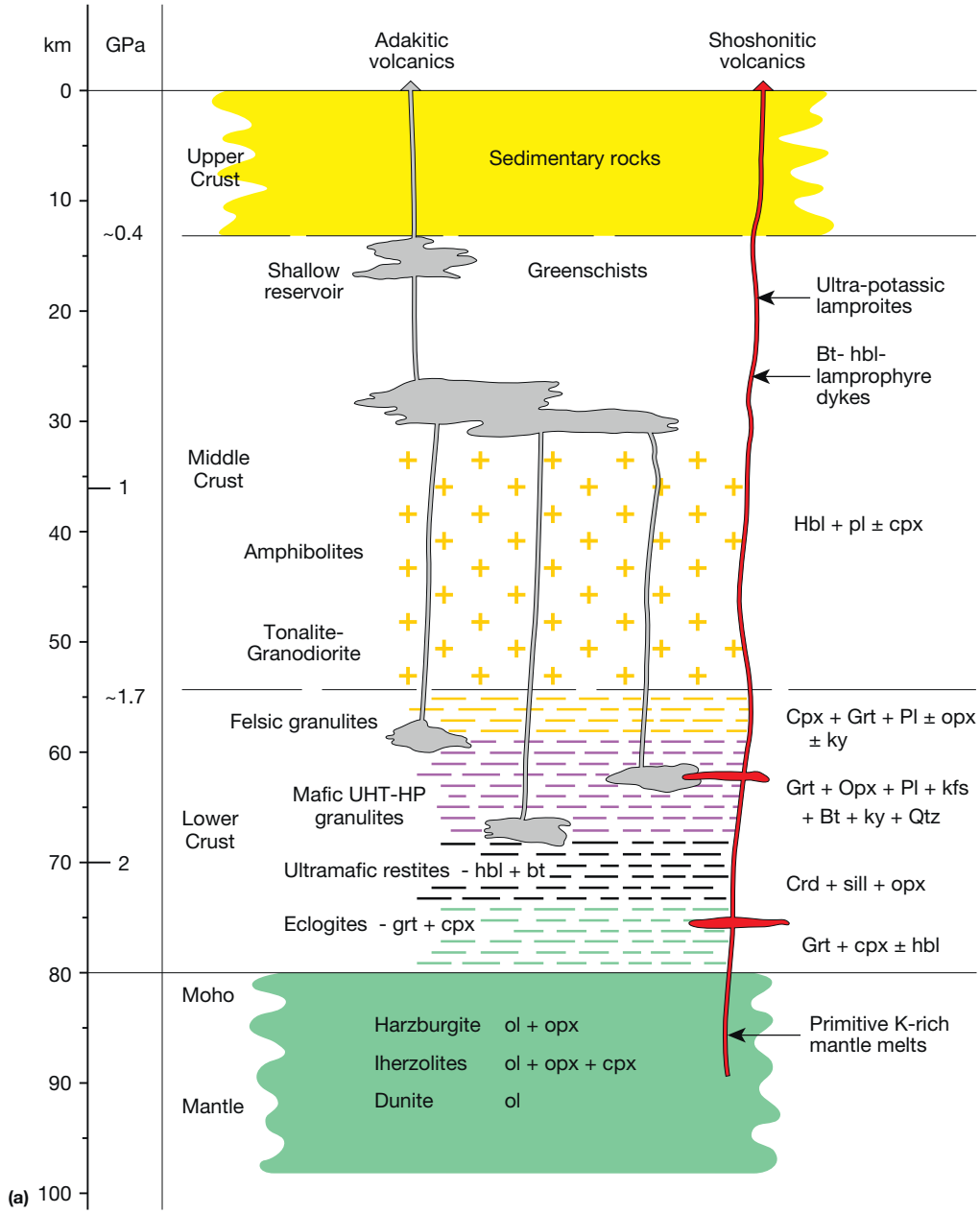

Figure 22 (a) Schematic crustal section through Tibet illustrating a model showing the proposed origin and emplacement of postcollisional adakites and shoshonites, after Searle et al. (2011). Crustal thickness is from Owens and Zandt (1997), Schulte-Pelkum et al. (2005), and Nábelek et al. (2009). Depths of adakite reservoirs and sources are from Guo et al. (2007). Mineral compositions of lower crust granulites and eclogites and ultramafic restites are from xenoliths entrained in shoshonitic dikes (Chan et al., 2009; Hacker et al., 2000). (b) Field photo of a typical adakitic dike intruding the Lhasa Block. (c) Shoshonitic dike from near Xigase, SW Tibet.

6.11.5.4 Strike-Slip Faults in Tibet

Large-scale strike-slip faults extend across the Tibetan Plateau, but their importance in terms of geologic offsets, timing of motion, slip rates, and extent of their depth has remained controversial. The original continental extrusion hypothesis for Tibet (Avouac and Tapponnier, 1993; Molnar and Tapponnier, 1975; Tapponnier et al., 1982, 2001) suggested that the boundaries of the extruding thickened crust were the right-lateral Karakoram fault along the SW and the left-lateral Altyn Tagh and Kunlun faults along the north. The latter two faults bound the Qaidam Basin and extend east beyond the boundary of Tibetan thick crust. Only the Altyn Tagh fault actually bounds the thickened crust of Tibet; all the other strike slips in Tibet have thick crust on both sides of the fault or cut through areas of thick crust. The thickest crust known, up to 90 km, occurs along the northern Karakoram (Wittlinger et al., 2004) to the west of the Karakoram strike-slip fault. The Kunlun, Xianshuihe, and Jiale faults curve around the eastern Himalayan syntaxis and record the major right-lateral shear and clockwise rotations around the SE parts of Tibet.

A detailed review of all Tibetan strike-slip faults has recently been published in Searle et al. (2011). Interpreting the history of slip along these faults depends on the timescale. Active motion over decadal timescales can be inferred from GPS and InSAR measurements. Late Quaternary slip rates can be inferred from dating of offset surface features using *in situ* cosmogenic nuclides and radiocarbon dates. Long-term geologic slip rates can be derived from U–Th–Pb dating of accurately mapped offset granitoids or metamorphic rocks.

6.11.5.4.1 Karakoram fault

The Karakoram fault in far SW Tibet and northern Ladakh (India) is the most extensively mapped and studied of all these Tibetan strike-slip faults (**Figure 23**). The ~700 km long NW-SE (~140°) striking vertical Karakoram fault runs from the Tashkurgan region of the northeastern Pamir to the Kailash region of SW Tibet (**Figure 1**). The fault cuts obliquely across the geologic terranes of the Pamir, Karakoram–Qiangtang, and Ladakh–Gangdese Ranges (Searle and Phillips, 2007). The northwestern end terminates in a series of contractional faults in the central Pamir where mapping has demonstrated that major gneiss domes (e.g., Kongur and Muztagh Ata) are not offset across the fault (Robinson, 2009a,b; Robinson et al., 2007). The southeastern end of the Karakoram fault merges into the Indus–Yarlung Tsangpo suture zone south of Mount Kailash, where north-directed backthrusting occurs along the northern margin of the Indian Plate (Searle, 1996; Searle et al., 1997a,b) and north–south extensional faulting occurs in the Purang graben (Murphy et al., 2000). The Karakoram fault forms one major strand along the Nubra Valley in Ladakh, but in the Tangtse region, the fault splays into two branches, the Tangtse fault strand to the SW and the Pangong fault strand to the NE, both of which display spectacular mylonites (**Figure 23**). Between the two strands, the Pangong range is an exhumed metamorphic complex comprising amphibolites, hornblende-biotite diorites, orthogneisses, migmatites, and abundant leucogranite dikes. Stretching lineations plunge between 0 and 20°NW along the Nubra Valley sector and ~30°NW at Tangtse, suggesting increasing vertical exhumation as well as dextral strike-slip in this region. In the central part, the fault cuts through numerous lithologic units, including precollisional Cretaceous hornblende–biotite granodiorites, granulite- and amphibolite facies metamorphic rocks, and a prominent leucogranite dike network.

Structural mapping combined with U–Pb dating shows that metamorphic rocks and almost all granites exhumed along the Karakoram fault formed prior to strike-slip shearing along the fault (Phillips et al., 2004; Searle, 1996; Searle et al., 1998; Streule et al., 2009) and not during strike slip (Lacassin et al., 2004; Valli et al., 2007, 2008; Weinberg and Mark, 2008; Weinberg et al., 2009). Both metamorphic rocks and granites extend west into the Baltoro region of north Pakistan, well away from the Karakoram fault. U–Pb ages of amphibolite facies metamorphic rocks cut by the Karakoram fault at K2 (Searle and Phillips, 2004) and Pangong (Streule et al., 2009) are Cretaceous. Geologic markers (notably the intrusive margins of the Baltoro and Nubra–Siachen granites) have been offset dextrally between 25 km (minimum) and 120–150 km (maximum) since 17 Ma (Phillips and Searle, 2007; Searle and Phillips, 2007; Searle et al., 2010a, 2011). A few late-stage leucogranite dikes cut the mylonite fabric, providing an upper age on the ductile shearing that formed mylonites. Phillips et al. (2004), and Phillips and Searle (2007) carried out detailed mapping combined with U–Pb ID-TIMS dating of granitoids along the shear zone. They concluded that ductile shearing along the Tangtse strand of the fault occurred between 15.68 and 13.73 Ma, based on U–Pb ages determined from early deformed protomylonitic leucogranites parallel to the mylonite foliation and late leucogranite dikes that cut the mylonite fabric. Brittle faults along the margins of the shear zone cut all rocks and prominent pseudotachylytes within the ductile shear zone indicate paleoearthquake ruptures. Using ^{40}Ar–^{39}Ar dating, Dunlap et al. (1998) demonstrated two phases of rapid exhumation, a dominantly transpressional phase from 17 to 13 Ma and a dominantly strike-slip phase of motion after 13 Ma.

The Karakoram fault does not appear to be particularly active today and has almost no historic earthquake activity, despite being a major geomorphological feature. The fault also shows little, if any, Quaternary offset (Robinson, 2009a,b). Present-day slip rates measured from InSAR and GPS (<7 mm year^{-1}; Wright et al., 2004) and Altyn Tagh fault (~11 mm year^{-1}; Elliott et al., 2008) and long-term geologic rates can only account for limited eastward extrusion of Tibet since Middle Miocene time. The relatively minor geologic offsets and low slip rates do not support large-sale continental extrusion of Tibetan crust along the Karakoram fault.

6.11.5.4.2 Altyn Tagh fault

The Altyn Tagh fault is a large-scale left-lateral strike-slip fault stretching for over 2000 km along the northern margin of the Tibetan Plateau and south of the Tarim Basin (**Figure 1**). It extends eastward beyond the limits of thickened Tibetan crust and runs along the northern boundary of the Qaidam Basin. Tapponnier et al. (1982) first proposed 500–700 km of left-lateral offset along the Altyn Tagh fault but provided no details of offset markers. Peltzer and Tapponnier (1988) proposed an ~500 km displacement of Paleozoic granodiorites between the western and eastern Kunlun Shan based upon Chinese

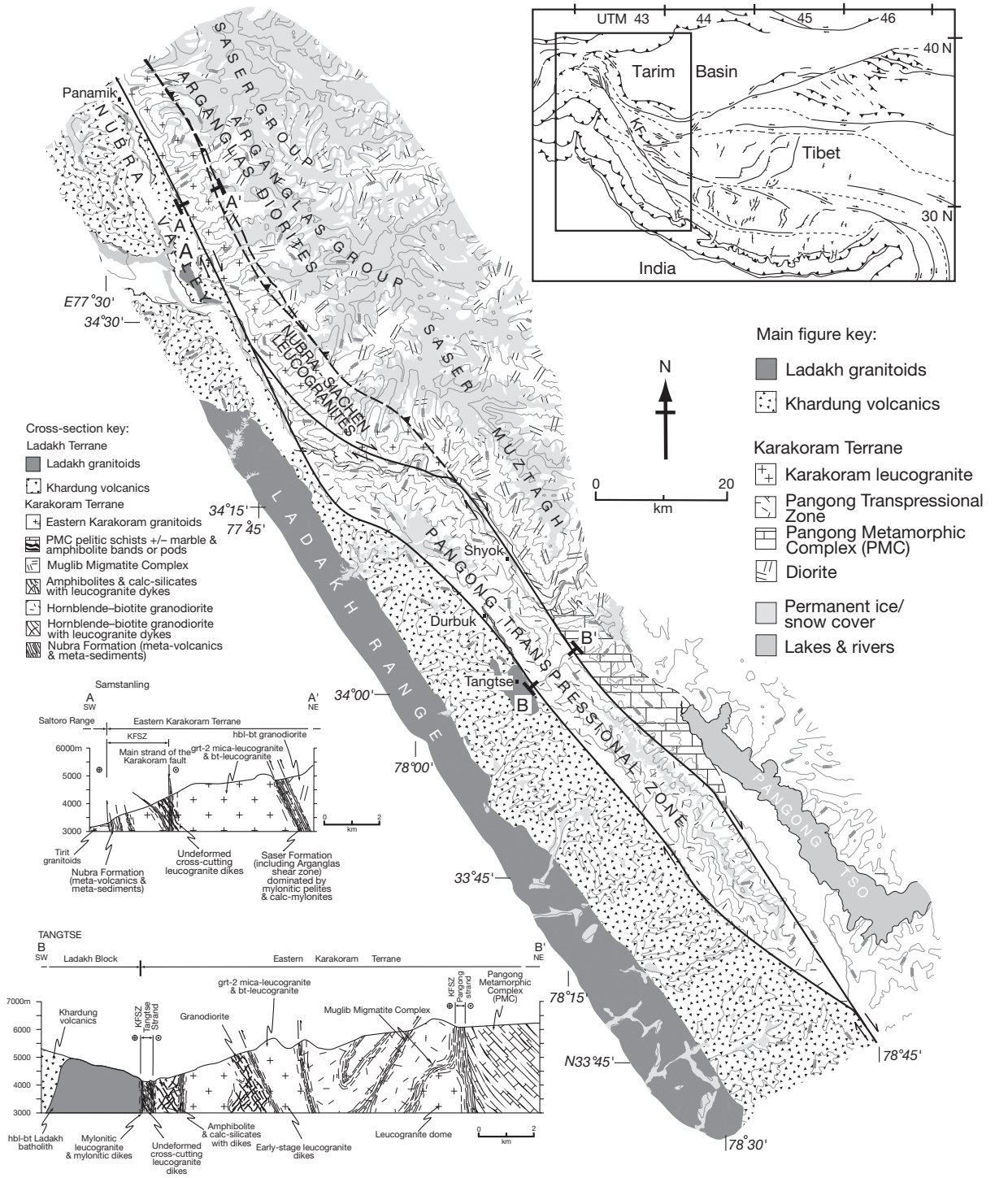

Figure 23 Geologic map and cross section of the Karakoram fault in northern Ladakh (India). Reproduced from Phillips RJ, Parrish RR, and Searle MP (2004). Age constraints on ductile deformation and long-term slip rates along the Karakoram fault zone, Ladakh. *Earth Planetary Science Letters* 226: 305–319; Phillips RJ, Searle MP, and Parrish RR (2013). The geochemical and temporal evolution of the continental lithosphere and its relationship to continental-scale faulting: The Karakoram Fault, eastern Karakoram, NW Himalayas. *Geochemistry*, *Geophysics*, *Geosystems* 14, http://dx.doi.org/10.1002/ggge.20061.

geologic mapping. Wang (1997) proposed a late Cenozoic left-slip offset of 69–90 km at 94°E, but due to a poorly constrained initiation of major faulting, the range of slip rates is 7–45 mm year^{-1}. However, Ritts et al. (2004) argued that this measurement is inaccurate due to mismatched offsets. Yin and Harrison (2000) calculated an average slip rate of 7–9 mm year^{-1} from an estimated left slip of ~280 ± 30 km since the Early Oligocene (~30 Ma) based on a piercing point defined by Cenozoic thrusts. Ritts and Biffi (2000) proposed ~400 km of left-lateral offset along the ATF based on an offset north–south aligned Jurassic paleoshoreline and ~360 km offset of Paleozoic felsic plutons. These authors and Yue et al. (2001, 2003) suggested a long-term Cenozoic slip rate of 12–16 mm year^{-1}, calculated from these stratigraphically correlated basin units. These offsets and slip rates are similar to the ~425 km proposed by Cowgill et al. (2003) for early Paleozoic piercing points. Initiation of slip along the Altyn Tagh fault is thought to have been Late Oligocene–Early Miocene (~23 Ma) from strata in the Xorkol basin bounding the fault at 92°E (Yue et al., 2001, 2003). However, Yin et al. (2002) estimated a significantly earlier age of fault initiation at 49 Ma with a total slip of ~470 ± 70 km, yielding a rate of 9 ± 2 mm year^{-1}. Provenance matching using zircon dating of Miocene conglomerate clasts constrains the long-term slip rate to <10 mm year^{-1} (Yue et al., 2003). However, this requires an accelerated slip rate between 25 and 17 Ma of 300 km offset (~40 mm year^{-1}). Therefore, a two-stage evolution in fault kinematics has been suggested with fast slip and extrusion during Late Oligocene–Early Miocene, changing to slow slip and crustal thickening up to the present (Ritts et al., 2004; Yue et al., 2001, 2003). Quaternary and active slip rates measured from InSAR and GPS are between 5 and 15 mm year^{-1}, but decrease toward the east (Elliott et al., 2008; Jolivet et al., 2008; Wright et al., 2004) and are not high enough to support large-scale continental extrusion.

6.11.5.4.3 Haiyuan fault

The most prominent faults in eastern Tibet are the Haiyuan, Xianshuihe, and Jiale faults that originate on the high plateau but extend east, curving around the eastern Himalayan syntaxis. The Haiyuan fault is a vertical left-lateral strike-slip fault that runs for ~1000 km from the northeastern part of the Tibetan Plateau, north of the Qaidam Basin across, to the Ordos Block (**Figure 1**). Burchfiel et al. (1991) suggested only 10.5–15.5 km offset along the Haiyuan fault by matching geologic markers across the fault. They showed that progressively smaller offsets occurred on younger rock units and proposed an average Pleistocene slip rate of 5–10 mm year^{-1} assuming that faulting started at the end of the Pliocene. In contrast, Gaudemer et al. (1995) estimated an offset of 95 km with a much older initiation age of 10 Ma, which also suggests a slip rate of ~10 mm year^{-1}. Ding et al. (2004) estimated ~60 km of left-lateral strike-slip offset along the Haiyuan fault zone since Upper Miocene by summing the offsets of three classes of pull-apart basins developed during different periods, giving an average rate of 6.5 mm year^{-1}.

Estimates of Late Pleistocene and Holocene slip rate for the Haiyuan fault based on ^{10}Be and ^{26}Al cosmogenic dating of offset moraines and alluvial terrace and riser offsets dated with ^{14}C ages (Lasserre et al., 1999; Zhang et al., 1988) range from 12 ± 4 to 19 ± 5 mm year^{-1}. The current slip rate estimated from InSAR is 4–8 mm year^{-1} (Cavalie et al., 2008) and is in near agreement with 8.6 mm year^{-1} derived from GPS observations (Gan et al., 2007). Microplate models for Tibet from Meade (2007) and Thatcher (2007) estimated fault slip rates of 9 and 6 mm year^{-1}, respectively.

6.11.5.4.4 Kunlun fault

The left-lateral Kunlun fault marks the northern boundary of the high-elevation, low-relief main part of the Tibetan Plateau for nearly 1500 km (**Figure 1**). The timing of initiation of strike-slip shearing and the finite displacement along the fault are both poorly constrained. Some authors have suggested 85 km of deflection of the Yellow River along the eastern segment of the fault (Gaudemer et al., 1989). Fu and Awata (2007) suggested a maximum offset of basement rocks of ~100 km and a maximum timing of shearing of 10 ± 2 Ma, giving a long-term slip rate of ~10 mm year^{-1}. In contrast, Jolivet et al. (2003) suggested that strike-slip motion in the western Kunlun ranges started at least by the Late Eocene, simultaneously with Eocene to Oligocene SW–NE compression. At ~15 Ma, extension resulted in pull-apart basins possibly concomitant with subduction of Tarim–Qaidam lithosphere southward beneath the Kunlun.

Slip rates along the Kunlun fault also vary considerably between short-term geodetic and long-term geologic rates. Quaternary slip rates along the Kunlun fault are, however, better constrained. Kirby et al. (2002) suggested that slip rates decrease systematically eastward along the eastern segment of the fault from >10 to <2 mm year^{-1}. These authors also showed that slip along the fault ends in the thickened crust of the plateau and that therefore any eastward extrusion must be absorbed by internal deformation in the plateau. This is supported by further observations east of 99°E, showing a lower slip rate of 2–6 mm year^{-1} for the easternmost portion of the fault (Harkins et al., 2010). The decrease in slip rate from ~10 mm year^{-1} to near zero over the last ~200 km of the eastern portion of the fault mirrors that observed for the eastern portion of the Altyn Tagh fault at 95–97°E (Zhang et al., 2007). Geodetic observations of 8–11 mm year^{-1} from GPS are in agreement for the western portion of the fault (Zhang et al., 2004). More recent GPS measurements also show a decrease in slip rate from 96 to 106°E of 14 to 2 mm year^{-1}. The microplate model of Thatcher (2007) suggests a uniform slip of 6–7 mm year^{-1} along the fault, whereas that from Meade (2007) suggests 10–11 mm year^{-1} for the western portion and 6–7 mm year^{-1} for the eastern segment. He and Chery (2008) in their mechanical model got consistent slip rates between 92 and 101°E of 8–12 mm year^{-1}, assuming a low effective fault friction.

6.11.5.4.5 Xianshuihe fault

The left-lateral active Xianshuihe fault cuts diagonally through the Songpan–Ganzi terrane, south of the Qaidam Basin in northeast Tibet southwest of the Longmenshan and Sichuan Basin, and curves around to north–south strike in western Yunnan (**Figure 1**). It appears to be one of the most active of all Tibetan faults, with several large earthquakes along it, including 8M7+ events since 1725 (Allen et al., 1991). West of 100°E, this activity appears to step left onto the

Ganzi–Yushu fault, which is also the locus of historical M ~ 7+ earthquakes, including the recent 2010 Yushu event.

The Xianshuihe fault cuts the eastern margin of the large Gongga Shan (7756 m) granite, a batholith-size body that includes early hornblende- and biotite-bearing diorites, granodiorites, and tonalites as well as later garnet-bearing two-mica granites. Roger et al. (1995) published a U–Pb zircon crystallization age of 12.8 ± 1.4 Ma but no information about precisely which phase of granite was dated. The Xianshuihe fault clearly cuts across the granite bodies with relatively minor offsets, so accurate U–Pb age on each granite phase is required before a detailed structural analysis can be made.

Geologic offsets of ~60 km for the last 2–4 Myr imply a long-term slip rate of 15–30 mm year^{-1} (Wang and Burchfiel, 2000). However, from thermochronology measurements dating the onset of fault activity at 13 Ma, Wang et al. (2009b) derived a long-term slip rate of 5.4 ± 0.8 mm year^{-1} based upon the 60–80 km offset and assuming an age of initiation (~13 Ma) based on K–Ar mica and apatite fission track ages. Holocene slip rates from radiometric dating are estimated to be 15 ± 5 mm year^{-1} in the northwest and 5 mm year^{-1} in the southeast Allen et al. (1991), with reestimates of the data yielding 14 ± 2 mm year^{-1} and 9.6 ± 1.7 mm year^{-1}, respectively (Xu et al., 2003). GPS measurements suggest an ~10 mm year^{-1} slip rate along the fault between 29 and 32°N with the rate decreasing to 4–7 mm year^{-1} as it runs north–south. Wang et al. (2009a) found a joint GPS and InSAR geodetic rate across the left-lateral fault at 101°E of 9–12 mm year^{-1} with a locking depth of 3–6 km.

The Kunlun and Xianshuihe faults rotate clockwise about a vertical axis showing that as India indented into Tibet, the eastern margin of the plateau was a large-scale zone of distributed right-lateral shear (Cobbold and Davy, 1988; England and Molnar, 1990). The eastern margin of the Tibetan Plateau (Longmenshan) shows no evidence of outward easterly crustal flow like the Himalaya; on the contrary, the margin appears to have been passively uplifted along steep west-dipping thrust faults such as those that ruptured during the Wenchuan earthquake.

6.11.5.4.6 Jiale fault

The right-lateral Jiale fault is the most prominent strike-slip fault of SE Tibet, running for at least 800 km WNW–ESE from the Bangong suture zone to the Burma–Yunnan border (**Figure 1**). North of the eastern Himalayan syntaxis, the fault splays into two branches, the northern Parlung fault that continues southeastward into the Gaoligong fault and the southern Puqu fault that swings around the syntaxis to align north–south and connect with the northern Sagaing Fault in Burma. The active deformation and GPS patterns (**Figure 20**) suggest a clockwise rotation around the eastern Himalayan syntaxis, with extruding crust bounded by the right-lateral Jiale, Gaoligong, and Sagaing faults in the west and the left-lateral Xianshuihe, Xiaojiang, and Dien Bien Phu faults in the east.

Armijo et al. (1989) proposed ~450 km of right-lateral offset along the Jiale fault without accurately dated markers or pinning points. Precise dating and mapping of offset geologic markers along the Jiale fault remain poorly defined. The Jiale fault cuts obliquely across the eastern Gangdese belt and cuts Cretaceous granites with U–Pb zircon ages of 136–113 Ma (Chiu et al., 2009). ^{40}Ar/^{39}Ar ages suggest that the main phase of strike-slip shearing was ~18–12 Ma (Lee et al., 2003; Lin et al., 2009). This age range overlaps with active shearing along ductile shear zones along the Gaoligong fault (Akciz et al., 2008; Lin et al., 2009) and the Sagaing Fault in Burma (Searle et al., 2007). It is also similar to the main strike-slip phase of motion along the Karakoram fault (Dunlap et al., 1998; Searle et al., 1998). Therefore, all the dated strike-slip faults in southern Tibet appear to have initiated more than 30 million years after the India–Asia collision.

6.11.5.5 East–West Extension in Tibet

The Tibetan Plateau is transacted by seven major north–south trending rift valley systems that were first identified from seismicity and Landsat imagery by Tapponnier and Molnar (1977), Molnar and Tapponnier (1978), and Ni and York (1978). Field investigations by Tapponnier et al. (1982) and Armijo et al. (1988, 1989) confirmed that north of the Himalaya in southern Tibet, east–west extension occurs on north–south normal faults, with rifts postdating contractional structures. These observations led to the idea of 'orogenic collapse' (Dewey, 1988). It is now known, however, that normal faults in the upper crust of Tibet were active synchronously with contractional structures and, because of the continuous underthrusting of Tibet by Indian lower crust (and to a lesser extent Tarim crust in the north), do not require a lowering of surface elevation or a decrease in crustal thickening. Armijo et al. (1988, 1989) noted the kinematic link between the northern limit of north–south rifts and the southern limit of northwest-striking right-lateral strike-slip faults. They explained the rifting as due to right-lateral transtension in southern Tibet along the Karakoram–Jiale fault zone, a series of WNW–ESE aligned strike-slip faults roughly along the Bangong suture zone that terminated in the south in the north–south-aligned grabens. They proposed that the Karakoram–Jiale fault system accommodated large-scale eastward extrusion of the Tibetan rigid block. North Tibet was therefore decoupled from South Tibet, allowing for the eastward extrusion of the northern plateau with respect to India, but not the Lhasa Block.

The rift valleys so prominent in South Tibet extend north into the Qiangtang terrane, where they form less prominent geomorphic features. Early knowledge about the more northerly rifts was based upon earthquake focal-plane solutions and limited Landsat imagery interpretation (Armijo et al., 1988; Molnar and Lyon-Caen, 1989). However, more recent field observations from northern Tibet (Yin et al., 1999) found significant north–south striking active normal faults, similar to those in the south, with up to 4–8 km displacements. The age of slip onset is uncertain, but Yin et al. (1999) estimated a minimum slip rate of 2 mm year^{-1}. This is similar to estimates from Armijo et al. (1988) of several kilometers of offset with slip rates of 1–4 mm year^{-1} for faults in southern Tibet. In a mirror image to the connection of strike-slip faults to the southern Tibet rifts, the rifts of northern Tibet are connected at their southern end to left-lateral strike-slip faults (Taylor et al., 2003). This forms a set of conjugate strike-slip faults, which accommodates the coeval north–south shortening and east–west extension of the plateau (Taylor and Peltzer, 2006; Taylor et al., 2003). McCaffrey and Nabelek (1998)

suggested that the driving force for the extension in southern Tibet was basal shear from the oblique sliding of the Indian Plate beneath the plateau. They noted the similarities with subduction along a curved boundary and the radial divergence of slip vectors along the Himalaya. However, the India–Asia collision is widely thought to have been orthogonal and not oblique, and there is no evidence of diachroneity in the timing of major events along the strike of the Himalaya (collision, peak metamorphism, anatexis, etc.) to suggest a diachronous or oblique collision.

Kapp and Guynn (2004) noted that the strikes of the rifts approximately fan outward from the Himalayan front. They suggested that the collisional stress of India forcing into Tibet caused the orientation of stress axes to be such that the intermediate stress σ_2 fans outward and that the strikes of normal faults will be similarly orientated. Kapp et al. (2007) noted low-angle normal faults flanking the Yadong–Gulu rift near Lhasa and the Lunggar rift in west-central Tibet but suggested that these faults originated at steep dips and were passively rotated with increased extension. Yin et al. (1999) observed normal faults in northern Tibet similar to those in the south, leading them to suggest that a regional boundary condition for the whole of eastern Asia was responsible for extension for the last 10 Myr, such as may be responsible for the Baikal Rift. Because the regional boundary forces would be expected to die out exponentially to the north, it seems unlikely that the Baikal Rift could be directly related to the Indian collision.

Elliott et al. (2010) recalculated the contribution of normal faulting to the extension of the plateau to be 15–20% using InSAR-derived measurements and body-wave seismology of eight recent moderate to large earthquakes across the plateau. By reexamining the location of different focal mechanisms with plateau elevation, they found that 85% of the moment release by normal faulting over the past 43 years is constrained to regions above 5 km, lending weight to the suggestion that this widespread faulting across the plateau is a result of variations in the gravitational potential energy of the lithosphere.

6.11.6 Tectonic Evolution of the Karakoram

The Karakoram terrane across northern Pakistan is the geologic equivalent of the Qiangtang terrane in central Tibet. South of the Karakoram lies the Shyok suture zone separating the Karakoram–Qiangtang terrane from the Kohistan–Ladakh arc-batholith and Gangdese batholiths of the Lhasa Block. Whereas the Qiangtang terrane is topographically high but has low relief, exposing mainly upper crustal sedimentary and volcanic rocks, the Karakoram has extremely high relief and is deeply eroded and exposes mostly deep crustal metamorphic rocks and granites (Fraser et al., 2001; Rolland et al., 2001; Searle, 1991; Searle and Tirrul, 1991; Searle et al., 1992, 2010a). Extensive field mapping combined with thermobarometry and U–Th–Pb dating of metamorphic and magmatic phases (**Figures 24** and **25**) has revealed a complex and long-lived thermal history that can be broadly summarized as precollisional (India–Kohistan arc–Asia collision) and postcollisional. The Kohistan arc together with the various ophiolite complexes (Sapat, Spontang, etc.) was obducted southward onto the Indian continental margin immediately prior to the closing of Tethys at ~50 Ma and the main India–Asia collision. A summary of all the U–Pb age data from metamorphic and igneous rocks along the Karakoram is shown in **Figure 26**.

6.11.6.1 Precollisional Magmatism and Metamorphism

Prior to the collision of the Kohistan arc and India with Asia, the southern margin of Asia was an Andean-type tectonic setting with subduction-related I-type granite batholiths and calc-alkaline magmatism above a north-dipping Tethyan oceanic subduction zone. The older components of the Karakoram batholith include I-type diorites, granodiorites, and hornblende- and biotite-bearing granites that have been subsequently deformed and metamorphosed to amphibolites (Hushe gneisses). The main component of the Karakoram batholith in the Hunza region (**Figure 27**) is the Hunza granodiorite with a U–Pb zircon age of 105.7 ± 0.5 Ma (Fraser et al., 2001). Similar belts of highly deformed and metamorphosed subduction-related rocks include the Muztagh Tower unit and K2 gneiss, north of the batholith (Crawford and Searle, 1992, 1993; Searle et al., 1989, 1990, 2010a). Part of the southern Karakoram metamorphic complex includes regional low-pressure andalusite-grade metamorphic rocks that are thought to be related to widespread Andean-type granite magmatism prior to the India–Asia collision (Searle and Tirrul, 1991). Recent thermobarometric studies have revealed andalusite and cordierite inclusions together with monazite inclusions within garnet that has a U–Pb age of 105.5 ± 0.8 Ma (Palin et al., 2012).

6.11.6.2 Postcollisional Metamorphism

Following the accretion of the Kohistan arc (and Ladakh–Lhasa terranes) to the Karakoram and the India–Asia collision, crustal thickening occurred along the Karakoram. Although some high-grade gneisses in the Hunza region have pre- or syncollisional U–Pb ages, most of the southern Karakoram metamorphic complex is composed of high-grade kyanite and sillimanite gneisses that have U–Pb zircon and monazite ages spanning the Oligocene to Early Miocene (c. 28–22 Ma; Fraser et al., 2001; Searle et al., 2010a). In the Baltoro region, two kyanite metapelites reached peak P–T conditions of 640–660 °C and ~7.4 kbar at c. 22 Ma (Palin et al., 2012), simultaneous with widespread crustal melting along the Baltoro granite batholith (Searle et al., 2010a). In the Hunza region, a kyanite-grade overprint (~7–8 kbar; 645 °C) on earlier sillimanite gneisses occurred at c.28.2 Ma (Palin et al., 2012).

The deepest exposed structural levels of the Karakoram crust are gneiss domes (e.g., Dassu dome) that are composed of sillimanite-grade gneiss with abundant migmatites that have Pliocene (~5.4–3.5 Ma) U–Pb ages (Fraser et al., 2001; Searle and Tirrul, 1991). These migmatites have been intruded by a network of tourmaline-bearing pegmatites, the youngest metamorphic–partial melting event recorded along the Karakoram. Because the crust may be as thick as 85–90 km beneath the Karakoram (Wittlinger et al., 2004), it is likely that folding, thrusting, crustal shortening and thickening, and high-grade metamorphism are all active today (**Figure 28**).

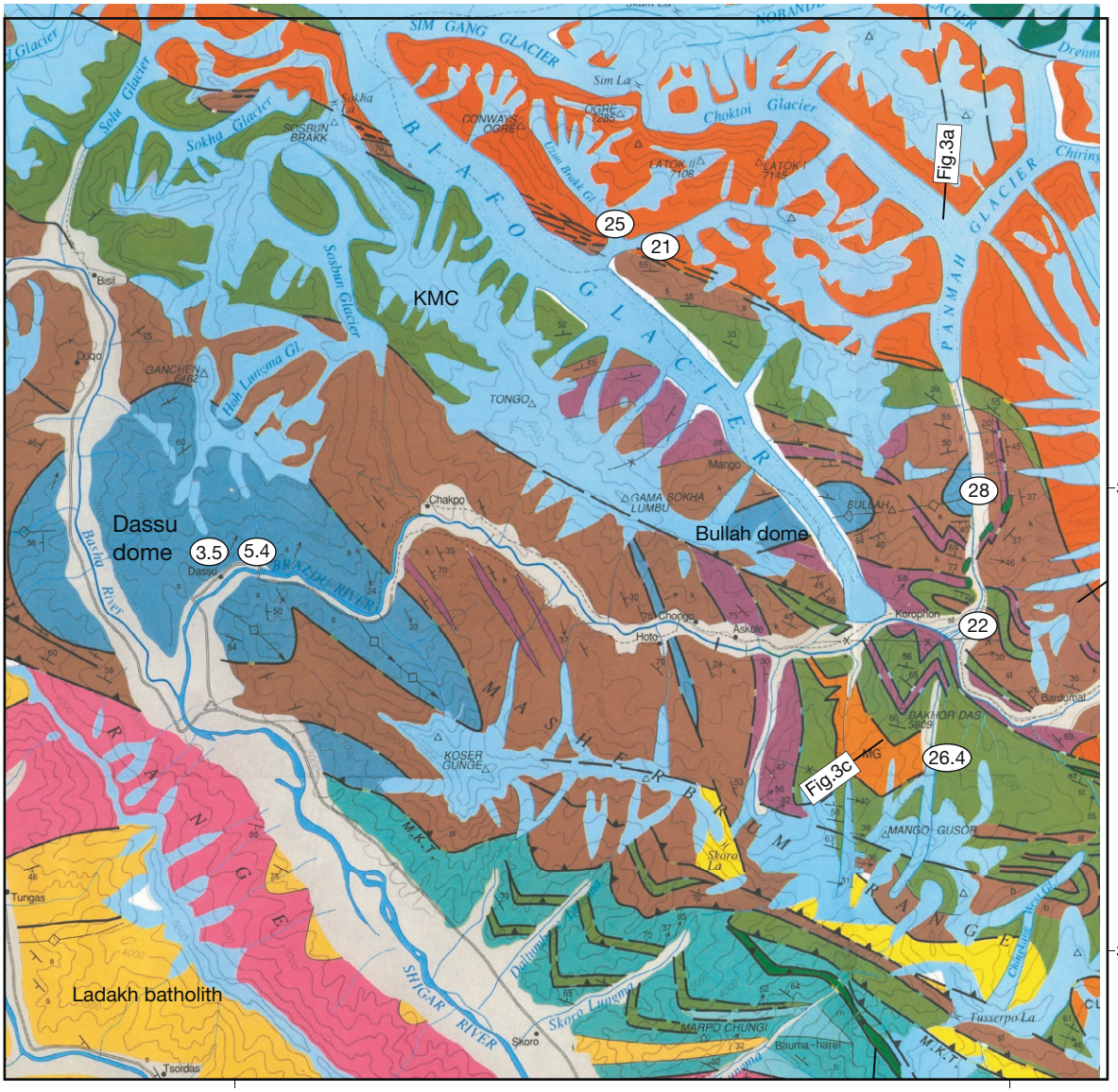

Karakoram Metamorphic Complex

- Panmah ultramafic mafic unit
- Askole amphibolite
- Ganschen paragneiss Bullah orthogneiss
- Dumordu marble
- Dassu gneiss
- (28) U–Pb age

Baltoro Granites

- MG / CL Mango Gusar Chinkiang-la granites
- Baltoro granites
- Masherbrum gneiss
- K / H Kande orthogneiss Hushe orthogneiss

Northern Karakoram

- Aghil Fm. (Tr. – Jr.)
- Shaksgam Fm. (Pm.)
- Baltoro Fm. black shales (Carb.)
- Doksam schists Mitre aureole
- Muztagh Tower gneiss
- Broad Peak quartzite diorite

0 5 10 km

Figure 24 (Continued)

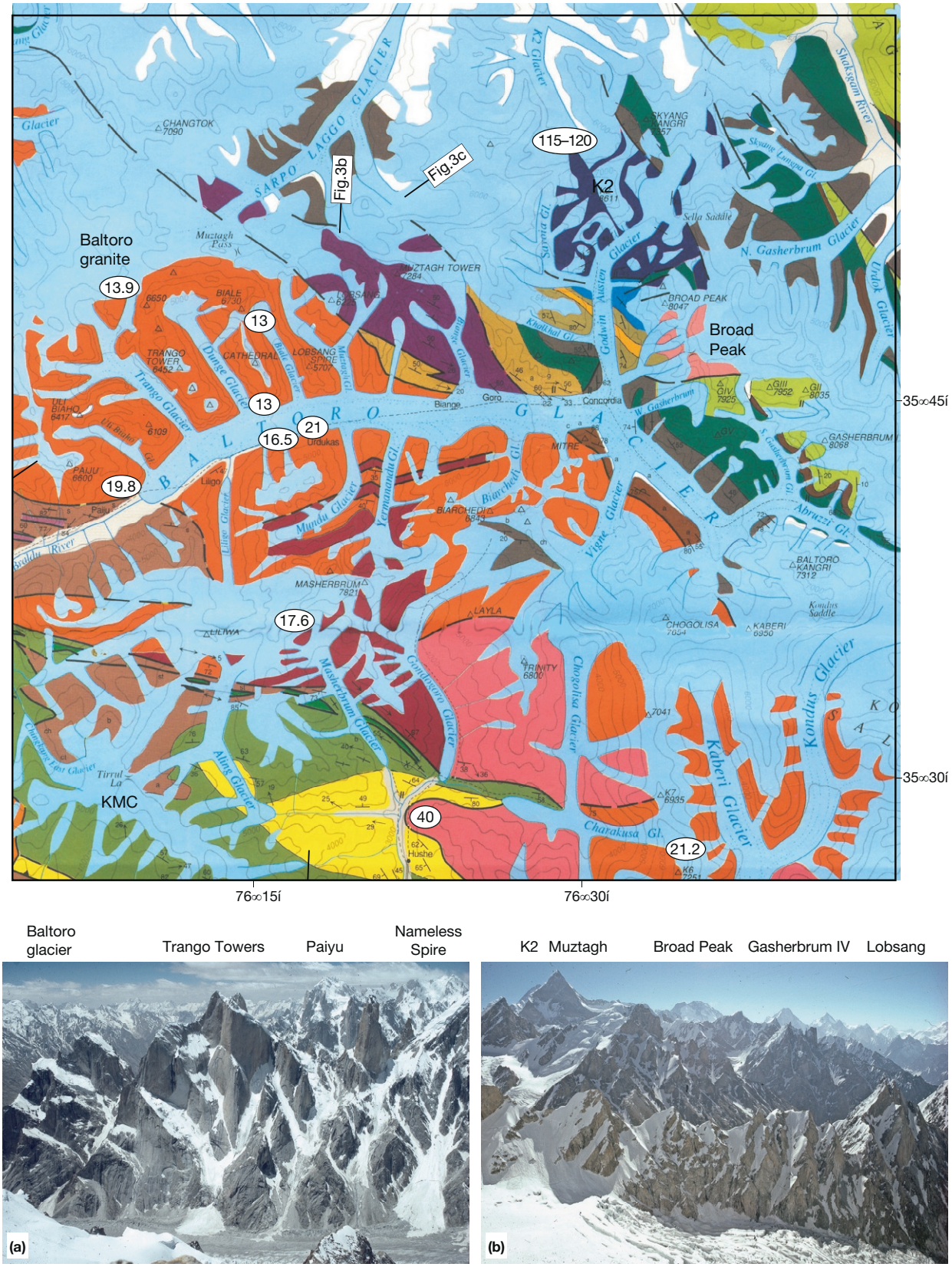

Figure 24 (a) Geologic map of the Baltoro Karakoram, north Pakistan, after Searle (1991) and Searle et al. (2010a) showing locations of U–Pb dated samples. KMC, Karakoram metamorphic complex; MKT, Main Karakoram Thrust. (b) Massive homogeneous leucogranites of the Baltoro batholith exposed in 2 km high cliff faces of the Trango Towers, above the Dunge glacier (photo taken from Biale Peak). (c) Baltoro granite batholith view north from Biale Peak. The Pakistan–China border lies along the K2–Broad Peak–Gasherbrum range at the head of the Baltoro glacier.

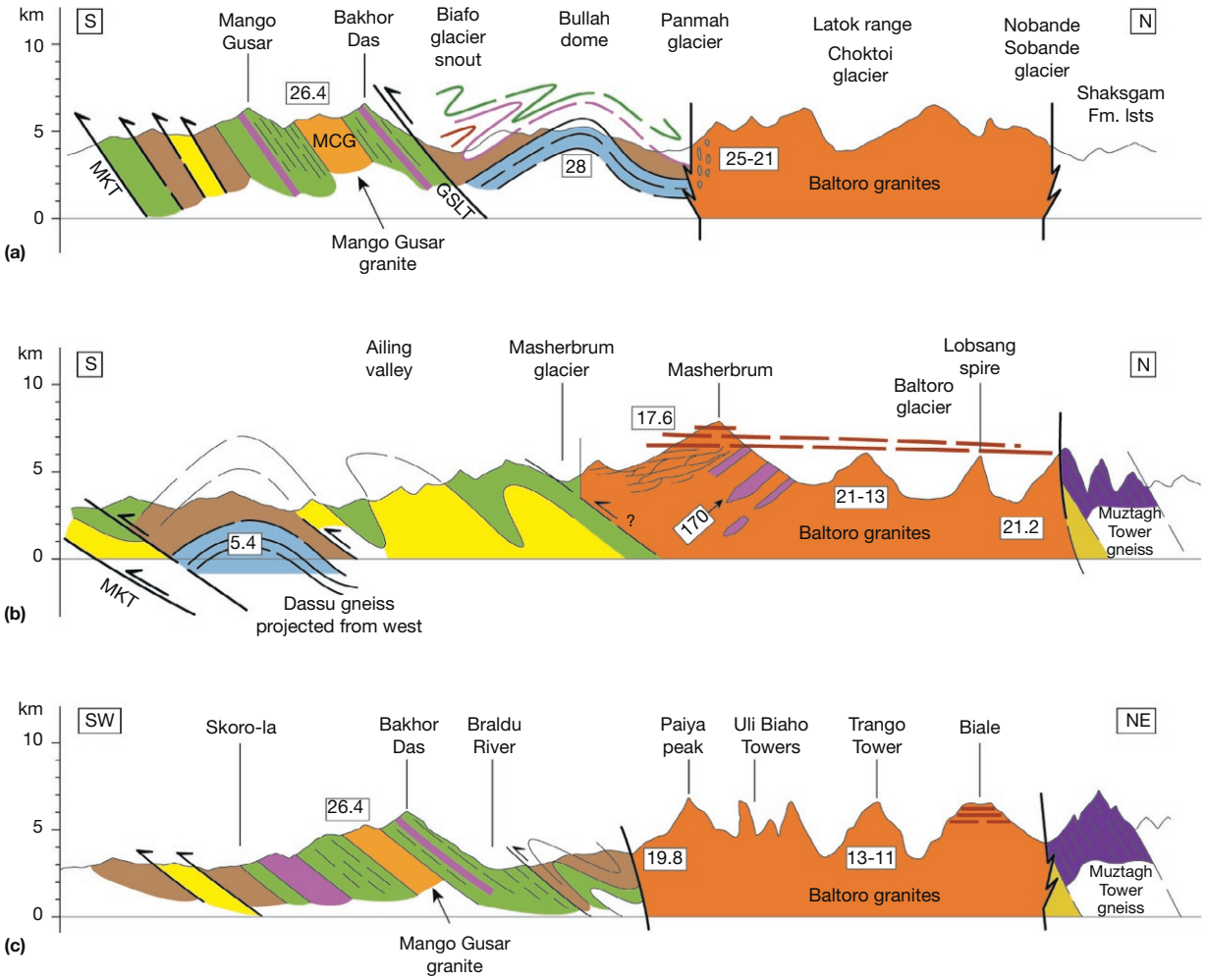

Figure 25 Cross sections of the Baltoro Karakoram, north Pakistan. Lines of sections are shown in **Figure 24**. Numbers refer to U–Pb ages of individual plutonic rocks and ages of peak metamorphism in the metamorphic rocks. Reproduced from Searle MP, Parrish RR, Thow AV, Noble SR, Phillips RJ, and Waters DJ (2010a) Anatomy, age and evolution of a collisional mountain belt: The Baltoro granite batholith and Karakoram Metamorphic complex, Pakistani Karakoram. *Journal of the Geological Society*, *London*, 167: 183–202, http://dx.doi.org/10.1144/0016-76492009-043; Searle MP, Cottle JM, Streule MJ, and Waters DJ (2010b) Crustal melt granites and migmatites along the Himalaya: Melt source, segregation, transport and granite emplacement mechanisms. *Transactions of the Royal Society of Edinburgh* 100: 219–233, http://dx.doi.org/10.1017/S175569100901617X.

6.11.6.3 Postcollisional Crustal Melting

The 700 km long Baltoro granite batholith lies north of the Karakoram metamorphic complex and forms most of the high peaks along the central Karakoram Range. In the Hunza section, much of the batholith is composed of precollisional mid-Cretaceous I-type hornblende-bearing granodiorites that are intruded by a large-scale network of leucocratic dikes, the Hunza dikes. Two sets of Hunza dikes have U–Pb zircon ages of 52–50 Ma (set 1) and 35.0 ± 1.0 Ma (Fraser et al., 2001). The latter age on undeformed dikes that cut regional schistosity and folds constrains the minimum age of regional deformation in the Hunza section. In the Baltoro region of the Karakoram, the batholith is composed mainly of postcollisional crustally derived biotite monzogranites to two-mica garnet leucogranites. The granites have a mildly peraluminous geochemistry and lower $^{87}Sr/^{86}Sr$ initial than Himalayan leucogranites (~0.71–0.72) and are interpreted as lower crustal melts derived from biotite dehydration of a dominantly metapelitic source (Searle et al., 1992, 2010a). The volume of leucogranite along the Karakoram is far greater than along the Himalaya. The sheer scale of crustal melting combined with the presence of concomitant lamprophyric dikes derived from the mantle suggests that there was a significant mantle heat source in addition to the crustal melting. The Baltoro granites are mainly undeformed and have vertical intrusive contacts along both northern and southern margins. Although some U–Pb zircon ages extend to ~24 Ma, the majority of ages span from ~22 Ma to as young as 14–13 Ma (Fraser et al., 2001; Parrish and Tirrul, 1989; Searle et al., 2010a).

In summary, the deep crustal metamorphic and granitic rocks of the Karakoram record extensive precollisional magmatism associated with low-pressure andalusite- and sillimanite-grade metamorphism followed by postcollisional regional crustal thickening, kyanite- and sillimanite-grade metamorphism, and

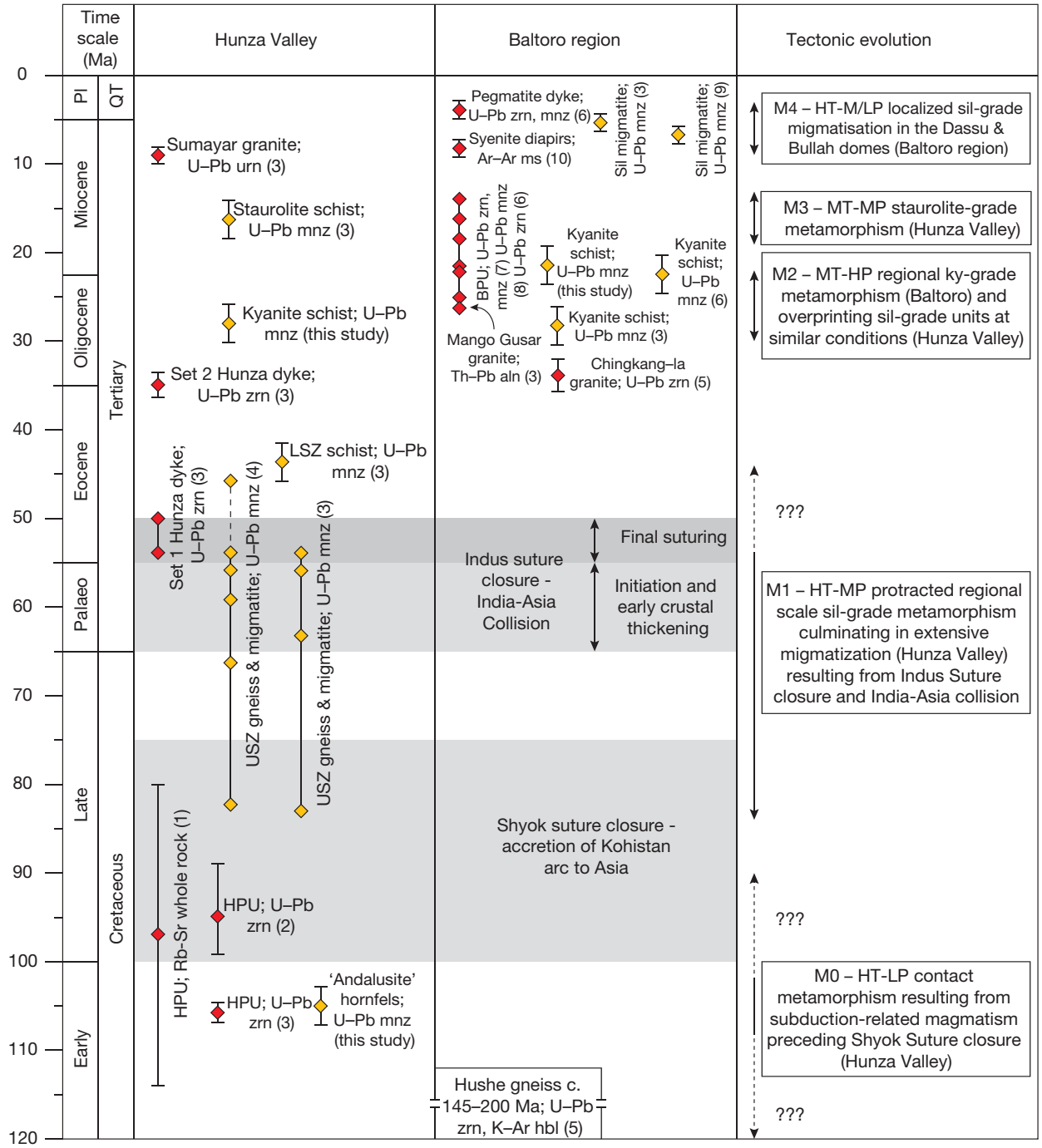
Time scale (Ma)
Hunza Valley
Baltoro region
Tectonic evolution
0
10
20
30
40
50
60
70
80
90
100
110
120
Pl
QT
Miocene
Oligocene
Eocene
Palaeo
Late
Early
Tertiary
Cretaceous
Sumayar granite; U–Pb urn (3)
Staurolite schist; U–Pb mnz (3)
Kyanite schist; U–Pb mnz (this study)
Set 2 Hunza dyke; U–Pb zrn (3)
Set 1 Hunza dyke; U–Pb zrn (3)
LSZ schist; U–Pb mnz (3)
USZ gneiss & migmatite; U–Pb mnz (4)
USZ gneiss & migmatite; U–Pb mnz (3)
HPU; Rb-Sr whole rock (1)
HPU; U–Pb zrn (2)
HPU; U–Pb zrn (3)
'Andalusite' hornfels; U–Pb mnz (this study)
Pegmatite dyke; U–Pb zrn, mnz (6)
Syenite diapirs; Ar–Ar ms (10)
Sil migmatite; U–Pb mnz (3)
Sil migmatite; U–Pb mnz (9)
BPU; U–Pb zrn, mnz (7) U–Pb mnz (8) U–Pb zrn (6)
Kyanite schist; U–Pb mnz (this study)
Kyanite schist; U–Pb mnz (6)
Kyanite schist; U–Pb mnz (3)
Mango Gusar granite; Th–Pb aln (3)
Chingkang–la granite; U–Pb zrn (5)
Final suturing
Indus suture closure - India-Asia Collision
Initiation and early crustal thickening
Shyok suture closure - accretion of Kohistan arc to Asia
Hushe gneiss c. 145–200 Ma; U–Pb zrn, K–Ar hbl (5)
M4 – HT-M/LP localized sil-grade migmatisation in the Dassu & Bullah domes (Baltoro region)
M3 – MT-MP staurolite-grade metamorphism (Hunza Valley)
M2 – MT-HP regional ky-grade metamorphism (Baltoro) and overprinting sil-grade units at similar conditions (Hunza Valley)
???
M1 – HT-MP protracted regional scale sil-grade metamorphism culminating in extensive migmatization (Hunza Valley) resulting from Indus Suture closure and India-Asia collision
???
M0 – HT-LP contact metamorphism resulting from subduction-related magmatism preceding Shyok Suture closure (Hunza Valley)
???

Figure 26 Time chart showing all U–Pb age data for the Hunza and Baltoro Karakoram with interpreted tectonic evolution; see Palin et al. (2012) for sources of data. Age data from multiple studies: (1) Debon et al. (1987); (2) Le Fort et al. (1983); (3) Fraser et al. (2001); (4) Foster et al. (2004); (5) Searle et al. (1989); (6) Searle et al. (2010a); (7) Parrish and Tirrul (1989); (8) Schärer et al. (1990); (9) Smith (1993); (10) Villa et al. (1996). Error bars represent quoted uncertainty, where applicable, but are not added to ranges. See Searle et al. (2010a) for sources of data. HPU = Hunza Plutonic Unit, BPU = Baltoro Plutonic Unit, LSZ = Lower sillimanite zone, USZ = Upper sillimanite zone, Palaeo = Palaeocene, QT = Quaternary, Pl = Pliocene/Pleistocene.

extensive lower crust partial melting. The Baltoro granites are volumetrically very large, are mainly undeformed, and are intruded into high-grade metamorphic rocks to the south and Carboniferous to Jurassic sedimentary rocks to the north.

6.11.7 Discussion: Lithospheric Models

There is increasing evidence that the Tibetan Plateau region was topographically high, at least along the southern part, the

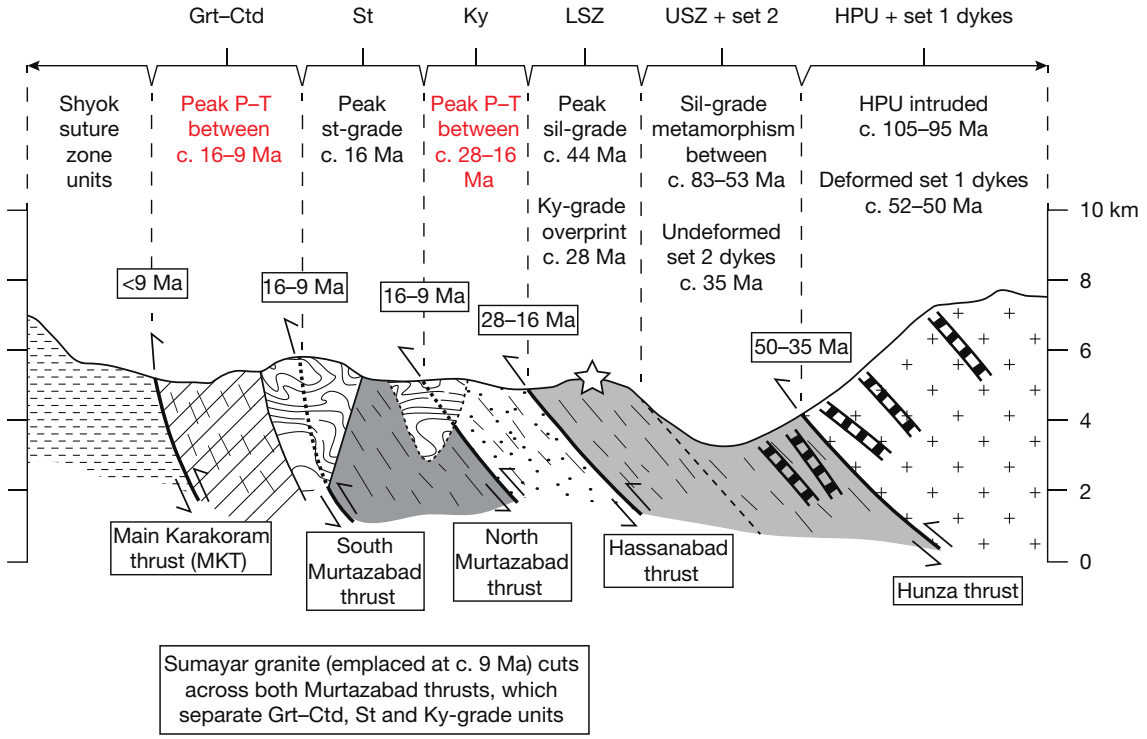

Figure 27 Schematic cross section through the Hunza valley in the Pakistan Karakoram showing metamorphic grade and U–Pb age data of each tectonic unit. Reproduced from Palin RM, Searle MP, Waters DJ, Horstwood MSA, and Parrish RR (2012). Combined thermobarometry and geochronology of peraluminous metapelites from the Karakoram metamorphic complex, north Pakistan: New insights into the tectonothermal evolution of the Baltoro and Hunza regions. *Journal of Metamorphic Geology*, http://dx.doi.org/10.1111/j.1525-1314.2012.00999.x.

Lhasa Block, during the Late Cretaceous prior to the ~50 Ma India–Asia collision. This thickening was related to magmatic intrusions of the Andean-type subduction-related granite batholiths along the Kohistan, Ladakh, and Gangdese granite belts. Calc-alkaline andesites, dacites, and rhyolites (Linzizong volcanics) are the subaerial component of the I-type granites. A regional unconformity plaining off folds in the Takena Formation redbeds beneath suggest that crustal shortening of southern Tibet must have occurred prior to the 60 Ma base of the Linzizong volcanics. The closing of the Tethys ocean that lay between India and Asia occurred during the Early Eocene; the youngest marine sedimentary rocks in Ladakh and in southern Tibet have Early Eocene foraminifera belonging to planktonic foraminiferal zone P8 and shallow benthic zone SBZ10 dated at 50.5 Ma (Garzanti et al., 1987; Green et al., 2008; Rowley, 1998; Zhu et al., 2005).

Following the India–Asia collision, the continuing northward drift of India and its penetration into Asia resulted in continued and accelerated crustal thickening and uplift of the plateau. The distribution and ages of mantle-derived shoshonitic and ultrapotassic volcanic rocks across Tibet suggest that 'hot' Asian mantle was progressively shunted northward by the underthrusting 'cold' Indian mantle lithosphere. Most of the geology across Tibet shows old (precollisional) deformation, metamorphism, and magmatism. These data support the Argand-type underthrusting models where Asian crust is passively lifted by underplating of Indian lithosphere (Argand, 1924; Searle et al., 2011). The paucity of Cenozoic deformation, metamorphism, and crustal shortening and thickening across the whole plateau does not support continuum (pure shear) models for Tibet (Dewey and Burke, 1973; England and Houseman, 1989; England and McKenzie, 1982).

Lower crustal flow models for eastern Tibet (Clark and Royden, 2000; Royden et al., 1997) mimic the GPS flow lines from active surface 'flow' of material eastward away from the high plateau toward Southeast Asia (Gan et al., 2007). However, there is no geologic evidence for any middle or lower crust flow eastward within the Longmenshan. If lower crust had been removed from the Tibet plateau region, a lower surface elevation would be expected, contrary to low-temperature thermochronology data across the plateau that show the plateau has been at elevations similar to the present since at least the Late Eocene (Hetzel et al., 2011). Much of the geology along the Longmenshan and in East Tibet shows Triassic–Early Jurassic Indosinian deformation and metamorphism with very little Cenozoic effects. Active east-directed thrusting is known from earthquakes such as the Wenchuan earthquake (Hubbard and Shaw, 2009) where steep thrust faults bound the margin of the thick crust. None of these structures, however, support lower crust flow models.

The Himalayan channel flow model of a 10–20 km thick section of partially middle crustal rocks being extruded to the south and bounded by crustal-scale ductile shear zones above and below is consistent with all geologic, metamorphic, and geochronological data. The south-directed MCT bounds the extruding channel below and the STD low-angle normal fault bounds the channel above. Both these structures and the ages of the migmatites and leucogranites within the channel show

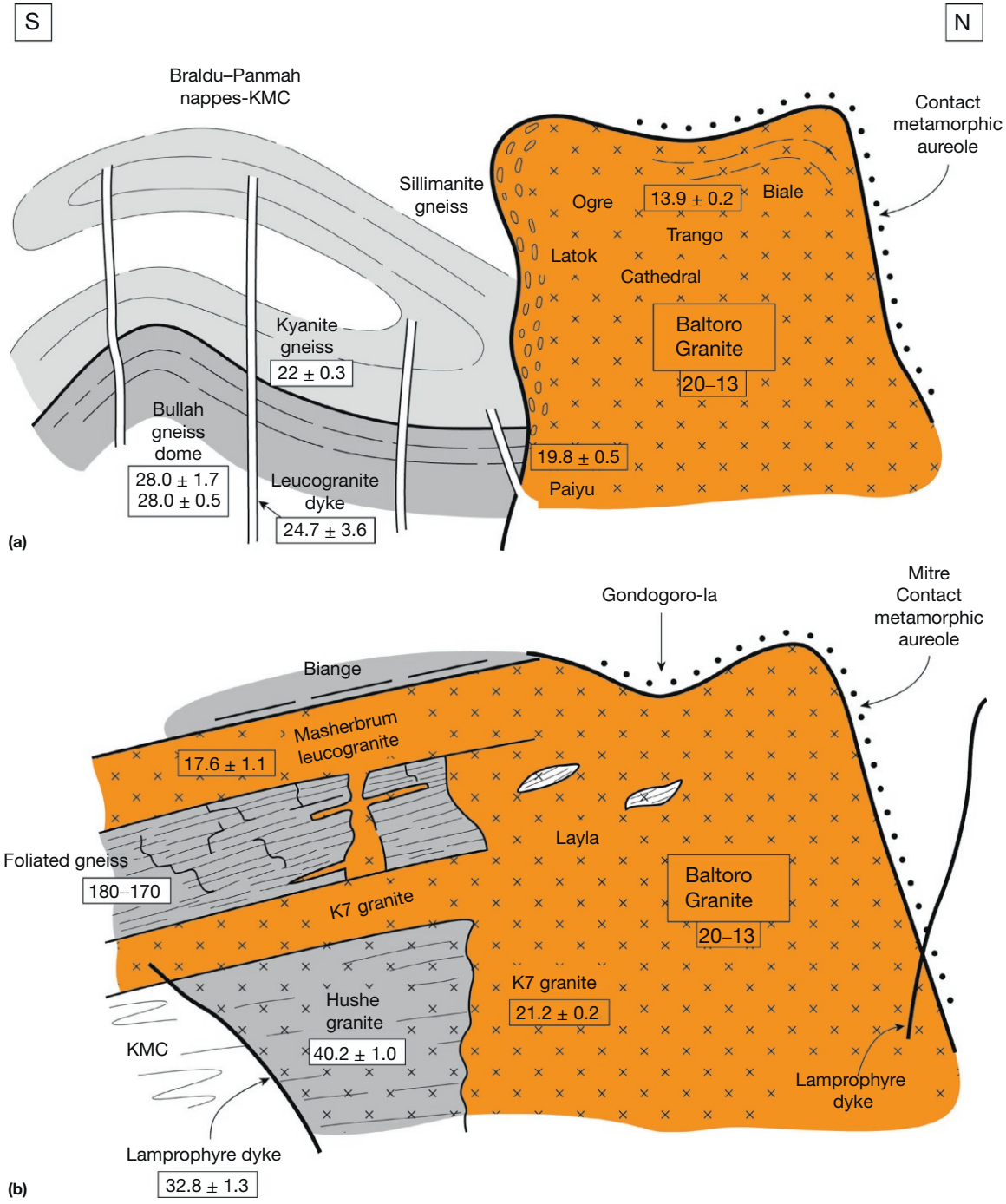

Figure 28 Schematic profiles across the Baltoro Karakoram showing the general anatomy of the Baltoro granite batholith and Karakoram metamorphic complex to the south, after Searle et al., (2010a); (a) across the Latok–Paiyu region and (b) across Masherbrum–Hushe area (see **Figure 24** for locations). Also shown are the age spans of magmatism as defined by U–Pb ages.

that channel flow was active during the Miocene (from c. 24–14 Ma), but is not active today. The material within the channel is all Indian Plate upper crustal rocks (Neoproterozoic and younger) that have been subducted to kyanite- and sillimanite-grade depths and returned to the surface by a general shear mechanism involving south-directed simple shear with a component of pure shear flattening.

6.11.8 Conclusions

1. Geologic, seismic, and magnetotelluric data from the Himalaya and southern Tibet clearly show that the crust is rheologically layered and decoupled along major subhorizontal shear zones. The brittle, seismogenic upper crust of Tibet is presently undergoing east–west extension, the

ductile-deformed midcrustal layer of South Tibet was and may still be at temperatures high enough to induce partial melting, while the dry granulite (or high-temperature eclogite) facies lower crust of South Tibet is underthrusting northward. The deepest earthquakes in Tibet at 75–85 km probably occur along the lower crust-upper mantle interface. Clearly, the Tibetan geotherm is not a simple linear depth profile.

2. The Himalayan midcrustal 'channel flow' model is supported by extensive structural, metamorphic, thermobarometric, and geochronological data. During the Miocene, a partially molten layer of middle crust was extruded >100 km south between two c. 1 km thick ductile shear zones, the overlying north-dipping low-angle STD normal fault and the south-directed MCT below. All the evidence points to the fact that both ductile shear zones and faults were active during the period c. 24–14 Ma, synchronously with the formation of the Himalayan leucogranites. There is no seismic or structural evidence that either fault is active today.
3. The model of lower crustal flow in eastern Tibet (Clark and Royden, 2000; Royden et al., 1997) mimics the GPS flow lines (Gan et al., 2007), but has no geologic evidence to support it. The active eastern margin of the Tibetan Plateau shows none of the attributes of the Himalaya. There is very little Neogene crustal shortening, no Cenozoic metamorphism or melting, no exposed rocks recording east-directed ductile flow, and only steep east-directed thrusts such as recorded by the Wenchuan earthquake (Hubbard and Shaw, 2009). If the lower crust was actively flowing east around the stable Sichuan basin, the upper crust that used to overlie this should be actively thickening and deforming.
4. The continental extrusion model whereby the thickened Tibetan crust was extruded eastward along bounding strike-slip faults away from the Indian indentor is responsible for only up to c. 100 km of extrusion, not the >1000 km as originally proposed (Armijo et al., 1989; Avouac and Tapponnier, 1993; Lacassin et al., 2004; Tapponnier et al., 1982, 2001). Motion on the Karakoram fault is less than 120 km and timing is restricted to the Upper Miocene (Phillips et al., 2004, 2013), long after the India–Asia collision (c. 50 Ma). Strike-slip faults cutting the thick crust of Tibet, such as the Karakoram fault, are mainly upper crustal structures that do not continue down to the deepest levels of the crust. Long-term slip rates derived from offset, precisely dated preshearing granites, and GPS active slip rates are compatible at 3–7 mm year^{-1}. Quaternary slip rates derived from cosmogenic dating of boulders in moraines along the Karakoram fault are not accurate because of the incorrect assumption that ^{10}Be ages of boulders are the same as the age of the landform. Accurate geologic offsets and long-term slip rates along the Altyn Tagh, Kunlun, Xianshuihe, and Jiale faults remain unknown.
5. High topography and thick crust along the Himalaya have almost certainly persisted for at least 35–40 million years as recorded by U–Th–Pb monazite dating of kyanite-, sillimanite-, and cordierite-bearing gneisses, migmatites, and crustal melt leucogranites (Palin et al., 2012; Searle et al., 2010b). Active crustal thickening and regional kyanite metamorphism also imply thick crust and high topography at that time.
6. High topography and thick crust in the Tibetan Plateau are known from geologic data and U–Th–Pb zircon and monazite dating of the deep crustal rocks in the Karakoram (geologically the western extension of the central Tibetan Qiangtang terrane), where 10–14 kbar (~30–45 km deep) crust metamorphism extends almost continually from the Late Cretaceous (65 Ma) to Pliocene (4–3 Ma) times (Searle et al., 2010a).
7. There is geologic evidence that Tibet was a high Altiplano-like feature before the India–Asia collision (e.g., England and Searle, 1986; Kapp et al., 2007). Thermochronological and cosmogenic nuclide data suggest a regional rather stable Eocene peneplain carved into Cretaceous granitoids and Jurassic sedimentary rocks across the Lhasa and Qiangtang terranes indicating a high plateau by 45 Ma (Hetzel et al., 2011; Rohrmann et al., 2012). Tibetan crust was at least 80 km thick by 17–14 Ma as shown by pressure and temperature conditions of felsic and mafic granulites from the lower crust preserved as small xenoliths in Upper Miocene ultrapotassic dikes. These granulites record temperatures of 1330–1130 °C and pressures of 26–22 kbar and were formed 16.8 ± 0.9, 15.6 ± 0.6, and 14.4 ± 0.4 Ma from ^{206}Pb/^{238}U dating of zircons (Chan et al., 2009).
8. Mantle-derived shoshonitic potassic and ultrapotassic volcanics requiring a hot mantle source erupted extensively across the Tibetan Plateau between 50 and 13 Ma (Chung et al., 2005). Adakitic dikes and lavas, requiring a garnet-bearing eclogite or amphibolite lower crust source, were intruded from at least 47 Ma in the Qiangtang block, central Tibet, and from at least 30 Ma in the Lhasa Block, South Tibet (Chung et al., 2003). The age, source rocks, and spatial distribution of these volcanic and intrusive rocks suggest that the crust must have been thick enough to have an eclogitic root from at least 47 Ma and that the mantle was heterogeneous and hot from the timing of India–Asia collision 50 Ma onward. Tibetan hot mantle was shunted to the north as Indian lithospheric mantle was progressively underthrust from the south.
9. The 40 km thick Indian Plate underthrusting the Himalaya and southern Tibet is clearly strong and rigid enough to support the load above it. The Indian Plate Neoproterozoic and Phanerozoic upper crust has been scraped off and shortened by about 800–1000 km to form the Himalaya, but the mainly old, cold, and dry granulites of the Indian Shield lower crust have been underthrust to the north beneath the Himalaya and South Tibet. Bouguer gravity anomalies associated with the flexure beneath the Ganges foreland basin and the Himalaya require a T_e of ~70 km in the subducting Indian Plate (Jordan and Watts, 2005).
10. Neither the 'jelly sandwich' nor the 'crème brûleé' models adequately explain all the features of the Himalayan–Tibetan lithosphere. The upper, middle, and lower crusts beneath southern Tibet are decoupled, each layer bounded by major subhorizontal shear zones or detachments. The upper crust has suffered N–S shortening during the Late Eocene to early Miocene, followed by late Neogene E–W extension. The middle crust has undergone

widespread Late Eocene–Oligocene kyanite-grade metamorphism, followed by HT/LP sillimanite–cordierite-grade metamorphism, muscovite and biotite dehydration melting, and southward-directed channel flow. The lower crust, comprising old, cold, anhydrous Precambrian granulites, has underthrust Tibet to the north and been re-metamorphosed to high-pressure granulite or eclogite facies in the Neogene.

Acknowledgments

Thanks to NERC for funding several expeditions to the Himalaya, Karakoram, and Tibet over the last 30 years and to Peter Molnar, Rick Law, Dave Waters, Randy Parrish, Steve Noble, Marc St-Onge, Sun-Lin Chung, Asif Khan, Qasim Jan, Tony Watts, and many others for detailed discussions. Thanks to Bradley Hacker for a detailed, comprehensive review and to editor Tony Watts for advice.

References

Akciz S, Burchfiel BC, Crowley JL, Jiyun Y, and Zhong C (2008) Geometry, kinematics and regional significance of the Chong Shan shear zone, Eastern Himalayan Syntaxis, Yunnan, China. *Geosphere* 4: 292–314. http://dx.doi.org/10.1130/GES00111.1.

Allen CR, Zhuoli L, Hong Q, Xueze W, Huawei Z, and Weishi H (1991) Field study of a highly active fault zone: The Xianshuihe fault of southwestern China. *GSA Bulletin* 103: 1178–1199. http://dx.doi.org/10.1130/0016-7606.

Argand E (1924) Le tectonique de l'Asie. In: *Proc. 13th Int. Geol. Congress, Brussels, vol. 7*, pp. 171–372.

Armijo R, Tapponnier P, Mercier JL, and Tonglin H (1988) Quaternary extension in Southern Tibet. *Journal of Geophysical Research* 91: 13803–13872.

Armijo R, Tapponnier P, and Tonglin H (1989) Late Cenozoic right-lateral strike-slip faulting in Southern Tibet. *Journal of Geophysical Research* 94: 2787–2838.

Austrheim H (1987) Eclogitisation of lower crustal granulites by fluid migration through shear zones. *Earth and Planetary Science Letters* 81: 221–232.

Austrheim H and Boundy TM (1994) Pseudotachylytes generated during seismic faulting and eclogitisation of the deep crust. *Science* 265: 82–83.

Avouac J-P and Tapponnier P (1993) Kinematic model of active deformation in Central Asia. *Geophysical Research Letters* 20: 895–898.

Beaumont C, Jamieson RA, Nguyen MH, and Lee B (2001) Himalayan tectonics explained by extrusion of a low-velocity channel coupled with focused surface denudation. *Nature* 414: 738–742.

Beaumont C, Jamieson RA, Nguyen MH, and Medvedev S (2004) Crustal channel flows: 1. Numerical models with applications to the tectonics of the Himalayan-Tibetan orogen. *Journal of Geophysical Research* 109: B06406. http://dx.doi.org/10.1029/2003JB002809.

Booth AL, Chamerlain CP, Kidd WSF, and Zeitler PK (2008) Constraints on the metamorphic evolution of the eastern Himalayan syntaxis from geochronologic and petrologic studies of Namche Barwa. *Geological Society of America Bulletin*. http://dx.doi.org/10.1130/B26041.1.

Brace WF and Kohlstedt DL (1980) Limits on lithostatic stress imposed by laboratory experiments. *Journal of Geophysical Research* 85: 6248–6252.

Burchfiel BC, Zhang P, Wang Y, et al. (1991) Geology of the Haiyuan Fault zone, Ningxia-Hui autonomous region, China, and its relation to the evolution of the Northeast margin of the Tibetan Plateau. *Tectonics* 10: 1091–1110.

Burov EB (2010) The equivalent elastic thickness (Te) seismicity and the long-term rheology of continental lithosphere: Time to burn out "crème brûlee"? Insights from large-scale geodynamic modelling. *Tectonophysics* 484: 4–26.

Burov EB and Watts AB (2006) The long-term strength of the continental lithosphere: "jelly sandwich" or "crème-brûleé"? *GSA Today* 16. http://dx.doi.org/10.1130/1052-5173.

Cavalie O, Laserre C, Doin M-P, et al. (2008) Measurement of interseismic strain across the Haiyuan fault (Gansu, China), by InSAR. *Earth and Planetary Science Letters* 275: 246–257. http://dx.doi.org/10.1016/j.epsl.2008.07.057.

Chan GH-N, Waters DJ, Searle MP, et al. (2009) Probing the basement of southern Tibet: Evidence from crustal xenoliths entrained in a Miocene ultrapotassic dyke. *Journal of the Geological Society, London* 166: 45–52.

Chen W-P and Molnar P (1983) Focal depths of intra-continental and intra-plate earthquakes and their implications for the thermal and mechanical properties of the lithosphere. *Journal of Geophysical Research* 88: 4183–4214.

Chen WP and Yang Z (2004) Earthquakes beneath the Himalaya and Tibet. Evidence for strong lithospheric mantle. *Science* 304: 1949–1952.

Chen Z, Burchfiel BC, Liu Y, et al. (2000) Global Positioning System measurements from eastern Tibet and their implications for India/Eurasia intercontinental deformation. *Journal of Geophysical Research* 105: 16215–16228. http://dx.doi.org/10.1029/2000JB900092.

Chiu H-Y, Chung S-L, Wu F-Y, et al. (2009) Zircon U–Pb and Hf isotopic constraints from eastern Transhimalayan batholiths on the precollisional magmatic and tectonic evolution in southern Tibet. *Tectonophysics*. http://dx.doi.org/10.1016/j.tecto.2009.02.034.

Chu M-F, Chung S-L, Song B, et al. (2006) Zircon U–Pb and Hf isotope constraints on the Mesozoic tectonics and crustal evolution of southern Tibet. *Geology* 34(9): 745–748.

Chung S-L, Lo C-H, Lee T-Y, et al. (1998) Diachronous uplift of the Tibetan Plateau starting 40 Myr ago. *Nature* 394: 769–773.

Chung S-L, Liu D, Ji J, et al. (2003) Adakites from continental collision zones: Melting of thickened lower crust beneath southern Tibet. *Geology* 31(11): 1021–1024.

Chung S-L, Chu M-F, Zhang Y, et al. (2005) Tibetan tectonic evolution inferred from spatial and temporal variations in post-collisional magmatism. *Earth Science Reviews* 68: 173–196.

Chung S-L, Chu M-F, Ji J, et al. (2009) The nature and timing of crustal thickening in Southern Tibet: Geochemical and zircon Hf isotopic constraints from postcollisional adakites. *Tectonophysics* 477: 36–48.

Clark MK and Royden LH (2000) Topographic ooze: Building the eastern margin of Tibet by lower crustal flow. *Geology* 28: 703–706.

Cobbold PR and Davy P (1988) Indentation tectonics in nature and experiment, 2. Central Asia. *Bulletin of the Geological Institutions of Uppsala* 14: 143–162.

Corfield RI and Searle MP (2000) Crustal shortening estimates across the north Indian continental margin, Ladakh, NW India. In: Khan MA, Treloar PJ, Searle MP, and Jan MQ (eds.) *Tectonics of the Nanga Parbat Syntaxis and the Western Himalaya*, vol. 170, pp. 395–410. London: Geological Society, Special Publication.

Corfield RI, Searle MP, and Pedersen RB (2001) Tectonic setting, origin and obduction history of the Spontang Ophiolite, Ladakh Himalaya, NW India. *Journal of Geology* 109: 715–736.

Cottle JM, Jessup MJ, Newell DL, Searle MP, Law RD, and Horstwood MSA (2007) Structural insights into the early stages of exhumation along an orogen-scale detachment: The South Tibetan Detachment System, Dzachaa Chu, Eastern Himalaya. *Journal of Structural Geology* 29: 1781–1797.

Cottle JM, Searle MP, Horstwood MSA, and Waters DJ (2009) Timing of midcrustal metamorphism, melting and deformation in the Mount Everest region of Southern Tibet revealed by U(–Th)–Pb geochronology. *Journal of Geology* 117: 643–664.

Cowgill E, Yin A, Harrison TM, and Feng WX (2003) Reconstruction of the Altyn Tagh fault based on U–Pb geochronology: Role of backthrusts, mantle sutures and heterogeneous crustal strength in the forming the Tibetan plateau. *Journal of Geophysical Research* 108. http://dx.doi.org/10.1029/2002JB002080.

Crawford MB and Searle MP (1992) Field relationships and geochemistry of pre-collisional (India-Asia) granitoid magmatism in the central Karakoram. *Tectonophysics* 206: 171–192.

Crawford MB and Searle MP (1993) Collision-related granitoid magmatism and crustal structure of the Hunza Karakoram, north Pakistan. In: Treloar PJ and Searle MP (eds.) *Himalayan Tectonics*, vol. 74, pp. 53–68. London: Geological Society, Special Publication.

Crowley JL, Waters DJ, Searle MP, and Bowring SA (2009) Pleistocene melting and rapid exhumation of the Nanga Parbat massif, Pakistan: Age and P–T conditions of accessory mineral growth in migmatite and leucogranite. *Earth and Planetary Science Letters* 288: 408–420.

De Sigoyer J, Chavagnac V, Blichert-Toft A, et al. (2000) Dating the Indian continental subduction and collisional thickening in the northwest Himalaya: Multichronology of the Tso Morari eclogites. *Geology* 28: 487–490.

Dewey JF (1988) Extensional collapse of orogens. *Tectonics* 7: 1123–1139.

Dewey J and Burke K (1973) Tibetan, Variscan and Precambrian basement reactivation: Products of a continental collision. *Journal of Geology* 81: 683–692.

Dhuime B, Bosch D, Bodinier J-L, et al. (2007) Multistage evolution of the Jijal ultramafic–mafic complex (Kohistan, N. Pakistan): Implications for building the roots of island arcs. *Earth and Planetary Science Letters* 261: 179–200.

Ding G, Chan J, Tian Q, Shan X, Xing C, and Wei K (2004) Active faults and magnitudes of left-lateral displacement along the northern margin of the Tibetan Plateau. *Tectonophysics* 380: 243–260. http://dx.doi.org/10.1016/j.tecto.2003.09.022.

Ducea MN, Lutkov V, Minaev VT, et al. (2003) Building the Pamirs: The view from the underside. *Geology* 31: 849–852.

Dunlap WJ, Weinberg RF, and Searle MP (1998) Karakoram fault zone rocks cool in two phases. *Journal of the Geological Society, London* 155: 519–538.

Dupont-Nuvet G, Lippert PC, van Hinsbergen DJJ, Meijers MJM, and Kapp P (2010) Palaeolatitude and age of the India-Asia collision: Palaeomagnetic constraints. *Geophysical Journal International* 182: 1189–1198.

Elliott JR, Biggs J, Parsons B, and Wright TJ (2008) InSAR slip rate determination on the Altyn Tagh fault, northern Tibet, in the presence of tomographically correlated atmospheric delays. *Geophysical Research Letters* 35: L12309. http://dx.doi.org/10.1029/2008GL033659.

Elliott JR, Walters RJ, England PC, Jackson JA, Li Z, and Parsons B (2010) Extension on the Tibetan plateau: Recent normal faulting measured by InSAR and body wave seismology. *Geophysical Journal International* 183: 503–555. http://dx.doi.org/10.1111/j.1365-246X.2010.04754.x.

England P and Houseman G (1989) Extension during continental convergence with application to the Tibetan Plateau. *Journal of Geophysical Research* 94: 17561–17579.

England P and McKenzie D (1982) A thin viscous sheet model for continental deformation. *Geophysical Journal Royal Astronomical Society* 70: 295–321.

England P and Molnar P (1990) Right-lateral shear and rotation as the explanation for strike-slip faulting in east Tibet. *Nature* 344: 140–142.

England P and Searle M (1986) The Cretaceous–Tertiary deformation of the Lhasa Block and its implications for crustal thickening in Tibet. *Tectonics* 5: 1–14.

Foley S, Tiepolo M, and Vannucci R (2003) Growth of early continental crust controlled by melting of amphibolite in subduction zones. *Nature* 417: 837–840.

Fraser JE, Searle MP, Parrish RR, and Noble SR (2001) Chronology of deformation, metamorphism, and magmatism in the southern Karakoram Mountains. *Geological Society of America Bulletin* 113: 1443–1455.

Fu B and Awata Y (2007) Displacement and timing of left-lateral faulting in the Kunlun fault zone, northern Tibet, inferred from geological and geomorphic features. *Journal of Asian Earth Sciences* 29: 253–265.

Gan W, Zhang P, Shen Z-K, et al. (2007) Present-day crustal motion within the Tibetan Plateau inferred from GPS measurements. *Journal of Geophysical Research* 112: B08416. http://dx.doi.org/10.1029/2005JB004120.

Gariepy C, Allegre CJ, and Ronghau X (1985) The Pb isotope geochemistry of granitoids from the Himalaya-Tibet collision zone: implications for crusted evolution. *Earth and Planetary Science Letters* 74: 220–234.

Garrido CJ, et al. (2006) Petrogenesis of mafic garnet granulite in the lower crust of the Kohistan Palaeo-arc complex (Northern Pakistan): Implications for intra-crustal differentiation of island arcs and generation of continental crust. *Journal of Petrology* 47: 1873–1914.

Garrido CJ, et al. (2007) Origin of the island arc Moho transition zone via melt-rock reaction and its implications for intracrustal differentiation of island arcs: Evidence from the Jijal complex (Kohistan complex, northern Pakistan). *Geology* 35: 683–686.

Garzanti E, Baud A, and Mascle G (1987) Sedimentary record of the northward flight of India and its collision with Eurasia (Ladakh Himalaya, India). *Geodynamica Acta* 1: 297–312.

Gaudemer Y, Tapponnier P, and Turcotte DL (1989) River offsets across active strike-slip faults. *Annules Tectonicae* 3: 55–76.

Gaudemer Y, Tapponnier P, Meyer B, et al. (1995) Partitioning of crustal slip between linked, active faults in the Eastern Qilian Shan and evidence for a major seismic gap, the Tianzhu gap, on the western Haiyuan fault, Gansu (China). *Geophysical Journal* 120(3): 599–645.

Godin L, Parrish RR, Brown RL, and Hodges KV (2001) Crustal thickening leading to exhumation of the metamorphic core of the central Nepal Himalaya: Insight from U–Pb and $^{40}Ar/^{39}Ar$ thermochronology. *Tectonics* 20: 729–747.

Godin D, Grujic D, Law RD, and Searle MP (2006) Channel flow, ductile extrusion and exhumation in continental collision zones: An introduction. In: Law RD, Searle MP, and Godin L (eds.) *Channel Flow, Ductile Extrusion and Exhumation in Continental Collision Zones*, vol. 268, pp. 1–23. London: Geological Society, Special Publication.

Goetz C and Evans B (1979) Stress and temperature in the bending lithosphere as constrained by experimental rock mechanics. *Geophysical Journal of the Royal Astronomical Society* 59: 463–478.

Gordon SM, Luffi P, Hacker B, et al. (2012) The thermal structure of continental crust in active orogens: Insight from Miocene eclogite and granulite xenoliths of the Pamir Mountains. *Journal of Metamorphic Geology* 30: 4133–4434.

Grasemann B, Fritz H, and Vannay J-C (1999) Quantitative kinematic flow analysis from the Main Central Thrust zone (NW Himalaya, India): Implications for a decelerating strain path and the extrusion of orogenic wedges. *Journal of Structural Geology* 21: 837–853.

Green OR, Searle MP, Corfield RI, and Corfield RM (2008) Cretaceous-Tertiary carbonate platform evolution and the age of the India-Asia collision along the Ladakh Himalaya (Northwest India). *Journal of Geology* 116: 331–353.

Grujic D, Hollister L, and Parrish R (2002) Himalayan metamorphic sequence as an orogenic channel: Insight from Bhutan. *Earth and Planetary Science Letters* 198: 177–191.

Guo Z, Wilson M, and Liu J (2007) Post-collisional adakites in south Tibet: Products of partial melting of subduction-modified lower crust. *Lithos* 96: 205–224.

Hacker B, Gnos E, Ratschbacher L, et al. (2000) Hot and dry deep crustal xenoliths from Tibet. *Science* 287: 2463–2466.

Hacker B, Luffi R, Lutkov V, et al. (2005) Near ultrahigh pressure processing of continental crust: Miocene crustal xenoliths from the Pamir. *Journal of Petrology* 46: 1661–1687.

Haines SS, Klemperer SL, Brown L, et al. (2003) INDEPTH III seismic data: From surface observations to deep crustal processes in Tibet. *Tectonics* 22. http://dx.doi.org/10.1029/2001TC001305.

Harkins N, Kirby E, Shi X, Wang E, Burbank D, and Chun F (2010) Millennial slip rates along the eastern Kunlun fault: Implications for the dynamics of intracontinental deformation in Asia. *Lithosphere* 2: 247–266. http://dx.doi.org/10.1130/L85.

Harris NBW and Inger S (1992) Trace Element Modeling of pelite-derived granites. *Contributions to Mineralogy and Petrology* 110: 46–56.

Harris NBW and Massey J (1994) Decompression and anatexis of Himalayan metapelites. *Tectonics* 13: 1537–1546.

Harris NBW, Ayres MW, and Massey J (1995) Geochemistry of granitic melts produced during the incongruent melt of muscovite: implications for the extraction of Himalayan leucogranite magmas. *Journal of Geophysical Research* 100: 15767–15777.

He J and Chery J (2008) Slip rates of the Altyn Tagh, Kunlun and Karakorum faults (Tibet) from 3D mechanical modeling. *Earth and Planetary Science Letters* 274: 50–58. http://dx.doi.org/10.1016/j.epsl.2008.06.049.

Hetényi G, Cattin R, Brunet F, et al. (2007) Density distribution of the India plate beneath the Tibetan Plateau: Geophysical and petrological constraints on the kinetics of lower crustal eclogitization. *Earth and Planetary Science Letters* 264: 226–244.

Hetzel R, et al. (2011) Low slip rates and long-term preservation of geomorphic features in Central Asia. *Nature* 417: 428–432.

Hodges KV (2000) Tectonics of the Himalaya and southern Tibet from two perspectives. *Geological Society of America Bulletin* 112: 324–350.

Houseman G, McKenzie D, and Molnar P (1981) Convective instability of a thickened boundary layer and its relevance for thermal evolution of continental convergent belts. *Journal of Geophysical Research* 86: 6115–6132.

Hubbard J and Shaw JH (2009) Uplift of the Longmen Shan and Tibetan Plateau, and the 2008 Wenchuan (M=7.9) earthquake. *Nature* 458. http://dx.doi.org/10.1038/nature07837.

Jackson J (2002) Strength of the continental lithosphere: time to abandon the jelly sandwich? *GSA Today:* 4–9.

Jackson J, McKenzie D, Priestley K, and Emmerson B (2008) New views on the structure and rheology of the lithosphere. *Journal of the Geological Society, London* 165: 453–465.

Jagoutz O and Schmidt MW (2012) The formation and bulk composition of modern juvenile continental crust: The Kohistan Arc. *Chemical Geology* 298(9): 79–96.

Jagoutz O, Müntener O, Burg J-P, Ulmer P, and Jagoutz E (2007) Lower continental crust formation through focussed flow in km-scale melt conduits: the zoned ultramafic bodies of the Chilas complex in the Kohistan island arc (NW Pakistan). *Earth and Planetary Science Letters* 242: 320–342.

Jamieson RA, Beaumont C, Medvedev S, and Nguyen MH (2004) Crustal channel flow: 2. Numerical models with implications for metamorphism in the Himalaya-Tibetan orogen. *Journal of Geophysical Research* 109, B06407.

Jan MQ and Howie RA (1981) The mineralogy and geochemistry of the metamorphosed basic and ultrabasic rocks of the Jijal Complex, Kohistan, NW Pakistan. *Journal of Petrology* 22: 85–126.

Jessup MJ, Law RD, Searle MP, and Hubbard MS (2006) Structural evolution and vorticity of flow during extrusion and exhumation of the Greater Himalayan Slab, Mount Everest massif, Tibet/Nepal: implications for orogen-scale flow partitioning. In: Law RD, Searle MP, and Godin L (eds.) *Channel Flow, Ductile Extrusion, and Exhumation in Continental Collision zones*, vol. 268, pp. 379–413. London: Geological Society, Special Publication.

Jessup MJ, Cottle JM, Searle MP, et al. (2008) P-T-t-D paths of Everest Series schist, Nepal. *Journal of Metamorphic Geology* 26: 717–739.

Jolivet M, Brunel M, Seward D, et al. (2003) Neogene extension and volcanism in the Kunlun Fault zone, northern Tibet: New constraints on the age of the Kunlun Fault. *Tectonics* 22: TC1052. http://dx.doi.org/10.1029/2002TC001428.

Jolivet R, Cattin R, Chamot-Rooke N, Lasserre C, and Peltzer G (2008) Thin-plate modeling of interseismic deformation and asymmetry across the Altyn Tagh fault zone. *Geophysical Research Letters* 35: L02309. http://dx.doi.org/10.1029/2007GL031511.

Jordan TA and Watts AW (2005) Gravity anomalies, flexure and the elastic thickness structure of the India-Eurasia collision system. *Earth and Planetary Science Letters* 236: 732–750.

Kaneko Y, Katayama I, Yamamoto H, et al. (2003) Timing of Himalayan ultrahigh-pressure metamorphism: Sinking rate and subduction angle of the Indian continental crust beneath Asia. *Journal of Metamorphic Geology* 21: 589–599.

Kapp P and Guynn JH (2004) India punch rifts Tibet. *Geology* 32: 993–996.

Kapp P, Yin A, Harrison TM, and Ding L (2005) Cretaceous-Tertiary shortening, basin development and volcanism in central Tibet. *Geological Society America Bulletin* 117: 865–878.

Kapp P, DeCelles PG, Gehrels G, Heizler M, and Ding L (2007) Geological records of the Lhasa-Qiangtang and Indo-Asian collisions in the Nima area of central Tibet. *Geological Society America Bulletin* 119: 917–932.

Kay RW and Kay SN (2002) Andean adakites: Three ways to make them. *Acta Petrologica Sinica* 18: 303–311.

Khan MA, Jan MQ, and Weaver BL (1993) Evolution of the lower arc crust in Kohistan, N. Pakistan: Arc magmatism through early, mature and intra-arc rift stages. In: Treloar PJ and Searle MP (eds.) *Himalayan Tectonics*, vol. 74, pp. 123–138. London: Geological Society, Special Publication.

Kirby E, Reiners PW, Krol MA, et al. (2002) Late Cenozoic evolution of the eastern margin of the Tibetan Plateau: Inferences from $^{40}Ar/^{39}Ar$ and (U–Th)/He thermochronology. *Tectonics* 21: TC1001. http://dx.doi.org/10.1029/2000TC001246.

Klemperer SL (2006) Crustal flow in Tibet: Geophysical evidence for the physical state of Tibetan lithosphere, and inferred patterns of active flow. In: Law RD, Searle MP, and Godin L (eds.) *Channel Flow, Ductile Extrusion and Exhumation in Continental Collision Zones*, vol. 268, pp. 39–70. London: Geological Society, Special Publication.

Kosarev G, Kind R, Sobolev S, Yuan X, Hanka W, and Oreshin S (1999) Seismic evidence for a detached Indian lithospheric mantle beneath Tibet. *Science* 283: 1306–1308.

Lacassin R, Valli F, Arnaud N, et al. (2004) Large-scale geometry, offset and kinematic evolution of the Karakoram Fault, Tibet. *Earth and Planetary Science Letters* 219: 255–269.

Lasserre C, Morel P-H, Gaudemer Y, et al. (1999) Postglacial left slip rate and past occurrence of M>8 earthquakes on the western Haiyuan fault, Gansu, China. *Journal of Geophysical Research*, 104. http://dx.doi.org/10.1029/1998JB900082.

Law RD, Searle MP, and Simpson RL (2004) Strain, deformation temperatures and vorticity of flow at the top of the Greater Himalayan Slab, Everest massif, Tibet. *Journal of the Geological Society, London* 161: 305–320.

Law RD, Searle MP, and Godin L (2006) *Channel Flow, Ductile Extrusion and Exhumation in Continental Collision Zones*, vol. 268, p. 620. London: Geological Society, Special Publication.

Law RD, Jessup MJ, Searle MP, Francsis MK, Waters DJ, and Cottle JM (2011) Telescoping of isotherms beneath the South Tibetan Detachment system, Mount Everest massif. *Journal of Structural Geology* 33: 1569–1594.

Lee H-Y, Chung S-L, Wang J-R, et al. (2003) Miocene Jiale faulting and its implication for Tibetan tectonic evolution. *Earth and Planetary Science Letters* 205: 185–194.

Lee H-Y, Chung S-L, Lo C-H, et al. (2009) Eocene Neotethyan slab breakoff in southern Tibet inferred from the Linzizong volcanic record. *Tectonophysics* 477: 20–35.

Leier AL, DeCelles PG, Kapp P, and Ding L (2007) The Takena Formation of the Lhasa terrane, southern Tibet: Record of a Late Cretaceous retroarc foreland basin. *Geological Society of America Bulletin* 119: 31–48.

Liang X, Sandvol E, Chen J, et al. (2012) A complex Tibetan upper mantle: A fragmented Indian slab and no south-verging subduction of Eurasian lithosphere. *Earth and Planetary Science Letters* 333: 101–111.

Lin T-H, Lo C-H, Chung S-L, et al. (2009) $^{40}Ar/^{39}Ar$ dating of the Jiale and Gaoligong shear zones: Implications for crustal deformation around the Eastern Himalayan Syntaxis. *Journal of Asian Earth Sciences* 34: 674–685.

Maggi A, Jackson J, McKenzie D, and Preistley K (2000) Earthquake focal depths, effective elastic thickness and the strength of the continental lithosphere. *Geology* 28: 495–498.

Martin H (1988) Adakite magmas: Modern analogues of Archean granitoids. *Lithos* 46: 411–429.

McCaffrey R and Nabelek J (1998) Role of oblique convergence in the active deformation of the Himalayas and southern Tibetan plateau. *Geology* 26: 691–694.

McKenzie D and Priestley K (2008) The influence of lithospheric thickness variations on continental evolution. *Lithos* 102: 1–11.

McKenzie D, Jackson J, and Priestley K (2005) Thermal structure of oceanic and continental lithosphere. *Earth and Planetary Science Letters* 233: 337–349.

Meade BJ (2007) Present-day kinematics at the India-Asia collision zone. *Geology* 35: 81–84.

Mo XX, Hou ZQ, Niu YL, Dong GC, Zhao ZD, and Yang ZM (2007) Mantle contributions to crustal thickening during continental collision: Evidence from Cenozoic igneous rocks in southern Tibet. *Lithos* 96: 225–242.

Mo XX, Niu YL, Dong GC, et al. (2008) Contribution of syn-collisional felsic magmatism to continental crust growth: A case study of the Palaeogene Linzizong volcanic succession in southern Tibet. *Chemical Geology* 250: 49–67.

Molnar P and Lyon-Caen H (1989) Fault plane solutions of earthquakes and active tectonics of the Tibetan Plateau and its margins. *Geophysical Journal International* 99: 123–153.

Molnar P and Tapponnier P (1975) Cenozoic tectonics of Asia: Effects of a continental collision. *Science* 189: 419.

Molnar P and Tapponnier P (1978) Active tectonics of Tibet. *Journal of Geophysical Research* 83: 5361.

Monsalve G, McGovern, and Sheehan A (2009) Mantle fault zones beneath the Himalayan collision: Flexure of the continental lithosphere. *Tectonophysics* 477: 66–76.

Mukherjee B, Sachan H, and Ahmad T (2005) A new occurrence of microdiamond from Indus Suture Zone, Himalaya, possible origin. In: Mascle G and Lavé J (eds.) *20th Himalaya-Karakoram-Tibet Workshop Abstracts*, vol. 44, 136.

Murphy MA, Yin A, Kapp P, Harrison TM, Ding L, and Jinghua C (2000) Southward propagation of the Karakoram Fault, southwest Tibet: Timing and magnitude of slip. *Geology* 28: 451–454.

Nábelek J and Hetényi G and the HiCLIMB team (2009) Underplating in the Himalaya-Tibet collision zone revealed by the Hi-CLIMB experiment. *Science* 325: 1371–1374.

Najman Y, et al. (2010) Timing of India-Asia collision: Geological, biostratigraphic and palaeomagnetic constraints. *Journal of Geophysical Research* 115: B12416. http://dx.doi.org/10.1029/2010JB007673.

Nelson KD, Zhao W, Brown LD, et al. (1996) Partially molten middle crust beneath Southern Tibet: Synthesis of Project INDEPTH results. *Science* 274: 1684–1688.

Ni J and York JE (1978) Cenozoic extensional tectonics of the Tibetan Plateau. *Journal of Geophysical Research* 83: 5377–5384.

Nomade S, Renne PR, Mo X, Zhao Z, and Zhou S (2004) Miocene volcanism in the Lhasa block, Tibet: Spatial trends and geodynamic implications. *Earth and Planetary Science Letters* 221: 227–243.

O'Brien PJ, Zotov N, Law R, Khan MA, and Jan MQ (2001) Coesite in Himalayan eclogite and implications for models of India-Asia collision. *Geology* 29: 435–438.

Owens TJ and Zandt G (1997) Implications of crustal property variations for models of Tibetan plateau evolution. *Nature* 387: 37–42.

Palin RM, Searle MP, Waters DJ, Horstwood MSA, and Parrish RR (2012) Combined thermobarometry and geochronology of peraluminous metapelites from the Karakoram metamorphic complex, North Pakistan: New insights into the tectonothermal evolution of the Baltoro and Hunza regions. *Journal of Metamorphic Geology*. http://dx.doi.org/10.1111/j.1525-1314.2012.00999.x.

Palin RM, Searle MP, St-Onge MR, et al. (2013) Monazite geochronology and petrology of kyanite- and sillimanite-grade migmatites from the northwestern flank of the eastern Himalayan syntaxis. *Gondwana Research*. http://dx.doi.org/10.1016/j.gr2013.06.022.

Parrish RR and Tirrul R (1989) U–Pb age of the Baltoro granite northwest Himalaya, and implications for zircon inheritance and monazite U–Pb systematics. *Geology* 17: 1076–1079.

Parrish RR, Gough SJ, Searle MP, and Waters DJ (2006) Plate velocity exhumation of ultrahigh-pressure eclogites in the Pakistan Himalaya. *Geology* 34: 989–992.

Passchier CW and Trouw RAJ (1996) *Microtectonics*. p. 278. Berlin: Springer.

Pedersen RB, Searle MP, and Corfield RI (2001) U–Pb zircon ages from the Spontang Ophiolite, Ladakh Himalaya. *Journal of Geological Society, London* 158: 513–520.

Peltzer G and Tapponnier P (1988) Formation and evolution of strike-slip faults, rifts and basins during the India-Asia collision: An experimental approach. *Journal of Geophysical Research* 93: 15085–15117.

Pettersen MG and Treloar PJ (2004) Volcanostratigraphy of arc volcanic sequences in the Kohistan arc, North Pakistan: Volcanism within and island arc, back-arc basin and intra-continental tectonic settings. *Journal of Volcanology and Geothermal Research* 130: 147–178.

Phillips RJ and Searle MP (2007) Macrostructural and microstructural architecture of the Karakoram fault: Relationship between magmatism and strike-slip faulting. *Tectonics* 26: TC3017. http://dx.doi.org/10.1029/2006TC00946.

Phillips RJ, Parrish RR, and Searle MP (2004) Age constraints on ductile deformation and long-term slip rates along the Karakoram fault zone, Ladakh. *Earth Planetary Science Letters* 226: 305–319.

Phillips RJ, Searle MP, and Parrish RR (2013) The geochemical and temporal evolution of the continental lithosphere and its relationship to continental-scale faulting: The Karakoram Fault, eastern Karakoram, NW Himalayas. *Geochemistry, Geophysics, Geosystems* 14. http://dx.doi.org/10.1002/ggge.20061.

Priestley K and McKenzie D (2006) The thermal structure of the lithosphere from shear wave velocities. *Earth and Planetary Science Letters* 244: 285–301.

Priestley K, Jackson J, and McKenzie D (2008) Lithospheric structure and deep earthquakes beneath India, the Himalaya and southern Tibet. *Geophysical Journal International* 172: 345–362.

Pullen A, Kapp P, Gehrels G, Ding L, and Zhang Q (2011) Metamorphic rocks in central Tibet: Lateral variations and implications for crustal structure. *Geological Society of America Bulletin* 123: 585–600. http://dx.doi.org/10.1130/B30154.1.

Rai S, Priestley K, Gaur V, Mitra S, Singh M, and Searle MP (2006) Configuration of the Indian Moho beneath the Northwest Himalaya and Ladakh. *Geophysical Research Letters* 33. http://dx.doi.org/10.1029/2006GL026076.

Ritts BD and Biffi U (2000) Magnitude of post-Middle Jurassic (Bajocian) displacement on the central Altyn Tagh fault system, northwest China. *Geological Society America Bulletin* 112: 61–74. http://dx.doi.org/10.1130/0016-7606.

Ritts BD, Yue Y, and Graham S (2004) Oligocene-Miocene tectonics and sedimentation along the Altyn Tagh fault, northern Tibetan plateau: Analysis of the Xorkol, Subei, and Aksay basins. *Journal of Geology* 112(2): 207–229. http://dx.doi.org/10.1086/381658.

Robinson AC (2009a) Geologic offsets across the Karakoram Fault: Implications for its role and terrane correlations in the western Himalayan-Tibetan orogen. *Earth and Planetary Science Letters* 279: 123–130.

Robinson AC (2009b) Evidence against Quaternary slip on the northern Karakoram Fault suggests kinematic reorganization at the western end of the Himalayan-Tibetan orogen. *Earth and Planetary Science Letters* 286: 15118–15170.

Robinson AC, Yin A, Manning CE, Harrison TM, Zhang S-H, and Wang X-F (2007) Cenozoic evolution of the eastern Pamir: Implications for strain accommodation mechanisms at the western end of the Himalayan-Tibetan orogen. *Geological Society of America Bulletin* 7(8): 882–896.

Roger F, Calassou S, Lancelot J, et al. (1995) Miocene emplacement and deformation of the Konga Shan granite (Xianshui He fault zone, west Sichuan, China): Geodynamic implications. *Earth and Planetary Science Letters* 130: 201–216.

Rohrmann A, Kapp P, Carrapa B, et al. (2012) Thermochronological evidence for plateau formation in central Tibet by 45 Ma. *Geology* 40: 187–190.

Rolland Y, Maheo G, Guillot S, and Pêcher A (2001) Tectono-metamorphic evolution of the Karakoram Metamorphic Complex (Dassu-Askole area, NE Pakistan): Exhumation of mid-crustal HT-MP gneisses in a convergent context. *Journal of Metamorphic Geology* 19: 717–737.

Rowley DB (1998) Minimum age of initiation of collision between India and Asia north of Mount Everest. *Journal of Geology* 106: 229–235.

Royden LH, Burchfiel BC, King RW, et al. (1997) Surface deformation and lower crust flow in Eastern Tibet. *Science* 276: 788–790.

Royden LH, Burchfiel BC, and Van der Hilst RD (2008) The geological evolution of the Tibetan Plateau. *Science* 321: 1054–1058.

Schärer U, Copeland P, Harrison TM, and Searle MP (1990) Age, cooling history and origin of postcollisional leucogranites in the Karakoram batholith, a multisystem isotope study. *Journal of Geology* 98: 233–251.

Schmidt J, Hacker BR, Ratschbacher L, et al. (2011) Cenozoic deep crust in the Pamir. *Earth and Planetary Science Letters* 312: 411–421.

Schulte-Pelkum V, Monsalve G, Sheehan A, et al. (2005) Imaging the Indian subcontinent beneath the Himalaya. *Nature* 435: 1222–1225.

Searle MP (1986) Structural evolution and sequence of thrusting in the High Himalaya, Tibetan-Tethys and Indus suture zones of Zanskar and Ladakh, Western Himalaya. *Journal of Structural Geology* 8: 923–936.

Searle MP (1991) *Geology and Tectonics of the Karakoram Mountains*. Chichester, UK: John Wiley & Sons, 358 pp, Geological Map of the Central Karakoram Mountains, scale 1:250,000.

Searle MP (1996) Geological evidence against large-scale pre-Holocene offsets along the Karakoram Fault: Implications for the limited extrusion of the Tibetan Plateau. *Tectonics* 15: 171–186.

Searle MP (2007) *Geological Map of the Mount Everest – Makalu Region, Nepal – South Tibet Himalaya. Scale 1:100,000*. UK: Oxford University.

Searle MP (2010) Low-angle normal faults in the compressional Himalayan orogen: Evidence from the Annapurna-Dhaulagiri Himalaya, Nepal. *Geosphere* 6: 296–315.

Searle MP and Phillips RJ (2004) A comment on "Large-scale geometry, offset and kinematic evolution of the Karakoram Fault, Tibet" *Earth & Planetary Science Letters* 229: 155–158.

Searle MP and Phillips RJ (2007) Relationships between right-lateral shear along the Karakoram Fault and metamorphism, magmatism, exhumation and uplift: evidence from the K2-Gasherbrum-Pangong Ranges, north Pakistan and Ladakh. *Journal of the Geological Society, London* 164: 439–450.

Searle MP and Rex AJ (1989) Thermal model for the Zanskar Himalaya. *Journal of Metamorphic Geology* 7: 127–134.

Searle MP and Szulc AG (2005) Channel flow and ductile extrusion of the high Himalayan slab – the Kangchenjunga – Darjeeling profile, Sikkim Himalaya. *Journal Asian Earth Sciences* 25: 173–185.

Searle MP and Tirrul R (1991) Structural and thermal evolution of the Karakoram crust. *Journal of the Geological Society, London* 148: 65–82.

Searle MP and Treloar PJ (2010) Was Late Cretaceous-Palaeocene obduction of ophiolite complexes the primary cause of crustal thickening and regional metamorphism in the Pakistan Himalaya? In: Kusky TM, Zhai M, and Xiao W (eds.) *The Evolving Continents – Understanding Processes of Continental Growth*, vol. 338, pp. 345–359. London: Geological Society, Special Publications.

Searle MP, Cooper DJW, and Rex AJ (1988) Collision tectonics in the Ladakh-Zanskar Himalaya. *Philosophical Transactions of the Royal Society, London* A326: 117–150.

Searle MP, Rex AJ, Tirrul R, Rex DC, and Barnicoat A (1989) *Metamorphic, Magmatic and Tectonic Evolution of the Central Karakoram in the Biafo-Hushe Regions of N. Pakistan*, vol. 232. Geological Society of America, pp 47–74, Special Paper.

Searle MP, Parrish RR, Tirrul R, and Rex DC (1990) Age of crystallisation and cooling of the K2 gneiss in the Baltoro Karakoram. *Journal of the Geological Society, London* 147: 603–606.

Searle MP, Crawford MB, and Rex AJ (1992) Field relations, geochemistry, origin and emplacement of the Baltoro granite, central Karakoram. *Transactions of the Royal Society of Edinburgh* 83: 519–538.

Searle MP, Parrish RR, Hodges KV, Hurford A, Ayres MW, and Whitehouse MJ (1997a) Shisha Pangma leucogranite, South Tibetan Himalaya: Field relations, geochemistry, age, origin and emplacement. *Journal of Geology* 105: 295–317.

Searle MP, Corfield RI, Stephenson BJ, and McCarron J (1997b) Structure of the North Indian continental margin in the Ladakh-Zanskar Himalayas: Implications for the timing of obduction of the Spontang ophiolite, India-Asia collision and deformation events in the Himalaya. *Geological Magazine* 134: 297–316.

Searle MP, Weinberg RF, and Dunlap WJ (1998) Transpressional tectonics along the Karakoram fault zone, northern Ladakh: Constraints on Tibetan extrusion, in Holdsworth. In: Strachan RE and Dewey JF (eds.) *Continental Transpressional and Transtensional Tectonics*, vol. 135, pp. 307–326. Geological Society of London, Special Publication.

Searle MP, Khan A, Fraser JE, and Gough SJ (1999) The tectonic evolution of the Kohistan-Karakoram collision belt along the Karakoram Highway transect, north Pakistan. *Tectonics* 18: 929–949.

Searle MP, Simpson RL, Law RD, Parrish RR, and Waters DJ (2003) The structural geometry, metamorphic and magmatic evolution of the Everest massif, High Himalaya of Nepal – South Tibet. *Journal of the Geological Society, London* 160: 345–366.

Searle MP, Law RD, and Jessup MJ (2006) Crustal structure, restoration and evolution of the Greater Himalaya in Nepal – South Tibet: Implications for channel flow and ductile extrusion of the middle crust. In: Law RD, Searle MP, and Godin L (eds.) *Channel Flow, Ductile Extrusion and Exhumation in Continental Collision Zones*, vol. 268, pp. 355–378. London: Geological Society, Special Publication.

Searle MP, Noble SR, Cottle JM, et al. (2007) Tectonic evolution of the Mogok metamorphic belt, Burma (Myanmar) constrained by U–Th–Pb dating of metamorphic and magmatic rocks. *Tectonics* 26: TC3014. http://dx.doi.org/10.1029/2006TC002083.

Searle MP, Law RD, Godin L, et al. (2008) Defining the Himalayan Main Central Thrust in Nepal. *Journal of the Geological Society, London* 165: 523–534. http://dx.doi.org/10.1144/0016-76492007-081.

Searle MP, Parrish RR, Thow AV, Noble SR, Phillips RJ, and Waters DJ (2010a) Anatomy, age and evolution of a collisional mountain belt: the Baltoro granite batholith and Karakoram Metamorphic complex, Pakistani Karakoram. *Journal of the Geological Society, London* 167: 183–202. http://dx.doi.org/10.1144/0016-76492009-043.

Searle MP, Cottle JM, Streule MJ, and Waters DJ (2010b) Crustal melt granites and migmatites along the Himalaya: Melt source, segregation, transport and granite emplacement mechanisms. *Transactions of the Royal Society of Edinburgh* 100: 219–233. http://dx.doi.org/10.1017/S175569100901617X.

Searle MP, Elliott JR, Phillips RJ, and Chung SL (2011) Crustal-lithospheric structure and continental extrusion of Tibet. *Journal of the Geological Society, London* 168: 633–672. http://dx.doi.org/10.1144/0016-76492010-139.

Sibson R (1983) Continental fault structure and the shallow earthquake source. *Journal of the Geological Society, London* 140: 741–767.

St-Onge MR, Rayner N, and Searle MP (2010) Zircon age determinations for the Ladakh batholith at Chumatang (Northwest India): Implications for the age of the India-Asia collision in the Ladakh Himalaya. *Tectonophysics* 495: 171–183.

St-Onge MR, Rayner N, Palin RM, Searle MP, and Waters DJ (2013) Integrated pressure–temperature–time constraints for the Tso Morari dome (Northwest India): Implications for the burial and exhumation path of UHP units in the Western Himalaya. *Journal of Metamorphic Geology*, http://dx.doi.org/10.1111/jing12030.

Stearns MA, Hacker BR, Ratschbacher L, Lee J, Cottle JM, and Kylander-clarke A (2013) Synchronous Oligocene-Miocene Metamorphism of the Pamir and north Himalaya driven by Plate Scale dynamics. *Geology*. http://dx.doi.org/10.1130/G34451. 1.

Streule MJ, Phillips RJ, Searle MP, Waters DJ, and Horstwood MSA (2009) Evolution and chronology of the Pangong Metamorphic Complex adjacent to the Karakoram fault, Ladakh: Constraints from thermobarometry, metamorphic modeling and U–Pb geochronology. *Journal of the Geological Society, London* 166: 919–932.

Streule MJ, Searle MP, Waters DJ, and Horstwood MSA (2010) Metamorphism, melting and channel flow in the Greater Himalayan sequence and Makalu leucogranite: Constraints from thermobarometry, metamorphic modelling and U–Pb geochronology. *Tectonics* 29: TC5011. http://dx.doi.org/10.1029/TC002533.

Streule MJ, Carter A, Searle MP, and Cottle JM (2012) Constraints on brittle field exhumation of the Everest-Makalu section of the Greater Himalayan sequence: Implications for models of crustal flow. *Tectonics* 31: TC3010. http://dx.doi.org/10.1029/2011TC003062.

Tapponnier P and Molnar P (1977) Active faulting and tectonics in China. *Journal of Geophysical Research* 82: 2905–2930.

Tapponnier P, Peltzer G, Ledain AY, Armijo R, and Cobbold PR (1982) Propagating extrusion tectonics in Asia: New insights from simple experiments with plasticine. *Geology* 10: 611–616.

Tapponnier P, Peltzer G, Ledain AY, Armijo R, and Cobbold PR (1982) Propagating extrusion tectonics in Asia: New insights from simple experiments with plasticine. *Geology* 10: 611–616.

Tapponnier P, Zhiqin X, Roger F, et al. (2001) Oblique stepwise rise and growth of the Tibet Plateau. *Science* 294: 1671–1677.

Taylor M and Peltzer G (2006) Current slip rates on conjugate strike-slip faults in central Tibet using synthetic aperture radar interferometry. *Journal of Geophysical Research* 111: B12402. http://dx.doi.org/10.1029/2005JB004014.

Taylor M and Yin A (2009) Active structures of the Himalayan-Tibetan orogen and their relationships to earthquake distribution, contemporary strain field and Cenozoic volcanism. *Geosphere* 5: 199–214.

Taylor M, Yin A, Ryerson FJ, Kapp P, and Ding L (2003) Conjugate strike-slip faulting along the Bangong-Nujiang suture zone accommodates coeval east–west extension and north–south shortening in the interior of the Tibetan Plateau. *Tectonics* 22(4): 18. http://dx.doi.org/10.1029/2002TC001361.

Thatcher W (2007) Microplate model for the present-day deformation of Tibet. *Journal of Geophysical Research* 112: B01401. http://dx.doi.org/10.1029/2005JB004244.

Tilmann F, Ni J, and INDEPTH III Seismic team (2003) Seismic imaging of the downwelling Indian lithosphere beneath Central Tibet. *Science* 300: 1424–1427.

Turcotte DL and Schubert G (2002) *Geodynamics*, 2nd edn., p. 456. Cambridge University Press.

Valli F, Arnaud N, Leloup PH, et al. (2007) Twenty million years of continuous deformation along the Karakorum fault, western Tibet: A thermochronological analysis. *Tectonics* 26: TC4004. http://dx.doi.org/10.1029/2005TC001913.

Valli F, Leloup PH, Paqquette J, et al. (2008) New U–Th/Pb constraints on timing of shearing and long-term slip-rate on the Karakorum fault. *Tectonics* 27: TC5007. http://dx.doi.org/10.1029/2007TC002184.

Van Hinsbergen DJJ, Steinberger B, Doubrovine PV, and Gassmöller R (2011a) Acceleration and deceleration of India–Asia convergence since the Cretaceous: Roles of mantle plumes and continental collision. *Journal of Geophysical Research* 116: B06101. http://dx.doi.org/10.1029/2010JB008051.

Van Hinsbergen DJJ, Kapp P, Dupont-Nivet G, Lippert PC, Decelles P, and Torsvick TH (2011b) Restoration of Cenozoic deformation in Asia and the size of Greater India. *Tectonics* 30: TC5003. http://dx.doi.org/10.1029/2011TC002908.

Vergne J, Whittlinger G, Hui Q, et al. (2002) Seismic evidence for stepwise thickening of the crust across NE Tibetan Plateau. *Earth and Planetary Science Letters* 221. http://dx.doi.org/10.1016/j.epsl. 2003.12.012.

Walker JD, Martin MW, Bowring SA, Searle MP, Waters DJ and Hodges KV (1999) Metamorphism, melting and extension: age constraints from the High Himalayan Slab of SE Zanskar and NW Lahoul. *Journal of Geology*, 107: 473–495.

Walker CB, Searle MP, and Waters DJ (2001) An integrated tectono-thermal model for the evolution of the High Himalaya in western Zanskar with constraints from thermobarometry and metamorphic modeling. *Tectonics* 20: 810–833.

Wang E (1997) Displacement and timing along the northern strand of the Altyn Tagh fault zone, Northern Tibet. *Earth and Planetary Science Letters* 150: 55–64. http://dx.doi.org/10.1016/S0012-821X(97)00085-X.

Wang E and Burchfiel BC (2000) Late Cenozoic to Holocene deformation in Southwestern Sichuan and adjacent Yunnan, China and its role in the formation of the southeastern post of the Tibetan Plateau. *Geological Society of America Bulletin* 112: 413–423.

Wang Q, Zhang PZ, Freymueller JT, et al. (2001) Present-day crustal deformation in China constrained by global positioning system measurements. *Science* 294: 574–577.

Wang H, Wright TJ, and Biggs J (2009) Interseismic slip rate of the northwestern Xianshuihe fault from InSAR data. *Geophysical Research Letters* 36. http://dx.doi.org/10.1029/2008GL036560.

Wang Q, Whyman DA, Li ZX, et al. (2010) Eocene north–south trending dikes in central Tibet: New constraints on the timing of east–west extension with implication for early plateau uplift. *Earth and Planetary Science Letters*. http://dx.doi.org/10.1016/j.epsl.2010.07.046.

Watts AB (2001) *Isostasy and Flexure of the Lithosphere*. Cambridge, New York: Cambridge University Press.

Watts AB and Burov E (2003) Lithospheric strength and its relationship to the elastic and seismogenic layer thickness. *Earth and Planetary Science Letters* 213: 113–131.

Weinberg RF and Mark G (2008) Magma migration, folding, and disaggregation of migmatites in the Karakoram Shear Zone, Ladakh, NW India. *Geological Society of America Bulletin*. http://dx.doi.org/10.1130/B26227.

Weinberg RF, Mark G, and Reichardt H (2009) Magma ponding in the Karakoram shear zone, Ladakh, NW India. *Geological Society of America Bulletin*. http://dx.doi.org/10.1130/B26358.

Weller OM, St-Onge MR, Watess DJ, et al. (2013) Quantifying barrovian metamorphism in the Danba Structural Culmination of eastern Tibet. *Journal of Metamorphic Geology*. http://dx.doi.org/10.1111/jmg.12050.

Wen D-R, Liu D, Chung S-L, et al. (2008a) Zircon SHRIMP U–Pb ages of the Gangdese Batholith and implications for Neotethyan subduction in southern Tibet. *Chemical Geology* 252: 191–201.

Wen D-R, Chung S-L, Song B, et al. (2008b) Late Cretaceous Gangdese intrusions of adakitic geochemical characteristics, SE Tibet: Petrogenesis and tectonic implications. *Lithos*. http://dx.doi.org/10.1016/j.lithos.2008.02.005.

Wittlinger G, Vergne J, Tapponnier P, et al. (2004) Teleseismic imaging of subducting lithosphere and Moho offsets beneath western Tibet. *Earth and Planetary Science Letters* 221: 117–130.

Wright TJ, Parsons B, England PC, and Fielding EJ (2004) InSAR observations of low slip rates on the major faults of western Tibet. *Science* 305: 236–240.

Xu X, Wen X, Zheng R, Ma W, Song F, and Yu G (2003) Pattern of latest tectonic motion and its dynamics for active blocks in Sichuan-Yunnan region, China. *Science in China* 46: 210–226. http://dx.doi.org/10.1360/03dz0017.

Xu WC, Zhang HF, Parrish RR, Harris N, Guo L, and Yuan HL (2010) Timing of granulite facies Metamorphism in the eastern Himalayan syntaxis and its tectonic implications. *Tectonophysics* 485: 231–244.

Yang J, Xu Z, et al. (2009) Discovery of an eclogite belt in the Lhasa block, Tibet: A new border for Palaeo-Tethys?. *Journal of Asian Earth Sciences* 34: 76–89.

Yin A and Harrison TM (2000) Geological evolution of the Himalayan–Tibetan orogen. *Annual Reviews of Earth Planetary Sciences* 28: 211–280.

Yin A, Kapp PA, Murphy MA, et al. (1999) Significant late Neogene east–west extension in northern Tibet. *Geology* 27: 787–790.

Yin A, Rumelhart PE, Butler R, et al. (2002) Tectonic history of the Altyn Tagh fault system in northern Tibet inferred from Cenozoic sedimentation. *Geological Society America Bulletin* 114: 1257–12295.

Yue Y, Ritts BD, and Graham SA (2001) Initiation and long-term slip history of the Altyn Tagh fault. *International Geological Review* 43: 1087–1093.

Yue Y, Ritts BD, Graham SA, Wooden JL, Gehrels GE, and Zhang Z (2003) Slowing extrusion tectonics: lowered estimate of post-Early Miocene slip rate for the Altyn Tagh fault. *Earth and Planetary Science Letters* 217: 111–122.

Zeitler PK, Meltzer AS, Koons PO, et al. (2001a) Erosion, Himalayan geodynamics and the geomorphology of metamorphism. *GSA Today* 11: 4–9.

Zeitler PK, et al. (2001b) Crustal reworking at Nanga Parbat, Pakistan: Metamorphic consequences of thermal-mechanical coupling facilitated by erosion. *Tectonics* 20: 712–728.

Zhang P, Molnar P, Burchfiel BC, et al. (1988) Bounds on the Holocene Slip Rate of the Haiyuan Fault, North-Central China. *Quaternary Research* 30: 151–164.

Zhang P, Shen Z, Wang M, Gan WJ, Burgman R, and Molnar P (2004) Continuous deformation of the Tibetan Plateau from global positioning system data. *Geology* 32: 809–812.

Zhang P, Molnar P, and Xu X (2007) Late Quaternary and present-day rates of slip along the Altyn Tagh Fault, northern margin of the Tibetan Plateau. *Tectonics* 26. http://dx.doi.org/10.1029/2006TC002014.

Zhang H, Harris N, Guo L, and Xu W (2009) The significance of Cenozoic magmatism from the western margin of the eastern syntaxis, southeast Tibet. *Contributions to Mineralogy and Petrology*. http://dx.doi.org/10.1007/s00410-009-0467-5.

Zhang ZM, Zhao GC, Santosh M, Wang JL, Dong X, and Liou JG (2010) Two stages of granulite facies metamorphism in the eastern Himalayan syntaxis, south Tibet: Petrology, zircon geochronology and implications for the subduction of Neo-Tethys and the Indian continent beneath Asia. *Journal of Metamorphic Geology* 28: 719–733.

Zhao W and Nelson WDProject INDEPTH team (1994) Deep seismic reflection evidence for continental underthrusting beneath Tibet. *Nature* 366: 557–559.

Zhu B, Kidd WSF, Rowley DB, Currie BS, and Shafique N (2005) Age of initiation of the India–Asia collision in the east-central Himalayas. *Journal of Geology* 113: 265–285.

This page intentionally left blank

6.12 Tectonic Models for the Evolution of Sedimentary Basins

S Cloetingh, Utrecht University, Utrecht, The Netherlands
PA Ziegler[†], University of Basel, Basel, Switzerland
F Beekman, Utrecht University, Utrecht, The Netherlands
EB Burov, Université Pierre et Marie Curie, Paris, France; Centre National de la Recherche Scientifique, Paris, France
D Garcia-Castellanos, Instituto de Ciencias de la Tierra Jaume Almera, Barcelona, Spain
L Matenco, Utrecht University, Utrecht, The Netherlands

© 2015 Elsevier B.V. All rights reserved.

This chapter is a revision of the previous edition chapter by S.Cloetingh and P.A. Ziegler, volume 6, pp. 485–611, © 2007, Elsevier B.V.

6.12.1 Introduction 513
6.12.2 Rheological Controls on Basin Evolution 516
6.12.2.1 Rheological Stratification of the Lithosphere 516
6.12.2.2 Rheological Controls on Basin Evolution: Europe's Continental Lithosphere 517
6.12.2.3 Loading, Flexure, and Rheology of the Lithosphere 519
6.12.3 Extensional Basin Systems 525
6.12.3.1 Modes of Rifting and Extension 528
6.12.3.1.1 Atlantic-type rifts 528
6.12.3.1.2 Back-arc rifts 528
6.12.3.1.3 Synorogenic rifting and wrenching 528
6.12.3.1.4 Postorogenic extension 528
6.12.3.2 Thermal Thinning and Stretching of the Lithosphere 529
6.12.3.3 Synrift Subsidence and Duration of Rifting Stage 531
6.12.3.4 Postrift Subsidence 533
6.12.3.4.1 Shape and magnitude of rift-induced thermal anomalies 534
6.12.3.4.2 Stretching factors derived from quantitative subsidence analysis 534
6.12.3.4.3 Postrift compressional reactivation potential 536
6.12.3.5 Finite Strength of the Lithosphere in Extensional Basin Formation 538
6.12.3.6 Rift Shoulder Development and Architecture of Basin Fill 539
6.12.3.7 Back-Arc Extensional Basins 541
6.12.3.7.1 Black Sea basin 542
6.12.3.7.2 Pannonian–Transylvanian Basin system 547
6.12.4 Compressional Basin Systems 554
6.12.4.1 Flexural Foreland Basins 554
6.12.4.1.1 Role of preorogenic extension and late-stage compression 559
6.12.4.1.2 Feedback between lithospheric and surface processes 560
6.12.4.2 Compressional Basin Formation by Lithospheric Folding 564
6.12.4.2.1 The role of lithospheric rheology 566
6.12.4.2.2 Observations 567
6.12.4.2.3 Basin geometry and accommodation space 574
6.12.4.2.4 Thermal regime 575
6.12.4.2.5 Modes of brittle deformation and faulting 576
6.12.4.2.6 Interaction of folding with other tectonic processes 577
6.12.5 General Conclusions and Future Perspectives 578
6.12.5.1 Future Perspectives 579
Acknowledgments 580
References 580

6.12.1 Introduction

Understanding the processes that drive sedimentary basin formation (e.g. Cloetingh et al., 1994; Ziegler, 1994) is a key element in elucidating the geologic evolution of the continental lithosphere. During the last decades, substantial progress was made in the understanding of thermomechanical properties and processes controlling the evolution of sedimentary basins and the isostatic response of the lithosphere to surface loads such as sedimentary basins. Much of this progress stems from improved insights into the mechanical properties of the lithosphere, from the development of new modeling techniques, and from the evaluation of new, high-quality datasets from previously inaccessible areas of the globe. The focus of this chapter is on tectonic models for

[†]Deceased.

 http://dx.doi.org/10.1016/B978-0-444-53802-4.00117-2

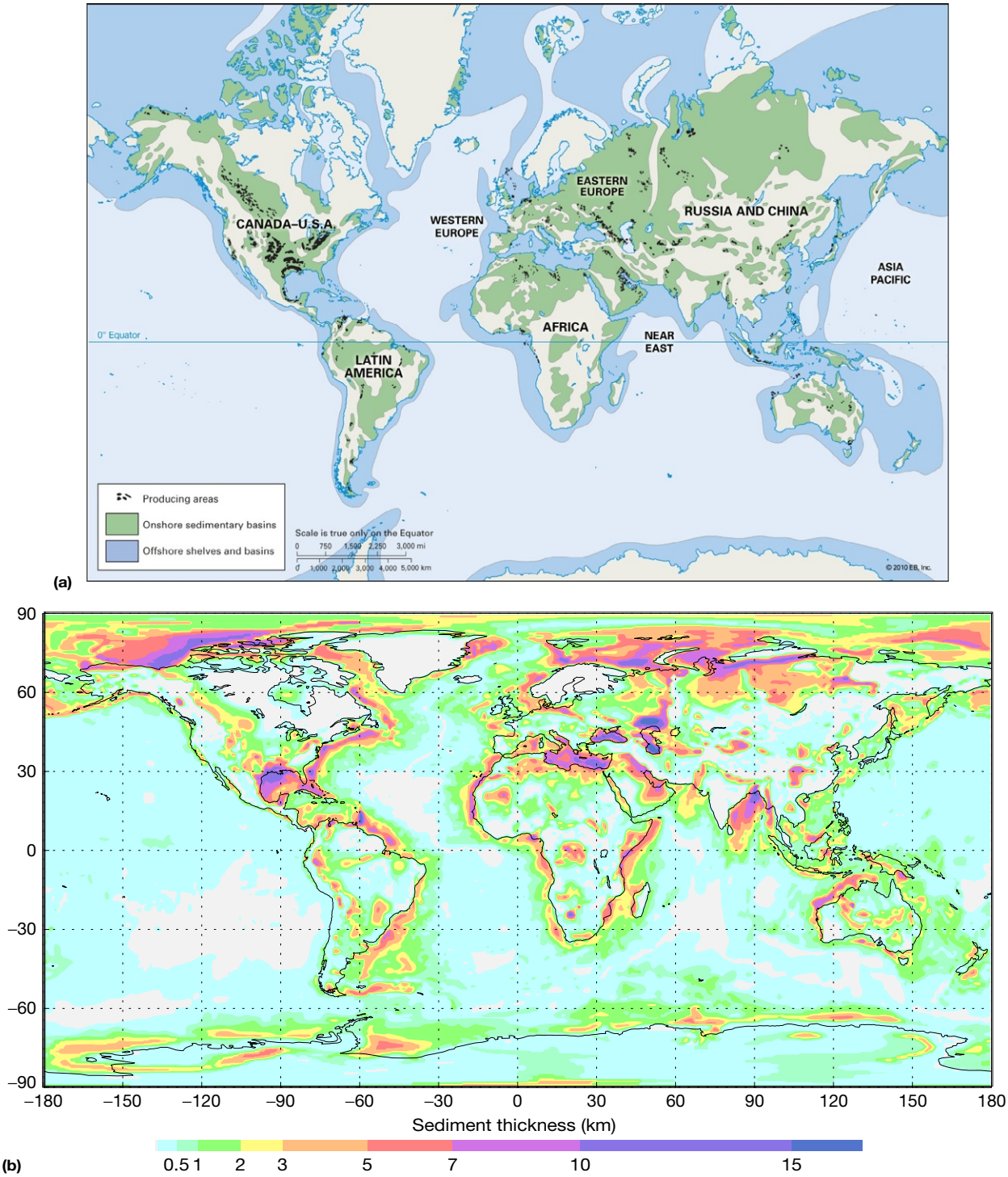

Figure 1 (a) Sedimentary basins and petroleum-producing areas of the world (the sizes of petroleum-producing areas are exaggerated in this map). (Adapted from Petroleum Publishing Co./PenWell (1970) Worldwide offshore activity and sedimentary basins. Oil and Gas Journal.) (b) Global map of sediment thickness, outlining the major onshore and offshore sedimentary basins of the world (reproduced from Laske G and Masters G (1997) A global digital map of sediment thickness. *Eos, Transactions of the American Geophysical Union* 78: F483).

processes controlling the evolution of sedimentary basins around the globe (Figure 1).

After the realization that subsidence patterns of Atlantic-type margins, corrected for effects of sediment loading and paleobathymetry, displayed the typical time-dependent decay characteristic of ocean-floor cooling (Sleep, 1971), a large number of studies were undertaken that aimed at restoring the quantitative subsidence history of basins on the basis of well data and outcropping sedimentary sections. With the introduction of backstripping analysis algorithms (Bond and Kominz, 1984; Steckler and Watts, 1982), the late 1970s and early 1980s marked a phase during which basin analysis

essentially stood for backward modeling, namely, reconstructing the tectonic subsidence from sedimentary sequences. These quantitative subsidence histories provided constraints for the development of conceptually driven forward basin models. For extensional basins, this commenced in the late 1970s with the appreciation of the importance of the lithospheric thinning and stretching concepts in basin subsidence (Salveson, 1976). After initiation of mathematical formulations of stretching concepts in forward extensional basin modeling (McKenzie, 1978), a large number of basin fill simulations focused on the interplay between thermal subsidence, sediment loading, and eustatic sea-level changes. To arrive at commonly observed more episodic and irregular subsidence curves, the smooth postrift subsidence behavior was modulated by changes in sediment supply and eustatic sea-level fluctuations. Another approach frequently followed was to input a subsidence curve, thus rendering the basin modeling package essentially a tool to fill in an adopted accommodation space (Burton et al., 1987; Lawrence et al., 1990). For the evolution of extensional basins, this approach made a clear distinction between their synrift stage and postrift stage, relating exponentially decreasing postrift tectonic subsidence rates to a combination of thermal equilibration of the lithosphere–asthenosphere system and lithospheric flexure (Watts et al., 1982).

A similar set of assumptions were made to describe the synrift phase. In the most simple version of the stretching model (McKenzie, 1978), lithospheric thinning was described as resulting from more or less instantaneous extension. In these models, a component of lithospheric mechanics was obviously lacking. On a smaller scale, tilted fault block models were introduced for modeling of the basin fill at the scale of half-graben models. Such models essentially decouple the response of the brittle upper crust from deeper lithospheric levels during rifting phases (e.g., see Kusznir et al., 1991).

A noteworthy feature of most modeling approaches in the 1990s was their emphasis on the basin subsidence record and their very limited capability to handle differential subsidence and uplift patterns in a process-oriented, internally consistent manner (e.g., see Doré et al., 1993; Kusznir and Ziegler, 1992; Larsen et al. 1992). More recently, increasing evidence is accumulating for compressional reactivation of extensional basins (e.g., Cloetingh et al., 2008; Johnson et al., 2008).

Compressional basin modeling also underwent a change in focus. The importance of the lithospheric flexure concept, relating topographic loading of the crust by an overriding mountain chain to the development of accommodation space, was recognized as early as 1973 by studying the foreland of the Canadian Rocky Mountain thrust belt (Price, 1973). Also here it took several years before quantitative approaches started to develop, investigating the effects of lithospheric flexure on foreland basin stratigraphy (Beaumont, 1981). The success of flexural basin stratigraphy modeling, capable of incorporating subsurface loads related to plate tectonic forces operating on the lithosphere (e.g., Peper et al., 1995; Van der Beek and Cloetingh, 1992), led in the 1990s to the need to incorporate more structural complexity in these models, also in view of implications for the simulation of thermal maturation and fluid migration (e.g., Parnell, 1994). The necessary understanding of lithospheric mechanics and basin deformation was subsequently developed after a bridge was established between researchers studying deeper lithospheric processes and those who analyzed the record of vertical motions, sedimentation, and erosion in basins (e.g., Cloetingh et al., 2007; Cloetingh and Negendank, 2010; Garcia-Castellanos and Cloetingh, 2012). This permitted the development of basin analysis models that integrate structural geology and lithosphere tectonics (see Roure et al, 2010c for an overview).

In the following sections of this chapter, we review recent advances in modeling the initiation and evolution of sedimentary basins in their lithospheric context on a global and more regional scale. To the latter purpose, we follow a natural laboratory approach selecting some well-documented basins of Europe. In this way, a review of recent advances and data interactive modeling integrating process modeling with geologic and geophysical data is given, covering key aspects of extensional basins, foreland basins, and basins formed by lithospheric folding. As will become clear from these sections, polyphase evolution of basin systems is the rule rather than an exception. Another important aspect has been the quantification of mechanical coupling of lithospheric processes to the near-surface expression of tectonic controls on basin fill. This invoked a process-oriented approach, linking different spatial and temporal scales in the basin record. Crucial in this was the testing and validation of modeling predictions in natural laboratories for which high-quality databases were available at deeper crustal levels (deep reflection and refraction seismic) and the basin fill (reflection seismic, wells, and outcrops), demanding a close cooperation between academic and industrial research groups (e.g., Roure et al., 2010c).

In **Section 6.12.2**, we first analyze the finite strength of the lithosphere, which plays an important role in the development of both extensional and compressional basins. This applies both to the geometry of the basin shape and to the record of vertical motions during and after rifting. We highlight the connection between the bulk rheological properties of the lithosphere and the evolution of some of Europe's main sedimentary basins. These include some of the best-documented sedimentary basin systems of the world.

In **Section 6.12.3**, we start with a review of the dynamics of extensional basin systems. First, we discuss the genetic types of extensional basins followed by an overview of the characteristics of thermal thinning of the lithosphere, doming and flood basalt extrusion, and aspects of particular importance to volcanic-rifted margins. We examine the record of vertical motions during and after rifting in the context of stretching models developed to quantify rifted basin development. We also address the tectonic control on postrift evolution of extensional basins. In **Section 6.12.3.7**, we develop the treatment of polyphase deformation of extensional basins by reviewing two European back-arc basin systems as natural laboratories: the Black Sea basin system and the Pannonian–Carpathian Basin system, both located in eastern Europe. We concentrate on rheological controls on basin formation and its consequences for large-scale basin stratigraphy and rift-shoulder dynamics. We also discuss the role of intraplate stresses and lithospheric strength evolution during the postrift phase and implications for neotectonic reactivation of the Black Sea basin system. The Pannonian–Carpathian Basin system is the site of pronounced contrasts of lithospheric strength between the Pannonian area, which is probably underlain by the hottest and weakest lithosphere of Europe,

and the particularly strong East European Platform lithosphere bounding the Carpathian arc to the east. Noteworthy features of the Pannonian system are the short duration of rifting phases in a back-arc setting affected by extensional collapse and subsequent compressional reactivation.

In Section 6.12.4, we review the development and evolution of compressional basins in a lithospheric context. We focus on foreland basins and basins that evolved as a result of large-scale compressional folding of intraplate continental lithosphere and present and discuss examples of both types of basins in the first part of the section. In the first part of Section 6.12.4, we address the role of flexure in compressional basin evolution and the interplay between lithosphere dynamics and topography in compressional basin systems. Basins developed on folded continental lithosphere have characteristic features. We illustrate this in the second part of Section 6.12.4 by the basins of central Asia, the folded lithosphere of Iberia, the NW European Platform, the Pannonian Basin and the South Caspian Basin.

The closing Section 6.12.5 draws some general conclusions and addresses future perspectives.

6.12.2 Rheological Controls on Basin Evolution

6.12.2.1 Rheological Stratification of the Lithosphere

The strength of *continental* lithosphere is controlled by its depth-dependent rheological structure in which the thickness and composition of the crust, the thickness of the lithospheric mantle, the potential temperature of the asthenosphere, and the presence or absence of fluids, as well as strain rates, play a dominant role (Burov, 2007; Cloetingh and Burov, 1996; Kusznir and Park, 1987; Watts, 2001, 2007; see also Watts, Chapter 6.01 and Burov, Chapter 6.03). Rheological models indicate that thermally stabilized continental lithosphere typically consists of the mechanically strong upper crust, which is separated by a weak lower crustal layer from the strong upper part of the mantle–lithosphere that in turn overlies the weak lower mantle–lithosphere (Figure 2).

By contrast, *oceanic* lithosphere has a more homogeneous composition and is characterized by a much simpler rheological structure. The strength of *oceanic* lithosphere depends mainly on its thermal regime, which controls its essentially

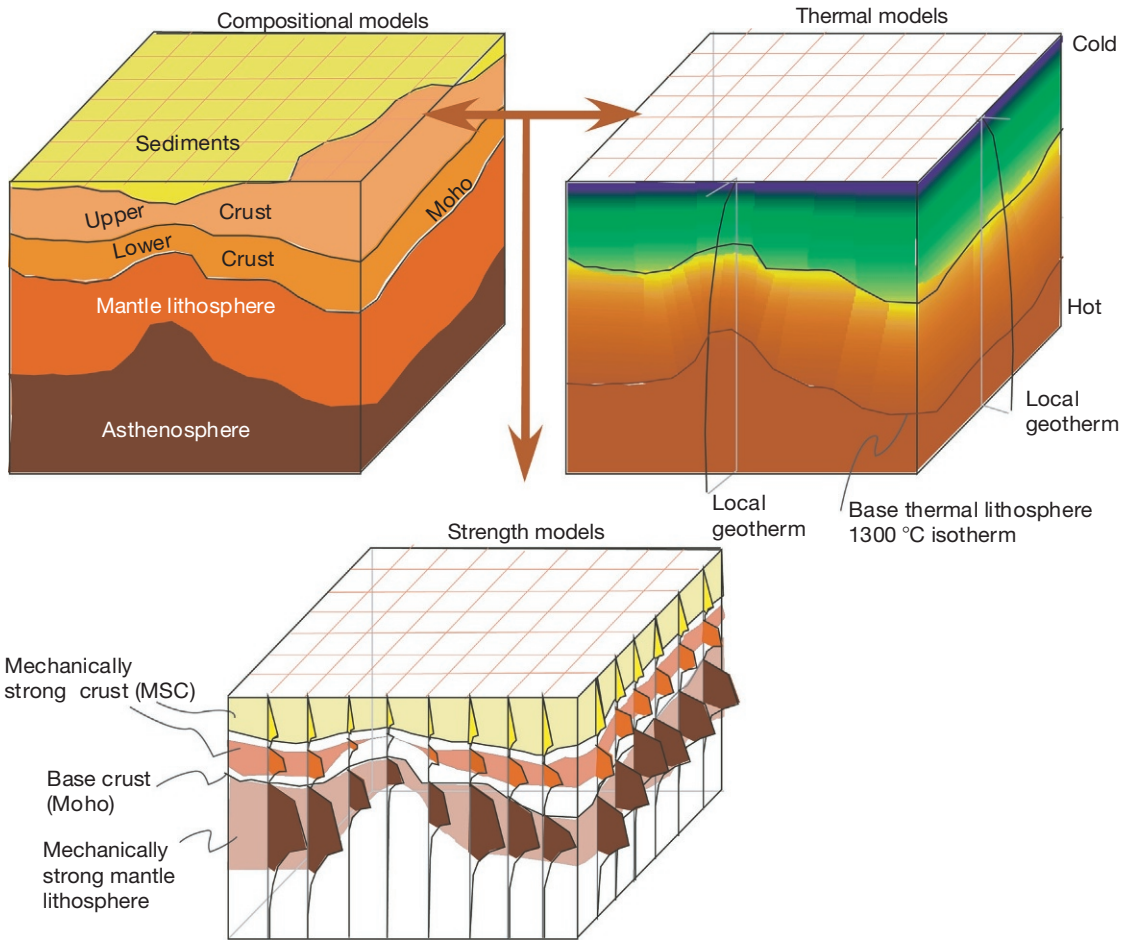

Figure 2 From crustal thickness (top left) and thermal structure (top right) to lithospheric strength (bottom): conceptual configuration of the thermal structure and composition of the lithosphere, adopted for the calculation of 3-D strength models. Reproduced from Cloetingh S, Ziegler PA, Beekman F, Andriessen PAM, Hardebol N, and Dèzes P (2005) Intraplate deformation and 3D rheological structure of the Rhine Rift System and adjacent areas of the northern Alpine foreland. *International Journal of Earth Sciences* 94: 758–778.

age-dependent thickness. Rheologically speaking, thermally stabilized oceanic lithosphere is considerably stronger than all types of continental lithosphere.

The strength of continental crust depends also on the availability of preexisting crustal discontinuities (Burov, 2007; see also Burov, this volume). Deep-reaching crustal discontinuities, such as thrust and wrench faults, cause significant weakening of the otherwise mechanically strong upper parts of the crust. As such discontinuities are apparently characterized by a reduced frictional angle, particularly in the presence of fluids (Van Wees, 1994), they are prone to reactivation at stress levels that are well below those required for the development of new faults. Deep reflection-seismic profiles show that the crust of late Proterozoic and Paleozoic orogenic belts is generally characterized by a monoclinal fabric that extends from upper crustal levels down to the Moho either at which it soles out or by which it is truncated (see Ziegler and Cloetingh, 2004). This fabric reflects the presence of deep-reaching lithologic heterogeneities and shear zones.

The strength of the continental upper lithospheric mantle depends to a large extent not only on the thickness of the crust but also on its age and thermal regime (Jaupart and Mareschal, 2007; see Jaupart and Mareschal, this volume). Thermally stabilized stretched continental lithosphere with a 20 km thick crust and a 50 km thick lithospheric mantle is mechanically stronger than unstretched lithosphere with a 30 km thick crust and a 70 km thick lithospheric mantle. Extension of stabilized continental crustal segments precludes ductile flow of the lower crust, and faults will be steep to listric and propagate toward the hanging wall, that is, toward the basin center (Bertotti et al., 2000). Under these conditions, the lower crust will deform by distributing ductile shear in the brittle–ductile transition domain. This is compatible with the occurrence of earthquakes within the lower crust and even close to the Moho (e.g., southern Rhine Graben: Bonjer, 1997; East African Rift: Shudofsky et al., 1987).

On the other hand, in young orogenic belts, which are characterized by crustal thicknesses of up to 60 km and an elevated heat flow, the mechanically strong part of the crust is thin and the lithospheric mantle is also weak. Extension of this type of lithosphere, involving ductile flow of the lower and middle crust along pressure gradients away from areas lacking upper crustal extension into zones of major upper crustal extensional unroofing, can cause crustal thinning and thickening, respectively. This deformation mode gives rise to the development of core complexes with faults propagating toward the hanging wall (e.g., Basin and Range Province: Bertotti et al., 2000; Buck, 1991; Wernicke, 1990). However, crustal flow will cease after major crustal thinning has been achieved, mainly due to extensional decompression of the lower crust (Bertotti et al., 2000).

Generally, the upper mantle of thermally stabilized, old cratonic lithosphere is considerably stronger than the strong part of its upper crust (Moisio et al., 2000). However, the occurrence of upper mantle reflectors, which generally dip in the same direction as the crustal fabric and probably are related to subducted oceanic and/or continental crustal material, suggests that the continental lithospheric mantle is not necessarily homogenous but can contain lithologic discontinuities that enhance its mechanical anisotropy (Vauchez et al., 1998; Ziegler et al., 1998). Such discontinuities, consisting of eclogitized crustal material, can potentially weaken the strong upper part of the lithospheric mantle. Moreover, even in the face of similar crustal thicknesses, the heat flow of deeply degraded late Proterozoic and Phanerozoic orogenic belts is still elevated as compared to adjacent old cratons (e.g., Pan-African belts of Africa and Arabia; Janssen, 1996). This is probably due to the younger age of their lithospheric mantle and possibly also to a higher radiogenic heat generation potential of their crust. These factors contribute to weakening of former mobile zones to the end that they present rheologically weak zones within a craton, as evidenced by their preferential reactivation during the breakup of Pangaea (Janssen et al., 1995; Ziegler, 1989b; Ziegler et al., 2001).

From a rheological point of view, the thermally destabilized lithosphere of tectonically active rifts, as well as of rifts and passive margins that have undergone only a relatively short postrift evolution (e.g., 25 Ma), is considerably weaker than that of thermally stabilized rifts and of unstretched lithosphere (Ziegler et al., 1998). In this respect, it must be realized that during rifting, progressive mechanical and thermal thinning of the lithospheric mantle and its substitution by the upwelling asthenosphere is accompanied by a rise in geotherms causing progressive weakening of the extended lithosphere. In addition, its permeation by fluids causes its further weakening. Upon decay of the rift-induced thermal anomaly, rift zones are rheologically speaking considerably stronger than unstretched lithosphere. However, the accumulation of thick syn- and postrift sedimentary sequences can cause by thermal blanketing a weakening of the strong parts of the upper crust and lithospheric mantle of rifted basins (Stephenson, 1989). Moreover, as faults permanently weaken the crust of rifted basins, they are prone to tensional and compressional reactivation (Ziegler et al., 1995, 1998, 2001, 2002).

In view of its rheological structure, the continental lithosphere can be regarded under certain conditions as a two-layered viscoelastic beam (Reston, 1990; Ter Voorde et al., 1998). The response of such a system to the buildup of extensional and compressional stresses depends on the thickness, strength, and spacing of the two competent layers and on stress magnitudes and strain rates and the thermal regime (Watts and Burov, 2003; Zeyen et al., 1997). As the structure of continental lithosphere is also laterally heterogeneous, its weakest parts start to yield first once tensional and compressional intraplate stress levels equate their strength.

6.12.2.2 Rheological Controls on Basin Evolution: Europe's Continental Lithosphere

Studies on the rheological properties of the European lithosphere revealed a direct link between its thermotectonic age and bulk strength (Cloetingh and Burov, 1996; Cloetingh et al., 2005a,b; Pérez-Gussinyé and Watts, 2005). On the other hand, inferences from *P*- and *S*-wave tomography (Goes et al., 2000a,b; Ritter et al., 2000, 2001) and thermomechanical modeling (Garcia-Castellanos et al., 2000) point to a pronounced weakening of the lithosphere in the Lower Rhine area owing to high upper mantle temperatures. However, the late Neogene and Quaternary tectonics of the Ardennes–Lower Rhine area appears to form part of a much wider neotectonic deformation system that overprints the late Paleozoic and Mesozoic basins of NW Europe. This is supported by

geomorphological evidence and the results of seismicity studies in Brittany (Bonnet et al., 2000) and Normandy (Lagarde et al., 2000; Van Vliet-Lanoë et al., 2000) and by data from the Ardennes–Eifel region (Van Balen et al., 2000), the southern parts of the Upper Rhine Graben (Nivière and Winter, 2000), the Bohemian Massif (Ziegler and Dèzes, 2005, 2007), and the North German Basin (Bayer et al., 1999).

Lithospheric-scale folding and buckling, in response to the buildup of compressional intraplate stresses, can cause uplift or subsidence of relatively large areas at timescales of a few My and thus can be an important driving mechanism of neotectonic processes. For instance, the Pliocene–Pleistocene accelerated subsidence of the North Sea basin is attributed to downbuckling of the lithosphere in response to the buildup of the present-day stress field (Van Wees and Cloetingh, 1996). Similarly, uplift of the Vosges–Black Forest Arch, which at the level of the crust–mantle boundary extends from the Massif Central into the Bohemian Massif, commenced during the Burdigalian (±18 Ma) and persisted until at least Early Pliocene times. Uplift of this arch is attributed to lithospheric folding controlled by compressional stresses originating at the Alpine collision zone (Dèzes et al., 2004; Ziegler and Dèzes, 2005, 2007; Ziegler et al., 2002).

An understanding of the temporal and spatial strength distribution of continental lithosphere (e.g., Cloetingh and Van Wees, 2005; Cloetingh et al., 2005a,b, 2006, 2007, 2011, 2013; Tesauro et al., 2007, 2009b, 2012b, 2013) may offer quantitative insights into the patterns of its intraplate deformation (basin inversion and upthrusting of basement blocks) and particularly into the pattern of lithospheric-scale folding and buckling. So far, strength envelopes and the effective elastic thickness (EET) of the lithosphere have been calculated for a number of locations in Europe (e.g., Cloetingh and Burov, 1996). However, as such calculations were made for scattered points only, or along transects, they provide limited information on lateral strength variations of the lithosphere. Although lithospheric thickness and strength maps have already been constructed for the Pannonian Basin (Lankreijer et al., 1999) and the Baltic Shield (Kaikkonen et al., 2000), such maps were until recently not yet available for all of Europe.

As evaluation and modeling of the response of the lithosphere to vertical and horizontal loads require an understanding of its strength distribution, dedicated efforts were made to map the strength of the European foreland lithosphere by implementing 3-D strength calculations (Cloetingh et al., 2005a,b; Tesauro et al., 2009b). Owing to the large amount of high-quality geophysical data acquired during the last 20 years in Europe, its lithospheric configuration is rather well known though significant uncertainties remain in many areas about the seismic and thermal thickness of the lithosphere (Artemieva, 2006, 2011; Artemieva and Mooney, 2001; Artemieva et al., 2006; Babuska and Plomerova, 1992). Nevertheless, available data help to constrain the rheology of the European lithosphere, thus enhancing our understanding of its strength.

Strength calculations of the lithosphere depend primarily on its thermal and compositional structure and are particularly sensitive to thermal uncertainties (Burov and Diament, 1995; Ranalli, 1995; Ranalli and Murphy, 1987). For this reason, the workflow aimed at the development of a 3-D strength model for Europe was twofold: (1) constructing a 3-D compositional model and (2) calculating a 3-D thermal cube. The final 3-D strength cube (**Figure 2**) was obtained by calculating 1-D strength envelopes for each lattice point (x,y) of a regularized raster covering NW Europe. For each lattice point, the appropriate input values were obtained from a 3-D compositional and thermal cube. A geologic and geophysical geographic database was used as reference for the construction of the input models.

For continental realms, a 3-D multilayer compositional model was constructed, consisting of one mantle–lithosphere layer, 2–3 crustal layers, and an overlying sedimentary cover layer, whereas for oceanic areas, a one-layer model was adopted. For the depth to the different interfaces, several regional- or European-scale compilations were available that are based on deep seismic reflection and refraction or surface wave dispersion studies (e.g., Artemieva et al., 2006; Blundell et al., 1992; Calcagnile and Panza, 1987; Du et al., 1998; Panza, 1983; Suhadolc and Panza, 1989; Tesauro et al., 2008). For the Moho depth, we relied on the EuCRUST-07 model of Tesauro et al. (2008) (**Figure 3**). Regional compilation maps of the seismogenic lithospheric thickness were used as reference to the base of the thermal lithosphere in subsequent thermal modeling (Babuska and Plomerova, 1993, 2001; Plomerova et al., 2002; Tesauro et al., 2010a,b).

Figure 4(a) shows the integrated strength under compression of the entire lithosphere of western and central Europe (Tesauro et al., 2009b), whereas **Figure 4(b)** displays the integrated strength of the crustal part of the lithosphere. As evident from **Figure 4**, European lithosphere is characterized by major spatial mechanical strength variations, with a pronounced contrast between the strong Proterozoic lithosphere of the East European Platform to the east of the Teisseyre–Tornquist Line and the relatively weak Phanerozoic lithosphere of western Europe. A similar strength contrast occurs at the transition from strong Atlantic oceanic lithosphere to the relatively weak continental lithosphere of western Europe. Within the Alpine foreland, pronounced northwest–southeast trending weak zones are recognized that coincide with such major geologic structures as the Rhine Graben system and the North Danish–Polish Trough that are separated by the high-strength North German Basin and the Bohemian Massif. Moreover, a broad zone of weak lithosphere characterizes the Massif Central and surrounding areas.

The presence of thickened crust in the area of the Teisseyre–Tornquist suture zone (**Figure 3**) gives rise to a pronounced mechanical weakening of the lithosphere, particularly of its mantle part. Whereas the lithosphere of Fennoscandia is characterized by a relatively high strength, the North Sea rift system corresponds to a zone of weakened lithosphere. Other areas of high lithospheric strength are the Bohemian Massif and the London–Brabant Massif, both of which exhibit low seismicity (**Figure 5**). A pronounced contrast in strength can also be noticed between the strong Adriatic indenter and the weak Pannonian Basin area.

Comparing **Figure 4(a)** with **4(b)** reveals that the lateral strength variations of Europe's intraplate lithosphere are primarily caused by variations in the mechanical strength of the lithospheric mantle, whereas variations in crustal strength appear to be more modest. The variations in lithospheric mantle strength are primarily related to variations in the thermal structure of the lithosphere that can be related to thermal perturbations of the sublithospheric upper mantle imaged by seismic tomography (Goes et al., 2000a), with lateral variations in crustal thickness

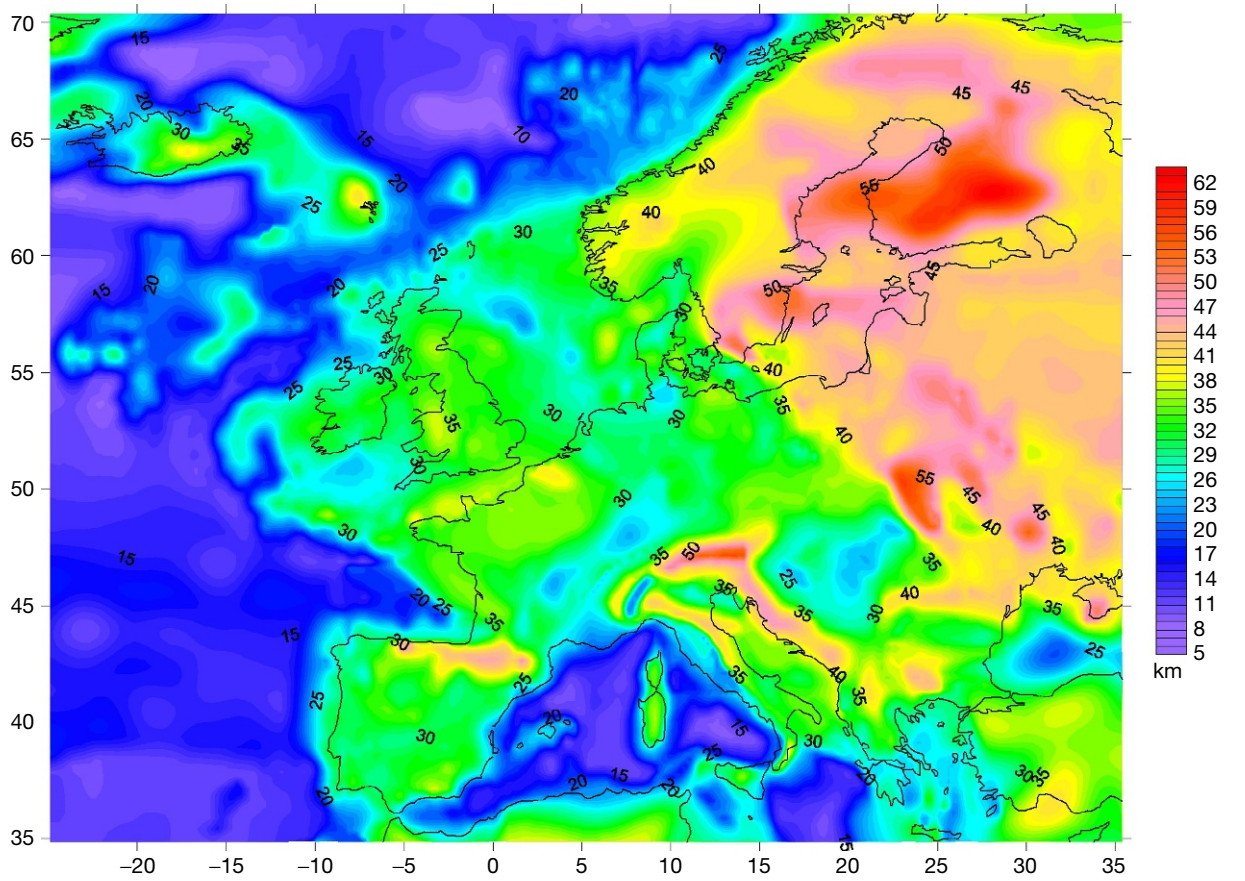

Figure 3 Map of Moho depth discontinuity for western Europe, constructed by integration of published regional maps. Reproduced from Tesauro M, Kaban MK, and Cloetingh SAPL (2008) EuCRUST-07: A new reference model for the European crust. *Geophysical Research Letters* 35: L05313.

playing a secondary role, apart from Alpine domains that are characterized by deep crustal roots. High strength in the East European Platform, the Bohemian Massif, the London–Brabant Massif, and the Fennoscandian Shield reflects the presence of old, cold, and thick lithosphere, whereas the European Cenozoic Rift System coincides with a major axis of thermally weakened lithosphere within the Northwest European Platform. Similarly, weakening of the lithosphere of southern France can be attributed to the presence of tomographically imaged plumes rising up under the Massif Central (Granet et al., 1995; Wilson and Patterson, 2001).

The major lateral strength variations that characterize the lithosphere of extra-Alpine Phanerozoic Europe are largely related to its late Cenozoic thermal perturbation and to Mesozoic and Cenozoic rift systems and intervening stable blocks and not so much to the Caledonian and Variscan orogens and their accreted terranes (Dèzes et al., 2004; Ziegler and Dèzes, 2006). These lithospheric strength variations are primarily related to variations in the thermal structure of the lithosphere and, therefore, are compatible with inferred variations in the EET of the lithosphere (see Cloetingh and Burov, 1996; Pérez-Gussinyé and Watts, 2005). The most important strong inliers in the lithosphere of the Alpine foreland lithosphere correspond to the early Paleozoic London–Brabant Massif and the Variscan Armorican, Bohemian, and west Iberian Massifs. The strong Proterozoic Fennoscandian–East European Craton flanks the weak Phanerozoic European lithosphere to the northeast, whereas the strong Adriatic indenter contrasts with the weak lithosphere of the Mediterranean collision zone.

Spatial variations in lithospheric strength and relatively hot upper mantle under the lithosphere of central and western Europe can lead to ductile crustal flow not only on continental scale in European lithosphere (Tesauro et al., 2011) but also on the scale of rifted margin systems such as the southern Norwegian rifted margin (Pascal and Cloetingh, 2009).

6.12.2.3 Loading, Flexure, and Rheology of the Lithosphere

The major, directly measurable proxy for the integrated strength of the lithosphere is its EET (or T_e, see Watts, 2001 and references therein). By comparing observations of flexure in the region of long-term loads such as ice, sediment, and volcanoes to the predictions of elastic plate flexure models, T_e of the lithosphere in a wide range of geologic settings could be estimated (Table 1). Flexure studies on oceanic lithosphere suggest that its T_e ranges between 2 and 40 km and depends on plate age and sedimentary load. The T_e of continental lithosphere ranges

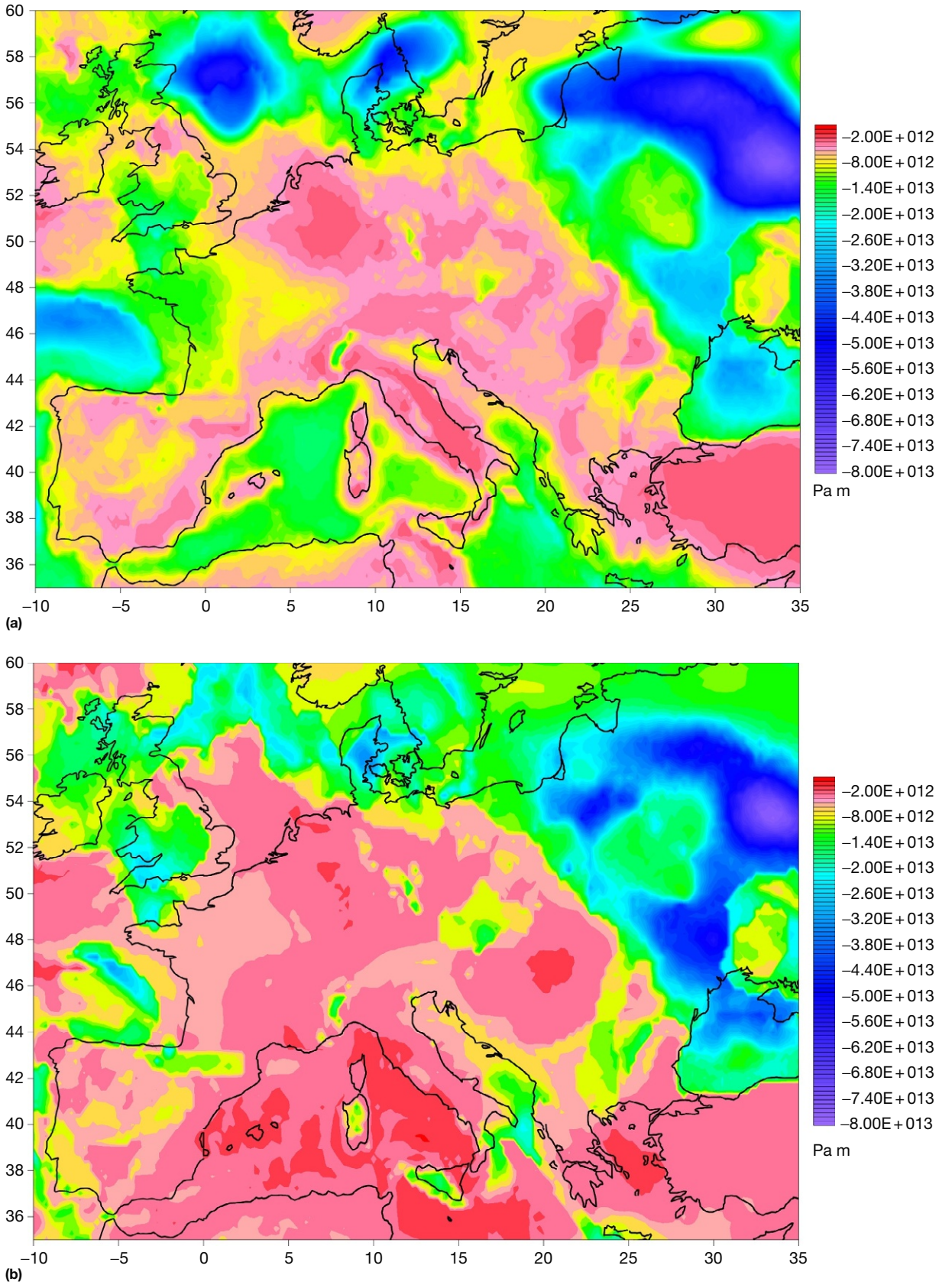

Figure 4 Integrated strength maps for intraplate Europe. Contours represent integrated strength in compression for (a) total lithosphere and (b) crust. Reproduced from Tesauro M, Kaban MK, and Cloetingh SAPL (2009a) A new thermal and rheological model of the European lithosphere. *Tectonophysics* 476: 478–495.

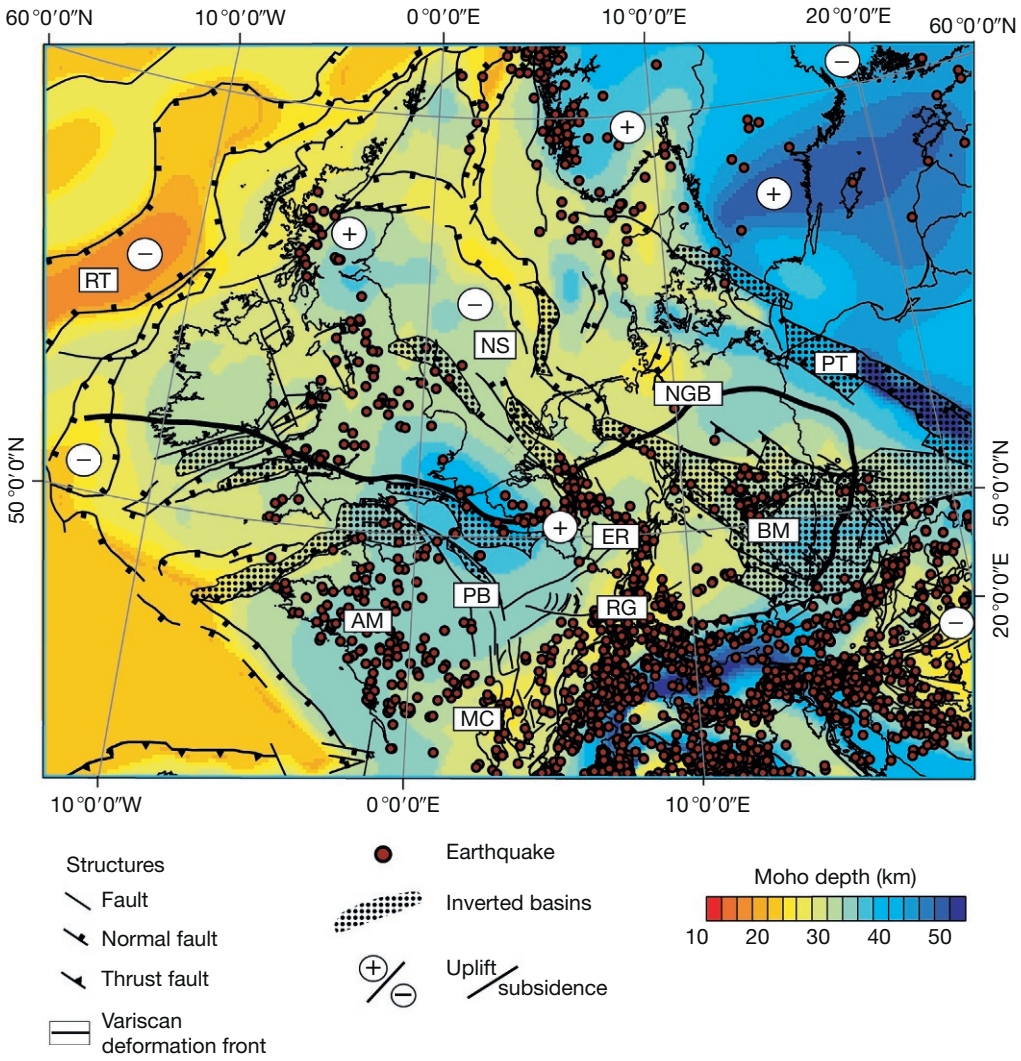

Figure 5 Seismicity (after Grünthal et al., 1999) superimposed on map of depth to Moho (reproduced from Ziegler PA and Dèzes P (2006) Crustal evolution of Western and Central Europe. *Geological Society, London, Memoirs* 32: 43–56) of northwest Europe. Neogene uplift and subsidence anomalies are indicated by circled plus and minus symbols, respectively (cf. Japsen and Chalmers, 2000). Also shown are locations of inverted basin structures (modified from Brun JP and Nalpas T (1996) Graben inversion in nature and experiments. *Tectonics* 15: 677–687). Note concentrations of intraplate seismicity in areas of crustal thickness contrast between basinal and Paleozoic massif areas, as well as in areas of crustal contrast along northeastern Atlantic rifted margins. Notable exception is seismicity along neotectonically active Rhine Graben (RG). BM, Bohemian Massif; ER, Eifel region; MC, Massif Central; NS, North Sea basin; NGB, North German Basin, PB, Paris Basin; PT, Polish Trough; RT, Rockall Trough; AM, Armorican Massif. Reproduced from Cloetingh S and Van Wees JD (2005) Strength reversal in Europe's intraplate lithosphere: Transition from basin inversion to lithospheric folding. *Geology* 33: 285–288.

from 0 to 100 km and shows no clear relationship with the consolidation age of the crust (Watts, 2001).

The thermomechanical age concept provides the framework for EET estimates of the lithosphere. Figure 6 (Cloetingh et al., 2013) illustrates the general trend of increasing elastic plate thickness with increasing thermomechanical age. Also plotted are predictions for the bulk rheology of the lithosphere based on extrapolations from rock-mechanical data, constrained by crustal geophysical data and thermal models. A characteristic feature of these models is the incorporation of a quartz-dominated upper crustal rheology and an olivine-controlled mantle rheology. These models are cast in terms of the depth to the base of the mechanically strong upper part of the crust (MSC) and the mechanically strong part of the upper mantle–lithosphere (MSL). The analysis of Figure 6 demonstrates that the mechanical properties of the crust are little affected by its age-dependent cooling, whereas the thickness and strength of the lithospheric mantle are very strongly age-dependent.

Oceanic flexural studies have shown that EET increases as the tectonic plate becomes older and gradually decreases after load emplacement ceases, because viscous stress relaxation makes the plate appearing weaker (Nádai, 1963). However, these relationships remain often unclear for continents (Watts, 2001). Adopting a quartz–diabase–olivine composition, the intrinsic strength of upper crust, lower crust, and lithospheric mantle increases with depth, in competition with

Table 1 Compilation of elastic thicknesses (EET) obtained from forward flexural modeling of foreland basins (see also **Figure 6**)

Plate	*Load/orogen*	*Basin*	*EET (km)*	*Error ± (km)*	*Source*
South Iberia	Betics W	Guadalquivir	10.0	5.0	Van der Beek and Cloetingh (1992) and Garcia-Castellanos et al. (2002)
South Iberia	Betics E	Guadalquivir	2.5	2.5	Van der Beek and Cloetingh (1992) and Garcia-Castellanos et al. (2002)
Central Iberia	Iberian Central System	Duero/Tajo/Madrid	7.0	5.0	Andeweg (2002)
North Iberia	Pyrenees, Iberian Chain, CCR	Ebro	22.5	10.0	Gaspar-Escribano et al. (2001) and Zoetemeijer et al. (1990)
W European Platform	Pyrenees	Aquitaine	25.5	5.0	Brunet (1986)
W European Platform	W Alps	North Alpine	25.0	15.0	Gutscher (1995), Macario et al. (1995), Stewart and Watts (1997), Ford et al. (1999), and Karner and Watts (1983)
W European Platform	E Alps	North Alpine	35.0	12.0	Gutscher (1995), Steward and Watts (1997), and Karner and Watts (1983)
Adriatic N	Alps/Apennines	Po west	20.0	5.0	Carrapa and Garcia-Castellanos (2005) and Kroon (2002)
Adriatic N	Alps/Apennines	Po east	10.0	8.0	Tang et al. (1992), Kroon (2002), and Barbieri et al. (2004)
Adriatic N	Apennines	Adriatic	28.0	3.0	Kroon (2002)
Adriatic center	Apennines	Adriatic	6.5	3.5	Kroon (2002)
Adriatic	Apennines/Dinarides	Apennine–Dinaridic	14.0	10.0	Royden (1988a,b) and Kruse and Royden (1994)
Adriatic S	Apennines		28.0	3.0	Kroon (2002)
Adriatic S	Calabria–Hellenides/Sicily		11.0	8.0	Cogan et al. (1989) and Moretti and Royden (1988)
Moesian Platform	S Carpathian	Getic Depression	11.0	2.0	Matenco et al. (1997a,b)
E European Platform	SE Carpathian	E Carpathian	12.0	5.0	Matenco et al. (1997a,b) and Steward and Watts (1997)
E European Platform	Carpathian		35.0	10.0	Royden and Karner (1984), Roure et al. (1993), and Raileanu et al. (1993)
E European Platform	NE Carpathian	E Carpathian	18.0	7.0	Matenco et al. (1997a,b), and Oszczypko et al. (2005)
E European Platform	NW Carpathian	W Carpathian	12.0	4.0	Oszczypko et al. (2005)
E European Platform	E Caucasus	N Caucasian	55.0	15.0	Ruppel and McNutt (1987) and Ershov et al. (1999)
E European Platform	W Caucasus	N Caucasian	70.0	15.0	Ruppel and McNutt (1987) and Ershov et al. (1999)
E European Platform	Urals		75.0	25.0	Kruse and McNutt (1988)
E European Platform	Urals		120.0	20.0	Piwowar and LeDrew (1996)
Scandinavia	Caledonian	Caledonian	87.0	20.0	Samuelsson and Middleton (1999)
Scandinavia	Caledonian	Caledonian	39.0	31.0	Poudjom-Djomani et al. (1999)
Mongolia, central			7.0	3.0	Bayasgalan et al. (2005)
Mongolia, south	Gobi-Altai		15.0	5.0	Bayasgalan et al. (2005)
Mongolia, west			40.0	10.0	Bayasgalan et al. (2005)
Siberian Platform	Verkhoyansk	Verkhoyansk	50.0	10.0	McNutt and Kogan (1987) and McNutt et al. (1988)
Arabian Shield	Zagros		50.0	25.0	Snyder and Barazangi (1986)
Arabian Shield	Oman mountain	N Oman	13.0	3.0	Ravaut et al. (1993)
Turkmenistan–Iran	Kopet Dag	Trans-Caspian	25.0	5.0	Artemjev et al. (1994)
Asia	Karakoram		121.0	10.0	Caporali (1995)
Tarim S	Kunlun	Tarim	44.0	25.0	Lyon-Caen and Molnar (1984), Fan and Ma (1990), and Teng (1991)
Tarim N	Tian Shan	Tarim	53.0	20.0	McNutt and Kogan (1987), McNutt et al. (1988), and Liu et al. (2006)
Dzungarian		Junggar	12.5	12.5	Burov et al. (1990), Burov and Kogan (1990)
Tadjik depression	Pamirs		15.0	5.0	McNutt et al. (1988)
China	Indosinian orogeny	Longmenshan	48.0	5.0	Yong et al. (2003)

(*Continued*)

Table 1 (Continued)

Plate	*Load/orogen*	*Basin*	*EET (km)*	*Error ± (km)*	*Source*
Indian shield	Karakoram		99.0	10.0	Caporali (1995)
Indian shield	Himalayas E	Ganges	90.0	15.0	Karner and Watts (1983), Lyon-Caen and Molnar (1985), and Royden (1993)
Indian shield	Himalayas W	Ganges	34.0	6.0	Karner and Watts (1983), Lyon-Caen and Molnar (1985), and Royden (1993)
Indian shield	Himalayas	Ganges	25.0	5.0	Hetényi et al. (2006)
Taiwan W	Taiwan	W Taiwan	15.0	6.5	Grotzinger and Royden (1990) and Lin and Watts (2002)
Papua New Guinea E			20.0	10.0	Haddad and Watts (1999)
Papua New Guinea W			75.0	10.0	Haddad and Watts (1999)
New Zealand		Wanganui	17.0	8.0	Holt and Stern (1991) and Stern et al. (1993)
E Australia	New Zealand (S Island)		22.5	12.5	Stern (1995)
N Australia	Banda Arc (Timor)		79.1	10.0	Londoño and Lorenzo (2004) and Tandon et al. (2000)
NW Australia	Banda Arc (Timor)		55.0	25.0	Lorenzo et al. (1998)
East Antarctic			62.0	37.0	Bott and Stern (1992)
S Am. Platform	Burdwood Bank	South Falkland	13.0	7.0	Bry et al. (2004)
S Am. Platform (Arg.)	E Andes? Volcanic?		14.0		Bahlburg and Furlong (1996)
S Am. Platform (Arg.)	Andes	Ordovician Puna	14.0		Bahlburg and Furlong (1996)
S Am. Platform (Arg.)	Andes	Puna 22,24 N	20.0		Prezzi (1999)
S Am. Platform (Bolivia)	Andes	Chaco	30.5	0.5	Coudert et al. (1995)
S Am. Platform (Peru)	Andes		40.0	15.0	Fan et al. (1996)
S Am. Platform (Ecuador)	Andes		25.0	20.0	Stewart and Watts (1997)
S Am. Platform (Colombia)	Andes	Llanos	70.0		Cardozo (1997)
S California	Transverse Ranges N		50.0	5.0	Sheffels and McNutt (1986)
S California	Transverse Ranges S		10.0	5.0	Sheffels and McNutt (1986)
N Am. Platform	Appalachians		105.0	25.0	Karner and Watts (1983), Hinze and Braile (1988), and Rankin et al. (1991)
N Am. Platform	Appalachians		70.0	15.0	Steward and Watts (1997)
N Am. Platform	Rocky Mountains (Paleozoic and Ancestral)	Pennsylvanian–Permian Paradox	25.0		Barbeau (2003)
N Am. Platform W		Idaho Wyoming	22.0		Jordan (1981)
N Am. Platform NW	Arctic Alaska	Colville	65.0	5.0	Nunn et al. (1987)

Reproduced from Garcia-Castellanos D and Cloetingh S (2012) Modeling the interaction between lithospheric and surface processes in foreland basins. In: Busby C and Azor A (eds.) *Tectonics of Sedimentary Basins: Recent Advances*, pp. 152–181.

the weakening induced by the geothermal gradient. This can lead to two weak zones, capable of mechanically decoupling the upper crust, the lower crust, and the lithospheric mantle. Burov and Diament (1992, 1995) provided a formulation to capture the dependence of EET on the degree of coupling between these layers and on inelastic (plastic) failure during plate bending. For a lithosphere behaving as three completely welded elastic plates, the EET (T_e) would be the addition of the individual thicknesses:

$$T_e = h_{UC} + h_{LC} + h_{ML}$$

where h_{UC}, h_{LC}, and h_{ML} are the mechanical thicknesses of the upper crust, lower crust, and mantle–lithosphere, respectively. If these three layers are completely decoupled, then

$$T_e = \sqrt[3]{h_{UC}^3 + h_{LC}^3 + h_{ML}^3}$$

The EET bands for the mechanically strong upper crust and upper lithospheric mantle (**Figure 6**) describe the integrated EET of the lithosphere that has a bearing on its response to loads imposed on it. The degree of coupling and/or decoupling between these two mechanically strong layers and the scatter of data points reflects to a large extent the importance of mechanical weakening of the lower crust by tectonic stresses (Cloetingh and Burov, 1996). Burov and Diament (1995) showed that a rheological model in which a weak lower crust is sandwiched between a strong brittle–elastic upper crust and an elastic–ductile mantle ('jelly sandwich' model; Jackson, 2002) accounts for the wide range of lithospheric T_e values

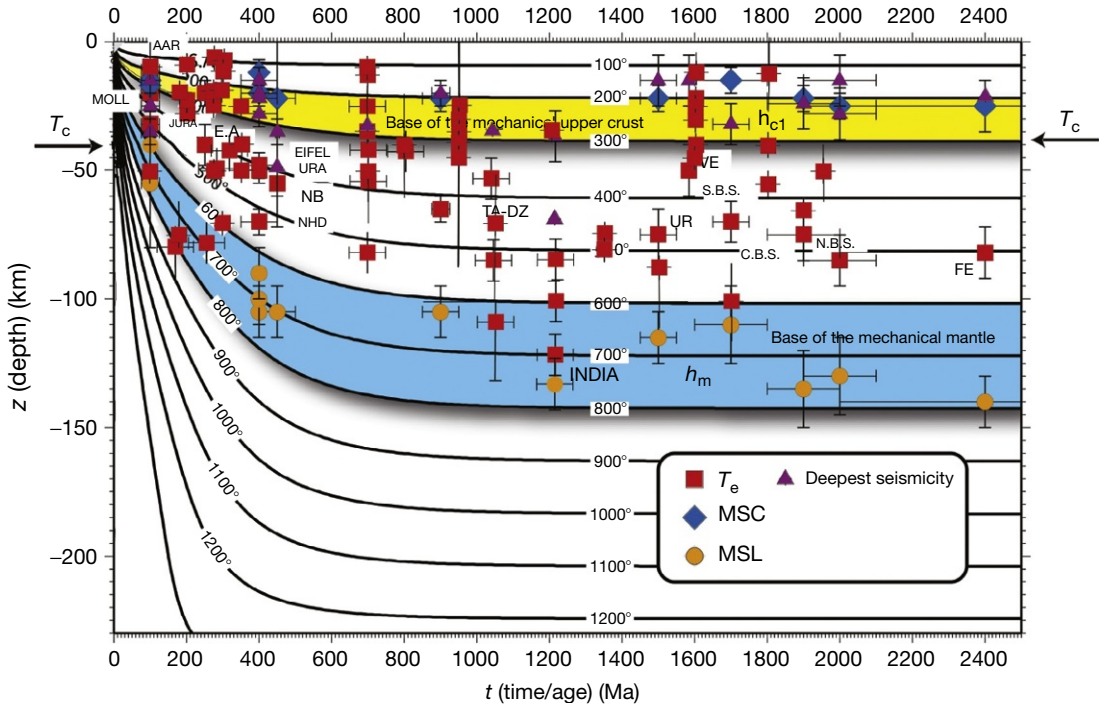

Figure 6 Compilation of observed and predicted values of effective elastic thickness (T_e, EET), depth to bottom of mechanically strong crust (MSC), and depth to bottom of mechanically strong lithospheric mantle (MSL) plotted against the age of the continental lithosphere at the time of loading and comparison with predictions from thermal models of the lithosphere. Labeled contours are isotherms. Isotherms marked by 'solid lines' are for models that account for additional radiogenic heat production in the upper crust. 'Dashed lines' correspond to pure cooling models for continental lithosphere. The equilibrium thermal thickness of the continental lithosphere is 250 km. 'Shaded bands' correspond to depth intervals marking the base of the mechanical crust (MSC) and the mantle portion of the lithosphere (MSL). 'Squares' correspond to EET estimates, 'circles' indicate MSL estimates, and 'diamonds' correspond to estimates of MSC. 'Bold letters' correspond to directly estimated EET values derived from flexural studies on, for example, foreland basins. 'Thinner letters' indicate indirect rheological estimates derived from extrapolation of rock-mechanics studies. The dataset includes (I): old thermomechanical ages (1000–2500 Ma): northernmost (N.B.S.), central (C.B.S.), and southernmost Baltic Shield (S.B.S.); Fennoscandia (FE); Verkhoyansk plate (VE); Urals (UR); Carpathians; Caucasus, (II): intermediate thermomechanical ages (500–1000 Ma): North Baikal (NB); Tarim and Dzungaria (TA-DZ); Variscan of Europe: URA, NHD, EIFEL; and (III): younger thermomechanical ages (0–500 Ma): Alpine belt: JURA, MOLL (Molasse), AAR; southern Alps (SA) and Eastern Alps (EA); Ebro basin; Betic rifted margin; Betic Cordilleras. Reproduced from Cloetingh S, Burov E, Matenco L, Beekman F, Roure F, and Ziegler PA (2013) The Moho in extensional tectonic settings: Insights from thermo-mechanical models. *Tectonophysics* 609: 558–604.

observed due to wide variations in crustal thickness and composition and geothermal gradients. At the same time, it was realized that rheological decoupling of the upper crust and lithospheric mantle also plays an important role in the structural style of intraplate compressional deformations (e.g., Rocky Mountains and Bohemian Massif; Ziegler et al., 1995, 2002).

Rheological decoupling of the crust and mantle parts of the lithosphere can contribute to the spread in EET values (Figure 6). However, a precise interpretation of continental EET is not trivial in the absence of a simple method to estimate an a priori EET based on regional parameters such as plate age and/or load age (Watts, 2001). At the same time, forward modeling of integrated lithospheric strength based on an integration of available constraints on lithospheric structure, thermal regime, and composition has provided a quantitative framework for present-day lithospheric strength on a continental scale (e.g., Cloetingh et al., 2005a,b; Tesauro et al., 2009a). Such an approach has demonstrated strong lateral heterogeneity in EETs in Europe (Figure 7), with low values in the Cenozoic rifts and relatively high values eastward of the Trans-European Suture Zone (see also Perez-Gussinyé and Watts, 2005).

Recently, the first global EET distributions have been published based on both admittance study approaches (Audet and Burgmann, 2011) and forward modeling of rheology (Tesauro et al., 2012a, 2013). A subsequent comparison of rheological and inverse approaches has demonstrated the existence of fairly robust spatial patterns in strength, with high values of EET associated with cratons and relatively low values of EET associated with rifts and convergence zones (Tesauro et al., 2009b, 2012a,b).

Sedimentary basins and continental topography are intrinsically coupled. This is the case not only in terms of the transfer of sediments from their source areas to the basins but also in terms of the support of surface loads by the underlying lithosphere. In discussions on the nature of controls on dynamic topography (e.g., Moucha and Forte, 2011), the role of spatial variations in structure and mechanical properties of the lithosphere (e.g., Tesauro et al., 2012a,b) is not always recognized. Constraints on upper mantle and crustal structure are of paramount importance in deciphering dynamic topography

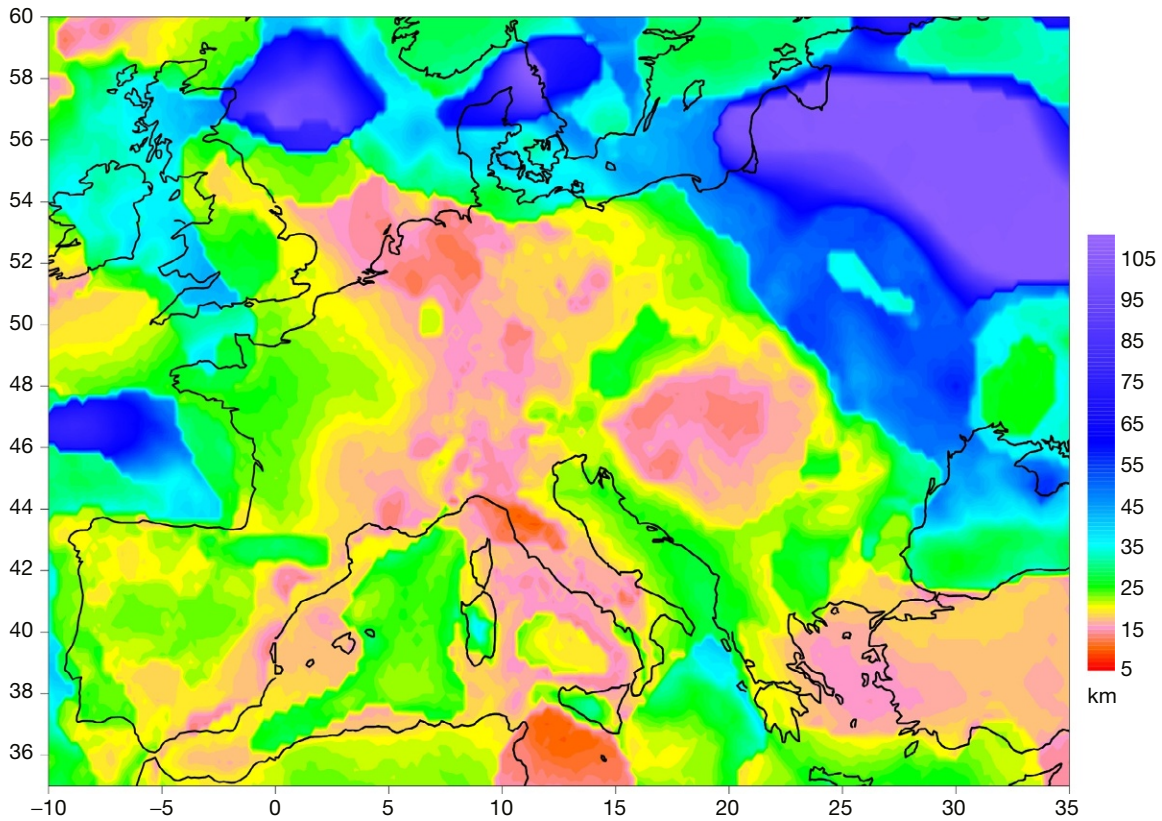

Figure 7 Effective elastic thickness (T_e) distribution of the European lithosphere derived from integrated strength of the lithosphere (km). Reproduced from Tesauro M, Kaban MK, and Cloetingh SAPL (2009) How rigid is Europe's lithosphere? *Geophysical Research Letters* 36: L16303.

attributed to mantle convective processes (Boschi et al., 2010). These authors predict for the Mediterranean area patterns in residual topography inferred from mantle flow (Faccenna and Becker, 2010) characterized by overall uplift of Iberia and overall subsidence in the eastern Mediterranean area. In contrast, predictions for basins in western Mediterranean area and Anatolia show striking differences dependent on the assumed crustal models (**Figure 8**). Availability of reliable crustal models is also crucial in separating the static isostatic and dynamic components of the topographic signal (Flament et al., 2013). This shows the need for more detailed models for crustal and upper mantle structures in the assessment of the relative contribution of mantle convection to regional-scale topography and the evolution of long-wavelength vertical motions in sedimentary basin systems.

6.12.3 Extensional Basin Systems

Tectonically active rifts, paleorifts, and passive margins form a group of genetically related extensional basins that play an important role in the spectrum of sedimentary basin types (Bally and Snelson, 1980; Buck, 2007; Ziegler and Cloetingh, 2004; see also **Chapter 6.08**). Extensional basins cover large areas of the globe and contain important mineral deposits and energy resources, including geothermal energy (e.g., Cloetingh et al., 2010; Lenkey et al., 2002). A large number of major hydrocarbon provinces are associated with rifts (e.g., North Sea, Sirte, and West Siberian basins and Dnieper–Donets and Gulf of Suez grabens) and passive margins (e.g., Campos Basin; Gabon, Angola, mid-Norway, and NW Australian shelves; and Niger and Mississippi Deltas; Ziegler, 1996). On these basins, the petroleum industry has acquired large databases that document their structural styles and allow detailed reconstruction of their evolution. Academic research programs have provided information on the crustal and lithospheric configuration of tectonically active rifts, paleorifts, and passive margins (e.g., Abadi et al., 2008; Beglinger et al., 2012a,b,c,d; Corver et al., 2009, 2011; Dupré et al., 2007, 2011). Petrologic and geochemical studies have advanced the understanding of rift-related magmatic processes. Numerical models, based on geophysical and geologic data, have contributed at lithospheric and crustal scales toward the understanding of dynamic processes that govern the evolution of rifted basins. In the succeeding text, we summarize basic concepts on dynamic processes that control the evolution of extensional basins.

A natural distinction can be made between tectonically active and inactive rifts and rifts that evolved in continental and oceanic lithosphere. Tectonically active intracontinental (intraplate) rifts, such as the Rhine Graben, the East African Rift, the Baikal rift, and the Shanxi Rift of China, correspond to important earthquake and volcanic hazard zones.

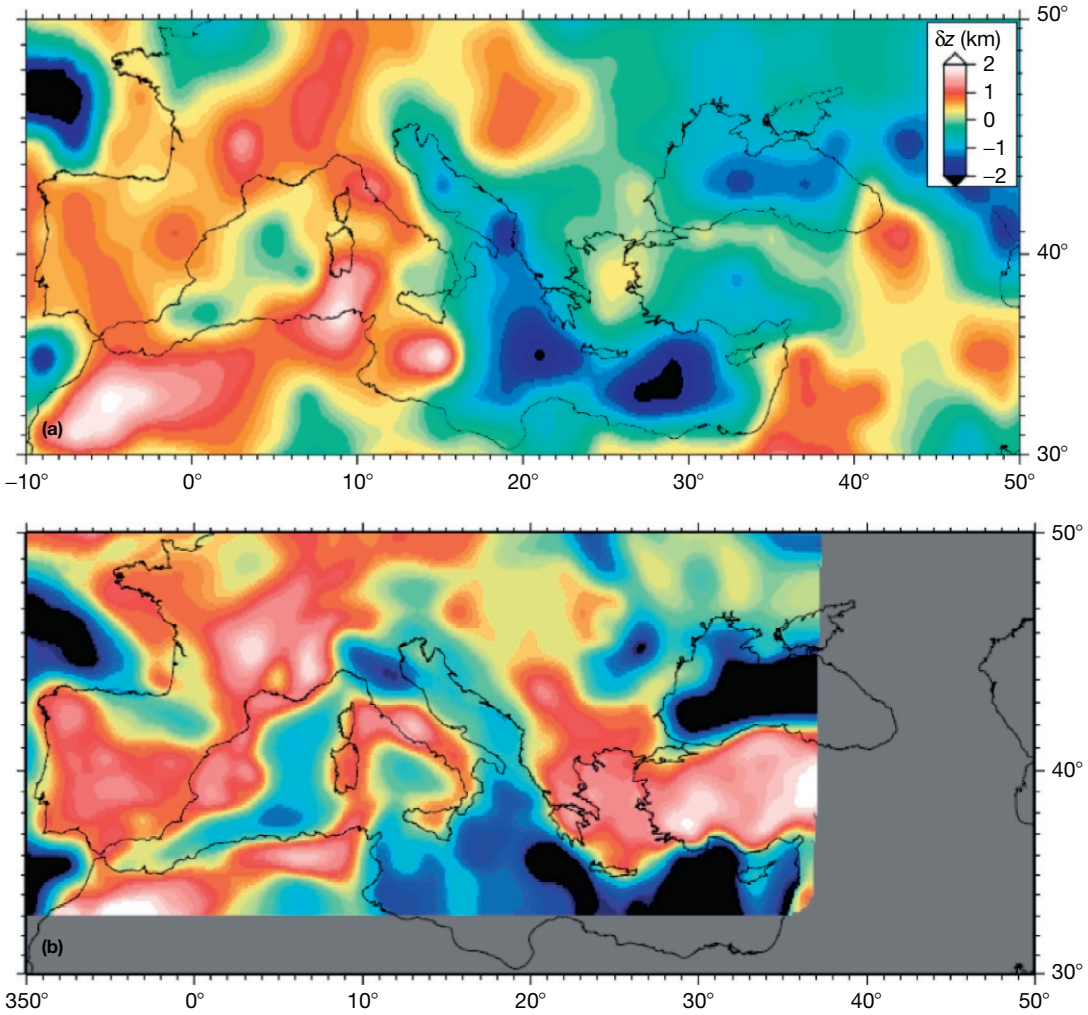

Figure 8 (a) Residual topography after correcting for isostatic adjustment based on the crustal model CRUST 2.0 (Bassin, 2000). (b) Same as (a), isostatic adjustment computed from EuCRUST-07 (Tesauro et al., 2008), with density values taken, again from CRUST 2.0. Reproduced from Boschi L, Faccenna C and Becker TW (2010) Mantle structure and dynamic topography in the Mediterranean Basin. *Geophysical Research Letters* 37: L20303.

The globe-encircling mid-ocean ridge system forms an immense intraoceanic active rift system that encroaches onto continents in the Red Sea and the Gulf of California. Rifts that are tectonically no longer active are referred to as paleorifts, aulacogens, inactive or aborted rifts, and failed arms, in the sense that they did not progress to crustal separation. Conversely, the evolution of successful rifts culminated in the breakup of continents, the opening of new oceanic basins, and the development of conjugate pairs of passive margins.

In the past, a genetic distinction was made between 'active' rifting and 'passive' rifting (Olsen and Morgan, 1995; Sengör and Burke, 1978). 'Active' rifts are thought to evolve in response to thermal upwelling of the asthenosphere (Bott and Kusznir, 1979; Dewey and Burke, 1974), whereas 'passive' rifts develop in response to lithospheric extension driven by far-field stresses (McKenzie, 1978). It is, however, questionable whether such a distinction is justified as the study of Phanerozoic rifts revealed that rift-related volcanic activity and doming of rift zones are basically a consequence of lithospheric extension and are not the main driving force of rifting. The fact that rifts can become tectonically inactive at all stages of their evolution, even if they have progressed to the Red Sea stage of limited seafloor spreading (e.g., Bay of Biscay–Pyrenean rift), supports this concept. However, as extrusion of large volumes of rift-related subalkaline tholeiites must be related to a thermal anomaly within the upper mantle, a distinction between 'active' rifting and 'passive' rifting is to a certain degree still valid, though not as 'black and white' as originally envisaged.

Rifting activity preceding the breakup of continents is probably governed by forces controlling the movement and interaction of lithospheric plates. These forces include plate boundary stresses, such as slab pull, slab rollback, ridge push, and collisional resistance, and frictional forces exerted by the convecting mantle on the base of the lithosphere (Bott, 1993; Forsyth and Uyeda, 1975; Wessel and Müller, 2007; Ziegler, 1993a,b; see also **Chapter 6.02**). On the other hand, deviatoric tensional stresses, inherent to the thickened lithosphere of young orogenic belts, as well as those developing in the lithosphere above upwelling mantle convection cells and mantle plumes (Bott, 1993), do not appear to cause, on their own, the

breakup of continents. However, if such stresses interfere constructively with plate boundary and/or mantle drag stresses, the yield strength of the lithosphere may be exceeded, thus inducing rifting (**Figure 9**).

It must be understood that mantle drag forces are exerted on the base of a lithospheric plate if its velocity and direction of movement differ from the velocity and direction of the mantle flow. Mantle drag can constructively or destructively interfere with plate boundary forces and thus can either contribute toward plate motion or resist it. Correspondingly, mantle drag can give rise to the buildup of extensional as well as compressional intraplate stresses (Artemieva and Mooney, 2002; Bott, 1993; Forsyth and Uyeda, 1975; Warners-Ruckstuhl et al., 2012). Although the present lithospheric stress field can be readily explained in terms of plate boundary forces (Cloetingh and Wortel, 1986; Richardson, 1992; Zoback, 1992), mantle drag probably contributed significantly to the Triassic–Early Cretaceous breakup of Pangaea, during which Africa remained nearly stationary and straddled an evolving upwelling and radial outflowing mantle convection cell (Pavoni, 1993; Ziegler, 1993a,b; Ziegler et al., 2001).

Mechanical stretching of the lithosphere and thermal attenuation of the lithospheric mantle are associated with the development of local deviatoric tensional stresses, which play an increasingly important role during advanced rifting stages (Bott, 1992; Ziegler, 1993a,b). This has led to the development

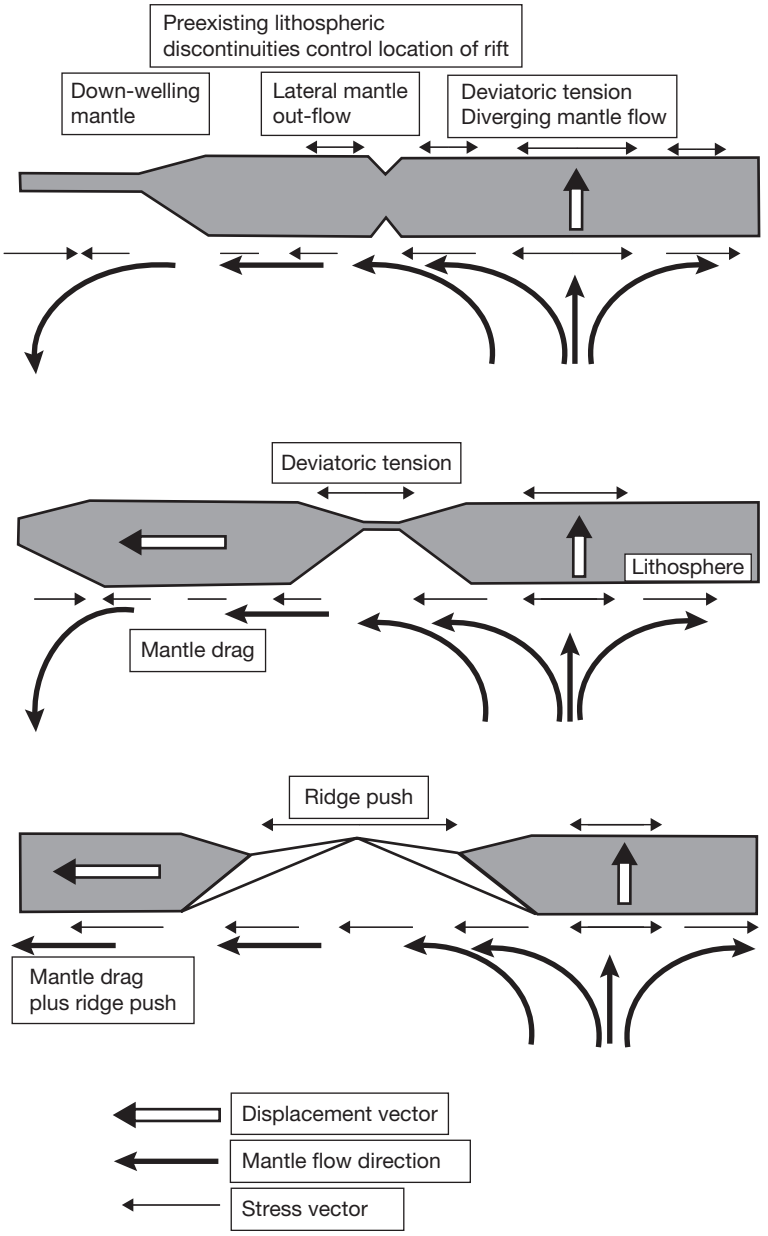

Figure 9 Diagram illustrating the interaction of shear traction exerted on the base of the lithosphere by asthenospheric flow, deviatoric tension above upwelling mantle convection cells, and ridge push forces. Reproduced from Ziegler PA, Cloetingh S, Guiraud R, and Stampfli GM (2001) Peri-Tethyan platforms: Constraints on dynamics of rifting and basin inversion. *Mémoires du Muséum national d'histoire naturelle* 186: 9–49.

of the concept that many rifts go through an evolutionary cycle starting with an initial 'passive' phase that is followed by a more 'active' stage during which magmatic processes play an increasingly important role (Burov and Cloetingh, 1997; Huismans et al., 2001a; Wilson, 1993a).

6.12.3.1 Modes of Rifting and Extension

6.12.3.1.1 Atlantic-type rifts

Atlantic-type rift systems evolve during the breakup of major continental masses, presumably in conjunction with a reorganization of the mantle convection system (Ziegler, 1993a,b). During early phases of rifting, large areas around future zones of crustal separation can be affected by tensional stresses, giving rise to the development of complex graben systems. In time, rifting activity concentrates on the zone of future crustal separation, with tectonic activity decreasing and ultimately ceasing in lateral graben systems. In time and as a consequence of progressive lithospheric attenuation and ensuing crustal doming, local deviatoric tensional stresses play an important secondary role in the evolution of such rift systems. Upon crustal separation, the diverging continental margins (pericontinental rifts) and the 'unsuccessful' intracontinental branches of the respective rift system become tectonically inactive. However, during subsequent tectonic cycles, such aborted rifts can be tensional and compressional-reactivated (Cloetingh et al., 2008; Johnson et al., 2008; Ziegler et al., 1995, 1998, 2001, 2002). The development of Atlantic-type rifts is subject to great variations mainly in terms of duration of their rifting stage and the level of volcanic activity (Ziegler, 1988, 1990a, 1996a).

6.12.3.1.2 Back-arc rifts

Back-arc rifts are thought to evolve in response to a decrease in convergence rates and/or even a temporary divergence of colliding plates, ensuing steepening of the subduction slab and development of a secondary upwelling system in the upper plate mantle wedge above the subducted lower plate lithospheric slab (Uyeda and McCabe, 1983). Changes in convergence rates between colliding plates are probably an expression of changes in plate interaction. Back-arc rifting can progress to crustal separation and the opening of limited oceanic basins (e.g., Sea of Japan, South China Sea, and Black Sea). However, as convergence rates of colliding plates are variable in time, back-arc extensional basins are generally short-lived. Upon a renewed increase in convergence rates, back-arc extensional systems are prone to destruction by back-arc compressional stresses (e.g., Variscan Rhenohercynian Basin, Sunda Arc and East China rift systems, and Black Sea domain; Cloetingh et al., 1989; Jolivet et al., 1989; Letouzey et al., 1990; Nikishin et al., 2001; Uyeda and McCabe, 1983; Ziegler, 1990a).

6.12.3.1.3 Synorogenic rifting and wrenching

Synorogenic rift/wrench deformations can be related to indenter effects and ensuing escape tectonics, often involving rotation of intramontane stable blocks (e.g., Pannonian Basin: Royden and Horváth, 1988; Late Carboniferous Variscan fold belt: Ziegler, 1990b), and to lithospheric overthickening in orogenic belts, resulting in uplift and extension of their axial parts (Peruvian and Bolivian Altiplano: Dalmayrac and Molnar, 1981; Mercier et al., 1992). Furthermore, collisional stresses exerted on a craton may cause far-field tensional or transtensional reactivation of preexisting fracture systems and thus the development of rifts and pull-apart basins. This model may apply to the Late Carboniferous development of the Norwegian–Greenland Sea rift in the foreland of the Variscan orogen, the Permo-Carboniferous Karoo rifts in the hinterland of the Gondwanaland orogen, the European Cenozoic Rift System in the Alpine foreland, and the Neogene Baikal rift in the hinterland of the Himalayas (Dèzes et al., 2004; Ziegler et al., 2001). Under special conditions, extensional structures can also develop in fore-arc basins (e.g., Talara Basin, Peru; see Ziegler and Cloetingh, 2004).

6.12.3.1.4 Postorogenic extension

Extensional disruption of young orogenic belts, involving the development of grabens and pull-apart structures, can be related to their postorogenic uplift and the development of deviatoric tensional stresses inherent to orogenically overthickened crust (Dewey, 1988; Sanders et al., 1999; Stockmal et al., 1986). The following mechanisms contribute to postorogenic uplift: (1) locking of the subduction zone due to decay of the regional compressional stress field (Whittaker et al., 1992), (2) rollback and ultimately detachment of the subducted slab from the lithosphere (Andeweg and Cloetingh, 1998; Bott, 1993; Fleitout and Froidevaux, 1982), and (3) retrograde metamorphism of the crustal roots, involving in the presence of fluids the transformation of eclogite to less dense granulite (Le Pichon et al., 1997; Straume and Austrheim, 1999). Although tensional collapse of an orogen can commence shortly after its consolidation, for example, the Variscan orogen (Ziegler, 1990a; Ziegler et al., 2004), it may be delayed by as much as 30 My, as in the case of the Appalachian–Mauritanides (Ziegler, 1990a). The Permo-Triassic West Siberian basin that is superimposed on the juncture of the Uralides and Altaides is in an example of a postorogenic tensional basin that began to subside shortly after the consolidation of these orogens (Nikishin et al., 2002; Vyssotski et al., 2006). In addition, modifications in the convergence direction of colliding continents and the underlying stress reorientation can give rise to the development of wrench fault systems and related pull-apart basins, controlling early collapse of an orogen, such as the Devonian collapse of the Arctic–North Atlantic Caledonides (Ziegler, 1989b; Ziegler and Dèzes, 2006) or the Stephanian–early Permian disruption of the Variscan fold belt (Ziegler et al., 2004).

The Basin and Range Province of North America is a special type of postorogenic rifting. Oligocene and younger collapse of the US Cordillera is thought to be an effect of the North American craton having overridden at about 28 Ma the East Pacific Rise in conjunction with rapid opening of the Atlantic Ocean (Verrall, 1989). In the area of the southwestern US Cordillera, regional compression waned during the late Eocene and the orogen began to collapse during late Oligocene with main extension occurring during the Miocene and Pliocene (Parsons, 1995). By contrast, the Canadian Cordillera remained intact. During the collapse of the US Cordillera, the heavily intruded, at middle and lower levels, ductile crust of the Basin and Range Province was subjected to major extension at high strain rates, resulting in uplift of ductilely deformed core complexes by 10–20 km. The area affected by extension, crustal thinning, volcanism, and uplift measures 1500×1500 km

(Wernicke, 1990). The Eocene–Oligocene magmatism of the Basin and Range Province bears a subduction-related signature, suggestive of an initial phase of back-arc extension, whereas lithospheric mantle- and asthenosphere-derived magmas play an increasingly important role from Miocene times onward, presumably due to the opening of asthenospheric windows in the Farallon slab during its detachment from the lithosphere and gradual sinking into the mantle (Parsons, 2006).

6.12.3.2 Thermal Thinning and Stretching of the Lithosphere

Mechanical stretching of the lithosphere, triggering partial melting of its basal parts and the upper asthenosphere, is followed by the segregation of melts and their diapiric rise into the lithosphere, an increase in conductive and advective heat flux, and consequently an upward displacement of the thermal asthenosphere–lithosphere boundary. Small-scale convection in the evolving asthenospheric diapir may contribute to mechanical thinning of the lithosphere by facilitating lateral ductile mass transfer (**Figure 10**; Mareschal and Gliko, 1991; Richter and McKenzie, 1978). Progressive thermal and mechanical thinning of the higher-density lithospheric mantle and its replacement by lower-density asthenosphere induces progressive doming of rift zones. At the same time, deviatoric tensional stresses developing in the lithosphere contribute to its further extension (Bott, 1992).

Although major hot-spot activity is thought to be related to a thermal perturbation within the asthenosphere caused by a deep mantle plume, smaller-scale 'plume' activity may also be the consequence of lithospheric stretching triggering partial melting by adiabatic decompression in areas characterized by an anomalously volatile-rich asthenosphere/lithosphere (Wilson, 1993a; White and McKenzie, 1989). In this context, it is noteworthy that extension-induced development of a partially molten asthenospheric diapir that gradually rises into the lithosphere causes by itself further decompression of the underlying asthenosphere and consequently more extensive partial melting and melt segregation at progressively deeper levels. Thus, the evolving diapir may grow not only upward but also downward. Similarly, acceleration of plate divergence and the ensuing increase in seafloor spreading rates probably cause at spreading axes partial melting and melt segregation at progressively deeper asthenospheric levels reaching down to 80–100 km, as imaged by seismic tomography (Anderson et al., 1992).

Melts, which intrude the lithosphere and pond at the crust/mantle boundary, provide a further mechanism for thermal doming of rift zones (**Figure 10**). Emplacement of such asthenoliths, consisting of a mixture of indigenous subcrustal

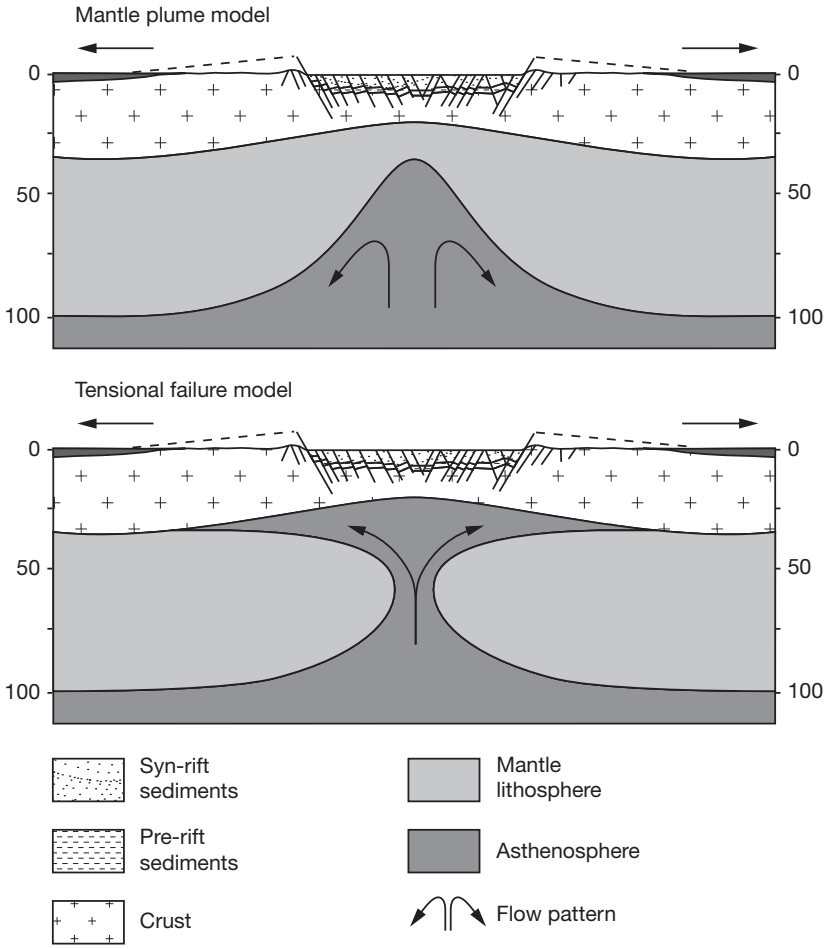

Figure 10 Rift models.

mantle material and melts extracted from deeper lithospheric and upper asthenospheric levels, may cause temporary doming of a rift zone and a reversal in its subsidence pattern, such as the Mid-Jurassic central North Sea arch (Ziegler, 1990a) or the Neogene Baikal arch (Suvorov et al., 2002).

Volcanic-rifted margins cannot always be linked directly to hot-spot areas. Different rifts show a wide range in lag time between rifting and the impingement of plumes on zones of crustal extension (Franke, 2013): nearly synchronous in the South Atlantic and Labrador Sea, while with a lag of 15 My in the Central Atlantic, 70 My in the Indian Ocean, and as long 280 My of intermittent crustal extension in the Norwegian–Greenland Sea (Nikishin et al., 2002; Ziegler and Cloetingh, 2004). Ziegler and Cloetingh (2004) concluded that initial magma generation in intracontinental rifts generally occurs in the 100–200 km depth range, corresponding to the lower parts of the lithosphere and the upper asthenosphere (Wilson, 1997). Moreover, several observations are difficult to reconcile with a deep mantle origin of the melts (Franke, 2013). Gradual changes of mantle properties and dynamics should generate a smooth transition from magma-starved to volcanic rifting over at least a hundred or a few hundreds of kilometers. However, observations of abrupt change in emplaced magmatic volume argue against the hypothesis that gradual along-margin variations in the thermal regime of the lithosphere and sublithospheric mantle (the traditional plume-driven model) are solely responsible for the formation of volcanic-rifted margins (Franke, 2013).

Depending on the applicability of the 'pure shear' (McKenzie, 1978) or the 'simple shear' model (Wernicke, 1985), or a combination thereof (Kusznir et al., 1991), the zone of upper crustal extension, corresponding to the subsiding rift, may coincide with the zone of lithospheric mantle attenuation (pure shear and combined shear) or may be laterally offset from it (simple shear; see **Figure 11**). Under conditions of pure

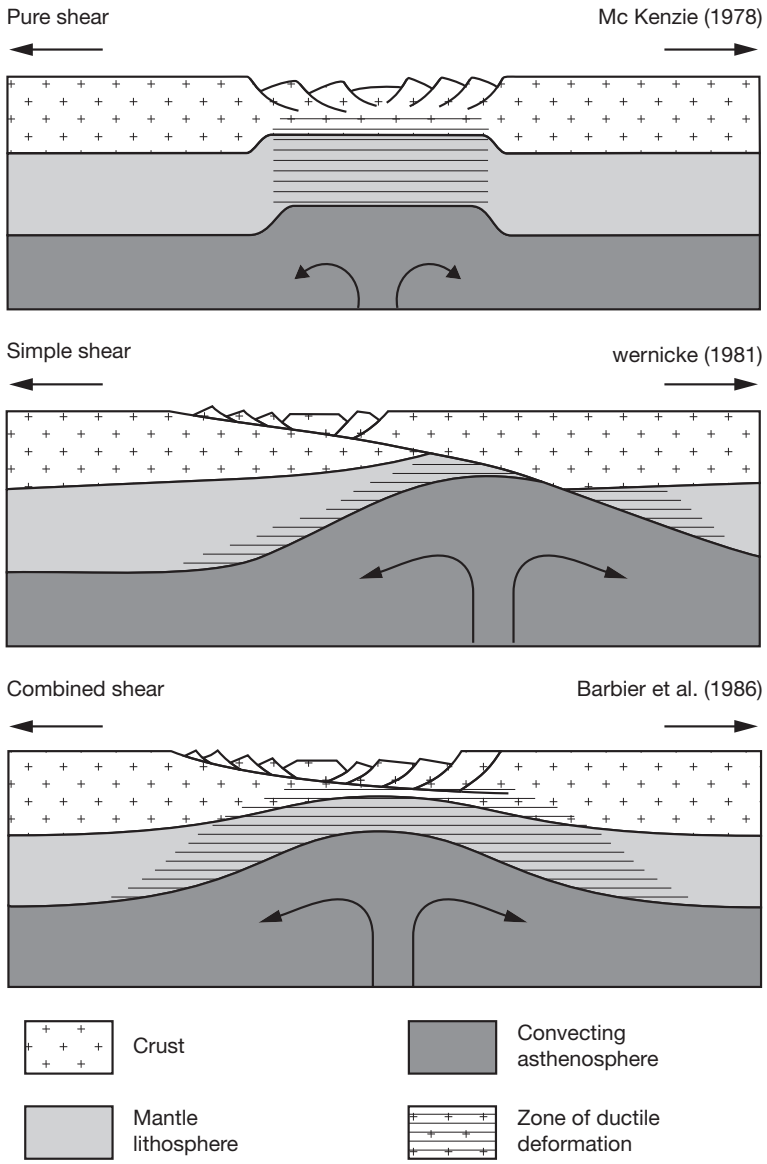

Figure 11 Lithospheric shear models.

shear lithospheric extension, magmatic activity should be centered on the rift axis where in time also mid-oceanic ridge basalt (MORB)-type magmas can be extruded after a high degree of extension has been achieved. By contrast, under simple shear conditions, magmatic activity is asymmetrically distributed with respect to the rift axis, and MORB-type extrusives may occur on one of the rift flanks (e.g., the Basin and Range Province (Jones et al., 1992), the Red Sea (Favre and Stampfli, 1992), and the Ethiopian Rift (Kazmin, 1991)).

A modification to the pure shear model is the 'continuous depth-dependent' stretching model that assumes that stretching of the lithospheric mantle affects a broader area than the zone of crustal extension (**Figure 12**; Rowley and Sahagian, 1986). In both models, it is assumed that the asthenosphere wells up passively into the space created by mechanical attenuation of the lithospheric mantle. In depth-dependent stretching models, this commonly gives rise to flexural uplift of the rift shoulders, whereas in the flexural cantilever model, which assumes ductile deformation of the lower crust, this produces footwall uplift of the rift flanks and intrabasin fault blocks (Kusznir and Ziegler, 1992). By the same mechanism, the simple shear model predicts asymmetrical doming of a rift zone or even flexural uplift of an arch located to one side of the zone of upper crustal extension (Wernicke, 1985). A modification to the simple shear model envisages that massive upper crustal extensional unloading of the lithosphere causes its isostatic uplift and passive inflow of the asthenosphere (Wernicke, 1990).

The structural style of rifts, as defined at upper crustal and synrift sedimentary levels, is influenced by the thickness and thermal state of the crust and lithospheric mantle at the onset of rifting, by the amount of crustal extension and the width over which it is distributed, the mode of crustal extension (orthogonal or oblique and simple shear or pure shear), and the lithologic composition of the pre- and synrift sediments (Cloetingh et al., 1995b; Ziegler, 1996a).

A major factor controlling the structural style of a rift zone is the magnitude of the crustal extensional strain that was achieved across it and the distance over which it is distributed (δ factor). Although quantification of the extensional strain and of the stretching factor δ is of basic importance for the understanding of rifting processes, there is often a considerable discrepancy between estimates derived from upper crustal extension by faulting, the crustal configuration, and quantitative subsidence analysis (Ziegler and Cloetingh, 2004).

6.12.3.3 Synrift Subsidence and Duration of Rifting Stage

The balance of two mechanisms controls the synrift subsidence of a sedimentary basin. Firstly, elastic/isostatic adjustment of the crust to stretching of the lithosphere and its adjustment to sediment loading causes subsidence of the mechanically thinned crust (**Figures 11** and **12**; Jarvis and McKenzie, 1980; Keen and Boutilier, 1990; McKenzie, 1978). Depending on the depth of the lithospheric necking level, this is accompanied by either flexural uplift or downwarping of the rift zone (**Figure 13**; Braun and Beaumont, 1989; Kooi, 1991; Kooi et al., 1992). Secondly, uplift of a rift zone is caused by upwelling of the asthenosphere into the space created by mechanical stretching of the lithosphere, thermal upward displacement of the asthenosphere–lithosphere boundary, thermal expansion of the lithosphere, and intrusion of melts at the base of the crust (**Figure 10**; Turcotte and Emerman, 1983). Thus, the geometry of a rifted basin is a function of the elastic/isostatic

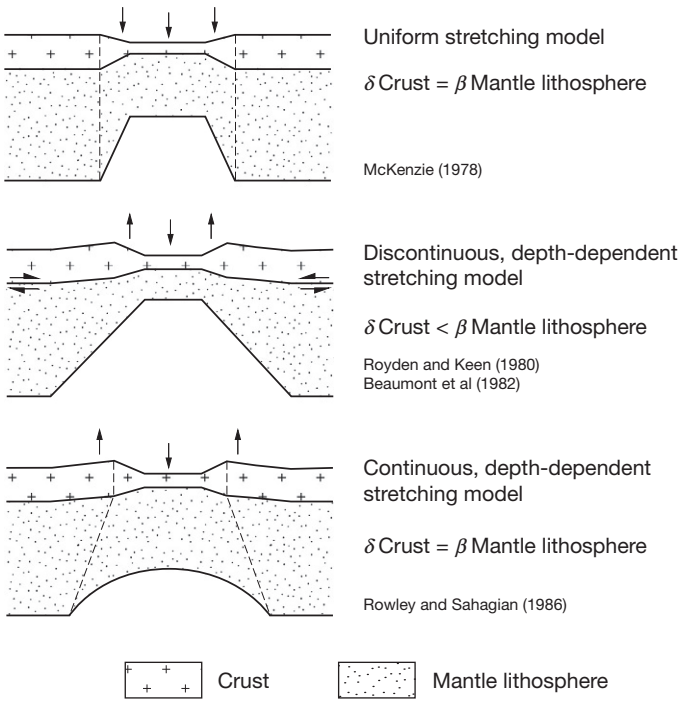

Figure 12 Lithospheric stretching models.

response of the lithosphere to its mechanical stretching and related thermal perturbation (Van der Beek et al., 1994).

The duration of the rifting stage of intracontinental rifts (aborted) and passive margins (successful rifts) is highly variable (**Figures 14** and **15**; Ziegler, 1990a; Ziegler and Cloetingh, 2004; Ziegler et al., 2001). Overall, it is observed that in time, rifting activity concentrates on the zone of future crustal separation with lateral rift systems becoming inactive. However, as not all rift systems progress to crustal separation, the duration of their rifting stage is obviously a function of the persistence of the controlling stress field. On the other hand, the time required to achieve crustal separation is a function of the strength (bulk rheology) of the lithosphere, the buildup rate, magnitude and persistence of the extensional stress field, constraints on lateral movements of the diverging blocks (on-trend coherence, counteracting far-field compressional stresses), and apparently not so much of the availability of preexisting crustal discontinuities that can be tensionally reactivated.

Crustal separation was achieved in the Liguro–Provençal Basin after 9 My of crustal extension and in the Gulf of

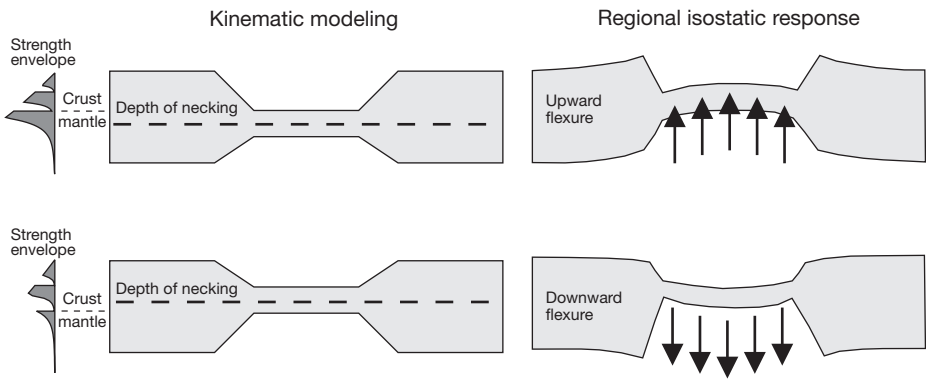

Figure 13 Concept of lithospheric necking. The level of necking is defined as the level of no vertical motions in the absence of isostatic forces. (left) Kinematically induced configuration after rifting for different necking depths. (right) Subsequent flexural isostatic rebound.

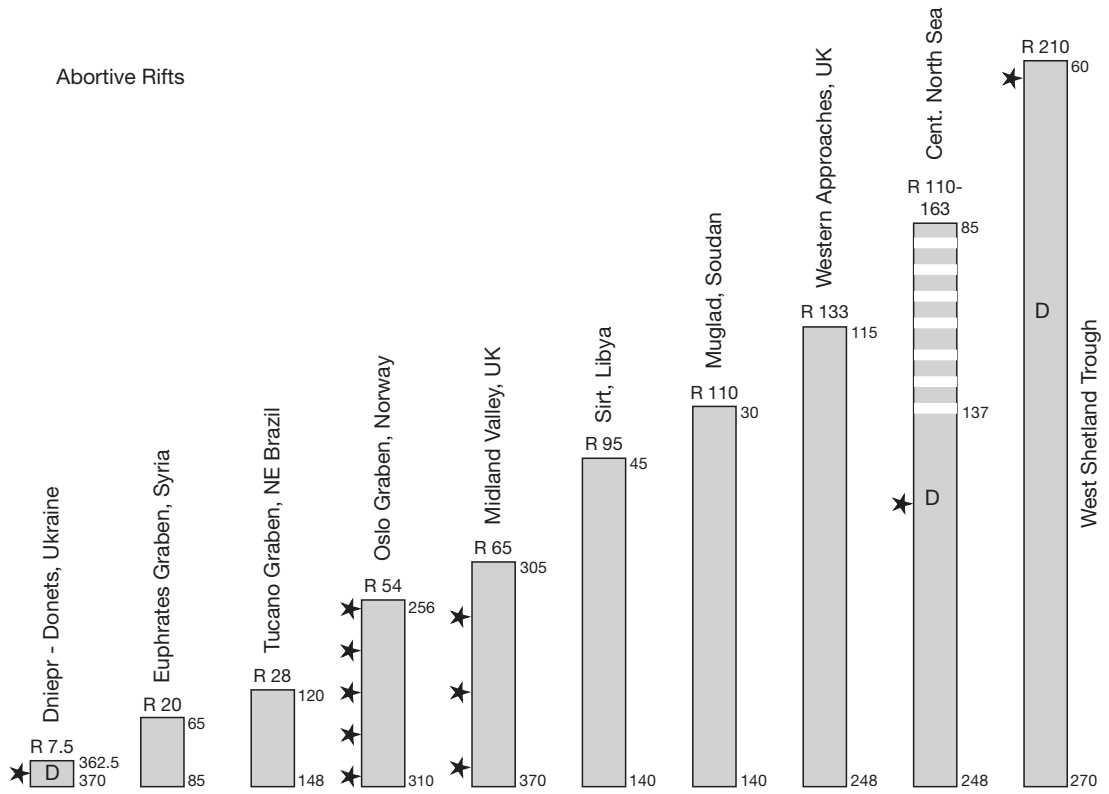

Figure 14 Duration of rifting stage of 'abortive' rifts (paleorifts and failed arms). Vertical columns in My; numbers on side of vertical columns indicate onset and termination of rifting stage in My; numbers under R on top of each column give the duration of rifting stage in My; stars indicate periods of main volcanic activity; D indicates periods of doming. Reproduced from Ziegler PA and Cloetingh S (2004) Dynamic processes controlling evolution of rifted basins. *Earth-Science Reviews* 64: 1–50.

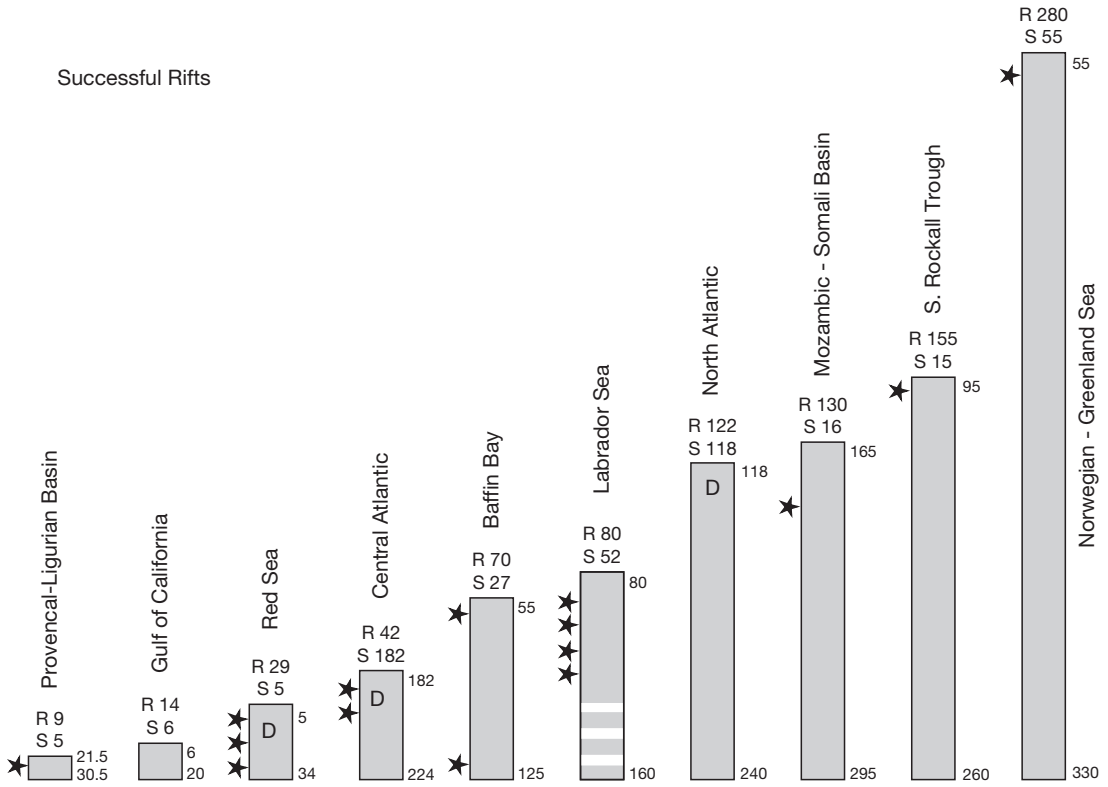

Figure 15 Duration of rifting stage of 'successful' rifts. Legend same as **Figure 14**. Numbers beside letter 'S' indicate duration of seafloor spreading stage in My. Reproduced from Ziegler PA and Cloetingh S (2004) Dynamic processes controlling evolution of rifted basins. *Earth-Science Reviews* 64: 1–50.

California after about 14 My of rifting, whereas opening of the Norwegian–Greenland Sea was preceded by an intermittent rifting history spanning some 280 My (Ziegler, 1988; Ziegler and Cloetingh, 2004). There appears to be no obvious correlation between the duration of the rifting stage (R) of successful rifts (**Figure 15**), which are superimposed on orogenic belts (Liguro–Provençal Basin, Pyrenees $R = 9$ My; Gulf of California, Cordillera $R = 14$ My; Canada Basin, Innuitian fold belt $R = 35$ My; Central Atlantic, Appalachians $R = 42$ My; and Norwegian–Greenland Sea, Caledonides $R = 280$ My), and the duration of those that developed within stabilized cratonic lithosphere (southern South Atlantic $R = 13$; northern South Atlantic $R = 29$ My; Red Sea $R = 29$ My; Baffin Bay $R = 70$ My; and Labrador Sea $R = 80$ My). This suggests that the availability of crustal discontinuities, which regardless of their age (young orogenic belts and old Precambrian shields) can be tensionally reactivated, does not play a major role in the time required to achieve crustal separation. However, by weakening the crust, such discontinuities play a role in the localization and distribution of crustal strain. Moreover, by weakening the lithosphere, they contribute to the preferential tensional reactivation of young and old orogenic belts (Janssen et al., 1995; Ziegler et al., 2001).

6.12.3.4 Postrift Subsidence

Similar to the subsidence of oceanic lithosphere, the postrift subsidence of extensional basins is mainly governed by thermal relaxation and contraction of the lithosphere, resulting in a gradual increase of its flexural strength, and by its isostatic response to sedimentary loading. Theoretical considerations indicate that subsidence of postrift basins follows an asymptotic curve, reflecting the progressive decay of the rift-induced thermal anomaly, the magnitude of which is thought to be directly related to the lithospheric stretching value (Beaumont et al., 1982; McKenzie, 1978; Royden et al., 1980; Sleep, 1973; Steckler and Watts, 1982; Watts et al., 1982). During the postrift evolution of a basin, the thermally destabilized continental lithosphere reequilibrates with the asthenosphere (McKenzie, 1978; Steckler and Watts, 1982; Wilson, 1993b). In this process, in which the temperature regime of the asthenosphere plays an important role, new lithospheric mantle consisting of solidified asthenospheric material is accreted to the attenuated old continental lithospheric mantle (Ziegler et al., 1998). In addition, densification of the continental lithosphere involves crystallization of melts that accumulated at its base or were injected, subsequent thermal contraction of the solidified rocks, and under certain conditions their phase transformation to eclogite facies. The resulting negative buoyancy effect is the primary cause of postrift subsidence.

However, in a number of basins, significant departures from the theoretical thermal subsidence curve are observed. These can in some cases be explained as effects of compressional intraplate stresses and related phase transformations (Cloetingh and Kooi, 1992a,b; Lobkovsky et al., 1996; Van Wees and Cloetingh, 1996). It appears that in many areas,

the postrift evolution is characterized by initial rift-related subsidence, sometimes followed by accelerated subsidence of the central parts of an extensional sedimentary basin, simultaneously occurring with broad uplift in adjacent areas flanking the depocenter. Examples can be found in the Atlantic margin of Morocco (Ghorbal et al., 2008; Gouiza et al., 2010), the southern Atlantic rifted margins (Beglinger et al., 2012a,b,c,d; Dupré et al., 2007, 2011), and the Sirte Basin in Libya (Abadi et al., 2008).

6.12.3.4.1 Shape and magnitude of rift-induced thermal anomalies

The shape and dimension of rift-induced asthenosphere–lithosphere boundary anomalies essentially control the geometry of the evolving postrift thermal sag basin (**Figure 11**). Thermal-sag basins associated with aborted rifts are broadly saucer-shaped and generally overstep the rift zone, with their axes coinciding with the zone of maximum lithospheric attenuation.

Pure shear-dominated rifting gives rise to the classical 'steer's head' configuration of the syn- and postrift basins (White and McKenzie, 1989) in which both basin axes roughly coincide, with the postrift basin broadly overstepping the rift flanks. This geometric relationship between syn- and postrift basins is frequently observed (e.g., North Sea rift: Ziegler, 1990b; West Siberian basin: Artyushkov and Baer, 1990; Dnieper–Donets graben: Kusznir et al., 1996; Stephenson et al., 2001; Gulf of Thailand: Hellinger and Sclater, 1983; Watcharanantakul and Morley, 2000; and Sudan rifts: McHargue et al., 1992). Such a geometric relationship is compatible with discontinuous, depth-dependent stretching models that assume that the zone of crustal extension is narrower than the zone of lithospheric mantle attenuation (**Figure 12**). The degree to which a postrift basin oversteps the margins of the synrift basin is a function of the width difference between the zone of crustal extension and the zone of lithospheric mantle attenuation (White and McKenzie, 1988) and the EET of the lithosphere (Watts et al., 1982).

Conversely, simple shear-dominated rifting gives rise to a lateral offset between the syn- and the postrift basin axes. An example is the Tucano graben of northeastern Brazil, which ceased to subside at the end of the rifting stage, whereas the coastal Jacuipe–Sergipe–Alagoas Basin, to which the former was structurally linked, was the site of crustal and lithospheric mantle thinning culminating in crustal separation and subsequent major postrift subsidence (Chang et al., 1992; Karner et al., 1992). Moreover, the simple shear model can explain the frequently observed asymmetry of conjugate passive margins and differences in their postrift subsidence pattern (e.g., Central Atlantic and Red Sea: Favre and Stampfli, 1992). Discrepancies in the postrift subsidence of conjugate margins are attributed to differences in their lithospheric configuration at the crustal separation stage. At the end of the rifting stage, a relatively thick lithospheric mantle supports lower plate margins, whereas upper plate margins are underlain by a strongly attenuated lithospheric mantle and partly directly by the asthenosphere. Correspondingly, lower plate margins are associated at the crustal separation stage with smaller thermal anomalies than upper plate margins (Stampfli et al., 2001; Ziegler et al., 1998). These differences in lithospheric configuration of conjugate simple shear margins have repercussions on their rheological structure, even after full thermal relaxation of the lithosphere, and their compressional reactivation potential (see succeeding text; Ziegler et al., 1998).

The magnitude of postrift tectonic subsidence of aborted rifts and passive margins is a function of the thermal anomaly that was introduced during their rifting stage and the degree to which the lithospheric mantle was thinned. Most intense anomalies develop during crustal separation, particularly when plume-assisted and asthenospheric melts well up close to the surface. The magnitude of thermal anomalies induced by rifting that did not progress to crustal separation depends on the magnitude of crustal stretching (δ-factor) and lithospheric mantle attenuation (β-factor), the thermal regime of the asthenosphere, the volume of melts generated, and whether these intruded the lithosphere and destabilized the Moho (**Figure 10**).

About 65% (after 60 My) and about 95% (after 180 My) of deep-seated thermal anomalies associated with a major pull-up of the asthenosphere–lithosphere boundary have decayed (mantle plume model; **Figure 10**). Thermal anomalies related to intralithospheric intrusions (tensional-failure model; **Figure 10**) have apparently a faster decay rate. For instance, the Mid-Jurassic North Sea rift dome had subsided below the sea level, 20–30 My after its maximum uplift, that is, well before crustal extension had terminated (Underhill and Partington, 1993; Ziegler, 1990a).

6.12.3.4.2 Stretching factors derived from quantitative subsidence analysis

The thickness of the postrift sedimentary column that can accumulate in passive margin basins and in thermal-sag basins above aborted rifts is a function not only of the magnitude of the lithospheric mantle and crustal attenuation factors β and δ but also of the crustal density and the water depth at the end of their rifting stage, as well as of the density of the infilling postrift sediments (carbonates, evaporites, and clastics). Moreover, it must be kept in mind that during the postrift cooling process, the flexural rigidity of the lithosphere increases gradually, resulting in the distribution of the sedimentary load over progressively wider areas.

Quantitative postrift subsidence analyses of extensional basins, neglecting intraplate stresses, are thought to give a measure of the thermal contraction of the lithosphere and, conversely, of lithospheric stretching factors, as suggested by the McKenzie (1978) model and its early users (e.g., Barton and Wood, 1984; Sclater and Christie, 1980). Such analyses, assuming Airy isostasy, yield often considerably larger δ-factors than indicated by the populations of upper crustal faults (Watcharanantakul and Morley, 2000; Ziegler, 1983, 1990a). This discrepancy is somewhat reduced when flexural isostasy is assumed (Roberts et al., 1993). However, as during rifting attenuation of the lithosphere is achieved not only by its mechanical stretching but also by convective and thermal upward displacement of the asthenosphere–lithosphere boundary, the magnitude of a thermal anomaly derived from the postrift subsidence of a basin cannot be directly related to a mechanical stretching factor. Moreover, intraplate compressional stresses and phase transformations in the lower crust and lithospheric mantle have an overprinting effect on postrift subsidence and can cause significant departures from a purely thermal subsidence curve

(Cloetingh and Kooi, 1992a,b; Lobkovsky et al., 1996; Van Wees and Cloetingh, 1996).

Furthermore, during rifting, the ascent of mantle-derived melts to the base of the crust can cause destabilization of the Moho, magmatic inflation of the crust, and its metasomatic reactivation and secondary differentiation (Morgan and Ramberg, 1987; Mohr, 1992; Stel et al., 1993; Watts and Fairhead, 1997). For instance, lower crustal velocities of 6.30–7.2 km s^{-1} and densities of 3.02×10^3 kg m^{-3} characterize the highly attenuated crust of the Devonian Dnieper–Donets rift almost up to the base of its synrift sediments, probably owing to its synrift permeation by mantle-derived melts (Stephenson et al., 2001; Yegorova et al., 1999).

Moreover, the accumulation of very thick postrift sedimentary sequences can cause phase transformation of crustal rocks to granulite facies, with the resulting densification of the crust accounting for accelerated basin subsidence. This process can be amplified in the cases of eclogite transformation of basaltic melts that were injected into the lithospheric mantle or that had accumulated at its base (Lobkovsky et al., 1996). However, it is uncertain whether large-scale eclogite formation can indeed occur at crustal thicknesses of 30–40 km (Carswell, 1990; Griffin et al., 1990). Although phase transformations, entailing an upward displacement of the geophysical Moho, are thought to occur under certain conditions at the base of very thick Proterozoic cratons (increased confining pressure due to horizontal intraplate stresses and/or ice load and possible cooling of asthenosphere; Cloetingh and Kooi, 1992a,b), it is uncertain whether physical conditions conducive to such transformations can develop in response to postrift sedimentary loading of paleorifts and passive margins as, for example, suspected for the East Newfoundland Basin (Cloetingh and Kooi, 1992a,b) and the West Siberian basin (Lobkovsky et al., 1996).

As rifting processes can take place intermittently over very long periods of time (e.g., Norwegian–Greenland Sea rift: Ziegler, 1988, 1989a), thermal anomalies introduced during early stretching phases start to decay during subsequent periods of decreased extension rates. Thus, the thermal anomaly associated with a rift may not be at its maximum when crustal stretching terminates and the rift becomes inactive. Similarly, late rifting pulses and/or regional magmatic events may interrupt and even reverse lithospheric cooling processes (e.g., Paleocene thermal uplift of northern parts of Viking Graben due to Iceland plume impingement: Nadin and Kusznir, 1995; Ziegler, 1990a). Therefore, analyses of the postrift subsidence of rifts that have evolved in response to multiple rifting phases spread over a long period need to take their entire rifting history into account.

Intraplate compressional stresses may cause amplification of the deflection of the lithosphere under basins and thus can overprint the thermal subsidence of postrift basins (Cloetingh et al., 1985; Zoback et al., 1993). The example of the Pliocene–Pleistocene evolution of the North Sea shows that the buildup of regional compressional stresses can cause a sharp acceleration of postrift subsidence (**Figure 16**; Cloetingh, 1988; Cloetingh et al., 1990; Kooi and Cloetingh, 1989; Kooi et al., 1991; Van Wees and Cloetingh, 1996). Similar contemporaneous effects are recognized in North Atlantic passive margin basins (Cloetingh et al., 1987, 1990) as well as in the Pannonian Basin (Horváth and Cloetingh, 1996). Also the late Eocene accelerated subsidence of the Black Sea basin can be

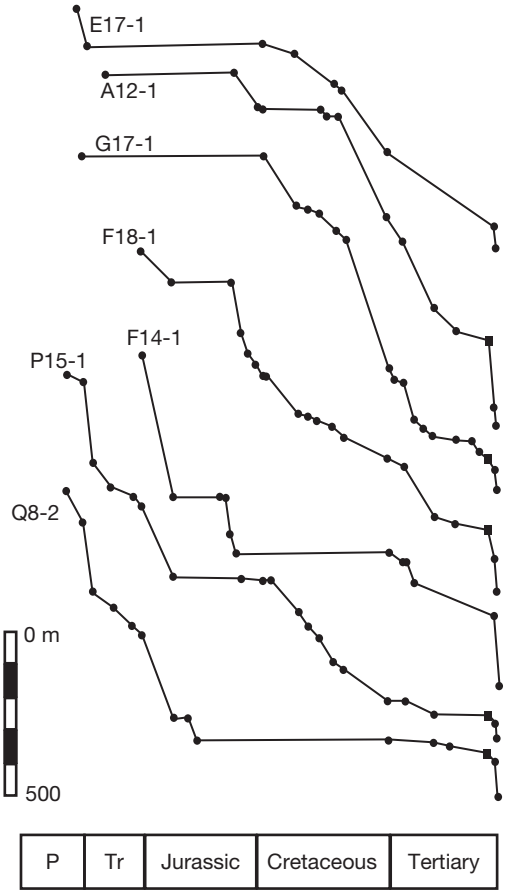

Figure 16 Tectonic subsidence curves of southern North Sea, showing accelerated subsidence during Pliocene–Pleistocene. Postrift stage starts during the Cretaceous. Reproduced from Kooi H (1991) *Tectonic Modelling of Extensional Basins*: *The Role of Lithospheric Flexure*, *Intraplate Stress and Relative Sea-level Change*, 183 pp. PhD Thesis, VU University, Amsterdam.

attributed to the buildup of a regional compressional stress field (Cloetingh et al., 2003; Robinson et al., 1995).

At present, many extensional basins are in a state of horizontal compression as documented by stress indicators summarized in the World Stress Map (Zoback, 1992) and the European Stress Map (e.g., Gölke et al., 1996). The magnitude of stress-induced vertical motions of the lithosphere during the postrift phase, causing accelerated basin subsidence and tilting of basin margins, depends on the ratio of the stress level and the strength of the lithosphere inherited from the synrift phase. Moreover, horizontal stresses in the lithosphere strongly affect the development of diapirism, accounting for local subsidence anomalies (Cloetingh and Kooi, 1992a,b), and have a strong impact on the hydrodynamic regime of rifted basins (Van Balen and Cloetingh, 1993, 1994) by contributing to the development of overpressure, as seen in parts of the Pannonian Basin (Van Balen et al., 1999). Glacial loading and unloading can further complicate postrift lithospheric motions, a better insight into the nature of which is required (Solheim et al., 1996).

These considerations indicate that stretching factors derived from the subsidence of postrift basins must be treated with reservations. Nevertheless, quantitative subsidence studies,

combined with other data, are essential for the understanding of postrift subsidence processes by giving a measure of the lithospheric anomaly that was introduced during the rifting stage of a basin and by identifying deviations from purely thermal cooling trends.

6.12.3.4.3 Postrift compressional reactivation potential

Paleostress analyses give evidence for changes in the magnitude and orientation of intraplate stress fields on timescales of a few My (Bergerat, 1987; Dèzes et al., 2004; Letouzey, 1986; Philip, 1987). Thus, in an attempt to understand the evolution of a postrift basin, the effects of tectonic stresses on subsidence must be separated from those related to thermal relaxation of the lithosphere (Cloetingh and Kooi, 1992a,b). In response to the buildup of far-field compressional stresses, rifted basins, characterized by a strongly faulted and thus permanently weakened crust, are prone to reactivation at all stages of their postrift evolution, resulting in their inversion (Ziegler, 1987, 1990a; Ziegler et al., 1995, 1998, 2001). Only under special condition can gravitational forces associated with topography around a basin cause its inversion (Bada et al., 2001).

Rheological considerations indicate that the lithosphere of thermally stabilized rifts, lacking a thick postrift sedimentary prism, is considerably stronger than the lithosphere of adjacent unstretched areas (Ziegler and Cloetingh, 2004). This contradicts the observation that rift zones and passive margins are preferentially deformed during periods of intraplate compression (Ziegler et al., 2001). However, burial of rifted basins under a thick postrift sequence contributes by thermal blanketing to weakening of their lithosphere (Stephenson, 1989; Van Wees, 1994), thus rendering them prone to tectonic reactivation.

In order to quantify this effect and to assess the reactivation potential of conjugate simple shear margins during subduction initiation, their strength evolution was modeled and compared to that of oceanic crust (Ziegler et al., 1998). By applying a 1-D two-layered lithospheric stretching model, incorporating the effects of heat production by the crust and its sedimentary thermal blanketing (**Table 2**), the thermomechanical evolution of the lithosphere was analyzed in an effort to predict its paleorheology (Bertotti et al., 1997; Van Wees et al., 1996).

For modeling purposes, a time frame of 100 My was chosen. Of this, the first 10 My (between 100 and 90 My in **Figure 17**) corresponds to the rifting stage, culminating in the separation of the conjugate upper and lower plate margins, and the following 90 My to the seafloor spreading stage during which oceanic lithosphere is accreted to the diverging plates. For modeling purposes, it was assumed that the prerift crustal and lithospheric mantle thicknesses are 30 and 70 km, respectively, and that at the end of the rifting stage, the upper plate margin has a crustal thickness of 15 km ($\delta = 2$) and a remaining lithospheric mantle thickness of 7 km ($\beta = 10$) (δ and β are, respectively, the crustal and subcrustal stretching factors (Royden and Keen, 1980)), while the lower plate margin has a crustal thickness of 10 km ($\delta = 3$) and a lithospheric mantle thickness of 63.6 km ($\beta = 1.1$; **Figure 17(a)** and **17(b)**). Results show that through time, the evolution of strength envelopes for lower and upper plate passive margins differs strongly. In principle, during rifting, increased heating of the lithosphere causes its weakening; this effect is most pronounced at the moment of crustal separation. However, upper and lower plate margins show a very different evolution, both during the rifting and postrift stage.

Table 2 Rheological and thermal parameters of crust and lithospheric materials, adopted for the rheological models shown in **Figure 17**

Layer	*Rheology*	*Conductivity* ($W\,m^{-1}\,K^{-1}$)	*Heat production* ($10^{-6}\,W\,m^{-3}$)
Sediments (models A, B, and C)	Quartzite	2	0.2
Sediments (model D)	Quartzite	1.4	1.8
Upper crust	Quartzite	2.6	1.88
Lower crust	Diorite	2.6	0.5
Lithospheric mantle	Olivine	3.1	0

At the moment of crustal separation, upper plate margins are very weak due to strong attenuation of the mantle–lithosphere and the ascent of the asthenospheric material close to the base of the crust. During the postrift evolution of such a margin, having a crustal thickness of 15 km, the strength of the lithosphere increases gradually as new mantle is accreted to its base and cools during the reequilibration of the lithosphere with the asthenosphere (**Figures 17(a)** and **18(a)**). In contrast, the evolution of a sediment-starved lower plate margin with a crustal thickness of 10 km is characterized by a synrift strength increase due to extensional unroofing of the little attenuated mantle–lithosphere; the strength of such a margin increases dramatically during the postrift stage due to its progressive cooling (**Figures 17(b)** and **18(b)**). At the time frame of 0 My, a sediment-starved lower plate margin is considerably stronger than the conjugate upper plate margin for which a sedimentary cover of about 7 km was assumed. The strength evolution of an upper plate margin is initially controlled by the youthfulness of its lithospheric mantle and its thicker crust and subsequently by the thermal blanketing effect of sediments infilling the available accommodation space. On the other hand, the strength of oceanic lithosphere that is covered by thin sediments only increases dramatically during its 90 My evolution and ultimately exceeds the strength of both margins, even if these are sediment-starved (**Figures 17(c)** and **18**). However, the strength of 90 My old oceanic lithosphere that has been progressively covered by very thick sediments is significantly reduced (**Figure 17(d)**) to the point that it approaches the strength of a sediment-filled lower plate margin (**Figure 18**).

To test the effects of sediment infill and thermal blanketing on the strength evolution of upper and lower plate passive margins, a wide range of models was run assuming that sediments completely fill the tectonically created accommodation space (sediment overfilled; **Figure 18**), adopting different sediment densities and corresponding sediment thickness variations (**Table 2**). Results show that a thick syn- and postrift sedimentary prism markedly reduces the integrated strength of a margin. However, despite the strong sediment fill effect on the integrated strength, earlier identified first-order differences between upper and lower plate margins remain. Compared to oceanic lithosphere, with both a 1 km sedimentary cover (**Figures 17(c)** and **18**) and a 15 km thick cover (**Figure 17(d)**), a sediment

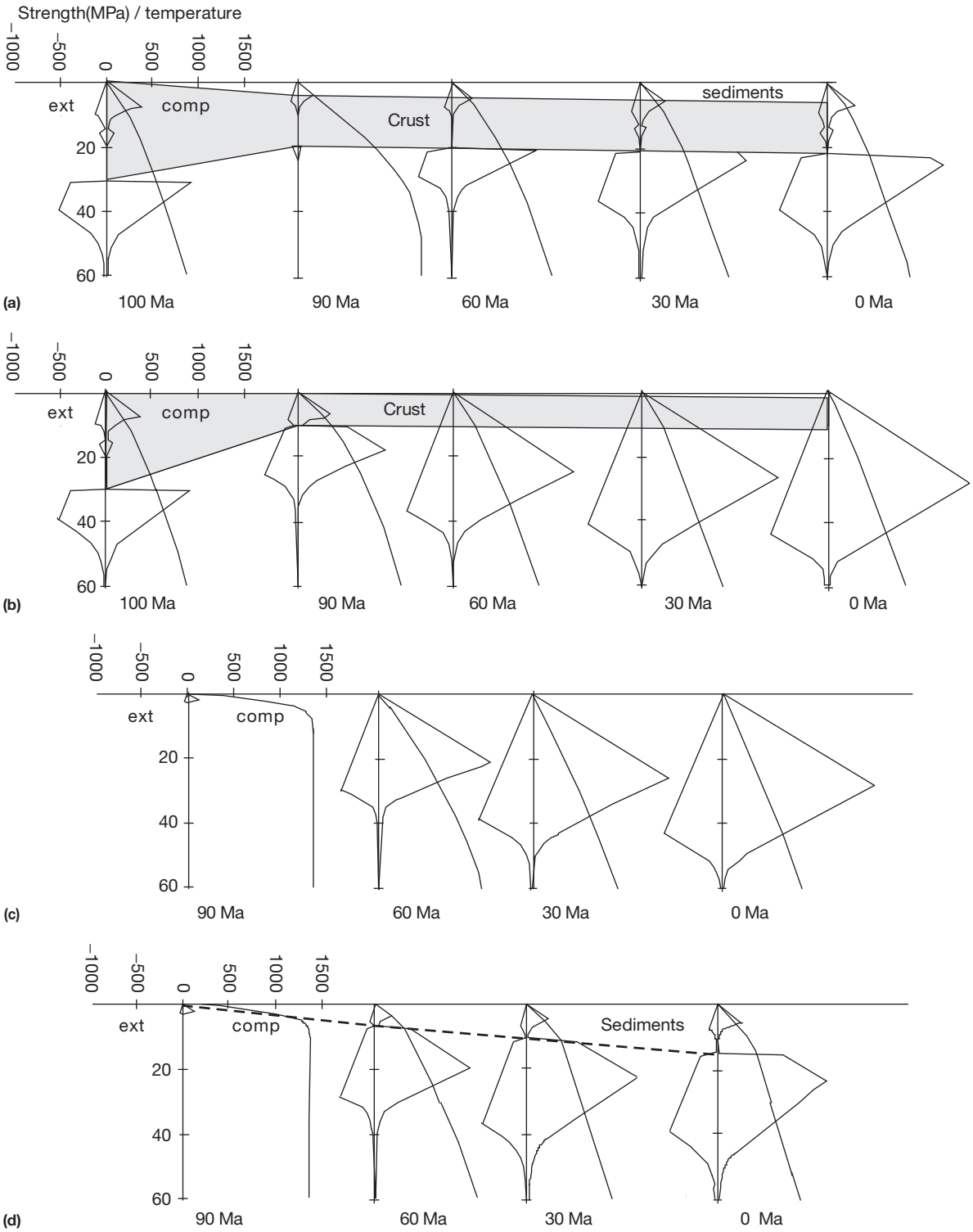

Figure 17 Depth-dependent rheological models for the evolution of lower plate and upper plate passive margins and oceanic lithosphere. For modeling parameters, see **Tables 2** and **3**. (a) Upper plate passive margin ($\delta = 2$, $\beta = 10$), characterized at the end of postrift phase by complete sediment fill of accommodation space ($\rho_s = 2100$ kg m^{-3}, 7.084 km sediments). (b) Lower plate passive margin ($\delta = 3$, $\beta = 1.1$), marked by sediment starvation at the end of postrift phase (1 km sediments). (c) Oceanic lithosphere with a thin sedimentary cover of 1 km. (d) Oceanic lithosphere with a gradually increasing sedimentary cover reaching a maximum of 15 km. Reproduced from Ziegler PA, Van Wees JD, and Cloetingh S (1998) Mechanical controls on collision-related compressional intraplate deformation. *Tectonophysics* 300: 103–129.

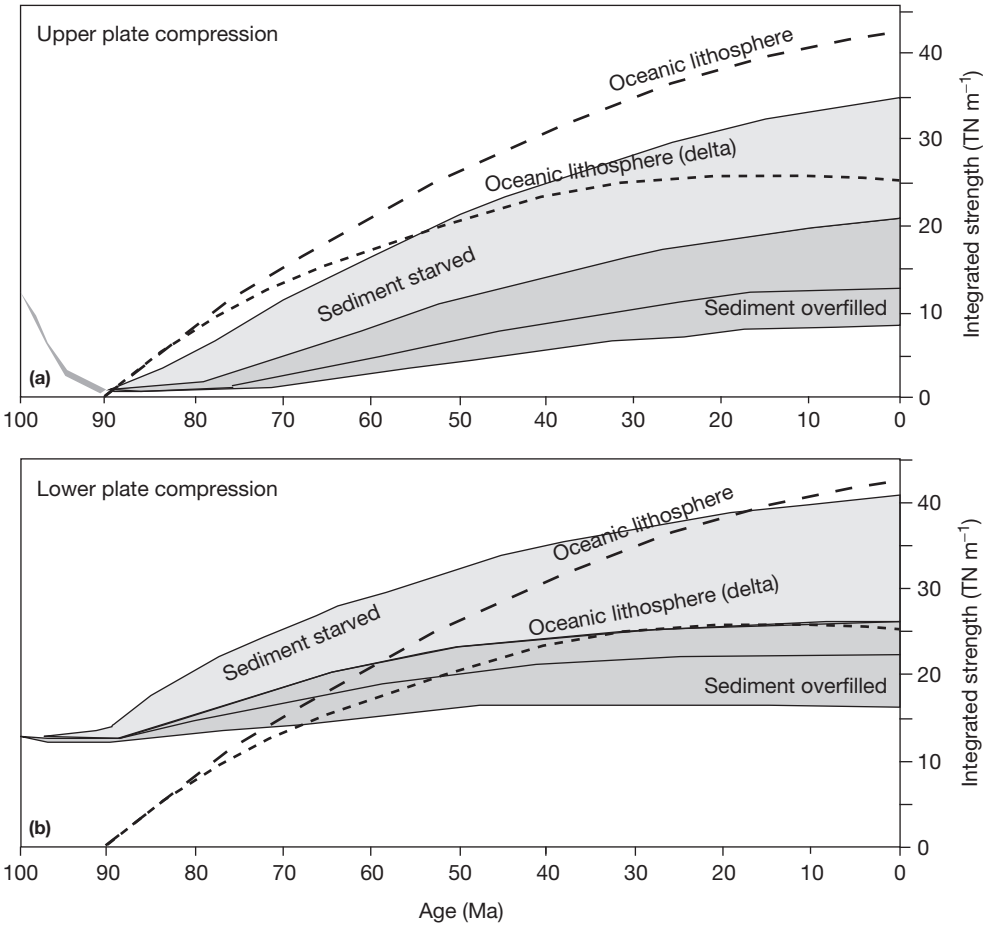

Figure 18 Integrated compressional strength evolution of sediment-starved and sediment-filled (a) upper plate and (b) lower plate passive margins, compared to the integrated strength evolution of oceanic lithosphere with thin and thick sediment cover as in **Figure 17**. Shaded areas demonstrate strong sensitivity of integrated strength to sediment infilling, ranging from sediment starvation (highest strength values) to complete fill of accommodation space (dark shading, lowest strength values). Curves in dark-shaded area correspond to different sediment densities and related range in sediment thickness (see **Table 3**). Reproduced from Ziegler PA, Van Wees JD, and Cloetingh S (1998) Mechanical controls on collision-related compressional intraplate deformation. *Tectonophysics* 300: 103–129.

overfilled upper plate margin (applying $\rho_s = 2100\ \mathrm{kg\ m^{-3}}$) is characterized by lower integrated strength values throughout its evolution. However, for a lower plate margin, conditions are dramatically different. Up to 20–70 My after rifting, the lower plate integrated strength values are significantly higher than those for oceanic lithosphere, with both a thin sedimentary cover and a thick sedimentary cover.

From these strength calculations, it is evident that at any stage, the upper plate margin is weaker than oceanic lithosphere and the conjugate lower plate margin. This suggests that the upper plate margin is the most likely candidate for compressional reactivation and the initiation of a subduction zone. For realistic sediment density and infill values ($\rho_s <= 2500\ \mathrm{kg\ m^{-3}}$), also, the upper plate margin tends to grow stronger in time, indicating that after a prolonged postrift stage (>70 My), localization of deformation and subduction along such a margin, instead of on the adjacent continent, should be facilitated by weakening mechanisms that are not incorporated in our standard rheological assumptions for the lithosphere, such as preexisting crustal and mantle discontinuities and the boundaries between old and newly accreted lithospheric mantle.

The modeling shows that the compressional yield strength of passive margins can vary considerably, depending on their lithospheric configuration, sedimentary cover, and thermal age. Lower plate margins, at which much of the old continental mantle–lithosphere is preserved, are considerably stronger than upper plate margins at which asthenospheric material has been accreted to the strongly attenuated old mantle–lithosphere. Although mature oceanic lithosphere is characterized by a high compressional yield strength, it can be significantly weakened in areas where thick passive margin sedimentary prisms or deep-sea fans prograde onto it (e.g., Gulf of Mexico: Worrall and Snelson, 1989; Niger Delta: Doust and Omatsola, 1989; Bengal fan: Curray and Moore, 1971).

6.12.3.5 Finite Strength of the Lithosphere in Extensional Basin Formation

In recent approaches to extensional basin modeling, the implementation of finite lithospheric strengths is an important step forward (see **Section 6.12.3** for a review). Advances in the understanding of lithospheric mechanics (e.g., Burov and

Table 3 Sediment-overfilled scenario (up to water surface), adopted in **Figure 18**

			Accumulated sediment fill (m)		
		Tectonic air-loaded subsidence (m)	$\rho_s = 2100\ kg\ m^{-3}$	$\rho_s = 2500\ kg\ m^{-3}$	$\rho_s = 2650\ kg\ m^{-3}$
Upper plate	Synrift	1474	4396	7065	9148
	Postrift	2375	7084	11384	14739
Lower plate	Synrift	2599	7752	7752	16130
	Postrift	3332	9939	15972	20679

Diament, 1995; Ranalli, 1995) demonstrate that early stretching models that assumed zero lithospheric strength during rifting are not valid. Moreover, the notion of a possible decoupling zone between the strong upper crust and the strong upper lithospheric mantle (see **Section 6.12.3.1**) is also important in the context of extensional basin formation. During the past decades, the relative importance of pure shear (McKenzie, 1978) and simple shear (Wernicke, 1985) mode of extension has been a matter of debate. In the presence of a weak lower crustal layer decoupling of the mechanically strong upper crust from the even stronger upper lithospheric mantle, the zone and symmetry of upper crustal extension do not necessarily have to coincide with the zone and symmetry of lithospheric mantle extension. This is particularly the case if the upper crust is weakened by preexisting discontinuities favoring its simple shear extensional deformation (Ziegler, 1996). A better appreciation of the role played by rheology during basin formation and the advent of corresponding modeling capabilities during the past few years has increasingly shifted the focus of attention away from these end-members of lithospheric extension. Finite element models have explored the large-scale implications of a finite lithospheric strength and particularly its sensitivity to the presence of fluids in the crust and lithospheric mantle (Bassi, 1995; Braun and Beaumont, 1989; Dunbar and Sawyer, 1989; Govers and Wortel, 1993). These dynamic models, which require intensive computing, are expensive to run and thus are not suitable for an industry user-oriented environment. However, they have provided the background for a more user-friendly class of kinematic models targeted at modeling rift-shoulder uplift and basin fill (Cloetingh et al., 1995c). These kinematic models invoke the concept of lithospheric necking around one of its strong layers during extensional basin formation (see Braun and Beaumont, 1989; Kooi et al., 1992; Spadini et al., 1995b). **Figure 13** illustrates the basic features of these models and their relation to the strength distribution within the lithosphere. In the presence of a strong layer in the subcrustal mantle, the level of lithospheric necking is deep, inducing pronounced rift-shoulder topography. This type of response is to be expected if extension affects cold and correspondingly strong intracontinental lithosphere; it is commonly observed in intracratonic rifts and rifted margin such as the Red Sea and the Transantarctic Mountains (Cloetingh et al., 1995a).

For Alpine/Mediterranean basins, which developed on a weak lithosphere with a thickened crust, the necking level is generally located at shallower depths). An example of such a situation is found in the Pannonian Basin (Horváth and Cloetingh, 1996; Van Balen et al., 1995, 1999) where the necking level is located at depths between 5 and 10 km within the upper crust. In this case, the strength of the lithospheric upper mantle has decreased to almost zero (see also **Figure 13**). Important exceptions to this general pattern do occur, however, such as in the southern Tyrrhenian Sea for which our modeling indicates a deep necking level to fit observational data (Spadini and Podladchikov, 1996; Spadini et al., 1995a,b). This is primarily attributed to the fact that the southern Tyrrhenian Basin developed essentially on Hercynian lithosphere with significant bulk strength of its mantle component. In other areas, this concept has led to a better understanding of lateral variations in basin structure and sedimentary fill within one and the same basin. This is exemplified by the Black Sea (see **Section 6.12.5**), where modeling deciphered important variations in necking level and thermal conditions between its eastern and western subbasins that can be attributed to differences in the timing and mode of their development (Cloetingh et al., 2003; Robinson et al., 1995; Spadini et al., 1996, 1997).

The interdependence of the necking depth and such parameters as prerift crustal and lithospheric thicknesses, the EET of the lithosphere, and strain rates was investigated in a comparative study on several basins, using the same modeling technology (Cloetingh et al., 1995a,b). Results of this study are summarized in **Figure 19**, illustrating that for Alpine/Mediterranean basins, the position of the necking level depends primarily on the prerift crustal thickness and strain rate, whereas the key controlling factors in intracratonic rifts appear to be the prerift lithospheric thickness and strain rate. This figure also illustrates where other basin formation processes have played a role. For instance, the Saudi Arabia–Red Sea margin is characterized by the presence of plume-related activity in the upper mantle that explains the systematic misfit of this case. The importance of the prerift lithospheric rheology for the subsequent basin geometry and the patterns of vertical motions are evident from these models. Moreover, they demonstrate that the better we are able to constrain the prerift evolution of an area, the greater the chance we have to define the parameter range that has to be to adopted for large-scale synrift mechanics.

6.12.3.6 Rift Shoulder Development and Architecture of Basin Fill

As discussed earlier, the finite strength of the lithosphere has important implications for the crustal structure of extensional basins and the development of accommodation space in them. The development of significant rift-shoulder topography in response to lithospheric extension has drawn attention to the need to constrain the coupled vertical motion of the shoulders and the subsiding basin (Kusznir and Ziegler, 1992). Whereas

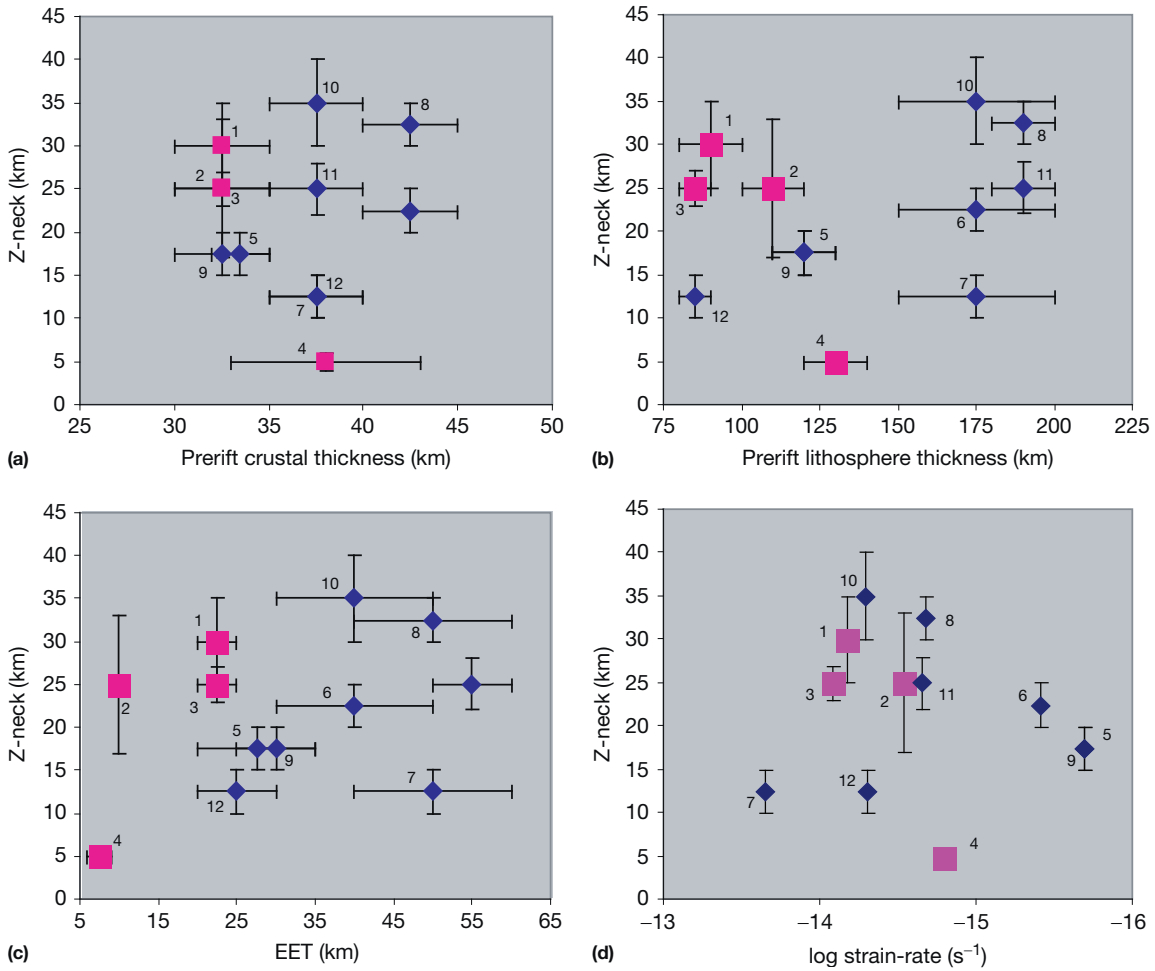

Figure 19 Correlation diagrams for the relationship between (a) necking depth and prerift crustal thickness, (b) necking depth and prerift lithospheric thickness, (c) EET and necking depth, and (d) necking depth and strain rate. *Circles* and *diamonds* indicate data from Alpine/Mediterranean basins and intracratonic rifts, respectively. Numbers refer to the following basins: *1* Gulf of Lion; *2* Valencia trough; *3* southern Tyrrhenian Sea; *4* Pannonian Basin; *5* North Sea; *6* Baikal rift; *7* Saudi Arabia Red Sea; *8* Transantarctic Mountains; *9* Barents Sea; *10* East African Rift; *11* western Black Sea; *12* eastern Black Sea. Reproduced from Cloetingh S, DArgenio B, Catalano R, Horvath F, and Sassi W (1995) Interplay of extension and compression in basin formation: Introduction. *Tectonophysics* 252: 1–5.

the standard approach in basin analysis focused until recently primarily on the subsiding basin, treating sediment supply as an independent parameter, necking models highlight the need for linking sediment supply to the rift-flank uplift and erosion history. To this end, a twofold approach was followed. The first research line aimed at constraining the predicted uplift histories by geothermochronology. Modeling of the distribution of fission-track length permits to back-stack the eroded sediments from their present position in the basin to their source on the rift shoulder in an effort to obtain a better reconstruction of the rift-shoulder geometries (e.g., Rohrman et al., 1995; Van der Beek et al., 1995). This has led to a better understanding of the timing and magnitude of rift-shoulder uplift, for example, on the Norwegian margin, shedding light on the observed relationship between onshore uplift and the presence of thick late Cenozoic sedimentary wedges in the adjacent offshore basin.

A second research line focused on the development of a model for basin fill simulation, integrating the effects of rift-shoulder erosion through hillslope transport and river incision with sediment deposition in the basin. As illustrated in Figure 20 (see Van Balen et al., 1995), these models predict the progradation of sedimentary wedges into extensional basins and the development of hinterland basins having a distinctly different stratigraphic signature than predicted by standard models, which invoke stretching and postrift flexure and which are commonly applied in the existing packages. Testing of this new model against a number of rifted margins around the world demonstrates that erosion of the rift-shoulder topography, created during extension of a lithosphere with a finite strength, eliminates to a large extent the need to invoke eustatic sea-level changes to explain the most commonly encountered large-scale stratigraphic features of rifted basins and associated hinterland basins.

On the scale of individual half-grabens, faulting exerts the main control on the basin architecture. Modeling studies have focused on the coupling of fault block tilting and the flexural behavior of the extending lithosphere. In a first step, modeling technology was developed to quantify the thermal effects of faulting on an extending lithosphere (Ter Voorde and Bertotti, 1994; Ter Voorde et al., 2007). Subsequently, models were

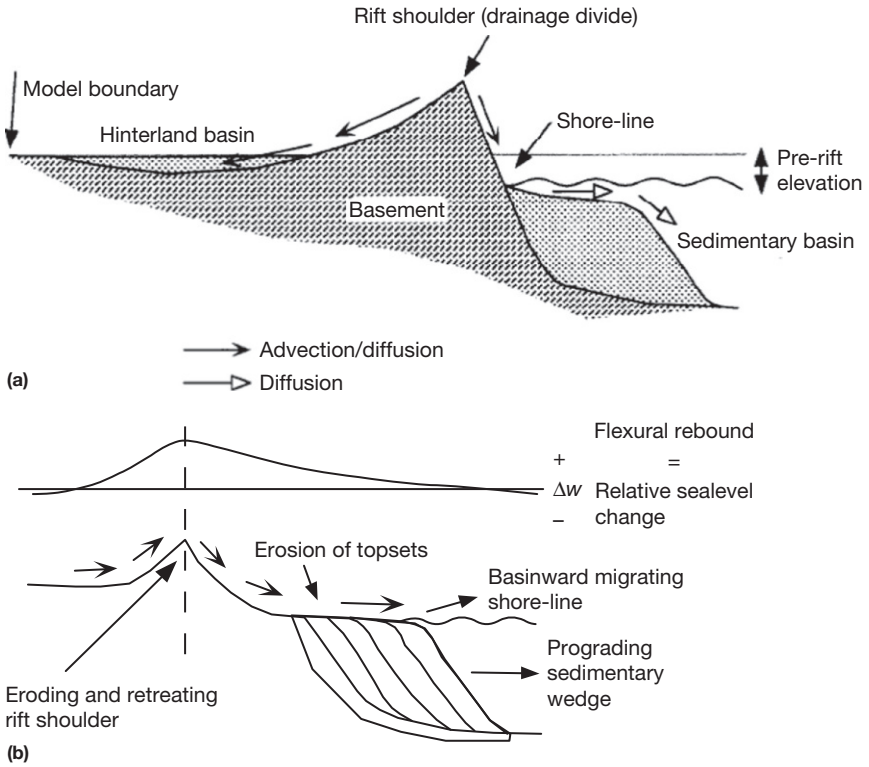

Figure 20 (a) Cartoon of the rift-shoulder erosion model. The isostatic response to necking of the lithosphere during extension causes a flexurally supported rift shoulder. In a landward direction, the rift shoulder is flanked by a flexural downwarp, the hinterland basin. The erosion products of the rift shoulder are transported to the offshore rifted basin and the hinterland basin. When the hinterland basin is completely filled, the sediments are taken out at the location indicated by 'model boundary.' These sediments are reintroduced into the model at the shoreline position in the offshore basin, establishing conservation of mass in the model. (b) Cartoon illustrating the mechanism of initial postrift coastal offlap at passive margins. Flexural rebound in response to erosional unloading at the rift shoulder causes uplift extending far into the offshore basin. The uplift causes erosional truncation of the topsets of the sedimentary wedge. Coastal onlap will occur when the rate of erosion-induced uplift is less than the subsidence caused by sedimentary loading, thermal contraction, and the flexural response to the increase in rigidity. Δw shows the instantaneous flexural uplift (+) and subsidence (−) pattern caused by rift-shoulder erosion. Reproduced from Van Balen RT, Vanderbeek PA, and Cloetingh SAPL (1995) The effect of rift shoulder erosion on stratal patterns at passive margins – Implications for sequence stratigraphy. *Earth and Planetary Science Letters* 134: 527–544.

developed that link the evolution of individual half-grabens to the extensional response of the deeper lithospheric (Ter Voorde and Cloetingh, 1996). The second step aimed at validating and testing these models against closely constrained natural examples, such as the well-exposed Mesozoic southern Alpine rifted margin, where extensive radiometric dating and the application of Ar/Ar laser-probing techniques permitted to constrain with high accuracy the thermal evolution of the extending lithosphere at subbasin and basin-wide scales (Bertotti and Ter Voorde, 1994). Testing and validation of the stratigraphic modeling component were carried out by a case-history study of the Oseberg field in the Norwegian part of the Viking Graben (Ter Voorde et al., 1997). This study demonstrated the need to establish a regional framework, linking the mechanics of the Oseberg block to the crustal evolution of adjacent areas, as a prerequisite for more detailed reservoir modeling.

Considering the notion that in synrift basins, different spatial and temporal scales are by their very nature linked, ignorance of constraints and structural information on surrounding areas will severely limit the quality of reservoir modeling. Modeling provides a quantitative tool to assess tectonic controls on synrift depositional sequences at a subbasin scale (see also Nottvedt et al., 1995). The amount of footwall uplift of an individual fault block appears to depend directly on the lithospheric necking level, controlling the large-scale response of the lithosphere to extension, and, therefore, should not only be attributed to factors restricted to the subbasin scale.

6.12.3.7 Back-Arc Extensional Basins

Back-arc extensional basins evolve in response to a decrease in the convergence rate or even a temporary divergence of colliding plates, causing steepening and rollback of the subducting lower plate lithospheric slab and the development of a secondary upwelling system in the upper plate mantle wedge above the subducting slab (e.g., Doglioni et al., 2007; Uyeda and McCabe, 1983). Back-arc basins can be developed over oceanic and continental lithosphere. Continental back-arc rifting can progress to the opening of limited oceanic basins (e.g., Sea of Japan, Black Sea, and South China Sea). However, as convergence rates between colliding plates vary in time, back-arc extensional basins are generally short-lived. Upon a renewed increase in convergence rates and shallowing of the subducting lower plate lithospheric slab, back-arc extensional basins are subjected to compressional stresses that can lead to their inversion and closure. Typical examples may include the Variscan

geosyncline, Sunda Arc and East China, or the Black Sea (Cloetingh et al., 1989; Hall et al., 2011; Jolivet et al., 1989; Munteanu et al., 2011; Nikishin et al., 2012; Uyeda and McCabe, 1983; Ziegler, 1990b). The sedimentary geometry and architecture of back-arc basins are controlled by such parameters as the age of subducted lithosphere, the subduction direction, the type of underlying lithosphere (oceanic versus continental), or the uplift of the orogenic arc (e.g., Dewey, 1980; Doglioni et al., 2007; Mathisen and Vondra, 1983; Uyeda and Kanamori, 1979). These parameters control the large variety of back-arc basins of various ages presently overlying different types of crust, such as the Caribbean, Banda–Sunda back-arcs, or the Black Sea basin (e.g., Hall et al., 2011; Meschede and Frisch, 1998; Munteanu et al., 2011; Spakman and Hall, 2010).

An observation that is common to many extensional back-arc basins floored by continental crust is the discrepancy between the observed amounts of crustal and lithospheric mantle stretching as derived from the magnitude, the upper crustal faulting and crustal/lithospheric thicknesses, and thus major differences between the corresponding stretching factors. This type of back-arc basin is often characterized by a much thicker postrift basin fill than predicted by synrift stretching as seen in the Pannonian Basin (Lenkey, 1999; Horváth et al., 2006). Such contrasting features occur in the hinterland of subduction-driven orogens (sensu Doglioni et al., 2007; Royden and Burchfiel, 1989), as, for example, the case of subduction driving the highly arcuate Mediterranean orogens (e.g., the Pannonian–Transylvanian system, the Aegean Sea, or the western Mediterranean, Faccenna et al., 2004; Jolivet and Brun, 2010; Krézsek and Bally, 2006; Matenco and Radivojević, 2012) or SE Asia subduction zones (e.g., the Malay and Pattani Basins; Morley and Westaway, 2006).

In the following, two large-scale extensional back-arc basins that underwent significant amounts of inversion postdating extensional episodes are discussed: the Black Sea and the Pannonian–Transylvanian Basin system of central Europe.

6.12.3.7.1 Black Sea basin

The Black Sea is superimposed on the Euxinus orogenic system that developed along the southern margin of the East European Craton during the closure of the Rheic and Paleo-Thethys Oceans. The Euxinus orogen was repeatedly subjected to back-arc extension and compression during the Triassic to Early Cretaceous final closure of the Paleo-Tethys Ocean and the opening of the Neo-Tethys Ocean (**Figure 21**; e.g., Nikishin et al., 2012; Okay et al., 1996; Robinson et al., 1996; Saintot et al., 2006; Şengör, 1987; Stephenson et al., 2004). The western Black Sea opened in Late Cretaceous times (e.g., Finetti et al., 1988; Görür, 1988; Munteanu et al., 2011; Nikishin et al., 2001, 2012), commonly interpreted as an extensional back-arc basin related to the N-ward subduction of the Neo-Tethys (e.g., Letouzey et al., 1977; Nikishin et al., 2012; Okay et al., 1994). Although a coeval opening of all domains of the Black Sea during Late Cretaceous times has been inferred (e.g., Nikishin et al., 2003; Zonenshain and Le Pichon, 1986), most studies agree that the eastern Black Sea has opened later, during Paleocene–Eocene times (e.g., Banks, 1998; Kazmin et al., 2000; Robinson et al., 1996; **Figure 21**; see also Okay et al., 1994), creating thinned continental to oceanic crust (Edwards et al., 2009; Shillington et al., 2008). The Early Cretaceous opening of the western Black Sea took place in a number of deformation phases (Munteanu et al., 2011) creating possibly oceanic crust, followed by overall seafloor spreading and subsidence during Late Cretaceous and Cenozoic times (Finetti et al., 1988; Görür, 1988; Nikishin et al., 2012; Starostenko et al., 2004). The Early Cretaceous back-arc opening was followed by a main Late Cretaceous extensional episode in the Pontides (Görür, 1988; Yilmaz et al., 1997). This can be followed laterally also onshore in the Balkanides (e.g.,

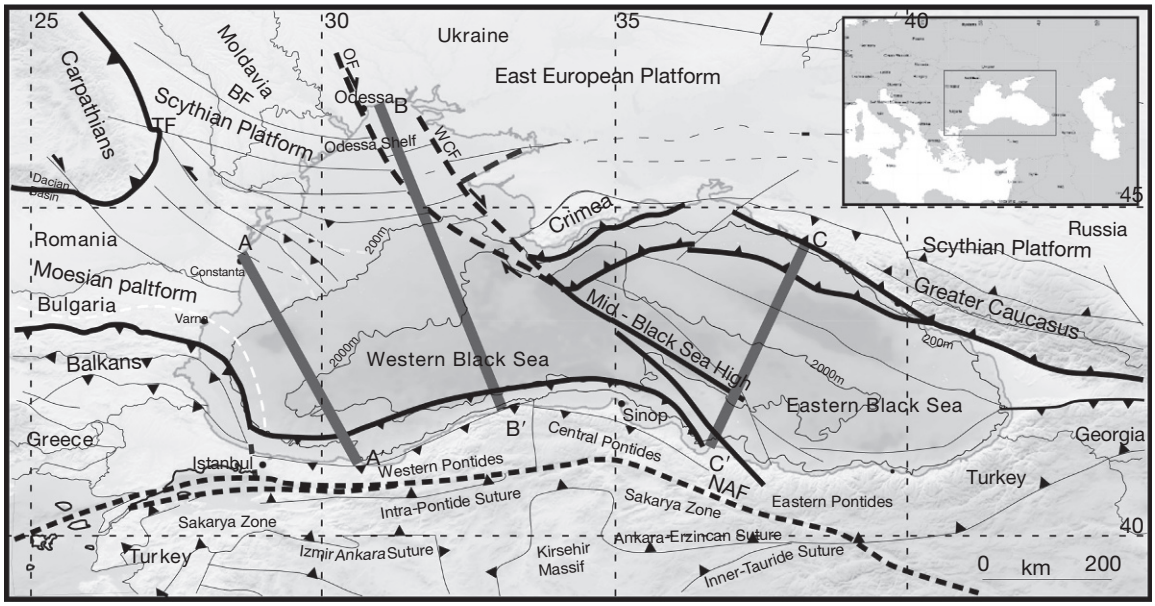

Figure 21 Tectonic map of the Black Sea and adjacent areas (simplified and modified from Munteanu, 2012) with the location of profiles shown in **Figure 22**. Reproduced from Munteanu I (2012) *Evolution of the Western Black Sea*: *Kinematic and Sedimentological Inferences from Geological Observations and Analogue Modelling*. Dissertation, Utrecht University.

Georgiev et al., 2001). The Eocene opening of the eastern Black Sea (e.g., Görür, 1988) has induced renewed extension in the western basin (e.g., Robinson et al., 1996; Dinu et al., 2005; Munteanu et al., 2011; Tari et al., 2009). The passive margin evolution that is interrupted by the late (middle) Eocene collision recorded the major tectonic units of the Pontides and Taurides (Okay et al., 1994; Şengör and Yilmaz, 1981). The major contraction taking place at the southern margin of the Black Sea led to the onset of inversion recorded in the extensional basins and to the formation of other foreland and thrust-sheet top basins (e.g., Dinu et al., 2005; Finetti et al., 1988; Nikishin et al., 2003; Robinson et al., 1996; Sunal and Tüysüz, 2002). In the western Black Sea basin, the contraction gradually migrated in time N-ward until the Odessa shelf (Munteanu et al., 2011), where the shortening continued during Miocene–Pliocene times (Khriachtchevskaia et al., 2009). The eastern Black Sea was inverted with an opposite polarity, the Crimean and Caucasus orogens being thrusted S-ward over the Black Sea domain starting with Oligocene times (e.g., Munteanu et al., 2013; Stovba et al., 2009). The change in polarity is accommodated by the transcurrent movements recorded by the Odessa–West Crimean fault system and along the Mid-Black Sea High (Munteanu et al., 2011, 2014).

In the context of the endemic Eastern Paratethys, the Neogene evolution of the western Black Sea basin is of special interest (Popov et al., 2006; Vasiliev et al., 2013). While fine clastic to pelagic Lower–Middle Miocene sediments are generally thin throughout the western Black Sea, higher subsidence rates are recorded during latest Miocene–Quaternary times (Cloetingh et al., 2003; Munteanu et al., 2012; Nikishin et al., 2003). The sea-level drop of the Messinian Salinity Crisis in the Mediterranean (e.g., Krijgsman et al., 1999) is recorded in the Black Sea by large-scale shelf erosion and massive progradation of clastics during the lower Pliocene transgressive and highstand, the estimated sea-level drop probably exceeding 1 km (e.g., Bartol and Govers, 2009; Bartol et al., 2012; Gillet et al., 2007; Hsü and Giovanoli, 1979; Munteanu et al., 2012). Rapid sea-level changes are also inferred for the Pliocene–Quaternary evolution of the western Black Sea (Lericolais et al., 2013; Winguth et al., 2000). Consequently, thick successions of mass-transport and turbiditic deposits are observed along a number of deep-sea fans in front of modern rivers discharging into the Black Sea (e.g., Popescu et al., 2001).

In the succeeding text, we address the relationship between the prerift finite strength of the lithosphere and the geometry of extensional basins in the Black Sea area and discuss the effects of differences in prerift rheology on the Mesozoic–Cenozoic stratigraphy of the western and eastern Black Sea basin. These findings raise important questions on postrift tectonics and on intraplate stress transmission into the Black Sea basin from its margins.

6.12.3.7.1.1 Rheology and back-arc rift basin formation

Inferred differences in the mode of basin formation between the western and eastern Black Sea basins can be largely explained in terms of paleorheologies. The prerift lithospheric strength of the western Black Sea (**Figure 22**) appears to be primarily controlled by the combined mechanical response of a strong upper crust and strong upper mantle (Spadini et al., 1996). The shallow necking level in the eastern Black Sea is compatible with a prerift strength controlled by a strong upper crust decoupled from the weak hot underlying mantle (**Figure 22**). These differences point to important differences in the thermotectonic age of the lithosphere of the two subbasins (Cloetingh and Burov, 1996). The inferred lateral variations between the western and eastern Black Sea suggest thermal stabilization of the western Black Sea prior to rifting, while the lithosphere of the eastern Black Sea was apparently already thinned and thermally destabilized by the time of Eocene rifting. The inferred differences in the necking level and in the timing of rifting between the western and eastern Black Sea suggest an earlier and more pronounced development of rift shoulders in the western Black Sea basin as compared with the eastern Black Sea (Robinson et al., 1995).

6.12.3.7.1.2 Strength evolution and neotectonic reactivation during the postrift phase

Automated backstripping studies and results of forward models of lithospheric stretching (Van Wees et al., 1998) provide estimates of the integrated lithospheric strength at various syn- and postrift stages. Top panel in **Figure 23** shows a comparison of observed and forward modeled tectonic subsidence curves for the center of the western Black Sea basin. Automated backstripping yields a stretching factor of 6. Modeling fails, however, to predict the pronounced late Neogene subsidence acceleration, documented by the stratigraphic record that may be attributed to late-stage compression. As postrift cooling of the lithosphere leads in time to a significant increase in its integrated strength, its early postrift deformation is favored. Present-day lithospheric strength profiles calculated for the center and margin of western Black Sea (Figure 23 bottom panels) show a pronounced difference. On the contrary, the onset of the basin inversion during late Middle Eocene times at short times after the extension ceased earlier during Middle Eocene means that the lithosphere was weak when compression was activated. The presence of relatively strong lithosphere in the basin center in the very late stages of Pliocene inversion and weaker lithosphere at the basin margins favors the deformation of the latter during late-stage compression.

In **Figure 24**, (top panel) the observed and forward modeled tectonic subsidence curves for the center of eastern Black Sea basin are compared, adopting for modeling a stretching factor of 2.3 that is compatible with the subsidence data and consistent with geophysical constraints. During the first 10 My of postrift evolution, integrated strengths are low but subsequently increase rapidly owing to cooling of the lithosphere. This would correspond to the initial moments of post-Middle Eocene inversion.

At short time after the ultimate cessation of rifting (~10 My) in Middle Eocene times, the basing was still underlain by very weak and extended lithosphere. This is the moment when the entire Black Sea basin was inverted due to the collision recorded in the Pontides domain (e.g., Nikishin et al., 2012). It should be noted, however, that with a cooling-related progressive increase of the integrated lithospheric strength, with time increasingly higher stress levels are required to cause large-scale deformation (**Figures 23** and **24**, middle panels). This is probably why the amplitude of contractional deformation decreases in time in the western Black Sea basin (Munteanu et al., 2012). Important in this context is also that, due to substantial crustal thinning, a strong upper mantle layer is present in the central part of the basin at relatively shallow depths that may contrast substantially with an inherited weaker

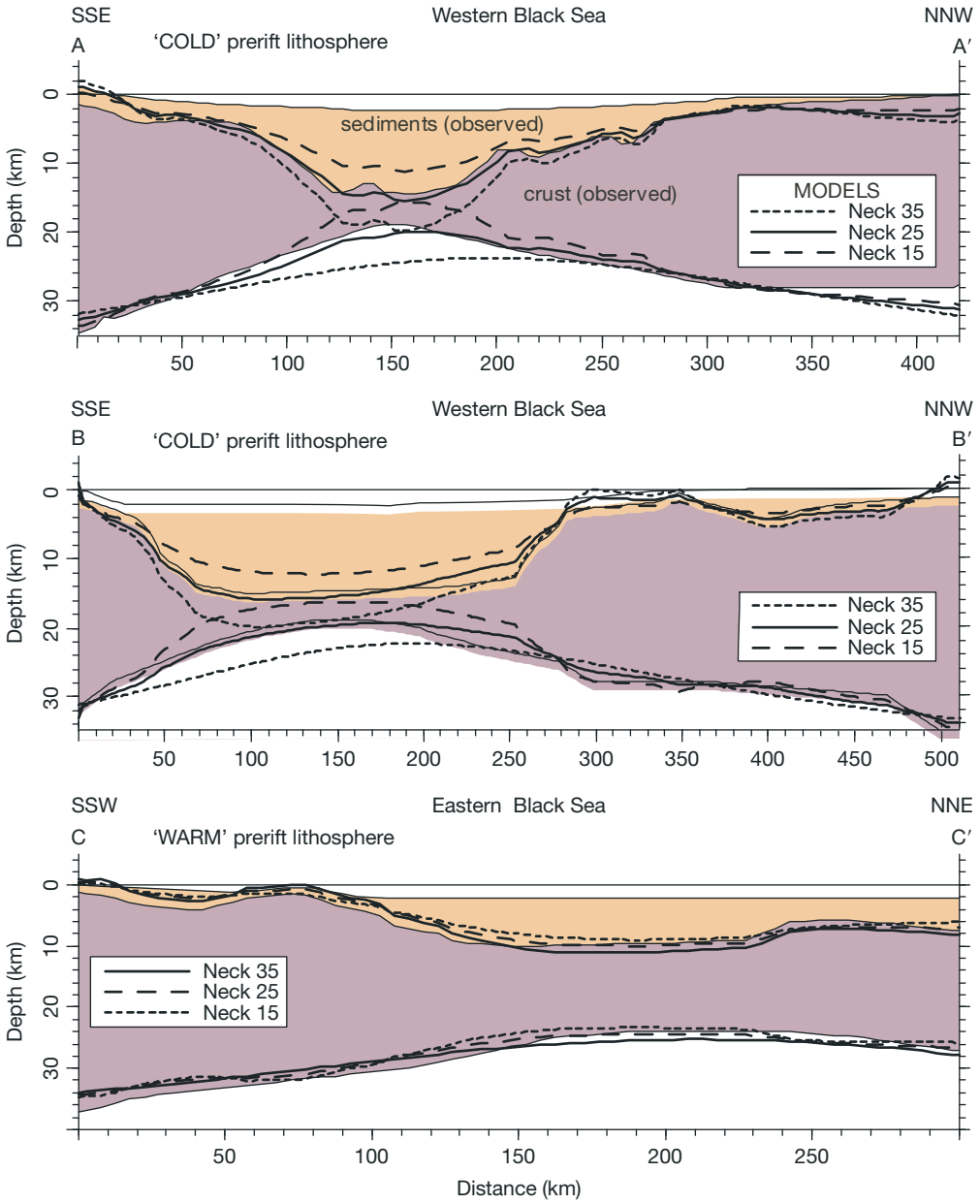

Figure 22 Crustal-scale models for basin evolution for the western and eastern Black Sea. For location of cross sections, see **Figure 21**. A comparison of predicted and observed Moho depths provides constraints on levels of necking and thermal regime of the prerift lithosphere. The models support the presence of cold prerift lithosphere compatible with a deep necking level of 25 km in the western Black Sea. For the eastern Black Sea, the models suggest the presence of a warm prerift lithosphere with a necking level of 15 km. Reproduced from Cloetingh S, Spadini G, Van Wees JD, and Beekman F (2003) Thermo-mechanical modelling of Black Sea Basin (de)formation. *Sedimentary Geology* 156: 169–184.

lower crust and, therefore, favor the transmission of contractional stresses over large distances (Munteanu, 2012).

Based on the present thermomechanical configuration (Figures 23 and 24) with relatively strong lithosphere in the basin center and relatively weak lithosphere at the basin margins, we predict that the bulk of shortening will be taken up in the margins of the basin during the initial phase of shortening, while the late-stage shortening induced by orogenic activity in the surrounding areas will be taken up along the basin center. The relative difference in rheological strength of the marginal and central parts of the basin is more pronounced in the eastern than in the western Black Sea. These predictions are in agreement with data mapping deformation in the Black Sea (e.g., Dondurur et al., 2013; Munteanu et al., 2012).

Basement and surface heat flow in the eastern and western Black Sea show markedly different patterns in timing of the rift-related heat flow maximum. The predicted present-day heat flow is considerably lower in the western than in the eastern subbasin. This is attributed to the presence of more heat-producing crustal material in the eastern than in the western Black Sea that is partly floored by oceanic crust. In heat flow modeling studies, the effects of sedimentary blanketing were

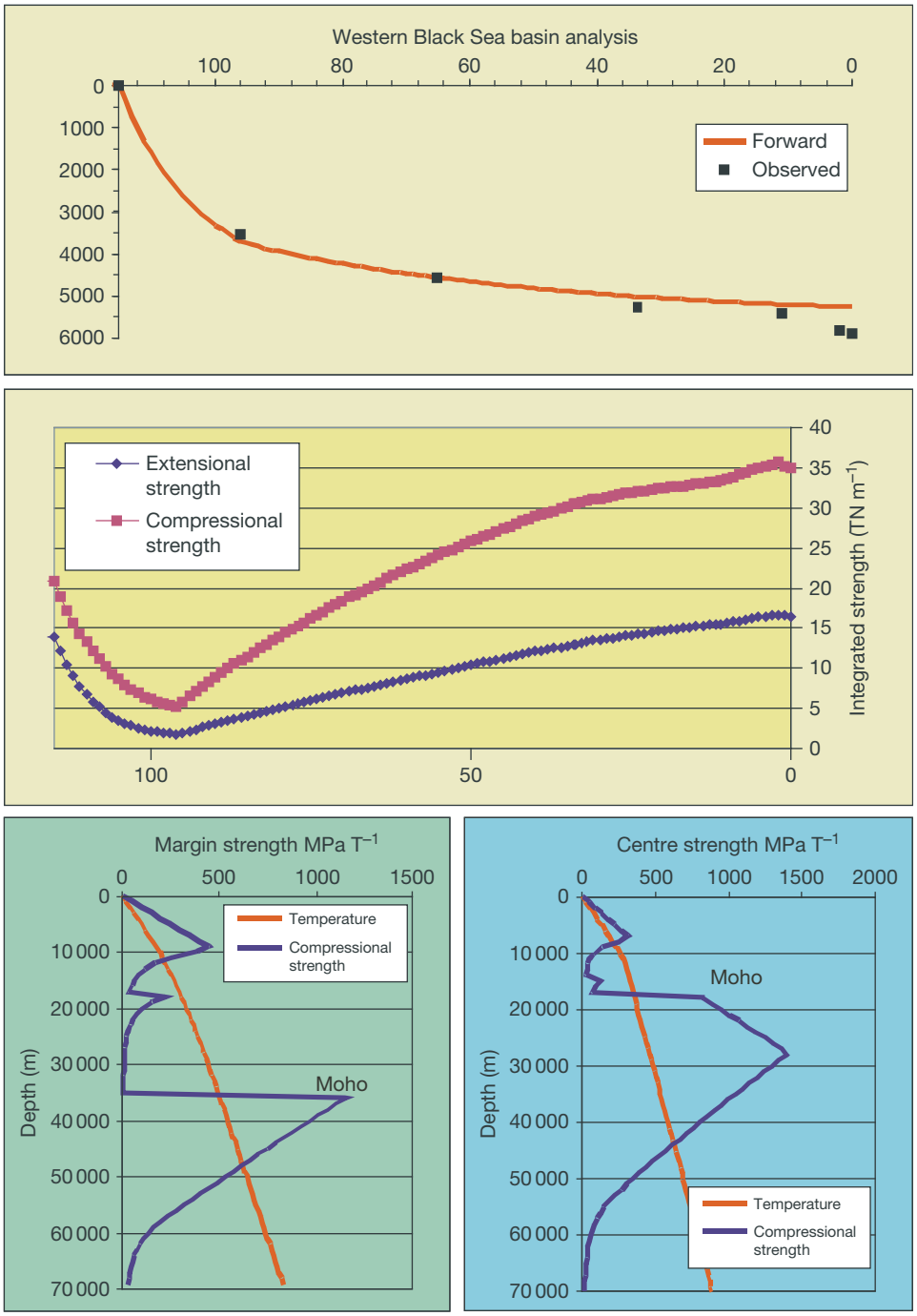

Figure 23 (Upper panel) Comparison of observed and forward modeled tectonic subsidence for the western Black Sea basin center. Automated backstripping yields an estimated stretching factor of 6. Postrift cooling leads in time to a significant increase in the predicted integrated strength for both compressional and extensional regimes (middle panel; 1 TN $m^{-1} = 10^{12}$ N m^{-1}). (Middle panel) Present-day lithospheric compressional strength profiles calculated for the center and margin of western Black Sea show with depth a pronounced difference (bottom panels). Temperature profiles (in ^{o}C) and Moho depth are given for reference. Note the important role of the actual Moho position in terms of mechanical decoupling of the upper crust and mantle parts of the Black Sea lithosphere. Reproduced from Cloetingh S, Spadini G, Van Wees JD, and Beekman F (2003) Thermo-mechanical modelling of Black Sea Basin (de)formation. *Sedimentary Geology* 156: 169–184.

taken into account (Van Wees and Beekman, 2000). Heat flow values vary between 30 mW m^{-2} in the center of the basins and up to 70 mW m^{-2} at the Crimean and Caucasus margins (Nikishin et al., 2003). With its sedimentary thickness of up to 15 km, thermal blanketing has a pronounced effect on the heat flow in the western Black Sea. As a result, its present-day integrated strength is not that much higher than its initial strength. By contrast, the integrated strength of the eastern

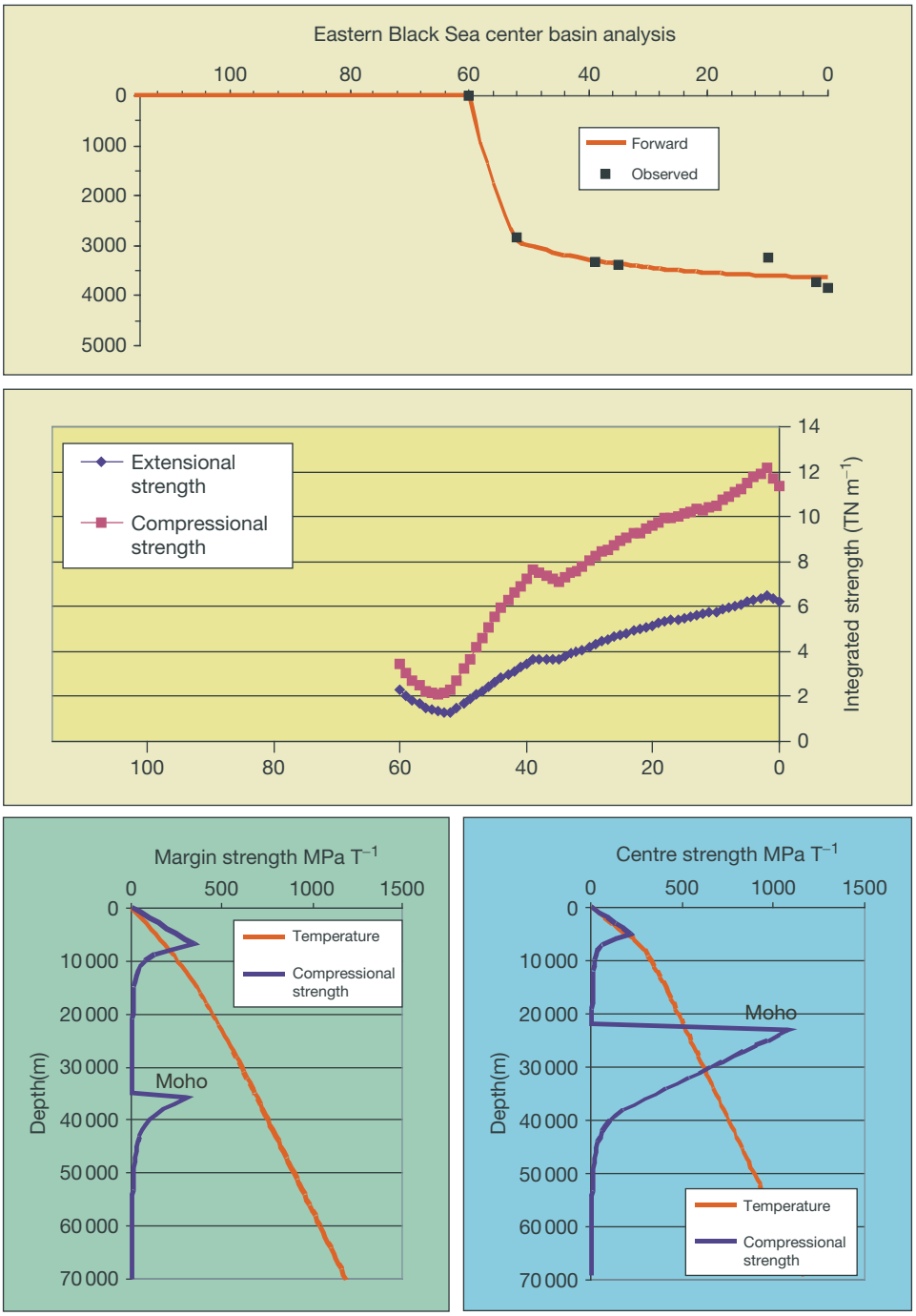

Figure 24 Comparison of observed and forward modeled tectonic subsidence for the eastern Black Sea basin center. Automated backstripping yields an estimated stretching factor of 2.3 (upper panel). Postrift cooling leads in time to a significant increase in the predicted integrated strength for both compressional and extensional regimes (middle panel 1 TN $m^{-1} = 10^{12}$ N m^{-1}). Present-day lithospheric strength profiles calculated for the center and margin of the eastern Black Sea show with depth a pronounced difference (bottom panels). Reproduced from Cloetingh S, Spadini G, Van Wees JD, and Beekman F (2003) Thermo-mechanical modelling of Black Sea Basin (de)formation. *Sedimentary Geology* 156: 169–184.

Black Sea is much higher than its initial strength as the blanketing effect of its up to 12 km thick sedimentary fill is less pronounced and as water depths are greater.

The western Black Sea center is marked by a thermomechanical age of around 100 My with rheological modeling indicating mechanical decoupling of the crust and lithospheric mantle (see Figures 23 and 24). These models imply an EET of at least 40 km (Burov and Diament, 1995) and folding wavelengths of 100–200 km for the mantle and 50–100 km for the upper crust (Cloetingh et al., 1999). For the eastern Black Sea, a probably significantly younger thermomechanical lithospheric age of 55 My implies an EET of no more than 25 km and indicates mantle folding at wavelengths of 100–150 km and a crustal folding wavelength similar to the western Black Sea.

The large dimension of the preexisting rift basin causes during the late stages of inversion a pronounced increase in the wavelength of the stress-induced downwarp (Cloetingh et al., 1999; Munteanu et al., 2011). This effect has been observed in the North Sea basin (Van Wees and Cloetingh, 1996) and the Pannonian Basin (Horváth and Cloetingh, 1996), both of which are characterized by large sediment loads and a wide rift basin. This provides an alternative to previous explanations for recent differential motions in the northern Black Sea basin (Smolyaninova et al., 1996) that were attributed to convective mantle flow.

6.12.3.7.2 Pannonian–Transylvanian Basin system

The Pannonian–Transylvanian Basin system is surrounded by the Carpathian and Dinaridic orogens (**Figure 25**) and has been the focus of major research efforts integrating a wide range of geophysical and geologic data, thus representing a key area for quantitative basin studies and the study of the dynamics of basin–orogen interaction (see Cloetingh et al., 2006; Horváth et al., 2006; Neubauer et al., 1997; Schmid et al., 2008, for recent reviews). A vast geophysical and geologic database has been established during the last decades as a result of major international research collaborations in this area, largely carried out in the framework of European programs such as the EU Integrated Basin Studies project (Cloetingh et al., 1995b; Durand et al., 1999), the EUROPROBE–PANCARDI (Decker et al., 1998) programs, the Peri-Tethys Programme (Brunet and Cloetingh, 2003; Ziegler and Horváth, 1996b; Ziegler and Roure, 1996), and more recently the ESF EUROCORES TOPO-EUROPE initiative and its dedicated subprojects, such as the Source–Sink and TOPO-Alps projects (Cloetingh et al., 2007; Matenco et al. (2013)).

An important asset of this natural laboratory is the high-quality constraints both on the evolution of Neogene basins such as the Pannonian or Transylvanian Basins and on the mechanics of surrounding orogens (see Cloetingh et al., 2006; Horváth et al., 2006; Leever et al., 2011; Matenco et al., 2010). A focal area has been the Vrancea seismogenic area of the SE Carpathians that displays a high-velocity teleseismic intermediate mantle anomaly commonly related to the rapid rollback evolution of a slab inherited from the evolution of the Alpine Tethys (e.g., Cloetingh et al., 2004; Ismail-Zadeh et al., 2012; Martin and Wenzel, 2006, and references therein). This anomalous seismicity can be related with significant recent tectonic activity and associated natural hazards (e.g., Cloetingh et al., 2005a,b; Matenco et al., 2007; Merten et al., 2010; Necea et al., 2005).

In the Pannonian–Transylvanian Basin system, extensive industrial reflection-seismic coverage and well data acquired in the context of petroleum exploration and surface studies permitted to construct a high-resolution kinematic, structural, sedimentologic, and stratigraphic framework (e.g., Bada et al., 2007; Horváth et al., 2006; Krezsek and Bally, 2006; Krezsek et al., 2010; Matenco and Radivojević, 2012; Sacchi et al., 1999; Sztanó et al., 2013; Tari et al., 1999; Tilita et al., 2013; Vasiliev et al., 2010) that set the stage for numerical and analog modeling (e.g., Bada et al., 1998; Dombradi et al., 2010; Jarosinski et al., 2011).

The Pannonian–Carpathian system, therefore, permits to test models for the development of sedimentary basins and their subsequent deformation and for ongoing continental collision. The lithosphere of the Pannonian Basin is a particularly sensitive recorder of changes in lithospheric stress induced by near-field intraplate and far-field plate boundary processes (Bada et al., 2001).

6.12.3.7.2.1 Neogene development and evolution of the Pannonian Basin

The Pannonian Basin of central Europe (**Figure 25**) is a classical extensional back-arc basin formed during Miocene times in

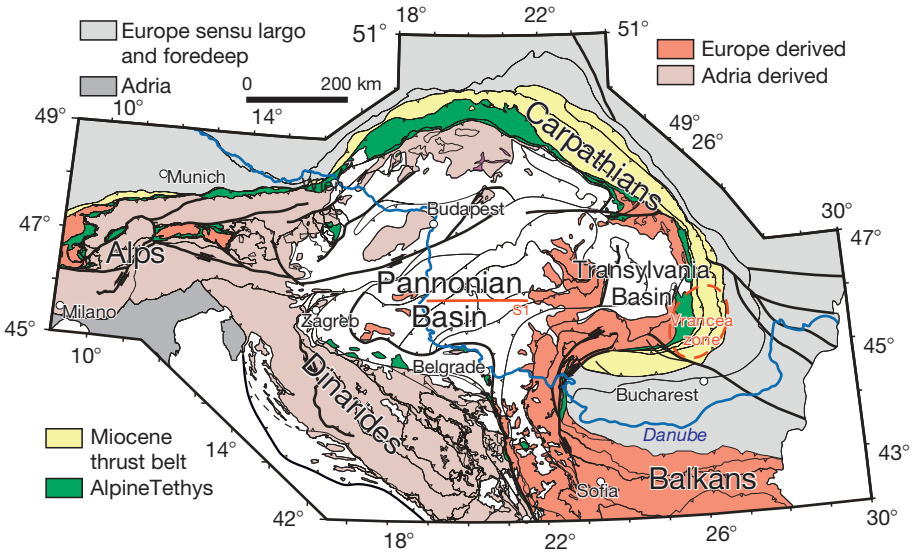

Figure 25 Tectonic map of the Alpine–Carpathian–Dinaridic system with the extent of the large Pannonian and Transylvanian back-arc basins and the location of other Miocene basins superposed over the Dinarides and Carpathians structures. Red line S1 indicates location of transect shown in Figure 28. Reproduced from Matenco L and Radivojević D (2012) On the formation and evolution of the Pannonian Basin: Constraints derived from the structure of the junction area between the Carpathians and Dinarides. *Tectonics* 31: TC6007 and Schmid SM, Bernoulli D, Fugenschuh B, et al. (2008) The Alpine-Carpathian-Dinaridic orogenic system: Correlation and evolution of tectonic units. *Swiss Journal of Geosciences* 101: 139–183.

response to the rapid rollback of a slab attached to the European continent, which is still underlain by highly thinned continental lithosphere (e.g., Balla, 1986; Cloetingh et al., 2006; Horváth, 1993; Horváth et al., 2006; Royden, 1988a,b). The rollback is partly responsible for the creation of the highly arcuate geometry of the Carpathian Mountains (e.g., Matenco et al., 2010), a process that is common with many other Mediterranean orogens (e.g., Faccenna et al., 2004; Jolivet and Faccenna, 2000). The Pannonian Basin is spatially juxtaposed over an orogenic area that formed in Cretaceous–Paleogene times in response to the subduction and closure of a number of oceanic domains that were kinematically linked with the evolution of the larger Alpine Tethys and Neo-Tethys oceans (e.g., Csontos and Voros, 2004; Schmid et al., 2008). Evolutionary models of the Pannonian Basin assume the onset of extension at ~20 Ma, subsequently followed by a peak tectonic activity along normal faults during Middle Miocene times, followed by a postrift, thermal-sag phase starting in Late Miocene times (e.g., Tari et al., 1999 and references therein). A latest Miocene–Quaternary contractional event has subsequently overprinted the basin during the translation and counterclockwise rotation of the Adriatic indenter (Bada et al., 2007; Fodor et al., 2005; Horváth, 1995; Horváth and Cloetingh, 1996; Pinter et al., 2005).

6.12.3.7.2.2 Dynamic models of basin formation

Several models have been proposed to explain the dynamics of Neogene rifting in the Pannonian Basin (Bada and Horváth, 2001), which take into account such prominent features of the Pannonian–Carpathian system as thinned and hot versus thickened and colder lithosphere in its central and peripheral sectors, respectively. Some of these models have proposed the presence of a mantle diapir beneath the intra-Carpathian area. Other models proposed rifting as the driving mechanism for the Pannonian Basin (Horváth et al., 1975), attributed to thermal thinning of the Pannonian lithosphere in response to upwelling of the mantle above the subducted European and Adriatic lithospheric slabs that dip beneath the Pannonian domain.

At a different scale and with a different mechanical behavior, the plume model has been also recently inferred by Burov and Cloetingh (2010) to be responsible for the formation of the asthenospheric upwelling beneath the Pannonian Basin and the initiation of subduction in neighboring Carpathian and Dinaridic orogens.

Other models stress the back-arc position of the Pannonian domain with respect to the Carpathian arc and postulate that gravity-driven passive rollback of the subducting European lithospheric slab is the driving force for the tensional subsidence of the Pannonian Basin (e.g., Csontos, 1995; Csontos et al., 1992; Horváth, 1993; Linzer, 1996; Royden and Horváth, 1988; Royden and Karner, 1984). In a modification of this model, eastward mantle flow is thought to control rollback of the subducted slab and related retreat of its hinge line.

Based on thermomechanical finite element modeling, Huismans et al. (2001b) were able to simulate temporal changes in rifting style in the Pannonian Basin, suggesting a two-phase evolutionary scheme for the system. According to their model, the initial early Middle Miocene basin subsidence was driven mainly by passive rifting in response to rollback of the subducted Carpathian slab, involving gravitational collapse of the thickened prerift Pannonian lithosphere. This triggered small-scale convective upwelling of the asthenosphere that has favored the late-stage thermal subsidence (Horváth, 1993) and the compressional inversion of the Pannonian domain during Late Miocene–Pliocene times (e.g., Bada et al., 1999; Fodor et al., 2005).

Another category of models involves lithospheric mantle instabilities for the formation of the asthenospheric up rise beneath the Pannonian Basin and the high-velocity anomalies observed by teleseismic tomography in neighboring orogens (e.g., Dando et al., 2011; Gemmer and Houseman, 2007; Houseman and Gemmer, 2007; Ren et al., 2012). These models assume a convective mantle removal beneath the Pannonian Basin, correlated with high heat flow and interpreted as upwelling asthenosphere correlated with a fast anomaly extending outward as far as the Carpathians, the Dinarides, and the Eastern Alps. This higher velocity mantle material is interpreted as being produced by a mantle downwelling, whose detachment from the lithosphere above may have triggered the extension of the Pannonian Basin.

6.12.3.7.2.3 Stretching models and subsidence analysis

Sclater et al. (1980) were the first to apply the stretching model of McKenzie (1978) to the intra-Carpathian basins. They found that the development of peripheral basins could be fairly well simulated by the uniform pure shear extension concept with a stretching factor of about 2. For the more centrally located basins, however, their considerable thermal subsidence and high heat flow suggested unrealistically high stretching factors up to 5. Thus, they postulated differential extension of the Pannonian lithosphere with moderate crustal stretching (δ factor) and larger stretching of the lithospheric mantle (β factor). Building on this and using a wealth of well data, Royden et al. (1983) introduced the nonuniform stretching concept according to which the magnitude of lithospheric thinning is depth-dependent. This concept accounts for a combination of uniform mechanical extension of the lithosphere and thermal attenuation of the lithospheric mantle (Ziegler, 1992, 1996b; Ziegler and Cloetingh, 2004). This is compatible with the subsidence pattern and thermal history of major parts of the Pannonian Basin that suggest a greater attenuation of the lithospheric mantle as compared to the finite extension of the crust. Horváth et al. (1988) further improved this concept by considering radioactive heat generation in the crust and the thermal blanketing effect of basin-scale sedimentation. By reconstructing the subsidence and thermal history, and by calculating the thermal maturation of organic matter in the central region of the Pannonian Basin (Great Hungarian Plain), a major step forward was made in the field of hydrocarbon prospecting by means of basin analysis techniques.

These studies highlighted difficulties met in explaining basin subsidence and crustal thinning in terms of uniform extension and point toward the applicability of anomalous subcrustal mantle thinning. This issue was central to subsequent investigations involving quantitative subsidence analyses (backstripping) of an extended set of Pannonian Basin wells and cross sections and their forward modeling (Juhász et al., 1999; Lankreijer et al., 1995; Lenkey, 1999; Sachsenhofer et al., 1997). Kinematic modeling, incorporating the concept of necking depth and finite strength of the lithosphere during and after rifting (Van Balen et al., 1999), as well as dynamic modeling studies (Huismans et al., 2001b), suggested that the

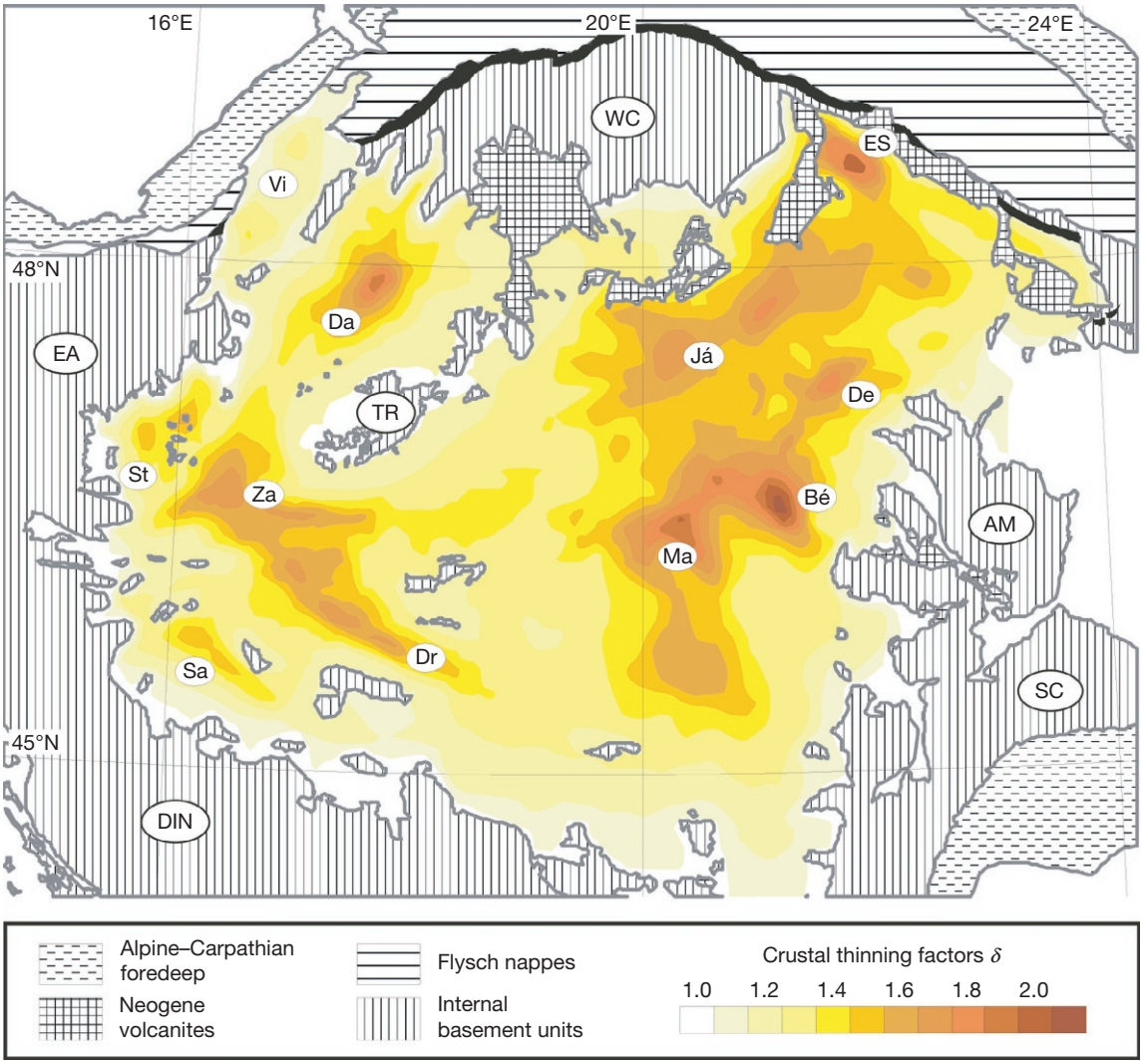

Figure 26 Crustal thinning factors calculated by forward modeling for the Pannonian Basin applying the nonuniform stretching concept and taking the effects of lateral heat flow and flexure of the lithosphere into account. Note the pronounced lateral variations in crustal extension controlling the development of deep subbasins separated by areas of limited deformation. AM, Apuseni Mts.; DIN, Dinarides; EA, Eastern Alps; TR, Transdanubian Range; SC, WC, Southern and Western Carpathians, respectively. Local depressions of the Pannonian Basin system: Be, Békés; Da, Danube; De, Derecske; Dr, Drava; ES, East Slovakian; Ja, Jászság; Ma, Makó; Sa, Sava; St, Styrian; Vi, Vienna; Za, Zala. Reproduced from Lenkey L (1999) Geothermics of the Pannonian Basin and Its Bearing on the Tectonics of Basin Evolution, 215 pp. PhD Thesis, VU University, Amsterdam.

transition from passive to active rifting was controlled by the onset of subcrustal flow and small-scale convection in the asthenosphere. In order to quantify basin-scale lithospheric deformation, Lenkey (1999) carried out forward modeling applying the concept of nonuniform lithospheric stretching and taking into account the effects of lateral heat flow, flexure, and necking of the lithosphere. Calculated crustal thinning factors (δ) indicate large lateral variation of crustal extension in the Pannonian Basin (**Figure 26**). This is consistent with the areal pattern of the depth to the pre-Neogene basement (Horváth et al., 2006). The indicated range of crustal thinning factors of 10–100% crustal extension is in good agreement with the prerift palinspastic reconstruction of the Pannonian Basin and the amount of cumulative shortening in the Carpathian orogen (e.g., Fodor et al., 1999; Roure et al., 1993).

As a major outcome of basin analysis studies, Royden et al. (1983) provided a two-stage subdivision for the evolution of the Pannonian Basin with a synrift (tectonic) phase during Early to Middle Miocene times and a postrift thermal subsidence phase during the Late Miocene–Pliocene. Further development of the stratigraphic database, however, demonstrated the need to refine this scenario. According to Tari et al. (1999), the regional Middle Badenian unconformity, marking the termination of the synrift stage, is followed by a postrift phase that is characterized by only minor tectonic activity. Nevertheless, the subsidence history of the Pannonian Basin can be subdivided into three main phases that are reflected in the subsidence curves of selected subbasins (**Figure 27**). The initial synrift phase is characterized by rapid tectonic subsidence, starting synchronously at about 20 Ma in the entire Pannonian Basin. This phase of pronounced crustal extension is recorded everywhere in the basin system and was mostly limited to relatively narrow, fault-bounded grabens or subbasins. During the subsequent postrift phase, much broader areas began to subside, reflecting

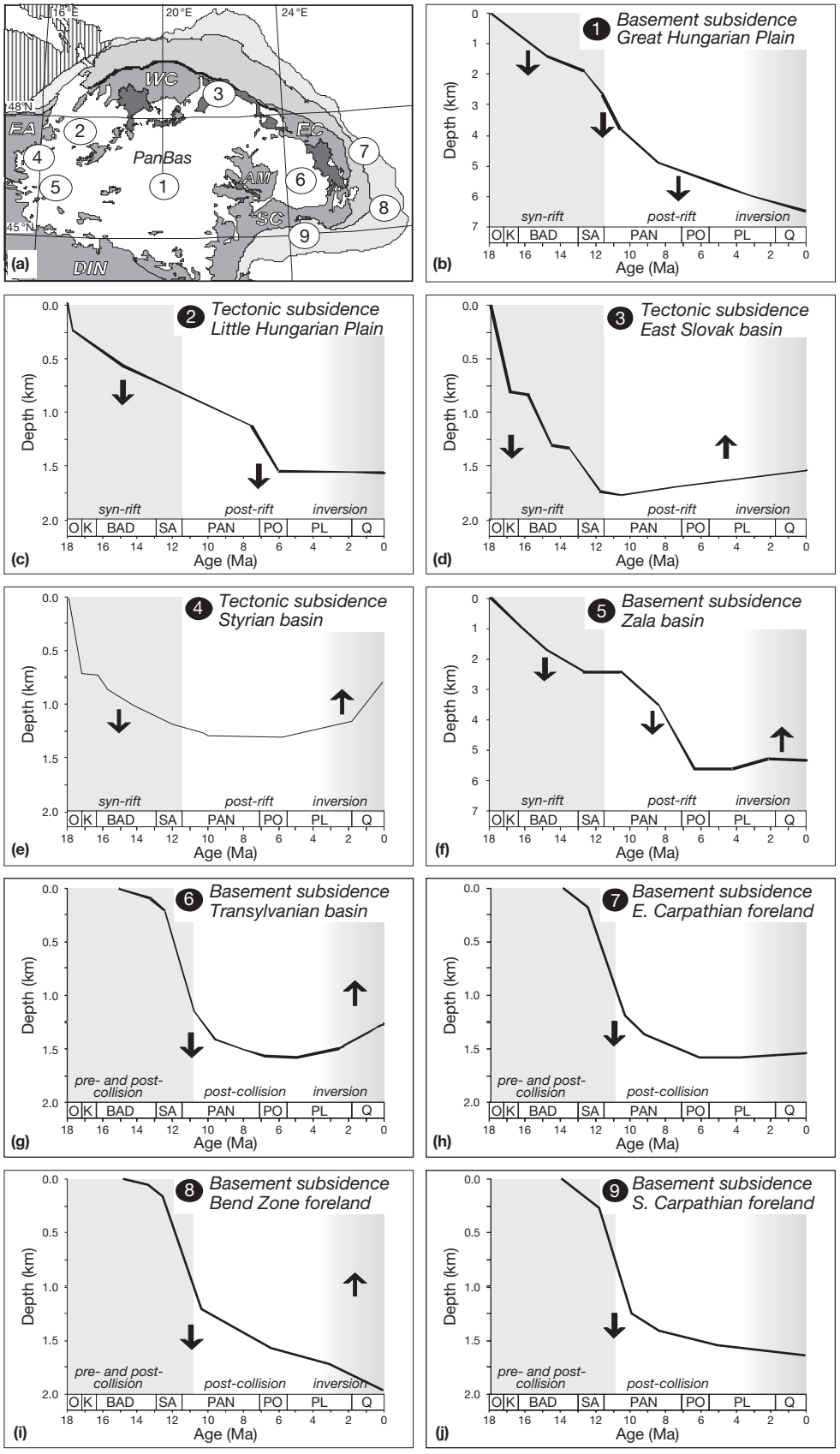

Figure 27 Subsidence curves for selected subbasins of the Pannonian Basin and the Carpathian foreland. Note that after a rapid phase of general subsidence throughout the entire Pannonian Basin, the subbasins show distinct subsidence histories from Middle Miocene times onward. Arrows indicate generalized vertical movements. O, K, Ottnangian and Karpatian, respectively (Early Miocene); BAD, SA, Badenian and Sarmatian, respectively (Middle Miocene); PAN, PO, Pannonian and Pontian, respectively (Late Miocene); PL, Pliocene; Q, Quaternary. AM, Apuseni Mts.; DIN, Dinarides; EA, Eastern Alps; PanBas, Pannonian Basin; SC, WC, Southern and Western Carpathian foreland basins, respectively. Reproduced from Cloetingh S, Bada G, Matenco L, Lankreijer A, Horváth F, and Dinu C (2006). Thermo-mechanical modelling of the Pannonian-Carpathian system: Modes of tectonic deformation, lithospheric strength and vertical motions. In: Gee D and Stephenson R (eds.) *European Lithosphere Dynamics*, Geological Society, London, Memoirs 32: 207–221.

general downwarping of the lithosphere in response to its thermal subsidence. This is particularly evident in the central parts of the Pannonian Basin, suggesting that in this area, synrift thermal attenuation of the lithospheric mantle played a greater role than in the marginal areas (e.g., Royden and Dövényi, 1988; Sclater et al. (1980)). The third and final phase of basin evolution is characterized by the gradual structural inversion of the Pannonian Basin system during the Late Pliocene–Quaternary. During these times, intraplate compressional stresses gradually built up and caused basin-scale buckling of the Pannonian lithosphere that was associated with late-stage subsidence anomalies and differential vertical motions (Horváth and Cloetingh, 1996). As evident from subsidence curves (**Figure 27**), accelerated late-stage subsidence characterized the central depressions of the Little and Great Hungarian Plains (**Figure 27(b)** and **27(c)**), whereas the peripheral Styrian and East Slovakian subbasins were uplifted by a few hundred meters after mid-Miocene times (**Figure 27(d)** and **27(e)**) and the Zala basin during the Pliocene–Quaternary (**Figure 27(f)**). The importance of tectonic stresses, during both the rifting phase (extension) and subsequent inversion phase (compression), is highlighted by this late-stage tectonic reactivation, as well as by other episodic inversion events in the Pannonian Basin (Fodor et al., 1999; Horváth, 1995).

A more recent analysis of the subsidence evolution of the Pannonian Basin in the sector connecting the Carpathians with the Dinarides has observed significant discrepancies with the aforementioned models by analyzing the development of syn- and postrift sedimentation (Matenco and Radivojević, 2012). This study has documented large-scale erosional unconformities between the classically defined syn- and postrift phases that migrate in time from the Dinarides to the Carpathians, while the postrift deposition for the Early and Middle Miocene rifting is largely missing (**Figure 28**). Therefore, these authors propose that the low-angle Early–Middle Miocene normal faults responsible for the basin formation are connected to a lower crustal detachment that was prolonged eastward beneath the Apuseni Mountains and affected the mantle–lithosphere below the Transylvanian Basin. The coupling between the mechanical extension of the Pannonian Basin and its thermal effects recorded in the Transylvanian Basin should have taken place in such a way that the intervening Apuseni Mountains did not underwent any significant Miocene vertical movements. The related exhumation and large-scale domal structure is mainly the effect of Cretaceous–Paleogene deformations (Merten et al., 2011). In contrast to earlier periods of extension, massive thermal-sag sedimentation is observed in direct relationship with and postdating the Pannonian–Lower Pontian detachments and/or normal faults (such as the Makó depression, **Figure 28**). The main depocenters of the thermal-sag sedimentation overlie these asymmetrical extensional structures. Furthermore, this thermal-sag sedimentation has a far larger areal extent than one of the half-grabens, covering an area that corresponds to the asthenospheric up rise presently observed beneath the Pannonian Basin (Horváth et al., 2006; Matenco and Radivojević, 2012).

These studies demonstrated the close relationship that existed between the timing and the nature of stress changes in extensional basins and structural episodes in the surrounding thrust belts, pointing to mechanical coupling between the orogen and its back-arc basin. In parallel, significant efforts have been devoted to reconstruct the spatial and temporal variations in thrusting along the Carpathian orogen (Matenco and Bertotti, 2000; Matenco et al., 2007; 2010; Roure et al., 1993; Schmid et al., 1998) and its relationship to foredeep depocenters (Cloetingh et al., 2005a,b; Matenco et al., 2003; Meulenkamp et al., 1996; Necea et al., 2005; Tarapoanca et al., 2004), changes in foreland basin geometry, and lateral variations in the flexural rigidity of the foreland lithosphere.

6.12.3.7.2.4 Lithospheric strength in the Pannonian–Carpathian system

The Pannonian–Carpathian system shows remarkable variations in crustal thickness (**Figure 29**) and thermomechanical properties of the lithosphere. Lithospheric rigidity varies in space and time, giving rise to important differences in the tectonic behavior of different parts of the system. As rheology controls the response of the lithosphere to stresses, and thus the formation and deformation of basins and orogens, the characterization of rheological properties and their temporal changes has been a major challenge to constrain and quantify tectonic models and scenarios. This is particularly valid for the Pannonian–Carpathian region where tectonic units with a different history and rheological properties are in close contact.

By conversion of strength predictions to EET values at a regional scale, Lankreijer (1998) mapped the EET distribution for the entire Pannonian– Carpathian system (**Figure 30**). Calculated EET values are largely consistent with the spatial variation of lithospheric strength of the system. Lower values are characteristic for the weak central part of the Pannonian Basin

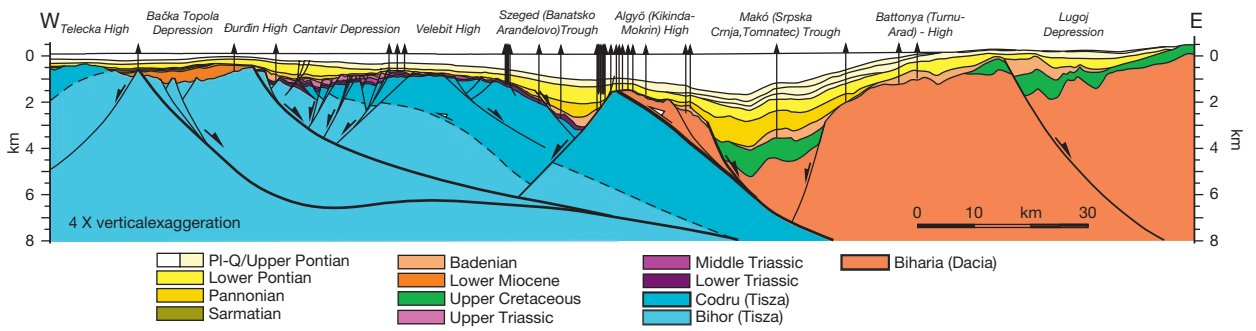

Figure 28 Depth converted regional transects over the Pannonian Basin of Serbia and Romania. Location of the transect is indicated in Figure 25. Reproduced from Matenco L and Radivojević D (2012) On the formation and evolution of the Pannonian Basin: Constraints derived from the structure of the junction area between the Carpathians and Dinarides. *Tectonics* 31: TC6007.

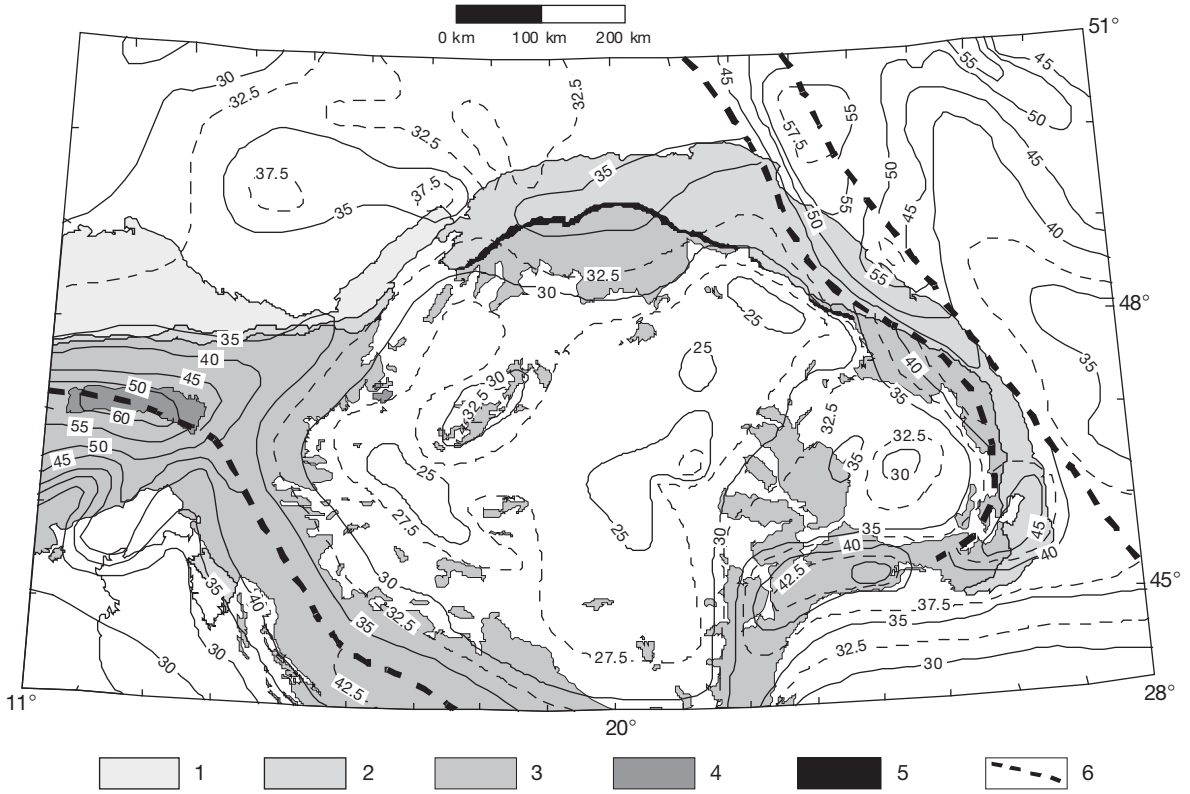

Figure 29 Crustal thickness in the Pannonian Basin and the surrounding mountains. Values are given in km. 1, foreland (molasse) foredeep; 2, flysch nappes; 3, pre-Tertiary units on the surface; 4, Penninic windows; 5, Pieniny Klippen Belt; 6, trend of abrupt change in crustal thickness. Reproduced from Horváth F, Bada G, Szafián P, Tari G, Ádám A, and Cloetingh S (2006) Formation and deformation of the Pannonian Basin: Constraints from observational data. *Geological Society, London, Memoir* 32: 191–206.

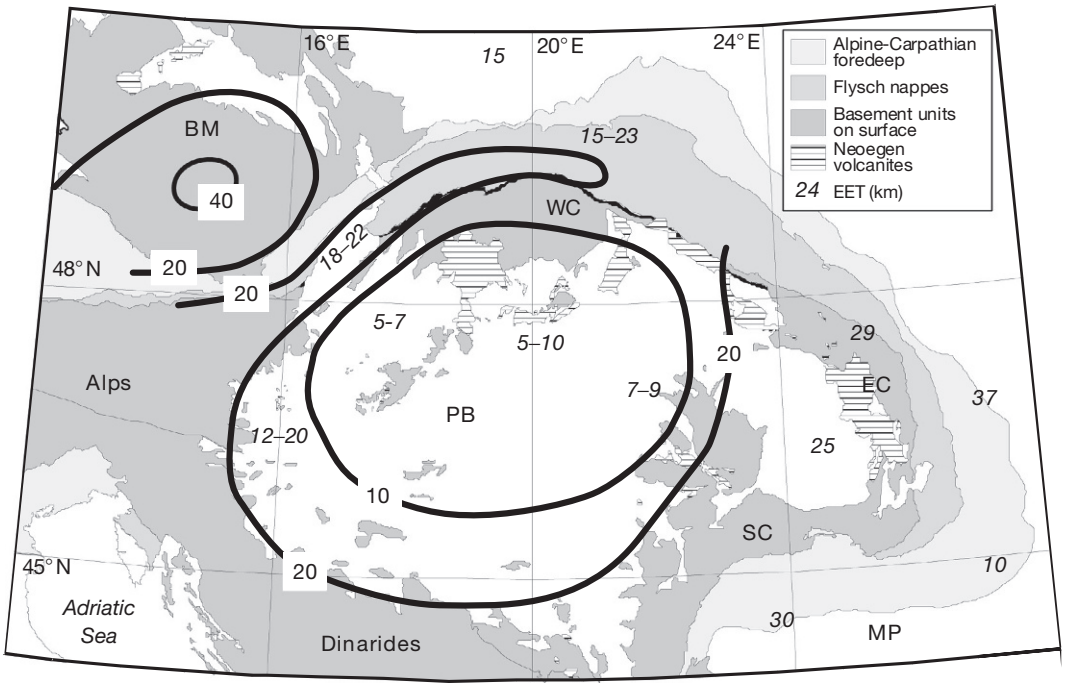

Figure 30 Effective elastic thickness (EET – in km) of the lithosphere in and around the Pannonian Basin predicted from rheological calculations. BM, Bohemian Massif; MP, Moesian Platform; PB, Pannonian Basin; EC, SC, WC, Eastern, Southern, and Western Carpathians, respectively. Reproduced from Lankreijer AC (1998) Rheology and Basement Control on Extensional Basin Evolution in Central and Eastern Europe: Variscan and Alpine-Carpathian-Pannonian Tectonics, 158 pp. PhD Thesis. VU University, Amsterdam.

(5–10 km), whereas EET increases toward the Dinarides and Alps (15–30 km) and particularly toward the Bohemian Massif and Moesian Platform (25–40 km). This trend is in good agreement with EET estimates obtained from flexural studies and forward modeling of extensional basin formation. Systematic differences, however, can occur and may be the consequence of significant horizontal intraplate stresses (e.g., Cloetingh and Burov, 1996) or of mechanical decoupling of the upper crust and uppermost mantle that can lead to a considerable reduction of EET values.

The range of calculated EET values reflects the distinct mechanical characteristics and response of the different domains forming part of the Pannonian–Carpathian system to the present-day stress field. These characteristics can be mainly attributed to the memory of the lithosphere. In this respect, it must be kept in mind that the tectonic and thermal evolution of these domains differed considerably during the Cretaceous–Neogene Alpine development of both the outer and the intra-Carpathian units and the Neogene extension of the Pannonian Basin, resulting in a wide spectrum of lithospheric strengths. These, in turn, exert a strong control on the complex present-day pattern of ongoing tectonic activity.

6.12.3.7.2.5 Deformation of the Pannonian–Carpathian system

The present-day deformation pattern and related topography development in the Pannonian–Carpathian system is characterized by pronounced spatial and temporal variations in the stress and strain fields (Figure 31; e.g., Cloetingh et al., 2006). Horváth and Cloetingh (1996) established the importance of Late Pliocene and Quaternary compressional deformation of the Pannonian Basin that explains its anomalous uplift and subsidence, as well as intraplate seismicity. Based on the case study of the Pannonian–Carpathian system, these authors established a novel conceptual model for the structural reactivation of back-arc basins within orogens. At present, the Pannonian Basin has reached an advanced evolutionary stage as compared to other Mediterranean back-arc basins (e.g., Bache et al., 2010) in so far as it has been partially inverted during the last few million years. Inversion of the Pannonian Basin can be related to temporal changes in the regional stress field, from one of tension that controlled its Miocene extensional subsidence to one of Pliocene–Quaternary compression resulting in deformation, contraction, and flexure of the lithosphere associated with differential vertical motions.

Model calculations are in good agreement with the overall topography of the system (Figure 31). Several flat-lying, low-elevation areas (e.g., Great Hungarian Plain and Sava and Drava troughs) subsided continuously since the Early Miocene beginning of basin development and contain 300–1000 m thick Quaternary alluvial sequences. By contrast, the periphery of this basin system, as well as the Transdanubian Range, the Transylvanian Basin and the adjacent Carpathians underwent late-stage uplift. Therefore, the spatial distribution of uplifting and subsiding areas within the Pannonian Basin can be interpreted as resulting from the buildup of intraplate compressional stresses, causing large-scale positive and negative

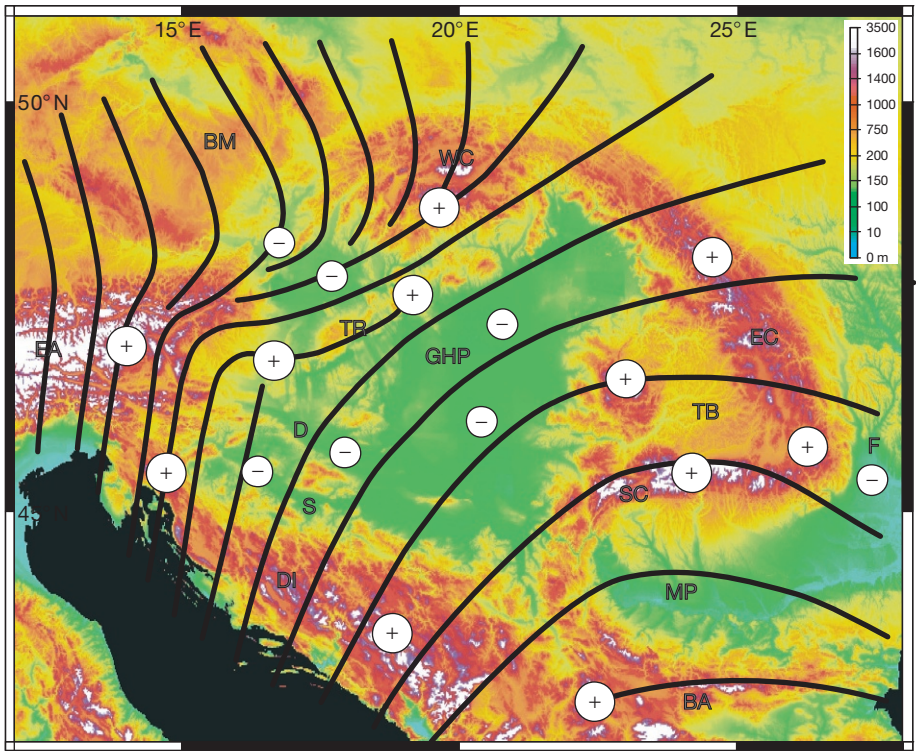

Figure 31 Topography of the Pannonian–Carpathian system showing present-day maximum horizontal stress (SHmax) trajectories (Reproduced from Bada G, Horváth F, Cloetingh S, Coblentz DD, and Toth T (2001) Role of topography-induced gravitational stresses in basin inversion: The case study of the Pannonian basin. *Tectonics* 20: 343–363). '+' and '−' symbols denote areas of Quaternary uplift and subsidence, respectively. BA, Balkanides; BM, Bohemian Massif; D, Drava trough; DI, Dinarides; EA, Eastern Alps; EC, Eastern Carpathians; F, Focşani Depression; MP, Moesian Platform; PB, Pannonian Basin; S, Sava trough; SC, Southern Carpathians; TB, Transylvanian Basin; TR, Transdanubian Range; WC, Western Carpathians. Reproduced from Cloetingh et al. (2006).

deflection of the lithosphere at various scales. This includes basin-scale positive reactivation of Miocene normal faults, and large-scale folding of the system leading to differential uplift and subsidence of anticlinal and synclinal segments of the orogen which were uplifted and considerably eroded from Late Miocene–Pliocene time onward (see **Figure 31**). Quantitative subsidence analyses confirm that late-stage compressional stresses caused accelerated subsidence of the central parts of the Pannonian Basin (Van Balen et al., 1999), while the Styrian Basin (Sachsenhofer et al., 1997), the Vienna and East Slovakian Basins (Lankreijer et al., 1995), and the Transylvanian Basin (Ciulavu et al., 2002) were uplifted by several hundred meters starting in Late Miocene–Pliocene times (**Figure 31**). The mode and degree of coupling of the Carpathians and Dinarides with their foreland control the Pliocene to Quaternary deformation patterns in their hinterland in the Pannonian–Transylvanian Basins (Ciulavu et al., 2002; Dombradi et al., 2007; Jarosinski et al., 2011). These findings can be related to the results of seismic tomography that highlight upwelling of hot mantle material under the Pannonian Basin and progressive detachment of the subducted lithospheric slab that is still ongoing in the Vrancea area (Wenzel et al., 2002; Wortel and Spakman, 2000).

In summary, results of forward basin modeling show that an increase in the level of compressional tectonic stress during Pliocene–Quaternary times can explain the first-order features of the observed pattern of accelerated subsidence in the center of the Pannonian Basin and uplift of basins in peripheral areas. Therefore, both observations and modeling results lead to the conclusion that compressional stresses can cause considerable differential vertical motions in the Pannonian–Carpathian back-arc basin–orogen system (Dombradi et al., 2007; Horváth et al., 2006; Jarosinski et al., 2011).

6.12.4 Compressional Basin Systems

In this section, we discuss basic concepts and observations for large-scale compressional basin systems. In doing so, we focus on flexural foreland basins (**Section 6.12.4.1**) and basins initiated by lithospheric folding (**Section 6.12.4.2**).

Flexural foreland basins are dynamic systems that provide key information on the interplay between lithospheric and surface processes (see also Garcia-Castellanos and Cloetingh, 2012, for a recent review). Their evolution can be constrained by various types of observations, including structural, paleogeographic, sedimentologic, paleoclimatic, potential field (gravity and geoid), and seismic data. These data allow extraction of the thermomechanical properties of the underlying continental lithosphere and are crucial in reconstruction of continental paleotopography. Flexural isostasy is a simple model and will certainly remain valid and useful as a first approach to isostasy, for example, to study first-order interactions with other processes based on synthetic experiments (e.g., Garcia-Castellanos, 2002; Pelletier, 2007). By their nature, foreland basins are in general undergoing a polyphase evolution, to a large extent conditioned by their overall regional tectonic setting. Of particular importance are the associated temporal and lateral variations in plate rigidity and stress fields. These features explain deviations in their record of vertical motions and basin geometries from predictions from simple foreland flexural models. Lateral variations in lithospheric rigidity are also of significant influence for the drainage history of foreland basins and their connectivity with adjacent back-arcs. Temporal variations in rigidity associated with preorogenic extension have a profound effect on the subsequent foreland basin subsidence. This feature is highly relevant in the context of subsidence histories of retro-foredeep basins with a subsidence history strongly deviating from predictions of flexural foredeep models (Naylor and Sinclair, 2008). Flexural forebulges are highly sensitive to changes in tectonic regime and inherited lateral lithospheric heterogeneities and might be enhanced by the progressive viscous relaxation of stresses during and after tectonic loading. Forebulges can in some cases determine the drainage history of the basin. Strong feedbacks exist between lithospheric and surface processes in foreland basins. The integration of numerical and analog modeling (Athmer et al., 2010; Persson et al., 2004) appears to be particularly promising to explore the coupling of tectonics and climate in orogenic foreland basin systems. A different example of inherited properties strongly affecting the basin development is provided by topography. Preflexural topography can not only modify estimates of tectonic load in flexural calculations but also overprint the effects of tectonic vertical motions on drainage development.

Sedimentary basins controlled by lithospheric folding are characterized by a number of features in their basin architecture, subsidence history, thermal evolution, and faulting patterns, making them distinctly different from other basin systems (see also Cloetingh and Burov, 2011, for a recent review). Of particular importance are the relatively short temporal scales involved in their evolution, whereas their spatial scales vary from tens to several hundreds of km, depending on the rheological stratification of the lithosphere and its thermomechanical age. Subsidence patterns are characterized by an acceleration of subsidence in the depocenters during compressional basin formation, occurring simultaneously with accelerated uplift of and erosion from flanking basin highs. In contrast with asymmetrical foreland basins, basins on folded lithosphere are symmetrical with equal dimensions for linearly trending topographic highs and lows. The thermal history of these basins is not characterized by an initial thermal perturbation, unless folding occurs in interaction with plume activity. In the absence of interplay with lithospheric-scale thermal perturbations, their thermal evolution will be primarily controlled by the burial history of the sediments deposited in the accommodation space created by the folding process. Intrabasinal faulting and the formation of pop-up structures and inverted basins at upper crustal levels are important in the structural evolution of these basin systems. The intensity of the brittle deformation peaks with ongoing shortening of the lithosphere during folding, but faulting activity is dramatically reduced after the cessation of folding. At this stage, with equilibrium between sedimentation and erosion, minor faulting occurs as a result of stress relaxation due to erosion of folded highs. During overall uplift of basins on folded lithosphere, their accommodation space is further reduced by unflexing and associated stress release through faulting.

6.12.4.1 Flexural Foreland Basins

Foreland basins owe their existence to the capacity of the lithosphere to support loads, such as the topography of

orogenic wedges or subducted lithospheric slabs (Garcia-Castellanos and Cloetingh, 2012). The lithosphere deforms by flexurally bending downward over areas often exceeding the spatial scale of these loads (**Figure 32**). The width of the resulting depression, the foreland basin, provides information on the mechanical strength of the underlying lithosphere. Under an imposed load, a zero-strength lithosphere would simply sink vertically into the mantle (Airy isostasy), thus not accounting for the development of a foreland basin. By contrast, a mechanically strong lithosphere, characteristic of cratonic forelands, allows for the subsidence of wide and relatively shallow foreland basins (flexural isostasy). Such wide foreland basins are associated with the Canadian Rocky Mountains of Alberta and British Columbia and the Appalachian fold-and-thrust belts (**Figure 33**) that are superimposed on the North American Proterozoic cratonic crust (e.g., Beaumont, 1981; Quinlan and Beaumont, 1984). By contrast, the much narrower Alpine foreland basins of Europe (**Figure 33**; Mascle, 1998) developed on considerably younger lithosphere that equilibrated with the asthenosphere after the Variscan orogeny and was modified by Mesozoic rifting activity. The time elapsed between rifting and the synorogenic flexural deformation of this foreland lithosphere was very variable (Pyrenees: *c.*30 Ma; Apennines: *c.*130 Ma). The relatively modest widths of the foreland basins of the Carpathians (Matenco et al., 1997a,b; Zoetemeijer et al., 1999), Pyrenees (Millan et al., 1995), the Betic Cordillera (Van der Beek and Cloetingh, 1992), the Apennines (Zoetemeijer et al., 1993), and the Eastern Alps (Andeweg and Cloetingh, 1998) reflect a relatively weak lithosphere.

In addition to topographic loading by orogenic wedges and loading by the sedimentary fill of the foreland basins, additional forces operate on the lithosphere, such as slab pull, slab detachment, and slab rollback, and play an important role in shaping the geometry of prowedge and retrowedge foreland basins (**Figure 34**; e.g., Millan et al., 1995; Ziegler et al., 2002). Moreover, depending on mechanical coupling/decoupling of the orogenic wedge and the foreland lithosphere, horizontal compressional stresses can be exerted onto the latter, influencing the geometry of an evolving flexural foreland basin (Ziegler et al., 2002).

In a first generation of flexural foreland basin models, the different loading components and forces were represented by a system of vertical loads, shear forces, and bending moments (Royden, 1988a,b, 1993). This approach is illustrated in **Figure 32**. A characteristic feature of these models is that horizontal stresses were neglected. Nevertheless, these have been shown to play a potentially important role in the geometry of foreland basins and the architecture of their sedimentary fill (Peper et al., 1995). These models were utilized to extract information on the mechanical properties of the lithosphere that was treated as an elastic plate rather than as a depth-dependent rheologically stratified beam. Consequently, the models yielded rough estimates for the EET of the lithosphere and a first approximation for the bulk rheology of the continents. This approach permitted to examine the effect of the time elapsed since the last

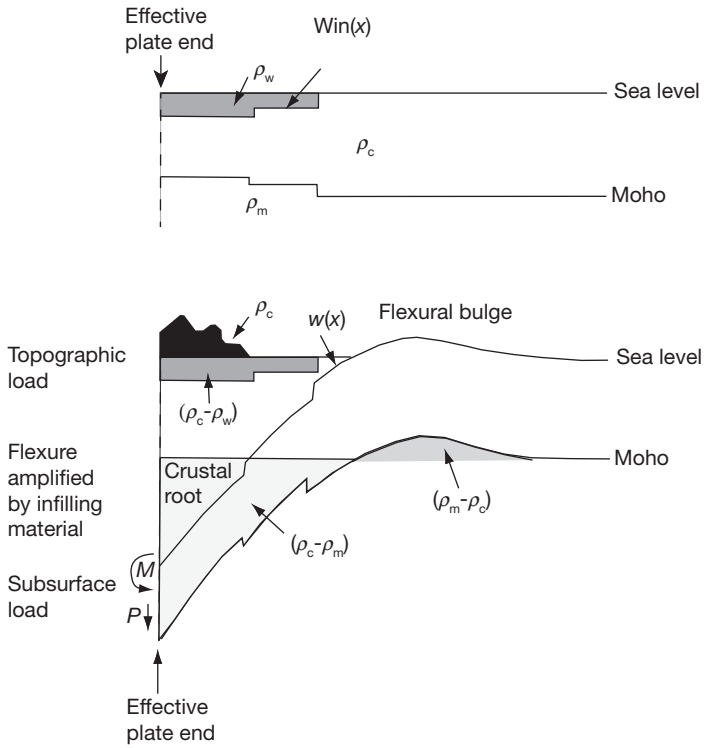

Figure 32 Concept of lithospheric flexure during foreland basin evolution. Deflection of the subducting lower plate lithosphere is the combined result of topographic loading by the mountain chain of the upper plate, the weight of the sediments in the foreland basin, and the weight of the subducted slab. The shape of the flexural foreland depression is controlled by the interplay between the lithospheric strength of the lower plate, the magnitude of the differential loads imposed on it, and the level of collision-related compressional stresses transmitted into it (see also Ziegler et al., 2002). Reproduced from Royden LH (1993) The tectonic expression slab pull at continental convergent boundaries. *Tectonics* 12: 303–325.

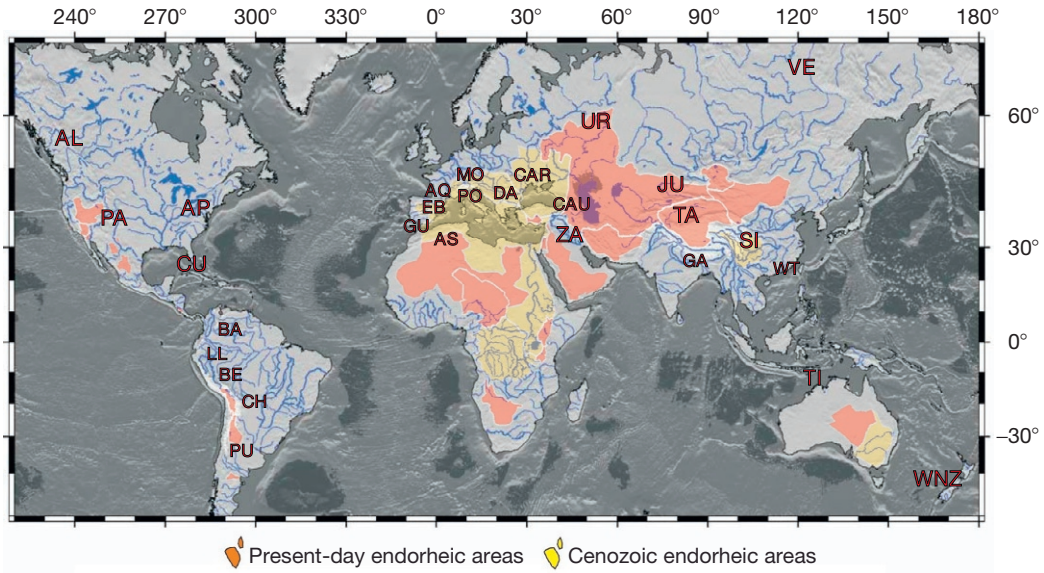

Figure 33 Location of the main foreland basins discussed in this study. Present-day endorheic areas and examples of areas that underwent endorheism during the Cenozoic are indicated by the color shading. Their singularity in terms of sediment transport affects a significant part of these basins. Foreland basins from west to east: AL, Alberta Basin; PA, Paradox Basin; AP, Appalachian; CU, Cuba; LL, Llanos (Andes); BA, Barinas; BE, Beni; CH, Chaco (Andes); PU, Puna (Andes); GU, Guadalquivir (Betics); EB, Ebro (Pyrenees); AQ, Aquitaine; AS, Algerian–Saharan Atlas; MO, Molasse (North Alpine); PO, Po and Piedmont (South Alpine); DA, Dacic Basin (South Carpathian); CAR, Subcarpathian; CAU, Caucasian; ZA, Zagros; UR, Uralian; JU, Junggar; TA, Tarim; GA, Ganges; SI, Sichuan; VE, Verkhoyansk; WT, west Taiwan; TI, Timor; WNZ, West New Zealand. Reproduced from Garcia-Castellanos D and Cloetingh S (2012) Modeling the interaction between lithospheric and surface processes in foreland basins. In: Busby C and Azor A (eds.) *Tectonics of Sedimentary Basins: Recent Advances*, pp 152–181.

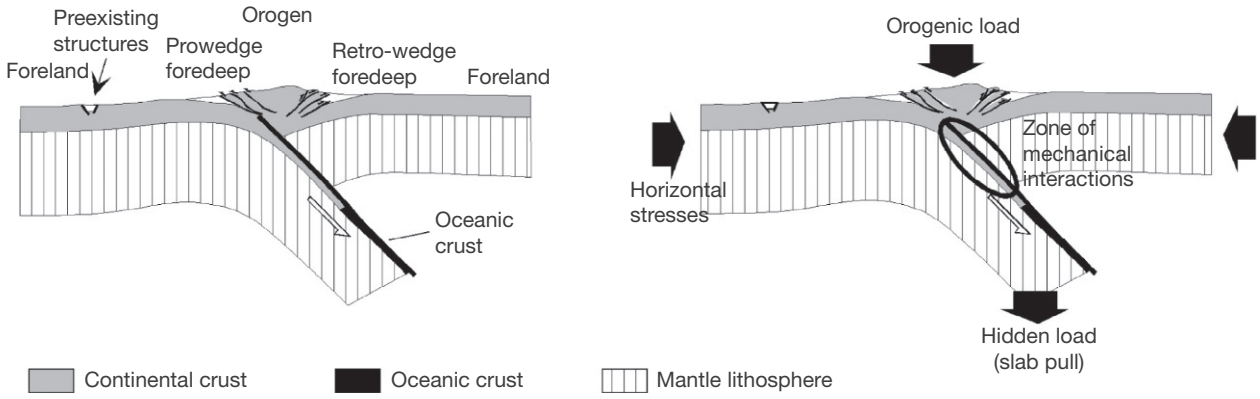

Figure 34 Conceptual model illustrating forces controlling the subsidence of retro- and prowedge foreland basins and showing zone of potential mechanical coupling between the upper and the lower plate. Reproduced from Ziegler PA, Bertotti G, and Cloetingh S (2002) Dynamic processes controlling foreland development Â the role of mechanical (de) coupling of orogenic wedges and forelands. In: *Stephan Mueller Special Publication Series*, vol. 1, 17–56.

thermal perturbation of the lithosphere (generally a rift phase) on its deflection during the subsequent foreland basin development phase. In this respect, Desegaulx et al. (1991) explained the rapid Cenozoic subsidence of the Aquitaine foreland basin (SW France) in terms of preorogenic synrift extensional thinning and associated thermal perturbation of the lithosphere and its postrift thermal subsidence and sedimentary loading.

The term foreland basin was introduced by Dickinson (1974) to refer to thick sediment accumulations in the undeformed areas (*forelands*) bounding orogens resulting from compressional tectonics. He proposed two broad categories: *peripheral foreland basins* related to continent–continent collision (e.g., the Indo-Ganges basin and the North Alpine basin; Figure 33) and *retroarc foreland basins* related to the subduction of oceanic lithosphere (e.g., the late Mesozoic–Cenozoic Rocky Mountain basins). Foreland basins are strongly asymmetric in cross section, with maximum depths next to the orogen and a wedge shape along its passive (undeformed) margin (Allen et al., 1986). Inspired by the early findings of marine geologic and geophysical studies (Vening-Meinesz, 1941), it soon

became widely accepted that foreland basins form primarily by flexural isostatic subsidence of the foreland (plate bending), in response to the growing weight of the tectonic units stacked by shortening in the orogen (Price, 1973). Presently, the weight of sediments and water in the foredeep and horizontal compression, slab pull, and, in the case of slab retreat, lateral asthenospheric push during the opening of the back-arc and delamination of the retreating delaminated mantle–lithosphere are all recognized as important ingredients for driving flexural subsidence in foreland basin settings (**Figure 35**).

More recent modeling studies implementing the initiation of subduction during continental collision (starting by Johnson and Beaumont, 1995) suggested that peripheral foreland basins can be further classified into retroforeland (forming on the overriding plate, e.g., the Aquitaine Basin, not to be confused with retroarc basins defined earlier) and proforeland basins (forming on the underthrusting plate, e.g., the Ebro basin and northern Pyrenees).

Various types of foreland basins have also been differentiated in relationship to the position of the Moho underlying the orogenic belt and the position of the backstop (the overriding plate). True subduction applies only for oceanic lithosphere, where also the crust is recycled in the mantle. Retroforeland basins, like the Canadian Rocky Mountain foreland basin (e.g., Hardebol et al., 2009, 2013), develop at the rear of an oceanic subduction zone. In the Canadian example, there is a complete preservation of the continental crustal thickness, the Moho being continuous from the foreland to the hinterland, perhaps indicating absence of continental subduction and only a limited amount of lateral flow in the lower crust. In collisional orogens, such as the Alps or the Pyrenees, the Moho is offset by a mantle indenter, the Moho of the lower plate deepening toward the plate boundary and accounting for a crustal root where most of the lower crust of the downgoing plate is progressively stacked (Roure et al., 1989, 2010b). In the case of slab retreat and back-arc development (i.e., Carpathians (Tomek, 1993), Apennines (Patacca et al., 2008), and Brooks Range in Alaska (Fuis et al., 1997)), there is no vertical offset of the Moho under the orogen, as in the Canadian Rocky Mountains. A possible interpretation for this is the delamination of the mantle–lithosphere (see also Bocin, 2010; Matenco et al., 2010).

Consistent with their flexural origin, foreland basins are generally characterized, in comparison with other sedimentary basins, by an overall acceleration of tectonic subsidence (i.e., *convex-up* subsidence curve), though eventually reflecting the periodicity of thrust loading (e.g., Xie and Heller, 2009) and with a less clear pattern in the case of retroforeland and retroarc basins (Naylor and Sinclair, 2008; see **Figure 36**). Many foreland basins have experienced a polyphase evolution characterized by preorogenic extension that might introduce a thermal, convex-down component in their subsidence record, which affects their vertical motions during the foreland basin stage. Examples are found in the Aquitaine Basin (southern France; Desegaulx et al., 1991) and the Romanian Carpathian foredeep (Tarapoanca et al., 2004). Alternatively, numerous foreland basins have recorded late-stage episodes of vertical uplift and unroofing, for instance, in the North American Cordillera, from the Canadian Rocky Mountains in the north (Hardebol et al., 2013) to the Mexican Cordoba Platform in the south (Roure, 2008; Roure et al., 2009), where uplift might be related to mantle convection at the rear of the Pacific subduction. Other examples can be found in United Arab Emirates, north

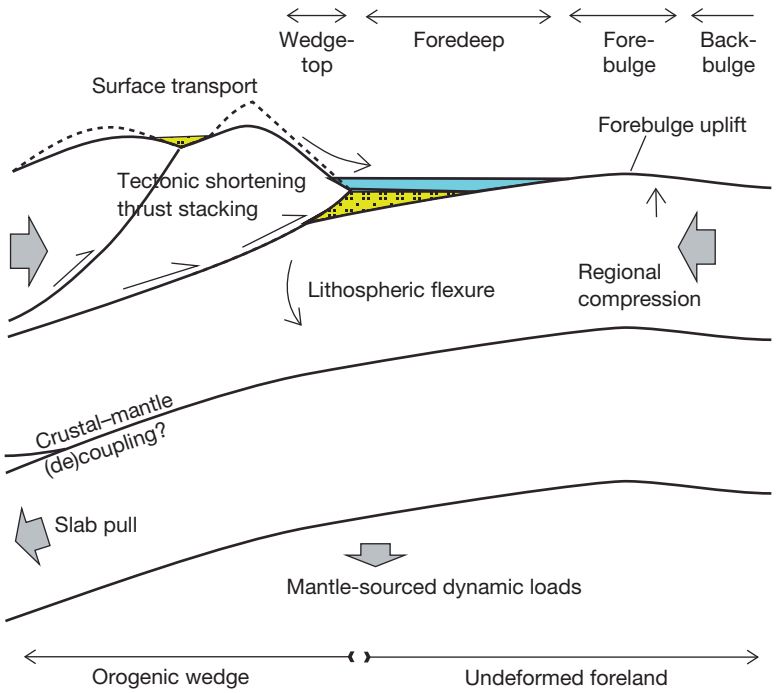

Figure 35 Simplified cartoon (not to scale) showing the standard partition of foreland basins and the main processes involved in their evolution. The crustal/mantle segment of the sketch applies mainly to retroarc basins and not to configurations with a true backstop. Reproduced from Garcia-Castellanos D and Cloetingh S (2012) Modeling the interaction between lithospheric and surface processes in foreland basins. In: Busby C and Azor A (eds.) *Tectonics of Sedimentary Basins: Recent Advances*, pp. 152–181.

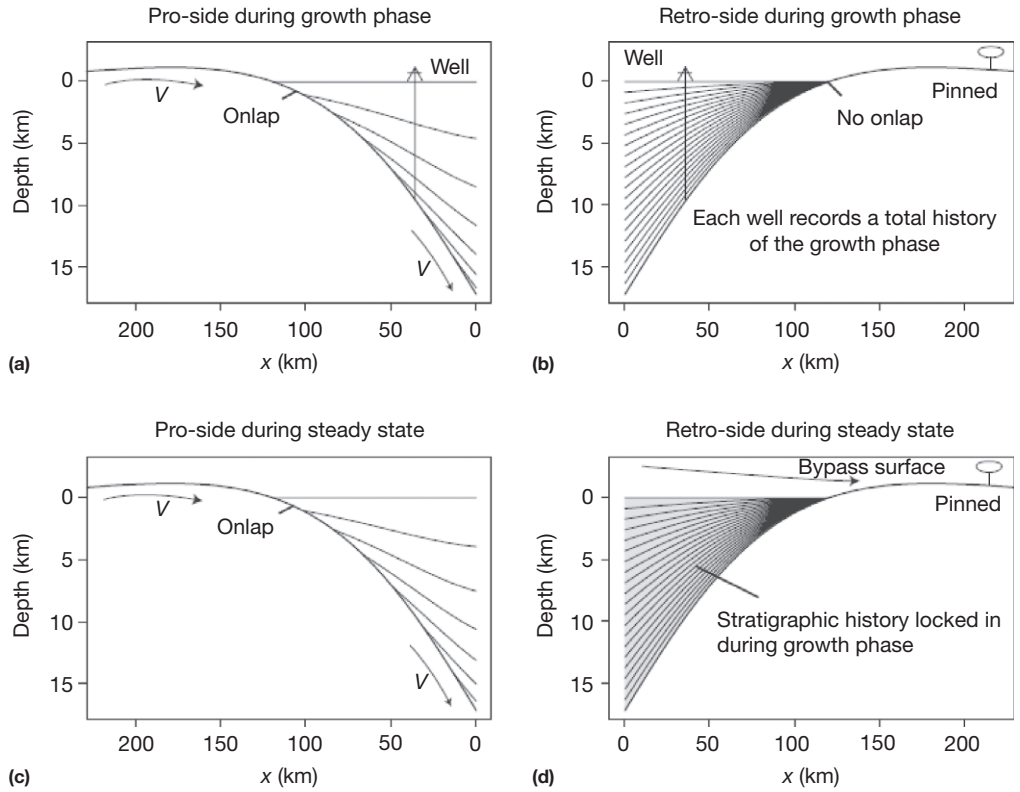

Figure 36 Typical basin fill geometries obtained from flexural modeling for pro- and retroforeland basins. A vertical end load is applied at x = 0 during the growth phase (a and b) and during the steady-state phase (c and d). The stratigraphic horizons are spaced at 3.55 My intervals, with a total duration for each simulation of 71 My. A synthetic well drilled in the retrobasin records the entire growth phase, whereas in the proside, it records only the recent advection of the basin. Reproduced from Naylor M and Sinclair HD (2008) Pro- vs. retro-foreland basins. *Basin Research* 20: 285–303.

Algeria, and the Apennines, where recent uplift relates to slab detachment and back-arc asthenospheric upwelling (Ali and Watts, 2009; Roure et al., 2010a; Tarapoanca et al., 2010; Van der Meulen et al., 1999).

The equation governing the bending of a thin elastic plate resting on an inviscid fluid (Turcotte and Schubert, 2014) is often used as a proxy for lithospheric flexure on the asthenosphere. This model shows that the flexural subsidence next to the orogenic wedge is wider and shallower for larger plate thicknesses and predicts a small uplift (forebulge) of the undeformed plate (foreland) of a few hundreds of meters or less (Turcotte and Schubert, 2014). Marine geophysical studies of plate flexure seaward off trenches and under volcanic island chains provide an interesting analog for the height of the foreland bulge not affected by surface erosion (e.g., Watts, 2001). These studies have drawn attention to the order in magnitude difference between the height of the bulge and the depth of adjacent flexural depocenter. Although the same is true for the relationship between the magnitude of the foreland bulge and the depth of foreland depocenter, subaerial erosion of the bulge usually hampers accurate estimates of bulge height. Integrating this model with field observations brings to the distinction of four depozones in foreland basins (DeCelles and Giles, 1996) sketched in **Figure 35**: wedge-top (sediments deposited on top of the deformation wedge, including piggyback basins), foredeep (sediments at the maximum flexural subsidence), forebulge (sedimentary cover of the foreland basin, if any), and backbulge (sedimentary cover beyond the forebulge, if any).

The first foreland basin modeling studies (Beaumont, 1981; Jordan, 1981, 1982; Flemings and Jordan, 1989; Sinclair et al., 1991) provided the numerical methods to calculate the EET of the continental lithosphere and established general relationships between sedimentary infill and tectonic shortening implied by simple flexural isostatic models. The simple approaches adopted for surface transport and tectonic deformation could only capture first-order interactions between these processes. For example, Beaumont (1981) showed that a purely elastic lithosphere bending under a prograding wedge would normally produce a prograding onlapping stratigraphy, while viscous relaxation of stress within the lithosphere might induce large-scale offlapping geometries and shift of depocenters toward the orogen. This latter geometric relationship was observed at that time in the Alberta Basin and later documented in many foreland basin settings (e.g., Carrapa and Garcia-Castellanos, 2005). The basin infill geometries predicted by those models were, however, subject to their 2-D nature (they modeled a vertical cross section) and the lack of mass conservation between erosion and sedimentation at the scale of the orogen–basin system.

The polyphase nature of foreland basins explains deviations in the geometry and record of vertical motions from predictions from simple flexural models of foreland basin evolution

(e.g., Cloetingh and Ziegler, 2007; Roure, 2008; Roure et al., 2010b). This is particularly important for the interpretation of EET values extracted from the geometry of the foredeeps or their gravity field. Temporal and spatial variations of EET (e.g., Prezzi et al., 2009) as well as temporal variations in horizontal stress are leading to a natural spread of EET when compared to the depth of isotherms in the lithosphere.

6.12.4.1.1 Role of preorogenic extension and late-stage compression

Many present-day foreland basins have been formed at the sites of preexisting rifts or rifted continental margins (Stockmal et al., 1986; Desegaulx et al., 1991). This fact has a number of important implications not only for the mode of shortening of the lithosphere but also for its subsidence history and thermal evolution. **Figure 37** illustrates the temporal evolution from rift to foredeep as reconstructed for the Aquitaine Basin (Desegaulx et al., 1991), which is the *retro*foreland basin of the Pyrenees. At the onset of foreland basin formation, the heat impulse in the lithosphere generated by preorogenic extension of the Gulf of Biscay region (**Figure 37**) was not yet relaxed. As a result, this basin has experienced considerable postrift thermal subsidence (**Figure 38**). In this case, a further complication comes from the obliquity of the rifting with respect to the main axis of subsequent compression, with a lateral movement during the Albian, prior to Late Cretaceous to Eocene frontal collision. The Romanian Carpathian foredeep also was affected by preorogenic extension (Tarapoanca et al., 2004). The superposition of preorogenic extension and foreland flexure results in subsidence patterns that deviate from predictions of standard flexural foreland basin models (Cloetingh and Ziegler, 2007). Furthermore, lateral variations in rheological properties in the downflexed lithosphere also occur in this situation, strongly affecting the subsidence patterns.

In addition to preorogenic extension, foreland subsidence can also be enhanced by late-stage compression associated with changes in the convergence rate. Examples can be found in the Aquitaine Basin and the Carpathian foredeep (Tarapoanca et al., 2004), as well as in the Alpine Piedmont Basin (Carrapa and Garcia-Castellanos, 2005). As pointed out by Cloetingh et al. (2004), slab detachment during final stages of continental collision can lead toward drastic changes in stress regime in the overriding plate with high levels of compression. In the case of the Romanian Carpathian foredeep, this has led to a more symmetrical shape of the foredeeps than predicted by foreland flexure alone. The superposition of preorogenic extension, foreland flexure, and late-stage compression also provides an explanation for cases of ultradeep foredeeps. An example of this is the Romanian Carpathians, with more than 12 km of Neogene sediments accumulating in the Focşani Depression flanked by the Carpathian orogen, where geothermochronology studies have provided evidence

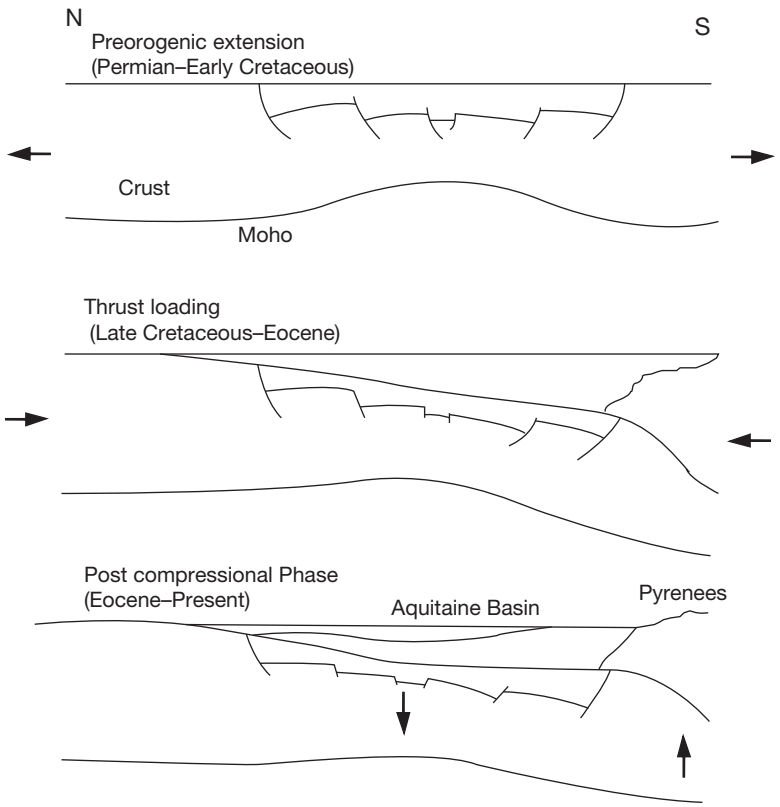

Figure 37 Schematic evolution of the Aquitaine foreland basin. (top) (Permian–Early Cretaceous) preorogenic extension phase; rifting of the European domain. (middle) (Late Cretaceous–Eocene) compression; formation of the Aquitaine foredeep. (bottom) (Eocene–present) postcompressive phase associated with unflexing. Reproduced from Desegaulx P, Kooi H, and Cloetingh S (1991) Consequences of foreland basin development on thinned continental lithosphere – Application to the aquitaine basin (Sw France). *Earth and Planetary Science Letters* 106: 116–132.

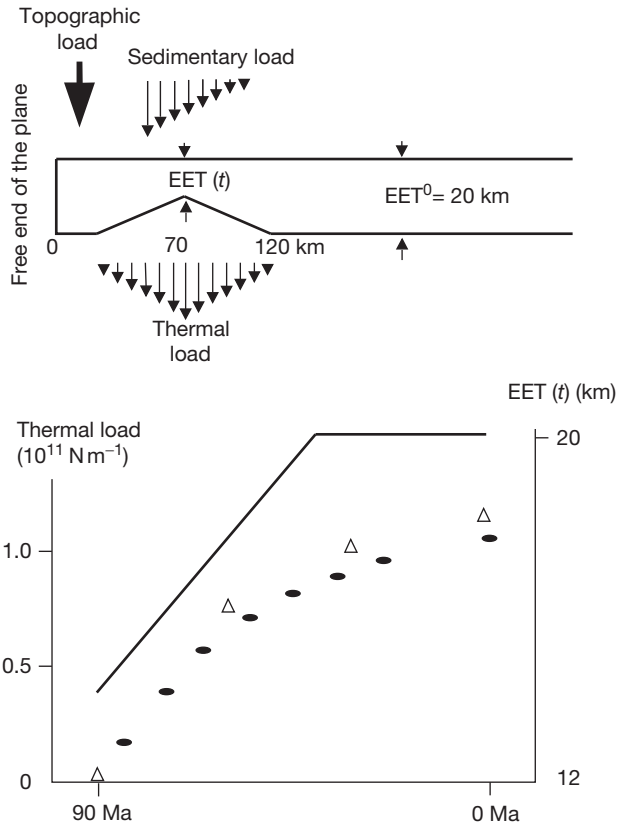

Figure 38 Cartoon illustrating the effect of extensionally induced weakening and ongoing thermal subsidence on foreland basin subsidence. (top) Thinning of the elastic plate coincides in space with the thermal load. A prograding topographic (thrust) load is applied. (bottom) Triangles denote the change of plate thickness through time EET (*t*) for the center of the preorogenic basin. Dotted line shows the evolution of thermal loading. Reproduced from Desegaulx P, Kooi H, and Cloetingh S (1991) Consequences of foreland basin development on thinned continental lithosphere – Application to the aquitaine basin (Sw France). *Earth and Planetary Science Letters* 106: 116–132.

for erosion of more than 4 km during the last 12 My (Merten et al., 2010; Necea, 2010; Sanders et al., 1999).

The Tertiary Piedmont Basin is the retroforeland basin of the Western Alps characterized by a noncylindrical geometry due to the superposition with the Ligurian Alps, oriented in an oblique direction (Bertotti and Mosca, 2009; Bertotti et al., 2006). Within the limitations imposed by this, cross-sectional modeling suggests that the presence of a compressional horizontal force during the formation of that basin enhanced the remarkable *toplap* sedimentary geometry shown in **Figure 39** (Carrapa and Garcia-Castellanos, 2005), with younger sediment filling only the basin areas closer to the Alps and gradually older sequences outcropping further toward the foreland.

6.12.4.1.2 Feedback between lithospheric and surface processes

Much effort in foreland basin modeling has been directed to understanding landscape evolution and surface processes (e.g., Bonnet, 2009 and references therein). A by-product of these studies is the development of a series of models integrating 3-D surface sediment transport with the dynamics of basin evolution (Johnson and Beaumont, 1995). Computer simulations coupling planform flexural isostasy and 3-D fluvial sediment erosion/transport have shown that river transport, on its own, is not capable of producing significant sediment accumulation on the foreland in the absence of flexural subsidence at intermediate EET values (Garcia-Castellanos, 2002). These findings are similar to the classical notion that, to generate significant accommodation space, kilometer-scale tectonic subsidence by lithospheric downflexing over a sizable area in front of the orogen is a prerequisite. More specifically, if the strength of the lithosphere is too low or too high, the creation of accommodation space next to the orogen becomes negligible, and rivers will transport their sediment load out of the orogen–basin system.

Whereas early diffusive models for erosion (Flemings and Jordan, 1989; Sinclair et al., 1991) produced significant amounts of sediment accumulation even for large rigidities, the more sophisticated models show that river transport does not allow such sediment accumulation in the absence of differential vertical motions, as in the case of very high rigidity. The dependence between the basin volumes predicted by these models and EET shows a remarkable similarity with the observed EET histogram (Garcia-Castellanos, 2002). This suggests that the EET *measurements* might be biased by a focus of studies on large sedimentary basins. An open question is to what extent the presence of middle EET values (20–40 km), responsible for 'large' sedimentary basins, is overestimated relative to larger and smaller values, which generate small basins. An example of this could be the Atlas orogen in Morocco, for which no forward flexural modeling has been performed in the tiny foreland basins formed in the vicinity. The absence of modeling is probably due to the fact that the associated foreland basin is relatively insignificant in both sedimentary thickness (<700 m) and width (<35 km in Ouarzazate). Preliminary flexural models of the Ouarzazate basin yield EET values below 4 km (Teson et al., 2006), a low value that may be linked to a mantle upwelling under the Moroccan Atlas Mountains, which would also explain the high topography relative to the small amounts of shortening, and the spatial coincidence of a gravity low and a geoid high in this orogen (Teixell et al., 2005). Other examples are the small Klagenfurt and Styrian Basins (Austrian Eastern Alps), where EET values between 1 and 5 km have been linked to strong decoupling of the upper crust (Nemes et al., 1997; Sachsenhofer et al., 1997).

6.12.4.1.2.1 Modeling the sedimentary infill geometry

Several researchers have focused numerical models to non-instantaneous orogenic loading, incorporating some simplified approach to fault propagation within the basement and the sediment (Garcia-Castellanos et al., 1997; Sassi et al., 1993; Sassi and Rudkiewicz, 2000; Toth et al., 1996). These studies aim to better constrain the tectonic evolution based on the sedimentary record or vice versa. To that purpose, a pure elastic plate responding instantaneously to loading is insufficient, and the transient viscous response of the lithosphere must be considered (Beaumont, 1981). Viscous relaxation during basin development induces basin narrowing and deepening, similar to the result of an EET reduction through time. The application of a viscoelastic model to the Guadalquivir Basin (Garcia-Castellanos et al., 2002) and the Tertiary Piedmont Basin (Carrapa and Garcia-Castellanos, 2005) shows that viscous

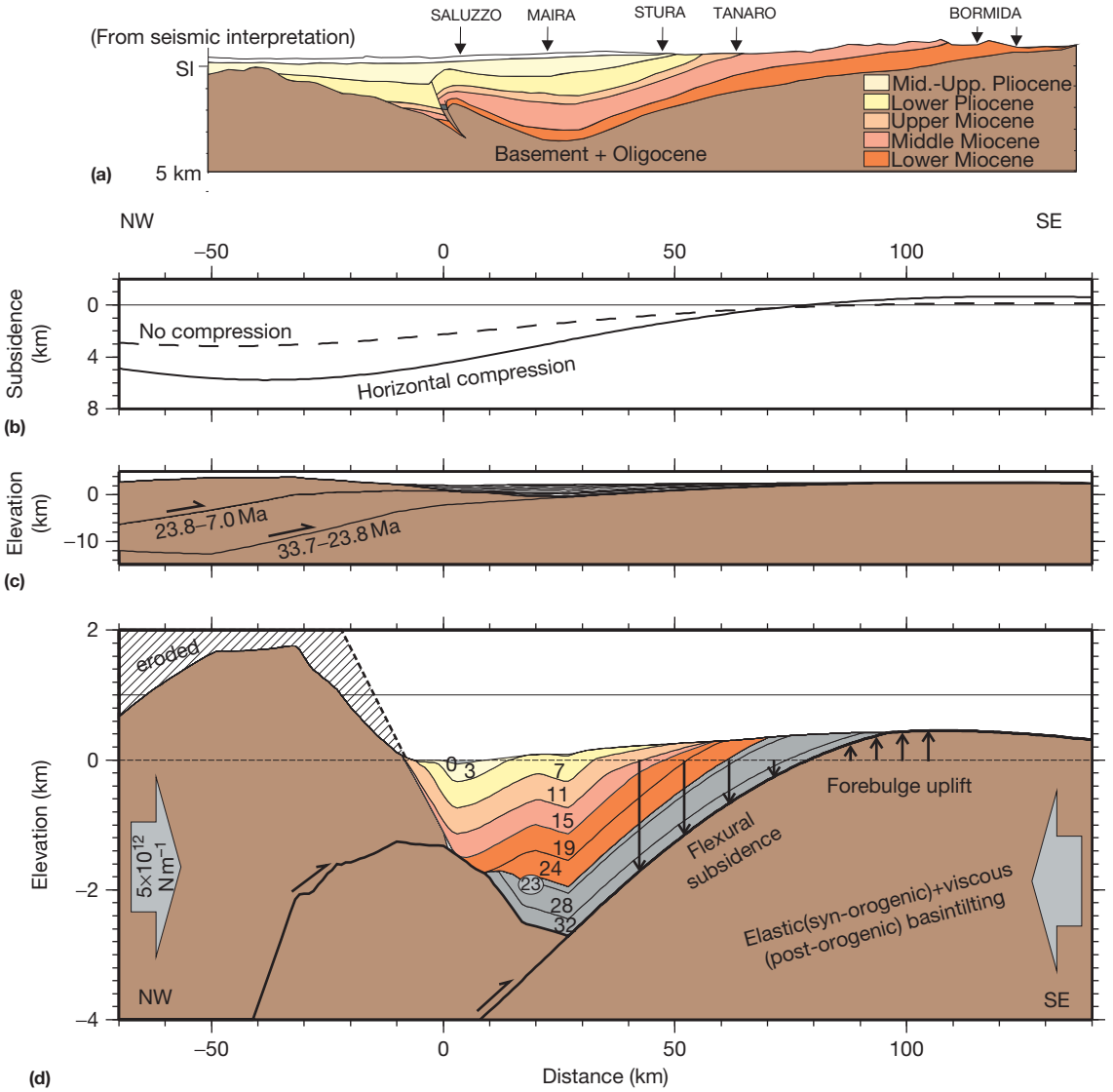

Figure 39 (a) Sedimentary infill geometry of the Piedmont Basin constrained by seismic surveys (see for location **Figure 33**). (b) Calculated vertical motions. Dashed line corresponds to an identical model without horizontal compression. (c) Final model geometry (no vertical exaggeration) obtained from a viscoelastic flexural model. (d) Basin geometry (vertically exaggerated). Reproduced from Carrapa B and Garcia-Castellanos D (2005) Western Alpine back-thrusting as subsidence mechanism in the Tertiary Piedmont Basin (Western Po Plain, NW Italy). *Tectonophysics* 406: 197–212.

basin narrowing may exceed the velocity of wedge motion, inducing a retreat of the subsiding area toward the orogen. Under such circumstances, older sedimentary units may outcrop in the distal parts of the foreland basin (**Figure 39**). A shift toward the orogen of the pinch out of sedimentary units is observed in the previously mentioned foreland basins and also in the Alberta Basin (Beaumont, 1981) and the Swiss Molasse basin (Schlunegger et al., 1997). In the Alberta Basin, the entire lithosphere, in both the foreland and the hinterland, has been uplifted (Hardebol et al., 2013). In the Swiss Molasse basin, the pinch out relates partially to post-Messinian inversion of Paleozoic grabens beneath the Jura Mountains, which accounts for a refolding of the intra-Triassic decollement, and differential topography between the Jura and the Molasse basin (Philippe, 1994; Roure et al., 1994). Models incorporating viscous relaxation, therefore, still require these mechanisms or the additional vertical or horizontal forces mentioned in the previous section to be able to fit the basin architecture.

6.12.4.1.2.2 Forebulge uplift

The magnitude of the forebulge might fluctuate with time as a result of temporal variations in regional stress fields (Cloetingh et al., 1989), stress accumulation and relaxation prior and upon thrusting (Peper et al., 1992), and spatial variations in rheology of the lithosphere underlying the foreland basin (Waschbusch and Royden, 1992). Numerical modeling has shown that the position of the forebulge should not be expected to migrate steadily toward the foreland even when the tectonic wedge does. Instead, this shift might slow down or accelerate if lateral EET variations are present (*Waschbusch and Royden, 1992*) or even

reverse direction and move toward the orogen due to viscous relaxation of stresses (Beaumont, 1981; Garcia-Castellanos et al., 2002). Forebulge uplift is therefore not necessarily stationary in time and space. In fact, the presently active forebulge might mark the current limit of the flexural basin geometry, whereas the basin fill might also have recorded an older forebulge, which is now buried under the foredeep depocenter.

In parallel, results from 3-D computer experiments (Garcia-Castellanos, 2002) show that forebulges may not easily be represented as drainage divides, since limited amounts of inherited (preflexural) topographic relief may be more decisive in determining the future drainage network than the vertical uplift associated with the forebulge (usually smaller than 200 m). This can be further complicated by the discrete localization of the forebulge as the front of deformation jumps toward the foreland. Still, these models do not exclude that forelands with small inherited topographic gradients and an initially poorly incised river network can develop drainage patterns that reflect forebulge uplift of a few hundred meters or even backbulge subsidence in the order of tens of meters (Horton and DeCelles, 1997; Roddaz et al., 2005). Such topographic anomalies can also occur in relation to foreland basement inversion such as documented for the US Rocky Mountains, Mérida Andes, and Saharan Atlas, which generate high topography inside a formerly continuous foreland (Colletta et al., 1997; Gries, 1983; Roure et al., 1997; Roure et al., 2010b).

In some foreland basins, such as along the eastern flank of the Andes, the sedimentary infill has overflowed the forebulge crest and the subsequent sedimentary cover extends beyond that. Computer simulations (**Figures 39** and **40**) show that changes in the balance between tectonic equilibrium and erosional equilibrium (in absence of eustatic base level changes or independent subsidence of the foreland) cannot result in overflowing an active forebulge (a forebulge being still uplifted by tectonic loading). As long as the basin is continental and exorheic, the drainage network generally adapts to these changes and copes with any increase in sediment delivery from the orogen or with any reduction in the rate of generation of accommodation space, transporting along-strike the excess mass to the open ocean (Garcia-Castellanos, 2002). Thus, forebulges buried under basin sediments are either a relic of former stages when the tectonic load was more distant from the foreland or active forebulges subdued below sea level by other subsidence mechanisms. This later interpretation is consistent with the notion by Dávila et al. (2007) that dynamic loading sourced in the mantle produced additional subsidence of the sub-Andean peripheral bulge allowing it to be overlain by later sediments. In addition to static loads, dynamic loading underneath the basin (e.g., viscous mantle corner flow above a subducting plate; Catuneanu et al., 1997) may cause long-wavelength subsidence and forebulge sediment overflow. Our understanding of these dynamic forces as the result of mantle convection has improved in the last years (e.g., Pysklywec and Mitrovica, 1997). The interaction of static (isostatic) and dynamic (e.g., coupling with mantle flow) forces might also be responsible for the formation and preservation of stacking patterns that do not conform to the predictions of simple elastic flexural models (Catuneanu et al., 1997). A more detailed possibly quantitative implementation of regional upper mantle flow studies in the analysis of foreland basins could provide additional understanding of these systems in the future.

6.12.4.1.2.3 Basin exhumation

Modeling studies during the last two decades have shown that erosion and deposition strongly influence tectonic processes, tuning the style of deformation in compressional belts (Avouac and Burov, 1996; Beaumont et al., 1992; Willett, 1999) and demonstrating the importance of feedback between uplift and erosion as well as deposition in the foredeep and the return flow in the lower crust (Garcia-Castellanos, 2002). The feedback between surface processes, isostatic reaction, and subsurface crustal flow can result in accelerated growth of topography in the area of strongest subsurface uplift. Examples are central Asia, the Cordilleran–Sub-Andean basins, and areas with lithospheric delamination, as all the crust remains attached to the upper plate. This mechanism is probably also important in the Eastern Alps where only the mantle–lithosphere is downthrusted, as proposed by Laubscher (2010). The lower crust in this case can then be viewed as rather ductile and flowing between the brittle upper crust and the underlying brittle mantle.

Similar feedback relationships between thrusting dynamics, foreland basin formation, and accretionary wedges have received considerable attention from numerical (e.g., Braun, 2006; Garcia-Castellanos, 2002; Garcia-Castellanos and Cloetingh, 2012; Simpson, 2006) and analog (e.g., Persson and Sokoutis, 2002; Smit et al., 2003, 2013) modelers. Combination of analog and numerical modeling benefits from the 3-D capabilities of analog tectonic experiments to implement preexisting structures, as well as the capability of numerical models to handle 3-D surface mass redistribution. The validation of modeling results requires the availability of high-quality datasets, including deep seismic profiles (Roure et al., 1989, 1996; Tomek, 1993), seismostratigraphic interpretations, and paleothermometers (Roure et al., 2010a).

The reciprocal interactions between surface and tectonic processes have been studied through hybrid numerical–analog models, fully coupling the dynamics of an analog deformation model (sandbox) and the fluvial transport numerical model (**Figure 40**; Athmer et al., 2010; Persson et al., 2004). In this technique, a backstop acts as an indenter at the upper boundary, compressing the initially flat sand layers. During shortening, a scanner is used to digitize the sandbox topography, which is then scaled and passed to the numerical surface process model. The calculated erosion and deposition are then downscaled and mechanically applied to the sandbox by respectively subtracting and adding sand to its surface. The drainage pattern evolving on top of the topography induces lateral differences in surface sediment redistribution, which disrupts the lateral (along-strike) symmetry of the initial setting. The modeling approach used in **Figure 40** is similar to that in Persson et al. (2004), except that here, a computer-calculated flexural isostasy is applied, which permits the formation of large flexural sedimentary basins. The initial topography is slightly tilted (0.5 degrees) toward the west (left). During the experiment, episodic sediment delivery toward the basin results from drainage reorganizations in the orogen and not from changes in tectonic shortening rates, which are not incorporated to this model. Hence, drainage reorganization is a mechanism of episodic sediment delivery, alternative to tectonic or climatic periodicity (Sobel et al., 2003). The forebulge is not migrating continuously toward the foreland, but in fact records two stages of discrete localization at a distance of ~300 and 150 km from the lower boundary of the model, linked with

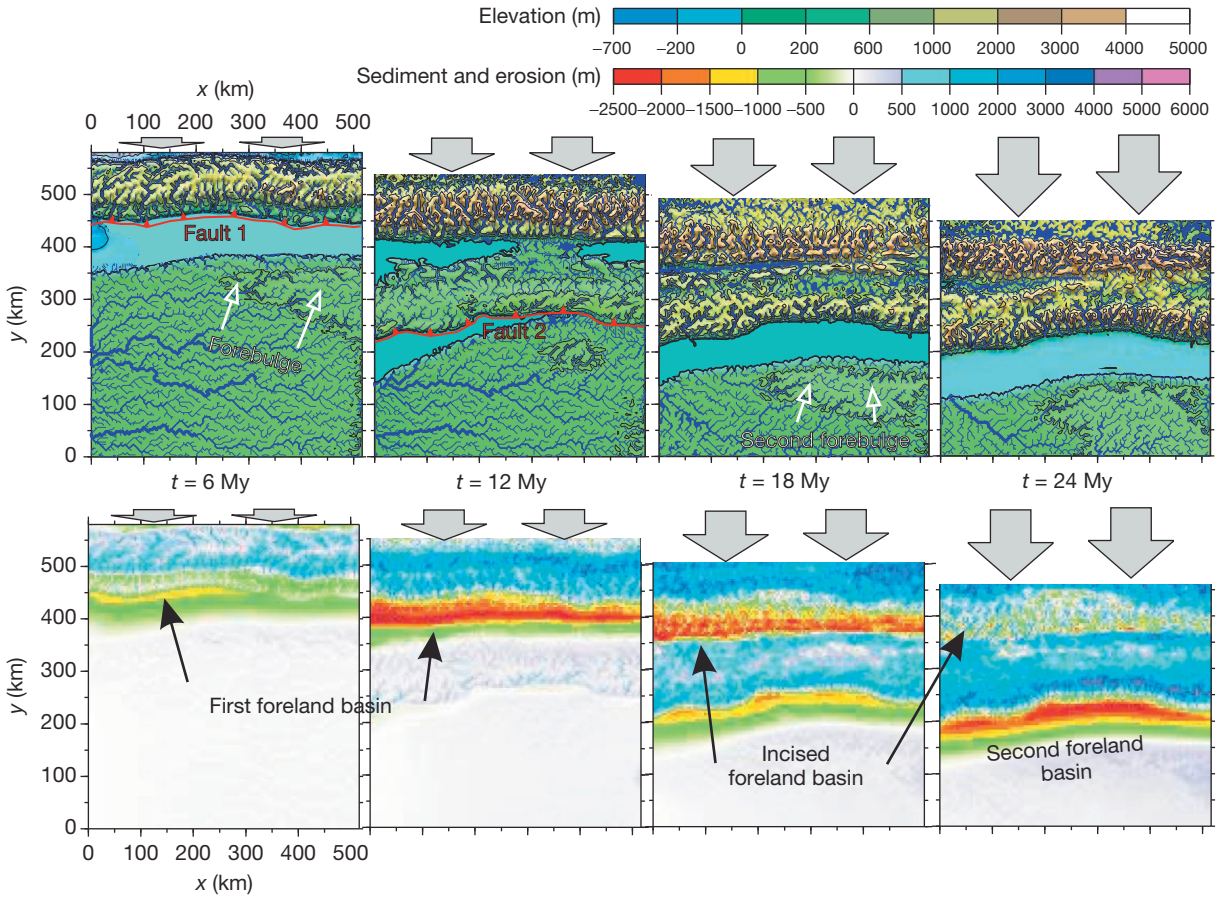
Elevation (m)
−700 −200 0 200 600 1000 2000 3000 4000 5000
Sediment and erosion (m)
−2500 −2000 −1500 −1000 −500 0 500 1000 2000 3000 4000 5000 6000
x (km)
0 100 200 300 400 500
y (km)
0 100 200 300 400 500
Fault 1
Fault 2
Forebulge
Second forebulge
t = 6 My
t = 12 My
t = 18 My
t = 24 My
First foreland basin
Incised foreland basin
Second foreland basin

Figure 40 Results from a combined analog–numerical model following a technique similar to Persson et al. (2004) but here incorporating flexural isostasy for the calculation of topography. The formation of topography and tectonic load is simulated with a sandbox compressed from the northern (upper) boundary. Gray arrows indicate cumulative backstop motion. The sand surface is scanned and passed to a computer program (*TISC*), which calculates river incision and sediment transport (Garcia-Castellanos et al., 2002). The calculated erosion/deposition is then downscaled and manually applied to the analog experiment. Four stages are shown at 6, 12, 18, and 24 My. The initial stage (0 My) consists of a flat surface with a slight tilt toward the left boundary, 100 m lower than the right one. Within the orogen, the drainage network develops in N–S direction, perpendicular to the tectonic structures, until a second major thrust develops in the sand ($t = 12$ My) further toward the south. The topography generated by this new fault induces a large drainage reorganization in the direction along the strike of the orogen ($t = 18$ and 24 My). The sediment accumulation produced in the foreland basin is *cannibalized* as the tectonic shortening is accommodated further to the south, as observed in a variety of geologic settings (e.g., DeCelles and Giles, 1996). Two major forebulge areas are uplifted in response to the two major deformation fronts. Both forebulges become drainage divides between the basin and the foreland, although the initial E–W drainage trend is essentially not modified. Cannibalization of piggyback basins and episodic motion of the forebulge is consistent with observations by, for example, Hippolyte et al. (1994) in the southern Apennines. Reproduced from Garcia-Castellanos D and Cloetingh S (2012) Modeling the interaction between lithospheric and surface processes in foreland basins. In: Busby C and Azor A (eds.) *Tectonics of Sedimentary Basins: Recent Advances*, pp. 152–181.

successive offsets of the active thrust front and flexed domain. Hippolyte et al. (1994) and Casero (2004) proposed such successive lateral jumps for the Messinian to Middle Pliocene depocenters in the Apennines. These experiments also show that lateral heterogeneities in erosion and sediment transport induce lateral tectonic diachronism and perturb the initial E–W symmetry of the sandbox setting, affecting the distribution of deformation in a way similar to that described through earlier 2-D numerical models of orogenesis (Willett, 1999). The experiments performed by Persson et al. (2004) and the one shown in **Figure 40** account for 3-D river sediment transport and suggest that axial transport in the orogen and along the foreland basin may induce lateral changes in the tectonic evolution of the orogen–basin system. An obvious challenge is to separate in the field these effects from those induced by inherited heterogeneities and lateral changes in the tectonic forcing.

To improve our understanding of the dynamics of foreland basins, future basin models must incorporate the full dynamics of lithospheric deformation (lithospheric flexure and folding, crustal thrusting, sediment deformation, subduction of the lithospheric mantle, and lower crustal and asthenospheric flow) and surface processes (incorporating to some degree climatic processes). Dynamic tectonic models have improved significantly our understanding of orogenesis (Burov and Toussaint, 2007; Garcia-Castellanos, 2007; Jiménez-Munt et al., 2005; Whipple, 2009; Willett, 1999; Willett et al, 2006) and currently start to contribute similarly at the basin scale (Simpson, 2010). These models are currently moving into 3-D (Braun, 2006),

incorporating more realistic surface processes. Surface process models have shown that there is substantial information waiting in the landscape record, which can contribute to a better quantitative understanding of orogen–basin systems.

6.12.4.2 Compressional Basin Formation by Lithospheric Folding

Folding of the lithosphere, involving positive and negative deflections (Figure 41), appears to be of more importance in the large-scale deformation of intraplate domains than hitherto realized (Cloetingh and Burov, 2011; Cloetingh et al., 1999). As discussed by Cloetingh and Burov (2011), folding can be observed at different spatial scales. At the scale of a microcontinent that was affected by a succession of collisional events, Iberia illustrates lithospheric folding and interplay between neotectonic and surface processes (Cloetingh et al., 2002). An important factor favoring a lithosphere-folding scenario for Iberia is the compatibility of the thermotectonic age of its lithosphere and the wavelength of observed deformations. Other well-documented examples of continental lithospheric folding occur in other regions across the globe (Figure 42). Prominent examples occur in central Asia and surrounding regions (e.g., Delvaux et al., 2013; Smit et al., 2013) involving a lithosphere with thermotectonic ages from 150 Ma (Kazakh shield, Fergana and Tadjik basins, and likely Dzungarian Basin) to 400 Ma (Tarim Basin). In this area, mantle and crustal wavelengths are 360 and 50 km, respectively, with a shortening rate of ~10–20 mm year^{-1} and 200–250 km of shortening during 10–15 My (Burov and Molnar, 1998; Burov et al., 1993). Three-dimensional fold structures in the Tibetan Plateau have been inferred from GRACE satellite gravity data, demonstrating prevailing fold wavelengths of 300–420 km (Shin et al, 2009).

Although the India–Eurasia collision is by far the most dominating factor in the eastern segment of the Alpine–Himalayan collision belt (e.g., Hatzfeld and Molnar, 2010), the contribution of the Arabian indenter to the deformation of western central Asia cannot be neglected. The stress system generated by both indenters is affecting the intraplate topography of (western) central Asia up to distances of the order of a few thousands of kilometers, leading to significant differential

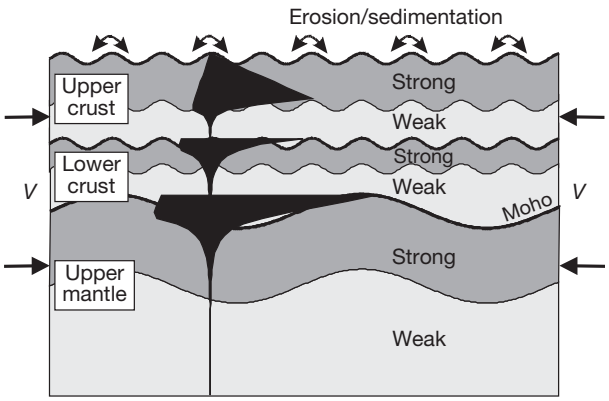

Figure 41 Concepts of folding in rheologically stratified lithosphere and feedback with sedimentation in downfolded areas and erosion of adjacent highs. Different simultaneously occurring wavelengths of crustal and mantle folding are a consequence of the rheological stratification of the lithosphere. Surface wavelengths can be affected also by feedback with surface processes.

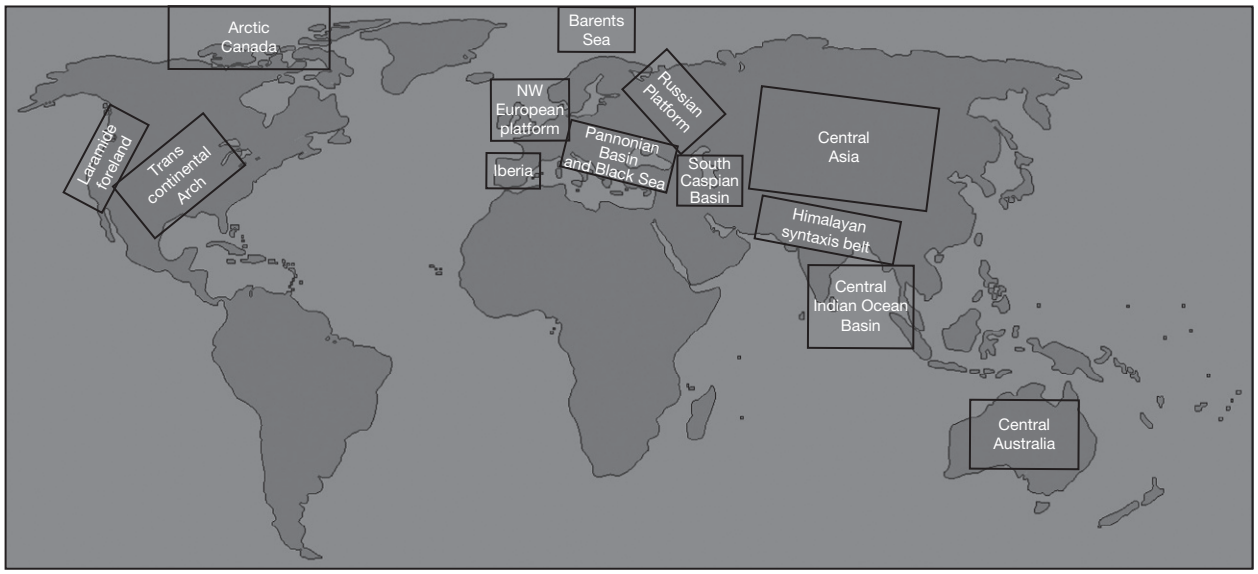

Figure 42 Map with examples of well-documented areas affected by lithospheric folding. Areas: Central Indian Ocean Basin (CIOB) (Geller et al., 1983; Stein et al., 1989); NW European Platform (Bourgeois et al., 2007; Lefort and Agarwal, 1996; Marotta et al., 2000); Pannonian Basin (Dombradi et al., 2010); Iberia (Cloetingh et al., 2002; De Vicente et al., 2007; Fernández-Lozano et al., 2011, 2012); central Asia (Burov et al., 1993; Nikishin et al., 1993; Burov and Molnar, 1998); Tibetan/Himalayan syntaxis belt (Burg and Podlachikov, 1999; Shin et al., 2009); Central Australia (Stephenson and Lambeck, 1985; Lambeck, 1983); Arctic Canada (Stephenson et al., 1990); Transcontinental Arch of North America (Ziegler et al., 1995); South Caspian Basin (Guest et al., 2007); Laramide foreland (the United States) (Tikoff and Maxson, 2001); Barents Sea (Ritzmann and Faleide, 2009).

vertical motions. Smit et al. (2013) pointed out that collision of the Eurasian plate with the Arabian and Indian Plates generates folding of the Eurasian lithosphere in two different directions with their interference manifested in the regional geology, gravity, and topography. The wavelengths of the observed lithospheric deformation are consistent with the inferences from thermomechanical models constructed for the lithosphere in western central Asia. Differences in the convergence velocities of the Indian and Arabian indenters with respect to Eurasia and spatial variations in thermomechanical structure of the lithosphere west and east of the Kugitang–Tunka Line appear to be of key importance.

The inferred wavelength of these neotectonic lithospheric folds is consistent with the general relationship between the wavelength of lithospheric folds and the thermotectonic age of the lithosphere shown by a global inventory of lithospheric folds (**Figure 43**; Cloetingh and Burov, 1996; Cloetingh et al., 2005a,b). In some other areas of continental lithospheric folding, smaller wavelength crustal folds have also been detected (Burov et al., 1993; Nikishin et al., 1993). Thermal thinning of the mantle–lithosphere, often associated with volcanism and doming, enhances lithospheric folding and appears to affect the wavelengths of folds (Burov and Cloetingh, 2009).

As has been shown (Burov et al., 1993; Cloetingh et al., 1999; Gerbault et al., 1999; Nikishin et al., 1993; Schmalholz and Podladchikov, 2000), viscoelastic folding starts to develop from the onset of compression and, in contrast to elastic folding, does not require specifically large intraplate stresses. Folding may continue until the background strain-rate drops, for example, due to the localization of deformation in a specific area or to reduction of far-field forces. Such intraplate deformation results from transmission of intraplate stress fields away from plate boundaries into continental forelands (Tesauro et al., 2005; Van der Pluijm et al., 1997; Ziegler et al., 1998).

In continental lithosphere, several wavelengths of folding are expected to develop as a result of the presence of several rheologically competent layers decoupled from each other by weak layers (**Figures 41** and **43**). Crustal folding can be traced from the surface topography, neotectonic movements, and free air gravity. The crust–mantle boundary (Moho) topography reflects mantle folding, because the mantle strength is highest at this interface, and thus, the geometry of Moho deflection is most likely to correspond to that of mantle folding. This wavelength can be traced from Bouguer gravity anomalies because the crust–mantle boundary represents also the main density contrast in the lithosphere. It is to be expected that the base of the mechanical lithosphere (MLB) has roughly the same geometry as the Moho deflection. Likely, the lithosphere–asthenosphere boundary (LAB) has little to do with mantle–lithospheric folding except some specific cases, as the MLB (roughly corresponding to 700 °C depth) is found well above the LAB (1330 °C). Consequently, the low-viscosity zone between MLB and LAB may damp the deformation in a way that the LAB remains even flat. Due to the low viscosity of gravitating mantle between the LAB and the MLB, the LAB is not necessarily advected or downwarped with deflection of the MLB, or at least the relations between the deformation of the MLB and that of LAB are not straightforward. In particular,

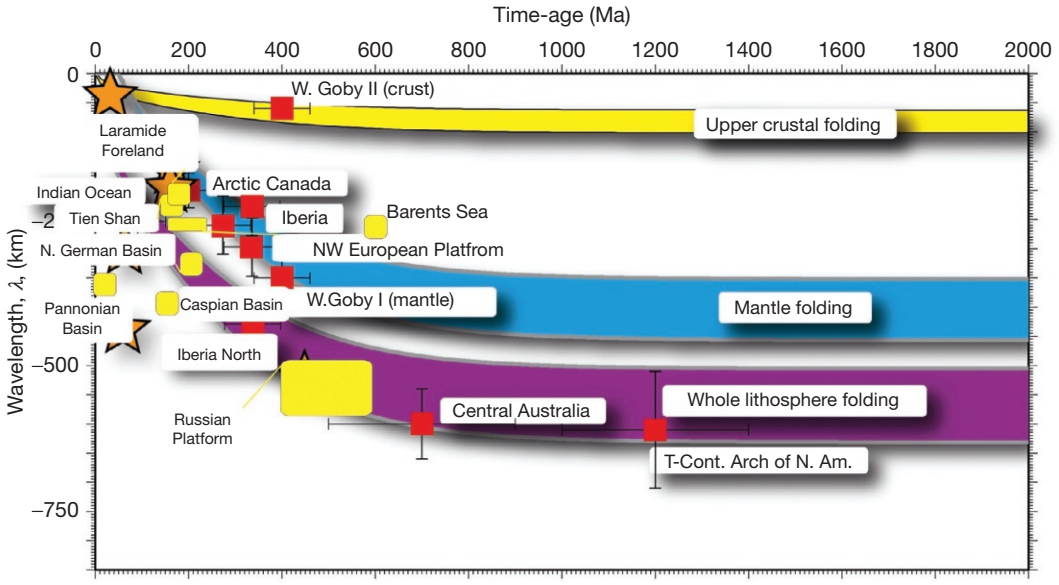

Figure 43 Characteristics of lithospheric folding. Polyharmonic folding concept: due to rheological stratification, the lithosphere can develop different folding wavelengths in response to tectonic compression. Surface topography will reflect superposition of different wavelengths. The colored zones correspond to theoretically folding wavelengths derived for the upper crust, mantle, and coupled whole mantle folding, based on an analytic model that accounts for strength variations as a function of thermomechanical age. Theoretically predicted wavelengths as function of thermotectonic age (for different lithospheric layers as well as whole-lithospheric folding) are compared to observed wavelengths and thermotectonic ages. See also **Table 4**. Reproduced from Cloetingh S, Burov E, and Poliakov A (1999) Lithosphere folding: Primary response to compression? (From central Asia to Paris basin). *Tectonics* 18: 1064–1083; Cloetingh S and Burov E (2011) Lithospheric folding and sedimentary basin evolution: A review and analysis of formation mechanisms. *Basin Research* 23: 257–290.

Table 4 Wavelengths and ages of basins located on folded lithosphere (see Figure 42 for locations)

	Area	*Thermotectonic age (Ma)*	*Folding wavelength λ (km)*	*References*
1	Tian Shan	175	200–250	Burov and Molnar (1998) and Burg et al. (1994)
2	Western Gobi	175–400	300–360	Nikishin et al. (1993) and Burov et al. (1993)
3	Central Asia	370–430	50–70 (crust) 300–400 (lithosphere–mantle)	Nikishin et al. (1993) and Burov et al. (1993)
4	Himalayan syntaxis belt	8–10	150	Burg and Podladchikov (1999)
5	Central Australia	500–900	550–650	Lambeck (1983), Stephenson and Lambeck (1985), and Beekman et al. (1997)
6	Russian Platform	400–600	500–600	Nikishin et al. (1997)
7	South Caspian Basin	125–155	350–450	Guest et al. (2007)
8	Eastern Black Sea	40–80	50–100 (crust) 100–150 (lithosphere–mantle)	Cloetingh et al. (2008)
9	Western Black Sea	75–125	50–100 (crust) 100-200 (lithosphere–mantle)	Cloetingh et al. (2008)
10	Pannonian Basin system	20	200–250	Horváth and Cloetingh (1996), Matenco et al. (2007), and Dombradi et al. (2010)
11	NW European Platform	180–230	270	Bourgeois et al. (2007)
12	Brittany	210–290	225–275	Bonnet et al. (2000)
13	Iberia	330–370	40–80 (crust) 125–275 (lithosphere–mantle)	Cloetingh et al. (2002)
14	Barents Sea	215–245	550–650	Ritzmann and Faleide (2009)
15	Canadian Arctic	150–250	170–230	Stephenson et al. (1990)
16	Transcontinental Arch of North America	1000–1400	500–700	Ziegler et al. (1995)
17	Laramide foreland (the United States)	175–225	190	Tikoff and Maxson (2001)

gravity instabilities or convective movements not related to folding can perturb the LAB without impact on the MLB.

Folding has important implications for vertical motions, sedimentary basin architecture, and the evolution of hydrocarbon systems (Ziegler et al., 1995; 1998). The large wavelength of vertical motions associated with lithospheric folding necessitates the integration of data from large areas (Allen and Davies, 2007; Elfrink, 2001), often beyond the scope of regional structural and geophysical studies that target specific structural provinces. Recent studies on the North German Basin show neotectonic reactivation by lithospheric folding (Marotta et al., 2000). Similarly, acceleration of the Pliocene–Pleistocene subsidence in the North Sea basin is attributed to stress-induced buckling of its lithosphere (Van Wees and Cloetingh, 1996). Folding of the Variscan lithosphere has been documented for Brittany (Bonnet et al., 2000; Lagarde et al., 2000), the adjacent Paris Basin (Lefort and Agarwal, 1996), and the Vosges–Black Forest Arch (Bourgeois et al., 2007; Dèzes et al., 2004; Ziegler and Dèzes, 2007). Lithospheric folding, therefore, appears to be an effective mechanism for the propagation of tectonic deformation from active plate boundaries far into intraplate domains (e.g., Burov et al., 1993; Stephenson and Cloetingh, 1991; Ziegler et al., 1995, 1998).

6.12.4.2.1 The role of lithospheric rheology

Folding is commonly associated with periodic deformation of layered structures with contrasting mechanical properties. As a consequence, the harmonic spatial periodicity is often believed to be its primary, almost synonymous, identifying factor. However, from a mechanical point of view, constant wavelength is not a necessary requirement. Folding is a compressional instability developing in stiff layers embedded in a weaker material. The harmonic solution of the equilibrium and conservation equations is a possible solution (Burov and Molnar, 1998; Cloetingh et al., 1999; Muhlhaus et al., 1998). The physical mechanism of folding is well understood. In a continuously layered medium, the stresses and strains must be continued across the interfaces between the layers. In multilayer systems with contrasting mechanical properties (e.g., strong and weak layers), this requirement may be difficult to satisfy, because the same amount of shortening in a stiffer layer would require much larger stress than in the neighboring weaker layer. The system becomes unstable and, in attempting to reduce the stress and strain unconformities at the interfaces between the layers, starts to fold (or buckle) in response to very small perturbations. In nonelastic media with strain-dependent properties, locally increased flexural strain at the fold limbs can create weakened zones that significantly facilitate further deformation. These weak or softened plastic or viscous zones are often referred to as inelastic hinges, since the system easily folds at such weakened zones. Homogeneous shortening of the lithosphere under horizontal compression requires more work than required by an equivalent amount of shortening by folding. However, shortening by underthrusting/subduction of the lithosphere may be more mechanically efficient than folding but may be blocked or unable to start immediately after the onset of shortening. For this reason, folding is likely to be a primary and common response to tectonic compression. Folding probably may continue, in an attenuated form, even after the beginning of subduction (Cloetingh et al., 1999) or reappear when the subduction channel is locked or during the aftermath of collision (Cloetingh et al., 2004; Matenco et al., 2007).

The rheological structure of the lithosphere (see Section 6.12.2) is a key factor in lithospheric folding (Watts and Burov, 2003). Compressional stresses must build up to a level comparable with the integrated strength of the lithosphere in order to induce folding. Prior to the advent of rheological models based on extrapolation of laboratory experiments (Carter and Tsenn, 1987; Goetze and Evans, 1979), lithospheric stresses were thought to be incapable of reaching the failure levels required for folding (Turcotte and Schubert, 2014).

The simplest expression of the folding process is in oceanic lithosphere, characterized by an absence of a rheological stratification, and with thermomechanical ages spanning a limited age window with a maximum of 200 My (Geller et al., 1983). Because weak lithosphere is easier to fold than strong lithosphere, one would expect the first observations of lithospheric folding from the rheologically weak continental plate interiors. However, the observation of folding of the relatively strong lithosphere of the central Indian Ocean with a thermomechanical age of 80 Ma and with wavelengths of 200-250 km (Bull and Scrutton, 1992; Geller et al., 1983; McAdoo and Sandwell, 1985; Stein et al., 1989) triggered the interest in this mode of deformation. There may be two reasons for this. First, the recognition of folding, by mapping of basin reflectors and gravity anomalies, requires spatial scales of several hundreds of kilometers. This is feasible with marine geophysical surveys but generally in excess of the spatial scales covered by land surveys. An exception has been the systematic mapping of basins in Central Australia, located on strong lithosphere with a thermomechanical age of ~700 Ma (Lambeck, 1983; Stephenson and Lambeck, 1985). The Indo-Australian Plate is under an exceptionally high level of compression (Stein et al., 1989), as a result of its collision with the Eurasian Plate. Under these conditions, high stresses might have been more important than the rheology of the plate interior (Beekman et al., 1996; Gerbault, 2000; Gerbault et al., 1999).

Secondly, folding in oceanic lithosphere is not affected by surface erosion, making it relatively easy to recognize. The presence of only one dominant folding wavelength characteristic of nonstratified oceanic lithosphere also facilitated a quantitative interpretation. Following the early studies in the Indian Ocean and in Central Australia in the rear of the Indian–Eurasian collision, attention shifted to the other side of the plate contact in central Asia. Large-scale folding patterns were recognized through the analysis of geophysical data, including gravity and topography (Burov et al., 1993; Burov and Molnar, 1998; Nikishin et al., 1993) as well as detailed geologic studies (Cobbold et al., 1993).

6.12.4.2.2 Observations

On the basis of an inventory of currently available results of studies of folded *continental* lithosphere, it appears that in general, the observed wavelengths of folding follow theoretical predictions for wavelengths as a function of thermomechanical age remarkably well (see Figure 43). Basins that developed on folded continental lithosphere have characteristic features. We illustrate this by largely concentrating on the basins of central Asia, the folded lithosphere of Iberia, the NW European Platform, the Pannonian Basin, and the South Caspian Basin.

6.12.4.2.2.1 Compressional basins of central Asia (Tian Shan and Fergana)

The young Fergana and Tadjik basins are compressional basins northwest and north of the Pamirs and south of the Tian Shan ranges (Burov and Molnar, 1998; Delvaux et al., 2013; Smit et al., 2013). In this area, the lithosphere underwent Jurassic reactivation and is characterized by relatively young thermomechanical ages (175 Ma; Burov and Molnar, 1998; Burg et al., 1994). In addition to having undergone thermal weakening, the lithosphere underlying these basins also probably has a weak, quartz-dominated lower crustal rheology. This has resulted in low values for the effective elastic plate thickness (EET) of the order of 15 km.

The central Tian Shan consists of an alternation of ranges and basins separated by reverse faults. The Tian Shan terminates west of the right-lateral Talas–Fergana Fault by splaying into two narrow mountain chains that surround the Fergana Valley. A narrow belt of mountains parallel to the central section of the fault slopes downward to the Fergana Valley, underlain by a deep basin with as much as 8 km of Cretaceous–Cenozoic sediments (Cobbold et al., 1993). Gravity data suggest that the Fergana and Tadjik basins are gravitationally overcompensated. The negative Bouguer gravity anomalies indicate a Moho several km deeper than predicted by models of local Airy isostasy (Burov and Molnar, 1998). This points to Moho downwarping due to nonisostatic processes and most probably, in this compressional context, to lithospheric folding. As demonstrated by numerical thermomechanical experiments (Burov and Molnar, 1998), the approximately north–south shortening of the relatively thin lithosphere could have created central downwarping and anticline mountains north and south of the basin. According to this model, this shortening has produced a folding instability in the mantle–lithosphere that has warped the basement immediately surrounding the basin upward and has forced the basin floor down beneath the Fergana Valley (with an estimate for the folding wavelength of the order of 200–250 km), possibly also producing deep mantle faulting (seen as Moho offsets in seismic reflection data).

Preexisting thermal structure and variations in crustal thickness have played a major control on the styles and distribution of faulting in this region (Figure 44; see also Burov and Molnar, 1998; Cobbold et al., 1993; Delvaux et al., 2013). Primary faults appear before the folding develops with a spacing that is proportional to brittle layer thickness. Subsequently, the two processes, faulting and folding, coexist in such a way that faults localize at the inflection points of folds. At this stage, the appearance of faults does not significantly influences the wavelength of folding. Because of the weakness of the lower crust, the upper crust should be completely decoupled from the mantle and interact with it only by flow in the lower crust. Lower crustal flow changes the wavelength and amplitude of the surface folding, which is terminated by the development of a single downwarped megafold (Cloetingh et al., 1999).

Liu et al. (2007) reported evidence for lithospheric folding in the central/north China Tarim Basin region, initiated during Pliocene times, with good time constraints provided by Ar/Ar dating. Two wavelengths are found of 30 and 400 km. The thermomechanical age of the lithosphere is estimated to be 250 Ma, as the main thermal perturbation was associated with

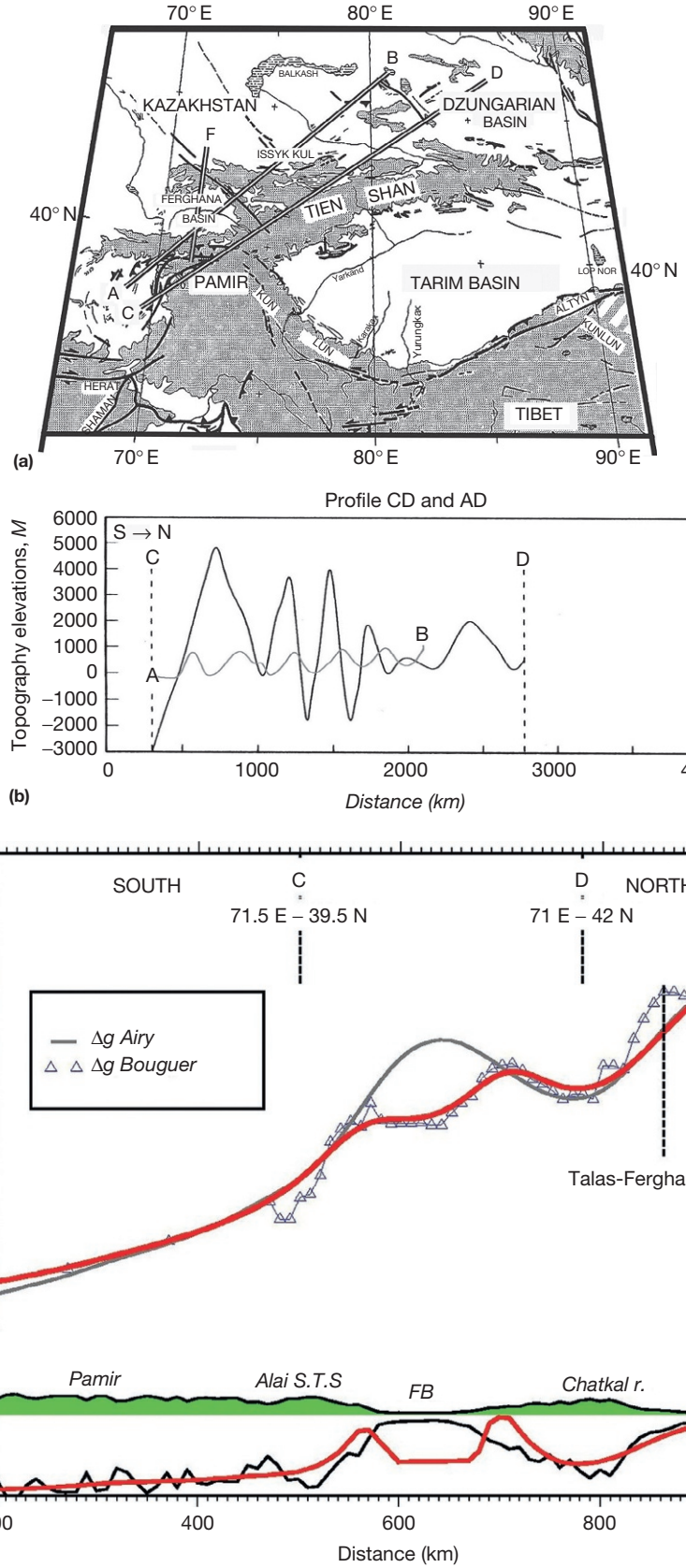

Figure 44 (a) Map showing major tectonic features of Tian Shan area of central Asia, with location of folding profiles discussed in Burov et al. (1993), Burov and Molnar (1998), and Cloetingh et al. (1999). (b) Neotectonic movements along the profiles AD and CD (Burov et al., 1993). (c) Measured and calculated Bouguer gravity anomalies for lithosphere under horizontal compression along profile F across the Fergana basin with corresponding topography profile. (d) Predicted topography and Moho geometry for Airy and best-fitting folding scenario. During compression, the amplitude of plate deflection changed significantly, while the wavelength of folding stayed constant (Burov and Molnar, 1998). Red lines are Bouguer anomaly predicted by folding model and Moho depression, respectively. Solid gray line is Airy isostasy. Solid black line is Airy Moho. Triangles indicate observed Bouguer anomaly. Green is topography above sea level. FB, Fergana basin. Reproduced from Cloetingh S, Burov E, and Poliakov A (1999) Lithosphere folding: Primary response to compression? (from central Asia to Paris basin). *Tectonics* 18: 1064–1083.

a major orogenic phase at 250 Ma ago. These findings are consistent with models in which decoupled lithospheric folds with 30 and 400 km wavelength correspond to, respectively, crustal folding and mantle folding. Deep seismic data for basins north of and within the Tibetan Plateau (Liu et al., 2006; Zhao et al., 2006) show that folding is not limited to the Tibetan Plateau (see also Shin et al, 2009).

6.12.4.2.2.2 Folded lithosphere of Iberia

As reviewed by Cloetingh et al. (2002), Tertiary lithospheric folding of Iberia occurs in Variscan lithosphere with wavelengths of 300 km, leading to the development of a system of parallel trending basins and highs (**Figure 45(a)**). This folding generated the distribution of basins and mountain chains, bounded by folds and faults (Cloetingh et al., 2002; De Vicente et al., 2007). The regularity of the fluvial network pattern of the central-western part of Iberia also indicates large-scale lithospheric folding. Alpine (mainly Cantabrian–Pyrenean-related) compressional tectonics was the principal factor for closing internally drained sedimentary basins, including the Ebro, Duero, and Tagus basins (Casas-Sainz and De Vicente, 2009).

A large body of geophysical and geologic observations is available on the crustal geometries and stress regimes of Iberia (De Vicente et al., 2007, 2008). This is supplemented by geothermochronology data (De Bruijne and Andriessen, 2000, 2002; Ter Voorde et al., 2004, 2007), demonstrating accelerated uplift of the highs during Late Miocene–Pliocene times. In spite of the existence of recent localized volcanism in the inner part of the Iberian plate, an important contribution from thermal uplift is questionable due to the distribution of crustal thickness (Casas-Sainz and De Vicente, 2009). Fernández-Lozano et al. (2011, 2012) have constructed a three-layer analog model consisting of brittle upper crust, ductile lower crust, and ductile upper mantle for Iberia. These models show that folding is associated with the deformation of narrow mountain ranges separated by basins (see **Figure 45(b)**). The narrow mountain ranges representing upper crustal pop-ups form the main topographic reliefs. Shortening is accommodated within the viscous crust beneath the pop-ups leading to lateral thickness variations of the ductile crust. These results are consistent with seismic and gravity data collected in the Cantabrian Mountains, the Spanish Central System, and the Toledo mountains (see also **Figure 45(a)**).

Serpelloni et al. (2013) recently carried out an extensive analysis of continuous Global Positioning System (GPS) data to constrain present-day vertical deformation rates in the Mediterranean region. Their study demonstrates the existence of long-wavelength undulations of vertical velocities in Iberia (**Figure 46**) at spatial scales compatible with predictions from models of lithospheric folding presented earlier.

6.12.4.2.2.3 The European Alpine foreland

Geophysical and geomorphological studies (e.g., Lefort and Agarwal, 1996; 2000; 2002; Marotta et al., 2000) indicate large-scale compressional deformation of the European Alpine foreland lithosphere. Although different in structural grain and rheological structure (Cloetingh et al., 2005a,b; Tesauro et al., 2007) inherited from differences in their Paleozoic–Mesozoic history, different segments of the lithosphere in the northern Alpine European foreland share many similarities in their Cenozoic intraplate deformation. Seismic and geologic evidence shows that the North German Basin cannot be explained by classical models of basin formation (Marotta et al., 2000). The basin underwent a polyphase history (Scheck and Bayer, 1999; Littke et al., 2008) of extension in the Late Triassic followed by lithospheric-scale folding in the Late Cretaceous–early Cenozoic (Mazur et al., 2005; Marotta et al., 2000). 3-D volumetric analysis shows that the compressional event was followed by faster subsidence during the Cenozoic (Scheck and Bayer, 1999). A similar observation was made by Van Wees and Cloetingh (1996) for the North Sea basin. Lithospheric folding modified a basin formed initially by deep-seated thermal perturbations (Scheck and Bayer, 1999) with a thinned crust and shallow Moho. The Moho updoming with a high of 3 km for the height of the bulge in the southern part of the North German Basin appears to be the consequence of flexural buckling of the previously thinned lithosphere by a compressive stress perpendicular to the strike of the basin.

From earliest Triassic to Late Jurassic, the Paris Basin (**Figure 47(a)**) subsided in an extensional framework and was larger than the present basin (Guillocheau et al., 2000). The western margin of the Paris Basin and the rifted Atlantic margin of France were subject to thermal rejuvenation during Mesozoic extension related to North Atlantic rifting (Robin et al., 2003; Ziegler and Dèzes, 2006). Subsequent compressional intraplate deformation (Ziegler et al., 1995) also affected the Paris Basin (Lefort and Agarwal, 1996). Numerical modeling indicates that the amplitude of the compression-induced vertical deflection in the Paris Basin is relatively small, requiring additional mechanisms such as flexure due to the load by the Alpine system (Bourgeois et al., 2007; Ziegler and Dèzes, 2007). However, periodic deformation at the same wavelength occurs northwest of the Paris Basin (**Figure 47(a)**, Bourgeois et al., 2007), which would not be the case if the northeastern part of the basin was flexed down by the load of the Alps. Bourgeois et al. (2007) carefully analyzed basement geometry and timing of vertical motions in the NW European Platform. They separated the contributions from the European Cenozoic Rift System (ECRIS) and the contributions from long-wavelength folding striking NE and located between the Alpine front and the North Sea. According to their analysis, the ECRIS developed mostly between 37 and 17 Ma, whereas lithospheric folds developed between 17 Ma and present, with a wavelength of 270 km and amplitude of 1500 m (see **Figure 47(b)**).

Quaternary folding of the Variscan lithosphere in the area of the Armorican Massif (Bonnet et al., 2000) developed folds with a wavelength of 250 km, pointing to a lithospheric mantle control on deformation. The timing and spatial pattern of uplift inferred from river incision studies in Brittany are incompatible with a glacioeustatic origin. Therefore, Bonnet et al. (2000) related the vertical motions to the deflection of the lithosphere by the present-day NW–SE-directed compressional intraplate stress field. Stress-induced uplift of the area appears to control fluvial incision rates and the position of the main drainage divides. Leveling studies (LeNotre et al., 1999) indicate its ongoing deformation.

6.12.4.2.2.4 The South Caspian Basin

The South Caspian Basin with an estimated sedimentary thickness up to 20 km (Brunet and Cloetingh, 2003; Egan et al.,

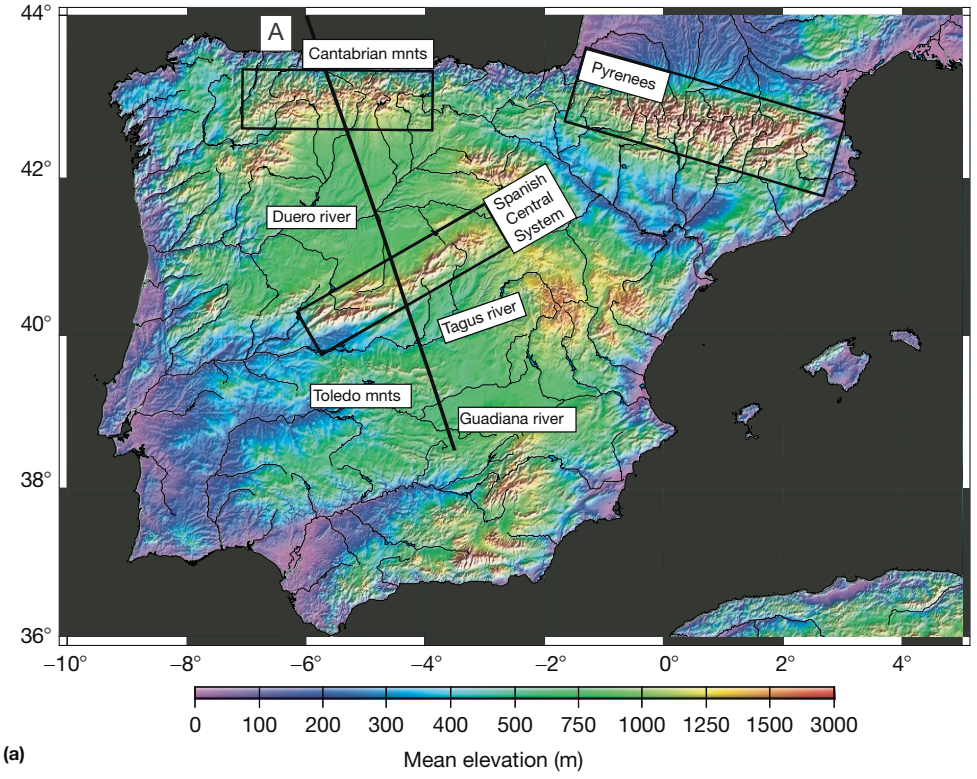

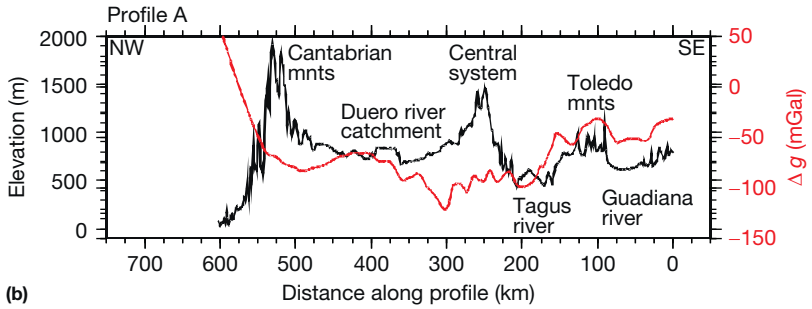

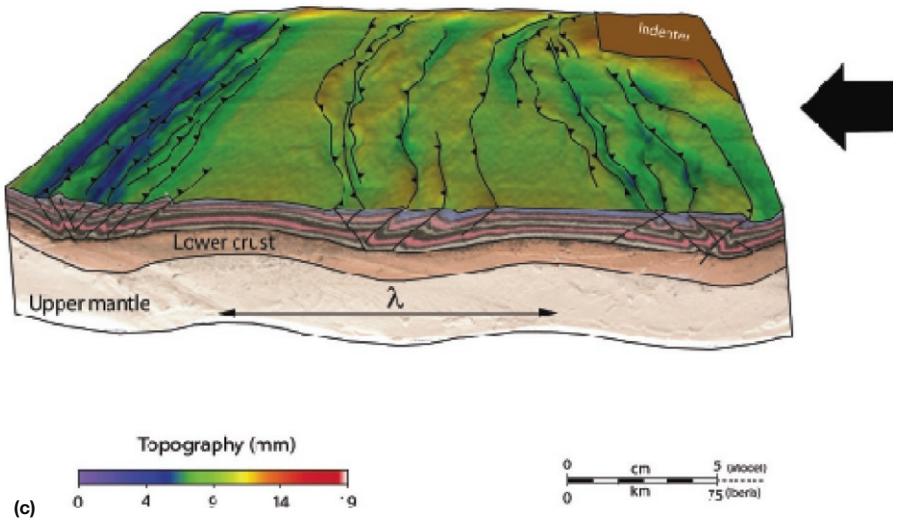

Figure 45 (a) First-order features of basin geometry of folded lithosphere of Iberia. (b) Topography displaying cylindrical patterns of alternating parallel trending highs and lows and corresponding gravity anomalies (red line) (see Cloetingh et al., 2002). (c) Results from analog modeling experiments, displaying pop-up structures underlying topographic highs, accompanied by folding of the Moho (Fernández-Lozano et al., 2011, 2012). Top panel shows final top view of the analog model and location of the cross section shown below. Arrow indicates the direction of the moving wall. λ is the wavelength of folding.

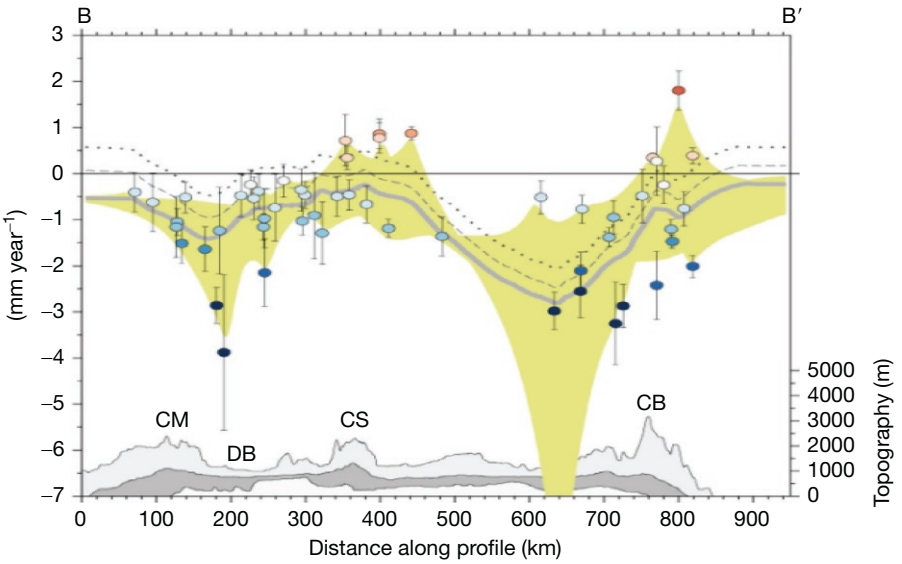

Figure 46 Observed vertical velocity field over the Iberian region (after Serpelloni E, Faccenna C, Spada G, Dong D, and Williams SD (2013) Vertical GPS ground motion rates in the Euro-Mediterranean region: New evidence of vertical velocity gradients at different spatial scales along the Nubia-Eurasia plate boundary. *Journal of Geophysical Research: Solid Earth* 118: 6003–6024). The cross section of the observed vertical velocities (colored circles), with 1σ uncertainty error bars, of GPS stations along cross section B–B′ in **Figure 45(a)**. The gray line shows the median value estimated from the smoothed spline fit of the vertical velocity field, while the yellow envelope shows the minimum and maximum vertical rates values in the swath, filtered using a 10 km Gaussian filter. Dark gray profile shows the average (median) topography, while the light gray and white profiles show the maximum and minimum elevations, respectively. The dotted and dashed lines show the median value estimated from the smoothed spline fit of the vertical velocity field corrected for the GIA component using two different models. DB, Duero basin; CS, Central System; CM, Cantabrian Mountains; and CB, Betic Cordillera.

2009) is probably one the deepest basins in the world. It is flanked by the Alborz Mountains to the south, with an elevation of 2–4 km (see **Figure 48**). The transition between basin and flanking high is abrupt and coincides with a coastline bounded by a major fault system. The formation of the South Caspian Basin is enigmatic. Attempts to explain it as an extensional basin or as a foreland basin have been unsuccessful. There is a lack of evidence for basin extension, and both stretching models and topographic loads and slab pull operating on downflexed lithosphere in foreland basin systems cannot explain differential vertical motions of this order of magnitude. As a result, phase changes in continental crust have been proposed as a mechanism for the formation of this superdeep basin (Artyushkov, 2007). A limitation in conclusively resolving the basin formation mechanism is the lack of multichannel seismic reflection data capable of imaging crustal structure below the thick sedimentary sequences. Over the last few years, however, other constraints on the area have become available (e.g., Guest et al., 2007).

Figure 48 presents a cross section of northern Iran and the South Caspian Basin (Guest et al., 2007). As shown, wavelengths for compressional folding of the lithosphere are typically in the range of 400 km. Although the actual basin formation mechanism for the Caspian Basin is not well resolved (e.g., Artyushkov, 2007), late Neogene folding has been affecting a lithosphere probably thermally reset by middle Late Jurassic marginal basin formation (Guest et al., 2007) with a thermomechanical age at the onset of collision of 130–150 Ma. Satellite data demonstrate an exceptionally large gravity anomaly over the basin (Kaban, 2002). Seismic tomography shows slab detachment under the Iranian plateau (Alinaghi et al., 2007; Hafkenscheid et al., 2006) beginning at about 10–15 Ma.

Basin analysis has shown that basement inversion has occurred 20 Ma ago, simultaneously with the slowing of Arabian/Eurasian Plate convergence and the onset of accumulation of Neogene clastics in foreland basins (e.g., Fakhari et al., 2008). By 10 Ma, contraction occurred by underplating of the Arabian crustal units beneath the Iranian Plate. Estimated shortening rates from current geodetic surveys (Vernant et al., 2004) are 7 mm year^{-1}. Results from geothermochronology demonstrate rapid uplift of the Alborz Mountains, with rates of 0.7 km My^{-1} exhumation between 6 and 4 Ma (Axen et al., 2001), implying ~10 km of uplift. This uplift was nearly synchronous with rapid South Caspian subsidence (Nadirov et al., 1997) and subsequent folding (Devlin et al., 1999). South Caspian sedimentation rates locally increased more than tenfold at ca 6 Ma, with more than 10 km of sediments deposited since then. Axen et al. (2001) argued that if ~10 km of post-6 Ma sediments is present in this basin, then as much as 20 km (equivalent to 80%) of the structural relief of about 25 km between the high Alborz and the southernmost Caspian basement may be younger than 6 Ma.

Folds in the southernmost Caspian Basin (Devlin et al., 1999) and in the Neogene of the northern Alborz foothills imply contraction. The lack of a crustal root under the Alborz Mountains also points to a flexural support by the South Caspian basement (Axen et al., 2001). The simultaneous reversal of Zagros strike slip and extrusion of central Iran, coarse Zagros molasse deposition, Dead Sea transform reorganization, and Red Sea oceanic spreading (Chu and Gordon,

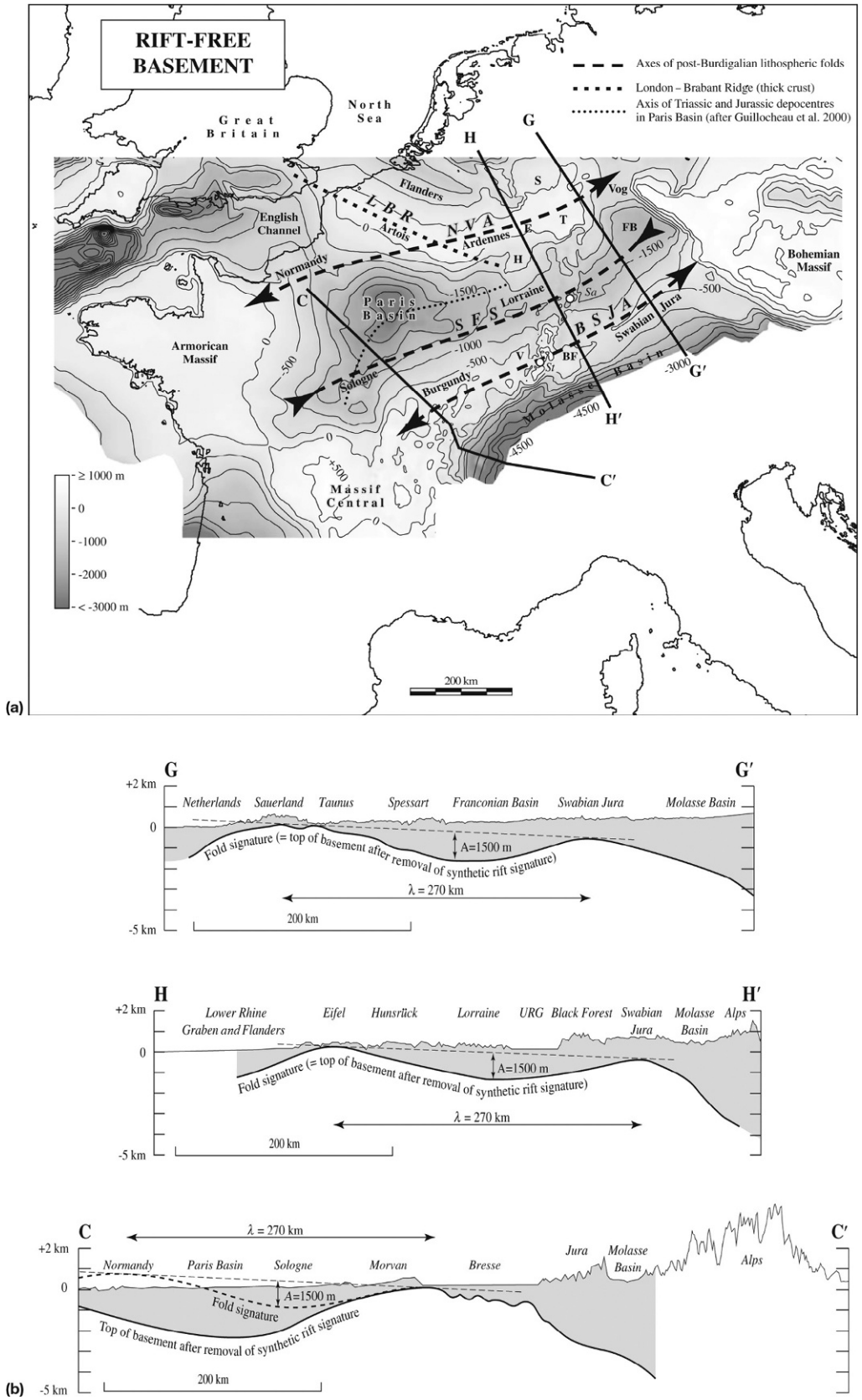

Figure 47 (a) Map of elevation of basement in the NW Alpine foreland with rift signature removed from the map of actual basement (reproduced from Bourgeois O, Ford M, Diraison M, et al. (2007) Separation of rifting and lithospheric folding signatures in the NW-Alpine foreland. *International Journal of Earth Sciences* 96: 1003–1031). Dashed lines show axes of late Neogene lithospheric folds, with a succession of anticlines and synclines: the Normandy–Vogelsberg anticline (NVA), Sologne–Franconian Basin Syncline (SFS), and the Burgundy–Swabian Jura Anticline (BSJA). LBR, London–Brabant Ridge with thick crust; BF, Black Forest; FB, Franconian Basin; E, Eifel; H, Hunsrück; S, Sauerland; T, Taunus; V, Vosges. (b) Cross sections of top basement in the NW Alpine foreland with rift signatures removed (Bourgeois et al., 2007; see for location Figure 47(a)). Thin line: Actual topography surface. Bold line: Elevation of top basement as predicted in the absence of rifting. Fold signatures are similar with a wavelength λ of 270 km and amplitude A of 1500 m in the Franconian Basin (cross section G–G′) and in the upper Rhine Graben area (cross section H–H′). In the Paris Basin, the development of folds with assumed same wavelength and amplitude (stippled bold line in cross section C–C′) implies subsidence of Sologne and uplift of Normandy.

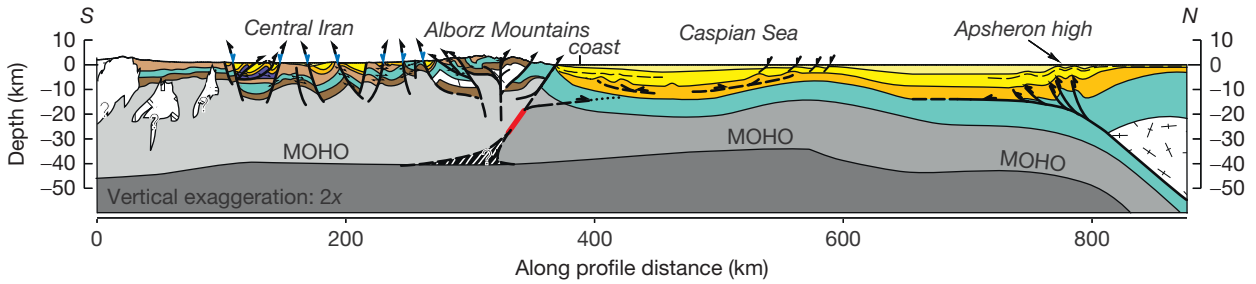

Figure 48 Schematic north–south trending cross section illustrating the basic tectonic setting for northern Iran and the South Caspian Basin (Guest et al., 2007), illustrating basin inversion of the central Iranian basin, pronounced differential topography at the transition of the Alborz Mountains, with a topographic high of several kilometers and the South Caspian Basin with about 20 km of sedimentary infill.

1998) all initiated around 5 ± 2 Ma (e.g., Axen et al., 2001; Smit et al., 2008a,b, 2010), was interpreted by these authors in terms of a widespread tectonic event. Slab detachment could explain part of the recent uplift of Iran, but does not directly explain the simultaneous dramatic subsidence in the adjacent Caspian Basin. However, slab detachment could have an indirect effect if reducing slab pull forces acting on the downgoing lithosphere promote the development of compressional stresses in both the downgoing and the overriding plates (Cloetingh et al., 2004; Matenco et al., 2007).

Guest et al. (2007) argued in favor of compressional deformation of the South Caspian Basin/Alborz Mountains. This interpretation was largely based on available industrial seismic reflection data and gravity data for the basin and followed a similar proposition made for the late-stage deformation of the adjacent Black Sea (Cloetingh et al., 2008; Nikishin et al., 2003). Guest et al. (2007) presented kinematic models, without addressing the reason for the difference in the order of magnitude of the basin depression and the adjacent high. Analog experiments (Sokoutis et al., 2005) show that when compression acts on two blocks with contrasting thickness (and rigidity), a major syncline will develop on top of the suture zone separating these blocks, flanked by an anticline of much lower amplitude. These results are consistent with predictions from folding theory that as a result of the acting gravity field, downwarping is mechanically more effective than upwarping against the action of gravity forces.

6.12.4.2.2.5 Basins on folded lithosphere in Eurasia

Comparison of lithospheric deformation in central Asia, Iberia, the NW European Alpine foreland, and the South Caspian Basin demonstrates common features compatible with an interpretation in terms of basins developed on folded lithosphere. Among these are their symmetrical shape, dimensions, and the temporal association of their basin formation history with the buildup of intraplate stresses. Important differences can be observed between the central Asian and Iberian basins and the South Caspian Basin on one side and the European Alpine foreland on the other side.

The central Asian basins and the basins of the Iberian Plate were initiated by Tertiary folding, whereas the European Alpine foreland underwent a polyphase history, following Carboniferous and Triassic stretching (Le Solleuz et al., 2004; Scheck and Bayer, 1999), prior to Late Cretaceous–early Cenozoic folding. The origin of the South Caspian Basin is not well resolved, but km-scale vertical motions are compatible with a megafold as a prime control on present-day basin geometry. These differences in evolution have a pronounced impact on basin dimensions and on the nature of basin fill. The central Asian basins, the folded basins of Iberia, and the South Caspian Basin have a wavelength compatible with theoretical predictions. In contrast, the fold wavelengths of the European Alpine foreland appear to be primarily controlled by the preexisting geometry of the sediment–basement interface and preexisting Moho topography inherited from the prefolding stage.

Differences occur also in the development of the ranges flanking the basins. In central Asia and Iberia, these highs have amplitudes and widths comparable to the prediction for periodic folding, whereas in the Paris Basin and the North German Basin, these highs are less well developed. The ratio of the depth of the South Caspian Basin to the height of the flanking Alborz Mountains is compatible with a megafold under this area of dramatic differential topography. The large amplitudes of folding at the flanks of the Pannonian Basin system are compatible with its extremely weak rheology. Differences in the amplitude of the highs might also partly result from the differences in neotectonic shortening. The highs bounding the basins of Iberia, South Caspian Basin, and central Asia, located relatively close to the site of ongoing convergence, are still experiencing active uplift. This is much less the case for the low-strain-deforming areas of the NW European Platform and the North German Basin where the peak compression occurred during Late Cretaceous–early Cenozoic. Another difference occurs in the depositional regime prevailing in these basins. The closed basin systems of central Asia and Iberia are dominated by continental and lacustrine deposits, whereas capture is usually a late-stage feature of these basins. The Paris Basin of the NW European Platform has a basin fill largely dominated by marine sediments deposited during the prefolding stage of their evolution, followed by marine Tertiary successions in the basin center with truncated basin margins. The creation of basin highs in this case was in general not capable of interrupting open connections to marine environments.

A general observation for all these basin systems is the flatness of sedimentary sequences in the depocenters. Faulting plays a minor role in the basin development. Faulting appears to be concentrated at the basin margins, with a highly variable depth extent, varying from upper crustal-scale faults bounding pop-up structures in the Iberian Central System to minor faulting in the basement of the North German Basin. The thermal regimes of the basins are similar with thermal histories strongly affected by subsidence and sediment deposition on downflexed lithosphere, preconditioned by its thermomechanical age.

6.12.4.2.3 Basin geometry and accommodation space

6.12.4.2.3.1 Basin shape

Folding of the lithosphere leads to a symmetrical pattern of downwarped areas (synclines) flanked by highs (anticlines) of similar amplitude and wavelength, like the Fergana basin in central Asia (Burov and Molnar, 1998). This symmetry is in marked contrast to the asymmetrical shape of foreland basins, formed by flexure in front of an orogenic wedge, which are flanked by a flexural bulge of which the amplitude is only up to 10% of the maximum depth of the foreland depression (Royden, 1988a,b; Zoetemeijer et al., 1999). Both types of compressional basins show linear nature alignment of parallel depocenters and flanking highs. An important difference is the presence of parallel trending depocenters for lithospheric folding, whereas foreland flexural basins have a single depositional system. In addition, basins developed on folded lithosphere have a static location of the axis of their depocenters, in contrast to foreland basins, where the axis of depocenters can migrate with time (e.g., Zoetemeijer et al., 1993).

In both cases, the integrated strength of the lithosphere (Tesauro et al., 2007; Watts and Burov, 2003) defines the characteristic width of the basins. For folding, the basin width roughly corresponds to one-half of the fold wavelength (λ), which equals 5–10 times the thickness of the strong core of the lithospheric plate, h ($h = 10$–100 km, i.e., $\lambda = 50$–1000 km). In the case of crust–mantle decoupling, which occurs in relatively young plates, two dominant folding wavelengths develop (typically 250–400 km and 50–100 km). Thus, two basin populations may be observed, one imbricated within the other. In the case of flexural foreland deformation, the width of the basin is controlled by the flexural parameter and is thus of the same order as the largest fold wavelength.

6.12.4.2.3.2 Subsidence patterns

Lithospheric folding results from an instability in the lithosphere due to stress/strain incompatibilities that develop in rheologically stratified layers under compressive strain. This process typically operates with timescales of the order of 1–10 My (Cloetingh et al., 1999). The preservation of lithospheric folds appears to depend strongly on the thermomechanical age of the underlying lithosphere (Cloetingh et al., 1999). Folds in young lithosphere will not be preserved upon relaxation of the stress field, whereas ones in cratonic lithosphere will be well preserved (Cloetingh et al., 1999).

Figure 49(a) displays characteristic basin subsidence patterns predicted by folding of 150 and 300 Ma old lithosphere due to a 3 cm year^{-1} shortening rate. As illustrated (**Figure 49(b)**), the differential motions occur in three distinct phases:

- *Stage 1* is the basin formation phase, coinciding with the initiation and development of folding, which is marked by an acceleration of subsidence in the basin and uplift in the flanking highs. As a result of the time lag between sediment supply and the creation of accommodation space, during the few My needed to form the basin, deposition cannot keep up with subsidence causing sediment-starved basins. A similar pattern occurs in pull-apart basins (Pitman and Golovchenko, 1983), which are also associated with ultrarapid subsidence in their formation stage also lasting only a few My.

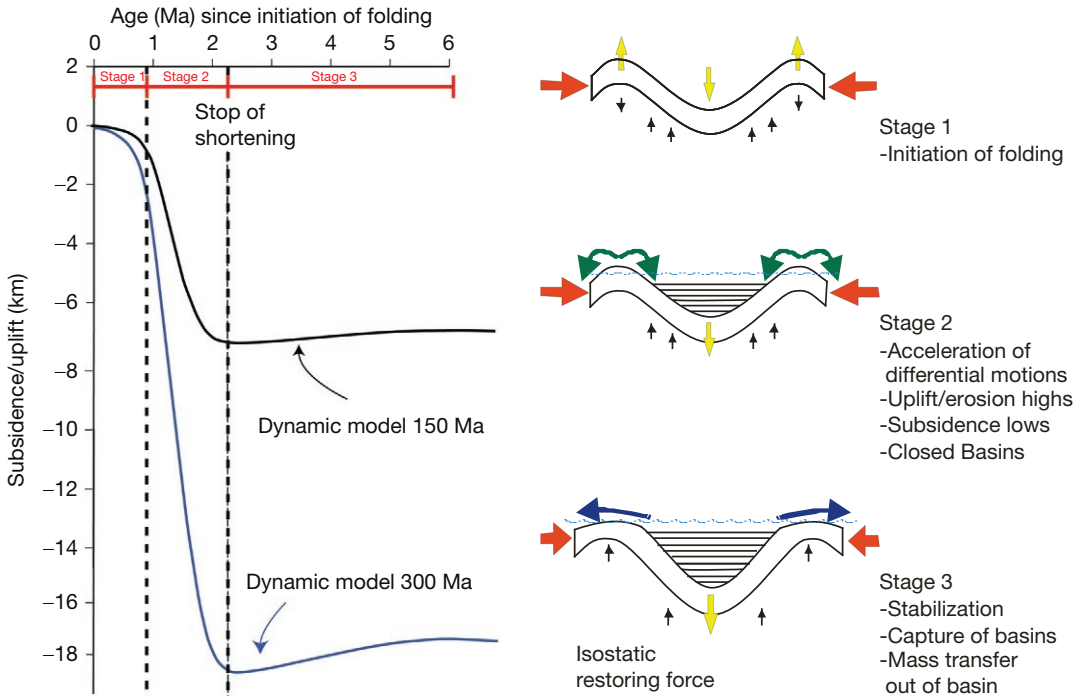

Figure 49 (a) Characteristic subsidence patterns in center of synclinal depression for thermomechanical age of 150 and 300 Ma, respectively. Shortening rate is 3 cm year^{-1}. (b) Characteristic stages in the evolution of a basin formed by lithospheric folding. Stage 1: Basin formation stage, acceleration of subsidence and uplift during folding. Stage 2: Steady state: equilibrium between tectonic subsidence and sediment supply from eroding highs. Stage 3: Capture of folded basin: overall uplift and erosion. Wiggled waved blue line marks position of base level. Reproduced from Cloetingh S and Burov E (2011) Lithospheric folding and sedimentary basin evolution: A review and analysis of formation mechanisms. *Basin Research* 23: 257–290.

- *Stage 2* is the basin preservation stage, where equilibrium develops between sediment supply and sediment deposition. As a result, the basin will be rapidly filled to overfilled.
- *Stage 3* is the basin destruction phase, characterized by basin capture and removal of sediments to areas outside the folding system. During this phase, the size of the accommodation space is reduced and erosion occurs on both flanks and depocenter. Thus, the net effect of these three stages is that lithospheric folding will lead to the development of distinct depositional–erosional cycles.

Characteristic patterns for vertical motions for folding of continental lithosphere of 150 and 300 Ma old (**Figure 49**) demonstrate a remarkably short timescale in which substantial amounts of tectonic subsidence are induced by the process of lithospheric folding. As shown by **Figure 49**, within 1 My after the initiation of folding induced by shortening the lithosphere at a rate of 3 cm year^{-1}, subsidence rates are in the order of 5–15 km My^{-1}, depending on the thermomechanical age of the lithosphere. Thus, folding appears to be more effective in middle-aged lithosphere of 300 Ma than in lithosphere of younger ages (Cloetingh et al., 1999; Burov and Cloetingh, 2009). After 2 My, a slow uplift phase starts of relatively minor magnitude of the order of a few hundreds of meters to a km. The predicted subsidence in **Figure 49** is for the center of the syncline. As pointed out earlier, erosion of the uplifted flanks is taken into account, adopting a diffusive equation approach to erosion (see Burov and Cloetingh, 1997; Cloetingh et al., 1999, for further details).

The alignment of parallel highs and basins of similar dimensions has an important consequence for the areal extent of the source areas for sediments available for deposition in the folded depressions. In comparison with foreland basins, the distribution of sources is more symmetrical, superseding the volume of sediments that can be eroded from, for example, the flexural foreland bulge. As noted earlier, erosion reduces the contribution of gravity-dependent terms and accelerates local deformation. Erosion, therefore, has an important feedback with the geometry of the accommodation space in changing the spectrum of wavelengths (Cloetingh et al., 1999). Erosion acts as a filter, suppressing the shorter wavelengths in folded basin topography. Strong erosion, insufficiently compensated by tectonic deformation, can even wipe out most of the topography. However, if the erosion is tuned to the average elevation rates (**Figure 50**), it may dramatically accelerate folding (Cloetingh et al., 1999).

There has been a rapid development in the application of stratigraphic modeling packages to sequence stratigraphy over the last two decades (e.g., Alzaga-Ruiz et al., 2009; Cross, 1990). Among the different types of modeling programs, the forward stratigraphic modeling approach has been applied extensively by basin modelers from academia and petroleum industry (e.g., Lawrence et al., 1990; Roure et al., 2010b). Forward stratigraphic modeling commonly starts with an estimate of the initial conditions related to an adopted basin formation mechanism and controlling parameters, followed by a forward prediction in time. Most of these software packages are based on sequence stratigraphic concepts (Wilgus et al., 1988). Assumptions for initial subsidence are either ad hoc or related to stretching (e.g., Lawrence et al., 1990) or foreland flexure (Garcia-Castellanos et al., 1997), but to date do not include lithospheric folding as a basin formation mechanism.

6.12.4.2.4 Thermal regime

Lithospheric folding is controlled by the interplay of lithospheric stresses and inherited strength of the lithosphere. The thermal regime controls the rheological profile and differs between folded basins developed in young lithosphere and basins in cratonic lithosphere. The latter are associated with much lower thermal gradients than basins developed on young continental lithosphere. As for foreland basins, the initiation

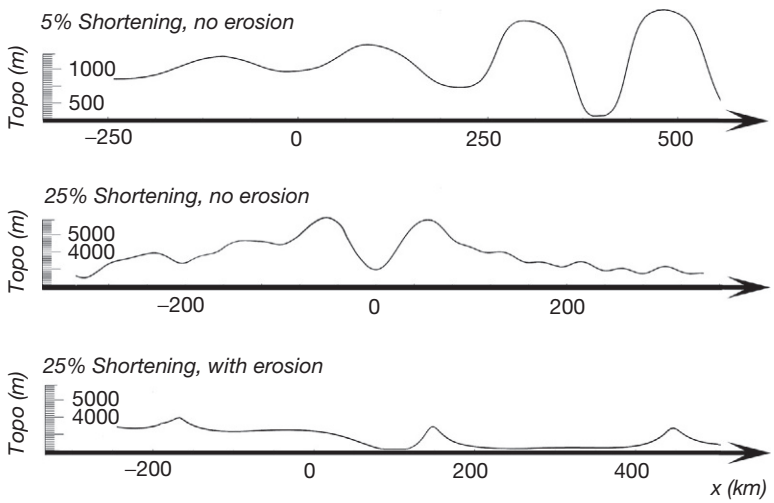

Figure 50 Illustration of the effect of erosion, which acts as a filter suppressing the short wavelengths. In this case, the wavelength and amplitude vary along the cross section at different stages of deformation due to a partial crust–mantle coupling and strain localization for a 400 Ma old lithosphere with weak quartz-dominated rheology. After 5% shortening (top), after 25% shortening (middle), after 25% shortening (bottom), strong zero order diffusional erosion (Avouac and Burov, 1996) tuned to keep mean elevation at the level of 3000 m. Erosion reduces the contribution of gravity-dependent terms (middle wavelength) and accelerates local deformation. Strong erosion, insufficiently compensated by the tectonic deformation wipes out most of the topography. Reproduced from Cloetingh S, Burov E, and Poliakov A (1999) Lithosphere folding: Primary response to compression? (From central Asia to Paris basin). *Tectonics* 18: 1064–1083.

of folding is not associated with a thermal instability, unless folding occurs in conjunction with plume activity (Burov and Cloetingh, 2009). Following the deposition of radiogenic sediments in the folded depression, sediment blanketing will affect the heat flow (Lavier and Steckler, 1997; Stephenson et al., 1990; Van Wees et al., 2009), modifying the surface heat flow in the basin center. As pointed out by Lavier and Steckler (1997) and Ziegler et al. (1998), the effect of sediment fill is to weaken the lithosphere. The low thermal conductivities of the sediments lead to high temperatures in the upper lithosphere and consequently low local yield strength. During basin subsidence, sediments deposited in the central parts of the basin might be exposed to temperature windows corresponding to hydrocarbon generation. At the same time, sediments predating the folding may have undergone extra burial due to synfolding sedimentation. An example is the Paris Basin, where source rocks of Toarcian age were folded in Cenozoic time (Guillocheau et al., 2000; Le Solleuz et al., 2004).

During basin capture, overall cooling takes place. This effect is illustrated by characteristic thermal evolution for different thermotectonic ages of 150 and 300 Ma of the folded continental lithosphere (**Figure 51**), incorporating radioactive heat production in the sediments filling in the synclinal basement depression (**Figure 49(b)**). Subsidence induced by folding is calculated for the center of the basin. Basins developing on folded lithosphere are characterized by their relatively low heat flow at the onset of folding, followed by a steady increase with time, doubling the heat flow over a time interval of the order of 5 My following the cessation of shortening. This increase is primarily due to the contribution of radioactive heat production in the very substantial pile of sediments accumulating in a relatively short time interval. The patterns of heat flow are similar for different thermomechanical ages of the lithosphere, with the oldest lithosphere having the lower heat flow. Older ages enhance the accommodation space and the contribution of the sediments to heat flow but are compensated by a larger decrease in heat flow with aging lithosphere. Another important factor is the mode of folding. Crustal-scale folding, which is characteristic for Lake Issyk-Kul, will be associated with shorter wavelengths, shallower basin depths, and thinner sequences of heat-producing sediments than for mantle–lithospheric folding. This effect might explain the relatively low heat flow observed in Lake Issyk-Kul (Vermeesch et al., 2004).

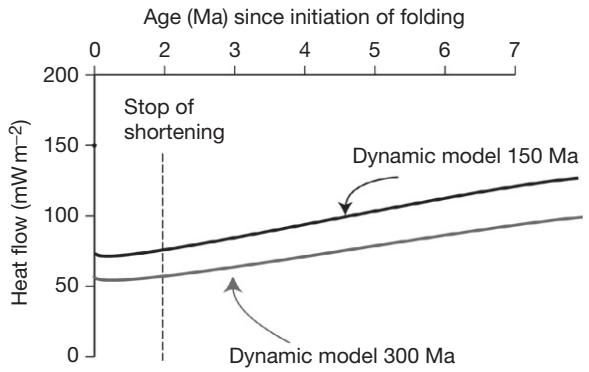

Figure 51 Thermal consequences of lithospheric folding and associated basin evolution depicted in **Figure 49**. The heat flow response is marked by an initial decrease in heat flow as a consequence of rapid sedimentation, followed by a progressive long-term heat flow increase after termination of shortening. Thermal conductivity of sediments is 2.5 Wm^{-1} C^{-1}. Surface radiogenic heat production H_s is 9.5×10^{-10} W kg^{-1}. Concentration of radiogenic heat sources within sedimentary basin fill is homogeneous. Exponential decay of heat production is assumed for underlying crustal rocks. Note that the figure shows only 7 Ma of thermal evolution. The heat flow does not increase anymore after some tens of Ma and subsequently decreases at later stages. Reproduced from Cloetingh S and Burov E (2011) Lithospheric folding and sedimentary basin evolution: A review and analysis of formation mechanisms. *Basin Research* 23: 257–290.

6.12.4.2.5 Modes of brittle deformation and faulting

The role of preexisting faults on the development of folding has been investigated through numerical experiments on folding of brittle–elastoviscous lithosphere (Beekman et al., 1996; Cloetingh et al., 1999; Gerbault et al., 1999) and through analog experiments on plastic–elastic lithosphere (e.g., Martinod and Davy, 1992; Sokoutis et al., 2005). These studies show that lithospheric folding and faulting can develop simultaneously and that preexisting crustal-scale faults do not prevent but instead promote the development of folding instabilities. The instabilities, in turn, can initiate the formation of new faults at the inflection points of the folds. Although the usual expectation is that faulting prevents folding, this view neglects the role of the gravity and friction on faults in the behavior of the large-scale fault-and-fold systems. As also observed in analog experiments (Martinod and Davy, 1992), this continuous behavior of faulted lithosphere can be explained by fault locking due to gravity and friction. After some sliding (uplift) on a fault, the potential gravitational energy working against friction generated by horizontal shortening forces becomes too high. As a result, the fault locks and the rock mass transmits horizontal stresses as a continuous medium. As the compression continues, one of the folds finally starts to grow faster than others, resulting in a loss of the periodicity and the formation of a megafold (see also the discussion in the context of the Fergana and Tadjik basins of central Asia).

Following the initiation of folding and the further buildup of compressional stresses, folding, therefore, will usually be accompanied by brittle deformation and faulting in the crust and upper lithosphere. The surface expression of folding in uniform lithosphere is frequently in the form of fault-controlled pop-up and pop-down structures and inverted basins (e.g., Cobbold et al., 1993), accompanied by the development of imbrications of bivergent thrust wedges at the areas where shortening is applied (Sokoutis et al., 2005). These findings (see **Figure 52**) are corroborated by observations in the Iberian Central System, where folding of Variscan lithosphere with a thermomechanical age of 280 Ma occurs (Cloetingh et al., 2002). Here, the brittle deformation associated with crustal-scale folding expressed by a folded Moho is mechanically decoupled from folding of the mantle–lithosphere (Fernández-Lozano et al., 2011, 2012; see **Figure 45(b)**).

Crustal and mantle faults may develop as a result of folding (Burov and Molnar, 1998; **Figure 53**). Folding can continue after these faults develop, and folding and faulting can coexist for times of several My (**Figure 45(b)**). For crust–mantle decoupling, a complex distribution of crustal faults and surface undulations can be expected, with crustal faults not necessarily connected to mantle faults. Numerical experiments suggest

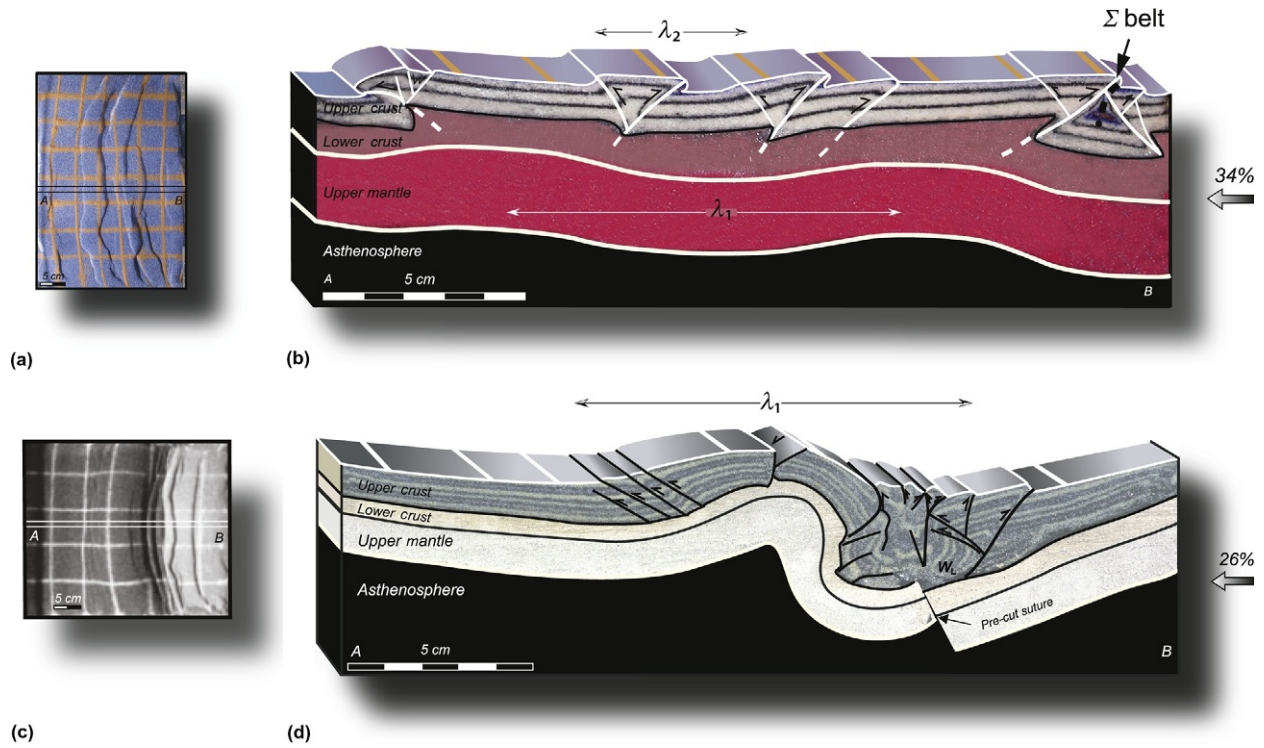

Figure 52 Results of analog tectonic experiments for lithospheric folding. (Top) Folding of uniform lithosphere. Cross section demonstrating pop-up structures in the upper crust above highs induced by lithospheric folding. λ_1 and λ_2 indicate first-order and second-order wavelengths, respectively. Imbrication of bivergent thrust wedges is responsible for the relatively high-topography belt ($\sum$-belt) at the right hand of the model and closure of prismatic basins with a rather undisturbed bottom. The progressive sinking of the prismatic basin allows transferring of the crustal material (i.e., cover sediments) that was initially situated at the surface of the model down to significant depth. (a) Final top view of model after 34% of bulk shortening. (b) Cross section located on the top view. Arrows indicate the direction of the moving wall. Note the similarity to central Iberia (**Figure 45**). (Bottom): Geometries predicted by analog experiment, shortening a lithosphere with two contrasting blocks, bounded by suture. A deep synclinal depocenter develops over the suture zone, flanked by an anticline of smaller amplitude. (c) Final top view of model after 26% of bulk shortening. (d) Cross section located on the top view. λ_1 indicates a first-order wavelength of the folding. Note the striking similarity to the configuration of the South Caspian Basin/Alborz mountain system displayed in **Figure 48**. Reproduced from Sokoutis D, Burg JP, Bonini M, Corti G, and Cloetingh S (2005) Litho spheric-scale structures from the perspective of analog continental collision. *Tectonophysics* 406: 1–15.

that mantle faults are unlikely to be longer than a few km in depth (Burov and Molnar, 1998). Such faults may also not develop at longer wavelengths of folding connected with stronger lithosphere. However, deep-seated faults in mantle–lithosphere can develop when cratonic lithosphere is folded (Cloetingh et al., 1999). The mode of faulting, depth extent, and spacing of faults depend on the thermomechanical age of the lithosphere. Once the development of folding begins in a basin, the intensity and depth penetration of faulting will accelerate. The mode of decoupling between crustal folding and mantle folding is crucial. Discontinuities within the folded lithosphere will localize the development of deep synclines, flanked by more modest anticlines (Sokoutis et al., 2005), and affect the distribution of faulting (**Figure 52**).

During the next phase of basin evolution, when a steady state is reached between the creation of accommodation space and sediment supply, only minor faulting will occur. This is in marked contrast with the later phase of basin capture, which is in general characterized by erosion and narrowing of the basin. Due to erosional unloading, stress relaxation will occur, manifested in upward propagating faults.

6.12.4.2.6 Interaction of folding with other tectonic processes

Folding, in addition to being a basin-forming mechanism, frequently interacts with other tectonic processes. As pointed out by Cloetingh (1988), intraplate compression can modify preexisting basins. As discussed earlier, the Pannonian Basin of central Europe created by Miocene back-arc extension appears to be an example of such a configuration, characterized by atypical aperiodic folding. Other examples are cratonic sag basins where intraplate compression (Cloetingh, 1988) is thought to occur in interaction with phase changes in the lithosphere (Artyushkov, 2007). Examples of these might be the Barents Sea (Ritzmann and Faleide, 2009) and possibly the South Caspian Basin, although in the latter case, preorogenic extension cannot be ruled out (Guest et al., 2007). Basins exposed to changes in tectonic regime will have a polyphase record (Cloetingh and Ziegler, 2007), characterized by a superposition of more than two regimes, such as preorogenic extension, foreland flexure, and late-stage folding. This sequence appears to be characteristic for some very deep foreland basins, such as the Focşani Depression of the Romanian Carpathians,

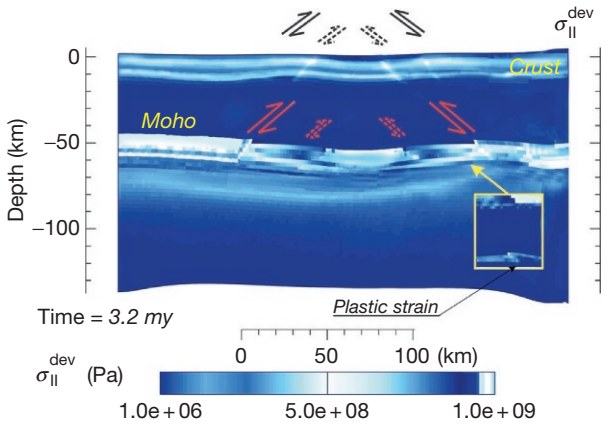

Figure 53 Numerical experiment on faulting developed in folded continental lithosphere of 150 Ma. Note different wavelengths of the crustal and mantle part of the lithosphere and differences in spacing and character of faults that are conditioned by folding. In each layer, two fault spacings occur: A shorter one proportional to layer thickness (also controlled by the strength contrast between the stiff layer and embeddings) and the longer wavelength controlled by the wavelength of folding. The insert shows plastic (brittle) strain localization characterizing initialization of mantle faulting. Reproduced from Burov EB and Molnar P (1998) Gravity anomalies over the Ferghana Valley (central Asia) and intracontinental deformation. *Journal of Geophysical Research-Solid Earth* 103: 18137–18152.

with more than 16 km of sediments, which was affected by extension due to the opening of the Black Sea basin, followed by foreland flexure and overprinted by Late Miocene compression (Tarapoanca et al., 2003). As pointed out earlier (Ziegler and Dèzes, 2007), the northwestern European foreland indicates folding, overprinting, rifting, and foreland flexure. Quantification of the topographies created by rifting and foreland flexure and correcting for them is essential to reconstruct the shape of the additional accommodation shape created by subsequent lithospheric folding (Bourgeois et al., 2007).

The impingement of plumes on the base of continental lithosphere can induce differential topography similar to the surface deflections characteristic for lithospheric folds (Burov et al., 2007; Guillou-Frottier et al., 2007). Plumes and lithospheric folds frequently interact in space and time in the geologic record (Burov and Cloetingh, 2009; Ziegler and Dèzes, 2007). Therefore, the evolution of folded lithosphere basins can be overprinted by the signatures of a plume or vice versa. This will lead to an amplification of the induced vertical motions, particularly significant for young and intermediate age lithosphere. Emplacement of hot upper mantle material will raise temperatures in the lithosphere and increase heat flow. Due to the lag time in the propagation of heat, the effect at the surface might become manifest only after several tens of My. Plume emplacement might also weaken the lithosphere, making it more prone to compressional fault reactivation after cessation of the folding.

Thermomechanical modeling illustrates the relative effectiveness of amplification of lithospheric deformation and topographic effects induced by plumes though folding and vice versa and consequences for basin evolution. Burov and Cloetingh (2009) examined the response times and time lags involved and whether small plumes were more efficient in localizing deformation than large plumes. Plume-affected folding appears to accelerate differential vertical motions (uplift and subsidence) in sedimentary basins. For the discrimination of plumes and folding as mechanisms for sedimentary basin formation, it is critical to access constraints on the presence or absence of radial versus linear symmetry, heat flow anomalies, and gravity and geoid data. Plume activity facilitates folding, by dramatically lowering the stress levels required (Burov and Cloetingh, 2009). Plume impact also reduces the fold wavelength and localizes folding above the plume impact area, with important consequences for the geometry of sedimentary basins.

6.12.5 General Conclusions and Future Perspectives

Sedimentary basin systems are sensitive recorders of dynamic processes controlling the deformation of the lithosphere and its interaction with the deep mantle and surface processes. The thermomechanical structure of the lithosphere exerts a prime control on its response to basin-forming mechanisms, such as rifting and its deflection under vertical loads, as well as its compressional deformation. Table 5 illustrates differences and similarities in basin shape, dimensions, subsidence characteristics, thermal evolution, and faulting histories between various basin types. Polyphase deformation is a common feature of some of Europe's best-documented sedimentary basin systems. The relatively weak lithosphere of intraplate Europe renders many of its sedimentary basins prone to neotectonic reactivation. Tectonic processes operating during basin formation and during the subsequent deformation of basins can generate significant differential topography in basin systems. As there is a close link between erosion of topographic highs and sedimentation in subsiding areas, constraints are needed on uplift and coeval subsidence to validate quantitative process-oriented models for the evolution of sedimentary basins. Integration of analog and numerical modeling provides a novel approach to assess the feedback mechanisms between deep mantle, lithospheric, and surface processes. The analysis of European basin systems demonstrates the importance of preorogenic extension of the lithosphere in the evolution of flexural foreland basins. Furthermore, compressional reactivation of extensional basins during their postrift phase appears to be a common feature of Europe's intraplate rifts and passive margins, reflecting temporal and spatial changes in the orientation and magnitude of the intraplate stress regime. Moreover, in the intraplate domain of continental Europe, which was thermally perturbed by Cenozoic upper mantle plume activity, lithospheric folding plays an important role and strongly affects the pattern of vertical motions, in terms of both the basin subsidence and the uplift of broad arches.

The development of sedimentary basins is, therefore, the intrinsic result of the interplay between lithospheric stresses and rheology and thermal perturbations of the lower lithosphere–upper mantle. The elucidation of paleostresses, paleotemperatures, and paleorheologies of the lithosphere is vital for the reconstruction of dynamically supported paleotopography. Rift shoulder topography and flexural topography

Table 5 Key characteristic features of different classes of sedimentary basins

Basin type	*Basin shape*	*Dimensions*	*Subsidence characteristics*	*Thermal evolution*	*Faulting history*
FLB	Symmetrical	Width: 50–600 km Depth: up to 20 km	Accelerated subsidence, timescales 1–10 My, simultaneously uplift at highs	No initial heating; heat flow increases in first 10s My with sediment deposition and burial and subsequently decreases	Intensive deformation, accelerating trough basin formation phase
FB	Asymmetrical	Width: 50–250 km Depth: up to 10 km	Linear subsidence, interrupted by short-lived faster subsidence during thrusting phases; timescales 10–100 My; simultaneously uplift from thrust front and foreland bulge	No initial heating; heat flow increases with time with sediment deposition and burial	Faulting and thrusting limited to orogenic wedge; minor deformation through faulting in foreland
EB	Symmetrical (pure shear); asymmetrical (simple shear)	Width: 30–500 km Depth up to 10 km	Rapid initial subsidence, followed by postrift decay in subsidence; in case of multiple rifting repeated accelerated subsidence; timescales for postrift subsidence of the order of 70 My. At rifting stage, development takes place of asymmetrical rift-shoulder topography, flanking the rift	Initial heating event, followed by decaying heat flow	Extensional faulting limited to basin formation phase; during postrift absence of faulting
PAB	Symmetrical	Width: 20 km Depth: up to 10 km	Very rapid initial subsidence, followed by postrift decay in subsidence, timescales: 1–10 My. In early stage, sedimentation cannot keep up with subsidence	Initial heating event, followed by very rapid decay in heat flow	Extensional faulting limited to basin formation phase; during postrift absence of faulting
ICB	Symmetrical	Width: 500–1000 km Depth: up to 10 km	Slow subsidence, punctuated by periods of faster subsidence, possibly related to large-scale tectonic events; characteristic timescales: 500–800 My	In the absence of understanding of basin formation mechanism, no prediction for initial heat flow; heat flow at later stage dominated by burial history	Very low level of faulting throughout tectonic history

Reproduced from Cloetingh S and Burov E (2011) Lithospheric folding and sedimentary basin evolution: A review and analysis of formation mechanisms. *Basin Research* 23: 257–290.

in compressional systems are directly linked to the thermomechanical properties and rheological stratification of the underlying lithosphere. The temporal evolution of the strength of continents and the spatial variations in stress and strength at continental margins, rifts, and orogenic belts govern the mechanics of basin development and destruction in time and space. Structural discontinuities and preexisting weakness zones are prone to reactivation in response to the buildup of extensional stresses and thus play an important role in the localization of rifts and related transfer zones. Similarly, their reactivation in response to the buildup of compressional stresses propagating from plate boundaries into continental platform areas controls the inversion of extensional basins and the upthrusting of basement blocks and contributes to the localization of lithospheric folding. The timing and nature of underlying changes in the controlling stress field and the resulting deformation processes can be unraveled by quantitative analyses of the stratigraphic record and the architecture of such complex polyphase sedimentary basins. This permits to assess systematic differences in the timing of the transition from rifting to intraplate compression and the development of foreland fold–thrust belts and lithospheric folds and vice versa.

Sedimentary basin systems are, by their nature, prone to tectonic reactivation and, therefore, frequently characterized by a polyphase evolution. Extensional basins are, for example, often formed in areas previously thickened by tectonic compression and subsequently often subject to late-stage compression. Examples include the Pannonian Basin of Hungary and the North Atlantic rifted margins. Similarly, foreland basins are frequently characterized by preorogenic extension. Examples include the Carpathian foredeep and the Aquitaine Basin of southern France, which was the retroarc foreland basin of the Pyrenees. The actual subsidence patterns of these polyphase systems are often more complex than predicted by the end-member models that only consider the basin formation mechanism.

6.12.5.1 Future Perspectives

The study of sedimentary basins demands added focus on surrounding highs that act as sediment sources as it is recognized that also uplifted/uplifting areas contain valuable information concerning, for instance, underlying deep-seated processes (Cloetingh et al., 2007, 2009, 2011, 2012, 2013;

Matenco et al., 2013). State-of-the art geothermochronology and the study of erosion and river pattern evolution provide major constraints on uplift histories. To elucidate the contribution of internal lithospheric processes and external forcing toward rates of erosion and sedimentation, therefore, presents a major challenge for sedimentary basin studies. This is particularly so as the sedimentary cover of the lithosphere provides a high-resolution record of the changing environment and of deformation and mass transfer at the surface and at different depth levels in the crust, lithosphere, and mantle system. With recent advances in seismic tomography and the development of full-waveform inversion methodologies, our understanding of crust–mantle interactions and their impact on sedimentary basins can be expected to further increase. Particularly striking in this effect is the rapid increase in spatial resolution capable, for example, to image in great detail the presence of mantle plumes in the northern Atlantic (Rickers et al., 2013), which will provide new constraints on the evolution of extensional basin systems in this area.

Tectonic reactivation has strongly affected the structure and fill of many sedimentary basins. The long-lasting rheology memory of the lithosphere appears to play a far more important role in basin reactivation than hitherto assumed. For present-day rheological strength distributions in the lithosphere, regional- and global-scale models have been developed recently (e.g., Tesauro et al., 2009a,b, 2012a,b, 2013). A better understanding of the 3-D linkage between basin formation and basin deformation would also benefit from establishing robust models for paleostrength distributions. Moreover, structural analysis of the basin architecture, including paleostress assessment, will provide important constraints on the transient nature of intraplate stress fields and their effects on the evolution of sedimentary basins (e.g., Roure et al., 2012).

Monitoring lithospheric deformation and its sedimentary record provides constraints on past and present-day structures and on deformation rates. Whereas in the past, tectonics, eustasy, and sediment supply have been commonly treated as separate factors in sedimentary basin analyses, nowadays, an integrated source–sink approach, constrained by fully 3-D quantitative subsidence and exhumation history analyses in carefully selected natural laboratories, is possible and ought to be further pursued (Cloetingh and Willett, 2013; Matenco et al., 2013).

In doing so, future researchers will build on the legacy of Peter Ziegler, coauthor of this chapter, who passed away on 19 July 2013 after the submission of this chapter. Peter Ziegler has been a pioneer in integrating geologic and geophysical information for elucidating lithosphere evolution in space and time. He successfully connected research on sedimentary basins carried out by the energy industry and academia. Peter's fundamental contribution to the paleogeography of Europe and the northern Atlantic and his seminal studies on sedimentary basins will be a solid base for the years to come. Peter's immense overview of the geologic record provided the background for his *Geological Atlas of Western and Central Europe*, which for long has served as a fundamental resource for scientists. Peter Ziegler early understood the importance of integrating different sources of information and that the whole crust and lithosphere are involved in tectonic evolution of basins.

Acknowledgments

The research on sedimentary basin systems reviewed in this chapter was largely carried out in the framework of the International Lithosphere Program (ILP) and the ESF EUROCORES TOPO-EUROPE program. We acknowledge the contributions and efforts made by coworkers from various research institutes in Europe to these projects. Martijn Vlieg is thanked for technical assistance.

References

Abadi AM, Van Wees JD, Van Dijk PM, and Cloetingh SAPL (2008) Tectonics and subsidence evolution of the Sirt Basin, Libya. *AAPG Bulletin* 92: 993–1027.

Ali MY and Watts AB (2009) Subsidence history, gravity anomalies and flexure of the United Arab Emirates (UAE) foreland basin. *GeoArabia* 14: 17–44.

Alinaghi A, Koulakov I, and Thybo H (2007) Seismic tomographic imaging of P- and S-waves velocity perturbations in the upper mantle beneath Iran. *Geophysical Journal International* 169: 1089–1102.

Allen MB and Davies CE (2007) Unstable Asia: Active deformation of Siberia revealed by drainage shifts. *Basin Research* 19: 379–392.

Allen PA, Homewood P, and Williams GD (1986) Foreland basins: An introduction. In: *Foreland Basins*, pp. 3–12. Oxford: Blackwell Publishing Ltd.

Alzaga-Ruiz H, Granjeon D, Lopez M, Seranne M, and Roure F (2009) Gravitational collapse and Neogene sediment transfer across the western margin of the Gulf of Mexico: Insights from numerical models. *Tectonophysics* 470: 21–41.

Anderson DL, Zhang Y-S, and Tanimoto T (1992) Plume heads, continental lithosphere, flood basalts and tomography. *Geological Society, London, Special Publications* 68: 99–124.

Andeweg B (2002) *Cenozoic tectonic evolution of the Iberian Peninsula: Effects and causes of changing stress fields*. Published PhD thesis, Vrije Universiteit Amsterdam, the Netherlands, pp. 178.

Andeweg B and Cloetingh S (1998) Flexure and 'unflexure' of the North Alpine German-Austrian Molasse Basin: Constraints from forward tectonic modelling. *Geological Society, London, Special Publications* 134: 403–422.

Artemieva IM (2006) Global 1 degrees x 1 degrees thermal model TC1 for the continental lithosphere: Implications for lithosphere secular evolution. *Tectonophysics* 416: 245–277.

Artemieva I (2011) *The Lithosphere: An Interdisciplinary Approach*. New York: Cambridge University Press.

Artemieva IM and Mooney WD (2001) Thermal thickness and evolution of Precambrian lithosphere: A global study. *Journal of Geophysical Research-Solid Earth* 106: 16387–16414.

Artemieva IM and Mooney WD (2002) On the relations between cratonic lithosphere thickness, plate motions, and basal drag. *Tectonophysics* 358: 211–231.

Artemieva IM, Thybo H, and Kaban MK (2006) Deep Europe today: Geophysical synthesis of the upper mantle structure and lithospheric processes over 3.5 Ga. *Geological Society, London, Memoirs* 32: 11–41.

Artemjev ME, Kaban MK, Kucherinenko VA, Demyanov GV, and Taranov VA (1994) Subcrustal density inhomogeneities of Northern Eurasia as derived from the gravity data and isostatic models of the lithosphere. *Tectonophysics* 240: 249–280.

Artyushkov EV (2007) Formation of the superdeep South Caspian basin: Subsidence driven by phase change in continental crust. *Russian Geology and Geophysics* 48: 1002–1014.

Artyushkov EV and Baer MA (1990) Formation of hydrocarbon basins: Subsidence without stretching in West Siberia. In: *The Potential of Deep Seismic Profiling for Hydrocarbon Exploration*, pp. 45–61. Paris: Technip.

Athmer W, Groenenberg RM, Luthi SM, et al. (2010) Relay ramps as pathways for turbidity currents: A study combining analogue sandbox experiments and numerical flow simulations. *Sedimentology* 57: 806–823.

Audet P and Burgmann R (2011) Dominant role of tectonic inheritance in supercontinent cycles. *Nature Geoscience* 4: 184–187.

Avouac JP and Burov EB (1996) Erosion as a driving mechanism of intracontinental mountain growth. *Journal of Geophysical Research-Solid Earth* 101: 17747–17769.

Axen GJ, Lam PS, Grove M, Stockli DF, and Hassanzadeh J (2001) Exhumation of the west-central Alborz Mountains, Iran, Caspian subsidence, and collision-related tectonics. *Geology* 29: 559–562.

Babuska V and Plomerova J (1992) The lithosphere in central-Europe – Seismological and petrological aspects. *Tectonophysics* 207: 141–163.
Babuska V and Plomerova J (1993) Lithospheric thickness and velocity anisotropy – Seismological and geothermal aspects. *Tectonophysics* 225: 79–89.
Babuska V and Plomerova J (2001) Subcrustal lithosphere around the Saxothuringian-Moldanubian Suture Zone – A model derived from anisotropy of seismic wave velocities. *Tectonophysics* 332: 185–199.
Bache F, Olivet JL, Gorini C, et al. (2010) Evolution of rifted continental margins: The case of the Gulf of Lions (Western Mediterranean Basin). *Earth and Planetary Science Letters* 292: 345–356.
Bada G, Cloetingh S, Gerner P, and Horváth F (1998) Sources of recent tectonic stress in the Pannonian region: Inferences from finite element modelling. *Geophysical Journal International* 134: 87–101.
Bada G and Horváth F (2001) On the structure and tectonic evolution of the Pannonian basin and surrounding orogens. *Acta Geologica Hungarica* 44: 301–327.
Bada G, Horváth F, Cloetingh S, Coblentz DD, and Toth T (2001) Role of topography-induced gravitational stresses in basin inversion: The case study of the Pannonian basin. *Tectonics* 20: 343–363.
Bada G, Horváth F, Dovenyi P, et al. (2007) Present-day stress field and tectonic inversion in the Pannonian basin. *Global and Planetary Change* 58: 165–180.
Bada G, Horváth F, Gerner P, and Fejes I (1999) Review of the present-day geodynamics of the Pannonian basin: Progress and problems. *Journal of Geodynamics* 27: 501–527.
Bahlburg H and Furlong KP (1996) Lithospheric modeling of the Ordovician foreland basin in the Puna of northwestern Argentina: On the influence of arc loading on foreland basin formation. *Tectonophysics* 259: 245–258.
Balla Z (1986) Paleotectonic reconstruction of the Central Alpine Mediterranean belt for the neogene. *Tectonophysics* 127: 213–243.
Bally AW and Snelson S (1980) Realms of subsidence. *Memoirs Canadian Society of Petroleum Geology* 6: 9–94.
Banks CJ (1998) Basins and thrust belts of the Balkan coast of the Black Sea. *Memoirs-American Association of Petroleum Geologists* 68: 115–128.
Barbeau DL (2003) A flexural model for the Paradox Basin: Implications for the tectonics of the Ancestral Rocky Mountains. *Basin Research* 15: 97–115.
Barbieri C, Bertotti G, Di Giulio A, Fantoni R, and Zoetemeijer R (2004) Flexural response of the Venetian foreland to the Southalpine tectonics along the TRANSALP profile. *Terra nova* 16: 273–280.
Bartol J and Govers R (2009) Flexure due to the Messinian-Pontian sea level drop in the Black Sea. *Geochemistry, Geophysics, Geosystems* 10: Q10013.
Bartol J, Matenco L, Garcia-Castellanos D, and Leever K (2012) Modelling depositional shifts between sedimentary basins: Sediment pathways in Paratethys basins during the Messinian Salinity Crisis. *Tectonophysics* 536: 110–121.
Barton P and Wood R (1984) Tectonic evolution of the north-sea basin – Crustal stretching and subsidence. *Geophysical Journal of the Royal Astronomical Society* 79: 987–1022.
Bassi G (1995) Relative importance of strain-rate and rheology for the mode of continental extension. *Geophysical Journal International* 122: 195–210.
Bassin C (2000) The current limits of resolution for surface wave tomography in North America. *Eos, Transactions of the American Geophysical Union* 81: F897.
Bayasgalan A, Jackson J, and McKenzie D (2005) Lithosphere rheology and active tectonics in Mongolia: Relations between earthquake source parameters, gravity and GPS measurements. *Geophysical Journal International* 163: 1151–1179.
Bayer U, Scheck M, Rabbel W, et al. (1999) An integrated study of the NE German Basin. *Tectonophysics* 314: 285–307.
Beaumont C (1981) Foreland basins. *Geophysical Journal of the Royal Astronomical Society* 65: 291–329.
Beaumont C, Fullsack P, and Hamilton J (1992) Erosional control of active compressional orogens. In: McClay KR (ed.) *Thrust Tectonics*, pp. 1–18. London: Chapman & Hall.
Beaumont C, Keen CE, and Boutilier R (1982) On the evolution of rifted continental margins – Comparison of models and observations for the Nova-Scotian margin. *Geophysical Journal of the Royal Astronomical Society* 70: 667–715.
Beekman F, Bull JM, Cloetingh S, and Scrutton R (1996) Crustal fault reactivation facilitating lithospheric folding/buckling in the central Indian Ocean. *Geological Society, London, Special Publications* 99: 251–263.
Beekman F, Stephenson RA, and Korsch RJ (1997) Mechanical stability of the Redbank Thrust Zone, central Australia: Dynamic and rheological implications. *Australian Journal of Earth Sciences* 44: 215–226.
Beglinger SE, Corver MP, Doust H, Cloetingh S, and Thurmond AK (2012a) A new approach of relating petroleum system and play development to basin evolution: An application to the conjugate margin Gabon coastal and Almada-Camamu basins. *AAPG Bulletin* 96: 953–982.
Beglinger SE, Doust H, and Cloetingh S (2012b) Relating petroleum system and play development to basin evolution: Brazilian South Atlantic margin. *Petroleum Geoscience* 18: 315–336.
Beglinger SE, Doust H, and Cloetingh S (2012c) Relating petroleum system and play development to basin evolution: West African South Atlantic basins. *Marine and Petroleum Geology* 30: 1–25.
Beglinger SE, Van Wees JD, Cloetingh S, and Doust H (2012d) Tectonic subsidence history and source-rock maturation in the Campos Basin, Brazil. *Petroleum Geoscience* 18: 153–172.
Bergerat F (1987) Stress-fields in the european platform at the time of Africa-Eurasia collision. *Tectonics* 6: 99–132.
Bertotti G and Mosca P (2009) Late-orogenic vertical movements within the arc of the SW Alps and Ligurian Alps. *Tectonophysics* 475: 117–127.
Bertotti G, Mosca P, Juez J, et al. (2006) Oligocene to present kilometres scale subsidence and exhumation of the Ligurian Alps and the Tertiary Piedmont Basin (NW Italy) revealed by apatite (U–Th)/He thermochronology: Correlation with regional tectonics. *Terra Nova* 18: 18–25.
Bertotti G, Podladchikov Y, and Daehler A (2000) Dynamic link between the level of ductile crustal flow and style of normal faulting of brittle crust. *Tectonophysics* 320: 195–218.
Bertotti G and Ter Voorde M (1994) Thermal effects of normal faulting during rifted basin formation, 2. The Lugano-Val grande normal-fault and the role of preexisting thermal anomalies. *Tectonophysics* 240: 145–157.
Bertotti G, Ter Voorde M, Cloetingh S, and Picotti V (1997) Thermomechanical evolution of the South Alpine rifted margin (North Italy): Constraints on the strength of passive continental margins. *Earth and Planetary Science Letters* 146: 181–193.
Blundell DJ, Freeman R, Mueller S, and Button S (1992) *A Continent Revealed: The European Geotraverse, Structure and Dynamic Evolution*. Cambridge: Cambridge University Press, 275 pp.
Bocin A (2010) *Crustal Structure of the SE Carpathians and Its Foreland from Densely Spaced Geophysical Data*, 124 pp. PhD Thesis, VU University Amsterdam, Amsterdam.
Bond GC and Kominz MA (1984) Construction of tectonic subsidence curves for the early paleozoic Miogeocline, southern Canadian rocky mountains – Implications for subsidence mechanisms, age of breakup, and crustal thinning. *Geological Society of America Bulletin* 95: 155–173.
Bonjer KP (1997) Seismicity pattern and style of seismic faulting at the eastern borderfault of the southern Rhine Graben. *Tectonophysics* 275: 41–69.
Bonnet S (2009) Shrinking and splitting of drainage basins in orogenic landscapes from the migration of the main drainage divide. *Nature Geoscience* 2: 766–771.
Bonnet S, Guillocheau F, Brun JP, and Van den Driessche J (2000) Large-scale relief development related to Quaternary tectonic uplift of a Proterozoic-Paleozoic basement: The Armorican Massif, NW France. *Journal of Geophysical Research: Solid Earth* 105: 19273–19288.
Boschi L, Faccenna C, and Becker TW (2010) Mantle structure and dynamic topography in the Mediterranean Basin. *Geophysical Research Letters* 37: L20303.
Bott MHP (1992) Modeling the loading stresses associated with active continental rift systems. *Tectonophysics* 215: 99–115.
Bott MHP (1993) Modeling the plate-driving mechanism. *Journal of the Geological Society* 150: 941–951.
Bott MHP and Kusznir NJ (1979) Stress distributions associated with compensated plateau uplift structures with application to the continental splitting mechanism. *Geophysical Journal of the Royal Astronomical Society* 56: 451–459.
Bott MHP and Stern TA (1992) Finite element analysis of Transantarctic Mountain uplift and coeval subsidence in the Ross Embayment. *Tectonophysics* 201: 341–356.
Bourgeois O, Ford M, Diraison M, et al. (2007) Separation of rifting and lithospheric folding signatures in the NW-Alpine foreland. *International Journal of Earth Sciences* 96: 1003–1031.
Braun J (2006) Recent advances and current problems in modelling surface processes and their interaction with crustal deformation. *Geological Society, London, Special Publications* 253: 307–325.
Braun J and Beaumont C (1989) A physical explanation of the relation between flank uplifts and the breakup unconformity at rifted continental margins. *Geology* 17: 760–764.
Brunet MF (1986) The influence of the evolution of the Pyrenees on adjacent basins. *Tectonophysics* 129: 343–354.
Bry M, White N, Singh S, England R, and Trowell C (2004) Anatomy and formation of oblique continental collision: South Falkland basin. *Tectonics* 23.
Brunet M-F and Cloetingh S (2003) Integrated peri-Tethyan basins studies (peri-Tethys programme). *Sedimentary Geology* 156: 1–10.

Buck WR (1991) Modes of continental lithospheric extension. *Journal of Geophysical Research: Solid Earth* 96: 20161–20178.

Buck WR (2007) The dynamics of continental break-up and extension. In: Watts AB (ed.) *Treatise on Geophysics*. *Crust and Lithosphere Dynamics*, vol. 6, pp. 335–376. New York: Elsevier.

Bull JM and Scrutton RA (1992) Seismic-reflection images of intraplate deformation, central Indian-ocean, and their tectonic significance. *Journal of the Geological Society* 149: 955–966.

Burg J-P and Podladchikov Y (1999) Lithospheric scale folding: Numerical modelling and application to the Himalayan syntaxes. *International Journal of Earth Sciences* 88: 190–200.

Burg JP, Van den Driessche J, and Brun JP (1994) Syn-thickening to post-thickening extension – Mode and consequences. *Comptes Rendus de l'Académie des Sciences – Series II* 319: 1019–1032.

Burov EB (2007) Plate rheology and mechanics. In: Watts AB (ed.) *Treatise on Geophysics*. *Crust and Lithosphere Dynamics*, vol. 6, pp. 99–151. Amsterdam: Elsevier.

Burov E and Cloetingh S (1997) Erosion and rift dynamics: New thermomechanical aspects of post-rift evolution of extensional basins. *Earth and Planetary Science Letters* 150: 7–26.

Burov E and Cloetingh S (2009) Controls of mantle plumes and lithospheric folding on modes of intraplate continental tectonics: Differences and similarities. *Geophysical Journal International* 178: 1691–1722.

Burov E and Cloetingh S (2010) Plume-like upper mantle instabilities drive subduction initiation. *Geophysical Research Letters* 37: L03309.

Burov EB and Diament M (1992) Flexure of the continental lithosphere with multilayered rheology. *Geophysical Journal International* 109: 449–468.

Burov EB and Diament M (1995) The effective elastic thickness (T-E) of continental lithosphere – What does it really mean. *Journal of Geophysical Research: Solid Earth* 100: 3905–3927.

Burov E, Guillou-Frottier L, d'Acremont E, Le Pourhiet L, and Cloetingh S (2007) Plume head-lithosphere interactions near intra-continental plate boundaries. *Tectonophysics* 434: 15–38.

Burov EB, Kogan MG, Lyon-Caen H, and Molnar P (1990) Gravity anomalies, the deep structure, and dynamic processes beneath the Tien Shan. *Earth and Planetary Science Letters* 96: 367–383.

Burov EB and Kogan MG (1990) Mechanical-gravitational model of the interaction of continental plates in the Tien-Shan region. *Doklady Akademii NAUK SSS* 313: 1439–1444.

Burov EB, Lobkovsky LI, Cloetingh S, and Nikishin AM (1993) Continental lithosphere folding in central-Asia. 2. Constraints from gravity and topography. *Tectonophysics* 226: 73–87.

Burov EB and Molnar P (1998) Gravity anomalies over the Ferghana Valley (central Asia) and intracontinental deformation. *Journal of Geophysical Research: Solid Earth* 103: 18137–18152.

Burov E and Toussaint G (2007) Surface processes and tectonics: Forcing of continental subduction and deep processes. *Global and Planetary Change* 58: 141–164.

Burton R, Kendall CGSC, and Lerche I (1987) Out of our depth – On the impossibility of fathoming eustasy from the stratigraphic record. *Earth-Science Reviews* 24: 237–277.

Calcagnile G and Panza GF (1987) Properties of the lithosphere-asthenosphere system in Europe with a view toward earth conductivity. *Pure and Applied Geophysics* 125: 241–254.

Caporali A (1995) Gravity anomalies and the flexure of the lithosphere in the Karakoram, Pakistan. *Journal of Geophysical Research: Solid Earth (1978–2012)* 100: 15075–15085.

Cardozo N (1997) Thermomechanical Modeling of the Llanos Basin Colombia, South America. *American Geophysical Union Spring meeting*. Baltimore: Ohio University.

Carrapa B and Garcia-Castellanos D (2005) Western Alpine back-thrusting as subsidence mechanism in the Tertiary Piedmont Basin (Western Po Plain, NW Italy). *Tectonophysics* 406: 197–212.

Carswell DA (1990) *Eclogite Facies Rocks*. New York: Blackie.

Carter NL and Tsenn MC (1987) Flow properties of continental lithosphere. *Tectonophysics* 136: 27–63.

Casas-Sainz AM and de Vicente G (2009) On the tectonic origin of Iberian topography. *Tectonophysics* 474: 214–235.

Casero P (2004) Structural setting of petroleum exploration plays in Italy. *Special Volume of the Italian Geological Society for the IGC* 32: 189–199.

Catuneanu O, Beaumont C, and Waschbusch P (1997) Interplay of static loads and subduction dynamics in foreland basins: Reciprocal stratigraphies and the "missing" peripheral bulge. *Geology* 25: 1087–1090.

Chang HK, Kowsmann RO, Figueiredo AMF, and Bender AA (1992) Tectonics and stratigraphy of the East Brazil Rift System – An overview. *Tectonophysics* 213: 97–138.

Chu DZ and Gordon RG (1998) Current plate motions across the Red Sea. *Geophysical Journal International* 135: 313–328.

Ciulavu D, Dinu C, and Cloetingh S (2002) Late Cenozoic tectonic evolution of the Transylvanian basin and northeastern part of the Pannonian basin (Romania): Constraints from seismic profiling and numerical modelling. *EGU Stephan Mueller Special Publication Series* 3: 105–120.

Cloetingh S (1988) Intraplate stresses: A new element in basin analysis. In: Kleinspehn K and Paola C (eds.) *Frontiers in Sedimentary Geology – New Perspectives in Basin Analysis*, pp. 205–230. New York: Springer.

Cloetingh S and Burov EB (1996) Thermomechanical structure of European continental lithosphere: Constraints from rheological profiles and EET estimates. *Geophysical Journal International* 124: 695–723.

Cloetingh S and Burov E (2011) Lithospheric folding and sedimentary basin evolution: A review and analysis of formation mechanisms. *Basin Research* 23: 257–290.

Cloetingh S, Beekman F, Ziegler PA, et al. (2008) Post-rift compressional reactivation potential of passive margins and extensional basins. *Geological Society, London, Special Publications* 306: 27–70.

Cloetingh S, Burov E, Beekman F, et al. (2002) Lithospheric folding in Iberia. *Tectonics* 21: 1041.

Cloetingh SAPL, Burov E, Matenco L, et al. (2004) Thermo-mechanical controls on the mode of continental collision in the SE Carpathians (Romania). *Earth and Planetary Science Letters* 218: 57–76.

Cloetingh S, Burov E, Matenco L, et al. (2013) The Moho in extensional tectonic settings: Insights from thermo-mechanical models. *Tectonophysics* 609: 558–604.

Cloetingh S, Burov E, and Poliakov A (1999) Lithosphere folding: Primary response to compression? (from central Asia to Paris basin). *Tectonics* 18: 1064–1083.

Cloetingh S, Cornu T, Ziegler PA, and Beekman F (2006) Neotectonics and intraplate continental topography of the northern Alpine Foreland. *Earth-Science Reviews* 74: 127–196.

Cloetingh S, D'Argenio B, Catalano R, Horváth F, and Sassi W (1995a) Interplay of extension and compression in basin formation: Introduction. *Tectonophysics* 252: 1–5.

Cloetingh S, Durand B, and Puigdefabregas C (eds.) (1995c) Special Issue on integrated basin studies (IBS) – A European Commission (DGXII) project. *Marine and Petroleum Geology* 12(8): 787–963.

Cloetingh S, Gallart J, de Vicente G, and Matenco L (2011) TOPO-EUROPE: From Iberia to the Carpathians and analogues. *Tectonophysics* 502: 1–27.

Cloetingh S, Gradstein FM, Kooi H, Grant AC, and Kaminski M (1990) Plate reorganization: A cause of rapid late Neogene subsidence and sedimentation around the North Atlantic? *Journal of the Geological Society* 147: 495–506.

Cloetingh S and Kooi H (1992a) Intraplate stresses and dynamic aspects of rifted basins. *Tectonophysics* 215: 167–185.

Cloetingh S and Kooi H (1992b) Intraplate stresses and dynamical aspects of rifted basins. *Tectonophysics* 215: 167–185.

Cloetingh S, Lambeck K, and McQueen H (1987) Apparent sealevel fluctuations and a paleo-stress field for the North Sea region. In: Brooks J and Glennie K (eds.) *Petroleum Geology of NorthWest Europe*, pp. 49–55. London: Graham and Trotman.

Cloetingh S, Mcqueen H, and Lambeck K (1985) On a tectonic mechanism for regional sealevel variations. *Earth and Planetary Science Letters* 75: 157–166.

Cloetingh S and Negendank JFW (2010) *New Frontiers in Integrated Solid Earth Sciences*, pp. 414. Springer.

Cloetingh S, Sassi W, Stephenson RA, et al. (1994) The origin of sedimentary basins – A status-report from the task-force of the international lithosphere program. *Marine and Petroleum Geology* 11: 659–683.

Cloetingh S, Spadini G, Van Wees JD, and Beekman F (2003) Thermo-mechanical modelling of Black Sea Basin (de)formation. *Sedimentary Geology* 156: 169–184.

Cloetingh S, Thybo H, and Faccenna C (2009) TOPO-EUROPE: Studying continental topography and Deep Earth-Surface processes in 4D. *Tectonophysics* 474: 4–32.

Cloetingh S, Tibaldi A, and Burov E (2012) Coupled deep earth and surface processes and their impact on geohazards. *Global and Planetary Change* 90–91: 1–19.

Cloetingh S, Van Balen RT, Ter Voorde M, Zoetemeijer BP, and Den Bezemer T (1997) Mechanical aspects of sedimentary basin formation: Development of integrated models for lithospheric and surface processes. *Geologische Rundschau* 86: 226–240.

Cloetingh S and Van Wees JD (2005) Strength reversal in Europe's intraplate lithosphere: Transition from basin inversion to lithospheric folding. *Geology* 33: 285–288.

Cloetingh S, Van Wees JD, Van der Beek PA, and Spadini G (1995b) Role of pre-rift rheology in kinematics of extensional basin formation – Constraints from

thermomechanical models of Mediterranean and Intracratonic basins. *Marine and Petroleum Geology* 12: 793–807.
Cloetingh S, Van Wees JD, Ziegler PA, et al. (2010) Lithosphere tectonics and thermomechanical properties: An integrated modelling approach for Enhanced Geothermal Systems exploration in Europe. *Earth-Science Reviews* 102: 159–206.
Cloetingh S and Willett SD (2013) TOPO-EUROPE: Understanding of the coupling between the deep Earth and continental topography. *Tectonophysics* 602: 1–14.
Cloetingh S and Wortel R (1986) Stress in the Indo-Australian plate. *Tectonophysics* 132: 49–67.
Cloetingh S, Wortel R, and Vlaar NJ (1989) On the initiation of subduction zones. *Pure and Applied Geophysics* 129: 7–25.
Cloetingh S and Ziegler PA (2007) Tectonic models for the evolution of sedimentary basins. In: Watts AB, Schubert G, Watts AB, and Schubert G (Eds.) *Treatise on Geophysics* 6: 485–611.
Cloetingh S, Ziegler PA, Beekman F, et al. (2005a) Intraplate deformation and 3D rheological structure of the Rhine Rift System and adjacent areas of the northern Alpine foreland. *International Journal of Earth Sciences* 94: 758–778.
Cloetingh S, Ziegler PA, Beekman F, et al. (2005b) Lithospheric memory, state of stress and rheology: Neotectonic controls on Europe's intraplate continental topography. *Quaternary Science Reviews* 24: 241–304.
Cloetingh SAPL, Ziegler PA, Bogaard PJF, et al. (2007) TOPO-EUROPE: The geoscience of coupled deep Earth-surface processes. *Global and Planetary Change* 58: 1–118.
Cobbold PR, Davy P, Gapais D, et al. (1993) Sedimentary basins and crustal thickening. *Sedimentary Geology* 86: 77–89.
Cogan J, Rigo L, Grasso M, and Lerche I (1989) Flexural tectonics of southeastern Sicily. *Journal of geodynamics* 11: 189–241.
Colletta B, Roure F, DeToni B, et al. (1997) Tectonic inheritance, crystal architecture, and contrasting structural styles in the Venezuela Andes. *Tectonics* 16: 777–794.
Corver MP, Doust H, Van Wees JD, Bada G, and Cloetingh S (2009) Classification of rifted sedimentary basins of the Pannonian Basin System according to the structural genesis, evolutionary history and hydrocarbon maturation zones. *Marine and Petroleum Geology* 26: 1452–1464.
Corver MP, Doust H, Van Wees JD, and Cloetingh S (2011) Source-rock maturation characteristics of symmetric and asymmetric grabens inferred from integrated analogue and numerical modeling: The southern Viking Graben (North Sea). *Marine and Petroleum Geology* 28: 921–935.
Coudert L, Frappa M, Viguier C, and Arias R (1995) Tectonic subsidence and crustal flexure in the Neogene Chaco basin of Bolivia. *Tectonophysics* 243: 277–292.
Cross TA (1990) *Quantitative Dynamic Stratigraphy*. New Jersey: Prentice-Hall.
Csontos L (1995) Tertiary tectonic evolution of the Intra-Carpathian area. *Acta Vulcanologica* 7: 1–14.
Csontos L, Nagymarosy A, Horváth F, and Kovac M (1992) Tertiary evolution of the intra-Carpathian area – A model. *Tectonophysics* 208: 221–241.
Csontos L and Voros A (2004) Mesozoic plate tectonic reconstruction of the Carpathian region. *Palaeogeography Palaeoclimatology Palaeoecology* 210: 1–56.
Curray JR and Moore DG (1971) Growth of Bengal Deep-Sea Fan and denudation in Himalayas. *Geological Society of America Bulletin* 82: 563–572.
Dalmayrac B and Molnar P (1981) Parallel thrust and normal faulting in Peru and constraints on the state of stress. *Earth and Planetary Science Letters* 55: 473–481.
Dando BDE, Stuart GW, Houseman GA, et al. (2011) Teleseismic tomography of the mantle in the Carpathian-Pannonian region of central Europe. *Geophysical Journal International* 186: 11–31.
Dávila FM, Astini RA, Jordan TE, Gehrels G, and Ezpeleta M (2007) Miocene forebulge development previous to broken foreland partitioning in the southern Central Andes, west-central Argentina. *Tectonics* 26: T05016.
De Bruijne CH and Andriessen PAM (2000) Interplay of intraplate tectonics and surface processes in the Sierra de Guadarrama (central Spain) assessed by apatite fission track analysis. *Physics and Chemistry of the Earth, Part A: Solid Earth and Geodesy* 25: 555–563.
De Bruijne CH and Andriessen PAM (2002) Far field effects of Alpine plate tectonism in the Iberian microplate recorded by fault-related denudation in the Spanish Central System. *Tectonophysics* 349: 161–184.
De Vicente G, Cloetingh S, Munoz-Martin A, et al. (2008) Inversion of moment tensor focal mechanisms for active stresses around the microcontinent Iberia: Tectonic implications. *Tectonics* 27: TC1009.
De Vicente G, Vegas R, Martin AM, et al. (2007) Cenozoic thick-skinned deformation and topography evolution of the Spanish Central System. *Global and Planetary Change* 58: 335–381.
DeCelles PG and Giles KA (1996) Foreland basin systems. *Basin Research* 8: 105–123.
Decker K, Lillie RJ, and Tomek C (1998) In: *Dynamics of the Pannonian-Carpathian-Dinaride System*, *PANCARDI: The Lithospheric Structure and Evolution of the Pannonian-Carpathian-Dinaride Region: Selected Papers from the PANCARDI Workshop 1996*, Amsterdam: Elsevier.
Delvaux D, Cloetingh S, Beekman F, et al. (2013) Basin evolution in a folding lithosphere: Altai-Sayan and Tien Shan belts in Central Asia. *Tectonophysics* 602: 194–222.
Desegaulx P, Kooi H, and Cloetingh S (1991) Consequences of foreland basin development on thinned continental lithosphere – Application to the Aquitaine Basin (Sw France). *Earth and Planetary Science Letters* 106: 116–132.
Devlin W, Cogswell J, Gaskins G, et al. (1999) South Caspian basin: Young, cool, and full of promise. *GSA Today* 9: 1–9.
Dewey JF (1980) Episodicity, sequence and style at convergent plate boundaries. In: Strangway DW (ed.) *The Continental Crust and Its Mineral Deposits*. Geological Society of Canada.
Dewey JF (1988) Extensional collapse of orogens. *Tectonics* 7: 1123–1139.
Dewey JF and Burke K (1974) Hot spots and continental break-up: Implications for collisional orogeny. *Geology* 2: 57–60.
Dèzes P, Schmid SM, and Ziegler PA (2004) Evolution of the European Cenozoic Rift System: Interaction of the Alpine and Pyrenean orogens with their foreland lithosphere. *Tectonophysics* 389: 1–33.
Dickinson WR (1974) Plate tectonics and sedimentation. *The Society of Economic Paleontologists and Mineralogists (SEPM)* 22: 1–27.
Dinu C, Wong HK, Tambrea D, and Matenco L (2005) Stratigraphic and structural characteristics of the Romanian Black Sea shelf. *Tectonophysics* 410: 417–435.
Doglioni C, Carminati E, Cuffaro M, and Scrocca D (2007) Subduction kinematics and dynamic constraints. *Earth-Science Reviews* 83: 125–175.
Dombradi E, Sokoutis D, Bada G, Cloetingh S, and Horváth F (2010) Modelling recent deformation of the Pannonian lithosphere: Lithospheric folding and tectonic topography. *Tectonophysics* 484: 103–118.
Dombradi E, Timar G, Bada G, Cloetingh S, and Horváth F (2007) Fractal dimension estimations of drainage network in the Carpathian-Pannonian system. *Global and Planetary Change* 58: 197–213.
Dondurur D, Küçük HM, and Çifçi G (2013) Quaternary mass wasting on the western Black Sea margin, offshore of Amasra. *Global and Planetary Change* 103: 248–260.
Doré A, Auguston J, Hermanrud C, Stewart D, and Sylta O (1993) In: *Basin Modelling: Advances and Applications*. Amsterdam: Elsevier, Applications. Norwegian Petroleum Society Special Publication 3.
Doust H and Omatsola E (1989) Niger delta. *Memoir American Association of Petroleum Geologists* 48: 201–238.
Du ZJ, Michelini A, and Panza GF (1998) EurID: A regionalized 3-D seismological model of Europe. *Physics of the Earth and Planetary Interiors* 106: 31–62.
Dunbar JA and Sawyer DS (1989) How preexisting weaknesses control the style of continental breakup. *Journal of Geophysical Research-Solid Earth and Planets* 94: 7278–7292.
Dupré S, Bertotti G, and Cloetingh S (2007) Tectonic history along the South Gabon Basin: Anomalous early post-rift subsidence. *Marine and Petroleum Geology* 24: 151–172.
Dupré S, Cloetingh S, and Bertotti G (2011) Structure of the Gabon Margin from integrated seismic reflection and gravity data. *Tectonophysics* 506: 31–45.
Durand B, Jolivet L, Horváth E, and Seranne M (eds.) (1999) *The Mediterranean Basins: Tertiary Extension Within the Alpine Orogen*. Geological Society of London, Special Publications 159.
Edwards R, Scott C, Shillington D, et al. (2009) Wide-angle seismic data reveal sedimentary and crustal structure of the Eastern Black Sea. *The Leading Edge* 28: 1056–1065.
Egan SS, Mosar J, Brunet M-F, and Kangarli T (2009) Subsidence and uplift mechanisms within the South Caspian Basin: Insights from the onshore and offshore Azerbaijan region. *Geological Society, London, Special Publications* 312: 219–240.
Elfrink N (2001) Quaternary groundwater avulsions: Evidence for large-scale midcontinent folding. *Association of Engineering Geologists News* 44: 60.
Ershov AV, Brunet M-F, Korotaev MV, Nikishin AM, and Bolotov SN (1999) Late Cenozoic burial history and dynamics of the Northern Caucasus molasse basin: Implications for foreland basin modelling. *Tectonophysics* 313: 219–241.
Faccenna C and Becker TW (2010) Shaping mobile belts by small-scale convection. *Nature* 465: 602–605.
Faccenna C, Piromallo C, Crespo-Blanc A, Jolivet L, and Rossetti F (2004) Lateral slab deformation and the origin of the western Mediterranean arcs. *Tectonics* 23: TC1012.
Fakhari MD, Axen GJ, Horton BK, Hassanzadeh J, and Amini A (2008) Revised age of proximal deposits in the Zagros foreland basin and implications for Cenozoic evolution of the High Zagros. *Tectonophysics* 451: 170–185.

Fan P and Ma BL (1990) General petroleum geology of the Tarim Basin. *Academia Sinica* 1: 1–21.

Fan G, Wallace TC, Beck SL, and Chase CG (1996) Gravity anomaly and flexural model: Constraints on the structure beneath the Peruvian Andes. *Tectonophysics* 255: 99–109.

Favre P and Stampfli GM (1992) From rifting to passive margin – The examples of the Red-Sea, Central Atlantic and Alpine Tethys. *Tectonophysics* 215: 69–97.

Fernández-Lozano J, Sokoutis D, Willingshofer E, Cloetingh S, and De Vicente G (2011) Cenozoic deformation of Iberia: A model for intraplate mountain building and basin development based on analogue modeling. *Tectonics* 30: TC1001.

Fernández-Lozano J, Sokoutis D, Willingshofer E, et al. (2012) Integrated gravity and topography analysis in analog models: Intraplate deformation in Iberia. *Tectonics* 31: TC6005.

Finetti I, Bricchi G, Del Ben A, Pipan M, and Xuan Z (1988) Geophysical study of the Black Sea. *Bollettino di Geofisica Teorica ed Applicata* 30: 197–324.

Flament N, Gurnis M, and Müller RD (2013) A review of observations and models of dynamic topography. *Lithosphere* 5: 189–210.

Fleitout L and Froidevaux C (1982) Tectonics and topography for a lithosphere containing density heterogeneities. *Tectonics* 1: 21–56.

Flemings PB and Jordan TE (1989) A synthetic stratigraphic model of foreland basin development. *Journal of Geophysical Research: Solid Earth (1978–2012)* 94: 3851–3866.

Fodor L, Bada G, Csillag G, et al. (2005) An outline of neotectonic structures and morphotectonics of the western and central Pannonian Basin. *Tectonophysics* 410: 15–41.

Fodor L, Csontos L, Bada G, Györfi I, and Benkovics L (1999) Tertiary tectonic evolution of the Pannonian Basin system and neighbouring orogens: A new synthesis of palaeostress data. *Geological Society, London, Special Publications* 156: 295–334.

Ford M, Lickorish WH, and Kusznir NJ (1999) Tertiary foreland sedimentation in the Southern Subalpine Chains, SE France: A geodynamic appraisal. *Basin Research* 11: 315–336.

Forsyth D and Uyeda S (1975) Relative importance of driving forces of plate motion. *Geophysical Journal of the Royal Astronomical Society* 43: 163–200.

Franke D (2013) Rifting, lithosphere breakup and volcanism: Comparison of magma-poor and volcanic rifted margins. *Marine and Petroleum Geology* 43: 63–87.

Fuis GS, Murphy JM, Lutter WJ, et al. (1997) Deep seismic structure and tectonics of northern Alaska: Crustal-scale duplexing with deformation extending into the upper mantle. *Journal of Geophysical Research: Solid Earth* 102: 20873–20896.

Garcia-Castellanos D (2002) Interplay between lithospheric flexure and river transport in foreland basins. *Basin Research* 14: 89–104.

Garcia-Castellanos D (2007) The role of climate during high plateau formation. Insights from numerical experiments. *Earth and Planetary Science Letters* 257: 372–390.

Garcia-Castellanos D and Cloetingh S (2012) Modeling the interaction between lithospheric and surface processes in foreland basins. In: Busby C and Azor A (eds.) *Tectonics of Sedimentary Basins: Recent Advances*, pp. 152–181.

Garcia-Castellanos D, Cloetingh S, and Van Balen R (2000) Modelling the middle pleistocene uplift in the Ardennes-Rhenish Massif: Thermo-mechanical weakening under the Eifel? *Global and Planetary Change* 27: 39–52.

Garcia-Castellanos D, Fernandez M, and Torne M (1997) Numerical modeling of foreland basin formation: A program relating thrusting, flexure, sediment geometry and lithosphere rheology. *Computers & Geosciences* 23: 993–1003.

Garcia-Castellanos D, Fernandez M, and Torne M (2002) Modeling the evolution of the Guadalquivir foreland basin (southern Spain). *Tectonics* 21: 1018.

Gaspar-Escribano JM, Van Wees JD, Ter Voorde M, et al. (2001) Three-dimensional flexural modelling of the Ebro Basin (NE Iberia). *Geophysical Journal International* 145: 349–367.

Geller CA, Weissel JK, and Anderson RN (1983) Heat-transfer and intraplate deformation in the central Indian-Ocean. *Journal of Geophysical Research* 88: 1018–1032.

Gemmer L and Houseman GA (2007) Convergence and extension driven by lithospheric gravitational instability: Evolution of the Alpine-Carpathian-Pannonian system. *Geophysical Journal International* 168: 1276–1290.

Georgiev G, Dabovski C, and Stanisheva-Vassileva G (2001) East Srednogorie-Balkan rift zone. *Mémoires du Muséum national d'histoire naturelle* 186: 259–293.

Gerbault M (2000) At what stress level is the central Indian Ocean lithosphere buckling? *Earth and Planetary Science Letters* 178: 165–181.

Gerbault M, Burov EB, Poliakov ANB, and Daignières M (1999) Do faults trigger folding in the lithosphere? *Geophysical Research Letters* 26: 271–274.

Ghorbal B, Bertotti G, Foeken J, and Andriessen P (2008) Unexpected Jurassic to Neogene vertical movements in 'stable' parts of NW Africa revealed by low temperature geochronology. *Terra Nova* 20: 355–363.

Gillet H, Lericolais G, and Rehault JP (2007) Messinian event in the black sea: Evidence of a Messinian erosional surface. *Marine Geology* 244: 142–165.

Goes S, Govers R, and Vacher P (2000a) Shallow mantle temperatures under Europe from P and S wave tomography. *Journal of Geophysical Research, Solid Earth* 105: 11153–11169.

Goes S, Loohuis JJP, Wortel MJR, and Govers R (2000b) The effect of plate stresses and shallow mantle temperatures on tectonics of northwestern Europe. *Global and Planetary Change* 27: 23–38.

Goetze C and Evans B (1979) Stress and temperature in the bending lithosphere as constrained by experimental rock mechanics. *Geophysical Journal of the Royal Astronomical Society* 59: 463–478.

Gölke M, Cloetingh S, and Coblentz D (1996) Finite-element modelling of stress patterns along the Mid-Norwegian continental margin, 62 degrees to 68 degrees N. *Tectonophysics* 266: 33–53.

Görür N (1988) Timing of opening of the Black-Sea Basin. *Tectonophysics* 147: 247–262.

Gouiza M, Bertotti G, Hafid M, and Cloetingh S (2010) Kinematic and thermal evolution of the Moroccan rifted continental margin: Doukkala-High Atlas transect. *Tectonics* 29: 1–22.

Govers R and Wortel MJR (1993) Initiation of asymmetric extension in continental lithosphere. *Tectonophysics* 223: 75–96.

Granet M, Wilson M, and Achauer U (1995) Imaging a mantle plume beneath the French Massif Central. *Earth and Planetary Science Letters* 136: 281–296.

Gries R (1983) Oil and gas prospecting beneath Precambrian of foreland thrust plates in rocky mountains. *Bulletin-American Association of Petroleum Geologists* 67: 1–28.

Griffin WL, O'Reilly SY, and Pearson NJ (1990) Eclogite stability near the crust-mantle boundary. In: Carswell DA and Carswell DA (eds.) *Eclogite Facies Rocks*, pp. 291–314.

Grotzinger J and Royden L (1990) Elastic strength of the Slave craton at 1.9 Gyr and implications for the thermal evolution of the continents. *Nature* 347: 64–66.

Grünthal G (1999) Seismic hazard assessment for Central, North and Northwest Europe: GSHAP Region 3. *Annali Di Geofisica* 42: 999–1011.

Guest B, Guest A, and Axen G (2007) Late Tertiary tectonic evolution of northern Iran: A case for simple crustal folding. *Global and Planetary Change* 58: 435–453.

Guillocheau F, Robin C, Allemand P, et al. (2000) Meso-Cenozoic geodynamic evolution of the Paris Basin: 3D stratigraphic constraints. *Geodinamica Acta* 13: 189–245.

Guillou-Frottier L, Burov E, Nehlig P, and Wyns R (2007) Deciphering plume-litho sphere interactions beneath Europe from topographic signatures. *Global and Planetary Change* 58: 119–140.

Gutscher M-A (1995) Crustal structure and dynamics in the Rhine Graben and the Alpine foreland. *Geophysical Journal International* 122: 617–636.

Haddad D and Watts AB (1999) Subsidence history, gravity anomalies, and flexure of the northeast Australian margin in Papua New Guinea. *Tectonics* 18: 827–842.

Hafkenscheid E, Wortel MJR, and Spakman W (2006) Subduction history of the Tethyan region derived from seismic tomography and tectonic reconstructions. *Journal of Geophysical Research: Solid Earth* 111: B08401.

Hall R, Cottam MA, and Wilson MEJ (2011) The SE Asian gateway: History and tectonics of the Australia–Asia collision. *Geological Society, London, Special Publications* 355: 1–6.

Hardebol NJ, Beekman F, and Cloetingh SAPL (2013) Strong lateral strength contrasts in the mantle lithosphere of continents: A case study from the hot SW Canadian Cordillera. *Tectonophysics* 602: 87–105.

Hardebol NJ, Callot JP, Bertotti G, and Faure JL (2009) Burial and temperature evolution in thrust belt systems: Sedimentary and thrust sheet loading in the SE Canadian Cordillera. *Tectonics* 28: TC3003.

Hatzfeld D and Molnar P (2010) Comparisons of the kinematics and deep structures of the Zagros and Himalaya and of the Iranian and Tibetan plateaus and geodynamic implications. *Reviews of Geophysics* 48: RG2005.

Hellinger SJ and Sclater JG (1983) Some comments on 2-layer extensional models for the evolution of sedimentary basins. *Journal of Geophysical Research* 88: 8251–8269.

Hetényi G, Cattin R, Vergne J, and Nábělek JL (2006) The effective elastic thickness of the India Plate from receiver function imaging, gravity anomalies and thermomechanical modelling. *Geophysical Journal International* 167: 1106–1118.

Hinze WJ and Braile LW (1988) Sedimentary cover of the North American Craton. In: *The geology of North America* 2, pp. 5–24. Geological Society of America.

Hippolyte JC, Angelier J, and Roure F (1994) A major geodynamic change revealed by quaternary stress patterns in the Southern Apennines (Italy). *Tectonophysics* 230: 199–210.
Holt WE and Stern TA (1991) Sediment loading on the western platform of the New Zealand continent: Implications for the strength of a continental margin. *Earth and planetary science letters* 107: 523–538.
Horton BK and DeCelles PG (1997) The modern foreland basin system adjacent to the Central Andes. *Geology* 25: 895–898.
Horváth F (1993) Towards a mechanical model for the formation of the Pannonian basin. *Tectonophysics* 226: 333–357.
Horváth F (1995) Phases of compression during the evolution of the Pannonian basin and its bearing on hydrocarbon exploration. *Marine and Petroleum Geology* 12: 837–844.
Horváth F, Bada G, Szafián P, et al. (2006) Formation and deformation of the Pannonian Basin: Constraints from observational data. *Geological Society, London, Memoir* 32: 191–206.
Horváth F and Cloetingh S (1996) Stress-induced late-stage subsidence anomalies in the Pannonian basin. *Tectonophysics* 266: 287–300.
Horváth F, Stegena L, and Géczy B (1975) Ensimatic and ensialic interarc basins: Comments on 'Neogene Carpathian Arc: A continental arc displaying the features of an island arc' by M. D. Bleahu, M. Boccaletti, P. Manetti, and S. Peltz. *Journal of Geophysical Research* 80: 281–283.
Houseman GA and Gemmer L (2007) Intra-orogenic extension driven by gravitational instability: Carpathian-Pannonian orogeny. *Geology* 35: 1135–1138.
Hsü KJ and Giovanoli F (1979) Messinian event in the Black-Sea. *Palaeogeography Palaeoclimatology Palaeoecology* 29: 75–93.
Huismans RS, Podladchikov YY, and Cloetingh S (2001a) Transition from passive to active rifting: Relative importance of asthenospheric doming and passive extension of the lithosphere. *Journal of Geophysical Research: Solid Earth (1978–2012)* 106: 11271–11291.
Huismans RS, Podladchikov YY, and Cloetingh S (2001b) Dynamic modeling of the transition from passive to active rifting, application to the Pannonian basin. *Tectonics* 20: 1021–1039.
Ismail-Zadeh A, Matenco L, Radulian M, Cloetingh S, and Panza G (2012) Geodynamics and intermediate-depth seismicity in Vrancea (the south-eastern Carpathians): Current state-of-the art. *Tectonophysics* 530–531: 50–79.
Jackson J (2002) Strength of the continental lithosphere: Time to abandon the jelly sandwich? *GSA Today* 12: 4–9.
Janssen ME (1996) *Intraplate Deformation in Africa as a Consequence of Plate Boundary Changes*: *Inferences from Subsidence Analysis and Tectonic Modelling of the Early and Middle Cretaceous Period*, 161 pp. PhD Thesis, VU University, Amsterdam.
Janssen ME, Stephenson RA, and Cloetingh S (1995) Temporal and spatial correlations between changes in plate motions and the evolution of rifted basins in Africa. *Geological Society of America Bulletin* 107: 1317–1332.
Japsen P and Chalmers JA (2000) Neogene uplift and tectonics around the North Atlantic: Overview. *Global and Planetary Change* 24: 165–173.
Jarosinski M, Beekman F, Matenco L, and Cloetingh S (2011) Mechanics of basin inversion: Finite element modelling of the Pannonian Basin System. *Tectonophysics* 502: 121–145.
Jarvis GT and Mckenzie DP (1980) Sedimentary basin formation with finite extension rates. *Earth and Planetary Science Letters* 48: 42–52.
Jaupart C and Mareschal JC (2007) Heat flow and thermal structure of the lithosphere. *Treatise on Geophysics*, vol. 6, pp. 217–251. The Netherlands: Elsevier.
Jiménez-Munt I, Garcia-Castellanos D, Negredo AM, and Platt JP (2005) Gravitational and tectonic forces controlling postcollisional deformation and the present-day stress field of the Alps: Constraints from numerical modeling. *Tectonics* 24: 1–15.
Johnson DD and Beaumont C (1995) Preliminary results from a planform kinematic model of orogen evolution, surface processes and the development of clastic foreland basin stratigraphy. In: Doborek SL and Ross GM (eds.) *Stratgraphic evolution of foreland basins, 52, pp. 3–24*. Society of Economic Palaeontologists and Mineralogists Special Publications.
Johnson H, Dore AG, Gatliff RW, et al. (2008) In: *The Nature and Origin of Compression in Passive Margins*. London: Geological Society, Special Publications, 306.
Jolivet L and Brun JP (2010) Cenozoic geodynamic evolution of the Aegean. *International Journal of Earth Sciences* 99: 109–138.
Jolivet L and Faccenna C (2000) Mediterranean extension and the Africa-Eurasia collision. *Tectonics* 19: 1095–1106.
Jolivet L, Huchon P, and Rangin C (1989) Tectonic setting of western Pacific marginal basins. *Tectonophysics* 160: 23–47.
Jones CH, Wernicke BP, Farmer GL, et al. (1992) Variations across and along a major continental rift – An interdisciplinary study of the Basin and Range Province, western USA. *Tectonophysics* 213: 57–96.
Jordan TE (1981) Thrust loads and foreland basin evolution, cretaceous, western United-States. *Bulletin of the American Association of Petroleum Geologists* 65: 2506–2520.
Jordan TE (1982) Tectonic loading and foreland basin subsidence. *International Congress on Sedimentology* 11: 131.
Juhász E, Phillips L, Müller P, et al. (1999) Late Neogene sedimentary facies and sequences in the Pannonian Basin, Hungary. *Geological Society, London, Special Publications* 156: 335–356.
Kaban MK (2002) A gravity model of the north Eurasia crust and upper mantle: 2. The Alpine-Mediterranean fold-belt and adjacent structures of the southern former USSR. *Russian Journal of Earth Sciences* 4: 19–33.
Kaikkonen P, Moisio K, and Heeremans M (2000) Thermomechanical lithospheric structure of the central Fennoscandian Shield. *Physics of the Earth and Planetary Interiors* 119: 209–235.
Karner GD and Watts AB (1983) Gravity anomalies and flexure of the lithosphere at mountain ranges. *Journal of Geophysical Research: Solid Earth (1978–2012)* 88: 10449–10477.
Karner GD, Egan SS, and Weissel JK (1992) Modeling the tectonic development of the Tucano and Sergipe-Alagoas rift basins, Brazil. *Tectonophysics* 215: 133–160.
Kazmin VG (1991) The position of continental flood basalts in rift zones and its bearing on models of rifting. *Tectonophysics* 199: 375–387.
Kazmin VG, Schreider AA, and Bulychev AA (2000) Early stages of evolution of the Black Sea. *Geological Society, London, Special Publications* 173: 235–249.
Keen CE and Boutilier R (1990) Geodynamic modelling of rift basins: The syn-rift evolution of a simple half-graben. In: *The Potential of Deep Seismic Profiling for Hydrocarbon Exploration*, pp. 23–33. Paris: Technip.
Khriachtchevskaia O, Stovba S, and Popadyuk I (2009) Hydrocarbon prospects in the Western Black Sea of Ukraine. *The Leading Edge* 28: 1024–1029.
Kooi H (1991) *Tectonic Modelling of Extensional Basins*: *The Role of Lithospheric Flexure, Intraplate Stress and Relative Sea-level Change*, 183 pp. PhD Thesis, VU University, Amsterdam.
Kooi H and Cloetingh S (1989) Intraplate stresses and the stratigraphic evolution of the North Sea Central Graben. In: Tankard AJ and Balkwill HR (eds.) *Extensional Tectonics and Stratigraphy of the North Atlantic Margins*, pp. 49–72 Memoirs American Associations of Petroleum Geologists.
Kooi H, Cloetingh S, and Burrus J (1992) Lithospheric necking and regional isostasy at extensional basins. 1. Subsidence and gravity modeling with an application to the Gulf of Lions Margin (Se France). *Journal of Geophysical Research: Solid Earth* 97: 17553–17571.
Kooi H, Hettema M, and Cloetingh S (1991) Lithospheric dynamics and the rapid pliocene quaternary subsidence phase in the southern north-sea basin. *Tectonophysics* 192: 245–259.
Krezsek C and Bally AW (2006) The Transylvanian Basin (Romania) and its relation to the Carpathian fold and thrust belt: Insights in gravitational salt tectonics. *Marine and Petroleum Geology* 23: 405–442.
Krezsek C, Filipescu S, Silye L, Matenco L, and Doust H (2010) Miocene facies associations and sedimentary evolution of the Southern Transylvanian Basin (Romania): Implications for hydrocarbon exploration. *Marine and Petroleum Geology* 27: 191–214.
Krijgsman W, Hilgen FJ, Raffi I, Sierro FJ, and Wilson DS (1999) Chronology, causes and progression of the Messinian salinity crisis. *Nature* 400: 652–655.
Kroon IC (2002) *Strength of the Adriatic lithosphere: Inferences from tectonic modelling*, 112 pp. Published PhD thesis. Vrije Universiteit Amsterdam, the Netherlands.
Kruse SE and Royden LH (1994) Bending and unbending of an elastic lithosphere: The Cenozoic history of the Apennine and Dinaride foredeep basins. *Tectonics* 13: 278–302.
Kusznir NJ, Marsden G, and Egan SS (1991) A flexural-cantilever simple-shear/pure-shear model of continental lithosphere extension: Applications to the Jeanne d'Arc Basin, Grand Banks and Viking Graben, North Sea. *Geological Society, London, Special Publications* 56: 41–60.
Kusznir NJ and Park RG (1987) The extensional strength of the continental lithosphere: its dependence on geothermal gradient, and crustal composition and thickness. *Geological Society, London, Special Publications* 28: 35–52.
Kusznir NJ, Stovba SM, Stephenson RA, and Poplavskii KN (1996) The formation of the northwestern Dniepr-Donets Basin: 2-D forward and reverse syn-rift and post-rift modelling. *Tectonophysics* 268: 237–255.

Kusznir NJ and Ziegler PA (1992) The mechanics of continental extension and sedimentary basin formation – A simple-shear pure-shear flexural cantilever model. *Tectonophysics* 215: 117–131.

Lagarde JL, Baize S, Amorese D, et al. (2000) Active tectonics, seismicity and geomorphology with special reference to Normandy (France). *Journal of Quaternary Science* 15: 745–758.

Lambeck K (1983) The role of compressive forces in intracratonic basin formation and mid-plate orogenies. *Geophysical Research Letters* 10: 845–848.

Lankreijer AC (1998) *Rheology and Basement Control on Extensional Basin Evolution in Central and Eastern Europe*: *Variscan and Alpine-Carpathian-Pannonian Tectonics*, 158 pp. PhD Thesis. VU University, Amsterdam.

Lankreijer A, Bielik M, Cloetingh S, and Majcin D (1999) Rheology predictions across the western Carpathians, Bohemian massif, and the Pannonian basin: Implications for tectonic scenarios. *Tectonics* 18: 1139–1153.

Lankreijer A, Kovac M, Cloetingh S, et al. (1995) Quantitative subsidence analysis and forward modelling of the Vienna and Danube basins: Thin-skinned versus thick-skinned extension. *Tectonophysics* 252: 433–451.

Larsen RM, Brekke H, Larsen BT, and Talleraas E (1992) *Structural and Tectonic Modelling and its Applications to Petroleum Geology*. 549 pp. Norwegian Petroleum Society Special Publications.

Laske G and Masters G (1997) A global digital map of sediment thickness. *Eos, Transactions of the American Geophysical Union* 78: F483.

Laubscher H (2010) Jura, Alps and the boundary of the Adria subplate. *Tectonophysics* 483: 223–239.

Lavier LL and Steckler MS (1997) The effect of sedimentary cover on the flexural strength of continental lithosphere. *Nature* 389: 476–479.

Lawrence DT, Doyle M, and Aigner T (1990) Stratigraphic simulation of sedimentary basins – Concepts and calibration. *Bulletin of the American Association of Petroleum Geologists* 74: 273–295.

Le Solleuz A, Doin MP, Robin C, and Guillocheau F (2004) From a mountain belt collapse to a sedimentary basin development: 2-D thermal model based on inversion of stratigraphic data in the Paris Basin. *Tectonophysics* 386: 1–27.

Leever KA, Matenco L, Garcia-Castellanos D, and Cloetingh SAPL (2011) The evolution of the Danube gateway between Central and Eastern Paratethys (SE Europe): Insight from numerical modelling of the causes and effects of connectivity between basins and its expression in the sedimentary record. *Tectonophysics* 502: 175–195.

Lefort JP and Agarwal BNP (1996) Gravity evidence for an Alpine buckling of the crust beneath the Paris Basin. *Tectonophysics* 258: 1–14.

Lefort JP and Agarwal BNP (2000) Gravity and geomorphological evidence for a large crustal bulge cutting across Brittany (France): A tectonic response to the closure of the Bay of Biscay. *Tectonophysics* 323: 149–162.

Lefort JP and Agarwal BNP (2002) Topography of the Moho undulations in France from gravity data: Their age and origin. *Tectonophysics* 350: 193–213.

Lenkey L (1999) *Geothermics of the Pannonian Basin and Its Bearing on the Tectonics of Basin Evolution*, 215 pp. PhD Thesis, VU University, Amsterdam.

Lenkey L, Dövényi P, Horváth F, and Cloetingh S (2002) Geothermics of the Pannonian basin and its bearing on the neotectonics. *Neotectonics and Surface Processes: The Pannonian Basin and Alpine/Carpathian System*, vol. 3, 29–40.

Lenotre N, Thierry P, Blanchin R, and Brochard G (1999) Current vertical movement demonstrated by comparative levelling in Brittany (northwestern France). *Tectonophysics* 301: 333–344.

Le Pichon X, Henry P, and Goffé B (1997) Uplift of Tibet: From eclogites to granulites—implications for the Andean Plateau and the Variscan belt. *Tectonophysics* 273: 57–76.

Lericolais G, Bourget J, Popescu I, et al. (2013) Late Quaternary deep-sea sedimentation in the western Black Sea: New insights from recent coring and seismic data in the deep basin. *Global and Planetary Change* 103: 232–247.

Letouzey J (1986) Cenozoic Paleostress pattern in the alpine foreland and structural interpretation in a platform basin. *Tectonophysics* 132: 215–231.

Letouzey J, Biju-Duval B, Dorkel A, et al. (1977) The Black Sea: A marginal basin; geophysical and geological data. In: Biju-Duval B and Montadert L (eds.) *Structural History of the Mediterranean, Basins*, pp. 363–376. Paris: Technip.

Letouzey J, Werner P, and Marty A (1990) Fault reactivation and structural inversion. Backarc and intraplate compressive deformations. Example of the eastern Sunda shelf (Indonesia). *Tectonophysics* 183: 341–362.

Linzer HG (1996) Kinematics of retreating subduction along the Carpathian arc, Romania. *Geology* 24: 167–170.

Lin AT and Watts AB (2002) Origin of the West Taiwan basin by orogenic loading and flexure of a rifted continental margin. *Journal of Geophysical Research: Solid Earth (1978–2012)* 107: ETG-2.

Littke R, Bayer U, Gajewski D, and Nelskamp S (2008) In: *Dynamics of Complex Intracontinental Basins: The Central European Basin System*. Heidelberg: Springer, 520 pp.

Liu MJ, Mooney WD, Li SL, Okaya N, and Detweiler S (2006) Crustal structure of the northeastern margin of the Tibetan plateau from the Songpan-Ganzi terrane to the Ordos basin. *Tectonophysics* 420: 253–266.

Liu YJ, Neubauer F, Genser J, et al. (2007) Geochronology of the initiation and displacement of the Altyn Strike-Slip Fault, western China. *Journal of Asian Earth Sciences* 29: 243–252.

Lobkovsky LI, Cloetingh S, Nikishin AM, et al. (1996) Extensional basins of the former Soviet Union – Structure, basin formation mechanisms and subsidence history. *Tectonophysics* 266: 251–285.

Londoño J and Lorenzo JM (2004) Geodynamics of continental plate collision during late tertiary foreland basin evolution in the Timor Sea: constraints from foreland sequences, elastic flexure and normal faulting. *Tectonophysics* 392: 37–54.

Lorenzo JM, O'Brien GW, Stewart J, and Tandon K (1998) Inelastic yielding and forebulge shape across a modern foreland basin: North West Shelf of Australia, Timor Sea. *Geophysical Research Letters* 25: 1455–1458.

Lyon-Caen H and Molnar P (1984) Gravity anomalies and the structure of western Tibet and the southern Tarim Basin. *Geophysical Research Letters* 11: 1251–1254.

Lyon-Caen H and Molnar P (1985) Gravity anomalies, flexure of the Indian plate, and the structure, support and evolution of the Himalaya and Ganga basin. *Tectonics* 4: 513–538.

Macario A, Malinverno A, and Haxby WF (1995) On the robustness of elastic thickness estimates obtained using the coherence method. *Journal of Geophysical Research: Solid Earth (1978–2012)* 100: 15163–15172.

Mareschal JC and Gliko A (1991) Lithospheric thinning, uplift, and heat-flow preceding rifting. *Tectonophysics* 197: 117–126.

Marotta AM, Bayer U, and Thybo H (2000) The legacy of the NE German Basin – Reactivation by compressional buckling. *Terra Nova* 12: 132–140.

Martin M and Wenzel F (2006) High-resolution teleseismic body wave tomography beneath SE-Romania - II. Imaging of a slab detachment scenario. *Geophysical Journal International* 164: 579–595.

Martinod J and Davy P (1992) Periodic instabilities during compression or extension of the lithosphere 1. Deformation modes from an analytical perturbation method. *Journal of Geophysical Research: Solid Earth* 97: 1999–2014.

Mascle A (ed.) (1998) *Cenozoic Foreland Basins of Western Europe*: Geological Society of London, Special Publications 134.

Matenco L, Andriessen P, and Network S (2013) Quantifying the mass transfer from mountain ranges to deposition in sedimentary basins: Source to sink studies in the Danube Basin-Black Sea system. *Global and Planetary Change* 103: 1–18.

Matenco L and Bertotti G (2000) Tertiary tectonic evolution of the external East Carpathians (Romania). *Tectonophysics* 316: 255–286.

Matenco L, Bertotti G, Cloetingh S, and Dinu C (2003) Subsidence analysis and tectonic evolution of the external Carpathian-Moesian Platform region during Neogene times. *Sedimentary Geology* 156: 71–94.

Matenco L, Bertotti G, Dinu C, and Cloetingh S (1997a) Tertiary tectonic evolution of the external South Carpathians and the adjacent Moesian platform (Romania). *Tectonics* 16: 896–911.

Matenco L, Bertotti G, Leever K, et al. (2007) Large-scale deformation in a locked collisional boundary: Interplay between subsidence and uplift, intraplate stress, and inherited lithospheric structure in the late stage of the SE Carpathians evolution. *Tectonics* 26: TC4011.

Matenco L, Krezsek C, Merten S, et al. (2010) Characteristics of collisional orogens with low topographic build-up: An example from the Carpathians. *Terra Nova* 22: 155–165.

Matenco L and Radivojević D (2012) On the formation and evolution of the Pannonian Basin: Constraints derived from the structure of the junction area between the Carpathians and Dinarides. *Tectonics* 31: TC6007.

Matenco L, Zoetemeijer R, Cloetingh S, and Dinu C (1997b) Lateral variations in mechanical properties of the Romanian external Carpathians: Inferences of flexure and gravity modelling. *Tectonophysics* 282: 147–166.

Mathisen ME and Vondra CF (1983) The fluvial and pyroclastic deposits of the Cagayan Basin, Northern Luzon, Philippines – An example of non-marine volcaniclastic sedimentation in an interarc basin. *Sedimentology* 30: 369–392.

Mazur S, Scheck-Wenderoth M, and Krzywiec P (2005) Different modes of the Late Cretaceous-Early Tertiary inversion in the North German and Polish basins. *International Journal of Earth Sciences* 94: 782–798.

Mcadoo DC and Sandwell DT (1985) Folding of oceanic lithosphere. *Journal of Geophysical Research-Solid Earth and Planets* 90: 8563–8569.

McHargue TR, Heidrick TL, and Livingston J (1992) Episodic structural development of the Central African Rift in Sudan. *Tectonophysics* 213: 187–202.

Mckenzie D (1978) Some remarks on development of sedimentary basins. *Earth and Planetary Science Letters* 40: 25–32.

McNutt MK and Kogan MG (1987) Isostasy in the USSR I: Admittance data. *Composition, Structure and Dynamics of the Lithosphere-Asthenosphere System* 16: 301–307.
McNutt MK, Diament M, and Kogan MG (1988) Variations of elastic plate thickness at continental thrust belts. *Journal of Geophysical Research: Solid Earth (1978–2012)* 93: 8825–8838.
Mercier JL, Sebrier M, Lavenu A, et al. (1992) Changes in the tectonic regime above a subduction zone of andean type – The andes of Peru and Bolivia during the Pliocene-Pleistocene. *Journal of Geophysical Research: Solid Earth* 97: 11945–11982.
Merten S, Matenco L, Foeken JPT, and Andriessen PAM (2011) Toward understanding the post-collisional evolution of an orogen influenced by convergence at adjacent plate margins: Late Cretaceous-Tertiary thermotectonic history of the Apuseni Mountains. *Tectonics* 30: TC6008.
Merten S, Matenco L, Foeken JPT, Stuart FM, and Andriessen PAM (2010) From nappe stacking to out-of-sequence postcollisional deformations: Cretaceous to Quaternary exhumation history of the SE Carpathians assessed by low-temperature thermochronology. *Tectonics* 29: TC3013.
Meschede M and Frisch W (1998) A plate-tectonic model for the Mesozoic and Early Cenozoic history of the Caribbean plate. *Tectonophysics* 296: 269–291.
Meulenkamp JE, Kovac M, and Cicha I (1996) On Late Oligocene to Pliocene depocentre migrations and the evolution of the Carpathian-Pannonian system. *Tectonophysics* 266: 301–317.
Millan H, Den Bezemer T, Vergés J, et al. (1995) Paleo-elevation and effective elastic thickness evolution at mountain ranges: Interference from flexural modelling in the Eastern Pyrenees and Ebro Basin. *Marine and Petroleum Geology* 12: 917–928.
Mohr P (1992) Nature of the crust beneath magmatically active continental rifts. *Tectonophysics* 213: 269–284.
Moisio K, Kaikkonen P, and Beekman F (2000) Rheological structure and dynamical response of the DSS profile BALTIC in the SE Fennoscandian Shield. *Tectonophysics* 320: 175–194.
Moretti I and Royden L (1988) Deflection, gravity anomalies and tectonics of doubly subducted continental lithosphere: Adriatic and Ionian Seas. *Tectonics* 7: 875–893.
Morgan P and Ramberg IB (1987) Physical changes in the lithosphere associated with thermal relaxation after rifting. *Tectonophysics* 143: 1–11.
Morley CK and Westaway R (2006) Subsidence in the super-deep Pattani and Malay basins of Southeast Asia: A coupled model incorporating lower-crustal flow in response to post-rift sediment loading. *Basin Research* 18: 51–84.
Moucha R and Forte AM (2011) Changes in African topography driven by mantle convection. *Nature Geoscience* 4: 707–712.
Muhlhaus HB, Sakaguchi H, and Hobbs BE (1998) Evolution of three-dimensional folds for a non-Newtonian plate in a viscous medium. *Proceedings of the Royal Society A Mathematical Physical and Engineering Sciences* 454: 3121–3143.
Munteanu I (2012) *Evolution of the Western Black Sea*: *Kinematic and Sedimentological Inferences from Geological Observations and Analogue Modelling*. Dissertation, Utrecht University.
Munteanu I, Matenco L, Dinu C, and Cloetingh S (2011) Kinematics of back-arc inversion of the Western Black Sea Basin. *Tectonics* 30: TC5004.
Munteanu I, Matenco L, Dinu C, and Cloetingh S (2012) Effects of large sea-level variations in connected basins: The Dacian-Black Sea system of the Eastern Paratethys. *Basin Research* 24: 583–597.
Munteanu I, Willingshofer E, Sokoutis D, Matenco L, Dinu C, and Cloetingh S (2013) Transfer of deformation in back-arc basins with a laterally variable rheology: Constraints from analogue modelling of the Balkanides–Western Black Sea inversion. *Tectonophysics* 602: 223–236.
Munteanu I, Willingshofer E, Matenco L, Sokoutis D, and Cloetingh S (2014) Far-field contractional polarity changes in models and nature. *Earth and Planetary Science Letters* 395: 101–115.
Nádai A (1963) *Theory of flow and fracture of solids*. New York: McGraw-Hill.
Nadin PA and Kusznir NJ (1995) Paleocene uplift and Eocene subsidence in the northern North-Sea Basin from 2D forward and reverse stratigraphic modeling. *Journal of the Geological Society* 152: 833–848.
Nadirov RS, Bagirov E, Tagiyev M, and Lerche I (1997) Flexural plate subsidence, sedimentation rates, and structural development of the super-deep South Caspian Basin. *Marine and Petroleum Geology* 14: 383–400.
Naylor M and Sinclair HD (2008) Pro- vs. retro-foreland basins. *Basin Research* 20: 285–303.
Necea D (2010) *High-Resolution Morpho-Tectonic Profiling Across an Orogen*: *Tectonic-Controlled Geomorphology and Multiple Dating Approach in the SE Carpathians*, 147 pp. PhD Thesis, VU Vrije Universiteit, Amsterdam.
Necea D, Fielitz W, and Matenco L (2005) Late Pliocene-Quaternary tectonics in the frontal part of the SE Carpathians: Insights from tectonic geomorphology. *Tectonophysics* 410: 137–156.
Nemes F, Neubauer F, Cloetingh S, and Genser J (1997) The Klagenfurt Basin in the Eastern Alps: An intra-orogenic decoupled flexural basin? *Tectonophysics* 282: 189–203.
Neubauer F, Cloetingh S, Dinu C, and Mocanu V (1997) Tectonics of the Alpine-Carpathian-Pannonian region: Introduction. *Tectonophysics* 272: 93–96.
Nikishin AM, Brunet MF, Cloetingh S, and Ershov AV (1997) Northern Peri-Tethyan Cenozoic intraplate deformations: Influence of the Tethyan collision belt on the Eurasian continent from Paris to Tian-Shan. *Comptes rendus de l'Académie des sciences. Série 2, Sciences de la terre et des planètes* 324: 49–57.
Nikishin AM, Cloetingh S, Lobkovsky LI, Burov EB, and Lankreijer AC (1993) Continental lithosphere folding in Central-Asia.1. Constraints from geological observations. *Tectonophysics* 226: 59–72.
Nikishin AM, Korotaev MV, Ershov AV, and Brunet MF (2003) The Black Sea basin: Tectonic history and Neogene-Quaternary rapid subsidence modelling. *Sedimentary Geology* 156: 149–168.
Nikishin AM, Ziegler PA, Abbott D, Brunet MF, and Cloetingh S (2002) Permo-Triassic intraplate magmatism and rifting in Eurasia: Implications for mantle plumes and mantle dynamics. *Tectonophysics* 351: 3–39.
Nikishin A, Ziegler P, Bolotov S, et al. (2012) Late Paleozoic to Cenozoic evolution of the Black Sea-Southern Eastern Europe Region: A view from the Russian Platform. *Turkish Journal of Earth Sciences* 21: 571–634.
Nikishin AM, Ziegler PA, Panov DI, et al. (2001) Mesozoic and Cainozoic evolution of the Scythian platform-Black Sea-Caucasus domain. *Memoires du Museum National d'Histoire Naturelle* 186: 295–346.
Nivière B and Winter T (2000) Pleistocene northwards fold propagation of the Jura within the southern Upper Rhine Graben: Seismotectonic implications. *Global and Planetary Change* 27: 263–288.
Nottvedt A, Gabrielsen RH, and Steel RJ (1995) Tectonostratigraphy and sedimentary architecture of rift basins, with reference to the northern north-sea. *Marine and Petroleum Geology* 12: 881–901.
Nunn JA, Czerniak M, and Pilger RH (1987) Constraints on the structure of Brooks Range and Colville Basin, northern Alaska, from flexure and gravity analysis. *Tectonics* 6: 603–617.
Okay AI, Satir M, Maluski H, et al. (1996) Paleo-and Neo-Tethyan events in northwestern Turkey: Geologic and geochronologic constraints. In: Yin A and Olsen KH (eds.) *The Tectonic Evolution of Asia*, pp. 420–441. Cambridge: Cambridge University Press.
Okay AI, Sengor AMC, and Görür N (1994) Kinematic history of the opening of the Black-Sea and its effect on the surrounding regions. *Geology* 22: 267–270.
Olsen KH and Morgan P (1995) Introduction: progress in understanding continental rifts. In: Olsen KH (Ed.) Developments in Geotectonics: Continental Rifts: Evolution, Structure, *Tectonics* 25: 3–26.
Olsen KH and Morgan P (2006) Chapter 1 Introduction: Progress in understanding continental rifts. In: Olsen KH (ed.) *Developments in Geotectonics*, vol. 25, pp. 3–26. Amsterdam: Elsevier.
Oszczypko N, Krzywiec P, Popadyuk I, and Peryt T (2005) Carpathian Foredeep Basin (Poland and Ukraine) - Its sedimentary, structural and geodynamic evolution. In: Golonka J and Picha FJ (eds.) *The Carpathians and their foreland: Geology and hydrocarbon resources* 84, pp. 293–350. AAPG.
Panza GF (1983) Lateral variations in the European lithosphere and seismic activity. *Physics of the Earth and Planetary Interiors* 33: 194–197.
Parnell J (1994) Geofluids: Origin migration and evolution of fluids in sedimentary basins. *Geological Society, London, Special Publications* 78: 1–372.
Parsons T (1995) The Basin and Range Province. In: Olsen KH (ed.) *Developments in Geotectonics, 25: Continental Rifts: Evolution, Structure, Tectonics,* pp. 227–324. Amsterdam: Elsevier.
Parsons T (2006) The basin and range province. In: Olsen KH (ed.) *Developments in Geotectonics*, vol. 25, p. 277. Amsterdam: Elsevier.
Pascal C and Cloetingh SAPL (2009) Gravitational potential stresses and stress field of passive continental margins: Insights from the south-Norway shelf. *Earth and Planetary Science Letters* 277: 464–473.
Patacca E, Scandone P, Di Luzio E, Cavinato GP, and Parotto M (2008) Structural architecture of the central Apennines: Interpretation of the CROP 11 seismic profile from the Adriatic coast to the orographic divide. *Tectonics* 27: TC3006.
Pavoni N (1993) Pattern of mantle convection and Pangaea break-up, as revealed by the evolution of the African plate. *Journal of the Geological Society* 150: 953–964.
Pelletier JD (2007) Erosion-rate determination from foreland basin geometry. *Geology* 35: 5–8.
Peper T, van Balen RT, and Cloetingh S (1995) Implications of Orogenic wedge growth, intraplate stress variations and eustatic sea-level change for Foreland Basin Stratigraphy—Inferences From Numerical Modeling. In: Dorobek S and Ross G (eds.) Stratigraphic developments in foreland basins, pp. 25—35. *Special Publications of Society for Sedimentary Geology 52*.

Peper T, Beekman F, and Cloetingh S (1992) Consequences of thrusting and intraplate stress fluctuations for vertical motions in foreland basins and peripheral areas. *Geophysical Journal International* 111: 104–126.

Pérez-Gussinyé M and Watts AB (2005) The long-term strength of Europe and its implications for plate-forming processes. *Nature* 436: 381–384.

Persson KS, Garcia-Castellanos D, and Sokoutis D (2004) River transport effects on compressional belts: First results from an integrated analogue-numerical model. *Journal of Geophysical Research: Solid Earth* 109: B01409.

Persson KS and Sokoutis D (2002) Analogue models of orogenic wedges controlled by erosion. *Tectonophysics* 356: 323–336.

Petroleum Publishing Co./PenWell (1970) Worldwide offshore activity and sedimentary basins. *Oil and Gas Journal*.

Philip H (1987) Plioquaternary evolution of the stress-field in mediterranean zones of subduction and collision. *Annales Geophysicae, Series B: Terrestrial and Planetary Physics* 5: 301–319.

Philippe Y (1994) Transfer Zone in the Southern Jura Thrust Belt (Eastern France): Geometry, development, and comparison with analogue modeling experiments. In: Mascle A (ed.) *Hydrocarbon and Petroleum Geology of France*, pp. 327–346. Heidelberg: Springer Berlin, Special Publication of the European Association of Petroleum Geoscientists 4.

Pinter N, Grenerczy G, Weber J, and Medak D (2005) *The Adria Microplate: GPS Geodesy, Tectonics and Hazards*, vol. 61, p. 414. Netherlands: Springer.

Pitman WC and Golovchenko X (1983) The effect of sealevel change on the shelfedge and slope of passive margins. *Special Publications of SEPM* 33: 41–58.

Piwowar JM and LeDrew EF (1996) Principal components analysis of Arctic ice conditions between 1978 and 1987 as observed from the SMMR data record. *Canadian journal of remote sensing* 22: 390–403.

Plomerova J, Kouba D, and Babuska V (2002) Mapping the lithosphere-asthenosphere boundary through changes in surface-wave anisotropy. *Tectonophysics* 358: 175–185.

Popescu E and Radulian M (2001) Source characteristics of the seismic sequences in the Eastern Carpathians foredeep region (Romania). *Tectonophysics* 338: 325–337.

Popescu I, Lericolais G, Panin N, Wong HK, and Droz L (2001) Late Quaternary channel avulsions on the Danube deep-sea fan, Black Sea. *Marine Geology* 179: 25–37.

Popov SV, Shcherba IG, Ilyina LB, et al. (2006) Late Miocene to Pliocene palaeogeography of the Paratethys and its relation to the Mediterranean. *Palaeogeography Palaeoclimatology Palaeoecology* 238: 91–106.

Poudjom Djomani YH, Fairhead JD, and Griffin WL (1999) The flexural rigidity of Fennoscandia: Reflection of the tectonothermal age of the lithospheric mantle. *Earth and Planetary Science Letters* 174: 139–154.

Prezzi CB (1999) Diacronismo en la deformación Mio-Pliocena de la Puna Argentina: Un modelo flexural. *Actas Congreso Geologico Argentino* 14: 197–200.

Prezzi CB, Uba CE, and Gotze HJ (2009) Flexural isostasy in the Bolivian Andes: Chaco foreland basin development. *Tectonophysics* 474: 526–543.

Price RA (1973) Large-scale gravitational flow of supracrustal rocks, southern Canadian Rockies. In: Jong K and Scholten RA (eds.) *Gravity and tectonics*, pp. 491–502. New York: John Wiley & Sons.

Pysklywec RN and Mitrovica JX (1997) Mantle avalanches and the dynamic topography of continents. *Earth and Planetary Science Letters* 148: 447–455.

Quinlan GM and Beaumont C (1984) Appalachian thrusting, lithospheric flexure, and the paleozoic stratigraphy of the eastern interior of north-America. *Canadian Journal of Earth Sciences* 21: 973–996.

Raileanu V, Taloş D, Varodin V, and Stiopol D (1993) Crustal seismic reflection profiling in Romania on the Urziceni-Mizil line. *Tectonophysics* 223: 401–409.

Ranalli G (1995) *Rheology of the Earth*. London: Chapman & Hall, 413 pp.

Ranalli G and Murphy DC (1987) Rheological stratification of the lithosphere. *Tectonophysics* 132: 281–295.

Rankin DW, Dillon WP, Black DFB, et al. (1991) *Central Kentucky to the Carolina Trough*. Geological Society of America.

Ravaut P, Alyahyaey A, Bayer R, and Lesquer A (1993) Isostatic response of the Arabian Platform to Ophiolitic Loading in Oman. *Comptes Rendus - Acadamie des Sciences* 317: 463–470.

Ren Y, Stuart GW, Houseman GA, et al. (2012) Upper mantle structures beneath the Carpathian-Pannonian region: Implications for the geodynamics of continental collision. *Earth and Planetary Science Letters* 349: 139–152.

Reston TJ (1990) The lower crust and the extension of the continental lithosphere - Kinematic analysis of birps deep seismic data. *Tectonics* 9: 1235–1248.

Richardson RM (1992) Ridge forces, absolute plate motions, and the intraplate stress-field. *Journal of Geophysical Research: Solid Earth* 97: 11739–11748.

Richter F and Mckenzie D (1978) Simple plate models of mantle convection. *Journal of Geophysics* 44: 441–471.

Rickers F, Fichtner A, and Trampert J (2013) The Iceland-Jan Mayen plume system and its impact on mantle dynamics in the North Atlantic region: Evidence from full-waveform inversion. *Earth and Planetary Science Letters* 367: 39–51.

Ritter JRR, Achauer U, Christensen UR, and the Eifel Plume T (2000) The teleseismic tomography experiment in the eifel region, central Europe: Design and first results. *Seismological Research Letters* 71: 437–443.

Ritter JRR, Jordan M, Christensen UR, and Achauer U (2001) A mantle plume below the Eifel volcanic fields, Germany. *Earth and Planetary Science Letters* 186: 7–14.

Ritzmann O and Faleide JI (2009) The crust and mantle lithosphere in the Barents Sea/Kara Sea region. *Tectonophysics* 470: 89–104.

Roberts AM, Yielding G, Kusznir NJ, Walker I, and Dorn-Lopez D (1993) Mesozoic extension in the North Sea: Constraints from flexural backstripping, forward modelling and fault populations. *Geological Society, London, Conference series* 4: 1123–1136.

Robin C, Allemand P, Burov E, et al. (2003) Vertical movements of the Paris Basin (Triassic-Pleistocene): From 3D stratigraphic database to numerical models. *Geological Society, London, Special Publications* 212: 225–250.

Robinson AG, Rudat JH, Banks CJ, and Wiles RLF (1996) Petroleum geology of the Black Sea. *Marine and Petroleum Geology* 13: 195–223.

Robinson A, Spadini G, Cloetingh S, and Rudat J (1995) Stratigraphic evolution of the Black-Sea – Inferences from basin modeling. *Marine and Petroleum Geology* 12: 821–835.

Roddaz M, Viers J, Brusset S, Baby P, and Herail G (2005) Sediment provenances and drainage evolution of the Neogene Amazonian foreland basin. *Earth and Planetary Science Letters* 239: 57–78.

Rohrman M, Vanderbeek P, Andriessen P, and Cloetingh S (1995) Meso-Cenozoic morphotectonic evolution of southern Norway – Neogene domal uplift inferred from apatite fission-track thermochronology. *Tectonics* 14: 704–718.

Roure F (2008) Foreland and Hinterland basins: What controls their evolution? *Swiss Journal of Geosciences* 101: S5–S29.

Roure F, Alzaga-Ruiz H, Callot JP, et al. (2009) Long lasting interactions between tectonic loading, unroofing, post-rift thermal subsidence and sedimentary transfers along the western margin of the Gulf of Mexico: Some insights from integrated quantitative studies. *Tectonophysics* 475: 169–189.

Roure F, Andriessen P, Callot JP, et al. (2010a) The use of palaeo-thermo-barometers and coupled thermal, fluid flow and pore-fluid pressure modelling for hydrocarbon and reservoir prediction in fold and thrust belts. *Geological Society, London, Special Publications* 348: 87–114.

Roure F, Brun JP, Colletta B, and Vially R (1994) Multiphase Extensional structures, fault reactivation, and petroleum plays in the alpine foreland basin of southeastern France. In: Mascle A (ed.) *Hydrocarbon and Petroleum Geology of France*, pp. 245–268. Springer Berlin Heidelberg, Special Publication of the European Association of Petroleum Geoscientists 4.

Roure F, Casero P, and Addoum B (2012) Alpine inversion of the North African margin and delamination of its continental lithosphere. *Tectonics* 31: TC3006.

Roure F, Choukroune P, Berastegui X, et al. (1989) Ecors deep seismic data and balanced cross-sections – Geometric constraints on the evolution of the pyrenees. *Tectonics* 8: 41–50.

Roure F, Choukroune P, and Polino R (1996) Deep seismic reflection data and new insights on the bulk geometry of mountain ranges. *Comptes rendus de l'Académie des sciences. Série 2, Sciences de la terre et des planètes* 322: 345–359.

Roure F, Cloetingh S, Scheck-Wenderoth M, and Ziegler P (2010b) Achievements and challenges in sedimentary basin dynamics: A review. In: Cloetingh S and Negendank J (eds.) *New Frontiers in Integrated Solid Earth Sciences International Year of Planet Earth*, pp. 145–233. Netherlands: Springer.

Roure F, Colletta B, DeToni B, et al. (1997) Within-plate deformations in the Maracaibo and East Zulia basins, western Venezuela. *Marine and Petroleum Geology* 14: 139–163.

Roure F, Roca E, and Sassi W (1993) The Neogene evolution of the outer Carpathian flysch units (Poland, Ukraine and Romania) – Kinematics of a foreland fold-and-thrust belt system. *Sedimentary Geology* 86: 177–201.

Roure F, Scheck-Wenderoth M, Gahnoog A, and Pharaoh T (2010c) Lithosphere dynamics and sedimentary basins: The Arabian plate and analogues. *Arabian Journal of Geosciences* 3: 327–329.

Rowley DB and Sahagian D (1986) Depth-dependent stretching – A different approach. *Geology* 14: 32–35.

Royden L (1988a) Flexural behavior of the continental lithosphere in Italy – Constraints imposed by gravity and deflection data. *Journal of Geophysical Research-Solid Earth and Planets* 93: 7747–7766.

Royden LH (ed.) (1988b) *The Pannonian Basin*. Tusla, OK: American Association of Petroleum Geologists, AAPG Memoirs 45.

Royden LH (1993) The tectonic expression slab pull at continental convergent boundaries. *Tectonics* 12: 303–325.

Royden L and Burchfiel BC (1989) Are systematic variations in thrust belt style related to plate boundary processes – (the Western Alps Versus the Carpathians). *Tectonics* 8: 51–61.
Royden LH and Dövényi P (1988) Variations in extensional styles at depth across the Pannonian basin system. *American Association of Petroleum Geologists* 45: 235–255.
Royden LH and Horváth F (eds.) (1988) *The Pannonian Basin: A case study in basin evolution,* American Association of Petroleum Geologists, AAPG Memoir 45.
Royden L, Horváth F, Nagymarosy A, and Stegena L (1983) Evolution of the Pannonian basin system. 2. Subsidence and thermal history. *Tectonics* 2: 91–137.
Royden L and Karner GD (1984) Flexure of the continental lithosphere beneath Apennine and Carpathian foredeep basins. *Nature* 309: 142–144.
Royden L and Keen CE (1980) Rifting process and thermal evolution of the continental-margin of eastern Canada determined from subsidence curves. *Earth and Planetary Science Letters* 51: 343–361.
Royden L, Sclater JG, and Von Herzen RP (1980) Continental-margin subsidence and heat-flow – Important parameters in formation of petroleum-hydrocarbons. *American Association of Petroleum Geologists Bulletin* 64: 173–187.
Ruppel C and McNutt M (1987) An elastic plate model for the Caucasus. *Eos Transactions AGU* 68: 420.
Sacchi M, Horváth F, and Magyari O (1999) Role of unconformity-bounded units in the stratigraphy of the continental record: A case study from the Late Miocene of the western Pannonian Basin, Hungary. *Geological Society, London, Special Publications* 156: 357–390.
Sachsenhofer RF, Lankreijer A, Cloetingh S, and Ebner F (1997) Subsidence analysis and quantitative basin modelling in the Styrian basin (Pannonian basin system, Austria). *Tectonophysics* 272: 175–196.
Saintot A, Brunet M, Yakovlev F, et al. (2006) The Mesozoic-Cenozoic tectonic evolution of the Greater Caucasus. *Geological Society, London, Memoirs* 32: 277.
Salveson JO (1976) Variations in the oil and gas geology of rift basins. In: *Egyptian General Petroleum Corporation, 5th Exploration Seminar, Cairo, Egypt*.
Samuelsson J and Middleton MF (1999) The Caledonian foreland basin in Scandinavia: Constrained by the thermal maturation of the alum shale. A reply. *Journal of the Geological Society of Sweden (GFF)* 121: 157–159.
Sanders CAE, Andriessen PAM, and Cloetingh SAPL (1999) Life cycle of the East Carpathian orogen: Erosion history of a doubly vergent critical wedge assessed by fission track thermochronology. *Journal of Geophysical Research: Solid Earth* 104: 29095–29112.
Sassi W, Colletta B, Bale P, and Paquereau T (1993) Modeling of structural complexity in sedimentary basins – The role of preexisting faults in thrust tectonics. *Tectonophysics* 226: 97–112.
Sassi W and Rudkiewicz JL (2000) *Computer Modelling of Petroleum Systems Along Regional Cross-Sections in Foreland and Fold-and-Thrustbelts*. In: Proceedings of the conference on geology and petroleum geology of the Mediterranean and circum Mediterranean Basins. Malta: EAGE.
Scheck M and Bayer U (1999) Evolution of the Northeast German Basin – Inferences from a 3D structural model and subsidence analysis. *Tectonophysics* 313: 145–169.
Schlunegger F, Jordan TE, and Klaper EM (1997) Controls of erosional denudation in the orogen on foreland basin evolution: The Oligocene central Swiss Molasse basin as an example. *Tectonics* 16: 823–840.
Schmalholz SM and Podladchikov YY (2000) Finite amplitude folding: Transition from exponential to layer length controlled growth (vol 179, pg 363, 2000). *Earth and Planetary Science Letters* 181: 617–633.
Schmid SM, Bernoulli D, Fugenschuh B, et al. (2008) The Alpine-Carpathian-Dinaridic orogenic system: Correlation and evolution of tectonic units. *Swiss Journal of Geosciences* 101: 139–183.
Schmid SM, Berza T, Diaconescu V, Froitzheim N, and Fügenschuh B (1998) Orogen-parallel extension in the Southern Carpathians. *Tectonophysics* 297: 209–228.
Sclater JG and Christie PAF (1980) Continental stretching – An explanation of the post-mid-cretaceous subsidence of the central north-sea basin. *Journal of Geophysical Research* 85: 3711–3739.
Sclater J, Royden L, Horváth F, Burchfiel B, Semken S, and Stegena L (1980) The formation of the intra-Carpathian basins as determined from subsidence data. *Earth and Planetary Science Letters* 51: 139–162.
Şengör AMC (1987) Tectonics of the tethysides – Orogenic collage development in a collisional setting. *Annual Review of Earth and Planetary Sciences* 15: 213–244.
Sengör AMC and Burke K (1978) Relative timing of rifting and volcanism on earth and its tectonic implications. *Geophysical Research Letters* 5: 419–421.
Şengör AMC and Yilmaz Y (1981) Tethyan evolution of Turkey – A plate tectonic approach. *Tectonophysics* 75: 181–241.
Serpelloni E, Faccenna C, Spada G, Dong D, and Williams SD (2013) Vertical GPS ground motion rates in the Euro-Mediterranean region: New evidence of vertical velocity gradients at different spatial scales along the Nubia-Eurasia plate boundary. *Journal of Geophysical Research: Solid Earth* 118: 6003–6024.
Sheffels B and McNutt M (1986) Role of subsurface loads and regional compensation in the isostatic balance of the Transverse Ranges, California: Evidence for intracontinental subduction. *Journal of Geophysical Research: Solid Earth (1978–2012)* 91: 6419–6431.
Shillington DJ, White N, Minshull TA, et al. (2008) Cenozoic evolution of the eastern Black Sea: A test of depth-dependent stretching models. *Earth and Planetary Science Letters* 265: 360–378.
Shin YH, Shum CK, Braitenberg C, et al. (2009) Three-dimensional fold structure of the Tibetan Moho from GRACE gravity data. *Geophysical Research Letters* 36: L01302.
Shudofsky GN, Cloetingh S, Stein S, and Wortel R (1987) Unusually deep earthquakes in east-Africa – Constraints on the thermomechanical structure of a continental rift system. *Geophysical Research Letters* 14: 741–744.
Simpson GDH (2006) Modelling interactions between fold-thrust belt deformation, foreland flexure and surface mass transport. *Basin Research* 18: 125–143.
Simpson GDH (2010) Influence of the mechanical behaviour of brittle-ductile fold-thrust belts on the development of foreland basins. *Basin Research* 22: 139–156.
Sinclair HD, Coakley BJ, Allen PA, and Watts AB (1991) Simulation of Foreland Basin stratigraphy using a diffusion-model of mountain belt uplift and erosion – An example from the central Alps, Switzerland. *Tectonics* 10: 599–620.
Sleep NH (1971) Thermal effects of formation of atlantic continental margins by continental break up. *Geophysical Journal of the Royal Astronomical Society* 24: 325–350.
Sleep NH (1973) Crustal thinning on Atlantic continental margins: Evidence from older margins. In: Tarling DH and Runcorn SK (eds.) *Implications of Continental Drift to the Earth Sciences*, vol. 2, 685–692.
Smit J, Brun JP, Cloetingh S, and Ben-Avraham Z (2008a) Pull-apart basin formation and development in narrow transform zones with application to the Dead Sea Basin. *Tectonics* 27: 257–290.
Smit J, Brun JP, Cloetingh S, and Ben-Avraham Z (2010) The rift-like structure and asymmetry of the Dead Sea Fault. *Earth and Planetary Science Letters* 290: 74–82.
Smit J, Brun JP, Fort X, Cloetingh S, and Ben-Avraham Z (2008b) Salt tectonics in pull-apart basins with application to the Dead Sea Basin. *Tectonophysics* 449: 1–16.
Smit JHW, Brun JP, and Sokoutis D (2003) Deformation of brittle-ductile thrust wedges in experiments and nature. *Journal of Geophysical Research: Solid Earth* 108: ETG 9.
Smit JHW, Cloetingh SAPL, Burov E, et al. (2013) Interference of lithospheric folding in western Central Asia by simultaneous Indian and Arabian plate indentation. *Tectonophysics* 602: 176–193.
Smolyaninova EI, Mikhailov VO, and Lyakhovsky VA (1996) Numerical modelling of regional neotectonic movements in the northern Black Sea. *Tectonophysics* 266: 221–231.
Sobel ER, Hilley GE, and Strecker MR (2003) Formation of internally drained contractional basins by aridity-limited bedrock incision. *Journal of Geophysical Research: Solid Earth* 108: ETG 9.
Sokoutis D, Burg JP, Bonini M, Corti G, and Cloetingh S (2005) Lithospheric-scale structures from the perspective of analogue continental collision. *Tectonophysics* 406: 1–15.
Solheim A, Riis F, Elverhøi A, et al. (1996) Impact of glaciations on basin evolution: Data and models from the Norwegian margin and adjacent areas – Introduction and summary. *Global and Planetary Change* 12: 1–9.
Spadini G, Bertotti G, and Cloetingh S (1995a) Tectono-stratigraphic modelling of the Sardinian margin of the Tyrrhenian Sea. *Tectonophysics* 252: 269–284.
Spadini G, Cloetingh S, and Bertotti G (1995b) Thermomechanical modeling of the Tyrrhenian Sea – Lithospheric necking and kinematics of rifting. *Tectonics* 14: 629–644.
Spadini G and Podladchikov Y (1996) Spacing of consecutive normal faulting in the lithosphere: A dynamic model for rift axis jumping (Tyrrhenian Sea). *Earth and Planetary Science Letters* 144: 21–34.
Spadini G, Robinson A, and Cloetingh S (1996) Western versus Eastern Black Sea tectonic evolution: Pre-rift lithospheric controls on basin formation. *Tectonophysics* 266: 139–154.
Spadini G, Robinson AG, and Cloetingh SAPL (1997) Thermomechanical modeling of black sea basin formation, subsidence, and sedimentation. *American Association of Petroleum Geologists Memoir* 68: 19–38.
Spakman W and Hall R (2010) Surface deformation and slab-mantle interaction during Banda arc subduction rollback. *Nature Geoscience* 3: 562–566.
Stampfli GM, Borel GD, Cavazza W, Mosar J, and Ziegler PA (2001) Palaeotectonic and palaeogeographic evolution of the western Tethys and PeriTethyan domain (IGCP Project 369). *Episodes* 24: 222–228.

Starostenko V, Buryanov V, Makarenko I, et al. (2004) Topography of the crust-mantle boundary beneath the Black Sea Basin. *Tectonophysics* 381: 211–233.

Steckler MS and Watts AB (1982) Subsidence history and tectonic evolution of Atlantic-type continental margins. *Dynamics of Passive Margins*, vol. 6, pp. 184–196. American Geophysical Union.

Stein CA, Cloetingh S, and Wortel R (1989) Seasat-derived gravity constraints on stress and deformation in the northeastern Indian-Ocean. *Geophysical Research Letters* 16: 823–826.

Stel H, Cloetingh S, Heeremans M, and Van der Beek P (1993) Anorogenic granites, magmatic underplating and the origin of intracratonic basins in a non-extensional setting. *Tectonophysics* 226: 285–299.

Stephenson RA (1989) Beyond first-order thermal subsidence models for sedimentary basins. In: *Quantitative Dynamic Stratigraphy*, pp. 113–125. Prentice Hall, New Jersey: Englewood Cliffs.

Stephenson RA and Cloetingh SAPL (1991) Some examples and mechanical aspects of continental lithospheric folding. *Tectonophysics* 188: 27–37.

Stephenson R and Lambeck K (1985) Isostatic response of the lithosphere with inplane stress – Application to Central Australia. *Journal of Geophysical Research-Solid Earth and Planets* 90: 8581–8588.

Stephenson RA, Mart Y, Okay A, et al. (2004) TRANSMED Section VIII; East-European Craton-Crimea-Black Sea-Anatolia-Cyprus-Levant Sea-Sinai-Red Sea. In: Cavazza W, Roure F, Spakman W, Stampfli GM, and Ziegler PA (Eds.) *The TRANSMED Atlas: The Mediterranean Region from Crust to Mantle*, pp. 77–98. Berlin: Springer.

Stephenson RA, Ricketts BD, Cloetingh SA, and Beekman F (1990) Lithosphere folds in the Eurekan Orogen, Arctic Canada. *Geology* 18: 603–606.

Stephenson RA, Stovba SM, and Starostenko VI (2001) Pripyat-Dniepr-Donets basin: Implications for dynamics of rifting and the tectonic history of the northern peri-Tethyan platform. *Memoires du Museum National d'Histoire Naturelle* 186: 369–406.

Stern TA (1995) Gravity anomalies and crustal loading at and adjacent to the Alpine Fault, New Zealand. *New Zealand Journal of geology and geophysics* 38: 593–600.

Stern TA, Quinlan GM, and Holt WE (1993) Crustal dynamics associated with the formation of Wanganui Basin, New Zealand. *Sedimentary Basins of the World* 2: 213–223.

Stewart J and Watts AB (1997) Gravity anomalies and spatial variations of flexural rigidity at mountain ranges. *Journal of Geophysical Research: Solid Earth (1978–2012)* 102: 5327–5352.

Stockmal GS, Beaumont C, and Boutilier R (1986) Geodynamic models of convergent margin tectonics – Transition from rifted margin to overthrust belt and consequences for foreland-basin development. *Bulletin of the American Association of Petroleum Geologists* 70: 181–190.

Stovba S, Khriachtchevskaia O, and Popadyuk I (2009) Hydrocarbon-bearing areas in the eastern part of the Ukrainian Black Sea. *Leading Edge (Tulsa, OK)* 28: 1042–1045.

Straume AK and Austrheim H (1999) Importance of fracturing during retro-metamorphism of eclogites. *Journal of Metamorphic Geology* 17: 637–652.

Suhadolc P and Panza GF (1989) Physical properties of the lithosphere-asthenosphere system in Europe from geophysical data. *The lithosphere in Italy* 80: 15–40.

Sunal G and Tüysüz O (2002) Palaeostress analysis of Tertiary post-collisional structures in the Western Pontides, northern Turkey. *Geological Magazine* 139: 343–359.

Suvorov VD, Mishenkina ZM, Petrick GV, et al. (2002) Structure of the crust in the Baikal rift zone and adjacent areas from Deep Seismic Sounding data. *Tectonophysics* 351: 61–74.

Snyder DB and Barazangi M (1986) Deep crustal structure and flexure of the Arabian plate beneath the Zagros collisional mountain belt as inferred from gravity observations. *Tectonics* 5: 361–373.

Sztanó O, Szafián P, Magyar I, et al. (2013) Aggradation and progradation controlled clinothems and deep-water sand delivery model in the Neogene Lake Pannon, Makó Trough, Pannonian Basin, SE Hungary. *Global and Planetary Change* 103: 149–167.

Tandon K, Lorenzo JM, and O'Brien GW (2000) Effective elastic thickness of the northern Australian continental lithosphere subducting beneath the Banda orogen (Indonesia): Inelastic failure at the start of continental subduction. *Tectonophysics* 329: 39–60.

Tang J, Lerche I, and Cogan J (1992) An inverse method for calculating basement geometries in foreland basins. *Journal of geodynamics* 15: 85–106.

Tarapoanca M, Andriessen P, Broto K, et al. (2010) Forward kinematic modelling of a regional transect in the Northern Emirates using geological and apatite fission track age constraints on paleo-burial history. *Arabian Journal of Geosciences* 3: 395–411.

Tarapoanca M, Bertotti G, Matenco L, Dinu C, and Cloetingh SAPL (2003) Architecture of the Focsani Depression: A 13 km deep basin in the Carpathians bend zone (Romania). *Tectonics* 22: 13.

Tarapoanca M, Garcia-Castellanos D, Bertotti G, et al. (2004) Role of the 3-D distributions of load and lithospheric strength in orogenic arcs: Polystage subsidence in the Carpathians foredeep. *Earth and Planetary Science Letters* 221: 163–180.

Tari G, Dövényi P, Dunkl I, et al. (1999) Lithospheric structure of the Pannonian basin derived from seismic, gravity and geothermal data. *Geological Society Special Publication* 156: 215–250.

Tari G, Nemcok M, Tari G, and Nemcok M (2009) Introduction to this special section: The Black Sea Region. *Leading Edge* 28: 1022–1023.

Teixell A, Ayarza P, Zeyen H, Fernandez M, and Arboleya ML (2005) Effects of mantle upwelling in a compressional setting: The Atlas Mountains of Morocco. *Terra Nova* 17: 456–461.

Teng JW (1991) Geophysical fields and hydrocarbon prospects of the Tarim Basin. *Academia Sinica* 2: 24–40.

Ter Voorde M and Bertotti G (1994) Thermal effects of normal faulting during rifted basin formation, 1. A finite difference model. *Tectonophysics* 240: 133–144.

Ter Voorde M and Cloetingh S (1996) Numerical modelling of extension in faulted crust: Effects of localized and regional deformation on basin stratigraphy. In: *Modern Developments in Structural Interpretation, Validation and Modelling*, pp. 283–296. London: Geological Society of London, Special Publication 99.

Ter Voorde M, De Bruijne CH, Cloetingh SAPL, and Andriessen PAM (2004) Thermal consequences of thrust faulting: Simultaneous versus successive fault activation and exhumation. *Earth and Planetary Science Letters* 223: 395–413.

Ter Voorde M, Gaspar-Escribano JM, Juez-Larre J, et al. (2007) Thermal effects of linked lithospheric and upper crustal-scale processes: Insights from numerical modeling of the Cenozoic Central Catalan Coastal Ranges (NE Spain). *Tectonics* 26: TC5018.

Ter Voorde M, Ravnås R, Færseth R, and Cloetingh S (1997) Tectonic modelling of the Middle Jurassic synrift stratigraphy in the Oseberg-Brage area, northern Viking Graben. *Basin Research* 9: 133–150.

Ter Voorde M, Van Balen RT, Bertotti G, and Cloetingh SAPL (1998) The influence of a stratified rheology on the flexural response of the lithosphere to (un)loading by extensional faulting. *Geophysical Journal International* 134: 721–735.

Tesauro M, Audet P, Kaban MK, Burgmann R, and Cloetingh S (2012a) The effective elastic thickness of the continental lithosphere: Comparison between rheological and inverse approaches. *Geochemistry, Geophysics, Geosystems* 13: Q09001.

Tesauro M, Burov EB, Kaban MK, and Cloetingh SAPL (2011) Ductile crustal flow in Europe's lithosphere. *Earth and Planetary Science Letters* 312: 254–265.

Tesauro M, Hollenstein C, Egli R, Geiger A, and Kahle HG (2005) Continuous GPS and broad-scale deformation across the Rhine Graben and the Alps. *International Journal of Earth Sciences* 94: 525–537.

Tesauro M, Kaban MK, and Cloetingh SAPL (2008) EuCRUST-07: A new reference model for the European crust. *Geophysical Research Letters* 35: L05313.

Tesauro M, Kaban MK, and Cloetingh SAPL (2009a) A new thermal and rheological model of the European lithosphere. *Tectonophysics* 476: 478–495.

Tesauro M, Kaban MK, and Cloetingh SAPL (2009b) How rigid is Europe's lithosphere? *Geophysical Research Letters* 36: L16303.

Tesauro M, Kaban M, and Cloetingh SPL (2010a) 3D crustal model of western and central Europe as a basis for modelling mantle structure. In: Cloetingh S and Negendank J (eds.) *New Frontiers in Integrated Solid Earth Sciences*, pp. 39–69. Dordrecht: Springer Heidelberg.

Tesauro M, Kaban M, and Cloetingh SPL (2010b) Thermal and rheological model of the European lithosphere. In: Cloetingh S and Negendank J (eds.) *New Frontiers in Integrated Solid Earth Sciences*, pp. 71–101. Dordrecht: Springer Heidelberg.

Tesauro M, Kaban MK, and Cloetingh SAPL (2012b) Global strength and elastic thickness of the lithosphere. *Global and Planetary Change* 90–91: 51–57.

Tesauro M, Kaban MK, and Cloetingh SAPL (2013) Global model for the lithospheric strength and effective elastic thickness. *Tectonophysics* 602: 78–86.

Tesauro M, Kaban MK, Cloetingh SAPL, Hardebol NJ, and Beekman F (2007) 3D strength and gravity anomalies of the European lithosphere. *Earth and Planetary Science Letters* 263: 56–73.

Teson E, Teixell A, García-Castellanos D, and Amrhar M (2006) *Geometry and Evolution of the Ouarzazate Basin in the Foreland of the High Atlas Mountains (Morocco)*. Vienna: EGU.

Tikoff B and Maxson J (2001) Lithospheric buckling of the Laramide foreland during Late Cretaceous and Paleogene, western United States. *Rocky Mountain Geology* 36: 13–35.

Tilita M, Matenco L, Dinu C, Ionescu L, and Cloetingh S (2013) Understanding the kinematic evolution and genesis of a back-arc continental "sag" basin: The Neogene evolution of the Transylvanian Basin. *Tectonophysics* 602: 237–258.

Tomek C (1993) Deep-crustal structure beneath the central and inner west Carpathians. *Tectonophysics* 226: 417–431.
Toth J, Kusznir NJ, and Flint SS (1996) A flexural isostatic model of lithosphere shortening and foreland basin formation: Application to the Eastern Cordillera and Subandean belt of NW Argentina. *Tectonics* 15: 213–223.
Turcotte DL and Emerman SH (1983) Mechanisms of active and passive rifting. *Tectonophysics* 94: 39–50.
Turcotte DL and Schubert G (2014) *Geodynamics*. Cambridge: Cambridge University Press.
Underhill JR and Partington MA (1993) Jurassic thermal doming and deflation in the North Sea: Implications of the sequence stratigraphic evidence. *Petroleum Geology Conference Proceedings*, vol. 4, pp. 337–345.
Uyeda S and Kanamori H (1979) Back-arc opening and the mode of subduction. *Journal of Geophysical Research* 84: 1049–1061.
Uyeda S and McCabe R (1983) A possible mechanism of episodic spreading of the Philippine Sea. In: Hashimoto M and Uyeda S (eds.) *Accretion Tectonics in the Circum-Pacific Regions*, pp. 291–306. Tokyo: TerraPub.
Van Balen RT and Cloetingh SAPL (1993) Stress-induced fluid flow in rifted basins. In: Horbury AD and Robinson A (eds.) *Diagenesis and Basin Development, Studies in Geology* 38, pp. 9–26. American Association of Petroleum Geologists.
Van Balen R and Cloetingh S (1994) Tectonic control of the sedimentary record and stress-induced fluid flow: Constraints from basin modelling. *Geological Society Special Publication* 78: 9–26.
Van Balen RT, Houtgast RF, Van der Wateren FM, Vandenberghe J, and Bogaart PW (2000) Sediment budget and tectonic evolution of the Meuse catchment in the Ardennes and the Roer Valley Rift System. *Global and Planetary Change* 27: 113–129.
Van Balen RT, Lenkey L, Horváth F, and Cloetingh SAPL (1999) Two-dimensional modelling of stratigraphy and compaction-driven fluid flow in the Pannonian Basin. *Geological Society Special Publication* 156: 391–414.
Van Balen RT, Vanderbeek PA, and Cloetingh SAPL (1995) The effect of rift shoulder erosion on stratal patterns at passive margins – Implications for sequence stratigraphy. *Earth and Planetary Science Letters* 134: 527–544.
Van der Beek P, Andriessen P, and Cloetingh S (1995) Morphotectonic evolution of rifted continental margins – Inferences from a coupled tectonic-surface processes model and fission-track thermochronology. *Tectonics* 14: 406–421.
Van der Beek PA and Cloetingh S (1992) Lithospheric flexure and the tectonic evolution of the Betic Cordilleras (Se Spain). *Tectonophysics* 203: 325–344.
Van der Beek P, Cloetingh S, and Andriessen P (1994) Mechanisms of extensional basin formation and vertical motions at rift flanks – Constraints from tectonic modeling and fission-track thermochronology. *Earth and Planetary Science Letters* 121: 417–433.
Van der Meulen MJ, Kouwenhoven TJ, Van der Zwaan GJ, Meulenkamp JE, and Wortel MJR (1999) Late Miocene uplift in the Romagnan Apennines and the detachment of subducted lithosphere. *Tectonophysics* 315: 319–335.
Van der Pluijm BA, Craddock JP, Graham BR, and Harris JH (1997) Paleostress in cratonic North America: Implications for deformation of continental interiors. *Science* 277: 794–796.
Van Vliet-Lanoë B, Laurent M, Everaerts M, Mansy J-L, and Manby G (2000) Évolution néogène et quaternaire de la Somme, une flexuration tectonique active. *Comptes Rendus de l'Académie des Sciences – Series IIA – Earth and Planetary Science* 331: 151–158.
Van Wees JD (1994) *Tectonic Modelling of Basin Deformation and Inversion Dynamics: The Role of Pre-existing Faults and Continental Lithosphere Rheology in Basin Evolution*. PhD Thesis, VU University, Amsterdam.
Van Wees JD, Arche A, Beijdorff CG, Lopez-Gomez J, and Cloetingh SAPL (1998) Temporal and spatial variations in tectonic subsidence in the Iberian Basin (eastern Spain): Inferences from automated forward modelling of high-resolution stratigraphy (Permian-Mesozoic). *Tectonophysics* 300: 285–310.
Van Wees JD and Beekman F (2000) Lithosphere rheology during intraplate basin extension and inversion – Inferences from automated modeling of four basins in western Europe. *Tectonophysics* 320: 219–242.
Van Wees JD and Cloetingh S (1996) 3D Flexure and intraplate compression in the North Sea Basin. *Tectonophysics* 266: 343–359.
Van Wees JD, Stephenson RA, Stovba SM, and Shymanovskyi VA (1996) Tectonic variation in the Dniepr-Donets Basin from automated modelling of backstripped subsidence curves. *Tectonophysics* 268: 257–280.
Van Wees JD, Van Bergen F, David P, et al. (2009) Probabilistic tectonic heat flow modeling for basin maturation: Assessment method and applications. *Marine and Petroleum Geology* 26: 536–551.
Vasiliev I, de Leeuw A, Filipescu S, et al. (2010) The age of the Sarmatian-Pannonian transition in the Transylvanian Basin (Central Paratethys). *Palaeogeography Palaeoclimatology Palaeoecology* 297: 54–69.
Vasiliev I, Reichart GJ, and Krijgsman W (2013) Impact of the Messinian Salinity Crisis on Black Sea hydrology – Insights from hydrogen isotopes analysis on biomarkers. *Earth and Planetary Science Letters* 362: 272–282.
Vauchez A, Tommasi A, and Barruol G (1998) Rheological heterogeneity, mechanical anisotropy and deformation of the continental lithosphere. *Tectonophysics* 296: 61–86.
Vening-Meinesz FA (1941) Gravity over the Hawaiian archipelago and over the Madeira area: Netherlands Acad. *Proceedings of the Netherlands Academie van Wetenschappen* 44: 1–12.
Vermeesch P, Poort J, Duchkov AD, Klerkx J, and de Batist M (2004) Lake Issyk-Kul (Tien Shan): Unusually low heat flow in an active intermontane basin. *Geologiya i Geofizika* 45: 616–625.
Vernant P, Nilforoushan F, Hatzfeld D, et al. (2004) Present-day crustal deformation and plate kinematics in the Middle East constrained by GPS measurements in Iran and northern Oman. *Geophysical Journal International* 157: 381–398.
Verrall P (1989) Speculations on the Mesozoic-Cenozoic tectonic history of the western United States. *The American Association of Petroleum Geologists* 46: 615–631.
Vyssotski AV, Vyssotski VN, and Nezhdanov AA (2006) Evolution of the West Siberian Basin. *Marine and Petroleum Geology* 23: 93–126.
Warners-Ruckstuhl KN, Govers R, and Wortel R (2012) Lithosphere-mantle coupling and the dynamics of the Eurasian Plate. *Geophysical Journal International* 189: 1253–1276.
Waschbusch PJ and Royden LH (1992) Episodicity in foredeep basins. *Geology* 20: 915–918.
Watcharanantakul R and Morley CK (2000) Syn-rift and post-rift modelling of the Pattani Basin, Thailand: Evidence for a ramp-flat detachment. *Marine and Petroleum Geology* 17: 937–958.
Watts AB (2001) *Isostasy and Flexure of the Lithosphere*. Cambridge: Cambridge University Press, 458 pp.
Watts AB (2007) An overview. *Treatise on Geophysics*, vol. 6, pp. 1–48. The Netherlands: Elsevier.
Watts AB and Burov EB (2003) Lithospheric strength and its relationship to the elastic and seismogenic layer thickness. *Earth and Planetary Science Letters* 213: 113–131.
Watts AB and Fairhead JD (1997) Gravity anomalies and magmatism along the western continental margin of the British Isles. *Journal of the Geological Society* 154: 523–529.
Watts AB, Karner GD, and Steckler MS (1982) Lithospheric flexure and the evolution of sedimentary basins. *Philosophical Transactions of the Royal Society A: Physical, Mathematical and Engineering Sciences* 305: 249–281.
Wenzel F, Sperner B, Lorenz F, and Mocanu V (2002) Geodynamics, tomographic images and seismicity of the Vrancea region (SE-Carpathians, Romania). *EGU Stephan Mueller Special Publication Series* 3: 95–104.
Wernicke B (1985) Uniform-sense normal simple shear of the continental lithosphere. *Canadian Journal of Earth Sciences* 22: 108–125.
Wernicke B (1990) The fluid crustal layer and its implications for continental dynamics. In: Salisbury MH and Fountain DM (eds.) *Exposed Cross-Sections of the Continental Crust*, pp. 509–544. The Netherlands: Springer.
Wessel P and Müller RD (2007) Plate tectonics. *Treatise on Geophysics*, vol. 6, pp. 49–98. The Netherlands: Elsevier.
Whipple KX (2009) The influence of climate on the tectonic evolution of mountain belts. *Nature Geoscience* 2: 97–104.
White N and Mckenzie D (1988) Formation of the steers head geometry of sedimentary basins by differential stretching of the crust and mantle. *Geology* 16: 250–253.
White RS and Mckenzie DP (1989) Volcanism at rifts. *Scientific American* 261: 62–71.
Whittaker A, Bott MHP, and Waghorn GD (1992) Stresses and plate boundary forces associated with subduction plate margins. *Journal of Geophysical Research: Solid Earth* 97: 11933–11944.
Wilgus CK, Hastings BS, Kendall CGSC, et al. (1988) Sea-level changes: An integrated approach. *Special Publications – Society of Economical Paleontologists and Mineralogists* 42: 402.
Willett SD (1999) Orogeny and orography: The effects of erosion on the structure of mountain belts. *Journal of Geophysical Research: Solid Earth* 104: 28957–28981.
Willett SD, Schlunegger F, and Picotti V (2006) Messinian climate change and erosional destruction of the central European Alps. *Geology* 34: 613–616.
Wilson M (1993a) Geochemical signatures of oceanic and continental basalts – A key to mantle dynamics. *Journal of the Geological Society* 150: 977–990.

Wilson M (1993b) Magmatism and the geodynamics of basin formation. *Sedimentary Geology* 86: 5–29.
Wilson M (1997) Thermal evolution of the Central Atlantic passive margins: Continental break-up above a Mesozoic superplume. *Journal of the Geological Society* 154: 491–495.
Wilson M and Patterson R (2001) Intraplate magmatism related to short-wavelength convective instabilities in the upper mantle: Evidence from the Tertiary-Quaternary volcanic province of western and central Europe. *Special Paper of the Geological Society of America* 352: 37–58.
Winguth C, Wong HK, Panin N, et al. (2000) Upper Quaternary water level history and sedimentation in the northwestern Black Sea. *Marine Geology* 167: 127–146.
Worrall DM and Snelson S (1989) Evolution of the northern Gulf of Mexico, with emphasis on Cenozoic growth faulting and the role of salt. *The Geology of North America*, vol. 1, pp. 97–138. Boulder, Colorado: Geological Society of America.
Wortel MJR and Spakman W (2000) Geophysics – Subduction and slab detachment in the Mediterranean-Carpathian region. *Science* 290: 1910–1917.
Xie X and Heller PL (2009) Plate tectonics and basin subsidence history. *Geological Society of America Bulletin* 121: 55–64.
Yegorova TP, Stephenson RA, Kozlenko VG, Starostenko VI, and Legostaeva OV (1999) 3-D gravity analysis of the Dniepr-Donets Basin and Donbas Foldbelt, Ukraine. *Tectonophysics* 313: 41–58.
Yilmaz Y, Tuysuz O, Yigitbas E, Genc SC, and Sengor AMC (1997) Geology and tectonic evolution of the Pontides. *Regional and Petroleum Geology of the Black Sea and Surrounding Region*, vol. 68, pp. 183–226, American Association of Petroleum Geologists Memoir.
Yong L, Allen PA, Densmore AL, and Qiang X (2003) Evolution of the Longmen Shan foreland basin (western Sichuan, China) during the Late Triassic Indosinian orogeny. *Basin Research* 15: 117–138.
Zeyen H, Volker F, Wehrle V, et al. (1997) Styles of continental rifting: Crust-mantle detachment and mantle plumes. *Tectonophysics* 278: 329–352.
Zhao JM, Mooney WD, Zhang XK, et al. (2006) Crustal structure across the Altyn Tagh Range at the northern margin of the Tibetan plateau and tectonic implications. *Earth and Planetary Science Letters* 241: 804–814.
Ziegler PA (1983) Crustal thinning and subsidence in the North-Sea. *Nature* 304: 561.
Ziegler PA (1987) Compressional intraplate deformations in the Alpine foreland – An introduction. *Tectonophysics* 137: 1–5.
Ziegler PA (1988) Evolution of the arctic-North Atlantic and the western Tethys – A visual presentation of a series of paleogeographic-paleotectonic maps. *Memoirs – American Association of Petroleum Geologists* 43: 164–196.
Ziegler PA (1989a) Evolution of Laurussia. In: *A Study in Late Paleozoic Plate Tectonics*. Dordrecht: Kluwer Academic.
Ziegler PA (1989b) Evolution of the North Atlantic – An overview. *The American Association of Petroleum Geologists* 46: 111–129.
Ziegler PA (1990a) Collision related intra-plate compression deformations in Western and Central-Europe. *Journal of Geodynamics* 11: 357–388.
Ziegler PA (1990b) *Geological Atlas of Western and Central Europe*. Shell Internationale Petroleum Maatschappij BV/Geological Society of London, Amsterdam: Elsevier, 239.
Ziegler PA (1992) Geodynamics of rifting and implications for hydrocarbon habitat. *Tectonophysics* 215: 221–253.
Ziegler PA (1993a) Smith, William Lecture 1992 – Plate-moving mechanisms – Their relative importance. *Journal of the Geological Society* 150: 927–940.
Ziegler PA (1993b) Plate-moving mechanisms: Their relative importance. *Journal of the Geological Society* 150: 927–940.
Ziegler PA (1994) *Geodynamic Processes Governing Development of Rifted Basins*. Paris: Technip.
Ziegler PA (1996a) Hydrocarbon habitat in rifted basins. In: Roure F, Ellouz N, Shein VS, and Skvortsov I (eds.) *Geodynamic Evolution of Sedimentary Basins*, pp. 85–94. Paris: Technip.
Ziegler PA (1996b) Geodynamic processes governing development of rifted basins. In: Roure F, Shein VS, Ellouz-Zimmermann N, and Skvortsow L (eds.) *Geodynamic Evolution of Sedimentary Basins*, pp. 19–67. Paris: Technip.
Ziegler PA, Bertotti G, and Cloetingh S (2002) In: *Dynamic processes controlling foreland development Â the role of mechanical (de) coupling of orogenic wedges and forelands*. *Stephan Mueller Special Publication Series*, vol. 1, pp. 17–56.
Ziegler PA and Cloetingh S (2004) Dynamic processes controlling evolution of rifted basins. *Earth-Science Reviews* 64: 1–50.
Ziegler PA, Cloetingh S, Guiraud R, and Stampfli GM (2001) Peri-Tethyan platforms: Constraints on dynamics of rifting and basin inversion. *Mémoires du Muséum national d'histoire naturelle*, vol. 186, pp. 9–49.
Ziegler PA, Cloetingh S, and Van Wees JD (1995) Dynamics of intra-plate compressional deformation: The Alpine foreland and other examples. *Tectonophysics* 252: 7–59.
Ziegler PA and Dèzes P (2005) Evolution of the lithosphere in the area of the Rhine Rift System. *International Journal of Earth Sciences* 94: 594–614.
Ziegler PA and Dèzes P (2006) Crustal evolution of Western and Central Europe. *Geological Society, London, Memoirs* 32: 43–56.
Ziegler PA and Dèzes P (2007) Cenozoic uplift of Variscan Massifs in the Alpine foreland: Timing and controlling mechanisms. *Global and Planetary Change* 58: 237–269.
Ziegler PA and Horváth E (1996a) Hydrocarbon habitat in rifted basins. In: Roure F, Ellouz N, Shein VS, and Skvortsow I (eds.) *Geodynamic Evolution of Sedimentary Basins*, pp. 19–67. Paris: Technip.
Ziegler PA and Horváth E (1996b) Peri-Tethys Memoir 2: Structure and prospects of Alpine basins and forelands. *Mémoires du Muséum national d'histoire naturelle*, vol. 170, p. 547.
Ziegler PA and Roure F (1996) Architecture and petroleum systems of the Alpine orogen and associated basins. *Mémoires du Muséum national d'histoire naturelle*, vol. 170.
Ziegler PA, Schumacher ME, Dèzes P, Van Wees JD, and Cloetingh S (2004) Post-Variscan evolution of the lithosphere in the Rhine Graben area: Constraints from subsidence modelling. *Geological Society, London, Special Publications* 223: 289–317.
Ziegler PA, Van Wees JD, and Cloetingh S (1998) Mechanical controls on collision-related compressional intraplate deformation. *Tectonophysics* 300: 103–129.
Zoback ML (1992) 1st-order and 2nd-order patterns of stress in the lithosphere – The World Stress Map Project. *Journal of Geophysical Research: Solid Earth* 97: 11703–11728.
Zoback MD, Stephenson RA, Cloetingh S, et al. (1993) Stresses in the lithosphere and sedimentary basin formation. *Tectonophysics* 226: 1–13.
Zoetemeijer R, Desegaulx P, Cloetingh S, Roure F, and Moretti I (1990) Lithospheric dynamics and tectonic-stratigraphic evolution of the Ebro Basin. *Journal of Geophysical Research: Solid Earth (1978–2012)* 95: 2701–2711.
Zoetemeijer R, Cloetingh S, Sassi W, and Roure F (1993) Modeling of Piggyback-Basin stratigraphy – Record of tectonic evolution. *Tectonophysics* 226: 253–269.
Zoetemeijer R, Tomek C, and Cloetingh S (1999) Flexural expression of European continental lithosphere under the western outer Carpathians. *Tectonics* 18: 843–861.
Zonenshain LP and LePichon X (1986) Deep basins of the Black-Sea and Caspian Sea as remnants of Mesozoic Back-Arc basins. *Tectonophysics* 123: 181–211.

6.13 Landscape Evolution

GE Tucker, Cooperative Institute for Research in Environmental Sciences (CIRES), Boulder, CO, USA; University of Colorado, Boulder, CO, USA

© 2015 Elsevier B.V. All rights reserved.

6.13.1	**Introduction**	593
6.13.2	**Global Overview**	594
6.13.3	**Major Controls on Continental Denudation**	594
6.13.3.1	Relief: Gravitational Potential Energy Gradients	595
6.13.3.2	Climate	602
6.13.3.3	The 'Glacial Buzzsaw' Hypothesis	604
6.13.3.4	Late Cenozoic Climate Change and Global Erosion	604
6.13.3.5	Lithology	606
6.13.3.6	Tectonic Processes	607
6.13.4	**Process Mechanics and Landscape Evolution Theory**	607
6.13.4.1	Weathering, Rock Damage, and Sediment Production	608
6.13.4.2	Gravitational Transport on Hillslopes	609
6.13.4.3	Glacial Erosion	611
6.13.4.4	Drainage Network Structure and Development	612
6.13.4.5	Dynamics of Channel Networks	614
6.13.4.5.1	Fluvial sediment transport	614
6.13.4.5.2	Channel incision into bedrock	616
6.13.4.6	Landscape Evolution Models	618
6.13.5	**Feedbacks Between Erosion, Climate, and Tectonics**	618
6.13.5.1	Erosion and Isostasy	618
6.13.5.2	Feedback and Steady State in Compressional Orogens	619
6.13.5.3	Tectonic Aneurysms	620
6.13.6	**Tectonics from Topography**	620
6.13.7	**Summary, Retrospect, and Prospect**	622
Acknowledgments		622
References		622

6.13.1 Introduction

The power of erosion on the Earth's continents is evident even from space. Nearly all of the Earth's landmasses are etched by valley networks, bearing evidence of surface modification and mass redistribution from flowing water or ice. Although erosion takes place at the Earth's surface, its effect is more than skin deep. Patterns of metamorphic and intrusive igneous rocks in shield areas and in the cores of orogens imply erosional exhumation to depths on the order of tens of kilometers – a substantial fraction of the continental crustal thickness. With a typical orogen erosion rate of order 10^{-3} m year^{-1}, kilometers of rock can be shaved off the crust in only a few million years. The rate and spatial patterns of erosion and sedimentation are large enough to influence crustal deformation, through feedbacks between rearrangement of crustal mass, buoyancy, and stresses. Thus, erosion, transport, and deposition at the Earth's surface play both direct and indirect roles in modifying the thickness (and to some extent the composition) of the Earth's crust. At long wavelengths (>100 km), continental topography reflects crustal thickness and density, as well as the density structure of the upper mantle. At shorter wavelengths, topography is shaped by surface processes acting on heterogeneous materials and structures created by brittle deformation of the upper crust.

To understand the origin, evolution, and significance of the Earth's continental topography, it helps adopt the same sort of perspective that astrophysicists and cosmologists routinely use: in explaining the biggest and most ancient features in the universe, they turn to small-scale process physics for a foundational theory. In deciphering landscape evolution, we do not normally need to zoom down to the scale of quarks (fortunately), and we have the further advantage of being able to observe processes more directly. Nonetheless, there is a great deal to be learned by considering the mechanics and chemistry of the surface processes that sculpt topography. In keeping with this philosophy, this chapter reviews some of what we presently know about landscape evolution from the perspective of rates, controls, and process mechanics, rather than with an emphasis on particular regions or landforms. We begin with an overview of rates and patterns of erosion and sedimentation on the continents. We then explore some of the major controls on rates of erosional exhumation. This sets us up to consider some of the physics behind geomorphic processes and their quantitative expression. We review the role of feedbacks between tectonics, climate, and erosion in shaping continental topography. Finally, we will briefly explore how landscape evolution theory provides a basis for deciphering tectonics from topography.

6.13.2 Global Overview

The vast majority of the Earth's land area is dissected by drainage networks (Figure 1). Drainage basins and their networks span at least twelve orders of magnitude in scale, from the roughly 6×10^{12} m^2 area of the Amazon basin to the few-square-meter basins that form in badlands and disturbed landscapes (Figure 1). Large river networks collect water and sediment over subcontinental regions and funnel them through channels toward sedimentary basins. Each year, the world's major drainage networks funnel some 40 000 km^3 of water from land to sea (Vörösmarty and Sahagian, 2000).

How much sediment does all this water carry? One estimate comes from Syvitski et al. (2005), who combined data on sediment flux, climate, and relief with semiempirical models to compare the modern and prehuman global sediment flux patterns. Their calculations indicated a total pre-Anthropocene riverine sediment flux to the oceans of about 15.5 GT year^{-1}. This figure is the equivalent of a globally averaged continental denudation rate of roughly 50–60 μm per year – a rate that, if sustained, would erode through 30 km thick continental crust in about 500 My. The greatest sediment yield derives from erosion in the tropical mountainous regions of Indonesia and Oceania, while the lowest yield comes from circum-arctic regions (Milliman and Syvitski, 1992; Syvitski et al., 2005). Overall, high mountain regions (above 3000 m average altitude) contribute about 60% of the global sediment yield.

Rates of denudation vary markedly across the continents. For example, a study of denudation rates in the central Himalayas using cosmogenic radionuclides found an average denudation rate of 1.3 m ky^{-1} (Lupker et al., 2012). (To put this rate in perspective, note that 1 km My^{-1} = 1 m ky^{-1} = 1 mm year^{-1}.) At the east and west ends of the Himalayan orogen (the syntaxes), low-temperature thermochronology reveals sustained rates of erosional exhumation on the order of several meters per thousand years (e.g., Zeitler et al., 2001a). Erosion in the Taiwan orogen is similarly impressive. One study based on fission-track analysis, for example, estimated island-wide average exhumation at ~2.3 m ky^{-1} (Fuller et al., 2006).

By contrast, the Dry Valleys region of Antarctica appears to have a remarkably low rate of denudation. One study using cosmogenic ^{21}Ne suggested maximum lowering rates on slopes between 0.26×10^{-3} and 1.02×10^{-3} m ky^{-1}, while rates on high-elevation surfaces were estimated at 0.133×10^{-3} to 0.164×10^{-3} m ky^{-1}. Similarly low rates ($0.3–5.7 \times 10^{-3}$ m ky^{-1}) have been identified on Australian bedrock landforms (Bierman and Caffee, 2002), while the rugged Cape Fold Belt mountains of South Africa are also wearing down at millimeter-per-millennium rates, despite their substantial relief (Scharf et al., 2013). Hence, regional exhumation rates on the continents, assessed on timescales of thousands to millions of years, appear to vary over about four orders of magnitude.

6.13.3 Major Controls on Continental Denudation

Among the various controls on denudation rate, four stand out: relief, climate, lithology, and tectonics. Relief appears as a surrogate for gravitational potential energy. As discussed in the succeeding text, it can be defined in a variety of ways, and it

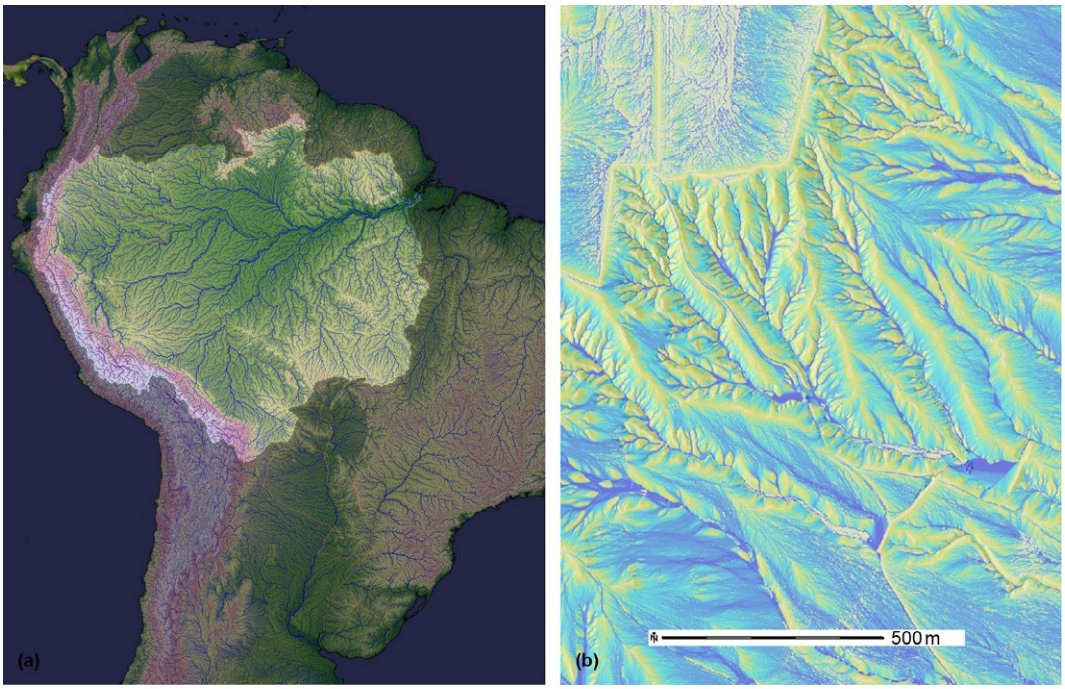

Figure 1 Continental topography is organized around drainage basins and networks. (a) The Amazon River drainage basin. (b) Small drainage basins on the eastern plains of Colorado, USA (color indicates upstream contributing drainage area). Note similarity in basin and network forms across scales. Amazon basin NASA image by Jesse Allen, using SRTM topography data provided of the University of Maryland's Global Land Cover Facility, and river data provided courtesy of the World Wildlife Fund HydroSHEDS Project; gully image by author, derived from 1 m lidar DEM of terrain near West Bijou Creek, Colorado.

correlates closely with mean surface slope angle. Climate encompasses a host of environmental factors, including precipitation, temperature, humidity, and their variation in time and space. Climate is also closely linked with the nature and density of plant and animal life, which can influence denudation through a variety of mechanisms, many of which are still poorly understood.

Studies of the major controls on continental denudation have traditionally relied on contemporary measurements of sediment flux from drainage basins. These measurements are expensive to make, and for this reason, such data are relatively sparse and tend to emphasize relatively large drainage basins. Modern sediment flux data can also be influenced by human activity, which can either accelerate natural sediment fluxes (mainly through deforestation and agriculture) or reduce them (through sediment retention behind dams and as a result of irrigation and flow regulation) (Walling and Webb, 1996). Nonetheless, as we will see shortly, analyses of sediment flux data can reveal the major trends and natural controls on landscape erosion.

The development of improved analytic techniques for cosmogenic nuclide analysis in the early to mid-1990s (e.g., Lal, 1991) provided a way to estimate catchment-averaged erosion rates on timescales of 10^3–10^5 years (Bierman and Steig, 1996; Brown et al., 1995; Granger et al., 1996). The method relies on the fact that cosmic-ray bombardment produces exotic nuclides within the upper meter or so of the Earth's surface, at rates that depend on latitude, altitude, and topography. The concentration of cosmogenic nuclides in detrital mineral grains at the outlet of a drainage basin varies inversely with the rate of denudation and can be inverted to solve for the rate. The method can provide denudation rate estimates on timescales that are much longer than historic records of sediment flux.

Together, estimates of denudation rate obtained from historic sediment flux and from cosmogenic nuclide analysis provide a means of assessing the relative importance of relief, climate, lithology, and tectonics. In the next sections, we explore these controls in turn.

6.13.3.1 Relief: Gravitational Potential Energy Gradients

Many erosional processes function by converting gravitational potential energy into work, with the net result that mass is transported downslope. One measure of the gravitational potential energy available is relief, which is defined as the difference between maximum elevation and minimum elevation in a particular area. Because relief is a scale-dependent quantity – it tends to grow with increasing horizontal measurement scale (e.g., Chase, 1992; Lyew-Ayee et al., 2007) – it is often expressed as *local relief*, which is the maximum altitude difference within an area of specified size and location. Another popular measure of relief is the relief ratio, defined as the maximum elevation difference within a drainage basin divided by the basin's Euclidean length.

Relief was introduced as a morphometric index before the advent of digital elevation models (DEMs), because it was relatively easy to measure from paper topographic maps. Not surprisingly, relief is highly correlated with average slope angle (Ahnert, 1970; DiBiase et al., 2010; Montgomery and Brandon, 2002), which is a more direct expression of the gravitational potential energy gradient experienced by surface materials.

Studies of modern sediment flux have consistently shown a strong correlation with various measures of relief (**Figure 2**). For example, Ahnert (1970) compared the denudation rate with mean local relief (defined in 20×20 km windows) in twenty midlatitude drainage basins and found a strong linear correlation. Schumm (1963) examined sediment flux data from small drainage basins in the Western United States and noted an exponential relation between relief and denudation rate. Subsequent investigations of local- to regional-scale sediment flux have shown similarly strong correlations with relief

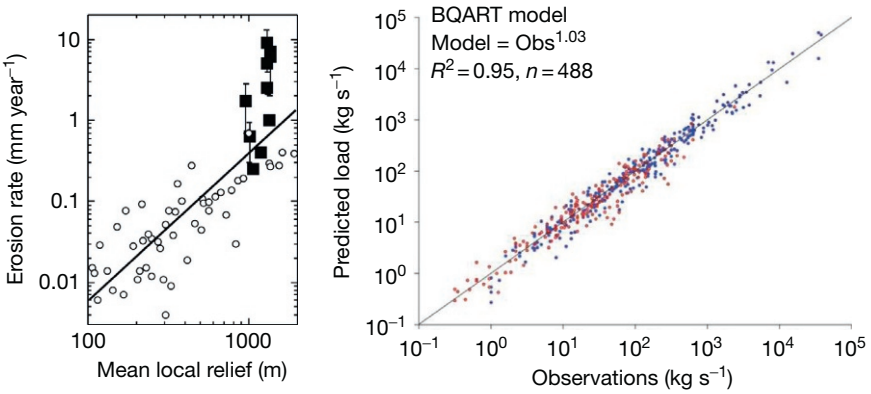

Figure 2 Relationship between erosion rate and relief. Left: plot from Montgomery and Brandon (2002) Topographic controls on erosion rates in tectonically active mountain ranges. *Earth and Planetary Science Letters* 201(3–4): 481–489; showing compilation of data on erosion rate versus mean local relief. Open circles show estimates derived from modern sediment yield data from locations around the world. Solid squares show mostly long-term thermochronological estimates from tectonically active settings (areas include the New Zealand Southern Alps, central Himalayas, Indus River basin, Olympic Mountains, Taiwan, Denali region (Alaska), Alps, and the Ganges and Brahmaputra basins). Line shows power-law regression $E = 1.4 \times 10^{-6} R^{1.8}$ (E in millimeter per year and R in meter). Right: test of the BQART model, which predicts a linear correlation between erosion and relief (eqn [1]), from Syvitski and Milliman (2007). The test compares model prediction with observations of sediment flux from 488 globally distributed rivers (colors represent two different data sets).

(e.g., Montgomery and Brandon, 2002). Likewise, sediment yield in the world's largest river basins is highly correlated with relief and relief-related metrics (Hovius, 1998; Pinet and Souriau, 1988; Summerfield and Hulton, 1994). Very large river basins such as the Amazon can encompass mountainous and lowland terrain. In an analysis of 280 river basins, Milliman and Syvitski (1992) concluded that small, mountainous rivers, particularly in Southern Asia and Oceania, contribute a disproportionate amount of sediment to the world's oceans. This finding illustrates the importance of steep channels and hillslopes.

Steady improvements in the quantity and quality of data on sediment flux, topography, climate, and other factors have enabled the development of empirical models of continental erosion. For example, Syvitski and Milliman (2007) used a database of 488 rivers to derive the 'BQART' model, which relates the average rate of erosion in a drainage basin, E, to relief, runoff, temperature, and basin area:

$$E \propto BQ^{0.31}A^{-0.5}RT \qquad [1]$$

where $R[L]$ is the maximum relief in the basin, $Q[L^3T^{-1}]$ is the mean annual discharge at the river basin outlet, $A[L^2]$ is the basin area, T is the mean annual temperature (the influence of which applies for $T \geq 2\,^{\circ}C$), and B is a factor that combines lithologic, glacial, and anthropogenic effects. Throughout the development of this and similar empirical models, relief consistently emerges as a key variable (Mulder and Syvitski, 1996). Even without accounting for the lithologic, glacial, or human effects (i.e., setting $B = 1$), Syvitski and Milliman (2007) found that eqn [1] accounted for 68% of the variation in sediment flux among rivers in their database (which encompass about 63% of the externally drained area of the continents). When B is defined so as to incorporate lithologic, human, and glacial influences, the equation accounts for 96% of the variance in sediment flux, though there remains up to an order of magnitude residual for any given measurement point (**Figure 2**, right). The linear dependence on R in eqn [1] represents a global average (Syvitski et al., 2003), with some climate zones showing a nonlinear dependence on R. As discussed further later, smaller-scale data sets show evidence for a strongly nonlinear relationship between erosion rate and relief in mountainous regions where slopes are close to their limit of mechanical stability.

Historical sediment fluxes represent only a short time window, and the influence of human activity can be difficult to isolate. Analysis of cosmogenic nuclide concentration in river sediment provides a way to estimate basin-averaged denudation rates on a much longer timescale (Bierman and Steig, 1996; Brown et al., 1995; Granger et al., 1996). Bombardment by high-energy cosmogenic particles produces a variety of exotic nuclides in minerals near the Earth's surface. For example, cosmic rays can gradually convert a small fraction of the oxygen and silicon atoms in quartz into ^{10}Be and ^{26}Al atoms, respectively. Despite the extremely low production rates and concentrations of these exotic nuclides, they can be measured accurately with accelerator mass spectrometry. The attenuation length, z_*, for cosmic-ray penetration is on the order of a meter for rock and soil; the nuclide production rate is greatest at or very near the land surface and falls off exponentially with depth over the length scale z_*. (The exact nature of the production rate decay function depends on the mechanism and target atom.) The concentration of cosmogenic nuclides within a mineral grain therefore depends mainly on the amount of time that the grain spends within the near-surface 'production window,' minus any accrued decay. Assuming that the speed of a mineral grain's approach to the surface is constant and that the time it spends in the river system after erosion is negligible, the concentration can be inverted for either an *in situ* denudation rate (for a surface sample collected in bedrock) or a catchment-wide average denudation rate (for a sample of alluvium, in which case one relies on mixing of sediment by the river system to produce an average value; cf. Von Blanckenburg, 2005). The timescale of averaging is set by the ratio of the penetration length scale, z_*, to the erosion rate. For erosion rates ranging from 10^{-3} to 10^{-5} m year^{-1}, the corresponding timescale ranges from about 1000 to 100 000 years.

In general, in landscapes with low to moderate relief, studies of cosmogenic nuclides in river sediment show a positive correlation between erosion rate and relief (Schaller et al., 2001; Von Blanckenburg, 2005; Wittmann et al., 2007) and/or between erosion rate and mean slope angle (Palumbo et al., 2010; Portenga and Bierman, 2011; Vanacker et al., 2007) (**Figure 3**). However, as Von Blanckenburg (2005) noted, there are some interesting exceptions. A study of the southern Appalachian Mountains by Matmon et al. (2003) revealed that basin-average erosion rate has no apparent correlation with relief or lithology, though they did discover a significant correlation with mean hillslope angle. The authors interpreted the lack of correlation between relief and erosion rate as evidence for Hack's concept of dynamic equilibrium, in which the various elements of the landscape tend, over time, to adjust toward a condition of space–time uniformity in denudation rate (Hack, 1960). A similar interpretation was made by Riebe

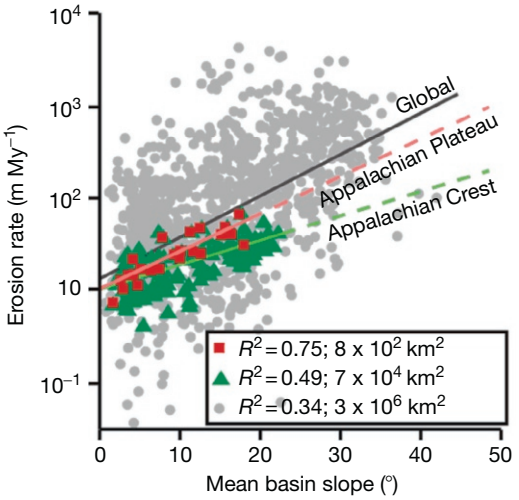

Figure 3 Global compilation by Portenga and Bierman (2011) of erosion rate estimates from cosmogenic isotope analyses of river sediment, showing correlation with mean basin slope. Erosion rates span four orders of magnitude. Reproduced from Portenga E and Bierman P (2011) Understanding earth's eroding surface with ^{10}Be. *GSA Today* 21(8): 4–10, Figure 5.

et al. (2000), who reported cosmogenically derived erosion rates from seven drainages in the Sierra Nevada. Those catchments that were close to active fault scarps and other signs of tectonic activity showed a positive correlation between relief and erosion rate, while those more distant showed only a weak correlation, consistent with an adjustment between relief, denudation, and lithology (perhaps in the form of variations in fracture density). In general, then, findings from cosmogenic nuclide analysis of river sediment support the notion that the erosion rate is sensitive to relief but that this sensitivity is masked in landscapes that have had sufficient time to evolve into a condition of dynamic equilibrium. More broadly, the development of cosmogenic nuclide techniques has allowed quantification of erosion rates and patterns in a wide variety of scales and contexts. Reviews of the technique and its applications are provided by Bierman and Nichols (2004) and Von Blanckenburg (2005).

Relief is generally well correlated with surface slope angle (Ahnert, 1970), which has a more direct link with sediment transport. Clearly, steeper slopes are likely to erode more rapidly and transport more sediment than more gentle ones, all else being equal, but what does the functional relationship between slope and erosion rate look like and under what circumstances? Ahnert's (1970) famous analysis implied a linear relationship between denudation rate and mean slope angle, with mean slope angles ranging from about 1° to 24°. On the other hand, in steeper terrain, hillslopes are often observed both to be relatively straight and to have angles that cluster around values that are consistent with mechanical stability limits (e.g., Burbank et al., 1996; Carson and Petley, 1970; Montgomery, 2001; Schmidt and Montgomery, 1995; Selby, 1982; Strahler, 1950, and references therein) (**Figure 4**). These observations are consistent with the expectation that there should be an upper limit to hillslope relief and gradient that reflects the bulk mechanical strength of rocks and/or soils. The connection between terrain steepness and mechanical failure is nicely illustrated by recent data from west-central Taiwan, which show that the modal hillslope angle is only slightly lower than the modal angle of slopes that experienced landsliding during the 1999 *M* 7.6 Chi-Chi earthquake (Hovius and Meunier, 2012) (**Figure 5**).

One implication of the threshold-hillslope hypothesis is that regions undergoing very rapid denudation should show little correlation between denudation rate and mean slope. Several studies have borne this out. In the northwestern Himalayas, where thermochronology and other lines of evidence imply regional variations in denudation rate of about a factor of 6, Burbank et al. (1996) reported that hillslope angles tend to be both steep (30–40°) and regionally uniform (**Figure 4**). Analysis of topography and thermochronology in the Olympic Mountains (Northwestern United States) by Montgomery (2001) and Montgomery and Brandon (2002) showed a similar pattern of spatially uniform slope-angle frequency distributions across an approximately twofold variation in long-term exhumation rates. Montgomery (2001) also showed that in the Oregon Coast Range, where rock uplift rates are generally lower than in the Olympic Mountains, there exist regional variations in mean slope angle (calculated from individual DEM cells) that mirror the inferred rates of rock uplift, suggesting that at least portions of this mountain range lie below the effective strength threshold.

Analyses of cosmogenic nuclides (chiefly ^{10}Be) in river sediment have done a great deal to illuminate the relationships among slope, relief, and denudation rate. Cosmogenic estimates of erosion rate in basins with mean slopes greater than about 25–30° typically show little correlation between slope and erosion rate, consistent with the threshold hypothesis (Densmore et al., 2009; Safran et al., 2005; Wittmann et al., 2007). On the other hand, data from multiple basins that span gradients above and below 25–30° show a strongly nonlinear relationship between erosion rate and mean hillslope angle (**Figure 6**) (Binnie et al., 2007; DiBiase et al., 2010, 2012; Norton et al., 2011; Ouimet et al., 2009; Palumbo et al.,

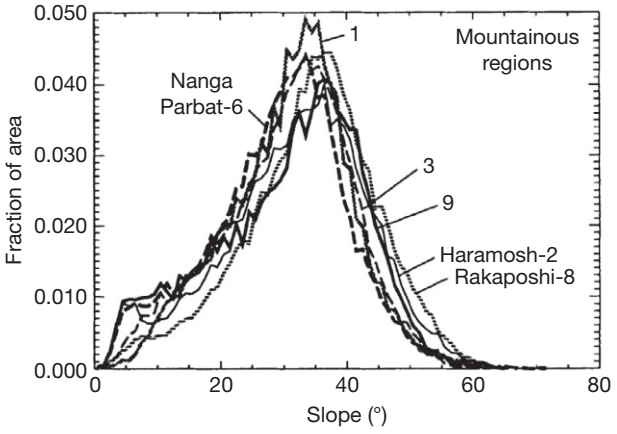

Figure 4 Slope frequency distributions from mountainous areas near Nanga Parbat, western Himalayas, derived from a 90 m-resolution digital elevation model. Regions with high denudation rate (curves 1, 2, and 6) have slope frequency distributions that are indistinguishable from regions with lower denudation rate (other curves). Reproduced from Burbank D, Leland J, Fielding E, et al. (1996) Bedrock incision, rock uplift and threshold hillslopes in the northwestern Himalayas. *Nature* 379(6565): 505–510.

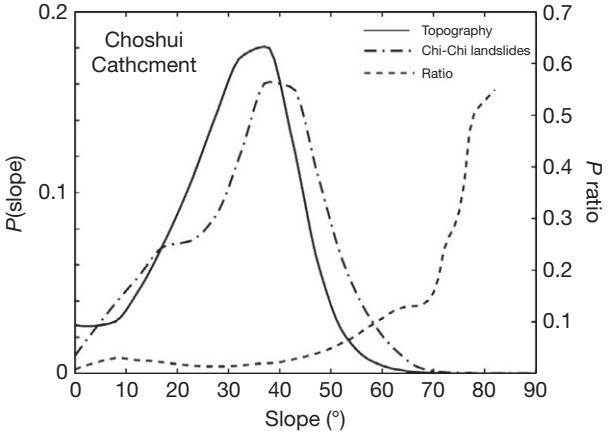

Figure 5 Slope-angle frequency data from the Choshui River basin, west-central Taiwan, comparing the distribution of slopes that failed during the 1999 *M* 7.6 Chi-Chi earthquake (dot-dash) with the distribution of all slopes in the catchment (solid line). Reproduced from Hovius N and Meunier P (2012) Earthquake ground motion and patterns of seismically induced landsliding. In: Clague J and Stead D (eds.) *Landslides: Types*, *Mechanisms*, *and Modeling*, pp. 24–36. Cambridge: Cambridge University Press.

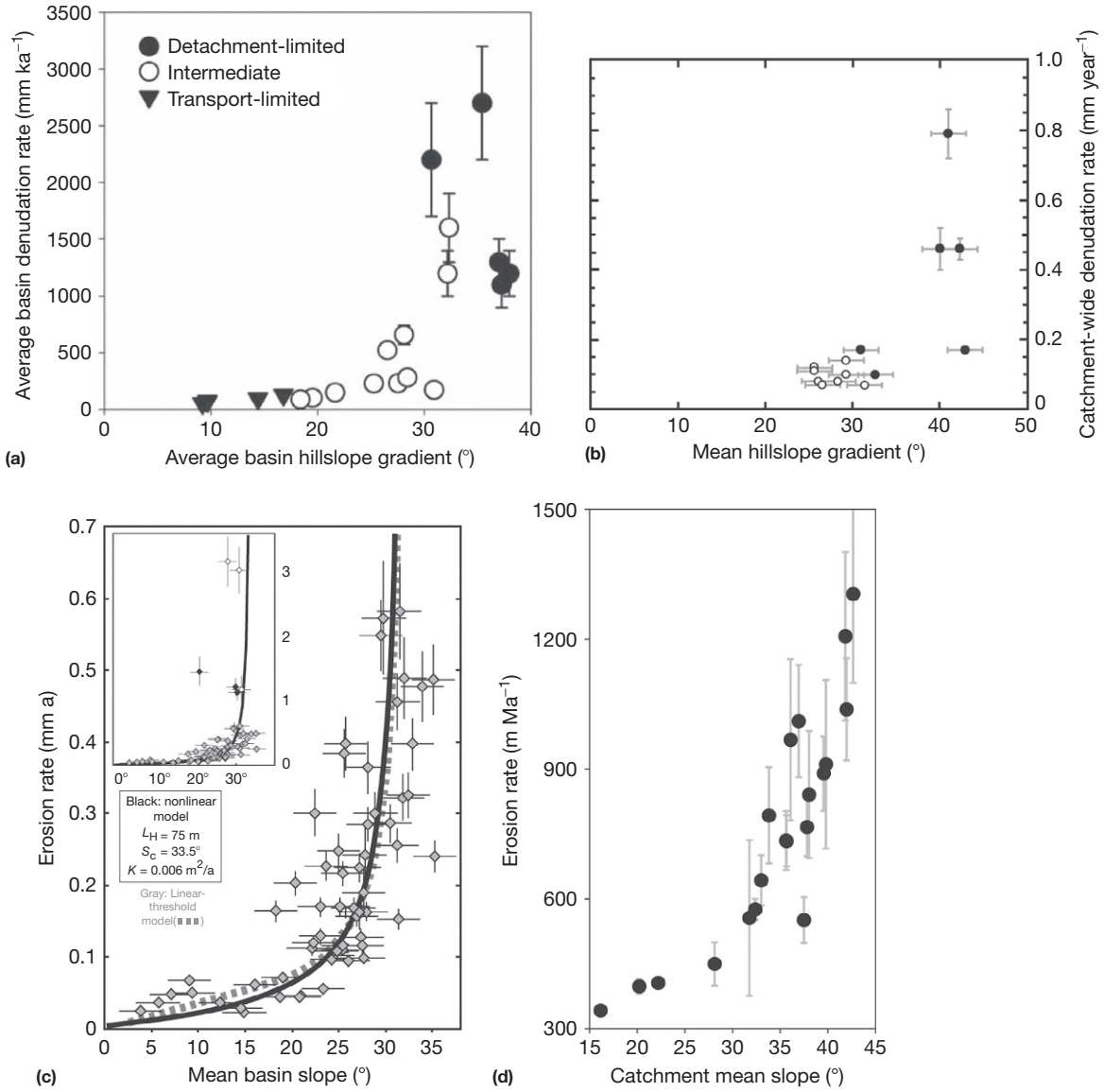

Figure 6 Examples of the relationship between erosion rate and mean slope, as deduced from cosmogenic nuclide analysis. (a) San Bernardino Mountains, California, USA (reproduced from Binnie SA, Phillips WM, Summerfield MA, and Fifield LK (2007) Tectonic uplift, threshold hillslopes, and denudation rates in a developing mountain range. *Geology* 35(8): 743–746. http://dx.doi.org/10.1130/G23641A.1). (b) Wasatch Mountains, USA (reproduced from Stock G, Frankel K, Ehlers T, Schaller M, Briggs S, and Finkel R (2009) Spatial and temporal variations in denudation of the Wasatch Mountains, Utah, USA. *Lithosphere* 1(1): 34–40). (c) Eastern margin of the Tibetan Plateau (reproduced from Ouimet WB, Whipple KX, and Granger DE (2009) Beyond threshold hillslopes: Channel adjustment to base-level fall in tectonically active mountain ranges, *Geology* 37(7): 579–582. http://dx.doi.org/10.1130/G30013A.1.). (d) San Gabriel Mountains, California, USA (modified from DiBiase R, Heimsath A, and Whipple K (2012) Hillslope response to tectonic forcing in threshold landscapes. *Earth Surface Processes and Landforms* 37: 855–865).

2011; Stock et al., 2009; Wittmann et al., 2007). Erosion rate data become increasingly scattered above 25–30°, consistent with the threshold hypothesis. For example, data from the San Gabriel and San Bernardino Mountains (Binnie et al., 2007; DiBiase et al., 2010, 2012) in Southern California, United States, show a pattern in which erosion rate varies roughly linearly with mean slope angle up to about 30°, at which point the data curve sharply upward (**Figure 6(a)** and **6(d)**).

It has been suggested that the transition to threshold hillslopes coincides with erosion rates that are faster than the maximum rate at which regolith (or 'soil' in the most generic sense) can be produced (Heimsath et al., 2012; Ouimet et al., 2009). Maximum rates of regolith production from bedrock have been estimated, from cosmogenic nuclide analysis, to be on the order of 0.1–0.3 m ky^{-1} (Heimsath et al., 1997, 2000, 2001), though Heimsath et al. (2012) recently suggested that the maximum rate may itself depend on topography and landslide frequency.

The finding of a strongly nonlinear erosion–slope relationship in steep terrain has several important implications for

landscape evolution. It suggests, for one thing, that in steep regions where erosion is dominated by landsliding, variations in erosion rate in space or time will tend to be accommodated by variations in landslide frequency rather than slope angle (e.g., Hovius et al., 1997; Montgomery and Brandon, 2002). In addition, it implies that there may be an effective upper limit to relief that reflects the maximum strength of rock and soil at the hillslope scale (Schmidt and Montgomery, 1995).

Hillslopes do not tell the whole story, however. A substantial fraction of regional relief in a typical mountain landscape reflects relief within the channel network. Most of the Earth's continental topography is organized around self-organized dendritic drainage networks (**Figure 1**). Although channels make up only a small fraction of the land surface, the planform shape of their networks sets the structure of the landscape, dividing terrain into hillslopes and valleys (**Figure 7**). The networks' third dimension, reflected in the longitudinal profiles of valleys, commonly forms the basic skeleton for topography. If one looks at the total relief within a given region, part of the elevation range will represent the height of hill crests above the adjacent channels, and part will arise from the altitude difference between the highest and lowest portions of the channel network. Relief on the channel network can make up 70–90% or more of total landscape relief (Whipple, 2004; Whipple and Tucker, 1999).

A useful way to describe the relief structure of a channel network is to examine the relationship between the slope of a channel segment, S, and the drainage area, A, of the basin upstream. In many basins, the slope–area relationship is well described by a power law (known as Flint's law, after Flint (1974))

Figure 7 Perspective image of a subcatchment of the Hualien River basin, Taiwan. The catchment has a drainage area of 447 km^2 and relief of 3580 m. Solid lines show the channel network, identified here as points with a drainage area >0.8 km^2. Reproduced from Whipple KX (2004) Bedrock rivers and the geomorphology of active orogens. *Annual Review of Earth and Planetary Sciences* 32: 151–185.

$$S = k_s A^{-\theta} \quad [2]$$

As one progresses downstream, the drainage area grows, while the gradient generally becomes smaller (**Figure 8**). The parameter k_s describes the gradient of a channel at unit drainage area, and for this reason, it is known as the *steepness index*. The rate of downstream gradient decrease is described by θ, and because a downstream-decreasing gradient describes a concave-upward longitudinal profile shape, the exponent θ is referred to as the concavity index (Whipple and Tucker, 1999). Values of the concavity index vary from basin to basin but in general tend to fall in the range of 0.2 to 1.0; values in the vicinity of 0.5 are especially common (Kirby et al., 2003; Tarboton et al., 1989; Tucker and Whipple, 2002; Whipple, 2004). The fact that most stream profiles are concave-upward is thought to reflect a condition of grade, in which a channel is able to accomplish similar work (sediment transport and/or bedrock incision) with a lower gradient when it has a larger basin and hence a higher water discharge (e.g., Howard, 1980; Mackin, 1948; Sinha and Parker, 1996; Snow and Slingerland, 1987; Willgoose et al., 1991a).

The slope–area scaling described by Flint's law has a lower limit that marks the degree of landscape dissection (e.g., Montgomery and Dietrich, 1992). For example, Tarboton et al. (1989) and Tarboton et al. (1992) examined slope–area scaling in DEMs from a variety of settings and found a break in scaling that corresponds approximately with the hillslope–channel transition. Others have recognized multiple-scale breaks that seem to reflect transitions in the dominant geomorphic process (Ijjasz-Vasquez and Bras, 1995; Montgomery and Dietrich, 1994; Tucker and Bras, 1998). In steep terrain, for example, one often observes a transition in scaling, from the inverse slope–area relation of eqn [2] to a near-constant gradient that corresponds to steep colluvial channels (DiBiase et al., 2012) (**Figure 8**). Such channels may be dominated by debris-flow scour rather than more typical fluvial processes (Montgomery and Foufoula-Georgiou, 1993; Seidl and Dietrich, 1992; Sklar and Dietrich, 1998; Stock and Dietrich, 2003).

The portion of a channel network that obeys Flint's law is often referred to as the fluvial (as opposed to colluvial) network, and relief formed by elevation differences within it is referred to as fluvial relief (Whipple, 2004). Fluvial relief within a catchment is described by the steepness index; all else equal, drainage networks with higher steepness indices contain greater relief (**Figure 8**).

In a review of data on steepness indices from a variety of settings, Whipple (2004) noted that when a reference concavity of 0.45 is used, k_s values from a variety of regions around the world vary by only about a factor of 30. This result is somewhat surprising, given the 1000-fold variation in rates of denudation noted earlier, and it may hint at a nonlinear relationship between channel slope and erosion rate. To investigate the nature of this relationship, several studies have estimated k_s in drainage networks for which independent estimates of erosion rate are available. Correlation between channel steepness and erosion rate has been demonstrated in a variety of tectonically active regions (DiBiase et al., 2010; Duvall et al., 2004; Harkins et al., 2007; Kirby and Ouimet, 2011; Kirby and Whipple, 2001; Kirby et al., 2003; Ouimet et al., 2009; Safran

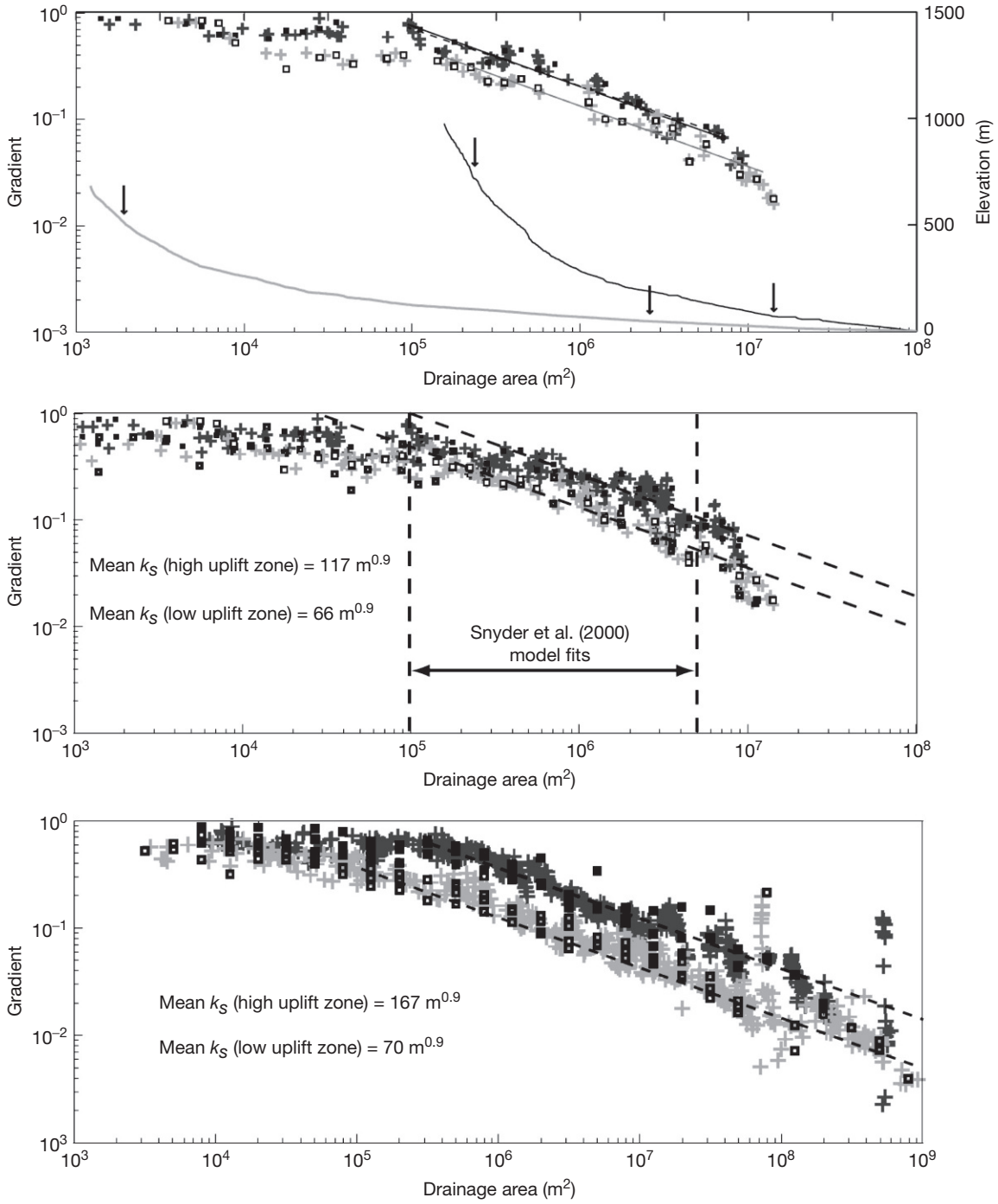
Gradient
Elevation (m)
Drainage area (m²)
Mean k_s (high uplift zone) = 117 m$^{0.9}$
Mean k_s (low uplift zone) = 66 m$^{0.9}$
Snyder et al. (2000) model fits
Mean k_s (high uplift zone) = 167 m$^{0.9}$
Mean k_s (low uplift zone) = 70 m$^{0.9}$

Figure 8 Examples of the relationship between slope and drainage area. Top: Longitudinal profiles (lines) and corresponding slope–area data (symbols) for two drainage basins in the King Range, USA. Middle: Slope–area data from six rivers in the King Range. Bottom: Slope–area data from the San Gabriel Mountains, USA. In both the King Range and San Gabriel Mountains, catchments undergoing more rapid rates of rock uplift and denudation, as determined from dated marine terraces and thermochronometry (respectively), have steeper channels. Reproduced from Wobus C, Whipple K, Kirby E, et al. (2006) Tectonics from topography: Procedures, promise, and pitfalls. *Tectonics*, *Climate and Landscape Evolution*, pp. 55–74.

et al., 2005; Snyder et al., 2000; Wobus et al., 2006a) (**Figure 9**). In some cases, the data show a nonlinear relationship in which a relatively small change in channel slope corresponds to a proportionally larger change in erosion rate (DiBiase et al., 2010; Harkins et al., 2007; Snyder et al., 2000). For example, in an analysis of the King Range (US west coast), Snyder et al. (2000) found that normalized channel gradients varied by about a factor of two between regions in which the estimated rate of channel incision varied by a factor of 8. Working further south along the US west coast, Duvall

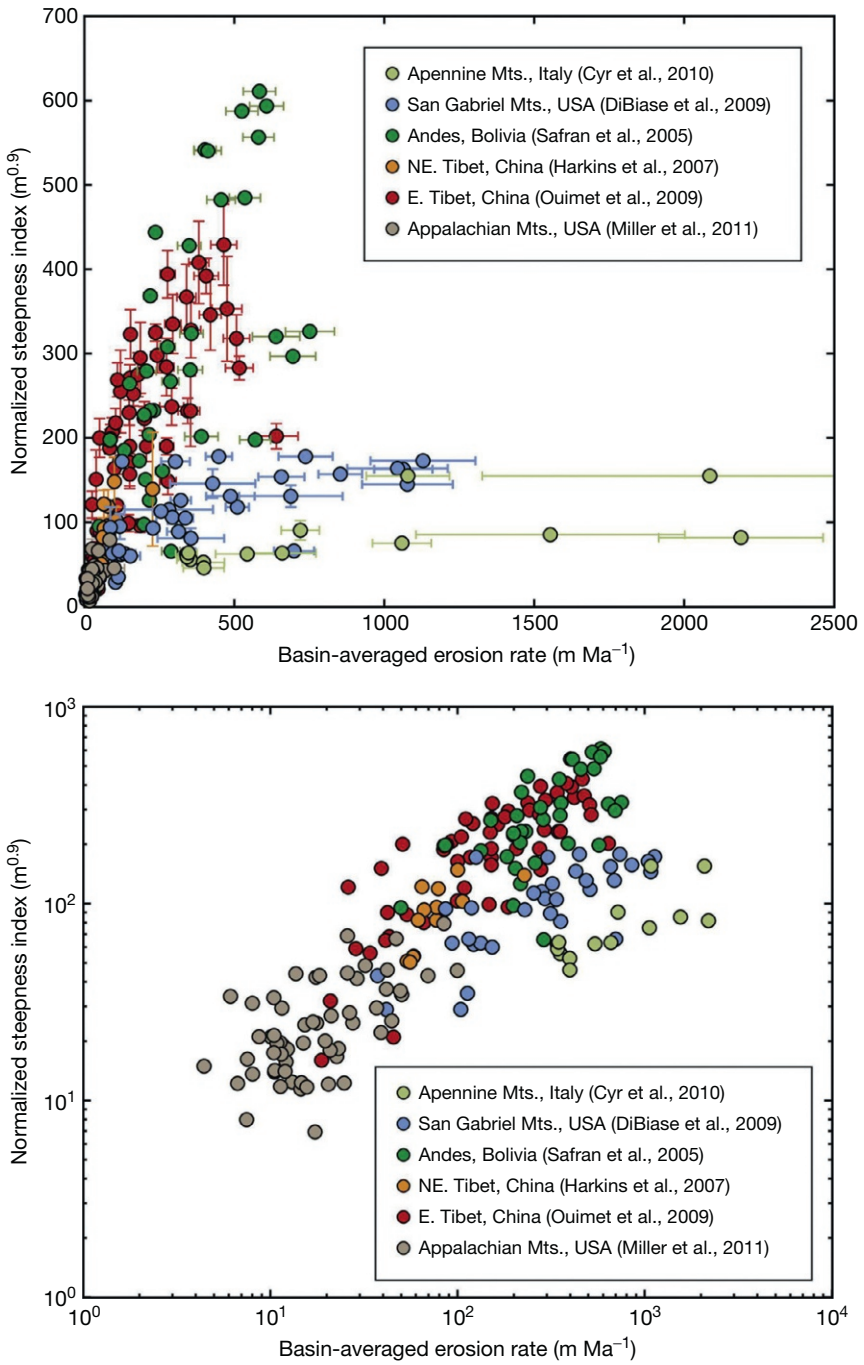
Normalized steepness index ($m^{0.9}$)
Basin-averaged erosion rate (m Ma^{-1})
Apennine Mts., Italy (Cyr et al., 2010)
San Gabriel Mts., USA (DiBiase et al., 2009)
Andes, Bolivia (Safran et al., 2005)
NE. Tibet, China (Harkins et al., 2007)
E. Tibet, China (Ouimet et al., 2009)
Appalachian Mts., USA (Miller et al., 2011)
Normalized steepness index ($m^{0.9}$)
Basin-averaged erosion rate (m Ma^{-1})
Apennine Mts., Italy (Cyr et al., 2010)
San Gabriel Mts., USA (DiBiase et al., 2009)
Andes, Bolivia (Safran et al., 2005)
NE. Tibet, China (Harkins et al., 2007)
E. Tibet, China (Ouimet et al., 2009)
Appalachian Mts., USA (Miller et al., 2011)

Figure 9 Relationship between erosion rate and steepness index k_s for several active tectonic regions. Reproduced from Kirby E and Whipple (2012) Expression of active tectonics in erosional landscapes. *Journal of Structural Geology* 44(5): 4e75.

et al. (2004) found a similar pattern. The causes of nonlinearity are still a matter of debate. Potential contributing factors include thresholds for sediment transport and erosion (DiBiase and Whipple, 2011; Lague et al., 2005; Molnar et al., 2006; Snyder et al., 2003c; Tucker, 2004; Tucker and Bras, 2000) and dynamic adjustments in channel width (Attal et al., 2008; Duvall et al., 2004; Finnegan et al., 2005; Lavé and Avouac, 2001; Yanites and Tucker, 2010; Yanites et al., 2010a). Interestingly, the correlation between channel gradient and erosion rate appears to extend beyond the erosion rate at which hillslopes achieve threshold gradients (DiBiase et al., 2010, 2012; Ouimet et al., 2009); in other words, hillslopes reach a threshold slope before channels do.

In summary, the rate at which continental topography is worn down and crustal material is recycled depends strongly on topographic relief. When relief is relatively high, both hillslopes and stream channels appear to exhibit a nonlinear relationship between relief and denudation rate. On hillslopes,

this manifests as an upper threshold to mean slope angle. Whether channel networks exhibit a similar upper limit remains to be demonstrated, but theory and observations suggest that as relief increases, the density of fluvial channels may decrease in favor of colluvial channels and/or hillslopes (DiBiase et al., 2012; Howard, 1997; Tucker and Bras, 1998), which may be dominated by debris-flow erosion (Stock and Dietrich, 2003). One interesting consequence of a nonlinear erosion–relief relation is that old mountain belts may take much longer to decay than linear models would predict (Baldwin et al., 2003). The strong connection between relief and denudation rate also leads to the possibility of quasi-steady states in mountain belts, a concept we explore further in the succeeding text. First, we consider three other major controls on continental erosion: climate, lithology, and tectonic processes.

6.13.3.2 Climate

There is ample reason to believe that climate should have a strong influence on landscape evolution. Yet in contrast to the strong direct link between erosion rate and relief, the role of climate in landscape evolution is less clear. In part, this reflects the fact that climate involves a range of different factors, including precipitation, temperature, and their variability in time and space. Climate is also clearly linked with ecosystems, such that it is often difficult to disentangle the direct role of climate from the role of biota, which are themselves influenced by climate. In this section, we explore what is known about the role of climate and life in governing landscape evolution.

The basic idea that climate should influence the rate and nature of landscape evolution comes partly from the simple observation that certain climate regimes are associated with distinctive processes and landforms (e.g., Büdel et al., 1982; Gutiérrez, 2005). For example, cold regions exhibit ice-related weathering and erosion processes (including, of course, glaciation) that are not found in warmer climates, whereas eolian transport is restricted to deserts and coasts where the vegetation cloak is thin or absent. Moreover, geomorphic and sedimentary records commonly show a distinct impact of glacial–interglacial cycles. For instance, many river terraces around the world have a documented association with late Quaternary climate variations, presumably reflecting changes in water and sediment supply (e.g., Bull, 1991). Other studies have demonstrated changes in hillslope erosion and sediment transport that are linked to glacial–interglacial shifts (Hughes et al., 2009; Roering et al., 2004; Tucker et al., 2011). In general, the case that climate influences processes and landforms is clear.

Nonetheless, there is still a great deal that we do not understand about the degree and manner in which factors such as precipitation and temperature influence the erosion of the Earth's continents. Consider first the case of precipitation. Many geomorphic processes involve water. Rivers are the principal agents for transporting debris from continents to oceans. Glacial valley erosion relies on a source of atmospheric water. Chemical weathering of rock is mediated by aqueous reactions underground. Freezing of water in rock and soil damages rock and transports sediment downhill (e.g., Anderson et al., 2012a). Weathering and transport by living things – from rock fracture by root growth to soil creep by animal burrowing – depend on the presence of water. Water in the subsurface reduces the stability of rock and soil on hillslopes, reducing the effective gradient at which landsliding may be triggered (e.g., Gabet et al., 2004). Likewise, the presence and magnitude of an erosion-resistant and water-absorbing plant carpet rely on water. It is reasonable to suppose, therefore, that the rate and nature of erosion on the continents should be correlated in some fashion with precipitation.

Studies of modern river sediment discharge often show some degree of correlation between sediment flux and factors related to runoff and precipitation (Hicks et al., 1996; Hovius, 1998; Jansson, 1988; Ludwig and Probst, 1998; Phillips, 1990; Syvitski and Milliman, 2007). For example, Hicks et al. (1996) reported a strong correlation between sediment yield and mean annual precipitation in a population of about 200 New Zealand drainage basins that spanned over an order of magnitude in precipitation rate (**Figure 10**). Similarly, the empirical global sediment yield model of Syvitski and Milliman (2007) predicts a correlation between sediment yield and mean annual runoff; recast in terms of average runoff, $P[L/T]$, the BQART model describes unit sediment yield, Y_s, as

$$Y_s = BP^{0.31}A^{-0.19}RT \qquad [3]$$

implying that mechanical erosion rate varies with about the cube root of average annual precipitation.

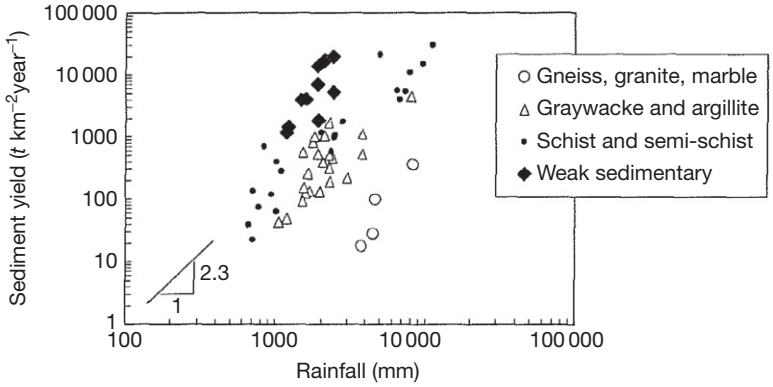

Figure 10 Sediment yield versus mean annual rainfall for basins in New Zealand, categorized among different lithologies. Reproduced from Hicks D, Hill J, and Shankar U (1996) Variation of suspended sediment yields around New Zealand: The relative importance of rainfall and geology. In: DE Walling and B Webb (eds.) *Erosion and Sediment Yield: Global and Regional Perspectives*, pp. 149–156. IAHS Publication.

Many data sets suggest only a weak correlation between sediment yield and precipitation (or runoff) (Aalto et al., 2006; Milliman and Syvitski, 1992; Pinet and Souriau, 1988; Summerfield and Hulton, 1994). In a study of sediment flux in rivers draining the Bolivian Andes, where sediment storage is minimal, Aalto et al. (2006) reported a strong correlation between sediment yield and relief but surprisingly little relation with precipitation. They suggested that the role of precipitation may be masked by covariation with relief, but in general, their result is typical in that studies that jointly examine relief and precipitation find stronger correlation with the former.

Estimates of long-term denudation from cosmogenic nuclide analysis show a similar ambiguity. Bierman and Caffee (2002) compared rates of rock lowering across arid and tropical sites in Australia and found a strong correlation between erosion rate and mean annual precipitation. On a global basis, however, the correlation that Bierman and Caffee (2002) observed is not seen. Von Blanckenburg et al. (2004) compiled denudation rate estimates obtained from cosmogenic nuclide analysis in river sediment from catchments underlain by crystalline rock. The data span annual precipitation rates from 30 to over 1000 mm $year^{-1}$ and temperatures from −0.4 to 25 °C. No simple correlation is apparent between erosion rate and precipitation rate. They highlight the case of Sri Lanka, a tropical setting characterized by moderately high relief and annual precipitation up to 5 m $year^{-1}$. Despite the high rainfall, estimated rates of denudation in Sri Lanka are only on the order of 0.002–0.011 m ky^{-1}.

Data on rates of chemical weathering, derived from solute loads in rivers (e.g., Gaillardet et al., 1999; White and Blum, 1995) and mass balance analysis of saprolite (e.g., Riebe et al., 2001), tell a somewhat similar story. Typically, rates of chemical denudation make up a relatively small fraction of total denudation (Summerfield and Hulton, 1994), except in regions of unusually low total erosion rate such as Sri Lanka (Von Blanckenburg et al., 2004). In a study of solute flux in 68 relatively small granitoid catchments, White and Blum (1995) found positive correlations between flux and precipitation, runoff, and temperature. These observations reflect the critical role of water in modulating chemical weathering reactions, as well as the effect of temperature on reaction kinetics. A similar weak but positive correlation with precipitation and/or runoff has been noted in other studies (e.g., Pinet and Souriau, 1988; Summerfield and Hulton, 1994; Von Blanckenburg, 2005; West et al., 2005). On the other hand, Riebe et al. (2001) found little correlation between chemical weathering and climate factors in a study of catchments on similar lithology in the Sierra Nevada of California. Thus, while there appears to be a tendency for wetter climates to produce more rapid rates of chemical denudation and weathering, the subtle nature of the correlation (even within similar lithologies) implies that other factors are at play.

Some of the ambiguity undoubtedly reflects the dual role of precipitation in providing energy for erosion and transport and in nourishing a plant canopy that shields the land surface from erosion. In an analysis of the variation between sediment yield and mean annual precipitation, Langbein and Schumm (1958) found that the highest yields were associated with semiarid regions. Subsequent data sets (reviewed, e.g., by Summerfield (1991)) show a similar pattern, with a second peak in very wet regions and a minimum in temperate, moderate-rainfall zones. The pattern has been attributed to changes in the balance between water availability (which enhances erosion) and vegetation (which retards it) and is consistent with models of runoff generation and wash erosion on hillslopes (Kirkby, 1995). In addition, it is not simply the mean annual precipitation that influences rates of denudation; precipitation variability plays a role as well (e.g., DiBiase and Whipple, 2011; Lague et al., 2005; Molnar, 2001; Tucker, 2004; Tucker and Bras, 2000) and may act to confound simple correlations between erosion and mean annual precipitation.

Many geomorphic processes are temperature-sensitive. Ice-related processes, such as glacial erosion, have an obvious temperature control. The chemical weathering of unstable minerals formed at depth also depends on temperature, through the Arrhenius relation. A number of geomorphic processes are sensitive to the time variability of temperature, as in the case of soil creep driven by repeated freezing and melting of ice lenses in the soil column (Anderson et al., 2012a). Thus, temperature and its variability should all be expected to have an influence on landscape evolution. The BQART model developed by Syvitski and Milliman (2007) predicts a linear correlation between sediment flux and mean annual temperature for regions above 2 °C. Perhaps this reflects the predicted exponential (Arrhenius) increase in rates of chemical weathering (and presumably clastic sediment production) with temperature, as suggested by data on solute fluxes (e.g., West et al., 2005; White and Blum, 1995). However, the correlation between temperature and erosion rate is typically weak (e.g., Summerfield and Hulton, 1994), suggesting that its overall role is not straightforward.

One obvious means by which temperature influences landscape evolution is in setting the conditions for glacial and periglacial erosion. We explore the role of glaciation further in **Sections 6.13.3.3** and **6.13.4.3**.

Living organisms influence landscape evolution through a variety of mechanisms, many of which remain poorly understood. Vegetation can limit erosion by adding cohesion to soil through root reinforcement, increasing soil infiltration and water-storage capacity, and dissipating fluid friction. Conversely, plants can accelerate rock damage through root growth and increase the rate of hillslope soil creep through bioturbation (e.g., Gabet et al., 2003). Riparian vegetation can alter the power of rivers and streams by influencing channel width and planform pattern (e.g., Tal and Paola, 2007). Plant roots also influence rates of chemical weathering by increasing soil–water acidity and possibly through symbiosis with mycorrhizal fungi. Burrowing animals are also known to facilitate soil motion on hillslopes through bioturbation (Gabet et al., 2003; Yoo et al., 2005). The role of microbiota is less clear, but the possibility exists for microbially enhanced chemical weathering of rocks (e.g., Templeton and Knowles, 2009). In general, the influence of biota in landscape evolution is an active research frontier. There is as yet no comprehensive theoretical framework for life's influence on landscape evolution, though as noted later, the role of plants and animals in governing individual geomorphic processes has begun to be addressed in landscape evolution theory (e.g., Collins et al., 2004; Gabet et al., 2003; Istanbulluoglu and Bras, 2005; Kirkby, 1995; Yoo et al., 2005).

In summary, whereas relief clearly exerts a strong and fairly straightforward control on the rate at which continents are worn down, climate variation, while influential, appears to play a more complex role. There is a need for mechanistic models that account for the effects of specific climate-related factors at the level of individual processes. Likewise, there is a need for models that explicitly address the action of living organisms in governing landscape evolution. Examples of progress toward these ends are reviewed in **Section 6.13.4**.

6.13.3.3 The 'Glacial Buzzsaw' Hypothesis

The dramatic scenery of glaciated landscapes testifies to the erosional power of moving ice. The obvious effectiveness of glaciers in sculpting landforms raises the question of whether glaciers are significantly more efficient as erosional agents than rivers, all else being equal. Suspended sediment yield from glaciated drainage basins is among the highest in the world and often higher than that from nonglaciated basins of comparable size (Gurnell et al., 1996; Hallet et al., 1996). Very rapid short-term rates of glacial bedrock erosion – on the order of tens of millimeter per year – have been documented during glacial surges (e.g., Humphrey and Raymond, 1994). On the other hand, these high rates appear to be relatively transient (decade-to-century scale) phenomena associated with surges or with transient rapid retreat of tidewater glaciers (Koppes and Hallet, 2002), rather than sustained long-term averages. Moreover, as Koppes and Montgomery (2009) pointed out, the highest documented rates of glacial erosion are comparable to the highest rates of river erosion, which can also can reach rates on the order of a centimeter per year or higher (e.g., Cook et al., 2013; Lavé and Avouac, 2001; Yanites et al., 2010a,b). Thus, studies of short-term sediment yield and erosion do not provide a clear answer as to the relative erosive power of rivers and glaciers.

One way to frame the question is to ask whether, for a given precipitation and erosion rate, a glaciated drainage basin would require more, less, or the same relief as a nonglaciated basin of the same size. Brocklehurst and Whipple (2002) addressed this question by comparing the relief and longitudinal profiles of basins with and without significant Pleistocene glaciation in the eastern Sierra Nevada. Their results implied that glacial erosion can indeed be more efficient than fluvial erosion in a temperate alpine environment.

The notion that glaciers beat rivers in the game of erosion has led to the startling hypothesis that glaciation may impose an upper limit on the height of mountain ranges. Working in the northwestern Himalayas, Brozović et al. (1997) noted a striking correlation between the altitude of the snow line, which rises to the northeast in concert with a decline in precipitation, and the modal elevation. Thermochronometry implies substantial variations in long-term exhumation across the region, but surprisingly, these variations appear to be uncorrelated with topography and relief. These observations led Brozović et al. (1997) to suggest that "in mountain belts that intersect the snow line, glacial and periglacial processes place an upper limit on altitude, relief, and the development of topography irrespective of the rate of tectonic processes operating." Essentially, according to this hypothesis, any topography that rises above the equilibrium-line altitude becomes efficiently eroded, as if it were impinging on the blades of an electrical circular (or 'buzz') saw; hence, the concept has come to be known as the glacial buzzsaw hypothesis.

Similar correlations between mountain height and the modern and Pleistocene equilibrium-line altitudes have been reported in the Andes (Montgomery et al., 2001), the Chugach–St. Elias Range (Spotila et al., 2004), Cascade Range (Mitchell and Montgomery, 2006), northeastern Basin and Range Province (Western United States) (Foster et al., 2008), and the southern Swiss Alps (Anders et al., 2010) (**Figure 11(a)** and **11(b)**). The correlation is also apparent in a global compilation by Egholm et al. (2009) (**Figure 11(c)**). These settings often show a similar lack of correlation between topography and long-term exhumation rate. One contributing factor that has been suggested is the tendency of glaciated valleys to be wider than fluvial valleys (presumably because of their greater effectiveness at lateral erosion), which should promote narrower and lower surrounding ridgelines (e.g., Anders et al., 2010; Brocklehurst and Whipple, 2002; Mitchell and Montgomery, 2006). Hales and Roering (2009) offered an interesting variation in suggesting that intense weathering by ice-wedge growth in fractures ('frost cracking') also contributes to rapid erosion at altitudes above the freezing point. Despite the appeal of the glacial buzzsaw hypothesis, it remains to be proven. One open question is the degree to which altitude influences near-surface temperature through surface heating. If the surface lapse rate is influenced by topography, then we might expect to see a correlation between equilibrium line altitude (ELA) and topography independent of any buzzsaws. Minder et al. (2010) showed that the mean annual lapse rate in the Cascade Mountains is significantly smaller than the commonly assumed surface lapse rate of 6.5 °C km^{-1}, which hints at the possibility of a general correlation between topography and lapse rate. Nonetheless, the glacial buzzsaw remains an intriguing possibility.

6.13.3.4 Late Cenozoic Climate Change and Global Erosion

Many of the world's mountain ranges and their sedimentary basins record evidence for unusually intense erosion and sedimentation during the past few million years. A reconstruction by Hay et al. (1988) of global rates of sediment accumulation during the Cenozoic found that the sedimentation rate during the past five million years was more than twice as great as that of any preceding five million-year period. Although traditionally these records had been interpreted as indicating the onset or acceleration of tectonic activity in various individual mountain ranges, Molnar and England (1990) proposed that they actually record a global increase in rates of erosion brought about by global cooling. Compilations of sediment accumulation records from around the world (Molnar, 2004a; Zhang et al., 2001) show a globally consistent increase in both the grain size and volume of sediment younger than a few million years (**Figure 12**). Molnar and England (1990) noted that there is no evidence for a global change in the speed or orientation of plate tectonics and argued that global climate cooling represents the only plausible source. The fact that the signal includes continental interior basins that are cut off from the oceans implies that eustatic sea-level fall cannot be the sole cause. Enhanced glacial and periglacial erosion is an obvious

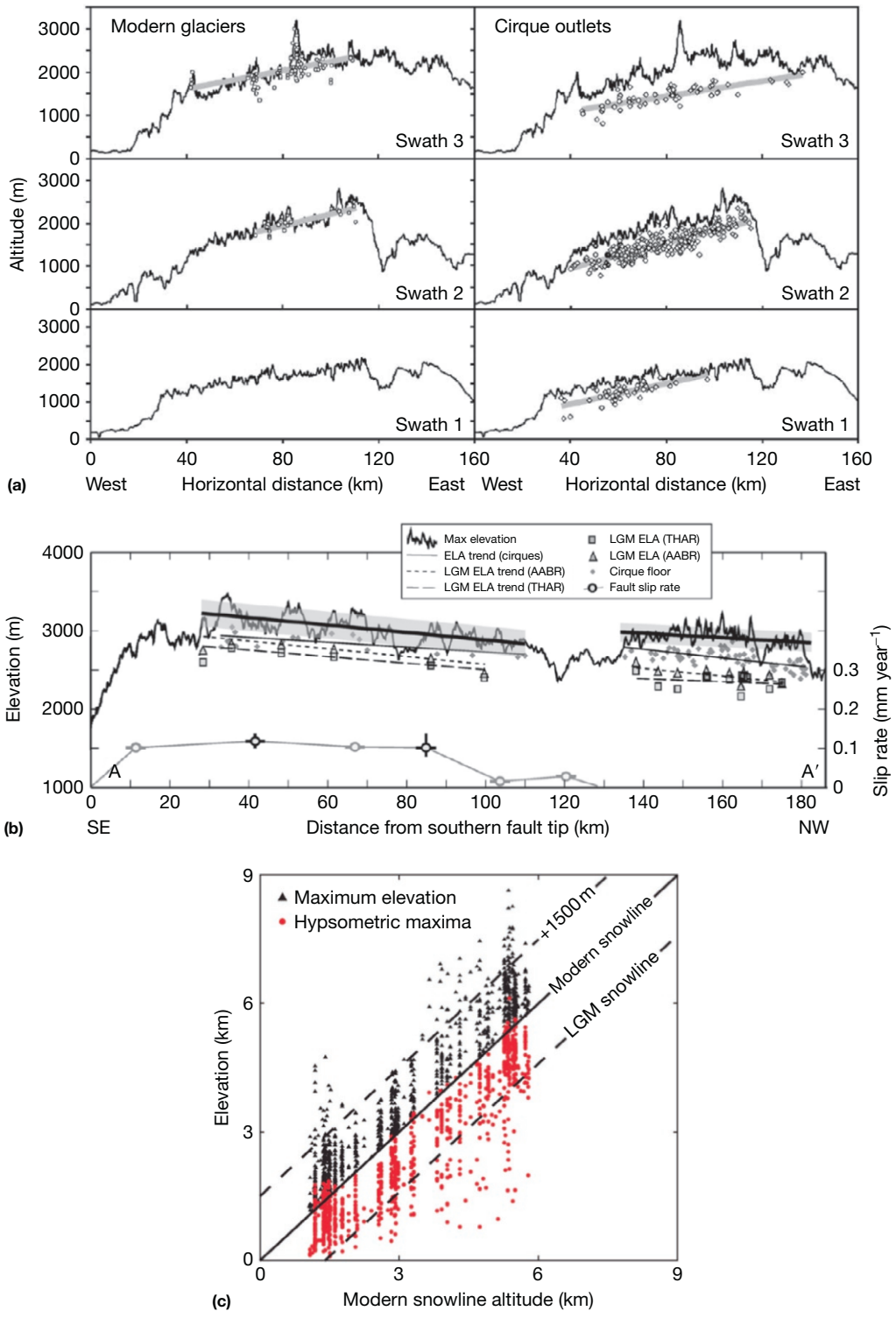

Figure 11 Examples of correlation between topography and snow-line altitude. (a) Topographic swath profiles from the Cascade Mountains, USA, compared with average glacier (left) and cirque outlet (right) altitudes (reproduced from Mitchell S and Montgomery D (2006) Influence of a glacial buzzsaw on the height and morphology of the Cascade Range in central Washington State, USA. *Quaternary Research* 65(1): 96–107). (b) Along-strike topographic profile compared with fault slip rate, cirques, and equilibrium-line altitudes along the Beaverhead–Bitterroot Mountains, an active normal-fault footwall in the western USA (reproduced from Foster D, Brocklehurst S, and Gawthorpe R (2008) Small valley glaciers and the effectiveness of the glacial buzzsaw in the northern Basin and Range, USA. *Geomorphology* 102(3): 624–639). (c) Correlation between peak altitude (triangles) and hypsometric peak (circles) with snow line, from a global database (reproduced from Egholm D, Nielsen S, Pedersen VK, and Lesemann J-E (2009) Glacial effects limiting mountain height. *Nature* 460(7257): 884–887).

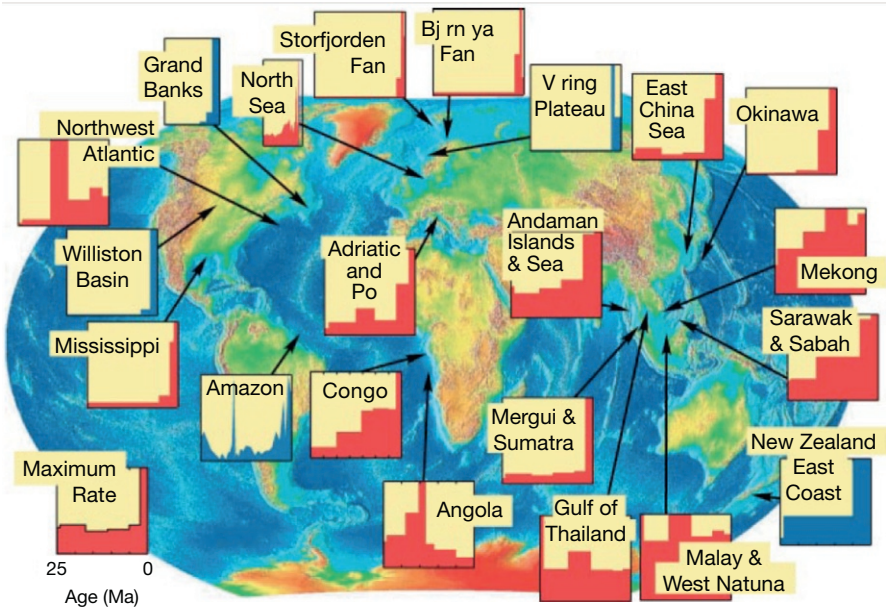

Figure 12 Map showing reconstructions of sedimentation rate since 25 Ma in basins around the world. Red diagrams show accumulation rates over the area of each basin; blue diagrams show point measurements (see original reference for sources and further information). Reproduced from Molnar P (2004) Late Cenozoic increase in accumulation rates of terrestrial sediment: How might climate change have affected erosion rates? *Annual Review of Earth and Planetary Sciences* 32: 67–89. http://dx.doi.org/10.1146/annurev.earth.32.091003.143456.

possibility, but cannot explain increased late Cenozoic sedimentation in tropical, unglaciated regions such as Northern Australia (Nott and Roberts, 1996). Rather, Zhang et al. (2001) and Molnar (2004a) suggested that while glacial erosion and sea-level fall are likely contributors, an additional factor is increased climate variability associated with the onset of strong ice age cycles, as indicated by the Cenozoic oxygen isotope record. Because geomorphic systems often exhibit threshold responses and other forms of nonlinearity, an oscillating climate is likely to drive more rapid erosion than a stable one, all else being equal (e.g., Molnar et al., 2006; Tucker, 2004).

The hypothesis of a global late Cenozoic increase in erosion and sedimentation rates was challenged by Willenbring and von Blanckenburg (2010). Their analysis was based in part on records of the ratio of the beryllium isotopes ^{9}Be and ^{10}Be retrieved from marine sediment cores and spanning about the past 10 My. ^{10}Be is produced and delivered to the oceans mainly through bombardment of atmospheric oxygen by cosmic rays, and its production rate is presumed to be roughly constant on million-year timescales. Its sister isotope, ^{9}Be, is derived mainly from weathering on the continents. Willenbring and von Blanckenburg (2010) proposed that any substantial changes in erosion should be reflected in similar changes in chemical weathering, and these in turn should show up as variations in the ^{10}Be/^{9}Be ratio. Because the cores they examined showed no major variations in this ratio during the past ten million years, they argued that the hypothesized global increase in rates of erosion and weathering did not occur. This argument, however, assumes a link between the continental erosion recorded in basin stratigraphy and the chemical weathering signal recorded in isotopic ratios; at present, this link remains poorly understood. If indeed there were a one-to-one relation between the two proxies, then why do they appear to show such different patterns? Willenbring and von Blanckenburg (2010) suggested that the unusually large volume of late Cenozoic sediment reflects the so-called Sadler effect, which describes a statistical tendency for depositional systems to preserve younger sediments, simply because they are less likely to have been remobilized than older sediments are (Sadler, 1999; Schumer et al., 2011).

The potential for the Sadler effect to produce the illusion of increasing sedimentation rates over time is an important cautionary note. On the other hand, surely some sedimentary basins really do record accelerations in deposition, and we do not yet have a reliable way to distinguish between real and apparent changes in sedimentation. The beryllium isotopic method used by Willenbring and von Blanckenburg (2010) is still relatively new, and its fidelity in recording global weathering rates remains to be explored. In the meantime, we are left with a question mark over the existence and potential causes of a worldwide erosion and sedimentation rate increase during the past several million years.

6.13.3.5 Lithology

The mechanical strength and chemical stability of rocks and soils clearly influence erosion rates and mechanisms, as well as the nature of the landforms that emerge. As one might expect, poorly consolidated sedimentary rocks tend to produce higher erosion rates than massive crystalline rocks, all else being equal (Dadson et al., 2003; Hicks et al., 1996; Inman and Jenkins, 1999; Pinet and Souriau, 1988; Schaller et al., 2001; Syvitski and Milliman, 2007). Among studies of catchment-wide sediment yield, Pinet and Souriau (1988) reported a sevenfold difference between basins containing massive and poorly consolidated rocks. Syvitski and Milliman (2007) found that by

using a lithology factor that varied by a factor of 6 between weak and resistant rocks, they could account for about 8% of the variability in sediment flux in a global data set. Approximately, a threefold difference in erosion rate between crystalline and sediment rocks was reported by Schaller et al. (2001). In a comparison of erosion rates among New Zealand catchments, Hicks et al. (1996) found that weak sedimentary lithologies erode as much as 1000 times faster than crystalline rocks (though differences in land use among lithologies may also contribute to this striking contrast) (**Figure 10**). Cosmogenic nuclide-derived estimates of erosion rate along the northern edge of the Tibetan Plateau led Palumbo et al. (2010) to conclude that sedimentary rocks tend to produce greater variability in erosion rate than more intensely metamorphosed rocks, perhaps reflecting variations in fracture density. Lithology has also been linked to variations in stream gradient (e.g., Duvall et al., 2004; Jansen et al., 2010; Johnson et al., 2009; Tucker and Slingerland, 1996).

Quantifying lithologic effects remains a frontier research area. Simply measuring rock resistance to erosion has proven to be challenging. The bulk strength of a fractured rock mass may be considerably lower than the intact rock strength that one measures in the lab or field (e.g., Schmidt and Montgomery, 1995). Moreover, the properties that determine a rock's susceptibility to weathering and erosion depend on the nature of the process. For example, the resistance of a rock mass to chemical dissolution by acidic pore water depends on the stability of its constituent minerals, whereas its resistance to hydraulic plucking depends on the spacing of fractures and/or bedding planes (e.g., Whipple et al., 2000). Likewise, the ability of rivers to transport eroded sediment depends strongly on grain size, which is influenced by lithology through factors such as rock fracture density and resistance to abrasion.

The need to measure these diverse lithologic properties in the context of landscape evolution has spurred efforts to quantify rock resistance. Shallow geophysics provides one promising approach. This method relies on linking attributes such as seismic velocity with bedrock fracture density (Clarke and Burbank, 2010) and degree of chemical weathering (Befus et al., 2011). Abrasion-mill experiments have also shown promise in quantifying the wear resistance of water-worked sediment (Attal and Lavé, 2006, 2009; Attal et al., 2006; Sklar and Dietrich, 2001).

6.13.3.6 Tectonic Processes

At first glance, it might seem odd to include tectonic process in the list of factors that influence the erosion of the continents. Although tectonic processes keep mountains aloft, one might think that their influence shows up in relief and perhaps lithology, which we have already considered. In fact, however, erosion and sediment yield data often show a correlation with tectonic activity that goes beyond relief and lithology (Dadson et al., 2003; Hovius, 1998; Pinet and Souriau, 1988; Portenga and Bierman, 2011; Vanmaercke et al., 2014; Von Blanckenburg, 2005). There are several likely explanations. In regions where topography lies close to a threshold for landsliding, as noted earlier, relief and erosion rate tend to become decorrelated; instead, the rate of denudation reflects the rate of rock uplift relative to the regional base level (Binnie et al., 2007; Burbank et al., 1996; DiBiase et al., 2010; Koppes and Montgomery, 2009; Montgomery and Brandon, 2002; Norton et al., 2011; Ouimet et al., 2009; Safran et al., 2005; Wittmann et al., 2007). The rejuvenation of relief by earthquakes, through the formation of fault scarps, can raise erosion rates as the geomorphic system responds (Cook et al., 2013; Yanites et al., 2010b). Tectonic processes also involve mechanical weakening of rock (Clarke and Burbank, 2011; Dühnforth et al., 2010; Koons et al., 2012; Molnar et al., 2007), in a manner that is often not apparent on regional geologic maps and therefore not counted in lithology indices. Seismic shaking during earthquakes can trigger widespread landsliding (Dadson et al., 2004), with an erosional impact that can persist long after the earthquake (Hovius et al., 2011; Yanites et al., 2010b, 2011), potentially leading to a net decline in relief despite the tectonic input (Hovius et al., 2011; Parker et al., 2011). Tectonically active regions often go hand in hand with volcanism, which can produce easily eroded volcaniclastic sediment (e.g., Gran et al., 2011; Major et al., 2000).

Finally, there is also a more subtle potential reason why tectonic activity correlates with denudation rate independent of relief or lithology. Given sufficient time, landscapes tend to adjust toward a condition that Hack (1960) termed *dynamic equilibrium*, in which various elements of the terrain adjust slopes and relief such that erosion rates become roughly uniform in space. As a result, areas underlain by more resistant lithologies tend to develop steeper slopes, as in the famous example of the Appalachian Ridge and Valley Province that Hack (1960) studied. One outcome of this tendency toward equilibration is a decorrelation between erosion rate and either relief or lithology, which has been observed in cosmogenic nuclide studies of tectonically quiet regions (Matmon et al., 2003; Riebe et al., 2000).

6.13.4 Process Mechanics and Landscape Evolution Theory

A comprehensive theory for the evolution of the Earth's land surface should be able to account for the shape of terrain, its rates and patterns of change, and the nature of its response to changes in climate, lithology, biota, and tectonics. A central challenge in formulating such a theory is the broad range of scales involved. Spatial scales vary from the smallest turbulent eddies in a stream (order 10^{-3} m) to the scale of a tectonic structure (order 10^4–10^5 m). The corresponding range in timescales varies from the duration of a turbulent burst (order 10^{-7} years) to the lifetime of a fault or fold (order 10^6 years). A mechanistic understanding of topography and its dynamics requires well-founded, quantitative theory of the governing processes. In this section, we briefly review progress toward this end and identify some remaining open questions.

A starting point for building a quantitative, mechanistic theory of landscape evolution is the continuity equation for a column of crustal rock or sediment with elevation η:

$$\frac{\partial \eta}{\partial t} = U - \frac{1}{1-\phi}\nabla \mathbf{q}_s \qquad [4]$$

Here, t is time, ϕ is porosity of the eroding material, and U represents vertical motion of rock relative to a specified

base-level reference frame (such as sea level, the geoid, the surface of a normal-fault hanging wall, or the bed of a large river adjacent to the landscape in question). The vector $\mathbf{q_s}$, with dimensions of length squared per time $[L^2/T]$, represents the horizontal flow of sediment and/or solutes per unit width. A specification of $\mathbf{q_s}$ for a particular process is known as a geomorphic transport law, which Dietrich et al. (2003) defined as "a mathematical statement derived from a physical principle or mechanism, which expresses the mass flux or erosion caused by one or more processes in a manner that: 1) can be parameterized from field measurements, 2) can be tested in physical models, and 3) can be applied over geomorphically significant spatial and temporal scales." The mass continuity formulation in eqn [4] assumes that the Earth's surface can be represented as a single-valued function of two horizontal dimensions plus time; that is, $\eta = f(x,y,t)$. This continuity law is limited in that it effectively ignores horizontal tectonic motions (though these can be added via an advection term (e.g., Miller et al., 2007)) and cannot deal with the motion of near-vertical surfaces such as channel banks, waterfalls, and sea cliffs. Nonetheless, it is widely used and suitable for our purposes. In this section, we examine some of the major processes that drive the topographic evolution of the continents, summarizing what is known (or not known, as the case may be) about the operative geomorphic transport laws.

6.13.4.1 Weathering, Rock Damage, and Sediment Production

Rocks seldom reach the Earth's surface unscathed. En route, they are subject to a range of alteration processes, most of which weaken them mechanically or chemically and make them easier to mobilize as they approach the surface. Very often, the material that lies just below the soil (or more generally *mobile regolith*) is not unaltered rock, but rather saprolite – rock that has been chemically altered and possibly fractured, but not otherwise physically disturbed (e.g., Anderson et al., 2012c). There is some evidence that the degree of saprolite weathering correlates with the rate at which the saprolite is entrained into mobile regolith (Burke et al., 2007; Dixon et al., 2009), though the cause–effect mechanisms remain something of a mystery. Note that while we usually associate chemical weathering with rock weakening, one counterexample is the cementation of near-surface soil and sediment due to chemical precipitation of mobile elements, as in the formation of duricrusts (e.g., Dixon and McLaren, 2009; Goudie, 1985).

In addition to chemical weakening, rocks can accumulate damage through fracturing. The role of tectonic extensional or shearing stresses in fracturing rocks has already been noted (Clarke and Burbank, 2011; Koons et al., 2012; Molnar, 2007). Topographic stresses have been linked to near-surface rock fracturing (Leith et al., 2014; Miller and Dunne, 1996), though the occurrence and rates appear sensitive to topographic configuration and Poisson's ratio, making it difficult to formulate a general theory (Molnar, 2004b). Similarly, sheeting joints in massive rocks, which were once widely attributed to unloading, are now understood to form where topographic curvature in the presence of 'residual' compressional stress creates strong surface-normal tension (Martel, 2006).

Wedging of cracks by growing tree roots or ice crystals can also propagate fractures in the upper few meters of the Earth's surface. Particular attention has been paid to fracture propagation by segregation ice growth, or 'frost cracking,' in which ice lenses within fractures grow by migration of thin films of supercooled liquid water (Anderson, 1998; Hales and Roering, 2007; Hallet et al., 1991; Murton et al., 2006; Walder and Hallet, 1985, 1986).

There is as yet no general agreement on how the chemical and physical damage to rocks should be described mathematically. One ideally needs to specify measurable properties of the weathered rock that evolve over time, and formulate equations to describe this transformation. One such property is the volumetric proportion of unaltered parent material (Kirkby, 1985); another is the frequency distribution of particle sizes within a weathered rock mass, the dynamics of which can be represented by transition matrix (Cohen et al., 2009). Anderson et al. (2012a) formulated rock weakening in terms of a generalized measure of damage, D, and damage rate $\dot{D}$. Damage may be defined according to any of several properties; for example, it could reflect the total surface area of fractures per unit volume and hence have dimensions of inverse length. Anderson et al. (2012a) proposed a general expression for damage evolution in which the damage rate declines exponentially with depth (reflecting depth decay in the activity of processes such as frost cracking) and becomes ineffective beyond a critical damage, D_{crit} (representing the notion that it is hard to break or dissolve what is already broken or dissolved):

$$\dot{D} = \dot{D}_0 e^{-(z/z_d)} \left[1 - \frac{D}{D_{crit}}\right] \quad [5]$$

According to this framework, the depth and extent of rock damage depend on the maximum damage rate D_0 and the depth decay length scale z_d; the damage rate vanishes as the rock approaches a state of critical (maximum) damage, D_{crit}. Interestingly, recent studies have independently documented the existence of a near-surface zone of damaged rock on the order of 5–15 m deep in disparate locations around the world (e.g., Befus et al., 2011; Clarke and Burbank, 2011) (**Figure 13**). We are only just beginning to understand quantitatively the controls on the properties and thickness of this near-surface damage zone.

Above the zone of damaged but in situ rock lies the *mobile regolith*, which might be defined as granular material in which grains have been displaced relative to their neighbors by more than their own diameter. Processes capable of entraining weathered rock into the mobile regolith layer include plant and animal activity, abiotic disturbance processes such as frost heave, and, in steep terrain, bedrock-involved landsliding and earthflows. Evidence from cosmogenic nuclide analyses supports the hypothesis of Gilbert (1877) that the entrainment rate varies inversely with mobile regolith thickness (e.g., Heimsath et al., 1997; McKean et al., 1993; Small et al., 1999), presumably because deeper regolith more effectively shields the underlying rock from disturbance. Data are generally consistent with the exponential form suggested by Ahnert (1976):

$$P = P_0 \exp(-z/z_*) \quad [6]$$

where P is the rate of lowering of the bedrock–regolith interface relative to the rock reference frame ('production rate'), P_0 is the maximum (bare bedrock) rate, z is regolith thickness, and z_* is

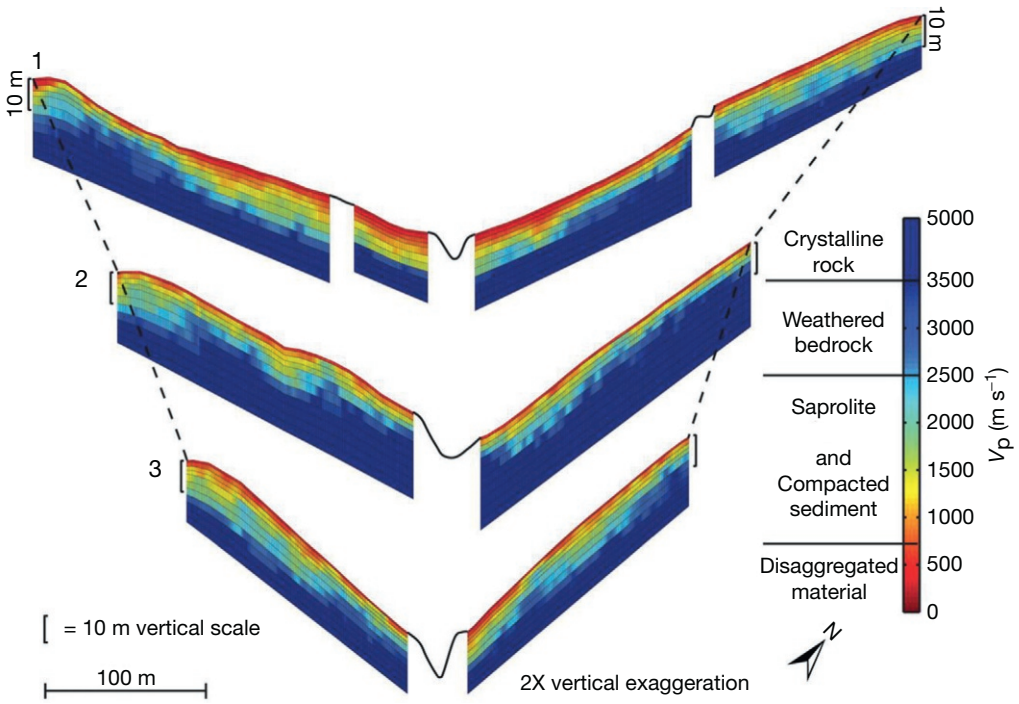

Figure 13 Shallow seismic velocity images showing distribution of soil, saprolite, and bedrock at the Boulder Creek Critical Zone Observatory, USA. Reproduced from Befus K, Sheehan A, Leopold M, Anderson S, and Anderson R (2011) Seismic constraints on critical zone architecture, Boulder Creek Watershed, Front Range, Colorado. *Vadose Zone Journal* 10(3): 915–927.

a depth decay scale on the order of a meter or less (e.g., Rosenbloom and Anderson, 1994). Some data sets also suggest that the maximum entrainment rate may occur under a small but finite mobile regolith cover, reflecting the retention of water and ability to host plants (Heimsath et al., 2009). When regional denudation is faster than the maximum rate of regolith production by small-scale disturbance processes such as animal burrowing, the regolith cover tends to become patchy and discontinuous, and bedrock landsliding presumably plays an increasingly important role in turning weathered rock into mobile sediment (Heimsath et al., 2012).

6.13.4.2 Gravitational Transport on Hillslopes

Gravity's tug on hillslope materials plays out in a remarkable variety of ways. On slopes that lie well below the angle of repose, mobile regolith is transported downslope by repeated episodes of disturbance, each of which has a higher probability of moving material down than up, with the net result that over many years the soil appears to creep downhill. Disturbance processes can include animal burrowing (Black and Montgomery, 1991; Gabet et al., 2003; Yoo et al., 2005), the growth and fall (or decay) of trees (Hughes et al., 2009; Roering et al., 2010), raindrop impact (Furbish et al., 2007), and frost heave (Anderson et al., 2012a), among others. There is now strong support for the hypothesis of Davis et al. (1892), Gilbert (1909), and Culling (1960, 1963) that the net average transport rate on relatively gentle, soil-mantled slopes depends on local gradient, leading to a transport law of the form

$$\mathbf{q}_s = -\kappa \nabla \eta \qquad [7]$$

where κ is a transport coefficient with dimensions of L^2/T and $\nabla\eta$ is the local hillslope gradient. When combined with mass conservation, one obtains a diffusion-like equation:

$$\frac{\partial \eta}{\partial t} = \kappa \frac{\rho_s}{\rho_b}, \nabla \eta_2 \qquad [8]$$

where ρ_s/ρ_b is the ratio of sediment grain to soil bulk density. Because of the diffusion form, disturbance-driven soil creep is sometimes referred to as 'geomorphic diffusion.' In fact, the analogy extends beyond this: just as classical Fickian diffusion arises from the statistics of molecular motion, the slope-dependent transport law can arise as the net effect of a directional bias in the statistics of particle displacement (Furbish and Haff, 2010; Furbish et al., 2009; Jyotsna and Haff, 1997; Tucker and Bradley, 2010). Disturbance events are limited in their depth of penetration, which may be set by either the nature of the process (such as the characteristic depth of root penetration) or the thickness of the soil (e.g., Braun et al., 2001; Furbish et al., 2009; Heimsath et al., 2005). The linear diffusion model predicts rounded, parabolic hillslopes (**Figure 14**, top).

For soil-mantled slopes steeper than perhaps 20° or so, there is evidence of a greater-than-linear functional relationship between soil transport rate and slope angle (Andrews and Bucknam, 1987; Roering, 2008; Roering et al., 1999). This nonlinear relationship reflects, in part, increasing displacement distance of disturbed particles (e.g., Furbish and Haff, 2010; Tucker and Bradley, 2010). The behavior can be approximated by models of the form

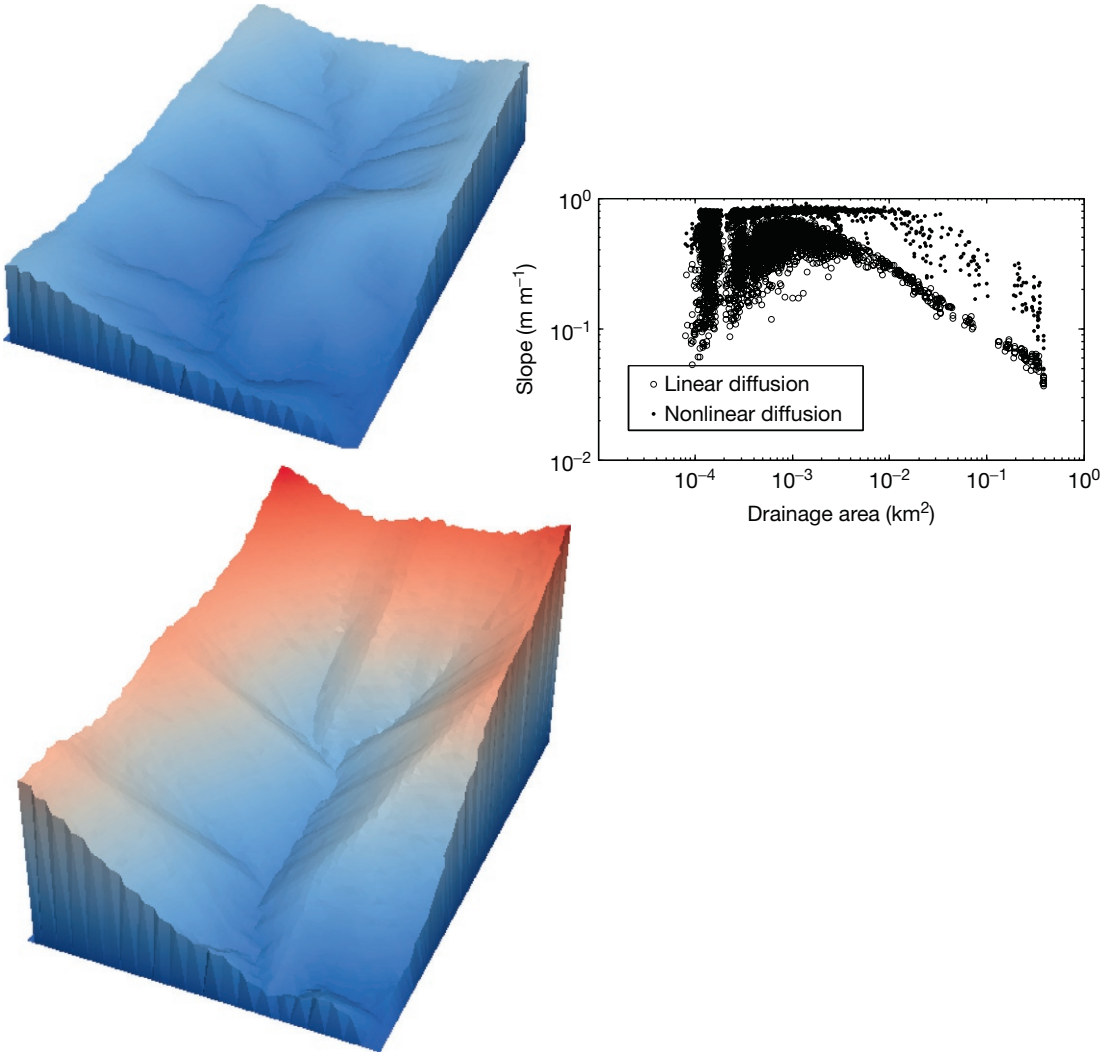

Figure 14 Numerical simulation showing hypothetical topography under the influence of water erosion (discussed below) and either linear (top) or nonlinear (bottom) soil creep. Rate of base-level lowering is eight times higher in bottom model. Simulations created using CHILD model (Tucker et al., 2001b).

$$\mathbf{q_s} = -\kappa \frac{1}{1-(\nabla\eta/S_c)^2}\nabla\eta \qquad [9]$$

where S_c represents an effective failure angle (Pelletier and Cline, 2007; Roering, 2008; Roering et al., 1999, 2001). The obvious divergence around $|\nabla\eta| = S_c$ indicates that this model is generally inapplicable to slopes that exceed a nominal angle of repose for soil. The model also assumes an unlimited availability of soil. Roering (2008) and others suggested a modified form of this model in which transport rate depends on soil thickness and vanishes as the soil cover tends toward zero. The various forms of nonlinear diffusion model have a further limitation in that they assume purely local transport (in other words, that flux at a point is solely a function of slope angle at that point); more general expressions have been suggested to account for nonlocal, long-distance transport on steep slopes (Foufoula-Georgiou et al., 2010; Furbish and Haff, 2010; Tucker and Bradley, 2010). The nonlinear diffusion model predicts relatively planar hillslopes with rounded ridge lines (**Figure 14**, bottom).

Thick and mechanically weak material in steep, humid terrain may undergo the creeping, quasi-viscous style of deformation known as earthflow. Booth and Roering (2011) recently introduced a geomorphic transport law for earthflows, in which the material is treated as a thin, viscous, non-Newtonian fluid similar to bed-frozen glacial ice.

Very steep hillslopes are susceptible to direct mechanical failure, when gravitational stress exceeds frictional and cohesive strength. Slope failure gives rise to a plethora of different forms of landsliding. The abrupt and episodic nature of landslides does not lend itself to the continuum-mechanics language of geomorphic transport laws like eqn [7]. Although theories for static slope stability are well developed, we presently lack geomorphic transport laws, or their stochastic

Figure 15 (a) Debris flow at Chalk Cliffs, Colorado, in September 2009. Note 50 cm high rain gauge (gray cylinder mounted on instrument bridge) for scale (photo courtesy Jeff Coe, USGS). (b) Channel erosion in the aftermath of debris flows, and damage to erosion-monitoring bolts placed in the channel floor (reproduced from McCoy S, Tucker G, Kean J, and Coe J (2013) Measurements of basal force from natural debris flows that incised bedrock. *Journal of Geophysical Research: Earth Surface*. 118: 1–12).

equivalents, that describe the long-term integrated action of abrupt mass-failure processes.

Debris flows act as both hillslope and channel processes: often triggered by intense runoff and/or landsliding on hillslopes, but cascading down the headwater hollows and low-order channels of mountainous landscapes (**Figure 15**). A debris flow is a powerful surge of water and sediment in which both fluid and granular forces contribute to motion (Iverson, 1997). Headwater channels frequented by debris flows tend to show relatively constant slope angles; this fact, combined with observations of rapid sediment entrainment and bedrock wear in the wake of natural debris flows (McCoy et al., 2012, 2013; Stock and Dietrich, 2006), leads to the hypothesis that debris flows can act as unique and powerful landscape evolution agents in steep terrain. Stock and Dietrich (2006) suggested a geomorphic transport law for the cumulative effect of debris flows, in which principal factors include shear rate, drainage area, and effective grain size. Refinement of this concept awaits a deeper understanding of sediment entrainment and bedrock erosion by debris flows (Hsu et al., 2008; Hungr et al., 2005; Iverson, 2012b; Iverson et al., 2010; McCoy et al., 2012, 2013).

6.13.4.3 Glacial Erosion

We have already seen evidence that glacial erosion is quite efficient, to the extent that it may outpace fluvial erosion in otherwise similar circumstances. Glaciers erode rock through *abrasion* by glacially entrained sediment and by *quarrying* (or 'plucking') of fracture-bounded blocks (cf. Cuffey and Paterson, 2010). In addition, subglacial streams may also contribute to sediment removal and bed erosion, and subglacial weathering may contribute to glacial erosion by dissolving or otherwise weakening rock at the glacier's bed. Mass wasting processes also contribute to glacial valley evolution and therefore both rock mass strength and the state of stress within the rock matter (Augustinus, 1995).

Several attempts have been made to model the physics of glacial abrasion. Hallet (1979) developed a theory that predicts that abrasion rate depends on sliding velocity and on basal melting rate (because basal melting drives englacial rocks toward the bed where they provide abrasive tools). In some cases, the supply of rock fragments, from sources such as frost weathering of valley sides, may be a limiting factor (Lliboutry, 1994).

In jointed rocks, quarrying may be the more important process (Glasser et al., 1998), particularly where joint density is relatively high (Dühnforth et al., 2010). Quarrying involves the removal of rock fragments by ice entrainment on the downstream end of a step in the rock beneath a glacier. The process requires either that fractures with spacing comparable to the step dimensions already exist in the rock mass or that the weight of the ice on the step induces fracture growth. Hallet (1996) developed a theory of glacial quarrying by fracture propagation and clast removal, which predicts that erosion rate depends sensitively on effective pressure and sliding velocity (both of which regulate ice-bed contact area). Fluctuations in water pressure can facilitate quarrying by providing stress for crack propagation behind steps (when water pressure is low and differential stress is high) and facilitating removal by pressure freezing and sliding (when water pressure is high) (Hallet, 1996; Hooke, 1991; Iverson, 1991; Rothlisberger and Iken, 1981).

Process models for glacial abrasion and quarrying focus on a representative element of the glacier bed, such as a single idealized step. This approach is necessary to make the problem tractable, but it leaves open the question of how one scales up the essential physics to treat landscape evolution. Models of glacial landscape evolution contain two basic elements: the physics of ice and the physics of erosion. The physics of ice flow is reasonably well understood. The main limitation for numerical models of glacial landscape evolution is the computational cost of solving the full mass and momentum balance for ice flow. For this reason, ice dynamics are often represented

using the shallow-ice approximation, in which flow is treated as a thin, non-Newtonian viscous sheet. Nonetheless, Egholm et al. (2012) showed that higher-order ice dynamics, and in particular the horizontal stress gradients that are commonly neglected, can influence landscape evolution by producing wider, shallower glacial valleys than thin-ice models typically predict. Glacial hydrology also appears to play an important role in governing glacial valley erosion (Herman et al., 2011).

The effective large-scale physics of glacial erosion remain incompletely understood. Often, total glacial erosion (combining all processes) is approximated as a power-law function of sliding velocity (Anderson et al., 2012b; Braun et al., 1999; Egholm et al., 2012; Harbor, 1992; Harbor et al., 1988; Herman and Braun, 2008; Kaufmann and Romanov, 2012; MacGregor et al., 2000; Oerlemans, 1984; Pelletier et al., 2010; Tomkin, 2007) and/or ice discharge (Anderson et al., 2006; Jamieson et al., 2008; Kessler et al., 2008), with exponents typically assumed to be in the range 1–4 (**Figure 16**). In many cases, a linear relation is assumed for the sake of simplicity. Iverson (2012a) presented a probabilistic model of erosion by glacial quarrying in which both rock strength and subglacial step size are treated as random variables. The model predicts that erosion rate should indeed scale as a power law of sliding velocity. Those accustomed to the idea that exponents express 'fundamental,' immutable physical relationships (such as the inverse-square law in Newton's theory of gravity) might be surprised at Iverson's findings, however. His analysis implies that the effective exponent should depend on the degree of rock-strength heterogeneity: for relatively homogeneous rock, erosion varies as the square of sliding velocity, while for more heterogeneous rock, the implied exponent is less than half. The latter is consistent with Amundson and Iverson (2006), who estimated that ice age glacial erosion rates in tributary and trunk glaciers in the Canadian Rockies correlated with about the 1/3 power of average ('balance') ice velocity.

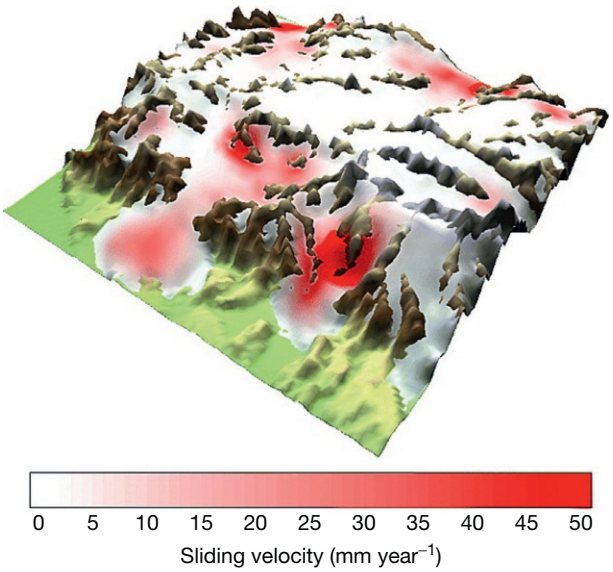

Figure 16 The numerical model of glacial flow and erosion in the Southern Alps, New Zealand. Erosion rate is assumed to be proportional to sliding velocity. Reproduced from Herman F and Braun J (2008) Evolution of the glacial landscape of the Southern Alps of New Zealand: Insights from a glacial erosion model. *Journal of Geophysical Research: Earth Surface* 113(F2): F02009.

Several other studies have explored more elaborate glacial erosion models. For example, some have separated abrasion and quarrying (Hildes et al., 2004; MacGregor et al., 2009). Finally, while most models of glacial landscape evolution have focused on valley deepening, there is mounting evidence that glacial headwall retreat may be at least as important as valley deepening (Brocklehurst and Whipple, 2002; Naylor and Gabet, 2007; Oskin and Burbank, 2005; Shuster et al., 2011), at least in the early stages of glacial landscape modification.

Overall, while a consensus theory of large-scale glacial erosion has yet to emerge, the outlines of such a theory are gradually coming into focus. It is clear, for example, that glacial landscape evolution is strongly influenced by sliding velocity, subglacial hydrology, and lithology. The problem of glacial headwall retreat in particular needs focused research.

6.13.4.4 Drainage Network Structure and Development

One of the most striking features of terrestrial landscapes is the organization of terrain around dendritic channel and valley networks. Drainage network formation lies at the heart of why mountains appear jagged rather than smooth. Branching networks are found not only on the Earth's continents but also on Mars and Titan. The ubiquity of network structures in nature, which gives us tree branches, roots, blood vessels, and other forms, has motivated considerable research into their origins.

One might ask why runoff on the continents organizes itself into networks, rather than flowing in thin, broad sheets of water across the landscape. An insightful theoretical analysis by Smith and Bretherton (1972) revealed that network formation will naturally arise from runoff when the ability of water to transport sediment increases more than linearly with the water discharge. Where this is true, an unchanneled land surface becomes subject to an instability: any perturbation that causes water to converge will tend to produce more rapid erosion at the point of flow convergence. The resulting depression collects more water, creating a positive feedback that leads ultimately to the formation of channel networks. Subsequent work has elaborated on the Smith–Bretherton channel initiation mechanism (Birnir et al., 2001; de Gennes, 2000; Fowler et al., 2007; Izumi and Fujii, 2006; Izumi and Parker, 2000; Kirkby, 1993; Loewenherz, 1991; Smith, 2010; Smith and Bretherton, 1972; Smith and Merchant, 1995; Smith et al., 1997; Sólyom, 2011). More generally, it is now clear that drainage networks will tend to arise wherever two units of water flow together can perform more erosion than the same two units separately.

River networks, like other network forms in nature, exhibit self-similarity (e.g., Rodriguez-Iturbe and Rinaldo, 1997; Veneziano and Niemann, 2000). Viewed from above without a scale bar, it is virtually impossible to tell the difference between the Amazon drainage and a network formed in a hectare of badlands. The fractal, self-similar nature of river networks and their basins is consistent with the hypothesis that, over time, networks evolve toward a state in which energy dissipation tends to be minimized (Colaiori et al., 1997; Errera and Bejan, 1998; Howard, 1990; Molnár and Ramirez, 1998;

Rodriguez-Iturbe and Rinaldo, 1997). A trajectory toward minimization of energy dissipation can be seen to arise from an erosional feedback mechanism: all else being equal, segments of a river network with locally high energy dissipation rate will tend to erode more rapidly (because part of the hydraulic energy is expended on erosion and sediment transport), which tends to reduce the local energy gradient and dissipation rate. River networks are, however, constrained by the topography that they carve and hence may evolve toward a state that Rodriguez-Iturbe and Rinaldo (1997) termed 'feasible optimality,' rather than a true global minimum.

Hillslopes and first-order channels mark the lower-scale limit of landscape dissection. A fundamental measure of landscape dissection is the drainage density (Horton, 1932), classically defined as the total length of channels, L, divided by the surface area that they span, A:

$$D_d = L/\sqrt{A} \quad [10]$$

The drainage density is one of several related measures of landscape dissection, including valley density (length of valleys per unit area) (Montgomery and Dietrich, 1994) and average flow-path distance to the nearest channel (Tucker et al., 2001a). Values of drainage density vary widely (**Figure 17**). For example, Lin and Oguchi (2004) reported drainage density of up to 160 km^{-1} in badlands formed in recently disturbed landscapes in Japan, while data from the Eastern United States presented by Horton (1945) have D_d values on the order of 0.5 km^{-1}.

What sets the limit to landscape dissection? The analysis of Smith and Bretherton (1972) predicted that the finest scales should grow the fastest, leading to the paradoxical outcome of an infinitely dissected landscape. In fact, a range of different factors are understood to limit the extent of channel dissection and set the hillslope scale. These include thresholds for erosion and sediment movement (Horton, 1945; Izumi and Parker, 2000), infilling of small incipient channels by various forms of gravitational (or eolian) transport (Kirkby, 1993; Loewenherz, 1991; Perron et al., 2009; Simpson and Schlunegger, 2003), limited overland flow generation (Dietrich et al., 1992, 1993), limited duration of runoff events (which prevents runoff from aggregating downslope) (Dunne, 1991), hydrodynamic diffusion (Izumi and Parker, 2000), and destruction of incipient channels by landslides (Tucker and Bras, 1998). In each case, there is a competition between erosion by concentrated running water (which tends to excavate channels) and channel infilling or stabilization. One can ask: how does the balance of power between these competing processes vary as a function of factors such as relief, material properties, vegetation, and climate? Several studies have addressed this question theoretically, finding that the relationship between drainage density and various potential controlling factors depends on the nature of the processes and materials involved (Collins and Bras, 2010; Howard,

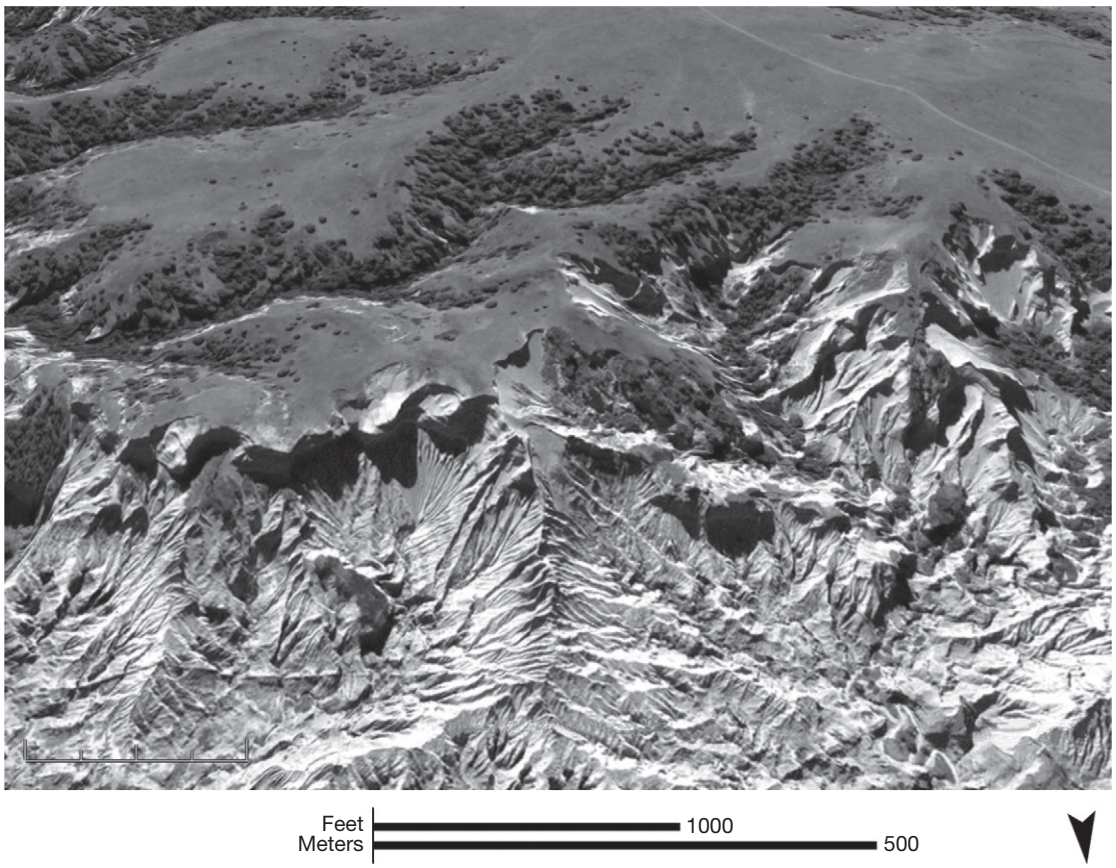

Figure 17 Example of dramatic spatial variation in drainage density. Perspective image of Badlands National Park, USA. Image obtained from Google Earth; imagery date April 2012.

1997; Istanbulluoglu and Bras, 2005; Kirkby, 1987; Moglen et al., 1998; Tucker and Bras, 1998). For example, drainage density may increase or decrease as a function of relief. Although some progress has been made in identifying major controls on drainage density using digital terrain data (e.g., Lin and Oguchi, 2004; Montgomery and Dietrich, 1989; Oguchi, 1997), a comprehensive and well-tested theory of drainage density is still needed.

What we know, then, amounts to basically the following: Drainage networks arise because there is generally a positive feedback between the collection of water and the rate of erosion by channelized flow. This feedback leads to surprising regularity and self-similarity in drainage network structures, as reflected in relationships between quantities such as drainage area and mainstream length. At small (meter to kilometer) wavelengths, a close competition between channel formation and channel erasure leads to a transition to relatively smooth, undissected hillslopes. The precise scale at which this transition takes place is set by the nature of the processes, the relief, and the materials involved. All else being equal, for example, the scale of landscape dissection tends to be finer when materials are relatively impermeable, grain size is relatively low, and/or rainfall intensity is relatively high.

6.13.4.5 Dynamics of Channel Networks

In landscapes with minimal glacial imprint, the fluvial system is usually the dominant geomorphic agent, responsible for incising into rock, etching a valley network, and creating the local relief that contributes to erosion on hillslopes. For this reason, a quantitative understanding of the dynamics of fluvial erosion and transport over long timescales, grounded in the governing physics and chemistry, represents a crucial element in any comprehensive model of landscape evolution. In addition, because the fluvial system derives its water and sediment from hillslopes, the nature of the interaction between channels and hillslopes is also a critical feedback.

In order to carve a valley, a river must accomplish two things. First, it must remove sediment produced within its catchment. Second, any bedrock underlying the channel must be broken down into pieces that are small enough to transport with the available hydraulic power. Depending on the circumstances, either one of these requirements might prove to be the limiting factor. Imagine, for example, an erosional landscape forming in an uplifted sedimentary basin composed mainly of unlithified sand deposits. In that case, the material is already fragmented, and the river network carves relief simply by washing the sand out. This is a very different picture from the case of an uplifted batholith made of massive, unfractured granite. Here, the excavation of a valley requires either hydraulic abrasion of granite through impact wear, or fragmentation of the granite by weathering processes, or some combination of the two. As a third example, imagine a landscape composed of uplifted, highly cohesive but uncemented marine mud deposits. Cohesion lends strong resistance to hydraulic detachment, yet once they become detached, the particles are quite easy to transport. Finally, consider the case of fully lithified but heavily fractured and highly heterogeneous sedimentary rocks. Here, the limiting factor could be plucking of joint-bounded blocks, which may come in a broad range of shapes and sizes. Alternatively, breakdown of the rock into smaller sizes by various weathering processes could be rate-limiting.

A reasonably comprehensive theory for fluvial landscape evolution must be able to honor all of these cases. Furthermore, such a theory should indicate *which* processes are the most critical and under what circumstances. Although we are still some distance from achieving this goal, current models have shown some success in accounting for first-order features of fluvial topography and dynamics. A few of these models are reviewed next.

6.13.4.5.1 Fluvial sediment transport

Sediment transport by water currents is reasonably well understood, even if the complexity of the problem makes accurate prediction difficult. Putting sediment into motion requires overcoming the immersed weight and macroscopic bed roughness that hold grains in place. Following the pioneering work by Shields (1936), the initiation of sediment motion is conventionally expressed in terms of an experimentally determined critical boundary shear stress, τ_c. This threshold depends on grain size, grain density, gravitational acceleration, and the size and configuration of other roughness elements on the bed. In the context of long-term landscape evolution, the nonlinearity that arises from this effective transport threshold has important implications for the scaling of relief and erosion rate (DiBiase and Whipple, 2011; Snyder et al., 2003a; Tucker, 2004), the response of fluvial systems to climate change (Lague et al., 2005; Molnar, 2001; Molnar et al., 2006; Rinaldo et al., 1995; Tucker, 2004; Tucker and Bras, 2000; Tucker and Slingerland, 1997), and the life span of decaying orogens (Baldwin et al., 2003).

When sediment grains are subjected to fluid shear, they experience lift and drag forces that cause them to move in the direction of the local current. Larger and/or denser grains tend to maintain close contact with the bed (and hence are referred to as bed load), while finer and/or less dense grains are partially or wholly held aloft by fluid turbulence. The literature is replete with models that predict fluvial sediment *transport capacity*. The capacity is normally defined in terms of a local equilibrium, in which the entrainment of grains from the bed is balanced by gravitational settling (disentrainment) of mobile particles. Because it involves rates of mobilization and settling, the transport capacity depends not only on the flow hydraulics and bed roughness but also on the sediment properties. One cannot speak meaningfully of transport capacity without reference to the nature of the available sediment.

For purposes of modeling long-term landscape evolution, engineering timescale formulas are typically simplified into a form such as the following:

$$Q_c = K_f W \left(K_t \left[\frac{Q}{W} \right]^M S^N - \Omega_c \right) \qquad [11]$$

where Q_c is the river's volumetric sediment transport capacity $[L^3/T]$, Q is water discharge, S is channel slope, W is channel width, Ω_c is an entrainment threshold below which transport rate is zero, and the rest are parameters. In this type of formulation, the first term in parentheses represents a particular hydrodynamic quantity such as shear stress or stream power per unit bed area, and the exponents are chosen to reflect the

appropriate scaling. For example, in the particular case of unit stream power, $M = N = 1$, and K_t is the unit weight of water (for other examples of casting sediment transport models into a form like eqn [11] see Howard (1980), Willgoose et al. (1991b), Howard (1994), Tucker and Bras (1998), and Tucker (2004)). Often, the threshold term is omitted, based on the argument either that transport tends to occur at high stages or that the stream width adjusts to maintain a fixed ratio of boundary shear stress to threshold shear stress (Paola et al., 1992).

River discharge typically fluctuates on a daily to hourly basis, which raises the question of how one chooses a value that is representative of long-term landscape evolution. Various approaches have been used. One popular approach is the concept of an effective discharge (Wolman and Miller, 1960), which represents the integrated result of the full natural sequence of flows, and to further assume that this discharge can be represented as a power function of drainage area, A (e.g., Willgoose et al., 1991b). A weakness of this approach is that the effective discharge itself may vary in space and time as topography evolves (Huang and Niemann, 2006; for further discussion of hydrologic approximations used in landscape evolution theory, see Tucker and Hancock (2010) and references therein).

For a river flowing on a bed of unconsolidated alluvium, conservation of mass dictates that the time rate of change of bed elevation is

$$\frac{\partial \eta}{\partial t} = B - \frac{1}{W(1-\phi)}\frac{\partial Q_c}{\partial x} \qquad [12]$$

where x is the distance along the stream channel and ϕ is the bed sediment porosity. Simplifying to omit the threshold and expressing Q in terms of A, this can be written in terms of two topographic (rather than strictly hydrological) parameters, area A and slope S:

$$\frac{\partial \eta}{\partial t} = B - \frac{1}{W(1-\phi)}\frac{\partial A^{M'} S^{N}}{\partial x} \qquad [13]$$

A defensible choice for N is unity (Tucker, 2004). The equation therefore describes a strongly diffusive behavior, in which sharp steps in the longitudinal profile of a river will be rapidly smoothed out.

Fluvial sediment transport models like eqn [13] make interesting predictions about the structure of drainage basin topography. For example, imagine a situation in which the following assumptions apply: transport rate per unit width is proportional to unit stream power above a threshold ω_c for sediment motion, effective discharge is proportional to drainage area times an effective runoff rate, channel width scales with the square root of basin area, grain size is uniform over space and time, and the rate of sediment delivery to the fluvial system per unit drainage area is steady and uniform. It can be shown (e.g., Tucker and Bras, 1998) that the relationship between channel slope and basin area under these conditions is

$$S = aE + b\omega_c A^{-1/2} \qquad [14]$$

where a and b are constants that reflect hydrology and channel geometry. The equation predicts longitudinal channel profiles that are straight to concave-upward, with a concavity index that ranges between 0 and 0.5, depending on the relative magnitudes of the two terms on the right-hand side (see also Willgoose, 1994 for in-depth analysis of slope–area scaling for transport-limited fluvial systems). **Figure 18** shows an example of a numerical simulation of two drainage networks for which a variant of eqn [14] applies. The roughness of the terrain is directly related to the concavity index (Tucker and Whipple, 2002), which in turn reflects the degree to which the threshold term (second on right) dominates. The illustration in **Figure 18** is a somewhat extreme example because the sediment is homogeneous; incorporating multiple grain sizes reduces the variation in concavity because the bed composition provides an extra degree of freedom for adjustment (Gasparini et al., 1999, 2004).

An exciting aspect of models like eqn [14] is that they make a direct connection between the physics of sediment transport and the large-scale morphology of the Earth's surface. At this point, the biggest limitation is uncertainty about the degree to which the various assumptions are justified. Even for the relatively simple case of a demonstrably transport-limited drainage network with a spatially uniform denudation rate, there are still at least three elements of the system that could influence

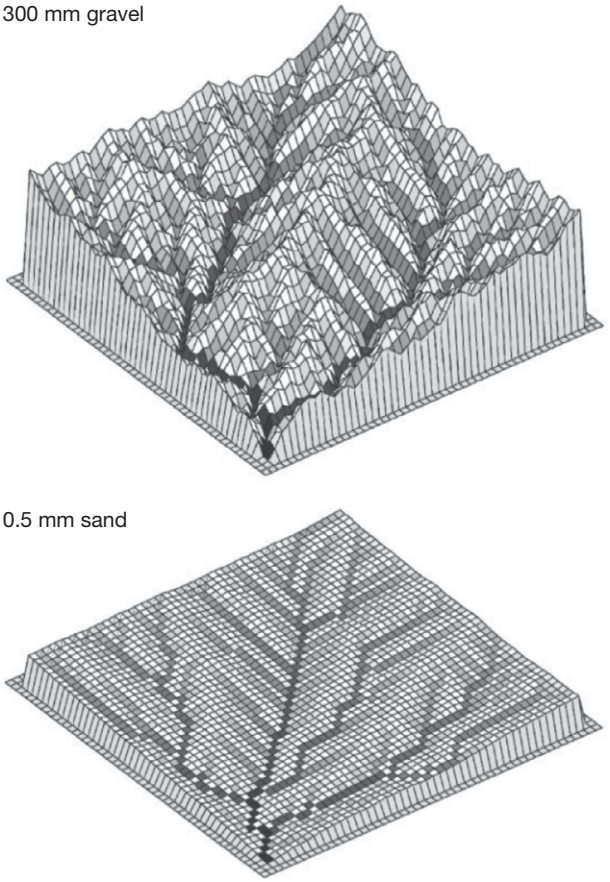

Figure 18 Numerical models of hypothetical topography formed by uplift and erosion of unconsolidated sediment. Reproduced from Gasparini N, Tucker G, and Bras R (2004) Network-scale dynamics of grain-size sorting: Implications for downstream fining, stream-profile concavity, and drainage basin morphology. *Earth Surface Processes and Landforms* 29(4): 401–421. http://dx.doi.org/10.1002/esp.1031.

the network topography in ways that are presently poorly understood. Drainage basin hydrology can clearly influence the space–time distribution of boundary shear stress and unit stream power, which may in turn influence the structure of topography (Huang and Niemann, 2006; Roe et al., 2002; Sólyom and Tucker, 2004). For example, a network dominated by episodic flash floods may behave very differently than one dominated by prolonged seasonal snowmelt. The geometry and roughness of channels, which are both tightly coupled to hydrology and boundary stress, have a profound influence on sediment transport rates. Finally, downstream fining of sediment through abrasion and fragmentation can have a major influence on the size distribution of the sediment load and hence on the relative mobility of sediment (Attal and Lavé, 2006, 2009; Le Bouteiller et al., 2011). Each of these issues represents a research frontier.

6.13.4.5.2 Channel incision into bedrock

The fluvial sediment transport theory reviewed in the preceding section applies to landscapes in which the production of unconsolidated sediment by weathering equals or exceeds the denudation rate or in which the substrate itself consists of unconsolidated sediment. In many parts of the world, these conditions are not met. Instead, in order to carve relief, the fluvial system must incise into the bedrock. Bedrock incision may be accomplished by one or more of three processes: plucking of fracture-bounded blocks, abrasion of rock by the impact of grains in transport, or fragmentation of rock along the channel bed and banks by weathering processes (Whipple, 2004). The first two of these represent direct bedrock erosion by the fluvial system. The simplest models to describe the resultant large-scale landscape evolution are based on the hypothesis that the rate of bedrock lowering, E, scales with either the cross section-averaged channel boundary shear stress, τ, or the rate of hydraulic energy dissipation per unit bed area (unit stream power), ω:

$$E \propto \tau - \tau_c = \left(\rho g^{2/3} C_f^{1/3}\right)[qS]^{2/3} - \tau_c \text{ Shear stress} \qquad [15]$$

$$E \propto \omega - \omega_c = (\rho g) qS - \omega_c \text{ Unit stream power} \qquad [16]$$

where q is discharge per unit channel width, ρ is the density of the fluid (water plus sediment), g is gravitational acceleration, and C_f is a roughness factor that has a weak dependence on flow depth. In both cases, there is a simple relationship between long-term average incision rate and the effective discharge-slope product (note that E is zero when the stress or power falls below the threshold). If one assumes that q scales as a power law with drainage basin area A, then both of these equations can be cast in terms of the topographic variables slope and area:

$$E = KA^m S^n - \Phi_c \qquad [17]$$

where K is a coefficient that lumps together climate, rock erodibility, and other factors, while Φ_c is a threshold (with dimensions of L/T) that depends on rock properties. The slope exponent n is either 1 or 2/3, while the value of m depends on the hydrology and channel geometry but is expected to be on the order of $n/2$ (Tucker, 2004; Whipple and Tucker, 1999). Because this equation can be derived from the hypothesis that erosion rate is proportional to stream power, eqn [17] has come to be known as the 'stream power model' (even if it strictly only represents stream power when $n = 1$).

In the case of a drainage basin with steady and uniform erosion rate (perhaps equal to the long-term average rock uplift rate relative to the geoid), the slope–area relationship is given by

$$S = \left(\frac{E + \Phi_c}{K}\right)^{1/n} A^{-m/n} \qquad [18]$$

The predicted value of $m/n \approx 1/2$ is consistent with the observation that many drainage basins, and notably those in which there is evidence for spatially uniform long-term erosion rates, have a concavity index close to 1/2 (e.g., Snyder et al., 2000; Tucker and Whipple, 2002). The stream power model also implies that the steepness index depends on the erosion rate, the effective erosion threshold, and the efficiency factor. In fact, as noted earlier, observations in settings where variations in E are known suggest a nonlinear (greater than unity) relationship between erosion rate and steepness index (Binnie et al., 2007; DiBiase et al., 2010; Duvall et al., 2004; Snyder et al., 2000, 2003a), whereas eqn [18] implies a linear relationship with a positive intercept. Such a nonlinearity can be accommodated by modifications to eqn [17] that take into account flow variability (Lague et al., 2005; Tucker, 2004) and/or dynamic adjustment in channel width (Duvall et al., 2004).

Equation [17] is often referred to as a detachment-limited model (Howard, 1994) because it assumes that the limiting factor for streambed incision is the initial liberation of particles from the bed, rather than the transport of detached particles. Whereas transport-limited models imply that channel network evolution should have a strongly diffusive character, stream power theory describes a wavelike response to perturbations (Tucker and Whipple, 2002; Weissel and Seidl, 1998; Whipple and Tucker, 1999; Whipple and Tucker, 2002) (**Figure 19**).

A third class of models builds on the notion that there is a continuum between sediment-saturated and sediment-poor conditions and that, all else being equal, a high sediment concentration will tend to inhibit bedrock erosion because alluvium shields the bed from wear (Beaumont et al., 1992; Chase, 1992; Davy and Lague, 2009). A general model of this type was introduced by Davy and Lague (2009), though the general concept had previously been used in short-term models of soil erosion (e.g., Nearing et al., 1989). The evolution equation can be written as

$$(1 - \phi)\frac{\partial \eta}{\partial t} = U + E_r\left(\frac{q_s}{q_c} - 1\right) \qquad [19]$$

where q_c is a transport capacity, defined as that transport rate for which the entrainment rate E_r and the sediment settling rate are equal:

$$q_c = \frac{qE_r}{\beta v_s} \qquad [20]$$

Here, the settling rate is the product of particle settling velocity and a dimensionless factor β (of order unity) that describes the enrichment in sediment concentration near the bed. The entrainment rate can then be modeled using eqn [15] or [16].

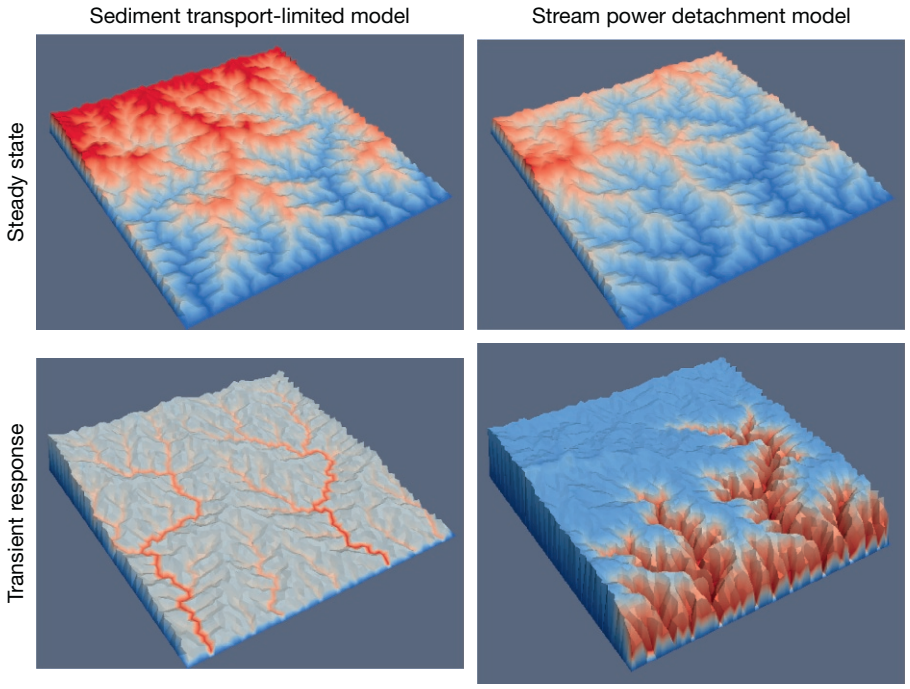

Figure 19 Numerical models of hypothetical topography, at steady state (top) and in response to a step increase in the rate of base-level lowering (bottom). Models on the left have a loose sediment substrate, which is represented using a form of eqn [13]. Models on the right assume that the rate of erosion is limited by the rate of detachment/entrainment of bedrock, which is proportional to excess shear stress (eqn [17]).

The success of this model in describing long-term channel network dynamics has not been extensively tested, but it has the advantage of smoothly transitioning between the transport-limited and detachment-limited end-member cases.

One weakness of all the foregoing models is that they ignore the contribution of mobile sediment grains to the impact wear of bedrock. A striking illustration of the importance of coarse, mobile sediment comes from a recent study of a 10 m high knickpoint generated by the 1999 Chi-Chi earthquake (M_ω 7.6) in Taiwan (Cook et al., 2013). For 5 years after the earthquake, bed-load sediment was trapped by a shallow depression upstream, and the knickpoint experienced relatively little erosion. After the sediment trap had filled and the stream resumed bed-load transport across the newly formed waterfall, incision proceeded quite rapidly, with over 600 m headward migration and the formation of a 20 m deep gorge in about 4 years. Clearly, the availability of bed-load sediment can make a difference.

Sklar and Dietrich (2004) and Chatanantavet and Parker (2009) developed long-term erosion laws that describe bedrock abrasion by saltating bed-load grains. The two models are similar. The Sklar–Dietrich saltation–abrasion model describes the rate of bed incision as the product of three factors: the frequency of bed impacts per unit area (I), the volume of rock removed per impact (V), and the average fraction of the bed exposed to impact wear (F):

$$E = IVF \qquad [21]$$

An intriguing implication of saltation–abrasion theory is that there is a 'sweet spot' for erosion: too much sediment will shield the bed from wear, while too little will produce few impacts. Curiously, the saltation–abrasion model also predicts that the erosion rate can sometimes actually decrease with slope angle, because the increase in saltation hop length and therefore impact frequency outweighs the increased impact velocity. Recent work by Huda and Small (2014) suggests that this behavior may be an artifact of the assumption of a planar bed. A key frontier in the modeling of long-term bedrock erosion by impact abrasion lies in addressing the roles of bed topography and turbulent flow structures.

Each of the families of stream erosion model is successful in the sense that each predicts concave-upward river profiles. Beyond this simple test, several studies have compared the predictions of one or more models with field case studies in which the initial and/or boundary conditions are known well enough to provide a feasible test (Attal et al., 2008, 2011; Cowie et al., 2008; Duvall et al., 2004; Hobley et al., 2011; Kirby and Whipple, 2001; Lavé and Avouac, 2001; Loget et al., 2006; Snyder et al., 2000, 2003a,b; Stock and Montgomery, 1999; Tomkin et al., 2003; Tucker, 2009; Valla et al., 2010; van der Beek and Bishhop, 2003; Whittaker et al., 2007a,b, 2008; Yanites et al., 2010a). In a test case of fluvial incision into carbonate bedrock, for example, both the detachment-limited and saltation–abrasion models proved to be consistent with observations, whereas transport-limited models clearly failed (Attal et al., 2008, 2011; Cowie et al., 2008; Whittaker et al., 2007b) (**Figure 20**). On the other hand, there have also been some surprising results, in which the transport-limited theory seems to describe the incision of hard metamorphic rock (Valla et al., 2010) and detachment-limited theory fits the erosion of loose glacial deposits (Hobley et al., 2011). There are good mechanical reasons for these seemingly paradoxical results, but

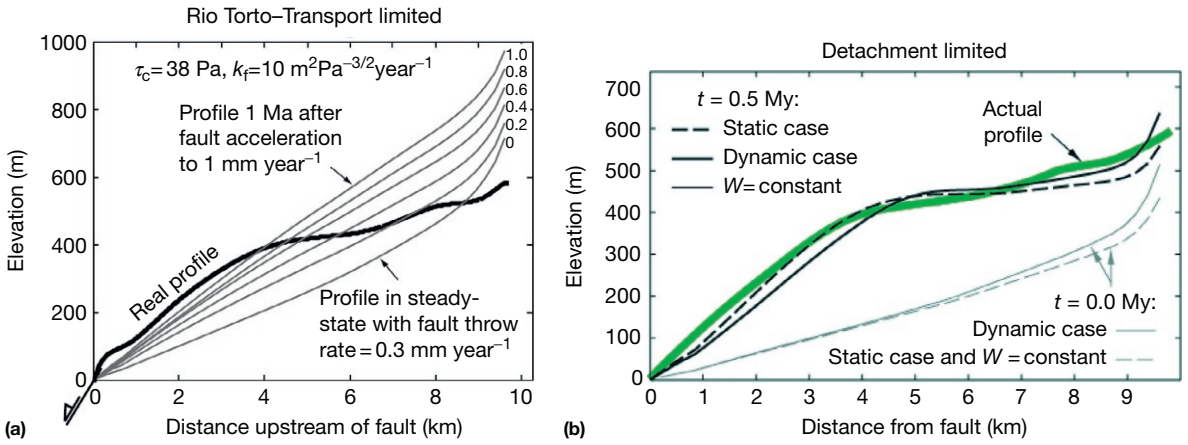

Figure 20 Comparison of observed and modeled longitudinal profiles along the Rio Torto, a bedrock stream draining an active extensional footwall in the Italian central Apennines. Convexity in the profile is interpreted as resulting from acceleration in slip rate beginning in the mid-Pleistocene (Whittaker et al., 2007b). (a) Transport-limited models fail to reproduce prominent channel convexity (reproduced from Attal M, Cowie P, Whittaker A, Hobley D, Tucker G, and Roberts G (2011) Testing fluvial erosion models using the transient response of bedrock rivers to tectonic forcing in the Apennines, Italy. *Journal of Geophysical Research* 116(F2): F02005). (b) The stream power erosion model is consistent with observed profile shape (modified from Attal M, Tucker GE, Whittaker AC, Cowie PA, and Roberts GP (2008) Modeling fluvial incision and transient landscape evolution: Influence of dynamic channel adjustment. *Journal of Geophysical Research* 113: F03013).

nonetheless, there is clearly more to be done in refining models of fluvial incision into bedrock and exploiting natural-experiment test cases.

One open question in long-term river erosion is understanding controls on channel geometry. The width of a stream is analogous to the sharpness of a knife: the narrower the channel, the more focused the friction and energy dissipation. Studies of a variety of actively incising channels reveal that channel geometry can and does vary systematically (Harbor, 1998; Montgomery and Gran, 2001) and in particular that channels tend to be narrower where the slope is steeper (Amos and Burbank, 2007; Duvall et al., 2004; Finnegan et al., 2005; Kirby and Ouimet, 2011; Lavé and Avouac, 2001; Turowski et al., 2006; Whittaker et al., 2007a; Yanites et al., 2010a). Although preliminary quantitative models for the evolution of bedrock channel shape and its influence on fluvial bedrock erosion have been suggested (Attal et al., 2008; Finnegan et al., 2005; Stark, 2006; Turowski et al., 2007, 2009; Wobus et al., 2006b; Yanites and Tucker, 2010), we still lack a comprehensive, mechanistic theory of bedrock channel geometry.

6.13.4.6 Landscape Evolution Models

The advent of geomorphic transport laws like those reviewed in the preceding section makes it possible to construct numerical models for the evolution of topography, known variously as landscape evolution models (LEMs) or surface-process models. Figures 14, 16, and 18–20 show various examples of LEM calculations. LEMs essentially help to provide a quantitative, theoretical underpinning for landscape evolution and allow one to visualize landform dynamics. Although they vary widely in their governing equations and target applications, the essence of all such models is that they compute the time evolution of topography by calculating erosion and sediment flux across a matrix of cells that represents the Earth's surface. The fundamental ingredients include a gridded (regular or irregular) representation of topography, routing of water across the terrain, conservation of sediment and/or rock mass, and a set of geomorphic transport laws to represent a particular collection of processes. LEMs have been applied to a wide variety of problems, from orogen evolution to gully network dynamics. The basis and applications of LEMs are the subject of several relatively recent review articles, to which the reader is referred (Beaumont et al., 2000; Bishop, 2007; Codilean et al., 2006; Coulthard, 2001; Martin and Church, 2004; Tucker and Hancock, 2010; van der Beek, 2012; Willgoose, 2005).

6.13.5 Feedbacks Between Erosion, Climate, and Tectonics

The exposure of high-grade metamorphic rocks at the Earth's surface testifies to the power of erosion. One of the exciting discoveries in the last few decades has been the recognition that the rearrangement of crustal mass by erosion can have a profound influence on continental dynamics. Erosion can influence crustal tectonic motion both passively, through isostatic rebound, and actively, by altering the stress field in a compressional orogen. Because climate and erosion are both influenced by topography, there is the potential for a dynamic feedback between crustal motion, climate, and surface erosion (or deposition). In this section, we explore some of the manifestations of this feedback.

6.13.5.1 Erosion and Isostasy

The isostatic response to erosional unloading represents the simplest form of erosion–tectonic feedback. It is a feedback with some fascinating consequences for landscape evolution. When erosional loading is focused in a particular area, such as a large river or glacier valley, the surrounding region will rise isostatically. Molnar and England (1990) hypothesized that

this phenomenon could lead to the uplift of mountain peaks when the valleys between them are deeply eroded. Because valley deepening is one potential outcome of climate change, there exists a potential mechanism for climatically driven surface uplift of summits. The actual magnitude and occurrence of this effect are matters of debate (Brocklehurst and Whipple, 2002; Gilchrist et al., 1994a; Lane et al., 2008; Menéndez et al., 2008; Montgomery, 1994; Montgomery and Greenberg, 2000; Pelletier, 2004; Small and Anderson, 1995; Stern et al., 2005; Whipple et al., 1999), but there is little doubt that the incision of a major valley can lead to some degree of isostatic surface uplift of the surrounding terrain.

Rifted continental margins present a fascinating case study in erosion–isostasy feedback. Relatively young rifts, such as the Eastern Africa and Red Sea extensional regions, have asymmetrical rift shoulders that presumably reflect thermal isostatic uplift. Many older passive margins show a similar geometry, with a seaward-facing escarpment(s) and an inland plateau that slopes gently toward the interior (Ollier, 1985; Weissel and Karner, 1989). Thermochronology data from passive margins such as Southern Africa (Brown et al., 1990, 2002), southeastern Brazil (Gallagher et al., 1994, 1995), eastern Australia (Moore et al., 1986), Western India (Widdowson, 1997), and the Red Sea (Abbate et al., 2002; Bohannon et al., 1989) show a postrift phase of substantial erosion on the seaward side of the escarpment (Gallgher and Brown, 1997). This observation supports the hypothesis that upwarps and escarpments along ancient rifted margins arise from an erosion–isostasy feedback: erosion focused along the rift leads to isostatic uplift that is focused along the margin, such that the area inland of an escarpment is tilted toward the interior (Gilchrist and Summerfield, 1990; Ollier, 1985; Partridge and Maud, 1987; Stüwe, 1991; ten Brink and Stern, 1992; van der Beek et al., 1995). This tilting inhibits drainage capture from the interior and can therefore help sustain a drainage divide that parallels the margin (Gilchrist et al., 1994b; Kooi and Beaumont, 1994; Sacek et al., 2012; Tucker and Slingerland, 1994; van der Beek et al., 2002). It is widely assumed that margin-parallel drainage divides originate during the rift phase, though Sacek et al. (2012) proposed that passive-margin escarpments and drainage divides may actually be the legacy of an interior flexural bulge, rather than the initial rift shoulder itself.

6.13.5.2 Feedback and Steady State in Compressional Orogens

At the time of the discovery of plate tectonics, it was widely believed that erosion was a prolonged but tectonically inconsequential aftermath of mountain building. For example, Schumm (1963) concluded that rates of tectonic motion generally outpace rates of erosion, suggesting that "rapid orogeny [is] accompanied and followed by relatively slower denudation." Evidence that began to emerge in the 1980s, however, changed that view. Adams (1980) was among the first to present evidence for a potential balance between erosion and rock uplift, based on a case study of the New Zealand Southern Alps. Adams noted that an estimated 25 km of exhumation produced only about 2.5 km of topographic relief, implying that some 90% of the advected rock has been eroded. Meanwhile, as we saw in **Section 6.13.3.1**, it was becoming increasingly clear that the rate of denudation is strongly sensitive to relief, implying that there ought to be a natural tendency for rates of erosion to come into balance with rock uplift. As the number and quality of low-temperature thermochronology analyses from active orogens grew, it became increasingly apparent that sustained rates of denudation could be substantially higher than was previously imagined: high enough, in fact, to rival even the fastest-growing orogens. When thermochronometric methods such as fission-track and (U–Th)/He analyses are applied to active orogens, they often show that rocks found at the surface today were exhumed from depths of 2–4 km within the past several million years – within the lifetime of the orogen. For example, apatite fission-track samples from northern Taiwan reported by Willett et al. (2003) implied the removal of 2–4 km of rock in less than a million years and nearly 25 km over the short life of the orogen. Studies such as this one suggested that, for many active mountain ranges, the amount of rock eroded is similar to the amount added over the system's lifetime, implying that some form of dynamic equilibrium – whether in flux, topography, temperature, or exhumation (Willett and Brandon, 2002) – is likely.

The realization that erosion can compete with tectonics inspired modeling studies designed to explore how erosion influences orogen mechanics. The critically tapered wedge model of Davis et al. (1983), for example, predicts that erosion plays a fundamental role in setting the wedge geometry and influencing deformation patterns. One fascinating aspect of steady states in orogens is the potential for feedback between tectonics and climate. Beaumont et al. (1992) and Willett et al. (1993) used finite-element deformation models to explore the evolution of a hypothetical orogen undergoing surface erosion. Inspired by the example of the New Zealand Southern Alps, where the rain shadow effect produces an enormous difference in precipitation between the windward and leeward sides, they compared models in which erosion is concentrated on one or the other side of the evolving orogen. The calculations predicted striking differences in topography, deformation patterns, and metamorphic grades. In essence, their theory predicts that when a growing mountain chain harvests water from the atmosphere, it creates an erosional asymmetry powerful enough to alter the motion of rocks deep in the crust. Hoffman and Grotzinger (1993) proposed that the legacy of ancient rain shadow effects remains visible in the metamorphic roots of ancient orogens in Eastern North America.

Analytic theory of eroding critical wedges also makes the startling prediction that climate can influence the width of an active orogen (Hilley and Strecker, 2004; Roe et al., 2008; Whipple and Meade, 2004). In a steady-state critical wedge, the net erosional mass flux (not including sediment recycled back into the wedge) must balance the convergence flux. When a wet climate or weak rocks make erosion relatively efficient, this balance can be achieved with a relatively narrow mountain belt. When the climate and/or rocks are poorly conducive to erosion, a wider orogen is required to achieve the same balance. One fascinating implication is that a change in climate or exposed rock type can drive dynamic widening or narrowing (e.g., Thomson et al., 2010), with consequent shifts in the loci of deformation (Upton et al., 2009).

6.13.5.3 Tectonic Aneurysms

Some of the highest long-term erosion rates in the world are found at the opposite ends of the Himalayan orogen: in the vicinity of the Nanga Parbat massif in the west and the Namcha Barwa peak in the east. Zeitler et al. (2001b) drew attention to several common aspects of these two Himalayan syntaxes. In both regions, powerful rivers, namely, the Tsangpo in the east and the Indus in the west, sweep around the adjacent massif. Each has over 6 km of relief between peak and river valley, over a horizontal distance of <30 km. The antiformal massifs are made of deeply and rapidly exhumed igneous and metamorphic rocks. In and around Nanga Parbat, for example, 15–20 km of rock has been exhumed in less than three million years. Zeitler et al. (2001a,b) proposed that these features are the hallmarks of what they termed a 'tectonic aneurysm' (**Figure 21**). Intense erosion by the major orogenic river and its tributaries leads to focused inflow and uplift of hot, weak crustal material. The process, according to their interpretation, is enhanced by rheological feedback in which focused erosion effectively weakens the surrounding rocks by removing mechanically strong upper crustal material, drawing in hot, lower crustal rock and raising the local isotherms (Koons et al., 2002). This upward deflection of the isotherms promotes rapid, localized deformation. The resulting fast rock uplift enhances the relief that sustains rapid erosion. Thus, the Himalayan syntaxes appear to offer two particularly striking examples of erosion–tectonic feedback.

6.13.6 Tectonics from Topography

Tectonic motion is hard to measure. Thanks to GPS technology, we can detect displacements on the order of centimeters accumulated over years to decades, but longer-term motion usually has to be inferred indirectly. The use of thermochronology, which can record cooling due to erosional exhumation, is a case in point: typically, cooling is assumed to have occurred because vertical motion ('uplift') of rocks created high relief and hence rapid unroofing (England and Molnar, 1990).

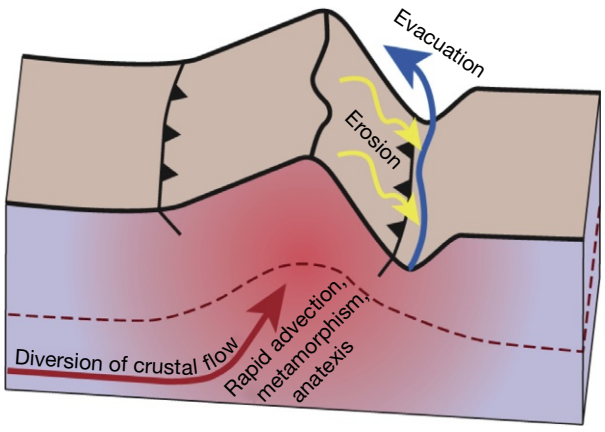

Figure 21 Cartoon illustrating the concept of a tectonic aneurysm. Reproduced from Zeitler PK, et al. (2001) Erosion, Himalayan geodynamics, and the geomorphology of metamorphism. *GSA Today* 11(1): 4–9.

The discovery that rates of erosion and rock uplift have a tendency to come into balance opened up another potential avenue for inferring rates tectonic motion: use the topography itself to deduce variations in rate of erosion, by measuring variations in the slopes of rivers. As discussed earlier, the rate of river incision into bedrock is strongly correlated with unit stream power and boundary shear stress, which in turn are closely linked with channel-bed slope, S, and drainage basin area, A (eqn [17]). Both of the latter quantities are relatively straightforward to measure from a DEM.

Imagine a landscape in which the rate of stream erosion, E, is roughly equal to the long-term rate of rock uplift, U. Stream-incision theory (eqn [18]) leads us to expect that the rock uplift rate in such a situation should be related to slope and drainage basin area by

$$S = \left(\frac{U + \Phi_c}{K}\right) A^{-m/n} \qquad [22]$$

The ratio m/n is equivalent to the concavity index, θ, while the factor in parentheses corresponds to the steepness index, k_s, and represents a measure of channel gradient that has been normalized to account for variations in basin size (Whipple and Tucker, 1999; Willgoose, 1994; Willgoose et al., 1991a). Both parameters can be estimated by a curve-fit to slope and area data derived from digital elevation data (e.g., Snyder et al., 2000). The procedure is reviewed by Wobus et al. (2006a). The steepness index depends on rock resistance, mean annual runoff, runoff variability, channel geometry (including roughness), bed sediment grain size (via Φ_c), and rock uplift rate (if the assumption of uplift–erosion balance is satisfied) (Tucker, 2004). Note that often, the threshold factor Φ_c is assumed to be negligible, though the finding of a strongly nonlinear relationship between gradient and incision rate (noted in **Section 6.13.3.1**) casts doubt on this assumption.

One application of slope–area analysis is to generate maps showing the spatial distribution of steepness index (**Figure 22**). If the climate and the rock and alluvium are spatially uniform, then any spatial variations in k_s ought to reflect variations in erosion rate, which in turn might correlate closely with rock uplift rate. Tests of this approach in regions with well-constrained tectonics have shown that the expected correlation between k_s and U shows up quite clearly (DiBiase et al., 2010; Duvall et al., 2004; Kirby and Whipple, 2001; Snyder et al., 2000, 2003a; Whittaker et al., 2008). Inspired by these success stories, quantitative stream-profile analysis has been used to identify patterns of rock uplift in a variety of active tectonic settings (Harkins et al., 2007; Hu et al., 2010; Kirby et al., 2003, 2007; Papanikolaou et al., 2012; Ponza et al., 2010; Robl et al., 2008; Shahzad et al., 2009; Wobus et al., 2003; Yanites et al., 2010a; Zhang et al., 2011). In addition to using steepness index as an indicator of relative erosion rates, the concavity index can also provide information about the geometry of deformation: when incision rates are greater in the headwaters, a profile will tend to be more concave, and vice versa (Kirby and Whipple, 2001).

In addition to providing information about the spatial distribution of incision and perhaps also rock uplift, stream-profile analysis can lend insight into timing and dynamics. Models for detachment-limited fluvial incision predict that abrupt changes in tectonic motion will produce

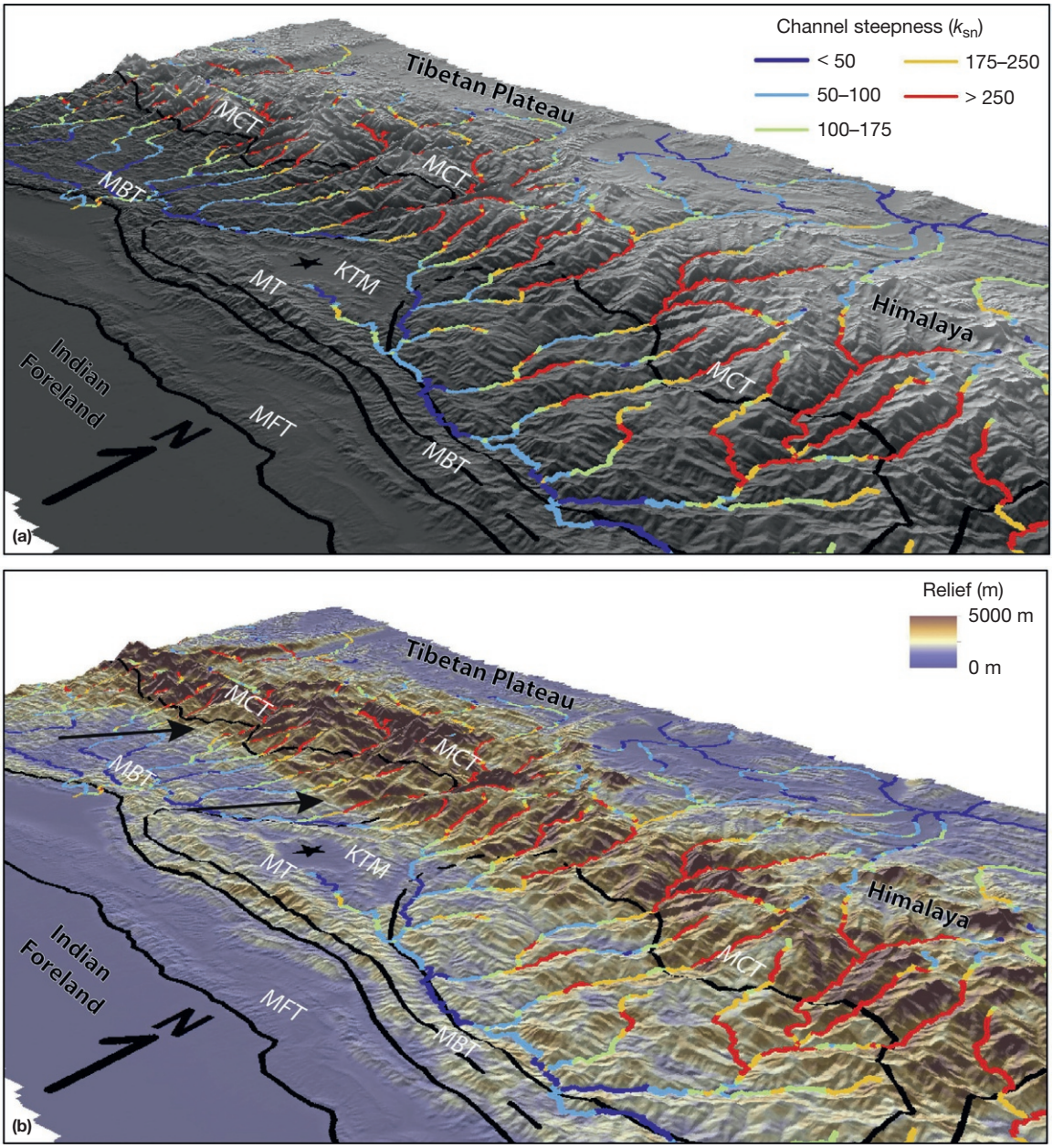

Figure 22 Perspective image highlighting steepness index values along channels in the central Nepal Himalayas (reproduced from Kirby E and Whipple KX (2012) Expression of active tectonics in erosional landscapes. *Journal of Structural Geology* 44(5): 4e75) (1.5 × vertical exaggeration; KTM = Kathmandu). White labels denote major thrusts: Main Central Thrust (MCT), Mahabharat Thrust (reference concavity = 0.4(MT), Main Boundary Thrust (MBT), and Main Frontal Thrust (MFT). (a) Topography and channel steepness index 5). (b) Topography color-coded by local relief within 2.5 km radius.

corresponding steps in a channel profile that migrate upstream (Tucker and Whipple, 2002; Whipple and Tucker, 1999, 2002). In particular, a rapid increase in the rate of rock uplift relative to local base level is predicted to generate convex-upward channel segments (knickzones), and indeed, such features have been observed where independent data on tectonic history imply that they should (e.g., Attal et al., 2011; Whittaker et al., 2007b). In essence, eqn [17] implies that the history of base-level motion is recorded in a train of upstream-traveling erosional waves. Patterns of gradient variation along channel profiles have been used as evidence of transient geomorphic and tectonic history in a variety of settings (Antón et al., 2012; Berlin and Anderson, 2009; Boulton and Whittaker, 2009; Castillo et al., 2012; Cook et al., 2009; Densmore et al., 2007; Foster and Kelsey, 2012; Hoke et al., 2007; Kirby and Whipple, 2012; Kirby et al., 2007; Miller et al., 2012, 2013; Molin et al., 2012; Morell et al., 2012; Olivetti et al., 2012; Pederson and Tressler, 2012; Roberts and White, 2010; Schildgen et al., 2012; Yildirim et al., 2011).

One limitation with slope–area analysis is that it effectively ignores variations in channel width, which can influence hydraulic power. For example, a case study of the Peikang River in west-central Taiwan showed that millennial-scale incision rate correlates closely with stream power and shear stress but that variations in these hydraulic quantities are more strongly reflected in width than in gradient (Yanites et al., 2010a). There is an interesting frontier to be explored in combining slope–area analysis with estimates of channel width derived from DEMs.

6.13.7 Summary, Retrospect, and Prospect

The Earth's combination of plate tectonics and a vigorous erosional engine makes our planet different from other bodies in the solar system. Continental crust can wear down at rates that range from millimeters to tens of meters per millennium, comparable to rates of crustal thickening and rock uplift. The rate of erosional unroofing depends strongly on topographic relief. It turns out that the relief–erosion relationship can be strongly nonlinear, such that in mountainous terrain, a relatively modest increase in relief can bring about a large increase in denudation rate. Because of this strong sensitivity to relief, there is a natural tendency for tectonically active landscapes to approach a state of balance between erosion and rock uplift. Thermochronology data from active orogens bear this out by demonstrating that exhumation and accretion are often of comparable magnitude. The similarity in rates of denudation and rock uplift, together with the importance of gravitational forces in governing crustal motion, means that erosional exhumation is not a geologic afterthought but rather an integral part of a coupled system. Examples of feedbacks between erosion and tectonics include isostasy on continental margins, climate controls on the width of active tectonic wedges, and the 'tectonic aneurysms' of the Himalayan syntaxes.

Climate plays a central role in landscape evolution by supplying water and energy and by nourishing biota. There is no doubt that changes in climate over time can play a major role in setting rates and patterns of erosion in specific circumstances, such as the incision of deep glacial valleys during ice ages. The hypothesis that global climate change caused a worldwide increase in sediment volume during the late Cenozoic is compelling but remains debated. Here, it is not so much a question of whether the Earth's climate plays a role in landscape evolution; clearly, our planet has a surface environment that is far more conducive to weathering and erosion than, say, the surface of Mars. Rather, it is a question of how much variation in geomorphic effectiveness there is among the Earth's different climate states (or oscillations between climate states), both present and past. To answer the question, we need to understand more deeply the mechanistic links between climate variables and geomorphic processes.

Glaciation provides one of the most striking examples of how climate can influence erosional processes. Mountain ranges often show a striking correlation between peak elevation and the glacial equilibrium-line altitude, consistent with the hypothesis that glacial erosion is powerful enough to prevent mountains from rising much higher than this. On the other hand, the null hypothesis – that higher land-surface altitude leads to a slower lapse rate and hence a higher ELA – has yet to be convincingly rejected.

Lithology is an obvious control on landscape evolution, yet we know surprisingly little at a quantitative level about its effects and importance. Erosion is often described in terms of driving and resisting forces, with most research efforts focused on the driving forces. There are hints, however, that differences in material properties could account for orders of magnitude of variation in resisting force. There is already one aspect of geomaterials – the grain size of fragmented rock – that is well known as a first-order control on resistance to detachment. Lithology, long relegated as a detail to be sorted out later, may well turn out to be a major character. Moreover, material properties are not truly independent variables; because rock strength depends partly on tectonic history and on topographic stress, there is a potential for feedback between tectonics, lithology, and erosion. One of the current challenges lies simply in identifying what are the key quantifiable properties that determine rock resistance to weathering and erosion and how to measure these.

Quantitative, theoretical understanding of landscape evolution is expressed by geomorphic transport laws. Significant progress has been made in formulating and testing transport laws for a variety of common processes, most notably soil creep and stream incision. For many processes, the transport laws contain 'black boxes' that still need to be opened. For other processes, such as those pertaining to bedrock landscapes and debris flows, geomorphic transport laws still need to be formulated and tested.

Geomorphic transport laws provide the process ingredients for comprehensive numerical models of landscape evolution. These models provide the 'theory engines' for landscape evolution. The current generation of models succeeds in capturing many common aspects of erosional topography, such as dendritic drainage networks, hillslope–valley topography, concave-upward channel profiles, knickpoints, convex-upward and planar hillslopes, and alluvial fans. There remains a need for more quantitative testing of landscape models, both through testing of individual geomorphic transport laws and by comparison to natural-experiment case studies.

Acknowledgments

The author is grateful for research support from the National Science Foundation (EAR-1246546, ACI-1147454, and EAR-0952247). Niels Hovius kindly provided a review that led to an improved manuscript and Gerard Roe provided helpful ideas and references on lapse rates and glacial buzzsaws.

References

Aalto R, Dunne T, and Guyot J (2006) Geomorphic controls on Andean denudation rates. *Journal of Geology* 114(1): 85–99.

Abbate E, Balestrieri ML, and Bigazzi G (2002) Morphostructural development of the Eritrean rift flank (southern Red Sea) inferred from apatite fission track analysis. *Journal of Geophysical Research* 107(B11): 2319.

Adams J (1980) Contemporary uplift and erosion of the Southern Alps, New Zealand. *Geological Society of America Bulletin* 91(1 Part II): 1–114.

Ahnert F (1970) Functional relationships between denudation, relief, and uplift in large, midlatitude drainage basins. *American Journal of Science* 268(3): 243.

Ahnert F (1976) Brief description of a comprehensive three-dimensional process-response model of landform development. *Zeitschrift für Geomorfologie, Supplementband* 25: 29–49.

Amos CB and Burbank DW (2007) Channel width response to differential uplift. *Journal of Geophysical Research: Earth Surface (2003–2012)* 112(F2): F02010, http://dx.doi.org/10.1029/2006JF000672.

Amundson J and Iverson N (2006) Testing a glacial erosion rule using hang heights of hanging valleys, Jasper National Park, Alberta, Canada. *Journal of Geophysical Research: Earth Surface (2003–2012)* 111(F1): F01020, http://dx.doi.org/10.1029/2005JF000359.

Anders A, Mitchell S, and Tomkin J (2010) Cirques, peaks, and precipitation patterns in the Swiss Alps: Connections among climate, glacial erosion, and topography. *Geology* 38(3): 239–242.

Anderson R (1998) Near-surface thermal profiles in alpine bedrock: Implications for the frost weathering of rock. *Arctic and Alpine Research* 30(4): 362–372.

Anderson S, Anderson R, and Tucker G (2012a) Landscape scale linkages in critical zone evolution. *Comptes Rendus Geoscience* 344: 586–596.

Anderson RS, Anderson SP, and Tucker GE (2012b) Rock damage and regolith transport by frost: An example of climate modulation of the geomorphology of the critical zone. *Earth Surface Processes and Landforms* 38(3): 299–316.

Anderson RS, Dühnforth M, Colgan W, and Anderson L (2012c) Far-flung moraines: Exploring the feedback of glacial erosion on the evolution of glacier length. *Geomorphology* 179: 269–285.

Anderson RS, Molnar P, and Kessler MA (2006) Features of glacial valley profiles simply explained. *Journal of Geophysical Research, Earth Surface* 111(F1): F01004. http://dx.doi.org/10.1029/2005JF000344.

Andrews D and Bucknam RC (1987) Fitting degradation of shoreline scarps by a nonlinear diffusion model. *Journal of Geophysical Research* 92(B12): 12857–12867.

Antón L, Rodés A, De Vicente G, et al. (2012) Quantification of fluvial incision in the Duero Basin (NW Iberia) from longitudinal profile analysis and terrestrial cosmogenic nuclide concentrations. *Geomorphology* 165: 50–61.

Attal M, Cowie P, Whittaker A, Hobley D, Tucker G, and Roberts G (2011) Testing fluvial erosion models using the transient response of bedrock rivers to tectonic forcing in the Apennines, Italy. *Journal of Geophysical Research* 116(F2): F02005.

Attal M and Lavé J (2006) Changes of bedload characteristics along the Marsyandi River (Central Nepal): Implications for understanding hillslope sediment supply, sediment load evolution along fluvial networks, and denudation in active orogenic belts. *GSA Special Papers* 398: 143–171.

Attal M and Lavé J (2009) Pebble abrasion during fluvial transport: Experimental results and implications for the evolution of the sediment load along rivers. *Journal of Geophysical Research* 114: F04023.

Attal M, Lavé J, and Masson J (2006) New facility to study river abrasion processes. *Journal of Hydraulic Engineering* 132(6): 624–628.

Attal M, Tucker GE, Whittaker AC, Cowie PA, and Roberts GP (2008) Modeling fluvial incision and transient landscape evolution: Influence of dynamic channel adjustment. *Journal of Geophysical Research* 113: F03013.

Augustinus PC (1995) Glacial valley cross-profile development: The influence of in situ rock stress and rock mass strength, with examples from the Southern Alps, New Zealand. *Geomorphology* 14(2): 87–97.

Baldwin J, Whipple K, and Tucker G (2003) Implications of the shear stress river incision model for the timescale of postorogenic decay of topography. *Journal of Geophysical Research* 108(B3): 2158. http://dx.doi.org/10.1029/2001JB000550.

Beaumont C, Fullsack P, and Hamilton J (1992) Erosional control of active compressional orogens. In: KR McClay (ed.) *Thrust Tectonics*, vol. 99, pp. 1–18. Chapman & Hall.

Beaumont C, Kooi H, and Willett S (2000) Coupled tectonic-surface process models with applications to rifted margins and collisional orogens. In: Summerfield MA (ed.) *Geomorphology and Global Tectonics*, pp. 29–56. Chichester: Wiley.

Befus K, Sheehan A, Leopold M, Anderson S, and Anderson R (2011) Seismic constraints on critical zone architecture, Boulder Creek Watershed, Front Range, Colorado. *Vadose Zone Journal* 10(3): 915–927.

Berlin MM and Anderson RS (2009) Steepened channels upstream of knickpoints: Controls on relict landscape response. *Journal of Geophysical Research: Earth Surface (2003–2012)* 114(F3): F03018, http://dx.doi.org/10.1029/2008JF001148.

Bierman P and Caffee M (2002) Cosmogenic exposure and erosion history of Australian bedrock landforms. *Geological Society of America Bulletin* 114(7): 787–803.

Bierman P and Nichols K (2004) Rock to sediment-slope to sea with ^{10}Be-rates of landscape change. *Annual Review of Earth and Planetary Sciences* 32: 215–255.

Bierman P and Steig E (1996) Estimating rates of denudation using cosmogenic isotope abundances in sediment. *Earth Surface Processes and Landforms* 21(2): 125–139.

Binnie SA, Phillips WM, Summerfield MA, and Fifield LK (2007) Tectonic uplift, threshold hillslopes, and denudation rates in a developing mountain range. *Geology* 35(8): 743–746. http://dx.doi.org/10.1130/G23641A.1.

Birnir B, Smith TR, and Merchant GE (2001) The scaling of fluvial landscapes. *Computers and Geosciences* 27(10): 1189–1216.

Bishop P (2007) Long-term landscape evolution: Linking tectonics and surface processes. *Earth Surface Processes and Landforms* 32: 329–365.

Black T and Montgomery D (1991) Sediment transport by burrowing mammals, Marin County, California. *Earth Surface Processes and Landforms* 16(2): 163–172.

Bohannon RG, Naeser CW, Schmidt DL, and Zimmermann RA (1989) The timing of uplift, volcanism, and rifting peripheral to the Red Sea: A case for passive rifting? *Journal of Geophysical Research: Solid Earth (1978–2012)* 94(B2): 1683–1701.

Booth A and Roering J (2011) A 1-d mechanistic model for the evolution of earthflow-prone hillslopes. *Journal of Geophysical Research* 116(F4): F04021.

Boulton S and Whittaker A (2009) Quantifying the slip rates, spatial distribution and evolution of active normal faults from geomorphic analysis: Field examples from an oblique-extensional Graben, southern Turkey. *Geomorphology* 104(3–4): 299–316.

Braun J, Heimsath AM, and Chappell J (2001) Sediment transport mechanisms on soil-mantled hillslopes. *Geology* 29: 683–686.

Braun J, Zwartz D, and Tomkin JH (1999) A new surface-processes model combining glacial and fluvial erosion. *Annals of Glaciology* 28(1): 282–290.

Brocklehurst S and Whipple K (2002) Glacial erosion and relief production in the eastern Sierra Nevada, California. *Geomorphology* 42(1): 1–24.

Brown RW, Rust DJ, Summerfield MA, Gleadow AJ, and Wit MC (1990) An early cretaceous phase of accelerated erosion on the south-western margin of Africa: Evidence from apatite fission track analysis and the offshore sedimentary record. *Nuclear Tracks and Radiation Measurements* 17: 339–350.

Brown E, Stallard R, Larsen M, Raisbeck G, and Yiou F (1995) Denudation rates determined from the accumulation of in situ-produced ^{10}Be in the Luquillo Experimental Forest, Puerto Rico. *Earth and Planetary Science Letters* 129(1): 193–202.

Brown RW, Summerfield MA, and Gleadow AJ (2002) Denudational history along a transect across the Drakensberg escarpment of southern Africa derived from apatite fission track thermochronology. *Journal of Geophysical Research* 107(B12): 2350.

Brozović N, Burbank D, and Meigs A (1997) Climatic limits on landscape development in the northwestern Himalaya. *Science* 276(5312): 571–574.

Büdel J, Fischer L, and Busche D (1982) *Climatic Geomorphology*. Princeton: Princeton University Press.

Bull W (1991) *Geomorphic Responses to Climatic Change*. New York, NY: Oxford University Press.

Burbank D, Leland J, Fielding E, et al. (1996) Bedrock incision, rock uplift and threshold hillslopes in the northwestern Himalayas. *Nature* 379(6565): 505–510.

Burke B, Heimsath A, and White A (2007) Coupling chemical weathering with soil production across soil-mantled landscapes. *Earth Surface Processes and Landforms* 32(6): 853–873.

Carson M and Petley D (1970) The existence of threshold hillslopes in the denudation of the landscape. *Transactions of the Institute of British Geographers* 49: 71–95.

Castillo M, Bishop P, and Jansen JD (2012) Knickpoint retreat and transient bedrock channel morphology triggered by base-level fall in small bedrock river catchments: The case of the Isle of Jura, Scotland. *Geomorphology* 181–182: 1–9.

Chase CG (1992) Fluvial landsculpting and the fractal dimension of topography. *Geomorphology* 5: 39–57.

Chatanantavet P and Parker G (2009) Physically based modeling of bedrock incision by abrasion, plucking, and macroabrasion. *Journal of Geophysical Research: Earth Surface (2003–2012)* 114(F4): F04018, http://dx.doi.org/10.1029/2008JF001044.

Clarke B and Burbank D (2010) Bedrock fracturing, threshold hillslopes, and limits to the magnitude of bedrock landslides. *Earth and Planetary Science Letters* 297(3): 577–586.

Clarke B and Burbank D (2011) Quantifying bedrock-fracture patterns within the shallow subsurface: Implications for rock mass strength, bedrock landslides, and erodibility. *Journal of Geophysical Research* 116(F4): F04009.

Codilean AT, Bishop P, and Hoey TB (2006) Surface process models and the links between tectonics and topography. *Progress in Physical Geography* 30: 307–333.

Cohen S, Willgoose G, and Hancock G (2009) The mARM spatially distributed soil evolution model: A computationally efficient modeling framework and analysis of hillslope soil surface organization. *Journal of Geophysical Research* 114(F3): F03001.

Colaiori F, Flammini A, Maritan A, and Banavar JR (1997) Analytical and numerical study of optimal channel networks. *Physical Review E* 55(2): 1298.

Collins D and Bras R (2010) Climatic and ecological controls of equilibrium drainage density, relief, and channel concavity in dry lands. *Water Resources Research* 46(4): W04508.

Collins D, Bras R, and Tucker G (2004) Modeling the effects of vegetation–erosion coupling on landscape evolution. *Journal of Geophysical Research, Earth Surface* 109(F3): F03004. http://dx.doi.org/10.1029/2003JF000028.

Cook KL, Turowski JM, and Hovius N (2013) A demonstration of the importance of bedload transport for fluvial bedrock erosion and knickpoint propagation. *Earth Surface Processes and Landforms* 38(7): 683–695.

Cook KL, Whipple KX, Heimsath AM, and Hanks TC (2009) Rapid incision of the Colorado River in Glen Canyon – Insights from channel profiles, local incision rates, and modeling of lithologic controls. *Earth Surface Processes and Landforms* 34(7): 994–1010.

Coulthard TJ (2001) Landscape evolution models: A software review. *Hydrological Processes* 15: 165–173.

Cowie P, Whittaker A, Attal M, Roberts G, Tucker G, and Ganas A (2008) New constraints on sediment-flux-dependent river incision: Implications for extracting tectonic signals from river profiles. *Geology* 36(7): 535.

Cuffey KM and Paterson W (2010) *The Physics of Glaciers*. Amsterdam: Academic Press.

Culling W (1960) Analytical theory of erosion. *Journal of Geology* 68: 336–344.

Culling W (1963) Soil creep and the development of hillside slopes. *Journal of Geology* 71: 127–161.

Dadson SJ, et al. (2003) Links between erosion, runoff variability and seismicity in the Taiwan Orogen. *Nature* 426: 648–651.

Dadson S, et al. (2004) Earthquake-triggered increase in sediment delivery from an active mountain belt. *Geology* 32(8): 733–736.

Davis D, Suppe J, and Dahlen F (1983) Mechanics of fold-and-thrust belts and accretionary wedges. *Journal of Geophysical Research: Solid Earth (1978–2012)* 88(B2): 1153–1172.

Davis W, et al. (1892) The convex profile of bad-land divides. *Science (New York, NY)* 20(508): 245.

Davy P and Lague D (2009) Fluvial erosion/transport equation of landscape evolution models revisited. *Journal of Geophysical Research, Earth Surface* 114(F3): F03007.

de Gennes P-G (2000) Effect of topographic convergence on erosion processes. *Journal of Physics: Condensed Matter* 12(8A): A499.

Densmore A, Gupta S, Allen P, and Dawers N (2007) Transient landscapes at fault tips. *Journal of Geophysical Research, Earth Surface* 112: F03S08.

Densmore A, Hetzel R, Ivy-Ochs S, Krugh W, Dawers N, and Kubik P (2009) Spatial variations in catchment-averaged denudation rates from normal fault footwalls. *Geology* 37(12): 1139–1142.

DiBiase R, Heimsath A, and Whipple K (2012) Hillslope response to tectonic forcing in threshold landscapes. *Earth Surface Processes and Landforms* 37: 855–865.

DiBiase R and Whipple K (2011) The influence of erosion thresholds and runoff variability on the relationships among topography, climate, and erosion rate. *Journal of Geophysical Research* 116(F4): F04036.

DiBiase R, Whipple K, Heimsath A, and Ouimet W (2010) Landscape form and millennial erosion rates in the San Gabriel Mountains, CA. *Earth and Planetary Science Letters* 289(1–2): 134–144.

Dietrich WE, Bellugi DG, Sklar LS, Stock JD, Heimsath AM, and Roering JJ (2003) Geomorphic transport laws for predicting landscape form and dynamics. In: Wilcock P and Iverson R (eds.) *Prediction in Geomorphology. Geophysical Monograph Series*, vol. 135. Washington, DC: AGU. http://dx.doi.org/10.1029/135GM09.

Dietrich W, Wilson C, Montgomery D, and McKean J (1993) Analysis of erosion thresholds, channel networks, and landscape morphology using a digital terrain model. *Journal of Geology* 101(2): 259–278.

Dietrich W, Wilson C, Montgomery D, McKean J, and Bauer R (1992) Erosion thresholds and land surface morphology. *Geology* 20(8): 675.

Dixon J, Heimsath A, Kaste J, and Amundson R (2009) Climate-driven processes of hillslope weathering. *Geology* 37(11): 975–978.

Dixon J and McLaren S (2009) Duricrusts. In: Parsons AJ and Abrahams AD (eds.) *Geomorphology of Desert Environments*, pp. 123–151. Springer.

Dühnforth M, Anderson R, Ward D, and Stock G (2010) Bedrock fracture control of glacial erosion processes and rates. *Geology* 38(5): 423–426.

Dunne T (1991) Stochastic aspects of the relations between climate, hydrology and landform evolution. *Transactions of Japanese Geomorphological Union* 12: 1–24.

Duvall A, Kirby E, and Burbank D (2004) Tectonic and lithologic controls on bedrock channel profiles and processes in coastal California. *Journal of Geophysical Research* 109(F3): F03002.

Egholm D, Nielsen S, Pedersen VK, and Lesemann J-E (2009) Glacial effects limiting mountain height. *Nature* 460(7257): 884–887.

Egholm D, Pedersen VK, Knudsen MF, and Larsen NK (2012) On the importance of higher order ice dynamics for glacial landscape evolution. *Geomorphology* 141: 67–80.

England P and Molnar P (1990) Surface uplift, uplift of rocks, and exhumation of rocks. *Geology* 18: 1173.

Errera M and Bejan A (1998) Deterministic tree networks for river drainage basins. *Fractals* 6(03): 245–261.

Finnegan NJ, Roe G, Montgomery DR, and Hallet B (2005) Controls on the channel width of rivers: Implications for modeling fluvial incision of bedrock. *Geology* 33(3): 229–232.

Flint J (1974) Stream gradient as a function of order, magnitude, and discharge. *Water Resources Research* 10(5): 969–973.

Foster D, Brocklehurst S, and Gawthorpe R (2008) Small valley glaciers and the effectiveness of the glacial buzzsaw in the northern Basin and Range, USA. *Geomorphology* 102(3): 624–639.

Foster MA and Kelsey HM (2012) Knickpoint and knickzone formation and propagation, South Fork Eel River, northern California. *Geosphere* 8(2): 403–416.

Foufoula-Georgiou E, Ganti V, and Dietrich W (2010) A nonlocal theory of sediment transport on hillslopes. *Journal of Geophysical Research* 115: F00A16.

Fowler A, Kopteva N, and Oakley C (2007) The formation of river channels. *SIAM Journal on Applied Mathematics* 67(4): 1016–1040.

Fuller C, Willett S, Fisher D, and Lu C (2006) A thermomechanical wedge model of Taiwan constrained by fission-track thermochronometry. *Tectonophysics* 425(1): 1–24.

Furbish D and Haff P (2010) From divots to swales: Hillslope sediment transport across divers length scales. *Journal of Geophysical Research* 115(F3): F03001.

Furbish D, Haff P, Dietrich W, and Heimsath A (2009) Statistical description of slope-dependent soil transport and the diffusion-like coefficient. *Journal of Geophysical Research* 114: F00A05.

Furbish D, Hamner K, Schmeeckle M, Borosund M, and Mudd S (2007) Rain splash of dry sand revealed by high-speed imaging and sticky paper splash targets. *Journal of Geophysical Research* 112: F01001.

Gabet E, Pratt-Sitaula B, and Burbank D (2004) Climatic controls on hillslope angle and relief in the Himalayas. *Geology* 32(7): 629–632.

Gabet E, Reichman O, and Seabloom E (2003) The effects of bioturbation on soil processes and sediment transport. *Annual Review of Earth and Planetary Sciences* 31(1): 249–273.

Gaillardet J, Dupré B, Louvat P, and Allegre C (1999) Global silicate weathering and CO_2 consumption rates deduced from the chemistry of large rivers. *Chemical Geology* 159(1): 3–30.

Gallagher K, Hawkesworth C, and Mantovani M (1994) The denudation history of the onshore continental margin of SE Brazil inferred from apatite fission track data. *Journal of Geophysical Research: Solid Earth (1978–2012)* 99(B9): 18117–18145.

Gallagher K, Hawkesworth C, and Mantovani M (1995) Denudation, fission track analysis and the long-term evolution of passive margin topography: Application to the southeast Brazilian margin. *Journal of South American Earth Sciences* 8(1): 65–77.

Gallgher K and Brown R (1997) The onshore record of passive margin evolution. *Journal of the Geological Society* 154(3): 451–457.

Gasparini N, Tucker G, and Bras R (1999) Downstream fining through selective particle sorting in an equilibrium drainage network. *Geology* 27(12): 1079.

Gasparini N, Tucker G, and Bras R (2004) Network-scale dynamics of grain-size sorting: Implications for downstream fining, stream-profile concavity, and drainage basin morphology. *Earth Surface Processes and Landforms* 29(4): 401–421. http://dx.doi.org/10.1002/esp.1031.

Gilbert G (1877) *Report on the geology of the Henry Mountains: U.S. Geographical and Geological Survey, 160*, Rocky Mountain Region.

Gilbert G (1909) The convexity of hilltops. *Journal of Geology* 17(4): 344–350.

Gilchrist AR, Kooi H, and Beaumont C (1994a) Post-Gondwana geomorphic evolution of southwestern Africa: Implications for the controls on landscape development from observations and numerical experiments. *Journal of Geophysical Research* 99: 739–742.

Gilchrist AR and Summerfield MA (1990) Differential denudation and flexural isostasy in the formation of rifted-margin upwarps. *Nature* 346: 739–742.

Gilchrist A, Summerfield M, and Cockburn H (1994b) Landscape dissection, isostatic uplift, and the morphologic development of orogens. *Geology* 22(11): 963–966.

Glasser NF, Crawford KR, Hambrey MJ, Bennett MR, and Huddart D (1998) Lithological and structural controls on the surface wear characteristics of glaciated metamorphic bedrock surfaces: Ossian Sarsfjellet, Svalbard. *Journal of Geology* 106(3): 319–330.

Goudie A (1985) Duricrusts and landforms. In: Richards KS, Arnett RR, and Ellis S (eds.) *Geomorphology and Soils*, pp. 37–57. George Allen and Unwin.

Gran K, Montgomery D, and Halbur J (2011) Long-term elevated post-eruption sedimentation at Mount Pinatubo, Philippines. *Geology* 39(4): 367–370.
Granger D, Kirchner J, and Finkel R (1996) Spatially averaged long-term erosion rates measured from in situ-produced cosmogenic nuclides in alluvial sediment. *Journal of Geology* 104(3): 249–257.
Gurnell A, Hannah D, and Lawler D (1996) Suspended sediment yield from glacier basins. In: *IAHS' Publications-Series of Proceedings and Reports-Intern Assoc Hydrological Sciences, No. 236,* pp. 97–104.
Gutiérrez M (2005) *Climatic Geomorphology*. Amsterdam: Elsevier.
Hack J (1960) Interpretation of erosional topography in humid temperate regions. *American Journal of Science* 258-A: 80–97.
Hales T and Roering J (2007) Climatic controls on frost cracking and implications for the evolution of bedrock landscapes. *Journal of Geophysical Research* 112: F02033.
Hales T and Roering J (2009) A frost "buzzsaw" mechanism for erosion of the eastern Southern Alps, New Zealand. *Geomorphology* 107(3–4): 241–253.
Hallet B (1979) A theoretical model of glacial abrasion. *Journal of Glaciology* 23: 39–50.
Hallet B (1996) Glacial quarrying: A simple theoretical model. *Annals of Glaciology* 22: 1–8.
Hallet B, Hunter L, and Bogen J (1996) Rates of erosion and sediment evacuation by glaciers: A review of field data and their implications. *Global and Planetary Change* 12(1): 213–235.
Hallet B, Walder J, and Stubbs C (1991) Weathering by segregation ice growth in microcracks at sustained subzero temperatures: Verification from an experimental study using acoustic emissions. *Permafrost and Periglacial Processes* 2(4): 283–300.
Harbor JM (1992) Numerical modeling of the development of U-shaped valleys by glacial erosion. *Geological Society of America Bulletin* 104(10): 1364–1375.
Harbor DJ (1998) Dynamic equilibrium between an active uplift and the Sevier River, Utah. *Journal of Geology* 106(2): 181–194.
Harbor JM, Hallet B, and Raymond CF (1988) A numerical model of landform development by glacial erosion. *Nature* 333: 347–349.
Harkins N, Kirby E, Heimsath A, Robinson R, and Reiser U (2007) Transient fluvial incision in the headwaters of the Yellow River, northeastern Tibet. *Journal of Geophysical Research* 112: F03S04.
Hay W, Sloan J II, and Wold C (1988) Mass/age distribution and composition of sediments on the ocean floor and the global rate of sediment subduction. *Journal of Geophysical Research* 93(B12): 14933–14940.
Heimsath AM, Chappell J, Dietrich WE, Nishiizumi K, and Finkel RC (2000) Soil production on a retreating escarpment in southeastern Australia. *Geology* 28(9): 787–790.
Heimsath A, DiBiase R, and Whipple K (2012) Soil production limits and the transition to bedrock-dominated landscapes. *Nature Geoscience* 5(3): 210–214.
Heimsath A, Dietrich W, Nishiizumi K, and Finkel R (1997) The soil production function and landscape equilibrium. *Nature* 388(6640): 358–361.
Heimsath AM, Dietrich WE, Nishiizumi K, and Finkel RC (2001) Stochastic processes of soil production and transport: Erosion rates, topographic variation and cosmogenic nuclides in the Oregon Coast Range. *Earth Surface Processes and Landforms* 26(5): 531–552.
Heimsath AM, Fink D, and Hancock GR (2009) The 'humped' soil production function: Eroding Arnhem Land, Australia. *Earth Surface Processes and Landforms* 34(12): 1674–1684.
Heimsath AM, Furbish DJ, and Dietrich WE (2005) The illusion of diffusion: Field evidence for depth-dependent sediment transport. *Geology* 33(12): 949–952.
Herman F, Beaud F, Champagnac J-D, Lemieux J-M, and Sternai P (2011) Glacial hydrology and erosion patterns: A mechanism for carving glacial valleys. *Earth and Planetary Science Letters* 310(3): 498–508.
Herman F and Braun J (2008) Evolution of the glacial landscape of the Southern Alps of New Zealand: Insights from a glacial erosion model. *Journal of Geophysical Research, Earth Surface* 113(F2): F02009.
Hicks D, Hill J, and Shankar U (1996) Variation of suspended sediment yields around New Zealand: The relative importance of rainfall and geology. In: DE Walling and B Webb (eds.) *Erosion and Sediment Yield: Global and Regional Perspectives*, pp. 149–156. IAHS Publication.
Hildes DH, Clarke GK, Flowers GE, and Marshall SJ (2004) Subglacial erosion and englacial sediment transport modelled for North American ice sheets. *Quaternary Science Reviews* 23(3): 409–430.
Hilley G and Strecker M (2004) Steady state erosion of critical coulomb wedges with applications to Taiwan and the Himalaya. *Journal of Geophysical Research* 109(B1): B01411.
Hobley DE, Sinclair HD, Mudd SM, and Cowie PA (2011) Field calibration of sediment flux dependent river incision. *Journal of Geophysical Research: Earth Surface (2003–2012)* 116(F4): F04017, http://dx.doi.org/10.1029/2010JF001935.
Hoffman PF and Grotzinger JP (1993) Orographic precipitation, erosional unloading, and tectonic style. *Geology* 21(3): 195–198.
Hoke GD, Isacks BL, Jordan TE, Blanco N, Tomlinson AJ, and Ramezani J (2007) Geomorphic evidence for post-10 ma uplift of the western flank of the central Andes 18 30–22 s. *Tectonics* 26(5).
Hooke RL (1991) Positive feedbacks associated with erosion of glacial cirques and overdeepenings. *Geological Society of America Bulletin* 103(8): 1104–1108.
Horton RE (1932) Drainage-basin characteristics. *Transactions of the American Geophysical Union* 13: 350–361.
Horton RE (1945) Erosional development of streams and their drainage basins. *Geological Society of America Bulletin* 56: 275–370.
Hovius N (1998) Controls on sediment supply by large rivers. *SEPM Special Publication* 59: 3–16.
Hovius N and Meunier P (2012) Earthquake ground motion and patterns of seismically induced landsliding. In: Clague JJ and Stead D (eds.) *Landslides: Types, Mechanisms, and Modeling*, pp. 24–36. Cambridge: Cambridge University Press.
Hovius N, Meunier P, Lin C, et al. (2011) Prolonged seismically induced erosion and the mass balance of a large earthquake. *Earth and Planetary Science Letters* 304(3): 347–355.
Hovius N, Stark CP, and Allen PA (1997) Sediment flux from a mountain belt derived by landslide mapping. *Geology* 25(3): 231–234.
Howard A (1980) Thresholds in river regimes. In: Coates DR and Vitek JD (eds.) *Thresholds in Geomorphology*, pp. 227–258. Allen and Unwin.
Howard AD (1990) Theoretical model of optimal drainage networks. *Water Resources Research* 26(9): 2107–2117.
Howard AD (1994) A detachment-limited model of drainage basin evolution. *Water Resources Research* 30(7): 2261–2285.
Howard A (1997) Badland morphology and evolution: Interpretation using a simulation model. *Earth Surface Processes and Landforms* 22(3): 211–227.
Hsu L, Dietrich WE, and Sklar LS (2008) Experimental study of bedrock erosion by granular flows. *Journal of Geophysical Research* 113(F2): F02001.
Hu X, Pan B, Kirby E, Li Q, Geng H, and Chen J (2010) Spatial differences in rock uplift rates inferred from channel steepness indices along the northern flank of the Qilian Mountain, northeast Tibetan plateau. *Chinese Science Bulletin* 55(27–28): 3205–3214.
Huang X and Niemann J (2006) An evaluation of the geomorphically effective event for fluvial processes over long periods. *Journal of Geophysical Research* 111(F3): F03015.
Huda SA and Small EE (2014) Modeling the effects of bed topography on fluvial bedrock erosion by saltating bed load. *Journal of Geophysics Research Earth Surface* 119: 1222–1239, http://dx.doi.org/10.1002/2013JF002872.
Hughes M, Almond P, and Roering J (2009) Increased sediment transport via bioturbation at the last glacial–interglacial transition. *Geology* 37(10): 919–922.
Humphrey N and Raymond C (1994) Hydrology, erosion and sediment production in a surging glacier: Variegated glacier, Alaska, 1982–83. *Journal of Glaciology* 40(136): 539–552.
Hungr O, McDougall S, and Bovis M (2005) Entrainment of material by debris flows. In: Jakob M and Hungr O (eds.) *Debris-Flow Hazards and Related Phenomena*, pp. 135–158. Springer.
Ijjasz-Vasquez E and Bras R (1995) Scaling regimes of local slope versus contributing area in digital elevation models. *Geomorphology* 12(4): 299–311.
Inman D and Jenkins S (1999) Climate change and the episodicity of sediment flux of small california rivers. *Journal of Geology* 107(3): 251–270.
Istanbulluoglu E and Bras RL (2005) Vegetation-modulated landscape evolution: Effects of vegetation on landscape processes, drainage density, and topography. *Journal of Geophysical Research* 110: F02012.
Iverson NR (1991) Potential effects of subglacial water-pressure fluctuations on quarrying. *Journal of Glaciology* 37(125): 27–36.
Iverson RM (1997) The physics of debris flows. *Reviews of Geophysics* 358: 245–296.
Iverson NR (2012a) A theory of glacial quarrying for landscape evolution models. *Geology* 40(8): 679–682.
Iverson RM (2012b) Elementary theory of bed-sediment entrainment by debris flows and avalanches. *Journal of Geophysical Research* 117(F3): F03006.
Iverson RM, Reid ME, Logan M, LaHusen RG, Godt JW, and Griswold JP (2010) Positive feedback and momentum growth during debris-flow entrainment of wet bed sediment. *Nature Geoscience* 4(2): 116–121.
Izumi N and Fujii K (2006) Channelization on plateaus composed of weakly cohesive fine sediment. *Journal of Geophysical Research, Earth Surface* 111(F1): F01012, http://dx.doi.org/10.1029/2005JF000345.
Izumi N and Parker G (2000) Linear stability analysis of channel inception: Downstream-driven theory. *Journal of Fluid Mechanics* 419: 239–262.

Jamieson SS, Hulton NR, and Hagdorn M (2008) Modelling landscape evolution under ice sheets. *Geomorphology* 97(1): 91–108.

Jansen JD, Codilean AT, Bishop P, and Hoey TB (2010) Scale dependence of lithological control on topography: Bedrock channel geometry and catchment morphometry in western Scotland. *Journal of Geology* 118(3): 223–246.

Jansson M (1988) A global survey of sediment yield. *Geografiska Annaler: Series A, Physical Geography*: 81–98.

Johnson JPL, Whipple KX, Sklar LS, and Hanks TC (2009) Transport slopes, sediment cover, and bedrock channel incision in the Henry Mountains, Utah. *Journal of Geophysical Research* 114: F02014.

Jyotsna R and Haff P (1997) Microtopography as an indicator of modern hillslope diffusivity in arid terrain. *Geology* 25(8): 695–698.

Kaufmann G and Romanov D (2012) Landscape evolution and glaciation of the Rwenzori Mountains, Uganda: Insights from numerical modeling. *Geomorphology* 138(1): 263–275.

Kessler MA, Anderson RS, and Briner JP (2008) Fjord insertion into continental margins driven by topographic steering of ice. *Nature Geoscience* 1(6): 365–369.

Kirby E, Johnson C, Furlong K, and Heimsath A (2007) Transient channel incision along Bolinas ridge, California: Evidence for differential rock uplift adjacent to the San Andreas Fault. *Journal of Geophysical Research: Earth Surface (2003–2012)* 112(F3): F03S07, http://dx.doi.org/10.1029/2006JF000559.

Kirby E and Ouimet W (2011) Tectonic geomorphology along the eastern margin of Tibet: Insights into the pattern and processes of active deformation adjacent to the Sichuan basin. *Geological Society, London, Special Publications* 353(1): 165–188.

Kirby E and Whipple K (2001) Quantifying differential rock-uplift rates via stream profile analysis. *Geology* 29(5): 415–418.

Kirby E and Whipple KX (2012) Expression of active tectonics in erosional landscapes. *Journal of Structural Geology* 44(5), 4e75.

Kirby E, Whipple K, Tang W, and Chen Z (2003) Distribution of active rock uplift along the eastern margin of the tibetan plateau: Inferences from bedrock channel longitudinal profiles. *Journal of Geophysical Research* 108(B4): 2217.

Kirkby M (1985) A basis for soil profile modelling in a geomorphic context. *Journal of Soil Science* 36(1): 97–121.

Kirkby MJ (1987) Modelling some influences of soil erosion, landslides and valley gradient on drainage density and hollow development. *Catena Supplement* 10: 1–11.

Kirkby M (1993) Long term interactions between networks and hillslopes. In: Beven K and Kirkby MJ (eds.) *Channel Network Hydrology*, pp. 255–293. John Wiley & Sons.

Kirkby M (1995) Modelling the links between vegetation and landforms. *Geomorphology* 13(1): 319–335.

Kooi H and Beaumont C (1994) Escarpment evolution on high-elevation rifted margins: Insights derived from a surface processes model that combines diffusion, advection, and reaction. *Journal of Geophysical Research* 99: 12191–12209.

Koons P, Upton P, and Barker A (2012) The influence of mechanical properties on the link between tectonic and topographic evolution. *Geomorphology* 137(1): 168–180.

Koons P, Zeitler P, Chamberlain C, Craw D, and Meltzer A (2002) Mechanical links between erosion and metamorphism in Nanga Parbat, Pakistan Himalaya. *American Journal of Science* 302(9): 749–773.

Koppes M and Hallet B (2002) Influence of rapid glacial retreat on the rate of erosion by tidewater glaciers. *Geology* 30(1): 47–50.

Koppes M and Montgomery D (2009) The relative efficacy of fluvial and glacial erosion over modern to orogenic timescales. *Nature Geoscience* 2(9): 644–647.

Lague D, Hovius N, and Davy P (2005) Discharge, discharge variability, and the bedrock channel profile. *Journal of Geophysical Research* 110: F04006. http://dx.doi.org/10.1029/2004JF000259.

Lal D (1991) Cosmic ray labeling of erosion surfaces: In situ nuclide production rates and erosion models. *Earth and Planetary Science Letters* 104(2): 424–439.

Lane N, Watts A, and Farrant A (2008) An analysis of Cotswold topography: Insights into the landscape response to denudational isostasy. *Journal of the Geological Society* 165(1): 85–103.

Langbein W and Schumm S (1958) Yield of sediment in relation to mean annual precipitation. *Transactions of the American Geophysical Union* 39(6): 1076–1084.

Lavé J and Avouac J (2001) Fluvial incision and tectonic uplift across the Himalayas of central Nepal. *Journal of Geophysical Research* 106(B11): 26561.

Le Bouteiller C, Naaim-Bouvet F, Mathys N, and Lavé J (2011) A new framework for modeling sediment fining during transport with fragmentation and abrasion. *Journal of Geophysical Research: Earth Surface (2003–2012)* 116(F3): F03002, http://dx.doi.org/10.1029/2010JF001926.

Leith K, Moore JR, Amann F, and Loew S (2014) In situ stress control on microcrack generation and macroscopic extensional fracture in exhuming bedrock. *Journal of Geophysical Research, Solid Earth* 119: 594–615.

Lin Z and Oguchi T (2004) Drainage density, slope angle, and relative basin position in Japanese bare lands from high-resolution DEMs. *Geomorphology* 63(3): 159–173.

Lliboutry L (1994) Monolithologic erosion of hard beds by temperate glaciers. *Journal of Glaciology* 40(136): 433–450.

Loewenherz DS (1991) Stability and the initiation of channelized surface drainage. A reassessment of the short wavelength limit. *Journal of Geophysical Research: Solid Earth (1978–2012)* 96(B5): 8453–8464.

Loget N, Davy P, and Van Den Driessche J (2006) Mesoscale fluvial erosion parameters deduced from modeling the Mediterranean sea level drop during the Messinian (late Miocene). *Journal of Geophysical Research: Earth Surface (2003–2012)* 111(F3): F03005, http://dx.doi.org/10.1029/2005JF000387.

Ludwig W and Probst J (1998) River sediment discharge to the oceans: Present-day controls and global budgets. *American Journal of Science* 298: 265–295.

Lupker M, Blard P, Lavé J, et al. (2012) ^{10}Be-derived Himalayan denudation rates and sediment budgets in the Ganga Basin. *Earth and Planetary Science Letters* 333: 146–156.

Lyew-Ayee P, Viles H, and Tucker G (2007) The use of GIS-based digital morphometric techniques in the study of cockpit karst. *Earth Surface Processes and Landforms* 32(2): 165–179.

MacGregor KR, Anderson R, Anderson S, and Waddington E (2000) Numerical simulations of glacial-valley longitudinal profile evolution. *Geology* 28(11): 1031–1034.

MacGregor KR, Anderson RS, and Waddington ED (2009) Numerical modeling of glacial erosion and headwall processes in alpine valleys. *Geomorphology* 103(2): 189–204.

Mackin J (1948) Concept of the graded river. *Geological Society of America Bulletin* 59(5): 463.

Major J, Pierson T, Dinehart R, and Costa J (2000) Sediment yield following severe volcanic disturbance—A two-decade perspective from Mount St. Helens. *Geology* 28(9): 819–822.

Martel S (2006) Effect of topographic curvature on near-surface stresses and application to sheeting joints. *Geophysical Research Letters* 33(1): L01308.

Martin Y and Church M (2004) Numerical modelling of landscape evolution: Geomorphological perspectives. *Progress in Physical Geography* 28: 317–339.

Matmon A, Bierman P, Larsen J, et al. (2003) Erosion of an ancient mountain range, the Great Smoky Mountains, North Carolina and Tennessee. *American Journal of Science* 303(9): 817–855.

McCoy S, Kean J, Coe J, Tucker G, Staley D, and Wasklewicz T (2012) Sediment entrainment by debris flows: In situ measurements from the headwaters of a steep catchment. *Journal of Geophysical Research* 117(F3): F03016.

McCoy S, Tucker G, Kean J, and Coe J (2013) Measurements of basal force from natural debris flows that incised bedrock. *Journal of Geophysical Research, Earth Surface* 118: 1–12.

McKean J, Dietrich W, Finkel R, Southon J, and Caffee M (1993) Quantification of soil production and downslope creep rates from cosmogenic ^{10}Be accumulations on a hillslope profile. *Geology* 21(4): 343–346.

Menéndez I, Silva PG, Martín-Betancor M, Perez-Torrado FJ, Guillou H, and Scaillet S (2008) Fluvial dissection, isostatic uplift, and geomorphological evolution of volcanic islands (Gran Canaria, Canary Islands, Spain). *Geomorphology* 102(1): 189–203.

Miller SR, Baldwin SL, and Fitzgerald PG (2012) Transient fluvial incision and active surface uplift in the woodlark rift of eastern Papua New Guinea. *Lithosphere* 4(2): 131–149.

Miller D and Dunne T (1996) Topographic perturbations of regional stresses and consequent bedrock fracturing. *Journal of Geophysical Research* 101(B11): 25523–25525.

Miller SR, Sak PB, Kirby E, and Bierman PR (2013) Neogene rejuvenation of central Appalachian topography: Evidence for differential rock uplift from stream profiles and erosion rates. *Earth and Planetary Science Letters* 369: 1–12.

Miller SR, Slingerland RL, and Kirby E (2007) Characteristics of steady state fluvial topography above fault-bend folds. *Journal of Geophysical Research* 112: F04004.

Milliman JD and Syvitski PM (1992) Geomorphic/tectonic control of sediment transport to the ocean: The importance of small mountainous rivers. *Journal of Geology* 100: 525–544.

Minder J, Mote P, and Lundquist J (2010) Surface temperature lapse rates over complex terrain: Lessons from the cascade mountains. *Journal of Geophysical Research* 115(D14): D14122.

Mitchell S and Montgomery D (2006) Influence of a glacial buzzsaw on the height and morphology of the Cascade Range in central Washington State, USA. *Quaternary Research* 65(1): 96–107.

Moglen GE, Eltahir EA, and Bras RL (1998) On the sensitivity of drainage density to climate change. *Water Resources Research* 34(4): 855–862.

Molin P, Fubelli G, Nocentini M, et al. (2012) Interaction of mantle dynamics, crustal tectonics, and surface processes in the topography of the Romanian Carpathians: A geomorphological approach. *Global and Planetary Change* 90: 58–72.
Molnar P (2001) Climate change, flooding in arid environments, and erosion rates. *Geology* 29(12): 1071–1074.
Molnar P (2004a) Late Cenozoic increase in accumulation rates of terrestrial sediment: How might climate change have affected erosion rates? *Annual Review of Earth and Planetary Sciences* 32: 67–89. http://dx.doi.org/10.1146/annurev.earth.32.091003.143456.
Molnar P (2004b) Interactions among topographically induced elastic stress, static fatigue, and valley incision. *Journal of Geophysical Research, Earth Surface* 109(F2): F02010. http://dx.doi.org/10.1029/2003JF000097.
Molnar P (2007) An examination of evidence used to infer late Cenozoic "Uplift" of mountain belts and other high terrain: What scientific question does such evidence pose? *Journal of the Geological Society of India* 70(3): 395–410.
Molnar P, Anderson RS, and Anderson SP (2007) Tectonics, fracturing of rock, and erosion. *Journal of Geophysical Research, Earth Surface* 112(F3): F03014. http://dx.doi.org/10.1029/2005JF000433.
Molnar P, Anderson R, Kier G, and Rose J (2006) Relationships among probability distributions of stream discharges in floods, climate, bed load transport, and river incision. *Journal of Geophysical Research, Earth Surface* 111(F2): F02001. http://dx.doi.org/10.1029/2005JF000310.
Molnar P and England P (1990) Late Cenozoic uplift of mountain ranges and global climate change—Chicken or egg? *Nature* 346(6279): 29–34.
Molnár P and Ramirez JA (1998) Energy dissipation theories and optimal channel characteristics of river networks. *Water Resources Research* 34(7): 1809–1818.
Montgomery DR (1994) Valley incision and the uplift of mountain peaks. *Journal of Geophysical Research: Solid Earth (1978–2012)* 99(B7): 13913–13921.
Montgomery DR (2001) Slope distributions, threshold hillslopes, and steady-state topography. *American Journal of Science* 301: 423–454.
Montgomery D, Balco G, and Willett S (2001) Climate, tectonics, and the morphology of the Andes. *Geology* 29(7): 579–582.
Montgomery D and Brandon M (2002) Topographic controls on erosion rates in tectonically active mountain ranges. *Earth and Planetary Science Letters* 201(3–4): 481–489.
Montgomery DR and Dietrich WE (1989) Source areas, drainage density, and channel initiation. *Water Resources Research* 25(8): 1907–1918.
Montgomery DR and Dietrich WE (1992) Channel initiation and the problem of landscape scale. *Science* 255: 826–830.
Montgomery D and Dietrich W (1994) Landscape dissection and drainage area-slope thresholds. In: Kirkby MJ (ed.) *Process Models and Theoretical Geomorphology*, pp. 221–246. Wiley.
Montgomery D and Foufoula-Georgiou E (1993) Channel network source representation using digital elevation models. *Water Resources Research* 29(12): 3925–3934.
Montgomery DR and Gran KB (2001) Downstream variations in the width of bedrock channels. *Water Resources Research* 37(6): 1841–1846.
Montgomery DR and Greenberg HM (2000) Local relief and the height of Mount Olympus. *Earth Surface Processes and Landforms* 25(4): 385–396.
Moore ME, Gleadow AJ, and Lovering JF (1986) Thermal evolution of rifted continental margins: New evidence from fission tracks in basement apatites from southeastern Australia. *Earth and Planetary Science Letters* 78(2): 255–270.
Morell KD, Kirby E, Fisher DM, and Soest M (2012) Geomorphic and exhumational response of the Central American volcanic arc to Cocos Ridge subduction. *Journal of Geophysical Research: Solid Earth (1978–2012)* 117(B4): B04409, http://dx.doi.org/10.1029/2011JB008969.
Mulder T and Syvitski J (1996) Climatic and morphologic relationships of rivers: Implications of sea-level fluctuations on river loads. *Journal of Geology* 104: 509–523.
Murton J, Peterson R, and Ozouf J (2006) Bedrock fracture by ice segregation in cold regions. *Science* 314(5802): 1127.
Naylor S and Gabet EJ (2007) Valley asymmetry and glacial versus nonglacial erosion in the Bitterroot Range, Montana, USA. *Geology* 35(4): 375–378.
Nearing M, Foster G, Lane L, and Finkner S (1989) A process-based soil erosion model for USDA-water erosion prediction project technology. *Transactions of the ASAE* 32(5): 1587–1593.
Norton K, von Blanckenburg F, DiBiase R, Schlunegger F, and Kubik P (2011) Cosmogenic ^{10}Be-derived denudation rates of the eastern and southern European Alps. *International Journal of Earth Sciences* 100(5): 1163–1179.
Nott J and Roberts R (1996) Time and process rates over the past 100 my: A case for dramatically increased landscape denudation rates during the late quaternary in northern Australia. *Geology* 24(10): 883–887.
Oerlemans J (1984) Numerical experiments on glacial erosion. *Zeitschrift für Gletscherkunde und Glazialgeologie* 20: 107–126.
Oguchi T (1997) Drainage density and relative relief in humid steep mountains with frequent slope failure. *Earth Surface Processes and Landforms* 22(2): 107–120.
Olivetti V, Cyr AJ, Molin P, Faccenna C, and Granger DE (2012) Uplift history of the Sila Massif, southern Italy, deciphered from cosmogenic ^{10}Be erosion rates and river longitudinal profile analysis. *Tectonics* 31(3): TC3007, http://dx.doi.org/10.1029/2011TC003037.
Ollier CD (1985) Morphotectonics of continental margins with great escarpments. In: Morisawa M and Hack JT (eds.) *Tectonic Geomorphology, Binghamton Symposium in Geomorphology*, pp. 3–25. Boston: Allen and Unwin.
Oskin M and Burbank DW (2005) Alpine landscape evolution dominated by cirque retreat. *Geology* 33(12): 933–936.
Ouimet WB, Whipple KX, and Granger DE (2009) Beyond threshold hillslopes: Channel adjustment to base-level fall in tectonically active mountain ranges. *Geology* 37(7): 579–582. http://dx.doi.org/10.1130/G30013A.1.
Palumbo L, Hetzel R, Tao M, and Li X (2010) Topographic and lithologic control on catchment-wide denudation rates derived from cosmogenic ^{10}Be in two mountain ranges at the margin of NE Tibet. *Geomorphology* 117(1): 130–142.
Palumbo L, Hetzel R, Tao M, and Li X (2011) Catchment-wide denudation rates at the margin of NE Tibet from in situ-produced cosmogenic ^{10}Be. *Terra Nova* 23(1): 42–48.
Paola C, Heller PL, and Angevine CL (1992) The large-scale dynamics of grain-size variation in alluvial basins, 1: Theory. *Basin Research* 4(2): 73–90.
Papanikolaou ID, Roberts G, Deligiannakis G, Sakellariou A, and Vassilakis E (2012) The Sparta Fault, Southern Greece: From segmentation and tectonic geomorphology to seismic hazard mapping and time dependent probabilities. *Tectonophysics* 597–598: 85–105.
Parker R, Densmore A, Rosser N, et al. (2011) Mass wasting triggered by the 2008 Wenchuan earthquake is greater than orogenic growth. *Nature Geoscience* 4(7): 449–452.
Partridge TC and Maud RR (1987) Geomorphic evolution of southern Africa since the Mesozoic. *South African Journal of Geology* 90(2): 179–208.
Pederson JL and Tressler C (2012) Colorado river long-profile metrics, knickzones and their meaning. *Earth and Planetary Science Letters* 345: 171–179.
Pelletier JD (2004) Estimate of three-dimensional flexural-isostatic response to unloading: Rock uplift due to late Cenozoic glacial erosion in the western United States. *Geology* 32(2): 161–164.
Pelletier JD and Cline ML (2007) Nonlinear slope-dependent sediment transport in cinder cone evolution. *Geology* 35(12): 1067–1070.
Pelletier JD, Comeau D, and Kargel J (2010) Controls of glacial valley spacing on earth and mars. *Geomorphology* 116(1): 189–201.
Perron JT, Kirchner JW, and Dietrich WE (2009) Formation of evenly spaced ridges and valleys. *Nature* 460(7254): 502–505.
Phillips J (1990) Relative importance of factors influencing fluvial soil loss at the global scale. *American Journal of Science* 290: 547–568.
Pinet P and Souriau M (1988) Continental erosion and large-scale relief. *Tectonics* 7(3): 563–582.
Ponza A, Pazzaglia FJ, and Picotti V (2010) Thrust-fold activity at the mountain front of the northern Apennines (Italy) from quantitative landscape analysis. *Geomorphology* 123(3): 211–231.
Portenga E and Bierman P (2011) Understanding earth's eroding surface with ^{10}Be. *GSA Today* 21(8): 4–10.
Riebe C, Kirchner J, Granger D, and Finkel R (2000) Erosional equilibrium and disequilibrium in the Sierra Nevada, inferred from cosmogenic ^{26}Al and ^{10}Be in alluvial sediment. *Geology* 28(9): 803–806.
Riebe C, Kirchner J, Granger D, and Finkel R (2001) Strong tectonic and weak climatic control of long-term chemical weathering rates. *Geology* 29(6): 511–514.
Rinaldo A, Dietrich W, Vogel S, Rigon R, and Rodriguez-Iturbe I (1995) Geomorphic signatures of varying climate. *Nature* 374: 632–636.
Roberts GG and White N (2010) Estimating uplift rate histories from river profiles using African examples. *Journal of Geophysical Research: Solid Earth (1978–2012)* 115(B2): B02406, http://dx.doi.org/10.1029/2009JB006692.
Robl J, Stüwe K, and Hergarten S (2008) Channel profiles around Himalayan river anticlines: Constraints on their formation from digital elevation model analysis. *Tectonics* 27(3).
Rodriguez-Iturbe I and Rinaldo A (1997) *Fractal River Networks: Chance and Self-organization*. Cambridge University Press.
Roe GH, Montgomery DR, and Hallet B (2002) Effects of orographic precipitation on the concavity of steady-state river profiles. *Geology* 30: 143–146. http://dx.doi.org/10.1130/0091-7613.

Roe GH, Whipple KX, and Fletcher JK (2008) Feedbacks among climate, erosion, and tectonics in a critical wedge orogen. *American Journal of Science* 308(7): 815–842.

Roering J (2008) How well can hillslope evolution models "explain" topography? Simulating soil transport and production with high-resolution topographic data. *Geological Society of America Bulletin* 120(9–10): 1248–1262.

Roering J, Almond P, Tonkin P, and McKean J (2004) Constraining climatic controls on hill-slope dynamics using a coupled model for the transport of soil and tracers: Application to loess-mantled hillslopes, South Island, New Zealand. *Journal of Geophysical Research* 109(F1): F01010.

Roering J, Kirchner J, and Dietrich W (1999) Evidence for nonlinear, diffusive sediment transport on hillslopes and implications for landscape morphology. *Water Resources Research* 35(3): 853–870.

Roering J, Kirchner J, Sklar L, and Dietrich W (2001) Hillslope evolution by nonlinear creep and landsliding: An experimental study. *Geology* 29(2): 143–146.

Roering J, Marshall J, Booth A, Mort M, and Jin Q (2010) Evidence for biotic controls on topography and soil production. *Earth and Planetary Science Letters* 298(1): 183–190.

Rosenbloom NA and Anderson RS (1994) Hillslope and channel evolution in a marine terraced landscape, Santa Cruz, California. *Journal of Geophysical Research* 99: 14013–14029.

Rothlisberger H and Iken A (1981) Plucking as an effect of water-pressure variations at the glacier bed. *Annals of Glaciology* 2(1): 57–62.

Sacek V, Braun J, and van der Beek P (2012) The influence of rifting on escarpment migration on high elevation passive continental margins. *Journal of Geophysical Research: Solid Earth (1978–2012)* 117(B4). http://dx.doi.org/10.1029/2011JB008547.

Sadler P (1999) The influence of hiatuses on sediment accumulation rates. *GeoResearch Forum* 5: 15–40.

Safran E, Bierman P, Aalto R, Dunne T, Whipple K, and Caffee M (2005) Erosion rates driven by channel network incision in the Bolivian Andes. *Earth Surface Processes and Landforms* 30(8): 1007–1024.

Schaller M, Von Blanckenburg F, Hovius N, and Kubik P (2001) Large-scale erosion rates from in situ-produced cosmogenic nuclides in European river sediments. *Earth and Planetary Science Letters* 188(3): 441–458.

Scharf TE, Codilean AT, de Wit M, Jansen JD, and Kubik PW (2013) Strong rocks sustain ancient postorogenic topography in southern Africa. *Geology* 41(3): 331–334.

Schildgen T, Cosentino D, Bookhagen B, et al. (2012) Multi-phased uplift of the southern margin of the central Anatolian Plateau, Turkey: A record of tectonic and upper mantle processes. *Earth and Planetary Science Letters* 317: 85–95.

Schmidt KM and Montgomery DR (1995) Limits to relief. *Science* 270: 617–620.

Schumer R, Jerolmack D, and McElroy B (2011) The stratigraphic filter and bias in measurement of geologic rates. *Geophysical Research Letters* 38(11): L11405.

Schumm S (1963) The disparity between present rates of denudation and orogeny. *USGS Professional Paper 454H*.

Seidl MA and Dietrich WE (1992) The problem of channel erosion into bedrock. *Catena Supplement* 23: 101–124.

Selby MJ (1982) Controls on the stability and inclinations of hillslopes formed on hard rock. *Earth Surface Processes and Landforms* 7: 449–467.

Shahzad F, Mahmood SA, and Gloaguen R (2009) Drainage network and lineament analysis: An approach for Potwar Plateau (northern Pakistan). *Journal of Mountain Science* 6(1): 14–24.

Shields A (1936) Anwendung der ähnlichkeits-Mechanik und der Turbulenzforschung auf die Geschiebebewegung. *Preussische Versuchsanstalt für Wasserbau und Schiffbau* 26: 524–526.

Shuster DL, Cuffey KM, Sanders JW, and Balco G (2011) Thermochronometry reveals headward propagation of erosion in an alpine landscape. *Science* 332(6025): 84–88.

Simpson G and Schlunegger F (2003) Topographic evolution and morphology of surfaces evolving in response to coupled fluvial and hillslope sediment transport. *Journal of Geophysical Research* 108(B6): 2300.

Sinha S and Parker G (1996) Causes of concavity in longitudinal profiles of rivers. *Water Resources Research* 32(5): 1417–1428.

Sklar L and Dietrich W (1998) River longitudinal profiles and bedrock incision models: Stream power and the influence of sediment supply. *Rivers over Rock: Fluvial Processes in Bedrock Channels*, vol. 107, pp. 237–260. Washington, DC: American Geophysical Union.

Sklar L and Dietrich W (2001) Sediment and rock strength controls on river incision into bedrock. *Geology* 29(12): 1087–1090.

Sklar L and Dietrich W (2004) A mechanistic model for river incision into bedrock by saltating bed load. *Water Resources Research* 40(6): W06301.

Small E and Anderson R (1995) Geomorphically driven late Cenozoic rock uplift in the Sierra Nevada, California. *Science* 270: 277–280.

Small E, Anderson R, and Hancock G (1999) Estimates of the rate of regolith production using ^{10}Be and ^{26}Al from an alpine hillslope. *Geomorphology* 27(1): 131–150.

Smith TR (2010) A theory for the emergence of channelized drainage. *Journal of Geophysical Research: Earth Surface (2003–2012)* 115(F2): F02023, http://dx.doi.org/10.1029/2008JF001114.

Smith TR, Birnir B, and Merchant GE (1997) Towards an elementary theory of drainage basin evolution: I. The theoretical basis. *Computers & Geosciences* 23(8): 811–822.

Smith TR and Bretherton FP (1972) Stability and the conservation of mass in drainage basin evolution. *Water Resources Research* 8(6): 1506–1529.

Smith TR and Merchant GE (1995) Conservation principles and the initiation of channelized surface flows. In: JE Costa, AJ Miller, KW Potter, and PR Wilcock (eds.) *Natural and Anthropogenic Influences in Fluvial Geomorphology* 89: 1–25 Washington, DC: American Geophysical Union. http://dx.doi.org/10.1029/GM089p0001.

Snow R and Slingerland R (1987) Mathematical modeling of graded river profiles. *Journal of Geology* 95: 15–33.

Snyder N, Whipple K, Tucker G, and Merritts D (2000) Landscape response to tectonic forcing: Digital elevation model analysis of stream profiles in the Mendocino triple junction region, northern California. *Bulletin of the Geological Society of America* 112(8): 1250.

Snyder N, Whipple K, Tucker G, and Merritts D (2003a) Importance of a stochastic distribution of floods and erosion thresholds in the bedrock river incision problem. *Journal of Geophysical Research* 108(B2): 2117. http://dx.doi.org/10.1029/2001JB001655.

Snyder N, Whipple K, Tucker G, and Merritts D (2003b) Channel response to tectonic forcing: Field analysis of stream morphology and hydrology in the Mendocino triple junction region, northern California. *Geomorphology* 53(1–2): 97–127.

Snyder NP, Whipple KX, Tucker GE, and Merritts DM (2003c) Channel response to tectonic forcing: Analysis of stream morphology and hydrology in the Mendocino triple junction region, northern California. *Geomorphology* 97–127.

Sólyom PB (2011) A channel head stability criterion for first-order catchments. *Earth Surface Processes and Landforms* 36(4): 533–546.

Sólyom P and Tucker G (2004) Effect of limited storm duration on landscape evolution, drainage basin geometry, and hydrograph shapes. *Journal of Geophysical Research* 109: 13.

Spotila J, Buscher J, Meigs A, and Reiners P (2004) Long-term glacial erosion of active mountain belts: Example of the Chugach-St. Elias range, Alaska. *Geology* 32(6): 501–504.

Stark CP (2006) A self-regulating model of bedrock river channel geometry. *Geophysical Research Letters* 33: L04402.

Stern T, Baxter A, and Barrett P (2005) Isostatic rebound due to glacial erosion within the Transantarctic mountains. *Geology* 33(3): 221–224.

Stock J and Dietrich W (2003) Valley incision by debris flows: Evidence of a topographic signature. *Water Resources Research* 39(4): 1089.

Stock JD and Dietrich WE (2006) Erosion of steepland valleys by debris flows. *Geological Society of America Bulletin* 118(9–10): 1125–1148.

Stock G, Frankel K, Ehlers T, Schaller M, Briggs S, and Finkel R (2009) Spatial and temporal variations in denudation of the Wasatch Mountains, Utah, USA. *Lithosphere* 1(1): 34–40.

Stock JD and Montgomery DR (1999) Geologic constraints on bedrock river incision using the stream power law. *Journal of Geophysical Research: Solid Earth (1978–2012)* 104(B3): 4983–4993.

Strahler A (1950) Equilibrium theory of erosional slopes approached by frequency distribution analysis. Part I. *American Journal of Science* 248: 673–696.

Stüwe K (1991) Flexural constraints on the denudation of asymmetric mountain belts. *Journal of Geophysical Research: Solid Earth (1978–2012)* 96(B6): 10401–10408.

Summerfield M (1991) *Global Geomorphology: An Introduction to the Study of Landforms*. Harlow, New York: Longman Scientific & Technical, Wiley.

Summerfield M and Hulton N (1994) Natural controls of fluvial denudation rates in major world drainage basins. *Journal of Geophysical Research* 99(B7): 13871–13883.

Syvitski J and Milliman J (2007) Geology, geography, and humans battle for dominance over the delivery of fluvial sediment to the coastal ocean. *Journal of Geology* 115(1): 1–19.

Syvitski J, Peckham S, Hilberman R, and Mulder T (2003) Predicting the terrestrial flux of sediment to the global ocean: A planetary perspective. *Sedimentary Geology* 162(1–2): 5–24.

Syvitski J, Vörösmarty C, Kettner A, and Green P (2005) Impact of humans on the flux of terrestrial sediment to the global coastal ocean. *Science* 308(5720): 376–380.

Tal M and Paola C (2007) Dynamic single-thread channels maintained by the interaction of flow and vegetation. *Geology* 35(4): 347.

Tarboton D, Bras R, and Rodriguez-Iturbe I (1989) Scaling and elevation in river networks. *Water Resources Research* 25(9): 2037–2051.

Tarboton D, Bras R, and Rodriguez-Iturbe I (1992) A physical basis for drainage density. *Geomorphology* 5(1): 59–76.
Templeton A and Knowles E (2009) Microbial transformations of minerals and metals: Recent advances in geomicrobiology derived from synchrotron-based x-ray spectroscopy and x-ray microscopy. *Annual Review of Earth and Planetary Sciences* 37: 367–391.
ten Brink U and Stern T (1992) Rift flank uplifts and hinterland basins: Comparison of the Transantarctic Mountains with the great escarpment of southern Africa. *Journal of Geophysical Research: Solid Earth (1978–2012)* 97(B1): 569–585.
Thomson SN, Brandon MT, Tomkin JH, Reiners PW, Vasquez C, and Wilson NJ (2010) Glaciation as a destructive and constructive control on mountain building. *Nature* 467(7313): 313–317.
Tomkin JH (2007) Coupling glacial erosion and tectonics at active orogens: A numerical modeling study. *Journal of Geophysical Research: Earth Surface (2003–2012)* 112(F2): F02015, http://dx.doi.org/10.1029/2005JF000332.
Tomkin JH, Brandon MT, Pazzaglia FJ, Barbour JR, and Willett SD (2003) Quantitative testing of bedrock incision models for the Clearwater River, NW Washington state. *Journal of Geophysical Research* 108: 2308.
Tucker G (2004) Drainage basin sensitivity to tectonic and climatic forcing: Implications of a stochastic model for the role of entrainment and erosion thresholds. *Earth Surface Processes and Landforms* 29(2): 185–205. http://dx.doi.org/10.1002/esp.1020.
Tucker GE (2009) Natural experiments in landscape evolution. *Earth Surface Processes and Landforms* 34(10): 1323–1460. http://dx.doi.org/10.1002/esp.1833.
Tucker G and Bradley D (2010) Trouble with diffusion: Reassessing hillslope erosion laws with a particle-based model. *Journal of Geophysical Research* 115: F00A10.
Tucker GE and Bras RL (1998) Hillslope processes, drainage density, and landscape morphology. *Water Resources Research* 36: 1953–1964.
Tucker GE and Bras RL (2000) A stochastic approach to modeling the role of rainfall variability in drainage basin evolution. *Water Resources Research* 36(7): 1953–1964.
Tucker GE, Catani F, Rinaldo A, and Bras RL (2001a) Statistical analysis of drainage density from digital terrain data. *Geomorphology* 36(3): 187–202.
Tucker GE and Hancock GR (2010) Modelling landscape evolution. *Earth Surface Processes and Landforms* 46: 28–50.
Tucker GE, Lancaster ST, Gasparini NM, and Bras RL (2001b) The channel-hillslope integrated landscape development (CHILD) model. In: Harmon RS and Doe WW (eds.) *Landscape Erosion and Evolution Modeling*, pp. 349–388. Dordrecht: Kluwer.
Tucker G, McCoy S, Whittaker A, Roberts G, Lancaster S, and Phillips R (2011) Geomorphic significance of postglacial bedrock scarps on normal-fault footwalls. *Journal of Geophysical Research* 116(F1): F01022.
Tucker GE and Slingerland RL (1994) Erosional dynamics, flexural isostasy, and long-lived escarpments: A numerical modeling study. *Journal of Geophysical Research* 99: 12229–12243.
Tucker GE and Slingerland RL (1996) Predicting sediment flux from fold and thrust belts. *Basin Research* 8: 329–349.
Tucker GE and Slingerland RL (1997) Drainage basin response to climate change. *Water Resources Research* 33: 2031–2047.
Tucker G and Whipple K (2002) Topographic outcomes predicted by stream erosion models: Sensitivity analysis and intermodel comparison. *Journal of Geophysical Research* 107(B9): 2179.
Turowski JM, Lague D, Crave A, and Hovius N (2006) Experimental channel response to tectonic uplift. *Journal of Geophysical Research: Earth Surface (2003–2012)* 111(F3): F03008, http://dx.doi.org/10.1029/2005JF000306.
Turowski JM, Lague D, and Hovius N (2007) Cover effect in bedrock abrasion: A new derivation and its implications for the modeling of bedrock channel morphology. *Journal of Geophysical Research, Earth Surface* 112(F4): F04006, http://dx.doi.org/10.1029/2006JF000697.
Turowski JM, Lague D, and Hovius N (2009) Response of bedrock channel width to tectonic forcing: Insights from a numerical model, theoretical considerations, and comparison with field data. *Journal of Geophysical Research, Earth Surface* 114(F3): F03016, http://dx.doi.org/10.1029/2008JF001133.
Upton P, Mueller K, and Chen Y (2009) Three-dimensional numerical models with varied material properties and erosion rates: Implications for the mechanics and kinematics of compressive wedges. *Journal of Geophysical Research* 114(B4): B04408.
Valla P, van der Beek P, and Lague D (2010) Fluvial incision into bedrock: Insights from morphometric analysis and numerical modeling of gorges incising glacial hanging valleys (Western Alps, France). *Journal of Geophysical Research* 115(F2): F02010.
van der Beek P (2012) Modelling landscape evolution. In: Wainwright J and Mulligan M (eds.) *Environmental Modelling: Finding Simplicity in Complexity*, p. 309. Wiley-Blackwell.
van der Beek P, Andriessen P, and Cloetingh S (1995) Morphotectonic evolution of rifted continental margins: Inferences from a coupled tectonic-surface processes model and fission track thermochronology. *Tectonics* 14(2): 406–421.
van der Beek P and Bishhop P (2003) Cenozoic river profile development in the Upper Lachlan catchment (SE Australia) as a test quantitative fluvial incision models. *Journal of Geophysical Research* 108: 2309. http://dx.doi.org/10.1029/2002JB002125.
van der Beek P, Summerfield M, Braun J, Brown R, and Fleming A (2002) Modeling postbreakup landscape development and denudational history across the southeast African (Drakensberg Escarpment) margin. *Journal of Geophysical Research* 107(B12): 2351.
Vanacker V, von Blanckenburg F, Hewawasam T, and Kubik P (2007) Constraining landscape development of the Sri Lankan escarpment with cosmogenic nuclides in river sediment. *Earth and Planetary Science Letters* 253(3): 402–414.
Vanmaercke M, Kettner AJ, Van Den Eeckhaut M, et al. (2014) Moderate seismic activity affects contemporary sediment yields. *Progress in Physical Geography*, 38(2): 145–172. http://dx.doi.org/10.1177/0309133313516160.
Veneziano D and Niemann JD (2000) Self-similarity and multifractality of fluvial erosion topography: 2. Scaling properties. *Water Resources Research* 36(7): 1937–1951.
Von Blanckenburg F (2005) The control mechanisms of erosion and weathering at basin scale from cosmogenic nuclides in river sediment. *Earth and Planetary Science Letters* 237(3): 462–479.
Von Blanckenburg F, Hewawasam T, and Kubik P (2004) Cosmogenic nuclide evidence for low weathering and denudation in the wet, tropical highlands of Sri Lanka. *Journal of Geophysical Research* 109(F3): F03008.
Vörösmarty C and Sahagian D (2000) Anthropogenic disturbance of the terrestrial water cycle. *BioScience* 50(9): 753–765.
Walder J and Hallet B (1985) A theoretical model of the fracture of rock during freezing. *Bulletin of the Geological Society of America* 96(3): 336.
Walder J and Hallet B (1986) The physical basis of frost weathering: Toward a more fundamental and unified perspective. *Arctic and Alpine Research* 18: 27–32.
Walling D and Webb B (1996) Erosion and sediment yield: A global overview. In: *IAHS' Publications-Series of Proceedings and Reports-Intern Assoc Hydrological Sciences, No. 236,* pp. 3–20.
Weissel JK and Karner GD (1989) Flexural uplift of rift flanks due to mechanical unloading of the lithosphere during extension. *Journal of Geophysical Research* 94(B10): 13919–13950.
Weissel JK and Seidl MA (1998) Inland propagation of erosional escarpments and river profile evolution across the southeast Australian passive continental margin. In: Tinkler KJ and Wohl EE (eds.) *Rivers Over Rock: Fluvial Processes in Bedrock Channels. Geophysical Monograph,* 107: Washington, DC: AGU.
West A, Galy A, and Bickle M (2005) Tectonic and climatic controls on silicate weathering. *Earth and Planetary Science Letters* 235(1): 211–228.
Whipple KX (2004) Bedrock rivers and the geomorphology of active orogens. *Annual Review of Earth and Planetary Sciences* 32: 151–185.
Whipple KX, Hancock GS, and Anderson RS (2000) River incision into bedrock: Mechanics and relative efficacy of plucking, abrasion, and cavitation. *Geological Society of America Bulletin* 112: 490–503.
Whipple KX, Kirby E, and Brocklehurst SH (1999) Geomorphic limits to climate-induced increases in topographic relief. *Nature* 401(6748): 39–43.
Whipple KX and Meade BJ (2004) Controls on the strength of coupling among climate, erosion, and deformation in two-sided, frictional orogenic wedges at steady state. *Journal of Geophysical Research* 109: F01011. http://dx.doi.org/10.1029/2003JF000019.
Whipple KX and Tucker GE (1999) Dynamics of the stream-power river incision model: Implications for height limits of mountain ranges, landscape response timescales, and research needs. *Journal of Geophysical Research* 104: 17661–17674.
Whipple KX and Tucker GE (2002) Implications of sediment-flux-dependent river incision models for landscape evolution. *Journal of Geophysical Research* 107. http://dx.doi.org/10.1029/2000JB000044.
White A and Blum A (1995) Effects of climate on chemical, weathering in watersheds. *Geochimica et Cosmochimica Acta* 59(9): 1729–1747.
Whittaker A, Attal M, Cowie P, Tucker G, and Roberts G (2008) Decoding temporal and spatial patterns of fault uplift using transient river long profiles. *Geomorphology* 100(3–4): 506–526.
Whittaker A, Cowie P, Attal M, Tucker G, and Roberts G (2007a) Bedrock channel adjustment to tectonic forcing: Implications for predicting river incision rates. *Geology* 35(2): 103.

Whittaker A, Cowie P, Attal M, Tucker G, and Roberts G (2007b) Contrasting transient and steady-state rivers crossing active normal faults: New field observations from the Central Apennines, Italy. *Basin Research* 19(4): 529–556.

Widdowson M (1997) Tertiary palaeosurfaces of the SW Deccan, western India: Implications for passive margin uplift. *Geological Society, London, Special Publications* 120: 221–248.

Willenbring JK and von Blanckenburg F (2010) Long-term stability of global erosion rates and weathering during late-Cenozoic cooling. *Nature* 465: 211–214.

Willett S, Beaumont C, and Fullsack P (1993) Mechanical model for the tectonics of doubly vergent compressional orogens. *Geology* 21(4): 371–374.

Willett SD and Brandon MT (2002) On steady states in mountain belts. *Geology* 30(2): 175–178.

Willett SD, Fisher D, Fuller C, En-Chao Y, and Chia-Yu L (2003) Erosion rates and orogenic-wedge kinematics in Taiwan inferred from fission-track thermochronometry. *Geology* 31(11): 945–948.

Willgoose G (1994) A physical explanation for an observed area–slope-elevation relationship for catchments with declining relief. *Water Resources Research* 30(2): 151–159.

Willgoose G (2005) Mathematical modeling of whole landscape evolution. *Annual Review of Earth and Planetary Sciences* 33: 14.1–14.17.

Willgoose G, Bras RL, and Rodriguez-Iturbe I (1991a) A physical explanation of an observed link area–slope relationship. *Water Resources Research* 27(7): 1697–1702.

Willgoose G, Bras RL, and Rodriguez-Iturbe I (1991b) A coupled channel network growth and hillslope evolution model: 1. Theory. *Water Resources Research* 27(7): 1671–1684.

Wittmann H, von Blanckenburg F, Kruesmann T, Norton KP, and Kubik PW (2007) Relation between rock uplift and denudation from cosmogenic nuclides in river sediment in the Central Alps of Switzerland. *Journal of Geophysical Research* 112: F04010. http://dx.doi.org/10.1029/2006JF000729.

Wobus CW, Hodges KV, and Whipple KX (2003) Has focused denudation sustained active thrusting at the Himalayan topographic front? *Geology* 31(10): 861–864.

Wobus C, Tucker G, and Anderson R (2006a) Self-formed bedrock channels. *Geophysical Research Letters* 33: 1–6.

Wobus C, Whipple K, Kirby E, et al. (2006b) Tectonics from topography: Procedures, promise, and pitfalls. In: *Tectonics, Climate and Landscape Evolution*, pp. 55–74.

Wolman MG and Miller JP (1960) Magnitude and frequency of forces in geomorphic processes. *Journal of Geology* 68: 54–74.

Yanites B and Tucker G (2010) Controls and limits on bedrock channel geometry. *Journal of Geophysical Research* 115(F4): F04019.

Yanites BJ, Tucker GE, Hsu H-L, Chen C-C, Chen Y-G, and Mueller KJ (2011) The influence of sediment cover variability on long-term river incision rates: An example from the Peikang River, central Taiwan. *Journal of Geophysical Research, Earth Surface* 116(F3): F03016.

Yanites B, Tucker G, Mueller K, and Chen Y (2010a) How rivers react to large earthquakes: Evidence from central Taiwan. *Geology* 38(7): 639.

Yanites B, Tucker G, Mueller K, et al. (2010b) Incision and channel morphology across active structures along the Peikang River, central Taiwan: Implications for the importance of channel width. *Geological Society of America Bulletin* 122(7–8): 1192.

Yildirim C, Schildgen TF, Echtler H, Melnick D, and Strecker MR (2011) Late Neogene and active orogenic uplift in the central Pontides associated with the north Anatolian Fault: Implications for the northern margin of the central Anatolian plateau, Turkey. *Tectonics* 30(5): TC5005.

Yoo K, Amundson R, Heimsath A, and Dietrich W (2005) Process-based model linking pocket gopher (*Thomomys bottae*) activity to sediment transport and soil thickness. *Geology* 33(11): 917–920.

Zeitler PK, et al. (2001a) Erosion, Himalayan geodynamics, and the geomorphology of metamorphism. *GSA Today* 11(1): 4–9.

Zeitler PK, et al. (2001b) Crustal reworking at Nanga Parbat, Pakistan: Metamorphic consequences of thermal-mechanical coupling facilitated by erosion. *Tectonics* 20(5): 712–728.

Zhang P, Molnar P, and Downs W (2001) Increased sedimentation rates and grain sizes 2–4 Myr ago due to the influence of climate change on erosion rates. *Nature* 410: 599–604. http://dx.doi.org/10.1038/35073504.

Zhang H-P, Zhang P-Z, Kirby E, Yin J-H, Liu C-R, and Yu GH (2011) Along-strike topographic variation of the Longmen Shan and its significance for landscape evolution along the eastern Tibetan plateau. *Journal of Asian Earth Sciences* 40(4): 855–864.